

REPORT DOCUMENTATION PAGE			Form Approved OMB No. 0704-0188	
Public reporting burden for this collection of information is estimated to average 1 hour per response, including the time for reviewing instructions, searching existing data sources, gathering and maintaining the data needed, and completing and reviewing the collection of information. Send comments regarding this burden estimate or any other aspect of this collection of information, including suggestions for reducing this burden to Washington Headquarters Services, Directorate for Information Operations and Reports, 1215 Jefferson Davis Highway, Suite 1204, Arlington, VA 22202-4302, and to the Office of Management and Budget, Paperwork Reduction Project (0704-0188), Washington, DC 20503.				
1. AGENCY USE ONLY (Leave blank)	2. REPORT DATE  5 September 1997	3. REPORT TYPE AND DATES COVERED  Conference Proceedings		
4. TITLE AND SUBTITLE  Challenges in Propellants and Combustion 100 Years after Nobel		5. FUNDING NUMBERS  F6170896W0125		
6. AUTHOR(S)  Conference Committee				
7. PERFORMING ORGANIZATION NAME(S) AND ADDRESS(ES)  MEGA Energy Technology Furudalsvagen 10 Vasterhaninge S - 137 34 Sweden		8. PERFORMING ORGANIZATION REPORT NUMBER  N/A		
9. SPONSORING/MONITORING AGENCY NAME(S) AND ADDRESS(ES)  EOARD PSC 802 BOX 14 FPO 09499-0200		10. SPONSORING/MONITORING AGENCY REPORT NUMBER  CSP 96-1027		
11. SUPPLEMENTARY NOTES				
12a. DISTRIBUTION/AVAILABILITY STATEMENT  Approved for public release; distribution is unlimited.			12b. DISTRIBUTION CODE  A	
13. ABSTRACT (Maximum 200 words)  The Final Proceedings for Fourth International Symposium on Special Topics in Chemical Propulsion 4-ISICP, 27 May 1996 - 31 May 1996  The Topics covered include: chemical kinetics of propellant combustion, environmental considerations in combustion of solid and liquid propellants, commercial application in the combustion of energetic materials, effective utilization of propellants, combustion diagnostics, recycling.				
14. SUBJECT TERMS			15. NUMBER OF PAGES  1181	
			16. PRICE CODE N/A	
17. SECURITY CLASSIFICATION OF REPORT  UNCLASSIFIED	18. SECURITY CLASSIFICATION OF THIS PAGE  UNCLASSIFIED	19. SECURITY CLASSIFICATION OF ABSTRACT  UNCLASSIFIED	20. LIMITATION OF ABSTRACT  UL	

# CHALLENGES IN PROPELLANTS AND COMBUSTION

---

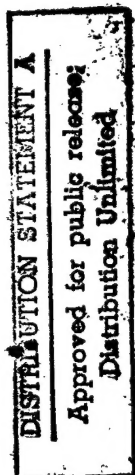
100 YEARS AFTER NOBEL

*EDITOR*

Kenneth K. Kuo

*ASSOCIATE EDITORS*

Thomas B. Brill • Rose A. Pesce-Rodriguez  
Alexander R. Mitchell • Josephine Covino  
S.K. Chan • Arie Peretz • Nils-Erik Gunners  
Stefan T. Thynell • S.H. Chan



19971002 131



begell house, inc.  
new york • wallingford (u.k.)

FROM CHALLENGE TO SOLUTION



## **Challenges in Propellants and Combustion**

### **100 Years After Nobel**

**Copyright © 1997 by Begell House, Inc. All rights reserved.**

Neither this book nor any part may be reproduced or transmitted in any form or by any means, electronic or mechanical, including photocopying, microfilming, and recording, or by any information storage or retrieval system, without prior permission in writing from the publisher.

Authorization to photocopy items for internal or personal use, or the personal or internal use of specific clients, may be granted by Begell House, Inc., provided that \$0.50 per page photocopied is paid directly to Copyright Clearance Center, 27 Congress Street, Salem, MA 01970 USA. The fee code for users of the Transactional Reporting Service is ISBN 1-56700-092-4/97\$0.00+\$0.50. The fee is subject to change without notice. For organizations that have been granted a photocopy license by the CCC, a separate system of payment has been arranged.

Begell House, Inc.'s consent does not extend to copying for general distribution, for promotion, for creating new works, or for resale. Specific permission must be obtained in writing from Begell House for such copying.

Direct all inquiries to Begell House, Inc., 79 Madison Ave., New York, NY 10016.

International Standard Book Number 1-56700-092-4  
Printed in the United States of America

## CONTENTS

<b>Preface</b>	<b>xi</b>
<b>Symposium Committee</b>	<b>xv</b>
<b>Historical Lecture on Alfred B. Nobel</b> Alfred Nobel: From Gunpowder to Ballistit <i>by Prof. Bertil Enoksson</i>	<b>xvii</b>

### AREA 1: CHEMICAL KINETICS OF PROPELLANT COMBUSTION

#### **Invited Paper**

Advances in Combustion-Like Kinetics and Mechanisms of Polymeric Binders <i>T.B. Brill, H. Arisawa, and P.E. Gongwer</i>	3
---	---

#### **Contributed Papers**

Unusual Combustion Behavior of Nitramines and Azides <i>R.L. Simmons</i>	24
Study of Flame Structure, Kinetics and Mechanism of the Thermal Decomposition of Solid Propellants by Probing Mass Spectrometry <i>O.P. Korobeinichev, L.V. Kuibida, A.A. Paletsky, and A.G. Shmakov</i>	38
Theoretical Study of HONO Reactions with H, OH, NO and NH <sub>2</sub> Radicals <i>C.-C. Hsu, J.W. Boughton, A.M. Mebel, and M.C. Lin</i>	48
Gas-Phase Reaction Mechanisms for Nitramine Combustion: On the Development of a Comprehensive Reaction Mechanism for Hydrogen/Nitrous Oxide Kinetics <i>R.A. Yetter, M.T. Allen, and F.L. Dryer</i>	58
Mechanistic Studies of Low-Pressure Flames Supported by Nitrogen Oxides <i>J.J. Cor, C.B. Dreyer, and M.C. Branch</i>	70

### AREA 2: ENVIRONMENTAL CONSIDERATIONS IN COMBUSTION OF SOLID AND LIQUID PROPELLANTS

#### **Invited Paper**

Towards the Development of "Clean Burning", Low Flame Temperature Solid Gun Propellants <i>R.A. Pesce-Rodriguez, R.A. Fifer, and J.M. Heimerl</i>	83
--	----

#### **Contributed Papers**

Effects of Rocket Exhaust on the Launch Site Environment and Stratospheric Ozone <i>R.R. Bennett, J.R. Wimpey, R. Smith-Kent, and A.J. McDonald</i>	92
--	----

Environmental Impact Assessment of Solid Rocket Motors Ground Tests <i>T. Aguesse</i>	106
On Thermochemical Characteristics of AP/NSAN/HTPB Composite Propellants <i>L. Araújo and O. Frota</i>	118
Realisation of an Eco-Friendly Solid Propellant Based on HTPB-HMX-AP System for Launch Vehicle Applications <i>Rm. Muthiah, T.L. Varghese, S.S. Rao, K.N. Ninan, and V.N. Krishnamurthy</i>	129
Soil Contaminated with Explosives: A Search for Remediation Technologies <i>J. Hawari, C.W. Greer, A.M. Jones, G.I. Sunahara, C.F. Shen, S.R. Guiot, G. Ampleman, and S. Thiboutot</i>	135
Solid Propellant Utilization by the Burning Propellant-Coal and Propellant-Peat Mixtures <i>A.V. Ananiev, A.G. Istratov, V.I. Kolesnikov, A.I. Kurochkin, V.N. Marshakov, G.V. Melik-Gaikazov, A.V. Rotshin, L.N. Stesik, and V.A. Teselkin</i>	145

### AREA 3: RECYCLING OF ENERGETIC MATERIALS

#### **Invited Paper**

Conversion of High Explosives <i>P. Wanninger</i>	155
--	-----

#### **Contributed Papers**

Boiler Fuel as a Recycling Option for Energetic Materials <i>L. Baxter, S. Huey, J. Lipkin, D. Shah, J. Ross, and G. Sclipa</i>	167
Recycling of Excess and Demilitarized Energetic Materials in Commercial Explosive Applications <i>O. Machacek, J.B. Gilion, G. Eck, J. Lipkin, R. Michalak, R. Perry, A. McKenzie, and L. Morgan</i>	177
Recent Studies on the Chemical Conversion of Energetic Materials to Higher Value Products <i>A.R. Mitchell, P.F. Pagoria, and R.D. Schmidt</i>	189
Recycling Propellants and Explosives into the Commercial Explosive Industry <i>M.E. Morgan and P.L. Miller</i>	199
Processing of Trinitrotoluene-Water Emulsions for Recycling <i>U. Teipel and H. Krause</i>	205
Pilot-Scale Base Hydrolysis Processing of HMX-Based Plastic-Bonded Explosives <i>R.L. Flesner, P.C. Dell'Orco, T. Spontarelli, R.L. Bishop, C.B. Skidmore, K. Uher, and J.F. Kramer</i>	213
Cryogenic Washout of Solid Rocket Propellants <i>J.P. Elliott, J.M. McNair, M.H. Spritzer, J.A. Hurley, and S.A. Rising</i>	221

AREA 4: NEW TECHNIQUES AND IMPROVED SAFETY IN COMBUSTION OF ENERGETIC MATERIALS

**Invited Paper**

- The Hazards of Solid Propellant Combustion 233  
*T.L. Boggs*

**Contributed Papers**

- Atomic Force Microscopy of Hot Spots in RDX and AP Crystals 268  
*J. Sharma and C.S. Coffey*
- The Importance of Mononitroso Analogues of Cyclic Nitramines to the Assessment of the Safety of HMX-Based Propellants and Explosives 278  
*R. Behrens and S. Bulusu*
- Ignition of Liquid and Solid Nitrocompounds at Fast Compressions of Gas Intrusions 290  
*B.N. Kondrikov, E.I. Dorofeev, and Yu.N. Polikarpov*
- Effect of  $\text{Fe}_2\text{O}_3$  on the Material Properties of AP/Al/HTPB Based Propellants 302  
*J.M. Boteler, J. Covino, and A.J. Lindfors*
- Thermomechanical Aspects of Energetic Crystal Combustion 313  
*R.W. Armstrong, W.L. Elban, A.L. Ramaswamy, and C.Cm. Wu*
- Insensitive Munitions Propulsion Progress 337  
*S.C. DeMay and C.J. Thelen*
- Combustion Roles in Safety of Less Explosively Sensitive Class 1.3 Propellants 345  
*C. Merrill*
- Propensity of Flame Spreading into Propellant Slits under Simulated Rocket-Motor Environments 356  
*K.K. Kuo, Y.C. Lu, and S.J. Ritchie*
- Evaluation of the Effectiveness of an Industrial Repair Procedure for Solid Propellant Grains 368  
*D. Cohen, K.K. Kuo, S.J. Ritchie, and Y.C. Lu*
- Solid Solution Formation Between RDX and Common Solid Propellant Binders 387  
*E. Boyer, P.W. Brown, and K.K. Kuo*
- Characterization of Waxes for Desensitization of Explosive Compositions 395  
*T. Chen, C. Campbell, and Y. Liang*

AREA 5: COMMERCIAL APPLICATION IN THE COMBUSTION OF ENERGETIC MATERIALS

**Invited Papers**

- Advances in Energetic Materials Manufacturing Technologies at ICI 413  
*S.K. Chan, G.A. Leiper, and R. Olive*

"Clean" Propellants for Commercial Applications <i>G.M.H.J.L. Gadiot, D.W. Hoffmans, P.A.O.G. Korting, and A.P.M. Leenders</i>	430
---	-----

#### **Contributed Papers**

Clean Liquid and Hybrid Gas Generator Systems for Inflating Car Airbags <i>J. Kishimoto, T. Saitoh, and A. Iwama</i>	442
Future Trends in Gas Generator Systems <i>H. Schubert and H. Schmid</i>	453
Utilization of Propellants for Inflator and Belt Restraint Systems <i>F. Volk</i>	457
Experimental Study of Flame-Spreading Processes over Mg/PTFE/Mg Thin Foils <i>C.L. Yeh, M.M. Mench, K.K. Kuo, and S.K. Chan</i>	465
Combustion and Detonation in Pulsed Power Generators <i>V.E. Fortov, V.B. Mintsev, and V.A. Zeigarnik</i>	476
Two-Phase Flames -- A Potential Method for Manufacturing Submicron Metal Oxide Powders <i>N. Ageev, S. Kyro, and Yu. Kostishin</i>	486

#### **AREA 6: IGNITION AND COMBUSTION PERFORMANCE OF PROPELLANTS FOR ROCKET PROPULSION**

##### **Invited Papers**

A Survey of Pressure-Driven Burning of Energetic Solids with Arrhenius Surface Pyrolysis <i>L. De Luca, M. Verri, F. Cozzi, A. Jalongo, and G. Colombo</i>	493
Recent Developments and Challenges in the Ignition and Combustion of Solid Propellants <i>G. Lengellé</i>	515

##### **Contributed Papers**

Recent Developments in Gun Propellants and Gun Propulsion Research at S.N.P.E. <i>J. Reynaud</i>	549
Combustion Behavior and Thermochemical Properties of JA2 Propellant <i>C. Kopicz, T.J. Watson, K.K. Kuo, and S.T. Thynell</i>	559
Ballistic and Microstructural Properties of a Highly Filled Gun Propellant with Varying Thicknesses of Inert Surface Coating <i>S.M. Caulder, F.S. Kim, and B.K. Moy</i>	574
Improvement of Ballistic Characteristics of Gun Propellants and Charges Using Metallic Additives <i>I.G. Assovskii, O.T. Chizhevskii, and V.V. Sergeev</i>	587

Burn Rate Studies of Gas Generator Propellants Containing AP/RDX <i>A.N. Nazare, S.N. Asthana, P.G. Shrotri, and H. Singh</i>	594
Mass Balance in Deterrent Coating of Smokeless Powders <i>J. Zigmund</i>	607
ADN: A New High Performance Oxidizer for Solid Propellants <i>A. Langlet, N. Wingborg, and H. Östmark</i>	616
ADN Propellant Technology <i>M.L. Chan, A. Turner, L. Merwin, G. Ostrom, C. Mead, and S. Wood</i>	627
"Activated" Aluminum as a Stored Energy Source for Propellants <i>G.V. Ivanov and F. Tepper</i>	636
High Burning Rate Solid Rocket Propellants <i>G. Doriath</i>	646
Experimental Analysis of a Minimum Smoke Propellant Ignition Characterization <i>L. Du, M. Song, H. Wang, and W. Yang</i>	661
A Solid-Phase Model for Plasma Ignition of Solid Propellant <i>R. Alimi, C. Goldenberg, L. Perelmutter, D. Melnik, and D. Zoler</i>	668
New Insights into the Combustion of AP/HTPB Rocket Propellants: The Catalyst Active Sites and a Combustion Flame Model for the Ferrocene-Catalysed Combustion <i>T.T. Nguyen</i>	679
Experimental Studies of Aluminum Agglomeration in Solid Rocket Motors <i>J. Duterque</i>	693
PolyNIMMO, a Candidate Binder for Solid Fuel Gas Generator Propellants <i>P.J. Honey, D.W. Anderson, G.A. Spinks, A.V. Cunliffe, and D.A. Tod</i>	706
Instantaneous Regression Behavior of HTPB Solid Fuels Burning with GOX in a Simulated Hybrid Rocket Motor <i>M.J. Chiaverini, N. Serin, D.K. Johnson, Y.C. Lu, and K.K. Kuo</i>	719
Real Gas Effects Simulation in a Model $\text{GH}_2/\text{O}_2$ Rocket Thrust Chamber <i>V.I. Golovitchev and G. Krülle</i>	734
Effects of Flame Behavior on a Gaseous Methane/Oxygen Small Thruster Performance <i>H. Kato, T. Ikezaki, and S. Yuasa</i>	743
Combustion Characteristics in a Gaseous Hydrogen/Oxygen Small Thruster <i>S. Yuasa, S. Kubota, and M. Fujita</i>	753
The Effect of Chemically Induced Stresses and Deformations on the Ignition of Solid Propellants <i>A.G. Knyazeva and V.E. Zarko</i>	762

Mathematical Modeling of Operation of an Acoustic Damper with Gas in its Internal Cavity <i>N.G. Alkov</i>	774
Ignition of Propellants: Shaping and Development of Burning Wave and its Characteristics <i>V.S. Abruikov, S.V. Ilyin, and V.M. Maltsev</i>	783
On Chemical Kinetics of the Ignition of AP/NSAN/Inert Binder Composite Propellants <i>O. Frota and L. Araújo</i>	793

#### AREA 7: COMBUSTION DIAGNOSTICS

##### **Invited Paper**

Propellant Combustion Diagnostics via Multichannel Absorption Spectroscopy <i>J.A. Vanderhoff, A.J. Kotlar, S.H. Modiano, and M.W. Teague</i>	807
--	-----

##### **Contributed Papers**

Optical Diagnostics of Atomization and Combustion for Cryogenic Liquid Rocket Propulsion <i>M. Oschwald, R. Lecourt, U. Brummund, A. Cessou, and O. Haidn</i>	825
Diagnostics of Non-Reacting and Reacting Supersonic Flows in a SCRAMJET Model Combustor Using Non-Intrusive Spectroscopic Methods <i>R. Höning, D. Theisen, R. Fink, G. Kappler, D. Rist, and P. Andresen</i>	837
Gas Temperature Measurements in a Flat Flame by Tunable Diode Laser Spectroscopy <i>M. Charpenel and C. Brossard</i>	849
The Response of a Pyrotechnic Powder under Dynamic Loading Conditions <i>A.I. Atwood, C.F. Price, S.A. Finnegan, P.O. Curran, and J. Wiknich</i>	863
Overtone Absorption Spectroscopy of Solid Propellant Flames: CO and N <sub>2</sub> O Concentrations <i>J.A. Vanderhoff, S.H. Modiano, B.E. Homan, and M.W. Teague</i>	876
Determination of Temperature and OH Concentration Profiles of RDX/CAB Pseudo Propellants Using UV/Visible Absorption Spectroscopy <i>A. Ulas, Y.C. Lu, and K.K. Kuo</i>	885
Combustion Phenomena of Boron Containing Propellants <i>W. Eckl, N. Eisenreich, W. Liehmann, K. Menke, Th. Rohe, and V. Weiser</i>	896
Characterization of Condensed-Phase Chemical Reactions of RDX and Nitramine-Based Propellants <i>E. Boyer, Y.C. Lu, and K.K. Kuo</i>	906
X-Ray Diagnostics for Local Burning Rate Measurements of Solid Propellants <i>M. Kohno, A. Volpi, and S.-I. Tokudome</i>	918

Spectroscopic Investigation of Solid Rocket Signatures <i>L. Deimling, W. Eckl, N. Eisenreich, W. Liehmann, and M. Weindel</i>	927
CARS Measurements of Temperature Fluctuations in a High Pressure Gas Turbine Combustor <i>B. Hemmerling, R. Bombach, and W. Kreutner</i>	934
Diagnostics and Active Control of Acoustic Instabilities in Combustors by Electrical Discharges and Plasma Jets <i>V.V. Afanasiev, V.A. Frost, N.I. Kidin, A.K. Kuzmin, and A.A. Terentiyev</i>	943
Composite Propellant Extinction by Laser Energy Pulse <i>C. Zanotti and P. Giuliani</i>	962
In-Cylinder Measurements of NO in a Running Diesel Engine by means of LIF Diagnostics <i>G.G.M. Stoffels, Th.M. Brugman, C.M.I. Spaanjaars, N. Dam, W.L. Meerts, and J.J. ter Meulen</i>	972

**AREA 8: THEORETICAL MODELING AND NUMERICAL SIMULATION OF COMBUSTION PROCESSES OF ENERGETIC MATERIALS**

***Invited Paper***

Numerical Simulation of Detonations: Fundamentals and Application <i>E.S. Oran</i>	985
---	-----

***Contributed Papers***

Some Dynamics of Acoustic Oscillations with Nonlinear Combustion and Noise <i>V.S. Burnley and F.E.C. Culick</i>	998
Modeling of Transient Combustion Regimes of Energetic Materials with Surface Evaporation <i>V.E. Zarko, L.K. Gusachenko, and A.D. Rychkov</i>	1014
Anomalous Group Combustion Theory: Transient Duality in Group Combustion <i>H.H. Chiu, C.L. Lin, and T.S. Li</i>	1026
A Phenomenological Theory of Propellants' Ignition and Subsequent Unsteady Combustion in High Pressure Chambers <i>I.G. Assovskii</i>	1035
Ignition and Unsteady Combustion of AP-based Composite Propellants in Subscale Solid Rocket Motors <i>A. Bizot</i>	1046
Evaluation of Thermochemical Erosion of the Solid Propellant Rocket Graphite Nozzle Throats by Integral Boundary Layer Technique <i>H. Vural and M.A. Ak</i>	1062
A Numerical Study on Unsteady Pressure Fluctuations of Davis Gun <i>H.-C. Cho, J.-K. Yoon and H.D. Shin</i>	1072



Unsteady Combustion of Homogeneous Energetic Solids <i>M.Q. Brewster and T.B. Schroeder</i>	1082
Improvements to Modeling of Hot Fragment Conductive Ignition of Nitramine-Based Propellants <i>E.S. Kim, S.T. Thynell, and K.K. Kuo</i>	1093
An Eigenvalue Method for Computing the Burning Rates of RDX and HMX Monopropellants <i>K. Prasad, R.A. Yetter, and M.D. Smooke</i>	1104
A Comparison of Solid Monopropellant Combustion and Modeling <i>M.W. Beckstead, J.E. Davidson, and Q. Jing</i>	1116
Modeling and Numerical Simulation of Physicochemical Processes Occurring in the Two-Phase Foam Layer of Burning RDX <i>K.K. Kuo, Y.C. Lu, and Y.S. Tseng</i>	1133
Nonlinear Transient Burning of Composite Propellants: The Effect of Solid Phase Reactions <i>J. Louwers and G.M.H.J.L. Gadiot</i>	1146
The Model of Porous Carbonized Particle Combustion <i>V.M. Gremyachkin</i>	1157
Numerical Simulation of the Nonstationary Spatial Gasdynamics Processes Accompanying the Pelletized Solid Propellant Combustion in a Gas Generator <i>A.M. Lipanov, A.N. Lukin, and A.V. Aliyev</i>	1164
<b>Authors Index</b>	1179

## PREFACE

Great challenges still exist in the area of propellant and combustion research 100 years after the passing of Alfred B. Nobel, who deserves to be called the "father of propellant science." Among Nobel's many breakthroughs and patented inventions, his development of ballistite, the first double-base propellant, has had a profound and lasting impact upon the propellant field. To commemorate Nobel's pioneering and innovative contributions to the development of explosives, pyrotechnics, and propellants, the Fourth International Symposium on Special Topics in Chemical Propulsion: *Challenges in Propellants and Combustion 100 Years After Nobel*, was held in Stockholm, Sweden, from the 27th through the 31st of May, 1996. The Symposium highlighted the substantial advancements made in propellant and combustion science during the last several decades, and also allowed for the exchange of information about current and future developments and research topics.

The International Symposium had several major objectives. These were: 1) to promote communication between researchers, designers, and manufacturers regarding state-of-the-art approaches in the field of propellants and combustion; 2) to discuss new and improved safety techniques in the combustion of energetic materials; and 3) to recommend future directions for research in combustion and chemical reaction systems. The Symposium also addressed several pressing global issues: a) the resolution of environmental issues in the combustion of energetic materials; b) the need for economical utilization of finite fuel resources; c) the production of power using existing or newly synthesized energetic materials; and d) the development of adequate techniques for disposal of surplus propellants and explosives for demilitarization purposes.

The Symposium was attended by 167 participants from 21 countries. In total, there were 127 technical papers, including 83 oral presentations and 44 poster papers. Of these, 100 (including the historical lecture on Nobel) were selected for publication in this edited book. All papers were reviewed using the same comprehensive procedures employed by respected journals in this field. Therefore, this volume should be considered an edited book of carefully reviewed and selected technical papers, rather than a collection of Symposium proceedings. The recent advances, future directions, and special challenges in each of the eight technical areas covered in this book are described below.

*Area 1: Chemical Kinetics of Propellant Combustion.* Major advancements have been made in the past decade in the use of detailed kinetics to model the combustion processes of various energetic materials. Incorporation of elementary reactions with specific rate constants is a common practice in the simulation of gas-phase reaction processes. The determination of rate constants for many elementary reactions between fragmented and decomposed species from propellant ingredients is a major task for propellant chemists. For the condensed phase, the diagnostics are much more limited than those for the gas phase. Theories for condensed phase reactions contain many more uncertainties. As kinetics for both the gaseous and condensed phases become available, it may be possible to understand and control transient events, such as ignition and combustion instability, at the molecular level.

*Area 2: Environmental Considerations in Combustion of Solid and Liquid Propellants.* Significant progress has been made towards the modeling of combustion products and phenomena which may affect the environment at both the ground and atmospheric levels. In many cases, the practical solution to combustion-related environmental hazards has been to design propellants in such a way as to avoid the generation of ecologically harmful ingredients. This is usually not a simple matter, as the formulator must identify

substitute ingredients which not only create no hazardous products themselves, but also possess the chemical and physical properties necessary to deliver the required performance. The most serious concern in recent years, the generation of hydrochloric acid (HCl) by solid propellants, has been lessened by the partial substitution of either nitramine crystals (HMX or RDX) or ammonium nitrate for ammonium perchlorate crystals. In both cases, the generation of HCl has been significantly reduced, but these substitutions result in greater production of NO<sub>2</sub>, which is thought to be of comparable toxicity to HCl. The task confronting "environmentally-minded" propellant designers is indeed challenging, since a favorable balance of performance and environmental safety cannot be easily achieved.

*Area 3: Recycling of Energetic Materials.* Since the end of the Cold War, disarmament of nuclear and conventional munitions has produced hundreds of millions of pounds of surplus propellants, explosives, and pyrotechnics worldwide. Historically, surplus energetic materials have been disposed of by open burning/open detonation (OB/OD). The disposal of these materials by OB/OD is becoming unacceptable due to public concerns and increasingly stringent environmental regulations. The proposed recycling of energetic materials as chemical feedstocks for the production of higher value chemicals potentially represents a "win-win" situation, since liabilities (surplus munitions) are converted to assets (useful products), sparing the environment the burden of present destructive disposal practices. The recycling of energetic materials will also play an important role in the formulation of new propellants and explosives. The goal is to demonstrate that pollution from the destruction of surplus propellants can be reduced by as much as 90% using life-cycle assessment methodologies and suitable recycling technologies.

*Area 4: New Techniques and Improved Safety in Combustion of Energetic Materials.* Due to demilitarization and the extension of lives of propulsion systems, the study of hazards and safety of energetic materials has become more important during the past decade. The ignition, decomposition, and mechanical damage of energetic materials can result in hazards such as explosions, deflagration-to-detonation transition (DDT), cook-off, and delayed detonation by unknown mechanisms (XDT). Incidents caused by these hazards have resulted in the loss of lives and the destruction of billions of dollars worth of propulsion equipment. The international community has performed significant research in the areas of DDT, XDT, cook-off, decomposition, ignition, electrostatic discharge, combustion and damage-induced reactions. These studies are intended to improve, mitigate and predict the overall safety of various propulsion systems. In order to reduce the probability of system hazards, future trends in the development of propulsion systems should incorporate design considerations for mechanical protection and thermal insulation of new and existing devices.

*Area 5: Commercial Application in the Combustion of Energetic Materials.* The advent of airbag technology and the widespread popularization of fireworks displays in many countries has led to an increase in the commercial use of propellants and pyrotechnics. The public's awareness of the use of such energetic materials has grown significantly with these and other commercial applications. In private industry, however, there is a lack of communication about important technological problems, largely due to the perceived need for corporate secrecy. One solution is to increase cooperation between academic institutes and industry, so that program managers and engineers in private industry will become more aware of the potential of advanced technologies, related background research, and the benefits of information exchange.

*Area 6: Ignition and Combustion Performance of Propellants for Rocket Propulsion.*

Knowledge of the performance of propellants and their ingredients is very important for the proper design and utilization of chemical rocket propulsion technologies. Current and near-future trends in this area include: a) further characterization of propellants using new energetic ingredients, such as ADN, CL-20, BAMO, GAP, and Alex (ultra-fine aluminum particles made by plasma explosion processes); b) extension of theoretical models to simulate combustion processes of propellants containing these new ingredients; c) further modification of models for simulation of the combustion and agglomeration of aluminum additives in solid propellants; d) development of more reliable models for the study of dynamic and unstable burning phenomena of solid propellants; e) extension of boundary-layer type of erosive burning models to include propellants containing new ingredients; f) the use of PolyNIMMO (3-Nitratomethyl-3-methyloxetane) polymer as an energetic binder in ramrocket gas-generator propellants; and g) the effect of chemically induced stresses on the ignition and combustion of solid propellants.

*Area 7: Combustion Diagnostics.* The development of new diagnostic techniques and the utilization of existing advanced instruments for the study of propellant flames and combustion phenomena in motors and engines continue to challenge the combustion community. Propellant flames often involve short residence times, large temperature and species concentration gradients in both condensed and gas phases, high pressures, and elevated temperatures. The data obtained from intrusive and non-intrusive techniques are crucial for several reasons. First, it is desirable to acquire a thorough fundamental understanding of the combustion behavior of energetic materials through in-depth data interpretation and mechanistic studies. Second, efforts at several institutions in the U.S. and abroad are underway to develop and validate comprehensive models describing the complex processes of heat transfer and finite-rate chemical kinetics during ignition and steady deflagration of energetic materials. To validate such models, data from carefully conducted experiments are needed for a broad range of test conditions. Recent advances and applications of non-intrusive diagnostic methods include multi-channel IR, tunable laser, UV/visible and X-ray absorption spectroscopy, and CARS and LIF spectroscopic techniques.

*Area 8: Theoretical Modeling and Numerical Simulation of Combustion Processes of Energetic Materials.* With the advent of the digital computer, the numerical simulation of physicochemical processes has become increasingly important in the design of combustion systems and prediction of combustion processes. The increased reliance upon computer-based predictions in design is largely the result of economic pressures. Not only is numerical simulation more economical than experimentation, but also the cost of performing a given calculation has decreased significantly over the years. This is mainly due to tremendous increases in computer speed and memory capacity with limited increases in overall computer costs. Numerical CFD simulations involving full sets of chemical reactions have now become possible. Whenever it is presently not economical or practical to utilize full numerical simulation free of empiricism, phenomenological models have been adopted to make possible numerical predictions of complex processes in various combustion devices. Therefore, modeling and numerical simulation are indispensable to the prediction of combustion processes of energetic materials.

Special thanks are due to those who acted as both Area Co-Organizers and Volume Associate Editors: Prof. Thomas B. Brill (Kinetics); Dr. Rose A. Pesce-Rodriguez (Environment); Dr. Alexander R. Mitchell (Recycling); Dr. Josephine Covino (Safety); Dr. S. K. Chan (Commercial Applications); Dr. Arie Peretz and Tekn. Lic. Nils-Erik Gunners (Performance); Prof. Stefan T. Thynell (Diagnostics); and Prof. S. H. Chan (Modeling/Numerical Simulation). The dedicated assistance of these Associate Editors in

processing technical reviews, editing and ensuring the uniformity of the manuscripts, and communicating with the authors for manuscript modification is greatly appreciated. Without their help, it would have been impossible to achieve the high quality of this volume.

Co-sponsorship of the Symposium itself was provided by the U.S. Air Force European Office of Aerospace Research & Development (EOARD), UK/USA; the U.S. Army Research Development and Standardization Group, UK/USA; the Institute of Applied Mechanics, Russia; MEGA Energy Technology, Sweden; National Cheng Kung University, Taiwan, ROC; National Defence Research Establishment (FOA), Sweden; National Tsing Hua University, Taiwan, ROC; Office of Naval Research (ONR), USA; Office National d'Etudes et de Recherches Aéropatiales (ONERA), France; the Pennsylvania State University, USA; the Russian Academy of Sciences, Russia; Société National Des Poudres et Explosifs (SNPE), France; the U.S. Army Research Laboratory, USA; China Aerospace Corporation, China; ICI Explosives, UK; Universal Tech Corporation, USA; Korea Advanced Institute of Science and Technology, Korea; and the Russian Foundation for Basic Research (RFBR), Russia. Since the Symposium and the compilation of this edited book would not have been possible without generous financial assistance, the support of these diverse organizations is greatly appreciated.

Major organizational responsibilities for the Symposium were divided among myself and the Co-Chairs, Tekn. Lic. Nils-Erik Gunnars of MEGA Energy Technology, Västerhaninge, Sweden, and Prof. George B. Manelis of the Russian Academy of Sciences, Chernogolovka, Moscow Region, Russia. In addition to the two Co-Chairs and the Associate Editors, I would also like to express my particular gratitude to Prof. Ronald W. Armstrong, Prof. Luigi De Luca, Dr. Robert A. Fifer, Dr. Guy Lengellé, Dr. Carl F. Melius, Dr. Richard S. Miller, Dr. Mark E. Morgan, Dr. Elaine S. Oran, Dr. Timothy P. Parr, Dr. Roland Pein, Prof. Dr. Hiltmar Schubert, and Dr. Robert W. Shaw, for serving as Area Co-organizers. An International Advisory Committee composed of more than one hundred distinguished members also furnished invaluable assistance. A complete list of International Advisory Committee members is given at the front of this volume.

Prof. Bertil Enoksson of the Department of Physical Chemistry at Uppsala University, Sweden is to be thanked for the invited contribution of his historical lecture on Alfred B. Nobel, which I have included at the beginning of the book. I would also like to acknowledge the administrative and technical assistance of Constance Tammerk, Faithann VanNess and Benjamin P. Perry. Finally, I give thanks to my wife, Olivia, and my daughters, Phyllis and Angela, whose loving support, understanding, and patience have made this work possible.

Kenneth K. Kuo  
Symposium Chairman  
and Volume Editor

### SYMPOSIUM CHAIR AND CO-CHAIRS

Prof. Kenneth K. Kuo Symposium Chair 140 Research Bldg. East Pennsylvania State University University Park, PA 16802- 2320 U.S.A. Phone: (1-814) 863-6270 Fax: (1-814) 863-3203 E-mail: kkkper@engr.psu.edu	Tekn. Lic. Nils-Erik Gunners Symposium Co-Chair MEGA Energy Technology Furudalsvägen 10 S-137 34 Västerhaninge SWEDEN Phone: (46-8) 500-208-27 Fax: (46-8) 500-208-27 E-mail: negunners@swipnet.se	Prof. George B. Manelis Symposium Co-Chair Institute of Chemical Physics Russian Academy of Sciences Chernogolovka, Moscow Region, RUSSIA 142432 Phone: (7-095) 913-23-10 Fax: (7-096) 51-535-88 E-mail: manelis@icp.ac.ru
---	--	--

### INTERNATIONAL ADVISORY COMMITTEE

Prof. Ronald W. Armstrong, USA* - 4	Prof. Guenter Klingenberg, Germany - 6,7
Dr. Igor Assovskii, Russia - 6	Prof. Boris N. Kondrikov, Russia - 1,6
Dr. Ezra Bar-Ziv, Israel - 6,7	Mr. Paul Korting, Netherlands - 2,5
Prof. Merrill W. Beckstead, USA - 1,6,8	Prof. Herman Krier, USA - 6
Dr. Michael Berman, USA - 1	Dr. V.N. Krishnamurthy, India - 6
Prof. Robert W. Bilger, Australia - 2,7	Prof. S. Krishnan, India - 6,7
Prof. Roland Borghi, France - 6,8	Dr. N. Kubota, Japan - 4,6
Prof. Derek Bradley, UK - 2,8	Dr. Paul Kuentzmann, France - 6,7
Prof. Melvyn C. Branch, USA 1,5	Prof. C.K. Law, USA - 6,8
Prof. K.N.C. Bray, UK - 1,8	Prof. John H. Lee, Canada - 6,8
Prof. Thomas B. Brill, USA* - 1,7	Dr. Guy Lengellé, France* - 6
Dr. J.B. Canterberry, USA - 3,4,5	Prof. M.C. Lin, USA - 1,8
Prof. Wen-Hwa Chen, Taiwan, ROC - 4	Dr. Joel Lipkin, USA - 2,3,6
Prof. S.H. Chan, USA* - 8	Prof. Alexey M. Lipanov, Russia - 6
Dr. S.K. Chan, Canada* - 5	Dr. David M. Mann, USA - 6
Prof. Paul H.H. Chiu, Taiwan, ROC - 2,8	Dr. Mark Maurice, USA@UK - 6
Dr. Josephine Covino, USA* - 4	Dr. Ingo May, USA - 1,2,7
Dr. Fred E.C. Culick, USA - 1,6,8	Dr. Carl F. Melius, USA* - 1
Dr. Alain Davenas, France - 6	Prof. A. G. Merzhanov, Russia - 1,5,6
Dr. Marc Defourneaux, Belgium - 4	Dr. Richard S. Miller, USA* - 6
Prof. Luigi DeLuca, Italy* - 6,8	Dr. Alexander R. Mitchell, USA* - 3
Dr. David R. Dillehay, USA - 2,6	Dr. Mark Morgan, USA* - 3
Prof. Lei Du, China - 4,6	Dr. Tam Nguyen, Australia - 1,2,6,7
Prof. Gerald M. Faeth, USA - 6,8	Prof. Takashi Niioka, Japan - 6
Prof. Chang-Gen Feng, China - 4,6	Dr. Helena Nilsson, Sweden - 6
Dr. Robert A. Fifer, USA* - 1,2	Prof. Boris V. Novozhilov, Russia - 8
Prof. Yuri V. Frolov, Russia - 6	Dr. Elaine S. Oran, USA* - 8
Prof. Wei Biao Fu, China - 2,6	Dr. Timothy P. Parr, USA* - 7
Prof. Alon Gany, Israel - 6	Dr. Roland Pein, Germany* - 6
Dr. W.L. Grosshandler, USA - 4	Dr. Arie Peretz, Israel* - 6
Prof. Ronald K. Hanson, USA - 7	Dr. Rose A. Pesce-Rodriguez, USA* - 1, 2
Dr. Jan Hansson, Sweden - 6	Dr. Roy E. Reichenbach, USA@UK - 1,6
Prof. Manuel V. Heitor, Portugal - 4,7	Mr. Jean-Paul Reynaud, France - 6
Prof. T. Hirano, Japan - 2	Dr. Juan De Dios Rivera, Chile - 2,5
Mr. Albert W. Horst, USA - 1,7	Prof. Oleg Ya Romanov, Russia - 6,7,8
Prof. Akira Iwama, Japan - 1,7	Prof. Hiltmar Schubert, Germany* - 1
Dr. Bo Janzon, Sweden - 6,7	Mr. Carlos Schüller, Spain - 6
Prof. Yoo Kim, Korea - 6	Dr. Robert W. Shaw, USA* - 1
Dr. I.J. Kirby, Scotland/UK - 6,8	Dr. H.F.R. Schoeyer, Holland - 6,8
Mr. Marion D. Kitchens, USA - 5	Dr. Haridwar Singh, India - 1,3,5,6
Dr. Rudolf Klemens, Poland - 1,2	Mr. Benjamin Stokes III, Belgium - 4,6

Prof. Alexey A. Sulimov, Russia - 6  
 Dr. D. Sutton, UK - 5  
 Mr. Hiroshi Tamura, Japan - 6  
 Prof. Stefan T. Thynell, USA\* - 7  
 Dr. Allen J. Tulis, USA - 1,5,6  
 Mr. Nico H.S. Van Ham, Netherlands - 6  
 Dr. John A. Vanderhoff, USA - 7  
 Prof. Pierre Van Tiggelen, Belgium - 7  
 Dr. Fred Volk, Germany - 1,5,6  
 Prof. Hüseyin Vural, Turkey - 5,6,8  
 Prof. H.G. Wagner, Germany - 1,4,7

Prof. J.H. Whitelaw, UK - 2,6,7  
 Prof. Forman A. Williams, USA - 6,8  
 Mr. Stig Wretling, Sweden - 6  
 Prof. Xiping Wu, China - 5,6,7  
 Prof. Jing-Tang Yang, ROC - 6,8  
 Dr. Richard Yetter, USA - 1,7,8  
 Dr. Claudio Zanotti, Italy - 6,7  
 Prof. V.E. Zarko, Russia - 5,6  
 Prof. Anatoli A. Zenin, Russia - 4,6,7  
 Dr. Ben T. Zinn, USA - 7,8  
 Prof. Andrey N. Zolotko, Ukraine - 2,7,8

(\* Denotes Area Co-Organizer)

### **TOPIC AREAS**

- (1) . . . . . Chemical Kinetics of Propellant Combustion
- (2) . . . . . Environmental Considerations in Combustion of Solid and Liquid Propellants
- (3) . . . . . Recycling of Energetic Materials
- (4) . . . . . New Techniques and Improved Safety in Combustion of Energetic Materials
- (5) . . . . . Commercial Application in the Combustion of Energetic Materials
- (6) . . . . . Ignition and Combustion Performance of Propellants for Rocket Propulsion
- (7) . . . . . Combustion Diagnostics
- (8) . . . . . Theoretical Modeling and Numerical Simulation of Combustion Processes of Energetic Materials

## **ALFRED NOBEL: FROM GUNPOWDER TO BALLISTIT**

**Bertil Enoksson**

Department of Physical Chemistry, Uppsala University, Uppsala, Sweden

**ABSTRACT:** Alfred Nobel was an inventor in many different fields who possessed a rare creative power. His scientific contributions were above all others in the explosives area with epoch-making results also of technical and economic importance: the introduction of high explosives, invention of the detonator, dynamite, blasting gelatin, gelatinous explosives, double base propellant, and progressive powder.

### **INTRODUCTION**

Alfred Bernhard Nobel was born in Stockholm, Sweden, on 21 October 1833. He died at San Remo, Italy, on 10 December 1896.

During his lifetime, Alfred Nobel was honored in many ways, but he accepted few official distinctions and complained that none of his orders had any foundation in explosives. Nonetheless, he highly appreciated his membership in the Royal Academy of Sciences, Stockholm, and the honorary degree of Doctor of Philosophy, which he received in 1893 at the University of Uppsala.

It is obvious that Alfred Nobel wanted to be remembered foremost for his scientific contributions in the field of explosives. Therefore, to commemorate Alfred Nobel, I will recount the struggle in the explosives market among blackpowder, cellulose nitrate and glycerol trinitrate, emphasizing the contributions made by Alfred Nobel.

In his teenage years in St. Petersburg, Alfred Nobel got to know about explosives and their possibilities. His father, Immanuel Nobel, managed a foundry and wheel factory, where among many other items, he also manufactured land and sea mines. In 1850, Alfred Nobel was sent to study in Sweden, Prussia, France, and North America. He spent most of his time abroad in Paris studying chemistry, partly at the laboratory of the famous Jules Pelouze. Alfred Nobel became familiar with the science of the time and learned about esterification with nitric acid. This knowledge was to be of vital importance to his work with nitroglycerin.

When back in St. Petersburg in 1854, Alfred Nobel was employed by his father's company, Nobel et Fils, which prospered as a consequence of the large orders by the Russian state during the Crimean War. But when the war came to an end in 1856, the company soon became insolvent. Alfred was sent to bankers in London and Paris in search of a loan. No one was willing to grant credit to the Nobels. Immanuel Nobel was bankrupt, and in 1859 he returned to Stockholm. His three eldest sons, Robert, Ludvig, and Alfred, stayed in St. Petersburg, where they operated a small workshop.



## BLACKPOWDER

Immanuel in Stockholm and Alfred Nobel in St. Petersburg, each individually, tried to find an explosive more effective than blackpowder. For more than 500 years, blackpowder had held its ground as the only propellant. Originally blackpowder consisted of approximately 40% saltpeter, 30% charcoal, and 30% sulphur, intimately ground together. Later normal gunpowder comprised 75% potassium nitrate, 15% charcoal and 10% sulphur, each component finely ground before moistened and mixed together.

If blackpowder is burned in a confined space, e.g., in a borehole, the pressure increases and so does the rate of burning to such a high value that it can be used for blasting. From the seventeenth century onward, blackpowder was applied to industrial blasting in mining. By varying the composition, granulation, and glazing, the blackpowder was adapted to the special use for which it was intended. Cheaper powder was produced in which potassium nitrate was replaced by sodium nitrate. Blackpowder slowly and only partly replaced the older fire-setting method, in which a fire was set against the rock face and then water was dashed onto the heated rocks. The broken rock could then be dug out.

Many additions were made to blackpowder in order to improve its properties. Other components were tested, but for a very long time blackpowder was the only explosive of importance on the market. No explosive has been or will be used for as many different applications as blackpowder. But times changed and blackpowder met a new threat from more specialized chemical agents and detonating explosives, such as nitrocellulose and nitroglycerin.

## NITROCELLULOSE

Cellulose nitrate was the first serious rival to compete with blackpowder for the commercial explosive market. In 1845, Christian Friedrich Schönbein, professor of chemistry at Basel, discovered a way to produce nitrocellulose by immersing cotton or paper into a mixture of nitric and sulphuric acids. This invention was made during his research about ozone and "active oxygen." Schönbein immediately recognized the possibilities of the product obtained by esterification of cotton with nitric acid and patented it as guncotton. He expected that his guncotton would soon replace gunpowder as a propellant. However, the nitrated cotton was unstable. Disastrous explosive accidents occurred during the manufacture and storage of guncotton. Furthermore, the enormous pressure generated by firing guncotton charges damaged and sometimes even blew up the guns used. For this reason, the manufacture of guncotton was officially prohibited and the development was very much delayed.

## NITROGLYCERIN

Soon, another high explosive appeared in the field. In 1846, Ascanio Sobrero, professor of industrial chemistry at Turin, discovered nitroglycerin. He slowly added glycerol to a pre-cooled mixture of nitric and sulphuric acids while stirring. When the reaction mixture was poured into water, nitroglycerin, an oil heavier than water, precipitated. It was purified by washing with a large amount of water.

Sobrero found nitroglycerin so unpredictable and frightening that he warned against its use. Although nitroglycerin showed its explosive strength, the danger seemed too great. It was only used in small quantities as a diluted alcoholic solution for a heart medicine.

It demanded a person with an extraordinary far-seeing spirit, ingenuity, courage, and an untiring energy to succeed in finding practical applications for this violent explosive. Alfred Nobel was that man.

## NOBEL'S DETONATOR

Remarkably, the first main difficulty encountered with nitroglycerin was in detonation. A spark or contact with a flame caused it to burn calmly without detonating. Immanuel Nobel in Stockholm tried mixtures of blackpowder and nitroglycerin. He got a increase in the strength of blackpowder, but the inconveniences of both ingredients remained. Alfred Nobel in St. Petersburg started in the same way, but showed more creativity. He initiated nitroglycerin by a shock from an explosive charge smaller than the main blasting load. In its first form, this detonator consisted of gunpowder compressed in a wooden cylinder which was closed by two plugs. Into one of them a safety fuse with blackpowder had been inserted. Later, this led to a blasting cap with an initiating explosive which reacts violently when heated, such as mercury fulminate. This brilliant way to ignite high explosives to detonation was the first epoch-making invention by Alfred Nobel. It opened the era of high explosives in the blasting industry, from the heaving action of blackpowder at a low, sustained pressure causing minimum fragmentation, to the great possibilities of high explosives of widely different weight strength, detonation velocity and pressure, loading density and blasting action.

## NOBEL'S BLASTING OIL

Alfred Nobel joined his father in Stockholm in 1863. Now, when he could initiate the detonation of nitroglycerin with unfailing certainty, he was ready to introduce nitroglycerin into blasting practice. His patented blasting oil was far superior in explosive power to ordinary gunpowder and had many advantages. Large savings in drilling labor and cost were achieved and the time required for much engineering work could be shortened tremendously. A growing demand for access to this effective explosive arose quickly. Military experts, however, declared that an explosive with such enormous strength was too dangerous to use in warfare.

The nitroglycerin was manufactured at the Nobels' pilot plant at Heleneborg in south Stockholm. Here, at the same time, work proceeded on improvements in the method of manufacturing nitroglycerin. On 3 September 1864, the temperature in the nitrating vessel rose out of control. A most terrible explosive accident followed, in which the whole factory was wiped out and five people were killed. Among the dead was Alfred Nobel's younger brother, Emil.

Now, there was no way back for Alfred Nobel. He had to show the world that his own faith in the usefulness and future of nitroglycerin was right. He needed to show that by his inventions, more people would be saved than lost by the introduction of high explosives into blasting techniques. This inspired him to do impressive, untiring work, in which he shrank from no difficulties for the betterment of mankind.

A ban was put on the manufacture and storage of nitroglycerin within populated areas. Alfred Nobel acted swiftly. Within a month after the accident, he was producing his blasting oil aboard a barge anchored on Lake Mälaren outside the bounds of Stockholm. In November 1864, Alfred Nobel founded his first limited company, Nitroglycerin AB. The following year, the company was granted a permit to build a nitroglycerin factory at a then-desolate creek of Mälaren, southwest of Stockholm.

## DYNAMITE

At the start of his nitroglycerin business, Alfred Nobel was already fully aware of the disadvantages of the liquid form of the blasting oil. It led to accidents in transportation and use. The nitroglycerin ran into fissures in the rock and could cause explosions when the broken rock was picked out.

Alfred Nobel worked persistently to find a means to make nitroglycerin safer. At first, he tried to reduce the dangers by transporting nitroglycerin dissolved in methanol. However, this method proved to be inadequate, and Alfred Nobel found it necessary to add the blasting oil in another form. He turned his attention to adsorbing the nitroglycerin in fibrous or porous substances such as nitrocellulose, paper, charcoal, and sawdust. He decided on kieselguhr, a fine, porous deposit of cell walls of diatoms. Seventy-five percent nitroglycerin adsorbed in 25% calcined kieselguhr formed an easy-to-handle plastic explosive. Guhr dynamite was patented in 1867 and is the best known of Alfred Nobel's inventions.

The guhr dynamite aroused enormous interest all over the world in mining and communication industries. Alfred Nobel founded companies and built nitroglycerin and dynamite plants in many places in different countries. He wanted his explosives to be manufactured as near the place of consumption as possible. In 1865, Alfred Nobel moved to Hamburg and lived there until 1873, experimenting for safer and more efficient explosives at his laboratory at Krummel.

The nitroglycerin explosives made possible enterprises which had been unthought of with gunpowder. However, Alfred met unexpected competition from miners who used his blasting oil because they found guhr dynamite too weak, since it had only about 60% of the blasting effect of pure nitroglycerin. Nevertheless, the strength of dynamite was many times that of blackpowder.

More serious was the struggle with nitrocellulose, particularly in Britain. Guncotton with about 20% water was packed in the bore hole and initiated by a primer of dried, compressed nitrocellulose, which, ironically, was fired by a Nobel detonator.

To succeed, it was necessary to increase the strength of dynamite. As a step in this direction, in 1869 Alfred Nobel patented the use of active adsorbents, which in contrast to the heat-absorbing kieselguhr, contribute to explosive energy. Straight dynamite could comprise nitroglycerin adsorbed in wood pulp, sodium nitrate and, as a stabilizer, calcium carbonate. But Alfred Nobel was not satisfied. He wanted something really new, a very powerful explosive, safer to handle than guhr dynamite and resistant to water and moisture.

## BLASTING GELATIN

In 1873, Alfred Nobel left Hamburg for Paris. He bought an elegant mansion on Avenue Malakoff and added a winter garden to his taste, stables for his horses, and a chemical laboratory for his research.

Alfred Nobel and his assistant, Georges Fehrenbach, made many tests with different explosive substitutes for kieselguhr, which was inert and also had the disadvantage of binding water better than nitroglycerin. From the outset they tried mixtures of nitroglycerin and nitrocellulose, but they got only suspensions of fibrous guncotton in the blasting oil and no coherent mass. Nitrocellulose adsorbs only small amounts of nitroglycerin. How to incorporate nitrocellulose with nitroglycerin and make nitrocellulose soluble in nitroglycerin? One day Alfred Nobel poured collodion, a solution of low-nitrogen nitrocellulose in ether-alcohol, into nitroglycerin. When most of the volatile solvents had evaporated, a rather stiff gel remained. His goal was within reach. However, many tests and much work had to be done before the invention was suited for presentation on the market. Only nitrocellulose with

a nitrogen content of about 12.2% is directly soluble in nitroglycerin. With a 7 to 8% collodion nitrocotton in nitroglycerin, a tough, viscoelastic gel is formed in a few hours. This gel, blasting gelatin was patented in 1876.

A competitor to Alfred Nobel declared Nobel's blasting gelatin, in every respect, to be the most perfect explosive known. Blasting gelatin is slightly stronger than pure nitroglycerin, as the oxygen excess of the nitroglycerin is utilized by the nitrocellulose and gives an additional contribution to the explosive energy. By the detonation of 1 kg well confined blasting gelatin 6.5 MJ is released. In less than 1 ps the pressure at the detonation front rises to over 20 GPa and the temperature to about 5,000 K. The detonation velocity is near 8 km/s.

Blasting gelatin is a superior explosive, which was used for such demanding tasks as blasting the hardest rock and under-water blasting. But blasting gelatin was more important as the basis of the gelatinous explosives which rapidly came into wide use. With less nitrocellulose, a thinner and softer gelatin was obtained, in which mixtures of oxidizing agents and combustibles were incorporated. These plastic explosives could easily be packed in a bore hole and they also stayed in holes directed upwards. In addition, the gelatinous blasting explosives were cheaper and safer and still had a good resistance to water. Ammon gelatin, in which the oxidizer is ammonium nitrate, was patented by Alfred Nobel in 1879.

Nitroglycerin explosives, due to Alfred Nobel's inventions and research, became the choice of the civil blasting market. The properties of the gelatins and dynamites could be modified in many ways. It was even possible to develop explosives which, when fired in coal mines, did not ignite firedamp or coal dust. However, so far, nitroglycerin had little military importance, and blackpowder still controlled the propellant business.

### **BALLISTIT**

The Nobel dynamite companies provided peaceful tools, not weapons. According to Alfred Nobel, blasting gelatin would propel not only the projectile, but also break the gun itself into fragments. Guncotton was tried as a propellant, but was unreliable. In spite of this, new lighter weapons were designed for more powerful propellants, which gave the bullet a much higher muzzle velocity than gunpowder could give. But the propellant with an easily controlled rate of burning was lacking.

While engaged in the development of blasting gelatin, Alfred Nobel began to think of a propellant consisting of nitroglycerin and nitrocellulose. His thoughts led him to celluloid, which has as two-thirds of its weight nitrocellulose and one-third camphor. Celluloid is too slow to propel projectiles and, besides, cannot burn without access to oxygen. Alfred Nobel thought that if the camphor was substituted partly or wholly with nitroglycerin, the burning rate would increase. The consistency would be retained, thus making it possible to form the powder in a proper way with a regulated surface and burning rate.

After many years of fundamental research and testing, Alfred Nobel finally introduced ballistit in 1888. It originally contained 60% nitrocellulose and 40% nitroglycerin and a small addition of diphenylamine as stabilizer. Ballistit was the first double base propellant. It produces great power and leaves no deposits and is nearly smokeless.

Ballistit was the last of the epoch-making discoveries by Alfred Nobel. It instantly aroused great interest. In scientific circles, Alfred Nobel's results were considered most remarkable and surprising. That two violent high explosives could combine into a propellant, which upon ignition burns with good

stability and precision, was indeed impressive. It was also striking that ballistit could be rolled between hot rollers or pressed under heat into different shapes.

Alfred Nobel had once more shown how two competing chemical substances, nitrocellulose and nitroglycerin, can work together and take the market from the earlier dominating blackpowder. He was not so successful with people and governments. When they learned about the new smokeless powder, they feared that their weapons would become inferior to those of others. His laboratory at Sevran was closed by the French authorities, who would not tolerate any rivals to their own single base powder. Alfred Nobel left Paris in 1891 and settled down in San Remo, Italy. In the United Kingdom, ballistit had to compete with cordite, a nitroglycerin powder which was based on Alfred Nobel's own ideas and research. This was a very hard blow for Alfred Nobel personally and a loss of an enormous sum of money in royalties to him, and later on to the Nobel Foundation.

Alfred Nobel was very active with experiments, research, and development work in San Remo, Italy, and at Björkborn and Bofors, Sweden, until his death in 1896. His last discovery in the realm of explosives was progressive smokeless powder (Swedish patent in 1896). Thin sheets of more slowly burning powder were rolled or pressed on each side of a faster burning one.

### EXPLOSIVE ENGRAVING OF ALFRED NOBEL

Alfred Nobel disliked all forms of personal attention and publicity. He wanted to be left in peace. Not even did he have his picture painted. How can I then dare to illustrate my lecture with a portrait of Alfred Nobel?

The metal plate for this picture of Alfred Nobel was produced by detonating a layer of explosive on a sheet of polymethyl methacrylate placed onto the painting on the plate. This explosive engraving method was developed by the artist Verner Molin in collaboration with Nitro Nobel, Alfred Nobel's first company. Thus this print has an explosive past and may be accepted in my lecture.

I will feel honored if this picture of Alfred Nobel could stay at this Symposium on Special Topics in Chemical Propulsion and later at the Workshop on Peaceful Utilization of Energetic Materials in St. Petersburg, where I hope it will remain.

### REFERENCES

- Bergengren, E., *Alfred Nobel: The Man and His Work*, Thomas Nelson and Sons, London, 1960.
- Enoksson, B., The Cordite Case in View of Modern Physical Chemistry, *7th Symposium on Chemical Problems Connected with the Stability of Explosives*, ed. Hansson, J., Detonik och Förbränning, Sundbyberg, 1985, 1-17.
- Enoksson, B., Gummidynamiten-Världens Första Explosiva Gelatin, *Svensk Kemisk Tidskrift-Kemiteknik*, Vol. 88, No. 12, 1976, 26-30.
- Marshall, A., *Explosives: History and Manufacture*, Vol. 1, P. Blakistone's Son and Co., Philadelphia, 1917.
- Miles, F.D., Cellulose Nitrate, *The Physical Chemistry of Cellulose Nitrate, its Formation and Use*, Oliver and Boyd, Edinburgh, 1955.
- Naoum, P., Nitroglycerine and Nitroglycerine Explosives, *Baillière, Tindall and Cox*, London, 1928.
- Nobel, A., *Improvements in the Manufacture of Explosives*, G.B. Patent No. 1471., 1888.
- Reader, W.J., *Imperial Chemical Industries, A History*, Vol. 1: *The Forerunners*, Oxford University Press, London, 1970.

- Romocki, S.J., Geschichte der Explosivstoffe II, *Die rauchschwachen Pulver in ihrer Entwicklung*, Robert Oppenheim, Berlin, 1896.
- Schück, H. and Sohlman, R., *The Life of Alfred Nobel*, William Heinemann, London, 1926.
- Storm, C.G., Smokeless Powder, *Colloid Chemistry*, ed. Alexander, J., The Chemical Catalog Company, New York, 1932, 101-116.
- Strandh, S., *Alfred Nobel*. Mannen, Verket, Samtiden, Natur och Kultur, Stockholm, 1983.
- Widman, O., Det Gamla och Det Nya Krutet, *P.A. Norstedt och Söners Förlag*, Stockholm, 1899.



Explosive Engraving of Alfred B. Nobel  
(Explosive Engraving Method Developed by Verner Molin, in collaboration with Nitro Nobel Co.)



***Area 1:***  
***Chemical Kinetics***  
***of***  
***Propellant Combustion***



## ADVANCES IN COMBUSTION-LIKE KINETICS AND MECHANISMS OF POLYMERIC BINDERS

Thomas B. Brill, Haruyuki Arisawa, and Polly E. Gongwer

Department of Chemistry, University of Delaware, Newark, DE 19716 USA

### ABSTRACT

The pyrolysis kinetics and mechanisms of polymeric organic binder/fuels are largely unknown at the conditions of combustion. New insights into this complex subject are coming to light by the use of T-jump/FTIR spectroscopy. An overview of findings for polymethylmethacrylate, cellulose acetate butyrate, polyethyleneglycol, and hydroxyl-terminated polybutadiene is presented. The main advances are: (1) Flash pyrolysis work has been achieved for the first time in which kinetics and reaction details for the formation of individual products are determined; (2) A switch in the controlling mechanism is observed from bulk-phase decomposition reaction control to desorption control at about 500°C; and (3) Kinetic models are given which contain the desorption-decomposition processes and apply to non-energetic polymers.

### INTRODUCTION

The combustion characteristics of formulated energetic materials, such as rocket propellants, explosives and gas generators, are unquestionably dominated by the energetic components. Consequently, most investigations of kinetics and mechanisms in the solid propellant and explosives field have focused on the pure energetic components. However, it is well-known that the polymeric binder, which provides both mechanical strength and fuel to the formulation, significantly contributes to the combustion and explosion characteristics. Most of what is known about the kinetics and pathways of thermal decomposition of binders has been obtained in temperature, pressure, and heating rate regimes that are very far from the combustion or explosion conditions. In addition, the chemical processes which occur during thermal decomposition of organic polymers can be extremely complicated. Their description exceeds the capability of most conventional experimental methods.

Advances in the chemistry of flash-heated polymers have recently become possible by using T-jump/FTIR spectroscopy [1]. T-Jump/FTIR spectroscopy simulates combustion conditions in the pyrolysis zone, and enables the products and their rates of formation to be determined in near real-time. This article addresses the chemistry of non-energetic binders about which comparatively little is known at combustion conditions.

## POLYMERS AND COMBUSTION-LIKE PYROLYSIS METHODS

A very large number of organic polymeric substances have been processed with energetic compounds to achieve the desired properties of a formulation. Curing agents, plasticizers, and stabilizers are frequently also incorporated. Table 1 lists some of the non-energetic and energetic polymers which have found application in recent years. Boileau [2] recently wrote about the synthesis and applications of several energetic binders. No generalized overview of synthesis and application of non-energetic binders was located. The combination of the wide variety of polymers and the many variables for a given polymer (molecular weight, dispersity, tacticity, etc.) explains this absence of generalized discussions. Articles about thermal decomposition tend to focus on one compound or class of compounds. For example, Beck [3] reviewed work up to 1987 on several polybutadienes.

Table 1  
Some Binder/Fuels used in Propellants and Explosives Formulations

<u>"Non-Energetic"</u>	
<u>Synthetic Hydrocarbons</u>	
HTPB (hydroxyl-terminated polybutadiene)	PS (polystyrene)
CTPB (carboxyl-terminated polybutadiene)	Vistac
Polyisobutylene	Wax
<u>Ethers</u>	
PEG (polyethyleneglycol)	PPG (polypropyleneglycol)
<u>Polyesters</u>	
Nylon	Laminac
<u>Cellulose</u>	
CAB (cellulose acetate butyrate)	CA (cellulose acetate)
<u>Copolymers</u>	
PBAA (polybutadiene acrylic acid)	
PBAN (polybutadiene acrylic acid acrylonitrile)	
<u>Fluorocarbons</u>	
Kel-F	Viton
<u>Others</u>	
PMMA (polymethylmethacrylate)	polysulfide
polycaprolactone	asphalt
polyurethane (estane)	silicone resins
<u>"Energetic"</u>	
<u>Nitrate esters</u>	
NC (nitrocellulose)	PVN (polyvinyl nitrate)
PGN (polyglycidynitrate)	Poly-NMMO (polynitratomethylmethyl oxetane)
CAN (cellulose acetate nitrate)	
<u>Nitroaliphatics</u>	
DNPS (dinitrophenylstyrene)	PNP (polynitrophenylene)
DNPA (dinitropropanol acrylate)	
<u>Azides</u>	
GAP (glycidyl azide polymer)	BAMO (bisazidomethyl oxetane)
AMMO (azidomethylmethyl oxetane)	-THF copolymer

Extensive literature exists on slow, controlled, thermal decomposition of organic polymers. For example, more than fifty publications dealing directly with the kinetics and mechanism of thermal decomposition of polymethylmethacrylate have appeared, and PMMA has one of the simplest decomposition mechanisms of all organic polymers!

Substantially less literature exists on pyrolysis chemistry of polymers at the heating rates and temperatures resembling combustion conditions. Essentially five methods of flash-heating have been used for non-energetic polymers: hot plate [4,5], hot gas and diffusion flames [6,7], arc image [8,9], filament heating [1,10-14], and laser heating [15-17]. Filament heating offers the best independent control over the heating rate and pyrolysis temperature. Most flash pyrolysis studies are not designed to provide a chemical analysis simultaneously with the pyrolysis process. If a flame is actually produced, then the most interesting near-surface species usually react before they can be identified. Hence, flash pyrolysis at combustion conditions is desirable, followed by quenching in an inert environment and immediate detection by a fast-response method. For example, rapid-scan FTIR spectroscopy or any other time-resolved spectral method can be used to identify and quantify the major products as they form. Therefore, a brief description is given here of T-jump/FTIR spectroscopy by which a film of a polymer is flash-heated to set temperatures representative of those at the surface during combustion, while mid-IR spectra are recorded of the evolved and quenched products.

#### T-JUMP/FTIR SPECTROSCOPY

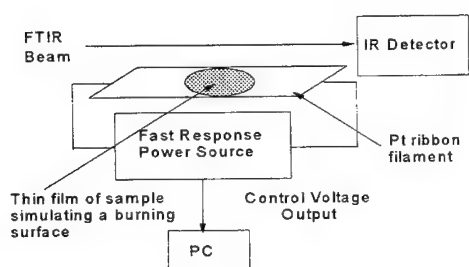


Figure 1. A schematic of T-Jump/FTIR spectroscopy

T-Jump/FTIR spectroscopy is an elaborate technique [1], but the essential features are illustrated in Figure 1. Approximately 200 $\mu$ g of the polymer was cast as a film on the center of a polished Pt ribbon filament. Catalysis by the Pt filament has been shown to be minimal in both oxidizing and reducing environments [18,19]. The filament was arranged inside of a gas-tight cell so that the beam of a rapid-scanning FTIR spectrometer passes about 3mm above the surface.

The cell was purged with Ar and pressurized to 1, 2 or 11 atm. By using a high-gain, fast-response power supply, the filament was heated at 2000°C/s and then held at a chosen temperature in the 350-610 $\pm$ 2°C range for 20s. The relationship between the applied voltage and the resultant filament temperature was determined for all experimental conditions by using melting point standards.

Although 2000°C/s is the filament heating rate, the sample heats at about 600-1000°C/s to the set temperature because of limitations in the rate of heat transfer [20,21]. After the initial 0.5s, the characteristic thermal diffusion time, which is the time required for one face of the film to sense a temperature transient at the other, is about 25ms [20]. This time is much faster than the data collection rate. As a result, the small changes in control voltage applied to the filament can be used to track the endothermic and exothermic events of the sample. An exotherm produces a negative deflection in the control voltage trace. Transmission IR spectra of the gaseous products were recorded every 100ms at 4cm<sup>-1</sup> resolution simultaneously with the control voltage measurement. These data provide the gas evolution rate and outline the chemistry taking place in the film, which is a "snapshot" simulation of the burning surface.

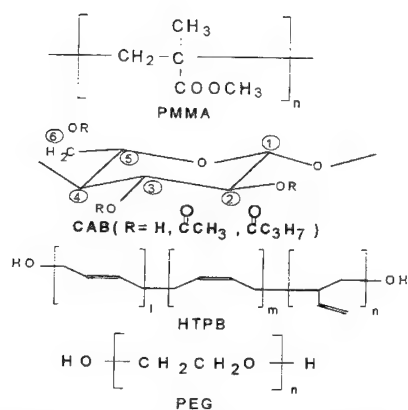


Figure 2. Structures of the polymers described herein.

The combustion-like pyrolysis process for polymers is illustrated in this article with the four polymers shown in Figure 2. These are polymethylmethacrylate (PMMA) with  $M_w = 2000$ , polyethyleneglycol (PEG) with  $M_w = 2090$ , cellulose acetate butyrate (CAB) with  $M_w = 75,000$ , and hydroxyl-terminated polybutadiene (HTPB) with  $M_w = 2,500$ . All of these compounds find application in consumer and industrial products, as well as in fuel/binders for the propulsion and energetic materials fields. For example, PMMA and HTPB are fuels for hybrid rockets. HTPB is also one of the most commonly used binders in composite propellants. PEG has been used in minimum smoke propellants as well as smoke generators. CAB is a binder for low vulnerability propellants.

### DATA ANALYSIS

T-Jump/FTIR spectroscopy enables kinetic determinations to be made because many of the temporally-resolved volatile products have characteristic absorbances at  $600\text{--}4000\text{cm}^{-1}$ . However, interference makes measurement of their concentrations by the absorbance at a single wavelength impossible. On the other hand, concentrations can be determined for all species simultaneously when all wavelengths are used. This procedure uses multivariate statistical and mathematical methods to maximize chemical details, and is known as chemometrics.

An absorptivity-concentration calibration relationship is first constructed for each pure product. For those products which are gaseous at  $20^\circ\text{C}$  and 1 atm, the three-dimensional matrix of absorbance, concentration and wavelength was measured at different partial pressures of Ar. For products which are liquid at  $20^\circ\text{C}$  and 1 atm, the calibration matrix was determined from the vapor spectrum at vapor-liquid equilibrium.

Second, for a time series of IR spectra during pyrolysis of HTPB and CAB, the time dependence of the concentration of each product was calculated by using non-negative least squares regressions of eq. 1 [22].

$$\mathbf{m} = \mathbf{K}\mathbf{c}(t) - \mathbf{r}(t) \quad (1)$$

Equation 1 is subject to the condition that the concentration,  $\mathbf{c}(t)$ , is  $\geq 0$ . The coefficient matrix  $\mathbf{K}$  contains the absorptivity spectra of the thermolysis products, and the vector  $\mathbf{r}(t)$  contains the IR spectrum of the thermolysis products at time  $t$ . The calculated vector  $\mathbf{c}(t)$  is the concentration of each product at  $t$  in which  $\mathbf{m}$  is minimized. Baseline corrections were required because smoke particles scatter IR radiation at shorter wavelengths.

For PEG and PMMA, quasi-Newtonian optimization (expression 2) was used because additional constraints could be placed on the concentration relationships [23].

$$\underset{\mathbf{c}(t)}{\text{minimize}} \left\{ \frac{1}{2} \mathbf{c}(t)^T \mathbf{H} \mathbf{c}(t) + \mathbf{g}(t)^T \mathbf{c}(t) \right\} \text{ subject to } \mathbf{A} \mathbf{c}(t) \geq 0 \quad (2)$$

$\mathbf{H} = 2\mathbf{K}^T\mathbf{K}$  and  $\mathbf{g}(t) = -2\mathbf{K}^T\mathbf{r}(t)$ , where  $\mathbf{A}$  is the constraint matrix which imposes the concentration conditions. The superscript  $T$  is the transpose of the matrix. The details of these procedures require much more discussion [22,23], but an outline of the method is summarized in Figure 3.

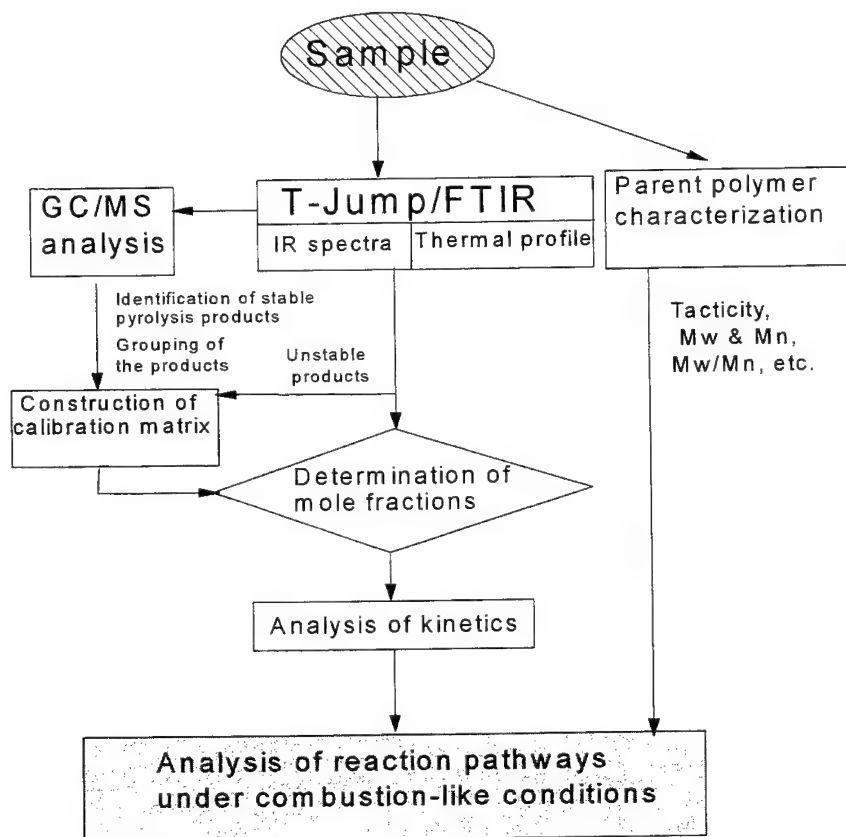


Figure 3. Algorithm for data analysis.

### THERMOCHEMISTRY OF POLYMERS

It is important to point out that HTPB and possibly PEG are cured during processing of a formulation. This is usually done by adding an isocyanate-containing compound such that the hydroxyl groups of the polymer and the isocyanate groups react to form urethane groups. This cross-linking process converts the formulation into the desired consistency and provides structural integrity. However, in the present article, pyrolysis of uncross-linked polymers is described. We believe that this departure from reality is reasonable based on comparisons of the pyrolysis kinetics and products from flash-heated HTPB in the free and urethane cross-linked forms [24]. When urethane cross-linked HTPB is pyrolyzed, urethane bonds are the first to cleave. The isocyanate cross-linking agent was found to volatilize and leave the parent HTPB to decompose as though it had never been cross-linked [24]. Consequently, pyrolysis of uncross-linked HTPB appears to be relevant to the combustion process.

As discussed above, the control voltage of the Pt filament, which the control circuit adjusts at a very fast rate in order to maintain a constant temperature (constant integrated resistance of Pt) during pyrolysis, provides a sensitive overall indication of the thermochemistry of the polymer film. Figure 4 shows the difference voltage trace of the four polymers which were heated at 600-1000°C/s to 500°C. In all cases, excess heat must be initially supplied due to polymer "melting" and the relatively large heat capacity of organic polymers. The fast oscillations which are superimposed on the traces of HTPB, PMMA and CAB are due to the formation and bursting of micro bubbles of decomposition and other volatile products which

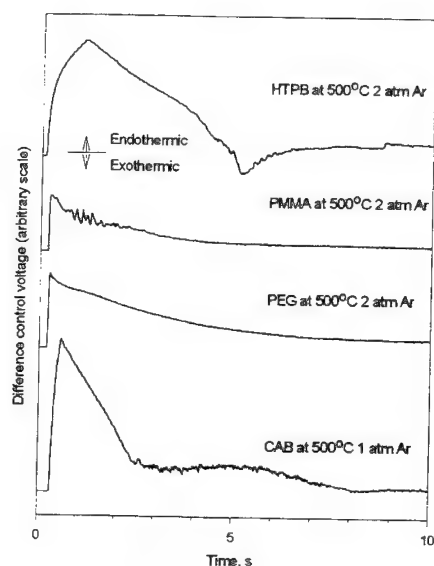


Figure 4. Control voltage difference traces showing the overall heat flow after heating the polymer films at 600-1000°C/s to 500°C.

materials [13]. Organic polymer pyrolysis, on the other hand, is somewhat more complex despite the fact that a repeating unit exists in the backbone. However, the "zip length",  $Z$ , has long been known to play a role in whether the monomer building blocks or other fragments from polymer pyrolysis dominate the vapor phase. Broadly, the zip length refers to the number of monomer units that are formed per initiation reaction event. Equation 3 defines the zip length when the rates of the decomposition reactions,  $k_d$ , are grouped as one rate and termination reactions,  $k_t$ , are grouped as one rate.

$$Z = \frac{k_d}{k_t} \quad (3)$$

The termination reactions include all radical recombinations, such as cyclization, H-scavenging, and multiple bond formation. Each of these processes could be first or second order and may contain a concentration dependence.

Table 2  
Zip Length of Several Polymers<sup>25</sup>

Polymer	$Z$
PMMA	$\sim 10^3$
Poly( $\alpha$ -methyl styrene)	$\sim 10^3$
Polystyrene	$\sim 5$
PTFE	$\sim 3$

hand, the tertiary carbon atom of PMA is not blocked and so a small zip length is expected. HTPB, PEG and CAB can be expected to release an extensive variety of products in part because of the large number of labile H atoms in the backbone of each polymer.

are released as the film viscosity decreases. Only HTPB exhibits any exothermicity as evidenced by the negative valley at about 5s. This release of heat by the sample is partly due to formation of *trans*-butadiene oligomers whose heats of formation are negative. These oligomers are major products of HTPB under flash pyrolysis conditions. The decomposition of the other three polymers is overall endothermic.

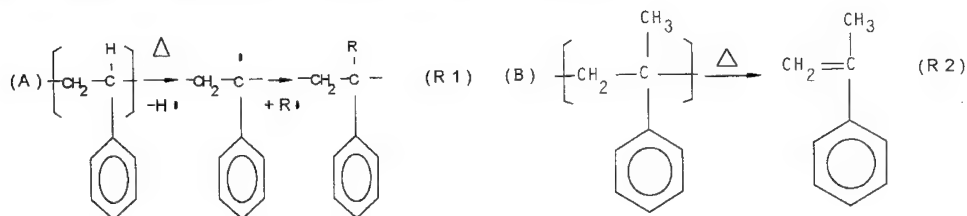
The temperatures for flash pyrolysis that were chosen for these studies are in the 370-600°C range. This range is believed to be representative of the temperatures at the surface of burning solid propellants. Therefore, the results should be applicable to describing the pyrolysis chemistry of polymers during combustion.

#### RELATIONSHIP BETWEEN POLYMER STRUCTURE AND PYROLYSIS PRODUCTS

The relationship between the parent molecular structure and the flash pyrolysis gases has been established in a qualitative way for many energetic

Table 2 gives the zip lengths of several polymers [25]. It is interesting to compare polystyrene (A) to poly( $\alpha$ -methylstyrene) (B). In case of A the zip length is short because the tertiary H atom is labile and so the tertiary site is readily attacked by other radicals which will terminate the depolymerization process (R1). On the other hand, B has no tertiary H atom and so the position is blocked from radical attack in favor of depolymerization (R2) into  $\alpha$ -methylstyrene. The same can be said for PMMA compared to polymethylacrylate (PMA). The tertiary carbon atom of PMMA is blocked by  $\text{CH}_3$ , which produces a large zip length. On the other

Figure 5 is a panel of plots showing the mole fractions of the major products from each polymer as a function of temperature, which were obtained by using T-jump/FTIR spectroscopy and the chemometrics methods of analysis noted above. Each of these will now be discussed.



#### PMMA-2000

Of the polymers shown in Figure 2, the gaseous products from flash pyrolysis of PMMA are the simplest. They consist only of MMA and CO<sub>2</sub>[26]. The simplicity of the product mixture and the dominance of MMA is directly attributable to the large zip length of PMMA. Different pyrolysis temperatures in the 460-600°C range have little effect on the mole fractions. Consequently, only two main reactions having

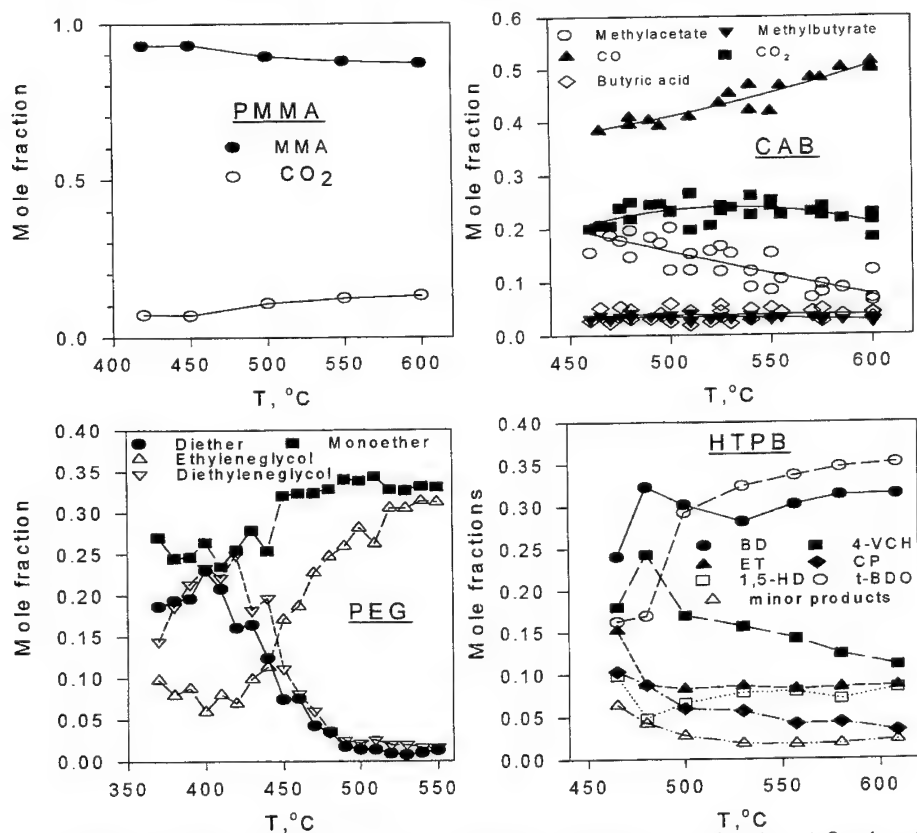


Figure 5. Mole fractions of the major volatile products at 2 atm Ar after flash-heating to the temperatures shown.

relatively similar rates occur simultaneously, i.e., random C-C homolysis and side-chain decarboxylation. Other minor products including  $\text{CH}_4$ ,  $\text{CH}_3\text{OH}$  and  $\text{CO}$  have been reported at lower heating rates and temperatures [27-29] than were used here. These were not detected in our work, however, some char remains on the filament which accounts for the stoichiometry imbalance resulting from the liberation of  $\text{CO}_2$ . Because no other IR-active gaseous products are produced, it is reasonable to assume that the mole fraction of char approximately equals that of the  $\text{CO}_2$  liberated.

#### CAB-75000

Although glucose-like monomers probably form upon thermal decomposition, they react further to form other volatile products rather than volatilize themselves [30]. Thus, an extensive variety of products can be expected upon flash pyrolysis of CAB. In addition to the major products shown in Figure 5, CAB oligomers (0.03), formaldehyde (0.03), ethyl ketene (0.03), ketene (0.03), acetic acid (0.01), and acetaldehyde (<0.01) also form [31]. The parenthetical numbers give the mole fraction of each.

CAB contains randomly substituted butyryl (1.66), acetyl (0.96), and hydrogen (0.38) groups at the 3R sites identified in Figure 2. Most of the vaporized products from flash pyrolysis of CAB are recognizable fragments of the polymer, especially with regard to the pendant groups. The major products  $\text{CO}$  and  $\text{CO}_2$  probably form from scission of the  $\text{CO}$  and  $\text{OCO}$  linkages in the anhydroglucose backbone [32] and by decarboxylation and decarbonylation of the ester groups.  $\text{CO}$  could also form from the  $\text{C}(2,3)\text{-O}$  linkages. Methyl butyrate and methyl acetate probably originate from  $\text{C}(5)\text{-C}(6)$  homolysis with H transfer. The carboxylic acids form from  $\text{C}(2,3)\text{-O}$  and  $\text{C}(6)\text{-O}$  homolysis with H transfer. Unlike the esters, the concentration of butyric acid is about twice that of acetic acid at all temperatures in accordance with the approximate relative concentrations of the esters in the parent polymer.

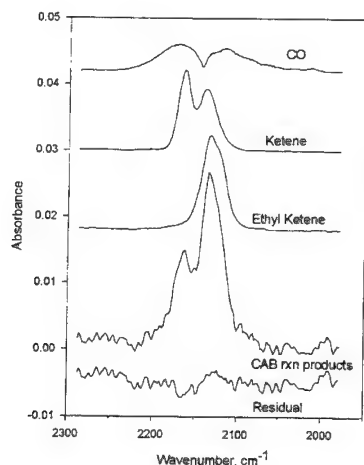


Figure 6. Deconvolution of the pyrolysis gases of CAB into the ketene components and  $\text{CO}$ .

The most interesting products not heretofore detected from substituted cellulose molecules are ketene [ $\text{CH}_2\text{C}=\text{O}$ ] and ethyl ketene [ $\text{CH}_3\text{CH}_2\text{C}(\text{H})=\text{O}$ ]. Figure 6 shows the resolution of ketene, ethyl ketene, and  $\text{CO}$  from the  $2050\text{--}2200\text{ cm}^{-1}$  region of the spectrum. Also shown is the residual  $m$  (equation 1). These ketene products probably arise from  $\text{O-C}$  homolysis of the  $\text{O-C}(\text{O})\text{R}$  pendant groups, which liberates  $-\text{C}(\text{O})\text{R}$ . This fragment can rearrange to ketene when  $\text{R} = \text{CH}_3-$  and ethyl ketene when  $\text{R} = \text{C}_2\text{H}_5-$ . Ketene and ethyl ketene have similar concentrations despite the fact that the butyryl group is more prevalent than the acetyl group in CAB.  $\text{CH}_3\text{C}(\text{O})\text{H}$  could result from  $\text{O-C}(\text{O})\text{CH}_3$  homolysis, as does ketene, but rather than losing H to form  $\text{H}_2\text{C}=\text{O}$ , the  $-\text{C}(\text{O})\text{CH}_3$  fragment could abstract H to form  $\text{CH}_3\text{C}(\text{O})\text{H}$ .  $\text{H}_2\text{CO}$  plausibly arises from the non-esterified  $-\text{OH}$  groups of CAB. IR absorbances closely matching those of the parent CAB are present, and most likely arise from oligomers of CAB resulting from random  $\text{C}(1)\text{-O}$  homolysis with H transfer.

A small amount of residue remained on the filament, which is brown at  $525^\circ\text{C}$ , but brown-black with a sooty appearance at  $540^\circ\text{C}$ . The formation of H- and O-rich volatile products in Figure 5 will leave a carbon-rich residue.



In general, the ring opening reactions of CAB and the presence of thermally removable pendant groups define many of the products of thermolysis. At 460°C, discrepancy exists between the butyryl/acetyl ratio in the parent polymer (=1.7) and the ratio of products attributable to the butyryl group (butyric acid, butyl acetate, and ethyl ketene) and the acetyl group (methyl acetate, acetic acid, acetaldehyde, and ketene) (=0.8). At 600°C, the concentration ratio of these products (=1.3) more nearly resembles the ratio in the parent polymer.

#### PEG-2090

PEG is a straight chain polymer having only secondary carbon atoms. The conditions for a long zip length are absent in the parent polymer. Accordingly, Figure 5 reveals that monoether oligomers ( $\text{CH}_3\text{CH}_2\text{O}[\text{CH}_2\text{CH}_2\text{O}]_n\text{H} + \text{CH}_3\text{O}[\text{CH}_2\text{CH}_2\text{O}]_n\text{H}$ ), diether oligomers ( $\text{CH}_3\text{CH}_2\text{O}[\text{CH}_2\text{CH}_2\text{O}]_n\text{CH}_3 + \text{CH}_3\text{O}[\text{CH}_2\text{CH}_2\text{O}]_n\text{CH}_3 + \text{CH}_3\text{CH}_2\text{O}[\text{CH}_2\text{CH}_2\text{O}]_n\text{CH}_2\text{CH}_3$ ), diethyleneglycol, and ethyleneglycol are the major products of flash thermolysis [23]. The mono- and diethers along with diethyleneglycol dominate the 370-430°C range. The average value of  $n$  for the monoethers is  $\leq 1.75$  in this temperature range. The monoether oligomers and ethyleneglycol are the most abundant products at 450-550°C. The average value of  $n$  for the monoethers is about 2.5 in this range. Five other products are also found but appear in lower concentration. These are 1,3-dioxolane, 2-methoxy-1,3-dioxolane, methyl vinyl ether, ethyl vinyl ether, and 4-butenal.

The marked shift in the composition of the volatile products at  $450 \pm 30^\circ\text{C}$  is a new observation. The probable reason is that below the transition temperature, the products primarily reflect the pyrolysis of the parent PEG polymer with formation of the residue. Above the transition temperature, products from both the parent polymer and the residue form simultaneously.

Thus, an important feature in the pyrolysis of PEG is the formation of a colorless, glassy residue on the filament below about 500°C. The greatest amount of residue was left after pyrolysis at lower temperatures. The different pyrolysis characteristics of PEG heated in the 370-550°C range appear to be related to the release of volatile products from the parent sample of PEG in competition with the formation and pyrolysis of this residue. From spectral evidence, the residue has few end-chain hydroxyl groups, and based on its glassy appearance, it probably has a higher degree of polymerization and/or different microstructure. For example, radical recombination in competition with radical production could produce an entangled, high Mw, polymer network in the residue. The fact that the monomer, ethyleneglycol, becomes a major product from this residue suggests that the zip length of the residue is higher than that of the parent polymer.

In general, the products of pyrolysis of PEG are recognizable oligomers in which O-C and C-C homolysis have occurred along with H-transfer. The ethyleneglycol monomer is a major product above about 450°C which suggests that a modified form of the PEG polymer forms during decomposition in competition with the volatilization of oligomers from the parent PEG-2090. This modified PEG polymer apparently has a higher zip length than the parent polymer.

#### HTPB-2500

As shown in Figure 4, HTPB is the only polymer of the four discussed here which exhibits exothermicity during decomposition. The volatile decomposition products begin to form during the exotherm. The zip length of HTPB is not known, but examination of its structure suggests that it is probably not large. Nevertheless, according to Figure 5, a significant amount butadiene (BD) monomer is released. The other major products are the stabilized dimer (4-vinyl-2-cyclohexene, 4-VCH) and *trans*-butadiene oligomers (t-BDO), both of which occur by random chain scission and H-transfer. In addition, to these main products, other products shown in Figure 5 form along with seven other minor products: 1,3-cyclohexadiene, toluene, benzene, vinyl-butadiene oligomers, *cis*-butadiene oligomers, propene, and dimethyl ether [22].

The products liberated by HTPB upon flash pyrolysis reveal why HTPB is somewhat exothermic upon decomposition. To understand the thermochemistry, the heat of formation of HTPB-5500 was estimated to be about -770 kcal/mol based on carboxyl-terminated polybutadiene data [33].  $\Delta H_f^\circ$  of BD, 4-VCH, and most of the minor products are positive. By Hess' Law, the thermal decomposition of HTPB, which is experimentally shown in Figure 4 to be exothermic, could not be exothermic with these products alone. On the other hand,  $\Delta H_f^\circ$  of t-BDO is negative. The approximate values for t-BDO,  $\text{CH}_3[-\text{CH}_2\text{CH}=\text{CHCH}_2-]_n\text{CH}_3$  (n values given parenthetically), are -11.1(1), -27.5(2), -52(3), -77(4) kcal/mol, etc. Because the mole fraction of t-BDO is substantial (especially at higher temperature), these oligomers readily offset the negative  $\Delta H_f^\circ$  of HTPB and produce the exothermicity demonstrated in Figure 4. The decomposition of HTPB is endothermic above 400°C when heated at a slow rate [34]. Thus, there are significant differences between the decomposition process of HTPB at low and high heating rates.

The product concentrations in Figure 5 depend on the pyrolysis temperature below  $515 \pm 15^\circ\text{C}$ . Under these conditions heterogeneous, bulk-phase processes (*cis-trans* isomerization, cross-linking, cyclization, and chain scission) dominate [35-43]. Thus, numerous competitive reactions, each having a specific rate constant, combine to produce the products observed, so that the product concentrations display the complex behavior of Figure 5. On the other hand, when  $530 < T < 609^\circ\text{C}$ , the product concentrations are less sensitive to the pyrolysis temperature. A plausible explanation for this insensitivity is that the heterogeneous-phase thermolysis reactions reach their maximum rate and cease to be sensitive to temperature. This idea has support in observations of an upper temperature limit of thermal decomposition of a polymer. For example, at  $dT/dt = 100^\circ\text{C/s}$ , most polymers have a limiting temperature of decomposition of  $480\text{--}530^\circ\text{C}$  [44]. The crossover for HTPB from temperature sensitivity in the product distribution to relative insensitivity occurs at  $515 \pm 15^\circ\text{C}$ . Above this temperature range, the rate of deconsolidation controls the process rather than the bulk-phase decomposition reaction rate.

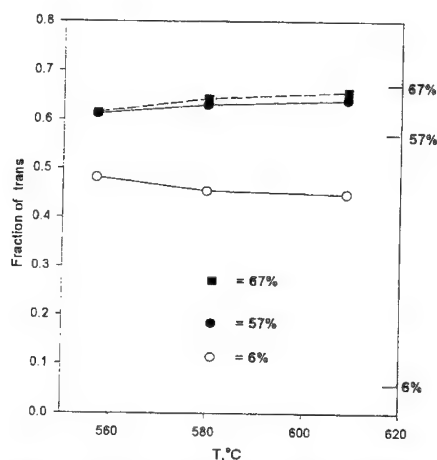


Figure 7. The fraction of *trans* groups in the gas phase following flash pyrolysis compared to the percentage of *trans* groups in the parent polymer (right side scale)

One of the few structure-decomposition relationships which is apparent for HTPB is the relationship of the concentration of the *trans*-butadiene component of several different polybutadiene polymers to the t-BDO concentrations in the gas phase. Three polybutadienes with different percentage of the *trans* unit were compared. Figure 7 shows that above  $560^\circ\text{C}$ , the fraction of *trans*-butadiene units in the gas phase resembles that in the parent (right side of Figure 7), if the parent polymer begins with a high percentage of *trans*-units. However, when the polymer begins with mostly *cis*-units (e.g. 92%), *cis*→*trans* isomerization must occur during the random chain scission process. Others have noted that an early chemical event in *cis*-polybutadiene upon heating is *cis-trans* isomerization leading to a 31:69 *cis:trans* ratio [39]. This previous finding is supported by the results in Figure 7. The retention of the *trans*-butene conformation when the gaseous products are formed implies that the remaining *cis*-butene and vinyl groups are mainly responsible for

the lesser products shown Figure 5. Sterically speaking, the *cis*-butene and vinyl groups of HTPB are already positioned for cyclization, whereas the *trans*-butene linkage is not.

The major role that t-BDO plays in the gas phase at high heating rates requires the formation of a residue with excess carbon content. This is because t-BDO has a higher H/C ratio compared to that of HTPB.

Indeed, a small amount of a carbonaceous residue remains on the filament following pyrolysis below 600°C.

### EFFECT OF PRESSURE ON THE SPECIES LIBERATED

The pyrolysis characteristics discussed above were determined at 1 or 2 atm of Ar. PMMA, PEG and HTPB were also investigated at 11 atm Ar to determine the effect of the external pressure on the species formed. Figure 8 is a panel of plots at 11 atm showing the temperature dependence of the mole fractions of the major species. These plots are to be compared with those in Figure 5 at 2 atm. The effect of pressure is negligible in the case of PMMA and is relatively weak in the case of HTPB. The main effect for HTPB is that the concentration of the monomer (BD) increases at the expense of the dimer (4-VCH). For PEG the effect of pressure on the products liberated is larger, but again, the main general effect is that lower Mw products increase in concentration at the expense of higher Mw products.

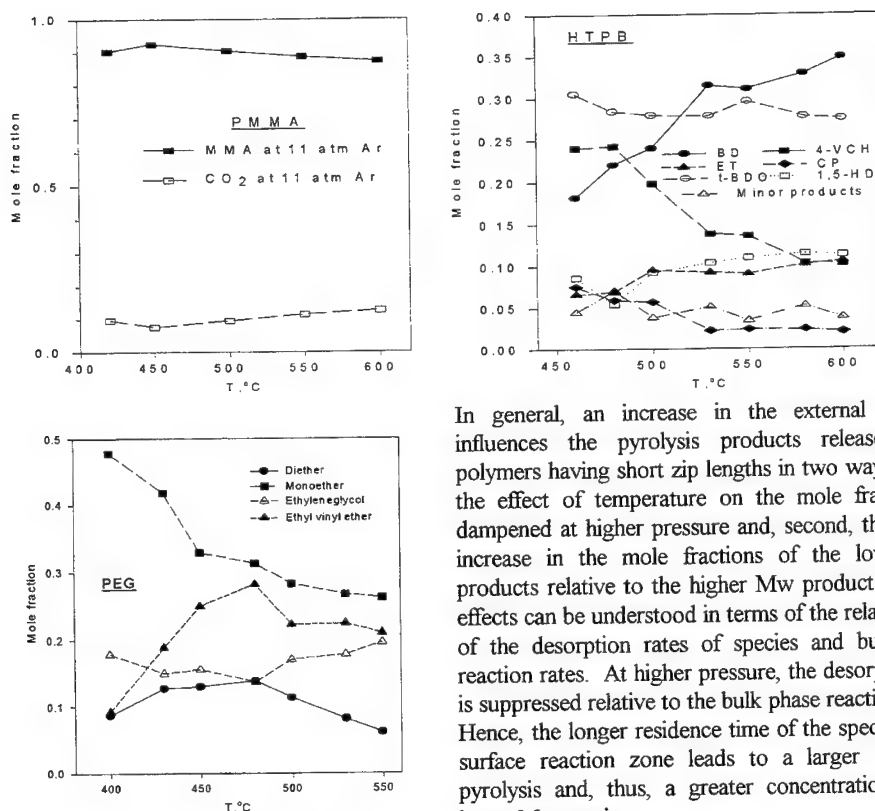


Figure 8. Mole fractions of the major volatile products at 11 atm Ar after flash-heating to the temperature shown.

In general, an increase in the external pressure influences the pyrolysis products released from polymers having short zip lengths in two ways. First, the effect of temperature on the mole fractions is dampened at higher pressure and, second, there is an increase in the mole fractions of the lower Mw products relative to the higher Mw products. These effects can be understood in terms of the relative roles of the desorption rates of species and bulk phase reaction rates. At higher pressure, the desorption rate is suppressed relative to the bulk phase reaction rates. Hence, the longer residence time of the species in the surface reaction zone leads to a larger extent of pyrolysis and, thus, a greater concentration of the lower Mw species.

### KINETICS OF EVOLUTION OF INDIVIDUAL GASEOUS PRODUCTS

The rate of increase in the IR absorbance intensity of the individual volatile products from flash pyrolysis of polymers leads to the rate constants for their evolution to the flame zone. The required concentrations can be determined separately as a function of time, temperature, and pressure. The importance of having rate constants for liberation of individual species, as opposed to simply the global rate of decomposition, is that

transient phenomena, such as ignition and combustion instability, potentially can be modeled with chemical details.

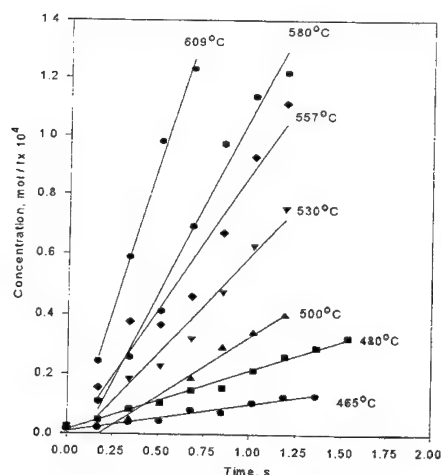


Figure 9. Rate plots for the formation of BD from HTPB flash heated to the temperatures shown.

As an example of the calculation of rate constants from T-jump/FTIR spectra, Figure 9 shows the rate of growth of BD from flash-pyrolysis of HTPB at the temperatures shown. The regression lines were obtained from the zeroth-order rate equation 4, where  $c_\infty$  is the measured concentration of the species after complete pyrolysis.

$$\frac{d(c/c_\infty)}{dt} = k \quad (4)$$

Zeroth-order kinetics fit the rate of growth of all products from PMMA, CAB, PEG, and HTPB. The fact that zeroth-order kinetics fit the experimental data is partly the result of the use of a film of about 50  $\mu\text{m}$  thickness as a "snapshot" simulation of the binder on the burning surface of formulated energetic materials. In effect, the "concentration" of the parent polymer remains essentially constant throughout the pyrolysis

process. This is the same condition that exists on the surface of a steadily burning material and explains why certain combustion parameters, such as the linear regression rate, also follow zeroth-order kinetics.

### PMMA

The Arrhenius plots for formation of MMA monomer and  $\text{CO}_2$  from PMMA-2000 at 2 atm are shown in Figure 10. Table 3 gives the Arrhenius activation energies,  $E_a$ , and pre-exponential factors,  $\ln A$ . It is instantly evident from Figure 10 that two different processes determine the rate of product evolution depending on the temperature. In the 380–460°C range, the Arrhenius parameters for MMA formation resemble those reported for random C–C scission in PMMA [45–47], e.g. 49.5–64.1 kcal/mol and  $\ln(A/\text{s}) = 31.8$ –45.9. The Arrhenius parameters for  $\text{CO}_2$  evolution in the 380–500°C range resemble those for decarboxylation of organic compounds. For example,  $E_a = 39.3$  kcal/mol and  $\ln(A/\text{s}) = 26$  is given for but-3-enoic acid [48] and  $E_a = 57$  kcal/mol is given for acetic acid [49]. In the 500–600°C range, the  $E_a$  values more closely resemble those reported for diffusion and desorption processes [4,50,51], e.g.,  $E_a = 7$ –20 kcal/mol. An increase in pressure to 11 atm causes a modest increase in the Arrhenius parameters [26].

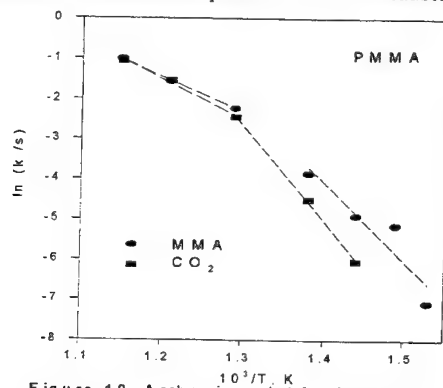


Figure 10. Arrhenius plot for formation of volatile products from PMMA at 2 atm Ar.

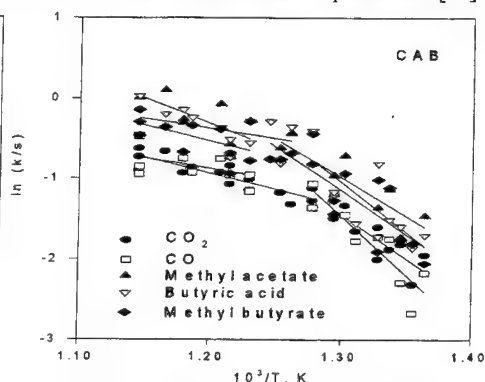


Figure 11. Arrhenius plot for formation of the major volatile products from CAB at 1 atm Ar.

Table 3  
Arrhenius Parameters for Flash Pyrolysis

Product	P, atm	E <sub>a</sub> , kcal/mol	ln(A/s)	E <sub>a</sub> , kcal/mol	ln(A/s)
<u>PMMA-2000</u>					
		<u>T=380-460°C</u>		<u>T=500-600°C</u>	
MMA	2	43±5	26±3	16±1	8.4±0.5
CO <sub>2</sub>	2	46±1 <sup>a</sup>	27±1 <sup>a</sup>	19±0.4	9.8±0.2
MMA	11	49±9	29±6	28±2	15±1
CO <sub>2</sub>	11	45±3 <sup>a</sup>	26±2 <sup>a</sup>	30±2	17±1
global	2	45±4	27±3	17±1	8.6±0.5
global	11	53±7	33±5	27±3	15±2
<u>CAB-75000</u>					
		<u>T=465-510°C</u>		<u>T=510-600°C</u>	
methyl acetate	1	19±4	11±2.5	13±5	8±3
methyl butyrate	1	22±4	13±3	8±4	4±2
acetic acid	1	40±8	25±5	2±2	2±1
butyric acid	1	24±7	15±5	5±3	3±2
formaldehyde	1	28±7	17±5	8±5	4±3
CO <sub>2</sub>	1	22±5	13±3	8±1	4±1
CO	1	29±5	17±3	5±3	2±2
ketene	1	20±3	12±2	4±2	2±1
ethyl ketene	1	21±4	12±2	7±2	3±1
CAB oligomers	1	13±3	7±2	13±3	7±2
global	1	22±6	13±4	6±1.5	3±1
<u>PEG-2090</u>					
		<u>T=370-440°C</u>		<u>T=370-550°C</u>	
monoether oligomers	2	---	---	25±2	14±1
ethyleneglycol	2	---	---	29±0.4	17±0.2
diether oligomers	2	16±1	10±1	---	---
diethylene glycol	2	20±8	12±6	---	---
ethyl vinyl ether	2	---	---	22±3	13±2
global	2	7±8	1±6	22±4 <sup>b</sup>	12±3 <sup>b</sup>
global	11	---	---	52±0.3 <sup>c</sup>	32±0.2 <sup>c</sup>
<u>HTPB-2500</u>					
		<u>T=450-530°C</u>		<u>T=530-600°C</u>	
BD	2	72±8	46±5	16±1	9±1
4-VCH	2	78±5	50±3	8±4	4±2
t-BDO	2	71±5	44±3	12±3	7±2
ET	2	70±5	44±4	24±2	13±1
CP	2	12±3	7±2	12±3	7±2
1,5-HD	2	28±1	16±1	28±1	16±1
BD	11	20±1	11±1	20±1	11±1
4-VCH	11	7±1	3±1	7±1	3±1
t-BDO	11	12±2	7±1	12±2	7±1
ET	11	19±3	10±2	19±3	10±2
CP	11	-6±9	-5±5	-31±26	-20±16
1,5-HD	11	18±2	10±1	18±2	10±1
global	2	58±4	36±4	13±3	8±2
global	11	13±2	7±1	13±2	7±1

<sup>a</sup>T=420-500°C; <sup>b</sup>T=480-550°C; <sup>c</sup>T=400-550°C

## CAB

Figure 11 shows the Arrhenius plots for several of the major products liberated by CAB and Table 3 contains the Arrhenius parameters. As with PMMA, it is obvious that the processes which control the gasification rates change in the  $510 \pm 20^\circ\text{C}$  range. Below this range, the values of the Arrhenius parameters suggest that the condensed-phase reactions are significant factors. For instance  $E_a = 30\text{--}35$  kcal/mol has been reported for decomposition of cellulose above  $325^\circ\text{C}$  [52,53]. Above  $510 \pm 20^\circ\text{C}$ , desorption is mainly controlling the rate of product evolution.

## PEG

In the discussion of the identity of the products liberated by PEG, it was noted that radical recombination reactions which compete with the fragmentation and volatilization process produce the hard, glassy residue having a Mw higher than the parent sample. Above the transition temperature range in Figure 5, pyrolysis of both the parent sample of PEG and this glassy residue contribute to the volatile products observed. Hence, the mole fractions in Figure 5 and the kinetics differ above and below the transition temperature range. Figure 12 displays the Arrhenius plots for the products shown in Figure 5, and Table 3 gives their Arrhenius constants. The magnitude of  $E_a$  suggests that desorption or a mixture of desorption and bulk-phase decomposition rates dominate the rate of product volatilization throughout the entire temperature range of study. This description of the pyrolysis process for PEG is consistent with the kinetics of weight loss by PEG oligomers having Mw=200-600, which have been heated at  $2^\circ\text{C}/\text{min}$  in a vacuum [54]. Values of  $E_a = 10$  kcal/mol (Mw = 200), 9 kcal/mol (Mw = 400) and 17 kcal/mol (Mw = 600) were reported. The implication of these low values of  $E_a$  is that desorption/evaporation of PEG oligomers, rather than condensed-phase thermal decomposition processes, dominates gasification when low Mw samples are heated. The fact that  $E_a$  increases as the Mw increases implies that condensed phase reactions begin to contribute to the rate of product volatilization.

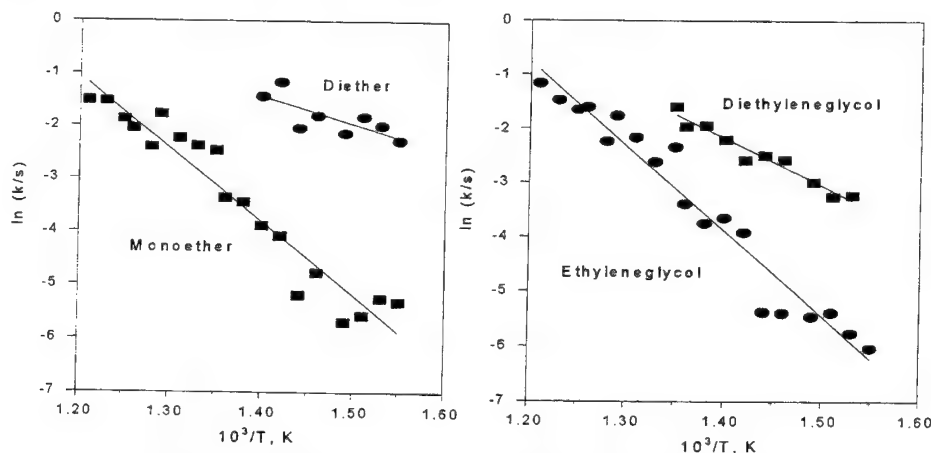


Figure 12. Arrhenius plot for the formation of the major volatile products from PEG at 2 atm.

## HTPB

Figure 13 shows the Arrhenius plots for the formation of products shown in Figure 5. Table 3 contains the Arrhenius constants. Except for CP and 1,5-HD, which are products of lesser concentration, the crossover from bulk chemical reaction control at lower temperatures to desorption control at higher temperatures is very similar to the behavior of PMMA and CAB. In the lower temperature range the Arrhenius parameters resemble the values for chain scission measured at much lower heating rates [43], e.g.  $41\text{--}62 \pm 4$

kcal/mol. Above the transition temperature, the Arrhenius parameters fall into the range of control by desorption of products from the surface. An increase in pressure to 11 atm causes a decrease in the Arrhenius parameters [22], which is opposite of the behavior of PMMA.

In general, clear evidence exists that desorption/evaporation rates rather than bulk phase decomposition rates control the rate of evolution of volatile products above  $500 \pm 30^\circ\text{C}$  for PMMA, CAB and HTPB. Below this temperature range condensed-phase reactions dominate the rate of product evolution. Desorption dominates PEG volatilization over the entire temperature range. These controlling processes are even more evident when the global kinetics are considered.

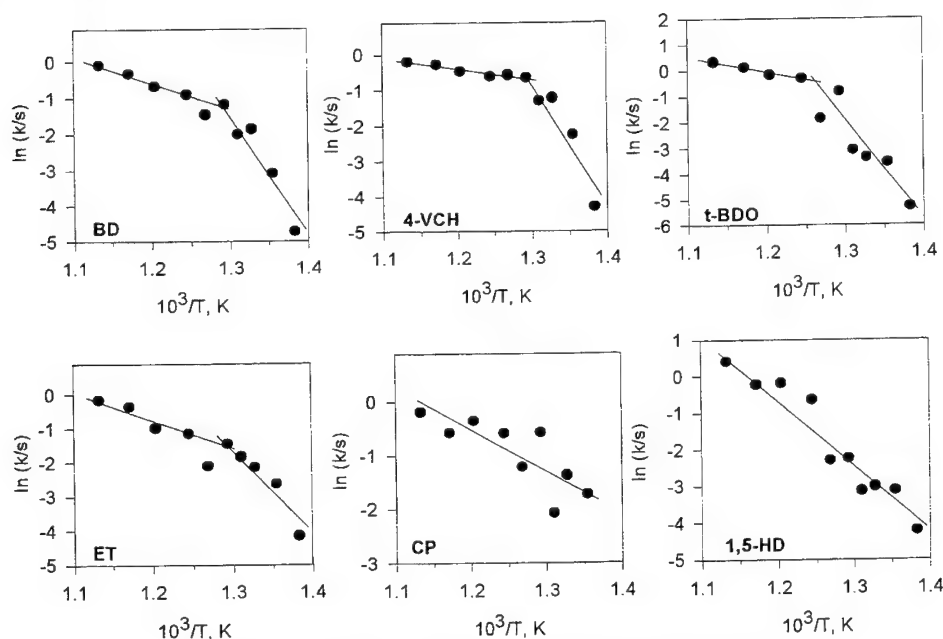


Figure 13. Arrhenius plots for the formation of the major volatile products from HTPB at 2 atm.

### GLOBAL KINETICS OF VOLATILIZATION

The global kinetics of volatilization are obtained by summing the concentrations of all of the volatile products. Figure 14 shows the resulting individual Arrhenius plots for the four polymers at 1-2 atm. In Figure 15, these plots are overlayed on the same scale for comparison. It is apparent that HTPB and CAB volatilize somewhat faster than PMMA and PEG. Table 3 contains the global Arrhenius constants. PMMA, CAB and HTPB resemble each other in that the Arrhenius constants show the dominance of bulk phase reaction control of volatilization below  $460\text{--}530^\circ\text{C}$  depending on the polymer, and desorption/evaporation control above this temperature range. PEG is somewhat unique in that desorption/evaporation mainly controls the rate of volatilization over the full  $370\text{--}550^\circ\text{C}$  range of study. However, the parent PEG polymer and the residue, which forms concurrently with selected volatile products, have somewhat different rates of volatilization. The bulk-phase reactions play a moderately greater role in the volatilization rate than they do for the parent polymer.

These findings indicate that the desorption kinetics of PMMA, CAB and HTPB should be used to describe vaporization when the surface temperature during combustion exceeds the  $460\text{--}530^\circ\text{C}$  range. If the surface temperature is less than this range, then bulk-phase decomposition reaction kinetics should be used

to describe the volatilization process. For PEG, desorption kinetics mainly describe the entire temperature range. Figure 5 shows that the distribution among the mole fractions of the products for HTPB and PEG also shifts in the transition temperature range.

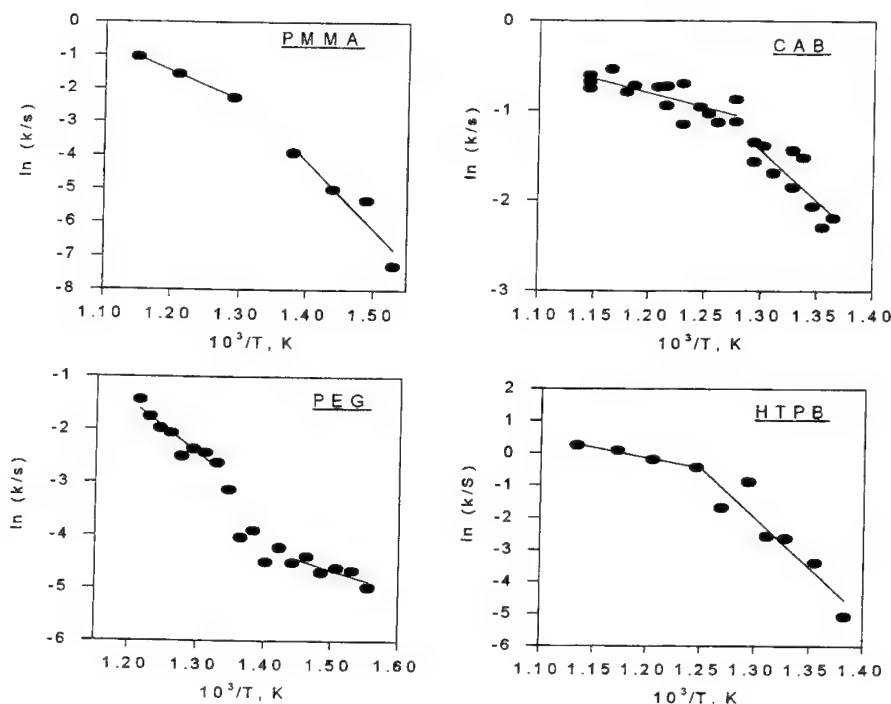


Figure 14. Global Arrhenius plots for the volatilization of all of the products from the polymers studied.

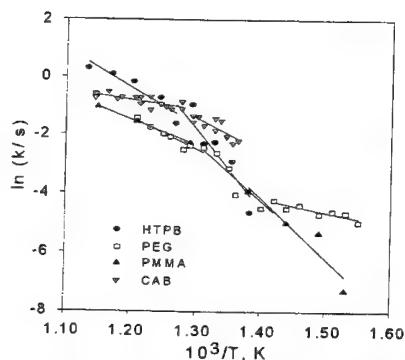


Figure 15. The composite plot of global Arrhenius plots in Figure 14 for overall comparison.

The temperature range where we observe the condensed-phase decomposition reaction rates to give way to desorption/evaporation rates is similar to the 480-520°C range which Shlensky, et al [44], proposed to be the limiting temperature for decomposition of polymers heated at rates up to 50,000°C/s. Above this temperature range the condensed-phase decomposition reactions occur faster than the desorption rate. Hence, the desorption and deconsolidation process controls the rate of volatilization at high temperature.

#### MODELS OF VOLATILIZATION KINETICS OF POLYMERS

To conclude this article, several kinetic models are described which include the decomposition and desorption kinetics and approximately reproduce the experimental trends in Figure 14 for PMMA, CAB, and HTPB. Because the Arrhenius parameters for PEG apparently result from competitive pyrolysis of two forms of the polymer, PEG is not considered further in this section.



To capture the significant curvature in the Arrhenius plots in Figure 14, a fractional form of the overall rate equation is needed which combines the main kinetic terms of desorption and decomposition. Chaiken, et al [4], presented such an equation based on the Langmuir theory of adsorption. They assumed that the limiting process at the surface was diffusion of the polymer fragments to the surface. In contrast, Lengellè [55] derived a pyrolysis equation without a fractional form which gives linear Arrhenius behavior and does not incorporate competitive processes. The Lengellè treatment applies at the limit of large  $E_a$ , i.e., when bulk-phase reactions are controlling. Therefore, it fails to reproduce our experimental results at higher temperatures.

In the model of Chaiken, et al [4], the relation between the observed rate of gaseous product evolution,  $k$ , and the rate of desorption,  $k_s$ , is expressed by equation 5, where  $\theta$  is the fraction of desorption sites. Following Chaiken et al [4], we take the  $k_s$  to be the first-order rate of desorption. Equation 6 applies in steady state, where  $J$  is the rate of diffusion and  $\xi$  is the same as the  $k_s$ , but with units of mol/cm<sup>2</sup> sec. The total number of desorption sites is the  $(\rho/Mw)^{2/3}$ , where  $\rho$  is the density and  $Mw$  is molecular weight. If  $n_s$  represents the number of desorption sites, then  $\theta = n_s(\rho/Mw)^{-2/3}$ . Therefore, equation 7 follows from equation 6. In turn, equation 8 applies so that  $\xi$  can be defined by equation 9.

$$k = \theta k_s \quad (5)$$

$$(1 - \theta)J = \theta \xi \quad (6)$$

$$k = \left( \frac{J / \xi}{1 + J / \xi} \right) A_s e^{-E_s/RT} \quad (7)$$

$$-\frac{dn_s}{dt} = k_s n_s = \theta \xi \quad (8)$$

$$\xi = \frac{k_s n_s}{\theta} = k_s \left( \frac{\rho}{Mw} \right)^{2/3} \quad (9)$$

In a modification of the assumption about the controlling surface process [4], we assumed that condensed phase decomposition as well as desorption could be operative, which leads to equation 10.  $\beta$  is a proportionality constant,  $k_d$  is the rate of bulk phase decomposition, and  $c_0$  is the concentration of the polymer in the bulk phase.

$$J = \beta k_d c_0 \quad (10)$$

$$\frac{J}{\xi} = \beta c_0 \left( \frac{Mw}{\rho} \right)^{2/3} \frac{k_d}{k_s} \quad (11)$$

Equation 11 follows from equations 9 and 10. In turn, equation 12 is obtained by substituting equation 11 into 7 and setting  $\alpha = \beta c_0 (Mw/\rho)^{2/3} A_d/A_s$ . As was previously done [4],  $\alpha$  can be thought of as an adjustable parameter. The remaining terms in equation 12 are the experimentally determined total rate parameters given in Table 3.

$$k = \alpha A_s e^{-E_d/RT} / (1 + \alpha e^{-(E_d - E_s)/RT}) \quad (12)$$

Figures 16 and 17 compare the experimental data to the predictions of equation 12 for PMMA at 2 and 11 atm and CAB at 1 atm. The values of  $\alpha$  are given on the plot. The smaller value of  $\alpha$  for PMMA at 11 atm compared to 2 atm implies that more desorption sites exist at 11 atm. This result could be understood by the existence of bubbles in the film (observed) and on the surface which are larger in number and smaller in diameter at 11 atm than at 2 atm. This would produce a larger effective surface area over which desorption can occur.

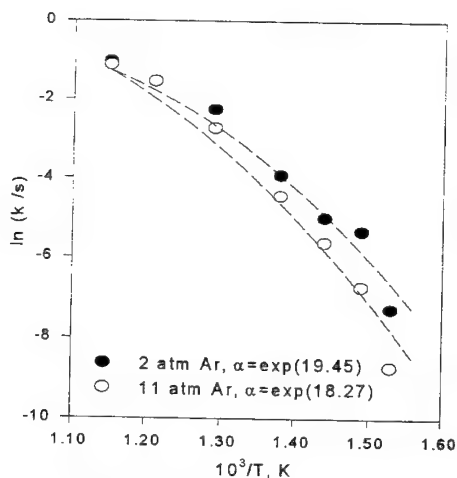


Figure 16. The experimental rate of vaporization of PMMA at 2 and 11 atm compared to the predictions of equation 12 with adjustable  $\alpha$  values.

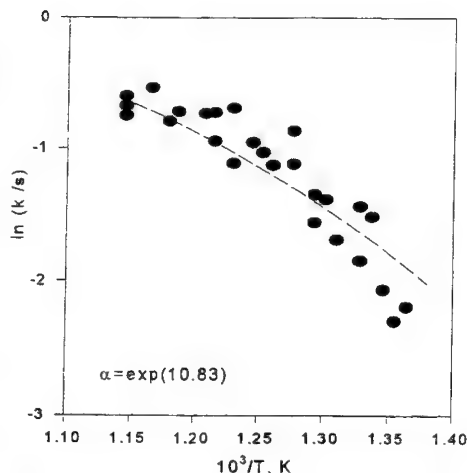


Figure 17. The experimental rate of vaporization of CAB at 1 atm compared to the predictions of equation 12.

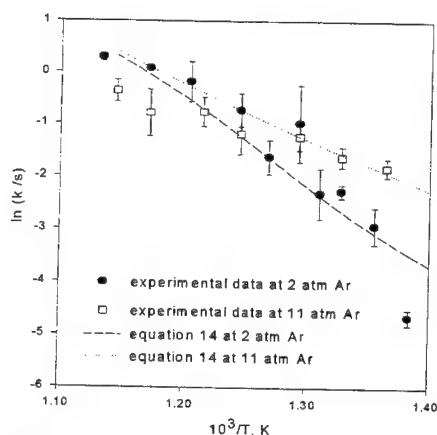


Figure 18. The experimental rate of data for HTPB at 2 and 11 atm compared to the predictions of equation 14 with no adjustable parameters.

Equation 12 fails to account for the behavior of HTPB in that neither the curvature in Figure 14 is captured nor is the fact that the desorption process is *enhanced* rather than suppressed by an increase in the pressure from 2 to 11 atm [22]. The behavior of HTPB is explained by modifying equation 6 to include the rate of adsorption,  $k_a$ , and the concentration of gaseous products,  $c_g$ . Equation 13 is the results. With the derivation given above and assumptions of the ideal gas law ( $c_g = P/RT$ ),  $k_a \approx k_s$ , and  $c_0 \approx n_s$ , equation 14 is obtained from equations 5 and 13. Figure 18 shows the fit of equation 14 to the experimental data for HTPB, without any adjustable parameters.  $T_0$  was chosen to be 298 K because the gaseous products are quenched in the T-jump/FTIR spectroscopy experiment.

$$(k_a c_g + k_d c_0)(1 - \theta) = \theta k_s n_s \quad (13)$$

$$k = \frac{k_s c_g + k_d c_0}{c_0 + c_g + (k_d / k_s) c_0} \quad (14)$$

At the present time no single equation will describe the combustion-like pyrolysis kinetics of the non-energetic polymers described here. Their behaviors are simply too diverse. However, the kinetic equations for vaporization that rest on the Langmuir theory of surface processes do capture the non-linear Arrhenius behavior. This non-linear behavior is consistent with the dominance of control by the desorption process at higher temperature and the dominance of control by the bulk-phase decomposition kinetics at lower temperature.

### ACKNOWLEDGMENTS

We are grateful for financial support from the Air Force Office of Scientific Research (Aerospace Sciences) and the Army Research Office on a subcontract from Pennsylvania State University. Support for H. Arisawa from the Technical Research and Development Institute, Japan Defense Agency was appreciated. Discussion with Drs. Rose Pesce-Rodriguez and Steven D. Brown was enlightening.

### REFERENCES

1. Brill, T. B., Brush, P. J., James, K. J., Shepherd, J. E. and Pfeiffer, K. J., 1992. Appl. Spectrosc. **46**, 900-911.
2. Boileau, J., 1996. in "Decomposition, Combustion, and Detonation Chemistry of Energetic Materials". Materials Research Society Vol. 418, T. B. Brill, T. P. Russell, W. C. Tao and R. B. Wardle, Eds. Pittsburgh, PA, pp. 91-102.
3. Beck, W. H., 1987. Combust. Flame, **70**, 171-190.
4. Chaiken, R. F., Anderson, W. H., Barsh, M. K., Mischuck, E., Moe, G. and Schultz, R. D., 1950. J. Chem. Phys., **32**, 141-146.
5. Coates, R. L., 1965. AIAA J., **3**, 1257-1261.
6. McAlevy, III, R. F. and Hansel, J. G., 1965. AIAA J., **3**, 244-249.
7. Blaskowski, W. S., Cole, R. B. and McAlevy, III, R. F., 1973. 14th Symp. (Int.) Combustion, The Combustion Institute, Pittsburgh, PA, p. 1177-1186.
8. Cohen, N. S., Fleming, R. W. and Derr, R. L., 1974. AIAA J., **12**, 212-218.
9. Bouck, L. S., Baer, A. D. and Ryan, N. N., 1973. 14th Symp. (Int.) Combustion, The Combustion Institute, Pittsburgh, PA, p. 1165-1176.
10. Oyumi, Y. and Brill, T. B., 1985. Combust. Flame, **62**, 213-224.
11. Cronin, J. T. and Brill, T. B., 1987. Appl. Spectrosc., **41**, 1147-1151.
12. Timken, M. D., Chen, J. K. and Brill, T. B., 1990. Appl. Spectrosc., **44**, 701-706.
13. Brill, T. B., 1992. Prog. Energy Combust. Sci., **18**, 91-116.
14. Ericsson, I., 1978. J. Chromatog. Sci., **16**, 340-344.
15. Brauman, S. K., 1988. J. Polym. Sci. Part B., **26**, 1159-1171.
16. Brewster, M. Q., Son, S., Hites, M. and Esker, D., 1992. 2nd Int. Conf. Laser Adv. Processes, Nagoaka, Niigata, Japan.
17. Lee, I-Y. S., Wen, X., Tolbert, W. A., Dlott, D. D., Doxtader, M. and Arnold, D. R., 1992. J. Appl. Phys., **72**, 2240-2448.
18. Brill, T. B., Brush, P. J. and Patil, D. G., 1993. Combust. Flame, **94**, 70-76.
19. Williams, G. K. and Brill, T. B., 1995. Combust. Flame, **102**, 418-426.
20. Shepherd, J. E. and Brill, T. B., 1993. 10th Int. Symp. Detonation, NSWC, White Oak, MD, p. 849-855.
21. Thynell, S. T., Gongwer, P. E. and Brill, T. B., 1996. J. Propuls. Power, **12**, 933-939.
22. Arisawa, H. and Brill, T. B., 1996. Combust. Flame, **106**, 131-143.
23. Arisawa, H. and Brill, T. B., 1996. Combust. Flame, in press.
24. Chen, J. K. and Brill, T. B., 1991. Combust. Flame, **87**, 217-232.
25. Wall, L. A., 1972. Nat. Bur. Stds. Spec. Publ. 357, 47-60.
26. Arisawa, H. and Brill, T. B., 1996. Combust. Flame, in press.
27. Kashiwagi, T., Inabi, A. and Hamins, A., 1989. Polym. Deg. Stab., **26**, 161-184.
28. Madorsky, S. L., 1953. J. Polym. Sci., **11**, 491-506.
29. Lomakin, S. M., Brown, J. E., Breese, R. S. and Nyden, M. R., 1993. Polym. Deg. Stab., **41**, 229-243.
30. Conley, R. T., 1970. Thermal Stability of Polymers Vol. 1, Marcel Dekker, Inc, New York, p. 523-547.

31. Gongwer, P. E., Arisawa, H. and Brill, T. B., 1996. Decomposition, Combustion and Detonation Chemistry of Energetic Materials, Materials Research Society Vol. 418, T. B. Brill, T. P. Russell, W. C. Tao, and R. B. Wardle, Eds. Pittsburgh, PA, pp. 233-238.
32. Scotney, A., 1972. Europ. Polym. J., **8**, 185-195.
33. Meyer, R., 1987. Explosives, 3rd Ed., VCH Publishers, New York, p. 357.
34. Haeusler, K. G., Schroeder, E. and Wege, F. W., 1977. Plaste Kautsch., **24**, 175-179.
35. Chen, J. K. and Brill, T. B., 1991. Combust. Flame, **87**:217-232.
36. Tamara, S. and Gillham, J. K., 1978. J. Appl. Polym. Sci., **22**, 1867-1884.
37. Rama Rao, M. and Radhakrishnan, T. S., 1990. J. Appl. Polym. Sci., **41**, 2251-2263.
38. Thomas, T. J., Krishnamurthy, V. N. and Nandi, U. S., 1979. J. Appl. Polym. Sci., **24**, 1797-1808.
39. Golub, M. A. and Gargiulo, R. J., 1972. J. Polym. Sci. Polym. Lett., **10**, 41-49.
40. Schneider, B., Doskocilova, D., Stokr, J. and Svoboda, M., 1993. Polymer, **34**, 432-436.
41. Grassie, N. and Heaney, A., 1974. J. Polym. Sci. Polym. Lett., **12**, 89-94.
42. McCreedy, K. and Keskkula, H., 1989. Polymer, **20**, 1155-1159.
43. Du, T., 1989. Thermochim. Acta, **138**, 189-197.
44. Shlensky, O. F., Matyukhin, A. A. and Varynshteyn, E. F., 1986. J. Thermal Anal., **31**, 107-115.
45. Clark, J. E. and Jellinck, H. H. G., 1965. J. Polym. Sci., **3**, 1171-1184.
46. Jellinck, H. H. G. and Luh, M. D., 1966. J. Phys. Chem., **70**, 3672-3680.
47. Hirata, T., Kashiwagi, T. and Brown, J. E., 1985. Macromolecules, **18**, 1410-1418.
48. Smith, G. G. and Blau, S. E., 1964. J. Phys. Chem., **68**, 1231-1234.
49. Blake, P. G. and Jackson, G. E., 1968. J. Chem. Soc. B., 1153-1155.
50. Jellinck, H. H. G. and Kachi, H., 1968. J. Polym. Sci. C, **23**, 87-95.
51. Kachi, H. and Jellinck, H. H. G., 1965. J. Polym. Sci., **A3**, 2714-2717.
52. Roberts, A. F., 1970. Combust. Flame, **14**, 261-272.
53. Milosavljevec, I. and Suuberg, E. M., 1994. Preprints of ACS Division of Fuel Chemistry, **39**, 860-864.
54. Ishikawa, M., 1985. The Bulletin of Aichi University of Education (Natural Science), **19**, 257-260.
55. Lenggè, G., 1970. AIAA J., **8**, 1989-1996.

## COMMENTS

*Josephine Covino-The Pentagon, Washington, DC, USA.* How do these kinetics apply to plasticized, binder-filled (i.e. "real propellants") formulations?

*Author's Reply.* "Real propellants" add a number of physical and chemical variables to the issue of pyrolysis of the pure components. Among the chemical issues are the rates of the reactions in binary and ternary phases, the role of interface chemistry, and the expansion of reaction pathways. Among the physical effects are the potentially different rates of heat and mass transfer. Pyrolysis kinetics of the pure components are only the first step to understand the behavior of a binary system. The binary system is, in turn, only a step along the way to a basic understanding of the real propellant. Hopefully, as we take these steps, we will discover that the real propellant is not as complex as it might seem based on the many possible contributing issues.

*Stefan Thynell-Pennsylvania State University, University Park, PA, USA.* Surface temperature of burning RDX is in the range from 650 to 700 K. For RDX-composite propellants, such as the LOVA series, the surface temperatures are 50 to 70 K lower. Your pyrolysis temperature range was 773 K to 900 K, much higher than the typical surface temperatures of the LOVA series. To what extent does the CAB component decompose in the condensed phase? Is it possible that large CAB (polymer) molecules depart from the surface and decompose largely in the primary reaction zone?

*Author's Reply.* After completion of this paper, we conducted experiments in which RDX and CAB were intimately mixed and flash pyrolyzed. The results suggest that RDX and CAB decompose more or less independently of one another and that the surface temperature is, therefore, controlled mostly by the RDX chemistry. As you suggest, this means that mesoscopic particles of CAB, which is rather thermally stable at the surface temperature of burning RDX, could be blown off the surface by the mass flux and thereby pyrolyze, not on the surface, but mostly in the near-field flame zone.

*Luigi Deluca-Politecnico di Milano, Italy.* I liked very much your presentation; in particular I appreciated you emphasis on pressure effects. We believe that a consistent implementation of even the simplest Arrhenius expression (i.e. zero-order) requires a pressure dependence. Can you comment on this?

*Author's Reply.* I agree that the zeroth-order surface gasification process of a polymer will have a pressure dependence. From the point of view of the effect on the chemistry, the surface can be thought of as a flow reactor in which the effect of increasing the pressure is to increase the density of the reacting species and increase their residence time in the surface reaction zone. Consequently, the spatial dimensions of the chemical zones (those of reactions and degree of heat release) are affected by the applied pressure, irrespective of the global order of the process.

*Vladimir E. Zarko-Institute of Chemical Kinetics and Combustion, Novosibirsk, Russia.* You made a conclusion on the important (major) role of evaporation/desorption at high temperature in the decomposition of polymers. Do you have independent additional evidence of the existence of these processes? Is it possible that the low effective energy of activation resulted from complex kinetics of chemical reactions?

*Author's Reply.* With regard to your first question, one of the more convincing items of data that supports the desorption/evaporation hypothesis is Reference 54. Ishikawa determined the evaporation kinetics of several pure PEG oligomers. The Arrhenius parameters are very similar to those for PEG in Table 3 at 2 atm. Your second question has merit in the sense that it is very difficult to dissect complex kinetics from the role of desorption. For example, in the case of HTPB, simple Hückel MO concepts suggest that the apparent activation energy of chain scission decreases with increasing chain length of the oligomers released. This pattern applies, however, only to an unsaturated polymer like HTPB, and not to the other saturated polymers discussed.

*Rose Pesce-Rodriguez-US Army Research Laboratory, Aberdeen, MD, USA.* Regarding your comments on cross-linking of PEG on thermolysis, I suggest that the process that is actually occurring is chain transfer, rather than cross-linking. Oxygen-centered radicals will attack carbons in the backbone of another PEG chain, displace a neighboring oxygen, and result in the formulation of a new  $-(C-O)-$  bond. It is possible to increase chain length through this process.

*Author's Reply.* Your comment on the mechanism is certainly reasonable. The main point is that the Mw increases during pyrolysis by this mechanism, which is what is observed experimentally.

## UNUSUAL COMBUSTION BEHAVIOR OF NITRAMINES AND AZIDES

**R. L. Simmons**

Naval Surface Warfare Center

Indian Head, MD 20640

301-743-4521

FAX 301-743-4775

e-mail: TMBJ00A@prodigy.com

**ABSTRACT:** This paper is a brief review of the molecular structure effects, notably nitrate ester versus nitramine and azide, on the linear burning rate of nitrocellulose-based solid propellants. Furthermore, these effects have been observed at pressures up to 350 MPa. Where traditionally the linear burning rate is a direct function of the flame temperature, some nitramines and azides display significant burning rate increases with decreasing flame temperature --- seemingly contrary to the standard combustion theories and explanations.

### INTRODUCTION

In the homogeneous nitrocellulose-nitroglycerin (NC-NG) double-base propellant system, it has long been known that the linear burning rate is a direct function of the flame temperature ( $T_p$ ) and heat of explosion ( $Q_{ex}$ ). If one wants faster burning, one simply uses a hotter and more energetic propellant --- usually one with a higher concentration of nitrogen in the NC or more NG. This behavior was clearly recognized when NC-based propellants were introduced in 1880, and has been well documented over the years <sup>1,2,3,4,5,6</sup>.

During work with aliphatic nitramines and azides at Eglin AFB in the early 1980s, it was discovered that many of these compounds gave behavior quite contrary to that expected solely on the basis of flame temperature and/or heat of explosion -- and it is the object of this paper to discuss this unusual combustion behavior. In general, the Eglin results have not been widely reported or readily available to researchers previously. One unique aspect about the Eglin burning rates is that they were obtained in a high pressure strand burner at pressures up to 350 MPa. Illustrative of the burning rates obtained from 20 MPa to 350 MPa are those shown in Figure 1.

Typically, linear burning rates are measured in a strand bomb at relatively low rocket pressures of only 3 to about 30 MPa. However, for gun propellant applications, it is necessary to measure the burning rate at significantly higher pressures --- and up to 350 MPa is desirable since it approximates the average pressure encountered during the typical gun ballistic cycle. It is believed that the strand burning rates measured at Eglin at 350 MPa are truly unique in this respect.

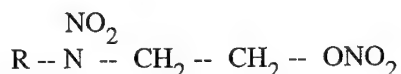
Of course, linear burning rates at pressures of 500 to 800 MPa would be even better, since current high performance guns operate at these higher peak pressures -- but no such high pressure strand burners are known to exist -- and derivation of linear burning rates from mass burning rates measured in closed bomb firings of granular propellants are usually subject to interpretation because of the complex perforated grain geometry, non-isochronic ignition effects (all grain surfaces do not ignite simultaneously), and the perforations are not perfectly centered..

## DISCUSSION OF RESULTS

The types of compounds observed to display burning rate behavior seemingly contradictory to that of normal double-base (increasing rate with decreasing flame temperature) were of two general categories: nitramines and azides, and the nitramines in turn were of two different varieties -- those with and without nitrate esters. Those with nitrate esters were known as NENAs (alkyl nitrate ethyl nitramine).

### NENAs

NENAs <sup>7,8</sup> are alkyl nitrate ethyl nitramines with the following structural formula:



Where R = an alkyl group such as methyl, ethyl, propyl, butyl, and pentyl. Note that the NENAs have both a nitramine + nitrate ester moiety. NENAs are completely miscible in NC (of 12.6% nitrogen) in all proportions to form homogeneous single-phase systems with no solid phases. Though the methyl derivative is a solid melting at 38-40°C, it is completely soluble in NC.

When examined at various concentrations in NC, it was found that not only did the burning rate change in direct proportion to the individual heat of explosion (Q<sub>ex</sub>) of the NENA studied -- but more importantly, the burning rate (in some cases) increased as the flame temperature (T<sub>p</sub>) decreased.

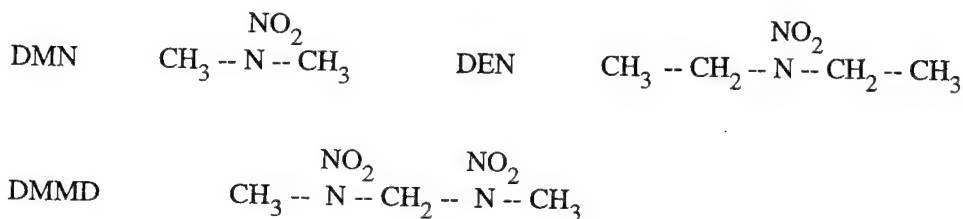
In summary, the following burning behavior was observed at 350 MPa:

<u>NENA</u>	NENA	<u>Admixed with 12.6%N NC:</u>			Pressure <u>Exponent</u>
	<u>Q<sub>ex</sub></u> <u>J/g</u>	<u>Q<sub>ex</sub></u> <u>J/g</u>	<u>T<sub>p</sub></u> <u>°K</u>	<u>Rate</u> <u>mm/sec</u>	
40% methyl	4657	4155	2489	232	0.941
40% ethyl	3335	3628	2179	192	1.005
40% propyl	2105	3134	1931	153	1.022
40% butyl	1084	2728	1758	127	1.006
50% butyl	1084	2435	1680	123	1.024
20% pentyl	197	3134	1961	136	0.844
40% pentyl	197	2372	1657	110	1.001
NC control	---	3891	2458	155	0.883

These results are plotted in Figure 2, where the unusual behavior of the NENAs can be seen compared to the typical NC-NG behavior expected. Note that in the case of ProNENA, the flame temperature decreased by over 500°K, yet the burning rate remained essentially unchanged. Even more unusual is the behavior of EtNENA where the flame temperature decreased by almost 300°K, and the burning rate increased by nearly 25%. MeNENA represents another case of unusual burning where the flame temperature increased very slightly (only 31°K), yet the burning rate increased by almost 50%. It is estimated that the burning rate of neat MeNENA (T<sub>p</sub> = 2588°K) should be 450-500 mm/sec at 350 MPa, compared to the NC-NG rate of 170-180 mm/sec. No actual burn rate measurement of neat MeNENA is known, but clearly, the nitramine moiety contributes to faster burning.

### Nitramines

Perhaps even more dramatic than the NENAs were three "all-nitramine" compounds where there were no nitrate ester or other energetic moieties present in the structure. These three nitramines were: dimethyl nitramine (DMN), diethyl nitramine (DEN), and dimethyl methylene dinitramine (DMMD) with the following structural formulas:



Because of the lower flame temperature (and reduced energy) of DMN and DEN, they were examined at a lower concentration in NC than the NENAs. In all instances, these nitramines were completely soluble in 12.6% N NC to form a single-phase homogeneous system, even though both DMN and DMMD are solids melting at 57°C and 49°C, respectively.



When added to NC, DEN lowered the flame temperature (by more than 500°K) without affecting the burning rate --- in much the same fashion as ProNENA --- only at a lesser concentration. For example, the following behavior was observed at 350 MPa:

<u>Nitramine</u>	<u>Qex</u> <u>J/g</u>	<u>Tp</u> <u>°K</u>	<u>Rate</u> <u>mm/sec</u>	<u>Pressure</u> <u>Exponent</u>
NC control	3891	2458	155	0.883
15% DEN	3067	1923	158	0.998
40% ProNENA	3134	1931	153	1.022

DMN, having a more favorable oxygen balance than DEN, was slightly hotter and faster burning than DEN --- not entirely unexpected. When added to NC, DMN lowered the flame temperature (by more than 400°K) and increased the burning rate by almost 20%. In a sense, DMN behaved intermediately between EtNENA and ProNENA --- only at a lesser concentration. The following behavior was observed at 350 MPa:

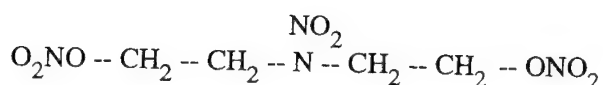
<u>Nitramine</u>	<u>Qex</u> <u>J/g</u>	<u>Tp</u> <u>°K</u>	<u>Rate</u> <u>mm/sec</u>	<u>Pressure</u> <u>Exponent</u>
NC control	3891	2458	155	0.883
30% DMN	3330	2009	184	0.940
40% EtNENA	3628	2179	192	1.005
40% ProNENA	3134	1931	153	1.022

DMMD with two nitramine groups per molecule is more energetic than either DMN or DEN. At a concentration of 50% in NC, it burned slightly faster than MeNENA -- and cooler by more than 250°K. The following behavior was observed at 350 MPa:

<u>Nitramine</u>	<u>Qex</u> <u>J/g</u>	<u>Tp</u> <u>°K</u>	<u>Rate</u> <u>mm/sec</u>	<u>Pressure</u> <u>Exponent</u>
NC control	3891	2458	155	0.883
50% DMMD	3736	2227	249	1.008
40% MeNENA	4155	2489	232	0.941

It is estimated that the burning rate of neat DMMD ( $T_p = 2106^\circ\text{K}$ ) should be about 300 mm/sec at 350 MPa, compared to the NC-NG rate of about 100 mm/sec (for the same  $T_p$ ). All three nitramines DMN, DEN, and DMMD appear to be excellent ingredients for adjusting the burning rate of NC propellants --- with little or no effect on flame temperature. Figure 3 illustrates this behavior where the effect of nitramine concentration is quite obvious.

In addition, the well known nitramine DINA <sup>9,10</sup> was also examined. It is perhaps closer related to the NENAs, but contains two nitrate esters plus a single nitramine moiety. It can be considered a derivative of DEN with a nitrate ester on each end of the ethyl linkages --- or as a derivative of EtNENA with a second nitrate ester, as shown in the following formula:



Although DINA is a solid melting at 52°C, it is soluble in 12.6% N NC in all proportions, yielding a single-phase homogeneous system just like the NENAs, DEN, DMN, and DMMD. When added to NC, DINA increased the flame temperature considerably (by almost 300°K) --- but did not burn appreciably faster than DMMD which is 500°K cooler. It appears that the two nitrate ester groups (in DINA) increased the flame temperature appreciably, but with little effect on burning rate over that expected from a simple increase in  $T_p$ . The results observed at 350 MPa are as follows:

<u>Nitramine</u>	<u>Q<sub>ex</sub></u> <u>J/g</u>	<u>T<sub>p</sub></u> <u>°K</u>	<u>Rate</u> <u>mm/sec</u>	<u>Pressure</u> <u>Exponent</u>
NC control	3891	2458	155	0.883
40% DINA	4531	2735	260	0.923
50% DMMD	3736	2227	249	1.008

The burning rate of neat DINA ( $T_p = 3135^\circ\text{K}$ ) is estimated to be about 400 mm/sec at 350 MPa, compared to the NC-NG rate of about 330 mm/sec (at the same  $T_p$ ).

### Azides

Azides are popular energetic ingredients which have attracted considerable attention world-wide during the past decade. The combined effects of azide + nitramine in the same molecule make extremely impressive energetic molecules. One diazido nitramine of interest is the liquid known as DANPE <sup>11</sup> (and previously as DIANP <sup>12</sup>), which readily plasticizes NC in all proportions to form single-phase systems.

An interesting homologous nitramine series can be arranged leading from DEN to DANPE as follows:

DEN	H --- CH <sub>2</sub> -- CH <sub>2</sub> -- N -- CH <sub>2</sub> -- CH <sub>2</sub> --- H	
EtNENA	H -	- ONO <sub>2</sub>
DINA	O <sub>2</sub> NO -	- ONO <sub>2</sub>
DANPE	N <sub>3</sub> -	- N <sub>3</sub>

with the following burning rate behavior observed at 350 MPa:

<u>Nitramine</u>	<u>Q<sub>ex</sub></u> <u>J/g</u>	<u>T<sub>p</sub></u> <u>°K</u>	<u>Rate</u> <u>mm/sec</u>	<u>Pressure</u> <u>Exponent</u>
15% DEN	3067	1923	159	0.998
40% EtNENA	3628	2179	192	1.005
40% DINA	4531	2735	260	0.923
40% DANPE	3473	2246	363	0.822

In this comparison, it is seen that the addition of a nitrate group (in EtNENA) increased the burning rate about 20%, while adding a second nitrate (in DINA) produced an additional 35% increase in burning rate. Even more impressive is the substitution of azide for nitrate (in DANPE) produced an additional 40% increase in rate --- with a simultaneous reduction in flame temperature of almost 500°K. This effect is illustrated in Figure 4.

It would be interesting to examine higher concentrations of DANPE in NC, however, because DANPE is so oxygen-deficient, the oxygen/carbon (O/C) ratio of the system is less than 1.00 beyond 60% DANPE (where  $T_p = 2243^\circ\text{K}$ ), and solid carbon would be formed during combustion.

The reduction in pressure exponent that occurred as the systematic changes were made to the molecular structure is believed to be significant, and it is concluded that azides inherently have slightly lower exponents (at least at these high pressures) than either nitramines or nitrate esters.

Another popular azide whose combustion was examined at high pressure is glycidyl azide plasticizer/polymer, commonly known as GAP --- and is soluble in NC in all proportions. The burning rate behavior noted was as follows:

<u>% GAP</u>	<u>Q<sub>ex</sub></u> <u>J/g</u>	<u>T<sub>p</sub></u> <u>°K</u>	<u>Rate</u> <u>mm/sec</u>	<u>Pressure</u> <u>Exponent</u>
NC control	3891	2458	155	0.883
20% GAP	3038	1980	160	0.823
30% GAP	2561	1773	181	0.766
neat GAP	---	≈1600	325*	0.692*

The data for neat GAP was taken from the latest Russian computer program FLAME and extrapolated to 350 MPa [*this is the only instance of extrapolation used*]. From these data, it is readily seen that the burning rate increases as the flame temperature decreases --- much like DANPE. See Figure 5. The pressure exponent also decreased - - much more than was seen for DANPE. Like DANPE, GAP is also oxygen-deficient and the O/C ratio quickly drops below 1.00 above 40% GAP in NC.

It is also believed to be significant that no slope breaks or pressure exponent changes were observed with any of these homogeneous nitramine and azide propellants over the entire pressure range tested, which typically was 15 to 350 MPa.

## CONCLUSIONS

Through carefully controlled changes in chemical composition and molecular structure, it is clear that nitramines burn faster than their nitrate ester counterparts --- and azides burn even faster --- when compared at the same flame temperature. The burning rate of azides also appears to be less sensitive to pressure. These classes of ingredients now offer the propellant formulator a dynamic range of burning rates without sacrifices or trade-offs in flame temperature or heat of explosion.

It is also concluded that high pressure strand burning rates --- where no geometry imperfections or ignition flame spreading effects have to be taken into account --- are very desirable and important --- especially in a regime where strand burning rates have not previously been measured. It is strongly recommended that linear burn rates and the combustion of propellants intended for use in high performance guns be determined at pressures up to 800-900 MPa.

Furthermore, this collection of high pressure combustion information on homogeneous propellants with no solid phases present, should provide new or additional data for the combustion modelers to consider --- especially where it may conflict with accepted theory.

It is recommended that high pressure burning studies be expanded to include other energetic molecular structures (of current interest) such as: TAG salts, caged nitramines and azides, ADN and dinitramide derivatives, TNAZ and derivatives, and tetrazoles. It is recommended that the study also include molecules which could retard burning with minimal effect on flame temperature.

## ACKNOWLEDGMENTS

The author gratefully acknowledges the efforts of the following people who contributed immensely to this paper in the way of assistance, suggestions, and inspiration: Otto K. Heiney (dec), Bertram K. Moy, Joseph F. Flanagan, Hays Zeigler, Gilbert B. Lancaster (dec), J. Robert Martin (dec), Joseph M. Heimerl, Arpad Juhasz, Rose Pesce-Rodriguez, and Vaslav Egorshof (of the Mendeleeff Institute).

## GLOSSARY

<u>Term</u>	<u>Definition</u>
ADN	Ammonium dinitramide
BuNENA	Butyl nitrate ethyl nitramine
DANPE	1,5-diazido-3-nitrazapentane; also known as DIANP
DEN	Diethyl nitramine

DIANP	1,5-diazido-3-nitrazapentane; also known as DANPE
DINA	1,5-dinitrato-3-nitrazapentane; dinitrato ethyl nitramine
DMN	Dimethyl nitramine
EtNENA	Ethyl nitrato ethyl nitramine
GAP	Glycidyl azide polymer/plasticizer
MeNENA	Methyl nitrato ethyl nitramine
N	Nitrogen content
NC	Nitrocellulose
NENA	Nitrato ethyl nitramine moiety
NG	Nitroglycerin
PeNENA	Pentyl nitrato ethyl nitramine
ProNENA	Propyl nitrato ethyl nitramine
Q <sub>ex</sub>	Heat of explosion; also known as HOE
TAG	Triamino guanidine
TNAZ	1,3,3-trinitro azetidine
T <sub>p</sub>	Isobaric flame temperature in °K

## REFERENCES

1. **Muraour, H.**, On the relation between the temperature of explosion of a propellant and its rate of burning, *Comptes Rendus de l'Academie des Sciences*, 187, 289, 1928.
2. **Gibson, R. E.**, Rocket fundamentals, *OSRD Report 3992*, The George Washington University, Allegany Ballistics Laboratory, 1944.
3. **Crawford, B. L., Huggett, C., and McBrady, J. J.**, Mechanism of burning of double-base propellants, *Journal of Physical and Colloid Chemistry*, 54, June 1950.
4. **Beckstead, M. W., Derr, R. L., and Price, C. F.**, A model of solid propellant combustion based on multiple flames, *AIAA Journal*, Volume 8, No. 12, 1970.
5. **Fifer, R. A.**, Chemistry of nitrate ester and nitramine Propellants, *Fundamentals of Solid Propellant Combustion*, AIAA Series, Volume 90, 1984.
6. **Kubota, N.**, Combustion characteristics of rocket propellants, *Fundamentals of Solid Propellant Combustion*, AIAA Series, Volume 90, 1984.
7. **Simmons, R. L.**, NENAs - New energetic plasticizers, *ADPA International Symposium on Energetic Materials Technology*, Orlando, FL, March 21-24, 1994.
8. **Simmons, R. L.**, NENA plasticizers, *NIMIC Workshop on Insensitive Munitions and New Energetic Molecules*, NATO HQ, Brussels, Belgium, June 22-24, 1994.

9. **Wright, G. F. and Chute, W. J.**, Nitramines and their preparation - DINA, *US Patent 2,461,582*, February 15, 1949.
10. **Kincaid, J. F.**, Flashless propellant with DINA, *US Patent 2,698,228*, December 28, 1954.
11. **Flanagan, J. E., Wilson, E. R., and Frankel, M. B.**, 1,5-Diazido-3-nitrazapentane (DANPE) and method of preparation, *US Patent 5,013,856*, May 7, 1991.
12. **Simmons, R. L. and Young, H. L.**, Azido nitramine 1,5-diazido-3-nitrazapentane (DIANP), *US Patent 4,450,110*, May 22, 1984.

### COMMENTS

J. P. Reynaud, SNPE Centre de Recherches du Bouchet, France. You said you prefer strand-burner techniques to closed bomb method for gun propellant burning rate measurements at high pressures. Don't you think that for composite gun propellants, because their non-uniaxial combustion process (with respect to NC propellant), the inhibition of lateral combustion of the strand could affect the representativity of the measure ? In a closed vessel, you have not this inconvenience, and at high pressure, I think we can assume the effect of bad ignition to be negligible. You can also deal with bad grain geometry data using a large volume closed vessel to statistically minimize this problem. What is your opinion on that ?

Author's Reply: Whenever possible, I prefer strands over perforated granules to determine linear burn rate --- to avoid complications which arise from assumptions about grain geometry and slivering after perforation burn-out. I realize that one can use a larger volume bomb with an associated larger number of grains (at constant loading density), however the problem of off-center perforations and slivering (which occur long before P max) still remains. Ignition and associated flame spreading into the perforations does not occur until about 30 MPa, and so the low pressure portion can be neglected --- however this will affect slivering and lead to non-uniformity of burning, and difficulty in determining the true linear burn rate. Unfortunately, propellant granules do not always have perfect geometry, and this non-uniformity (coupled with non-uniform flame spread) can lead to erroneous linear burn rates.

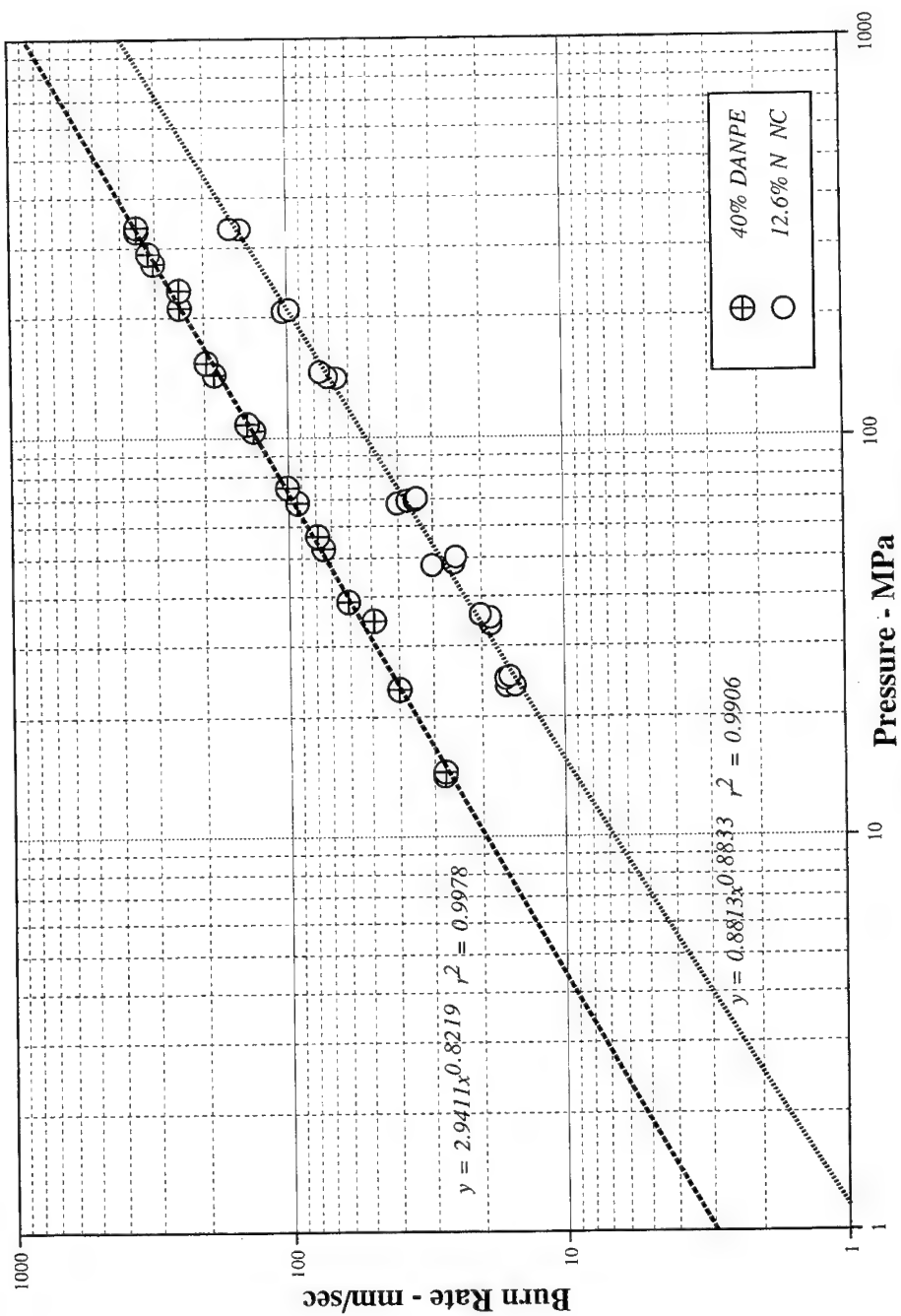


Figure 1. High pressure strand burning rates

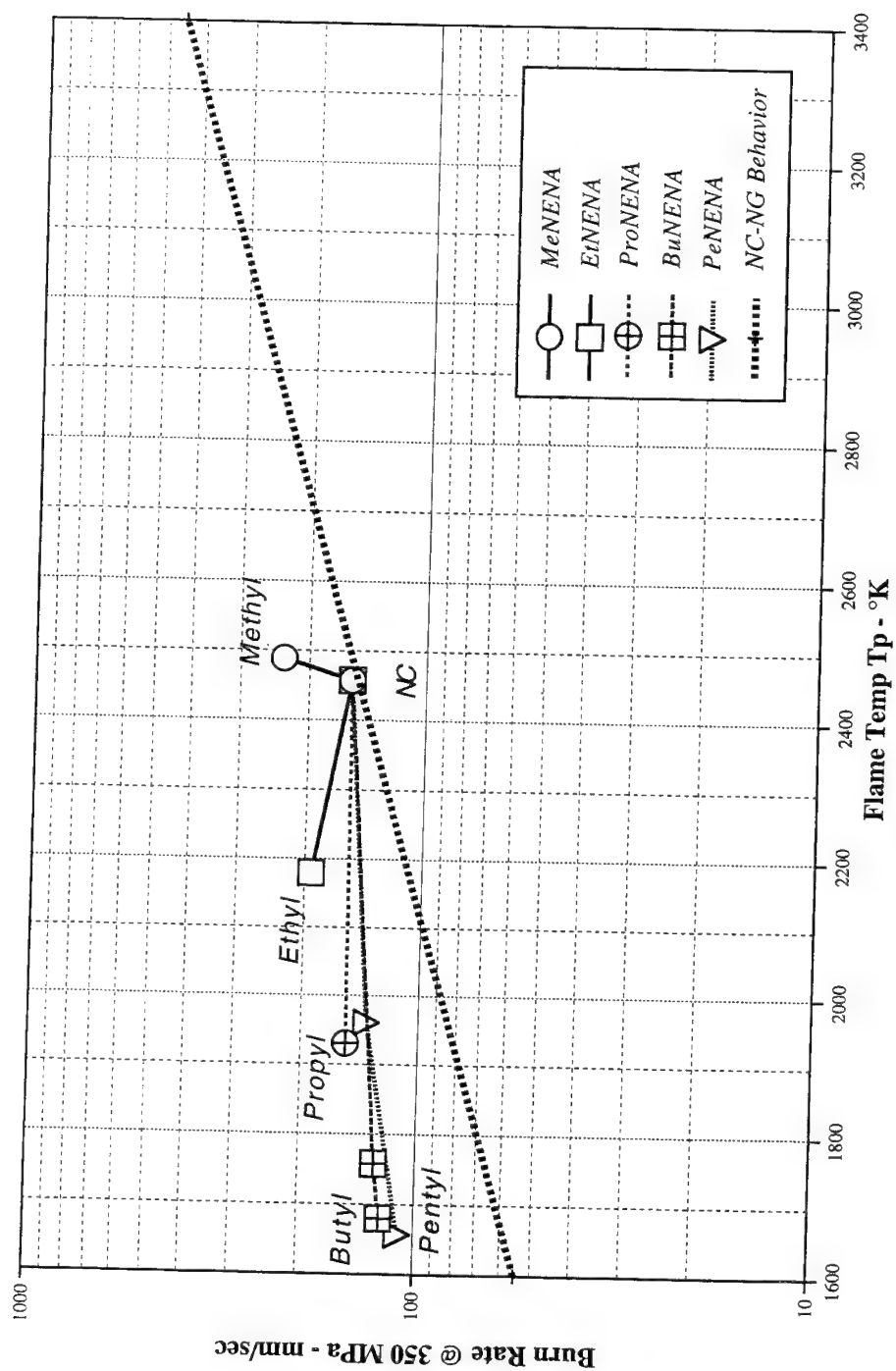


Figure 2. NENA behavior



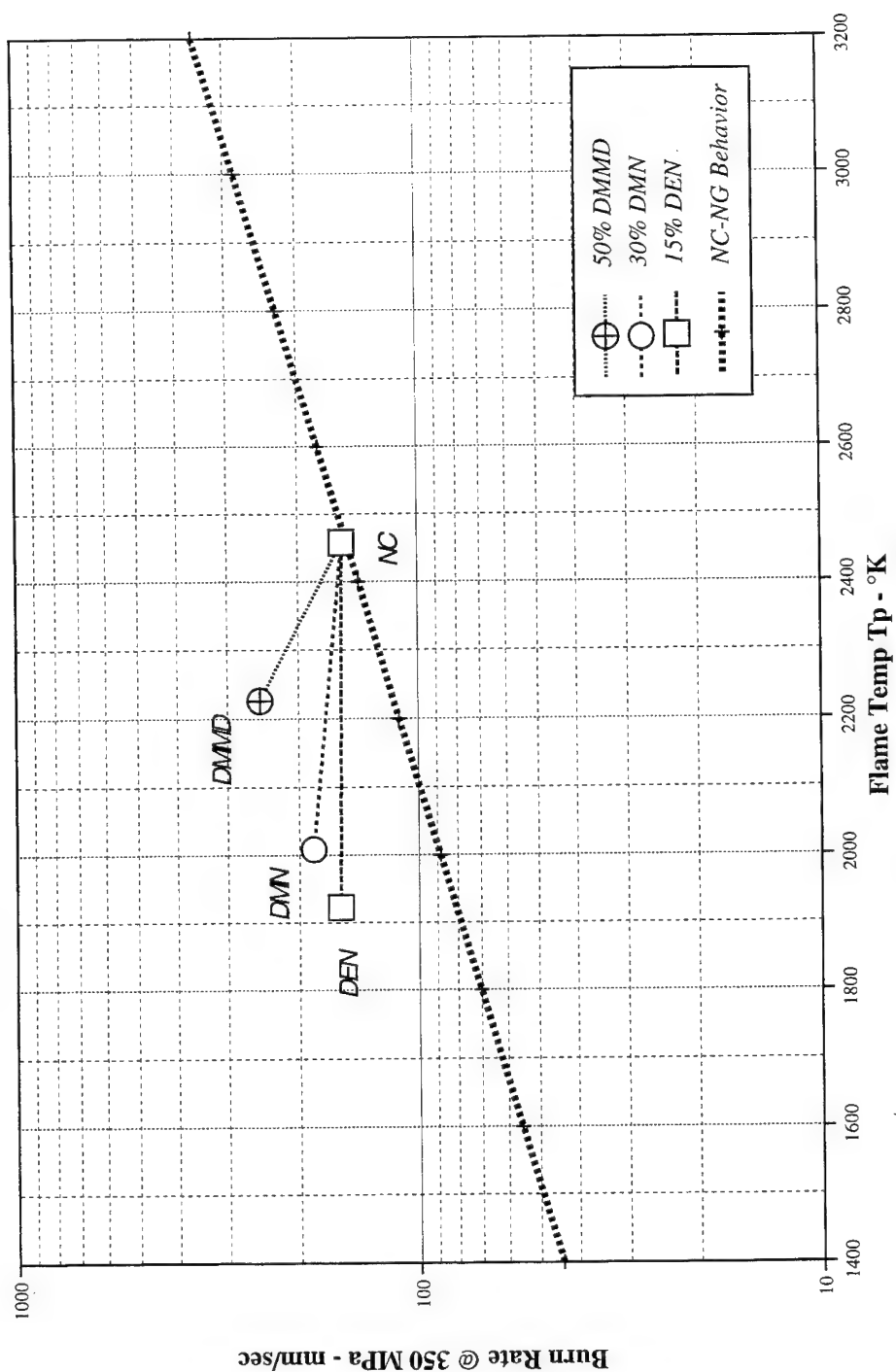


Figure 3. Nitramine behavior

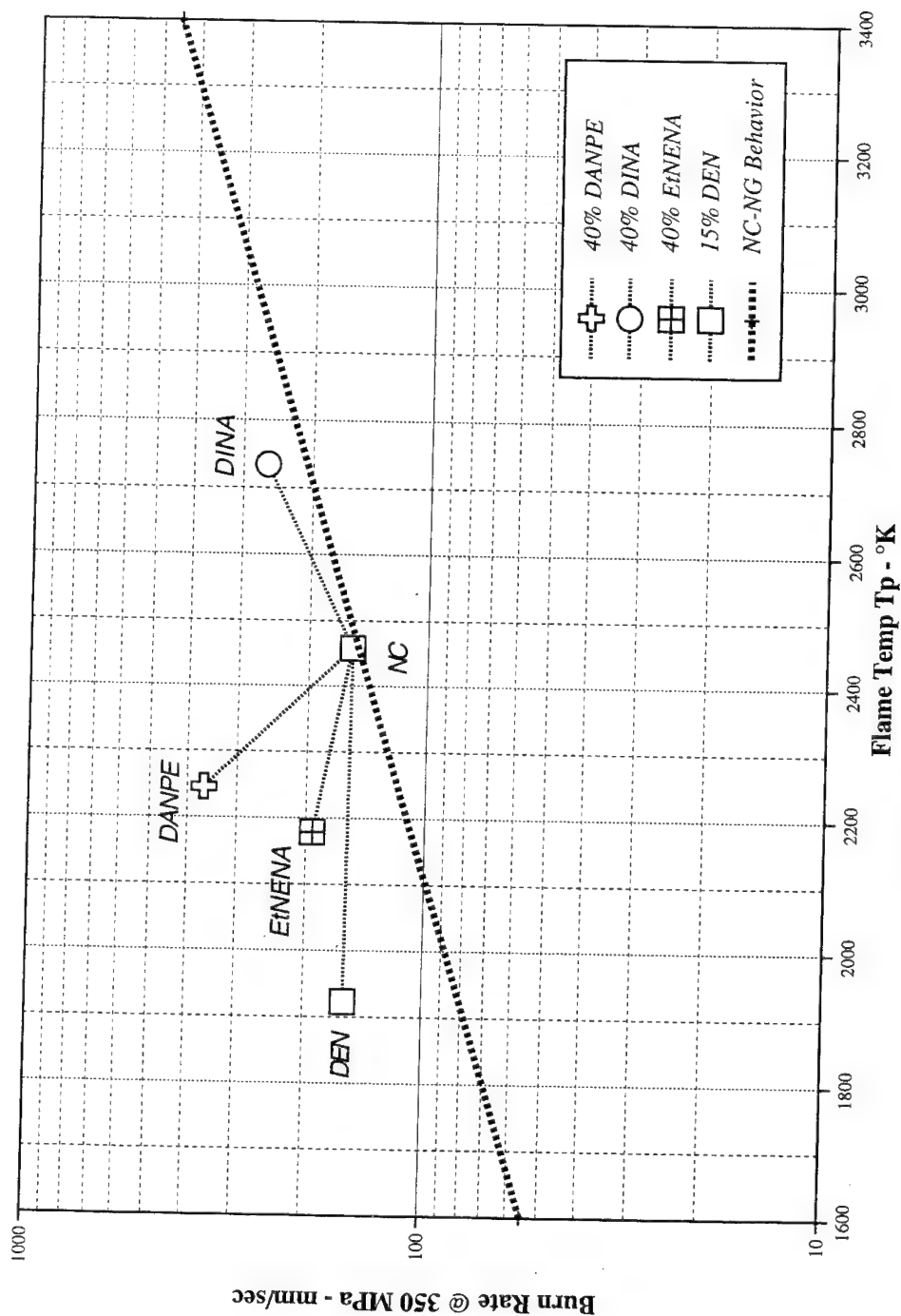


Figure 4. Changing chemical structure

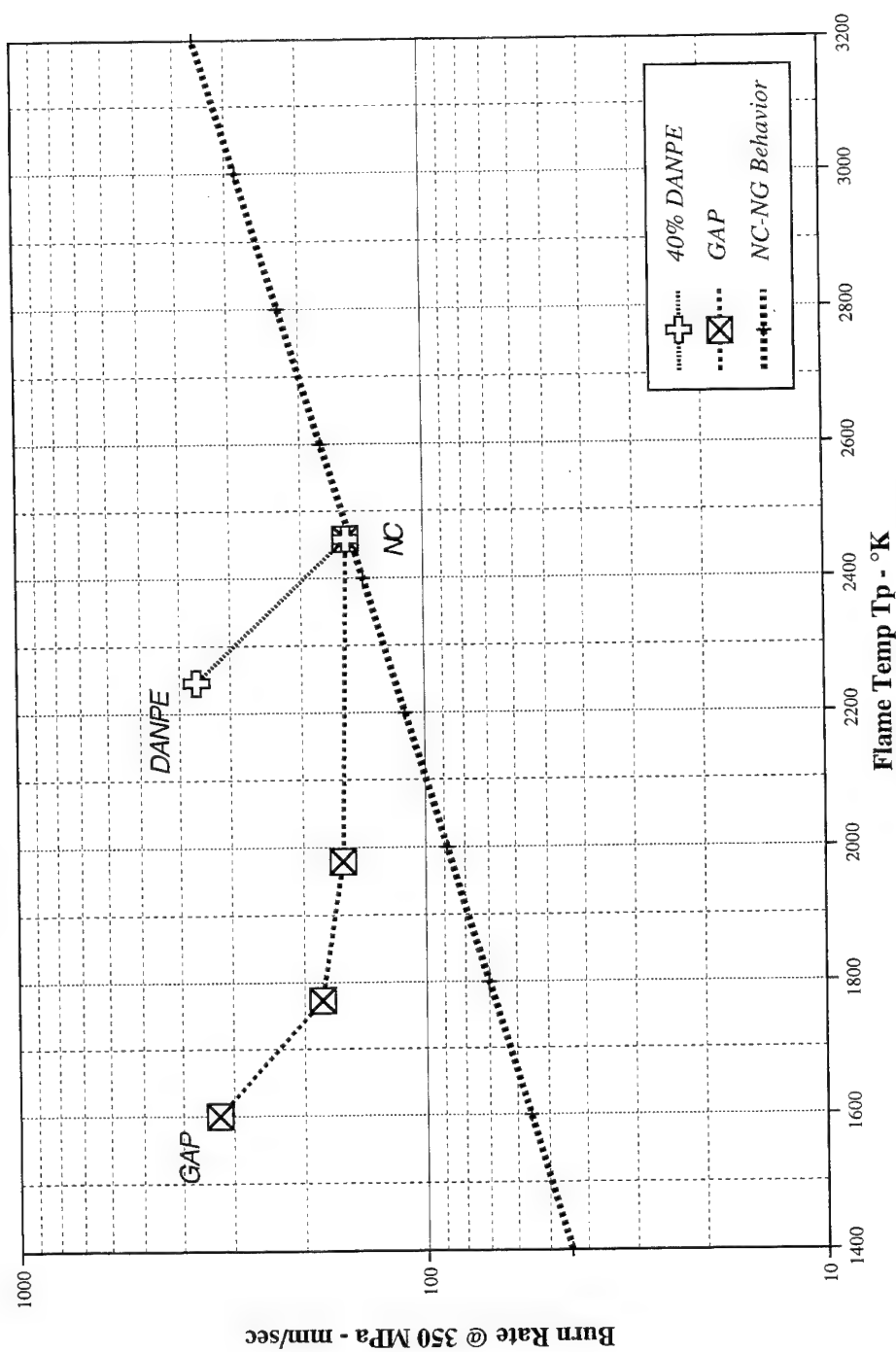


Figure 5. Behavior of azides

# STUDY OF FLAME STRUCTURE, KINETICS AND MECHANISM OF THE THERMAL DECOMPOSITION OF SOLID PROPELLANTS BY PROBING MASS SPECTROMETRY.

O.P.Korobeinichev, L.V.Kuibida, A.A.Paletsky, A.G.Shmakov

Institute of Chemical Kinetics and Combustion  
Siberian Branch Russian Academy of Sciences  
630090 Novosibirsk, Russia, korobein@kinetics.nsk.su

**ABSTRACT:** The methods for the study of flame structure and kinetics of the thermal decomposition of solid propellant (SP) by probing mass spectrometry (PMS) are described. Several types of setups based on microprobe and molecular beam mass spectrometric probing for the study of SP flame structure at high (10 atm) and low ( $\leq 1$  atm) pressures have been developed. An installation for studying thermal decomposition of SP at the high heating rate of SP specimen up to 20-100 degree/s under the condition approximately similar to those present in the condensed phase in the vicinity of the burning surface is described. The results of the investigation of the flame structure of SP ingredients (RDX, ADN), sandwich systems are presented. Profiles of the species concentrations in flames have been measured. The main reaction in high temperature zone of RDX and ADN flames has been determined. The results of RDX flame structure modeling are in a good agreement with the experimental ones. The results of probing gas phase zone at ADN deflagration at 1, 3 and 6 atm. are presented. Flame structure studies of sandwich based on AP allowed a confirmation of multizone structure and step-by-step mechanism of reactions in AP flame. A study of thermal decomposition of ammonium dinitramide (ADN) by molecular beam mass spectrometry has been carried out. The products of ADN thermal decomposition and products release rates on heating rate of 20 deg/s has been obtained. Data obtained by PM at the SP combustion and decomposition chemistry are discussed and compared with literature data.

## INTRODUCTION

It is generally believed that future progress in the understanding of solid propellant (SP) combustion is to arise from a clearer picture of the chemistry and physics taking place in SP flames. The combustion chemistry of solid propellants is not well understood. Much more detailed information is required to provide progress in the understanding of SP combustion. It is important to understand the combustion chemistry since it is the type of information a propellant formulator or a chemist may use to tailor and (or) to improve the performance of the propellant [1]. The main source of our knowledge on the combustion chemistry of SP is the results of flame structure studies: spatial distributions of temperature and species concentration in flames.[2-4] The main methods applied to the investigation of chemical and thermal flame structure of SP are the following: 1) probing mass-spectrometry, 2) spectroscopic methods - absorption and emission; planar laser induced fluorescence (PLIF); Spontaneous Raman Scattering (SRS), Coherent Anti-Stokes Raman Spectroscopy (CARS); 3) microthermocouple technique. [1-10]

Until recently there were few works on SP flame structure. However, the improvement of experimental technique, the development of works on flame structure modeling and the rise of interest to SP combustion chemistry, increased the number of works in this field.

At present one of the most effective and universal experimental technique for studying SP flame structure is the method of mass spectrometric probing of SP flames (MSPSPF) which was improved.[11] It allows the detection of all stable species present in the flame as well as the structure of SP flames. The PMS method consists in the following: a burning strand of SP moves at a speed exceeding the burning rate toward a probe so, that the probe is continuously sampling gaseous species from all the zones including those adjacent to the burning surface. The sample is transported to an ion source of a time-of-flight (TOF) or quadrupole mass spectrometer. Mass spectra of samples are recorded with simultaneous filming of the probe and burning surface. The data allow identification of stable components, determination of their concentrations and spatial distributions, i.e. the study of flame microstructure. The method of probing mass spectrometry is successfully applied also for the study of kinetics and mechanism of SP thermal decomposition. Thermal decomposition of SP is one of the most important stages of SP combustion process. The reactions taking place in the surface layer of burning SP are suppliers of gas products which subsequent reactions result in heat release sustaining the combustion process. Therewith kinetics and reaction mechanism of SP thermal decomposition and their ingredients at the temperature close to the one at the burning surface are necessary to an understanding of combustion mechanism and development of SP combustion model. Such information can result from using Rapid-Scan FTIR spectroscopy, SMATCH/FTIR, T-Jump/FTIR, developed by T.Brill as well as the method of differential mass-spectrometric thermal analysis (DMTA).[12,13] It allows the acquisition of information about the products of SP decomposition as well as the rate of evolving each product as a function of time. The purpose of this work is to describe mass spectrometric probing technique, to demonstrate its application with some examples for the study of SP flame structure and thermal decomposition.

## EXPERIMENTAL TECHNIQUES

Two types of apparatuses have been developed to study flame structure. The sample is transported to an ion source as a molecular flow using a microprobe with the inlet orifice of 10-20  $\mu\text{m}$  in the first type of

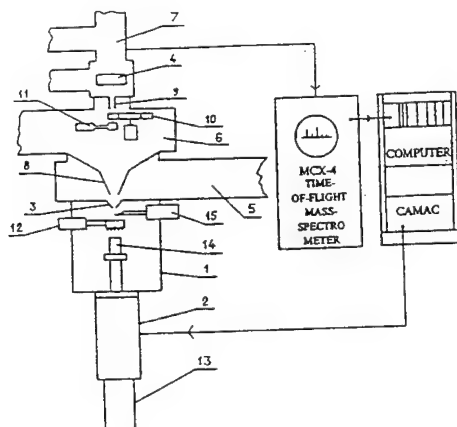


Figure 1. MBMS system for studying the flame structure of solid propellants with TOFMS.

- 1) combustion chamber; 2) scanning system; 3) probe;
- 4) ion source; 5) skimmer chamber; 6) collimator;
- 10) slotted disk; 11) electromagnetic chopper.
- 12) ignition spiral; 13) stepper motor;
- 14) burning strand; 15) thermocouple.

setup and as a molecular beam using a sonic probe with the inlet orifice of 20-200  $\mu\text{m}$  in the second type. The former setup has a high spatial resolution and just slightly disturbs the flame allowing study of the flame with a narrow combustion zone up to 0.1 mm. However, in this case radicals recombine and quenching can become a problem. The latter setup with molecular beam mass spectrometric (MBMS) sampling allows detection of radicals, but more strongly disturbs the flame, and therefore, has a reduced spatial resolution.

Figure 1 shows the MBMS system, which has been used to examine flame structures of RDX, ADN.[2-4] It includes: an apparatus for probing a flame containing a molecular beam sampling system, a time-of-flight mass spectrometer (TOFMS) type MSKh-4 as a detector, a combustion chamber, a scanning system, a data-acquisition system and an experiment controller based on CAMAC equipment and a computer. A probe produces a molecular beam which passes to an ion source.

The flame is sampled with a probe (3), a 25 mm high cone with a  $50^\circ$  external angle, a  $40^\circ$  internal angle, and a 50-100  $\mu\text{m}$  diameter orifice at the apex (at 1 atm). The ignition spiral (12) is automatically removed from the combustion zone after ignition. To scan SP flame a control system and a stepper motor (13) are required. The burning strand (14) is moved with a motor (13). Thermocouple (15) serves to measure temperature profile in flame. A strand is moved at a speed less than 10 mm/s and is driven by a stepper motor, one step is 1.25  $\mu\text{m}$ . The data acquisition and control system consists of computer AT486, a CAMAC apparatus, a double-beam oscilloscope, a scanner control, and a printer. To study the flame structure at high pressure by MBMS quartz probe with the inner angle of  $40^\circ$  with the orifice of 50  $\mu\text{m}$  at 3 atm, 20  $\mu\text{m}$  at 6 atm and wall thickness near the probe tip of 25  $\mu\text{m}$  has been used. For visualization of combustion process video camera Panasonic NV - M3000 EN have been used. The study of  $\text{H}_2/\text{O}_2/\text{Ar}$  (0.1/0.05/0.85) flame structure stabilized on flat burner at 10 atm has been carried out to demonstrate the possibility of MBMS application for the study of flame structure at high pressure.[14] For the investigation of sandwich systems the setup of the first type with microprobe sampling was used. The combustion products were sampled using a quartz probe with sampling orifice 20  $\mu\text{m}$ . For obtaining mole fraction of products calibration on individual substances and their mixes has been carried out.

Temperature profiles have been measured in some cases with an immovable thermocouple, in others cases - thermocouple moving toward burning surface of a strand with a scanning device at the rate, exceeding the burning rate. Pt-Pt(10%)Rh and W-WRe thermocouples with the wire diameter of 20-30  $\mu\text{m}$  were used. The time constant for Pt-PtRh thermocouple 20  $\mu\text{m}$  in diameter, 3 mm in length has been found to be 0.004 s. Temperature in ADN combustion products was measured with a thermocouple Pt-Pt(10%)Rh  $\sim 120$  microns in total diameter. The width of thermocouple wires was 50 microns. The thermocouple was protected with a noncatalytic coating Ceramobond 569. The coating width was 35 microns. The thermocouple arm length was 2 mm. Thermocouple outlets were placed in quartz capillaries 5 mm in length and 0.5 mm in diameter and fastened to the ceramic tube. Thermocouple was inserted between igniter loops made from nichrome wire (Figure 2). Thermocouple junction was situated within  $\sim 1$ -2 mm below the plane, in which igniter loops are located. The distance between the thermocouple and ADN strand surface is comprised  $\sim 0.2$ -0.5 mm.

The setup for mass spectrometric investigations of the kinetics of SP thermal decomposition under the conditions approximately similar to those present in the condensed phase in the vicinity of the SP burning surface and the method itself are detailed early.[2] The study of ADN thermal decomposition was conducted through their heating at the rate of about 20 degree/s in an oxidized crucible and analysis of decomposition products with molecular-beam mass spectrometry (Figure 3). The crucible was produced from aluminum.

There is a hollow at its upper side 4 mm in diameter and  $\sim 2$  mm in depth for the installation of ADN crystals. There is an aperture in the crucible, where a thermocouple is clamped to conduct measurements of the sample sublayer temperature. The crucible is oxidized through electroplating, the width of  $\text{Al}_2\text{O}_3$  coating comprising  $\sim 50$ -100 microns. It protects against an electric contact of

thermocouple and electrical furnace winding with the crucible. The crucible is externally heated with a winding from nichrome wire. The crucible is fastened to a ceramic tube installed into a glass tube 10 mm in diameter, through which argon flow is fed. The crucible is located within ~1-2 mm from the tip of quartz sampler.

## RESULTS

The study of combustion chemistry, RDX and ADN flames structure is of interest for two reasons. First, they present an alternative to ammonium perchlorate (AP) as ecologically pure oxidizers in solid propellants. Secondly, a detailed study of their combustion mechanism on a molecular level and development of models of their combustion seem to be possible owing to the simplicity of their chemical structure and relatively small number of possible products.

### RDX Flame Structure.

Figure 4 represents concentration profiles of the reacting components in RDX flame at  $p=0.5$  atm, found on RDX flame probing with MBMS and on modeling by Ermolin et al. [15,16] They are in a good agreement with each other. The results of modeling conducted by Mellius are in a better agreement with the above experimental results. [17] The experiment shows oxidation of cyanohydrogen HCN with nitrogen oxide to be responsible for the heat release in flame and to effect RDX burning rate.

### ADN Flame Structure.

Ammonium dinitramide (ADN) is a new energetic material which can be used as an oxidizer in solid rocket propellants with high environmental safety. [18] ADN is more simple in its chemical structure and number of involved elements than RDX. ADN decomposition chemistry was studied by the method T-Jump FTIR at 260°C at 1 atm. Ar. [12] The decomposition process becomes strongly exothermic as the first gas products are detected. The first detected products are mostly  $\text{HNO}_3$ ,  $\text{NH}_3$  and  $\text{N}_2\text{O}$  in roughly similar amounts. Minor quantities of  $\text{NO}_2$ , ammonium nitrate (AN) and  $\text{H}_2\text{O}$  are also present in the initial spectrum. Gas product ratio has also been obtained on a laser-pyrolyzed strand of ADN with the use of a quartz microprobe mass spectrometer MPMS and are comparable to those obtained by IR spectroscopy. ADN material was received as a crystalline powder and was pressed into cylindrical pellets 0.64 cm in diameter, 0.4-0.9 cm long with a consolidation pressure of about 500 atm. Pellet densities were approximately of  $1.5 \text{ g/cm}^3$ . Regression rates of ADN pellets

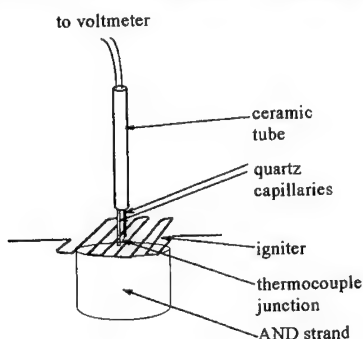


Figure 2. Installation for temperature measurements at ADN combustion at 3 and 6 atm

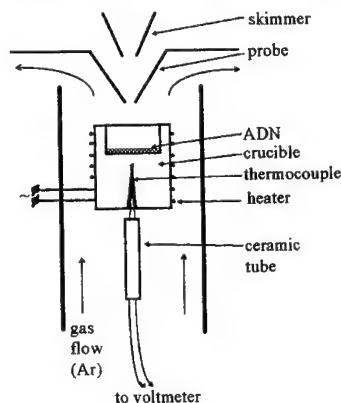


Figure 3. Installation for mass spectrometric thermal analysis

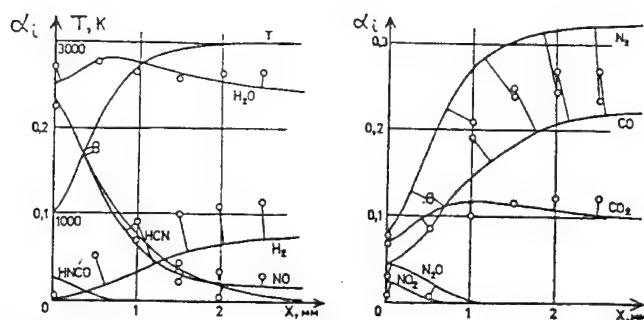


Figure 4. Temperature and species mole fractions profiles in RDX flame at 0.5 atm.  
Dots - experiment, solid line - modeling

under 1 atm increased from 0.5 cm/s to 0.7 cm/s as the incident heat flux was increased from 50 W/cm<sup>2</sup> to 300 W/cm<sup>2</sup>. [6] Temperature measurements using fine-wire thermocouples indicated a surface temperature of 570-580K at 1 atm. MPMS technique did not allow HNO<sub>3</sub> detection in products of laser pyrolysis of ADN. Self-sustaining deflagration of ADN under 1-6 atm have been studied in this work by MBMS. First our results on study of ADN flameless deflagration at 1 atm have been presented earlier. [19] ADN used in this work have been synthesized at Zelinsky Institute of Organic Chemistry Russian Academy of Sciences by the method described earlier. [20] The purity of ADN is 97%. The main impurity is AN (about 3%). Melting starts at 90-94°C. Decomposition starts at 130-135°C. Specific density of ADN crystal is 1.82 g/cm<sup>3</sup>. ADN strands 21 mm in length, 10 mm in diameter, of specific density of 1.79 g/cm<sup>3</sup> pressed using the pressure of 7000 atm. They burn steadily and flamelessly at 1 and 3 atm. The flame appears at the ADN deflagration at 6 atm. Different methods were applied to measure the burning rate: those based on signals from thermocouples and mass-spectra of a strand ignition or extinction (at 1, 3, 6 atm) and on video-recording data as well (at 6 atm). The results of studying burning rate and final burning temperature at different pressures (1-6 atm) are tabulated in Table 1.

Table 1

Burning Rate U and Final Temperature of ADN Combustion Products T<sub>c</sub> in Relation to Pressure p

p, atm	1	3	6
U, mm/s	3.44±0.05	12±1	19±2
T <sub>c</sub> , °C	320-370	550±80	1080±30

Two types of experiments on mass spectrometric probing of ADN burning zone have been conducted: a) A strand mounted at the distance of 1 mm from the probe is immovable. Burning surface is moving outward from the probe at ADN burning rate; b) burning strand is moving toward the probe at the rate exceeding ADN burning rate. Both methods were used when determining combustion products composition at 1 atm. In the experiment of the first type the following masses have been detected in mass spectra of samples with drawn from combustion products: 46 (NO<sub>2</sub>, HNO<sub>3</sub>), 30 (NO, N<sub>2</sub>O, NO<sub>2</sub>, HNO<sub>3</sub>), 44 (N<sub>2</sub>O), 17 (NH<sub>3</sub>, H<sub>2</sub>O), 28 (N<sub>2</sub>, N<sub>2</sub>O), 18 (H<sub>2</sub>O), 63 (HNO<sub>3</sub>). Mass-spectrum of ADN combustion products at 1 atm is represented in Table 2.

Table 2

Relative Peak Intensities I<sub>i</sub>/I<sub>44</sub> in the Mass-Spectrum of ADN Combustion Products at 1 atm

m/e	17	18	28	30	44	46	62	63
I <sub>i</sub> /I <sub>44</sub>	0.78	0.35	0.26	1.4	1	1.3	6.3·10 <sup>-3</sup>	1.1·10 <sup>-3</sup>



Along with the above-mentioned mass peaks a peak 62 amu was found, its intensity exceeded the peak at 63 amu by a factor of 5-6. The peak of 62 amu has not been identified yet. It is supposedly assigned to nitramide  $\text{NH}_2\text{NO}_2$ . Identification requires calibration for this specific compound. We supposed the detection of peak of mass 124, attributable to molecular ion ADN, and those of 106 and 107 attributable to molecular and fragmentary ions of dinitramide. However these peaks have not been found even in the mass-spectra of samples taken within 0.2 mm from the burning surface. The nature of peaks behavior with time (seldom sharp fluctuations) is indicative of the formation of AN aerosol both from the reaction in condensed phase and from  $\text{NH}_3$  and  $\text{HNO}_3$  reaction in gas phase. We have made verification of heat balance conservation at condensed phase surface on ADN flameless burning at 1 atm as a result of ADN thermal decomposition, accounting for mole fractions and enthalpies of the reaction products, temperature of ADN burning surface ( $320^\circ\text{C}$ ). It demonstrated that heat balance at the burning surface is conserved if it is supposed that AN is available in gas phase in the concentration of 0.05 (mole fractions). The composition of products of ADN flameless burning at the pressure of 1 atm calculated from samples mass-spectra and calibrations from combustion products is tabulated in Table 3.

Table 3

The Composition of Products of ADN Flameless Burning (Mole Fractions) at the Pressures of 1 and 3 atm

p, atm	$\text{NH}_3$	$\text{H}_2\text{O}$	NO	$\text{N}_2\text{O}$	$\text{NO}_2$	$\text{HNO}_3$	$\text{N}_2$	Balance H:O:N
1	0.18	0.17	0.01	0.16	0.38	0.07	0.03	0.95:1.31:1.02
3	0.08	0.27	0.23	0.23	0.07	0.035	0.08	0.82:0.98:1.04

A comparison with the data on thermal decomposition and laser-pyrolysis of ADN (received from another source and possibly having distinctive characteristics) showed some difference from them.[12,6] Table 3 tabulates data on the composition of products of ADN flameless burning at the pressure of 3 atm as well. They resulted from the experiments on ADN combustion products probing at 3 atm, where the strand face to be ignited was situated within 2 mm from the probe and ADN burning surface was moving outward from the probe at the rate of ADN burning. Typical

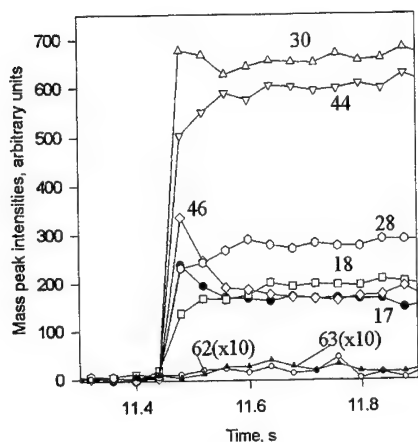


Figure 5. Typical mass peak intensity dependencies from time at probing ADN combustion zone at 3 atm.

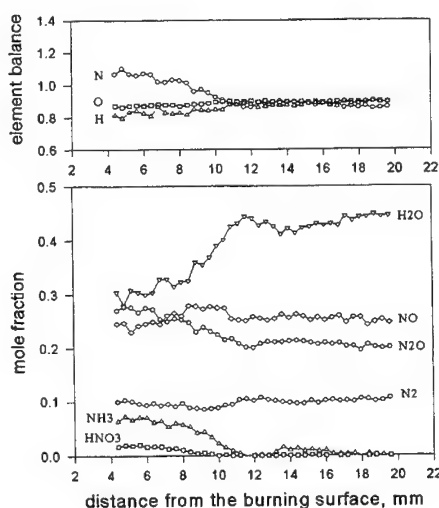


Figure 6. Species mole fraction profiles and element balances in ADN flame at 6 atm. ( $u = 20.3$  mm/s)

dependencies of mass-peaks intensities on time in mass-spectra of samples taken from the locations at different distances from the surface of ADN "flameless" burning at 3 atm are represented on Figure 5. One can see that apart from the periods of strand ignition intensities of all mass peaks are nearly constant in time. The peak of  $m/e=62$  was not found in samples mass-spectra at 3 atm. Table 3 makes clear that mole fractions of  $\text{NH}_3$ ,  $\text{HNO}_3$  and  $\text{NO}_2$  are decreasing and the ones of  $\text{H}_2\text{O}$ ,  $\text{NO}$ ,  $\text{N}_2\text{O}$ ,  $\text{N}_2$  are increasing with pressure rise. It is interesting to note that the strand failed to be ignited at 2 atm.

We did not study the zone located at the distance less than 2 mm from the surface. The possibility of a narrow zone of "low temperature" flame in the vicinity to the burning surface at 3 atm should not be excluded. Concentration profiles of ADN flame species at the pressure of 6 atm, starting at the distance of 4 mm from the burning surface, and element balances are represented on Figure 6. It is obvious that ammonia ( $\text{NH}_3$ ) oxidation with  $\text{HNO}_3$  and  $\text{N}_2\text{O}$  is the main reaction to result in heat release in gas phase. This reaction gives  $\text{NO}$ ,  $\text{N}_2$ ,  $\text{H}_2\text{O}$  as products. Data on the products composition in ADN flame at 6 atm at the distance 4.4 and 19.6 mm from the burning surface are tabulated in Table 4.  $\text{NO}_2$  is absent at the distance of 4.4 mm.

Table 4

Products Composition (in Mole Fractions) in ADN Flame at 6 atm at the Different Distances L from the Burning Surface

L, mm	$\text{NH}_3$	$\text{H}_2\text{O}$	$\text{NO}$	$\text{N}_2\text{O}$	$\text{N}_2$	$\text{HNO}_3$
4.4	0.07	0.31	0.23	0.28	0.10	0.02
19.6	0	0.45	0.25	0.20	0.11	0

Lack of mass balance by elements throughout the burning zone is 10-20%. The data of two experiments on temperature profile measurements in ADN flame at 6 atm are represented on Figure 7. One can suggest that the zones of "low temperature" (cool) flames are not percent near the ADN burning surface, although it requires verification to be performed in future. Components concentration (from 4 mm) and temperature profiles obviously testify that temperature and components concentration gradients are low (nearly absent) nearby the burning surface at the distance above 2 mm, however near to a surface significant temperature and components concentration gradients can exist. It means that the reaction zone in condensed phase controls the rate of ADN deflagration at  $p < 6$  atm. The flame lifts off the burning surface and exists under selfignition conditions.

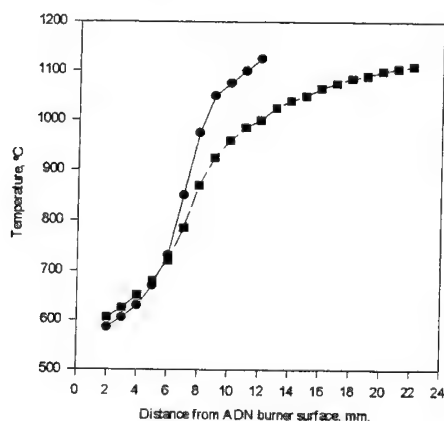


Figure 7. Temperature profiles (two experiments) in ADN flame at 6 atm.

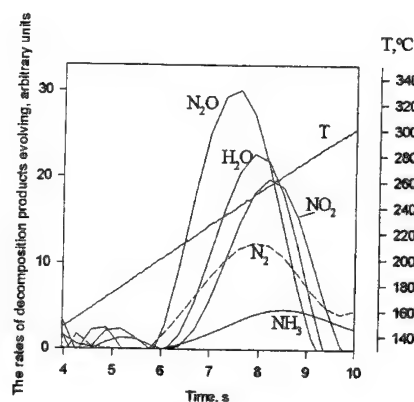


Figure 8. The rates of decomposition products evolving and temperature as a function of time at ADN decomposition at 1 atm.

### Study of ADN Thermal Decomposition Using Mass Spectrometric Thermal Analysis.

As ADN thermal decomposition controls its deflagration rate at  $p \leq 6$  atm as it was shown above and it is a very important stage, a study of ADN thermal decomposition was carried out. Figure 8 represents the results on ADN mass-spectrometric thermal analysis at the heating rate of about 20 degrees/sec at 1 atm. Decomposition of one ADN crystal weighing less than 1 mg was studied. Maximums of  $N_2O$  and  $N_2$  evolution rates are obviously found at a lower temperature ( $\sim 245^\circ C$ ) than those of other products -  $NO_2$ ,  $H_2O$ ,  $NH_3$  ( $255^\circ C$ ). The rate of  $NO$  evolution is rather low. Evolution of  $HNO_3$  takes place as well, but the accuracy in  $HNO_3$  peak measurements was rather low under these conditions. The ratio between the amounts  $m_i$  of the resulting decomposition products (the area under each curve)  $m_{N_2O} > m_{H_2O} > m_{NO_2} > m_{N_2} > m_{NH_3}$  is the same as when decomposing ADN at  $260^\circ C$  and 1 atm in the experiments of T. Brill et al. carried out using T-Jump FTIR procedure.[12] Further investigations should be aimed at the determination of kinetic parameters of ADN thermal decomposition at different pressures and the determination of their relation to ADN deflagration rate.

### Sandwich Flame Structure.

The study of combustion mechanism of systems of sandwich type, of their flames structure is of interest in connection with the necessity to understand and describe processes taking place at the surface of oxidizer-"base" contact in propellant, which is of importance for the creation of a realistic model of composite solid propellants combustion models.[21] A study of flame structure of sandwich systems has been carried out. Oxidizer - "base" sandwiches are the best models of composite propellants. The structure of subatmospheric flames of sandwich-type systems consisting of alternating laminae of ammonium perchlorate (AP) and "base" has been studied.[22] "Base" is a polymerized mixture of fine-grained AP (particle size  $< 50 \mu m$ ) and polybutadiene binder (PB). A "base" of the following composition was used: 54% AP + 46% PB. Sandwiches consisted of five alternating laminae: three AP laminae and two "base" laminae. An AP-based sandwich was prepared of pressed AP plates (density  $1.85 g/cm^3$ , thickness 1.3 mm) and a laminae (thickness 1.0 mm) of polymer "base". Thermal structure of flames was studied using thermocouples (tungsten-rhenium wires 30 and 50  $\mu m$  in diameter) embedded in propellant samples. Chemical structure of flame was analyzed by mass spectrometric probing (using a microprobe) similar to the one described earlier.[23] Quartz cones had a 15-20  $\mu m$  sampling orifice. In order to study the structure of the burning surface and the shape of an oxidizer and "base" laminae, samples were quenched using rapid depressurization.

At low pressures AP-lamina were found to protrude above "base" lamina approximately by 0.5 of lamina thickness and have a shape close to circle segment. Figure 9 shows surface profiles of quenched strands for sandwiches. The profiles of concentrations for 17 stable components and of temperature for three cross-sections corresponding to the middle of "base" lamina, and to the interface between the laminae have been determined. The following components have been found in the sandwich flames:  $H_2$ ,  $NH_3$ ,  $H_2O$ ,  $C_2H_2$ ,  $HCN$ ,  $CO$ ,  $N_2$ ,  $NO$ ,  $HCl$ ,  $CO_2$ ,  $N_2O$ ,  $NO_2$ ,  $ClOH$ ,  $O_2$ ,  $C_2H_6$ ,  $ClO_2$ ,  $Cl_2$ ,  $HClO_4$ . Mole fractions and temperature profiles for the cross-sections corresponding to the middle of AP and "base" laminae are shown in Figure 9. The analysis of the obtained data testifies that there are two zones in flame in the cross section corresponding to the middle of AP lamina. The first zone adjoining the burning surface of AP is a narrow (about 0.2 mm) AP flame zone wherein ammonia is oxidized by  $HClO_4$  and  $ClO_2$  to yield  $NO$ ,  $O_2$ , and other substances. In the second wider (about 3 mm) zone  $O_2$  and  $NO$  are consumed. Oxygen and nitric

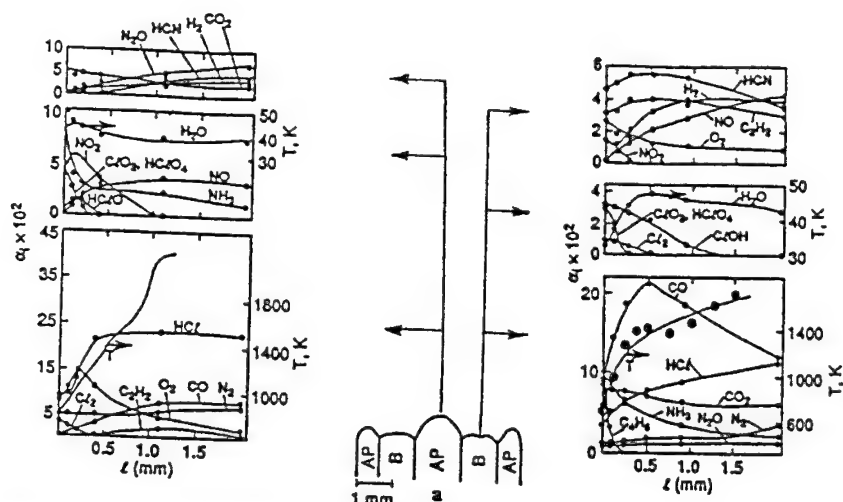


Figure 9. Profiles of temperature and species concentration profiles at sandwich flame probing

oxide are consumed in oxidation reaction of carbon monoxide with  $\text{CO}_2$  and  $\text{N}_2$  formation; HCN,  $\text{C}_2\text{H}_2$  and  $\text{H}_2$  are slowly oxidized. It should be noted that fuel components, i.e. products of "base" destruction, HCN and  $\text{C}_2\text{H}_2$  penetrated right up to the oxidizer surface due to diffusion: there is a concentration gradient of the components, directed to the burning surface. These products can react with AP, that may be an additional source of heat release on the burning surface.

## CONCLUSIONS

The method of flames study by probing mass spectrometry is an important instrument for the study of chemistry of solid propellants combustion and thermal decomposition. It is a good addition to the spectroscopic methods of flames investigation and such methods of the investigation of SP thermal decomposition under the conditions close to those of combustion as SMATCH/FTIR, T-Jump/FTIR. These types of experiments will lead to a better basic understanding of solid propellants combustion, which in its turn facilitates propellants formulation and the prediction of propellants ballistic behavior.

## REFERENCES

1. Edwards, T., 1988. "Solid Propellant Flame Spectroscopy". Report. AFAL-TR-88-076, Edwards AFB, CA, pp. 219.
2. Korobeinichev, O.P., 1988. "Dynamic Probe Mass Spectrometry of Flames and the Decomposition of Condensed Systems", *Combustion, Explosion and Shock Waves*, Vol. 23, pp. 565-576.
3. Korobeinichev, O.P., 1993. "A Study of Condensed System Flame Structure", *Pure & Appl. Chem.*, Vol. 65, pp. 269-276.
4. Korobeinichev, O.P., Kuibida, L.V., Paletsky, A.A., Chernov, A.A., 1996. "Study of Solid Propellant Flame Structure By Mass-Spectrometric Sampling", *Combustion Science and Technology* (in press).
5. Litzinger, T.A., Lee, Y.J., Tang, C.J., 1994. "A Study of Solid Propellant Combustion Using a Triple Quadrupole Mass Spectrometer with Microprobe Sampling", in *Proceedings Workshop on*

- Application of Free-Jet, Molecular Beam, Mass Spectrometric Sampling*, Estes Park, Colorado, October 11-14, pp.128-135.
6. **Fetherolf, B.L., Litzinger, T.A.**, 1992. "Physical and Chemical Processes Governing the CO<sub>2</sub> Laser-Induced Deflagration of Ammonium Dinitramide (ADN)". *Proceeding of the 29th JANNAF Combustion Meeting*, pp. 329-338.
  7. **Vanderhoff, J.A., Teague, M.W., Kotlar, A.J.**, 1992. "Absorption Spectroscopy Through the Dark Zone of Solid Propellant Flame.", *Ballistic Research Laboratory Report BRL-TR-3334*, pg. 41.
  8. **Parr, P., Hanson-Parr, D.**, 1994. "Solid Propellant Flame Chemistry and Structure." in *Non-Intrusive Combustion Diagnostics*, edited by Kenneth K.Kuo; associate editor Timothy P.Parr, Begell House Publishing Co. and CRC Press, pp.517-599.
  9. **Stufflebeam, J.H., and Eckbreth, A.C.**, 1989. "CARS Diagnostics of Solid Propellant Combustion at Elevated Pressure", *Combustion Science and Technology*, Vol.66, pp.163-179.
  10. **Zenin, A.A.**, 1966. "The Temperature Distribution Structure in the Steady Burning of Double-Base Propellants", *Fizika Gorenia i Vzriva*, Vol.2, No.3, pp.67-76[in Russian].
  11. **Korobeinichev, O.P., Tereshchenko, A.G.**, 1976. "Mass Spectrometric Study of Distribution of Concentrations In Combustion Zones of Condensed Systems." *Dokl. Akad. Nauk USSR*, vol.231, No.5, pp.1159-1161.[in Russian].
  12. **Brill, T.B., Brush, P.J., Patil D.G.**, 1993. "Thermal Decomposition of Energetics Materials 58. Chemistry of Ammonium Nitrate and Ammonium Dinitramide Near the Burning Surface Temperature", *Combustion and Flame*, Vol.92, pp.178-186.
  13. **Korobeinichev, O.P., Anisiforov, G.I.**, 1974. "Mass Spectrometric Thermal Analysis Using the Time-of-Flight Mass Spectrometer", *Izv. Sib. Otd. Akad. Nauk USSR, Ser. Khim. Nauk*, Vol.4, pp.38-41 [in Russian].
  14. **Korobeinichev, O.P., Paletsky, A.A., Kuibida, L.V., Bolshova, T.A. and Fristrom, R.M.**, 1996. "Study of the Structure of A Ten Atmosphere H<sub>2</sub>/O<sub>2</sub>/Ar Flame Using Molecular Beam Inlet Mass Spectrometric Probing", *Fizika Gorenia i Vzriva*, Vol.32(3)[in press] [in Russian].
  15. **Korobeinichev, O.P., Kuibida, L.V., Orlov, V.N., Tereshchenko, A.G., Kytsenogii, K.P., Mavliev, R.A., Ermolin, N.E., Fomin, V.M., Emel'yanov, I.D.**, 1985. "Mass Spectrometric Probe Study of the Flame Structure and Kinetics of Chemical Reactions in Flame.", in: *Mass-spectrum. Khim. Kinet.*, editor Tal'roze, V.L., Nauka, Moscow, pp.73-93[in Russian].
  16. **Ermolin, N.E., Korobeinichev, O.P., Kuibida, L.V., Fomin, V.M.**, 1985. "Processes in Hexogene Flames.", *Comb., Expl. and Shock Waves*, Vol.24, pp.400-406.
  17. **Melius, G.F.**, 1988. "The Gas-Phase Flame Chemistry of Nitamine Combustion", *25th JANNAF Combust. Mtg.*, Vol.2, pp.155-162.
  18. **Pak, Z.**, 1993. "Some Ways to Higher Environmental Safety of Solid Rockets Propellant Application", *AIAA Paper*, pp.93-1755.
  19. **Korobeinichev, O.P., Kuibida, L.V., Paletsky, A.A., Shmakov, A.G.**, 1996. "Combustion Chemistry of Energetic Materials Studied by Probing Mass Spectrometry", in *Decomposition, Combustion and Detonation Chemistry of Energetic Materials, Proceeding MRS Symposium*, editors: Brill T.B., Russell T.P., Tao W.C., Wardle R.B., Vol.418.
  20. **Luk'yanov, A.O., Gorelik, V.D., Tartakovsky, V.A.**, 1994. "Dinitramide and its Salts", *Izv. Akad. Nauk, Ser. Khim.*, Vol.1, pp.94-97[in Russian].
  21. **Price, E.W.**, 1995. "Effect of Multidimensional Flamelets in Composite Propellant Combustion.", *Journal of Propulsion and Power*, Vol.11, pp. 717-728.
  22. **Korobeinichev, O.P., Tereshchenko, A.G., Shvartsberg, V.M., Chernov, A.A., Zabolotny, A.E., Makhov, G.A.**, 1991. "A Study of Flame Structure of Sandwich Systems Based on Ammonium Perchlorate, HMX, and Polybutadiene Binder" in *Flame Structure*, editor Korobeinichev O.P., Vol.2, pp.262-267.
  23. **Korobeinichev, O.P., Tereshchenko, A.G.**, 1976. "Mass Spectrometric Study of Distribution of Concentrations in Combustion Zones of Condensed Systems.", *Dokl. Akad. Nauk USSR*, Vol.231, No.5, pp.1159-1161[in Russian].

## THEORETICAL STUDY OF HONO REACTIONS WITH H, OH, NO AND NH<sub>2</sub> RADICALS

C.-C. Hsu, J. W. Boughton, A.M. Mebel and M.C. Lin  
Department of Chemistry, Emory University, Atlanta, GA 30322, USA

**ABSTRACT.** Four HONO reactions of importance in the combustion of nitramines involving H, OH, NO and NH<sub>2</sub> have been studied by ab initio molecular orbital calculations. The results of these calculations, using the Gaussian-2 and modified Gaussian-2 methods, indicate that all of the reactions except NH<sub>2</sub> + HONO occur by both direct abstraction and indirect metathetical reactions. Take the H + HONO reaction, for example, the direct abstraction process producing H<sub>2</sub> + NO<sub>2</sub> appears to be the least important channel, whereas the attack of the H atom at the N site producing HNO + OH via the excited HN(O)OH intermediate is the dominant channel. The theoretically computed molecular structures, vibrational frequencies and energies for the reactants and transition states were used to calculate rate constants for different product channels of these reactions employing the conventional transition-state theory or the canonical variational transition-state theory (depending on reaction barriers involved) for direct abstraction reactions and using the RRKM theory for complex-forming indirect metathetical processes.

### 1. INTRODUCTION

Nitrous acid (HONO) is a key intermediate in the decomposition reactions of ammonium nitrate (AN), ammonium dinitramide (ADN) and RDX/HMX propellants. Because of its relatively weak H-O bond, with  $D(\text{H-ONO}) = 327.5 \pm 2.1$  kJ/mole,<sup>1</sup> HONO may be an effective radical scavenger for reactive species such as H, OH and NH<sub>2</sub>:

- (1)  $\text{H} + \text{HONO} \rightarrow \text{H}_2 + \text{NO}_2, \text{H}_2\text{O} + \text{NO}, \text{etc.}$
- (2)  $\text{OH} + \text{HONO} \rightarrow \text{H}_2\text{O} + \text{NO}_2$
- (3)  $\text{NH}_2 + \text{HONO} \rightarrow \text{NH}_3 + \text{NO}_2$

These exothermic reactions convert more reactive chain carriers to the comparatively less reactive NO<sub>2</sub> molecule. With few exceptions,<sup>2</sup> the kinetics and mechanisms of most HONO reactions in the gas phase have not been thoroughly and quantitatively investigated. For example, the rate constant for the simplest HONO metathetical reaction (1), has not yet been directly determined and the product of the reaction has been invariably assumed to be H<sub>2</sub> + NO<sub>2</sub> in computer modeling of complex systems. The results of our recent ab initio molecular orbital calculations reveal, however, the presence of other potential product channels, which may occur with smaller reaction barriers.

The objective of this article is to use the recently developed high-level ab initio molecular orbital calculation techniques for elucidation of the mechanisms of these and other related HONO reactions. The rate constants for their low-energy reaction paths will be calculated with various statistical theories and recommended for future applications.

## 2. COMPUTATION METHODS

### 2.1. Ab Initio MO Calculations

The geometries and energies of the reactants, products, intermediates and transition states for all of the systems studied have been calculated with the Gaussian-2 (G2)<sup>3</sup> or the modified Gaussian-2 (or G2M) method.<sup>4</sup> With the former method, developed by Pople and coworkers,<sup>3</sup> geometries were optimized at the UMP2/6-311G(d,p) level of theory and the calculated frequencies and zero-point energy (ZPE) corrections were scaled by 0.95.<sup>3</sup> With the G2M method developed by Mebel et al.,<sup>4</sup> geometries of various species and transition states involved were optimized at the hybrid density functional<sup>5,6</sup> B3LYP/6-311G(d,p) level of theory. The B3LYP vibrational frequencies were calculated for ZPE-corrections and for transition state theory (TST) and Rice-Ramsperger-Kassel-Marcus (RRKM) calculations without scaling.

The energies of various species including TS's were further improved with higher levels of theoretical calculations as described in the G2<sup>3</sup> and G2M<sup>4</sup> schemes. The G2 scheme consists of a series of calculations to approximate the QCISD(T)/6-311+G(3df,2p) energy<sup>3</sup> using U(R) MP2 geometries, whereas the G2M scheme uses a similar series of calculations to approximate the RCCSD(T)/6-311+G(3df,2p) energy<sup>7,8</sup> with B3LYP geometries.<sup>4</sup> Several approximations to the G2M (RCC) scheme can be made for systems as high as six to seven heavy atoms (such as N, C and O). A detailed description of the scheme can be found in Ref. 4. All calculations were carried out with the MOLPRO94<sup>8</sup> and Gaussian 92<sup>9</sup> programs.

Since the reactivity of HONO in its cis-form is invariably greater than its trans-isomer, all the theoretical results presented here correspond to those of cis-HONO. Kinetically, the omission of contributions from trans-HONO is not expected to lead to any error because the cis  $\rightleftharpoons$  trans isomerization through the ON-OH torsional vibration occurs readily above room temperature.

### 2.2. TST and RRKM calculations

According to the general transition state theory, the rate constant for a direct bimolecular metathetical reaction or reactions of any order occurring under high-pressure conditions can be calculated with the equation:<sup>10,11</sup>

$$k(T) = l_a \frac{k_B T}{h} e^{-\Delta G^\ddagger / RT} \quad (1)$$

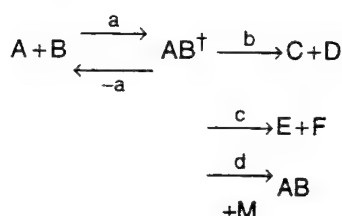
where  $l_a$  is the reaction path degeneracy,  $k_B$  is the Boltzmann constant,  $h$  is the Planck constant and  $\Delta G^\ddagger$  is the Gibbs free energy of activation at the transition state.

For a reaction with a well-defined TS, the location of  $\Delta G^\ddagger$  on its potential energy surface coincides with the col of the energy barrier. Equation (1) can be readily calculated with

the conventional TST using a computed energy barrier ( $E_0 = \Delta H^\ddagger$ ) and molecular parameters (moments of inertia and vibrational frequencies).<sup>10,11</sup>

For a reaction with a poorly defined TS, because of a negligibly small reaction barrier such as  $\text{NH}_2 + \text{NO}_x$  and  $\text{OH} + \text{HONO}$ , the location of  $\Delta G^\ddagger = \Delta H^\ddagger - T\Delta S^\ddagger$  varies with temperature. It should be searched and calculated variationally along the reaction path so as to compute  $k(T)$  by eq. (1). This approach has been referred to as canonical variational TST (cVTST).<sup>10,11</sup>

Both situations described above occur in the reactions of interest in the present study. For a reaction taking place via one or more long-lived intermediates, such as



multichannel RRKM calculations should be carried out for the formation of various products and the disappearance of the reactant A or B. In the above scheme,  $\text{AB}^\ddagger$  represents the vibrationally excited AB intermediate. Reactions of this type have been routinely encountered in combustion systems. The theory gives good results, provided that the transition states for the association step (a) and decomposition steps (b) and (c) are well-defined and that their energies and molecular parameters are reliably calculated by ab initio MO methods. If any of the above reaction steps has a poorly defined TS, the canonical variational approach mentioned above can be applied.<sup>12,13</sup> Recently, the alternative, mathematically more rigorous, microcanonical approach<sup>14-16</sup> has been extended by Diau and Smith<sup>17</sup> to treat a multichannel system containing two long-lived intermediates.

For the typical reaction scheme given above, the steady-state treatment for  $\text{AB}^\ddagger$  gives rise to:<sup>18</sup>

$$k_i(T) = I_a \frac{k_B T}{h} \frac{Q_i^\ddagger Q_r^\ddagger}{Q_A Q_B} e^{-E_a/RT} \int_0^\infty \frac{k_{E_i} \Sigma P_a(E_a^\ddagger) e^{-E_a^\ddagger/RT}}{\Sigma_i k_{E_i} + \omega} \frac{dE_a^\ddagger}{RT} \quad (2)$$

$$k_d(T) = I_a \frac{k_B T}{h} \frac{Q_i^\ddagger Q_r^\ddagger}{Q_A Q_B} e^{-E_a/RT} \int_0^\infty \frac{\omega \Sigma P_a(E_a^\ddagger) e^{-E_a^\ddagger/RT}}{\Sigma_i k_{E_i} + \omega} \frac{dE_a^\ddagger}{RT} \quad (3)$$

where  $i = -a, b$ , and  $c$  and  $I_a$  is the reaction path degeneracy for the formation of  $\text{AB}^\ddagger$  via step (a).  $Q_A$  and  $Q_B$  are the total partition functions of A and B, respectively.  $Q_i^\ddagger$  and  $Q_r^\ddagger$  are the translational and rotational partition functions, respectively, of the transition state  $\text{AB}^\ddagger$  for step (a), which has a zero-point energy (ZPE) corrected energy barrier  $E_a$  at 0 K. In the integral,  $\omega$  is the effective collision frequency for the deactivation of  $\text{AB}^\ddagger$  by step (d), and

$$k_{E_i} = C_i \Sigma P(E_i^\ddagger) / h N(E) \quad (4)$$



is the specific rate constant for the decomposition of  $AB^\ddagger$  by steps (-a), (b) and (c). In eq. (4),  $C_i$  is the product of statistical factor  $l_i$  and the ratio of the overall rotational partition functions of the transition state for step (i) and the AB intermediate.  $\Sigma P_i(E_i^\ddagger)$  is the sum of states of transition state for step (i) and  $N(E)$  is the density state of AB having a total energy  $E$ .

The applications of these equations to the systems involving long-lived intermediates as revealed by ab initio MO calculations will be illustrated later.

### 3. RESULTS AND DISCUSSION

Four bimolecular reactions of HONO involving H, OH, NO and  $NH_2$  have been studied by ab initio MO and statistical-theory calculations. The majority of these reactions, except  $OH + HONO$ , have not been measured experimentally, despite their apparent practical importance to the  $NH_3$  - de $NO_x$  and propulsion processes. The results of our calculations are summarized below.

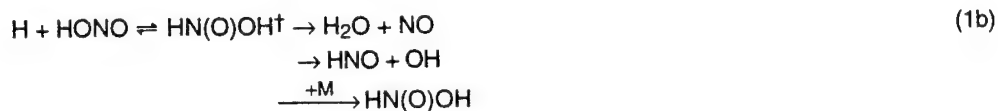
#### 3.1. $H + HONO \rightarrow$ products:

The potential energy of the  $H + HONO$  system obtained by the G2 method<sup>3</sup> is presented in Fig. 1. The reaction appears to be far more complicated than has been commonly assumed to occur solely by direct abstraction:



The reaction has a barrier as high as 30 kJ/mole, in close agreement with 34 kJ/mole calculated by Melius using the BAC-MP4 method.<sup>19</sup>

The lowest energy path was found to occur via H-addition to the N atom of HONO (TS2) producing the excited  $HN(O)OH$  intermediate with 140 kJ/mole of internal energy. The excited  $HN(O)OH$  can undergo either  $H_2O$  elimination via TS5 with 96 kJ/mole of reaction barrier or OH elimination producing HNO via TS6, which has no reverse barrier and is, therefore, poorly defined. For the formation of  $HNO + OH$ , we must employ the variational TST method to calculate  $\Delta G$  along the reaction coordinate leading to products. At a specific temperature, the location at which the maximum Gibbs free energy ( $\Delta G^\ddagger$ ) appears, corresponds to TS6. Using Eq. (1), one can obtain the first-order rate constant for  $HN(O)OH \rightarrow HNO + OH$ . Because of the presence of the long-lived  $HN(O)OH$  adduct, RRKM calculations were carried out with the multichannel mechanism:



which is essentially the same as the general scheme presented above for  $A + B$ .

A similar calculation was made for the third  $H + HONO$  reaction path, which occurs by H-addition to the terminal O atom via TS5, producing another long-lived intermediate  $HONOH$ , dihydroxyl amino radical. The addition process has a barrier of 42 kJ/mole, also

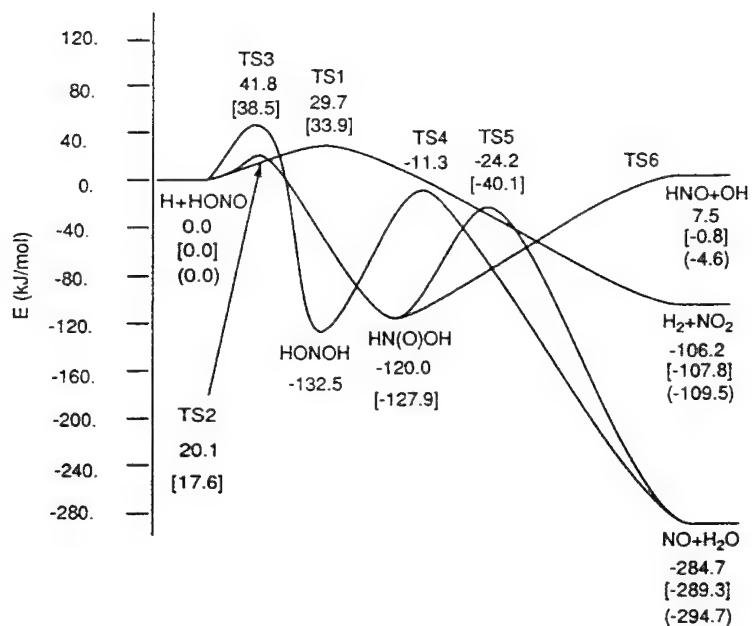


Fig. 1. Energy diagram for the H + HONO reaction. The energies were computed by G2/B3LYP/6-311G(d,p); those given in brackets are BAC-MP4 results<sup>19</sup> and those in parentheses are JANAF values.<sup>20</sup>

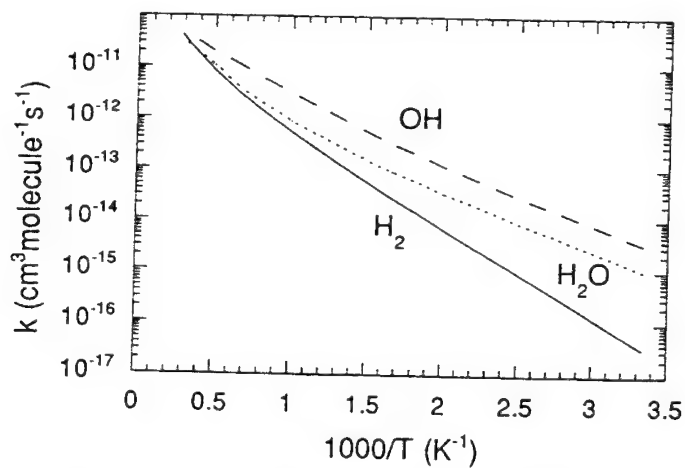


Fig. 2 Arrhenius plots for the formation of various products in the H + HONO reaction.

agreeing closely with the BAC-MP4 value of 39 kJ/mole by Melius.<sup>19</sup> The excited N(OH)<sub>2</sub> radical can readily eliminate H<sub>2</sub>O via a 4-centered TS<sub>4</sub>, which is calculated to be 121 kJ/mole above N(OH)<sub>2</sub>. The RRKM calculation, based on the mechanism:



using eqs. (2)-(4) with one less product channel gives the rate constants for H<sub>2</sub>O + NO formation and for the production of the association product, N(OH)<sub>2</sub>. Under combustion conditions, the formation of stabilized N(OH)<sub>2</sub> and HN(O)OH is relatively unimportant.

The above calculations by the conventional TST for (1a) and by RRKM theory for (1b) and (1c) give the following rate constant expressions for production of H<sub>2</sub> + NO<sub>2</sub>, H<sub>2</sub>O + NO and HNO + OH, respectively:

$$k_{\text{H}_2} = 3.3 \times 10^{-16} T^{1.55} e^{-3329/T}$$

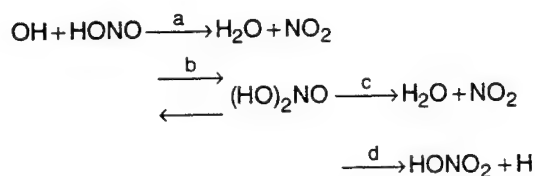
$$k_{\text{H}_2\text{O}} = 1.4 \times 10^{-17} T^{1.89} e^{-1936/T}$$

$$k_{\text{OH}} = 9.4 \times 10^{-14} T^{0.86} e^{-2500/T}$$

in units of cm<sup>3</sup>/molecule·s for 300-3000 K. The rate constant for H<sub>2</sub>O + NO production includes those from channels (1b) and (1c). As shown in Fig. 2, the direct abstraction reaction (1a) is the least important channel, whereas the H-for-OH indirect displacement process dominates the reaction throughout the temperature range calculated. This is a very interesting and unexpected result, indeed.

### 3.2. OH + HONO → H<sub>2</sub>O + NO<sub>2</sub>:

Similar to the H + HONO reaction discussed above, our ab initio MO calculations for the OH - HONO system reveal the presence of an indirect metathetical channel (b) which, however, has a much higher reaction barrier than the direct abstraction process (a), as shown below:



The corresponding energy diagram is shown in Fig. 3.

The conventional TST calculations for (a) and (d) as well as the RRKM calculations for (b), (c), (c) via (b) and (d) via (b), give the following rate constants:

$$k_a = 5.10 \times 10^{-20} T^{2.39} e^{+22.97/T} \text{ cm}^3/\text{molecule}\cdot\text{s (tentative),}$$

$$k_b = 2.21 \times 10^7 T^{-6.49} e^{-6170/T} \text{ cm}^3/\text{molecule}\cdot\text{s}$$

$$k_c = 1.25 \times 10^{19} T^{-2.96} e^{-7842/T} \text{ 1/s}$$

$$k_d = 5.0 \times 10^{10} T^{0.683} e^{-20751/T} \text{ 1/s}$$

$$k_{b-c} = 5.03 \times 10^{-20} T^{2.18} e^{-6653/T} \text{ cm}^3/\text{molecule}\cdot\text{s}$$

$$k_{b-d} = 9.37 \times 10^{-28} T^{4.09} e^{-15138/T} \text{ cm}^3/\text{molecule}\cdot\text{s}$$

For channel (a), the G2M energy optimized at RCCSD(T)/6-311G(d,p)//UMP2-6-311G(d,p) has a distinct barrier of 4.0 kJ/mole, which together with the generally tighter MP2 structure, led to a smaller rate constant than observed experimentally.<sup>2</sup>

On the other hand, the B2LYP/6-311G(d,p) optimized structure and energy shows no saddle point. In order to obtain a more reliable potential energy surface, calculations are underway with a higher level of theory such as the QCISD(T) method.

### 3.3. $\text{NO} + \text{HONO} \rightarrow \text{HNO} + \text{NO}_2$ :

The four species involved in this reaction are known to coexist in most H/N/O-systems. The reverse of this process,  $\text{HNO} + \text{NO}_2 \rightarrow \text{NO} + \text{HONO}$ , may be an important sink for  $\text{NO}_2$  which is more reactive than HONO during the initial phase of nitramine combustion reactions. The rate constant for either forward or reverse direction has not been experimentally measured.

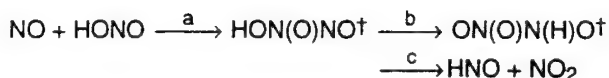
The result of our calculation with the G2M method<sup>4</sup> gives a reaction barrier of 153.5 kJ/mole and endothermicity of 131.3 kJ/mole, which is in reasonable agreement with the JANAF value, 119.2 kJ/mole.<sup>20</sup> The largest error in the JANAF value may arise from the heat of formation of HNO, which has an expected error of  $\pm 8$  kJ/mole.

A TST calculation with eq. (1) using the computed energies for the reactants ( $\text{NO} + \text{cis-HONO}$ ) and the transition state gives

$$k_3 = 1.0 \times 10^{-26} T^{4.41} e^{-16,020/T} \text{ cm}^3/\text{molecule}\cdot\text{s}$$

for the temperature range of 300-3000 K.

An alternative reaction path involving the formation of the association complex:



has to overcome a large barrier (190 kJ/mole) for the H-migration step (b). Therefore, it is insignificant to the overall reaction.

### 3.4. $\text{NH}_2 + \text{HONO} \rightarrow \text{NH}_3 + \text{NO}_2$ :

To our knowledge, there is no rate constant measurement for this exothermic reaction, which is expected to be a key  $\text{NH}_2$  removal process in the AN and ADN systems. Because of the high number of heavy atoms involved in the reaction, the energies of the reactants, TS and products were computed with the G1,<sup>21</sup> instead of the G2 scheme<sup>3</sup> using either the UMP2/6-311G(d,p) or B3LYP/6-311G(d,p) level of theory for structural optimization and frequency calculations.<sup>22</sup> The former gave rise to a significantly tighter TS structure which led to a much smaller rate constant. From the calculated energies and molecular structures with the two methods using eq. (1), we obtained:

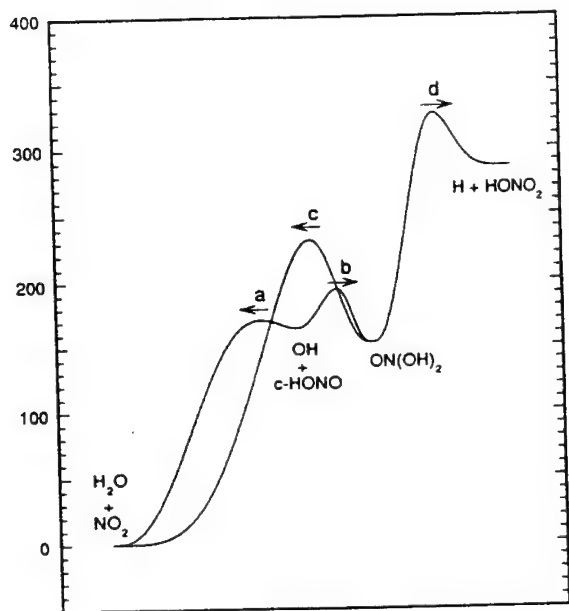


Fig. 3. Zero-point energy diagram for the OH + HONO reaction system.

$$k_4 (\text{UMP2}) = 3.5 \times 10^{-23} T^{2.93} e^{+2600/T} \text{ cm}^3/\text{molecule}\cdot\text{s}$$

$$k_4 (\text{B3LYP}) = 1.2 \times 10^{-22} T^{3.02} e^{+2487/T} \text{ cm}^3/\text{molecule}\cdot\text{s}$$

for the temperature range of 300-3000 K. The latter expression was found to be in closer agreement with the kinetically modeled rate constant for the  $\text{NH}_3 + \text{NO}_2 \rightarrow \text{NH}_2 + \text{HONO}$  reaction.<sup>23</sup>

#### ACKNOWLEDGMENTS

The authors gratefully acknowledge the support of this work by the Office of Naval Research (contract no. N00014-89-J-1949) under the direction of Dr. R. S. Miller. We thank the Cherry L. Emerson Center for Scientific Computation for the use of computing facilities and various programs.

#### References

1. Kerr, J. A., 1988. Strengths of Chemical Bonds, in *Handbook of Chemistry and Physics*, CRC Press, Inc., pp. F174-F189.
2. Tsang, W. and Herron, J. T., Chemical Kinetic Data Base for Propellant Combustion I. Reactions Involving NO, NO<sub>2</sub>, HNO, HNO<sub>2</sub>, HCN and N<sub>2</sub>O, *Journal of Physical Chemistry Reference Data*, 20, 609-663, 1991.

3. **Curtiss, L. A., Raghavachari, K., Trucks, G. W. et al.**, Gaussian-2 theory for molecular energies of first- and second-row compounds, *Journal of Chemical Physics*, 94, 7221-7230, 1991.
4. **Mebel, A. M., Morokuma, K. and Lin, M. C.**, Modification of GAUSSIAN-2 Theoretical Model: The Use of Coupled-Cluster Energies, Density-Functional Geometries, and Frequencies, *Journal of Chemical Physics*, 103, 7414-7421, 1995.
5. **Becke, A. D.**, Density-Functional Thermochemistry. III. The Role of Exact Exchange, *Journal of Chemical Physics*, 98, 5648-5652, 1993.
6. **Lee, C., Yang, W. and Parr, R.G.**, Development of the Colle-Salvetti Correlation-Energy Formula into a Functional of the Electron Density, *Physical Review*, B37, 785-789, 1988.
7. **Purvis, G. D. and Bartlett, R. J.**, A Full-Coupled Cluster Singles and Doubles Model: The Inclusion of Disconnected Triples, *Journal of Chemical Physics*, 76, 1910-1918, 1992.
8. **Hampel, C., Peterson, K. A. and Werner, H.-J.**, A Comparison of the Efficiency and Accuracy of the Quadratic Configuration Interaction (QCISD), Coupled Cluster (CCSD), and Brueckner Coupled Cluster (BCCD) Methods, *Chemical Physics Letters*, 190, 1-12, 1992.
9. **Frisch, M. J., Trucks, G. W., Head-Gordon, M. et al.**, GAUSSIAN 92/DFT (Gaussian, Inc., Pittsburgh, PA, 1993).
10. **Laidler, K. J.**, 1987, *Chemical Kinetics*, 3rd ed., p. 124, Harper and Row, NY.
11. **Truhlar, D.G., and Garrett, B.C.**, Variational Transition State Theory, *Annual Review of Physical Chemistry*, 35, pp. 159-189, 1984.
12. **Hsu, C.-C.**, Theoretical Studies of Reactions of Molecular Oxygen with Formyl and Methyl Radicals, M.S. thesis, Emory University, March 1996.
13. **Hsu, C.-C., Mebel, A. M. and Lin, M. C.**, 1996. *Ab Initio* Molecular Orbital Study of the  $\text{HCO} + \text{O}_2$  Reaction: Direct vs. Indirect Abstraction Channels, *Journal of Chemical Physics*, in press.
14. **Wardlaw, D. M. and Marcus, R. A.**, Unimolecular Reaction Rate Theory for Transition States of Partial Looseness. II. Implementation and Analysis with Applications to  $\text{NO}_2$  and  $\text{C}_2\text{H}_6$  Dissociations, *Journal of Chemical Physics*, 83, 3462-3480, 1985.
15. **Klippenstein, S. J. and Marcus, R. A.**, Application of Unimolecular Reaction Rate Theory for Highly Flexible Transition States to the Dissociation of  $\text{CH}_2\text{CO}$  into  $\text{CH}_2$  and  $\text{CO}$ , *Journal of Chemical Physics*, 91, pp. 2280-2292, 1989.
16. **Smith, S. C.**, Microscopic Rate Coefficients in Reactions with Flexible Transition States: Analysis of the Transitional-Mode Sum of States, *Journal of Chemical Physics*, 95, pp. 3404-3430, 1991.
17. **Diau, E. W. G. and Smith, S. C.**, 1996. Temperature Dependence of Rate Coefficients and Branching Ratios for the  $\text{NH}_2 + \text{NO}$  Reaction via Microcanonical Variation Transition State Theory, *Journal of Physical Chemistry*, submitted.
18. **Berman, M. R. and Lin, M. C.**, Kinetics and Mechanisms of the  $\text{CH} + \text{N}_2$  Reaction. Temperature- and Pressure-Dependence Studies and Transition-State-Theory Analysis, *Journal of Physical Chemistry*, Vol 87, pp. 3933-3942, 1983.
19. **Melius, C. F.**, 1993. *BAC-MP4 Heats of Formation and Free Energies*, Sandia National Laboratories, Livermore, CA.

20. Chase, M.W., Jr., Davies, C. A., Downey, J. R. et al., *JANAF Thermochemical Tables*, Journal of Physical Chemistry Reference Data, 14, Suppl. No. 1, pp. 1-1856, 1985.
21. Pople, J. A., Head-Gordon, M., Fox, D. J. et al., Gaussian-1 Theory: A General Procedure for Prediction of Molecular Energies, *Journal of Chemical Physics*, 90, pp. 5622-5629, 1989.
22. Mebel, A. M., Diau, E. W. G., Lin, M. C. et al., 1996. Theoretical Rate Constants for the  $\text{NH}_3 + \text{NO}_x \rightleftharpoons \text{NH}_2 + \text{HNO}_x$  ( $x=1,2$ ) Reactions by ab Initio MO/VTST calculations, *Journal of Physical Chemistry*, in press.
23. Thaxton, A. G. and Lin, M.C., 1996. Rate Constant for the  $\text{NH}_3 + \text{NO}_2 \rightarrow \text{NH}_2 + \text{HONO}$  Reaction: Comparison of Kinetically Modeled and Theoretically Predicted Results, *International Journal of Chemical Kinetics*, in preparation.

## Gas-Phase Reaction Mechanisms for Nitramine Combustion: On the Development of a Comprehensive Reaction Mechanism for Hydrogen/Nitrous Oxide Kinetics

Richard A. Yetter,<sup>1</sup> Mark T. Allen,<sup>2</sup> and Frederick L. Dryer<sup>1</sup>

<sup>1</sup>Princeton University, Princeton, NJ;

<sup>2</sup>SciTec, Inc., Princeton, NJ

**ABSTRACT:** As part of a research effort to develop comprehensive gas-phase reaction mechanisms for nitramine combustion, the present paper reports on recent sub-model development of  $H_2/N_2O$  kinetics. A single reaction mechanism, based on literature thermochemical and kinetic data and developed from intermediate temperature flow reactor studies, is tested against previous high temperature shock tube data, low temperature static bulb reactor data, and laminar premixed flame speed data. Model predictions are found to be in good agreement with the shock tube and flow reactor data, but too fast when compared against the bulb data. In addition, predicted flame speeds are found to be ~ 15% lower than those measured experimentally. The present results further indicate the importance of the branching channels of the  $H + N_2O$  reaction over the entire temperature range as well as secondary reactions involving  $NH$ , and suggest that, at high temperatures, the rate constant for the direct reaction of  $CO + N_2O$  is lower than predicted from extrapolation of previous evaluations.

### INTRODUCTION

The assembly and validation of comprehensive gas-phase kinetic mechanisms with nitrous oxide as the oxidizer are important sub-model components for understanding the fundamental chemical processes occurring during combustion of nitramine propellants and explosives and for developing engineering models. The resulting mechanisms provide useful tools in determining what elementary reactions require improved definition, in acting as benchmarks against which lumped chemistry models can be developed and tested, and in evaluating the interactions of chemistry and transport phenomena in simple one-dimensional systems. Moreover, comprehensive mechanisms, evaluated and validated over large ranges in pressure, temperature, and equivalence ratio are required for simulating more practical combustion environments where gas phase chemistry is intimately coupled with chemical processes occurring at the material surface.

The mechanism for the hydrogen - nitrous oxide reaction is an integral part of all energetic polycyclic nitramine decomposition mechanisms, just as its analog, the  $H_2/O_2$  system is for all hydrocarbon oxidation mechanisms. Unlike the highly chain-branched  $H_2/O_2$  system, the  $H_2/N_2O$  system is dominated by straight chain kinetics. Furthermore,  $H_2/N_2O$  kinetics do not form the  $HO_2$  radical. However,  $NH$  radicals can be formed, which significantly increase the complexity of the  $N_2O$  system.

The kinetics of hydrogen - nitrous oxide mixtures have been studied extensively over the last forty years. These studies have included homogeneous kinetic studies at high temperatures<sup>1-8</sup> and at low



temperatures<sup>9,10</sup> and studies with coupled chemistry and transport.<sup>11-23</sup> From these studies, most of the important elementary reactions are reasonably well known over an extended temperature range. However, past modeling studies have generally focused on a particular temperature regime and consequently a single reaction mechanism has never been tested against the widest range of available experimental data. Moreover, the collection of reactions and rates used to describe a mechanism has differed significantly from investigator to investigator. In the present paper, a single reaction mechanism for  $H_2/N_2O$  kinetics, based on literature thermochemical and kinetics parameters, is tested against experimental data covering the temperature range of 813 - 3075 K and pressure range from 0.56 - 3 atm.

### MECHANISM DEVELOPMENT AND VALIDATION

In the present work, reaction mechanisms are developed systematically,<sup>24,25</sup> beginning with the simplest species and reactions which are common sub-elements in the combustion of more complex species, and sequentially constructed by incorporating new species and reactions in order of increasing complexity. At each level, the newly added portions of the mechanism are tested and validated by thorough comparison between numerically predicted and experimentally observed results. Identification of the important features and rate controlling processes is achieved through application of sensitivity analysis and reaction flux techniques.

The validation at each level of development of a reaction mechanism requires experimental data from several sources such as shock tubes, flow reactors, and static reactors because different elementary reactions can be dominant under different experimental conditions. For example, some reactions are negligible except under high temperature shock tube conditions, while others become unimportant for temperatures above 1000 K. Validation of coupled gas-phase heat release rates and gas-phase transport is required to complete the development and validation of a comprehensive gas-phase thermochemical, kinetics and transport model. Data from premixed flames are necessary to validate heat release rates and flame speed predictions. Data from diffusion flames are necessary to validate transport and extinction phenomena, in addition to gas-phase kinetics and heat release rates. The entire procedure is hierarchical and illustrated in Figure 1.

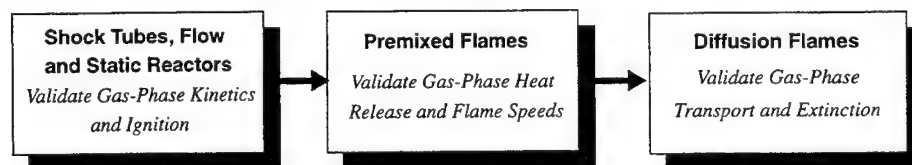


Figure 1. Hierarchical development and validation of gas-phase submodels.

### REACTION MECHANISM

The reaction mechanism is based on recent literature review and from flow reactor studies by Allen<sup>26</sup> and Allen et al.<sup>10,27</sup> This mechanism consists of sub-mechanism development from separate studies on  $H_2/O_2$  kinetics,<sup>28,29</sup>  $CO/H_2/O_2$  kinetics,<sup>30,31</sup> and  $N_2O$  decomposition.<sup>32</sup> A listing of the reaction mechanism and the literature sources for the thermochemical and kinetic parameters can be found in Allen et al.<sup>27</sup> The only modifications made to the mechanism in the present study relative to that of Allen et al.<sup>27</sup> are the efficiency factors for various collision partners of the  $N_2O$  thermal decomposition reaction and the rate constant for the reaction between  $CO$  and  $OH$ . In the work of Allen et al.,<sup>27</sup> a revised rate constant for the reaction between  $H + NO + M \rightarrow HNO + M$  at intermediate temperatures is reported, and thus, the present work also serves to further investigate this evaluation at low and high temperatures. Carbon monoxide and  $CO_2$  have been included in  $H_2/N_2O$  mixtures of several

earlier studies to enable in-situ diagnostics (via the flame band signal and CO<sub>2</sub> emission), to perturb the kinetic system, and to change the thermophysical properties of the mixture.

Efficiency factors for collision partners in the thermal decomposition of N<sub>2</sub>O have been reported in the literature; the results from some of these studies are given in Table 1.

TABLE 1. Efficiency Factors for N<sub>2</sub>O(+M) ⇌ N<sub>2</sub>+O(+M)

Ref	Ar	He	N <sub>2</sub>	H <sub>2</sub> O	CO <sub>2</sub>	N <sub>2</sub> O	O <sub>2</sub>	CO	NO
33	1		1.5		5-6				
34	1		1.7	12	3		1.4		
1,23	1					10			
35	1	3.3	1.25	7.5	6.6	5	1.15		
36	1	4.2	1.74		4	6.9	1.3	3	3
36	1	.7-1.2	1.2	2.9	2.4	2	1-1.2		
this work	1	1.6	1.6	12	3	3	1.6	1.6	1.6

The values used in the present work are listed at the bottom of the table. As discussed by Yetter et al.,<sup>30</sup> the rate constant reported for CO + OH in Allen et al.<sup>27</sup> is not sufficient for temperatures greater than 2000 K. Since many of the experiments modeled here are for T > 2000 K, the alternative expression from Baulch<sup>37</sup> ( $k_{\text{CO+OH}} = 6.75 \times 10^{10} \exp[0.000907 \times T] \text{ mol}^{-1} \text{ cm}^3 \text{ s}^{-1}$ ) was used here in the form of a double exponential. Neither of these modifications affect the results of Allen et al.<sup>10,27</sup> and Allen<sup>26</sup> where studies were conducted at intermediate temperatures and the mixtures were highly diluted with N<sub>2</sub>.

## RESULTS

### High Temperature Homogeneous Kinetics

A number of high temperature shock tube experiments, both incident and reflected wave, have been performed on H<sub>2</sub>/N<sub>2</sub>O mixtures.<sup>1-8</sup> These experiments have varied from studies on specific reaction rate constants, in which the H<sub>2</sub>/N<sub>2</sub>O reaction was used as a source of O-atoms, to studies that characterize mechanistic behavior of the system. The works considered here include those of Pamidmukkala and Skinner,<sup>6</sup> Borisov et al.,<sup>5</sup> Hidaka et al.,<sup>8</sup> Dean,<sup>3</sup> and Dean et al.<sup>4</sup> Recently, Anderson et al.<sup>38</sup> have modelled the shock tube studies of Henrici and Bauer<sup>1</sup> and Hidaka et al.<sup>8</sup> using a reaction mechanism in general agreement with the present mechanism, and their findings are discussed in the next section. We have chosen to include the work of Dean et al.<sup>4</sup> on H<sub>2</sub>/N<sub>2</sub>O/CO/Ar mixtures in the present study because of the strong coupling between H<sub>2</sub> and moist CO kinetic systems and because of our prior extensive model development and validation of H<sub>2</sub>/O<sub>2</sub> and CO/H<sub>2</sub>O/O<sub>2</sub> kinetic systems.

The study of Pamidmukkala and Skinner<sup>6</sup> report resonance absorption spectroscopy measurements of O-atom concentrations behind reflected shock waves over the temperature range of 1919-2781 K. Highly dilute and fuel-rich conditions for two mixture compositions were chosen to isolate a few reactions from which the rate constant of H<sub>2</sub> + O → OH + H was measured.

Oxygen atom concentrations from two of these experiments are shown in Figure 2 for a mixture consisting of 100 ppm H<sub>2</sub>, 20 ppm N<sub>2</sub>O, with the balance Ar. Part (a) of the figure is for a shock temperature/pressure of 2249 K / 1.28 atm and part (b) is for a shock temperature/pressure of 2419 K / 1.48 atm. The symbols are the experimental data and the lines the corresponding model predictions. Primary sensitivity to all conditions studied was to the reaction rate constants of N<sub>2</sub>O + Ar → N<sub>2</sub> + O + Ar and H<sub>2</sub> + O → OH + H, which are directly responsible for the formation and removal of O-atoms

during the first 300  $\mu$ s. At longer extents of reaction, the rate coefficients for  $\text{H} + \text{O}_2 \rightleftharpoons \text{OH} + \text{O}$  and the reverse of  $\text{H}_2 + \text{O} \rightleftharpoons \text{OH} + \text{H}$  become important.

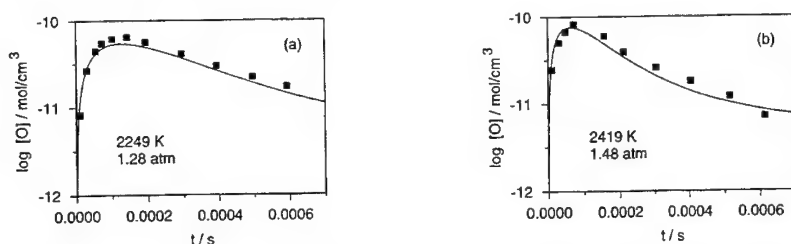


Figure 2. Comparison of O-atom concentrations from reflected shock tube experiments;<sup>6</sup> Initial mixture composition,  $X(\text{H}_2) = 100 \text{ ppm}$ ,  $X(\text{N}_2\text{O}) = 20 \text{ ppm}$ , balance Ar. (a)  $T = 2249 \text{ K}$ ,  $P = 1.28 \text{ atm}$ , (b)  $T = 2419 \text{ K}$ ,  $P = 1.48 \text{ atm}$ .

Borisov et al.<sup>5</sup> report ignition delay times of  $\text{H}_2/\text{N}_2\text{O}$  mixtures behind reflected shock waves over the temperature range of 1200 - 2000 K and reflected wave pressures,  $P_5$ , of 1 - 12 atm. The measurements reported were scaled to  $P_5 = 1 \text{ atm}$  using a linear dependence. The ignition delays were determined from absorption of  $\text{N}_2\text{O}$  at 2537 Å and emission in the visible region as the time from the moment of passage of the impact wave into the observation zone to the start of rapid decay in  $\text{N}_2\text{O}$  concentration or an increase in emission of the reaction. Experimental and numerical results for two mixtures, both fuel lean, are given in Figure 3. Ignition delays were defined in the modeling calculations as the time at which the tangent to the  $\text{N}_2\text{O}$  - time plot intercepted the t-axis located at the level of the initial  $\text{N}_2\text{O}$  concentration. Symbols are the experimental data and lines the corresponding calculations.

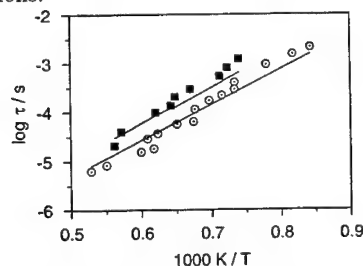


Figure 3. Comparison of ignition delays<sup>5</sup> for various temperatures at 1 atm. Initial mixture compositions: squares;  $X(\text{H}_2) = 0.05$ ,  $X(\text{N}_2\text{O}) = 0.05$ , balance Ar, circles;  $X(\text{H}_2) = 0.05$ ,  $X(\text{N}_2\text{O}) = 0.15$ , balance Ar.

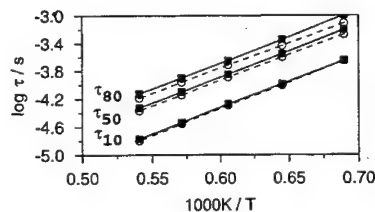


Figure 4. Comparison of  $\text{N}_2\text{O}$  consumption times<sup>8</sup> for various temperatures at 3 atm. Initial mixture composition:  $X(\text{H}_2) = 0.01$ ,  $X(\text{N}_2\text{O}) = 0.005$ , balance Ar.

Hidaka et al.<sup>8</sup> studied the  $\text{H}_2/\text{N}_2\text{O}$  reaction behind both incident and reflected shock waves in the temperature range 1450-2200 K and pressure range 0.6 - 3.5 atm using both single pulse and time resolve techniques. A computer simulation was performed to determine rate constants for the reactions of  $\text{O} + \text{N}_2\text{O} \rightarrow \text{N}_2 + \text{O}_2$ ,  $\text{O} + \text{N}_2\text{O} \rightarrow 2\text{NO}$ , and  $\text{H} + \text{N}_2\text{O} \rightarrow \text{N}_2 + \text{OH}$ . Unfortunately, the experimental conditions were not sufficiently reported to model individual experimental data. However, a comparison of predictions between the two models at conditions that closely replicate their experiments are presented in Figure 4. The open symbol/dashed lines are predictions with the model of Hidaka et al.<sup>8</sup> and the solid symbol/solid lines are the present predictions. The times  $\tau_{10}$ ,  $\tau_{50}$ , and  $\tau_{80}$  correspond to 10%, 50%, and 80% consumption of the initial  $\text{N}_2\text{O}$  concentration. The observed differences are approximately the same size as the scatter in the experimental data.

Dean<sup>3</sup> has monitored  $\text{N}_2\text{O}$  decay via infrared emission at 4.65  $\mu\text{m}$  in reacting mixtures of  $\text{N}_2\text{O}/\text{H}_2/\text{Ar}$  behind reflected shock waves over the temperature range of 1950 - 3075 K with total concentrations ranging from  $1.2$  to  $2.5 \times 10^{18} \text{ molec/cm}^3$ . Nitrous oxide was observed to decay exponentially and an

overall rate constant was determined. The overall rate constant was defined as  $k_{\text{obs}} = -[d \ln (\text{IR})/dt] / [M]$  where IR is the observed  $\text{N}_2\text{O}$  infrared signal and  $[M]$  the total gas concentration. Values of  $k_{\text{obs}}$  for each experiment were obtained from the linear portion of the semilog plot only when the region of linearity covered at least a factor of two change in the infrared signal. Comparison of experimental and model results for a series of temperatures with the same initial mixture composition are shown in Fig. 5.

In another shock tube study, Dean et al.<sup>4</sup> have reported kinetic results on  $\text{H}_2/\text{N}_2\text{O}/\text{CO}/\text{Ar}$  mixtures behind reflected shock waves over the temperature range of 2000 - 2850 K and total concentrations near  $5 \times 10^{18}$  molec/cm<sup>3</sup>. Emissions at 450 nm ( $[\text{CO}][\text{O}]$ ) and  $4.27 \mu\text{m}$  ( $[\text{CO}_2]$ ) were measured to

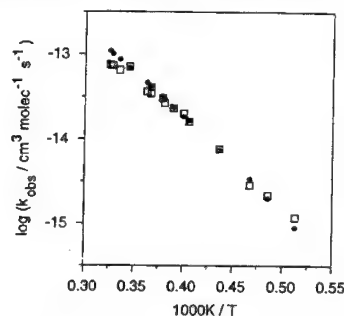


Figure 5. Comparison of  $k_{\text{obs}}$  from experimental data (open squares) and numerical prediction (solid circles) for various temperatures and total concentrations. Initial mixture composition:  $X(\text{H}_2)=0.00101$ ,  $X(\text{N}_2\text{O})=0.0102$ , balance Ar. Initial pressure and temperature data can be found in Table 1 of Dean.<sup>3</sup>

obtain concentration - time data for both oxygen atoms and carbon dioxide. Figure 6a shows the comparison of  $\text{CO}_2$  data versus reaction time obtained from the same mixture with different shock temperatures. The mixture consisted of 0.05%  $\text{H}_2$ , 1.01%  $\text{N}_2\text{O}$ , and 2.99%  $\text{CO}$  with the balance Ar. The time  $\tau'$  (circles) is the time at which the  $\text{CO}_2$  concentration equaled  $4 \times 10^{15}$  molecules/cm<sup>3</sup> and  $\tau''$  (squares) is the time at which the  $\text{CO}_2$  concentration equaled  $1 \times 10^{16}$  molecules/cm<sup>3</sup>.

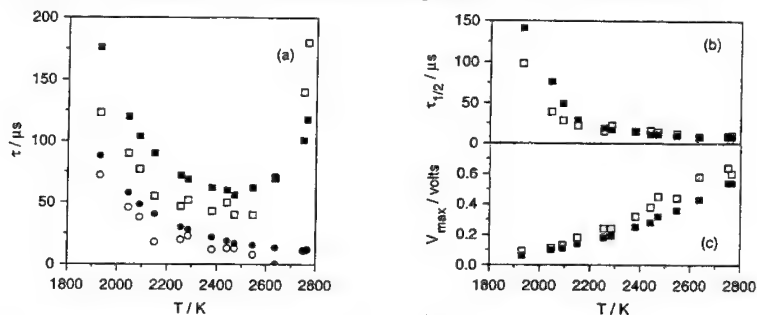


Figure 6. (a) Comparison of  $\text{CO}_2$  emission data.  $\tau'$  (circles) and  $\tau''$  (squares) are defined in the text. Initial mixture composition:  $X(\text{H}_2)=0.0005$ ,  $X(\text{N}_2\text{O})=0.0101$ ,  $X(\text{CO})=0.0299$ , balance Ar. Initial pressure and temperature data can be found in Table 3 of Dean et al.<sup>4</sup> (b) Comparison of  $\tau_{1/2}$ , defined in text. (c) Comparison of  $V_{\text{max}}$ , defined in text. The solid symbols are the calculated values and the open symbols are the experimental data.

Experimental observations of the flame band signal included the time  $\tau_{1/2}$ , defined as the time at which the flame band signal equaled one half the maximum and the maximum signal  $V_{\text{max}}$  which was observed as a constant for long reaction times. In order to compare model predictions to the flame band signal data, Dean et al. applied partial equilibrium technique to shock heated mixtures of  $\text{H}_2/\text{O}_2/$

CO/CO<sub>2</sub>/Ar of near equilibrium composition. From these experiments, a calibration factor relating the observed constant signal to the quasi-equilibrium concentrations of CO and O was obtained.

In the present study, partial equilibrium was not assumed, and the calibration factor was obtained from modeling the calibration experiments with the complete mechanism.<sup>29</sup> The product [CO][O], corresponding to the experimentally measured signal, for the calibration factor was taken at the peak O-atom concentration. After this peak, the product [CO][O] was observed to slowly decrease with time, i.e., a constant signal was not observed for hundreds of microseconds as in the experiments. The resulting calibration curve was  $3.45 \times 10^{-34} \exp(-3125 \text{ cal mole}^{-1}/RT) \text{ V cm}^6 \text{ molec}^{-2}$ . Comparison of predicted and experimental flame band signals are shown in Figures 6b and 6c.

Figure 7 reports the results from another mixture initially of 0.049% H<sub>2</sub>, 1.04% N<sub>2</sub>O, and 12.01% CO with the balance Ar. The fuel/oxidizer equivalence ratio of this mixture is approximately 4 times greater than the equivalence ratio of the previous mixture. For this mixture,  $\tau'$  corresponds to [CO<sub>2</sub>] =  $5 \times 10^{15}$  molecules/cm<sup>3</sup> and  $\tau''$  to [CO<sub>2</sub>] =  $2.0 \times 10^{16}$  molecules/cm<sup>3</sup>.

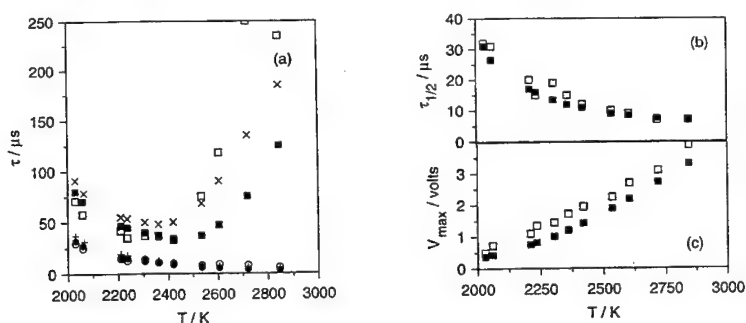


Figure 7. (a) Comparison of CO<sub>2</sub> emission data.  $\tau'$  (circles) and  $\tau''$  (squares) are defined in the text. Initial mixture composition:  $X(\text{H}_2)=0.00049$ ,  $X(\text{N}_2\text{O})=0.0104$ ,  $X(\text{CO})=0.1201$ , balance Ar. Initial pressure and temperature data can be found in Table 3 of Dean et al.<sup>4</sup> (b) Comparison of  $\tau_{1/2}$ , defined in text. (c) Comparison of  $V_{\text{max}}$ , defined in text. The solid symbols are the calculated values and the open symbols are the experimental data.

### Intermediate and Low Temperature Homogeneous Kinetics

Below 1000 K, three of the more recent studies on the H<sub>2</sub>/N<sub>2</sub>O reaction have been reported by Baldwin et al.,<sup>9</sup> Allen et al.,<sup>10</sup> and Borisov et al.<sup>5</sup> Allen et al.<sup>10</sup> studied dilute mixtures of H<sub>2</sub> and N<sub>2</sub>O in N<sub>2</sub> in a flow reactor at 3 atm and 995 K. The consumption and formation of H<sub>2</sub>, N<sub>2</sub>O and H<sub>2</sub>O were measured as well as intermediate species profiles of NH<sub>3</sub> and NO. Species concentrations were obtained by probe sampling and quenching a small portion of the gases along the reactor centerline. These gases were then analyzed with a FTIR for N<sub>2</sub>O, H<sub>2</sub>O, NO, and NH<sub>3</sub> and a selective thermal conductivity detector for H<sub>2</sub>. A comparison of model and experiment is shown in Figure 8 for an initial mixture composition of 0.53% H<sub>2</sub> and 1.1% N<sub>2</sub>O with the balance N<sub>2</sub>. Additional comparisons of this model with experimental data can be found in Allen et al.<sup>10</sup>

The study of Baldwin et al.<sup>9</sup> on H<sub>2</sub>/N<sub>2</sub>O/He mixtures was conducted at 813 and 873 K in a bulb reactor at 0.66 atm. The reaction was followed by sampling the gas after a known time and then determining the N<sub>2</sub> content by gas chromatography. Changing the vessel surface from pyrex to silica to a boric acid coated vessel indicated no effect on the N<sub>2</sub> formation rate. Nitric oxide concentration was also measured showing the production and consumption of NO. Comparisons of model predictions with these data showed the model predictions to be too fast ranging from about a factor of 15 at 873 K to factors of 36-50 at 813 K. Predicted NO concentrations were about a factor of 6 too small at 873 K.

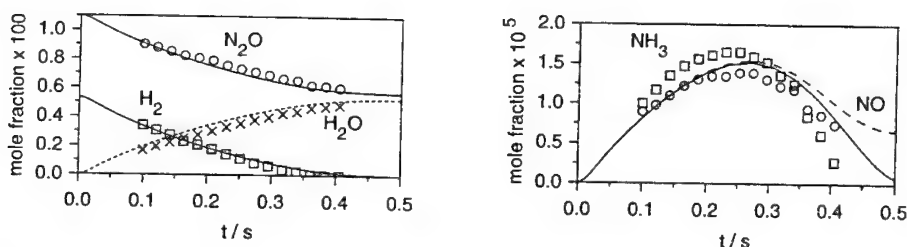


Figure 8. Comparison of model (lines) and experiment (symbols) from flow reactor studies.<sup>10</sup> In part (b), the circles and dashed lines correspond to the NO mole fraction.

### Laminar Premixed Flame Speeds

Premixed flame speeds of  $H_2/N_2O$  mixtures have been studied by several investigators.<sup>11-23</sup> Duval and VanTiggelen,<sup>15</sup> using the flame cone technique, have reported flame speeds for a wide range of equivalence ratios and dilution with different inert gases. Figure 9 presents experimental and numerical speeds for various equivalence ratios with three levels of  $N_2$  dilution. Figure 10 presents a comparison of flame speeds with different diluents at the same equivalence ratio. With the exception of the Ar diluted flames, the numerical flame speeds are approximately 15% lower than the experimentally measured flame speeds.

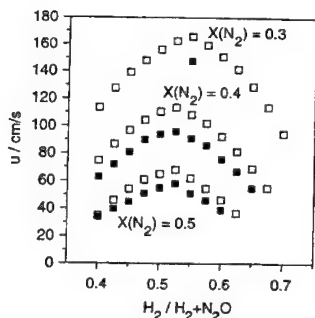


Figure 9. Comparison of flame speeds<sup>15</sup> as a function of equivalence ratio and  $N_2$  dilution. Solid symbols - model, open symbols - experiment.

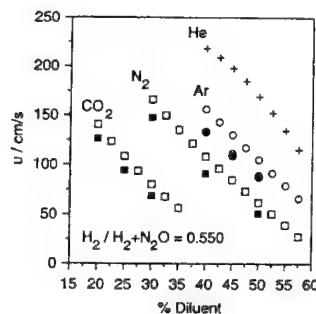


Figure 10. Comparison of flame speeds<sup>15</sup> as a function of dilution for different inert gases. Solid symbols - model, open symbols - experiment.

### DISCUSSION AND CONCLUSIONS

Agreement between model and experiment is generally found to be good. The experiments of Pami-dimukkala and Skinner<sup>6</sup> were mainly sensitive to the  $N_2O$  thermal decomposition reaction and reactions of the  $H_2/O_2$  system. Thus, the agreement here further validates these sub-mechanisms. The experimental results of Borisov et al.,<sup>5</sup> Hidaka et al.,<sup>8</sup> and Dean,<sup>3</sup> however, are sensitive to several reactions of the  $H_2/N_2O$  system including those of H atoms with  $N_2O$  (Table 2). The results of Dean were also found to be sensitive to the reactions of O atoms with  $N_2O$ . The rate constants used in the present mechanism for the  $O+N_2O$  reactions are from Baulch et al.<sup>36</sup> Dean analyzed his results for these rate constants and found that they should be about a factor of five lower than those recommended by Baulch et al. In contrast, Hidaka et al., as well as the similar studies of Henrici and Bauer,<sup>1</sup> found from analysis of their data that the  $O+N_2O$  reactions should be 5 to 7 times larger than the rec-

ommendations from the Baulch review. The present results show that both sets of experimental data can be reasonably predicted with the Baulch et al. rates. Anderson et al.<sup>38</sup> have also modelled the data of Hidaka et al. and Henrici and Bauer and have found equally good agreement between model prediction and experiment. Their analysis clearly showed for the first time that the  $O + N_2O$  reaction was not the major source of NO in these experiments. Nitric oxide was reported to form through the  $H + N_2O \rightarrow NO + NH$  reaction, either by its direct formation or indirectly via later reactions of NH. Thus, Anderson et al. concluded that the evaluations of the rate constants for the  $N_2O + O$  reactions by Hidaka et al. and Henrici and Bauer, both of which were carried out under similar experimental conditions, are invalid. As is evident from Table 2, our findings are in agreement with those of Anderson et al. showing the  $N_2O$  consumption times to be sensitive to several reactions that control the fate of NH, which were not included in the original mechanism of Hidaka et al. The high sensitivity of the  $H_2/N_2O$  reaction rate to  $N_2H_3$  and  $NH_3$  reactions was also recently demonstrated by Allen et al.<sup>10</sup> at lower temperatures.

TABLE 2. Sensitivity of ignition delay times and  $N_2O$  consumption times to rate constants of the mechanism. Normalized sensitivities below 0.01 are not listed.

Reaction (duplicate reactions listed below have a double exponential rate expression)	Borisov et al. <sup>5</sup> 1780 K	Borisov et al. <sup>5</sup> 1380 K	Hidaka et al. <sup>8</sup> 1600 K			Dean <sup>3</sup> 2640 K
	$\frac{\partial \ln \tau}{\partial \ln k}$	$\frac{\partial \ln \tau}{\partial \ln k}$	$\frac{\partial \ln \tau_{10}}{\partial \ln k}$	$\frac{\partial \ln \tau_{50}}{\partial \ln k}$	$\frac{\partial \ln \tau_{80}}{\partial \ln k}$	$\frac{\partial \ln \tau_{30\mu s}}{\partial \ln k}$
$O+H_2 \rightleftharpoons H+OH$	-0.116	-0.037	-0.030	-0.019	-0.017	-0.055
$H+O_2 \rightleftharpoons O+OH$						
$OH+H_2 \rightleftharpoons H_2O+H$	-0.071	-0.061	-0.050	-0.062	-0.066	
$H_2O+O \rightleftharpoons 2OH$						
$NH+NO \rightleftharpoons N_2O+H$	-0.022	0.029	0.011	0.070	0.116	-0.056
$NH+NO \rightleftharpoons N_2O+H$				-0.018	-0.030	0.016
$N_2O+O \rightleftharpoons N_2+O_2$						-0.033
$N_2O+O \rightleftharpoons 2NO$						-0.026
$N_2O+H \rightleftharpoons N_2+OH$	-0.209	-0.392	-0.388	-0.465	-0.541	-0.093
$N_2O(+M) \rightleftharpoons N_2+O(+M)$		-0.012		-0.021	-0.021	
$NH+OH \rightleftharpoons HNO+H$				0.011	0.018	
$NH+NO \rightleftharpoons N_2+OH$				-0.014	-0.022	
$NH_2+H \rightleftharpoons H_2+NH$			-0.019	-0.016		
$NH_3+H \rightleftharpoons NH_2+H_2$				-0.021	-0.016	
$NH_3+OH \rightleftharpoons NH_2+H_2O$					0.013	
$N_2H_3+M \rightleftharpoons N_2H_2+H+M$				-0.015	-0.032	
$N_2H_3+M \rightleftharpoons NH_2+NH+M$					0.014	
$N_2H_2+M \rightleftharpoons NNH+H+M$					-0.018	
$NH_3+NH_2 \rightleftharpoons N_2H_3+H_2$				0.037	0.072	

The agreement between model and experiment for the  $H_2/N_2O/CO$  mixtures of Dean et al. was not as good. For temperatures below 2500 K, the differences in relative times (i.e.,  $\tau''/\tau'$ ) were less than 25% for the mixture with 12% CO (Fig. 7) and varied from 25 to 50% for the mixture with 3% CO (Fig. 6), with the model predictions consistently too long. Above 2500 K,  $\tau'$  was in good agreement for both mixtures, whereas  $\tau''$  was 30-50% too small for the model predictions. The sensitivity of  $\tau'$  and  $\tau''$  to various rate constants of the mechanism for the high and low temperature experiments with each mixture are reported in Table 3. For the high temperature experiments, the direct reaction between CO and  $N_2O$  is found to be important. The rate constant used for  $CO+N_2O$  in the present work is from Loiret et al.<sup>39</sup> and is in good agreement with that of Zaslonko et al.<sup>40</sup> At temperatures above 2500 K, extrapolations from these rate expressions ( $E_a \sim 45$  kcal/mol) yield rate constants which exceed those recommended by Fujii et al.<sup>41</sup> and Milks and Matula<sup>42</sup> (with  $E_a \sim 20$  kcal/mol). Figure 7 shows the results of calculations with the  $CO + N_2O$  reaction removed from the mechanism (in the figure,  $+ = \tau'$  and  $x = \tau''$ ), also suggesting that the rate constants of Loiret et al. and Zaslonko et

al. are too high above 2500 K. Below about 2500 K, the present analysis cannot yield any new information on this rate constant because of its decreased sensitivity. However, it should be noted that the rate constants with the lower  $E_a$  yield too high a rate constant below 1200 K. As indicated from our own work<sup>27</sup> and the recent theoretical and experimental work of Lin and Melius,<sup>43</sup> this reaction is likely extremely slow. Consequently, the high temperature rate of this reaction (near 2000 K) is still in question, particularly with regard to the flame studies of Dinhi et al.<sup>44</sup> where a high value for this rate constant is necessary to model their results.<sup>27</sup> Additional studies are required to resolve these discrepancies. In addition to the high sensitivity to the  $\text{CO} + \text{N}_2\text{O}$  reaction, Table 3 also shows  $\tau'$  and  $\tau''$  to be sensitive to many other reactions of the  $\text{H}_2/\text{N}_2\text{O}$  system, with  $\text{O} + \text{H}_2 \rightleftharpoons \text{H} + \text{OH}$ ,  $\text{H} + \text{N}_2\text{O} \rightleftharpoons \text{N}_2 + \text{OH}$  and  $\text{CO} + \text{OH} \rightleftharpoons \text{CO}_2 + \text{H}$  being the most sensitive. Refinements in these latter rate constants to match the high temperature data would also significantly modify the lower temperature comparisons.

TABLE 3. Sensitivity of  $\tau'$  and  $\tau''$  to rate constants of the mechanism for the experiments of Dean et al.<sup>4</sup> Normalized sensitivities below 0.01 are not listed.

Reaction (duplicate reactions listed below have a double exponential rate expression)	T=1930 K Fig. 6		T = 2790K Fig. 6		T=2030 K Fig. 7		T = 2870K Fig. 7	
	$\frac{\partial \ln \tau'}{\partial \ln k}$	$\frac{\partial \ln \tau''}{\partial \ln k}$	$\frac{\partial \ln \tau'}{\partial \ln k}$	$\frac{\partial \ln \tau''}{\partial \ln k}$	$\frac{\partial \ln \tau'}{\partial \ln k}$	$\frac{\partial \ln \tau''}{\partial \ln k}$	$\frac{\partial \ln \tau'}{\partial \ln k}$	$\frac{\partial \ln \tau''}{\partial \ln k}$
$\text{O} + \text{H}_2 \rightleftharpoons \text{H} + \text{OH}$	-.24	-.17	-.22	-.31	-.25	-.19	-.22	-.19
$\text{H} + \text{O}_2 \rightleftharpoons \text{O} + \text{OH}$	.06	.09	.21	-.26	.02	.04	.04	-.03
$\text{OH} + \text{H}_2 \rightleftharpoons \text{H}_2\text{O} + \text{H}$	.05	.11	.04	.03	.02	.06	.01	.01
$\text{H}_2\text{O} + \text{O} \rightleftharpoons 2\text{OH}$	.03	.07	.02	.01		.02		
$\text{NH} + \text{NO} \rightleftharpoons \text{N}_2\text{O} + \text{H}$	.06	.07	.06	.38	.05	.10	.03	.45
$\text{NH} + \text{NO} \rightleftharpoons \text{N}_2\text{O} + \text{H}$	-.02	-.02	-.02	-.11	-.01	-.03		-.13
$\text{N}_2\text{O} + \text{O} \rightleftharpoons \text{N}_2 + \text{O}_2$	.02	.02	-.02	-.75	.02	.02		-.42
$\text{N}_2\text{O} + \text{O} \rightleftharpoons 2\text{NO}$	.02	.02	.02	.27	.02	.03	.01	.33
$\text{N}_2\text{O} + \text{H} \rightleftharpoons \text{N}_2 + \text{OH}$	-.19	-.23	-.38	-.15	-.21	-.38	-.14	-.91
$\text{CO} + \text{OH} \rightleftharpoons \text{CO}_2 + \text{H}$	-.37	-.57	-.49	-.47	-.17	-.30	-.47	-.11
$\text{CO} + \text{OH} \rightleftharpoons \text{CO}_2 + \text{H}$	-.05	-.08	-.30	-.29	-.03	-.06	-.10	-.07
$\text{CO} + \text{N}_2\text{O} \rightleftharpoons \text{CO}_2 + \text{N}_2$	-.06	-.07	-.35	-.37	-.15	-.12	-.50	-.68
$\text{NO}_2 + \text{H} \rightleftharpoons \text{NO} + \text{OH}$				-.03				-.02
$\text{NH} + \text{O} \rightleftharpoons \text{NO} + \text{H}$			-.03	-.04	-.02			
$\text{NH} + \text{OH} \rightleftharpoons \text{HNO} + \text{H}$				.02		.01		
$\text{NH} + \text{NO} \rightleftharpoons \text{N}_2 + \text{OH}$				-.02				-.02
$\text{N}_2\text{O} (+\text{M}) \rightleftharpoons \text{N}_2 + \text{O} (+\text{M})$				.02				
$\text{CO} + \text{O} (+\text{M}) \rightleftharpoons \text{CO}_2 (+\text{M})$				-.03				

At low and intermediate temperatures, the agreement with the flow reactor studies of Allen et al.<sup>10</sup> are good. The analysis of these results can be found in Allen et al.<sup>10</sup> Significant discrepancy still remains in the agreement between the present model predictions and the bulb experiments of Baldwin et al.<sup>9</sup> Bozzelli et al.<sup>45</sup> have theoretically analyzed the branching channels of the  $\text{H} + \text{N}_2\text{O}$  reaction using QRRK theory and suggest that HNNO stabilization may be important at low temperatures and can be used to explain the experimentally observed curvature in the overall rate constant. However, Diau and Lin<sup>46</sup> have reported on the importance of tunneling in this reaction, which can not be neglected when analyzing the curvature in the temperature dependent rate constant. To investigate the possible role of HNNO stabilization, we have included the branching ratios of Bozzelli et al.<sup>45</sup> in the present model along with secondary reactions for the formation and consumption of HNNO, HNOH, and  $\text{NH}_2\text{OH}$ .<sup>47</sup> Although inclusion of these reactions did decrease the amount of discrepancy between model and experiment, the agreement was still poor. These latter results did show minor sensitivity to consumption of HNNO and HNOH by H atoms. Hence, both experimental aspects, e.g., the role of wall reactions, and model parameter uncertainties need further examination. An improved understanding of low temperature kinetics is especially important with regard to near surface propellant modelling.



Finally, the flame speed measurements are about 15% faster than those predicted by the current model. The trends of these results are consistent with previous flame modeling studies,<sup>19</sup> and with the homogeneous kinetic results that predict slower rates at high temperature and faster rates at low temperature. The agreement here is well within the error limits of the experiments.

The authors wish to acknowledge support for this work from the Office of Naval Research, under Contract No. N00014-90-J-4062, and to acknowledge Dr. R.S. Miller as Technical Monitor.

## REFERENCES

1. **Henrici, H. and Bauer, S.H.**, 1969. "Kinetics of the Nitrous Oxide - Hydrogen Reaction," *J. Chem. Phys.*, Vol. 50, pp. 1333-1342.
2. **Soloukhin, R.I.**, 1973. "High Temperature Oxidation of Hydrogen by Nitrous Oxide in Shock Waves," *14th Symp. (Int.) on Combustion*, The Combustion Institute, Pittsburgh, pp. 77-82.
3. **Dean, A.M.**, 1976. "Shock Tube Studies of  $N_2O/Ar$  and  $N_2O/H_2/Ar$  Systems," *Int. J. Chem. Kinet.*, Vol. 8, pp. 459-474.
4. **Dean, A.M., Steiner, D.C., and Wang, E.E.**, 1978. "A Shock Tube Study of the  $H_2/O_2/CO/Ar$  and  $H_2/N_2O/CO/Ar$  Systems: Measurement of the Rate Constant for  $H+N_2O=N_2+OH$ ," *Combust. Flame* Vol. 32, pp. 73-83.
5. **Borisov, A.A., Zamanskii, V.M., and Skachkov, G.I.**, 1978. "Kinetics and Mechanism of Reaction of Hydrogen with Nitrous Oxide," *Kinet. Catal.*, Vol. 19, pp. 26-32.
6. **Pamidimukkala, K.M. and Skinner, G.B.**, 1982. "Resonance Absorption Measurements of Atom Concentrations in Reacting Gas Mixtures. VIII," *J. Chem. Phys.*, Vol. 76, pp. 311-315.
7. **Hidaka, Y., Takuma, H., and Suga, M.**, 1985. "Shock Tube Study of the Rate Constant for Excited  $OH^+(^2\Sigma^+)$  Formation in the  $N_2O-H_2$  Reaction," *J. Phys. Chem.*, Vol. 89, pp. 4903-4905.
8. **Hidaka, Y., Takuma, H., and Suga, M.**, 1985. "Shock Tube Studies of  $N_2O$  Decomposition and  $N_2O-H_2$  Reaction," *Bull. Chem. Soc. Jpn.*, Vol. 58, pp. 2911-2916.
9. **Baldwin, R.R., Gethin, A., Plaistowe, J., and Walker, R.W.**, 1975. "Reaction Between Hydrogen and Nitrous Oxide," *Chem. Soc., Faraday Trans. 1*, Vol. 71, pp. 1265-1283.
10. **Allen, M.T., Yetter, R.A., and Dryer, F.L.**, 1997. "Kinetics of Hydrogen-Nitrous Oxide Mixtures- Implications of  $N_xH_y$  Chemistry," *Combust. Flame*, in press.
11. **Van Wouterghem, J. and Van Tiggelen, A.**, 1955. "Flame Propagation in Gaseous Mixtures Containing Nitrous-Oxide as Oxidant," *Bull. Soc. Chim. Belg.*, Vol. 64, p. 780.
12. **Dixon-Lewis, G., Sutton, M.M., and Williams, A.**, 1964. "Stability of Hydrogen-Nitrous Oxide-Nitrogen Flames on a Flat Flame Burner," *Combust. Flame*, Vol. 8, pp. 85-87.
13. **Dixon-Lewis, G., Sutton, M.M., and Williams, A.**, 1965. "Some Reactions of Hydrogen Atoms and Simple Radicals at High Temperatures," *Tenth Symposium (International) on Combustion*, The Combustion Institute, Pittsburgh, PA, pp. 495-502.
14. **Dixon-Lewis, G., Sutton, M.M., and Williams, A.**, 1965. *J. Chem. Soc. Lond.*, pp. 5724-5729.
15. **Duval, A. and Van Tiggelen, P.J.**, 1967. "Kinetical Study of Hydrogen-Nitrous Oxide Flames," *Bull. Acad. Roy. Belges*, Vol. 53, pp. 366-402.
16. **Balakhnine, V.P., Van Dooren, J., and Van Tiggelen, P.J.**, 1977. "Reaction Mechanism and Rate Constants in Lean Hydrogen-Nitrous Oxide Flames," *Combust. Flame*, Vol. 28, pp. 165-173.
17. **Cattolica, R.J., Smooke, M.D., and Dean, A.M.**, 1982. "A Hydrogen-Nitrous Oxide Flame Study," Sandia National Laboratories Report No. SAND82-8776. Also Western States Section Meeting of the Combustion Institute, 1982. Paper No. WSS/CI 82-95.
18. **Vanderhoff, J.A., Bunte, S.W., Kotlar, A.J., and Beyer, R.A.**, 1986. "Temperature and Concentration Profiles in Hydrogen-Nitrous Oxide Flames," *Combust. Flame*, Vol. 65, pp. 45-51.
19. **Coffee, T.P.**, 1986. "Kinetic Mechanisms for Premixed, Laminar, Steady-State Hydrogen/Nitrous Oxide Flames," *Combust. Flame*, Vol. 65, pp. 53-60.
20. **Anderson, W.R., and Faust, C.M.**, 1992. "Modelling of  $H_2/N_2O$  Flames," Proceedings 29th JANNAF Combustion Subcommittee Meeting, CPIA Publication 593, Vol. II, p. 205.
21. **Sausa, R.C., Anderson, W.R., Dayton, D.C., Faust, C.M. and Howard, S.L.**, 1993. "Detailed Structure of a Low Pressure, Stoichiometric  $H_2/N_2O/Ar$  Flame," *Combust. Flame*, Vol. 94, p. 407.

22. Dayton, D.C., Faust, C.M., Anderson, W.R., and Sausa, R.C., 1994. "Flame Structure Measurements of a Lean  $H_2/N_2O/Ar$  Flame Employing Molecular Beam Mass Spectroscopy and Modeling," *Combust. Flame*, Vol. 99, p. 323.
23. Brown, M.J., and Smith, D.B., 1994. "Aspects of Nitrogen Flame Chemistry Revealed by Burning Velocity Modelling," *Twenty-Fifth Symposium (International) on Combustion*, The Combustion Institute, Pittsburgh, PA, pp. 1011-1018.
24. Westbrook, C.K. and Dryer, F.L., 1984. "Chemical Kinetic Modeling of Hydrocarbon Combustion," *Progress in Energy and Combustion Science*, Vol. 10, pp. 1-57.
25. Yetter, R.A., Dryer, F.L., Allen, M.T., and Gatto, J., 1995. "Development of Gas-Phase Reaction Mechanisms for Nitramine Combustion," *J. Propulsion and Power*, Vol. 11, pp. 685-697.
26. Allen, M.T., June 1996. Ph.D. Thesis, Princeton University, T-2069, Princeton, NJ 08544.
27. Allen, M.T., Yetter, R.A. and Dryer, F.L., 1997. "High Pressure Studies of Moist Carbon Monoxide/Nitrous Oxide Kinetics," *Combust. Flame*, in press.
28. Yetter, R.A., Yetter, R.A., and Rabitz, H., 1990. "Flow Reactor Studies of Carbon Monoxide/Hydrogen Kinetics," *Combust. Sci. Technol.*, Vol. 79, pp. 129-140.
29. Kim, T., 1992., M.S. Thesis, Princeton University, Princeton, NJ 08544.
30. Yetter, R.A., Dryer, F.L., and Rabitz, H., 1990. "A Comprehensive Reaction Mechanism for Carbon Monoxide/Hydrogen/Oxygen Kinetics," *Combust. Sci. Technol.*, Vol. 79, p. 129.
31. Kim, T. Yetter, R.A., and Dryer, F.L., 1994. "New Results on Moist CO Oxidation: High Pressure, High Temperature Experiments and Comprehensive Kinetic Modeling," *25th Symposium (International) on Combustion*, The Combustion Institute, Pittsburgh, PA, pp. 759-766.
32. Allen, M.T., Yetter, R.A., and Dryer, F.L., 1995. "The Thermal Decomposition of Nitrous Oxide at  $1.5 < P < 10.5$  atm and  $1103 < T < 1173$  K.," *Int. J. Chem. Kinet.*, Vol. 27, p. 883.
33. Tsang, W. and Herron, J.T., 1991. "Chemical Kinetic Data Base for Propellant Combustion: I," *J. Phys. Chem. Ref. Data*, Vol. 20, pp. 609-664.
34. Glarborg, P., Johnsson, J.E., and Dam-Johansen, K., 1994. "Kinetics of Homogeneous Nitrous Oxide Decomposition," *Comb. Flame*, Vol. 99, pp. 523-533.
35. Volmer, M. and Bogdan, Z., 1933. *Z. Phys. Chem.* Vol. 21, p. 257.
36. Zamansky, V.M. and Borisov, A.A., 1989. "Mechanism and Promotion of Self-Ignition of Prospective Fuels," in *Itogi Nauki i Tekhniki, seriya Kinetika i Kataliz*, Vol. 19, Moscow, 1989.
37. Baulch, D.L., Drysdale, D.D., Duxbury, J., and Grant, S.J., 1976. *Evaluated Kinetic Data for High Temperature Reactions*, Vol. 3, Butterworths, London.
38. Anderson, W.R., Ilincic, and Seshadri, K., 1994. "Studies of Reactions Pertaining to and Development of a Reduced Mechanism for the Double Base Propellant Dark Zone," *Proceedings 31st JANNAF Combustion Subcommittee Meeting*, CPIA Publication 620, Vol. II, p. 387.
39. Loirat, H. Caralp, F., and Destriau, M., 1983. *J. Phys. Chem.*, Vol. 87, p. 2455.
40. Zaslanko, I.S., Losev, A.S., Mozzhukhin, E.V., and Mukoseev, Yu. K., 1979. *Kinet. Catal.*, Vol. 20, p. 1144.
41. Fujii, N., Kakuda, T., Takeishi, N., and Miyama, H., 1987. *J. Phys. Chem.* Vol. 91, p. 2144.
42. Milks, D. and Matula, R., 1972. *14th Symposium (International) on Combustion*, The Combustion Institute, Pittsburgh, PA, p. 84.
43. Lin, M.C. and Melius, C.F., 1992. unpublished results, personal communication with M.C.L.
44. Dinhi, H., Tsai, H.-M., and Branch, M.C., 1991. "Combustion Mechanism of Carbon Monoxide-Nitrous Oxide Flames," *Combust. Flame*, Vol. 87, p. 13.
45. Bozzelli, J.W., Chang, A.Y., and Dean, A.M., 1994. "Analysis of the Reactions  $H+N_2O$  and  $NH+NO$ : Pathways and Rate Constants over a wide Range of Temperature and Pressure," *25th Symposium (International) on Combustion*, The Combustion Institute, Pittsburgh, PA, p. 65-974.
46. Diau, E.W.G. and Lin, M.C., 1995. "Theoretical Study of  $H(D) + N_2O$ : Effects of Pressure, Temperature, and Quantum-Mechanical Tunneling on  $H(D)$ -Atom Decay and  $OH(D)$ -Radical Production," *J. Phys. Chem.*, Vol. 99, pp. 6589-6594.
47. Diau, E.W.G., Lin, M.C., He, Y., and Melius, C.F., 1995. "Theoretical Aspects of H/N/O-Chemistry Relevant to the Thermal Reduction of NO by  $H_2$ ," *Prog. Energy Combust. Sci.* Vol. 21, pp. 1-23.

## COMMENTS

A. Koichi Hayashi, Aoyama Gakuin University, Tokyo, Japan:

How do you account for the dependence upon pressure of the rates of your mechanism? I am especially interested in high pressure applications, such as SCRAMJET combustion.

Authors' Reply:

The pressure effects of uni-molecular and three body recombination reactions are modeled with high and low pressure limit rate constants, including Troe fall-off expressions.

## MECHANISTIC STUDIES OF LOW-PRESSURE FLAMES SUPPORTED BY NITROGEN OXIDES \*

J. J. Cor, C. B. Dreyer and M. C. Branch  
Center for Combustion Research  
University of Colorado  
Boulder, Colorado

**ABSTRACT:** The development of detailed models of solid propellant combustion requires detailed information on the gas-phase chemistry occurring above the propellant surface. Different flame systems have been identified as important to study in order to gain greater understanding of solid propellant gas-phase chemistry. In particular, systems which need study are flames of carbon monoxide and hydrocarbons burning with nitrogen oxides. Since both premixed and diffusion flame chemistries exist above the propellant surface, premixed and diffusion flames involving these reactants need to be studied. In the past decade, several experimental studies have been made of premixed flames consisting of these reactants. More recently, counterflow diffusion flames consisting of these reactants have been studied as well. In the present work, several different premixed and counterflow diffusion flames have been modeled using a common, 275-reaction mechanism.

Solid propellant combustion models require gas-phase chemical kinetic mechanisms which are as small as possible. Therefore, for each premixed flame system studied, sensitivity and rate generation analyses have been used to identify which reactions in the detailed mechanism are critical to each system. Based on these analyses, and comparisons with the experimental data, reduced mechanisms, consisting of only the essential chemical reactions for each flame system, have been developed. These reduced mechanisms have been combined into a comprehensive, reduced mechanism consisting of 42 reactions. In general, this reduced mechanism models the flames' chemistry as accurately as the full mechanism does.

The full and reduced mechanisms have also been used to model methane-nitrous oxide and carbon monoxide-nitrous oxide counterflow diffusion flames. From comparisons with the experimental data, it is determined that, in general, the full mechanism and the reduced mechanism model the diffusion flame chemistry as accurately as they modeled the premixed flame chemistry. Also, in the diffusion flames, there is reasonable agreement between the modeling results using the full and reduced mechanisms.

The problem of  $N_2O$  decomposition remains a key area requiring further study. The rate constants for this reaction had to be modified to model the  $CO-N_2O$  flames and the  $CH_4-N_2O$  diffusion flame accurately. The reason for this discrepancy is still to be determined, but future studies of the  $N_2O$  decomposition reaction are suggested.

\* This work was sponsored by the Air Force Office of Scientific Research under Grand DOD-F49620-93-0430.

## INTRODUCTION

Solid rocket propellant is composed of numerous oxidizer particles of varying sizes and shapes which are bound together by fuel binder. Complex physical and chemical processes occur as each particle burns with the surrounding binder. The processes include decomposition of the solid phase, burning of the oxidizer decomposition products in a monopropellant flame, and burning of the oxidizer and fuel decomposition products in diffusion flames. These processes also interact with the dynamics of the rocket chamber. The fundamental understanding of these processes is incomplete; this lack of fundamental understanding makes the synthesis of new propellants a largely empirical process, causing successful formulation of new propellants to be time-consuming and even dangerous tasks. Therefore, the development of a predictive capability for solid propellant combustion is extremely desirable.

The models which have been developed to predict the combustion characteristics of solid rocket fuel are semi-empirical in nature, and in general contain only rudimentary surface- and gas-phase chemistry.<sup>1-3</sup> They have been successful in showing trends in solid propellant combustion, but a truly predictive capability has not been achieved. In order to develop this predictive capability, more detailed and realistic physics and chemistry are needed. However, due to the complex nature of solid propellant combustion, different aspects of it -- including the gas-phase chemistry -- must be studied separately and then integrated into an overall combustion model.

Yetter et al.<sup>4</sup> suggested a three-tiered, systematic study of the gas phase chemistry involved in solid propellant combustion. The first tier data, obtained from shock tubes and flow reactors, is used to validate gas-phase kinetics and ignition. The second tier of data, obtained from premixed flame studies, is used to validate gas-phase kinetic mechanisms as they affect one-dimensional heat release and flame speeds. The final tier of data, obtained from diffusion flames, is used to evaluate mechanisms in an environment involving multidimensional transport processes and flame extinction. Yetter et al. specifically identified flame systems requiring detailed study, which, among others, included  $\text{CH}_4\text{-N}_2\text{O}$ ,  $\text{CO-N}_2\text{O}$ ,  $\text{C}_2\text{H}_2\text{-NO}_2$  and  $\text{CH}_2\text{O-NO}_2$ . Mechanisms need to be developed which can accurately predict the chemistry of these systems in shock tubes, premixed flames and diffusion flames. Further, these mechanisms should ideally consist of a small number of chemical reactions, so that global modelers, who must simulate the entire solid propellant combustion process, can keep the computational requirements of the gas-phase chemistry to a minimum.

The present study focuses on the second and third tiers of data identified by Yetter et al.<sup>4</sup> Premixed flames  $\text{CH}_4\text{-N}_2\text{O}$ ,  $\text{CO-N}_2\text{O}$ ,  $\text{C}_2\text{H}_2\text{-NO}_2$  and  $\text{CH}_2\text{O-NO}_2$  have been modeled using a common, detailed mechanism and compared to measurements. For each of these flames, the mechanism has then been reduced to the minimum number of reactions which still capture all of the essential features of the flame structure. These reduced mechanisms have then been combined into a comprehensive, reduced mechanism which can model all of the premixed flames of this study. The full mechanism and the comprehensive, reduced mechanism have also been used to model counterflow diffusion flames of  $\text{CH}_4\text{-N}_2\text{O}$  and  $\text{CO-N}_2\text{O}$ .

## RESULTS

### Premixed Flames

**$\text{CH}_4\text{-N}_2\text{O}$  Flames.** The first flame modeled in this study was a 30-torr, burner stabilized flame with a  $\text{CH}_4\text{-N}_2\text{O-Ar}$  molar ratio of 0.14-0.57-0.29. Experimental data for this flame were obtained from Vandooren et al.,<sup>5</sup> who measured the structure using molecular beam mass sampling, mass spectrometric analysis and thermocouples. The flame was modeled using the computer program

Premix.<sup>6</sup> This flame and all other flames in this study were modeled using the measured temperature profile as input to the program in lieu of solving the energy equation.

The mechanism first used to model the flame, developed by Branch and Cor,<sup>7</sup> consisted of 54 species and 272 reactions. Branch and Cor successfully used this mechanism to model several different premixed flame systems involving nitrogen oxides. However, Fig. 1 shows that this mechanism produced a calculated flame chemistry which proceeded too slowly relative to the measurements of Vandooren et al.<sup>5</sup> To understand the cause of this discrepancy, sensitivity analysis was performed to determine which reactions were dominating the flame's structure. The concentrations of almost every major species in the flame was found to be highly dependent on the  $N_2O$  decomposition reaction,  $N_2O + M = N_2 + O + M$ , which is Reaction 37 in Table 1. The rate constants Branch and Cor used for this reaction are also those given in Table 1. The literature on this reaction was reviewed and various recommended rate constants were input into the mechanism with the goal of bringing the modeling into closer agreement with the measurements. However, no rate constants recommended in the literature were fast enough to achieve this goal.

Another attempt to improve agreement between modeling and measurements was made by adding the radical reaction  $N_2O + CH_3 = N_2 + CH_2O + H$  to the mechanism of Branch and Cor.<sup>7</sup> This reaction was added because of the relatively high concentration of  $CH_3$  found in the measurements and modeling. Adding this reaction produced only a slight improvement between the measurements and the modeling; however, since it did improve the modeling results, the reaction was included in the mechanism, resulting in a 273-reaction mechanism. More significantly, the pre-exponential factor for  $N_2O$  decomposition was then made a factor of eight larger than the value used by Branch and Cor.<sup>7</sup> This value was in excess of the highest recommended values in the literature, but the effect of using this value in the 273-reaction mechanism produced a significant improvement between measurement and modeling for almost all of the species measured in the flame.

The need to accelerate the rate constant for  $N_2O$  decomposition in this manner suggested that there are factors relating to  $N_2O$  decomposition not adequately addressed in the mechanism of Branch and Cor.<sup>7</sup> Therefore, a second approach to modifying the mechanism was to keep the rate constants for  $N_2O$  decomposition unchanged from those given for Reaction 37 Table 1, and instead include additional  $N_2O$  decomposition pathways. The first change was to add enhancement factors to  $N_2O$  decomposition as suggested by Van Tiggelen.<sup>8</sup> These factors are shown below Reaction 37 in Table 1. Also, it was considered that when  $N_2O$  collides with itself, it is possible for both molecules to decompose, via the reaction  $2N_2O = 2N_2 + 2O$ , which is Reaction 38 in Table 1. Therefore, the enhancement factor for  $N_2O$  was set to zero for Reaction 37, and Reaction 38 was added to the mechanism. Finally, it was considered that unimolecular  $N_2O$  decomposition could also exist. Therefore, the NIST Chemical Kinetic Reference Base<sup>9</sup> was reviewed for rate constant data for first-order  $N_2O$  decomposition at low pressure. A curve fit through the available data produced the rate constants given for Reaction 39 in Table 1.

These combined changes relating to  $N_2O$  decomposition resulted in a 275-reaction mechanism. As shown in Fig. 1, this mechanism produced results in marked improvement over those obtained using the original mechanism of Branch and Cor.<sup>7</sup> Also, the results using the 275-reaction mechanism were in very close agreement with the results from the 273-reaction mechanism described above, which included the artificially enhanced pre-exponential factor for  $N_2O$  decomposition. Since the changes made to achieve the 275-reaction mechanism are less arbitrary than those used to obtain the 273-reaction mechanism, subsequent analyses in this review are presented based on using the 275-reaction mechanism. It is noted, however, that results are virtually the same using either mechanism.

Rate generation and sensitivity analyses were performed on the 275-reaction mechanism as it was used to model the  $CH_4$ - $N_2O$  flame of Vandooren et al.<sup>5</sup> The rate generation analysis determined

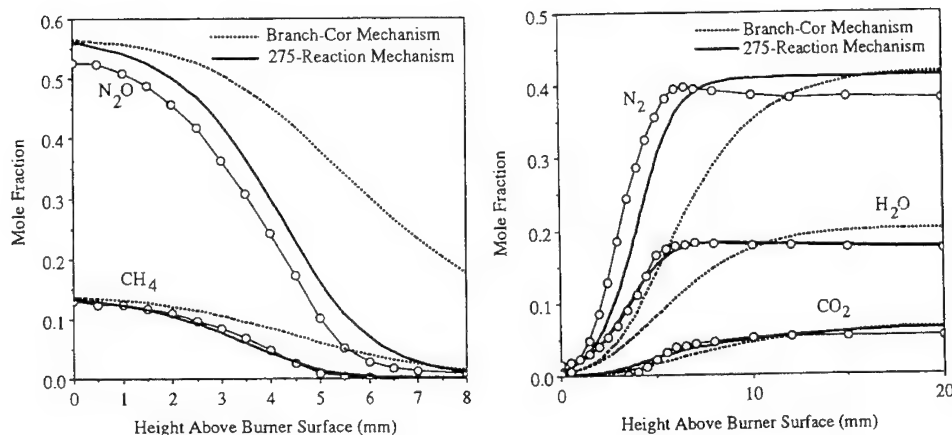


Figure 1. Measured (circles) and modeled (lines) concentration profiles of  $\text{CH}_4$ ,  $\text{N}_2\text{O}$ ,  $\text{N}_2$ ,  $\text{H}_2\text{O}$  and  $\text{CO}_2$  in 50-torr,  $\text{CH}_4$ - $\text{N}_2\text{O}$ -Ar flame measured by Vandooren et al.<sup>5</sup>  $\text{CH}_4$ - $\text{N}_2\text{O}$ -Ar molar ratio is 0.14-0.57-0.29 and total reactant volumetric flowrate is 14.2 standard liters per minute (slm). Flame is modeled using mechanism developed by Branch and Cor<sup>7</sup> and 275-reaction mechanism developed in this study.

which reactions are producing each species at each point in the flame, and the sensitivity analysis determined the reactions to which the species concentration is most sensitive at each point in the flame. All reactions not found to be significant in either the rate generation or sensitivity analyses were removed from the mechanism. After this analysis was completed, further reduction in the size of the mechanism was done more subjectively, by removing additional reactions involving species of low concentration. The final reduced mechanism consisted of 17 species and 22 reactions. The modeling results using this mechanism were in very close agreement with the results obtained from the full, 275-reaction mechanism. In Fig. 1, the 22-reaction data would lie almost exactly on top of the 275-reaction data which have been plotted.

The 275- and 22-reaction mechanisms were also used to model a 50-torr,  $\text{CH}_4$ - $\text{N}_2\text{O}$  flame with an equivalence ratio of 1.13, whose structure was measured by Habeebullah et al.<sup>10</sup> In the measurements, probe sampling and gas chromatographic analysis were used for stable species, laser-induced fluorescence (LIF) was for unstable species, and LIF and thermocouples were used for temperatures. Measurement results and modeling results are shown in Fig. 2. It can be seen that the modeling results are in close agreement with the measurements for the majority of species in this flame, and that the full and reduced mechanisms are once again in close agreement with each other.

**$\text{C}_2\text{H}_2$ - $\text{NO}_2$  Flame.** The 275-reaction mechanism was used to model a 25-torr flame with a  $\text{C}_2\text{H}_2$ - $\text{NO}_2$ -Ar molar ratio of 0.201-0.548-0.251 whose structure was measured by Volponi and Branch.<sup>11</sup> Stable species were measured using mass spectrometric analysis, unstable species were measured using LIF and temperatures were measured from thermocouples and OH rotational spectra. Measurements and modeling results, shown in Fig. 3, were in good agreement. Rate generation and sensitivity analysis were again performed on the 275-reaction mechanism as it was used to model this flame, and unnecessary reactions once again eliminated from the mechanism. Additional reactions involving species of low concentration were then also removed from the mechanism. The resulting reduced mechanism consisted of 19 species and 16 reactions, and as can be seen in Fig.

3, was in good agreement with the full, 275-reaction mechanism.

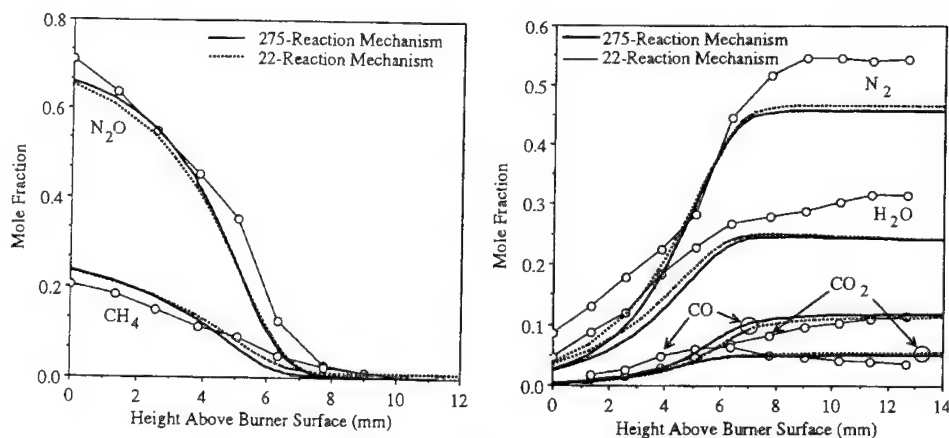


Figure 2. Measured (circles) and calculated (lines) profiles of  $\text{CH}_4$ ,  $\text{N}_2\text{O}$ ,  $\text{CO}$ ,  $\text{CO}_2$ ,  $\text{H}_2\text{O}$  and  $\text{N}_2$  in 50 torr,  $\text{CH}_4$ - $\text{N}_2\text{O}$  flame measured by Habeebullah et al.<sup>10</sup> Flame equivalence ratio is 1.13 and reactant flowrate is 2.22 slm. Flame is modeled using 275- and 22-reaction mechanisms developed as part of this study.

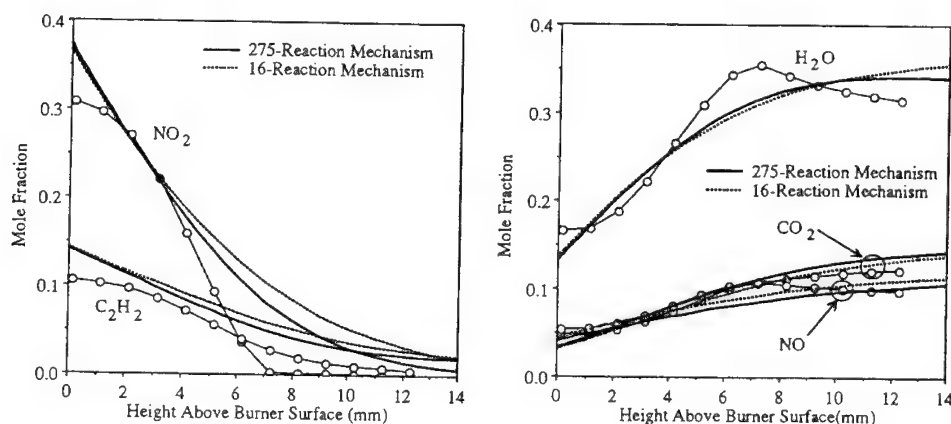


Figure 3. Measured (circles) and modeled (lines) profiles of  $\text{C}_2\text{H}_2$ ,  $\text{NO}_2$ ,  $\text{H}_2\text{O}$ ,  $\text{CO}_2$  and  $\text{NO}$  in 25-torr  $\text{C}_2\text{H}_2$ - $\text{NO}_2$ -Ar flame measured by Volponi and Branch.<sup>11</sup>  $\text{C}_2\text{H}_2$ - $\text{NO}_2$ -Ar molar ratio is 0.201-0.548-0.251 and reactant flowrate is 4.01 slm. Flame is modeled using 275- and 16-reaction mechanisms developed as part of this study.

**$\text{CH}_2\text{O}$ - $\text{NO}_2$  Flame.** The 275-reaction mechanism was used to model a 55-torr flame with a  $\text{CH}_2\text{O}$ - $\text{NO}_2$ - $\text{O}_2$  molar ratio of 0.247-0.627-0.126, whose structure was measured by Branch et al.<sup>12</sup> Stable species were measured using probe extraction and gas chromatography, intermediate species were measured using LIF, and temperatures were measured using thermocouples. Due to measurement problems involving recombination of species within the measurement probe, only a limited comparison between measurements and modeling was possible. This comparison is shown in Fig. 4. The modeled profiles for  $\text{CO}$  are in reasonable agreement with the experimental data,



while the measured  $\text{CH}_2\text{O}$  and  $\text{CO}_2$  profiles are less well-predicted. Despite the limited data available, sensitivity and rate generation analyses were performed on the 275-reaction mechanism modeling the  $\text{CH}_2\text{O}-\text{NO}_2-\text{O}_2$  flame. When unnecessary reactions were eliminated, a 15-species, 15-reaction mechanism resulted, and as can be seen in Fig. 4, the modeling results using this mechanism were in good agreement with those obtained using the full mechanism.

***CO-N<sub>2</sub>O Flame.*** The 275-reaction mechanism was used to model a 50-torr, stoichiometric  $\text{CO}-\text{N}_2\text{O}$  flame whose structure was measured by Dindi et al.<sup>13</sup> Species were measured using probe extraction and gas chromatography and temperatures were measured by a thermocouple. The chemistry proceeded too rapidly relative to the measurements using the 275-reaction mechanism. Therefore, the 272-reaction mechanism of Branch and Cor, which does not contain the enhancement factors shown for Reaction 37 in Table 1, and also does not contain Reactions 38 and 39, was used to model the flame. As seen in Fig. 5, the 272-reaction mechanism produced results which were in better agreement with the experimental data than the results obtained using the 275-reaction mechanism.

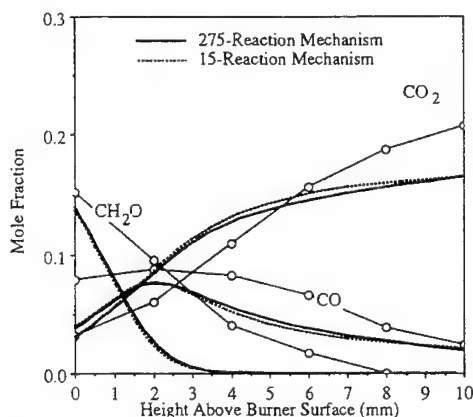


Figure 4. Measured (circles) and modeled (lines) species concentration profiles in 55-torr,  $\text{CH}_2\text{O}-\text{NO}_2-\text{O}_2$  flame measured by Branch et al.<sup>12</sup>  $\text{CH}_2\text{O}-\text{NO}_2-\text{O}_2$  molar ratio is 0.247-0.627-0.126 and reactant flowrate is 2.15 slm. Flame is modeled using 275- and 15-reaction mechanisms developed as part of this study.

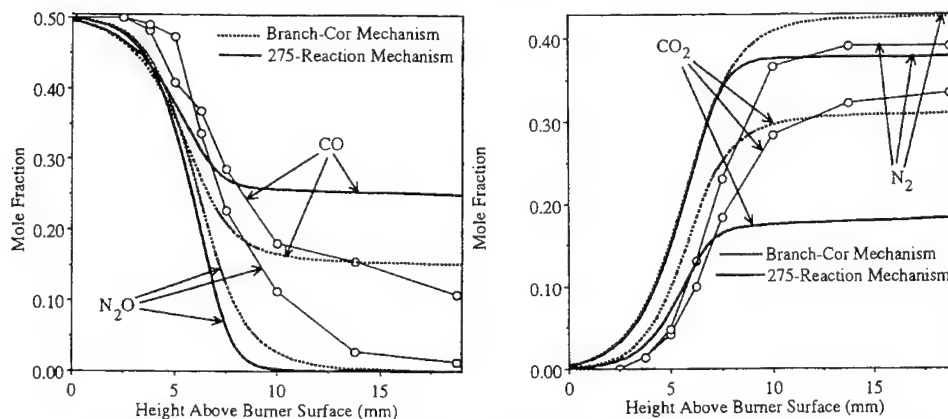


Figure 5. Measured (circles) and calculated (lines) concentration profiles for  $\text{CO}$ ,  $\text{N}_2\text{O}$ ,  $\text{CO}_2$  and  $\text{N}_2$  in 50-torr, stoichiometric  $\text{CO}-\text{N}_2\text{O}$  flame measured by Dindi et al.<sup>13</sup> Reactant flowrate is 2.1 slm. Flame is modeled using mechanism developed by Branch and Cor<sup>7</sup> and 275-reaction mechanism developed as part of this study.

Dindi et al.<sup>13</sup> developed a seven-species, four-reaction mechanism to model this flame. These four reactions are Reactions 37, 40, 41 and 42 in Table 1. The modeling of the flame was repeated using these four reactions with the rate constants given in Table 1. Results were in very close agreement with the full, 272-reaction mechanism of Branch and Cor.<sup>7</sup>

*Combined, Reduced Mechanism.* The reduced mechanisms which were developed for the CH<sub>4</sub>-N<sub>2</sub>O, C<sub>2</sub>H<sub>2</sub>-NO<sub>2</sub>, CH<sub>2</sub>O-NO<sub>2</sub> and CO-N<sub>2</sub>O premixed flames were combined to produce a comprehensive, reduced mechanism which could model any of these four systems. Since many of the reactions were common among the four reduced mechanisms, the combined mechanism consisted of only 42

TABLE 1  
Comprehensive, Reduced Chemical Kinetic Mechanism

REACTIONS	K = A T <sup>b</sup> exp(-E/RT)			Applicable Flame Systems			
	A (mole-cm-sec-K)	b	E (cal/mole)	CH <sub>4</sub> -N <sub>2</sub> O	C <sub>2</sub> H <sub>2</sub> -NO <sub>2</sub>	CH <sub>2</sub> O-NO <sub>2</sub>	CO-N <sub>2</sub> O
1. CH <sub>2</sub> O+OH=HCO+H <sub>2</sub> O	3.43E+09	1.2	-447.0			X	
2. CH <sub>2</sub> O+H=HCO+H <sub>2</sub>	2.19E+08	1.8	3000.0	X		X	
3. HCO+M=H+CO+M	2.50E+14	.0	16802.0	X		X	
CO Enhanced by	1.900E+00						
H <sub>2</sub> Enhanced by	1.900E+00						
CO <sub>2</sub> Enhanced by	3.000E+00						
H <sub>2</sub> O Enhanced by	5.000E+00						
4. CO+OH=CO <sub>2</sub> +H	1.51E+07	1.3	-758.0	X	X	X	
5. HO <sub>2</sub> +NO=NO <sub>2</sub> +OH	2.11E+12	.0	-479.0		X	X	
6. NO <sub>2</sub> +H=NO+OH	3.50E+14	.0	1500.0		X	X	
7. NO <sub>2</sub> O=NO+O <sub>2</sub>	1.00E+13	.0	600.0			X	
8. NO <sub>2</sub> +NO <sub>2</sub> =NO+NO+O <sub>2</sub>	2.00E+12	.0	26824.0		X	X	
9. NO <sub>2</sub> +CO=NO+CO <sub>2</sub>	1.20E+14	.0	31600.0		X	X	
10. OH+NO+M=HONO+M	5.10E+23	-2.5	-68.0		X	X	
11. HONO+OH=H <sub>2</sub> O+NO <sub>2</sub>	1.30E+10	1.0	35.0		X	X	
12. HO <sub>2</sub> +NO <sub>2</sub> =HONO+O <sub>2</sub>	4.64E+11	.0	-479.0			X	
13. NO+NO=N <sub>2</sub> +O <sub>2</sub>	1.30E+14	.0	75630.0			X	
14. HCO+NO <sub>2</sub> =CO+HONO	1.50E+13	.0	-430.0			X	
15. C <sub>2</sub> H <sub>2</sub> +O=CH <sub>2</sub> +CO	1.02E+07	2.0	1900.0		X		
16. C <sub>2</sub> H <sub>2</sub> +O=HCCO+H	1.02E+07	2.0	1900.0		X		
17. OH+C <sub>2</sub> H <sub>2</sub> =C <sub>2</sub> H+H <sub>2</sub> O	3.37E+07	2.0	14000.0		X		
18. C <sub>2</sub> H+O <sub>2</sub> =2CO+H	3.52E+13	.0	.0		X		
19. 2OH=O+H <sub>2</sub> O	6.00E+08	1.3	.0		X		
20. HCN+OH=CN+H <sub>2</sub> O	1.45E+13	.0	10929.0		X		
21. NO <sub>2</sub> +M=NO+O+M	1.10E+16	.0	66000.0		X		
22. CH <sub>2</sub> +NO=HCN+OH	1.39E+12	.0	-1100.0		X		
23. CN+NO=N <sub>2</sub> +CO	1.07E+14	.0	8000.0		X		
24. CH <sub>4</sub> +H=CH <sub>3</sub> +H <sub>2</sub>	2.20E+04	3.0	8750.0	X			
25. CH <sub>4</sub> +OH=CH <sub>3</sub> +H <sub>2</sub> O	1.60E+06	2.1	2460.0	X			
26. CH <sub>4</sub> +O=CH <sub>3</sub> +OH	1.02E+09	1.5	8604.0	X			
27. CH <sub>3</sub> +O=CH <sub>2</sub> O+H	8.00E+13	.0	.0	X			
28. OH+H <sub>2</sub> =H <sub>2</sub> O+H	1.17E+09	1.3	3620.0	X			
29. O+OH=O <sub>2</sub> +H	4.00E+14	-5	.0	X			
30. O+H <sub>2</sub> =OH+H	5.06E+04	2.7	6290.0	X			
31. OH+HO <sub>2</sub> =H <sub>2</sub> O+O <sub>2</sub>	7.50E+12	.0	.0	X			
32. H+HO <sub>2</sub> =2OH	1.40E+14	.0	1073.0	X			
33. H+HO <sub>2</sub> =H <sub>2</sub> +O <sub>2</sub>	1.25E+13	.0	.0	X			
34. NH+NO=N <sub>2</sub> O+H	2.40E+15	-8	.0	X			
35. N <sub>2</sub> O+OH=N <sub>2</sub> +HO <sub>2</sub>	1.00E+13	.0	10000.0	X			
36. N <sub>2</sub> O+H=N <sub>2</sub> +OH	1.50E+14	.0	15090.0	X			
37. N <sub>2</sub> O+M=N <sub>2</sub> +O+M	4.90E+14	.0	57500.0	X			
H <sub>2</sub> O Enhanced by	7.500E+00						
NO Enhanced by	2.000E+00						
CO Enhanced by	2.000E+00						
CO <sub>2</sub> Enhanced by	2.000E+00						
N <sub>2</sub> O Enhanced by	0.000E+00						
38. N <sub>2</sub> O+N <sub>2</sub> O=2N <sub>2</sub> +2O	4.90E+15	.0	57500.0	X			
39. N <sub>2</sub> O=N <sub>2</sub> +O	8.80E+10	.0	65100.0	X			
40. N <sub>2</sub> O+O=N <sub>2</sub> +O <sub>2</sub>	7.00E+14	.0	28200.0	X			
41. N <sub>2</sub> O+O=2NO	5.60E+14	.0	28200.0	X			
42. CO+N <sub>2</sub> O=N <sub>2</sub> +CO <sub>2</sub>	2.00E+12	.0	17300.0	X			

reactions and 26 species. This mechanism is shown in Table 1. This table also identifies which flame system individual reactions are applicable to. Results using the combined mechanism in Table 1 were in very close agreement with the modeling results obtained using any of the four reduced mechanisms developed to model the individual flame systems.

## Diffusion Flames

The 275-reaction mechanism was also used to model two counterflow diffusion flames whose structure was measured by Cor and Branch.<sup>14</sup> The first was a 165-torr flame with a  $\text{CH}_4\text{-N}_2\text{-N}_2\text{O}$  molar ratio of 1.0-1.58-2.77 and the second was a 85-torr flame with a  $\text{CO-CH}_4\text{-N}_2\text{O}$  molar ratio of 1.0-0.01-1.01. Temperatures were measured using thermocouples and stable species concentrations were measured using probe extraction and gas chromatography. The flame was modeled using the computer program Oppdif, developed by Kee et al.<sup>15</sup> As in the premixed flame modeling, the measured temperature profiles were used as input to the model in lieu of solving the energy equation.

Using the 275-reaction mechanism, the chemistry proceeded too rapidly relative to the measurements in both diffusion flames. Therefore, the 272-reaction mechanism of Branch and Cor<sup>7</sup> was used to model the flames instead. The measured and calculated species profiles are given in Figures 6 and 7. Reasonable agreement between measurements and modeling was achieved for most species in these flames. In Fig. 6, it can be seen that the agreement between measurements and modeling is generally as accurate as was found in the premixed  $\text{CH}_4\text{-N}_2\text{O}$  flames shown in Figures 1 and 2. Oxygen is, however, greatly overpredicted in the diffusion flame, which is not the case for the premixed flame.

A comparison between the modeling results obtained in the premixed  $\text{CO-N}_2\text{O}$  flame of Dindi et al.,<sup>13</sup> shown in Fig. 5, and the  $\text{CO-N}_2\text{O}$  flame of Cor and Branch,<sup>14</sup> shown in Fig. 7, is made difficult because of the need to premix a small amount of  $\text{CH}_4$  with the  $\text{CO}$  in the diffusion flame. This small amount of  $\text{CH}_4$  was required to get the fuel to decompose and burn in the diffusion flame. Still, modeling of the diffusion flame was as successful as the modeling of the premixed flame, as can be seen from a comparison of the common species in Figures 5 and 7.

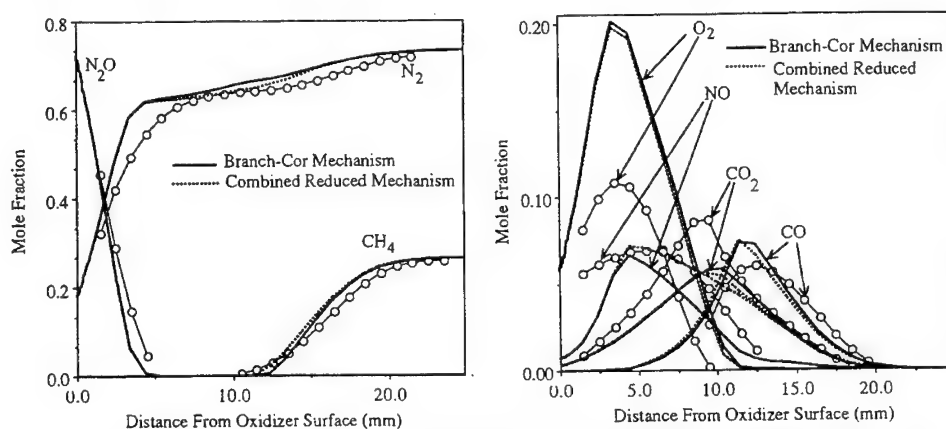


Figure 6. Measured (symbols) and calculated (lines) concentration profiles of  $\text{CH}_4$ ,  $\text{N}_2\text{O}$ ,  $\text{N}_2$ ,  $\text{O}_2$ ,  $\text{NO}$ ,  $\text{CO}_2$  and  $\text{CO}$  in a 165-torr  $\text{CH}_4\text{-N}_2\text{-N}_2\text{O}$  counterflow diffusion measured by Cor and Branch.<sup>14</sup> Flow rate from the oxidizer surface is 4.68 slm  $\text{N}_2\text{O}$  and flowrate from fuel surface is 2.96 slm  $\text{CH}_4$  and 8.37 slm  $\text{N}_2$ . Burner surface diameters are 67.4 mm and separation distance is 24.8 mm. Flame is modeled using the mechanism of Branch and Cor,<sup>7</sup> and mechanism in Table 1, excluding Reactions 38 and 39 and without enhancement factors for Reaction 37.

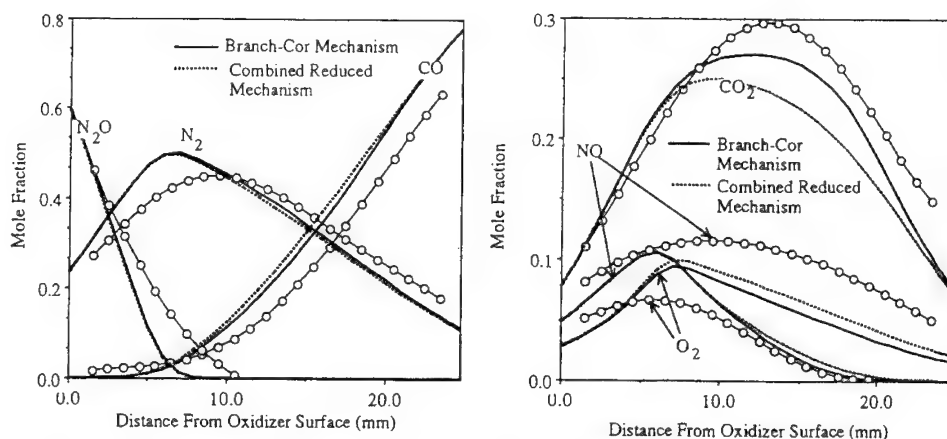


Figure 7. Measured (symbols) and calculated (lines) concentration profiles of CO, N<sub>2</sub>O, NO, CO<sub>2</sub>, NO and O<sub>2</sub> in a 85-torr CO-CH<sub>4</sub>-N<sub>2</sub>O counterflow diffusion flame measured by Cor and Branch.<sup>14</sup> Flowrate from the oxidizer surface is 1.69 slm N<sub>2</sub>O and flowrate from the oxidizer surface is 0.017 slm CH<sub>4</sub> and 1.67 slm CO. Burner surface diameters are 67.4 mm and separation distance is 24.8 mm. Flame is modeled using the mechanism of Branch and Cor,<sup>7</sup> and mechanism in Table 1, excluding Reactions 38 and 39 and enhancement factors for Reaction 37.

The mechanism of Table 1, minus the enhancement factors for Reaction 24, and also minus Reactions 25 and 26, was also used to model the diffusion flames of Cor and Branch.<sup>14</sup> Fig. 6 shows that for the CH<sub>4</sub>-N<sub>2</sub>O diffusion flame, reasonable agreement with the full mechanism was obtained using this reduced mechanism, with the exception of some discrepancy in modeling the NO profile. Fig. 7 shows that the agreement between the full and reduced mechanism in the CO-N<sub>2</sub>O diffusion flame was reasonable except for some discrepancy in modeling the CO<sub>2</sub> concentration profile.

## DISCUSSION

The decomposition reaction for N<sub>2</sub>O, N<sub>2</sub>O+M=N<sub>2</sub>+O+M is critical to modeling premixed and diffusion flames containing N<sub>2</sub>O as a reactant. In the current study, two different approaches were used to model the chemistry involving this reaction in order to obtain good agreement across the range of experimental data. The N<sub>2</sub>O decomposition was required to be faster in the premixed CH<sub>4</sub>-N<sub>2</sub>O flames than in the premixed CO-N<sub>2</sub>O flame or either of the counterflow diffusion flames. A consistent mechanism for handling N<sub>2</sub>O decomposition, applicable to the entire range of experimental flames modeled in this study, was not obtained.

The reason for a slower N<sub>2</sub>O decomposition in the CO-N<sub>2</sub>O premixed flame and both diffusion flames than needed for the CH<sub>4</sub>-N<sub>2</sub>O premixed flames in this study has yet to be determined. It is possible that N<sub>2</sub>O decomposition is enhanced by the presence of certain hydrocarbon or hydrogen species, which would have been absent during the N<sub>2</sub>O decomposition in the premixed CO-N<sub>2</sub>O flame and the diffusion flames. Data on enhancement factors for hydrocarbon species and hydrogen species might be especially valuable in trying to develop a comprehensive mechanism consistent across all flames studied. Therefore, it is recommended that N<sub>2</sub>O decomposition be more thoroughly studied, with a

determination made of the enhancement factors for as many different collisional partners as possible. Low-pressure, unimolecular  $\text{N}_2\text{O}$  decomposition should be carefully studied as well.

The comprehensive, reduced mechanism shown in Table 1 contains 42 reactions. This mechanism has been developed to model four different flame systems. However, the systems modeled here are only a small subset of the number of flames which were identified as being important by Yetter et al.<sup>4</sup> Undoubtedly more chemistry will be needed to model all system identified by Yetter et al. It appears, therefore, that a comprehensive mechanism, even of reduced size, which can be used by global modelers of solid propellant combustion, will contain a substantial number of reactions, and will require a great deal of computational power for any global, solid propellant combustion model.

### REFERENCES

1. Beckstead, M. W., Derr, R. L. and Price, C. F., 1970. "A Model of Composite Solid Propellant Combustion Based on Multiple Flames," *AIAA Journal*, Vol. 8, No. 12, pp. 2200-2207.
2. King, M. ., 1974. "Model for Steady State Combustion of Unimodal Composite Solid Propellants," AIAA Paper No 78-216, *AIAA 16th Aerospace Science Meeting*, Huntsville, Alabama.
3. Cor, J. J. and Renie, J. P., 1987. "A Continuous Oxidizer Regression Model for the Combustion of Composite Solid Propellants," *Western States Section/The Combustion Institute 1987 Spring Meeting*, Provo, Utah, Paper 87-17.
4. Yetter, R. A., Dryer, F. L., Allen, M. et al., 1991. "Development of Gas-Phase Reaction Mechanisms Important to the Combustion Process of High Energy Density Materials," *28th JANNAF Combustion Meeting*, Vol. 2, CPIA Publication 573, pp. 307-322.
5. Vandooren, J., Branch, M. C. and Van Tiggelen, P. J., 1992. "Comparisons of the Structure of Stoichiometric  $\text{CH}_4\text{-O}_2\text{-Ar}$  and  $\text{CH}_4\text{-N}_2\text{O-Ar}$  Flames by Molecular Beam Sampling and Mass Spectrometric Analysis," *Combustion and Flame*, Vol. 90, pp. 247-258.
6. Kee, R. J., Grcar, J. F., Smooke, M.D., et al., 1985. "A Fortran Program for Modeling Steady Laminar One-Dimensional Premixed Flames," *Report SAND 85-8240*, Sandia National Laboratories, Livermore, CA.
7. Branch, M. C. and Cor, J. J., 1993. "Structure and Chemical Kinetics of Flames Supported by Nitrogen Oxides," *Pure and Applied Chemistry*, Vol. 65, pp. 277-283.
8. Van Tiggelen, P. J., 1995. Laboratoire de Physico-Chimie de la Combustion, Université Catholique de Louvain, Belgium, Personal Communication.
9. Mallard, W. G., Westley, F., Herron, J. T., et al., 1994. *NIST Standard Reference Database 17*, Distributed by NIST Standard Reference Data, Gaithersburg, MD, USA.
10. Habeebullah, M. B., Alasfour, F. N., and Branch M. C., 1990. "Structure and Kinetics of  $\text{CH}_4/\text{N}_2\text{O}$  Flames," *Twenty-Third Symposium (International) on Combustion*, The Combustion Institute, Pittsburgh, PA, pp. 823-831.
11. Volponi, J. V. and Branch, M. C., 1992. "Flame Structure of  $\text{C}_2\text{H}_2\text{-O}_2\text{-Argon}$  and  $\text{C}_2\text{H}_2\text{-NO}_2\text{-Argon}$  Laminar Premixed Flames," *Twenty-Fourth Symposium (International) on Combustion*, The Combustion Institute, Pittsburgh, PA, pp. 823-831.

12. Branch, M. C., Sadeqi, M. E., Alfarayedhi, A. A. *et al.*, 1991. "Measurements of the Structure of Laminar, Premixed Flames of  $\text{CH}_4/\text{NO}_2/\text{O}_2$  and  $\text{CH}_2\text{O}/\text{NO}_2/\text{O}_2$  Mixtures," *Combustion and Flame*, Vol. 83, pp. 228-239.
13. Dindi, H., Tsai, H. -M. and Branch, M. C., 1991. "Combustion Mechanism of Carbon Monoxide-Nitrous Oxide Flames," *Combustion and Flame*, Vol. 87, pp. 13-20.
14. Cor, J. J. and Branch, M. C., 1996. "Studies of Counterflow Diffusion Flames at Low Pressures," *Combustion Science and Technology*, under review.
15. Kee, R. J., Miller, J. A., Evans, G. H., *et al.*, 1988. "A Computational Model of the Structure and Extinction of Strained, Opposed Flow, Premixed Methane-Air Flames," *Twenty Second Symposium (International) on Combustion*, The Combustion Institute, pp. 1479-1494.

### COMMENTS

J. Vanderhoff, Army Research Laboratory, Aberdeen Proving Ground, Maryland. Differences exist between the flame species experimental data and the model predictions for the  $\text{CH}_2\text{O}/\text{NO}_2$  flame. It is suggested that the differences are due to experimental difficulties. What is your opinion of the extent to which an incomplete reaction set is responsible for the differences?

Author's Reply. The differences could very well arise because of experimental uncertainty or because of an incomplete reaction mechanism or uncertainties in the rate data. Our confidence in the experimental data in the flame with  $\text{CH}_2\text{O}$  is not as great as with the other flames largely due to the experimental difficulties in generating pure, gaseous  $\text{CH}_2\text{O}$  in the laboratory and in calibration for this species and  $\text{NO}_2$ . These two species pose special challenges due to the fact that they polymerize if not kept heated prior to introduction into the flame. Another contributing factor is that the measurements of  $\text{CH}_2\text{O}$  containing flames are at much higher concentrations than previous measurements of  $\text{CH}_2\text{O}$  as an intermediate in hydrocarbon combustion systems.

***Area 2:***

***Environmental Considerations  
in Combustion of Solid  
and Liquid Propellants***

## TOWARDS THE DEVELOPMENT OF "CLEAN BURNING", LOW FLAME TEMPERATURE SOLID GUN PROPELLANTS<sup>1</sup>

R. A. Pesce-Rodriguez, R. A. Fifer, and J. M. Heimerl  
U.S. Army Research Laboratory

**ABSTRACT:** As part of an effort to develop "clean burning" solid propellants, an investigation into the use of agents which would eliminate nitrogen oxide from propellant pyrolysis products was performed. Urea was found to reduce both flame temperature and the level of nitrogen oxide. Unfortunately, it also decreased the theoretical performance of propellants to which it was added. While such formulations would never qualify for use in actual weapon systems, they suggest that a "clean" gun propellant *could* also fill a more traditional need of the Army, i.e. lengthening the service life of gun barrels by reduction of flame temperature. A useful lesson for researchers investigating the development of environmentally-friendly propellants is that performance will always be *the* determining factor in selection of propellants. Perhaps the most useful outcome of this effort was the stimulation of renewed interest in agents to reduce flame temperatures.

### INTRODUCTION

There are several challenges posed by solid propellants in the Army's current gun systems. Not least among these are the need for reduced flame temperatures (to extend gun barrel service life), and the need for reduced toxic gas production, especially under pyrolysis conditions. Incomplete combustion of solid gun propellants is a common occurrence during the firing of both experimental and fielded gun systems. Included among the products of this phenomenon are nitrogen oxides and carbon monoxide. Carbon monoxide, CO, poses the most serious health hazard [1], and is found at such dangerously high levels that health agencies may impose restrictions on the number of test firings that be performed per day. Unfortunately, elimination of CO from gun propellant combustion products is not feasible from a ballistic standpoint. However, the corrosive nature of nitrogen oxides (NOx's) also makes them a matter of concern for both users and environmental/health-related agencies. A. Snelson *et al.* [2] measured breech NOx concentrations that were  $10^5$  times greater than predicted by thermochemical calculations, indicating that the actual problem may be more serious than many users suspect. While it may be argued that bore evacuators protect tank crews against toxic combustion products, this is true only when the evacuators are functioning properly and when intact. It has been reported that a hole as small as 2 cm is sufficient to allow dangerously high levels of toxic gases into the crew compartment. It has been suggested that even

---

<sup>1</sup>A modified version of this manuscript has been published in the *Journal of Energetic Materials*, Vol 14, 173-191 (1996).



intact evacuator systems do not keep tank compartments free of propellant combustion gases. Exposure of test crews to combustion gases is becoming increasingly more common as test site personnel resort to enclosed (muffled) bays to reduce noise levels near urban populations. At such sites, large fans must ventilate the test bay for several minutes to remove toxic vapors before testing can resume.

Solid residues resulting from incomplete combustion also pose significant safety and environmental concerns. For example, smoldering residues remaining after firing often result in significant quantities of smoke. This low pressure pyrolysis generates much larger quantities of NO<sub>x</sub> and other non-equilibrium gases than does high pressure combustion. Re-ignition of propellant residue in fielded tanks has been reported. Propellant residue in breeches is also said to be responsible for the creation of sealing problems.

As discussed above, incomplete combustion of solid propellants can pose a significant hazard to the health and safety of military and civilian personnel. The work presented here summarizes efforts intended to address and reduce this hazard by identifying solid propellant formulations which will generate less NO<sub>x</sub>, especially under pyrolysis conditions, while at the same time meeting the Army's need for propellants with reduced flame temperature.

## BACKGROUND

It has been known for some time that M30 gun propellant (composed of nitrocellulose, nitroguanidine and nitroglycerine) differs from other NC-based propellant in that its flame temperature is relatively cool and that it exhibits no "dark zone", i.e. no non-luminous zone [3-7]. Dark zone chemistry is dominated by the chemistry of NO - more specifically, by the slow conversion of NO to N<sub>2</sub> [8]. Much attention has been given to this chemistry because of its potential importance to delayed ignition [5,6]. It was proposed by Anderson [9] that the absence of the dark zone in M30 might suggest that nitroguanidine was behaving as a "De-NO<sub>x</sub> agent", i.e. and species capable of reducing NO<sub>x</sub> to N<sub>2</sub>.

A proposed mechanism for the removal of NO<sub>x</sub>'s by amines is described in Figure 1 [10]. De-NO<sub>x</sub> agents have been shown to be effective in eliminating NO<sub>x</sub> production in internal combustion engines and other devices. In these applications, the agents are ammonia- or amine-producing species which reduce NO to N<sub>2</sub>. In nitrate ester- or nitramine-based solid gun and rocket propellants, NO is produced from the -NO<sub>2</sub> groups in the energetic oxidizer (e.g., RDX), polymer (e.g., nitrocellulose NC), or plasticizer (e.g., nitroglycerine, NG). The concept for the current work is based on the use of De-NO<sub>x</sub> agents in solid propellants to reduce NO to N<sub>2</sub> at or near the burning propellant surface; the increased near-surface energy release should also lead to more complete combustion (i.e. more equilibrium products and less solid residue) and reduction of other products of a toxic or carcinogenic nature. In addition to reducing NO<sub>x</sub> levels in the combustion products of solid gun propellants, burn rate modification by De-NO<sub>x</sub> agents is also possible. Previous attempts to "catalyze" the burning of solid propellants have made use of oxidizing agents (e.g. PbO), rather than reducing agents (e.g. NH<sub>3</sub>). (Note: An exception to this has been found, Fifer and McBratney [11], and Fifer and Cole [12].) If De-NO<sub>x</sub> agents can effectively eliminate NO<sub>x</sub> from the combustion products of solid propellants, they may also serve as effective burning rate "catalysts", thereby simultaneously preventing pollution (by both NO<sub>x</sub> and heavy metals) and enhancing performance.

Based on this background information, an investigation into the effects of ammonia- and amine-generating compounds on solid propellant combustion and pyrolysis products was undertaken. In an examination of the pyrolysis products of M30 (a triple-base propellant) and two "nitroguanidine-free" nitrocellulose-based propellants (M9 and M10, double- and single-base propellants, respectively), it was observed that M30 actually generates more NO than do the propellants without nitroguanidine. These results suggest that while nitroguanidine might participate in the elimination of NO under high pressure combustion conditions, it does not do so at atmospheric pressure. Results to be presented below indicate that while nitroguanidine does generate NH<sub>3</sub>, it also generates significant quantities of NO and is therefore an

unsuitable agent for reduction of NO<sub>x</sub> production under pyrolysis conditions.

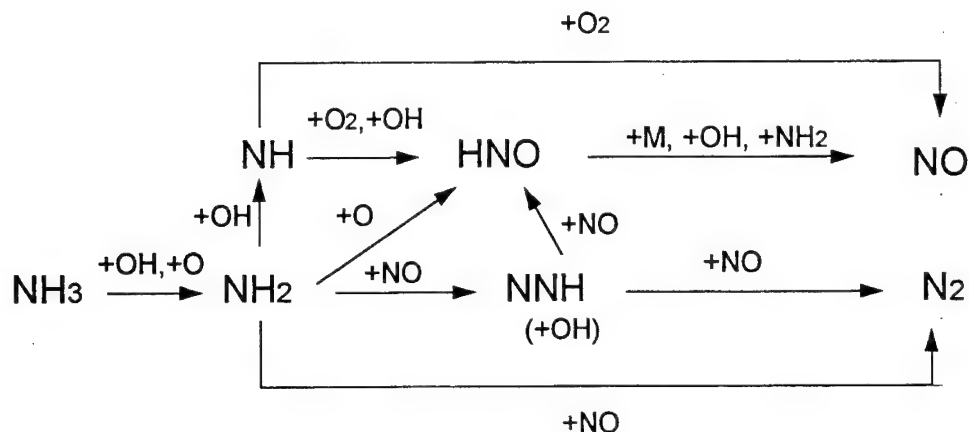


Figure 1. The thermal De-NO<sub>x</sub> process [10]

The specific focus of the present work is on the use of urea as an agent for reduction of both flame temperature and NO<sub>x</sub> production under pyrolysis conditions. Acknowledgement of the existence of superior agents for both individual objectives is freely given. The primary objective of this paper and of the presentation made at the Fourth International Symposium on Special Topics in Chemical Propulsion is to stimulate discussion on the subject of "clean burning" propellants with reduced flame temperatures. Limited success in this area has already been observed. In recent months, both the US Army and Navy have demonstrated a renewed interest in agents for flame temperature reduction. Interest in cleaner burning solid gun propellants is limited to only those formulations that in no way compromise performance.

## EXPERIMENTAL

### Samples

Experimental quantities of a double-base, JA2-like solid propellant were fabricated by handmixing acetone solutions of JA2 with ground urea. Pyrolysis samples were prepared by casting films of the handmixed propellants on aluminum foil. Candidate De-NO<sub>x</sub> agents included triaminoguanidine nitrate (TAGN), nitroguanidine (NQ), triamino-trinitro-benzene (TATB), ammonium carbonate, and urea. Structures of these compounds are given in Figure 2.

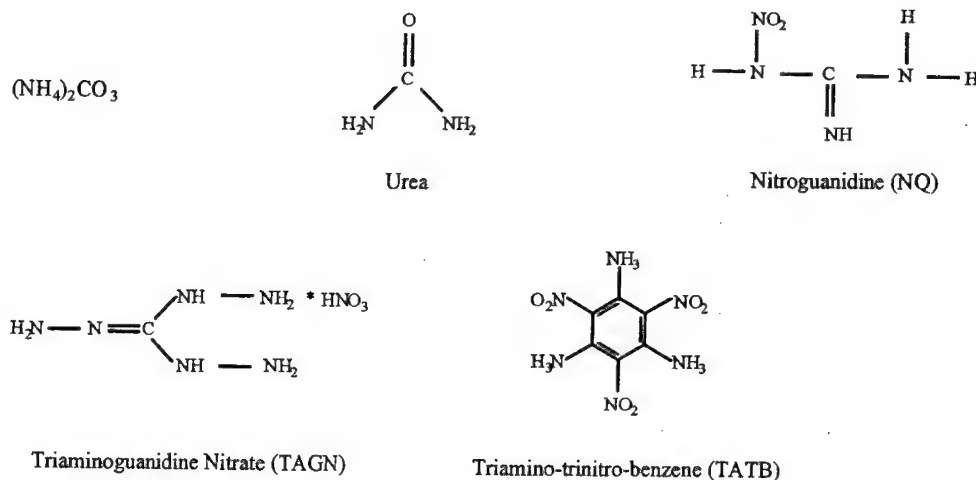


Figure 2. Structure of several candidate De-NOx agents

### Chromatographic Instrumentation

Analyses of pyrolysis products were conducted using a Hewlett Packard 5965 Gas Chromatograph ("GC") interfaced to a Hewlett Packard Model 5965A infrared detector, "IRD", and 5970 Mass Spectrometric Detector, "MSD" (only MS results are reported here). Chromatographic conditions: Quadrex capillary column 0.32 mm x 25 m x 3  $\mu\text{m}$  OV-17 film; oven program: 50° C for 3 min, then 50° C to 200° C at 10 deg/min; injector and interface chamber held at 200° C.

### Pyrolysis experiments

Samples were placed in quartz tubes and held in place with plugs of glass wool. Tubes were inserted into a coil-type Pyroprobe (Chemical Data Systems, CDS, Model 122) which was connected via a heated CDS interface chamber to the splitless injector of the GC. The heated GC interface was continuously swept with helium carrier gas. Approximately 0.6 mg of sample was pyrolyzed for each analysis. All samples were pulse-pyrolyzed at 1000° C.

### Calculations

Blake (13) calculations were performed using a value of -80.227 kcal/g-mol for the heat of formation of urea, and "standard" library values for JA2 propellant.

## RESULTS AND DISCUSSION

Screening runs of potential agents for reduction of NO<sub>x</sub> generation were performed by pyrolyzing the materials at 1000°C. The primary basis for acceptance during screening runs was that the materials thermally decompose to generate ammonia or amines. Results of screening tests, as well as the melting (or decomposition) temperatures for the several candidate agents, are given in Table 1. Based on the information in Table 1, it was concluded that the energetic materials (TAGN, NQ, and TATB) were unsuitable agents. The basis for this conclusion is that while those agents do generate ammonia, they also generate significant quantities of NO, suggesting that while they may reduce flame temperatures, they will not reduce NO<sub>x</sub> generation under pyrolysis conditions (as was observed for pyrolysis of M30 gun propellant). Ammonium carbonate was eliminated from further consideration because of its low decomposition temperature.

**Table 1**

Relative Pyrolysis Yields and Melting/Decomposition Temperatures for Several Candidate Agents

Compound	Relative Pyrolysis Yield		T <sub>m</sub> (°C)	Comments
	NH <sub>3</sub> *	NO*		
Ammonium Carbonate	329	0	58 (d)	good De-NO <sub>x</sub> agent, but hygroscopic
Urea	101**	0	133	good thermal stability, compatible with NC
TAGN	281	111	216 (d)	generates NO on pyrolysis
NQ	66	194	225-250 (d)	generates NO on pyrolysis
TATB	33	174	325 (d)	generates NO on pyrolysis

(d) Decomposes

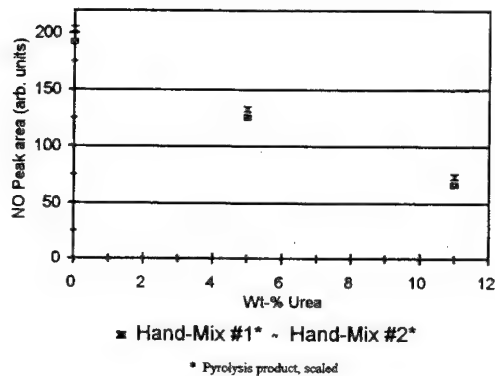
\* Pyrolysis at 1000° C. Peak area determined by pyrolysis/GC-MS; sample mass = 0.3 mg

\*\* Urea also generated "large" pyrolysis products (e.g. vapor phase urea). It is expected that under combustion conditions, more NH<sub>3</sub> will be generated.

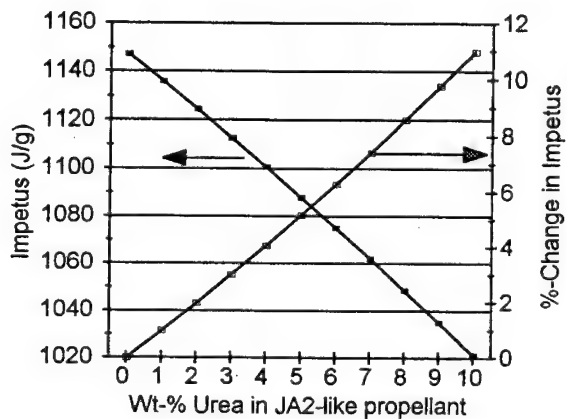
Figure 3 shows the experimental results for pyrolysis of JA2-like propellants containing urea. Levels of NO generated from pyrolysis of two different hand-mixes of JA2/urea propellants are shown. Figures 4 and 5 show impetus and flame temperatures, respectively, calculated using the Blake code. As expected, the impetus is observed to decrease as the percentage of urea in the formulation increases. The net change in impetus for a JA2-like propellant containing 4 wt-% urea is approximately 4% relative to neat JA2. The flame temperature of the JA2/urea propellant containing 4 wt-% urea is approximately 200°K lower than that of neat JA2. The decrease in projectile velocity for the same JA2/urea propellant is expected to be approximately 2% (considering that muzzle velocity can be approximated by the square root of the impetus).

Of course, a decrease in performance even as small as 2% is completely unacceptable for a new propellant formulation. However, the potential for flame temperature reduction offered by urea is quite attractive, and if nothing else, leads to the consideration of other possible agents. A recent paper by Juhasz et al. [14] is closely related to the work presented here, and reports on 12 additives considered as potential agents for reduction of flame temperature. Results of thermochemical calculations for a JA2-like propellant

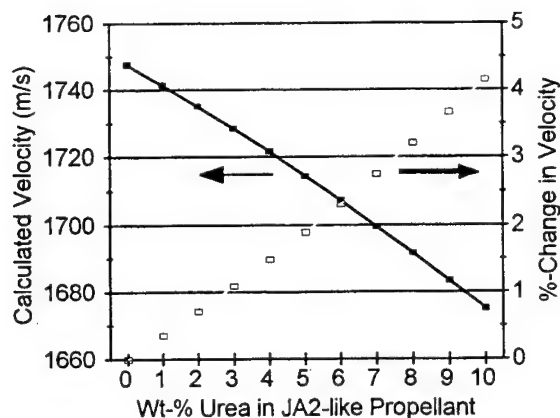
containing these agents indicate that performance need not suffer at the expense of reduced flame temperature. Investigation of the effect the agents on propellant pyrolysis studies have not yet been performed.



**Figure 3.** NO produced from pyrolysis of JA2/Urea propellant (\*: scaled)



**Figure 4.** Calculated flame temperature for JA2/Urea propellant. Based on BLAKE calculations at 0.2 g/cc nominal gas phase density.



**Figure 5.** Calculated impetus for JA2/Urea propellant; from Blake calculations at 0.2 g/cc gas phase density.

### CONCLUSION

Based on the results presented here, it is concluded that urea is an attractive agent for decreasing *both* flame temperature and production of NO under pyrolysis conditions. It effectively reduces the level of NO generated by pyrolysis of JA2-like propellants, yet has little effect on performance when used at low levels of incorporation. Flame temperature reductions achievable with an agent such as urea are expected to significantly extend the life of gun barrels. An added benefit of the use of urea is that it has been reported to be a successful flash suppressant [15]. Results reported for the use of polyurethane additives in double-base propellants [16] suggest a similar flame temperature suppression and concomitant wear reduction.

While the results reported here are certainly insufficient to justify the fielding of a new propellant, they do provide encouragement in the search for agents that will not only reduce flame temperatures of solid propellants and thereby extend gun barrel service life, but also provide a safer environment for testing and military personnel. Discussions and investigations stimulated by these early results are already taking place in the United States. It is hoped that this manuscript and the presentation made at the Fourth International Symposium on Special Topics in Chemical Propulsion will stimulate others in the field of gun propellant development to consider environmental and health aspects, as well as performance aspects, when designing new propellant formulations.

### ACKNOWLEDGMENTS

The authors would like to thank Dr. Anthony Kotlar for his assistance in running Blake calculations.

## REFERENCES

1. **Weyandt, T.B. and Ridgeley, C.D.**, Carbon monoxide, Chapter 11, pp 397-427, in *Textbook of Military Medicine, Part III, Disease in the Environment*, Vol. 2. Office of the Surgeon General, Department of the Army of the United States of America., R. Zajchuk, D.P. Jenkins, and R.F. Bellamy, Eds, 1993.
2. **Snelson, A., Ase, K., Taylor, K., Gordon, S.**, Combustion product evaluation of various charge sizes and propellant formulations, Final report, April 1989, Contract No. DAMD17-88-C-8006.
3. **Vanderhoff, J.A.**, Spectral studies of propellant combustion. I: Experimental details and emission results for M30 propellant, BRL-MR-3714, Dec 1988.
4. **Vanderhoff, J.A.**, Spectral studies of propellant combustion. II. Emission and absorption results for M30 and HMX1 propellant, BRL-TR-3055, Dec 1989.
5. **Vanderhoff, J.A.**, Species profiles in solid propellant flames using absorption and emission Spectroscopy, Comb. and Flame, 84, 1991a. pp. 73-92.
6. **Vanderhoff, J.A., Teague, M.W., Kotlar, A.J.**, Absorption spectroscopy through the dark zone of propellant flames, BRL-TR-3334, April 1992.
7. **Teague, M.W., Singh, G., Vanderhoff, J.A.**, Spectral studies of propellant combustion. IV: Absorption and burn rate results for M43, MX39, and M10 propellant, ARL-TR-180. Aug 1993.
8. **Vanderhoff, J.A., Teague, M.W., Kotlar, A.J.**, Determination of temperature and NO concentration through the dark zone of solid-propellant flames, Proceedings of the 24th Symposium (International) on Combustion, The Combustion Institute, 1991b. pp 1915-1922
9. **Anderson, W.R.**, various private communications with members of ICB/IBC/BRL during the period of 1987-1988.
10. **Miller, J.A. and Bowman, C.T.**, Mechanisms and modeling of nitrogen chemistry in combustion, Prog. Energy Combust. Sci. 15 (1989). pp. 287-338.
11. **Fifer, R.A. and McBratney, W.F.**, Catalysis of nitramine propellants by metal borohydrides, ARBRL-MR-03300, ADA, 133 215, July 1983.
12. **Fifer, R.A. and Cole, J.E.**, Catalysts for nitramine propellants, disclosure submitted July 1980, US Patent 4,379,007.
13. **Freedman, E.**, "BLAKE - A thermodynamics code based on Tiger - User's guide and manual, ARBRL-TR-02411, July 1981.
14. **Juhasz, A., Heimerl, J., Pesce-Rodriguez, R. and Simmons, R.**, Additives to reduce flame temperatures of advanced gun propellants, Proceedings of the 1996 JANNAF Combustion Subcommittee & Propulsion Systems Hazards Joint Meeting, Naval Post Graduate School, Monterey, CA, 4-8 November 1996, CPIA Pub., in press. Companion paper: **Heimerl, J.M., Juhasz, A., Pesce-Rodriguez, R., Kotlar, A.J., and Cumpton, R.**, A critical comparison of theoretical performance calculations obtained from BLAKE and MCVEC thermochemical codes, Proceedings of the 1996 JANNAF Combustion Subcommittee & Propulsion Systems Hazards Joint Meeting, Naval Post Graduate School, Monterey, CA, 4-8 November 1996, CPIA Pub., in press.
15. **Klingenberg, G. and Heimerl, J.M.**, Review of French Work, Chapter 13 in *Gun Muzzle Blast and Flash*, Progress in Astronautics and Aeronautics, Volume 139, p. 290. 1992.
16. **Huwei, L. and Ruonong, F.**, Application of pyrolysis-gas chromatography in explosive and propellant analysis", Journal of Beijing Institute of Technology, 1992 (1), pp. 13-18.

## COMMENTS

1. Dr. Tung-ho Chen, U.S. Army Armament Research, Development, and Engineering Center, Picatinny Arsenal, New Jersey. To the best of my knowledge, there are no internationally accepted criteria for determining compatibility by DSC. It is therefore recommended that the standard compatibility test (90 °C for 40 hours, in this case) be performed in the studies of this subject.

Authors' Reply. Yes, you are correct. The DSC results presented do not confirm long-term compatibility. The samples with which we performed our investigations were all very small (less than one gram in size) hand-mixes that could be easily screened for *gross incompatibility* by DSC. Regarding the compatibility of the specific JA2/Urea formulation, we have been told by several individuals with first or second-hand knowledge of previous work with such a formulation that the materials are NOT compatible when tested by other methods.

2. Prof. M.C. Lin, Emory University, Atlanta, GA. Cyanuric acid, an efficient source of HNCO, has been used by Sandia National Labs (Livermore) for the rapid reduction of NO<sub>x</sub> (RAPRENO<sub>x</sub>). Have you studied its effect on NO<sub>x</sub> reduction in gun propellant combustion reactions?

Authors' Reply. Actually, the focus of this work was *pyrolysis* of gun propellants rather than combustion. We did consider cyanuric acid, but spent most of our time screening materials that were thought to be good sources of ammonia and/or amines, rather than HNCO. Your suggestion is a good one. Given the opportunity to spend more time on this project, we would certainly give this candidate a second look.



## EFFECTS OF ROCKET EXHAUST ON THE LAUNCH SITE ENVIRONMENT AND STRATOSPHERIC OZONE

Robert R. Bennett, Jay R. Whimpey, Randall Smith-Kent, Allan J. McDonald  
Thiokol Corp., Brigham City, Utah

**ABSTRACT:** Three independent studies regarding the environmental impacts of testing and launching rockets were published in the 1991 - 1992 time frame. Each of these studies concluded that these impacts are quite minor. Since these studies were published, there has been additional work in exhaust cloud modeling, ozone depletion predicted by atmospheric models, and in alternate propellant development.

This paper discusses the conclusions of the three earlier studies in light of the most recent data. The long term impact of launching nine Shuttles and three Titan IV rockets annually is predicted to be a global stratospheric ozone depletion of 0.006 - 0.02 percent. Local and regional effects are predicted to be higher.

While a considerable amount of work has been done to understand the impacts of rockets on the environment near the launch site, one of the potentially toxic species produced in the atmosphere during a rocket launch,  $\text{NO}_2$ , has been given little treatment. Recent calculations show that  $\text{NO}_2$  produced from afterburning and atmospheric oxidation of some liquid rocket exhaust clouds may be of comparable toxicity to  $\text{HCl}$  plus  $\text{NO}_2$  from some solid rockets.

### BACKGROUND

The environmental impacts of chemical propulsion continue to be an area of research and concern from time to time. Three independent reviews<sup>1,2,3</sup> were published in the 1991 - 92 time frame which summarized the data available at that time regarding the atmospheric effects of launching rockets. Additional studies were published previous to that time,<sup>4,5</sup> and have included the impacts of launching and testing rockets on both the atmosphere and on the biota in the vicinity of the launch or test site. The American Institute of Aeronautics and Astronautics (AIAA) sponsored a workshop on the atmospheric effects of chemical rocket propulsion in Sacramento in June, 1991. Representatives from the propulsion industry, the National Aeronautics and Space Administration (NASA), the Department of Defense (DoD), the Environmental Protection Agency (EPA), environmental groups, the Library of Congress, and the atmospheric science community all helped to produce a position paper. The paper was published in October 1991 after approval by all parties concerned. The conclusions of the study regarding the magnitude of the effects were:

1. Using a launch model of nine Shuttles and six Titans per year, on a global basis, stratospheric ozone depletion was calculated to range from 0.0065% to 0.024%. Depletion is expected to be somewhat higher in the northern mid-latitudes, where most of the launches occur. In the near

vicinity of the plumes, ozone depletion may be high (>80%), but recovery occurs rapidly. Global ozone depletion due to heterogeneous reactions that may take place on the surfaces of alumina, soot, or ice is expected to be small if the chemistry associated with rocket particulates is the same as that of natural stratospheric particulates.

2. The global contribution to anthropogenic sources of acid rain by chemical rockets is estimated to be less than 0.01%. Current data suggest that local effects are confined to areas less than 2,500 feet from the launch site.

3. The contribution of chemical rockets to global warming is minute.

4. The extensive experience base in rocket testing and flights suggests that concerns with toxicity of rocket ingredients or effluents are manageable by proper operational controls.

The AIAA report recognizes that there are many areas which have not received adequate research. For example, the global, regional, and local stratospheric ozone effects cited are almost all calculated effects based on atmospheric models. There is very little experimental data available on either measurement of the exhaust species themselves, or their effects. The AIAA recommended that research be conducted on both stratospheric ozone effects and on local tropospheric air and ground effects. While there has been some research in these areas since the publication of the AIAA report, there has not been a concerted, focused effort, primarily due to a lack of funding.

Shortly after the publication of the AIAA report, the World Meteorological Organization (WMO) issued its 1991 assessment on the state of knowledge of stratospheric ozone depletion.<sup>2</sup> The WMO report includes a chapter on the effects of rockets on stratospheric ozone. This chapter was included because of a request by the Russians to do so. It was the conclusion of this study that the impact of chemical rockets, particularly the Space Shuttle, on global stratospheric ozone is, at most, a third order effect, and not of great concern. It also included a discussion on local ozone effects, concluding that while there may be significant ozone depletion in the air around the rocket plume, the atmosphere recovers rapidly. An upper limit of local ozone destruction following a Shuttle launch was obtained by satellite data showing no ozone depletion within the detection limits of the Total Ozone Mapping Spectrometer (TOMS) instrument.

The third of the major studies conducted<sup>3</sup> was sponsored by the European Space Agency (ESA), and concerned the impacts of Ariane V launches on the stratosphere. The assessment was based on launching 10 Ariane V rockets per year, every year for 20 years. The conclusions in this study were very similar to those of the other two studies, and ESA did not recommend any changes in launch vehicles for environmental reasons.

As with the AIAA report, the ESA and the WMO reports recognize the limitations of the measured data obtained to date. The ozone depletion data reported were all calculations based on homogeneous chemistry. Without conducting a rigorous global model on rocket exhaust impacts, it is estimated that the inclusion of potential heterogeneous chemistries would at most double the stratospheric ozone depletion from rockets.

## DISCUSSION AND RESULTS

### Update on the Stratospheric Impacts of Rockets

In the years since the AIAA, WMO, and ESA reports were issued, our understanding of atmospheric processes has improved, and additional refinements to the global models have been made. Additional modeling studies on the effects of rockets on stratospheric ozone have been published.<sup>6,7,8,9,10,11,12,13,14,15</sup> These studies have mainly focused on local stratospheric impacts of the exhaust cloud from a single launch. There is some question as to the constituents of the exhaust cloud, particularly the distribution of chlorine between HCl (by far the major chlorine species at ground level), and Cl<sub>2</sub>. Some models suggest that chlorine from rocket exhaust is distributed about equally between Cl<sub>2</sub> and HCl with afterburning under stratospheric conditions. Molecular chlorine will be photolyzed within minutes or hours, whereas HCl remains intact for days or weeks, but eventually releases its chlorine after reacting with a hydroxyl radical. On a regional or global basis, this is irrelevant, since in either case, the chlorine will eventually be released as free atomic chlorine.

On a local basis, an increase in the Cl<sub>2</sub>/HCl ratio could lead to more significant ozone depletion within the plume. However, Karol et al.<sup>16</sup> cited in the WMO report and in the AIAA report, predict that even without free chlorine, the bulk of the ozone in the plume of a solid or liquid rocket may be depleted for a few hours due to the production of NO with afterburning. Karol used the U.S. Space Shuttle as a test case for a mostly solid propulsion system, and the Russian Energya for an all liquid system. There has been some debate on the quantity of NOx (odd nitrogen species, mainly NO and NO<sub>2</sub>) species produced in the afterburning region of rocket plumes, particularly at stratospheric altitudes,<sup>17</sup> with predicted NOx emission indices ranging from 0.06<sup>9</sup> to 33 g NOx/kg fuel,<sup>15</sup> depending on the type of rocket and the model used. Obviously, the extent of NOx production will directly affect the relative contribution of chlorine species in solid rocket exhaust to the total ozone destruction resulting from the rocket. For the maximum stratospheric NOx production scenario, the overall impact on the total ozone column from the Space Shuttle was calculated by Karol to be at most an 8 percent decrease, which recovers after a few hours. Of the total ozone destroyed, about 25 percent was calculated to be due to HCl, and 75 percent to NOx.

Regardless of which, if any, model is most accurate, an upper limit on total column ozone destruction after a single launch can be established based on the work by McPeters et al.,<sup>18</sup> and Kruger et al.<sup>7,12</sup> using data from the Total Ozone Mapping Spectrometer (TOMS). The TOMS instrument has passed over the southeast U.S. on several occasions within several hours after Space Shuttle launches and detected no ozone decrease. The TOMS instrument does not have an extremely high resolution footprint, but should be able to detect a column ozone decrease of about 10 percent over a 20x20 km area.

Larger decreases in the total local ozone column within a Space Shuttle exhaust cloud than Karol calculates have been predicted by Ross,<sup>19</sup> who estimates up to 30 percent decreases in the total ozone column may be observed if wind conditions are such that the exhaust contrail is 'stacked' vertical by atmospheric winds. They predict that the bulk of the ozone destruction will be due to free chlorine, produced from the photolysis of Cl<sub>2</sub>, which, in turn, was produced during the afterburning from HCl. As a consequence of this prediction, and the limitations in the resolution of the TOMS instrument, the Aerospace Corp. has designed and built a new high resolution ozone imager (HIROIG), which has a much narrower field of view in order to focus on point sources of ozone depletion. This instrument has yet to be placed on a space platform, but has been used on the ground in an attempt to measure column ozone depletion following a Shuttle launch. The HIROIG instrument was deployed at the Kennedy Space Center for the July 1994 launch, and collected data under nearly ideal conditions for ozone depletion measurements. The Shuttle was launched around noon on a clear day, with upper atmospheric

winds blowing such that the contrail did stack back on itself, and the whole cloud drifted to a position nearly directly above the HIROIG. The final report on the HIROIG measurements has not yet been released, but preliminary indications are that no alarming ozone depletion was observed.

The identification of the central role of heterogeneous processes in the formation of the Antarctic ozone hole has been well documented in recent years. Condensation of HCl and NO<sub>2</sub> onto polar stratospheric cloud (PSC) aerosols, and the subsequent release of active chlorine into a denitrified atmosphere are the most significant chemistries leading to the nearly complete depletion of stratospheric ozone at some altitudes during the Antarctic spring. Jackman et al.,<sup>15</sup> have recently calculated the added effect of stratospheric aerosols on the regional and global ozone depletion due to rocket launches. Using the same launch scenario proposed by Prather<sup>5</sup> of nine Shuttles and six Titans, Jackman calculates the global ozone depletion due to rockets to be 0.0056% when only homogeneous chemistry is included, and 0.014% when stratospheric aerosols of both sulfuric acid and polar stratospheric clouds (ice and hydrated nitric acid) are included. It has been pointed out<sup>20</sup> that the propellant mass of a Titan rocket used by Prather is low by a factor of two, so the actual launch scenario used was nine Shuttles and three Titans.

The possibility of additional ozone depletion due to heterogeneous chemical reactions occurring on the condensed phase species (Al<sub>2</sub>O<sub>3</sub>, H<sub>2</sub>O, soot) produced by rockets has been raised. It is not currently known whether or not chemistries similar to those occurring on PSCs can occur on alumina from rockets. However, calculations by Carrier et al.<sup>8</sup> suggest that even with a high rate of reaction, the plume disperses too rapidly for significant ozone destruction by heterogeneous processes.

Another area of recent research has been the question of halocarbon (CFC) reactions on the alumina from solid rockets.<sup>11</sup> It has been suggested that alumina surfaces may act as catalytic sites for the decomposition of CFCs. If this is the case, then alumina could cause the CFCs to release their chlorine more rapidly than they otherwise would. This would result in the overall active chlorine burden in the stratosphere being increased in the short term, but decreased in the long term. Robinson's work indicates that CFCs in contact with alumina may indeed be decomposed. However, this study was performed using pure, single crystal alumina. The alumina from a rocket motor may be very different. In addition, if the alumina decomposes CFCs in the stratosphere, it should do the same in the troposphere, and would therefore prevent those CFCs from reaching the stratosphere and releasing their chlorine into the ozone destruction cycle. It is therefore not clear what the overall impact catalytic CFC decomposition on the surfaces of rocket exhausted alumina would have on stratospheric ozone.

While only a limited amount of experimental work specifically focused on the stratospheric impacts of chemical propulsion has been done, the evidence linking the Antarctic ozone hole in particular, and global stratospheric ozone depletion in general to the tropospheric emission of CFCs and other ozone depleting substances (ODSs) continues to grow. The link between active stratospheric chlorine species and the nearly complete removal of ozone from the Antarctic stratosphere at certain altitudes and seasons has been firmly established.<sup>21</sup> The efforts of the parties involved in the Montreal Protocol to eliminate the production and release of ODSs have begun to bear fruit. The rate of increase of the concentration of the most abundant CFCs has begun to slow, while the atmospheric concentration of trichloroethane has actually begun to drop. This is significant for chemical propulsion in that the same models and scientific understanding which led to the provisions of the Montreal Protocol were used to draw the conclusions in the papers cited above.

### Local Launch Site Issues

Virtually all of the studies which have been done on the effects of rocket effluents around the launch site have focused on solid rockets, and in particular, the HCl and aluminum oxide emissions.<sup>22,23</sup> The one

exception is that the impacts of a catastrophic failure of a liquid rocket using  $N_2O_4$ /Aerozine have been evaluated, since both of these ingredients are quite toxic. Aerozine is a mixture of approximately 50 percent unsymmetrical dimethyl hydrazine (UDMH) and 50 percent hydrazine. The studies which have been done show that plant and animal mortalities resulting from the HCl in the exhaust cloud of a Shuttle launch are limited to a region within about 1/2 mile of the launch pad. Leaf spotting from acidic deposition occurs up to several miles away, but the effects are temporary.

Because of the toxicity of HCl at concentrations greater than about 10 ppm, and the ceiling limit of 5 ppm under EPA and the National Institute of Occupational Safety and Health (NIOSH), launch criteria have been established for ground level HCl concentrations. Prior to each launch at either Vandenberg Air Force Base (VAFB) or Cape Canaveral Air Station (CCAS), local meteorological data and calculated rocket exhaust products are input into the Rocket Exhaust Effluent Dispersion Model (REEDM), which calculates the maximum ground level concentrations of the exhaust species over the surrounding area. These data are used to assess the advisability of launching from a toxicological exposure basis. The Air Force has defined Toxic Hazard Corridor Tier levels, to which toxicological data can be applied to assess the potential danger to individuals near the launch site. The tier levels are defined as follows:<sup>24</sup>

Tier I: A zone for which certain sensitive individuals (asthmatics and those with pulmonary difficulties) may be at some risk from exposure.

Tier II: A zone that represents the concentration level above which there may be significant or irreversible effects from exposure.

Tier III: A zone that represents the concentration level which is immediately dangerous to life and health.

The Air Force policy at VAFB has been to consider a Tier I condition predicted to impact the general populace or on base housing as a 'no go' for launch. The Tier I criteria have undergone three revisions in the past year, changing from 10 ppm time weighted average (TWA) for 30 minutes, to 1 ppm instantaneous (Oct. 27, 1994), to 1 ppm TWA for 1 hour (Dec. 30, 1994),<sup>25</sup> and finally to 2 ppm TWA for 1 hour or 10 ppm instantaneous (June 7, 1995).<sup>26</sup> The consequence of the Oct. 27, 1994 change to 1 ppm maximum peak concentration was a reduction in launch probability at VAFB of all launch vehicles using solid rocket motors. For example, the Titan vehicle launch probability was reduced to 27 percent based on the HCl restrictions alone. Realizing the hardship imposed on rocket launching by this very conservative restriction, a reassessment was made, resulting in the guidelines of 30 Dec. and 7 June.

One area, which appears to have been mostly overlooked, are the tropospheric NO<sub>x</sub> emissions of rockets. Most of the calculations have used as input to the exhaust cloud dispersion models the species at the nozzle exit plane, which have not taken into account afterburning, and the possible production of NO<sub>x</sub>'s. Those studies which have considered afterburning and NO<sub>x</sub> production have mainly focused on the stratospheric ozone effects of the major NO<sub>x</sub> constituent, NO. NO<sub>x</sub> effects have not been of serious concern in the launch site models because NO is fairly innocuous compared with HCl or NO<sub>2</sub>. Calculations of afterburning chemistry at sea level show that fairly high levels (on the order of 2-3 percent of the total exhaust) of NO<sub>x</sub> are predicted when afterburning is completed, and that about the same amount is produced in both liquid and solid rockets.

A study to calculate the relative concentrations of HCl, NO, and NO<sub>2</sub> in the exhaust clouds of various rocket motors as the clouds diffuse and strike the ground has been conducted recently. As discussed above, there are regulations in place for maximum predicted HCl concentrations, and launches and tests have been delayed on this basis. Since NO<sub>2</sub> is at least as toxic as HCl, based on its permissible exposure

limit (PEL) of 1 ppm, and on toxicological studies, it was felt that it was important to calculate their relative concentrations for different launch vehicles.

Table I shows the calculated exhaust products of many of the current U.S. launch vehicles. Two columns are shown for each vehicle, the first giving the nozzle exit plane species, and the second, the species predicted after the completion of the afterburning reactions in which oxygen from the air further oxidizes hydrogen, carbon monoxide. The values shown are in grams of products per 100 grams of propellant. The total of all products is greater than 100 grams for the afterburning cases because oxygen and nitrogen from the atmosphere are incorporated into some of the species. In the case of water, some is produced within the rocket chamber, as is reflected in the exit plane columns, some is produced when hydrogen and hydroxyl are oxidized, and some is present in the ambient air. The values given for water in the afterburning columns include as much water as would be present in air at 25°C and 46% relative humidity.

From an environmental perspective, the most significant change in exhaust species with afterburning is the production of nitrogen oxides. The computer model used for these calculations predicts that all of the rocket motors shown produce between 2.3 and 3.5 grams NO<sub>x</sub> per 100 grams of fuel during the afterburning process, with more than 99 percent in the form of NO, with only a trace of NO<sub>2</sub>. While NO is classified as a toxic chemical, it is less toxic than either HCl or NO<sub>2</sub>. Its Occupational Safety and Health Administration (OSHA) TWA permissible exposure limit (PEL) is 30 mg/m<sup>3</sup>, with no ceiling limit listed. This is similar to the toxicity of carbon monoxide. The OSHA ceiling value for HCl is 7 mg/m<sup>3</sup> (5 ppm), and for NO<sub>2</sub> is 1.8 mg/m<sup>3</sup> (1 ppm).

Although NO is the species immediately produced in the afterburning of the rocket, measurements suggest that a significant fraction of the NO is converted to NO<sub>2</sub> within several minutes.<sup>27</sup> NO, NO<sub>x</sub> and ozone measurements were made by an instrumented aircraft which flew through the exhaust cloud of a Titan III launch in 1974. The passes were made at T+5 and T+34 minutes, and showed increasing levels of NO<sub>2</sub>. At T+5 minutes, about 22 percent of the NO<sub>x</sub> was NO<sub>2</sub> while at T+34 minutes, this had increased to about 32 percent. Assuming that the calculations are correct, and there is little NO<sub>2</sub> immediately after the launch, an excellent fit of the NO<sub>2</sub>/NO<sub>x</sub> ratio vs. log(time) can be made. This is shown in Figure 1. The significance of these data is that within several minutes after the rocket launch, a significant portion of the NO has been converted to a species of much greater toxicity.

While concern has been expressed over the past several years about the potential for public exposure to unacceptable levels of HCl from solid rocket motors containing AP, NO<sub>2</sub> has not been an issue even though it is potentially more toxic than HCl. This is largely because even with afterburning considered, NO<sub>2</sub> is only a very minor constituent of rocket exhaust. It is only when the conversion of NO to NO<sub>2</sub>, and the relative rise rates of different exhaust clouds are included that NO<sub>2</sub> becomes significant. It is important to remember that for the regulatory limits, the real concern is not maximum exhaust cloud concentrations, but rather the maximum concentrations observed on the ground as the exhaust cloud disperses over the nearby landscape.

Calculations were performed for all of the launch vehicles listed in Table 1 using the EPA approved INPUFF computer model to predict the maximum concentrations of important exhaust species impacting the ground as a function of distance from the launch site for various meteorological conditions. In order to make comparisons between different rocket motors, the results were normalized to equivalent thrust. Figure 2 shows a comparison between the maximum ground concentration of NO<sub>2</sub> from a single Space Shuttle Main Engine (SSME), and the NO<sub>2</sub> plus HCl from a Space Shuttle Solid Rocket Booster (SRB) as a function of distance from the launch site, as calculated by the INPUFF program. The NO<sub>2</sub> concentration was estimated from the calculated NO<sub>x</sub> concentration, and was based on the Titan data from Figure 1. The principal reason that the NO<sub>2</sub> ground concentration from the SSME may be just as high at some locations as the HCl plus NO<sub>2</sub> ground concentration of the SRB is the relative plume rise.

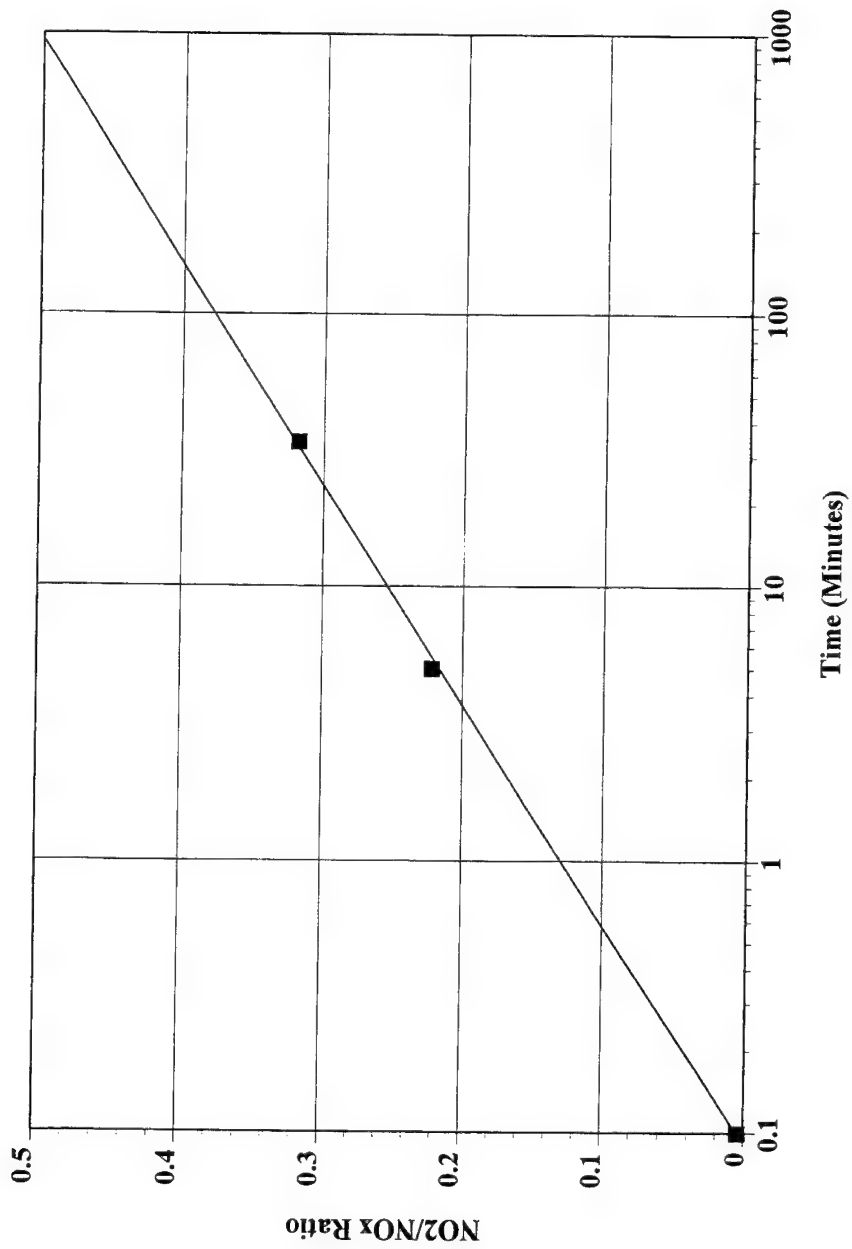


Figure 1. Titan III Launch: time evolution of  $\text{NO}_2/\text{NO}_x$  ratio in the exhaust cloud. Zero time point is calculated.

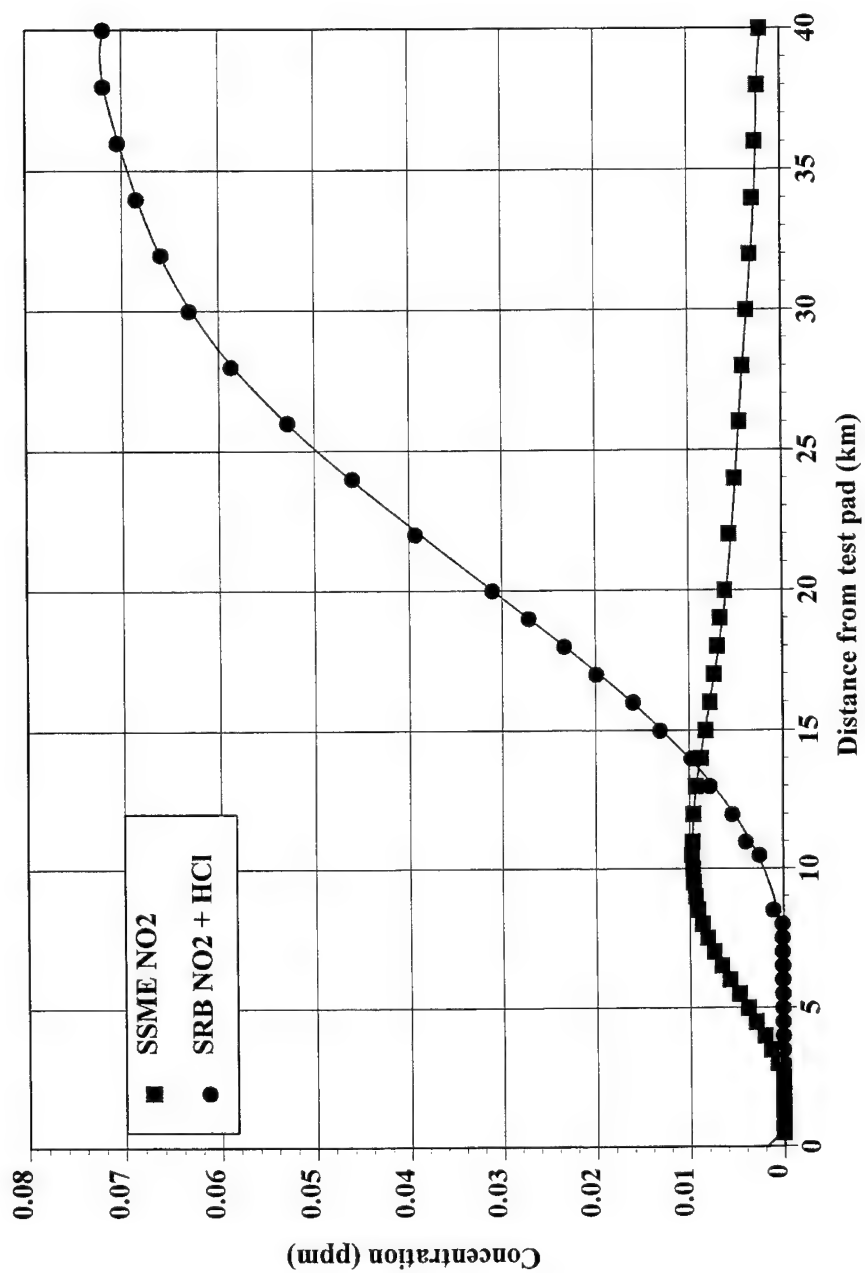


Figure 2. Comparison of NO<sub>2</sub> from an SSME static test with NO<sub>2</sub> plus HCl from an SRB static test.  
Maximum ground concentrations as a function of distance from rockets.



TABLE 1  
Exhaust Species from U.S. Space Launch Vehicles

Vehicle	Space Shuttle				Titan				Delta			
	SRBs Solid PBAN/AP/Al		SSMEs Liquid LO <sub>2</sub> /LH <sub>2</sub>		SRMU Solid HTPB/AP/Al		LR87 Liquid N <sub>2</sub> O <sub>4</sub> /Aerozine		GEM Solid HTPB/AP/Al		RS-27 Liquid LO <sub>2</sub> /RP1	
Species	exit plane	with after- burning	exit plane	with after- burning	exit plane	with after- burning	exit plane	with after- burning	exit plane	with after- burning	exit plane	with after- burning
Al <sub>2</sub> O <sub>3</sub>	29.32	29.32			34.19	34.19			34.26	34.26		
CO	24.59	0.0			21.41	0.0	5.38	0.0	21.42	0.01	47.30	0.04
CO <sub>2</sub>	2.76	41.25			2.05	35.42	16.81	24.49	2.05	35.49	22.92	93.90
Cl	1.30	0.06			1.65	0.02		0.0	1.60	0.13		
Cl <sub>2</sub>	0.004	1.08			0.005	1.37		0.0	0.005	1.92		
H	0.102	0.0	0.155	0.018	0.14	0.0	0.046		0.14	0.0	0.18	0.0
H <sub>2</sub>	1.99	0.0	3.60	0.157	2.00	0.0	0.25		2.05	0.0	1.20	0.0
H <sub>2</sub> O	6.69	52.18*	92.38	119.39*	8.62	69.19*	34.75	87.67*	8.77	64.94*	25.80	55.49
HCl	19.41	19.55			18.31	18.52			18.55	18.03		
N <sub>2</sub>	8.72	mixes with air			8.29	mixes with air	21.83	mixes with air	8.31	mixes with air	0.0	
NO	0.043	2.87		2.98	0.06	3.28	2.74	2.54	0.06	2.31	0.0	3.50
NO <sub>2</sub>	0.0	0.001		0.002	0.0	0.01	0.007	0.01	0.0	0.008		0.008
O	0.021	0.0	0.158	0.46	0.038	0.0	0.997	0.0	0.04	0.0	0.218	0.01
OH	0.37	0.0	3.35	3.14	0.50	0.0	4.98	0.0	0.48	0.0	2.021	0.13
O <sub>2</sub>	0.009	mixes with air	0.36	mixes with air	0.014	mixes with air	12.18	mixes with air	0.013	mixes with air	0.414	mixes with air

\*Total water with afterburning includes atmospheric water. Assume 14,500 ppm water in ambient air (equivalent to 46% RH at 25°C).

Motors with very high thrust such as seen in SRBs have a large heat release concentrated in a single plume. The plume from the SRB is predicted to rise higher than that of the SSME, and therefore become more dispersed prior to impacting the ground.

Figure 3 represents an attempt to include the relative toxicities of the two species with the concentration data in order to get a 'toxicity ratio'. Since  $\text{NO}_2$  has a PEL about four times lower than that of HCl, equivalent toxicity would be faced at 1/4 of the  $\text{NO}_2$  concentration. Thus, for any value greater than 1 on the curve in Figure 3, a person on the ground would be exposed to a more toxic exhaust cloud from an SSME firing than from an SRB firing. For this scenario, this would be the case for locations from 2 to 9 km from the rocket motor. It must be noted that the conversion of NO to  $\text{NO}_2$  is likely to be dependent on the type of launch vehicle and on local meteorological conditions. Applying the rate of NO to  $\text{NO}_2$  conversion from the Titan vehicle to other rocket motors is therefore only an approximation, but lacking other data, it is the best that can be done.

Normalizing launch systems to equivalent thrust for comparisons is difficult. For example if it is desirable to compare the SRB exhaust cloud with the cloud formed by a combination of several SSMEs, one must assume a cluster of SSMEs in some configuration. If the SSMEs are arranged such that the plumes mix little before combining with ambient air, the exhaust clouds may have a rise height similar to that from a single motor, and therefore have ground impact concentrations much higher than a single motor due to the increased mass of exhaust products. On the other hand, if the plumes from the individual motors combine to form one large plume with a buoyancy equivalent to one large motor, the  $\text{NO}_2$  concentration from the SSME cluster would be similar to that of the SRB. Figure 4 shows the worst case scenario for an SSME cluster, and assumes that the separate exhaust plumes do not combine early to contribute to each other's buoyancy, but do eventually mix to give a single large exhaust cloud. In this scenario, the exhaust cloud from the SSME cluster has a ground cloud toxicity equivalent to, or greater than that of the SRB out to about 22 km from the launch/test site. It is likely that in reality, some mixing would occur in the hot SSME plumes, and the plume rise would be somewhat higher than that calculated for a single SSME. The concept of large hot plumes giving more dispersed ground impacts than smaller, less buoyant plumes is analogous to the construction of tall smokestacks at power plants. When the air pollutants are released at a high altitude, they are dispersed to harmless concentrations by the time they impact the ground, whereas if they were released at ground level, their concentrations would be significantly higher.

These findings are only relevant on a relative sense. None of the concentrations predicted by the INPUFF code exceed the PELs for any rocket exhaust species. Note that the concentrations of the two species of concern are predicted to be less than 0.1 ppm at all locations (Figure 2), much less than the respective 1 or 5 ppm PELs for  $\text{NO}_2$  and HCl. However, decisions or recommendations of preferred rocket propulsion chemistry have been made in the past on the basis of predicted ground concentrations, and in fact, launches and static tests of solid rocket motors have been delayed at times. What these data suggest is that one of the proposed solutions for making rocket exhaust clouds less toxic, switching from solid to liquid booster rockets, may not improve the situation at all.

## CONCLUSIONS

The environmental impacts of chemical rocket propulsion have continued to be investigated in recent years. The recent data have tended to support the conclusions of the reviews which were published in the 1991-92 time frame. The global impacts of rockets at current or projected launch rates on the stratospheric ozone layer are very small, on the order of a few thousandths to one or two hundredths of a percent. Regional effects were predicted to be somewhat higher in regions of high launch activities, while local effects were calculated to be rather high immediately following a launch, but recovered to

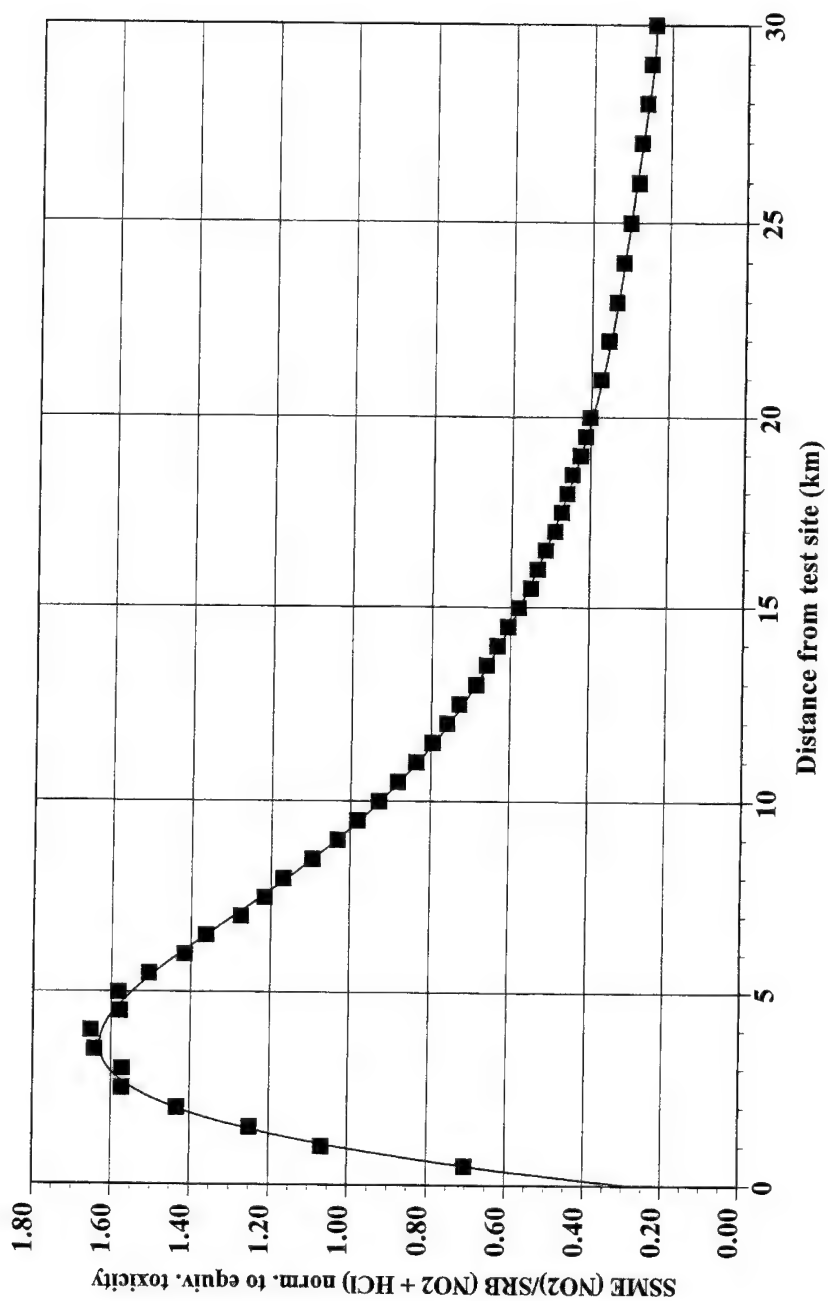


Figure 3. Relative toxicity of SSME vs. SRB exhaust clouds. Exhaust species as calculated - no normalization to equivalent thrust.

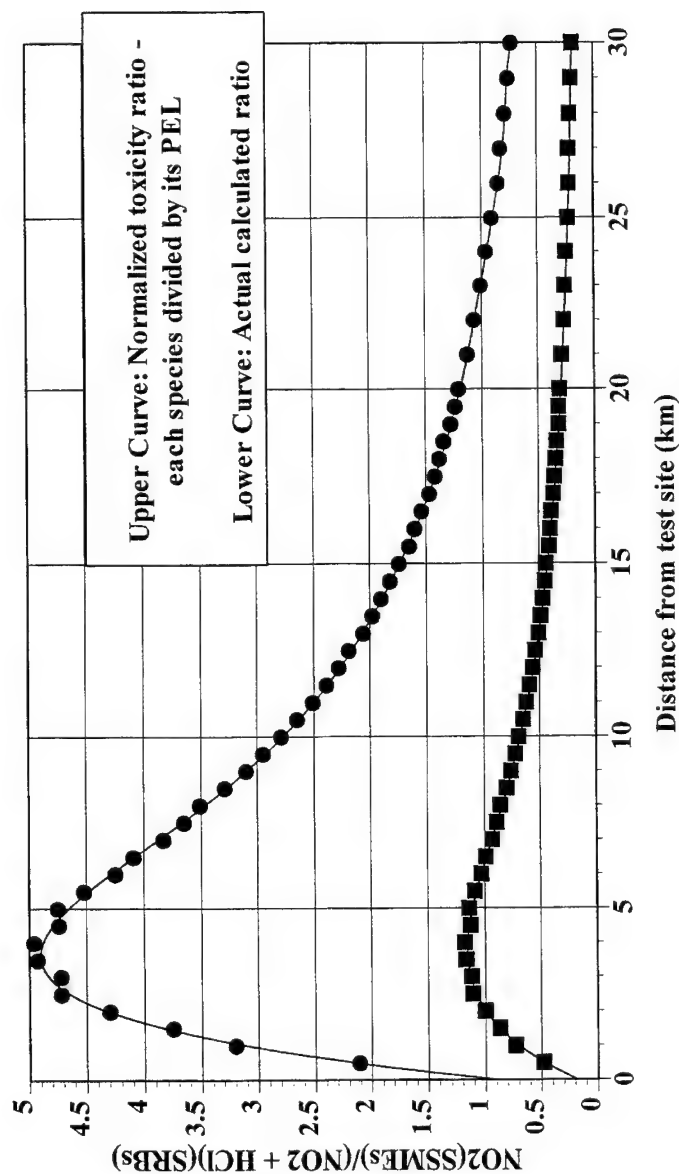


Figure 4. Calculated ground cloud concentrations of  $\text{NO}_2$  from SSMEs vs.  $(\text{HCl} + \text{NO}_2)$  from SRBs at equivalent thrust. Worst case scenario.

Assumptions:

1.  $\text{NO}_2/\text{NO}_x$  ratio derived from Titan measurements (see Fig. 1)
2. Equivalent thrust levels
3. Ground concentrations calculated using EPA approved INPUFF model
4. Assume meteorological condition C, wind speed = 5 m/s

near prelaunch levels within a few hours. Most of the recent work on the impact of rocket motors has focused on local ozone effects in the vicinity of the exhaust cloud. Model calculations have been performed in Germany and in the U.S. and confirm the earlier predictions of high local ozone depletion, but disagree to some degree on the chemical species responsible for the ozone destruction, and on the length of time required for recovery.

Although it has been argued for years that solid rocket clouds containing HCl present no threat to the public health, even on a local level, there have always been concerned parties that have argued that less toxic exhaust clouds can be produced by switching to liquid propulsion. The data presented above show that this may not necessarily be the case, and that to the contrary, at many locations the toxicity of liquid rocket exhaust clouds may exceed that of solid rockets. Since neither exhaust cloud presents a real threat to safety, decisions on the choice of propulsion system should be made on the basis of cost, reliability, and safety, and not on the basis of local environmental impacts. In connection with this, launch site range safety should not focus entirely on HCl as it has done in the past, but should also consider NO<sub>2</sub> from all rockets in the test or launch decision.

#### ACKNOWLEDGMENTS

The authors would like to acknowledge David Pray of Secor for performing the INPUFF calculations cited in the text.

#### REFERENCES

1. Anon., Atmospheric effects of chemical rocket propulsion, *American Institute of Aeronautics and Astronautics Report*, 1991.
2. Harwood, R. S., Jackman, C. H., Karol, I. L., *et al.*, Scientific assessment of ozone depletion: 1991. Chapter 10: "Predicted rocket and shuttle effects on stratospheric ozone," *World Meteorological Organization Ozone Report No. 25*, 1992.
3. Jones, A. E., Bekki, S. and Pyle, J. A., Modelling assessment of the atmospheric impact of exhaust products (chlorine, H<sub>2</sub>O, Al<sub>2</sub>O<sub>3</sub>) from Ariane 5 rocket launches, *Report to the European Space Agency*, University of Cambridge, United Kingdom, 1993. Although the official publishing date was 1993, early drafts were available in 1991.
4. Anon., Space Shuttle Environmental Impact Statement, *NASA*, 1978. and references therein.
5. Prather, M., Garcia, M. M., Douglass, A. R., *et al.*, The space shuttle's impact on the stratosphere, *J. Geophys. Res.*, 95, 583, 1990.
6. Denison, M. R., Lamb, J. J., Bjorn Dahl, *et al.*, Solid rocket exhaust in the stratosphere: plume diffusion and chemical reactions, Paper no. AIAA 92-3399, *AIAA/SAE/ASME/ASEE 28th Joint Propulsion Conference and Exhibit*, Nashville, Tennessee, July 6-8, 1992.
7. Craggier, B. C., Hirschberg, M. M., and Fabian, P., Effects of solid-fueled rocket exhausts on the stratospheric ozone layer, *Ber. Bunsenges. Phys. Chem.*, 96(3), 268, 1992.
8. Carrier, G. F., Fendell, F. E., and Dahbura, R. S., Chlorine production by particle-catalyzed reaction between rocket-exhaust and ambient-stratospheric reservoir species, Paper no. AIAA-92-3505, *AIAA/SAE/ASME/ASEE 28th Joint Propulsion Conference and Exhibit*, Nashville, Tennessee, July 6-8, 1992.
9. Leone, D. M., and Turns, S. R., Oxides of nitrogen formation in rocket plumes, *Proceedings of 4th Annual Symposium of the Propulsion Engineering Research Center*, Marshall Space Flight Center, Huntsville, Alabama, Sept. 9-10, 1992, 89-94.

10. Cohen, R. B., Learning about potential effects of solid propellant exhaust on the stratosphere, *Air Force Phillips Laboratory Solid Propellant Environmental Issues Technical Interchange Meeting and Conference*, Ogden, Utah, March 24-25, 1994.
11. Robinson, G. N., Freedman, A., Kolb, C. E., and Worsnop, D. R., Decomposition of halomethanes on  $\alpha$ -alumina at stratospheric temperatures, *Geophys. Res. Lett.* 21(5), 377, 1994.
12. Krüger, B. C., Ozone depletion in the plume of a solid-fueled rocket, *Ann. Geophys.*, 1994.
13. Cofer, W. R. III, Purgold, G. C., and Edahl, R. A., Solid propellant exhausted aluminum oxide and hydrogen chloride: environmental considerations, Paper no. AIAA 93-0305, *31st Aerospace Sciences Meeting and Exhibit*, Reno, NV, Jan. 11-14, 1993.
14. Leone, D. M., and Turns, S. R., Active chlorine and nitric oxide formation from chemical rocket plume afterburning, Paper no. AIAA 94-0788, *32nd Aerospace Sciences Meeting and Exhibit*, Reno, NV, Jan. 10-13, 1994.
15. Jackman, C. H., Considine, D. B., and Fleming, E. L., The Space Shuttle's Impact on the Stratosphere: An Update, *J. Geophys. Res.*, in press, 1996.
16. Karol, I. L., Ozolin, Y. E., and Rozanov, E. Y., Effects of space rocket launches on ozone and other atmospheric gases, *European Geophysical Association Conference*, Wiesbaden, Germany, 1991.
17. Bennett, R. R., and McDonald, A. J., The atmospheric impacts of chemical rocket motors, *International Scientific Colloquium on the Impact of Emissions from Aircraft and Spacecraft Upon the Atmosphere*, Köln, Germany, 1994.
18. McPeters, R., Prather, M. J. and Doiron, S., Reply to Steven Aftergood comment on "The space shuttle's impact on the stratosphere," *J. Geophys. Res.* 96, 17379, 1991.
19. Ross, M., Local effects of solid rocket motor exhaust on stratospheric ozone, *J. Spacecraft and Rockets*, 33(1), 144, 1996.
20. Brady, B. B., Fournier, E. W., Martin, L. R., and Cohen, R. B., Stratospheric ozone reactive chemicals generated by space launches worldwide, *Aerospace Report* No. TR-94(4231)-6, November 1, 1994.
21. For example, see Jones, A. E. and Shanklin, J. D., Continued decline of total ozone over Halley, Antarctica since 1985, *Nature*, 376(6539), 409, 1995, and Vonder Gathen, P., et al., Observational evidence for chemical ozone depletion over the Arctic in winter 1991-92, *Nature* 375(6527), 131, 1995.
22. Anderson, B. J., and Keller, V. W., A field study of solid rocket exhaust impacts on the near-field environment, *NASA Tech. Mem.* 4172, 1990.
23. Schmalzer, P. A., Hinkle, C. R., and Breininger, D., Effects of space shuttle launches STS-1 through STS-9 on terrestrial vegetation of John F. Kennedy Space Center, Florida, *NASA Tech. Mem.* 83103, 1985.
24. Partee, L. C., Col. USAF, *Memorandum* dated June 9, 1995.
25. Leibrecht, M. E., Col. USAF, *Memorandum* dated December 30, 1994.
26. Leibrecht, M. E., Col. USAF, *Memorandum* dated June 7, 1995.
27. Stewart, R. B., and Gomberg, R. I., The production of nitric oxide in the troposphere as a result of solid-rocket-motor afterburning, *NASA TND-8137*, 1976.

## **ENVIRONMENTAL IMPACT ASSESSMENT OF SOLID ROCKET MOTORS GROUND TESTS**

**Aguesse, T.,  
DGA, Direction des Missiles et de l'Espace  
Centre d'Achèvement et d'Essais des Propulseurs et Engins  
B.P. 2, 33165 Saint-Médard-en-Jalles Cédex, FRANCE**

**ABSTRACT:** It is usually recognized that the impact of solid rocket propulsion on the environment lies in the interaction between exhaust gases and upper atmosphere layers (greenhouse effect or ozone layer's destruction). The fact remains that local pollution near test benches, may occur if meteorological conditions are bad. In order to grant test permission, we studied the environmental impact of a given test. Indeed, industrial and urban areas located in the neighbourhood, require that acid rain phenomenon should be taken into account. Achieved at the shortest delay before the tests, this environmental impact assessment is carried out by computed simulations. Results have been gradually adjusted thanks to various tests up to the ARIANE V booster scale. Recently new work was done on the ascensive phase of exhausts and a new model, derived from G.A. BRIGGS' model, was developed. Theoretical work is presented.

### **INTRODUCTION**

The CAEPE is a French Ministry of Defense ground testing center for ballistic and tactical missiles. In particular, it specializes in bench-testing the various solid rocket motors for the French Nuclear Deterrent. These ground tests, involving high tonnage rocket motors, require increasingly strict precautions whenever firing authorizations are requested, as the test area is under pressure from urban expansion in neighboring towns.

The harmful side-effects of rocket ground testing may be divided into three categories :

- exhaust gases containing hydrochloric acid vapor and dust
- the likelihood of acid rain under the trajectory of the effluent gases
- high-intensity noise pollution.

The first point would seem to be the most difficult to resolve, as the standards for atmospheric pollution are becoming increasingly strict. In fact, the risk of acid rain and noise pollution causes greater concern. Furthermore, although it would seem difficult to eliminate the hydrochloric acid content in the exhaust gases, it is possible to avoid acid rain or concentrated noise pollution in a restricted area. This is achieved by authorizing test firing subject to the results of mathematical simulations to forecast the extent of the various risks in function of the actual meteorological conditions in the vicinity of the test zone.

It is immediately obvious that the most difficult aspect is developing sufficiently fast calculations to provide real assistance in decision-making before the weather conditions change.

Following some general remarks about rocket exhaust, this article presents details of the most complex part of the simulation : modeling the rising and diffusion of the plume of exhaust fumes. A brief presentation of the acoustic simulation is included at the end of the article.

## **GENERAL DESCRIPTION OF EFFLUENT GASES FROM SOLID ROCKET MOTORS**

Over the past thirty years, many authors have analyzed the environmental impact of solid rocket motors. The most delicate area, considered to be the major pollutant, that has given rise to a long-standing controversy, is the interaction between space rocket launcher exhaust gases and the stratospheric ozone layer. Indeed, as A. DAVENAS remarked, it would seem that the international community now agrees that "the impact of rocket motors is extremely low, or even negligible, as compared to other sources of compounds likely to react with ozone".<sup>1</sup> The affect on the atmosphere as a whole may also be considered negligible. As a ground test of a military rocket motor generates much less pollution than a shuttle launch, there is no reason to suppose that there would be any significant pollution of the lower layers of the atmosphere in the area around the test center (the lower level of the atmosphere is from 1,000 to 2,000 meters : as the exhaust consists of very hot gases it rises very rapidly, then stabilizes in this layer). This is due to the fact that the exhaust cloud is very small in atmospheric terms ( $10^5 - 10^7 \text{ m}^3$ ) so it dissipates very rapidly.

In practice, although the CAEPE is about ten kilometers upwind from a METEO-FRANCE weather station in the prevailing wind, no atmospheric pollution has ever been detected.

As far as compliance with atmospheric pollution standards is concerned, the CAEPE must remain below a threshold set by the Classified Installations Department (for information, the CAEPE's pollution levels are approximately 1/10 of the threshold). The threshold is expressed as an annual quantity of hydrochloric acid released into the atmosphere. (It is equivalent to the pollution released by 4 1-meter diameter smokestacks producing air contaminated with HCl at a rate of 10 m/s, and complying with instantaneous emission standards).

The quantity of gas emissions is not, therefore, harmful to the environment. On the other hand, as was mentioned in the introduction, it is necessary to take steps to prevent acid rain.

## **MODELING THE RISK OF ACID RAIN**

Acid droplets are not formed systematically within the emission cloud. As has been mentioned in other publications the firing of a rocket motor is not usually capable of producing acid rain on its own.<sup>2-4</sup> However, the meteorological situation and water injection systems used to protect some facilities may aggravate the risk to a considerable extent.

### **General Characteristics**

The objective of this model is to forecast the risks generated in an area close to the point of emission (with a radius of a few kilometers). Its intended operational use (authorizing test-firings) precludes any elaborate system requiring long calculation times. This model only takes a few minutes to run. It is initialized by means of a weather radiosonde operated by CAEPE staff, making it possible to produce a realistic simulation in under half an hour.



The calculations are divided into two stages, first modeling the emission cloud as it rises and stabilizes, then calculating its diffusion. The second stage will not be described in detail in this article.<sup>5</sup> It should also be noted that the two stages in the model are not equally important from an operational point of view. It is quite clear that producing an accurate diffusion model is not very useful unless the trajectory is reliable. It is much more important to have a model capable of predicting as accurately as possible the altitude at which the cloud of exhaust fumes will stabilize (and, thus, the cloud's trajectory), although it may be necessary to weight the rain parameters as we can be satisfied with a succinct diffusion survey. The vital parameter in our simulation is the stabilization altitude, determined in function of local meteorological conditions.

### Rising Phase

Although the way the plume of smoke rises is influenced by the aerodynamic configuration of the ground around the test site (buildings around the test bench, local relief in the form of protective mounds, etc.), we make the (realistic) assumption that the influence of these factors is negligible by comparison with the direct upward force of the plume of smoke. This force is produced by the initial vertical velocity of the exhaust, combined with its high temperature, which creates a significant difference in density between the gaseous effluent and the surrounding air.

When the test firing takes place in a horizontal configuration (on a deflector) or "nozzle down" (in a trench deflector), the simulation is no longer bound by the very complex aerodynamic interactions with the ground as the position of the discharge source may be considered to be the deflector or trench deflector outlet.

In all these configurations, the data are then restricted to an initial, purely vertical, velocity ( $w_0$ ), a geometrical parameter (initial radius of the gas cloud,  $r_0$ ) and a thermodynamic parameter describing the initial heat flow rate,  $Q_{H_0}$ , in the rocket exhaust.

The weather radiosonde provides a description of atmospheric conditions, which are then divided into layers where the normal variables (temperature, pressure, humidity, wind speed and direction) change in a linear manner.

### Model

In the most general case, the mass-conservation equations for momentum and energy (considered here in the form of enthalpy), may be expressed as follows :

$$\frac{\partial \rho}{\partial t} + \text{div}(\rho \vec{V}) = 0 \quad (\text{mass conservation}) \quad (3.1)$$

$$\rho \frac{D\vec{V}}{Dt} + \text{div} \vec{\Phi}_b, \vec{v} = \rho \vec{f} \quad (\text{momentum}) \quad (3.2)$$

$$\rho \frac{Dh}{Dt} + \text{div} \vec{\Phi}_b, ei = \frac{Dp}{Dt} + p \cdot \text{div} \vec{V} - \vec{\Phi}_b, \vec{v} \cdot \vec{\text{grad}} \vec{V} \quad (\text{enthalpy}) \quad (3.3)$$

where :  $\rho$  represents the local density of the fluid

$\vec{V}$  the velocity

$h = ei + \frac{p}{\rho}$	the enthalpy of the internal energy fluid $ei$ at pressure $p$
$\overline{\Phi_{D, \bar{v}}}$	the most general way of expressing the momentum diffusion flux density
$\overline{\Phi_{D, ei}}$	the most general way of expressing the internal energy diffusion flux density
$\frac{D}{Dt}$	the special derivative (total derivative).

In the mechanics of continuous media, it is shown that the momentum diffusion flux density is identified with the tensor  $\overline{\bar{P}}$  of the stresses within the fluid.

Finally, the internal energy diffusion flux density takes into account the flow of heat through the fluid by conduction (Fourier's law), physical diffusion (Fick's law), radiation, etc.

*Simplifying assumptions.* - The only external force applying to the fluid is due to gravity:

$$\rho \bar{f} = \rho \bar{g} \quad (3.4)$$

- The fluid is Newtonian and non-viscous:

$$\text{div } \overline{\Phi_{D, \bar{v}}} = \overline{\text{grad } p} \quad (3.5)$$

- The processes are adiabatic:

$$\overline{\Phi_{D, ei}} = 0 \quad (3.6)$$

This last assumption takes into account :

- negligible conductive heat flux (perfectly justified)
- low radiant flux (also justified, in the case of mainly gaseous exhaust fumes, with a low particle content)
- no convective flux, which is logical, given that the initial model was based on the assumption of a non-viscous fluid, that would, therefore, be incapable of producing turbulence.

It is, however, quite clear, that experimental observations reveal a highly turbulent plume, that draws in outside air as it expands.

To solve this problem, we adopted the TAYLOR model (also used by G.A. BRIGGS). He suggested closing the model with a geometrical equation describing the development of the plume as it rises, and the effect by which it absorbs outside air. A simple equation (development of the plume in a cone shape) is sufficient on its own for modeling the viscous effects and provides an adiabatic boundary.

The model can then be summed up in the following equations :

$$\frac{\partial \rho}{\partial t} + \text{div}(\rho \bar{V}) = 0 \quad (\text{mass conservation}) \quad (3.7)$$

$$\rho \frac{D\bar{V}}{Dt} = \rho \bar{g} - \overline{\text{grad } p} \quad (\text{momentum}) \quad (3.8)$$

$$\rho \frac{Dh}{Dt} = \frac{Dp}{Dt} \quad (\text{enthalpy}) \quad (3.9)$$

$$r = r_0 + \gamma \cdot z \quad (\text{geometry}) \quad (3.10)$$

where  $r$  is the radius of the plume at altitude  $z$ .

By making use of the notion of potential temperature  $\theta$  that remains constant in an adiabatic evolution, the enthalpy equation is replaced by (combined with the perfect gases law) :

$$\frac{D\theta}{Dt} = 0 \quad (3.11)$$

The attempt to identify a stationary solution leads to the following :

$$\text{div}(\rho \bar{\mathbf{V}}) = 0 \quad (3.12)$$

$$\rho(\bar{\mathbf{V}} \cdot \text{grad}) \bar{\mathbf{V}} = \rho \bar{g} - \text{grad } p \quad (3.13)$$

$$(\bar{\mathbf{V}} \cdot \text{grad}) \theta = 0 \quad (3.14)$$

$$\mathbf{r} = r\theta + \gamma \cdot \mathbf{z} \quad (3.15)$$

*Standard solution.* The solution proposed by BRIGGS leads to the following equations:<sup>6-7</sup>

$$\frac{dFm}{dt} = F \quad (3.16)$$

$$\frac{dF}{dt} = -s \cdot Fm \quad (3.17)$$

$$\mathbf{r} = r\theta + \gamma \cdot \mathbf{z} \quad (3.18)$$

with the following parameters :

$$F = g \cdot \frac{\theta - \theta_{ex}}{\theta_{ex}} \cdot u \cdot r^2 = g \cdot \frac{Q_H}{\pi \rho_{ex} c_p T_{ex}} \quad (3.19)$$

$$Fm = uwr^2 \quad (3.20)$$

$$s = \frac{g}{\theta_{ex}} \frac{\partial \theta_{ex}}{\partial z}, \quad \text{stability parameter for the outside atmosphere}$$

$u$  = horizontal velocity of the fluid (affected by the wind)

$w$  = vertical velocity

$T$  = temperature of the fluid

$c_p$  = heat capacity of the surrounding air, at constant pressure

$Q_H$  = heat flow rate (logically related to the velocity,  $u$ , according to equation (3.19))

(the "ex" indices refer to the fluid outside the cloud)

Equation (3.16) is derived from the conservation of momentum and equation (3.17) from the conservation of potential temperature.

We immediately observe that the dependence on  $u$  (outside wind velocity) raises a major physical problem when  $u$  is zero.

However, this solution does make it possible to obtain the following :

- in a neutral layer :

$$z(t) = \left( \frac{3F_0}{2\gamma^2 u} t^2 + \frac{3F_{m0}}{\gamma^2 u} t + \left( \frac{r_0}{\gamma} \right)^3 \right)^{1/3} - \frac{r_0}{\gamma} \quad (s = 0) \quad (3.21)$$

- in a stable layer :

$$z(t) = \left( \frac{3F_{m0}}{\gamma^2 \sqrt{s} u} \sin(\sqrt{s} t) + \frac{3F_0}{\gamma^2 s u} (1 - \cos(\sqrt{s} t)) + \left( \frac{r_0}{\gamma} \right)^3 \right)^{1/3} - \frac{r_0}{\gamma} \quad (s > 0) \quad (3.22)$$

It should be noted that these equations are obtained by assuming that at the initial moment,  $F_0$  and  $F_{m0}$  must be independent of  $u$ . Briggs therefore rewrote equations (3.19) and (3.20), replacing  $u_0$  with  $w_0$ , showing a realistic dependence on the initial velocity that is, in fact, purely vertical:

$$F_0 = g \cdot \frac{\theta_0 - \theta_{ex}}{\theta_{ex}} \cdot w_0 \cdot r_0^2 \quad (3.23)$$

$$F_{m0} = w_0^2 r_0^2 \quad (3.24)$$

In this case, integrating equations (3.16) and (3.17), where  $u = \text{constant}$  in each layer of the atmosphere, produces equations (3.21) and (3.22). These have the advantage of showing a simple dependency of the altitude expressions on the wind velocity. However, as has already been mentioned, this dependence is inconvenient in that the results tend to diverge when wind velocity is low.

*Another solution.* Another solution may, apparently, be put forward for the momentum conservation equation (3.13).

Assuming that the discharge does not rotate (no vorticity), equation (3.13) becomes :

$$\rho \cdot \text{grad} \frac{V^2}{2} = \rho \bar{g} - \text{grad } p \quad (3.25)$$

By integrating on the surface  $S = \pi r^2$ , represented by the intersection of the plume with the horizontal plane at altitude  $z$ , equation (3.25) may then be expressed as :

$$\int_S \rho \frac{\partial(1/2(u^2 + w^2))}{\partial z} dS = \int_S g(\rho - \rho_{ex}) dS \quad (3.26)$$

where  $u$  and  $w$  are the horizontal and vertical components of the velocity, respectively.

As the characteristics of the fluid are assumed to be constant across the entire surface  $S$ , the first element may also be expressed as :

$$\begin{aligned} \int_S \rho \frac{\partial(1/2(u^2 + w^2))}{\partial z} dS &= \rho \frac{d(1/2(u^2 + w^2))}{dz} \int_S dS \\ &= \rho \frac{d(1/2(u^2 + w^2) \int_S dS)}{dz} \end{aligned} \quad (3.27)$$

$$d\left(\int_S dS\right)$$

(the term in  $\rho \frac{S}{dz}$  is negligible if the cone has a small angle).

This gives :

$$\begin{aligned} \frac{d(1/2(u^2 + w^2)r^2)}{dz} &= g \cdot \frac{\rho - \rho_{ex}}{\rho} r^2 \\ &\approx g \cdot \frac{\rho - \rho_{ex}}{\rho_{ex}} r^2 \end{aligned} \quad (3.28)$$

or :

$$\frac{d(1/2(u^2 + w^2)r^2)}{dt} = g \cdot \frac{\rho - \rho_{ex}}{\rho_{ex}} w \cdot r^2 \quad (3.29)$$

$$\Rightarrow \frac{d(1/2(u^2 + w^2)r^2)}{dt} = \frac{gQ_H}{\pi\rho_{\text{ex}}c_p T_{\text{ex}}} \quad (3.30)$$

where  $Q_H$  is now the rate at which the heat crosses the surface  $\pi r^2$  at velocity w.

Lastly, the momentum conservation equation is expressed as :

$$\frac{d\mathcal{J}_m}{dt} = \mathcal{J} \quad (3.31)$$

with the following parameters:

$$\mathcal{J}_m = 1/2(u^2 + w^2)r^2 \quad (3.32)$$

$$\mathcal{J} = F = \frac{gQ_H}{\pi\rho_{\text{ex}}c_p T_{\text{ex}}} \quad (3.33)$$

The energy conservation equation found by Briggs :<sup>7</sup>

$$\frac{dF}{dt} = -s.Fm \quad (3.34)$$

may be described in physical terms as a friction that absorbs the buoyancy force. Experience has shown that it is a good description of reality at the level of interest in this case. It may be expressed as:

$$\frac{d\mathcal{J}}{dt} = -s.\mathcal{J}_m \quad (3.35)$$

*Summary of the model.* Three equations are used to build a simple model of the phenomenon:

$$\frac{d\mathcal{J}_m}{dt} = \mathcal{J} \quad (3.36)$$

$$\frac{d\mathcal{J}}{dt} = -s.\mathcal{J}_m \quad (3.37)$$

$$r = r_0 + \gamma.z \quad (3.38)$$

with the following parameters:

$$\mathcal{J}_m = 1/2(u^2 + w^2)r^2 \quad (3.39)$$

$$\mathcal{J} = F = \frac{gQ_H}{\pi\rho_{\text{ex}}c_p T_{\text{ex}}} \quad (3.40)$$

where  $Q_H$  is the heat flow crossing the intersection of the plume with a horizontal plane at local vertical velocity  $w$ , and  $u$  represents the velocity of the fluid in the horizontal plane, corresponding to the atmospheric wind velocity at the altitude under consideration.

By solving this system, the following equations are derived, giving the equations for the change in altitude  $z$  over time :

$$\left(\left(\frac{dz}{dt}(t)\right)^2 + u^2\right)(r_0 + \gamma.z(t))^2 = 2f(t) \quad (3.41)$$

where the function  $f(t)$  is equal to :

- in the case of a neutral atmosphere ( $s = 0$ )

$$f(t) = f_0 \cdot t + f_{m0} \quad (3.42)$$

- in the case of a stable atmosphere ( $s > 0$ )

$$f(t) = f_{m0} \cdot \cos(\sqrt{s}t) + \frac{f_0}{\sqrt{s}} \cdot \sin(\sqrt{s}t) \quad (3.43)$$

The case of an unstable atmosphere ( $s < 0$ ) theoretically indicates an increase in the buoyancy force. However, in our situation, the phenomenon whereby outside air is drawn into the plume tends to counterbalance that effect. This case is therefore treated as a neutral atmosphere.<sup>7</sup>

### Examples of Results

The graphs below (Figures 1 - 4) show the behavior of the Briggs and CAEPE models, respectively. These graphs have been obtained for the usual type of plume produced on our scale, where the initial data are on the following scale :

$$F_0 = 20,000 \text{ m}^4\text{s}^{-3}$$

$$r_0 = 10 \text{ m}$$

$$w_0 = 15 \text{ ms}^{-1}$$

The same drawing coefficient ( $\gamma = 0.5$ ) was used to test both models.

The curves in Figures 1 and 2 show the influence of the wind in a neutral case ( $s = 0$ )

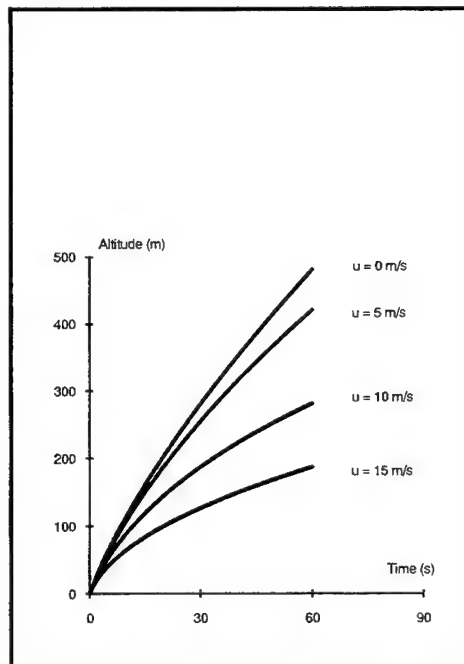
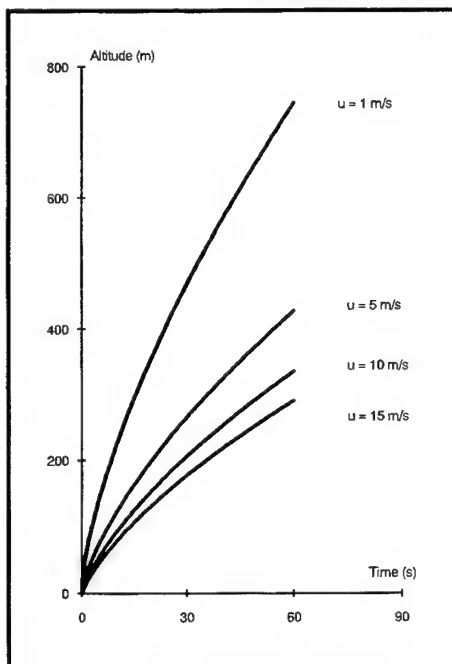
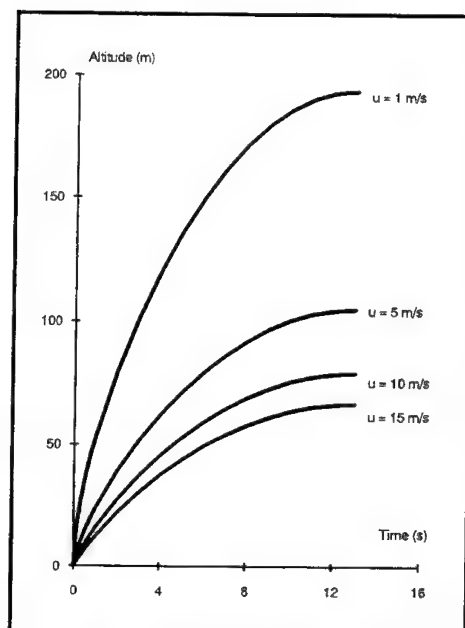


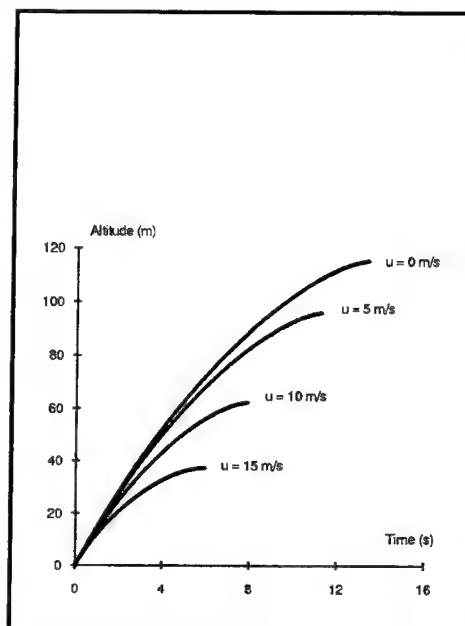
Figure 1. Neutral atmosphere, Briggs model

Figure 2. Neutral atmosphere, CAEPE model

and the curves in Figures 3 and 4 describe a similar case with a stable atmosphere ( $s = 0.05 \text{ s}^{-2}$ )



**Figure 3.** Stable atmosphere, Briggs model



**Figure 4.** Stable atmosphere, CAEPE model

This comparison demonstrates the following types of behavior :

- On the same basis in a single-layer atmosphere, the CAEPE model always gives a stabilization altitude (in a stable case), or an altitude at a given time (in a neutral case), lower than that of the Briggs model, although the variation equations are fairly similar. (Because of differences in w variation, note that it is impossible to affirm such conclusions for multi-layer atmosphere cases).
- A very interesting aspect of our model is to give variable stabilization times according to the wind velocity. These times are always shorter than those obtained using the Briggs model. This point correlates very well with our experience.<sup>2</sup>
- The case where there is no wind is obtained normally. The known divergence from the Briggs model at low wind velocities is therefore eliminated.
- Finally, the initial data are naturally dependent on  $w_0$  and the wind at ground level (Brigg's assumption that  $u_0 = w_0$  is not necessary) and, whatever the wind at ground level, the slope at the origin of the altitude variation equation is in keeping with the initial vertical velocity,  $w_0$ .

A comparison with experimental observations was presented in a previous article.<sup>2</sup> It was established that, in the new model, calculations were coherent with all experimental results, even in cases that were incompletely described by the Briggs model. The proposed equations would seem to provide an accurate macroscopic description of the way the plume of exhaust fumes moves through an atmospheric layer of given stability. It is, therefore, important to model a series of sufficiently thick layers so that these good equations are not only used in the vicinity of the origin. Current research is aimed at dividing the atmosphere into appropriate layers, using simple criteria, on the basis of data collected by the on-site radiosonde.

### Diffusion Phase

Once the plume of exhaust fumes reaches its stabilization altitude, or the vertical velocity becomes much lower than the horizontal velocity, the air absorption phenomenon analyzed in the previous paragraph becomes negligible, by comparison with those of turbulent diffusion and drift.

These phenomena are then described by the general diffusion equation. Work in this field has been carried out by ONERA and a summary of the assumptions is included in our previous article.<sup>8,2</sup>

By applying this cloud model, and including a rain parameter, it is possible to forecast the risk of acid rain.

### Rain Parameter

The effluent cloud is, in fact, a ternary mixture of alumina, hydrochloric acid and water, with a highly complex evolution.

The research carried out by ONERA has made it possible to develop an elaborate calculation code for modeling the formation of a liquid phase in the cloud.<sup>9</sup> This is calculated on the basis of the quantities of water present (from the combustion process, injected deliberately, and in the atmosphere absorbed by the cloud) and the degree of risk of the formation of a liquid phase in the mixture.

The possibility of nucleation followed by growth of the aerosol thus formed have also been studied.<sup>10</sup> The equations used to calculate growth are derived from those of Fukuta and Walter.<sup>11</sup>

As a result, the time required for the calculation is rather long, making it unsuitable for operational use.

With the help of this code, observations made on a small-scale model, and the results of tests carried out at the CAEPE, a set of criteria for the development of acid rain has been developed.

The areas at risk are then located on a map.<sup>12</sup>

## NOISE POLLUTION

Although the risk of acid rain is the major concern of the test manager, a certain amount of unavoidable noise pollution is also generated during static tests of rocket motors. Although it does not last very long (usually on the order of one minute), this may cause considerable nuisance.

Once again, it is necessary to analyze the interaction with the environment in order to make a realistic forecast. This is due to the fact that certain atmospheric conditions (wind, temperature) set up acoustic focus zones. The noise levels in these zones may be as high as 150 dBa at some considerable distance from the source (several hundred meters).

The model used at the CAEPE is based on research carried out at the Saint-Louis Franco-German Institute. Only the main characteristics are presented in this article.<sup>12-14</sup> The calculation is based on the phenomenon of acoustic energy being carried by sound waves, as identified by ray trajectography.

The acoustic intensity is calculated for focus zones by making use of the phenomenon of energy conservation along elementary tubes based on the acoustic rays.<sup>2</sup>

The intensity is then corrected for atmospheric absorption phenomena (affected by humidity) according to AFNOR tables.<sup>15</sup>

The CAEPE provided noise forecasts for the first launches of the ARIANE V solid-fueled rocket at Kourou. Table 1 and Figure 5 show the iso-intensity graphs (100 dBa and 80 dBa) as well as the correlation between the measured intensity and calculation results at several significant points.



Distance	Azimuth	Calculation Results	Measured Intensity
1250 m	90°	103 dB	106 dB
4250 m	30°	79 dB	70 dB
5300 m	60°	73 dB	52 dB (*)
7650 m	225°	100 dB	70 dB (**)
9500 m	115°	58 dB	60 dB
14.1 km	255°	76 dB	53 dB (**)
15.2 km	90°	Backgr. noise	63 dB
15.7 km	300°	85 dB	53 dB (**)
29.2 km	300°	Backgr. noise	60 dB
30.0 km	240°	Backgr. noise	63 dB

(\*) building mask

(\*\*) reducing effect of tropical forest

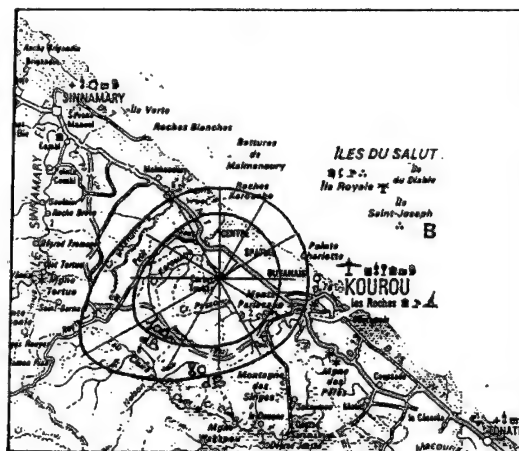


Table 1. Table of results

Figure 5. Example showing mapping of acoustic levels (forecast for short dry season)

## CONCLUSION

In view of the necessity of updating their calculation codes, the CAEPE recently revised their research on exhaust plume models. A model derived from the Briggs system would currently appear to provide very realistic results.

Further testing will be required to confirm the validity of this model, which has the advantage of compensating for the inadequacies of the Briggs model in certain special cases, while the results are otherwise fairly similar.

As they have been in use for several years under a wide range of meteorological conditions, the CAEPE simulations have reached a good level of maturity, both in estimating the formation of acid rain and the problem of noise pollution, and this is by no means their only advantage.

1. Davenas, A., Environmental aspects of rocket and gun propulsion, *Technical Evaluation Report of the 84th AGARD Symposium (Propulsion and Energetic Panel)*, Aalesund, Norway, August 29 - September 2, 1994.
2. Aguesse, T., Moreau, S., Evaluation de l'impact sur l'environnement des essais statiques de propulseurs à propergol solide, *84th AGARD Symposium (Propulsion and Energetic Panel)*, Aalesund, Norway, August 29 - September 2, 1994.
3. Sauvel, J., L'examen des pollutions liées aux moteurs-fusées, *Nouvelle Revue d'Aéronautique et d'Astronautique*, n° 3, 1993.
4. Bouchardy, A.M., Larue, P., Verdier, C., Etude des effluents émis par les tirs au point fixe de gros propulseurs à propergol solide, *ONERA. RT n° 3/3401 EYP*, 26 Mars 1979.
5. Bouchardy, A.M., Modèle de prévision de la pollution atmosphérique due à une source de polluants, *La Recherche Aérospatiale*, n° 3, 169-175, 1980.
6. Briggs, G.A., Plume rise, *U.S. Atomic Energy Commission, Division of Technical Information*, TID 25075, 1969.
7. Briggs, G.A., A simple model for bent-over plume rise, *Pennsylvania State University, Ph. D. Thesis*, December 1970.

8. **Bouchardy, A.M., Pillot, P., Verdier, C.,** Prediction and measurements of the transport of solid rocket motor exhaust effluents during eight static tests, *ONERA. RT n° 6/3401 EYP*, December 1979.
9. **Bouchardy, A.M., Verdier, C.,** Etude des effluents émis par les tirs au point fixe de gros propulseurs à propergol solide, *ONERA. RT n° 8/3401 EYP*, 28 Septembre 1980.
10. **Bouchardy, A.M., Verdier, C.,** Etude des effluents émis par les tirs au point fixe de gros propulseurs à propergol solide, *ONERA. RT n° 11/3401 EYP*, 24 Décembre 1982.
11. **Fukuta, N., Walter, L.A.,** Study of basic theories of water condensation, *Denver Research Institute*, Report n° DRI 2532, January 1970.
12. **Gnemmi, P., Vermorel, J.,** Modélisation bi-dimensionnelle du calcul des rayons acoustiques se propageant dans la basse atmosphère, *Rapport ISL RT 504/87*, 1987.
13. **Gnemmi, P., Vermorel, J.,** Les effets des conditions météorologiques sur la propagation acoustique dans la basse atmosphère, *Rapport ISL RT 519/88*, 1988.
14. **Sauvel, J., Vermorel, J.,** An operational prediction for far field airblast effects: practical experience at CAEPE, *Twenty-fourth D.O.D. Explosives Safety Seminar*, Saint-louis, USA, August 28-31, 1990.
15. **AFNOR,** Atténuation du son dans l'air, *Norme Française S 30.009*, 1980.

## COMMENTS

Dr. Robert R. Bennett, Thiokol Corporation:

1) Does the computer code presented predict ground concentration of exhaust species? If yes, do you have examples of any field data? 2) How were exhaust cloud heights determined? 3) Are all static tests vertical? Does it matter? 4) Do you have further plans for field validation? 5) Will model be available for others to use?

Author's Replies:

- 1) At the very beginning, the code was able to perform such predictions (in fact just as REEDN does). But during the validation phase (1978) it was decided to use rain criteria which were expected to be more significant according to our problem. Thus the code calculates parameters according to whether acid rain is present or not. Our go/no go test criterium became rain/no rain criterium over definite zones in the neighborhood.
- 2) They were determined by triangulation and in some cases by direct measurement with the help of an airplane altimeter. Thus triangulation technique was shown to be quite correct.
- 3) The code uses the assumption that the initial velocity of the exhaust is purely vertical. But it does not mean that the test must be vertical. Indeed the aerodynamic configuration of every test site imposes free vertical velocity at the exit of the test bench (thanks to deflector).
- 4) On one hand our go/no go criterium imposes that no rain could occur over specific zones. Therefore ground concentration of exhaust species is not interesting for our studies. On the other hand stabilisation validation must be carried on. Present work deals with atmosphere stratification.
- 5) Calculations could be done with external radiosondage.

## ON THERMOCHEMICAL CHARACTERISTICS OF AP/NSAN/HTPB COMPOSITE PROPELLANTS

Araújo<sup>1</sup>, Luis and Frota<sup>2</sup>, Octávia

1 - National Institute of Engineering and Industrial Technology, Az. dos Lameiros Est. Paço do Lumiar - 1699 Lisboa Codex, Portugal; 2 - Laboratory of Energetic and Detonic - 3150, Condeixa, Portugal

**ABSTRACT.** The first part of the work concerned the evaluation of the environmental impact of ammonium perchlorate / non-stabilised ammonium nitrate / hydroxyl terminated polybutadiene composite propellants and determination the HCl concentration in the combustion products of the propellants. The results, obtained by electrometry and precipitation titration, were compared with those obtained with a numeric code that allows to consider up to  $m$  ( $m < 20$ ) reacting atomic species and the possibility of formation of  $n$  ( $n < 40$ ) chemical components, by combination of the  $m$  atomic species. There is good correlation between experimental and theoretical values. The influence of non-stabilised ammonium nitrate content on linear regression rates of the propellants was assessed. The experimental results, obtained in a classic Crawford bomb by the fuse wires method, allowed the determination of the  $V_r(P)$  evolution of the formulations. The ignition delay,  $\tau_i$ , of the formulations was also studied. Small test samples of the propellants were submitted to radiative heating in an electrical furnace. The ignition instant was determined by the simultaneous obtainement of a sharp rise of the output of a thermocouple and a minimum surface temperature. The analysis of the results showed that increasing weight content of non-stabilised ammonium nitrate originates shorter values of  $\tau_i$ . Further interpretation showed that the evolution of  $\ln \tau_i$  could be described in two linear Phases. The transition temperatures between Phases were calculated, and the results obtained showed that partial substitution of ammonium perchlorate by non-stabilised ammonium nitrate increased the domain of occurrence of homogeneous ignition.

### 1 - INTRODUCTION

The growing utilisation of rocket motors in non - military utilisations has put increased urgency in the development of low polluting propulsive compositions, that simultaneously present reduced sensitivity to slow and fast cook-off and shock generating stimuli [1, 2, 3]. As the exhaust gases resulting from the combustion of ammonium perchlorate based (AP) composite propellants include a large amount of hydrogen chloride and other chlorine components which are the main source of high levels of toxicity for most living forms and equipment corrosion damages, partial substitution of ammonium perchlorate by non-stabilised ammonium nitrate (NSAN) is under study at the Laboratory of Energetic and Detonic [4, 5, 6, 7]. The use of NSAN is not free of problems. Nevertheless, its low sensitivity to impact and friction and the absence of chlorine in its composition, make this component

an attractive oxidiser candidate, namely for those applications where increased insensitivity and a significant reduction of the emissions of acid compounds, specially HCl, are of concern and high specific impulse is not a determining parameter. This work concerns the influence of increasing NSAN weight content on the composition of the combustion products, linear burning rates and ignition characteristics of AP/NSAN/HTPB composite propellants.

## 2 - PROPELLANTS COMPOSITION AND PREPARATION

All the compositions were formulated with 80 % weight of solid oxidant charge and 20 % weight of bulk (pre polymer, plasticizer and curing agent) binder system. The cases of 0 %, to 80 % of non-stabilised ammonium nitrate weight content, of the total solid oxidant charge, were assessed in this work (Table 1).

**Table 1**  
Weight Composition of the Propellants

PROPELLANT	COMPOSITION (% wt)
C1	80 AP / 20(HTPB + IPDI + DOA)
C2	72 AP / 8 NSAN / 20 (HTPB + IPDI + DOA)
C3	64 AP / 16 NSAN / 20 (HTPB + IPDI + DOA)
C4	56 AP / 24 NSAN / 20 (HTPB + IPDI + DOA)
C5	48 AP / 32 NSAN / 20 (HTPB + IPDI + DOA)
C6	40 AP / 40 NSAN / 20 (HTPB + IPDI + DOA)
C7	32 AP / 48 NSAN / 20 (HTPB + IPDI + DOA)
C8	24 AP / 56 NSAN / 20 (HTPB + IPDI + DOA)
C9	16 AP / 64 NSAN / 20 (HTPB + IPDI + DOA)

Compositions containing AP only were bimodal with a 50 % fine/coarse weight proportion of the AP particles, but in the formulations including NSAN the compositions used were trimodal, with the same fine/coarse AP weight composition.

The particle size distribution curves of both oxidisers were established by Laser Diffraction Spectrometry. The particle sizes presented in Table II were obtained by sieving and kept at  $333 \pm 5$  K and  $11 \pm 2$  % relative humidity for the propellants formulations.

**Table 2**  
Particle Sizes Used in the Formulations

AP fine	$45 < d_{AP} < 90 \mu\text{m}$
AP coarse	$106 < d_{AP} < 150 \mu\text{m}$
NSAN	$150 < d_{NSAN} < 180 \mu\text{m}$

The propellants were obtained by mixing under vacuum at 333 K in an anchor blade type mixer, cast in small boxes (100 mm  $\times$  50 mm  $\times$  30 mm) and cured at 333 K for five days. The test samples were cut from the cured propellant blocks and its uniformity was verified by optical microscopy and bulk density measurements of the various strands.

### 3 - ENVIRONMENTAL IMPACT

#### Experimental

For the analysis of the influence of the NSAN content of the propellants on the global acidity of the combustion products, small samples ( $1.20 \times 10^{-3}$  kg) of compositions C1 to C7 were ignited, by means of an electrically heated coiled wire, in a closed combustion chamber that was previously flushed with nitrogen (Figure 1). After complete combustion of the sample, the gaseous mixture of the combustion products was transferred to a sealed reservoir, under vacuum, containing 100 ml of bi-distilled water. An aqueous solution was obtained by mechanical agitation of the container. All the experiments were made at atmospheric pressure ( $P_{N_2}=10^5$  Pascal).

The measure of the HCl concentration and of the global acidity of the solution of the combustion products was made by titrimetric and electrometric analysis. Precipitation titration - argentimetric process, according to the Mohr procedure, was used for measures concerning HCl only. The solution of the combustion products was neutralised with a NaOH solution (0.01 M). For the precipitation titration an  $AgNO_3$  solution (0.01 M) and a  $K_2CrO_4$  solution (0.005 M) as indicator was used.

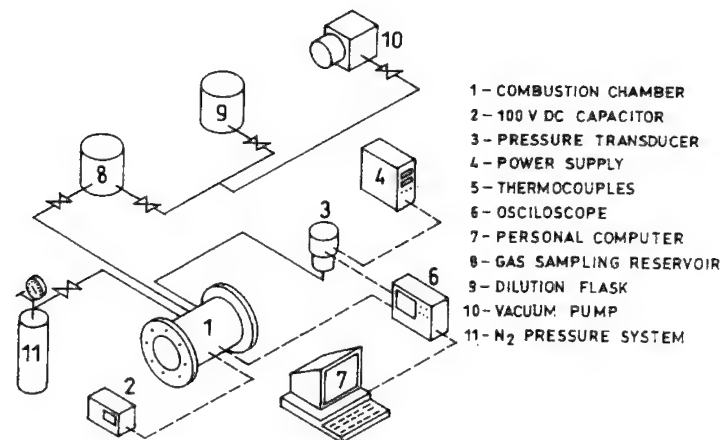


Figure 1. Environmental impact and HCl concentration. Experimental apparatus.

The results obtained (Figure 2) show the expected decrease of the HCl concentration with the increase of NSAN content of the propellants. The maximum and minimum values measured, 6.64 and 2.62 moles of HCl per kg of propellant, were obtained for compositions C1 and C7, respectively. A Metrohm pH meter with a glass electrode was used for the electrometric measures. The measures of the global  $[H^+]$  values of the solutions allowed us to calculate in each case the correspondent acidity (Figure 3). Assuming that the formation of  $HCO_3^-$  in the solution of the combustion products was the only chemical mechanism, along with the presence of HCl, with a significant contribution to the global values obtained, carbon dioxide was eliminated from the initial solution for the measurements concerning HCl concentrations.

A decrease of both global acidity and HCl emissions was observed with the increase of the NSAN content of the compositions. The reduction of the global acidity of the solutions was almost constant in all cases representing 20 % of the initial. As expected, the maximum and minimum values measured were obtained for compositions C1 and C7, respectively:

$$\begin{aligned}
[H^+]_{C1} &= 2.18 \times 10^{-2} \text{ g dm}^{-3} \\
[H^+]_{C7} &= 1.09 \times 10^{-2} \text{ g dm}^{-3} \\
[\text{moles HCl/kg prop}]_{C1} &= 6.71 \\
[\text{moles HCl/kg prop}]_{C7} &= 2.08
\end{aligned}$$

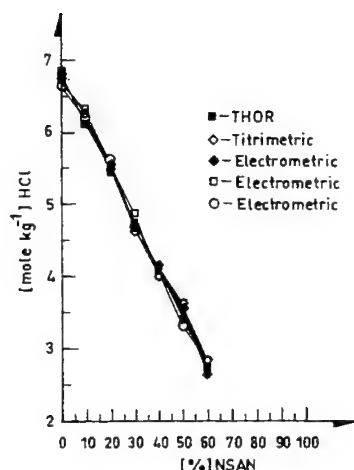


Figure 2. HCl concentration, as a function of NSAN content.

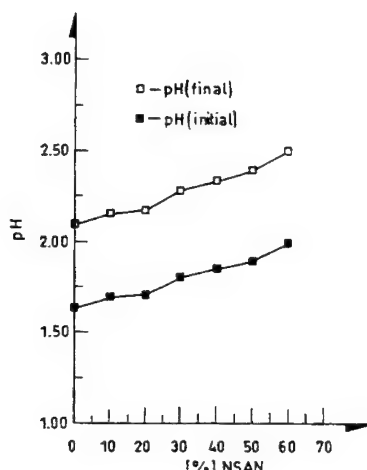


Figure 3. Global acidity of the solution of the combustion products, as a function of NSAN content.

### Theoretical

The theoretical prediction of the composition and thermodynamic properties of the gaseous mixtures of the combustion products, for isobaric adiabatic conditions, was made using the THOR code [8]. This code allows to consider up to  $m$  atomic species ( $m \leq 20$ ) and the possibility of formation of  $n$  ( $n \leq 40$ ) reaction products by combination of these atomic species. Among the  $n$  chemical components,  $m$  are considered *basic*, as they constitute the starting composition for the calculations. The selection of the  $m$  components depends on the equivalence ratio, related to stoichiometry, of the initial reacting mixture, and they should be those which are expected to have a more significant concentrations in the combustion products mixture. The species mass balance yields a linear system involving  $m$  equations, the remaining  $n-m$  equations needed to solve the problem are obtained using the method of Lagrange multipliers or the equilibrium constants. In order to calculate the chemical concentrations of the  $n$  components, for given  $P_0$  and  $T_0$  initial conditions, the system composed by the  $m$  basic components is solved and one or more possible components are added with optimisation of the relative concentration inside the group related to the same atomic species, for the minimum value of the Gibbs free energy  $G = \sum x_i \mu_i$ , with the free energy of each component expressed as  $\mu_i = G_{0i}(T) + RT \ln P + RT \ln (x_i)$ . The values of  $G_{0i}(T)$ , are obtained from the JANNAF Tables and from the polynomial expressions of Gordon and McBride [9, 10]. The solution of the composition problem involves simultaneously the thermodynamic equilibrium, obtained with the mass and species balances, the equilibrium condition  $G = G_{\min}(P, T, x_i)$ , the thermal equation of State (EoS) and the energetic EoS, related to the internal energy  $E = \sum x_i e_i(T) + \Delta e$ . The calculations of the final equilibrium compositions and correspondent combustion temperature were performed using the ideal gas EoS, for isobaric and adiabatic conditions in the pressure interval  $10^5 \text{ Pascal} \leq P \leq 10^7 \text{ Pascal}$ , assuming the possibility of formation of  $\text{CO}_2$ ,  $\text{CO}$ ,  $\text{H}_2\text{O}$ ,  $\text{OH}$ ,  $\text{N}_2$ ,  $\text{O}_2$ ,  $\text{H}_2$ ,  $\text{NO}$ ,  $\text{NO}_2$ ,  $\text{H}$ ,  $\text{N}$ ,  $\text{O}$ ,  $\text{NH}_2$ ,  $\text{HCl}$  and  $\text{CH}_2$  as reaction products.

## Correlation of Results

There is a good agreement between the values calculated with the THOR numeric code and the experimental results obtained using both techniques (Figure 2). The partial substitution of ammonium perchlorate by ammonium nitrate in the oxidant charge of composite propellants reduces in a very effective way the emissions of acid components during combustion, namely the formation of hydrochloric acid. The results obtained emphasise the contribution of carbon dioxide to the global acidity of the combustion products. Care must be taken in eliminating carbon dioxide before measuring the HCl values once the acidity values of the aqueous solution of the combustion products decreases significantly, about 20 % of the initial values (Figure 3).

## 4 - LINEAR REGRESSION RATES

### Experimental

The measurement of the linear regression rates of compositions C1, C4, C6 and C9, in the pressure range  $10^5 \text{ Pascal} < P < 10^7 \text{ Pascal}$ , was made by the classic fuse wires method, using a Crawford bomb, that was flushed and pressurised with nitrogen to the desired level, before each test (Figure 4).

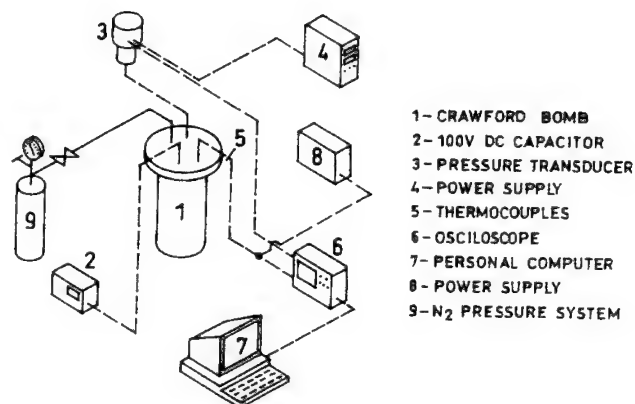


Figure 4.  $V_r(P)$  measurements. Experimental apparatus.

Propellant samples of formulations were temperature conditioned to  $298 \pm 3 \text{ K}$  before testing. The strands of each composition (70 mm x 10 mm x 10 mm), inhibited with an epoxy resin, were ignited by a resistive wire glued on its top and a 100 V DC discharge system. A pressure transducer connected with the bomb measured the internal pressure during the combustion of the sample. All the data (electrical tension and time) was registered in a 500 Msamples/s oscilloscope (Tektronix 320 TDS) and transferred to a personal computer for further analysis. The results obtained (Figure 5) show that the values of  $V_r(P)$  decrease with increasing content of NSAN.

The evolution of the linear regression rates of the compositions in function of pressure, follow the De Vieille burning rate laws ( $V_r = a P^n$ ) shown in Table 3. The pressure exponent  $n$  and the  $a$  constant also decrease when the content of NSAN is increased showing a progressive pressure insensitivity of the formulations' burning rates, for increasing NSAN weight contents.

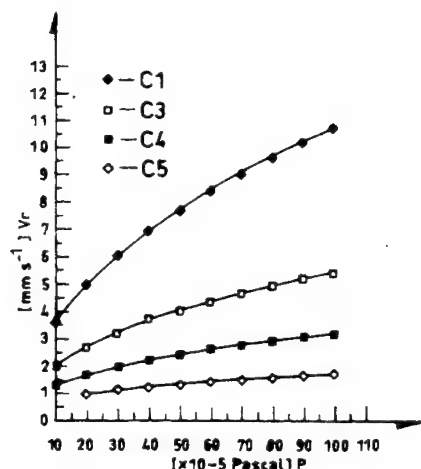


Figure 5. Evolution of the linear regression rate, as a function of pressure and NSAN content.

Table 3  
De Vieille Laws of the Propellants

Propellant	$V_r(P)$
C1	$V_r = 1.18 P^{0.48}$
C3	$V_r = 0.74 P^{0.43}$
C4	$V_r = 0.49 P^{0.41}$
C5	$V_r = 0.32 P^{0.37}$

## 5 - IGNITION CHARACTERISTICS

### Experimental

The test samples, cut from the strands of compositions C1, C3, C4 and C6, were circular pellets of propellant 10 mm in diameter and 0.8 mm thick. In order to reduce the existence of ignition spots, that would increase data scatter, the surface of the samples was rubbed with fine emery paper and brushed to dust out any loose particles. The test samples were conditioned at  $298 \pm 2$  K and  $11 \pm 2$  % relative humidity before testing.

The experimental apparatus (Figure 6) used in this work for the measurement of ignition delays of the propellants, in ambient air and at atmospheric pressure, is essentially composed of an electrical furnace, a pneumatic system for rapid introduction of the propellant samples and peripheral devices allowing real time control of the process and data acquisition. The furnace, composed of a ceramic ignition chamber, cylindrical, 115 mm long and 65 mm in diameter, heated by a 650 Watt electrical element and externally isolated with ceramic, has a maximum temperature of 1573 K. The temperature of the ignition chamber is controlled by an PID temperature controller associated with a Chromel-Alumel thermocouple.

In order to optimise the temperature uniformity, axial and radial measurements of the temperature were made inside the furnace using a K type thermocouple that was displaced one millimetre between measurements.

The results of this calibration process identified a cylindrical test zone (10 mm high and 20 mm in diameter), where the maximum axial and radial temperature gradients proved to be always less than 0.05 % of the lower test temperature. During the ignition tests the temperature of the measuring zone was monitored by a shielded K type thermocouple perpendicular to its axis. A pneumatic cylinder was used for the rapid introduction of the propellant samples in the test zone. The test samples were fixed to the extremity of a thin wire isolated with Teflon, that was axially connected with the piston of the pneumatic cylinder. The length of the wire is such that at the piston maximum displacement the sample is positioned at the centre of the furnace measuring zone. The time evolution of the surface temperature of the sample was measured with a 78  $\mu$ m K type thermocouple. A detailed view of the sample and thermocouple installation can be seen in Figure 7.



The electrical output of the thermocouples was amplified by an AD595AQ RS Data Control K type thermocouple amplifier, with cold junction compensation, and registered by a Tektronix 320 TDS oscilloscope.

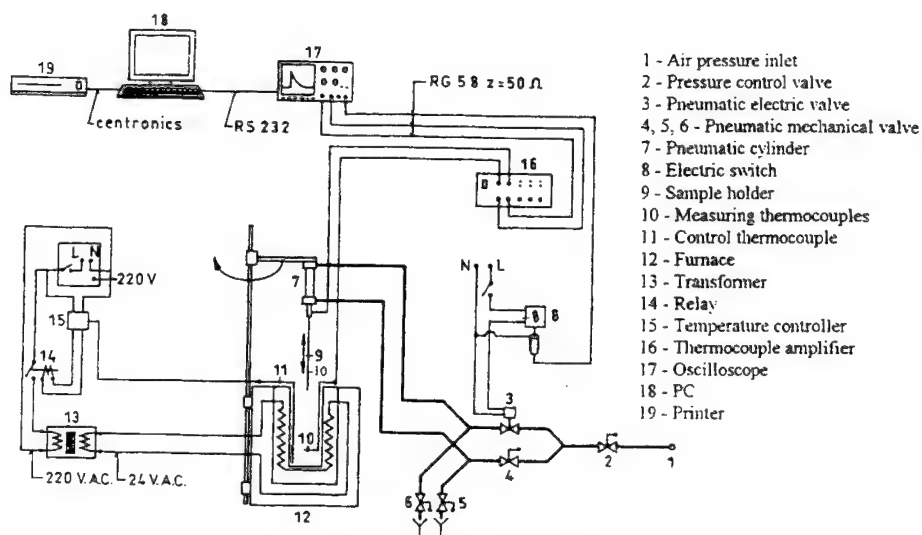


Figure 6. Experimental apparatus.

*Time response of the equipment.* Calibration tests were performed in order to measure the time response of the measuring equipment,  $\Delta t$ , that should be deducted from the experimental ignition delay measurements:

$$\Delta t = \delta t_1 + \delta t_2 \quad (5.1)$$

$\delta t_1$  and  $\delta t_2$  being, respectively the mechanical time of injection of the test sample inside the furnace and the time delay characteristic of the measuring chain.

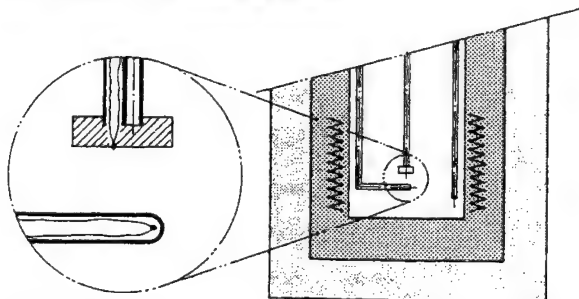


Figure 7. Position of the thermocouple in the test sample.

The time delay of the measuring chain,  $\delta t_2$ , was identified with the time interval between the moment of contact of the thermocouple with the free surface of three molten standard phase change substances ( $t_0$ ) and the moment when the temperature measured by the thermocouple was 95 % of the characteristic phase change temperature of the substance ( $t_f$ ), being the final value of  $\delta t_2$  the

arithmetic mean of the results obtained in each case. This procedure proved that the  $\delta t_2(T)$  evolution was linear and could be represented by the equation:

$$\delta t_2 = 53.189 - 0.049 T \text{ (ms)} \quad (5.2)$$

and that the mechanical injection time was  $\delta t_1 = 38 \pm 2$  ms.

*Ignition tests.* The procedure to obtain ignition delay data started with the radial displacement of the injection system, followed by the heating period of the ignition chamber up to the desired temperature. The measuring thermocouple was threaded through the sample and the pellet was positioned on the support wire. Once thermal equilibrium inside the furnace was attained, the injection cylinder was displaced to the furnace axis and the propellant sample was injected into the measuring zone until ignition occurred. The obtained data was transferred to a personal computer for further analysis.

As the temperature of thermal degradation of NSAN (443 K) is significantly lower than the correspondent for AP (713 K), and in agreement with several authors, the ignition instant of the sample was determined by the simultaneous obtainement of a sharp rise of the output of the measuring thermocouple and a minimum surface temperature,  $T_s \geq T_{mNSAN}$ , being  $T_{mNSAN}$  the melting temperature of NSAN [11].

### Theoretical

The ignition delay data obtained for the propellants is plotted in Figure 8. The ignition delays, in function of temperature, were calculated using the equation:

$$\tau_i(T) = \Delta t_{exp}(T) - \delta t_1 - \delta t_2(T) \quad (5.3)$$

A first showed that, as expected, the ignition delay,  $\tau_i$ , of all the tested propellants increases for decreasing temperature levels. Considering the effect of the oxidiser composition alone, it is also apparent from Figure 8 that increasing weight content of non-stabilised ammonium nitrate originates shorter values of  $\tau_i$  for the same temperature levels.

Further interpretation of the experimental data was made considering a bulk analysis of the ignition phenomena, that is, assuming a first order rate controlling reaction with constant reactants' consumption during the pre-ignition period [12]. The reaction rate can thus be correlated by an Arrhenius law:

$$\frac{d[X]}{dt} = K[X] e^{-\frac{E}{RT}} \quad (5.4)$$

where  $[X]$  represents the reactants concentration,  $K$  the pre-exponential Arrhenius constant,  $T$  the temperature of the measuring zone and  $E$  the activation energy of ignition. Based on the simple assumption that the ignition delay is, in a first analysis, inversely proportional to  $d[X]/dt$ ,  $\tau_i$  can be expressed

$$\tau_i = \beta e^{\frac{E}{RT}} \quad (5.5)$$

where  $\beta$  is a constant, related to the pre-exponential Arrhenius constant, for each formulation. A  $\ln \tau_i$  vs.  $1/T$  plot will thus originate a straight line expressed by the equation

$$\ln \tau_i = \ln \beta + \frac{E}{RT} \quad (5.6)$$

The application of this type of analysis to the experimental results showed that, in all formulations, the evolution of  $\ln \tau_i = \ln \tau_i(1/T)$  presented in fact a discontinuity and could be described in two linear Phases (Figure 9), with different values of the activation energy and  $\beta$  factor.

As the calculated values of the activation energy for Phase I of the evolution  $\ln \tau_i = \ln \tau_i(1/T)$  are always inferior to those of Phase II (Table 4), and keeping in mind that homogeneous gas phase reactions generally occur at higher temperatures, with high levels of activation energy, whereas heterogeneous reactions, with lower activation energy, predominate at lower temperatures, this type of evolution seems to indicate that the ignition mechanism of AP/NSAN/HTPB composite propellants is strongly dependent on the heating rate, corresponding Phase I to the occurrence of heterogeneous ignition reactions while homogeneous gas phase ignition reactions are characteristic of Phase II [14].

The transition temperatures ( $T_{tr}$ ) between Phases I and II were calculated solving the system of equations formed by the polynomial regression of the experimental results, identified as belonging to each phase. The results obtained (Table 4) clearly show that partial substitution of ammonium perchlorate by of non-stabilised ammonium nitrate in the propellants' formulation shifts the transition temperature to lower levels, increasing in this way the domain of occurrence of homogeneous ignition.

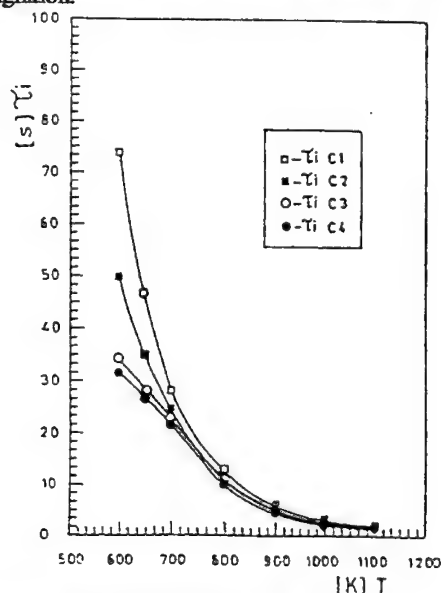


Figure 8. Experimental results. Evolution of  $\tau_i(T)$  of the propellants.

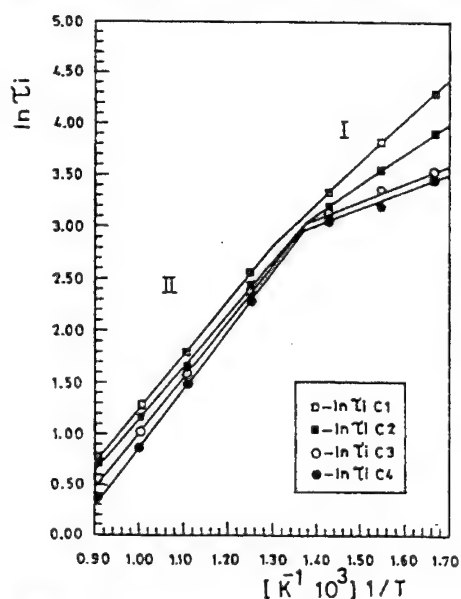


Figure 9. Evolution of  $\ln \tau_i (1/T)$ . Definition of Phases I and II.

Table 4

Calculated Values of  $E$  and  $\beta$  for Phases I and II and Transition Temperatures Between Heterogeneous and Homogeneous Ignition Mechanisms

PROPELLANT	$E_I$ (kJ mol <sup>-1</sup> )	$\beta_I$ (s)	$E_{II}$ (kJ mol <sup>-1</sup> )	$\beta_{II}$ (s)	$T_{tr}$ (K)
C1	33.6	$0.86 \cdot 10^{-1}$	43.3	$1.90 \cdot 10^{-2}$	767
C2	24.6	$3.59 \cdot 10^{-1}$	41.8	$2.07 \cdot 10^{-2}$	726
C3	14.2	1.96	44.4	$1.77 \cdot 10^{-2}$	727
C4	13.6	2.05	47.0	$0.85 \cdot 10^{-2}$	730

The values of the activation energy and of the experimental factor  $\beta$  are also affected by the presence of NSAN (Table 4). In fact, for both types of composite propellants, the calculated values present a significant decrease of  $E$  values of Phase I while  $\beta_I$  factors are increased. A similar analysis of the results obtained for Phase II shows that, after an initial slight decrement of  $E_{II}$  due to the presence of NSAN, the values of this parameter increase, becoming superior to the correspondent of the formulation with AP only. This same type of function can be observed for the  $\beta_{II}$  factor which values decrease, after a minimum value for formulations containing 20 % NSAN, becoming inferior to the  $\beta_{II}$  of the formulation with AP only.

## 6 - SYNTHESIS

All the compositions were formulated with 80 % weight of solid oxidant charge and 20 % weight of bulk (pre-polymer, plasticizer and curing agent) binder system. The cases 0 % to 80 % of NSAN weight content, of the total solid oxidant charge, were studied.

The first part of the experimental work concerned the determination of the HCl concentration in the combustion products. Small samples of the formulations were ignited in a combustion chamber, previously flushed with nitrogen, and the reaction products diluted in bi-distilled water, in order to obtain an aqueous solution. The experimental values were obtained using the classic processes of electrometry and precipitation titration.

The results obtained allowed the determination of the evolution of the HCl concentration and of the global acidity of the combustion products' solution.

The experimental results were compared with those obtained using the numeric code THOR that allows the calculation of the equilibrium composition of the combustion products of the propellants. The final composition and correspondent combustion temperature were calculated using the ideal gas E.o.S, considering the possibility of formation of  $\text{CO}_2$ ,  $\text{H}_2\text{O}$ ,  $\text{N}_2$ ,  $\text{CO}$ ,  $\text{HCl}$ ,  $\text{O}_2$ ,  $\text{CH}_4$ ,  $\text{OH}$ ,  $\text{NO}$ ,  $\text{H}_2$ ,  $\text{N}$ ,  $\text{O}$ ,  $\text{C}$ ,  $\text{H}$ ,  $\text{NH}_3$  and  $\text{C}_{\text{soI}}$  as combustion products.

There is a good agreement between the values calculated with the numeric code and the experimental results obtained using both techniques. The partial substitution of ammonium perchlorate by non-stabilised ammonium nitrate reduces in a very effective way the emission of acid components during combustion, namely the formation of hydrochloric acid.

The linear regression rates of the propellants were assessed. The experimental measurement of the linear regression rate ( $V_r$ ), obtained in a conventional strand-burner, allowed the determination of the  $V_r(P)$  evolution of the formulations, as a function of non-stabilised ammonium nitrate weight content of the propellants.

The results showed a progressive pressure insensitivity of the formulations' burning rates, for increasing NSAN weight contents.

The ignition delay of the AP/NSAN/HTPB formulations was studied in the next phase of this work. Test samples were submitted to radiative heating in an electrical furnace, until ignition occurred. As the temperature of thermal degradation of NSAN (443 K) is significantly lower than the correspondent for AP the ignition instant of the sample was determined by the simultaneous obtainement of a sharp rise of the output of the measuring thermocouple and a minimum surface temperature,  $T_s \geq T_{\text{mNSAN}}$ , being  $T_{\text{mNSAN}}$  the melting temperature of NSAN.

The results obtained showed that increasing weight content of NSAN originate shorter values of  $\tau_i$ . Further interpretation of the experimental data, assuming a first order rate controlling reaction, showed that the evolution of  $\ln \tau_i = \ln \tau_i (1/T)$  presented a discontinuity and could be described in two linear Phases correspondent to the occurrence of heterogeneous ignition and homogeneous gas phase ignition reactions, indicating that the ignition mechanism of AP/NSAN/HTPB composite propellants is strongly dependent on the heating rate.

The transition temperatures ( $T_{tr}$ ) between the two ignition mechanisms were calculated, and the results obtained clearly show that partial substitution of AP by NSAN shifts the transition temperature to lower levels, increasing the domain of occurrence of homogeneous ignition.

## REFERENCES

1. Hawk, C., Environmental effects of solid rocket propellants, *Proceedings of the AGARD Conference on Environmental Aspects of Rocket and Gun Propulsion, Propulsion and Energetics Panel (PEP) 84th Symposium*, Aalesund, Norway, 1994, 1/1-1/12.
2. Pérut, C., Bodart, V. and Cristofoli, B., Propergols solides pour lanceurs spatiaux générant pas ou peu de gaz chloridrique, *Proceedings of the AGARD Conference on Environmental Aspects of Rocket and Gun Propulsion, Propulsion and Energetics Panel (PEP) 84th Symposium*, Aalesund, Norway, 1994, 4/1-4/12.
3. Manelis, G. B., Possible ways of development of ecologically safe solid rocket propellants, *Proceedings of the AGARD Conference on Environmental Aspects of Rocket and Gun Propulsion, Propulsion and Energetics Panel (PEP) 84th Symposium*, Aalesund, Norway, 1994, 13/1-13/6.
4. Araújo, L. and Frota, O., Low pollution of AP/AN based composite propellants, *Proceedings of the 2nd International Conference on Combustion Technologies for a Clean Environment*, 2, 9-14, 1993.
5. Araújo, L. and Frota, O., Thermochemical characteristics of AP/AN based composite propellants, *Proceedings of the 25th International Annual Conference of ICT (Energ. Mater. - Analysis, Characterisation and Test Techniques)*, Karlsruhe, Germany, 1994, 47/1-47/8.
6. Frota, O. and Araújo, L., Rheologic characteristics of HTPB/Al/AP dispersions, *Proceedings of the 25th International Annual Conference of ICT (Energ. Mater. - Analysis, Characterisation and Test Techniques)*, Karlsruhe, Germany, 1994, 51/1-51/11.
7. Campos, J., Araújo, L., Góis, J. C., Pires, A., Mendes, R. and Nina, M., Gas pollutants from ammonium nitrate based propellants, *Proceedings of the AGARD Conference on Environmental Aspects of Rocket and Gun Propulsion, Propulsion and Energetics Panel (PEP) 84th Symposium*, Aalesund, Norway, 1994, 18/1-18/7.
8. Campos, J., Thermodynamic calculation of solid and gas pollutants using different equations of state, *Proceedings of the First International Conference on Combustion Technologies for a Clean Environment*, Vilamoura, Portugal, 1991.
9. JANNAF, *Thermochemical Tables*, National Bureau of Standards, 1971.
10. Gordon, S. and McBride, B.J., Report NASA SP273, 1971.
11. Kishore, K. and Gayathri, V., Chemistry of ignition and combustion of ammonium perchlorate based propellants, *Fundamentals of Solid Propellant Combustion*, AIAA, 90; 1984.
12. Girdhar, H. L. and Arora, A. J., Ignition delay of composite solid propellants by the hot plate technique, *Combustion and Flame*, 31, 245-250, 1978.
13. Frota, O. and Araújo, L., Chemical kinetics in the ignition of AP/AN based composite propellants, *Tenth Symposium on Chemical Problems Connected With the Stability of Explosives*, Margreterorp, Sweden, 1995.

## COMMENTS

**Dr. Rose Pesce-Rodriguez** - Can You describe the intended applications for the propellant systems discussed in your presentation?

**Ms. Octávia Frota** - As referred in the introduction of this paper, there is in Portugal a strong interest in the development of low polluting propulsive compositions. As the generality of the new low polluting oxidizers still present high levels of sensitivity to both shock and heat, ammonium nitrate still is a natural candidate for the substitution of ammonium perchlorate. The propellants discussed in this paper are in fact baseline formulations, which energetic characteristics are flexible enough to allow tailoring according with the specifications of the end user.

## **REALISATION OF AN ECO-FRIENDLY SOLID PROPELLANT BASED ON HTPB -HMX-AP SYSTEM FOR LAUNCH VEHICLE APPLICATIONS**

**Rm.Muthiah, T.L.Varghese, S.S.Rao, K.N.Ninan & V.N.Krishnamurthy**  
Propellants, Polymers, Chemicals and Materials Entity  
Vikram Sarabhai Space Centre,  
Trivandrum 695 022  
India

**ABSTRACT:** An eco-friendly higher solid loaded HTPB propellant with improved energetics has been realised in small scale by incorporating 10-20% by weight of a high energy material namely, HMX. This propellant with 88% solid loading has given good processability, mechanical properties and reduced pressure index. Pollution due to HCl smoke in the rocket exhaust is reduced by 20 to 30% by weight. This propellant is expected to give a vacuum specific impulse of 293 seconds at an operating pressure of 70 ksc and an area ratio of 10. Sub Scale motors of 2kgs size have been successfully static tested to evaluate the performance.

### **INTRODUCTION**

Hydroxyl terminated polybutadiene (HTPB) based composite propellant is the present work horse propellant for the solid rocket motors of the Indian Launch Vehicles. This propellant has undergone various stages of development and qualification tests and is being successfully used in the various stage solid motors of Augmented Satellite Launch Vehicle (ASLV) and Polar Satellite Launch Vehicle (PSLV). The successful scale-up and productionisation of 129-tonne booster motor of PSLV, the third largest solid booster and the first largest operational HTPB based solid rocket motor has established ISRO's (Indian Space Research Organisation) capability in solid rocket technology.

The main constituents of this HTPB propellant are hydroxyl terminated polybutadiene (HTPB) as binder, ammonium perchlorate(AP) as oxidizer and powder grade aluminium(Al) as metallic fuel along with other additives such as plasticizer, wetting/bonding agents, cross linker, curatives, stabilizers, burn rate modifiers, etc. The major component of the propellant is AP which is present to an extent of about 70% . During the propellant combustion, large amounts of HCl gas and other chlorine compounds are generated in the motor exhaust. These gases are highly corrosive and toxic in nature and they form semi-opaque clouds under humid conditions. During the firing of large size boosters of launch vehicles such as Space Shuttle Booster (503 tonnes) enormous quantity of HCl (above 100 tonnes) is produced and let to the atmosphere. This may lead to " heavy acid rain" polluting the environment and also cause depletion of the ozone layer. These aspects are a subject of concern among the scientists in recent times, even though the quantities of harmful exhausts from rockets is orders of magnitude lower than that produced from automobiles. Efforts have been made for the development of alternate propellants which are environmental friendly and are equally or more energetic to meet the future space requirements.

Various alternatives have been reported<sup>1</sup> to reduce the concentration of harmful exhaust products in solid propellants. The use of non-HCl generating oxidizers such as ammonium nitrate (AN) has been thought of. The phase change occurring at 32°C and the low oxidizing potential leading to lesser energetics are the inherent problems with AN. Another approach<sup>2</sup> is to partially substitute AP with AN or nitramine compounds such as HMX (Cyclo tetramethylene tetranitramine) or RDX (Cyclo trimethylene trinitramine) so that the extent of HCl pollution can be reduced. Recent literature reports use of ADN<sup>3</sup> (ammonium dinitramide) and HNF<sup>4</sup> (hydrazinium nitroformate) as eco-friendly oxidizers in solid propellants.

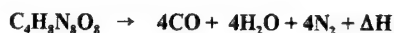
In this paper, we report the development of an environmental friendly propellant based on HTPB binder with partial substitution of AP by nitramine compound, HMX. Incorporation of 10-20% by weight of HMX reduces the HCl smoke by 20-30% by weight at the same time improving the specific impulse. The research programme has led to the development of a high performance eco-friendly propellant for future space applications.

## EXPERIMENTAL

### Materials

HTPB used in this study has been made in-house by the free radical solution polymerization technique. Two grades of HMX of average particle size 60 and 220 microns and AP of 40 and 300 microns were used in the propellant composition.

HMX is a high explosive generally used in explosive charges. But in solid propellant, it acts as a slow explosive as it is diluted with other propellant components. The characteristic feature of high sensitivity to friction of HMX is reduced by wet handling with suitable plasticizer. Processing of HMX-based HTPB propellant upto 20% HMX has been done without any problem in smaller scale. However, incorporation of HMX beyond 10% in large scale processing in tonnage has to be done with adequate precaution. HMX is a stoichiometrically balanced material constituted of C, H, N and O and is expected to give higher energy release<sup>5</sup>.



### Performance Analysis

Performance evaluation of HTPB propellant containing HMX at concentration level up to 30% by weight has been carried out using standard computational programme. The effect of HMX loading on HCl smoke in the motor exhaust and the energetics in terms of specific impulse, flame temperature and mean molecular weight of combustion gases are shown in Fig.1 (A and B).

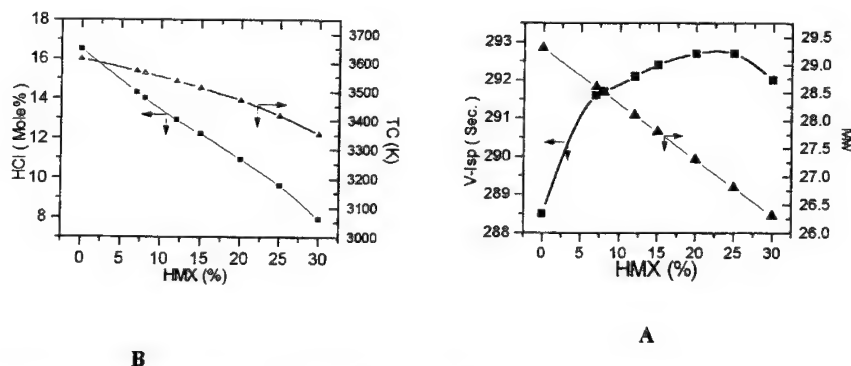


Figure 1. Effect of HMX on A- Hcl Smoke and Flame Temperature, B. - Vacuum Isp and Mol.Wt.

The figure shows that HCl smoke in the motor exhaust decreases with increase in HMX concentration. Flame temperature ( $T_c$ ) and mean molecular weight of exhaust gases ( $M_w$ ) show a gradual decrease as the HMX loading is enhanced. However specific impulse and vacuum specific impulse ( $I_{sp}$ ) which are the indices of energy content, increase to the maximum level at about 20-25% loading of HMX and thereafter show a decreasing trend.

The effect of HMX loading at 0, 10, 20, 25 and 30% levels on HCl smoke,  $I_{sp}$ ,  $T_c$  and  $M_w$  is shown in Table 1. It can be seen that at 20% level of HMX where the energetics is maximum, a reduction of 30% by weight of HCl smoke in the motor exhaust could be realized. The lower flame temperature also is advantageous in reducing the dead weight of insulation, inhibition etc of the rocket motor. The reduction in the mean molecular weight of exhaust gases also improves the motor efficiency. This leads to a low pollution propellant with improved energetics, i.e. an increase in vacuum  $I_{sp}$  by 4.2 seconds. The increase in  $I_{sp}$  could be explained by the fact that HMX is a stoichiometrically balanced material and that the major products of combustion are lighter molecules like CO and  $H_2$ , which contribute more towards propulsive energy.

**TABLE 1**  
**Effect of HMX Loading on HCl Smoke,  $I_{sp}$ ,  $T_c$  &  $M_w$**

Solid Loading : 88% (18%Al)  
HTPB Binder : 12%  
AP + HMX : 70%

HMX loading (wt.%)	HCL content in exhaust (wt.%)	Reduction of HCL (wt.%)	$I_{sp}$ at 70 ksc (sec)	Vacuum $I_{sp}$ at 70 ksc (sec)	$T_c$ (K)	$M_w$
0	20.6	0	265.0	288.5	3613	28.3
10	17.4	15.5	266.8	291.9	3550	28.3
20	14.6	30.0	268.0	292.7	3469	27.3
25	13.1	36.4	268.1	292.7	3417	26.8
30	11.0	46.6	267.7	292.0	3354	26.3

### Propellant Processing and Characterisation

An 88% solid loaded HTPB propellant formulation containing 18% Al was selected for this study. HMX was incorporated as a partial substitute of AP. The propellant ingredients were mixed in a 3 litre capacity sigma mixer. The processability of the slurry was monitored by measuring the end-of-mix viscosity (EOM) and viscosity build up for a period of 3 hours. The propellant slurry was vacuum cast either as cartons for evaluation of mechanical properties and strand burn rate or as 100 mm diameter tubular grains weighting about 2 kilogrammes of propellant for static firing. The mechanical properties of cured propellant samples were evaluated using dumb-bells conforming to ASTM standards D-412-68 (Type-C) at a cross head speed of 50 mm/minute at 25°C. The burn rate of the cured propellant strands was determined using Acoustic Emission Technique at different pressures varying from 30 to 70 Ksc.



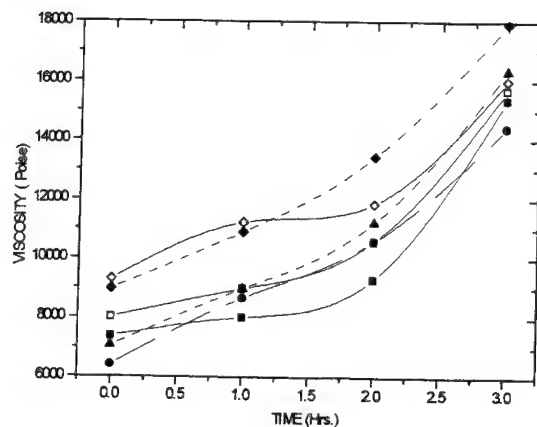
**TABLE 2**  
**Propellant composition**

Ingredients	Percentage by weight					
	1*	2	3	4	5	6
HTPB + plasticizer + TDI + additives	12	12	12	12	12	12
Al (15 microns)	18	18	18	18	18	18
HMX( 220 microns)	0	0	10	10	0	20
HMX( 60 microns)	0	10	0	10	20	0
AP (300 microns)	56	48	48	50	50	40
AP (40 microns)	14	12	12	0	0	10

\* Blank (without HMX)

## RESULTS AND DISCUSSION

The slurry characteristics of HMX loaded (20%) HTPB propellant and blank are shown in Fig.2.



**Figure 2.** Effect of HMX loading on slurry viscosity for various compositions, ■ - 1, ◆ - 2, ◇ - 3, ▲ - 4, ● - 5, □ - 6 ( ref. Table 2)

The viscosity build-up data of the propellant slurry in Fig.2 show good processability with HMX loaded propellant and are quite comparable to those of the blank.

The mechanical properties of the cured propellant such as tensile strength, elongation, modulus, hardness, density

and burn rate are listed in Table 3.

**TABLE 3**  
**Effect of 10- 20% HMX Loading on HTPB Propellant Properties**

Properties	Composition					
	1 *	2	3	4	5	6
<b>Mechanical</b>						
Tensile strength (ksc)	7.6	7.4	7.2	7.5	8.0	8.2
Elongation (%)	33	35	37	36	36	41
Modulus (ksc)	47	45	43	48	45	53
Hardness (Shore A)	70	70	70	70	70	72
Density (gm/cc)	1.800	1.795	1.795	1.790	1.790	1.790
<b>Ballistic</b>						
Strand burn rate at 70 ksc,mm/sec.	6.90	6.15	5.90	5.30	5.25	5.50
Burn rate pressure index 'n'	0.44	0.35	0.34	0.33	0.30	0.31

\* Blank (without HMX)

The mechanical properties of the blank and the five different formulations with different combinations of AP coarse and fine, and HMX coarse and fine show more or less similar results. This shows good manoeuvrability of the propellant formulation with different particle sizes of AP and HMX.

HMX propellant shows slower burn rate compared to blank as seen from the burn rates of 10% and 20% HMX loaded propellant. The effect of particle size of HMX seems to be negligible. The burn rate pressure index was found to be lower with HMX propellant. This could be due to the melting of HMX and formation of melt layer of HMX-HTPB binder, acting as a thick barrier between AP particles. This causes a decrease in the diffusion rate of fuel to the diffusion flame. The burn rate and combustion index are mainly controlled by the diffusion flame produced by the decomposition products of AP and binder<sup>6</sup>. PEM motor ballistic performance of 20% HMX loaded HTPB propellant is shown in Fig.3. PEM motor is our ballistic evaluation test motor having 100 mm diameter and 200 mm length with a circular port and propellant loading of 2 kilogrammes. The thrust - time curves show similar pattern with increased burn time for HMX propellant. The smooth combustion of HMX-based HTPB propellant has been established in this sub-scale motor. Scale up version of this motor is under way. The extent of exact increase in energetics can be assessed better with large size motors.

### CONCLUSION

Development of an eco-friendly high performance propellant containing 20% HMX was realized in sub-scale mixing. Processability and mechanical properties are quite comparable to HTPB propellant (blank). Burn rate and burn rate pressure index are found to be lower than those of the blank. This novel formulation is expected to give a 30% (by weight) reduction of HCl smoke in the exhaust, improved vacuum specific impulse by 4.2 seconds and reduction in the flame temperature by 144 K.

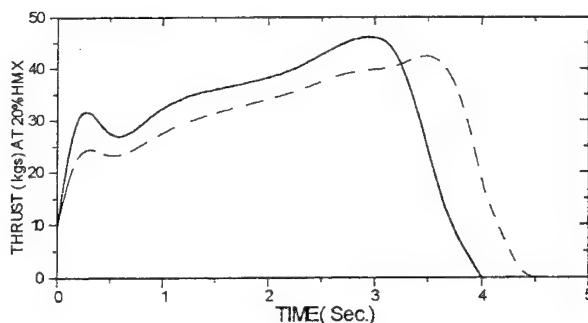


Figure. 3. Thrust-Time profile for PEM motors, — standard, --- with 20% HMX

#### ACKNOWLEDGEMENTS

The authors are grateful to Director, VSSC for the permission to present the paper. Thanks are also due to many colleagues who helped in characterization and manuscript preparation.

#### REFERENCES

1. Korting, P.A.O.G, Zee, F.W.M. and Meulenbrugge, J.J., Performance of No Chlorine Containing Composite Propellants With Low Flame Temperatures, *ALAA-1987-1803*.
2. Doll, D.W., Hendrickson R.R. and Cragun, R.B., Low Cost Propellant for Large Booster Applications, *ALAA-1986-1706*.
3. Borman, Stu., Advanced Energetic Materials Emerge for Military and Space Applications, *C & EN*, January 17, 1994, Washington.
4. Schoyer, H.F.R, Schnorhk, A.J., Korting, P.A.O.G. et al., High Performance Propellants based on Hydrazinium Nitroformate, *J. Propulsion and Power*, Vol. 11, No.4, July-August, 1995.
5. Sofue, T., Takahashi, M., Funo, Y. et al., A High Performance Apogee Boost Motor Using HMX Composite Propellants, *Proceedings of the Fifteenth International Symposium on Space Science and Technology*, Tokyo, Vol. 1, pp.271-276, 1986.
6. Mitani, T., Takahashi, M., Niioka, T. et al., Combustion Characteristics of AP/HMX Composite Propellants, *ibid*, pp.237-242, 1986.

## SOIL CONTAMINATED WITH EXPLOSIVES: A SEARCH FOR REMEDIATION TECHNOLOGIES<sup>§</sup>

J. Hawari,\* C. W. Greer, A. M. Jones, G. I. Sunahara, C. F. Shen, and S. R. Guiot  
Biotechnology Research Institute, National Research Council,  
6100 Royalmount Av, Montreal (PQ), H4P 2R2, CANADA

G. Ampleman and S. Thiboutot,  
Defence Research Establishment Valcartier,  
2459, boul. Pie XI Nord, C.P. 8800, Courcellette (PQ), G0I 1R0, CANADA

### 1. ABSTRACT

A multidisciplinary approach involving chemistry, microbiology, ecotoxicology and environmental engineering was undertaken by the Defence Research Establishment of the Department of National Defence (DREV/DND) and the Biotechnology Research Institute of the National Research Council of Canada (BRI/NRC) to characterize and to optimize the biodegradation potential of TNT and RDX in pure form and in soil. The nature and level of contamination by RDX and TNT in various soils were determined in an interlaboratory study involving both organizations using EPA Method # 8330. Microorganisms were isolated from the native soils and found to be capable of mineralizing ( $^{14}\text{CO}_2$  liberation) RDX under aerobic conditions when the latter was used as sole nitrogen source. RDX disappearance was accompanied by the elimination of toxicity associated with RDX, as determined by the Microtox test. Studies are underway to use the isolated indigenous strain as a bioaugmentation agent for future site application. Thus far TNT showed more toxic effects than RDX and metabolic analysis showed that TNT was biotransformed into the more toxic amine metabolites. In soil these amine metabolites react with humic acids to give recalcitrant and intractable products. To eliminate problems associated with TNT mineralization in soil we thus undertook a study to first wash TNT out of the soil using several water additives and then treat the TNT washings. Preliminary data showed that mineralization of TNT using sewage sludge under both aerobic and anaerobic conditions was enhanced in the presence of cyclodextrins. Further enhancement in the mineralization rate of TNT was obtained after subjecting the soil extract to photolysis. In an integral study, soil heavily contaminated with RDX (2000 ppm) and TNT (1000 ppm) was treated in bioslurry reactors supplemented with sewage sludge under both aerobic and anaerobic conditions. The biological performance of these reactors was monitored using microcosms spiked with  $^{14}\text{C}$ -labelled TNT or RDX. Preliminary data showed that RDX was almost completely mineralized. TNT rapidly disappeared (biotransformation to amino derivatives) with little mineralization. The data obtained from the present aerobic, soil washing and bioslurry reactors studies will be used for the development of practical soil remediation technologies.

<sup>§</sup> NRCC Publication # 34544

\* corresponding author

## 2. INTRODUCTION

Presently, contamination of soils by RDX and TNT and other energetic organonitro compounds, generated as wastes from the munitions and defence industries, is a significant worldwide environmental problem. These compounds are mutagenic, toxic, and have the tendency to persist in the environment [1,2]. Incineration has been suggested as a remediation technology but is considered costly and may produce toxic chemicals if not carefully controlled [3]. Although composting is relatively cheap and explosives disappear at relatively fast rate, the fate of these compounds is complicated by the presence of excessive amounts of other organic compounds in the compost [4]. Bioremediation is considered to be feasible under aerobic conditions [5], however, the body of literature reports indicates that a significant portion of the explosive undergoes biotransformation particularly with TNT. Biotransformation leads to the formation of toxic amino analogs that may react with soil humic acids to form covalently-bound complex structures that are intractable and difficult to mineralize [6,7]. This clearly explains why complete mineralization ( $\text{CO}_2$  liberated) of the explosive is difficult to attain in a soil environment. We have recently observed that biodegradation of RDX and TNT under both aerobic and anaerobic conditions using soil indigenous bacteria produce mineralization in addition to other transformation products [8].

To minimize the problems associated with the formation of such transformation products during soil remediation and to improve mineralization we believe that a soil pretreatment process such as soil washing is necessary. Thus soil washing of explosives using surfactants and cyclodextrins (CDs) will be described. It is planned that data obtained will be used as part of a joint soil washing/biodegradation process for total mineralization of explosives. The present study thus describes recent advances made toward characterizing and degrading RDX and TNT in soil using multidisciplinary protocols involving chemistry, microbiology, ecotoxicology and environmental engineering.

## 3. EXPERIMENTAL

### 3.1 Materials and methods

Lignosol XD was from Reed Lignin, Quebec (PQ), Canada; sodium lignosulfonate (Lignisite 458) was from Burlington, Washington, USA. *B*-cyclodextrin, hydroxypropyl-*B*-cyclodextrin (hp-*B*-CD) with a degree of substitution (ds) of 7 hydroxypropyls/cyclodextrin (American Maize, Hammond, IN), methyl-*B*-cyclodextrin (Me-*B*-CD) (ds 12.6), sodium dodecyl sulfate (SDS) and Tween-80 were from Aldrich, Milwaukee, WI.  $^{14}\text{C}$ -substrate were prepared by the method of Ampleman et al. [9].

**3.2 Soil sampling and extraction.** Soil samples were collected at three contaminated sites from depths of 15 to 45 cm. Two sites were chosen for specific contamination by RDX and TNT. The third site, a disposal site for energetic compounds treated by "open-pit burning," was suspected of being contaminated with various energetic compounds. Soils were extracted and analyzed for the extent of RDX and TNT contamination by HPLC as described by EPA Method # 8330 [10]. DREV and BRI performed an interlaboratory study, based on the the EPA method, to analyze RDX and TNT in pure form and in soil using various concentrations (0.5 to 20,000 ppm). The technique was accurate (>90% recovery), sensitive (DL 0.5 ppm) and precise (RSD  $\pm$  2%). The experiments regarding the effect of additives on the extractability (washing) of RDX and TNT were carried out as described earlier [11].

**3.3 Isolation and enrichment of bacteria.** To isolate bacteria from contaminated soil capable of degrading the energetic compounds, enrichment cultures were prepared using a minimal salts medium, MSM, [12] containing the energetic compound (100 mg/L) as either sole nitrogen or carbon source. Laboratory-scale microcosms enriched with  $^{14}\text{C}$ -substrates were used to assess spontaneous mineralization, as determined by liberated  $^{14}\text{CO}_2$ , in contaminated soils, and to study bioaugmentation of RDX and/or TNT contaminated soil with an actively degrading bacterium. In the latter microcosms, an aqueous suspension of washed cells was added to the surface of soil to yield an initial inoculum density of  $10^8$  colony-forming units (CFU)/g soil. Uninoculated soils acted as negative controls. All incubations were in the dark at 25 to 27°C.

**3.4 Bioslurry reactors.** Two bioslurry reactors with a working volume of 4 litres each were used in the biodegradation study of RDX and TNT and operated under both aerobic and anaerobic conditions. The aerobic reactor was supplemented with activated sludge and the anaerobic one with anaerobic sludge. Each of the two bioslurry reactors was charged with dry weight agricultural soil 40%, sludge 20 % and a Carbon Oxygen Demand concentration of 5 g COD/L. The total reactor volumes were completed with distilled water. The concentration of TNT and RDX in the soil was artificially amended at values of 1000 and 2000 ppm, respectively. The performance of each reactor was monitored by conducting the following tests: COD, Total Suspended Solids (TSS), Sulfate (for anaerobic reactors), Volatile Fatty Acids, explosive, metabolites and redox potential.

**3.5 Typical microcosms to assess mineralization potential in bioslurry reactors.**

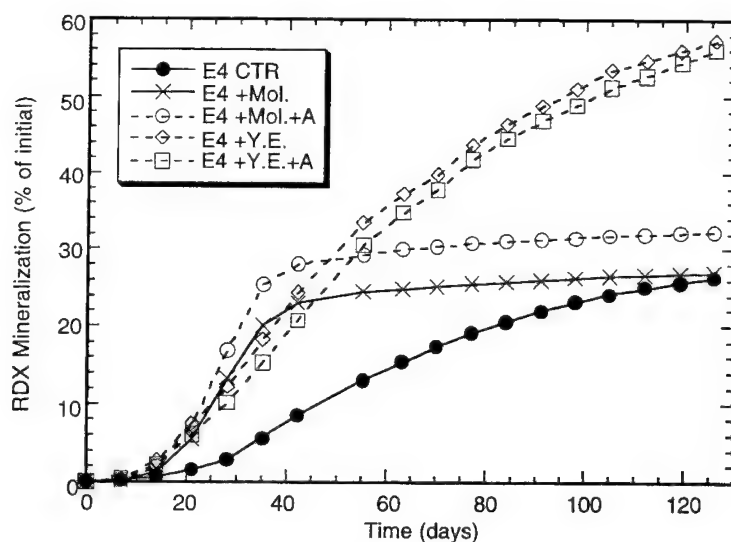
The soil samples were incubated in 100 ml glass vials equipped with a CO<sub>2</sub>-trap containing 0.5 ml of 5 N KOH. The soil-to-mineral media ratio was 30% (by weight) and the initial concentrations of RDX and TNT varied depending on the experiment. Each vial was sealed by a Teflon-lined stopper and wrapped in aluminum foil to prevent photodegradation and placed in a shaking water bath set at 100 rpm and 25°C. At given intervals, the KOH solution were sampled under positive gas pressure, oxygen for aerobic vials and nitrogen for anoxic ones. The extracted alkali was then mixed with 15 ml of scintillation cocktail (ACS, Amersham, Arlington Heights, Ill., USA) and tested for radio-activity using a scintillation counter (Packard Tri-Carb model 4530, Downers Grove, Ill., USA).

**3.6 Metabolite analysis.** The culture medium was extracted with ethyl acetate and analyzed by HPLC (EPA Method # 8330)<sup>10</sup> or GC/MS (Varian GC/MS equipped with a Saturn II ion trap detector). Alternatively, in the case of TNT, the amino-TNT metabolites were analyzed directly in the culture medium using the new solid phase microextraction technique (SPME) in combination with a GC/MS (see below) [13,14].

## **4. RESULTS AND DISCUSSION**

### **4.1 Aerobic Biodegradation of RDX and TNT.**

Soil contaminated with RDX (9640 mg/kg) yielded a microbial consortium with the ability to mineralize RDX when provided as the sole nitrogen source for growth. A bacterial strain, identified as *Rhodococcus* SP, was latter isolated from the this consortium. With glucose as a carbon source, this bacterium was able to mineralize 35% RDX as determined by the amount of liberated <sup>14</sup>CO<sub>2</sub> using a [<sup>14</sup>C]RDX tracer under aerobic incubation in 48 h. The biodegradation of RDX to CO<sub>2</sub> established the aerobic biodegradation potential of RDX, and suggested that aerobic remediation of RDX-contaminated soil is feasible. Binks et al.<sup>15</sup> have identified a strain of bacteria (*Stenotrophomonas maltophilia* PBI) that can degrade RDX under aerobic and nitrogen-limiting conditions. This is in contrast to the biodegradation of RDX under anaerobic conditions that produces mutagenic or carcinogenic hydrazine and dimethylhydrazines [16]. Recently, Crawford has reported research data on the biodegradation of nitrated munition compounds by obligately anaerobic bacteria [17]. When an agricultural soil was artificially amended with pure RDX (50 or 100 mg/kg,) and inoculated with strain, mineralization (liberated <sup>14</sup>CO<sub>2</sub>) increased as compared to uninoculated control soils. However, the ability of this organism to degrade RDX in soil may be influenced by the concentration of RDX, soil/contaminant interactions, and/or nutrient limitation. The effect of pH, RDX/TNT concentration, and the presence of additives such as yeast extract are presently under investigation. Preliminary observations indicate that slightly alkaline pHs favor RDX biodegradation. Also biostimulation with other nutrients (C-source) enhanced mineralization of RDX in soil using the added bacterium (Figure 1) and also minimized the negative effect of TNT on the mineralization of RDX. On the other hand, TNT is a more recalcitrant compound, and thus far the substrate has been demonstrated to undergo extensive biotransformation with minimal ring cleavage to CO<sub>2</sub> [18,19] Microcosms, containing soils contaminated with TNT (25 to 12,000 mg/kg) and spiked with [<sup>14</sup>C]TNT showed that only the soil with the lowest TNT concentration exhibited mineralization activity (<10%). Mineralization was dependent on TNT concentration and stopped when the TNT concentration reached 100 mg/kg. Neither nutrient enhanced the rate of mineralization in the soil. A strain was later isolated from a soil consortium developed from the soil using low concentrations of TNT (5 mg/L) as the sole nitrogen source



**Figure 1.** Mineralization of RDX in soil (19,056 ppm RDX), with or without amendments or bioaugmentation (+ A); E4 is soil identity, ctr: control, mol: nutrient, and YE: nutrient)

In axenic liquid culture containing ammonium sulfate (250 mg/L) as a conitrogen source and glucose as a carbon source, this isolated strain rapidly transformed TNT (5 mg/L) within 26 h to monoamino- and diamino-TNT derivatives as determined by Solid Phase Microextraction combined (SPME) with GC/MS. SPME uses a fine fused silicon-fiber with a polymeric coating to extract organic compounds from their matrix and directly transfer them into the injector of a gas chromatograph (GC) for chemical desorption and analysis [13,14]. The technique allows the detection of transient metabolites at trace level to help in the study of the metabolic pathways. Figure 2 A and B is a typical SPME/GC/MS spectra of TNT metabolites formed under aerobic conditions, namely, 2-amino-4,6-di-nitro-toluene, 4-amino-2,6-di-nitro-toluene and 2,4-di-amino-6-nitro-toluene and 2,6-di-amino-4-nitro-toluene.

The present study confirms that in the case of TNT, biotransformation, rather than mineralization, is the main biodegradation pathway under both aerobic or anaerobic conditions. Earlier reports have also indicated that biotransformation is the main pathway for TNT biodegradation [18,19,20]. The limitation imposed on TNT mineralization is possibly due to the high oxidative properties of TNT and also to the steric hindrance imposed on the carbon-backbone of TNT by the  $\text{NO}_2$  groups. Another difficulty encountered in TNT biodegradation in soil is the interactions between TNT (and its amino metabolites) with soil constituents such as humic acids (humification) resulting in the loss of TNT and its metabolites within the soil environment. This explains why in spite of TNT disappearance very little carbon dioxide is formed. With these difficulties in TNT biodegradation at hand, studies are underway to enhance bioavailability of TNT (and its metabolites) to the degrading microorganisms in soil. Also other avenues are being explored to enhance mineralization of TNT (and RDX) such as the use of bioslurry reactors (described below) and joint soil washing/biodegradation processes.

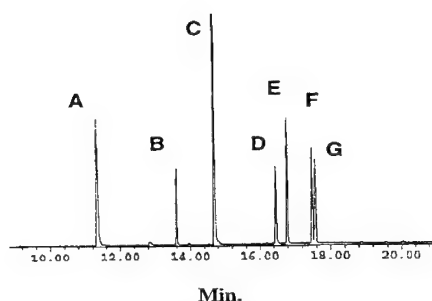


Figure 2A: SPME/GC/MS Total Ion Chromatogram of Aerobic TNT Metabolites A: Recovery Standard (2,4-dinitrotoluene), B: TNT (trinitrotoluene), C: IS (Dibenzothiophene), D: 2,4-diamino-6-nitrotoluene; E: 2-amino-4-dinitrotoluene; F: 4-amino-2,6-dinitrotoluene and G: 2,6-diamino-4-nitrotoluene.

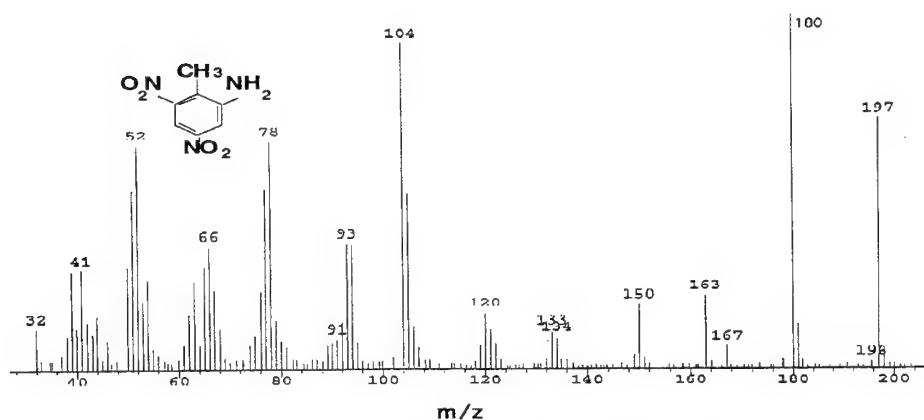


Figure 2B. A typical SPME/GC/MS of 2-NH<sub>2</sub>-4,6-di-NO<sub>2</sub>-toluene

#### 4.2 Removal of RDX and TNT from soil by washing:

As the previous study indicated, the aerobic mineralization of TNT in soil is poor and mineralization is often hampered by the formation of intermediate products (amine derivatives). Apart from being toxic to microorganisms these intermediates interact with soil constituents such as humic acid (humification) and produce intractable products that are not available to the degrading microorganism. We therefore undertook a study to first wash the explosive out of the soil using several additives then biotreat the soil washing using bacteria and/or fungi.

In an earlier report [11] we found that one washing cycle of the soil (2 g, 1000 ppm) with acetonitrile (10 mL) extracted most of the RDX (99 %). Whereas in the case of water at least 4 washing cycles were needed to recover RDX from the soil. However, in the presence of 0.1 w/v of the nonionic cyclodextrins hp-B-CD and Me-B-CD the recovery of RDX increased to 2.4 and 1.5-fold of that of pure water (37,7 mg/L), respectively. Cyclodextrins have been used in the past to enhance the solubility of PAHs and are recommended to be used to facilitate the removal of contaminants from soil [21]. We thus selected hp-B-CD, and studied the effect of increasing its concentration on the recovery of RDX. Increasing the concentration of the CD from 0.1 % to 1 %, 2.5 %, 5 %, and 10 % w/v led to an increase in the recovery of RDX from 45.4 % to 49.4 %, 82.8 % and 87.3 %, respectively. Since high concentrations of the CD is neither cost effective nor environmentally acceptable a CD concentration ranging from 0.1 to 1 % w/v would constitute the most reasonable



hydraulic based system for the removal of RDX from soil. Under these conditions at least two washing cycles would be needed to wash out RDX, i. e. 10 mL solvent/2 g contaminated soil (1,000 ppm).

In the case of TNT, a heavily contaminated soil was used (5265 ppm) and portions of the soil were washed with several water based solutions ranging from water, lignosulfonate, quaternary ammonium salt, Tween-80, to CDs (Table 1). The use of 1 % w/v of either additive did not drastically enhance the recovery of TNT from soil. In all cases the amounts of extracted TNT was close to that obtained using water alone, i.e., concentration of TNT was ca 90 ppm. The amounts of extracted TNT could be increased by increasing the amounts of the additive. For example, TNT recovery increased by a factor of 4 (Tween-80) and 5 (quaternary ammonium salt) by increasing additive concentration to 4 % w/v. Interestingly, the amounts of TNT recovered using pure water did not reach the normal solubility of TNT (140 mg/L). This is attributed to the adsorption/desorption behavior of TNT in a soil/water system. These interactions between TNT and soil constituents are considered critical in determining the fate (biodegradability/mineralization) of TNT in the soil. Earlier batch sorption experiments in flooded soil showed that biodegradation kinetics of nitrogen-substituted naphthalene's are controlled by the adsorption/desorption behavior of the substrate in the soil [22,23]. Electron-donor-acceptor complexes, formed between the electron-deficient polynitroorganics and the e-rich mineral surfaces such as soil clay, may significantly influence the transport and fate of such compounds in the soil. For instance, about 20 % of TNT (initial concentration 16 mg/mL<sup>-1</sup> of soil/solution slurry) stays in the soil after three sequential desorption cycles [7].

Table 1.

Recovery of TNT from contaminated soil (1 g) using water (10 mL) and different cosubstrates (0.1 %v/w)

Solvent (0.1 % w/w)	[TNT] ppm (RSD)	Solvent (4 % w/w)	[TNT] ppm (RSD)
Water	89.2 (0)	Water	89.2 (0)
Lignosulfonate	75.5 (0)	Lignosulfonate	191.1 (1)
SDS	94.8 (4)	SDS	426.3 (10)
Tween-80	112.8 (3)	Tween-80	370.0 (2)
Carboxymethyl- β-cyclodextrin	90.4 (2)	Carboxymethyl- β-cyclodextrin	88.4 (3)
Hydroxypropyl- β-cyclodextrin	81.0 (2)	Hydroxypropyl- β-cyclodextrin	151.1 (2)
Dimethyl- β-cyclodextrin	96.5 (1)	Dimethyl- β-cyclodextrin	268.0 (1)

EPA Method 8330 showed 5265 ppm, RSD: relative standard deviation (based on triplicates)

The enhancement in the water solubility of organic compounds in the presence of CDs is attributed to the formation of inclusion complexes involving the CD host cavity and the guest molecule mainly through hydrophobic interactions. While our objective in the present study was not to investigate the nature and the structure of explosive/CD complexes we believe that such a study will help optimize the removal of explosives from soil. Thus far very little information is available in the literature on the CD/explosive inclusion complexes. The nature of these complexes (e. g., CD/RDX ratio) and the mechanisms of interactions among the species are not fully understood. Recently Cahil et al [24,25] have used <sup>1</sup>H-NMR Spin-Lattice relaxation time to study inclusion complexes that form between explosives of the nitramine family (e.g. RDX) and CDs (α, β, and γ).

As we mentioned earlier, one of the frequently encountered problems during biodegradation of TNT in soil is the formation of intermediate amine metabolites that interact with soil humic acid and form

intractable complexes.. Cyclodextrins are used to minimize these problems and thus to enhance mineralization. Observations from preliminary microcosm experiments showed that the presence of Hp- $\beta$ -CD (1 % w/v) in TNT washings (50 ppm) slightly enhanced mineralization (from 1 % to 3 % in 5 months) using both aerobic and anaerobic sludges. However, photolytical pretreatment (300 nm, 15 h) of TNT washings (> 80 % of TNT disappeared) showed that mineralization increased from 1 % to 15 % using aerobic sludge. Under anaerobic conditions the photolyzed mixture showed only 5 % mineralization as determined by liberated  $^{14}\text{CO}_2$ . More work is underway to study the effect of several other additives on the recovery of TNT from soil and on its mineralization.

#### 4.3 Biodegradation of RDX and TNT Using Bioslurry Reactors.

Mineralization of explosives, particularly TNT in soil is found to be difficult to attain due to the presence of severe interactions between the explosives and their metabolites with soil constituents. Also the previous study demonstrates that the biodegradability of the explosive is affected in the presence of other explosives. To clarify these problems and to enhance mineralization of explosives a study was initiated to develop bioslurry reactors that can degrade relatively high concentration of RDX and TNT either separately or in the same bioreactor.

Preliminary results (Figures 3 and 4) indicate that TNT (initial concentration 1,000 ppm) was very rapidly removed in both the anaerobic and aerobic bioslurry reactors. The removal of RDX (initial concentration 2,000 ppm) in the reactor supplemented with anaerobic sludge illustrated a lag period up to two weeks, then RDX was completely removed during three weeks. These results may indicate that the RDX degrading activity of anaerobic sludge was not inhibited by the high concentrations of TNT and RDX in the slurry reactor. The explosive degrading bacteria in the anaerobic sludge were able to adapt to the toxicity of both TNT and RDX. The RDX concentrations in the reactor supplemented with activated sludge and operated under aerobic conditions indicate removal of RDX was very poor under aerobic conditions.

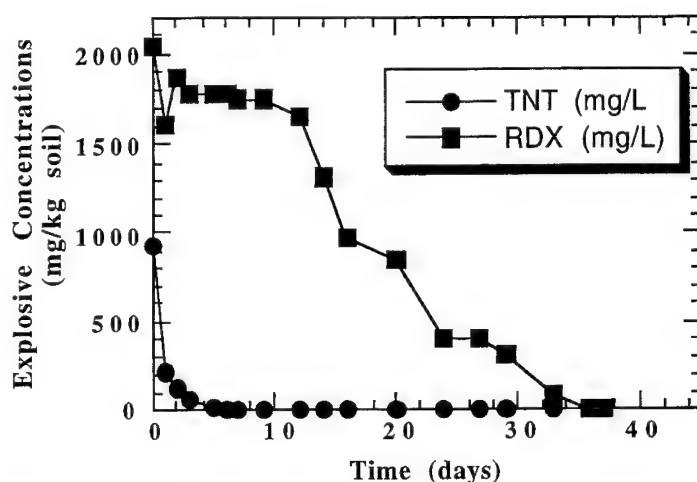
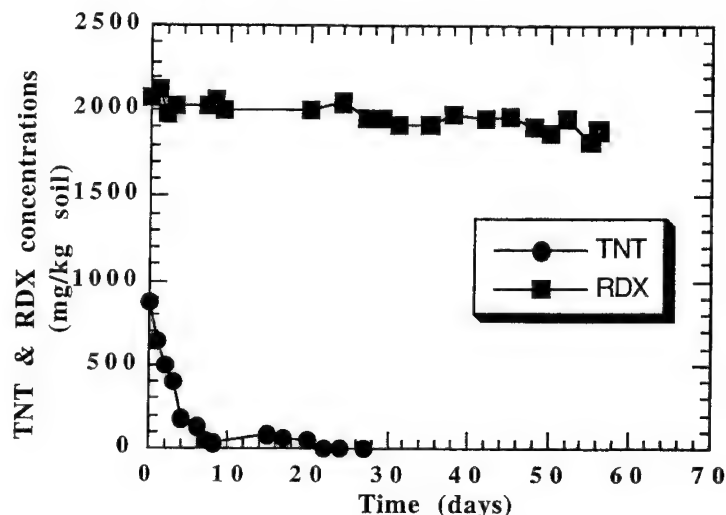


Figure 3. Explosive removal in a bioslurry reactor supplemented with anaerobic sludge operated under anaerobic conditions.

Microcosm tests simulating the bioslurry reactors using  $^{14}\text{C}$ -labeled TNT and RDX were conducted to see if TNT and RDX removal from the slurry reactors is attributed to mineralization to  $\text{CO}_2$  and furthermore to determine the synergetic or antagonistic effect of TNT and RDX on mineralization. In general TNT mineralization was found to be very poor under both aerobic and anaerobic conditions. Supplements of activated or anaerobic sludge did not improve the mineralization rates of TNT. These results suggest that TNT removal in the bioslurry reactors under both aerobic and anaerobic conditions were merely due to biotransformation. This was in fact the case since very little  $^{14}\text{CO}_2$  was detected

and several intermediate amino-TNT metabolites are formed.

On the other hand, soil slurry microcosms conducted under aerobic conditions showed that 10 % of the RDX was mineralized by soil indigenous microbes after 8 weeks of incubation and that the supplement of activated sludge in the soil slurry microcosms increased RDX mineralization to 18 %. This value is far below the 60 % mineralization level achieved for RDX in microcosms using activated sludge only, indicating that the presence of soil inhibited the RDX degrading activity of activated sludge. Furthermore, the antagonistic effect of TNT on the RDX mineralization was clearly revealed by a drop in the mineralization rate of RDX from 16% to 4% after the addition of TNT to the microcosms.



**Figure 4. Explosive removal in a bioslurry reactor supplemented with aerobic sludge operated under aerobic conditions.**

Similar to the microcosms conducted under aerobic conditions, soil indigenous microbes were able to mineralize RDX up to 15% under anaerobic conditions, the mineralization rate of RDX however was greatly enhanced by the supplement of municipal anaerobic sludge, reaching 60% in the microcosms with soil, RDX and anaerobic sludge. Mineralization of RDX was boosted when the microcosms, initially incubated under anaerobic conditions, were switched to aerobic conditions and amended with 10% activated sludge. The boost in RDX mineralization, as determined by liberated  $\text{CO}_2$ , is apparently due to further degradation of RDX metabolites to  $\text{CO}_2$  since RDX was found to mineralize poorly under aerobic conditions.

#### 4.4 Ecotoxicology

One of our objectives is to develop toxicological tools to assess the effectiveness of remediation technologies for sites contaminated with energetic substances, such as TNT and RDX, and their metabolites. In addition to the environmental concerns, we have also recently addressed some other problems such as genotoxicity. This toxicological issue may be problematic since there is the possibility that the biodegradation of certain energetic substances may lead to poorly characterized and potentially toxic compounds which are not easily identifiable by routine analytical methods. For this purpose, a suite of bioassays (including tests for bacterial and mammalian cytotoxicity and genotoxicity, green algae growth inhibition, and earthworm survival) is being used to develop a databank which characterizes the toxicological effects of these soil contaminants. Preliminary results indicate that TNT and not RDX, is mutagenic on TA98 (frameshift) and TA100 (basepair substitution) variants, using the Fluctuation test. On the other hand, TNT is negative using the SOS Chromotest. Mammalian cytotoxicity and mutagenicity tests using cultured V79 Chinese hamster fibroblasts indicate that RDX was clearly less toxic than TNT (at equivalent concentrations) and that TNT metabolites were generally less toxic than the parent compound when tested at short exposure periods. The genotoxicity

of these energetic compounds showed that both TNT and RDX were weakly mutagenic. Studies are being continued to further broaden our knowledge of the mechanisms of toxicity of these soil and groundwater contaminants which ultimately may have long-term environmental impacts at different terrestrial organismal levels.

## 5. CONCLUSION

The challenge in solving problems associated with the biodegradation of explosives in soil is how to render the substrate bioavailable to the degrading microorganisms and amenable to mineralization. Bioavailability can be enhanced through the use of additives such as CDs, anionic or neutral surfactants and biodegradability can be facilitated and enhanced by physicochemical pretreatment (e.g. photolysis) techniques. In the case of TNT, minimizing the number of the steric and highly oxidized NO<sub>2</sub> groups on the aromatic ring facilitate bacterial attack on the carbon backbone of the ring and thus enhance mineralization. In the case of RDX, however, mineralization is possible under aerobic conditions but the extent of mineralization is dependent on the concentration of the explosive. Preliminary data showed that bioslurry reactors and a combined anaerobic/aerobic strategy are promising approaches to remediate soil contaminated with relatively high concentrations of RDX (2,000 ppm) and TNT (1,000 ppm). The present study clearly demonstrates that no single technology may be universally feasible to clean soil contaminated with explosives. A multidisciplinary approach is needed depending on the type of soil and type and extent of contamination. Subsequently, aerobic biodegradation of RDX in soil, joint soil washing/biodegradation and bioslurry reactors are all important and worthy of continued development.

## 6. ACKNOWLEDGEMENTS

The authors would like to thank the following: A. Halasz, S. Dodard, E. Zhou, A. Renoux, B. Lachance, S. Labelle, A. Mihoc, A. Gagnon and H. Gagnon for their technical assistance

## 7. BIBLIOGRAPHY

1. Gorontzy, T., Drzyzga, O., Kahl, M. K., Bruns-Nagel, D., Breitung, J., Von Loew, E. and Blotevogel, K. H., Microbial degradation of explosives and related compounds, *Critical Reviews in Microbiology*, 20(4), 265-284, 1994.
2. Kaplan, D.L., Biological degradation of explosives and chemical agents, *Curr. Opin. Biotechnol.*, 3, 253-260, 1992.
3. Kaplan, D.L. and Kaplan, A.M., Thermophilic biotransformation of 2,4,6-trinitrotoluene under simulated composting conditions. *Appl. Environ. Microbiol.*, 44, 757-760, 1982.
4. Williams, R.T., Ziegenfuss, P.S. and Sisk, W.E., Composting of explosives and propellant contaminated soils under thermophilic and mesophilic conditions, *J. Ind. Microbiol.*, 9, 137-144, 1992.
5. Haigler, B. E., Wallace, W. H. and Spain, J. C., "Biodegradation of 2-nitrotoluene by *Pseudomonas* sp. strain JS42." *Appl. Environ. Microbiol.* 60: 3466-3469, 1994.
6. Kaplan, David L. and Kaplan, Arthur M., 2,4,6-trinitrotoluene-surfactant complexes: decomposition, mutagenicity and soil leachnig studies., *Environ. Sci. Technol.*, 16, 566-571, 1982.
7. Pennington, J. C. and William, H. P. Jr., Adsorption and desorption of 2,4,6-trinitro-toluene by soil., *J. Environ. Qual.*, 19, 559, 1990.
8. Jones, A., Ampleman, J. G., Thiboutot, S., Lavigne, J., Greer, C., Hawari, J., Biodegradability of Highly energetic chemicals under aerobic conditions., "In *Bioremediation of Recalcitrant Organics*," Ed. Robert Hinchee, Ronald E. Hoeppel and Daniel B. Anderson, Battelle Press, Columbus, Richland, US, 3(7), 251-257, 1995.
9. Ampleman, G., Thiboutot, S., Lavigne, J., Marois, A., Hawari, J., Jones, A. M. and Rho, D., "Synthesis of <sup>14</sup>C-labelled hexahydro-1,3,5-trinitro-1,3,5-triazine (RDX), 2,4,6-trinitrotoluene (TNT), nitrocellulose (NC) and glycidyl azide polymer (GAP) for use in assessing the biodegradation potential of these energetic compounds." *J. Labelled Compd Radiopharm.* V. 36 (6), 559-77, 1995.
10. U.S. Environmental Protection Agency. Nitroaromatics and Nitramines by HPLC. Second Update SW846, Method # 8330, 1990.
11. Hawari, J., Halasz, A., E. Zhou and Zilber B., Enhanced recovery of the explosive 1,3,5-tri-aza-1,3,5-tri-nitrocyclohexane, *Chemosphere*, 22, 1929-1936, 1996,

12. Greer, C. W., Hawari, J. and Samson, R., Influence of environmental factors on 2,4-dichlorophenoxyacetic acid degradation by *Pseudomonas cepacia* isolated from peat, *Arch. Microbiol.*, 154, 317-322, 1990.
13. Zhang, Z., Yang, M. Pawliszyn, J. Solid Phase Microextraction., *Anal. Chem.*, 66 (17), 844A-852A, 1994
14. Pawliszyn, J. New Directions in Sample Preparation for Analysis of Organic Compounds., 14, 113-122, 1995,
15. Binks, B. R., Nicklin, S., and Bruce, C. Neil, Degradation of hexahydro-1,3,5-trinitro-1,3,5-triazine (RDX) by *Stenotrophomonas maltophilia* PBI, 61 (4), 1318-1322, 1995.
16. McCormick, N. G., Cornell, J. H. and Kaplan, A. M., Biodegradation of hexahydro-1,3,5-trinitro-1,3,5-triazine. *Appl. Environ. Microbiol.*, 42, 817-823, 1981.
17. Crawford, R. L. Biodegradation of nitrated munition compounds and herbicides by obligately anaerobic bacteria., "In "Biodegradation of nitroaromatic compounds" Ed. J. C. Spain, Plenum Press., N. Y. 87-98, 1995.
18. McCormick, N. G., Feeherry, F. E. and Levinson, J. S., Microbial transformation of 2,4,6-trinitrotoluene and other nitroaromatic compounds, *Appl. Environ. Microbiol.*, 31, 949-958, 1976.
19. Boopathy, R., Wilson, M., Montemagno, C. D., Manning, J. F. Jr., and Kulpa, C. F., Biological transformation of 2,4,6-trinitrotoluene (TNT) by soil bacteria isolated from TNT-contaminated soil. *Bioresource Technol.*, 47, 19-24, 1994.
20. Schackmann, A., and Müller, R., Reduction of nitroaromatic compounds by different *Pseudomonas* species under aerobic conditions. *Appl. Microbiol. Biotechnol.*, 34, 809-813, 1991.
21. Wang, X. and Breausseau, M., Simultaneous complexation of organic compounds and heavy metals by a modified cyclodextrin, *J. Environ. Sci Technol.*, 29, 2632-2635, 1995.
22. Bashir B., Hawari J. A, Leduc, R. and Samson, R., Behavior of Nitrogen-substituted PAHs in Soil: Part I Sorption/Desorption and Biodegradation, *Water Research*, 28, 1817-1825, 1994.
23. Bashir B., Hawari J. A, Leduc, R. and Samson, R., Behavior of Nitrogen-substituted PAHs in Soil: Part II Effect of Sorption/desorption on Aerobic Biodegradation Kinetic, *Water Research*, 28, 1827-1833, 1994.
24. Cahil, S., Rinzler, A. G., Owens, F. J. and Bulusu, S., Molecular complexes of explosives with cyclodextrins, *J. Phys Chem.*, 98, 7095-7100, 1994.
25. Cahil, S. and Bulusu, S., Molecular complexes of explosives with cyclodextrins, *J. Mag. Res.*, 31, 731-735 1993.

## SOLID PROPELLANT UTILIZATION BY THE BURNING PROPELLANT-COAL AND PROPELLANT-PEAT MIXTURES.

Ananiev, A.V., Istratov, A.G., Kolesnikov, V.I., Kurochkin<sup>1</sup>, A.I., Marshakov, V.N.,  
Melik-Gaikazov, G.V., Rotshin, A.V., Stesik<sup>2</sup>, L.N., Teselkin, V.A.

Institute of Chemical Physics, Russian Academy of Sciences, 4 Kosygin St., Moscow 117977,  
Russia;

<sup>1</sup> Krzhizhanovsky Institute of Energy

<sup>2</sup> Institute of Chemical Physics in Chernogolovka

**ABSTRACT:** The investigation of the combustion of the mixtures of propellant-coal and propellant-peat for both composite and double-base propellants was performed in a laboratory reactor and in a model industrial bed-burning furnace. The mechanism of combustion of the bricks was studied for various contents (propellant concentration) for the safe and ecologically clean combustion in furnaces. The flammability and explosion limits for the coal-propellant mixtures were determined. It was showed that the energetic advantage and technological possibility of preparation and combustion of bricks made from the propellant-coal and propellant-peat mixtures in the regime of layer combustion.

### INTRODUCTION

The propellant destruction (or utilization) problem arises when dealing with waste and scrap in propellant industry and also considering disarmament. The possibility of using briquetted mixtures of propellant crumb with low-value coal or peat for bed-burning furnace for these purposes is of great importance.

In 1992 the researchers from the Semenov Institute of Chemical Physics and the Krzhizhanovsky Institute of Energy proposed the destruction of used double-based propellant (DBP) and composite solid rocket propellant (CP) in composite fuel materials based on natural fuels such as brown coal and peat.

The results of the thermodynamic computations of the combustion temperature of brown coal and its mixtures with CP (AP - 68% , binder - 14% , Al - 18% ) and DBP N ( NG - 28% , NC - 57% , DNT - 11% ) are presented in Fig. 1 as a function of the air equivalence ratio,  $\alpha$ , i.e. the ratio of the amount of supplied air to the stoichiometric amount of air. In accordance with the data provided by the Institute of Energy, the brown coal used in our studies ( averaged over the Moscow coal basin) consists of: water (  $W^r$  ) - 8.16 % , ashes (  $A^r$  - 37.28 % ,  $C^r$  - 36.54 % ,  $H^r$  - 3.09 % ,  $S^r$  - 2.99% ,  $O^r$  - 11.31 % and  $N^r$  - 0.63 %; calorificity -

9.88 MJ/kg. One can easily notice that adding propellant to the coal increases the energy characteristics of the fuel, though not too much - at the 5-10% level.

Let us now compare the energy characteristics of the solid natural fuels with propellants. The burning of natural fuel is performed under supply of sufficient amount of air: about 5 kg of air for 1 kg of the coal. The calorific value of the Moscow Region brown coal is around 10 MJ/kg so that calorificity per unit mass will be near 1.6 MJ/kg. On the other hand, the propellants are highly filled with their own oxygen and their combustion products are able to burn when mixed with the air. Therefore, if the heat of combustion of the propellant is 4.2 MJ/kg, then the full oxidation of all the compounds requires almost 2 kg of extra air, and the combustion of the burned gases will give around the same 1.6 MJ/kg. One should consider this a positive result since the combustion the propellant-coal mixtures in the furnace will not require upgrading the furnaces to accommodate a higher level of thermal stress and loading.

## METHODS OF RESEARCH

The composite fuel materials (CFM) can be used as bricks pressed from the powder coal and propellant where the size of the coal and propellant particles should not exceed 3 mm. The study of the mechanism of CFM combustion was performed on cylindrical samples 12 mm in diameter and 10-13 mm high (1.6 grams) and cubic bricks having a 20 mm edge of (12 grams). The combustion of samples was studied both in laboratory reactors and in a bed-burning furnace. The main experiments were performed in the laboratory reactor modeling the combustion conditions in the furnace.

The laboratory reactor consists of the horizontal tube 150 mm long with the internal diameter of 33 mm heated up to the temperature of 750K. The sample was suspended by the W-Re5 - W-Re20 thermocouple 100  $\mu$ m in diameter with the help of ceramic tubes. Open ends of the tube ensured the free air supply. The reactor was placed on the VLZ-type automatic scales. Thus the permanent recording of the weight of the sample and the temperature in its center was ensured.

## RESULTS AND DISCUSSION

The experiments demonstrated that the coal brick with the 20 mm edge completely burns in ~140 min., the brick with the 20% of the N-propellant in ~100 min., and the one with 40% of N-propellant in ~80 min. These burning times are proportional to the percent of coal in the brick.

Fig. 2 shows the history of the relative mass loss of the sample in percent (Fig. 2a) and the temperature in the center of the sample (Fig. 2b) in the time period from 0 to 30 min for different mixtures of N-propellant in coal. It is necessary to point out the existence of extremes on the curves at 780-790 K. These extremes correspond to the full combustion of the propellant and light volatile components of the coal: for example for pure coal the extreme of the first curve in Fig. 2b ( $t = 10$  min.) corresponds to the relative mass loss of 26% on the first curve in Fig. 2a. This quantity coincides with the known percent of light volatile compounds in the Moscow Region brown coal. For the 40% propellant-coal mixture (curves number 5) at the temperature 780 K ( $t = 4$  min.) the mass loss is 55%, being the sum of the weights of the propellant (40%) and volatile compounds (15%). The same

analysis is valid for the other curves. The shape of the curves after the extremes points represents relatively slow coal combustion. This phase corresponds to the known percent of the mineral part (slag) in the coal. The analysis of the curves 1-5 in Fig. 2 suggests the existence of two different burning regimes — "layer" and "relay-race". When the amount of propellant is under 20% (curves 1-3) one has the "layer" regime where the full combustion of the propellant and volatile components (everywhere  $t = 10$  min.) takes place under relatively slow heating of the sample from the external heater and energy excitation near the surface. This regime is similar to the usual diffusion regime of the coal combustion. The curves 4-5 (when the amount of propellant is 30 and 40% ) demonstrate the possibility of fast penetration of combustion inside the sample ( $t < 6$  min.) by the "relay-race" transfer of the combustion wave by the propellant particles. The relay-race mechanism for the bricks made from particles less than 1 mm starts to work near 30% of the N-propellant part. The existence of the relay-race mechanism is also verified by faster growth of the temperature in the center of the brick and the possibility of combustion of the brick with 40% of propellant concentration in open air without preheating and burning by open fire. Under such conditions the brick with less than the 40% concentration does not burn.

In Fig. 3 one can find the results of combustion of the bricks made of the same size powders of coal and CP. The history of relative weight loss of the brick (Fig. 3a) and the temperature in the center of the brick (Fig. 3b) is presented. The curves 1-4 correspond to the CP concentration in the mixture of 10, 15, 20 and 30%. The process of the combustion for the bricks with CP is similar to the one with the N-propellant, i.e. it also has two phases. The first one is full combustion of the CP and light volatile compounds and the second is full combustion of the coal in two regimes of "layer" and "relay-race" combustion. The layer regime is typical for the bricks with 10 and 15% CP concentration (curves 1 and 2) while the relay-race one - for the 20 and 30% concentration of CP (curves 3 and 4). The difference between the combustion of the CP bricks compared to that for the N-propellant bricks is explained by the fact that CP burns for shorter times and heats coal to higher temperatures.

More detailed study showed that the relay-race combustion starts when the volume fraction of the propellant in the mixture achieves the so called percolation limit (or percolation crisis) corresponding to  $16 \pm 3\%$  of the volume - when there is the geometric possibility for continuous combustion channels through the sample. The results of this research are contained in the papers of the authors to be published in the Journal of Chemical Physics, v. 15, N 9, pp. 143-147 (Russian). In this paper one can also find a discussion of the paradox as to why the relay-race combustion is possible even when the size of the propellant particles is below the critical diameter of the propellant combustion - the role of burning elements is then played by accidental clusters of small propellant particles (cluster fragments) where the critical diameter of combustion is essentially lower than the critical diameter for the pure propellant sample.

## FIRE AND EXPLOSION SAFETY

In the relay-race regime one has burning gas formation at high speeds beyond the capabilities of usual furnaces. Therefore, decreasing of the propellant percentage to the level that guarantees the absence of the relay-race regime is mainly a matter of safety. For this reason the external heat and mechanical action tests (uniform heating of the powder specimen by sand bath, open fire action and drop-weight machine testing) were performed. All tests showed that the compositions with less than 30% of propellant content



gave a flash in the course of uniform heating to the temperature over 430K and did not lead to combustion in the whole bulk. The compositions with the propellant content more than 40% can burn in an open fire, though only the propellant and light components of the brick really burn.

The explosion safety of the bricks was estimated by studying the sensitivity to mechanical impact of pressed samples of 10 mm diameter and thickness from 0.1 to 1 mm, with the size of the particles less than 0.4 mm. The tests were performed at the vertical K-44-P drop weight machine using the tensometric technique with the photo-electric recording of the moment of the explosion. The mass of the falling hammer was 10 kg and the drop height was 25 cm. In experiments we measured the pressure of destruction of samples as a function of their thickness. The critical pressure of explosion initiation  $P_{cr}$  was evaluated from this dependence as a pressure corresponding to the boundary between the purely mechanical fracture of the sample and destruction attended by explosion. This approach allows us to compare the sensitivity of the mixtures to the mechanical actions with those of known explosives. The results of comparison are presented in the following table:

TABLE 1  
The Characteristics of Explosion Initiation

Explosive	$P_{cr}$ , kBar ( $10^3$ atm)
TNT	10.5
propel.H/coal 30/70	$10.7 \pm 0.2$
propel.H/coal 50/50	$9.6 \pm 0.2$
picric acid	9.5
comp.propel./coal 20/80	$9.2 \pm 0.2$
perchlorate ammonia	$8.5 \pm 0.2$
RDX	7.4
comp.propel./coal 40/60	$7.3 \pm 0.3$
propellant H	$4.9 \pm 0.2$
composite propellant	3.2

The following conclusions can be made based on data presented in the table:

- (1) When "diluting" both ballistic and mixed propellants with the coal there is a strong decrease in the sensitivity of these compositions. The mixtures with CP possess greater sensitivity than those with ballistic propellant;
- (2) The sensitivity even of the composites with CP (with the coal content more than 60%) is less than that of ammonium perchlorate but more than that of TNT.

#### ECOLOGY

From the point of view of ecology, the most danger from the burning gases comes from the nitrogen ( $NO_x$ ) and sulfur ( $SO_x$ ) oxides. While the  $SO_x$  originate from the compounds of the coal, the  $NO_x$  come from the air nitrogen and are produced in the highest temperature

parts of the combustion zone where their concentration approaches the thermodynamic equilibrium ( $< 1\%$  in volume). They more or less decompose when the burned gases cool down. The computation of the equilibrium composition of the burned products of the coal-propellant mixtures showed that adding propellant to the coal in the amount of 10-20% does not significantly change the concentration of the nitrogen oxides since such modification does not change the burning temperature significantly while the amount of nitrogen is greater in the air than in the coal or propellant.

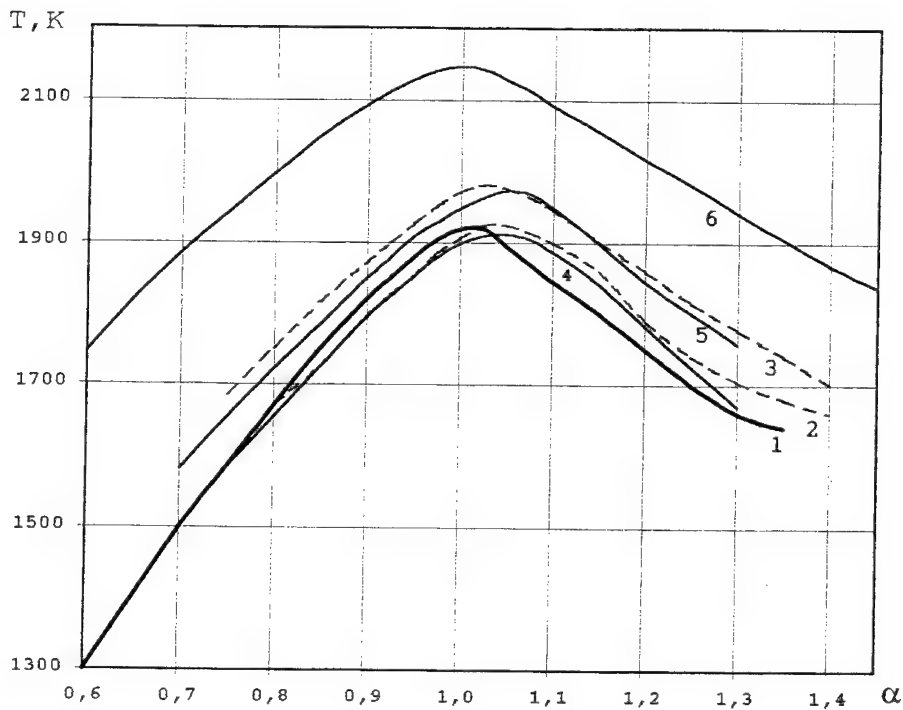
Special attention is paid to the HCl present in the burned gases of CP based on ammonium perchlorate. The thermodynamic calculations showed that the concentration of the HCl in the burned gases of the mixture of CP with coal is approximately the same as that of  $\text{SO}_x$  and  $\text{NO}_x$ . The computations showed also that adding potash ( $\text{K}_2\text{CO}_3$ ) to the composition in an amount corresponding to the stoichiometric ratio of K and Cl decreases the level of the concentration of HCl the burned gases by the factor of 7. The experimental detection of the amount of HCl the burned gases of CP-coal mixtures showed that at least half of the HCl is absorbed by the mineral part of the coal. Adding of potash enhances adsorption. After the combustion of the CP-peat mixtures the HCl does not appear at all in significant concentrations since it is coupled by iron existing in the mineral part of the peat. Thus, using the optimal compositions of propellant-natural fuels for combustion together with the traditional methods against acid components of burned gases allow one to ensure the necessary level of ecological norms.

#### COMBUSTION IN BED - BURNING FURNACE

To support the conclusions of the laboratory experiments, the tests in a model industrial bed-burning furnace were also performed. In these tests the 300 gram bricks made of the pure coal as well as the bricks of the N-propellant mixed with the coal in the ratio 20/80 and 40/60, the bricks of the CP mixed with coal in the ratio 20/80, 20/72+8% of potash, 30/70, 30/57+13% of potash and the bricks of pure peat and CP mixed with peat in the ratio 20/80 were investigated. The fire-chamber had a furnace-bar with dimensions of 200×235 mm and a height of 385 mm from the furnace-bar to the diversion channel of the burned gases, and had the air supply system under the fire-bar lattice. First the layer of the brown coal was burned on the fire-bar lattice. After the steady combustion of the coal in the bricks was established, i.e. the light fractions burned away, the set of bricks was loaded to the overheated upper layer. We recorded the temperature in the burning layer and burned gases and burnt gases were sampled for the chemical analysis. These studies demonstrated the significant influence of the propellant compounds to the burning and combustion of bricks. With an increase in propellant concentration in a composition the temperature level at the first stage of combustion increased 50-200 degrees and the time of combustion became shorter. The propellant combustion in bricks can either heat the coal making the process of coal combustion easier with propellant concentrations up to 20-25% and so-called layer combustion, or, with propellant concentrations more than 30% gives rise to the additional development of "heat" porosity simplifying the diffusion of oxygen inside the brick. The analysis of burned gases demonstrated that the concentration of ecologically dangerous oxides  $\text{CO}_x$ ,  $\text{NO}_x$  in the burned gases of bricks containing CP (especially with extra potash) were virtually the same as in combustion of the natural fuels.

## CONCLUSION

Thus, our investigations showed the energetic advantage and technological possibility of preparation and combustion of bricks made from propellant-coal and propellant-peat mixtures in the regime of layer combustion.



**Figure 1.** Temperature of the burned gases of mixtures of brown coal with CP and N-propellant as a function of the air equivalence ratio  $\alpha$ . Curve 1 - coal; Curves 2 and 3 - coal with 20% and 30% CP composition respectively; Curves 4,5 and 6 - coal with 10%, 20%, and 50% of N-propellant respectively.

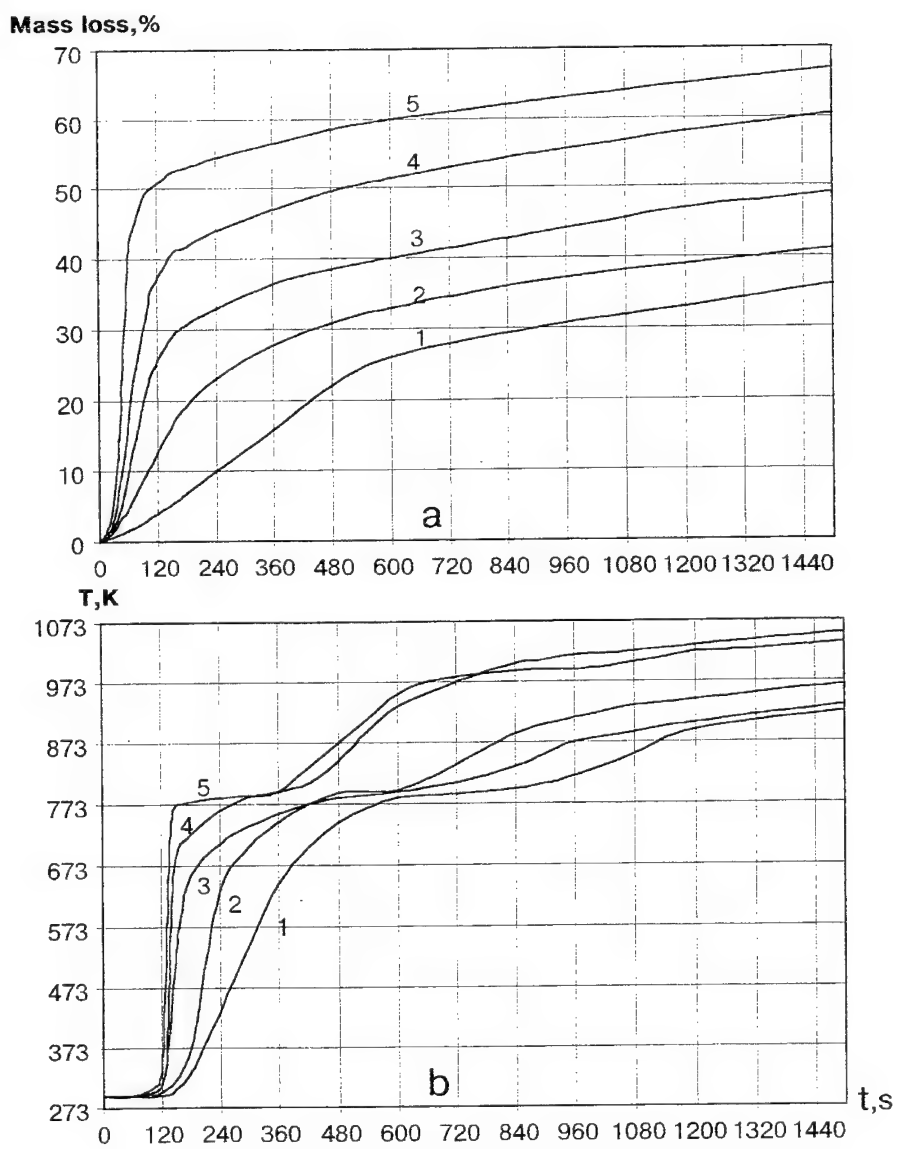


Figure 2. a) Sample percent mass loss; b) Temperature in the center of the sample as a function of time,  $t$ . Curve 1-5 correspond to the concentration of the propellant of 0%, 10%, 20%, 30%, and 40% in the brown coal-N-propellant composition.

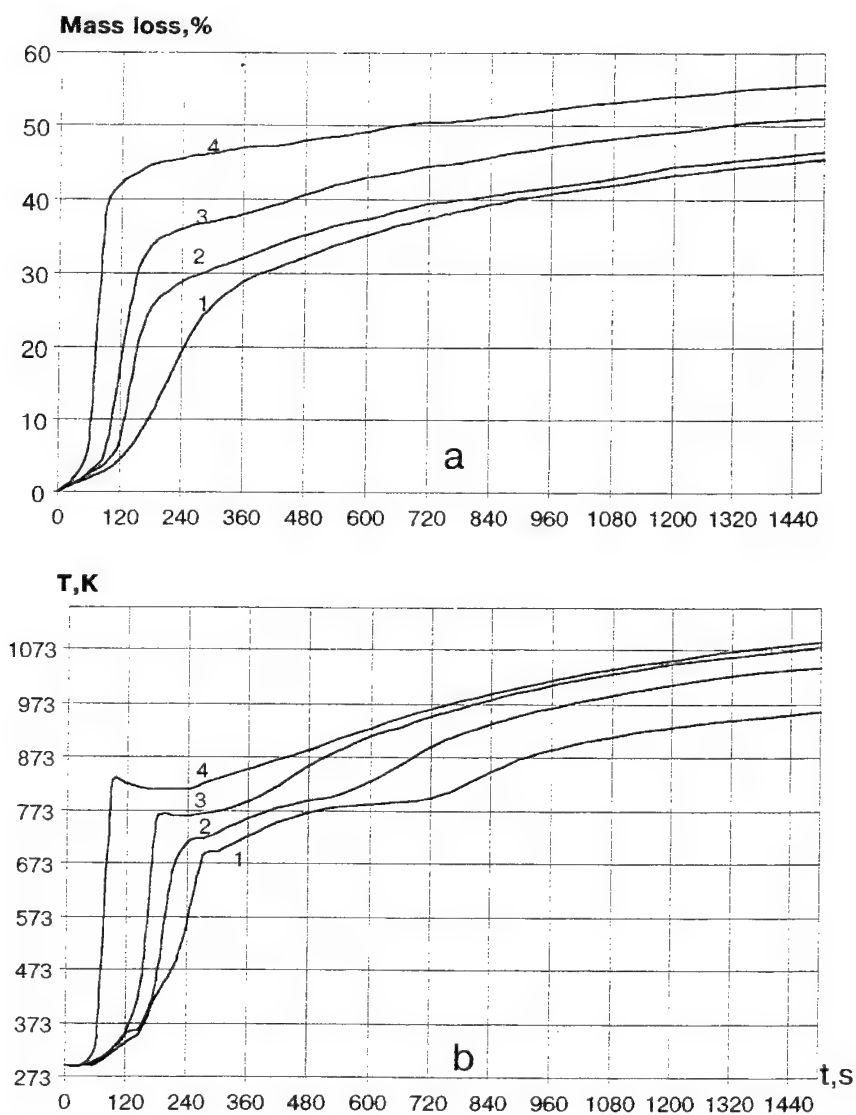


Figure 3. a) The relative percent weight loss of a sample; b) Temperature in the center of the sample as a function of time,  $t$ . Curves 1-4 correspond to the concentrations of propellant of 10%, 15%, 20%, and 30% in the coal-CP composition.

***Area 3:***  
***Recycling***  
***of***  
***Energetic Materials***

## **CONVERSION OF HIGH EXPLOSIVES**

**Paul Wanninger**

Dynamics Division, TDW, PO Box 1340  
86523 Schrobenhausen, Germany

**ABSTRACT:** The disposal of high explosives was not a problem prior to German reunification. Large quantities (300,000 tons) of old and substandard munitions were acquired when the former German Democratic Republic (GDR) was reunited with the Federal Republic of Germany (FRG). This paper evaluates processes available for the conversion of high explosives, and concludes that an affordable and readily available method for the destruction of high explosives from old ordnance is controlled burning.

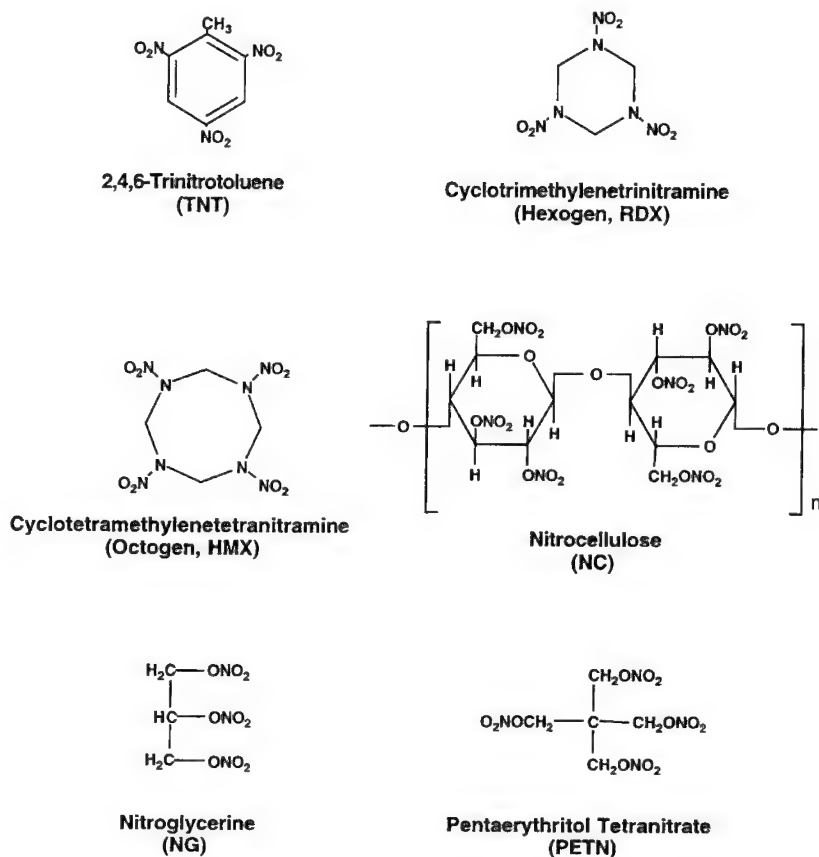
### **INTRODUCTION**

Military high explosives are made in order to provide a propelling effect (propulsion) or a destructive effect (detonation) in munitions. The most commonly used high explosives are summarized in Figure 1. High explosives, rocket propellants or propellant powders seldom contain only pure high explosives. Normally they are present in mixtures which have to be separated into their individual components when preparing them for conversion. This is relatively simple in the case of high explosive charges and still feasible for single base propellants, but is very difficult for double base propellants since these usually exist as compacted propellant mixtures. The dissolution and separation of such propellants are very expensive and time consuming.

The idea of disposing of or converting high explosives into harmless products first occurred in 1989, after Germany's reunification, when old high explosives stored in the former GDR turned out to be available in enormous quantities. About 300,000 tons of ammunition had to be disposed of. The ammunition did not comply with Western safety standards and, according to international standards, had been stored for too long.

The usual disposal procedure used by the German Armed Forces was disassembly of the munitions, which means that they separated the high explosives from the metal parts and then crushed them for burning in the open air. This combustion is uncontrolled and entails considerable emission

of harmful material into the air, especially nitrogen monoxide. Demilitarization means in this case classification of the ammunition, and removal of detonators and H.E. charges. For the removed H.E. charges, there are different possibilities, e.g. recycling, chemical conversion into valuable products, etc.



**Figure 1.** Commonly used high explosives

From a chemical point of view, most explosives are highly nitrated aromatic compounds, highly nitrated heterocycles or nitric acid esters. Due to the large number of reactive functional groups, the old high explosives could obviously be regarded as valuable raw material for chemical synthesis. Chemical reactions are in most cases reduction, oxidation or hydrolysis of a molecule. In the case of nitroaromatics, only the reduction process renders a valuable product.



## CHEMICAL CONVERSION

The most important of the nitrated aromatics is 2,4,6 trinitrotoluene, generally known as TNT. TNT, with its reactive nitro groups, is especially suited for chemical conversion. To eliminate the explosive characteristics from this compound, the  $\text{NO}_2$ -groups have to be removed or converted. This is best achieved by catalytic reduction which employs hydrogen,  $\text{H}_2$ . The resulting 2,4,6-triaminotoluene (TAT) has no explosive character. Reaction is achieved with 98% efficiency and was first carried out in laboratory scale by Heim and Wagner.<sup>1</sup> In the 1970's BASF looked at this process to manufacture isocyanates to serve as precursors for polyurethane.<sup>2,3</sup> Beginning in 1990, the armament industry (Rheinmetall and Dasa) installed pilot plants to hydrogenate TNT.<sup>4,5</sup> Hydrogenation of TNT leads to 2,4,6-triaminotoluene in a single step. Then, using  $\text{NaBH}_4$  and applying harsh conditions like high temperature and pressure, it is possible to hydrogenate the aromatic ring to 2,4,6-triaminomethylcyclohexane (TAMC) as illustrated in Figure 2.

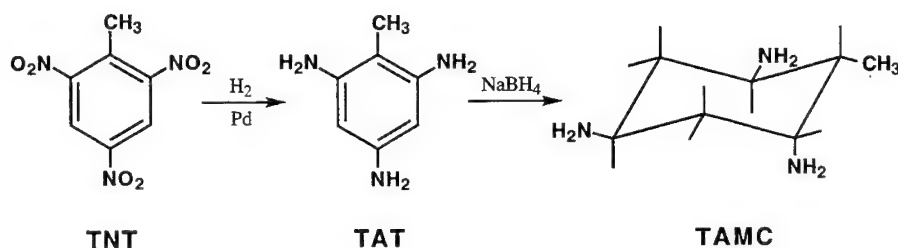


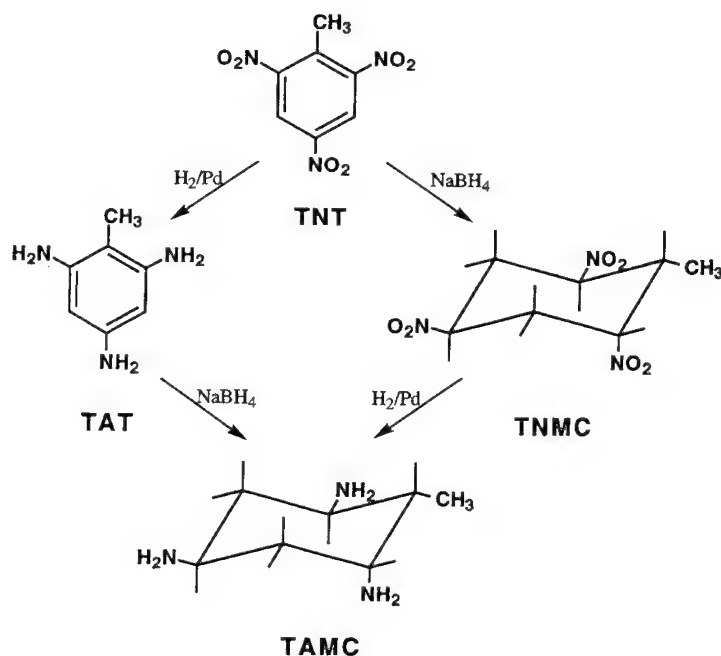
Figure 2. Hydrogenation of TNT

Hydrogenation of TNT is achieved in polar solutions by adding a catalyst with intensive stirring under simultaneous introduction of hydrogen. The reaction can be observed with  $^1\text{H}$ -NMR and IR spectroscopy or with thin layer chromatography. Hydrogenation is achieved in several steps, reaction velocity being a function of temperature and catalyst to a large extent. Low temperatures are sufficient to obtain a reaction. The hydrogen consumption at 25 to 35°C is very high, and at 60°C the reaction velocity and the desorption of hydrogen compete. Of the 4 types of catalysts investigated (Pd, Rh, Raney Ni and Ru), palladium was by far the most efficient. However, with 2% palladium catalyst relative to the TNT mass, the reaction can no longer be controlled. The strongly exothermic reaction ( $\Delta H = -1850 \text{ kJ/mol}$  TNT =  $-8145 \text{ kJ/kg}$  TNT) requires small reactor volumes and large heat exchange surfaces for cooling.<sup>6,7</sup>

The reaction rate is strongly solvent-dependent, proceeding most rapidly in methanol, slower in ethanol and isopropanol, and slowest in THF. The consumption of hydrogen is used as a measurement unit for the reaction

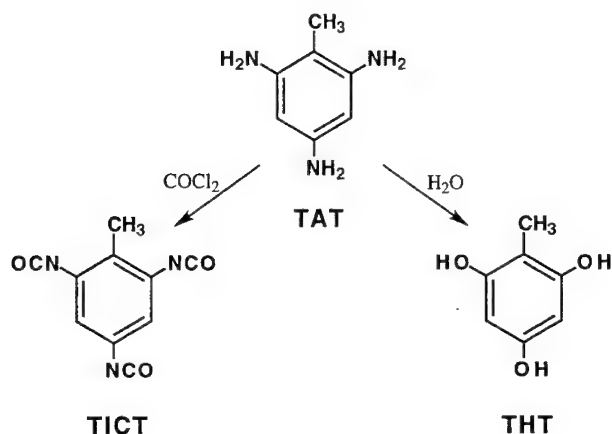
velocity. Over a wide range, the reaction velocity is directly proportional to the amount of catalyst. To control the reaction, carefully controlled temperatures and low percentages of catalyst are advisable. A continuous installation for the hydrogenation of TNT in which TNT is dissolved in relatively small amounts, is recommended. In a solution of 5 - 10% there is no danger of detonation or deflagration.

Hydrogenation of the benzene core of 2,4,6-triaminotoluene or TNT is achieved by the reaction with  $\text{NaBH}_4$  (Figure 3).<sup>8,9</sup> This creates trinitromethylcyclohexane (TNMC) where there are eight possible stereoisomers (Figure 3 shows only one stereoisomer). The use of  $\text{NaBH}_4$  to achieve core hydrogenation, however, proves to be very expensive. Trials to convert TNT directly into methyltriaminocyclohexane (TAMC) using hydrogen in the presence of catalysts supplied only unsatisfactory yield.<sup>8</sup>



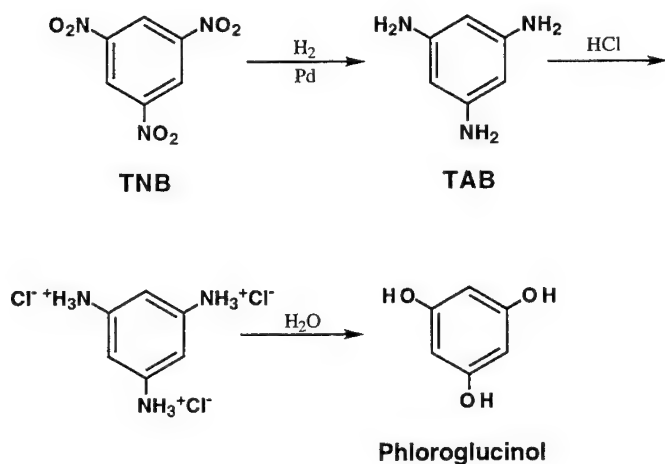
**Figure 3.** Conversion of TNT to TAMC

TAT is very reactive and not stable at higher humidity. Interesting synthetic possibilities involving TAT are the conversion with phosgene ( $\text{COCl}_2$ ) into 2,4,6-toluenetriisocyanate (TICT)<sup>10</sup> or hydrolysis into 2,4,6-trihydroxytoluene (THT) (Figure 4). Since triisocyanates permit polymerization in three dimensions, they can be used in place of diisocyanates like hexamethylene



**Figure 4.** TAT reaction products

diisocyanate in polyurethane formulations in order to influence the characteristics of the plastics. As core-hydrogenated isocyanates are considerably less sensitive against UV radiation than aromatic isocyanates (the secondary chain is stabilised against attack by radicals), a simple catalytic hydrogenation of TNT to TAMC is desirable.<sup>11</sup>



**Figure 5.** Preparation of phloroglucinol from TNB

The synthesis of 1,3,5-trihydroxybenzene (phloroglucinol) obtained from 2,4,6-trinitrobenzene (TNB) is achieved in the same way as the synthesis of 2,4,6-trihydroxytoluene (Figure 5).

Another example of the chemical conversion of high explosives is hydrolysis of glycerinetritrate. In this case, the major product is glycerol, a commodity chemical. Hydrolysis leads to useful products, however, only in the case of nitrates. Nitramines such as RDX are decomposed into formaldehyde and ammonia with this type of conversion.<sup>12</sup>

### COMMERCIAL ASPECTS OF CHEMICAL CONVERSION

The products obtained from the chemical conversion of high explosives are all classical chemical raw materials which are already produced in large quantities. The market possibilities are correspondingly unfavorable. This applies most of all for 2,4,6-toluenetriisocyanate, cellulose, glycerine, pentaerythritol and ammonium nitrate.

Phloroglucinol serves as a synthetic building block in the pharmaceuticals industry and moreover as an additive for cosmetics and photo developers. The price for phloroglucinol is about 180 to 220 DM per kg. A new synthesis of this valuable product would be interesting. As, however, the worldwide demand for phloroglucinol is about 150 to 200 tons annually, provision of 15 to 20 million DM investment funds required for the establishment of a plant to manufacture phloroglucinol from trinitrobenzene is uninteresting.<sup>13</sup>

The development of a chemical process using high explosives as raw materials will require time, as well as experience in the handling and chemical processing of high explosives.

### BIOLOGICAL DECOMPOSITION OF HIGH EXPLOSIVES

Decomposition of high explosives using bacteria is conceivable. However, the problem is the low solubility of the high explosives in water, the medium which the bacteria need. To be able to dissolve TNT (TNT solubility in water is about 0.5 mmol/L) in a measurable time, feeding of 20mmol glucose and ammonium sulfate each is necessary. TNT is soluble up to 50 mmol/L in alcohol/water solutions.

The low solubility, requirement for temperature control of the solution at 35 - 40°C as well as addition of glucose, ethanol and other nitrogenous or carbonic nutrients needed by the bacteria result in an enormous expenditure of funds, such that a large-scale plant for the biological decomposition of high explosives appears impossible. The biological conversion of TNT works only if the process is split up into two different processes, an anaerobic and an aerobic process with two different types of bacteria and process parameters. In addition, about one-third of the formulation is reduced only partially.<sup>14</sup> The metabolites which still contain nitro groups are much more

toxic than TNT. Other explosives like HMX and RDX are not processible because they are nearly insoluble in water.<sup>14</sup>

Another disadvantage is the fact that high explosives are usually available as mixtures so that intensive processing and chemical pre-treatment is necessary, in order to have the substances ready for biological decomposition.<sup>15</sup> For example, a typical double base propellant contains lead and copper salts which are highly toxic to all bacteria. A separation of these materials is feasible but not economical.

In summary, the problems with the biological treatment of H.E. are the low solubility in water, the high energy and nutrient consumption, the sensitivity of the bacteria to metal salts and the incomplete degradation of the high explosives which yields very toxic metabolites.

### **RECYCLING OF HIGH EXPLOSIVES**

Military high explosives are normally solid organic compounds, which can be recrystallised. Recycling, i.e., cleaning and recovery of high explosives like TNT, HMX, and RDX is possible in principle, but the value of these substances has to be considered. One kilogram of TNT for civilian or military purposes is available on the world's markets for 1 to 5 DM, depending on quality, RDX for about 25 to 30 DM and HMX for about 60 to 80 DM. Thus, recycling appears sensible only for HMX, as large quantities of solvents as well as suitable facilities with all the necessary licenses required for the processing of high explosives. Recovered high explosives then have to be re-qualified for military or commercial use, which means that they have to pass a comprehensive acceptance test procedure.

### **USE IN CIVILIAN EXPLOSIVES**

It has often been suggested that military H.E. charges could be crushed and the residues added to civilian explosives. Unfortunately, different regulations and requirements apply to military and civilian explosive charges and their various qualification methods.

TNT for example presents a very negative oxygen balance (-74%) which permits adding TNT only in small quantities to explosives used for mining purposes. The CO percentage admissible after firing is extremely limited because of the risk of firedamp.<sup>16</sup> Adding TNT to H.E. charges used in openpit mining is, in principle, possible. Military high explosives, however, show a very high brisance and can be added to slurry explosive charges only in small quantities since this usually changes the particle size distribution of the blasted minerals considerably. Slurry explosive charges are compounds that can be transferred in pumps and consist of oxidizing agents (in most cases ammonium nitrate), water and fuels, and are used exclusively for civilian

purposes. The requirement of extensive safety approvals allows only extremely small amounts of military high explosives to be processed in civilian high explosive charges.

### THERMAL DISPOSAL OF HIGH EXPLOSIVES

Uncontrolled burning of propellants and explosives pollutes the air with various gases like  $\text{NH}_3$ ,  $\text{HCN}$  and  $\text{NO}$  and also produces soot which is contaminated with highly toxic aromatic compounds. Controlled combustion of high explosives offers a series of advantages. Mixtures which are difficult to separate can be burned. The energy contents of high explosives are for the most part overrated. Table 1 contains a comparison of the caloric content of several high explosives to those of normal fuels. To reach the temperatures that are required for complete combustion of high explosives, it is necessary to supply external energy. This can be achieved by controlled burning in a rotary kiln with subsequent flue gas purification. This, however, leads to high investment and maintenance cost due to the applicable safety and environment regulations that have to be observed. A high explosives combustion plant has been running smoothly in Saxony, Germany, since mid-1994.<sup>17</sup>

**Table 1**  
Thermal Decomposition of Explosives  
Combustion Enthalpy (kJ/kg)

Explosives		Fuels	
TNT	15,146	WOOD	15,700
RDX	9,560	CHARCOAL	31,000
HMX	9,883	DIESEL OIL	43,960
NC	9,677	ETHYLENE	50,790
NG	6,761	AMMONIA	22,360

### OUTLOOK AND ASSESSMENT OF PROCESSES

When looking at the individual processes for the conversion of high explosives, one must yield to a variety of technical and commercial considerations. Recycling in the form of re-use is given a very high priority by our society, but has to remain affordable. Consequently, its use is excluded for cheap and dangerous products and comes into consideration only for expensive high explosives like HMX. The chemist's dream of syntheses using old high explosives as starting materials fails because of the immense

investments required to build facilities for the conversion of these substances and because of the surplus of products found on the world's markets.

At first glance, the biological decomposition of high explosives appears to be a promising idea. It is, however, very expensive as it must start with pure substances and leads to product compounds that are very difficult to separate. Controlled burning is the only remaining affordable way to destroy high explosives extracted from old ordnance. The summary in Table 2 shows that the desire for the complete protection of the environment and preservation of resources is not always economically sensible or feasible.

**Table 2**  
Disposal of Explosives  
Evaluation of Different Processes

Material	Recycling	Chemical Conversion	Biological Degradation	Burning
<u>High Explosives</u>				
TNT	# Ø	# O	# Ø	# O
RDX	# Ø	+ Ø	+ Ø	# O
HMX	# O	+ Ø	-	# Ø
TNT/RDX	# Ø	# Ø	+ Ø	# O
TNT/HMX	# O	# O	-	# O
<u>Propellants</u>				
NC	-	+ Ø	# Ø	# O
NG	# Ø	+ Ø	+ Ø	# O
AP	# O	+ Ø	-	# O
Single Base	+ Ø	+ Ø	+ Ø	# O
Double Base	-	+ Ø	-	# O
Composite	# Ø	+ Ø	-	# O
<u>Key to Symbols</u> # = large scale production possible + = feasible - = not feasible O = useful business management Ø = not useful business management				

## APPENDIX: LIST OF TERMS

Propellants consist of different high explosives and are sub-divided into:

**Single base propellants:** Cellulose nitrate (nitrocellulose) serves as the sole energy carrier. A radical scavenger (diphenylamine) protects against aging.

Typical composition:

- 98% Nitrocellulose with varying nitrification degrees (11.6 - 13.3%).
- 2 % Diphenylamine as radical scavengers for  $\text{NO}_2$  radicals.

Main use: propellant for small calibered munition.

**Double base propellants:** The two high explosives cellulose nitrate (nitrocellulose) and glycerine nitrate (nitroglycerine) serve as energy carriers.

Typical composition:

- 50% Nitrocellulose
- 40% Nitroglycerine
- 1% Copper salicylate (combustion moderator)
- 2.5 % Lead resorcinate (combustion moderator)
- 2 % 2,4 dinitrodiphenylamine (radical scavenger)
- 4 % Di-n-propyladipate (additive)
- 0.5% Potassium kryolithe  $\text{K}_3\text{AlF}_6$  (flame suppression)

Main use: rocket motors for military purposes.

**Triple base propellants:** Three energy carriers define the formulation.

Typical composition:

- 50% Nitrocellulose
- 20% Nitroglycerine
- 20% Nitroguanidine
- 2% Akardite (diphenylmethyl urea)
- 0.5% Potassium kryolithe ( $\text{K}_3\text{AlF}_6$ )

Main use: propellant for large caliber munition.

**Composite propellants:** In contrast to the homogeneous single, double and triple base propellants, composite propellants are regarded as heterogeneous. They consist of an oxidizing agent, an inorganic salt and a plastic component - in most cases this is a polyurethane which acts simultaneously as binding agent and as fuel. In many cases, ferrous oxides are used to serve as a combustion moderator.



Typical composition:

- 85% Ammonium perchlorate
- 13% Polyurethane/hydroxy terminated polybutadiene and isophorone diisocyanate
- 2% Ferrous (III) oxide

Main use: military and civil long range rocket motors (e.g. space shuttle propulsion).

**Oxygen balance:** This represents the percentage of oxygen (in percent by weight) available during detonation upon conversion of the energetic material into  $H_2O$ ,  $CO_2$ ,  $NO_2$ ,  $Al_2O_3$  etc. When the percentage of oxygen bound in the high explosive is insufficient to ensure a complete conversion this is regarded a negative oxygen balance; when the percentage of oxygen is sufficient or is in excess, this is regarded a positive oxygen balance.

Examples:

TNT ( $C_2H_5O_6N_3$ )	-74.0 %
Nitroglycerine ( $C_3H_5O_9N_3$ )	+ 3.5 %
Ammonium Nitrate ( $NH_4NO_3$ )	+20.0%

## REFERENCES

1. **Hein, F. and Wagner, F.**, *Ber. Dtsch. Chem. Ges.*, 68, 856, 1935.
2. **BASF AG**, DE 3218665, 1981; *Chem. Abstr.*, 98, 106961z, 1981.
3. **BASF AG**, DE 3132923, 1981; *Chem. Abstr.*, 98, 197770d, 1981.
4. **Lübben, M., Scholles, H., Reichelt, K. and Kluger, K. M.**, "Utilization of TNT through Hydrogenation"; Presentation at the 23rd Annual ICT, Karlsruhe, 8-1, 1992.
5. **Wanninger, P.**, "Energetic and Inert Admixtures in Propelling and Explosive Charges; Problems with Disposal"; Presentation at the 23rd Annual ICT, Karlsruhe, 27-1, 1992.
6. **Kaiser, M.**, "Investigation of Environmentally Relevant TNT Decomposition Products"; Poster, 22nd Annual ICT, Karlsruhe, 1991.
7. **Westerterp, K. R., von Gelder, K. B., Damhof, J. K. and Krojenga, P. J.**, *Chem. Eng. Sci.*, 45, 3159, 1990.
8. **Kitzelmann, E.**, Dissertation, Technical University of Munich, 1993.
9. **Sokolova, V. A., Blodiyev, M. D., Gidasov, B. V. and Timofeeva, T. N.**, *Zh. Org. Khim.*, 8, 1243, 1972; *J. Org. Chem. USSR (English Translation)*, 8, 1257, 1972.
10. **Sundermann, R.**, Bayer AG, personal communication.
11. **Dieterich, D.**, *Chem. unserer Zeit*, 24, 135, 1990.
12. **Hoffsommer, J. C., Kubose, D. A. and Glover, D. J.**, *J. Phys. Chem.*, 81, 380, 1977.

13. "Phenol Derivatives", in *Ullmanns Enzykl. Tech. Chem.* 4th Edition, volume 13, p. 223., 1979.
14. **Knackmus, H. J.**, Project Report, Institute of Microbiology, University of Stuttgart, August 28, 1991.
15. **Felber, K. A.**, "Biological Decomposition of TNT"; Proceedings of the 23rd Annual ICT, Karlsruhe, 1992, 33-1.
16. **Meyer, R.**, *Explosives* (3rd ed.), VCH: Weinheim, Germany, 1987.
17. **Rosendorfer, T.**, "Continuous Burning of Explosives"; Presentation at the 84th AGARD Symposium, Alesund, 1994.

### COMMENTS

*B.N. Kondrikov, Mendeleev University of Chemical Technology, Russia.* Ten years ago in the USSR we were using 1.5 - 2 million tons of commercial explosives (including 0.2 million tons of pure TNT and 0.3 - 0.4 million tons TNT mixed with ammonium nitrate) on an annual basis. We are still using a lot of TNT and gun propellants for rock blasting in Russia despite numerous difficulties. The 0.3 million tons of ammunition to be demilitarized in Germany represents an explosives consumption of three months for our mining industry. The use of demilitarized ammunition in commercial explosives is not a dream in Russia, it is reality.

*Author's reply.* In principle it is possible to use TNT in open pit mining. However, I cannot agree on the use of double base propellants in such operations because of the especially toxic dusts (particle size < 1 micron) of PbO, CuO, etc. that would be released following detonation.

## BOILER FUEL AS A RECYCLING OPTION FOR ENERGETIC MATERIALS

Larry Baxter, Sid Huey, Joel Lipkin, Devang Shah,  
James Ross, and Gian Sclippa

Combustion Research Facility, Sandia National Laboratories  
Livermore, CA 94550

**ABSTRACT:** This investigation addresses the combustion-related aspects of the reapplication of energetic materials as fuels in boilers as an economically viable and environmentally acceptable use of excess energetic materials. The economics of this approach indicate that the revenues from power generation and chemical recovery approximately equal the costs of boiler modification and changes in operation. The primary tradeoff is the cost of desensitizing the fuels against the cost of open burn/open detonation (OB/OD) or other disposal techniques. Two principal combustion-related obstacles to the use of energetic-material-derived fuels are  $\text{NO}_x$  generation and the behavior of metals.  $\text{NO}_x$  measurements in a small pilot-scale combustor were obtained as a function of fuel composition and operating conditions using calibrated, research-quality NDIR analysis of sampled gases. These data indicate that the nitrated components (nitrocellulose, nitroglycerin, etc.) of energetic materials decompose with  $\text{NO}_x$  as the primary product.  $\text{NO}_x$  levels are sensitive to local stoichiometry and temperature and subject to the same controls as are common for traditional fuels. Class 1.3 materials also produce higher  $\text{NO}_x$  compared to traditional fuels, primarily due to the temperature of the burning aluminum particles. The behavior of inorganic components in energetic materials tested in this investigation could lead to boiler maintenance problems such as deposition, grate failure, and bed agglomeration. The root cause of the problem is the potentially extreme temperature generated during metal combustion. While these behaviors represent important considerations for the reapplication of energetic materials as fuels, none is insurmountable. The reuse of energetic materials as fuels is viewed as a realistic and economical alternative to OB/OD and most other technologies.

### INTRODUCTION

Significant amounts of energetic material (EM) await reapplication or reuse in the US and abroad. The institutions primarily responsible for this material include US DoD, US DOE, NASA, US DOT (Coast Guard), explosives and propellant manufacturing companies, and corresponding institutions in countries other than the US. The sources of this material include reduction of weapon inventories (conventional and nuclear) and manufacturing waste. Definitive estimates of the total amount of material are not available, but our estimate is that the US DOE material awaiting disposition is 3 million kg and growing at a rate of 50,000 kg/yr. The material for which the DoD has responsibility is estimated at 376 million kg, growing at a rate of 73 million kg/yr. In addition to logistic problems caused by this stockpile, compliance and negotiations of arms control agreements with the States of the former Soviet Union are currently being affected by lack of an appropriate means for EM reapplication. Environmentally acceptable means of disposing of this material have not yet been identified.

Because of public and regulatory concerns, open burning and detonation of these materials is becoming increasingly less acceptable. Since disposal costs are approaching \$2000 per metric ton, reapplication of this material in a manner avoiding disposal fees is highly desirable. Potential reapplication technologies include use as explosives in mining and excavation and processing to withdraw high-value commercial chemicals. Some of these processes result in byproducts that could

be used as boiler fuels. In addition, the EM can be converted entirely to boiler fuel by desensitization processes. Such fuels are hereafter referred to as EM-derived fuel (EMDF). The focus of this investigation is co-firing EMDF with coal, biomass, or other fuels in boilers or industrial furnaces. Recent economic analyses indicate that such a process could compete with open burning and open detonation if the cost of preparing EMDF can be held below the cost of open burning or open detonation. Revenues from chemical recovery and power generation approximately equal costs of boiler modifications and maintenance of new fuel feedlines [Shah, 1994]. Many of these facilities are designed to burn a wide variety of materials such as grasses, agricultural wastes, urban wood waste, and coal, and have feed systems that accommodate wide fluctuations in fuel composition and morphology. Much of the EMDF of interest could be handled in these facilities at much lower cost than current disposal processes and in a more environmentally benign fashion than either open burning or open detonation. Establishing the reapplication of energetic materials as fuels as a viable technology option depends in large measure on characterizing the fuels and their combustion properties, which is the focus of this investigation.

## FUELS AND FACILITIES

EMDF describes two types of materials produced by established industrial processes and distinguished largely by the energetic material from which they are derived. All of the materials are rendered nonexplosive, and are characterized by transportation and storage hazards similar to traditional fuels, before being classified as EMDF. EMDF samples formed from double-base propellants or primary explosives (Figure 1) reported here are generated in an industrial (Alliant Techsystems Inc.) process that results in an emulsion of water ( $\approx 30\%$ ), kerosene ( $\approx 65\%$ ), and energetic material ( $\approx 5\%$ ). EMDF from propellant materials is derived from industrially treated rocket motor propellant (Thiokol) as moist, porous rubber (polybutadiene) with imbedded aluminum and small amounts of residual ammonium perchlorate. Hazard Classes have been developed to use as a guide in transport and storage of these materials. Primary explosives are in Hazard Class 1.1 whereas solid propellants are generally in Hazard Class 1.3. While the classes were originally intended to distinguish the materials based on handling and storage properties, they are useful in their chemical distinction as well and are used here to classify the material according to combustion behavior. Both forms of EMDF have little in common with the materials from which they are derived. The properties of these fuels are discussed separately.

### Primary Explosives and Double-Base Propellants

Some potential combustion issues associated with these materials can be appreciated by examining their chemical structures, as are illustrated in Figure 1. The materials for which data are later presented include emulsions of nitroglycerin and nitrocellulose, both of which are illustrated in the figure. The forms of nitrogen in explosives or double-base propellants (Hazard Class 1.1 materials) are predominately either nitrate groups or in physical proximity to nitrate groups. This contrasts with nitrogen in traditional fuels, which is dominated by pyrrolic and pyridinic nitrogen in coal, for example, (also illustrated in the figure). The tendency for EMDF to form  $\text{NO}_x$  will be shown to be much higher for EMDF than for traditional fuels, and these chemical differences are believed to be the primary cause of the observed differences in effluent  $\text{NO}_x$  concentrations.

A second major difference in the chemical structures of explosive and double-base propellant EMs compared with traditional fuels is the high oxygen concentration of the former. These high oxygen contents affect important combustion properties such as heating value (Figure 2), amount of required excess air, and stability/storage. The heating value results can be misleading. Standardized heating value analyses are based on energy content of the fully oxidized material per unit mass of fuel. In the case of EM, most of the oxidizer is contained in the sample. A more insightful comparison is the energy content (designated EC in the figure), in which we normalize everything by the mass of fuel plus oxidizer. The energy content is a better indicator of relative combustion properties such as flame temperature than is the heating value. Assuming air is used as the oxidizer, the energy content values for oil and coal are approximately 3.0 and 2.8 MJ/kg, respectively, whereas TNT and RDX are approximately 3.6 and 4.6 MJ/kg, respectively.

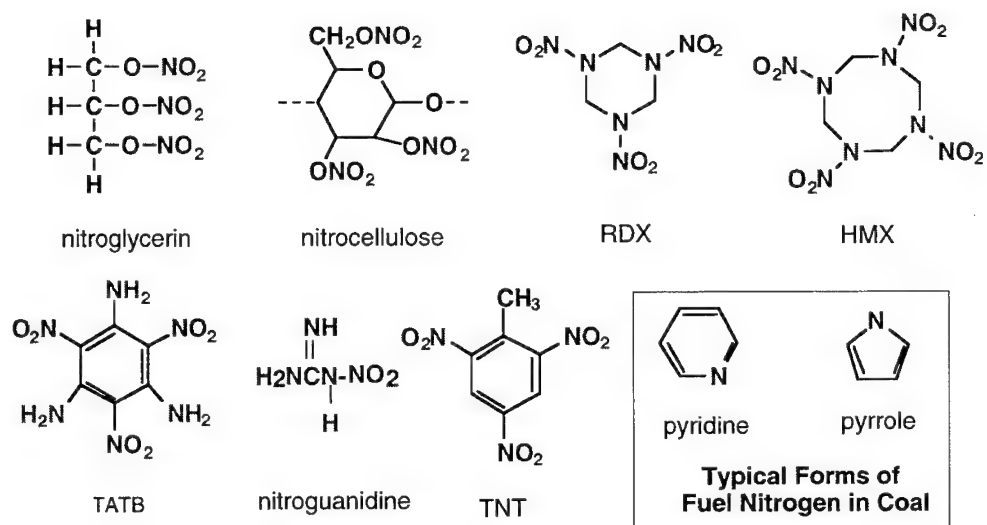


Figure 1. Chemical structures of many significant forms of energetic materials found in explosives and double-base propellants. Chemical structures for the dominant forms of nitrogen in coal are illustrated for comparison in the box.

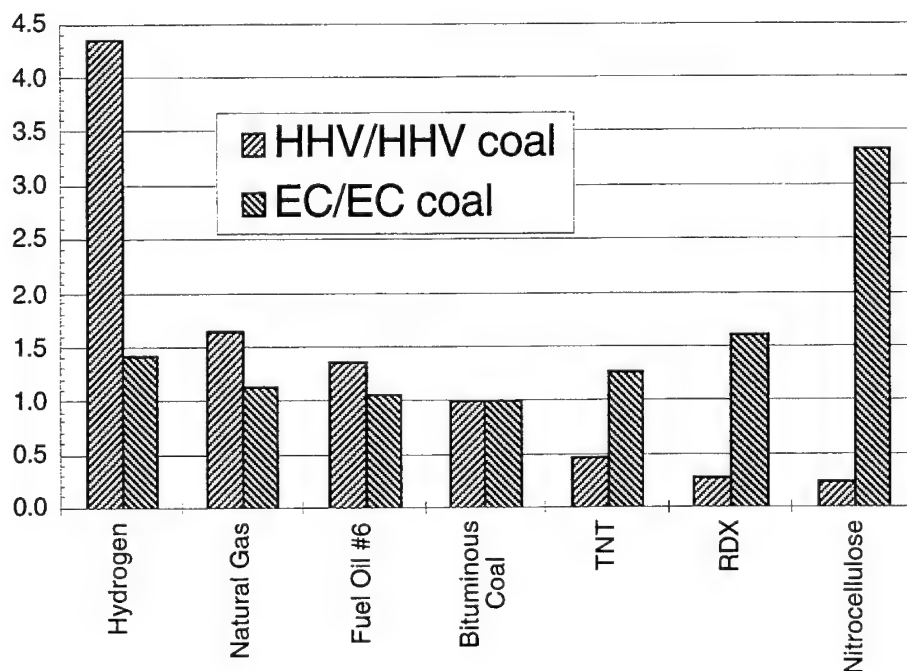


Figure 2. Heating values of traditional fuels compared with energetic materials.

All EMDFs used in this investigation are blended with other fuels or are chemically altered so as to produce more stable materials. In addition, EMDF use is envisioned as a component ( $\approx 10\%$ ) of a feed stream containing predominately traditional fuels. In general, the EMDFs potentially contribute as much or slightly more energy to a combustion system as traditional fuels.

### Rocket Motor Propellant Binder

A second major class of fuel is derived from processed rocket motors. These typically are obtained from ammonium-perchlorate-based propellant binders. After ammonium perchlorate (AP) is extracted through water washing, the residual binder is used as a fuel. The binder is typically polybutadiene, often with as much as 65% aluminum imbedded in the form of  $30\text{ }\mu\text{m}$  or smaller particles. Residual AP in the fuel is less than 10%, with 3% being a representative amount. The fuel also retains significant ( $\approx 25\%$ ) moisture from the washout process. The primary combustion issues associated with this fuel include pollutant formation and the behavior of the aluminum.

In comparison to the double-base materials,  $\text{NO}_x$  emissions from this fuel are expected to be lower and to arise less from fuel  $\text{NO}_x$  mechanisms and more by thermal and prompt mechanisms. The only nitrogen in the fuel is from the residual AP, which would amount to less than 0.4% N in a typical formulation (3% AP residual in fuel) as opposed to  $\approx 1\text{--}2\%$  N in double-base materials (5% EM in emulsion). The nitrogen present also is less likely to form  $\text{NO}_x$  because of its chemical form.

The behavior of the aluminum in the fuel poses a potential equipment problem. Aluminum melts at a relatively low temperature ( $660\text{ }^\circ\text{C}$ ) and burns at potentially high temperatures (adiabatic flame temperature  $> 3000\text{ }^\circ\text{C}$ ), typically established in practice by mass transfer limitations and gas dissociation. These characteristics illustrate the potential for molten aluminum forming ash deposits or oxidizing aluminum damaging components of a boiler due to the extreme temperature.

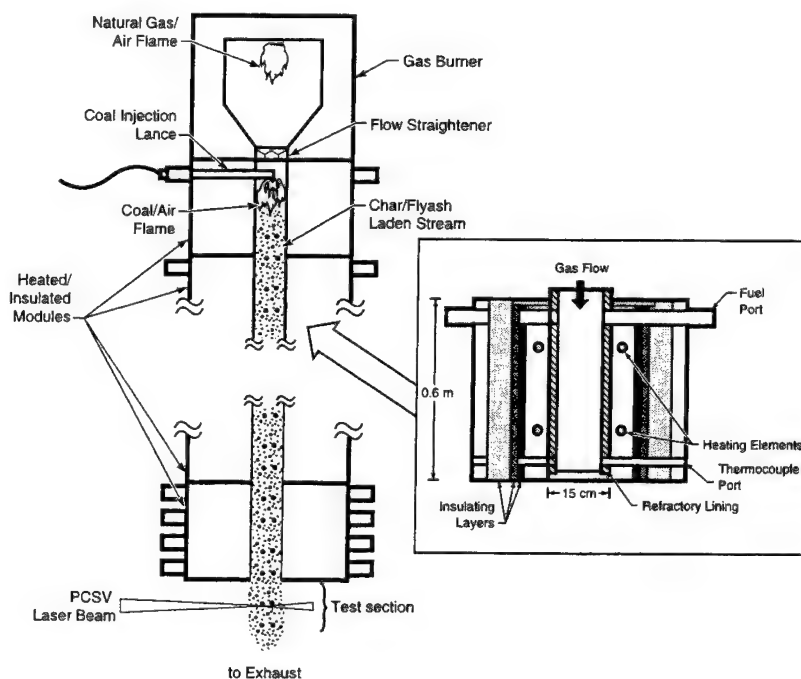


Figure 3. Schematic diagram of Sandia's Multifuel Combustor.

## Combustion Facilities

Most of the data reported herein were collected from Sandia's Multifuel Combustor (MFC, Figure 3). The MFC is a two-story, small pilot-scale ( $\approx 100,000$  Btu/hr, depending on fuel type) facility that simulates the local environment to which fuel particles are exposed as they pass through commercial-scale, entrained-flow combustion systems. Fuel is inserted through any of a series of ports along the length of the combustor, allowing variation of residence time from a few milliseconds to 4-5 seconds. The combustor wall temperature in each of the modular sections is independently controllable up to  $1400^\circ\text{C}$  in sustained tests. The MFC allows experiments to be performed under well-known and well-controlled conditions while simulating most of the important characteristics of commercial-scale boilers fired with solid, liquid, or gaseous fuels. Particle and gas residence times, temperature histories, and local stoichiometry histories are independently controllable in the MFC.

In addition, experiments were conducted on a low-density mat of alumina fibers suspended in a laminar flow of combustion gases in Sandia's Char Combustion Laboratory (CCL) using the captive particle imaging (CPI) system. This system monitors individual particle behavior for particles at least  $80\text{ }\mu\text{m}$  in diameter. Particle temperature is also monitored throughout the particle combustion history.

## RESULTS AND DISCUSSION

The issues and, in particular, the mechanisms of  $\text{NO}_x$  formation associated with Hazard Class 1.1 and 1.3 materials are quite different and are discussed separately.

### Fuels Derived from Hazard Class 1.1 Energetic Materials

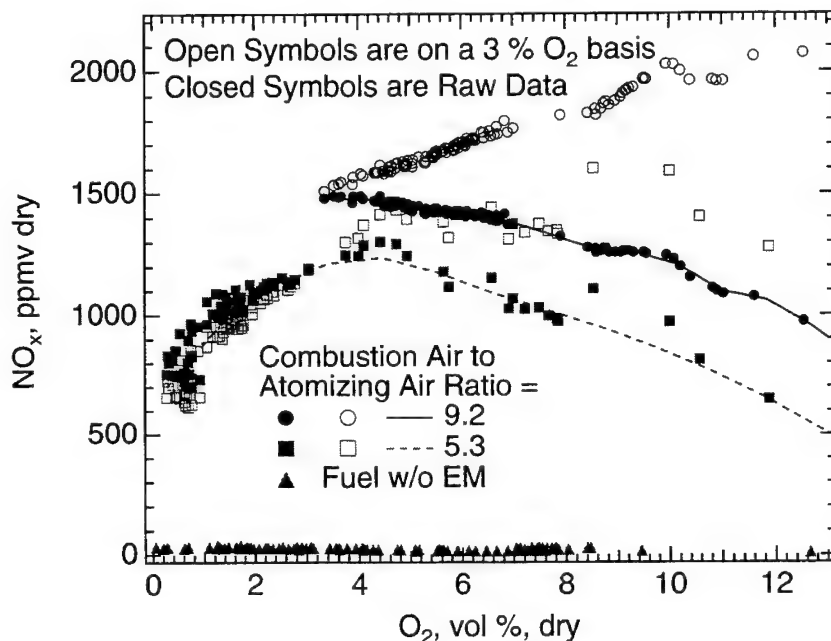
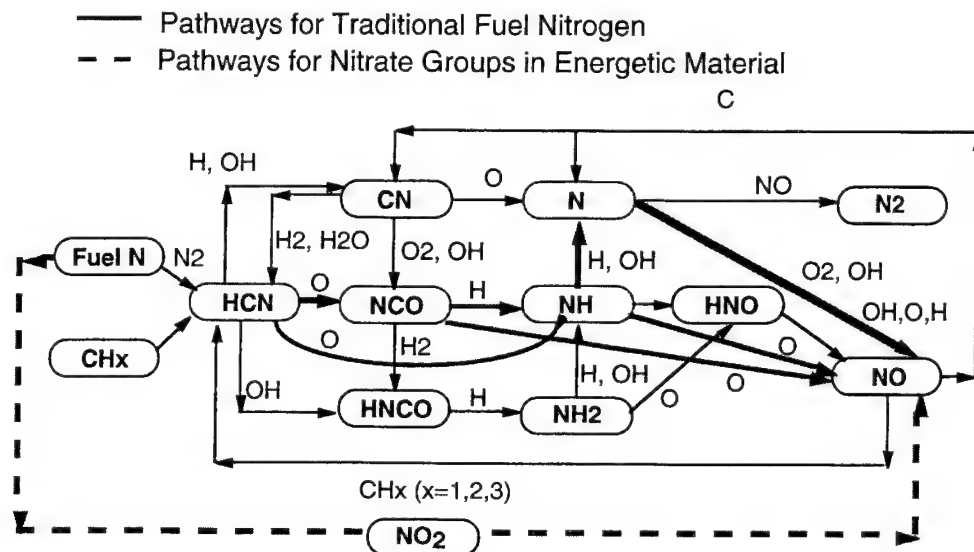


Figure 4.  $\text{NO}_x$  emissions from double-base energetic material as a function of exit  $\text{O}_2$  concentration, presence of energetic material, and combustion air to atomizing air flow rates.

Figure 4 summarizes  $\text{NO}_x$  data for the double-base EMDF under different operating conditions and as a function of exit  $\text{O}_2$  concentration. Data from samples of the emulsion containing EM are compared with data from identically prepared material without EM. The base case (without EM) indicates less than  $20\text{ ppmv NO}_x$  under all conditions. The EMDF comprises 5 % of a mixture of nitroglycerin and

The data indicate high  $\text{NO}_x$  emissions, as expected, with  $\text{NO}_x$  decreasing with increasing atomizing air flowrates. The trends are consistent with  $\text{NO}_x$  chemistry [Bowman, 1991], but the magnitudes provide interesting contrast to traditional flames. The increase in observed  $\text{NO}_x$  concentrations with the inclusion of energetic material in the emulsion attests to the efficient conversion of EM-bound nitrogen to  $\text{NO}_x$ . These data represent total  $\text{NO}_x$  measurements. Our measurements of  $\text{NO}_2$  vs NO indicate that at this temperature the NO accounts for over 90% of total  $\text{NO}_x$ .

A schematic illustration of the formation of  $\text{NO}_x$  from EMDF is presented in Figure 5 and contrasted with the traditional chemistry of fuel nitrogen. As seen,  $\text{NO}_2$  and  $\text{NO}$  are primary products of nitrate decomposition in energetic materials. These compounds often



172



## Fuels Derived from Hazard Class 1.3 Energetic Materials

Figure 6 illustrates similar data for the polybutadiene material mixed with coal at several mass ratios. In its raw form, the binder material is a porous, adherent, rubber material that is exceptionally difficult to handle. It cannot be maintained at reasonably small particle sizes without coating it with a powder or similar material to prevent reagglomeration. In these experiments, we used pulverized coal (utility grind 70% through 200 mesh) as the powder. The dominant source of fuel nitrogen in this experiment was the coal.

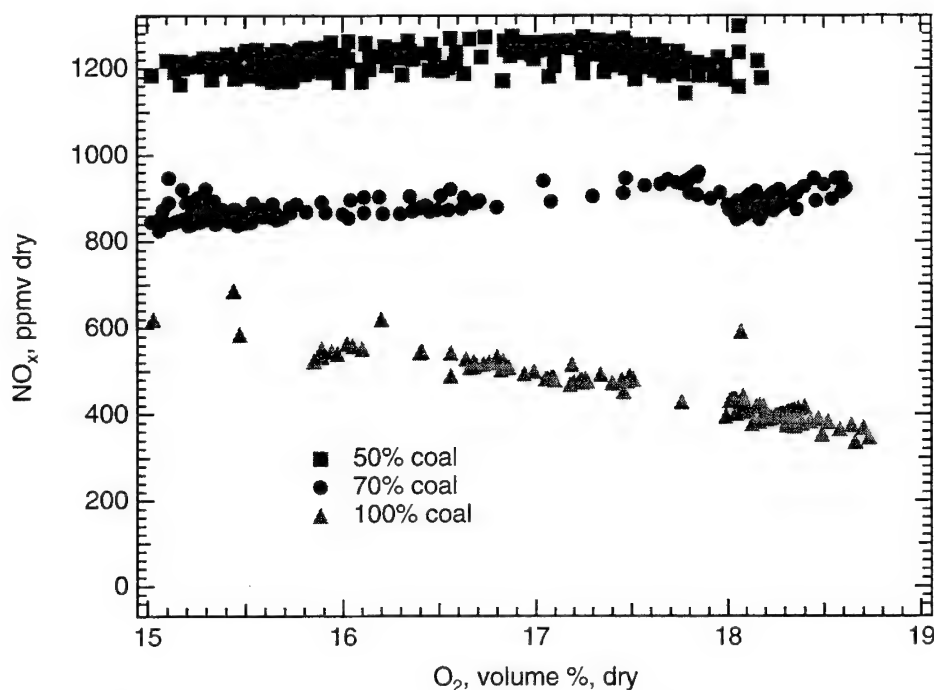


Figure 6. NO<sub>x</sub> emissions from propellant binder material blended with coal as a function of exit O<sub>2</sub> concentration and blend ratio.

The data in the figure illustrate increasing NO<sub>x</sub> concentrations with increasing fraction of energetic material derived fuel in the blend. The coal contains approximately 1.2% nitrogen by mass whereas the energetic material contains just trace amounts of residual ammonium perchlorate. The data suggest that the dominant mechanisms of NO<sub>x</sub> formation does not involve the fuel nitrogen. The aluminum particles in the binder attain temperatures higher than those found in any fossil fuel combustion process under similar conditions. Experiments in both the MFC and the CCL indicate that aluminum particle temperatures exceed 2300 °C under typical combustion conditions. In the captive particle imaging system, temperatures are measured optically and calibrated with a blackbody system. The highest temperature we could achieve in the blackbody was 1700 °C, establishing the high limit of our temperature monitoring capability. Experiments were conducted in environments with oxygen concentrations ranging from 1% O<sub>2</sub> to 20% O<sub>2</sub>. Under all conditions, the particle temperature exceeded the upper limit of our diagnostic. During 12% O<sub>2</sub> experiments in the CPI, the particles melted through the alumina mat used to hold them. The Al<sub>2</sub>O<sub>3</sub> melting point is approximately 2000 °C, depending on crystalline structure. At 6% O<sub>2</sub>, the temperature was again higher than 1700 °C, but the particles did not melt through the mat. Coating of particles with coal reduced their temperatures, but never below 1700 °C. Observations at the remaining oxygen concentrations were made in the MFC and particle temperatures were high judging from particle emission, but particles were not stationary during individual shutter cycles so no reliable temperature estimate could be made. These high

temperatures are believed to induce significant  $\text{NO}_x$  formation through thermal and prompt mechanisms in the particle boundary layer. The precise amount of the  $\text{NO}_x$  recorded in Figure 5 associated with non-fuel  $\text{NO}_x$  is difficult to determine, but it should slightly exceed the difference between the pure coal case and the two cases in which energetic material derived fuel was used. Combustion conditions were nominally identical for all three cases.

Observed  $\text{NO}_x$  concentrations are much lower as compared to double-base material (Figure 4), consistent with the lower nitrogen content of the fuel and the mode of occurrence of nitrogen. An interesting observation is that the  $\text{NO}_x$  levels observed for the double-base material exceed equilibrium  $\text{NO}_x$  at the prevailing oxygen concentrations even at the highest anticipated flame temperatures (1400 °C) of the system. This suggests that the decomposition of the energetic material proceeds through a primary product of NO, creating super-equilibrium concentrations of NO throughout the flame. This is in contrast to traditional flames, where  $\text{NO}_x$  concentrations are below their equilibrium values in the early stages of flame development and in the flame front itself. The  $\text{NO}_x$  data from the binder appear much more consistent with traditional fuel behavior [Bowman, 1992].

The MFC results also indicated that molten aluminum particles exist in flows well after 1.5 s of residence time. This sustained presence of molten material presents some deposition threat to the system. In addition, the large amount of inorganic material in the fuel (60% aluminum by weight) could overwhelm particulate cleanup systems if a high percentage of EMDF were fired in a boiler.

$\text{NO}_x$  emissions from energetic materials and the potential for particle deposition and damage to grates or other equipment from aluminum are genuine concerns in the reapplication of energetic materials as fuels, but both issues can be managed by blending the EMDF with other fuels and by judiciously choosing the boiler design and operating conditions with which to treat the material. In particular,  $\text{NO}_x$  emissions in a 10% blend of EMDF with traditional fuel would be treatable using existing technology on many biomass and coal boilers, ammonia injection being the most common. It is not clear that  $\text{NO}_x$  emissions would be as controllable using low  $\text{NO}_x$  burners as with coal since the data suggest that the nitrogen quantitatively converts to NO during thermal decomposition. If this is the case, the greatest reduction would be achieved by accelerating the  $\text{NO}_x$  reduction kinetics in and near the flame. Aluminum-containing fuels may best be used in entrained-flow facilities rather than on grates due to their extremely high combustion temperatures. However, the difficulty of reducing the particle size to entrainable values complicates its use in entrained flow systems. The ash formed after complete combustion is benign and should not pose a problem for any combustor except for its quantity.

In addition to  $\text{NO}_x$  issues and the behavior of aluminum, the possible formation air toxics are an issue for the combustion of energetic material-derived fuels. The air toxics are conveniently discussed in the categories of inorganic and organic toxics and are delineated in the 1990 amendment to the Clean Air Act [1989]. Inorganic toxics of relevance to combustion of energetic material derived fuels include beryllium, lead, and trace or impurity amounts of the remaining toxic inorganics. We have analyzed representative samples of energetic materials for their total inorganic concentrations using neutron activation analysis (NAA). The concentrations are near or below detection limits for all of the compounds and samples analyzed thus far, none of which include either lead or beryllium as intentionally added materials. EMDFs containing either lead or beryllium in more than impurity concentrations (ppm or less) are poor candidates for use as fuels.

Organic air toxics of principle concern include chlorinated aromatic hydrocarbons in the forms of dioxins, furans, pcbs or their precursors. There is a possibility of the formation of these compounds when fuels including residual chlorine are used, such as binders from ammonium-perchlorate-based rocket motors. Because chlorinated aromatic compounds are rare in the fuel, the formation of the compounds, if any, would occur as combustion gases cool in the post-flame environment. This issue has been addressed for incineration of these materials [Biagioni Jr., 1994], but has not been addressed in combustion or power generation systems. In incinerators, the total production of furans and dioxins was below regulatory limits. We anticipate similar results for combustion systems and are continuing work in this area.

## CONCLUSIONS

The potential for reapplication of excess energetic materials as boiler fuels has been economically and experimentally explored. The economics suggest that the cost of such disposal techniques could be approximately equivalent to the cost of constructing and operating the facility that removes the material and desensitizes it. Revenues gained from power generation and chemical recovery are approximately equal to expenses of boiler modifications and operation of new feedlines.

Combustion issues include the formation of pollutants, especially  $\text{NO}_x$ , and the behavior of aluminum.  $\text{NO}_x$  emissions from combustion of double-base material are notably higher than from combustion of traditional fuels with similar nitrogen contents. Essentially all of this  $\text{NO}_x$  is formed through fuel-bound  $\text{NO}_x$  mechanisms. The data suggest that thermal decomposition of the EMDF leads to essentially quantitative formation of  $\text{NO}_x$  from fuel nitrogen, unlike traditional fuels. Nevertheless, the  $\text{NO}_x$  should be treatable by the same down-stream treatment techniques as are effective with other fuels, i.e., selective noncatalytic reduction by injecting, for example, ammonia. When blended with traditional fuels,  $\text{NO}_x$  emissions from double-base materials will not be prohibitive.

$\text{NO}_x$  emissions from propellant binders are much lower than for double-base materials, but still are appreciable. The data suggest much greater contributions from thermal and prompt mechanisms, possible because of extremely high aluminum particle temperatures. These issues are also not prohibitive if the EMDF is blended in modest quantities with traditional fuels.

Management of the inorganic portions of some EMDFs may pose potential deposition and equipment problems. Aluminum particles attain high temperatures, well above their melting points, and remain at high temperatures for 1.5 s or more, which is long compared to residence times available in the furnace sections of most commercial boilers. Extreme temperatures of aluminum particles could pose some hazard to grates and kilns, where they are in potential intimate contact with surfaces. In our experiments, aluminum-containing EMDFs exposed to greater than 12%  $\text{O}_2$  melted through alumina fibers on a mat. Careful management of the fuel on a grate or in a kiln or combustion in suspension may prevent damage to systems at commercial scale. The large quantities of aluminum (60% of fuel mass) in many EMDFs could potentially overwhelm particle cleanup devices, even though the particles tend to form large and easily collected fly ash. These issues could be managed by limiting the fraction of EMDF in the blended boiler fuel.

## ACKNOWLEDGMENTS

The cooperation of James Persoon (Alliant Techsystems Inc., Hopkins, MN) and John Slaughter (Thiokol Corp., Brigham City, UT) in obtaining samples of EMDF for this project are appreciated. The support and management of Don Hardesty and Jack Swearengen is also appreciated.

## REFERENCES

1. (1989). "Federal Register: Part III; Air Contaminants" (Final Rule No. 29 CFR Part 1910).
2. Behrens Jr., R. (1990). "Thermal Decomposition of Energetic Materials: Temporal Behaviors of the Rates of Formation of the Gaseous Pyrolysis Products from Condensed-Phase Decomposition of Octahydro-1,3,5,7-tetranitro-1,3,5,7-tetrazocine." *Journal of Physical Chemistry*, 94(17), 6706-6718.
3. Behrens Jr., R., and Bulusu, S. (1991). "Thermal Decomposition of Energetic Materials: 2. Deuterium Isotope Effects and Isotopic Scrambling in Condensed-Phase Decomposition of Octahydro-1,3,5,7-tetranitro-1,3,5,7-tetrazocine." *Journal of Physical Chemistry*, 95(15), 5838-5845.
4. Behrens Jr., R., and Bulusu, S. (1992a). "Thermal Decomposition of Energetic Materials. 3. Temporal Behaviors of the Rates of Formation of the Gaseous Pyrolysis Products from Condensed-Phase Decomposition of 1,3,5-Trinitrohexahydro-s-triazine." *Journal of Physical Chemistry*, 96(22), 8877-8891.

5. Behrens Jr., R., and Bulusu, S. (1992b). "Thermal Decomposition of Energetic Materials. 4. Deuterium Isotope Effects and Isotopic Scrambling (H/D,  $^{13}\text{C}/^{18}\text{O}$ ,  $^{14}\text{N}/^{15}\text{N}$ ) in Condensed-Phase Decomposition of 1,3,5-Trinitrohexahydro-s-triazine." *Journal of Physical Chemistry*, 96(22), 8891-8897.
6. Biagioni Jr., J. R. (1994). "An Environmentally Acceptable System for the Disposal of Energetic Materials". In *Demil '94*, .
7. Bowman, C. T. (1991). "Chemistry of Gaseous Pollutant Formation and Destruction." In W. Bartok and A. Sarofim (Eds.), *Fossil Fuel Combustion: A Source Book* (pp. 866). New York: John Wiley & Sons.
8. Bowman, C. T. (1992). "Control of Combustion-Generated Nitrogen Oxide Emissions: Technology Driven by Regulation". In *Twenty-Fourth Symposium (International) on Combustion*, (pp. 859-878). Sydney, Australia: The Combustion Institute.
9. Shah, D. S. (1994). "Analysis of Propellants, Explosives, and Pyrotechnics Co-Combustion in Fossil Fuel and Biomass Boilers as Means of Resource Recovery and Recycle" No. White Paper.

#### COMMENTS

H. Krause, *Fraunhofer-Institut für Chemische Technologie (ICT), Germany*. Our data suggest overall conversion efficiencies of nitrate groups of 1/10 for neat nitrocellulose and 1/3 for neat TNT, both at stoichiometric ratio of 1.5 and 2.0 (fuel lean). These are lab-scale experiments using 10-150 g of material and using a methane-air flame to stabilize the combustor.

*Author's reply.* The data between our laboratories are probably consistent. We do believe that virtually every nitrate group forms an  $\text{NO}_x$  compound as an initial product during decomposition in a combustion environment, and this is consistent with fundamental MBMS investigations as cited. However, the fate of the  $\text{NO}_x$  compound is determined by the same complex gas-phase chemistry as characterizes traditional  $\text{NO}_x$  behavior. In particular, heavily nitrated compounds will easily exceed the equilibrium gas-phase  $\text{NO}_x$  concentrations during combustion, resulting in the kinetics going backwards from the traditional view and destroying  $\text{NO}_x$  as it drives toward equilibrium. As temperatures drop, these kinetics slow and the ultimate exit  $\text{NO}_x$  concentration is determined by the relationship between kinetics (temperature/stoichiometry driven) and temperature history/residence time. The data presented in our investigation indicate final nitrogen conversion efficiencies ranging from 0.3 to 0.9, depending on stoichiometry and residence time. This was using fuels sometimes containing less than 5% energetic material. If we used neat fuels, the absolute  $\text{NO}_x$  concentrations would be higher but the conversion efficiencies would be much lower (we have demonstrated this by testing different concentrations of TNT in toluene). I believe our data are possibly consistent with your data. We are confident in our results in any case.

## **RECYCLING OF EXCESS AND DEMILITARIZED ENERGETIC MATERIALS IN COMMERCIAL EXPLOSIVE APPLICATIONS**

**Dr. Oldrich Machacek, J. Brent Gillion, Gary Eck**  
Universal Tech Corporation

**Dr. Joel Lipkin**  
Sandia National Laboratories

**Ron Michalak, Robert Perry, Al McKenzie, Larry Morgan**  
United Technologies Chemical Systems Division

**ABSTRACT:** Universal Tech Corporation, has achieved considerable success in the area of recycling excess and demilitarized energetic materials. The recycling of these materials into commercial explosive formulations for use in mining and quarrying has proven to be a viable option for handling excess and demilitarized energetic materials. The focus of this paper will be on describing the Propellant/Explosive Evaluation Model (PEEM), which Universal Tech utilizes when developing a recycling method for a particular energetic material. In particular, details will be given concerning the results of a study project which Universal Tech conducted for Sandia National Laboratories. In this study project, Sandia provided Universal Tech with cryogenically downsized particles of two rocket propellants. Universal Tech successfully developed commercial explosive formulations using both of the propellants.

### **INTRODUCTION**

For many years, the most common disposal method of energetic materials has been open burning/open detonation (OB/OD). Examples of more modern methods of disposal are incineration, thermal treatment, ingredient reclamation and biodegradation. Each of these methods are disposal techniques for a hazardous waste material. They each require expensive permitting and operational costs as well as carrying less than favorable public opinion. The presented study describes the Propellant/Explosive Evaluation Model (PEEM), which Universal Tech uses to evaluate energetic materials for recycling applications. Specific results are given from a study performed in cooperation with Sandia National Laboratories in which two solid propellants were evaluated for use in commercial explosive formulations. The results presented herein indicate that the incorporation of both types of propellants as ingredients in commercial explosive formulations proved to be a safe, inexpensive (as compared to other methods) and environmentally sound method for the alternate use of the materials.

## DESCRIPTION OF COMMERCIAL EXPLOSIVES STUDIED

Universal Tech Corporation possesses considerable expertise in the field of watergel slurry explosives. It is estimated that 300-350 million pounds of watergel slurry explosives are used in the United States each year. The work Universal Tech has done with energetic materials recycling has been focused in the watergel slurry arena. A list of the typical ingredients used in watergel slurry formulations appears below.

### Watergel Slurries

<u>Ingredients</u>	<u>Use</u>
Ammonium Nitrate	Oxidizer
Sodium, Calcium Nitrate	Oxidizer
Methylamine Nitrate	Sensitizer, Fuel
Hexamethylenetetramine	Sensitizer, Fuel
Aluminum (Coarse, Atomized)	Fuel, Sensitizer
Ethylene glycol	Fuel
Water	Fluidizer
Guar Gum	Gelling Agent
Ammonium, Potassium, Sodium Perchlorate	Oxidizer, Sensitizer
Glass Microspheres	Sensitizer

The production of a watergel slurry explosive is a relatively simple process which incorporates two basic steps. First, a Mother Solution, or liquid phase, (which normally constitutes 30-60% of the final product) is produced. The second step involves the blending of the Mother Solution with any additional dry oxidizer (nitrate) salts, aluminum powders (if necessary) and gelling+crosslinking agents. The blending process is utilized to homogenize the mixture and most importantly to entrain air into the mixture (unless chemical gassing is used). Air is entrained until the desired density of the product is achieved. When ready to package, the mixture has the consistency of thick oatmeal which is easily pumped into packages. The required equipment consists of temperature controlled liquid storage tanks, oxidizer (nitrate) storage bins, a mixing chamber, and packaging equipment. The process is easily made to be closed-loop with no effluents being presented for treatment or disposal. All scrap or off-spec materials are recycled as is any wash water which might be generated. The production process can be made modular, completely contained and is inexpensive to capitalize. Production facilities can easily be established in the same area as the demilitarization operation to increase the economy of the approach.

## PROPELLANT/EXPLOSIVE EVALUATION MODEL

The evaluation of a particular energetic material for use as an ingredient follows a simple model, which has come to be called the Propellant/Explosive Evaluation Model (PEEM). The PEEM is described as follows:

### **Step 1. Initial Safety Review**

This step is accomplished by reviewing all available safety and sensitivity test data for the energetic material. This information is used to do an informal hazards analysis and to ensure that all following work will be done in a safe manner.

### **Step 2. Laboratory Formulation**

In a controlled laboratory setting and in less than 1000 gram batches, several preliminary screening tests are conducted. The efforts include tests for 1) chemical compatibility between the ingredients of the watergel slurry formulation and the energetic material as well as any processing intermediates and the energetic material, 2) thermal stability at, 75°C as a check for any undesirable high temperature reactions, 3) mixing rheology as a check of the formulations producibility based on the particle size and level of incorporation of the energetic material.

### **Step 3. Safety Tests**

This step includes the safety testing of the energetic material, any processing intermediates which would be involved with the production of the final product, and the final blended product. The data from these tests are used as indicators for the development of safe handling, storage and processing practices. They also allow for process safety management decisions to be made.

### **Step 4. Pilot Plant Scale-Up**

In this step, efforts are scaled-up to 100 kg batches of the candidate formulations, which were developed in the previous laboratory scale efforts. The scale-up mixing is done to observe for any differences between the small scale batches and the larger batches in the area of rheology. Once completed, the pilot plant scale batches are tested for explosive characteristics, such as unconfined velocity of detonation, critical diameter, cold temperature sensitivity (to initiation) and underwater energy release. These tests are conducted on the freshly made batches as well as aged portions of the batches. This step is where the optimization work is done, which results in the best possible formulation for using a particular energetic material with the factors of production, end-use, market development, economics and others being considered.

### **Step 5. Department of Transportation Shipping Classification Tests**

This step is required for all new explosive formulations in the United States. It is required that a series of tests be conducted to determine the shipping classification of the new explosive. These tests are listed in the 49 CFR and described in the United Nations Test Manual<sup>1</sup> for the Transport of Hazardous Goods.

## **Step 6. Production Scale-Up**

This step involves the scale-up to full production of the propellant/explosive blended products. Observations as to rheology and producability are made. The scaled-up products are then taken to the field and tested in actual production blasts at a working mine.

## **TEST DESCRIPTION/RESULTS ON SANDIA NATIONAL LABORATORIES PROJECT**

On May 12, 1995, UTeC received samples of two propellant types from Sandia National Laboratories. The propellant samples were submitted for the development and demonstration of recycling applications in commercial blasting explosives. For the purpose of this paper, the samples will be called Propellant A and Propellant B. The propellants were originally used in two different tactical missiles. The propellants were derived from a cryocycling process, which Sandia had been developing in cooperation with Global Environmental Solutions, Inc.. In order to successfully conduct this work, UTeC utilized the Propellant/Explosive Evaluation Model mentioned above.

### **1.0 Initial Safety Review**

The results of the Initial Safety Review were conclusive in establishing the fact the each propellant was a double base propellant containing certain quantities of nitroglycerin and nitrocellulose. The particle size of the propellant particles was such that they were suitable for use with no further downsizing required. Past work with other double base propellants indicated that some incompatibility could exist between the nitroesters and the hexamethylenetetramine (hexamine), which is normally used in Universal Tech's products as a fuel ingredient. No other safety concerns or hazards were identified that would have hindered subsequent efforts. Therefore the second step of the Propellant Evaluation Model was began.

### **2.0 Laboratory Formulation**

A simple particle size check using standard sieve analysis showed each propellant to have been broken into 0.25 to 1.75 cm chunks by the cryocycling process. Transparent pieces of case liner with an amber tint were observed in the drums of each propellant. Initially, the oxygen balance (approximate) of each propellant was calculated based upon the major components. From this approximation, it was observed that both propellants had similar oxygen balance values. Using an oxygen balance value of  $-23\text{gO}_2/100\text{g}$ , formula calculations were made using the propellants at equal values. These formulations were calculated in a manner which used the complete fuel value of the propellants. Formulations containing 20%, 30% and 40% of each propellant were calculated. Formulations containing hexamine and ethylene glycol were calculated. Table I lists the initial formulations.



TABLE I

Formulations for Laboratory Scale Development. Values shown are percent by weight.

## Ethylene glycol Based Formulations

<u>Ingredient</u>	<u>Standard</u>	<u>20%</u> <u>Prpint</u>	<u>30%</u> <u>Prpint</u>	<u>40%</u> <u>Prpint</u>
Water	13.00	13.00	13.00	13.00
Ammonium Nitrate	17.00	17.00	17.00	17.00
Sodium Nitrate	05.00	05.00	05.00	05.00
Ammonium Perchlorate	04.00	04.00	04.00	04.00
<u>Sodium Acetate</u>	<u>01.00</u>	<u>01.00</u>	<u>01.00</u>	<u>01.00</u>
Total Mother Solution	(40.00)	(40.00)	(40.00)	(40.00)
Dry Ammonium Nitrate	47.00	33.00	26.00	12.00
Dry Sodium Nitrate	00.00	00.00	00.00	05.00
Ethylene glycol	12.00	06.00	03.00	02.00
Guar Gum	00.90	00.90	00.90	00.90
Crosslinker	00.10	00.10	00.10	00.10
<u>Propellant</u>	<u>00.00</u>	<u>20.00</u>	<u>30.00</u>	<u>40.00</u>
Total	100.00	100.00	100.00	100.00
Oxygen Balance gO <sub>2</sub> /100g	-1.2	-0.9	-0.7	-2.2

## Hexamine Based Formulations

<u>Ingredient</u>	<u>Standard</u>	<u>20%</u> <u>Prpint</u>	<u>30%</u> <u>Prpint</u>	<u>40%</u> <u>Prpint</u>
Water	13.00	13.00	13.00	13.00
Hexamethylenetetramine	08.50	04.00	03.00	02.00
Nitric Acid (100%)	03.76	01.77	01.33	00.90
Ammonium Perchlorate	04.00	04.00	04.00	04.00
Sodium Nitrate	00.00	00.00	00.00	05.00
<u>Ammonium Nitrate</u>	<u>10.74</u>	<u>17.23</u>	<u>18.67</u>	<u>15.10</u>
Total Mother Solution	(40.00)	(40.00)	(40.00)	(40.00)
Dry Ammonium Nitrate	59.00	39.00	29.00	14.00
Dry Sodium Nitrate	00.00	00.00	00.00	05.00
Guar Gum	00.90	00.90	00.90	00.90
Crosslinker	00.10	00.10	00.10	00.10
<u>Propellant</u>	<u>00.00</u>	<u>20.00</u>	<u>30.00</u>	<u>40.00</u>
Total	100.00	100.00	100.00	100.00
Oxygen Balance gO <sub>2</sub> /100g	-0.7	-0.2	-2.4	-2.0

Using the above formulations, a total of 14 lab scale mixes were made. Each mix was observed for physical characteristics as well as being subjected to a simple compatibility test. Table II below gives the mix identifications and descriptions for each of the 14 lab scale mixes mentioned above.

TABLE II  
Mix Identifications and Descriptions of Lab Scale Development Mixes.

<u>Mix I.D.</u>	<u>Description</u>	<u>Mix pH</u>	<u>Density (g/cc)</u>
6-6-01	Ethylene glycol (EG) Standard	5.2	1.20
6-6-02	EG + 20% Propellant A	5.2	1.17
6-6-03	EG + 30% Propellant A	5.2	1.21
6-6-04	EG + 20% Propellant B	5.1	1.21
6-6-05	EG + 30% Propellant B	5.2	1.20
6-6-06	Hexamethylenetetramine Std.(HEX)	5.1	1.21
6-6-07	HEX + 20% Propellant A	5.2	1.18
6-6-08	HEX + 30% Propellant A	5.1	1.19
6-6-09	HEX + 20% Propellant B	5.2	1.21
6-6-10	HEX + 30% Propellant B	5.1	1.13
6-7-01	EG + 40% Propellant A	5.2	1.20
6-7-02	EG + 40% Propellant B	5.1	1.17
6-7-03	HEX + 40% Propellant A	5.2	1.22
6-7-04	HEX + 40% Propellant B	5.1	1.19

The compatibility test was conducted at three temperatures: ambient (20-25°C), 40°C and 50°C. The ambient and 40°C temperatures represented normal and maximum expected explosive storage magazine temperatures. The 50°C temperature represented an extreme situation not usually observed in normal explosive storage conditions. The test apparatus involved no instrumentation. A known volume of each sample was placed in a glass jar. The original volume was noted with a mark on the outside of the jar. The lid of the jar was placed loosely so as to allow for any gasses to escape, thus avoiding any pressure rupture of the jar during storage. A sample of each formulation was placed at each of the three test temperatures. Initially, the jars were observed daily. After the first week, the jars were observed weekly. An observation was made to check the level of the sample within each jar. Any changes in volume were noted in the data record. No attempts were made to analyze any generated gases resulting from possible reaction between incompatible ingredients of the propellant and watergel slurry matrix.

*Compatibility tests results at ambient (20-25°C).* None of the samples of ethylene glycol based mixes had exhibited any volume change due to off-gassing after 7 weeks of storage at this temperature. Each hexamine based mix containing propellant exhibited some volume change due to off-gassing. The volume change was slight and occurred after 3-4 weeks of storage. The incompatibility between the hexamine based mixes and the propellants was expected and verified past results that have indicated an incompatibility between the hexamine and some nitro esters.

*Compatibility tests results at 40°C.* The hexamine based samples exhibited significant volume change, and thus, significant incompatibility. The reaction and resultant volume change was observed to take several days to occur. However, it did occur and the samples were removed from the test. These results verified past work that heat is a catalyst for the incompatibility reaction of hexamine and nitro esters. No volume change was observed for any of the ethylene glycol samples at this temperature after 7 weeks of storage.

*Compatibility tests results at 50°C.* All of the hexamine based mixes gassed significantly. The volume of the HEX + Propellant A samples had grown by up to 40% on the fourth day of observation. The HEX + Propellant B samples exhibited the same characteristics, with a volume change of up to 47% on the 12th day of observation. The level of volume change due to off-gassing was unacceptable for useful shelf-life and storage characteristics of a commercial blasting product. Some slight volume change was observed for the ethylene glycol samples at this temperature after 7 weeks of storage. The volume changes were minimal and did not present any undue concerns for safe shipment and storage of these products.

### 3.0 Safety Tests

*Blasting cap sensitivity.* The first test conducted was cap sensitivity. This test was conducted in 7.62 cm diameter X 15.24 cm long charges. A #8 strength electric blasting cap was inserted approximately 2.54 cm into one end of the charge. Each propellant was tested dry, wetted with Mother Solution, and blended with the ethylene glycol based watergel slurry matrix. Neither of the propellants detonated with the blasting cap when dry. However, they did ignite and burn. This was witnessed by finding charred cardboard tube remnants in the test area. The ignition did not occur in every test. In several repetitions of the test the sample container and propellant were simply blown apart by the blasting cap. When wetted with 50% Mother Solution, the propellants did not detonate or ignite in the blasting cap test. Samples of the ethylene glycol based watergel slurry product containing 30% of each of the propellants were also found not to detonate or ignite in the blasting cap test.

*Deflagration to Detonation (DDT).* This test measured the tendency for the propellant to undergo transition from deflagration to detonation. Each propellant was tested dry, wetted with Mother Solution, and blended with the ethylene glycol based watergel slurry matrix as a finished product. When tested dry, Propellant A did not transition to detonation according to the test procedure. However, the test pipe was broken and peeled back at the capped end. No hole was blown in the witness plate. The Propellant B propellant also did not transition to detonation. The test pipe was left in-tact, with the cap being blown off. The witness plate was not punctured, but was dented. When wetted with 30% Mother Solution (by weight), the Propellant A sample blew the test pipe into several pieces. The witness plate was not punctured, but was severely dented. A repeat of this test with 50% Mother Solution resulted in the pipe being left in tact. Pieces of the propellant were retrieved from the test area as well as from inside of the pipe. Propellant B, when wetted with 50% Mother Solution, did not DDT. The test pipe in both trials was left in-tact with propellant remaining inside and on the ground in the test area. The finished product samples, with the propellants being blended at a 30% level with the ethylene glycol based watergel slurry matrix, were not reactive. The test pipes from these samples were retrieved in-tact with considerable amounts of the test sample still in the pipe.

### 4.0 Pilot Plant Formulation

Based on the results of the chemical compatibility tests, which were conducted during the Laboratory Scale work, the ethylene glycol based formulations were selected as the most favorable for use with both of the propellants. Initially, in the Pilot Plant, four small batches

(10kg) containing each of the propellants were made to verify the sensitivity to initiation and velocity of detonation of the formulations developed at the Lab Scale. Each of these formulations was based on using the propellants as true fuel in the formulation and holding the water content of the formulation constant. This method of using the propellant did not allow for the slurry portion of the formulation to be oxygen balanced. Due to the lack of oxygen balance, the slurry portion of the formulation was not actually an optimum formulation on its own. The intent was that the propellant would provide sufficient fuel value to the formulation to give it the desirable detonation characteristics. However, upon the completion of these detonation tests, it was noted that each formulation lacked sufficient sensitivity.

Next, due to the lack of sensitivity and less than desirable detonation characteristics of the formulations discussed above, it was decided to use additional ethylene glycol to oxygen balance the slurry portion of the formulation; thereby, no longer using the propellants as true fuel sources. It was anticipated that by oxygen balancing the slurry portion, and thus, attempting to make it a viable explosive formulation on its own, this would increase the sensitivity and velocity of detonation of the resultant formulations. Also, the water content of the formulations was decreased from 13% to 9.1%. In effect, it was supposed that the propellants would be used as extenders of an explosive formulation and would enhance the detonation characteristics of the blended product over that of the standard slurry formulation. Subsequently, and in order to test this theory, three more small batches (16 kg) were made. Only Propellant A was used for these formulations. A standard formula containing no propellant was used, a formula with the slurry portion of the product which was oxygen balanced and to which 30% of Propellant A was added, and a formula for which the overall formulation was oxygen balanced and contained 30% of Propellant A. From detonation tests, it was observed that the mix, which consisted of the propellant being added to an already oxygen balanced slurry, exhibited acceptable detonation characteristics. The standard slurry, which contained no propellant, proved to be very insensitive, with low detonation velocity results, as did the mix which contained the propellant as a complete source of fuel.

Based on these findings, a total of five 120 kg batches were made in the Pilot Plant mixer. In these mixes, the slurry portion of each of the formulations was oxygen balanced. Thus, as described above, the propellants were actually added to the formulations as extenders of a base explosive formulation. A standard slurry was made which contained no propellant, and four slurries were made which contained different levels of the two propellants. Mixes were made which contained 15% of each of the propellants individually, and which contained 30% of each of the propellants. The formulations for these mixes are recorded in Table III. . The mixes were packaged in various diameter cardboard tubes for explosive characteristics testing. The following detonation tests were conducted: **Unconfined Velocity of Detonation** at two temperatures, **Critical Diameter**, and **Underwater Energy**. These tests were conducted on unconfined charges in all cases. A description of the explosive characteristics test procedures follows:

*Unconfined velocity of detonation.* The unconfined velocity of detonation was measured by utilizing a standard point-to-point chronograph "make-circuit" measurement system. In this test two sets of insulated wires are placed in the charge a known distance apart. As the detonation wave travels through the charge, the wire sets are shorted together, causing a current flow. By measuring the time between the "making" of the circuit, velocity is easily calculated.

*Critical diameter.* The velocity of detonation of most explosive formulations is affected by the charge diameter. Thus, it is important to know at what minimum diameter the formulation can be reliably initiated with a chosen initiating primer. This critical diameter was measured by detonating various diameter charges of the formulations, beginning with 15cm and working down, until a failure was observed. The last diameter at which a reliable detonation was received was taken to be the critical diameter. The velocity of detonation test was used as a witness of detonation. This test was conducted at both 20° and 4°C.

*Underwater energy<sup>3</sup>.* This test allowed for the measurement of the energy release of an explosive formulation. The test was conducted underwater due to the high consistency and repeatability of the water as a test medium. The unconfined charges were packaged in 6 inch diameter, one gallon cans. All of the charges were initiated with a one pound cast primer.

The five mixes described previously were subjected to the tests just described. The results of these tests were recorded in Table IV.

TABLE III  
Pilot Plant Mix Formulations

Standard Product Solution		Product Propellant Solution
<u>Ingredient</u>	<u>Weight %</u>	<u>Weight %</u>
Water	28.90	26.00
Ammonium Nitrate	48.90	51.10
Sodium Nitrate	15.60	14.30
Ammonium Perchlorate	04.40	05.70
Sodium Acetate + HNO <sub>3</sub>	02.20	02.90
Total	100.0	100.0
pH	5.0 at 110°F	5.1 at 100°F

Slurry Formulations (16000g batches were made in Hobart Mixer)

<u>Ingredient</u>	<u>Standard</u> <u>8-9-01</u>	<u>15% Prp B</u> <u>8-14-02</u>	<u>15% Prp A</u> <u>8-14-01</u>	<u>30% Prp B</u> <u>8-10-01</u>	<u>30% Prp A</u> <u>8-11-01</u>
Std. Mother Solution	45.00	--	--	--	--
Propellant Mother Soln.	--	40.00	40.00	35.00	35.00
Ground Amm. Nitrate	33.40	25.0	25.00	17.40	17.40
Ammonium Perchlorate	08.00	08.00	08.00	08.00	08.00
Ethylene glycol	12.00	10.50	10.50	08.40	08.40
Guar Gum	01.40	01.30	01.30	01.10	01.10
Crosslinker	00.20	00.20	00.20	00.10	00.10
Propellant (N-8)	00.00	15.00	00.00	30.00	00.00
Propellant (JPN)	00.00	00.00	15.00	00.00	30.00
Total	100.00	100.00	100.00	100.00	100.00
Density (g/cc)	1.20	1.15	1.15	1.15	1.15
pH	4.9 at 70°	5.3 at 77°	5.3 at 77°	5.4 at 75°	5.1 at 74°

TABLE IV  
Explosive Characteristics Data for Pilot Plant Scale Batches from Table III.

The tests which were conducted on the products were Velocity of Detonation at two temperatures, Critical Diameter, and Underwater Energy. These tests were conducted on unconfined charges in all cases. Additionally, each mix was tested for initiation sensitivity with a #8 strength Electric Blasting Cap. All tests were conducted on unconfined charges.

8-9-01 = Standard Slurry (no propellant)  
8-14-01 = 15% Propellant A  
8-11-01 = 30% Propellant A

8-14-02 = 15% Propellant B  
8-10-01 = 30% Propellant B

A. Velocity of Detonation/Critical Diameter. A one pound cast primer was used for initiation in all of these tests. Data are in meters per second ( $\pm 100$  meters/sec)

**Charge Diameters in Centimeters**

20°C						40°C			
<u>Mix No.</u>	<u>15.24</u>	<u>12.7</u>	<u>10.16</u>	<u>7.62</u>	<u>6.35</u>	<u>15.24</u>	<u>12.7</u>	<u>10.16</u>	<u>7.6</u>
8-9-01	4965	4790	4420	3730	fail	fail	—	—	—
8-14-02	5330	5080	4450	3800	3315	fail	—	—	—
8-14-01	5425	5200	4600	4235	3730	4470	4495	4090	fail
8-10-01	5445	4960	4780	3365	3000	fail	—	—	—
8-11-01	5600	5380	5255	5060	4700	5560	5440	4820	fail

B. Cap Sensitivity Test. A #10 Electric Blasting Cap was used in these tests. The charge temp. was 31°C.

<u>Mix No.</u>	<u>7.62 cm x 20.32 cm Charge</u>	
8-9-01	fail	
8-14-02	fail	
8-14-01	fail	
8-10-01	fail	
8-11-01	detonation	fail at 27°C

C. Underwater Energy (cal/gm)( $\pm 2.5\%$ )

<u>MIX #</u>	<u>DEN</u>	<u>VOD</u>	<u>DP</u>	<u>SLF</u>	<u>SSE</u>	<u>CSE</u>	<u>BUB</u>	<u>TOT</u>
ANFO	900	3506	27.7	1.31	260	341	519	860
8-9-01	1200	4966	74.0	1.70	200	340	431	771
8-14-02	1200	5331	85.3	1.74	204	355	434	790
8-14-01	1200	5427	88.4	1.75	214	375	433	807
8-10-01	1200	5447	89.0	1.76	201	354	427	781
8-11-01	1200	5604	94.2	1.78	234	417	456	873

DEN = Density in kg/cc  
VOD = Velocity of Detonation in meters/second  
DP = Detonation Pressure in kBars as approximated by  $0.25 \times \text{density} \times \text{VOD}^2$   
SLF = Shock Loss Factor (calculated from detonation pressure and velocity of detonation, allows for approximation of the amount of energy in the shock wave which is lost between the point of detonation and the point of pressure measurement)  
SSE = Specific Shock Energy measured at the transducer  
CSE = Corrected Shock Energy,  $\text{SSE} \times \text{SLF}$   
BUB = Bubble (Gas) Energy  
TOT = Total Available Work Energy,  $\text{CSE} + \text{BUBBLE}$

### **5.0 Department of Transportation Shipping Approval<sup>2</sup>**

The shipping approval tests were conducted for and witnessed by the Bureau of Explosives in early 1996. The tests concluded that the formulations containing the propellants would be classified as Class 1.5D Blasting Agents. The formal assignment of EX numbers by the United States Department of Transportation is pending.

### **6.0 Full Scale Demonstration**

A 4500 kg batch of the formulation which contained 30% of Propellant A was manufactured and field tested. The results of the test showed the explosive to be highly successful in breaking and displacing the blasted media. The test was conducted at a rock quarry in northeast Oklahoma in early 1996.

## **CONCLUSIONS**

### **Propellant A**

The velocity of detonation data (at 20 and 4°C) and the underwater energy data indicated that the incorporation of Propellant A was more beneficial at the higher 30% level. At the 15% level, propellant A also proved to be a useful ingredient. However, the 30% level exhibited greater increases in velocity of detonation, sensitivity, energy release and cold temperature sensitivity. Either of the propellant slurry formulations, 15% or 30%, would offer excellent detonation characteristics for use in both cool temperature environments and warm temperature environments. The high velocity of detonation results would allow them to be a good explosive for most hard rock mining applications.

### **Propellant B**

The results of the 20°C velocity of detonation and underwater energy tests indicated that Propellant B was a more beneficial ingredient in the slurry explosive when added at a 15% level, as compared to a 30% level. This was attributed to a lack of sensitivity on the part of Propellant B. Although Propellant B, when added at either level did increase the velocity of detonation of the blended product over that of the standard product in large charge diameters, it was not sensitive enough to sustain these increases in smaller charge diameters. The 15% propellant slurry also offered both greater sensitivity (as witnessed by

higher detonation velocity data) and greater energy release than the standard slurry product. The velocity of detonation results at 4°C also indicated a lack of sensitivity on the part of Propellant B in that the blended products, regardless of propellant level. This lack of cold temperature sensitivity would preclude the use of Propellant B as an additive to the test slurry matrix in cold temperature applications. In other words, the formula which was developed would be a viable formulation with very good detonation characteristics at warm temperatures. This fact would simply dictate the use of this formulation in warmer regions of the country and in larger charge diameters.

### **Overall**

From the test data generated in this study, it was obvious that both propellants were capable of performing as an energetic fuel/sensitizer ingredient in a suitable commercial watergel slurry explosive. This fact makes the propellants useful materials and removes their connotation as a hazardous waste. These results also indicated that the recycling of the propellants into commercial explosives offered a viable alternative to the open burning/open detonation disposal methods.

1. United Nations Recommendations for the Transport of Dangerous Goods, Tests and Criteria, Second Edition
2. 49 CFR § 173.57(a) and 173.58(b)
3. Bjarnholt, "Suggestions on Standards for Measurement and Data Evaluation in the Underwater Explosion Test. 8th Meeting for the Standardization of the Methods of Testing Explosives. Oct 3-6, 1978 Tatranska Lomnica, Czechoslovakia



## RECENT STUDIES ON THE CHEMICAL CONVERSION OF ENERGETIC MATERIALS TO HIGHER VALUE PRODUCTS

Alexander R. Mitchell, Philip F. Pagoria, and Robert D. Schmidt  
Energetic Materials Center, Lawrence Livermore National Laboratory  
MS L-282, P.O. Box 808, Livermore, California 94550, USA

**ABSTRACT:** The use of energetic materials as chemical feedstocks for higher value products potentially provides environmentally sound and cost-effective alternatives to disposal by open burning/open detonation. The conversion of UDMH (unsymmetrical dimethylhydrazine) and Explosive D (ammonium picrate) to higher value explosives such as 1,3,5-triamino-2,4,6-trinitrobenzene (TATB) and 1,3-diamino-2,4,6-trinitrobenzene (DATB) illustrates our approach. We have developed a new synthesis of TATB that utilizes surplus UDMH (propellant) and Explosive D (high explosive) as starting materials. Methyl iodide reacts with UDMH to provide TMHI (1,1,1-trimethylhydrazinium iodide) which serves as a reagent for the amination of nitroaromatic substrates via Vicarious Nucleophilic Substitution (VNS) of hydrogen. The reaction of picramide (obtained from Explosive D) with TMHI gives TATB or DATB in 95% and 75% yields, respectively. This synthesis should offer significant savings in the production of TATB thereby making this insensitive high explosive more accessible for civilian applications.

### 1. INTRODUCTION

The demilitarization of nuclear and conventional munitions is producing millions of pounds of surplus explosives (energetic materials). Historically, surplus explosives have been disposed of by open burning/open detonation (OB/OD). The disposal of these materials by OB/OD is becoming unacceptable due to public concerns and increasingly stringent environmental regulations. Environmentally sound and cost-effective alternatives to OB/OD are needed. We are investigating the chemical conversion of energetic materials to higher value products. This paper focuses on the use of a surplus propellant (UDMH) and high explosive (Explosive D) as chemical precursors to higher value explosives (DATB and TATB).

### 2. TATB

TATB is a reasonably powerful high explosive whose thermal and shock stability is considerably greater than that of any other known material of comparable energy.<sup>1</sup> It is used in military applications because of its

significant insensitivity to thermal and shock environments. There is also interest in employing TATB in the civilian sector for deep oil well explorations where heat-insensitive explosives are required. TATB had been priced at \$20 to \$50 per pound when it was being produced on an industrial scale in the U.S. TATB is currently available to customers outside of the Department of Energy (DOE) for \$100 per pound.<sup>2</sup> This paper describes a new synthesis of TATB developed at Lawrence Livermore National Laboratory (LLNL) that utilizes inexpensive starting materials and mild reaction conditions.

## 2.1 Current Preparation of TATB

TATB is produced in the USA by nitration of the relatively expensive and domestically unavailable 1,3,5-trichlorobenzene (TCB) to give 2,4,6-trichloro-1,3,5-trinitrobenzene (TCTNB) which is then aminated to yield TATB (Figure 1).<sup>3</sup> Elevated temperatures (150 °C) are required for both reactions. The major impurity encountered in this process is ammonium chloride. The inclusion of 2.5% water during the amination step significantly reduces the ammonium chloride content of the TATB.<sup>4</sup> Low levels of chlorinated organic impurities have also been identified. These impurities include 2,4,6-trichloro-1,3,5-trinitrobenzene (TCTNB), 1,3-dinitro-2,4,5,6-tetrachloro-benzene, 1,3-dinitro-2,4,6-trichlorobenzene and their partially aminated products.<sup>5</sup> A synthesis of TATB that replaces TCTNB with a non-chlorinated starting material is clearly desirable.

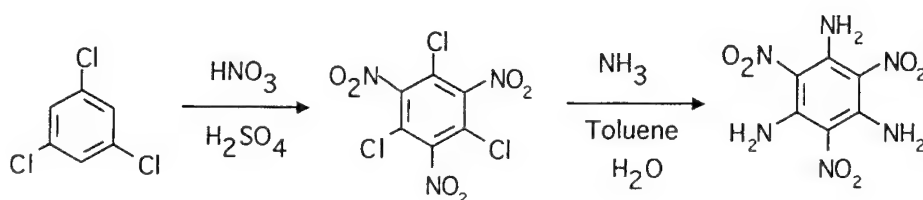


Figure 1. Current synthesis of TATB

## 2.2 Vicarious Nucleophilic Substitution of Hydrogen

Vicarious nucleophilic substitution (VNS) of hydrogen is a well-established procedure for the introduction of carbon nucleophiles into electrophilic aromatic rings.<sup>6,7</sup> The reaction involves the addition of a carbanion bearing a leaving group (X) to an electrophilic aromatic ring and subsequent rearomatization by loss of the leaving group through elimination as HX (Figure 2, Z=CH<sub>2</sub>). This reaction has been applied to a wide variety of

nitroarenes and nitro-substituted heterocycles.<sup>7</sup>

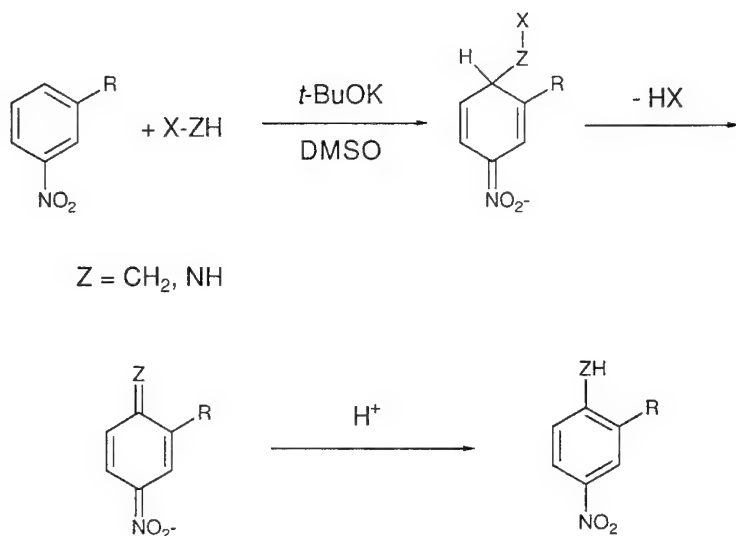


Figure 2. Vicarious nucleophilic substitution of hydrogen

By analogy, VNS reactions can also take place with amine nucleophiles. Such reagents are of the common form  $\text{X-NH}_2$ , where X is an auxiliary group capable of stabilizing a negative charge, thus driving rearomatization of the  $\sigma$ -intermediate adduct (Figure 2,  $Z=\text{NH}$ ). One of the first examples of amination by VNS of hydrogen was provided by Meisenheimer and Patzig who reacted 1,3-dinitrobenzene with hydroxylamine in the presence of strong base to yield 2,4-dinitrophenylene-1,3-diamine.<sup>8</sup> Recently, a number of more active aminating reagents such as 4-amino-1,2,4-triazole<sup>9</sup> and substituted sulfenamides<sup>10</sup> have been developed. These reagents were designed to be good nucleophiles that easily add to electrophilic aromatic rings and also possess good leaving groups (Figure 2,  $\text{X}=1,2,4\text{-triazole, RS}$ ).

### 2.3 Use of 1,1,1-Trimethylhydrazinium Iodide as a VNS Reagent

Although quaternary hydrazinium compounds have been known for over one hundred years,<sup>11,12</sup> they have not been employed as VNS reagents. We examined 1,1,1-trimethylhydrazinium iodide (TMHI)<sup>13</sup>  $[(\text{CH}_3)_3\text{N}^+-\text{NH}_2 \text{ I}^-]$  for use as a VNS reagent. We reasoned that TMHI would be sufficiently nucleophilic to substitute into nitro-substituted aromatic rings but would be superior to the previous examples because the leaving group would be the neutral trimethylamine instead of a stabilized anionic species. In addition,

there was a possibility that the hydrazinium halide would react with base to form the neutral ylide species,  $[(CH_3)_3N^+-NH^-]$ , which may be the reactive species in the amination process. Indeed, when TMHI was reacted with various nitro-substituted aromatics the amino functionality was introduced in good to excellent yields.

A study of product yields and distribution of various 3-substituted nitrobenzene derivatives was performed using TMHI (Figure 3 and Table 1).

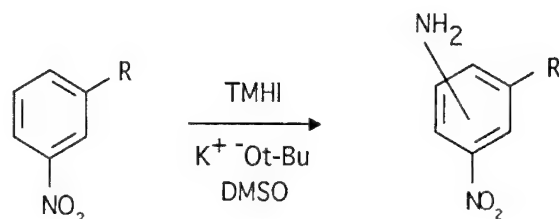


Figure 3. Amination of 3-substituted nitroaromatics

Table I  
Amination of 3-Substituted Nitrobenzenes

R	Total Yield (%)	Position of NH <sub>2</sub> <sup>a</sup>	% Isomer
H	85	2	61
		4	39
CH <sub>3</sub>	84	2	38
		4	35
Cl	82	6	27
		2	32
		4	49
COOH	95	6	19
		4	71
OCH <sub>3</sub>	66	6	29
		2	90
F	84	4	10
		2	45
		4	47
I	76	6	8
		2	45
		4	38
CN	41	6	17
		2	20
		4	44
		6	36

<sup>a</sup> Relative to NO<sub>2</sub>

The results of our study were compared with the findings reported for 4-amino-1,2,4-triazole (ATZ).<sup>9</sup> ATZ was found to be regioselective, giving substitution para- to the nitro group exclusively. TMHI gave all possible product isomers thereby showing no selectivity but presumably greater reactivity. There was a general tendency for TMHI to yield products in which the amine substitution occurs predominantly ortho- to the nitro group although some exceptions were noted.<sup>14</sup> We are currently investigating the use of more sterically crowded 1,1,1-trialkylhydrazinium halides derived from UDMH in an attempt to influence the regioselectivity of the aminating reagent.

## 2.4 Starting Materials for TATB Synthesis

This project originally began as part of demilitarization activities related to the chemical conversion of energetic materials into higher value products.<sup>15,16</sup> Consequently, our synthesis of TATB has been designed so

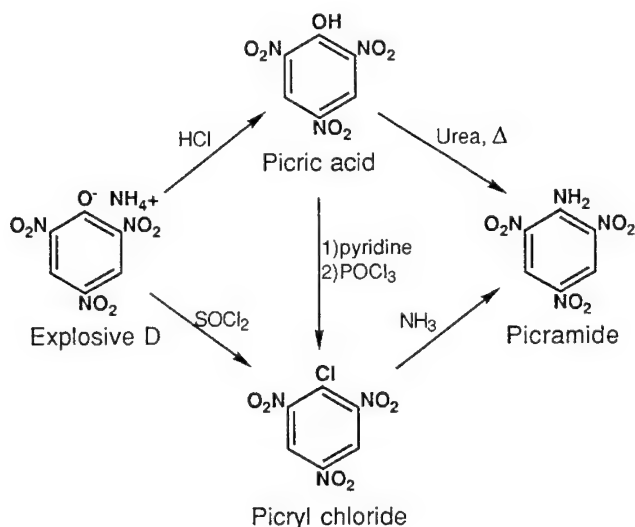


Figure 4. Synthesis of picramide from Explosive D

that either surplus energetic materials or inexpensive, commercially available chemicals can be used to make the necessary starting materials. Several million pounds of ammonium picrate (Explosive D) are available for disposal in the USA. Ammonium picrate can be converted to 2,4,6-trinitroaniline (picramide) by the pathways shown in Figure 4. The reaction of picric acid with urea at elevated temperature (173 °C) has been reported to provide picramide in 88% yield.<sup>17</sup> The analogous reaction of Explosive D

with urea to directly provide picramide has not been reported. Picramide is also readily accessible from nitration of the commercially available and relatively inexpensive 4-nitroaniline.<sup>18</sup>

1,1-Dimethylhydrazine (unsymmetrical dimethylhydrazine, UDMH) has been used as a liquid rocket propellant. Thirty thousand metric tons of UDMH in Russia are available for disposal in a safe and environmentally responsible manner.<sup>19</sup> 1,1,1-Trimethylhydrazinium iodide (TMHI), our VNS reagent of choice, is readily prepared through the alkylation of UDMH by methyl iodide.<sup>20</sup> Alternatively, TMHI can be prepared directly from hydrazine and methyl iodide.<sup>13</sup>

## 2.5 Amination of Picramide by Hydroxylamine Derivatives

We initially explored the conversion of picramide to DATB and TATB using hydroxylamine (Figure 5, R = H) and aqueous base as reported for the conversion of 4,6-dinitrobenzofuroxan (DNBF) to give 5,7-diamino-4,6-dinitrobenzofuroxan (CL-14).<sup>21</sup> DATB was obtained in a low yield (16%) after removal of unreacted picramide.

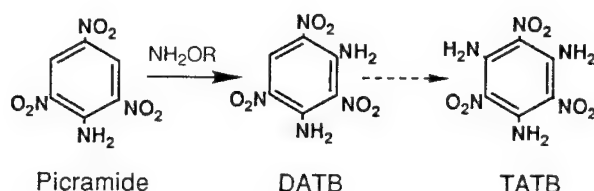
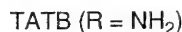


Figure 5. Reaction of picramide with  $\text{NH}_2\text{OR}$  (R = H,  $\text{CH}_3$ ,  $\text{C}_6\text{H}_5\text{CH}_2$ )

The replacement of aqueous base with sodium methoxide in anhydrous methanol or DMSO raised the yield of DATB from 16% to over 50%. The use of alkoxy derivatives (R =  $\text{CH}_3$ ,  $\text{C}_6\text{H}_5\text{CH}_2$ ) gave exclusively DATB in 87-91% crude yields. The reaction of picramide with hydroxylamine or its O-alkyl derivatives never yielded more than trace quantities of TATB.

## 2.6 Amination of Picramide by ATZ

Picramide reacts with 4-amino-1,2,4-triazole (ATZ) in dimethylsulfoxide in the presence of strong base (NaOMe or  $\text{KOt-Bu}$ ) at room temperature (24 h) to yield, depending on the quantity of ATZ used, either DATB or TATB and 1,2,4-triazole (TZ) (Figure 6).



## 2.7 Amination of Picramide by TMHI

$$\begin{array}{ccccccc}
 \text{O}_2\text{N} & & \text{NH}_2 & & \text{NO}_2 & & \\
 | & & | & & | & & \\
 \text{C}_6\text{H}_2 & + & \text{CH}_3\text{-N}^+\text{(CH}_3)_3\text{-NH}_2\text{ } \Gamma^- & \xrightarrow[\text{DMSO}]{\text{NaOCH}_3} & \text{O}_2\text{N} & & \text{NH}_2 & & \text{NO}_2 & & \text{CH}_3\text{-N}^+\text{(CH}_3)_3 & + & \text{CH}_3\text{-N}^+\text{(CH}_3)_3\text{ } \Gamma^- \\
 | & & | & & | & & | & & | & & | & & | \\
 \text{NO}_2 & & & & \text{H}_2\text{N} & & \text{NO}_2 & & \text{R} & & & & \\
 | & & & & | & & | & & & & & & \\
 \text{NO}_2 & & & & \text{NO}_2 & & & & & & & & \\
 \text{Picramide} & & \text{TMHI} & & \text{DATB (R = H)} & & \text{TMA} & & & & & & \\
 & & & & \text{TATB (R = NH}_2\text{)} & & & & & & & & 
 \end{array}$$
$$\begin{array}{ccccccc} \begin{array}{c} \text{CH}_3 \\ | \\ \text{CH}_3-\text{N} \\ | \\ \text{CH}_3 \end{array} & + & \text{Cl}-\text{NH}_2 & \longrightarrow & \begin{array}{c} \text{CH}_3 \\ | \\ \text{CH}_3-\text{N}^+-\text{NH}_2 \\ | \\ \text{CH}_3 \end{array} \text{Cl}^- & \xrightarrow{\text{HI}} & \begin{array}{c} \text{CH}_3 \\ | \\ \text{CH}_3-\text{N}^+-\text{NH}_2 \\ | \\ \text{CH}_3 \end{array} \text{I}^- \\ \text{TMA} & & & & \text{TMHCl} & & \text{TMHI} \end{array}$$

195

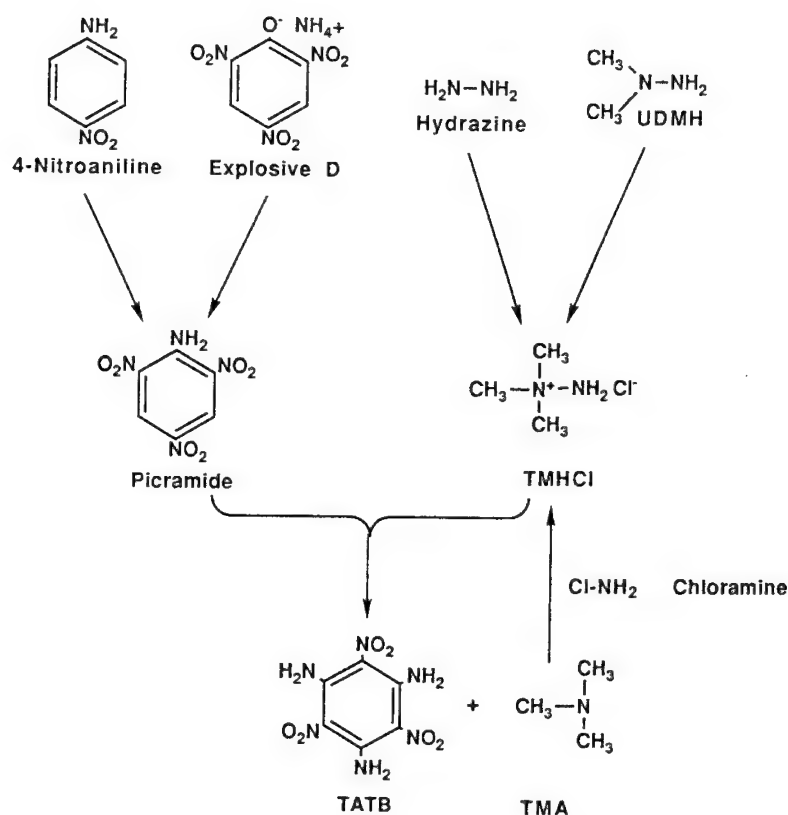


Figure 9. Synthesis of TATB from inexpensive starting materials.

bench to pilot plant is outlined in Figure 9. The starting materials are relatively inexpensive and can be obtained from demilitarization programs (Explosive D, UDMH) or commercial sources (4-nitroaniline, hydrazine). We have eliminated the use of chlorinated arenes in response to environmental concerns and will recycle solvents and materials whenever possible.<sup>23</sup> Trimethylamine (TMA), a noxious and moderately toxic gas (bp 3 °C) released during the VNS reaction, will be reacted with chloramine to regenerate the TMHCl consumed in the synthesis of TATB.

### 3. Summary and Conclusions

We have described the use of a surplus rocket propellant (UDMH) to prepare TMHl, a novel and highly reactive VNS aminating reagent. TMHl allows the direct amination of nitroarenes. We have developed a new and improved synthesis of TATB using TMHl and relatively inexpensive starting materials. We are currently investigating the use of TMHl and other quaternary



hydrazinium compounds derived from UDMH to prepare new energetic materials useful for military and civilian applications.

#### 4. Acknowledgement

This work was performed under the auspices of the U.S. Department of Energy by Lawrence Livermore National Laboratory under Contract No. W-7405-ENG-48.

#### 5. References

1. Rice, S.F. and Simpson, R.L., "The Unusual Stability of TATB: A Review of the Scientific Literature", Lawrence Livermore National Laboratory, Livermore, CA, Report UCRL-LR-103683, 1990.
2. Simpson, R.L., Energetic Materials Center, Lawrence Livermore National Laboratory, personal communication.
3. Benziger, T.M., "Manufacture of Triaminotrinitrobenzene," in *Chemical and Mechanical Technologies of Propellants and Explosives, Proc. 1981 Intl. Annual Conference of ICT*, Karlsruhe, Germany, 1981, 491-503.
4. Benziger, T.M., *Method for the Production of High-Purity Triamino-trinitrobenzene*, U. S. Patent No. 4,032,377, 1977.
5. Yasuda, S. K., "Identification of 1,3,5-Triamino-2,4,6-trinitrobenzene Impurities by Two-Dimensional Thin-Layer Chromatography," *J. Chromatogr.*, 71, 481-486, 1972.
6. Makosza, M. and Winiarski, J., "Vicarious Nucleophilic Substitution of Hydrogen," *Acc. Chem. Res.*, 20, 282-289, 1987.
7. Chupakhin, O. N., Charushin, V. N. and van der Plas, H. C., *Nucleophilic Aromatic Substitution of Hydrogen*, Academic Press, San Diego, CA, 1994, 59-66.
8. Meisenheimer, J. and Patzig, E., "Directe Einführung von Aminogruppen in den Kern aromatischer Körper", *Ber.*, 39, 2533-2542, 1906.
9. Katritzky, A.R. and Lorenzo, K. S., "Direct Amination of Nitrobenzenes by Vicarious Nucleophilic Substitution," *J. Org. Chem.*, 51, 5039-5040, 1986.
10. Makosza, M. and Bialecki, M., "Amination of Nitroarenes with Sulfenamides via Vicarious Nucleophilic Substitution of Hydrogen," *J. Org. Chem.*, 57, 4784-4785, 1992.
11. Fischer, E., "Über aromatische Hydrazinverbindungen," *Ber.*, 9, 880-891, 1876.
12. Sisler, H. H. and Omietanski, G., "The Chemistry of Quaternized Hydrazine Compounds," *Chem. Rev.*, 57, 1021-1047, 1957.
13. Harries, C. and Haga, T., "Über die Methylierung des Hydrazinhydrats," *Ber.*, 31, 56-64, 1898.

14. Pagoria, P. F., Mitchell, A. R. and Schmidt, R. D., "1,1,1-Trimethylhydrazinium Iodide (TMHI): A Novel, Highly Reactive Reagent for Aromatic Amination via Vicarious Nucleophilic Substitution (VNS)", *J. Org. Chem.*, 61, 2934-2935, 1996.
15. Pruneda, C. O. , Mitchell, A. R. and Humphrey, J., "Reusing the High Explosives from Dismantled Nuclear Weapons," *Energy and Technology Review*, Lawrence Livermore National Laboratory, Livermore, CA, UCRL-52000-93-11-12, 19-26, 1993.
16. Mitchell, A. R. and Sanner, R. D., "Chemical Conversion of Energetic Materials to Higher Value Products," in *Energetic Materials- Insensitivity and Environmental Awareness, Proc. 24th Intl. Annual Conference of ICT*, edited by Ebeling, H., Karlsruhe, Germany, 1993, 38:1-38:6.
17. Spencer, E. Y. and Wright, G. F., "Preparation of Picramide," *Can. J. Research*, 24B, 204-207, 1946.
18. Holleman, A. F., "1,3,4,5-Tetranitrobenzene," *Rec. trav. chim.*, 49, 112-120, 1930.
19. *Chemical and Engineering News*, May 8, 1995, p.21.
20. Westphal, O., "Über die Alkylierung des Hydrazins," *Ber.*, Vol. 74, 759-776, 1941.
21. Norris, W. P. and Chafin, A. P., "CL-14, A New Dense, Insensitive, High Explosive," Naval Weapons Center, China Lake, CA, NWC TP 6597 (publication UNCLASSIFIED), 1985.
22. Omietanski, G. M. and Sisler, H. H., "The Reaction of Chloramine with Tertiary Amines. 1,1,1-Trisubstituted Hydrazinium Salts," *J. Am. Chem. Soc.*, 78, 1211-1213, 1956.
23. Graedel, T. E. and Allenby, B. R., *Industrial Ecology*, Prentice Hall, Englewood Cliffs, NJ, 1995.

## **RECYCLING PROPELLANTS AND EXPLOSIVES INTO THE COMMERCIAL EXPLOSIVE INDUSTRY**

**Mark E. Morgan and Paul L. Miller**

Global Environmental Solutions, Alliant Techsystems Operation  
4100 South 8400 West, Annex 16, Magna, Utah 84044, USA

**ABSTRACT:** As part of environmentally safe recycling of unwanted ordnance, the commercial blasting industry is a significant potential user of recovered energetic materials. This industry utilizes significant quantities of explosive materials on an annual basis and can easily become an even larger consumer of military energetics if their requirements are properly addressed. Significant quantities of solid rocket motor propellant are about to emerge in the world market as a product requiring recycling. The commercial explosive market is a willing consumer of these materials, albeit at a very low price. The majority of the world's supply of solid propellants contain high value explosives, fuels and oxidizers. A challenge for the technical community is to develop products or processes that can return higher values because of the constituent propellant ingredients.

### **BACKGROUND**

Alliant Techsystems and Global Environmental Solutions (GES) are world leaders in both the manufacture of conventional ordnance and in the environmentally safe conversion of military materials into civilian uses. Our commercial efforts in the Former Soviet Union (FSU) have been showcase operations demonstrating that environmentally safe conversion of military ordnance is not only possible, but, based on reclamation values alone, can be economically profitable. Our commercial efforts in the FSU are internally funded and not funded by the U.S. government.

Global Environmental Solutions has been a driving force in the development of high-pressure fluids for energetics removal and the safe conversion of explosive ordnance. Our independent research performed in 1991-1992 demonstrated that high-pressure fluids could be controlled to safely cut explosives ranging from PETN to TNT at pressures of up to one gigapascal (147,000 psig). The results of testing on the first 178,000 high-explosive projectiles were presented to the United States Department of Defense Explosive Safety Board (DDESB) in the summer of 1992. Since then GES recycling efforts have expanded significantly so that we currently count in metric tons rather than individual units.

Current Recycling operations are centered in two major facilities located in the countries of Belarus and Ukraine. From these operations GES is processing large caliber artillery rounds through joint ventures with these two nations' governments. The operations are reclaiming valuable metals, such as brass, copper, and steel from the unexpended ordnance. Even more important for environmental considerations is conversion of the recovered propellants and high explosives for use in Belarus' and

Ukraine's commercial blasting industries. These recycling efforts have been very successful on the pilot scale and are transitioning to full-scale production. Within three years over 5000 metric tons of propellant have been converted into commercial mining explosive. These activities have been a substantial benefit for Belarus' and Ukraine's mining industry. The net results of these munition conversion efforts include:

- an environmentally safe conversion of excess and obsolete munitions
- employment for countries converting their military to market economy businesses
- an improved mining product to improve production yields
- a profitable revenue for all participants

Facilities in the Ukraine and Belarus each have the capability of processing approximately 25 metric tons of TNT per day while recycling nearly all of the water used in the Fluidjet washout systems. The remaining water is lost through evaporation or as water taken out with the explosives. The explosive is then de-watered and processed for use in the local commercial blasting industry. As a basis for the comparison of the production line's size, TNT manufacturing lines<sup>1</sup> in the United States during the Second World War were rated at only 59 metric tons per day.

Global Environmental Solutions' experiences in the FSU and research and experience in the United States converting nitrocellulose propellants and high explosives into commercial explosives have allowed the following observations:

#### **Historical Perspective on Conversion of Smokeless Powders and High Explosives for Commercial Mining**

The use of smokeless powders, high explosives and propellants for commercial blasting goes back at least 30 years to the major expansion efforts on the Mesabi and Vermilion iron ore deposits of northern Minnesota.

Post-World War II availability of propellants and explosive materials allowed entrepreneurial blasters to mix differing proportions of propellants and explosive materials with oxidizers and blending agents to form high grade blasting slurries that could outperform either dynamite or ammonium nitrate/fuel oil (ANFO).

The early 1960s saw a tremendous rise in the use of government surplus smokeless powders being used in the manufacture of slurried explosives. Both single based and double based propellants were extensively used by the entrepreneurial explosive companies to gain market advantage over established explosive industries. Today most all of the explosives used in mining are variations on ANFO, slurries and, most recently, emulsions. The use of smokeless powder and high explosives in slurries diminished during the mid-1960s. As government surplus supplies diminished, the cost of the materials became uneconomical compared to other materials.

The mixtures of fuels, oxidizers and additives that can make an effective slurry explosive are almost infinite. An amazing amount of historical data exists on the use of surplus smokeless powders, high explosives and rocket fuels for use in the formation of commercial explosives. A brief compilation of mixes is given in Table I.

TABLE 1  
Common Explosive Mixtures Using Surplus Energetic Materials

Designation	Sensitizer	Water
Slurry Exp. - TNT	17 to 60% TNT	8 to 40%
Slurry Exp. - Comp B	15 to 35% Comp B	12 to 16%
Slurry Exp. - Single Base	20 to 60% SB Prop.	2 to 20%
Slurry Exp. - Dbl Base	20 to 60% Dbl Base	2 to 20%
Slurry Exp. - TNT/Al	5-25/0.5-40% TNT/Al	10 to 30%
Slurry Exp. - Propellant/Al	10-25/1-40 Prop./Al	12 to 30%
Zernogranulite 50/50V <sup>3</sup>	50% TNT	
Zernogranulite 30/70V	70% TNT	
Akvatol 65/356	27 to 30% TNT	
Akvatol M-15	21 to 22% TNT	

Since Global Environmental Solutions' goals are for an environmentally safe and yet profitable solution to the demilitarization of conventional weapons, the recycling of the salvaged smokeless powders and high explosives into commercial mining explosives is an ideal fit. The FSU has been willing to experiment with a small tonnage of material that has been recycled and have found these mixes ideal for use in their aboveground quarrying industry. The use of quarries for test shots to evaluate explosive materials is identical to the process that the Bureau of Mines follows in the United States.

The result of testing in the FSU is that the recycled energetic materials can substantially improve mining industry's efforts to become profitable. Since slurry explosives use up to 30% explosive and up to 20% water, ammonium nitrate supplies can be stretched to make about twice the amount of mining explosives than they previously had. One of the more interesting items of our research to date is the need for larger explosive particle sizes for successful slurry explosives. This was especially beneficial as it is both easier and safer to process energetic materials to coarse pellets than to fine powders.

#### **Current Problems with the Conversion of Smokeless Powders and High Explosives for Commercial Mining in the United States**

Several barriers exist in the United States that inhibit the use of recycled propellants and explosives into the commercial mining industry. First, the reclaimed energetic materials cannot be economically used if the EPA identifies them as hazardous waste. If the material is considered a hazardous waste, the burden of regulatory compliance far outweighs any cost benefit that could be realized through recycling. The second major issue is that even minor changes in propellant feedstock technically identifies the blended slurry material as a "new" explosive requiring full recertification by the Department of Transportation, both to transport propellant and the subsequent explosive. The third major problem is the lack of adequate quantities of ordnance being released into the demilitarization market to supply sufficient explosive and propellant materials for the consumers. Information from the explosives market, indicates that the typical explosive blender would need to be able to contract for at least 1.6 million pounds of smokeless powder a year. Current U.S. government demilitarization

policies and practices are not making these quantities of energetic material available to the industrial base.

### **International Efforts to Convert Smokeless Powders and High Explosives to Commercial Mining Products**

In contrast with the problems in the United States, the state committees of the Eastern European countries are working pro-actively to assist efforts to recycle these munition materials into the commercial marketplace. These countries have assisted in coordinating the packaging, transportation and field use of the explosives. Because of this close cooperation, no specific waivers have been required for use of the recycled explosive. In addition to helping eliminate bureaucratic "red-tape," the countries are providing sufficient surplus munition and (soon) rocket motors containing solid propellant.

### **Use of Solid Rocket Motor Propellants in Commercial Explosives**

Work performed in the United States by Slaughter et al<sup>4</sup>, and Gilion of Universal Tech Corporation have shown conclusively that solid rocket motor propellants are an efficient and desirable additive to commercial slurry explosives used by the mining industry. This work shows that solid propellant of various types, when added in the range of 20%-36%, actually increases the performance of the explosive. To date, the primary drawback to exploiting these developments has been an insufficient supply of solid propellant for recycling.

An analysis of the currently available data on solid rocket motors shows that at least 44,000 metric tons of propellant could be available for recycling through the year 2000 (Table 2). Of note in these quantities is that the solid rocket motors listed for Russia and Ukraine comprise only those required to be eliminated by treaty. Not included in Table 2 are the worldwide, non-treaty covered strategic missiles and all worldwide tactical rocket motors outside the United States.

**TABLE 2**  
**Potential Solid Rocket Propellant for Demilitarization**

Country	Quantity (metric tons)
Russian Solid Rockets <sup>5</sup>	25,135
Ukrainian Solid Rockets <sup>5</sup>	5,640
U.S. Solid Rockets <sup>6</sup>	13,073
Total	43,848

Even considering the enormous potential quantity of solid rocket propellant, the worldwide annual consumption of explosives, Table 3, at almost 500,000 metric tons, dwarfs the amount of available solid propellant. Table 3 shows explosives as generic grades, with "grade A" representing a premium quality primary explosive, and "grade F" a bulk commodity commercial explosive such as ANFO. The split between primary and secondary explosives is approximately between grades "C" and "D". Solid rocket propellant could most likely displace a 20%-30% fraction of explosives in grades "E" and "F". Calculating this quantity at 119,250 metric tons, the worldwide commercial explosives industry could easily consume the worldwide stockpile of solid rocket propellant.

TABLE 3 Estimated Worldwide Consumption for Explosives		
Explosive Grade	Estimated Worldwide Consumption per Year (metric tons)	Potential Market Value \$(U.S.)/metric ton
"A"	114	\$28,600
"B"	228	\$11,000
"C"	3,477	\$1,430
"D"	6,136	\$440
"E"	136,000	\$220
"F"	341,000	\$132
TOTAL	486,955	

The positive aspect of this consumption capability is that there is a readily available market, with demonstrated technology, that is able to accept this material. The market is so sizable that full consumption of the solid propellant will not have a negative impact on the business or economics of the explosives industry or suppliers of commodities and chemicals to these explosives companies.

There are negative aspects, however. This ready and willing industry is fiercely competitive! Values paid for solid rocket propellant will, at best, be pennies/kg. In addition, tipping fees may be required if the propellant quantities are not large and in steady supply.

The low value of propellant means that the cost to remove propellant from rocket motor cases will not be covered. This gives no incentive to the governments owning rocket motor assets to stop the environmentally controversial practice of destruction by open burning/open detonation. Additionally, use of the propellant in low value mining products ignores the fact that propellants may have explosive compounds (such as HMX) worth up to \$31,000 (U.S.)/metric ton.

The challenge for solid propulsion industry then becomes finding higher value uses for solid rocket motor propellants. Creative solutions are required, especially those that may lead outside the current bounds of the energetics/explosives industry. The conversion of propellants and explosives from conventional ammunition presents significant challenges even though potentially useful chemical conversions are known. The lure for developing conversion technologies for solid rocket propellants resides in the large quantities of higher value products that are potentially available.

The rewards for successful new ideas to deal with solid rocket propellants will be the ability to encourage governments away from open burning/open detonation, the motivation for the industrial base to capitalize for these processes at production scale, and the more sound economic use of expensive, useful propellant ingredients.

To the commercial explosives industry, do not fear. Ties with the propulsion industry will grow stronger as these assets come into the industrial base for demilitarization. Even the non-valuable propellants an/or residual materials will make good fuel additives to commercial explosives. For a sizable fraction of the rocket motor arsenal the commercial mining industry will be the most logical solution to a pressing problem, and the propulsion industry will be thankful for an industry and products that can consume these propellants.

## CONCLUSIONS

Global Environmental Solutions has demonstrated that the technologies currently exist for the environmentally safe and profitable demilitarization of ordnance, including the conversion of smokeless powders, explosives and solid propellants into commercially desirable mining explosives. Administrative and regulatory issues must be addressed to exploit recycling these materials into North American markets.

## REFERENCES

1. **Kay, S.**, Encyclopedia of Explosives and Related Items, Vol. 9, p. T-236, ARRADCOM, Dover, New Jersey, 1980.
2. **Cook, M.A.**, The Science of Industrial Explosives, p.19, Ireco Chemicals, Salt Lake City, Utah, 1974.
3. **Rossi, B.**, Commercial Explosives and Initiators - A Handbook, Nedra Press, Moscow, 1971.
4. **Slaughter, J.A., Munson, W.O. and Bonner, C.**, The Use of Reclaimed Solid Rocket Propellant in Commercial Explosives, 3rd Global Demil Symposium, American Defense Preparedness Association, pp.357-364, 1995.
5. **START**, Treaty Between the United States of America and the Union of Soviet Socialist Republics on the Reduction and Limitation of Strategic Offensive Arms, 1991.
6. Joint Ordnance Commanders Group Munitions Demil Disposal Subgroup, September 1995, Joint Demilitarization Study, Demil Technology Office, U.S. Army Defense Ammunition Center and School, pp. II 2-8 - II-2-11, 1995.



## PROCESSING OF TRINITROTOLUENE-WATER EMULSIONS FOR RECYCLING

Ulrich Teipel and Horst Krause

Fraunhofer Institut für Chemische Technologie (ICT), D-76318 Pfinztal, Germany

**ABSTRACT:** When disposing of trinitrotoluene (TNT), the TNT-melt must be pretreated. One possibility is to emulsify the melt in water after the TNT has been dismantled from the explosive charge. Production of these emulsions can be accomplished using emulsifying machines based on the rotor-stator principle, e.g., ring gear dispersion machines or colloid mills. Droplet size reduction results from the normal and tangential stresses applied to the droplet as it is subjected to laminar or turbulent flow fields. Knowledge of the droplet size and droplet size distribution of the dispersed phase is important to determine the quality of an emulsion and the emulsification process. In this paper, results from the discontinuous production of TNT-water emulsions are presented. In addition, the use of laser diffraction spectrometry for analyzing TNT droplet size is described.

### 1. INTRODUCTION

When disposing of explosive materials, the dismantled ammunition must be pretreated prior to being chemically transformed (via, e.g., hydration, hydrolysis, combustion, etc.). Pretreatment makes it possible to introduce the treated material continuously into a reactor vessel. In pretreating trinitrotoluene (TNT), the TNT-melt can be emulsified in water after it has been dismantled from the explosive charge. Production of a TNT-water emulsion desensitizes the explosive melt and also increases the specific surface area of the explosive phase, resulting in improved kinetics of the subsequent decomposition reactions. In addition, producing an emulsion allows one to control more effectively the material's rheological behavior compared to the pure explosive melt.<sup>1,2</sup> For characterizing an emulsion and the emulsification process, besides the process variables, the most important quantities to measure are the droplet size and droplet size distribution of the emulsion.

### 2. FUNDAMENTALS

Emulsions are multiple-phase disperse systems consisting of at least two immiscible fluids. The dispersed phase exists as droplets in the continuous phase. One of the phases is hydrophilic (polar), while the other is hydrophobic (nonpolar), the simplest case being oil in water. Fundamentally, based on the material comprising the dispersed phase, emulsions are differentiated, as either oil-in-water (O/W) or water-in-oil (W/O) emulsions. Dispersed systems in which the dispersed phase consists of droplets that are themselves emulsions are termed polyphasic or multiple emulsions.<sup>3</sup>

Depending on the emulsification technique, the droplet diameter of the dispersed phase ranges from  $0.1 \text{ mm} \leq x \leq 100 \mu\text{m}$ . These materials, termed macroemulsions, are thermodynamically unstable, i.e., due to the surface energy between the two phases, the surface area of the dispersed phase will tend toward a minimum, resulting in coalescence of the droplets. The ultimate result may be sedimentation or bulk separation of the two phases due to density differences between the two fluids. This is termed instability.

An emulsion is considered stable if the distribution of the dispersed phase remains constant over a given time period, i.e. there is no change in the droplet size distribution and no development of gradients in the dispersed phase distribution. The duration of the time period depends on the particular application in question.

Another type of emulsion is the micro or colloidal emulsion which has a very low interfacial energy between the dispersed and continuous phase. These emulsions can therefore be produced using very low mechanical energy. The average droplet size of these extremely stable emulsions is smaller than  $0.1 \mu\text{m}$ .

### 3. PROCESSING OF EMULSIONS

When processing emulsions, the oil, water and emulsifying agent are premixed prior to emulsification. Through mechanical agitation (mixing or stirring) the inner phase is dispersed to form a coarse emulsion. During subsequent emulsification, shear and normal stresses deform the coarse droplets and, when a critical deformation is exceeded, the droplets break-up.

#### 3.1 Emulsifying Machines

A wide variety of different emulsifiers are available for making emulsions. Among the most important, in particular with respect to the emulsification of explosive materials, are stirring devices and rotor-stator systems, such as ring gear dispersion machines and colloid mills.

*Ring gear dispersion machines.* Ring gear dispersion machines have a rotor and stator that are both slit, with the rotor turning at a high rate. The coarse emulsion is introduced into the center of the rotor-stator system and is dispersed in the radial direction. Because the fluid is centrifugally accelerated by the rotor motion, this type of dispersion machine also functions as a pump. The disruption of the droplets is primarily achieved by turbulence.

*Colloid mills.* In colloid mills, the dispersed phase is primarily broken up through shearing in the conical annular gap between the rotor and the stator. As the coarse emulsion enters the colloid mill, it is accelerated in the circumferential direction by the rotor. This tangential shear flow (Couette flow) is combined with an axial pipe flow (Hagen-Poiseuille flow). There are currently no results on how effective this combination of flows is in breaking up droplets.

Axial adjustment of the rotor and stator can be used to vary the gap width and, in turn, the residence time and intensity of the deformation field in the gap. To obtain an emulsion with a narrow possible droplet size distribution, the energy density of mechanical energy must be as uniform as possible within the gap.

#### 4. DROPLET SIZE ANALYSIS

Knowledge of the droplet size and droplet size distribution of the dispersed phase is important to determine the quality of an emulsion. A variety of different techniques are available for determining the particle or droplet size and size distribution of the disperse phase. These techniques differ not only in their physical principles, but also in their measuring capacity. In this paper, the use of laser diffraction spectrometry is described. In this method, particle size information is obtained by measuring the laser beam's diffusion as a result of its interaction with suspended particles.

##### 4.1 Laser Diffraction Spectrometry

The scattered light beam resulting from a particle's interaction with a light source can be characterized with a quantity called the "Mie-parameter,"  $\alpha$ .

$$\alpha = \frac{\pi \cdot x}{\lambda} \quad (1)$$

The scattering behavior can be categorized into the following ranges, based on the wavelength of the light  $\lambda$  and the particle diameter  $x$ :

$\alpha \ll 1$	Rayleigh scattering
$0.1 < \alpha < 10$	Mie scattering
$\alpha \gg 1$	Fraunhofer scattering

Rayleigh scattering is characterized by symmetry in the scattered light, i.e., light is scattered equally in the forward and reverse directions. Because of the scattering symmetry, particle size analysis cannot be performed in the Rayleigh regime.

In the Mie range, size analysis is possible for particles larger than 0.1  $\mu\text{m}$ . As the Mie-parameter  $\alpha$  increases, light scattered in the forward direction increases in intensity, while the intensity of the back-scattered light decreases.

When beam optics is valid ( $\alpha \gg 1$ ), particle size analysis via scattering is straightforward. The narrowest region of forward scattering ( $\phi \rightarrow 0$ ) is primarily determined by diffraction. Contributions from scattering due to refraction and reflection are negligible. In this region, the diffraction is nearly identical to that which occurs when light interacts with a disk (also known as Fraunhofer diffraction).<sup>4</sup>

Laser diffraction spectrometers are available for measuring particle sizes from 0.1 to 2000  $\mu\text{m}$ . The measurement range using a single detector can be set by varying its focal length. Figure 1 shows the schematic of a laser diffraction particle sizing instrument.

The device consists of a He-Ne laser that transmits at a wavelength  $\lambda = 632.8 \text{ nm}$  and a receiver that contains an optical imaging system and detector electronics. In measuring emulsions and suspensions, the expanded parallel light beam is directed at a cuvette through which the dispersion flows. Light diffracted from the particles or droplets forms a radial symmetric Fraunhofer diffraction pattern on the semi-circular detector. For spherical particles, this diffraction pattern consists of concentric, alternating light and dark rings (diffraction rings) with a bright circle in the center.

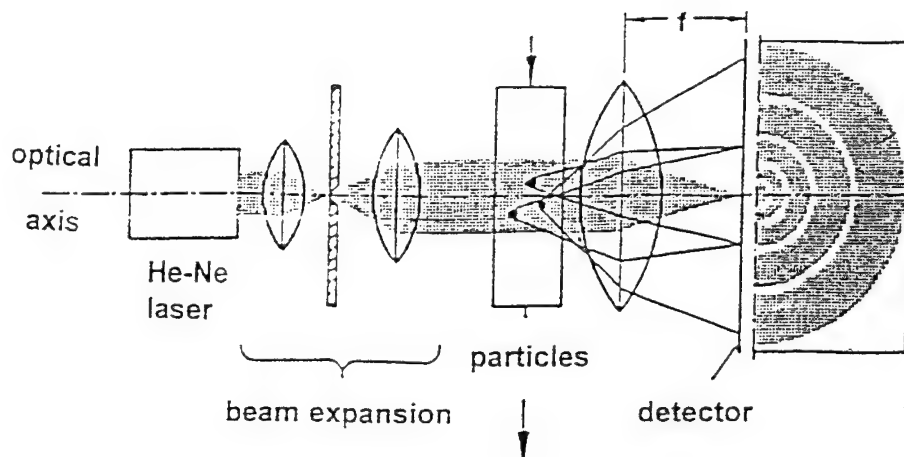


Figure 1. Schematic of a laser diffraction particle sizing instrument

Equation 2 describes the intensity distribution of the diffraction pattern  $I(r,x)$  as a function of particle diameter  $x$  and the radial distance  $r$  to the optical axis.

$$I(r, x) = I_0 \cdot \left( \frac{\pi x^2}{4\lambda f} \right)^2 \cdot \left( \frac{2J_1 \left( \frac{\pi x r}{\lambda f} \right)}{\left( \frac{\pi x r}{\lambda f} \right)} \right) \quad (2)$$

Here,  $f$  is the focal length and  $J_1$  is the Bessel function of first art and first order.

Measurement of a collection of particles results in additive overlapping of the scattered light intensity from each individual particle. The particle size distribution can be calculated from the measured intensity distribution of the scattered light.<sup>5</sup> A major advantage of laser diffraction spectrometry is the relatively short measurement time required compared to non-optical techniques.

## 5. EXPERIMENTAL AND RESULTS

The trinitrotoluene-water emulsions described here were produced in a discontinuous emulsifier illustrated in Figure 2. Following pre-emulsification with a stirrer, which produced a droplet size from 80 to 150  $\mu$ , the emulsion was introduced into a ring gear dispersion unit for fine emulsification. This unit had a rotor with a diameter  $d = 16$  mm and a gap width  $s$  of 0.8 mm. The rotor rotation rate was variable between 5000 and 18000 rpm. Temperature control was achieved using a double-walled agitated tank fitted with a thermostat. The particle size distribution of the TNT-droplets was determined via laser diffraction spectrometry as described in section 4.1. The spectrometer was equipped with a dispersion unit as well as an electrical heating system.

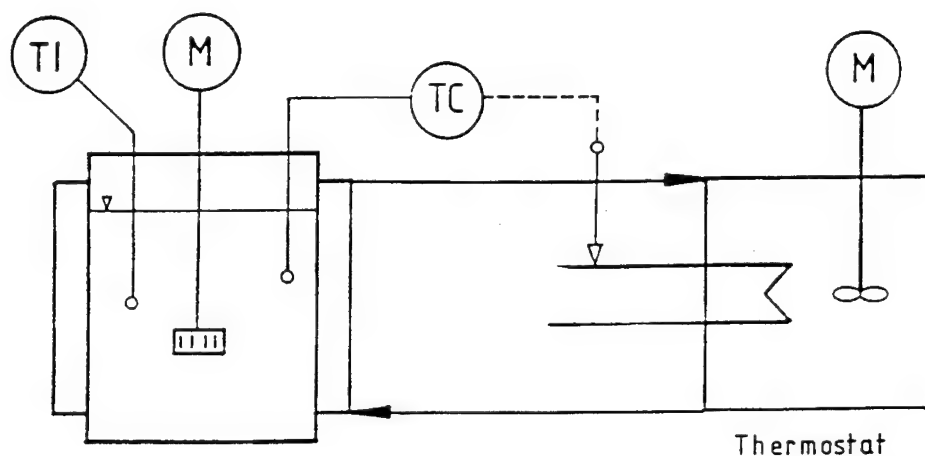


Figure 2. Discontinuous emulsification machine

Because 2,4,6 trinitrotoluene has a melt temperature  $v_m$  of approximately  $80^\circ\text{C}$ , the temperature used for producing and characterizing the TNT-water emulsion was always greater than  $80^\circ\text{C}$ .

A qualitative assessment of the emulsion's stability was obtained through sedimentation experiments as well as cooling experiments, in which the temperature of the agitated tank was continuously lowered. The cooling experiments showed that a TNT-water emulsion with an initial temperature of  $85^\circ\text{C}$  remained fluid down to  $\sim 75^\circ\text{C}$ , using a moderate cooling rate of  $dv/dt = -0.5^\circ\text{C}/\text{min}$ . At this temperature, the TNT droplets began to sediment, due to their higher density compared to water. At  $v = 70^\circ\text{C}$ , TNT crystals (needles) form beginning at the free surface, and finally at  $v \cong 60^\circ\text{C}$  all of the TNT exists in solid form.

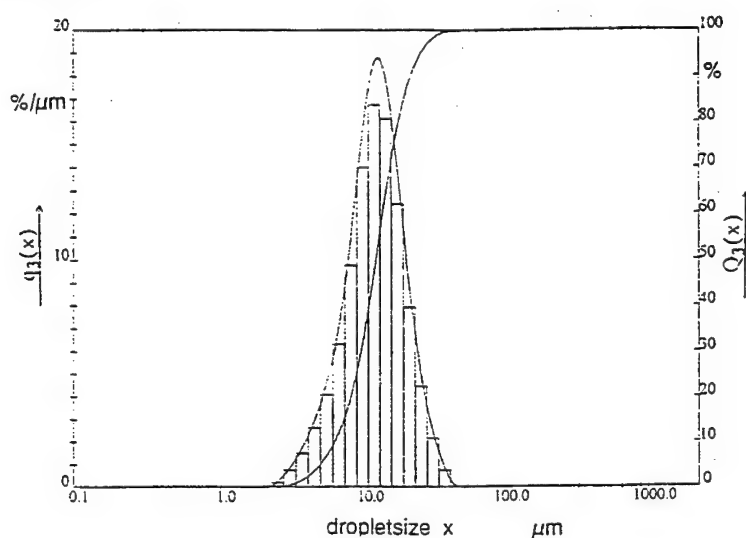


Figure 3. Droplet size distribution of a TNT-water emulsion

The sedimentation experiments showed that at  $v_m = 85^\circ\text{C}$ , approximately 10 volume percent of the dispersed phase had sedimented within 10 minutes. After 20-25 minutes a sedimentation layer consisting of approximately 20% of the TNT had formed at the bottom of the agitated tank. In the TNT-concentration range examined (from 5 to 25 weight percent), there was no difference in the sedimentation behavior resulting from restricted motion of the droplets.

Figure 3 shows an example of the droplet size characterization of a TNT-water emulsion using laser diffraction spectrometry. The volume sum distribution  $Q_3(x)$  and the volume density distribution  $q_3(x)$  are plotted for an emulsion with a TNT concentration of 20 wt. percent that was manufactured using a rotor speed of 10000 rpm and an emulsification time  $\Delta t = 180$  s. The median droplet size  $x_{50,3}$  was  $11.45\text{ }\mu\text{m}$ , and the mean diameter  $\bar{x}$  was  $10.03\text{ }\mu\text{m}$ .

The following set of experiments was conducted to determine the parameters and operating conditions that are most effective in achieving small droplet size in a discontinuous emulsion process. The influence of these parameters and operating conditions on the ultimate droplet size distribution were also examined. At a constant rotation rate  $n$  of 12000 rpm, the final droplet diameter was measured as a function of emulsification time. It is shown in Figure 4 that the droplet size does not significantly change for emulsification times greater than 90 s. The droplet size approaches an asymptotic value of 3 to 5  $\mu\text{m}$ .

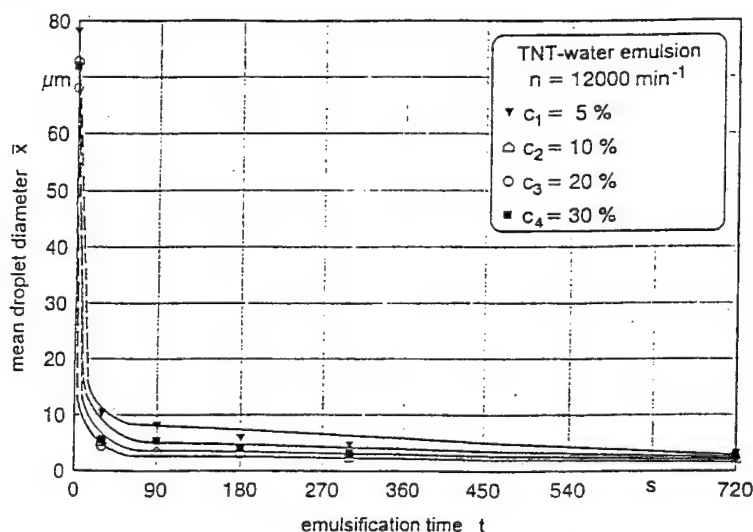


Figure 4. Mean droplet diameter as a function of emulsification time

The dependence of the droplet size on TNT concentration is shown in Figure 5 for three different rotation rates. There is no significant concentration dependence over the range from 5 to 30 weight percent TNT.

The dependence of the droplet size on the Reynolds number in the annular gap is shown in Fig. 6. Assuming simple Couette flow, the Reynolds number in the gap can be calculated as follows:

$$\text{Re} = \frac{\rho_k \cdot \pi \cdot D_R \cdot n \cdot s}{\eta_k} \quad (3)$$

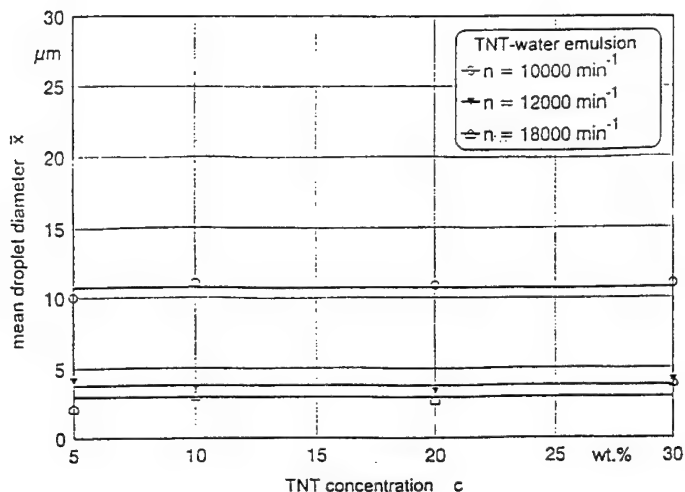


Figure 5. Mean droplet diameter as a function of TNT concentration

It is clear from Fig. 6 that smaller drop sizes are obtained as the Reynolds number increases. The size approaches a limiting value of  $\bar{x} = 3 \mu\text{m}$ . At smaller values of the Reynolds number (i.e., a given machine geometry and given material, dispersed at lower rotation rates) the average droplet diameter for this system (TNT-water) is 20-25  $\mu\text{m}$ .

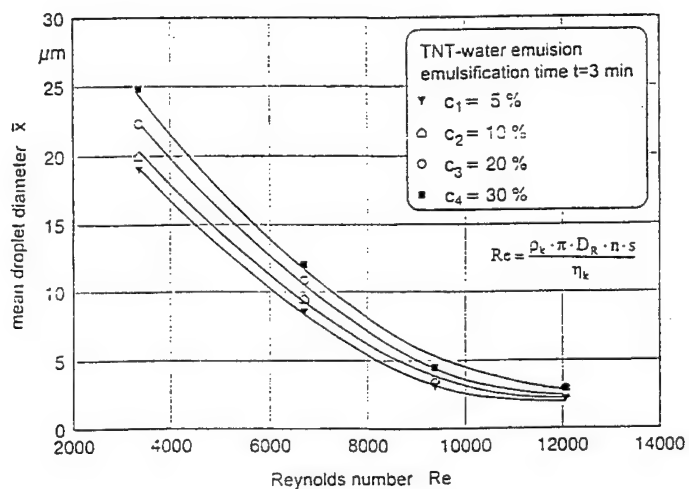


Figure 6. Mean droplet diameter as a function of Reynolds number

From the results shown in these Figures, it is concluded that ring gear dispersion units can be used to manufacture TNT-water emulsions with an optimum droplet size for subsequent disposal in chemical reactions such as hydration or hydrolysis.

## 6. REFERENCES

1. **Teipel, U. and Löffler, F.**, Aufbereitung von Explosivstoffschmelzen durch Emulsionsherstellung am Beispiel Trinitrotoluol-Wasser, *Proc. 23rd Intern. Annual Conference of ICT*, Karlsruhe, 1992.
2. **Teipel, U.**, Processing of Emulsions of Explosive Melt, *Propellants, Explosives, Pyrotechnics*, 17, 214-217, 1992.
3. **Becher, P.**, Encyclopedia of Emulsion Technology, Vol.1, Marcel Dekker Inc., New York, Basel, 1983.
4. **Kerker, M.**, The Scattering of Light, Academic Press, New York and London, 1969.
5. **Heuer, M. and Leschonski, K.**, Results obtained with a New Instrument for the Measurement of Particle Size Distributions from Diffraction Patterns, *Part. Charact.*, 2, 7-13, 1985.



## PILOT-SCALE BASE HYDROLYSIS PROCESSING OF HMX-BASED PLASTIC-BONDED EXPLOSIVES

R.L. Flesner, P.C. Dell'Orco, T. Spontarelli, R.L. Bishop, C.B. Skidmore, K. Uher, and J.F. Kramer

Explosives Technology and Safety, Los Alamos National Laboratory, Los Alamos, NM 87545

**ABSTRACT:** Los Alamos National Laboratory has demonstrated that many energetic materials can be rendered non-energetic via reaction with sodium hydroxide or ammonia. This process is known as base hydrolysis. A pilot scale reactor has been developed to process up to 20 kg of plastic bonded explosive in a single batch operation. In this report, we discuss the design and operation of the pilot scale reactor for the processing of PBX 9404, a standard Department of Energy plastic bonded explosive containing HMX and nitrocellulose. Products from base hydrolysis, although non-energetic, still require additional processing before release to the environment. Decomposition products, destruction efficiencies, and rates of reaction for base hydrolysis will be presented. Hydrothermal processing, previously known as supercritical water oxidation, has been proposed for converting organic products from hydrolysis to carbon dioxide, nitrogen, and nitrous oxide. Base hydrolysis in combination with hydrothermal processing may yield a viable alternative to open burning/open detonation for destruction of many energetic materials.

## INTRODUCTION

### Bench and Pilot-Scale Base Hydrolysis of HMX Based Explosives

The safe disposal of excess high explosives has become increasingly important in recent years due to the disassembly of large quantities of Cold War munitions. Thus far, the primary disposition of waste high explosives has been open burning/open detonation (OB/OD). Due to noise concerns and the dispersion of undesirable burning products, OB/OD has recently fallen out of favor with state and federal regulatory agencies. This has prompted the development of safe and environmentally benign disposal alternatives. One high explosive disposal alternative being developed in parallel by industry and Los Alamos National Laboratory is base hydrolysis.

Base hydrolysis is a process whereby explosives are reacted with concentrated base solutions (1-8 M) at elevated temperatures (80°C to 150°C) to produce non-energetic, water soluble reaction products. At temperatures above the normal solution boiling point, the process is carried out in pressurized reactors. Bases used include sodium hydroxide, potassium hydroxide, ammonium hydroxide, and sodium carbonate; although water is the most commonly used solvent, other solvents (i.e., ethanol, DMSO) may be used neat or in combination with water to reduce mass transfer resistances to reaction. Several different reaction paths occur in the hydrolysis process, including hydrolysis, oxidation/reduction, and substitution/elimination. These reaction paths produce a product stream which largely consists of simple carboxylic acids, amines, sodium salts, ammonia, and gaseous nitrogen/nitrous oxide. In general, hydrolysis reactions consist of parallel mass transfer and reaction kinetic steps; the temperature, pressure, and solvent combination determine whether mass transfer or reaction kinetics is the rate limiting step.

A variety of explosives has been successfully treated using base hydrolysis.<sup>1</sup> Both nitramines and nitroaromatics are converted to water soluble, non-energetic products. When high volume loadings of base-resistant binders are present in a formulation, solvents generally have to be added to swell the binder, thus allowing base access to the high explosive. In addition to bulk explosives, base hydrolysis has also been shown to be effective in regenerating explosive-laden activated carbon,<sup>2</sup> and in treating HE contaminated rags and soils.

Base hydrolysis has been successfully transitioned to large scale operations. Currently, two large-scale units are scheduled for implementation later this year at Eglin Air Force Base and the Pantex Plant in Amarillo, Texas. An ammonia-based hydrolysis process is operational at Thiokol to treat CYH rocket propellant.<sup>3</sup> In addition, Chemical Systems Division, a propellant manufacturer in northern California, is currently using base hydrolysis to destroy some of their waste energetic materials.<sup>4</sup>

The objective of this paper is to summarize research efforts in the base hydrolysis of HMX formulations at Los Alamos National Laboratory (LANL). Research at LANL has been primarily focused on PBX's from Department of Energy dismantlement programs. Specifically, we have focused on PBX 9404, a 94% HMX composition. Both bench and pilot-scale studies have been conducted, with the purpose of developing a prototype reactor for use at the DOE's dismantlement plant at Amarillo, Texas. Atmospheric and pressurized hydrolysis processes have been evaluated in the laboratory. Results from the testing of a pilot-scale atmospheric hydrolysis reactor for PBX 9404 will be presented here. Ongoing work includes further investigation of mass transfer resistances as a function of temperature, pressure, and base composition, and the development of a pilot-scale pressurized hydrolysis reactor for use in DOE dismantlement activities.

## EXPERIMENTAL METHODS

A pilot-scale batch reactor was constructed for the purpose of hydrolyzing large explosive pieces into water soluble, non-explosive products. PBX 9404 (94% HMX, 3% nitrocellulose binder, 3% chloroethylphosphate plasticizer, and 0.1% diphenylamine (nitrocellulose stabilizer)) was used in this study. Two forms of explosive were studied: molding powder and consolidated charges. Molding powder consisted of small particles or pieces of plastic-covered explosive up to 0.5-1 cm in diameter. Consolidated pieces were manufactured by pressing molding powder in high pressure hydrostatic presses at elevated temperatures.

A stainless steel 55-gallon container was used as the basis of the reactor system. Two 7.5 KW Tempco electric circulation heaters (model # CR3N-4008-4G 7.5) were used to heat the fluid (NaOH, 0.8-1M) up to 90°C. Hydrolysis liquor was circulated through the heaters using a Wilden M-1 stainless steel/Teflon air operated diaphragm pump (model # M1/ST/TF/TF/ST). Hydrolysis liquor was pumped from the bottom of the reactor, into the diaphragm pump, through the heaters, and then back into the sides of the reactor. A schematic of the initial reactor configuration is shown in Figure 1. The flow pattern and design of the reactor were later modified to alleviate solid accumulation problems, as discussed later.

An experiment was initiated by filling the reactor with a base solution. Either molding powder or a consolidated piece were placed in a stainless steel basket inside of the reactor. For the molding powder experiments, only one basket was used. For the first consolidated piece experiment, a cage was used to initially place the explosive inside the reactor. This cage rested on the bottom of the steel basket inside the reactor. In an attempt to increase the mass transfer in the reactor and therefore the overall reaction rate, the steel basket was not used in the second consolidated piece experiment. The steel cage merely rested on the bottom of the reactor immediately above an air sparge.

Mixing in the reactor was accomplished by pump circulation and an air sparge. One inch stainless steel tubing and Swagelok fittings were used as plumbing between the reactor, pump, and circulation heaters. Paddlewheel flowmeters (Omega, model #FP-5300) measured flow through either side of the reactor. Type K thermocouples were used to monitor temperature at various points in the reactor and in the heater's thermowells. Viatran pressure transducers (model 244) measured head pressure of the liquid inside the reactor.

The system was monitored remotely during experiments using a Stanford SR630 thermocouple monitor, an Apple Macintosh computer with a National Instruments GPIB board, and National Instruments LabVIEW software. Thermocouple, flow, and pressure measurements were all monitored at the computer, and this data was all logged to the hard drive as an ASCII file. In addition, the LabVIEW program controlled the

Liquid samples were analyzed by ion chromatography (IC) for anions and cations, total organic carbon (TOC) and total inorganic carbon (TIC), and by a pH meter. The IC anion analysis determined acetate, formate, nitrite, nitrate, oxalate, and glycolate. Cations measured were ammonia, sodium, and methylamine.

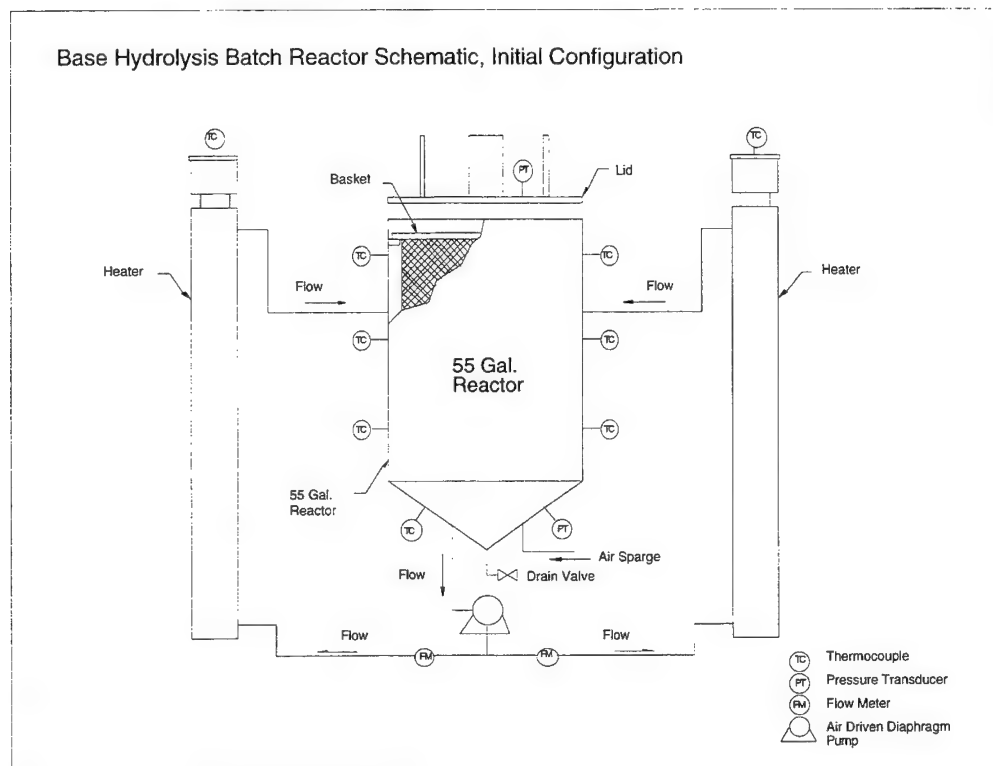


Figure 1. Base hydrolysis batch reactor, initial configuration. This configuration was used only during the first 30 pound molding powder experiment.

## RESULTS AND DISCUSSION

**PBX 9404 molding powder.** Two experiments were performed using 30 lb of molding powder. In the first experiment, significant solids accumulation occurred. This accumulation severely choked fluid flow through the heaters. In the original plumbing scheme (Figure 1), the powder was pumped from the bottom of the reactor, into the pump, and then through the external circulation heaters. The nitrocellulose in the powder reacts relatively fast (within minutes at 80°C),<sup>5</sup> and most of the HMX accumulated in the pumps and the plumbing near the bottom of the reactor. Within the first 40 minutes of operation, the reactor plugged. The bulk fluid temperature at the time of plugging was 68°C. Although serious plugging occurred throughout the bottom of the reactor system, no serious exotherms were detected in any part of the reactor.

Because of the serious nature of the solids accumulation, the reactor was reconfigured so that fluid was pumped from the side of the reactor, into the diaphragm pump and to the heaters before being returned to the

bottom of the reactor. The new pumping scheme is shown in Figure 3. The advantage of this pumping scheme is that HMX powder that has not yet reacted in the tank will not settle and plug the reaction pumping system and heaters. The disadvantage is that since the pump inlet is taking fluid from the sides of the reactor, a minimum amount of liquid must be maintained in the reactor for the system to work properly. This minimum amount is approximately 40 gallons.

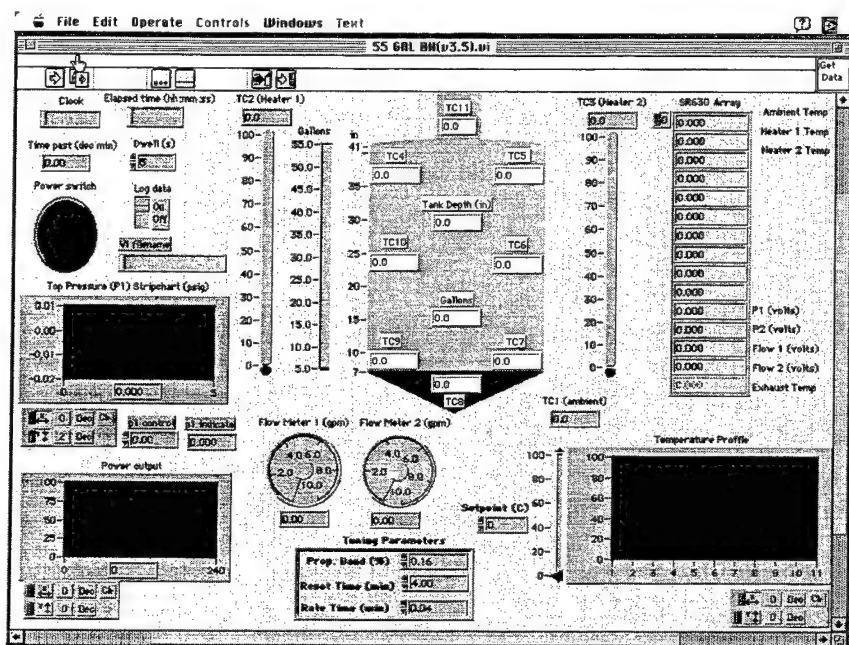


Figure 2. LabVIEW control panel for computer control of pilot-scale base hydrolysis unit. LabVIEW was run on an Apple Macintosh IIfx computer.

Another 30 lb molding powder experiment was conducted with the configuration displayed in Figure 3. In this second molding powder experiment, the fluid was heated from 30°C to 85°C in approximately 1.6 hours. Similar to the first experiment, by the time the solution reached 85°C, most of the nitrocellulose had reacted releasing the fine HMX powder. At this point, possible intermittent plugging was observed in one of the flow lines, which continued for about 70 minutes. Instead of plugging, the paddle of one of the flowmeters may have caught itself during this time on a plastic insertion fitting. The reaction time-temperature history is shown in Figure 4. In this figure, the heater temperature, the bulk fluid temperature, and the set point temperature are shown. Approximately 2 hours after the experiment began, one of two flow sensors indicated that intermittent plugging or flowmeter measurement problems were taking place. When this was observed, the heaters were completely turned off. This is indicated by the abrupt change in temperature set point at approximately 3 hours time, (dashed line, Figure 4). After the heating power was turned off, a slight exotherm of approximately 4°C was also observed and is indicated on the graph. Most likely, some nitrocellulose continued to hydrolyze and caused the temperature increase.

*PBX 9404 consolidated pieces.* This reactor was originally designed to remediate large pressed pieces of PBX 9404, not molding powder. Much of the DOE's remediation mission is to get rid of large pressed pieces. These pieces require a longer reaction time since the system is mass transfer limited, which leads to less powder present at any one time, reducing the chance of plugging. Furthermore, the slower reaction rate will cause the exotherm created by the degradation of nitrocellulose to be much less. The molding powder experiments were judged to be a worst case reaction scenario for solids loading in the reactor. They were carried out to both illustrate the robust capabilities of the system, and to give the system a thorough safety test.

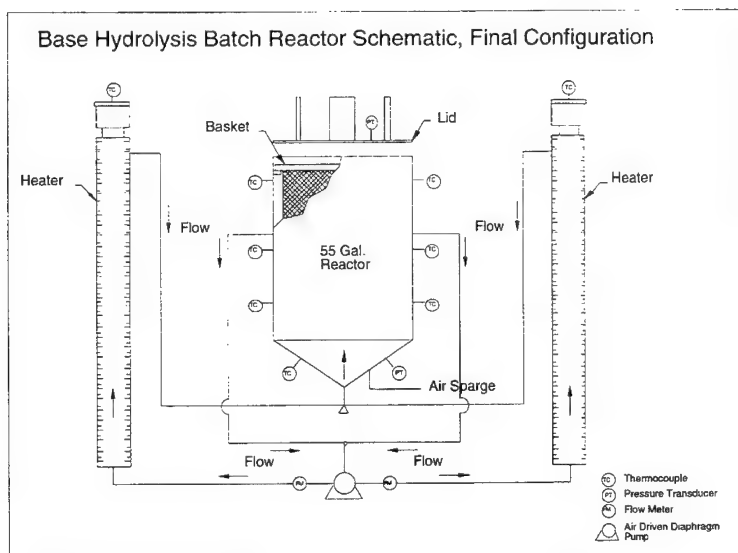


Figure 3. Base hydrolysis reactor schematic, final configuration. This configuration was used after the reactor plugged significantly in the first molding powder experiment.

Consolidated pieces were hydrolyzed in two different experiments. Each experiment involved a single pressed PBX 9404 piece made from molding powder. In the first experiment, a charge weighing less than 35 lb was hydrolyzed in 45 gal of 1 M NaOH. The fluid was initially heated to near 90°C and then held above 80°C for 9 hours. The reactor was allowed to cool overnight. The next morning, the basket was taken out of the reactor, and a significant quantity of the pressed piece remained. The piece was not weighed at this point, but was returned back to the reactor and heated again that day. The reactor was held above 80°C for an additional 8.7 hours. The reactor was then allowed to cool overnight. The time-temperature history of the reaction is shown in Figure 5. The following morning, a small piece was removed. The solution was then drained and filtered, and a small amount of additional HMX powder was recovered (100-200g). The total amount left was 6% of the starting material. The rest of the explosive had been converted to base hydrolysis products (i.e., water soluble aqueous compounds, and  $N_2$ ,  $N_2O$ , and  $NH_3$ ).

In the second experiment, we attempted to increase the mixing and therefore the overall mass transfer of the solid explosive into the surrounding base solution. We achieved this by removing the basket that held the explosive as previously described in the Experimental Methods section. It was hoped that the additional mixing created by having the air sparge near the explosive would cause the explosive to hydrolyze faster. This was not necessarily the case. In the second experiment, we achieved approximately 87% destruction. This was less than the first experiment, where we achieved 94% destruction, however the reaction was not held at temperature as long. These results are summarized in Table 1.

TABLE 1  
Destruction Percentage of Consolidated PBX 9404 High Explosive

Experiment Number	Time above 80°C (h)	High Explosive Destruction %
Consolidated Exp #1	21	94
Consolidated Exp #2	18	87

Both experiments proceeded at approximately the same rate. If the rate is assumed to be approximately linear for the whole reaction, the amount of explosive hydrolyzed per unit time in the second experiment is slightly more (4.9% reacted per hour vs. 4.6% for the first experiment). This assumption is not completely true; past experiments have shown that the reaction rate is not linear with time.<sup>5</sup> The reaction slows somewhat as it proceeds, both due to the depletion of hydroxide ion as the reaction progresses and to the increased

concentration of soluble salts in the liquid that tend to "salt out" organic species, thus reducing their solubility. Approximate reaction rates of the two consolidated pieces are reported in Figure 6. Also shown in Figure 6 is the overall reaction rate of the second molding powder experiment and a comparison to experiments performed in a lab scale reactor at 90 and 150°C. In one of the lab-scale experiments (indicated by 150-P on the x-axis), a single consolidated piece (2" diameter by 3" high cylinder) weighing a total of 284 g was used. In this experiment, the temperature was raised to 150°C for 53 min. At the end of the experiment, 99.8% of the explosive had been destroyed.

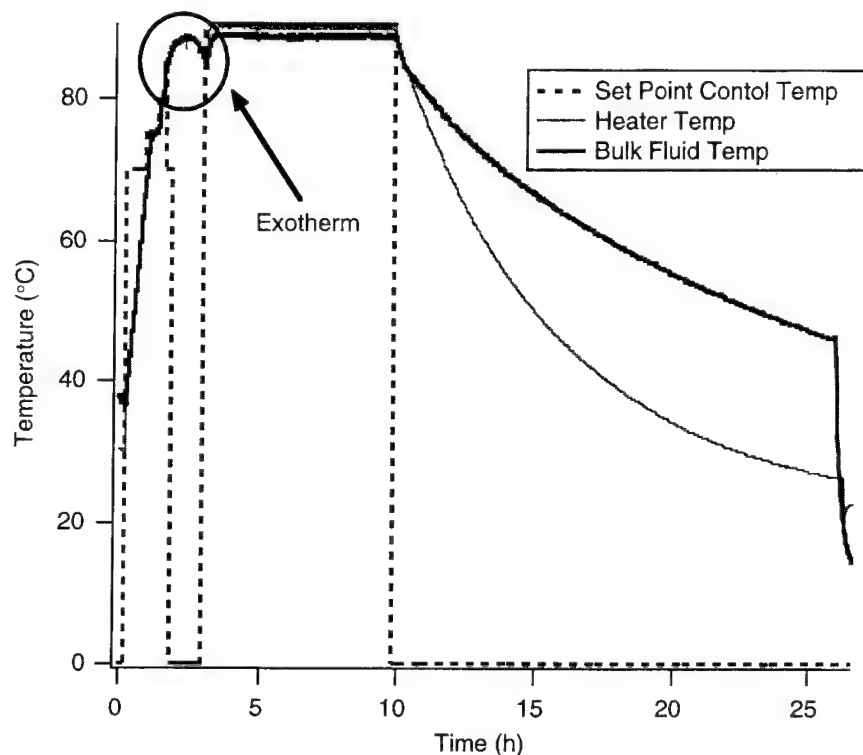


Figure 4. Second PBX 9404 molding powder Experiment. Thirty pounds of PBX 9404 molding powder were hydrolyzed in 45 gal of 1.0 M NaOH.

Figure 6 shows a qualitative comparison in reaction rates between molding powder and consolidated pieces at both small and large scales. Since this is a mass transfer limited reaction, the available explosive surface area plays a large role in the rate. This is reflected in the faster reaction rate for molding powder compared to the consolidated pieces. The high temperature experiments are included to show the increase in mass transfer (even without stirring), and therefore the overall increase in reaction rate. A direct comparison of rates for consolidated pieces shows that destruction rates increase nearly 2 orders of magnitude when the temperature is increased from 90°C (mixed) to 150°C (with no mixing). We do not expect that reaction rates will scale linearly with respect to explosive size because of the general decrease in ratio of surface area to volume when larger consolidated pieces are used. Preliminary estimates indicate that a large scale charge may take from 2 to 4 times longer than the small scale piece treated at 150°C. Mixing should also significantly increase mass transfer at the higher temperatures as well.

**Product analysis.** Major carbon products in solution consist of sodium formate and sodium acetate. These two products account for approximately 40 to 50% of the total carbon from the high explosive. Sodium nitrite is the major nitrogen product in solution accounting for approximately 20% of the nitrogen in the explosive.

Gas data were not collected in these experiments. In previous experiments,<sup>6</sup> nitrogen gas, nitrous oxide, and ammonia are released in the reaction, and account for about half of the nitrogen in the explosive. Total carbon and total organic carbon were also measured at the end of each experiment. These results are summarized in Table 2, which presents Ion Chromatography results for both sets of experiments. We are also aware that sodium glycolate is present in our product mixture, but glycolate and acetate elute out at similar retention times in our IC analysis.

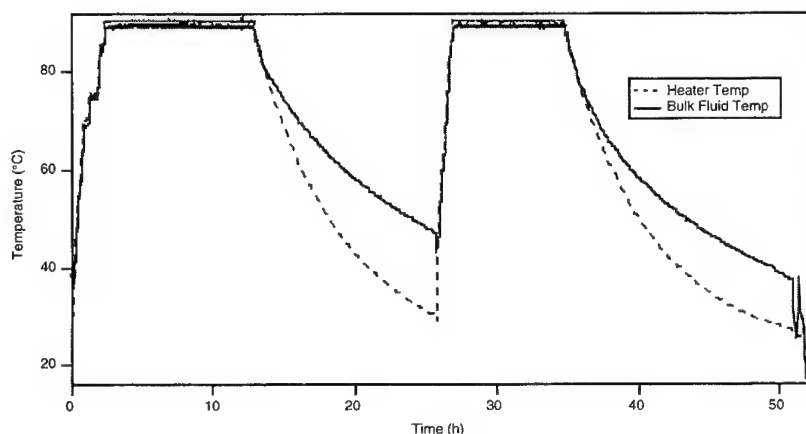


Figure 5. First PBX 9404 consolidated piece experiment. One PBX 9404 pressed piece (weighing less than 35 lb) was hydrolyzed in 45 gal of 1.0 M NaOH.

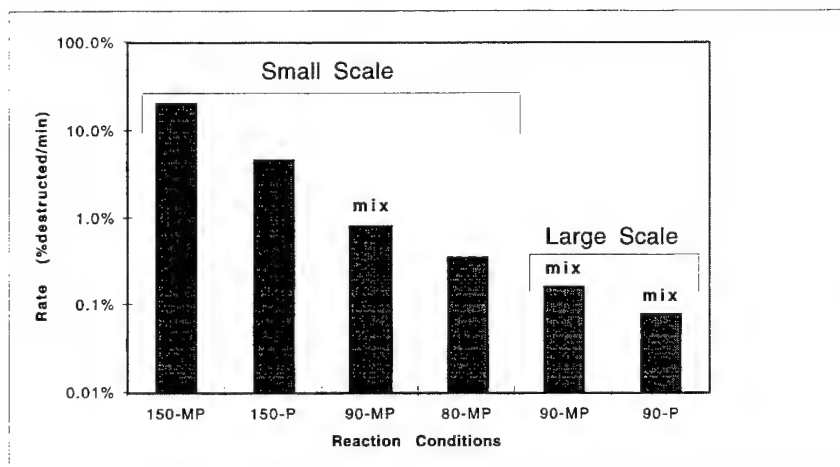


Figure 6. Reaction rate comparison between small and large scale reactions. Temperature (°C) and explosive form are indicated on the x-axis. MP refers to molding powder and P refers to consolidated pieces. Mixing was carried out in some experiments and is indicated.

The products shown in Table 2 are amenable to treatment by hydrothermal oxidation. Indeed, we have had success mineralizing organic carbon using nitrite and nitrate available in the solution.<sup>1</sup> Hydrothermal oxidation experiments performed on PBX 9404 hydrolysate indicated that organic carbon conversions greater

than 99% were achieved at relatively mild operating conditions (374°C, 300 bar). To completely mineralize the organic carbon, additional oxidant such as hydrogen peroxide must be added to the hydrothermal system.<sup>1</sup>

TABLE 2  
Ion Chromatography Results for PBX 9404 Pilot Scale Hydrolysis

IC products (% of C or N in explosive processed)	Molding powder 2	Consol. piece 1	Consol. piece 2
Acetate	19%	22%	25%
Formate	16%	21%	23%
Nitrite	20%	19%	20%
Nitrate	0.7%	0.5%	0.7%
Organic carbon	99%*	93%	101%
Inorganic carbon	1.1%*	1.4%	1.8%

\* - Mass balances based on Total Carbon analytical results rather than amount of explosive left at end of experiment.

## CONCLUSIONS

We have successfully hydrolyzed HMX plastic bonded pressed explosives at a pilot scales of less than 35 lb of explosive. Reaction rates are slower than similar bench scale experiments due to decreases in mixing efficiency at larger scales. Times up to 20 hours are required to destroy 90% of the explosive. Major aqueous carbon products include sodium acetate, formate, and glycolate, all of which are amenable to hydrothermal oxidation. Lab scale experiments at higher temperatures (e.g., up to 150°C) indicate that destruction rates may be an order of magnitude faster than reactions carried out at 90°C. More work is needed to quantify scale-up data for these higher temperatures.

## ACKNOWLEDGMENTS

We would like to thank the DOE/DoD Memorandum of Understanding for funding this research.

## REFERENCES

1. Flesner, R.L., Dell'Orco, P.C., Spontarelli, T., *et al.*, Pressurized Alkaline Hydrolysis and Hydrothermal Oxidation of HMX based Energetic Materials as an Integrated Process for EM Disposal. Submitted to *Proceedings of the JANNAF Propulsion and Subcommittee Joint Meetings*, Tampa, Florida, December 4-8, 1995.
2. Heilmann, H.M., Strenstrom, M.K., Hesselmann, R.P.X., *et al.*, *Wat. Sci. Tech* 30, 53, 1994.
3. Cannizzo, L. F.; Mower, G. L.; Hunstman, L. R., *et al.*, *J. Energ. Mater.* 13, 331, 1995.
4. Borcherdig, R., Treatment of Solid Propellant Manufacturing Wastes, Base Hydrolysis as an Alternative to Open Burning, *Proceedings of the JANNAF Safety and Environment Protection and Propellant Development and Characterization Subcommittee Joint Meetings*, San Diego, California, July 13-14, 1995.
5. Spontarelli, T., Buntain, G. A., Sanchez, J. A., *et al.*, Destruction of Waste Energetic Materials Using Base Hydrolysis, *Proceedings of the 12th (1993) Incineration Conference*, Knoxville, Tennessee, May 3-7, 1993, 787.
6. Flesner, R. L.; Spontarelli, T.; Dell'Orco, P. C., *et al.*, Base Hydrolysis and Hydrothermal Processing of PBX 9404, *ACS Symposium Series, Emerging Technologies in Hazardous Waste Management VI*. Sept. 19-21, Atlanta, GA, 1994, 225.



## CRYOGENIC WASHOUT OF SOLID ROCKET PROPELLANTS\*

J. P. Elliott<sup>1</sup>, J. M. McNair, M. H. Spritzer, J. A. Hurley<sup>2</sup>, S. A. Rising

General Atomics<sup>1</sup>, San Diego, California;

U. S. Air Force<sup>2</sup>, Armstrong Laboratory/EQS, Tyndall AFB, Florida

**ABSTRACT:** Cryogenic washout (U.S. Patent No. 5025632) is a process using liquid nitrogen (LN<sub>2</sub>) as a washout medium to remove propellant from within solid rocket motors. The process is environmentally clean and produces dry, size-reduced particles that are well suited for disposal or for reuse in applications such as commercial explosives.

A prototype cryogenic washout facility has been constructed for washout of Minuteman II Stage 3 solid rocket motors under a contract with the U.S. Air Force. Design support testing on a bench-scale system has been completed. Workup and subscale safety tests are in progress.

The design support testing included laboratory and bench-scale testing on Hazard Class 1.1 and 1.3 propellants. The laboratory tests established that essentially no change in the sensitivity of the test propellants occurred between ambient and cryogenic temperatures.

This paper describes prototype equipment design and presents a summary of the testing performed.

### INTRODUCTION

During the past four years, cryogenic washout has been under development for the Air Force Environics Directorate of Armstrong Laboratory by General Atomics (GA). A cryogenic safety data base was acquired under Contract No. F08635-91-C-0179 for impact, friction, low level shock, electrostatic discharge, and finally high pressure LN<sub>2</sub> jet impact, with no initiations.

Through sponsorship from Joint Ordnance Commanders Group, GA was awarded a follow-on contract (F08635-92-C-0075) from the Air Force to design, build, and test a prototype system for Class 1.1 solid rocket motor propellant disposal. GA's subcontractors are Alliant TechSystem Inc., Thiokol Corporation, El Dorado Engineering, Eco Waste Technologies together with the University of Texas Balcones Research Center, and Fluor Daniel. Two innovative technologies will be used for the prototype system: (1) cryogenic washout for propellant removal and size reduction and

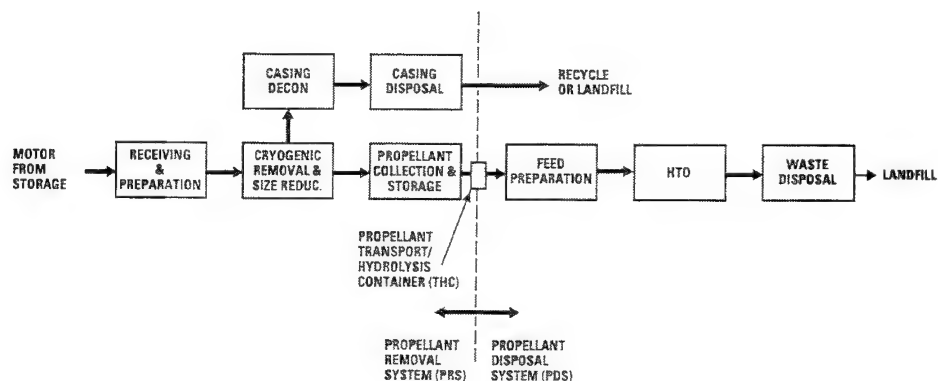
<sup>^</sup>Approved for public release; distribution is unlimited.

<sup>\*</sup>Work performed under U.S. Air Force Contract Nos. F08635-91-C-0179 (completed) and F08635-92-C-0075 (ongoing) with General Atomics, San Diego, CA.

(2) hydrothermal oxidation (HTO) for propellant disposal. HTO, also known as supercritical water oxidation (SCWO), uses supercritical water as a medium in which these hazardous materials are completely oxidized in a fully contained system. In combination, these technologies provide an environmentally safe and cost-effective system for disposal of these propellants.

### PROTOTYPE CRYOGENIC WASHOUT SYSTEM DESCRIPTION

The current cryogenic washout system is structured to solve, in a near-optimum manner, the end-to-end problem of Class 1.1 propellant removal, size reduction, reuse, or disposal. A prototype system has been constructed to remove and size reduce propellant using cryogenic washout and to destroy the propellant by means of HTO. The prototype system consists of the process elements shown in Figure 1. The prototype system was designed to handle the Minuteman II Stage 3 rocket motor (see Figure 2).



K-620(1)  
8-2-94

Figure 1. Block flow diagram for prototype Class 1.1 propellant demilitarization system

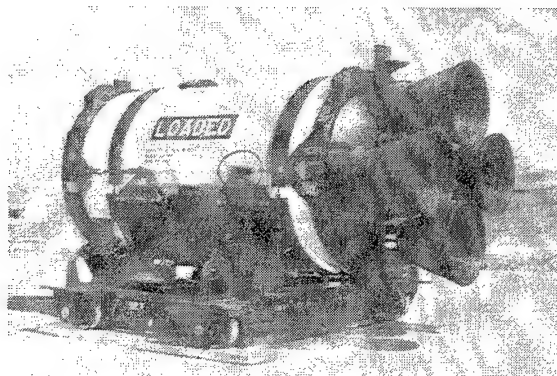


Figure 2. Minuteman II Stage 3 Motor

The general arrangement of the prototype PRS is shown in Figure 3. The rocket motor is mounted in a fixture that supports the motor and provides torque transmission, riding rings, and a seal surface. The fixture is mounted on an incline in a frame that incorporates a rotary drive mechanism and rollers that mate with the riding rings on the fixture. The seal ring mates with a seal flange on the washout enclosure. The washout enclosure collects and directs propellant particles and residual  $\text{LN}_2$  into the transport/hydrolysis container. The gas is ducted to the gas filter assembly before discharge to the atmosphere. The  $\text{LN}_2$  washout lance passes through the washout enclosure where a boot is used to provide a seal and accommodate the axial and radial translation of the lance. The high-pressure  $\text{LN}_2$  supply (9,000 to 30,000 psi) is connected to the drive end of the lance with flexible connections.

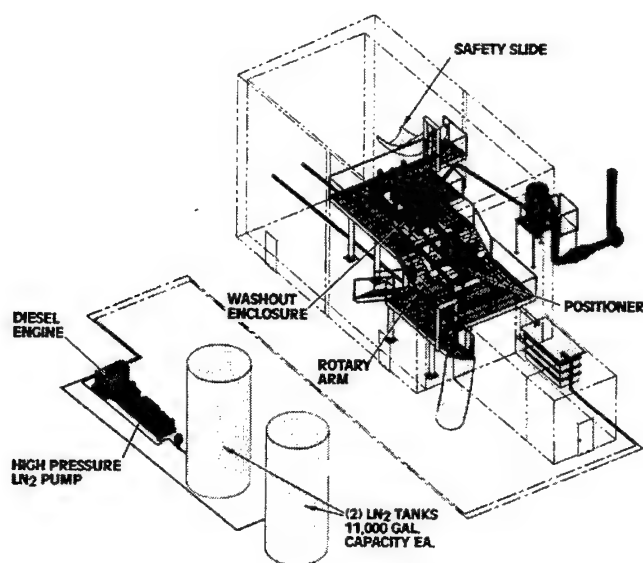


Figure 3. PRS equipment arrangement (looking north)

### INITIAL SAFETY TESTS

The initial prototype design support tests included safety testing to characterize the CYH and DDP Class 1.1 propellant types contained in the Minuteman II, Stage 3 motor. These tests, performed by Alliant TechSystem and Thiokol Corporation (TC), included initiation sensitivity, electrical properties, material compatibility, combustion, dust explosibility, shock sensitivity, photomicroscopy, angle of repose, and packing fraction. Follow-up testing was then performed by both Alliant TechSystem and TC to determine initiation sensitivity. Tests included the Hercules-modified Bureau of Mines impact test, the Hercules Allegany Ballistics Laboratory (ABL) sliding friction test, and the ABL electrostatic discharge (ESD) test. Impact tests establish threshold initiation level (TIL) and probability of initiation (probit) data to calculate safety margins for various process conditions. The TIL corresponds to the highest energy level at which no initiations would be expected in twenty trials. Statistically, this corresponds to 0.034 probit. Friction tests establish pressure and velocity TILs and probits to calculate safety margins for process conditions. All Hercules testing was done at a sliding velocity of 8 fps (TC conducts friction testing at 8, 6, and 3 fps.). ESD tests determine what level of ESD energy will initiate the material. A summary of the test results for CYH propellant is listed in Table 1.

TABLE 1  
Sensitivity Comparison for CYH Propellant

Material	Temperature	Probit TILs		
		Impact (J/m <sup>2</sup> )	Friction (N/m <sup>2</sup> )	ESD (J)
Cryo-fines (<20 mesh)	ambient (~72°F)	3.59 X 10 <sup>3</sup>	1.63 X 10 <sup>4</sup>	8.07 X 10 <sup>-1</sup>
	-94°F to -124°F	1.01 X 10 <sup>4</sup>	3.17 X 10 <sup>4</sup>	1.25
	-300°F to -320°F	9.96 X 10 <sup>3</sup>	3.00 X 10 <sup>4</sup>	1.29
Slices (0.333-in. thk.)	ambient (~72°F)	1.86 X 10 <sup>4</sup>	5.16 X 10 <sup>4</sup>	5.05 X 10 <sup>-1</sup>
	-94°F to -124°F	1.38 X 10 <sup>4</sup>	4.92 X 10 <sup>4</sup>	7.30 X 10 <sup>-1</sup>
	-300°F to -320°F	1.82 X 10 <sup>4</sup>	5.20 X 10 <sup>4</sup>	5.17 X 10 <sup>-1</sup>
Wiley mill (<20 mesh)	ambient (~72°F)	3.45 X 10 <sup>3</sup>	1.55 X 10 <sup>4</sup>	5.05 X 10 <sup>-1</sup>

TC categorizes tested samples as Green Line (GL) — safe, Yellow Line (YL) — somewhat hazardous, and Red Line (RL) — very hazardous, based on characteristics of Minuteman Stage I propellant. Materials found to be RL require special precautions or rules developed to handle the material. The limits of each classification are delineated in Table 2. The TC test methods are for 50% values. These are determined using the Bruceton method. The ABL tests are for TILs, which are the values at which 20 consecutive no-fires occur.

TABLE 2  
Thiokol Material Sensitivity Classification

Test	Line Limits		
	Red	Yellow	Green
TC Impact (in.)	≤ 4	4 < YL < 11	≥ 11
TC Friction (lb)	≤ 10	10 < YL < 35	≥ 35
ABL Impact (cm)	< 3.5	3.5 ≤ YL < 6.9	≥ 6.9
ABL Friction (lb @ fps)	< 50@3	50@3 ≤ YL < 100@8	≥ 100@8
TC ESD (J)	≤ 0.06	0.06 < YL < 8	≥ 8
SBAT (°F)	≤ 225	225 < YL < 300	≥ 300

During hydrolysis studies of CYH/DDP propellants, several initiation sensitivity tests were performed. Table 3 presents the results of testing CYH and DDP chips. Table 4 shows the results of meshed and hydrolyzed CYH. For both of these tables, YL and RL values are shown with a double border around the cell; GL values have single borders. The simulated bulk autoignition test (SBAT) involves the slow warming of a sample until self-heating is observed.

TABLE 3  
Initiation Testing of CYH/DDP Chips

Test	Date		
	2/7/91	5/3/93	
Propellant	CYH	CYH	DDP
TC Impact (in.)	25.55	----	16.4
TC Friction (lb)	60.8	62.3	----
ABL Impact (cm)	3.5	6.9	11.0
ABL Friction (lb @ fps)	130@8	50@6	100@8
TC ESD (J)	> 8	2.88	> 8
SBAT (°F)	----	248	245

TABLE 4  
Initiation Testing of Meshed and Hydrolyzed CYH

Test	Date			
	5/3/93	4/ /93	5/3/93	
Mesh	10	40	40	Hydrolyzed
TC Impact (in.)	----	----	----	> 46
TC Friction (lb)	63	----	62.6	> 64
ABL Impact (cm)	6.9	1.0	3.5	----
ABL Friction (lb @ fps)	100@6	25@8	25@8	----
TC ESD (J)	3.25	4.27	6.42	> 8
SBAT (°F)	248	248	262	330

#### Effect of Particle Size

Most sensitivities increase for small particles. Testing was performed on 0.033-in.-thick slices (Bureau of Mines Tests) and 20-mesh (approximately 0.040 in maximum particle size) cryogenic washout particles. Previous work had determined that the slices have sensitivities similar to bulk material. The following conclusions can be drawn from these tests:

- DDP sensitivities to impact are increased by a factor of 1.4 to 4.4 for 20-mesh particles relative to slices.
- CYH sensitivities to impact are increased by a factor of 1.8 to 5.2 for 20-mesh particles relative to slices.
- DDP sensitivities to friction are increased by a factor of 1.5 to 2.4 for 20-mesh particles relative to slices.
- CYH sensitivities to friction are increased by a factor of 1.7 to 3.6 for 20-mesh particles relative to slices.
- ESD sensitivities are inconsistent as a function of particle size.
- Wiley milled particles (which are cryogenically prepared) have the same characteristics as cryogenic washout propellant particles.
- Hand ground particles prepared at room temperature have unchanged sensitivities, relative to unground material.

### **Effect of Temperature**

The following points are apparent:

- Sample sizes 0.033-in.-thick have little change in sensitivity as a function of temperature.
- Hand-ground propellant particles prepared at room temperature have little change in sensitivity as a function of temperature.
- Impact, friction, and ESD sensitivities for cryogenic washout propellant particles are decreased by a factor of 2 to 4 at LN<sub>2</sub> temperature (-320°F) compared with ambient temperature particles.

### **GL, YL, and RL Sensitivity Criteria**

Cryogenic washout propellant particles have the following sensitivities, relative to RL and YL:

- Impact sensitivities for CYH and DDP at room temperature are between RL and YL.
- Impact sensitivities for CYH and DDP at LN<sub>2</sub> temperature are on the safe side of YL.
- Friction sensitivities for CYH and DDP vary between GL and the safe side of YL.
- ESD sensitivities for CYH and DDP vary between GL and the safe side of YL.

## **OTHER SAFETY TESTS**

### **Electrical Properties**

Electrical properties tests consisted of determining volume resistivity, dielectric constant, and dielectric breakdown. Testing was performed with both solid and crumb propellant at ambient temperature and at -150°F.

Both CYH and DDP became much less conductive at cryogenic temperature. Volume resistivity increased from about 10<sup>3</sup> ohm-cm at ambient temperature to about 10<sup>15</sup> ohm-cm at -150°F. This tended to slow charge dissipation through the propellant at cryogenic temperatures.

Typical for relatively conductive propellants like CYH and DDP, dielectric constants decrease in magnitude at lower temperatures and increase at lower applied frequencies. Dielectric constants are lower for cryo-removed crumb vs. solid propellant.

Dielectric breakdown voltages were higher at cryogenic temperature than at ambient. In addition, some of the samples shattered into small pieces at -150°F. No ignitions occurred during any of the dielectric breakdown testing with CYH or DDP propellant. Some other propellant types can ignite and burn vigorously as a result of dielectric breakdown testing.

### **Material Compatibility**

To date, 38 materials have been tested for compatibility with CYH/DDP. One of two test methods were used. The Hercules Modified Taliani test was performed on materials that decompose to form NO<sub>x</sub> gas. The Differential Scanning Calorimeter (DSC) was used on materials that do not form NO<sub>x</sub> on decomposition. Of the 38 materials tested, 30 are considered compatible.

## Propellant Combustion

Two types of tests were performed to determine propellant combustion characteristics: unconfined burn and Russian deflagration-to-detonation transition (DDT).<sup>1</sup>

The unconfined burn test was performed on both solid 2-in. X 2-in. X 1.5 in. CYH and DDP propellant samples and cryo-removed fines. None of the unconfined burning tests detonated. For the solid samples, DDP burned faster (23 sec) than CYH (38 sec), and more sparks were seen with the DDP. Propellant fines were placed in paper ice cream buckets to simulate burning ground conditions for disposal of dry propellant. The burning was vigorous and intense, but the confinement provided by the bucket was insufficient for transition to detonation.

Compared to conventional DDT tests, the Russian version uses relatively small sample sizes, but gives comparable results. Both CYH and DDP fines detonated after ~10 in. of confined run-up. The results were unaffected by propellant temperature (ambient and -300°F). The results of these tests indicate that cryogenic washout particle fines require much more containment to detonate than 32  $\mu$  RDX and 5  $\mu$  HMX, which are handled routinely by TC and Hercules. Solid propellant samples and water-wet fines (75% propellant, 25% water) did not detonate.

## Dust Explosibility

Propellant fines removed by the LN<sub>2</sub> jet at Pit 38 were characterized for dust explosibility in the Hartmann test apparatus. The 20-mesh samples of CYH and DDP propellant fines did not react in either the minimum concentration or the minimum energy testing in the Hartmann test. When the samples were screened to 42-mesh (i.e., particles  $\leq 0.014$ -in.), CYH propellant reacted in the minimum concentration test at 800 mg and DDP reacted at 600 mg.

## Shock Sensitivity

Card gap tests determine material sensitivity to shock pressure. In all cases, CYH and DDP fines required less shock for detonation than solid propellant. In all cases, CYH and DDP fines required more shock for detonation at -300°F than at 72°F, i.e., they were less sensitive at cryogenic temperatures. In addition, in the most sensitive case, both CYH and DDP fines at 72°F were nearly identical to dry HMX (16.1 kilobars vs. 16.4 kilobars), which is handled routinely by TC and Hercules.

## Photomicroscopy

Photomicroscopy determines by visual examination the physical properties of the removed propellant crumb to understand any mechanical phenomena or evidence of initiation. The following

---

<sup>1</sup> Russian DDT is a trademark of Thiokol Corporation.

conclusions are based on representative photomicrographs of the screened 20-mesh and virgin propellant samples.

- Small, white-colored patches on the cryo-removed samples and the Wiley-milled samples are believed to be ammonium perchlorate (AP) leached from the matrix by water that came from thawing the sample after exposure to ambient air at cryogenic temperatures. This should not occur in the prototype unless the washout box or THC is opened before reaching room temperature.
- There appears to be an insignificant difference between cryo-removed propellants and propellant mechanically ground inside the Wiley mill. This can be useful for future work with propellant fines, because additional samples can be prepared without using the LN<sub>2</sub> jet for size reduction. This conclusion is also supported by the sensitivity data.
- There are no signs of initiation or combustion in any of the samples. Dark spots are believed to be remnants of either insulator rubber or adhesive.
- There are no signs of migration, separation, or crystallization of nitroglycerin (NG) or of any other volatile materials. This conclusion is also supported by many years of freezing propellants with dry ice or LN<sub>2</sub> before machining operations or storage.
- There are loose crystals of ammonium perchlorate (AP) and HMX as a result of the large surface area generated during removal. This should be anticipated in the prototype operation.

#### CONCLUSIONS FROM SAFETY TESTING

The results show no change or a decrease in sensitivity for low temperatures and generally increased sensitivity for cryogenic washout particles, compared with propellant slices. In addition, testing has been performed to determine how the propellants will react if initiated. These data indicate that the size-reduced propellants can detonate if initiated in the cryogenic washout process; however, size-reduced ambient temperature propellant requires more confinement to detonate than the ambient temperature HMX and RDX powders that TC and Hercules handle routinely.

#### DESIGN SUPPORT TESTS AT PIT 38

Additional design support tests were performed at the Alliant TechSystems Pit 38 test site in Magna, Utah (see Figure 4). These tests were performed with an improved LN<sub>2</sub> high-pressure system, improved nozzle design and a wider range of performance parameters. The resultant performance parameters are summarized in Figures 5, 6, and 7. The maximum rate of propellant removal was about 0.1 Kg/s (765 lb/hr).



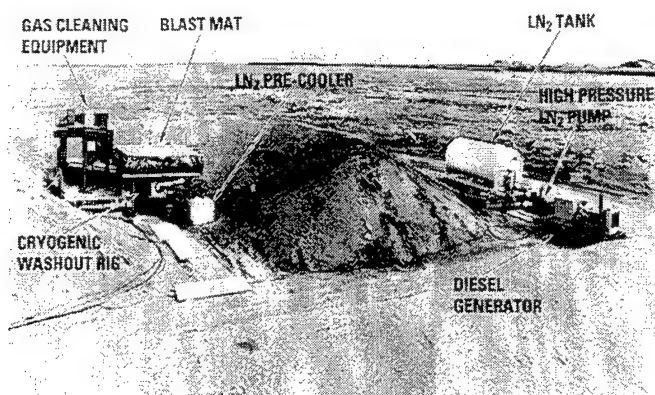


Figure 4. Bench-scale cryogenic washout site at Pit 38, Hercules, Inc., Magna, Utah

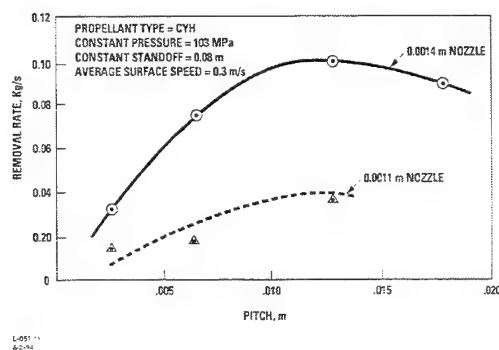


Figure 5. Effect of pitch and nozzle size on cryogenic washout of propellant

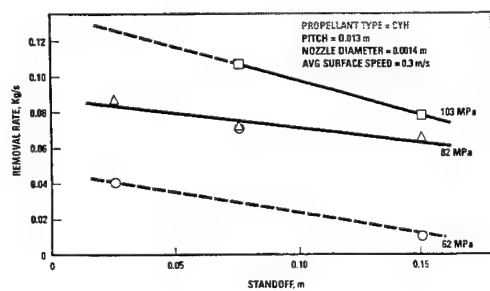


Figure 6. Effect of standoff and pressure on cryogenic washout of propellant

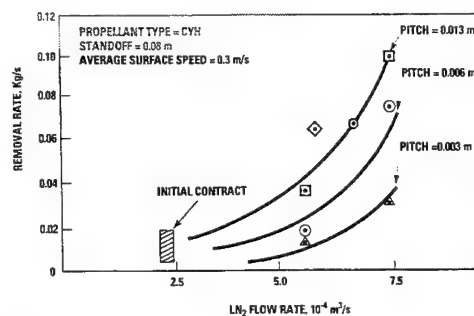


Figure 7. Effect of flow and pitch on propellant removal rate

There was no indication of initiation or combustion of propellant during the design support tests at Pit 38. Evidence of minor electrostatic charging was detected by remote electrometer sensing of streaming current. Electrostatic potentials of up to 16,000 volts were measured on the outside surfaces of the washout enclosure. Unlike the test rig, which had transparent sides, the outside surfaces on the solid rocket motor disposal prototype system will be aluminum and it is not expected that charging voltages will be as high.

The hazards testing at Pit 38 was designed to exceed the expected exposure time of the propellant to the jet stream. Dwell tests were performed using a 0.044-in.-diameter jet orifice to simulate abnormal process conditions where the jet was allowed to remain in one location for up to 15 minutes. Because of physical limitations, the maximum pressure from the HP pump was ~17,000 psig. These conditions did not result in propellant ignition. The surfaces of the removed propellant were inspected using a microscope and there were no signs of microscopic initiation.

### PROTOTYPE PRS TESTING

There are other factors that may or may not bear on the safety of the PRS process, including: (1) effect of propellant exposure to moist air; (2) composition of propellant talc; (3) high pressure LN<sub>2</sub> initiation of propellant; (4) friction initiation of entrapped propellant particles; (5) ESD initiation of cryowashed propellant; (6) bulk propellant fracture from cryogenic exposures; (7) lance impingement with propellant; (8) motor case cryojel blow-through; and (9) propellant initiation from drop into THC.

A series of process-simulation and subscale tests were planned to answer these questions and to permit washout of a full motor. These tests included (1) supplemental DDT and mini card gap tests on propellant fines and (2) 25mm gun impact tests, LN<sub>2</sub> jet impact tests, variable cold temperature (i.e., "glass-transition") drop tests, and subscale tests. The subscale tests consisted of 75g, 1000g, and 50 lb tests in the prototype facility under the maximum LN<sub>2</sub> jet pressures achievable. The results of the process-simulation and subscale tests revealed no new hazards. During subsequent testing on a full-scale motor, an initiation event occurred involving approximately 8–9 grams of propellant. Detailed investigations failed to determine the exact cause of initiation, so additional process-simulation and subscale tests were conducted. The initial efforts focused on determining if ESD was the principal cause of the 8–9 gram initiation event. After considerable testing and study, it was concluded that ESD was probably not the cause of the initiation. The focus then shifted to "impact" as being the likely cause of the event.

Subsequent subscale tests performed under actual LN<sub>2</sub> jet washout conditions revealed that very small nonpropagating initiations were occurring at the test chamber walls. These were detected using very sensitive light measurement instrumentation. It was believed these initiations were caused by high-speed propellant particles impacting the chamber walls. A decision was made to reduce the LN<sub>2</sub> jet pressures and repeat the subscale tests under closely monitored conditions. Upon conclusion of the subscale tests at the lower LN<sub>2</sub> jet pressures, a decision will be made regarding washout of a full Minuteman II Stage 3 motor. Those tests are currently underway; and the initial results are looking favorable.

***Area 4:***

***New Techniques and  
Improved Safety in Combustion  
of Energetic Materials***

## THE HAZARDS OF SOLID PROPELLANT COMBUSTION

**Thomas L. Boggs**

Research and Technology Division  
Naval Air Warfare Center Weapons Division  
China Lake, California, USA 93555-6100

**ABSTRACT:** Decomposition, ignition, and combustion reactions can result in hazards such as explosions, deflagration-to-detonation transition (DDT), cookoff and delayed detonation (XDT). These hazards have caused the loss of many lives and destroyed many millions of dollars worth of ships and aircraft. This paper discusses some of the accidents, and the decomposition, ignition, combustion, DDT, XDT, and cookoff research being performed to address these hazards.

### INTRODUCTION

When I was invited to present this plenary address, a complete overview of the hazards associated with solid propellant combustion, coupled with an extensive bibliography seemed appropriate. That is until the reality of page limitations was considered. For example, the extensive bibliography took up over 30 pages, even using abbreviated format for the citations. Similarly, a complete description of all of the research in all of the technical areas would greatly exceed the page limitations. For example, Reference 1 alone has almost 200 pages.

Thus, this paper is highly condensed, and refers to other longer, more comprehensive documents.<sup>1-3</sup> It presents research, much of it conducted within the Engineering Sciences Branch at China Lake, to illustrate points being made--it is not a survey of all similar work.

This paper concentrates on hazards of solid propellant combustion. While the emphasis is on solid propellants some discussion of explosives is also included. In the past there was a clearer distinction between propellants and explosives, but today high performance minimum smoke propellant looks much like a plastic bonded explosive, and some underwater explosives look much like aluminized ammonium perchlorate based propellants. And we all know that propellants can detonate/explode.

The emphasis is on combustion and associated hazards, and therefore "normal" combustion phenomena are not discussed. While shock-to-detonation transition of propellants is also an important consideration, it is not discussed here either.

In many fields of science and technology we make use of the logic: sample + stimulus + environment -> response. We try to control the sample, stimuli, and environment; change one variable at a time; and determine the response. Unfortunately, in hazards work, we often get an undesired response--fire, explosion, detonation--and must infer the conditions of sample, stimuli, and environment that produced that response. It is not easy, and often impossible, to discern the causative factor(s), especially if a detonation or explosion destroyed much of the evidence. The problem is made worse if

Approved for public release; distributions is unlimited.

there was significant loss of life and equipment resulting in litigation, and secrecy. If the above was not bad enough, it is compounded by hazards being probabilistic, occurring once in hundred (severe risk), once in a million (often felt to be acceptable risk, depending on severity of accident.) Because all up weapons are expensive, there is a tendency to test as few of them as possible. This may give a false sense of security because of the probabilistic nature of the hazard response. As discussed in Ref. 1, in order to exceed the 50% probability of seeing an explosion in two tests, the probability of explosion in one test must be 3 in 10.

Members of the energetic materials community, whether working on propellants and/or explosives, have always been keenly aware of the hazards in working with these materials. There has been increased emphasis in the last decade due to Insensitive Munition programs in various countries. In the US, the Navy's Insensitive Munitions Advanced Development program has made significant progress in decreasing the violence associated with hazard response (from detonation, explosion, or severe deflagration to burning reaction), and provided the ship's crew additional time to try to contain and mitigate the hazard response. The program has led the way to standardized consideration of the IM issues. MIL-STD 2105A defined the hazard areas of bullet impact, fragment impact, fast cookoff, slow cookoff, and sympathetic reaction; presented standardized tests and methods, and described pass/fail criteria. The follow-on MIL-STD-2105B improved the methods by increasing emphasis on Threat Hazard Analyses (THA), and allowing the THAs to define more realistic hazard test conditions, rather than just relying on the generic tests called out in 2105A.

In addition to the efforts of the Insensitive Munitions programs, other, complementary efforts were being conducted. One of these efforts was the development of Hazard Assessment Protocols.<sup>4</sup>

The authors of Ref. 1 thought that a program leading to mechanistic understanding of reactions and the ability to predict hazard response was required. It was felt that the traditional, standard go/no-go tests did not provide this understanding nor the predictive capability. A hazard assessment method that considered classes of output (detonation, explosion, burning, and no reaction) in terms of input stimulus and target (includes sample and environment) was developed after many discussions. Key to this effort was the hazard assessment protocol. At that time, in a separate effort within The Technical Cooperation Panel (TTCP), hazard assessment protocols were being developed.

A hazard assessment protocol is a logic process presented in flow chart form that enables the user to assess the likely hazard responses of his sample (or munition) subjected to various levels of stimuli in a given environment. Because the protocol is in flow chart form, it directs the user into the logic paths most likely to be encountered for that combination of sample, stimuli and environment. Other combinations of sample, stimuli and environment may require using other logic paths. The protocol also indicates what information must be obtained to perform the assessment of probable outcome (detonation, explosion, burn or no reaction) for any given path. Because the hazard assessment is based on logic and directly associated with the sample, in a real environment, and subject to real threats, it has more value than the results of a few go/no-go tests using standard stimuli (such as one fragment size and velocity). The hazard assessment approach, more extensively discussed in Refs. 1 and 4, and the individual protocols for different hazard types are currently available from the NATO Insensitive Munitions Information Center.

As described in Ref. 4, information from the hazard assessment protocols can be used to determine hazard response plots showing what conditions (such as fragment mass and velocity) may cause detonation, burning or no reaction for a given sample. Reference 4 also shows how threat maps may be overlaid on the hazard response plots to determine vulnerability of a sample or munition to threats. In this regard, the hazard assessment protocols are very much like the Threat Hazard Assessments.

While progress has been significant, much remains to be done. The specifics are discussed in the following sections. One general area of concern that still remains is fire, especially fire on board ships. While the Insensitive Munitions programs have reduced severity of reaction (in some cases from detonation and violent explosions down to burning), and provided valuable increased time for the ship crew to mitigate reactions, fire, while passing the IM requirements, remains a major concern.

Historically many ships have been lost to fire, often after surviving the blast and fragments from the warhead.

The experience of the United Kingdom in the Falklands conflict is an example. The British lost a total of six ships with several others damaged. The HMS SHEFFIELD was a 4100 ton destroyer that was struck by an Exocet missile. The missile struck her amidships, penetrated a fuel tank, and smashed into the machinery spaces. The Exocet's 360 pound warhead apparently did not detonate. Burning residual fuel from the missile motor ignited fuel fires, resulting in thick, acrid smoke being spread through the ship's ventilation system. The ship's company fought the fires for 4 1/2 hours before the ship had to be abandoned. Twenty men were lost in the fire. The ship subsequently sank several days later while under tow in heavy seas. The merchant ship ATLANTIC CONVEYOR was struck by one, and possibly two Exocet missiles, whose warheads are believed not to have detonated. She was loaded with aluminum freight containers, aircraft and combustible materials, including ammunition and fuel. She was quickly engulfed in flames and burned out, sinking three days later. Three Royal Navy and nine merchant marine personnel were killed. The HMS ARDENT was hit by a 1000 pound bomb and Snake-eye bombs which caused a runaway ammunition fire. Twenty two men were killed, 30 injured and the ship sank. The HMS COVENTRY was hit by a 1000 pound bomb that induced runaway fires. Twenty one men were killed and the ship sank. The HMS PLYMOUTH was hit by multiple small bombs that induced severe fires, severely disabling the ship. The RFA SIR GALAHAD was hit by multiple bombs, inducing an ammunition fire. Fifty one men were killed and the ship sank. The RFA SIR TRISTRAM was hit by multiple bombs which induced fires and severely disabled the ship. The hanger and the helicopter of the 6200 ton HMS GLAMORGAN destroyer were destroyed by fire caused by unspent propellant from an Exocet motor (All 13 casualties were caused by the shrapnel from the detonating warhead.). The HMS ANTELOPE was struck by a bomb that did not explode. It sank due to fires, caused by the detonation of the bomb while being defused, that spread to the main magazines.

On 17 May 1987, the USS STARK was hit by two Exocet missiles while operating in the Persian Gulf. The warhead of the first missile did not detonate, but the missile did penetrate approximately 80 feet into the ship, spreading approximately 120 pounds of burning propellant. The propellant used in the Exocet missiles burns at temperatures estimated at 3000-3500°F. Heat and acrid smoke immediately began filling the surrounding area impeding personnel from escaping the affected compartments. The second missile penetrated the hull and detonated about 5 feet inside the hull, ripping a large hole in the hull. This large hole allowed air to ventilate from the outside, and helped in igniting and burning combustibles. The initial blast and fragments ruptured the port side firemain. Loss of the firemain and the intense heat and smoke from the burning propellant and burning combustibles, including PVC wire insulation, severely impeded the fire fighting efforts. The intense heat also resulted in vertical fire spread by ignition of combustibles in compartments directly above the main blaze. The initial blast and fires killed 37 men and injured several others. Men were trapped in the berthing space directly below the compartment engulfed by fire.

### DECOMPOSITION

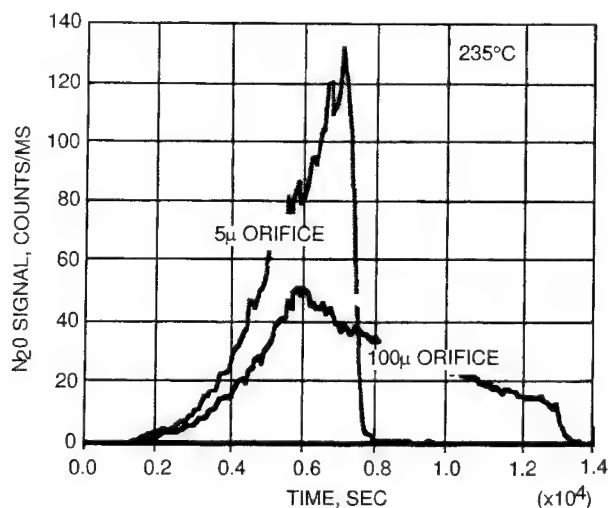
Decomposition, while usually not a hazard in itself unless it produces hazardous or toxic by-products, is an important first step in the response to thermal stimuli. This is especially true if confinement of product gases causes pressure increase and acceleration in the rate of decomposition, and damage to the sample causes increased shock sensitivity due to voids and increased burn area.

Much work has been done in the last 50 years in this area. There have been several surveys presented.<sup>5-7</sup> Since those surveys were published much additional work has been done that elucidates detailed reaction steps, reaction products, and reaction rates. These later studies have helped resolve many of the controversies presented in the earlier surveys.

Behrens and Bulusu, separately and together, have extensively studied the thermal decomposition of RDX and HMX (also with isotope labeling), in the solid and liquid phases, under very slow heating

rates. See for example Ref. 8. Their results include the decomposition products; an induction period, followed by two acceleratory periods; the Arrhenius parameters for each of these periods, decomposition mechanisms, and how the data can be used to calculate the time and temperature to decompose an amount of HMX, and to estimate the extent of decomposition expected under normal storage conditions. The studies suggest that the process controlling the early stages of HMX decomposition is scission of the N-NO<sub>2</sub> bond, reaction of the NO<sub>2</sub> within a "lattice cage" to form the mononitroso analog of HMX, followed by decomposition of the mononitroso HMX within the HMX lattice to form gaseous products that are retained in bubbles or diffuse into the surrounding lattice. Behrens has also studied the effects of confinement of decomposition products by changing the orifice size in his cell from 100 microns to 5 microns. The results for N<sub>2</sub>O are shown in Figure 1. The increase in concentration and the decrease in time is marked.

Erickson also worked with Behrens and Bulusu in developing rate expressions for the decomposition of RDX. In Ref. 9, they compared their results to those obtained by Trott, Renlund and Erickson using infrared analysis of confined thin films subjected to a variety of heating conditions. In these latter studies additional condensed phase reaction products were found, and the authors attributed the additional products to the differences in sample confinement. In the latter studies the decomposition products were in intimate contact with the decomposing solid.



**Figure 1.** The ion signal Measured with a Mass Spectrometer that Originates from the N<sub>2</sub>O Evolving from HMX at an Isothermal Temperature of 235°C. Results are shown from experiments using a 5 μm and 100 μm reaction cell orifice. The higher rate of gas formation and the shorter duration for decomposition in the experiment with the 5 μm orifice show the effect of containing the decomposition products on the reaction rate. The isothermal temperature was attained at 2500 seconds, average particle diameter is 150 μm.<sup>8</sup>

Brill and co-workers have studied the decomposition of many energetic materials using a rapid, isothermal pyrolysis technique coupled with an FT-IR spectrometer (called T-Jump/FT-IR spectroscopy). For HMX,<sup>10</sup> the gas product data strongly indicate two parallel decomposition reactions:

$\text{HMX} \rightarrow \text{intermediate states} \rightarrow 4(\text{NO}_2 + \text{HCN} + \text{H})$  or  $4(\text{HONO} + \text{HCN})$  at high temperatures,

and

$\text{HMX} \rightarrow \text{intermediate states} \rightarrow 4(\text{N}_2\text{O} + \text{CH}_2\text{O})$  at low temperature.

Litzinger et al. have investigated laser-induced decomposition of RDX.<sup>11</sup> Species detected above the bubbling surface of the RDX include  $\text{N}_2$ ,  $\text{CO}$ ,  $\text{H}_2\text{O}$ ,  $\text{NO}_2$ ,  $\text{H}_2$ , perhaps  $\text{CH}_2\text{O}$ , but only small amounts of  $\text{HCN}$  and  $\text{NO}$ .

The effects of confinement of decomposition products is dramatically shown by Lee of China Lake, for both AP and propellants based on AP. As an example, Figure 2 shows the difference in behavior for AP decomposition with no confinement, with some confinement, and in a hermetically sealed container. All of the samples show the 240°C orthorhombic to cubic phase change endotherm, and the first exotherm. The uncovered sample does not show the second exotherm, while both confined samples show the second exotherm with the increased confinement of the hermetically sealed sample causing the second exotherm to occur at significantly lower temperature.

All of the above studies, and there are many others, show the effects of confining the decomposition products. These results apply to later discussions of ignition, combustion, cookoff and deflagration-to-detonation transition.

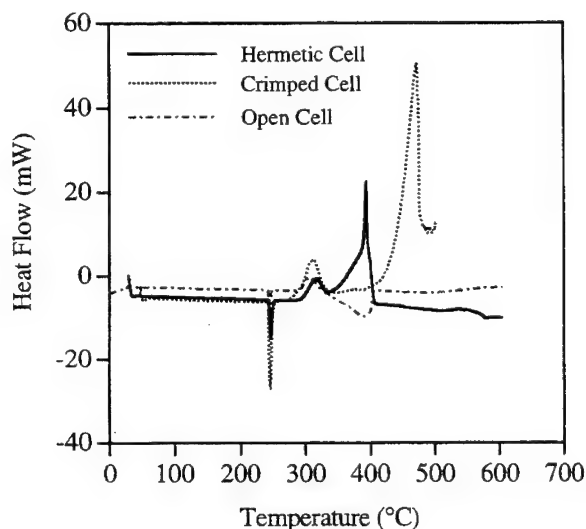


Figure 2. Decomposition of ammonium perchlorate in various containers.



In extrapolating decomposition results to ignition and combustion, care must be taken. Often the conditions are very much different between the regimes, and the results may not extrapolate. For example, Ref. 7b presents many examples where the results of burn rate additives affects the decomposition in one way, e.g., increasing or decreasing the decomposition rate, while the effect on combustion is just the opposite.

Future work needs to focus on the decomposition of propellants, not just ingredients. This is a challenge, especially for those propellants incorporating significant amounts of ammonium perchlorate (AP). Much of the instrumentation and test equipment is sophisticated and expensive, and research personnel do not like to expose their equipment to the corrosive products from AP decomposition, or the decomposition of propellants containing AP. Research on decomposition of propellants needs to be extended to higher pressure and confinement of decomposition products.

### IGNITION

Ignition is the beginning of every combustion process. Hence it must be handled effectively when a controlled combustion process is to be initiated, and it must be prevented reliably if accidental fires and explosions, such as the inadvertent ignition of catocene propellants that caused fatalities, are to be avoided. This process is also important in laboratory investigations to look into the ignition process itself, to classify the sensitivity of propellants with respect to planned or accidental ignition stimuli, to classify additives, or to assess the influence of external parameters.

Solid propellant ignition is both a process and the successful completion of that process. As a propellant sample is externally heated, there is an increase in the surface temperature and a build up of a thermal profile within the sample. When gasification of the sample begins, the gaseous products begin to react exothermically. This heat release increases the gas temperature, and thus, the reaction rates. With additional heating and accumulation of gas phase species the flame will "snap back" toward the propellant surface. At this point, the flame provides sufficient energy for propellant pyrolysis, the external heat source is no longer necessary, and ignition is complete. These processes are graphically illustrated in the general log flux-log time, ignition plot shown in Figure 3.

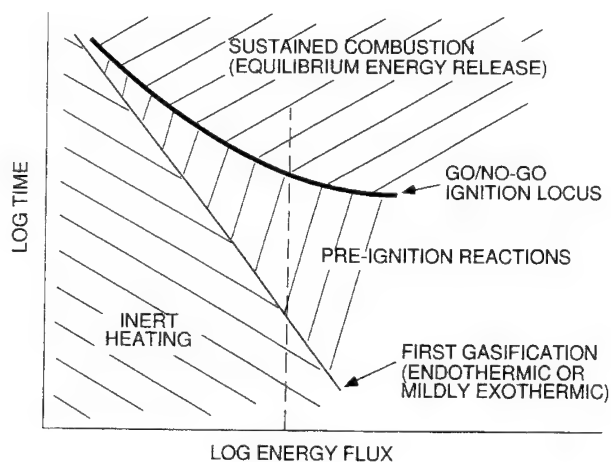


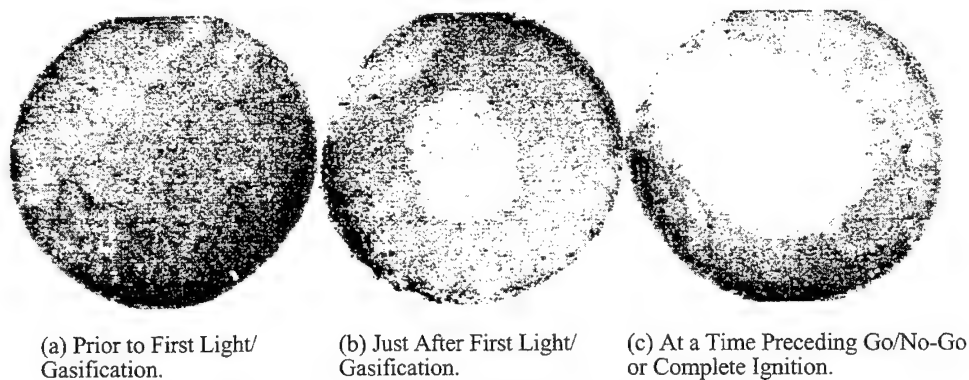
Figure 3. General log energy flux versus log time plot of ignition process.

For a given energy level (the dotted line in Figure 3) a series of events are shown at various times when the sample is subject to the flux. For some initial time, nothing appears to be happening. If the energy flux is terminated during this time and the sample examined, no significant decomposition of the exposed surface is seen. Figure 4a shows a sample of a high energy propellant containing nitramine which was subjected to  $200 \text{ cal/cm}^2\text{sec}$  for a time just prior to first gasification (evidenced by "first light" detected by a photodiode). No significant reaction occurred but a thermal profile was being established within the solid. It is not until the "first gasification" time is achieved that the sample starts to significantly decompose. The flux established and deepened the thermal profile in the solid until a surface temperature was reached that caused significant ablation/decomposition at the surface. For exposures slightly longer than the time necessary for this initial gasification, the sample continued to gasify but did not ignite in the classic sense of ignition. That is, if the external energy flux was removed, the sample would cease gasifying, the temperature profile in the solid will collapse, and the sample would cease regressing. Figure 4b is a sample subjected to  $200 \text{ cal/cm}^2\text{sec}$  at a time just after first gasification (as evidenced by "first light") and shows some decomposition of the surface, while Figure 4c shows another sample at  $200 \text{ cal/cm}^2\text{sec}$  and a time just less than that required for "go/no-go" ignition. This sample shows significant decomposition. Ignition was not achieved until the conditions of flux-time associated with the line indicated as "go/no-go ignition" on Figure 3 were achieved. At this time, and for longer exposure times, the sample was ignited in the sense that if the external energy flux was removed, the sample would continue to burn by itself without the external stimulus.<sup>12</sup> There is another region of "overdriven" combustion--higher fluxes and steeper thermal profiles, where sudden removal of the flux will also cause the sample to extinguish.<sup>6</sup>

Figure 3 is a generalized depiction of the ignition process. It defines three regions separated by two lines:

- Inert heating region
- First gasification line
- Pre-ignition region
- Go/no-go ignition curve
- Self-sustained combustion region

The location of these lines and their relationship to the described regions is dependent on many variables. Propellant formulations, external energy level, and test pressure all affect the time relationship between the establishment of the thermal profile and self-sustained combustion.



**Figure 4.** Nitramine based propellant exposed to radiant energy flux.

Exposing a solid propellant to high energy levels may not be sufficient to initiate combustion. The pre-ignition region is important in that it is in this region that the solid has gasified into reactive intermediate species (pyrolysis products), but these intermediate species have not reacted to final products; thus self-sustained combustion has not been attained. Unfortunately, many investigators view propellant ignition as simply a switch based on a critical surface temperature of the solid. When this "ignition criteria" is satisfied, these people assume an instantaneous change is made from a nonreacting inert solid to burning at steady-state with fully reacted gases at the equilibrium flame temperature. While this criteria may be useful, in some cases of ammonium perchlorate-rubber propellants where the samples ignite almost immediately after first gasification, it does not match reality for all solid propellants and test conditions.<sup>13</sup> Concepts such as minimum ignition energy or ignition temperatures have been introduced. In some limited instances, they have certain merit in spite of the fact that their meaning is equivocal and important boundary conditions are usually ignored when applying the data in other situations. In general, AP-based propellants tested at low flux levels and high ambient pressures show little or no detectable difference between go/no-go and first light/first gasification. Nitramine based propellants under similar conditions, display significant pre-ignition behavior.<sup>14</sup> Pre-ignition behavior can be demonstrated in the AP-based propellants by increasing the flux level and decreasing the test pressure.<sup>14</sup>

The effects of flux and of pressure are shown in Figure 5 for a predominantly AP-HTPB binder propellant. The effect of flux is clearly seen for the first gasification line and the various go/no-go lines. The effect of pressure is also clearly shown. Since the first gasification is essentially the ablation of the solid and primarily dependent on surface temperature, pressure should have little or no effect on this line. However, the rate of conversion of pyrolysis products to final reaction products is very pressure dependent and the go/no-go ignition locus reflects that pressure dependence. The region of pre-ignition reactions discussed earlier (the difference between first gasification and go/no-go lines) is clearly evident for the 50 psia case, as is the diminishment of the pre-ignition region with pressure increase to 100 and 200 psia.

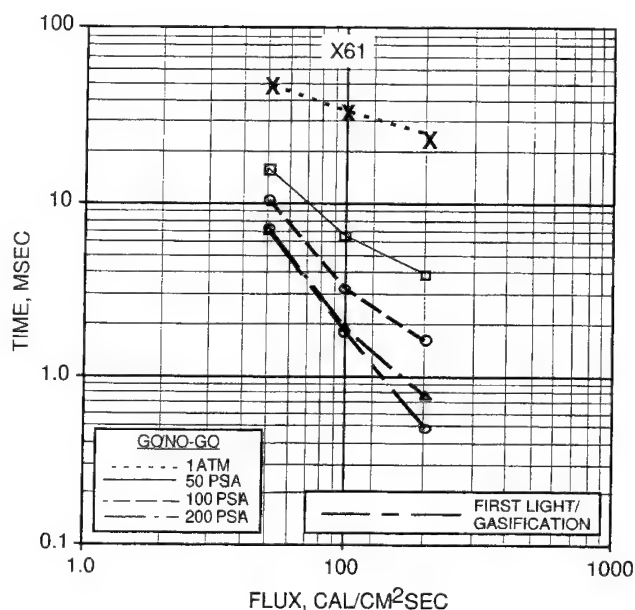
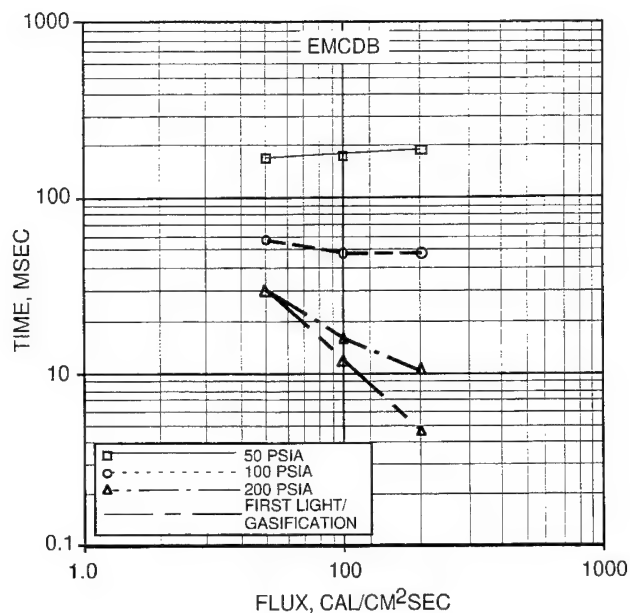


Figure 5. Effect of flux and pressure on ignition of ammonium perchlorate-HTPB propellant.



**Figure 6.** Effect of flux and pressure on ignition of cast modified double base propellant.

Similar behavior, but with even more pronounced preignition behavior, is shown in the ignition map for a cast modified double base propellant, Figure 6. Propellants incorporating high nitramine loading also display this pronounced preignition behavior.

The implications of the pre-ignition region on deflagration to detonation transition and other transient combustion related hazards has been discussed in Refs. 6, 8, and 9, and is shown in the later section on deflagration-to-detonation transition.

This is a general overview of ignition due to thermal flux delivered to the surface (the examples given were for radiant flux).

### Ignition Due to Electrostatic Discharge

As shown in Ref. 1 direct thermal ignition is not the only hazard concern. Ignition caused by impact, friction and/or electrostatic discharge (ESD) are also of concern. Ignition due to impact and friction will not be covered in this paper. However inadvertent ignition associated with ESD is discussed below.

On 11 January 1985, in Heilbron, Germany, a Pershing II missile having an AP/hydroxyl-terminated polybutadiene (HTPB)/aluminum propellant loaded in a Kevlar case, ignited and killed three people. A probable cause was electric charge build-up caused by separation of dissimilar dielectric materials in a cold, dry environment. Another incident, involving the pulling of the mandrel from a large cast HTPB propellant motor, also resulted in fatalities. This was also attributed to ESD. Recorded electrical potentials on a mandrel core may exceed several thousand volts at the end of the mandrel pulling operation.

Much work has been done to investigate the susceptibility of propellants to ESD, and the works of Kent and Rat, SNPE, France; Hammett of the UK; Dreitzler of US Army Missile Command; Lee of the Naval Surface Warfare Center, Raun of Hercules (now Alliant Tech); and others should be consulted. At China Lake, Covino and Hudson performed work summarized in Ref. 15 and discussed below.

When a missile motor is charged to a potential where breakdown occurs, or when a change in grounding conditions allow breakdown of the material, electrical discharge can occur. Discharge generates charge carriers which reduce the impedance of the energetic material and results in rapid current increase. This can lead to arcing, establishment and growth of further discharge, followed by catastrophic discharge. The discharge releases energy, converting a small volume of propellant to gas. If enough material is converted and enough heat generated by this decomposition, then the propellant may ignite, often with severe consequences.

The major determinants for ESD sensitivity are: volume resistivity, di-electric constant, and di-electric strength. At China Lake, Covino and Hudson measured these parameters for HTPB binder, inert HTPB propellants, and live propellants. The volume resistivities were measured as a function of temperature, voltage, time of voltage application, relative humidity and sample thickness. The dielectric constant for these materials was measured as a function of temperature, relative humidity, sample thickness and frequency. Neglecting the effects of breakdown voltage, the higher the dielectric constant the more energy can be stored in the propellant, and hence increased susceptibility to ESD. This coupled with the low dissipation factor for HTPB causes ESD problems. The dielectric breakdown voltage is the voltage that may be sustained across the sample just prior to the transition from non-conductive to conductive. The dielectric strength is the dielectric breakdown voltage divided by the sample thickness.

The results of Covino and Hudson's work was applied using the "percolation" calculations advocated by Kent and Rat. The results show that the overall electrical properties of the propellant was most influenced by the HTPB binder, and to a lesser extent by the concentration and particle size of the aluminum powder. The contribution of the oxidizer particles was primarily in determining the spacing of the aluminum particles and the thickness of binder layer between particles.

This work, along with that of others mentioned above was used to develop ESD hazard assessment protocols as part of the Technical Cooperation Panel, and through various Joint Army Navy NASA Air Force (JANNAF) activities.

### **Other Ignition Hazard Considerations**

In addition to a basic understanding of ignition, there exist several rules of thumb that people sometimes use. Two such "rules" that are sometimes helpful are:

(1) Propellants based on ammonium perchlorate often ignite as soon as the stimulus causes rapid gasification of the propellant. Remember AP propellants usually have less of a pre-ignition region than do double-base or nitramine based propellants.

(2) Within a family of propellants, the faster the burning rate the easier it is to ignite the propellant. Thus propellants incorporating burn rate accelerators, such as catocene, may be very easy to ignite.

As with all "rules of thumb," the above rules should not be blindly used.

What are some of the implications for hazards based on the above discussion of ignition? Obviously propellants that do not ignite at low pressures (i.e., do not sustain) have some advantages in several hazard areas. Several times in the last year I have heard people refer to hazard class 1.3 propellants as being inherently safer than hazard class 1.1 propellants, with the implications that this is true for all

situations. While this is true when we are considering mechanical shock stimuli of tens of kilobar magnitude, it is not always true when other stimuli are considered. Referring back to the sample, stimuli, environment yielding response discussion at the beginning of this paper, and considering the information presented in the ignition and combustion sections of this paper, we see that in many instances the 1.3 propellants can be more hazardous than 1.1 propellants. We have seen that AP based propellants (almost always class 1.3), are often easier to ignite in terms of energy flux necessary to cause decomposition, and in producing go/no-go ignition almost simultaneously with decomposition. Contrast that with the nitramine based propellants (often class 1.1) that show large, pressure dependent delays between decomposition and self-sustained (go/no-go) combustion. The AP based propellants usually burn quite well at one atmosphere, while nitramine propellants often do not burn well, if at all, at one atmosphere. (See the paper by Merrill in this Symposium for additional, collaborating data, and a discussion of deaths in incidents with 1.3 propellant.) As an aside, in my Branch several people involved with daily operations involving propellant have stated that they would rather work with 1.1 propellant, than 1.3.

As discussed earlier, many of the AP/HTPB/Al propellants show high ESD sensitivity, and may result in incidents and deaths.

There are other sample types that may have relatively high hazards in some situations, even though they have a hazard class 1.3. For example, some AP based propellants containing catalysts such as catocene, or some AP based propellants incorporating fine aluminum fuel.

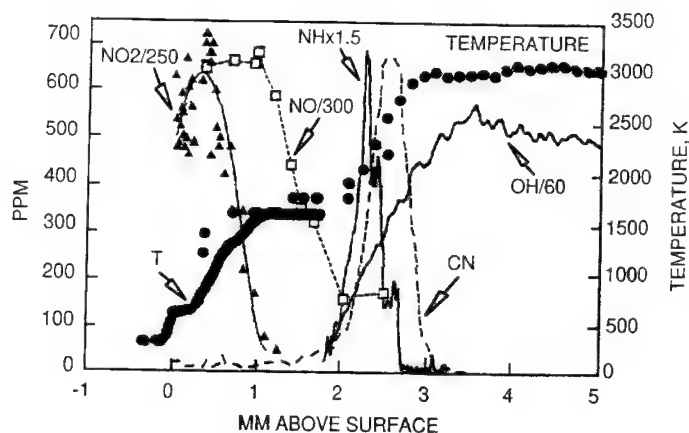
The purpose of these remarks is not to say that one material is safer than another: there are hazards associated with **all** propellants and they must be handled accordingly. I want to dispel the idea that, just because a propellant is classed as 1.3, does not mean that it is insensitive to all hazard stimuli. You cannot treat it as if it were inert.

As will be briefly shown later, and in more detail in Ref. 1, propellants with significant preignition behavior, friability, and shock sensitivity are extremely susceptible to deflagration to detonation transition (DDT) and other forms of delayed detonation.

## LASER ASSISTED COMBUSTION

Laser assisted combustion has been used to study the gas phase reactions of RDX, HMX, and various double base and nitramine based propellants. In these tests CO<sub>2</sub> lasers are used to provide energy flux of sufficient magnitude (higher than that used in laser induced decomposition studies.) to allow ignition of the sample. Since these tests are performed at low pressures (up to one or two atmospheres), the flame zone is stretched in distance and can be studied using techniques such as fine wire thermocouples, triple quadrupole mass spectrometry, time-of-flight mass spectrometry, planar laser induced fluorescence, and absorption spectroscopy. These techniques, used by Parr, Hanson-Parr, and Litzinger and co-workers in the US, and Korobeinichev and Zenin in Russia, provide valuable measurements of flame structure, temperature and species. The following results are illustrative of the type of research being conducted.

The Parrs working in the Combustion Diagnostics Laboratory at China Lake have made extensive measurements of the species and temperature profiles above solid propellants during laser ignition, laser supported deflagration, and self deflagration.<sup>16-19</sup> Energetic materials studied included RDX, HMX, CL-20, TNAZ, ADN, HNF, and AP. Advanced laser diagnostics, such as Planar Laser Induced Fluorescence, were used to make temporally and spatially resolved measurements of the flame structure. Many of these materials have two stage flames not unlike double base propellants. For example, RDX shows a two stage flame under laser supported deflagration (Figure 7). The primary flame raises the temperature to about 1500K and is only about 100-200 microns thick even at 1 ATM. There is an extended "dark zone" where the temperature is relatively constant. The species in this dark zone include NO and HCN. NO<sub>2</sub> was found to convert to NO early in the dark zone. Indeed the cause of the dark zone is the slow reduction kinetics of NO. Beyond the dark zone a secondary flame



**Figure 7.** Temperature and species profile for laser-supported deflagration of RDX at 1 ATM. Laser flux of  $400\text{W}/\text{cm}^2$ .

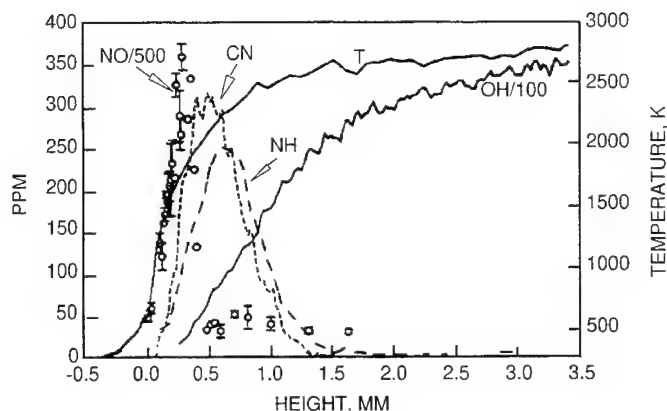
forms, shown by peaks in the radical concentrations CN and NH, the consumption of the NO (and, by other measurements, HCN), and the rapid rise in temperature as well as OH. This flame is about 2.5 mm away from the surface under these conditions.

The dark zone of RDX collapses even at 1 ATM when the laser supporting flux is removed (Figure 8). The primary and secondary flames essentially merge and the temperature profile rises monotonically. Although the dark zone for HMX is present at 1 ATM for self deflagration, it too collapses at elevated pressures. Despite this behavior, the presence of the dark zone indicates two stage chemistry and this is just what is seen in ignition studies: the dark zone species form and accumulate *before* the secondary flame ignites. In a hazard scenario this means it is possible for explosive premixed gases (mostly HCN,  $\text{H}_2\text{CO}$ , NO,  $\text{NO}_2$ , and  $\text{N}_2\text{O}$ ) to accumulate in the rocket motor or within the cracks of a damaged grain. Substantial energy remains for conversion of these dark zone gases to final products. These gases may lead to or enhance the violence of a transition to detonation. In deflagration the temperature rises from 1500K to 2920K, so somewhat more than half the total energy release is available.

The above is illustrative of research being conducted at China Lake. Litzinger et al.,<sup>20</sup> also used laser assisted combustion of RDX and saw evidence of a primary reaction zone involving consumption of  $\text{NO}_2$ , and the reaction in the luminous flame zone consumes HCN, NO, and  $\text{N}_2\text{O}$ . These examples are presented to illustrate the type research being conducted. The reader should consult the references for further detail, and for the work of others. For example, Ref. 19 provides description of some of the diagnostic techniques.

These experimental data are combined with analytic modeling (e.g., the work of Yetter and Dryer<sup>21</sup> and work at China Lake) and are yielding outstanding results. These studies are meaningful in helping understand the pre-ignition, ignition and transient combustion behavior that are described in later sections dealing with ignition, combustion, deflagration-to-detonation transition, and cookoff. The existence of reactive intermediate species play a significant role in these processes.

Future work should see these type experiments applied to propellants, and to higher pressures. Unfortunately some limitations are currently found, especially with AP based propellants and at high pressures for all propellant types, due to the very small distance between the regressing surface and the final flame zone.



**Figure 8.** PLIF measured and absorption calibrated species and temperature profiles for *self* deflagration of RDX at 1 ATM (no external laser heating flux). Temperatures below 0.3 mm come from 5 micron thermocouple. Without substantial external laser flux the dark zone temperature plateau disappears due to the diffusive smearing caused by the close proximity of the radical profiles of the secondary flame.

## COMBUSTION

The pressure-time history due to burning propellant in a closed (or semi closed) container is a function of several considerations and can result in propulsion, explosion, and even transition to detonation. As shown in the fragment impact hazard analysis protocol,<sup>1,4</sup> the balance between gas generation vs. gas venting determines whether an explosion can occur. Similarly a deflagration to detonation transition can occur if several conditions, some related to ignition and combustion, are met.

The pressure-time history is a function of the mass burning rate which in turn is a function of the propellant density, burning surface areas and surface regression rate (often called the linear burn rate or simply burn rate)

$$p, t = f(\dot{m}, \dots)$$

$$\dot{m} = \rho r A_b$$

However, the surface regression rate is a function of pressure, often given as  $r = C_p^n$ . There are several factors involved with the combustion of a confined energetic material, and how that combustion can lead to hazardous situations. The pressure-time produced from the combustion of the energetic material must be compared to the dynamic mechanical behavior of the case, with proper consideration of the venting, to determine the overall response. Again, the gas production rate produced by the propellant is a function of: (1) The surface regression rate of the propellant, which in turn is a function of the pressure, and (2) the burn surface area of the propellant which is in turn a function of the surface regression history.

The following sections briefly discuss burn rate and burn area considerations, as well as providing references to more detailed discussions.



## Burn Rates of Energetic Materials

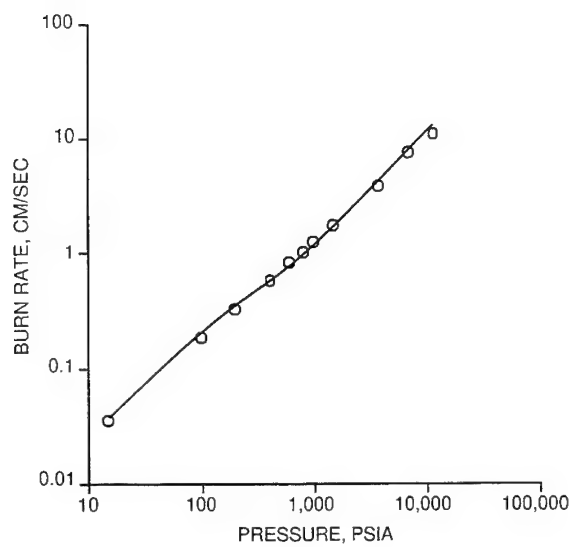
The rate at which a solid is converted to gas during combustion is commonly called the burn rate and is a function of pressure as discussed above, initial sample temperature, and boundary considerations such as flow past the surface (often called erosive burning). Data from Atwood and Curran show the effects of pressure and initial sample temperature on burn rate (Figure 9a and b). Figure 9a shows the burn rate of ambient temperature RDX from 1 atmosphere up to 10,000 psi, while Figure 9b shows the burn rates for RDX samples initially at 223, 298, 373, and 423 K. The symbols on the plots are the experimental data, and the lines are the results of calculations using the "frozen" kinetic parameters discussed below.

Burn rate data are required for hazard assessment protocol considerations discussed earlier, and in other protocols presented in Ref. 1. The data are used in other not so obvious ways: (1) the slope of the burn rate-pressure curve, when plotted logarithm burn rate-logarithm pressure is the burn rate exponent ( $n$  in the expression  $r = Cp^n$ ) and can give some indication of potential hazards, and (2) the temperature and pressure sensitivity of burn rate, coupled with ignition data, can be used to evaluate kinetic parameters, that are, in turn, "frozen" input variables to be used in transient combustion codes to predict convective combustion and deflagration-to-detonation transition.

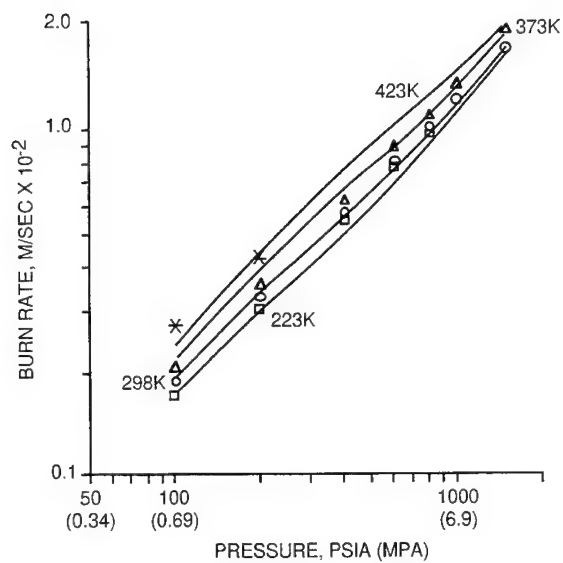
Burn rate exponents very near unity and above are to be avoided since a small increase in pressure has a corresponding larger effect on burn rate, which increases the pressure, and increases the burn rate and so on until a case failure or explosion results. In rocket propellants slope breaks as illustrated in Figure 10 often occur at high pressures. Many times the high pressure portion of the burn rate curve has a burn rate exponent very near or slightly greater than one.

The transient combustion analyses, developed by Price at China Lake, are used to model high rate combustion phenomena such as deflagration to detonation. In fact, transient combustion analyses must be used, as opposed to combustion descriptions such as  $r = Cp^n$ , if one is to fully predict the various aspects of DDT (a later section will discuss this subject). This is because the plots of Figure 9 are essentially the "steady state" values of burn rate-pressure, and may be altered in very rapidly changing environments such as present in DDT experiments. A mistake often made by analysts is to try to apply steady state data to a highly transient situation - almost implying that the transient is a special case of steady state, when in reality steady state is the special case of fully transient.

If one keeps the above consideration in mind one can use the burn rate data and ignition data as special cases to determine kinetic data. Briefly, these models are based on two competing solid to pyrolysis product reactions (similar to Brill's work on nitramine decomposition), followed in each path by sequential pyrolysis product to final product second order gas phase reactions. The kinetic parameters of Arrhenius pre-factor and activation energy (four pre-factors and four activation energies) together with corresponding energy release are determined by evaluating what values give the best fit to actual burn rate [ $r = r(p, T_0)$ ] data and flux-time-pressure ignition data. The values determined for RDX are given in Table 1. These parameters are then "frozen" and used in other experiments to predict laser augmented burn rate, convective combustion, and DDT. The goodness of fit can be appreciated by comparing the results predicted using the set of "frozen parameters" to the actual data (solid curves). As seen in Figure 9a the fit is outstanding over this large pressure range, while Figure 9b shows the excellent agreement, using the same "frozen" parameters, for the temperature sensitivity. These same frozen parameters applied to the ignition data for RDX show the same good fit.



(a) Burn Rate of RDX at Ambient Temperature.



(b) Burn Rate at Various Temperatures.

Figure 9.

TABLE 1  
RDX Kinetic Parameters.

Reaction 1a, Solid to Reactive Intermediate Gases	Reaction 1b Intermediate to Final Products
Prefactor $4.95\text{E}+20 \text{ sec}^{-1}$	Prefactor $1.48\text{E}+11 \text{ cm}^3/\text{mole sec}$
Activation Energy 48.6 kcal/mole	Activation Energy 19.4 kcal/mole
Reaction 2a, Solid to Reactive Intermediate Gases	Reaction 2b Intermediate to Final Products
Prefactor $4.40\text{E}+18 \text{ sec}^{-1}$	Prefactor $1.92\text{E}+14 \text{ cm}^3/\text{mole sec}$
Activation Energy 44.3 kcal/mole	Activation Energy 25.9 kcal/mole

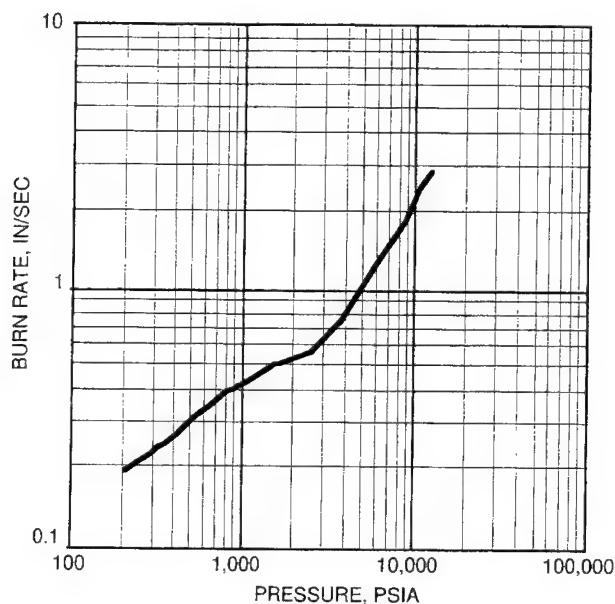


Figure 10. Burn rate as a function of pressure, showing a slope break at high pressure.

### Burn Area

Burn area is an extremely important determinant of the hazard severity given inadvertent ignition of the propellant. References 22 and 23 present extensive surveys of combustion into defects in energetic materials. Damage is involved in many hazard scenarios such as bullet fragment impact, ESD, and some slow cook-off areas. The damage can be pre-existing before ignition/combustion, or it may accompany the ignition/combustion. The burning of pre-strained (hence, in some cases, pre-damaged propellant) is described below.

### The Effects of Strain on the Burning Rates of High Energy Solid Propellants

High energy propellants usually have a high solids loading (the portion of solid ingredients such as ammonium perchlorate (AP), cyclotetramethylenetetranitramine (HMX), aluminum and other

ingredients such as solid catalysts) as compared to the polymeric binder. An obvious condition accompanying high solids loading is that there is less polymeric binder "glue" to hold the solid particles together to form propellants having acceptable mechanical properties. Given these highly loaded propellants, one would like to know such things as how far can a propellant be strained before ballistic anomalies (such as burn rate augmentation) become significant.

The burning rate of a high energy propellant as a function of strain is presented in Figure 11. [Note: The propellant was strained prior to burning. Thus any damage was pre-existing and held open.] The data show that no significant augmentation of burning rate occurs for pressures below 500 psi regardless of strain (the samples fail at approximately 25% strain). At higher pressures ( $p \geq 750$  psi) burn rate augmentation appears for strains above approximately 8%. At 1500 psi and strains above approximately 12%, the sample burns in a vigorous and nonplanar fashion precluding meaningful measurement of a linear surface regression.

Data for several types of propellants show burn rate increase at pressures and strains greater than some threshold values. (The magnitude of the threshold values depends on the propellant.) It should be emphasized that both threshold values (pressure and strain) have to be exceeded, exceeding just one is not sufficient. For example, high strain but low pressure will not cause augmentation nor will high pressure but low strain.

The mechanical response of the propellants to strain was studied using a binocular microscope. These studies showed, using the propellant of Figure 11 as an example, that at 4% strain, debonds (separation, on a micro-scale, of the solid particle from the polymeric binder) between ingredients occurs, between 9-11% strain these debonds are often fully developed cracks, with the walls of the crack in close proximity. At approximately 16% these cracks are open voids; that is, the walls of the crack are no longer in contact with one another. At approximately 24% the sample is often riddled with large cracks and the sample fails.

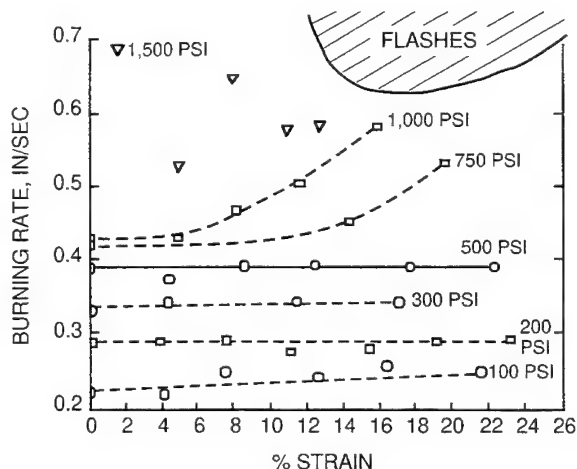
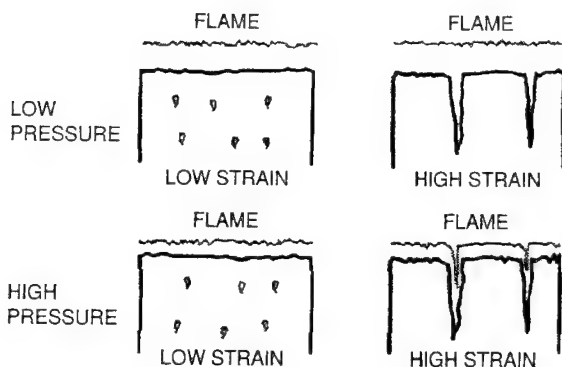


Figure 11. Burning rate of a high energy propellant as a function of pressure and strain.



**Figure 12.** A Mechanism for the Augmentation of Burning Rate Due to Pressure and Strain.

The above, coupled with our knowledge of flame stand-off distance decrease with pressure increase, provides a mechanistic understanding for the burn rate augmentation due to strain and pressure. The mechanism is shown in Figure 12. At low strain values the propellant is not significantly damaged and so regardless of the flame stand-off (Figure 12. (top)), augmentation will not occur. When the propellant is highly strained and fissured, augmentation occurs if the flames can penetrate into those fissures. At low pressures the flame stands too far from the surface to allow penetration, but at high pressures the flame is close enough to the surface to penetrate the fissures and cause burn rate augmentation.

Since flame penetration into the defects seems to be required for burn rate enhancement, a study was done using propellants that had been strained almost to failure and then the tension removed. The voids closed and when those samples with the closed voids were burned, the burn rate was identical to the undamaged propellant burned at that pressure.

These data indicate that under certain conditions strain can cause damage, and if that damage is sufficient and open, and if the pressure is high enough to allow flame penetration into the defects, then burn rate enhancement can occur.

Professor Kuo and co-workers at Pennsylvania State University have studied the combustion of propellants with various cracks and other defects, observing crack growth during combustion. Their extensive publications, for example Ref. 24, should be consulted for more information.

In addition to the growth of cracks during combustion there are other dynamic effects. As burn rate increases the thermal zone gets thinner and the thermal gradient gets steeper. Under these conditions many samples, and ingredients within samples, crack, allowing combustion into these fissures. Under some conditions the cracking is so severe that the sample actually comes apart. Robert Fifer and his colleagues at the Army Research Laboratory have extensively studied this deconsolidation, and the reader is referred to their works.

If the propellant undergoes significant break-up then DDT or other burn to violent reactions may occur. Ensuing sections of this paper briefly discuss these possibilities.

#### **DEFLAGRATION-TO-DETONATION TRANSITION (DDT)**

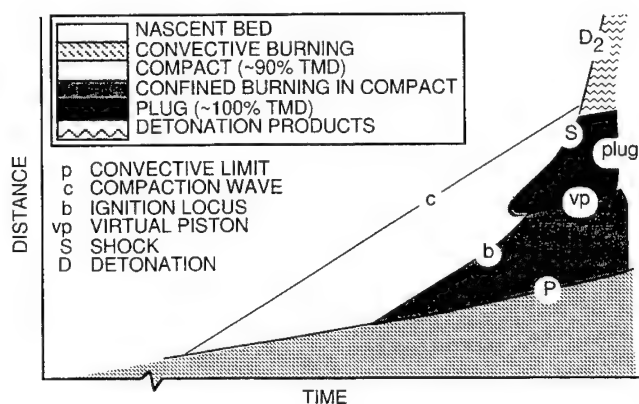
DDT has occurred during firing of rocket motors. In the early 1960s at Hercules, Kenvil, NJ, a ten pound charge of slurry cast cross linked composite modified double base containing AP and HMX

was observed to DDT during routine static firing. The cause was attributed microporosity in the grain.<sup>25</sup> In May 1974, at Hercules, Bacchus, UT, a second stage Trident C4 motor underwent DDT during a routine static test firing. The cause was attributed to a region of highly damaged propellant produced when the nozzle blew out and the motor case "snapped back." DDT has also been observed in granular systems such as gun propellant.

DDT reactions have been widely studied in the laboratory and described in extensive analytical modeling. The excellent experimental work conducted at Naval Surface Warfare Center (Bernecker, Price, Sanduskey, Glancy), at Hercules (now Alliant TechSystems, by Butcher and Keefe), at Los Alamos (McAfee, Asay, Campbell, Ramsay, Son, and Bdzil), at LLNL (Green, Lee), and the excellent analytical work of Baer, Nunziato, Krier, Beckstead, Butler, Kooker, Weston, Son, Kim and Cowperthwaite should be consulted. Many of these works have been published in the International Detonation Symposia proceedings. [Again, this is not meant to be a complete listing.] We, at China Lake, have also been strongly involved in these efforts, and results of our work are presented later in this section.

Bernecker<sup>26</sup> has listed the stages of DDT mechanism for porous charges as: (1) Pre-ignition, (2) Ignition/Conductive Burning, (3) Convective (Reaction) Burning, (4) Compressive (Hot Spot) Burning, (5) Shock Formation, (6) Compressive Burning, and (7) Detonation. McAfee et al.<sup>27</sup> has depicted these stages (combining 1-3 and using slightly different nomenclature) in the distance-time plane as shown in Figure 13.

Whether or not a propellant reaction can transition from a burning reaction to a detonation is determined by several considerations. The key requirement for this transition to occur is a sufficient surface to volume ratio and porosity of the energetic sample either through manufacture and loading, in the case of some gun propellants, or through large scale damage in the case of missile propellants. For missile propellants the first consideration then is the likelihood of the propellant being damaged either before or during the burn. This is a critical consideration because, with rare exceptions, it is nearly impossible for a consolidated propellant at near theoretical maximum density (TMD) to undergo a DDT reaction.



**Figure 13.** Schema of the DDT process in granular HMX.

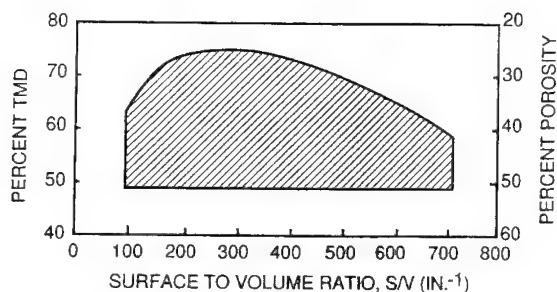


Figure 14. Limits of DDT or granulated propellant samples.<sup>28</sup>

Figure 14 presents the limits of DDT for granulated propellant samples of a given type.<sup>11</sup> This plot shows that you must have sufficient TMD - for this propellant formulation and confinement about 49% TMD; any less will not sustain and accelerate the reaction. If the sample is too dense, the DDT reaction will not occur. Similarly there is a range of surface to volume required (100-700 inches<sup>-1</sup>) if DDT is to occur. If these conditions, or similar conditions for other samples, are not met then a DDT reaction, for this propellant, is extremely improbable. Although transition to detonation may not be probable, an explosion may still occur. In order to determine whether an explosion may occur, the pressure and the rate of pressurization caused by gasification must be determined and compared to the rupture characteristics of the motor case.

If the propellant is damaged and if the resulting %TMD and surface-to volume ratio are in the "right" range then DDT is extremely likely. Whether or not the DDT occurs is determined by the pressure and pressurization rate within the vessel and the rupture characteristics of vessel (motor case). If the motor case ruptures "too soon," then confinement is lost and the DDT reaction becomes unlikely. (The rupture may be a violent explosion.) The rupture characteristics of the vessel need to be determined experimentally and/or analytically but will not be discussed further in this paper.

The distance time history of a DDT reaction of 1080  $\mu$ m HMX powder, originally loaded in a heavy walled tube to 61% TMD is shown in Figure 15. The figure shows the x-t location of the luminous front, the weak compaction wave, and the strong compaction wave and the build up of detonation that occurs 104 mm down the tube and after approximately 400  $\mu$ seconds. [Note: in this experiment, time = 0 was taken to be first detection of luminosity at the igniter interface, not necessarily first reaction of the igniter.] After this transition the detonation wave moves through the rest of the sample at 5.9 mm/ $\mu$ sec. The location of the lines in the x-t plane are strongly influenced by several considerations. These include the degree of confinement, the strength or "brisance" of the ignition stimulus, the sample thermochemical and physical characteristics, the charge dimensions (diameter and column length), and the intrinsic detonability of the material. The physical characteristics of the sample include the size and shape of the damaged pieces, the porosity and gas permeability, and the compressibility. The thermochemical considerations include the chemical composition of propellant, pyrolysis products, and final products; the kinetics and energetics associated with the pyrolysis process (solid propellant going to reactive intermediate species), and the kinetics and energetics associated with the conversion of the reactive intermediate gases to final products.

It must be stressed that the above items are listed separately but in fact the DDT process is a highly coupled interaction of these various considerations.

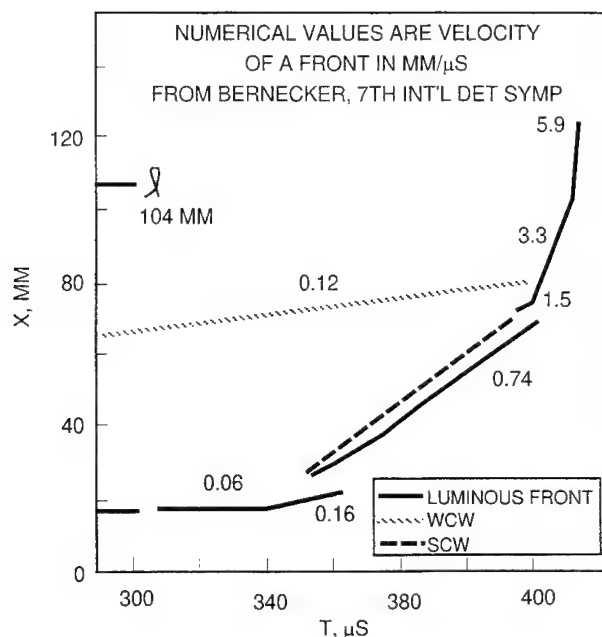


Figure 15. Wave front velocities for a DDT reaction (from Bernecker<sup>29</sup>).

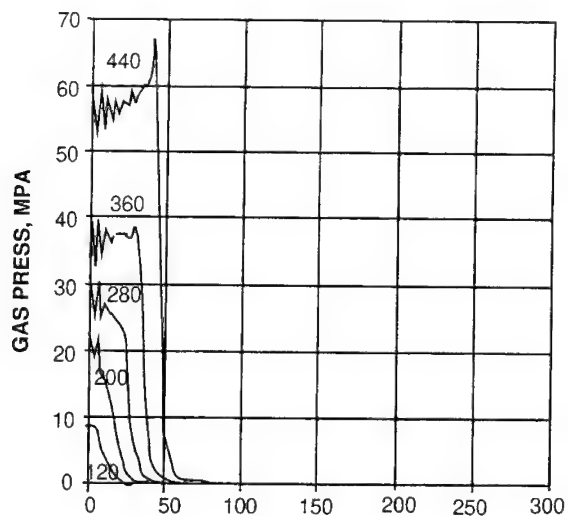
From the above discussion it can be seen that the following types of data are necessary in order to predict whether DDT is likely to occur:

- Strength and brisance of ignition stimulus
- Confinement and rupture characteristics of the case
- Compaction behavior of the sample - how the %TMD changes with pressure
- The compaction/drag/permeability - the compaction is caused by an imbalance of forces between the drag of the gases flowing over the particles and the particles ability to resist compression. As the sample is compacted, the permeability (the ability of gas to flow through the sample) is changed
- The kinetics and energetics associated with the pyrolysis and conversion to final products
- The compressive ignition characteristics of the compacted material
- The detonability of the propellant

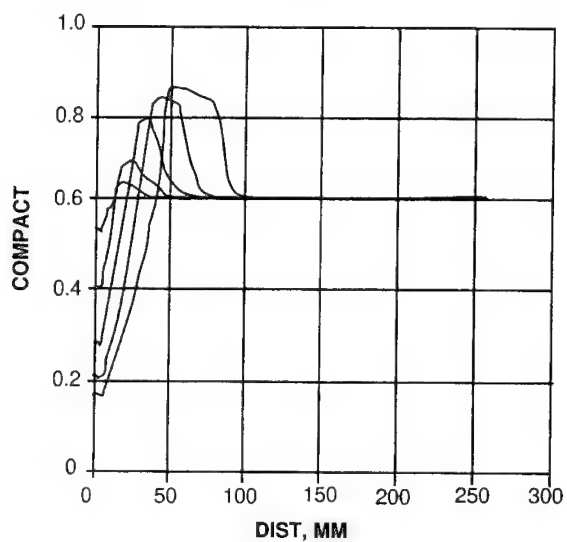
Reference 1 discusses the various test techniques used in conjunction with DDT studies, as well as providing references to detailed analytical studies.

Previous sections mentioned that the ignition flux-pressure-time data, together with burn rate-pressure-initial sample temperature data, are used to determine kinetic parameters in a transient global kinetics combustion code. At China Lake, this transient combustion code is then used in a larger DDT code to predict aspects of (a) gas pressure in the tube as a function of location and time, (b) compaction profiles in distance and time, (c) amount of solid pyrolyzed, and amount of pyrolysis products reacted to final products, and (d) thermally and mechanically (piston) stimulated DDT. A few examples are shown here in Figures 16 through 18.





(a) Pressure.



(b) Compaction.

**Figure 16.** Pressure and compaction profiles at beginning of DDT process.

The analytical modeling of DDT performed at China Lake has been described in Ref. 30. This modeling is based on much of the work presented in earlier sections of this paper. For example, it uses the kinetics and energetics determined for ignition and combustion, as described earlier, to describe the combustion behavior in the DDT process. In addition it uses the drag and compaction

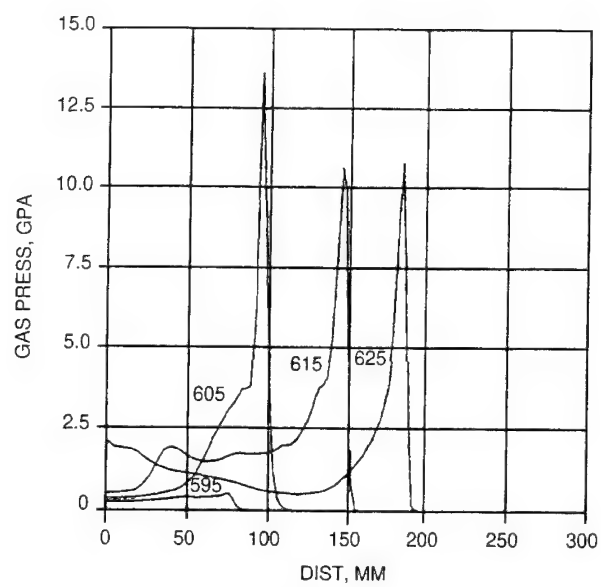
data determined at Naval Surface Weapons Center and at China Lake. The following presents typical results of our calculations.

Figure 16a presents the predicted gas pressure-distance profiles at 120, 200, 280, 360, and 440  $\mu$ seconds, showing a relatively slow build-up in pressure, for 1080 $\mu$ m HMX burning in a heavy walled tube (essentially the same conditions of the actual experiments shown in Figure 15). Figure 16b shows the corresponding compaction profiles. At  $t = 0$ , the tube is uniformly filled at 61% TMD. As the first material reacts, some of the material is gasified, and starts pushing adjacent material down the tube. As the reactions continue, more and more of the powder is compacted by, and ahead of, the pressure wave, and a plug of approximately 85% TMD is formed.

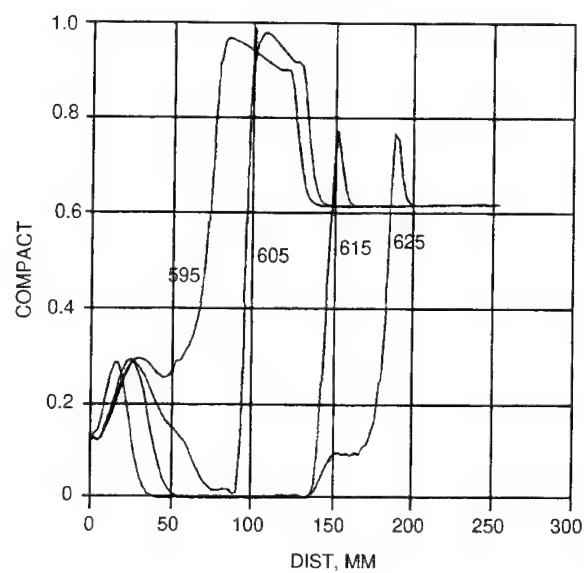
Figure 17a presents the gas pressures at the transition at 595, 605, 615, and 624  $\mu$ seconds. When this plot is compared with Figure 17a two observations are made: in Figure 16a the pressure slowly builds (the time steps were 80  $\mu$ s) to a modest pressure (60-70 MPa) while in Figure 17a the gas pressure goes from less than 1 GPa to over 12 GPa in 10  $\mu$ seconds - a tremendous acceleration. Figure 17b presents the corresponding compaction plots. At 595  $\mu$ s the reactions have caused an almost impermeable plug of approximately 95% TMD. As the reactions continue that plug is rapidly consumed with the TMD going to zero in the area of reaction.

Figure 18 is a plot of the location of the leading edge of the compaction profile as a function of time. The solid curve is for the calculations presented in Figs. 16 and 17, and shows transition to detonation at approximately 125 mm and 600  $\mu$ seconds. These values can be compared to the experimental values of 104 mm and approximately 430  $\mu$ seconds from first luminosity presented in Figure 16. [Note: The time differences are not unexpected. The calculations set  $t = 0$  to be when the igniter is initiated, while  $t = 0$  for the experiment was when first illumination out of the igniter was observed.] The dashed curve is for the case where the prefactors for the gas phase reactions were increased by 3 orders of magnitude (from  $10^5$  to  $10^{11}$ , for one reaction path, and from  $10^{11}$  to  $10^{14}$  in the other gas phase reaction path). As can be seen this change to faster kinetics produces significant change. The transition to detonation occurs too quickly, but more importantly it occurs in the wrong place. Predictions for other cases bear out the tremendous importance of the gas phase kinetics if experiments are to be properly modeled. As mentioned earlier these kinetic parameters are independently determined from the burn rate as a function of pressure and initial sample temperature coupled with the ignition flux-time-pressure data.

*Critical impact velocity.* Before leaving this section on DDT, I would like to comment on the use, or rather misuse, of the term critical impact velocity. The term refers to an impact velocity in the shot gun test, that produces enough damage to the sample, so that the damaged sample will experience a DDT reaction in the DDT tube test. This part is relatively straight forward; the problem comes with an intermediate step--closed bomb firings. Butcher and Keefe, burned their shotgun damaged samples in a 91cc closed bomb. They found that when the samples were damaged enough to produce a pressure rise rate of  $2.5 \times 10^6$  psi/sec in that 91cc closed bomb, then similar damaged material would transit to detonation in the DDT tube experiment. By plotting impact velocity and pressurization rate as measured in the closed bomb, and using this  $2.5 \times 10^6$  psi/sec pressurization rate they determined the corresponding "critical impact velocity" for that propellant. The problem today is that people do not remember that the CIV values that Butcher and Keefe reported were for that one propellant, or for a family of propellants of very similar composition, tested in that one closed bomb. You cannot compare data if propellants have significant differences in surface burn rate, burn surface area, or density (see earlier discussion on pressurization). Similarly you can't make comparisons if the closed bombs are different volumes and/or design. This is mentioned because recently some people looked at some closed bomb data of an AP based propellant, a propellant that produced a rather high  $dp/dt$  in a closed bomb, and deduced that this propellant would have a DDT problem because it exceeded the critical impact velocity. This was not necessarily true because this propellant had a higher burn rate, and was more friable (more burn surface area) than the propellants studied by Butcher and Keefe.

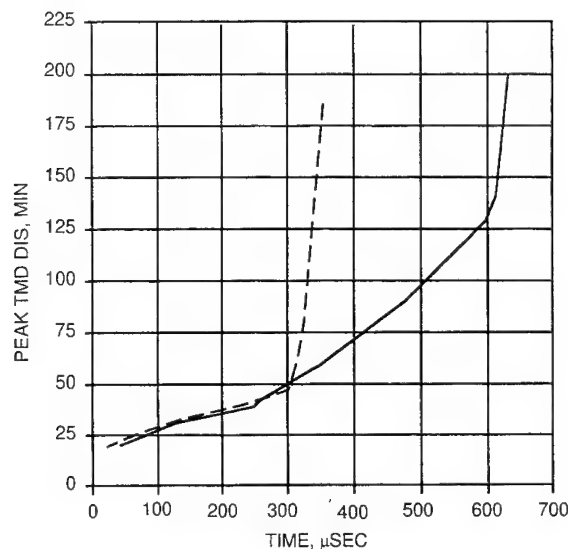


(a) Pressure.



(b) Compaction.

Figure 17. Pressure and compaction profiles at onset of transition to detonation.



**Figure 18.** Location of leading edge of the compaction profile as a function of time.

#### **DELAYED DETONATION (OFTEN REFERRED TO AS XDT)**

There are many examples of delayed detonation phenomena. Delayed in this context refers to detonation occurring at times longer than associated for prompt shock to detonation transition (SDT). The early work of Green, et al.<sup>31</sup> and Keefe<sup>32</sup> should be consulted. Since those early works, much additional work has been performed, showing delayed detonations in many different instances. A recent joint NATO Insensitive Munitions Information Center/The Technical Cooperation Panel (NIMIC/TTCP) workshop held at China Lake (in conjunction with the NIMIC/TTCP cookoff workshop described later), resulted in 8 different XDT scenarios: (1) rocket motor bore effects, (2) bullet/fragment impact on high explosives and some propellants, (3) gap tests, (4) shot gun tests, (5) pick up tests, (6) sometimes in sympathetic detonation tests, (7) cavitation in liquid explosives, and (8) flyer plate impact tests.

Items (1) and (2) are of concern with respect to rocket motors having some form of a center perforation as observed by Nouguez and co-workers at SNPE.<sup>33</sup> When they fired a bullet through the propellant web it caused no detonation, while a similar bullet, at the same velocity, when fired so that it went through the bore caused detonation. At China Lake, Finnegan and co-workers investigated a similar phenomena in an idealized one dimension geometry. They fired fragments at a target consisting of metal cover to simulate the motor case, slab of propellant, air gap, propellant, and metal. They found that as the projectile penetrated the first slab of propellant it damaged the propellant and a debris cloud moved across the air gap. When this debris cloud impacted the second propellant slab it usually ignited and depending on the gap and the propellant material would either burn vigorously or detonate. Finnegan found that there were three regimes of detonation reaction depending on the bore spacing: one region of prompt, shock induced reaction and two regions of delayed ( $50+ \mu$ s after debris cloud impacted second surface). From these studies Finnegan concluded that (1) some confinement was necessary to achieve these delayed detonations, (2) the second surface did not have to be "live"—it could be inert and still cause the delayed detonation, and (3) the reaction required the live debris cloud, the second surface and the projectile. Tests with a hole on the second side, so that the debris cloud ahead of the projectile, and the projectile, would pass through the hole and not impact

the second side resulted in no delayed detonations. In addition Finnegan performed a limited number of tests where the second side was either concave or convex.

Finnegan's test is of interest because so far it mimics responses of ordnance items to bullet and fragment impact. Those items that detonate in the large-scale test, also detonate in Finnegan's test, while those that violently burn in the large-scale tests also do so in Finnegan's test.

These phenomena have been incorporated into the bullet/fragment impact hazard assessment protocol.

### COOKOFF

As mentioned earlier, fire is a major concern on-board ship, especially for the large aircraft carriers. Operations on board a carrier deck are carefully orchestrated events, many of them occurring simultaneously, especially during combat. There is the launching of aircraft with the high g forces associated with catapult launch; there are the hard, high speed landings on a moving, small deck (when compared to normal landing fields) with rapid deceleration when the tail hook engages the arresting cable (sometimes referred to as "controlled crashes"); there is the race between launching aircraft, and recovering aircraft, often low on fuel, from the previous launches; there are often many planes on deck, in various stages of readiness--some being re-fueled, some being re-armed; there are often "bomb farms" (stockpiled weapons stores on the deck) because you do not have time to move enough ordnance from the magazines to the deck and onto the planes without stockpiling the items on deck, there are hot gas "huffers" used to start engines, there is handling equipment, and there are people, all on deck, all moving around. The potential for fire is extremely high and the potential of weapons to be caught in that fire is also relatively high. And there is no place to run and hide.

As presented by Beauregard<sup>34</sup> from October 1966 to May 1981 there were four aircraft carrier accidents that resulted in fires and munition explosions. Two hundred and twenty sailors and naval aviators were killed and seven hundred and eight were injured. In terms of 1990 dollars, there were 478 million dollars in ship damage, and 1,958 million dollars in aircraft damage. The following descriptions of the events were excerpted from Ref. 34.

On 26 October 1966, two sailors aboard the USS Oriskany were re-stowing aircraft flares from an aircraft returning from a mission over Vietnam. One of the sailors dropped a flare that actuated. One of the sailors picked up the actuated flare, threw it in the locker, and closed the door. Unfortunately there were some 2.75 inch rocket warheads in the locker. A warhead detonated spreading the fire. A second warhead detonated, followed by explosion of a liquid oxygen tank. Forty four sailors were killed and 156 injured. Two helicopters and four aircraft were severely damaged. The Navy spent over \$48 million repairing the ship.

On 29 July 1967, onboard the USS FORRESTAL, a ZUNI rocket was accidentally fired from an aircraft being readied for a mission. The rocket crossed the flight deck, struck another aircraft, and ignited a fuel fire. Ninety seconds after the fire started, a bomb detonated, killing or wounding most of the fire fighting crews. The detonation ruptured the flight deck, and burning fuel spilled into the lower decks. Bombs, warheads, and rocket motors reacted with various degrees of violence. There were 134 deaths and 161 injured. Twenty one aircraft were destroyed and the repair to the ship cost over \$758 million.

On 15 January 1969, onboard the USS ENTERPRISE, the exhaust from an aircraft engine starter unit impinged onto a pod containing four ZUNI rockets, causing one of the warheads to detonate. Fragments ruptured the aircraft's fuel tanks and a fire ensued. Less than one minute after the first explosion, three more ZUNI warheads detonated, blowing holes in the flight deck and allowing burning fuel to pour into the lower level. In all there were 18 munition explosions, and 8 holes were blown through the flight deck. There were 28 deaths and 344 injuries. Fifteen aircraft were destroyed and the ship repair cost over \$487 million.

On 26 May 1981, an EA-6B aircraft returning to the USS NIMITZ at night, struck a helicopter, other aircraft, and a tow tractor before coming to rest. The ensuing fuel fire was contained and the order was given to begin the clean-up. As men approached, a SPARROW warhead buried amongst the hot debris detonated and re-kindled the fire. Three more warheads detonated before the fire could be extinguished. There were 14 sailors killed and 39 injured. Three aircraft were destroyed and 9 damaged. Repair to the ship cost over \$58 million.

Lest anyone think that cookoff only happens on ships, or is just a Navy problem, consider the Roseville, California rail yard fire, and various ammunition dump explosions (also taken from Beauregard<sup>34</sup>). At Roseville, on 28 April 1973, a boxcar carrying bombs caught fire and caused the bombs to explode. In the next few hours 18 boxcars exploded in succession. Fortunately no one was killed but 48 people were injured and there was \$24 million in property damage. In 1965 the ammunition dump at Bien-Hoa, Vietnam air base was destroyed by fire and secondary explosions. In March 1965, the Viet Cong attacked the munition storage area at Qui Nhon. The fire and secondary explosions killed 3 and injured 34, and many tons of ammunition were destroyed. Also in 1965 fires and secondary explosions at Da Nang destroyed more than \$123 million of ammunition. Two incidents in Desert Storm reveal that cookoff problems still exist. During the war a SCUD missile landed a few hundred yards from where tons of US ammunition were stored. Fortunately, the missile did not directly hit the site. After the war there was a fire in a transport vehicle at the Army's Camp Doha in Kuwait. An explosion spread the fire, causing secondary explosions. The Army lost more tanks in that accident than in the entire war against Iraq. Fifty-two soldiers were injured in the incident and three were killed while clearing damaged ordnance.

There are obviously many cookoff situations to be considered, but much of the attention falls at the two ends of the spectrum: fast cookoff when ordnance is subject to direct fire such as burning aircraft fuel or a bonfire, and slow cookoff. The MIL-STD-2105A defined the fast cookoff and slow cookoff tests for the US. While the conditions for fast cookoff are widely accepted, those for slow cookoff have been in almost constant debate. The prescribed 6°F/hr heating rate (3.3°C/hr) has been the topic of heated debate in many cookoff workshops. Many feel that it is not representative of any real threat, that it takes too long to run the test (sometimes days), that the test keeps going until a reaction occurs regardless if that is a realistic time duration, that it gives worst case reaction (almost thermal explosion) because of the low temperature gradient (although some tests, using a higher heating rate, seem to indicate that in some instances a more violent reaction occurred), and that we waste much money trying to design weapons to this unrealistic test. Others defend the test, saying that some criteria is needed, and it has often been said that while it may not be the best test, there is an extensive data base. While I tend to be in the first group, often countering with "What good is an extensive data base, if almost everything fails?" For example, of 25 motors tested for slow cookoff at 6°F/hr, only one passed, and it was an unusual geometry. I also facetiously compare continuously using this heating rate simply because we have a data base to the example of the fellow looking for his wallet under the street lamp, not because he lost it there but because it was the only place he could see in the darkness. I believe that there is hope to resolve this issue, and get on with more important technical issues. The MIL-STD 2105B allows for a Threat Hazard Assessment (THA) to be made. This THA looks at the weapons system from "cradle to grave" and tries to describe the environments the weapons system is likely to encounter, the hazards associated with the environment, the stimulus levels likely to be seen in those encounters, the probability of being subject to the event(s), and the likely reactions. From this THA comes recommendations of what stimuli and levels the munition should be tested for. This THA can be used to recommend that some slow cookoff heating rate other than 6°F/hr. is more realistic for that weapon and its life cycle exposure, and that the weapon should be tested at this more realistic condition. Some of the THA that I have reviewed are recommending higher slow cookoff heating rates (e.g., 50°F/hr, 52.8°F/hr—not sure where this level of accuracy came from, and 75°F/hr).

Much work has been done in the cookoff area (see for example various works by Pakulak of NAWC China Lake, Butcher of Alliant TechSystems, Tarver of Lawrence Livermore National Laboratory). From these many studies, the temperature and time to reaction can be predicted for many materials. However the ability to predict violence of reaction is still a goal, and reflects the complex interaction between the sample, the stimulus and the environment. For cookoff, the stimulus and environment are

obviously intertwined. The sample is also difficult to describe at times because it changes as it decomposes, and the decomposition products may play a significant role. In the US, various laboratories and investigators are working together on what has been termed "The Cookoff Grand Challenge." This cooperative effort seeks to join experiments with analytical modeling. Fundamental parameters needed for the modeling have been identified and are being measured. These data are given to the modelers for use in their codes. Benchmark tests are also being proposed. These tests will be "proof of principle" tests where those doing analytical modeling will attempt to predict the results before the experiments are run. The results of the experiments will then be compared to the analytical predictions. Hopefully interactions between the groups will enhance progress toward the goal of being able to predict violence of reaction as well as time to and temperature of reaction.

As part of this "Grand Challenge" various laboratories are investigating the behavior of a series of propellants, that have controlled formulation changes. These propellants are summarized in the following table:

TABLE 2  
PS Propellants

Weight % Ingredients	PS1	PS2	PS13	PS4
R-45/IPDI	7.77	7.77	5.77	7.77
DTBH	0.05	0.05	0.05	0.05
Flexone	0.05	0.05	0.05	0.05
Tepanol	0.12	0.12	0.12	0.12
AL (29 $\mu$ m)	20.00	20.00	20.00	20.00
AP (400 $\mu$ m)		50.00		
AP (200 $\mu$ m)	50.00		50.00	48.80
AP (20 $\mu$ m)	20.00	20.00	20.00	20.00
Dioctyl Sebacate	2.00	2.00		2.00
Isodecyl Pelargonate			4.00	
Iron Oxide, Fe <sub>2</sub> O <sub>3</sub>				1.20
DDI				

Work on this same series of propellants is presented by others at this meeting (Merrill; Boteler, Covino and Lindfors; and Tao et al). The decomposition behavior of some of these propellants as determined by Lee, was discussed earlier. Fundamental data being obtained for these propellants include thermal conductivity, thermal diffusivity and coefficient of thermal expansion as a function of temperature, decomposition behavior (with and without confinement of products), and the burn rates as a function of pressure and sample temperature. In addition other laboratory scale experiments are being conducted to obtain mechanistic understanding of the important parameters. One example of these type experiments are those being conducted at China Lake by Dimaranan, Hudson and Lee, using the PS series of propellants. One such experiment uses a small "gun" device. The propellant samples are heated at a constant rate, and when the propellant "cooks off" the resultant gases expel the pellet, and the pellet velocity is measured. The velocity of the propellant, like violence of reaction is determined by the pressure-time history, except in the case of the gun, part of the confinement is released, giving a measure of the violence of the energetic material. Propellants PS 1 and PS4, identical except for the addition of iron oxide in PS4, show effects of composition. Figure 19 shows that both materials produce approximately the same pellet velocity at cookoff, but that the cookoff of PS4 occurs at approximately 250°C while the cookoff of PS1 occurs at approximately 320°C. Also shown on the plot is the minimal differences of heating at 10 or 15°C/min. The difference in decomposition is graphically illustrated by scanning electron micrographs (SEM) of samples heated to a temperature, then cooled and examined using SEM. The samples heated to 245°C show marked differences. PS4 samples show cracking of AP crystals and decomposition of propellant while the PS1 samples do not show this decomposition. This shows the importance of a small change in formulation, and the importance of gaseous decomposition products for PS4.

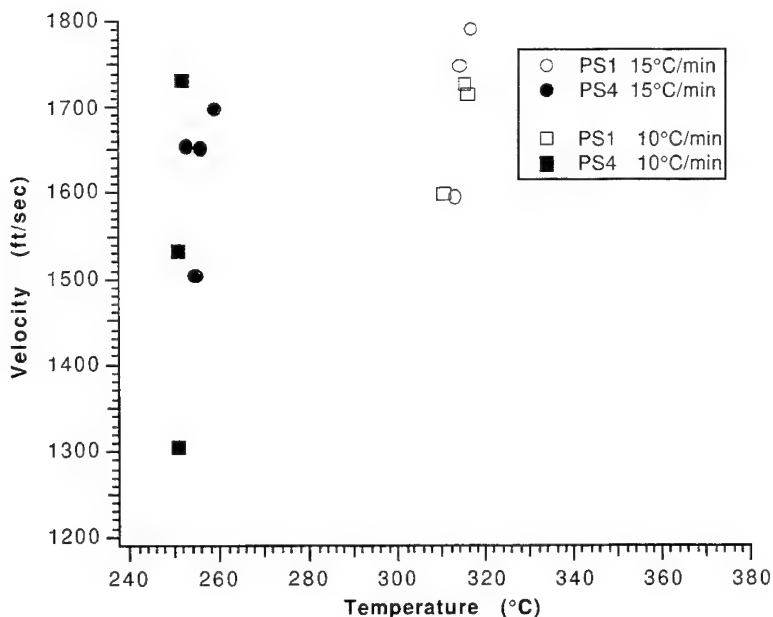


Figure 19. Velocity vs. cookoff temperature for PS1 & PS4.

The apparatus is designed so that the propellant can be ignited at a temperature lower than the cookoff temperature. The goal is to determine if the cookoff event is related to the temperature sensitivity of burn rate, or if other factors dominate. As shown in Figure 20a and 20b, when the propellants are ignited at lower temperatures the velocities are only modestly increasing with temperature. However at temperatures below, but approaching the cookoff temperature, the pellet velocity of the ignited sample is similar to that of the cookoff sample. This may have implications if you want to reduce the cookoff violence by intentionally lighting the propellant before it cooks off. The propellant may have to be ignited at some temperature much lower than the cookoff temperature, and there is obviously a trade off between igniting at this lower temperature vs. letting the sample heat further, increasing the violence of reaction but also "buying time" to try to mitigate the reaction. In another series of tests designed to partially answer the question of how much time can be used, the samples were heated at a rate to a given temperature and then held at that temperature. The results are shown in Figure 21 plotted as hold time after reaching temperature, and the temperatures. As shown, the closer to the cookoff temperature the shorter time before the sample will cook off anyway. But as the temperatures are lowered the times increase markedly, until at some temperature the reaction takes a very long time to occur, if at all. Firefighters often want to know: "How much time do I have to fight the fire, given a certain temperature of the propellant?" These are just examples of the type of work being conducted in our laboratories in support of the Grand Challenge.

The analytical modeling studies conducted at Sandia and LLNL as part of the Grand Challenge are somewhat different in their approach, but both have shed valuable insight into the cookoff violence. Both consider not only the energetic material reactions and state of the energetic material and its products, but also consider the thermomechanical effects of the surrounding confinement. The Sandia approach is a multidimensional model coupling thermal, chemical and mechanical response of reactive and nonreactive components. In this model, TREX3D is analysis software which links reactive heat transfer with mechanics. It uses an operator splitting technique whereby thermal/chemical fields are



advanced for a fixed mechanics field, then the mechanics field is advanced over the same time interval using the updated thermal/chemical fields. The elements are the JAS quasi-static finite element mechanics solver which feeds stress/strain data to the COYOTE finite element thermal/chemical solver which in turn feeds temperature and fraction of material decomposed a reactive, elastic-plastic constitutive model, REP. JAS and REP are coupled to give equilibrated stress fields.<sup>35</sup> This code, and its earlier one dimensional version, has been used to model the behavior of the NAWC small scale cookoff bomb with AP based propellant, the LLNL ODTX experiment, the Naval Surface Warfare Center Variable Confinement Cookoff Test, the French cookoff experiment, a 3D rocket motor with star grain, and the Sandia hot cell experiment of Renlund. The application of the model to Renlund's hot cell experiment was used to improve the experiment--a nice coupling between analysis and experiment.<sup>36</sup>

LLNL uses the ALE 3D code to describe various cookoff situations. These modeling capabilities include thermal diffusion and convection to transport heat to the energetic material in the weapons system, temperature based chemical reaction modeling of the decomposition, and mechanical modeling of both the metal casing and the unreacted and decomposed energetic material.<sup>37</sup> Nichols has applied the modeling to describe the reaction of energetic material in the Variable Confinement Cookoff Test developed at the Naval Surface Warfare Center.

There are several other analytical tools available. See for example, Ref. 38.

The NATO Insensitive Munitions Information Center (NIMIC) and the Technical Cooperation Panel (TTCP) recently held a workshop on cookoff at China Lake. There were presentations of current work followed by three "splinter session" working groups. Each group was to define the most important issues in the cookoff area, and determine what work needs to be done in the future. The following is a very brief overview of these discussions, and provides a list of future cookoff considerations.

All three groups recognized the need for mechanistic understanding of cookoff and the capability to predict the violence of reaction. The responses of the three groups, and their emphases, varied, but there was much similarity. Part of their responses can be grouped into the sample + stimuli + environment ----> response notion presented at the beginning of this paper. Obviously, all of the groups were concerned with the violence of the reactions in terms of metal acceleration (size and shape of fragments, fragment velocity) and blast wave (pressure wave impulse, structure and velocity), and the resulting inflicted damage.

Samples range from undamaged, pristine propellants to degraded samples that have undergone significant mechanical and chemical changes. These samples need to be described in terms of: (1) physical description of the sample, both energetic material and confining material(s) as they change due to the thermal insult (porosity, specific surface, density, thermal expansion, mechanical properties such as stress-strain, fracture state/morphology). These data need to be as a function of temperature, (2) thermal properties, such as conductivity and diffusivity, of the solid, gaseous decomposition products and confining medium, again as a function of temperature, and (3) thermochemical properties such as reaction rates (kinetic parameters, burn rates) for the undamaged and damaged materials, in various degrees of confinement, all considered at temperatures and pressures.

All three groups when discussing stimuli, questioned the relevance of the 6°F/hr (3.3°C/hr) heating rate requirement. The groups also indicated that the Threat Hazard Assessments should determine what heating rates should be used for testing. However much improvement to the THA approach must be made, again changes based on mechanistic understanding of cookoff.

Environmental considerations such as confinement and resulting pressure, and the complex coupling with the reaction of the sample, must be understood if significant progress is to be made. It was also suggested that the fire fighting and user communities help define the environmental considerations.

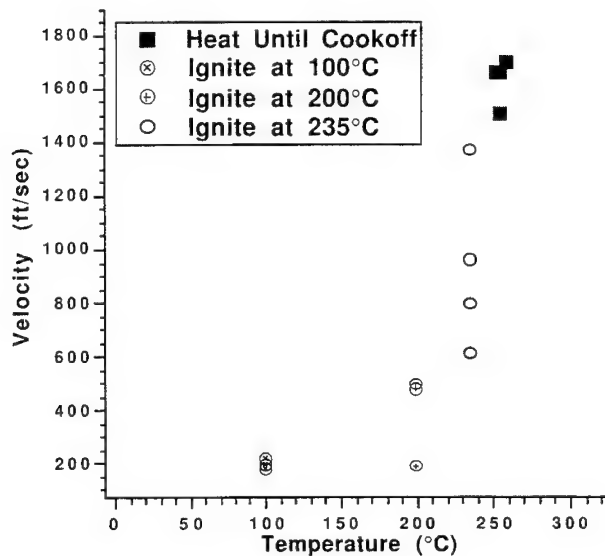


Figure 20a. Velocity vs. ignition temperature PS4.

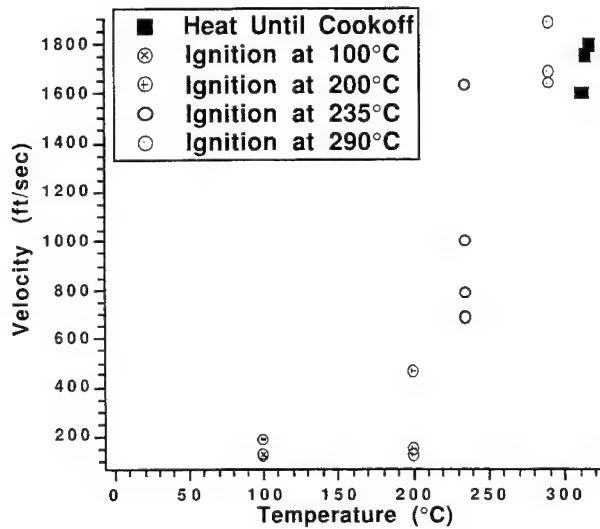


Figure 20b. Velocity vs. ignition temperature PS1.

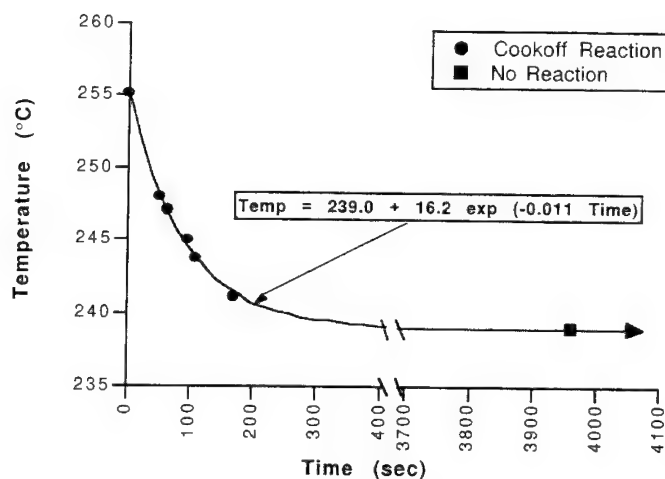


Figure 21. Temperature vs. hold time PS4.

Obviously much work, both experimental and analytical modeling, is needed, and these areas were extensively discussed. There is a significant need for standardized bench mark tests. While one test with many samples, heating rates, variable confinement, etc. would be desirable, the groups felt that it may be an illusive goal, and that probably multiple tests would be required. These tests should have: known and controlled boundary conditions, well characterized geometry with known material properties, variable and reliable confinement capacity, and a complete diagnostics package. This diagnostics package should include the capability to measure: in situ pressure, in situ but non-interfering temperature, strain, material state (porosity, surface area), boundary temperatures and heating rates, and once reaction occurs, wall velocity, fragment number, fragment size, and fragment velocities. Obviously no one test is likely to provide all of these data.

Such tests are needed, not only to gain mechanistic understanding but also to serve as tests for the analytical modeling.

While the needs list is extensive, the workshop participants thought that a cooperative effort could increase the ability to achieve the goals of mechanistic understanding and prediction of cookoff violence. Hopefully the extension of the Grand Challenge to the NIMIC/TTCP communities may provide this increased cooperation.

## IN CONCLUSION

Much of this paper is already a summary of work presented in more detail in Ref. 1 and the other documents cited in Ref. 1. The attempt here has been to provide a brief introduction and overview and hope that the reader will turn to the references for more detail. It presents much work that has been performed at China Lake in this area over the past couple of decades. While the paper presents work primarily performed at China Lake, it should be remembered that we do not work in a vacuum. We are indebted to our many colleagues who have shared their ideas and their work.

## REFERENCES

This is not a complete listing of references. Many investigators were named as performing work similar to that being discussed in the text, and it was suggested that the reader might want to consult the works of these authors. Because of space limitations, those citations are not mentioned in this list of references.

1. Boggs, T.L. and Derr, R.L., eds., 1990. "Hazard Studies for Solid Propellant Rocket Motors," in *AGARDograph No. 316*, 202 pp.
2. Victor, A. C., 1996. "Insensitive Munitions Technology for Tactical Rocket Motors," to be published in *ALAA Progress Series* Volume.
3. Mellor, A.M., Boggs, T.L., Covino, J., Dickinson, C.W., Dreitzler, D., Thorn, L.B., Frey, R.B., Gibson, P.W., Roe, W.E., Kirshenbaum, M., and Mann, D.M., 1988. "Hazard Initiation in Solid Rocket and Gun Propellants and Explosives," *Progress in Energy & Combustion Science*, Vol 14, No. 3, pp. 213-244. (See also Mellor, A.M., Mann, D.M., Boggs, T.L., Dickinson, C.W., and Roe, W.E., 1987. "Hazard Initiation in Energetic Materials: Status of Technology Assessment," *Combustion Science and Technology*, Vol. 54, pp. 203-215.)
4. Boggs, T.L., 1991. "Combustion and Safety of Solid Propellant Rocket Motors," in *Combustion of Solid Propellants*, NATO Advisory Group for Aerospace Research and Development, AGARD-LS-180, pp. 9/1-9/14.
5. Fifer, R.A., 1984. "Chemistry of Nitrate Ester and Nitramine Propellants," *Fundamentals of Solid-Propellant Combustion, Progress in Astronautics and Aeronautics*, Vol. 90, edited by Kuo, K.K. and Summerfield, M., pp. 177-237.
6. Boggs, T.L., 1984. "Thermal Behavior of RDX and HMX," *Fundamentals of Solid-Propellant Combustion, Progress in Astronautics and Aeronautics*, Vol. 90, pp. 121-175.
- 7a. Jacobs, P.W.M. and Whitehead, H.M., 1969. *Chemical Reviews*, Vol. 69, p. 551.
- 7b. Boggs, T.L., Zurn, D.E., Cordes, H.F., and Covino, J., 1988. "The Combustion of Ammonium Perchlorate and Various Inorganic Additives," *Journal of Propulsion and Power*, Vol. 4, No. 1, pp. 27-40.
8. Behrens, R. and Bulusu, S., 1995. "Thermal Decomposition of HMX: Low Temperature Reaction Kinetics and their Use for Assessing Response in Abnormal Thermal Environments and Implications for Long-term Aging," presented at *1995 Fall Materials Research Society Meeting*, Boston, MA.
9. Erickson, K.L., Behrens, R., Bulusu, S., 1992. "Development of Rate Expressions for the Thermal Decomposition of RDX," *29th JANNAF Combustion Subcommittee Meeting*, Hampton, VA.
10. Brill, T.B., 1995. "Multiphase Chemistry Considerations at the Surface of Burning Nitramine Monopropellants," *Journal of Propulsion and Power*, Vol. 11 No. 4, pp. 740-751.
11. Litzinger, T.A., Fetherolf, B.L., Lee, Y.J., Tang, C-J, 1995. "Study of the Gas-Phase Chemistry of RDX: Experiments and Modeling," *Journal of Propulsion and Power*, Vol. 11, No. 4, pp. 698-703.
12. Boggs, T.L., Price, C.F., and Derr, R.L., 1984. "Transient Combustion: An Important Consideration In Deflagration to Detonation Transition," *Propulsion and Energetics Panel 63(A)th Meeting*, Lisse, Netherlands, AGARD Conference Proceedings, AGARD CP-367, pp. 12-1 thru 12-2.
13. Boggs, T.L., Atwood, A.I., Graham, K.J., Lepie, A.H., Price, C.F., Richter, H.P., and Zurn, D.E., 1985. "Hazards of Solid Rocket Propellants," *Proceedings of the Eastern States Combustion Institute*, Physical and Chemical Processes in Combustion, Philadelphia, PA, pp. B1-12.
14. Boggs, T.L., Price, C.F., Atwood, A.I., Zurn, D.E., and Derr, R.L., 1982. "Role of Gas Phase Reactions in Deflagration-to-Detonation Transition," *Seventh Symposium (International) on Detonation*, Naval Surface Weapons Center, NSWC MP 82-834, pp. 216-224.
15. Covino, J., and Hudson, F.E., 1991. "Current Assessment Methodology for Electrostatic Discharge Hazards of Energetic Materials," *Journal of Propulsion*, Vol. 7, No. 6, pp. 894-903.

16. Parr, T.P. and Hanson-Parr, D.M., 1993. "Solid Propellant Flame Chemistry and Structure," Invited paper at the *Third International Symposium on Special Topics in Chemical Propulsion: Non-Intrusive Combustion Diagnostics*, Schevenigen, The Netherlands.
17. Hanson-Parr, D.M. and Parr, T.P., 1994. "RDX Flame Structure," *Twenty-Fifth International Symposium on Combustion*, The Combustion Institute, p. 1635.
18. Parr, T.P. and Hanson-Parr, D.M., 1995. "Solid Propellant Flame Structure," *Proceedings of the Materials Research Society Fall Meeting*, Symposium on the Decomposition, Combustion, and Detonation of Energetic Materials.
19. Parr, T.P. and Hanson-Parr, D.M., 1992. "Advanced Diagnostic Techniques for NonSteady Burning of Solid Propellants," in *Progress in Astronautics and Aeronautics*, Eds. L. De Luca, E. Price, and M. Summerfield, Vol. 143, pp. 261-324.
20. Tang, C-J, Lee, Y.J., Kudva, G., and Litzinger, T.A., 1995. "A Study of the Gas Phase Chemical Structure During CO<sub>2</sub> Laser Assisted Combustion of HMX," *1995 JANNAF Combustion Subcommittee Meeting*.
21. Yetter, R.A. and Dryer, F.L., cited in Ref. 16.
22. Belyaev, A.F., et al., 1973. "Transition from Deflagration to Detonation in Condensed Phases," translated by Israel Program for Scientific Translations, Springfield, VA, National Technical Information Service, (1975 translation).
23. Bradley, H.H., Jr., and Boggs, T.L., 1978. "Convective Burning in Propellant Defects: A Literature Review," Naval Weapons Center, NWC TP 6007, 96 pp.
24. Kuo, K.K., and Kooker, D.E., 1992. "Coupling between Nonsteady Burning and Structural Mechanics of Solid Propellant Grains," in *Nonsteady Burning and Combustion Instability of Solid Propellants*, *Progress in Astronautics and Aeronautics*, Vol. 143, pp. 465-517.
25. Simmons, R.L., personal communication, 14 Feb. 1996.
26. Bernecker, R.R., "DDT Studies of a High Energy Spherical Ball Propellant," *Ninth Symposium (International) on Detonation*, Office of the Chief of Naval Research, OCNR 113291-7, Vol. I, pp. 354-362.
27. McAfee, J.M., Asay, B.W., Bdzil, J.B., "Deflagration-to-Detonation in Granular HMX: Ignition, Kinetics, and Shock Formation," *Tenth International Detonation Symposium*, Office of Naval Research, ONR 33395-12, pp. 716-723.
28. Butcher, A.G., Hopkins, B.D., and Robinson, N.J., as presented in R. R. Bernecker, 1984. "The DDT Process in High Energy Propellants," in *Hazard Studies for Solid Propellant Rocket Motors*, NATO AGARD Conference Proceedings, AGARD-CP-367, pp. 14-1 to 14-16.
29. Bernecker, R.R., Sandusky, H.W., and Clairmont, A.J., Jr., 1982. "Deflagration-to-Detonation Transition Studies of Porous Explosive Charges in Plastic Tubes," *Seventh Symposium (International) on Detonation*, NSWC MP 82-334, pp. 119-138.
30. Price, C.F. and Boggs, T.L., "Transient Combustion of Solid Propellants: An Important Aspect of Deflagration-to-Detonation Transition," in *Nonsteady Burning and Combustion Stability of Solid Propellants*, Vol. 143, pp. 441-464. (See also Price, C.F., Atwood, A.I., and Boggs, T.L. "An Improved Model of the Deflagration-to- Detonation Transition in Porous Beds," *The Ninth Symposium (International) on Detonation*, pp. 363-376.)
31. Green, L.G., James, E., Lee, E.L., Chambers, E.S., Tarver, C.M., Westmoreland, C., Weston, A.M., Brown, B., 1982. "Delayed Detonation in Propellants from Low Velocity Impact," *Seventh Symposium (International) on Detonation*, NSWC MP 82-334, pp. 256-264.
32. Keefe, R., "Delayed Detonation in Card Gap Tests," *Seventh Symposium (International) on Detonation*, pp. 265-272.
33. Noguez, B., Berger, H., Gondouin, B., and Brunet, J., 1989. "An Odd Bore Effect on Bullet Induced Detonation of High Energy Propellant Grains," *American Defense Preparedness Association Symposium on Compatibility of Plastics and Other Materials with Explosives, Propellants and Pyrotechnics*.
34. Beauregard, R. "Insensitive Munitions--Are They Worth the Cost?"
35. Hobbs, M.L., and Baer, M.R., 1995. "Multidimensional Fully-Coupled Thermal/Chemical/Mechanical Response of Reactive Materials," *1995 JANNAF Propulsion Systems Hazards Subcommittee Meeting*.

36. Renlund, A.M., Miller, J.C., Hobbs, M.L., and Baer, M.R., 1995. "Experimental and Analytical Characterization of Thermally Degraded Energetic Materials," *1995 JANNAF Propulsion Systems Hazards Subcommittee Meeting*.
37. Nichols, A.L. III, 1995. "Coupled Thermal/Chemical/Mechanical Modeling of Insensitive Explosives in Thermal Environments," *1995 APS Topical Conference on Shock Compression of Condensed Matter*.
38. Victor, A.C., 1996. "Simple Calculation Methods for Munitions Cookoff Times and Temperatures," accepted for publication in *Propellants, Explosives, and Pyrotechnics*. (See also, Victor, A.C., 1994. "Exploring Cookoff Mysteries," *1994 JANNAF Propulsions Systems Hazards Subcommittee*.)

## ATOMIC FORCE MICROSCOPY OF HOT SPOTS IN RDX AND AP CRYSTALS

J. Sharma<sup>1</sup> and C.S. Coffey<sup>2</sup>

<sup>1</sup> Naval Surface Warfare Center, Carderock Division, West Bethesda, MD 20817 USA;

<sup>2</sup> Naval Surface Warfare Center, Indian Head Division, Indian Head, MD 20640 USA.

**ABSTRACT:** An atomic force microscope has been used to reveal the structure of residual sub-micron size reaction sites in drop weight impacted RDX and in laser heated AP crystals. The smallest reaction sites in impacted RDX were hemispherical craters of 20-300 nm size. On a somewhat larger scale, hillocks of 200-1000 nm were observed, their shape giving evidence of internal reaction and ballooning. At some sites large (1000-3000 nm) volcano-like hot spots from which gases had escaped and where melting had taken place, were observed. Even a mild impact disrupts the periodicity of the RDX lattice, the molecules get displaced from their normal sites by as much as 20 % and sometimes get re-oriented. In AP, laser heating produced cracks and also trumpet shaped 50-200 nm craters, most of which supported a crystallographically oriented square lid on top of them, formed from the wellknown orthorhombic to cubic(rocksalt) phase transition at 240° C.

## INTRODUCTION

In order to explain the easy ignition of explosives by different stimuli, Bowden and Yoffe [1] invoked the idea of hot spots. They proposed that no matter how energy is supplied to an explosive, it gets localized in small reaction sites( 0.1-10 microns), which may develop into hot spots capable of causing the whole explosive to go off. It is believed that the reaction sites grow from crystal defects which are even smaller. Since these defects are believed to control the sensitivity of the explosive and play important role in the ignition process, it is important to know their structure and to understand how they grow. So far, the specific defects critical to the sensitivity of an explosive have not been identified and simple facts such as batch to batch variation in sensitivity has escaped explanation. The smallness of the reaction sites has prevented us from knowing their structure. The advent of the Atomic Force Microscope (AFM), which can see even atoms, has removed this obstacle and has opened up the possibility of following the growth of hot spots from their smallest size and earliest stage.

In the present work an atomic force microscope (AFM) has been used to reveal residual sub-micron size reaction sites and hot spots in impacted RDX and in laser heated AP. Crystals of RDX have been impacted in a drop test machine and the resulting reaction sites in them have been studied. Starting from the general disorder and dislocations created in the lattice at molecular level by mild impact, various kinds of reaction sites including the development of large (2-3 micron size) volcano-like hot spots have been followed. Micro Munroe jets (10 microns in length), which were so far considered as mere speculations, have for the first time been observed [2]. Dislocation densities of  $10^{12} \text{ cm}^{-2}$  have been seen, and it has been found that the lattice gets severely disrupted at an impact level much below that of reaction, by displacements of the molecules from their regular positions. The molecules get displaced randomly by 20 % of their molecular distances, in all directions. In the

ensuing rearrangement some of the molecules get also re-oriented. The AFM results bring out the point that the RDX lattice is a molecular lattice, and it behaves like one. The ideas of dislocations based on atomic lattices may have to be revised for the case of molecular crystals.

The smallest reaction sites observed in RDX were hemispherical craters, 20 nm in diameter comprising of roughly 10,000 molecules. These might represent the smallest hot spots possible. Reaction hillocks with bumps as on a custard apple have been seen roughly in the 200-1000 nm size. They may be arising from reaction taking place in the interior, leading to melting and ballooning. Finally volcano-like large reaction sites which emitted out gaseous products have been seen. Evidence of melting and decomposition, producing sponge-like RDX particles, has also been seen in severely affected areas.

In the case of AP crystals, laser action produced trumpet-shaped craters typically of 100-200 nm size, as mentioned in Reference [3]. Most of them were crowned with square blocks or lids perched on the top, sticking higher than the crystal surface and all oriented in the same direction. In the region of higher action, the cubic blocks got eroded and became conical in appearance, leaving in some cases a crater with square cross-section. One micron wide cracks, produced due to the heating of the laser, were found to follow the orthorhombic directions of the original crystal.

## EXPERIMENTAL

Sugar-like crystals of RDX, 50-300 microns in size, were sandwiched between sheets of heat sensitive film or between cleaved sheets of mica. A 10 KG weight was dropped in the BIC machine of C.S. Coffey [4], from a chosen height (ranging between 20-150 cm) and the samples were picked up at different distances from the center of the impact pattern. Both "go" and "no go" samples were investigated. For the study in ammonium perchlorate (AP), a single crystal was irradiated on (001) crystal plane with a 8 ns pulse from a Nd/Yag laser (1064 nm in wavelength) with a 0.25 J of energy focussed over an area of 2 mm diameter. The deposited energy was sufficient to cause large scale cracking and the formation of a crater. A Digital Instruments Nanoscope II, Scanning Probe Microscope was used in the present work. The measurements were carried out in air at room temperature using a 100 micron cantilever with an oxygen sharpened silicon nitride tip hopefully only tens of Angstroms wide at the point of contact with the sample. The cantilever was used in height mode and rather a high force of  $10^{-8}$ - $10^{-7}$  N was used to obtain the images.

## RESULTS AND DISCUSSION

The present study has shown that RDX shows molecular disarrays even when it is mildly impacted. Figure 1 is an image of a control RDX crystal showing molecules arranged in regular arrays, each white spot representing a molecule. (RDX crystals proved to be very soft and tend to have secondary growth, therefore large area image with perfect periodicity could not be obtained.) Figures 2,3 and 4 are images of very mildly impacted RDX (23 cm drop height), showing that the rigid periodicity of the lattice surface is disrupted at many places. Although the overall periodic arrangement is maintained, wiggles in the lines are seen. If a wiggle is an evidence of a dislocations, then dislocation density of  $10^{12}$  cm<sup>-2</sup> is apparent. Figure 5 is a lineplot of the control crystal emphasizing the periodicity in a clear way. Compared to that, Figure 6 shows the effect of mild impact. The image of Figure 6 shows clearly the violations of periodicity. In the disarray (Figure 6), the molecules get displaced from their regular sites by as much as 20 %. This displacement has been found to be in the x-y plane as well as in the z-plane which is evident from the sinking and lifting up of the molecules from their regular sites. It appears that some bunching takes place in these displacements. The displacements of individual molecules gives the message that RDX is a



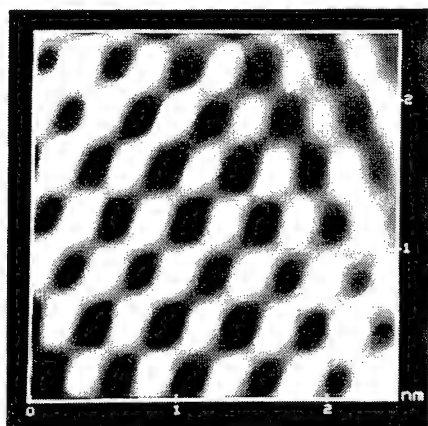


Figure 1. (Left) An AFM image of the surface of a control crystal of RDX, probably (001) plane, showing the periodic arrangement of the molecules, each white blob representing a molecule.

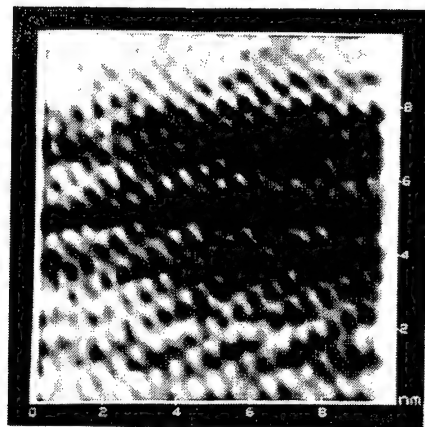


Figure 2. (Right) An AFM image of mildly impacted RDX showing molecular disarrays and jogs. The surface does not terminate in a crystal plane. Some of the molecules are lifted up, while some are sunk-in. Near the bottom left, a few rows show formation of Y's, representing dislocations.

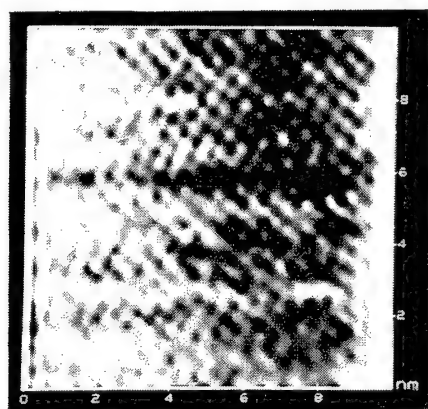


Figure 3. (Left) An AFM image of mildly impacted RDX showing molecules at different heights and forming incomplete rows.

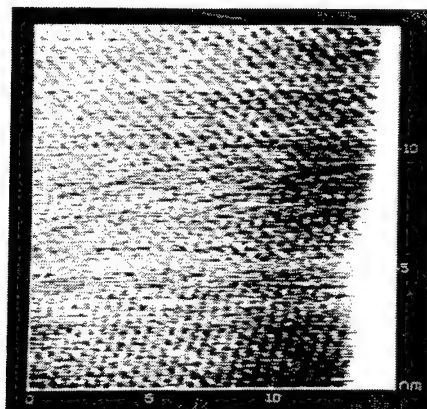


Figure 4. (Right) An AFM image of mildly impacted RDX showing jogs and irregularities in rows of molecules, as evidence of dislocations.

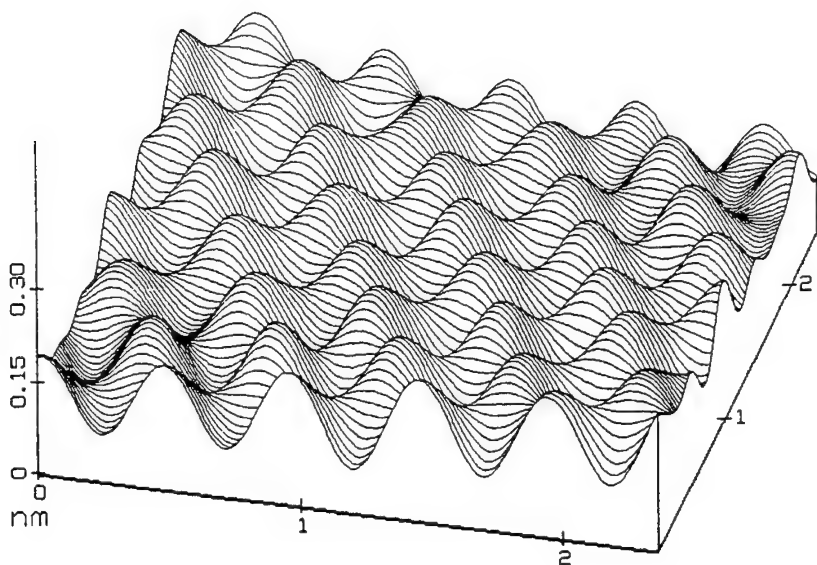


Figure 5. A magnified line plot of control crystal face of RDX, bringing out the perfect periodicity of the molecular arrays in x,y and z-directions.

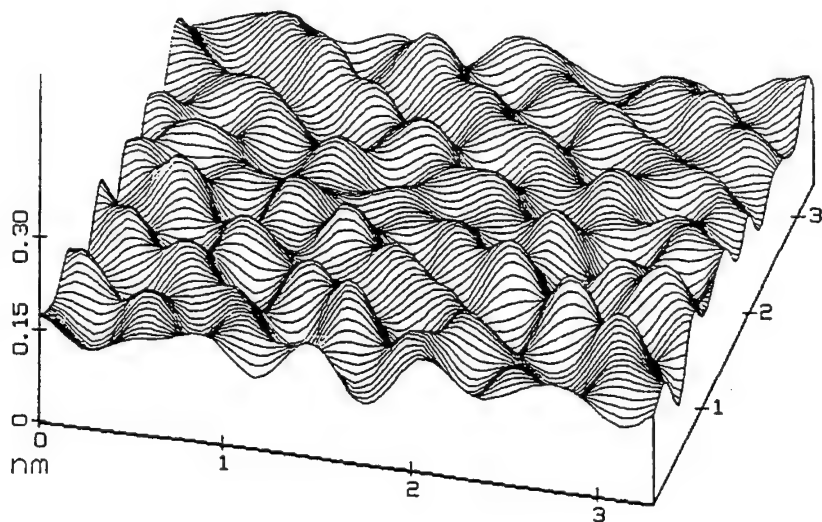


Figure 6. A magnified line plot of impacted RDX, showing clearly the irregularities produced in the molecular arrangement. The molecules show displacements in x,y and z-directions away from their expected positions. Some of them appear to have rotated into new orientations.

molecular solid in which the molecule as an entity can seek new positional equilibria, after the lattice has been effected by the impact. Figures 2, 3, and 4 show that the molecules can form incomplete rows and layers with various kinds of imperfections in them. In the bottom part of Figure 4, a few Y's can be seen which can be direct evidences of dislocations.

From the shape of the individual bumps in Figure 6, it is also obvious that some of the molecules are re-oriented. In other words, the molecular displacements are accompanied with molecular re-orientations, for some of the molecules. To explain the re-orientation one can imagine that the violation of rigid periodicity can give larger volume to some molecules which can re-orient themselves. Another attractive explanation that can be suggested is that some of the molecules are chemically changed from the mild impact. According to the findings of Behrens and Bulusu [5] and those of Sharma et al [6] and Hoffsommer et al [7], the nitroso derivatives could be produced. These molecules will be smaller than RDX molecules from the loss of oxygen atoms in the nitro groups, so that they can easily re-orient themselves. The AFM is blind to chemical changes but may show differences based on the size of the molecules.

AFM images of particles picked up from different parts of the impact pattern have revealed that in the center area the primary effect of the impact is crushing of the crystallites from the original 50-300 micron size to a few micron size. The powder still retains its crystal shape as shown in Figure 7. However, the particles after being driven out radially, get changed in external morphology, they become like pebbles (Figure 8) and furthermore, the ratio of the height to lateral size decreases by an order of magnitude as they reach the end of their radial tracks. The top surface of the pebbles end in a molecularly rough surface, not in a flat crystal face. The pebble like appearance may be the result of friction, deformation and also sublimation. As mentioned by Coffey and Jacobs [8], it is at the end of the tracks that reaction is generally initiated. In the present set of experiments it has been noticed that if the drop height is large, the action can start at a relatively smaller distance from the central area but it starts farther away if the drop height is small. In the areas where action takes place, various kinds of reaction sites have been observed with the help of the AFM. Volcano-like large craters (200-1000 nm) with holes in them, from which reaction products in the form of gases have escaped, have been seen. Evidence of melting and liquid splattering is clear. At some places spongy masses of RDX (Figure 9), made so from gases escaping, have also been observed. Since the decomposition temperature of RDX is quite close to the melting point, this is not surprising. These images make the point that major action in RDX, during thermal ignition, takes place in the molten state. At other places, closer to the center of the impact pattern, reaction sites in the shape of ballooned hillocks were seen (Figure 10). This is evidence of internal reaction and the bumpy appearance of the hills again supports the point that melting has taken place. Attempts were made to scrape the top of the hills to see if they are hollow, so far the attempts have not succeeded. At some places in the sample picked up from the "go" experiments, very small reaction sites in the form of hemispherical craters have been observed as shown in Figure 11. They ranged in diameter from 20 to 100 nm, roughly. The 20 nm crater represents the smallest site seen so far, produced by the loss of approximately 10,000 molecules from the hemisphere. It would be interesting to pose the question whether this represents the lowest limit for the formation of a hot spot in an explosive. Since action in explosives always starts at hot spots, the question of the smallest possible hot spot, below which the lattice dissipates away the energy without any action, has often been raised [see Boddington [9]]. This argument has been used to explain why explosives on the shelf, are not initiated by highly energetic cosmic rays or background nuclear radiations [10]. It is believed that the size of a viable hot spot has to be larger than a critical size. The smallest size of 20 nm diameter, found in the present measurements, agrees well with the calculations of Armstrong et al [11] who came out with the number 3,500 molecules per molecular plane, for the smallest hot spot in RDX, with 40 ns as a characteristic time.

In the case of laser heated ammonium perchlorate (AP), the effect seems to be controlled and

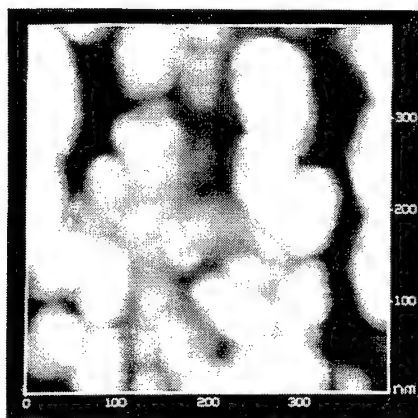
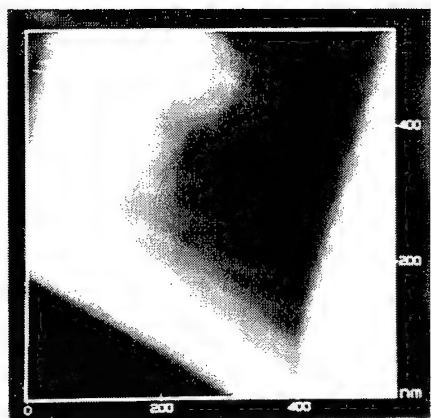


Figure 7. (Left) An AFM image of a crushed RDX particle from the central part of the impact pattern, retaining some semblance of crystal appearance.

Figure 8. (Right) An AFM image of particles of RDX picked up from near the outer tip of the radial impact pattern, showing the formation of pebbles, due to the action of friction, deformation and probably also sublimation.

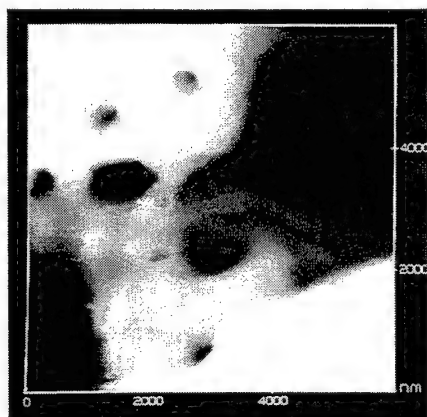


Figure 9. An AFM image from the outer radial area of an impact pattern where reaction took place, giving evidence of melting and gaseous decomposition of RDX.

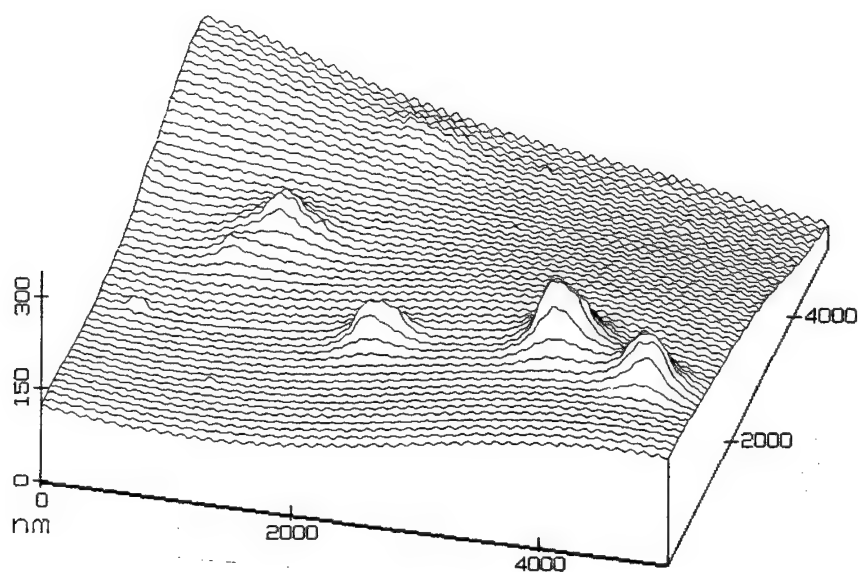


Figure 10. An AFM image of impacted RDX showing the formation of ballooned hillocks, observed in some areas. The irregular shape of the hillocks indicates non-uniformity of reaction even inside one hillock.

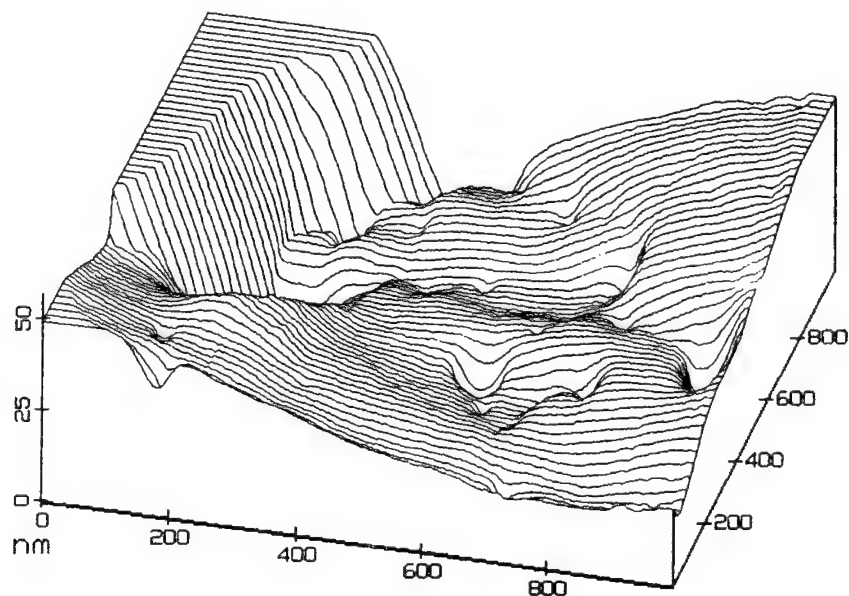


Figure 11. The hemispherical craters shown, from which the material has disappeared, represent smaller of the reaction sites seen so far. The smallest crater observed was approximately 20 nm in diameter, representing perhaps the smallest hot spot in RDX, produced by the loss of approximately 10,000 molecules.

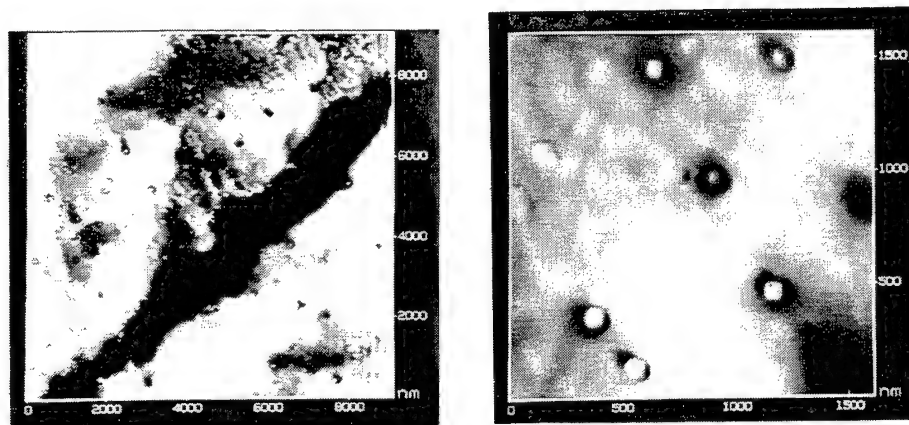


Figure 12. (Left) Laser produced reaction sites on the surface of an ammonium perchlorate (AP) crystal, as tiny white specks and craters. A crack which is approximately a micron wide, follows the orthorhombic direction of the crystal and has ragged banks.

Figure 13. (Right) Magnification of the image of Figure 12, shows that the white specks are square blocks perched on top of trumpet shaped craters. The square blocks give evidence of phase transition into cubic (rocksalt) structure, known to take place in AP at 240 C. The square blocks are lined up in the same direction, indicating that the original crystal surface must be playing important role in the phase transformation.

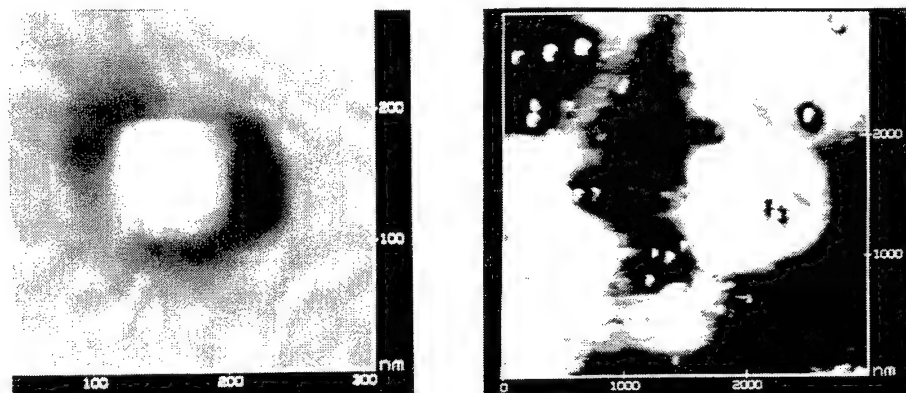


Figure 14. (Left) Further magnification of the square block shows that the crystal surface around it develops a square depression and the top of the square block is higher (brighter) than the surrounding surface of the original crystal.

Figure 15. (Right) In the area of more intense action of the laser, the square blocks get eroded into conical shapes, leaving behind square holes, in many cases.

dominated by the wellknown crystallographic phase transformation from orthorhombic to cubic (rocksalt) phase that takes place at 240° C. As a result of laser irradiation very large number of reaction sites showed up as tiny specks, as seen in Figure 12. Magnification showed that each speck actually consists of a squarish crater housing a square lid or block on top of it (Figure 13). The square lids or blocks are roughly 70-100 nm on each side and about 50 nm high, each perched on a crater, as seen in Figures 13 and 14. Sometimes the lid is found to have moved out of the crater, resting on the surface of the original crystal, not far from the crater, as seen in Figure 13. The square lids were found to be all oriented in the same direction (Figure 13), indicating that their growth is controlled by the original crystal direction. The area near the square blocks seemed eroded and it sometimes showed a square depression. The top surface of the block sticks out slightly higher than the general surface of the crystal. The square shape of the blocks is an evidence of phase transition into the cubic form. Boggs and Kraeutle [12], reported the formation of the square and rectangular holes on the surface of thermally decomposed AP. Since they used a scanning electron microscope in their study, they could see the holes after the holes had grown to larger than microns size. It is likely that the sub-micron size craters with square blocks, reported in this paper, seen through the atomic force microscope, are precursors of the large rectangular holes reported by Boggs and Kraeutle [12].

The heating of the laser caused cracks to develop (as seen in Figure 12), which were found to be roughly one micron thick and which followed the orthorhombic directions of the original crystal. The sides of the cracks showed right angle steps and inside the cracks many square blocks could be seen. From these images it is clear that the phase transition of AP is playing important role. It seems that in the area of intense heat, the square blocks got changed into conical shape, as seen in Figure 15, due to their erosion and decomposition.

### CONCLUSIONS

It can be said that the application of AFM has given some valuable information about the formation of hot spots, and reaction sites in the nm size range, showing their earlier stages of development. It has shown that in RDX even mild impact causes the molecular arrays of the lattice to be disrupted. Displacements of the molecules are large and are sometimes associated with re-orientation of the molecules. This should be taken into consideration in future modelling, not only of explosives but also for molecular crystals in general. The smallest reaction site to date is about 20 nm in size and comprises roughly 10,000 molecules. Larger reaction sites in the form of ballooned hillocks and volcanoes result from more intense action in the peripheral area of the impact pattern. Evidence of melting is frequent. In the laser heated AP, the orthorhombic to cubic phase transition seems to play important role in the thermal damage.

### ACKNOWLEDGEMENT

This work was supported by U.S. Office of Naval Research, Contract No. N00014-96-WX-20538.

## REFERENCES

1. **Bowden, F.P. and Yoffe, Y.D.**, *Initiation and Growth of Explosion in Liquids and Solids*, Cambridge University Press, 1952, London, 64-65.
2. **Sharma, J. and Coffey, C.S.**, Nature of Ignition Sites and Hot Spots, Studied by Using an Atomic Force Microscope, *Proc. of APS-Shock Compression of Condensed Matter*, Seattle, Wa. 1995, 811-814.
3. **Sharma, J., Coffey, C.S., Ramaswamy, A.L., et al.**, Atomic Force Microscopy of Hot Spot Reaction Sites in Impacted RDX and Laser Heated AP, *Mat. Res. Soc. Symp. Proc.* 418, 257-264, 1996.
4. **Coffey, C.S., De Vost, V.F. and Woody, D.L.**, Towards Developing the Capability to Predict the Hazard Response of Energetic Materials Subjected to Impact, in *Proc. of Ninth Symposium (International) on Detonation*, Vol. II, 1243-1253, 1989.
5. **Behrens, R. and Bulusu, S.** Thermal Decomposition of Energetic Materials, III, IV, *J. Phys. Chem.*, 96, 8877-8897, 1992.
6. **Sharma, J., Hoffsommer, J.C., Glover, D.J., et al.**, Sub-Ignition Reactions at Molecular Levels in Explosives Subjected to Impact and Underwater Shock, *Proc. Eight (International) Detonation Symposium*, Albuquerque, NSWC MP86-184, 725-733, 1985.
7. **Hoffsommer, J.C., Glover, D.J. and Elban, W.L.**, Quantitative Evidence for Nitroso Compound Formation in Drop-Weight Impacted RDX Crystals, *J. Energetic Materials*, Vol. 3(2), 149-167, 1985.
8. **Coffey, C.S. and Jacobs, S.J.**, Detection of Local Heating in Impact or Shock Experiments with Thermally Sensitive Films, *J. Appl. Phys.*, 52, 6991- 6993, 1981.
9. **Boddington, T.**, The Growth and Decay of Hot Spots and the Relation Between Structure and Stability, in *Ninth Symposium (International) on Combustion*, (Academic Press, New York), 287-293, 1981.
10. **Mallay, J.F., Prask, H.J. and Cerny, J.**, Inadequacy of Thermal Initiation Theory in Interpreting the Results of Fission Fragment Irradiation of Explosives at Elevated Temperatures, *Nature*, 203, No. 4944, 473-476, 1964.
11. **Armstrong, R.W., Coffey, C.S., De Vost, C.S. et al.**, Crystal Size Dependence for Impact Initiation of Cyclotrimethylenetrinitramine Explosive" *J. Appl. Phys.*, 68(3), 979-984, 1990.
12. **Boggs, T.L. and Kraeutle, K.J.**, Role of Scanning Electron Microscope in the Study of Solid Rocket Propellant Combustion, Ammonium Perchlorate Decomposition and Deflagration, *Combustion Science and Technology*, 1, 75-93, 1969.



# The Importance of Mononitroso Analogues of Cyclic Nitramines to the Assessment of the Safety of HMX-Based Propellants and Explosives

Richard Behrens<sup>1</sup> and Suryanarayana Bulusu<sup>2</sup>

<sup>1</sup>Sandia National Laboratories, Combustion Research Facility, Livermore, California;

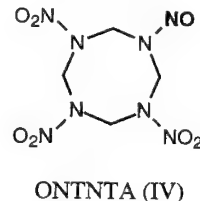
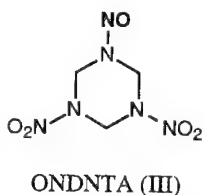
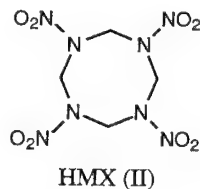
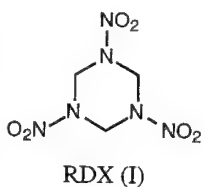
<sup>2</sup>U.S. Army, ARDEC, Dover, New Jersey

**ABSTRACT:** A summary of the thermal decomposition behaviors of HMX, RDX and 1-nitroso-3,5-dinitro-s-triazine (ONDNTA) as determined from simultaneous thermogravimetric modulated beam mass spectrometry (STMBMS) measurements is presented. A qualitative model of the physical and chemical processes that control decomposition of HMX in the solid phase, based on results from all three compounds, is described. Its implications for the response of systems containing these materials to abnormal thermal environments, such as fire, is discussed.

## INTRODUCTION

Cyclic nitramines, such as RDX (I) and HMX (II), are high energy containing compounds that are used extensively in both propellant and explosive formulations. These formulations are found in devices ranging from rocket motors to explosives. Typically, these devices are not used for long periods of time after they are initially manufactured and in many cases they are destroyed or recycled before ever being used. During the life of these devices, they are transported and stored in different environments. It is important that these devices remain safe throughout this life cycle. To assess the safety of these devices during the life cycle, it is necessary to understand how they will respond to their environment. In this regard, two main areas are of interest. First, how will the device respond in an abnormal environment, such as a fire? Second, what effect does aging in the various environments have on the properties and behavior of the device? For example, does the thermal, impact, or shock sensitivity increase with age? To address these issues from a scientific point of view requires an increased understanding of the chemical and physical processes that occur in the energetic materials found in these devices.

Recent efforts to develop models, that will describe the response of a munition in a "slow-cookoff" situation, associated with a fire, strive to use a fundamental understanding of the chemical and physical processes that occur in energetic materials to predict the time to ignition of the event and the degree of violence after ignition.<sup>1</sup> Significant success has been obtained in predicting the time to ignition but less success has been achieved in predicting the degree of violence. The degree of violence may be characterized by relatively benign event, such as a deflagration, or a more serious event, characterized by an explosion or detonation. The success achieved in modeling



the time to ignition arises, in part, from the empirical characterization of one-dimensional time-to-explosion data collected on various energetic materials.<sup>2</sup> However, predicting the degree of violence of the event requires a more in depth understanding of the processes that control the reaction of the material after ignition. The degree of violence of this event will be controlled by the combustion process and the interaction of the combustion process with the extent of confinement of the reacting material. For example, with higher degrees of confinement the pressure at which the combustion occurs will be higher, and thus, the burn rates should be higher.

Measurement of the pressure dependence of burn rates of energetic materials associated with propellants has been done extensively in pressure ranges associated with both rocket motors and guns. Modeling these processes in an empirical fashion has been quite successful<sup>3</sup> and more recent modeling on a molecular level in the gas phase and to a lesser extent in the condensed phase have had good success. However, little work has been done on burn rates under highly confined conditions, although several recent measurements have been made on burn rates of energetic materials between 200 and 400 MPa.<sup>4</sup>

Characterizing the response of a munition in a "slow-cockoff" situation poses a more difficult problem than that associated with the confined combustion problem. This increased difficulty is due to the degradation of the material prior to ignition. This degradation process can lead to the formation of both gaseous and condensed phase products that are not present under normal conditions. As these products are produced in the decomposition process, they may lead to the formation of bubbles and pores within the energetic material or possibly form solutions between the normal material and its decomposition products. Basically this changes the physical and chemical characteristics of the bed of energetic material. The extent of change of the chemical and physical properties is dependent on both time and the temperature field within the material prior to ignition.

Therefore, developing models for predicting the response of a munition in a "slow-cockoff" situation, or even developing experiments to characterize the combustion process requires a good understanding of the decomposition process. Ultimately, one should understand both the chemical and physical changes that occur in the materials, where they occur within the materials and how fast they occur. In this paper we address the decomposition chemistry associated with two materials used extensively in propellants and explosives, RDX and HMX.

Over the past ten years we have conducted extensive thermal decomposition studies on HMX<sup>5,6</sup> and RDX<sup>7,8</sup> and several less extensive studies on other cyclic nitramines having five-, six- and seven-member rings. In all of these studies we have found that the mononitroso analogue (e.g., ONDNTA (III) and ONTNTA (IV) for RDX and HMX, respectively) of the parent compound is formed in the decomposition process. The identity and relative amounts of the gaseous decomposition products (i.e., NO<sub>2</sub>, HCN, N<sub>2</sub>O, CH<sub>2</sub>O, NO, H<sub>2</sub>O, CO) depends on whether these products are formed directly from the cyclic nitramine or through the mononitroso intermediate. We have also found that the mononitroso intermediate plays a significant role in the decomposition of HMX and RDX in the solid phase. As a consequence of our findings on the decomposition of HMX and RDX, we have undertaken a study of the decomposition of the independently synthesized mononitroso analogue of RDX, ONDNTA.<sup>9</sup>

From our STMBMS measurements on ONDNTA, we have found that its decomposition is quite complex. It decomposes in two different temperature regimes and its decomposition rate and mechanism are very sensitive to the extent of interaction between ONDNTA and its decomposition products. The higher temperature decomposition regime commences at approximately 170 C, the melting point of ONDNTA and is autocatalytic in nature. The lower temperature regime occurs up to ~140 C and the extent of decomposition in this regime is very sensitive to interaction with product gases.

The highlights of our experiments that led to our current understanding of the decomposition mechanisms of RDX and HMX along with implications for possible changes in the sensitivity of RDX and HMX will be discussed in this paper.

## EXPERIMENTAL

### Instrument Description

The STMBMS apparatus and basic data analysis procedure have been described previously.<sup>10</sup> This instrument allows the concentration and rate of formation of each gas-phase species in a reaction cell to be measured as a function of time by correlating the ion signals at different  $m/z$  values measured with a mass spectrometer with the force measured by a microbalance at any instant. In the experimental procedure, a small sample (~10 mg) is placed in an alumina reaction cell that is then mounted on a thermocouple probe that is seated in a microbalance. The reaction cell is enclosed in a high vacuum environment ( $< 10^{-6}$  torr) and is radiatively heated by a bifilar-wound tungsten wire on an alumina tube. The molecules from the gaseous mixture in the reaction cell exit through a small diameter orifice (2.5 to 970  $\mu$  in these experiments, orifice length is 25  $\mu$ ) in the cap of the reaction cell, traverse two beam-defining orifices before entering the electron-bombardment ionizer of the mass spectrometer where the ions are created by collisions of 20 eV electrons with the different molecules in the gas flow. A relatively low electron energy of 20 eV (compared to 70 eV used on normal mass spectrometry measurements) is used to reduce the extent of fragmentation of the higher molecular weight ions and thus, limit their contribution to ion signals measured at lower  $m/z$  values that are associated with the thermal decomposition products. The background pressures in the vacuum chambers are sufficiently low to eliminate significant scattering between molecules from the reaction cell and background molecules in the vacuum chambers. The different  $m/z$ -value ions are selected with a quadrupole mass filter and counted with an ion counter. The gas flow is modulated with a chopping wheel and only the modulated ion signal is recorded. The containment time of gas in the reaction cell is a function of the orifice area, the free volume within the reaction cell, and the characteristics of the flow of gas through the orifice. The reaction cell used in the experiments has been described previously,<sup>7</sup> and the cap in the reaction cell is now sealed using vacuum grease and an o-ring between the taper plug and the gold foil pinhole orifice. The time constant for exhausting gas from the cell is small compared to the duration of the experiments ( $> 1000$  sec). Note that the containment time of gas within the reaction cell is short once the gas molecules are in the free volume of the cell, but it may be much longer if the gas is trapped in the condensed-phase of the material within the cell. The pressure of the gas products within the reaction cell range from less than 1 torr for experiments with the larger diameter orifices (970  $\mu$ ) to greater than 1000 torr for experiments with the smallest diameter orifices (2.5  $\mu$ ).

### Sample Preparation

The syntheses of RDX(I), HMX(II) and their isotopic analogues were described in previous papers<sup>5-8</sup>. ONDNTA (III) and deuterium labeled, ONDNTA- $d_6$ , which are intermediates in the decomposition of RDX and RDX- $d_6$  respectively, were prepared according to previously known methods<sup>11</sup> starting with the corresponding hexahydro-1,3,5-trinitroso-s-triazine analogue. The deuterated version of the hexahydro-1,3,5-trinitroso-s-triazine was prepared by the base catalyzed deuterium exchange method described in an earlier paper<sup>8</sup>. The ONDNTA samples were characterized by NMR and IR measurements and their mass spectra indicated a purity greater than 99% with ~0.25% RDX contamination. The samples melt between 165 and 170°C.

### RDX AND HMX DECOMPOSITION.

The decomposition of both RDX and HMX is a complex process that is controlled by multiple reaction pathways whose behavior depends on both the individual properties of the molecules themselves, as well as the physical state of the sample. The global chemical reaction pathways that control the decomposition process in the liquid phase are shown in Figure 1 for the case of RDX. Important physical processes in the decomposition of material in the solid phase are illustrated in Figure 3 for the case of HMX.

## RDX Decomposition

Four primary reaction pathways control the decomposition of RDX in the liquid phase between 200 and 215°C (Fig. 1). Two pathways are first order reactions solely in RDX. One of these produces predominantly OST, NO, and H<sub>2</sub>O and accounts for approximately 30% of the decomposed RDX and the other produces predominantly N<sub>2</sub>O and CH<sub>2</sub>O with smaller amounts of NO<sub>2</sub>, CO, and NH<sub>2</sub>CHO and accounts for 10% of the decomposed RDX. The third pathway consists of formation of ONDNTA by reaction between NO and RDX, followed by the decomposition of ONDNTA to predominantly CH<sub>2</sub>O and N<sub>2</sub>O. The nature of the fourth reaction pathway is less certain. From our original experiments on RDX, we proposed that in the fourth pathway RDX decomposes by reaction with a catalyst that is formed from the decomposition products of RDX. This pathway is based on the temporal behaviors of the gas formation rates of the decomposition products. However, from more recent experiments with the independently synthesized mononitroso analogue of RDX, ONDNTA, it appears that this fourth channel may also involve the ONDNTA intermediate. The third and fourth reaction channels each account for approximately 30% of the decomposed RDX.

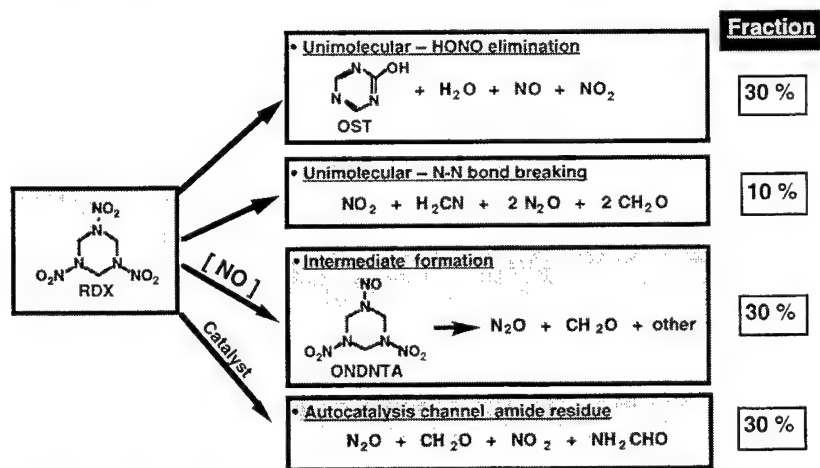


Figure 1. Decomposition pathways for RDX in the liquid phase. (Data from Ref. 7)

Experiments with solid-phase RDX at 190 C have shown that its decomposition rate is very much slower than that of liquid phase RDX as can be seen in Figure 2. ONDNTA is the only product that appears to be formed during the early stages of the decomposition of RDX in the solid phase. As the solid-phase decomposition progresses, N<sub>2</sub>O and lesser amounts of CH<sub>2</sub>O start to evolve and their rates of evolution increase slowly until products associated with the liquid-phase RDX decomposition appear and the rates of gas formation of all products rapidly increase. This behavior strongly suggests that the decomposition of solid RDX occurs through formation of ONDNTA within the lattice. Its subsequent decomposition within the lattice to N<sub>2</sub>O and CH<sub>2</sub>O, followed by the dispersion of CH<sub>2</sub>O in the RDX, leads to the eventual liquefaction of the remaining RDX and the onset of the associated liquid-phase decomposition reactions.

## HMX Decomposition.

Physical processes also play a role in controlling the rates of thermal decomposition for HMX and RDX. A model of these physical processes, based on the identities of the decomposition products and the temporal behaviors of their gas formation rates as determined from our experiments with HMX and

RDX, is illustrated in Fig. 3. An illustration of the typical observed data from the decomposition of HMX below its melting point is shown in Figure 4.

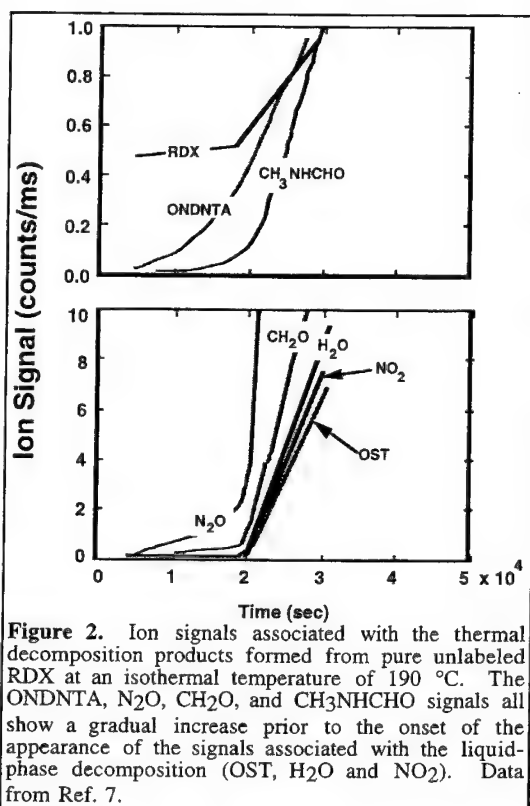
The first step in the decomposition of HMX in the solid phase is illustrated in Figure 3. As the solid HMX is heated, a quasi-equilibrium is established between the gas and solid phase HMX. During the initial period, decomposition of HMX in the gas phase occurs and the decomposition products are observed directly as the gas exits the reaction cell. Concurrently, decomposition of HMX occurs in the solid phase, first forming the mononitroso analogue of HMX, ONTNTA (IV), which then decomposes to lower molecular weight decomposition products. Both the ONTNTA and its decomposition products remain trapped within the HMX particles during the initial stages of the decomposition. These processes are illustrated in the first two diagrams in Fig. 3. These aspects of the model are based on the following results:

- 1) Gas-phase decomposition contributes to the decomposition products as can be seen from the gas formation rates of  $\text{CH}_2\text{O}$  and  $\text{N}_2\text{O}$ , shown in Fig. 4b, which are constant and proportional to the vapor pressure of HMX. The duration of the constant gas formation rate of  $\text{N}_2\text{O}$  is referred to as the induction period.

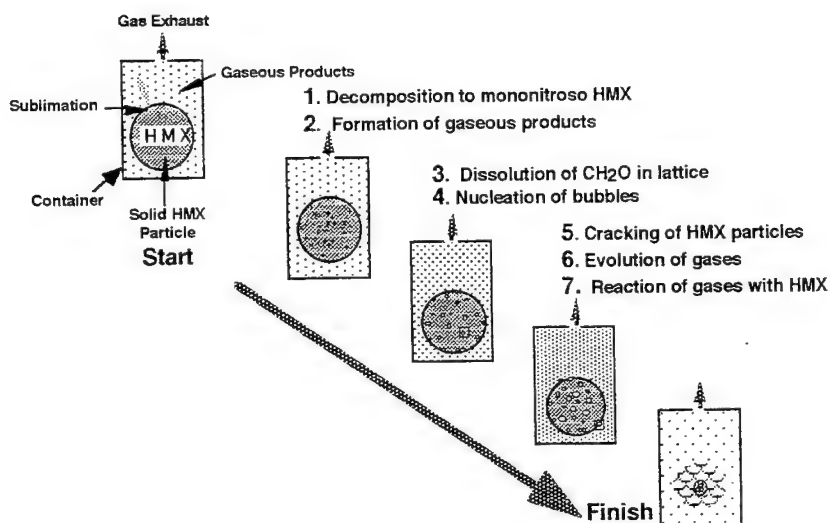
- 2) By analogy, during the decomposition of RDX in the solid phase only ONDNTA and its decomposition products are observed.<sup>7</sup>

HMX continues to decompose in the solid phase through the mononitroso intermediate. Decomposition of the mononitroso intermediate produces low molecular weight products, such as  $\text{N}_2\text{O}$  and  $\text{CH}_2\text{O}$ , and a polymeric product. The low-molecular-weight products move within and interact with the surrounding HMX lattice, to form bubbles, containing primarily  $\text{N}_2\text{O}$ , and solutions between the HMX and  $\text{CH}_2\text{O}$ , which may be localized in the volumes surrounding the bubbles. A polymeric product is also formed in the region of the bubbles and itself undergoes a thermal decomposition process yielding both lower molecular weight decomposition products and other polymeric products. Eventually, the size and pressure within the bubbles grows, leading to cracking of the HMX particles and release of the trapped products. These aspects of the model are based on the following results:

- 1) At the end of the induction period there is a rapid rise in the rate of release from the solid of  $\text{N}_2\text{O}$  followed some time later by a rise in the rate of release of formaldehyde ( $\text{CH}_2\text{O}$  in Fig. 4). This along with similar results for decomposition of RDX in the solid phase and the fact that the mononitroso analogue of RDX forms mostly  $\text{N}_2\text{O}$  and  $\text{CH}_2\text{O}$  when decomposed under high confinement (see ONDNTA results below) strongly supports this mechanism.



**Figure 2.** Ion signals associated with the thermal decomposition products formed from pure unlabeled RDX at an isothermal temperature of 190 °C. The ONDNTA,  $\text{N}_2\text{O}$ ,  $\text{CH}_2\text{O}$ , and  $\text{CH}_3\text{NHCHO}$  signals all show a gradual increase prior to the onset of the appearance of the signals associated with the liquid-phase decomposition (OST,  $\text{H}_2\text{O}$  and  $\text{NO}_2$ ). Data from Ref. 7.



**Figure 3.** Schematic representation of the processes involved in the decomposition of a particle of HMX. The particle is in a container that is representative of the reaction cell used in the STMBMS thermal decomposition experiments.

- 2) At the completion of a decomposition experiment, at isothermal temperatures below the melting point of HMX, an orange-brown residue remains that retains the same shape as the original HMX particles ( $\sim 150 \mu\text{m}$  diameter) and upon examination with transmission electron microscopy was found to be composed of broken spherical shaped shells ranging in size from  $\sim 0.1 \mu\text{m}$  to  $\sim 5 \mu\text{m}$ . This residue is a form of polyamide that decomposes to formamide, N-methylformamide, and N,N-dimethylformamide, as well as several other lower molecular weight species upon further heating.<sup>5</sup> This supports the idea of bubble formation, as well as polymerization, in the decomposition process.
- 3) The fact that 75% of the ONTNTA formed in the decomposition of HMX in the solid phase does not undergo scrambling of the N-NO bond (Ref. 6) compared to complete scrambling of the N-NO bond in ONDNTA in the decomposition of RDX in the liquid phase (Ref. 7) suggests that formation of ONTNTA in the solid phase occurs at individual sites in the lattice. After the ONTNTA decomposes at the lattice site, the lower molecular weight products disperse in the lattice to expand existing bubble sites or create new nucleation centers.
- 4) The observation of the formation of dimethylnitrosamine,  $(\text{CH}_3)_2\text{NNO}$ , from the decomposition of HMX in the solid phase, as well as from the unusual decomposition process of ONDNTA under high confinement (see below), suggests that the mononitroso analogue of HMX plays a very important role in its decomposition in the solid phase.

The increase in the rate of decomposition after the induction period suggests an autocatalytic process, as can be seen from Fig. 4. The processes that occur in the early stages of decomposition continue, but now the decomposition process is affected by the reaction of gaseous decomposition products with the remaining HMX. This effect can be seen from a comparison of the rate of decomposition, as characterized by the rate of formation of  $\text{N}_2\text{O}$ , from experiments in which the pressure of the decomposition products in the reaction cell was varied by using orifices with diameters of 5 and  $100 \mu\text{m}$  as can be seen from the results in Figure 5. The higher pressure of contained gaseous products in the experiment with the  $5 \mu\text{m}$  diameter orifice increases the rate of decomposition of the HMX sample.

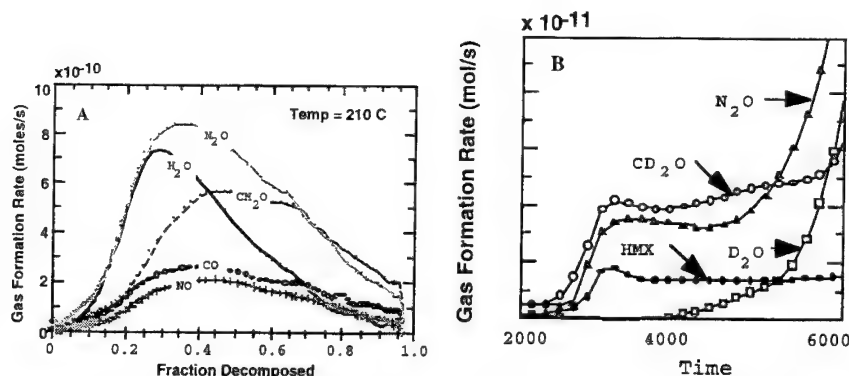


Figure 4. a) Gas formation rates of the products from the thermal decomposition of HMX at 210°C. The duration of the decomposition process is about 37000 seconds. b) Gas formation rates of thermal decomposition products from HMX-d8 during the induction period and first stage of the acceleratory period.

#### ONDNTA DECOMPOSITION

In the case of the intermediate in RDX decomposition, ONDNTA, we have been able to independently synthesize it and study its decomposition mechanisms separately.<sup>9</sup> Analysis of the details of its decomposition behavior are currently underway and only a brief summary of the results are presented here. This nitramine decomposes in two separate temperature regions sequentially, one between 95 and 145 °C and the other between 155 and 210 °C. An illustration of this behavior is shown in Figure 6 for the decomposition of ONDNTA in a reaction cell with a 50  $\mu\text{m}$  diameter orifice and held at two different isothermal temperatures of 115 and 175 °C. The major decomposition products are  $\text{N}_2\text{O}$ ,  $\text{CH}_2\text{O}$ ,  $\text{CO}/\text{N}_2$  ( $m/z=28$ ) and  $\text{NO}_2$  and the minor decomposition products include several formamides and dimethylnitrosamine,  $(\text{CH}_3)_2\text{NNO}$ . The

products obtained from both regions are very similar to those obtained from the decomposition of HMX and RDX in the solid phase with some variation between the two channels of ONDNTA decomposition. Careful examination of the ONDNTA sample by IR, NMR and mass spectrometry show no evidence of any major impurity that would account for the decomposition products observed in the lower temperature channel of the decomposition. Furthermore, examination of samples that were held at temperatures associated with the lower temperature decomposition region (125 °C) stopped producing decomposition products and when the remaining sample was evaporated only the reactant, ONDNTA, was detected with the STMBMS. It is not understood why the decomposition stops in the lower temperature region. However, it is surmised that in this temperature region there is a competition between two competing processes. One is an autocatalytic process in which contained gas-phase decomposition products accelerate the decomposition process and the second is some undetectable phase transition that leads to a more stable phase of ONDNTA that is not susceptible to autocatalysis.

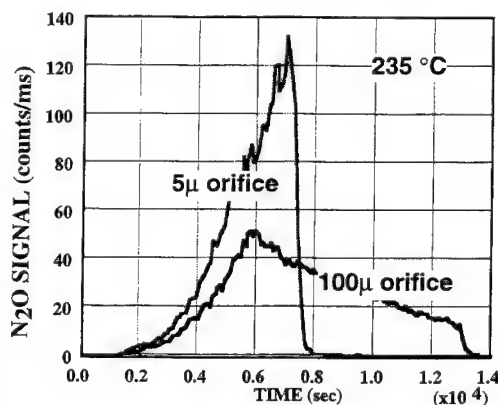
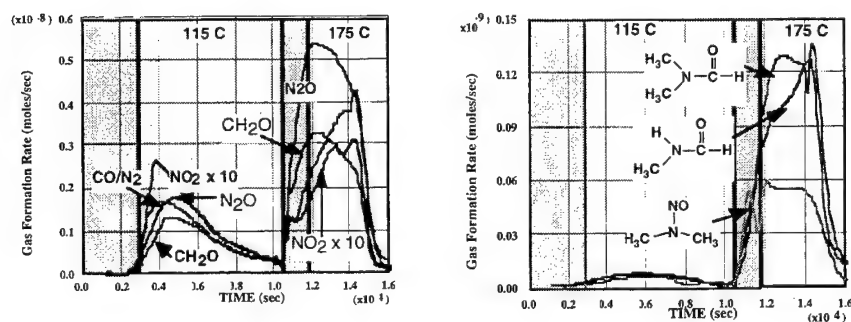


Figure 5. The effect of containment of gaseous decomposition products on the decomposition of HMX in the solid phase is illustrated with the ion signals associated with the rate of formation of  $\text{N}_2\text{O}$  formed during the decomposition in two different experiments with HMX at 235 °C and using orifice diameters of 100  $\mu\text{m}$  and 5  $\mu\text{m}$ .

This competition between autocatalytic decomposition and stabilization of the ONDNTA is illustrated quite dramatically by the results of an experiment using a smaller, 5  $\mu\text{m}$  diameter orifice that raises the partial pressures of the decomposition products within the reaction cell. A comparison between the gas formation rates and the associated partial pressures of the decomposition products for experiments carried out with 50 and 5  $\mu\text{m}$  diameter orifices is shown in Figure 7. Decomposition of ONDNTA in the experiment conducted with a 5  $\mu\text{m}$  diameter orifice occurs much more rapidly than with a 50  $\mu\text{m}$  diameter orifice. In the experiment with the 5  $\mu\text{m}$  diameter orifice, the pressures of the decomposition products are about 1000 times higher, the ONDNTA decomposes approximately 100 times as fast, and the entire sample is consumed in the low temperature channel. Thus, the increased pressure of the



**Figure 6.** Gas formation rates of decomposition products from the thermal decomposition of ONDNTA in a reaction cell with a 50  $\mu\text{m}$  orifice at isothermal temperatures of 115 C and 175 C.

decomposition products appears to increase the rate of the autocatalytic decomposition to such an extent that it overcomes the process that leads to a more stable form of ONDNTA. Details of this unusual behavior and the kinetics of the decomposition will be the subject of another paper.

These results indicate that as ONDNTA decomposes it releases gaseous products and also forms a nonvolatile compound (possibly polymeric) that is relatively stable. The first step in the process may be scission of the N-NO<sub>2</sub> bond as evidenced by the NO<sub>2</sub> signal, followed immediately by loss of CO/N<sub>2</sub>, N<sub>2</sub>O and CH<sub>2</sub>O as indicated by the simultaneous rapid rise in these signals. Two different explanations may be made for the sharper decrease in the CO/N<sub>2</sub> and NO<sub>2</sub> signals compared to the N<sub>2</sub>O and CH<sub>2</sub>O signals. The first explanation is that the ONDNTA sample is rapidly converted to a nonvolatile product (the rate of conversion is characterized by the NO<sub>2</sub> or CO/N<sub>2</sub> signals) that then undergoes a slower decomposition to form N<sub>2</sub>O and CH<sub>2</sub>O. The second possible explanation is that the nonvolatile decomposition product interacts with the remaining ONDNTA, thus providing another decomposition pathway that leads to the release of N<sub>2</sub>O and CH<sub>2</sub>O. The fact that there is an abrupt appearance of a new set of decomposition products later in the process suggests that the first explanation may be more likely. This is based on the fact that the abrupt appearance of these new products occurs in both the thermal ramp and isothermal experiments. It suggests that the nonvolatile product formed in the initial decomposition of ONDNTA itself decomposes, releasing N<sub>2</sub>O and CH<sub>2</sub>O until it reaches a point at which the nonvolatile product becomes sufficiently unstable that it starts to decompose more rapidly into water, dimethylnitrosamine and the formamides. This process is quite consistent with the observed data. A discussion of details of this process will be presented in a future paper.



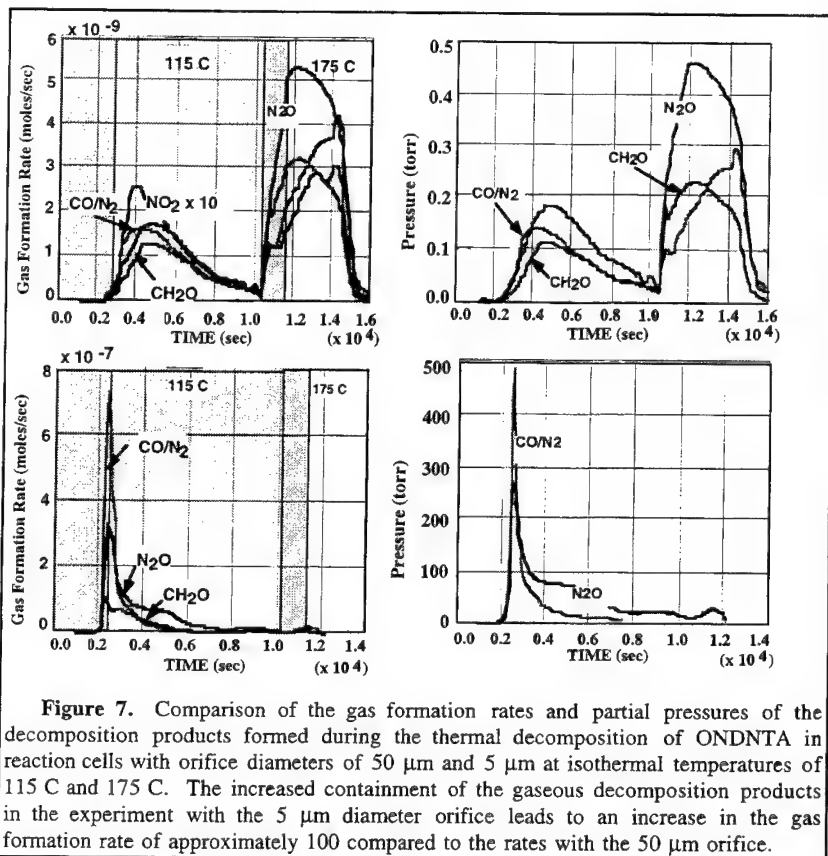


Figure 7. Comparison of the gas formation rates and partial pressures of the decomposition products formed during the thermal decomposition of ONDNTA in reaction cells with orifice diameters of 50  $\mu\text{m}$  and 5  $\mu\text{m}$  at isothermal temperatures of 115 C and 175 C. The increased containment of the gaseous decomposition products in the experiment with the 5  $\mu\text{m}$  diameter orifice leads to an increase in the gas formation rate of approximately 100 compared to the rates with the 50  $\mu\text{m}$  orifice.

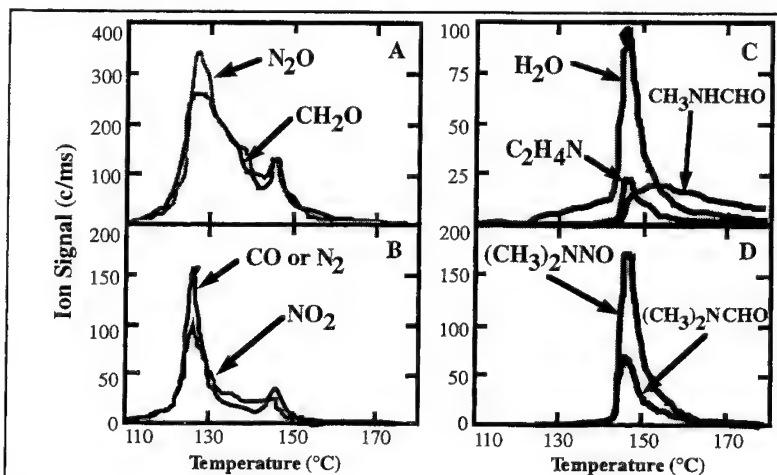


Figure 8. Ion signals formed in the mass spectrometer from thermal decomposition products from ONDNTA under conditions of high confinement. The heating rate is 2°C/min.

## IMPLICATIONS OF THE RESULTS FROM HMX, RDX AND ONDNTA ON THE HMX DECOMPOSITION PROCESS

The similarities between the products and their sequence of formation in the thermal decomposition of ONDNTA under high confinement conditions and the products observed in the decomposition of HMX in the solid phase are quite striking. First, the major products formed in the decomposition are the same, namely  $\text{N}_2\text{O}$ ,  $\text{CH}_2\text{O}$  and  $\text{CO/N}_2$ . Second, the products that originate from the decomposition of the nonvolatile product formed in the decomposition of ONDNTA are the same as those observed in the decomposition of HMX in the solid phase ( $\text{H}_2\text{O}$ ,  $(\text{CH}_3)_2\text{NNO}$ ,  $\text{CH}_3\text{NHCHO}$ , and  $(\text{CH}_3)_2\text{NCHO}$ ). Third, a stable residue remains after the decomposition of both materials. One notable difference between the decomposition of these two materials is the observation of  $\text{NO}_2$  during the decomposition of ONDNTA and the absence of  $\text{NO}_2$  as an observed product during the decomposition of HMX. However, since HMX decomposes at higher temperatures and the process occurs within the HMX particles it is quite likely that the  $\text{NO}_2$  reacts within the HMX particles to form  $\text{NO}$  and thus  $\text{NO}_2$  is not observed in our experiments with HMX. One other difference between the decomposition of ONDNTA and HMX is the presence of  $\text{HCN}$  in the decomposition of HMX and its absence in the decomposition of ONDNTA. Although  $\text{HCN}$  is not one of the more abundant products observed in the solid-phase decomposition of HMX, its presence indicates that a pathway, similar to the OST pathway observed in the liquid-phase decomposition of RDX, occurs during the decomposition of HMX, but with only a minor contribution. This behavior is also supported by our previous work on decomposition of HMX in the liquid phase<sup>12</sup> in which OST and other products formed from the HMX ring ( $\text{H}_2\text{C}_2\text{N}_2\text{O}$ ,  $m/z=70$ ) were observed.  $\text{HCN}$  will be formed upon further decomposition these products.

From this qualitative description of the decomposition of HMX, RDX and ONDNTA, the following model of the decomposition of HMX in the solid phase can be constructed.

- 1) HMX decomposes to its mononitroso analogue at individual lattice sites within the particles.
- 2) The mononitroso analogue decomposes to gaseous products ( $\text{CO/N}_2$ ,  $\text{N}_2\text{O}$  and  $\text{CH}_2\text{O}, \dots$ ).
- 3) The gaseous products move within and interact with the lattice. Initially the  $\text{CO/N}_2$  and  $\text{N}_2\text{O}$  coalesce to form bubbles and the  $\text{CH}_2\text{O}$  dissolves in the HMX lattice.
- 4) Weakening of the HMX lattice due to dissolved  $\text{CH}_2\text{O}$  allows dissociation associated with liquid-phase decomposition to occur. This leads to the formation of  $\text{HCN}$  from the ring and  $\text{HONO}$  and its decomposition products,  $\text{H}_2\text{O}$ ,  $\text{NO}$  and  $\text{NO}_2$ .
- 5) Formation of the HMX mononitroso analogue, ONTNTA, and its subsequent decomposition continues. The ONTNTA now decomposes to  $\text{CO/N}_2$ ,  $\text{N}_2\text{O}$  and  $\text{CH}_2\text{O}$  and a nonvolatile product that may be polymeric. This nonvolatile product itself undergoes decomposition to  $\text{CH}_2\text{O}$  and  $\text{N}_2\text{O}$  and eventually becomes unstable and decomposes to formamides and dimethylnitrosamine. This nonvolatile product may be a catalyst for the decomposition.
- 6) The size and gas pressure within the bubbles grow eventually leading to cracking of the HMX particles and release of the gaseous products.
- 7) The gaseous products interact with the remaining HMX sample to accelerate its decomposition. The reactions responsible for this aspect of the process have not yet been determined.
- 8) Finally the HMX is depleted and a residue with polyamide characteristics remains.

This model summarizes the global chemical reaction pathways and physical processes that we believe control the decomposition of HMX in the solid phase. Clearly more work needs to be done to probe aspects of both the chemical reaction pathways, such as catalysis by gaseous decomposition products, and the physical processes, such as bubble growth and gas release from the particles. In addition, we need to develop models to accurately represent these processes so that these results may be used in models addressing issues of long-term aging and response of these materials in abnormal environments such as fires.

## SUMMARY AND IMPLICATIONS FOR COOKOFF RESPONSE.

Understanding the physical and chemical changes that occur prior to ignition in energetic materials in munitions that are subjected to abnormal thermal environments is important for developing reliable models for characterizing the violence of the resulting event. HMX and RDX are usually but one ingredient in a propellant or explosive formulation, and therefore, it is important to understand how their behavior may be influenced by other components of the formulation. The results of our work on these materials indicates that several of the decomposition processes occur within the solid particles and thus should not be significantly influenced by other ingredients in the formulation, whereas, other aspects of the results suggest that interactions with other ingredients may be important.

The important aspects of the decomposition of HMX that may be independent of other ingredients involve the formation and decomposition of the mononitroso analogue of HMX. The formation of ONTNTA in the lattice of HMX and its subsequent decomposition to gaseous products will create more localized defects within the HMX particles, thus increasing the density of potential "hot spots" and possibly increasing the shock or impact sensitivity. Further degradation of HMX within the particles leads to formation of bubbles within the particles and eventual fracture of the particles, creating smaller particles with more edges. This may also increase the impact or shock sensitivity of the material. As the decomposition progresses the material becomes porous as the HMX decomposes. Its pores being filled by its thermal decomposition products (i.e.,  $N_2O$ ,  $CH_2O$ , etc.), which still contain a large fraction of the energy originally stored in the HMX. Ignition of the material in this porous condition may lead to a more violent event.

The important aspects of the decomposition of HMX that may be dependent on other ingredients in a formulation are associated with the influence of thermal decomposition products on the rate of decomposition of HMX in an autocatalytic manner. This interaction may manifest itself by either an increase or a decrease in the rate of decomposition of HMX depending on whether the other ingredients increase or decrease the amount of the species responsible for autocatalysis. Neither the identity of the autocatalyst nor how it may interact with other components in a formulation are known at present.

Future work in this area involves developing models to represent the decomposition processes outlined in this paper and investigating the role of autocatalysis by the gaseous decomposition products.

## ACKNOWLEDGMENTS

The authors wish to thank D.M. Puckett for assistance in collecting the mass spectrometry data. This work was supported by the Memorandum of Understanding between the Office of Munitions and the U.S. DOE, the U.S. Department of Energy under Contract DE-AC04-94AL85000, the U.S. Army ARDEC, and the U.S. Army Research Office under contract 33655-CH.

<sup>1</sup> a) **M. Baer, E. Hertel and R. Bell**, "Multidimensional DDT Modeling of Energetic Materials" and **M. Baer, M. Hobbs, R.J. Gross, D.K. Gartling and R.E. Hogan**, "Modeling of Thermal/Chemical/Mechanical Response of Energetic Materials" in Proceedings of 26th International Conf. of ICT, 1995, Karlsruhe, FRG; b) **M. Baer and M. Hobbs**, "Multidimensional Fully Coupled Thermal/Chemical/Mechanical Response of Reactive Materials", Proceedings of the JANNAF Hazards Subcommittee, Huntsville, Alabama, October, 1995.

<sup>2</sup> **McGuire, R. R. and Tarver, C.M.**, Seventh Symposium (International) on Detonation, NSWC MP 82-334, Annapolis, Maryland, 56 (1981).

<sup>3</sup> "Fundamentals of Solid-Propellant Combustion," Kuo, K. K. and M. Summerfield eds.; Progress in Astronautics and Aeronautics Vol. 90., p. 121, AIAA Inc., New York, NY, 1984.

<sup>4</sup> **J. Maienschein**, Lawrence Livermore National Laboratory, private communication.

<sup>5</sup> **R. Behrens, Jr.**, "Thermal Decomposition of Energetic Materials: Temporal Behaviors of the Rates of Formation of the Gaseous Pyrolysis Products from Condensed-Phase Decomposition of HMX", *J. Phys. Chem.* **94**, 6706-6718, 1990.

<sup>6</sup> **R. Behrens, Jr. and S. Bulusu**, "Thermal Decomposition of Energetic Materials. 2. Deuterium Isotope Effects and Isotopic Scrambling in Condensed-Phase Decomposition of Octahydr-1,3,5,7-tetranitro-1,3,5,7-tetrazocine (HMX)", *J. Phys. Chem.* **95**, 5838-5845, 1991.

<sup>7</sup> **R. Behrens, Jr. and S. Bulusu**, "Thermal Decomposition of Energetic Materials III: Temporal Behaviors of the Rates of Formation of the Gaseous Pyrolysis Products from Condensed-Phase

Decomposition of 1,3,5-Trinitro-hexahydro-s-triazine (RDX)", J. Phys. Chem. 96, 8877-8891, 1992.

<sup>8</sup> **R. Behrens, Jr. and S. Bulusu**; "Thermal Decomposition of Energetic Materials IV: Deuterium Isotope Effects and Isotopic Scrambling (H/D,  $^{13}\text{C}/^{18}\text{O}$ ,  $^{14}\text{N}/^{15}\text{N}$ ) in Condensed Phase Decomposition of 1,3,5-Trinitro-hexahydro-s-triazine (RDX)", J. Phys. Chem. 96, 8891-8897, 1992.

<sup>9</sup> **Behrens, R. Jr., Land, T., Bulusu, S.**, *Proceedings of the 30th JANNAF Combustion Meeting*, Monterey, CA., November 1993.

<sup>10</sup> a) **Behrens, Jr., R.**, *Rev. Sci. Instrum.*, 1986, **58**, 451; b) **Behrens, Jr. R.**, "The Application of Simultaneous Thermogravimetric Modulated Beam Mass Spectrometry and Time-of-Flight Velocity Spectra Measurements to the Study of the Pyrolysis of Energetic Materials." In *"Chemistry and Physics of Energetic Materials"*, Bulusu, S.N., Ed.; Proceedings of the NATO Advanced Study Institute, Vol. 309, Kluwer Academic Publishers, Netherlands, 1990, p. 327; c) **Behrens, Jr., R.**, "Identification of Octahydro-1,3,5,7-tetranitro-1,3,5,7-tetrazocine (HMX) Pyrolysis Products by Simultaneous Modulated Beam Mass Spectrometry and Time-of-Flight Velocity-Spectra Measurements", *Int. J. Chem. Kinetics*, 1990, **22**, 135.

<sup>11</sup> **Brockman, F. J., Downing, D. C. and Wright, G. F.**, *Canadian J. of Research*, 1949, **27B**, 469.

<sup>12</sup> **R. Behrens and S. Bulusu**, "Recent Advances in the Decomposition of Cyclic Nitramines", *Proceedings of the Materials Research Society Symposium*, Vol 296, 13 - 24, 1992.

## IGNITION OF LIQUID AND SOLID NITROCOMPOUNDS AT FAST COMPRESSION OF GAS INTRUSIONS

**B.N.Kondrikov, E.I.Dorofeev, Yu.N.Polikarpov**  
Mendeleev University of Chemical Technology,  
9 Miusskaya Sq., Moscow 125047, Russia

**ABSTRACT:** Initiation of explosion of liquid and solid explosives by rapid compression of gas intrusions has been the subject of extensive study during at least half of century. However only limited quantitative both theoretical and phenomenological description of the process till now is reached. This work is devoted to elaboration and application of two experimental procedures of the energetic materials initiation by means of the gas cavities compression. One of them named method U-shaped tube was used to generate data which revealed the role of air inclusions in causing ignitions during the rapid compression of a liquid in the broad range of conditions of its production or transportation. Another procedure consists of employment of fallhammer impact machine equipped with the impact device containing a layer of explosive on the bottom of the hole filled by air to investigate sensitivity of solid energetic materials, and to simulate possible conditions of in-bore premature explosions. Critical pressure of initiation is determined for many liquid explosives, preeminently nitrocompounds, in U-shaped tube. Dependence of critical pressure on the hole depth is estimated in fallhammer apparatus. The approximate theoretical relations are developed to describe the experimental facts.

### 1. INTRODUCTION

The liquid nitrocompound, nitroglycerin, introduced into practice by Alfred Nobel a century ago made the Revolution in the field of technology of explosives, in rock blasting, and in propellants manufacturing and application. This fact evokes the greatest respect bearing in mind that nitroglycerin is one of the most dangerous chemical substances, and all the history of its production and application is nothing but continuous chain of the accidental, sometimes catastrophic explosions. It was precisely Alfred Nobel who understood also that this behavior was connected at least partly with liquid state of aggregation of the compound, and found out two paradoxical ways to decrease sensitivity of the liquid at first by mixing nitroglycerin with the mineral substance, kieselguhr, and then by introducing into it some amount of nitrocellulose, also very hazardous substance, as a result decreasing danger of the explosive drastically.

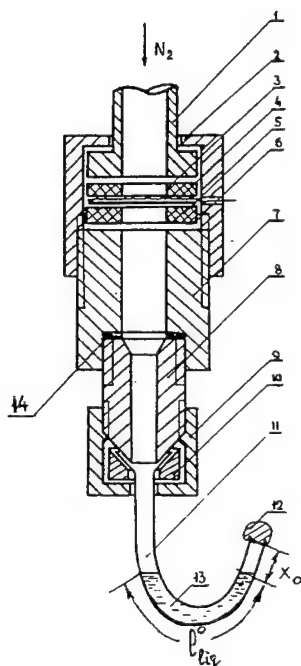
The main source of higher danger of liquid energetic materials (LEM) is ignition and explosion at fast compression of gas inclusions. We have investigated ignition and explosion at quick compression of gas cavities of a row of LEM using two experimental procedures. One of them consists of application of U-shaped tube from steel or perspex one end of which is connected through the socket and the plastic disc with a receiver containing compressed nitrogen. Another end of the tube is sealed. Explosive liquid is immersed in the lower section of the tube. When the disc is ruptured the liquid in the tube is set to motion by jet of nitrogen rushing into the tube, and impinges upon the tube

end. The procedure in outlines reproduces the method described elsewhere. [1] Another procedure consists of employment of fallhammer impact machine (36 kg falling weight, 1.5 m height limit). Impact device of the machine contains a hole of definite diameter and depth at bottom of which a small portion of explosive is pressed. The plastic substance, ceresine (wax from ozocerite) flows into the hole during impact, and compresses air inside it. Critical pressure necessary for ignition of EM is determined in both the methods used.

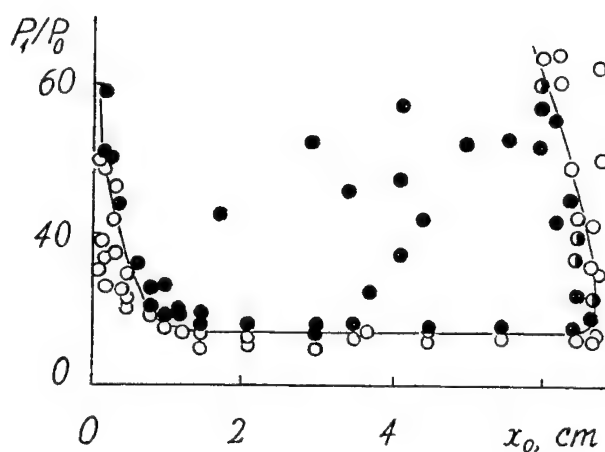
## 2. EXPERIMENTAL

### 2.1. U-shaped Tube Method and Results

Schematic drawing of U-shaped tube apparatus used for LEM testing is shown in Figure 1. Receiver of 0.25 l volume is attached through a sleeve (1) and the union nut (2) to thick walled socket (7). Plastic disc (5) inserted between rings (3) and (6) separates regions of high and low pressure. Nichrome wire 0.1 mm diameter (4) passing through the small electrically isolated orifice in the nut (2) is placed between the disc and the emery paper ring which fixes the wire location and provides uniform rupture of the disc. Steel reducer (8) made airtight by means of the TEFLON ring (14) is screwed in the socket (7). Bottom part of the reducer is connected with the rolled out end of U-shaped tube (11) fixed by the union nut (9) and made tight by means of the copper collar (10).



**Figure 1.** U-shaped tube test assembly. Explanation of the numbers, see text



**Figure 2.** Results of NGL investigation in U-shaped tube (version 2): ● - explosion, ○ - no ignition, ◐ - ignition without explosion

Tube of stainless steel, 4 mm diameter, 2 mm wall thickness, was bent to form U-shaped channel. One end of the tube was rolled out on the lathe. After that the tube was placed in concentrated nitric acid and kept there about 24 hours to remove traces of oil and dirt. Then it was flushed and dried out, and sealed immersing the other end of it into the small crucible filled by melted solder providing after cooling strong reliable connection of the plug (12) with the tube walls and flat smooth surface of the bottom of the channel. Firmness of the plug/tube connection was high enough to ensure its retention even at explosion, if depth of section of the plug inside the tube were at least 5 mm. When it was smaller the plug could be removed from the tube during pressurization, and process of explosion extinguished. Column of a liquid tested ( $l_{liq}^0$ ) (13) occupied the lower section of U-shaped tube providing some space filled by air between surface of the liquid and bottom of the channel ( $x_0$ ). After necessary pressure in the receiver was attained the disc (5) was ruptured, and compressed nitrogen from the receiver aspired into the tube. The column of the liquid was set to motion, and at the same time the jet of nitrogen penetrated into it forming a cone head part of which had velocity higher than velocity of the whole mass of the liquid.

During the work, even at explosions, when U-shaped tube was destroyed, the TEFLON ring (6) and the emery paper ring, as well as the copper collar (10) were preserved, usually without any visible changes, and could be reused. The TEFLON ring (14) on the contrary was deformed after every run, and must be replaced. By the special experiments with four nitric esters, and some other substances it was shown that absence of the tightening ring 14 resulted in difference only about 2 atm in critical pressure necessary for ignition  $P_{cr}$ . Correspondingly experiments were carried out in some cases without the ring. This version of the experimental procedure is denoted below as version 2 as distinguished it from the first, basic modification. Variants 3 and 4, with the ring 14 but without the receiver, and without both the ring and the receiver gave very big difference in  $P_{cr}$ , and were not recommended as the test methods.

V-shaped channel in transparent block was used to visualize the process. Channel 4 or 7 mm diameter was drilled in the perspex block of about 90×80×30 (mm). It was polished after drilling using dichloroethane and dried out. One end of the channel was supplied by the threaded joint to connect it with the reducer (8). The other end was tightly closed by a bolt. Process of a liquid motion was photographed by means of the high speed framing camera SKS-2M (2,000 to 4,000 frames per second) against background of a bright screen. The processes of ignition, DDT, and detonation were registered by the streak camera JFR-2. The limit of pressure at application both U- and V-shaped tubes was about 100 atm, i.e. pressure in commercial nitrogen cylinder.

SKS-2M framing camera records demonstrate movement of the liquid column surface exposed to the bottom of the channel of V-shaped tube as well as motion of the head part of the jet inside the column. Velocity of the head portion of the jet is higher than velocity of the surface of the column exposed to bottom of the tube. The results of the frames elaboration were drawn in form of the curves in  $t-x$  plane. Intersection point of the curves represents a state when the jet of nitrogen breaks through the layer of liquid into cavity and no essential compression of the air bubble (and accordingly ignition of the liquid) is possible.

Figure 2 shows a line that separates region of explosions (solid circles inside the zone confined by the curve) and region of non explosions (open circles outside the explosion zone). Half-open circles correspond to experiments where ignition take place but U-shaped tube is found unchanged or only slightly deformed. The right upward branch of the curve Fig. 2 demonstrates in fact locus of the points of intersection of the curves one of which represents the head of the jet motion, and the other reflects the surface of the liquid migration. Left branch of the curve demonstrates  $P_{cr}$  change probably connected with heat losses at low  $x_0$  values.

Streak camera records show that at pressure of nitrogen in the receiver close to  $P_{cr}$  low and sometimes even high velocity detonation develops after ignition. Retonation wave also can be observed. At higher pressures detonation and retonation processes are suppressed in some cases, and only quick burning of LEM is registered.

**TABLE 1**  
**Critical Pressures of Ignition of LEM in U-shaped Tube**

N	Explosive	Version			
		1	2	3	4
1	Methylnitrate	8	10	12.5	18
2	Allylnitrate	10	-	-	-
3	Nitroglycerin (NG)	11	13	15	23
4	NG/DGDN (60/40)	11	-	-	-
5	Nitroglycol (NGL)	12.5	14	17	27
6	Diethyleneglycoldinitrate (DGDN)	11(?)	15	18	25
7	AEDAP	15	-	-	-
8	AEDAT	15	-	-	-
9	FEFO	16	17	20	28
10	TNM/Benzene (90/10)	20	-	-	-
11	DINA	21.5	-	-	-
12	BTNENA	23	27	31	39
13	ADN	23	-	-	-
14	2,4-DNT/HNO <sub>3</sub> (70/30)	60	-	-	-
15	TNT	80	82	83	86
16	Nitromethane (NM)	>100	-	-	-
17	Tetranitromethane (TNM)	>100	-	-	-
18	TNT/RDX (70/30)	>100	-	-	-
19	Alumotol (15/85)	>100	-	-	-
20	Methylamineperchlorate/H <sub>2</sub> O (65/35)	-	>100	-	-
21	Ethylenediaminediperchlorate/ H <sub>2</sub> O(70/30)	-	>100	-	-

Notes: Versions 1 - 4 are described in text. All the solid at usual conditions substances are tested at temperature 5 - 10K higher their melting points.

AEDAP is 2-azidoethoxy-1,3-diazidopropane. AEDAT is 2-(2-azidoethoxy)-4,6-diazido-1,3,5-triazine. FEFO is bis (2-fluoro-2,2-dinitroethyl) formal. BTNENA is bis (2,2,2-trinitroethyl) nitroamine.

Table 1 presents the data obtained at testing of LEM in U-shaped tube. Quite naturally methylnitrate having nitric esters kinetics, very high burning rate, and high vapor pressure is ignited best of all, at the smallest pressure in the receiver. Allylnitrate is the second LEM in this respect, and nitroglycerin is the third. All these substances have noticeably higher tendency to ignition than that of nitroglycol which is characterized by the highest among the usual nitric esters heat of explosion. Two azides are ignited approximately as nitric esters but burn more quietly, very often ignition without explosion is observed. ADN behaves about as BTNENA and DINA, although it has at least twice as low heat of explosion than these nitrocompounds.

Conditions of trinitrotoluene ignition are close to the limit of applicability of this test method:  $P_{cr}$  is about 80 atm. Nitromethane, tetranitromethane, and some other slow burning liquids may not be initiated in U-shaped tube. Suspensions, TNT/Al (85/15) (15% of pigment grade aluminum in the mixture) and TNT/RDX (70/30) also do not explode, probably due to very high viscosity. The jet of



the compressed gas just breaks through the layer of the suspension, and the gas in the cavity may not be compressed sufficiently.

Mixing an explosive liquid with non-explosive organic diluents results in augmentation of  $P_{cr}$  (Table 2). The most important characteristic of the diluent is probably its specific heat  $C_p$ . Critical concentration of chloroform and bromoform, the substances characterized by the very low  $C_p$  values, is several times higher, than that of methanol and acetone.

**TABLE 2**  
**Effect of Solvents on Sensitivity of NGL in U-shaped Tube:  $P_{cr}$ , atm, (Version 2)**

Solvent conc., %	Methanol	Acetone	Chloroform	Bromoform
0	13.5	13.5	13.5	13.5
5	15.5	15.5	13.5	13.5
10	20	20	13.5	13.5
15	26.5	26.5	14.5	14.5
20	47	50	14.5	14.5
25	71	>100	14.5	14.5
30	>100	-	15	15
40	-	-	17.5	15
50	-	-	22.5	15.5
60	-	-	39	16
70	-	-	95	16.5
78	-	-	>100	60

Influence of initial temperature on  $P_{cr}$  of one of the nitric esters, diethyleneglycoldinitrate DGDN, was also estimated.  $P_{cr}$  rises from 7 to 24 atm at initial temperature from +100 to -15°C decrease.

## 2.2. Fallhammer method and results

Estimation of sensitivity of solid explosives to compression of gas intrusions was carried out using fallhammer apparatus ( $m = 36$  kg,  $H_{max} = 1.5$  m). Small (about 0.01 g) portion of explosive tested was thoroughly pressed into a hole of  $d \approx h$  drilled in the plastic disc inserted, bottom of the hole up, into the steel heavy confinement cylinder enclosing hardened steel driving and backup pistons. A layer of ceresine was located on the backup piston under the hole. Another steel cylinder filled by oil was used as a damper to increase time and to decrease maximal pressure of impact. Pressure transducer, amplifier and oscillograph were employed to measure pressure-time dependence during impact. Time of the gas compression as well as time of pressure decrease due to the falling weight rebound was  $1.5 \pm 0.4$  ms. The apparatus was constructed to meet circumstances of quick compression of gas inclusions and possible ignition at in-bore premature explosion of a charge of explosive fill in an artillery projectile at gunshot.

Results of the experiments for phlegmatized RDX (about 6% of hydrocarbon desensitizer added) are presented in Figure 3. The every point is a result of the experiment at the definite height of the falling weight impact.

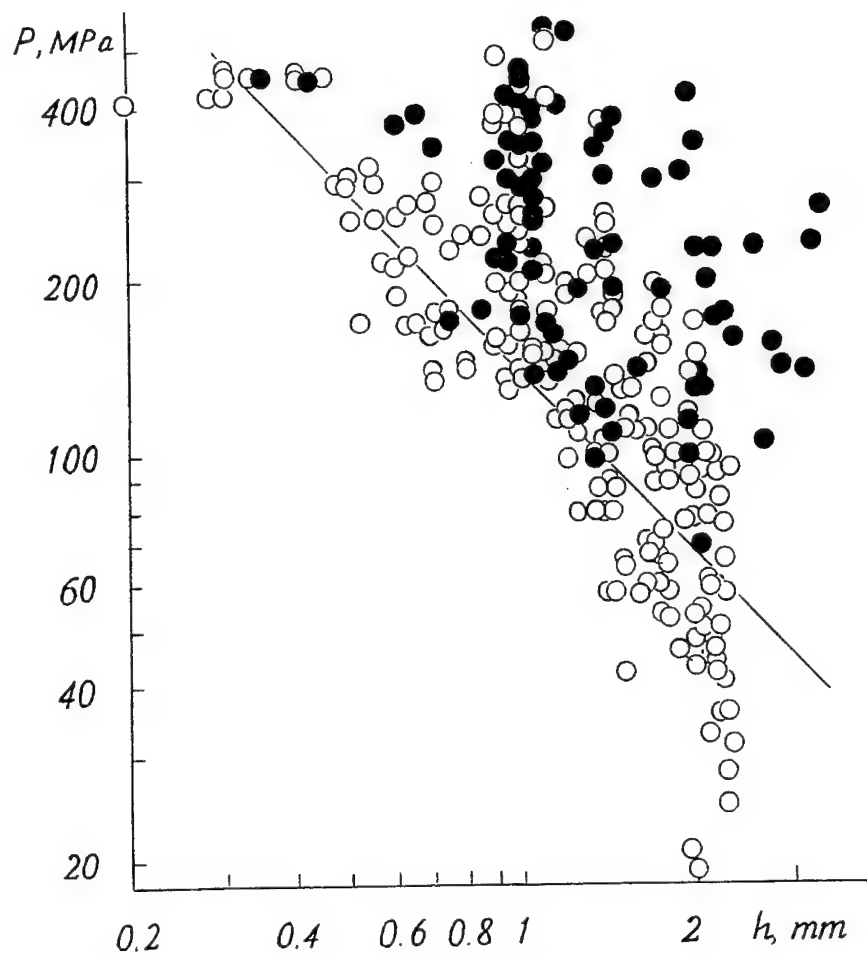


Figure 3. Limiting pressure of ignition versus depth of the hole. Experiments on fallhammer apparatus with phlegmatized RDX: ● - ignition, ○ - no ignition.

The line separating the region where ignition can occur is

$$\log_{10} P_{cr} = 2.13 - \log_{10} h \quad (P_{cr} \text{ in MPa, } h \text{ in mm}) \quad (2.1)$$

Obviously at the conditions of the experiment it would be very difficult to reproduce the results of compression of the very small ( $0.3\text{--}20 \text{ mm}^3$ ) gas intrusions. The main source of scattering is the leak of air from the hole through the small cracks or pores. Accordingly probability of ignition even at pressures twice as big as the value of  $P_{cr}$  is merely about 50%, and only at relatively big dimensions of the hole and at pressures of about  $3 P_{cr}$  the probability seems to be close to 100%.

### 3. DISCUSSION

As it has been mentioned in our previous work Yuly B.Khariton was among the first to pay attention to the fact that ignition of a liquid by weak mechanical impact occurs as a result of compression and heating of gas inclusions.[1] That time the authors might not refer however that about two years before the experiments carried out by Yuly B.Khariton the young, modest military engineer Khariton M.Lavrik had proposed compression of the gas intrusions as the only real source of in-bore premature explosions of high explosive shells, very serious problem in defense industry of USSR in the course of the Soviet-Finnish war of 1939/1940. The proposals of Kh.M.Lavrik were of prime importance, during few years, on several proving grounds, some thousand projectiles of different caliber were tested by proof-firing, and no one of them gave premature explosion after the changes in filling technology which were implemented by manufacturers in correspondence with Kh.M.Lavrik suggestions. Some thirty years after, it was again Dr.Kh.M.Lavrik who managed to solve, at participation of the authors of this paper, the same problem as applied to 125-mm shaped charge projectiles for the smooth-bore tank gun.

Comprehensive work on investigation of the gas bubbles compression at initiation of explosives by impact was carried out during and after the World War II in Prof.F.P.Bowden Laboratory, Cambridge, England.[2] Many valuable investigations were performed later in this and other scientific sites.[3-7] As to premature explosions of artillery projectiles is concerned it would be necessary to note extensive experimental and analytical study at the Ballistics Research Laboratory (BRL) as well as experiments on NSWC setback shock simulator.[8,9] However till now detailed theoretical description of ignition of explosive at rapid compression of gas cavities is still not reached. The analytical model with due regard for heat losses into steel driving piston was developed to elucidate experimental findings.[8] Very big difference between calculated and experimental data, however, was observed.

In this work we attempted to exclude examination of the heat exchange processes between hot compressed gas and metal surfaces. This might be implemented in principle quite easily because even the very thin, about 10 mcm, film of explosive or some other substance of low heat conductivity on metal surface prevents heat transfer to the metal during 0.1 to 1 ms, characteristic time of the hot compressed gas in the cavity existence. In any case, the gas from the system leakage is assumed to be more substantial source of energy losses and ignition threshold augmentation than the heat exchange influence. Consequently pure adiabatic model is considered.

In framework of classic theory of ignition the energy consumption necessary to produce the ignition zone near surface of reactive substance at conditions of the experiment in U-shaped tube is

$$\frac{P_1 x_0}{2} = k \left[ (T_s - T_0) \left( \sqrt{(\pi/4) \lambda c \rho t_i} \right) \right] \quad (3.1)$$

where  $P_1$  is pressure of compressed gas in the receiver,  $x_0$  is the distance between the surface of a liquid and the bottom of the tube,  $\lambda$ ,  $c$ ,  $\rho$  are the heat conductivity coefficient, specific heat, and density of a substance ignited correspondingly,  $T_s$  and  $T_0$  are surface temperature at the moment of ignition and initial temperature of the substance;  $t_i$  is ignition delay time, and  $k$  is a proportionality coefficient. Denominator 2 in (3.1) reflects the fact that only one half of heat of the compressed gas filled in the gap can be used for producing of the preheated layer near surface of LEM.

Formula (3.1) is derived from the usual expression

$$t_i = \pi \lambda c \rho (T_s - T_0)^2 / 4q^2 \quad (3.2)$$

where  $q$  is the mean value of heat of flux assumed to be proportional to the energy consumption  $P_1 x_0 / 2$ . The final gap width  $l_f$  between the bottom of the channel and the surface of explosive at the moment of collapse of the gas (air) inclusion is neglected in (3.1) as compared to the initial air gap dimension  $x_0$ .

The usual one-dimensional model considers a piston compressing gas in space  $0 < x < x_0$  under influence of the force  $P_1 S$ , where  $S$  is the plug cross section area. The equation of the plug motion with due regard for the resistance of a gas in compressed cavity, but neglecting expansion of the tube, compression of the liquid, and penetration of the jet of nitrogen into the liquid, has a form

$$-\rho l^0 \frac{d^2 x}{dt^2} = P_1 - P = P_1 - P_0 (x_0 / x)^\gamma \quad (3.3)$$

$$(t = 0, x = x_0, x' = 0)$$

where  $\gamma$  is the polytropic exponent of the gas,  $P$  is pressure of air in the cavity,  $P_0$  is the initial pressure ( $10^5$  Pa),  $P_1$  is pressure of nitrogen in the receiver.

The first integral of (3.3) at  $dx/dt=0$  has two solutions corresponding to initial and to final conditions of the first half-phase of the piston motion. The first solution is trivial, at  $t = 0$ ,  $P = P_0$ . The second solution gives parameters of the gas in the gap between bottom of the tube and the surface of the piston as well as the gap width at the moment of collision, when again  $dx/dt=0$  (all the variables at  $x'=dx/dt=0$  are noted by index  $f$ )

$$P_f = P_0 l_f^{-\gamma}; \quad \frac{T_f}{T_0} = \theta_f = l_f^{-(\gamma-1)} \approx \left(1 + P_1(\gamma-1)/P_0\right) \quad (3.4)$$

The final gap relative width  $l_f = x_f/x_0$  is calculated from equation

$$l_f = 1 - \frac{P_0}{P_1(\gamma-1)} \left( \frac{1}{l_f^{\gamma-1}} - 1 \right) \approx \left[ 1 + P_1(\gamma-1)/P_0 \right]^{-\frac{1}{\gamma-1}} \quad (3.5)$$

The maximal heat flux at the moment of impingement is

$$q_m = (2\lambda / x_f)(T_f - T_s^0) \quad (3.6)$$

where  $T_s^0$  is temperature of the surface of explosive at the outset of the ignition process

$$\frac{T_s^0}{T_0} = \theta_s^0 = (b + \theta_f)(b + 1)^{-1} \quad (3.7)$$

where  $b = \left[ (\lambda c \rho)_s / (\lambda c \rho)_g \right]^{1/2}$

Indices  $g$  and  $s$  relate to the gas in the cavity and to the surface of EM correspondingly.

Combining equations (3.1) and (3.4)-(3.7) we have

$$P_{cr} / P_0 = \frac{1}{A} \left( \frac{\pi k \lambda c \rho (T_s - T_0)^2}{4 P_0 \lambda_g T_0} \right)^{\frac{\gamma-1}{2\gamma-1}} \quad (3.8)$$

where

$$A = (\gamma - 1)^{\frac{\gamma}{2\gamma-1}} \left[ 1 - \frac{P_0 (\theta_s^0 - 1)}{P_1 (\gamma - 1)} \right]^{\frac{\gamma-1}{2\gamma-1}} \left[ 1 + \frac{P_0}{P_1 (\gamma - 1)} \right]^{\frac{1}{2\gamma-1}}$$

In the range of  $10 \leq P_1 \leq 20$  atm  $1/A = 1.90 \pm 0.05$ .

Constant  $k$  in (3.1) and (3.8), on the one hand, includes the heat losses at ignition, and, on the other hand, it allows to correct the heat flux value which probably is higher than the value given by the expression (3.6).

Assuming for nitroglycol (NGL) the constants  $\lambda = 0.25$  W/(m.K),  $c = 1.6$  kJ/(kg.K),  $\rho = 1500$  kg/m<sup>3</sup>,  $T_s = 640$  K (approximate value of the critical temperature of NGL),  $T_0 = 293$  K,  $k = 1$ , and for gas in the cavity  $\gamma = 1.4$ , and  $\lambda_g = 0.1$  W/(m.K) we obtain from (3.8)  $P_{cr} = 16P_0$ . It is almost exactly the critical pressure necessary for ignition of NGL at version 2 of U-shaped tube method (see Table 1, and Figure 2). For all the other substances under consideration  $P_{cr}$  varies in the narrow limits of  $16 \pm 4$  atm. It is absolutely staggering result, the very simple model gives in outlines the very good correlation with experiment. It should be stressed that equation (3.8) in full accordance with Figure 2 demonstrates independence of  $P_{cr}$  on  $x_0$ . However this relates only to the first group of LEM tested, precisely to the sensitive substances having  $P_{cr}$  in the range of 8 to 23 atm. Moreover, this approach does not allow to distinguish the sensitivities of different explosives inside the group.

Formula (3.8) presumably gives just an estimation of the critical condition of ignition. As a matter of fact it shows only that in principle ignition and burning of a liquid are possible at pressure on the order of  $P_{cr}$ . Real development of burning is connected eventually with conditions of deflagration to detonation transition (DDT). It is not possible now to estimate DDT critical parameters. However the necessary condition of burning and DDT might be determined. Obviously it would be such a velocity of gas and heat evolution after ignition at which burning could not extinguish as a result of pressure drop at the liquid piston rebound.

Consequently the rate of pressure rise in any case must be not less than absolute value of the pressure drop velocity due to gas in the cavity expansion. Rate of pressure decrease in turn is approximately  $P_f$  divided by time of expansion, and correspondingly it is a function of  $P_f$ . Mean value of the rate is about 0.3 GPa/ms. Suggesting dependence of  $dP/dt$  on  $P_f$  say in form of  $P' = P'_0 (P_f/P_0)^n$ , we obtain

$$\frac{dP}{dt} = P' = P'_0 \left( \frac{P_f}{P_0} \right)^n = u_m \frac{RT_p}{x_f}$$

and correspondingly

$$\frac{P_{cr1}}{P_0} = \left[ \left( \frac{x_0 P'_0}{u_0 \rho R T_p} \right)^{\frac{\gamma-1}{\gamma(\gamma-1)+1}} - 1 \right] (\gamma-1)^{-1} \quad (3.9)$$

where  $R$  is the specific gas constant ( $\sim 300$  J/(kg K)),  $T_p$  is the adiabatic temperature of burning,  $u_0$  and  $v$  are constants of the burning rate versus pressure law.

The calculation results at  $x_0=0.04$  m,  $n=1/2$ ,  $R=300$  J/(kgK) and  $P'_0=0.015$  GPa/ms (corresponding to the mean value  $P_f/P_0 \approx 400$ ) are collected in Table 3.

**TABLE 3**  
**Comparison of the Results of  $P_{cr}$  Experimental and Theoretical Evaluation**

LEM	$P_{cr \text{ exp.}}/P_0$		$\rho$ g/cm <sup>3</sup>	$T_p$ K	$u_0$ mm/s	$v$	$P_{cr1}/P_0$
	version 1	version 2					
Methylnitrate	8	10	1.2	3371	1.2	1.0	7.8
Nitroglycerin	11	13	1.6	3415	1.34	0.956	10.5
Nitroglycol	12.5	14	1.5	3417	0.29	0.89	13.5
AEDAP	15	-	1.33	2300	4	0.5	16.9
DINA	21.5	-	1.5	3080	0.4	0.7	19.7
ADN	23	-	1.6	2053	6	0.39	19.7
TNT	80	82	1.47	2042	0.07	0.95	21.1

Notes:  $x_0=0.04$  m,  $T_p$ ,  $u_0$ ,  $v$  for all the substances except ADN and AEDAP are taken from one of the author's compilation.[10] For ADN A.P.Denisyuk data are utilized, for AEDAP our estimations are used.[11,12]

For all the representatives of the first group the calculation gives rather good fit to the experimental results. TNT as well as the second group LEM representatives ignition can not be described by the equation (3.9). Presumably it would be necessary to take into account reaction of the tube walls and compression of the liquid at very high pressure  $P_f$ . Of course this means also that still more simple approach employing equation (3.1) can be utilized only for very crude estimations.

Such an estimation probably could be implemented however to explain the results obtained with the fallhammer technique. Curves  $P(t)$  show that time of pressure rise varies in the range of  $1.5 \pm 0.4$  ms, in fact independently of the load drop height. Period of approximate constancy of pressure near the top of  $P(t)$  curve, which is supposed to be the ignition characteristic time, is about 0.5 ms, again independently of  $P_{cr}$ . In that event equation (3.1) can be used to calculate  $P_f(x_0)$  dependence in form

$$P_{cr} = \frac{B}{x_0}$$

that qualitatively corresponds to the experimental relation (2.1). At thermal constants used above, and at  $t_i=0.5$  ms,  $P_f=P_{cr}$ ,  $\Delta T = 400$  K and  $\rho=1.7$  g/cm<sup>3</sup> we have

$$P_f x_0 / k = 4 \sqrt{(\pi/4) \lambda c \rho \Delta T^2 t_i} = 2.6 \cdot 10^4 \text{ Pa m}$$

Comparing this with formula (2.1) we get  $k \approx 5$ .

Obviously the very big energy losses (due to viscous resistance of the plastic material, its heating and possible vaporization, friction between details of the impact system, etc.) take place in this case. Meanwhile it would be necessary to note that very good correlation between results of this test and the real conditions of ignition at proof-firing are observed.

#### 4. CONCLUSIONS

Careful measurements of critical pressure necessary for ignition, burning and explosion of a row liquid energetic materials in U-shaped steel tube under influence of a jet of compressed gas are performed. They show that most of liquids capable to ignition at these conditions have critical pressure in the range of 8 to 23 atm. After that the jump of  $P_{cr}$  is observed, in the region of 23 to 100atm only two explosives, melted TNT, and solution of DNT in nitric acid are located. The liquids sensitivity of which is lower than that of TNT are not ignited in U-shaped tube.

The usual model including compression of a gas between the flat smooth surfaces unexpectedly gives in general terms rather good accordance with the mean value of  $P_{cr}$  for the group of the most sensitive LEM.

Thorough examination of the possible ways of ignition conducted in framework of general ideas of the burning theory leads to conclusion that main in this respect feature of a liquid is burning rate versus pressure dependence. High burning rate, and a big exponent of  $u(P)$  law provide easy positive reaction of a liquid at the test and give low  $P_{cr}$  amplitude. As these characteristics of burning determine also probability of burning to detonation transition both ignition and DDT usually are observed simultaneously.

The experimental data received at fall hammer apparatus application show that in outlines they are consistent with the usual notions of ignition theory, on the one hand, and with practice of in-bore premature explosions prevention, on the other hand.

#### ACKNOWLEDGEMENT

This work was sponsored by the Russian Foundation of Fundamental Investigations (RFFI), Project N 96-03-32858.

#### REFERENCES

1. Dorofeev, E.I. and Kondrikov, B.N., Ignition of a liquid in an evacuated glass tube under the effect of an air jet, *Sov. Chem. Phys.* 2, 446-450, 1985.
2. Bowden, F.P. and Ioffe, A.D., *Initiation and growth of explosion in liquids and solids*, Cambridge, At the University Press, 1952.
3. Levine, D. and Boyars, K., The sensitivity of nitroglycerin to impact, *Comb. and Flame*, 9, 131-140, 1965.
4. Johansson, C.N. and Persson, P.-A., *Detonics of high explosives*, Academic Press, London and New York, 1970.

5. Coley, G.D. and Field, J.E., The role of cavities in the initiation and growth of explosion in liquids, *Proc.Roy. Soc. London*, A 335, 67-86, 1973.
6. Field, J.E., Swallowe, G.M. and Heavens, S.N., Ignition measurements of explosives during mechanical deformation, *ibid*, A 382, 231-244, 1982.
7. Dubovik, A.V. and Bobolev, V.K., *Tchuvstvitelnost zhidkikh vzrivchatykh system k udaru (Sensitivity of liquid explosive systems to impact)*, Nauka, Moscow, 1978.
8. Starkenberg, J., Ignition of high explosives by rapid compression of an adjacent gas layer, *The 7th Symposium (Int.) on Detonation*, Annapolis, Maryland, NSWC MP 82-334. Dahlgren, Virginia - White Oak, Maryland, June 16-19, 1981, 3-16.
9. Myers, T.F. and Hershkowitz, J., The effect of base gaps on setback-shock sensitivities of cast composition B and TNT as determined by the NSWC setback-shock simulator, *ibid.*, 914-923.
10. Kondrikov, B.N., *Ignition and burning of nitrocompounds*, MIGHT, Moscow, 1985.
11. Denisuk, A.P., private communication, 1995.
12. Kondrikov, B.N., Burning of droplets and particles of explosives, *Europyro 95*, 6<sup>e</sup> Congres International de Pyrotechnie, Tours, France, 1995, 525-532.



## EFFECT OF $\text{Fe}_2\text{O}_3$ ON THE MATERIAL PROPERTIES OF AP/AL/HTPB BASED PROPELLANTS

J. M. Boteler\*, J. Covino, and A. J. Lindfors  
Shock/Detonation Laboratory  
Research Department  
NAWC, China Lake, Ca.

**ABSTRACT:** Catalytic quantities of  $\text{Fe}_2\text{O}_3$  are frequently added to certain propellant formulations to facilitate the characteristic burn rate. Past studies have demonstrated that the addition of less than 2%  $\text{Fe}_2\text{O}_3$  in Ammonium Perchlorate (AP) based propellants may result in a significant increase (60-70%) in the burn rate. The mechanistic interpretation for this increase is not well understood. Indeed, very little is known regarding the role  $\text{Fe}_2\text{O}_3$  plays in the combustion process or what effect it's inclusion may have on the mechanical properties of this class of propellants. With this motivation a comprehensive study of both the combustion and dynamic properties of selected AP/Al/HTPB propellants was undertaken at NAWC. Initial measurements using the closed bomb technique indicate that the increase in burn rate is pressure dependent for these propellants and any catalytic effect due to  $\text{Fe}_2\text{O}_3$  is lost above 0.3 Kbar. To address the safety issue of these propellants it is desirable to examine the material response due to dynamic loading and high strain-rate. These type experiments closely approximate the likely hazard scenarios which the energetic material may experience. For example, shock experiments are typified by large non-hydrostatic stresses and very rapid loading rate such as that imparted by fragment impact.

Three formulations differing only in coarse AP particle size and the addition of less than 1.2% of  $\text{Fe}_2\text{O}_3$  formed the basis of this study. A total of twelve shock loading experiments were performed for input pressures to 200 Kbar ( $2.9 \times 10^6$  psi). Shock Hugoniot relationships for the three formulations were determined and compared to the Hugoniot for high density ( $\approx 94\%$  TMD) AP. The experimental Hugoniots for the formulations without  $\text{Fe}_2\text{O}_3$  were in good agreement with the AP Hugoniot. The formulation with  $\text{Fe}_2\text{O}_3$  demonstrated a larger impedance than the PS1 and PS2 formulations. This latter result is consistent with the high strain-rate experiments performed on a Split Hopkinson Bar (SHB) in the compression mode. The yield and failure stress plotted as a function of strain-rate were consistently higher for the propellant with  $\text{Fe}_2\text{O}_3$ . The experimental results thus demonstrate that the addition of a small amount of  $\text{Fe}_2\text{O}_3$  can measurably affect the mechanical response of the propellant host material. Since the shock experiments attain pressures much greater than the closed bomb experiments, this result also suggests that a different mechanism may be affecting the mechanical response.

## INTRODUCTION

In recent years extensive experimental studies have generated a wealth of information regarding the inherent risk and performance tradeoffs of certain Class 1.1 propellant formulations. To date, the more common Class 1.3 propellants, have not been afforded such treatment. In contrast to the Class 1.1 propellants, 1.3 propellants are widely believed to be non-detonable and essentially unreactive at low pressure. In this latter class of propellants the Al/AP/HTPB (Hydroxy-Terminated-Poly-Butadiene)

formulations are of special interest due to their widespread usage. In the last decade there have been several incidents involving the inadvertent ignition of aluminized AP/HTPB propellant grains. These incidents have occurred both in military and industrial settings and have given rise to concern among the propulsion community regarding the safety and hazard potential for deployed systems using these formulations. The physical conditions which may drive these systems to unintentional ignition fall into three categories: 1) electrostatic discharge (ESD) phenomena, 2) thermal (cookoff) processes, and 3) impact induced effects.

Significant static electric charge may accumulate during the routine handling and manufacture of solid rocket motors. For example, potential charge build-up exceeding several thousand volts has been reported at the end of a mandrel pull-out operation [1]. Several comprehensive studies have explored ESD and have been instrumental in implementing extensive changes in both government and industrial facilities to reduce ESD hazards.

Cook-off is defined as the violent response of energetic materials in weapon systems exposed to abnormal thermal environments [2]. Several accidents involving fire on aircraft carrier decks leading to cook-off have occurred in the past. Thermal hazard tests have been performed by the Department of Defense and the Department of Energy over the past 30 years. Such tests are costly, extremely complicated and conducted in the latter stages of a weapons development when design changes are not easily made. It is thus prudent to assess the hazard potential of an energetic formulation prior to it being deployed into new or existing weapons platforms [2].

Impact of a bullet or fragment against a solid rocket motor can cause a response ranging from no reaction to full-up detonation depending on the impact geometry as well as the velocity and mass of the projectile. For very sensitive propellants (Class 1.1), a sufficiently energetic fragment can produce a shock-to-detonation (SDT) type reaction upon impact. In addition, a delayed detonation may result from deflagration (DDT) or other mechanism (XDT). Although the physical processes involved in SDT and to a lesser extent DDT are reasonably well understood, much effort has been devoted recently to the XDT reactions which may be far more violent.

In this work we consider the results of high strain-rate and shock loading experiments performed on three AP/Al/HTPB propellant formulations, one of which included  $\text{Fe}_2\text{O}_3$  as a burn rate catalyst. Of particular interest in this study was the role of Ammonium Perchlorate (AP) particle size and the function of  $\text{Fe}_2\text{O}_3$  in the material response. We report on the unreacted Hugoniot relationships and discuss recent results on pre-damaged propellant samples. The results reported here suggest that  $\text{Fe}_2\text{O}_3$  may also play a role in the mechanical response of the propellant in addition to its better known role as a burn-rate modifier.

## EXPERIMENTAL

### Sample Formulation and Preparation

All propellant samples used for the high strain-rate and shock impact studies were formulated at NAWC. The three propellants discussed here are designated as PS1, PS2, and PS4. composition is given in Table 1.

**TABLE 1**  
Propellant Composition and Measured Density

	AP (Fine) $\mu\text{m}/\% \text{ wt.}$	AP (Coarse) $\mu\text{m}/\% \text{ wt.}$	Al $\mu\text{m}/\% \text{ wt.}$	Burn Mod. Type/ $\% \text{ wt.}$	% Solids	Binder	Plasticizer	Density g/cc
PS1	20/20	200/50	29/20	none	90	HTPB	DOS	1.841
PS2	20/20	400/50	29/20	none	90	HTPB	DOS	1.836
PS4	20/20	200/48.8	29/20	$\text{Fe}_2\text{O}_3$	90	HTPB	DOS	1.853

As can be seen by inspection of this table, all propellant samples contained 20% weight of 29  $\mu\text{m}$  aluminum, HTPB binder, and DOS (Dioctyl Sebacate) plasticizer. The distinction between the PS1 and PS2 formulations was solely in the coarse AP particle size. The PS1 and PS4 formulations were almost identical with the exception of a small amount ( $\approx 1.2\%$ ) of  $\text{Fe}_2\text{O}_3$  as a burn rate modifier. The iron oxide was provided by JPL and composed of at least 99%  $\text{Fe}_2\text{O}_3$  with particle size on the order of a few microns. All formulations contained 90% solids and the measured densities are provided in the last column of this table.

For the Compression Hopkinson bar experiments, the propellant samples submitted for use were cut in the shape of disks from uniform slabs of propellant which had been pre-cut to the desired thickness. The aspect ratio was determined by using the results of Davies and Hunter [3] who derived an expression for the optimum diameter-to-thickness ratio from basic energy considerations and stress nonuniformities induced by inertia. They found that an acceptable design criterion for the sample aspect ratio is given by,

$$\frac{\text{diameter}}{\text{thickness}} = \frac{2}{\sqrt{3\nu}} \approx 2.31 \quad (1)$$

where  $\nu$  is Poisson's ratio and is taken to be 0.5 for the purposes of this study (see for example [4]). Although we attempted to adhere to Eqn. (1), the material pliability resulted in a 10-15 % scatter about the 2.31 value. In addition, to minimize frictional effects between the bars and the sample, a very thin layer of molybdenum disulfide was used to coat the loading surfaces.

Target samples for the shock impact experiments were either guillotined, or machined from bulk blocks, into 100 mm diameter slabs 6.25 mm thick (nominal). Prior to target assembly, the samples were measured for uniformity and ambient density. All samples for each propellant formulation were obtained from the same material batch in order to minimize density fluctuations.

### High Strain-Rate Experiments

The high strain-rate experiments were performed at NAWC on a split Hopkinson bar (SHB) operated in the compression mode. The bar was manufactured by California Research and Technology and is of typical design. A schematic of the NAWC Split-Hopkinson Bar (SHB) apparatus is shown in Fig.1.

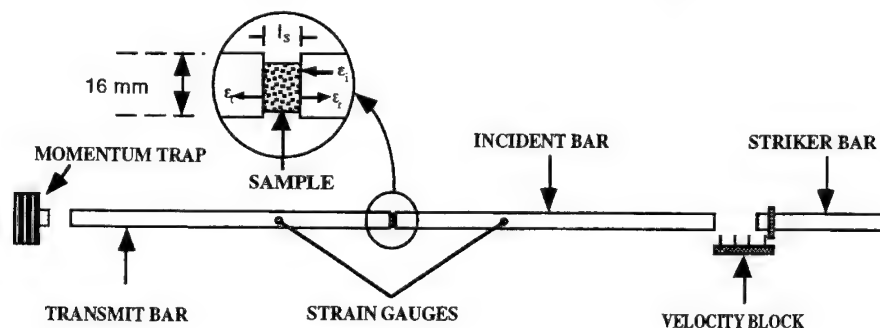


FIGURE 1. Schematic of Hopkinson Bar Instrument

The sample to be studied, with thickness  $l_s$ , diameter  $d_s$ , and cross-section area  $A_s$  was sandwiched between two steel bars 16 mm in diameter labeled in the figure as the incident and transmit bars. These bars are fabricated from 4150 steel with a measured density of 7.828 g/cc and sound velocity of 5 Km/s. Two pairs of strain gauges are located on the bars equidistant from the sample. The two strain gauges comprising each pair are bonded to the bar opposite to each other to

effectively cancel out any bending wave contribution. Each gauge pair is connected to a balanced bridge network and the output is displayed on a digitizing oscilloscope. For each experiment the striker bar is accelerated by a compressed gas gun and impacts the incident bar with a velocity  $V_0$  measured by an interval counter. A one dimensional compression wave propagates down the incident bar with amplitude  $\epsilon_i$  and a pulse length that is large compared to the sample thickness  $l_s$ . Upon reaching the test sample, part of the compressive pulse is transmitted through the sample with amplitude  $\epsilon_t$  and part is reflected with amplitude  $\epsilon_r$  due to the impedance mismatch. The stress within the sample is considered to be uniformly distributed. It is easily shown [5] that three equations may be derived to describe the stress, strain rate and resultant strain within the sample. These are given by,

$$\sigma(t) = E_0 \left( \frac{A_0}{A_s} \right) \epsilon_t(t), \quad \dot{\epsilon}(t) = - \left( \frac{2C_0}{l_s} \right) \epsilon_r, \text{ and } \epsilon(t) = - \left( \frac{2C_0}{l_s} \right) \int_0^t \epsilon_r dt \quad (2)$$

Where,  $\sigma(t)$  is the stress in the sample at time 't',  $E_0$  is Young's modulus,  $A_0$  and  $A_s$  are the cross-sectional areas of the bar and sample and  $C_0$  is the sound speed in the bar. The strain is determined by integrating over the duration of the compressive pulse, which is 280  $\mu$ s for the NAWC Hopkinson bar.

### Shock Loading Experiments

The unreacted Hugoniot of the three class 1.3 propellants were investigated by shock loading experiments. Shock waves were generated by planar impact in a 75 mm single stage powder gun. *In Situ* manganin and PVDF stress gauges recorded pressure-time histories up to 200 Kbar.

The target assembly consisted of a buffer plate (driver) and two or more propellant slabs. Teflon armored gauge packages were placed at each interface. For longitudinal stress less than 75 Kbar, piezoresistive manganin gauges were used; otherwise, Bauer type PVDF piezoelectric gauges were employed. The stress gauges provided time of arrival for the shock wave in addition to the pressure histories. A small layer of urethane adhesive was used to fill any surface voids and bond the slabs together.

Impact configurations were planar and symmetric. Tilt was measured to be 1 miliradian or less. In order to achieve the desired stress range, three impact/buffer materials were used: PMMA, 2024T-4 aluminum (Al), and 304 stainless steel (SS). With these materials, and projectile velocities approaching 1.9 mm/ $\mu$ s, peak input pressures to 140 Kbar were attained. Data from two shots performed at LLNL extended the data set to roughly 200 Kbar For PS1 and PS2 [6].

## EXPERIMENTAL RESULTS AND ANALYSIS

### Hopkinson Bar

Because the strain rate is not truly constant for the entire pulse duration, care must be exercised in assigning a value. Figure 2. (a) & (b) show graphically how the strain rates were determined for PS-4. The strain rate was determined from the slope of the strain *versus* time plots presented in Fig.2.(a) The most linear portion of this curve was selected as the value to be used. This section is highlighted in Fig. 2.(a) by the darker line and the dotted lines in Fig. 2. (b) representing the strain rate *versus* time profiles. In the latter figure the strain-rate values have been annotated above each curve. Inspection of Fig.2 (a & b) also shows the nonlinear variation of strain rate which occurs early in the compressive pulse. Note that the dotted lines in Fig 2 (b) have been extrapolated to the axis edge for convenience of viewing. Discussion of wave dispersion and other contributing factors to the nonlinearity may be found in several published works [7, 8]. Similar plots are found for the PS1 and PS2 samples for approximately the same strain rates.

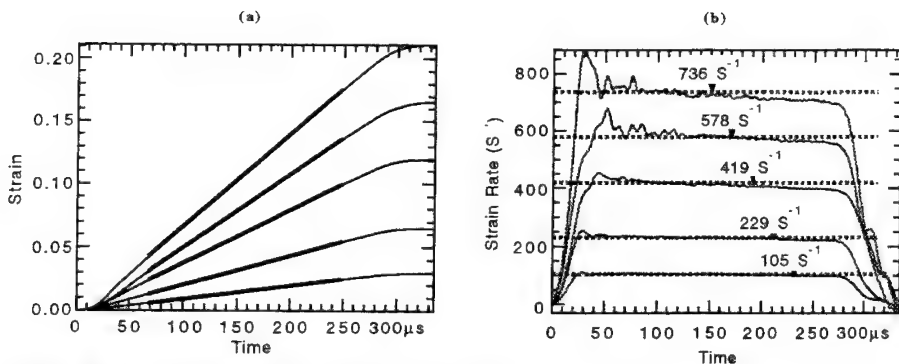


FIGURE 2. (a) Strain versus Time plot for PS4, (b) Strain Rate versus Time plot for PS4.

The stress-strain behavior was calculated as a function of time using Eqns. (1). The stress-strain curves for PS-1, PS-2, and PS-4 formulated propellants are shown in Figs. 3 a,b,c respectively. For each propellant formulation, the figure shows a family of curves, one at each strain rate. Note that each curve in this figure was averaged over several experiments conducted at the same strain rate.

A typical stress-strain curve exhibits a brief elastic response before a yield point. A fairly sharp maximum is reached immediately preceding a negative downward slope. It should be noted that no attempt has been made to correct for wave dispersion or nonuniform deformation. The stress is considered to be the average stress throughout the sample. The true stress may be calculated from the engineering stress;  $\sigma_T = \sigma_{Eng} (1 - \epsilon)$ .

#### ANALYSIS OF SHB RESULTS

As noted in the preceding section the stress-strain curves display several features which are worth investigating. The parameters which may be measured from the stress-strain curves are illustrated in the generic curve shown in Fig. 4. This figure was provided by Lieb [9]. The elastic modulus ( $E$ ) corresponds to the linear (Hookian) portion of the curve which begins to yield at a certain stress  $\sigma_Y$ , and strain  $\epsilon_Y$ . A typical curve will also exhibit a maximum stress and strain ( $\sigma_m$ ,  $\epsilon_m$ ) and a failure stress and strain ( $\sigma_f$ ,  $\epsilon_f$ ). The data collected in this study were examined for these principle features. The oscillations at the leading edge of the compression pulse are called Pochhammer-Chree oscillations (see for example Fig. 2.b). They are due to dispersion of the initial

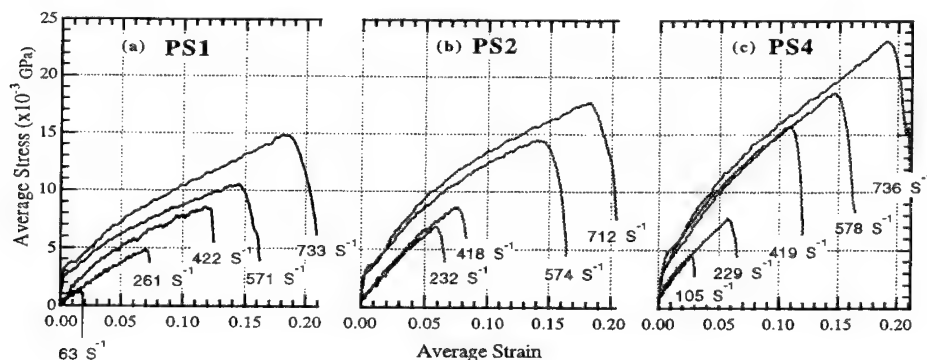


FIGURE 3. Average Stress-Strain Curves for (a) PS1, (b) PS2, and (c) PS4.

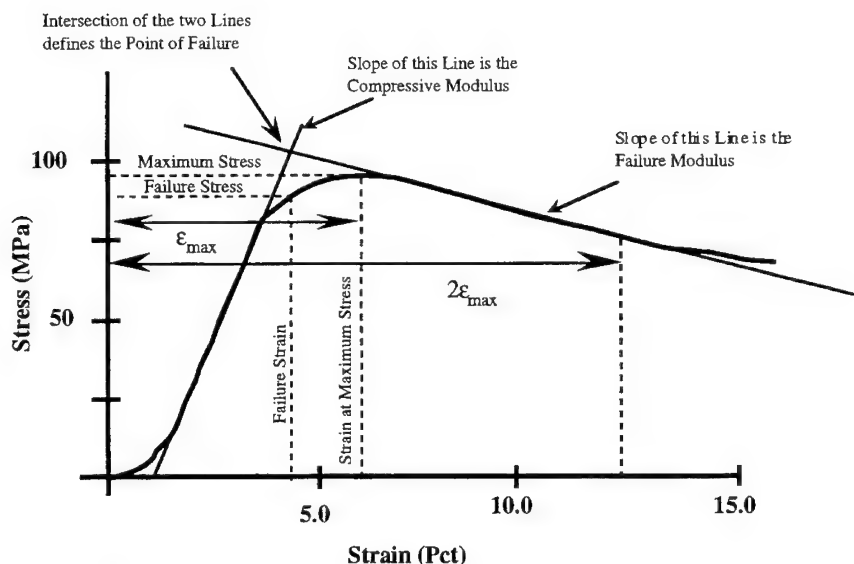


FIGURE 4. Diagram of a Generic Stress-Strain Curve Indicating Parameters of Interest [9].

wave. These nonlinearities made determination of the elastic modulus unreliable and will not be reported here. The yield stress for each curve was determined and is plotted as a function of strain rate in Fig. 5 a. The stress-strain figures also indicate what appears to be a failure stress which has been plotted for each curve and is presented in Fig. 5 b. The least square fit for each data set is indicated in these figures by the dotted lines with the corresponding goodness of fit provided in the figure legend. Trends in the plotted data are readily apparent in these figures. The average yield stress and fail stress are observed to increase with strain rate. The largest yield and fail stress is exhibited by the PS-4 formulation. Although we have identified failure stress on the curves, it is not clear that they indicate true material failure since they occur near the end of the pulse when the energy is rapidly diminishing [10]. The plastic portion of the stress strain curves suggests that work hardening is taking place similar to that shown by certain thermoplastic elastomer (TPE) propellant formulations utilizing CL-20 and TNAZ [10].

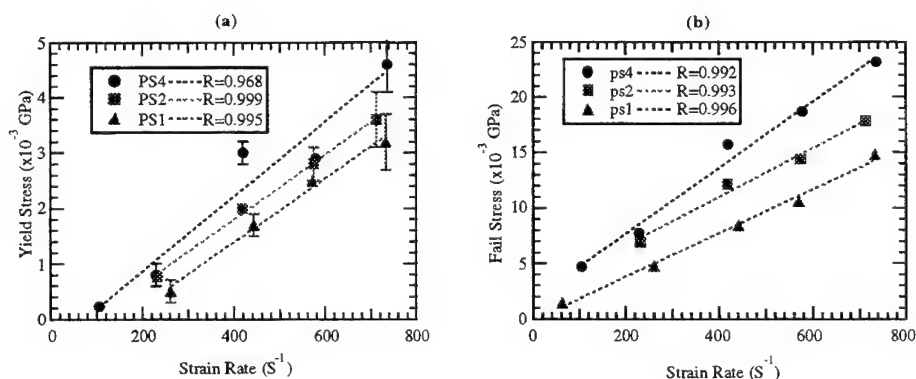


FIGURE 5. (a) Yield Stress and (b) Fail Stress *versus* Strain Rate.

### Results of Impact Experiments

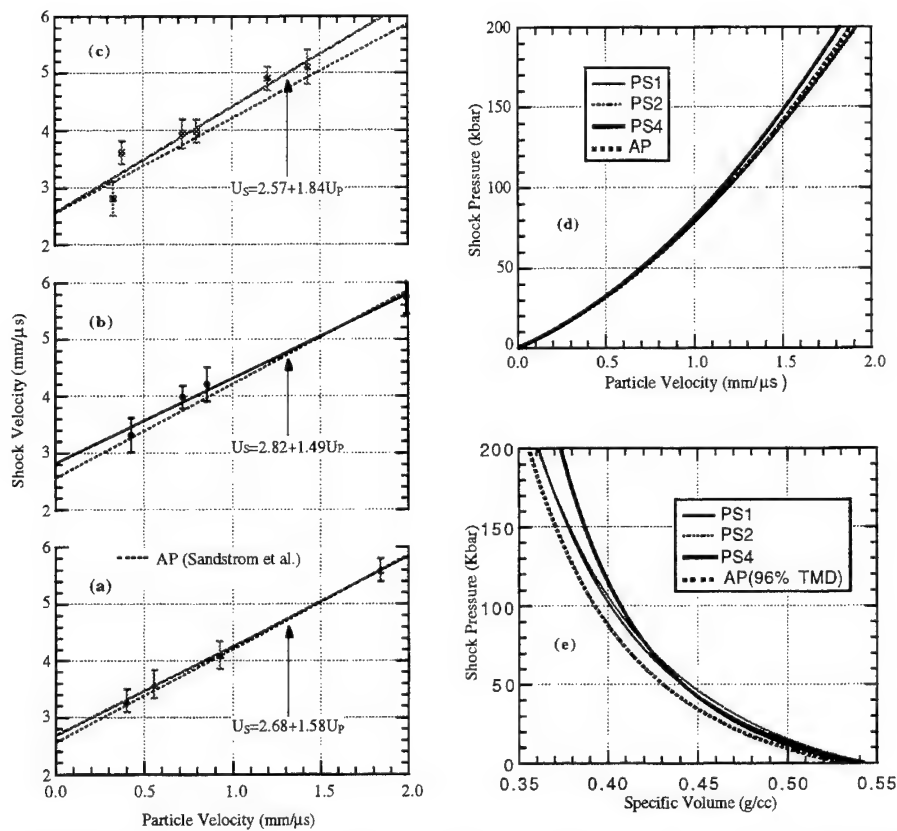
A total of seventeen shock experiments were performed in the course of this study; twelve experiments to establish the unreacted Hugoniot of the three propellants, and five experiments to explore the dynamic response of pre-damaged propellant samples. In this report we address only the unreacted Hugoniot. A discussion of the damaged propellant response may be found elsewhere [11].

Experimental results for the pristine samples are given in Table 3. The shot number given in column 1 and the impactor/buffer material type is indicated in column 2. Projectile velocity, shock velocity, particle velocity and peak pressure are given in columns 3-6, respectively. The peak pressure was measured at the buffer-sample interface. The best fit, linear  $U_S$ - $U_P$  relationship for each propellant is indicated in Figures 6 a, b and c. The error in shock velocity is due to the uncertainty in arrival time. The PS1 and PS2 Hugoniot include two high pressure data points provided by LLNL [6]. Our results compare favorably with the shock Hugoniot for pure AP (TMD=1.95 g/cc) as reported by Sandstrom et al. [12]. This is indicated by the dotted lines in this figure. Below 50 Kbar the three Hugoniot are indistinguishable from the AP Hugoniot, within experimental error. At higher input pressure the PS4 Hugoniot begins to diverge, becoming stiffer at higher pressure. This observation is consistent with the reported stress-strain data for this material [13]. For completeness, the Hugoniot for all three propellant formulations are plotted in Figures 6 (d) and (e) in both P- $U_P$  and P-V space.

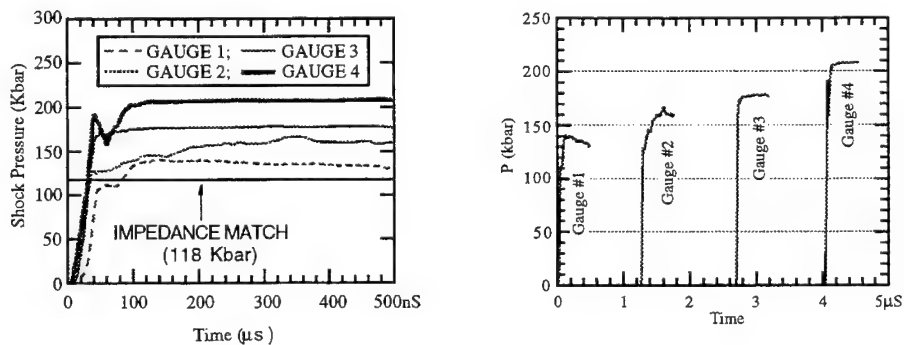
**TABLE 3**  
Experimental Results For Undamaged Materials

SHOT	FLYER/BUFFER MATERIAL	IMPACT VELOCITY (mm/ $\mu$ s)	SHOCK VELOCITY (mm/ $\mu$ s)	PARTICLE VELOCITY (mm/ $\mu$ s)	SHOCK PRESSURE (Kbar)
2PS1	2024Al/2024Al	1.37	4.11	0.93	70
3PS1	PMMA/PMMA	1.04	3.30	0.40	27
4PS1	PMMA/PMMA	1.41	3.59	0.56	38
1PS2	PMMA/PMMA	1.06	3.32	0.43	26
2PS2	2024Al/2024Al	1.26	4.20	0.86	66
3PS2	2024Al/2024Al	1.05	3.98	0.72	52
1PS4	PMMA/PMMA	0.76	2.82	0.33	17
2PS4	PMMA/PMMA	1.06	3.62	0.38	26
3PS4	2024Al/2024Al	1.07	3.99	0.72	54
4PS4	2024Al/2024Al	1.16	3.94	0.80	59
5PS4	304SS/304SS	1.66	4.90	1.20	109
6PS4	304SS/304SS	1.60	5.10	1.43	135

The last experiment in the shock series (Shot 6PS4) was designed to search for any evidence of reactivity in the pristine PS4 material. Four PVDF gauges were embedded between four PS4 samples nominally 6.25 mm thick. Figure 7 represents the pressure time histories for this experiment. For clarity, the records have been truncated to show only the first 0.5  $\mu$ s of gauge response. The measured input pressure at gauge # 1 is 135 Kbar and grows to 210 Kbar at gauge # 4 after the shock has transited 19 mm of material. Such a pressure evolution is indicative of chemical reactivity feeding the shock front. These observations are in agreement with the findings of Bai and Ding [14], Bai et al. [15] and Huang et al. [16] for a similar propellant formulation. These studies suggest that AP/Al/HTPB type propellants begin to decompose behind a 140 Kbar shock front. Bai et al. [15] observed two distinct peaks in the pressure-time profiles, one at or near the shock front and a second occurring 1-2  $\mu$ s later. They conclude that the observed increase of pressure behind the shock front (first peak) is primarily due to the shock decomposition of AP and HTPB, and the second peak is due to the reaction between these products and the Al.



**FIGURE 6.** Hugoniot Relationships for (a) PS1, (b) PS2, and (c) PS4. (d) Peak stress is shown as a function of particle velocity  $U_p$  and (e) specific volume  $V_s$ .



**FIGURE 7.** Embedded Gauge Experiment on PS4



## DISCUSSION

The experimental data which we have presented for the  $\text{Fe}_2\text{O}_3$  formulated propellant strongly suggests that the dynamic mechanical response differs measurably from similar formulations without  $\text{Fe}_2\text{O}_3$ . Split Hopkinson Bar data indicates that at equivalent strain rates the PS4 formulation appears more stiff than the PS1 and PS2 formulations, yielding at a larger stress and strain. Similarly the shock compression studies show a Hugoniot for PS4 which is characteristic of a material of higher impedance than PS1, PS2, or solid AP. In contrast, within experimental error, the PS1 and PS2 formulations do not appreciably differ from the solid AP Hugoniot as reported by Sandstrom [12]. These results suggest that the effect of AP particle size on shock response is negligible in comparison to the addition of  $\text{Fe}_2\text{O}_3$  which appears to "stiffen" the host material. This latter result is consistent with the recent findings of DeFusco and Shanholtz at the Allegany Ballistics Laboratory [17]. They found that the elastic modulus increased in AP/AL/HTPB class propellants containing  $\text{Fe}_2\text{O}_3$ . The modulus was also observed to increase with increasing  $\text{Fe}_2\text{O}_3$  content (0.2-1.5 % by weight).

One of the authors (A.J.L.) has recently conducted shock experiments on the PS2, and PS4 formulations (PS1 series is in progress) which have been subjected to tensile strain of 5%, 10%, and 15 % along an axis orthogonal to the shock loading direction. The introduction of voids *via* de-wetting is expected to facilitate hot-spot development and hence increase propellant sensitivity. Indeed the "damaged" PS2 formulation clearly demonstrates a more shock sensitive system and a family of porous Hugoniots which reflect the induced void content (see for example Boteler and Lindfors [11]). By contrast, the PS4 formulation which also demonstrates increased reactivity, displays nearly the same Hugoniot as the pristine material irrespective of the measured void content, again suggesting that the PS4 formulation is mechanically different due to the  $\text{Fe}_2\text{O}_3$ .

$\text{Fe}_2\text{O}_3$  is normally added to the propellant formulation as a burn rate catalyst. Low pressure closed-bomb experiments performed by Atwood et al. [18] and Paull et al. [19] confirm the catalytic effect at both ambient and elevated temperatures. However, as pointed out by Paull [19], at roughly 0.3 Kbar ( $\approx 4000$  psi) the burn rates for all three formulations merge, signifying the apparent loss of any catalytic effect due to the  $\text{Fe}_2\text{O}_3$ . Although the mechanism responsible for this behavior is not understood, it would appear to be different from the mechanism responsible for the PS4 dynamic response, or possibly a different manifestation of the same mechanism. When comparing the low pressure closed-bomb studies to the shock experiments it is important to point out that the former are essentially hydrostatic whereas the latter are highly nonhydrostatic. This difference is nontrivial and may account for some of the observed behavior.

In summary, we have found that the inclusion of  $\text{Fe}_2\text{O}_3$  into the formulation not only influences the propellant burn rate but its mechanical properties as well. Similarly, the coarse AP particle size for PS1 (200  $\mu\text{m}$ ) and PS2 (400  $\mu\text{m}$ ) also affects the burn rate with the PS1 burn rate slightly faster than the PS2 [19]. However, the AP particle size has little effect on the dynamic response for the strain-rates and longitudinal stresses considered in this study. Thus, when considering hazard scenarios it is important to take into account all material responses. The addition of even very small amounts of a substance to impart a desired effect may also alter the mechanical response of the material making it stronger or more vulnerable.

Future experimental and computational work is necessary on the  $\text{Fe}_2\text{O}_3$ -HTPB system to identify the bonding chemistry. In addition to NMR, EPR, and magnetic susceptibility experiments, molecular orbital calculations would be very useful.

## ACKNOWLEDGMENTS

The authors wish to thank the Defense Nuclear Agency for their support of this work. We also wish to thank Scott Pockrandt, Frank Hudson, and Rodney Robbs for their assistance in conducting some of the experimental measurements reported here.

## REFERENCES

1. Covino, J. and F. Hudson. *Electrostatic Discharge (ESD) Hazards of Energetic Materials*. Tenth International Detonation Symposium. 1993, Boston, Mass., 936-943.
2. *Cook-Off Mechanistic and Predictive Capabilities* 1992, CPIA Publication #586.
3. Davies, E.D. and S.C. Hunter, *The Dynamic Compression Testing of Solids by the Method of the Split Hopkinson Pressure Bar*. J. Mech. Phys. Solids, **11**, p. 155-179, 1963.
4. Oberth, A.E., *Principles of Solid Propellant Development*, 1987.
5. Meyers, M.A., *Dynamic Behavior of Materials*. First ed. 1994, John Wiley & Sons. 305-307.
6. Urtiew, P., LANL, *Private Communication* 1995.
7. Lifshitz, J.M. and H. Leber, *Data Processing in the Split Hopkinson Bar Tests*. Int. J. Impact Eng., **15**(6), p. 723-733, 1994.
8. Follansbee, P.S. and C. Frantz, *Wave Propagation in the Split Hopkinson Bar*. Transactions of the ASME, **105**, pp.61-67, 1983.
9. Lieb, R.J., *High Strain Rate Response of Gun Propellants Using the Hopkinson Split Bar*. Army Ballistic Research Laboratory, 1991.
10. Lieb, R., Army Research Laboratory, *Private Communication*, 1996.
11. Boteler, J.M. and A. J. Lindfors, *Shock Loading Experiments on Selected AP/Al/HTPB Propellants*. Proceedings of the 1995 Conference on Shock Compression of Condensed Matter, Seattle, Washington, Schmidt and Tao Ed., AIP press, Vol. 2, pp. 767-770.
12. Sandstrom, F.W., P.A. Persson, and B. Olinger. *Isothermal and Shock Compression of High Density Ammonium Nitrate and Ammonium Perchlorate*. Proceedings of the 1993 Conference on Shock Compression of Condensed Matter. 1993, Colorado Springs, Colorado, Schmidt Ed., AIP Press. 1409-1412.
13. Boteler, J.M. and A.J. Lindfors. *High Strain-Rate Mechanical Properties of PS1, PS2, and PS4 Propellants*. DNA Propellant Review, May 24. 1995.
14. Bai, C. and J. Ding. *Response of Composite Propellants to Shock Loading*. Ninth International Symposium on Detonation. 1989, Portland, Oregon, pp. 879-885.
15. Bai, C., F. Huang, and J. Ding. *Behavior of Ammonium Perchlorate Under Shock Loading*. Proceedings of the 1991 Conference on Shock Compression of Condensed Matter. 1991, Williamsburg, Virginia, Schmidt Dick Forbes & Tasker Eds., North Holland press. pp. 651-653.
16. Huang, F., C. Bai, and J. Ding. *Mechanical Response of a Composite Propellant to Dynamic Loading*. Proceedings of the 1991 Conference on Shock Compression of Condensed Matter. 1991, Williamsburg, Virginia, Schmidt Dick Forbes & Tasker Eds., North Holland press. pp. 491-494.
17. DeFusco, A. and C.E. Shanholz, Alliant Techsystems, Allegany Ballistics Laboratory, *Private Communication*, 1996.
18. Atwood, A.I., et al., *Shotgun Testing for the Propellant Sensitivity Program* NAWC, China Lake, NAWCWPNS TM 7876, 1995.
19. Paull, D.G. *Burn Rate Measurements of AP/HTPB Propellants at Ambient and Elevated Temperatures*. in JANNAF Propulsion Systems Hazards Subcommittee. 1995, Huntsville, Alabama,.

## COMMENTS

1. Mr. G. Doriath, SNPE. Centre de Recherches du Bouchet, France.

Why is it necessary to offer a chemical explanation for the interaction between HTPB binder and  $\text{Fe}_2\text{O}_3$ ? As  $\text{Fe}_2\text{O}_3$  particles are much smaller than AP and Aluminum particles, they could induce a high strain rate "physical" effect which also increases the stiffness of the propellant. If we consider a chemical effect, it could be due to the contribution of the bonding agent.

Authors' Reply:

One must be careful when making a distinction between "physical" and "chemical" effects.  $\pi$ -bonding is common to physicists as well as chemists. The  $\text{Fe}_2\text{O}_3$  particles used in this study were  $\sim 5\mu\text{m}$  in size. For a sufficient quantify, the impedance mismatch could account for an apparent "stiffening" of the material. However, it is unlikely that 1.2% by weight is an adequate quantity. In the Authors' opinion, the  $\pi$ -bonding scheme is a more likely explanation, though either may easily be tested for. Since the same bonding agent was added to both PS-1 and PS-4 formulations, it is not clear to the Authors how it may contribute to the observed differences. Your comment is appreciated.

2. Dr. H. Singh, HEMRL Pune, India.

Any specific reason for choosing  $\text{Fe}_2\text{O}_3$ -based compositions? Copper chromite and Butyl ferrocene-based compositions produce better burn rates (catalysts). How are the rates generated with  $\text{Fe}_2\text{O}_3$  comparable with those generated with the above catalysts?

Authors' Reply:

The effects of Copper chromite were not studied.

## THERMOMECHANICAL ASPECTS OF ENERGETIC CRYSTAL COMBUSTION

R.W. Armstrong<sup>1</sup>, W.L. Elban<sup>2</sup>, A.L. Ramaswamy<sup>1</sup>, and C.Cm. Wu<sup>3</sup>

<sup>1</sup>University of Maryland, College Park, MD 20742; <sup>2</sup>Loyola College, Baltimore, MD 21210; <sup>3</sup>Naval Research Laboratory, Washington, DC 20375.

**ABSTRACT:** The lower thermal conductivity, larger elastic compliance, and greater brittleness of a typical energetic crystal contribute to the importance of thermomechanical influences on combustion and initiation of explosion behavior. For example, recent laser-induced localized heating experiments conducted on RDX and AP crystal surfaces have revealed networks of microscopic cracks in association with the initiation of chemical decomposition. The crystallographically-determined ultrafine crack networks (that have been traced in AP to the orthorhombic to rocksalt structure-type phase transformation as well) are associated, in turn, with the greater hardnesses of energetic crystals. The coupled hardness and brittleness properties are attributed to the difficulty of initiating viscoplastic flow by dislocation movement, as illustrated on a hardness stress-strain basis. In this respect, recent results obtained here that show comparable hardnesses of ADN and RDX crystals are in agreement with a report of comparable drop-weight impact sensitivities. A dislocation pile-up avalanche explanation of such drop-weight impact sensitivity measurements is related to model calculations of thermally induced explosive decompositions. The dependence of impact sensitivity on crystal size is of special interest because of the possibility of relation to crystal size effects that are reported for the pressure dependencies of burning rates.

### Introduction

Early work on the safe, effective, use of explosives was based in chemistry, say, stemming from the time of Nobel, whose inventions of a mercury percussion cap, kieselguhr dynamite (nitroglycerine), and blasting gelatine, were coupled with a business acumen that provided for a number of continuing Nobel enterprises, not the least of which is the world reknown Nobel Prize activity [1]. The first Nobel prizes in 1901: in chemistry to J.H. van't Hoff for chemical reaction studies and osmotic pressure; and, in physics to W.C. Roentgen for the

discovery of x-rays, represented fundamental research accomplishments that continue to provide a basis for modern research activities aimed at achieving a better understanding of, and improving upon, the properties of energetic materials and chemical propulsion systems. S.A. Arrhenius received the third Nobel prize in chemistry in 1903. The powerful secondary explosives, cyclotrimethylenetrinitramine (RDX), cyclotetramethylenetetranitramine (HMX), and pentaerythritol tetranitrate (PETN), were synthesized near to the turn of the century.

Modern challenges in propellant system development cover a wide range of considerations. On the experimental frontier: a start has been made in applying x-ray diffraction imaging (topography) to the systematic characterization of growth sector and dislocation structures that are produced within the volumes of energetic crystals conventionally grown from supersaturated solvent solutions [2]; mass spectrometry observations are being made of reaction products generated at the initial stages of chemical decomposition under controlled temperature and pressure conditions [3]; laser-induced fluorescence imaging absorption diagnostics are being applied to studying the chemical evolution of reactant species near to the combustion interface [4]; nanoscale atomic force microscopy methods are being applied to assessing thermally- or mechanically-induced damage mechanisms within affected energetic material systems [5]; and, engineering test systems are being designed, and evaluated, to track the relevant scale of potentially hazardous events occurring in propellant system operations [6].

On the theoretical frontier, extensive work is being done to establish the hierarchical set of chemical reactions that are potentially involved in energetic material decompositions [7]. Consideration of the fastest chemical reaction rates, suggestive of starvation kinetics [8], or the possibility of even faster physical kinetics [9] or mechano-electronic excitations at a propagating shock front [10-12] are active research topics. And, then, there are special considerations particular to the model lattice and structural defect characteristics of energetic crystal behaviors when subjected to thermal or mechanical forces, say, as invoked in the proposed "steric hindrance" of energetic crystal lattices under shock deformation conditions [13] and, also, assessment of relative stress levels involved in the competition between viscoplastically hindered dislocation motion on limited deformation systems and dislocation crack-producing reactions on potential cleavage systems [14].

#### Crystal Morphologies and Internal Structures

Different crystallographic surfaces and internal perfections are produced during the conventional growth of energetic crystals from a variety of supersaturated solvent solutions. RDX, with an orthorhombic crystal structure, provides an important example system that has been studied by a number of investigators [15-18]. Figure

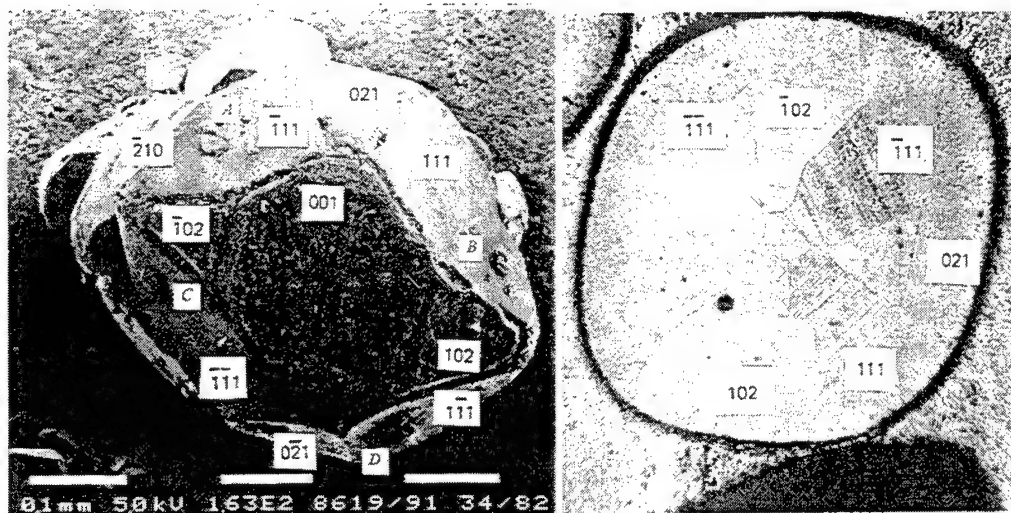


Figure 1a. Identification of growth surfaces after solution growth.  
Figure 1b. Identification of internal growth sector plane traces.

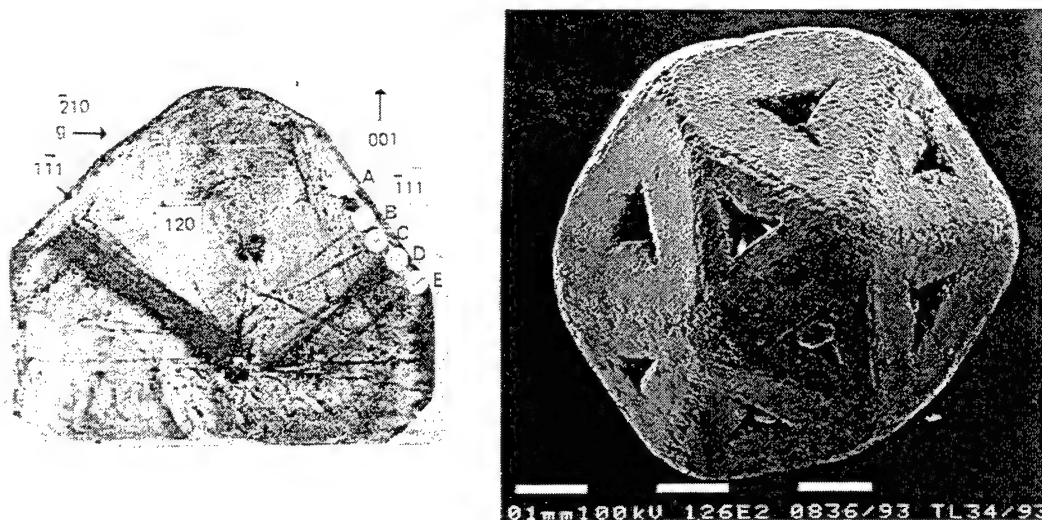


Figure 1c. ( $\bar{2}10$ ) x-ray diffraction image of dislocation bundles.  
Figure 1d. Crystal with triangular pits at exposed growth surfaces.  
Figure 1. RDX crystal morphologies, growth sectors and dislocations.

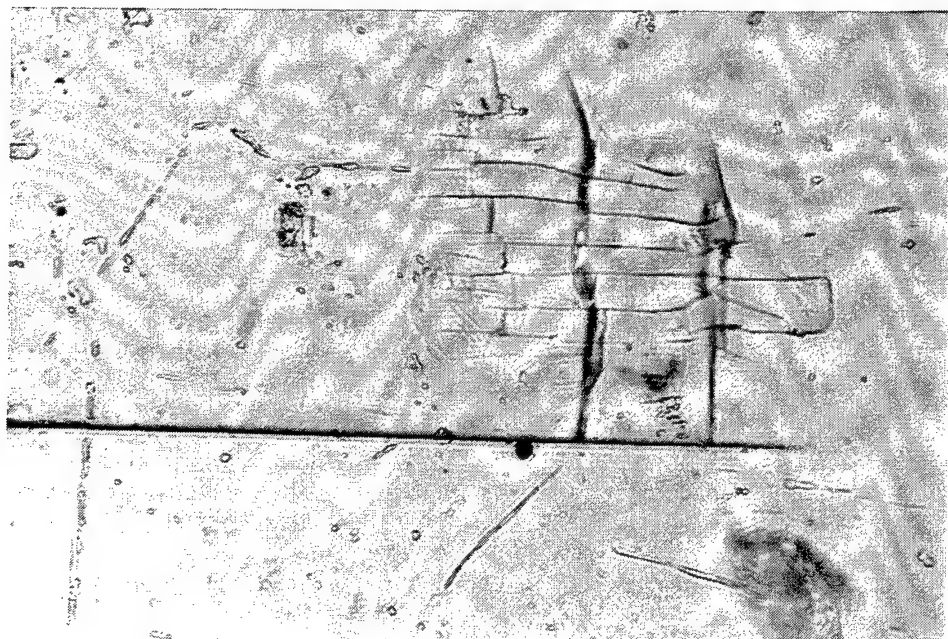
1a shows a typical commercial crystal growth morphology for a crystal of several hundred micrometers size and, 1b, growth sectors within a sectioned crystal [15]. The external growth planes and their internal traces within the individual growth sectors have been

identified in Figure 1 on the basis of a stereographic projection method of analysis [17].

Figure 1c shows by comparison with 1a,b an internal dislocation growth structure that has been revealed by Lang transmission x-ray diffraction imaging [16]. The surface-terminating dislocation lines are proposed to have participated in the crystal formation process by producing a spiral terraced structure of ledges that propagated, in normal fashion, rather more slowly across the  $\{111\}$ -type surface planes [19]. Returning to Figure 1a, then, four probable dislocation emergence sites are identified by the letters A-D at "pill box" structures on the identified  $\{111\}$  surface planes. The reversed situation is shown for another RDX crystal [20] in Figure 1d whereby the spread of terraced ledges across  $\{111\}$  and, presumably,  $\{102\}$  planes must be relatively fast so that apparent pits are produced at the dislocation emergence sites. In either case, the external growth morphologies of energetic crystals are shown to be indicative also of particular dislocation distributions within the crystals [21].

#### Laser-Induced Thermomechanical Influences

A fundamental role for the involvement of viscoplastic deformation and cleavage cracking in the thermal decomposition of laboratory-grown RDX crystals was established for localized melting induced by a grazing laser beam impinging on pre-damaged hardness indentation sites [22]. Figure 2 shows a smaller, thermally-induced, microcracking network



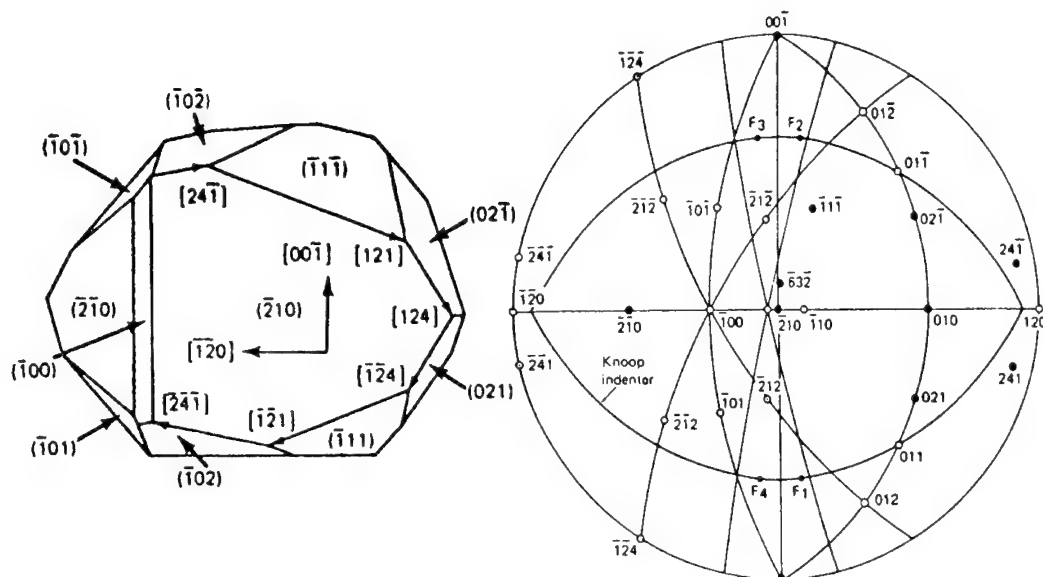


Figure 2. Laboratory-produced RDX crystal of 1.0 cm size, with identified growth surfaces and stereographic projection for planes (closed circles), directions (open circles), and Knoop indentation experiment shown below where laser heating has produced localized decomposition in the indentation strain field.

initiated within a larger laser-irradiated area encompassing the top edge of the tip of a pre-indented horizontal Knoop microhardness impression. A schematic view of the crystal and matching stereographic projection description for the irradiated  $(\bar{2}10)$  surface containing the Knoop indentation are shown also in the Figure. The long axis of the Knoop indentation is aligned along the  $[120]$  direction. A vertical spacing of approximately 10 micrometers applies for the smallest, horizontal,  $(00\bar{1})$  cleavage cracks that are joined by nearly vertical, and deeper,  $(010)$  and  $(24\bar{1})$  cleavage cracks. The experiment demonstrated that pre-existent defect structures are preferred sites for chemical decomposition. Similar results have been reported for shock-loaded crystals of AP [23].

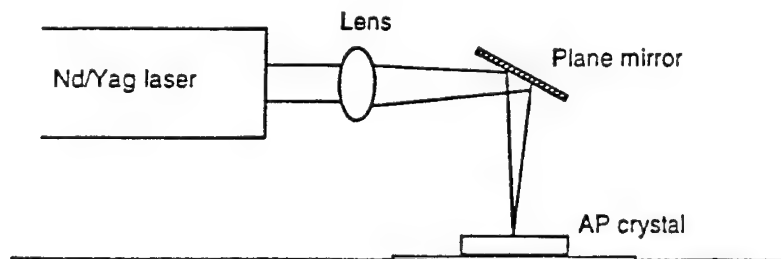


Figure 3a. Schematic of 8 ns, amplified 160-250 mJ, laser experiment



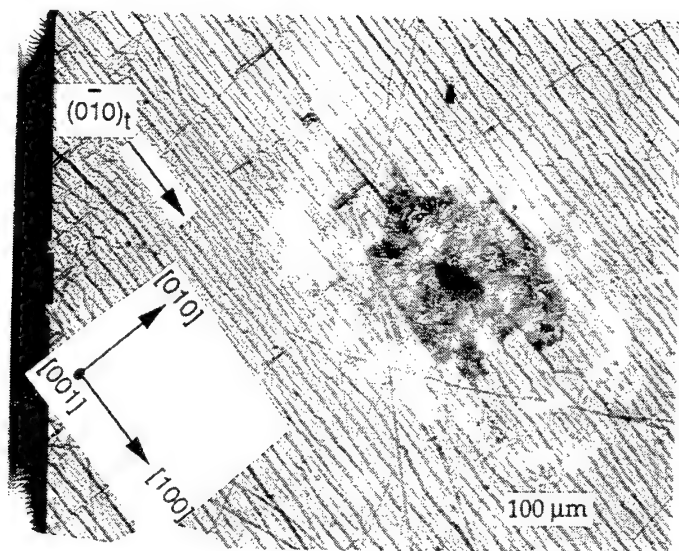


Figure 3b.  $(0\bar{1}0)_t$  and subsurface  $(001)$  laser damage in AP crystal

Figure 3. Nanosecond laser-induced cracking and decomposition in AP

A more detailed study has been made of laser-induced chemical decomposition on laboratory-grown ammonium perchlorate (AP) crystal surfaces [24]. Figure 3a shows the schematic experiment, in this case, for direct focusing of the laser beam onto the top  $(001)$  surface of the orthorhombic AP crystal structure. The near-macroscopic consequence of laser irradiation is shown at relatively low magnification in Figure 3b. The inclined black line stripes of the easy  $(0\bar{1}0)$  cleavage faces are identified in the Figure. A whitish halo from sub-surface  $(001)$  cleavage cracking is recognizable at the fragmented laser damage site. At larger magnification, the speckled background pattern that is just recognizable in Figure 3b is shown in Figure 4a to be composed of a finer microcracking network of  $\{010\}$  cracks generated after the thermally-induced AP orthorhombic-to-cubic-rocksalt lattice transformation had occurred. The transformation temperature is reported to be 240 C and the cubic phase has a lower density [25].

In Figure 4a, the smaller squarish pattern of residual rocksalt-type  $\{010\}$  cleavage cracks is lined up with the  $\langle 100 \rangle$  cube axes that are shown to be rotated about the common  $[001]$  direction in both the cubic and orthorhombic lattice systems. In the  $(001)$  plane, the  $[010]$  cube direction is parallel to the orthorhombic  $[\bar{1}20]$  direction. The microcracks, that are almost optically invisible in the finer network, have a spacing of approximately 2-10 micrometers and estimated depths of 0.1-2.3 micrometers. Figure 4b shows a complementary scanning electron microscope (SEM) picture of the microcracked region. A

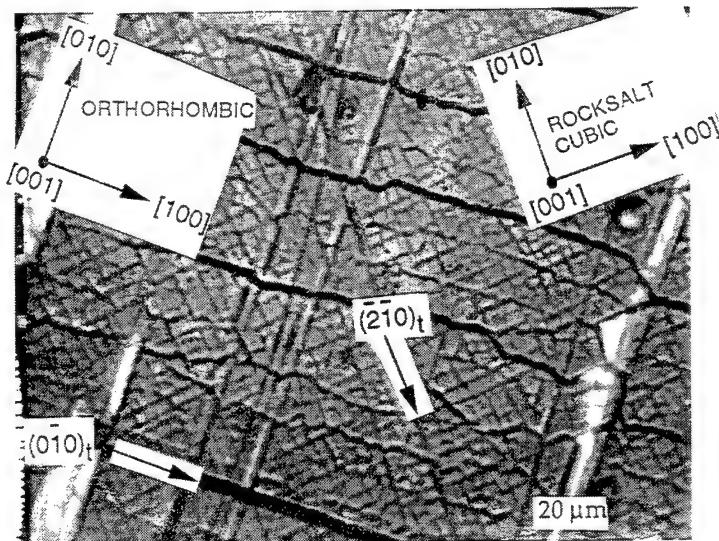


Figure 4a. Orthogonal  $\{100\}$  cracking pattern from AP transformation

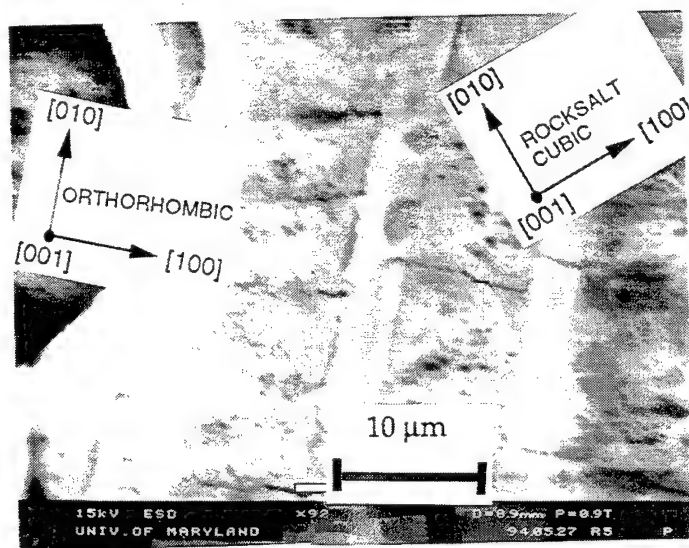
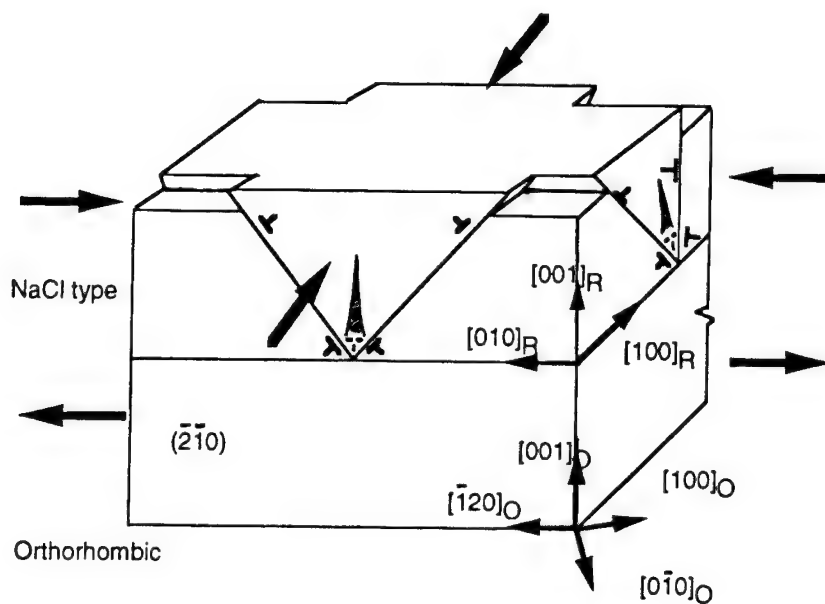


Figure 4b. SEM picture of decomposition sites at crack intersections

Figure 4. Residual cubic microcracking and decomposition sites in AP

subsurface, squarish, pattern of dark holes marks the AP decomposition sites in Figure 4b, taken to be associated with the formation of chlorate product detected by x-ray photoelectron spectroscopy measurements [24,26] and known to be characteristic of thermal



DISLOCATION MECHANISM FOR CRACKING. R=ROCKSALT  
O=ORTHORHOMBIC

Figure 5. Dislocation mechanics description of  $\langle 110 \rangle \{011\}$  slip-induced microcracking on  $\{100\}$  cleavage planes in cubic AP

degradation in AP. The SEM pattern of decomposition sites appears to match the intersection lines of the microcrack network and, hence, there is an indicated relationship between the microcrack network and the earliest stage of thermomechanically-induced AP decomposition.

Figure 5 shows a dislocation mechanics based model that is proposed to describe these individual crystal decomposition observations. The thermal expansion accompanying localized heating of a surface region produces a biaxial compressive stress in the affected surface layer [22]. The 240 C orthorhombic-to-cubic phase transformation in AP enhances the compressive stress state because of the lower density of the cubic phase [25]. Dislocation slip is initiated in the affected, thin, surface layer on established  $\langle 110 \rangle$  slip directions in conjugate  $\{110\}$  slip planes of the cubic structure. At the internal intersection of slip systems, the lead dislocations will react to produce an embryonic dislocation-crack nucleus in accordance with dislocation vector reactions of type:

$$(a/2) [01\bar{1}] (011) + (a/2) [011] (0\bar{1}1) = a[010] (001).$$

The prescribed dislocation reaction applies for the front (100) crystal face of Figure 5. The reacted [010] dislocation represents a compressive crack, with local tensile stress between it and the free surface, as indicated in the Figure. Under sufficient "driving force" from other dislocations piled-up behind on the same slip systems, the embryonic crack will propagate upwards to the crystal surface. In addition, a substantial hydrostatic component of stress is generated in the surface layer at the intersection of the orthogonal lines of reacted dislocations, say, at the intersection between the [100] line direction for the reacted dislocation on the front face of Figure 5 and the [010] line direction for the reacted dislocation shown on the side (010) face. The consequence is to set-up a favorable stress state for AP decomposition in this surface layer and, thus, a thermomechanical influence on the decomposition process. The viscoplastic slip and related cracking behavior of the energetic materials is not dissimilar to the mechanical property behavior of ceramic crystals.

#### Crystal-based Strength and Cracking Properties

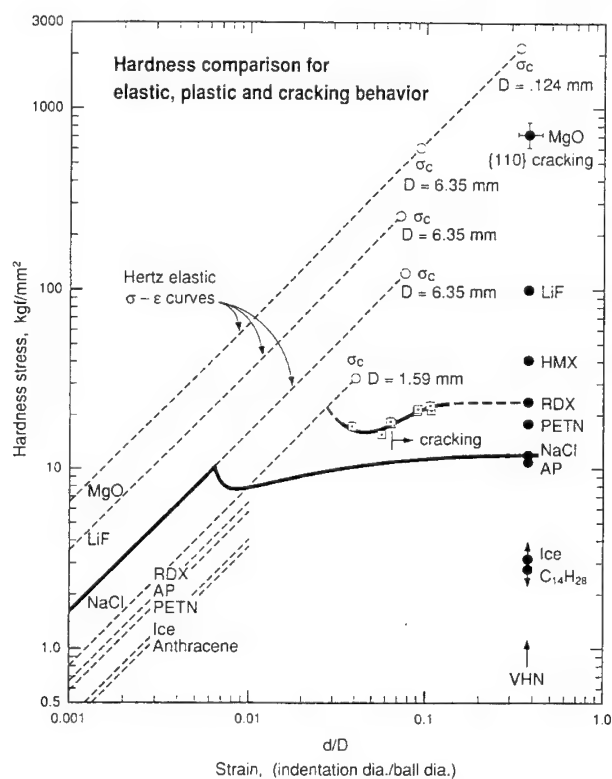


Figure 6. Hardness stress-strain description of elastic, plastic and cracking behavior in RDX, PETN, AP and related inert materials

The relatively high hardnesses of energetic crystals, with their various degrees of compliant molecular, hydrogenic and ionic bonding in the different lattice structures, are proposed to obtain for two related crystal structure based reasons: (1), there is a limited availability of slip and/or deformation twinning systems to relieve the application of mechanical forces; and, (2), dislocation movement on the limited deformation systems is particularly difficult because of intermolecular blockages between adjacent outcropping units of nearest neighbor molecules, in line with the consideration mentioned earlier of "steric hindrance" [13]. The energetic materials are known to be relatively brittle and to fail by cleavage. Their indentation hardness properties are of special interest because the technique provides measureable permanent deformation while constraining the extent of cracking and, also, the hardness test provides an index of mechanical behavior that has been correlated experimentally with sensitivity to initiation of decomposition, say, in drop-weight impact tests.

Figure 6 gives evidence on an indentation hardness stress-strain basis [27] for the observation that energetic crystals have relatively high hardnesses. A sequential elastic-plastic-cracking dependence is shown on a graphical log-log comparison for a hypothetical ball indentation testing procedure. The hardness stress is the effective mean pressure on the ball and the hardness strain is the ratio of the surface-projected contact diameter and ball diameter. For a plastic indentation, the hardness stress is obtained from the remnant areal diameter or by converting the size of a polygonal indentation to an effective ball diameter using the "cone angle" of the sharp indenter. In this way, diamond pyramid (Vickers) hardness numbers (VHN) are estimated to correspond to a ball indentation strain of 0.375, as shown at different vertical locations for the VHN values on the right side of the Figure.

The solid and dashed lines beginning from the lowest hardness stress-strain values in Figure 6 are for the predicted Hertzian elastic behavior for a ball indentation test. The lines are shifted upwards according to the smaller elastic compliances (greater stiffnesses) of the (steel) ball and indented materials. For example, RDX and PETN each have lower elastic moduli, hence, greater elastic compliances, than sodium chloride (NaCl). However, the typical VHN value shown for the hardness of NaCl is significantly less (on this logarithmic scale) than that of either RDX or PETN. A number of ball indentation test measurements are shown (as open square points) for RDX, including a mark at the hardness strain where cracking first appeared. The estimated theoretical elastic Hertzian stress at which cracking should appear for the ball indentation test (with ball diameter,  $D = 1.59$  mm), in the absence of plastic deformation, is also shown at the terminal point on the dashed line for RDX. Thus, plastic deformation is indicated to occur in RDX at just less than the theoretical elastic fracture stress and to promote subsequent cracking of the material at

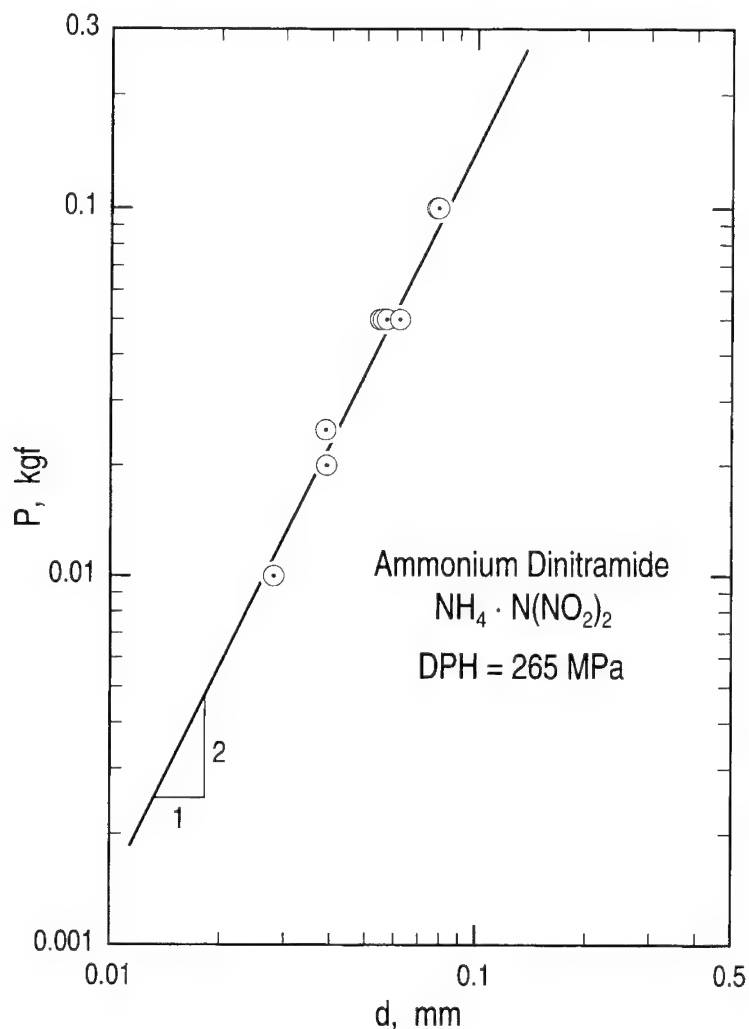


Figure 7a. Load (P) versus diagonal length (d) measurements for ADN

a lower hardness stress than the theoretical value.

Figure 7a shows recent measurements of indentation load (P) versus residual diamond pyramid diagonal length (d) values for microhardness indentations put onto the (100) surface of an ammonium dinitramide (ADN) crystal. A model representation of the monoclinic ADN crystal structure is shown in Figure 7b. The measurements were obtained under low humidity conditions because of the hygroscopic nature of ADN. From the defined microhardness pressure relationship,  $DPH = 1.8544 P/d^2$ , a relatively high value of 27 kgf/mm<sup>2</sup> (265 MPa) was determined. The microhardness value is very nearly the same as the typical value

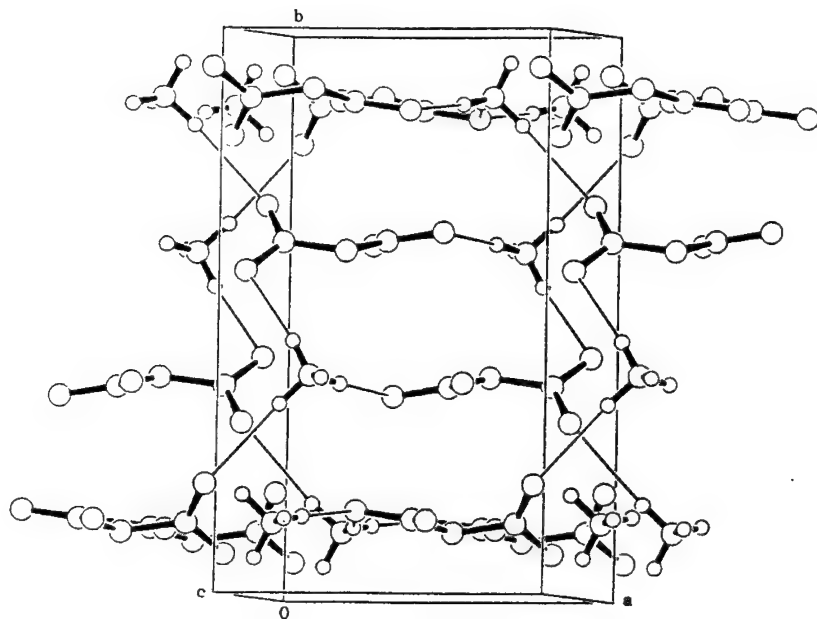


Figure 7b. Unit cell structure for ADN with bond length connections

shown for RDX in Figure 6. The comparable hardness values for ADN and RDX are in line with a recent report of comparable drop weight impact sensitivities for the two materials [28], and are similarly out of line, in agreement with the comparison made in Figure 6, with conventional correlations of strength properties and melting temperature. The hardness of ADN is about 2.5 times greater than that of NaCl.

An indication of the molecular interactions involved in establishing the presumed anisotropic strength properties of ADN is given in the unit cell characterization of Figure 7b. Figure 8 gives an analogous description for RDX: in 8a, of the orthorhombic unit cell; in 8b, showing a proposed model of the  $[\bar{1}00]$  dislocation Burgers vector for (040) planar slip; and, in 8c, an example of adjacent molecular interactions involved in  $[100]$  direction slip occurring on the identified (02 $\bar{1}$ ) slip plane [17]. In Figure 8c, strong interactions are indicated for outcropping oxygen atoms which, if dissociated from their respective molecules, would produce the dinitroso compounds that have been detected as a decomposition product in deformed RDX after near critical drop-weight impact tests [29]. The consideration provides further evidence for the importance of mutual blockages between adjacent molecules during dislocation movement in determining the relatively high strength properties of energetic crystals, in this

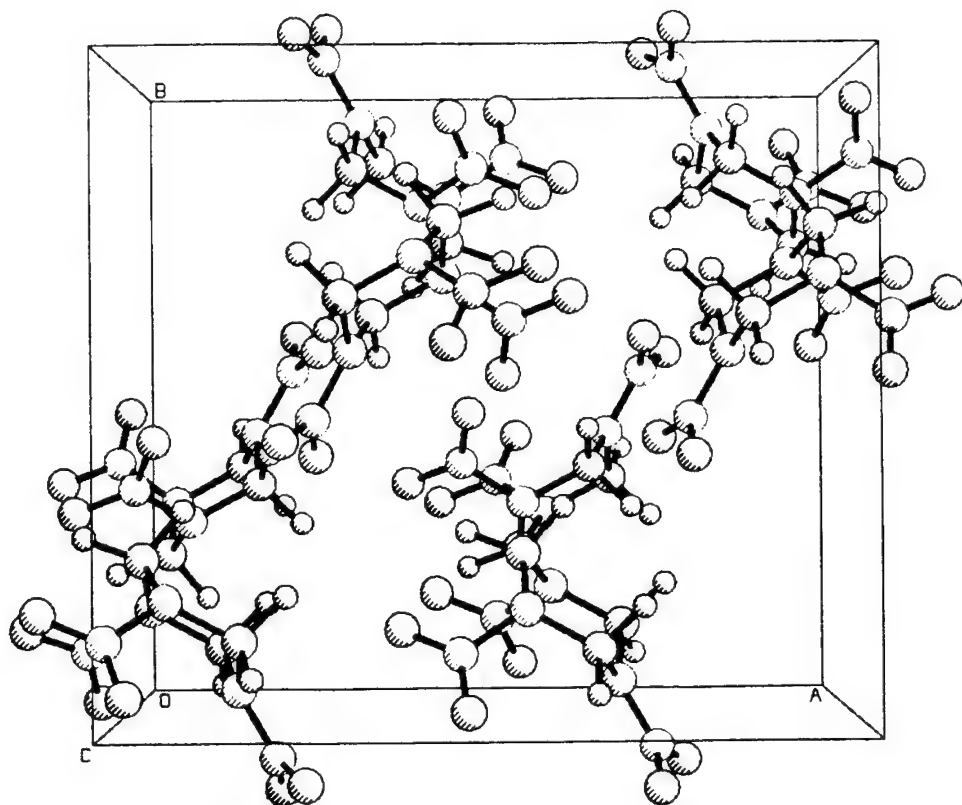


Figure 8a. RDX unit cell

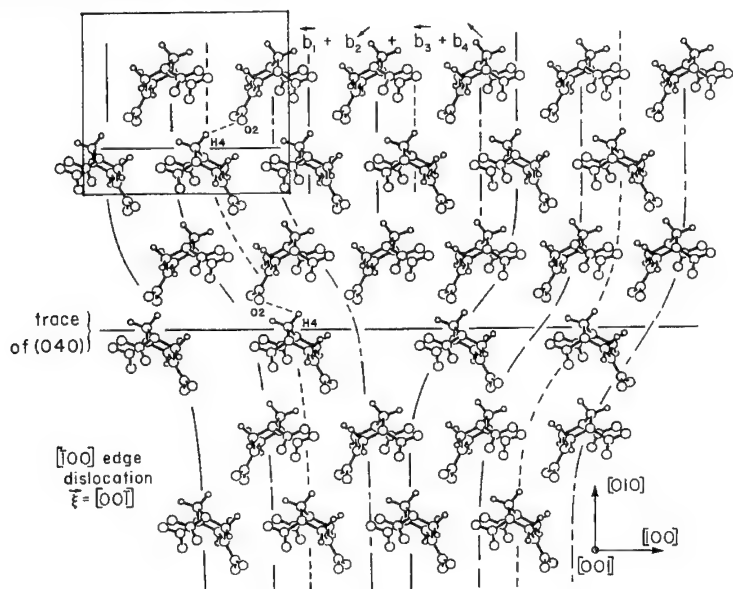


Figure 8b. Schematic (002) RDX slice of  $[100]$  (040) slip dislocation



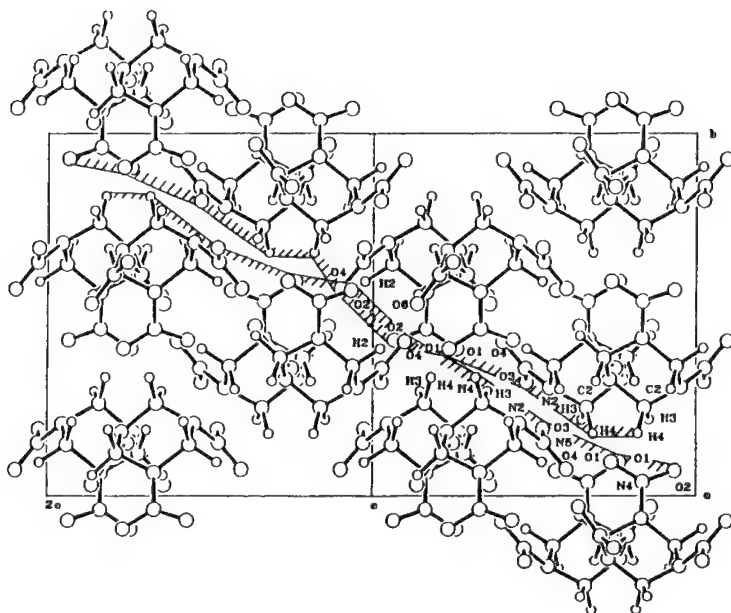


Figure 8c. Dinitroso molecule interactions for  $[100](02\bar{1})$  slip in RDX

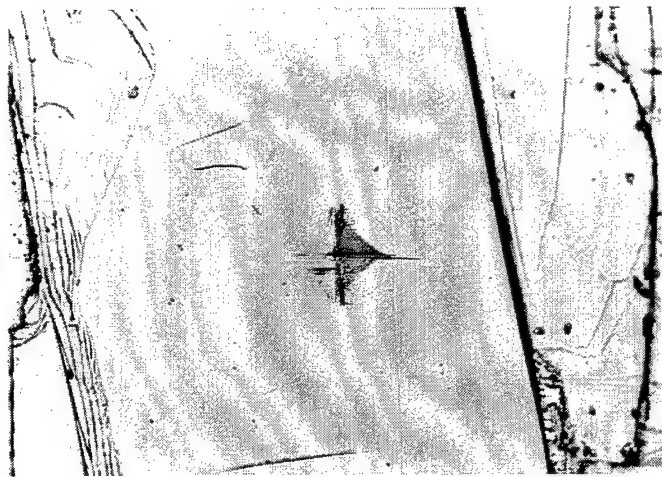
case relating to a chemical reaction pathway for molecular decomposition.

Figures 9a-c show optical and x-ray diffraction images of  $(00\bar{1})$  cleavage cracking initiated by dislocation slip at a microhardness indentation on the orthorhombic  $(\bar{2}10)$  cleavage surface of an AP crystal. The deformation zone around the indentation is seen in the optical micrograph of Figure 9a to be plastically anisotropic. Recognizable slip system traces are seen to be inclined to the indenter facet edges; and, the larger facets in the two lower indentation quadrants are the result of greater deformation having occurred there. The important indication, in line with the elastic, plastic and cracking sequence established for Figure 6, is that the  $(00\bar{1})$  cleavage crack has been initiated by plastic flow by slip on the indicated plane traces. The dislocation reaction

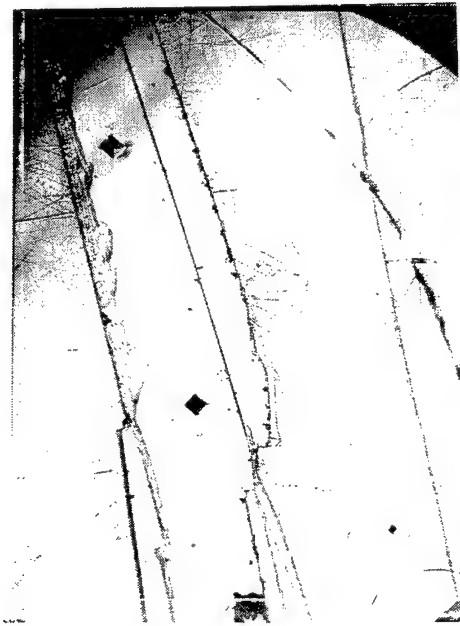
$$[\bar{1}0\bar{1}](\bar{1}11) + [10\bar{1}](\bar{1}\bar{1}\bar{1}) = [00\bar{2}](\bar{1}\bar{1}0)$$

has been proposed for the mechanism of crack nucleation [30].

Figures 9b,c are matching optical and  $(\bar{5}23)$  x-ray diffraction images, at lower magnification, of the indentation that has been described (on the left) and another one placed further along the same  $(\bar{2}10)$  plane surface on the right. The x-ray topograph of Figure 9c shows, by virtue of the (white) reduction in reflected x-ray intensity extending far below the indentations, the far reaching effect of the significantly greater deformation that has occurred around the lower



9a. DPH microindentation at 100 gf  
on  $(\bar{1}10)$  surface in AP



9b. Optical micrograph of diamond pyramid microindentations



9c.  $(\bar{1}23)$  x-ray image of cumulative dislocation strains

Figure 9. Dislocation slip induced  $(00\bar{1})$  cleavage cracking in AP

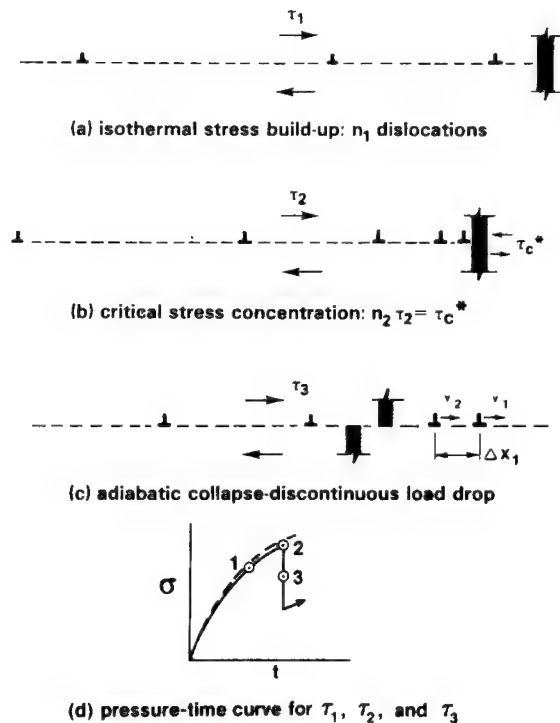


Figure 10. Dislocation pile-up avalanche model for deformation induced hot spots

indenter facets. The x-ray image gives emphasis to the cumulative strains generated by multiple dislocation displacements occurring within a normal slip band structure. The cumulative dislocation displacements in blocked slip bands are modeled in terms of dislocation pile-ups that produce substantial localized stresses at the pile-up tips.

#### Hot Spots at Dislocation Pile-up Avalanches

Very significant localized heating has been demonstrated theoretically to accompany the release of a dislocation pile-up, particularly, in association with the formation of a cleavage crack [31]. Figure 10 shows schematically the proposed sequence of events leading to hot spot heating on this basis. First, there is the isothermal build-up of the slip band structure during initial straining of the material, then leading to impingement of the propagating slip band at an obstacle, which, for most effective hot spot heating, involves crack formation and consequent adiabatic dissipation of the stored elastic strain energy in the pile-up. The released dislocations at the pile-up tip are driven at extremely high velocity by the effective applied stress magnified by the number of dislocations following behind.

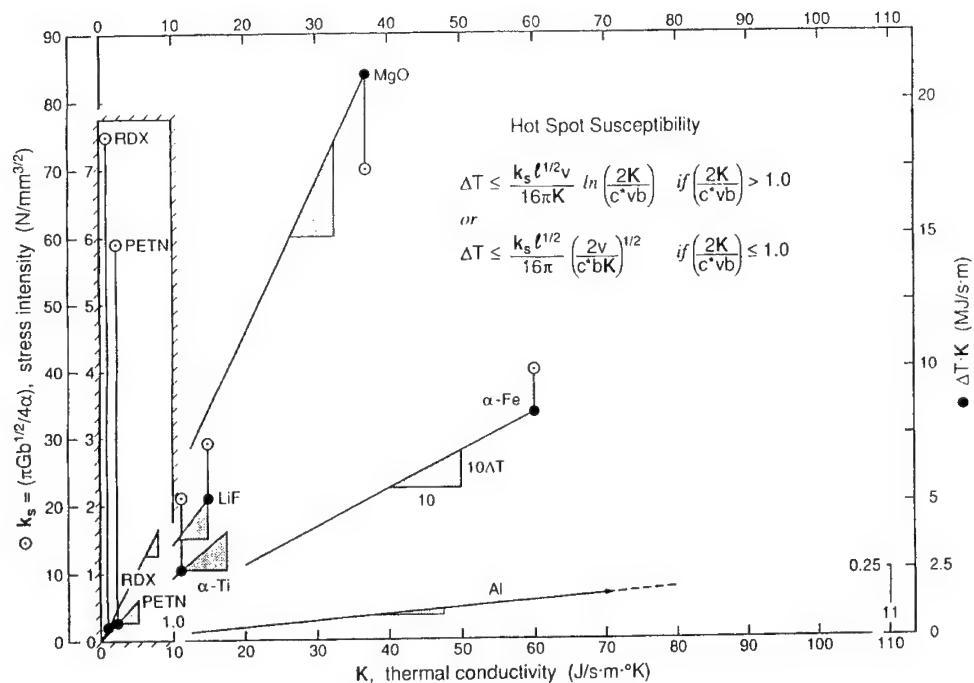


Figure 11. Graphical description of (microstructural stress intensity)/(thermal conductivity) ratio for hot spot susceptibility

Several consequences of the dislocation pile-up mechanism for hot spot heating appear to be in agreement with experimental observations. Those materials susceptible to hot spot heating have exhibited discontinuous load drop responses in drop-weight impact tests [32] and that is the expected behavior indicated in Figure 10 for the dislocation pile-up avalanche model. A model calculation for the upper limiting temperature rise is given in Figure 11 for which the ratio of the microstructural stress intensity measuring the local obstacle strength,  $k_s$ , and the thermal conductivity,  $K$ , are the main parameters separating the predicted behavior of different materials, in apparent agreement with the relative importance of adiabatic heating effects.

#### Hot Spot Relation to the Combustion Pressure Exponent?

A first connection of the dislocation pile-up avalanche model and predicted thermal explosion temperatures [33] was made for RDX on a graphical basis relating to Figure 12 [34]. Results for PETN, AP and ammonium nitrate (AN) particles of 1.0 mm size, equivalent to that

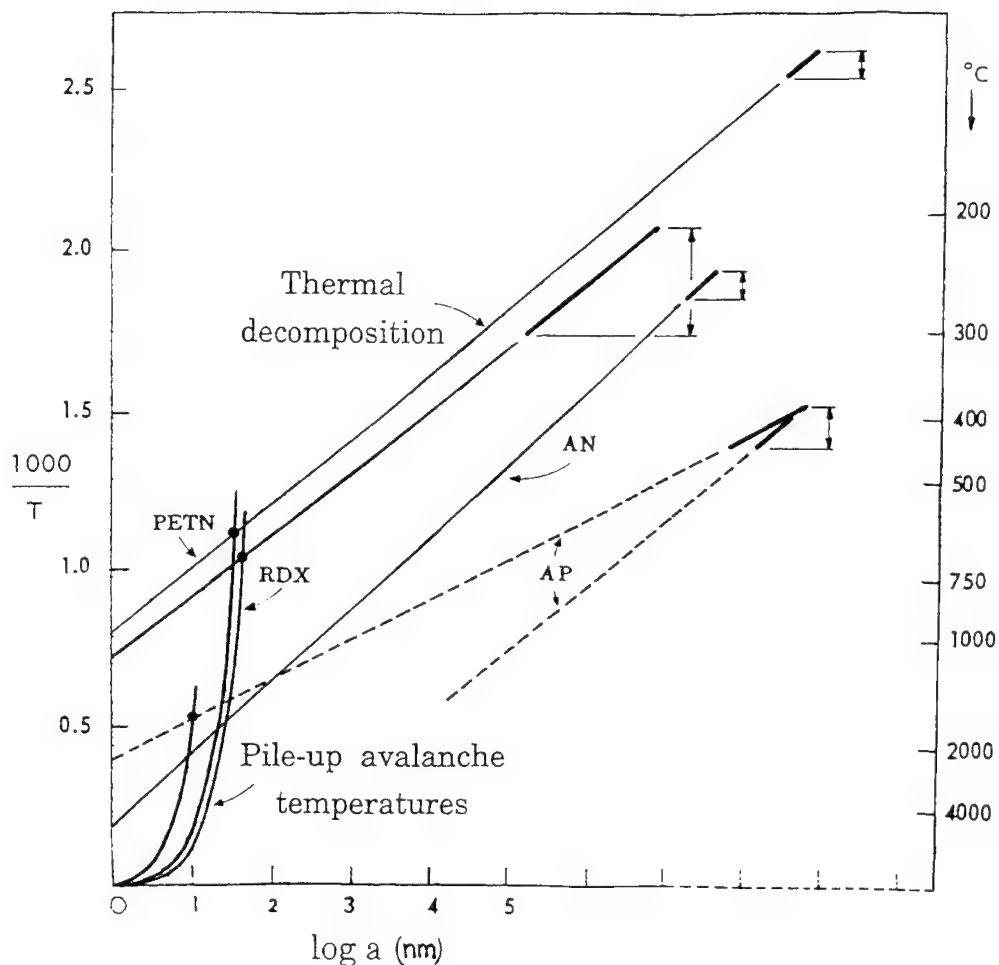


Figure 12. Pile-up avalanche temperatures relating to thermal explosion temperatures, also connecting with the temperature ranges employed in determining the Arrhenius parameters for the thermal explosion calculations

presumed for the shown RDX result, have been added here along with extension of the thermal explosion temperature dependencies to the temperature ranges (indicated by the vertical dimension markers) for determining the Arrhenius parameters involved in the thermal explosion calculations. Larger particle, or defect sizes, will move the curves to the right, thus producing lower required hot spot temperatures for explosion, possibly relating to more macroscopic engineering considerations [35]. PETN is predicted to be somewhat more impact sensitive than RDX, despite its greater thermal conductivity, because of its (Arrhenius-determined) thermal explosion properties [36,37].

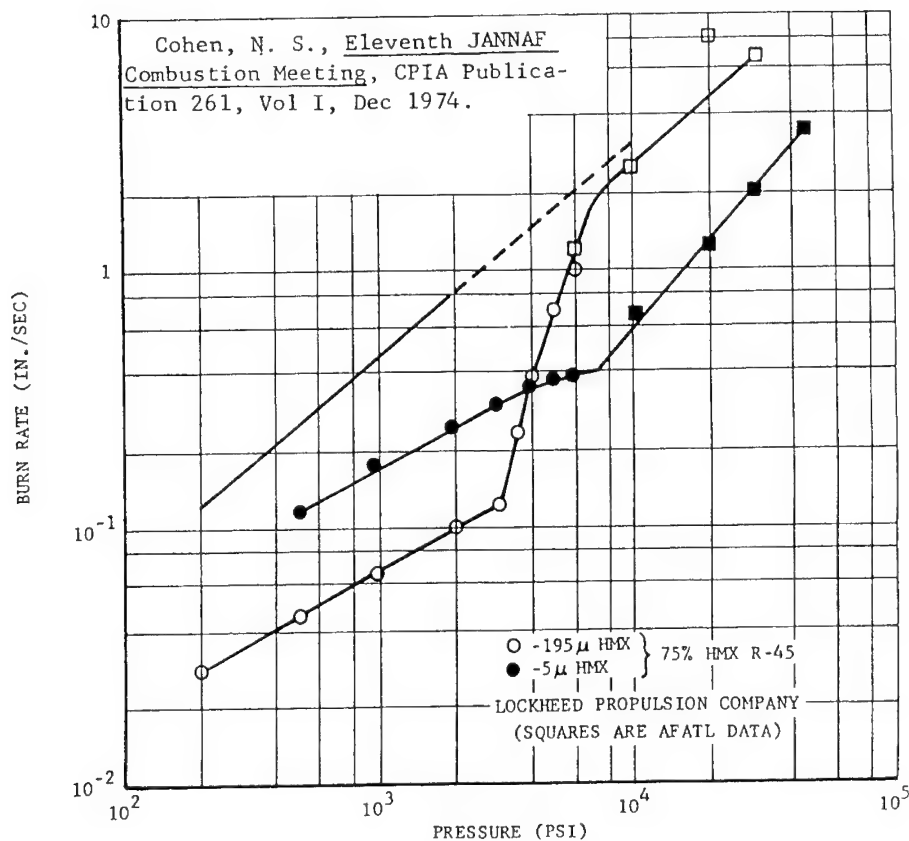


Figure 13. Burn rate versus pressure measurements reported for HMX

A substantial variation occurs in the Arrhenius parameters reported for AP [38]. For the lowest AP slope in Figure 12, corresponding to a highest activation energy, AP is predicted to be more impact sensitive than AN, as indicated in experimental tests although both materials are sufficiently impact insensitive, compared to RDX and PETN, as to be at the limit of most impact tester reliabilities.

A different interesting connection of such thermomechanical considerations, particularly relating to particle size effects, concerns the possibility of hot spot behavior being involved in the sudden change of the pressure exponent measured in propellant combustion experiments. A review has been given of the coupled exponential pressure and Arrhenius dependencies involved in such combustion studies [39], that should probably be explained ultimately on a van't Hoff reaction isotherm basis. Figure 13 shows experimental results reported in a pioneering study of two cyclotetramethylenetetranitramine (HMX) composite systems compared with an indicated smooth burn rate for pure HMX [40]. Similar modern results, involving unstable combustion of larger 150 micrometer HMX

particles in a polymeric binder system, have been reported with the suspicion of particle fracturing as the cause of abnormal burning behavior [41]. On the basis of a pile-up avalanche explanation for the behavior, one should expect cracking to occur at a greater pressure for the smaller particle size, in line with the experimental results shown in Figure 13. Otherwise the combustion surface temperature and thermal gradient properties of the composite system, and material variations also involving porosity, are additional important variables to investigate.

#### Summary

Modern energetic crystal results have been described as part of the continuing theoretical and experimental challenges that apply for the safe, effective, use of explosive crystals in propellant formulations. The varying energetic crystal morphologies are indicated to be dependent upon the internal dislocation defect structure that determines, in turn, the material viscoplastic deformation behavior and, particularly, crystal cracking properties. Laser-induced heating effects in RDX and AP crystals are shown to be associated with evident thermomechanical cracking influences on the decomposition behavior.

New microhardness measurements on an ADN crystal give a high value of  $27 \text{ kgf/mm}^2$ , essentially equivalent to that for RDX, and consistent with a report of approximately equivalent impact sensitivities for the two materials. Hot spot behavior is associated with cumulative dislocation behavior in a slip band, modeled as a dislocation pile-up, and this provides an explanation of crystal size effects on thermomechanical properties. Smaller crystals are better. The pile-up model predictions are related to a theoretical description of thermal explosion behavior. The new possibility is raised of such considerations relating to a thermomechanical viscoplastic/cracking influence on producing an undesired sudden increase in the pressure exponent used to characterize combustion behavior.

#### Acknowledgments

The authors are grateful to K.K. Kuo for the invitation to participate in the 4-ISICP program. A.C. van der Steen has supplied information about the TNO Prins Maurits Laboratory research effort on the morphologies and internal growth structures of RDX crystals. RDX crystals employed here were supplied by H.H. Cady, Los Alamos National Laboratory; and, AP crystals were supplied by T.L. Boggs, Naval Weapons Center, China Lake. The AP laser experiments were performed in the laboratory of C.H. Lee, Dept. of Electrical Engineering, University of Maryland. AP x-ray diffraction images were obtained in the

laboratory of W.T. Beard, Jr., Laboratory for Physical Sciences, College Park, MD. ADN crystals from the Stanford Research Institute were supplied by W.M. Koppes, Naval Surface Warfare Center, Indian Head Division. Unit cell structures for the various crystals were supplied by H.L. Ammon and Z.Y. Du, Dept. of Chemistry and Biochemistry, University of Maryland. T.B. Brill, University of Delaware, is thanked for calling attention to pioneering work on the HMX combustion pressure exponent. This research effort has been supported by ONR Contract N00014-86-K-0286, managed by R.S. Miller.

#### References

1. "Nobel: The Man and His Prizes", H. Schück, R. Sohlman, A. Österling, G. Liljestrang, A. Westgren, M. Siegbahn, A. Schou, and N.K. Ståhle (Elsevier Publishing Company, Amsterdam, 1962).
2. P.J. Halfpenny, K.J. Roberts and J.N. Sherwood, *Philos. Mag.* A53, 531 (1986).
3. R. Behrens Jr. and S. Bulusu, *J. Phys. Chem.* 96, 8877 (1992).
4. T.P. Parr and D.M. Hanson-Parr, in "Decomposition, Combustion, and Detonation Chemistry of Energetic Materials", Vol. 418, eds. T.B. Brill, T.P. Russell, W.C. Tao and R.B. Wardle (Mater. Res. Soc., Pittsburgh, PA, 1996) p. 207.
5. J. Sharma, C.S. Coffey, A.L. Ramaswamy and R.W. Armstrong, in "Decomposition, Combustion, and Detonation Chemistry of Energetic Materials", Vol. 418, eds. T.B. Brill, T.P. Russell, W.C. Tao and R.B. Wardle (Mater. Res. Soc., Pittsburgh, PA, 1996) p. 257.
6. K.K. Kuo, T.A. Litzinger and W.H. Hsieh, in "Structure and Properties of Energetic Materials", eds. D.H. Liebenberg, R.W. Armstrong and J.J. Gilman (Mater. Res. Soc., Pittsburgh, PA, 1993) p. 331.
7. C.F. Melius, in "Approches Microscopique et Macroscopique des Detonations", ed. S. Odier, *J. de Phys. IV*, Colloque C4, suppl. au *J. de Phys. III*, Vol. 5, p. C4-535 (1995).
8. H. Eyring, *Science* 199, 740 (1978).
9. F.E. Walker, in "Approches Microscopique et Macroscopique des Detonations", ed. S. Odier, *J. de Phys. IV*, Colloque C4, suppl. au *J. de Phys. III*, Vol. 5, p. C4-309 (1995).
10. W.L. Faust, *Science* 245, 37 (1989).
11. A. Tokmakoff, M.D. Fayer and D.D. Dlott, *J. Phys. Chem.* 97, 1901 (1993).



12. J.J. Gilman, *Philos. Mag.* B71, 1057 (1995).
13. J.J. Dick, R.N. Mulford, W.J. Spencer, D.R. Pettit, E. Garcia and D.C. Shaw, *J. Appl. Phys.* 70, 3572 (1991).
14. R.W. Armstrong and W.L. Elban, in "Energetic Material Fundamentals Workshop", Los Alamos National Laboratory, 1986 (Chemical Propulsion Information Agency Publication 475, 1987) p. 177.
15. W. Connick and F.G.J. May, *J. Cryst. Growth* 5, 65 (1969).
16. I.T. McDermott and P.P. Phakey, *J. Appl. Cryst.* 4, 479 (1971).
17. W.L. Elban, J.C. Hoffsommer and R.W. Armstrong, *J. Mater. Sci.* 19, 552 (1984).
18. A.C. van der Steen and W. Duvalois, "What Do Explosive Particles Look Like?", Preprints Vol. 3, ONR/TNO Workshop on Desensitization of Explosives and Propellants, ed. A.C. van der Steen (Prins Maurits Laboratory, Rijswijk, The Netherlands, 1991) p.1.
19. F.C. Frank, *Acta Cryst.* 4, 497 (1951).
20. A.C. van der Steen, private communication (1993).
21. H. Klapper, in "Characterization of Crystal Growth Defects", eds. B.K. Tanner and H.K. Bowen (Plenum Press, N.Y., 1980) p. 133.
22. R.W. Armstrong, A.L. Ramaswamy and J.E. Field, in "ONR/SNPE/ONERA Workshop on Combustion Mechanisms", ONREUR Report 91-02-W, ed. R.W. Armstrong (U.S. Office of Naval Research European Office, London, U.K., 1991), p. 168.
23. H.W. Sandusky, B.C. Glancy, D.W. Carlson, W.L. Elban and R.W. Armstrong, *J. Prop. Power* 7, 518 (1991).
24. A.L. Ramaswamy, H. Shin, R.W. Armstrong, C.H. Lee and J. Sharma, "Nanosecond and Picosecond Laser-induced Cracking and Ignition of Single Crystals of Ammonium Perchlorate", *J. Mater. Sci.* 31, 6035 (1996).
25. F. Solymosi, "Structure and Stability of Salts of Halogen Oxyacids in the Solid Phase" (John Wiley and Sons, N.Y., 1977) p. 195.
26. B.C. Beard and J. Sharma, in "Structure and Properties of Energetic Materials", Vol. 246, eds. D.H. Liebenberg, R.W. Armstrong and J.J. Gilman (*Mater. Res. Soc.*, Pittsburgh, PA, 1993) p. 257.

27. B.L. Hammond and R.W. Armstrong, *Philos. Mag. Lett.* 57, 41 (1988).
28. A. Langlet, N. Wingborg and H. Östmark, "ADN - A New and Promising Oxidizer for Composite Rocket Propellants", Fourth International Symposium on Special Topics in Chemical Propulsion (4-ISICP): "Challenges in Combustion and Propellants 100 Years after Nobel", Stockholm, Sweden, May 27-31, 1996).
29. J.C. Hoffsommer, D.J. Glover and W.L. Elban, *J. Energetic Mater.* 3, 303 (1985).
30. W.L. Elban, P.J. Coyne, Jr., H.W. Sandusky, B.C. Glancy, D.W. Carlson and R.W. Armstrong, "Investigation of the Origin of Hot Spots in Deformed Crystals: Studies on Ammonium Perchlorate and Reference Inert Materials", Naval Surface Warfare Center Report NSWC MP 88-178, April 1988.
31. R.W. Armstrong, C.S. Coffey and W.L. Elban, *Acta Metall.* 30, 2111 (1982).
32. S.N. Heavens and J.E. Field, *Proc. Roy. Soc. (London)* A338, 77 (1974).
33. R.W. Armstrong, C.S. Coffey, V.F. DeVost and W.L. Elban, *J. Appl. Phys.* 68, 979 (1990).
34. T. Boddington, Ninth Symposium (International) on Combustion (Academic Press, N.Y., 1963) p. 287.
35. D. Cohen, K.K. Kuo, S.J. Ritchie and Y.-C. Lu, "Evaluation of the Effectiveness of an Industrial Repair Procedure for Solid- Propellant Grains", Fourth International Symposium on Special Topics in Chemical Propulsion (4-ISICP): "Challenges in Combustion and Propellants 100 Years after Nobel", Stockholm, Sweden, May 27-31, 1996.
36. R. Meyer, "Explosives", 2nd ed., (Verlag Chemie, Deerfield Beach, FL, 1981).
37. Engineering Design Handbook, Explosives Series, U.S. Army Materiel Command, AMC Pamphlet AMCP 706-177 (1971).
38. P.W.M. Jacobs and H.M. Whitehead, *Chem. Rev.* 69, 551 (1969).
39. L. De Luca, M. Verri, F. Cozzi and G. Colombo, "A Survey of Pressure-Driven Burning of Energetic Solids with Arrhenius Surface Pyrolysis", Fourth International Symposium on Special Topics in Chemical Propulsion (4-ISICP): "Challenges in Combustion and Propellants 100 Years after Nobel", Stockholm, Sweden, May 27-31, 1996.

40. N.S. Cohen, Eleventh JANNAF Combustion Meeting, CPIA Publication 261, Vol. I (1974); results quoted by K.P. McCarty, "HMX Propellant Combustion Studies", Air Force Rocket Propulsion Laboratory Report AFRPL-TR-76-59, December 1976.

41. W.C. Tao, M.S. Constantino and A.M. Frank, "A Macroscopic and Microscopic Look into the Fundamentals of Vulnerability", Preprints Vol. 2, ONR/TNO Workshop on Desensitization of Explosives and Propellants, ed. A.C. van der Steen (Prins Maurits Laboratory, Rijswijk, The Netherlands, 1991).

## INSENSITIVE MUNITIONS PROPULSION PROGRESS

S. C. DeMay,<sup>1</sup> C. J. Thelen<sup>2</sup>

<sup>1</sup>Naval Air Warfare Center Weapons Division, China Lake;

<sup>2</sup>Sverdrup Technology, Inc., NAWC Division

**ABSTRACT:** Increasing interest in the application of thrust-managed, solid-propellant rocket motors for future missiles has prompted a desire to learn how these motors might react to the stimuli involved in the MIL-STD 2105B<sup>1</sup> insensitive munitions (IM) hazards tests. An opportunity became available for the Insensitive Munitions Advanced Development (IMAD) Propulsion Project to obtain four experimental, dual-pulse (two chamber) rocket motors; these motors were subjected to the fast cookoff, slow cookoff, bullet impact, and fragment impact IM hazards tests. These motors had steel cases with a bulkhead separating one pulse from the other. The propellant for each pulse grain was a nitrate-ester-plasticized, reduced-smoke, hydroxyl-terminated polyether (HTPE) propellant.

Reactions in the IM hazards tests were classified as follows: fast cookoff, deflagration (fail); slow cookoff, explosion (fail); bullet impact, burn (pass); and fragment impact, explosion (fail). In the cookoff tests, the aft pulse (pulse 1) reacted first followed by the forward pulse (pulse 2). Delay times between the reaction of pulse 1 and pulse 2 were 5 seconds for the fast cookoff and 45 seconds for the slow cookoff tests. It was unexpected when pulse 1 reacted first, because this pulse's chamber consisted of thicker insulation. In the impact tests, the projectiles and fragments were aimed at the pulse 2 chamber resulting in the reaction of this pulse with no accompanying reaction from pulse 1. The implication of these results is that separate chamber, pulsed motors containing a relatively insensitive propellant such as the HTPE propellant will probably provide less collateral damage than motors in which an equivalent amount of propellant is contained in one chamber.

\* Approved for public release; distribution is unlimited.

\*\* This effort was supported by the Insensitive Munitions Advanced Development (IMAD) Program (Don Porada, cognizant technology manager).

## INTRODUCTION

Since the establishment of the Navy's insensitive munitions (IM) initiative in 1984, a relatively large number of rocket motors have been subjected to the MIL-STD 2105<sup>2</sup> fast cookoff, slow cookoff, bullet impact, and fragment impact IM hazard tests. All of these motors were single-chamber motors; a few of these were dual-thrust motors. Recently, the Navy completed the design, fabrication, and static firing of a 7-inch-diameter, dual-pulse (two chamber) motor<sup>3</sup> under its Multimission Propulsion Technology-Advanced Technology Demonstration (MMPT-ATD) Program. This provided the Insensitive Munitions Advanced Development (IMAD) Propulsion Project an opportunity to obtain and IM hazards test dual-pulse rocket motors and, thereby, add a different motor configuration to the hazards test database. Using the MMPT-ATD contract, four additional dual-pulse rocket motors were procured and subjected to the aforementioned IM hazards tests. This paper describes the results of these tests and compares them to the test results of the same propellant in several other motor configurations.

## ROCKET MOTOR DESCRIPTION

The purpose of the MMPT-ATD rocket motor concept was to provide multimission propulsion capability through energy management using a dual-pulse (two chamber) motor having a 7-inch-diameter steel (D6AC) case and an integrated aerodynamic-thrust vector control (TVC) system for attitude control. To minimize program cost, the steel cases for the test motors were fabricated from reconditioned Advanced Medium-Range Air-to-Air Missile (AMRAAM) lot acceptance test (LAT) cases; a "doubler" section was electron-beam-welded between two halves of an AMRAAM case.

To minimize cost, the 7-inch-diameter motors used in the IM hazard tests had an aft-end bulkhead simulating a nozzle entrance section and throat instead of having a blast tube and TVC nozzle. They also had a stainless steel bulkhead insulated with MX-2646 silica phenolic approximately at their mid-section; this bulkhead separated the two propellant grains. The bulkhead had a nickel rupture disk designed to release at 350-500 psi. The pulse chambers of the motors were insulated with R-181 elastomeric insulation applied to the inner wall of the case. To thermally protect the aft pulse 1 section of the case during operation of pulse 2, an elastomerized silica phenolic sleeve was added to the aft chamber. R-181 insulated the simulated nozzle internally and a phenolic disk sealed its throat. To minimize a chance for a heat path through this simulated nozzle, its external surface was coated with room temperature vulcanizing (RTV) rubber. The propellant grains were fabricated from an IM reduced-smoke, hydroxyl-terminated polyether (HTPE) propellant developed by Alliant Techsystems under an IMAD Propulsion Project contract.<sup>4</sup>

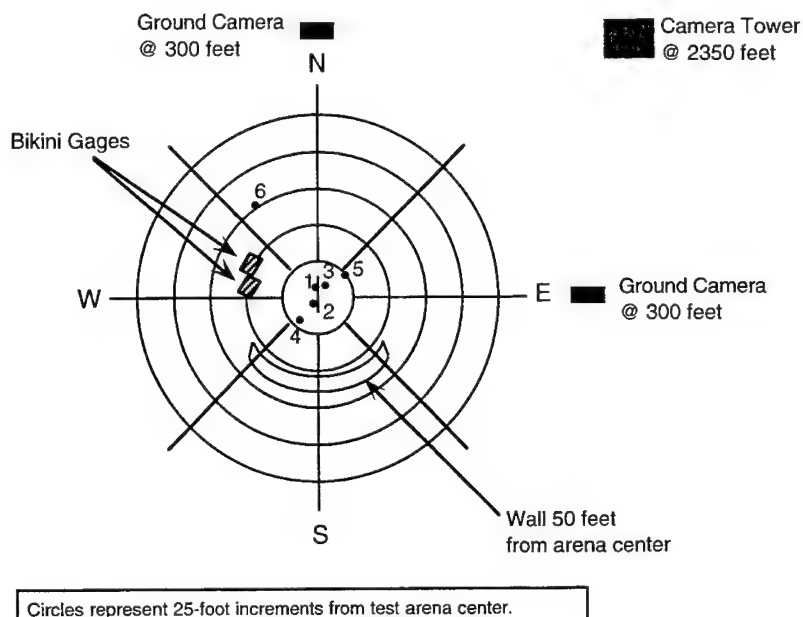
## IM HAZARD TESTS

The fast cookoff, slow cookoff, bullet impact, and fragment impact IM hazards tests were conducted in accordance to MIL-STD 2105B; however, only one test for each hazard was conducted instead of the duplicate tests required by the military standard. The Ordnance Hazards Evaluation Board (OHEB) has reviewed the test results and assigned reaction classifications.

### Fast Cookoff

Pulse 1 (aft pulse) reacted at 69 seconds in the test, rupturing the aft section of the case. Five seconds later, pulse 2 (forward pulse) reacted and vented through the mid-section bulkhead. After completion of the test, unburned pieces of propellant were found out to 310 feet from the test center. A piece of

pulse 1 case section was located at 75 feet and another at 8 feet. The case's nozzle section was at 50 feet from the test center. A piece of the rupture disk sealing the case's mid-section bulkhead was found underneath the "A" frame used to support the motor, and another piece was located at 22 feet. No overpressure was recorded by the Bikini gauges (50 feet from test center), and 95% of the motor's non-energetic material was recovered. Figure 1 shows the debris map for this fast cookoff test. This motor's reaction was classified as a deflagration (fail).



Recovered fragments from fast cookoff test.

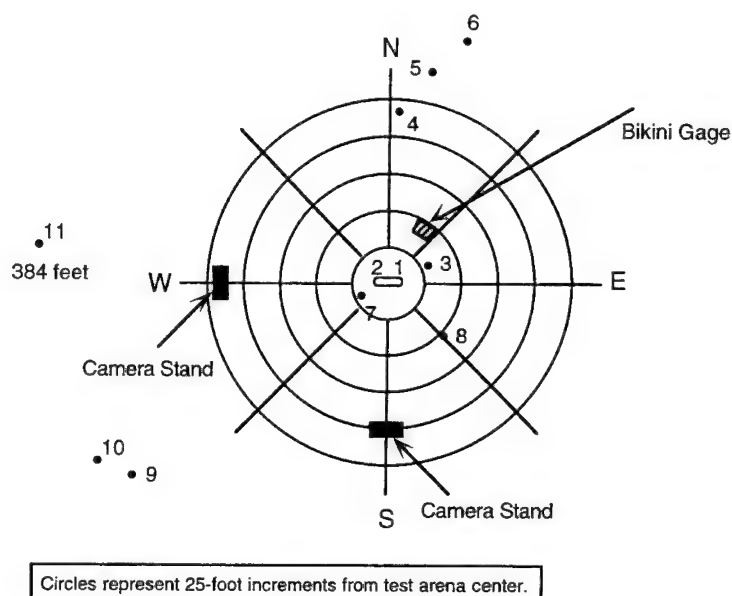
DESCRIPTION	SIZE, in	WEIGHT, lb	LOCATION
1. Motor forward end	37.75 x 7 diameter	34.65	on the "A" frame
2. Rupture disk	3 x 2.5	0.06	under the "A" frame
3. Piece of motor case	10 x 28	5.77	8 feet
4. Rupture disk	4 x 2.5	0.07	22 feet
5. Motor aft end	6 x 7 diameter	18.64	50 feet
6. Piece of motor case	27.5 x 10	5.47	75 feet
Small pieces of unburned propellant	varied	7.57	scattered as far as 310 feet from arena center

Figure 1. Debris map of fast cookoff test.

### Slow Cookoff

Pulse 1 reacted at a case surface temperature of 271°F; as a result of this reaction, the aft section of the case was blown to pieces. A second reaction (pulse 2) occurred 44 seconds later; this reaction also resulted in several pieces of the case being thrown away from the test site; however, the forward end of the pulse 2 motor section remained on the "A" frame and burned. No propellant exudation or other physical events were recorded by the internal oven TV camera prior to the reaction of pulse 1. After the test, a section of the motor case just forward of the nozzle end was found under the "A" frame, and

the nozzle end was found at 384 feet from the test center. Other pieces of the motor case were found from 18 to 211 feet of the test site; the bulkhead separating the pulse propellant grains was found at 51 feet from the test center. Small pieces of unburned propellant were spread out to 200 feet. Figure 2 shows a map of the debris collected after the test. The weight of the non-energetic motor material recovered was 77% of its original weight. The maximum overpressure measured by Bikini gauges at 50 feet from the test center was between 1.9 and 2.8 psi. The test's horizontal witness plate exhibited no damage. This motor's reaction was classified as an explosion (fail).



Recovered fragments from slow cookoff test.			
DESCRIPTION	SIZE, in	WEIGHT, lb	LOCATION
1. Motor forward end	23.5 x 7 diameter	14.41	On "A" frame
2. Motor case piece	18.5 x 4.5	4.05	Under "A" frame
3. Motor case piece	0.75 x 7.25	0.02	33 feet
4. Motor case piece	7 x 11.5	5.52	120 feet
5. Motor case piece	4.75 x 6.5	0.59	141 feet
6. Motor case piece	10.5 x 11	1.91	162 feet
7. Motor case piece	4.5 x 0.5	0.35	18 feet
8. Bulkhead	2 x 6.5 diameter	3.92	51 feet
9. Motor case piece	8 x 17	1.89	201 feet
10. Motor case piece	3 x 4	0.20	211 feet
11. Motor aft end	9 x 7 diameter	19.10	384 feet
Small unburned propellant pieces	varied	1.67	Within 200 feet

Figure 2. Debris map for the slow cookoff test.

### Bullet Impact

The the .50-caliber bullet impacts were aimed (spaced one inch apart) to the mid-length of the pulse 2 (forward) section of the motor. Upon the impact of the first projectile, which traveled at 2841 ft/s, a piece of the case in the target area broke away leaving bare propellant or insulation/liner as the target

for the following two projectiles. The motor case with a piece missing from its forward section, an unreacted pulse 1 (aft), and an undamaged mid-section bulkhead remained on the "A" frame. That part of the pulse 2 propellant grain that had remained in the case ignited and burned. After the test, the other piece of the case was found at 32 feet from the test center. Unburned pieces of the pulse 2 propellant grain were found out to 94 feet. Figure 3 shows the debris map of this test. The recovered two pieces of case represented 99% of the motor's non-energetic material initial weight. No overpressure was measured by the Bikini gauges situated at 50 feet from the test center, and the test's witness plate exhibited no damage. Based upon these results, this motor's reaction was classified as a burn (pass).

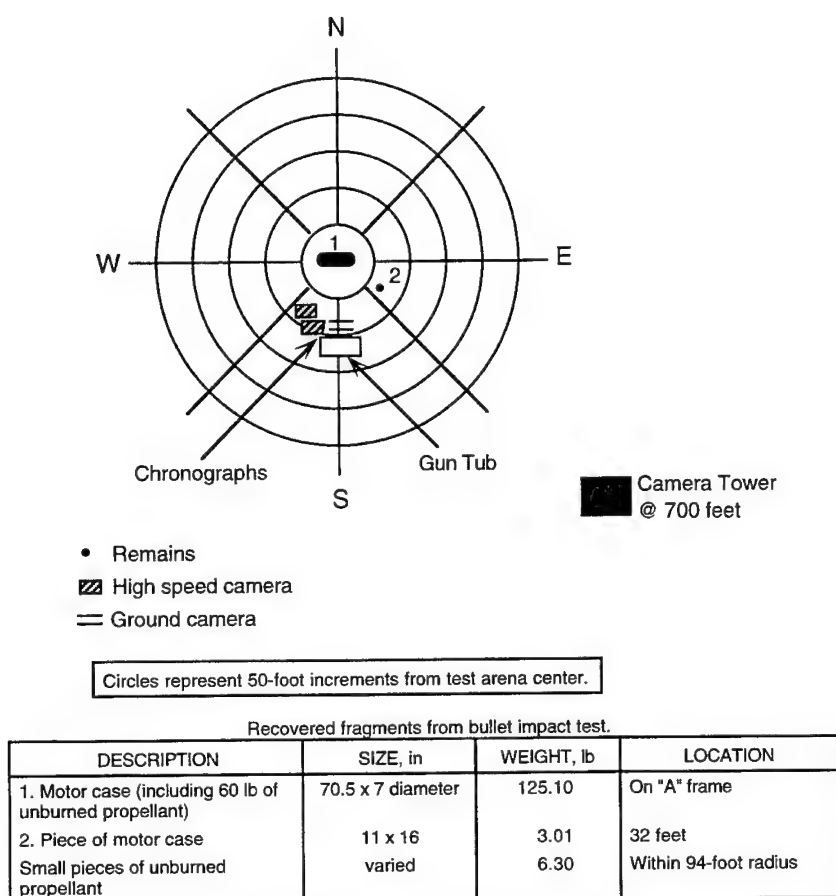


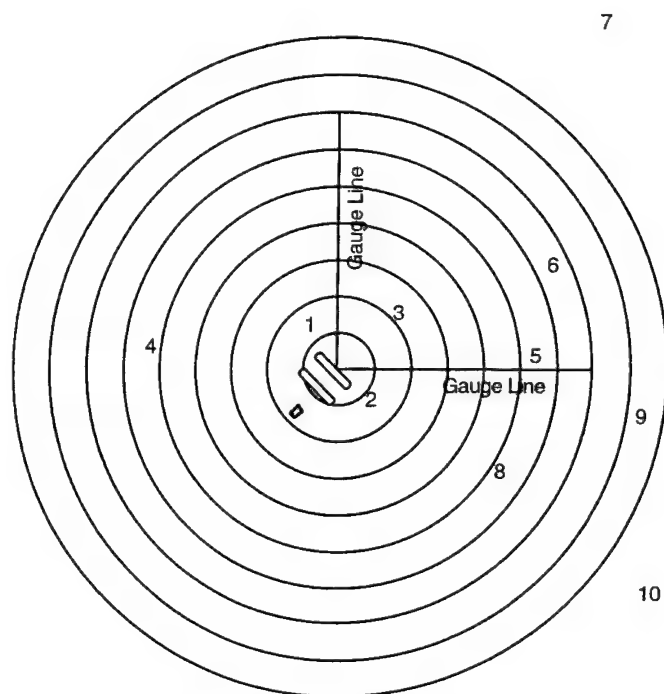
Figure 3. Debris map for the bullet impact test.

### Fragment Impact

An explosive, five-cube projector was aimed at the mid-length of the pulse 2 (forward) section of the motor. The projector was placed 17 feet from the motor. From film taken with a high speed camera, it was determined that four out of the five 0.5-inch mild steel cubes in the projector impacted the motor. On impact, the motor broke into two major pieces; the forward piece was thrown 11 feet from the test site with its propellant burning. The other major case piece containing pulse 1 and a part of pulse 2



was thrown 15 feet aft of the test center, with the propellant unreacted. Five case fragments were found from 20 to 190 feet, with the heaviest (2.75 lb) at the greatest distance. Three relatively large pieces of unburned propellant were found at 21, 53, and 56 feet from the test center. The test's horizontal witness plate exhibited no damage, but the vertical witness plate exhibited several holes and marks. The pressures measured with the airblast overpressure gauges were attributed to the blast from the fragment projector with no augmentation by the motor's reaction. The debris map for this test is shown in Figure 4. This motor's reaction was classified as a explosion (fail).



Circles represent 10-foot increments from test arena center.

Recovered fragments from fragment impact test.

DESCRIPTION	SIZE, in	WEIGHT	LOCATION
1. Forward motor closure	15 x 7	10 lb 4 oz	11 feet
2. Nozzle end of motor with propellant	43.5 x 7	125 lb 6 oz	15 feet
3. Propellant	7 x 4.5	2 lb	21 feet
4. Propellant	10 x 5.5	2 lb 2 oz	53 feet
5. Propellant	4 x 4	12 oz	56 feet
6. Motor casing	11 x 5.5	12 oz	61 feet
7. Motor casing	17 x 18	2.75 lb	190 feet
8. Motor casing	8 x 4	8 oz	50 feet
9. Motor casing	7 x 3.5	6 oz	90 feet
10. Motor casing	6.25 x 2.5	4 oz	160 feet

Figure 4. Debris map of the fragment impact test.

## DISCUSSION AND CONCLUSIONS

The investigators in charge of this effort were surprised to find that pulse 1 (aft pulse) reacted first in the cookoff tests; this section had extra insulation to protect the case during operation of pulse 2 (forward pulse). While significant temperature differences possible in a fast cookoff test could have partially explained this result, the thermocouples around the motor did not indicate that this was probable. Moreover, the slow cookoff test result indicates that other factors may be involved. Apparently, there is an unknown heat path to the pulse 1 propellant grain that is possibly associated with either the case's simulated nozzle closure or more probably with its mid-section bulkhead.

Another surprising result was that pulse 1 survived when pulse 2 was impacted by either the .50-caliber projectiles or the 0.5-inch steel cubes and that the case's mid-section bulkhead remained intact. From this result, one could infer that the pressures resulting from the pulse 2 reaction were below the 350-500 psi required to rupture the bulkhead disk. However, the cases fractured on impact, providing a large venting area which significantly moderated the pressure arising from the propellant reaction.

The reaction classification assigned to the fragment impact test is of concern. While the OHEB's reaction classification is appropriate based on some of the event criteria defined by MIL-STD 2105B, we believe that the degree of hazard contributed by the motor was less than what implied by the explosion classification. Based on the test report, the motor was impacted by four of the five 0.5-inch steel cubes that were explosively projected at an average speed of 8300 ft/s; this event by itself would have caused a considerable amount of case fragmentation without any energy input from propellant reaction. Moreover, the survival of the pulse 1 section with the mid-section bulkhead and its rupture disk intact in both the bullet and fragment impact tests seems to indicate that the propellant's reaction to impact is relatively slow and that significant localized pressurization could not develop under the case venting that occurred. This characteristic would minimize the amount of case fragmentation contributed by the propellant reaction. In addition, based on the fact that the horizontal witness plate was undamaged and the vertical witness plate exhibited a large hole in the area where it backed the aim point on the pulse 2 section of the motor, we believe that the major source of fragmentation energy came from the projector and the momentum of the fragments. Further support to this theory is provided by a statement in the test report indicating that "...the airblast peak overpressure values were what was expected from the fragment projector with no augmentation by the propellant's reaction."

Recent IM studies conducted by the Navy Sidewinder Program Office indicated that the fragment impact test is one of the most difficult of the IM tests to pass. The Naval Air Warfare Center Weapons Division's (NAWCWPNS) Sidewinder Project's representatives recently ran a fragment impact test at the New Mexico Tech's Energetic Materials Research and Testing Center (Socorro, NM) to ensure the accuracy of their fragment projector (smooth-bored 57-mm M2 gun), check the speed of the fragments, and establish a baseline reaction. The target for this test was an inert Mk 36 Sidewinder motor containing an unknown simulant propellant (believed to be a polyurethane simulant propellant). Two fragments were aimed at the center of the motor approximately 1.5 inches apart; when the fragments traveling at 8528 ft/s impacted, the motor broke into two major pieces. Unfortunately, a debris map was not prepared after the test, but approximately 5 inches of the motor's center section were missing. One large piece of simulated propellant was found at 70 feet from the test center and two smaller pieces at 60 and 55 feet. The only case fragments recovered were found within 3 feet of the motor. Extrapolating these data to a test that uses an explosive-driven, 5-cube fragment projector and in which at least two or more cubes strike a motor, it is hard to believe that any steel-cased motor would be able to survive or pass the fragment impact test. Perhaps a basic investigation should be conducted on the fragment impact test to revise the passing criteria and possibly recommend eliminating the use of an explosive-driven, multifragment projector as a test option.

Overall, the reaction classifications assigned to the IM hazards tests of the 7-inch-diameter, dual-pulse motor were more violent than expected. Table 1 compares these with the reactions of the same propellant in other motor configurations.<sup>5</sup> As can be seen, the reactions are more violent than those experienced by an 8-inch-diameter, steel-cased motor. However, as expected, the reaction violence is greatly decreased when the propellant is encased in composite cases and cylinders.

TABLE 1  
IM Hazard Test Results of IM HTPE (GHE) Propellant in Several Motor Configurations.

Motor Configuration	Reaction Classification			
	Fast Cookoff	Slow Cookoff	Bullet Impact	Fragment Impact
7-inch, dual-pulse motor	Deflagration	Explosion	Burn	Explosion
5-inch, composite case motor	Burn	Explosion	Burn	Burn
5-inch, composite cylinder	Burn	Burn	Burn	Burn
8-inch, steel case motor	Burn	Deflagration	Burn	Explosion
10-inch, composite case motor	Burn/Deflag	Deflagration	Burn	Deflagration
10-inch, composite cylinder	Burn	Burn	Burn	Explosion

The dual-pulse motor filled with a relatively insensitive propellant such as HTPE appears to provide an advantage when exposed to bullet or fragment impact stimuli because it limits the amount of reacting propellant. Moreover, the delay in the reaction of the pulses during cookoff may be of some advantage because it also limits the amount of propellant that reacts at any one time. These characteristics should help limit the extent and area of collateral damage resulting from the motor's reaction due to fast and slow cookoff or bullet and fragment impact hazard stimuli.

## REFERENCES

1. MIL-STD-2105B. *Military Standard, Hazard Assessment Tests for Non-Nuclear Munitions*, 12 January 1994. Publication UNCLASSIFIED.
2. MIL-STD-2105A, *Military Standard, Hazard Assessment Tests for Non-Nuclear Munitions*, 8 March 1991. Publication UNCLASSIFIED.
3. Florian, S., Carreno, D., Gehris, A. P. and Thompson, A. M. "Multimission Propulsion Technology—Advanced Technology Demonstration (MMPT-ATD) Program—Seven-Inch-Diameter Demonstration and Study," *Proceedings of the 1995 JANNAF Propulsion Meeting*, Tampa, FL, 4-7 December 1995. Paper UNCLASSIFIED.
4. Alliant Techsystems, Allegany Ballistics Laboratory (formerly Hercules, Inc.). *Final Report Advanced Development of Insensitive Munitions IM Sidewinder (Contract N60530-91-C-0214)*, in process.
5. DeMay, S. C., Smith, A. O. and Thelen, C. J. "IM Propulsion: Progress and Problems," *Proceedings of the 1995 JANNAF Propulsion Meeting*, Tampa, FL, 4-7 December 1995. Paper UNCLASSIFIED.

## COMBUSTION ROLES IN SAFETY OF LESS EXPLOSIVELY SENSITIVE CLASS 1.3 PROPELLANTS

Claude Merrill, US Phillips Laboratory, Edwards Air Force Base

**ABSTRACT:** During the decade of the 1980s, a number of people died manufacturing and mission suitability testing Explosive Class 1.3 solid propellants. During the same time frame no one was fatally injured in the United States in Explosive Class 1.1 solid propellant incidents. This incongruence of fatal injury incidents with the "explosively safer" Class 1.3 propellants rather than with Class 1.1 propellants was due to the relative burning rates of Class 1.1 and Class 1.3 propellants at low pressures of one atmosphere or slightly higher. Explosive safety problems with Class 1.3 propellants can also occur in the high pressure regimes with rapid acceleratory burn rates above the so called burn rate exponent slope break for ammonium perchlorate oxidized compositions. An enormous explosive threat can occur when large Class 1.3 solid propellant motors used for space launches experience early flight failures and motors or motor fragments crash to earth at high velocities. When propellant quantities are in the range of roughly 50 to nearly 500 metric tons per booster motor, there is a great blast potential. Preliminary screening of a few booster compositions in low and ultrahigh pressure regimes has produced hope that careful selection of combustion traits and propellant materials might substantially improve large rocket motor safety.

### INTRODUCTION

The relative safety of Explosive Class 1.3 rocket motors is largely driven by solid propellant low pressure and ultrahigh pressure combustion characteristics. In this article the relationship between fire and explosive safety for low speed burn rate (less than 13 mm/sec at 6.9 MPa) hydrocarbon / aluminum (Al) / ammonium perchlorate (AP) types of Explosive Class 1.3 solid propellants will be discussed. Hydrocarbon/Al/AP propellants have complex combustion behavior usually divided into at least three distinct types that are associated with different and, often variable, pressure ranges. These ranges are (a)

a low pressure zone near one atmosphere that can have a high, variable burn rate pressure exponent, (b) an intermediate, motor pressure operating range between 2 and 15 megapascals (MPa), (300 to 2200 pounds per square inch usually associated with a constant burn rate pressure exponent, psi), and (c) a high pressure zone above the motor operating pressure range including the so called "burn rate pressure exponent break" or "exponent break" where the burn rate pressure exponent is higher than in the motor operational pressure range. The pressure at which the low burn rate pressure exponent observed at motor operating pressures transitions to a higher burn rate pressure exponent varies. Occasionally, it occurs near or below 15 MPa (2200 psi), but it can occur at 100 MPa (15,000 psi) or more. The pressure at which the burn rate pressure exponent break takes place is highly dependent on the propellant formulation. Although the relationship of propellant composition and burn rate pressure exponent break pressure is not a topic of this discussion, the high burn rate pressure exponent at high pressures should be noted for its strong relationship to propellant explosiveness.

Different types of polybutadiene rubber binder solid propellants are used as combustion gas generators for a majority of rocket motor systems, especially for large rocket booster applications. These propellants have modest cost due to market availability of ingredients, are readily mixed and cast into motor grains, possess controllable cure traits, have solids contents and energetics for favorable thrust performance, show good combustion characteristics for motor operation at adequate burn rates and low burn rate pressure exponents, meet strength and elasticity rocket motor demands, and have low explosive hazards. Polybutadiene type booster propellants usually contain plasticized or nonplasticized curable binders filled with Al powder fuel and multimodal, granulated AP oxidizer. Total solids content of booster propellants range from 84 to 90%. Examples of curable butadiene rubber binders include carboxy-terminated polybutadiene (CTPB), hydroxy-terminated polybutadiene (HTPB), polybutadiene-acrylonitrile (PBAN, carboxy terminated), and polybutadiene-acrylonitrile acrylic acid (PBAA). These can be indicated as CTPB/Al/AP, etc.. Some rocket booster systems are very large. The new Titan IV solid rocket motor upgrade (SRMU) space launch booster system will contain more than 600 metric tons of HTPB/Al/AP solid propellant, and the Space Shuttle launch system contains more than 1000 metric tons of PBAN/Al/AP solid propellant.

Polybutadiene type binder propellants are usually classified as Class 1.3 explosives since they primarily experience fire hazards rather than explosive hazards. When compared with Explosive Class 1.1 propellants, the slow burning, hydrocarbon type, Explosive Class 1.3 solid propellants are normally considered quite safe. In the relatively small amounts required for motors less than 0.3 m (13 inch) diameter, most hydrocarbon binder/Al/AP propellants are very safe. However, in recent years despite their greater deflagrative and detonative safety, low burn rate hydrocarbon binder propellants have been involved in many more serious accidents than the highly explosive Class 1.1 solid propellants. The size of some of the large booster motors and the large amounts of solid propellant they contain reduce the margin of safety in ways that are not well understood. Quantitative risk assessment as motor size varies is lacking. Decreased safety for large booster motors has been observed during manufacturing, qualification testing, transportation, and field operations. In addition, observation of missile fallbacks early in a launch sequence has forced the user community to recognize that very substantial explosions can be produced by very large Class 1.3 solid propellant motors. Even explosively benign solid propellants acquire explosive traits when propellant grains are large and undergo adequately dynamic mistreatment. For a rocket launch system containing up to 1000 metric

tons of solid propellant unacceptable air shocks can be experienced at distances greater than two kilometers.

For personnel, the most serious solid propellant accidents were caused by small energy stimulations producing fires that rapidly escalated over a large number of propellant pieces or fragments or caused containment vessel bursts. We have concentrated our safety efforts on explosive safety and, as shown in the evidence of accidents and their nature, inadequately paid attention to fire safety.

Normal combustion characteristics of the hydrocarbon/Al/AP, Class 1.3, booster solid propellants at low pressures near one atmosphere and at ultrahigh pressures involved in crashes are responsible for most accidental hazardous fire and explosive events. Limited experimental data indicates that these hazardous combustion traits differ from one propellant composition to another. Ordinarily, combustion of a specific propellant is studied over a narrow pressure range associated with rocket motor function without considering propellant combustion actions outside that range. Observing how a number of propellants burn under low and very high pressures revealed remarkable differences. Certain propellant compositions exhibit slower burning rates at one atmosphere and others exhibit smaller burn rate pressure exponents at pressures above the slope break region. Combustion differences affecting propellant safety are produced by changes in normal propellant ingredients such as plasticizer content, plasticizer material, solid filler particle sizes, curatives, and minor additives. The differences are so large that carefully selecting propellant compositions should greatly improve propellant safety.

In the discussions below, only generic descriptions of propellant formulations will be given. This not only avoids exposure of proprietary material, but allows showing how propellant combustion characteristics can vary. A focused search to find a safer hydrocarbon/Al/AP, booster solid propellant composition seems possible based on the limited data available.

## DISCUSSION

Figure 1 shows a log-log plot of burn rate (RB) versus pressure for a HTPB/Al/AP propellant that for this discussion is designated HTPB A. The combustion behavior is quite complex with three or more different burn rate pressure exponents over the range of pressures. Burn rate data for Figure 1 are listed in Table 1. Some gun propellant burn rate pressure plots, once the minimum burn sustaining pressure is attained, exhibit monotonous straight line log-log behavior indicating a constant burn rate pressure exponent up to 100 MPa or more. It is the relatively large variance in behavioral changes at the low pressure and high pressure regions from one rocket propellant to another which indicates that safer propellant formulations can be selected once an adequate understanding of the relationship between combustion characteristics and propellant composition is obtained.

Between pressures of about 1.5 and 30 MPa (200 and 4500 psi) the burn rate of propellant HTPB A follows the equation:

$$R_B \text{ (mm/s)} = 4.314 [P \text{ MPa}]^{0.32} \quad (1)$$

Using the burn rate equation above, the calculated burn rate at one atmosphere is 2.08 mm/s (0.082 ips). This is much faster than the measured 0.84 mm/s burn rate at atmospheric pressure.

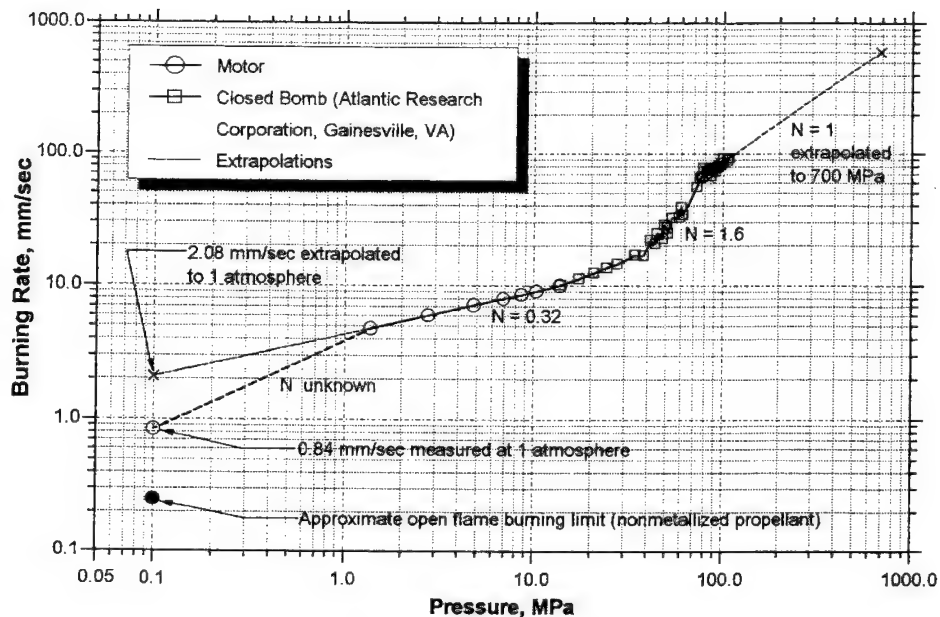


Figure 1. Burn Rate Versus Pressure for HTPB A Propellant.

Table 1. HTPB A Propellant Strand Burning Data by Atlantic Research Corp., Gainesville, VA (1)

Burn Rate		Pressure		Burn Rate		Pressure	
mm/s	(ips)	MPa	(psi)	mm/s	(ips)	MPa	(psi)
10.1	(0.399)	13.79	( 2000)	74.7	(2.941)	81.43	(11810)
11.3	(0.445)	17.24	( 2500)	71.1	(2.801)	82.46	(11960)
12.5	(0.492)	20.68	( 3000)	75.7	(2.981)	84.53	(12260)
13.7	(0.540)	24.13	( 3500)	74.3	(2.927)	85.56	(12410)
14.6	(0.575)	27.58	( 4000)	77.8	(3.064)	86.39	(12530)
17.0	(0.668)	33.99	( 4930)	67.9	(2.674)	86.77	(12585)
16.9	(0.666)	37.85	( 5490)	75.7	(2.981)	88.67	(12860)
22.0	(0.865)	41.26	( 5985)	78.2	(3.080)	89.49	(12980)
20.8	(0.817)	43.78	( 6350)	78.6	(3.096)	90.53	(13130)
24.9	(0.980)	44.75	( 6490)	72.9	(2.869)	90.60	(13140)
22.6	(0.891)	47.92	( 6950)	78.6	(3.096)	91.22	(13230)
28.7	(1.131)	48.85	( 7085)	78.6	(3.096)	92.77	(13455)
27.3	(1.076)	50.61	( 7340)	79.2	(3.118)	93.22	(13520)
24.9	(0.980)	51.02	( 7400)	79.9	(3.146)	94.25	(13670)
32.5	(1.279)	53.71	( 7790)	81.2	(3.197)	95.28	(13820)
33.0	(1.298)	58.67	( 8510)	82.1	(3.232)	97.42	(14130)
39.3	(1.548)	60.05	( 8710)	82.1	(3.232)	97.42	(14130)
34.0	(1.337)	60.95	( 8840)	85.4	(3.361)	98.25	(14250)

Table 1. HTPB A Propellant Strand Burning Data by Atlantic Research Corp., Gainesville, VA  
(1) (concluded)

Burn Rate		Pressure		Burn Rate		Pressure	
mm/s	(ips)	MPa	(psi)	mm/s	(ips)	MPa	(psi)
55.8	(2.195)	72.39	(10500)	93.4	(3.678)	99.52	(14435)
65.3	(2.569)	75.50	(10950)	85.9	(3.381)	100.25	(14540)
67.9	(2.674)	77.43	(11230)	89.5	(3.522)	105.73	(15335)
67.1	(2.642)	77.98	(11310)	89.5	(3.522)	105.73	(15335)
78.6	(3.095)	78.94	(11450)	93.4	(3.676)	107.80	(15635)
Extrapolation				602	(23.70)	689	(100000)

The central portion of the Figure 1 plot exhibiting linear behavior at a slope or burn rate pressure exponent of  $\sim 0.32$  between  $\sim 1.5$  and 30 MPa (200 to 4500 psi) is the operating region for rocket motors. Our standard 6.9 MPa (1000 psi) burn rate for HTPB A propellant was 8.0 mm/second (0.32 ips). A portion of this region is usually measured to see if propellant burn rate appropriately matches that needed for a particular motor application. Combustion data would be measured at pressures exceeding maximum expected motor operating pressure (MEOP) to see if a potentially troublesome exponent break occurred near the projected MEOP.

Since motor chuffing often occurs below  $\sim 1.5$  MPa, burn rates are seldom measured in the lower pressure zone between roughly 10 atmospheres and one atmosphere pressure. However, the Department of Transportation in the United States requires that solid propellants burn time be measured for a single 50.8 mm (2.0 inch, in.) propellant cube and a group of four cubes in fuel oil or kerosene engulfing fires on a bed of wood sawdust. Measurable time lag usually takes place before propellant cubes begin burning. The time difference between the first signs of a propellant fire to the last visible evidence of propellant burning is designated as the propellant cube burn duration. Since all sides of the propellant cube can burn, the propellant burn duration is that required to traverse 25.4 mm of propellant. Although one atmosphere cube burn rate data can be subject to a number of errors, differences in burn rates are readily observable. Cube burning data is rarely available to the researcher because it is seldom published in circulated reports or assembled in collections of propellant cube burn data. The Department of Transportation propellant cube burn tests allowed recognition that the actual one atmosphere burn rate for propellant HTPB A, 0.84 mm/s (0.033 ips), was so much slower than the extrapolated value, 2.08 mm/s (0.082 ips), from the burn rate equation for motor burn rates.

Burn rate lag below the calculated one atmosphere burn rate is a feature that should be maximized to increase work place protection against accidental fires. If flame spreading could be greatly inhibited, more personnel could escape from areas with many propellant pieces exposed. As low pressure propellant burn rates decrease, minimum stimulation required to initiate fire by friction, mechanical impact, and electrostatic discharge should increase. Serious fires with rapid flame spreading have happened with Class 1.3 solid propellants with one atmosphere burn rates above 1.5 mm/s (0.06 ips). No serious accidents have occurred with solid propellants with one atmosphere burn rates below 1.5 mm/s for either Explosive Class 1.1 or 1.3 propellants. Slow burning, high energy, Explosive Class 1.1, nitrate ester propellants often have one atmosphere burn rates in the range from 0 to 0.64 mm/s (0.025 ips). These Class 1.1 propellants are relatively insensitive to ignition by the minor stimulations that might be found in manufacturing, operational suitability testing, and motor movements. I have not heard of low rate, high energy, Class 1.1 solid propellants being ignited by accidental minor friction, impact, and electrostatic discharge events during the last 25 years in the



United States. Since Class 1.1 propellants with quite low or absent one atmosphere burn rates are relatively fire safe, enhanced fire safety is predicted for Class 1.3 propellants with very low one atmosphere burn rates.

A valuable characteristic for a propellant atmospheric conditions would be a lack of burning or one atmosphere flame extinguishment. A series of nonmetallized HTPB solid propellants with increasing flame retardant content demonstrated a lower open flame combustion limit of about 0.25 mm/s (0.01 ips). This burn rate is indicated near the bottom of Figure 1. Metallized solid propellants may have somewhat lower extinguishment limits, but a 0.25 mm/s burn rate might be selected as a goal for hydrocarbon/Al/AP low burn rate booster propellants.

In Figure 1, the burn rate pressure exponent break point above 40 MPa indicates the start of the third combustion range. The highly acceleratory propellant burning promoted by an elevated burn rate pressure exponent above the slope break may be the primary cause for the explosive properties exhibited by AP oxidized solid propellants. If the elevated burn rate exponent could be reduced, the propellant burn rates associated with transitory high pressures in missile fallback events might be reduced enough to avoid violent explosions. The HTPB A propellant burn rate pressure exponent between ~40 and 80 MPa pressure is near 1.6. Above ~80 MPa to 107 MPa, the highest experimental pressure, an additional combustion behavior zone exhibiting a burn rate pressure exponent of ~1.0 may have occurred, but the scattered, strand burning, combustion bomb data obscures results. To be sure whether a change from a burn rate pressure exponent of 1.6 to 1.0 occurs, more experimental burn rate measurements at even higher pressures are needed.

If the burn rate pressure exponent changes to 1.0 at ~80 MPa pressure, an extrapolation to ~700 MPa (100,000 psi) would indicate a burn rate of ~600 mm/s (24 ips). Failed launch fallback crashes could produce shocks in the propellant as high as 300 to 1000 MPa. In this pressure region above the propellant slope break point for AP oxidized propellants, the accelerated burn rate associated with the increased burn rate pressure exponent should be a driver for propellant explosiveness. The very high burn rates at extreme pressures should be related to critical diameter, the minimum propellant diameter that can sustain a self-propagating detonation. Reduction of propellant burn rates at slope break pressure and burn rate pressure exponents above the slope break might greatly increase propellant critical diameters and, correspondingly greatly reduce booster propellant explosiveness in failed launch fallbacks.

Burn rates for Class 1.3, booster propellants at 6.9 MPa are typically in the range from 8 to 13 mm/s. Measured burn rates at one atmosphere, for propellants with burn rate pressure exponents of ~0.3 to 0.4, are often only slightly lower than a burn rate estimate derived by extrapolation. Propellant HTPB A is a relatively unusual propellant since its measured burn rate at one atmosphere is much slower than for many hydrocarbon/Al/AP propellants. Figure 2 compares the low pressure burn rate data of HTPB A propellant with a more normal propellant called HTPB B. The burn rate as a function of pressure between ~1 and 15 MPa (150 to 2200 psi) for HTPB B propellant is:

$$R_B = 6.218 P^{0.37} \quad (2)$$

The measured one atmosphere burn rate of HTPB B propellant was 2.54 mm/s (0.100 ips). This burn rate is very close to the 2.67 mm/s (0.105 ips) one atmosphere burn rate calculated for HTPB B propellant using equation 2. With HTPB B propellant the measured one atmosphere burn rate is near one fifth that of the propellant burn rate at 6.9 MPa. Many HTPB propellants have similar one atmosphere/6.9 MPa burn rate ratios.

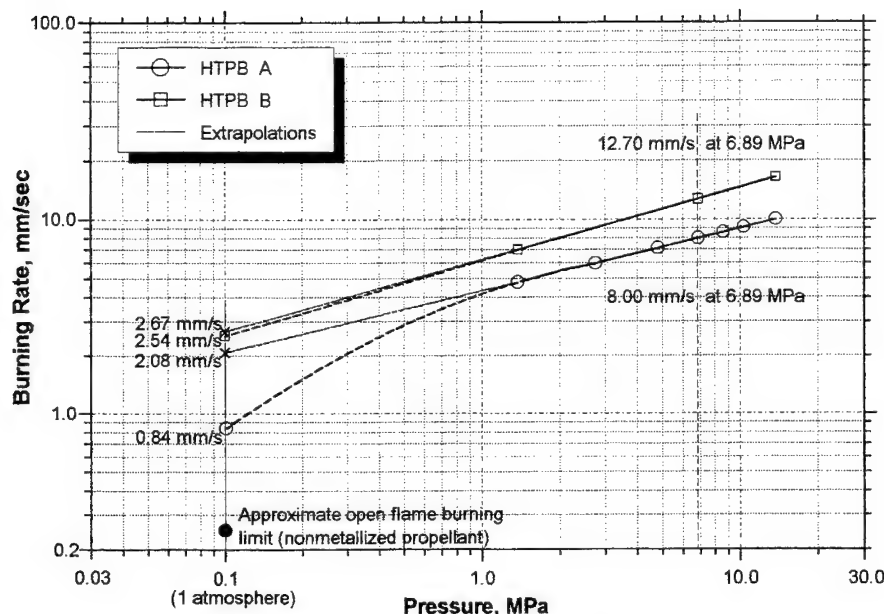


Figure 2. Low Pressure Burn Rate Comparison of HTPB A and HTPB B Propellants.

Another Class 1.3 propellant which exhibits an even larger decrease in one atmosphere burn rate versus the burn rate calculated using the burn rate equation in the motor operating pressure region is a glycidyl azide polymer (GAP)/76% AP propellant. The GAP binder did not include a nitrate ester plasticizer. Figure 3 plots the burn rate versus pressure, and Table 2 lists the burn rate data. The 6.9 MPa burn rate was faster than for either HTPB A or B propellants at 15.8 mm/s. At ~1.2 MPa pressure the measured motor burn rate begins to fall below the linear burn rate slope of 0.236 determined at pressures above 1.25 MPa and less than ~8.25 MPa. With the low burn rate exponent, the burn rate at one atmosphere burn rate was calculated as 5.8 mm/s and measured as 0.64 mm/s. If the GAP/AP propellant was formulated for a 6.9 MPa burn rate of 8.0 mm/s as with propellant HTPB A, the measured one atmosphere burn rate may have approached the lower burning rate limit determined in nonmetallized HTPB gas generator grains with flame inhibitors. A large falloff for one atmosphere burn rate compared with the calculated rate shows that propellant compositions other than nitrate ester formulations can experience sharp burn rate slumps at low pressures.

Table 2. GAP/76% AP Measured Burn Rates at Various Pressures, Motors and Cubes

Burn Rate		Chamber Pressure		
mm/s	(ips)	MPa	(psi)	
0.64	(0.025)	0.097	( 14)	Propellant cube burning
9.04	(0.356)	0.834	( 121)	
10.5	(0.414)	1.23	( 178)	$R_B = 9.986 P^{0.236}$ mm/s between 1.25 and 8.25 MPa
11.9	(0.470)	2.03	( 295)	
14.1	(0.554)	4.24	( 615)	

Table 2. GAP/76% AP Measured Burn Rates at Various Pressures, Motors and Cubes  
(concluded)

Burn Rate		Chamber Pressure	
mm/s	(ips)	mm/s	(psi)
14.9	(0.588)	5.39	( 782)
15.5	(0.610)	6.37	( 924)
16.5	(0.648)	8.16	(1184)
18.1	(0.712)	9.93	(1440)
24.3	(0.957)	14.18	(2057)
5.76	(0.226)	0.10	( 14)

15.8 mm/s (0.62 ips) at 6.89 MPa

Extrapolated from higher pressures

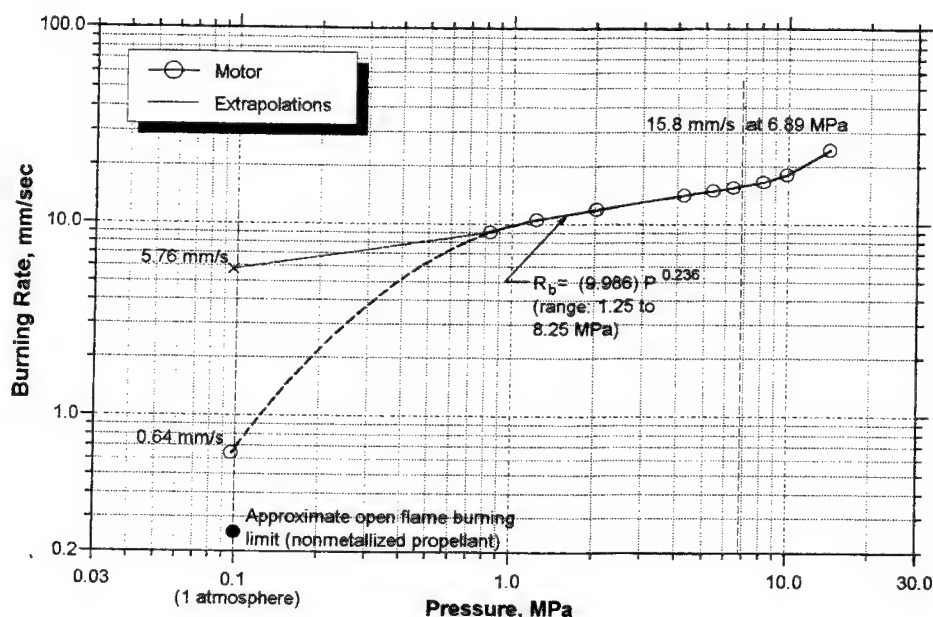


Figure 3. GAP/76% AP Propellant Burn Rate Versus Pressure

Burn rate data above the burn rate pressure slope break for HTPB/Al/AP propellants are difficult to find. Alice Atwood (2) of China Lake, CA has obtained burn rate data for HTPB A propellant and another called HTPB C using a combustion bomb technique. Reduction of closed bomb data transforms a measured pressure-time history into a mass regression rate through the application of the Noble-Able covolume equation of state (3). Their equation is used in the differentiated form along with a differentiated energy balance to derive the propellant mass regression rate as a function of time. Mass regression rate of a propellant is equal to the product of the burning surface area (input as geometric form function), the sample density, and the linear burning rate. For undamaged materials the propellant density and burn area are known and the linear burn rate as a function of pressure is determined. Cylindrical samples of HTPB A and HTPB C propellants about 25 mm in length and weighing about 8.1 grams were burned in a 90.5 ml volume bomb. By using the measured surface area, inputting the sample shape and density, burn rate data were determined from the recorded pressure and time behavior. Figure 4 shows plots of HTPB A and HTPB C propellant

burn rates versus pressure and Table 3 contains the closed bomb burn rate numerical data. Although this method yields numerical data somewhat different from motor firing data, relative combustion behavior between propellants obtained by this technique can be noted. The two propellants behave quite differently above burn rate pressure exponent break pressures in that HTPB A propellant has a much larger burn rate pressure exponent. How the two propellants react above 83 MPa is unknown, but the initially slower burning HTPB A propellant equals the HTPB C burn rate at about 83 MPa pressure. It seems that HTPB A propellant might be as explosive or more explosive than HTPB C propellant. We might have expected the two propellants to have parallel burn rate pressure behavior throughout the entire pressure range. If this had happened, the slower burning propellant would always be somewhat less explosive because of its lower burn rate.

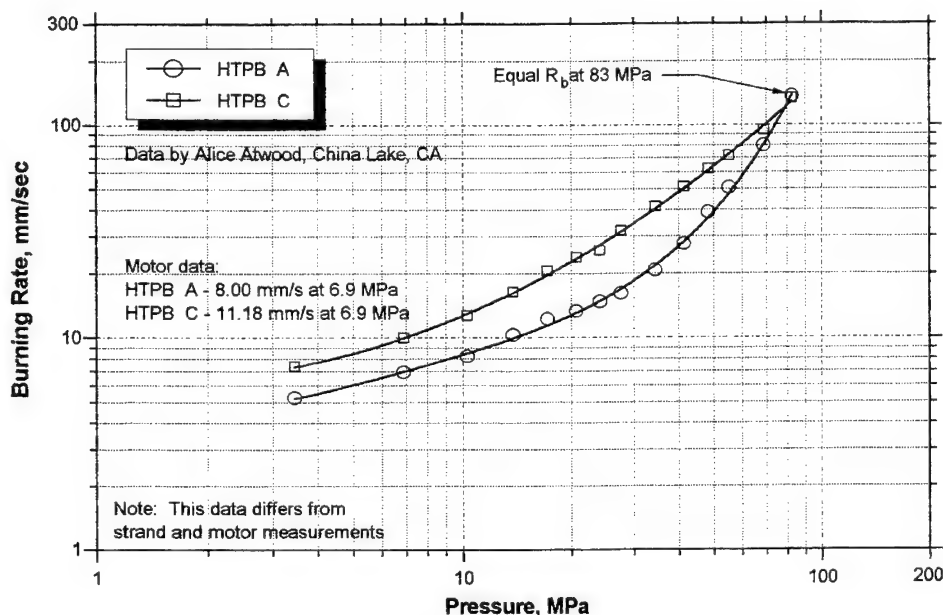


Figure 4. HTPB A and HTPB C Closed Bomb Burn Rates Versus Pressure

Table 3. HTPB A and HTPB C Closed Bomb Burn Rates vs. Pressure  
By Alice Atwood, China Lake, CA (2)

HTPB A Burn Rate, mm/s (ips)	HTPB C Burn Rate, mm/s (ips)	Pressure, MPa (psi)
5.25 (0.207)	7.36 (0.290)	3.45 ( 500)
6.93 (0.273)	10.0 (0.395)	6.89 ( 1000)
8.21 (0.323)	12.7 (0.500)	10.3 ( 1500)
10.3 (0.406)	16.4 (0.647)	13.8 ( 2000)
12.2 (0.480)	20.5 (0.807)	17.2 ( 2500)
13.3 (0.522)	23.9 (0.940)	20.7 ( 3000)
14.7 (0.577)	25.7 (1.10 )	24.1 ( 3500)
16.1 (0.634)	32.0 (1.26 )	27.6 ( 4000)

Table 3. HTPB A and HTPB C Closed Bomb Burn Rates vs. Pressures  
By Alice Atwood, China Lake, CA (2) (concluded)

HTPB A Burn Rate mm/s (ips)	HTPB C Burn Rate mm/s (ips)	Pressure MPa (psi)
20.7 (0.814)	41.4 (1.63 )	34.5 ( 5000)
27.6 (1.09 )	51.1 (2.01 )	41.4 ( 6000)
38.9 (1.53 )	61.9 (2.44 )	48.3 ( 7000)
50.7 (2.00 )	71.6 (2.82 )	55.2 ( 8000)
79.7 (3.14 )	94.1 (3.70 )	68.9 (10000)
136 (5.36 )	133 (5.25 )	82.7 (12000)

#### SUMMARY

The less sensitive, Explosive Class 1.3, AP oxidized, solid propellants combust in different ways at low pressures, at motor operational pressures, and at high pressures above the slope break. Usually, burn rate traits at pressures outside those suitable for rocket motor operation are not investigated. Very massive solid propellant motors have encountered serious problems in accidental fires and fallback explosive events that would not be serious for much smaller rocket motors. The occurrence of fire and explosive problems with our supposedly safer propellants has raised the importance of investigating propellant burn characteristics at pressures both below and above rocket motor operating pressures. Propellant combustion drives fire risk at pressures near one atmosphere, and it also drives the vigor of explosive events stimulated by motor fallbacks in failed launches of large space launch missile systems. Burning characteristics in these different regions are not the same for various hydrocarbon/Al/AP propellants. The large differences observed with occasional substantial burn rate lag at one atmosphere and tolerable burn rate pressure exponents above the burn rate pressure exponent break pressure seem to be caused by ordinary propellant formulation variables, such as plasticizers, solid particle sizes, curatives, and minor additives. These observations indicate that careful selection of propellant ingredients could result in low burn rate hydrocarbon/Al/AP propellants with reduced fire hazard and reduced explosive risk.

Reductions in one atmosphere burn rates are desired. HTPB A propellant with a 0.84 mm/s one atmosphere burn rate is a step in the right direction. Self extinguishment at one atmosphere would be even better. Many Explosive Class 1.1 solid propellants which have one atmosphere burn rates less than 0.65 mm/s have not been involved in accidental, small workplace stimuli fires in decades. If Explosive Class 1.3, hydrocarbon/Al/AP solid propellants had one atmosphere burn rates at 0.65 mm/s or less, their fire safety would be significantly improved. With lowered one atmosphere burn rates the minimum energetics for provoking propellant fire by friction, mechanical impact, and electrostatic discharge should be raised considerably making fires less likely to occur.

In the high pressure region above rocket motor operational pressures, Explosive Class 1.3 solid propellants typically experience a burn rate pressure exponent break characterized by a transition to a burn rate pressure exponent higher than observed in the motor operational pressure region. This enhanced burn rate pressure exponent can be as high as 1.6 (HTPB A) in the ~30 to 80 MPa pressure range. Some propellants do not have pressure burn rate exponents that high above the break, as indicated by HTPB C. If burn rate pressure exponents could be kept below ~0.7 at pressures above the break, the propellant would have much less propensity to explode violently in fallback events.

## REFERENCES

1. Private Communication, Atlantic Research Corporation, Gainesville, Virginia, March 1995.
2. Private Communication, Alice Atwood, China Lake, California, February 1996.
3. Corner, J., 1950. *Theory of the Interior Ballistics of Guns*, John Wiley and Sons, Inc., p. 100.

## ACKNOWLEDGMENTS

The author is grateful for support from the US Defense Nuclear Agency and the US Air Force Titan Systems Program Office.

## COMMENTS

Dr. Fred Volk, Fraunhofer-Institut für Chemische Technologie (ICT), Pfaffzettel, Germany:

- (1) What kind of computer program is being used to calculate burn rate as a function of pressure?
- (2) Will you have any problems with reproducibility of burn rate at very low pressures (e.g., 0.1 MPa)?

Author's Reply:

(1) The computer program takes into account change in surface area of a small right cylinder or propellant as combustion on all surfaces increases chamber pressure. This procedure was developed at the Naval China Lake (USA) facility. Alice Atwood of the Naval Air Warfare Center, China Lake, CA, USA, produced data used in the paper. (2) Reproducibility of one atmosphere burn rates with open burning of 50.8 mm propellant cubes in a quiet engulfing kerosene fire has been reproducible within 10% of the determined value. A strong wind can produce conditions where burn rate is considerably faster than in its absence.

Mr. Jean-Paul Reynaud, SNPE Defence Espace, Centre de Recherches du Bouchet, France:

Have you found consistent results in the overlapping regions of the two different burning rate measurement techniques employed?

Author's Reply:

A number of elevated burning rate techniques were used. These include small-scale motors (approximately 145 gms propellant), a closed high-pressure bomb by ARC, Inc., where inhibited burn strands were burned in oil at a series of imposed pressures, and the China Lake closed bomb technique, using combustion gases from a small right cylinder of propellant burning on all exposed surfaces to produce rapidly increasing chamber pressure. At 13.8 MPa, the ARC and China Lake methods provide burn rates matching those obtained by the small motors. As pressures are increased, burn rate values for the ARC and China Lake methods diverge. This divergence has not been investigated. Differences in the values may be related to differences in heat loss by the two propellant burning techniques.

## **PROPENSITY OF FLAME SPREADING INTO PROPELLANT SLITS UNDER SIMULATED ROCKET-MOTOR ENVIRONMENTS**

**Kenneth K. Kuo, Yeu-Cherng Lu, and Steven J. Ritchie**

Mechanical Engineering Department  
The Pennsylvania State University  
University Park, PA 16802, USA

**ABSTRACT:** This work was aimed to help identifying the possible cause of the Titan IV K-11 motor failure. A motor analog was used to evaluate the propensity of flame spreading into solid-propellant slits which simulated the knife-cuts resulting from the repair on one of the grain segments. Target test conditions were established to examine the validity of the test results. Experimental observations indicated that flame can indeed propagate into propellant slits even under compression, one of the test conditions controlled to simulate situations during the ignition transient of the Titan IV solid rocket motor. Based in part on the experimental evidence supported by this series of tests, it was concluded that flame spreading into the knife-cuts was the most probable scenario leading to the motor failure.

### **INTRODUCTION AND BACKGROUND**

Flame spreading into defect regions of a solid-propellant grain could cause very undesirable performance of a rocket motor due to the unexpected extra surface area available for burning. Therefore, the propensity of flame spreading into a flaw such as a crack or debond and the development of combustion process in the flaw have been studied extensively in the past (for example, see Refs. 1-21). However, because of the complex nature of the problem, no quantitative predictions from any existing theoretical models can be obtained to simulate a broad range of test conditions. It is inevitable that each investigation covers only a specific range of operation conditions. The specific objective of this study is directed at assisting the identification of the most probable cause for the failure of the Titan IV K-11 solid rocket motor (SRM) occurred on August 2, 1993.

Figure 1 represents a segment of the Titan IV SRM propellant grain (68% AP, 16% PBAN, 16% Al). The top surface of the propellant grain was initially inhibited by a layer of restrictor material (filled NBR rubber), which was in direct contact with a thin PBAN type liner. It was found that the interface between the restrictor and the propellant grain had some voids and debonds during the pre-firing inspection by a non-destructive ultrasonic technique. In order to salvage this segment from being scrapped, the propellant manufacturer performed a repair to the defect region.

In the repair procedure, a special knife was used to cut through the peripheral of the restrictor to be removed. The knife was used to make a series of 1.5" long cuts along the restrictor surface, and was allowed to penetrate the propellant grain a maximum depth of 0.5". However, this depth was only approximated by the technicians making the repairs and could not be measured following the repairs.

## Repaired Motor Segment

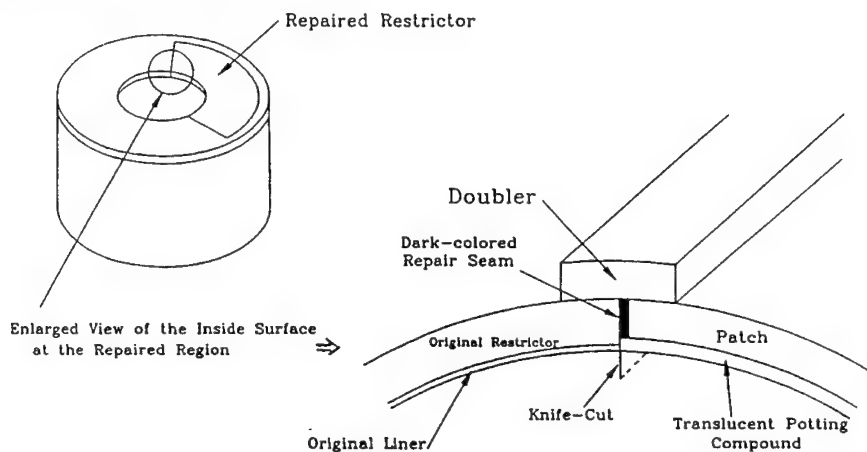


Fig. 1 Schematic diagram of a section of a repaired solid-propellant grain

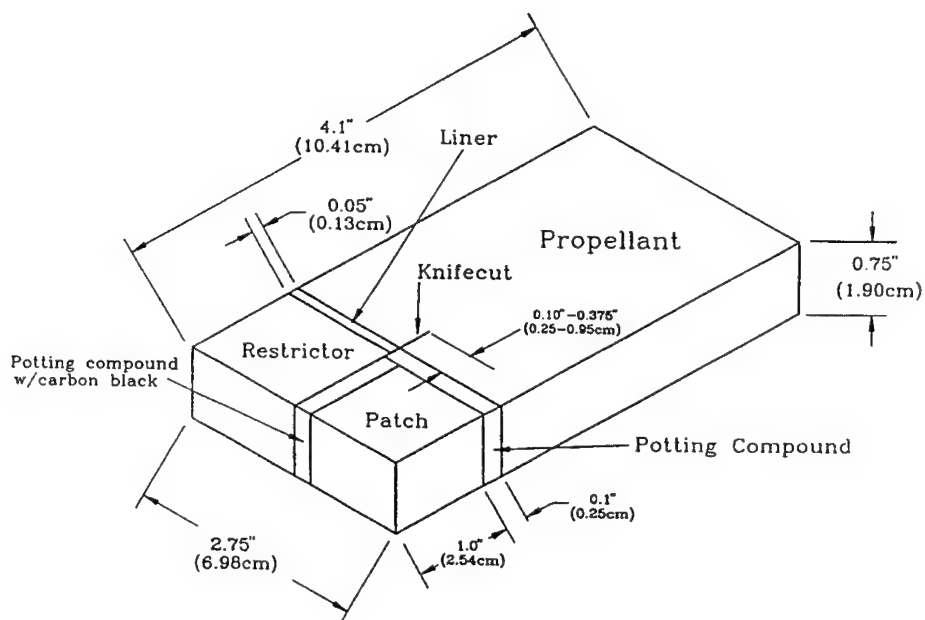


Fig. 2 Geometry of propellant samples supplied by UT/CSD



For this work, it was assumed that the actual maximum cut depth was 3/8".

The defect region was then removed by peeling off the cut slice. An epoxy cured versamid potting compound (AL227-70) was applied to the grain surface of the peeled-off section. No special precautions or treatments were used to prevent or enhance the flow of potting compound in the knife-cut areas. A repair "patch" made of filled NBR rubber was then placed onto the top of the potting compound to form a flat surface with the original, uncut restrictor surface. The interfaces between the patch and the original restrictor were also filled with potting compound, darkened with carbon black. A second patch called a doubler was used to cover the entire interfacial seam lines.

After the repair, the segment was used for the launching of the Titan IV vehicle. Unfortunately, the K-11 vehicle failed during the SRM burn. Following the failure, an investigation group (K-11 Test Team) was formed and scrutinized all of the preparation and motor-firing data for the cause of the incident. After their preliminary investigation, they suspected that flame spreading into the knife-cuts left after the repair of the segment be one of the potential causes for failure. In essence, these knife-cuts formed a continuous, artificial crack extending from the bore to within several inches of the case wall. This crack is a potential passage for flame spreading to occur during the motor operation. If the flame does propagate into the slit, the extra burning surface area could lead to a higher and faster pressure build-up in the chamber as well as an undesirable local pressure build-up in the slit caused by the extra amount of mass production from propellant surfaces along the cut. The extent of damages experienced by the motor depends upon many factors, including the geometry of the slit, motor operation conditions, and overall hardware structural integrity.

Therefore, to support the above speculation, it is very crucial to know if the flame can indeed propagate into the slit under conditions similar to that of the Titan IV SRM. This investigation was then initiated to provide relevant experimental evidence. Appropriate target chamber conditions were established to simulate the Titan IV SRM ignition transient and to examine the validity of test results.

## EXPERIMENTAL SETUP

The test chamber is essentially the one used in Ref. 4 and only a brief description is given with emphasis on the modifications. Propellant samples with the geometry shown in Fig. 2 were fabricated and supplied by United Technologies/Chemical Systems Division (UT/CSD). The samples have all the required features such as the restrictor, patch, knife-cut, and potting compound to simulate a portion of the repaired segment.

The width of the sample [2.75 inches (6.98 cm)] was intentionally made larger than the width of the sample holder [2.2 inches (5.59 cm)]; therefore, the sample could be trimmed from the original 2.75 inches to a dimension equal or larger than 2.2 inches. When the sample was placed into the sample holder, some degree of compressive effect was thus created on the sample, depending upon the final sample width. By varying this dimension, the amount of initial compression near the slit location can be controlled very precisely. The control of the degree of compression is very important to simulate the real Titan IV SRM conditions because the propellant grain was under compressive strain during the motor firing. The length scales of the cut region were measured under a microscope. The degree of compression was determined by the change of distance between two marked dots on each side of the cut before and after loading into the sample holder. In this series of tests, sample compression ranged from 0.0 to 1.17%. It is noted that the slit opening can be as large as 20 micrometers even under compression in some samples. This is caused by the contact of two cut surfaces which can never be perfectly even. Figures 3 and 4 are two sets of micrographs showing the slit regions before and after the compression for Tests # 15 and 17, respectively. It is evident that the slit was not totally closed under compression. A gap width of finite size was left in both samples.

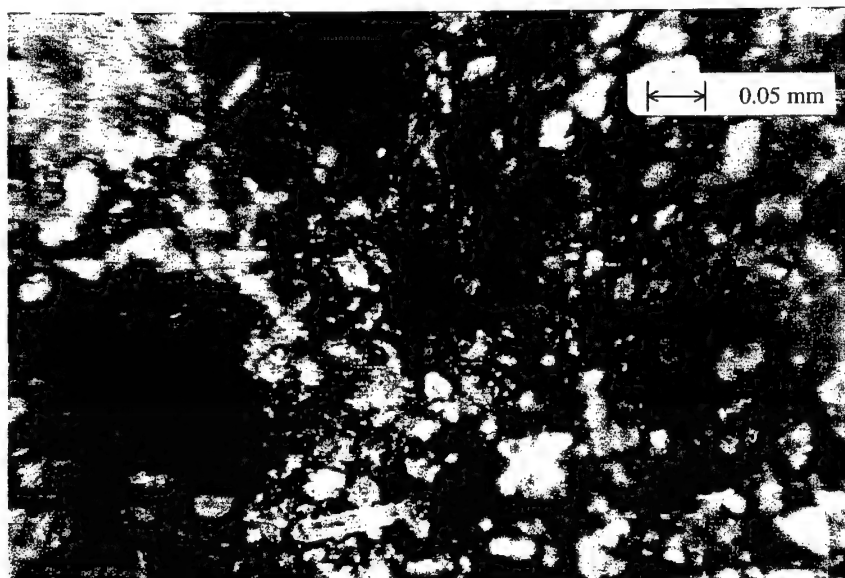


Fig. 3(a) Microscopic photograph of the flame-side slit with the sample under no compression for Test #15 (45x Magnification).

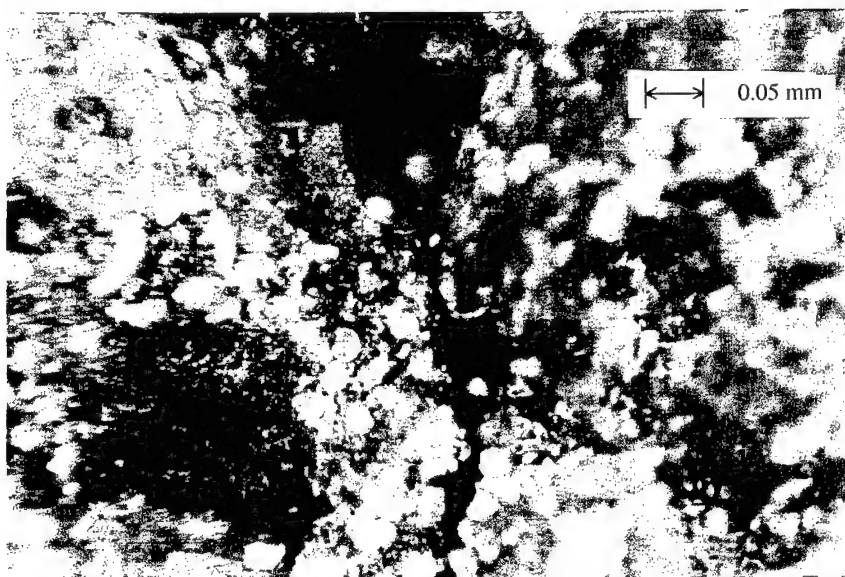


Fig. 3(b) Microscopic photograph of the flame-side slit with the sample under 0.36% compression for Test #15 (45x Magnification).

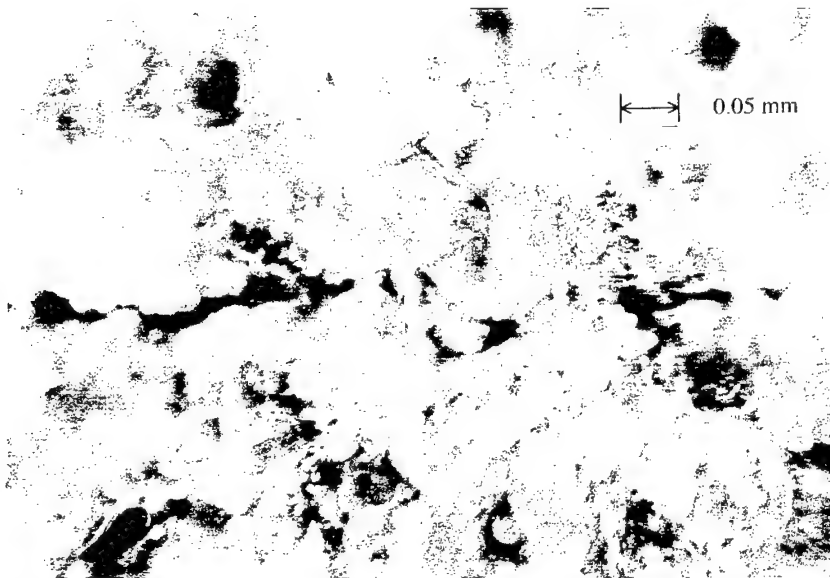


Fig. 4(a) Microscopic photograph of the flame-side slit with the sample under no compression for Test #17 (45x Magnification).

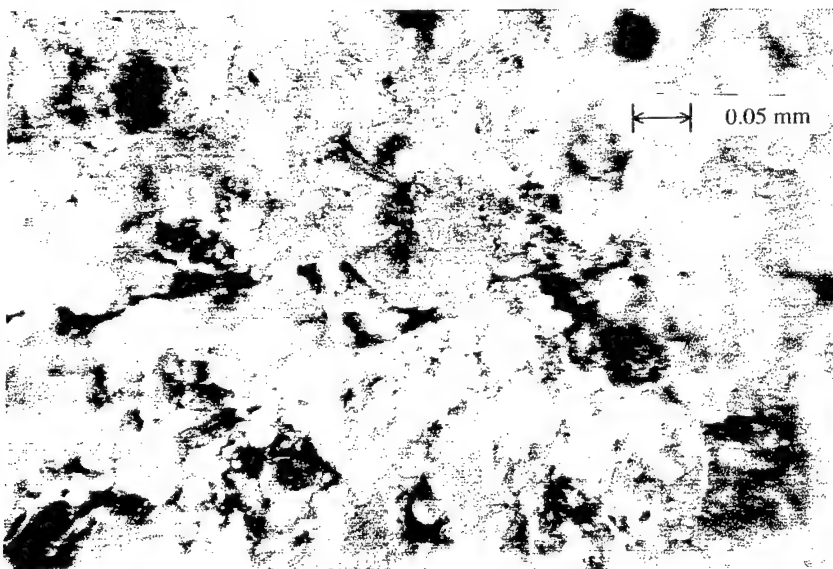


Fig. 4(b) Microscopic photograph of the flame-side slit with the sample under 0.41% compression for Test #17 (45x Magnification).

Figures 5(a) and 5(b) show the side and center-plane cross-sectional views of the test chamber with the propellant sample installed. The propellant sample was positioned flush against the plexiglass window of the chamber. The slit was positioned near the center of the window for photographic observation. The thickness of the channel in the sample holder is 1.0 inch (2.54 cm); the sample is initially 0.75 inch (1.90 cm) thick. This allows for an initial 0.25-inch (0.64 cm) flow passage between the back side of the sample and the instrument plate (opposite in position to the front window). Chamber venting occurred downstream of the sample through a graphite nozzle. The sample was held in place initially by two pieces of brackets. A layer of flame retardant grease was applied to the window side of the sample. With this configuration, there should be no observable light emission through the plexiglass window during the test until the flame penetrates through the slit or the sample burns out.

Ignition was achieved through an igniter system initiated by an electric match. The M105 electric match was enhanced by black powder (about 0.25 g) and propellant shavings (about 0.75 g), which were contained in a plastic bag and taped around the end of the match. This igniter assembly was used to ignite a small booster propellant charge [about 11/16" x 3/4" x 15/16" (1.75 cm x 1.90 cm x 2.38 cm)] located upstream of the propellant sample. The hot combustion products generated from the igniter and booster propellant charge in turn ignited the test sample.

Pressure transducers (Kistler 601B1 and 601B122) were installed at three locations along the flow passage on the back instrument plate. Pressure signals were amplified by Kistler 504E charge amplifiers and recorded by a Nicolet Multipro data acquisition system. Pressure levels were controlled by varying the throat area of the exit nozzle, the initial amount of propellant burning surface area, and the initial chamber volume. The test event was recorded by a HYCAM II high-speed 16 mm movie camera located about 4.5 feet (1.37 m) away from the front window with a framing rate of 1000 pictures/second. A Kodak Spin Physics SP2000 high-speed video camera was also used for backup purpose. Parameters varied in tests included the slit geometry (depth and width), chamber pressure, chamber pressurization rate, and degree of sample compression.

## RESULTS AND DISCUSSION

In order to achieve test conditions similar to the ignition transient of the Titan IV rocket motor, the following target chamber operational conditions were established for assisting the evaluation of test results.

- (1) Chamber pressure  $\leq 1000$  psia (6.89 MPa),
- (2) Chamber pressurization rate  $\leq 5500$  psi/s (37.92 MPa/s),
- (3) Sample compression strain  $\geq 0.3\%$ ,
- (4) Slit depth  $\leq 3/8$  inch (0.95 cm), and
- (5) Flame spreading through the cut must occur before the last 0.5 seconds of the sample burn-out.

These target test conditions were based on the data gathered on the Titan IV K-11 Solid Rocket Motor-1 during the actual firing.<sup>22</sup> The first two conditions were deduced from the recorded pressure-time trace. The compression strain on the propellant grain during ignition transient was calculated from finite element analysis. The 3/8-inch cut depth was considered to be the maximum depth incurred from the repair procedure. Since the propellant sample can lose its integrity near burn-out (i.e., too thin), the 0.5 second was considered to be an appropriate limit. If the flame spreading through the slit is seen in a test, the above five criteria have to be met in order to consider that particular test as a valid test for demonstrating the possibility of flame spreading into a slit under conditions similar to the ignition transient of the Titan IV SRM.

Because the test chamber had a very small volume and a complicated inner contour after installing the sample, holding brackets, igniter, booster propellant charge, and inhibiting EPDM layers in the sample holder, it was very difficult to exactly control the chamber pressure and pressurization rate. Also the

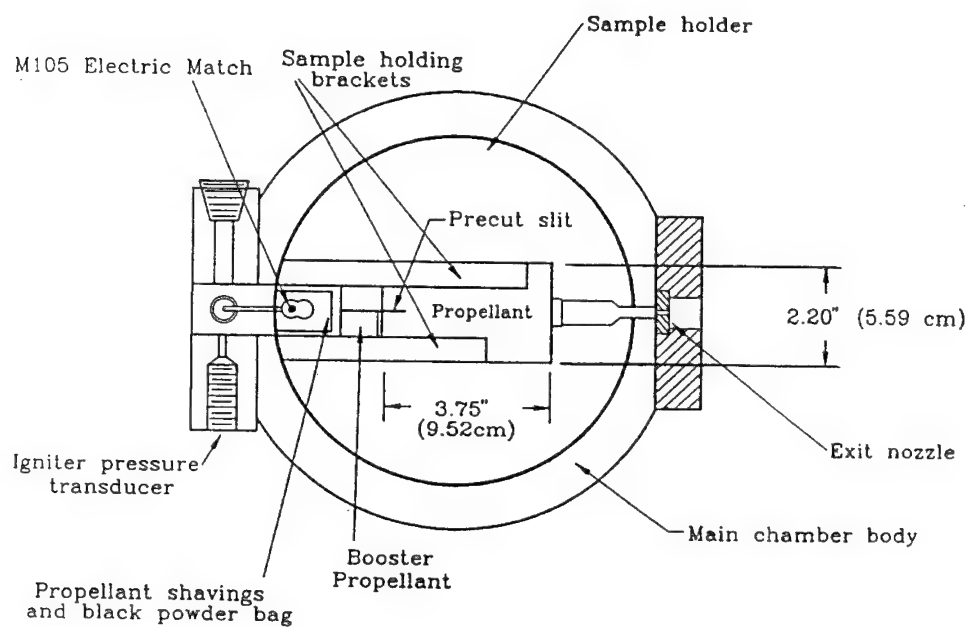


Fig. 5(a) Side view of test chamber with propellant sample installed

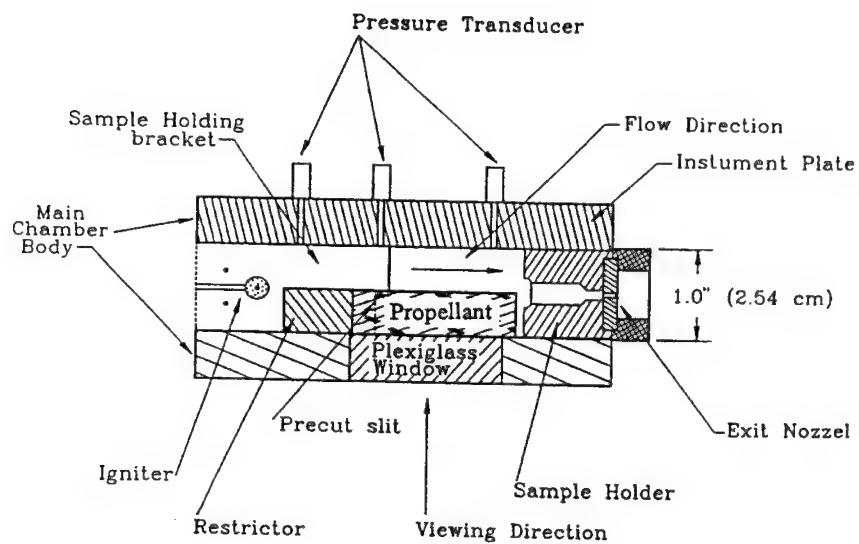


Fig. 5(b) Center-plane cross-sectional view of test chamber

evolution of flame on the booster-propellant surface and the ignition delay between the booster and main propellant grains were not easily predicted. All of these factors made fine adjustments of test setup (such as nozzle throat area and chamber free volume) between consecutive tests necessary to maneuver chamber conditions toward the target conditions.

In total, twenty tests were conducted and results of some of the tests are summarized in Table 1. The omitted tests were baseline tests and tests using another type of propellant conducted prior to the receipt of the Titan IV samples from CSD. As shown in Table 1, each test showed flame spreading into the slit. However, not all of them met the above five criteria.

- (1) Tests # 3, 5, and 7 met all other criteria except Item 3 since the samples were not under pre-compression strain in these three tests.
- (2) Tests # 13, 14, 16, 17, and 20 met all other criteria except Item 5 because the flame spreading was seen to occur near the end of the test run.
- (3) Tests # 11, 18, and 19 didn't meet more than one criteria.
- (4) Test # 12 met all other criteria except that the chamber pressure at the flame penetration was higher than 1000 psia.
- (5) Only Test #15 showed flame spreading through the propellant slit and met all of the above five criteria.

Figures 6 and 7 show time variations of pressure and pressurization rate of Tests # 12 and 15, respectively. The time of light emission seen on the window side of the sample is marked in these figures.

Based upon the above observations, it was found that the occurrence of flame spreading into a slit is possible in a motor analog environment under the test conditions similar to the ignition transient of the Titan IV SRM. Although it is difficult to make direct extrapolation of lab-scale tests to large-scale motor firings, this series of tests indeed provides localized experimental evidence of the possibility of flame spreading into a propellant slit and warrants appreciable considerations when dealing with actual SRMs. After evaluating test results of this study and their own investigations,<sup>23</sup> the K-11 Test Team concluded that the flame spreading into the knife-cuts resulting from the repair procedure was the most probable cause responsible for the Titan IV K-11 failure.

It is surprising to see that the flame spreading can still occur in samples under sufficient amounts of compression. This is because the slit was not totally closed even under compression (as shown in Figs. 3 and 4). Considering the fact that flame standoff distances are so small at high pressures (on the order of tens of micrometers), the best way to avoid flame spreading seems to be totally closing the gap width of the slit. Another way is to groove out the slit region and replace it with suitable inhibiting material which can adhere to the propellant surface.

## CONCLUSIONS

The propensity of flame spreading into slits under conditions similar to the ignition transient of the Titan IV SRM was evaluated using a motor analog. It was found that it is possible for flame spreading to occur under established target test conditions. Based on a series of studies, including this investigation, the Titan IV K-11 test team concluded that flame spreading into the knife-cuts left after an SRM propellant/restrictor repair was the most probable cause of the K-11 failure on August 2, 1993.

Even though applying certain degrees of compression to test samples could reduce the possibility of flame spreading, compression can not totally eliminate this possibility because gap widths of finite size could exist near the cut zones of the propellant sample. Since no cut surfaces can be perfectly flat, flame spreading could occur even under sufficient degrees of compressive strain. In general, it is believed that more extensive study is definitely necessary for establishing more comprehensive theories and working criteria for engineering applications.

TABLE 1  
Test Results of Flame Spreading into a Propellant Slit

Test No.	Slit Depth (in)	Sample Compression (%)	Slit Gap Width (mils)	Time* of Flame Penetration into Slit (sec)	Time* of Sample Burn-out (sec)	Valid Early Flame Penetration	Pressure at Penetration (P) or Max. Pressure (M) (psig)	dP/dt at Penetration (P) or Max. dP/dt (M) (psi/s)
3	0.36	0.0	n/a	n/a	n/a	yes	140 (P)	830 (P)
5	0.33	0.0	n/a	n/a	n/a	yes	220 (P)	5300 (P)
7	0.33	0.0	n/a	n/a	n/a	yes	220 (P)	1410 (P)
8	0.35	1.17	n/a	n/a	n/a	no	1150 (M)	5010 (M)
11	0.28	0.7-1.16	< 0.1	2.02	2.19	no	1900 (M)	9590 (M)
12	0.33	0.46-0.54	< 0.1	0.57	2.19	yes	1590 (P)	1705 (P)
13	0.30	0.47-0.56	< 0.1	2.92	3.05	no	625 (M)	3265 (M)
14	0.25	0.42-0.57	< 0.1	2.34	3.16	no	625 (M)	2675 (M)
15	0.21	0.36-0.51	0.25-0.1	0.90	3.04	yes	444 (P)	2385 (P)
16	0.24	0.50	< 0.1	2.40	2.90	no	900 (M)	2816 (M)
17	0.23	0.36-0.41	0.25-0.1	2.49	2.88	no	970 (M)	3400 (M)
18	0.21	0.34-0.44	< 0.1	2.87	3.00	no	1012 (M)	3484 (M)
19	0.19	0.43-0.60	0.25-0.1	2.43	2.66	no	1250 (M)	6500 (M)
20	0.23	0.41-0.54	0.25-0.1	2.72	2.78	no	740 (M)	2313 (M)

Note:

\* -- Time was measured from the initiation of ignition trigger

n/a -- not available (not recorded or not measured)

1 psi = 6894.7 Pa

1 in = 2.54 cm

1 mil = 0.001" = 0.00254 cm

#### ACKNOWLEDGEMENTS

This work was sponsored by Wyle Laboratories and U.S. Air Force. The encouragement and support of Steven T. Griswold of Wyle Lab, and Capt. Barry Portner and Stu Bridges of the Air Force are highly appreciated. In addition, the authors would also like to thank the input and useful discussion of the K-11 Test Team Members, including Robert Geisler, Jim McKinnis, Paul Willoughby, Barry Portner, Kirsten Pace, and S. R. Lin. The supply of propellant test samples, EPDM sheets, and potting compound by UT/CSD is also highly appreciated.

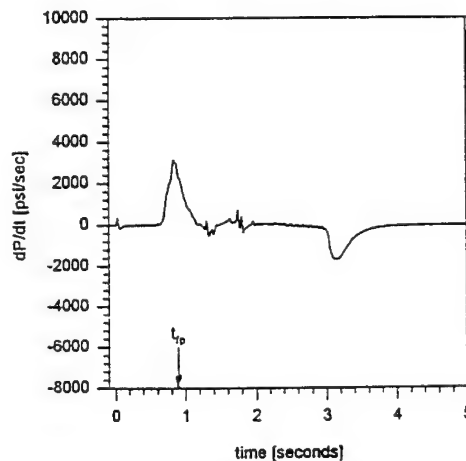
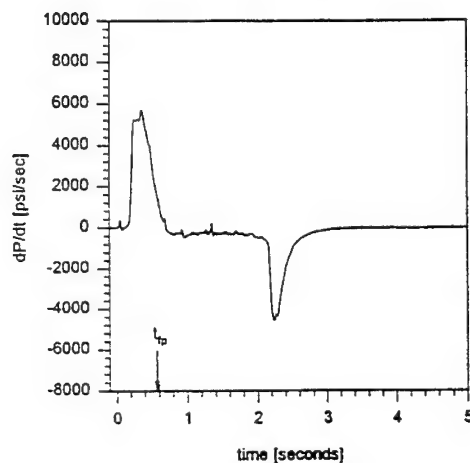
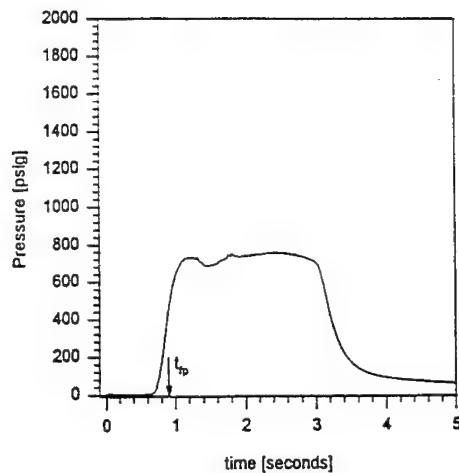
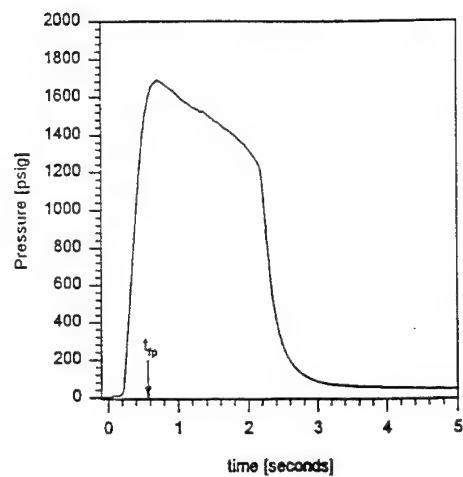


Fig. 6 Recorded time variations of pressure and pressurization rate near the crack entrance location (Test # 12). The arrows indicate the time of light emission seen on the window side of the cut slit.

Fig. 7 Recorded time variations of pressure and pressurization rate near the crack entrance location (Test # 15). The arrows indicate the time of light emission seen on the window side of the cut slit.



## REFERENCES

1. **K. K. Kuo and D. E. Kooker**, "Coupling between Nonsteady Burning and Structural Mechanics of Solid Propellant Grains," Chap. 11, *Nonsteady Burning and Combustion Stability of Solid Propellants*, edited by L. DeLuca and M. Summerfield, 1992.
2. **Y. C. Lu and K. K. Kuo**, "Modeling and Numerical Simulation of Combustion Process inside a Solid-Propellant Crack," *Propellants, Explosives, Pyrotechnics*, vol. 19, pp. 217-226, 1994.
3. **S. D. Heister and E. M. Landsbaum**, "Analysis of Ballistic Anomalies in Solid Rocket Motors," *Journal of Propulsion*, Vol. 7, No. 6, pp. 887-893, 1991.
4. **S. R. Wu, Y. C. Lu, K. K. Kuo, and V. Yang**, "Crack Initiation and Propagation in Burning Metalized Solid Propellants," *Proceedings of the 18th International Pyrotechnics Seminar*, pp. 985-1004, 1992.
5. **J. L. Prentice**, "Flashdown in Solid Propellants," U.S. Naval Ordnance Test Station, Rept. NAVWEPS 7964, China Lake, CA, NOTS TP 3009, Dec. 1962.
6. **V. K. Bobolev, A. D. Margolin, and S. V. Chuiko**, "The Mechanism by Which Combustion Products Penetrate into the Pores of a Charge of Explosive Material," *Doklady Akademii Nauk SSSR*, Vol. 162, pp. 388-391, May 1965.
7. **A. F. Belyaev, A. I. Korotkov, A. A. Sulimov, M. K. Sukoyan, and A. V. Obmenin**, "Development of Combustion in an Isolated Pore," *Combustion, Explosion, and Shock Waves*, Vol. 5, pp. 4-9, Jan.-Mar. 1969.
8. **A. F. Belyaev, V. K. Bobolev, A. I. Korotkov, A. A. Sulimov, and S. V. Chuiko**, "Development of Burning in a Single Pore," *Transition of Combustion of Condensed Systems to Detonation*, Science, Nauka, Moscow, Chap. 5, Pt. A, Sec. 22, pp. 115-134, 1973.
9. **A. D. Margolin and V. M. Margulis**, "Penetration of Combustion into an Isolated Pore in an Explosive," *Combustion, Explosion, and Shock Waves*, Vol. 5, pp. 15-16, Jan.-Mar. 1969.
10. **T. Godai**, "Flame Propagation into the Crack of a Solid-Propellant Grain," *AIAA Journal*, Vol. 8, No. 7, pp. 1322-1327, 1970.
11. **K. K. Kuo, A. T. Chen, and T. R. Davis**, "Convective Burning in Solid-Propellant Cracks," *AIAA Journal*, Vol. 16, No. 6, pp. 600-607, 1978.
12. **M. Kumar, S. M. Kovacic, and K. K. Kuo**, "Flame Propagation and Combustion Processes in Solid Propellant Cracks," *AIAA Journal*, Vol. 19, No. 5, pp. 610-618, 1981.
13. **M. Kumar and K. K. Kuo**, "Effect of Deformation on Flame Spreading and Combustion in Propellant Cracks," *AIAA Journal*, Vol. 19, No. 12, pp. 1580-1589, 1981.
14. **H. R. Jacobs, M. L. Williams, and D. B. Tuft**, "An Experimental Study of the Pressure Distribution in Burning Flaws in Solid Propellant Grains," Univ. of Utah, Final Report to Air Force Rocket Propulsion Lab., AFRTL-TR-72-108, UTEC DO 72-130, Salt Lake City, UT, Oct. 1972.
15. **Z. V. Kirsanova and O. I. Leipunskii**, "Investigation of the Mechanical Stability of Burning Cracks in a Propellant," *Combustion, Explosion, and Shock Waves*, Vol. 6, No. 1, pp. 68-75, 1970.
16. **G. P. Cherepanov**, "Combustion in Narrow Cavities," *Journal of Applied Mechanics and Technical Physics*, Vol. 11, No. 2, pp. 276-281, 1970.
17. **A. F. Belyaev, M. K. Sukoyan, A. I. Korotkov, and A. A. Sulimov**, "Consequences of the Penetration of Combustion into an Individual Pore," *Combustion, Explosion, and Shock Waves*, Vol. 6, pp. 149-153, Apr.-Jun. 1970.
18. **J. G. Siefert and K. K. Kuo**, "Crack Propagation in Burning Solid Propellants," *Dynamics of Shock Waves, Explosions, and Detonations*, edited by J. R. Bowen, N. Manson, A. K. Oppenheim, and R. I. Soloukhin, Vol. 94, Progress in Astronautics and Aeronautics, AIAA, New York, pp. 575-595, 1985.
19. **K. K. Kuo, J. A. Moreci, and J. Mantzaras**, "Different Modes of Crack Propagation in Burning Solid Propellants," *Journal of Propulsion and Power*, Vol. 3, No. 1, pp. 19-25, 1987.
20. **K. K. Kuo and J. A. Moreci**, "Crack Propagation and Branching in Burning Solid Propellants,"

*Proceedings of the 21st Symposium (International) on Combustion*, The Combustion Institute, Philadelphia, PA, pp. 1933-1941, 1986.

21. **K. K. Kuo, J. M. Char, J. Smedley, and J. Nimis**, "Dimensional Analysis and Experimental Observation of the Coupling Phenomena Between Combustion and Fracture of Damaged Propellant Samples," JANNAF Combustion Meeting, Monterey, CA, 1987.
22. Titan IV Recovery Test Team, private communications, Nov.-Dec. 1993.
23. A group of presentations on Titan IV solid rocket motor in an AIAA Conference on Large Solid Rockets: Advances Through Experiences, Oct. 4-6, 1994, Monterey, CA.

### COMMENTS

1. Professor Hiltmar Schubert, ICT, Fraunhofer, Germany:

I would like to remind the authors of a paper written about 25 years ago by a Japanese expert published in the JPL Journal about flames spreading into slits. He found that the slit has to be more than 0.1 mm wide for flames to spread.

Authors' Reply:

We are familiar with T. Godai's work in Japan on the subject of flame spreading into propellant cracks. He utilized the concept of *quenching distance* to arrive at a threshold distance below which the flames will not propagate into the propellant crack. This concept cannot be applied to the dynamic pressurization of propellant grains with defects, since the propellant material is viscoelastic and the defect region can expand to allow hot combustion product gases to penetrate into the cracked region, resulting in motor failure and subsequent explosion.

The Pennsylvania State University, University Park, PA 16802 USA

368

## INTRODUCTION

Flame spreading into propellant grain defect regions such as cracks and debonds can sometimes lead to very undesirable burning behavior during the operation of solid-propellant rocket motors (This topic has been studied by many notable researchers, as summarized by Kuo and Kooker<sup>1</sup> in their recent review article). Therefore, precautions must be taken to avoid the creation of any such defects during the manufacture, storage and transportation of propellant grains. In order to utilize propellant grains with moderate defects, an appropriate repair procedure has to be established and strictly followed to minimize the potential of flame spreading into the repaired regions. The effectiveness of any specific repair procedure has to be assessed thoroughly before it is accepted for application to field services.

Testing of a suggested repair procedure using a motor analog is the first step in the screening process and represents a very economical method. The information obtained from this study can not only demonstrate the effectiveness of a given repair procedure, but also assist in the establishment of a final, reliable repair procedure. The major objectives of this investigation are: (1) to provide experimental evidence showing that the occurrence of flame spreading into a properly repaired region can be avoided, and (2) to illustrate the abnormal burning behavior when flame propagates into an unrepaired crack region under operational conditions similar to those in SRMs.

Based upon the above mentioned motivation, unrepaired samples with slits were used for studying the flame spreading into cracks (FSIC) phenomena. Propellant samples repaired with a suggested procedure were tested to evaluate the effectiveness of the repair in preventing flame spreading from occurring. Aluminized AP/HTPB composite propellant samples were processed and supplied by UT/CSD. Tests were performed using a motor analog which can maintain a steady chamber pressure for a reasonable time duration (~20 seconds). Detailed experimental setup, data acquisition systems, test procedure, and test results are described in the following sections.

In a related investigation, Kuo, et al.<sup>2</sup> studied the propensity of flame to spread into propellant slits under pre-specified target test conditions simulating certain nominal Titan IV SRM ignition transient conditions. The motor analog was able to closely simulate the chamber pressure, pressurization rate, degree of sample compression prior to ignition, and sample cut depth. A series of tests were executed in a small windowed test chamber in order to estimate the influence of these test variables on flame penetration under these conditions. Results showed that flame spreading occurred in all tests with samples under no compression; flames penetrated slits at pressures between 1.0 - 1.5 MPa (140 - 220 psia), and pressurization rates between 5.7 - 36.5 MPa/s (830 - 5300 psi/s). Flame spreading into slits was observed in about 20% of the tests performed with the slit under compressive strain (0.3% - 1.2%). In view of this significant percentage of flame penetration, a repair procedure has been highly recommended. In this study, thirteen tests were performed in a large windowed test motor to evaluate the effectiveness of the repair procedure<sup>3</sup>. The following sections provide a detailed description of the experimental setup, sample preparation procedure, instrumentation, and test results.

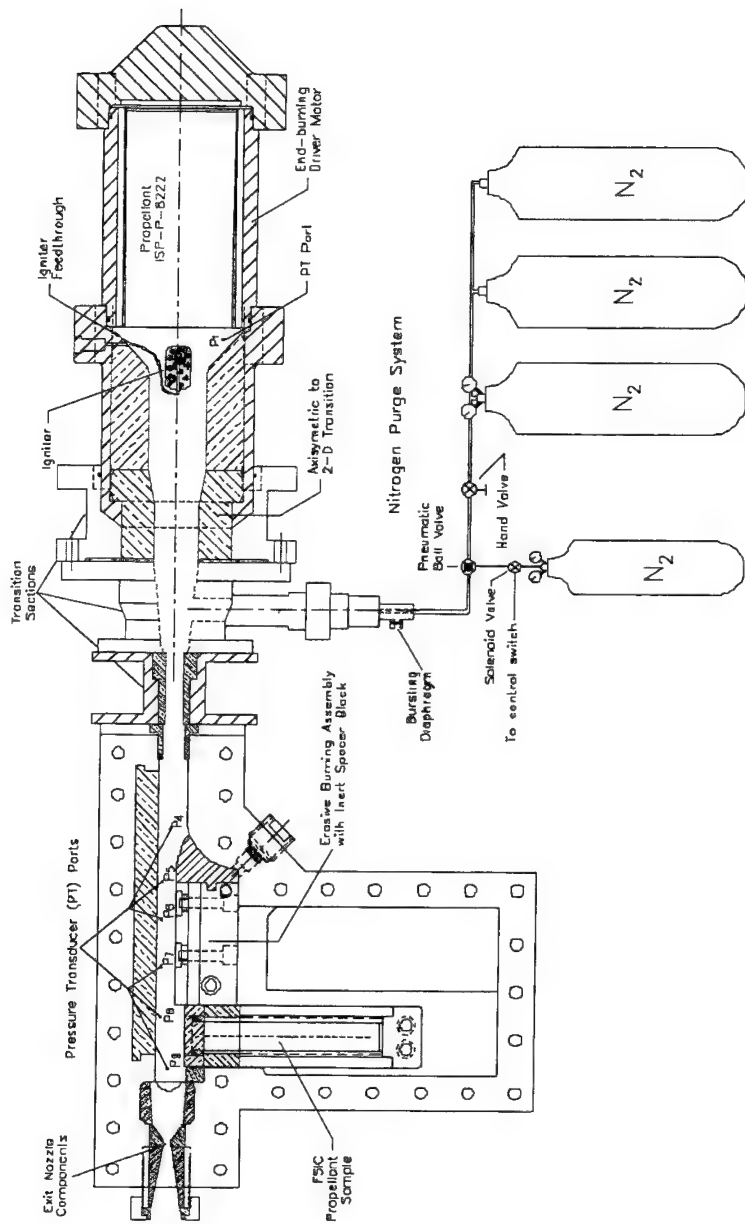


Fig. 1 Overall Assembly of FSIC Test Rig

## EXPERIMENTAL/ANALYTICAL APPROACH

The facility utilized for the FSIC study was an existing test rig originally designed for erosive burning investigations of solid propellants<sup>4</sup>. Figure 1 is a schematic diagram showing various components of the setup (drawn from the FSIC window side). Extensive modifications were made to the main combustion chamber to accommodate FSIC testing, with much of the chamber interior re-designed and the addition of a vertical window for observation of any abnormal flame spreading and propellant regression phenomena. The chamber consists of three large plates referred to as the "back", "middle", and "front" plates (see Fig. 2). As shown in both Figs. 1 and 2, FSIC observation is from the rear, via a vertical window port cut into the back plate. All chamber and test rig interfaces are sealed with Viton (fluorocarbon) O-rings. Most interior stainless steel surfaces are lined with ablative graphite material to avoid direct contact with corrosive combustion product gasses. In addition, the driver motor and exit nozzle components were modified. The graphite inserts downstream of the driver motor convert the axi-symmetric profile of the flow to a 2-D geometry. Ignition of the driver grain was accomplished via electrical initiation of a small ignition charge, via a feedthrough. The hot combustion gasses from the driver motor ignite the FSIC propellant sample rapidly. For the FSIC test series, an inert block replaced the propellant at the erosive burning location. The prepared FSIC sample assembly (in its holder with the attached sacrificial window) is placed, inset into the back chamber piece, as shown in Fig. 2. When the front chamber piece is fastened to the assembly, the entire sample window surface comes into contact with the main window.

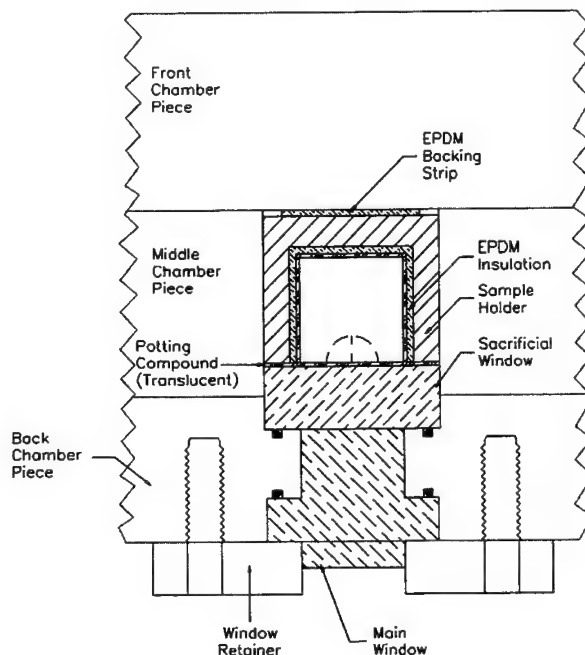


Fig. 2 Composite Cross-Section View of FSIC Chamber Assembly (from top)

Compressible EPDM rubber strips were mounted on the back of the sample holder in order to allow for minor tolerance variations as well as to achieve good contact between the propellant and sacrificial window during assembly. A double O-ring arrangement maintains the pressure seal between the windows and test chamber. Figure 2 describes this window arrangement with respect to the sample holder positioning. A gaseous purge system (as shown in Fig. 1) was used for post test chamber cool-down, and to eradicate harmful gases from the chamber.

### Driver Motor Description

End-burning driver grains manufactured by Industrial Solid Propulsion, Inc. were employed as gas generators for FSIC testing. These grains were supplied as cartridges made to fit the CP (Center-Perforated) Aerojet 5C3-9 motor hardware used in previous erosive burning tests. The driver grain is described in Table I. The end-burning cylindrical driver grain is slightly tapered (burning towards increased burning surface area) to partially compensate for nozzle erosion. An end-burning grain does not always burn back in a flat or even fashion due to coning or non-uniform ignition. This non-uniform burning can result in flame spreading to the head-end, and the resulting sudden increase in burning area could lead to an over-pressurization. Therefore, the head-end surface of the grain was inhibited with a restrictor material.

Table I. End-Burning Driver Grain Specifications

ISP-P-8222 (81.9% AP, 17% HTPB, 1% burn rate catalyst, 0.1% C)			
$\rho_P$	1.641 g/cm <sup>3</sup>	$a$	0.7172 cm/s·MPa <sup>-n</sup>
$T_f$	2580 K	$n$	0.284
MW	23.33 kg/kmol	$r_b @ P_{ref}^*$	1.165 cm/s
$\gamma$	1.22	$t_b @ P_{ref}^*$	19.74 s
$L_{G,DM}$	23.18	Avg. $D_{G,DM}$	11.57 cm

\* $P_{ref}$  is the reference test pressure of 5.52 MPa (800 psi)

The igniter was composed of an M-105 electric match surrounded by a plastic bag containing 2g of Boron potassium nitrate (BKNO<sub>3</sub>) granules. This assembly was enclosed in a larger bag containing 25g of BKNO<sub>3</sub> pellets in the form of tablets (D=0.63 cm, max. thickness = 0.34 cm). The igniter was positioned near the center of the initial burning surface, as shown in Fig. 1. This igniter composition was found to be effective in consistently igniting the end-burning driver grains with a very short ignition delay and suitable pressurization characteristics.

### Sample Preparation

A critical element for achieving successful tests is the sample preparation procedure. Five

system check-out tests were conducted to debug the test facility and to develop a reasonable sample preparation procedure as described below.

Most of the tests were carried out using propellant samples supplied by UT/CSD. The approximate (finished) dimensions of the UT/CSD samples are a 3.10 cm x 3.58 cm (1.22" x 1.41") cross-section by a 20.32 cm (8") length. The initial sample processing by UT/CSD involved several steps:

- (1) First, the propellant blocks were rough cut
- (2) A slit was cut 2.5 cm (1") from the sample top extending 1.3 cm (0.51") from the sample end, to a depth of about 0.8cm (0.39").
- (3) The slit was "removed" using a cylindrical blade. This resulted in a semi-cylindrical groove.
- (4) AL227-70 potting compound (a chemical product of UT/CSD) was poured into the repair groove and allowed to cure.
- (5) The propellant sample was then machined to its final dimensions.

The AL227-70 potting compound is an epoxy-like substance specially formulated for propellant repairs. It has mechanical properties similar to those of the propellant material, but it is essentially inert. For the cut samples utilized in tests #26 and #30, steps (3) and (4) were left out. For the translucent repair utilized in test #31, a grooved sample was repaired at PSU with potting compound without the carbon black opacifier. For a description of sample and cut/repair geometry, refer to Figure 3. In addition to the samples, UT/CSD supplied the potting compound and EPDM rubber insulation which were required to install the samples into the sample holder. The mass fraction composition of the material used for sample repairs was 69.75% AL227-70 (potting compound), 30% DER 332 (epoxy resin, a product of Dow Chemical), and 0.25% carbon black (opacifier). The standard composition was used in all repair tests, with the exception of test #31 where the carbon black was not used.

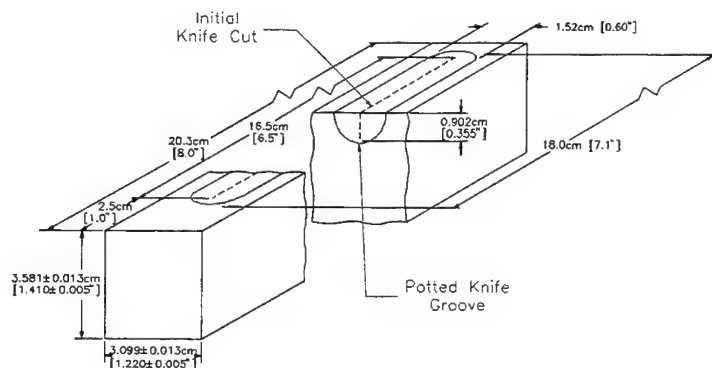


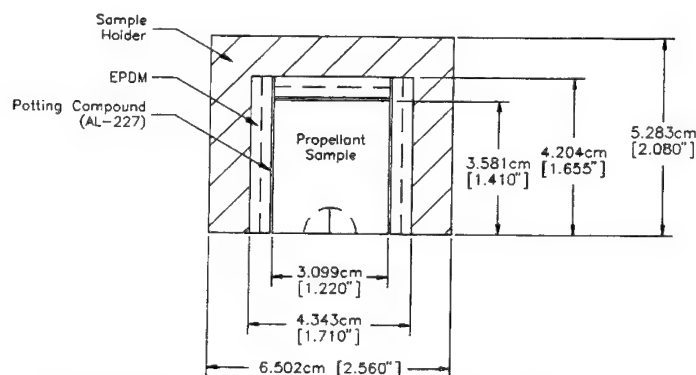
Fig. 3 Schematic Diagram of FSIC Sample



Four types of samples were tested for different purposes:

- Blanks, undamaged samples for system checkout/baseline testing
- Cut samples (unrepaired) - with a 0.95 cm (0.37") deep cut or slit extending 16.5 cm (6.5"), starting 2.5 cm (1") from the sample top, for flame spreading evaluation. See "Initial Knife Cut" in Fig. 3.
- Samples with standard repairs - propellant around the cut was grooved out and repaired with the standard opaque composition for repair validation. See "Potted Knife Groove" in Fig. 3.
- A sample with a translucent repair - same as above, except carbon black opacifier was eliminated from the repair composition.

The test sample installed in the sample holder is shown schematically in Figure 4 (top cross-sectional view) and Figure 5 (front and side views). The installation of the sample into the sample holder was carried out using a two-step procedure. The sample and the EPDM insulation material were glued into the sample holder using the potting compound (without opacifier). This assembly was allowed to cure for at least sixteen hours before the plexiglass window was glued into place on the front face of the sample. Metal shims were utilized to assure a uniform thickness of potting compound between the viewing sample surface and the sacrificial window. Prior to the window attachment, markings were painted on the front surface of the sample in order to aid focusing of the high-speed cameras. The translucent potting compound composition was used for adhering the sacrificial plexiglass window to the propellant sample. Also, for several tests, tracer chemicals were imbedded at various locations along the length of the sample near the repaired region.



**Fig. 4 Cross-sectional View of FSIC Propellant Sample Mounted in its Holder**

### Tracer Salt Technique

The tracer detection technique<sup>5,6</sup> involves the placement of a small quantity of the chemical tracer at known locations in the propellant grain. A few milliseconds after exposure to combustion gases, the salt tracer is thermally excited and emits radiation. The emission signal of the particular

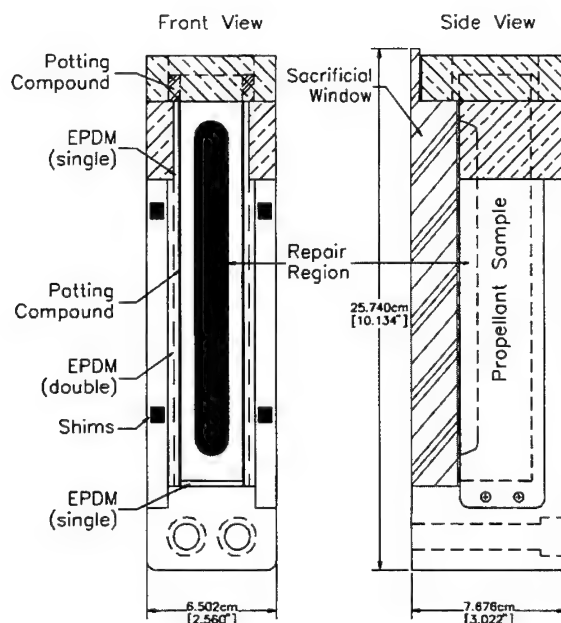


Fig. 5 FSIC Sample Holder Assembly

tracer is then detected in the plume. The approach adopted in this study involves the use of inexpensive photodiodes and narrow band-pass filters to restrict the detector's range to that of the emission wavelengths of the chemical tracer. A multichannel data acquisition system was used to continuously record the photodetector signals versus time. Correlating the known locations of the tracer salt samples along with the time of onset of the signals in the plume, the time of occurrence can be readily determined. Thus, this technique can be used to determine the flame front arrival times at specific locations. In this study, the technique was utilized to help determine the occurrence of flame spreading or failure of the repair. Because the standard repair material is opaque, one could not ordinarily observe flame spreading behind the repair by visual means - so this technique is particularly suitable. Several FSIC samples had rubidium sulfate ( $\text{Rb}_2\text{SO}_4$ ) or boron potassium nitrate ( $\text{BKNO}_3$ ) embedded at known locations during preparation. In the case of the cut samples, the tracer was inserted adjacent to the cut line and for the repaired sample, the tracer was inserted behind the repair material. Typical tracer data are presented along with the test results.

### Nozzle Sizing

Chamber pressure is controlled via a set of interchangeable graphite nozzles. The results of a simple nozzle sizing analysis for target chamber pressures based on mass balance in the test chamber, using an estimated graphite erosion rate of 0.15 mm/s (0.006 in/s) for class ATJ graphite and accounting for the motor grain taper, is given in Table II. The mass flow rate of the combustion

products through the nozzle are assumed to consist of mass burning rates of the driver motor grain and of the propellant sample. The choked flow equation was used to relate the throat areas with the chamber pressure and flow rate through the nozzle. The goal pressures at all three specified levels were typically met within  $\pm 0.34$  MPa ( $\pm 50$  psi) during the driver grain burn duration.

**Table II.** Nozzle Sizing Analysis

Chamber Pressure, MPa (psi)	5.52 (800)	6.90 (1000)	8.27 (1200)
Mass Generation Rate, kg/s (lbm/s)	0.216 (0.477)	0.230 (0.508)	0.242 (0.534)
Initial $A^*$ , $\text{cm}^2$ ( $\text{in}^2$ )	0.495 (0.0765)	0.456 (0.0707)	0.389 (0.0603)
Initial $D^*$ , cm (in)	0.794 (0.312)	0.762 (0.300)	0.704 (0.277)

### Instrumentation

Pressure measurement was carried out using several Kistler 601B1 and 601B122 piezoelectric pressure transducers mounted in water cooled jackets. Signals from these transducers were transmitted to Kistler 504E charge amplifiers by shielded high impedance cables. The voltage outputs of the charge amplifiers were captured on a Nicolet Multipro system (including an IBM compatible 486 computer controller). Pressure measurements were typically made at four locations: just downstream of the initial burning surface of the end-burning driver grain ( $P_1$ ), the test chamber entrance ( $P_4$ ), and two positions above the FSIC samples (represented as  $P_8$  and  $P_9$ ). These positions can be identified in the side-view schematic diagram that was presented in Figure 1, or from another perspective in Figure 6. In each test, P-t traces at these four locations tracked one another quite closely, within  $\pm 0.14$  MPa ( $\pm 20$  psi). Pressure data presented in this paper was taken from the most downstream transducer above the FSIC sample (i.e.,  $P_9$ ).

Each test event was recorded from several orientations using five separate cameras. Their locations relative to the test facility can be identified in Figure 6. The primary visual data was obtained by a 16mm HYCAM high-speed movie camera and a Spin Physics SP2000 high-speed video camera system. A view of the FSIC window by both cameras was made possible by turning the image path by  $90^\circ$ , using two mirrors. The first mirror is a semi-transmissive mirror that acts as a beam splitter reflecting 50% and also transmitting 4 to 8% of the incident light. This mirror was oriented in such a way that the reflected portion was observed and recorded by the HYCAM camera and the transmitted portion continued on to a second, fully reflective mirror. This second mirror is oriented towards the Spin Physics video camera. Behind the mirrors, a piece of black opaque cloth material was mounted to prevent stray light from behind the mirrors interfering with the transmitted image. Both of these cameras were focused on the propellant sample surface. The camera exposure settings were established during the system checkout runs and by estimations of light intensity. The HYCAM provided the most useful photographic data, with the only disadvantage being that it was required to wait for film processing. Thus, for backup purposes, and in order to know the outcome of each test immediately, the Spin Physics camera was also used. The Spin Physics has a lower resolution than the HYCAM, but it has the benefit of instant playback and the capacity for digitization and image processing. Most of the detailed analysis presented in the test summaries was based on the images recorded on HYCAM 16mm films. For the repair tests, the HYCAM and Spin Physics cameras operated at 2000 and 1000 pictures/second, respectively. For

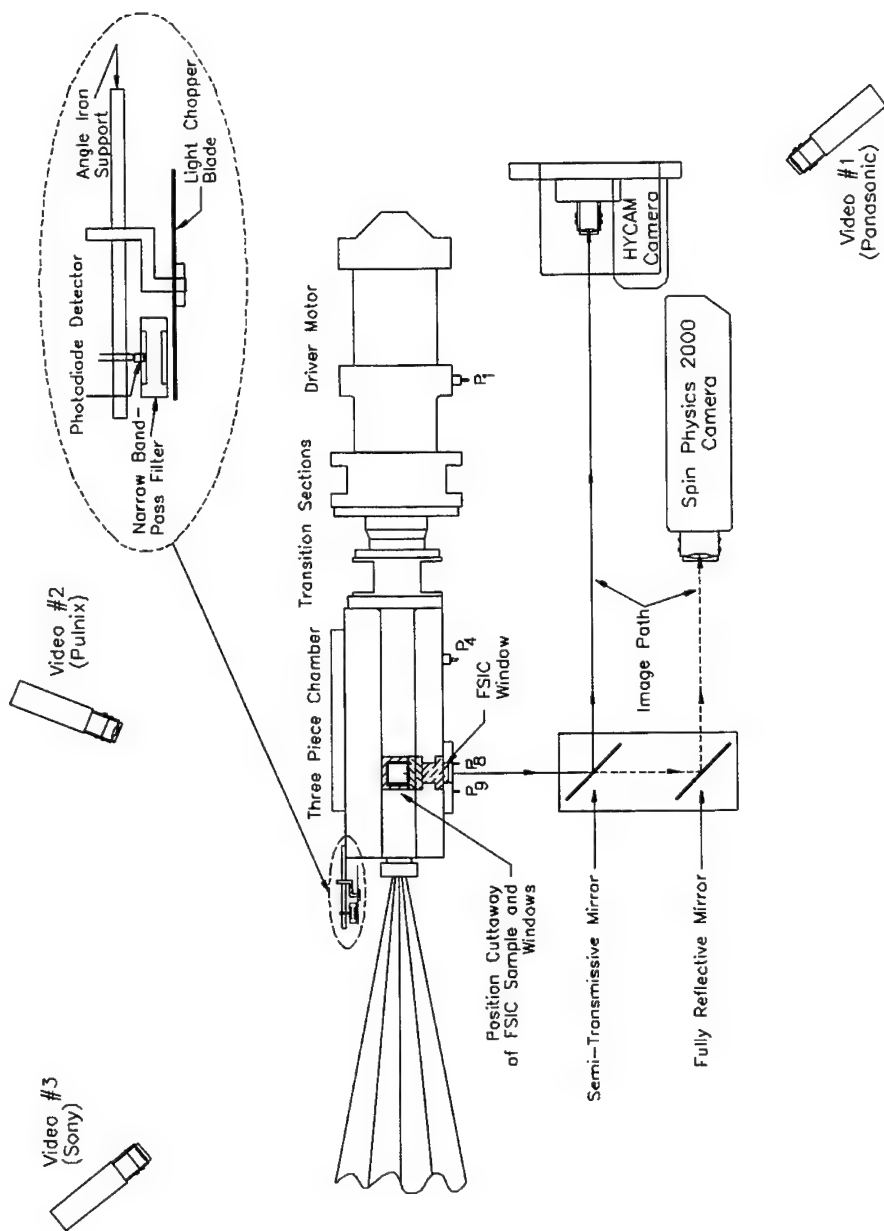


Fig. 6 Schematic of Top View of FSIC Test Facility Including Optics

the cut tests (where relatively faster events were anticipated), the HYCAM and Spin Physics cameras operated at 2800 and 1500 pictures/second, respectively. The remaining three video cameras were used to monitor the test rig for any unexpected problems or anomalies such as chamber leakage. They provided top, front, and downstream (including the exhaust plume) views of the test setup. Exhaust fans mounted on the rear of the test frame kept the camera views un-obstructed by any smoke drawn back from the exhaust plume.

Instrumentation for detection of chemical tracers in the plume included a silicon photo-diode detector, a light chopper, a narrow band filter (10 nm wide centered on the primary spectral line of each of the salts used), and a signal amplifier system. Spectral signal traces were acquired and recorded on a Nicolet Multipro multichannel digital oscilloscope. It was necessary to limit the detector sensitivity range to the tracer signal wavelengths via the narrow-band filters in order to mask out the intense background radiation which is present in the combustion product gases of aluminized propellant. The detector instrumentation is schematically drawn in an inset to Figure 6.

The remote control center, located outside the test cell consisted of a Nicolet Multipro data acquisition system, a computer controller, a set of six charge amplifiers, a Spin Physics video control unit, VCRs for recording images from Video #1 and Video #2, display monitors for live viewing of the test facility during the test run, and the ignition control switch panel. The ignition control circuit used in this investigation was designed not to directly initiate ignition of the igniter charge. Rather, the final switch in the ignition sequence was the HYCAM camera start switch. The ignition circuit was remotely activated by an event switch, which was triggered when the movie film passed a certain prespecified footage setting on the HYCAM camera. To assure the attainment of the desirable framing rate, the footage setting was chosen, so that the ignition was initiated after the initial acceleration period of the movie film. After a short delay, the driver motor was fully ignited, and then, the hot combustion products from the driver motor ignited the FSIC sample.

## Discussion of Experimental Results

Five system checkout tests (FSIC Test #21-#25) were carried out to debug the test facility. Over the course of these tests, several major system modifications were accomplished. Propellant samples used in tests #26 and #30 had cuts (but without any repair) prepared by UT/CSD. The purpose of these tests was to evaluate the propensity for flame to penetrate into and propagate through the cut region in this motor analog. Tests #27-#29 evaluated UT/CSD standard repair samples at the 5.52 MPa (800 psi) chamber pressure range, and tests #32 and #33 evaluated UT/CSD repair samples at pressures of 6.90 and 8.27 MPa (1000 and 1200 psi), respectively, in order to evaluate the effect of pressure on the effectiveness of the repair procedure. FSIC test #31 utilized a UT/CSD sample repaired at PSU with translucent potting compound and run at the standard test pressure of 5.52 MPa in order to evaluate the effect of an opacifier in the repair. These sample configurations, chamber pressures, and overall test results are summarized in Table III.

**Table III.** Summary of Test Results

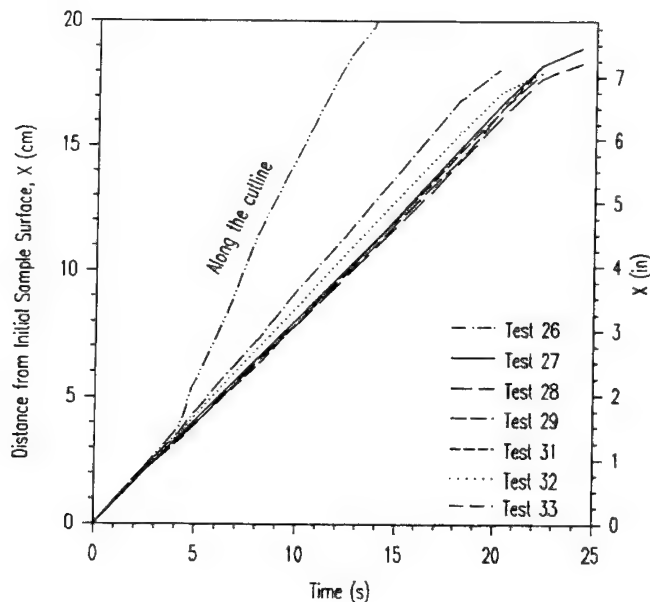
Test #	Sample Configuration	Pressure Specified MPa (psi)	Flame / Repair Status
21-25	Blank	5.52 (800)	System check-out
26	Cut along sample	5.52 (800)	Flame penetrates cut
27	Standard Repair	5.52 (800)	Repair is successful
28	Standard Repair	5.52 (800)	Repair is successful
29	Standard Repair	5.52 (800)	Repair is successful
30	Cut with Barrier	5.52 (800)	Flame "flash-down" into cut
31	Translucent Repair	5.52 (800)	Repair is successful
32	Standard Repair	6.90 (1000)	Repair is successful
33	Standard Repair	8.27 (1200)	Repair is successful

### Interpretation of Reduced Data

The reduced data for these tests was composed of P-t traces, flame front propagation charts (reduced from high-speed film data), and tracer emission plots. Some errors were potentially introduced in the film analysis. These errors could result from (1) image displacement caused by slight film motion during projection, (2) uncertainties regarding ignition delay times of the FSIC sample, (3) measurement error of length scale, and (4) unevenness of burning surface. Thus, the deduced flame front trajectories have some accuracy limitations; however the overall behavior is believed to be well represented, with an estimated total error of 6%. The flame front trajectories (the same as burning surface trajectories in the case of repaired samples) are presented in Figure 7 for tests #26-29 and #31-33. Test #30 was not included, since a very rapid flame spreading event precluded detailed observation of the flame front motion. In all repaired sample test cases, the speeds of the flame front displacement were quite constant until the burnout of the driver motor grain, which is observable by the slope change near the end of these test runs. For tests with similar pressure (#27, #28, #29, and #31), the burning surface trajectories are closely grouped (indicated good repeatability), while the higher pressure tests (#32 and #33) are clearly separated. For test #26, the non-constant flame propagation along the cut line is due to unsteady flame penetration along the slit. The instantaneous flame front contours of test #26 are shown in Figure 8. Typical instantaneous flame front contours for a repaired sample are shown in Figure 9. Comparing with Figure 8, the flame front contours are quite uniform; no preferential direction of burning surface advancement was observed. This result implies that the repaired region exhibited normal burning behavior.

### Testing of Repaired Samples

In most pressure-time traces for repaired samples, the driver-grain appears to burn slightly progressively. As was mentioned previously, the motor was tapered to compensate for nozzle erosion. However, actual nozzle erosion was less than predicted; as a result, the pressure increased slightly over the burn duration. Additionally, a small peak in each P-t trace was observed immediately prior to extinguishment of the driver grain. This is believed to be caused by a



**Fig. 7. Burning Surface Locations vs. Time**

momentary increase in burning surface area near the end of motor operation.

Pressure-time traces for the tests utilizing repaired samples (Tests #27-29 and #31-33) are presented in Figure 10. Little variation was observed in the burning of these samples. All the repair samples evaluated in the FSIC test series appeared to perform satisfactorily. No anomalous burning behavior such as preferential burning along the repair region, or unusual propagation phenomena were observed in these test runs. In Figure 10, the three distinct near steady-state pressure levels are apparent, with tests #27-31 clustered at the 5.5 MPa range, test #32 at the 7 MPa range and test #33 at the 8.3 MPa range. The pressure trace for test #32 does indicate some irregularities, however even in this case there was no evidence to indicate a propellant sample repair failure. We see pressure loss at 7.8, 10.1, and 11.2 seconds. The exact reason for these irregularities is not known. It is speculated they may be caused by either anomalous behavior of the driver motor or partial failure of the nozzle seals. These pressure anomalies are definitely not caused by the sample burning out prior to the driver motor grain. In all of the repair sample tests, the sample burned longer than the driver motor, as indicated by video records. The sample alone could only pressurize the chamber to 0.34 MPa, not the 5-6 MPa level where the pressure variations occurred. This type of behavior did not appear in any of the other tests. Based upon the data obtained from this set of tests, no noticeable difference was observed in the repair effectiveness as a result of the increased pressure levels. From the data gathered in these tests, it seems that the repair maintained integrity and effectiveness to at least the tested maximum pressure of 8.3 MPa (1200 psi).

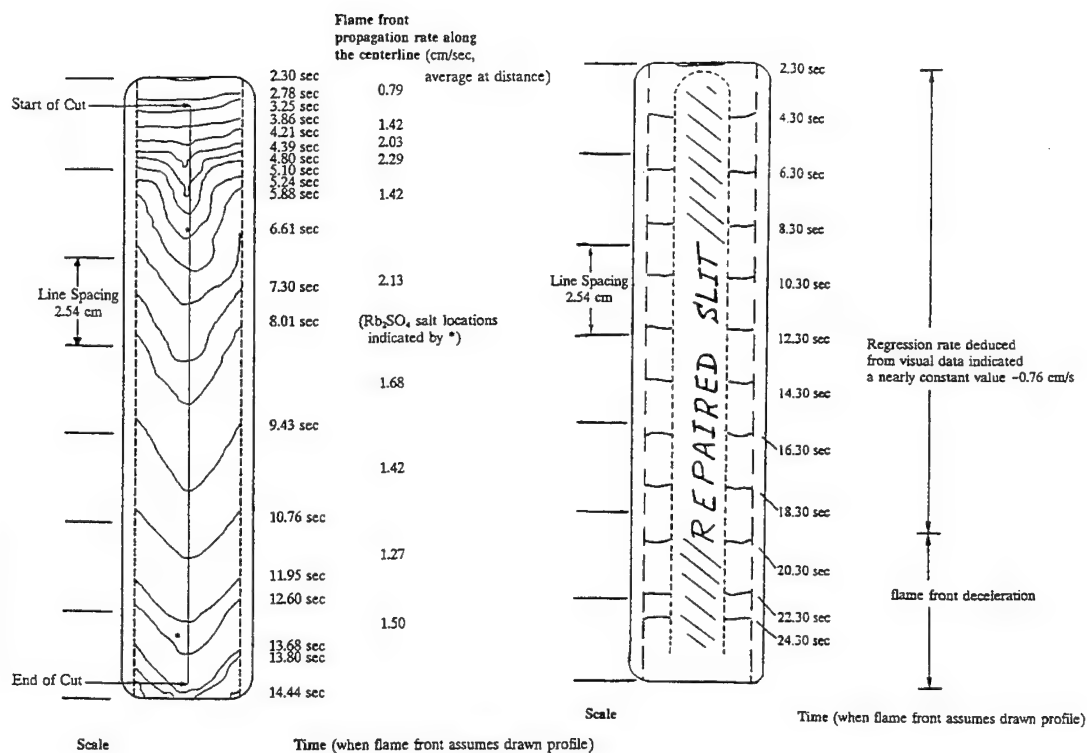


Figure 8. Instantaneous Flame Front Contours on the Viewing Surface of the Cut FSIC Sample (Test No. 26)

Figure 9. Instantaneous Flame Front Contours on the Viewing Surface of the Repaired Sample (Test No. 28)

In test #31, a translucent repair was utilized. Here as well, no noticeable difference was observed in the sample burning behavior of the transparent repair compared to those of the standard opaque repairs. The recovered repair material from test #31 was somewhat more eroded than those recovered from other tests. However, with only one test run using translucent repair material, there is insufficient data to make any conclusive statements regarding the effect of the opacifier in the repair. In addition, radiation effects may not scale linearly to the full scale scenario. Nevertheless, to eliminate in-depth radiation absorption, it is recommended that the repair material include an opacifier ingredient such as carbon black.

### Testing of Samples with Cuts

Pressure-time traces for the cut sample tests (Tests #26 and #30) are shown in Figure 11. During sample preparation for test #26, the window was directly glued to the sample surface. As a result, some potting compound was able to seep into the cut - resulting in an unintentional partial "repair"; consequently, the flame spread rate along the cut was not significantly different from that along the edge zones. Nevertheless, the uneven flame spreading phenomena resulted in increased burning surface area. This effect, together with a slightly undersized nozzle throat area resulted in



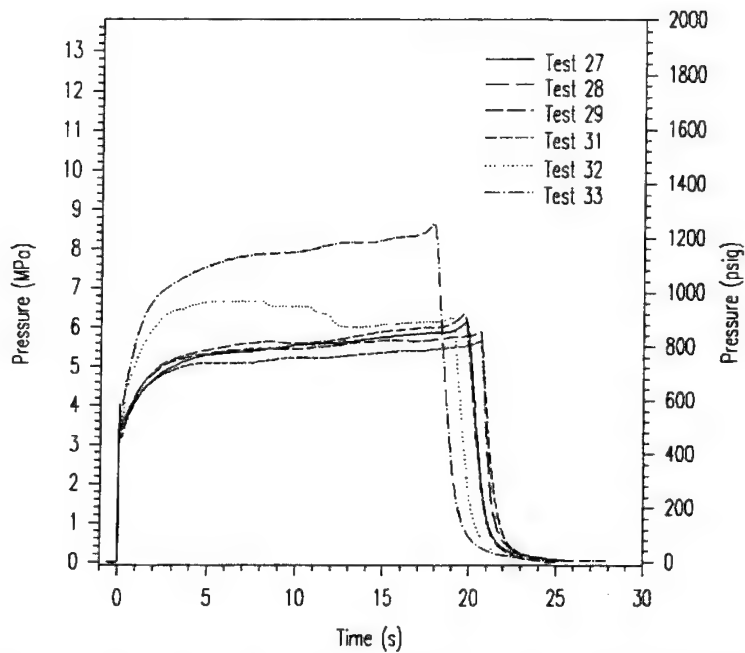


Fig. 10 Measured Pressure-Time Trace at the FSIC Sample Location (Tests with Repaired Samples)

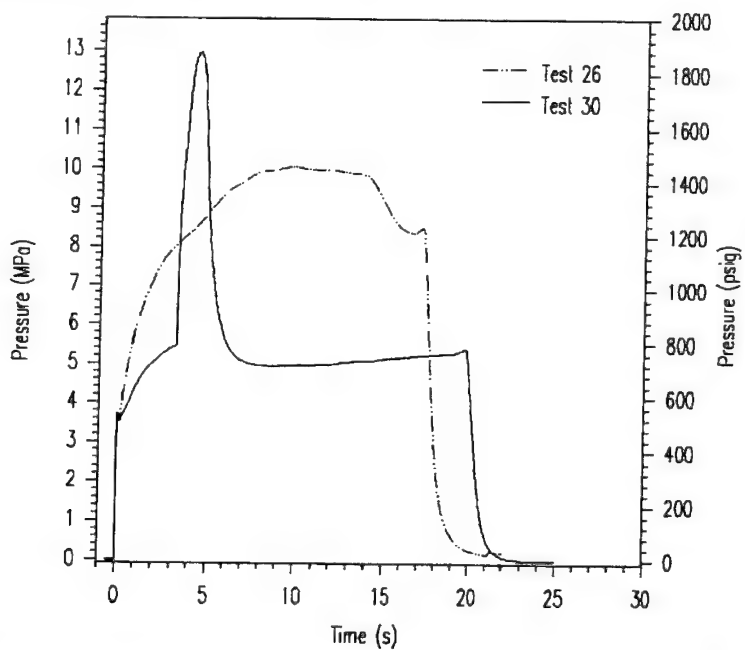
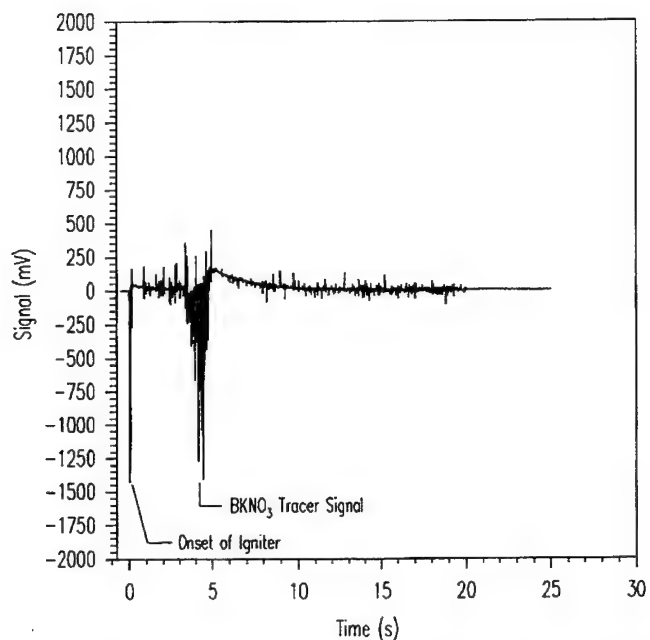
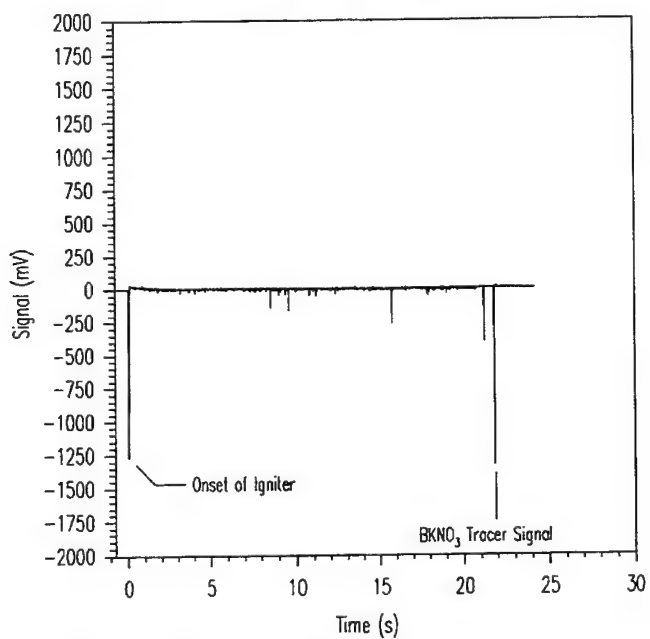


Fig. 11 Measured Pressure-Time Trace at the FSIC Sample Location (Tests with Cut Samples)



**Fig. 12 Recorded Time Variations of Tracer Signals from the Exhaust Plume in the Range  $\lambda = 780 \pm 5$  nm (Test No. 30)**



**Fig. 13 Recorded Time Variations of Tracer Signals from the Exhaust Plume in the Range  $\lambda = 780 \pm 5$  nm (Test No. 31)**

an elevated pressure level, causing a faster burning rate and a shorter total burn time. In the sample preparation for test #30, a very narrow pre-cast potting barrier strip (~0.6 mm in width x 0.5 mm in thickness) was placed over the cut to prevent potting compound from flowing in. When the potting compound was used to adhere the window to the test sample, this pre-cast strip fused with the potting compound, leaving no visible boundaries. The test results showed a dramatic difference in flame spreading behavior and pressurization characteristics in comparison with test #26. In this case, shortly after the flame reached the cut region, a rapid flame "flash-down" into the cut occurred, resulted in a pronounced pressure peak at around 4 seconds. The sample was completely consumed in about 6 seconds, long before the burnout time of the driver motor grain.

The cut sample tests clearly indicated that flame could propagate into an un-repaired slit in this motor-analog environment. This implies that any failure of a repaired sample would produce a pronounced flame spreading effect which can be detected from both visual records and P-t data. Hence, the tests with cut samples further serve to validate the success of the repair tests.

### Tracer Salt-Indicated Results

Recorded time variations of tracer signals in the wavelength range of 775 to 785 nm from the exhaust plume of FSIC tests #30 and #31 are presented in Figures 12 and 13, respectively. Because the detector is sensitive to combustion products of the igniter ( $\text{BKNO}_3$ ), the ignition event was generally accompanied by a large signal at the time of ignition. In test #30, a single  $\text{BKNO}_3$  tracer was imbedded at 17.8 cm from the sample top. The arrival time of the flame front at this location was 3.75 seconds (as indicated by film data), and the corresponding tracer signal was recorded at 3.85 seconds. In test #31,  $\text{BKNO}_3$  tracer material was inserted at 17.8 cm from the sample top. The arrival time of the flame front at this location, based on the high-speed movie film was 21.5 seconds, and the corresponding tracer signal was acquired at 21.7 seconds. In both of these tests, the tracer signals seem to produce consistent information on the arrival times of the flame front at the embedded tracer locations. This implies that the use of chemical tracer salts as an indicator of flame front position versus time in flame spreading studies could be a viable technique if sufficient attention is given to the following factors, including: tracer chemical selection, proper orientation of the detector, narrow band-pass filter selection based upon the tracer material and the aluminum content in the propellant grain, and elimination of any possible contaminants from the combustion chamber. In the FSIC test series, two chemical tracers were utilized: rubidium sulfate ( $\text{Rb}_2\text{SO}_4$ ) and boron potassium nitrate ( $\text{BKNO}_3$ ). Rubidium sulfate was found to be marginally detectable over background noise, while the boron potassium nitrate was more easily detectable due to its relatively high signal magnitudes.

### SUMMARY AND CONCLUSIONS

To evaluate the effectiveness of a proposed repair procedure for aluminized AP-based composite propellant used in Titan IV solid rocket motors, a series of tests was conducted in a motor analog simulating the chamber pressure level of actual Titan IV SRMs. A total of thirteen test firings was conducted in this study. Test results using repaired propellant samples were compared to those with unrepaired slit cuts.

- (1) The tests using cut samples clearly showed that flame could propagate into an unrepaired slit in the motor analog, resulting in easily observable abnormal flame spreading and burning behavior as well as chamber pressure overshoots. This flame spreading phenomena was especially pronounced in the test when the slit was not filled with any repair material during preparation.
- (2) All tests using repaired samples showed normal burning behavior up to the highest tested pressure level of 8.3 MPa (1200 psi). This indicates that the repair procedure proposed by UT/CSD, which was examined in this study, is successful in preventing the flame penetration into properly repaired regions of the propellant sample.
- (3) From the limited tests conducted, the opacity of the repair material seems to exhibit no effect on the burning behavior of the repaired propellant sample.
- (4) Embedded salt tracer materials (such as  $\text{BKNO}_3$  and  $\text{Rb}_2\text{SO}_4$ ) could be used as indicators for flame front locations if the tracer signals are properly detected in the exhaust plume jet.

Demonstration of the effectiveness of certain repair procedures is absolutely necessary to assure the proper recovery of damaged propellant grains from propulsion applications. Additionally, adequate criteria are necessary to determine which propellant defects are repairable.

### ACKNOWLEDGEMENTS

This work was sponsored by WYLE Laboratory through the office of Steven T. Griswold under a subcontract from Phillips Lab managed by Stu Bridges and the Titan Special Program Office of Capt. Barry Portner. Their support and encouragement are highly appreciated. The authors would like to acknowledge the input and useful discussion of the K-11 Test Team Members, especially Robert Geisler, Paul Willoughby, Jim McKinnis, Kirsten Pace, Capt. Barry Portner, Stu Bridges, Bill Mascio and S.R. Lin. The supply of propellant test samples, EPDM sheets, and potting compound by CSD is also highly appreciated. The help of Matt Mench and David Johnson of PSU in test preparation and test firings is also acknowledged.

### REFERENCES

1. Kuo, K.K., Kooker, D.E., "Coupling Between Nonsteady Burning and Structural Mechanics of Solid-Propellant Grains", *Nonsteady Burning and Combustion Stability of Solid Propellants, AIAA Progress Series in Astronautics and Aeronautics*, Vol. 143, ed. by L. DeLuca, E. Price, and M. Summerfield, 1990.
2. Kuo, K.K., Lu, Y.C., Ritchie, S.J., "Interim Report on Titan IV Flame Propagation Experiments and Numerical Simulation", Combustion Propulsion and Ballistic Technology Corp., February, 1994.
3. Kuo, K.K., Cohen, D., Ritchie, S.J., Lu, Y.C. "Final Report on Titan IV Flame Propagation Experiments and Numerical Simulation", Combustion Propulsion Ballistic Technology Corp., November, 1994.

4. Razdan, M.K., Kuo, K.K., "Erosive Burning of Composite Solid Propellants by Turbulent Boundary-Layer Approach", *AIAA Journal*, Vol. 17, No. 11, November 1979, pp. 1225-1233.
5. Willoughby, P.G., "Ablation Measurements in Solid Rocket Motors Using Alkali Metal Salt Tracers", *CPIA Publication 390, Vol. IV, JANNAF Propulsion Meeting*, February 1984.
6. Cohen, D. "Solid Propellant Regression Measurements Using Imbedded Chemical Tracers and Design of Test Program and Facilities for Investigation of the Erosive Burning and Flame Spreading Characteristics of the Solid Propellant Used in Advanced Solid Rocket Motors (ASRM)", M.S. Paper in Mechanical Engineering, The Pennsylvania State University, August, 1994.

### COMMENTS

Akira Iwama, Professor Emeritus, The Institute of Space and Astronautical Science:

Several years ago, we produced a test motor with diameter of 110 mm in order to investigate the possibility of flame spreading along the surfaces between poorly bonded propellant grains. We divided the casting process into two stages. After one grain had been cured completely, another batch of propellant dough was cut and cured. The composition of these two grains was similar. Upon firing, this motor recorded a significantly high pressure spike at around 5.0 MPa. I presume the minimum bonding strength is necessary between the repairing material and the damaged grain surface. Have you ever noted such an event and measured the bonding properties before an experiment?

Authors' Reply:

It is interesting to learn that you made such a study of poorly bonded surfaces between propellant grains. It is very likely that your observed high pressure spike was caused by the phenomena of flame propagating into the weakly bonded surface region. I do not have any data similar to what you describe, but I believe it will be useful to conduct further studies into this area.

## SOLID SOLUTION FORMATION BETWEEN RDX AND COMMON SOLID PROPELLANT BINDERS

E. Boyer,<sup>1</sup> P. W. Brown,<sup>2</sup> and K. K. Kuo<sup>1</sup>

<sup>1</sup>Department of Mechanical Engineering; <sup>2</sup>Department of Materials Science and Engineering  
The Pennsylvania State University, University Park, PA 16802

**ABSTRACT:** Because of many favorable characteristics, RDX has been extensively utilized as an ingredient in both gun and solid rocket propellants. Much work has been done on the decomposition and subsequent reactions involving RDX and other propellant ingredients, but very little attention has been given to the effects of solid-state interactions in the condensed phase. The combination of ingredients in solid propellants (e.g., oxidizer, binders, plasticizers, etc.) may not be adequately modeled as just a physical mixture since interactions between these components can change intermolecular forces in the propellant mixture, leading to changes in physical properties and combustion behavior. In this work, the solubilities of common propellant ingredients including acetyl triethyl citrate (ATEC), cellulose acetate butyrate (CAB), nitrocellulose (NC), and an energetic plasticizer (EP) and their effects on RDX unit cell dimensions were investigated. X-ray powder diffraction analysis showed that all binders tested formed a solid solution with RDX indicated by expansion of the RDX unit cell volume. CAB was found to have a solubility limit greater than 16 wt%, while EP had the least. NC and ATEC both showed solubility up to about the 9 wt% level. Changes in material and combustion properties due to the solid solution formation should therefore be closely examined in the modeling of combustion processes of RDX-based composite propellants.

### INTRODUCTION

Widely used as a high explosive, RDX (also known as hexogen, cyclonite, cyclotrimethylene trinitramine, hexahydro-1,3,5-trinitro-1,3,5-triazine, and hexahydro-1,3,5-trinitro-*s*-triazine) has been shown to be a very useful energetic ingredient in both gun and solid rocket propellant applications. Due to its relative insensitivity to accidental energy stimuli, it has been used in Low Vulnerability Ammunition (LOVA) formulations. In addition, the absence of HCl in RDX combustion products makes it desirable on an environmental basis.

Since the regression rate and burning behavior of solid propellant can be greatly influenced by processes occurring in the burning surface and subsurface regions, it is vital to obtain more knowledge about condensed-phase phenomena in order to better understand the combustion of nitramine-based solid propellants.

Because propellants consist of a combination of oxidizer, binders, plasticizers, and other ingredients it may not be adequate to model a composite propellant by treating it merely as a physical mixture. The formulation of a common RDX-based propellant, XM39, is shown in Table 1. Interactions between these components must be understood in order to create an accurate model. Changing intermolecular forces due to ingredient interactions can affect density, enthalpy of fusion, melting temperature, stability, aging characteristics, and general combustion characteristics. There has been much work done on decomposition and subsequent reactions involving RDX and other propellant ingredients,<sup>1-7</sup> but very little attention has been given to the effects of solid-state behavior and interactions in the condensed phase,<sup>8,9</sup> other than characterization of pure RDX.<sup>10-12</sup>

**Table 1**  
Ingredients in XM39 LOVA Propellant

Propellant	Material	%
XM39	RDX	76.0
	Cellulose Acetate Butyrate (CAB)	12.0
	Acetyl Triethyl Citrate (ATEC)	7.6
	Nitrocellulose (NC) (12.6% N)	4.0
	Ethyl Centralite (EC)	0.4

Effects of changing intermolecular forces due to transitions of pure phases of HMX (cyclotetramethylenetetranitramine), a high-energy material very similar to RDX, have been investigated previously and shown to be important,<sup>13</sup> but little work has been done on the effect of solid solutions between crystalline nitramines and binder materials. Some studies have found an effect on the melting and decomposition temperatures of RDX when mixed with other propellant ingredients.<sup>14-16</sup> Previously, X-ray diffraction (XRD) analysis of quenched samples of XM39 and another LOVA propellant (here called MZ) containing an energetic plasticizer by Wilson, et al.<sup>17,18</sup> showed evidence of the formation of RDX/binder solid solutions in both virgin and extinguished samples. Earlier results of this study demonstrated the formation of RDX/binder solid solutions in binary mixtures.<sup>19</sup> It has also been suggested that RDX/binder solid solutions may require consideration in propellant recycling and recovery procedures such as supercritical fluid extraction.<sup>20</sup> Therefore, it is important to gain a better understanding of the effects of solid solution formation on the combustion and other characteristics of propellant formulations. In this study, the interactions of the RDX and the ingredients in XM39 and MZ propellants are examined.

#### X-RAY DIFFRACTION PRINCIPLES

All crystalline materials (e.g., nitramines) consist of a regularly ordered arrangement of atoms or molecules commonly known as a lattice. The lattice contains many repeated units called the unit cells. Each unit cell is described by a set of parameters that is unique for every crystalline phase. Both material and thermal properties of the substance (e.g., density, strength, melting point, etc.) are functions of these parameters. Depending on orientation, many different parallel planes of atoms or molecules can be formed by the lattice. Through the use of X-ray diffraction analysis (XRD), the plane spacings present in a sample can be detected and used to ascertain the form and size of the unit cell(s) present, characterizing the material. A monochromatic beam of X-rays is directed at the material of interest and is scattered by the atoms or molecules present in the lattice. Due to the wave-like nature of X-rays, diffraction (constructive interference) occurs when the difference in path-lengths of X-rays scattering off different planes are integer multiples of the wavelength, therefore causing the scattered X-rays to be in phase with one another. Shown graphically in Fig. 1, this condition is known as the Bragg Law:

$$n\lambda = 2d \sin \theta \quad (1)$$

where  $n$  represents any positive integer,  $\lambda$  the wavelength,  $d$  the interplanar spacing, and  $\theta$  the angle of incidence. When the Bragg Law is met, a strong beam is returned, compared to weak scattering at other conditions.

The use of a diffractometer (Fig. 2) allows a range of X-ray incidence angles to be scanned automatically. A pattern can then be generated, with the strong reflections when the Bragg Law is met appearing as peaks plotted against the  $2\theta$  value. The location and spacing of the peaks in the pattern is unique to the planar spacings present in the sample.

When large crystals of a given material are difficult to obtain, the use of powdered samples in XRD has proven to be useful. Powder diffraction relies on a statistical sample of many randomly-oriented crystallites (small crystalline regions). All possible plane spacings are exposed to the beam at all times, so a strong diffraction peak is generated at any angle where the Bragg Law is met for the spacings present in the material. Since the crystallites are randomly arranged in the sample, the crystallographic

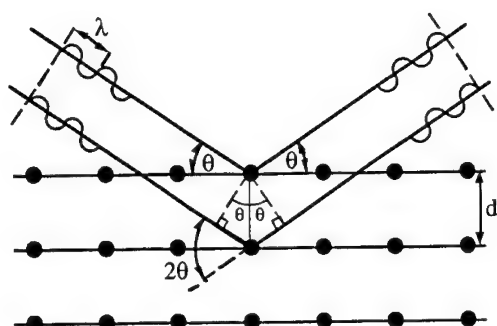


Figure 1. Diffraction of X-rays from planes in the crystal lattice

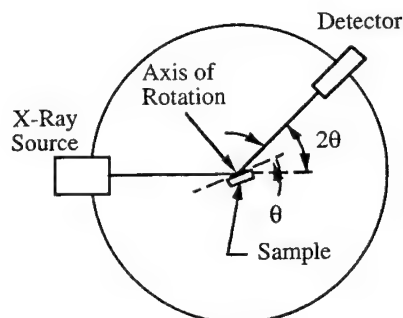


Figure 2. Schematic diagram of diffractometer.

orientations of the planes corresponding to particular diffraction peaks is not obvious from the pattern, but through careful analysis of the position and intensity of these peaks, the form and shape of the unit cell of the sample can be reconstructed.

Solid solutions are formed by the introduction of one type of molecule into a lattice made up of another. There are two possible forms: (1) interstitial, in which case molecules are inserted into existing spaces between molecules in the lattice, and (2) substitutional, where the molecules replace original molecules in the lattice. The presence of substituents in the lattice affects intermolecular forces, leading to a change in dimensions of the unit cell of the lattice that can be quantitatively measured using XRD techniques.<sup>21-23</sup>

### SAMPLE PREPARATION

One gram binary mixtures of the recrystallized RDX and the binder ingredients of interest were formulated to isolate the effects of individual propellant components. Since military grade RDX can contain a significant portion of HMX which would greatly affect this study, it was purified before the samples were made using an acetone recrystallization process.<sup>24</sup> CAB (Military Type II, Eastman CAB-381-20) was acquired through the Naval Surface Warfare Center-Indian Head from a lot used in MZ production. Since pure NC of the grade used in nitramine composite propellants was not available, it was obtained from M30 propellant, which is 98 wt% NC. The M30 was completely dissolved in acetone, then thoroughly washed in water to remove the  $K_2SO_4$  additive, a flash suppressant. Although the NC in M30 contains a different percent of nitration than that used in XM39 and MZ propellants, it is believed that the solid solution results should be essentially the same for both types.

Samples containing liquid ingredients were prepared slightly differently from those without any liquid ingredients. For mixes of RDX and solid binder materials, the desired proportions were first weighed out dry. Acetone was then added to the mixed powders until the sample was completely dissolved (approximately 20 mL). The solution was then shock precipitated into a large volume of water and the fine powders formed were allowed to settle to the bottom to facilitate filtering. The sample was separated from the liquid using vacuum filtration through fine (particle retention  $>2.5 \mu m$ ) filter paper. After filtration, the sample was placed in a drying oven at  $55^\circ C$  overnight to drive off any water or residual solvent. Measurements showed that this process yielded an approximately normal distribution of particle sizes around  $10 \mu m$  mean diameter.

Liquid ingredients proved to be more of a challenge since they could not be co-precipitated with RDX into water, both because of their liquid nature and solubility in water. Instead, the RDX was shock-precipitated separately and dried to obtain the fine particles desired. Then, after adding the desired proportion of the liquid ingredient, the sample was physically mixed by continuously compressing and stirring until the liquid was evenly distributed.

After the powdered samples were prepared, they were sealed in glass vials and aged at  $80^\circ C$  for 14 days to facilitate equilibration. After aging, but prior to X-ray analysis, approximately 5 wt% of a



silicon standard<sup>25</sup> was thoroughly mixed with the samples. The powdered samples containing the Si standard were packed into glass slides for use in the diffractometer. The standard used produced X-ray peaks at known positions, allowing the patterns obtained to be calibrated, eliminating instrument systematic errors.

### DATA ACQUISITION AND ANALYSIS

X-ray diffraction patterns were collected using a Philips APD3600 automated powder diffractometer controlled by the APD1700 software package running on a DEC VAXstation 3100/38 computer. Cu  $K_{\alpha}$  X-rays were used by this system at a wavelength of 1.54059 Å. After examination of initial fast scans, samples were scanned from 10 to 70 degrees  $2\theta$  with 2 second counts at 0.02 degree steps. Over this range, sufficient standard peaks existed to allow an accurate correction for instrument systematic error, and the higher-angle RDX peaks allowed the lattice parameters to be determined more accurately. Peak locations were found from the diffraction patterns using the SPECLOT computer program<sup>26</sup> and manually checked for accuracy. Lattice parameters were then determined using a least-squares fit, implemented in the Appleman program.<sup>27</sup>

### RESULTS

Typical X-ray patterns for pure RDX and an RDX/binder mixture are shown in Figs. 3 and 4, respectively. Although at first glance the patterns appear the same, upon closer examination, it can be seen that the RDX/binder mixture has a lower intensity at all points, and a higher background signal. This is because the binder is an amorphous (non-crystalline) material with no regular ordering, therefore no diffraction peaks are generated, only an amorphous hump. Also, some peak broadening can be seen in the RDX/binder pattern, probably caused by the formation of smaller particles during shock precipitation of the sample. Some of the peaks are shifted slightly due to solid solution formation, although this is more apparent through computer analysis of the entire pattern.

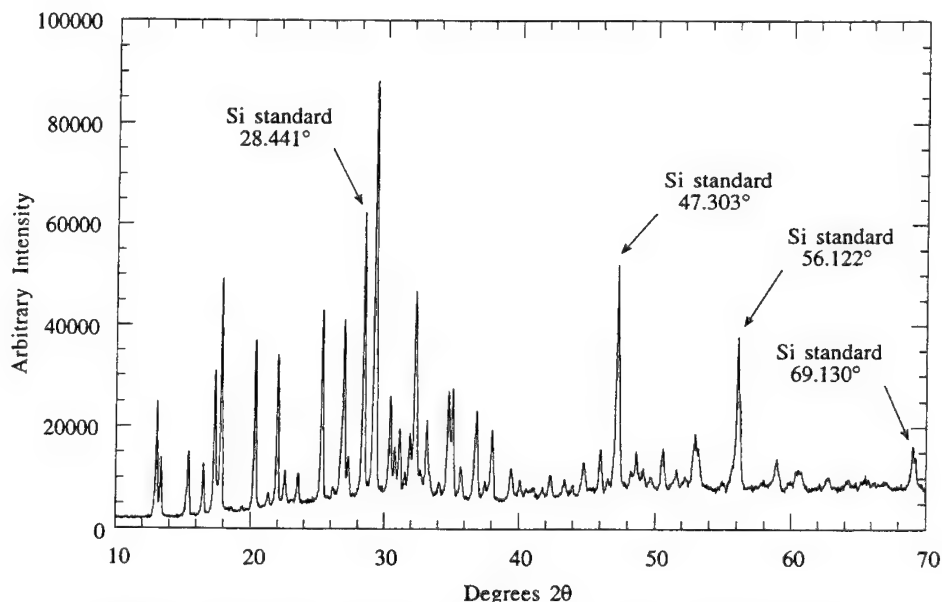


Figure 3. Typical X-ray diffraction pattern for pure RDX with Si standard

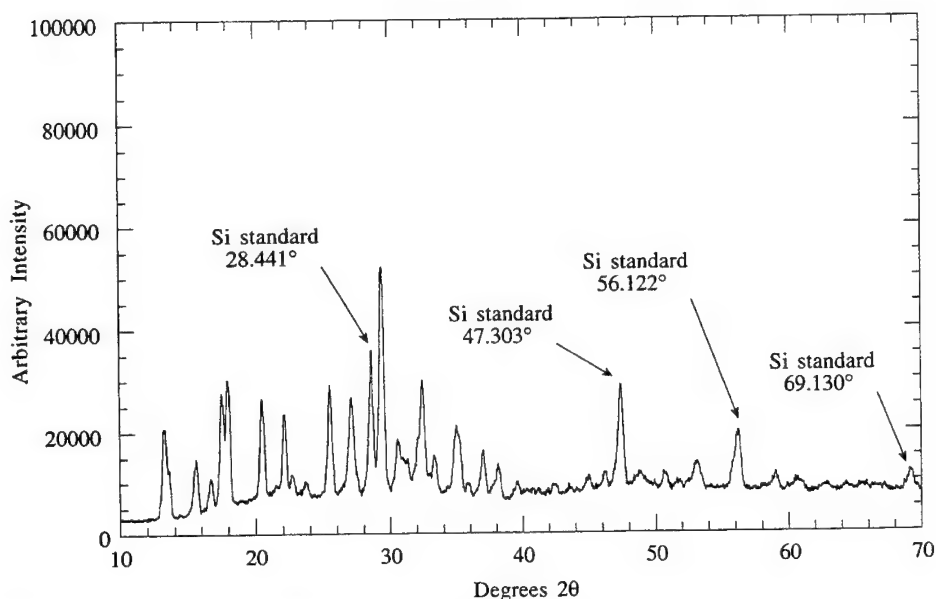


Figure 4. Typical X-ray diffraction pattern for RDX/binder (24% CAB) mixture with Si standard

For RDX/NC mixtures, all three lattice parameters elongate slightly (shown in the table in Fig. 5). Figure 5 shows the effect of these changing parameters on the unit cell volume, a continuous increase up the 9 wt% NC point. This indicates the upper limit for NC solid solubility in RDX. RDX/ATEC shows much the same behavior in the unit cell, with a slight increase in the B parameter (table in Fig. 6) causing the unit cell (Fig. 6) to grow until the 9 wt% ATEC point is reached, then leveling off. RDX/EP appears to be slightly soluble, up to the 3 wt% point, shown in Fig. 7. All the lattice parameters increase with the addition of CAB, yielding a nearly linear increase in the unit cell volume, as seen in Fig. 8. No plateau in cell volume was observed, indicating that the extent of CAB solubility in RDX may be greater than 16%. Mixtures with higher percentages of CAB were made, but due to the amorphous nature of CAB, did not yield usable results after the data reduction process. These results differ from those previously reported in Ref. 19 because of more precise sample preparation and analysis coupled with a new series of tests on a higher-performance diffractometer.

There appears to be more variability in the results of the liquid ingredients than solid ones. This is most likely due to some inhomogeneity in the samples due to the difficulty in the mixing process. The solid solutions would not have formed uniformly in the sample, influencing the results even though every effort was made to use a well-mixed, uniform sample.

## CONCLUSIONS

All the RDX/binder mixtures formed solid solutions to some extent, shown by expansion of the RDX unit cell. Addition of CAB had the greatest effect, with the solubility limit greater than 16 wt% CAB, while EP had the least. Due to the relative size of the RDX and binder molecules, all the solutions formed are believed to be substitutional. CAB, the largest molecule, had the greatest effect on the unit cell.

Analysis of the interactions between RDX and common propellant ingredients is important for many reasons. The changes in material properties should be closely examined in the future when modeling RDX-based composite propellants. Safe disposal and/or recovery and recycling may also be affected. X-ray techniques used to ascertain the purity of crystalline propellants by looking for the presence of another phase may not be as accurate as previously thought since a low percentage contaminant may be disguised by solid solution formation.

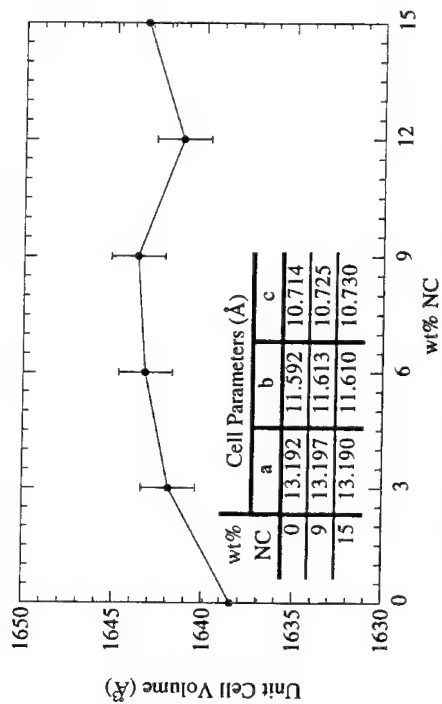


Figure 5. Effect of NC on RDX unit cell

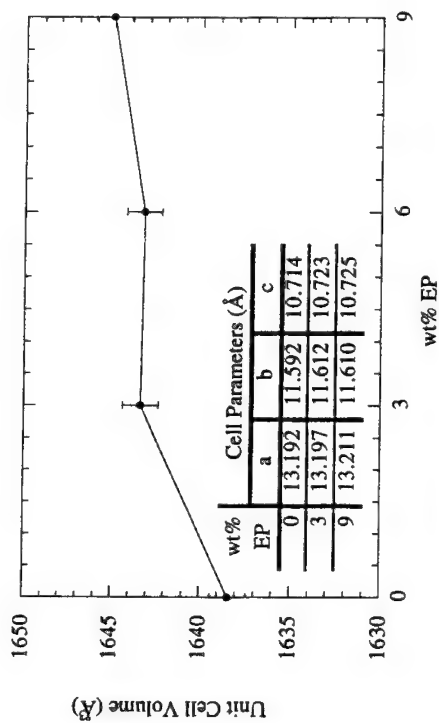


Figure 7. Effect of EP on RDX unit cell

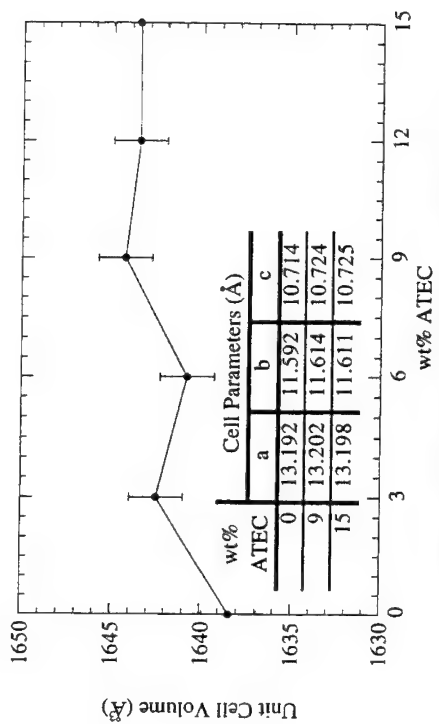


Figure 6. Effect of ATEC on RDX unit cell

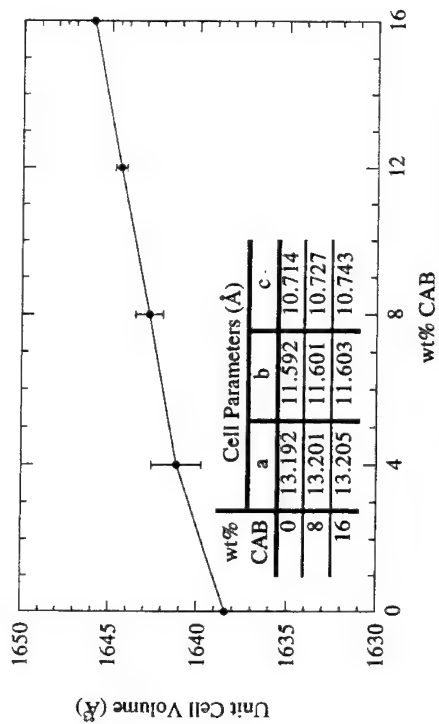


Figure 8. Effect of CAB on RDX unit cell

## FUTURE WORK

Work is currently underway to extend the present solid solution characterization study to systems of HMX (another energetic nitramine) and other propellant ingredients. Studying the HMX/RDX system can assist in better understanding the difference between military grade RDX, used in actual propellants, and pure RDX as commonly used in combustion models. Determining the change in thermal properties and the effect of temperature on solid solubility and constructing phase diagrams will greatly aid in integrating these results into combustion models.

## ACKNOWLEDGMENTS

This work has been sponsored by the Army Research Office under Contract Nos. DAAH04-93-G-0364 and DAAL03-92-G-0118. The interest and support of program manager Dr. Robert W. Shaw are gratefully acknowledged. Military grade RDX used was generously supplied by the Army Research Laboratory (ARL) in Aberdeen, Maryland with the assistance of Dr. Martin S. Miller. Dr. Rose Pesce-Rodriguez of ARL and Susan Peters of the Naval Surface Warfare Center-Indian Head were instrumental in obtaining the CAB. Finally, the assistance of Mr. Sean J. Wilson in the early start of this work and the continuing aid of Prof. Deane K. Smith, both from the Pennsylvania State University, are greatly appreciated.

## REFERENCES

1. **Boggs, T. L.**, The Thermal Behavior of Cyclotrimethylenetrinitramine (RDX) and Cyclotetramethylenetetranitramine (HMX), in *Fundamentals of Solid-Propellant Combustion (Progress in Astronautics and Aeronautics 90)*, edited by Kuo, K. K. and Summerfield, M., American Institute of Aeronautics and Astronautics, 1984, 121-175.
2. **Fifer, R. A.**, Chemistry of Nitrate Ester and Nitramine Propellants, in *Fundamentals of Solid-Propellant Combustion (Progress in Astronautics and Aeronautics 90)*, edited by Kuo, K. K. and Summerfield, M., American Institute of Aeronautics and Astronautics, 1984, 177-238.
3. **Behrens, Jr., R. and Bulusu, S.**, Thermal Decomposition of Energetic Materials. 3. Temporal Behaviors of the Rates of Formation of the Gaseous Pyrolysis Products from Condensed-Phase Decomposition of 1,3,5-trinitrohexahydro-s-triazine, *Journal of Physical Chemistry*, 96, 8877-8891, 1992.
4. **Schroeder, M. A., Fifer, R. A., Miller, M. S., et al.**, Condensed-Phase Processes During Solid Propellant Combustion. Part II: Chemical and Microscopic Examination of the Conductively Quenched Samples of RDX, XM39, JA2, M30, and HMX-Binder Composition, Technical Report BRL-TR-3337, Ballistic Research Laboratory, May 1992.
5. **Brill, T. B., Brush, P. J., Patil, D. G., et al.**, Chemical Pathways at a Burning Surface, in *Twenty-Fourth Symposium (International) on Combustion*, The Combustion Institute, 1992, 1907-1914.
6. **Brill, T. B. and Brush, P. J.**, Condensed Phase Chemistry of Explosives and Propellants at High Temperature: HMX, RDX, and BAMO, *Philosophical Transactions Royal Society of London A*, 339, 377-385, 1992.
7. **Melius, C. F.**, Thermochemical Modeling: II. Applications to Ignition and Combustion of Energetic Materials, in *Chemistry of Physics and Energetic Materials*, edited by Bulusu, S. N., Kluwer Academic Publishers, 1990, 51-78.
8. **Piermarini, G. J., Block, S., and Miller, P. J.**, The Diamond Anvil Cell for Physical and Chemical Investigations of Energetic Materials at High Pressures, in *Chemistry of Physics and Energetic Materials*, edited by Bulusu, S. N., Kluwer Academic Publishers, 1990, 369-389.
9. **Karpowicz, R. J. and Brill, T. B.**, Comparison of the Molecular Structure of Hexahydro-1,3,5-trinitro-s-triazine in the Vapor, Solution, and Solid Phases, *Journal of Physical Chemistry*, 88, 348-352, 1984.

10. McCrone, W. C., RDX, *Analytical Chemistry*, 22, 954-955, 1950.
11. Choi, C. S. and Prince, E., The Crystal Structure of Cyclotrimethylene-trinitramine, *Acta Crystallographica B*, 28, 2857-2862, 1972.
12. Sullenger, D. B., Cantrell, J. S., and Beiter, T. A., X-ray Powder Diffraction Patterns of Energetic Materials, *Powder Diffraction*, 9, 2-14, 1994.
13. Brill, T. B. and Karpowicz, R. J., Solid Phase Transition Kinetics. The Role of Intermolecular Forces in the Condensed-Phase Decomposition of Octahydro-1,3,5,7-tetranitro-1,3,5,7-tetrazocine, *Journal of Physical Chemistry*, 86, 4260-4265, 1982.
14. Quintana, J. R., Ciller, J. A., and Serna, F. J., Thermal Behaviour of HMX/RDX Mixtures, *Propellants, Explosives, Pyrotechnics*, 17, 106-109, 1992.
15. Hussain, G. and Rees, G. J., Thermal Decomposition of RDX and Mixtures, *Fuel*, 74, 273-277, 1995.
16. Reich, L., Compatibility of Polymers with Highly Energetic Materials by DTA, *Thermochemica Acta*, 5, 433-442, 1973.
17. Sean J. Wilson, The Surface Structure and Composition of the Foam Layers Recovered from RDX-based Materials after Laser Deradiation, Master's Thesis, The Pennsylvania State University, 1995.
18. Wilson, S. J., Brown, P. W., Thynell, S. T., et al., Surface Microstructure Resulting from Laser-Assisted Pyrolysis and Combustion of XM39 and MZ Propellants, in preparation.
19. Boyer, E., Brown, P. W., and Kuo, K. K., Phase Relationships Involving RDX and Common Solid Propellant Binders in *Decomposition, Combustion, and Detonation Chemistry of Energetic Materials (Volume 418 MRS Symposium Proceedings)*, edited by Brill, T. B., Russell, T. P., Tao, W. C., et al., Materials Research Society, 1996.
20. Liebman, S., Personal communication, 1995.
21. Cullity, B. D., *Elements of X-ray Diffraction*, Addison-Wesley Publishing Co., Inc., 1978, 81-88.
22. Goehner, R. P. and Nichols, M. C., X-ray Powder Diffraction, in *ASM Handbook Volume 10: Materials Characterization*, American Society for Metals, 1991, 333-343.
23. Callister, Jr., W. D., *Materials Science and Engineering: An Introduction*, John Wiley & Sons, Inc., 1991, 54-59.
24. Schroeder, M. A., Private communication, 1993.
25. National Bureau of Standards Standard Reference Material 640b Silicon Powder.
26. Goehner, R. P., SPECPLOT User's Manual: Revised 1/82 for DEC Operating Systems, General Electric Technical Information Report No. 82CRD114, May 1982.
27. Appleman, D. E. and Evans, Jr., H. T., Job 9214: Indexing and Least-Squares Refinement of Powder Diffraction Data, USGS Report GD-73-003, United States Geological Survey, 1973.

## CHARACTERIZATION OF WAXES FOR DESENSITIZATION OF EXPLOSIVE COMPOSITIONS

Tung-ho Chen<sup>1</sup>, Clement Campbell<sup>1</sup>, and Yu-long Liang<sup>2</sup>

<sup>1</sup>U. S. Army Armament Research, Development, and Engineering Center  
Picatinny Arsenal, New Jersey, 07806-5000, U. S. A.; <sup>2</sup>Geocenters, Inc.  
762 Route 15 South, Lake Hopatcong, New Jersey 07849, U. S. A.

**ABSTRACT:** For safe handling and use of high explosives, waxes have been used to desensitize military high explosive compositions consisting of relatively sensitive explosive ingredients. In addition to the principal purpose of desensitization, the waxes also act as binders, lubricants, and sealants. It is well known that the type of wax used in the desensitization of explosive compositions will affect the quality of cast explosives. The objective of this paper is to characterize two different waxes and examine the role of molecular weight. To this end, the experimental approaches capable of providing structural as well as molecular weight information were selected for this study. These are direct exposure probe mass spectrometry (DEPMS) and supercritical fluid chromatography (SFC). In addition, comparative differential scanning calorimetry (DSC) of both waxes was conducted to determine the melting and cooling characteristics of both waxes.

This paper will briefly describe the experiments and discuss the results obtained. The discussion will include the feasibility of using a 'designer wax' tailored for desensitizing any particular high explosive composition.

### INTRODUCTION

As early as 1892, it was indicated that the incorporation of waxes such as the paraffin waxes in explosive compositions results in reducing the sensitivity of the latter to mechanical stimuli<sup>1a</sup>. In addition to the principal role of desensitization, the waxes are also used as shock attenuators, binders, lubricants, sealants, fuels, and inert simulants<sup>1b</sup>. Furthermore, the presence of waxes in explosive compositions provides

other important benefits including wetting, coating, dispersion, thinning, void filling, and increased production rate<sup>2</sup>.

It is well known that the physico-chemical properties of waxes used in the desensitization of explosive compositions will affect the quality of cast explosives<sup>1c</sup>. The objective of this study is to characterize two saturated hydrocarbon waxes, Waxes A and B, and examine the role of molecular weight on the void formation in a cast explosive composition. The voids in explosive compositions are critical defects as they constitute potential hot spots giving rise to premature ignition of explosive compositions due to adiabatic compression of entrapped air in the cavities<sup>1a,3</sup>. It has been shown that the internal cavities ranging from 50 to 100 micrometers are the potential hot spots in the monomodal cast wax-bonded RDX formulations near the initiation threshold of the incident shock waves at 4 to 5 GPa<sup>4</sup>. To this end, the experimental approaches capable of providing structural as well as molecular weight information were selected for this study. These are direct exposure probe mass spectrometry (DEPMS) and supercritical fluid chromatography (SFC). In addition, comparative differential scanning calorimetry (DSC) of both waxes was conducted to determine the melting and cooling characteristics of both waxes.

In the past, various physico-chemical techniques have been used to characterize the desensitization waxes. These include melting point, penetration test, viscosity, methylethyl ketone extraction, sweating or exudation test, acid, ester, iodine, and saponification numbers, ash, flash point, thermogravimetric analysis, differential thermal analysis, DSC, gas chromatography, gel permeation chromatography<sup>1d,5,6,7</sup> and supercritical fluid extraction-supercritical chromatography combined with Fourier transform Infrared spectrometry<sup>8</sup>.

## EXPERIMENTAL

### Apparatus

A Finnigan OWA 1020-B Gas Chromatograph/Mass Spectrometer (GC/MS)

was operated in the positive ion chemical ionization (PCI) mode using methane as the reagent gas at 3-5 Torr for the DEPMS experiments. A Suprex MPS/225 Multi Purpose System was used in the SFC experiments. A Perkin-Elmer DSC-4 differential scanning calorimeter was used in the DSC experiments.

## Chemicals

Carbon dioxide used in the SFC experiments was SFC-Grade.

## RESULTS AND DISCUSSION

### DEPMS

Figures 1 and 2 exhibit the DEPMS spectra of Waxes A and B, respectively. The DEPMS probe was heated at 10 °C/min. to 1000 °C in approximately 2 minutes. The spectra show the respective profiles of the saturated hydrocarbon ion fragments,  $C_nH_{2n+1}^+$  ranging from  $C_3H_7^+$  ( $m/z = 43$ ;  $n = 3$ ) to  $C_{18}H_{37}^+$  ( $m/z = 253$ ;  $n = 18$ ). Quite clearly, Wax B contains a much greater fraction of high molecular weight hydrocarbon mixtures than Wax A.

### SFC

Figures 3 and 4 show the SFC chromatograms of Waxes A and B, respectively. SFC was operated in the pressure program mode and the SFC conditions are listed below.

#### SFC Conditions:

Column:	Nucleosil R C-18, 10 cm x 1.0 mm, 5 $\mu$ m, pore size, 100 Å
Oven Temperature:	75 °C
Pressure Programming:	Equilibrate at 125 atm
1.	Maintain at 125 atm for 2 min.
2.	Linear program up to 450 atm in



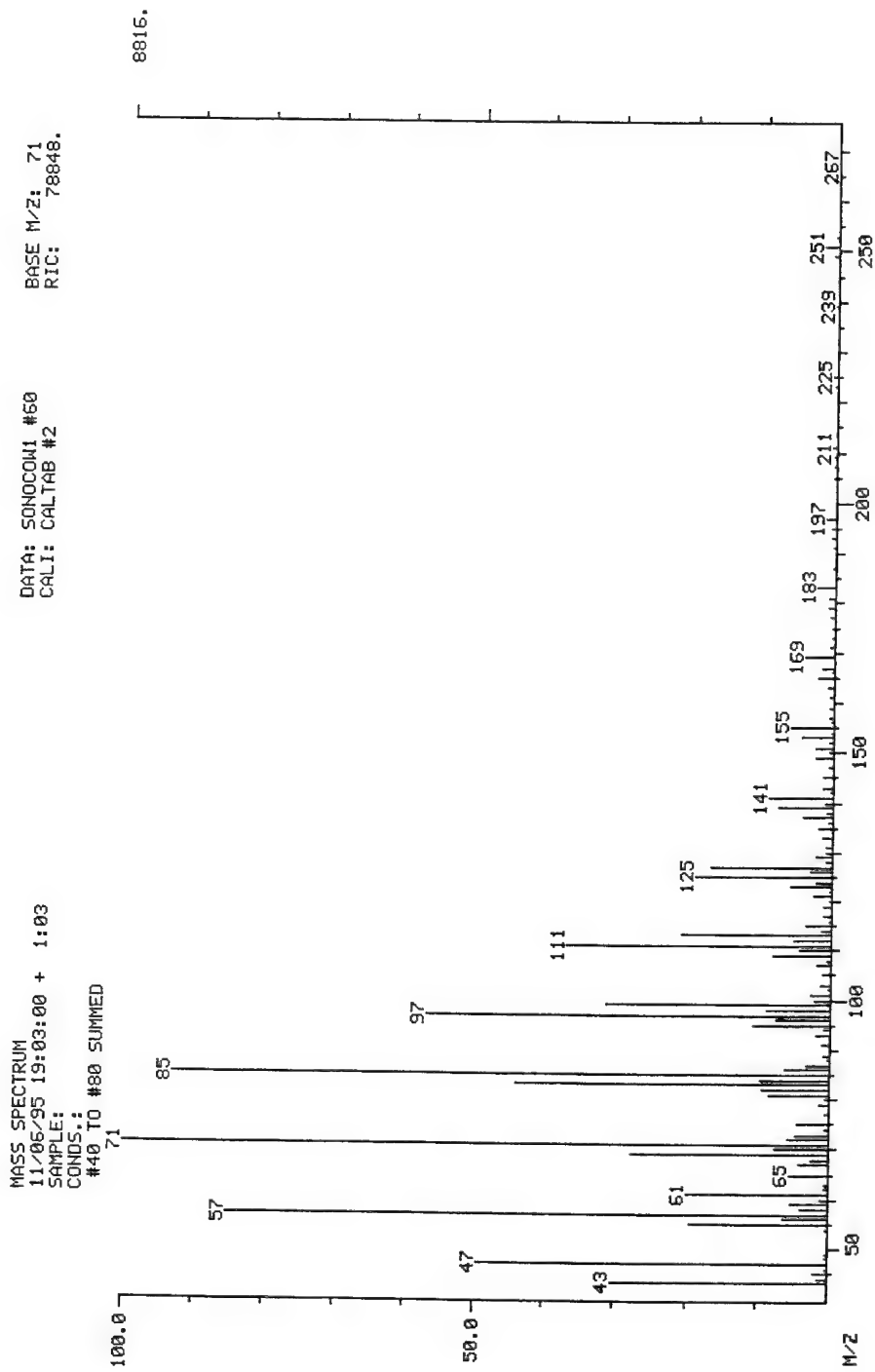


Figure 1. DEPMs Spectrum of Wax A

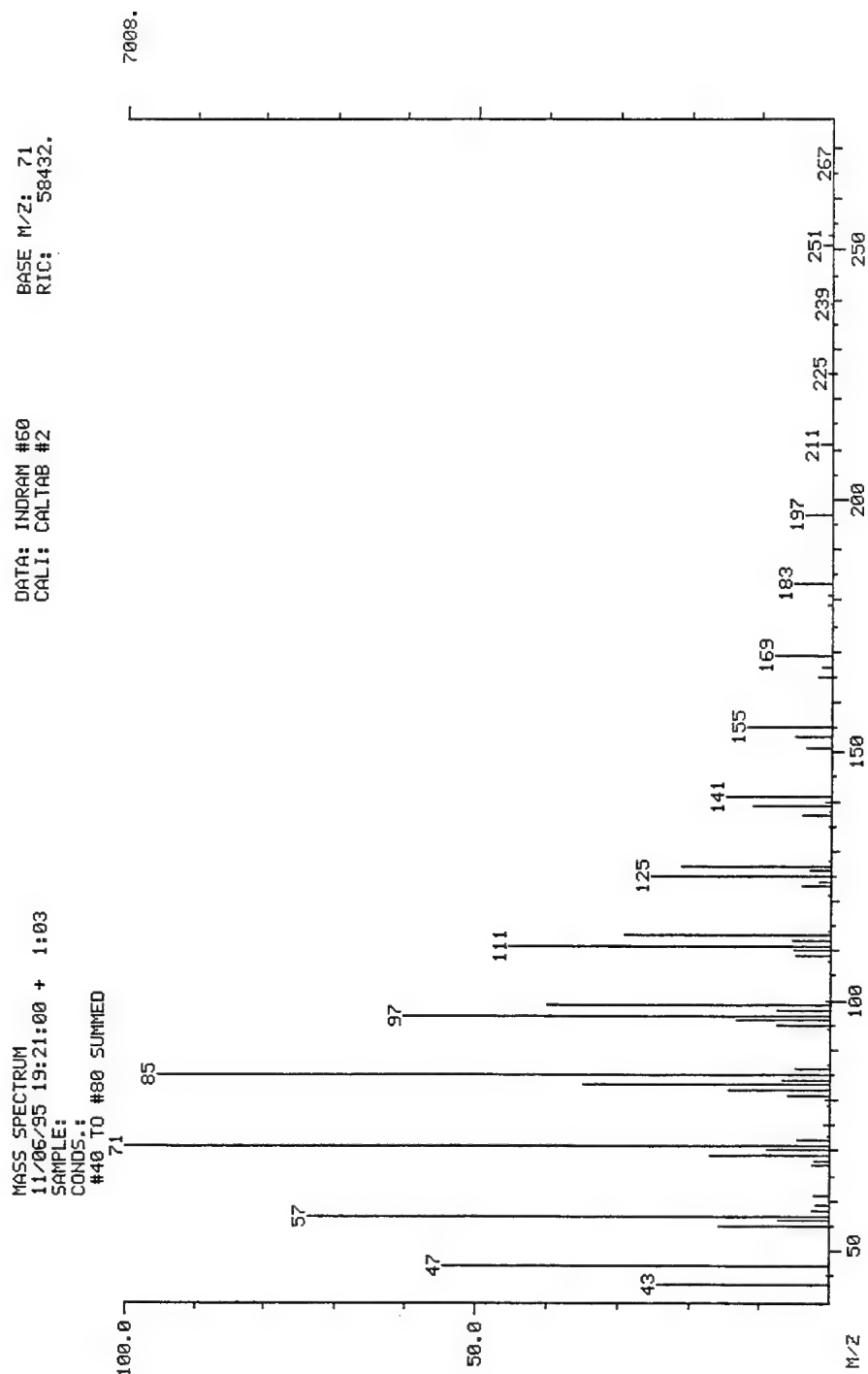


Figure 2. DEPMS Spectrum of Wax B



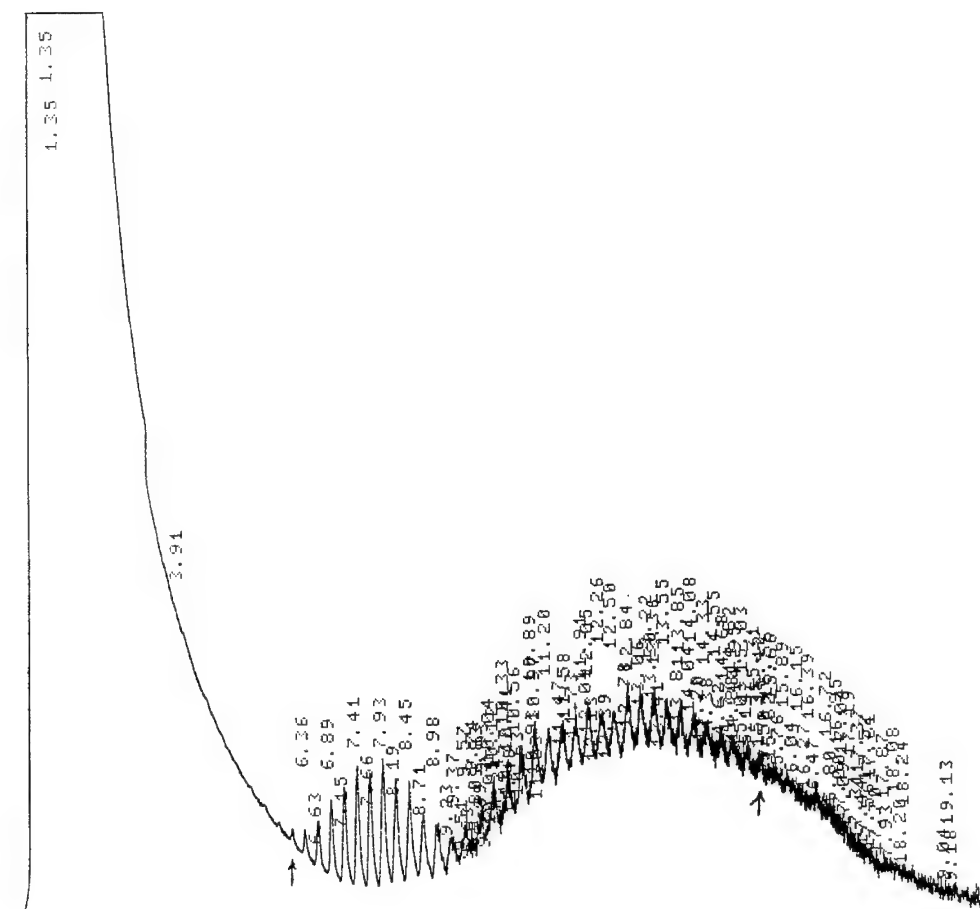


Figure 4. SFC Chromatogram of Wax B

3. 8 min.  
 Maintain at 450 atm for 2 min.  
 Sample Concentrations: Wax A, 0.1049 g/10 ml  
 cyclohexane; Wax B, 0.1059 g/10  
 ml cyclohexane. The samples are  
 soluble at 60 °C at these  
 concentrations.

These spectra support the DEPMS finding. Thus, the major fraction of Wax A ranges in molecular weight from 310 ( $C_{22}H_{46}$  = 310;  $n$  = 22) to 478 ( $C_{34}H_{70}$  = 478;  $n$  = 34) with 422 being approximately the most prominent molecular weight ( $C_{30}H_{62}$  = 422;  $n$  = 30) in this fraction. The molecular weights of Wax A are in the range of 310 ( $C_{22}H_{46}$  = 310;  $n$  = 22) to 674 ( $C_{48}H_{98}$  = 674;  $n$  = 48). In contrast, Wax B's main fraction shifts to a much higher molecular weight range relative to that of Wax A, i. e., from 492 ( $C_{35}H_{72}$  = 492;  $n$  = 35) to 800 ( $C_{57}H_{116}$  = 800;  $n$  = 57) with 702 ( $C_{50}H_{102}$  = 702;  $n$  = 50) being the most abundant molecular weight in this fraction. Wax B has a molecular weight range of 310 ( $C_{22}H_{46}$  = 310;  $n$  = 22) to 800 ( $C_{57}H_{116}$  = 800;  $n$  = 57). Therefore, Wax B should exhibit a higher melting range than that of Wax A.

## DSC

Indeed, DSC results (Figures 5 and 6) confirmed this conclusion. The melting point of Wax B ranges approximately from 40 - 88 °C which is about 10 °C higher than that of Wax A, i. e., 40 - 78 °C. The DSC thermograms were obtained at 2 °C/min. which was determined to be the optimum heating rate to obtain correct heating and cooling curves. The bottom traces represent the corresponding cooling curves in the figures.

Figure 7 shows the heating and cooling curves of Composition B obtained at the heating rates of 2.0 °C/min. and 0.1 °C/min., respectively. These rates were determined to be optimum. The heating curves obtained at the heating rates of less than 2.0 °C were virtually identical to the one shown in this figure (upper curve), while the lowest cooling rate of 0.1 °C/min. was necessary to obtain a reproducible crystallization

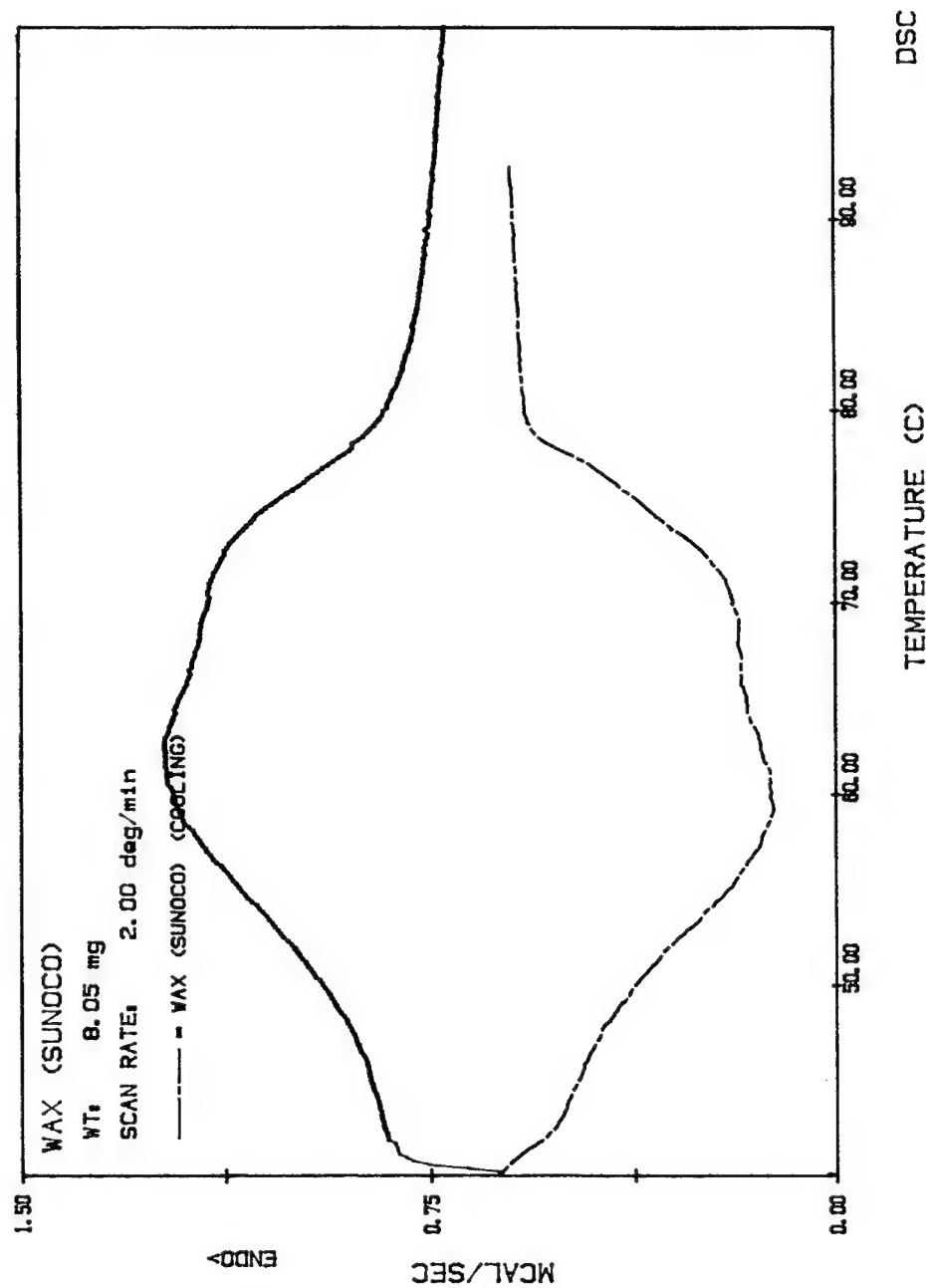


Figure 5. DSC Thermograms of Wax A

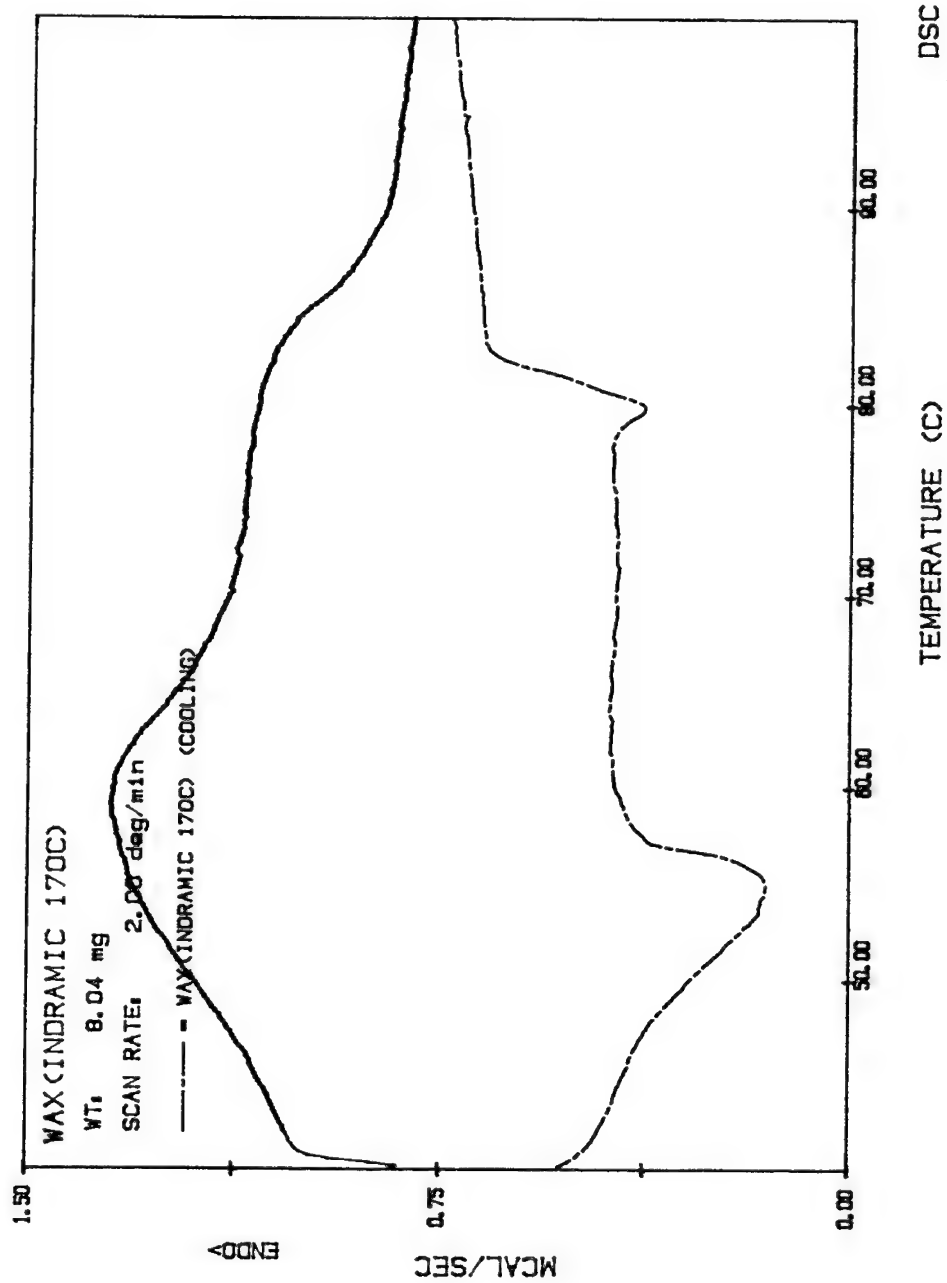


Figure 6. DSC Thermograms of Wax B

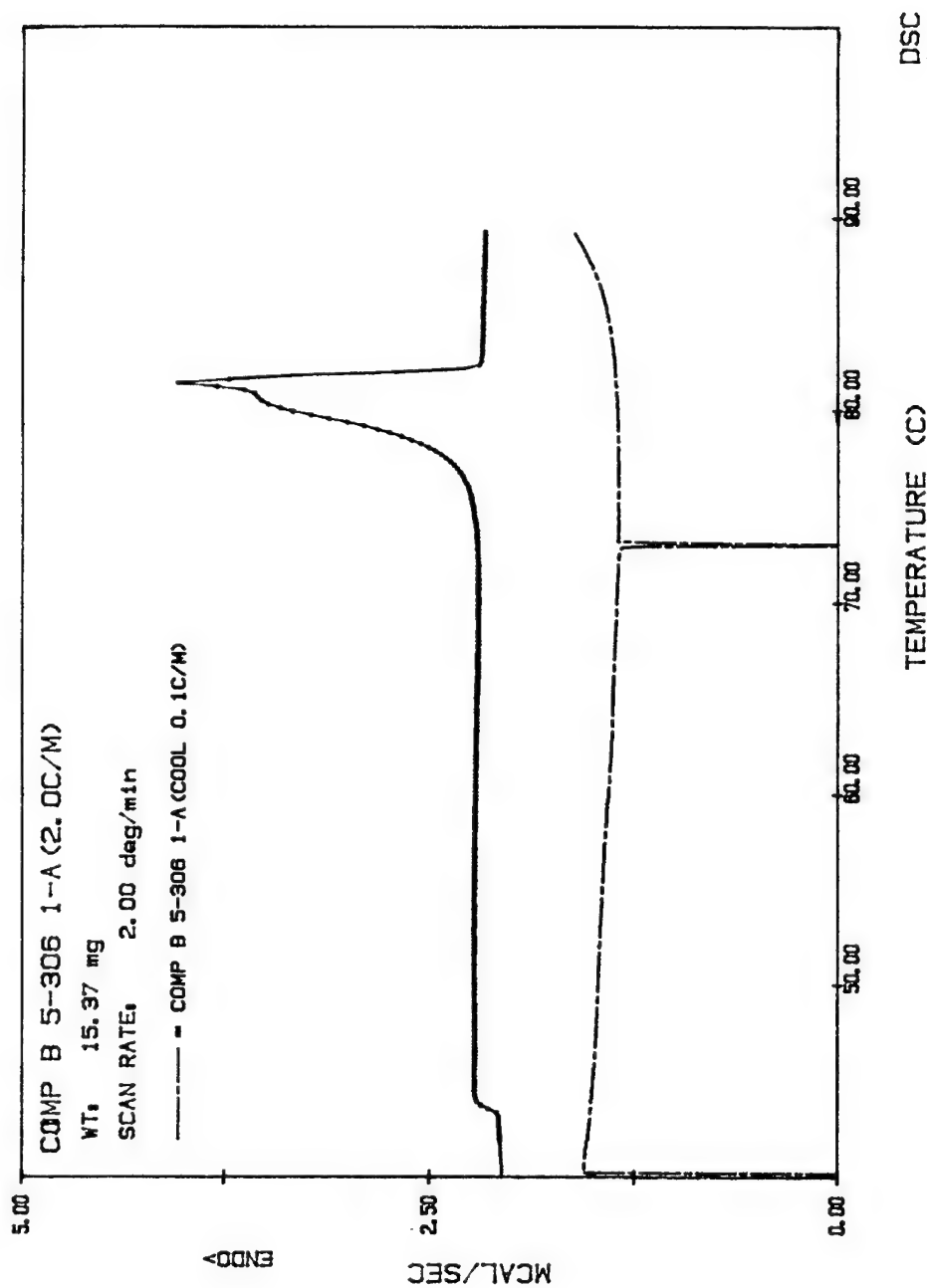


Figure 7. DSC Thermograms of Composition B



temperature of approximately 73 °C for 2,4,6-trinitrotoluene (TNT). The latter is erratic and non-reproducible at higher cooling rates and the supercooling of TNT persists to much lower temperatures. Quite obviously, the desensitization wax must have a substantial fraction melting below 73 °C to fill the voids formed during the sudden crystallization of TNT from the metastable supercooling state. The sharp exothermic peak of TNT with very low enthalpy change compared to the endothermic peak of TNT melting during the heating phase is attributed to the fact that the sudden release of heat from the supercooled TNT crystallization is much faster than the time constant of DSC, i. e., only part of the enthalpy change is sensed.

#### **Casting Quality of Composition B with Wax A or Wax B Desensitizers**

Recently, it has been demonstrated statistically that under identical casting conditions, the Composition B cast with Wax B exhibits much greater degree of void formations compared to that cast with Wax A, resulting in much higher rejection rates in numerous castings. Similar observations have been reported over a decade ago<sup>1e,9</sup>. In view of the findings in the present work, this can be clearly attributed to the fact that Wax B consists of higher molecular weight fractions than Wax A, causing the former to freeze at a higher temperature range relative to the latter. This in turn, results in greater void formations and much higher rejection rates actually observed, since the voids formed during the sudden crystallization of TNT are not adequately filled in due to the relative lack of the lower molecular weight fractions in Wax B.

#### **'Designer Wax'**

Studies have been made to explore the idea of 'designer wax', i. e., the optimum wax tailored for desensitizing any particular explosive composition. As a first step, only optimum melting range, among other parameters, is addressed here. Since Wax A is obviously superior to Wax B, attempts were made to remove the higher molecular weight fractions in the latter to match the upper melting range of the former. A crude heat fractionation technique employing an oven was found to be inadequate for this purpose. However, a solvent extraction technique proved to be

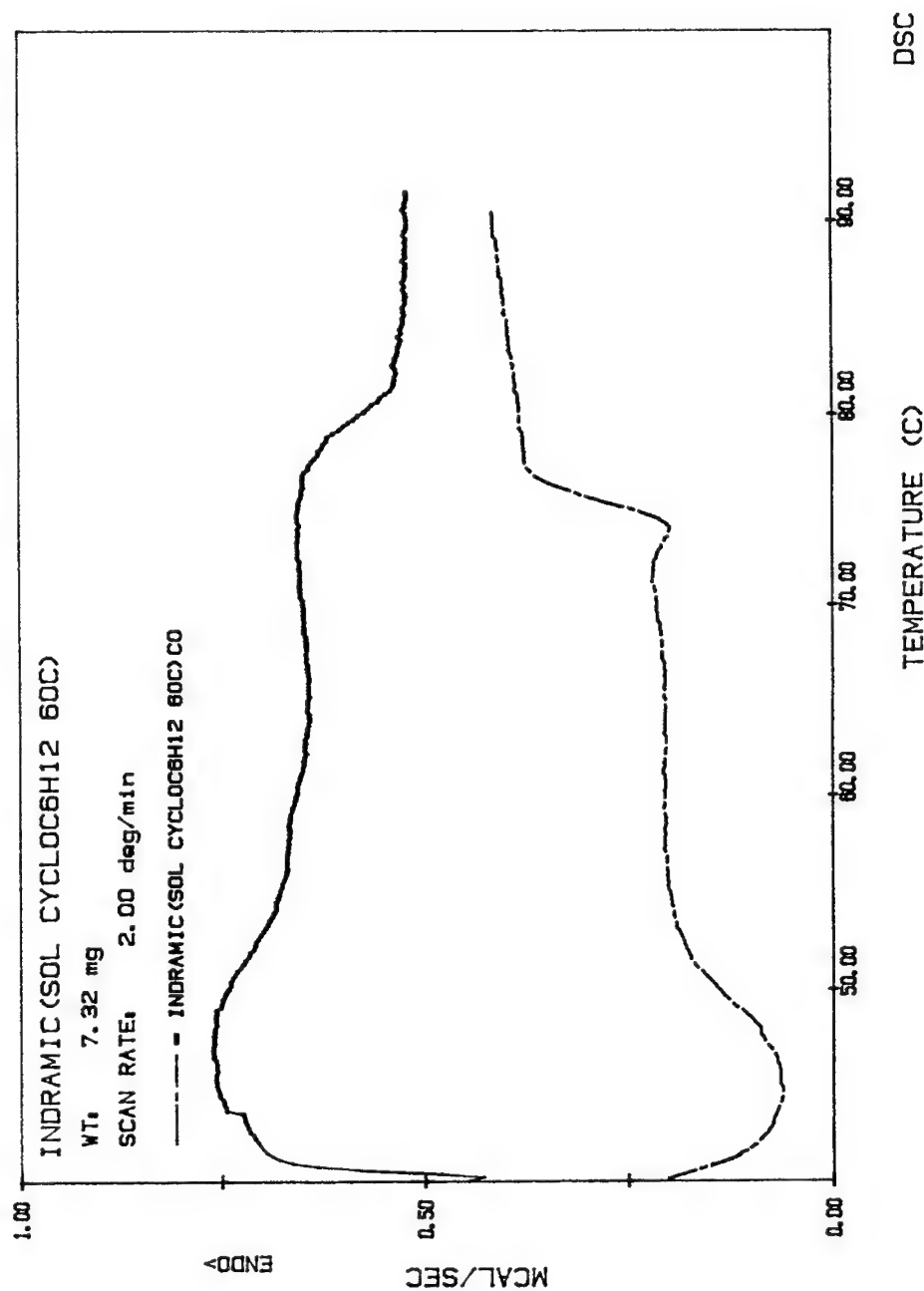


Figure 8. DSC Thermograms of the Cyclohexane Extract at 60 oC of Wax B

successful. Figure 8 shows the heating (upper curve) and cooling (lower curve) DSC thermograms of the cyclohexane extract at 60 °C of Wax B. It can be seen readily that the upper melting range is essentially reduced down to that of Wax A (see Figures 5 and 6) demonstrating the feasibility of tailoring the melting range of an inferior wax into a superior one for Composition B casting application.

### SUMMARY

DEPMS, SFC, and DSC clearly show that Wax B consists of higher molecular weight fractions than Wax A. This causes the former to freeze at a higher temperature range relative to the latter resulting in a much greater degree of void formations actually observed in the cast Composition B and much higher rejection rates. Obviously, Wax B contains a smaller fraction melting below 73 °C compared to Wax A to fill the voids formed during the sudden crystallization of TNT from the metastable supercooling state.

The feasibility of fashioning a 'designer wax' tailored for desensitizing any particular explosive composition has been demonstrated.

### REFERENCES

1. a. Seeger, D. E., 1983. Waxes-Use in Energetic Materials, *Encyclopedia of Explosives and Related Items*, PATR 2700, Volume 10, Edited by Kaye, S. M., Assisted by Herman, H. L., U. S. Army Armament Research and Development Command, Dover NJ, page W26; b. *ibid*, pp. W24-51; c. *ibid*, pp. W36-42; d. *ibid*, pp. W52-57. e. *ibid* pp. W53-54; Reference 88, 1983.
2. Statton, G. and Taylor R.C., Surfactants and Desensitizing Wax Substitutes for TNT-Based Systems, *Final Report, July 2, 1992-July 1, 1994*, Mach I, Inc., King of Prussia, PA.
3. Velicky, R. W., Effect of TNT Miscible Additives on the Mechanical Behavior and Shock Sensitivity of Composition B, *Report No. ARAED-TR-88031, January 1989*, U. S. Army Armament Research and Development Center, Dover, NJ.

4. **Borne, L.**, Influence of Intragranular Cavities of RDX Particle Batches on the Sensitivity of Cast Bonded Explosives, *Report No. ISL-PU-339/93, July 1993*, Institut Franco-Allemand de Recherches, Saint-Louis, France.
5. **Harris, J.**, Characterization of Four Montan Waxes, *Technical Report, October, 1993*, U. S. Army Armament Research Development and Engineering Center, Picatinny Arsenal, NJ.
6. **Kemp, R. T. and Anthony, F. B.**, Synthesis of Waxes for the Phlegmatization of Explosives, *Report No. NSWC/DL-TR-3364, December 1975*, Naval Surface Weapons center, Dahlgren, VA.
7. **Hogge, W. C. and Cousins, E. R.**, Evaluation of Synthetic Waxes for Desensitizing Explosives, *Interim Report for FY 1975*, November 1975, Naval Weapons Station, Yorktown VA.
8. **Ashraf-Khorassani, M. and Taylor, L. T.**, Analysis of Crude, Purified, and Synthetic Candelilla Wax Using Supercritical Fluids, *LC-GC, Volume 8, Number 4, 1990*, pp. 314-320.
9. **Pellen R. and Russell K.**, Study of Melt Loading the 105 MM M1 Projectile with Comp B Containing Grade B wax, *Report No. PA-TR-4854, September 1975*, Picatinny Arsenal, Dover, NJ.

***Area 6:***

***Ignition and Combustion  
Performance of Propellants  
for Rocket Propulsion***

## ADVANCES IN ENERGETIC MATERIALS MANUFACTURING TECHNOLOGIES AT ICI

S.K. Chan<sup>1</sup>, G.A. Leiper<sup>2</sup>, R. Olive<sup>3</sup>

1. ICI Explosives Canada

2. ICI Explosives, Automotive Products

3. ICI Engineering Technology

**ABSTRACT :** ICI Explosives has recently developed a number of novel manufacturing processes for energetic materials. These processes were highly successful in improving manufacturing efficiency, mixing efficiency, product quality and control, safety and environmental friendliness. The propellants and pyrotechnics produced by these processes have enhanced reaction rates and improved completeness of reaction as a result of the highly efficient mixing in the micron and submicron levels. The Microsaf™ Process is ICI's second generation sodium azide propellant technology. The active ingredients are either completely dissolved or mixed in water which allows the use of extremely fine insoluble ingredients. A free flowing powder with excellent product quality is produced by a spray drying process. All reject materials are entirely recyclable. The Freeze-Dry technology uses a fast freezing and vacuum freeze dry process to produce a flowable powder consisting of extremely fine crystals for the dissolved ingredients. The Enerfoil™ Process uses physical vapour deposition technology to coat magnesium on PTFE film. The Enerfoil™ film thus produced possesses unique properties of fast and controlled reaction, enhanced handling safety and ease of conversion to desirable shape for use in many applications such as ignition enhancer and hybrid inflator heating system for airbag inflators.

### INTRODUCTION

ICI Explosives has been a leader in the supply of advanced explosives and energetic products for over a century. For over 25 years, ICI Explosives has also been actively involved in the development and manufacture of many airbag inflator pyrotechnics systems. In all these activities, the safety, health and environmental effects (SHE) of any manufacturing process are among the highest priority concern during its design, selection and all subsequent stages. Since 1990 ICI Explosives Automotive Products has developed a number of new technologies to produce high quality products safely which are also cost effectively and environmentally friendly. ICI's new products include the second generation sodium azide Microsaf™ propellant and Enerfoil™ ignition film. Other potentially new products are being considered with a new technology under development which is based on the freeze drying technology. These new technologies demonstrate vividly that safety and efficiency can indeed be combined in high quality production processes if these objectives were kept clearly in mind during the design and formulation stages. These processes and the performance of the products are described in the present paper.

## MICROSAF™ PROPELLANT

In the early 1970's the airbag industry went through a very thorough analysis concluding that sodium azide was the most optimum propellant material because it produces non-toxic gas with relatively low temperatures of reaction and at reasonably high burn rates. Its high temperature of decomposition also contributes to the propellants' excellent long term storage stability which is essential for the reliability of the inflator for the life of the car. To date, the majority of the 50 million cars equipped with airbags still have sodium azide based inflators. ICI was one of the original developers of sodium azide based gas generant formulations for airbag inflators. One of the formulations (Ref. 1) was mass produced by ICI's subsidiary company, Sabag Inc., in the late 1980's and early 1990's for passenger side airbag inflators. The production was by means of traditional grind and mix technology widely used in the pyrotechnics industry. The formulation consisted of four major ingredients (sodium azide, iron oxide, sodium nitrate and bentonite) with graphite fibres added to increase the burn rate. It was one of the cleanest azide propellants in the industry. However, it was found to be too complex for the production process to produce consistent product performance. The final mixed powder was not sufficiently free flowing to guarantee even filling of the press mould which determines the pressed density and grain dimension. In the worst case, uneven filling could even damage the press tools. Like all other azide propellant manufacturers, the early operations suffered a few accidents. For these reasons, a program was launched in 1990 at ICI Explosives Canada to develop a new formulation and a new processes to produce the second generation sodium azide propellant. This resulted in the Microsaf™ propellant and process (Refs. 2-4).

### Propellant Formulation

Microsaf™ propellant has only three ingredients : sodium azide, iron oxide and silica. The particle sizes of the oxides (0.2 µm iron oxide, R-1599D from Harcros Pigments, Toronto Canada and 0.014 µm silica, Ca-O-Sil fumed silica from Cabot, Shakerheights, Ohio) were the finest commercially available. This formulation is one of the most desirable since it is relatively cool burning with the most desirable combustion products. The formulation produces products shown in the following equation :

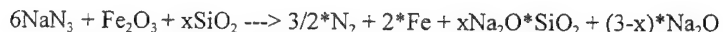


Figure 1 shows the predicted combustion products and experimental burn rates for a range of silica content, with fixed azide and iron oxide mass ratio of 2.326. Within a wide range of variation of the formulation, the combustion temperature (1250 - 1650 K ) remains below the melting point of iron and it stays as a solid clinker in the combustion chamber after the combustion. The silica reacts exothermically with part of the sodium oxide to form sodium silicate, which can be easily filtered. Thus the amount of undesirable, highly alkaline, sodium oxide is reduced to the minimum and theoretically to zero level above 14% of silica. The linear burn rate was experimentally measured by burning a pressed cylinder (12.7 mm diameter by 12.7 mm long) in nitrogen atmosphere at an initial pressure of 6.9 MPa in a 1.5 L high pressure vessel. The burn rates were found to depend on the process employed to produce the formulation. The values shown in Figs. 1 and 2 were obtained from powder produced by the spray dry process as described below. It was found to be proportional to the predicted heat of reaction as shown in Fig. 2. The burn rate could then be adjusted over a wide range of values from 20 to over 50 mm/s to suit customer's specifications. In practice, the most used formulation was  $\text{NaN}_3/\text{Fe}_2\text{O}_3/\text{SiO}_2$  63/29/8 in weight percentage.

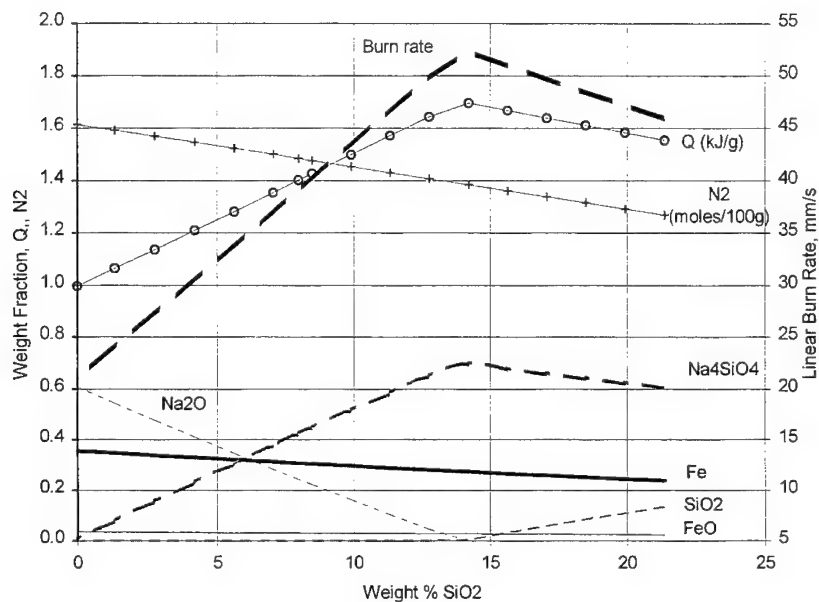


Fig. 1 Predicted combustion products and burn rates of Microsaf™ gas generant.

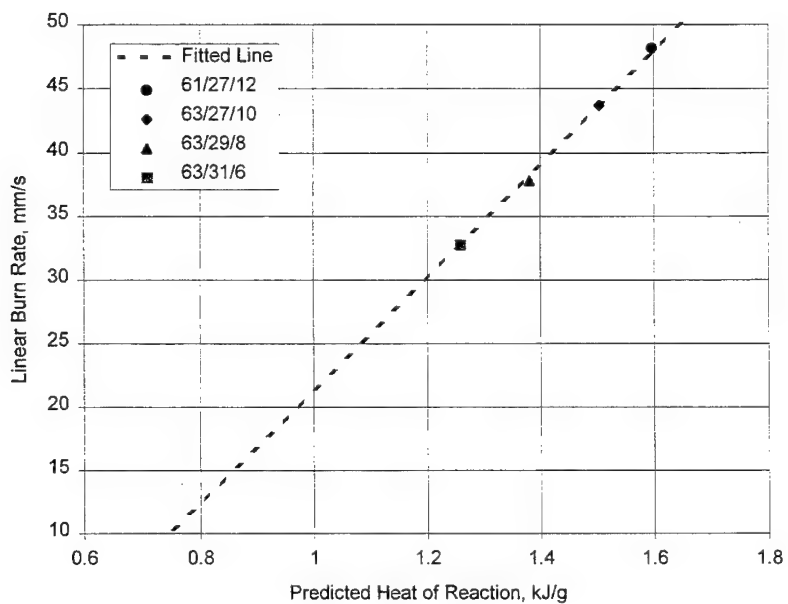


Fig.2 Correlation of experimental linear burn rates with predicted heat of reaction



## Manufacturing Processes

To avoid the high energy input and high frictional environment of standard grinding process, early on in the development program it was decided that a novel approach will be required to provide a safe and efficient mixing process to produce a product having the necessary small particle sizes and intimacy of mixing of the ingredients. The relatively high solubility of sodium azide (29.4 g/100 ml water) suggested a possibility of using a totally dissolved phase and precipitation technology to produce the propellant. Thus the sodium azide was dissolved completely in water and the oxides were mixed in forming a colloidal suspension. A high shear mixer was utilized to obtain a thorough dispersion of the oxide particles. The addition of the Cab-O-Sil increased the viscosity of the solution and helped to keep the iron oxide in suspension for a sufficiently long period of time to complete the subsequent process steps. The aqueous dispersion was passed through a spray dryer. In the spray dryer, the solution was pumped through nozzles to form streams of small droplets into a flowing current of hot air at a temperature in the range of 80-180° C, whereby the water inside the droplet was evaporated. The dried particles produced in the process comprise substantially spherical micro-porous aggregates of azide crystals with the oxide particles encapsulated by the azide particles. A scanning electron micrograph of a particle is shown in Fig. 3, which shows the particle to be about 40  $\mu\text{m}$  in diameter while the azide crystals are in platelet forms with a thickness of 0.5-1  $\mu\text{m}$ . Figure 3 also shows the x-ray concentration maps of the particle. These maps indicate the concentrations of the three elements Na, Fe and Si and provide visual proof of the high degree of uniformity of the distribution of the three ingredients,  $\text{NaN}_3$ ,  $\text{Fe}_2\text{O}_3$  and  $\text{SiO}_2$  respectively in the spray-dried granules. Such a high degree of intimacy of mixing guarantees the fast and complete reaction of the ingredients which eliminates the production of free sodium in the combustion products. Most commercially available azide propellants produce free sodium on combustion to a certain degree. It must be trapped inside the inflator and cannot be allowed to flow into the airbag due to the fact that it burns readily in air and produces toxic sodium oxide. In contrast, Microsaf™ propellant produces no free sodium after combustion.

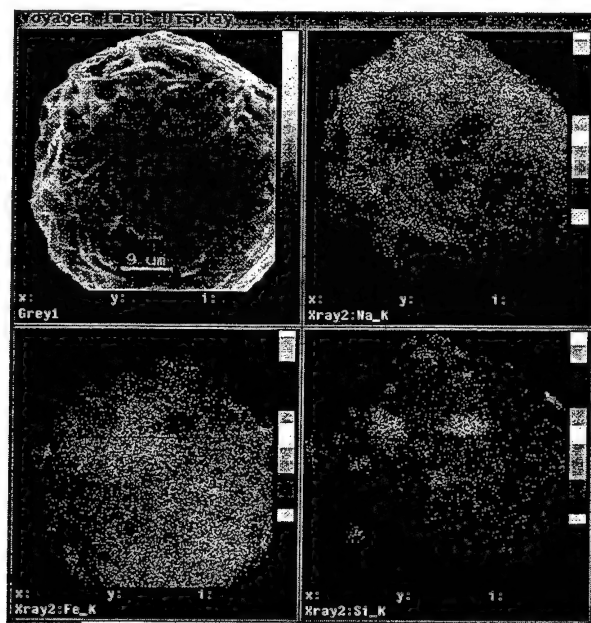


Fig. 3 SEM and X-ray concentration maps of Na, Fe and Si of a spray-dried Microsaf™ particle.

Due to the small sizes of the ingredient and their extremely high degree of mixing, the intrinsic reaction rate is also higher resulting in higher burn rates of Microsaf™ propellants. Table 1 provides examples of the burn rates of Microsaf™ propellant and the same formulation produced either by direct drying of the aqueous dispersion or by ball milling.

TABLE 1  
Comparison of Burn Rates of Microsaf™ Propellants Produced by Different Processes

Production process	Linear burn rate, mm/s
Microsaf™	40
Drying of aqueous dispersion	24.4
Ball Milling	33

A schematic of the complete Microsaf™ process is shown in Fig. 4. It illustrates the process steps involving slurring and mixing, spray drying, powder conditioning, tableting and pressed grain drying. The powder conditioning process depended on the requirements of the tableting process. It generally consisted of mixing in additional pressing aids, e.g. moisture or graphite powder. Since the starting material was in solution form, reject materials at any point in the process cycle could be reprocessed by re-dissolving in the slurring tank. This eliminated the need to burn the reject material, which was becoming more restrictive due to the strict environment laws in most areas in North America. Currently, commercial azide propellant producers have to reclaim the sodium azide from reject propellants by additional process steps. These add to the overall cost of production. Even with this, some of the ingredients cannot be recycled and must be disposed of and they add to the contamination of the environment. In contrast, the Microsaf™ process is totally recyclable and completely environmentally friendly.

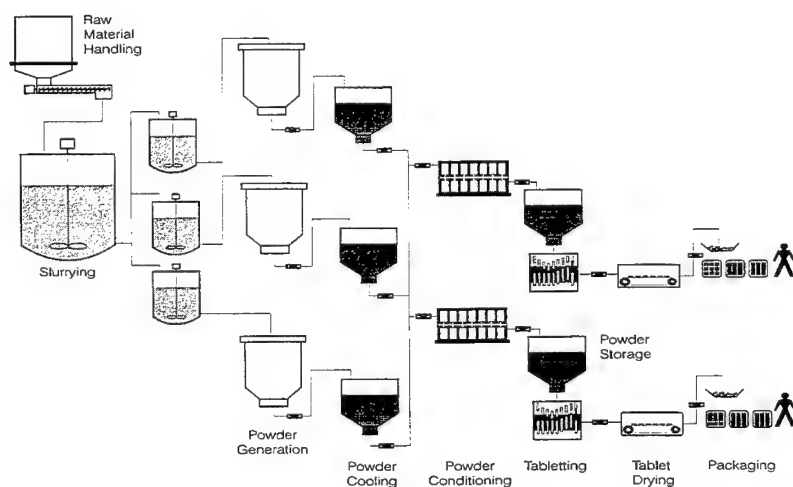


Fig. 4 Schematics of Microsaf™ Production Processes

A demonstration pilot scale plant was built and operated for over two years. The reliability of the Microsaf™ process was shown by the small variations in the compositions of a large number of batches, as shown in Fig. 5. The results show that the concentrations of all ingredients were kept to within  $\pm 1\%$ . The reproducible compositions and intimacy of mixing are also reflected in the measured linear burn rate of these batches as shown in Fig. 6. For the present formulation, the average linear burn rate was 37.8 mm/s with a standard deviation of 1.8 mm/s over all the batches examined. These batches were highly experimental in nature involving many process variations to evaluate process control parameters and included some recycled powder and recycled pressed grains. The ignition efficiency of the Microsaf™ propellant grains was also more consistent than powder produced by ball milling as demonstrated by the hot plate ignition delay times<sup>5</sup> of the two processes shown in Fig. 7. This again demonstrated the consistent and high degree of intimacy of mixing obtainable with the present process.

The highest priority requirement in process design was safety. The Microsaf™ solution process avoids the handling and mixing of dry pyrotechnic material which is in general very sensitive to friction and impact in the dry state. The high quantity of water eliminates the fire hazard. Due to its simplicity, reliability and recyclability, it is also potentially the lowest cost production process in the industry.

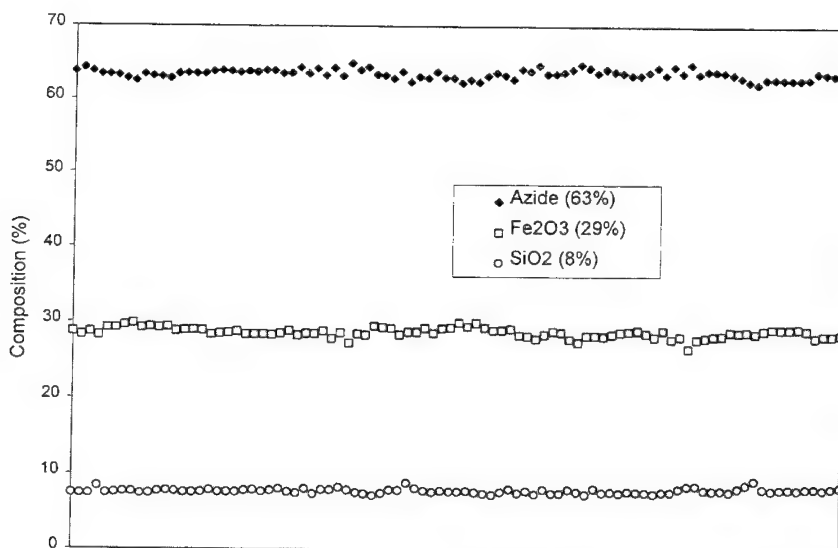


Fig. 5 Variation of Microsaf™ product composition over a number of batches.

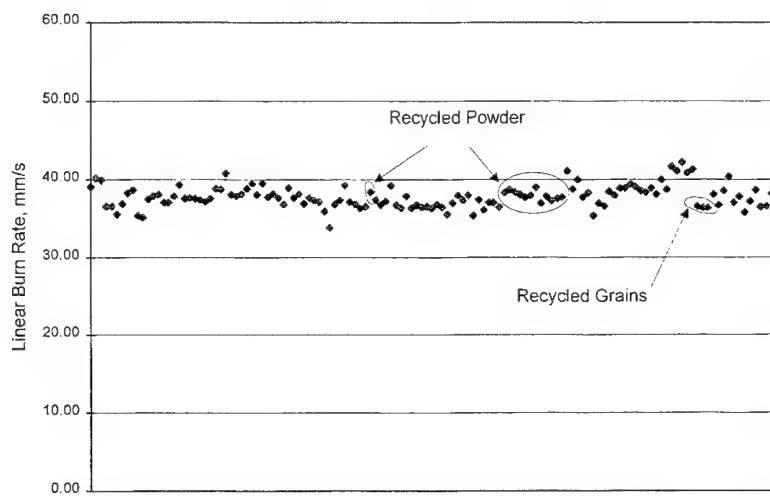


Fig. 6 Microsaf™ propellant burn rates from all experimental batches.

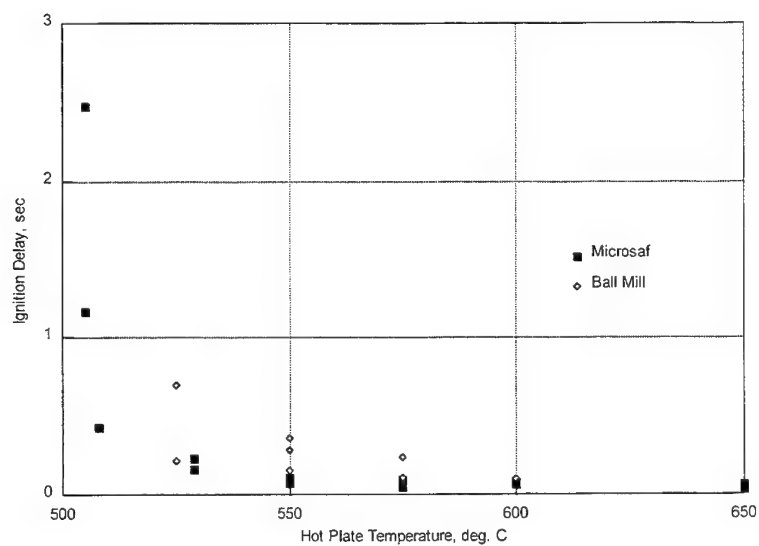


Fig. 7 Comparison of ignition delay times of sodium azide based propellants produced by different processes.

## FREEZE-DRY TECHNOLOGY

While spraying drying was shown to be adequate for the production of relatively temperature tolerant sodium azide base pyrotechnics, however, the process temperatures were too high for the stability of most energetic materials. The process was also not suitable for materials with a relatively low melting point. Furthermore, extraction of the solvent by evaporation creates a hollow spherical structure after the drying process. Such enclosed air voids can cause problems for fast pressing operations due to the resistance of the entrapped air. The progressive crystallization process can also cause segregation of the mixed solids from the crystallizing material. The relatively low concentration of the silica on the surface of the spray dried Microsaf<sup>TM</sup> particle seen in the X-ray energy dispersion spectra of Fig. 3 is evident of such segregation. For these and for the obvious reasons of safety in avoiding the use of excessively high temperature operations, an improved process was sought for the manufacture of Microsaf<sup>TM</sup> and other energetic materials. The new concept combined crash freezing and freeze-drying for the manufacture of energetic and other materials.

Freeze drying technology is a well known process in other industries where it is used for materials which deteriorate in high temperatures, e.g. instant coffee. The process is in principle also suitable for energetic materials for the same reasons. Furthermore, when combined with crashed freezing, the process was shown to be capable of producing ultra-fine crystals desirable for almost all energetic materials<sup>6</sup>. The freeze drying process concept is relatively straight forward. Its principle is illustrated in Fig. 8, which shows the phase diagram of an aqueous solution as a function of pressure and temperature. The starting point "A" in the diagram is the solution phase, or solution with

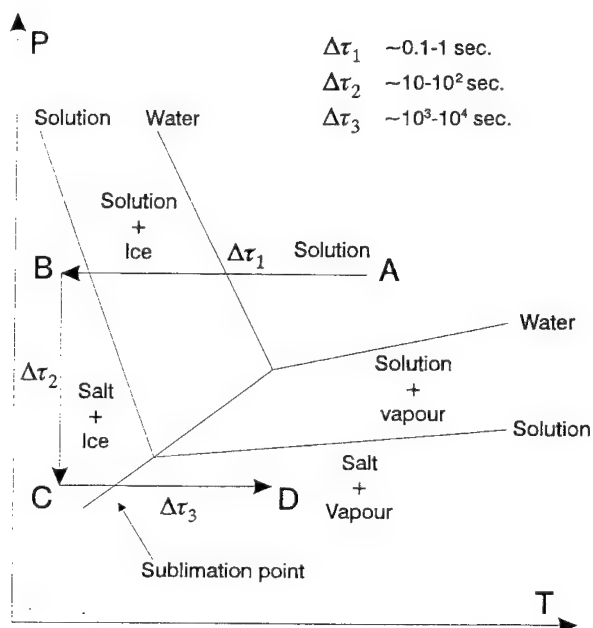


Fig. 8 Cryogenic powder synthesis phase diagram for aqueous solution

dispersed solids, at atmospheric pressure and room temperature. This solution is chilled rapidly to well below its freezing point "B". The frozen solid is then depressurized (point "C") in a vacuum chamber and heat is applied to it inside the vacuum chamber subliming the frozen solvent, resulting in a dried powder (point "D"). In practice, the solution ("A") is sprayed into a cold medium, e.g. cold nitrogen gas, as very small droplets. The large surface area and the large temperature difference between the nitrogen and the solution droplets ensures high heat transfer rate which reduces the crystal sizes. As an illustration, the freezing time is normally of the order of 0.1 - 1 second. The decompression time takes a few 10's of seconds and the vacuum drying time is the longest taking the order of an hour. Therefore, such crashed freezing and freeze drying processes can produce extremely small crystal sizes of the order of a few tens of nanometers. The very short freezing time also minimizes migration of the mixed solids, thus maintaining the uniformity of dispersion obtained in the solution mixing process. The ultra-fine crystals are preserved in the vacuum drying process as the frozen solvent is extracted by sublimation and diffusion through the inter-crystal spaces. The resultant freeze dried particle consists of a uniformly porous structure containing very fine crystals and the mixed solids.

In terms of the SHE effects, the freeze-dry process possesses all the advantages of the Microsaf<sup>TM</sup> spray dry process described above plus the improved safety by eliminating the high temperature spray drying step. Therefore, the process is theoretically the safest possible route of producing an energetic material. However, this is still a very new concept in the early stages of development. Presently, small pilot scale plants were built for experimental purpose. Nevertheless, many energetic materials have been produced with highly improved ballistic properties.

### Examples of Application

A few materials of interest to ICI have been investigated with our pilot freeze-dry process<sup>6</sup>. One of the first materials investigated with this new process was ammonium nitrate based propellants. Due to the environmental concerns of the combustion products of ammonium perchlorate based propellants, there is currently a lot of interest in propellants based on ammonium nitrate, which produces more environmentally friendly combustion products. Table 2 shows a comparison of the linear burn rates from materials produced by the freeze-dry process and by ball milling. There are significant increases in the burn rates of 35 - 65% for ammonium nitrate formulations from the ball milled materials. Similar increase was also obtained with Microsaf<sup>TM</sup>, although the burn rate from the freeze-dried material was similar to that from the spray dried material (Table 1). Freeze-dried black powder had a higher and more reproducible linear burn rate than that produced from conventional process. The literature reported burn rates<sup>7</sup> ranging from 10 to 30 mm/s, showing the difficulties of producing black powder with consistent performance. The present process overcomes that problem and is intrinsically safer.

TABLE 2  
Comparison of Propellants Linear Burn Rates (mm/s) at 6.9 MPa  
Produced by the Freeze Dry and Ball Milling Processes

Formulation	Freeze Dry	Ball Mill
AN/polyacrylamide/C	4.3	3.2
above + catalyst	6.3	3.8
Microsaf <sup>TM</sup> propellant	40	33
Black powder	20 (1.9 g/cc)	10-15 <sup>7</sup> (1.7 g/cc)

## ENERFOIL™ PYROTECHNIC FILM

The previous two processes had advanced the degree of mixing of fine solids in water or in the solution of the major ingredients. The resultant mixing scales in the final powder, however, still depends on the degree of dispersion in the solution and the degree of migration during the crystal formation step. In recent computer simulations in ICI<sup>8</sup>, they have clearly shown that, for random mixtures of poly-dispersed spherical particles, it is unlikely that a two component powder mixture of similar particle sizes can ever be uniform on the length scales characteristic in condensed phase combustion. In order to achieve a reasonable degree of uniformity of mixing, the sizes of the minor component must be much smaller than the major component. This is exactly the reason of choosing the very much smaller iron oxide and silica in the Microsaf™ formulation. Nevertheless, the degree of mixing is still dependent on the dispersion properties of these fine particles and the mixing process.

Recently a major advance in pyrotechnic process technology was invented at the Defence Research Agency (DRA) of the Ministry of Defence<sup>9,10</sup>, UK. This process produces thin film pyrotechnics by physical vapour deposition (PVD) of the reactant in vacuum. The process was in principle simple and highly controlled. Alternating layers of fuels and oxidizers were laid down on a substrate to form a sandwich of pyrotechnic material. The layer thickness, in effect the particle sizes, were controlled by the vapour deposition process and the intimacy of mixing by the creation of a laminar structure. Advantages of this novel process were immediately obvious. The randomness of mixing was eliminated and local stoichiometry guaranteed. Process dust generation was minimized. The reproducibility offered by PVD was high, promising a reduction in scrap material. Moreover, as the pyrotechnic material was manufactured in sheet form, subsequent handling did not rely on dispensing powder and pressing pellets, but on cutting strips and rolling film.

One interesting aspect of this technology was the production of a very reactive pyrotechnic material based on magnesium and PTFE. In powder form, this mixture was much used as rocket motor igniter material. Unfortunately, the powder was dangerous to manufacture and hazardous to handle and press, with approximately 1 in every 30,000 pellets spontaneously igniting. DRA found that when a piece of PTFE film was coated with magnesium, a fast burning composition resulted which showed much improved resistance to hazardous stimuli. ICI Explosives Automotive Products recognized the significance of such a process and the new material in their applications in automotive airbag inflators. An exclusive license was obtained in 1992 from the DRA and the UK authorities for the use of this material in automotive safety systems. ICI early on conceived of an ignition enhancer for sodium azide propellant gas generant and heating system in hybrid airbag inflators<sup>11-13</sup> made from such magnesium-PTFE pyrotechnic sheet, or Enerfoil™ film, as its trade name adopted by ICI.

Although initial feasibility was demonstrated by a simple vacuum coater built by the DRA, the quality of the Enerfoil™ film was poor and there was a lack of reproducibility in performance. However, no commercial manufacturing process existed for the film. ICI decided to design and build the world's first production scale roll coater for the production of the Enerfoil™ film, with input from experts from ICI Explosives, ICI Films, ICI Image Data and engineers from General Vacuum Equipment Ltd. (Heywood, Lancashire, UK). Special attentions were paid to safety issues during the development process and this has resulted in some innovative features<sup>14,15</sup>. Machine fabrication and commissioning was completed in 1994 and installation at ICI Explosives' Tamaqua (Pennsylvania, USA) site was completed in 1995. The process, product and some application results are briefly described in the following, more details can be found in Refs. 16-18.

## Vacuum Coating Process

The machine layout is shown in Fig. 9. The film winding mechanism was arranged so that the rewind zone was located at one end of the machine and was separated from the unwind zone. In the unwind (coating) zone, the PTFE feed reel unwound the roll of film which was wound on a first cooled coating drum for coating of the first side of the film and then wound onto the second drum for coating the opposite side. Beneath the two cooled drums were two identical magnesium sources. Each source consisted of a series of radiantly heated crucibles held in retorts. The retorts were arranged across the web and were equally spaced radially around the drum. Magnesium ingots were heated under high vacuum and sublimed to form vapour jets. The vapour jets were directed onto the substrate, where the vapour condensed on the web in contact with the chilled process drum. This coating was achieved with excellent uniformity. An accurate, non-contact, multi-point deposition monitor, which was specially adapted to this application, was installed after each process drum. They measured the thickness of the first and second coatings continuously. This data was then stored and used to control the evaporation sources and the stored data also provided product quality verification.

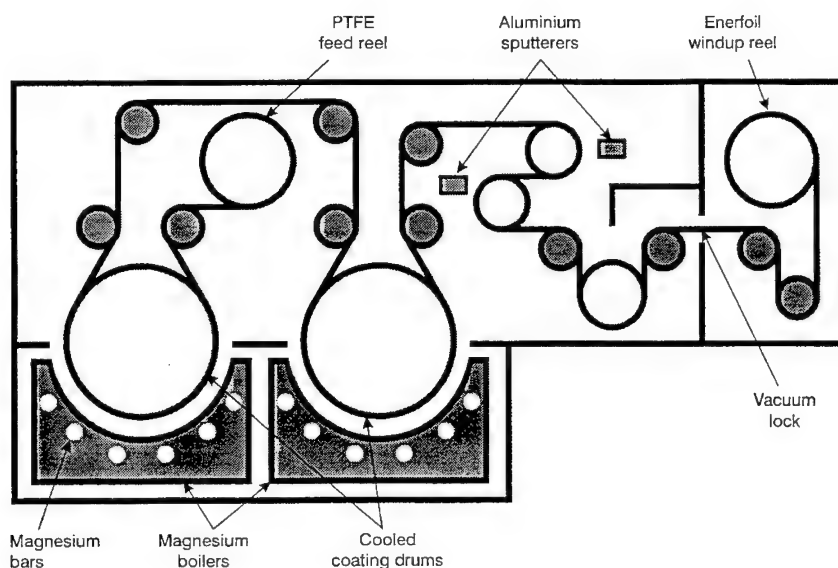


Fig. 9 Enerfoil™ vacuum coater schematic

After the coating of the magnesium layers, the film was then wound around two drums where a very thin coating of aluminum (20 nm) was coated on the magnesium surfaces. The aluminum coating helped to reduce surface oxidation rate of the Enerfoil™ in the presence of oxygen. After the aluminum coating, the film was then passed through a load lock which separated the coating chamber from the rewind chamber.

As usual, safety has been of paramount importance during the design and manufacture of this machine. This was achieved by incorporating automatic controls wherever possible and some proprietary design features. The load lock was one of these features.



### Enerfoil™ Film Properties

The magnesium crystal formed columnar structures on the PTFE surface, as can be seen in the scanning electron micrograph of Fig. 10. The magnesium layer was typically about 8  $\mu\text{m}$  thick with individual crystal sizes of about 1  $\mu\text{m}$  wide by 8  $\mu\text{m}$  long. The unique sandwich structure of this material with a continuous surface conductive metal layers rendered it very much safer in handling. Standard hazard tests on the film were carried out in our laboratories, and the results are summarized in Table 3. The data show that Enerfoil™ film is very insensitive to impact and friction and the electrostatic ignition threshold for sustained burning is exceptionally high. Thermal stability data were obtained by high temperature DSC and they showed the material to be extremely insensitive to heat. Together, these properties provided positive proves that Enerfoil™ film is much safer for subsequent processing and handling operations than that associated with powder systems. For example the spark sensitivity of the equivalent powder system is less than about 1 joule<sup>19</sup>.

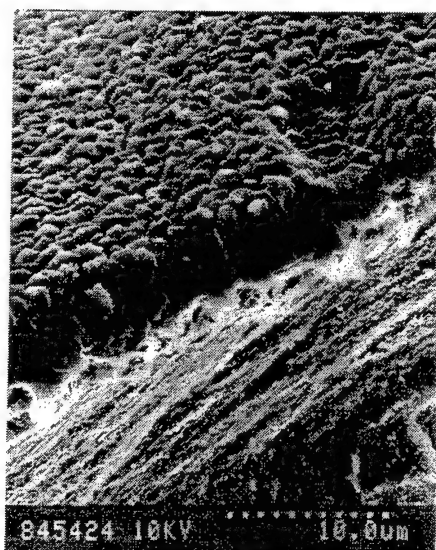


Fig. 10 SEM of Enerfoil™ surface showing the columnar structure of magnesium crystals

TABLE 3  
Hazard and Sensitivity Data for Enerfoil™ Pyrotechnic Film

BAM impact sensitivity	16 Joule
BAM friction sensitivity	> 360 N
Static ignition threshold	20 Joules
DSC thermal stability	> 450° C
Time to ignition at 550 ° C	30 sec

Ballistic properties have been computed by thermochemical calculations, and by calculation from closed vessel combustion tests. These are summarized in Table 4. The Enerfoil™ pyrotechnic film has a very high flame temperature and heat of reaction, but a very low force constant. Such a combination of properties is ideal for ignition systems, since these systems would generate very low

transient forces avoiding damages to the propellant grains. Ignition is primarily caused by the condensation of the reaction products onto the propellant, with the release of large amounts of energy. Flame spread rates across the film were measured and found to be sensitive to local pressure and geometry. Flame spread across an unconfined sheet occurred at about 1 m/s<sup>20</sup>. Upon confinement, the flame spread rate could reach close to sonic or even supersonic speeds.

TABLE 4  
Computed and Measured Ballistic Properties

Isochoric flame temperature	5010° K	Mass of gas. products	78% at flame temperature
Isobaric flame temperature	3800° K		0% at STP
Heat of reaction	9.6 MJ/kg	Flame spread rate	~ 1 m/s (combustion)
Force Constant	0.165 MJ/kg		~ 1000 m/s (detonation)
Linear burn rate <sup>21</sup>	16.9p(MPa) <sup>0.22</sup>		

In general there are three intrinsic energy release rates for a roll of combustible sheet material depending on the geometry of the roll. The energy release rate of a loosely wrapped roll, with optimum interply spaces, is governed by the speed of propagation of the combustion front through the interply spaces and the intrinsic burn rate of a single layer of Enerfoil™ film. Both of these rates are functions of the initial pressure only, for a given ambient gas composition. For example, it takes 0.6 ms to consume a 40 µm thick material at 20 MPa assuming the burn rate of Ref. 21. It takes 0.2 ms for the flame to propagate through 200 mm length of a typical ignition roll, when a strong ignition source is used generating a detonative combustion wave. (The latter is slower if a gentle ignition source is used generating a slower combustion flame propagating at about 1 m/s.<sup>20</sup>) Therefore, the overall energy release rate (< 1 ms) is determined by a combination of these two rates and is independent of the number of layers, or the total amount of material, in the roll. On the other hand, if the interply spaces are reduced to zero, prohibiting the free propagation of combustion products in the spaces, the roll possesses two other energy release rate. A second energy release rate is determined by the radial thickness of the roll and the linear burn rate of the material in the radial direction. The third energy release rate is given by the length of the roll and the linear burn rate of the roll in the axial direction. Obviously, an infinite number of energy release rates, from milliseconds to seconds, can be obtained by choosing one of these two modes with suitable dimensions for the roll. This illustrates the versatility of Enerfoil™ film in its potential applications.

### Enerfoil™ Commercial Applications

One of the first commercial applications of Enerfoil™ pyrotechnic film was developed by ICI Explosives Automotive Products in the area of ignition systems for sodium azide based passenger side airbag inflators. Airbag inflators require very fast functional times of between 30 - 60 ms. Uniform and prompt ignition of the gas generant grains are an absolute necessity. Previous commercial ignition systems were both expensive and hazardous in manufacturing and handling. ICI Explosives' Enerfoil™ ignition enhancer had overcome both the cost and handling hazards of these systems. Its performance was shown to be among the best in the industry<sup>18</sup>. The ignition enhancer was made from cut sheets of quadrilateral shaped Enerfoil™ film pre-embossed with rows of regularly spaced dimples. The sheet was wound to form a hollow coil with the desired interply separation distances of about 300 µm. The enhancer was inserted into a stack of propellant grains, with or without a confinement tube. The end of the enhancer with the internal helices was ignited by a squib. This resulted in extremely fast combustion time of the enhancer as shown in Fig. 11, which

shows the pressures inside the confining tube and in the propellant chamber filled with dummy grains. The total combustion time of the Enerfoil™ enhancer was only about 2.5 ms which corresponded to a linear burn rate of 8 mm/s for a 40  $\mu$ m thick film, assuming simultaneous combustion from both sides of the film. Similar burn rates (10 mm/s) were reported by Peretz<sup>20</sup> for Mg/PTFE at atmospheric pressure.

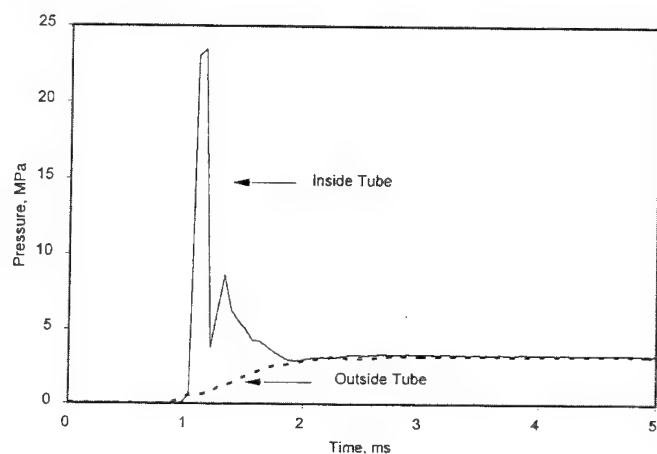


Fig. 11 Ballistic performance of Enerfoil™ ignition enhancer in a confinement tube.

Ignition of solid propellants depends strongly on the rate of heat transfer to the surface of the propellant, which depends on an efficient coupling between the propellant grain design and the function of the ignition system. ICI Explosives has developed a very efficient grain geometry which made full use of the very high energy flux from the Enerfoil™ ignition enhancers. The grains were wafers, pressed from Microsaf™ powder, having dimensions of 35 mm OD, 14 mm ID and 4 mm thick. One surface of the grain had 16 radial ridges (0.25 mm height) pressed on the grain. The experimental pressure in the enhancer confining tube, from a test using such a combination of enhancer and propellant grains, is shown in Fig. 12. Following the enhancer reaction spike, the rise

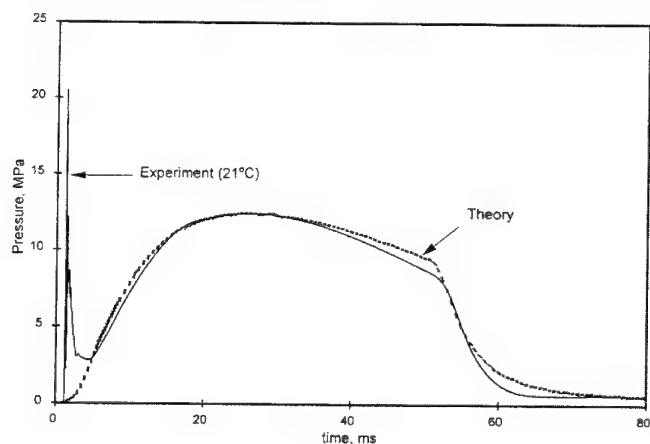


Fig. 12 Comparison of predicted and experimental inflator pressures.

in pressure at 4.2 ms is a result of the combustion of the propellant. Therefore, ignition of the grains were effected well before this time. This ignition delay ( $\sim 3 - 3.5$  ms) was found to be almost independent of initial inflator temperatures, which was unique among all existing commercial inflator ignition systems. The sharp change of slope at 51.5 ms was caused by the almost simultaneous completion of combustion of all propellant grains. This was an indirect proof that the propellant grain surfaces were ignited uniformly and simultaneously. This is further proven by the excellent fit between the experimental curve and the theoretical prediction<sup>18,22</sup>.

Another potential application of Enerfoil<sup>TM</sup> pyrotechnic film was its use as a heating source in hybrid inflators<sup>12</sup>. In this case, the Enerfoil<sup>TM</sup> heating system was housed inside a high pressure bottle, containing inert gases such as argon, helium or nitrogen. Oxygen was normally added to facilitate the reaction speed of the Enerfoil<sup>TM</sup> film and to increase the total energy output by reacting with the carbon from the combustion products. The latter reaction increased the theoretical heat of reaction from 9.6 kJ/g to 14.9 kJ/g. The desired Enerfoil<sup>TM</sup> film geometry depended on the energy release rate requirements. The geometry of a fast output charge differed only slightly from the ignition enhancer. However, for slower energy output rates, the other geometries mentioned above or combinations of them were needed. A single or multiple charges was used to phase out the energy release rate to provide programmed output for the next generation smart airbags. Fig. 13 is a plot of the bottle and output pressures in a 60 L tank for a single charge of 6 g of Enerfoil<sup>TM</sup> roll, made using the fastest burning geometry, burnt in a 0.5 L vessel containing argon and oxygen (90/10). Fig. 14 is a similar pressure plot for a dual charge system with one radially burning (tightly wrapped) roll and one fast burning Enerfoil<sup>TM</sup> roll. The ignition of the latter was delayed by 10 ms, which produced the desired slow and fast output pressures in the 60 L tank. Such programmability is required in the next generation of smart inflators and airbags.

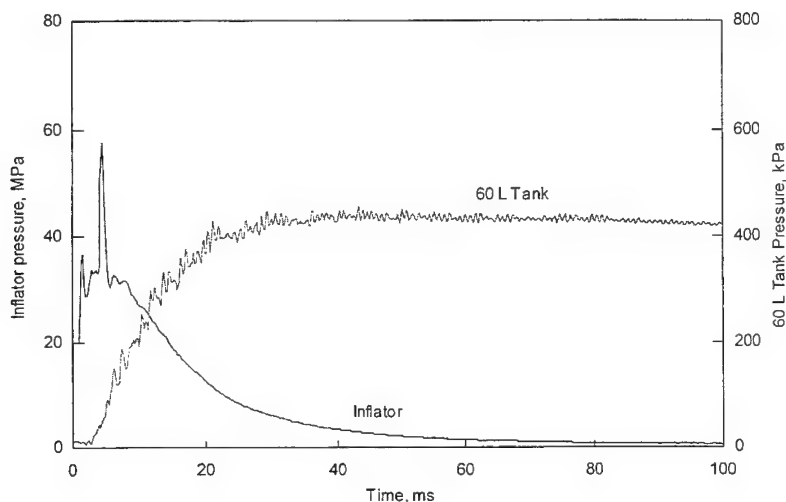


Fig. 13 Hybrid inflator output with one 6 g Enerfoil<sup>TM</sup> heating roll.

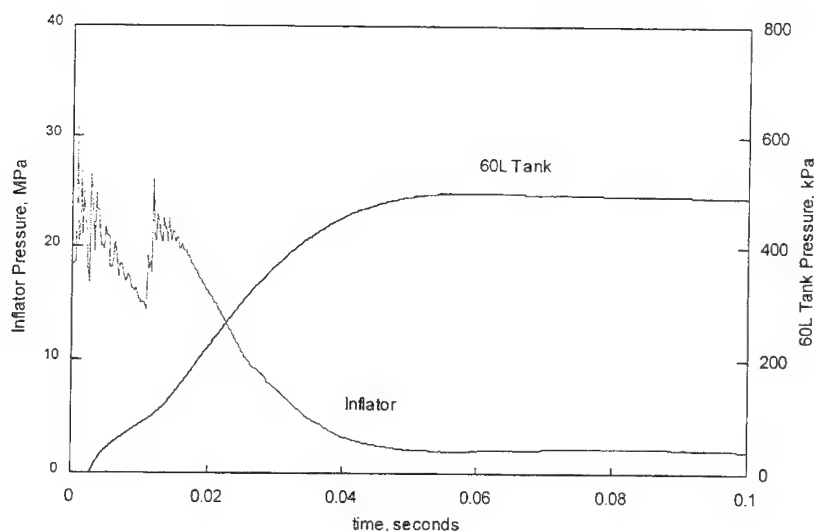


Fig. 14 Hybrid inflator and tank pressures with dual Enerfoil™ heating rolls.

## CONCLUSIONS

The present paper demonstrates clearly the possibility of designing new processes and formulations jointly for energetic materials to achieve the highly desirable features of improved reaction rate and completeness of reaction ( requiring small ingredient sizes with controlled and high degree of intimacy of mixing), with enhanced manufacturing efficiency and safety. At the same time a high degree of environmental friendliness can also be obtained with these new processes by reducing or eliminating material wastage through recycling. All three ICI processes described in this paper met some or all of these ideal process criteria.

The energetic materials industry has progressed a long way since Alfred Nobel's days. It is, with the new processes such as those described here, definitely going into the Twenty First Century with a new outlook and promise of ideal energetic materials with all desirable features that could only be dreamt of until now. The new processes will also allow the industry to produce new materials satisfying the most stringent environmental requirements in all countries by their inherent cradle to grave approach in integrated process and formulation design.

## ACKNOWLEDGMENTS

The different areas of work reported in this paper were the results of the diligent efforts by many people in ICI Explosives in North America and the U.K. and a few from ICI Engineering Technology and ICI Films, U.K. Their contributions are acknowledged with thanks. We are specially grateful to Dr. I.J. Kirby for his technical support and the numerous fruitful discussions. The authors would also like to thank ICI Explosives for its permission for the publication of this paper.

## REFERENCES

1. Utracki L., "Azide and doped iron oxide gas generating composition", U.S. Patent 4,243,443, 1981.
2. Chan S.K., "Pyrotechnic bodies", European Patent Application EP 0 576 161A1, 1993.
3. Chan S.K., Kirby I.J. and Oliver R., "Method of producing pyrotechnic masses", US Patent 5 449 424, 1995.
4. Chan S.K., Oliver R. and Hsu N., "Process for the preparation of gas-generating compositions", UK Patent Application 95-05623, 1995.
5. Chan S.K., "Hot plate ignition characteristics of a sodium azide propellant", Proceedings of the Sixteenth International Pyrotechnics Seminar, pp. 399-408, Jonkoping, Sweden, 1991.
6. Clarke, K.H., Graham, D.A. and Oliver, R., "Process for the production of an exothermically reacting composition", European Patent Application 95-305162, 1995.
7. a. Kroschwitz, J.I. ed., Kirk-Othmer Encyclopedia of Chemical Technology, Fourth Edition, John Wiley and Sons., vol. 10, p.111, 1993.  
b. Andreyev, K.K., "Thermal decomposition and combustion of explosive substances", NTIS AD-726573, 1966.
8. Sutton D., ICI Engineering Technology, private communications.
9. Alford, F., "Pyrotechnic materials", Patent WO 90/10724, 1990.
10. Alford F. and Place M., "The development and production of pyrotechnic systems from the vapour phase, Part 1, Thermite type materials", pp. 1-16; "Part 2, The production of bulk reactive materials", pp. 17-32, Proceedings of the 15th International Symposium on Pyrotechnics, Boulder, Co. U.S.A., 1990.
11. Chan S.K., Graham S.J. and Leiper G.A., "Gas generator ignited by lamina or film", US Patent 5 351 619, 1994.
12. Chan S.K., Kirby I.J., Graham S.J. and Leiper G.A., "Hybrid inflator", US Patent 5,411,290, 1995.
13. Chan S.K., Graham S.J. and Leiper G.A., "Pyrotechnic ignition device", UK Patent Application 95-09606, 1995.
14. Baxter I.K., Bishop C.A., McGee D.C. and Watkins K., "Evaporator for vacuum web coating", UK Patent Application 93-23033-2, 1993.
15. Baxter I.K., Bishop C.A., McGee D.C. and Watkins K., "Vacuum Web Coating", UK Patent Application 93-23034-0, 1993.
16. Fonseca J.J., Gorton W., "A novel roll coater for double sided heavy deposition of magnesium onto PTFE films", 37th Society of Vacuum Coating Annual Technical Conference Proceedings, p.218, 1994.
17. Chan S.K., Graham S.J. and Leiper G.A., "Enerfoil™ ignition film as an ignition charge", ICT 26th International Annual Conference, Pyrotechnics, Karlsruhe, July 4-7, 1995.
18. Chan S.K., Leiper G.A. and Underwood B., "Design and performance evaluation of Enerfoil™ ignition enhancers for passenger side airbag inflators", Proceedings of ADPA International Conference on Energetic Materials Technology, Phoenix, Arizona, pp.1-8, 1995.
19. McIntyre F.L., "A compilation of hazard and test data for pyrotechnic compositions", ARLCD-CR-80047, (AD A096248), 1980.
20. Yeh C.L., Mench M.M., Kuo K.K. and Chan S.K., "Experimental study of flame-spreading processes over Mg/PTFE/Mg thin foils", Fourth International Symposium on Special Topics in Chemical Propulsion : Challenges in Propellants and Combustion 100 Years After Nobel, Stockholm, Sweden, May 27-31, 1996.
21. Peretz A., "Investigation of pyrotechnic MTV compositions for rocket motor igniters", J.Spacecraft, v.21, No.2, pp. 222-224, 1984.
22. Chan S.K., "A lumped parameter airbag gas generator model", Proceedings of the Twentieth International Pyrotechnics Seminar, Colorado, pp. 153--166, 1994.

## **"CLEAN" PROPELLANTS FOR COMMERCIAL APPLICATIONS**

**G.M.H.J.L. Gadiot, D.W. Hoffmans, P.A.O.G. Korting and A.P.M. Leenders**  
TNO Prins Maurits Laboratory

**ABSTRACT:** Trends for solid propellant applications in the Netherlands during the last decade are described, especially focusing on new propellant formulations which are "clean".

In 1985 TNO Prins Maurits Laboratory (TNO-PML) became involved in the development of pyrogenic devices for Ariane 5's Vulcain engine HM 60, which developed into a production programme of AN based turbine pump starters and igniters for the European Space Agency (ESA).

During the development, it turned out that removing the hydrochloric acid has other advantages, e.g., less smoke in the rocket plume, while AN based formulations show better cook-off behaviour.

Another application of "clean" propellant technology is the development of a new "environmentally friendly and human friendly" gas generator composition for an airbag. This composition is based on AN with triaminoguanidine -nitrate (TAGN) or nitroguanidine (NQ) and has the advantage over sodium azide ( $\text{NaN}_3$ ) based gas generators that less toxic and corrosive products and much less solid reaction products are formed.

In a search for new "clean" high performance propellants, performed for the ESA, Hydrazinium Nitroformate (HNF) based propellants were identified as new interesting formulations, that offer a much higher specific impulse than obtained with conventional composite propellants.

Under sponsorship of ESA and the Netherlands Agency for Aerospace Programs a research programme was initiated, aiming at experimentally demonstrating the increased performance of HNF based propellants.

## **INTRODUCTION**

Until about ten years ago most of the activities in the area of solid propellants at TNO-PML were focused on their use in rockets and missiles for defence purposes.

This propellant technology may also be used for other (civil) applications, when there is a need to produce in a reliable way a large amount of gas in a very short time.

For example civil applications of energetic materials can be found in:

- propellants for propulsion devices (e.g. apogee kick-motors);
- igniters;
- gas generators (e.g. turbine pump starters);
- airbags;
- fire extinguishing/explosion suppression equipment;
- safety systems (e.g. pyrovalves);

- cutting devices (pyrocutters);
- separation charges.

In 1985 TNO-PML started development work, together with Stork Product Engineering (SPE), on a gas generator (turbine pump starter) and two igniters for the Ariane 5 Vulcain engine. For the propellant used in the devices, ESA required non-corrosive gases, which led to the development of AN based propellant.

Nowadays propellant grains for turbine pump starter and igniters are being produced at Aerospace Propulsion Products (APP), a company founded by TNO in 1989.

During the years, it became also clear that the environmental impact of space related activities led to an increasing concern about acid released into the atmosphere during launches. During one Space Shuttle launch about 250 tons of hydrochloric acid is formed, causing effects like acid rain and depletion of the ozone layer. Clean propellants will have an advantage in this respect. A disadvantage is that AN based conventional propellants have lower energetic properties than AP based propellants.

For rocket motor applications, a two-way technology approach has been chosen:

- extending the existing AN technology by introducing energetic binders like glycidyl azide polymer (GAP);
- development of a new technology based on a "new" chlorine free oxidizer hydrazinium nitroformate (HNF) with a very high specific impulse. This new oxidizer is now being produced by APP on pilot plant scale. Its synthesis method has been patented.

Also other applications of propellant technology have been pursued, like air bags, fire extinguishers, pyrovalves and pyrocutters.

For air bags a new solution, which is "environmentally friendly and human friendly", has been patented and will be further developed together with industry.

In this way propellant activities at TNO-PML in the last decade have undergone a shift, whereby about half of the activities is still for defence purposes and half for civil applications.

## DEVELOPMENT OF AN BASED PROPELLANTS

In 1985, SPE and TNO-PML submitted a joint proposal for the development of three pyrotechnic devices for the Vulcain engine. After a first feasibility study in 1987, a contract was awarded to SPE and TNO for the development and delivery of Turbopump Starters and Igniters for the Gas Generator and Thrust Chamber of the Vulcain engine. In this program, TNO developed propellants and booster charges for these devices, while SPE designed the metal casings. For safety reasons (in view of manned space flight double base propellants were considered too hazardous) and for technical reasons, chlorine free composite propellants based on ammonium nitrate (AN) were selected. Since then, TNO-PML has studied the use of AN as an oxidizer for solid propellants thoroughly.

Ammonium Nitrate is easily available and less hazardous than Ammonium Perchlorate (AP). However, the performance of AN based propellants is much lower, while in addition AN shows phase transitions with corresponding changes in volume in the temperature range of interest for practical applications. In-depth studies of AN phase transitions and the use of various compounds that may suppress phase transitions like diamine nickel nitrate have been made by the Institut für Chemische Technologie (ICT) in Germany [Engel]. This institute is one of the few producers of phase stabilized Ammonium Nitrate (psAN), that can be used as an oxidizer in propellant formulations. Since most of the phase stabilizers are carcinogenic or may cause an environmental problem this prohibits the widespread use of psAN. Therefore, research is directed towards more acceptable stabilizers; as water promotes phase transitions, the introduction of very dry AN may become an attractive alternative for AN stabilized with metal oxide. AN has other drawbacks, it is very hygroscopic and therefore requires the use of humidity controlled facilities. The burning rate of AN based propellants is low, typically 2-3 mm/s at 10 MPa, and is closely related to the decomposition mechanism of AN, which is known to be endothermic [Brill]. This also explains the



poor ignitability of AN propellants, although one may argue that this may be a clear advantage instead of a disadvantage. It is important to state that by increasing the pressure and temperature the decomposition of AN becomes less endothermic. Also the use of catalysts may change the decomposition mechanism of AN.

On the basis of psAN, TNO-PML developed a low temperature (1400 K) propellant for the Turbine Pump Starter and a relatively high temperature (2250 K) propellant for the Gas Generator Igniter and the Thrust Chamber Igniter for the Ariane 5 Vulcain engine. The Vulcain engine (Figure 1) is fed by liquid oxygen and liquid hydrogen and is designed to provide 1025 kN thrust during 600 s for the Ariane 5 launcher.

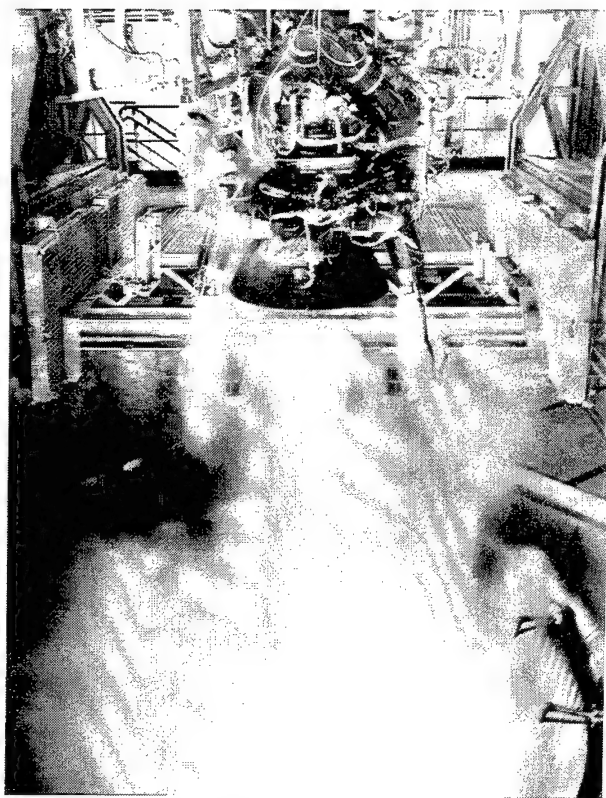


Figure 1. Testing of the Vulcain engine

The engine is a gas generator cycle engine with two high performance turbo pumps, one for liquid hydrogen and the other for liquid oxygen. A schematic view on the main components of the engine is shown in Figure 2. The specifications of the starter and ignition equipment do not allow for the production of corrosive gases by these devices as these would be detrimental for the engine's hardware. Part of the propellant development work by TNO-PML has been published in the open literature. In [Korting], the effect of various catalysts on burning rate behaviour has been studied. The results of an ignition research programme have been presented in [2x, de Valk en Mul]. Igniters for a fast and reliable ignition could be designed on the basis of the Magnesium Teflon Viton pyrogenic composition. The effect of moisture and ageing on AN based propellants were shown in a study

reported in [Miedema, Zee]. The effect of particle size distribution on the burn rate of AN based propellants was thoroughly investigated as to reduce propellant batch-to-batch variations when introducing new batches of psAN in the production of propellant. A better method was developed to relate burning rate to particle size distribution, see [Miedema, Klein].

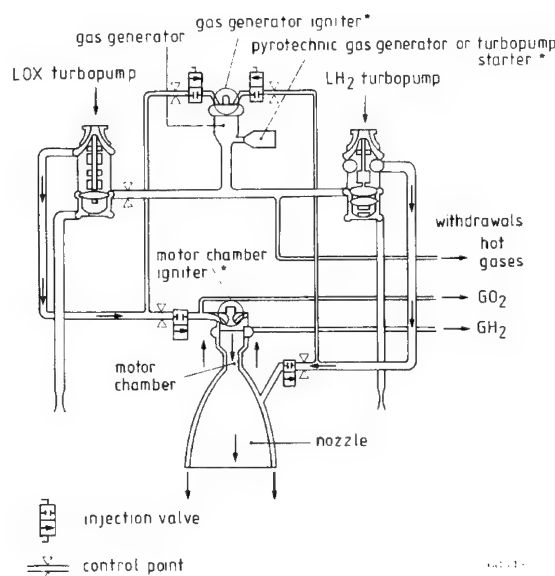


Figure 2. Hydraulic Scheme of Ariane 5's Vulcain engine

To further increase the knowledge level of psAN based propellants, a separate technology program was carried out during the period 1991 - 1995. Attention was paid to mechanical properties and glass transition point, and the effect of curing catalysts, anti-oxidant and NCO/OH on ageing. Also the effect of moisture and certain ingredients on thermal stability of AN propellants was studied. Through this knowledge the production process of AN based propellants could be controlled within narrow margins. A thorough study was performed to investigate the effect of various catalysts on burn rate and burn rate exponent. The ignition behaviour was also studied in more detail. In cooperation with the University of Milan (L. De Luca), a steady combustion model for AN based propellants has been developed, in which the effects of AN particle size and phase transitions on the combustion process is taken into account. The pyrolysis is modeled by considering the decomposition of AN and the binder separately. The physical description of the burning AN particle follows the Becksted, Derr & Price (BDP) model. As an example, Vieille's burning rate law derived by the model has been plotted for a propellant consisting of 75% AN and 25% HTPB, see Figure 3. The results are given for three different particle sizes. The trend of the pressure exponent vs. particle diameter at low and high AN loadings for three different propellant temperatures is plotted in Figure 4.

At present TNO-PML studies the use of AN in AP based solid propellant formulations to lower the hazard properties of systems using AP based propellant. For instance, an igniter equipped with a AN/AP based propellant, in combination with a conventional composite propellant grain, may significantly improve the Insensitive Munitions (IM) characteristics of the complete rocket motor when subjected to slow cook-off. This is due to the lower auto ignition temperature of the igniter propellant.

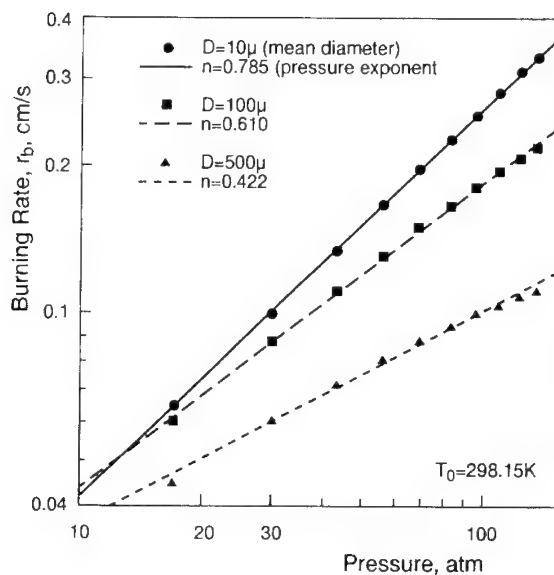


Figure 3. Derivation of Vieille's law for AN/HTPB 75/25 propellants with three different particle mean diameters

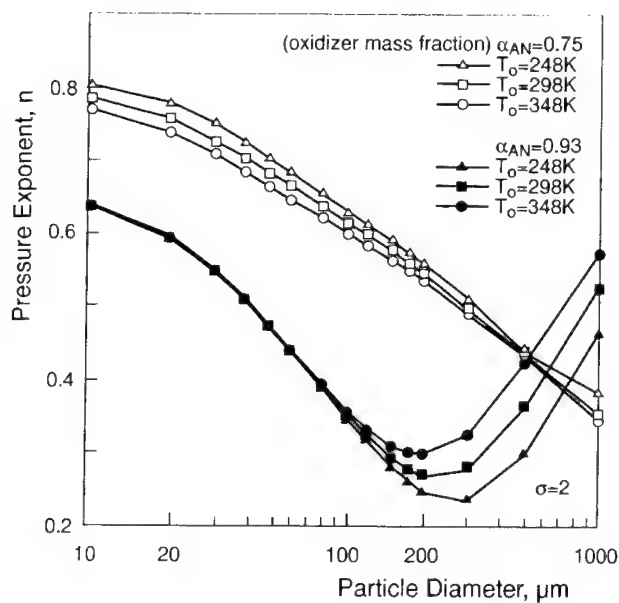


Figure 4. Trend of the pressure exponent with respect to the particle diameter at two oxidizer mass fractions and three initial temperatures

### SPIN-OFF OF AN TECHNOLOGY

Most gas generator compositions used nowadays in airbags are based on sodium azide,  $\text{NaN}_3$ . These compositions show drawbacks:  $\text{NaN}_3$  itself is a toxic compound and corrosive reaction products are formed. Half of the reaction products are solids which do not contribute to the gas production, but may cause scalds. Research is focused to replace  $\text{NaN}_3$  by other propellant formulations.

Also TNO-PML is involved in this research. Interesting formulations were developed that may overcome the disadvantages of  $\text{NaN}_3$ .

These compositions are based on AN/TAGN or AN/NQ, which are non-toxic raw materials. Primarily non-toxic gaseous products are formed, i.e.  $\text{N}_2$ ,  $\text{CO}_2$  and  $\text{H}_2\text{O}$ . Also some CO may be formed. Copper (II) oxide is added to these compositions to decrease the amount of CO formed and also to increase the burning rate.

Burning rate vs. pressure data were generated using a laboratory scale burner, while combustion products were analyzed immediately after disseminating the gases in a 50 l bag (see Figure 5). In addition to  $\text{N}_2$ ,  $\text{CO}_2$  and  $\text{H}_2\text{O}$ , the following gases were identified: CO, NO,  $\text{NO}_2$ , HCN and  $\text{NH}_3$ .

The amount of CO formed can be up to 10%. However, addition of CuO decreased this to approximately 2%. The amount of NO,  $\text{NO}_2$ , HCN and  $\text{NH}_3$  formed was acceptable, regardless whether CuO was added or not.

From Table 1 one may conclude that the gas formation of AN/TAGN or AN/NQ is approximately twice that of  $\text{NaN}_3$ ; that the amount of solid particles is derived from added CuO; and that the flame temperature is somewhat high. The consequences of the latter are being investigated.

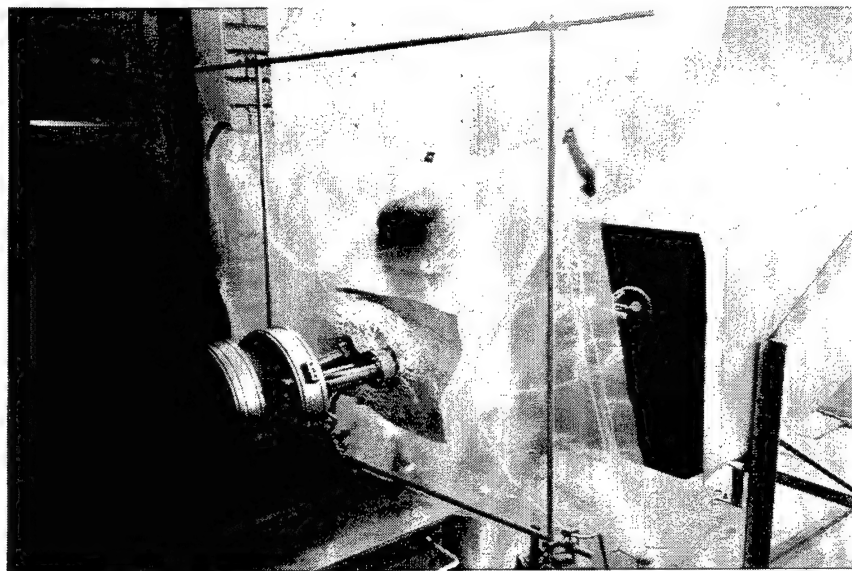


Figure 5. Test set-up for dissemination in a 50 l bag

**Table 1**

Theoretical predicted properties of AN/TAGN or AN/NQ compositions compared to  $\text{NaN}_3$

Properties (calculated)	$\text{NaN}_3$	AN/TAGN or AN/NQ composition
Gas formation (per 100 gram)	1.64 mole	2-5 mole
Formation of solid particles (per 100 gram)	50 gram	3-11 gram
Flame temperature	1300 K	2300 K

**Table 2**

Test results of AN/TAGN or AN/NQ compositions

Test results AN/TAGN or AN/NQ composition

Burning rate	10 - 25 mm/s, 10 MPa
CO formation in bag	appr. 2%
Vacuum stability test	0.1 - 1 ml/2.5 gram (40 hrs at 90°C)
Impact sensitivity	10-15 Nm
Friction sensitivity	216 N

Table 2 shows that the newly developed compositions are very promising for being actually used as a gas generator composition in an airbag. The composition has to be optimised for specific applications.

## DEVELOPMENT OF HNF BASED PROPELLANTS

In 1988, a study on a new storable high performance propellant was initiated at TNO-PML under funding of ESA and the Netherlands Agency for Aerospace Programs (NIVR).

In this study [Mul et al.] the combination of HNF, Al and GAP was identified as a very promising formulation for future solid propellants for application in space launcher boosters. When aluminium is not present in the formulation, a high performance minimum smoke propellant is obtained. HNF/Al/GAP propellants will have an enhanced performance in terms of specific impulse, and are environmentally friendly due to the absence of chlorine containing combustion products.

As a first step theoretical performance was calculated. Some relevant performance aspects and typical reaction products for advanced space and tactical propellants are compared in Table 3 to their conventional counterparts. The advanced propellant formulation has an enhanced performance in terms of specific impulse (Isp) of 6% for the space propellant and 8.5% for the tactical propellant. For space propellants a high specific impulse is the driving factor. For tactical propellants in missiles reduced plume signature is also a driving factor.

The advanced tactical propellant:

- generates no hydrogen chloride, preventing secondary smoke to form in the rocket plume;
- produces less carbon monoxide and hydrogen and hence, reduces the probability of after burning;
- contains no solid matter, preventing the occurrence of primary smoke.

These three aspects contribute to the largely improved signature of the advanced tactical plume.

As a second step availability of ingredients was considered. The main ingredients for the propellant are HNF and GAP. GAP is produced under license from Rockwell in the US, by SNPE in France. HNF was not commercially available at that time, but is presently produced on pilot scale (capacity 30 - 300 kg/year) at APP using an acid-base reaction between nitroform and hydrazine [Schöyer et

al.]. The product is recrystallized for improved purity. So far, two recrystallization methods have been developed; a solvent/nonsolvent method is employed for obtaining small HNF particles (average diameter~ 20  $\mu\text{m}$ ) and an evaporation method is used to obtain larger HNF particle sizes (average diameter~ 200  $\mu\text{m}$ ). In this way a bi-modal mixture was obtained. HNF particles are needle shaped. This is not desirable for propellant production with respect to impact and friction sensitivity and propellant solid loading. At present length to diameter ratios of 2 - 5 can be achieved for both particle sizes, but research at APP is focused to further reduce L/D ratios. A typical example of HNF recrystallized particle shape is given in Figure 6.

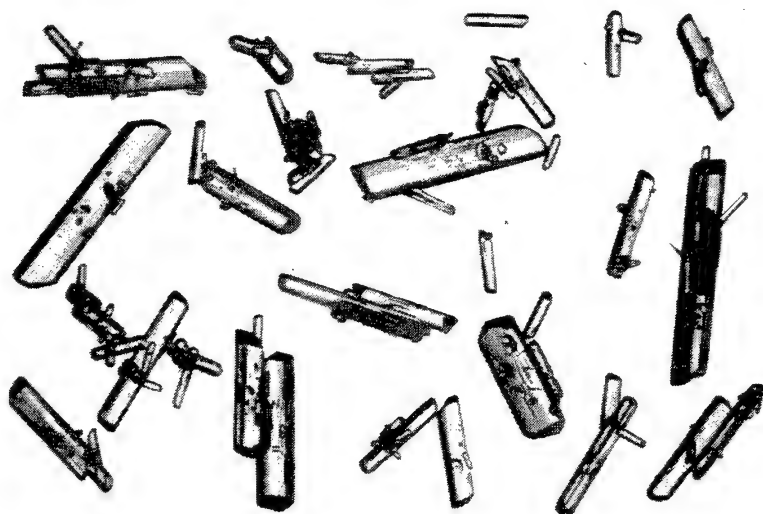


Figure 6. Re-crystallized HNF with Length over Diameter ratios 4 to 5 ( $\langle x \rangle = \sim 500 \mu\text{m}$ )

As a third step safety of handling and manufacturing, toxicity and compatibility of ingredients was considered. Some elementary properties of HNF and other common oxidizers are given in Table 4. The Table shows that the melting/decomposition temperature is similar for AP and HNF, whereas it is lower for ADN (ADN is also a new chlorine free oxidizer, studied primarily in the USA). With regard to impact and friction HNF propellants are somewhat more sensitive than AP or AN propellants, but the values are still acceptable for practical use. With regard to toxicity detailed laboratory investigations were made. The result was that HNF is not very toxic (comparable to RDX) and can be used in the chemical process with normal precautions. Detailed experiments on compatibility were performed and showed that the combination HNF/Al/GAP is a compatible system. Compatibility problems were only observed when introducing isocyanates, commonly used curing agents for GAP. Although the exact mechanism is still unknown, the incompatibility is caused by a competitive reaction between binder and HNF with the free isocyanate groups. Development work to find a good curing system identified curing agents and process conditions that resulted in a cured propellant with acceptable properties and stability.

**Table 3**  
Performance and reaction products of space and tactical propellants [Gadiot et al.]

Property		Conventional Space	Advanced Space	Conventional Tactical	Advanced Tactical
AP	[% by weight]	68	--	82	--
HNF	[% by weight]	--	59	--	85
Al	[% by weight]	18	21	4	--
HTPB	[% by weight]	14	--	14	--
GAP	[% by weight]	--	20	--	15
p <sub>c</sub>	[MPa]	10	10	10	10
A <sub>c</sub> /A <sub>t</sub>		100	100	10	10
T <sub>c</sub>	[K]	3378.09	3818.68	3016.02	3365.54
I <sub>sp</sub>	[m/s]	3096.6	3287.8	2498.2	2710.0
I <sub>vac</sub>	[m/s]	3217.0	3436.0	2686.5	2926.7
CO	[% by weight]	27.05	29.02	17.60	9.20
CO <sub>2</sub>	[% by weight]	3.88	0.33	19.03	32.49
HCl	[% by weight]	21.73	--	26.37	--
H <sub>2</sub>	[% by weight]	2.97	2.87	1.45	0.36
H <sub>2</sub> O	[% by weight]	3.94	0.68	21.20	28.92
N <sub>2</sub>	[% by weight]	5.37	22.45	6.51	29.02
Al <sub>2</sub> O <sub>3</sub> (A)	[% by weight]	35.04	44.66	7.84	--

**Table 4**  
Comparison of properties of AN, AP, RDX and HNF

Parameter	AN	AP	RDX	HNF	ADN
molecular formula	NH <sub>4</sub> NO <sub>3</sub>	NH <sub>4</sub> ClO <sub>4</sub>	C <sub>3</sub> H <sub>6</sub> N <sub>3</sub> (NO <sub>2</sub> ) <sub>3</sub>	N <sub>2</sub> H <sub>5</sub> C(NO <sub>2</sub> ) <sub>3</sub>	NH <sub>4</sub> N(NO <sub>2</sub> ) <sub>2</sub>
molecular weight, kg/kmol	80.04	117.5	222.1	183.09	124.06
density, kg/m <sup>3</sup>	1720	1950	1820	1872	1820
heat of formation, kJ/mol	-365	-296	+70.7	-72	-150.6
oxygen balance, %	20.0	34.0	-21.6	13.1	25.8
melting point, K	443	403	477	395	363
friction sensitivity, N	353	> 100	120	18 - 20	--
impact sensitivity, Nm	49	15	7.5	2 - 3	--
toxicity-LD <sub>50</sub> , mg/kg	not toxic	not toxic	100	128	--

As a fourth step an actual propellant was manufactured and tested to demonstrate the expected increase in performance. HNF based propellants with suitable curing behaviour, expressed by acceptable mechanical properties, have been produced for Proof of Concept (PoC) testing, and were fired in a laboratory scale burner. Initial HNF/Al/GAP formulations showed a pressure exponent of about 0.8 for HNF/GAP based formulations [Schöyer et al.], with a burning rate of 64 mm/s at 10 MPa. An exponent this high was termed unsuitable for PoC testing as it could result in an unstable test situation with respect to operating pressure. The introduction of a suitable burning rate modifier resulted in an exponent of about 0.6, with a burning rate of 40 mm/s at 10 MPa, which is suitable for PoC testing.

Theoretical and experimental characteristic velocities ( $c^*$ ) are given in Figure 7, showing the improved performance of the HNF/Al/GAP (59/21/20) propellant over the conventional AP/Al/HTPB, (68/18/14) propellant for space applications. With the HNF/Al/GAP propellant, the  $c^*$  values increase with pressure, probably due to the increase in the residence time of the combustion products in the combustion chamber with increasing pressure. Residence times for the conventional propellant are three times higher for similar conditions, showing the good combustion efficiency of the HNF/Al/GAP propellant.

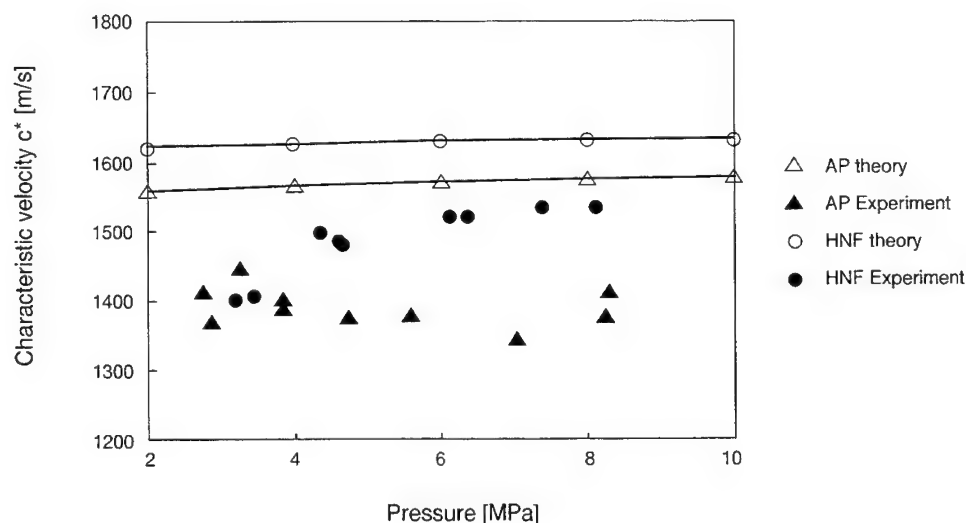


Figure 7. Theoretical and experimental  $c^*$  values for HNF/Al/GAP propellants compared to a conventional AP/Al/HTPB propellant.

As a fifth step is foreseen the industrialization of an advanced composite solid propellant based on HNF and energetic binders and metals like aluminium, in order to obtain a qualifiable propellant.

#### INDUSTRIALIZATION OF PROPELLANT PRODUCTION IN THE NETHERLANDS

For development, verification, testing and qualification of Ariane 5's Vulcain engine more than 2500 AN based propellant grains had to be manufactured up to 1995. To answer the need for a regular production of these propellant grains a company was founded by TNO in 1989. This company, Aerospace Propulsion Products BV, has its production site in a large forested area near Hoogerheide, the Netherlands. The production plant encompasses a propellant production and testing facility covering a floor surface of more than 500 m<sup>2</sup>. The propellant production facility is equipped with a special storage room for raw materials, a temperature and humidity controlled (the relative humidity is kept below 25%) propellant mixing room containing a 50 kg propellant mixer with casting equipment, and a propellant curing room. The propellant testing facility comprises equipment for non-destructive (ultrasonics and X-ray) and destructive (static firing, mechanical properties) testing.



## CONCLUSIONS

In the last decade in the Netherlands dual use of defence expertise has become more and more important. For that purpose about 10 years ago propellant technology at TNO-PML was also aimed at space applications.

Developmental and industrialization efforts have been successfully completed. Nowadays an industrial base for AN and HNF technology exists in the Netherlands and a big shift in activities at TNO-PML for the civil market has been realized.

## ACKNOWLEDGEMENT

Most of the research was funded by the European Space Agency (ESA) and by the Netherlands Agency for Aerospace Programs (NIVR)

## REFERENCES

- Brill, T.B., Brush, P.J. and Patil, D.G., Thermal Decomposition of Energetic Materials 58. Chemistry of Ammonium Nitrate and Ammonium Dinitramide Near the Burning Surface Temperature, *Combustion and Flame*, 92, pp 178-186, 1993.
- Engel, W., Eisenreich, N., Deimling, A., et al., Ammonium Nitrate - a Less Polluting Oxidizer, *24th International Annual Conference of ICT*, 29 June-2 July 1993, Karlsruhe, Germany, 1993.
- Gadiot, G.M.H.J.L., Mul, J.M., Lit, P.J. van, et al., Hydrazinium Nitroformate and its use as use as Oxidizer in High Performance Solid Propellants, Propulsion and Energetics Panel (PEP), *84th Symposium on "Environmental Aspects of Rocket and Gun Propulsion"*, Aalesund, Norway, 29 August - 2 September 1994.
- Gadiot, G.M.H.J.L., Mul, J.M. and Meulenbrugge, J.J., New solid propellants based on energetic binders and HNF, *43rd congress of the international astronautical federation*, August - September 1992, Washington D.C., USA.
- Korting, P.A.O.G., Zee, F.W.M. and Meulenbrugge, J.J., Combustion Characteristics of Low Flame Temperature Chlorine-Free Composite Propellants, *Journal of Propulsion and Power*, volume 26, Number 3, May-June 1990, pp 250-255.
- Miedema, J.R., Klein, A.J.J. and Zee, F.W.M., Particle Size Distribution Effect on Burn Rate of Ammonium Nitrate Based Propellant, *31st AIAA/ASME/SAE/ASEE Joint Propulsion Conference and Exhibit*, July 10-12, 1995/San Diego, CA.
- Miedema, J.R., Zee, F.W.M. and Meulenbrugge, J.J., Some Aspects of Aging of Ammonium-Nitrate Based Composite Rocket Propellants, Environmental Testing in the 90's, *20th International Conference of ICT*, June 27- June 30, Karlsruhe, Germany, 1989.
- Mul, J.M., Korting, P.A.O.G. and Schöyer, H.F.R., A Search for New Storable High-Performance Propellants, *ESA Journal*, Vol. 14, pp. 253-270, 1990.

**Mul, J., Meulenbrugge, J. and Valk, G. de,** Development of an MTV Composition as Igniter for Rocket Propellants, *International Pyrotechnic seminar*.

**Schöyer, H.F.R., Schnorhk, A.J., Korting, P.A.O.G., et al.,** High-Performance Propellants Based on Hydrazinium Nitroformate, *JPP*, Vol. 11, No. 4, July - August 1995.

**Valk, G.C. de, Zee, F.W.M. and Gadiot, G.M.H.J.L.,** HM-60 Pyrotechnic Igniters Ignition Improvement, AIAA/SAE/ASME/ASEE, *26th Joint Propulsion Conference*. July 16-18, 1990/Orlando, FL.

## **CLEAN LIQUID AND HYBRID GAS GENERATOR SYSTEM FOR INFLATING CAR AIRBAGS**

**JUNICHI KISHIMOTO\*, TAKEO SAITOH \*\* AND AKIRA IWAMA\***

**\*NIPPON KOKI COMPANY, SHIRAKAWA PLANT**

2-1, Aza Dobu, Nishigo-mura, Nishi-Shirakawa, Fukushima Pref. 961 Japan.

**\*\*THE INSTITUTE OF SPACE AND ASTRONAUTICAL SCIENCE, MINISTRY  
OF EDUCATION, SCIENCE AND CULTURE.**

3-1-1, Yoshinodai, Sagami-hara, Kanagawa, 229 Japan.

The need to clean and low cost gas generator systems for the use to inflate the airbags in motor vehicles has greatly increased. Aiming to avoid the disadvantages of solid azide- and tetrazol-based gas generants, and combinations of high pressure inert gas with solid propellants to be adapted in current and near-future airbags, this investigation has been carried out to manage to apply water solutions of stabilized hydrogen peroxide from 55 to 60wt% in concentration to the combustors to be integrated in airbag module. There are some favorable properties with such a low concentration  $H_2O_2$  solution: azeotropic behavior to suppress the freezing point lower than 233K, no hazard of causing the spontaneous explosion accident due to the self-accelerated decomposition during long time storage in confined vessel, low production cost and contribution to downsizing of the modules. First of all, however, it must be stressed that the decomposition products of  $H_2O_2$  emitted from airbags into the environment are only clean oxygen, water haze and dry vapor.

This paper reports the achievement of successfully combusting simple  $H_2O_2$  solution and hybrid propellant consisting of  $H_2O_2$  solution of achievement in the practical application of the combustors loading simple  $H_2O_2$  solution combined with pressurized oxygen to inflate airbags for passenger cars. In order to acquire the design data a series of investigation was conducted by means of heavy wall combustors to develop the starter for realizing the  $H_2O_2$  decomposition at the designated time sequence, and developed a two stage injection method which pours the incandescent combustion products into  $H_2O_2$  solution. At the event of collision the initiator should start, followed by firing the main booster. The initiator is the  $B/KNO_3$  pyrotechnic granules and pellets, catalyst powder and the booster is the pyrotechnics powder and highly energetic material. The total amount is approximately 3~7g. The combustor is divided to a primary reaction chamber in which gas generant cartridge is placed and a secondary decomposition chamber putting the catalyst net for completing  $H_2O_2$  decomposition. The experimental gas generator systems have proved to be capable of meeting the strict safety and environment standards and of corresponding to the time budget, which are requested in the deployment procedure items for 60 and 150 liter airbags at the temperature from 233 to 363K specified by Japanese Industrial Standards.

### **1. Introduction**

The very popular airbag systems are fast becoming the standard installations in passenger cars.

At the beginning of the 21st century, any protection system for car occupant safety will not only be limited to the airbags, they shall almost become mandatory requirements to protect against injuries to vital human body locations in collision accidents. Airbags have already demonstrated positively to be capable of protecting the car occupants. Presently, there are three types of gas generators being employed for this purpose [1].

The first generation of the gas generant is the consolidated pellets or thin wafers of a mixture of sodium azide and oxidizers which the present airbag modules employ mostly. However, this gas generant contains unfavorable combustion products in the emission, particularly sodium oxide and sodium hydroxide to react with air. Furthermore, a number of incidents have occurred in the various stages of production of this type of propellants. The hazard properties of these materials are still not fully understood. The search for other chemicals to replace sodium azide have become an urgent target in the airbag industry.

In order to satisfy this target requirement, tetrazoles and other organic compounds containing a high percentage of nitrogen are being developed as the second generation solid gas generant for airbags. Although these gas generants may contribute to the size reduction and higher performance of gas generators, there still exist some disadvantages such as inclusion of cyan compounds, nitrogen oxides and carbon monoxide in combustion products and too high combustion temperatures. Particularly, for the airbags more than 120 liter in capacity the emission amount of such toxic gases shall deviate from the acceptable limit.

The third generation of airbag inflator is based on the dispensation of nitrogen or other inert gas from high pressure vessels. For the reduction in temperature due to adiabatic expansion, 13~15g of solid propellant must be combusted in the inflator at the instant of event occurrence. An electric circuit and a mechanical device are installed in the bomb for quick gas port opening. At present many car manufacturers are introducing this type of inflators. Significant reduction of inflator weight and size, however, is too high a barrier to overcome in this system.

Brede [2] first presented a gas generator using a liquid triple-propellant composed of butane, dinitrogen monoxide and carbon dioxide. Regretfully, this combination must be operated at very high pressures over 100MPa and has a difficulty on the control of mass exhaust rate. It does not seem such a gas generant might liberate us from a pressure of the car maker on cost reduction and clean gas emission.

This paper reports a successful development of new automotive airbag systems using 50~60wt% water solution of hydrogen peroxide following the previous work [3]. This system can meet the time budget imposed by car makers at a wide environment temperature region, 233~373K. For example, the 60wt% water solution of hydrogen peroxide has a potential to generate 1.06 mole oxygen and 4.78 mole dry water vapor per 100 ml. The concentration is in a safety composition free of self-heating possibility, being lower than 64.5 wt%, as shown in Fig. 1. Therefore, neither explosion hazard nor rapid pressure elevation in a container should take place. Car production industries impose us the long term stability, 10 to 15 years, on the aging property of airbag gas generant. So far, it has been generally believed that the use of hydrogen peroxide as gas generant for airbag inflation is hopeless venture in practice because of the intrinsic property of the high spontaneous decomposition rate. However, addition of a stabilizer to water solution of  $H_2O_2$  and fluorohydrocarbon polymer coated container on the inner surface could promise a high stability over 10 years.

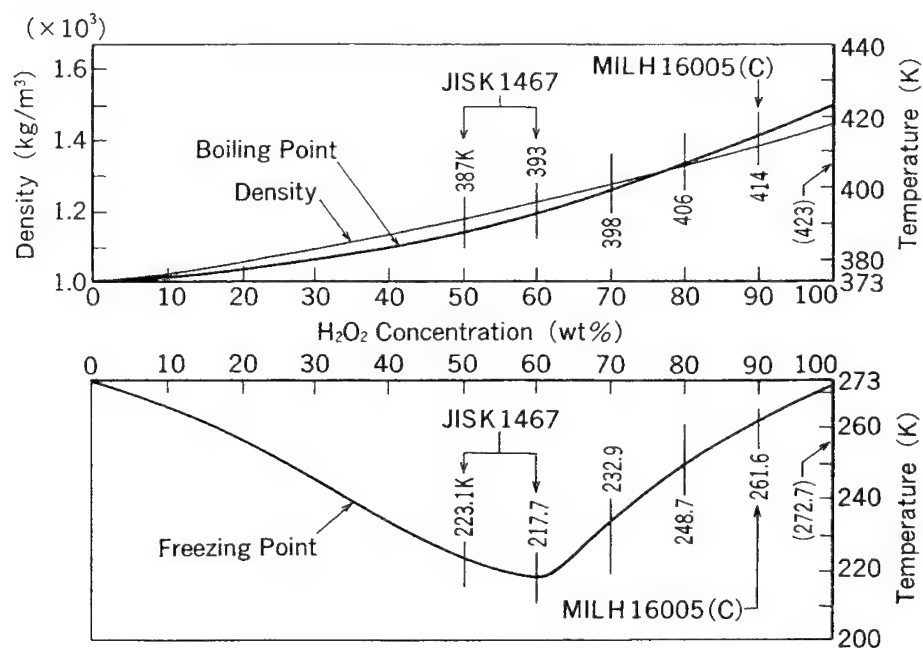


Figure 1. Phase diagram of the mixture of H<sub>2</sub>O<sub>2</sub> and H<sub>2</sub>O.

## 2. Gas generant

Stabilized 60wt% water solution of H<sub>2</sub>O<sub>2</sub> has been supplied by Mitsubishi Gas Chemical Industries Co. The freezing- and boiling point of water solution of H<sub>2</sub>O<sub>2</sub> in 55-60wt% in concentration are fortunately outside of the operation temperature zone(233K~363K) specified by car makers as shown in Fig. 1. However, the most serious problem of H<sub>2</sub>O<sub>2</sub> is the stability at high temperatures and aging property.

Table 1 demonstrates the aging deterioration in H<sub>2</sub>O<sub>2</sub> concentration before and after the test sample was maintained for 500 h at 383K.

Table 1 An Acceleration Aging Test Result

Stabilizer Content (ppm)	Initial H <sub>2</sub> O <sub>2</sub> Content (wt%)	Final H <sub>2</sub> O <sub>2</sub> Content (wt%)	Deterioration (wt%)
100	60.15	58.96	1.19
100	60.28	59.02	1.26
50	60.15	59.04	1.11
50	60.28	59.17	1.11

The selection of a suitable stabilizer gives an solution for the most serious problem of the poor stability inherent to  $\text{H}_2\text{O}_2$ . The performance test suggested the allowable deterioration is 5wt %. This acceptable limit would be reduced down to 50wt % if combined to a hybrid system that the pressurized gas can participate a role for airbag inflation.

Figure 2 shows another  $\text{H}_2\text{O}_2$  advantage of low concentration  $\text{H}_2\text{O}_2$ . There is no apprehension that explosion hazard may take place due to self-heating decomposition during storage. As the gas generant is loaded in a confined container, the concentration shall not be increased to a boundary line 64.5wt% over which the self-heating is accelerated once the spontaneous decomposition starts at the rate to a level.

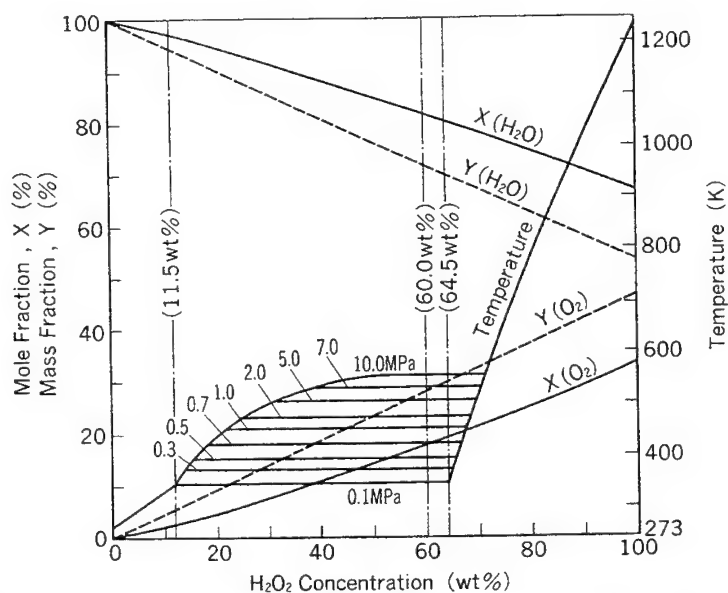


Figure 2. Temperature and composition of the decomposition products of the mixture of  $\text{H}_2\text{O}_2$  and  $\text{H}_2\text{O}$ .

### 3. Combustors

We prepared two different combustors with capacities to inflate 60 and 150 liter s airbags respectively as shown in Figs. 3 and 4. One is a heavy wall combustor for investigating the fundamental design parameters and it can be incorporated into both the driver- and passenger-side module. The reactors divided into two chambers by a partition with 2mm dia. four nozzles in order to complete  $\text{H}_2\text{O}_2$  decomposition. Also, an idea of two stage ignition has been proposed concerning the starter design.

Another is a prototype combustor developed for passenger-side airbag(150 liters) module. We have conducted environment test, putting special emphasis on the preservation of performance by minimizing the effect of ambient temperatures, to determine the capacities of the primary and secondary reactor chambers, the loading of the 60wt %  $\text{H}_2\text{O}_2$  solution, the void volume in the primary chamber, and the composition of starter ingredients.

It is well known that the heat of decomposition of  $H_2O_2$  is



The starter ingredients and quantity were calculated, based on Eq.(2) so that the liquid phase is maintained in the primary reactor and the exhaust water becomes dry vapor by setting the maximum temperature( $T_r$ ) of 500-650K which may be obtained from the initial temperature( $T_i$ ) in the primary chamber.

$$\Delta H_r M_r + \sum_{j=1}^j \Delta H_s^j M_s^j = \sum_{k=1}^k M_p^k (H_{T_f}^{0,k} - H_{T_i}^{0,k}) \quad (2)$$

where  $M_r$ ,  $M_s^j$  and  $M_p^k$  are the loaded mass of hydrogen peroxide solution,  $j$ -th starter component and  $k$ -th reaction products,  $\Delta H_r$  and  $\Delta H_s^j$  are the heat of reaction of hydrogen peroxide and  $j$ -th starter component,  $H_{T_f}^{0,k}$  and  $H_{T_i}^{0,k}$  is the heat content per unit mass at the initial and final temperature, respectively. The exothermicity of the starter was determined from a case at 237K initial condition.

The two phase flow composed of superheated liquid water and gaseous oxygen injected to the secondary reactor through the nozzle. Herein, unreacted reactant is converted to water and oxygen while it passes the  $KMnO_4$  attached copper net. In the primary reactor the state of superheated water in the reaction products is beyond the critical pressure(22.12MPa) but the maximum temperature may be in the vicinity of the critical temperature(647.3K). It depends upon the initial temperature, starter intensity and loading weight of gas generant.

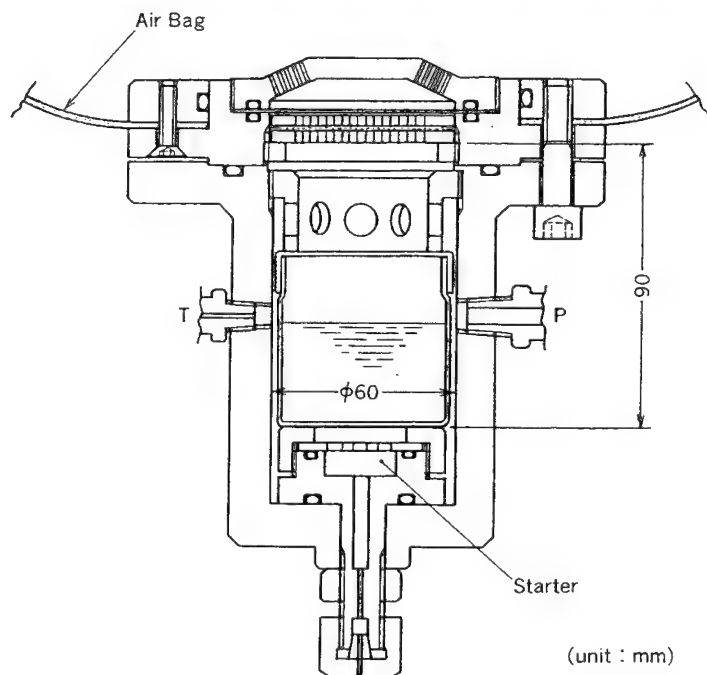


Figure 3. Versatile heavy wall combustor for developing both driver- and passenger(fellow driver)-side airbag module.

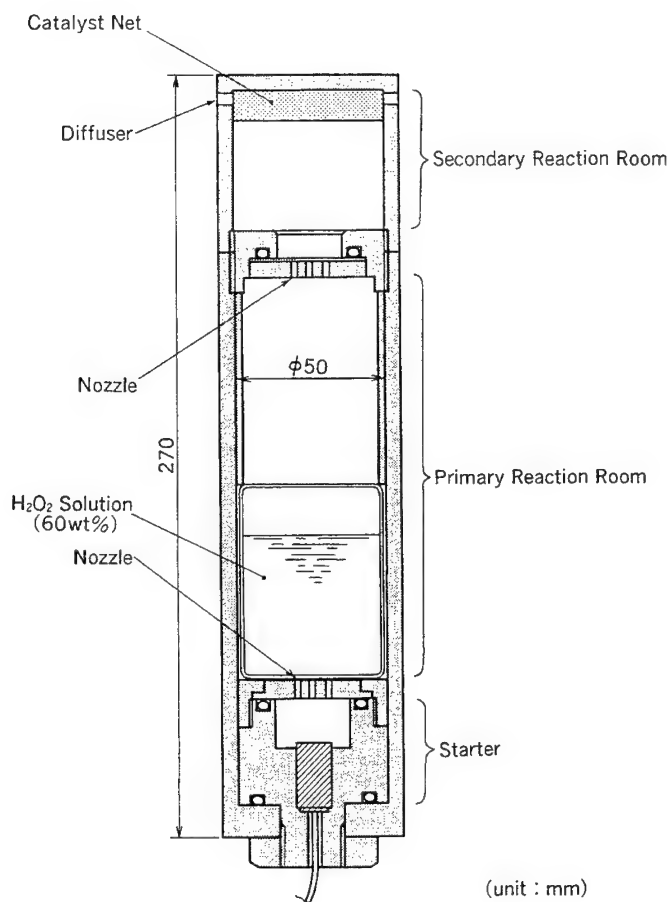


Figure 4. Prototype P-side combustor.

By assuming that the discharge gas must exceed the boiling point of water, the amount of gas generant and starter ingredients are determined to bring the dry water vapor and oxygen into the airbags under a wide range of ambient temperatures. Automobile industries have very demanding specifications that airbags must inflate completely in 233~363K. Both the driver- and passenger-side combustors were designed to produce dry water vapor with an exhaust temperature of 423K at 150 and 250kPa starting from an initial temperature of 243K.

For a passenger-side inflator a 110ml of cartridge loaded with 80~100ml of liquid gas generant is set in the primary combustor in which approximately 180ml of void space remains. Once pyrotechnic powders(3~7g) ignite, a needle penetrates into the cartridge with a very high force and introduce the incandescent particles of metal oxides and hot gases therein. For the starter of driver-side combustor,  $\text{KMnO}_4$  powder is included in the starter beside the pyrotechnic ingredients.



#### 4. Tuning to the time budget required for airbag inflation

The performance and suitability of the combustor as an airbag module was evaluated based on 60 liter constant volume tank tests. Figures 5 and 6 indicate the tuning zones to meet the movement of occupant during crash accident for both the driver- and passenger-side airbag modules. Nowadays, however, every car maker sets up different acceptable tuning zone for different car category, dimension and crash shock transmitting aspect inherent to the car structure. Therefore, commercially available airbag system is shifting to acceptable tuning zone far narrower than that shown in Figs. 5 and 6. The allocation of every event time during an airbag deployment sequence with this system is: 0~15ms for crash sensing, squib ignition and cartridge lid perforation. The driver-side airbag(60 liter) and passenger-side airbag(150 liter) must inflate fully in 45~60ms and 70~100ms respectively. At the rebound of occupant at 60~130ms, airbags must remain fully inflated followed by a rapid deflation.

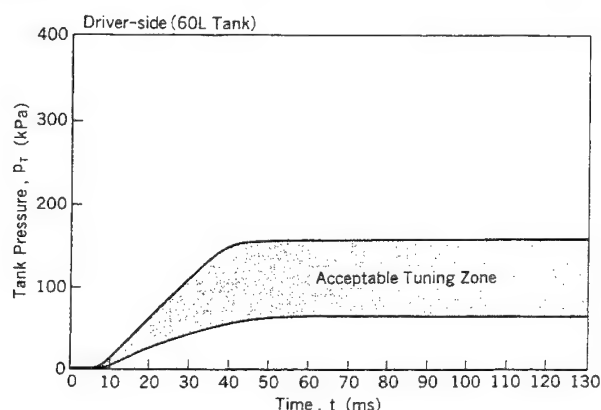


Figure 5. Tuning zone requested for D-side combustor in the range from 233~373K.

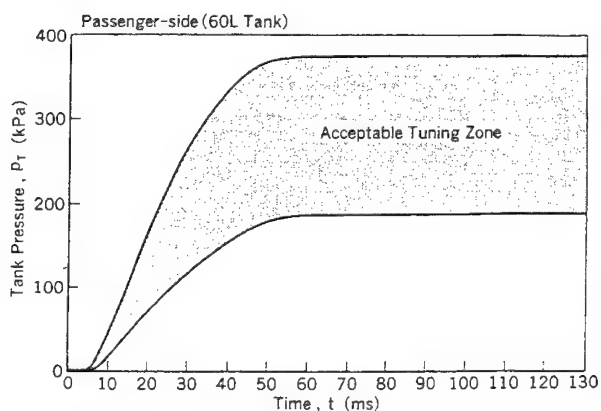


Figure 6. Tuning zone requested for P-side combustor in the range from 233~363K.  
Temperature-time history of the reacted products of 60wt%  $H_2O_2$  solution with the heavy wall combustor.

In the primary reaction chamber, superheated water of the reaction product is at a liquid state, being over the critical pressure(22.1MPa) and less than the critical temperature(647K) as shown in Fig.7. This suggests that adequate design, particularly the choices of all the reaction chamber dimensions in the combustor is an important issue in order to eliminate over-pressure in practice.

As shown in Figs. 8, 9 and 10, the pressure-time of the gaseous products discharged from a passenger-side combustor in 60 liter tank tests carried out at the low and high temperatures, can pass the tuning zone in Fig. 5. Tuning to the required time budget at driver-side airbag system can be accomplished easier. In this case, the decomposition rate of 60wt%  $H_2O_2$  which is initiated with a mixture of pyrotechnic powder and catalyst is sufficiently fast to pass the tuning zone shown in Fig. 6. Therefore, neither particular modification in term of combustor design nor investigation of starter ingredients is required for controlling the decomposition rate.

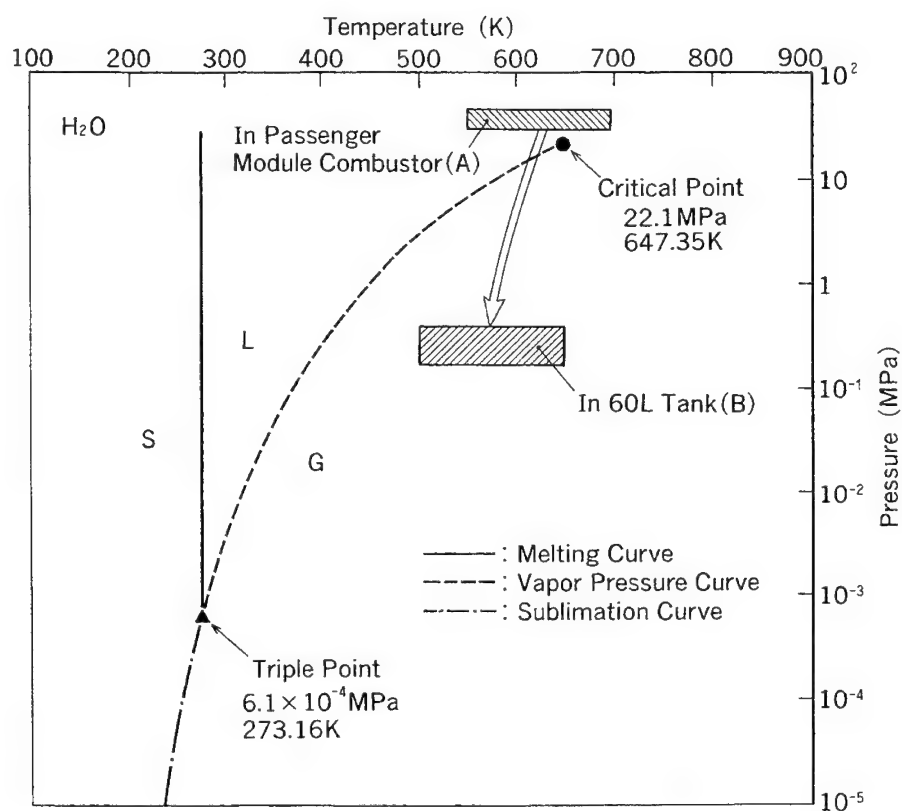


Figure 7. Phase diagram showing water properties in the primary reaction chamber and at the exit of the combustor.

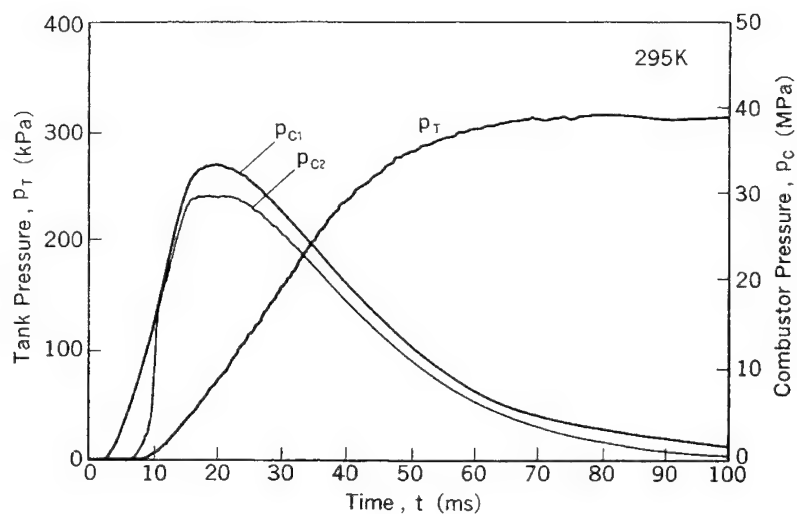


Figure 8. A Sixty liter tank test at room temperature(295K) in P-side combustor.  
Sample: 60wt% H<sub>2</sub>O<sub>2</sub> 100ml.

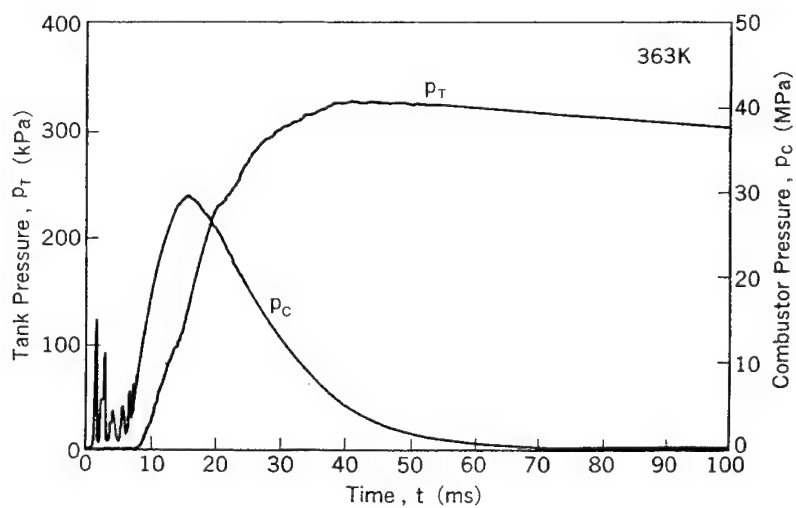


Figure 9. A sixty liter tank test at high ambient temperature(363K) in P-side combustor. Sample: 60wt% H<sub>2</sub>O<sub>2</sub> 100ml.

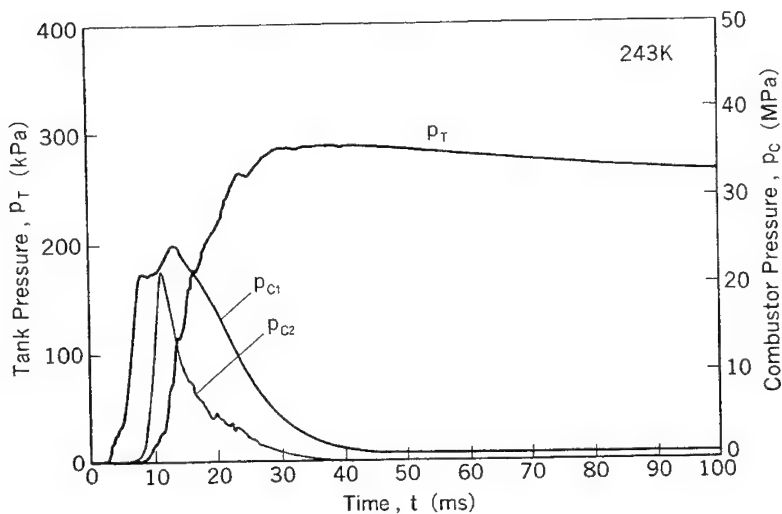


Figure 10. A sixty liter tank test at low temperature(243K).  
Sample: 60wt%  $\text{H}_2\text{O}_2$  100ml.

### 5. Hybrid type combustor

In automotive air bag applications, the hydrogen peroxide gas generator must have a void space in a primary chamber. Passenger-side combustor has a volume nearly twice that of the gas generant liquid. The exhaust gases should be choked at the diffuser for a passenger-side combustor system. Otherwise, at high ambient temperatures the peak pressure in operation might exceed 50MPa that we set as an upper limit. Figure 11 shows the introduction of 2MPa oxygen into the void space produces an increase in the peak pressure less than 2%.

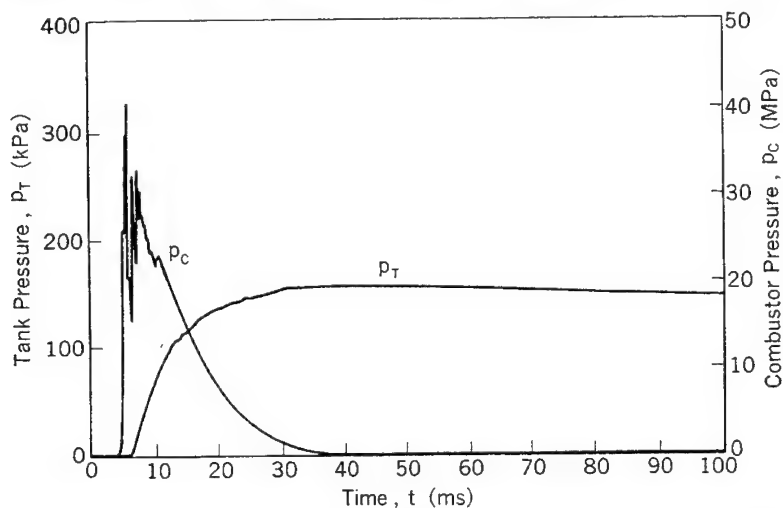


Figure 11. A sixty liter tank test for hybrid type D-side combustor at room temperature(295K).  
Sample: 60wt%  $\text{H}_2\text{O}_2$  70ml pressurized gas,  $\text{O}_2$ , 2MPa.

However, the void space pressurization should contribute to resist against cartridge can breaking by making a pressure balance between the inside and outside of cartridge, even if  $\text{H}_2\text{O}_2$  decomposition proceeds by several percent during a long time storage. The void space volume required for driver-side combustor is 30~50% of a cartridge since no choking is needed at the diffuser of the secondary reaction chamber.

## 6. Concluding remarks

The hydrogen peroxide airbag system produces clean gases as the main reaction products that are dry  $\text{H}_2\text{O}_2$  vapor and oxygen. It was noted the dry  $\text{H}_2\text{O}_2$  vapor condenses partially in the airbag and may play a role to prevent polyamide-fiber-made airbags from catching fire.

The amount of 60 wt %  $\text{H}_2\text{O}_2$  solution is 45~70ml and 80~100ml for the driver-side and passenger-side airbag modules respectively. The dimension of driver-side combustor may satisfy the need of down-size and cost reducing. However, passenger-side combustors have dimension similar to the present combustor loading sodium azide or tetrazol type solid gas generant though cost reduction can be achieved. We are continuing further investigation on the performance improvement in the application of 55~60wt% water solution of  $\text{H}_2\text{O}_2$  to new airbag system as well as the fundamental research.

## References

1. Karlow, James P., Jakovski, J. John, and Seymour, B. "Development of a New Downsized Airbag System for Use in Passenger Vehicles" 1994, Presented SAE International Congress and Exposition
2. Brede, U. "Liquid Propellant Inflators" 1994, Presented at the 2nd International Conference on Car Airbag Systems", Paper No.13, Karlsruhe, Germany
3. Tsujikado, N., Saitoh, T., Iwama, A., and Kazumi, T. A "Hybrid Gas Generator Using Low Concentration Hydrogen Peroxide Solution for Inflating Car Airbags", 1995, Presented at 26th International Annual Conference of ICT, Paper No. 6, Karlsruhe, Germany

## Future Trends in Gas Generator Systems

H. Schubert and H. Schmid

Fraunhofer Institut für Chemische Technologie (ICT)

### 1. Introduction

Gas generator systems are small aggregates for the single generating of working gas over relatively short periods. This working gas has different functions depending on the field of application. In contrast to rocket propulsion the gases do not escape with supersonic speed into the atmosphere for the generation of thrust, but gas generating takes place at low temperatures at subsonic speed.

The first solid fuels for such gas generators have been produced on the basis of single-, double- and triple base solid propellants for guns and rockets. For this reason they have been applied mainly in military fields. They have also been used in the military and civil space technology for auxiliary devices in space rockets or for the stabilization of satellites. Apart from small charges for starting piston engines the civil use of gas generators began only a few decades ago with the increasing application of airbags. This development has been the reason for producing gas generators of very different constructions for a large variety of applications. The gas generator system is a good example for conversion from military into civil fields.

Based on the state of technology the following contribution should demonstrate potentials in research and trends in developments and may also cause future innovations.

### 2. Areas of Application

#### 2.1 Airbag Systems

Nowadays airbag systems become extremely popular in the automotive market. Almost all automobile manufacturers offer them, either as an extra or as standard accessory. The predicted growth rates are enormous (Fig. 1). Airbag systems have passed their first crucial test: they work in practice and in large numbers as part of a comprehensive concept of occupant security. Airbag systems are basically comprised of gas generators in a pressure casing that has an opening and triggering mechanism. The terminology is currently being worked out by ISO (Fig. 2). Following this terminology the paper deals only with the inflator assembly and its components. The function of the gas inflator is the production of working gas to blow up the bag during a crash of an automobile to protect the occupant against impact. In practice we have to consider various crash situations belonging to the direction and energy of forces and the position and weight of the occupant. Therefore we distinguish between different types of airbag systems (front, side, head etc.) and according to the forces produced by the crash, position and weight of the occupant an adjustable sensor with a diagnostic module.

Wearing seat belts, the airbag should not work if the speed difference will be only 10 - 20 km/h. On the other hand a trend is to be observed that according to the different crash situations the pressure-time curve of the inflator can be changed, caused by different construction elements of the inflator assembly. The knowledge of interior ballistics of guns has contributed to this possibility for instance, the different charges of a howitzer.

The application of airbags outside the automobile to avoid a crash situation just before a collision may be a vision for the future. The function of such airbags has to be adapted according to the effective forces and very high demands are required of the sensors.

Beside the airbags for occupant protection systems in automobiles, protecting devices for motor-cyclists may be conceivable. Other applications of gas generator systems should be mentioned in this context. For instance, the large numbers of devices to inflate bags for rubber dinghies, dampers for release mechanisms, etc. are a few examples.

The technical demands for such gas generator systems are in average not so high as in the airbag systems.

## 2.2 Gas generators for the function mechanical devices.

Gas generators can also be used for starting up turbines, for the pressure generation of liquids, activation of mechanical devices. In this field belongs also the retracting device for the safety belt in the automobile. An interesting variant for the application of gas generators is an improved traction of the tyres, which may be achieved by short-term blowing away of the water film in case of aquaplaning or by scattering sand before the tyres in case of icy roads.

## 2.3 Fire extinguishing

In the area of fire extinguishing systems gas generators are used which can be operated with formulations without the ecologically harmful halons.

## 2.4 Suppression of gas and dust explosions

With the aid of gas generators, large volume of inert gas be introduced into deflagrating gas clouds to avoid dangerous reactions.

## 3. General technical requirements

Because of the close contact to the vehicle passenger the requirements on inflators for airbag systems are most severe compared with other applications.

The following requirements should be met by a gas inflator for airbags:

- Low combustion temperature ( $\approx$  1750 K)
- Low gas-pollutant concentration (CO, NO)
- High specific gas volume ( $\approx$  14 mol/kg)
- Appropriate and reproducible pressure-time curves (short-term Pmax)
- Wide temperature-function range
- Resistance against thermal and mechanical environmental influences
- Non-poisonous source materials
- Low production cost
- Long life and high reliability
- Disposal with minimal environmental impacts.

Today these requirements can be more or less fulfilled. The problem lies in finding the optimal combination for the desired function.

In general, it is desired to have future gas inflator systems that are smaller, lighter and cheaper while satisfying all the other requirements.

Parallel to this, low limits are assumed for the toxicity of gases in the vehicle passenger compartment, especially for:

CO: < 1000 ppm (in relation to a 50-liter test atmosphere)  
NO < 150 ppm (in relation to a 60-liter test atmosphere)

With regard to the dilution effect in a passenger compartment (approx. 3000 l) compared to the new VDI proposal „Maximal Emission Concentration“, these numbers appear very conservative. The hourly average value is 25 ppm. The short-term CO peak value should not exceed 300 ppm. Since the respective circumstances vary in an „event“, it is better to strive for the average values as limits. Looking at things this way, the air a smoker breathes with a maximum of 50 ppm even seems toxic.

These general technical requirements demand the optimal generation of gas, on the one hand, and a low combustion temperature and a low CO-NOx pollutant concentration, on the other hand. At this point, the development of N<sub>2</sub>O plays a subordinate role in comparison to the CO problematic, as long as one maintains a balanced oxygen equilibrium.

In Figure 3, the general technical requirements can be roughly assigned to the different applications considered here.

#### **4. Compositions and characteristics**

One must differentiate between gas inflator assemblies for the passenger compartment and for external use.

##### **4.1 Gas inflator assemblies for the passenger compartment**

###### **4.1.1 Solid fuel gas inflator assemblies**

For optimizing solid-fuel gas inflator assemblies the following options are available:

- Choice of nitrogen-containing compounds
- Choice of suitable oxidations
- Variation of the oxygen balance
- Utilization of coolants
- Utilization of catalysts.

Up to now, the most important development for airbag inflators is based on the carbon free system of sodium azide and various oxidizers which produces nitrogen gas for this purpose. However, the generation of alkaline particles presents a disadvantage, although the latter can be reduced through the formation of slag. A second disadvantage is connected with the disposal problem of the inflator assemblies which contain toxic sodium azide. For these reasons, other systems are in development which are rich in nitrogen but include compounds containing a small quantity of organic carbon. Chemical compounds, such as TAGN, NIGU, ATZ, GZT, etc. (Fig. 4), which are transformed with suitable oxidizers, offer an option. However, the price is an undesirable concentration of CO, CO<sub>2</sub> and NO<sub>x</sub>, which may be decreased by varying the temperature or by catalysts (Fig. 5).

###### **4.1.2 Liquid fuel inflator assemblies**

Through the application of liquid fuels as gas inflators, one might have the opportunity to take advantage of carbon-free compounds which even transform themselves into working atmospheres without leaving any residues. Systems and technologies originating in the aerospace field as well as examples from defense technology development exist.

Systems consisting of hydrazine nitrate, compounds including hydroxyl ammonium nitrate (HAN) and hydrogen peroxid are some of the examples. However, one creates a different drawback, for instance, an additional transport device and problems of long-term stability. Nonetheless, one should not exclude a practical application from the start.

###### **4.1.3 Hybrid gas inflator assemblies**

Systems of pressurized gases (e.g. air, nitrogen, argon) in pressure-vessels that, by opening a rupturable membrane, stream into the airbag are regarded as hybrid gas generators. A two-step pyrotechnic charge opens the membrane and heats the working atmosphere. Through this process, the cooling of the expanding gases is compensated or even overcompensated. One can design the amount of pyrotechnic charge, so that the developing carbon monoxide does not exceed the working atmosphere limit of 1000 ppm.

The greater weight created by the pressure bomb that must meet the pressure-vessel regulation, is the disadvantage of this version.

Systems like these have already been realized.

##### **4.2 Gas inflator assemblies for external use**

If one is not restricted by the CO concentration problem, then a realm of different propellant systems is opened to the inflator designer. Based on the present state of knowledge, solid fuel inflators are generally preferred. Propellant charges based on nitro-cellulose and composite types such as ammonium nitrate and HTPB based propellants with or without plasticizers can be used. Other propellants types with the addition of nitroguanidine and derivatives are other possibilities.

Since a phase stabilized spherical ammonium nitrate and spherical nitroguanidine is now available, most of the difficulties to use these propellant types are now overcome.

In this case, one will refer to developments and experiences in defense technology. Optimal adaptation for the specific application at the best possible price will have priority.



## **5. Handling and operational safety**

The electronic equipment in modern devices makes possible the monitoring of the operational safety of the individual systems. In most cases, safety is dependent on the foregoing life cycle, therefore on the experienced environmental impacts /2/. The most important of these are the mechanical (shock and vibration) and thermal impacts on the gas inflator assemblies. Gas inflator assemblies are energetic systems and consequently their life is limited. Known temperature stress and aging mechanisms would make it possible to have an indicator that warned of the end of a thermally-dependent operating life.

The presence of moisture reduces the operational safety of pyrotechnic and gas inflator generators. Consequently, an air-tight isolation from the outer-atmosphere is a basic requirement.

## **6. Disposal**

Comparing the production numbers of airbags in the future to other applications of gas generators, the airbag will play a dominant role also in the field of the disposal.

In the year 2000, an estimated 70 million airbag units will be produced worldwide. Therefore, future closed-loop economies will also demand concepts for the disposal or recycling of these safety systems in ways that create as few environmental impacts as possible and/or practical. To meet these demands, technical concepts need to be developed and responsibilities for disposal allocated.

## **7. Conclusion**

- Inflators and especially airbag systems are a typical conversion product of the defence industry.
- The use of inflators in airbag systems plays a dominant role compared with all other applications now and in the near future.
- Airbag systems have become an integrated part of the automobile safety management.
- Today's airbag-systems function properly but they are still representing the first phase of a technological development.
- Smart systems will dominate the future tailored to a specific type of crash and its severity, to a specific position of car occupants, to a specific safety management of a car.
- The development and great success of the airbag-system has given impulses to create other applications of inflator assemblies.
- Applied R and D will provide tailored solutions.

## **Bibliography**

- / 1/ Schubert, Hiltmar, „Risks and Chances of Technology - Contributions of Applied Research to Passenger Safety“, Airbag 2000 (1992); Proceedings.
- / 2/ Ziegahn, Karl-Friedrich, „Qualification of Airbag-Systems Tailored to the Automobile Environment“, Airbag 2000 (1992), Proceedings.

## UTILIZATION OF PROPELLANTS FOR INFLATOR AND BELT RESTRAINT SYSTEMS

FRED VOLK

*Fraunhofer Institut für Chemische Technologie (ICT)  
D-76327 Pfinztal*

### 1. Abstract

In the past, most airbag gas generators for inflator systems were based on sodium azide ( $\text{NaN}_3$ ) containing propellants. But in the meantime also azide-free propellants are being used such as nitrocellulose (NC) containing systems and double base propellants (Eurobag-gasgenerator).

At the Fraunhofer Institute in Pfinztal many investigations have been conducted for the qualification of different gas generators. In this connection, safety aspects, internal ballistics behavior, stability and life time of the propellants have been measured as well as the reaction products in order to find out the toxicity of the products.

The results of these investigations will be discussed in this paper.

### 2. Introduction

A gas generator propellant for air bags and belt restraint systems must fulfill the following requirements:

- capability of a very fast reaction of the propellant after ignition connected with the formation of a large enough gas volume,
- the gaseous and solid reaction products formed during the combustion should be characterized by a very low toxicity,
- the handling of the propellant should be without problems; this means the sensitivity to impact, to friction and to heat should not be dangerous,
- the propellant should exhibit a good thermal stability and a long life time,
- a disposal of the gas generator propellant should be compatible to the environment.

Most of the gas generator propellants being used today are based on sodium azide as a main propellant. As oxidizers usually

- potassium nitrate ( $\text{KNO}_3$ )
- sodium nitrate ( $\text{NaNO}_3$ )
- molybdenum disulfide ( $\text{MoS}_2$ )
- copper oxide ( $\text{CuO}$ )
- iron oxide ( $\text{Fe}_2\text{O}_3$ ) etc.

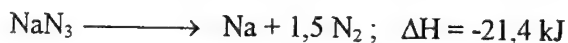
come into consideration.

Since about 5 years also propellants consisting of nitrate esters, such as nitrocellulose, have been used for air bags, although components of this kind are contained in propellants for belt restraint systems for many years.

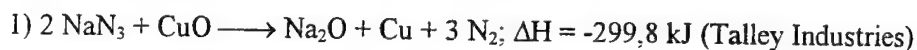
In this paper, testing methods are described for a better qualification of gas generator propellants. In this connection, not only the reaction behavior of different propellants will be discussed. Also the influence of different parameters such as impact, friction, heat and humidity onto the propellant will be described by testing a typical gas generator propellant.

### 3. Reaction behavior of components and propellants of air bag systems

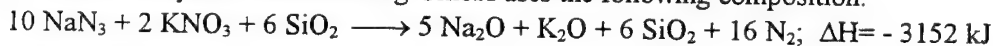
The basic substance of most gas generators is sodium azide ( $\text{NaN}_3$ ). It decomposes at  $275^\circ\text{C}$  in vacuum forming sodium ( $\text{Na}$ ) and nitrogen ( $\text{N}_2$ ):



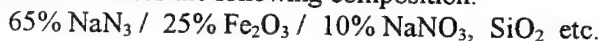
It reacts more easily by mixing with an oxidizer:



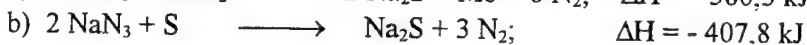
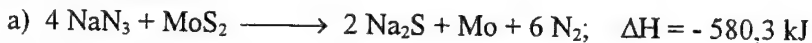
2) TEMIC Bayern-Chemie Airbag GmbH uses the following composition:



3) TRW - VSSI uses the following composition:



4) Morton International:



#### 4. Experimental results

Gas generators for air bags and belt restraint systems must exhibit safety and thermal properties which meet defined requirements. The most important tests for determining these properties are briefly discussed in this paper together with experimental results.

The following tests have been conducted in order to qualify an air bag gas generator propellant consisting of sodium azide ( $\text{NaN}_3$ ), molybdenum disulfide ( $\text{MoS}_2$ ) and sulfur. For this purpose,

- impact and friction sensitivity
- chemical stability
- combustion gas volume
- analysis of combustion gas and of the solid residue
- maximum pressure
- hygroscopicity

have been measured.

##### 4.1 IMPACT SENSITIVITY

The impact sensitivity of explosive substances is determined using the drop weight test developed by the German Federal Institute for Testing Materials (BAM, Berlin[1,2]. In this test, the minimum energy which causes at least one positive result from a set of six tests is determined.

<u>Result:</u>	<u>Impact sensitivity:</u>
- By using complete pellets:	No reaction
- By using small pieces:	7,5 Nm

##### 4.2 FRICTION SENSITIVITY

The friction sensitivity of explosive substances is determined using the friction tester developed by the BAM [1,2]. In this test, the minimum force (in Newton N) applied to a contact pin is determined, which causes at least one positive flame, crackle or explosion from a set of six tests.

Result: For this investigation, a sieve fraction of  $< 500 \mu\text{m}$  was taken. As result no friction sensitivity was found; this means no reaction was observed under a pistil load of  $\leq 360$  Newton (N).

##### 4.3 CHEMICAL STABILITY

###### 4.3.1 Dutch test at $110^\circ\text{C}$

The Dutch test was conducted at  $110^\circ\text{C}$  by an isothermal heating of two propellant samples of 4g according to the description TL 1376-950. Using this method, the weight loss between 8 and 72 hours of constant heating is measured.

Result:

Storage time (hours)	Weight loss (wt %)	
	sample A	sample B
0 - 8	0,18	0,19
0 - 72	0,29	0,30
8 - 72	0,11	0,11

The decomposition rate of 0,11% is very low; this means the propellant is very stable in this case.

#### 4.3.2 90° C Weight Loss Test

For determining the chemical stability of nitrocellulose containing gas generators, usually a 90° C test is being used. In this case, the time at 90° C ageing is measured up to an onset of an autocatalytic decomposition, which is characteristic for single base and double base propellants.

The beginning of a strong accelerated decomposition is equal to the end of the safe life time of a propellant.

The investigation of a double base propellant, which is being used as inflator system for the so-called Eurobag, exhibited an autocatalytic decomposition at 90° C after a storage time of 63 days.

#### 4.3.3 Service life determination of nitrocellulose containing propellants

The service life of nitrocellulose containing gas generators for air bags and belt restraint systems is determined by a storage of the propellant at different constant temperatures between 60° C and 90° C by measuring the stabilizer decrease down to a point at which 50% of the stabilizer has depleted. In this case, the so-called half-life time of the stabilizer is measured. Through extrapolation of the exponential relationship between temperature and stabilizer depletion rate, the service life at a lower storage temperature or under any given temperature profile is determined.

For example, the investigation of two single base propellants for belt restraint systems gave the following results with regard to a 50% depletion time of the stabilizer diphenylamine (DPA):

Temperature (°C)	50% depletion of DPA in days	
	Gas generators: B.C. 86/046	SNPE 94/86
90	2,3	2,5
80	7,9	7,7
70	30,9	31,3
↓	↓	↓
30	43,7 years	34,5 years

#### 4.4 MEASURING OF THE COMBUSTION GAS VOLUME

For the determination of the volume of the combustion gas, 2,5 grams of the air bag propellant were ignited in a calorimetric bomb exhibiting a chamber volume of 25 cm<sup>3</sup>. The combustion was initiated by the hot wire technique with a 12 Volt battery. After the shot, the product gas was measured using a graduated gas sample system. As a result, 375 to 385 cm<sup>3</sup> gas have been measured related to one gram of the propellant. The residue of solid products in the closed bomb was about 55 weight percent.

#### 4.5 COMBUSTION IN A 60 LITER VESSEL

For investigation the combustion behavior of complete gas generator systems without bag, a 60 l vessel was used. In this case usually the pressure-time plot or the maximum pressure is being determined. In addition, gaseous and solid reaction products are analyzed.

For the tests, three air bag gas generators A, B and C have been used.

##### 4.5.1 Pressure measurement

The gas generator mounted on the top of the vessel was ignited with a 12 Volt battery. The pressure was measured using a piezoresistive pressure gauge of Kistler Company, Germany. The following maximum pressures were measured:

Gas generator A:	1,9 bar,
Gas generator B:	2,0 bar,
Gas generator C:	1,9 bar.

##### 4.5.2 Analysis of the gaseous products

Three gas generators have been fired into a 60 l tank in order to analyze as well the reaction gas as the solid residue. After the shot, gas was taken using evacuated glass bottles and analyzed by gas chromatography and Draeger tubes for the trace analysis.

Analysis by gas chromatography in volume percent			
Gas generator:	A	B	C
H <sub>2</sub>	0,35	0,36	0,36
O <sub>2</sub>	14,44	14,53	14,37
N <sub>2</sub>	85,11	85,00	85,17
CO	0,08	0,09	0,08
CO <sub>2</sub>	0,01	0,01	0,01

Analysis by Draeger tubes in ppm			
Gas generator:	A	B	C
NO <sub>x</sub>	10	12	10
HCN	-	-	-
NH <sub>3</sub>	65	75	65
CO	500 - 600	600 - 700	600 - 700
H <sub>2</sub> S	?	?	?
SO <sub>2</sub>	-	-	-
CH <sub>2</sub> O	-	-	-

#### 4.5.3 Analysis of the solid reaction products

In order to analyze the solid reaction products of air bag shots, usually the following elements should be taken into account:

Sodium (Na)  
Potassium (K)  
Silicon (Si)  
Molybdenum (Mo)  
Iron (Fe)  
Copper (Cu).

After the combustion of the gas generator, the 60 l tank was treated with distilled water to wash out the solid products quantitatively. In order to get a complete solution, a treatment with HCl is necessary. Then the above mentioned elements, or other ones, will be determined quantitatively by Atomic Absorption Spectroscopy (AAS) or by Inductive Coupled Plasma Method (ICP).

Before treatment with hydrogen chloride, the p<sub>H</sub> - value of the water solution is measured.

The following concentrations have been measured using the AAS - method:

Analysis of the solid residue								
Gas generator	p <sub>H</sub> value	Solid residue (mg)	Na (mg)	K (mg)	Mo (mg)	Si (mg)	Fe (mg)	Cu (mg)
A	11,8	2316	599	51	263	4	0,5	1,2
B	11,0	1812	494	207	39	4	0,2	0,8
C	11,1	1689	501	116	43	4	0,7	0,5

We see that the p<sub>H</sub> - value is relatively high; the washing water exhibits a strong alkaline reaction, due to the formation of sodium hydroxide (NaOH).

#### 4.6 HYGROSCOPICITY

In order to measure the hygroscopicity, propellant samples were stored at a relative humidity of about 65% at room temperature in special climatic heating systems. In our case, glass tubes containing 3 grams of propellant samples were stored at 23° C. From time to time the mass of the tubes was determined in order to get the increase of humidity. The following table shows the result of humidity increase of three propellant samples stored at 65% relative humidity:

Storage time (days)	Humidity increase in weight %		
	Sample a	Sample b	Sample c
5	1,27	1,23	1,20
11	2,17	2,16	2,03
18	4,97	4,91	4,78
24	6,13	5,94	5,58

From the table we see an increase of humidity content after 24 days at 23° C of about 6%.

#### 4.7 BONFIRE TEST

In order to find out how a gas generator reacts when directly exposed to a flame, the Bonfire test should be conducted. In this test, the inflator system is exposed to hot exhaust gases from a gas burner until self-ignition occurs. The observation includes whether or not metallic fragments are formed during self-ignition and combustion. It is also important if the gas generator moves from its original position or not, this means if it is thrust neutral or not.

By testing different gas generators it was found that the results depend on the position of the flame. This means if the flame is directed onto the igniter side, in most cases a complete combustion of the propellant starts after a distinct time. If the flame is opposite to the igniter, usually the time is longer until a complete combustion has occurred.

#### 5. Disposal of gas generators

Most of the gas generators for air bag systems consist of sodium azide ( $\text{NaN}_3$ ) and oxidizers such as molybdenum disulfide ( $\text{MoS}_2$ ), potassium nitrate ( $\text{KNO}_3$ ), sodium nitrate ( $\text{NaNO}_3$ ), iron oxide ( $\text{Fe}_2\text{O}_3$ ) and other ingredients. From these substances, Sodium azide exhibits the most toxic properties. It is extremely poisonous: Ingestion of small quantities can cause nausea, vomiting, headache, diarrhea, difficulty in breathing and heart palpitations. A dangerous reaction product is hydrazoic acid, see data sheet of sodium azide.



Because of the poisonous behavior of sodium azide included in the propellant, gas generators should be fired for disposal purposes. The reaction products, consisting of  $\text{Na}_2\text{O}$ ,  $\text{K}_2\text{O}$ ,  $\text{Na}_2\text{S}$ ,  $\text{Mo}$ ,  $\text{MoS}$ ,  $\text{Cu}$ ,  $\text{CuO}$ ,  $\text{FeO}$  etc. are much less poisonous.

## 6. Conclusion

This paper deals with the investigation of gas generators for air bags and belt restraint systems. The reaction behavior of sodium azide and nitrocellulose based gas generators is described. Safety aspects during handling, thermal stability and life time of different propellants have been discussed. In addition, reaction products from shots in the 60 l vessel were analyzed.

## 7. References

1. Koenen, H. and Ide, K.H. , *Explosivstoffe* 9, page 4 - 13 and 30 - 42 (1961)
2. Meyer, K., *Explosives*, 3rd Edition, 1987, VCH Publishers, Weinheim, Germany
3. Technical Delivery Requirements (TL) 1376-950
4. Volk, F., Life time determination of a double base propellant for inflator systems  
20th Int. Pyrotechnics Seminar, 25-29 July 1994, Colorado Springs, USA
5. Volk, F., Investigation of gas generators for air bags and passive restraint systems  
9th Symp. Chem. Probl. Connected with the Stability of Explosives, August 1992, Margaretertorp, Sweden
6. Menke, K., Volk, F., Bucerius, K.M., Schmid, H., Production of explosives for air bags: An overview on special issues like safety, handling, and risks  
Int. Symposium on Sophisticated Car Occupant Safety Systems, November 2-3, 1992, Karlsruhe, Germany.

## EXPERIMENTAL STUDY OF FLAME-SPREADING PROCESSES OVER Mg/PTFE/Mg THIN FOILS

C. L. Yeh,<sup>1</sup> M. M. Mench,<sup>1</sup> K. K. Kuo,<sup>1</sup> and S. K. Chan<sup>2</sup>

<sup>1</sup> Department of Mechanical Engineering, The Pennsylvania State University  
University Park, PA 16802, U.S.A.

<sup>2</sup> ICI Explosives Canada, Technical Centre, McMasterville, Quebec, Canada J3G 6N3

### ABSTRACT

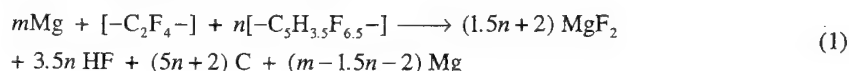
An experimental study of flame-spreading behavior over thin Mg/PTFE/Mg foils (called Enerfoil™ Pyrotechnic Film) with thicknesses of 10/25/10  $\mu\text{m}$  was conducted in an argon environment. This thin film pyrotechnic material has been designed to serve as an ignition enhancer in passenger-side airbag gas generators. The objective of this study was to determine the effects of initial chamber pressure and gap width between two foils on the intrinsic flame-spreading rate of Enerfoil™ films. In the experimental setup, the steady-state flame-spreading rate ( $V_{FS}$ ) was deduced from the flame-front trajectory measured by an array of fast-response Lead-Selenide (Pb-Se) IR photodetectors. The initial chamber pressure was varied from 0.1 to 10.5 MPa. Results indicated that for single-foil tests  $V_{FS}$  decreased as the initial chamber pressure was increased; this observed trend is believed to be caused by a greater heat loss to the ambient gas at higher pressures. An experimental correlation was developed with a pressure exponent of  $-0.118$ . For double-foil tests, the gap width between two adjacent foils was varied from 50 to 400  $\mu\text{m}$ . It was found that for double-foil tests there exists an optimal gap width for obtaining a maximum  $V_{FS}$  at a given initial chamber pressure. The optimal gap width appears to become smaller as the initial chamber pressure increases. For each gap width tested, there is also an optimal pressure at which the  $V_{FS}$  reaches a maximum. The existence of the optimal pressure and gap width is caused by the combination of several factors, including required physical space for complete gas-phase reactions, heat transfer rates to both unburned foils and ambient gases.

### INTRODUCTION

Pyrotechnic compositions based on the formulation of magnesium (Mg) and polytetrafluoroethylene [PTFE,  $(-\text{C}_2\text{F}_4-)_n$ ] have been utilized as a rocket motor igniter material due to several advantages<sup>1</sup>: high-energy content, low hygroscopicity, high degree of safety in preparation, low temperature and pressure dependence of the burning rate, easy fabrication of igniter pellet or grain, favorable aging characteristics, stable burning at low pressures, and low production costs. Viton copolymer,  $(-\text{C}_5\text{H}_3.5\text{F}_{6.5}-)_n$ , is frequently added to the conventional Mg-Teflon (MT) powder mixture to increase homogeneity and to facilitate product fabrication without producing any adverse effect on combustion thermochemistry. It is important to note that "soft" ignition (defined as low motor pressurization rate and absence of an ignition peak) of solid-propellant motors is readily obtainable with MT or MTV

(Mg-Teflon-Viton) pellets and granules.<sup>2</sup> The soft ignition feature is often desirable for certain propellant grain configurations.

A comprehensive thermochemical study was conducted by Peretz<sup>1</sup> for different MT and MTV formulations. A simplified combustion scheme of MTV compositions for both stoichiometric and Mg-rich formulations was expressed by the following reaction<sup>1</sup>:



Using 3.4 cm long tubular MTV pellets with inside and outside diameters of 1.05 and 2.35 cm, respectively, a series of ballistic tests was conducted by Peretz.<sup>1</sup> MTV pellets with a composition of 58% Mg, 38% PTFE, and 4% Viton showed fast flame spreading, stable burning and reproducible results. The burning rate law for test samples consolidated at 220 MPa with the above composition at ambient temperatures over the pressure range of 0.8 to 4.2 MPa was deduced to be:

$$r_b \text{ (cm/s)} = 1.69 P(\text{MPa})^{0.22} \quad (2)$$

No noticeable variation of the pressure exponent in the burning rate law with temperatures (-40 °C to 70 °C) was detected. Consolidation at lower pressures of 150 and 100 MPa was found to increase the burning rates by 4% and 15%, respectively.

The burning rate characteristics of Mg/PTFE/Viton pyrotechnic material were also studied by Kubota and Serizawa.<sup>3</sup> The burning rate of MTV pellets (7 mm in diameter and 30 mm in length) was determined in a chimney-type strand burner pressurized with nitrogen. Experimental results indicated that the burning rate increases with the increase in the weight fraction of Mg particles ( $\xi$ ) for samples with  $\xi$  from 0.2 to 0.7. The pressure exponent of the burning rate law is relatively constant for MTV pellets with a high concentration of Mg (60% and 70%); however, the pressure exponent increases rapidly with increasing pressure for pellets with a low concentration of Mg (20%, 30%, and 40%). The burning rate is also dependent on the particle sizes of Mg and PTFE; it is higher for pellets with either smaller Mg particles or larger PTFE particles.

Based upon their experimental observations, Kubota and Serizawa<sup>3</sup> proposed a combustion mechanism of Mg/PTFE pyrotechnics. It was postulated that Mg particles melt on the burning surface and are partially oxidized by fluorine which is produced by the thermal decomposition of PTFE particles. Subsequently, Mg particles on the burning surface are ejected into the gas phase where they react rapidly with fluorine.

Due to the broad utilization of PTFE in the industry, the thermal decomposition of PTFE has been studied extensively.<sup>4-8</sup> The decomposition of PTFE in vacuum or in inert gas (He and N<sub>2</sub>) environments yields mainly the monomer tetrafluoroethylene (C<sub>2</sub>F<sub>4</sub>).<sup>4-6</sup> However, carbonyl fluoride (COF<sub>2</sub>), carbon dioxide, and tetrafluoromethane (CF<sub>4</sub>) are major products when PTFE is decomposed in air or oxygen.<sup>6,7</sup> Below 650 °C, COF<sub>2</sub> appears to be the main product, and at higher temperatures it disproportionates to CO<sub>2</sub> and CF<sub>4</sub>. The thermal characteristics of the PTFE decomposition was investigated by Griffiths et al.<sup>8</sup> using a simultaneous DTA/DTG. It was found that the decomposition of PTFE is an endothermic process in argon and nitrogen but it becomes exothermic in air. The thermal decomposition of PTFE in the presence of magnesium was also studied by Griffiths et al.<sup>8</sup> Results indicated that the addition of Mg powders causes the purely endothermic decomposition of PTFE in argon and nitrogen to develop two exotherms at 570 °C and 630 °C. Development of these two exotherms represents the change of reaction mechanism between Mg and decomposed products of PTFE in the formation of carbon and magnesium fluoride. Moreover, complete decomposition can be achieved at a lower temperature in air than in the inert atmosphere and major decomposed products are magnesium fluoride, magnesium oxide, and unreacted magnesium.

Recently a new pyrotechnic technology was invented at the Defense Research Agency (DRA) of the Ministry of Defense, UK,<sup>9-11</sup> using a physical vapor deposition (PVD) technique to manufacture thin Mg/PTFE/Mg pyrotechnic foils. ICI Explosives has developed the invention further into a commercial

manufacturing process and built the world's first production scale roll coater for the manufacture of such pyrotechnic foils, called Enerfoil™ Pyrotechnic Film. The first commercial application of such material was to serve as an ignition enhancer in passenger-side airbag gas generators. The thickness of the Mg/PTFE/Mg film is typically around 10/25/10  $\mu\text{m}$ . The unique form of this material allows one to design an ignition train into a wide range of geometries through standard film processing techniques such as embossing, cutting, rolling, and cassetting. This high degree of automation in manufacture and conversion of Enerfoil™ films is highly beneficial for a large volume products with consistent quality. As a result, the Enerfoil™ pyrotechnic film has been considered to be an attractive candidate for a broad range of potential applications in both civil and military systems (e.g., enhancers for airbag inflator systems, gas generators, rocket motors, large caliber ordnance, signal transfer tubes, and flares).<sup>12</sup>

In a series of performance evaluation tests, Chan et al.<sup>12-14</sup> demonstrated that a wound roll of Mg/PTFE/Mg film can provide rapid and uniform ignition of sodium azide based propellants with minimum damage to the propellant grain structure. This novel material has been shown to have better performance than conventional pyrotechnic powders of an identical chemical composition in terms of ballistic, environmental, and cost considerations. The geometric configuration of Mg/PTFE/Mg films has been found to be an important parameter to obtain optimum performance. Experiments showed that the time to reach complete reaction of a wound Mg/PTFE/Mg roll depends strongly on the separation of adjacent layers and the confinement of the film element. With an optimum interply separation of about 300  $\mu\text{m}$  and proper confinement, full reaction of a Mg/PTFE/Mg coil (229 mm in length) was achieved in less than 4 ms in a cylindrical combustion vessel which simulated the physical dimensions of a typical passenger side airbag inflator.<sup>14</sup> However, it is hard to deduce the flame-spreading rate of the Enerfoil™ film from this type of tests. For achieving deeper understanding of ignition and flame-spreading processes of this new material, it is useful to obtain the intrinsic flame-spreading rate of Enerfoil™ film as well as the rate dependency on operating conditions.

Most of the previous research work, as mentioned above, was focused on the combustion of pyrotechnic pellets made of well-mixed powders, very little study aiming at the burning process of thin film pyrotechnics. The objective of the present study is to investigate the fundamental flame-spreading characteristics of thin Mg/PTFE/Mg foils under well-defined and -controlled test conditions using a non-intrusive optical diagnostic technique. This work includes a study of the effects of initial chamber pressure and gap width between adjacent foils on the flame-spreading rate of Mg/PTFE/Mg foils. In addition, correlations describing the steady-state flame-spreading rate of the Mg/PTFE/Mg foil as a function of operating conditions were developed.

## METHOD OF APPROACH

### Measurement of Flame-Spreading Rate

A schematic diagram of the experimental setup to measure the flame-spreading rate over Mg/PTFE/Mg thin foils is shown in Fig. 1. A high-pressure windowed stainless-steel chamber was used in this study. An array of infrared (IR) photodetectors, consisting of six fast-response lead-selenide (Pb-Se) IR photodetectors ( $< 10 \mu\text{s}$  temporal response; 1-4.5  $\mu\text{m}$  wavelength), was mounted on the top wall of the test chamber. These detectors were arranged adequately to cover the axial variations of light emission from the foil surface, for providing the ignition delay times of various sites of the test sample opposite to the photodetectors. The selection of IR photodetectors was based upon a study by Thynell et al.<sup>15</sup> using a Fourier-Transform Infrared (FT-IR) spectrometry to show that the optical signals from an ignited propellant surface could be distinctly differentiated from those of an unignited propellant surface, even in the presence of combustion product gases and metal-oxide particles in line-of-sight measurements. To use the emitted energy as a means for detecting the arrival of the flame front, Thynell et al.<sup>15</sup> outlined three criteria: (1) it is necessary to have optical access to the measurement location, (2) the emitted energy from the burning surface must be distinguishable from flowing combustion product gases, and (3) the measurement system must be capable of recording the rapidly changing event. All three criteria were satisfied in the experimental setup of this study.

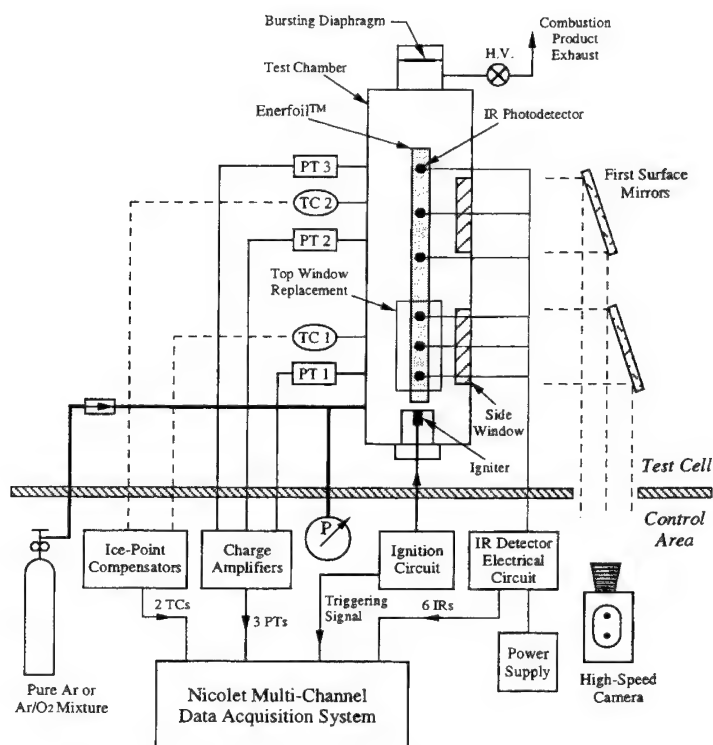


Figure 1. Schematic Diagram of Experimental Setup to Measure Flame-Spreading Rate of Mg/PTFE/Mg Foils

Six specially-designed photodetector holders, which contain quartz windows and window retainers, provide both the optical access of photodetectors to the sample surface and the tight seal for high-pressure tests. The electrical circuit for IR detectors consists of six parallel IR photodetectors and each detector is connected in series with a  $1\text{ M}\Omega$  resistor. An excitation voltage was supplied to the detector array and the voltage across each  $1\text{ M}\Omega$  resistor was recorded using a PC-based Nicolet multi-channel data acquisition system. The design was based upon the fact that as the photodetector senses a signal the resistance of the detector decreases, resulting in an increase in voltage across the  $1\text{ M}\Omega$  resistor.

The overall transient event of ignition and flame-spreading of a Mg/PTFE/Mg foil was recorded by a high-speed movie camera (Pulnix CCD camera or Spin Physics 2000 camera). As shown in Fig. 1, two first surface mirrors reflect the images from two side windows to the camera which is located in the control area.

Three fast-response pressure transducers (PT1, PT2, and PT3; Kistler Instrument Corp.) were mounted at upstream, midstream, and downstream locations along the test chamber to record the pressure-time history of the chamber during the burning of Mg/PTFE/Mg foils. Two fine-wire ( $25\text{ }\mu\text{m}$ ) Pt/Pt-10%Rh thermocouples (TC1 and TC2) were used to measure the surface temperature of Mg/PTFE/Mg foils and the gas-phase temperature during the flame-spreading event.

### Mg/PTFE/Mg Foil Sample and Igniter

Mg/PTFE/Mg foil samples with a layer thickness of 10/25/10  $\mu\text{m}$  were supplied and manufactured by ICI Explosives. These foils were treated with a very thin aluminum oxide coating to prevent the oxidation of Mg layers by ambient gases. The composition of Mg/PTFE/Mg foils is slightly Mg-rich and has a weight percentage of 31-35% Mg, 65-69% PTFE, and less than 1% Al. Test samples used in this study were 2.5 cm wide and 45 cm long; the reason for using long sample strips is to accurately determine the intrinsic flame-spreading rate.

In the experiment, the Mg/PTFE/Mg foil sample was mounted on a sample holder made of an ablative resistant material, MXB-360. The selection of MXB-360 was based upon its low thermal conductivity, high-temperature refractory nature, and material rigidity. The igniter was installed inside an igniter holder. Both sample holder and igniter holder were connected with a steel baseplate, permitting adjustment of the distance between the igniter tip and the sample surface. Results presented in this paper were obtained in test conditions with 3.4 mm between the igniter tip and the leading edge of test samples. The ignition circuit was designed to synchronously send out a firing current to the igniter and a triggering signal to the data acquisition system. Igniters used in this study were also manufactured and supplied by ICI Explosives. This type of igniters has an amount of pyrotechnic charge of 60 mg powders, consisting of zirconium, boron, and potassium perchlorate mixture.

### Test Conditions

Experiments were conducted with two different sample configurations: single foil and double foils. For single-foil tests, the sample was mounted on a horizontal sample holder with six photodetectors aimed at different axial locations along the centerline of the sample surface. For each double-foil test, two samples were mounted on two vertical sample holders with adjustable gap widths; the photodetector array was aligned along the gap between two foils.

All the tests were conducted in a pure argon environment. The test chamber pressure was varied from one atmosphere (0.1 MPa) to 10.5 MPa. For double-foil tests, the gap width between two adjacent foils was varied from 50 to 400  $\mu\text{m}$ .

## DISCUSSION OF RESULTS

### Single-Foil Tests

A typical set of IR photodetector responses signifying the arrival of flame front to the detector locations opposite to a single foil is shown in Fig. 2. The first abrupt rise in voltage output of each photodetector was treated as the onset of ignition. The flame front propagation velocity was then determined by a linear fit of the ignition front trajectory. It was found that in most of the tests the flame front signal is essentially linear for the last five detectors, indicating a steady-state flame-spreading rate in this region. (It should be noted that the sequential onset of IR signals does not appear to be linear in Fig. 2 due to a non-linear stagger of these traces, which does not correspond to the actual locations of IR detectors.) The first photodetector data was omitted from the linear fit due to the randomness associated with the pyrotechnic igniter discharge.

Figure 3 shows a plot of flame-front trajectories of a series of single-foil test runs at several different initial chamber pressures. The free volume inside the test chamber for single-foil tests was about 330  $\text{cm}^3$ . Steady-state flame-spreading rates ( $V_{FS}$ ) were then deduced from the linear fit of each flame-front trajectory. As indicated in Fig. 3,  $V_{FS}$  decreased as the initial chamber pressure was increased. It is believed that the steady-state propagation rate of a flame front depends on the energy transfer from the combustion products to the unburned foil. The observed trend can be explained by considering the amount of heat loss from the combustion products of a Mg/PTFE/Mg foil to the ambient gas. For higher initial chamber pressure, the gas density was higher and therefore the combustion products of Mg/PTFE/Mg foils were cooled more rapidly, resulting in a decrease in heat transfer rate to the unburned foil and flame-spreading rate.

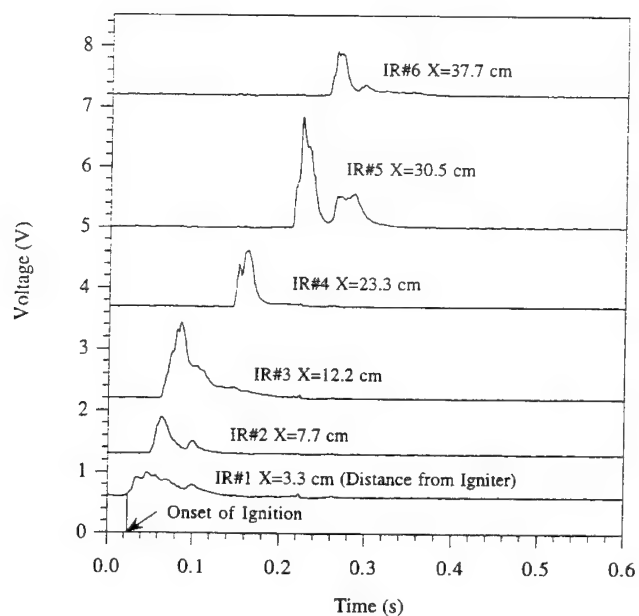


Figure 2. A Typical Set of IR Photodetector Responses

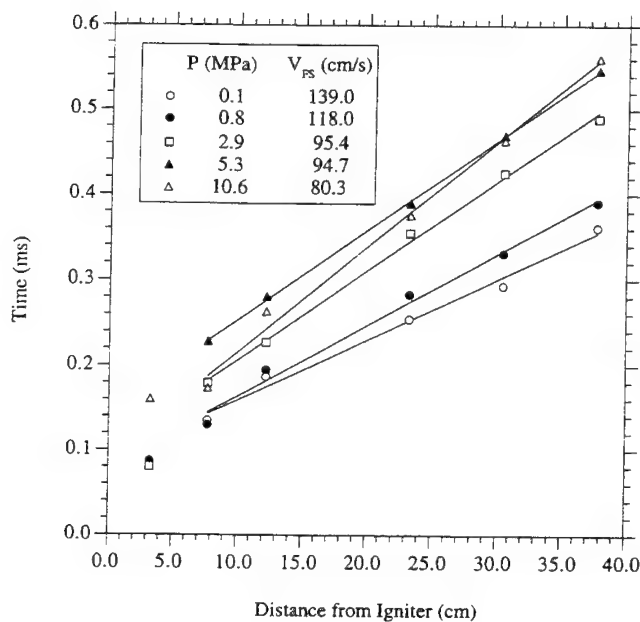


Figure 3. Flame Front Trajectories of Single Mg/PTFE/Mg Foils in 100% Ar at Different Initial Chamber Pressures

The following correlation was developed to relate the  $V_{FS}$  of single foils as a function of initial chamber pressure

$$V_{FS} \text{ (cm/s)} = 108.2 P(\text{MPa})^{-0.1184} \quad (3)$$

Figure 4 shows a comparison of the measured  $V_{FS}$  versus  $P$  data for single-foil tests with the correlation. It is evident that the correlation fits the measured data very well.

### Double-Foil Tests

Figure 5 shows a plot of deduced  $V_{FS}$  versus gap width for a series of double-foil tests at several different initial chamber pressures. Tests were conducted at gap widths of 51, 102, 204, 305, and 408  $\mu\text{m}$ . The gap width was controlled by using metal shims of different thicknesses between the opposing foils. The free volume inside the test chamber for double-foil tests was minimized for two reasons: (1) to reduce the amount of heat loss to non-reacting gases inside the test chamber and (2) to more closely simulate the confined conditions of Enerfoil<sup>TM</sup> pyrotechnic films used as an ignition enhancer in automobile airbag applications. The free volume for double-foil tests was about 100  $\text{cm}^3$ .

Steady-state flame-spreading rates ( $V_{FS}$ ) were deduced from the linear fit of each flame-front trajectory as described in the Single-Foil Tests section. Figure 5 reveals the existence of an optimal gap width for obtaining a maximum  $V_{FS}$  at a given initial chamber pressure. It is important to note that this optimal gap width is not constant and is a function of the initial chamber pressure. At a given pressure, the  $V_{FS}$  decreases at gap widths larger than the optimal value due to the increased heat loss to a larger amount of gases in the gap as well as the increased radiation heat loss to interior surfaces of the test chamber. It may also be caused by the fact that as the gap width increases the radiation shape factor from the burned foil to the unburned opposing foil decreases. When gap widths were smaller than the optimal value, the decrease of  $V_{FS}$  was caused by the lack of volume for the gas-phase reaction to reach a fully reacted state. These above effects result in an optimal gap width for a given initial chamber pressure.

As can be seen in Fig. 5, the optimal gap width appears to become smaller as the initial chamber pressure increases. This gap-width induced shift phenomenon can be explained by noting that as the initial chamber pressure increases, the collision frequency of gas molecules is higher and therefore gas-phase reactions require less space to reach a fully reacted state. Also, for regions beyond the optimal gap width, the decrease of  $V_{FS}$  with an increase in the gap width is more pronounced at higher pressures. This is believed to be caused by a greater heat loss from the combustion products to the ambient gas at higher initial chamber pressures. It is anticipated that as the gap width is increased to a certain extent, the value of  $V_{FS}$  should approach asymptotically to the single foil result. However, the current test matrix does not cover a very broad range of gap widths.

Figure 6 is a plot of the  $V_{FS}$  versus initial chamber pressure at several different gap widths. It is evident from Fig. 6 that for each gap width tested, there is also an optimal pressure at which the  $V_{FS}$  reaches a maximum. This phenomenon can be interpreted as the result of two competing effects. As the pressure increases, the heat transferred from combustion products to the unburned foil is enhanced by having higher Reynolds and Nusselt numbers, resulting in a larger local heat-transfer coefficient. However, the heat loss to the ambient gas is also increased at higher pressures. It is believed that the enhanced heat transfer to the unburned foil near the flame front dominates before the optimal pressure, after which the heat loss to the ambient gas becomes dominant.

A set of pressure-time ( $P-t$ ) traces obtained from a typical test run is shown in Fig. 7. (These two  $P-t$  traces were purposely offset for clarity.) The two gauges were located at 5 cm apart. Based upon the comparison of these traces, it is evident that the pressure wave phenomenon is not important during the transient event. The slight increase of pressure was caused by both an increase of the gaseous mass and heat generation due to foil combustion. However, the pressure rise is not very pronounced. The pressure decrease beyond the peak value at the end of foil combustion was caused by the cooling of product gases by the chamber walls.



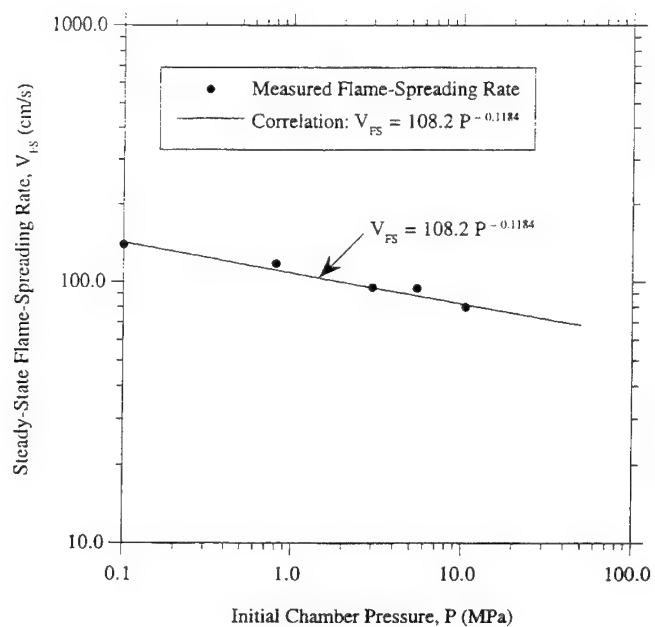


Figure 4. Measured and Correlated Flame-Spreading Rates of Single Mg/PTFE/Mg Foils in 100% Ar as a Function of Initial Chamber Pressure

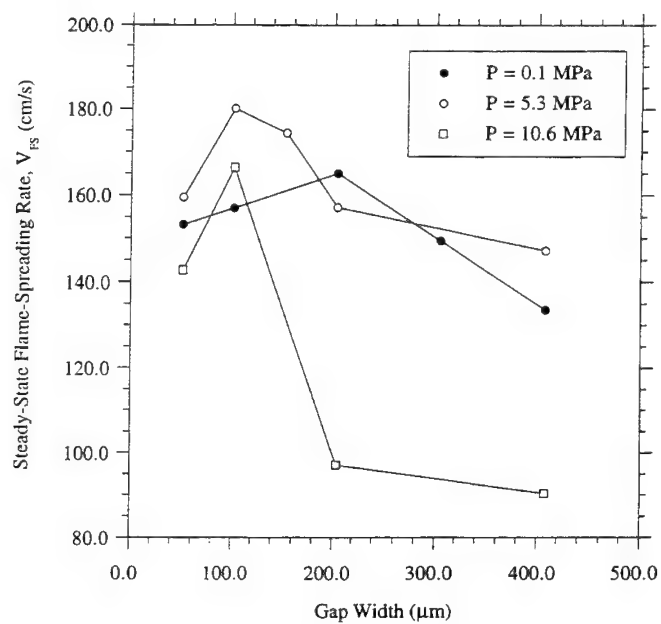


Figure 5. Deduced Steady-State Flame-Spreading Rate vs. Gap Width for Double-Foil Tests at Several Initial Chamber Pressures

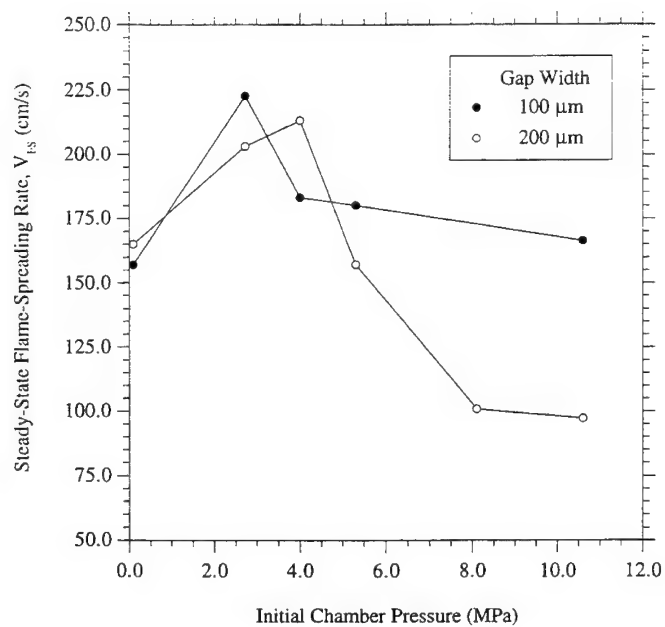


Figure 6. Deduced Steady-State Flame-Spreading Rate vs. Initial Chamber Pressure for Double-Foil Tests at Two Gap Widths

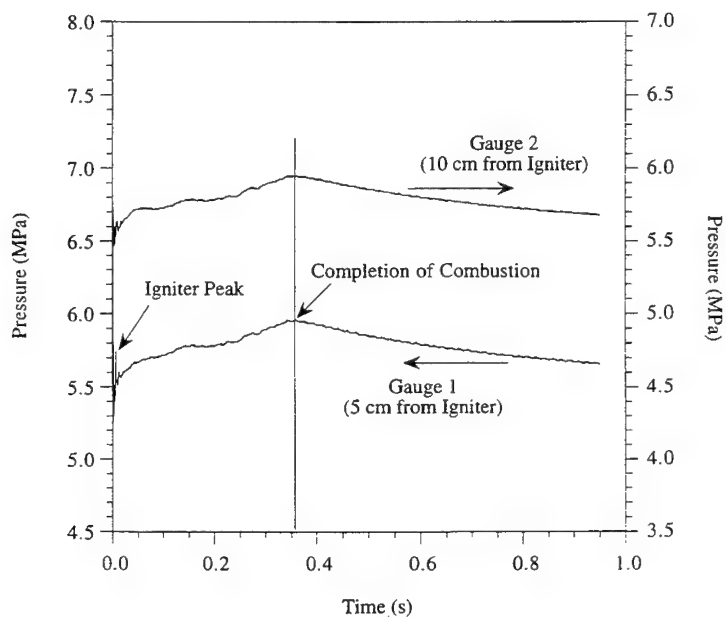


Figure 7. A Typical Set of Pressure-Time Traces Recorded in a Double-Foil Test (Initial Chamber Pressure = 5.3 MPa)

## CONCLUSION

Based upon the experimental measurements and observations of this study, several major findings are listed below.

1. For single-foil tests in an argon environment, results showed that the steady-state flame-spreading rate ( $V_{FS}$ ) decreased as the initial chamber pressure was increased. It is believed that for higher initial chamber pressures, the heat loss from the combustion products of Mg/PTFE/Mg foils to the ambient gas is greater, resulting in a decreased heat transfer rate to the unburned foil and a lower flame-spreading rate.
2. A correlation was developed to relate the  $V_{FS}$  as a function of initial chamber pressure for single foil tests. The pressure exponent was found to be  $-0.118$ .
3. For double-foil tests, an optimal gap width for obtaining a maximum  $V_{FS}$  at a given initial chamber pressure was observed. The decrease of  $V_{FS}$  at gap widths larger than the optimal value can be attributed to the increased heat loss to both a larger amount of gases in the gap and interior surfaces of the test chamber. When the gap widths were smaller than the optimal value, the decrease of  $V_{FS}$  is believed to be caused by the lack of volume for the gas-phase reaction to reach a fully reacted state.
4. The optimal gap width appears to become smaller as the initial chamber pressure increases. This gap-width induced shift phenomenon can be explained by considering the effect of initial chamber pressure on the physical space required to reach a fully reacted state.
5. For each gap width tested, there is also an optimal pressure at which the  $V_{FS}$  reaches a maximum. The existence of the optimal pressure is caused by two competing heat transfer rates; one from combustion products to the unburned foil and the other to the ambient gas. The first one dominates before reaching the optimal pressure. The heat loss to the ambient gas becomes dominant after the optimal pressure.

## ACKNOWLEDGMENTS

This work represents a part of the results obtained from the research project sponsored by ICI Explosives Canada. The technical input from Mr. E. R. Cox and Mr. T. V. Aukzemas of ICI Explosives is gratefully acknowledged. The supply of Enerfoil™ films and pyrotechnic igniters from ICI Explosives is also greatly appreciated.

## REFERENCES

1. Peretz, A., "Investigation of Pyrotechnic MTV Compositions for Rocket Motor Igniters," *Journal of Spacecraft and Rockets*, 21, 222-224, 1984.
2. Crosby, R., Mullenix, G. C. and Swenson, I., "Design and Development of a Hot Particle Igniter," *AIAA Paper 72-1196*, Nov. - Dec., 1972.
3. Kubota, N. and Serizawa, C., "Combustion of Magnesium/Polytetrafluoroethylene," *Journal of Propulsion and Power*, 3, 303-307, 1987.
4. Madorsky S. L. and Straus, S., "Note on the Thermal Degradation of Polytetrafluoroethylene as a First-Order Reaction," *Journal of Research of the National Bureau of Standards - A. Physics and Chemistry*, 64A, 513-514, 1960.
5. Siegle, J. C., Muus, L. T., Lin, T. and Larsen, H. A., "The Molecular Structure of Perfluorocarbon Polymers. II. Pyrolysis of Polytetrafluoroethylene," *Journal of Polymer Science: Part A*, 2, 391-404, 1964.
6. Morisaki, S., "Simultaneous Thermogravimetry-Mass Spectrometry and Pyrolysis-Gas Chromatography of Fluorocarbon Polymers," *Thermochimica Acta*, 25, 171-183, 1978.

7. **Paciorek, K. L., Kratzer, R. H. and Kaufman, J.**, "Oxidation Thermal Degradation of Polytetrafluoroethylene," *Journal of Polymer Science: Polymer Chemistry Edition*, 11, 1465-1473, 1973.
8. **Griffiths, T. T., Robertson, J. Hall, P. G. and Williams, R. T.**, "Thermal Decomposition of PTFE in the Presence of Magnesium," *Proceedings of the 16th International ICT-Jahrestagung combined with 10th International Pyrotechnics Seminar*, 19-1 to 19-10, 1985.
9. **Allford, F. G.**, "Pyrotechnic Materials," Patent No. WO 90/10724, 1990.
10. **Allford, F. G. and Place, M. S.**, "The Development and Production of Pyrotechnic Systems from the Vapor Phase: Part One – Thermite Type Materials," *Fifteenth International Pyrotechnics Seminar*, 1-16, 1990.
11. **Allford, F. G. and Place, M. S.**, "The Development and Production of Pyrotechnic Systems from the Vapor Phase: Part Two – The Production of Bulk Reactive Materials," *Fifteenth International Pyrotechnics Seminar*, 17-34, 1990.
12. **Chan, S. K., Graham, S. J. and Leiper, G. A.**, "Some Properties of Thin Film Pyrotechnics," *Twentieth International Pyrotechnics Seminar*, July, 1994.
13. **Chan, S. K., Graham, S. J. and Leiper, G. A.**, "Enerfoil™ Ignition Film as an Ignition Charge," *Proceeding of 26th International Annual Conference of ICT*, Karlsruhe, Germany, 58-1 to 58-14, 1995.
14. **Chan, S. K., Leiper, G. A. and Underwood, B.**, "Design and Performance Evaluation of Enerfoil™ Ignition Enhancers for Passenger Side Airbag Inflators," *ADPA International Symposium on Energetic Materials Technology*, Phoenix, AZ, 1995.
15. **Thynell, S. T., Huang, I. T., Kuo, C. S., Hsieh, W. H. and Kuo, K. K.**, "Approach to Measurements of Flame Spreading over Solid Propellants," *Journal of Propulsion and Power*, 8, 914-917, 1992.

## COMBUSTION AND DETONATION IN PULSED POWER GENERATORS

V.E.Fortov, V.B.Mintsev, V.A.Zeigarnik

High Energy Density Research Center, IVTAN-Association, Russian Academy of Sciences

**ABSTRACT:** High-power electrical sources are considered using powder fuels and explosives: pulse and explosive magnetohydrodynamic (MHD) generators and magnet flux cumulative (MC) generators. The powder MHD-generators are verified in field geophysical studies. Their further employment depends strongly on improvement of the combustion processes. Analysis is presented of ways to solve the problem. For the case where high-power pulses are needed with repetition frequencies of 1 to 1000 Hz, the use of explosive MHD-generators is promising. The MC-generators are particularly appropriate for superhigh-power supershort pulses for supplying vacuum diodes, railguns, electron and proton accelerators, powerful lasers, powerful microwave generators, etc. Various designs of such MC-generators are considered as well as their achievable parameters. A suggestion is made of their use in geophysics. The MC-generators are compared to the MHD-generators against their use as power supply for earth crust electromagnetic sounding and electrical prospecting.

### INTRODUCTION

Many new technologies need high power small bulk power supplies. Requirements for such supplies include self-sufficiency, transportability, and fast entering into issued operating regime. The most promising power supplies for such use are generators with explosives as the primary energy source. This is because the explosives accumulate energy up to 10 MJ/kg, that is 5-6 orders of magnitude higher than capacitors. Depending on the energy pulse duration required to be supplied in a load, either combustion or explosion is used. In particular, such devices are MHD-generators which in turn are classified as powder and explosive MHD-generators. The former were primarily taken up in geophysical investigations and thus were referred to as geophysical (pulsed) MHD-generators.

### GENERAL DESCRIPTION OF THE PULSED MHD-GENERATORS

The power that pulsed MHD-generators release into self-consistent load is within 10 to 100 MW, the pulse duration being within 10 s [1-3]. Such high output parameters allow electromagnetic soundings of the earth crust up to depths of 10 to 40 km to be performed. Over many years, such generators were used for the investigation the deep structure of the earth crust (experiments at the Kola Peninsula and at the Urals), for oil & gas prospecting in the Pre-Caspian and East Siberian regions, and also for earthquake prediction at the Pamirs and Tien Shan seismoactive regions. As a result of the investigations made by using

the MHD-generators, fundamentally new and important geological and geophysical data were obtained [4-6].

The requirements of self-consistence of MHD-generators as well as the requirement of fast (sufficiently less than the operating pulse duration) self-excitation impose rigid restrictions on the lower level of the so-called energy complex of the working fluid -  $\sigma W^2$ , where  $\sigma$  is electrical conductivity,  $W$  - flow velocity at the inlet to the electrode section of the MHD-channel:  $\sigma W^2 \geq 150-200 \text{ Sm/m} \cdot (\text{km/s})^2$ . This condition limits allowable types of working fluids to high energy chemical fuels with combustion temperatures of 3800-4000 K. The working fluid for the existing pulsed MHD-installations is combustion products of special-purpose powder plasmogenerating fuels, the  $\sigma W^2$  value being 350-400  $\text{Sm/m} \cdot (\text{km/s})^2$  at combustion temperatures within 3850-3950 K.

The experience accumulated in pulsed MHD-generator use for geophysical investigations shows that in order to strive for wider industrial use, it is necessary to decrease the cost of a single run of the MHD-facility. To do this would require increasing effectiveness of the fuel use as well as using alternative low-priced fuel compositions.

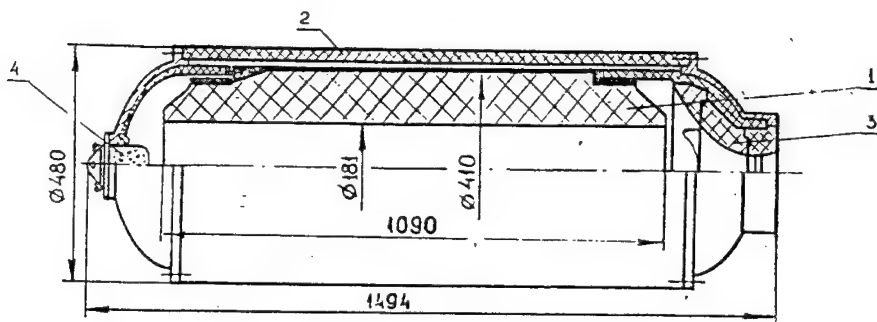
### FUEL AND COMBUSTOR OPTIMIZATION

To solve the problem, numerical and experimental study was performed intended to obtain full combustion of the fuel components and to achieve design thermodynamical and electrophysical parameters of powder plasmogenerating fuel (PPF) combustion products. The latter differ from solid rocket fuels by enlarged content of metal fuel (usually aluminium or aluminium-magnesium alloys) and low-ionized seed (potassium or cesium nitrates) to obtain high conductivity of the combustion products (more than 50  $\text{Sm/m}$ ). As the metal fuel content in the PPF may be as high as 27-28%, the process of metal particle agglomeration at PPF burning surface should go more intensively than the same for rocket fuel with metal content of 18-22%.

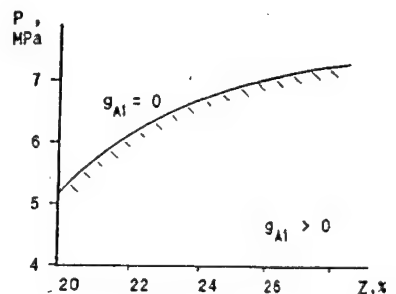
The experimental studies show that:

- 1) The agglomerate dimension is in about inverse proportion to the combustion pressure.
- 2) The distribution function of agglomerates by size is of bimodal pattern; the first mode particles (up to 10  $\mu\text{m}$  in size) consist completely of aluminium oxide; the second mode particles (up to 500  $\mu\text{m}$  in size) still contain a portion of active non-burnt aluminium.
- 3) With a pressure increase from 2 to 4 MPa, the large agglomerate content decreases rapidly in condensed combustion products, as does the content of active fuel. As pressure increases further, these dependencies become smoother and from 6 to 8 MPa these parameters do not vary at all. Thus, the most preferable PPF combustion pressure in the plasma generator, accounting for metal combustion completeness factor, is within the range of 5-7 MPa.

The completeness of metal combustion depends primarily on the size of the metal agglomerates dispersed from the burning PPF surface. The whole variety of factors influencing this process may be basically reduced to the two controlled parameters:  $Z$  - mass metal content in the PPF and  $P_k$  - pressure in the combustion chamber. To determine the dependence of non-burned metal content in condensed phase of combustion products on these two parameters,  $g(Z, P_k)$ , results of complex MHD-tests of various PPF with the metal content  $Z$  within 21 to 28% at pressures within 3 to 6 MPa in the full-scale GP-77 plasma generator with residence time of combustion products in the chamber of 20 ms were analyzed. Just such generators are incorporated into the "Pamir" type geophysical MHD-facilities [6]. Their schematics is shown at Figure 1 taken from [8].



**Figure 1.** Full-scale GP-77 plasma generator. 1 - propellant charge; 2 - body; 3 - nozzle; 4 - ignitor.



**Figure 2.** Determination of effective use field for plasmagenerating propellant [8].

The  $g(Z, P_k)$  is shown at Figure 2; this curve limits the optimum pressure area of PPF burning [8].

The experimental data obtained on PPF burning allow a physical model of combustion product plasma formation in the plasma generator to be proposed and also a numerical 1D model of working fluid creation in the pulse MHD-facilities to be developed; the model represents a joint equation system including hydrodynamics, heat and mass transfer, and chemical kinetics in multiphase media.

Another way of optimized PPF use is the use of combined plasma generators, where additional oxidizer is delivered into the combustion chamber [9]. Numerical and experimental studies were performed of such generator with nitrogen monoxide and air delivery into the combustion chamber. Such an approach provides 20 to 30% output power augmentation and allows output parameters to be stabilized or controlled within a wide range, thus reducing unit power cost released in the load. Another means of delivering additional oxidizer is to use specialized pyrotechnical oxygengenerating compositions (OGC) based on strontium nitrate. That way, the plasma generator is to include two fuel charges with an excess of fuel and oxidizer, respectively.

The OGC combustion products include 30-35% of nitrogen and 70-65% of oxygen at temperature 2000 K. Injection of such oxidizer into the combustor with the PPF charge provides the plasma temperature beyond 4000 K and about doubles electrical conductivity to the PPF combustion products. While burning the OGC, it is necessary to provide store of the condensed combustion products (slag) in a chamber separated from the main chamber containing the ballestite fuel charge thus preventing the MHD-channel from the slag fallout.

On this basis, the plasma generator with OGC is to be separately charged and to consist of two chambers: a hot oxygen generator chamber with the OGC grains (under pressures up to 10 MPa) and a plasma generator combustion chamber with powder plasmagenerating fuel charge (under pressures of 3-5 MPa); the two chambers to be connected in series via an interface nozzle unit.

The experimental finishing of such generator design has resulted in stable ignition and burning of the two charges. Thus, combined fire tests were performed of the separate charged plasma generator incorporated into the "Zond-1" laboratory MHD-facility.

Another way to create plasmogenerating fuels and combustors for pulsed MHD-generators, alternative to the existing PPF, is to use of powder-type fuel compositions an order of magnitude cheaper than PPF and providing similarly high output parameters. Besides, such fuel compositions may fit more strict requirements as to pulse duration, repetition frequency, and also provide operation duration of the MHD-facility of several tens of seconds, the last being highly conjectural for powder plasma generators.

Fuel compositions were considered based on carbon and solid hydrocarbons such as  $C_{10}H_8$  or  $C_{14}H_{10}$  with addition of high energy fuel (aluminium, magnesium, or zirconium) and low-ionized seed (potash) burned in gaseous (oxygen) or liquid (nitrogen tetroxide) oxidizer. The study shows that carbon particles are comparatively large in size (up to 50  $\mu m$ ); thus, due to heterogeneous burning, its complete after-burn does not take place, lowering the plasma electrophysical parameters. On the contrary, hydrocarbon fuel burning is preceded by their thermal decomposition producing gaseous and ultradisperse condensed products; thus, their energy potential may be almost completely realized at residence times in the combustor of about 1-3 ms.

On the basis of the numerical and experimental investigations, a full-scale plasma generator was installed where the preassigned combustion product conductivity level was attained. In the cases when pulses are needed with significantly (3-4 orders of magnitude) higher with drastically (5-6 orders) shorter duration, explosive MHD-generators or so-called explosive magnetic flux (the same: magnetic flux cumulative) generators may be employed.

### EXPLOSIVE MHD-GENERATORS

In the explosive MHD-generators, enthalpy conversion into electric energy takes place under the conditions of shock wave gas flow; the shock-wave-heated front has a specific heat content of about 20 times as great as that of the initial explosive. Six models of linear, disk, and radial explosive MHD-generator were investigated experimentally. Generalized criterion relationships have been obtained providing full-scale facility designing with preassigned parameters. Numerical models have been developed that satisfactorily account for the physical processes in the MHD-channel [10].

As the explosive MHD-generators are non-destructive energy supplies than they can operate in frequency (repetitive) mode provided by systems of mechanical charge replacement and electrical commutation (1 to 1000 Hz depending on the explosive charge scale). The specific energy release for each pulse is of about 1 kJ per 1 kg of the installation mass. Under electrical commutation condition a frequency of 1000 Hz and energy level of 20 kJ per pulse are achievable. For mechanical replacement of a charge these features are 5 Hz and 300 kJ. Design work shows that total 300 kJ pulse number may range up to 5, and 20 kJ pulses - up to 30.

### MAGNETIC FLUX CUMULATIVE GENERATORS

Magnetic flux cumulative (MC) generators may produce still more power than explosive MHD-generators [11-13].

The principle of MC action is based on the effect of magnetic cumulation during compression of magnetic flux by a metal conductor driven by the detonation products of

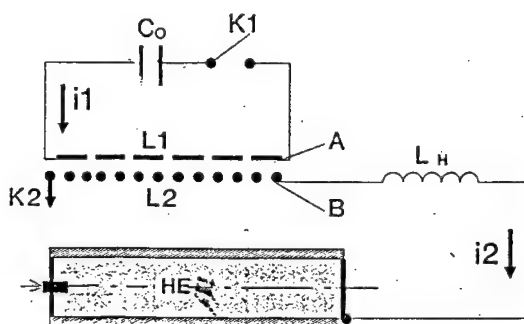


HE. A typical and the simplest construction consists of a helical coil wrapped around a copper cylinder filled with high explosives. Permanent magnets, piezoceramics or a small capacitor supplies an initial current of few hundred amps that creates an initial magnetic field in the gap between the coil and cylinder. The explosion compresses the magnetic field and pushes it out into the load, where a very short duration high-power electrical pulse is generated.

MC-generators are unique constructions for obtaining super high magnetic fields under the laboratory conditions. The record fixed values are as high as 25 MJ [11] and stable values of 10-14 MJ have been achieved [14] in volumes of several cubic centimeters. MC-generators have great possibilities as pulsed energy sources. Actually, levels of energy in the is load up to 100 MJ [12], currents up to 300 MA, voltages up to 1 MV, specific energies of 100 kJ/cm<sup>3</sup> and specific powers of 10 MW/cm<sup>3</sup> have been achieved. Maximum values of energy and power for special types of MC-generator are estimated to be as high as 1 GJ and 100 TW.

In the most experiments carried out to date, the MC-generators were connected to low-inductive loads (1-100 nH), resulting in high explosive chemical energy conversion efficiencies of up to 10% [12]. Recently, with advances in pulsed power technology, the great interest has been in the potential for MC-generator use as the energy source for non-traditional high impedance loads such as vacuum diodes [15, 16], railguns [17], electron and proton accelerators [18], powerful lasers [19] and powerful microwave generators [20-23]. To realize considerable power in such loads, the MC-generator must have large self inductance and produce high voltages of about 0.1-1 MV.

To achieve a wide range of parameters for various applications, lots of the MC-generator constructions were designed to solve special scientific problems. To convert the chemical HE energy into microwave radiation, three types of compact (mass of high explosive 200-700 g) high-voltage helical MC-generators with flux trapping were designed [24, 25]: cylindrical generators with simultaneous axial charge initiation and small-sized cylindrical and conical generators with moving contact point. The main feature of these MC-generators is their ability to produce high (50-200 KV) voltage pulses directly in the generator due to rapid (5-15 mcs) change in its high initial inductance.



**Figure 3.** Schematics of the MC- generator with flux trapping

The MC-generator with flux trapping (Figure 3) consists of an outer solenoid  $L_1$ , inner solenoid  $L_2$  and copper cylindrical armature  $L_3$  with HE charge inserted. The initial magnetic flux in the  $L_2$  solenoid is produced either by a current discharge via the  $C_0$  capacitor or using the  $L_p$  "booster" generator. The HE charge is initiated at the moment of the first current maximum. The detonation products expand the armature; the latter shorts out the secondary circuit; the magnetic flux is pressed and pushed out into the load. In the case of simultaneous axial initiation, the armature expands as a cylinder axial with the MC helices. In the case of

single point initiation, the armature takes a form of a cone; thus, with turns of the inner helix  $L_2$  are shorted out successively. The current rise time in the load is determined by the dynamics of the armature expansion.

For effective MC-generator operation, large values of the inner helix inductance are necessary. If the operation time is less than 10 mcs, high time derivatives occur of the magnetic field in the MC-generator volume occur; thus, a high electric field appears, resulting in breakdowns and great flux losses. Output voltages for desired parameters may reach the values as high as 50 KV. Thus, for effective MC-generator operation, it is necessary to ensure good turn-to-turn insulation, insulation between armature and inner helix, and interhelix insulation.

However, for the small-sized MC-generator, the more rigid requirements for the insulation, the smaller would be achievable inductance values. In a MC-generator with simultaneous axial initiation, there is no moving contact point; thus, the inner working helix was covered inside with thick layer of insulation.

The axial MC-generator consists of the three axis details: armature, inner solenoid and outer solenoid, 200 mm in length. The HE charge - powdered hexogen of  $m = 600$  g - explosion is initiated by a copper exploding wire placed in the axis of symmetry. In the cylindrical MC-generator with a moving contact point, the HE charge ( $m = 200-400$  g) explosion was initiated by an electric detonator placed at the butt-end.

The solenoids were wound up by copper ties or wires on PTFE tube with rectangular helical grooves, and then were glued by epoxy resin. The insulation between the inner and the outer solenoids was made as several turns of wide kapton film. To prevent surface breakdown, special insulating ribs were placed and glued over the generator. The armatures were made of copper tubes with outer diameter of 50-70 mm and 2.5 mm in thick. The tubes were stretched out on a mandrel and then were externally grind.

Conical MC-generators are faster than cylindrical ones. As the voltages developed in conical MC-generator are higher, fluoroplastic insulated wire was used to wind the helices. The axial length of conical solenoids was from 80 to 100 mm, the major diameter of the stator cone was 104 mm while the minor diameter varied within 80-100 mm. The HE charge mass was equal to 200-300 g.

Separate test series were carried out with axial, cylindrical, conical and two-cascade generators [22, 24, 25]. In the course of these experiments, currents were obtained of up to 90 kA in high inductive load  $L = 1-15$  mH within the time interval of 15 mcs, energy release in a pulse being as high as 12 kJ. The maximum flux amplifying coefficient obtained was equal to  $j = 6$ , with corresponding energy amplifying coefficient being  $y = 20$ . The shortest run time - of about 5.7 mcs - was realized in the conical MC-generators. As a whole, the conical MC-generators are characterized by energy amplification coefficients up to  $y = 2.3$ , that is closed to maximum value for this type of generator.

Current and voltage pulses obtained in axial MC-generators exhibit sharp trailing edges. Thus, to obtain high output voltage, one should use the residual inductance of the axial MC-generator as the inductive load. In the experiments with exploding wires, this device had stood up the voltage pulses up to 200 KV. However, because of small inductance reduction (of about 5) the energy conversion coefficient turns out to be small:  $y < 33\%$ .

Cylindrical MC-generators show high flux amplifying values,  $j = 6.1$  and energy amplifying  $y = 20$ . Such cylindrical devices provide up to 90% trapped flux. However, its run time is twice as great.

The MC-generators considered provide low energy amplification. They need to use special booster generators as a feeding system. To start up a MC-generator with simultaneous axial initiation, we have used a helical MC - generator [20] with an output energy of 60 kJ.

Thus, the magnetic generator with flux trapping works as a high voltage pulse forming system only. To start up a fast conical generator, we have used a cylindrical generator with

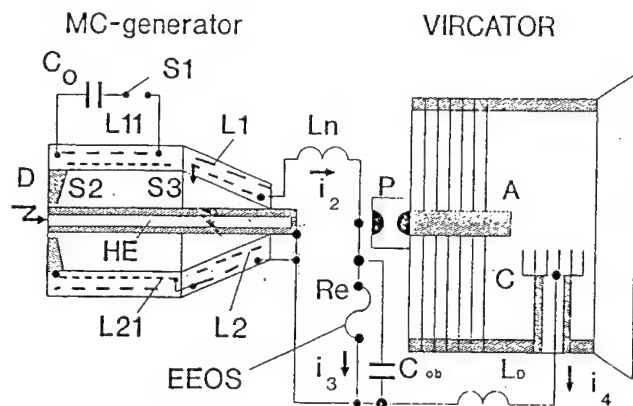


Figure 4. Experimental schematics.

storage of 5 mch. The total energy amplification coefficient for this generator is of about  $\gamma=10$ .

The most promising way to convert energy of high explosives into microwaves seems to be use of the MC-generator as a pulsed power feeding system for relativistic generators of coherent microwave radiation. In our experiments [20-22], vircator on the base of triode with virtual cathode was employed as a source of coherent microwave radiation at frequency of about 3 GHz. In that generator, oscillation of a relativistic electron beam between real and virtual cathodes produces high power microwave radiation. Note that the electron beam was successfully produced exceeding the space charge limiting current without any bulky system for external magnetic field.

Thus, the original transformerless electrical circuit was developed for the high power electron beam and microwave generation [20, 21] on the base of the high voltage MC-generator with flux trapping (Figure 4). A small capacitor  $C_0=100$  mcF charged up to 3 kV was used for current loading of the "booster" cylindrical generator with flux trapping  $L_{11}$  (high explosive charge mass being 200-700 g) and thus intensifying the electric energy of its load - the external coil of high voltage MC-generator  $L_1$  - up to 5 kJ.

In the experiments with the MC-generator with axial initiation, simple helical MC-generators with the load energy up to 60 kJ were used. The secondary circuit of the high voltage MC-generator was crowbarred at the moment of reaching the maximum current in the  $L_1$ . With the liner expansion of the high voltage generator, the magnetic flux is "trapped" by the  $L_2$  internal solenoid and thus produces the current in the initiation circuit - exploding wires. The high voltage MC-generator operates during 6-8 mcs giving the voltage up to 50-200 kV and the current up to 30 kA.

The switch consists of several tens of parallel copper wires, 40-50 mcm in diameter and with length of 0.5-1.0 m, immersed in nitrogen under pressure of 0.5 MPa. The wire sizes are chosen in such a way that maximum velocity of their electric resistance growing (the electrical explosion itself) is attained at the very end of the MC-generator operation. As the construction of the high voltage generator withstands the voltage only within 200 kV, the  $L_n$  inductive storage is inserted between the MC-generator and the exploding wires. The

flux trapping and an output energy up to 5 kJ [21, 22, 25]. Figure 4 shows the schematics of the two cascade (cylindrical-conical) generator with HE mass 550 g. Capacitor  $C_0=100$  mcF charged up to 3 kV was used as a source of initial magnetic field with an energy of about 400 J. The booster cylindrical generator with flux trapping enlarges the electric energy release in the load - the external coil of the fast MC-generator. The last cascade works during a time interval less than 10 mcs providing energy of 3-5 kJ in the inductive

overvoltage occurring at the current cutoff results in a spark in the gap, and the high voltage pulse enters vircator anode producing the exploding emission from the cathode, formation of electron beam and generation of microwave radiation.

Several sets of experiments were performed to generate electron beam and microwave radiation pulses using HE energy. The output currents obtained were up to 30 kA and the inductive load energy was up to 3 kJ. The exploding wire parameters were also varied because the most profitable regimes were searched for high voltage delivery to the vircator. The energy required for the wires explosion is of about 2-3 kJ; hence, the total MC-generator output energy does not exceed 2-3 kJ.

Thus, the high voltage pulses up to 600 kV with 180-500 ns duration and rise-time of about 60 ns are delivered to the vircator inlet. The triode current amplitude reaches 16 kA, that corresponds to a power of relativistic electron beam of about 10 GW. The peak power of microwave radiation into atmosphere has come to 100-120 MW at wavelength of  $10^{-5}$  cm, the signal duration being of 100-200 ns.

#### MC-GENERATOR USE IN GEOPHYSICS

Recently, a suggestion was put forward for use of MC-generators in geophysical investigations similarly to that of pulsed (geophysical) MHD-generators. The peculiarity of the MC-generator geophysical employment is simultaneous excitation of electromagnetic and seismic fields with adequate parameters for the geophysical applications.

The MC-generator may produce magnetic dipole moment up to  $10^8$  A·m<sup>2</sup> with pulse duration of about 0.1 s in a load (inductor) - horizontal circle loop, 10 m in diameter, with active resistance of  $10^{-4}$  Ohm. Sounding with such loop provides that the dipole condition is met beginning from distances of 50-100 m from the survey center. Then, elastic wave is generated with energy of about 1 MJ within time interval of about  $10^{-4}$  s. The seismic source represents horizontal force, that is axis symmetric pressure center; thus, requirements are met of joint-depth-point reflection seismic survey.

Under the condition of simultaneous electromagnetic and seismic excitation, a series of cross-effects (including those non-linear) may be manifested, that is seismo-electrical, seismo-magnetic, and electro-seismic effects. Such effects were always subject of special interest of geophysics because, along with fundamental knowledge, such effects may provide new information on fine structure of non-uniform crust media.

The table shows comparison of parameters of pulsed MHD-generator and MC-generators against their use for geophysical investigations.

From the above table, one may see that for a depth range a few kilometers, the MC-generators may turn out to be promising due to their small bulk and comparatively low cost. For deeper investigations (up to 10 km), MHD-generators beat MC-generators. Yet, more detailed comparative analysis of performance and cost-effectiveness for the two supplies lies ahead.

TABLE  
Comparative Parameters of the MHD-Generator and MC-Generator

	MHD-generator	MC-generator
Sounding available: electromagnetic seismic	+ —	+ —
Dipoles available: electrical magnetic	+ +	— +
Power produced	10–40 MW	1–10* GW
Pulse duration	up to 10 s	0.1–1* s
Energy release in the load	100 MJ	100 MJ
Load parameters: resistance inductance	0.02–0.1 Ohm 10 mH	0.0004 Ohm 0.01 mH
Size: electrical dipole magnetic dipole	10 km 2 x 2 km <sup>2</sup>	— 5 m radius
Magnetic dipole moment	10 <sup>10</sup> A·m <sup>2</sup>	10 <sup>8</sup> A·m <sup>2</sup>
Sounding depth	4–6 km	2–3 km
Survey mass	15 ton (without the load)	1 ton (with the load)

\* Parameters for prospective facilities

#### REFERENCES

1. Morokhov, I.D., Velikhov, E.P., and Volkov, Ju.M. Pulse MHD-Generators and deep electromagnetic structure of the earth crust, *Atomnaya Energiya*, 44, 213-219, 1978 (in Russian).
2. Velikhov, E.P. and Zeigarnik, V.A. MHD-technique of energy conversion in geophysics, *MHD - Theory, Energetics, Technology*, 1, 19-29, 1985 (in Russian).
3. Breev, V.V., Gubarev, A.V., and Panchenko, V.P. *Supersonic MHD-Generators*, Energoatomizdat, Moscow, 1988 (in Russian).
4. Velikhov, E.P. *et al.* Pulsed MHD Facilities: geophysical applications, *Magnetohydrodynamics*, 2, 27-33, 1989.
5. Velikhov, E.P., ed. *Geoelectrical Soundings Using High-Power Current Supply at the Baltic Shield*, Nauka, Moscow, 1989 (in Russian).
6. Velikhov, E.P. and Zeigarnik, V.A., eds. *Reflection of Geodynamic Processes in Geophysical Fields*, Nauka, Moscow, 1993 (in Russian).
7. Aitov, N.L., Zeigarnik, V.A., Novikov, V.A., *et al.* Overview of IVTAN's activity in the field of pulsed MHD power generation, *Proceedings of 32th SEAM*, Pittsburgh, June 28-30, 1993.

8. Novikov, V.A., Okunev, V.I., Babakov, Yu.P., *et al.* Increase of pulsed geophysical MHD installations specific power parameters by perfection of solid fuel plasma generators. *Proceedings of 11th Int. Conf. on Magnetohydrodynamic Electrical Power Generation*, Beijing, China, October 12-16, 1992, Vol. 2, 556-563.
9. Novikov, V.A. *et al.*, Low temperature plasma generator with pyrotechnic source of hot oxygen for pulsed MHD plants, *ibid*, Vol. 2, 564-569.
10. Asinovsky, E.I. *et al.* *Explosive MHD-Generators*, Institute for High Temperature, USSR Acad. Sci., Moscow, 1991 (in Russian).
11. Sakharov, A.D., Ludaev, R.Z., Smirnov, E.N., *et al.* Magnetic flux compressors. *Doklady Akad. Nauk SSSR*, 165, 65-71, 1965 (in Russian).
12. Pavlovski, A.I. and Ludaev, R.Z. *The Problems of Experimental and Theoretical Physics*, Nauka, Moscow, 1965 (in Russian).
13. Knoepfel, H. *Pulsed High Magnetic Fields*. Noth-Holland Publishing, Amsterdam-London, 1970.
14. Pavlovski, A.I., Kolokolchikov, N.P., *et al.* Cascade magnetocumulative generator of super high magnetic fields. in: *Ultrahigh Magnetic Fields. Physics. Technique. Application*, Nauka, Moscow, 1984, 19-22 (in Russian).
15. Freeman, B.L., Ericson, D.J., Fowler, C.M. *et al.* Magnetic flux compression powered electron beam experiments, in: *Megagauss Technology and Pulsed Power Applications*, Plenum Press, 1987, 729-735.
16. Pavlovskii, A.I., Popkov, N.F., Kargin V.I. *et al.* Magnetic cumulation generators as a power source to accelerate intense electron fluxes, in: *Megagauss Fields and Pulsed Power Systems*, Nova Science Publ., 1990, 449-452.
17. Fowler, C.M., Peterson, D.R., Kerrisk, J.F., *et al.* Explosive flux compression strip generators, in: *Megagauss fields. Physics. Technique. Application*, Nauka, Moscow, 1984, 282-291 (in Russian).
18. Pavlovski, A.I., Kuleschov, G.D., and Ludaev, R.Z. Linear inductive accelerators. *Atomnaya Energia*, 41, 228-242, 1976 (in Russian).
19. Jones, C.R., Fowler, C.M., and Ware, F.D. High-energy atomic iodine laser driven by magnetic flux compression generator, in: *Megagauss Technology and Pulsed Power Applications*, Plenum Press, 1987, 747-754.
20. Azarkevich, E.I., Didenko, A.N., Dolgoplov P.V. *et al.* Generation of pulsed microwave impulses with the aid of high explosive. *Doklady Akad. Nauk SSSR*, 319, 352-353, 1987 (in Russian).
21. Azarkevich, E.I., Didenko, A.N., Zherlitsin A.G. *et al.* Generation of microwave radiation with the aid of high explosive, *Preprint*: Chernogolovka, 1992 (in Russian).
22. Azarkevich, E.I., Didenko, A.N., Zherlitsin A.G. *et al.* Generation of high power electron beam and microwave radiation with the aid of high explosive. *High Temperatures*, 32, 127- 132, 1994.
23. Brodskiy, A.Y., Vdovin, V.A., Korznevskiy, A.V. *et al.* Transformation of energy of high explosive into electromagnetic radiation. *Doklady Akad. Nauk SSSR*, 314, 846-850, 1990 (in Russian).
24. Mintsev, V.B., Ushnurtsev, A.E., and Fortov, V.E. Models of magnetic flux compressors with flux trapping. *High Temperatures*, 31, 469-475, 1993.
25. Karpushin, Yu.V., Leont'ev, A.A., Mintsev, V.B. *et al.* Experimental investigations of compact magnetic flux compressors with flux trapping. *High Temperatures*, 31, 662-667, 1993.

## **TWO-PHASE FLAMES -- A POTENTIAL METHOD FOR MANUFACTURING SUBMICRON METAL OXIDE POWDERS.**

**N.Ageev, S.Kyro, Yu.Kostishin**  
Analog Co., Odessa, Ukraine

**ABSTRACT:** Submicron metal oxide powders formation was studied in premixed, two-phase flames of metal dust clouds in order to investigate the effect of the two-phase flame parameters: additional energy sources, reactant concentrations, thermodynamics, kinetics and diffusion properties of gas system on the physical-chemical properties of the final product. The results obtained showed that varying the flame parameters made it possible to change the burning mechanism from heterogeneous to vapor phase and, hence, to produce submicron oxide powders.

In recent times submicron metal oxide powders have found applications in an increasingly wider range of industrial processes, where their physical-chemical properties (particle size distribution, chemical purity, phase structure and other) are exploited. These properties are the fundamental driving force for researching new economical synthetic techniques for creating a number of metal oxides which do not exist in either the quantity or purity to be useful.

We propose to use two-phase flames of metal dust clouds for manufacturing submicron metal oxide powders. Almost all peculiarities of this method are caused by the greatly exothermic reactions involved in the oxide's synthesis. These cause high burning temperature, absence of outward energy expenses, high synthesis yields and a clean transmutation of the initial metals. An important feature of this method is that the synthesis process is stationary and self-heating, which leads to a good control of the phase, chemical composition and particle size dispersion of the oxides [1].

According to the mechanism of the metal particle's combustion in a two-phase flame we can note two limiting regimes for the oxide formation. In the first regime (heterogeneous mechanism of particles combustion, for example iron, zirconium) the oxide formation zone is localized on the particle surface - therefore the oxide and metal particles size distributions are rather similar; several crystalline and chemical oxide phases are observed in the final product. A rather different picture emerges in the second regime (vapor-phase mechanism of particle combustion, for example aluminum, boron, magnesium) - the oxide formation zone becomes localized in gas phase, potentially producing submicron metal oxide powders with high chemical and physical purity [2].

Therefore, in order to produce submicron, high-quality metal oxide powders, the particle must turn according to the vapor-phase mechanism. A basic requirement of this mechanism is the

proximity of the particle burning temperature to the metal's boiling point. This condition may be also achieved for metals which turn the heterogeneously by varying the two-phase flame parameters: additional energy sources, reactant concentrations, thermodynamics, kinetics and diffusion properties of the gas system.

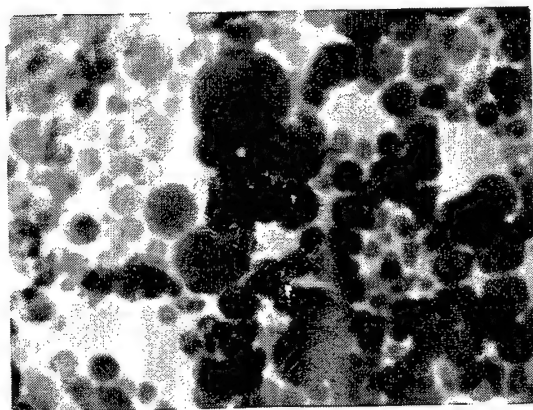
In this paper, we experimentally investigate the effect of these parameters on the physical-chemical properties of the final product.

Premixed, two-phase flames of metal dust clouds were studied in a special flame reactor: a detailed description of the reactor and the experimental methods have been presented in paper [2]. The particle size distributions of the samples were determine by counting the particles with an optical microscope ( $d > 0.5\mu$ ), or an electron microscope which had of magnification of 44200. The phase structure of the samples was determined by the X-ray Debay-Cherer method. The chemical composition of the samples was studies by two independent methods: by product spectrum and by active valence of metal. Zirconium, aluminum, and iron powders with average particle diameters of about 10 micron were used.

The effect of the thermal conductivity coefficient and initial dust cloud temperature was studied for premixed laminar flames in zirconium dust clouds ( $P_{O_2} = 0.2$ , mass zirconium concentration  $B = 600 \text{ mg/l}$ ). It was found that changing the carrier gas from mixtures of  $\text{He} + \text{O}_2$  to  $\text{Ar} + \text{O}_2$  gave an increasing particle burning temperature due to a lowering of the thermal conductivity coefficient. In this way, the portion of liquid zirconium which evaporated from the droplet surface increased and submicron oxide formed by vapor-phase reactions around the molten droplet.

For example, the mass portion of submicron zirconium oxide (particle diameter  $\sim 0.05\mu$ ) makes up 2-5% for  $\text{He} + \text{O}_2$  mixtures, whereas for  $\text{Ar} + \text{O}_2$  mixtures it is 40-50% -- Fig.1.

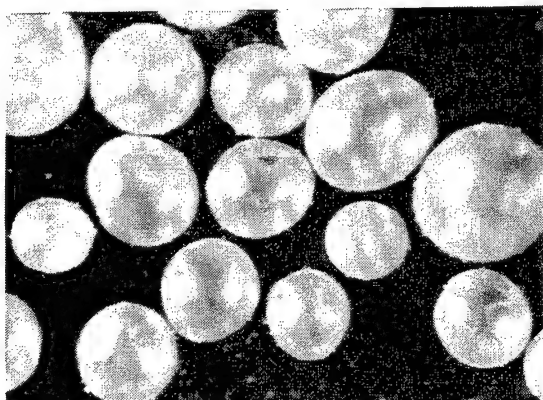
**Figure 1.** Electron micrograph (x44200) of particles of  $\text{ZrO}_2$   
average diameter  $0.043\mu$ .



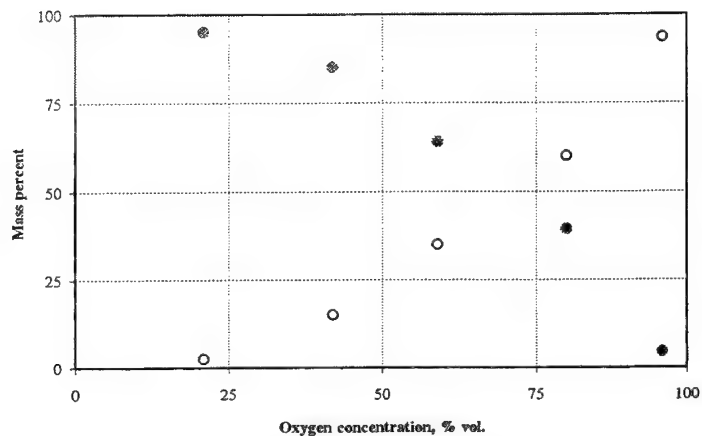


Increasing the initial dust cloud temperature (pre-heating to 500K) also led to an increased particle burning temperature and therefore the portion of submicron oxide in final product increased. It is interesting to note, that, under these conditions, hollow-microspheres of zirconium oxide appeared (mass portion more than 20%, average sphere diameter - 40 micron, wall thickness -  $0.3\mu$  -- Fig.2). This was caused by readily soluble gases in the initial zirconium particles inflating the liquid oxide cover. Hollow-microspheres of zirconium oxide are not formed by vacuum drying of the initial zirconium with temperature 400K.

**Figure 2.** Photograph of the hollow microspheres  $ZrO_2$ .



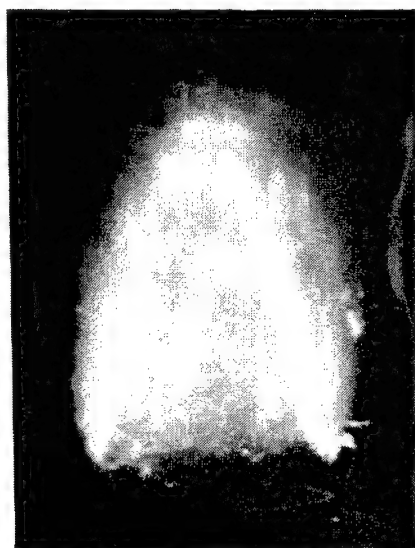
**Figure 3.** Effect of  $O_2$  concentration on mass-composition of final products. • -  $FeO$ ; ° -  $Fe_2O_3$ .



The effect of oxygen concentration on the characteristics of the final products was studied using premixed laminar flames of iron dust clouds ( $B = 400 \text{ mg/l}$ ). As may be seen from Fig.3, at low oxygen concentrations the final product is a fine powder of iron oxide FeO (average diameter  $2.4\mu$ ). A submicron powder of iron oxide  $\gamma\text{-Fe}_2\text{O}_3$  (average diameter  $0.044\mu$ ) appeared with increasing oxygen concentration. This product is the main one at  $\text{O}_2$  concentration more than 70%. This happens, because the iron particles' combustion mechanism changes from heterogeneous to gaseous with increasing oxygen concentration (increasing the particle burning temperature more than 200-500K). Note, that submicron powder of  $\gamma\text{-Fe}_2\text{O}_3$  have high magnetizability.

The effect of the velocity of the dust cloud flow ( $Re$ ) on the characteristics of final products was studied using premixed aluminum dust clouds flames. Chemical and dispersion analysis showed, that quality products (monodisperse powder, spherical particle, particle diameter -  $0.098\mu$ , chemical purity more than 99.9%) may be obtained only under laminar flow, i.e. in stable synthesis conditions (stationary temperature and concentrations fields) - Fig.4. In comparison with laminar flames, turbulent flames gave chemical purity of less than 98% and particle sizes from  $0.1\text{-}10 \mu$ .

**Figure 4.** The aluminum laminar conical dust flame in air, concentration of Al -  $300 \text{ g/m}^3$



The results obtained showed that varying the flame parameters made, it possible to change the burning mechanism from heterogeneous to vapor-phase and, hence, to produce submicron oxide powders. The two-phase flame method for manufacturing submicron metal oxides powders combines many important advantages, such as: the possibility of obtaining grain sizes and product purity, which are unattainable by the traditional methods; all-round ecological purity; high productivity; the possibilities to modify the particles sizes, crystal forms and powder colors within wide limits.

#### References.

1. Patent No 2021206 RU, C1 5 C01G25/20, 1990.
2. Goroshin, S., Shoshin, Yu., Ageev, N., Poletayev, N., The premixed aluminum dust laminar flame structure, *Flame Structure*, Vol.1, pp.213-217, 1991.

---

***Area 6:***

***Ignition and Combustion  
Performance of Propellants  
for Rocket Propulsion***



# A SURVEY OF PRESSURE-DRIVEN BURNING OF ENERGETIC SOLIDS WITH ARRHENIUS SURFACE PYROLYSIS

L. De Luca\*, M. Verri, F. Cozzi, A. Jalongo, and G. Colombo  
Politecnico di Milano, Facoltà di Ingegneria, 20133 Milan, MI, Italy

## Abstract

A survey of pressure-driven burning of solid energetic materials, with chemically inert condensed phase, is presented. External radiation, if any, and initial temperature are constant parameters. Intrinsic stability of this burning configuration is discussed by a host of analytical techniques, implementing the Flame Modeling method within an appropriate AQSHOD (Arrhenius surface pyrolysis, Quasi-Steady gas phase, Homogeneous condensed phase, One-Dimensional sample) framework. In particular, the effects of an explicit pressure dependence of the concentrated surface pyrolysis are assessed. The classical results by Denison-Baum and Zeldovich-Novozhilov of the corresponding linear adiabatic problem are fully recovered as special cases. By combining an exact analysis with an approximate nonlinear integral method, a possible extension of the steady working regime beyond the classical linear stability boundaries is revealed. In this regime, the common time-invariant steady burning is replaced by self-sustained oscillatory steady burning. This time-dependent steady regime is observed up to the proper deflagration limit for a number of operating parameters. Therefore, in general, for energetic solid materials the stability of steady burning is extended from the linear stability boundaries (of the time-invariant solution) to the deflagration boundaries (of the self-sustained oscillatory solution). For nonlinear transient burning, dynamic extinction boundaries are revealed as well. However, while stability boundaries are exactly defined, deflagration and dynamic extinction boundaries are only approximately determined.

## NOMENCLATURE

- $A, B \equiv$  nondim. functions defined by Eq. 7.1, Eq. 7.2  
 $\bar{A}_s \equiv$  function defined by Eq. 4.1, (cm/s)/(atm<sup>n\*</sup>)  
 $a, b \equiv$  nondim. functions defined by Eq. 3.2, Eq. 3.3  
 $\bar{a}_\lambda, \bar{r}_\lambda \equiv$  average volumetric absorption coefficient (cm<sup>-1</sup>), burning surface reflectivity (%)  
 $c \equiv$  specific heat, cal/g K  
 $\tilde{E}_{(\dots)} \equiv$  activation energy, cal/mole  
 $E_{(\dots)} \equiv \tilde{E}_{(\dots)}/R/T_{(\dots)}$ , nondim. activation energy  
 $F_s \equiv I_s/[\rho_c c_{ref} r_{b,ref}(T_{s,ref} - T_{ref})]$ , nondim. reference external radiant flux  
 $f(X) \equiv$  nondim. function describing spatial distribution of impinging radiation  
 $H_{(\dots)} \equiv Q_{(\dots)}/[c_{ref}(T_{s,ref} - T_{ref})]$ , nondim. reference heat release (positive if exothermic)  
 $I_s \equiv$  external radiant flux intensity, cal/cm<sup>2</sup>s  
 $i \equiv$  imaginary unit  
 $K \equiv$  nondim. function defined by Eq. 6.11  
 $k \equiv (\bar{T}_s - T_1)[\partial \ln \bar{m}/\partial T_1]_p$ , ZN steady sensitivity parameter  
 $k_{(\dots)} \equiv$  thermal conductivity, cal/cm s K

\* Copyright © 1996 by Luigi DeLuca, AIAA Associate Fellow. All rights reserved.

$m \equiv$  mass burning rate, g/cm<sup>2</sup>s  
 $n \equiv$  pressure exponent of steady burning rate; also: order of the disturbance thermal profile  
 $N \equiv$  numerator of the right hand side of Eq. 8.2  
 $N_s \equiv$  radiation fraction absorbed below reacting surface layer  
 $n_s \equiv$  pressure exponent of surface pyrolysis law defined by Eq. 4.1  
 $n_{T_s} \equiv$  pressure exponent of steady surface temperature dependence on pressure  
 $P \equiv p/p_{ref}$ , nondim. pressure  
 $p \equiv$  pressure, atm  
 $p_{ref}, T_{ref} \equiv$  reference temperature (300 K), reference pressure (68 atm)  
 $Q \equiv$  heat release, cal/g (positive if exothermic)  
 $q \equiv \tilde{q}/[\rho_c c_{ref} r_{b,ref} (T_{s,ref} - T_{ref})]$ , nondim. reference energy flux  
 $q_r \equiv (1 - \bar{\tau}_\lambda) I_s / [\rho_c c_{ref} \bar{r}_b (\bar{T}_s - T_{ref})]$ , absorbed nondim. external radiant flux  
 $r \equiv [\partial \bar{T}_s / \partial T_1]_p$ , ZN steady sensitivity parameter  
 $r_b \equiv$  burning rate, cm/s  
 $r_{b,ref}, T_{s,ref} \equiv$  reference burning rate  $r_b(p_{ref})$ , reference surface temperature  $T_s(p_{ref})$   
 $R \equiv r_b/r_{b,ref}$ , nondim. reference burning rate  
 $R_p \equiv$  mass burning rate response to pressure fluctuations, nondim.  
 $\mathcal{R} \equiv$  universal gas constant; 1.987 cal/mole K  
 $T \equiv$  temperature, K  
 $t \equiv$  time, s  
 $\langle t_g^\dagger \rangle, \langle \tau_g^\dagger \rangle \equiv$  dim. (g/cm<sup>2</sup>s)<sup>-2</sup>, nondim. average gas-phase characteristic time parameter  
 $u, u_X \equiv$  nondim. temperature disturbance, nondim. thermal gradient disturbance  
 $W_p, W_p(\gamma) \equiv$  nondim. functions defined by Eq. 6.10, Eq. 6.8  
 $X \equiv x r_{b,ref} / \alpha_c$ , nondim. reference space coordinate  
 $x \equiv$  space coordinate, cm

### Greek Symbols

$\alpha \equiv$  thermal diffusivity, cm<sup>2</sup>/s; also: temperature sensitivity of chemical reactions in Eq. 6.4  
 $\beta_g \equiv$  overall reaction order of gas-phase chemical reactions in Eq. 6.5  
 $\gamma \equiv$  flame elongation parameter for distributed flames  
 $\delta \equiv \partial(\ln \bar{m}, \bar{T}_s) / \partial(\ln p, T_1) = \nu r - \mu k$ , ZN steady parameter (pyrolysis Jacobian)  
 $\zeta_f \equiv m c_g / k_g x_f = m^2 \langle t_g^\dagger \rangle = R^2 \langle \tau_g^\dagger \rangle$ , a nondimensional quantity used in Eq. 4.4  
 $\Theta \equiv (T - T_{ref}) / (T_{s,ref} - T_{ref})$ , nondim. reference temperature  
 $\ell_r \equiv \bar{a}_\lambda \alpha_c / \bar{r}_b$ , nondim. ratio of conductive to radiant layer thickness  
 $\lambda_1 \equiv (1 + \sqrt{1 + 4i\Omega}) / 2$ , complex characteristic roots of fluctuating thermal profile  
 $\mu \equiv [\partial \bar{T}_s / \partial \ln p]_{T_1} / (\bar{T}_s - T_1)$ , ZN steady sensitivity parameter  
 $\nu \equiv [\partial \ln \bar{m} / \partial \ln p]_{T_1}$ , ZN steady sensitivity parameter; also: frequency, Hz  
 $\xi \equiv$  thermal disturbance layer thickness  
 $\rho \equiv$  density, g/cm<sup>3</sup>  
 $\sigma_p \equiv$  steady temperature sensitivity of burning rate, 1/K  
 $\tau \equiv t r_{b,ref}^2 / \alpha_c$ , nondim. reference time coordinate  
 $\Omega \equiv 2\pi \nu \alpha_c / \bar{r}_b^2$ , nondim. circular frequency  
 $\omega \equiv 2\pi \nu$ , circular frequency, rad/s

### Subscripts

bif  $\equiv$  bifurcation  
 c  $\equiv$  condensed phase  
 c,s  $\equiv$  burning surface from the condensed phase side  
 g  $\equiv$  gas phase  
 g,s  $\equiv$  burning surface from the gas phase side  
 p  $\equiv$  pressure  
 ref  $\equiv$  reference

$s \equiv$  burning surface  
 $-\infty \equiv$  far upstream  
 $(\dots)_0 \equiv$  initial value in time  
 $(\dots)_1 \equiv$  cold boundary value

#### Superscripts

$(\dots)' \equiv$  fluctuating value  
 $(\dots) \equiv$  steady-state value  
 $(\dots) \equiv$  dimensional value

## 1. BACKGROUND

Following the pioneering work by Zeldovich [1] in 1942, two main approaches, known as Zeldovich-Novozhilov (ZN) method and Flame Modeling (FM) method, have emerged to study unsteady combustion of solid propellants. Both share the basic assumptions of Quasi-Steady gas phase, Homogeneous condensed phase, and One-Dimensional propellant strand (QSHOD framework). Within this framework and for pressure perturbations only, linear stability analyses were first presented by Denison and Baum [2] in 1961 for premixed flames and Novozhilov (e.g.: [3] [4] [5]) in 1965 by the ZN method. Both papers, in the linear approximation of the problem, relaxed the assumption of constant surface temperature until then accepted. Systematic investigations were carried out by Culick for a variety of flame configurations (e.g.: [6] [7]) and Krier et al. (KTSS, [8]) for diffusive flames. A detailed experimental and theoretical investigation on pressure-driven frequency response was performed by Brown and Muzzy (BM, [9]) for a generic QSHOD flame. The results obtained by the writers for pressure-driven burning, by implementing an exact approach in the FM framework, were reported in [10]. Another approach was investigated by the senior author in the past [11] [12] [13]; this is based on an approximate integral method [14] fully preserving the nonlinear nature of the problem.

Most investigations in this area have resorted to a one-to-one correspondence between burning rate and surface temperature (no explicit dependence on operating parameters, such as pressure for example, would be considered). Following the recent critical revision of the Arrhenius pyrolysis law by Brewster and coworkers [15] [16] [17], a controversy arose as to the meaning and relevance of surface gasification processes depending not only implicitly but also explicitly on pressure (in particular). In technical jargon, the pyrolysis Jacobian is not necessarily zero. This point will be discussed in detail, but excluding possible explicit effects from other controlling parameters. Typically, radiation and initial temperature are considered constant parameters (not necessarily having standard values).

The purpose of this paper is to offer a survey of pressure-driven burning intrinsic stability by including the effects of explicit pressure dependence of surface gasification. The condensed phase is assumed chemically inert. The classical QSHOD assumptions are retained. The concentrated surface gasification, tacitly assumed in the QSHOD framework and anyway enforced by most investigators, is a pure phenomenological approach. No attempt is made in this paper to go beyond these phenomenological limits; for details, see [18].

## 2. FORMULATING THE MASTER QSHOD PROBLEM

A one-dimensional strand of homogeneous material is assumed burning with a quasi-steady gas phase subjected to changes in time of pressure only. Thermophysical properties are assumed to be at most pressure dependent. The strand is burning, with no velocity coupling, in a vessel at uniform pressure; radiation, if any, consists of a constant collimated radiant flux originated *exclusively* from a continuous external source of thermal nature and interacting *exclusively* with the condensed phase. Overall, assume no radiation scattering, no photochemistry, no condensed

phase chemical reactions, and no external forces. Define a Cartesian axis with its origin anchored at the burning surface and positive in the gas-phase direction. Nondimensional quantities are obtained by taking as reference those values, maybe only nominal, associated with the conductive thermal wave in the condensed phase under adiabatic burning at 68 atm.

Let the condensed phase ( $X < 0$ ) be a semi-infinite slab of uniform and isotropic composition, and  $\Theta_1$  a fixed value. The energy equation and associated conditions [10] [13] [19] [20] are

$$\frac{\partial \Theta}{\partial \tau} + R(\Theta_s) \frac{\partial \Theta}{\partial X} = \frac{\partial^2 \Theta}{\partial X^2} + N_s f(X)(1 - \bar{\tau}_\lambda) F_s(\tau) \quad (2.1)$$

$$\Theta(X, \tau = 0) = \Theta_0(X < 0) \quad (2.2)$$

$$\Theta(X \rightarrow -\infty, \tau) = \Theta_1 \quad (2.3)$$

$$q_{c,s} = q_{g,s} + R(\Theta_s) H_s + (1 - N_s)(1 - \bar{\tau}_\lambda) F_s(\tau) \quad (2.4)$$

where  $N_s = \exp[-\ell_r/E_s]$  as suggested in [21] and [16] based on [22]. The (net) heat release  $H_s$  of gasification reactions concentrated at the burning surface is

$$H_s(P, \Theta_s) = \bar{H}_s(\bar{P}) + \frac{c_g - c_c}{c_c} (\bar{\Theta}_s - \Theta_s) \quad (2.5)$$

where the dependence  $\bar{H}_s(\bar{P})$  under steady-state operations is assumed known. In this paper, only the particular case of pressure-driven burning (with or without a constant external radiation support) is considered. Under these circumstances, the nontrivial time-invariant steady-state solution is

$$\bar{\Theta}(X) = \Theta_1 + (\bar{\Theta}_s - \Theta_1) \exp(\bar{R}X) \quad (2.6)$$

In the QSHOD framework, analysis of the intrinsic stability for pressure-driven burning does *not* require formulating a specific pyrolysis law as long as the surface mass production is a mathematically smooth and monotonic increasing function of surface temperature, as in general observed for one-step, irreversible gasification processes. Likewise, a specific flame model is *not* required as long as the heat feedback is a mathematically smooth and unimodal function of burning rate (i.e., only a maximum value exists), as indeed observed for one-phase, laminar, nonviscous, low-subsonic, thermal flames. In this respect, the authors propose to call this general framework a master QSHOD model. The treatment will be conducted in general terms as far as possible. But specific submodels will be needed to assess quantitative trends.

### 3. EXACT INTRINSIC BURNING STABILITY

The master QSHOD problem is reformulated as an initial value problem for an abstract nonlinear parabolic equation, in an infinite-dimensional normed functional space (Banach space) consisting of thermal profiles. Assume that the initial thermal profile  $\Theta_0(X)$  deviates from the pertaining time-invariant steady profile by a small but finite disturbance  $u_0(X) \equiv \Theta_0(X) - \bar{\Theta}(X)$  and define the finite temperature disturbance, propagating inside the condensed phase, as

$$u(X, \tau) \equiv \Theta(X, \tau) - \bar{\Theta}(X) \quad (3.1)$$

The long time asymptotic behavior of  $u(X, \tau)$  is investigated using a generalized version of the linearized stability principle for semilinear parabolic equations [23] [24]. Under steady operating conditions, including any implicit and/or explicit pressure dependence of the surface pyrolysis, the QSHOD problem of Eqs. 2.1 - 2.4 admits a *unique* time-invariant steady-state nontrivial solution ( $\bar{R} > 0$ ) if the propellant burns under adiabatic conditions or subjected to a positive heat flux. For pressure-driven burning, the relevant stability properties can be collected under



only two nondimensional parameters,  $a$  and  $b$ , respectively defined in terms of burning surface and gas-phase properties [25] as

$$a \equiv \left[ (\Theta_s - \Theta_1) \frac{\partial \ln R}{\partial \Theta_s} \right]_{\Theta_s = \bar{\Theta}_s} \quad (3.2)$$

$$b \equiv \left[ \left( \frac{\partial q_{g,s}}{\partial R} + H_s \right) \frac{\partial \ln R}{\partial \Theta_s} \right]_{\Theta_s = \bar{\Theta}_s} - \frac{c_g - c_c}{c_c} \quad (3.3)$$

In general  $a > 0$  while  $-\infty < b < +\infty$ ; both parameters implicitly depend on the radiant flux as well (if any).

If the real part of one or both of the discrete eigenvalues of a suitably defined linear operator is positive, the solution is unstable; if the real part of all eigenvalues is negative or the discrete spectrum is empty, the solution is stable. If a pair of purely imaginary eigenvalues arises, then the nature of the intrinsically stable solution changes from time-invariant to self-sustained oscillatory; this switch of stability character for the steady solution is called *Hopf bifurcation* (for details, see [26] p. 333). In general, stability results can be summarized in a 3D plot where the intrinsic burning stability and instability regions are separated by a surface, across which Hopf bifurcation occurs, and a plane over which at least one eigenvalue is zero [19] [20]. For a full discussion, see [27]. For pressure-driven burning regime, the bifurcation *surface* reduces to a bifurcation *line*  $2a = b(b-1)$ ; likewise, the bifurcating frequency reduces to  $\Omega_{bif} = (b-1)/2\sqrt{b(b-2)}$ . The intrinsic burning stability condition for small but finite size disturbances is determined as:  $b < 1$  always stable, while

$$b > 1 \quad \text{stable if} \quad a > \max \left\{ b-1, \frac{b}{2}(b-1) \right\} \quad (3.4)$$

shown as a solid thick line on Fig. 1. The region between the straight line  $b = 1$  and the parabola  $4a = b^2$  is where eigenvalues with imaginary parts arise; the iso-frequency lines (constant  $\Omega$ ) lying in this region are indicated. Just at the stability boundary, this frequency pertains to the self-sustained oscillatory burning ( $\Omega = \Omega_{bif}$ ).

These findings exactly recover the classical parabolic pressure-driven linear stability boundaries first discovered by Denison and Baum for premixed flames [2] and Novozhilov by the ZN method (e.g.: [3] [4] [5]). Likewise, the boundaries determined by KTSS [8] and BM [9] respectively for distributed flames and a generic QSHOD flame are also recovered. In particular, the parabolic boundaries found by the FM and ZN methods are seen to exactly overlap in Fig. 1.

## 4. THE AQSHOD PROBLEM

To assess quantitative trends, specific submodels for the surface pyrolysis and gas-phase transient flame need to be implemented. The test case is a model propellant whose properties were listed in [10] p. 811.

### 4.1. Surface Pyrolysis

Let the burning surface be an infinitesimally thin planar surface subjected to one-step, irreversible gasification processes. The Arrhenius exponential law, commonly used for concentrated pyrolysis, in dimensional terms is

$$r_b(p, T_s) = \tilde{A}_s p^{n_s} \exp\left(-\frac{\tilde{E}_s}{RT_s}\right) \quad (4.1)$$

For the explicit pressure dependence, a power law with finite  $n_s$  is commonly accepted. In principle, the power  $n_s$  should be evaluated experimentally. But it is shown in a companion

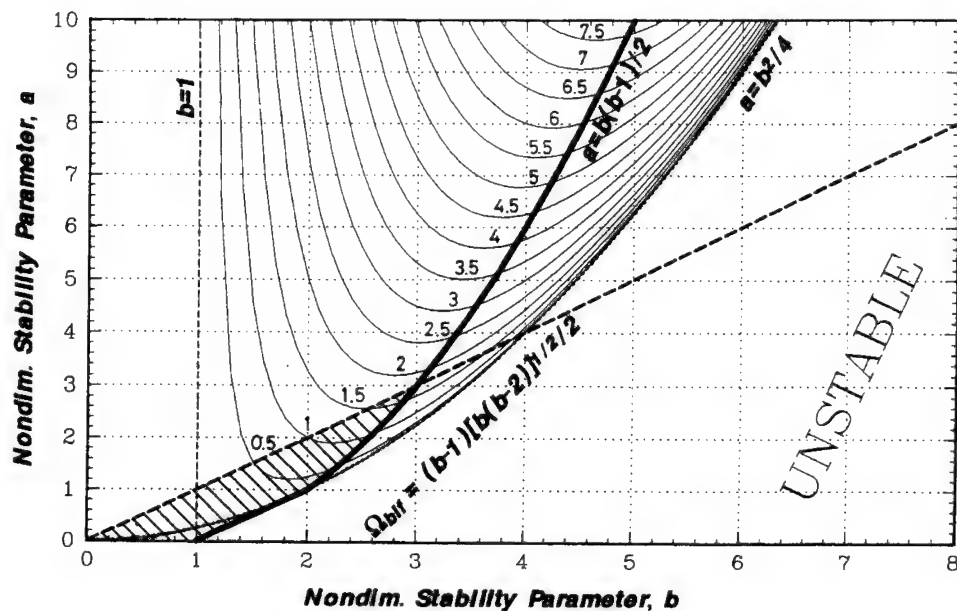


Figure 1. QSHOD intrinsic stability map for pressure-driven burning. The thick solid line is the exact linear stability boundary recovering the classical adiabatic FM results by Denison and Baum (sharp premixed flames) and ZN results by Novozhilov. Frequency of the self-sustained oscillatory burning is parametrically plotted.

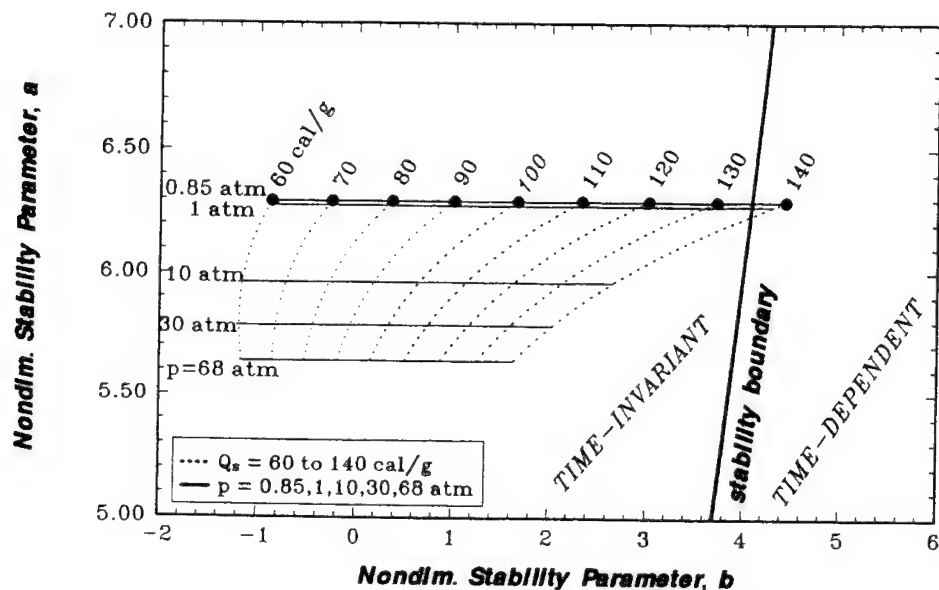


Figure 2. QSHOD intrinsic stability map for pressure-driven burning showing the effects of pressure and surface heat release with no pressure dependence of overall surface pyrolysis ( $n_s = 0$ ). Test propellant for the indicated set of operating parameters.

paper [18] that for piecewise continuous functions

$$n_s = n - n_{T_s} \frac{\tilde{E}_s}{\mathcal{R}\bar{T}_s} \quad (4.2)$$

being  $n$  and  $n_{T_s}$  evaluated, respectively by steady-state burning rate  $\bar{r}_b = r_{b,ref}(p/p_{ref})^n$  and surface temperature  $\bar{T}_s = T_{s,ref}(p/p_{ref})^{n_{T_s}}$  measurements, over each pressure interval obtained by properly splitting the whole pressure range of interest. This relationship can be seen, for Arrhenius pyrolysis, as the FM version of the ZN local relationship

$$\frac{\delta}{r} = \nu - \frac{\mu k}{r} \quad (4.3)$$

recently discussed by Brewster and coworkers [15] [16] [17] and in turn derived from the Jacobian  $\delta \equiv \partial(\ln \bar{m}, \bar{T}_s)/\partial(\ln p, T_1) = \nu r - \mu k$  of the four steady sensitivity parameters used in the ZN formulation (e.g., see [5]). Due to the practical importance of the Arrhenius kind of pyrolysis, this particular problem is conveniently called the AQSHOD (Arrhenius surface pyrolysis, Quasi-Steady gas phase, Homogeneous condensed phase, and One-Dimensional propellant strand) problem and will specifically be addressed in this paper.

#### 4.2. Transient Flame Model

This aspect of the problem, already described elsewhere [10] [20], is only quickly summarized here. The flow is assumed to be one-phase, laminar, nonviscous, low-subsonic, and with Lewis number = 1. For distributed flames of thickness  $x_f$  with the maximum heat release rate site approaching the burning surface, the nonlinear heat feedback [13] in nondimensional terms is

$$q_{g,s}(P, R) = RH_g \frac{\gamma + 1}{\zeta_f} F(\gamma) \quad (4.4)$$

where

$$F(\gamma) \equiv 1 - \frac{(-1)^\gamma \gamma!}{(\zeta_f)^\gamma} \exp(-\zeta_f) + \sum_{i=1}^{\gamma} \frac{(-1)^i \gamma!}{(\gamma - i)! (\zeta_f)^i} \quad (4.5)$$

being  $\zeta_f \equiv R^2 < \tau_g^\dagger >$  a quantity to be properly evaluated at the flame front. The additional assumption of flames *linearized* in the exponential term, i.e.,  $\zeta_f$  large, can be invoked to analytically compute frequency response functions. The parameter  $\gamma$  is used to describe the space elongation of the flame: for  $\gamma = 0$  the standard KTSS transient flame model is recovered, while  $\gamma > 0$  deals with distributed flames of larger thickness.

### 5. PRESSURE DEPENDENCE OF ARRHENIUS PYROLYSIS

The effects of finite  $n_s$  are now discussed. A critical revision of the commonly implemented Arrhenius pyrolysis law and importance of surface dynamics was recently conducted by Brewster and coworkers [15] [16] [17]. Their criticism of the current state of the art is at least partly shared, but no distributed gasification process is considered in this instance. Let us start by the simplest point of view: a constant value of  $n_s$  is enforced to describe a possible explicit pressure dependence of the surface pyrolysis. For the selected test propellant, the intrinsic stability map for  $n_s = 0$  is shown in Fig. 2, to be contrasted with Fig. 3 where  $n_s = -0.3$  and  $+0.3$  were enforced. In all figures, only pressure-driven burning is considered. From a visual inspection of these figures, the effect of parametrically variable  $n_s$  is clear: while a positive  $n_s$  sensibly favors stability, a negative  $n_s$  favors instability (in that the intrinsic stability boundary is past beyond). The same conclusion can be reached by analyzing the pressure-driven linear frequency response function; see Fig. 4. Although the detailed trends are complex, in general the values

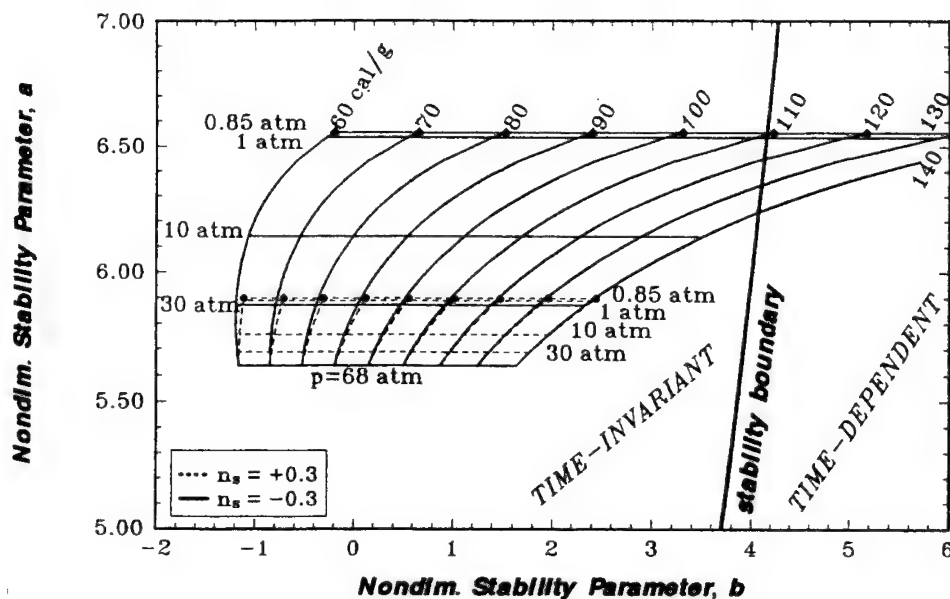


Figure 3. QSHOD intrinsic stability map for pressure-driven burning showing the effects of pressure and surface heat release with pressure dependence of overall surface pyrolysis ( $n_s \neq 0$ ). Instability is favored by negative values of  $n_s$  while stability is favored by positive values of  $n_s$ . Test propellant for the indicated set of operating parameters ( $n_s = -0.3$  and  $n_s = +0.3$ ).

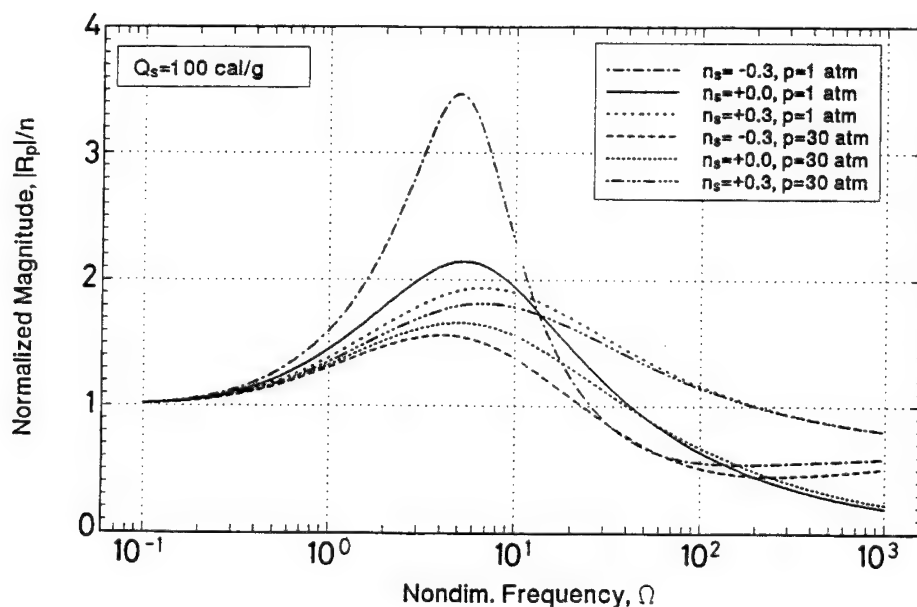


Figure 4. Linear pressure-driven frequency response function demonstrating effects of finite  $n_s$  values. Test propellant for the indicated set of operating parameters ( $n_s = -0.3, 0, +0.3$ ).

of  $Q_s$  forcing an unbounded limit of the frequency response confirm those expected from the stability plots: for  $n_s = -0.3, 0, +0.3$  the values  $Q_s = 111.99, 137.69, 171.95$  cal/g at 1 atm and  $Q_s = 173.85, 181.76, 190.42$  cal/g at 30 atm are found. Notice that increasing  $n_s$  also implies decreasing values of the resonance frequency; see Table 1.

Numerical simulations of relaxation transients confirm the validity of the analytical expectations; see Fig. 5. The critical values of  $Q_s$  at the crossing of the linear stability boundary can be assessed by a numerical go/no-go procedure. A very good agreement is found with the analytical expectations. For each tested value of  $n_s$ , a burning relaxation transient for  $Q_s$  less than the critical value always keeps its initial time-invariant steady configuration; for  $Q_s$  larger than the critical value, the burning relaxation transient sooner or later switches from its initially assigned (presumed time-invariant) steady configuration to a self-sustained oscillatory steady configuration. For example, for  $n_s = -0.3, 0, +0.3$  (see Fig. 5) the bracketing values at 1 atm were respectively determined as  $Q_s = 111-112, 137-138, 172-173$  cal/g, to be compared with the corresponding frequency response results in Table 1. Better accuracy would be gained by higher numerical precision. While the induction time for this combustion regime switch depends on the detailed burning history and in general cannot be predicted, burning frequencies agree well with the analytical expectations. Typical values are summarized in Table 1.

The same general trend is observed for pressure-driven burning under constant radiation. The effect of parametrically variable  $n_s$  is again tangible: while a positive  $n_s$  sensibly favors stability, a negative  $n_s$  favors instability. However, under constant radiation these effects are restricted to the low range of pressure and/or radiant flux explored. As matter of fact, for large pressures and even more so for large radiant flux, the gradual conversion of the radiation-sustained combustion wave into an ablation wave makes burning more and more stable (see detailed discussion in [19] and [20]). Larger values of radiant flux make pressure less influential. The same conclusion can be reached by analyzing the pressure-driven linear frequency response function in the presence of a constant radiant flux.

Table 1  
Computed Values (Frequency Response) of  $Q_s$  and  $\Omega$  at the Stability Boundary.

operating conditions		computed values	
p, atm	$n_s$	$Q_s$ critical, cal/g	$\Omega$ critical
1	-0.3	111.99	4.786
1	0	137.69	4.751
1	+0.3	171.95	4.169
30	-0.3	173.85	4.169
30	0	181.76	4.074
30	+0.3	190.42	3.981

What is a suitable value for  $n_s$ ? For piecewise continuous functions, the general expression of Eq. 4.2 [18] shows that  $n_s$  is a function of other surface steady parameters. As an example, the stability map of Fig. 6 was obtained for a modified test propellant ( $\tilde{E}_s = 16,100$  cal/mole, based on an industrial composite propellant of national production). The switch of the controlling mechanism from a diffusive to a premixed flame, for a pressure very close to the atmospheric value, is responsible of the apparent break of burning features and subsequent distinct  $n_s$  increase in the subatmospheric range. The dependence of  $n_s$  on operating conditions is illustrated in Table 2:  $n_s$  increases with increasing pressure and decreasing surface activation energy. However, under all tested circumstances, for pressure-driven burning  $n_s$  is found to feature limited values around zero. Yet its effects, although modest on steady-state burning, may be relevant for unsteady regimes, as shown next section. Similar remarks were made by Brewster and coworkers in the ZN framework [15] [16]; but differences too exist due to the overall Arrhenius pyrolysis used here. For details, see [18].

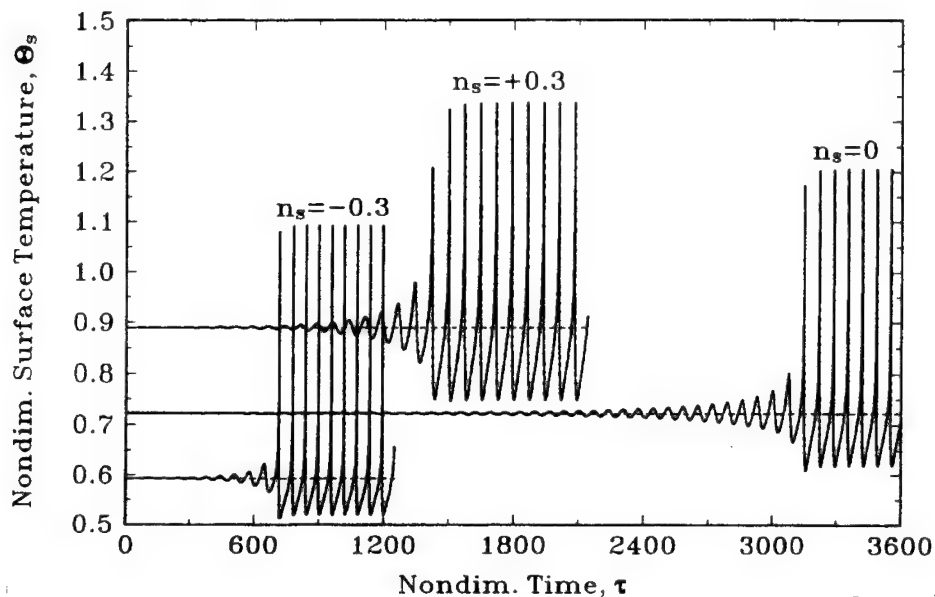


Figure 5. Go/no-go numerical validation showing agreement with analytical expectations (exact intrinsic stability theory and unbounded limit of linear frequency response). Test propellant for the indicated set of operating parameters (pressure-driven,  $n_s = -0.3, 0, +0.3$ ).

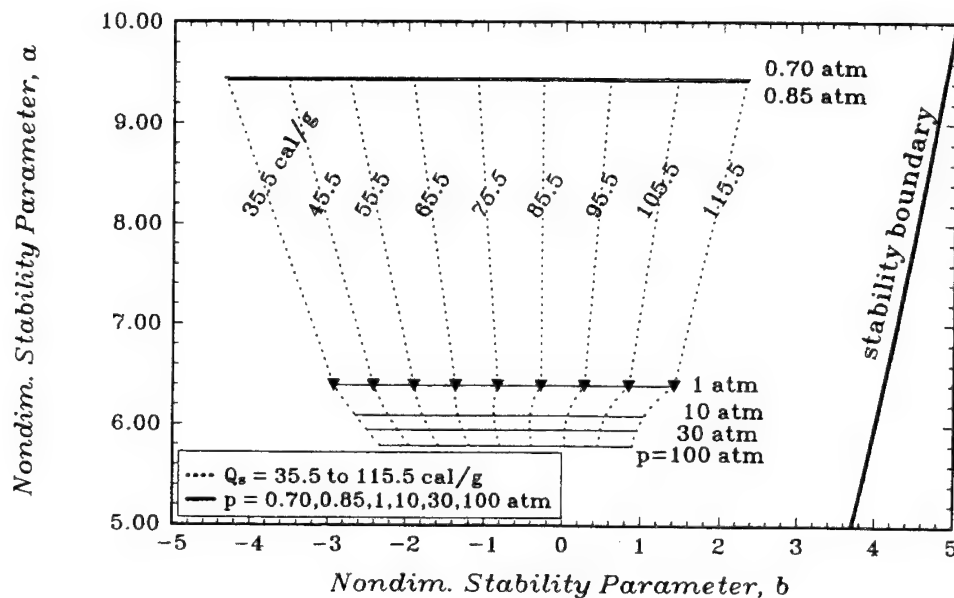


Figure 6. QSHOD intrinsic stability map for pressure-driven burning showing the effects of computed  $n_s$  over a large pressure range. Modified test propellant for the indicated set of operating parameters ( $\bar{E}_s = 16, 100$  cal/mole).

**Table 2**  
Illustrating  $n_s$  Dependence on Operating Conditions.

pressure	$n_s$	
p, atm	$E_s = 16,100$ cal/mole	$E_s = 20,000$ cal/mole
100	1.227E-01	2.558E-02
68	1.152E-01	1.623E-02
50	1.090E-01	8.653E-03
30	9.869E-02	-4.189E-03
10	7.556E-02	-3.290E-02
2	3.938E-02	-7.779E-02
1	2.292E-02	-9.821E-02
0.85	1.711E-01	2.608E-01
0.70	1.667E-01	2.571E-01

## 6. LINEAR FREQUENCY RESPONSE FUNCTION

Another way to assess intrinsic stability of a combustion configuration is by means of the unbounded response limit of the frequency response function for the linear approximation of the problem. Fluctuations of burning rate, subsequent to an externally controlled sinusoidal fluctuation of pressure with angular frequency  $\omega$ , are sought for. Thus, pressure-driven frequency response is a complex function defined as

$$R_p \equiv \frac{m'/\bar{m}}{p'/\bar{p}} \quad (6.1)$$

The basic mathematical assumption of linear theories is that all time-dependent variables (...) can be expressed as the sum of a steady-state value  $\overline{(...)}$  and a small disturbance of the type  $(...)' \cdot e^{i\omega t}$ , whose amplitude has to be determined but is always much smaller than the steady-state counterpart.

### 6.1. Standard "Two-Parameter" Form

All QSHOD frequency response functions, for both FM and ZN methods, can be cast in the standard "two parameter" form [6]. From a formal viewpoint, a "universal" law for pressure-driven frequency response functions can be established. Only parameter B (essentially related to the flame description) takes different values for different burning configurations, while parameter A (related to surface pyrolysis) is not affected; see also Section 7.

### 6.2. Pressure-Driven Frequency Response

For pressure fluctuations, a general expression allowing radiation background [15] [16] is

$$R_p(\omega) = \frac{nAB + n_s(\lambda_1 - 1)}{\lambda_1 + \frac{A}{\lambda_1} - (1 + A) + AB - A\bar{q}_r \frac{N_s(\lambda_1 - 1)}{\lambda_1(\ell_r + \lambda_1 - 1)}} \quad (6.2)$$

whose equivalent ZN expression, as re-formulated by Son and Brewster [21], is obtained with

$$A \equiv k/r, \quad B \equiv 1/k, \quad n \equiv \nu, \quad \text{and} \quad n_s \equiv \delta/r \quad (6.3)$$

At any rate, the static limit  $R_p(\omega \rightarrow 0) = n$  (FM) or  $\nu$  (ZN) is defined by the experimental steady burning rate law, while  $n_s$  (FM) or its equivalent  $\delta/r$  (ZN) play an explicit role.

- For adiabatic pressure-driven *sharp* flames, find

$$B = B_{sharp} \equiv \frac{c_g}{c_c} \frac{1}{A} \frac{2E_s - \frac{c_g \bar{T}_s}{Q_g - c_g(\bar{T}_f - \bar{T}_s)}}{\frac{(\alpha_g + E_g)\bar{T}_s}{\bar{T}_f} - \frac{c_g \bar{T}_s}{Q_g - c_g(\bar{T}_f - \bar{T}_s)}} \quad (6.4)$$

valid for arbitrary  $n_s$  if simultaneously

$$n_s = n + E_s(\beta_g - 2n) \frac{Q_g - c_g(\bar{T}_f - \bar{T}_s)}{c_g \bar{T}_s} \quad (6.5)$$

yielding, thanks to Eq. 4.2, the following constraint

$$\beta_g = 2n - n_{T_s} \frac{c_g \bar{T}_s}{Q_g - c_g(\bar{T}_f - \bar{T}_s)} \quad (6.6)$$

- For adiabatic pressure-driven *distributed* flames ( $\gamma = 0, 1$ ) with arbitrary  $n_s$ , find

$$B = B_{distributed} \equiv \frac{1}{n} [W_p(\gamma) + \frac{c_g n_s}{c_c A}] \quad (6.7)$$

$$W_p(\gamma) \equiv n \left[ 2(\gamma + 1) \left( 1 - \frac{2\gamma}{\zeta_f} \right) \frac{H_g}{\zeta_f} + \frac{c_g}{c_c} \frac{1 - n_s/n}{A} \right] \quad (6.8)$$

where both parameters are convenient generalizations of the corresponding quantities

$$B \equiv \frac{1}{n} [W_p + \frac{c_g n_s}{c_c A}] \quad (6.9)$$

$$W_p \equiv n [2(1 - \bar{H}_s) + \frac{c_g}{c_c} \frac{1 - n_s/n}{w_s}] \quad (6.10)$$

previously introduced by Culick (p. 26 of [7]).

- For radiation-assisted pressure-driven flames, whether sharp (see Eq. 6.4) or distributed (see Eq. 6.7), parameter  $B$  has to be augmented by  $\bar{q}_r$ .

### 6.3. Unbounded Response Limit

By putting the denominator of  $R_p = 0$  in Eq. 6.2, a complex equation is obtained. This defines the QSHOD stability boundaries and related frequency laws of pressure-driven linear burning for both FM and ZN approaches. These boundaries correspond to the condition of unbounded response of the burning propellant even for vanishing fluctuations of pressure and were first identified by Denison and Baum [2] for adiabatic sharp flames. In the FM approach [19] [20] with surface-driven burning (no radiation penetration, if any), the stability boundary is found as  $A = K(K - 1)/2$ , while the frequency of the unbounded response is given by  $\Omega_K = [(K - 1)/2] \sqrt{K(K - 2)}$  requiring  $K > 2$  for real  $\Omega$ . These results were separately obtained for sharp [28] and distributed [29] flames. As matter of fact, for both configurations [30] one can write

$$K = 1 + A - AB \quad (6.11)$$

but the actual expressions of  $K$  are different because the proper value of  $B$  has to be introduced (see Eq. 6.4 for sharp flames and Eq. 6.7 for distributed flames) possibly augmented by  $\bar{q}_r$ .



## 7. COMPARING AQSHOD INTRINSIC STABILITY

In their classical analysis of premixed flames Denison and Baum [2] introduced three parameters ( $A_{DB}$ ,  $\alpha_{DB}$ , and  $q_{DB}$ ) and formulated the instability condition for a steady-state burning propellant as  $q_{DB} > 1$  and  $q_{DB}^2 - q_{DB} - 2A_{DB} > 0$ , exactly matching the ZN stability conditions (see also p. 623 of [5]). A full discussion is reported by Williams [26]; see in particular pp. 330-335. Similar results were later found by KTSS [8] for diffusion flames and BM [9] for a generic QSHOD flame, again using three parameters (respectively  $w_s$ ,  $B_{KTSS}$ ,  $A_{KTSS}$  and  $A_{BM}$ ,  $B_{BM}$ ,  $R_{BM}$ ).

In the AQSHOD linear regime, a complete formal equivalence between FM and ZN frameworks exists, including the unbounded response limit of pressure-driven frequency responses, if one recognizes

$$A = A_{DB} = w_s = A_{BM} = a = \frac{k}{r} = \frac{\tilde{E}_s}{\Re \bar{T}_s} \frac{\bar{T}_s - T_1}{\bar{T}_s} \quad (7.1)$$

$$B = \alpha_{DB} = B_{KTSS} = \frac{B_{BM} - n_s}{n - n_s} = \frac{1 + A - K}{A} = \frac{1 + a - b}{a} = \frac{1}{k} = \frac{1}{\sigma_p(\bar{T}_s - T_1)} \quad (7.2)$$

$$K = q_{DB} = A_{KTSS} = R_{BM} = 1 + A - AB = b = 1 + \frac{k}{r} - \frac{1}{r} = 1 + \frac{\tilde{E}_s}{\Re \bar{T}_s} \frac{\sigma_p(\bar{T}_s - T_1) - 1}{\sigma_p \bar{T}_s} \quad (7.3)$$

where in general all parameters are pressure dependent. The positions in Eqs. 7.1 - 7.3 make all the relationships reported above for the stability boundary and oscillation frequency equivalent and interchangeable, and thus independent on the specific flame model or approach (ZN vs. FM).

Notice that actually only two parameters are needed, as first recognized in the ZN approach [3]. Indeed, all methods (each within its validity limits) yield the *same* linear intrinsic stability boundary as

$$a = \frac{b(b-1)}{2} \text{ (FM)} \quad \text{or} \quad r = \frac{(k-1)^2}{k+1} \text{ (ZN)} \quad (7.4)$$

and the *same* frequency of the oscillatory solution just at the stability boundary as

$$\Omega_{bif} = \frac{b-1}{2} \sqrt{b(b-2)} \text{ (FM)} \quad \text{or} \quad \Omega_{bif} = \sqrt{k} \frac{(k+1)}{(k-1)^2} \text{ (ZN)}$$

This last result recovers in particular the classical prediction  $\Omega_{bif} = A\sqrt{B}$  by Culick (p. 2251 of [6]) about the frequency of unbounded response. Notice also that the couple of parameters  $A, K$  appears more suitable to study linear frequency response than the commonly used  $A, B$  and, within the limits stated in Section 2, points out the irrelevance of the implemented flame model. Notice finally that allowing either infinitesimal (linear approximations) or small but finite disturbances (exact theory) yields the same linear intrinsic stability boundaries and frequencies. A summarizing overview of intrinsic burning stability in the broad QSHOD framework is shown in Fig. 1; applications are reported in Figs. 2, 3, 7.

## 8. AN APPROXIMATE NONLINEAR INTEGRAL METHOD

This method was first proposed to study dynamic extinction problems due to fast decrease of pressure and/or radiant flux, but in this paper only pressure-driven static (i.e., uncoupled) stability is of interest. Some features predicted by this nonlinear approach are of great interest in complementing the results produced by the stability theories so far mentioned. The technique can be applied to both FM and ZN approaches. No specific pyrolysis law or flame model need to be specified *a priori*; but notice that in principle only nonlinear transient flame models should

be implemented, since deviations from the pertaining steady-state solution can be sensible. A full exposure of the method was given in [11] [12] [13].

Assume that within a perturbed thermal layer of unknown thickness  $\xi(\tau)$ , the temperature disturbance defined by Eq. 3.1 has the form  $u(X, \tau) = u_s(\tau) \cdot u_c(X/\xi)$  for  $-\xi(\tau) \leq X \leq 0$ , where  $u_s(\tau)$  is left fully unknown while  $u_c(X/\xi) \equiv (1 + X/\xi)^n$  describes the monotonic decay in space of the temperature disturbance. The disturbance thickness  $\xi(\tau)$  can be evaluated as  $\xi(\tau) = nu_s/(u_X)_{c,s}$  being  $(u_X)_{c,s}$  the surface thermal gradient disturbance at the condensed phase side

$$(u_X)_{c,s} = [q_{g,s} + RH_s + (1 - N_s)F_s] - [\bar{R}(\bar{\Theta}_s - \Theta_1) - \bar{N}_s\bar{F}_s] \quad (8.1)$$

### 8.1. Intrinsic QSHOD Burning Stability

Let us examine in particular the problem of intrinsic burning stability. This implies that the operating pressure (and any other time dependent parameter, if any, possibly affecting the surface boundary condition) are maintained constant in time. By substituting the above defined disturbance quantities and integrating over the perturbed thermal layer of unknown thickness  $\xi(\tau)$ , the partial differential equation stating energy conservation for the condensed phase (Eq. 2.1) is reduced to an ordinary differential equation in time. By further assuming  $N_s = \bar{N}_s$  and for monotonic propagations of the disturbance layer thickness  $\xi(\tau)$ , find

$$\frac{d\Theta_s(\tau)}{d\tau} = \frac{-R[\Theta_s - \Theta_\xi] - \bar{R}[\Theta_\xi - \Theta_1] + q_{g,s} + RH_s + (1 - N_s)F_s}{\frac{2n}{n+1} \frac{\Theta_s - \bar{\Theta}_s}{(u_X)_{c,s}} \left\{ 1 - \frac{1}{2} \frac{\Theta_s - \bar{\Theta}_s}{(u_X)_{c,s}} \left[ \frac{\partial(u_X)_{c,s}}{\partial(\Theta_s)} \right]_P \right\}} \quad (8.2)$$

The intrinsic stability of a steady-state regime is investigated by accepting finite size perturbations, of monotonically decaying nature, overlapping the initial unperturbed steady profile and investigating their asymptotic behavior. Only the numerator  $N$  of the right hand side of Eq. 8.2 governs the algebraic roots of the restoring function (unless the denominator goes simultaneously to zero). For pressure-driven burning, the first derivative of the numerator  $N$  is

$$\begin{aligned} \frac{\partial N}{\partial \Theta_s} = & -\frac{\partial R}{\partial \Theta_s} [(\Theta_s - \Theta_1) - (\bar{\Theta}_s - \Theta_1) \exp(-\bar{R}\xi)] - R \left[ 1 + (\bar{\Theta}_s - \Theta_1) \bar{R} \frac{\partial \xi}{\partial \Theta_s} \exp(-\bar{R}\xi) \right] + \\ & + \bar{R}^2 (\Theta_s - \Theta_1) \frac{\partial \xi}{\partial \Theta_s} \exp(-\bar{R}\xi) + \frac{\partial R}{\partial \Theta_s} \left[ \frac{\partial q_{g,s}}{\partial \bar{R}} + \bar{H}_s + \frac{c_g - c_c}{c_c} (\bar{\Theta}_s - \Theta_s) \right] - R \frac{c_g - c_c}{c_c} \end{aligned}$$

where all partial derivatives are taken at constant pressure. The stability boundary is determined by the condition of zero slope of the numerator  $N$  at the steady-state root  $\Theta_s = \bar{\Theta}_s$ . This yields

$$\frac{1}{\bar{R}} \frac{\partial \bar{R}}{\partial \bar{\Theta}_s} \left[ \frac{\partial q_{g,s}}{\partial \bar{R}} + \bar{H}_s \right] - \frac{c_g - c_c}{c_c} - \frac{1}{\bar{R}} \frac{\partial \bar{R}}{\partial \bar{\Theta}_s} (\bar{\Theta}_s - \Theta_1) \left[ 1 - \exp \frac{-n\bar{R}}{\frac{\partial \bar{R}}{\partial \bar{\Theta}_s} \left[ \frac{\partial q_{g,s}}{\partial \bar{R}} + \bar{H}_s \right] - \bar{R} \frac{c_g - c_c}{c_c}} \right] = 1$$

or, in terms of the stability parameters defined by Eqs. 3.2 and 3.3,

$$a = \frac{b-1}{1 - \exp(-n/b)} \quad (8.3)$$

Therefore, the approximate integral technique exactly recovers the parabolic FM stability boundary of Eq. 7.4 for  $n = -b \ln(1 - 2/b)$ , implying  $n$  ranging from about 2.72 to 2.87 for the test model propellant nominally burning from 0.01 to 1000 atm. Likewise, the approximate integral technique exactly recovers the parabolic ZN stability boundary of Eq. 7.4 for  $n = 2k/(k-1) \ln k$ , implying  $n$  ranging from about 2.5 to 3.5 for the common  $k$  interval from 1 to 3. The particular case  $n = 3$  was already treated by Zarko et al. ([31] p. 387 and Fig. 12), showing close results with respect to the classical ZN stability boundary.

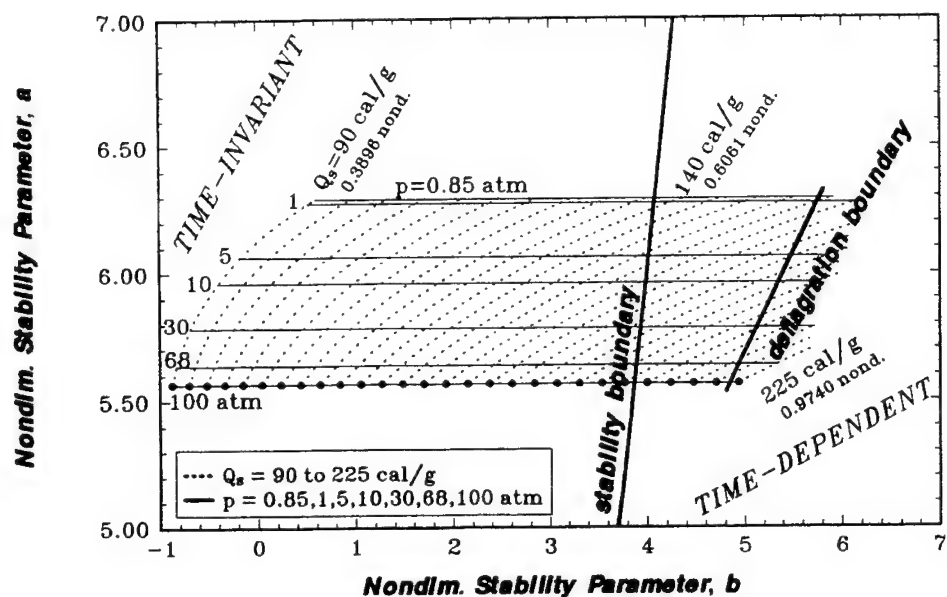


Figure 7. QSHOD intrinsic stability map for pressure-driven burning with  $Q_s$  parametrically varying from 90 to 225 cal/g (i.e., from 0.3896 to 0.9740 nondimensional). Test propellant for the indicated set of operating parameters ( $n_s = 0$ ).

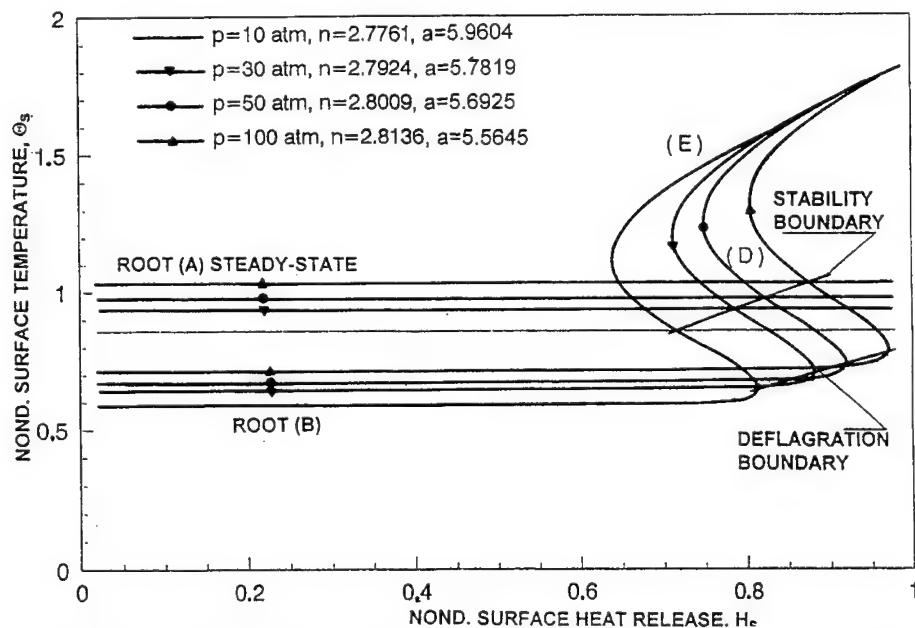


Figure 8. Bifurcation and deflagration boundaries as revealed by an approximate integral method implementing the exact value of the disturbance thermal profile  $n$  at each pressure. Test propellant for the indicated set of operating parameters ( $n_s = 0$ ).

## 9. DEFLAGRATION AND DYNAMIC EXTINCTION BOUNDARIES

All classical intrinsic stability boundaries, whether FM or ZN, are valid only for infinitesimal (linear approximation of the problem) or small but finite deviations (exact approach) from the stability boundaries. Thus, the self-sustained oscillatory regime revealed by classical analyses (for example [2] [3]) is expected to be true only at the stability boundary. Actually, numerical and experimental tests show that the self-sustained oscillatory burning regime may extend sensibly beyond the stability boundary. In fact, the approximate integral technique reveals the existence of a second boundary below which self-sustained oscillatory burning is found and beyond which no stable steady burning regime can be found. This second boundary is a *deflagration* boundary. Deflagration boundaries can be determined for both FM and ZN methods as hereafter described.

For convenience, consider the stability plots of Fig. 7 and Fig. 8, obtained for the selected test case respectively from the exact method and approximate integral method. In both figures, surface heat release is considered as the bifurcating parameter at several pressures ranging from 1 to 100 atm. In the stability plot of Fig. 7, at each operating pressure, while  $a$  is fixed  $b$  is seen to vary going from a first critical value (stability boundary, defined by Eq. 3.4) to a second critical value (deflagration boundary) which has been determined with the help of Fig. 8.

In the stability plot of Fig. 8, at each operating pressure, root A exactly corresponds to the proper steady-state time-invariant solution. Roots B, D, E are further roots produced by the integral method; for a full discussion see [13]. In this plot, the stability boundary is determined by the coalescence of roots A and D (zero slope of the time-invariant steady solution) while the deflagration boundary is determined by the coalescence of roots B and D. How does this translate into Fig. 7? Notice first that, at each operating pressure, root A also corresponds to a well defined  $a$ , while  $b$  varies going from a first critical value (stability boundary, see Eq. 8.3) to a second critical value (deflagration boundary). Thus, a precise one-to-one correspondence between the two stability plots exists for *each* time-invariant steady solution in terms of  $a$  and  $b$ ; this mapping can be used to locate the deflagration boundary in Fig. 7 from Fig. 8. Differently from previous applications of the integral method, the plot of Fig. 8 was obtained by implementing for the polynomial disturbance order the "exact" value of  $n$  as suggested in Eq. 8.3 at *each* operating pressure. Although no guarantee exists that this value keeps unchanged for varying surface heat release, this choice makes sure that at least the stability boundary thus determined precisely coincides with the one obtained via the exact approach.

Thus, by combining the exact analysis with the approximate integral method, the existence of two distinct boundaries is revealed: the first boundary holds true for the stable steady-state time-invariant burning (the line so far called linear stability boundary), while the second boundary holds true for the stable steady-state self-sustained oscillatory burning. Since no stable steady-state reacting solution is permitted beyond this second boundary, this takes the meaning of a *deflagration limit*. Therefore, a finite interval of operating conditions exists over which the stable steady-state reacting solution is time-dependent (oscillatory self-sustained) rather than time-invariant. The linear stability boundary of classical approaches corresponds to the incipient part of this interval (i.e., where the transition of the steady solution from time-invariant to self-sustained oscillatory burning occurs), while the second boundary corresponds to the end of the interval. In mathematical words, at the stability boundary a Hopf bifurcation occurs generating a stable limit cycle whose existence is bounded by the deflagration boundary. Notice that this possible extension of the steady working regime beyond the linear stability boundaries occurs for a number of operating parameters (not only surface heat release as shown in Figs. 7-8). In conclusion, for energetic solid materials the stability of steady burning may be sensibly widened from the stability boundaries (of the time-invariant solution) to the deflagration boundaries (of the self-sustained oscillatory solution).

By the same technique, the dynamic extinction boundary can be determined in the stability plot of Fig. 8. It is enough to connect, at any given operating pressure, roots B below which steady

reacting solutions are no longer allowed [11] [12] [13]. Thus, it is seen that the whole region in Fig. 8 below the dynamic extinction boundary (for each operating pressure) and deflagration boundary does not permit steady burning solutions, while the region between linear stability boundary and deflagration boundary permits only steady self-sustained oscillatory burning.

## 10. VALIDATION AND VERIFICATION

Validation analyses can be carried out analytically by cross-checking that at the predicted stability boundaries the linear frequency response functions does yield an unbounded response limit. This consistency test, most reassuring when applicable, was successfully performed in a number of cases. For details, see [10] p. 809.

Testing by numerical simulations is more suitable to verify a wide range of physical configurations. Systematic tests were conducted by integrating the governing set of equations by a standard finite difference scheme under a variety of operating conditions. The effects of several parameters were checked on both stability and deflagration boundaries, in general confirming the validity of the reported findings. Independent and systematic numerical tests in agreement with the conclusions of this paper were reported in [32].

Conclusive validation can only be obtained by experimental testing, in general less immediate than the above checks. By slowly lowering the operating pressure in a laboratory burner, before reaching the deflagration limits an oscillatory burning regime is well detectable for a variety of solid propellants [33]. More complex testing can be performed (for example, see [34] Figs. 6-8) by using external radiation, revealing oscillatory burning near the pressure deflagration limit in qualitative agreement with the findings of this paper. Both experimental approaches confirm the existence of distinct stability and deflagration boundaries. Systematic testing concerning the pressure-driven dynamic extinction, performed by a go/no-go technique [12], confirms the existence of neatly distinct dynamic extinction and pressure deflagration boundaries [35]. In this wide framework, specific effects due to pyrolysis and heterogeneity are not the purpose of this paper.

## 11. CONCLUSIONS AND FUTURE WORK

The effects of pressure dependent surface pyrolysis were investigated from several viewpoints: negative or positive values of  $n_s$  were respectively found to be destabilizing or stabilizing in the standard AQSHOD framework. However, for the simple pressure-driven burning configuration considered in this paper,  $n_s$  features a small value smoothly decreasing from positive to negative for decreasing pressure. But the effects of finite  $n_s$ , although modest on steady-state burning properties, may be relevant for unsteady and/or unstable regimes. Intrinsic combustion stability has been discussed by a host of analytical techniques: within the AQSHOD framework the exact abstract approach recovers all known results, including the classical boundaries by Denison-Baum and Zeldovich-Novozhilov of the related linear adiabatic problem, as special cases. Moreover, it was shown that the stability of steady-state regime is extended up to the deflagration boundaries, but a switch from time-invariant to self-sustained oscillatory steady burning (time-dependent) occurs at the linear stability boundary. Cross-checks with other analytical results, numerical simulations, and experimental observations in general agree with the proposed picture. Discussions of pyrolysis modeling and heterogeneity effects were outside the scope of this paper. But work on pyrolysis and surface layer structure is presently under progress.

### Acknowledgments

The financial support of INTAS-93-2560 and MURST 40% is gratefully acknowledged.

## References

- [1] Ya.B. Zeldovich. On the combustion theory of powders and explosives. *Journal of Experimental and Theoretical Physics*, 12:498–510, 1942.
- [2] M.R. Denison and E. Baum. A simplified model of unstable burning in solid propellants. *ARS Journal*, 31:1112–1122, 1961.
- [3] B.V. Novozhilov. Stability criterion for steady-state burning of powders. *Journal of Applied Mechanics and Technical Physics*, 6(4):157–160, 1965.
- [4] B.V. Novozhilov. *Nonstationary Combustion of Solid Rocket Fuels*. Nauka, Moscow, Russia, 1973. Translation AFSC FTD-MT-24-317-74.
- [5] B.V. Novozhilov. *Theory of Nonsteady Burning and Combustion Stability of Solid Propellants by the ZN Method*, volume 143 of *AIAA Progress in Astronautics and Aeronautics*, 'Nonsteady Burning and Combustion Stability of Solid Propellants', edited by L. DeLuca, E.W. Price, and M. Summerfield, chapter 15, pages 601–641. AIAA, Washington, DC, USA, 1992.
- [6] F.E.C. Culick. A review of calculations for unsteady burning of a solid propellant. *AIAA Journal*, 6(12):2241–2255, 1968.
- [7] F.E.C. Culick. Some problems in the unsteady burning of solid propellants. Technical Report NWC TP-4668, Naval Weapons Center, China Lake, CA, USA, 1969.
- [8] H. Krier, J.S. T'ien, W.A. Sirignano, and M. Summerfield. Nonsteady burning phenomena of solid propellants: Theory and experiments. *AIAA Journal*, 6(2):278–288, 1968.
- [9] R.S. Brown and R.J. Muzzy. Linear and nonlinear pressure coupled combustion instability of solid propellants. *AIAA Journal*, 8(8):1492–1500, 1970.
- [10] L. DeLuca, R. DiSilvestro, and F. Cozzi. Intrinsic combustion instability of solid energetic materials. *Journal of Propulsion and Power*, 11(4):804–815, 1995.
- [11] L. DeLuca. Nonlinear burning stability theory of heterogeneous thin flames. *18th Symposium International on Combustion*, pages 1439–1450, 1981.
- [12] L. DeLuca. *Extinction Theories and Experiments*, volume 90 of *AIAA Progress in Astronautics and Aeronautics*, chapter 12, pages 661–732. AIAA, Washington, DC, USA, 1984.
- [13] L. DeLuca. *Theory of Nonsteady Burning and Combustion Stability of Solid Propellants by Flame Models*, volume 143 of *AIAA Progress in Astronautics and Aeronautics*, 'Nonsteady Burning and Combustion Stability of Solid Propellants', edited by L. DeLuca, E.W. Price, and M. Summerfield, chapter 14, pages 519–600. AIAA, Washington, DC, USA, 1992.
- [14] T.R. Goodman. Application of integral methods to transient nonlinear heat transfer. In *Advances in Heat Transfer*, volume 1, pages 51–122. Academic Press, 1964.
- [15] M.Q. Brewster, M.A. Zebrowski, T.B. Schroeder, and S.F. Son. Unsteady combustion modeling of energetic solids. AIAA, Washington, DC, USA, 1995. AIAA Paper 95-2859.
- [16] M.Q. Brewster and S.F. Son. Quasi-steady combustion modeling of homogeneous solid propellants. *Combustion and Flame*, 103:11–26, 1995.
- [17] S.F. Son and M.Q. Brewster. Unsteady combustion of homogeneous energetic solids using the laser-recoil method. *Combustion and Flame*, 100:283–291, 1995.

- [18] L. DeLuca, M. Verri, F. Cozzi, and G. Colombo. Revising the pyrolysis jacobian. In *NATO Advanced Research Workshop (NATO-ARW) on Peaceful Utilization of Energetic Materials*, 1996. Fourth International Conference on Combustion (ICOC-96), Saint Petersburg, Russia, 3-6 Jun 1996.
- [19] L. DeLuca, P. Mazza, and M. Verri. Intrinsic stability of solid rocket propellants burning under thermal radiation. In *Proceedings of CNES - CNRS - ONERA Conference, Bordeaux, France, 11-15 Sep 1995*, volume 1, pages 77-90, 1995.
- [20] L. DeLuca, M. Verri, and Jalongo A. *Intrinsic Stability of Energetic Solids Burning under Thermal Radiation*, volume 173 of *AIAA Progress in Astronautics and Aeronautics "Progress in Combustion Science - in Honor of Ya.B. Zel'dovich"*, edited by W.A. Sirignano, A.G. Merzhanov, and L. DeLuca. AIAA, Washington, DC, USA, 1996. under press.
- [21] S.F. Son and M.Q. Brewster. Linear burning rate dynamics of solids subjected to pressure or external radiant flux oscillations. *Journal of Propulsion and Power*, 9(2):222-232, 1993.
- [22] M.M. Ibricu and F.A. Williams. Influence of externally applied thermal radiation on the burning rates of homogeneous solid propellants. *Combustion and Flame*, 24:185-198, 1975.
- [23] D. Henry. *Geometric Theory of Semilinear Parabolic Equations*, volume 840 of *Lecture Notes in Mathematics*. Springer-Verlag, New York, NY, USA, 1981.
- [24] C.M. Brauner, A. Lunardi, and C. Schmidt-Lainé. Stability of travelling waves with interface conditions. *Nonlinear Analysis*, 19:455-474, 1992.
- [25] C.D. Pagani and M. Verri. Stability analysis of the travelling wave solutions in burning solid propellants. In V. Lakshmikantham, editor, *Proceedings of the First World Congress of Nonlinear Analysts, Tampa, FL, USA, 19-26 Aug 1992*, pages 661-666. Walter de Gruyter, Berlin - New York, 1996.
- [26] F.A. Williams. *Combustion Theory*. The Benjamin/Cummings Publishing Company, Menlo Park, CA, 2nd edition, 1985.
- [27] M. Verri. Asymptotic stability of travelling waves in solid propellant combustion under thermal radiation. Preprint under preparation, Dipartimento di Matematica, Politecnico di Milano, Milan, Italy, 1997.
- [28] R. Cristiani. Stabilità lineare e non lineare della combustione stazionaria dei propellenti solidi. Master's thesis, Dipartimento di Energetica, Ingegneria Aeronautica, Politecnico di Milano, Milan, Italy, 1993.
- [29] F. Cozzi. Risposta in frequenza teorica e sperimentale di propellenti solidi soggetti a radiazione laser. Master's thesis, Dipartimento di Energetica, Ingegneria Aeronautica, Politecnico di Milano, Milan, Italy, 1993.
- [30] L. DeLuca, C.D. Pagani, and M. Verri. A review of solid rocket propellant combustion. In *Proceedings 19th International Symposium on Space Technology and Science, Yokohama, Japan*, pages 109-116, May 1994. Paper 94-a-30v, 1994.
- [31] V.E. Zarko, V.N. Simonenko, and A.B. Kiskin. *Radiation-Driven Transient Burning: Experimental Results*, volume 143 of *AIAA Progress in Astronautics and Aeronautics*, chapter 10, pages 363-398. AIAA, Washington, DC, USA, 1992.
- [32] D.E. Kooker and C.W. Nelson. Numerical solution of solid propellant transient combustion. *Journal of Heat Transfer*, 101:359-364, 1979.

- [33] C. Zanotti, U. Carretta, C. Grimaldi, and G. Colombo. *Self-Sustained Oscillatory Burning of Solid Propellants: Experimental Results*, volume 143 of *AIAA Progress in Astronautics and Aeronautics 'Nonsteady Burning and Combustion Stability of Solid Propellants'*, edited by L. DeLuca, E.W. Price, and M. Summerfield, chapter 11, pages 399-439. AIAA, Washington, DC, USA, 1992.
- [34] T. Saito and A. Iwama. Laser ignition behavior of ctpb/ap propellants at subatmospheric pressures. In *Proceedings of the ICT 10th Annual Conference*, pages 127-151, Karlsruhe, Germany, 1979.
- [35] C. Bruno, G. Riva, C. Zanotti, R. Dondé, C. Grimaldi, and L. DeLuca. Experimental and theoretical burning of solid rocket propellants near the pressure deflagration limit. *Acta Astronautica*, 12(5):351-360, 1985.

## COMMENTS

**M.Q. Brewster, UIUC, USA.** First, there are some subtle notational differences between the sensitivity parameter formulation used here and the definition under ZN theory. For example, the pressure exponent  $n$  defined by  $\bar{r}_b = r_{b,ref}(p/p_{ref})^n$  (following Eq. 4.2) is not in general the same as the ZN sensitivity parameter  $\nu$ . This distinction is contrary to Eq. 6.3, which assumes that  $n$  has the same ZN sensitivity parameter definition. If the former equation is used as the definition of  $n$  then  $n$  can only be thought of as the ZN sensitivity parameter if  $\nu \neq \nu(p)$ , which is often a reasonable approximation over limited pressure ranges but not near so-called "exponent breaks" or over large pressure ranges. Similar comments hold for  $n_{T_s}$ : according to  $\bar{T}_s = T_{s,ref}(p/p_{ref})^{n_{T_s}}$ ,  $n_{T_s}$  is equivalent to the ZN parameter  $\mu$  only when  $n_{T_s} \neq n_{T_s}(p)$ . The same can be said about the definition of  $n_s$  in Eq. 4.1, which is not the ZN sensitivity parameter  $\delta/r$  unless  $n_s \neq n_s(p)$  is assumed. It would seem that to obtain Eq. 4.2 requires assuming that  $n$ ,  $n_{T_s}$ , and  $n_s$  are all independent of pressure to the degree that the derivatives terms are negligible. However, demonstrating the pressure dependence of  $n_s$  is one of the paper's point. Some discussion is needed of the validity of implicitly assuming  $n_s \neq n_s(p)$  and then explicitly demonstrating the pressure dependence of  $n_s$  in Table 2.

The main question with this approach is the assumed Arrhenius surface pyrolysis law, Eq. 4.1; how well does Eq. 4.1 represent reality? That question can only be answered by comparison with observations and in that regard steady state measurement are necessary but not sufficient. Unsteady measurements are required. We have previously examined single-step, zero-order decomposition in the high activation energy limit (see Eq. 13 of Ref. 1 or Eq. 7 of Ref. 2 in this Proceedings) and found that it matches both steady state burning rate data and unsteady response function data for homogeneous materials when quasi-steady conditions are satisfied. What is needed is to put Eq. 4.1 to the same test. That can be done in part here by comparing the sensitivity parameter relation for large activation energy, zero-order decomposition,

$$n_s = \frac{-n}{k(2 - \bar{Q}_c - \bar{Q}_r) - 1} \quad (C1)$$

with Eq. 4.2. The zero-order relation Eq. C1 indicates that  $n_s$  and  $n$  should have opposite sign (the denominator is positive for realistic conditions). The behavior of Eq. 4.2 is quite different: when  $n$  is negative  $n_s$  must also be negative ( $n_{T_s}$  is presumably positive), and when  $n_s$  is positive  $n$  must also be positive. This alone shows that the two pyrolysis relations have very different behavior at the sensitivity parameter level. An additional difference is that Eq. 4.1 embodies a zero radiation Jacobian sensitivity parameter ( $\delta_q/r = [\partial \ln \bar{r}_b / \partial \ln \bar{q}]_{\bar{T}_s, \bar{p}}$ ) whereas zero order decomposition does not. Laser-recoil response function data obtained for AP and double base propellant are difficult to fit with  $\delta_q/r = 0$  but have shown favorable comparison



with zero order decomposition (see Refs. 1-2). Though radiation driven burning is not the emphasis in this paper, it still offers evidence on the issue of accuracy of a pyrolysis relation and the sensitivity parameters derived therefrom. Since sensitivity parameters are derivatives of a primary function (in this case a pyrolysis relation) and because the error in a function is amplified in its derivatives, the question of suitability of a pyrolysis relation must be addressed by considering not only the function but its derivatives. We think the evidence so far suggests that the formally derived zero-order decomposition relation is significantly more accurate at the sensitivity parameter than the *ad hoc* Arrhenius surface pyrolysis relation, Eq. 4.1 (even with  $n_s$ ).

The second main question has to do with the data used for comparison. Only materials that burn in a fashion which satisfies the classical quasi-steady assumptions should be expected to show correspondence with the theory. These assumptions include quasi-steady gas-phase, quasi-steady (i.e., vanishingly thin) condensed phase reaction zone, homogeneous propellant with constant properties, and one-dimensional heat feedback. Composite propellants which exhibit heterogeneous effects such as multi-dimensional heat transfer in both the solid and gas-phase violate these assumptions. Presumably AP composite propellants with fine enough AP at low pressure can be considered quasi-homogeneous for these purposes. The propellants used by Brown and Muzzy referred to in the presentation and the paper do not appear to be quasi-homogeneous. Neither do the industrial composite propellants referred to in the paper. Given the AP and binder have different chemical and thermophysical properties and therefore different activation energies and surface temperatures, how are the "homogeneous" properties of the present analysis to be viewed in context of a heterogeneous propellant? It also seems that important response mechanisms such as selective ingredient pyrolysis would be entirely missed by applying the homogeneous, one-dimensional analysis to such data.

#### References

- [1] M.Q. Brewster and S.F. Son. Quasi-steady combustion modeling of homogeneous solid propellants. *Combustion and Flame*, 103:11-26, 1995.
- [2] M.Q. Brewster and T.B. Schroeder. Unsteady combustion of homogeneous energetic solids. In *Challenges in Propellants and Combustion 100 Years After Nobel*. Proceedings of Fourth International Symposium on Special Topics in Chemical Propulsion (4-ISICP), Stockholm, Sweden, 27-31 May 1996. Begell House, Inc., 1997.

**Authors' Reply.** This paper, and the companion Ref. 1, are only the first reports of a much wider general revision on the basic internal ballistic laws (burning rate and surface temperature) commonly used in the literature. We are systematically testing all of them (actually, only a few) and under arbitrary combinations of pressure, initial temperature, and radiant flux. Besides the two papers already mentioned, other presentations were already given (see Refs. 2-3) and will be given in the near future covering other aspects of this general problem.

Within this framework, a detailed reply to the first part of the Comment is the following:

- The pressure exponent  $n$  is defined over each pressure subinterval, of the entire operating range, for which  $n = \text{const}$  (piecewise continuity). Near the "exponent breaks" the proper left or right limit has to be taken. Thus no difference arises with the ZN sensitivity parameter  $\nu$ , except when  $n$  continuously changes with pressure (a situation not yet met in this investigation). At any rate, no special difficulty arises in adopting the more general ZN definition (for example, see Ref. 3).
- The same remarks can be repeated for the exponent  $n_{T_s}$ .
- Concerning the exponent  $n_s$ , both approaches were followed:  $n_s$  piecewise continuous or continuously changing with pressure. In this paper, to be consistent with the rest of the manuscript and also recover previous results found long ago in our laboratory (as reported

in Ref. 1),  $n_s$  piecewise continuous with pressure was adopted. Equivalent results are found if  $n_s$  continuously changing with pressure is adopted.

- Having assumed piecewise continuity of the three exponents, all derivatives mentioned in the Comments should not appear.

The two "main" objections discussed in the second part of the Comment seem inappropriate, because beyond the scope of the paper. The objective of this paper (see last paragraph of the section Background on page 3 of the paper) was to show that a general nonlinear intrinsic stability analysis, recently put forward by the authors, does include surface pressure dependence effects and that several, distinct analytical techniques bring about exactly the same intrinsic stability boundary. The selection of the "best" pyrolysis law or consideration of heterogeneity effects are another matter. In particular:

- Concerning the Arrhenius surface pyrolysis, this is only one of the pyrolysis laws being examined in this investigation. The matter as to the most suitable pyrolysis law is under active investigation and it would be premature to discuss it at this time.
- Concerning the heterogeneity effects, no comparison of the stability analysis predictions with experimental results is reported but only analytical and numerical calculations. Anyway, the comment is well received and the test propellant, used to perform comparisons among the different theoretical approaches, has simply been called a "model propellant".

#### References

- [1] L. DeLuca, M. Verri, F. Cozzi, and G. Colombo. Revising the pyrolysis jacobian. In *NATO Advanced Research Workshop (NATO-ARW) on Peaceful Utilization of Energetic Materials*, 1966. Fourth International Conference on Combustion (ICOC-96), Saint Petersburg, Russia, 3-6 Jun 1996.
- [2] L. DeLuca, M. Verri, F. Cozzi, and G. Colombo. Surface pyrolysis of high energy materials. In *Seminar Handbook*, 1966. International Seminar on High Energy Materials, Pune, India, 19-21 Nov 1996.
- [3] L. DeLuca, M. Verri, F. Cozzi, G. Colombo, and E. Volpe. Adiabatic pyrolysis of solid propellants. AIAA Paper 97-0588 presented at the 35th AIAA Aerospace Sciences Meeting and Exhibit, Reno, USA, 6-9 Jan 1997.

**RECENT DEVELOPMENTS AND CHALLENGES  
IN THE IGNITION AND COMBUSTION  
OF SOLID PROPELLANTS**

**G. Lengellé  
Energetics Department**

**ONERA  
National Laboratory  
for Aerospace Research and Development of France**

**ABSTRACT**

It is of much interest to know (mostly from detailed experiments) the mechanisms involved in the combustion of solid propellants and as much as possible to describe them through modeling. The regimes thus investigated should be :

- ignition (reaching first decomposition and transitioning to fully developed flame),
- steady combustion (evolution with respect to pressure and initial temperature) resulting from the coupling between condensed and gaseous phases, including the behavior of added aluminium,
- response to erosive burning conditions,
- response to pressure (and velocity) oscillations,

(these last two topics being covered very briefly for the sake of space).

From such knowledge and modeling various results should be expected :

- orientations in the elaboration of new propellants for the tailoring of their combustion characteristics,
- prediction of the operation of compactly loaded motors (such as for hypervelocity missiles) which are submitted to erosive burning,
- prediction of the stability of the motor,
- prediction of the distributed combustion of aluminum, resulting in possible specific impulsion losses due to incomplete combustion, as well as in the accumulation of slag at the rear end of large boosters.

A conclusion is reached that much work has been accomplished, which has to be extended to the emerging propellants based on new ingredients, and which has to be integrated more and more, alongside the development of the description of the internal aerodynamics, into the prediction of the motor performance.

## INTRODUCTION

A review of our knowledge of the combustion of solid propellants is presented. It is conceived as a guide to the abundant literature on the subject, rather than an (impossibly) exhaustive analysis of the many works carried out. It is based in large part on work carried out at ONERA. However, there has always been an effort to incorporate results from other organizations and to thus synthesize the approaches.

Contacts have been made, to complement the knowledge largely acquired through the literature, through AGARD programs and a DEA with the USA, mostly through the literature for other countries (i.e., with the C.I.S.).

The scope of this paper is within the aim of integrating the knowledge and the accompanying modeling of the combustion in the description of the operation of motors. Therefore the models presented are those kept at a reasonable level of complexity. More detailed analyses are viewed as useful to validate the simplified approaches.

## COMPONENTS USED IN SOLID PROPELLANTS

Various types of the already existing propellants and their main characteristics and applications are summarized in Table 1. The newly developed ingredients considered, as compared to the existing ones, are found in Table 2 for oxidizers, Table 3 for polymers and Table 4 for plasticizers, along with an indication of improvements they should bring. The various ingredients, existing or under development, and the corresponding propellants will be reviewed in the following sections.

## IGNITION

The investigation of the ignition of solid propellants is of importance on two levels [1] :

- As such because it impacts on the starting of the motor. At high pressure, if the motor is closed by a rupture disk, the main ignition delay is essentially that necessary to reach the first decomposition of the active ingredient of the propellant. But for high heat fluxes and pressures around ambient, the transition delay to an established flame becomes important. The first ignition delay is shown in Fig. 1 for AP composite propellants and in Fig. 2 for double-base propellants (where  $\Gamma$  is the thermal effusivity). Results from Price [2] show clearly the importance of the establishment of the flame after first ignition, see Fig.3 ; this phenomenon is taken into account by Bizot [3] in his modeling. Ref. [4] should be looked upon on how to integrate such modeling in the description of the start-up of the motor.
- As a source of information for the condensed phase decomposition kinetics, as will be shown later.

Table 1

## Performance/Characteristics of Various Propellants

PROPELLANT	COMPOSITION (main ingredients)	$\rho_p$ g/cm <sup>3</sup>	$I_s(70/1)$ theor. (pract.)	APPLICATIONS/CHARACTERISTICS
Extruded DB	Nitrocellulose Nitroglycerin	$\leq 1.66$	$\leq 230$ s ( $\approx 10$ s)	- Anti-tank rockets and missiles - AS rockets - Some tactical missiles (SA) Minimum smoke
Powder cast DB	Nitrocellulose Nitroglycerin	$\leq 1.66$	$\leq 225$ ( $\approx 10$ s)	- Anti-tank missiles - Some tactical missiles (AS) Minimum smoke
AP composite	Ex : 88% AP - 12% HTPB	1.72	$\approx 250$ ( $\approx 10$ s)	- Some AS rockets - Some tactical missiles Reduced smoke (HCl-H <sub>2</sub> O)
AP composite with aluminum	Ex : 68 AP - 20 al. - 12 CTPB	$\approx 1.82$	265 ( $\approx 20$ s)	- AA tactical missiles - Anti-ship missiles (booster) - Tactical ballistic missiles - Strategic ballistic missiles - Apogee motors - Boosters for space launchers (Titan III, IV, Space Shuttle, Ariane V...) Smoky (Al <sub>2</sub> O <sub>3</sub> )
HMX (RDX) composite	HMX or RDX - XLDB binder	$< 1.75$	$< 255$ ( $\approx 15$ s)	- Anti-ship missiles (cruise) - SA missiles Minimum smoke (without AP)
HMX composite with aluminum	XLDB binder	1.87	273	- Strategic ballistic missiles (upper stages) (Trident, MX...) Smoky (Al <sub>2</sub> O <sub>3</sub> )

Sources : Air et Cosmos n° 1000, may 1984. Annales des Mines, jan-feb. 1986.  
Aéronautique et Astronautique, n° 138, 1989.

**Table 2**  
Typical New Propellant Oxidizers


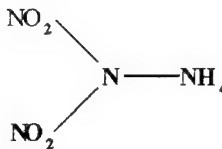
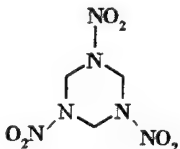
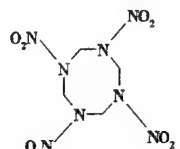
Structure	Characterization	Applications
<p>HNTW (CL20) caged nitramine</p>  <p>● N-NO<sub>2</sub></p>	<p>d = 2,04 ΔHf = + 225 cal/g</p>	<p>- impulsive and minimum smoke propellant</p>
<p>ADN</p> 	<p>d = 1,80 ΔHf = - 290 cal/g</p>	<p>- low vulnerability (?) - demilitarization - propellants for space launchers without HCl</p>
Comparison		
<p>RDX</p>  <p>HMX</p> 	<p>d = 1,91 ΔHf = + 68 cal/g</p>	<p>- for tactical missiles - for strategic missiles (USA)</p>
<p>Ammonium perchlorate NH<sub>4</sub>ClO<sub>4</sub></p>	<p>d = 1,95 ΔHf = - 600 cal/g</p>	<p>- for strategic missiles, launchers and boost stages of tactical missiles</p>

Table 3

## Typical New Propellant Polymers

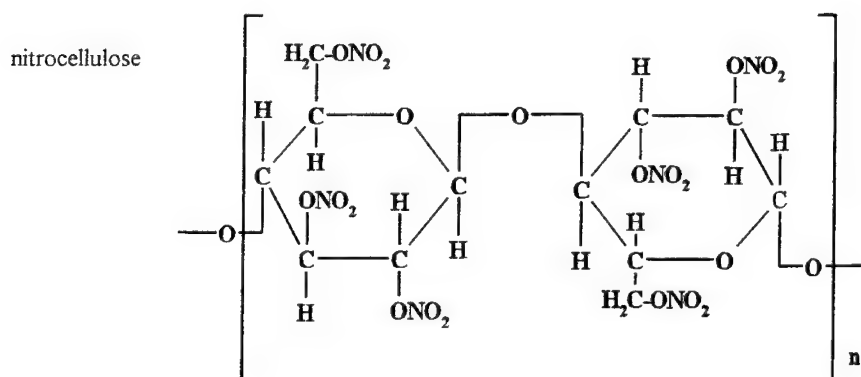
Structure	Characterization	Applications
<p>GAP</p> $\text{H} - \left[ \text{OCH}_2\text{CH} \begin{array}{c}   \\ \text{CH}_2 \\   \\ \text{N}_3 \end{array} \right]_n - \text{OH}$	<p><math>d = 1,28</math>  <math>\Delta H_f = + 280 \text{ cal/g}</math></p>	<p>- performance  - low vulnerability  - burning rate</p>
<p><math>(\text{BAMO})_n - (\text{AMMO})_m - (\text{BAMO})_n</math></p> <p>BAMO</p> $\text{HO} - \left[ \text{CH}_2 - \text{C} \begin{array}{c}   \\ \text{CH}_2\text{N}_3 \\   \\ \text{CH}_2\text{N}_3 \end{array} - \text{CH}_2 - \text{O} \right]_n - \text{H}$ <p>AMMO</p> $\text{HO} - \left[ \text{CH}_2 - \text{C} \begin{array}{c}   \\ \text{CH}_3 \\   \\ \text{CH}_2\text{N}_3 \end{array} - \text{CH}_2 - \text{O} \right]_n - \text{H}$	<p>thermoplastic elastomer  fusion <math>\leq 100^\circ\text{C}</math></p>	<p>- demilitarization  - continuous manufacturing</p>
Comparison		
Polybutadiene (HTPB)	<p><math>d = 0,90</math>  <math>\Delta H_f = +5 \text{ cal/g}</math></p>	<p>- for launchers, strategic  and tactical missiles</p>

Table 4

Typical New Propellant Plasticizers

Structure	Characterization	Applications
<p>GAPA</p> $\left[ \begin{array}{c} \text{N}_3\text{CH}_2\text{CHO} \\   \\ \text{CH}_2 \\   \\ \text{N}_3 \end{array} \right]_n \text{CH}_2\text{-CH}_2\text{-N}_3$	<p><math>d = 1,27</math>  <math>H_f = +537 \text{ cal/g}</math></p>	<p>- burning rate  - low vulnerability</p>
Comparison		
<p>NGL</p> $\text{O}_2\text{NO-CH}_2\text{-CH(ONO}_2\text{)-CH}_2\text{-ONO}_2$	<p><math>d = 1,60</math>  <math>H_f = -405 \text{ cal/g}</math></p>	<p>- plasticizer for tactical  and strategic missiles</p>

Reminder: Double-base propellants





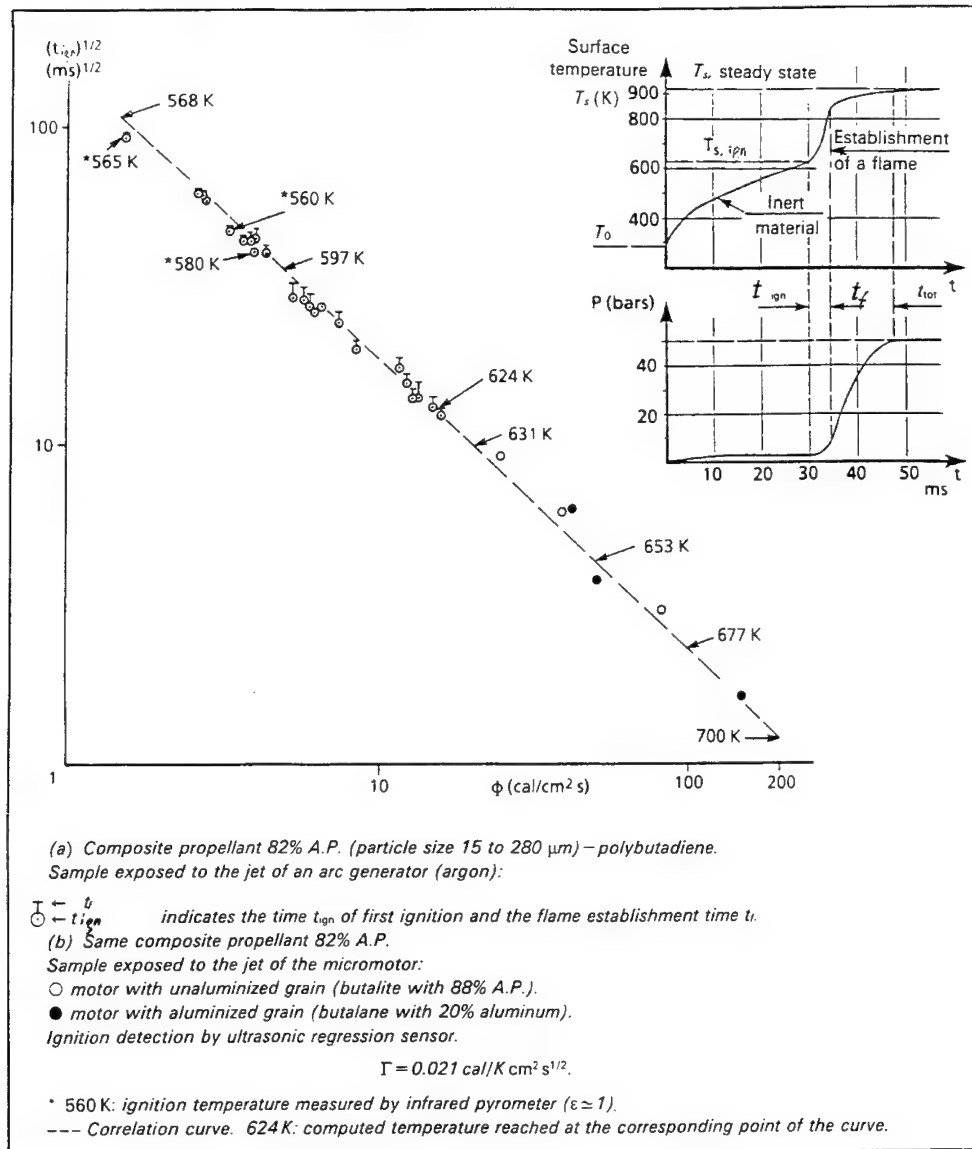
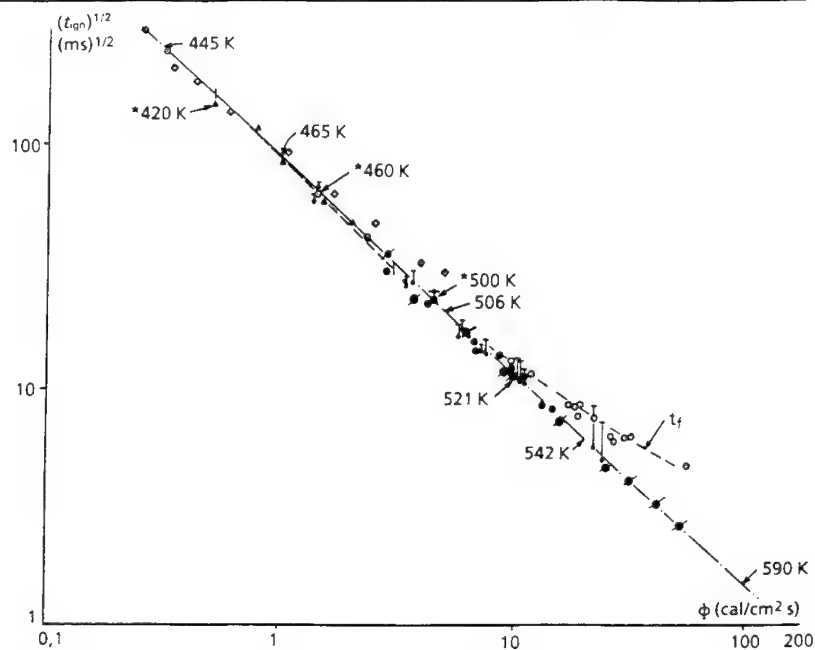


Figure 1. Ammonium perchlorate composite propellants



Results of Suh  $t_{\text{ign}} \blacktriangle$  | - - - - - | computed curve

Radiation flux  $0.5 < \Phi_0 < 2 \text{ cal/cm}^2 \text{ s}$ .

Pressure  $7 \times 10^{-2} \text{ atm}$ ; inert ambient gas.

Propellant  $M_2$  (1,060 cal/g); 0.3 % graphite;  $\beta = 250 \text{ cm}^{-1}$  (absorption coefficient).

Results given by the author  $E_p = 40 \times 10^3 \text{ cal/mole K}$ ;  $A = 10^{17} \cdot \text{s}^{-1}$ ;  $Q_s = 60 \text{ cal/g}$ .

\* 420 K: ignition temperature measured by thermocouple.

Results of Price  $t_{\text{ign}} \diamond$

Radiation flux  $0.25 < \Phi_0 < 5 \text{ cal/cm}^2 \text{ s}$ .

Pressure 1.05 atm; gas: ambient air.

J.P.N. propellant (1,230 cal/g). Nonopacified.

No values for  $E_p$  and  $A$  (influence of the absorption in depth beyond  $2 \text{ cal/cm}^2 \text{ s}$  probably too high).

Results of Niioaka  $\bigcirc$  —  $\bigcirc$  Average of the results.

Convection flux  $0.3 < \Phi_0 < 2.3 \text{ cal/cm}^2 \text{ s}$ .

Pressure 1 atm. Jet of air, helium or air + oxygen.

Cold propellant (753 cal/g).

Results given by the author  $E_p = 30,000 \text{ cal/mole K}$ ;  $\rho_p A Q_s = 8 \cdot 10^{13} \text{ cal/cm}^2 \text{ s}$ .

\* 460 K. measured by thermocouple

ONERA results  $\bullet$  —  $\bullet$   $t_{\text{ign}}$  pyrometer  $\bigcirc$  ultrasound.

Convection flux  $1.3 < \Phi_0 < 24 \text{ cal/cm}^2 \text{ s}$  and 60 by ultrasound.

Pressure  $\approx 1 \text{ atm}$ . Argon jet.

Hot propellant (1,100 cal/g). \* 500 K Measured ignition temperature

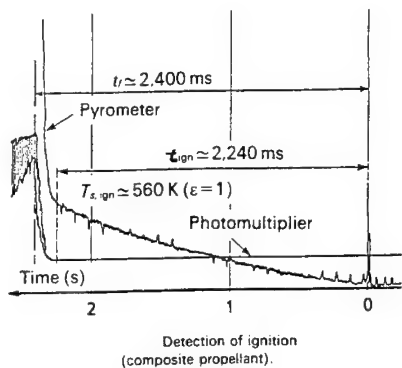
- - - Correlation curve. 521 K: computed temperature reached on the corresponding point of the curve.

$$\Gamma = 0.018 \text{ cal/K cm}^2 \text{ s}^{1/2}.$$

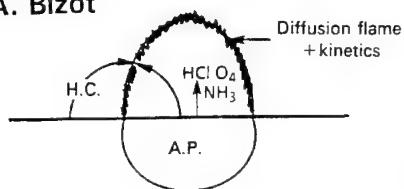
ENSTA/ONERA Results

$\bullet$   $\text{CO}_2$  laser, 1 bar, propellant 1,100 cal/g.

Figure 2. Double-base homogeneous propellants

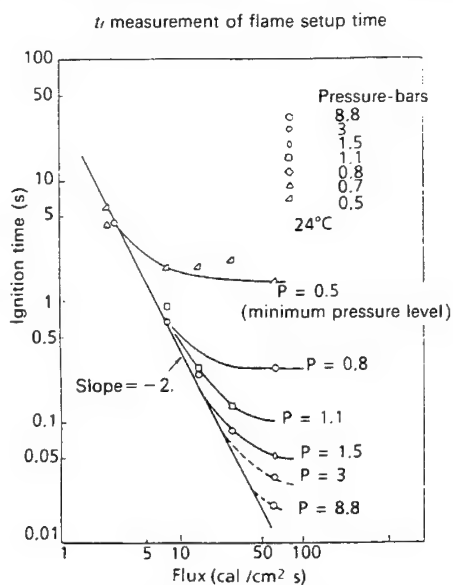


A. Bizot



$$\Phi_{\text{all}} = H_c (T_g - T_f)$$

$$H_c = 0.07 \text{ cal/cm}^2\text{/s/K}$$



A.P. composite propellant.

Influence of pressure on flame setup time.

E. W. Price

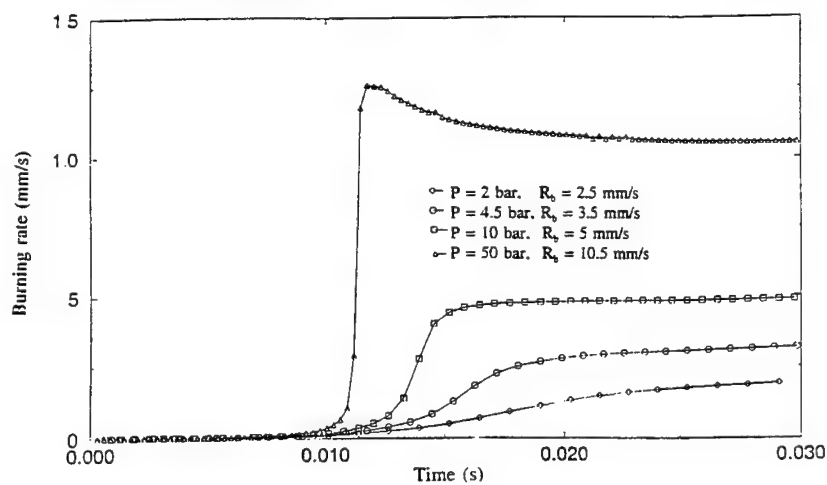


Figure 3. Transition to established flame

## CONDENSED PHASE PROCESS

The combustion of solid propellants results from the coupling between the condensed phase process and the gas flame heat flux reaching the surface.

The principles of the modeling of the condensed phase behavior are indicated in Fig. 4, as described in early work [5]. An overall vision can be reached, in particular for DB propellants, HMX, ADN and for polybutadiene and GAP binders, that the kinetics of the condensed phase decomposition under combustion conditions remains the same, all the way from that under DSC or thermogravimetry conditions, through ignition conditions. This can be found in Fig. 5 for polybutadiene, Fig. 6 for GAP, Fig. 7 for DB propellants [6] (Brewster has also adopted this viewpoint [7]). Finally in Figs. 8 and 9 it can be seen for HMX that the kinetics obtained under DSC conditions, confirmed for ignition, correlate very well the results obtained under combustion.

Recently Wight [8] has carried out an investigation of the condensed phase decomposition of ammonium dinitramide, ADN, using thermogravimetric techniques for low heating rates (at temperatures from 150 to 250°C) and thin film ( $< 1 \mu\text{m}$ ) laser pyrolysis for high heating rates (at temperatures around 450°C). The conclusion is reached that the nature of the gases evolved from the condensed phase,  $\text{NH}_3$ ,  $\text{H}_2\text{O}$ ,  $\text{NO}$ ,  $\text{N}_2\text{O}$ ,  $\text{NO}_2$ ,  $\text{HONO}$  and  $\text{HNO}_3$ , and the kinetics, with an activation energy of  $200 \pm 20$  kJ/mole (about 48 kcal/mole) associated with the breaking of the N-N bond, should remain the same over the wide temperature range and heating rates values (from  $10^{-2}$  to  $10^7$  °C/s !).

These results are one more indication that the initial step in the thermal decomposition of ingredients of propellants and the associated kinetic parameters can be the same at low temperatures and at high regression rates typical of combustion. This is far from obvious a priori and has to be proved for each ingredient considered. A well known counter-example is that of ammonium perchlorate, which undergoes low and high temperature surface sublimation- dissociation and, under combustion, which sustains a condensed phase decomposition in a superficial liquid layer.

Detailed investigations of the decomposition steps can be found for HMX, Brill [9], as well as for nitrate esters, Melius [10].

It has to be mentioned that the condensed phase process is of direct impact for the understanding and modeling of the response of solid propellants to pressure oscillations, one can see as an example the work of Brewster [7].

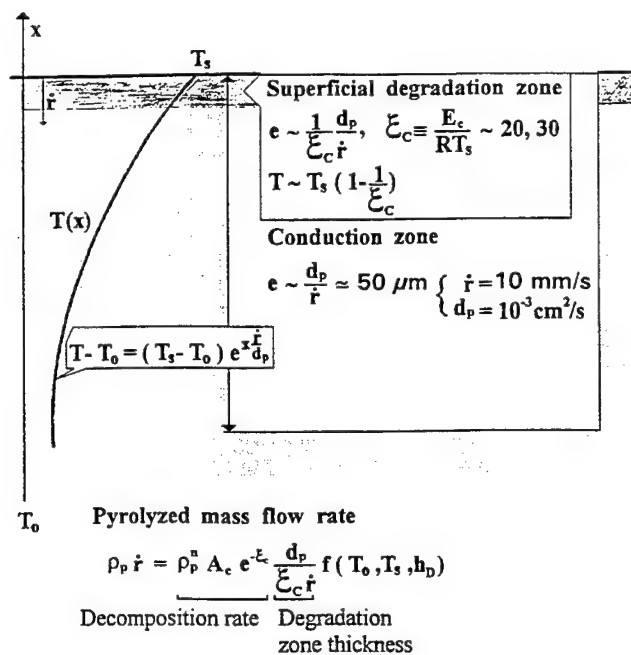


Figure 4. Principle of the modeling of the condensed phase behavior

$$E_c = 48.6 \text{ kcal/mole} \quad (T. \text{ Brill} \approx 46)$$

$$A_c = 2.63 \cdot 10^{12} \text{ s}^{-1}$$

$$d_p = 1 \cdot 10^{-3} \text{ cm}^2/\text{s} \quad h_D = 450 \text{ cal/g}$$

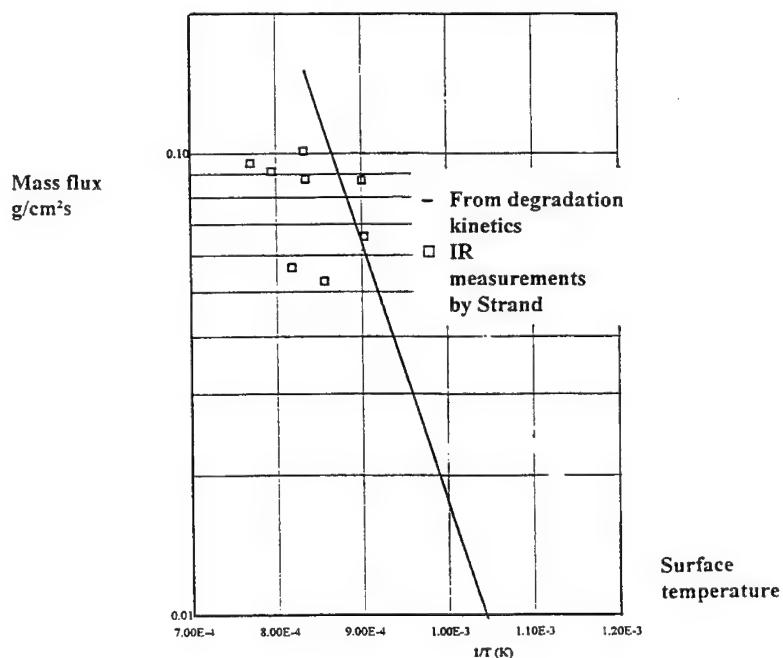
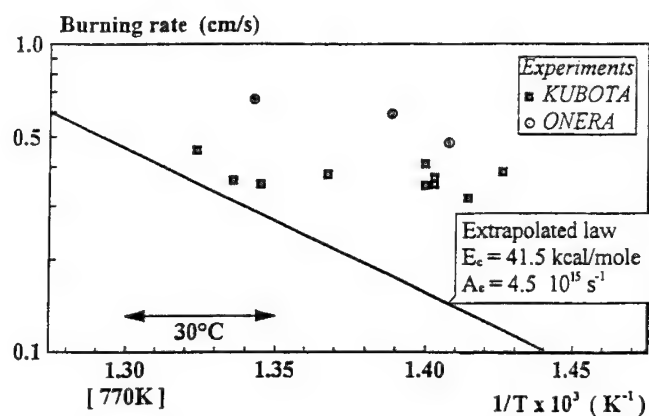


Figure 5. Pyrolysis law for HTPB



T. Brill  $39.4 \pm 1.1 \text{ kcal/mole}$   
(idem for AMMO BAMO 1991)

Figure 6. Correlation between burning rate and surface temperature for GAP

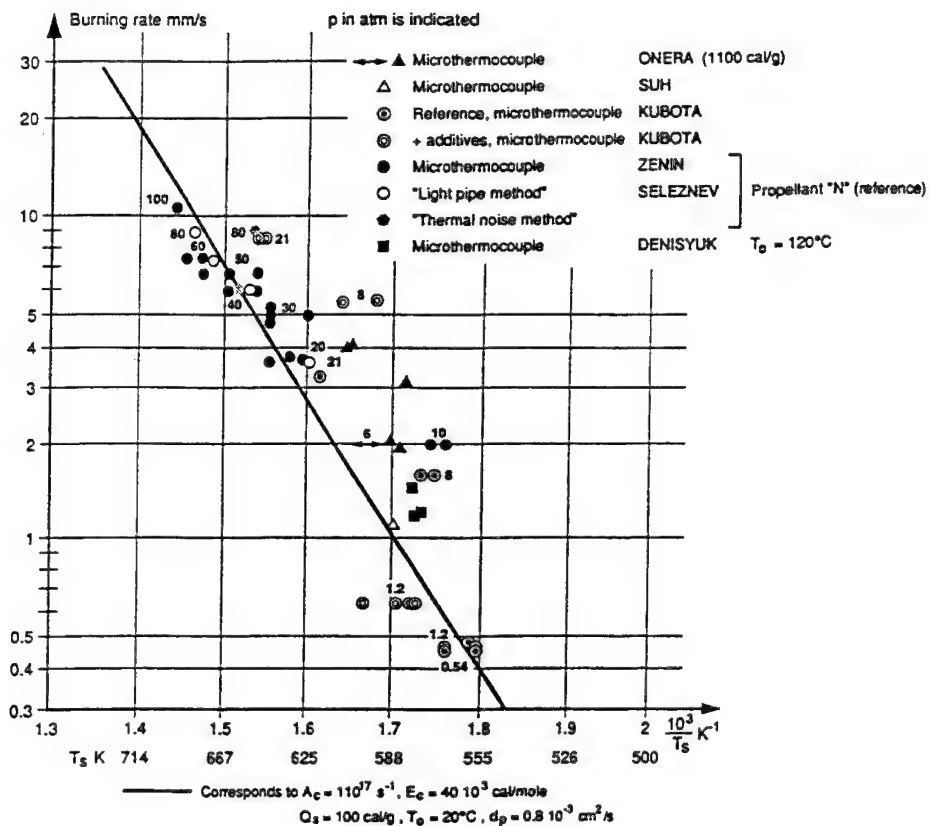


Figure 7. Pyrolysis law for double - base propellants

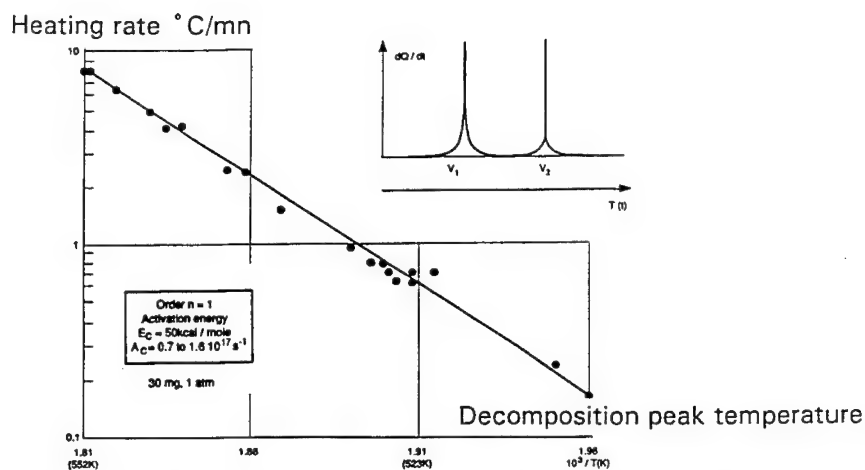


Figure 8a. Differential thermal analysis of HMX decomposition

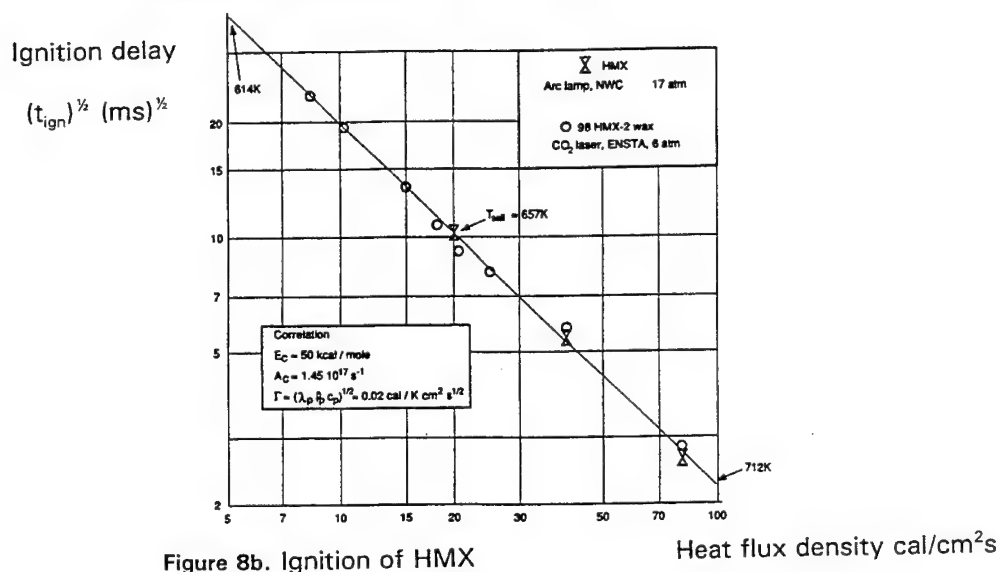


Figure 8b. Ignition of HMX

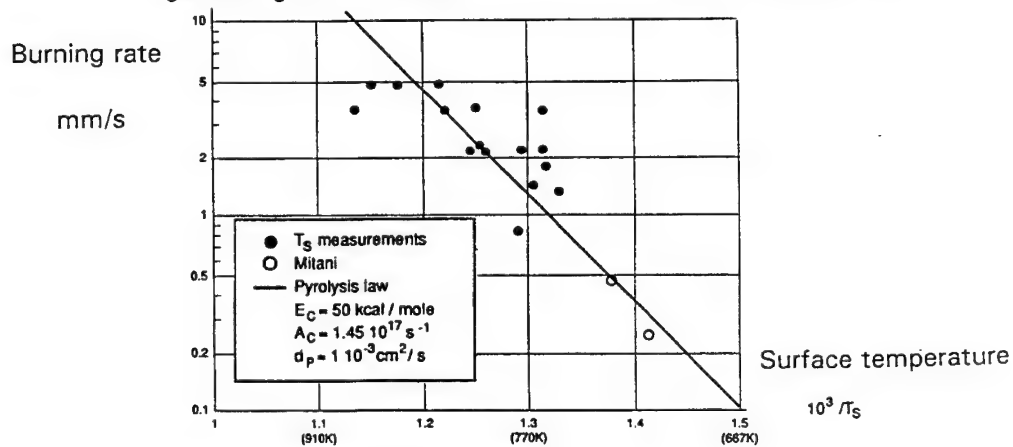


Figure 9. Pyrolysis law for HMX

## COMBUSTION OF PREMIXED PROPELLANTS OR MONOPROPELLANTS

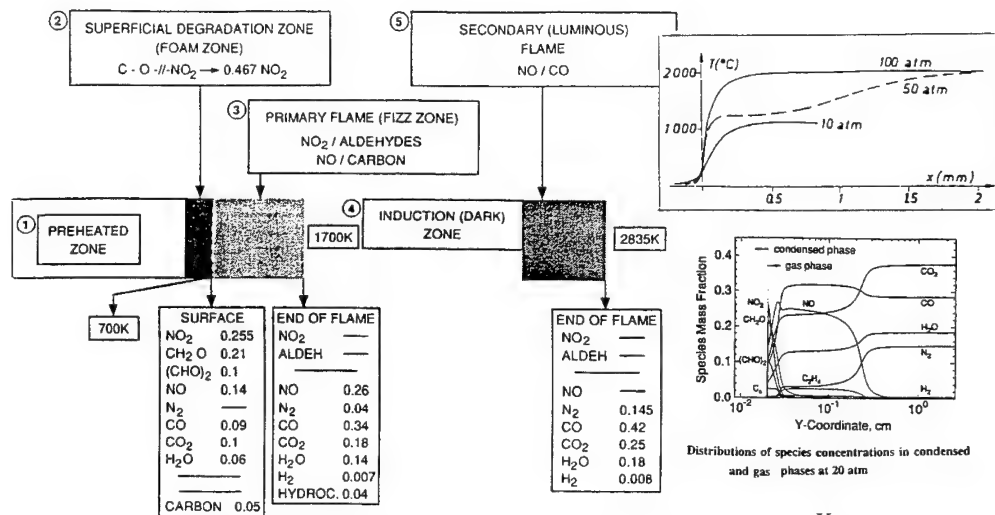
Double base propellants undergo a combustion governed by premixed primary and secondary flames, see Fig. 10. The nature of the gases involved has been established from sampling and mass spectrometry analysis [6]. Yang et al [11], in complete osmosis with the results of ONERA, have produced a model for the staged flames of these propellants (Fig. 10), to be then used in a description of the response to pressure oscillations. It is well known that the staged flame structure is such that adequate additives, salts of lead, copper, bismuth..., will enhance the secondary flame reactions, involving NO, close to the surface, creating super-rate effects and (sought after for operating stability reasons) plateau effects (corresponding to the secondary flame coming close to the surface anyway as pressure increases).

HMX has a behavior somewhat similar to that of a DB propellant, due to the fact that it creates gases which can produce primary and secondary flames, see Fig. 11. In this figure, a very simplified model, based on overall kinetics, shows that the secondary flame dominates the burning rate as soon as 20 to 30 atm (for DB propellants this occurs above 100 atm), in such a way that there is no possibility of creating a super-rate effect (and the accompanying plateau). A much more elaborate model, see Fig. 12, has been presented by Yang et al [12] for RDX. This model takes into account the two condensed phase decomposition paths suggested by Brill, but also incorporates a large amount of evaporation of the RDX (it has to be noted that in the case of HMX, referring to Figs. 8 and 9, the conclusion is reached that the condensed phase process under combustion corresponds to complete decomposition as observed under DSC conditions).

An RDX model has also been presented by Beckstead [13], by taking into account, as well as Yang, the detailed gas phase kinetics (more than 200 reactions) of Yetter [14], see also Branch [15] (both taking a large number of informations from Melius).

Results for the combustion of the caged nitramine HNIW, see Table 2, are presented in Fig. 13. It is seen that its behavior is similar to that of HMX (with a higher burning rate due to the higher energetic content), with possibly at pressure below about 20 atm a staged flame leading to a lesser pressure exponent. In any event, the observation that the secondary flame comes close to the surface above this pressure should exclude the possibility of creating super-rates in HNIW; such impossibility is also the case for HMX.





Figures for an 1100 cal/g propellant. Surface and primary flame (at 11 atm) mass fractions from gas analysis

Figure 10. Various zones in the combustion of a double-base propellant

NO <sub>2</sub>	NO	N <sub>2</sub> O	N <sub>2</sub>	CO <sub>2</sub>	CO	H <sub>2</sub> O	H <sub>2</sub>	HCHO	HCN
22.2	17.5	19.1	3	1.4	1.6	3.7	0.1	14.1	16.8

59 %

31 %

Gases evolved from the surface of HMX. Mass fractions

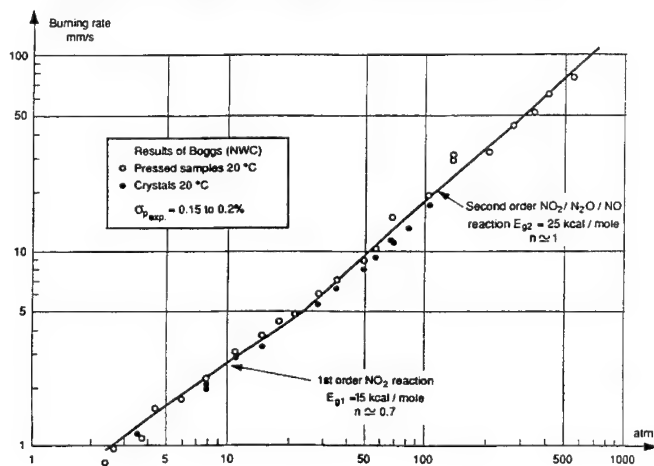
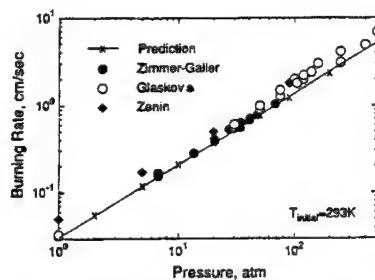
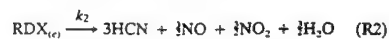
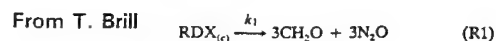
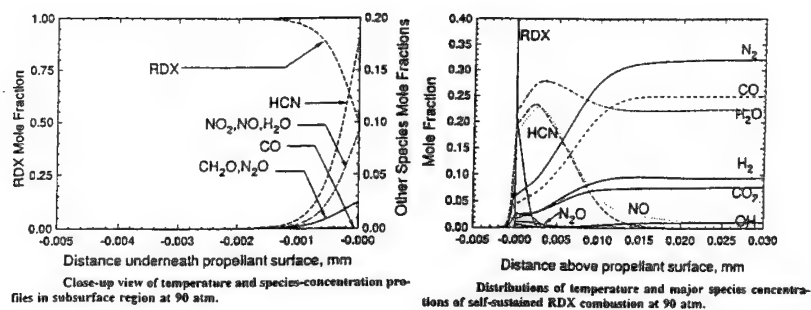


Figure 11. Burning rate of HMX



Effect of pressure on strand burning rate of RDX monopropellant.

Figure 12. Modeling of RDX combustion (V. Yang)

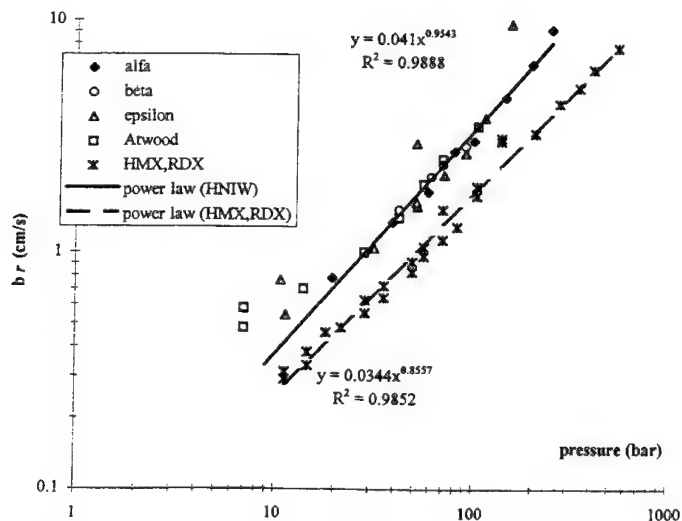


Figure 13. HNIW burning rate

## COMBUSTION OF COMPOSITE PROPELLANTS

Almost all propellants are composites of oxidizer particles with either an inert binder, such as polybutadiene, or an active binder including some nitric ester, see Fig. 14. The description of such AP-inert binder composite propellants was carried out early by Beckstead et al [16]. In this work a surface average is carried on the AP particles and the surrounding polybutadiene binder. This model was extended by Cohen [17]. Later, Beckstead [18] considering HMX with an active binder, taking into account the fact that both ingredients sustain self combustion, introduced the idea of the overall regression rate of the propellant resulting from the sequential burning of the two components. Finally, Blomshield considered a mix of surface average and sequential burning for AP-HMX-inert binder propellants [19].

A unified approach is proposed, based on the sequential burning viewpoint, for all propellants, see Fig. 14. In the case of AP-inert binder composites, a strong diffusion flame exists between excess  $O_2$  and hydrocarbons from the binder. In the case of nitramines with active binders not much diffusion flame can be envisioned. However the oxidizer reaching the surface, more or less at the binder surface temperature, needs to transition to its full combustion temperature (see [6] for the description of this delay) (in the case of AP the binder temperature is higher than that of the oxidizer and no transition delay should occur).

The sequential burning approach is first applied to AP-inert binder propellants, necessitating first a description of AP alone, refer to Figs. 15 and 16 (see also [6]). In particular in Fig. 16 the idea is expressed that the lower deflagration limit is due to the reaching of a surface temperature below the liquefaction temperature of 830 K. The work of Beckstead [20] on a detailed model of AP combustion should also be consulted (it includes a kinetic scheme for the gas phase reactions of about 100 steps).

In Fig. 17 the various values involved are indicated. In particular, it is considered that the AP premixed flame is very close to the surface and that there is no need to take into account a primary peripheral flame between the sublimation product  $HClO_4$  and hydrocarbons. Only the final flame  $O_2/HC$ , controlled by diffusion and kinetics, is considered. Results of such a model as compared to experimental measurements show a good agreement, as found in Fig. 18 (A nuance is added, see [6], that diffusion in the flame centered on the AP particle is enhanced at high pressures by some turbulent component. This allows to depict an increase in the pressure exponent of the burning rate above about 100 atm. However at higher pressures, above 300 atm, an extra break in the slope cannot yet be explained). In this figure the role of the additive is described by the hypothesis that the residue it leaves on the surface will act as a flame holder, bringing the diffusion flame closer to the surface.

The case of HMX-energetic binder compositions is displayed in Fig. 19. The sequential burning approach is again applied by taking into account the, experimental, burning rates of HMX and of the active binder, with, Fig. 14, the transition delay for HMX to reach its established combustion surface temperature. A good match with the measurements of the propellant burning rate is obtained, indicating that the physical idea of the sequential burning seems reasonable. An equally good agreement, Fig. 20, is seen for an HNIW -active, GAP+nitric ester, binder composition. For these types of propellants it has to be mentioned that their burning rates are very sensitive to pressure. As was mentioned earlier, there is not much hope to find additives that will act upon the oxidizer (the staged flames collapse into one at low pressure), the main action being with lead/copper salts creating semi-plateau effects in the binder.

Quite frequently aluminum is added as fuel, allowing an increase in temperature of about 1000 K. In Fig. 21, the first event of agglomeration at the surface is depicted [21]. About 40 % of the original aluminum is found to agglomerate into globules of about 125  $\mu\text{m}$ , which after burning will leave oxide particles of about 50  $\mu\text{m}$ , although in small amount. Indications on the combustion of the aluminum globules are found in Fig. 22, with a strong influence of the globule size and of the concentration of oxidizing species (from [22]) and a moderate influence of the pressure (from the early work of Davis), as reflected in the proposed correlation formula indicated. The theoretical description of the combustion process, by Beckstead [23] or Marion [24] (see Fig. 23), based on a droplet model, fails to represent the effect of the pressure. The added hypothesis of oxide diffusion back to the surface so as to increase the cap makes the combustion time even longer and does not seem to have to be taken into account. It is believed that the large,  $\approx 50 \mu\text{m}$ , oxide particles, see Fig. 21, result from the caps on the agglomerated aluminum particles and that the alumina in the cap is formed during the fairly long agglomeration process on the surface (rather than during combustion of the globule).

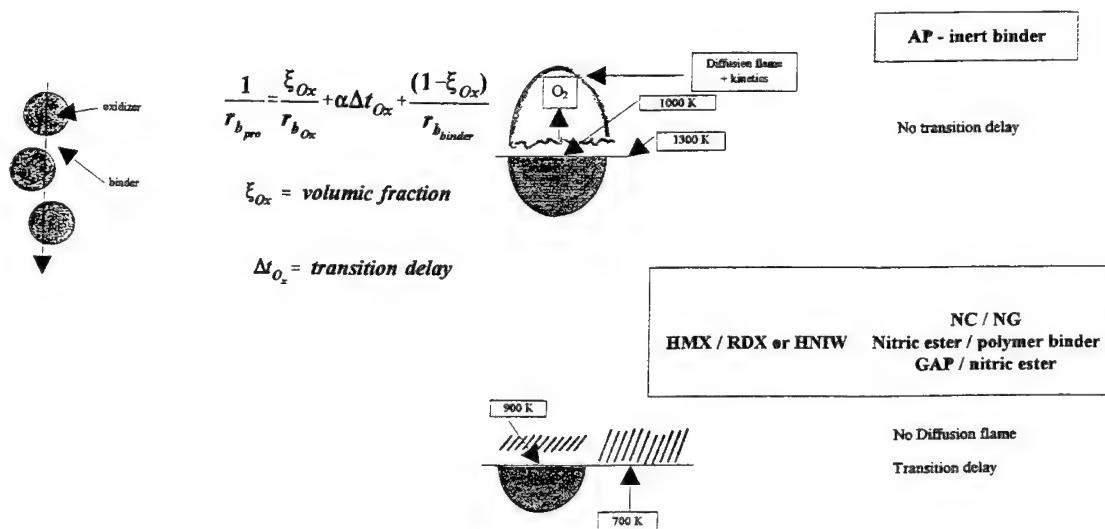
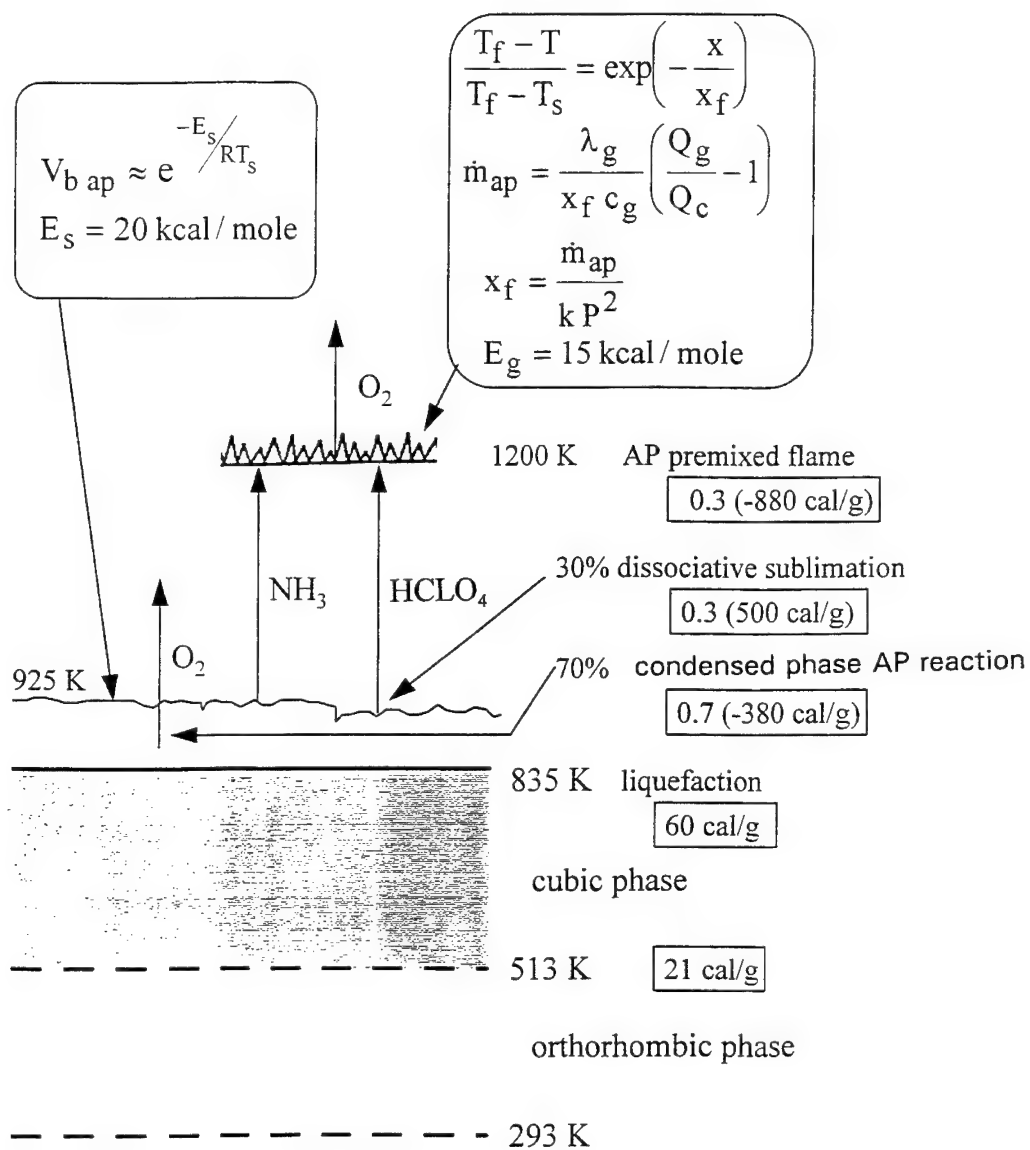
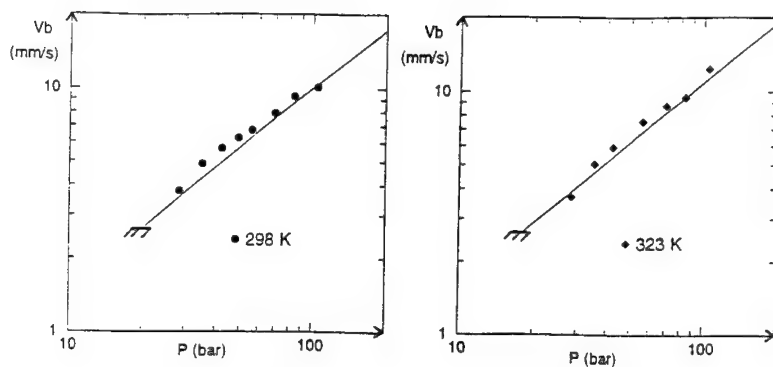


Figure 14. Unified approach to composite propellant modeling



In part from C.Guirao and F.A.Williams  
At 100 bar ~ 10 mm/s

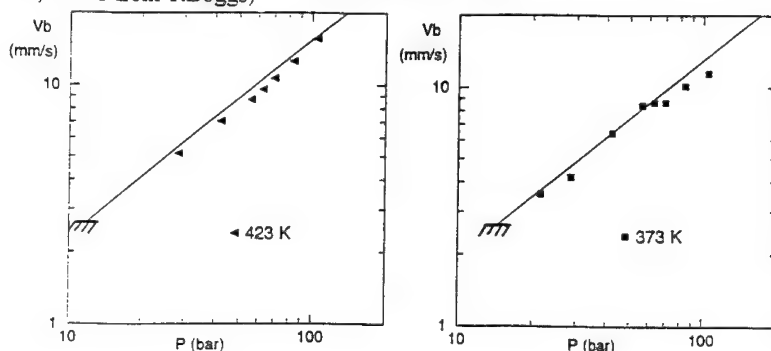
Figure 15. AP combustion model



$P_{crit}=20.2$  bar

$P_{crit}=18.1$  bar

(Exp. at 25, 50, 100, 150°C from T.Boggs)  $V_b$  critical=2.65 mm/s



$P_{crit}=11.9$  bar

$P_{crit}=14.6$  bar

Figure 16. AP burning rate versus  $T_0$

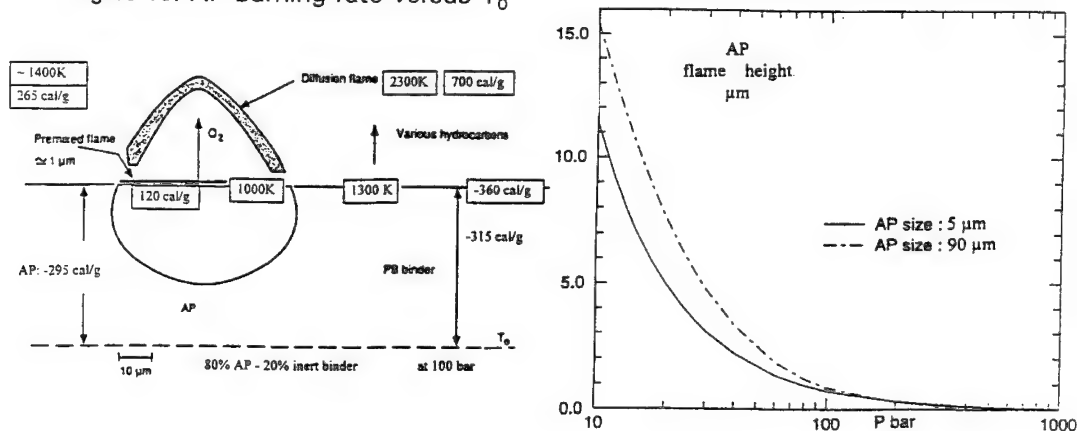


Figure 17. AP composite propellant flame structure

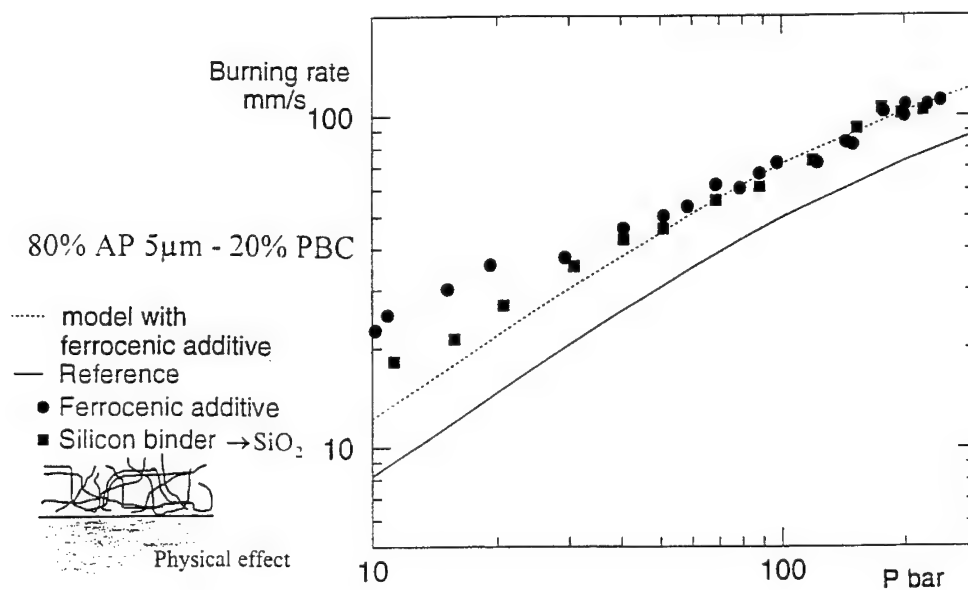
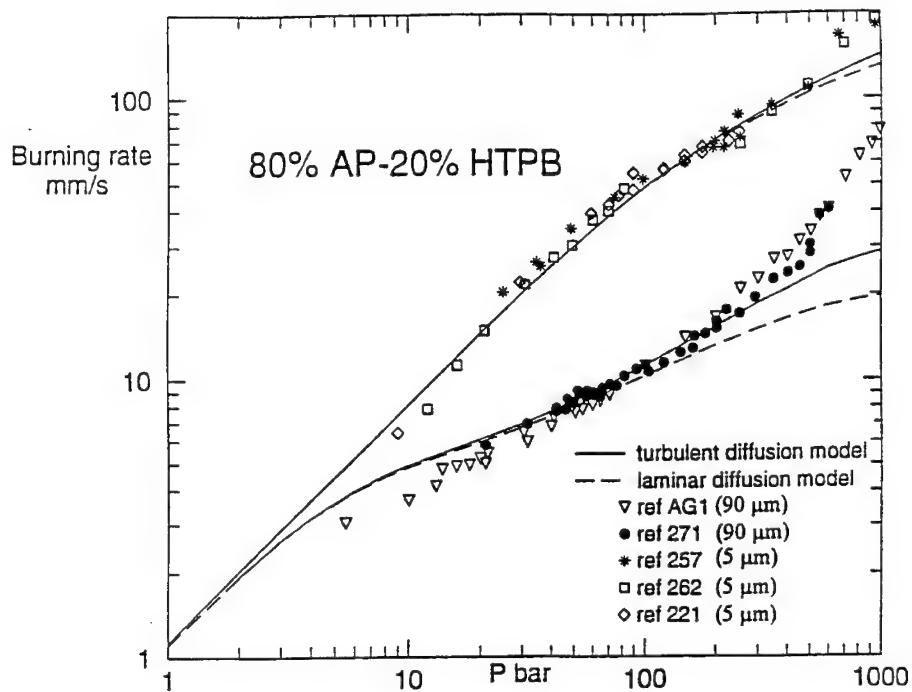
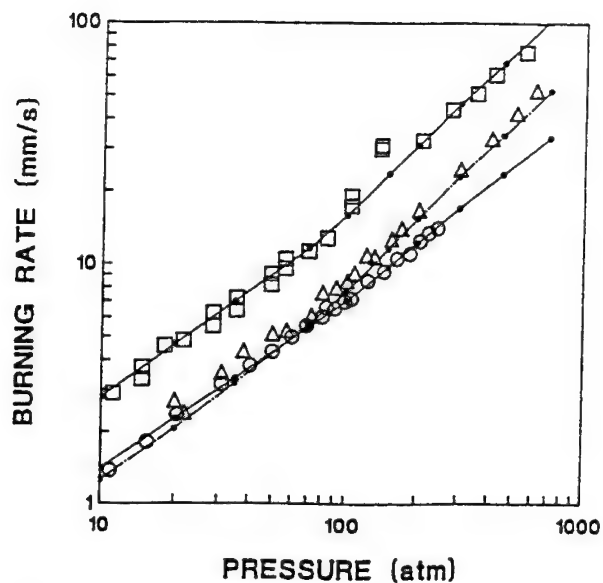


Figure 18. Burning rate of AP composite propellants



- HMX
- ENERGETIC BINDER (Heat of explosion=850 cal/g)
- △ 75% HMX [40 $\mu$ m(50%)+4.7 $\mu$ m(50%)] + 25% BINDER
- Computed burning rate

Figure 19. Experimental and computed burning rate of a nitramine based propellant

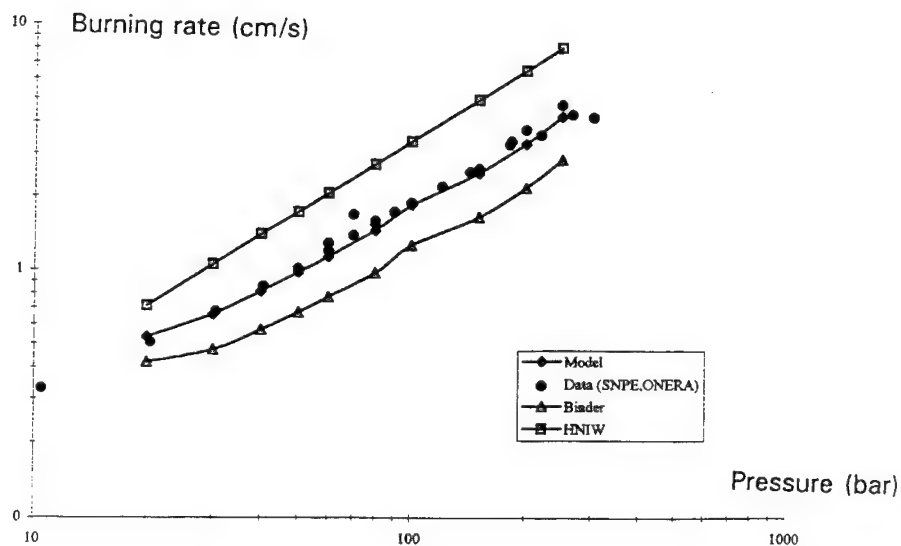


Figure 20. Burning rate of an HNIW propellant (60% HNIW (100  $\mu$ m) - GAP + nitric ester)



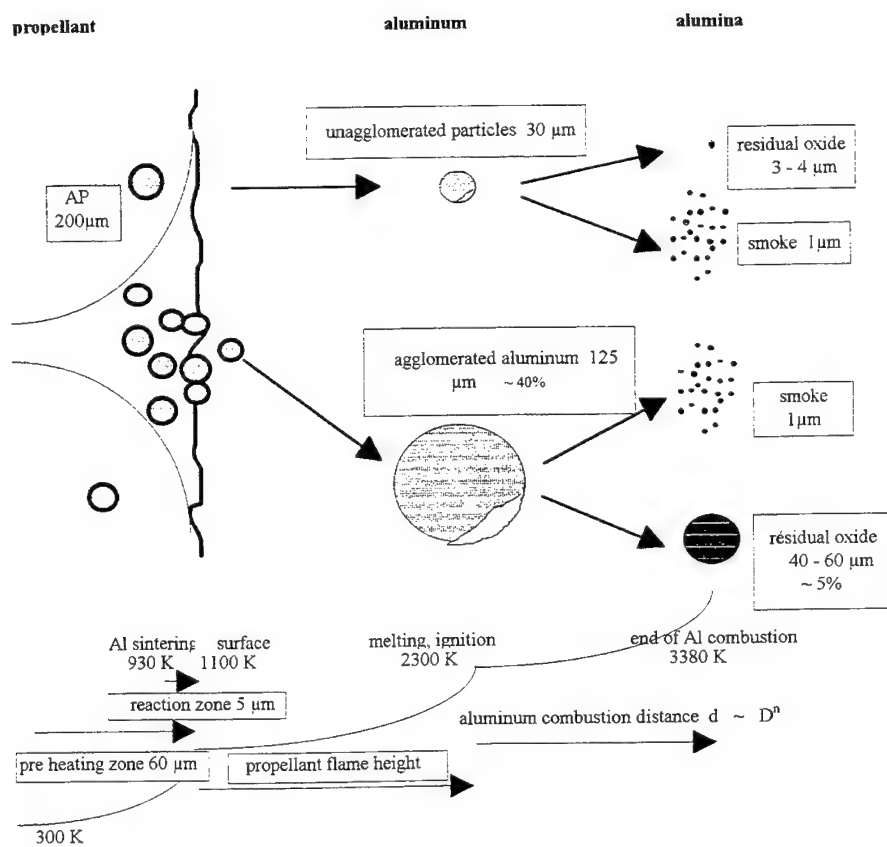
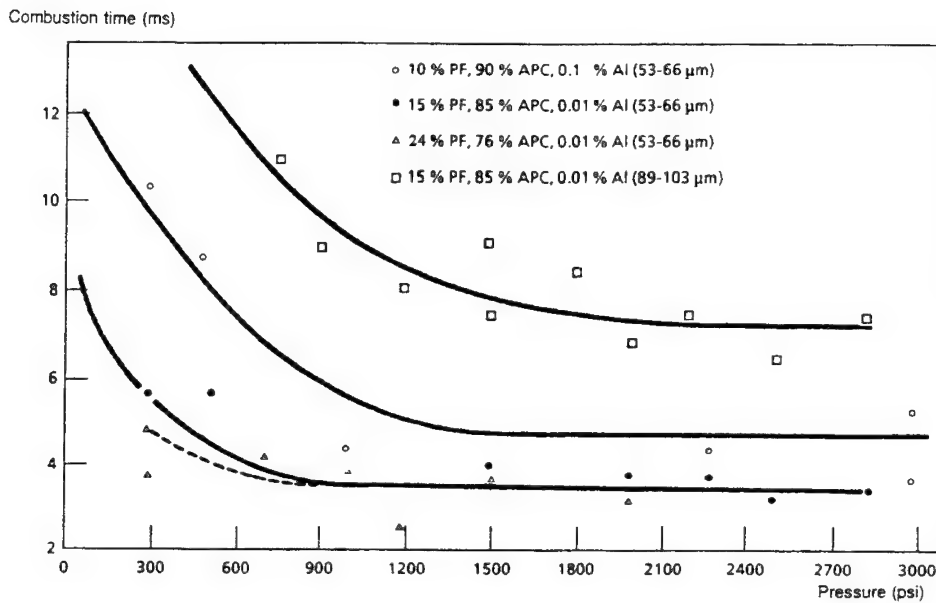


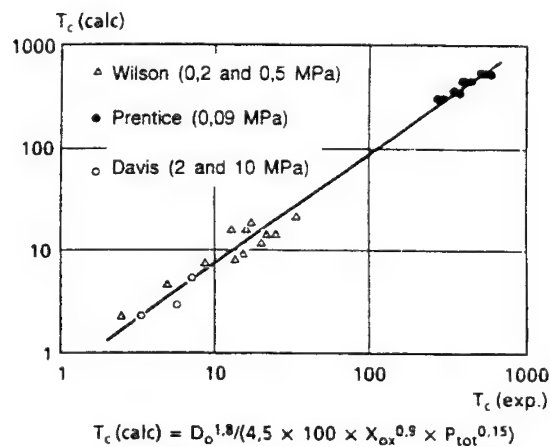
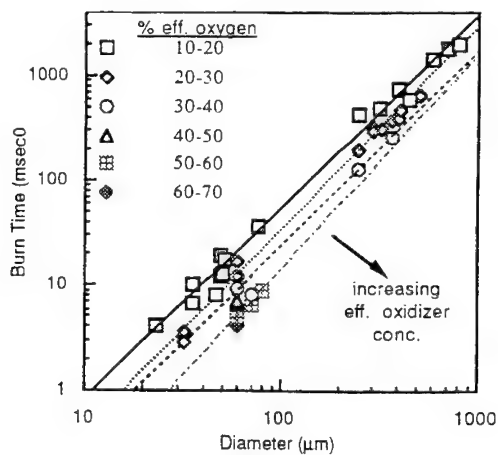
Figure 21. Scheme for aluminum agglomeration and combustion (J. Duterque)

Davis (1963), Olsen and Beckstead (1995)



Davis' results.

Influence of pressure ( $P < 90$  bar) and initial size ( $d_0 = 53-103 \mu\text{m}$ )



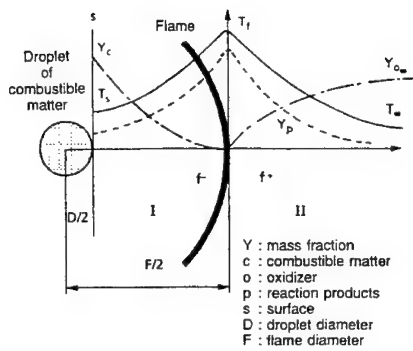
$$T_c(\text{calc}) = D_0^{1.8} / (4.5 \times 100 \times X_{\text{ox}}^{0.9} \times P_{\text{tot}}^{0.15})$$

Correlation of experimental results with different pressures.

Figure 22. Aluminum particles combustion in a propellant or in a burner

No pressure effect

### $D^2$ law



$$D^2 = D_0^2 - Kt$$

$$\frac{d}{dt}(D^2) = -\frac{\lambda_g}{\rho_c C_p} 8Ln(1+B) = -K$$

$$B = \frac{1}{H_v} [C_p(T_s - T_\infty) + Q_f \frac{Y_{O_2}}{r_{st}}]$$

$$Q_f = h^0_{cg} + r_{st} h^0_{og} - h^0_p (1 + r_{st})$$

### Model with retrocondensation of aluminum (Brooks and Beckstead, Marion et al.)

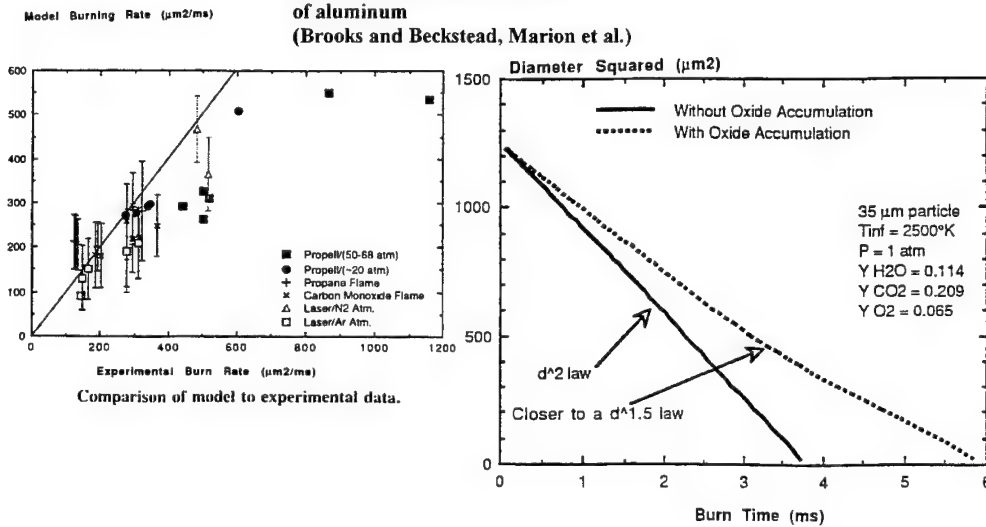


Figure 23. Aluminum combustion modeling

## THE ULTRASONIC MEASUREMENT OF THE BURNING RATE

The ultra-sonic technique developed at ONERA allows detailed measurements of the burning rate, see Fig. 24 [25]. This technique has been transferred at Penn State with Kuo and Micci and at University of Alabama with Frederick. It has been employed independently at TNO for ablatable fuels, as well as at Thiokol in fairly large hybrid motors. This technique replaces the strand burner and is particularly useful in erosive burning work since it allows local, instantaneous measurements in a motor.

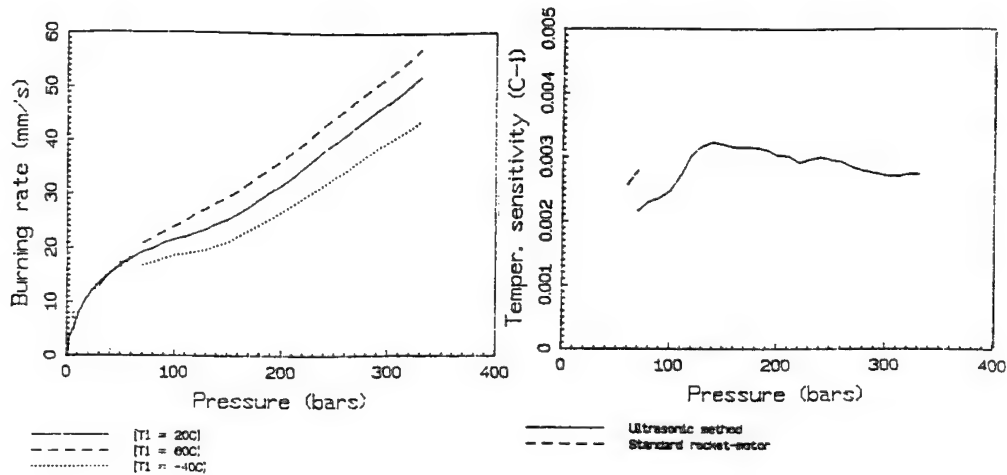
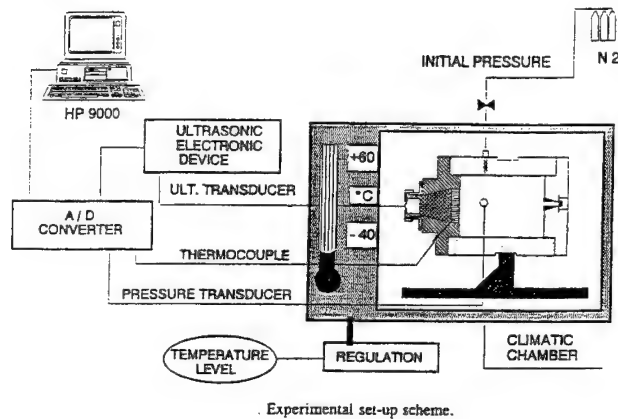


Figure 24. Determination of solid propellant burning rate sensitivity to the initial temperature by the ultrasonic method (F. Cauty, J.C. Demarais, Ch. Eradès)

## RESPONSE TO EROSIVE BURNING

Experiments and modeling of the erosive burning of solid propellants have been carried out by King [26], Kuo [27] and at ONERA [28,29] for double-base and composite propellants. It has been established quite convincingly that the mechanism is related to the penetration of turbulence from the external flow into the flame height of the propellant, with an enhancement of the flux from flame to surface and thus of the burning rate. The modelisation of this mechanism (requiring the treatment with a Couette approach of the zone close to the surface, containing the flame, and the matching with the external flow) results in an evaluation of the erosive burning rate in good agreement with the measurements (in particular with the ultra-sonic technique) [29]. In Fig. 25, as a summary of the approach of ONERA, the separation between non erosive and erosive domains as a function of the propellant base burning rate is displayed, showing that the specific mass flow rate, the burning rate (and the scale) are the main parameters in the erosive burning problem. The model adopted is amenable to being incorporated in a description of a motor operation.

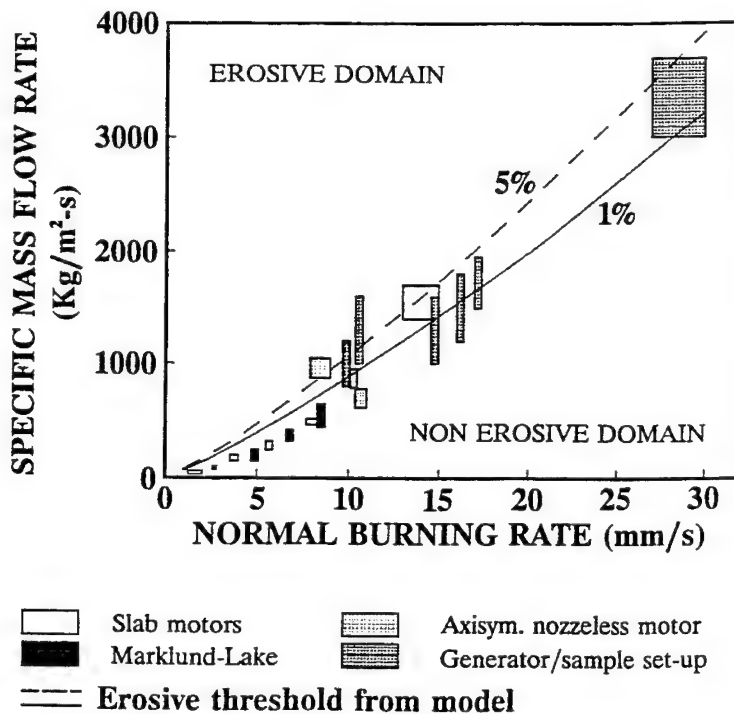


Figure 25. Erosive mass flow rate threshold as from the model and various small scale experiments

## RESPONSE TO PRESSURE AND VELOCITY OSCILLATIONS

The assessment of the stability of a motor requires the knowledge of the response of the propellant to pressure, and possibly velocity, oscillations.

Various techniques are used to measure the response to pressure oscillations : T-burner, modulated ejection motor with an indirect measurement or a direct measurement with the microwave or the ultrasonic techniques (limited to frequencies below 200 and 100 Hz). Comparative results are found as an example in Fig.26 [30]. The MHD technique has also been used with results which need to be confirmed [31]. Recent experiments have evidenced perturbative phenomena (thermo-electronic effects induced on the probes even without the magnetic field) which must be eliminated.

The modeling of the response is based on the idea that it comes from the unsteadiness of the condensed phase, with the flame zone responding instantaneously. Results from such a model for an AP composite propellant, as compared to measurements from the modulated exhaust motor, are indicated in Fig.27 (with values which need to be somewhat revised to be in harmony with more recent inputs in the stationary model). In Fig.28 model results obtained by Brewster [7] for DB propellants (with a description of the condensed phase in osmosis with that of ONERA) are favorably compared to T-burner measurements. These results are encouraging and should lead to a more systematic modeling effort of the response of the various propellants.

With respect to velocity coupling, an experimental work at ONERA [32] was carried out with an AP propellant on a slab motor (equipped with 5 ultrasonic transducers) with a modulated exhaust. Erosive burning factors up to 1.5 were obtained at the aft end of the motor (for a normal burning rate of about 5 mm/s), disappearing as the channel would open up and the specific mass flow rate would fall under the threshold value ( $\approx 250 \text{ kg/m}^2\text{s}$ ). In parallel, an extra response was measured at the aft end of the motor, as long as the erosive burning rate would persist, see Fig.29. Such results were taken as evidence that a velocity coupling corresponding to an unsteady erosive response exists.

A number of works have been performed about ideas of a velocity coupling mechanism existing even under conditions where no steady erosive burning occurs. Most typical is that of Beddini [33] for a reference double base-propellant. The mechanism put forward is that, under unsteady conditions, local instantaneous transverse gradients in the velocity profiles are created which can trigger turbulence and thus enhance the heat flux to the surface. This will correspond to a sensitivity to velocity oscillations. The conclusions are, it is believed, somewhat blurred by the taking into account of an important equivalent sand roughness of 100 to 150  $\mu\text{m}$  (as compared to a flame height of 10  $\mu\text{m}$ ), apt to start turbulence.

The recent work of Zarko [34] asserts that a homogeneous propellant with no steady-state erosion will not undergo unsteady response to cross-flow. For composite propellants however an idea is proposed for a response to velocity oscillations even without steady erosive burning, that of the protusion of the more thermally stable component of the propellant which would be sensitive to these velocity oscillations, thus bringing in one more mechanism for "velocity coupling".

# Real Part of Response

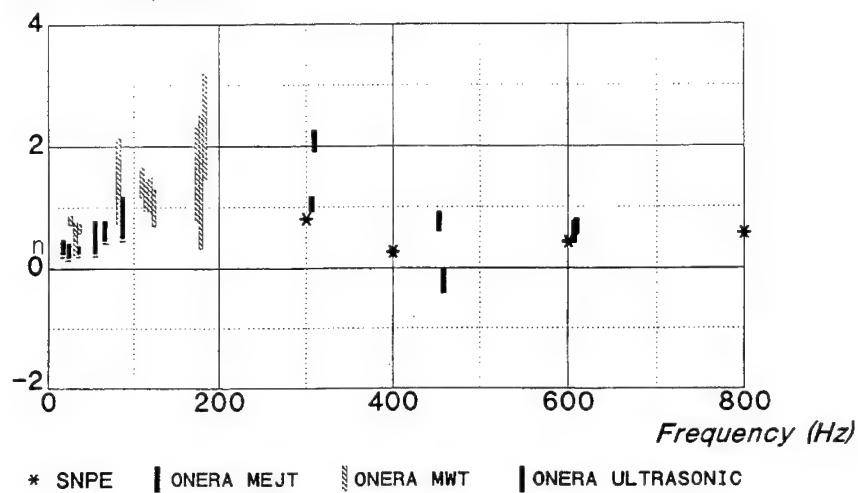


Figure 26. Summary of pressure-coupled response function results for the Ariane 5 propellant

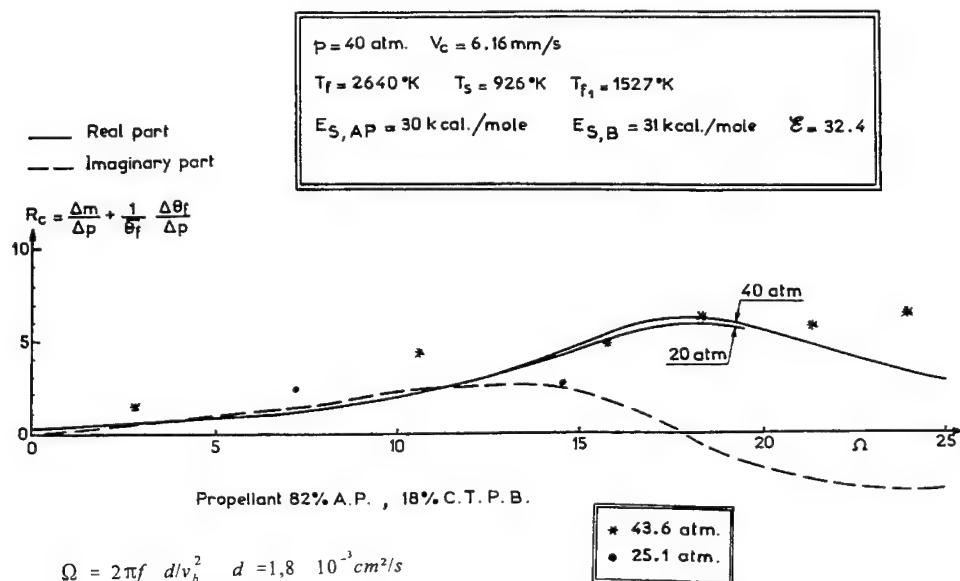


Figure 27. Response of the propellant as obtained from the theoretical description and with the modulated exhaust rocket motor

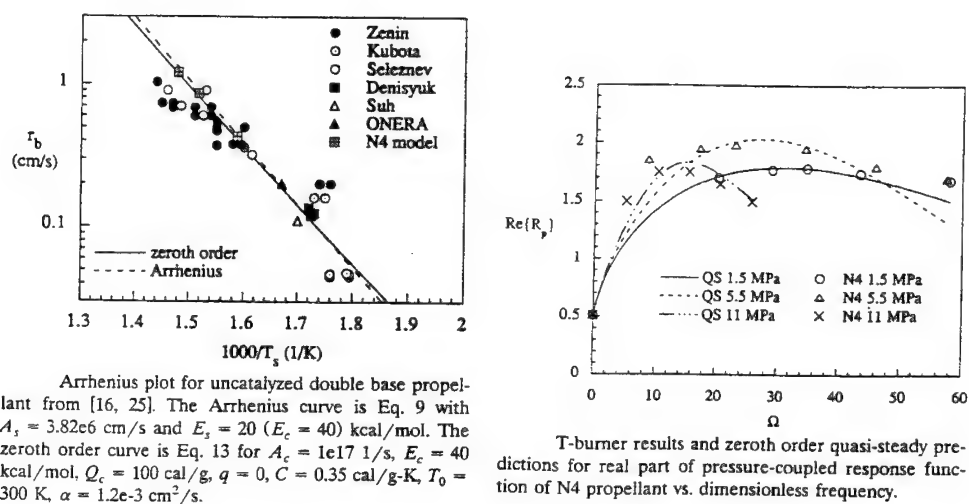


Figure 28. Combustion response modeling of homogeneous solid propellants (Q. Brewster)

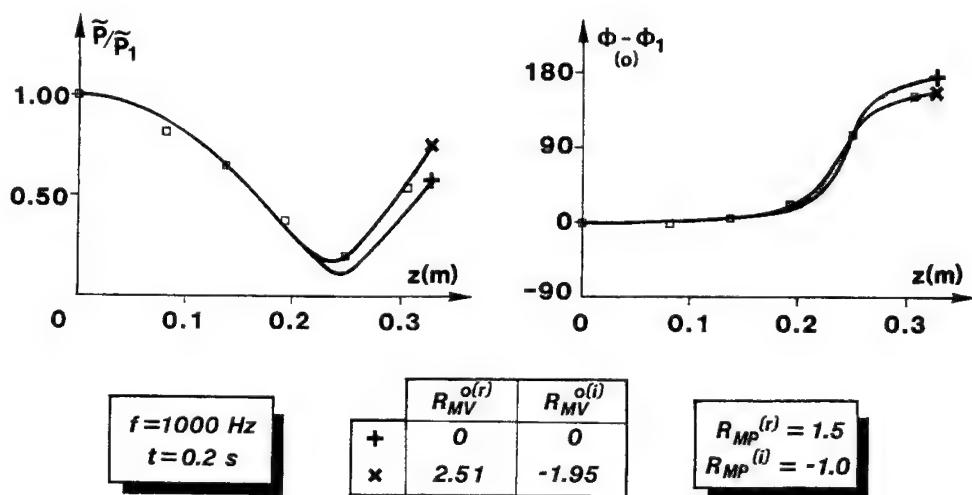


Figure 29. Velocity coupling results (G. Avalon)



## CONCLUSIONS

Some of the achievements and of the remaining challenges in the development of propellants and in the knowledge of their various combustion regimes are :

- Components of propellants : new ingredients are developed for improved characteristics (HNIW, ADN, GAP, GAPA...). More work remains to be done for obtaining thermally stable propellants meeting LOVA or IM requirements, for obtaining environmentally-friendly propellants for space launchers, military applications, gas generators, air bags... It is felt that the knowledge acquired should allow to progress rationally in the elaboration of these new propellants.
- Ignition : the ignition characteristics, for double-base propellants, AP-inert binder, or RDX/HMX-energetic binder composite propellants, are deemed to be known ; they can now be incorporated in the description of the motor ignition (see the presentation by A. Bizot). The measurements and the modeling should be extended to propellants based on the new ingredients (HNIW, ADN, GAP...).
- Condensed phase process : although some knowledge of the decomposition kinetics has been acquired, more work should be carried out to develop direct measurement techniques and modeling for a better understanding of the processes in the condensed phase (leading to ignition or during combustion), in particular relating to the chemical species.
- Steady combustion : it is estimated that the knowledge is fairly good for the individual components, AP, DB propellant or active binder, HMX-RDX, inert binder. There remains a need for detailed description of the flame structure (with a complete chemical reactions scheme) of the known components to start with, to be extended to the new ingredients. After much modeling work, it is believed that an approximate quantitative picture of the combustion of propellants has been acquired, again to be extended to propellants based on the new components. The particular case of aluminum, for which a semi-quantitative knowledge exists, needs further work to reach a predictive status for the agglomeration at the surface, the burning and the formation of the alumina smoke and residue, allowing in particular a better understanding of the slag accumulation in large motors.
- Response to erosive burning : much progress has been accomplished to measure and describe the erosive burning of DB, AP or RDX/HMX propellants, including the metalized propellants. It is now possible to incorporate such a description in the prediction of the operation of motors. The propellants based on the new ingredients remain to be considered with respect to experiments and modeling.
- Response to pressure (and velocity) oscillations : the measurements, with various techniques, of the response yield as yet fairly scattered results. The prediction through modeling, based on the knowledge of the steady combustion, is the object of renewed efforts. Such a modeling would help in correlating the measurements and in predicting the response of propellants still at the beginning of development. Possibly this would allow to change the composition of the propellant to calm down the instability. Some modeling work was carried out years ago on the response of propellants to velocity oscillations, as well as some experimental results. The debate with respect to the various "velocity couplings" remains open, various mechanisms being proposed. Experimental work remains the key point to determine the validity of these mechanisms.

**Acknowledgments** : Many people at ONERA contributed to this work : G. Avalon, R. Bellec, A. Bizot, F. Cauty, M. Charpenel, J. Duterque, J.F. Trubert, F. Vuillot... Financial support came in part from DGA, Délégation Générale à l'Armement.

## REFERENCES

- [1] G. Lengellé, A. Bizot, J. Duterque, J.C. Amiot, "Ignition of Solid Propellants", La Recherche Aérospatiale, Vol.2, 1991.
- [2] E.W. Price et al, "Theory of Ignition of Solid Propellants", AIAA Journal, July 1966, p.1153.
- [3] A. Bizot, "Ignition and Unsteady Combustion of AP-Based Composite Propellants", this volume.
- [4] A. Bizot, "Ignition and Unsteady Combustion of Composite Propellants in Subscale Solid Rocket Motors", to be presented at AIAA JPC, Seattle, July 1997.
- [5] G. Lengellé, "Thermal Degradation Kinetics and Surface Pyrolysis of Polymers" AIAA Journal, Vol.8, November 1970, p.1989.
- [6] G. Lengellé, J. Duterque, J.C. Godon, J.F. Trubert, "Solid Propellant Steady Combustion. Physical Aspects", AGARD, Lecture Series n° 180, 1991.
- [7] Q. Brewster, S.F. Son, "Quasi-Steady Combustion Modeling of Homogeneous Solid Propellants", Combustion and Flame, Vol.103, 1995, pp. 11-26.
- [8] C.A. Wight, S. Vyazorkin, "Kinetics and Mechanism of Thermal Decomposition of ADN", JANNAF Combustion Meeting, Monterey, November 1996.
- [9] T. Brill, "Multiphase Chemistry Considerations at the Surface of Burning Nitramine Monopropellants", Journal of Propulsion and Power, Vol.11, July 1995, p.740.
- [10] C. Melius, "Theoretical Study of the Reaction Mechanism of Nitrate Ester Decomposition", this volume.
- [11] T.S. Roh, I.S. Tseng, V. Yang, "Effects of Acoustic Oscillations on Flame Dynamics of Homogeneous Propellants in Rocket Motors", Journal of Propulsion and Power, Vol.11, July 1995, p.640.
- [12] Y.C. Liao, V. Yang, "Analysis of RDX Monopropellant Combustion with Two-Phase Subsurface Reactions", Journal of Propulsion and Power, Vol.11, July 1995, p.729.
- [13] J.E. Davidson, M.W. Beckstead, "Improvements to RDX Combustion Modelling", AIAA paper n° 96-0885, Aerospace Sciences Meeting, January 1996.
- [14] R.A. Yetter et al, "Development of Gas-Phase Reaction Mechanisms for Nitramine Combustion", Journal of Propulsion and Power, Vol.11, July 1995, p.683.

- [15] J.J. Cor, M.C. Branch, "Structure and Chemical Kinetics of Flames Supported by Solid Propellant Combustion", *Journal of Propulsion and Power*, Vol.11, July 1995, p.704.
- [16] M.W. Beckstead, R. Derr, C. Price, "A Model of Composite Solid-Propellant Combustion Based on Multiple Flames", *AIAA Journal*, Vol.8, 1970, pp.2200-2207.
- [17] N. S. Cohen, "Review of Composite Propellant Burn Rate Modeling", *AIAA Journal*, Vol.18, 1980, pp. 277-293.
- [18] M. W. Beckstead, "A Model for Composite Modified Double-Base Propellant Combustion", *JANNAF Combustion Meeting*, October 1989.
- [19] F. Blomshield, J. Osborn, "Nitramine Composite Solid Propellant Modelling", *AIAA paper n° 90-2311*, JP Conference, 1990.
- [20] M. W. Beckstead, "An Ammonium Perchlorate Model Based on a Detailed Kinetic Mechanism", *JANNAF Combustion Meeting*, November 1996.
- [21] J. Duterque, "Experimental Studies of Aluminum Agglomeration in Solid Rocket Motors", this volume.
- [22] S.E. Olsen, M. W. Beckstead, "Burn Time Measurements of Single Aluminum Particles in Steam and Carbon Dioxide Mixtures", *AIAA paper n° 95-2715*, JP Conference, 1995.
- [23] K.P. Brooks, M. W. Beckstead, "Dynamics of Aluminum Combustion", *Journal of Propulsion and Power*, Vol.11, July 1995, p.769.
- [24] M. Marion, C. Chauveau, I. Gökalp, "Studies on the Ignition and Burning of Levitated Aluminum Particles", *Combustion Science and Technology*, Vol.115, 1996, p.369.
- [25] F. Cauty, J.C. Démarais, C. Eradès, "Determination of Solid Propellant Burning Rate Sensitivity to the Initial Temperature by the Ultrasonic Method", *3<sup>rd</sup> International Symposium ICP*, May 1993.
- [26] M. K. King, "Erosive Burning of Solid Propellants", *Journal of Propulsion and Power*, Vol.9, November 1993, p.785.
- [27] M.K. Razdan, K.K. Kuo, "Turbulent Flow Analysis and Measurements of Erosive Burning Rates of Composite Solid Propellants", *AIAA Journal*, Vol.20, 1982, p.122.
- [28] J.C. Godon, J. Duterque, G. Lengellé, "Solid Propellant Erosive Burning", *Journal of Propulsion and Power*, Vol.8, July 1992, p.741.
- [29] J.C. Godon, J. Duterque, G. Lengellé, "Erosive Burning in Solid Propellant Motors", *Journal of Propulsion and Power*, Vol.9, November 1993, p.806.
- [30] J.C. Traineau, M. Prevost, P. Tarrin, "Solid Propellants Pressure-Coupled Response Function", *AIAA paper n° 94-3043*, JP Conference, 1994.

- [31] F. Cauty, P. Comas, F. Vuillot, M.M. Micci, "Magnetic Flow Meter Measurement of Solid Propellant Pressure-Coupled Responses Using an Acoustic Analysis", *Journal of Propulsion and Power*, Vol.12, March 1996, p.436.
- [32] G. Avalon, J. Pascal, F. Cauty, "Experimental Investigation of Solid Propellant Velocity Coupling", AIAA paper n° 87-1727, JP Conference, 1987.
- [33] T.A. Roberts, R.A. Beddini, "A Comparison of Acoustic and Steady-State Erosive Burning in Solid Rocket Motors", AIAA paper n° 89-2664, JP Conference, 1989. Also AGARD Mission at ONERA, April 1990.
- [34] L.K. Gusachenko, V.E. Zarko, "Possible Mechanism of Nonsteady-State Erosion Combustion of Composite Solid Propellants", *Combustion, Explosion and Shock Waves*, Vol.31, 1995, p.437.

#### COMMENT

Quinn Brewster, Department of Mechanical and Industrial Eng., University of Illinois, Urbana.

The correlation between temperature profile (dark zone) and pressure exponent break seems good for double base propellant ( $p \approx 100$  atm), but not so clear for HMX. Without external radiation HMX shows no dark zone even at 1 atm, yet you show a pressure exponent break at 20 atm, attributing it to merging flames, similar to DB. Please comment on the state of knowledge and similitary between HMX and DB two stage flames.

Authors's reply.

It is felt that the experimental results on the burning rate of HMX, see Fig. 11, show quite clearly a change in burning rate slope around 20 atm. However the main indication is from cinematography revealing a clearly detached luminous flame at pressures around a few atm. N. Kubota (see for example : *Propellants, Explosives and Pyrotechnics*, February 1989) has also shown such pictures. It is thus considered that HMX has a double flame structure like homogeneous propellants, but that this staged flame collapses into one very quickly for practical purposes.

## RECENT DEVELOPMENTS IN GUN PROPELLANTS AND GUN PROPULSION RESEARCH AT S.N.P.E.

**Jean-Paul REYNAUD**

SNPE / Advanced Technologies and Propulsion Division  
Centre de Recherches du Bouchet - BP N° 2  
91710 VERT-LE-PETIT, FRANCE

**ABSTRACT** This paper describes recent developments in gun propellants and gun propulsion research from the energetic material point of view, performed under French MOD sponsorship and directed toward providing technical solutions to new weapon system requirements.

The three main types of solid propellants on which research is conducted at SNPE are: conventional nitrocellulose-based and multibased propellants, composite gun propellants based on inert binder and composite gun propellants based on energetic binder. Recent results obtained for each kind are shown and discussed.

Common granulation propellants cannot offer required performance improvement. Modular charges, or charges in two pieces for large caliber guns, need higher loading density to get good ignition, to minimize pressure waves, and to reach required performance levels. Therefore, SNPE performed some studies on new partially-cut multi-perforated propellant sticks ("kerfed" sticks). Some results are presented showing their advantages in better ignition of a modular charge and vulnerability reduction.

For future 45 mm medium caliber guns, consolidated charges obtained by agglomeration of propellant grains with an energetic binder, provide up to a 40 % increase in volumetric loading. This configuration of grains allows caseless ammunition manufacturing and also charge arrangement for telescoped projectiles.

The paper also describes recent improvements in theoretical dimensioning tools developed by SNPE, which help in diagnosis, research orientation, and firing behavior prediction. The thermodynamics code BAGHEERA has been adopted by NATO, the chemical kinetic code BALOO takes into account new propellant types and gun barrel wear, the interior ballistic code family MOBIDIC has been selected at the French national level for future research. The last includes a version with internal boundaries and is able to take into account discontinuities.

## INTRODUCTION

Propulsion in guns is achieved through combustion gas generation. Energetic materials (propellants) serve to store the potential energy needed for propulsion. They are more often solids, but may be liquids or gels. When ignited, an energetic material burns under a self sustained type of combustion. It is also possible to drive combustion from the outside, for example, with a plasma, i.e. the electro-chemical concept. In the long term, one can imagine other types of energy storage, such as electrical, and the possibility of propulsion not based on gas generation. Electrical launchers are far in the future. Solid gun propellants still offer substantial opportunities to achieve significant gun system improvement in areas such as formulation, grain shape, and function.

Recent developments in solid gun propellants and gun propulsion research from the energetic materials point of view, performed at SNPE under French Ministry of Defence sponsorship, were directed toward providing technical solutions to new weapon systems requirements [1].

The three French main weapon programs are the 155 mm long-range field artillery gun, the 140 mm future main battle tank gun, and the 45 mm future medium caliber gun. Each of them is based on a new concept, respectively: modular charges, charge in two pieces and telescoped projectile. These concepts require advances in energetic materials to achieve performance, safety, stability, reliability, life cycle, and cost goals. They also require vulnerability and erosivity reduction (especially for high velocity projectile), process improvement, and environmental protection.

Within this context, research is performed by SNPE at Le Bouchet Research Center in three main directions: the formulation of new energetic materials for gun propulsion, the search for new gun propellant design (e.g., cut-up sticks, consolidated charges) and/or research for new charge design (e.g., modular charges). To help in diagnosis, research orientation and firing behavior prediction, theoretical dimensioning tools are simultaneously developed by SNPE. All these points will be successively detailed in the following.

## RESEARCH ON SOLID GUN PROPELLANT MATERIALS

The three main types of solid gun propellants on which research is performed at SNPE are:

✓ Conventional nitrocellulose based and multibased propellants (up to 65 % filler content)

✓ Composite gun propellants based on inert binder (usually filled with nitramine up to 85 %)

They provide the same performance level than conventional propellants with the advantages of more thermally stable materials, gains in vulnerability reduction and stability, with an erosivity level near that of conventional propellants.

✓ Composite gun propellants based on energetic binder (filled with 70 to 80 % of nitramine)

They make high performance possible and keep vulnerability and erosivity levels within specified limits.

In each of these three groups, formulation is based on a combination of binder, plasticizers and fillers.

Energetic binders used at SNPE include Nitrocellulose and Glycidyl Azide Polymer (GAP). Inert binders include Cellulose Acetate Butyrate (CAB) and Hydroxy Terminated Polybutadiene (HTPB). Some are thermoplastic, others crosslinked in each kind of binder.

As plasticizers, nitrated esters, BDNPA/F, GAPA, DANPE, NENAs can be associated with energetic binders or an inert binder like CAB, while only inert plasticizers are to be used with inert binders like HTPB.

Fillers include cyclic nitramines (RDX, HMX), linear nitramines (NQ), cage molecules (CL20) or ionic nitrate (TAGN). For each case, the choice is a compromise of thermodynamics, compatibility, feasibility, processing, firing characteristics and cost.

In the three following figures, conventional propellants are represented by a narrow rectangle in a diagram plotting impetus versus flame temperature. The problem is to find a compromise that will provide the best gun performance at an acceptable erosivity level.

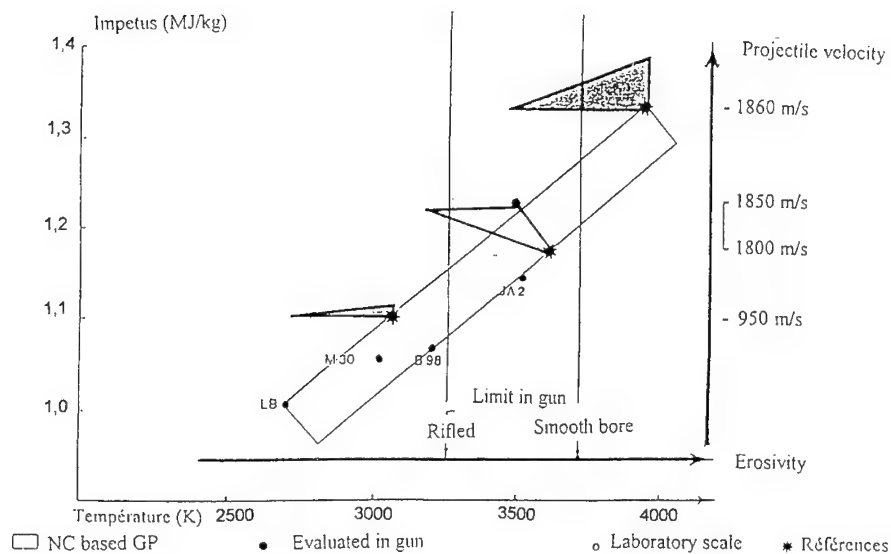


Figure 1. NC based gun propellants

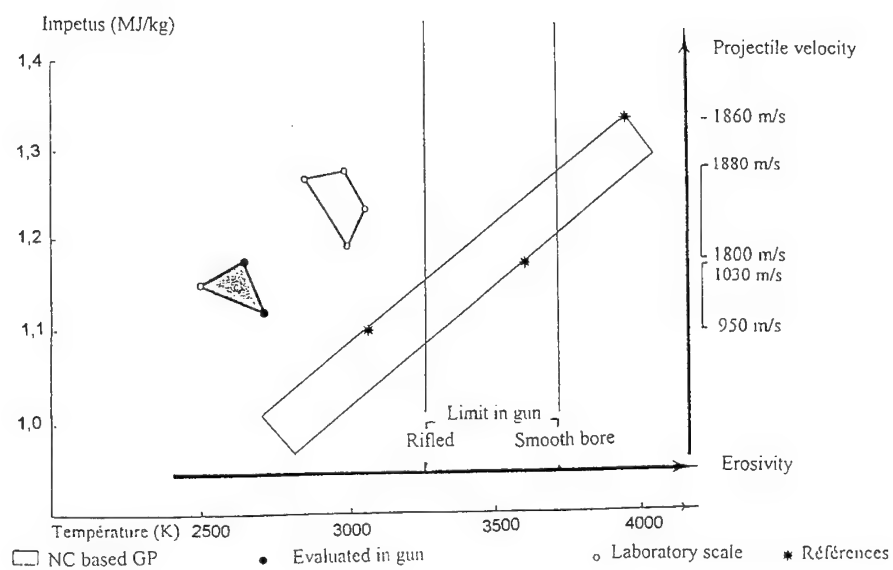


Figure 2. Inert binder based composite propellants

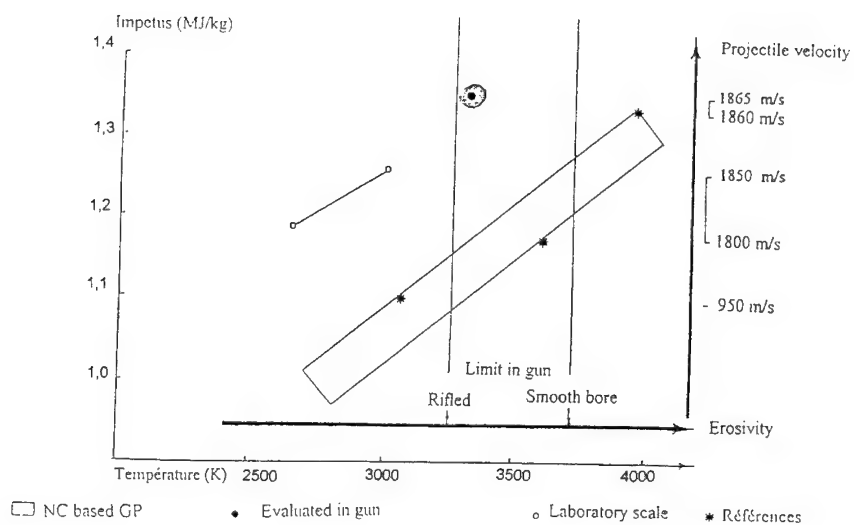


Figure 3. Energetic binder based composite propellants

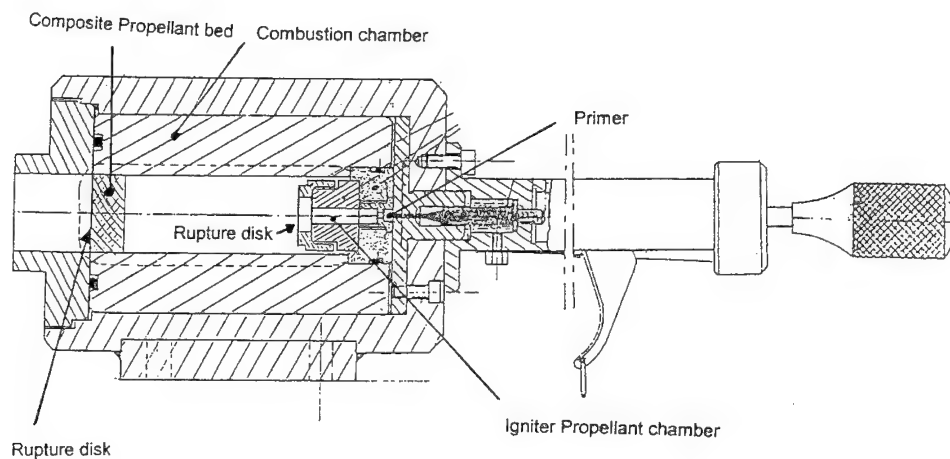


Figure 4. SID experimental device



✓ In Figure 1, filled multibase propellants promise a large reduction in erosivity through flame temperature reduction of 350 to 600 K in the 155 mm field artillery gun, 120 mm APFSDS and the 140 mm for tank guns. Projectile velocities are derived from ballistics computation. Erosivity reductions, related to flame temperature computed through the thermodynamic code BAGHEERA, are less precise and need to be experimentally verified.

✓ In Figure 2, inert binder-based composite propellants also lead to performance gains in 155 mm and 120 mm guns. Until now, there was no solution for the 140 mm gun because of a too-low impetus. Computed flame temperature reduction for composite propellants cannot be easily converted to erosivity reductions as for conventional propellants, due to the high individual flame temperature of the filler materials. The main gain is in the area of vulnerability reduction. Some ignition problems are on the way to being solved using adapted ignition powder.

For this group of composite propellants, the igniter propellant must be fitted to gun propellant composition. On a laboratory scale, good ignition delay for inert binder based composite propellant has been reached using different mixtures of porous Nitrocellulose with Nitroglycerine or TEGDN, Ammonium Perchlorate and several metallic charges. Table 1 gives relative ignition delay of a 7-gram RDX/PBHT propellant charge in front of a 350 mg igniter filled up with five different ignition propellants. (New adapted igniter propellants are identified by CIP1 to CIP3.) The device used for this experiment is shown in Figure 4. These new igniter propellants are under tests in operating guns.

Igniter Propellant	Black Powder	Boron / KNO <sub>3</sub>	CIP1	CIP2	CIP3
Standard Ignition Delay (ms)	145	14	9	2.5	2.8

**Table 1**  
Standard Ignition Delays for inert binder based composite propellant

✓ Figure 3 shows that energetic binder-based composite propellants make it possible to meet the higher performance needs, along with the possible erosivity reduction necessary to preserve the operational interests in those new systems.

## NEW PROPELLANT GRAIN DESIGN

### New Kerfed sticks [2]

Common granulation propellants cannot offer the performance improvements required for today's propelling charges. Calculations (Figure 5) show the correlation between progressivity with multiperforated grains and muzzle velocity of the projectile in a future 155 mm gun. To reach that goal value (more than 945 m/s) at the same time a higher loading weight than the maximum value reachable with grains is needed. Modular charges, or charges in two pieces, also need higher density or lower porosity to get good ignition and flame propagation, in order to minimize pressure waves and to reach required performance levels. That is the reason why SNPE performed work on new "kerfed sticks" (e.g., partially-cut multi-perforated propellant sticks) [3]. These geometries offer improvements over tubes, slotted tubes, and pre-fragmented sticks (see Figure 7).

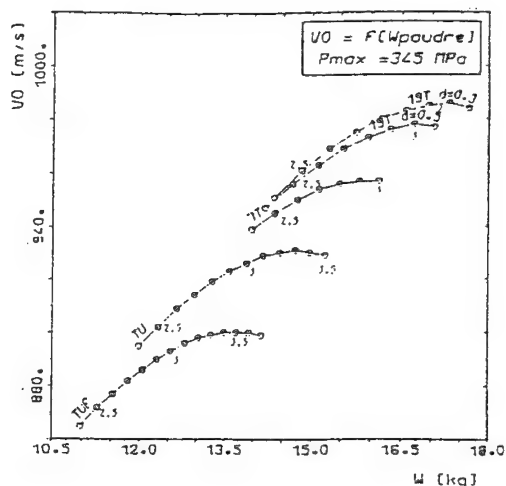


Figure 5. Theoretical performance of various gun propellant geometries for the 155 mm gun

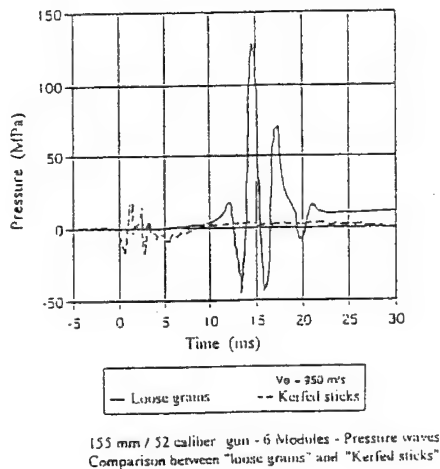


Figure 6. Pressure waves reduction

Kerfed sticks preserve better ignitability allowing the ammunition maker to utilize flat ignition systems, using weakened pressure waves as described in Figure 6. Negative  $\Delta P$  is lowered from 50 down to 15 MPa in the 155 mm gun loaded with six modular charges. Furthermore, kerfed sticks provide, through their multiperforation, better performance and behavior with regard to gun tube wear because they quickly become grains at the beginning of the ballistic cycle. Therefore, easier motion of grains behind the projectile avoid increased erosion due to heavy sticks standing in the combustion chamber. In the same way, improved loading configuration allows the use of lighter weight grains such as seven perforated grains instead of nineteen (usually used in artillery) and contributes to tube erosion reduction.

For vulnerability, kerfed sticks exhibit a critical diameter larger than 160 mm and no associated detonation in modular unicharge when made with double base (NC+NGI) propellant (web=2.55 mm, 19 perforations) adapted to the 155 mm gun.

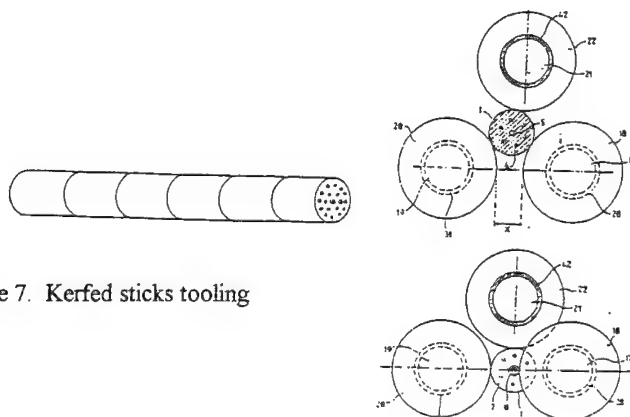


Figure 7. Kerfed sticks tooling

### Consolidated charges

Consolidated charges obtained by agglomeration of propellant grains with an energetic binder under compression provide up to a 40 % increase in volumetric loading. This arrangement of grains into blocks allows manufacture of charges for caseless ammunition, and also manufacture of moving charges or charges adapted to arrow type projectiles. Performance increase was measured to be near 10% with respect to projectile velocity at the same pressure level in a 30 mm gun, for example. In a 45 mm APFSDS, the results obtained with a consolidated single-base propellant are shown in the following table, where they can be compared to the reference propellant (bulk loaded deterred single-base). In both cases, the maximum pressure was 500 MPa.

	Propellant weight (g)	Muzzle velocity (m/s)	Action time (ms)	Negative $\Delta P$ (MPa)
Deterred Single-base (Bulk loaded)	740	1600	6.3	120
Single-base (consolidated)	830	1640	7.6	0

**Table 2**  
Consolidated charge 45 mm APFSDS experiments

Consolidated charge also makes it possible to organize the flow around a telescoped projectile. This is a technical key considering that the differential speed of propellant grains versus projectile fins is computed around 400 m/s. Today this technology seems of great interest for new generation of medium caliber guns of course, but it is also sought for large calibre gun applications and for electro-thermo-chemical gun propelling charges.

Consolidated igniter propellant tubes or discs are also an interesting means to improve ignition using the Combustible Unicharge Case (CUC) under development at SNPE. Grain sizes and the agglomeration process are adjusted in order to give required quickness and action time. With this technique, a lot of designs are possible e.g., tubes on one or both side of the CUC, base pad in the container.

### RECENT DEVELOPMENTS OF THEORETICAL TOOLS

Laboratory simulations and modelizations are useful to understand, predict and optimize new propellant charges behavior. Cost and duration of ammunition development can be significantly reduced by using theoretical dimensioning tools, resulting in recent improvements in the field of interior ballistics. Such tools developed by SNPE, under French MOD sponsorship, have been widely spread throughout French organizations and companies and even at international level; for example, the thermodynamic code BAGHEERA was adopted by NATO (STANAG 4400) and its latest version integrates a new equation of state for condensates at high pressure.

In the following recent developments of two other important theoretical tools, the chemical kinetic code BALOO and the interior ballistic code family MOBIDIC are described.

### Chemical kinetic code BALOO

The consideration of chemical reaction kinetics appeared to be very useful in improving the accuracy of interior ballistics codes. It is particularly true when the delay between the first propellant grain decomposition and the gaseous equilibrium is no longer negligible versus stay-time in the barrel. This problem is very crucial when using composite propellants based on inert binder. That is the reason why SNPE developed the chemical kinetic code BALOO. This code takes into account up to 150 species and 500 chemical reactions. It calculates chemical species production and consumption rates, temperature and pressure derivatives versus time and, explicitly, a chemical states succession. Time step is automatically fitted to chosen criteria, in order to get a regular main interior ballistics variables development. The model is numerically solved and under experimental validation. Predicted results for the example of RDX combustion in a closed vessel at a loading density of 200 kg/m<sup>3</sup> are given in Figures 9 and 10. For this calculation, the Glarborg, Miller and Kee scheme was used [4] [5].

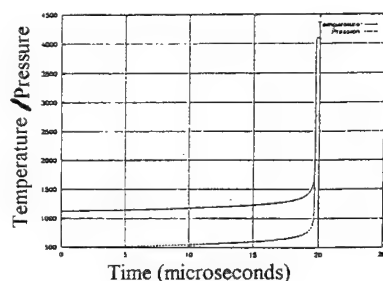


Figure 9. RDX combustion temperature and pressure

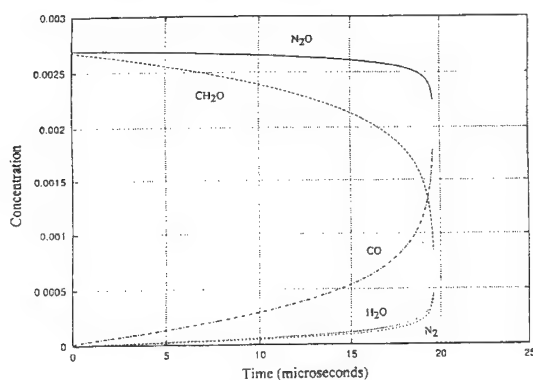


Figure 10. RDX combustion species concentration

The reaction mechanism and kinetic constant selection method was chosen to allow simplification, streamlining of the model. A simplified version of BALOO will then be used in coupling with interior ballistics code MOBIDIC. This coupling is of great interest to study the ignition phase of the gun propellant charge and for gun wear prediction.

### Last interior ballistic code improvement : MOBIDIC FI

The interior ballistics code family MOBIDIC was selected at the French national level for future research. Presently, this family includes a two-phase, two-dimensional code version with internal boundaries named MOBIDIC 2D-FI and is then able to take into account discontinuities as the NOVA code does. This will be essential for computing the three new ammunitions concepts which are: unimodular charges, charges in two pieces, and telescoped ammunition.

This theoretical model has been used, for example, to simulate ignition and combustion processes of modular charges for the 155 mm. A comparison between experimental and theoretical results is given in Figures 11 and 12. The experimental results were obtained in a transparent simulator, developed for that purpose, and also in a classical metallic simulator with rupture disk (Figure 13). Using high-speed cinematography, this new experimental tool gives information on flame spreading, gas flows, and mechanical behavior of combustible case walls. It can be used for

optimization of propellant charge and igniter design and to help select new energetic materials. It provided very interesting information about internal boundaries behavior useful for MOBIDIC-2D-FI validation [6] [7] [8].

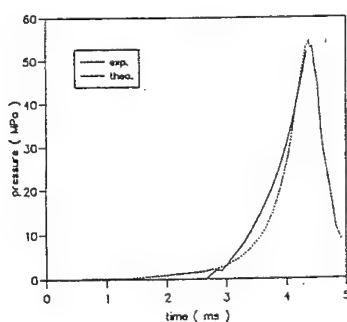


Figure 11. Comparison at P1 location

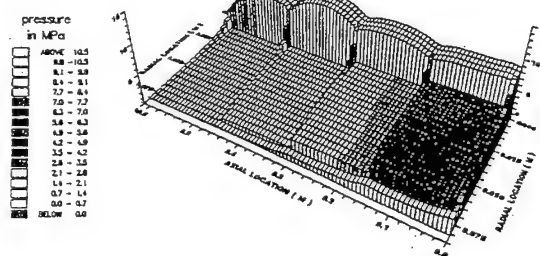


Figure 12. Gas pressure at time 0.58 ms

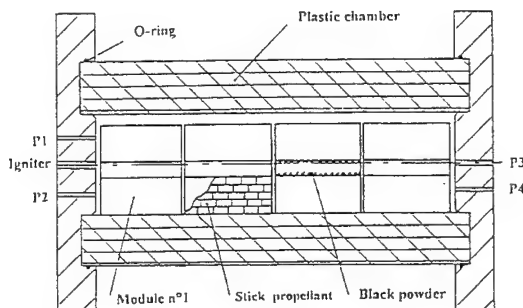


Figure 13. Transparent simulator

## CONCLUSION

The future of gun propellants and gun propulsion remains focused on the development of the above mentioned areas, particularly in the fields of propellant formulation, grain geometry and charge firing behavior. Recent improvements make it possible to propose viable and safe solutions for normal firing. They also allow both the understanding and the prediction of the consequences of accidental firing. Current research will continue in those fields and will progress in additional areas, such as processing, vulnerability, and erosivity reduction of propellant charge. This last point is becoming more and more important as performance increases.

In the distant future, another promising topic in the energetic materials area for gun propulsion is the use of gelled propellants in a conventional ammunition propelling charge. These propellants rank between solid and liquid propellants. They can develop a high thermodynamical performance level and their demonstrated ability to burn, following a parallel axial regression, makes them more adapted to ballistic adjustment than liquids. Some formulations have been already tested on a laboratory scale by SNPE, such as a combination of TEGDN, RDX and TAGN.

## REFERENCES

- [1] **Paulin, J.L.**, Evolutionary trends in gun propellants and gun propulsion, *National Defence and Technology*, 53-58, 1994.
- [2] **Martin, B., Paulin, J.L., Reynaud, C.**, Unicharge propellants and combustible cases systems, *International Gun Propellant Symposium*; Parsipanny, NJ, 1994.
- [3] **Boisseau, J., Paulin, J.L., Reynaud, C.**, Brins de poudre propulsive multiperforés et divisés, appareillage de fabrication et son utilisation, *French Patent 2679 992, US Patent 5 251 549*.
- [4] **Bac, J.P.**, Le code cinétique BALOO, *Internal SNPE report*.
- [5] **Glarborg, P., Miller, J.A., Lee, R.J.**, Kinetic Modelling and Sensitivity Analysis of Nitrogen Oxide Formation in Well-Stirred Reactor, *Combustion and Flame*, 65, 177-202, 1986.
- [6] **Reynaud, C., Reynaud, J.P., Roller, D., Rio, P.**, Visualisation of the ignition phase of a large calibre gun modular charge, *International Annual Conference of ICT*, 1994.
- [7] **Briand, R., Tissier, P.Y., Reynaud, C., Kuo, K.K.**, Theoretical modelling of ballistics processes of modular charges for large caliber guns, *13th International Symposium on Ballistics*, Stockholm, 1992.
- [8] **Ruth, C.R., Minor, T.C.**, Experimental study of flamespreading processes in 155 mm, XM216 modular propelling charges, *Memorandum report BRL-MR-3840*, 1990.

# COMBUSTION BEHAVIOR AND THERMOCHEMICAL PROPERTIES OF JA2 PROPELLANT

C. Kopicz<sup>1</sup>, T.J. Watson<sup>2</sup>, K.K. Kuo<sup>2</sup>, S.T. Thynell<sup>2</sup>

<sup>1</sup> Department of Aerospace Engineering; <sup>2</sup> Department of Mechanical Engineering  
The Pennsylvania State University  
University Park, PA 16802

**ABSTRACT:** JA2 is a commonly used gun propellant for various weapon systems. Knowledge of its combustion behavior is useful for system design application. The burn rate of JA2 propellant was determined as a function of pressure,  $0.69 \leq p \leq 41.4$  MPa ( $100 \leq p \leq 6,000$  psi), and initial temperature,  $25^\circ\text{C} \leq T_i \leq 60^\circ\text{C}$ . Burn rate plot shows slope breaks at 6.9 MPa (1,000 psi) and 4.5 MPa (650 psi) for the initial temperatures of  $25^\circ\text{C}$  and  $60^\circ\text{C}$ , respectively. At high pressures,  $P > 40$  MPa (6,000 psi), measured burn rates were found to agree with the Army's closed bomb data. The steady-state burn rates also agreed with the instantaneous burn rates obtained from X-ray radiography measurement conducted at various chamber pressurization rates. The burning surface temperature and temperature sensitivity ( $\sigma_p$ ) were also deduced. The rapid decay of  $\sigma_p$  with an increase in pressure for  $p < 20$  MPa and extremely low values of  $\sigma_p$  at pressures greater than 20 MPa explains the lack of dynamic burning of JA2 propellant.

## NOMENCLATURE

<u>Symbols</u>	<u>Description</u>
a	Pre-exponential for St. Robert's law
A	Pre-exponential of pyrolysis law
C	Heat capacity, J/(gm °C)
$E_a$	Activation energy, J/mole
k	Thermal conductivity, J/(cm s °C)
$\dot{m}_b''$	Mass burning flux, kg/(cm <sup>2</sup> s)
n	Burning rate exponent for St. Robert's law
p	Pressure, N/m <sup>2</sup> or MPa or atm
$\dot{q}''$	Heat flux, J/(m <sup>2</sup> · s)
Q	Heat release, J/(gm °C)
$Q_{TOT}$	Total heat release at constant volume in a combustion wave, J/(gm °C s)
$R_b$	Strand burning rate, cm/s
$R_u$	Universal gas constant, J/(mole K)
T	Temperature, °C
x	Axial coordinate, cm

#### Greek Symbols

$\alpha$	Thermal diffusivity, cm <sup>2</sup> /s
$\gamma$	Ratio of specific heats (C <sub>p</sub> /C <sub>v</sub> )
$\sigma_p$	Temperature sensitivity
$\rho$	Density, gm/cm <sup>3</sup>

#### Subscripts

$\Delta$	Ambient conditions
c	Solid (Condensed) phase
f	Flame
g	Gas
i	Initial
p	Propellant
ref	Reference value
s	Surface

### INTRODUCTION

JA2 is used in a variety of ballistic systems. Although JA2 burn rate data have been obtained from closed-bomb testing, no reliable data exist which describe the steady-state burning behavior of this propellant over a broad pressure range. For pressures below 62 MPa (9,000 psi), the results can be affected by the igniter, flame spreading over the propellant grain, and transient burning of the sample. It is also difficult to use closed-bomb tests to determine the burning surface temperature of the propellant. Reliable measurement of the steady-state burning rate and thermal-wave profile of the JA2 propellant will allow the chemical processes of the combustion of this propellant to be understood.

Many references can be found in the literature which address the combustion mechanisms of conventional double-base propellants [1-7]. JA2 is a modified double-base propellant consisting of three major ingredients: nitroglycerin (NG), nitrocellulose (NC), and diethylene glycol dinitrate (DEGDN). Table 1 lists the detail formulation of JA2 propellant. The solid JA2 propellant, its flame structure, and its thermal wave structure are homogeneous [2]. The adiabatic flame temperature of JA2, 2,883 K at P=100 atm, provides a relatively high impetus for the propellant without causing gun barrel erosion. From the mechanical property point of view, JA2 propellant grains are highly suited for ballistic applications, since they have very high resistances to fracture. In addition, the handling and packaging of JA2 propellants are relatively easy.

It is usually very difficult to obtain an accurate trace of the thermal wave profile inside a burning propellant. Properly mounting the thermocouple in the propellant strand, removing excess acetone from the sample, and securing thermocouple connections to the extension wire make the process a very tedious and challenging one [8,9]. At all test pressures, carbonaceous residues are observed to form on the surface and periodically flake off [10]. This can affect the thermocouple measurements near the burning surface. Measuring the thermal wave profile becomes more difficult as the test pressure increases due to increased burn rates. As the burning rate increases, less time is available for the thermal wave to form in the propellant. At some point, the thermal wave thickness is so small that the use of thermocouples is extremely difficult. Zenin and Finjabore [3,12], Klein, et al., [8], and Klager and Zimmerman [13] have made successful measurements of the thermal wave of double-base propellants using fine-wire micro-thermocouples with a bead size no greater than 5  $\mu$ m. Once a reproducible thermal wave was measured, the data were used to interpret the combustion



processes of the propellant and to determine certain important thermochemical parameters of the propellant, e.g., burning-surface temperature, thermal diffusivity, and thermal conductivity.

TABLE I  
Chemical Composition of JA2

Ingredient Name	Chemical Composition	Molecular Weight (kg/kmole)	Mass Fraction (%)
Nitrocellulose (13±.04 %N)	$[\text{C}_6\text{H}_7(\text{OH})_{0.42}(\text{ONO}_2)_{2.58}]_n$	$(246.255)_n$	59.50
Nitroglycerin	$\text{CH}_2(\text{ONO}_2)\text{CH}(\text{ONO}_2)\text{CH}_2(\text{ONO}_2)$	227.085	14.90
Diethylene glycol dinitrate (DEGDN)	$\text{O}_2\text{NOCH}_2\text{CH}_2\text{OCH}_2\text{CH}_2\text{ONO}_2$	196.115	24.80
N'-Methyl-N-N-Diphenylurea (Akardit II)	$\text{CH}_3\text{NHCON}(\text{C}_6\text{H}_5)_2$	226.270	0.70
Magnesium Oxide	MgO	40.304	0.05
Graphite	C	12.011	0.05

The purpose of this work is to investigate the combustion behavior of JA2 propellant. Specifically, the objectives of the research are:

- (1) to measure the steady-state burning rate at various operating conditions;
- (2) to determine the temperature sensitivity of the propellant burning rate;
- (3) to measure the thermal-wave structure and burning-surface temperature of the propellant using a fine-wire thermocouple;
- (4) to deduce various important thermochemical properties from the thermal-wave structure. These parameters include thermal diffusivity, activation energy and pre-exponential factor for the Arrhenius pyrolysis law, the burning rate exponent (n) and the coefficient (a) for the St. Robert's burning rate law; and
- (5) to compare and combine the results of this work with other companion research work conducted at the Pennsylvania State University to give a full description of the combustion behavior of JA2.

## EXPERIMENTAL APPROACH

### Experimental Apparatus for Strand Burner Tests

A windowed strand burner was used to study the combustion behavior of the JA2 propellant. Figure 1 shows a schematic diagram of the strand burner setup used to measure the burning rate and surface temperature of JA2 at various pressures. A piece of nichrome wire imbedded in a small strand of NOSOL 363 propellant was used as an igniter for the JA2 propellant. An electric current was sent through the nichrome wire by an external power supply to ignite the thin NOSOL 363 propellant for achieving uniform ignition and burning of the JA2 strand.

For pressures less than 13.8 MPa (2,000 psi), the chamber pressure was measured by a Validyne transducer (DP-215) and a carrier demodulator (CD15) with a frequency response of 1,000 Hz. To maintain the desired pressure level in the strand burner, an Omega solenoid valve (SV106) was used to control the flow rate of exhaust gases. For pressures above 13.8 MPa (2,000 psi), a Kistler pressure transducer and charge amplifier were used to measure the chamber pressure. At test pressures between 13.8 MPa (2,000 psi) and 41.4 MPa (6,000 psi), an Atkomatic solenoid valve was used to maintain desired pressures by exhausting excess gas. The voltage signal produced by the

pressure transducer was monitored by an IBM-AT personal computer, which controlled the solenoid valve and maintained the desired test pressure. For high pressure tests, the solenoid valve was replaced by a surge tank, and the IBM-AT PC controller was removed from the setup.

The Validyne and Kistler pressure transducers were calibrated by a high-accuracy Heise pressure gauge. The charge amplifier for the Kistler pressure transducer was calibrated by inputting a known voltage signal to the charge amplifier and adjusting the sensitivity until the output reached the desired level.

A silicon bath was used to condition the chamber to a desired test temperature. The silicon fluid was maintained at a desired temperature with a combination heating and cooling unit fitted with a magnetic stirrer. A pump attached to the unit circulated the silicon fluid through a copper jacket wrapped around the chamber.

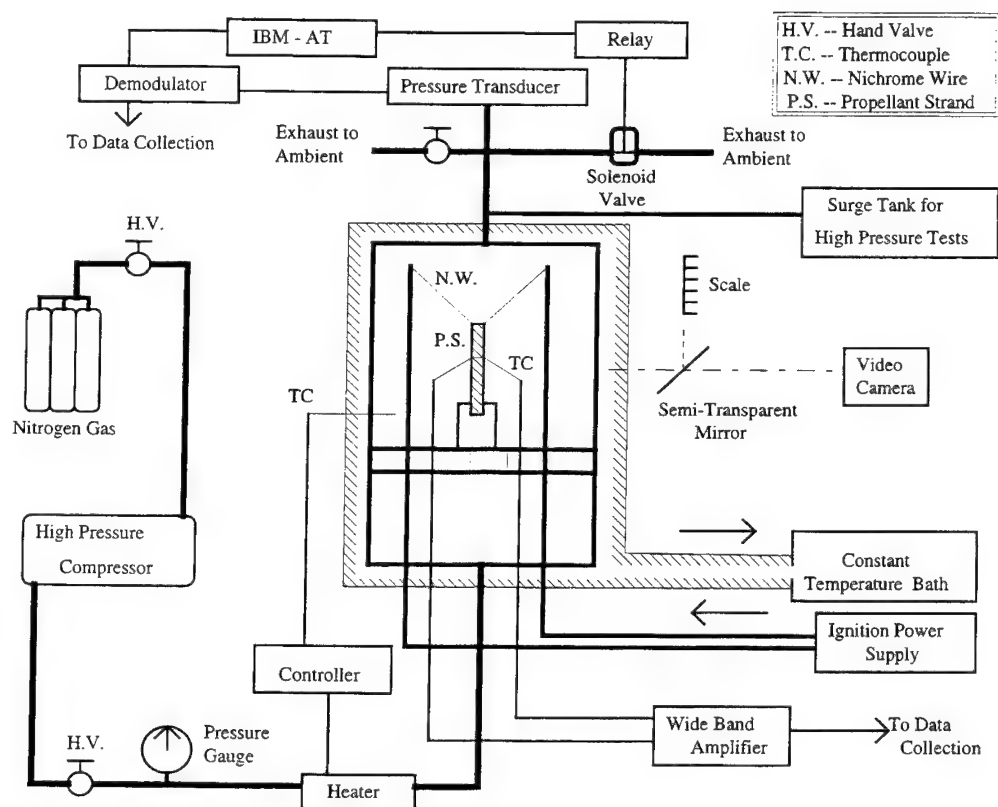


Figure 1. Schematic diagram of experimental apparatus used in strand burning tests

The nitrogen purge gas was adjusted with a resistant heating unit. When the propellant strand was exposed to the purge gas for a sufficient period of time, the temperature of the propellant strand became identical to the gas temperature. Thermocouple imbedded within the propellant indicated when this was achieved. To help maintain the propellant strand at a given temperature, the power delivered from the heater to the purge gas was regulated by a Honeywell temperature controller.

### Strand-Burning Rate and Thermal Wave Structure Measurements

A scale was optically superimposed on the image of the 6.25mm diameter propellant strand by a semitransparent mirror. A Panasonic VCR and camcorder were used to record the test sample image and superimposed scale through the chamber window at the rate of 30 frames/s. A clock superimposed on the image by the camera provided time of the burn. The length of the strand that burned in a certain amount of time was measured from the scale superimposed on the image to determine the burning rate.

The thermal wave structures of the JA2 propellant were measured under steady burning conditions by a thermocouple made from 25- $\mu\text{m}$  fine-wire rolled to a thickness of 5- $\mu\text{m}$ . The thermocouple was bent into the shape of an inverted U (see Fig. 2). The joint was positioned in the center of the flat portion of the U. This flat portion helped reduce conductive heat losses from the thermocouple [3, 9, 11, 12]. Empirical results showed that the most reproducible temperature-time traces were obtained when the flat portion of the U was about 0.4 mm (0.0157 in). This length provided sufficient distance to prevent heat loss from the thermocouple and still short enough to prevent excessive movement of the thermocouple bead when the burning surface passed by the thermocouple during testing. Figure 2 shows the general process of mounting the thermocouple. The method illustrated in Fig. 2 is similar to the method used by Zenin, et al [3]; and Klein, et al [8]. To embed the thermocouple in a strand, the propellant strand was split longitudinally, and the thermocouple was mounted in one half of the propellant with the base of the U parallel to the top and bottom surfaces of the strand and the leads of the thermocouple extending from each side. A small amount of acetone was applied in the neighborhood of the thermocouple junction to soften the propellant in that region. Acetone was also placed on the inner surface of each half of the propellant stick, and the two halves were pressed together to reform the strand. The sample was baked in an oven heated to 60 °C (140 °F) for 24 hours to remove as much of the acetone as possible. A few samples were baked under the same conditions for 48 hours. No noticeable differences were observed. Then the strand was mounted vertically in the windowed strand burner for testing.

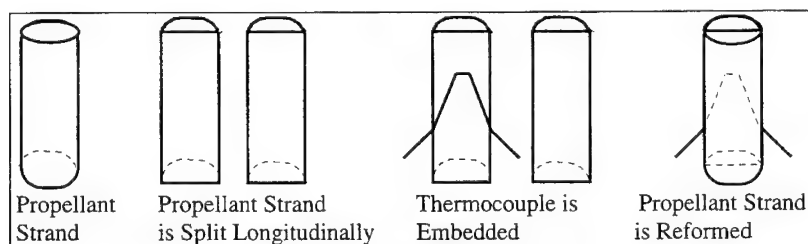


Figure 2. Thermocouple embedding process.

### Determination of the Physical and Thermochemical Properties of JA2 from Recorded Temperature-Time Traces

In this study, the characteristic time of the thermal wave, thermal diffusivity, and temperature sensitivity were determined by utilizing a one-dimensional, steady-state, energy-balance equation

[2,8,14]. The energy equation can be written as

$$\frac{d}{dx} \left( k \frac{dT}{dx} \right) - \rho_p r_b C_c \frac{dT}{dx} = 0 \quad (1)$$

Since JA2 propellant is opaque, in-depth radiation absorption is assumed to be negligible. In general, the thermal properties of the propellant are functions of temperature. Miller [16,17] showed that the values of  $\alpha$ ,  $k$ , and  $C_c$  vary to some extent with the propellant temperature (for  $-40 < T < 50$  °C). However, the assumption that the thermal properties of the propellant were constant was utilized. Using this assumption, Eq. (1) can be integrated with the following boundary conditions:

$$\begin{aligned} x=0 & \quad T=T_s \\ x=-\infty & \quad T=T_o \end{aligned}$$

to yield the exponential expression:

$$\frac{T-T_o}{T_s-T_o} = \exp\left(\frac{r_b \rho_p C_c x}{k}\right) \quad (2)$$

where  $-\infty < x \leq 0$ . The burning propellant surface corresponds to  $x = 0$ .

By measuring the burn rate of the JA2 propellant at various initial temperatures, the temperature sensitivity of the propellant ( $\sigma_p$ ) is determined from the following equation, based upon the definition of  $\sigma_p$  [15]:

$$\sigma_p \equiv \frac{1}{r_b} \left[ \frac{\partial r_b}{\partial T_o} \right]_p = \left[ \frac{\ln(r_b) - \ln(r_{b,ref})}{T - T_{ref}} \right]_p \quad (3)$$

According to Arrhenius law, the relationship between the surface temperature and the burning rate may be expressed [15, 24]:

$$r_b = A \exp\left(\frac{-E_a}{2R_u T_s}\right) \quad (4)$$

If the burn rate is transformed into a mass burn rate by multiplication of the burn rate by the propellant density, a different form of the gasification law [3] is:

$$\dot{m}_b'' = \rho_p r_b = \rho_p A \exp\left(\frac{-E_a}{2R_u T_s}\right) \quad (5)$$

To bypass the problem of determining the Arrhenius coefficient, the following relationship suggested by Zenin [24] for numerous double-base propellants is utilized:

$$\dot{m}_b'' = 1.8 \times 10^3 \exp\left(\frac{-5000}{T_s}\right) \quad (6)$$

This expression corresponds to an activation energy of 21 kcal/mole, and it implies that as soon as  $r_b$  is measured, the burning surface temperature is known.

Neglecting radiation effects, an energy balance at the burning surface may be written:

$$Q_s = \frac{1}{r_b \rho_p} \left[ (\dot{q}_p'' - \dot{q}_g'') + \rho_p r_b (T_s - T_{ref})(C_{p,s+} - C_{c,s-}) \right] \quad (7)$$

When the result of  $Q_s$  calculated from Eq. (7) is divided by the heat of explosion, it can be compared to that determined from the empirical relationship proposed by Zenin [3,24] expressing the amount of heat release from the condensed phase during the combustion of a double-base propellant:

$$\frac{Q_s}{Q_{TOT}} = 0.17 - 0.103 \cdot \exp\left(\frac{-0.02 \cdot p}{\sqrt{r_b}}\right) \quad (8)$$

where  $Q_{TOT}$  represents the total heat release at constant volume,  $r_b$  is the linear burn rate in cm/s, and  $p$  is the pressure in atmospheres.

## DISCUSSION OF RESULTS

### Thermal Wave Structures for Solid- and Gas- Regions

A typical thermocouple trace is shown in Fig. 3. A vertical line indicates the location of the burning surface. The burning surface temperature is labeled  $T_s$  and its value was estimated from Eq.(6). Points to the left of the burning surface reveal the thermal wave within the solid phase. These points decay somewhat in exponentially fashion from the surface temperature,  $T_s$ , to the initial temperature,  $T_0$ . The slight variation in the subsurface temperatures could have been caused by the changing properties of JA2 as the propellant was heated or by the presence of impurities.

Points to the right of the burning surface line indicates the thermal wave within the gas phase. The temperature-time trace in this region shows some minor fluctuation. In the vicinity of the burning surface, the thermal trace could have been affected by carbonaceous deposits that formed on the surface during combustion and then broke free of the surface [10]. As the thermocouple became more exposed to the combustion gasses, it was subjected to motion and flutter in the gas flow. The combustion products present in the gas phase are known to react in the presence of platinum. Because of the catalytic effects of platinum, Klein, et al [8] used a thermocouple coated with a thin layer of borax and measured a somewhat different gas-phase trace than was measured with an uncoated thermocouple. Because the aim of this study was to measure the thermal wave up to the burning surface of the propellant, uncoated thermocouples were used, and thus, the gas phase traces may not be accurate. In addition, luminous flame was not present at pressures below 1.03 MPa (150 psig); thus, only fizz burning occurred. At test pressures above 150 psig, the presence of a dark zone and luminous flame was observed. The dark zone was physically observable for pressures up to 3.10 MPa (450 psig).

Figure 4 is provided to illustrate the consistency achieved in measuring the thermal profile of the burning JA2 propellant. The profiles virtually overlay each other in the subsurface region. The average of these traces in the sub-surface region can be fitted with an exponential profile. The traces begin to diverge as the gas-phase region passes over the thermocouple and causes the thermocouple to experience some movement. The position of divergence is a good indication of the location of the burning surface and hence its surface temperature. The agreement between the measured and the predicted ones using eq. (6) is excellent.

### Burning Rate Characteristics

This study examined the dependency of JA2 burning rate on pressure ranging from 0.689 MPa (100 psi) to 41.4 MPa (6,000 psi). Figure 5 shows a log-log plot of the burn rate versus pressure. For data collected with an initial temperature of 25°C, the graph shows a slope break near 5.51 Mpa (800

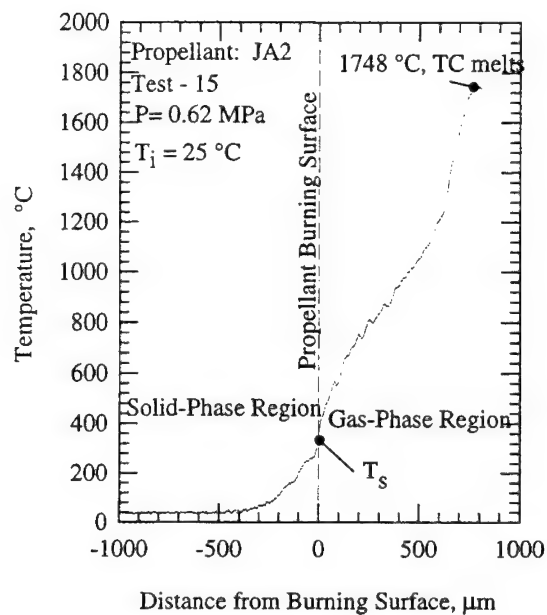


Figure 3. Typical thermocouple trace

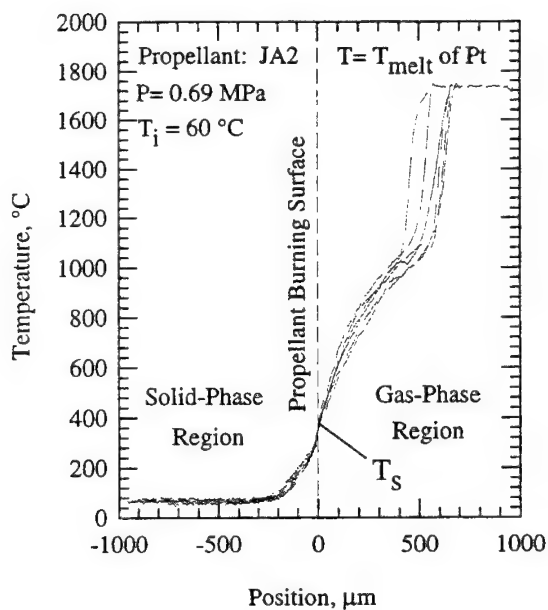


Figure 4. Overlay of thermal wave profiles

psi). Using St. Robert's burn rate formula ( $r_b = a \cdot p^n$ ), the pressure exponent,  $n$ , and the coefficient,  $a$ , can be determined for each curve shown on the plot. The coefficient ( $a$ ) was calculated from the y-intercept of the regression analysis. The pressure exponent ( $n$ ) was determined by the slope of the regression analysis. Data collected at various pressures with an initial propellant temperature of 60°C show a slope break at 4.5 MPa (650 psi).

When the results of the steady-state burning rate measurements of this work were compared to the interrupted burn rate measurements made by Watson, et al [18] and the closed-bomb tests of the Army [19], as shown in Fig. 6, good agreement is seen for pressures greater than 20.7 MPa (3,000 psi). For lower pressures there is a great disparity in the data. At low pressures the closed bomb data are subject to errors caused by the igniter and flame spreading processes. The instantaneous burn rates deduced from the interrupted burning tests conducted at PSU [18] are also plotted on the graph. In general, the instantaneous burn rate data are in good agreement with the steady-state data. This agreement shows the extraordinarily stable burning behavior of JA2. Detailed reasons are given by Watson, et al. [18].

Figure 7 shows the effect of initial temperature and chamber pressure on burning rate by combining PSU burn rate data (up to 41.4 MPa (6,000 psi)) with Army closed-bomb burn rate data. A slope break was observed in the data at 5.5 MPa (800 psi). For each curve shown in Fig. 7, a pressure exponent ( $n$ ) and coefficient ( $a$ ) for the St. Robert's law were calculated to describe the JA2 propellant burn rate for a broad range of pressures.

The data in Fig. 7 were used to generate the temperature sensitivity plot of shown in Fig. 8. In Fig. 8, there are two curves: the solid line represents the curve fits through the burn rate data collected at the initial temperatures of 25 °C and 60 °C, and the dashed line represents the curve fits through the burn rate data collected at the initial temperatures of 25 °C and -40 °C. The short dashed portion of the curve fit for the data collected at the initial temperatures of 25 °C and -40 °C at pressures below 20 MPa (2,900 psi) represents conjectured profile based upon the shape of the solid curve. For pressures above 20 MPa (2,900 psi), the value of  $\sigma_p$  is low. As the pressure increases from 0.69 MPa (100 psi) to 20 MPa (2,900 psi), the value of  $\sigma_p$  decreases rapidly to very low values. This decline in  $\sigma_p$  and the very low values of  $\sigma_p$  at higher pressures cause the lack of dynamic burning effect of JA2 propellant discussed by Watson, et al [18].

### Characterization of Thermochemical Behavior of JA2 Propellant

Surface temperature was determined from the temperature-time traces for comparison with eq. (6). To determine the surface temperature from the experimental data, a semi-log plot of the temperature-time trace was created. Data points in the sub-surface region of the trace formed a straight line on the semi-log plot. The point at which the trace made a break from its linearity was determined to be the location of the surface temperature [11,14]. When irregularities were observed in the subsurface plot, the break from linear had to be judged by using the data points above 150 °C (302 °F).

Because properties of the propellant (e.g., thermal conductivity, thermal diffusivity, and heat capacity) change with temperature, the surface temperature was in general difficult to determine. This graphical method of determining the surface temperature is subjective and can be ambiguous. The results of the data analysis were plotted in Fig. 9 with the predicted value of the surface temperature from Eq.(6). Figure 9 shows the good agreement between the experimentally determined and the predicted values of the surface temperature. Table 2 lists the pressures, predicted and experimentally deduced surface temperatures.

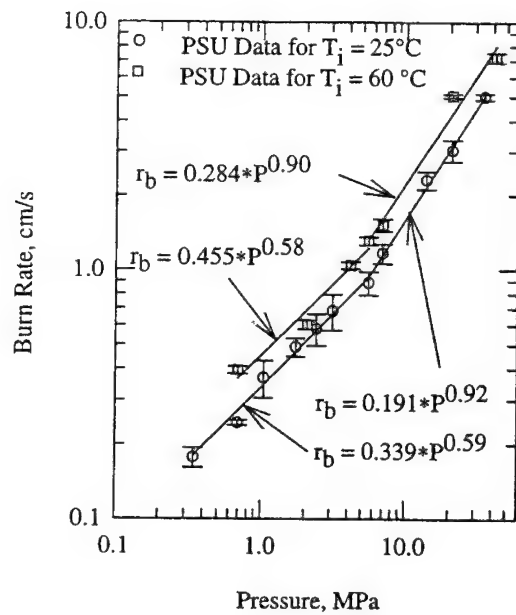


Figure 5. JA2 strand burn rates as a function of pressure and initial temperature

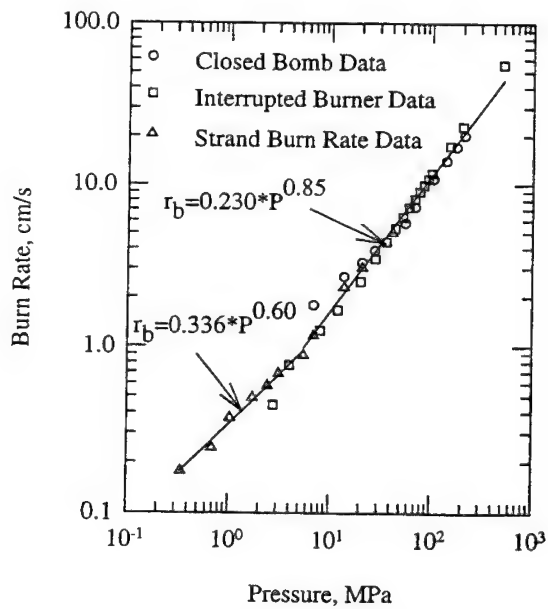


Figure 6. Comparison of JA2 strand burner burn rate data with those obtained from PSU interrupted burner [18] and Army closed bomb [19]



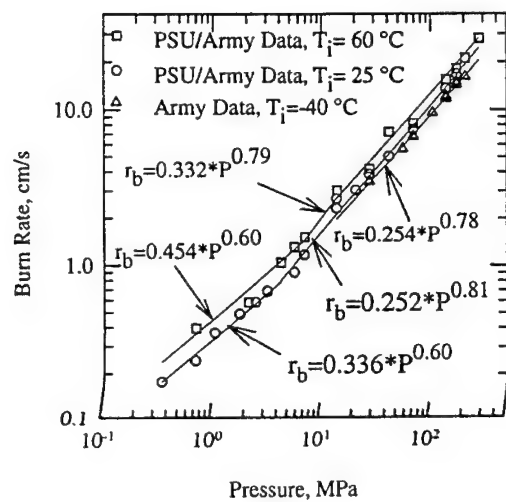


Figure 7. Burning rate expression generated from combined strand burner data of PSU and closed bomb data of Army [19] for JA2 propellant

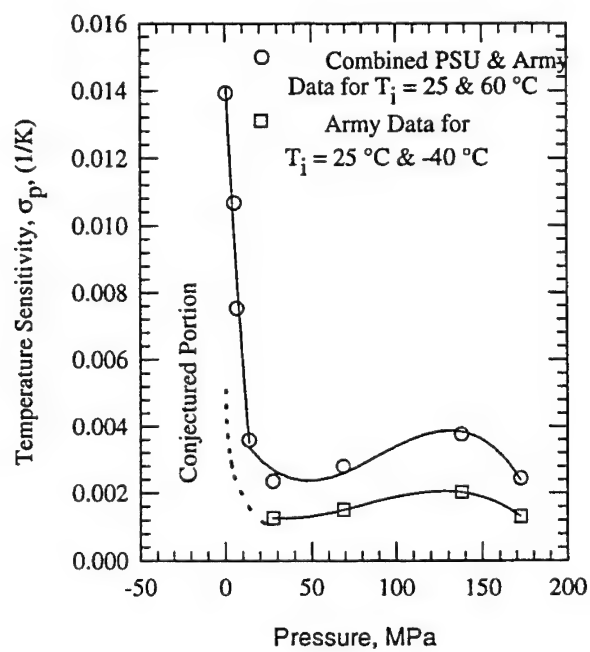


Figure 8. Temperature sensitivity of JA2

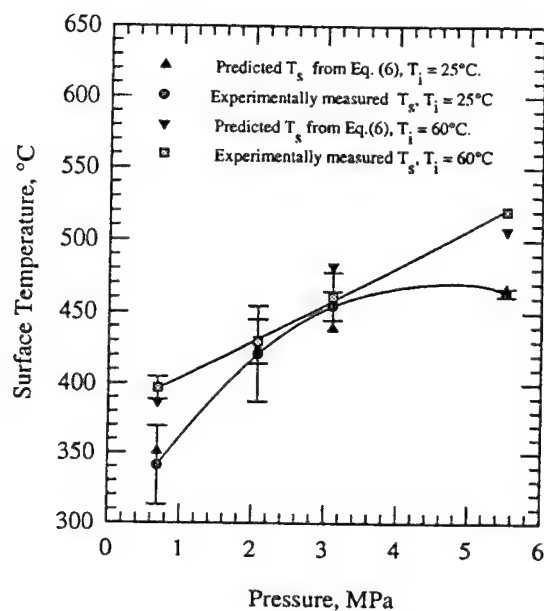


Figure 9. Dependence of surface temperature on pressure

TABLE 2  
Predicted and Experimentally Deduced Surface Temperatures for Test Pressures

Pressure MPa (psi)	Initial Temperature, $T_i = 25^\circ\text{C}$		Initial Temperature, $T_i = 60^\circ\text{C}$	
	Predicted Surface Temp From Eq.(6) (°C)	Deduced Surface Temp from T-t Traces (°C)	Predicted Surface Temperature (°C)	Deduced Surface Temp. from T-t Traces (°C)
0.69 (100)	351	334 ± 30	387	397 ± 10
2.06 (300)	424	445 ± 30	427	450 ± 20
3.10 (450)	439	454 ± 20	---	---
4.10 (600)	---	---	482	470 ± 20
5.15 (800)	465	465 ± 20	---	---

Figure 9 clearly shows that the temperature of the burning surface increases with increasing pressure. When the surface temperature was plotted versus the burn rate, as shown in Fig. 10, the activation energy of the propellant could be determined. By this method the activation energy of JA2 was determined to be 94.0 kJ/mole (22.4 kcal/mole). This value agrees quite well with the 21 kcal/mole activation energy used to predict the values of  $T_s$ . The pre-exponential constant for the pyrolysis law,  $A$ , is 18.54 m/s.

Figure 11 shows the deduced specific heat release at the burning surface ( $Q_s$ ), expressed in terms of a fraction of heat of explosion of the propellant ( $Q_{TOT}$ ), as a function of pressure. Values of  $Q/Q_{TOT}$  were deduced from Eq.(8) based upon measured quantities (such as burning-surface temperature, initial temperature, chamber pressure, propellant regression rate, and temperature gradients above and below the burning-surface) and calculated thermal properties of the solid- and gas- phases near the burning surface. The thermal diffusivity of the solid propellant was determined from the measured characteristic time of the thermal wave and the regression rate of the propellant. Thermal properties of the gas phase were determined by specifying the chamber pressure and burning-surface temperature for the CET86 computer code. These data were utilized in the evaluation of  $Q_s$  from Eq.(8). As shown in Fig. 11,  $Q_s$  generally increases with chamber pressure. The variation of the deduced data in Fig. 11 is believed to be caused by the variation in the surface temperature and the estimated values of the solid-phase thermal and transport properties. The predicted values of  $Q_s/Q_{TOT}$  versus pressure based upon Zenin's correlation for various double-base solid propellant [3,12,24] are superimposed on the same figure. In general, the predicted values using this correlation are within the experimental uncertainty.

The thermochemical properties deduced in this study are useful for analyzing the combustion performance of JA2 propellant and for gaining a better understanding of the characteristic behavior of this propellant. The values of thermochemical and physical properties obtained from literature and utilized in this study are presented in Table 3.

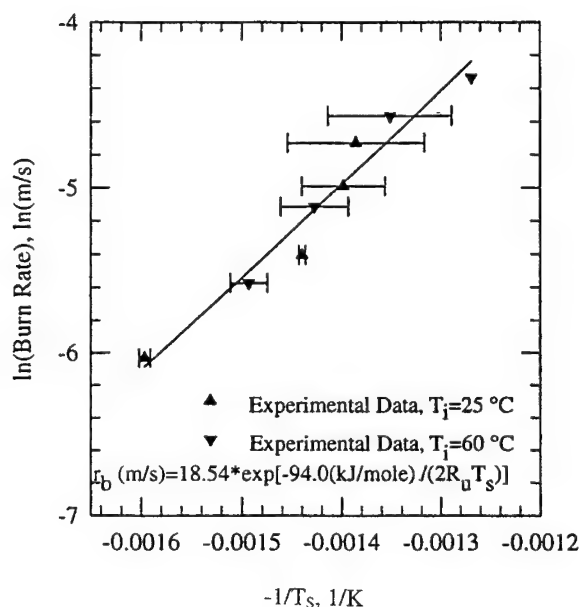


Figure 10. Relation between burn rate and burning surface temperature for JA2

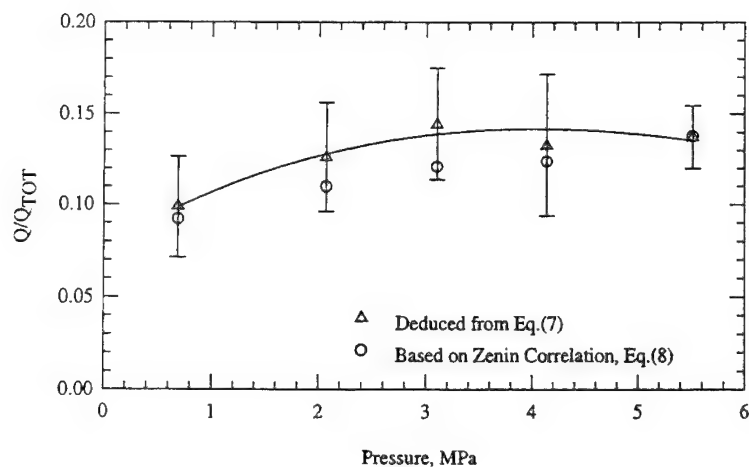


Figure 11. Heat release at the burning surface, expressed in fraction of heat of explosion of the propellant, as a function of pressure

TABLE 3  
Thermochemical and Physical Properties of JA2

Property	Value	Property	Value
$\rho_p$ , g/cc	1.595	$E_a$ , kJ/mole	94.0
$C_p$ , J/(gm °C)	0.40	Heat of Explosion, cal/gm	1117.3
$C_c$ , J/(kg K)	1341.8	Impetus, J/gm	1142.4
$\gamma$ for product gas	1.226	$T_f$ , K (p=100 atm)	2883
$\alpha_p$ (near surface), m <sup>2</sup> /s	$3.8 \times 10^{-7}$		

## SUMMARY AND CONCLUSIONS

In this study, the steady-state combustion characteristics of JA2 propellant have been studied at various pressures [0.69 MPa (100 psi) < p < 41.4 MPa (6,000 psi)]. JA2 propellant strands were burned in an optical strand burner. The propellant burning rates were deduced from the recorded video images of the burning surface regression using a superimposed scale. Thermal wave profiles were measured using fine-wire thermocouples at initial propellant temperatures of 25 °C and 60 °C for pressures from 0.69 MPa (100 psi) to 5.51 MPa (800 psi). Using reproducible results of the measured temperature-time traces, the burning-surface temperatures were determined for various test conditions. Several important thermochemical properties [such as the specific heat release at the surface ( $Q_s$ ), temperature sensitivity ( $\sigma_p$ ), and the activation energy ( $E_a$ )] were deduced from the measured temperature-time traces.

The major conclusions of this study:

1. Steady-state strand burn rate data agree very well with the burn rate data using either the PSU interrupted burner and the Army closed-bomb. This agreement clearly demonstrates the stable burning characteristic of JA2 propellant, i.e., its lack of dynamic burning behavior.

This observation can be explained by the sharp decrease of the temperature sensitivity ( $\sigma_p$ ) over the pressure range from 0.69 MPa to 20 MPa (100 psi to 3,000 psi) and the low values of temperature sensitivity for pressures above 20 MPa (3,000 psi).

2. The burn rate was determined as a function of pressure and initial temperature. Slope breaks in semi-log plots of the burn rate as a function of pressure and initial temperature were observed. Expressions of St. Robert's law to describe the burn rate behavior of JA2 above and below the slope breaks for each initial propellant temperature were determined. The values of the coefficient and pressure exponent for each expression of St. Robert's law were given as functions of initial temperature for initial propellant temperatures between  $-40^\circ\text{C}$  and  $60^\circ\text{C}$ .
3. Burning-surface temperature was determined from the measured thermal wave profiles. The burning-surface temperatures deduced from temperature-time traces agreed with the values predicted by an empirical rate expression of Zenin [3,24].
4. The activation energy of JA2 propellant associated with pyrolysis was determined to be 22.4 kcal/mole. The value compares quite closely with the average activation energy of 21 kcal/mole for numerous double-base propellants studied by Zenin.
5. Values of the specific heat release at the propellant burning surface,  $Q_s$ , were also determined for JA2 propellant. The value of  $Q_s$  increases slightly with pressure. When the comparing the  $Q_s$  values with the results of Zenin's relation for the heat release at the burning surface of double-base propellants, the heat release at the burning surface calculated by Zenin's relation is within the experimental error of the measurements of this study.

#### ACKNOWLEDGEMENT

This work was performed under contract DAAL03-92-0020 with the U.S. Army Research Office under the management of Dr. D. M. Mann. A part of the support and propellant samples were provided by Mr. Fred Robbins of the Army Research Laboratory. Their interest and support are greatly appreciated.

#### REFERENCES

1. Symposium on Kinetics of Propellants, *Journal of Physical and Colloid Chemistry*, Vol. 54, 1950, pp. 847-954.
2. Lengelle, G., Duterque, J., Verdier, C., Bizot, A., and Trubert, J.F., "Combustion Mechanism of Double Base Solid Propellants," *17th Symposium (International) on Combustion*, The Combustion Institute, Pittsburgh, PA, 1979, pp. 1443-1451.
3. Zenin, A.A., "Thermal Wave Profiling Measurements Using Fine Wire Thermocouples," URI Seminar presented at The Pennsylvania State University, Aug. 1994.
4. Beckstead, M.W., "Model for Double-Base Propellant Combustion," *AIAA Journal*, Vol. 18, No. 8, 1980, pp. 980-985.
5. Suh, N.P., Tsai, C.L., Thompson, C.L., and Moore, J.S., "Ignition and Surface Temperatures of Double-Base Propellants at Low Pressures I. Thermocouple Measurements," *AIAA Journal*, Vol. 8, No. 7, 1970, pp. 1501-1506.
6. Rogers, C.R., and Suh, N.P., "Ignition and Surface Temperatures of Double-Base Propellants at Low Pressures II. Comparison of Optical and Thermocouple Techniques," *AIAA Journal*, Vol. 8, No. 8, 1970, pp. 1314-1321.
7. Thompson, C.L., and Suh, N.P., "Gas Phase Reactions near the Solid-Gas Interface of a Deflagrating Double-Base Propellant Strand," *AIAA Journal*, Vol. 9, No. 1, 1971, pp. 154-159.

**BALLISTIC AND MICROSTRUCTURAL PROPERTIES  
OF A HIGHLY FILLED GUN PROPELLANT WITH VARYING  
THICKNESSES OF INERT SURFACE COATING**

**S. M. Caulder, F. S. Kim, and B. K. Moy**  
Indian Head Division, Naval Surface Warfare Center  
Indian Head, Maryland 20640-5035

**ABSTRACT:** A highly filled multiperforated gun propellant containing predominately RDX was spray coated on its surface with cellulose acetate butyrate (CAB). The coating thickness was either 1 or 2.4% by weight. The purpose of the coating was to lower the initial maximum peak pressure and impart a progressive burn rate to the gun propellant grains. The coated and uncoated propellant grains were combusted in a closed bomb. Pressure-time combustion curves were obtained. The homogeneity and thickness of the coatings were measured from photomicrographs and x-ray maps obtained using a differentially pumped scanning electron microscope (WET-SEM) equipped with a light element energy dispersive x-ray detector (EDS). The SEM and closed bomb results showed that the initial pressure-time ballistic traces could be lowered and retarded as a function of coating thickness.

**INTRODUCTION**

When a gun propellant burns in the barrel of a weapon, the internal ballistic energy of the propellant is best utilized if the gas pressure is kept as constant as possible up to the time the projectile emerges from the barrel. In order to best achieve this progressive burn one can impart a suitable shape to the grain as well as treating the surface of the grain with a suitable substance that retards initial combustion. By treating the surface with an inert substance one can lower the maximum peak pressure of the pressure-time curve in a gun chamber environment. This surface treatment will also alter the time trace in the low (< 1000 psi) pressure range.

Extruded single and double base gun propellants have traditionally had methyl and ethyl centralite driven into the exterior propellant surface to control the pressure peak maximum. This surface treatment slows the burning rate of the exterior surface with relationship to the inner surface, so that a more progressive ballistic behavior is achieved. The steeping method for diffusing the centralites into the propellant grain is not applicable to highly filled propellants.

This paper will discuss the research on highly filled nitramine gun propellant grains that were spray coated with an inert substance. The thickness of the coating was measured and correlated with pressure-time combustion curves obtained from closed bomb measurements.

## EXPERIMENTAL

### Method of Coating Gun Propellant Grains

Two different highly filled gun propellants were coated with cellulose acetate butyrate (CAB). The first gun propellant was a HELP-1 formulation designated M-43. This formulation contained the following ingredients: RDX, CAB, nitrocellulose (NC), ethyl centralite (EC), and a mixture of bis dinitro propyl acetal/formal (BDNPA/F). The second gun propellant was designated EX-97 and contained RDX, NC, CAB, EC, trimethylolethane trinitrate (TMETN) and triethyleneglycol dinitrate (TEGDN). The physical dimensions of the HELP-1 and EX-97 propellant grains are 0.504 in. diameter and 0.738 in. in length; 0.270 in diameter and 0.30 in. in length respectively. Both propellant grains were multiperforated.

The propellant grains were coated in a "sweetie" barrel with a solution containing cellulose acetate butyrate, ethyl acetate and ethanol. The coating procedure used an adjustable fan patten spray head and extension nozzle. The system uses a 5 gallon pressurized tank. The spray is air aspirated with a pressurized fluid feed from the tank. The theoretical coating thickness was determined by weighing coated grains and calculating the surface area of the grain from its measured dimensions. Using these measurements one can calculate the coating thickness, the actual coating thickness, and its uniformity was determined from photomicrographs and elemental oxygen and nitrogen x-ray maps of cross sectioned propellant grains obtained using a differentially pumped scanning electron microscope equipped with light element (C,N,O) energy dispersive x-ray microanalysis capabilities. Since a WET-SEM was used no additional sample preparation was necessary.

## RESULTS AND DISCUSSION

### Scanning Electron Microscopy

The photomicrographs of the microstructure of the two different formulations of gun propellant grains used in this investigation, EX-97 and HELP-1, were very similar in appearance. This is due to the fact that the solids loading is essentially the same for both formulations. SEM photomicrographs of the surface of an uncoated EX-97 grain magnified 100X and 1000X are shown in Figures 1 and 2 respectively. SEM photomicrographs of the surface of EX-97 grain that had been coated 1% by weight with CAB are shown in Figures 4 and 5. When comparing the SEM photomicrographs of the uncoated grains (Figures 1 and 2) with those of the 1% coated grains (Figures 4 and 5) one can readily see the differences in surface microstructure between the coated and uncoated grains. The micro-porosity seen in the uncoated grains has virtually disappeared in the coated grains. The structural characteristics of the RDX solids are visible in the uncoated grain (Figure 2) but are not discernable in the coated grain (Figure 4). SEM photomicrographs of fractured cross sections of the uncoated and 1% coated EX-97 grains are shown in Figures 3 and 6 respectively. When comparing the photomicrograph of the cross sections of the uncoated and coated grains one can see the thin coating on the 1% grain at this magnification. Measurements made at higher magnifications of the thickness of the coatings on the 1% coated grains showed small variations at different points on the grain. These small variations give an indication of the uniformities of the coating.

The microstructure of the surface of the EX-97 grain that had a 2.4% by weight coating is shown at 100X and 1000X in Figures 7 and 8. The 2.4% coated grains had a much more uniform coating over the entire grain surface when compared with the grains coated at the 1% level. The surface

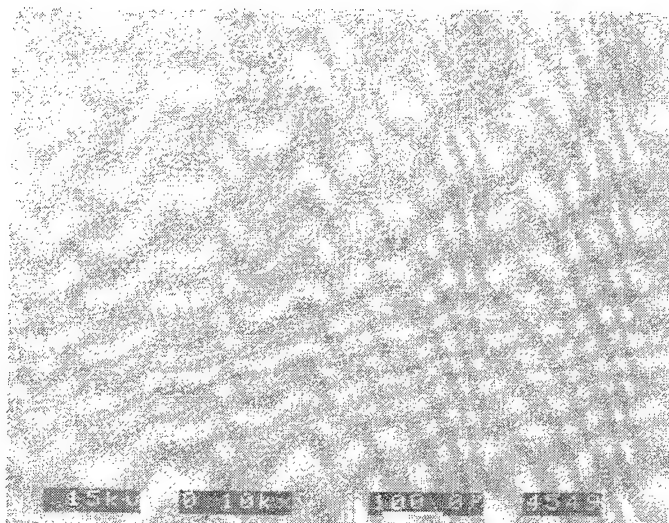


Figure 1. SEM photomicrograph surface of uncoated grain  
100X

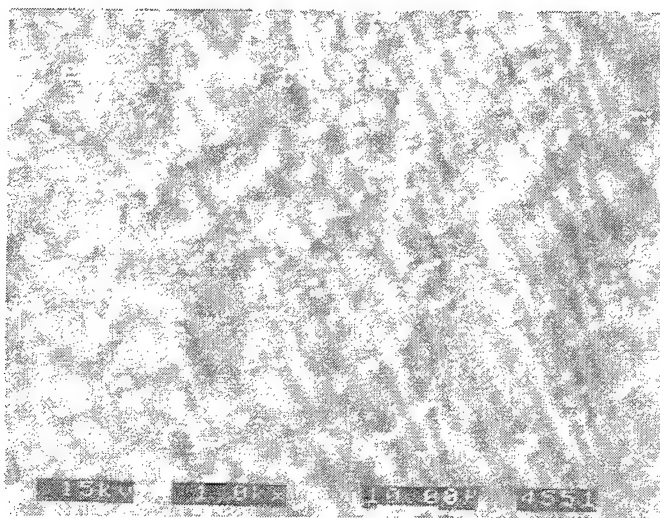


Figure 2. SEM photomicrograph surface of uncoated grain  
1000X



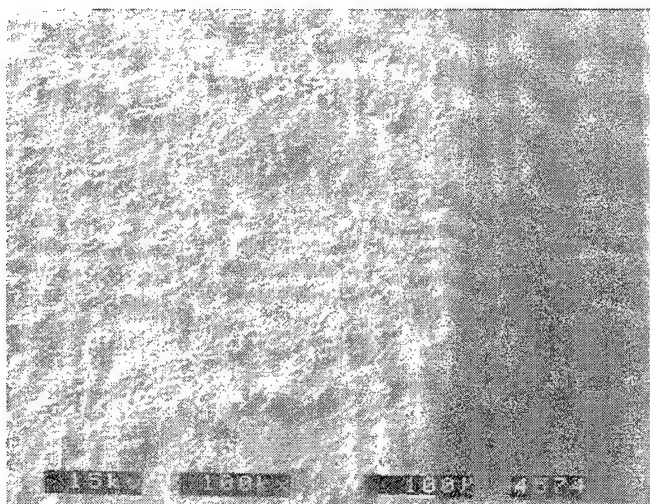


Figure 3. SEM photomicrograph cross section of uncoated grain  
100X

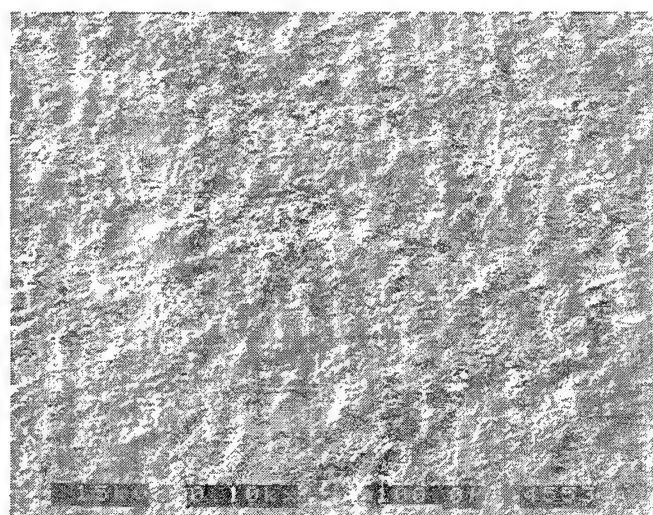


Figure 4. SEM photomicrograph surface of 1% CAB coated grain  
100X

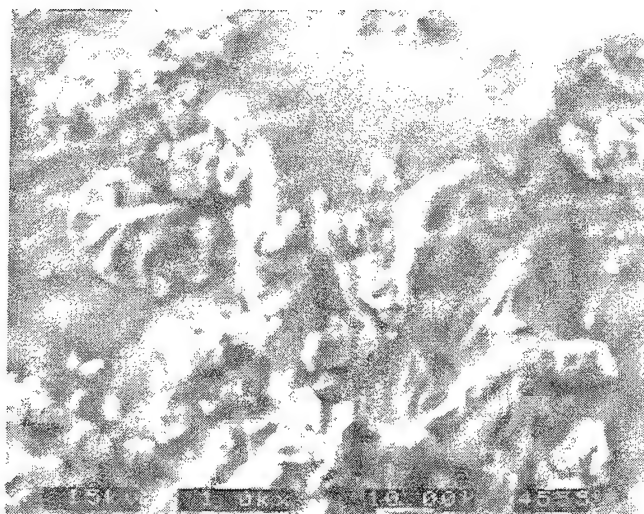


Figure 5. SEM photomicrograph surface of 1% CAB coated grain  
1000X

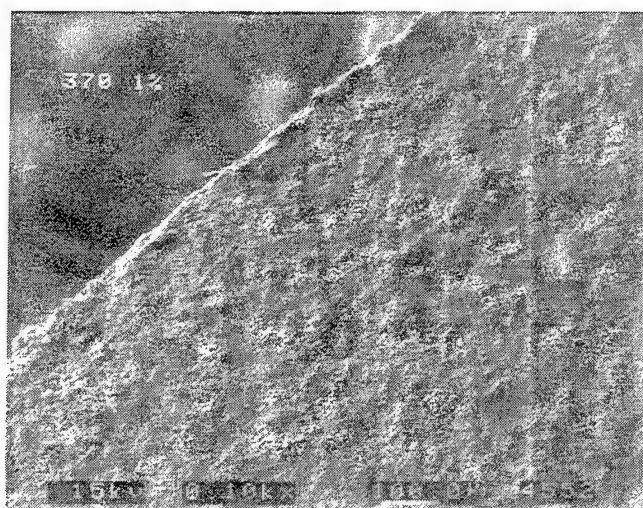


Figure 6. SEM photomicrograph cross section of 1% CAB coated grain  
100X

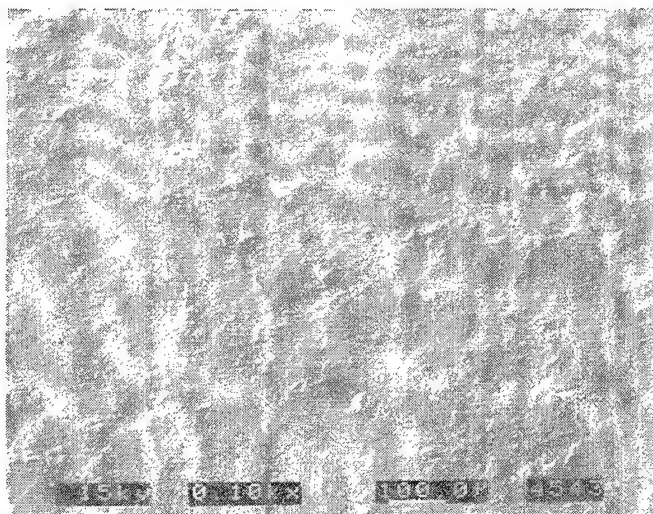


Figure 7. SEM photomicrograph surface of 2.4% CAB coated grain  
100X

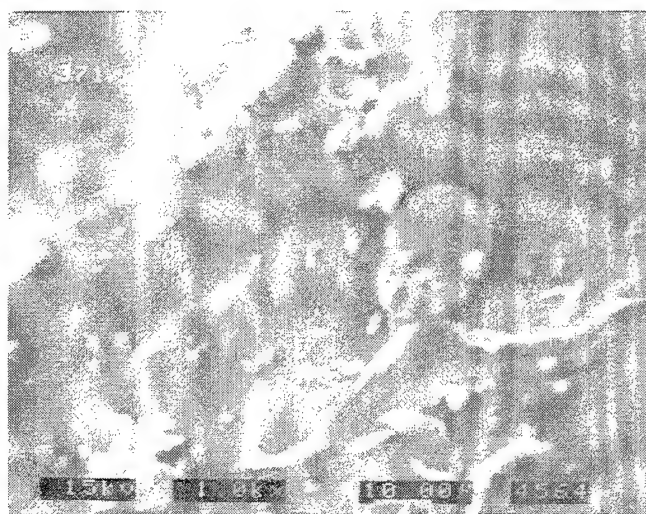


Figure 8. SEM photomicrograph surface of 2.4% CAB coated grain  
1000X

microstructure of the 2.4% coated grains were more glass-like in appearance than the 1% grains. This can be seen when comparing Figure 5 with Figure 8. The SEM photomicrograph shown in Figure 9 is of a 2.4% coated fractured grain cross section. In this photomicrograph one can very easily see the coating and measure its thickness. A number of thickness measurements made on several cross sectioned grains showed that the 2.4% coatings were much more uniform in thickness than the 1% coated samples.

While SEM can be used to measure coating thickness one needs to be certain that none of the energetic components of the grain formulation has diffused to the surface of the inert CAB coating. Components of the HELP-1 formulation, such as TMETN and TEGDN migrate as the grain ages. This migration can alter the intended purpose of the inert coating. In order to ascertain whether any of the energetic components have migrated to the surface one needs to look at the elemental composition of the surface of the coated grains with x-ray energy dispersive analysis (EDX).

### Energy Dispersive X-ray Microanalysis (EDX)

X-ray microanalysis can measure qualitatively and quantitatively the elements from atomic number 3 to 99. In this study of coated and uncoated gun propellants the two elements of interest are nitrogen and oxygen. Since the inert coating cellulose acetate butyrate contains carbon, hydrogen and oxygen the signal of interest is associated with oxygen. The energetic portion of the grain will have signals associated with carbon, nitrogen and oxygen. When a coated grain is fractured and a x-ray map is generated of the cross section, one can determine the thickness of the inert coating by measuring the difference between the synchronous cursors associated with the oxygen and nitrogen maps.

A reference oxygen and nitrogen map of a cross sectioned uncoated EX-97 grain is shown in Figure 10. As one would expect, there is no difference in the two maps since oxygen and nitrogen elements are uniformly distributed throughout the microstructure. Figure 11 shows separate oxygen and nitrogen maps associated with a cross sectional grain that had a 1% CAB coating. Since the CAB coating contains no nitrogen and the energetic portion of the rest of the grain does, the difference between the synchronized cursors provides a measure of the coating thickness. The measured coating thickness for a specific area of the 1% coated grain was found to be 18.90  $\mu\text{m}$ . This value varied slightly from grain to grain and from area to area within the same grain. The range observed for the average coating thickness from grain to grain varied between 16.20 and 19.00  $\mu\text{m}$ . The theoretical value assuming uniform coating thickness based on measured average weight gains of a number of 1% by weight coated grains and measured grain geometries was calculated to be 16.00  $\mu\text{m}$ . The oxygen and nitrogen maps associated with a cross sectioned 2.4% coated grain is shown in Figure 12. The average measured thickness for this coating was 32.50  $\mu\text{m}$ . The calculated theoretical value is 39.00  $\mu\text{m}$ . The coatings on these grains were more homogeneous than was observed on the 1% coated grains. There was also less grain to grain variation. A theoretically calculated plot of uniform coating thickness vs. weight % CAB is shown in Figure 13. X-ray analysis of the coated surfaces of a number of grains did not show evidence of a nitrogen signal. Thus during the time period of our experiments no nitrogen containing energetic material migrated to the CAB coated surface. Therefore, closed bomb experiments were expected to show a progressive burn as a function of coating thickness.

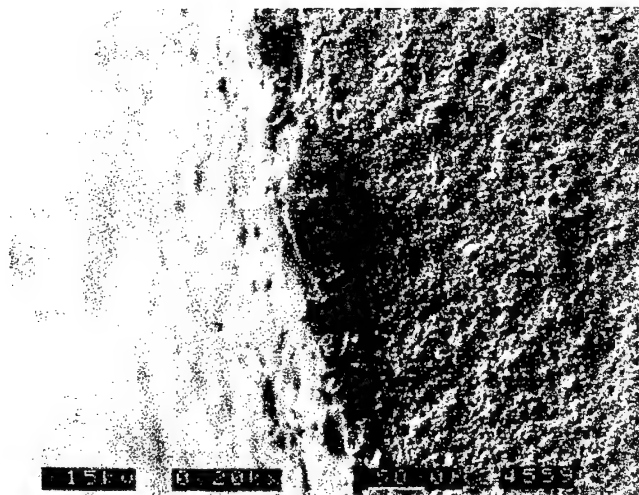


Figure 9. SEM photomicrograph cross section of 2.4% CAB coated grain  
200X

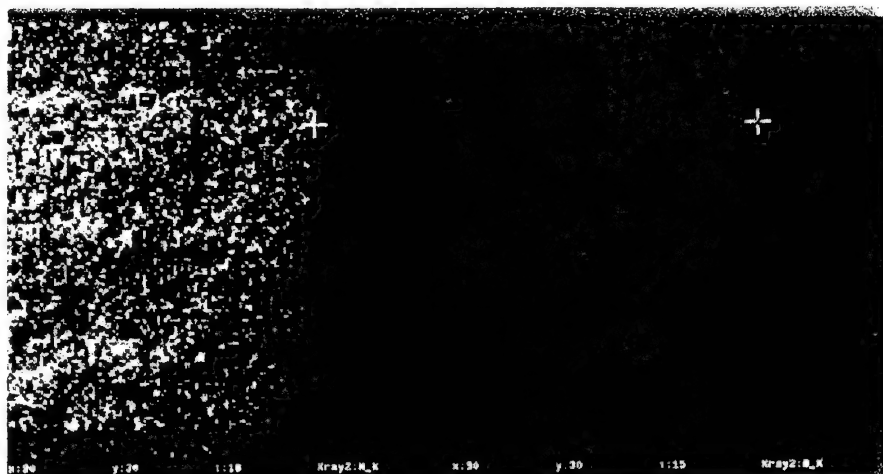


Figure 10. X-ray map of uncoated grain oxygen and nitrogen map

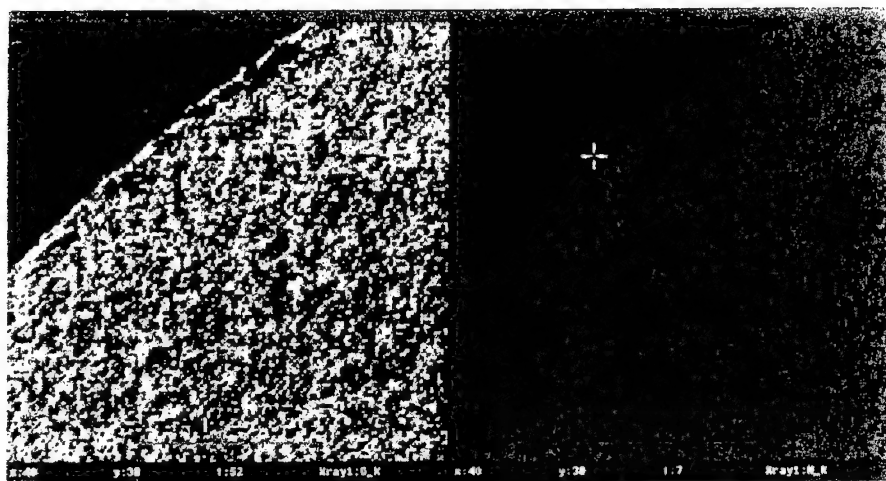


Figure 11. X-ray map of 1% CAB coated grain oxygen and nitrogen map

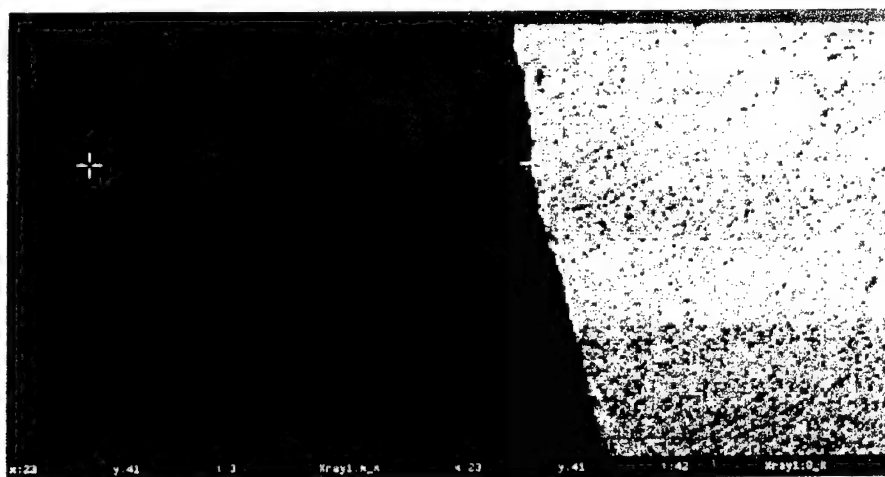


Figure 12. X-ray map of 2.4% CAB coated grain oxygen and nitrogen map

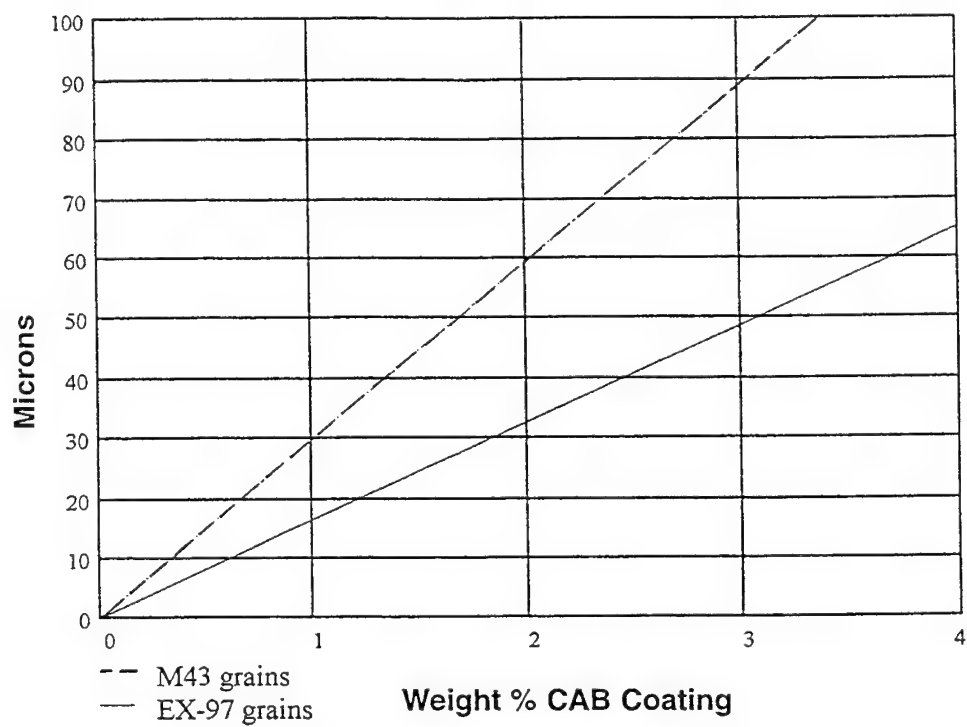


Figure 13. Theoretical coating thicknesses for 2 sample grain geometrics based on weight percent of CAB

### Closed Bomb Ballistic Results

The closed bomb was used to measure pressure-time characteristics of the uncoated and coated propellant grains. The pressure vs. time traces are shown in Figures 14 and 15. Figure 14 shows the pressure vs. time trace for the full pressure range up to 50,000 psi. Figure 15 shows the major time differences as a function of coating thickness at low pressures. As can be seen, and as expected, the thicker the inert coating, the slower the initial pressure rise becomes. Also, one can see that as you approach pressures of 2000 psi the relative quickness (RQ's ( $dp/dt$ )) becomes almost identical. A similar effect should occur in a gun barrel.

The pressure-time traces shown in Figures 14 and 15 are obtained in a 182 cc volume closed bomb instrument using 41 grams of test propellant. The curves indicate that there is a delayed gas generation event from the initiation of the igniter to the 3000 psi pressure measurement point in the closed bomb. This tells us that the coated outside surface of the grain is probably not igniting at the same time as the uncoated perforations are igniting. Only after the flame has thoroughly ignited the perforations does the coating begin to burn off and the outer surface of the grain begin to burn. These closed bomb pressure-time traces do not give us prediction of how the coated propellant will behave in a gun barrel, but only that the burn behavior of the coated propellant is probably suited to optimizing performance of gun systems. The actual time it would take in a gun system for the coating to burn off is undetermined with these preliminary tests; however, given the ability to apply differing coating thicknesses and the possibility of using other coating compounds, the necessary ballistic match could be readily tailored.

### CONCLUSIONS

A technique for imparting an inert coating to highly filled nitramine gun propellants has been developed. The characterization of the coated propellant samples by SEM and x-ray microanalysis showed that one can attain a uniform coating that will impart beneficial pressure-time characteristics when measured in a closed bomb. Similar characteristics should be observed in a gun barrel. This x-ray microanalysis technique can also be used to measure the diffusion of an energetic component into the inert coating. This type of measurement is beneficial when looking for changes in ballistic behavior as a function of aging of the propellant grains.



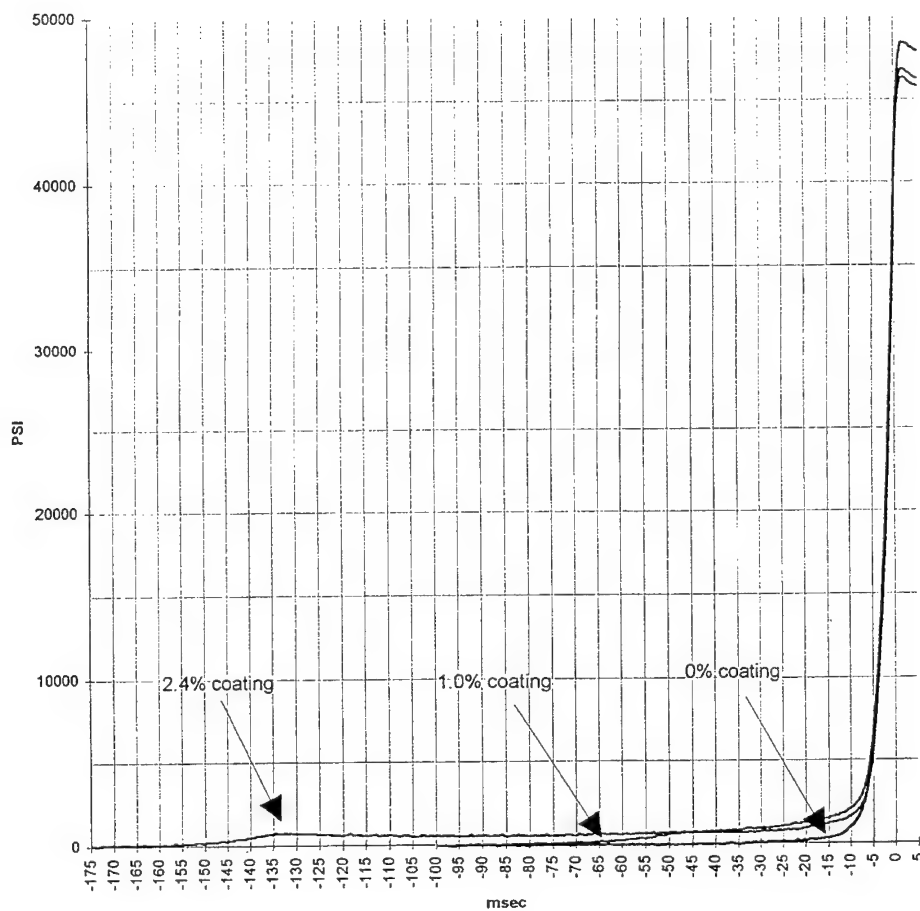


Figure 14. Closed bomb pressure vs. time traces  
0, 1, 2.4% CAB coatings, zero offset at 5000 psi

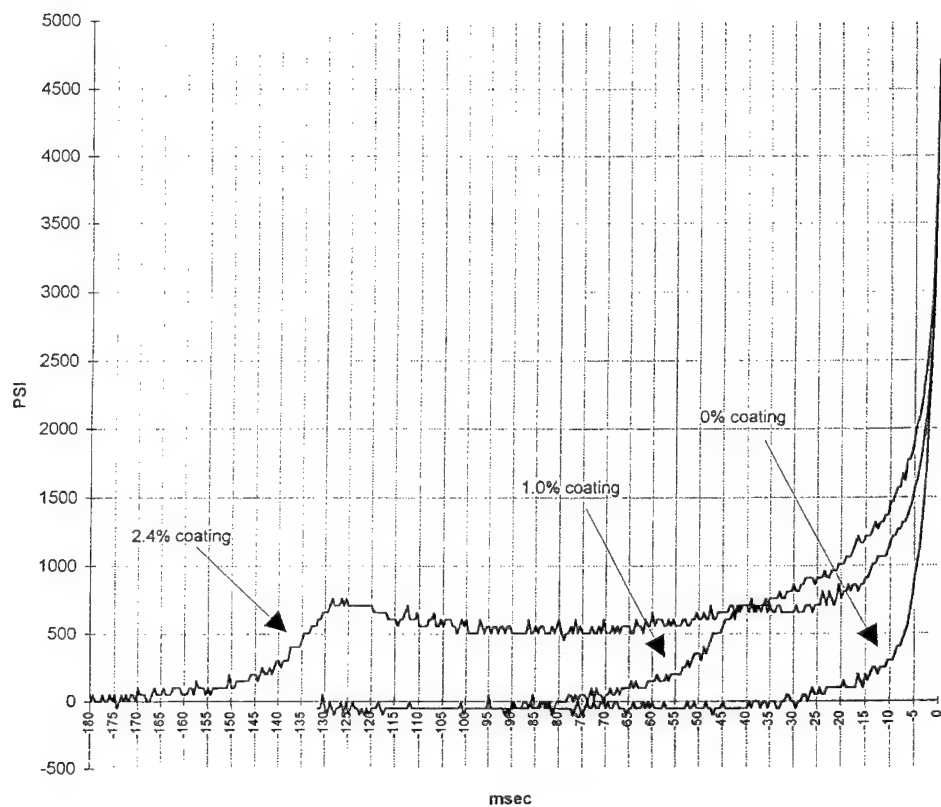


Figure 15. Closed bomb pressure vs. time traces  
0, 1, 2.4% CAB coatings, aero offset at 5000 psi

## IMPROVEMENT OF BALLISTIC CHARACTERISTICS OF GUN PROPELLANTS AND CHARGES USING METALLIC ADDITIVES

I.G. Assovskii<sup>1</sup>, O.T. Chizhevskii<sup>2</sup>, V.V. Sergeev<sup>2</sup>

<sup>1</sup>Semenov Institute of Chemical Physics RAS,  
Kosygin St. 4, Moscow 117977 Russia;

<sup>2</sup>GNPP "Pribor", Moscow 113519 Russia.

**ABSTRACT:** The purpose of this paper is to demonstrate the possibility of improving the ballistic properties of conventional gun propellants by adding fine grain metallic elements into the propellant composition or by including them as a separate component of gun charge. The primary focus is the improvement of single- and double-base gun propellants using either aluminum powder or foil. The possibility of obtaining improvements in the velocity of gun-launched projectiles has been proven theoretically by means of the thermodynamic calculations and numerical simulation of the interior ballistics process, and experimentally by firings, using 30-mm/75-caliber gun. The addition of aluminum particles into the propellant composition as well as into the gun-chamber was tested. The latter provides a rather simple method to improve the thermal characteristics of powder gases and optimize the heat-release process thereby improving the flatness of the gun pressure-time curve. This paper continues and summarizes the author's investigations published in [1,2].

### INTRODUCTION

Increased projectile velocity is a major objective of gun and rocket design. In order to achieve high speeds for projectile, a chemical propulsion system must use a hot light gas as driving agent because the attainable maximum of projectile velocity is proportional to the speed of sound in the working substance used [3-6]. Therefore by either increasing propellant energy or decreasing the average molecular weight of the combustion products one may improve interior ballistic characteristics for both conventional gun-tube and for rocket launchers [6-9].

Composite propellants containing metallic particles as energetic additives have long been used for solid-propellant rocket motors. It is customary to assume that application of high-energy propellants in gun-tube systems is extremely limited, as it is accompanied by increasing of gun barrel wear, which is proportional to the propellant flame temperature [10,11]. The hot combustion gases in ordnance are known to wear steel from the gun barrel, and eventually render the barrel unserviceable.

The experience of recent years indicates that gun tube erosivity depends on the composition of combustion products and on the bore surface state, as well as on the flame temperature (see, for example [11]). Therefore it is desirable to achieve the increase in projectile muzzle velocity by means of optimization of the combustion products composition, and keep the maximum gas temperature and pressure within the allowable limits. The theoretical and experimental results presented in this paper show that such approach can be realized using aluminum additives to conventional gun propellants.

### THERMODYNAMIC AND BALLISTIC CALCULATIONS

Thermodynamic properties of propellants include the flame temperature  $T_f$  and composition  $B_j$  of the combustion products, their specific heats, average molecular weight  $M$ , and covolume under certain conditions [4,6]. The method used to calculate these properties for propellants containing metallic additives has been published in [1]. The pressure of condensed products, caused by the Brownian movement of particles, is neglected.

The calculations were carried out for given gas-pressures assuming the equation of state corresponding to an ideal gas. This assumption is permissible, as comparisons of results, computed with the ideal gas equation of state and equations for real gases indicate that only relatively small differences arise in flame temperature and in average molecular weight of gas products [8,12]. Nevertheless, the calculation of gas-pressures for various loading densities  $D$  needs the state equation for a real gas, for example, a virial equation [4,7,12], taking into account covolume and other characteristics of real gas-state.

The trustworthiness of the numerical method [1] was evaluated by comparison of the combustion product composition as calculated for conventional gun powders and rocket solid propellants with appropriate literature data. A good agreement between calculated results and literature values justifies the method [1] used in this work.

The gross coefficients  $B_j$  of compositions for single- and double-base gun-propellants (pyroxylin and ballistite), with various contents of aluminum, and the enthalpies  $H$  of their formation under standard condition  $T = 298$  K, are presented in Table 1.

TABLE 1  
Summary of Compositions and Thermochemical Properties of the Propellants.

Powder		Pyroxilin				Ballistite			
Addition* of									
Al, %		0	5	10	15	0	5	10	15
Al		0	1.765	3.369	4.834	0	1.765	3.369	4.834
	O	36.78	35.03	33.44	31.98	36.39	34.66	33.08	31.64
$B_j$ ,	H	25.02	23.83	22.74	21.75	27.86	26.53	25.33	24.22
mol/kg	N	9.709	9.247	8.827	8.443	10.46	9.965	9.512	9.098
	C	20.84	19.85	18.94	18.12	20.24	19.28	18.40	17.60
Enthalpy,									
	-H, MJ/kg	2.364	2.251	2.149	2.056	2.096	1.996	1.905	1.823

\* It is the weight-ratio of the aluminum to the original propellant.

These thermochemical properties of propellants are the initial data for further thermodynamic and ballistic calculations. The results of thermodynamic and ballistic characteristics of original and metallized powders at pressure 3000 atm and temperature 298 K are shown in Table 2.

As we can see in Table 2, the introduction of aluminum leads to increasing maximum temperature  $T_f$  and powder force  $F=RT_f/M$ , where  $R$  is the universal gas constant. As a result, the corresponding increase in muzzle velocity  $V$  of projectile is provided. It is of great interest as an interior ballistic problem to estimate the variation of thermodynamic characteristics by pressure changes in ranges typical for gun-firings.

TABLE 2  
Thermodynamic and Ballistic Characteristics of Powders with Aluminum Additives

Powder	Pyroxilin				Ballistite			
Addition~ of Al, %	0	5	10	15	0	5	10	15
$T_f$ , K	2878	3152	3403	3634	2947	3212	3454	3676
M, g/mol:								
all products	26.27	27.60	28.92	30.25	25.48	26.77	28.06	29.35
gas-phase	26.27	25.11	23.95	22.80	25.48	24.36	23.24	22.12
Relative weight of $Al_2O_3$	0	0.090	0.172	0.246	0	0.090	0.172	0.246
of gas-products	1	0.956	0.912	0.868	1	0.956	0.912	0.868
Relative volume $W_{cond}/W_{prod}$ ( $Al_2O_3$ )	0	0.008	0.015	0.021	0	0.008	0.015	0.021
$(D_o-D)/D_o$ , %	0	3.29	5.39	6.89	0	2.85	4.75	5.70
$W_{charg}/W_{chamb}$	0.209	0.195	0.186	0.178	0.198	0.186	0.18	0.171
Density, g/cm <sup>3</sup>	1.60	1.65	1.70	1.74	1.60	1.65	1.70	1.74
Heat of explosion, cal/g	956	1086	1205	1313	1006	1134	1250	1357
Force F, J/g	911	1044	1181	1325	962	1096	1236	1382
$F/F_o$	1	1.146	1.30	1.46	1	1.14	1.29	1.44
$V/V_o$	1	1.047	1.09	1.124	1	1.044	1.08	1.12
Addition to covolum, cm <sup>3</sup> /kg	0	0.028	0.059	0.093	0	0.028	0.059	0.093

Towards this aim, the calculations of maximum temperatures  $T_f$  and powder forces  $F$  were carried out for pressure values up to 5000 atm. The results of calculations presented in Table 3 show that pressure influence is relatively small. So, the relative increase in temperature  $T_f$  by pressure variation from 40 to 5000 atm consists 1.7÷2.0%, and the maximum increase in powder force consists 1.0 %.

This increase in temperature,  $T_f$ , takes place due to the suppression of dissociation reactions, that simultaneously leads to some increase in average molecular weight  $M$  of gas mixture. The competing influence of these two factors leads to appearance of a maximum on the curve  $F(P)$  located in the pressure range between 1000-2000 atm.

TABLE 3  
Combustion Products Temperature  $T_f$  and Force  $F$  vs Pressure.

Powder	Pyroxilin				Ballistite			
Pressure, atm	40	100	1000	5000	40	100	1000	5000
$T_f$ , K	2833	2850	2872	2880	2890	2912	2940	2950
$F$ , J/g	903	907	911	910	952	957	962	961

The effect of dissociation suppression influences the temperature,  $T_f$ , and powder force mainly at pressures up to 1000 atm. This effect can be neglected in the field of relatively high pressures 1000-5000 atm. So, the estimations obtained for  $P=3000$  atm are true over a wide range of pressures. The weak dependence of powder force on pressure points indirectly to the possibility of using the equation of state for an ideal gas instead of one for real gas.

#### DISCUSSION OF THE CALCULATIONS RESULTS

The thermodynamic calculations testify that addition of aluminum to conventional gun-powders may be one of the potential methods for increasing their energy density. As we mentioned, the utilization of high-energy propellants (HEP) is usually accompanied by increasing in temperature  $T_f$  and, as result, in erosivity of powder gases. For example, HEP containing explosives usually have the high temperature,  $T_f$ , together with high molecular weight,  $M$ , of combustion products due to an increase in  $CO_2$  content in products. This circumstance is illustrated by thermochemical data for non-metallized powders, presented in Table 4.

It is desirable to make up the increase in powder force,  $F$ , and consequently in muzzle velocity of projectile,  $V \sim F$ , by decreasing the molecular weight  $M$ , but keeping the temperature,  $T_f$ , within the allowable limits. This purpose is served for conventional propellants by means of aluminum addition, as the data presented in Tables 2 and 4 show.

The energy increase for conventional propellants by introduction of aluminum leads simultaneously to a highly desirable lower molecular weight,  $M$ , of the working gas. This is due to the reduction of  $CO_2$  to  $CO$  by the oxidation of aluminum present as condensed phase  $Al_2O_3$ . On the basis of calculations, a significant effect on the projectile velocity,  $V$ , on the one hand, and on the life of gun barrel on the other hand, could be optimized by the content of aluminum in the powder [charge].

For traditional gun-propellant rounds, not more than 5-8 wt.% content of aluminum is acceptable. In such a case, one would expect a flame temperature increase up to 3100-3300 K, a powder force increase up to 15-20%, and a muzzle velocity increase up to 4-8%. These improvements are highly substantial in comparison with improvements made by other known methods, for example, the using of powder with fast-burning explosives.

TABLE 4

Thermochemical Characteristics and Compositions of Combustion Products of Metallized and Conventional Gun Propellants\*

Powder	T, K	F, J/g	M, g/mol	Composition of Products, mol/kg					
				CO	CO <sub>2</sub>	H <sub>2</sub> O	H <sub>2</sub>	N <sub>2</sub>	Al <sub>2</sub> O <sub>3</sub>
M1	2480	928	22.2	22.8	2.40	6.10	9.10	4.50	
P	2878	911	26.3	14.3	6.56	9.37	2.82	4.70	-
B	2947	962	25.5	14.3	5.92	10.2	3.34	5.05	-
M30	3021	1078	23.3	11.8	3.00	10.5	5.50	11.9	-
P+5%Al	3152	1044	25.1	15.3	4.50	7.99	3.50	4.43	0.09
B+5%Al	3212	1096	24.4	15.2	4.04	8.64	4.12	4.75	0.09
M5	3264	1079	25.1	16.5	4.90	9.30	4.00	4.90	-
P+10%Al	3403	1181	24.0	16.0	2.90	6.47	4.34	4.17	0.17
B+10%Al	3454	1236	23.2	15.8	2.60	6.94	5.06	4.47	0.17
P+15%Al	3640	1325	22.8	16.4	1.72	4.81	5.34	3.92	0.25
B+15%Al	3676	1382	22.1	16.0	1.56	5.14	6.12	4.20	0.25
M8	3716	1178	26.2	13.0	6.40	10.2	2.40	5.40	-

\* Note: P is pyroxilin; B is ballistite; M1 - M30 are the conventional US gun-propellants [8,11].

#### FIRING TESTS OF GUN-CHARGES CONTAINING ALUMINUM ADDITIVES

In order to experimentally verify the proposed method for increasing in muzzle velocities of projectiles, some firings were done with charges containing aluminum additives taken in excess of 100% of powder mass. An investigation of conventional charges containing aluminum powder ASD-1, or granulated aluminum AG-90 (on the base of 90% ASD-1 with 10% of pyroxylin), was performed.

Also examined were gun charges containing aluminum foil particles of different thickness. The aim of these tests was to identify both the optimum form for aluminum foil elements, and their distribution over the gun chamber volume. The trials were carried out using conventional 30 mm ballistic gun-tube. The measurements of projectile muzzle velocities were provided by solenoids. The maximum gas-pressure was measured by crusher gang and simultaneous measurement of the pressure curve  $P(t)$  was provided by means of the piezometric pickup T-6000.

The results of ballistic trials show that small additions of aluminum powder ASD-1 (or the composition of granulated aluminum AG-90) in amount of 2-6%, leads to an increase in the maximum pressure of powder gases. The more aluminum contained in the charge, the higher is the pressure increase. The addition of 4.4% aluminum powder ASD-1 leads to an increase in the muzzle velocity up to 6.3%, and a maximum pressure increase of up to 20%. The addition of

4.6% of granulated aluminum AG-90 of different fractions into the same charge leads to increase in the muzzle velocity of up to 2.5-6.0%, and a maximum pressure increase of up to 10-16%.

These experimental data confirm the theoretical forecast, and have been the basis for further optimization of the charge design to reduce temperature,  $T_f$ , keeping the increase in muzzle velocity,  $V$ . The main goal for subsequent experiments was the search for the optimum form of aluminum elements to improve thermodynamic characteristics of combustion products, and to optimize the dynamics of energy release during combustion of the metal-containing charges.

Results of these investigations for charges containing particles of aluminum foil indicate the peculiar dependence of the ballistic characteristics on foil thickness. So, the utilization of foils having the certain thickness ensures the smaller rate for the maximum pressure increase in comparison with the rate of the muzzle velocity increase. This unusual experimental observation can be explained by the influence of the time-delay of aluminum particles ignition, which depends on foil thickness.

A special investigation of the interior ballistic process was carried out to confirm this hypothesis and to compare the burning processes for conventional and metallized charges. These experiments were provided by synchronous measurement of pressure curves  $P(t)$  at five different cross sections along the barrel. The maximum pressure for the charge containing the aluminum foil elements (3% of charge mass) was slightly lower (0.9%), than that for a conventional charge. At the same time, the addition aluminum foil increased the muzzle velocity by up to 2.3%.

This effect is accompanied by an increase in the flatness of the pressure curves, i.e., the ratio of the mean pressure to the peak pressure. In the case of charges with aluminum foil, the pressure measured in the barrel, at the point 7.5 clb. from the chamber, is higher than the corresponding value for conventional charge by up to 8.3%. As the projectile moves along the bore, the pointed difference of pressures are decreased: at a distance of 26 clb. it is 3.3%, and near the muzzle end (75 clb) it is only 2.0%.

The ballistic efficiency of the aluminum addition can be also estimated by comparison of the pressure impulses for conventional and metallized charges. These values were derived according to experimental curves,  $P(t)$ , for different cross-sections of bore. For the point at a distance of 7.5 clb. from the chamber's bottom, the pressure impulse for the metallized charge exceeds the corresponding value for the regular charge by 14.4%. For the next section, corresponding to a distance of 26 clb., this value is lowered by up to 9.8%.

The high energy release by aluminum burning is favorable for total combustion of powder charge in the bore during the pressure decrease period of the shot cycle. The numerical estimation of consumed powder corroborates this effect. The long ignition-delay of aluminum foil changes the gas-temperature distribution along the bore. According to theoretical estimations taking into account the foil ignition-delay, the temperature-time curve has the second maximum as a result of aluminum burning. The optimization of aluminum content is directed to increase this second maximum of temperature but not exceed the level of first maximum gas temperature. In the case of the metallized charge, the descending part of the curve  $T(t)$ , next to the second maximum, falls above the same one for the original charge without aluminum.



## CONCLUSION

The results of experimental and theoretical investigations presented in this paper demonstrate the possibility of improving the ballistic characteristics of conventional gun-propellants by addition of small amounts of either aluminum powder or foil particles of certain thickness.

The interior ballistic process for gun-tube systems using the multi-phase combustion products of metallized charges as their working substance can be governed effectively by means of the amount & size/form of additives.

## REFERENCES

1. Assovskii I.G., Boborykin V.M., and Leipunskii O.I., Ballistic Characteristics of the Gun Propellants with Metallic Additives. The Thermodynamic Calculation, Report of Inst. Chem. Physics, The USSR AS, Moscow, 1983 [in Russian].
2. Assovskii I.G., Sergeev V.V., and Toporkov D.L., Ballistic Characteristics of the Gun Powders with Metal Elements, Proc. Int. Conf. on Combustion, Moscow - St. Petersburg, IPC RAS, 1993.
3. Serebryakov M. E., Interior Ballistics, Oborongiz, Moscow, 1949, [in Russian] .
4. Comer J., Theory of Interior Ballistics of Guns, Wiley, New York, 1950.
5. Landau L. D., and Lifshitz E. M., Hydrodynamics, Theoretical Physics, Vol. 6, Nauka, Moscow, 1986.
6. Sorkin R.E., Gas-thermodynamics of solid-propellant rocket motors, Nauka, Moscow, 1967 [in Russian].
7. Krier H. and Summerfield M. (eds.), Interior Ballistics of Guns, Progress in Astronautics and Aeronautics, Vol. 66, AIAA, Washington, D.C., 1979.
8. Stiefel L. Gun Propellants, pp. 307-324, *ibid*.
9. Kuo K.K., and Summerfield M. (eds.), Fundamentals of Solid Propellant Combustion, Progress in Astronautics and Aeronautics, Vol. 90, AIAA, Washington, D.C., 1984.
10. Orlov B.V., Larman E.K., and Malikov V.G., Arrangement and Design of Gun Barrels, Mashinostroenie, Moscow, 1976 [in Russian].
11. Ward J.R., Stobie I.C., Kaste R.P., and Bensinger B.D., Effect of Surface Oxide on Gun Barrel Wear, CorrosionNACE, Vol.39, No.10, pp. 384-385, (1983).
12. Baibuz V.F., Zitserman V.Yu., Golubushkin L.M., and Chernov Yu.G., Chemical Equilibrium in Nonideal Systems, Inst.of High Temperatures, AS USSR, Moscow, 1985.

## BURN RATE STUDIES OF GAS GENERATOR PROPELLANTS CONTAINING AP/RDX

A.N. Nazare, S.N. Asthana, P.G. Shrotri and Haridwar Singh  
High Energy Materials Research Laboratory  
Pune 411 021, India

**ABSTRACT:** This paper reports burn rate results of AP/RDX-based compositions with Epoxy / Epoxy-GAP binder. Bimodal AP composition with 40% Epoxy binder gave burn rates of 2.1-2.4 mm/s in the pressure range of 1-8.8 MPa and appeared to be suitable for the primary combustor in ramjet applications. Incorporation of 10-30% GAP at the cost of epoxy binder resulted in a 30-250% increase in burn rates, and replacement of coarse AP by fine AP (4 and 10 $\mu$ ) led to a 1.5-5 -fold increase in burn rates. Addition of 2 parts of copper chromite / ferric oxide as a catalyst resulted in a moderate increase in burn rates, while incorporation of butyl ferrocene led to a 1.3-3 -fold increase in burn rates. Ballistically modified AP/Epoxy/GAP compositions with burn rates ranging from 5-15 mm/s at 1 MPa to 15-30 mm/s at 8.8 MPa and moderate flame temperatures have potential for gas generator application. The effect of replacement of AP by RDX on burn rates was also studied during this work.

### INTRODUCTION

Research in the field of gas generators has gained tremendous momentum during recent years in view of their wide application as a source of power for a relatively short duration. Simplicity and lighter weight are other special features of gas generators as compared to conventional short duration power equipment. Gas generators are used extensively as base bleed units, to augment the range of gun-propelled projectiles by about 20-30%, and as a source of hot gas for driving the turbines of turbopumps in a liquid rocket and actuating catapults[1-2]. AP(ammonium perchlorate)-based compositions find wide applications as base bleed propellants, as they meet the basic requirement of combustion efficiency at subatmospheric pressures. The flame temperature (Tf) of practically useful base bleed units ranges from 1600K to 3300K with burn rates of 1-5 mm/s at atmospheric pressure[3-5]. Gas generators for air bag applications, turbine propulsion, and as aircraft starters demand clean burning with noncorrosive exhaust products without solid residues. The ballistic requirements of gas generators are low Tf (1000-2500 K), but efficient combustion in the pressure range of 2-6.9 MPa [6-8]. Ammonium nitrate(AN)- based systems meet these requirements. However, AN undergoes crystal phase transition at 32°C, leading to volume changes which are undesirable as grains undergo thermal cycling during exposure in the field. A number of additives are added to AN to make it phase stabilized. However, only a few compounds have been found effective[6]. Triamino guanidine nitrate (TAGN) has been found to be an attractive oxidizer for gas generators[7]. AN/TAGN-based gas generators having Tf of 1270-2400 K and burn rates of 1-10 mm/s at 6.9 MPa are reported in literature. Nitramines are considered potential oxidizers for gas generators, as they can offer clean burning with chlorine free exhaust. However, to the best of our information, no systematic study has been carried out on nitramine-based systems, probably due to the inherent problems of combustion inefficiency at low pressures. Various binders used for gas

generators so far include cellulose acetate, polyesters, polyethers, polybutadienes (HTPB/CTPB). Tetrazoles are expected to be highly useful as they decompose to give mainly  $N_2$ . Azido-polymers like glycidyl azide prepolymer (GAP) have acquired great importance as energetic binders/plasticizers for gas generators [6-8]. Epoxy binders, which may be of interest for gas generators in view of their superior tensile properties to polybutadiene-based polymers, have not been explored.

In view of the foregoing and because the search is on for combustion-efficient gas generators for various applications, the present work was undertaken to study and develop gas generators with AP and RDX as the oxidizer. The effect of selected catalysts, namely, ferric oxide, copper chromite and n-butyl ferrocene on the burn rates of AP / RDX compositions has also been studied. Low-molecular-weight GAP was used as a plasticizer to achieve high combustion efficiency. As low molecular weight GAP poses the problem of gasification as a plasticizer for HTPB due to its interaction with isocyanates curatives[9], epoxy binder which has found application for composite formulations[10,11] was selected.

### EXPERIMENTAL

Novolac epoxy resin-Dobekot E4 (epoxide equivalent  $330 \pm 35$ , viscosity  $17120 \pm 50$  cps, density  $1.06$  g/cc) cured with polyamide hardener-EH 411 (viscosity  $17750 \pm 50$  cps, density-  $0.97 - 0.99$  g/cc) supplied by M/s Dr Beck and Co (India) was used as binder. The energetic plasticizer GAP (molecular weight about 500, duly characterized) was synthesized as per the method described in reference[12]. AP of particle size 150-200  $\mu$  grounded to average particle size 10 and 4  $\mu$  using Jet-O-Mizer and RDX of particle size 25  $\mu$  obtained by reduction method were used as oxidizer. Ferric oxide of 0.6  $\mu$  size; copper chromite of particle size 3-4  $\mu$  and butyl ferrocene of 99% purity were used. Propellant compositions were prepared by slurry - cast technique[13]. The procedure involved the deaeration of a mixture of Dobekot E4 and GAP under agitation in a vertical mixer of 5 lit. capacity. Oxidizer (AP/RDX) was added to the deaerated mix. The mixing continued for one hour at room temperature. Subsequently, hardner EH 411 (E4 : EH411 ratio 60:40) added and additional mixing was carried out for 20-30 min. The slurry thus obtained was cast in the mould under vacuum (vacuum bell). The propellant was cured at  $40^\circ\text{C}$  for 5 d. The curing process involved reaction between  $-\text{NH}_2$  group of the polyamide and epoxy group of the resin.

Burn rates were determined in the pressure range of 1-8.8 MPa by employing Acoustic Emission (AE) technique. The method involved combustion of propellant strand in the nitrogen pressurized steel bomb using water as the media. Acoustic signals generated by the deflagrating sample were unidirectionally transmitted through the water and sensed by the transducer with resonance frequency of 200 kHz. The burn rates were computed from x-y chart record of acoustic signals.

The calorimetric values (cal-val) were obtained by using Julius Peters bomb calorimeter. Mechanical properties were determined on Universal Material Testing machine (INSTRON MODEL 1185).

In order to understand combustion behavior, extinguished propellant samples were subjected to Scanning Electron Microscopic (SEM) studies using equipment of JEOL make (Model- JSM-J 200). Propellant samples were ignited by means of ignition wire and quenched using liquid Nitrogen. The samples were coated with a thin layer of gold under vacuum and subjected to 25 kv acceleration voltage. Photographs were taken at the magnification level of  $\times 750$ .

### RESULTS AND DISCUSSION

#### AP- based gas generator compositions

In view of the superior mechanical properties and better density of epoxy resins as compared to HTPB, studies were conducted with epoxy as main fuel cum binder. Since it was not possible to

**TABLE 1**  
Comparative Data on Different Binder Systems

Binder system	Mechanical properties				
	Tensile strength (Mpa)	Elongation (%)	Compressive strength (MPa)	Compression (%)	Density (g/cc)
HTPB 50, Emolein 50 XL with TDI, NCO/OH=1	0.6	60	-	-	0.93
Epoxy 100(60% resin: 40% hardner)	6.3	35	76	60	1.03
Epoxy 75, GAP 25	0.8	20	1.2	30	1.1

incorporate more than 60% of oxidizer (particularly in fine size) in the epoxy matrix, experiments were restricted to 60% solid loading.

Burn rates obtained for the compositions containing 60% AP and 40% binder system are given in Figures 1-3. A composition containing bimodal (coarse and fine) AP (200u-70% : 10u-30%) with 40% epoxy binder was taken as the control, which gave burn rates of 2.1-2.4 mm/s in the pressure range of 1-8.8 MPa. On incorporation of 10, 20 and 30% GAP at the cost of epoxy binder, an increase in the burn rates of the order of 30-250% was obtained. With 10u AP, burn rates obtained were 1.5-2 times higher in comparison to corresponding bimodal AP-based compositions. On incorporation of AP of 4u size in place of AP of 10 u size, the increase in burn rates was 1.5-3.5 times for epoxy binder-based compositions and 1.5-4.7 times for 10-30% GAP based compositions. Pressure exponent 'n' values as calculated from plot of log of burn rate vs log of pressure (Figures 1-3) for bimodal AP compositions were 0.06-0.3 and for fine AP (10u and 4u) compositions in the range of 0.23 - 0.45.

The results on the effect of selected ballistic modifiers, namely, copper chromite, ferric oxide and butyl ferrocene, are given in Figures 4-6. While incorporation of 2 parts copper chromite and ferric oxide led to a marginal increase in burn rates (4-40%), butyl ferrocene addition resulted in a 1.3 - 3-fold enhancement in burn rates in the entire pressure range studied. The values of 'n' for ballistically-modified compositions ranged between 0.3 and 0.67 (Figures 4-6).

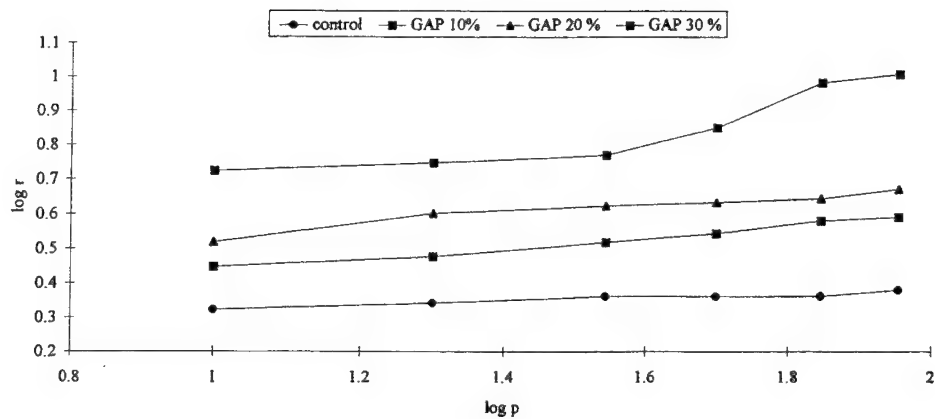
#### **RDX / AP-RDX- based Gas Generators**

RDX- based propellant compositions with 40% epoxy binder exhibited burn rates of 1.9-3.7 mm/s in the pressure range of 3.5-8.8 MPa. The increase in burn rates on incorporation of 10% GAP at the cost of epoxy resin was about 3-30% and on increase in GAP to 20% level, 21-90% burn-rate enhancement was obtained. The pressure index value for RDX- based compositions containing 40% epoxy binder, as well as 10% GAP : 30% epoxy combination, was 0.6-0.7, while for 20% GAP : 20% epoxy combination the 'n' value was 0.6 in 3.5-4.9 MPa pressure region and 1-1.5 in the pressure range of 4.9-8.8 MPa (Figure 7).

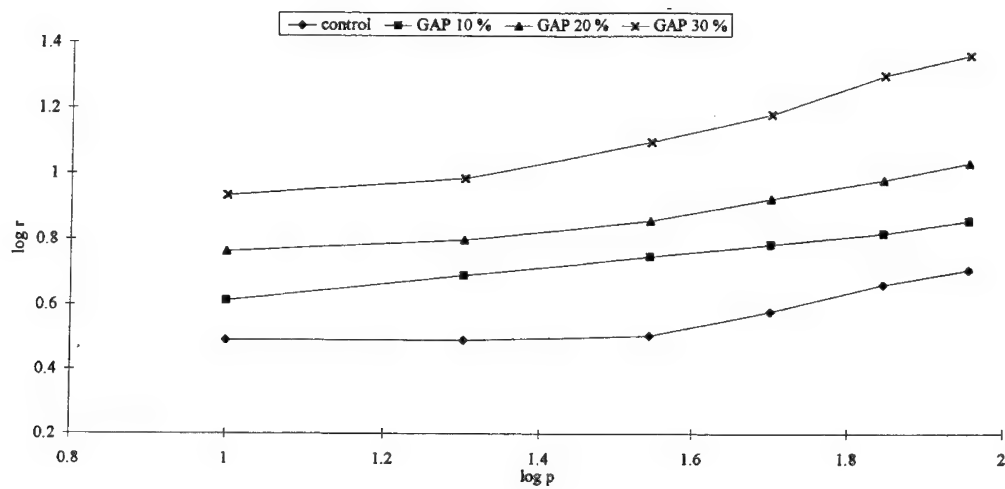
In order to achieve superior burn rates, part of RDX was replaced by AP. A 1:1 combination of AP and RDX (30% AP / 30% RDX) gave combustion rates intermediate to those for RDX and AP individually. Thus, with 20% epoxy binder and 20% GAP combination burn rates of 5-8 mm/s were obtained in the pressure range of 4.9-8.8 MPa. The corresponding burn rates with 10% epoxy binder and 30% GAP compositions were 6.4 - 14 mm/s. Ballistic modification of 1:1 AP-RDX composition containing 10% epoxy and 30% GAP binder with copper chromite, ferric oxide, and butyl ferrocene resulted in a marginal increase in burn rates (Figure 8).

#### **Combustion mechanism**

Burn rates of solid propellants depend on a number of factors, of which dependence on pressure is critical from a propulsion point of view. The burning process of a given propellant is defined in terms of combustion wave structure, which is a function of the propellant composition and operating conditions. At the propellant burning surface, referred to as condensed phase, an endothermic / exothermic decomposition reaction produces reactive gases. The interactions between the emitted gases in gas phase above the burning surface generate heat to form a luminous flame zone, where exothermic reactions are completed and final combustion products are formed. The heat feedback from high temperature gas phase to unburnt propellant surface raises its temperature to decomposition temperature resulting in gasification and subsequent exothermic chemical reactions. This successive heat feedback process results in steady-state combustion [14].



**Figure 1.** Burning Rates of AP (C:F-70:30) Based Gas Generating Compositions



**Figure 2.** Burning Rates of Ap (10 u) Based Gas Generating Compositions

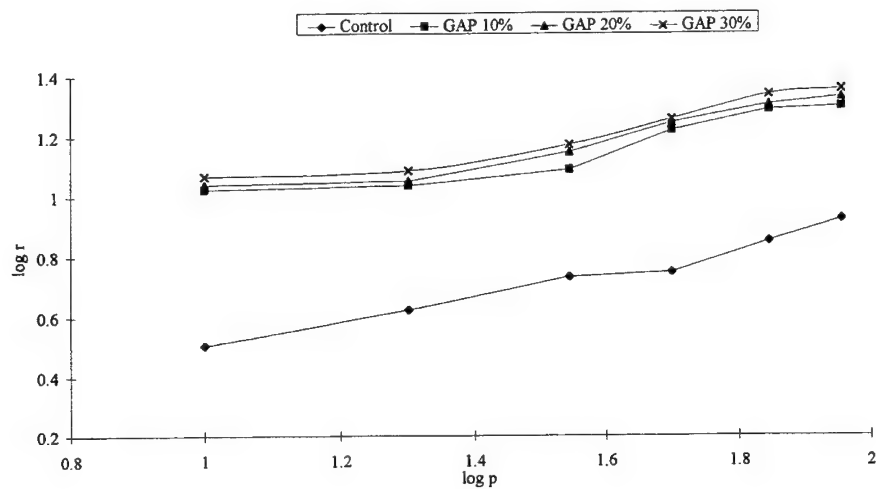


Figure 3. Burning Rates of AP (4u) Based Gas Generating Compositions

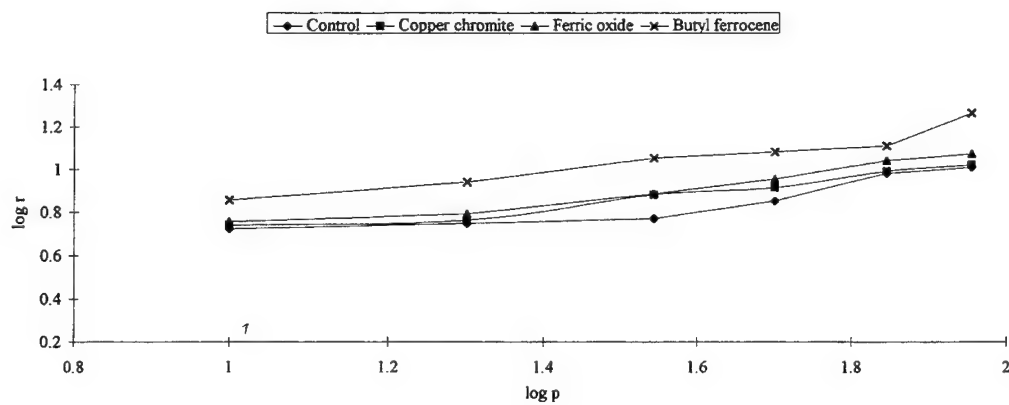
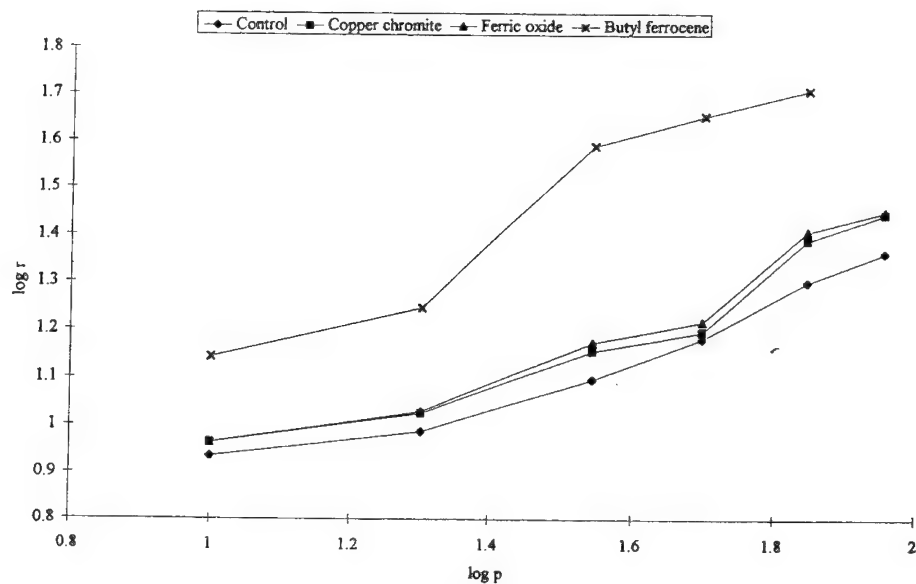
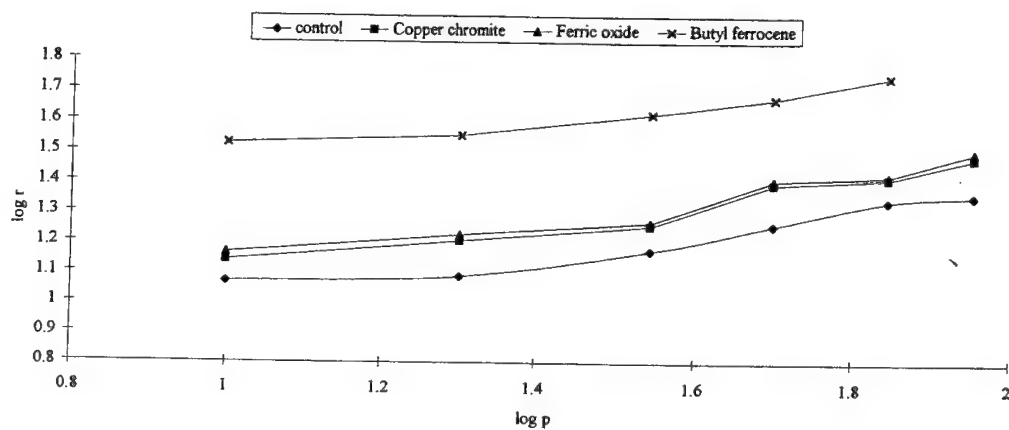


Figure 4. Burn Rates of AP (C:F-70:30) GAP Gas Generating Compositions with Selected Ballistic Modifiers



**Figure 5.** Burn Rates of AP (10 u) GAP Gas Generating Compositions with Selected Ballistic Modifiers



**Figure 6.** Burn Rates of AP (4 u) GAP Gas Generating Compositions with Selected Ballistic Modifiers



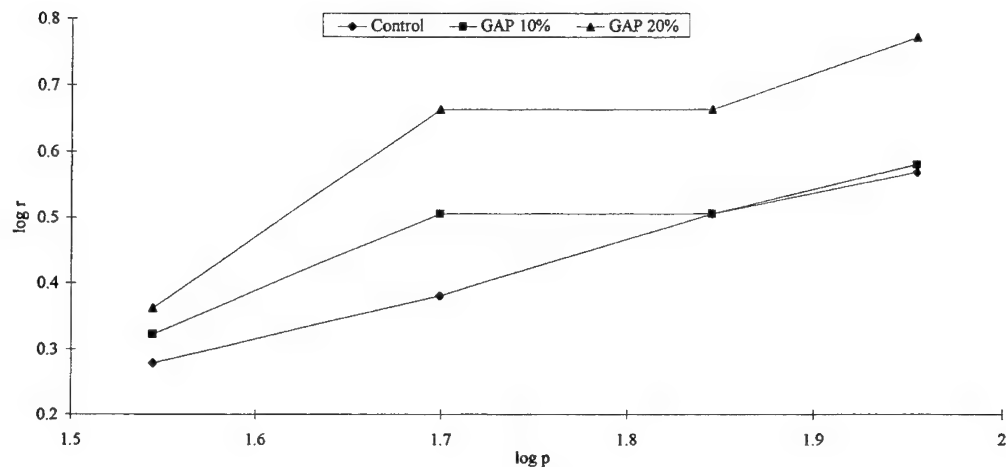


Figure 7. Burn Rates of RDX (25u) Based Gas Generating Compositions

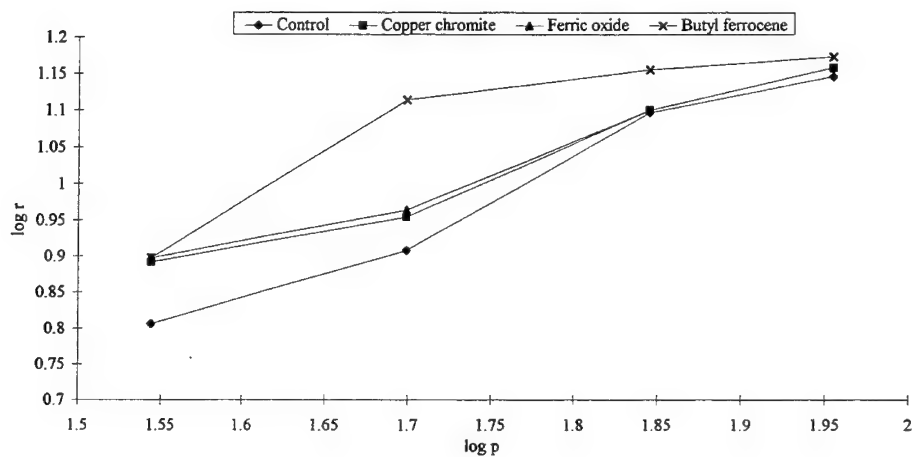


Figure 8. Burn Rates of AP (10u)/RDX (25u) Based Gas Generating Compositions with Selected Ballistic Modifiers

BDP model postulates the formation of multiple flames. AP burns as a monopropellant and another flame (primary flame) results from the immediate vicinity of the oxidizing species from AP flame to the fuel binder. The ultimate flame emanates from the combustion of fuel vapors with the oxidizer vapors unused in the earlier regions. Despite a evidence that the fuel binder and the oxidizer have different surface temperatures, the same average value of the surface temperature is assumed for both species. The model offers a means of computing burn rates, flame stand off distance, and flame heights. During the present work, burn rate predictions using BDP model[15] were made in the pressure range of 1-8.8 MPa. In the case of bimodal AP-containing compositions, predicted values were on the lower side in the pressure range of 3.5- 8.8 MPa, as compared to experimentally-determined values. However, a close agreement was obtained between predicted and determined values in the pressure range of 3.5-6.9 MPa for compositions containing 4 u AP. This may be due to the fact that when bimodal AP particles were used there was a variation of size over a wide range. In case of 4u AP the particles spectrum band was narrow[15]. While there was a marginal increase in surface temperature on decrease in particle size of AP, a considerable increase in height of AP monopropellant flame was observed. Regarding flame heights for oxidizer fuel primary flame, a marginal increase was observed on decrease in particle size. As per the model, monopropellant AP flame and primary flame compete for reactive oxidizer species. The final flame heights for compositions containing fine AP were found to be less than those for coarse AP[Table 2].

The higher burn rates for composite formulations with fine AP than with coarse AP may be explained on the basis of Sammons[16] model. As per this model, AP and binder decompose in the solid phase and the products obtained interact in the interstices between the AP particles and fuel, which increases burning surface temperature and the total heat release, as the AP particle size decreases.

It has been reported by various researchers that copper chromite catalyzes exothermic condensed phase reactions. However, iron catalysts have little effect on the condensed phase reaction and catalyze the primary flame reaction rather than AP decomposition[17]. It is believed that iron catalysts serve as a source of generation of ferric oxide particles. Consequently, ferric oxide particles eject into the burning flame and provide the effective site for the primary flame reaction by heterogeneous mechanism. The catalyst effectiveness depends on the way they are distributed, as well as on the Fe concentration. Flanagan[18] suggested that high efficiency of butyl ferrocene is due to the fact that the oxidation of butyl ferrocene results in the formation of extremely fine (<1000 Å) size ferric oxide. Addition of RDX resulted in low burn rates of compositions evaluated during this work, which may be attributed to the lower flame temperature of RDX-binder premixed flame than that of AP-binder diffusion flame[19]. The overall effect is reduced feedback to the propellant surface. GAP is known to undergo exothermic decomposition on / near the surface leading to an increase in propellant surface temperature and consequently, high burn rates [20].

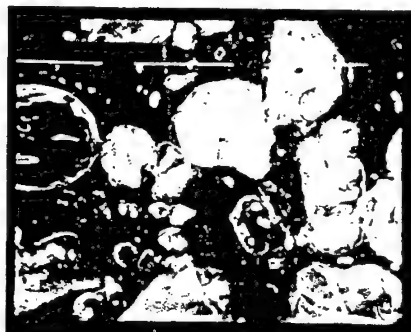
In order to gain insight on the combustion mechanism, the surface structure of the extinguished propellant in comparison to that of the unburned sample was studied by applying SEM. In the case of Bimodal AP/Epoxy system, large particles of AP protruding from the surface were observed as reported for AP/HTPB systems. This suggests that fuel evaporates more readily than the oxidizer. Incorporation of GAP results in a marked change in the surface structure. Thus, in place of protruding AP particles, cavities were observed on the surface, suggesting an increase in overall decomposition rate of propellant particularly that of AP. In the case of compositions with 4u AP, incorporation of GAP again appears to have a marked effect on increase in decomposition of AP / overall propellant as revealed by large and deep cavities on the extinguished propellant samples(Figure 9).

**TABLE-2**  
Burn Rates, Surface Temperature and Flame Heights of  
AP Based Gas Generating Compositions Computed from BDP Model

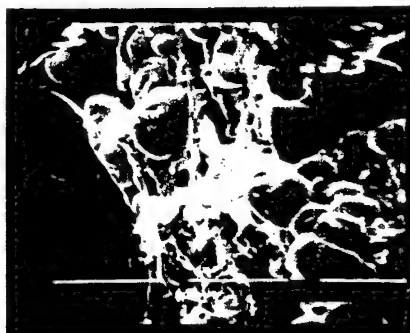
Composition		@MPa	Burn Rates (mm/s)		Surface Temperature (°C)	Flame Heights		
AP (%)	Epoxy Binder (%)		Predicted	Obtained		AP mono prop. flame (mm)	Primary flame (mm)	Final flame (mm)
60	40	1	1.5	2.1	785.9	11.19	20.56	18.85
(150- 200u)		2	2.1	2.2	820.3	7.46	21.22	19.14
		3.5	2.8	2.3	837.1	4.93	21.89	20.63
		4.9	3.3	2.3	850.4	3.51	22.06	21.79
		6.9	3.8	2.3	857.2	2.47	22.42	23.21
		8.8	4.1	2.4	864.7	1.81	22.48	24.10
60	40	1	1.7	3.2	800	15.80	20.14	15.97
(4u)		2	2.9	4.2	839.2	13.80	21.76	14.11
		3.5	4.5	5.4	862.6	12.56	23.55	13.06
		4.9	6	5.6	890.5	11.54	24.19	12.19
		6.9	7.9	7.1	905	10.84	25.30	11.71
		8.8	9.6	8.4	927.9	10.10	25.55	11.14

at Chamber Pressure 71 MPa

Figure 9. SEM Photographs of Gas Generator with AP 60% and Binder 40%

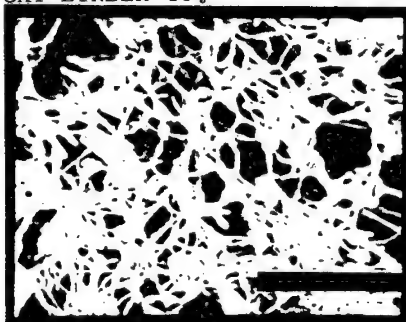


SAMPLE



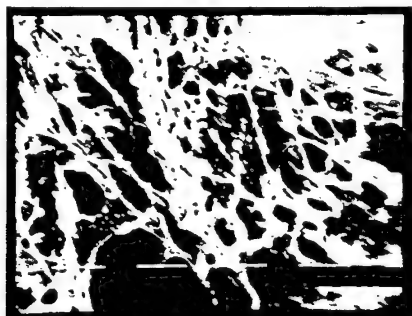
EXTINGUISHED SAMPLE

AP 60% (C:F-70:30), EPOXY BINDER 40%



EXTINGUISHED SAMPLE

AP 60% ( 4 u), EPOXY BINDER 40%



EXTINGUISHED SAMPLE

AP 60% (C:F-70:30), EPOXY 30%

GAP 10%



EXTINGUISHED SAMPLE

AP 60% ( 4 u), EPOXY 30%

GAP 10%

## CONCLUSIONS

- ◆ Replacement of 10-30 wt % Epoxy binder by GAP results in 1.5-2 -fold increase in burn rate for AP-Epoxy compositions incorporating bimodal or 10  $\mu$  AP.
- ◆ Composition containing 4  $\mu$  AP gave 1.5-5 -fold increase in burn rate on incorporation of 10-30 % GAP at the cost of Epoxybinder.
- ◆ Ferric oxide, copper chromite and butyl ferrocene were found to be effective ballistic modifiers for AP-Epoxy-GAP compositions. Butyl ferrocene gave the best results as revealed by 1.3-3-fold increase in burn rate of AP- based system on its incorporation.
- ◆ RDX/AP-RDX- based systems gave relatively lower burn rate than AP- based compositions.
- ◆ Burn rate results obtained can be explained on the basis of BDP model.

## REFERENCES

1. **Bull, G. N.**, Base bleed technology in perspective, *Proceedings of 1st International Symposium on Special Topics in Chemical Propulsion: Base bleed*, Greece, Nov. 23-25, 1988.
2. **Sutton, G. P.**, *Rocket propulsion elements*, 5th Ed., John Wiley and Sons, New York, 1986, 243-44.
3. **Zoshong, D., Yabel, L. and Shaosong, C.**, A study of drag reduction by base bleed at subsonic speeds, *Proceedings of 1st Int. Symp. on Special Topics in Chemical Propulsion: Base Bleed*, Greece, Nov. 23-25, 1988, III-3.
4. **Gauchoux, J., Couper, D. and Lecoustre, M.**, Base bleed solid propellant, properties and processability for industrial solid propellant, *Proceedings of 1st Int. Symp. on Special Topics in Chemical Propulsion: Base Bleed*, Greece, Nov. 23-25, 1988, I-1.
5. **Chargetique, D. and Couloumy, M. T.**, Base burn projectile: French projectile model, *Proceedings of 1st Int. Symp. on Special Topics in Chemical Propulsion: Base Bleed*, Greece, Nov. 23-25, 1988, II-9.
6. **Reed, Jr., R., Lie, B. Y. S., Henry, R. A. and Smith, I. O.**, *Proceedings of 6th International Pyrotechnics Seminar*, 1978, 503-518.
7. **Eisele, S., Volk, F. and Menke, K.**, Gas generators based on TAGN and polymeric binder system, *Inst. fur Chemische Technologie (ICT)*(Germany), 1990, 38/12 - 38/19.

8. **Helmy, A.M.**, AIAA / SAE / ASME / AMEE 23rd Joint Propulsion Conference, June 29-July 2, San Diego, California, 1987, 1-10.
9. **Misra, L. D., Rickerbaugh, D. E., Ashmore, C. I. and Mechrotrs, A. K.**, Development of GAP-TAGN-PEG propellants, Part I: Study of ingredients, *JANNAF Propulsion Meeting*, Vol. II, 1984, 153-180.
10. **Kammerer, A. and Reich, H.V.**, Study of the effect of binder on the combustion characteristics of composite solid propellants, *ICT-Explosivst*, Fraunhofer, Germany, 1974, 115-127.
11. **Malcolm, E.P., Wallace, J., McMichael and Elmer, L.P.**, 1964. *Solid combustible composition containing epoxy resins*, U. S. Pat. 3130096.
12. **Ahad, E.**, 1987. *Process for preparation of alkyl azido substituted hydroxy terminated polyethers*, Euro. Patent. 87310476.4.
13. **Gould, R. F.**, Propellants, Manufacture, Hazards and Testing, American Chem. Soc, Advanced Chem. Series., 1969.
14. **Kuo, K. K. and Summerfield, M.**, eds, Fundamentals of solid propellants combustion, *Progress in Astronautics and Aeronautics*, AIAA Inc., New York, 1984.
15. **Cohen, N. S.**, Review of composite propellant burn rate modeling, *AIAAJ*, Vol.18(3), 1969. 277-293.
16. **Sammons, D.**, AIAA Paper no. 69-504, 1969.
17. **Wang, S. Y., Wang, S. S. and Chiu, H. S.**, An investigation of catalysts in the combustion of iron catalyzed composite propellants, *Proceedings of 19th Int. Ann. Conf. on ICT*, 8/1-8/14, 1985
18. **Flanagan, D. A.**, 1967. AFRPL-TR-67-18
19. **Kuwahara, T., and Kubota, N.**, Combustion of RDX/AP composite propellants at low pressures, *J Spacecraft and Rockets*, Vol.21(5) 1984, 502-507.
20. **Nazare A. N., Asthana S. N. and Haridwar Singh**, Glycidyl azide polymer (GAP): an energetic component of advanced solid rocket propellants-a review, *J. of Energetic Materials*, Vol. 10, 1992, 43-63.

## MASS BALANCE IN DETERRENT COATING OF SMOKELESS POWDERS

Dipl. Eng. Jan Zigmund

SYNTHESIA a. s.  
Research Institute for Industrial Chemistry  
53217 Pardubice - Semtin  
CZECH REPUBLIC

**ABSTRACT:** Some experiments carried out on the research of deterrent coating of smokeless powders are described in this paper.

An emulsion procedure was used for deterrent coating (phlegmatization). Samples of both powder grains and the bath were withdrawn during the experiments and concentrations of the deterrent were determined. A simple balance model was made up on the basis of which the rate of penetration of deterrent into powder grain was estimated. The nitrocellulose of the powder grains proved to bind readily the deterrent that disappears out of the bath within a short time. The oversaturated layer (approximately 42%) then, with decreasing rate, spreads out into the grain and its propagation stops at concentration of about 27%.

At the industrial scale, the deterrent coating process is performed portionwise and this effect is even more distinctive. The deterrent disappears out of the bath within 2 to 5 minutes after dosing.

The assumption was introduced into the model of the mass balance that the deterrent concentration profile in the powder grain is steep. The literature data show that the deterrent coating mechanism is similar to that of dyeing of textile fibers with reactive dyestuff that is chemically bonded to the polymer matrix. Hydrogen bonds between the deterrent carbonyl group and unesterified -OH groups of nitrocellulose play this role in case of phlegmatization.

### Introduction

Deterrents are materials that, diffused into the powder grains, decrease the propellant burning rate during the early stages of a ballistic cycle when the powder charge surface is at maximum. After a projectile starts moving down the barrel, the undeterred, energetically richer grain cores burn at higher rate. In other words, deterrent coating serves to control and thus to improve the charge progressivity. Since small variations in depth of the deterred layer and the deterrent concentration in this layer have proven to be of significant influence to the ballistic properties of the powder, several experiments have been performed to study the kinetics of the phlegmatization process. The most known deterrent substances, e.g., Centralite I and II, Acardite I, Di-n-butylphthalate (DBP), Camphor, Diphenylurethane and some Acrylates have been used in the experiments. The rate of deterrent penetration into the grains, changes in deterrent layer concentrations and the deterrent bath exhaustion have been studied and a simple mathematical model for typical deterrent coating process carried out with CI has been utilized to describe the given effects.

## Theory

In principle the process of deterrent coating of powder grains is similar to that of dyeing textile fibers. In both cases this is a question of diffusion of a substance emulgated and dissolved in the bath into the polymer surface. Crank<sup>1</sup> made his contribution to the study of diffusion problems. It is a complicated task to give a detailed description of the effects accompanying dyeing process. Even the simplest arrangement, i.e., an isolated fiber in an infinite, perfectly stirred bath represents a mathematical system with at least 9 variables. In practice the dyeing models are simplified to three simultaneous actions:

- a) transport of the dyestuff to the fiber surface
- b) adsorption of the dyestuff on the fiber surface
- c) diffusion of the dyestuff from the surface into the fiber.

From the kinetic aspect the slowest action, i.e., the diffusion of the dyestuff into fiber or, in case of phlegmatization, the deterrent into powder grains, determines deterrent front propagation. In case of the one-dimensional diffusion in the chemically homogeneous polymer, the Fick law II is valid:

$$\frac{\partial c}{\partial t} = D \cdot \frac{\partial^2 c}{\partial x^2} \quad (1)$$

where:  $c$  - concentration,  $x$  - depth of deterred layer,  $t$  - time, and  $D$  - diffusion coefficient.

Furthermore, deterrent coating is a process when the deterrent molecules diffuse into the powder grain being hydrogen bonded to the unesterified  $-OH$  groups of nitrocellulose (Figure 1).

In this case the diffusion coefficient is not a constant and these cases are included among non-Fickian diffusions. A series of the possible dependencies  $D = f(c)$  has been suggested, e.g.:

$$D = D_0 \cdot e^{kc}; \quad D = D_0 \cdot c^k; \quad D = D_0 \cdot (1 + k \cdot c) \quad \dots$$

however, the equation (1) is difficult to solve and the analytical function  $c = f(x)$  has not been found at all.

Nakamoto<sup>2</sup> et al. engaged in investigation of the bond character and measured the  $O-H \cdots O$  bond stretching frequencies of a series of compounds. It was found that there is a wide range existing where the length of the hydrogen bond is linearly dependent on the stretching frequency shift but beyond the value of about 2.80 Å the sensitivity of the stretching frequencies shift decreases exponentially with the bond length.

Brodman<sup>3</sup> et al. used infrared spectrometry to study the hydrogen bond between the carbonyl group of DBP, Camphor, CI and CII and the unesterified  $-OH$  groups of nitrocellulose. On the basis of the graphical dependence of the length of the bond vs  $f(\text{wave number})$  published by Nakamoto, the authors determined the length and the strength of the hydrogen bond from the stretching frequencies shift.

It follows from their measurements that the bond strength is graded in the order: C I > C II > Camphor > DBP. The above mentioned hydrogen bond length/wave number dependence of the compounds determined by Nakamoto and complemented with measurements performed by Brodman is given in Figure 2.

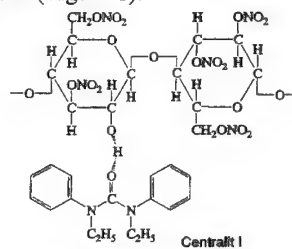


Figure 1. Hydrogen bond between nitrocellulose and CI

## Methods for measuring of the deterrent penetration depth

Several authors have engaged in measuring the deterrent penetration depth. The simplest way seems to be measuring of the layer transparency of the powder grain sections obtained by microtome cuts<sup>4</sup>. The so called autoradiography<sup>5</sup> is another more complicated way to determine the deterrent penetration depth. DBP containing radioactive carbon  $^{14}C$  was used by Brodman to phlegmatize the



powder. The coated grains were microtomed into sections of 30  $\mu\text{m}$  thickness and the concentration profile of the marked DBP in the section was contact - measured on film. The blackening of the film was observed by means of densitometer. However, it was found that almost 96% of the light-sensitive Ag particles in the film emulsion were struck within 5  $\mu\text{m}$  of the  $\beta$  particles source. Thus, the resolution of this method  $\pm 10 \mu\text{m}$  is determined and the  $\beta$  scattering is the greatest source of the measuring inaccuracy. A conclusion was formulated by Brodman that the optically determined depth of the deterred layer corresponds with the real depth of the detergent penetration.

The autoradiographic method was also used to study the detergent penetration depth of nitrocellulose tubular powder by Meier<sup>6</sup> et al. They deterred powder of the A 5020 type at various temperatures, time intervals taken by the coating process and concentrations of the radioactive  $^3\text{H}$  DBP,  $^3\text{H}$  Camphor,  $^3\text{H}$  CI,  $^{14}\text{C}$  DBP and their mixtures. The deterred layer thicknesses were measured in the same way as Brodman did using the film applied to the powder grain cuts. Their work also indicates an increasing detergent migration tendency in series  $\text{CI} < \text{DBP} < \text{Camphor}$ .

The problem of measuring of the detergent concentration profiles in a powder grain is shown in Figure 3. For the purposes of comparison the typical dyestuff concentration profile is given there, as well as a case of dyestuff diffusion when no interaction with the polymer fiber occurs.

Several other ways to measure the detergent concentration profiles can be found in literature, but the optical method being the simplest one has been chosen for our experiments. Thin sections of 50  $\mu\text{m}$  thickness were made of powder grains and the depth of the deterred layer was measured using the MITUTOYO profile-projector.

## Experimental

To perform phlegmatization experiments the spherical powder TR 42 with the following properties was used:

Table 1 Properties of the TR 42 powder

Centralite I	0.6	%
Dinitrotoluene	4.0	%
Nitrocellulose (13.0 % N)	82.5	%
Nitroglycerine	13.0	%
Water	0.6	%
Density	1.52	$\text{g}\cdot\text{cm}^{-3}$
Bulk density	97.05	$\text{g}\cdot(100 \text{ ml})^{-1}$
Heat of explosion	3902	$\text{kJ}\cdot\text{kg}^{-1}$
Average grain diameter	1.325	mm

The detergent coating experiments were, in the laboratory scale, performed in 3L heated glass vessel equipped with stirrer, thermometer, feeding funnel and an opening for sampling the contents. 2.3L hot water, 75 g spherical powder TR 42 and 1 g emulsifier were put into the vessel and the suspension heated to  $85 \pm 1^\circ\text{C}$  under stirring for 30 minutes. Then the suspension of detergent prepared from 3 g emulsifier, 5 g CI and 200 ml cold water was added into the stirred powder suspension. Then, 5 minutes after the addition of the detergent, 5 ml sample of phlegmatizing bath

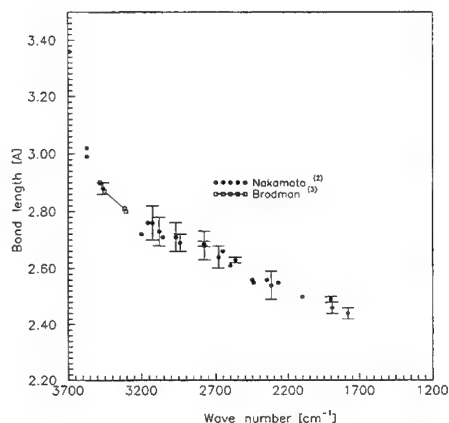


Figure 2. Length of hydrogen bond vs. stretching frequencies.

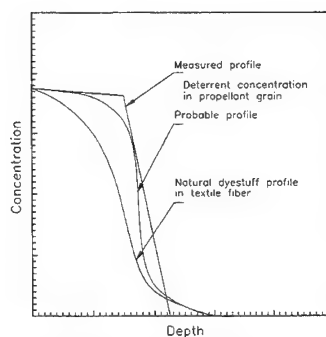


Figure 3. Concentration profiles in a polymer matrix

and 0.824 g sample of powder were withdrawn. The sampling of the phlegmatizing bath and powder was then repeated in the intervals as given in Table 2.

The last samples were withdrawn 3 hours after the phlegmatization process had started. The samples of the powder were dried at 65 °C for three hours in a hot-air dryer.

Four grains of approximately same dimensions were always used from each powder sample and from these grains the sections of 50 µm thickness were prepared.

The depth of the detergent layer was measured four times for each grain in two directions perpendicular to one another using MITUTOYO profile projector. The hundred - fold magnification was used for measuring the grain sections.

Chromatographic method was used to determine the CI concentration in both powder grains and phlegmatization bath. The samples of the bath were diluted and the precipitated CI dissolved in methanol.

The measured depths of detergent penetration into grains, the increase in the detergent concentration in the powder and its exhaustion from the bath are given in Table 2, Figure 4 and Figure 5.

Table 2 The measured dependencies in the detergent coating of TR 42 powder

Sample N°	Time [min]	Sample mass [g]	Concentration of CI in powder [%]	Concentration of CI in bath [g·L <sup>-1</sup> ]	Average depth of deterred layer [µm]
1	0	0.000	0.60	2.00	0.0
2	5	0.824	1.18	1.87	5.1
3	10	1.527	2.06	1.37	10.8
4	15	1.326	2.89	1.15	14.4
5	20	1.580	3.87	0.97	17.9
6	25	2.073	4.58	0.84	20.6
7	30	1.855	4.90	0.63	26.2
8	40	1.970	5.82	0.38	31.7
9	50	1.863	6.19	0.33	34.6
10	60	1.553	6.30	0.28	39.3
11	90	2.330	6.54	0.25	44.6
12	120	3.603	6.60	0.22	44.8
13	150	3.550	6.61	0.20	51.8
14	180	-	6.99	0.19	56.1

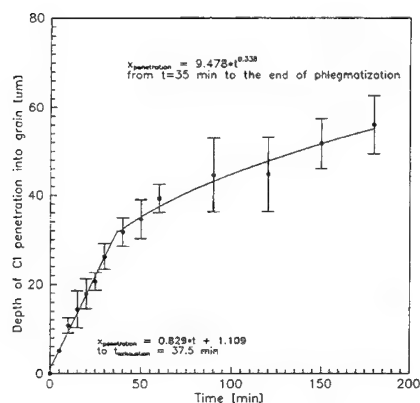


Figure 4. Detergent penetration depths into TR 42 powder grain/time dependence

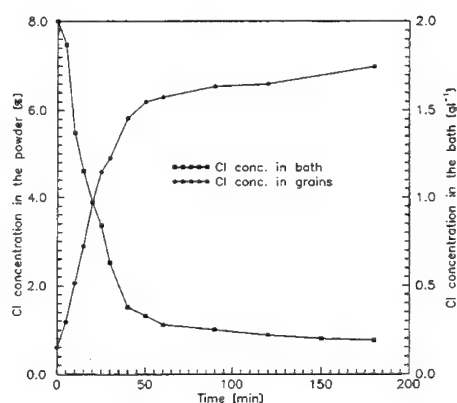


Figure 5. Detergent concentration in the TR 42 powder and bath/time dependence

To study the kinetics of phlegmatization process *carried out portionwise*, the usual laboratory scale detergent coating was performed as well.

1.8L hot water, 500 g spherical powder and 1g emulsifier were put into the heated and stirred laboratory vessel of 3L volume. The mixture in the vessel was heated to 90 °C and kept at this temperature during the whole experiment.

The deterrent coating was performed by successively adding six portions of suspension consisting of 0.5 g emulsifier and 5 g Centralite I in 33 ml cold water. After adding each portion of above mentioned suspension, samples of both powder and bath were taken from the vessel.

The time course of the sampling, the measured deterrent concentrations in the samples of the bath and the average deterrent penetration depths into grain are given in Figure 6 and Figure 7.

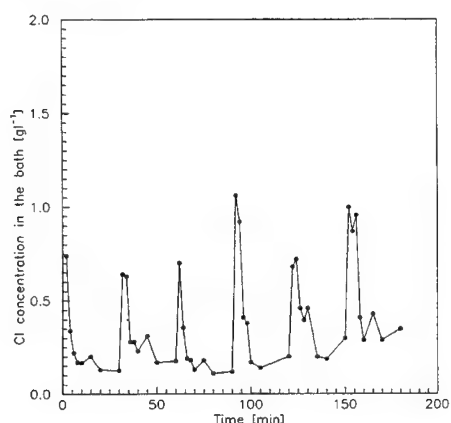


Figure 6. Detergent concentration in the bath/time dependence in the portionwise carried out deterrent coating

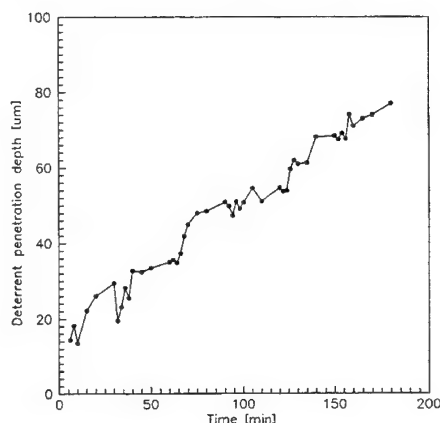


Figure 7. CI penetration depth into grain/time dependence in the portionwise carried out deterrent coating

To determine the depth of the deterrent penetration the average of 16 measurements performed using the MITUTOYO profile projector at 50x magnification was used.

It follows from the two foregoing experiments that the bath concentration of CI decreases quickly to the value of about 0.3 g·L<sup>-1</sup> (0.03%) remaining at this value until the experiment has finished. As given later, the deterrent concentration in the deterred layer after the bath has been exhausted amounts 42%. From this the deterrent equilibrium can be calculated as follows:

$$\frac{c_{\text{layer}}}{c_{\text{bath}}} = \frac{42}{0.03} = 1400$$

To achieve more accuracy in determining the  $c_{\text{layer}}/c_{\text{bath}}$  equilibrium, the deterrent coatings of a small quantity (1.5 g) of powder in a bath (2.5L volume) of low deterrent concentrations (the "infinite bath") has been performed consecutively as given in Table 3:

Table 3 The CI concentration changes in both, the bath and the powder of the PD 24 - 25 type.

Sample N <sup>o</sup>	Weight of CI [g]	Initial CI conc. in the bath [g·L <sup>-1</sup> ]	Final CI conc. in the bath [g·L <sup>-1</sup> ]	CI in the powder [%]
1	0.546	0.22	0.19	1.70
2	0.618	0.25	0.21	1.90
3	0.844	0.31	0.23	-
4	1.500	0.68	0.51	21.25
5	2.442	0.94	0.62	33.75
6	3.125	1.33	0.84	31.75
7	4.998	2.05	1.57	31.40

However, the depths of the layers have not been determined in those experiments. No deterred layer has originated in the bath of CI concentration up to  $\approx 0.3 \text{ g}\cdot\text{L}^{-1}$  and above this concentration a crust of CI has stuck on the powder grains thus resembling "snowballs" when examined under a microscope.

### Mass balance in deterrent coating process

The experiment concerning the deterrent coating of the TR 42 powder was designed to simplify the deterrent coating conditions as much as possible. In order to maintain the bath concentration at a constant level as long as possible a large bath volume to a small quantity of the powder ratio was chosen. Thus a constant "detering force" on the powder grain surface should have been ensured. The aim of this arrangement of the experiment was to exclude all disturbing effects in the normal performance of deterrent coating process, i.e., precipitating and adhering of the deterrent on the powder grain surface, changing deterrent concentration in the bath, etc.

The time dependent changes of CI concentration in both the powder and the bath, and the CI penetration depth into a powder grain reflect the fact that the coating mechanism is really non-Fickian as stated by Brodman and other authors.

In the above example the deterrent concentration in the powder increases from the initial value 0.6% up to 6% linearly (see Table 2 and Figure 5). Simultaneously the bath is exhausted to the concentration of about  $0.3 \text{ g}\cdot\text{L}^{-1}$  within approximately 35 minutes. The dependence of deterrent penetration depth into the powder grains upon time up to this point can also be considered as linear. Then, the deterrent concentration in the deterred layer should also remain constant until the moment of exhaustion of the bath.

The course of deterrent coating of powder grain can be simply described as follows:

- 1) the deterrent forms a layer of high concentration on the grain surface that advances at a constant rate into the powder grain until the bath has been exhausted;
- 2) after the deterrent content in the bath has been exhausted the deterrent affected layer advances at decreasing rate into the grain and its concentration decreases probably until all deterrent molecules have been hydrogen bonded on the unesterified  $-OH$  groups of nitrocellulose.

As given above (see Table 3), no "infinite bath" can be made and therefore, taking into account average grain diameter, time, velocity of deterrent front, volume of deterred layer, volume of deterrent bath, etc., we have suggested the following phlegmatization model:

#### 1) Before exhaustion of the bath

The dependence of deterrent penetration depth into a powder grain vs. time may be expressed as:

$$x = v_{\text{diff}} \cdot t \quad [\text{mm}]$$

The equation valid for the decrease of the deterrent concentration in a bath is:

$$c_{\text{bath}} = c_0 - \frac{m_d}{V_0}$$

The deterrent concentration in the deterred layer may be calculated from the overall concentration of CI adsorbed in propellant grain powered by the volume of the propellant grain of average diameter and divided by the volume of the deterred layer (see Table 1 and Table 2).

$$c_{\text{layer}} = \frac{5.4 \cdot 1.28}{0.166} \approx 42 \quad [\%]$$

The suggested model, taking into account the decrease in the powder mass in the phlegmatization bath due to sampling, was investigated using the constants for velocity of deterrent front:

$$v_{dif} = 0.829 \quad [\mu\text{m} \cdot \text{min}^{-1}]$$

The above given equations hold good until the moment when the bath has been exhausted, i.e., at the time  $t_{\text{exhaust}} = 35$  minutes.

## 2) After exhaustion of the bath

For the time period from the moment of exhaustion of the bath  $t_{\text{exhaust}}$  to the end of deterrent coating process  $t_{\text{end}} = 180$  min., making use of the equation valid for the deterrent front velocity it can be written that:

$$v_{dif} = 9.478 \cdot t^{-0.662} \quad [\mu\text{m} \cdot \text{min}^{-1}]$$

The courses of the calculated dependencies are given in Figure 8 - Figure 12.

The designation used in the equations:

$x$	- depth of deterrent layer	$[\mu\text{m}]$
$v_{dif}$	- velocity of deterrent front in powder grain	$[\mu\text{m} \cdot \text{min}^{-1}]$
$V_0$	- volume of deterrent bath	$[\text{L}], [\text{dm}^3]$
$t$	- time	$[\text{min}]$
$c_{\text{layer}}$	- concentration of CI in deterred layer	$[\%], [\text{g} \cdot \text{dm}^{-3}]$
$c_{\text{bath}}$	- concentration of CI in bath	$[\%], [\text{g} \cdot \text{dm}^{-3}]$
$c_0$	- initial concentration of CI in bath	$[\%], [\text{g} \cdot \text{dm}^{-3}]$
$m_a$	- mass of CI adsorbed to powder grains	$[\text{g}]$

## Conclusion

To understand the kinetics of the deterrent coating of powder grains, not only the deterrent penetration depth into a powder grain but also the increase in deterrent concentration in the powder together with its decrease in the bath have been studied.

The measured dependence  $x = f(t)$  (Figure 4) was fitted with simple regression curves and these were used in the program mathematically modelling diffusion of CI into the TR 42 powder grains. The decrease in the deterrent concentration in the bath and the increase in its concentration in the powder was then simply calculated from the mass balance of the deterrent coating course. Since during the experiment the powder mass decreased from 75 g to 50 g (by about 1/3) and the bath volume by 65 ml due to sampling during the experiment it was necessary to incorporate these facts into the program.

During the experiments it was found that:

- 1) The concentration of the deterrent in the deterred layer before exhaustion of the bath is so high (estimated approximately 42%, see Figure 10 and Figure 12) that no other explanation is possible except that its concentration is constant.
- 2) It is probable that the deterrent advances into a grain at a constant velocity until its concentration in the bath decreases to the critical value of approximately 0.03%.
- 3) After the bath has been exhausted the velocity of the deterrent front propagation decreases and its concentration in the deterred layer drops to the value of about 27% (Figure 10 and Figure 12). This is probably the value when all deterrent molecules are hydrogen bonded on the unesterified -OH groups of nitrocellulose. From this concentration the moving of the deterrent molecules in the nitrocellulose matrix of the grain is very limited.

- 4) In addition, by the precise measuring of the powder grain dimensions it was found that, relating to the amount of the detergent added, the grain volume increases by approximately 10%, i.e., that the deterred layer undergoes the process of swelling. This phenomenon brings considerable complications with respect to any advanced mathematic modelling of detergent coating process.

#### Calculated dependencies of mass balance in detergent coating of propellant TR 24

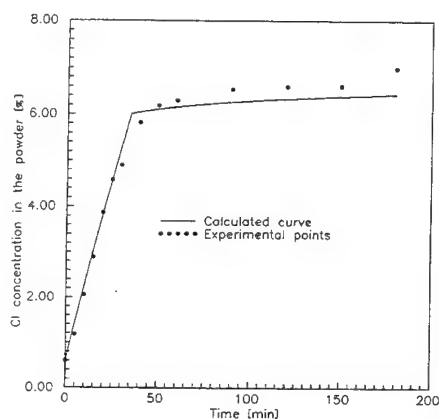


Figure 8. Cl concentration in powder/time-dependence (theor.)

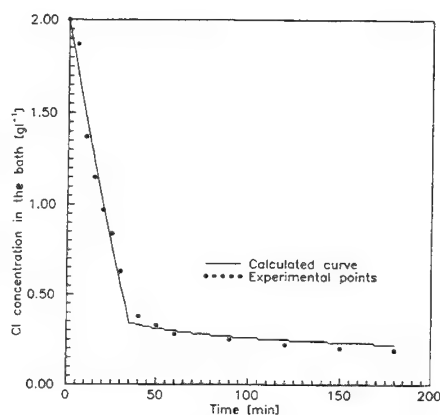


Figure 9. Cl concentration in the bath/time-dependence (theor.)

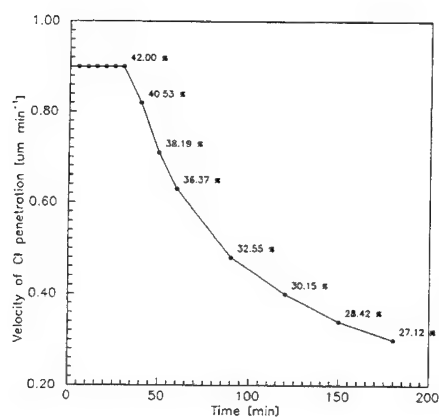


Figure 10. Velocity of Cl diffusion into powder grain/time-dependence (theor.)

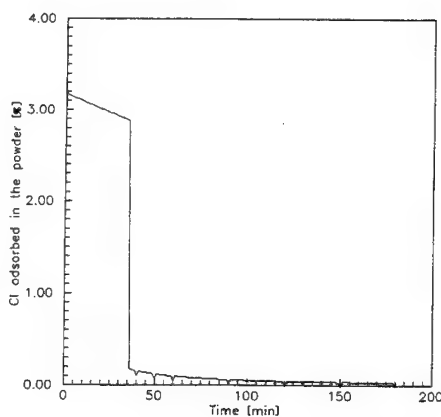


Figure 11. Cl adsorbed in the powder/time-dependence (theor.)

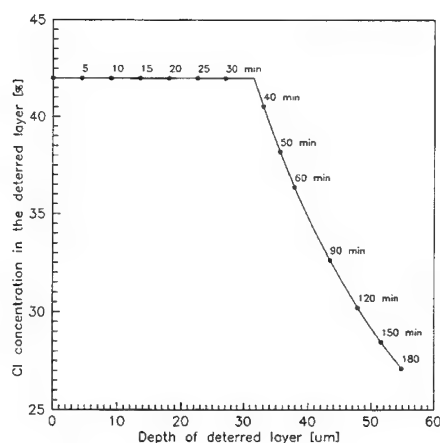


Figure 12. Concentration of Cl in the deterred layer vs. the thickness of the layer for the individual sampling times (theor.)

## References

1. (Book) **Crank, J., Park, G.S.**, 1968. *Diffusion in Polymers*, Academic Press, London and New York.
2. (Article in Journal) **Nakamoto, K., Marghoses, J. and Rundle, R.E.**, 1955. "Stretching Frequencies as a Function of Distance in Hydrogen Bonds," *J. Amer. Chem. Soc.*, Vol. 77, pp. 6480-6486.
3. (Article in Journal) **Brodman, B.W., Devine, M.P. and Gurbarg, M.T.**, 1974. "Hydrogen Bonding of Deterrents to Unesterified Hydroxyl Groups in Nitrocellulose," *J. Appl. Polym. Sci.*, Vol. 18, pp. 943-946.
4. (Article in Journal) **Fong, C.W. and Cooke, C.**, 1982. "Diffusion of Deterrents into a Nitrocellulose-Based Small Arms Propellant. The Effect of Deterrent Structure and Solvent," *J. Appl. Polym. Sci.*, Vol. 27, pp. 2827-2832.
5. (Article in Journal) **Brodman, B.W. and Devine, M.P.**, 1974. "Autoradiographic Determination of the Di-n-butyl Phthalate Concentration Profile in a Nitrocellulose Matrix," *J. Appl. Polym. Sci.*, Vol. 18, pp. 3739-3744.
6. (Technical Report) **Meier, H., Bosche, D., Zeitler, G., Zimmerhackl, E., Hecker, W.**, 1979, "Investigation of Surface Treatment of Propellant Grains Using Labeled Substances", *Report BMVg-FBWT-79-14*, Bundesministerium de Verteidigung, Bonn, Germany.

## ADN: A new high performance oxidizer for solid propellants

A. Langlet, N. Wingborg and H. Östmark  
Defence Research Establishment  
S-172 90 Stockholm, SWEDEN

### ABSTRACT

Ammonium dinitramide, or ADN ( $\text{NH}_4\text{N}(\text{NO}_2)_2$ ), is a new and promising oxidizer with high impulse and high burning rate. It is a potential replacement for ammonium perchlorate ( $\text{NH}_4\text{ClO}_4$  or AP). Since ADN does not contain chlorine, a composite rocket propellant containing ADN and a polymer binder will produce minimal smoke, and will be more environmentally friendly compared to propellants based on AP. There are, however, some drawbacks: ADN is relatively shock sensitive, it is also sensitive to light and moisture. Moreover, ADN has until now been very expensive to produce. This paper presents a study of the sensitivity, thermal stability, and some spectroscopic properties of ADN. The paper also presents a comparison of the impulse of composite propellants based on ADN and oxidizers such as AN, AP, CL-20 and HNF, with HTPB as a binder. The ADN used in this work was synthesized at the National Defence Research Establishment (FOA), by a new and much less expensive method. The friction sensitivity of ADN is much lower than that of RDX. The impact sensitivity of ADN is of the same magnitude as that of RDX but varies a great deal with the shape of the particles, e.g. prilled ADN is nearly twice as insensitive as RDX. The reaction of ADN is also less violent. The ignition temperature was determined to be 160°C (by Wood's metal bath). The thermal stability, measured with microcalorimetry, shows that ADN is stable to at least 80°C and that impurities cause decreased thermal stability. The activation energy ( $E_a=158$  kJ/mole) and frequency factor ( $K_0=6.0\cdot 10^{15}$  s<sup>-1</sup>) was determined from DSC data using the ASTM method E 698-79. It was also found that ADN in aqueous solution is sensitive to light.



## INTRODUCTION

In the search for replacement oxidizer for AP a number of new and interesting substances have been suggested: HNF[1], CL-20 [2,3], and ADN [4-6]. ADN is a new, and very promising, oxidizer with high performance which yet has some drawbacks, e.g. a fairly high sensitivity, a high price, and sensitivity to moisture and light.

Only a couple of papers on the thermal stability and sensitivity of ADN have yet been openly published [5-7]. It has been shown earlier that the thermal sensitivity can not be satisfactorily determined with only a few tests: in order to get the full picture a fairly large number of tests has to be performed. In a study on the thermal sensitivity and decomposition of new high explosives a more complete set of tests has been used [8,9]. In this paper data from the following tests and studies are presented: Drop weight test, friction test, ignition temperature test, DSC, microcalorimetry, FTIR and FT-Raman spectroscopy.

In Figure 1 the theoretical specific impulse for some theoretical propellants with different types of oxidizers are compared with each other. In all cases, the binder is based on HTPB and IPDI. Possible incompatibility between the oxidizers and the binder is not considered. The theoretical specific impulse (Ns/kg) was calculated by using the Gordon-McBride code [10]. It calculates the chemical equilibrium compositions by minimizing Gibb's free energy. It is assumed that all gases are ideal and that interactions among phases can be neglected. In all cases the pressure in the combustion chamber was 10 MPa and the gases were expanded in the nozzle, assuming shifting equilibrium composition, to a surrounding pressure of 0.1 MPa. The thermo-chemical data used is shown in Table 1 and is taken from Ref. [1] unless otherwise stated.

**Table 1.** Properties of oxidizers and binders.

Component	Sum formula	Density (g/cm <sup>3</sup> )	Heat of formation (kJ/mole)
AP	ClH <sub>4</sub> NO <sub>4</sub>	1.95	-296.00
ADN	H <sub>4</sub> N <sub>4</sub> O <sub>4</sub>	1.82-1.84	-150.60
CL-20	C <sub>6</sub> H <sub>6</sub> N <sub>12</sub> O <sub>12</sub>	2.04*	+415.47
HNF	CH <sub>5</sub> N <sub>5</sub> O <sub>6</sub>	1.87-1.93	-72.00
AN	H <sub>4</sub> N <sub>2</sub> O <sub>3</sub>	1.72	-365.04
HTPB+IPDI	C <sub>7.11</sub> H <sub>10.62</sub> N <sub>0.06</sub> O <sub>0.19</sub> *	0.924*	+0.88*

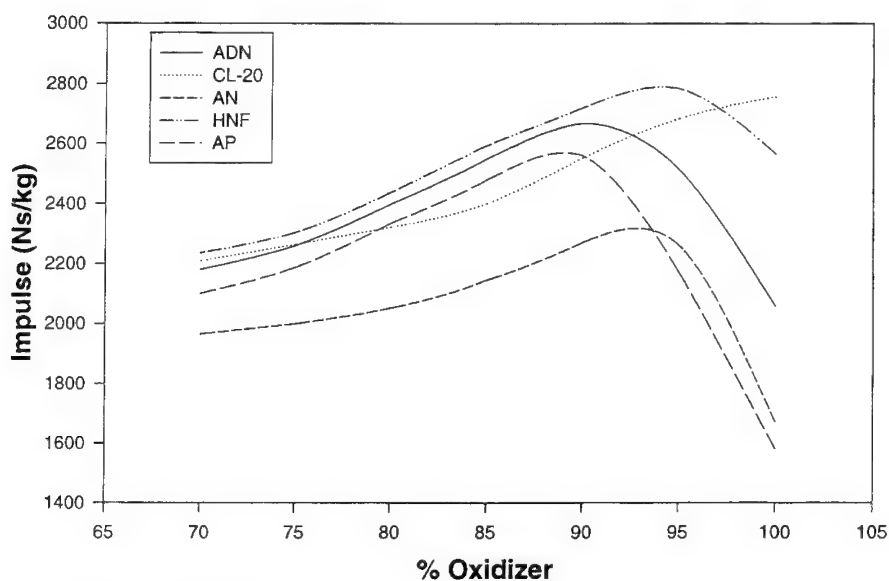
\* FOA data.

Since the oxidizers differ in density it is more correct to compare the impulse at an equal volume fraction. A volume fraction of 0.7 for AP corresponds to a weight fraction of 83%. It seems thus reasonable to compare the oxidizers at this volume fraction. This comparison is shown in Table 2.

**Table 2.** Oxidizer influence on propellant performance

Oxidizer	Impulse at vol. fraction 0.7 (Ns/kg)
AP	2429
ADN	2470
CL-20	2371
HNF	2516
AN	2072

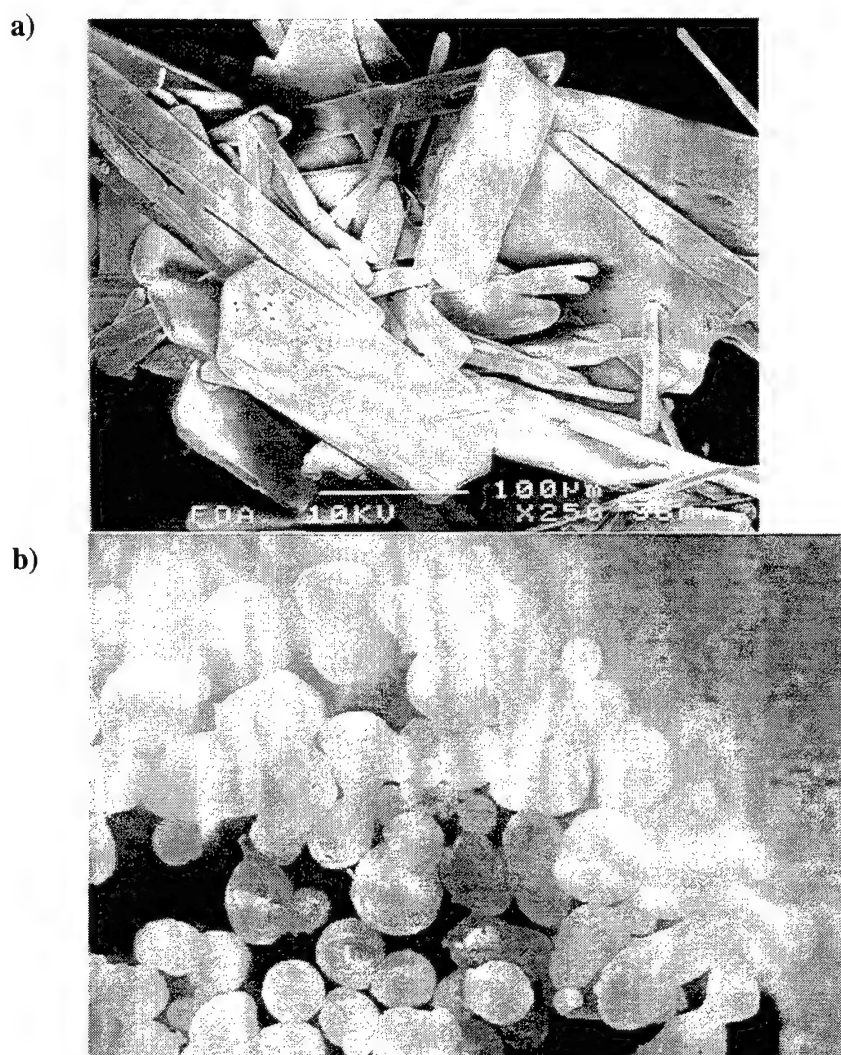
HNF has the highest impulse, approximately 2 % higher than ADN. To obtain a volumetric filling fraction of 0.7 it is necessary, however, that the oxidizer crystals have a spherical shape. At FOA we have been able to produce spherical ADN particles (see below). HNF forms needle shaped crystals with a length over diameter ratio ( $l/d$ ) of 2 to 5 [1]. In practice it is not yet proven that HNF-based propellants will have higher specific impulse than ADN-based propellants.



**Figure 1.** Propellant performance

## SYNTHESIS

The ADN used for this work was synthesized at FOA (National Defence Research Establishment) by a new and simple method. The particle shape from the synthesis could best be described as fluffy flakes and needles (see Figure 2 a). The density of ADN was measured with a helium pycnometer and found to be 1.82-1.84 g/cm<sup>3</sup>. In order to get better particle shapes for propellant use, a melt method for prilling ADN was tested. This method produced nice round particles with a diameter of about 700μm (see Figure 2 b).



**Figure 2.** ADN particle shapes: *a)re-crystallized, b)prilled.*

## SENSITIVITY TESTS

The drop-weight sensitivity as well as the friction sensitivity of ADN were measured. The impact sensitivity was measured with a 2 kg drop weight BAM apparatus. The results are based on tests on both sides of the 50% probability level using an up-and-down method. The friction sensitivity was measured with a BAM friction apparatus, using the same technique. The calculations were performed with the ML14 computer code. The results from these calculations can be found in Table 3 where data for RDX is also given for comparison.

**Table 3.** Sensitivity data for ADN and RDX.

Explosive	Drop height (cm)	Friction Test (kp)	Electrical Discharge	Comments
ADN	31	> 35		See fig. 2 a
prilled ADN	59			See fig. 2 b
RDX	38	12		

The results indicate that sensitivity to impact is greatly dependent on the shape of the ADN particles.

## DSC

The basic thermal stability of ADN was measured with DSC using a Mettler 30 instrument. The samples were heated from room temperature with a heating rate of 0.5-10° C/min. Figure 2 shows a plot of the natural logarithm of heating rate vs. 1/ temperature at max. isotherm. Using these data and the ASTM method E 698-79, the activation energy ( $E_a$ ) was measured and the frequency factor ( $K_0$ ) was calculated (temperature interval 165-200 °C), see Table 4. Compared to RDX, ADN has a smaller activation energy but also a smaller frequency factor.

**TABLE 4.** Kinetic parameters from DSC experiment on ADN

Explosive	$E_a$ (kJ/mole)	$\log (K_0)$ ( $K_0$ in $s^{-1}$ )	Comments
ADN	158	15.8	
RDX	201.5	18.8	[11]

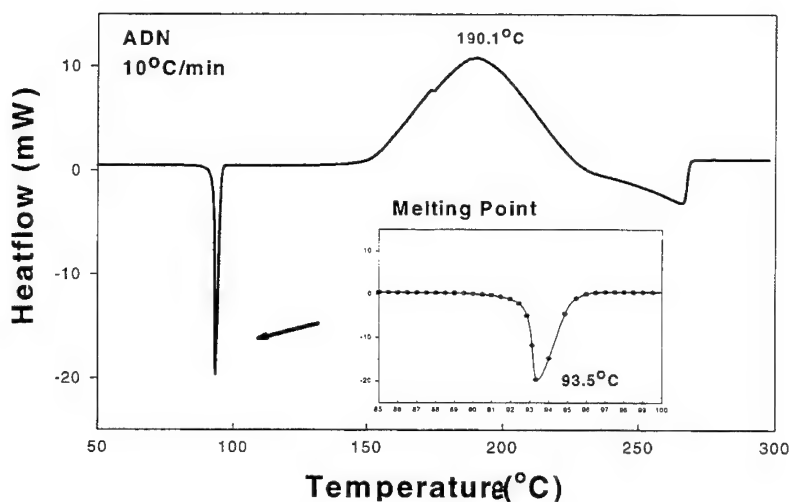


Figure 3a. Typical DSC curve for ADN.

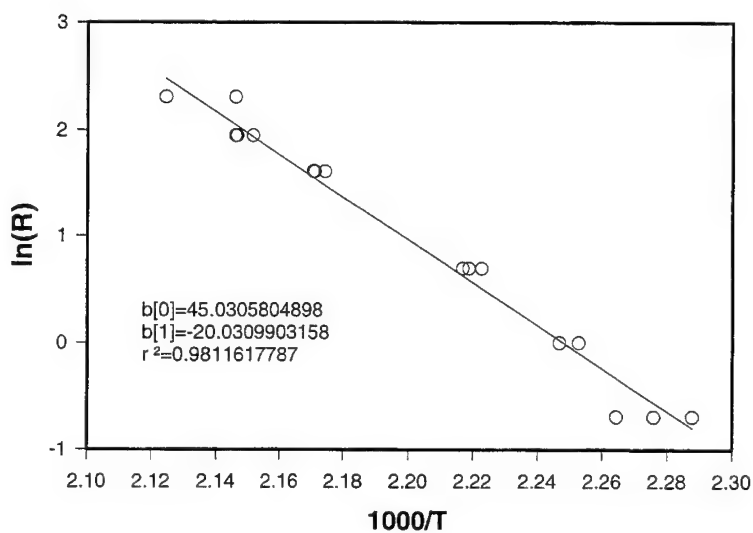
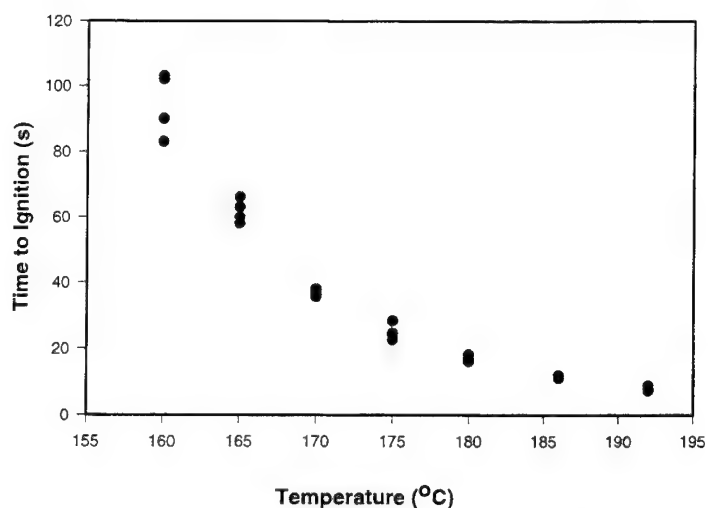


Figure 3. DSC plot of  $\ln$  heating rate vs.  $1/\text{temperature}$  at max. isotherm for ADN.

### IGNITION TEMPERATURE TEST

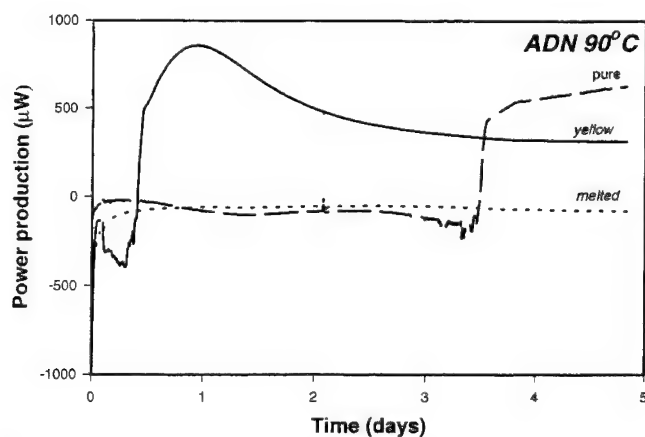
The sensitivity to thermal ignition was measured using Wood's metal bath. The ignition temperature was found to be 160°C. The ignition temperature measured for ADN is relatively low; Tetryl tested in the same apparatus under the same conditions gave a temperature of ignition at 207.5°C. The data is shown in Figure 4. From these measurements the activation energy was also determined,  $E_a = 127$  kJ/mole.



**Figure 4.** Time to ignition vs. temperature measured with Wood's metal bath.

#### MICROCALORIMETRY

An LKB Thermal Activity Monitor equipped with the BOMIC 2277 software was used to monitor the stability of ADN at 65, 80 and 90°C. A microcalorimeter measures the sum of all chemical and physical reactions that takes place in the sample. The apparatus used is very accurately thermostated and the accuracy of the apparatus is better than 1  $\mu$ W. In Figure 5 the activity at 65 and 90°C over a period of 5-21 days is shown for ADN. The batch denoted A is less pure than batch B. It can be seen here that the activity is significantly higher for less pure ADN and that water influences the thermal stability especially for less pure ADN. The melted (prilled) ADN also seems to be much more stable. We do not currently have any explanation for this.



**Figure 5a.** ADN Microcalorimetry at 90 °C.

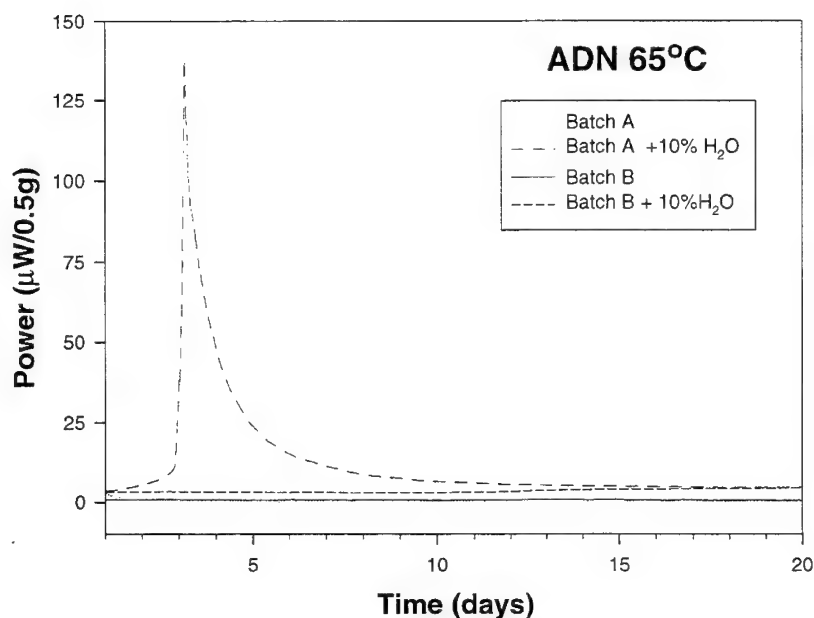
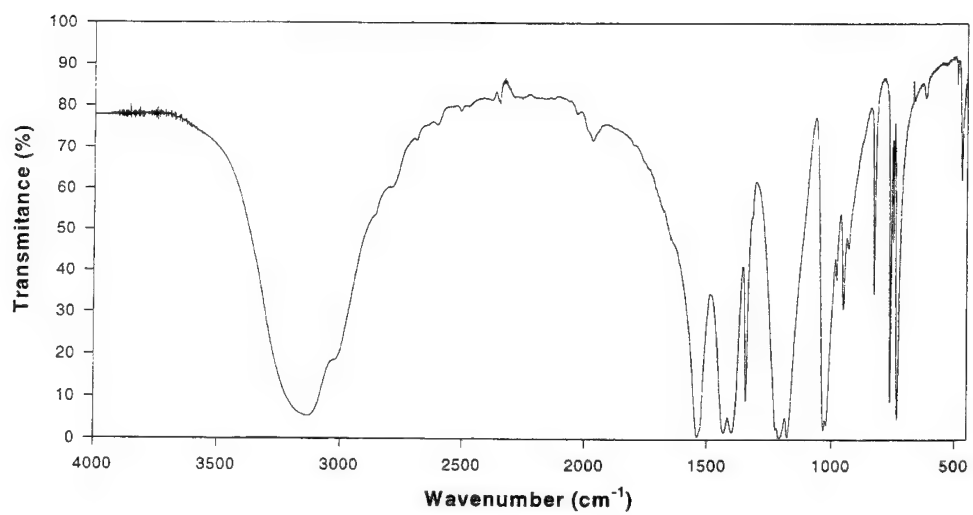


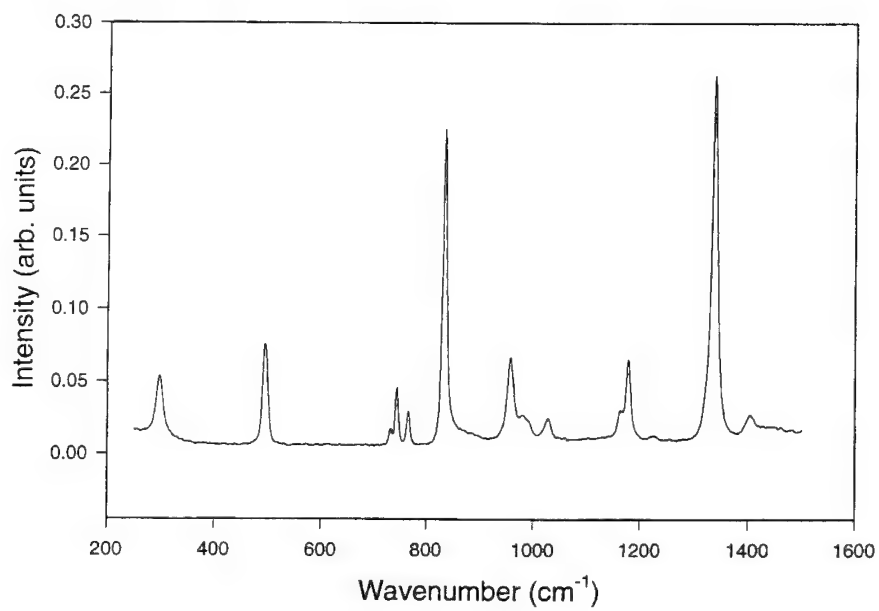
Figure 5b. ADN Microcalorimetry 65 °C

### FT-IR AND FT-RAMAN SPECTROSCOPY

The ADN was identified by FT/IR spectroscopy (reference spectra from [5,6]) which is so far the best routine method for identifying ADN. Recently, FT-Raman spectroscopy has emerged as an interesting complement to FTIR in explosives analysis [12]. This method uses only a small amount of solid sample (a few mg of powder) and is very easy to perform. Figure 6 shows the FTIR spectrum and Figure 7 shows FT-Raman spectra of ADN. The FT-IR/Raman spectra presented here were measured with a Bruker IFS 55 equipped with a Raman attachment. The excitation wavelength was 1064  $\mu\text{m}$  and the resolution used was  $2\text{ cm}^{-1}$ . The conclusion from the FT-Raman measurements is that FT-Raman gives a sharper peak and is easier to interpret.



**Figure 6** *FT-IR Spectrum of ADN.*

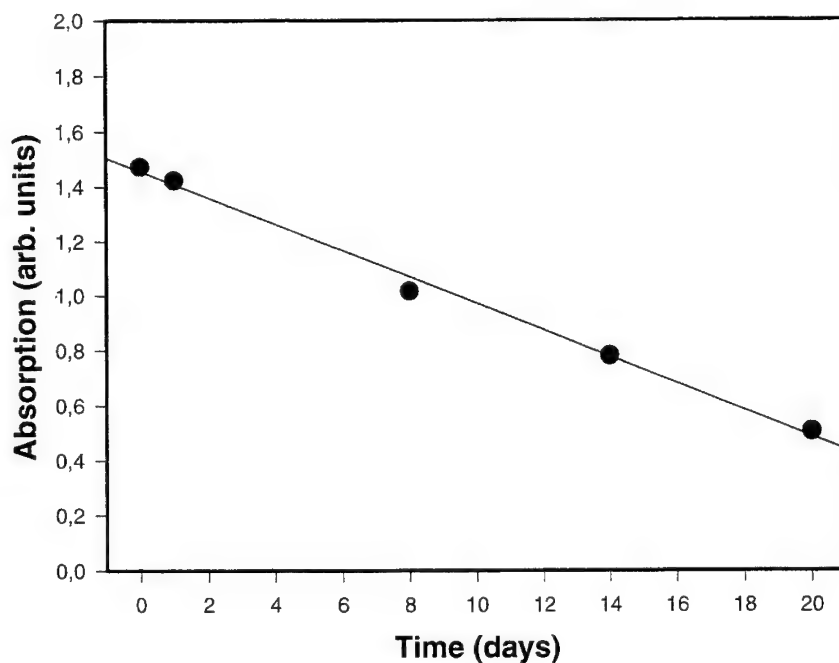


**Figure 7** *FT-Raman Spectrum of ADN*



## LIGHT SENSITIVITY

The light sensitivity of ADN was measured by allowing a solution of ADN to stand in daylight for three weeks. The results from these measurements are shown in Figure 8. The concentration was measured with UV-spectroscopy. In this figure is clearly seen that an ADN solution is unstable in light.



**Figure 8.** *ADN light sensitivity (in water solution). Concentration vs. number of days in day light.*

## DISCUSSION AND CONCLUSIONS

Some preliminary conclusions can be drawn from this initial study, as follows:

- ADN is thermally more unstable than RDX.
- The purity of ADN greatly influences its thermal stability.
- The impact sensitivity of ADN is greatly dependent on particle shape.
- In solution, ADN is sensitive to light.

The results in this paper clearly indicate that ADN is a very promising candidate for a new oxidizer, but that several important questions remain to be answered.

## ACKNOWLEDGEMENTS

We would like to thank Birgitta Persson for the splendid work with the microcalorimetry, the DSC and the SEM pictures, and Lars Bodin for the drop weight and friction tests.

## REFERENCES

1. Schröder, H.F.R., *et al.*, High-Performance Propellants Based on Hydrazonium Nitroformate, *J. Propulsion and Power*, 11, 856-869, 1995.
2. Foltz, M.F., *et al.*, The Thermal Stability of the Polymorphs of Hexanitrohexaazaisowurtzitane, Part I, Propellents, Explosives, Pyrotechnics, 19, 19-25, 1994.
3. Foltz, M.F., *et al.*, The Thermal Stability of the Polymorphs of Hexanitrohexaazaisowurtzitane, Part II, Propellents, Explosives, Pyrotechnics, 19, 133-144, 1994.
4. Bottaro, J.C., *et al.*, Methode of Forming Dinitramide Salts, US patent WO 91/19670, 1991.
5. Hatano, H., *et al.* New Synthetic Method and Properties of Ammonium Dinitramide (ADN), in *EuroPyro 95 6e Congrès International de Pyrotechnie*, Tours, France, 1995.
6. Rossi, M.J., J.C. Bottaro, and D.F. McMillen, The Thermal Decomposition of the New Energetic material Ammonium dinitramide ( $\text{NH}_4\text{N}(\text{NO}_2)_2$ ) in relation to Nitramide ( $\text{NH}_2\text{NO}_2$ ) and  $\text{NH}_4\text{NO}_3$ , *Int. J. Chem. Kinetics*, 25, 549-570, 1993.
7. Brill, T.B., P.J. Brush, and D.G. Patil, Thermal Decomposition of energetic Materials 58. Chemistry of Ammonium Nitrate and Ammonium Dinitramide Near the Burning Surface Temperature, Combustion and Flame, 92, 178-186, 1993.
8. Östmark, H., *et al.*, A Study of the Sensitivity and Decomposition of 1,3,5-trinitro-2-oxo-1,3,5-triazacyclo-hexane, *Thermochimica Acta*, 260, 201-216, 1995.
9. Östmark, H., H. Bergman, and G. Åqvist, The Chemistry of 3-nitro-1,2,4-triazole-5-one (NTO): Thermal Decomposition, *Thermochimica Acta*, 213, 165-175, 1993.
10. Gordon, S. and B.J. McBride, Computer Program for Calculation of Complex Chemical Equilibrium Compositions, Rocket Performance, Incident and Reflected Shocks, and Chapman-Jouguet Detonation, NASA, Washington, D.C., 1971.
11. Rogers, R.N. and L.C. Smith, Application of Scanning Calorimetry to the Study of Chemical Kinetics, *Thermochimica Acta*, 1, 1-9, 1970.
12. Östmark, H., H. Bergman, and P. Sjöberg. Sensitivity and Spectroscopic Properties of the  $\beta$ - and  $\epsilon$ -Polymorphs of HNIW, in *International Symposium on Energetic Materials Technology*, Phoenix, Arizona, 1995.

## ADN PROPELLANT TECHNOLOGY

May Lee Chan, Alan Turner, Larry Merwin,  
Gregory Ostrom, Carol Mead, and Stan Wood  
Naval Air Warfare Center Weapons Division  
China Lake, California USA

**ABSTRACT:** This paper discusses a number of issues critical to ammonium dinitramide (ADN) propellant technology. It also includes a survey of the chemical purity levels of ADN produced by different sources, the safety properties of ADN with different levels of water content, and the prilling of neat ADN to produce spherical particles. In addition, it discusses the aging stability and processing properties of propellants containing ADN and ADN prills. To qualify ADN as a propellant ingredient, these properties must be thoroughly characterized and understood, so that the properties of ADN propellants can be predicted when this compound is incorporated in the binder.

## INTRODUCTION

Ammonium dinitramide (ADN) is a very powerful organic oxidizer that can replace ammonium perchlorate (AP) in propellant compositions. Calculations have shown that, when incorporated in propellant formulations, ADN can make those propellants capable of performance equal to or higher than that of the conventional hydroxyl-terminated polybutadiene (HTPB)/AP propellants.<sup>1</sup> If ADN propellants are developed, they will not produce toxic HCl in the exhaust and will greatly minimize the secondary smoke problem that is caused by the nucleation of HCl. Because of their environmentally friendly characteristics and demonstrated low toxicity to humans,<sup>2-4</sup> ADN propellants are highly desirable.

Initial evaluation<sup>5</sup> of the ADN neat solid revealed that ADN is slightly more sensitive than cyclotrimethylenetrinitramine (RDX) in impact sensitivity and it is not very sensitive to friction or electrostatic discharge. ADN was also shown to be thermochemically compatible with a variety of binder materials.

\* Approved for public release; distribution is unlimited.

\*\* This effort was supported by the Insensitive Munitions Advanced Development (IMAD) Program (Don Porada, cognizant technology manager).

The undesirable crystal shape (thick plates or needle-like crystals) of ADN has caused many of the difficulties encountered in ADN propellant processing, especially for high solids loading (>70%). In addition to the undesirable shape, it has also been observed that ADN crystals recrystallized from organic solvents are prone to develop defects and crystal inhomogeneity. One of the ways developed to solve this problem has been to produce ADN prills from molten material. This process is similar to the one used in ammonium nitrate (AN) prilling technology, where prills can be made from molten AN. When conditions are monitored and controlled, spherical particles of ADN can be produced. A sphere is the most desirable shape for maximizing solid loading in propellant processing.

## EXPERIMENTAL RESULTS

### Source of ADN

The synthesis of ADN has been well documented by chemists both from the U.S. and Russia.<sup>6-10</sup> The ADN material used in the work described in this paper was purchased from SRI and Thiokol Co. The ADN material consists of either thick plates or needle-like crystals with high aspect ratio.

### ADN Prilling

According to Russian technology data,<sup>3,11</sup> the prilling process of ADN involves melting and shearing ADN to produce small droplets that cool rapidly to form hardened spheres.

A laboratory setup (Figure 1) was constructed to produce ADN prills in small scale. The setup consists of a fluted glass column equipped with a glass stirring rod with shearing baffles at the base. The rod is connected to a stirring motor. A liquid carrier fluid (an oil immiscible with molten ADN) is poured into the column. When the motor drives the stirring rod, high-shear conditions can be generated. ADN and small amounts of stabilizer (0.3% hexamine) were added to the carrier fluid; the carrier fluid was then heated in a oil bath to 105°C. After 10 minutes of gentle stirring, the ADN became molten (with dissolved thermal stabilizer). Upon high shearing, molten ADN droplets were quickly formed and quenched to hardened spheres. About 50 batches of ADN prills (2 to 3 grams per batch) were prepared and analyzed for safety, thermal, and morphological properties. Some of the processing variables were studied to find whether high shear is necessary to form the droplets of molten ADN. It was discovered that 110°C or less for up to 15 minutes is the safe temperature at which to melt ADN; a temperature higher than 120°C for any length of time decomposes ADN (fair amounts of gaseous bubbles are present in the hardened spheres). The addition of hexamine (0.3% by weight) serves to thermally stabilize the ADN melt. No safety problems were encountered while preparing the prills. However, additional studies are needed to ensure safe operation, especially on a larger scale. Data obtained on the melting characteristics of ADN, heating and cooling rates, and rates of shearing should be useful for designing a melt granulator for scaling up the process.

### Characteristics of ADN Prills

ADN prills produced with the laboratory setup described above were characterized for their properties. Under optical microscopic examination, the spheres are translucent to clear in appearance (Figure 2) and have high density (1.801 g/cm<sup>3</sup>). Scanning electron microscope (SEM) photomicrographs (Figure 3) showed spheres having a lava-like surface texture, which could be indicative of a melting and crash-cooling process.

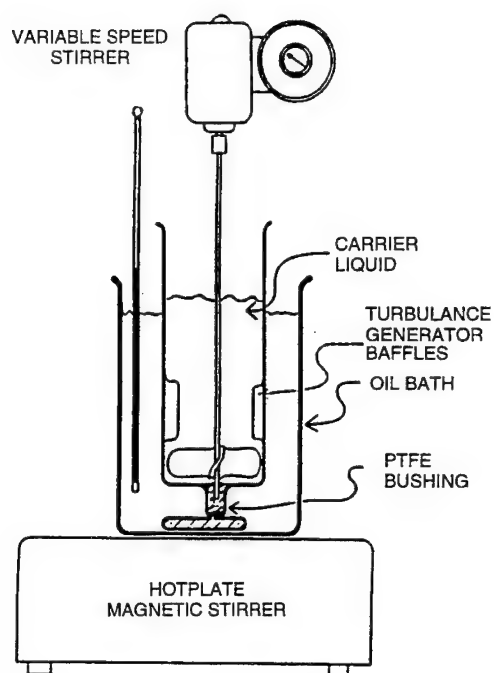


Figure 1. Small Laboratory Prilling Apparatus.

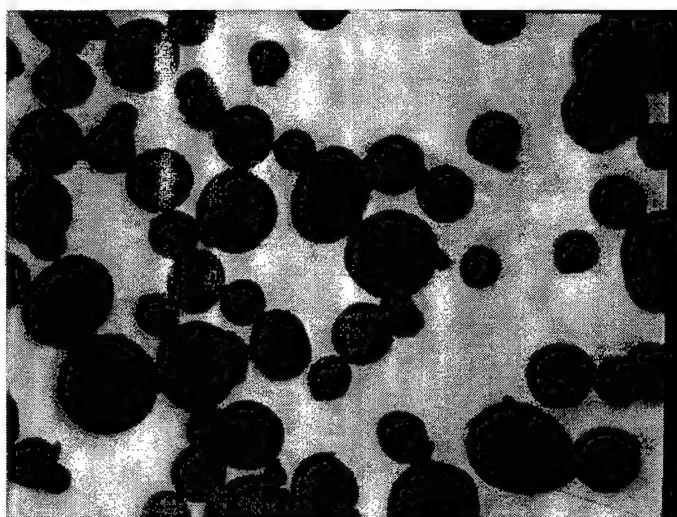


Figure 2. ADN Prills.

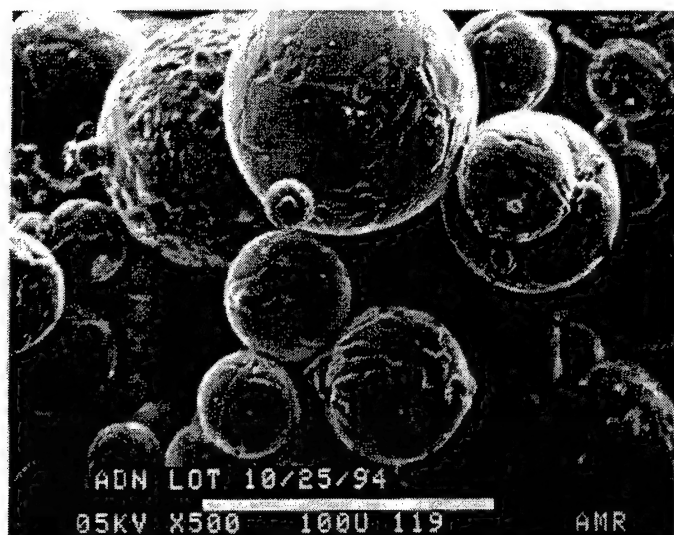


Figure 3. SEM Micrograph of ADN Prills.

The particle size distribution of prilled ADN, depending upon the shearing rate used during the prilling process, is typically in the range of 30 to 500  $\mu\text{m}$ . It was found that the spheres were very easy to sieve to obtain different lots with narrow particle size distribution. The spheres containing 0.3% hexamine exhibited excellent thermal stability when compared to the neat ADN. The results of vacuum thermal stability (VTS) tests conducted at 98°C (Figure 4) indicated a dramatic effect of hexamine stabilization, whereas neat ADN decomposed rapidly at this temperature.

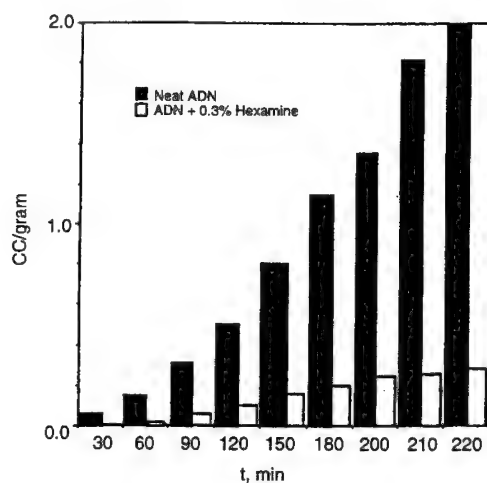


Figure 4. ADN Vacuum Thermal Stability Test Results.

Hexammonium dinitramide has been isolated in the ADN+hexamine mixtures; the presence of hexammonium dinitramide was further verified through nuclear magnetic resonance (NMR) techniques. The presence of hexamine may prevent dinitramic acid from attacking the rest of the ADN, thus preventing further ADN decomposition.

### Chemical Purity of Neat ADN and ADN Prills

The chemical purity of ADN produced from different sources has been analyzed by ion chromatography (IC) with the anion exchange Dionex column. The results of this analysis are indicated in Table 1. Most of the ADN samples were very pure; they typically contained only about 0.05 to 0.55% of ammonium nitrate (AN); no traces of nitrite were detected in any of the samples. Occasionally, a small percentage of ammonium nitrourethane (ANU) was detected; this compound is part of the starting material carried over in synthesis and scale-up. Although the effect of ANU on the curing and aging of ADN propellant is unknown, no problems are anticipated. During the synthesis scale-up of ADN, the pH of the reaction mixture was adjusted to 8.5 to 9.0 in the amination process; therefore, the nitric acid level should not be a concern.

TABLE 1  
Chemical Analyses of ADN Samples by IC.

ADN Sample	NO <sub>3</sub> , %	ANU, %
Norris-145154-1	0.11	--
Norris-145157-3	0.25	--
SRI PRD 5-23	0.26	--
SRI PRD 5-24	0.40	--
SRI PRD 50-31	0.55	0.52
ADN prills 3-14-95 (made from SRI PDR 50-31)	0.05	nil
ADN Thiokol 6-7-95	0.05	nil

ADN prills contain less AN than does the neat ADN; these data could indicate that, with the help of hexamine, little or no decomposition of ADN occurs during the melt phase of prilling. A similarly encouraging result was also obtained with the prills made with Thiokol Corporation's material.

### Effect of Water on Thermal and Safety Properties

Data obtained from Russian ADN literature<sup>3,4,11</sup> indicate that ADN is more thermally stable if the ADN crystal is slightly moist (at around 0.5% H<sub>2</sub>O). Because the climate at China Lake is very dry, the water content of ambient-stored ADN was measured regularly. The measurements indicated that ambient-stored ADN had a low water content of 0.02%. Various samples of ADN were equilibrated in constant humidity chambers at two different humidity levels (58 and 38%) for 95 hours to allow some water to be absorbed into the ADN crystals. The water content of the ADN samples equilibrated at different time intervals was then analyzed. The results, as indicated in Table 2, showed that ADN and ADN prills can quickly absorb water. It was found that their water content was 0.4% after 24 hours, and increased to 1.76% when stored over 95 hours in a chamber at 58% relative humidity. ADN samples can also desorb water quickly; in fact, samples previously stored at 58% relative humidity were transferred to ambient storage where their water content decreased to 0.07% after two weeks.

The results of the safety tests conducted at China Lake are summarized in Table 3. They show several important points: 1) ADN is slightly more sensitive than cyclotetramethylenetetranitramine (HMX) or cyclotrimethylenetrinitramine (RDX) in impact and friction tests (this fact is supported by other reports);<sup>12</sup> 2) ADN samples containing 0.5% water exhibit less sensitivity to impact than ADN samples containing 0.02% water; and 3) ADN prills containing 0.3% hexamine exhibit no deterioration

of safety properties when compared with the neat ADN solid. When prills were being produced, a sample containing 2% hexamine exhibited greater sensitivity during Allegany Ballistic Laboratory (ABL) friction testing, 87 pounds at 50% point (close to the sensitivity of pentaerythritol tetranitrate (PETN)) compared to the 295 to 355 pounds typically obtained for ADN prills containing 0.3% hexamine. It was concluded that ADN prills containing over 1 to 2% hexamine are most likely too friction sensitive to make or to process.

TABLE 2  
ADN Water Content.

Relative Humidity, %	Time, hrs	Water, %*
Neat ADN (SRI, >99% pure)		
10-15 (ambient storage)	--	0.02
58	3	0.03
58	4	0.07
58	16	0.25
58	24	0.40
58	95	1.76
58	14 + 2 wks ambient storage	0.07
38	94	0.06
38	336	0.08
38	1104	0.07
ADN Prills		
10-15 (ambient storage)	--	0.02

\* Water content measured by the Karl Fisher method.

TABLE 3  
ADN Safety Properties.

Material	Safety Tests		
	Impact (2.5 kg, 50%), cm	ABL Friction (50%), lbs	Electrostatic (0.25 J)
Neat ADN			
SRI-50-31	11-12	295-355	10/10 NF
SRI-50-31 (H <sub>2</sub> O = 0.25%)	11-12	295-355	10/10 NF
SRI-50-31 (H <sub>2</sub> O = 0.5%)	15	295-355	10/10 NF
Thiokol lot 6-7-95	--	--	--
ADN Prills			
from SRI-50-31 (0.3% hexamine)	11-12	295-355	10/10 NF
from SRI-50-31 (2.0% hexamine)	11	87	10/10 NF
from Thiokol (0.3% hexamine)	11-12	295-355	10/10 NF

NOTE: 1. All ADN samples have 0.02% water content except where otherwise noted.  
2. HMX (Class 1) has the following safety properties: Impact = 20 cm; ABL friction = 398 lbs; Electrostatic = 10/10 NF.



## ADN Propellant Aging

The thermal stability of ADN is an issue that has been the focus of study by many investigators.<sup>11,13,14</sup> It is known that ADN decomposes to form  $N_2O$ ,  $N_2$ ,  $NH_3$ , nitric acid, and ammonium nitrate. However, other questions, like the following, still remain unanswered. How does ADN propellant age? What is its shelf-life? Do hexamine-stabilized ADN prills provide better propellant shelf-life than the neat ADN crystals?

In an attempt to answer some of these questions, researchers at China Lake have made a number of propellant formulations using ADN material, both crystals and prills, in glycidyl azide polymer (GAP), poly(diethyleneglycol-4,8-dinitraza undecanate) (ORP-2), and polycaprolactone polymer (PCP) binders. These formulations were as follows: PCP/butanetriol trinitrate (BTTN)/neat ADN, PCP/BTTN/ADN prills, GAP/BTTN/neat ADN, GAP/BTTN/ADN prills, ORP-2/BTTN/neat ADN, ORP-2/BTTN/stabilized ADN. All of the propellants contained 65% solids loading, BTTN, and 0.8% n-methyl p-nitro aniline (MNA) as the stabilizer. The BTTN/polymer ratio was 2 to 2.5. An inert polymer (PCP) and two energetic polymers (GAP and ORP-2) were used in the aging study described herein; GAP/BTTN/HMX mixes were used as the baseline (since it is known that GAP, BTTN, and HMX form compatible mixtures). The ADN propellants were cured with either hexamethylene diisocyanate (HMDI) or a multifunctional isocyanate (N-100). The samples were subjected to 160°F (71°C) isothermal aging conditions. At the end of every two-week interval, the aged samples were removed, their stabilizer content was measured, and their physical properties were visually examined. The samples remained physically intact and no exudation or excess softening were observed. The aging samples were monitored for a total of eight weeks at the same temperature. The results, also shown in Figure 5, were as follows: 1) when compared to HMX-filled compositions, ADN propellants deteriorated more rapidly upon aging; 2) hexamine-stabilized ADN prills did not exhibit any advantage over neat ADN samples in long-term aging; 3) differences between the three binders used in the ADN formulations were observed—PCP appeared to be the best, followed by ORP-2 and GAP; and 4) all propellant samples met the shelf-life requirement set by weapon system developers (0.2% MNA remaining at the end of 4 weeks and 0.1% MNA remaining at the end of 8 weeks after aging at 160°F).

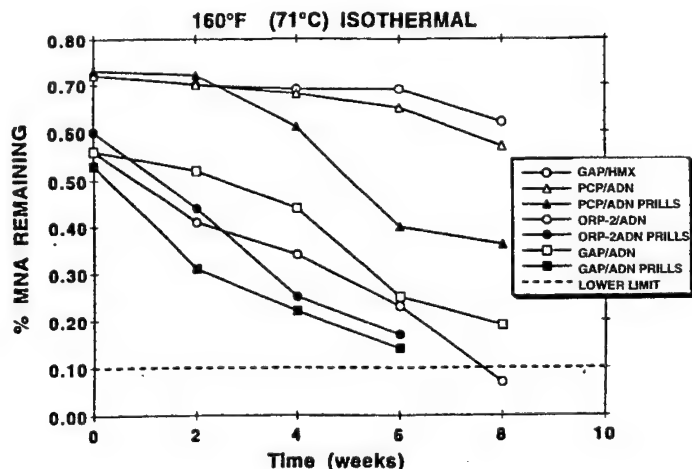


Figure 5. ADN Propellant Aging.

## SUMMARY AND CONCLUSION

The chemical purity of the ADN produced by SRI and Thiokol is very high. Less than 0.5% impurities were found in all the samples tested. During studies, it was learned that ADN absorbs and desorbs water freely; therefore, propellant processing needs to be conducted in a dry environment.

Upon aging, ADN propellants behave in a way similar to that of conventional nitrate-ester-containing propellants and can be stabilized by adding MNA to the propellant mix to prolong their shelf-life. Preliminary results indicate that high-energy ADN propellants can be made with sufficient shelf-life for incorporation in U.S. weapon systems. The presence of a chemical stabilizer within the crystal is not critical to obtaining good aging characteristics in propellants, but it is critical to use small amounts (0.3 to 0.5%) of hexamine or other stabilizer in the melt phase of the prilling process to ensure the safety and thermal stability of the ADN melt.

High-quality spherical ADN particles can be obtained through a granulation process in a small laboratory apparatus. This is an important technological development, because a sphere is the most desirable shape for good processing (ADN propellants with high solids loading can be obtained by using spherical ADN particles). A melt granulator is currently being designed and constructed to scale up the prilling process to produce ADN prills for propellant formulation.

## REFERENCES

1. **Atwood, A.I., Curran, P.O., Boggs, T.L., Hollins, R.A., Chan, M.L. and Wiknich, J.**, "ADN Combustion Studies," *Proceedings of the 30th JANNAF Combustion Subcommittee Meeting*, Monterey, Calif., November 1993. Paper UNCLASSIFIED.
2. **Chan, May L. and Demay, Susan C.**, "Development of Environmentally Acceptable Propellants," *Proceedings of the 84th Symposium of the Propulsion and Energetics Panel on the Environmental Aspects of Rocket and Gun Propulsion*, 29 August-2 September 1994, Alesund, Norway. Paper UNCLASSIFIED.
3. **Pak, Z.**, "Some Ways to Higher Environmental Safety of Solid Rocket Propellant Application," *AIAA/SAE/ASME/ASEE 29th Joint Propulsion Conference and Exhibit*, 28-30 June 1993, Monterey, Calif. Paper UNCLASSIFIED.
4. **Manelis, G.B.**, "Possible Ways of Development of Ecologically Safe Solid Rocket Propellants," *AIAA/SAE/ASME/ASEE 29th Joint Propulsion Conference and Exhibit*, 28-30 June 1993, Monterey, Calif. Paper UNCLASSIFIED.
5. **Chan, M.L., Turner, A. and Nadler, M.**, "Safety, Aging, and Thermocompatibility Issues of ADN and ADN Propellants," *Proceedings of the Joint JANNAF Propellant Development & Characterization and New Energetic Materials Workshop Meetings*, 18-19 April 1994, Kennedy Space Center, Fla. Paper UNCLASSIFIED.
6. **Tartakovsky, V.A.**, "Dinitramide Chemistry," *Lectures in Energetic Material Research by Russian Scientists*, 27-28 February and 1 March 1995, China Lake, Calif. Paper UNCLASSIFIED.
7. **Tartakovsky, V.A. and Luk'yanov, O.A.**, "Synthesis of Dinitramide Salts," *Proceedings of the 25th International Annual Conference of ICT*, 28 June-1 July 1994, Karlsruhe, Germany. Paper UNCLASSIFIED.
8. **Schmidt, R.J., Bottaro, J.C., Ross, D.S. and Penwell, P.E.**, "Dinitramide Salts and Method of Making Same," International Patent Application No. WO 91/19669, issued June 1990. US patent No. 5,254,324, issued 19 Oct. 1993. Patent UNCLASSIFIED.

9. **Schmidt, R.J., Bottaro, J.C., Penwell, P.E. and Bomberger, D.C.**, "Process for Forming A Dinitramide Salt or Acid," International patent application No. WO 93/16002, issued Aug 1993. Patent UNCLASSIFIED.
10. **Schmidt, R.J., Bottaro, J.C., Penwell, P.E. and Bomberger, D.C.**, "Process for Forming Ammonium Dinitramide Salt by Reaction Between Ammonia and A Nitronium-containing Compound," U.S. Patent No. 5,316,749, issued 31 May 1994. Patent UNCLASSIFIED.
11. **Manelis, G.B.**, "Thermal Decompositon of Dinitramide Ammonium Salt," *Proceeding of the 26th Annual Conference of ICT*, July 1995, Karlsruhe, Germany.
12. **Highsmith, T. and Wardle, R.**, "ADN Sensitivity," *Proceedings of the 1995 JANNAF Propellant Development and Characterization Subcommittee Meeting*, April 1995, Pasadena, Calif. (CPIA publication No. 625). Paper UNCLASSIFIED.
13. **Russell, T.P., Stern, A.G., Koppes, W.M. and Bedford, C.D.**, "Thermal Decomposition and Stabilization of Ammonium Dinitramide," *Proceedings of the 1992 JANNAF Combustion and Hazards Subcommitte Meeting*. (CPIA publication No. 593.) Paper UNCLASSIFIED.
14. **Boswell, R.F. and Tompa, A.S.**, "Thermal Compatibility Test for Energetic Materials," *Proceedings of the 1995 JANNAF Propellant Development and Characterization Subcommittee Meeting*, April 1995, Pasadena, Calif. (CPIA publication No. 625.) Paper UNCLASSIFIED.

#### COMMENTS

Dr. A. Peretz, Rafael, Haifa, Israel. 1. Can you comment on the ballistic and mechanical properties of ADN-based propellants? 2. What kind of problems need solutions before operational use of those propellants?

Author's Reply. We have typically found that ADN propellants burn about 1.5 to 2 times faster than the corresponding HMX compositions. Because the processing problems associated with ADN propellants have not been fully resolved, their mechanical properties have yet to be properly assessed and optimized.

Before ADN propellants are recommended for operational use, their properties—ballistic, mechanical, processing, and hazard—need to be fully assessed and optimized.

## **'ACTIVATED' ALUMINUM AS A STORED ENERGY SOURCE FOR PROPELLANTS**

**By Gennady V. Ivanov<sup>1</sup>, and Frederick Tepper<sup>2</sup>**

Institute of Petroleum Chemistry, Russian Academy of Sciences, Tomsk, Russia<sup>1</sup>;  
Argonide Corp, I-4 Industrial Park, Sanford, Florida, 32771, USA<sup>2</sup>

**ABSTRACT:** The process of electro-explosion of metal wires, which has been known for more than 200 years, has been adapted to the preparation of activated aluminum, called Alex. The process produces metallic particles of approximately 50-100 nanometers in size. X-ray diffraction studies both in Russia and the U. S. A. confirm the crystallites are aluminum, although one study shows a minor amount of an unknown phase, that is presumed to be oxide. The surface phase appears to be semiconductive in nature. The most unusual characteristic of this aluminum is the stored energy that is released upon reaching a threshold temperature. While this heat generation has been confirmed by other researchers, no one, including the authors has a proven theory for the source of this energy. Nevertheless, this material is suggested for use as a fuel in pyrotechnics, explosives and propellants.

### **DESCRIPTION OF THE PROCESS**

The electro-explosion of a metal wire (EEW) to produce aerosols was discovered in 1773 by Michael Faraday, but its practical application and detailed investigation didn't begin until after World War II. This was in connection with the study of detonators for atomic bombs and space rocket technology.

These investigations showed unusual behavior in the way current flowed through wires and a number of experimental research studies were then performed. The result is a picture of the electro-explosion process in which short powerful impulses of current generates a compressing electromagnetic field around the wire. The field keeps the metal together in the form of a cylinder even though the metal is extremely superheated. In addition, the flow of the current heats the wires up to 20,000 to 30,000 degrees and then its electrical resistance rises to infinity, causing interruption of the current flow. Then the supercompressed and superheated metal in the form of a plasma expands with supersonic velocity, creating a shock wave in the surrounding gas, and produces atomized nanosize metal crystallites.

The phenomenon of EEW was the subject of reports in four international symposia [1-4], and maybe hundreds or even thousands of articles were published in scientific magazines in the USA, Russia and elsewhere. But only four articles, published before 1970 [5-8] were dedicated to producing fine aerosols by the EEW process, and they didn't perform detailed research on the properties of the particles that were produced.

After 1970, the High Voltage Institute in Tomsk, Russia, studied the production of ultra-fine aluminum powders (Alex) by the EEW process. In these studies the explosion of the wire was done in a vessel filled with a non oxidizing gas of either hydrogen, argon or helium, and the particles were collected by sedimentation. A semi-automatic laboratory apparatus was constructed that produced grams of powder

per day, which provided sufficient material to initiate studies of physical and chemical properties of the powder.

### THE SHAPE AND SIZE OF THE PARTICLES

Early electron photomicrographs showed that the Alex particles are ideal spheres (Fig 1). The size of the particles depends on the length and diameter of the exploding wires, the voltage, the total quantity of electrical energy imparted to the wire, the characteristics of the impulse, the source of the wire and other parameters [ 9, 10]. Recently it was found that the spheres were formed as a result of melting and sintering under the action of the electron beam of the microscope. This change occurred over a period of 2 to 3 seconds after initial application of the beam to the field of view. Fig 2 shows the initial view and Fig 3 shows the view after several seconds. The formation of spherical balls as in Fig. 1 became apparent during continued viewing under the high energy beam. Electron microscopic views of the powder could be obtained without it being sintered through the use of the low energy scanning electron microscope (Fig 4), or by heat sinking or cooling the stage. In this case, the powder is seen as irregular clumps of very small particles of approximately 50 nanometers in size. This irregular collection of particles may be described by the theory of fractals. [11, 12].

### CHEMICAL COMPOSITION

Standard chemical analysis shows that Alex is approximately 92-95% aluminum. Using mass spectrometry and vacuum thermal desorption, while measuring weight loss (using a highly sensitive quartz spiral balance), and by measuring the volume of the desorbed gas, it was established that the powder contained 5-8% of adsorbed air components. First, moisture desorbed after the temperature of the sample reached 100 deg, nitrogen then desorbed in the interval 200-250 deg and oxygen desorbed at 300- 350 deg. Upon cooling in air, the sample readsorbed the same quantity of air as had been desorbed. Alex will absorb other gases, including chlorine, and so long as it is kept in a dry atmosphere the chlorine did not react chemically with the aluminum over a period of one year.

### STRUCTURE OF THE CRYSTAL LATTICE

The x-ray powder diffraction patterns of Alex are identical to that of crystalline aluminum. Prof. Randall German's group at Penn State Univ. also verified that no peaks were observed other than those of aluminum. They also calculated sizes for the crystal lattice to be 67 nanometers. More accurate measurement of Alex by Prof. Deane Smith of Penn State shows a minor phase barely discernable by x-ray, whose lines are unidentified, and is presumed to be an oxide.

### ELECTROCONDUCTIVITY

Pressed pellets of Alex have a room-temperature electrical resistivity of hundreds of millions of ohms, which depends upon the pressure that had been applied to the pellet to form it. At 200-300 deg, the resistance falls to 20,000 -30,000 ohms. Upon recooling to room temperature, the higher resistivity is restored to the initial level rather precisely. This phenomenon was repeated over several cycles of heating and cooling. Hall effect measurements were done that showed that the carriers of current are positive. This means that Alex behaves as a semi-conductor of holes. The data of chemical and x-ray analysis and the semiconductor behavior suggest that the particles are surrounded by a thin film of unusual oxide composition.

### STORED ENERGY

Figure 5 shows thermogravimetric analysis (TGA/DTA) plots on a sample of Alex, where:

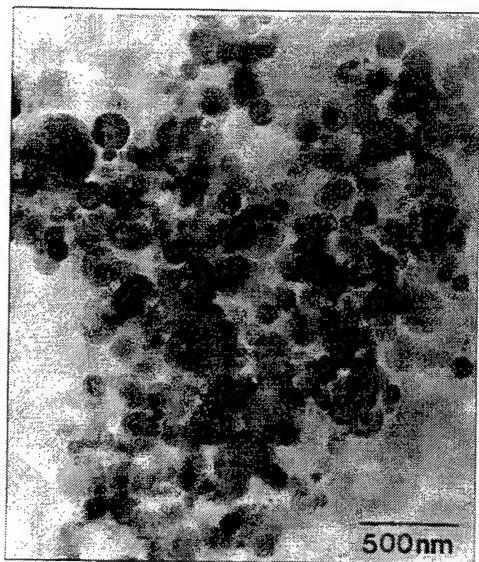


Figure 1  
TEM of ALEX.

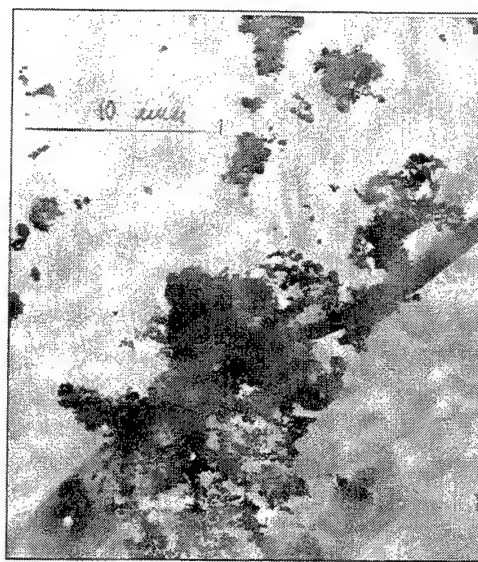


Figure 2  
SEM of Alex.  
(Early exposure.)

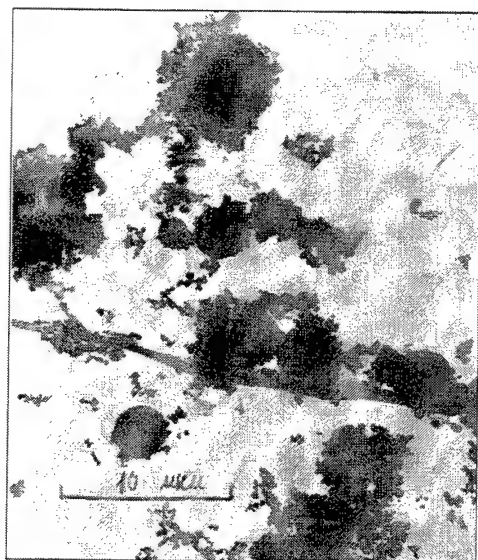


Figure 3  
SEM of Alex  
(Late exposure.)

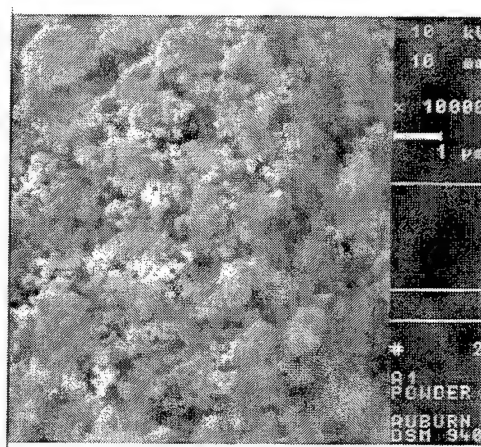


Figure 4  
Low energy SEM of Alex.

Curve 1 is the applied temperature  
Curve 2 is the change of temperature of the Alex sample  
Curve 3 is the change in weight of the sample  
Curve 4 is the differential of Curve 2.

An exotherm occurs at 450 degrees without any weight change, that is, without oxidation. The exotherm reaches a maximum at 550 deg, with partial oxidation occurring after 550-580 deg. There is an endotherm at 637 degrees corresponding to melting. There is a peak at 753 corresponding to fast oxidation.

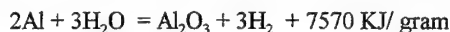
Microscopic observation and classical chemical analysis of the Alex sample after TGA shows that near 70% of it is bright metallic balls of pure aluminum and only 30% by weight is white oxide. When we spread Alex powder on a ceramic sheet and ignite it by a hot wire, it shows a two-step reaction. The first reaction produces a dull red light, which occurs across the powder layer. Then the material may cool and if reignited, there is a second step which is presumably the burning process that occurs with the generation of white light. But as with the TGA experiments, full oxidation is absent. We conclude that the process of self-heating and self-sintering of Alex particles is faster than the process of oxidation.

Pressed pellets of Alex were placed on a stainless steel plate inside a glass vacuum chamber and were heated. Using a thermocouple we measured the temperature of the steel plate, and with a second thermocouple measured the pellet temperature. At approximately 450-460 deg, the pellet starts to show signs of melting, while the second thermocouple detects a fast rise in temperature of the pellet to 900 deg. This process of fast-rising temperature over a two to three second duration corresponds to a process of heat explosion.

When one edge of a pressed pellet is placed on a hot plate there is a visible propagation of light across the pellet. Figure 6 is a cinematic view of the advance of the light wave. The moving of the wave transforms the dark material of the pressed pellet of Alex into bright monolith metal. So, releasing all the stored energy in Alex takes place in the form of heat explosions and heat waves [13 and 14].

### CHEMICAL PROPERTIES

The reaction of Alex with water is evident at 50 deg, and at 70-80 deg Alex will react within seconds in the form of heat explosions, which heat the water to boiling. The solid products of this reaction, as defined by x-ray diffraction, are  $\text{Al}(\text{OH})_3$ ,  $\text{AlOOH}$  and mostly  $\text{Al}_2\text{O}_3$ . The reaction



is very energetic and can be used for the generation of hydrogen. The energy available if the hydrogen is burned is 14,300 kJ/g. The surface area of the aluminum oxide that is produced is about 200  $\text{m}^2/\text{g}$ . We have found this alumina to be a very effective absorbent of different organic and inorganic impurities in the purification of water.

Stable gels can be formed by adding water containing 3% polyacrylamide to Alex. The gel of water in the polyacrylamide was mixed mechanically with Alex to yield a 1:1 molar mixture, which is paste-like. In the form of a gel, the water doesn't boil at 100 deg, and after ignition by a hot wire, the Alex/water gel will burn similarly as would paste propellants. The effect of pressure on the burning rate is seen in Fig 7. We used an argon-filled Crawford bomb, with a quartz tube of 1 cm inner diameter and 3 cm high filled with the paste. The burning rate curve can be described by the formula:

$$v = 0.183 (p/p_0)^{0.4} \text{ cm/sec, where } p_0 = 1 \text{ atm}$$

We also performed some experiments in a Viel bomb. A pressure of 600-700 atmospheres was formed

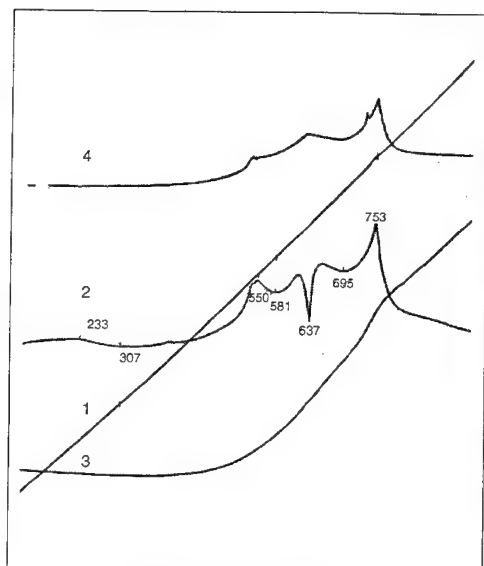


Figure 5  
TGA/DTA of Alex.

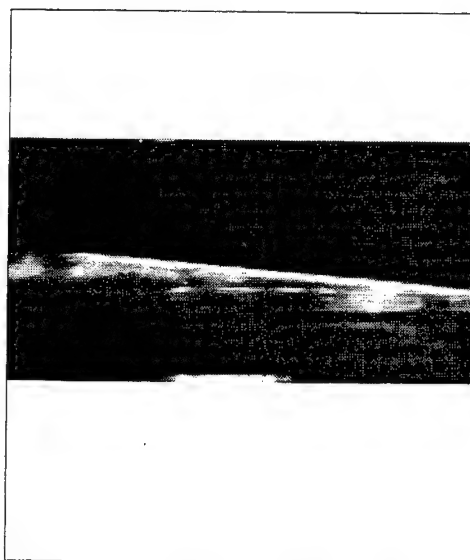


Figure 6  
Cinematic of light wave of Alex pellet.

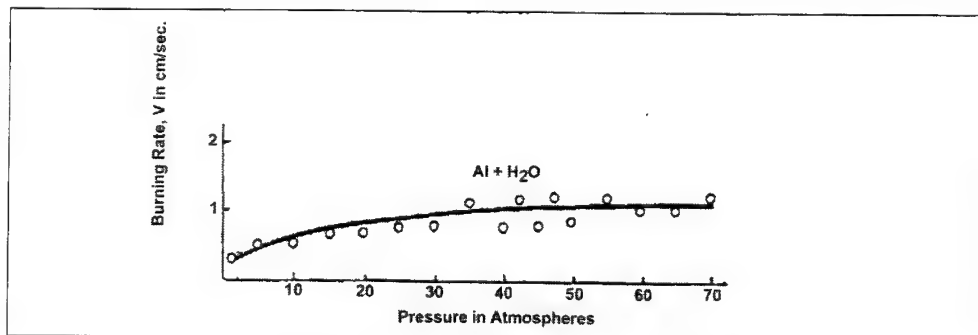


Figure 7. Burning rate for Alex gel.

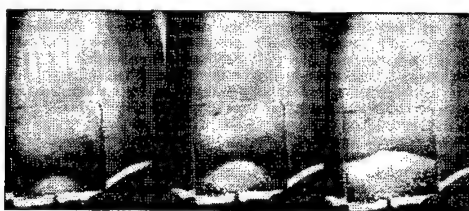


Figure 8. "Burning" of Alex in Nitrogen.



by bursts of the contents as if gun powder was ignited. The calculated temperature was in excess of 4000 deg, substantially above the melting point of the aluminum oxide, which melts at 2100 deg. The product of this reaction was a single transparent monolith. There was also some quantity of aluminum nitride as a result of the presence of the polyacrylamide. [15].

Alex, when contained in a Crawford bomb will ignite and 'burn' vigorously in pressurized (20-60 atm) nitrogen. Figure 8 shows the self-propagating wave during the synthesis of AlN. The resulting nitride product contains only 2-3% of unreacted Alex.

Pressed pellets (20 mm dia., 2-3 mm high) of mixtures of Alex with lead nitrate or barium nitrate were nested within massive steel blocks and covered by steel lids. After being impacted by shock waves from the explosions of hexamethyl-3 nitroaniline, chemical analysis shows that the resulting products contain no aluminum oxide, and the Alex was transformed into AlN. So, it appears that Alex reacts more readily and more quickly with nitrogen than with oxygen.

#### ALEX ADDITIONS TO EXPLOSIVES

The internal energy content of Alex can be utilized in explosives. For instance, Fig. 9 shows how the detonation velocity of hexamethyl-3-nitroamine changes versus Alex content. In these experiments we worked with charges 20 mm in diameter, 70 mm long that were pressed up to a density of 0.9. The velocity of the process was measured by the standard method of registration. The picture shows that the mechanisms have abnormal character. When the content of Alex was lower than 30%, the detonation velocity decreased from 5400 meters/sec to 4700 meters/sec, about equivalent to how industrial aluminum formulations behaved. But with additional Alex contents there was a very fast rise to 7000 meters/sec (at 50 % of Alex). This means that at these low concentrations, the energy of the particles didn't contribute to the explosion, but at higher contents there is a very large effect on increasing the speed of detonation. This is the first time that it has been noted that the speed of detonation can be increased by the addition of metal powders. It means that the individual particles react during the high speed detonation reaction, releasing their energy in the period less than one microsecond, which is similar to a micro-explosion. In our experiments with explosives, aluminum nitrides rather than oxides are formed in the detonation reaction. This reduces the amount of nitrogen oxides generated by the explosion [16].

#### STUDIES OF BINARY ALEX-OXIDIZER MIXTURES

Binary mixtures of Alex and ammonium perchlorate, potassium nitrate or sodium nitrate were pressed up to densities of 0.9-0.95 and inserted into transparent plexiglass tubes (inner diameter of 8 mm, wall thickness of 1 mm). The length of the charge was 10 mm. Samples were burned in a constant pressure bomb (Crawford bomb). The burning velocity was measured by photo registrations.

Figure 10 shows the burning velocity versus the percent of metal in the mixture containing ammonium perchlorate. (Note: There is a heat output for pure Alex because of its self-heating phenomena.) For mixtures of ammonium perchlorate and low contents of Alex and at a pressure of 40 atmospheres, the burning velocity was equal to or slightly lower than analogous mixtures based on industrial aluminum powder. However, with an increasing content of Alex, the burning velocity increased 10 to 20 times. Mixtures with 40% of industrial aluminum were not combustible, but mixtures with Alex had high burning rates when the aluminum content was between 42 to 95%.

For mixtures of Alex and potassium perchlorate ( Fig 11 ), there was also a sharp dependence of burning velocity on the Alex content. The burning velocity rose very quickly at 5 to 15% (Curve 1) and reached a maximum velocity of 180 mm/sec at metal contents near stoichiometry. Alex was also substituted for a part of the industrial aluminum. The addition of 30% Alex to industrial powder improves the burning of the mixture. The velocity of burning of activated aluminum with nitrates (Curve 3, Fig. 12) was also

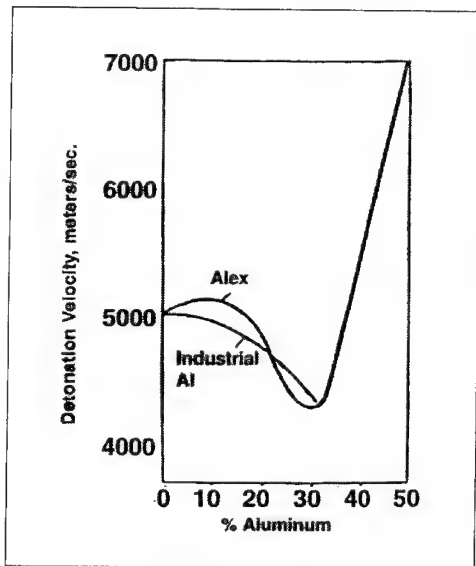


Figure 9  
Detonation velocity as a function of aluminum  
in an explosive.

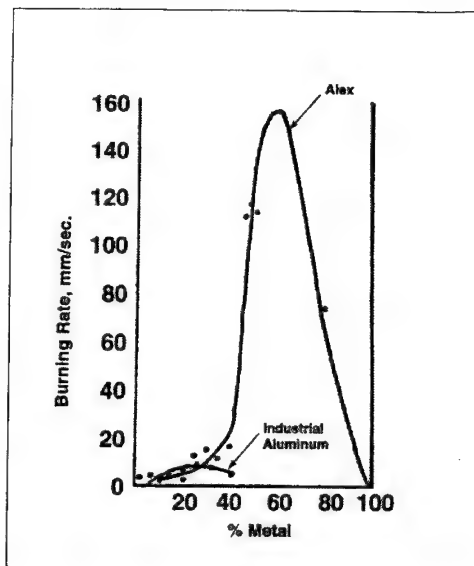


Figure 10  
Burning rate versus percent of Aluminum - Ammonium  
Perchlorate mixtures.

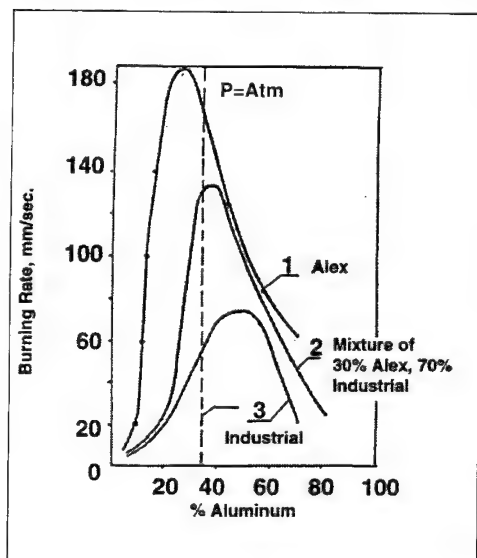


Figure 11  
Burning rate versus percent of Aluminum - Potassium  
Perchlorate mixtures.

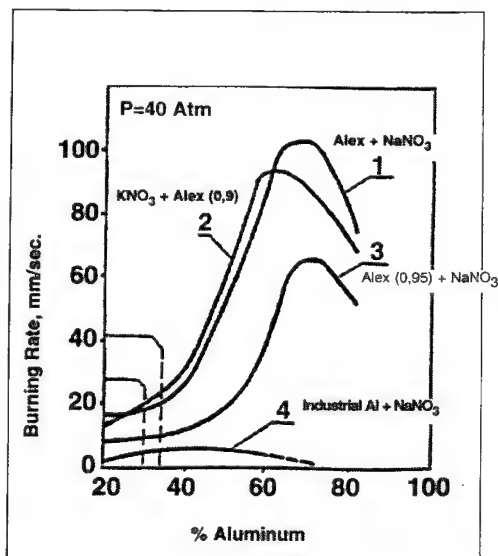


Figure 12  
Burning rate versus percent of Aluminum with nitrates.

ten times higher than analogous mixtures with industrial aluminum (Curve 4). In this case, the maximum burning rate is shifted to compositions greater than stoichiometric. Burning rate is a function of the packing density, with Curve 1 compacted to about 0.9 (90% of theoretical density), while curve 3 is compacted to a higher density - in excess of 0.95.

It is generally known that on the surface of burning a charge of propellant, the particles of aluminum melt and agglomerate to large droplets which have no time to fully oxidize within the throat of the engine. There are two modes of energy loss due to incomplete combustion - the loss of heat, and a reduction in gas velocity caused by the presence of the large heavy particles. Figure 13 shows a microcinema of the surface of a burning mixture of ammonium perchlorate, Alex and binder. This figure shows that the metal burns mainly on the surface and high dispersive particles of oxide are present in the flame, rather than burning droplets of aluminum as is the case when ordinary pyrotechnic aluminum is used.

It is also generally known that when samples of propellants burn while standing on massive metallic blocks there isn't full combustion. There is a thick film of unburnt substances on the metal block as a result of fast cooling of condensed phases of burning propellant. These sections of pyrotechnic mixtures (about 0.5 mm-1 mm thick on the surface of the blocks) were very visible and included droplets of metals and carbonized binder. On the other hand, mixtures with Alex don't produce any trace of residue, indicating their combustion was rather complete.

Charges of these mixtures were compressed into steel tubes and they were cooled by liquid nitrogen. At temperatures near -70 degrees the mixture with industrial aluminum didn't burn. But the mixture with Alex invariably burned reliably and completely all the time, even after keeping it 2-3 hours inside of a liquid argon-filled vessel.

It's obvious that using Alex in pyrotechnic mixtures changes the mechanism of burning. In usual mixtures, burning causes a flow of heat from the flame into the solid pyrotechnic and if the quantity of this heat is too small for gasification, as in sub-cooled conditions, then the combustion isn't self-propagating. With Alex, the conduction of heat releases the energy which is conserved in the particles, which causes initiation of burning processes, because the temperatures attained in the solid cause decomposition of ammonium perchlorate accelerating oxidation at the gas/solid interface.

Portions of 10 mg of stoichiometric mixtures of unpressed powders of ammonium perchlorate with three versions of Alex were put in small aluminum foil cups and put on a hot plate. Figure 14a shows curves of the explosion delay time versus the temperature of the hot plate. A sharp sound and destruction of the foil into very small fragments allowed us to conclude that these processes were not burning but detonation. We got analogous results with potassium chlorate and potassium perchlorate formulations. Mixtures with industrial aluminum flashed without any sound. The points on curve Fig 14b lie on straight lines in coordinates  $1/T \times 10^3 - \lg(t)$ . In Fig 14b, the slope shows the energy of activation is 5 or 6 Kcal per mole for each of the three oxidizer formulations. Such activation energies correspond to physical desorption, rather than chemical reaction. In this case, it is the activating character of the aluminum that is responsible for the low activation energy.

## CONCLUSIONS

Aluminum powder, formed by the process of electro-explosion of aluminum wire, has unusual physical and chemical properties, and has conserved energy which is useful in enhancing the performance of propellants and explosives. In addition, the enhanced reactivity of this material provides benefits in the direct synthesis of aluminum compounds such as AlN. The specific cause of the conserved energy has not yet been conclusively identified, and future studies are intended to elucidate this unusual behavior.

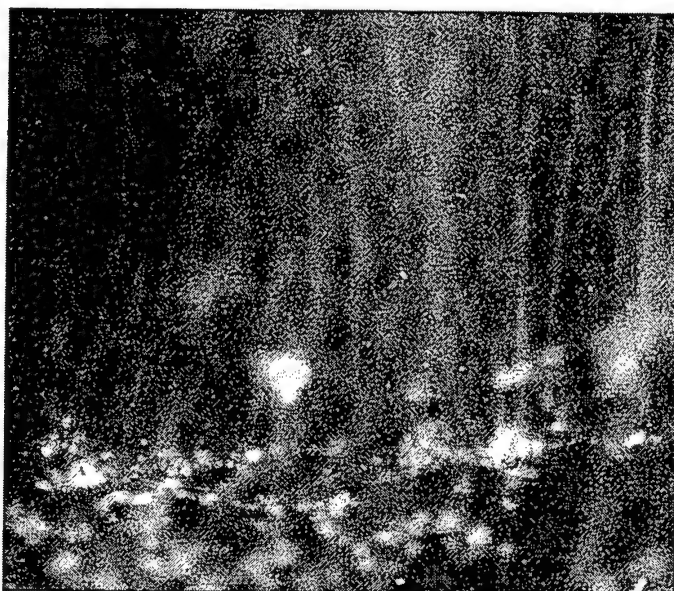


Figure 13. Microcinema of burning Alex/Ammonium Perchlorate mixture.

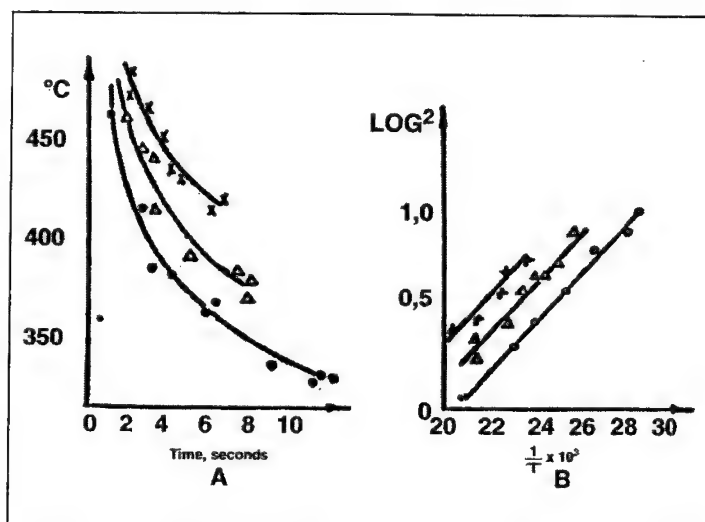


Figure 14. Explosion time versus temperature for Ammonium Perchlorate/Alex.

## REFERENCES

1. Chase, W. G. and Moore, H. K. - Conference on Exploding Wire Phenomenon, April 1959, Plenum Press, New York.
2. Chase, W. G. and Moore, H. K. - Conference on Exploding Wire Phenomenon, Nov. 1961, Plenum Press.
3. Chase, W. G. and Moore, H. K. - Conference on Exploding Wire Phenomenon, March, 1964, Plenum Press.
4. Chase, W. G. and Moore, H. K. - Conference on Exploding Wire Phenomenon, Oct. 1967, Plenum Press.
5. Kariotis, F. G., Fish, B. R. and Royster, G. W. - Aerosols from Exploding Wires - from Conference on Exploding Wire Phenomenon, Nov. 1961, p 299
6. Kaoru, K., Hiroshi, I., and Yasuo, M - Jour. Japan Soc. of Powder Metallurgy - April 1970, Vol. 16, pp 338-344.
7. *ibid*, July 1973, vol. 20, pp 67-708.
8. Tadao, K., Kenkichi, K., Izumi, F. - Synthesis of Metal Nitride Powder by Exploding Wire Phenomena., Proc. Japan Congress Material Research, Kyoto, Sept. 1976, Published by Soc. of Materials Science, Kyoto, Japan, 1977, pp 147-151.
9. Kotov, U. A. and Yavorovsky, N. A. - Research of Particles Produced by Electrical Explosion of Wires. - Physics and Chemistry of Materials Treatment - 1978 #4, pp 24-28
10. Zelinski, V. U., Yavorovsky, N. A., and Proskorovskaya, L. T. - Structure of Aluminum Powder Produced by Electrical Explosions - Physics and Chemistry of Materials Treatment - 1984, #1, pp 57-59.
11. Pietronero, L - Proceedings of the Sixth Trieste International Symposium on Fractals in Physics, ICTP, Trieste, Italy, July, 1985
12. Ivanov, A. G., Barachtin, V. T. - Structure and Properties of Ultra-fine Powders - Proc. of 4th European Conf. on New Technology - East-West - Oct 1993, Vol 2 - pg. 1-3, St. Petersburg Univ.
13. Ivanov, G. V. , Yavorovsky, N. A., Kotov, U.A., Davidovich, V. I., Melnikova, G. A. - Self Propagated Processes of Sintering of Ultra-Dispersive Metallic Powders. - Dokladi Akad. Nauk. SSR - 1984 - Vol 275, #4, pp 873-875.
14. Yavorovsky, N.A. Ilyin, A. P., Davidovich, V. I. Lerner, M. I., Proskorovskaya, L. T. - Phenomenon of Heat Explosions of Ultra-Dispersive Powders of Pure Metals - Proc. of First All-Union Symposium on Macroscopic Kinetics and Chemical Gas Dynamics - Oct. 1984 , Alma Ata, Vol 1 - pp 54-55.
15. Ivanov, V. G., Leonov, C. H., Savinov, G. L. , Gavriluk, O. V. and Glascov, O. V. - Burning of Mixtures of Ultra-Dispersive Aluminum with Gelled Water. Physics of Burning and Explosions, 1994, #4, pp 167-168.
16. Reshetov, A. A., Schneider, V. B. and Yavorovsky, N. A. - Influence of Ultra-Dispersive Aluminum on the Speed of Detonations of Hexamethy- 3-Nitroamine, Proc. of First All-Union Symposium on Macroscopic Kinetics and Chemical Gas Dynamics - Oct 1984, Alma Ata, Vol 1, 55-56.

## COMMENTS

A. Peretz, Rafael, Israel. 1. Have you considered quantitatively the applications of Alex to rocket propulsion? What will be the limitations of use in this case, if any? Another application to be considered may be FAE systems.

Author's Reply. We have in fact considered Alex's use in solid propellants, such as with ammonium perchlorate. There is some experimental work being done at a few U. S. government agencies and a few aerospace organizations in such applications and the results are promising. Substantial increases in burning rate were obtained. It was also noted that there was more uniformity in burning Alex, while coarser aluminum powder agglomerated during burning. Gels of Alex in water appear to be a promising monopropellant, but there has been no work done on such mixtures outside of our own studies. We believe that FAE is indeed a good application for Alex, but no work has been done.

## HIGH BURNING RATE SOLID ROCKET PROPELLANTS

G. DORIATH

PROPULSION RESEARCH MANAGER

SNPE RESEARCH CENTRE

91710 VERT-LE-PETIT - FRANCE

### ABSTRACT

The need for high velocity in ground to air missile applications which require a very short time of combustion for the rocket motor and for the thrusters piloting the trajectory, has prompted SNPE to study and develop under governmental funding new minimum and reduced smoke solid propellants with high burning rate which will be able to meet also the high energy and IM requirements. As it has already recently shown Butacene catalysed reduced smoke composite propellants are a good base to achieve high burning rate with a relatively reduced pressure exponent in a large range of operational pressure. The adjustment of the combustion characteristics may be obtained by controlling the content of Butacene in direct relationship with the content of iron, and the content of Ammonium Perchlorate and its particles size. The use of Ultra Fine Ammonium Perchlorate allows to achieve ultra high burning rates, between 50 mm/s to 200 mm/s in a very large range of pressure as the pressure exponent may stay under 0.5 until several hundreds of bars.

Unlike composite propellant for which it is relatively easy to achieve high burning rate as a lot of various catalysts act on the decomposition mechanism of the Ammonium Perchlorate oxidiser, minimum smoke XLDB propellants which use Nitramine (RDX) cannot be accelerated in a efficient way by the use of additives modifying the combustion of this "monopropellant" filler. Very few combustion catalysts of pure RDX exist and they are incompatible with the main energetic ingredients of the XLDB binders. Therefore the only practical ways to achieve high burning rate minimum smoke propellants are :

- to incorporate ballistic modifiers used in conventional double base propellants such as lead catalysts or more recently SNPE developed unleaded catalysts which act on the decomposition of the binder. But the effects on the burning rate stay at a limited level, which lags far from our goals. The low pressure exponents are nevertheless very attractive.
- to use new energetic ingredients, binder or filler, which burn by themselves faster than the conventional constituents. Some great results have been obtained with new formulations which use GAP binder and CL 20 as a main filler. Burning rate as high as 40 mm/s at operational pressure will be achievable in the next future if a good compromise with energetic properties and IM objectives may be found.

In conclusion, today, to achieve very high burning rates, specifically required for some thruster grain design, Butacene based reduced smoke propellants with Ultra Fine Ammonium Perchlorate are the only solution. But for the main propulsion which needs medium range of burning rate, minimum smoke propellants are available.

### 1 - HIGH BURNING RATE REDUCED SMOKE COMPOSITE PROPELLANT

A large increase of burning rate at operational pressure can be achieved by the use of catalysts of the decomposition of Ammonium Perchlorate used in large amount (more than 82 % in the conventional minimum smoke composite propellant. These catalysts are very well known : they are metallic derivatives, solid such as Copper Chromite or Ferric Oxide and liquid such as the ferrocenic compounds, Catocene and Butacene. The latter <sup>1,2</sup>, with its ferrocene groups attached to the backbone of the polymer is very attractive since it exhibits the same great efficiency as the liquid ferrocene catalysts without their main drawback which is a poor ageing due to their potential migration in the cured binder.

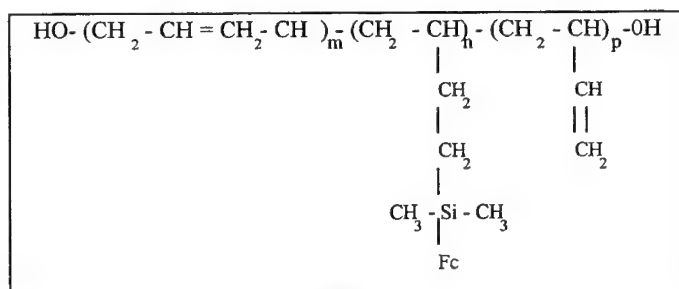
An other well known way to increase the burning rate of the minimum smoke composite propellants is the use of fine particles of Ammonium Perchlorate <sup>3, 4</sup>. At SNPE we have developed some grinding processes at industrial scale to get various grades of fine particles : 10 µm (conventional grinding), 3 µm (Fluid Energy Mill) and 1 µm (grinding process in a liquid suspension). Combinations of Butacene and these various grades of Ammonium Perchlorate have been mixed to try to get the higher burning rate achievable in composite propellants.

#### Effect of the Particle Size of Ammonium Perchlorate.

All the results presented have been obtained in propellants containing 86 % of solid:

- ♦ 85 % of A.P. and 1 % of Al (Table 1)
  - and ♦ 82 % of A.P. and 4 % of Al (Table 2)
- in a binder formulated with a mix of 50 % of Butacene Prepolymer and 50 % of HTPB. Butacene has been already described (Fig 1) :

**Figure 1.** Sketch of the Butacene Prepolymer.



It is a HTPB prepolymer with attached ferrocene groups <sup>2,5</sup> to avoid any possibility of migration of the catalyst and potential problems of ageing.

**Table 1**  
Burning rate of Reduced Smoke Propellants (A.P. 82 % ; Al 4 %)

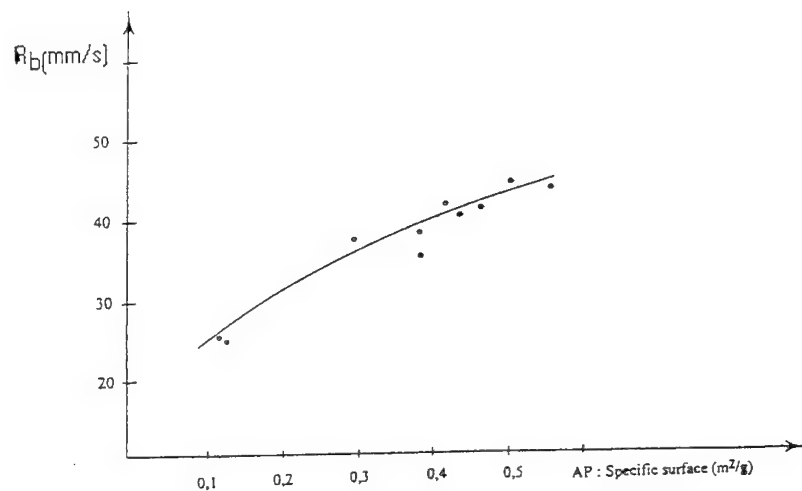
Grade of A.P. (%) (Mean Diameter in µm)					Burning rate* (7 MPa) mm/s	Pressure exponent (5 to 30 MPa)	Burning rate * (Ambient Pressure) mm/s	Specific Surface** m <sup>2</sup> /g
200	90	40	10	3				
34	20		28		25.4	0.27		0.11
52			30		25	0.28	3.1	0.12
	52			30	38.5	0.36	3.9	0.38
		62		20	37.8	0.40		0.29
		52		30	42.2	0.39		0.41

\* Ultrasonic or Strand Burner measurements.

\*\* Computed from the mean diameter.

These results obtained with castable compositions show that the increase of burning rate due to the increase of the specific surface of A.P. is relatively strong for the low value and becomes nearly flat with the use of Ultra Fine A.P. (Fig 2).

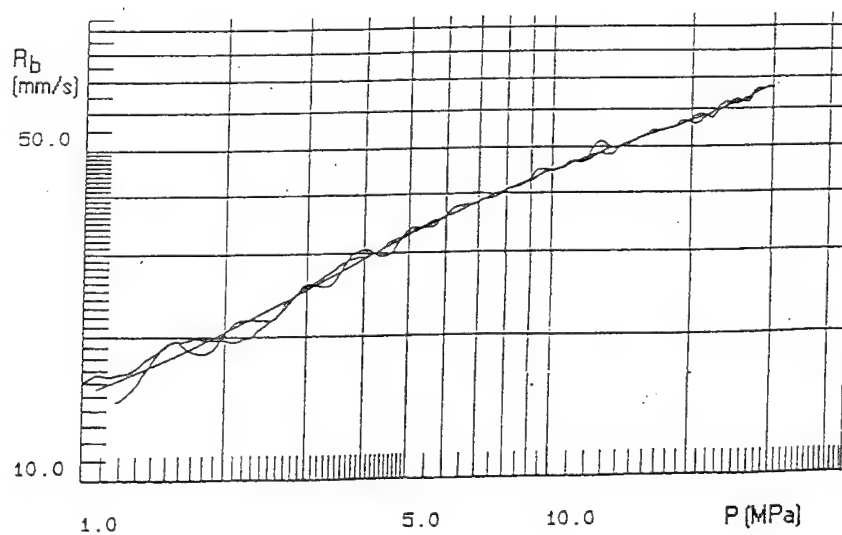
Figure 2. Influence of the Specific Surface of A.P. on the burning rate of Butacene based Propellants (86 % of fillers)



Ultrasonic and Strand Burner measurements

- o 82 % of A.P.
- \* 85 % of A.P.

Figure 3. Typical burning rate/pressure curve for a 82 % A.P. / 4 % Al / Butacene based propellants. (A.P. 90  $\mu$ m : 52 % ; A.P. 3  $\mu$ m : 30 %)



Ultrasonic measurement : 2 tests (oscillating curves) and the average curve.



**Table 2**  
Burning rate of Reduced Smoke Propellants (A.P. 85 % ; Al 1 %)

Grade of A.P. (%) (Mean Diameter in $\mu\text{m}$ )				Burning rate* (7 MPa) mm/s	Pressure exponent (5 to 30 MPa)	Burning rate * (Ambient Pressure) mm/s	Specific Surface** $\text{m}^2/\text{g}$
90	10	3	1				
55		30		36	0.36	5.9	0.48
34	23	28		43.8	0.37	6.2	0.50
55		22	8	43.6	0.37	9.3	0.55
37	20	28		41.9	0.36	6.4	0.46
37	23	25		40.8	0.36	4.8	0.43

\* Ultrasonic or Strand Burner measurements.

\*\* Computed from the mean diameter.

The upper limit of the burning rates achievable with this type of castable compositions (limited content of burning rate catalyst and fine A.P. for safety reasons, see hereinafter) is nearly 40 to 45 mm/s at 7 MPa and 70 to 75 mm/s at 25 MPa (see Fig 3 and 4) which comply with the requirements of the future motors. The pressure exponent remains low (between 0.35 to 0.4) for the considered range of pressure. A small decrease of this exponent is reported with the coarse A.P.

In the last column of the tables 1 and 2 are mentioned the burning rate at ambient pressure. This parameter is considered very important at SNPE for these compositions which are easy to ignite, for instance by friction (sensitivity : 50 to 60 N at Julius Peters Test). It is directly linked to the heat flux provided by the combustion of a propellant sample: in case of accidental ignition, higher is the ambient burning rate higher is the heat flux and more severe may be the eventual injuries of a present worker.

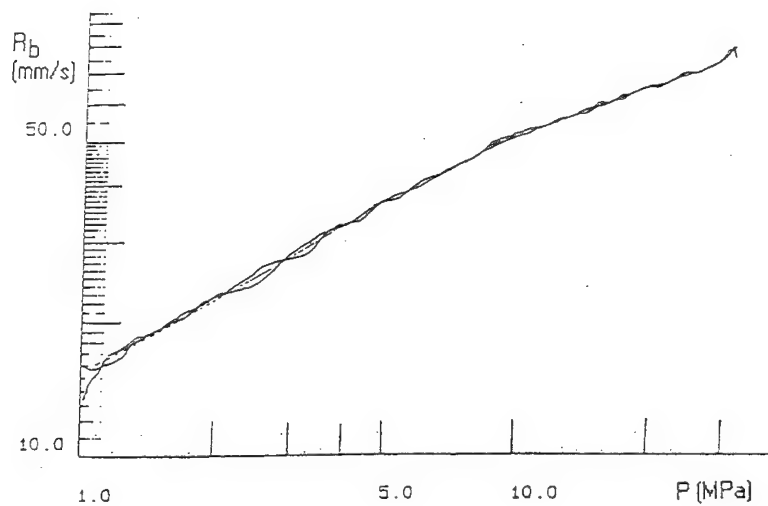
The long experience at SNPE of the manufacture of high burning rate composite propellants whatever the catalyst is used, solid or liquid, recommends not to exceed an ambient burning rate of 5 mm/s to respect reasonable safety conditions of handling of propellant. This parameter increases with the use of fine particles of A.P. until unacceptable level with propellants very rich in Fine (3  $\mu\text{m}$ ) or using Ultra Fine (1  $\mu\text{m}$ ) A.P. It can be noticed that the compositions with significant amount of Aluminium (4%) burn at a lower ambient burning rate. This statement remains to be confirmed. But the results are relevant with data obtained on aluminium rich compositions (85 % solids) in which the ambient burning rate is divided by a factor of nearly 2 for a maintained level of burning rate at operational pressure:

Composition:	Binder HTPB/Butacene 50/50	15 %
	A.P.	
	90 $\mu\text{m}$	23 %
	10 $\mu\text{m}$	25 %
	3 $\mu\text{m}$	20 %
	Aluminium	17 %
Burning rate at 7 MPa		44.8 mm/s
Burning rate at ambient pressure		3.8 mm/s

#### Use of Potassium Perchlorate (K.P.)

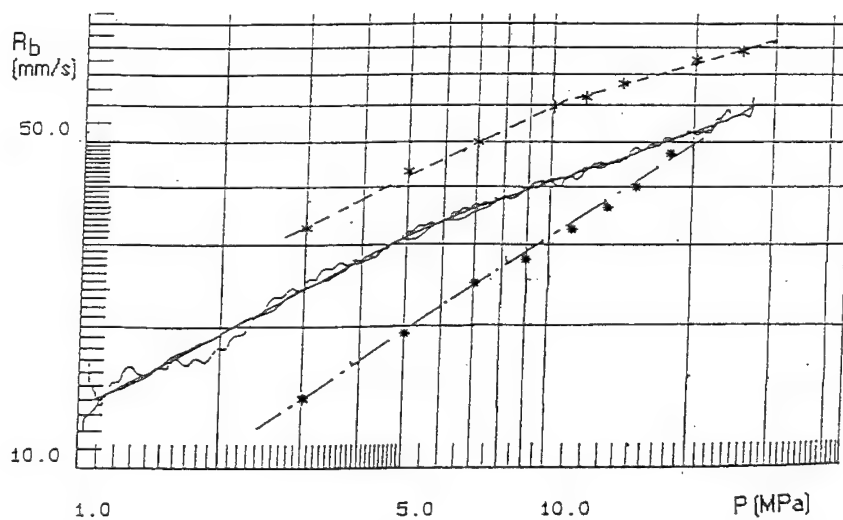
Attempts to find a better compromise between the burning rates at operational and ambient pressure have been conducted to the evaluation of compositions using a mix of A.P. and K.P., as Potassium Perchlorate is well known to give high burning rate at operational pressure. Besides a better behaviour at IM thermal stimuli, of the propellants could be expected <sup>6</sup>, in relationship with the high temperature

Figure 4. Typical burning rate/pressure curve for a 85 % A.P./Al/Butacene based propellant.  
(A.P. 55  $\mu\text{m}$  : 52 % ; A.P. 3 $\mu\text{m}$  : 22 % ; A.P. 1 $\mu\text{m}$  : 8 %)



Ultrasonic measurements: 2 tests (oscillating curves) and the average curve.

Figure 5. Burning rate of A.P./K.P./Butacene based propellants ; (86 % fillers)



Ultrasonic measurements: 2 tests for each composition

- Only A.P. oxidiser (mix of 90  $\mu\text{m}$  and 3  $\mu\text{m}$ )
- \* Only K.P. oxidizer (mix of 250  $\mu\text{m}$  and 30  $\mu\text{m}$ )
- x Mix of A.P. (10 and 3  $\mu\text{m}$ ) and of K.P. (250  $\mu\text{m}$ )

of decomposition (610°C) of this perchlorate more thermally stable than the Ammonium Perchlorate. Propellants which contain this oxidiser are still minimum smoke : they produce Potassium Chloride which is gaseous at the temperature of the exhaust gas.

Table 3 shows the results obtained on 86 % of solid propellant compositions with a small amount of aluminium (1 %). The binder has the same composition as the binder used in the propellants reported in the above paragraph : it contains 50 % of Butacene as burning rate catalyst.

**Table 3**  
Burning rate of A.P./K.P. Butacene/HTPB Reduced Smoke Propellants

Grade of K.P.(%) (Mean Diameter in µm)			Grade of K.P.(%) (Mean Diameter in µm)			Burning rate* (7 MPa) mm/s	Pressure exponent (10 to 30 MPa)	Burning rate * (Ambient Pressure) mm/s	Friction Sensitivity  N
250	110	30	90	10	3				
55		30				24.1	0.76	1.4	120
			55		30	36	0.36	5.9	50
	55				30	37.5	0.35	4.3	65
	37			20	28	42.2	0.37	5.0	63
		55			30	39.8	0.54	4.2	77
35				20	30	51.1	0.32	3.6	110
35		20			30	46	0.38	5.2	58
	35	20			30	46.1	0.39	3.1	50

\* Ultrasonic and Strand Burner measurements.

When K.P. is used alone (without A.P.) propellants exhibit a limited burning rate (roughly 25 mm/s), (the size of K.P. has a small effect on the burning rate), very high exponent (0.7 to 0.8) between 3 to 20 MPa (Fig 5). and attractive safety characteristics : low burning rate at ambient pressure and low sensitivity at friction. These results have induced formulators to try to evaluate compositions with a mix of A.P. and K.P.. Table 3 and Fig 5 show that high burning rates (45 to 50 mm/s at 7 MPa) can be achieved with K.P. when mixed with fine particles of A.P. with a relatively low exponent at pressure above 10 MPa. This reduction of the exponent could be linked with the presence of a break in the burning rate/pressure curve of the "only A.P." propellants at about 6 to 7 MPa. The combustion seems to be piloted by the couple A.P./Butacene. It may be assumed that the availability of higher burning rates with A.P./K.P. propellants at operational pressure is due to the addition of the accelerating effect of ferrocene catalysts on A.P. in a partially based HTPB/K.P. propellant which has an inherent high burning rate.

Unfortunately the good safety characteristics of the only K.P. based propellants are not totally kept when A.P. is added, even if a small gain may be expected (the data, a little bit scattered, need to be confirmed, mainly in friction).

#### Ultra high burning rates.

To achieve ultra high burning rates it is necessary :

➤ to increase the amount of catalyst in the binder (with the risk of increase the sensitivity of the propellant, but since the application considered use very small motors, the eventual effects are reduced and precautions can be easily taken to protect workers during handling of the propellant).

**Table 4**  
Ultra high burning rate Butacene bases Propellants

Composition A.P./Al Grades of A.P. (%)	Viscosity (end of mix) (hPl)	Burning rate * at P (MPa)			Pressure exponent (3 to 50 MPa)	Friction sensitivity (N)	Burning rate* at ambient pressure mm/s
		7	30	50			
86/2 D/M3	50	58	127	145	0.46	41	3.9
87/1 D/M3	46	84	146	194	0.43	62	9.4
86/2 D/F/M1	44	75	129	143	0.33		3.8
64 M1	17	90	153	192	0.38	160	24

\* Strand burner measurements

D : Mean diameter 90  $\mu$ m

M3 : Mean diameter 3  $\mu$ m

M1 : Mean diameter 1  $\mu$ m

➤ and to take benefit of the burning rate increase with the pressure in using high operational pressure. The very high pressures are not suitable for the conventional motors as they require too heavy high pressure resistant vessels, but they are compatible with very small motors like thrusters for pyrotechnic devices. Thus compositions have been tested with high level of Butacene (95 to 100 % of the prepolymer), and high level of fine particles of AP. The main results are reported in Table 4.

Despite a high content of AP and of fine particles the mix of these compositions is relatively easy. They need pressure assistance for casting and moulding of perforated grains. The burning rates obtained at 50 MPa comply with the objectives of 150 to 200 mm/s and the pressure exponent is low for a such range of high pressure. As expected the burning rate at ambient pressure is very high (incompatible with conventional motor grains) for the compositions burning the most rapidly. It should be noticed the ultra high burning rate, at operational pressure and unfortunately at ambient pressure, of the last composition of table 4, low content of solid (64 % of Ultra Fine AP only). Although insensitive to friction, due to the high level of binder, this composition is considered too hazardous to be made in industrial conditions.

## 2 - HIGH BURNING RATE HIGH ENERGY MINIMUM SMOKE PROPELLANTS.

Conventional minimum smoke propellant are homogeneous propellants which use Nitro-cellulose and nitrate ester plasticisers such as nitro-glycerine. The main types are E.D.B. propellants or extruded double base propellants and C.D.B. propellants, or cast double base propellants. High burning rates can be achieved with these propellants but they exhibit some handicaps : mechanical properties incompatible with the use in case bonded grain, and limited specific impulse. The increasing demand of more energy for low signature solid rocket motor has conducted to the development of new propellants. They are based on the energetic binder of the conventional E.D.B. and C.D.B. propellants modified by elastomeric polymers to achieve elastomeric modulus required by case bonded grains, and Nitramine fillers to meet with the energy requirements. On this basis SNPE, in France, has chosen to develop XLDB propellants which use the slurry process of the composite propellants ; the main ingredients of the binder are an inert hydroxyterminated polyester prepolymer crosslinked with a polyisocyanate and plasticised with nitrate ester plasticisers. The Nitramine fillers RDX or HMX used in these propellants, which burn very slowly and for which no efficient catalyst has been found, give to the propellant an inherent low burning rate, unsuitable for the future applications. So a lot of studies have been performed in order to find convenient ways to achieve the required level of burning rate.

### Use of burning modifiers.

On the basis of the conventional catalysts of the homogeneous propellant a solid lead catalyst (called J.L. in this document for restricted information reasons) have been selected and developed. It is now produced at full scale at SNPE. The efficiency of this catalyst is strongly dependant of the size of the particles, fig (6) and table (5), and of the amount of catalyst in the propellant (table 6).

**Table 5**  
Influence of the size of the catalyst particles.

Specific surface (m <sup>2</sup> /g)	Mean diameter (μm)	Burning rate 5 MPa (mm/s)	Burning rate 15 MPa (mm/s)	Burning rate increase at 7 MPa (%) (mm/s)	Pressure exponent 5 to 15 Mpa (mm/s)
No catalyst	/	4.6	11	0	0.77
0.2	10.5	4.4	12.3	-8	0.80
.3	6.2	6.2	12.8	+8	0.62
1.7	1.7	9.1	15.3	+68	0.46
9	0.54	9.3	15.9	+80	0.48
17.4	0.45	11	17.5	+103	0.42

Composition : Nitro-glycerine/Butanetrioltrinitrate plasticised polyester binder/RDX 55 %.  
Strand-Burner or Ultrasonic measurements.

Coarse particles of catalyst are roughly inefficient. But the diminution of the particle size may cause a doubling of the burning rate with a dramatic reduction of the pressure exponent. To meet full scale production reproducibility of the characteristics of the catalyst a specific surface of 9 to 10 m<sup>2</sup>/g is a satisfying compromise (Fig 7).

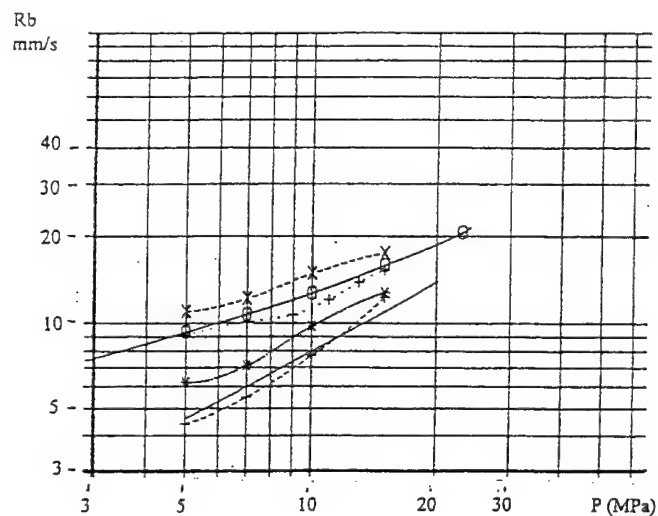
**Table 6**  
influence of the amount of catalyst

J.L. Catalyst %	Burning rate 5 MPa (mm/s)	Burning rate 15 MPa (mm/s)	Burning rate increase at 7 MPa (%)	Burning rate increase at 15 MPa (%)	Pressure exponent 5 to 15 MPa
0	4.6	11	Ref.		
2	6.9	17.8	96	45	0.6
3	12.2	19.1	130	55	0.4
4	13	19.4	146	58	0.35

Composition : Nitro-glycerine/Butanetrioltrinitrate plasticised polyester binder/RDX 50 %  
Ultrasonic measurements.

As expected the results reported in table 6 show the increasing effect of a increasing amount of the catalyst. The extent of this effect decreases at high pressure. At pressures above 20 MPa the effect is negligible. These results are totally consistent with the effects of this type of catalyst <sup>7,8</sup> in double base propellants in which an overburning rate is created at medium range of pressure with a low pressure exponent. On the contrary, since the burning rate at low and high pressures has the same values as the burning rate of the basic composition without catalyst the pressure exponent becomes very high at these pressures.

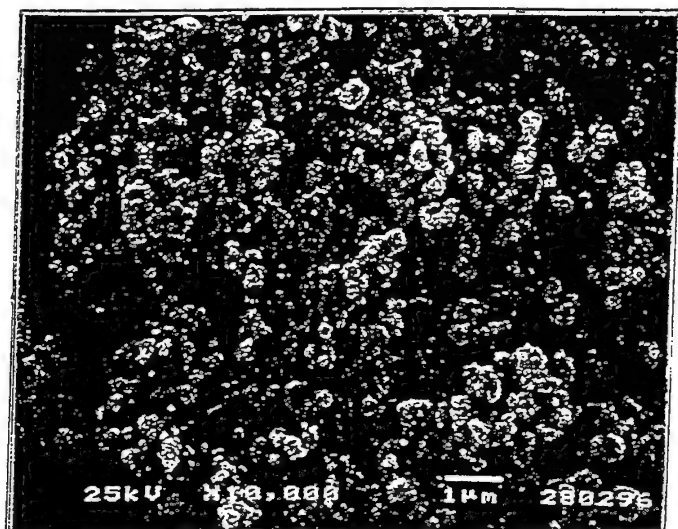
Figure 6. Effect of the particle size of the J.L. catalyst on a conventional XLDB propellant



Ultra sonic measurements

- Ref.: Polyester binder without catalyst/RDX 55 %
- 4 % of catalyst (0.2 m<sup>2</sup>/g)
- \*\* 4% of catalyst (0.3 m<sup>2</sup>/g)
- ++ 4 % of catalyst (1.7 m<sup>2</sup>/g)
- 0-0- 4% of catalyst (9 m<sup>2</sup>/g)
- xx 4% of catalyst (17.4 m<sup>2</sup>/g)

Figure 7. Micrography of J.L. Catalyst (10 m<sup>2</sup>/g)



#### *Effect of carbon black particles.*

Due to the similarity of the mechanism of action of this catalyst in XLDB propellants and in double base propellants it can be expected an additional increase of the burning rate with the addition of Fine Carbon Black particles with a very high Specific Surface. Table 7 shows that this effect exists only in the case of Ultra Fine Carbon Black particles (Specific Surface of 130 m<sup>2</sup>/g), but the burning rate increase is small (1 mm/s) on the whole range of tested pressure.

**Table 7**  
Effect of ultra fine carbon black

Carbon black %	Specific surface m <sup>2</sup> /g	Burning rate (mm/s) at P (MPa)				Pressure exponent
		5	10	15	20	
0		13	16.8	19.4	21.9	0.30
1	70	13	16.9	19.4	21.9	0.30
1	131	13.9	17.5	19.9	22.8	0.31

#### Ultrasonic measurements

Composition : Nitro-glycerine/Butanetrioltrinitrate plasticised polyester binder/RDX 50 % ; J.L. catalyst 4 %.

#### *Effect of the nature of the Nitrate ester plasticiser.*

All the previous results have been obtained with high energetic compositions with RDX, or better, HMX as energetic filler and a binder rich in nitro-glycerine. But to meet the I.M. requirements, mainly in case of shock aggression, it is necessary to remove nitro-glycerine from the binder. So a lot of formulations have been realised with a mix of Trimethyloltrinitrate and Butanetrioltrinitrate as energetic plasticisers of polyester binder. This change induces dramatic changes in the properties of the propellants (table 8) :

- Reduced level of energy: 6s of loss in specific impulse
- Lower burning rate: about 30 % at 7 MPa and a slight increase of pressure exponent,
- And as expected a strongly enhanced behaviour at the High Velocity Shot Gun Test.

**Table 8**  
main effects of the nature of the energetic plasticiser.

Plasticiser	Is 70/1 (s) (theoretical)	Burning rate 7 MPa (mm/s)	Pressure exponent	Critical impact Velocity XDT (m/s)
NG/BTTN	244.5	13.5	0.34	480
TMETN/BTTN	238.5	10.8	0.46	800

Composition : Energetic binder 33 %/Filler 63 %/J.L. Catalyst 4 %.

The Velocity Limit at which the XDT appears is nearly doubled. The very high values reached should warrant an acceptable behaviour (combustion) in bullet impact test on a tactical motor.

Despite having low burning rate these compositions with low sensitive plasticisers are attractive due to their good behaviour in IM testing, thermal or impact aggressions. So they have been largely developed and tested in generic motors. In the table (9) are given some results obtained at various temperatures in Bates 3"5 motors.

**Table 9**  
Temperature Sensitivity

$A_b/A_t$	P (MPa)	Temperature sensitivity %/°C	
		- 46 to + 20	+ 20 to + 65
225	6.8	0.16	0.19
300	10.5	0.17	0.16
420	17.2	0.21	0.31

Bates 3"5 measurements.

$A_b/A_t$  : ratio of Propellant Combustion Area/Throttle Area.

#### *Partial conclusions*

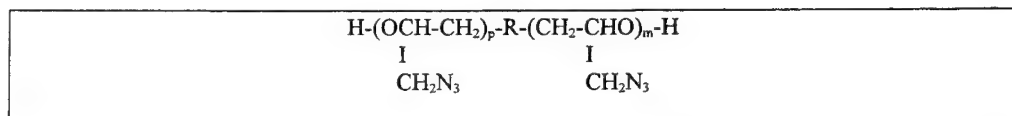
The above mentioned results show that high burning rates required for the future I.M. minimum signature rocket motors cannot be reached by the only use of conventional solutions. The only hope today, in the absence of efficient catalysts for RDX or HMX decomposition, is to find new energetic binder or/and fillers with high inherent burning rates. Some preliminary results obtained at SNPE Research Centre are presented hereinafter.

#### *Use of GAP*

##### GAP Prepolymer

GAP (fig 8) is based on a non oxidiser (less sensitive than  $\text{NO}_2$  groups) azide group, but very energetic due to its high enthalpy of formation. SNPE<sup>9</sup> is since 1990 licensed from Rocketdyne for production and selling of GAP in Europe. Today more than 2 t of GAP have been produced by batch of 150 kg in a pilot plant in Sorgues SNPE's facility near Avignon.

**Figure 8.** GAP Prepolymer



A particularity of this prepolymer is a fast burning rate by itself when ignited at ambient pressure and temperature. A burning rate increase of the propellant made of is eventually expected. Table (10) exhibits some results which demonstrate (in an "a priori" IM composition since it uses low sensitive plasticisers), the efficiency of GAP based binders (Is : + 3s and 16 % or burning rate increase at 15 MPa) and also an additional effect of the J.L. catalyst.

But this burning rate remains too low for our objectives. So some experiments are under way to test new energetic fillers.

#### *Use of CL 20.*

CL 20 is a new energetic oxidiser in development in many Countries. The most dense grade (e) is produced at SNPE in a pilot plant (25 Kg/batch) in Sorgues near Avignon. It is a very powerful oxidiser with safety characteristics still no completely satisfying, comparable with the most sensitive grades of HMX or RDX. Some first trials have been carried out in order to assess the achievable



burning rates in polyester and GAP binders based propellants. It is impossible at the time to tell if this type of propellant might comply with the IM requirements. But the energetic characteristics (Is 10 s above the most energetic IM Compositions) and the burning rate are very promising, as shown hereinafter.

**Table 10**  
Burning rate of RDX/GAP binder propellants.

Composition %	J.L. catalyst %	Burning rate			Pressure exponent 5 to 15 MPa
		at 7 Mpa mm/s	at 15 Mpa mm/s	increase at 15 Mpa (%)	
Ref.	4	10.8	15.5	/	0.46
GAP binder*	3	12.1	17.6	13.5	0.46
GAP binder**	4	14	18	16.1	0.40

Plasticisers : BTTN/TMETN

Ref : RDX 63 %, Is : 238 s

GAP binder compositions : RDX 60 %, Is : 241.5 s

\* Ultrasonic Results

\*\* Firing tests in Bates 3"5

Results of table (11) and Fig 9 and 10 indicate a strong effect on the burning rate of the use of CL20 as the only oxidiser instead of HMX.

**Table 11**  
Burning rate of CL20 propellants

Composition	Filler	Burning modifiers	Burning rate			Pressure exponent 5 to 15 MPa
			at 7 MPa mm/s	at 15 MPa mm/s	Increase at 15 MPa %	
Polyester binder	HMX	No	6	11	Ref.	0.89
Polyester binder	CL 20	No	11.5	23	132	0.92
GAP binder	HMX	No	7.2	13.6	24	0.91
GAP binder	CL20*	No	13.4	27.2	147	0.94
		No	10.0	26.0	136	0.95
GAP binder	CL20	J.L. + Carbon black	17	29.6	169	0.52 (1 to 9 Mpa) 0.84 (9 to 30 Map)

Strand Burner or Ultrasonic measurements

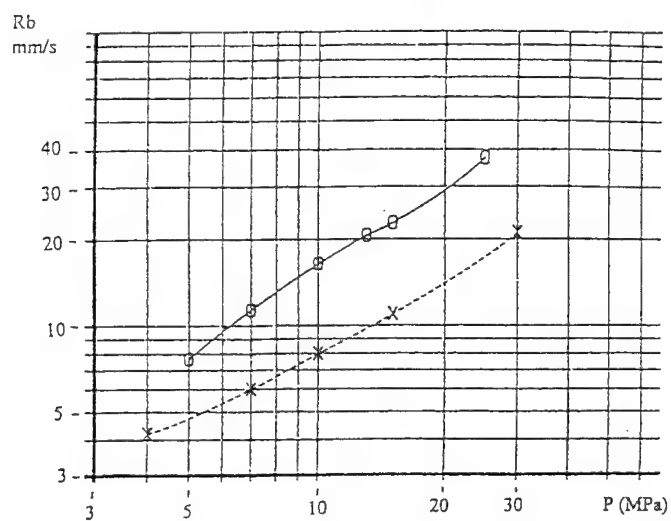
\* 2 lots of CL 20 (2 batches)

CL 20 Particles size : mix of 150 µm and 50 µm

Theoretical Is (70/1) of the GAP/CL 20 Compositions : 249 s

Density of the GAP/CL 20 Compositions : 1.78 to 1.81.g/cm<sup>3</sup>

Figure 9. Burning rate of no catalysed Polyester XLDB Propellants

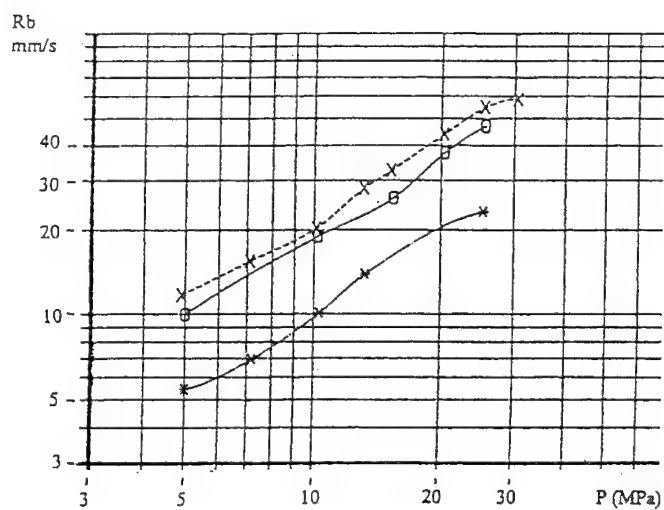


Strand burner measurements

$\times\times$  HMX 60 %

$oo$  CL20 60 %

Figure 10. Burning rate of GAP XLDB propellants



Strand burner measurements

$**$  Réf. GAP/HMX 60 %

$oo$  GAP/CL20 60 % Lot 725

$\times\times$  GAP/CL20 60 % Lot 801

But the pressure exponent of this no catalysed compositions are too much high for any application. Fortunately the same catalysts systems used in the more conventional compositions are very effective at low pressure, since the pressure exponent is lowered till nearly 0.5 under 10 MPa (last composition of the table 11 and Fig 11). It should be improved at high pressure, between 10 and 30 MPa, in the next future, by a optimisation of the catalysts and a necessary adaptation of the particles size and shape. But a major concern will remain to solve : what should be the compromise between the energetic performance and the IM characteristics ?.

### 3 - CONCLUSION

As it has been shown, the objectives of high burning rate required by the low signature future motors for tactical applications could be reached with the new propellants under development at SNPE.

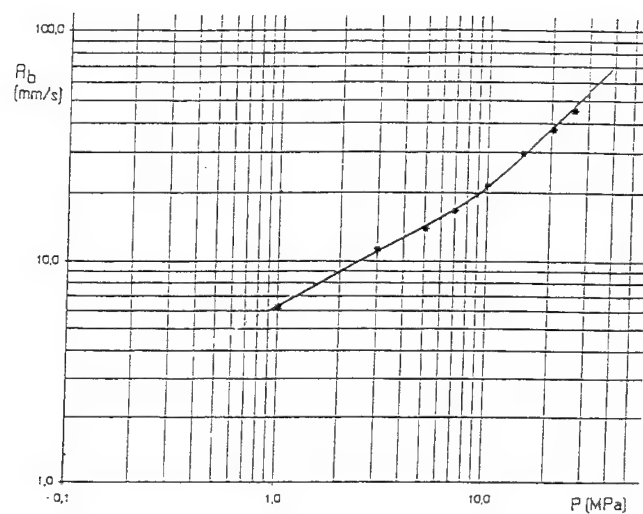
In reduced smoke composite propellant the association of Butacene prepolymer with Fine or Ultra Fine A.P. is an attractive solution. For the highest burning rate the violence of the combustion in case of accidental ignition ( a potential event since these propellants are friction sensitive) at ambient pressure may be a big concern for the present workers. If solutions cannot be found to protect people efficiently, compositions with a combination of A.P. and K.P. as main oxidisers in a Butacene based binder could be an other good way.

In minimum smoke propellant the conventional catalysts used in the double base propellant are not sufficient to reach the objectives of burning rate, and the task is complicated by the necessity to comply with the IM requirements, which oblige to use low sensitive energetic plasticisers. Solutions must be sought in the new energetic molecules such as GAP prepolymer and mainly CL20 which burn by themselves very rapidly and allow to reach high performance. But a necessary compromise with IM requirements remains also to be found.

### References

1. **Doriath, G.**, Energetic insensitive Propellants for Solid and Ducted Rockets, *Journal of Propulsion and Power*, Vol. 11, n° 4, pp 870 - 882.
2. **Fonblanc, G.**, The Maturity of BUTACENE R, Based Composite Propellants", *AIAA Paper* 94 - 3194, July 1994.
3. **Lijegren, T.**, Composite Propellants with High Burning Rates, *Report* (1990), FOA-C-20781-2.1 ; Order PB90 - 201526, 29 pp.
4. **Fink, B., and Mondet, J.C.**, Combustion of solid Composite Propellants Using a Ferrocene Derivative Grafted in the Binder, Karlsruhe, Germany, 1988.
5. **Raynal, S., and Doriath, G.**, New Functional Prepolymers for High Burning Rates Solid Propellants, *AIAA Paper* 86 - 1594, June 1986.
6. **Ahn N. Duong**, Desensitised Solid Rocket Propellant Formulation", *U.S. Patent* 5,574,625, Dec. 1995.
7. **Kubota, N., and al.**, The Mechanism of Super Rate Burning of Catalysed Double-Base Propellants, Report 1087, *Aerospace and Mechanical Sciences*, Princeton University, Princeton, N.J., Mar. 1973.
8. **Lengelle, G., and al.**, Mechanism of the Combustion of Double-Base Propellants", 17 th *Symposium international on Combustion* (Combustion Institute, Pittsburgh, Pa., 1979, pp. 289-293.
9. **Couturier, R.**, "New Molecules and New Propellants", *Entretiens Sciences et Defense*, 1993, Paris

Figure 11. Burning rate of J.L. catalysed GAP/CL20 Propellants (60 % of CL 20)



Ultrasonic measurements

## EXPERIMENTAL ANALYSIS OF A MINIMUM SMOKE PROPELLANT IGNITION CHARACTERIZATION

Lei Du, Mingde Song, Hui Wang, and Weidong Yang

The Fourth Academy of China Aerospace Coporation,  
P. O. Box 120, Xi'an, 710025, Shaanxi Province,  
The People's Republic of China.

**ABSTRACT:** The ignition characterization of a natramine minimum smoke HMX/AP/PPE propellant and an AP/HTPB propellant have been analyzed experimentally by a CO<sub>2</sub> laser generator and a Kodak Ektapro motion analysis workstation in this paper. Experiment results show that the ignition delay time, initial ignition flame structure and the steady combustion flame structure of the minimum smoke propellant are quite different from those of the AP/HTPB propellant. The results also indicate that the increasing of heat flux or ambient pressure lowered the ignition delay time.

### INTRODUCTION

Nitramine composite propellant is a kind of energetic material with high energy and reduced smoke. The propellant ignition characterization are somewhat different from the HTPB propellant. Therefore, the study of its ignition and combustion characterization is helpful in the study of its chemical kinetics mechanism.

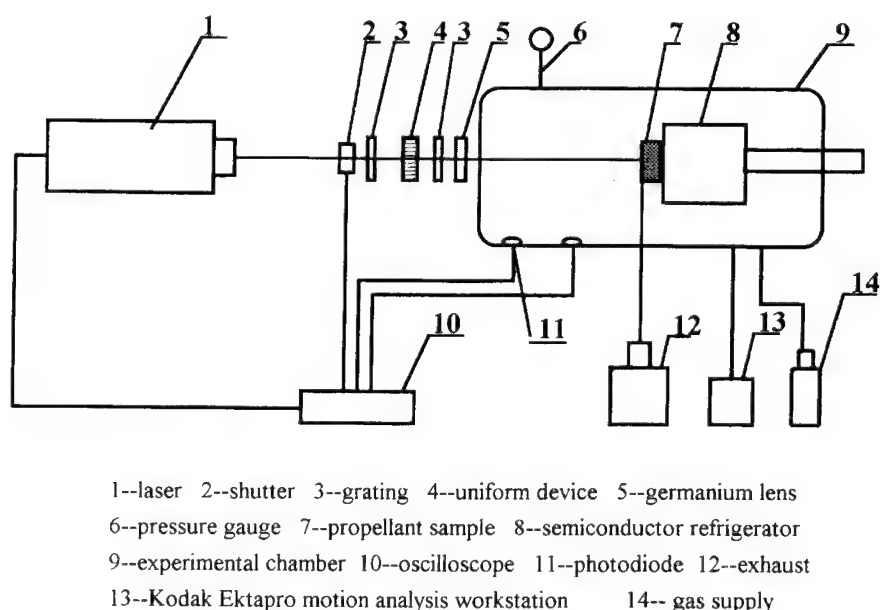
McCarty et al studied the effects of solid loading percentage and HMX particle size on the behavior of nitramine propellants. Kubota Cohen-Nir and Kuo studied the combustion of HMX containing propellant. These research achievements have been reviewed by Boggs and Fifer in reference<sup>1</sup>. However, some details of the propellant ignition process are still unknown, such as the thermal pyrolysis, flame initiation and structure of the reaction zone.

The CO<sub>2</sub> laser was widely used in propellant radiative ignition investigation due to its significant advantages<sup>2</sup>. Ohlemiller and Summerfield<sup>3</sup> performed early studies on laser ignition behavior of polymeric fuels. DeLuca et al<sup>4,5</sup> examined the radiative ignition characterization of several propellants

including HMX containing composite propellant, AP propellant and double base propellant. Kashiwagi<sup>6,7</sup> employed a CO<sub>2</sub> laser generator in the study of PMMA ignition. Ignition behavior of a HMX-based minimum smoke composite propellant and a HTPB/AP propellant have been analyzed experimentally by a CO<sub>2</sub> laser generator in this paper. The ignition process of the two propellants was recorded by a set of Kodak Ektapro high speed motion analysis workstation. The ignition delay time of the two propellants at different ambient pressure was also measured.

## EXPERIMENTATION

The experimentation of this paper consists of an experiment chamber, a CO<sub>2</sub> laser generator and a set of Kodak Ektapro motion analysis workstation. Figure 1 shows the diagram of the experimentation.



**Figure 1.** Diagram of Experimentation

The light path of the laser consists of a shutter for adjusting propellant sample expose time, two gratings for adjusting the light spot diameter and a special spinning device, which revolves at a speed of 25 rounds a second, to assure a uniform heat flux on the propellant sample surface.

The maximum power of the continuous wave CO<sub>2</sub> laser, used as ignition source in this study, is 40W. The wave length is 10.6 $\mu$ m. The power is also adjustable. The laser power can be measured in the experiments.

The experiment chamber, shown in figure 2, has two plexiglass windows, one is for the video camera to take pictures, the other is for a monochromometer and an oscilloscope to measure the ignition delay time. It also has a germanium lens window for concentrating the CO<sub>2</sub> laser. Only air is used in this study, though the pressure, temperature and the ambient atmosphere inside the chamber are adjustable. The ignition heat flux can be controlled and predicted by changing the position of the sample holder, because the position of propellant sample determines the distance between the propellant sample and the germanium lens, this distance affects the diameter of the light spot on the propellant sample, which is related to the heat flux on the propellant.

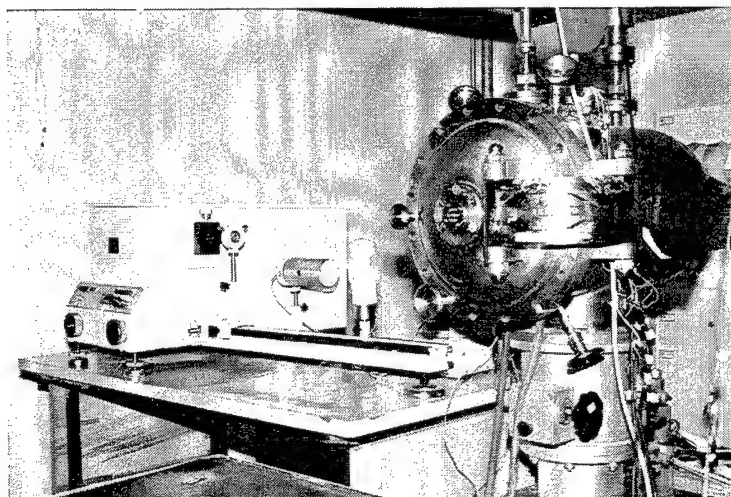


Figure 2. The experiment chamber

In the previous study, we measured the ignition delay time by measuring the temperature of micro-thermocouples imbedded in the propellant samples, however, in this study, we define it as the light emission time that self-sustained combustion can be maintained. When the propellant is ignited, the photodiode in the chamber senses the light emission, the laser was cut off when photodiode signals were strong enough, for example, three times greater than the average background level.

A Kodak Ektapro motion analysis workstation was also employed in this study, this high speed motion analyzer can record 1000 images per second, the information of the taken images can be also processed by the workstation. Thus, we can analyze the propellant ignition characterization more clearly and conveniently.

The ingredients of the two kinds of propellant samples used in this study are shown in Table 1. PPE is the plasticized polyether binder system. The propellant samples were glued on the chamber sample holder.

TABLE 1

## Ingradients of Test Propellants

HTPB/AP Propellant %			HMX/AP/ PPE Propellant %			
AP	HTPB	Al	AP	HMX	PPE	Al
70	13.5	16.5	15	44	24.5	16.5

## RESULTS AND DISCUSSION

It is generally regarded that HMX melt with the binder in propellant surface, its pyrolysis gaseous products are  $\text{NO}_2$ ,  $\text{N}_2\text{O}$ ,  $\text{NO}$  and  $\text{CH}_2\text{O}$ . The temperature of the propellant surface increases sharply as a result of the exothermic reactions induced by  $\text{NO}_2$  and  $\text{CH}_2\text{O}$ . Consequently, oxidizing reactions took place, the temperature increases slowly to a certain level, then a luminous flame appears. The location of flame is dependent on ambient pressure.

## Flame Observation

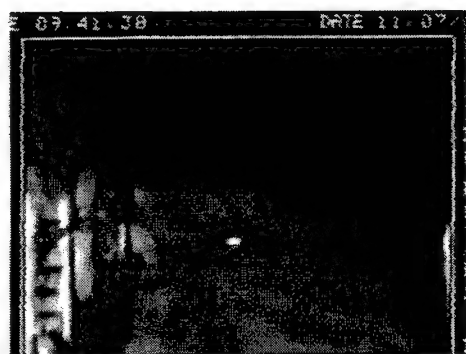
A series of images of the propellant have been taken during ignition process by the Kodak Ektapro motion analysis workstation. Figure 3 shows the typical pictures. Different locations and different shapes of luminous flames have been observed. Firstly, a rather weak flame appears in the gas phase distant from the sample surface (Figure 3a). The flame becomes larger and brighter, and moves slowly toward the propellant surface. Meanwhile, the luminosity of the propellant surface increases. This implies that there are some chemical reactions on the propellant surface. The products of these reactions interact continuously in the gas phase. (Figure 3b), The ejection of HMX particles have also been observed in this study (Figure 3c).

## Ignition Delay Time

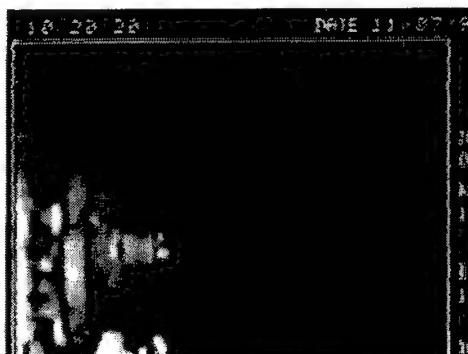
The ignition delay time of the two kinds of propellant samples at different ambient pressure and different radiative heat flux have been measured in this study. A negative ambient pressure was selected to investigate the gas phase effects. The results are shown in Figure 4 and Figure 5 respectively.

The ignition characterization of the two propellants show the same tendency. A decrease of ambient pressure leads to an increase of ignition delay time, and a decrease of radiative heat flux leads to an increase of ignition delay time. We can see that the ignition delay time of the two propellants is different in lower pressure and lower heat flux. The results indicates that the effects of ambient pressure on HMX propellant are greater than those on AP propellant. The difference lessens when pressure or heat flux increases. Figure 4 also implies that the ignition energy of HMX propellant is



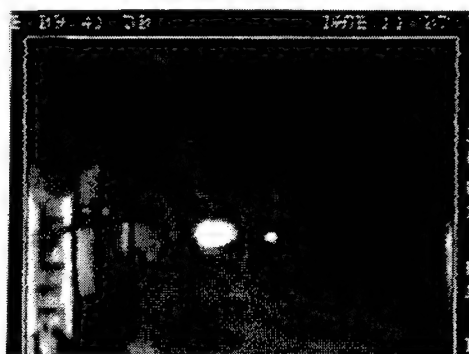


HMX/AP/PPE propellant

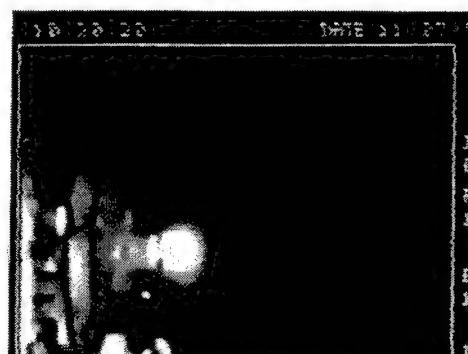


AP/HTPB propellant

a) Initial ignition flame structure



HMX/AP/PPE propellant



AP/HTPB propellant

b) Ignition flame structure



HMX/AP/PPE propellant

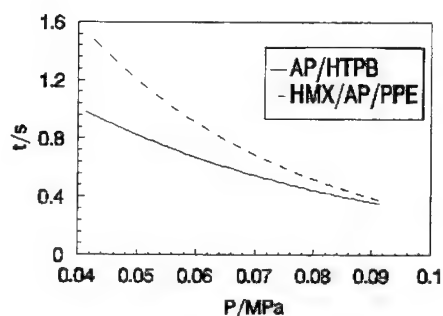


AP/HTPB propellant

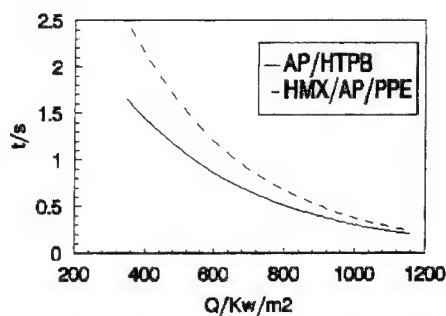
c) Steady flame structure

**Figure 3.** Ignition and combustion flame of the experiment propellants

greater than that of the AP propellant. De Luca<sup>4</sup> reported the same tendency. He found that HMX propellant was the most difficult to ignite, then AP propellant, then double base propellant.



**Figure 4.** Effects of ambient pressure on ignition delay time



**Figure 5.** Effects of ignition heat flux on ignition delay time

The decomposition reactive energy of HMX is generally regarded greater than that of the AP. The decomposition temperature of HMX is also greater than that of AP. Moreover, The decomposition products of HMX propellant are oxidizer-poor. The oxidizer density of AP propellant in the gas phase is higher than that of the HMX propellant. Roller et al<sup>1</sup> found that the LOVA propellants can be ignited more effectively using oxidizer-rich ignition materials. If the ambient pressure is not high enough, the oxidizer gas will not concentrate adequately. These are some of the reasons why HMX propellant ignites with difficulty. It also reminds us that an oxidizer-rich ignition charge and a higher critical pressure should be taken into account in nitramine propellant rocket motor designing.

It is generally regarded that the ignition characterization of energetic plasticizer containing propellants varies with ambient oxygen density much strongly. The HMX propellant used in this study contains considerable energetic plasticizer. This is why the test propellant relies on the gas phase strongly during ignition process in this study.

## CONCLUSION

The flame structure and ignition delay time of a kind of HMX minimum smoke propellant have been studied in this paper. We can draw the following conclusions from the experiment results. First, the ignition of HMX propellant is more difficult than that of the AP/HTPB propellant. Secondly, the ignition characterization of the HMX propellant studied is strongly affected by ignition heat flux and ambient pressure. This study also proves that the Kodak Ektapro motion analysis workstation is a very useful tool in solid propellant combustion diagnostics.

## REFERENCES

1. Kuo, K. and Summerfield, M., Fundamentals of Solid Propellant Combustion, *Progress in Aeronautics and Astronautics*, Vol. 90, 1984.
2. BenReuven, M. and Caveny, L., Nitramine Flame Chemistry and Deflagration Interpreted in Terms of a Flame Model, *AIAA 79-1113*, 1979.
3. Ohlemiller, T.J. and Summerfield, M., Radiative Ignition of Polymeric material in Oxygen/Nitrogen Mixture, *13th Symposium of Combustion*, 1971, 1087-1094.
4. DeLuca, L., et al, Radiative ignition of double base propellants: Some formulation Effects, *AIAA Journal*, Vol.14, No.7, July, 1976, 940-946.
5. DeLuca, L., et al, Radiative ignition of double base propellants: Preignition Events and Source Effects, *AIAA Journal*, Vol.14, No.8, August, 1976, 1111-1117.
6. Kashiwagi, T., Experimental Observation of Radiative Ignition Mechanism, *Combustion and Flame*, Vol.34, 1979, 231-244.
7. Kashiwagi, T., Effects of Attenuation of Radiation on Surface Temperature for Radiative Ignition, *Combustion Science and Technology*, Vol. 20, 1979, 225-234.

## A Solid-Phase Model for Plasma Ignition of Solid Propellant

R. Alimi, C. Goldenberg, L. Perelmutter, D. Melnik

Propulsion Physics Laboratory  
Physical Systems Division  
SOREQ NRC, Yavne 81800, Israel

D. Zoler

Raymond and Beverly Sackler Faculty of Exact Sciences  
School of Physics & Astronomy, Tel Aviv 69978, Israel

### Abstract

In this study we present a one-dimensional model that describes the ignition of solid propellant by a hot gas resulting from the mixing of a plasma jet with the air initially present in the combustion chamber. This model provides information about the ignition process, such as the ignition delay and the effect the physical properties of the ignition stimulus have on it.

Our model is based on a solid phase (thermal) model for ignition. The solid phase theory of propellant ignition is mostly successful in situations where the propellant is exposed to a strong flux of energy, and the velocity of the heating stimulus is high. Plasma ignition is such a situation.

The main conclusions that emerge from our study are the following: (i) Propellant ignition begins when the plasma energy and mass (partial density) in the combustion chamber reaches values that change only slightly with the level of input power density. (ii) The ignition time delay is mostly sensitive to the value of the plasma temperature at the capillary exit, and to a smaller extent to its exit velocity. (iii) For low velocities of the ignition stimulus, the radiative flux of energy is always the main factor leading to ignition. However, during the early moments of propellant heating, the convective energy flux is larger than the radiative one. The convective energy flux plays the role of a "pre-heating" factor. At higher velocities and for small values of the density of input energy, the convective energy flux can overcome the radiative one. (iv) The penetration depth of the heat wave into the propellant is very small up to ignition onset. It is larger for longer ignition time delays obtained with lower input powers. (v) Semi-quantitative agreement with experimental measurements was found.

## Nomenclature

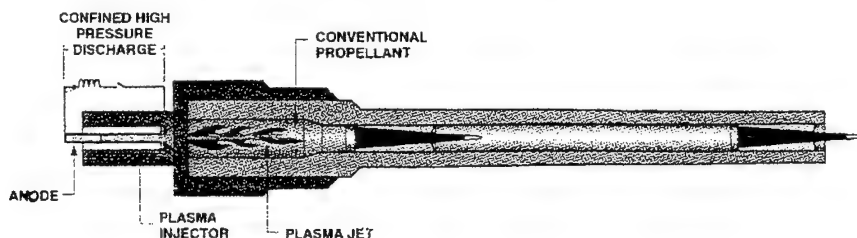
$c, c_{mix}$	specific heat of the propellant and igniting mixture ( $c=1.465$ kJ/kg/K)
$D_p$	effective diameter of the propellant grain ( $= 7 \cdot 10^{-3}$ m)
$E_a$	activation energy for the chemical reaction ( $= 1.67 \cdot 10^5$ J/mole)
$k, k_{oo}, k_{mix}$	thermal conductivity of propellant, neutral gas, and mixture ( $k = 0.314$ J/m K sec, $k_{oo} = 2.68 \cdot 10^{-2}$ J/m K sec)
$K_0$	pre-exponential Arrhenius factor ( $K_0 Q = 1.77 \cdot 10^{25}$ J/kg sec)
$m_{g0}, m_{pl}, m_{mix}$	mass of the neutral gas, plasma and mixture respectively ( $m_{pl} = 8.36 \cdot 10^{-27}$ kg, $m_{g0} = 49 \cdot 10^{-27}$ kg)
$n_{g0}, n_{pl}, n_{mix}$	number of density of the neutral gas, plasma and mixture respectively ( $n_{g0} = 2.46 \cdot 10^{25}$ m $^{-3}$ )
$P$	igniting mixture pressure (Pa)
$q_{ext}, q_{conv}, q_{rad}$	external, convective and radiative fluxes of energy, respectively
$Q, Q_c$	chemical reaction heat per unit volume, and rate of chemical heat production
$R$	universal gas constant ( $= 8.31$ J/mol.K)
$T_0, T, T_{pl}, T_{mix}$	initial, propellant, plasma and mixture temperature respectively ( $T_0 = 300$ K)
$t$	time variable (sec)
$u$	igniting mixture velocity (m/s)
$x$	space variable (m)
$Z$	plasma ionization degree
$\delta$	heat penetration length (m)
$\epsilon$	emissivity factor
$\rho, \rho_{mix}$	propellant and igniting mixture densities respectively ( $\rho = 1.6 \cdot 10^3$ kg/m $^3$ )
$\sigma_{SB}$	Stefan-Boltzmann radiative constant ( $5.67 \cdot 10^{-8}$ W/m $^2$ K $^4$ )
$\mu_{g0}, \mu_{mix}$	the neutral gas and igniting mixture viscosity coefficients ( $\mu_{g0} = 2.58 \cdot 10^{-5}$ kg/m.sec)
$\tau$	dimensionless time variable

## 1 Introduction

During the last decade a sustained research effort has been made in order to prove that plasma can be successfully used for accelerating projectiles to velocities larger than those reached with conventional devices and methods. One of the most promising propulsion concept, based on the use of a plasma source, is the solid propellant electrothermal chemical (SPETC) technology. The SPETC technology uses plasma as an additional source of energy for igniting a solid chemical propellant. It is also expected that, depending on the plasma thermodynamical and hydrodynamical properties, and on the duration of the plasma injection, the combustion process of the propellant can be controlled and enhanced.

The source of plasma generally used is a capillary built from a plastic material. At its closed end there is an anode and at the open end, a cathode. By applying a high energy (power) electrical pulse to this device, we get a high density flux of plasma characterized by temperatures of up to 5eV and velocities of more than 10km/sec. The pressure inside the capillary can reach values larger than 7kbar. The plasma results from the capillary material ablation, and from subsequent ionization by the mainly radiative flux of energy reaching its walls [1-9]. A schematic drawing of a SPETC gun is shown in Figure 1.

Fig.1 : Schematic drawing of A SPETC gun.



Recently many efforts have been devoted to building models able to simulate the internal ballistics of SPETC guns, and to clarify the role of the plasma in changing the propulsion characteristics [10-16]. In [16] the first experimental evaluations of the discharge process, ablative plasma parameters, together with some data concerning the propellant combustion (the pressure variation in the combustion chamber of the experimental facility and the burning rate) are presented.

In order to use the plasma source for better control of the propulsion processes, and to increase gun performances, one needs to investigate in greater detail the effect of the plasma on the ignition and combustion processes of solid propellant.

Until now, we have used the term "plasma" for the presumed ignition factor in the SPETC process. Let us be more specific on this point. In the experiment reported in [16] the ignition of the propellant is directly caused by the plasma jet generated in the capillary. In this case the initial pressure in the combustion chamber is rather low and the propellant sample is positioned in the near vicinity of the plasma source. Therefore the propellant is directly exposed to the plasma flux. However, in real cases the situation is rather different and certainly more complex. The plasma leaving the capillary enters initially into an "ullage tube" [13] (placed in the center of the combustion chamber). This tube allows the plasma to propagate through the propellant bed in the combustion chamber. The initial pressure in the combustion chamber is atmospheric. Therefore, even for very high energy discharges, the mass of plasma leaving the capillary will be only a small fraction of that of the gas surrounding the propellant. This will be especially true up to propellant ignition. It is therefore reasonable to assume that, in realistic situations, the propellant is not ignited directly by the plasma leaving the capillary, but rather by a "mixture" of the neutral gas initially present in the combustion chamber and the plasma. It is expected that this "mixture" will have thermodynamical and hydrodynamical properties different from those of the plasma at the capillary exit. A method of evaluating these characteristics has to be used in order to describe the ignition process correctly.

In this study we present a model able to describe the ignition of solid propellant by an ionized gas. This model provides ignition process data, such as the ignition delay and the effect the physical properties of the ignition stimulus have on the ignition delay.

Since the plasma flow is quasi-stationary [1,9], the plasma parameters generally change little inside the capillary and at its exit, their temporal dependence presenting extended plateaux. This, of course, will not be true for the "mixture" of neutral gas and plasma in the combustion chamber, the properties of which will probably change quite rapidly, depending on the mass of plasma leaving the capillary and its thermodynamical and hydrodynamical properties. In the frame of the present model, we will assume that the time of the mixing of the plasma and the air is much smaller than the ignition time delay. Time dependent expressions of the density, temperature, specific heat, molar mass, coefficient of thermal conductivity and coefficient of viscosity of the igniting mixture will be briefly presented.

The paper is organized as follows: in Section 2, we present the main assumptions and model equations; in Section 3 we present and analyze a selection of the results obtained by solving the set of equations of the model; in Section 4 we summarize the main conclusions.

## 2 Assumptions and Model Equations

The solid phase (thermal) ignition theory of solid propellants deals with phenomena that can be described by considering heat release and propagation only, without taking diffusion factors into account. Experimental results supporting the use of the solid phase ignition theory for our problem can be found in Ref. (17).

Our model equations are built in the frame of this theory on the basis of the following assumptions:

- (a) The propellant is heated by convective and radiative fluxes of energy coming from the hot igniting gas mixture.
- (b) The propellant is treated as a homogeneous, semi-infinite slab of material
- (c) The propellant and the surrounding gas are initially at thermal equilibrium.

- (d) The thermophysical properties of the propellant (the thermal conductivity, specific heat and density) are not temperature dependent.
- (e) The activation energy and the heat of reaction are also temperature independent.
- (f) Except for an exothermic chemical reaction of zero order there are no volume energy sources in the propellant which is externally heated only through its surface.
- (g) The chemical reaction resulting in the propellant ignition takes place in a thin heated subsurface layer. The thickness of the heated layer is considerably less than any spatial dimension of the propellant.
- (h) Negligible propellant surface regression occurs up to the ignition moment.
- (i) The propellant indepth absorption is not considered.

One of the most important issues in the ignition (either experimental or theoretical) is the choice of a so-called "ignition criterion". Obviously, this choice will affect the determination of the ignition time delay.

In this paper we will consider two ignition criteria. Both of them lead to the same prediction for the ignition time delay with a good degree of precision, in the range of a few microseconds.

The first and main criterion that was used in this work, states that the temperature of the propellant surface must reach a critical value. This value is usually known from experiments or from theoretical chemical considerations. The second criterion assumes that ignition occurs when the rate of heat production from the chemical reaction exhibits a very steep increase. This criterion provides (as we shall see later in Fig. 3) with a high degree of precision (a few microseconds) the same ignition time than the first criterion. The temperature of the propellant at the ignition time provided by the second criterion is very close to the threshold value used in the first criterion (see Table 2).

The purpose of calculations in the frame of solid phase ignition theory is to determine a non stationary temperature field in the propellant, the ignition delay time and how these parameters are affected by the heating conditions. The equations, the initial conditions and the boundary conditions that describe the propellant heating process up to ignition are similar to those used for this kind of theory when studying solid propellant ignition by conventional means, and can be written as follows [18,19]:

$$c\rho \frac{\partial T}{\partial t} = k \frac{\partial^2 T}{\partial x^2} + Q K_0 \exp(-E_a/RT) \quad (1)$$

$$-k \frac{\partial T}{\partial x} = q_{ext} = q_{rad} + q_{conv} : \text{at } x = 0 : \quad (2)$$

$$\frac{\partial T}{\partial x} = 0 : \text{at } x = \infty; T = T_0 \text{ at } t = 0 \quad (3)$$

$$q_{conv} = 0.4(T_{mix} - T)(k_{mix}\rho_{mix}u)^{2/3} \left( \frac{c_{mix}}{D_p \mu_{mix}} \right)^{1/3} ; q_{rad} = \sigma_{SB}(T_{mix}^4 - T^4) \quad (4)$$

Refer to the nomenclature for symbols definitions. The following assumptions have been made in the calculations of the mixture properties:

- The plasma leaving the capillary and the neutral gas are treated as ideal gases.
- The main plasma parameters leaving the capillary are varying as some prescribed functions of time that approximate the real shape of this variation in ablative capillary discharges.
- The mixing time between the plasma and neutral gas is much shorter than the heating time or the ignition time delay.
- The plasma temperature does not change due to expansion in the combustion chamber, but only by heat transfer to the neutral gas.

- At any time the ionized gas and its physical parameters are a result of the mixing between the neutral gas and the mass of plasma that left the capillary until this specific time.

In the following equations we provide expressions for some of the mixture properties. For the sake of shortness dimensionless expressions are given.

$$\tilde{n}_{mix}(\tau) = \frac{n_{mix}}{n_{g0}} = 1 + \tilde{n}_{pl}(\tau)(1 + Z) ; \quad n_{mix} = n_{g0} + n_{pl}; \quad \tilde{n}_{pl} = \frac{n_{pl}}{n_{g0}} \quad (5)$$

$$\tilde{T}_{mix}(\tau) = \frac{T_{mix}}{T_0} = \frac{\tilde{T}_g + \tilde{n}_{pl}(\tau)\tilde{T}_{pl}(\tau)(1 + Z)}{1 + \tilde{n}_{pl}(\tau)(1 + Z)} ; \quad \tilde{T}_g = \frac{T_{g0}}{T_0}; \quad \tilde{T}_{pl} = \frac{T_{pl}}{T_0} \quad (6)$$

Defining the average mass and density of the mixture particle as:

$$m_{mix} = \frac{m_{pl}n_{pl} + m_{g0}n_{g0}}{n_{pl} + n_{g0}} ; \quad \rho_{mix} = m_{mix} \cdot n_{mix} \quad (7)$$

we finally obtain the following dimensionless expressions:

$$\tilde{m}_{mix}(\tau) = \frac{m_{mix}}{m_{g0}} = \frac{1 + \frac{m_{pl}}{m_{g0}}\tilde{n}_{pl}(\tau)}{1 + \tilde{n}_{pl}(\tau)} ; \quad \tilde{\rho}_{mix}(\tau) = \frac{\rho_{mix}}{n_{g0}m_{g0}} = 1 + \frac{m_{pl}}{m_{g0}}\tilde{n}_{pl}(\tau) \quad (8)$$

$$\tilde{\mu}_{mix} = \frac{\mu_{mix}}{\mu_{00}} = \frac{\tilde{T}_g^{1/2}}{1 + 0.135\tilde{n}_{pl}[1 + 1.67 \cdot 10^2(\tilde{T}_g/\tilde{T}_{pl}^5)^{1/4}]^2} + \frac{1.48 \cdot 10^{-5}\tilde{n}_{pl}\tilde{T}_{pl}^{5/2}}{\tilde{n}_{pl} + 0.328[1 + 6 \cdot 10^{-3}(\tilde{T}_{pl}^5/\tilde{T}_g)^{1/4}]^2} \quad (9)$$

$$\tilde{k}_{mix} = \frac{k_{mix}}{k_{00}} = \frac{\tilde{T}_g^{1/2}}{1 + 0.135\tilde{n}_{pl}[1 + 1.67 \cdot 10^2(\tilde{T}_g/\tilde{T}_{pl}^5)^{1/4}]^2} + \frac{5.34 \cdot 10^{-3}\tilde{T}_{pl}^{5/2}\tilde{n}_{pl}}{\tilde{n}_{pl} + 0.328[1 + 6 \cdot 10^3(\tilde{T}_{pl}^5/\tilde{T}_g)^{1/4}]^2} \quad (10)$$

$$c_{mix} = 6.97 \cdot 10^2 \frac{1 + 0.168 \cdot \tilde{n}_{pl}}{1 + \tilde{n}_{pl}} \text{ J/(kgK)} \quad (11)$$

### 3 Results and Discussions

In the present study, we will analyze the ignition process of a propellant by plasma produced in the ablative capillary for four different pulses of input energy. The pulse duration in all four cases is 1 msec, and the maximum values of the input power during the discharge are 60 MW, 100 MW, 200 MW and 300 MW, respectively. The time profile of the main plasma parameters was chosen based on the fact that for a discharge in which the plasma flow at the open end is sonic (critical), it is similar with a good degree of precision to that of the input energy pulse [9]. In [2,3,8], a method was presented that allows us to evaluate the main plasma parameters at the capillary exit for a steady state ablative discharge. The same method can be used successfully for the evaluation of the maximum values of these parameters in a time dependent discharge.

Table 1 summarizes the maximum values of the main plasma parameters at the capillary exit for the four cases considered here.

The ignition mixture velocity  $u$  remains an undefined parameter. Recent preliminary experimental measurements performed at Soreq have shown that the value of the ignition stimulus velocity is, most probably, in the range 300-2000 meters per second. To our knowledge, no other published data is available. Therefore, a parametric study of the effect of  $u$  on the ignition process will be conducted using four different values:  $u = 300, 500, 1000$  and  $2000$  m/s.

A selection of the main results of this study can be found in Figs. 2 to 4 and in Table 2.



Table 1: The maximum values of the main plasma parameters at the capillary exit

Power (MW)	60	100	200	300
Temperature (K), $T_{m,e}$	$2.07 \cdot 10^4$	$2.35 \cdot 10^4$	$2.79 \cdot 10^4$	$3.09 \cdot 10^4$
Mass density ( $kg/m^3$ ) $\rho_{m,e}$	0.287	0.395	0.609	0.785
Exit velocity (m/sec) $V_{m,e}$	$9.28 \cdot 10^3$	$9.9 \cdot 10^3$	$1.08 \cdot 10^4$	$1.135 \cdot 10^4$
Mass flux (kg/sec) $\dot{m}_{m,e}$	0.228	0.333	0.561	0.760

Table 2: Some parameters of the igniting mixture and the plasma at ignition onset.  $T_s(t_i)$  - propellant surface temperature (K);  $\Delta t_i$  - the ignition delay ( $\mu$  sec);  $\Delta t_i(exp)$  - the upper bond experimental ignition delay ( $\mu$  sec);  $m(t_i)$  - mass of plasma in the combustion chamber (kg);  $T_{mix}(t_i)$  - igniting mixture temperature (K);  $\rho_{mix}(t_i)$  - igniting mixture density ( $kg/m^3$ );  $P(t_i)$  - igniting mixture pressure (MPa) and  $W_{int}(t_i)$  - plasma internal energy in the combustion chamber (kJ) for the four considered maximum values of the input power.

Power (MW)	$T_s(t_i)$	$\Delta t_i$	$\Delta t_i(exp)$	$m(t_i)$	$T_{mix}(t_i)$	$\rho_{mix}(t_i)$	$P(t_i)$	$W_{int}(t_i)$
60	458.5	505	-	$7.70 \cdot 10^{-5}$	3809	1.243	1.52	17
100	460.4	390	< 600	$7.47 \cdot 10^{-5}$	4031	1.243	1.61	18
200	463.0	284	< 450	$7.34 \cdot 10^{-5}$	4277	1.242	1.71	19
300	463.7	237	< 300	$7.17 \cdot 10^{-5}$	4413	1.242	1.77	20

### 3.1 Plasma and igniting mixture parameters values up to ignition onset

The following conclusions can be drawn: From Table 2, it seems that up to the onset of propellant ignition, the plasma partial density reaches almost the same value independently of the input energy. Since the neutral gas partial density is constant during the propellant ignition process and, since we assumed that the mass of gases leaving the propellant up to ignition is negligible, we conclude that the igniting mixture density and mass is almost the same at the ignition onset for all the input energies considered.

The main differences between the four ignition processes that lead to different ignition time delays seem to be connected to the partial temperature of the plasma component of the mixture.

As the maximum power of the input electrical pulse increases, higher plasma partial temperatures are reached, leading to higher temperature of the mixture (See Table 1 and 2).

Not only the plasma temperature, but also its density and velocity at the capillary exit depend on the input power. Therefore our results support the claim that using a plasma source for propellant ignition does indeed allow the control of the propellant ignition time delay.

Another conclusion can be drawn from Table 2. Using plasma as a primer for propellant ignition does not lead to large values of igniting mixture temperature. If the flame temperature for conventional igniters is approximately 3000K, we derive from Table 2 that, even for the largest maximum power used in our calculations, the mixture temperature at ignition is only 47% higher. The relatively small values of the mixture temperature can be explained by the small ratio of the partial densities of the plasma to the neutral gas in the combustion chamber.

### 3.2 The effect of convective and radiative heating

Two heating factors were considered in the present study: the convective and radiative fluxes of energy. We now address the important issue of evaluating the relative effect of these factors on the ignition process. It is also interesting to see how different velocities of the ignition stimulus affect the

ignition delay. The results plotted in Figs. 2a, 2b attempt to give an answer to these questions.

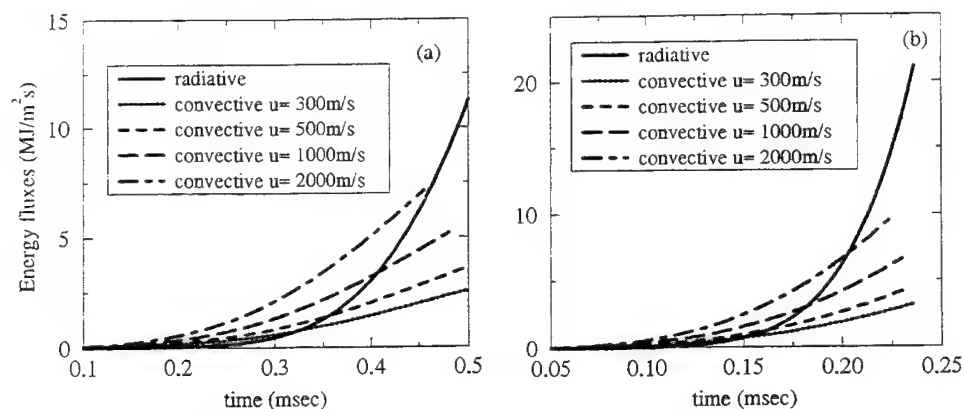


Fig. 2: The total energy fluxes for different velocities of the igniting mixture for maximum input power of 60 MW (a), and 300MW (b).

Figs. 2a and 2b represent the radiative flux of energy for the case of a maximum input power of 60MW and the corresponding convective energy fluxes for four different values of ignition stimulus velocity, as indicated in the figure. In Fig. 2b the same quantities were plotted but for a maximum input power of 300MW. The following conclusions can be drawn. In the earlier stages of the propellant heating the main role is played by the convective heating for all the cases presented in Figs. 2a and 2b. For relatively low velocities (less than 500m/s), the role of the convective heat flux is limited to that of a pre-heating factor and it remains lower than the radiative contribution for time moments near the ignition onset for all the studied cases. For velocities equal to, or larger than, 2000m/s (see in Fig. 2a the curve corresponding to  $u = 2000\text{m/s}$ ), the convective flux of energy becomes comparable to, or even larger than the radiative one during the entire time of propellant heating up to ignition onset. For high input powers (see Fig. 2b) the radiative component remains dominant, even for high velocities. The changes in the ignition delay are relatively modest when the velocity of the ignition stimulus increases. The maximum difference we find in the 60MW case is for a velocity of  $u = 2000\text{m/s}$ , where the ignition delay is 10% smaller than that for  $u = 300\text{m/s}$ . Therefore, we expect that the errors in the measurement of the parameter  $u$  will not change in a significant manner the ignition picture, at least regarding the ignition delay (compare, for example, the curves for  $u = 300$  and  $500\text{m/s}$  in Figs. 2a and 2b).

### 3.3 Ignition delay and ignition temperature

The discussion will be based on the results plotted in Fig. 3 and Table 2. In Fig. 2 the rate of chemically produced heat at the propellant surface  $Q_c$  are plotted as a function of time for each one the input power values we have considered. We note that at the time the chemically produced heat at the propellant surface suddenly presents a dramatic increase, the propellant surface temperature reaches a value of about 460K (which is accepted and experimentally determined as the ignition temperature for the kind of propellant we consider here).

The ignition time delay is one of the most important parameters characterizing the propellant and fuel ignition process. The capability of controlling the ignition time delay is strongly related to our ability to control the ignition process itself. We see in Table 2 that the ignition time delay decreases by almost 54% (from  $505\mu\text{sec}$  to  $237\mu\text{sec}$ ) as the maximum input power increases from 60MW to 300MW. At the same time the increase in the plasma energy entering the combustion chamber up to propellant ignition is only 18%. We can also conclude from Table 2 that the changes in the ignition

time delay are strongly related to those of the mixture temperature. However, the quantity of plasma inside the combustion chamber at ignition onset shows a very slight dependence on the input energy. This means that the ignition delay is practically determined by the temperature of the mixture which, in turn, is directly determined by the plasma temperature at the capillary exit. As already mentioned, the value of the plasma temperature at the capillary exit with a given geometry depends on the input power per unit volume [3,12,13]. This leads us to the conclusion that the time delay itself can be linked to the value of the input power. From the data presented in Table 2, we can build a simple empirical relation between the ignition delay,  $\Delta t_i$  and the input power ( $W_{inp}$ )

$$\Delta t_i \sim W_{inp}^{-\beta} \quad (12)$$

In our case  $\beta \approx 0.475$ . Our results also point to the possibility of minimizing the amount of energy needed to ignite the propellant. In other words, we can evaluate the minimal duration of an input energy pulse needed in order to ignite the propellant. On the other hand, for a pulse longer than the required minimum, we can evaluate the part of the input energy which will further contribute to the combustion process.

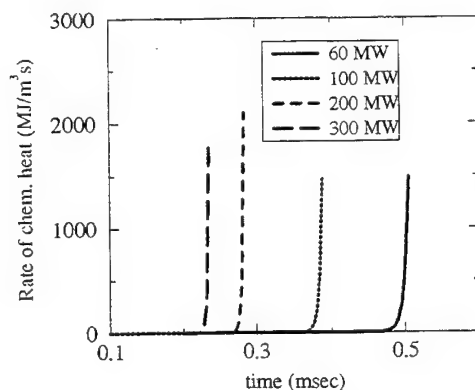


Fig. 3: Rate of chemical heat production at the propellant surface

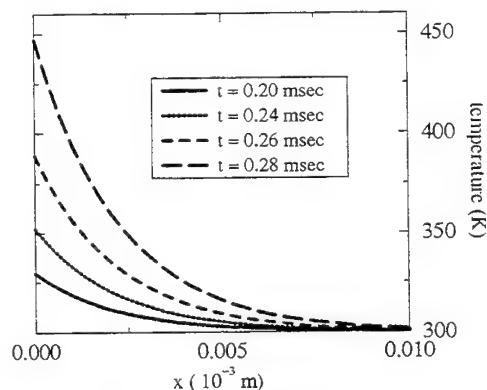


Fig. 4: Heat wave penetration inside the propellant (for 200 MW case)

### 3.4 The propellant spatial temperature profile

We now turn to the propagation of the heat wave in the propellant during the heating (induction) period up to ignition onset. The data are plotted for different times in Fig. 4 for the 200MW case. The main feature is the small thickness of the layer in which the temperature changes significantly. Let us define the penetration depth ( $\delta$ ) of the heat wave until ignition onset, as the value of the  $x$  coordinate at which the temperature changes by less than 0.3% with respect to the initial value. Then, up to the ignition onset, for the 60MW case  $\delta \approx 1.5 \cdot 10^{-5}$ m, for the 100MW case  $\delta \approx 1.2 \cdot 10^{-5}$ m; for the 200MW case  $\delta \approx 10^{-5}$ m and for the 300MW case  $\delta \approx 0.8 \cdot 10^{-5}$ m. All these values are much lower than the propellant web ( $1.37 \cdot 10^{-3}$ m). This fact supports a-posteriori two of our assumptions: the one-dimensionality of the ignition problem and the fact that until ignition onset the quantity of propellant which is gasified is very small.

### 3.5 Comparison with experiment

The experiments we compare to the model were not designed for being ignition experiments. Rather they are regular shots performed with the Soreq 105mm SPETC gun, in which, among other data, the breech pressure was recorded from the beginning of the ignition trigger. For this reason the ignition delay one can obtain from the rise of the pressure signal is only an upper bound of the

real time at which the first grains are starting to burn. Three shots were used. The shots differ only by the power of the electric pulse used for ignition (100, 200 and 300 MW respectively). The other shot parameters are the same and correspond to the data used in the model (propellant type and amount, chamber volume etc.) The results are shown in the fourth column of Table 2. We conclude to a good semi-quantitative agreement between the experimental and the prediction model values. In the next future a series of specially designed closed bomb experiments should be performed to check more quantitatively the predictions of our ignition model.

## 4 Conclusions

A one dimensional model for solid propellant ignition using a plasma source has been proposed. In the frame of the model assumptions the propellant is heated and ignited by convective and radiative fluxes of energy from a mixture between the plasma leaving an ablative discharge device and the neutral gas existing in the combustion chamber.

The main conclusions that emerge from our study are the following:

- Propellant ignition begins when the plasma energy and mass (partial density) in the combustion chamber reach values that change only slightly with the level of the input power density.
- The ignition time delay is mostly sensitive to the value of the plasma temperature at the capillary exit, and to a smaller extent to its exit velocity. Since the plasma temperature is directly related to the density of the input power, we can conclude that, indeed, we have a good tool for direct influence on the ignition process of the propellant and, in some respects, also to affect the propellant combustion.
- For low velocities of the ignition stimulus, the radiative flux of energy is always the main factor leading to ignition. However, during the early moments of propellant heating, the convective flux of energy is larger than the radiative one. The convective flux of energy plays the role of a "pre-heating" factor. At higher velocities and for small values of the density of input energy, the convective flux of energy can overcome the radiative one.
- The ignition criteria we use lead to the same ignition time delay. From the second criterion it also follows that the ignition temperature is approximately 460K. This result is in agreement with the experimental value for the propellant we used in this study.
- The depth of penetration of the heat wave into the propellant is very small up to ignition onset. It is larger for longer ignition time delays obtained with lower input powers. This result supports a posteriori two of the model assumptions, namely: the accuracy of the one-dimensional approach and neglecting the effect of propellant gasification up to ignition onset.
- We have also performed a parametric study of the effect of the emissivity on the ignition time delay. For the 60 MW case, we have checked the following values of  $\epsilon$ : 1, 0.8, 0.6, 0.4. The time delays were found to be 505, 522, 545, and 575  $\mu\text{sec}$  respectively. As one can see no significant changes (maximum 15%) were induced in the time delay when the emissivity factor was changed by 60%.
- The ignition stimulus temperature at ignition onset in plasma stimulated ignition is higher than the value reached in the conventional ignition processes, depending on the density of input power. This higher value of the ignition mixture temperature, even if not as high the temperature at the capillary exit, has a dramatic effect on the ignition delay and seems to be the main factor, in the frame of our model, that makes the difference between conventional propellant ignition and plasma stimulated propellant ignition.

- The predicted time ignition delays seem to be in good agreement with the measured values. although dedicated experiments are yet to be designed to get a cleaner basis for comparing between theory and experiment.

## References

1. Tidman, D.A., Thio, Y.C., Goldstein, S.A. and Spicer, D.S., 1986, "High Velocity Electrothermal Mass Launcher". *GT Devices Report*, 86-7.
2. Loeb, A. and Kaplan, Z., 1989. "A Theoretical Model for the Physical Processes in the Confined High Pressure Discharges of Electriothermal Launchers", *IEEE Trans. Magn.*, Vol. 25, pp. 342-346.
3. Mohanti, R.B. and Gilligan, J.G., 1990, "Electrical Conductivity and Thermodynamic Functions of Weakly Nonideal Plasmas". *J. Appl Phys.*, Vol. 68, p. 5044.
4. Burton, R.L., Wilko, B.K., Witherspoon, F.D. and Jaafari, G., 1991, "Energy Mass Coupling in High-Pressure Liquid Injected Arcs", *IEEE Trans. Plasma Sci.*, Vol 19, pp. 340-349.
5. Zoler, D. and Cuperman, S., 1992. "Quasi-one-dimensional Model Equations for Plasma Flows in High Pressure Discharges in Ablative Capillaries", *J. Plasma Phys.*, Vol. 42, pp. 215-227.
6. Bourham, M.A., Gilligan, J., Hankins, O., Eddy, W. and Hurley, J., 1992. *Proc. 9th International Conf. on High Power Particle Beams*, Washington D.C., Vol. III, p. 1979.
7. Powell, J.D. and Zielinski, A.E., 1993, "Capillary Discharge in the Electrothermal Gun", *IEEE Trans. Magn.*, Vol. 29, pp. 591-596.
8. Zoler, D., Cuperman, S., Ashkenazy, J., Caner, M. and Kaplan, Z., 1993. "Effect of a Non-Ideal State Equation on the Steady State Critical Flow Characteristics in Ablative Capillaries", *J. Phys. D: Appl. Phys.*, Vol. 26, pp. 657-660.
9. Zoler, D. and Alimi, R., 1995, "A Proof for the Need of Self-Consistent Treatment in Modelling of Capillary Ablative Discharges", *J. Phys. D: Appl. Phys.*, Vol. 28, pp. 1141-1152.
10. Oberle, W.F. and White, K.J., 1991 "Electrothermal Gun Technology and Performance: An Analysis of Small and Large Caliber Ballistic Data", *BRL-TR-3238, Ballistic Research Laboratory, Aberdeen Proving Ground, MD.*
11. McElroy, H.A., Grieg, J.R. and Juhasz, A.A., 1991, "Plasma Augmented Ball Propellant Ballistics", *Proc. of 5th International Gun Propellant and Propulsion Symposium.*
12. Morrison, W.F., Wren, G.P. and Oberle, W.F., 1992, "Modeling of the Interior Ballistic Process in a Hybrid Solid Propellant, Electrothermal-Chemical Gun", *BRL Technical Report. BLR - Aberdeen Proving Ground, MD.*
13. Kaplan, Z., Saphier, D., Melnik, D., Gorelik, Z., Ashkenazy, J., Sudai, M., Kimhe, D., Melnik, M., Smith, S. and Juhasz, A.A., 1993, "Electrothermal Augmentation of a Solid Propellant Launcher", *IEEE Trans. Magn.*, Vol. 29, p. 573.
14. Wren, G.P., Oberle, W.F., Sinha, N., Hosangadi, A., Dash, S.M., 1993, "U.S. Army Activities in Multidimensional Modeling of Electrothermal-Chemical Guns", *IEEE Trans. Magn.*, Vol. 29, p. 631.
15. Woodley, C.R., 1993, "A Parametric Study for an Electrothermal-Chemical Artillery Weapon", *IEEE Trans. Magn.*, Vol. 29, p. 625.

16. Edwards, C.M., Bourham, M.A. and Gilligan, J.G., 1995, "Experimental Studies of the Plasma-Propellant Interface for Electrothermal-Chemical Launchers", *IEEE Trans. on Magn.*, Vol. 31, p. 404.
17. Keller, J.A., Baer, A.D., and Ryan, N.W., 1966 "Ignition of Ammonium Perchlorate Composite Propellants by Convective Heating", *AIAA Journal*, Vol. 4, No. 8, 1358.
18. Merzhanov, A.G. and Averson, A.E., 1971, "The Present State of the Thermal Ignition Theory", *Combust. Flame*, Vol. 16, pp. 89-124.
19. Gough, P.S., 1983, "XNOVA - An Express Version of the NOVA Code", Final Report, Contract No 174-82-01-8048, Portsmouth, NH 03801.

#### Comments

**Qwinn Brewster - Univ. of Ill. Urbana, USA:** I think the effect of in-depth absorption of radiation may be very important in this situation. Even with opacifying carbon in the propellant, the photon mean free path (inverse absorption coefficient) for the characteristic plasma radiation will be at least of the order of the reported conduction penetration depths (microns). I suggest relaxing or at least investigating the surface absorption assumption.

**Authors' reply:** We totally agree with this observation. It is our intention to extend the present model in order to take into consideration the radiation in-depth absorption effect on the propellant ignition.

**Ashot Nazarian - SAIC/NIST USA:** 1. Is there any dependence of ignition parameters on plasma pulse duration?

2. What is the emissivity (non-black body) contribution to the accuracy of the calculation?

**Authors' reply:** 1. The answer is both yes and no. Yes if one remarks that the ignition parameters are mainly affected by the amount of energy provided by the plasma, that is the **time integral** of the pulse power. However, once ignition has occurred, and since the plasma ignites quite uniformly and simultaneously the whole propellant charge, the rest of the pulse (i.e. how long the pulse is *after* the ignition) does not affect the ignition process.

2. We of course agree with the fact that including the emissivity of propellant will affect the ignition time delays predicted in our model. To check quantitatively this effect, we have performed a series of calculations where we added an emissivity factor of 0.8, 0.6 and 0.4 (instead of 1). These calculations were done for the case of maximum input power of 60MW. In this case the ignition time delay  $\Delta t_i$  was 505  $\mu\text{sec}$ . The results are  $\Delta t_i = 522, 545$  and  $575 \mu\text{sec}$  respectively. Therefore changing by 60% the emissivity infers a change of about 15% in  $\Delta t_i$ .

**Jean-Paul Reynaud - SNPE - France:** You made some assumptions for radial and axial igniting mixture velocities values. Were they real assumptions or did you make some experimental measurements of this parameter? If yes, what kind of experiment?

**Authors' reply:** We have indeed performed in our laboratory some preliminary experiments to evaluate the axial and radial velocities of the igniting mixture of plasma/air. A detailed description of the experimental set-up, diagnostics and results will be presented in San Francisco at the next International Symposium on Ballistics. In summary, the results indicate that the axial velocity, at least during the ignition stage, is between 1500 and 2000 m/s, while the radial velocity rather ranges between 300 to 500 m/s. The velocity values in the above ranges depend mainly on the value of the electric input power.

**“New Insights into the Combustion of AP/HTPB Rocket Propellants:  
The Catalyst Active Sites and a Combustion Flame Model for  
The Ferrocene-Catalysed Combustion”**

**T.T. Nguyen**

Weapons Systems Division  
Defence Science & Technology Organisation (DSTO)  
P.O. Box 1500 Salisbury, South Australia 5108, Australia

**ABSTRACT:** The combustion of solid rocket propellants consisting of hydroxy-terminated polybutadiene (HTPB) as binder and ammonium perchlorate (AP) as oxidiser and incorporating the ferrocenic burn rate catalysts Catocene and Butacene was examined with a view to: (i) obtaining a better understanding of the propellant combustion behaviour and the prevailing mechanistic sites of burn rate catalysis, and (ii) determining the burn rate temperature sensitivity.

Examination revealed that the enhancing effect of 1% Catocene was equivalent to 0.5% Butacene. The combined experimental evidence (from burn rate measurements and scanning electron microscopy) provides insights into the possible sites of the catalytic action by the ferrocenic catalyst. The data were interpreted as indicating the catalyst acting predominantly in the binder, possibly to promote AP/binder reactions at the AP/binder interface, or to enhance the binder pyrolysis. There could be, possibly to a much less extent, active sites formed by iron particles ejected into the primary diffusion flame. There was no evidence suggesting the catalyst acting in the oxidiser to promote surface AP decomposition. The arguments support the logic that the combustion is controlled by the primary diffusion flame. A combustion flame model is proposed which shows the domed AP surface particle, undercutting along the AP particle boundary, and the primary diffusion flame bending across the AP/binder interface.

The burn rate temperature sensitivity value ( $\sigma_p$ ) at 10 MPa for the propellants containing 0.5% Catocene and 0.5% Butacene was 0.17 and 0.15%/°C, respectively. This represents a reduction of 40% and 35%, from the baseline non-catalyst value. The lowering of burn rate temperature sensitivity re-affirms the contention that a primary diffusion flame mechanism is operative for the ferrocene-catalysed combustion.

## INTRODUCTION

Propellant burn rate is an important characteristic of solid propellant combustion. A common method for enhancing burn rate is by the use of metal containing catalysts. Numerous mechanistic studies have shed some light about how these catalysts function. A great deal of effort has been focussed on the relative importance of the role played by the ammonium perchlorate (AP) oxidiser and the inert hydroxy-terminated polybutadiene (HTPB) binder. One school of thought advocates that burn rates of composite propellants are determined by the burn rates of the oxidiser AP and its catalysed decomposition reactions<sup>1-4</sup> while another puts more emphasis on the binder and its catalysed heterogeneous reactions with the oxidiser.<sup>4,5</sup>

Another long standing controversy has been the question as to whether gas-phase reactions, or condensed-phase (i.e. surface and sub-surface) reactions play a dominant role in burn rate enhancement.<sup>3,4,6</sup>

In favour of gas-phase reactions, Rastogi et al.<sup>7</sup> suggested that the actual species catalyzing the burn rates was the oxide derived from the original metal salt additive which functions by promoting the gas-phase reactions on the surface but not the exothermic reactions in the condensed phase. Others<sup>8-11</sup> suggested that iron-containing catalysts such as iron oxide and ferrocenes act in the gas phase to increase the reaction rate of perchloric acid and its initial decomposition products.

By contrast, condensed-phase reactions are shown to be important in the heterogeneous reactions between the binder and AP, or in the binder decomposition itself. From the observed undercutting along the boundary of the AP particles on the quenched propellant surfaces, Krishnan et al.<sup>12-14</sup> suggested that iron oxide and copper chromite catalysts enhance the propellant burn rates by promoting heterogeneous surface and sub-surface reactions between the binder and oxidiser. Similar observations were reported in other studies using sandwich propellants by Price et al.<sup>15-16</sup> Kishore et al.<sup>3,17,18</sup> concluded that more definite evidence for condensed-phase reactions came from the identification of peroxide intermediates in chemical analyses and infrared spectroscopy of quenched propellants. A model was put forward<sup>19</sup> to incorporate condensed-phase reactions where both AP and the binder decompose in the solid phase, and the products mix and interact in the interstices between the AP particles and the binder.

While the evidence is strong for condensed-phase reactions between the binder and oxidiser, evidence for catalyst enhanced binder degradation has been somewhat contradictory. On the one hand, binder thermal degradation has been claimed<sup>20</sup> to be the rate-limiting step in HTPB/AP combustion catalyzed by copper containing additives. Catalysis was found to increase the burn rate when copper chromite was pre-mixed into the binder, but not when it was pre-mixed into the AP.<sup>4,21</sup> On the other hand, no augmented binder pyrolysis was observed when catalysts known to enhance propellant burn rates were used.<sup>1,5</sup> Further, changes in the kinetics or heats of degradation of the polymeric binders have been shown not to have a significant effect on propellant burn rates,<sup>5,22</sup> and such negative results were interpreted as inferring the catalyst affects gas-phase AP decomposition reactions.<sup>5</sup>

The question of a dual role has also been raised. One study suggests copper chromite catalyst accelerates AP decomposition as well as promotes the oxidation of the fuel through heterogeneous reactions.<sup>23</sup> Another shows copper chromite does not promote heterogeneous reactions with solid fuel binder, nor modify binder pyrolysis, but it possibly enhances gas-phase reactions by its presence in the interface between the AP and binder.<sup>22</sup>

Because of the complex and confusing literature mentioned above, the present study aimed to obtain a better understanding of the propellant burning surfaces, their combustion behaviour and the prevailing mechanistic sites of ferrocenic burn rate catalysis. Evidence is presented from burn rate measurements



and burning surface characteristics that the ferrocenic catalysts act in the binder, possibly to promote the heterogeneous reactions between the binder and the AP, or to enhance binder pyrolysis. It is argued that condensed-phase reactions at the binder/AP interface are likely to be important for catalysing the primary diffusion flame. There is no evidence for catalysed AP decomposition reactions on the propellant burning surface.

## EXPERIMENTAL

### Materials

Bimodal blends of AP (source: Kerr-McGee) were used, consisting of a medium sized (200  $\mu\text{m}$ ) fraction and a small sized (20  $\mu\text{m}$ ) fraction. This combination was recommended as offering an optimum AP particle size width distribution to enable the best possible reduction of burn rate temperature sensitivity.<sup>24</sup> Particle size distributions were measured on a Malvern Mastersizer/E.

The non-catalysed propellant formulation contained 83% (weight fraction) AP (medium sized 65/small sized 35) and 17% HTPB (source: Elf-Atochem) including a small amount (approximately 3%) of a curing agent, DDI (Trademark of General Mills Inc.), which is a diisocyanate derived from a dimer acid  $\text{C}_{36}\text{H}_{64}\text{O}_4$ . In all other formulations, the binder level was kept unchanged at 17%, and the catalyst was added at the expense of the total AP solid loading (83%) while maintaining constant the medium sized/small sized AP ratio of 65 to 35.

Catocene (source: Thiokol) was kindly donated by the U.S. Department of the Navy, Naval Air Warfare Centre, China Lake, California. Butacene (source: SNPE) was an HTPB prepolymer with a ferrocenic moiety grafted through an alkyl silane group to the polymer backbone. It had an iron content of 8.10 % by weight, whereas the iron content in Catocene was 23.85 %. For comparative assessment, the propellants containing Butacene were prepared so that they contained the same amount of iron in the ferrocenic complex as that amount of iron in the catalyst Catocene incorporated in the corresponding propellants. In the following sections they are referred to as the 0.5 % (actual 1.5 % Fe) and 1.0 % (actual 2.9 % Fe) Butacene containing propellants for direct comparison with the corresponding propellants containing 0.5 and 1.0 % Catocene. Because Butacene also contained an amount of HTPB, this amount was taken into account in determining the 17% binder content of the propellant.

The detailed formulations of the propellants are summarised in Table 1.

TABLE 1  
Propellant Formulations (Weight %) Containing Various Catalysts at Different Concentrations

	Baseline propellant (No catalyst)	Catocene concetration			Butacene concentration		
		0.5%	1%	3%	0.5%	1%	3%
HTPB	13.79	13.79	13.73	13.79	12.42	11.18	5.91
AP (200 $\mu\text{m}$ )	53.95	53.63	53.30	52.00	53.95	53.95	53.95
AP (20 $\mu\text{m}$ )	29.05	28.87	28.70	28.00	29.05	29.05	29.05
Catocene	-	0.50	1.00	3.00	-	-	-
Butacene	-	-	-	-	1.47	2.95	8.83
DDI	3.21	3.21	3.27	3.21	3.11	2.87	2.26

## Propellant Processing and Manufacture

The propellants were manufactured in batch sizes using a 1-pint Baker Perkins planetary action mixer. All mixing was performed under reduced pressure at 60°C. After mixing, the propellant was top cast under reduced pressure into a rectangular mould and subsequently cured for one week at 60°C. The castability of the propellant and the rate of the early stage of the cure reaction were determined by measuring the viscosity of the propellant as a function of time. A Haake RV3 viscometer with a cup and rotor sensor was used for these measurements.

## Strand Burn Rate Measurements

The cured propellant slabs were machined into strands of dimensions 175 x 5 x 5 mm. The strands were inhibited with coatings of phenolic epoxy resin, or polyvinyl acetate paint. They were burned in a nitrogen pressurised Crawford-type bomb over a pressure range 2 to 18 MPa. All burn rate measurements were at 20°C; except in the determination of temperature sensitivity burn rates were measured at -20 and 55°C. Burn rates as a function of pressures were plotted and the curves of best fit through the data points were obtained by least square regression.

## Interrupt Bomb

An interrupt bomb, constructed from a modified version of the original design<sup>25</sup> by the U.S. Naval Weapons Centre, was employed in the quenching of burning propellants. A propellant strand (length 40 mm, cross section 5x5 mm) was burned in the bomb at a pressure in the range 2-10 MPa, and quenched by rapid depressurisation of the nitrogen. A stack of mylar disks (disk thickness 0.13 mm) was used as diaphragm in the combustion chamber. The propellant strand, mounted at the opposite end of the bomb, could be ignited by an igniter wire inserted through it. A nichrome wire, sandwiched between the mylar disks, was heated by a triggered capacitor discharge. The hot wire caused immediate rupture of the mylar disks, leading to a rapid drop in the chamber pressure which extinguished the propellant combustion. The number of mylar disks to be used was dependent on the bomb pressure under which the propellant burned. The rate of depressurisation was chosen to ensure that propellant burning was completely and permanently extinguished. Some alterations of the surface structures may have resulted from the quenching process, but the marked correlations established previously<sup>26</sup> indicated that any artifacts due to the quenching process would be of minor importance. The quenched propellant was examined by scanning electron microscopy.

## Scanning Electron Microscopy

Scanning electron microscopy (SEM) was carried out using a Jeol JSM 35 scanning electron microscope with a Tracor Northern microprobe attachment for qualitative element identification by Energy Dispersive Analysis. X-ray digital images of elements were constructed by a Tracor Northern X-Ray analyser coupled to the microscope. The X-Ray analyser used a Flexitran program called the Image Processing Program (IPP) to construct digital elemental X-ray maps according to the intensities of X-rays produced by the electron microscope.

A portion of the quenched propellant strand was cut and mounted on a sample holder for SEM examination. In order to prevent surface charging, i.e. build-up of electrostatic potential on the non-conducting propellant surface, the surface was coated with a thin layer of gold (a few hundred Angstrom thick) by vacuum deposition.

## RESULTS

### Burn Rate Measurements

Burn rates of the propellants containing 0.5, 1 and 3% Catocene showed enhancements with respect to the non-catalysed background propellant. At 1% Catocene concentration, a burn rate increase of up to 80% was observed. The enhancements, however, were not proportional to the catalyst concentrations.

Burn rates of the propellants containing 0.5, 1 and 3% Butacene were also measured, and found to be always higher than the corresponding Catocene propellant burn rates. The Butacene propellant burn rates are compared with the Catocene propellant burn rates in Figure 1, and summarised in Table 2.

Since the Butacene compound consists of a single ferrocenic moiety and a pre-polymer HTPB joined together through a silane-type linkage, the possible enhancing effect due to the linkage was examined. Burn rate measurements of the propellant containing 1% tetraethylsilane confirmed that there was no enhancing effect from the silane linkage. Thus the observed enhanced burn rates of the Butacene propellants originate from the catalytic effect of the ferrocenic moiety.

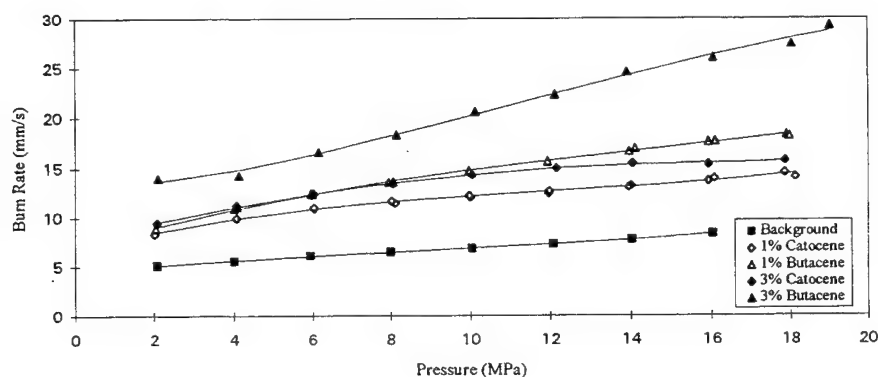


Figure 1. Plots of Burn Rates (mm/s) versus Pressures (MPa) of Propellants Containing Catocene and Butacene Catalyst at Various Catalyst Concentrations.

### Scanning Electron Microscopy

SEM photographs of the quenched burning surfaces of the propellants containing the ferrocenic catalysts all show undercuttings, to varying degrees, along the boundaries of AP surface particles where the oxidiser is in contact with the binder. This observation suggests heterogeneous reactions at the AP/binder interfacial region on the burning surface.<sup>12-14,27</sup> For the propellant containing 0.5% Butacene catalyst, the undercuttings were quite pronounced at both low (2 MPa) and high (10 MPa) pressures; see Figure 2. Another characteristic feature of the ferrocenic propellants is the domed, convex shape of the AP particle on the burning propellant surface. The protruding AP surface

suggests that the regression rate of the propellant as a whole is faster than that of the oxidiser particles.

TABLE 2  
Burn Rates (mm/s) of the HTPB/AP Propellants Containing Catocene and Butacene at Different Catalyst Concentrations.

Pressure (MPa)	Baseline Propellant	Propellant containing Catocene at indicated Catocene concentration			Propellant containing Butacene at indicated Butacene concentration		
	No Catalyst	0.5%	1%	3%	0.5%	1%	3%
2	5.08	7.95	8.45	9.38	7.77	8.97	13.60
4	5.62	9.39	9.84	11.04	9.54	10.80	14.75
6	6.08	10.41	10.86	12.39	10.79	12.35	16.29
8	6.48	11.10	11.61	13.47	11.62	13.66	18.13
10	6.87	11.58	12.18	14.29	12.17	14.77	20.15
12	7.27	11.97	12.65	14.89	12.55	15.75	22.25
14	7.74	12.39	13.11	15.30	12.89	16.63	24.32
16	8.29	12.95	13.66	15.55	13.30	17.47	26.26
18	8.97	13.77	14.39	15.66	13.91	18.32	27.97

The oxidiser particles were lagging behind the flame front of the regressing surface. For the Catocene and Butacene propellants this feature was observed throughout the pressure regime 2 to 10 MPa. Frothy, white areas indicating the presence of gaseous decomposition products from surface/sub-surface reactions were observed widely all over the binder surface, including the interfacial regions around small-sized (20  $\mu\text{m}$ ) AP particles. These features possibly suggest decomposition reactions of the binder taking place on the surface, and such binder pyrolysis could be promoted by the catalyst.<sup>4,15,21</sup> In addition, they may indicate binder/oxidiser reactions occurring along small-sized

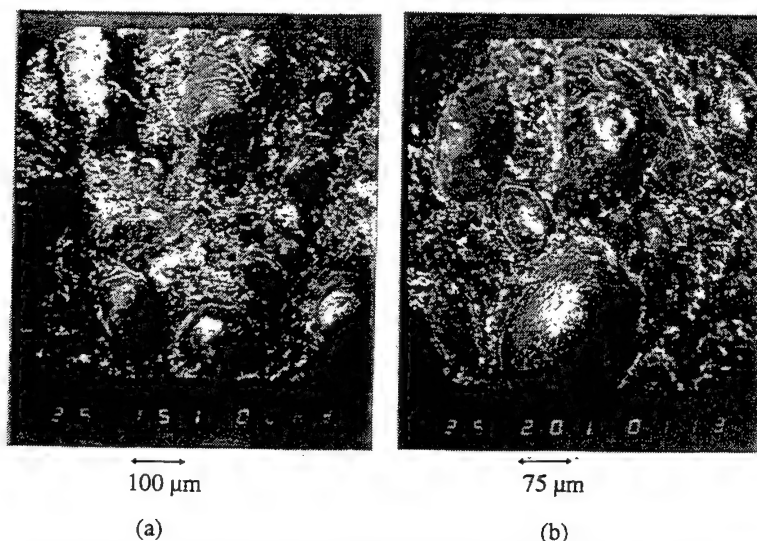


Figure 2. SEM Photographs Showing Undercuttings along the AP Particle Boundary on the Butacene-Containing Propellant Surface (a) Quenched at 2 MPa, and (b) Quenched at 10 MPa

AP/binder interfacial regions. These suggestions are supported by the SEM observation of iron containing particles (from the ferrocenic catalyst) dispersed in the binder phase (see below).

The features on the surface of the Butacene propellants were in sharp contrast with the burning surface of propellants containing carborane-type additives, which had a "rocky, pebbled" appearance, and was covered by a layer of viscous binder melt.<sup>28</sup>

Under high magnification, the SEM photographs (see Figure 3a) of the ferrocenic propellants show aggregations of vigorously reacting iron compounds displaying intensely frothy, white blooming areas. A careful search revealed no evidence of well-defined grape-like structures (see Figure 3b) such as those observed for aluminium in aluminised propellants.<sup>28</sup> X-ray photoelectron spectroscopy of the quenched propellants showed the Fe 2p peak at a binding energy of 712 eV, confirming the existence of iron oxide in the form of Fe<sub>2</sub>O<sub>3</sub> and/or Fe<sub>3</sub>O<sub>4</sub>. Iron oxide catalyst acts as a heat source to increase the propellant burn rates, contrasting to aluminium which acts a heat sink which has the effect of decreasing propellant burn rates.<sup>28</sup>

#### Burn Rate Temperature Sensitivity

The burn rate temperature sensitivity ( $\sigma_p$ , %/°C) for the propellants containing 0.5% Catocene and 0.5% Butacene was determined over the temperature range -20 to 55°C. At 10 MPa, the  $\sigma_p$  value for the 0.5% Catocene propellant and the 0.5% Butacene propellant was 0.17 and 0.15%/°C, respectively. These values represent a reduction of 40 and 35% from the baseline value of 0.23%/°C for the non-catalysed HTPB/AP propellant.

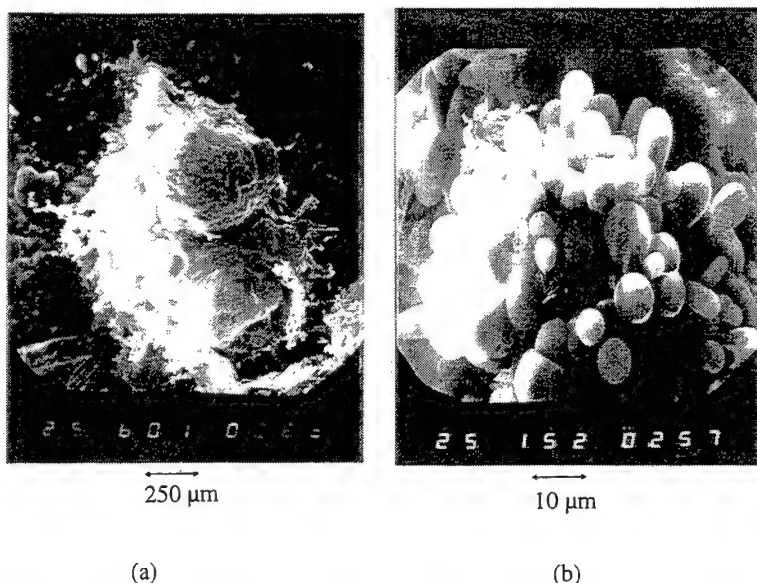


Figure 3. SEM photographs: (a) showing vigorously reacting iron compounds on the propellant (quenched at 3 MPa) containing the ferrocenic catalyst; and (b) showing an aggregate of aluminium oxide particles with cracks on the oxide skin and exudation of molten aluminium metal on an aluminised HTPB/AP propellant quenched at 3 MPa.

## DISCUSSION

### Burn Rate Enhancements

The Butacene propellants display considerably higher burn rates than those of the corresponding Catocene propellants containing the same amounts of iron. Further examination revealed that the effect of 0.5% Butacene is approximately equivalent to that of 1% Catocene in enhancing burn rates.

As noted before, Butacene contains a ferrocenic derivative chemically bonded onto the HTPB polymer backbone.<sup>29</sup> The substantial burn rate augmentation of Butacene propellants compared to Catocene propellants suggests that the ferrocenic catalyst functions more effectively when it is firmly immobilised in the binder. As advised by a reviewer of the paper, for a given iron concentration in the binder the difference in burn rates observed can be attributed at least partly, and probably mostly, to the presence of silicium, a well-known burn rate catalyst in Butacene (one silicon atom for every ferrocene group).

Evidence for the ferrocenic catalysts acting in the binder and the mechanistic sites of the ferrocene catalysis will be discussed in the following sections.

### Active Sites of Ferrocene Catalysis in AP/HTPB Propellant Combustion

In the present study, the combined experimental data give evidence that the potential sites of the ferrocenic catalysts are in the binder, which enhance reactions between the binder HTPB and oxidiser AP at the binder/oxidiser interface, or possibly promote the pyrolysis of the binder. The interfacial reactions and the binder pyrolysis were likely to occur on the surface/sub-surface of the burning propellant. The experimental evidence consists of the following.

- (i) Enhanced burn rates of the Butacene propellants over the Catocene propellants
- (ii) Iron containing particles observed in the HTPB binder of the quenched propellant surface
- (iii) Domed, protruding (sometimes apparently intact) shape of AP particle surface
- (iv) Undercutting along the boundary of surface AP particles.

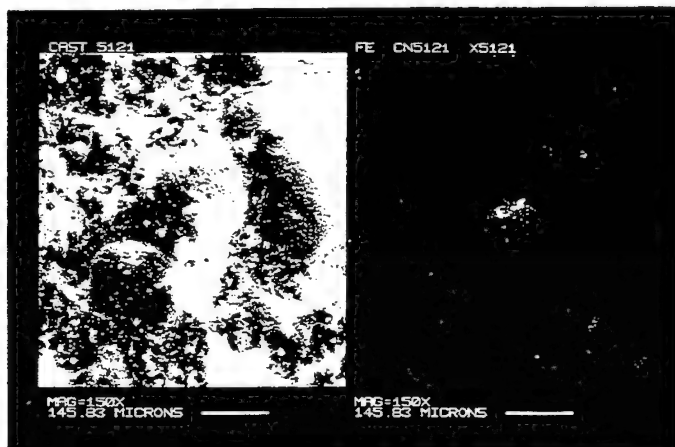
The arguments support the logic that the condensed-phase reaction products readily energise the primary diffusion flame (see later). There was no evidence suggesting that the catalyst acts in the oxidiser to promote surface AP decomposition reactions.

(i) *Enhanced burn rates of Butacene propellants.* Catocene itself is a good burn rate enhancing catalyst, but Butacene promotes even higher burn rates. This clearly indicates the ferrocenic catalyst functions more effectively when it is firmly bonded to the binder. Thus the catalytically active sites are likely to be in the binder.

(ii) *Iron particles observed in the binder.* The SEM X-ray elemental image analysis indicated the presence of iron containing particles dispersed in the binder of the quenched Catocene propellant (see Figure 4). X-ray photoelectron spectroscopy of the same quenched propellant sample confirmed the existence of iron oxide,  $\text{Fe}_2\text{O}_3$  and/or  $\text{Fe}_3\text{O}_4$ .

Oxidation of ferrocene and n-butylferrocene catalysts in burning propellants was found to yield finely divided iron (III) oxide.<sup>30</sup> According to Price and Sambamurthi,<sup>15</sup> iron oxide catalyzes the decomposition of fuel binders to more easily oxidisable forms, thereby bringing the primary diffusion flame closer to the surface and enhancing the burn rates. Using a different type of binder (i.e. PBAN)

in sandwich burning studies, Price<sup>31</sup> also reported concentrations of iron containing residue (from Catocene catalyst) in the binder surface.



(a) (b)  
Figure 4. SEM photographs (a) showing the quenched propellant surface at 2 MPa, and (b) the corresponding X-ray elemental image analysis showing iron particles dispersed in the binder of the same sample.

Further support can be gained from other studies. Wang<sup>32</sup> observed the dispersed iron compound on the burning surface of HTPB/AP propellants and suggested that the iron-containing catalysts serves as a source generating in-situ thermally stable  $\alpha\text{-Fe}_2\text{O}_3$  particles ( $>1000^\circ\text{C}$ ) which eject into the flame as the possible active sites. Lengelle et al.<sup>33</sup> suggested that iron oxide increases propellant burn rates by increasing the heat flux and through direct contact with the binder.

In the present study, all the combined evidence (i.e. enhanced burn rates of Butacene propellants, dispersed iron compounds in the binder phase, and the observed reactivities on the binder surface) indicate that the dominant active sites of the ferrocene catalyst are in the binder, either to enhance the binder pyrolysis,<sup>15,21,33</sup> or to promote binder/oxidiser reactions along the AP/binder interface (see below). Other possible active sites could be in the primary diffusion flame, as Wang<sup>32</sup> suggested above.

(iii) *The domed, convex shape of AP particle surface.* For the Catocene propellants and Butacene propellants, the shape of surface AP particles is domed, and the particles protrude from the propellant regressing surface. The AP was lagging behind the flame front. In some instances, the surface of the AP particles (for both particle sizes 400 and 80  $\mu\text{m}$ ) was domed, and appeared almost intact. However, intense surface reactivities were observed on the binder, particularly along the binder/AP interface, as indicated by white, frothy areas spreading widely on the binder surface (see Figure 5b). There was little evidence of any significant AP surface reactivities.<sup>34</sup>

In sharp contrast, for the propellants without catalyst, the AP particle surface (particle sizes 400 and 80  $\mu\text{m}$ ) was concave (i.e. dish-like), with strong surface reactivities near the middle of the AP particles (see Figure 5a). Yet the burn rates of the catalysed propellant were enhanced over the

propellant containing no catalyst. Thus the ferrocenic catalyst enhances the propellant burn rates, but does not promote surface decomposition reactions of the AP. The catalyst action sites are most likely in the binder, not in the AP.

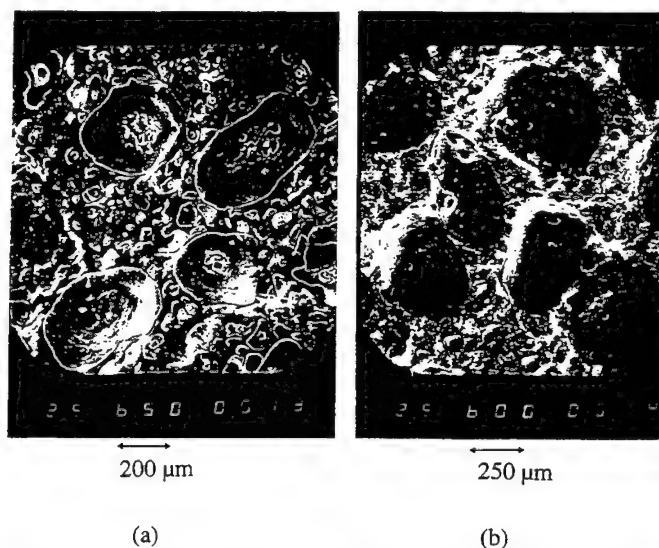


Figure 5. SEM photographs of the propellant quenched at 2 MPa: (a) without catalyst, and (b) containing the Catocene catalyst.

Theoretical calculations by Bilger, Jia, and Nguyen<sup>34</sup> in parallel with the present experiments confirmed that in the Catocene propellant the binder burns faster than the AP particle surface at both low (2 MPa) and high (7 MPa) pressures. Jia and Bilger<sup>35</sup> concluded that it is the diffusion process which has a strong influence on the combustion of mid-sized AP (e.g. 20 and 200  $\mu\text{m}$ ) and HTPB binder, while the combustion of coarse-sized AP (e.g. 400  $\mu\text{m}$ ) simply behaves like monopropellant AP combustion.

(iv) *Undercuttings along the AP particle boundaries.* The present SEM evidence shows undercuttings around the surface AP particles (see Fig 2). The intensity of the undercutting appeared to be pressure dependent, and it was more pronounced at low pressures. This observation has been described previously in both propellant-like sandwich systems,<sup>5,16</sup> and in actual propellants.<sup>12-14, 26,32</sup>

The undercutting is attributed to catalysed AP/binder heterogeneous reactions along the interface, in agreement with more recent studies by Krishnan<sup>12-14</sup> and Wang<sup>32</sup> for similarly catalysed propellant systems. For propellants containing no catalyst, undercutting along the interface and domed AP particles were also observed, but they were interpreted as indicating no interfacial binder/AP reactions.<sup>26</sup>

Using a different type of binder (i.e. PBAN) in propellant-like sandwich burning, Price contended that catalysts, including copper chromite, iron oxide and Catocene, do not promote interfacial binder/oxidiser reactions, nor enhance AP decomposition; but they may catalyse binder pyrolysis because of the observed concentrations of iron oxide residue (from the Catocene catalyst) in the binder laminates.<sup>31</sup> The different experimental conditions employed in the earlier studies (different binders, AP sizes and modes, and AP/binder ratios) would preclude attempts for any valid comparison with the present study.



### Primary Diffusion Flame Control

The evidence presented above suggests that possibly dominant sites for the ferrocenic catalyst are in the binder, not in the AP, to promote the heterogeneous binder/AP reactions along the AP particle boundaries. Such reactions at the interface would catalyse the primary diffusion flame because of the close proximity of the flame to the interface. The final diffusion flame would be too far away from the burning surface, whereas the AP monopropellant flame would be geometrically inaccessible to the catalyst particles.

Another factor enhancing the interaction between the primary diffusion flame and the interfacial binder/oxidiser reaction products is that the shape of the primary flame closes over the binder, flipping across the binder/oxidiser boundary.<sup>36,37</sup> As the combustion reaches a steady state, the AP particle is exposed to a more oxidiser-rich environment, and the primary flame shape will no longer close over the oxidiser crystal as in the case of a fuel-rich environment existing in the initial stage of the combustion.<sup>36</sup> The importance of such configuration of the primary diffusion flame has recently been re-affirmed by Beckstead.<sup>37</sup>

The domed, convex shape of the AP particle surface together with the undercutting along the AP particle boundaries suggest that the dominant heat feedback to the burning surface is from the primary diffusion flame. Most of the heterogeneous reaction products between the binder and the AP would be readily fed into the primary flame. If AP condensed-phase decomposition reactions had been of significance, these reaction products would have energised the AP monopropellant flame directly above the AP particle surface which would have caused<sup>38</sup> the particle surface shape to be recessed at the middle, rather than domed and protruding as consistently observed in the present study.

To rationalise the combined experimental evidence available from the present study, a combustion flame model, based on the original multiple flame model<sup>39</sup>, for the ferrocene-catalysed AP/HTPB propellant combustion is proposed (Figure 6).

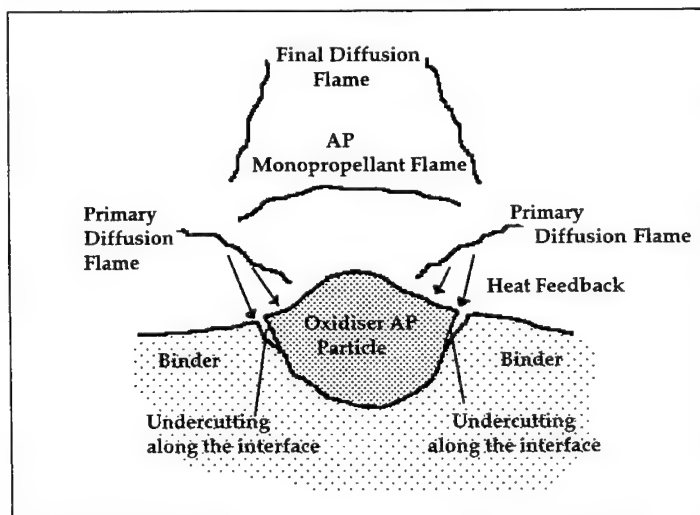


Figure 6. Combustion flame model of the ferrocene-catalysed propellant showing the domed, protruding surface of the AP particle, catalyst-promoted undercuttings along the oxidiser/binder interface, and the primary diffusion flame flipping across the interface.

The present model incorporates a domed AP particle surface, catalyst-promoted undercuttings along the AP/binder interface, and the primary diffusion flame bending across the interface.

In reviewing the mechanisms and models of burn rate temperature sensitivity, Cohen and Flanigan<sup>40</sup> concluded that diffusion flame control is less temperature sensitive than AP flame control. This notion is consistent with the theoretical view that the diffusion process is less temperature sensitive than the kinetic process, bearing in mind that the AP flame is a kinetically limited flame. Diffusion flame control is, therefore, the desirable mechanism for burn rate temperature sensitivity, and this has been borne out in the present study.

### Reduced Burn Rate Temperature Sensitivity

The contention<sup>41</sup> that the ferrocene-catalysed combustion is diffusion flame controlled was supported by the present results on the temperature sensitivity of propellant burn rates. The effect of the added catalysts Catocene and Butacene was to lower the burn rate temperature sensitivity of the HTPB/AP propellant. The lowering of  $\sigma_p$  appeared to be a true reduction and not an artifact associated with a lowering of the pressure exponent,<sup>40</sup> because the pressure exponents of the catalysed propellants were measured to be practically unchanged.<sup>42</sup>

## CONCLUSION

The present study on HTPB/AP propellants containing ferrocenic catalysts has shed new light on the ferrocene-catalysed combustion. The combined experimental evidence suggest that the potentially dominant sites of the catalyst are in the binder, to catalyse the reactions between the binder and oxidiser at the binder/oxidiser interface, or to promote the pyrolysis of the binder itself. There could be, possibly to a much less extent, active sites formed by iron particles ejected into the primary diffusion flame. There is little evidence of the ferrocenic catalyst enhancing the surface decomposition of AP. Under the burning surface conditions, and due to the close proximity of the primary flame to the interface, the combustion is controlled by the primary diffusion flame.

The mechanistic scheme proposed may be specific to the ferrocenic catalyst or at least iron-containing catalysts, and further studies are warranted for other metal-containing additives.

### Acknowledgments

The technical assistance of Peter Berry, of the DSTO Weapons Systems Division, in processing the propellants, operating the interrupt bomb, and in data reduction is acknowledged. Graham Fowler, of the DSTO Land, Space, and Optoelectronic Division, is thanked for collecting the SEM and related data. The US Naval Air Warfare Centre, China Lake is thanked for donation of the Catocene sample.

## REFERENCES

1. Kishore, K., and Sunitha, M.R., Effect of Transition Metal Oxides on Decomposition and Deflagration of Composite Solid Propellant Systems: A Survey, *AIAA Journal*, 17, 1118-1125, 1979.

2. Beckstead, M.W., A Model for Solid Propellant Combustion, *The 18th Symposium (International) on Combustion*, The Combustion Institute, Pittsburgh, 175-185, 1981.
3. Kishore, K., A Comprehensive View on the Combustion Models of Composite Propellants, *AIAA Journal*, 17, 1216-1224, 1979.
4. Kishore, K. and Gayathri, V., Chemistry of Ignition and Combustion of Ammonium Perchlorate Based Propellants, in: "*Fundamentals of Solid Propellant Combustion*", edited by Kuo, K.K. and Summerfield, M., AIAA, New York, 90, 53, 1984.
5. Cohen, N.S., Fleming, R.W., and Derr, R.L., Role of Binders in Solid Propellant Combustion, *AIAA Journal*, 2, 212-218, 1974.
6. Cohen, N.S., Review of Composite Propellant Burn Rate Modelling, *AIAA Journal*, 18, 277-293, 1980.
7. Rastogi, R.P., Singh, G., and Singh, R.R., Burn Rate Catalysis for Composite Propellants, *Combust. Flame*, 30, 117-124, 1977.
8. Pittman, C.U., Action of Burn Rates Catalysts in Composite Propellant Combustion, *AIAA Journal*, 7, 328-334, 1969.
9. Burnside, C.H., Correlation of Ferric Oxide Surface Area and Propellant Burning Rates, *AIAA Paper* 75-234, 1975.
10. Pearson, G.S., The Role of Catalysts in Ignition and Combustion of Solid Propellants, *J. Combust. Sci. Tech.* 3, 155-163, 1971.
11. Bakhman, N.N., Nikiforov, V.S., Avdyunin, V.I., Fogelzang, A.E., and Kichin, Y.S., Catalysed Burn Rate of Ammonium Perchlorate and Polymethylmethacrylate Mixture, *J. Catalysis*, 35, 383-389, 1974.
12. Krishnan, S., and Periasamy, C., Low Pressure Burning of Catalysed Composite Propellants", *AIAA Journal*, 24, 1670-1675, 1986.
13. Krishnan, S. and Jeenu, R., Subatmospheric Burning Characteristics of AP/CTPB Composite Propellants with Burning Rate Modifiers, *Combust. Flame*, 80, 1-6, 1990.
14. Krishnan, S., and Jeenu, R., Combustion Characteristics of AP/HTPB Propellants with Burn Rate Modifiers, *J. Propulsion and Power*, 8, 748-755, 1992.
15. Price, E.W. and Sambamurthi, J.K., Mechanism of Burn Rate Enhancement by Ferric Oxide, CPIA Publication 412, Chemical Propulsion Information Agency, John Hopkins University, Baltimore, Vol 1, 1984.
16. Hightower, J.D. and Price, E.W., Experimental Studies Relating to the Combustion Mechanism of Composite Propellants, *Astronaut. Acta*, 14, 11-21, 1968.
17. Kishore, K., Pai Veneker, V.R., Chaturvedi, B.K., and Gayathri, V., Mechanistic Studies of Composite Propellants, *AIAA Journal*, 15, 114-116, 1977.
18. Kishore, K., Pai Veneker, V.R. and Gayathri, B.K., Reaction Intermediates during Combustion of Some Model Solid Rocket Fuels, *Fuel*, 60, 164-167, 1981.
19. Sammons, G.D., Studies of Thermal Behaviour of Solid Propellants by Differential Scanning Calorimetry, *Analytical Chem.*, 305-311, 1968.
20. Fong, C.F. and Hamshire, B.L., Mechanism of Burn Rate Catalysis in Composite Propellant Combustion, *Combust. Flame*, 65, 61-69, 1986.
21. Nadaud, L., Models used at ONERA to Interpret Combustion Phenomenon in Heterogeneous Propellants, *Combust. Flame*, 12, 177-195, 1968.
22. Jones, H.E. and Strahle, W.C., Effects of Copper Chromite and Iron Oxide Catalysts in AP/CTPB Sandwich, *The 14th Symposium (International) on Combustion*, The Combustion Institute, Pittsburgh, 1287-1295, 1972.
23. Inami, S.H., Rajapakse, Saw, R., and Wise, H., Solid Propellant Kinetics: Part I. The Ammonium Perchlorate Copper Chromite Fuel System, *Combust. Flame*, 17, 189-196, 1971.
24. Nguyen, T.T., Burn Rate Temperature Sensitivity of Solid Rocket Propellants: An Overview of Current Status of Experimental Results, *Defence Science and Technology*

- Organisation (DSTO) Materials Research Laboratory, Technical Report No. MRL-TR-92-5, Australia, 1992.
25. Boggs, T.L., Crump, J.E., Krateutle, K.J., and Zurn, D.E., Cinephotomicrography and Scanning Electron Microscopy as used to Study Solid Propellant Combustion, in: *Experimental Diagnostics in Combustion of Solids*, AIAA, New York, Vol 63, pp. 20-48, 1978.
  26. Boggs, T.L., Derr, R.L., and Beckstead, M.W., Surface Structure of Ammonium Perchlorate Composite Propellants, *AIAA Journal*, 8, 370-372, 1970.
  27. Boggs, T.L., Zurn, D.E., Cordes, H.F., and Covino, J., Combustion of Ammonium Perchlorate and Inorganic Additives, *J. Propulsion Power*, 4, 27-40, 1988.
  28. Nguyen, T.T., The Effect of Ferrocenic and Carborane Derivative Burn Rate Enhancing Catalysts in AP-Composite Propellant Combustion: Mechanism of Ferrocene-Catalysed Combustion, Defence Science and Technology Organisation (DSTO), Technical Report DSTO-TR-121, Australia, 1994.
  29. Finck, B., and Mondet, J.C., Combustion of Solid Composite Propellants Using a Ferrocene Derivative Grafted in the Binder, *The 19th International Annual Conference of ICT*, 72.1-72.13, 1988.
  30. Flanigan, D.A., Analysis of AP Propellants Combustion Catalysed with NBF: A Limiting Case, Air Force Rocket Propulsion Laboratory Technical Report AFRPL-TR-67-18, 1967.
  31. Price, E.W., Review of Sandwich Burning, *30th JANNAF Combustion Meeting*, CPIA Publication No. 606, Vol II, 1993.
  32. Wang, S.Y., Wang, S.S., Liu, F., and Chiu, H.S., An Investigation of Catalysis in the Combustion of Iron Catalysed Composite propellants, *The 19th International Annual Conference of ICT*, 8.1-8.14, 1988.
  33. Lengelle G., Brulard, J., and Moutet, H., Combustion Mechanism of Composite Solid Propellants, *The 16th Symp (International) on Combustion*, 1257-1269, 1976.
  34. Bilger, R.W., Jia, X., and Nguyen, T.T., Theoretical and Experimental Study of Composite Solid Propellant Combustion. *J. Combust. Sci. Technology*, 115, 1-39, 1996.
  35. Jia, X. and Bilger, R.W., The Burke-Schumann Diffusion Flame with Zero Net Flux Boundary Conditions, *J. Combust. Sci. Technology*, 99, 371-376, 1994.
  36. Beckstead, M.W., Description of the Separate Surface Temperature Model for Solid Propellant Combustion, in : *Ballistic Control of Solid Propellants. Vol III.*, Air Force Rocket Propulsion Laboratory Technical Report No. AFRPL-TR-81-58, 1982.
  37. Beckstead, M.W., Solid Propellant Combustion Mechanisms and Flame Structures, *Pure & Applied Chemistry*, 65, 297-307, 1993.
  38. Quinn Brewster, M., Heat Transfer in Heterogeneous Propellant Combustion Systems, in: *Annual Review of Heat Transfer*, 4, 287-330, 1992.
  39. Beckstead, M.W., Derr, R.L., and Price, C.F., A Model for Composite Solid Propellant Combustion Based on Multiple Flame, *AIAA Journal*, Vol. 8, pp. 2200-2207, 1970.
  40. Cohen, N. and Flanigan, D.A., Mechanisms and Models of Solid Propellant Burn Rate Temperature Sensitivity: A Review, *AIAA Journal*, 23, 1538-1547, 1985.
  41. Beckstead, M.W., and Cohen, N., Temperature and Pressure Sensitivity of Composite Propellants", *7th JANNAF Combustion Meeting*, CPIA Publication 204, 2, 75-84, 1971.
  42. Nguyen, T.T., Reduced Burn Rate Temperature Sensitivity of Advanced Solid Rocket Propellants Containing Ferrocenic Catalysts, Defence Science and Technology Organisation (DSTO), Technical Report DSTO-TR-181, Australia, 1996.

## EXPERIMENTAL STUDIES OF ALUMINUM AGGLOMERATION IN SOLID ROCKET MOTORS

By J. DUTERQUE

Energetics Department ONERA - FRANCE

**ABSTRACT:** In a solid propellant containing an inert binder (polybutadiene), an oxidizer (ammonium perchlorate) and aluminum (15/ 20%), Al is introduced during the propellant formulation as single particles, the median diameter of which is typically between 5 and 40 microns. During the propellant combustion, some of the aluminum particles leave the combustion surface without agglomeration, while others coalesce and give globules, with diameters very different from the initial particle sizes. The relative proportions of unagglomerated particles and globules are poorly known.

The diameter and the mass fraction of large globules which leave the combustion surface immediately govern the Al combustion time and the diameter and mass fraction of the large  $Al_2O_3$  caps. Understanding of this last point is essential for large motors because these residues are liable to form  $Al_2O_3$  slag which accumulates at the motor aft end.

The experimental set-up is a pressurizable bomb (<10 MPa). The sample combustion surface is filmed with a high speed camera ( $\approx 2000$  f/s). Film utilization allows the determination of Al globule diameters just before ignition. For a classical composite propellant, a median value of 125  $\mu m$  was found, the combustion pressure being 4 MPa. By modifying some parameters (propellant formulation, combustion pressure), some factors able to modify the globule size were determined.

### NOMENCLATURE:

$A_o, A_i$ : aluminum agglomeration mass fraction ( mass of agglomerated Al/ mass of total Al)  
D: particle diameter ( $\mu m$ )  
 $d_p$ : thermal diffusivity ( $mm^2/s$ )  
f: mass fraction  
paG: large AP particles  
paF: fine AP particles  
 $R_b$ : propellant burning rate ( $mm/s$ )  
T: temperature (K)  
 $T_{react}$ : residence time(s)  
 $\rho$ : mass volumic ( $mg/mm^3$ )

### INTRODUCTION

Many large solid rocket motors use aluminized propellants and submerged nozzles. The positive effect is to increase energetic performance (aluminum combustion allows an increase in combustion temperature and the submerged nozzle improves the loading factor of the motor). The negative effect is slag formation at the motor aft end. Recently, M. Salita<sup>1</sup> has reviewed the problems related to the slag generation. Most of the liquid and gaseous combustion products are swept along by the flow stream and are ejected through the nozzle throat, but a part of the liquid residues (alumina droplets) are trapped behind the submerged nozzle. This entrapment occurs by impingement on the backface of the nozzle or by capture in a recirculation zone (Figure 1). Slag reduces motor performance and has been postulated to cause excessive erosion of aft-dome insulation. Also, a surprising dispersion of slag weight has occurred in many motors. For example, the measured slag weight for statically fired Space Shuttle Boosters (High Performance Motor version ) varied between 426 and 1407 kg. One of the important factors liable to act upon the entrapment of the droplets is the droplet diameter, because, in

a two phase flow, the large particles do not follow the stream lines. Any attempt to reduce the slag mass needs control of the alumina particle size.

In a solid propellant containing an inert binder (polybutadiene), an oxidizer (ammonium perchlorate) and aluminum (15/ 20%), Al is introduced during the propellant formulation as single-size particles, the median diameter of which is typically between 5 and 40 microns. During the propellant combustion, some of part of the aluminum particles leaves the combustion surface without agglomerating, the others one coalesce and give globules, with diameters very different from the initial particle sizes. The relative proportions of unagglomerated particles and globules are poorly known. After ignition, Al burns in the gas phase and the combustion time is strongly dependent on the initial diameter ( $D^2$  law). The condensed products of Al combustion are mostly alumina which is found with a bimodal repartition <sup>2-6</sup>. The first mode consists of sub or micronic  $Al_2O_3$  produced by the gas phase combustion of Al. The second one (40/60  $\mu m$ ) comes from the  $Al_2O_3$  protecting layer around the Al particles. This layer melts at the ignition time to give a cap attached to the globule surface. The cap size increases during agglomeration or combustion. A sketch of these processes is presented in Figure 2.

The repartitions given in the literature ( a survey of recent  $Al_2O_3$  droplet data is given in Reference 3) between large and fine alumina particles are not coherent. There is a strong dependence on the experimental set up. For propellant sample tests (quench bomb<sup>6</sup>), the results give a majority (70 - 80%) of fine particles ( $< 5\mu m$ ). The median diameter of large particles is between 40 and 50  $\mu m$ . With a dry bomb, Blomshield<sup>5</sup> gets about the same percentage of fine particles, but he finds an intermediary class at 20-25  $\mu m$  and the median diameter of large particles is about 100  $\mu m$ . Results obtained in micromotor tests are also scattered. Reference (2) gives 90% of large particles compared to 10% in Reference (4).

In order to evaluate these different results, it seems necessary to have a good knowledge of the aluminum globule size repartition just after they leave the combustion surface and just before ignition. Moreover, the comprehension of the agglomeration mechanism would be useful in order to decrease the mean globule size.

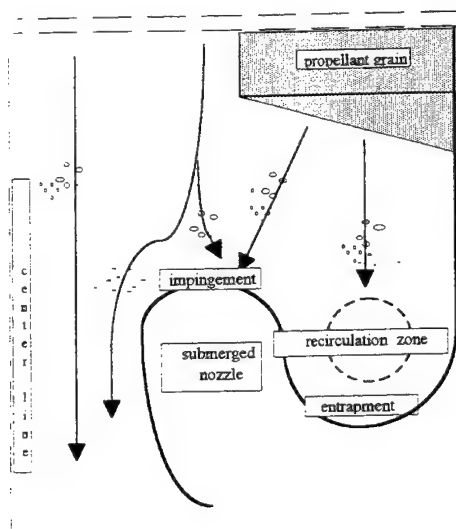


Figure 1. Scenario of slag accumulation

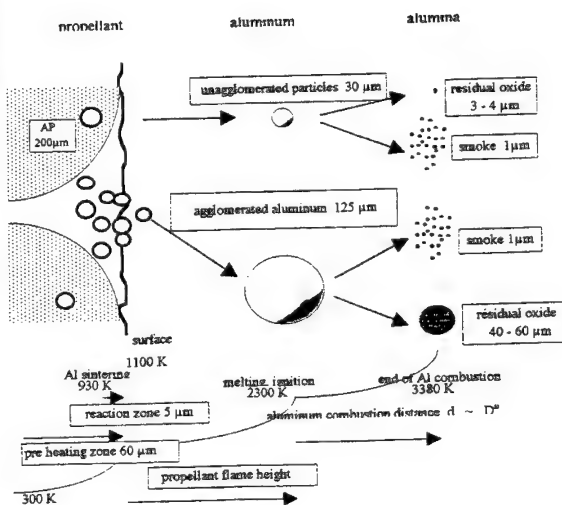


Figure 2. Scheme of Al agglomeration and Al combustion

## BACKGROUND

### Agglomeration Fraction

During propellant combustion, some aluminum particles emerge from the surface and enter into the gas phase at their original size (parent particles), while others will agglomerate into a much larger size. The main points are firstly, the mass fraction of agglomerated aluminum  $A_o$  and secondly, the size distribution of agglomerated aluminum.

Concerning the first point Beckstead<sup>7</sup> and Cohen<sup>8</sup> suggested two correlations based on experimental results. In the two cases, the data base<sup>9</sup> was the same (AP/Al/HTPB propellant). The main parameter was the ratio between fine and large AP particles ( $f_{paF} / f_{paG}$ ). The total AP mass fraction ( $f_{paT}$ ) was 70%. For some tests, combustion pressure and aluminum size were modified; aluminum mass fraction was 18%.

Beckstead's correlation

$$A_o = .0005 D_{paG} D_{Al}^{.25} \frac{1 + 30 \frac{f_{paF}}{f_{paG}}}{1 + 80 \left( \frac{f_{paF}}{f_{paG}} \right)^2}$$

Cohen's correlation:

$$A1 = \frac{f_{paF}}{f_{paT}} ((.38 \ln D_{paG} - 1.61) \frac{D_{paF}}{40} - .96 - \ln D_{paG} + 4.13)$$

$$A_o = A1 + .479 \ln D_{paG} + \frac{D_{paF}}{100} (2.01 - .48 \ln D_{paG}) - 1.964$$

Cohen suggested a more complex equation, because he believes that important effects of AP fine particles are not taken into account by Beckstead's correlation. Moreover he provided correction formulas for pressure and aluminum size variations.

As the propellant used in the two cases contained the same Al mass fraction, this factor does not enter in the correlations.

If we apply these correlations to different propellant compositions (Table 1), we note very strong differences depending on the propellant composition:

- $A_o$  is more dependent on the mass ratio of fine particles than their sizes,
- $A_o$  depends on the large AP particle sizes,
- for high  $A_o$  there is no difference between the two correlations,
- for low  $A_o$ , Beckstead's results are lower than Cohen's, but probably, experimental results of Reference 9 are not sufficiently precise to discriminate between the two correlations.

**Table 1**  
A<sub>o</sub> as function of the Propellant Compositions

Propellant	Shuttle <sup>(4)</sup>	Aerojet <sup>(9)</sup>			French Comp. 904118	French Comp. MY9406
binder	14%	12%			12%	12%
Aluminum	16% (23 μm)	18% (23 μm)			18% (30 μm)	18% (15 μm)
AP	200 μm 48.8%	200 μm	64%	47%	200 μm (58%)	100 μm (50%)
	30 μm 20.8%	6 μm	6%	23%	10 μm (10%)	10 μm (18%)
test pressure (MPa)	3.6	4.42			4	3
burning rate (mm/s)	8.8	Unknown			7	8.4
A <sub>o</sub> (Cohen)	25%		49%	24%	45%	17%
A <sub>o</sub> (Beckstead)	17%		46%	17%	42%	10%

One point of interest in these results is to emphasize the importance of the composition on the mass agglomeration fraction and probably on the slag mass. For propellants with approximately the same global AP mass fraction, it is possible to modify A<sub>o</sub>, just by modifying the ratio AP<sub>F</sub>/AP<sub>G</sub> and/or the AP<sub>G</sub> size.

In parallel with the empirical correlation, Cohen <sup>10</sup> has developed an analytical model (pocket model) to obtain A<sub>o</sub>. It is assumed that the large AP particles are regularly distributed in the propellant. The pockets formed between these particles are filled with binder, fine AP particles and aluminum (see fig. 2). Cohen defines as many free volumes (enclosed in each other) as there are large AP particles size modes. The diameter of the smallest volume obtained is the diameter of the cluster as long as the AP particle is notably bigger than that of the aluminum. These are aluminum particles, enclosed in a pocket, which are involved in the agglomeration process. By knowing the propellant composition and the different particle sizes, it is easy to determine the aluminum mass contained in each free volume defined by AP particles. It is hypothesized that the fraction agglomerated is proportional to the amount of aluminum that melts within an effective pocket.

To determine the melted fraction, Cohen supposes that in each pocket Al particles fall according to a certain distribution (possibly different from the propellant distribution). The basic idea is that, during the surface regression, Al particles go across the thermal profile established in the binder. Because there is a temperature gradient between binder and charges, the particles reach the binder temperature after a certain time. This time, proportional to the square diameter, has to compare with the residence time of the particle (function of the burning rate). From this comparison, Cohen determines a melting critical diameter. All aluminum particles below this diameter melt; unmelted particles leave the surface without agglomeration. The problem, according to Cohen, is that the aluminum size distribution in the pocket is unknown. This is why he does not compare the model with experimental results.



## Aluminum Size Distribution

A number of different analytical models<sup>11-13</sup> have been proposed to determine the Al agglomeration process and the Al globule size in composite propellants. A review is given in Reference 14. All these models start from the original idea, which is that the aluminum particles are enclosed in pockets formed by the coarse AP particles. The models differ mainly in the choice of fusion criterion, but they tend towards the same results. The decrease in globule sizes is given by:

- the increase in AP mass fraction, the fine AP diameter, fine AP/large AP ratio,
- the decrease in large AP diameter,
- the increase in burning rate.

The only conflict, between the models, is the effect of aluminum initial diameter.

Unfortunately, these models are rarely compared with usable experimental results; perhaps, it is difficult to get valuable data to define the temperature criterion? This is why, in the codes where the globule sizes are necessary, empirical correlations are used (Table 2).

**Table 2**  
Aluminum Agglomeration Correlations

D (microns), $R_b$ (mm/s)			
author	correlation	propellant	comments
Hermesen (15)	$D = \frac{907.43}{R_b f_{AP}}$	AP 400-200-8 $\mu\text{m}$ 68% PBAN binder 16%	f : mass fraction of total AP experimental data
Liu (16)	$D = \frac{118.8}{R_b f_{AP}^2} - 146.5$	AP 400-200-90-15 $\mu\text{m}$ RDX 10-50-15 $\mu\text{m}$ PBHT binder - Al 6 $\mu\text{m}$	f : mass fraction of total AP
Salita (3)	$D = \frac{869}{R_b f^2}$	shuttle propellant table 1	f : mass fraction of Al + AP experimental data

These correlations take into account the burning rate, but only make use of experimental results without physical interpretation. None of these three formulas consider the aluminum concentration. Using the geometric bases of the pocket model, ONERA tried to consider these two points (influence of the burning rate and Al concentration). Some tests were carried out with propellants 904118 and MY 9406 (Table 1). As the agglomeration process is a surface phenomenon (just below and just above), it is probably independent of the gas flow field in the motor, except perhaps in erosive conditions, so it is believed that sample tests are representative.

## EXPERIMENTAL RESULTS

### Experimental Set-up

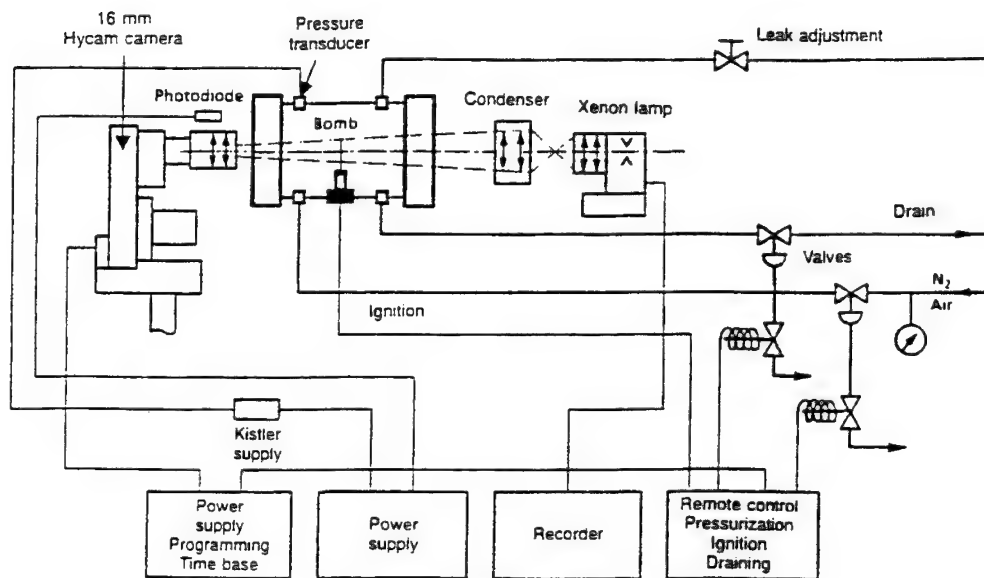


Fig. 3 - Visualization setup.

The test set-up (Fig. 3) is a pressurizable chamber with pressure control up to 10 MPa and specially designed for visualisations. A small sample of propellant ( $5 \times 5 \times 0.8$  mm) is placed on a support and ignited by a hot wire. The combustion surface is filmed with a high speed camera (1000 to 5000 f/s); this camera can be fitted with a normal or a microscopic objective lens. The exposure time can be varied down to as little as  $2 \cdot 10^{-6}$  s. The film exploitation allows one to count and to measure the aluminum globules just before ignition. For each test between 50 and 80 particles were counted. As the depth of the optical field is narrow, not the total of the globules were counted. Moreover, the resolution of the optical device does not permit distinguishing particles under  $20\text{--}30$   $\mu\text{m}$ . This set-up allows one to get the size distribution but not the agglomeration fraction ( $A_0$ ). So, by modifying the sample holder the particles are quenched in an alcoholic bath just after they leave the combustion surface. During a test, the distance of the combustion surface to the bath varied from 4 to 8 mm. After that, particles were studied by scanning electronic microscopy. For a few tests, a size distribution was measured with a Malvern granulometer.

### Results

In Figure 4, globule size distributions for different test pressures (0.2-4 MPa) are presented. Evolution of the median number diameter with the pressure is clearly seen. In fact, as the propellant

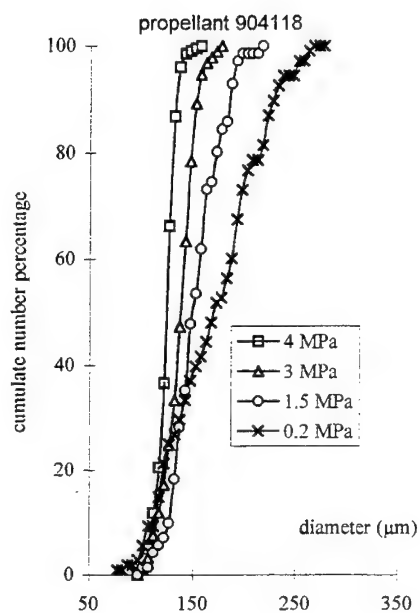


Figure 4. Pressure Influence on Globule Size

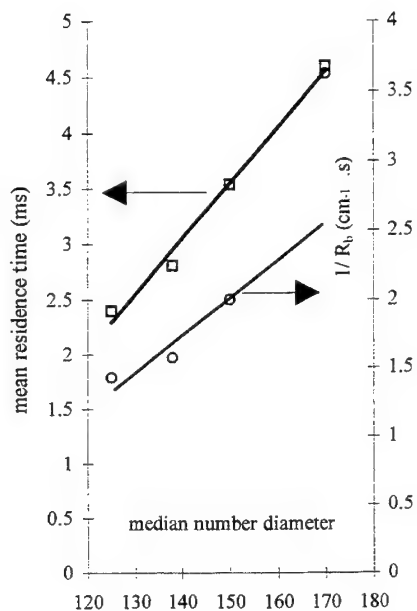


Figure 5. Comparative Evolution of Globule Diameter with the Residence Time and b.rate

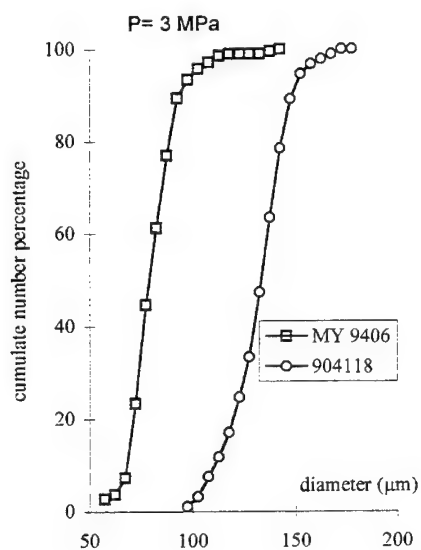


Figure 6. Formulation Influence on Globule Size

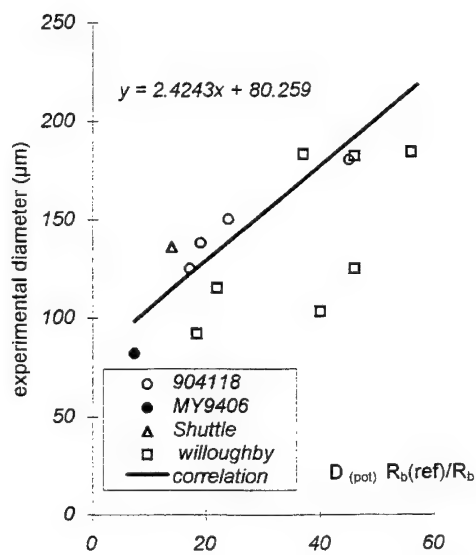


Figure 7. Measurement Correlation

was the same (904118), it is purely the burning rate effect on the globule size. One point of interest is that distribution heterogeneity increases as the burning rate diminishes. Another point is that, except for the lowest pressure, the minimal diameter (about 100  $\mu\text{m}$ ) is independent of the pressure (for all pressures, more than 90% of globules have a diameter above 110 $\mu\text{m}$ ).

We have also measured the residence time of the agglomerates at the surface (time between the appearance of aluminum particles and the melting process). There are noticeable dispersions in the measurements, but a true evolution with the burning rate is observed. In Figure 5, it is seen that the globule diameter is proportional to the residence time and, except for the lowest burning rates, approximately inversely proportional to the burning rate. Results are recapitulated in Table 3.

For another propellant (MY 9406), where the sizes and the fine/large AP particles ratio were modified, results (Figure 6) give a mean diameter notably smaller (80  $\mu\text{m}$  - 3MPa - 8.5 mm/s).

This set of results was interpreted by using the geometric conditions of the pocket model. Aluminum particles (with binder and fine AP particles) are included in the free volumes between large AP particles. Knowing the propellant formulation, it is possible to compute the mass of aluminum included in each pocket (details of this computation are given in Reference 14).

**Table 3**  
904118 propellant

test pressure (MPa)	burning rate (cm/s)	globule median diameter ( $\mu\text{m}$ )	mean residence time (ms)	dispersion (ms)
4	0.7	125	2.4	1 - 5
3	0.635	138	2.81	1 - 5
1.5	0.5	150	3.54	1 - 5
0.2	0.27	170	4.6	1 - 10

From this mass, we determine a potential diameter of the agglomerate:

$$D_{pot} = \left( \frac{f_{AP} \rho_{pa}}{f_{paG} \rho_{Al}} \right)^{\frac{1}{3}} D_{paG} \quad (1)$$

We have correlated the results of Table 3 with this potential diameter and, taking into account the experimental burning rate effect, we obtain (Figure 7):

$$D = 2.42 D_{pot} \frac{R_{br}}{R_b} + 80.26 \quad (2)$$

In this equation D is in microns and the burning rate in mm/s. The reference burning rate (to homogenize the equation) is 1 mm/s.

Other available results<sup>(4,17)</sup> are plotted on the same figure. Shuttle and MY 9406 propellants are in good agreement with the correlation, Willoughby's results are more dispersed, but the tendency remains very correct. The two most dispersed values correspond to a propellant containing very large AP particles (400 $\mu\text{m}$ ).

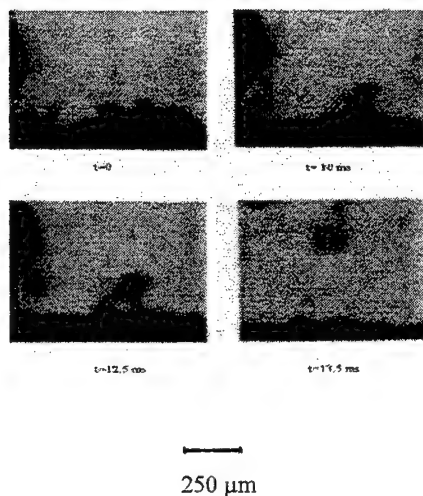


Figure 8. Globule Formation (0.2 MPa)

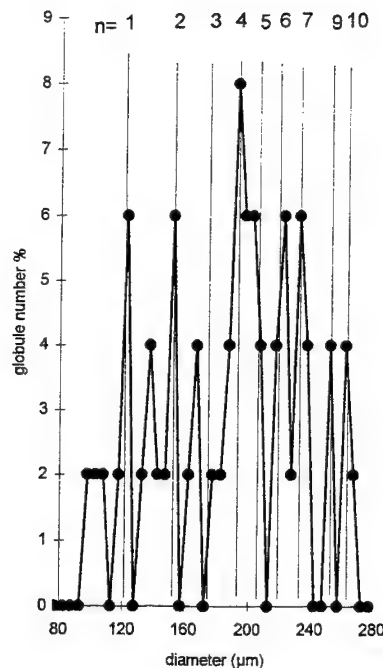


Figure 9 Correlation Between Exp. Diameters and Computed Diameters (from n pockets connection)

The film study shows (Figure 8) that the agglomerates are trapped on the surface during a few milliseconds (Table 3). This time must be compared with the residence time of Al particles in the subsurface zone. For a regressing propellant, the condensed phase processes have been described by Lengellé<sup>18</sup>. The thermal profile is given by:

$$\frac{T - T_o}{T_s - T_o} = \exp \left( -\frac{x R_b}{d_p} \right) \quad (3)$$

and the associated residence time is

$$\tau_{\text{res}} = \frac{x}{R_b} \quad (4)$$

Between surface temperature ( $T_s \sim 1200$  K) and initial temperature ( $T_o$ ), two characteristic temperatures have to be considered: the aluminum melting temperature (933 K) and the binder temperature degradation, the latter depending on the activation energy of the condensed phase degradation. With the data of Reference 18, we find that the residence time of aluminum between 933 and the surface is less than one millisecond (to be compared with the 4 or 5 ms at the surface). This time period is just sufficient to produce a softening of binder and aluminum particles which become sintered together (Price<sup>19</sup>). The main coalescence into one globule happens between the regression surface and the gas flame, (Figure 8).

Al particles contained in a pocket volume are the basic unit of agglomerates. When one

agglomerate arrives at the surface, a lapse of time is necessary to reach ignition. As the initial Al particle is always embedded in a protective alumina layer, the ignition temperature is probably close to 2300K. One argument in favor of this temperature is given by the comparison between the results of a gas phase temperature profile computation, in tests conditions, and the agglomerate melting distance. To reach 2300 K, computation gives about 150  $\mu\text{m}$ ; the measured distance (Figure 8) is comprised between 150 -200  $\mu\text{m}$ .

The surface residence time will depend on surface temperature, burning rate and also on the gas phase temperature profile. If this time is long, there is an increasing probability for the few elementary agglomerates to merge together and form a bigger globule. In Figure 9, we have correlated the experimental number diameter distribution with a computed diameter defined as being that of an aluminum globule resulting from the connection between "n pockets". We have obtained a good correlation between computed values and the most important distribution peaks. This test was specially chosen because the burning rate was very low (0.3 cm/s at 0.2 MPa), so the residence time was long.

The last studied point was the agglomeration fraction ( $A_0$ ) by quenching the agglomerates in an alcoholic bath. The distance of the combustion surface to the bath was comprised between 4 to 8 mm, corresponding to a combustion time below 2 ms. An example of the collected particles is shown in Figure 10. The spherical shape taken by the liquid globule during combustion (Figure 11) has been preserved by the quench. A few globules are superficially cracked (probably because of the strong thermal gradient); the number of exploded globules increases with pressure. On many globules the residual alumina lobe can be seen; this lobe is specially visible in Figure 11. If we examine the residues with strong magnification, micronics spherical particles are often visible on the surface of large particles. This is why it is difficult to determine a size distribution from SEM photography. Three tests (904118 propellant, 4 Mpa) were analyzed with a laser granulometer. The three tests give, in volume,  $20 \pm 2\%$  of fine particules (0.05 - 5  $\mu\text{m}$ ). Knowing that initial aluminum has a distribution between 5 and 100  $\mu\text{m}$ , we postulate that the fine ones are combustion products (alumina). If we correct this distribution by the different specific masses, we obtain an aluminum

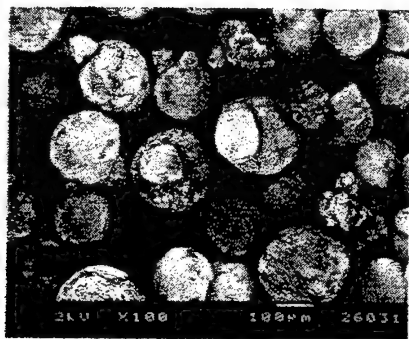
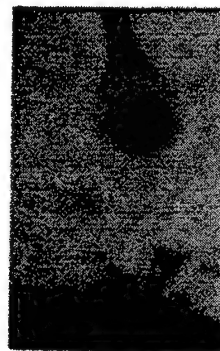


Figure 10. Quenched Globule (1.5 Mpa)



500  $\mu\text{m}$

Figure 11. 0.2 MPa  
Alumina Cap Visualisation

combustion ratio of about 15%. For the particles above  $5\mu\text{m}$ , we observe two distribution modes ( $\approx 20$  and  $100\text{--}200\mu\text{m}$ ). The first one was supposed to contain mainly initial aluminum ( $5\text{--}80\mu\text{m}$ ) and the second one ( $> 80\mu\text{m}$ ) to contain agglomerates. The repartition between these two modes has been evaluated (as the two modes are not separated, it is just an estimation). The three tests give respectively for  $A_0$ : 36, 36 and 51%. These values are comparable (for the same propellant) with the correlations of Table 1. In the same way, an estimation of the number median diameter of the  $100\text{--}200\mu\text{m}$  mode gives  $115\mu\text{m}$ , to be compared with the  $125\mu\text{m}$  measured during the combustion (we have taken into account, the specific mass differences due to the temperature differences).

More information can be obtained from the SEM and film pictures, relative to the residual alumina lobe. As shown by Fig. 2, there are two main size modes for the alumina residus ( $\approx 1$  and  $40\text{--}60\mu\text{m}$ ). The first one is a direct product of the Al vapor phase combustion, the second one comes from the initial  $\text{Al}_2\text{O}_3$  protective layer around the Al particle. The layer thickness depends on Al manufacture conditions, but it is rather low (a few nanometers). If we adopt a mean value ( $5\text{ nm}$ ), it is possible to determine the mass of alumina (and so, the diameter of a spherical residue) contained in an Al agglomerate (itself formed by the coalescence of some initial particles). For a  $125\mu\text{m}$  agglomerate we find  $\approx 15\mu\text{m}$  for the  $\text{Al}_2\text{O}_3$  residue. This value is notably lower than experimental results.<sup>(2-6)</sup> Law<sup>20</sup> supposes that, during combustion, a part of the fine particles retrodiffuses from the gas phase to the surface. But another possibility is that, during the agglomeration process, a part of the Al is oxidized through a solid-gas reaction. There are two arguments to support this hypothesis. The first one is that aluminum, trapped at the surface during a few milliseconds, is in a very oxidizing environment (combustion beginning); the second one is the strong thermal gradient around the agglomerate. So, because the strong difference between dilatation coefficients of Al and  $\text{Al}_2\text{O}_3$ , there is a constant renewal of the aluminum surface favoring new oxidation. In these conditions, the alumina cap size of aluminum globules, quenched close to the surface (before notable combustion), must be sensibly larger than the initial  $15\mu\text{m}$ . From the pictures of Fig. 10 and 11, it is possible to estimate the alumina cap size, by supposing the cap is the emergent part of a two sphere intersection. We find values comprised between  $30$  and  $70\mu\text{m}$ . These measurements are not very precise, but, in our opinion, sufficient to think that oxide cap formation is mainly achieved during agglomeration process, rather than during combustion.

The final objective is to know the mass fraction of large alumina residues able to generate slags. From results of this study, it is possible to give an estimation of this mass fraction. With the following assumptions:

Each large Al globule gives an alumina cap, the final diameter of which is  $60\mu\text{m}$ ;

The mean diameter of large agglomerated Al globules is  $125\mu\text{m}$ ;

The mass fraction of agglomerated aluminum is 40%;

the mass fraction of large  $\text{Al}_2\text{O}_3$  residues ( $60\mu\text{m}$ ) is about 5%. This estimation is in agreement with experimental results (dry bomb), given by Salita.<sup>3</sup>

## CONCLUSIONS

From a set of experimental results, it is possible to propose a physical interpretation of Al agglomeration process in solid propellant combustion. The size of Al globules depends on the AP size particles, AP mass fraction (especially fine AP-large AP ratio) and also on the propellant burning rate. This parameter acts by modifying the surface temperature and the gas phase profile temperature, which modifies the surface residence time of Al agglomerates. Some work is still necessary to "model" these interferences, but a correlation, grouping propellant formulation and burning rate, is proposed. Another result is that the formation of large ( $30\text{--}70\mu\text{m}$ ) alumina particles is mainly achieved at the combustion surface during agglomeration process. This point must be taken into account in aluminum combustion models. Finally, first results give an Al agglomeration fraction around 40%. This value is in agreement with correlations proposed by Beckstead and Cohen.

### Acknowledgment

This work was supported under Centre National d'Études Spatiales (CNES) contract.

We would like to thank the Dr Guy Lengellé for his particularly useful advice and D. Lambert for his important contribution in experimental work.

### References

- [1] Salita M., "Deficiencies and Requirements in Modeling of Slag Generation in Solid Rocket Motors", *Journal of Propulsion and Power*, Vol 11, N° 1, 1995.
- [2] Traineau J.C., Kuentzmann P., Prevost M., Tarrin P., Delfour A., "Particle Size Distribution in a Subscale Motor for the Ariane 5 Solid Rocket Booster", *AIAA Paper 92-3049*, 1992.
- [3] Salita M., "Survey of Recent  $Al_2O_3$  Droplet Size Data in Solid Rocket Chambers, Nozzles and Plumes", *31<sup>th</sup> JANNAF Combustion Meeting*, 1994.
- [4] Laredo D., McCrorie J.D., Vaughn J.K., Netzer D.W., "Motor and Plume Particle Size Measurements in Solid Micromotors", *J.P.P.*, Vol. 10, n° 3, 1994.
- [5] Blomshield F.S., Kraeutle K.J., Stalnaker R.A., "Shuttle RSRM Aluminum Oxide Investigations", *31<sup>th</sup> JANNAF Combustion Meeting*, 1994.
- [6] Braithwaite P.C., Christensen W.N., Daugherty V., "Quench bomb investigation of aluminum oxide formation from solid rocket propellants, (Part 1), *25<sup>th</sup> JANNAF Combustion Meeting*, 1988.
- [7] Beckstead M.W., "A Model for Solid Propellant Combustion", *14<sup>th</sup> JANNAF Combustion Meeting*, 1977.
- [8] Cohen N.S., Strand L.D., "A Model for the Burning Rate of Composite Propellants", *17<sup>eme</sup> JANNAF Combustion Meeting, CPIA Publication 329, Vol. 1*, 1980.
- [9] Micheli P.L., Schmidt W.G., "Behavior of Aluminum in Solid Rocket Motors", *AFRPL-TR-77-29, Aerojet Solid Propulsion Co., Sacramento, CA*, 1977.
- [10] Cohen N.S., "A Pocket Model for Aluminum Agglomeration in Composite Propellants", *AIAA Journal*, Vol 21 N° 5, 1983.
- [11] Grigorev V.G. and al., "Experimental Investigation of the Agglomeration of the Aluminum Particles in Burning Condensed Systems", *Fizika Gorenia i Vzryva*, vol 17 n° 4, 1981.
- [12] Leiji J., Shuffen Lo, "A Sponge model for Aluminum Agglomeration in Composite Propellant", *39<sup>th</sup> Congress of the International Astronautical Federation, Bangalore, India*, 1988.
- [13] Sambamurthi J.K. and al., "Aluminum Agglomeration in Solid Propellant Combustion", *AIAA Journal*, vol. 22 n° 8, 1984.
- [14] Duterque J., Hommel J., "Étude de l'agglomération et de la combustion de l'aluminium dans les propergols solides", *La Recherche Aérospatiale* n° 4, 1993.
- [15] Hermesen R. W., "Aluminum Combustion Efficiency in Solid Rocket Motors", *AIAA paper 81-0038*, 1981.
- [16] Liu t., Perng H., Luh S., Liu F., "Aluminum Agglomeration in an AP/RDX/Al/HPTB Propellant Combustion", *AIAA Paper 91-1870*, 1991.
- [17] Willoughby P. G., Baker K.L., Hermesen R.W., "Photographic Study of Solid Propellant Burning in an Acceleration Environment", *13<sup>th</sup> Symposium (Inter.) on Combustion, Pittsburgh*, 1981.
- [18] Lengellé G., Duterque J., Godon J.C. and Trubert J.F., "La combustion des propergols solides", *AGARD Lectures Series* n° 180, 1991.
- [19] Price E.W., "Combustion of Metalized Propellants", in *Fundamental of Solid-Propellant Combustion*, edited by Kuo K.K. and Summerfield M., Vol 90, AIAA Inc., pp. 479-513, 1984.
- [20] Law C.K., "A Simplified Theoretical Model for the Vapor Phase Combustion of Metal Particles", *Combustion Sciences and Technology*, Vol7, pp. 197-21, 1973.



## COMMENTS

Carlos Schuller, INTA, Spain. Do you think that the efficiency of combustion of high aluminum content composite propellants depends upon the initial particle size of the aluminum powder? If so, is small particle size aluminum better than large particle size in achieving better performance in ballistics?

Author's Reply. Al combustion efficiency depends on the ratio between aluminum combustion time and residence time of Al particles in the motor. Therefore, combustion efficiency is dependent more upon the large Al globules (about 100  $\mu\text{m}$ ) than the initial Al particle size (10-30  $\mu\text{m}$ ).

The size of the large Al globules depends upon the size of large AP particles and upon the AP and Al mass fraction. Perhaps the agglomeration fraction ( $A_o$  in the paper) depends upon the original aluminum particle size (smaller sizes favoring a larger dispersion out of the pockets during propellant formulation). This point has not been verified.

Frederick Tepper, Argonide Corporation, Pittsburgh, PA, U.S.A. The particle size of aluminum does appear to affect agglomeration, at least if the powder is sub-micron. As I reported yesterday, the aluminum described exotherms at about 400 °C and reacts in the solid phase, and little aluminum is left to agglomerate in the gas phase. Also, the sub-micron alumina particles are less likely to impact the wall of the rocket and accumulate as slag.

## POLYNIMMO, A CANDIDATE BINDER FOR SOLID FUEL GAS GENERATOR PROPELLANTS.

P J Honey, D W Anderson, G A Spinks, A V Cunliffe, D A Tod

WX4 Department, Defence Research Agency, Fort Halstead, Sevenoaks, Kent, TN14 7BP, England.

**ABSTRACT:** An investigation of polyNIMMO's potential, as both binder and oxidiser, in a high energy smokeless solid fuel gas generator propellant comprised part of a UK ramrocket development programme. The benchmark trial showed polyNIMMO's burn rate was considerably lower than GAP, or polyGLYN. The advantages and disadvantages of various binary mixtures of polyNIMMO with fuels, oxidisers, plasticisers and burn rate catalysts are discussed. The conclusions drawn from this study were applied to multiple component polyNIMMO formulations, with volumetric heat values of up to  $32200 \text{ MJ/m}^3$  ( $\sim 500 \text{ Btu/in}^3$ ). Difficulties with ignitability of fuel-rich systems were observed. Comparison of the chamber temperature (which varied, significantly, with pressure) with the burn rate proved to be a more suitable method for assessment of ignitability than the formulations temperature of ignition. The relationship observed between the calculated chamber temperature and experimental burn rate will be discussed in greater detail. This work has shown that the smokeless fuel-rich polyNIMMO gas generator compositions examined possess the basic characteristics required for an air-breathing radial-burner motor configuration. Effort is currently focused on achieving a smokeless fuel-rich formulation ( $\approx 32200 \text{ MJ/m}^3$ ) possessing a high pressure exponent ( $\sim 0.5-0.7$ ) with a slow, stable, burn rate ( $\sim 0.7 \text{ mm/s}$ ) at low pressure ( $< 3 \text{ MPa}$ ).

## INTRODUCTION

Research programmes are being undertaken in various countries on air-breathing rocket motors (ramjets), focusing on both both liquid fuelled ramjet and solid fuel ducted rocket (ramrocket) systems. A number of the requirements for a solid fuel gas generator for a ramrocket are: minimum signature, fuel richness ( $\geq 32200 \text{ MJ/m}^3$ ), tailorable gas delivery, insensitivity and high burn rates. To achieve these targets the propellants have mainly been designed around two basic configurations, (i) GAP/Carbon and (ii) HTPB/AP. The GAP/Carbon composition fulfils all requirements whilst the AP formulations tend to be reduced smoke. To achieve minimum signature for HTPB composite propellants the oxidiser AN would be needed - the resultant burn rates would be either too slow, or too fast, for, respectively, end-burner or radial-burner configurations.

The authors would like to thank V Carroll and J Campey for the temperatures of ignition and B Kelso, A Ross, R Jeffrey, E McLaughlin, I Sharp and G Bruce of DRA Bishopton for the strand burning results.

© - British Crown Copyright, 1996/DERA. Published with the permission of the Controller of Her Britannic Majesty's Stationery Office.

The Defence Research Agency are undertaking a five year technology research programme for the development of an appropriate UK ramrocket technology base. Part of this programme was the investigation into the potential of using polyNIMMO in a high energy smokeless solid fuel gas generator propellant. PolyNIMMO's potential is in the dual role of both binder and oxidiser, thus reducing the need for high percentages of oxidisers (which defeats the high energy requirement). A systematic study of the strand burn rates of binary mixtures of four types of additives was undertaken to provide a baseline picture of this potential. The additives were various hydrocarbon fuels, oxidisers, plasticisers and burn rate catalysts. The research was then expanded to investigate tertiary, quaternary and other multi-component systems (to produce a performance matched (32200 MJ/m<sup>3</sup>) composition). The results could also, hopefully, be used to prioritise the effects of specific additives. The strand burn rates of binary, tertiary and other multiple component systems are presented below.

Initially the data generated from these experiments were intended to address only the effect on burn rates, however, with the large quantity produced other aspects of fuel rich gas generator propellants were studied. Difficulties with ignition and sustainable burning of some formulations, mainly the very fuel-rich systems, were observed. A study of the temperatures of ignition showed that similar formulations followed a pattern but significant variations in composition did not seem to fit any specific relationship. The burn rates for various formulations compared well with oxygen balance but could not be related to sustainability as the oxygen balance did not vary with pressure. Theoretical chamber temperatures were calculated from the compositions thermochemistry and were seen to vary, significantly, with pressure for these oxidiser deficient formulations. Comparison with the burn rate data, for numerous compositions, provided a better method for the assessment of formulation ignitability. The simple relationship observed between the calculated chamber temperature and experimental burn rate will be discussed in greater detail.

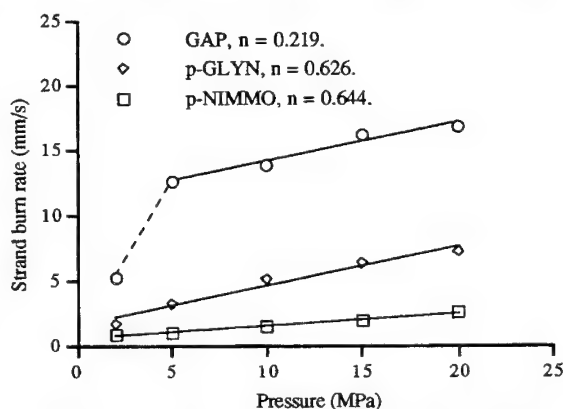
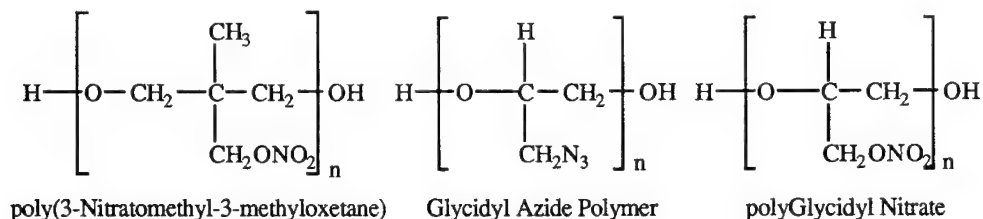


Figure 1. Burn rates of various energetic binders

## BINDERS

Strand (5 x 150 mm, d x l) firings<sup>1</sup> of N100 cured polyNIMMO provided the benchmark for comparison with those from the binary mixtures. Although polyNIMMO has a similar volumetric heat value (denoted here as 'Oe') as GAP (Oe = 24353 MJ/m<sup>3</sup> (378 Btu/in<sup>3</sup>) and Oe = 25193 MJ/m<sup>3</sup> (391 Btu/in<sup>3</sup>) respectively) the difference in chemical structure (see below) results in vastly different burn rates (Figure 1). However, polyNIMMO's advantage is that stable burning can be achieved at low pressures ( $\leq 2$ MPa). PolyGLYN's burn rates were approximately three times higher than for polyNIMMO but this advantage is traded-off through the reduction in energy (Oe = 17685 MJ/m<sup>3</sup>, 275 Btu/in<sup>3</sup>). Having determined the baseline burn rate of polyNIMMO binder a series of investigations into the various additives was undertaken.



## FUELS

The fuels chosen (polyStyrene, polyEthylene, poly- $\alpha$ -MethylStyrene (PAMS), HTPB and Carbon Black) would impart to polyNIMMO the extra energy desired but without compromising the smokeless requirement. The purpose was to determine the advantages/disadvantages of each fuel, with respect to percentage composition, by observing its effect on the burn rate. Thus a selection of w/w percentages were manufactured from available materials and, where necessary, milled to reduce the particle size. The results of the strand burn rate trials for the fuels are presented in Figures 2-6. PolyStyrene filled polyNIMMO showed a significant decrease in burn rate but sustained burning even at 25% loading. This was superior to both polyEthylene and PAMS which failed to sustain burning partially or completely. HTPB filled polyNIMMO showed notable reduction in burn rate and was sustainable at quite high loading's and low pressures. The carbon black selected (Raven 22, mono-modal ~62 nm) did not seem to affect the burn rate at low loading's however, the maximum was about 22 w/w% before the composition became too stiff to work. Bimodal carbon black could be used to achieve higher filling volumes/energy but unsustainable burning at the higher levels studied proved disadvantageous. At 15% loading PAMS and polyStyrene degraded the burn rate the least with HTPB showing the greatest abatement. At the higher loading's the order remained the same except the PAMS formulations ignited but failed to sustain burning (at all pressures). That ignition could be achieved suggested that something was snuffing-out the burning process and was later identified as being caused by the small particle size (<30 $\mu$ m) of the milled fuel. Thus, PAMS loaded polyNIMMO would continue to be investigated but the particle size/burn rate problem would have to be overcome.

## OXIDISERS

To reduce the hazards when formulating the composition only ammonium nitrate and ammonium perchlorate oxidisers

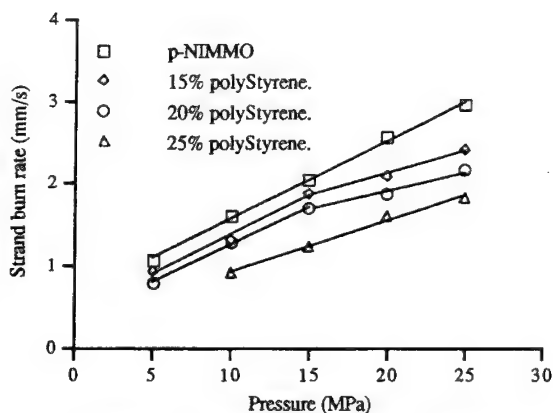


Figure 2. PolyStyrene filled polyNIMMO

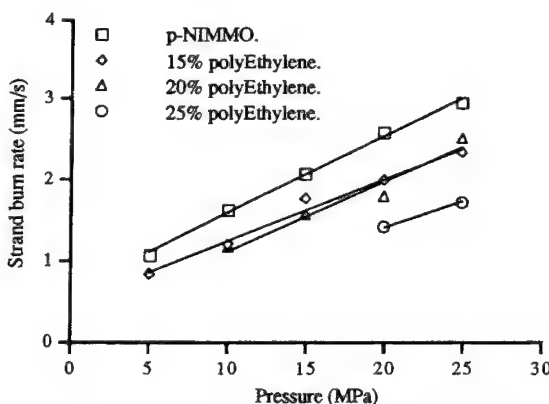


Figure 3. PolyEthylene filled polyNIMMO

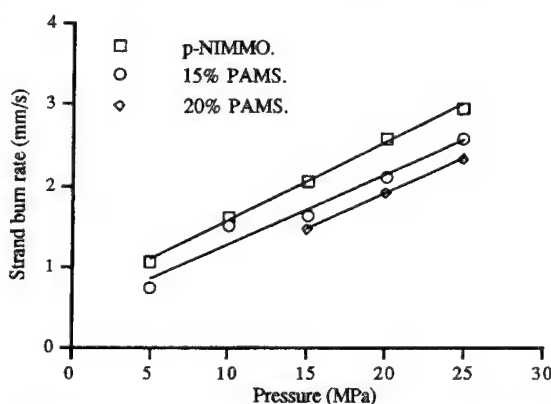


Figure 4. Poly- $\alpha$ -MethylStyrene filled polyNIMMO

were examined. Whilst HMX, or RDX, are higher in energy they are unlikely to provide sufficient additional advantage over ammonium perchlorate, or ammonium nitrate, at the projected low level being used. Whilst the colder burning ammonium nitrate conforms to the smokeless requirement ammonium perchlorate would result in a certain amount of smoke. However, at the percentage level envisaged in the final composition, for a target  $O_e$  of  $32200 \text{ MJ/m}^3$ , the propellant would be, at worst, reduced smoke. The increase in burn rate for multi-modal ammonium nitrate filled polyNIMMO showed (Figure 7) a steady progression for the 10 and 15% loading's with the 20% formulation displaying rates only slightly higher than the 15% filled sample. The multi-modal ammonium perchlorate formulations (Figure 8) differed inasmuch that the major change occurred between 0 and 5% with a steady progression up to 15%. No explanation can be offered but it is thought that a size change, from the multi-modal form added, to a smaller form is occurring in the curing polyNIMMO binder. Assuming the two oxidisers exhibit different solubility's they would thus show different burn rate characteristics, as they do. For 15% ammonium perchlorate filled polyNIMMO reducing the AP particle size gave the expected increase in burn rate, with micronised ( $2\text{-}3\mu\text{m}$ ) exhibiting (Figure 9) the fastest burn rate.<sup>2</sup>

## PLASTICISERS

The mechanical properties of cured polyNIMMO binder are such that a plasticiser would be needed to achieve a serviceable low glass transition temperature. A selection of energetic plasticisers are available, some having similar, or greater,  $O_e$ 's as polyNIMMO, which would help fulfil the high energy requirement. The strand burn rates (Figure 10) for various 5% plasticiser loaded samples show only minor increases compared to that of the baseline polyNIMMO binder rate. MEN42 plasticiser (ICI) showed the greatest increase but its lower energy makes the higher energy K10 plasticiser (Royal Ordnance) more attractive. The low 5% loading was only used to enable comparison of the different plasticisers and much higher loading's would be required to achieve the low glass transition temperature required for defence applications.

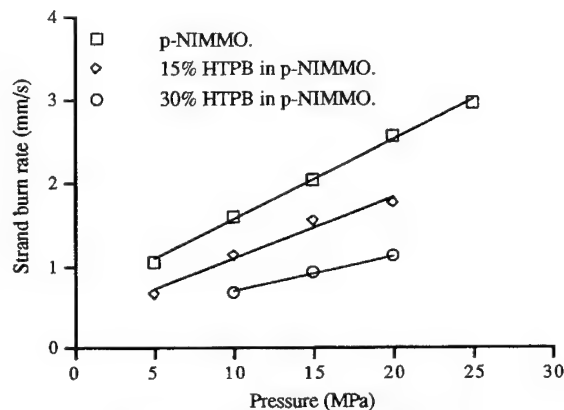


Figure 5. HTPB filled p-NIMMO

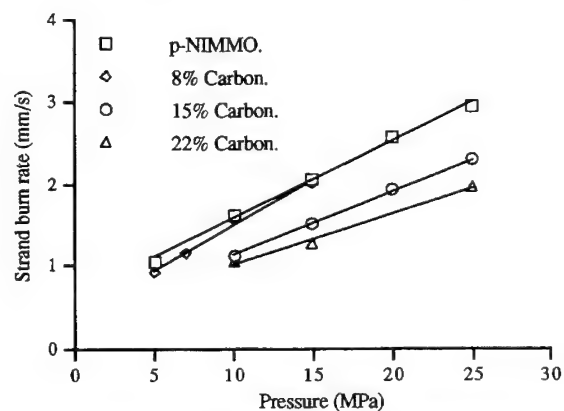


Figure 6. Carbon black filled polyNIMMO

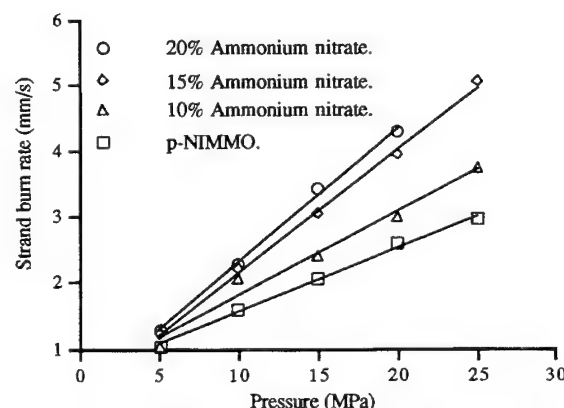


Figure 7. Ammonium nitrate filled polyNIMMO

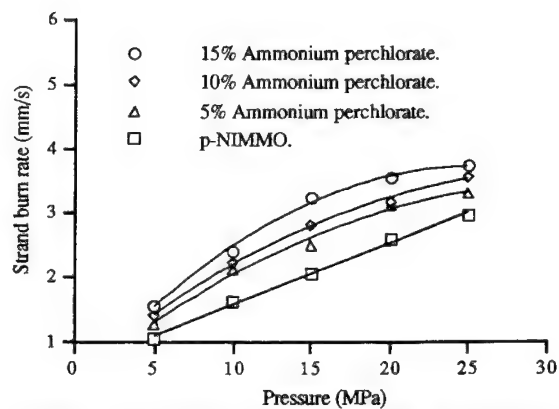


Figure 8. Ammonium perchlorate filled polyNIMMO

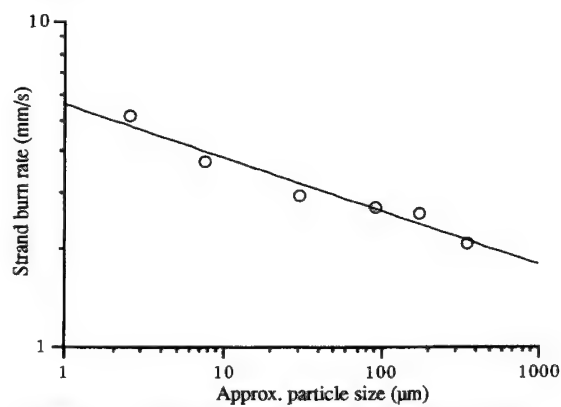


Figure 9. Effect of AP size on burn rate (10 MPa)

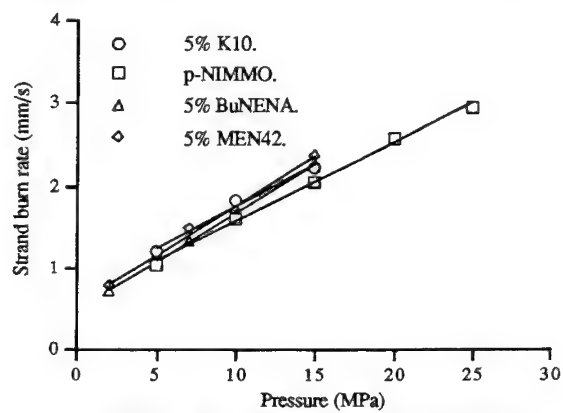


Figure 10. Plasticiser filled polyNIMMO

## BURN RATE CATALYSTS

The addition of burn rate catalysts were investigated for two reasons; (i) the potential increase in burn rate provided, and (ii) the potential stabilisation of burning at low pressures. Some of the catalysts would however have the disadvantage of increasing the smokiness. The effect of the burn rate catalysts are shown in Figure 11. At 15MPa pressure the 2% basic copper chromate samples showed the largest increase in burn rate with catocene exhibiting the next best enhancement; the remaining catalysts examined providing little, if any, improvement in burn rate. At 5MPa pressure all the catalysts failed to improve the polyNIMMO burn rate significantly which suggested that the combustion process was not being altered by the catalyst. Thus, the first aspect has been proven, albeit at higher pressures only. PolyNIMMO binder burns stably at 2MPa and hence examination of the effect of catalytic burning stabilisation needed a poor-burning fuel filled composition. Figure 12 shows the effect of basic copper chromate and catocene on the burn rate of 25% polyEthylene filled polyNIMMO, which had shown non-sustainable burning below 20MPa. Catocene showed a greater improvement in both burn rate and pressure range performance than basic copper chromate, the converse of that observed for the binary mixture. However, catocene caused this 25% polyEthylene filled polyNIMMO mixture to degrade (by cracking) after only three weeks at room temperature. No such degradation has, to date, been observed for the basic copper chromate formulation. Stabilisation of low pressure burning has been achieved for fuel filled polyNIMMO through using burn rate catalysts, however catocene caused unacceptable degradation of the physical properties.

## MULTIPLE COMPONENT FORMULATIONS

The effect of additives as binary mixtures with polyNIMMO on the burn rate have been studied. Experience with HTPB composite propellants indicated that there would be no simple translation of these effects to multiple component formulations. The catalyst/polyEthylene/ polyNIMMO work above suggested that polyNIMMO bound gas generator propellants were going to be no different. Using this work as a starting point for increasing the number of components the effect, on the burn rate, of adding plasticiser to a polyEthylene/catalyst system was studied (Figure 13).

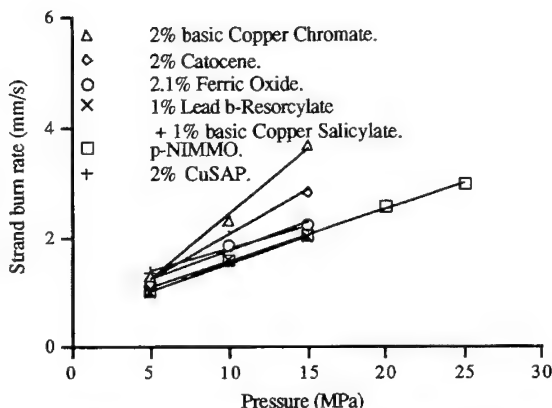


Figure 11. Burn rate catalyst filled polyNIMMO

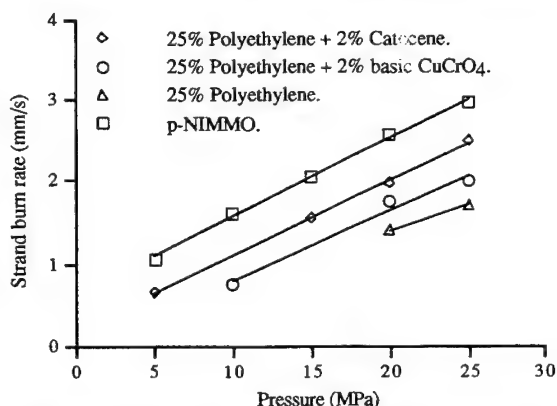


Figure 12. 25 w/w% Polyethylene (plus additives)

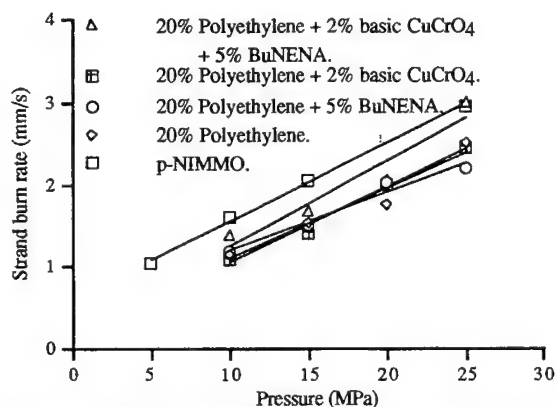


Figure 13. 20 w/w% PolyEthylene (plus additives)

As expected the 5% BuNENA plasticised polyEthylene/ polyNIMMO system showed little effect on the burn rate compared to the base 20% polyEthylene formulation (28700 MJ/m<sup>3</sup>). The basic copper chromate composition also exhibited little change, which was not as expected, but when both catalyst and plasticiser were added a significant enhancement in burn rate was observed, suggesting a potential synergy. However, the increase in burn rate caused by the catalyst and plasticiser was not enough to overcome the abatement caused by the polyEthylene fuel.

The next step was to prepare compositions of similar energy to the binary polyEthylene composition but using oxidiser (ammonium perchlorate), rather than catalysts, to provide the burn rate enhancement. The polyEthylene based mixed fuel system examined (Figure 14) showed that a high level of oxidiser (to balance high fuel loading) provided lower enhancements than the higher plasticiser loaded formulations. These compositions had better burn rates than polyNIMMO (but not as high as desired) and considerably better than equivalent energy binary fuel/polyNIMMO formulations, although at lower pressures some suffered non-sustainable burning. Replacement of polyEthylene with carbon black in an effort to formulate a performance matched ammonium perchlorate composition (i.e. 32200 MJ/m<sup>3</sup>) showed (Figure 15) that absence of plasticiser and higher fuel loading resulted in a dramatic abatement of burn rates, compared to the previous series of formulations. The pressure exponent had also decreased, from that experienced in all the previous compositions, and was assumed to have resulted from ammonium perchlorate dominating the combustion process. Enhanced burn rates have been achieved for K10/ammonium perchlorate formulations in median energy systems. The disadvantages of low burn rates and lack of a high pressure exponent for the performance matched ammonium perchlorate formulations suggests that ammonium nitrate may offer benefits.

The initial stage in investigating ammonium nitrate multiple component formulations was examination of improved oxygen balances, for various fuel filled polyNIMMO compositions, with Oe's in the 24100-27100 MJ/m<sup>3</sup> range. Predetermined concentrations of ammonium nitrate were added to

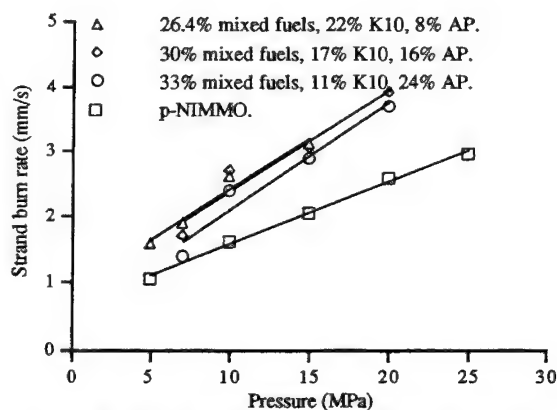


Figure 14. Mixed fuels (polyEthylene)/AP/K10

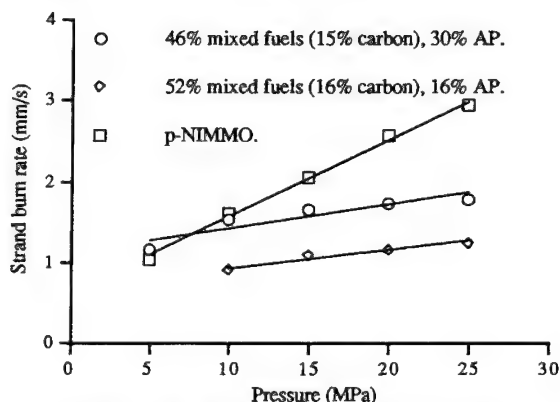


Figure 15. Mixed fuels (carbon black)/AP

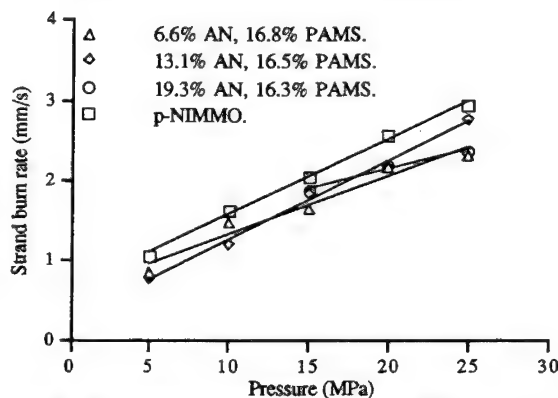


Figure 16. Effect of AN on PAMS based comps.



~15w/w% PAMS, polyStyrene and HTPB filled polyNIMMO formulations to give oxygen balances between the 15% fuel loading and polyNIMMO.

Figures 16 to 18 show the effects the ammonium nitrate had on the burn rate. Adding approximately 7% of ammonium nitrate to the PAMS composition had virtually no effect on the burn rate (compared to the binary 15% PAMS formulation, Figure 4). The poor continuity of the burn rates from the ~13% and ~19% loadings probably relates to a combination of effects (e.g. PAMS and ammonium nitrate particle size, ammonium nitrate colder burning nature). The ~15% polyStyrene series, unlike PAMS, showed a consistent degradation in burn rate and sustainability across the pressure range examined. However increasing oxygen balance resulted in a converse order to that expected, i.e. the highest loading (~19%) exhibiting the poorest performance and *visa versa*. The ~15% binary polyStyrene mixture displayed a burn rate between the ~7 and ~13% ammonium nitrate loaded compositions indicating that poorer oxygen balances are not directly related to burn rate. Although burn rates between the binary HTPB/polyNIMMO mixture and polyNIMMO were displayed by the ~15% HTPB/ammonium nitrate series, the amount of change between the ammonium nitrate levels was not very high. Also, the continuity in burn rate abatement seen for polyStyrene was not observed and excepting any experimental error the same size change seen for the binary ammonium nitrate/polyNIMMO formulations is the most probable explanation. Instead of prioritising the different fuels this work has shown that other properties (e.g. particle size) have a greater effect on the burn rate. Also polyNIMMO bound gas generator propellants are unlikely to burn fast enough for an end-burner configuration when ammonium nitrate oxidiser is used.

The emphasis thus changed from trying to achieve faster burn rates for an end-burner configuration to investigating suitable options for an ammonium nitrate filled radial-burning performance matched propellant composition. A high carbon black/fuel loaded (Oe ~32600 MJ/m<sup>2</sup>) ammonium nitrate

formulation (Figure 19) exhibited a sustainable burn rate of 0.86 mm/s at 5MPa but the pressure exponent was approximately half that required. The addition of basic copper chromate and BuNENA gave slightly increased burn rates, but failed to improve the pressure exponent. Attempts to recover the

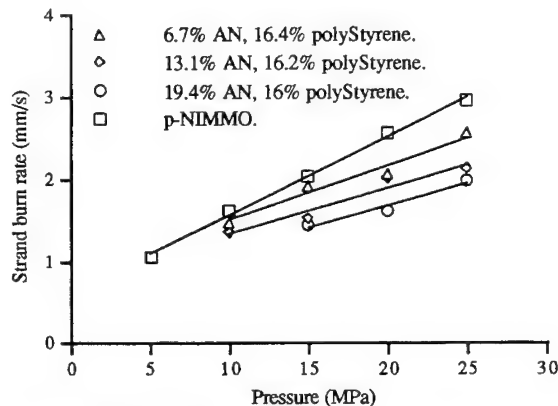


Figure 17. Effect of AN on p-Styrene based comps.

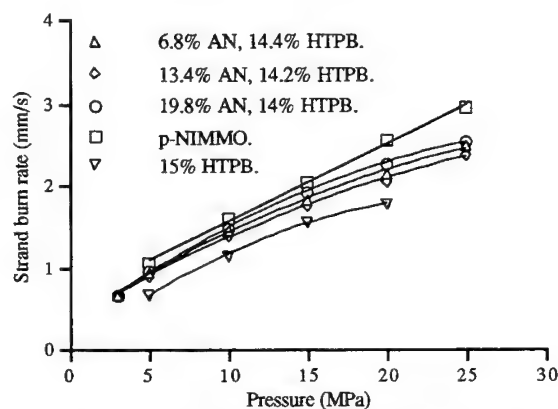


Figure 18. Effect of AN on HTPB based comps.

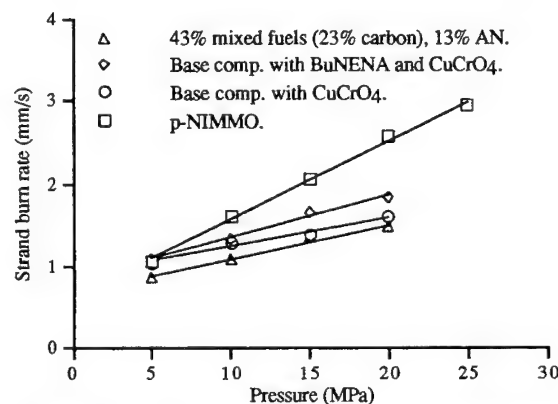


Figure 19. Performance matched AN compositions

pressure exponent along with other requirements for lower carbon black and higher plasticiser levels prompted two new series of experiments.

Replacement of some ammonium nitrate with K10 and carbon black with PAMS produced performance matched compositions which showed (Figure 20) better pressure exponents (0.5-0.6) without degrading the sustainable burn rate (at 5MPa). A similar concentration set of samples, but with polyStyrene replacing the PAMS, displayed (Figure 21) similar burn rate performances. These smokeless fuel-rich formulations ( $O_e \approx 32200 \text{ MJ/m}^3$ ) possess slow, stable, burn rates ( $\sim 0.8 \text{ mm/s}$ ) at low pressure (5MPa) with acceptable pressure exponents which fulfil the basic requirements for a radial-burner motor configuration. This work obviously needs to be developed further if compositions at larger grain sizes with similar properties are required to be formulated. Sustainable slower burn rates at lower pressures are desired but problems experienced so far suggest this may be very difficult to achieve.

## DATA MODELLING

Initially the data generated from these experiments were intended to address only the effect on burn rates, however, with the large quantity produced other aspects of fuel rich gas generator propellants were studied. Difficulties with ignition and sustainable burning of some formulations, mainly the very fuel-rich systems, were observed. A study of the temperatures of ignition was hoped would provide a reasoned explanation. Some of the performance matched compositions examined showed that similar formulations followed a pattern but significant variations in composition did not seem to fit any specific relationship (Figure 22). Comparison of the strand burn rates, for a variety of compositions, with their oxygen balance (weight oxygen required to combust 1kg of propellant) gave a reasonable relationship (Figure 23). The formulations oxygen balance however does not vary with pressure and also did not explain the poor combustion at lower pressures. Thus a different parameter, which varied with pressure, needed studying to describe the ignition/sustainability difficulties. Comparison of polyEthylene content with pressure showed (Figure 24) a sustain/ no-sustain relationship similar to

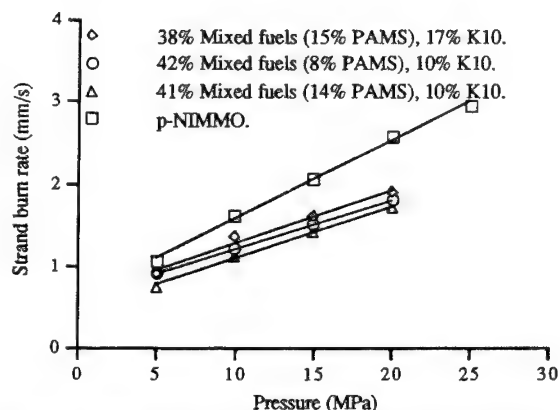


Figure 20. Performance matched (PAMS)/AN comps.

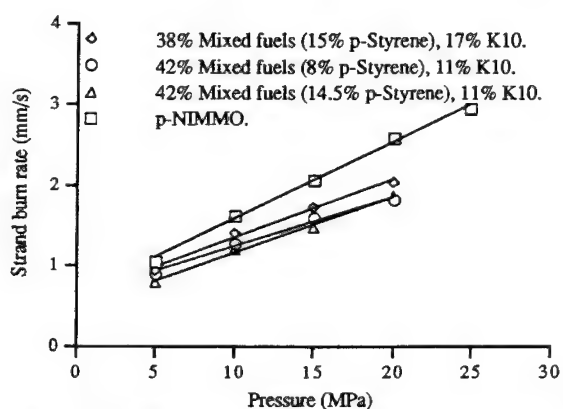


Figure 21. Performance matched (p-Styrene)/AN comps.

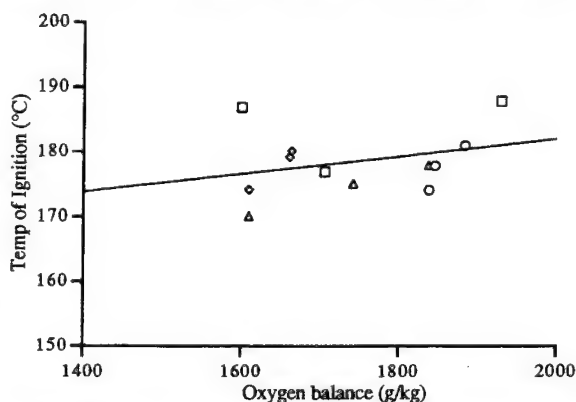


Figure 22. Effect of  $O_2$  bal. on temperature of ignition

that observed for ammonium perchlorate/PBAN compositions.<sup>3</sup> Flame temperatures for the AP/PBAN compositions varied with pressure and those formulations exhibiting lower values failed to sustain combustion.

Similar calculations (NASA Lewis CET89) for various polyEthylene content polyNIMMO samples showed that the lower values also displayed unsustainable burning (Figure 25). At the higher polyEthylene contents other factors (e.g. small particle size) have started to dominate the combustion, hence the unsustainable burning (at 10 and 15MPa) despite higher temperatures than 15% at 5MPa. As both burn rate and chamber temperature, for all the compositions investigated, seemed to vary with pressure the logical extension was to plot burn rate against chamber temperature (similar to burn rate vs pressure plots). For example, the binary polyStyrene mixtures displayed (Figure 26) similar burn rate relationships ( $r = a T_c^x$ ) as that observed for burn rates as a function of pressure ( $r = a P^n$ ). The variation between the percentage contents probably relates to changes in combustion processes (as shown by pressure exponent changes). Taking this into account the data could probably be fitted by the same function. Thus, all the binary fuel mixtures were plotted (Figure 27) and all exhibited a similar good fit. The various fuels also showed sustainable burning at chamber temperatures above 1240-1250K, i.e. slightly higher than for the AP/PBAN compositions.<sup>3</sup>

The three ammonium perchlorate binary formulations (Figure 28) showed even better correlation to a single burn rate/temperature equation. However, the increasing burn rates, for increasing ammonium nitrate content, were not reflected in higher chamber temperatures - rather, a cooling effect was observed - which accounts for the poor correlation. Application to both performance matched ammonium perchlorate (Figure 29) and ammonium nitrate (Figure 30) compositions again showed very good correlation. These ammonium perchlorate compositions failed to sustain burning at low pressures and they were found to possess chamber temperatures in the 1240-1250K region. The ammonium nitrate compositions achieved sustainable low burn rates at lower pressures and chamber temperatures as low as 1200K.

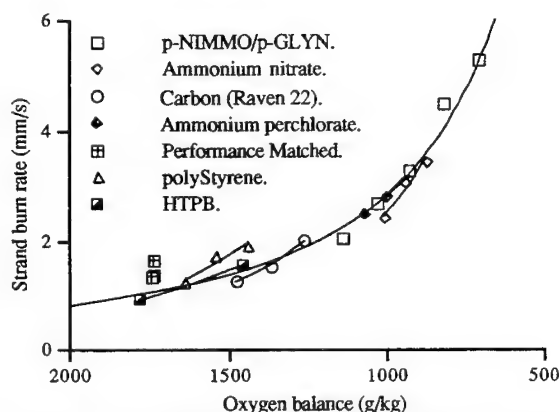


Figure 23. Effect of O<sub>2</sub> bal. on burn rates at 15 MPa

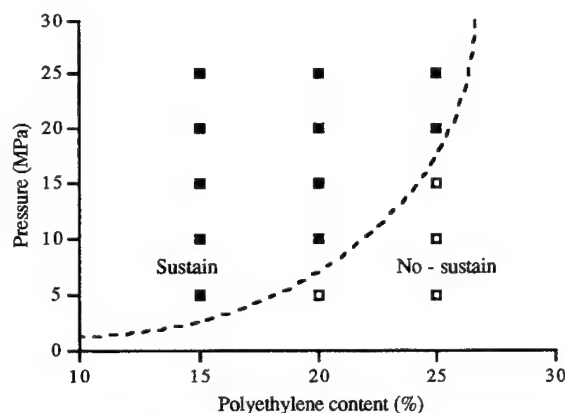


Figure 24. Effect of % polyEthylene on sustainability

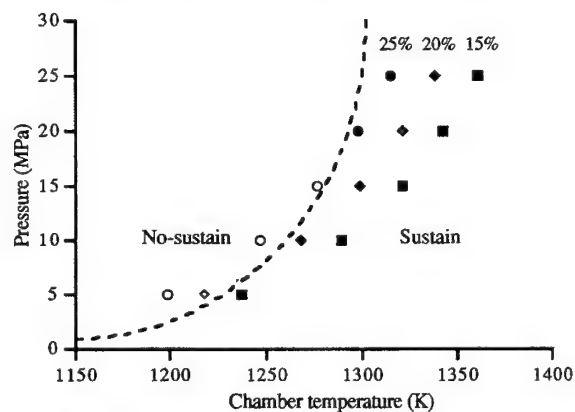


Figure 25. PolyEthylene chamber temp. vs sustain

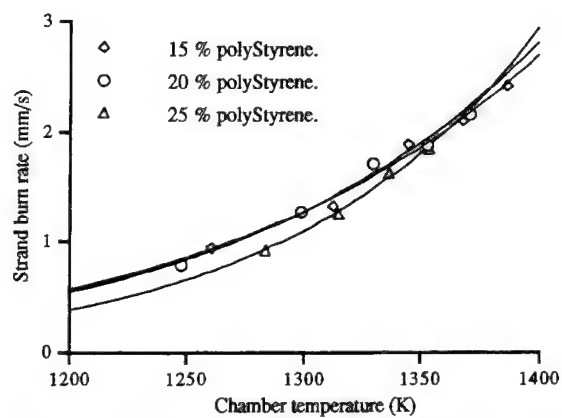


Figure 26. PolyStyrene filled polyNIMMO (Fig 2.)

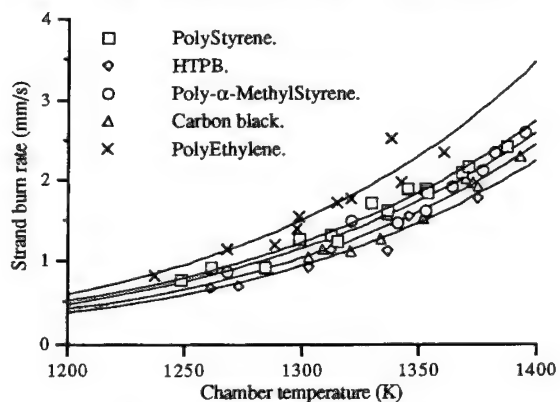


Figure 27. Fuel filled polyNIMMO

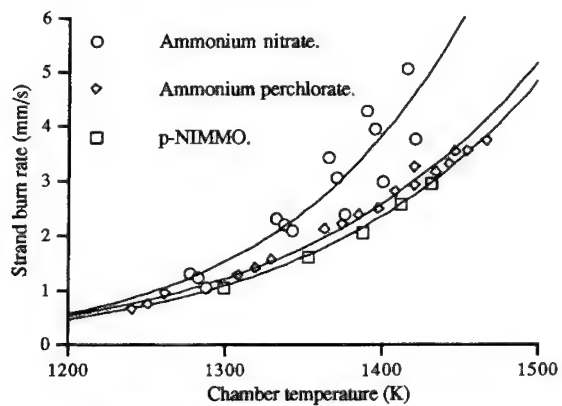


Figure 28. Oxidiser filled polyNIMMO

Thus, for polyNIMMO composite gas-generator propellants a chamber temperature in excess of  $\sim 1200\text{K}$  is required to achieve sustainable burning. This is close to that observed for other fuel-rich propellants.<sup>3</sup> A relationship, for the fuel-rich polyNIMMO formulations investigated, has been observed between chamber temperature and burn rate. This fits the same empirical formula observed for determining pressure exponents. The correlation is usually very good and quite large changes, within the same basic composition, can be made without affecting the fit. Hence, having obtained sufficient experimental burn rate data the empirical model can be used to re-formulate a composition to achieve a specific burn rate, or pressure, target. Factors such as particle size, percentages of burn rate catalysts, potential pressure exponent changes, ignitability, etc. must, however, be considered.

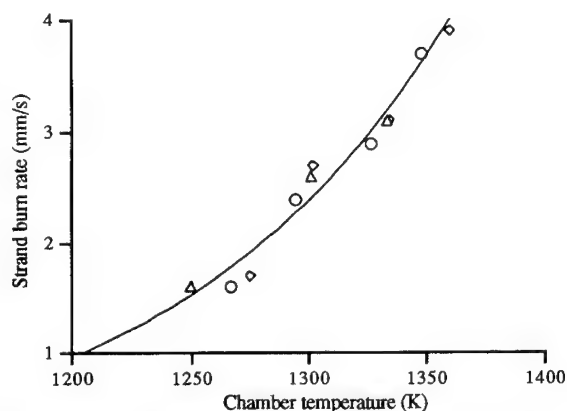


Figure 29. Perform. matched AP comps. (Fig. 14)

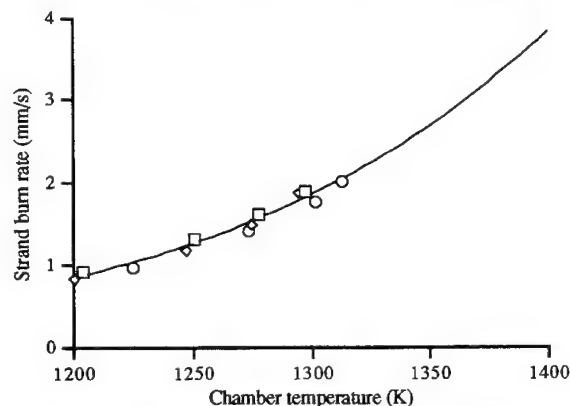


Figure 30. Perform. matched AN Comps. (Fig 21)

## CONCLUSIONS

The burn rate of polyNIMMO is significantly lower than that of GAP and to achieve the order of magnitude improvement to obtain similar values high levels of oxidisers would be needed. This would however reduce the volumetric heat value ('Oe'). The various fuels studied increased the Oe but were found to abate burn rates, although enhancements were seen for other additives. The enhancements were not great enough to overcome the adverse effect the fuels had on the burn rate for performance matched polyNIMMO formulations to be considered in an end-burner propellant configuration.

This work has shown that the smokeless fuel-rich ( $O_e \geq 32000 \text{ MJ/m}^3$ ) polyNIMMO gas generator compositions examined possess the basic characteristics (a slow, stable, burn rates ( $\sim 0.8 \text{ mm/s}$ ) at low pressure (5MPa) with acceptable pressure exponents) required for an air-breathing radial-burner motor configuration. This work obviously needs to be developed further if compositions at larger grain sizes with similar properties are required to be formulated. PolyStyrene and carbon black gave the best burn rate performance across the range of percentage compositions although polyEthylene provided the slowest burn rates. Poly- $\alpha$ -MethylStyrene was found not to sustain burning at high concentrations, especially at low pressures, because of the small particle size used. Thus effort is currently focused on achieving a smokeless fuel rich formulation ( $O_e \approx 32200 \text{ MJ/m}^3$ ) possessing a high pressure exponent ( $\sim 0.5-0.7$ ) with a slow, stable, burn rate ( $\sim 0.7 \text{ mm/s}$ ) at low pressure ( $\sim 3\text{MPa}$ ). An empirical model is being used to assist re-formulation studies.

## REFERENCES

1. Strand firings were obtained using equipment acceptable under proposed Def-Stan for strand burn rate testing. The proposed Def-Stan has been based on the current UK testing method (i.e. that used for these experiments). The summary for the method is; "The propellant is tested in the form of extruded strands 1/8 inch in diameter or machined strands 1/8 inch square. The strands are coated with an inhibitor before testing so that only axial (cigarette-type) burning can take place. After a conditioning period, three strands are mounted in a bomb pressurized with nitrogen and ignited electrically. The burning time for 5 inches of each strand is measured automatically and the burning time in inches per second is calculated."
2. **Kubota, N.**, Survey of Rocket Propellants and Their Combustion Characteristics, *Fundamental of Solid Propellant Combustion*, edited by Kuo, K. K. and Summerfield, M., Progress in Astronautics and Aeronautics, Vol. 90, AIAA, New York, 1-52, 1984.
3. **Shalom, A., Gany, A.**, Flammability Limits and Ballistic Properties of Fuel-Rich Propellants, *Propellants, Explosives, Pyrotechnics*, 16, 59-64, 1991.

## COMMENTS

G. Doriath, SNPE, Vert-Le-Petit, France. Do you think that you will have the same results of burning rate and limits of sustained and unsustained combustion for tests in motors?

Authors' reply. It is recognised that strand burn rates (obtained from static pressure measurements) are not truly representative of the burn rates observed for larger grain size test motors (i.e. a dynamic pressure test method). Sub-scale motor tests on several fuel-rich polyNIMMO compositions were sufficiently close to the strand burn rates for us to have confidence in our data. The observed variance we felt resulted from using different sources of oxidiser and fuel. We are confident that any digression from the desired burn rates for a smokeless fuel-rich polyNIMMO composite propellant can be overcome using the wealth of data and experience available. Our understanding of the physical factors affecting combustion will hopefully enable us to convert an unsustaining formulation to one that will sustain burning.

# INSTANTANEOUS REGRESSION BEHAVIOR OF HTPB SOLID FUELS BURNING WITH GOX IN A SIMULATED HYBRID ROCKET MOTOR

Martin J. Chiaverini, Nadir Serin, David K. Johnson, Yeu-Cherng Lu, and Kenneth K. Kuo

Department of Mechanical Engineering

The Pennsylvania State University

University Park, PA 16802 USA

## ABSTRACT

An experimental investigation using a high-pressure hybrid motor analog has been conducted to provide detailed solid fuel regression rate data at realistic operating conditions for both model validation and correlation development. The 2-D motor operated at a maximum pressure of 9 MPa (1300 psi) with maximum injected gaseous oxygen mass fluxes of  $420 \text{ kg/m}^2\text{-s}$  ( $0.6 \text{ lb}_m/\text{in}^2\text{-s}$ ). Hydroxyl-Terminated Polybutadiene (HTPB, R-45 M) cured with Isonate 2143L was used as the baseline solid fuel. Either carbon black powder or ultra-fine aluminum (UFAL) powder was added to the HTPB fuel during the processing stage for some tests. Both ultrasonic pulse-echo and real-time X-ray radiography techniques were used to determine the instantaneous regression rate. An array of fine-wire thermocouples was used to determine fuel surface temperatures and subsurface temperature profiles. The deduced instantaneous regression rates displayed a complex dependency on axial location and flow conditions. Close to the sample leading edge, the regression rate, governed by the mixing motion of the entering GOX flow, did not vary with time. Following this region, the regression rates exhibited strong dependency on both axial location and flow structure. When the GOX mass fluxes were below  $140 \text{ kg/m}^2\text{-s}$  ( $0.2 \text{ lb}_m/\text{in}^2\text{-s}$ ), gas-phase radiative heat transfer to the fuel surface was found to play a more important role in the regression of solid fuel. Solid fuel regression rates were found to correlate well with the injected oxidizer mass flux, chamber pressure, axial location, and port height. The addition of carbon black had no effect on regression behavior. Addition of 20% of UFAL powder, however, was found to increase the mass burning rate by 70%.

## NOMENCLATURE

<i>Symbols</i>		<i>Greek Symbols</i>	<i>Subscripts</i>
c speed of sound (m/s)	p pressure (MPa)	$\Delta$ change in value	b based on burning
$D_h$ hydraulic diameter (m)	r regression rate (mm/s)	$\kappa$ gas absorption	f fuel
G local mass flux ( $\text{kg/m}^2\text{-s}$ )	Re Reynolds number	coefficient ( $\text{MPa m}^{-1}$ )	o reference value
$G_o$ oxidizer mass flux ( $\text{kg/m}^2\text{-s}$ )	t time (s)	$\rho$ density ( $\text{g/cm}^3$ )	p based on pressure
h port height (m)	w web thickness (mm)	$\tau$ propagation time ( $\mu\text{s}$ )	x based on axial distance.
L fuel slab length (m)	x axial location (m)		i initial value

## INTRODUCTION

Hybrid rocket motors have unique operational and performance advantages over both liquid bi-propellant and solid propellant rockets. Several different types of hybrid rockets have been proposed over the years including the classical (solid fuel and liquid oxidizer), reverse (solid oxidizer and liquid fuel), and gas-generator (fuel-rich solid propellant grain with injected oxidizer) configurations [1].

Among these configurations, the classical hybrid rocket has received the most attention and is the primary focus of this study. Classical hybrid rocket systems offer several important advantages over their liquid and solid rocket counterparts [2,3]. First, hybrid rocket motors are less sensitive to cracks and imperfections in the solid-fuel grain than solid-propellant rocket motors, and are therefore much safer. Second, because only the oxidizer is stored in liquid form, hybrids require only half as much feed-system hardware as liquid propellant rockets. Third, hybrid rockets can easily be throttled for thrust control, maneuvering, motor shutdown and restart by adjusting only the oxidizer flow while avoiding the necessity of matching hydraulic characteristics with the fuel, as in liquid propellant rockets. Fourth, the solid phase fuel provides a convenient matrix for various additives for purposes such as plume signature tailoring for military applications and metal particles for high-performance missions. Fifth, hybrid rocket motor grains pose no explosion hazard during manufacture, transport, ground-test, and storage since the fuel and oxidizer are separated both physically and by phase. Finally, hybrid rockets, as opposed to solid rockets, are environmentally clean since their exhaust products contain no chlorine. Because of their inherent safety, hybrid rockets should be economic from both manufacturing and launching points of view. From a performance standpoint, hybrid rockets are comparable to both liquid- and solid-propellant rockets. Typical hybrid motors have greater specific impulse than solid propellant motors and greater density specific impulse than liquid propellant motors.

Several important theoretical and experimental studies were performed during the 1960s to study the regression behavior of solid fuels. For example, Marxman, Gilbert, Wooldridge, and Muzzy [4,5] developed an influential heat-transfer limited regression rate model. Their results showed that, in the absence of significant gas-phase radiation, the solid fuel regression rate was primarily a function of the local mass flux and axial position but not the motor pressure. Smoot and Price [6-8] conducted a large number of experiments using a lab-scale motor. They found that at low pressures ( $p < 1$  MPa) the average regression rates were independent of mass flux but strongly dependent on pressure, an effect attributed to presumed heterogeneous reactions on the solid fuel surface. It should be noted that both flow rates and pressures in Smoot and Price's experiments were somewhat low in comparison to those of practical hybrid rocket applications.

Although various regression rate analyses and correlations have been developed in the last few decades, the literature has historically lacked a sufficient amount of realistic empirical data with which to validate these models. Instantaneous regression rate data have been especially lacking, and, with a few exceptions [9,10], rarely been reported. In an attempt to provide more data for model validation and useful engineering correlations for design considerations, an experimental investigation using a lab-scale hybrid motor analog has been conducted in this investigation. The study focuses on the following objectives: 1) non-intrusive measurement of instantaneous and average solid-fuel regression rates under various operating conditions including GOX flux level, motor pressure, and fuel formulation, 2) determination of the solid-fuel surface temperatures and subsurface temperature profiles as a function of both operating conditions and axial locations, 3) investigation of the effects of solid-fuel additives on burning behavior, and 4) development of empirical correlations relating the regression rate to various operating conditions and geometric parameters.



## METHOD OF APPROACH

Figure 1 shows a schematic diagram of the windowed, high-pressure, 2-D slab motor used in this study. References [11,12] provide a more detailed description of the entire test rig.

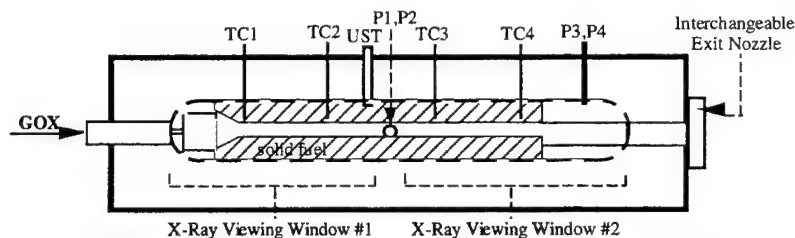


Fig. 1 Schematic diagram of hybrid motor with diagnostic devices

The main body of the motor was constructed of stainless steel, had an overall length of 1,067 mm, width of 178 mm, and height of 254 mm. It was designed to operate at a maximum pressure of 10 MPa. The operating chamber pressure of the motor was partially controlled using interchangeable graphite exit nozzles. Gaseous oxygen was injected at the head-end of the test chamber with a maximum flux of  $420 \text{ kg/m}^2\text{-s}$ . These operating conditions are within the range expected for sub-scale and full-scale hybrid motors [2,13]. The motor accommodates two opposing fuel slabs, 584 mm (23 in) long and 76 mm (3 in) wide. Hydroxyl-Terminated Polybutadiene (HTPB) was used as the baseline solid fuel. In several tests, either carbon black powder (CB) or ultra-fine aluminum powder (UFAL) was added to the HTPB during the processing stage. The carbon black powder was added to investigate the effect of an opacifying agent on fuel regression behavior, had a mean particle size of 75 nm, and accounted for 0.25% of the total solid fuel weight. The UFAL powder was added to evaluate its performance as a possible regression rate enhancing agent and had a mean particle size in the range of 50 to 100 nm. It was added in amounts of 4%, 12%, and 20% of the total fuel weight. Solid fuel slabs were processed at the Pennsylvania State University with fine-wire thermocouples embedded at various axial locations before curing. Although the total fuel slab thickness with the submerged sample retainer was 42.5 to 44 mm thick, the fuel slabs had usable web thicknesses between 17.5 mm (0.689 in) and 19 mm (0.748 in).

The motor was instrumented with a variety of diagnostic devices for determination of chamber pressure variations, subsurface thermal profiles at various axial locations, burning fuel surface temperature distribution, and instantaneous solid fuel web thickness profiles. Figure 1 shows the approximate locations of four of the seven thermocouples (TC), the pressure transducers (P) and the ultrasonic transducer (UST) in the instrumented motor. The instantaneous solid fuel regression rate was obtained using two independent techniques: ultrasonic pulse-echo method and real-time X-ray radiography. References [11,12,14,15] describe these techniques in detail. The ultrasonic pulse-echo method enabled determination of the instantaneous fuel web thickness at one of four selected axial locations with a maximum sampling frequency of 20 kHz. Normally, a frequency of 1 or 5 kHz is sufficient to accurately determine the instantaneous fuel web thickness. The X-ray radiography system captured real-time images of the regressing fuel slab surface over a region 165 mm long, and therefore provided axial, as well as temporal, variations in the fuel web thickness and regression rate. To the best of the authors' knowledge, this work represents the first application of real-time X-ray radiography for determination of instantaneous regression rates of solid fuel in a hybrid motor.

The global regression rate and the time-averaged, but axially-dependent regression rates were also determined for each test. The global regression rate was found by dividing the fuel mass difference before and after the test by the fuel burning time. The axially dependent regression rates

were found by dividing the local fuel web thickness difference before and after the test (in either 12.5 or 25 mm increments) by the burning time.

## RESULTS AND INTERPRETATIONS

Table 1 summarizes the test conditions of the 15 test firings conducted in this study. The pressure ranges given in the fourth column correspond to the maximum motor pressure and the minimum motor pressure just before shut down by terminating the GOX flow. The pressure drop was due mainly to erosion of the graphite nozzle throat. Test No. 4 had an unexpected maximum pressure level of 9 MPa caused by a momentary blockage of the nozzle by a piece of solid fuel torn from the fuel slab. After this test, extension pins were mounted to the ends of the fuel sample holders to provide extra support for the solid fuel slabs, which prevented the problem from recurring. The third column of Table 1 gives the initial GOX mass flux found by dividing the known GOX mass flow rate by the initial combustor port area. The last column gives the global regression rate of each test. Test No. 5 has a relatively high regression rate with large pressure oscillations observed during the firing. Others have reported similar finding for tests with substantial pressure oscillations [10]. Tests No. 9 and 11 were conducted using one translucent fuel slab and one fuel slab with 0.25 wt% carbon black. Test No. 10 was conducted using a totally different solid fuel, and therefore is not included in this Table. Tests No. 12, 13, and 14 were conducted using one pure HTPB slab and one fuel slab processed with UFAL mass fractions of 4, 12, and 20%, respectively.

TABLE 1  
Summary of Test Firings

TEST NO.	FUEL TYPE	$G_{o,i}$ , kg/m <sup>2</sup> -s (lb/in <sup>2</sup> -s)	Pressure, MPa (psia)	Burn Time (s)	$r_{global}$ , mm/s (in/s)
1	HTPB	337.8 (0.48)	8.55-2.31 (1240-335)	15.0	-
2	HTPB	68.3 (0.10)	2.07-2.05 (300-300)	2.7	-
3	HTPB	125.3 (0.18)	3.45-2.48 (500-360)	3.6	-
4	HTPB	166.8 (0.24)	8.96-1.79 (1300-260)	5.8	-
5	HTPB	158.3 (0.23)	5.31-2.82 (770-410)	4.1	1.4 (0.055)
6	HTPB	133.3 (0.20)	3.89-1.34 (565-195)	6.6	0.92 (0.036)
7	HTPB	102.3 (0.15)	3.65-1.72 (530-250)	8.9	0.76 (0.030)
8	HTPB	100.7 (0.15)	3.45-1.72 (500-250)	9.5	0.76 (0.030)
9	HTPB +0.25% CB	113.5 (0.17)	3.45-1.72 (500-250)	4.2	1.2 (0.047)
11	HTPB +0.25% CB	162.3 (0.24)	4.93-1.24 (715-180)	8.5	0.95 (0.037)
12	HTPB; HTPB+4%UFAL	196.9 (0.29)	3.72-2.07 (540-300)	4.0	1.13 (0.045) 1.29 (0.051)
13	HTPB; HTPB+12%UFAL	234.5 (0.35)	4.31-1.86 (625-270)	4.5	1.24(0.049) 1.49 (0.059)
14	HTPB; HTPB+20%UFAL	220.5 (0.33)	4.14-2.14 (600-310)	4.4	1.28(0.050) 1.57 (0.062)
15	HTPB	362.5 (0.54)	4.96-1.52 (720-220)	7.2	1.38 (0.054)
17	HTPB	369.9 (0.56)	4.62-1.52 (670-220)	6.1	1.43 (0.056)

## Deduction of Instantaneous Regression Rates

The comparison of data from real-time X-ray radiography and ultrasonic pulse-echo measurements indicated that the chamber pressurization and depressurization processes affected the web thickness and regression rate results. The top portion of Fig. 2 shows the time histories of motor pressure and burned web thickness for Test No. 9, while the regression rates deduced from the ultrasonic measurement are shown in the bottom portion of the Figure. The dashed curve indicates the uncorrected regression rate deduced directly from the ultrasonic measurement device, while the solid curve represents the corrected regression rate found by considering the mechanical deformation of the fuel slabs under pressure excursions. The correction procedure is discussed below. The ultrasonic transducer was located a distance of 178 mm downstream from the leading edge of the fuel slab. The times of GOX flow initiation, ignition of the solid fuel slabs, and GOX flow termination are indicated on the graph. Notice that at the start of GOX flow, but *before* ignition, the web thickness decreased due to the chamber pressurization, yielding a corresponding artificial regression rate of the fuel slab surface. This artificial regression rate reached a peak value of 0.9 mm/s, and then fell back to zero as the chamber pressure reached a steady level of about 0.6 MPa. This change of solid fuel web thickness and regression rate were not caused by burning, but induced by the mechanical compression of the fuel slabs. Since the motor underwent relatively rapid pressurization at ignition, the regression rates at the start of the tests were greatly influenced by the compression process. When the GOX flow was terminated, the motor underwent a depressurization process which caused an apparent increase in the instantaneous web thickness and a *negative* regression rate (not shown in the figure). These effects are also due to solid fuel deformation during the pressure excursions.

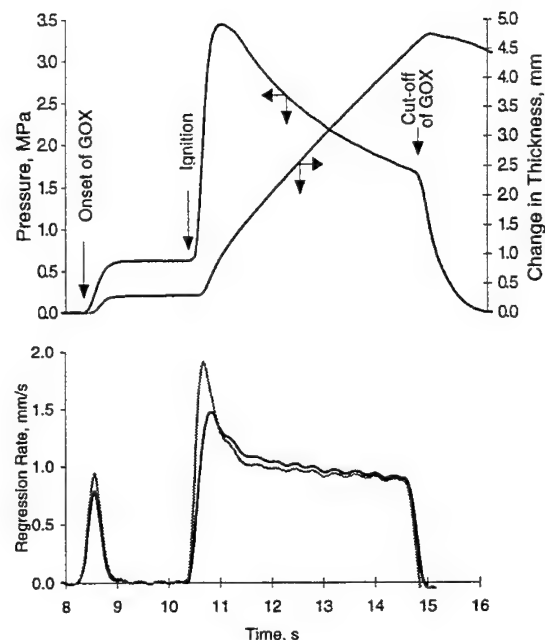


Figure 2. Time histories of motor pressure, web thickness, and the regression rate comparison from ultrasonic measurement (Test No. 9)

Notice that at the start of GOX flow, but *before* ignition, the web thickness decreased due to the chamber pressurization, yielding a corresponding artificial regression rate of the fuel slab surface. This artificial regression rate reached a peak value of 0.9 mm/s, and then fell back to zero as the chamber pressure reached a steady level of about 0.6 MPa. This change of solid fuel web thickness and regression rate were not caused by burning, but induced by the mechanical compression of the fuel slabs. Since the motor underwent relatively rapid pressurization at ignition, the regression rates at the start of the tests were greatly influenced by the compression process. When the GOX flow was terminated, the motor underwent a depressurization process which caused an apparent increase in the instantaneous web thickness and a *negative* regression rate (not shown in the figure). These effects are also due to solid fuel deformation during the pressure excursions.

In order to separate the effects of mechanical compression and true regression due to combustion, several calibration tests were conducted using cold flow to characterize the mechanical deformation behavior of the HTPB solid fuel slabs. A simple correlation was developed to relate the change in propagation time of the ultrasonic signal through the solid fuel with chamber pressure:

$$\Delta\tau/\tau_0 = 1.3893 \times 10^{-5} + 3.476 \times 10^{-3}P - 7.1371 \times 10^{-5}P^2 \quad (1)$$

where  $P$  is measured in MPa. In Eq. (1),  $\Delta\tau$  represents the change in propagation time due to pressurization, and  $\tau_0$  is the propagation time at the reference pressure of 0.1 MPa. As discussed in Ref. 14, the propagation time of the ultrasonic signal through the solid fuel provides the measurement of the web thickness. This equation was incorporated into the data analysis routine to correct the observed burned web thickness, and therefore the regression rate, for the

compression/decompression effect. It should be noted that Eq. (1) is applicable for quasi-steady conditions. Under highly transient operating conditions, other factors such as pressurization rates and visco-elastic material properties including shear modulus, creep compliance, and Poisson's ratio should be considered in the development of a further refined correction.

The amount of regression rate correction is shown as the difference between the two traces in the lower portion of Fig. 2. The artificial regression rate spike at the onset of GOX flow was not totally eliminated in this test, due to highly transient conditions not accounted for by Eq. (1), while in other tests the magnitude of the spike was substantially reduced after the correction.

The real-time X-ray radiography system was also used to determine solid-fuel regression rates. Figure 3 shows X-ray radiography images of a portion of the motor at three different times for Test No. 14. Images similar to these were used to determine the instantaneous web thickness and port cross sectional area at certain spatial intervals along the fuel slabs. The time resolution between images was usually about 135 ms, while web thickness measurements were made every 12.5 mm along the motor axis.

Figure 4 shows the chamber pressure time history and the changes in web thickness due to burning (closed circles), compression, and the sum of both effects (open circles) for Test No. 17 at one axial location. In order to find the web thickness change due to burning alone, the change due to compression was subtracted from the overall change measured from the X-ray images. The change due to compression was found using Eq. (1), but with the left hand side replaced by  $\Delta w_p/w_0$ , the strain, which is equivalent to  $\Delta \tau/\tau_0$  if there is no change in the speed of sound of HTPB under different pressures. When the variation in speed of sound,  $c$ , is important, the relationship between

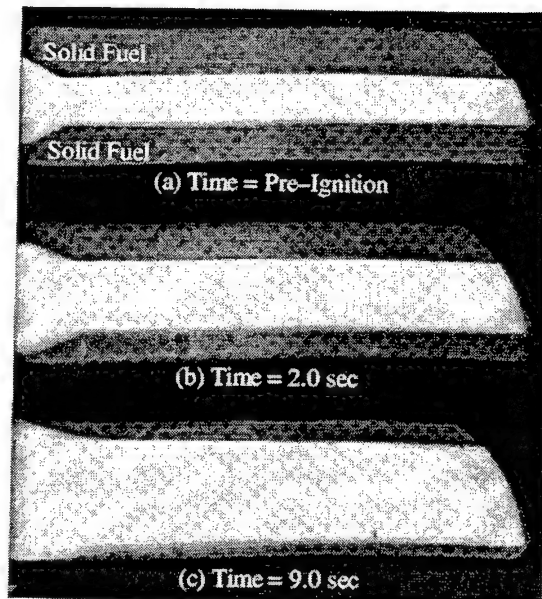


Figure 3. Images from X-ray radiography system

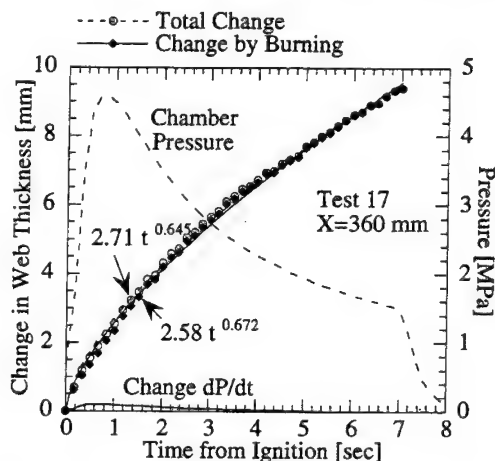


Figure 4. Changes in solid fuel web thickness due to burning and pressurization, from X-ray data

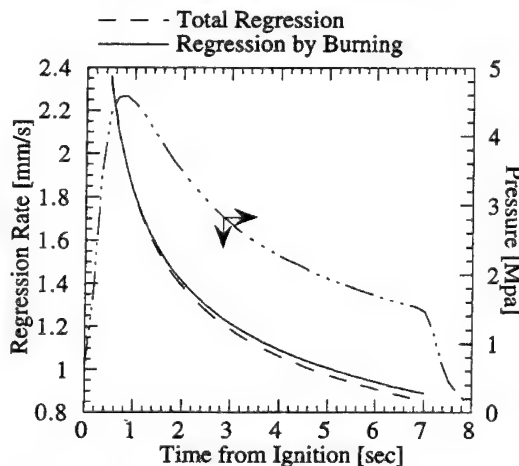


Figure 5. Comparison of corrected and uncorrected regression rates deduced from X-ray data

$\Delta w_p/w_0$  and  $\Delta\tau/\tau_0$  is given by

$$\Delta\tau/\tau_0 = 1 + (\Delta w_p/w_0 - 1)c_0/c \quad (2)$$

where the quantities with subscript "o" represent those at the reference condition (0.1 MPa). The quantity  $\Delta w_p$  represents the instantaneous web thickness change due to pressure excursions, which can be found since the measured web thickness change,  $w_0$ , and pressure,  $p$ , are known at all times. Therefore, as with the ultrasonic transducer data, the changes in web thickness due to compression and burning can be separated to find the true regression rate due to burning alone.

Figure 5 shows the regression rates corresponding to the total observed web thickness change and the change due to burning alone, along with the chamber pressure history. The regression rates were determined by curve-fitting the change in web thickness due to burning using a power-law equation of the form:

$$\Delta w_b = a + bt^k \quad (3)$$

which fits the experimental data quite well as shown in Fig. 4. In Eq. (3),  $\Delta w_b$  is given in mm and  $t$  is given in s. The corresponding regression rate is obtained by taking the time derivative of Eq. (3). Since  $\Delta w_b$  depends on axial location, the coefficients  $a$ ,  $b$ , and  $n$  in Eq. (3) also depend on axial location.

As the motor is pressurized just following ignition, the change in web thickness due to compression continues since the pressure continues to increase to the maximum pressure. During this time, the change in fuel web thickness due to compression is in the same direction as the change due to burning. Therefore, compression of the fuel slab makes the regression rate appear slightly higher than its true value, until maximum motor pressure,  $p_{max}$ , is reached. After reaching  $p_{max}$ , the motor pressure begins to drop due to erosion of the graphite nozzle and the increase in free volume of the chamber. The fuel slabs begin to expand due to chamber depressurization. During this time, the change in fuel web thickness due to depressurization is in the direction opposite that due to regression, so that X-ray analysis indicates a regression rate lower than the true value for the interval from  $p_{max}$  to GOX shut-off. Therefore, the true regression rate due to burning is higher than that given by the uncorrected data during the time between  $p_{max}$  and termination of the GOX flow, but slightly lower than that indicated by the uncorrected data over the interval from ignition to  $p_{max}$ .

The correction methods for the ultrasonic pulse-echo and real-time X-ray radiography systems discussed above were used to correct all instantaneous regression rate data discussed here. Direct comparison of the true regression rates determined by the two independent techniques were made for most of the tests over the time intervals between peak pressure and GOX shut off. The agreement between the two methods is usually within about  $\pm 4\%$ . Figure 6 compares the results of the two methods for Test No. 17. At this point, no attempt has been made to deduce the ignition transient (defined as the time interval between first increase in regression rate and peak regression rate) or the shut-down transient using the X-ray radiography system. However, the ultrasonic

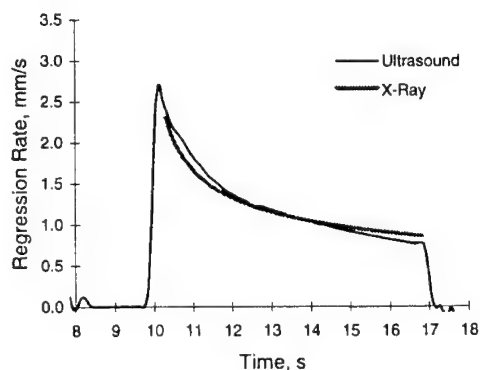


Figure 6. Regression rate comparison of ultrasound and X-Ray (Test No. 17)

pulse-echo method has sampling intervals of about 0.2 ms, and was used to determine the instantaneous regression rate over the entire test from ignition to motor shut down.

### Effects of Solid Fuel Additives

Carbon black powder or ultra-fine aluminum (UFAL) powder was added to the fuel slabs for several tests. In those tests, one fuel slab contained the additive at a certain weight percentage, while the other fuel slab was pure HTPB. This dual slab testing method allowed for a direct comparison of the pyrolysis behavior of the two different fuel formulations.

#### Carbon Black Powder

Carbon black represents a commonly used solid-fuel opacifier. The addition of carbon black makes the solid fuel opaque, which prevents in-depth radiation absorption. In order to determine the effect of carbon black on solid fuel regression rate and surface temperature, one of the fuel slabs was fabricated with 0.25% by weight carbon black additive during the fuel processing stage for two tests. The results of both tests indicated no significant difference in the regression rates of the slabs with carbon black compared to those of the translucent fuel slabs. For Test No. 9 (initial GOX flux of  $210 \text{ kg/m}^2\text{-s}$ ), both slabs had a global regression rate of  $1.2 \text{ mm/s}$  and displayed very similar time-averaged regression rate profiles. For Test No. 11 (initial GOX flux of  $170 \text{ kg/m}^2\text{-s}$ ) both slabs had nearly the same global regression rate of  $0.96 \text{ mm/s}$ . Again, the time-averaged regression rate profiles with respect to axial location were almost identical within experimental error. Figure 7 illustrates this result, along with the results of Test No. 14, discussed later. It is believed that a black char layer was formed on the surface of the translucent fuel slabs during burning, so that the radiative heat flux was absorbed only at the surface rather than in the interior of the slab. Such a char layer has been observed on the surfaces of all recovered HTPB fuel slabs.

From thermocouple measurements, the surface temperature of the slab with carbon black was about  $930 \text{ K}$  at a location  $300 \text{ mm}$  downstream from the leading edge of the fuel slab in Test No. 11. This result is consistent with previous surface temperature measurements, which indicate that the surface temperature of pure HTPB fuel slabs is between  $900$  and  $1050 \text{ K}$ , depending on operating conditions and axial location [12]. The subsurface thermal wave profiles of Test No. 6 (translucent slab) and No. 11 (black slab) are compared in Figure 8 since both tests had similar initial GOX mass fluxes ( $148$  and  $162 \text{ kg/m}^2\text{-s}$ , respectively), and global regression rates ( $0.92$  and  $0.95 \text{ mm/s}$ , respectively). As shown in Fig. 8, the surface temperatures and subsurface temperature profiles are also quite similar, giving further evidence that the addition of carbon black powder did not noticeably affect the regression.

The surface temperature, subsurface temperature profile, and heat flux to the solid fuel surface can change substantially with operating conditions, as shown in Figure 9. Figure 9 compares the temperature profiles from Test Nos. 6 and 17, both of which were conducted with translucent fuel slabs only. Test No. 6 (initial GOX flux of  $148 \text{ kg/m}^2\text{-s}$ ), has a surface temperature of  $950 \text{ K}$  and a thermal wave about  $0.125 \text{ mm}$  thick while Test No. 17 (initial GOX flux of  $394 \text{ kg/m}^2\text{-s}$ ), has a higher surface temperature of about  $1018 \text{ K}$  and

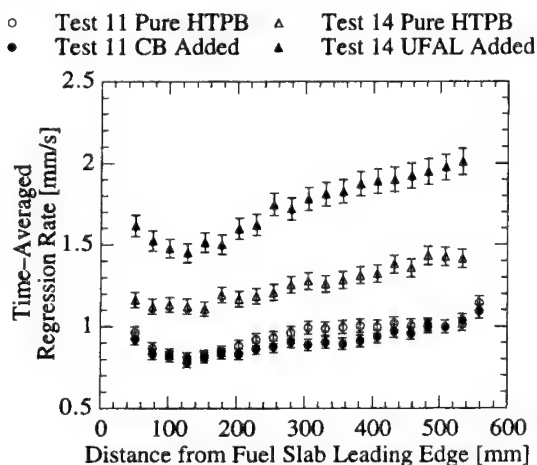


Figure 7. Time-averaged regression rate profiles showing effects of solid fuel additives

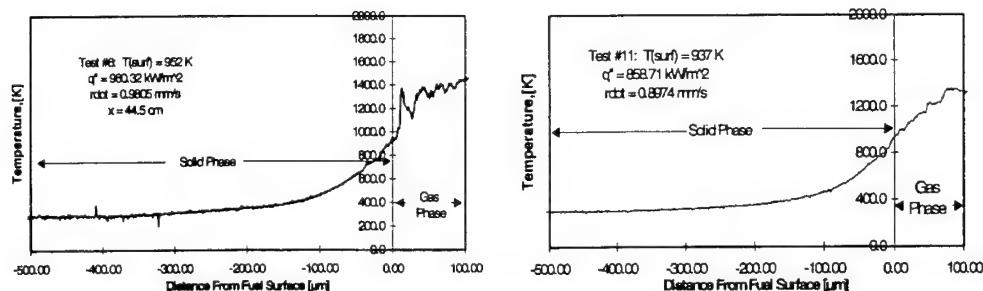


Figure 8. Temperature profiles for translucent and black fuel slabs under similar operating conditions

a thinner thermal wave of about 0.065 mm. In addition, the calculated heat flux into the fuel at the surface for Test No. 6 is 718 kW/m<sup>2</sup>, which is much lower than the value of 1500 kW/m<sup>2</sup> for Test No. 17 with much stronger convective shear flow.

#### Ultra-Fine Aluminum Powder

Ultra-fine aluminum powder (with a particle size of between 50 and 100 nm), also called Alex by Russian researchers, is a very fine powder manufactured in Russia by exploding thin aluminum wires in an Argon environment [16]. In order to assess the effects of ultra-fine aluminum powder (UFAL) on the burning rate of HTPB, several tests were conducted using one pure HTPB fuel slab and one HTPB fuel slab loaded with a certain mass fraction of UFAL.

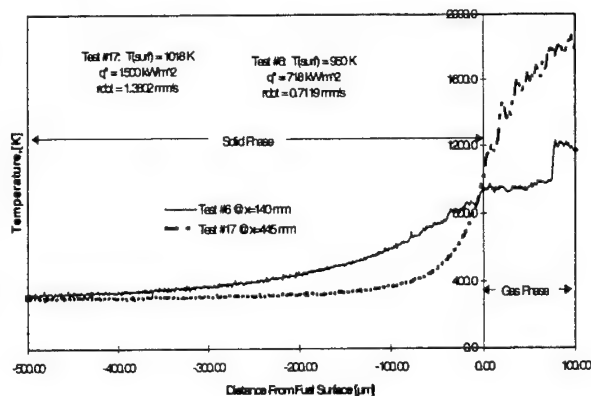


Figure 9. Temperature profiles for translucent fuel slabs

was added to one fuel slab in amounts under different operating conditions of 4, 12, and 20% of the total fuel

weight, respectively. In contrast to carbon black powder, the UFAL powder had a significant effect on the solid fuel regression rate. Figure 7 shows the time-averaged regression rate profiles of the pure HTPB slab and the HTPB/20%UFAL slab from Test No. 14. Though the two profiles have approximately the same shape, the fuel slab containing 20% UFAL consistently displays a much higher regression rate than the pure HTPB slab at the same axial location.

Figure 10 shows the increase in global regression rate and global mass burning rate with respect to pure HTPB versus %wt of UFAL in the fuel slab. Since UFAL has a higher density than HTPB, the increase in mass burning rate is even higher than the increase in regression rate for the same percentage of UFAL. Test No. 14 indicates that with 20% UFAL addition, the regression rate increased by almost 40% and the mass burning rate increased by approximately 70% over the pure HTPB slab. These values represent a significant change in performance since low regression rate is often cited as a major disadvantage of hybrid rocket motors.

As discussed in Ref. [12], the surface of recovered pure HTPB slabs exhibited different characteristics with axial distance: The front portion of the slab had a smooth surface, followed by a middle region of increasingly distinct transverse striations. The transverse striations developed into much more random patterns at distances further downstream. These fuel surface characteristics were attributed to the transition from laminar to turbulent flow in the boundary layer. The fuel slabs



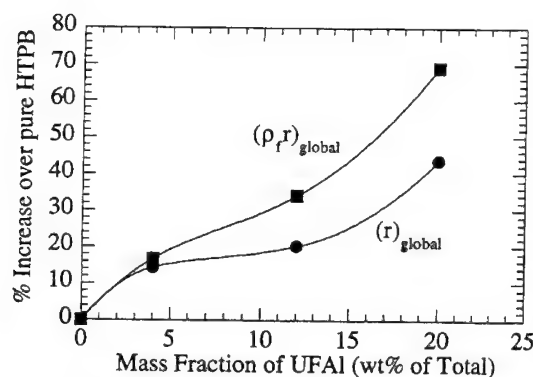


Figure 10. Effect of UFAL addition on global regression and mass burning rates

containing UFAL exhibited much different surface characteristics than the pure HTPB slabs. Figure 11 shows the fuel slabs from Test No. 13. The slab with 12% UFAL displayed a much smoother surface than the pure HTPB slab. This evidence suggests that some forms of heterogeneous reactions may exist near the surface region, and thereby contribute to the enhanced regression. Based on Ref. [16], it is believed that when subjected to a large enough heat flux, such as occur in a hybrid rocket motor, UFAL particles vaporize with an associated high heat release. Possibly, the unique UFAL manufacturing process allows the particles to form in a metastable state. When "disturbed" by heating, the particles vaporize and release their stored energy. This energy release causes a greater heat feedback to the fuel surface than that which occurs in pure HTPB, and increases the regression rate. It is useful to postulate another mechanism associated with microexplosions to explain the rapid reaction of the aluminum particles near the surface. During manufacturing, the UFAL particles were formed under a rapid cooling process. A shell-like crust may form on the surface of the particles as the outer region cools, inducing a high potential for built-in thermal stresses within the particle as the interior region cools to ambient conditions. When the UFAL particles are subjected to high temperatures near the fuel surface, the outer shell is heated and softened first. The internal material could then be ejected in the form of a microexplosion. Due to these unusual and promising characteristics of UFAL, much more research in this area is required.

#### Development of Regression Rate Correlations

One of the major goals of this study was to develop empirical correlations which relate the solid fuel regression rate to operating conditions and geometry of the motor. Accurate estimation of solid-fuel regression rate is needed for motor design, performance prediction, and low residual fuel sliver mass fraction.

Once the instantaneous regression rate has been deduced at known operating conditions, the data can be correlated with other instantaneous governing parameters such as  $G$  (or  $G_0$ ),  $P$ , and  $D_h$  to determine their functional relationships. In order to correlate experimental data over a broad range of oxidizer flux levels, the effect of gas-phase radiation on regression rate must be considered, as discussed in Ref. [17,18,19]. The radiative energy flux, though normally assumed a small fraction of the total energy feedback to the solid fuel, could be especially important at low oxidizer mass fluxes. Considering an approach similar to that taken

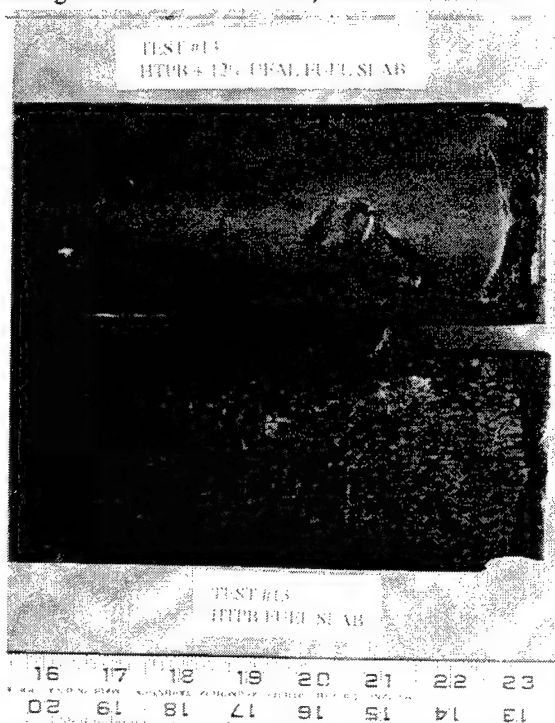


Figure 11. Surface characteristics of pure HTPB (bottom) and HTPB with 12% UFAL addition (top)



by Marxman et al [5], the following functional form was used to correlate instantaneous regression rate with instantaneous motor operating conditions and geometry:

$$\dot{r} = C_1 G_0^n x^m \left( \frac{C_2}{G_0^n x^{n-1}} (1 - e^{-\kappa p h}) + \exp \left[ \frac{-C_2}{G_0^n x^{n-1}} (1 - e^{-\kappa p h}) \right] \right) \quad (4)$$

where  $\kappa$  represents the gas absorption coefficient and  $h$  is the instantaneous port height between the fuel slabs. The dimensionless form of Eq. (4) is

$$\frac{\dot{r}}{G_0} = a_1 \text{Re}_x^{n-1} \left( \frac{a_2}{G_0 \text{Re}_x^{n-1}} (1 - e^{-\kappa p h}) + \exp \left[ \frac{-a_2}{G_0 \text{Re}_x^{n-1}} (1 - e^{-\kappa p h}) \right] \right) \quad (5)$$

In Eq. (4),  $\dot{r}$  is given in (mm/s),  $G_0$  in ( $\text{kg}/\text{m}^2\text{-s}$ ),  $p$  in (MPa),  $x$  in (m), and  $h$  in (m). The term  $(1 - e^{-\kappa p h})$  in Eq. (4) represents the emissivity of the gas phase [20], while the term  $C_1 G_0^n x^m$  represents the convective contribution to the regression rate. When  $\kappa p h$  is zero, there is no thermal radiation from the gas phase and the term in curly brackets becomes unity. In the process of correlation development, the data were compared to  $C_1 G_0^n x^m$  alone, which was not adequate to account for the regression rate values at the lower GOX mass fluxes. The more complicated form of Eq. (4) was necessary to adequately correlate the data.

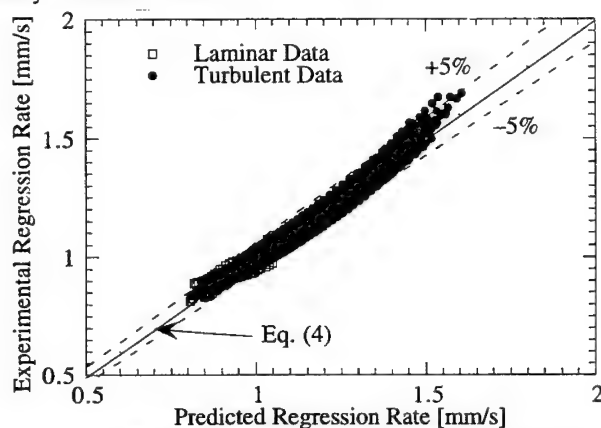


Figure 12. Regression rate correlation for HTPB

The parameters  $C_1$ ,  $C_2$ ,  $m$ ,  $n$ , and  $\kappa$  were found using a least squares analysis to minimize error. Figure 12 shows the experimental regression rate versus the predicted regression rate found using Eq. (4). Almost all the data lies within a  $\pm 5\%$  error band, indicating that the correlation properly represents the important physical processes governing solid fuel regression. However, it should be noted that the data shown in Fig. 12 represents two different correlations: one for the laminar flow regime and one for the turbulent flow regime. The parameters have different values in these two regimes as shown in Table 2.

TABLE 2  
Parameters for Correlations

Parameter	Laminar	Turbulent
$c_1$	0.1165	0.0158
$c_2$	6.632	84.389
$n$	0.50	0.90
$m$	0.313	0.344
$\kappa$	17.13	17.13

The value for  $n$  in the turbulent regime is slightly higher than the theoretical value of 0.8. Since  $G_0$  has been used here instead of the local flux,  $G$ , this difference is expected. However, the 0.5 power is also expected since the laminar region exists near the head end where  $G_0$  is quite close to  $G$ . According to convective theory, the regression rate should depend on axial position,  $x$ , to the  $-0.2$  power in the turbulent regime and  $-0.5$  in the laminar regime. Here, an overall positive power on  $x$  was found for both regimes. Since  $G_0$  has been used here instead of  $G$ , the positive power on  $x$  probably accounts for the increase in regression rate due to mass accumulation in the downstream direction.

Figure 13 shows the contribution of both convection and radiation to the regression rate versus oxidizer mass flux for Test No. 15. At higher mass fluxes, the radiative contribution accounts for about 6 or 7% of the total regression, but as mass flux decreases, the radiation becomes more important, eventually providing over 12% of the overall regression rate. At higher pressures, the radiative contribution should be even more prominent in the lower mass flux regime. The percentage of regression rate due to convection was evaluated as the ratio of  $C_1 G_0^n x^m$  to the left hand side of Eq. (4), the total regression rate. The percentage of regression due to radiation is the difference between 100 and the convection portion.

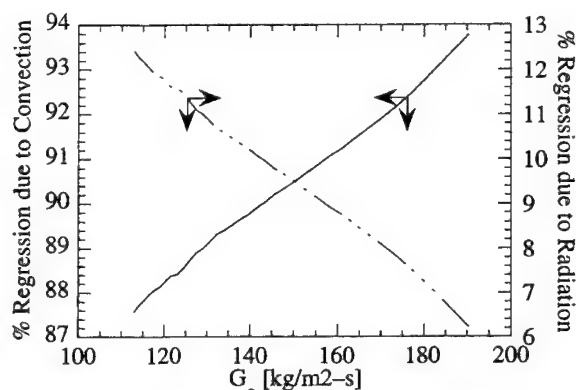


Figure 13. Radiative and convective contributions to regression rate

### CONCLUSIONS

Several conclusions can be drawn from the results of the study:

1. Mechanical deformation of the solid fuel slabs during the motor pressurization and depressurization stages can significantly influence the deduced instantaneous regression rate. This effect must be accounted for when analyzing instantaneous regression rate data. An accurate correction method has been developed in this investigation.
2. With the above factor considered, both real-time X-ray radiography and ultrasonic pulse-echo methods showed similar results for both the solid fuel instantaneous web thickness and instantaneous regression rate.
3. The addition of carbon black powder as an opacifying agent had no observable effect on either solid fuel regression rate or surface temperature. It is believed that a thin, sooty char layer, formed on the fuel surface during burning, has the same effect as adding carbon black to the solid fuel.

4. Addition of ultra-fine aluminum powder (UFAL) caused a significant increase in the solid fuel regression rate. The solid fuel mass burning rate was increased by up to approximately 70% with the addition of 20% by weight of UFAL (the maximum percentage tested). It is believed that UFAL increases the regression rate by enhancing the heat release at or near the solid fuel surface.

5. Regression rate measurements indicate that gas-phase radiation contributes in a non-negligible amount to regression of solid fuels at low oxidizer mass flux levels (below about  $140 \text{ kg/m}^2\text{-s}$ ). The motor pressure plays an important role in this regime; at higher pressures, gas-phase emission is more pronounced.

6. Taking into account the effects of gas-phase radiation, flow regime, and axial location, semi-empirical correlations have been developed to describe the regression rate of pure HTPB as a function of  $G_o$ ,  $P$ ,  $x$ ,  $h$ ,  $L$ , and  $Re_x$ . These variables represent *a priori* known design parameters. It is believed that the correlations presented here can be useful design tools to help predict motor performance and fuel utilization.

#### ACKNOWLEDGEMENT

The authors would like to thank NASA/MSFC for funding this work under Contract No. NAS 8-39945. The support and encouragement of Mr. Roger Harwell of MSFC and Mr. Marion D. Kitchens of NASA Headquarters are highly appreciated. We would like to thank Mr. Les Tepe of the Phillips Lab and Dr. David M. Mann of the Army Research Office for supporting the purchase of the Ultrasonic Measurement System from ONERA, France. The help of Mr. Franck Cauty of ONERA in the technology transfer of the ultrasonic pulse-echo technique to the research team is also greatly appreciated under the NATO/AGARD sponsorship. The authors also wish to thank TUBITAK of Turkey for sponsoring the scholarship of Mr. Nadir Serin which made his participation in this study possible. Mr. Grant Risha's assistance in performing this study is very highly appreciated.

#### REFERENCES

- [1] Green, L., 1963. "Introductory Considerations on Hybrid Rocket Combustion," *Heterogeneous Combustion*.
- [2] Sutton, G. 1992. *Rocket Propulsion Elements: An introduction to the Engineering of Rockets*, Sixth Edition, John Wiley & Sons.
- [3] Altman, D., 1991. "Hybrid Rocket Development History," AIAA Paper 91-2515.
- [4] Marxman, G. A., and Gilbert, M., 1963 "Turbulent Boundary Layer Combustion in the Hybrid Rocket," *Ninth International Symposium on Combustion*, Academic Press, Inc., pp. 371-383.
- [5] Marxman, G. A., Wooldridge, C. E., and Muzzy, R. J., 1964. "Fundamentals of Hybrid Boundary Layer Combustion," *Heterogeneous Combustion, Progress in Astronautics and Aeronautics*, Vol. 15, Academic Press, Inc., pp. 485-521.
- [6] Smoot, L. D., and Price, C. F., 1965. "Regression Rates of Nonmetalized Hybrid Fuel Systems," *AIAA Journal*, Vol. 3, No. 8.
- [7] Smoot, L. D., and Price, C. F., 1965. "Regression Rates of Metalized Hybrid Fuel Systems," *AIAA Journal*, Vol. 4.

- [8] Smoot, L. D., and Price, C. F., 1966. "Pressure Dependence of Hybrid Fuel Regression Rates," *AIAA Journal*, Vol. 5, No. 1.
- [9] Peck, M. V., and Houser, T. J., 1963. "Research in Hybrid Combustion," *Heterogeneous Combustion*, pp. 559-581.
- [10] Dijkstra, F., and Korting, P., 1990 "Ultrasonic Regression Rate Measurement in Solid Fuel Ramjets," AIAA 90-1963.
- [11] Chiaverini, M. J., Harting, G. C., Lu, Y. C., Kuo, K. K., Serin, N., and Johnson, D. K., 1995. "Fuel Decomposition and Boundary-Layer Combustion Processes of Hybrid Rocket Motors," AIAA 95-2686.
- [12] Chiaverini, M. J., Harting, G. C., Lu, Y. C., Kuo, K. K., Serin, N., and Johnson, D. K., 1995. "Combustion of Solid Fuel Slabs with Gaseous Oxygen in a Hybrid Motor Analog," presented at 32nd JANNAF Combustion meeting, Huntsville, AL.
- [13] Boardman, T. A., Carpenter, R. L., Goldberg, B. E., and Shaeffer, C. W., 1993 "Development and Testing of 11- and 24-Inch Hybrid Motors Under the Joint Government/Industry IR&D Program," AIAA 93-2552.
- [14] Cauty, F., et. al., 1994. "Determination of Solid Propellant Burning Rate Sensitivity to the Initial Temperature by the Ultrasonic Method", *Non-Intrusive Combustion Diagnostics*, Edited by K. K. Kuo and T. P. Parr, Begell House, Inc., New York.
- [15] Kuo, K. K. and Parr, T. P., eds., 1994. *Non-Intrusive Combustion Diagnostics*, Begell House, Inc., pp. 365-423.
- [16] Ivanov, G. V. and Tepper, F., 1996. "'Activated' Aluminum as a Stored Energy Source for Propellants", presented at the Fourth International Symposium on Special Topics in Combustion, Stockholm, Sweden.
- [17] Muzzy, R. J., 1972. "Applied Hybrid Combustion Theory," AIAA Paper No. 72-1143.
- [18] Estey, P. N., Altman, D., and McFarlane, J. S., 1991. "An Evaluation of Scaling Effects for Hybrid Rocket Motors," AIAA Paper No. 91-2517.
- [19] Strand, L., Jones, M. D., Ray, R. L., and Cohen, N. S., 1994. "Characterization of Hybrid Rocket Internal Heat Flux and HTPB Fuel Pyrolysis," AIAA 94-2876.
- [20] Incropera, Frank P. and DeWitt, David P., 1990. *Fundamentals of Heat and Mass Transfer*, 3rd ed., John Wiley & Sons .

#### COMMENTS

Mehmet Ali Ak, Middle East Technical University, Turkey:

Is the decrease in motor pressure really due to erosion of the graphite nozzle, or could it be caused by erosive burning of the solid fuel?

Author's Reply:

Normally, we see about a factor of 2 or 3 drop in pressure by the end of the test as compared to the peak pressure just after ignition, depending on the particular operating conditions and test duration. We have observed that the throat area increases by about a factor of 2 to 2.5 due to that erosion, so it seems logical that the pressure drop is due mainly to this effect. However, some of the decrease in

pressure is also caused by a decrease in overall mass flow rate (oxidizer plus fuel), which is caused by a decrease in instantaneous regression rate.

In order to see the relative importance of these two effects, we can use Test 17 as an example. The pressure ratio is the product of the mass flow rate and throat area ratios, in accordance with the steady state continuity equation applied to a control volume around the entire combustor port. For this particular case, the ratio of maximum to minimum pressure is about 3, the ratio of maximum to minimum mass flow rates is about 1.2, and the ratio of minimum to maximum throat area was measured to be about 2.5. Therefore, we find that the nozzle erosion accounts for about 83% of the pressure drop.

G.C. Schüller, I.N.T.A., Madrid, Spain:

Have you planned to try another fuel apart from HTPB? How were the combustion times of your tests?

Author's Reply:

The combustion times of our tests were about 6 to 12 seconds. Besides pure HTPB, we have already tested HTPB+0.25% carbon black and HTPB+4, 12, and 20% ultra-fine aluminum powder (UFAL). Some of these results are reported in the present article. In the future, it may be possible to test HTPB+Al as a comparison with the UFAL. An amount of JIRAD hybrid fuel is available and may also be tested in order to obtain empirical correlations of regression rate vs operating conditions.

# REAL GAS EFFECTS SIMULATION IN A MODEL $GH_2/O_2$ ROCKET THRUST CHAMBER

V.I. Golovitchev <sup>1</sup>, and G. Krülle <sup>2</sup>

<sup>1</sup> Chalmers University of Technology, S-412 96 Göteborg, Sweden; <sup>2</sup> Forschungszentrum Lampoldshausen, D-74239 Hardthausen, Germany

**ABSTRACT:** A CFD-model for a multicomponent reacting mixture of real gases at supercritical conditions is integrated into the KIVA-II code to analyze high pressure  $GH_2/O_2$  ignition processes in a model single injector rocket thrust chamber. The model incorporates mixture thermodynamic anomalies accounted for in terms of the Redlich-Kwong equation for  $O_2$ , while another species are treated as ideal, perfect gases, the  $k-\epsilon$  turbulent submodel for compressible media, and equilibrium and finite-rate combustion chemistry. The detailed mechanism of  $H_2/O_2$  oxidation is used to simulate ignition initiated by "hot spots". The "dense" gas formulation, in contrast to the ideal gas model, predicts mixing enhancement within the cylindrical part of the thrust chamber leading to a decrease in the oxygen jet core length, more stringent requirements for mixture flammability and reduced combustion efficiency. Using equilibrium chemistry, the model does not predict ignition and pressure rise time histories comparable to the results of calculation with finite-rate kinetics.

## NOMENCLATURE

$a, b$	constants of R-K eq.	$c$	molar density, constant
$d, D$	binary and effective diffusion	$e$	internal energy
$F$	heat flux	$h$	specific enthalpy
$J$	diffusion flux	$k$	turbulent energy
$M$	Mach number, molecular mass	$p$	static pressure
$Pr$	Prandtl number	$\dot{Q}_c$	heat release rate
$R_o$	gas constant	$t, T$	time, temperature
$U$	velocity	$u$	velocity components
$V$	molar volume	$x$	mole fraction, coordinates
$\delta$	Kronecker delta	$\epsilon$	dissipation rate
$\kappa$	conductivity	$\mu$	dynamic viscosity
$\nu$	kinematic viscosity	$\rho$	mass density
$\dot{\rho}$	production rate	$\sigma$	viscous stress
$\Omega_{a,b}$	constants of R-K eq.	$\nabla$	nabla operator
$\vec{\phantom{x}}$	vector quantity	$\hat{\phantom{x}}$	tensor quantity
$\bar{\phantom{x}}$	averaged quantity	$'''$	fluctuations

## INTRODUCTION

The need to improve the analysis of high pressure  $GH_2/LOX$  rocket engines with the help of computational fluid dynamics has been well recognized. The reliability of computer results depends on the physical models implemented to simulate the dominating in-chamber phenomena,

i.e., propellants injection, liquid component atomization and gasification, turbulent mixing and combustion [1]. To such a purpose, a theoretical model [2] based on the KIVA-II code [3] is developed and applied to a single injector model thrust chamber. In order to simulate the in-chamber processes, it was necessary to modify the grid generator, the boundary conditions, and to incorporate detailed, (8 species, 26 reactions), finite-rate  $H_2/O_2$  combustion chemistry, and models for the thermodynamic anomaly, as well as for compressible turbulence.

In fact, vaporized  $LOX$  near the faceplate is injected at supercritical conditions, thus involving substantial deviations of fluid properties from the ideal gas model. As a first step, the volumetric behavior of a mixture as a function of pressure, temperature and composition is described in terms of the Redlich-Kwong equation, with its parameters determined from the "mixing rules" of [4]. Compressibility effects are taken into account through the dilatation terms in the transport equation for the averaged turbulent kinetic energy and in the Newton's law analogue for turbulent fluid. A reduced, algebraic form of the turbulent kinetic energy dissipation rate is used in the simulations.

2D numerical modeling is applied to a single coaxial  $H_2/O_2$  injector reference thrust chamber, including the cylindrical combustor and a portion of the Laval nozzle. This chamber geometry is under experimental study at the DLR Lampoldshausen Research Center [5]. The numerical results presented here are time histories of flow parameters illustrating ignition development initiated by hot spots, i.e., internal energy sources at some points in the flowfield. Calculations are prolonged up to the "steady state" using both finite-rate and equilibrium chemistry for two thermodynamic models: the ideal gas, and the "dense" gas at supercritical conditions.

### DENSE GAS INJECTION MODEL

The compressible dense gas flow is governed by the conservation laws in the following form.

*Mass :*

$$\frac{\partial \rho}{\partial t} + \nabla \cdot (\rho \vec{U}) = 0 \quad (1)$$

where  $\vec{U}$  is the vector of fluid velocity, and  $\rho$  is the total fluid density.

*Momentum :*

$$\frac{\partial \rho \vec{U}}{\partial t} + \nabla \cdot (\rho \vec{U} \vec{U}) = -\nabla p + \nabla \cdot (\hat{\sigma}) \quad (2)$$

where  $p$  is the pressure, and  $\hat{\sigma}$  is the turbulent viscous stress tensor defined later.

*Energy :*

$$\begin{aligned} \frac{\partial \rho e}{\partial t} + \nabla \cdot (\rho e \vec{U}) &= -p \nabla \cdot \vec{U} + (1-f) \hat{\sigma} : \nabla \vec{U} \\ &+ f \rho \epsilon - \nabla \cdot (\vec{F}) + \dot{Q}_c \end{aligned} \quad (3)$$

where  $e$  is the internal, (exclusive of chemical), energy per unit mass,  $\epsilon$  is the turbulence kinetic energy dissipation rate,  $\vec{F}$  is the heat flux vector, and  $\dot{Q}_c$  is the volumetric chemical heat release rate. The factor  $f=0$  for laminar, and  $f=1$  for turbulent flows, indicate that for turbulent flows the term  $\hat{\sigma} : \nabla \vec{U}$  is a measure of  $k$  production, rather than a contribution to the internal energy.

*Species Concentration :*

$$\begin{aligned} \frac{\partial \rho_s}{\partial t} + \nabla \cdot (\rho_s \vec{U}) &= -\nabla \cdot (\vec{J}_s) + (\dot{\rho}_s)_c \\ s &= 1, N_s \end{aligned} \quad (4)$$

Here,  $\vec{J}_s$  is the diffusion mass flux of the  $s$ -species,  $N_s$  is the number of species, and  $(\dot{\rho}_s)_c$  are the chemical mass production terms.

The diffusion mass flux is used in a generalized form of the Fick's law

$$\begin{aligned}\vec{J}_s &= -cD_s\nabla(\rho_s/c) + (c\rho_s/\rho)\sum_i D_i\nabla(\rho_i/c) \\ D_s &= (1-x_s)\left(\sum_{i\neq s} \frac{x_i}{d_{is}}\right)^{-1}\end{aligned}\quad (5)$$

where  $d_{is}$  is the binary diffusivity for each pair  $(i, s)$  of species,  $x_s=c_s/c$  is the mole fraction,  $c_s=\rho_s/M_s$ , and  $M_s$  are the molar density and the molecular mass of species  $s$ , respectively.

The heat flux vector is given by

$$\vec{F} = -\kappa\nabla T + \sum_s h_s \vec{J}_s \quad (6)$$

where  $\kappa$  is the thermal conductivity of the mixture,  $h_s$  is the specific enthalpy of the  $s$ -species.

Molecular transport coefficients were calculated with the help of the CHEMKIN libraries [9].

Among existing two-constant equations of state [4], the Redlich-Kwong equation was selected as the most simple and accurate at high pressures. The Redlich-Kwong equation is:

$$\begin{aligned}p &= \frac{R_o T}{(V_i - b)} - \frac{a}{\sqrt{T}V_i(V_i + b)} \\ V_i &= \frac{M_i}{\rho_i}, a = \sum_{i=1}^{N_s} \sum_{j=1}^{N_s} x_i x_j a_{ij}, b = \sum_{i=1}^{N_s} x_i b_i \\ a_{ij} &= \sqrt{a_i a_j}, b_{ij} = \frac{b_i + b_j}{2} a_i = \frac{\Omega_a R_o^2 T_{ci}^{2.5}}{P_{ci}} \\ \Omega_a &= 0.4278, b_i = \frac{\Omega_b R_o T_{ci}}{P_{ci}}, \Omega_b = 0.0867\end{aligned}\quad (7)$$

where  $a$  and  $b$  are the R-K equation parameters.

The heat capacity of the mixture is calculated as a sum of the calorically perfect contribution [6] and a residual heat capacity evaluated with the help of a "departure function" expressed in terms of the R-K equation [7]. These data were stored in a tabular fashion and used in calculations. Figure 4 shows the density of mixture as a function of temperature for several different compositions at 100 atm. It illustrates that the "real gas" corrections are substantial at low temperatures and high concentrations of  $O_2$ . Figure 5 illustrates the anomaly in the heat capacity of oxygen in the vicinity of the critical point.

Turbulent mass, momentum and energy transport dominate in a rocket thrust chamber. Nevertheless, the entrainment rate of compressible flows is less than that of corresponding incompressible flows. To simulate stratified compressible turbulent flow, the transport  $k-\epsilon$  equations with some additional terms are solved

*Turbulent Kinetic Energy :*

$$\begin{aligned}\frac{\partial \bar{\rho} k}{\partial t} + \frac{\partial \bar{\rho} \tilde{u}_j k}{\partial x_j} &= \frac{\partial}{\partial x_j} \left[ \left( \frac{\mu_t}{Pr_k} + \mu \right) \frac{\partial k}{\partial x_j} \right] - \\ \bar{\rho} \tilde{u}_i \tilde{u}_j \frac{\partial U_i}{\partial x_j} - \bar{\rho} \epsilon &- \frac{\overline{u_i' \partial p'}}{\partial x_i} + \frac{\overline{\rho' u_i' \partial \bar{p}}}{\bar{\rho} \partial x_i}\end{aligned}\quad (8)$$

The superscript  $\sim$  refers to the mass-averaged values,  $Pr_k$  is the turbulent Prandtl number for  $k$ . The turbulent viscous stress tensor is given by

$$\sigma_{ij} = -\bar{\rho} \tilde{u}_i \tilde{u}_j = \mu_t \left( \frac{\partial U_i}{\partial x_j} + \frac{\partial U_j}{\partial x_i} - \frac{2}{3} \delta_{ij} \frac{\partial U_\ell}{\partial x_\ell} \right) - \frac{2}{3} \delta_{ij} \bar{\rho} k, \quad \mu_t = c_\mu \frac{\rho k^2}{\epsilon} \quad (9)$$

where  $\mu_t$  is the turbulent viscosity, and  $c_\mu$  is the model constant.



Compressibility effects are taken into account through the dilatation terms  $\nabla \cdot \vec{U}$  included into the transport equation for the averaged turbulent kinetic energy and Newton's law for a turbulent fluid. The turbulence production now contains the term  $-2/3 \bar{\rho} k \nabla \cdot \vec{U}$ , which behaves as a source in the compression flow regions ( $\nabla \cdot \vec{U} < 0$ ), and as a sink, when ( $\nabla \cdot \vec{U} > 0$ ). The compressible dissipation terms are assumed to depend on the local turbulent Mach number. The trace of the pressure-strain rate tensor, ("towards isotropy" term), is approximated in terms of the second order closure modeling [8], i.e.,

$$\overline{(p'u_i)_{,i}} \approx \bar{\rho} k \nabla \cdot \vec{U}, \quad \overline{p' \frac{\partial u_i}{\partial x_i}} = \overline{p'u'_{i,i}} \approx \bar{\rho} \epsilon M_t^2 \quad (10)$$

The original  $\epsilon$ -equation deduced from eq. (8) by dividing its terms by a time scale  $k/\epsilon$  demonstrates the canonical Landau nonlinearity, complicating an evolution of turbulence in the thrust chamber flow when the velocity changes from low subsonic to supersonic due to the compressibility effects. The result could be a quasi-periodic motion characterized by more and more periods appearing in succession; in the limit of  $Re \rightarrow \infty$  the number of periods becomes, likewise, infinitely large. This flow complexity cannot be reproduced on a coarse computational grid. Besides, in the limit of high  $Re$ , the  $\epsilon$ -equation reduces to a balance between the triple correlation of the velocity gradients and the second derivatives of the velocity

$$\nu \left( \frac{\partial^2 u_i}{\partial x_j \partial x_k} \right)^2 + \frac{\partial u_j}{\partial x_k} \frac{\partial u_i}{\partial x_j} \frac{\partial u_i}{\partial x_k} = 0 \quad (11)$$

from which, under certain assumptions [8], the expression follows which is formally consistent with the Kolmogorov's microscale definition.

Exploiting this circumstance, the grid size  $\Delta$  in the simulations is identified with the Kolmogorov's microscale  $\Delta = \ell_k = (\nu_*^3/\epsilon)^{1/4}$ , where  $\nu_* = c_\nu k^2/\epsilon$  is the "turbulent" kinematic viscosity, and used in order to calculate the dissipation rate from the  $\ell_k$  definition. The turbulent diffusion of mass and energy is simulated by means of appropriate turbulent Schmidt and Prandtl numbers. There is no intension to simulate turbulence/combustion interaction, although the importance of such a modeling is acknowledged.

## COMBUSTION MODEL

The finite-rate chemically reacting flow problem is difficult to solve because the mass balance equations are numerically stiff. The KIVA-II code facilitates the treatment of combustion chemistry by subdividing the mechanism into finite-rate and equilibrium reactions. The finite-rate  $H_2/O_2$  combustion mechanism, (8 species, 26 reactions), and reaction rate parameters in the Arrhenius form are listed in Table 1 and based mainly on the data in [10]. The third body concentrations  $M_i$  and chaperon efficiencies are defined by following expressions:  $M_i = \sum_s \alpha_{is} [X_s]$ , where  $[X_s]$  is a species molar density, and  $\alpha_{1,H_2} = \alpha_{2,H_2} = 2.5$ ,  $\alpha_{1,H_2O} = 12.0$ ,  $\alpha_{2,H_2O} = 15.0$ . Rate coefficients for the backward reactions are computed with the help of linear regression. The equilibrium combustion mechanism consists of stages 27-31 from Table 1. If the forward reaction rate coefficients are equal to 1.0, the regression procedure yields the corresponding equilibrium constants. The mechanism is used in conjunction with the ignition threshold and turns on when the temperature reaches the prescribed level.

A sensitivity analysis applied to this reaction scheme shows that at low pressure the ignition process is controlled well by the classic  $H_2/O_2$  combustion mechanism, (reaction 3 in Table 1 dominates), while at high pressures, the role of the trimolecular reaction 7 becomes more pronounced during the induction period. The competition between reactions 3 and 7 defines the non-monotonous dependence of ignition delays on the pressure. The mechanism was tested by comparing computed results with the experimental data [11] for the ignition delay times of

$H_2$ /Air mixtures at 2 atm, (see Figure 3). Although experimental data for rocket chamber conditions are not available, the computer results presented in Figure 3 demonstrate no substantial difference in the ignition mechanism in the case of high pressure.

**Table 1**  
Reaction Mechanism for  $H_2/O_2$  Combustion

Reaction	$a_f^r$	$\zeta_f^r$	$E_{af}^r$
1. $H_2 + O_2 \rightleftharpoons OH + OH$	$1.7 \cdot 10^{13}$	0.0	47780.
2. $H_2 + OH \rightleftharpoons H_2O + H$	$1.2 \cdot 10^{09}$	1.30	3626.
3. $O + OH \rightleftharpoons O_2 + H$	$4.0 \cdot 10^{14}$	-0.50	0.
4. $O + H_2 \rightleftharpoons OH + H$	$5.0 \cdot 10^{04}$	2.67	6290
5. $H + HO_2 \rightleftharpoons O + H_2O$	$3.1 \cdot 10^{10}$	0.0	3590.
6. $O + OH + M \rightleftharpoons HO_2 + M$	$1.0 \cdot 10^{16}$	0.0	0.
7. $H + O_2 + M_2 \rightleftharpoons HO_2 + M_2$	$3.6 \cdot 10^{17}$	-0.72	0.
8. $OH + HO_2 \rightleftharpoons H_2O + O_2$	$7.5 \cdot 10^{12}$	0.0	0.
9. $H + HO_2 \rightleftharpoons OH + OH$	$1.4 \cdot 10^{14}$	0.0	1073.
10. $O + HO_2 \rightleftharpoons O_2 + OH$	$1.4 \cdot 10^{13}$	0.0	1073.
11. $OH + OH \rightleftharpoons O + H_2O$	$6.0 \cdot 10^{08}$	1.3	0.
12. $H + H + M_1 \rightleftharpoons H_2 + M_1$	$1.0 \cdot 10^{18}$	-1.0	0.
13. $H + H + H_2 \rightleftharpoons H_2 + H_2$	$9.2 \cdot 10^{16}$	-0.6	0.
14. $H + H + H_2O \rightleftharpoons H_2 + H_2O$	$6.0 \cdot 10^{19}$	-1.25	0.
15. $H + OH + M \rightleftharpoons H_2O + M$	$1.6 \cdot 10^{22}$	-2.0	0.
16. $H + O + M \rightleftharpoons OH + M$	$6.2 \cdot 10^{16}$	-0.6	0.
17. $O + O + M \rightleftharpoons O_2 + M$	$1.9 \cdot 10^{13}$	0.0	-1788.
18. $H + HO_2 \rightleftharpoons H_2 + O_2$	$1.2 \cdot 10^{13}$	0.0	0.
19. $HO_2 + HO_2 \rightleftharpoons H_2O_2 + O_2$	$2.0 \cdot 10^{12}$	0.0	0.
20. $H_2O_2 + M \rightleftharpoons OH + OH + M$	$1.3 \cdot 10^{17}$	0.0	45500.
21. $H_2O_2 + H \rightleftharpoons HO_2 + H_2$	$1.6 \cdot 10^{12}$	0.0	3800.
22. $H_2O_2 + H \rightleftharpoons H_2O + OH$	$1.0 \cdot 10^{13}$	0.0	3590.
23. $H_2O_2 + OH \rightleftharpoons H_2O + HO_2$	$1.0 \cdot 10^{13}$	0.0	1800.
23. $H_2O_2 + H \rightleftharpoons H_2O + OH$	$1.0 \cdot 10^{13}$	0.0	3590.
24. $H_2O_2 + O \rightleftharpoons H_2O + O_2$	$8.4 \cdot 10^{11}$	0.0	4260.
25. $H_2O_2 + O \rightleftharpoons OH + HO_2$	$2.0 \cdot 10^{13}$	0.0	5900.
26. $HO_2 + H_2 \rightleftharpoons H_2O + OH$	$6.5 \cdot 10^{11}$	0.0	18800.
27. $O_2 \rightleftharpoons O + O$	1.0		
28. $H_2 \rightleftharpoons H + H$	1.0		
29. $H_2 + O_2 \rightleftharpoons OH + OH$	1.0		
30. $H_2O + OH \rightleftharpoons HO_2 + H_2$	1.0		
31. $H_2O + H_2O \rightleftharpoons H_2O_2 + H_2$	1.0		

The table consists of two blocks for elementary and equilibrium reactions, respectively. Rate coefficients, third body concentrations  $M_i$  and chaperon efficiencies are taken in the form of [10].

## REACTIVE FLOW SOLVER

Combustion in a rocket thrust chamber is characterized by the existence of vastly different time and length scales associated with convective, diffusive and chemical processes. The flow Mach number tends to zero near the injection plate and is supersonic at the nozzle exit. For density based algorithms, the numerical stability restrictions require very small time steps. To overcome this difficulty, the KIVA-II code uses the semi-implicit, pressure based algorithm coupling iteratively all Mach number fluid mechanics with global, finite-rate and partial equilibrium chemistry. The application of the solution procedure to the detailed mechanism of  $H_2/O_2$  combustion is relatively straightforward.

Each cycle of calculations is divided into three steps. Steps 1 and 2 constitute a Lagrangian stage in which the cell vertices move with the fluid. Step 1 of the computations accounts for the gas-phase chemical reactions. Step 2 computes the pressure gradients in the momentum equation and the velocity dilatation terms in the mass and energy equations, as well as viscous and diffusion terms. In Step 3, the frozen flow field is rezoned onto a fixed Eulerian grid. This step is equivalent to a convective "fluxing" using a quasi-second order upwind monotone scheme. The convection time increment satisfies the Courant stability condition.

The axisymmetric slice of the test geometry is modeled on a 26x2x31 grid. The boundary conditions are the specified inlet parameters and the pressure at the outflow boundary. The centerline of the flow is a symmetry condition, and the "law of the wall" model is used to simulate a near-wall boundary layer with a heat transfer. The inflow conditions are prescribed to distinguish between the ideal gas and the dense gas models. The mixture ratio  $O/F=6$  is kept constant for both cases. The chamber pressure is a self-adjusting function of time depending on turbulent mixing and heat release. The back pressure was calculated from 1D gasdynamics.

## RESULTS AND DISCUSSION

Numerical modeling was performed for a single coaxial injector reference thrust chamber, (see Figure 5), including the cylindrical combustor and a portion of the Laval nozzle. The model thrust chamber has the following main dimensions: the length and the radius of the cylindrical portion are .2 m and .015 m; the lengths and the critical radius of the Laval nozzle are .0269 m and .0592 m, respectively. The longitudinal position of the critical cross section is .2212 m. The injector radii are .0023 m, .0035 m and .004 m, respectively. Low temperature, (100 K), oxygen and hydrogen are injected at different velocities, (22 and 250 m/sec, respectively), into a high pressure, (20 bar), chamber environment. Calculations begin with the chamber full of stagnant nitrogen. The combustion process is initiated by "hot spots" at a prescribed instant, (6 msec), turned on for some time, ( $\sim 1$ -2 msec), and then turned off, simulating typical pyroforic ignition devices or sparks. The amount of the energy supplied must be sufficient to support the development of finite-rate ignition. The inlet level of turbulent kinetic energy is specified as 1-2% of the total flow kinetic energy, while the turbulent length scales are selected as fractions of the characteristic diameters of the injector elements.

A transient plot of the chamber pressures is shown in Figure 4 for the finite-rate and equilibrium chemistry models. The pressure rise is associated mainly with the heat release. In the case of "weak" ignition the combustion process cannot be initiated. The results presented in Figure 5 are typical transient plots of temperature corresponding to a low preturbulence level, ( $\sim 1\%$  of the total kinetic energy), in the mixing propellant jets, and illustrate the ignition development starting from the "hot spot", (plot 1, 7.26 msec), up to the steady-state combustion regime, (plot 4, 12.0 msec). During the transient computations, it was observed that the flow parameters were pulsating due to a "periodical" change in the intensity of the heat release. This phenomenon is indicative of a coupling between the combustion and fluid dynamics processes and is less pronounced in the ideal gas model. As a result, the temperature in plot 3, (9.26 msec), is lower than that in the earlier combustion stage. The flame length at this instant is the largest, as the reactants are consumed not only in the initial mixing zone, but also in the region where the cold mixture has had time to premix before ignition.

The supercritical "dense" fluid formulation, in contrast to the ideal gas model, yields significant changes in the thrust chamber flowfield. The correct  $O_2$  injection density  $\sim 1100 \text{ kg/m}^3$  enhances the mixing rate within the cylindrical part of the thrust chamber, especially at higher, ( $\sim 4\%$ ), preturbulence levels. Preturbulence leads to a rapid destruction of the cold oxygen jet core and therefore, results in a higher combustion efficiency. The steady-state mixture parameter, ( $H_2O$ ,  $H_2$ , and  $O_2$  mass fractions and temperature), plots for the ideal gas and equilibrium chemistry models are presented in Figure 6. A comparison of the temperature distribution 4 in

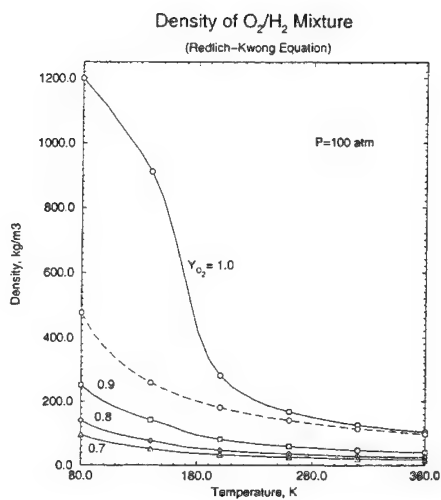


Figure 1. Density of  $O_2/H_2$  mixture at supercritical conditions. Dashed line corresponds to the ideal gas model for pure  $O_2$ .

IGNITION DELAY TIMES FOR  $H_2/Air$  MIXTURES  
( $H_2/O_2$  Mixtures at 100 atm)

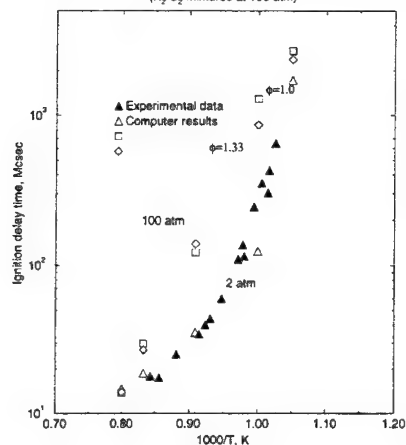


Figure 3. Ignition delay times for  $H_2/O_2$  mixtures at low and high pressures. Experimental data correspond to stoichiometric  $H_2/Air$  mixture at 2 atm.

Heat Capacity of Dense  $O_2$  at Constant Pressure  
(Redlich-Kwong Equation)

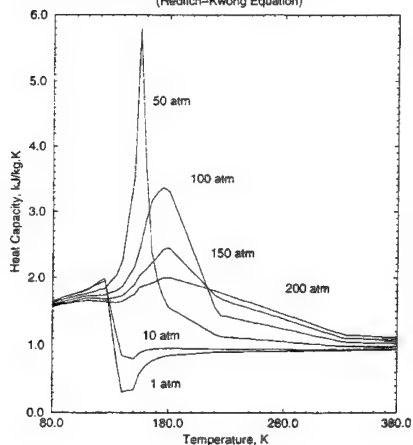


Figure 2. Variation of  $C_p$  of dense  $O_2$  as a function of temperature and pressure in terms of the real gas model.

High Pressure  $O_2/H_2$  Combustion Simulation  
(Pressure vs time history)

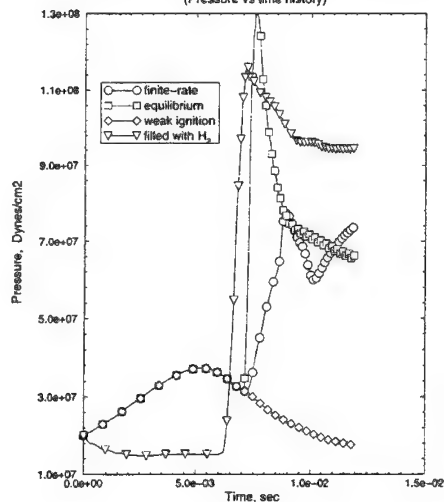


Figure 4. Chamber pressures as a function of time for different chemical models of ignition.

# REFERENCE $\text{GH}_2/\text{O}_2$ ROCKET THRUST CHAMBER

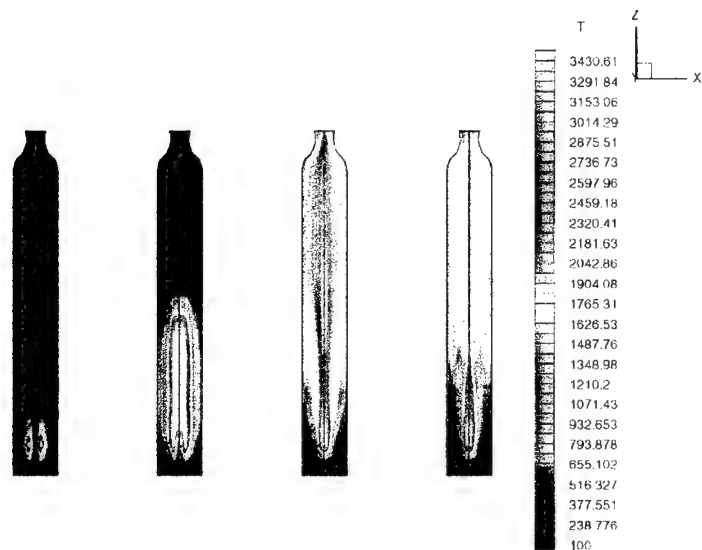


Figure 5. Temperature distributions at different instants:  $t_i = 7.26, 7.9, 9.26,$  and  $12.0$  msec, respectively. *Real* gas model.

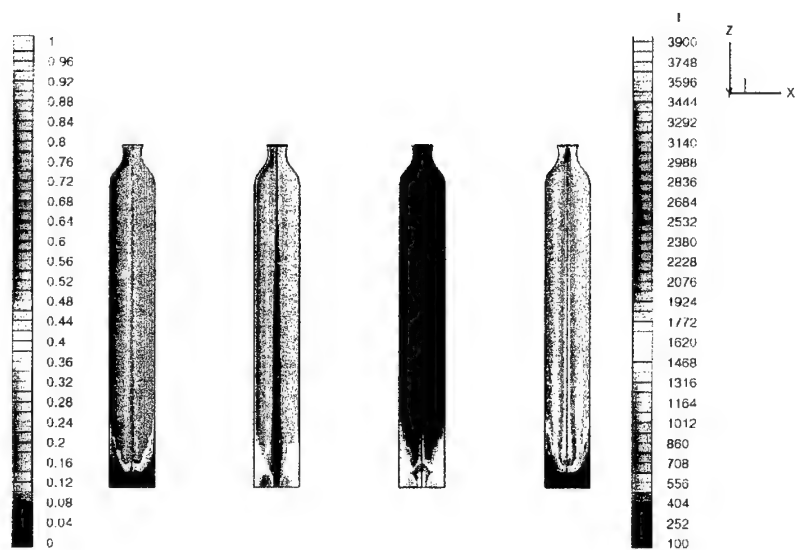


Figure 6. Steady-state flow parameter distributions:  $\text{H}_2\text{O}$ ,  $\text{H}_2$ ,  $\text{O}_2$ , and temperature, respectively. *Ideal* gas model.

Figure 6 with the temperature plot in Figure 5 confirms the aforementioned conclusion. The temperature peaks at 3856 K which is close to the equilibrium limit at constant volume.

If the simulation starts with the chamber full of moving  $H_2$ , the pressure vs time history does not show the initial rise as can be seen in Figure 4. Design chamber pressure, ( $\sim 100$  bar), was not reached in all cases because of incomplete combustion, a significant result associated with finite-rate kinetics.

## CONCLUSION

Numerical results show the essential role of finite-rate chemistry and thermodynamic non-ideal gas behavior in the simulation of high pressure  $H_2/O_2$  combustion. The enhanced mixing process determines the location of the combustion zone and yields a large difference for the in-chamber steady state solution in comparison with the ideal gas model. Even though the equilibrium model is used in conjunction with the temperature threshold, it does not simulate the ignition process comparable to that of finite-rate chemistry.

## References

- [1] Liang, P., and Ungewitter, R., Multi-Phase Simulations of Coaxial Injector Combustion, AIAA Paper 92-0345, 1992.
- [2] Golovitchev, V.I., and Schley, C.-A., Preliminary Modification of KIVA-II Code for Rocket Thrust Chamber Modeling, DLR IB 643-95-04, 1995.
- [3] Amsden, A.A., O'Rourke, P.J., and Butler, T.D., KIVA-II: A Computer Program for Chemically Reactive Flows with Sprays, Los Alamos Report LA-11560-MS, 1989.
- [4] Reid, R.C., Prausnitz, J.M., and Poling, B.E., The Properties of Gases & Liquids, 4th edition, McGraw-Hill Book Company, NY, 1986.
- [5] Schley, C.-A., Schik, A., and Krülle, G., Cryogenic High Pressure Coaxial Injection and Atomization: Experiments and Modeling, AIAA Paper 95-2556, 1995.
- [6] McBride, B.J., Reno, M.A., and Gordon, S., CET93 and CETPC: An Interim Updated Version of the NASA Lewis Computer Program for Calculating Complex Chemical Equilibria with Applications, NASA TM-4557, 1994.
- [7] Hendricks, R.C., Baron, A.K., and Peller, I.C., GASP - A Computer Code for Calculating the Thermodynamic and Transport Properties for Ten Fluids: Parahydrogen, Helium, Neon, Methane, Nitrogen, Carbon Monoxide, Oxygen, Fluorine, Argon, and Carbon Dioxide, NASA TN D-7808, 1975.
- [8] Golovitchev, V.I., and Bruno, C., Modeling of Parallel Injection Supersonic Combustion, ISTS Paper 94-a-08, Yokohama, Japan, May 15-24, 1994.
- [9] Kee, R.J., Dixon-Lewis, G., Warnatz, J., Coltrin, M.E., and Miller, J.A., A Fortran Computer Package for the Evaluation of Gas-Phase Multicomponent Transport Properties, SAND86-8246, 1986.
- [10] Miller, J.A., and Bowman, G.T., Mechanism and Modeling of Nitrogen Chemistry in Combustion, Prog. Energy Combust. Sci., 15, 287-338, 1989.
- [11] Jachimowski, C.A., An Analytical Study of the Hydrogen-Air Reaction Mechanism with Application to Scramjet Combustion, NASA TP 2791, 1988.

## EFFECTS OF FLAME BEHAVIOR ON A GASEOUS METHANE/OXYGEN SMALL THRUSTER PERFORMANCE

KATO Hideki, IKEZAKI Takashi, and YUASA Saburo  
Tokyo Metropolitan Institute of Technology,  
Asahigaoka 6-6, Hino-shi, Tokyo 191, JAPAN

**ABSTRACT:** This paper reports the experimental results of the basic performance of a  $\text{GCH}_4/\text{GO}_2$  small thruster with a swirl-coaxial injector. The effects of the equivalence ratio of  $\text{CH}_4/\text{O}_2$  mixtures and the swirl intensity of the  $\text{O}_2$  injector on the combustion characteristics of the combustion chamber were studied. It was found that applying swirl to the  $\text{O}_2$  jet greatly improved the thruster performance by increasing the mixing rate between the propellants. The performance was also influenced by the equivalence ratio. Direct observation in the combustion chamber showed that when the swirl intensity of the  $\text{O}_2$  jet was small, the flame lifted at low equivalence ratios and the rim stabilized flame was formed at high equivalence ratios. For higher swirl intensity, only a lifted flame was developed over the range of the equivalence ratio tested. The tendency is explained by the ratio of the angular momentum of the  $\text{O}_2$  jet to the linear momentum of  $\text{CH}_4$  jet. The lifted flames had a favorable effect on the mixing between the propellants, resulting in the good thruster performance. Emission spectra from the flame in the combustion chamber were measured to make the combustion process clear. The measurement showed that the various reactions including the generation of OH, CH and  $\text{C}_2$  initially proceeded on the injector side. The formation order and intensity variation of the species were discussed.

### INTRODUCTION

Hydrocarbon fuels are proposed for propellants of booster rocket engines to launch vehicles. Methane is denser than hydrogen, relatively cheap, and gives relatively good performance. With oxygen, therefore, it is a candidate propellant. It is well known that combustion in thrust chambers is strongly influenced by the design of injectors, though the detailed effects of injectors on combustion phenomena in a combustion chamber have not yet been clarified.

We developed a  $\text{GCH}_4/\text{GO}_2$  thruster for obtaining fundamental data and comparing to the  $\text{H}_2/\text{O}_2$  thruster.[1] The present experiments focused on the effects of  $\phi$  of  $\text{CH}_4/\text{O}_2$  mixtures and the swirl intensity of the injector on the combustion characteristics of the combustion chamber. The swirl intensity of the injector, represented by the swirl number  $S_g$ , was defined as the ratio of angular momentum flux to (radius x axial momentum flux), depending on the configurations of the  $\text{O}_2$  injector port.[2] Spectroscopic analysis was made to improve our understanding of the combustion phenomena.

### EXPERIMENTAL APPARATUS AND PROCEDURE

Figure 1 shows a cross-sectional view of the thruster used in this study, which is basically the same as that used for the  $\text{GH}_2/\text{GO}_2$  small thruster.[1] The chamber and

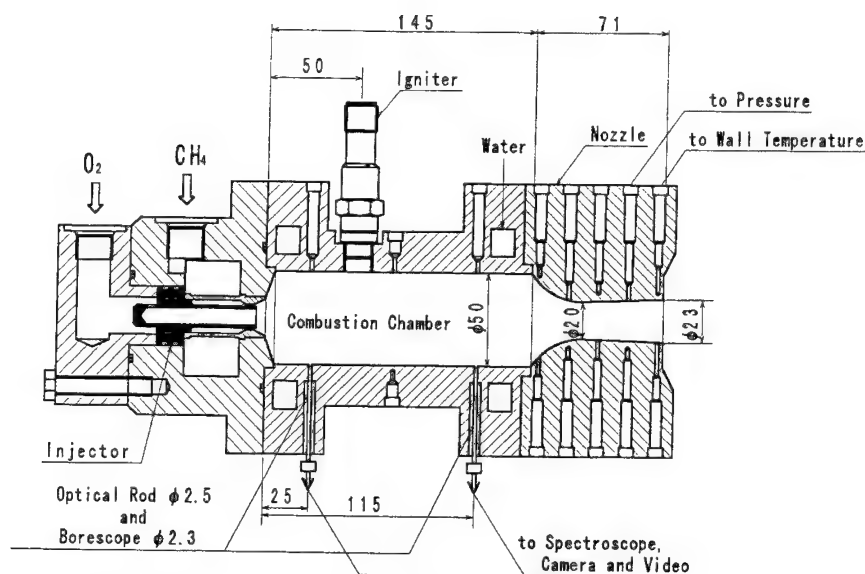


Figure 1. Cross-sectional view of the thrust chamber.

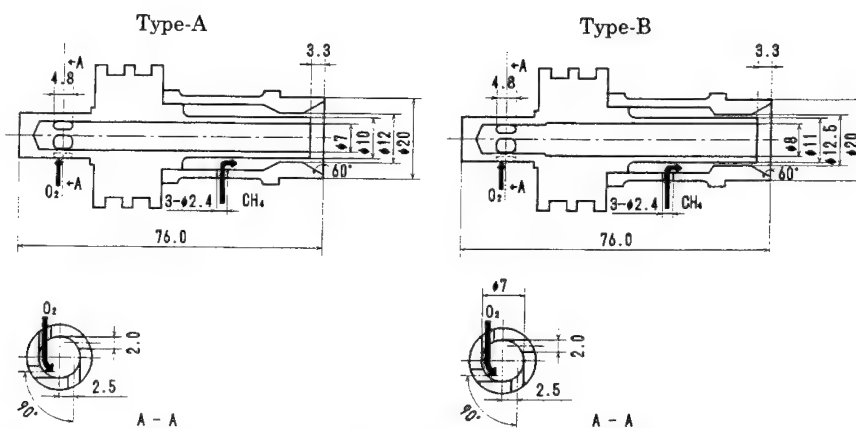


Figure 2. Schematic of the coaxial injectors: Type-A injector,  $S_g = 0.78$  and Type-B injector,  $S_g = 0.68$ .

the nozzle were fabricated from oxygen-free copper and were water cooled. Two small quartz glass windows were located at  $x = 25$  mm and  $x = 115$  mm downstream of the injector exit, which allowed the inside of the combustion chamber to be viewed. The propellants were ignited by a spark plug mounted on the middle part of the chamber wall. Gaseous methane and oxygen were introduced into the chamber through a single coaxial injector. To promote mixing between the propellants, swirling motion was applied to the  $O_2$  jet. Two types of injectors, Type-A and Type-B as shown in Fig. 2, were used to vary the injection velocity ratios between the propellants. The swirl numbers  $S_g$  are listed in Table 1. Flame appearances were photographed using a borescope, and emission spectra were measured through a quartz fiber using a multi-channel detector with a photodiode of 1024 channels.



Nominal chamber conditions and performances were as follows:

Chamber pressure	$P_c$	0.39	MPa ,
$\text{CH}_4$ mass flow rate	$\dot{m}_{\text{CH}_4}$	0.021	kg/s ,
$\text{O}_2$ mass flow rate	$\dot{m}_{\text{O}_2}$	0.051	kg/s ,
Equivalence ratio of propellants $\phi$			1.6,
Thrust	$F$	136	N ,
Specific impulse	$I_{sp}$	193	s .

The experiments were carried out by varying the equivalence ratio  $\phi$  in the range from 1.1 to 2.1. The time duration of a test firing was 12 seconds.

**Table 1**  
Injector Geometry

	Type-A	Type-B
Port area ( $\text{GO}_2$ ), $\text{mm}^2$	38.5	50.3
Annulus area ( $\text{GCH}_4$ ), $\text{mm}^2$	34.6	27.7
Geometric swirl number, $S_g$	0, 0.78, 1.40	0, 0.68

## EXPERIMENTAL RESULTS AND DISCUSSION

### Performance Evaluations

Figures 3 and 4 show  $I_{sp}$  and  $c^*$  efficiencies measured without the correction of heat losses.[3] In the case of Type-A injector at  $S_g = 0$ , the chamber pressure did not attain the design point and the maximum value of the pressure was only 0.29 MPa. At  $\phi$  ranging between 1.2 to 1.6, measured values of  $I_{sp}$  and  $c^*$  efficiencies tended to increase with increasing  $\phi$ . The maximum values were about 127 s and 0.72, respectively. These were far lower than the theoretical values because under no swirling condition the design chamber pressure could not be attained even at the design flow rates of  $\text{O}_2$  and  $\text{CH}_4$ . The low levels of the  $c^*$  efficiency indicate incomplete combustion. Ignition did not occur when  $\phi$  was larger than 1.6. With  $\text{O}_2$  swirl, the maximum values of  $I_{sp}$  and  $c^*$  efficiency were about 170 s and 0.91, respectively. For  $S_g = 0.78$   $I_{sp}$  attained a maximum value at  $\phi$  of about 1.5, which is smaller than the theoretically calculated ratio of 1.6. For higher swirl intensity,  $S_g = 1.40$ ,  $I_{sp}$  attained a maximum value at about  $\phi = 1.6$ .  $c^*$  efficiencies decreased from 0.93 to 0.89 if  $\phi$  was increased.

In the case of Type-B injectors at  $S_g = 0$ , the chamber pressure was 0.33 MPa. Though each performance value was improved slightly compared to that obtained by Type-A at  $S_g = 0$ ,  $c^*$  efficiency was still low. In the case of  $S_g = 0.68$ ,  $I_{sp}$  was almost the same value as that for Type-A with swirl up to  $\phi = 1.6$ , and was an intermediate value at higher  $\phi$ . There was no difference of  $c^*$  efficiency between Type-A and Type-B.

These results indicate that application of swirling motion to the  $\text{O}_2$  jet greatly improved the thruster performance. The performance was also improved by using Type-B injectors.

### Flame Configurations

In order to obtain a better understanding of the combustion behavior, photographs of the flames in the combustion chamber at  $x = 25$  mm and 115 mm from the injector exit were taken. Variations of flame configurations obtained in this study are summarized in Table 2.

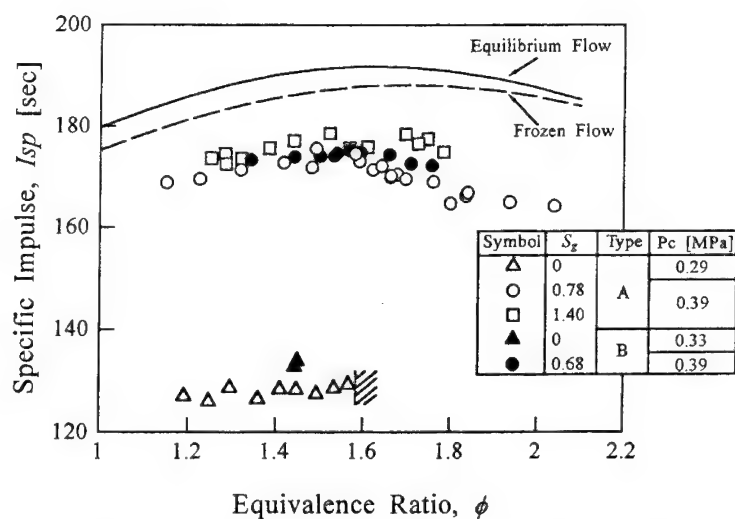


Figure 3. Variation of specific impulse with equivalence ratio.

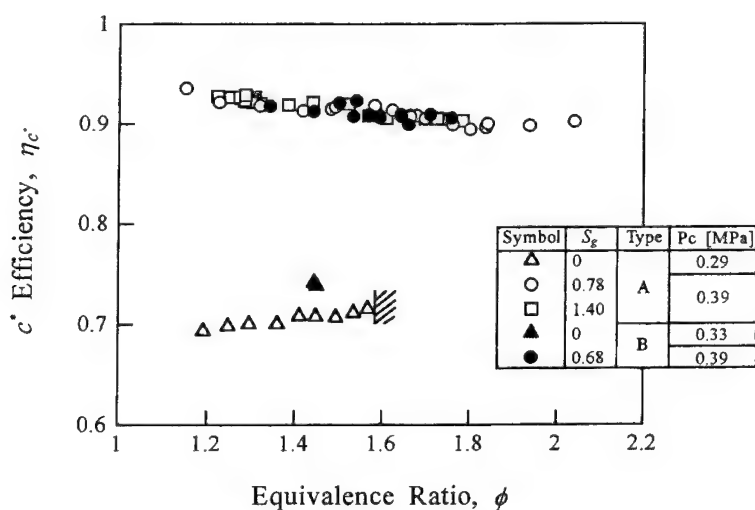


Figure 4. Variation of  $c^*$  efficiency with equivalence ratio.

Table 2  
Flame Configurations

	Geometric Swirl Number, $S_g$	Flame Configuration	
		$\phi = 1.3$	$\phi = 1.7$
Type-A	0	Jet Diffusion Flame	Non-ignition
	0.78	Lifted Flame	Rim-stabilized Flame
	1.40	Lifted Flame	
Type-B	0	Jet Diffusion Flame	-----
	0.68	Rim-stabilized Flame	

Figure 5 shows typical flame appearances observed for Type-A injectors. Under the condition of no swirling motion, a stable ordinary jet diffusion flame stabilized on the injector rim was formed (Fig.5-a). Even near the nozzle entrance, combustion was confined to the narrow region on the control axis. This suggests incomplete combustion in the chamber, resulting in decreases of the  $c^*$  efficiency and the chamber pressure. For  $Sg = 0.78$ , two typical configurations of the flames, a lifted and a rim-stabilized flame, were observed depending on  $\phi$ , as shown in Figs. 5-b and 5-c. When  $\phi$  was smaller than 1.3, the flame lifted (Fig.5-b). When  $\phi$  exceeded 1.7, only a rim-stabilized flame developed and had the characteristic shape of a diffusion flame (Fig.5-c). At  $x = 125$  mm, dark regions on the upper and lower sides of the photograph show that the flame remains narrow. Between these ratios, a lifted and a rim-stabilized flame formed alternately. It should be noted that the value of  $\phi$  at which the flame configuration transformed from a lifted flame to a rim-stabilized flame coincides with that giving the maximum value of  $I_{sp}$ . The period that the rim-stabilized flame was formed increased with an increase of  $\phi$ . In the case of  $Sg = 1.40$ , only a lifted flame was observed over the range tested (Fig.5-d). The flame configuration was essentially the same as the lifted flame for  $Sg = 0.78$  except that a small conical luminous region existed near the injector exit.

Based on these results and characteristic performances for Type-A injectors with a swirling motion of the  $O_2$  jet, we suggest the following: when the rim-stabilized flame develops, the flame becomes narrower due to diminution of the mixing rate. This reduces the degree of completeness of combustion in comparison with the lifted flame. Thus, for  $Sg = 0.78$  the change from the lifted flame to the rim-stabilized flame causes a decrease of  $I_{sp}$ . In the case of  $Sg = 1.40$ , on the contrary, only the lifted flame develops, so  $I_{sp}$  attains a relatively higher value. Combustion occurs near the chamber wall for the lifted flame spreading outside because the stronger swirling motion increases heat loss to the wall. This consideration shows that there are no differences in apparent  $c^*$  efficiencies between  $Sg = 0.78$  and 1.40 without the correction of heat loss because the combustion efficiency drop for a rim-stabilized flame is nearly equal to the increase of heat loss for the lifted flame.

Figure 6 shows photographs of the flames at  $x = 25$  mm, in the case of Type-B injectors at  $\phi = 1.4$ . When  $Sg = 0$ , a jet diffusion flame was observed. The diameter of the flame was larger than that of the flames for Type-A injectors at  $Sg = 0$  (Fig.6-a). For  $Sg = 0.68$ , a rim-stabilized flame was formed (Fig.6-b). The flame spread out wider and a conical strong luminous region was recognized. The shape of the flame differed from that of the rim-stabilized flame observed for Type-A injectors at  $Sg = 0.78$ .

Figure 7 shows injection velocities of the  $O_2$  and  $CH_4$  jets as a function of  $\phi$ . While for Type-A injectors  $u_{O_2}$  is higher than  $u_{CH_4}$  in the range of  $\phi$  below 1.8, for Type-B injectors  $u_{CH_4}$  is higher than  $u_{O_2}$ . The injection velocities influence the flame configuration even at the same swirl intensity. For Type-B injectors, the velocity increase of the  $CH_4$  jet impinging on the  $O_2$  jet spreading outside decreases the flame stability on the injector rim. This encourages turbulent mixing and the combustion process is improved.

The ratios of the angular momentum of the  $O_2$  jet to the linear momentum of the  $CH_4$  jet are plotted in Fig. 8 as a function of  $\phi$ . The momentum ratio is defined by the following equation:

$$\frac{\dot{m}_{O_2} \cdot u_{O_2} \cdot r_{O_2}}{\dot{m}_F \cdot u_F \cdot 2\sqrt{A_F/\pi}} \times Sg$$

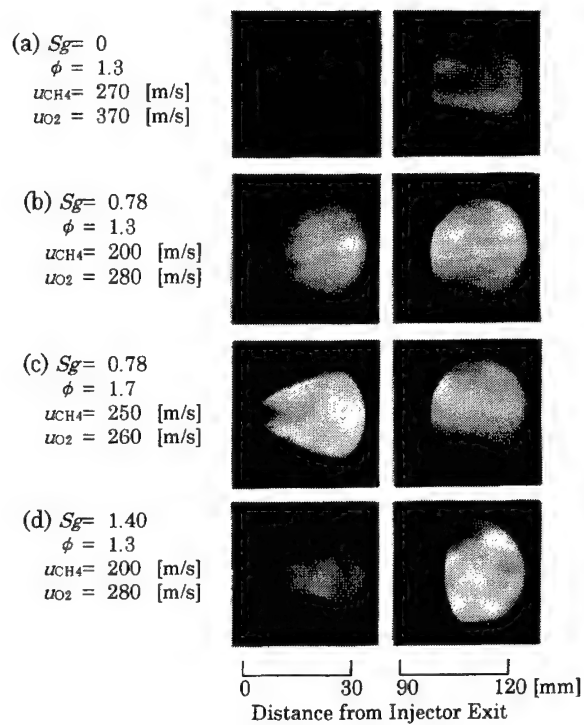


Figure 5. Typical flame appearance in the thrust chamber: Type-A injector.

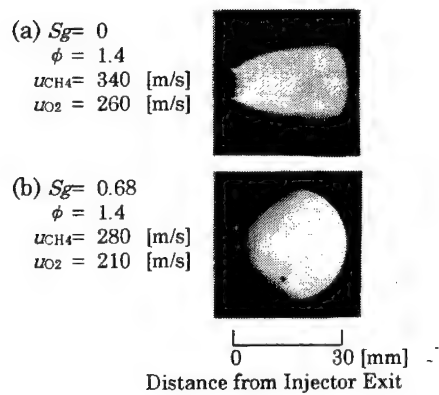


Figure 6. Typical flame appearance in the thrust chamber: Type-B injector.

where  $\dot{m}_{O_2}$  is the oxidant mass flow rate,  $\dot{m}_F$  is the fuel mass flow rate,  $u_F$  is the fuel injection velocity,  $r_{O_2}$  is the exit radius of the  $O_2$  port, and  $A_F$  is the area of the fuel injector port. For comparison, the momentum ratio for the  $H_2/O_2$  propellants[1] are also shown. The figure shows that with a decrease of  $\phi$ , the  $O_2$  angular momentum increases. Corresponding to this, the rim stability decreases. This relation implies that the radial velocity component of the  $O_2$  jet due to swirling motion acts on the  $CH_4$  jet as a cross flow, causing the  $CH_4/O_2$  flame to lift. For the lifted flame, the mixing between the propellants is promoted near the base of the flame to reduce the flame length, which was confirmed in a previous paper.[4] Thus, the lifting had favorable effects on the thruster performance due to the completeness of combustion in the chamber.

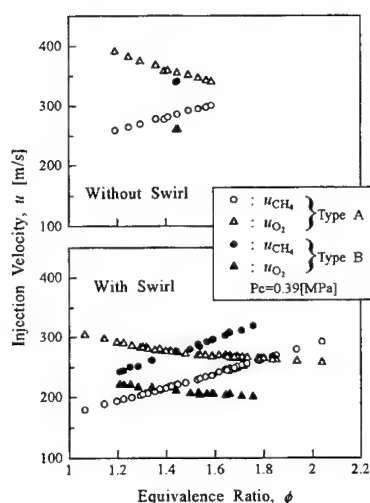


Figure 7. Injection velocities as a function of equivalence ratio.

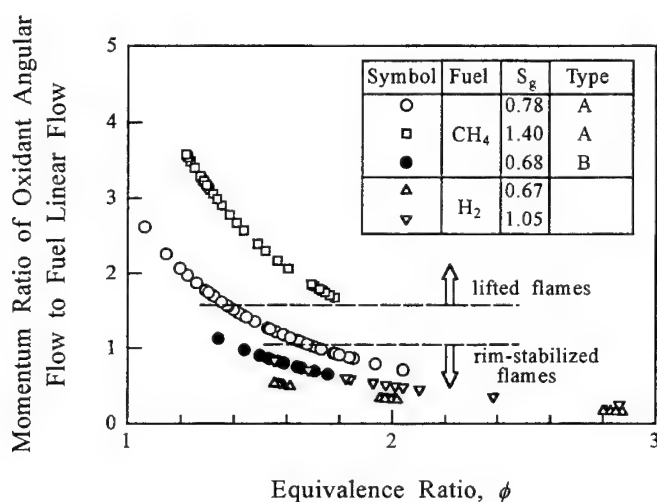


Figure 8. Momentum ratio of oxidant angular flow to fuel linear flow:  $P_c = 0.39$  MPa.

## Combustion Process

To examine the reaction process in the combustion chamber, spectroscopic analysis was performed (Type-A injector,  $Sg = 0.8$ , and  $\phi = 1.3$  and  $1.7$ ). Figures 9 and 10 show the emission spectra for two values of  $\phi$ , respectively, at two positions where photographs of the flames were taken: the injector side and the nozzle side in the combustion chamber. On the injector side of  $x = 25$  mm at  $\phi = 1.3$ , strong OH, CH and  $C_2$  bands, and continuous emission are recognized as shown in Fig.9-a. The continuous emission may be due to partially  $O_2$  Schumann-Runge bands and partially radiation of the reaction of CO and O.[5] On the nozzle side of  $x = 115$  mm, OH bands and continuous emission are stronger than those spectra on the injector side and CH bands are negligible (Fig.9-b). For  $\phi = 1.7$  at  $x = 25$  mm, OH and  $C_2$  bands and continuous emission are observed as shown in Fig.10-a. The CH band at  $\lambda = 431.5$  nm is the strongest in the region of wavelengths measured. On the nozzle side, OH bands and continuous emission become stronger than those on the injector side (Fig.10-b). This spectroscopic result of the intensity of the continuous emission coincides with the visual observation of luminosity in the combustion chamber.

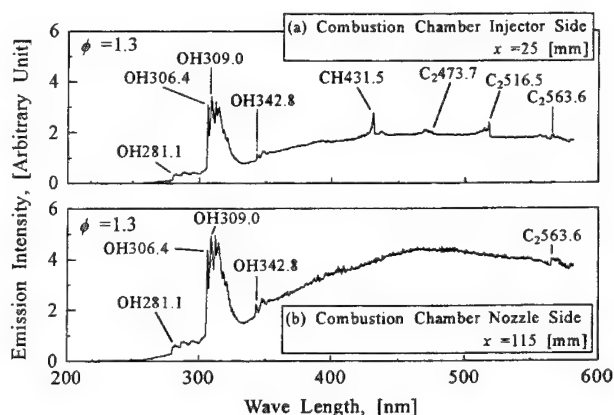


Figure 9. Variation of emission spectrum with axial position: Type-A injector,  $Sg = 0.78$ ,  $\phi = 1.3$ .

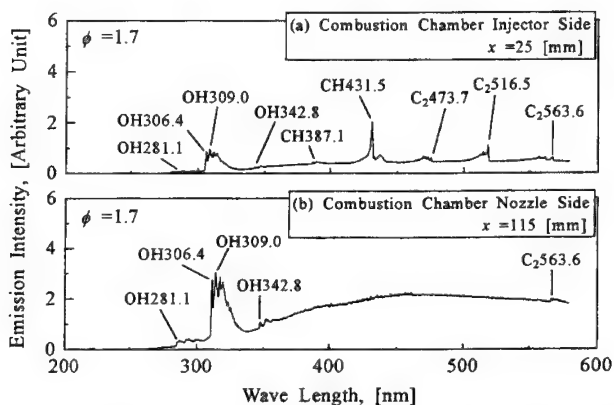


Figure 10. Variation of emission spectrum with axial position: Type-A injector,  $Sg = 0.78$ ,  $\phi = 1.7$ .

In order to improve our understanding of the above experimental results, the flame structure of  $\text{CH}_4/\text{O}_2$  one-dimensional premixed flames was calculated.[6] Figure 11 shows the concentration and temperature distributions calculated at  $\phi = 1.3$ . CH is produced in the main reaction region and is then consumed immediately. CH concentration is low. On the other hand, OH reaches a chemical equilibrium composition through the main reaction zone. The formation order and intensity variation obtained from the spectroscopic analysis agree with that of the calculated premixed flame. These results imply that the various reactions including the generation of CH due to decomposition of  $\text{CH}_4$  proceeded on the injector side, and that the final products and the OH persisting for a long while were produced from the intermediate downstream products in this rocket engine.

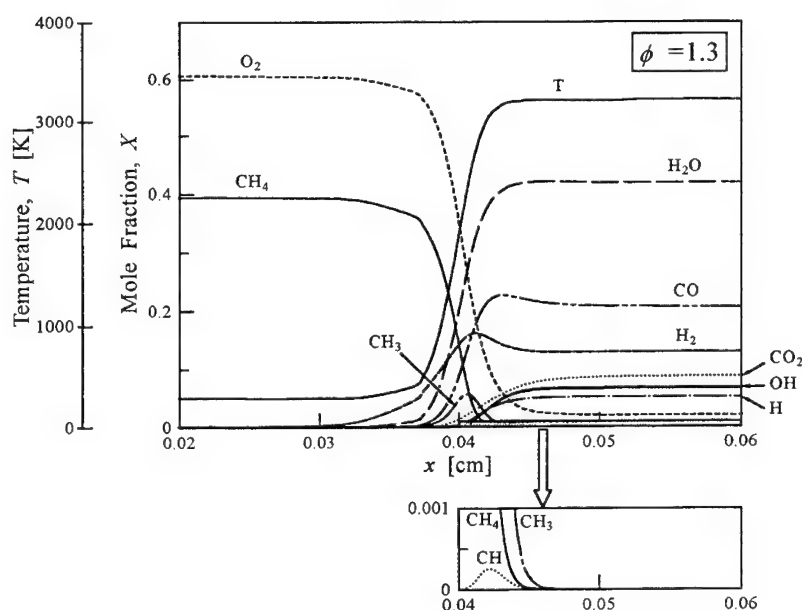


Figure 11. Concentration and temperature distributions in a one-dimensional  $\text{CH}_4/\text{O}_2$  premixed flame.

## CONCLUSIONS

- (1) Flame configurations were strongly influenced by the swirl intensity of the  $\text{O}_2$  jet and the equivalence ratio between the  $\text{O}_2/\text{CH}_4$  propellants. When the swirl intensity of the  $\text{O}_2$  jet was small, the flame lifted at low equivalence ratios and the rim stabilized flame was formed at high equivalence ratios. For higher swirl intensity, only the lifted flame was developed over the range of the equivalence ratio tested.
- (2) Applying swirl to the oxygen jet had favorable effects on the thruster performance due to the completeness of combustion in the chamber attributed to the mixing between the propellants. The lifting of the flame had the same effects on the performance as the swirling motion of the  $\text{O}_2$  jet.
- (3) Emission spectra of OH, CH and  $\text{C}_2$  were observed on the injector side insensitive to the equivalence ratio. Although CH and  $\text{C}_2$  consumed immediately, OH emission increased toward downstream.

### ACKNOWLEDGMENTS

This work was supported by the Grants-in-Aid for Special Project Research of Tokyo Metropolitan. The authors would like to express their sincere thanks to Mr. Imamura T. and Mr. Miyashita T. for their cooperation in conducting the experiment.

### REFERENCES

1. Yuasa, S., Kubota, S., and Fujita, M., Combustion Characteristics in a Gaseous Hydrogen/Oxygen Small Thruster, *Fourth International Symposium on Special Topics in Chemical Propulsion*, 1996.
2. Yuasa, S., Effects of Swirl on the Stability of Jet Diffusion Flames, *Combustion and Flame*, 66, 181-192, 1986.
3. Gordon, S. and McBride, B., Computer Program for Calculation of Complex Chemical Equilibrium Compositions, Rocket Performance, Incident and Reflected Shocks, and Chapman-Jouguet Detonations, *NASA SP-273*, 1971.
4. Hottel, H. C. and Hawthorne, W. R., Diffusion in laminar flame jets, *Third Symposium on Combustion and Flame Explosion Phenomena*, Williams & Wilkins, Baltimore, 254-266, 1949.
5. Gaydon, A. G. and Wolfhard, H. B., *Flames*, Chapman and Hall, London, 158-162, 1979.
6. Kee, R. J., Grcar, J. F., Smooke, M. D., et al., A Fortran Program for Modeling Steady Laminar One-Dimensional Premixed Flames, *Sandia Report, SAND85-8240*, 1985.



## COMBUSTION CHARACTERISTICS IN A GASEOUS HYDROGEN/OXYGEN SMALL THRUSTER

YUASA<sup>1</sup> Saburo, KUBOTA<sup>1</sup> Satoshi, and FUJITA<sup>2</sup> Masumi

<sup>1</sup>Tokyo Metropolitan Institute of Technology,  
Asahigaoka 6-6, Hino-shi, Tokyo 191, JAPAN ;

<sup>2</sup>National Space Development Agency of Japan,  
Hamamatsu-cho 1-29-6, Minato-ku, Tokyo 105, JAPAN

**ABSTRACT:** An experimental study on the combustion phenomena in a combustion chamber was performed by using a gaseous hydrogen/oxygen small rocket thruster with a single swirl-coaxial injector. The variables studied were the swirl intensity of the injector and the equivalence ratio between the propellants. Direct observation in the combustion chamber showed that a stable hydrogen/oxygen flame attached to the injector rim was formed independent of the swirl intensity. Applying swirl to the oxygen jet increased the flame diverging angle and decreased the flame length in the chamber, thus reducing the reaction time to reach completion of combustion. Measurements of the OH-radical intensity in the chamber revealed that the location of the actively reacting region moved with the swirl intensity and the equivalence ratio in the chamber. With oxygen swirl, high performance of  $I_{sp}$  and  $C^*$  was obtained, but without oxygen swirl the performance parameters decreased noticeably. This can be explained by the degree of completeness of combustion in the chamber attributed to the mixing between the propellants. The test results indicated that a small and simple thruster with a single swirl-coaxial injector offered good performance by increasing the mixing rate between the propellants.

### INTRODUCTION

The auxiliary propulsion system for the manned Space Station must have a long life and operate with high reliability and low maintenance. For this purpose, there has recently been interest in a small rocket engine using gaseous hydrogen/oxygen as propellants.[1,2] These propellants provide a simple combustor structure because of the excellent combustion characteristics of hydrogen, which is useful for the operation requirements. In addition, the hydrogen/oxygen system has cost and environmental merits because the propellants can be produced by electrolysis of waste water used in the Space Station and ensure a low contamination level for the Station.

We have developed a gaseous hydrogen/oxygen small and simple rocket thruster with a single swirl injector. The swirl intensity of the injector, represented by a geometrical swirl number  $S_g$  defined as the ratio of angular momentum flux to (radius x axial momentum flux),[3] was important factor in this study. The present study examined combustion phenomena in the thruster chamber to obtain fundamental data on small rocket combustion and to verify the good performance of the simple thruster.

## EXPERIMENTAL APPARATUS

Figure 1 shows the thick-walled, water-cooled thruster used in this study. The thruster was made of oxygen-free, high-conductivity copper. It contained a single swirl-coaxial injector with an outer hydrogen and an inner swirling oxygen jet and two optical ports for viewing the combustion process and measuring spectra from a flame in the combustion chamber. Several possible temperature and pressure measurement taps were also equipped, and the temperature and pressure values at the center of the chamber were monitored during a test run. Figure 2 shows a schematic of the swirl-coaxial injector. Hydrogen was supplied axially through an outer annulus. Oxygen was supplied tangentially through an inner tube with inlet slots. The initial temperatures of the propellants were room temperature. Three types of the injector, having the swirl number  $S_g$  of 0, 0.67 and 1.05 for the oxygen jets, were used in this study. (When  $S_g=0$ , oxygen without swirl was introduced axially without swirl.) Two small ports with quartz windows allowed the inside of the combustion chamber to be viewed. A bore scope system, shown in Fig. 3, and a quartz fiber system were used for observing the combustion phenomena and for measuring flame spectra in the chamber, respectively. No coolant was provided for the window surface. To measure the radial heat flux in the chamber wall, a thermocouple was embedded in the wall at the center with respect to the axial position, and was slid by 1-mm spaces in the wall every test runs. Thrust was measured by a calibrated load cell equipped in front of the thrust chamber.

The nominal mass flow rate of hydrogen was 10 g/s, while the oxygen flow rate was 40 g/s, resulting in an equivalence ratio of 2. These flow rates together with the nozzle configuration produced a chamber pressure of 0.39 MPa and a thrust level of 123 N. The primary variables studied here were the swirl intensity  $S_g$  of the oxygen jet and the equivalence ratio  $\phi$  for hydrogen/oxygen propellants.

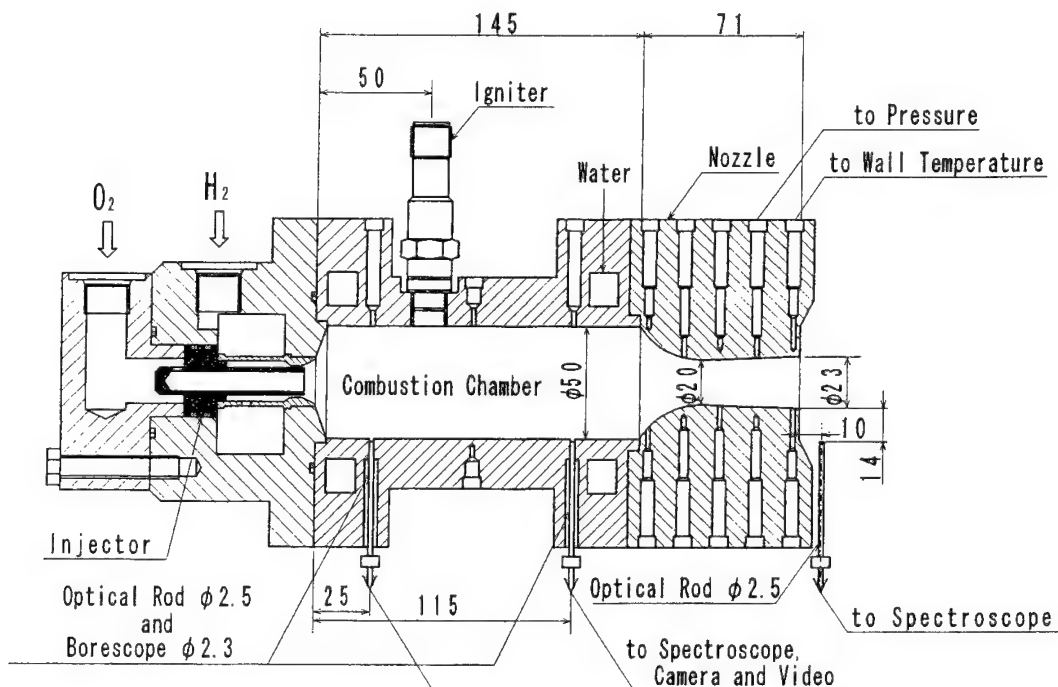


Figure 1. Schematic of small thruster chamber with a coaxial injector. Dimensions are in mm.

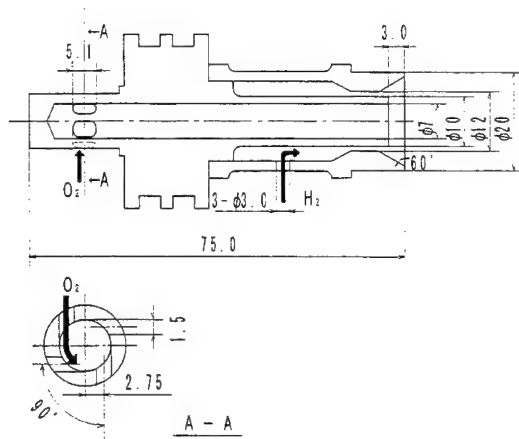


Figure 2. Schematic of the swirl-coaxial injector :Sg=1.05.

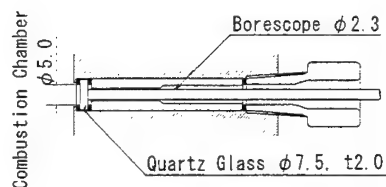


Figure 3. Schematic of the borescope.

## EXPERIMENTAL RESULTS AND DISCUSSION

### Time History of Thruster Parameters

In the present study, the overall firing duration was 12 seconds, which was decided by a compromise between the survivability of the optical systems without cooling and the time required for steady-state data to be reached. A typical history of several key operating parameters is presented in Fig.4. It can be seen that the parameters except the wall temperature achieved steady-state after the start transient. The wall temperature increased during the entire test run, but at the end of the test the increase was minimum. Thus, data of the operating parameters evaluated near the end of the run can be considered applicable to steady-state conditions. The specific impulse  $I_{sp}$ , the  $C^*$  efficiency  $\eta_{c^*}$  and the heat flux were calculated based on these data.

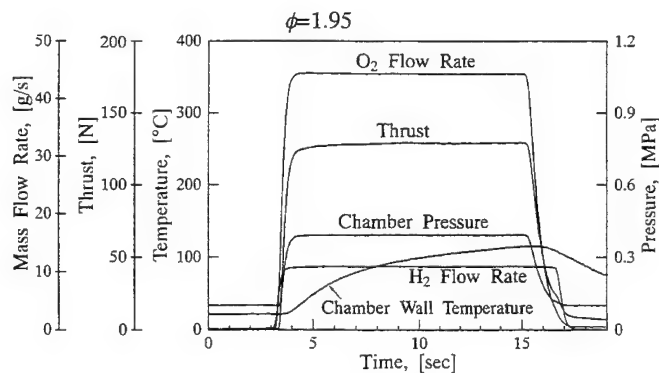


Figure 4. Typical time history of key operating parameters.

## Thruster Performance

Measured  $I_{sp}$  and  $\eta_{c^*}$  without correction for heat losses to the cooling water are plotted as a function of  $\phi$  in Fig. 5. When swirl was applied to the oxygen jet, measured  $I_{sp}$  increased with increasing  $\phi$ . This represents the same tendency as the theoretical values of  $I_{sp}$ .  $\eta_{c^*}$  varied a little with  $\phi$ , ranging from 0.91 to 0.94. This suggests that the combustion behavior in the chamber did not essentially vary with  $\phi$ . The apparent values of  $\phi$  and  $\eta_{c^*}$  obtained were independent of  $S_g$ . On the other hand, in the case without swirl of the oxygen jet, although the dependency of  $I_{sp}$  and  $\eta_{c^*}$  on  $\phi$  was almost the same as that with swirl, the absolute values were considerably lower than those with swirl. This suggests that combustion without swirl of the oxygen jet was not completed in the chamber.

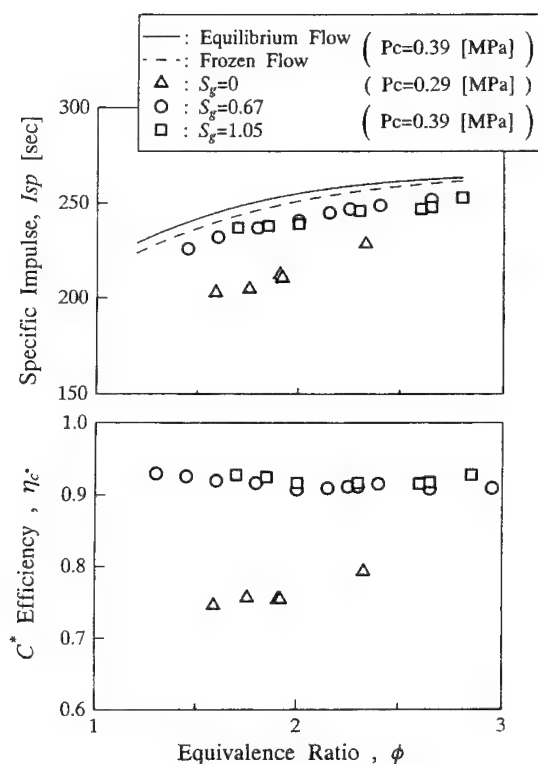


Figure 5. Measured specific impulse and  $C^*$  efficiency as a function of equivalence ratio

Table 1  
 $C^*$  efficiencies with corrections:  $P_c=0.39$  Mpa,  $\phi=2.0$ .

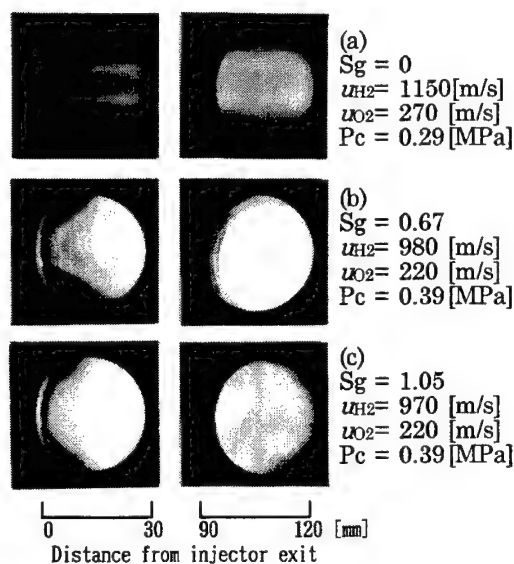
Swirl intensity of O <sub>2</sub> jet	Uncorrected $\eta_{c^*}$	Corrected $\eta_{c^*}$
$S_g = 0.67$	0.91	0.93
$S_g = 1.05$	0.92	0.99

Using the thermocouple data measured at 1-mm spaces in the chamber wall, the heat flux during a fire testing was calculated. The typical heat fluxes of the combustor at  $\phi = 2.0$  were  $2.33 \text{ MW/m}^2$  for  $S_g = 0.67$  and  $6.42 \text{ MW/m}^2$  for  $S_g = 1.05$ . It should be noted that the heat flux increased with a higher  $S_g$ . The present heat flux values are close to those previously reported for the small hydrogen/oxygen rocket engine with 414 kPa chamber pressure.[4]  $\eta c^*$  was corrected for the heat losses from the combustion chamber,[5]

assuming that the values of the losses were nearly equal to the heat fluxes obtained. The corrected values of  $\eta c^*$ , shown in Table 1, indicate that mixing and combustion with a strong swirl degree of the oxygen jet were mostly completed in the combustion chamber, and applying swirl to the oxygen jet effectively improved combustion performance. It is concluded that a small and simple thruster with a single swirl-coaxial injector may offer good performance.

### Flame Behavior in the Combustion Chamber

*Effects of swirl of oxygen jet.* Figure 6 shows the variation in shape of the flames formed in the chamber as a function of  $S_g$ . Two fields of view are shown from 0 mm to 30 mm and from 90 mm to 120 mm downstream of the injector exit, respectively. These photographs show that the stable hydrogen/oxygen flames, attached to the injector rim between the oxygen jet and the hydrogen jet, were formed in the combustion chamber independent of  $S_g$ . The flame without oxygen swirl was generally similar in shape to ordinary turbulent jet diffusion flames. Even near the nozzle entrance, combustion was confined to the narrow region on the central axis (Fig.6-a). Applying swirl to the oxygen jet increased the flame diverging angle and decreased the flame length (Fig.6-b and 6-c). It can be seen that a conical luminous region appeared at the location just downstream of the injector exit. This implied that due to the strong swirling motion of the oxygen jet a recirculation zone formed in the region, where mixing and combustion between the propellants proceeded actively. At the downstream region of the chamber, combustion might occur all over the chamber. With stronger swirl intensity of the oxygen jet, the flame diverging angle became wider. The luminous cone moved upstream, and thus the flame length became shorter. The change of the flame shape with  $S_g$  suggests that an increase of  $S_g$  decreased the boundary thickness over the chamber wall, resulting in higher heat flux from the combustion chamber.



**Figure 6.**  
Variation of flame  
configuration  
in the combustion  
chamber with swirl  
intensity of the oxygen jet:  $\phi = 2.0$ .

Figure 7 shows the emission spectra of a hydrogen/oxygen flame formed in the combustion chamber. The bands of OH are visible, in agreement with observations of ordinary hydrogen/oxygen flames formed at various conditions.[6] Figure 8 shows the intensities of OH-radical ( $\lambda = 306.3$  nm) along the axial distance from the injector exit for the three  $S_g$  values. (The intensities were normalized by the intensity of  $S_g=0.67$  at 25 mm from the injector exit.) It was found that the OH intensity for  $S_g=0$  was weakest for the three  $S_g$  values at 25 mm and increased toward the downstream. However, the intensity was strongest among the three  $S_g$  values at the exit of the thruster nozzle. The high level of OH-radical shows that the reaction between the propellants still proceeded substantially even at the exit of the nozzle. The OH intensity for  $S_g=1.05$  was the strongest of the three  $S_g$  values at the location closes to the injector and was reduced sharply toward the downstream, indicating that combustion mainly occurred in the upstream region of the combustion chamber as a result of the increased mixing rate between the propellants due to impingement of the outer hydrogen jet on the inner oxygen jet spreading outside by the swirling motion.

The flame observations and OH-radical intensity measurements indicated that the hydrogen/oxygen propellants without swirl formed a flame, similar to ordinary turbulent jet diffusion flames, which require a long residence time in the chamber to complete combustion, and hence the combustion reaction did not reach completion. On the other

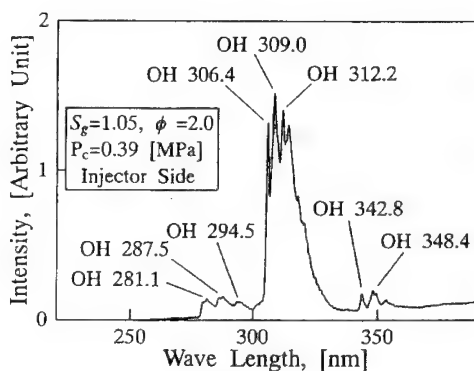


Figure 7. Emission spectra of a hydrogen/oxygen flame formed in the combustion chamber.

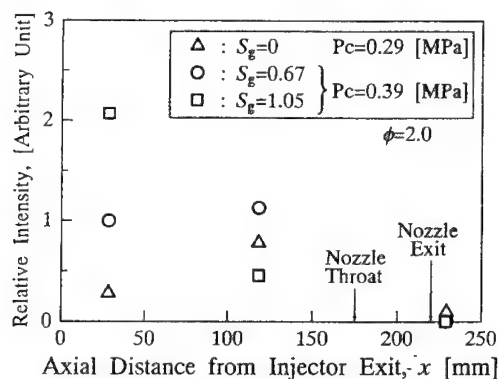
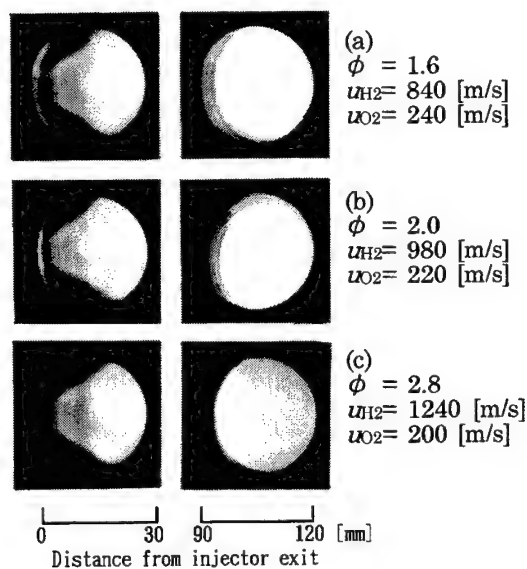


Figure 8. OH-radical intensity comparisons for the three swirl intensities of the oxygen jet.

hand, applying swirl to the oxygen jet increased the rate of turbulent mixing between the oxygen and the hydrogen jet, thus reducing the reaction time to reach completion of combustion in the chamber. It should be noted that in this thruster system infinitely fast mixing of the propellants and products, referred to as stirred reactor concept, did not occur, but the mixing between the propellants may be a controlling process of the combustion.

**Effects of equivalence ratio.** Figure 9 shows the shape variation of the swirling flames developed in the combustion chamber with  $\phi$  at a constant chamber pressure. The intensities of OH-radical ( $\lambda = 306.3$  nm) for the three flames at  $\phi = 1.6 \sim 2.8$  are plotted in Fig.10 against the axial distance from the injector exit. (The intensities were normalized by the intensity of  $\phi = 2.0$  at 25 mm downstream of the injector exit.) A stable hydrogen/oxygen flame, stabilized on the injector rim, developed over the range of  $\phi$  tested. Although the shape of the flame was mostly insensitive to  $\phi$ , the diverging angle of the flame at the injector exit slightly decreased with increasing  $\phi$ . On the contrary, the conical luminous region in the flame close to the injector became slightly wider and spread upstream, suggesting that the region where combustion proceeded actively moved upstream with an increase of  $\phi$ . The behavior of these flame configurations coincided well with the results of the OH-radical levels. At low  $\phi$  the radical intensity downstream of the chamber was higher than that upstream, and at high  $\phi$  the reverse tendency was obtained. Considering the injection velocities of the hydrogen and the oxygen jet as a function of  $\phi$ , as shown in Fig.11, the dependency of the flame shape and OH intensity on  $\phi$  may be explained as follows: with increasing  $\phi$ , the velocity of the hydrogen jet increases significantly, but the velocity of the oxygen jet remains almost constant. Since the outer hydrogen jet impinges on the inner swirling oxygen jet spreading outside, the velocity increase of the hydrogen jet reduces the divergence angle of the inner oxygen jet, and improves the turbulent mixing between the propellants. This effect promotes rapid completion of combustion in the chamber.



**Figure 9.** Variation of flame configuration in the combustion chamber with equivalence ratio:  $P_c = 0.39$  MPa.

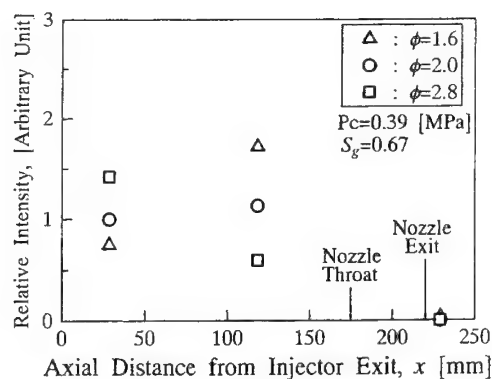


Figure 10. OH-radical intensity comparisons for the three equivalence ratios.

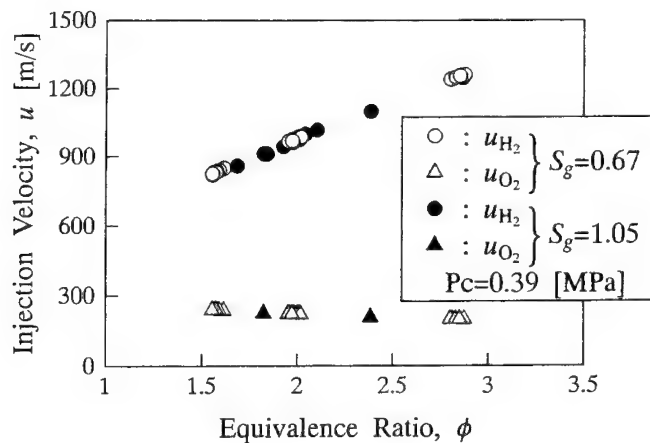


Figure 11. Injection velocities of the propellants as a function of equivalence ratio.

## CONCLUSION

- (1) A gaseous hydrogen/oxygen small and simple rocket thruster, containing a single swirl-coaxial injector with an outer hydrogen and an inner swirling oxygen jet and two optical ports for viewing combustion process and measuring spectra from a flame in the combustion chamber, has been developed.
- (2) The stable hydrogen/oxygen flame attached to the injector rim between the oxygen jet and the hydrogen jet was formed in the combustion chamber independent of  $S_g$ . The flame configuration was strongly sensitive to the swirl intensity of the oxygen jet.
- (3) Applying swirl to the oxygen jet increased the rate of turbulent mixing between the oxygen jet and the hydrogen jet, reducing the reaction time to reach completion of combustion in the chamber. In this thruster system, the mixing between the propellants may be a controlling process of combustion.
- (4) With oxygen swirl, high performance of  $I_{sp}$  and  $C^*$  efficiency was attained, but without oxygen swirl, the performance parameters decreased noticeably. A small and simple thruster with a single swirl-coaxial injector offered good performance.



### ACKNOWLEDGMENTS

This work was supported by the Grants-in-Aid for Special Project Research of Tokyo Metropolitan. The authors would like to express their thanks to Mr. Morita Y., Mr. Ikezaki T., Mr. Kato H., Mr. Imamura T. and Mr. Miyashita T. for their cooperation in conducting the experiment.

### REFERENCES

1. Finden, L. E., et al., 25-lbf  $\text{GO}_2/\text{GH}_2$  Space Station Thruster, *AIAA/ASME/SAE/ASEE 24th Joint Propulsion Conference*, AIAA 88-2793, 1988.
2. Kim, S. and VanOverbeke, T., Calculations of Gaseous  $\text{H}_2/\text{O}_2$  Thruster *AIAA/ASME/SAE/ASEE 26th Joint Propulsion Conference*, AIAA 90-2490, 1990.
3. Yuasa, S., Effects of Swirl on the Stability of Jet Diffusion Flames, *Combustion and Flame*, 66, 181-192, 1986.
4. Reed, B. D., Small Hydrogen/Oxygen Rocket Flowfield Behavior From Heat Flux Measurements, *AIAA/ASME/SAE/ASEE 29th Joint Propulsion Conference*, AIAA-93-2162, 1993.
5. Suzuki, A., et al., An Experimental Investigation of Combustion Performance of  $\text{LOX}/\text{GH}_2$  Rocket Combustor with Coaxial Injectors, *NAL TR-473*, 1976.
6. Gaydon, A. G., *The Spectroscopy of Flames*, Chapman and Hall, London, 1974.

## THE EFFECT OF CHEMICALLY INDUCED STRESSES AND DEFORMATIONS ON THE IGNITION OF SOLID PROPELLANTS

A. G. Knyazeva<sup>1</sup> and V. E. Zarko<sup>2</sup>

<sup>1</sup>Tomsk State University, Physico-Technical Faculty, Tomsk 634050, Russia; <sup>2</sup>Institute of Chemical Kinetics and Combustion, Russian Academy of Sciences, Novosibirsk 630090, Russia

**ABSTRACT:** A coherent physicochemical approach based on the coupling between chemical and mechanical processes in a solid material is applied to modeling the ignition of solid propellants. Governing equations are derived with account taken for the relationships of nonequilibrium thermodynamics. It is shown that using purely thermal models for the description of ignition of deformable energetic materials may lead to mistakes in determining the global reaction kinetic parameters. Accounting for the contribution of mechanical processes could change the value of the activation energy either in a positive or negative direction, depending on the conditions of heating.

### NOMENCLATURE

$c_E$	= specific heat under constant deformation
$E_0$	= activation energy of reaction
$f$	= free energy
$f^0$	= Helmholtz free energy
$F$	= vector of external mass forces
$g_{BA}$	= dimensionless coefficient of concentration expansion
$g_k$	= chemical potential (of components, vacancies, or dislocations)
$g_s$	= dimensionless coefficient of structural expansion
$J_k^0$	= total flux of component $k$
$J_k$	= diffusion flux of component $k$
$J_T$	= heat flux
$k_o$	= pre-exponent
$K$	= isothermal modulus of uniform compression
$m_k$	= molar mass of component $k$
$N_k$	= mass concentration of component $k$
$P$	= pressure
$P_0$	= empirical constant
$Q_o$	= thermal effect of global reaction
$r$	= damage extent
$R$	= universal gas constant
$S$	= specific entropy

$t^*$	= ignition moment
$t_a$	= period of adiabatic induction
$T$	= temperature
$T^*$	= ignition temperature
$T_a$	= adiabatic ignition temperature
$T_s$	= surface temperature
$U$	= specific internal energy
$v$	= velocity of the center of masses
$v_k$	= individual velocity of component $k$
$V_p$	= specific volume of damage
$y$	= transformation degree
$z$	= number of chemical reactions
$\alpha_a$	= coefficient of concentration expansion of a reagent
$\alpha_b$	= coefficient of concentration expansion of a product
$\alpha_T, \alpha_k, \alpha_S$	= coefficients of linear thermal, concentration, and structural expansion, respectively
$\chi_p$	= damage potential
$\gamma_{ki}$	= stoichiometric coefficient of component $k$ in the $i$ -th reaction
$\eta_0$	= initial porosity of material
$\varepsilon_{ij}$	= component of strain tensor
$\varepsilon_{kk}$ or $\varepsilon_{mm}$	= the first invariants of the strain tensor
$\varepsilon_{ij} \varepsilon_{ij}$	= second invariant of the strain tensor
$\varphi_i(y)$	= kinetic function
$\varphi_i$	= rate of the $i$ -th reaction
$\kappa$	= analogue of the coefficient of dynamic viscosity
$\lambda, \mu$	= Lamé coefficients
$\rho$	= density of medium
$\rho_k$	= density of component $k$
$\rho_0$	= initial density of medium
$\sigma$	= stress tensor
$\sigma_{ij}$	= component of stress tensor
$\sigma_k$	= source of component $k$
$\omega$	= coherence coefficient for strain and temperature fields

## INTRODUCTION

Historically, the physicochemical transformations which accompany combustion and ignition of solid propellants are modeled by methods that are similar to those used to construct the mathematical models of gas combustion. Such a traditional approach proved itself in the first approximation. Many qualitative peculiarities of the processes of solid propellant combustion were revealed and physical and mathematical similarities in various (at first glance) processes were established. A more profound approach to the study of solid-phase transformations must take into account the peculiarities of the motion of corresponding media and the interrelated character of various physical processes.

At the macrolevel this more detailed investigation is manifested in the interaction of heat-and-mass transfer with various mechanical processes which, generally speaking, are widely used in mechanics but sometimes without correct thermodynamic or statistical background. This is first observed in the neglect of both the specific features of chemical and physical transformations and the nonlinear feedback relations between chemical transformations and physical processes. The global models of solid media of different complexities which are available in thermomechanics are either not applied to real processes or are applied in very particular aspects. Obviously, the complexity and manifold of physicochemical processes in the combustion wave make it necessary to determine one or several effective stages of chemical reactions with some effective global kinetic parameters.<sup>1</sup>

However, attempts to use purely thermal models to treat and interpret experimental data often give very contradictory results because they neglect the fact that various nonlinear physical processes cannot be reduced to global kinetic dependencies. Using the methods of continuum medium mechanics, the approach has been proposed of modeling physicochemical transformations in the solid media which are accompanied by deformation and destruction.<sup>2,3</sup> The approach takes into account the peculiarities of solid-phase transformations when constructing the macrolevel models and has a fairly rigorous thermodynamic background. Additionally, it may readily be applied to complex media (non-isotropic, with inner parameters, memory, etc). Below, we consider the application of this approach to the modeling of solid propellant ignition.

## BASIC EQUATIONS

The basic equations used to construct particular ignition models are usually mechanical balance equations, supplemented with relations between thermodynamic fluxes and forces, various empirical laws (if necessary), and an equation of state. The latter is represented by the relation between the components of stress and strain tensors.

The continuity equation for mixture components has the form ( $\nabla \cdot \bar{A} = \text{div} \bar{A}$ ;  $\dot{\bar{A}} = \frac{d\bar{A}}{dt}$ ):

$$\frac{\partial \rho_k}{\partial t} + \nabla \cdot \bar{J}_k^0 = \sigma_k \quad k = 1, 2, \dots, n$$

or

$$\rho \dot{N}_k + \nabla \cdot \bar{J}_k = \sigma_k \quad (1)$$

Here  $\rho_k = \rho N_k$ ;  $\bar{J}_k^0$  is the total flux of component  $k$ ;

$$\dot{N}_k = \frac{dN_k}{dt} = \frac{\partial N_k}{\partial t} + N_k \nabla \cdot \bar{v} \quad (2)$$

$$\bar{J}_k^0 = \rho_k (\bar{v}_k - \bar{v}) + \rho_k \bar{v} = \bar{J}_k + \rho_k \bar{v}$$

$\bar{v}$  is the velocity of the center of masses determined as follows:

$$\rho \bar{v} = \sum_{k=1}^n \rho_k \bar{v}_k \quad \text{or} \quad \bar{v} = \sum_{k=1}^n N_k \bar{v}_k \quad (3)$$

$\sigma_k$  is the source of component  $k$ :

$$\sigma_k = \sum_{i=1}^Z \gamma_{ki} m_k \varphi_i \quad (4)$$

The equation of the mass continuity for a mixture as a whole is convenient to write in a form similar to Eq. (1):

$$\dot{\rho} + \rho \nabla \cdot \bar{v} = 0 \quad (5)$$

The equation of momentum conservation for the mixture (includes in common cases) the vector  $\bar{F}$  of external mass forces ( $\nabla \cdot \hat{\sigma} = \text{div } \hat{\sigma}$ ):

$$\rho \frac{d\bar{v}}{dt} = \rho \bar{F} + \nabla \cdot \hat{\sigma} \quad (6)$$

The equation of conservation of internal energy is of the form:

$$\rho \dot{U} = -\nabla \cdot \bar{J}_T + \sigma_U \quad (7)$$

where  $U$  is the specific internal energy in a local volume;  $\sigma_U$  is the corresponding source defined as:

$$\sigma_U = \hat{\sigma} \cdot \nabla \cdot \bar{v} + \sum_{k=1}^n \bar{J}_k \bar{F}_k$$

Here  $\hat{\sigma} \cdot \nabla \cdot \bar{v}$  is the double scalar production of tensors of stress and velocity of deformations;  $\bar{F}_k$  is the vector of external force which affects component with number  $k$ :

$$\bar{F} = \sum_{k=1}^n N_k \bar{F}_k$$

To construct particular combustion models we use the equation of thermal conductivity which is derived by generalizing the Gibbs equation with regard to a medium with additional parameters

$$\rho \frac{dS}{dt} = \frac{\rho}{T} \frac{dU}{dt} - \frac{\sigma_{ij}}{T} \frac{d\epsilon_{ij}}{dt} - \frac{\rho}{T} \sum_{k=1}^{n+2} g_k \frac{dN_k}{dt} - \frac{\chi_p \rho_o}{T} \frac{dV_p}{dt} \quad (8)$$

and the balance relationships for the other values .

In Eq. (8)  $S$  is the specific entropy for a local volume;  $g_k$  are the chemical potentials of components ( $k = 1, 2, \dots, n$ ), vacancies ( $k = n+1$ ), and dislocations ( $k = n+2$ ), respectively;  $\rho_o$  is the initial density of

the medium,  $V_p$  is the specific volume of damages (pores, cracks, etc). In the particular case of a symmetric stress tensor and an absence of external mass forces, the equation of thermal conductivity has the form:

$$\rho c_\epsilon \frac{dT}{dt} = -\nabla \cdot \vec{J}_T - \rho T \frac{d}{dt} \left[ \epsilon_{kk} \frac{\partial(Kw\rho^{-1})}{\partial T} \right] - \rho \sum_{k=1}^{n+2} g_k \frac{dN_k}{dt} - \chi_p \rho_0 \frac{dV_p}{dt} + \rho T \frac{d}{dt} \left[ \frac{\epsilon_{kk}^2}{2} \frac{\partial(\lambda\rho^{-1})}{\partial T} + \epsilon_{ij}\epsilon_{ij} \frac{\partial(\mu\rho^{-1})}{\partial T} \right] \quad (9)$$

which corresponds to the Helmholtz function of local specific free energy,  $f$ , written as follows:

$$f = f^0 - \rho^{-1} (Kw\epsilon_{kk} + \mu\epsilon_{ij}\epsilon_{ij} + \frac{\lambda}{2}\epsilon_{kk}^2) \quad (10)$$

Here  $f^0$  is the Helmholtz free energy in the standard state. In Eq. (9)  $K$  is the isothermal modulus of uniform compression,  $K = \lambda + 2\mu/3$ . Parameter  $w$  accounts for relative change in specific volume due to thermal, concentration and structural expansion with  $\sigma_{kk} = 0$ :

$$w = \frac{V - V_0}{V_0} = 3[\alpha_T(T - T_0) + \sum_{k=1}^{n+2} (N_k - N_{k0})\alpha_k + \alpha_s(V_p - V_{p0})]$$

$$\text{where } \alpha_T = \frac{1}{3V_0} \left( \frac{\partial V}{\partial T} \right)_{N_k, V_p}; \quad \alpha_k = \frac{1}{3V_0} \left( \frac{\partial V}{\partial N_k} \right)_{T, N_{j \neq k}, V_p}; \quad \alpha_s = \frac{1}{3V_0} \left( \frac{\partial V}{\partial V_p} \right)_{T, N_k}$$

As a relation between thermodynamic potentials and forces in this general formulation of the model we use the linear Onsager relations which are known to be suitable for description of different nonlinear irreversible processes in a wide range of the local thermodynamic variables.<sup>4,5</sup> We omit here the corresponding relations for scalar, vector and tensor values in order not to encumber the text. Note that the expressions for fluxes and forces are chosen in such a way that the local production of entropy, which is a positively determined quadratic form, is not negative and the system of the Onsager coefficients satisfies all necessary thermodynamic conditions including that for new terms (vacancies, dislocations and damages).<sup>4-6</sup> Expression for the local entropy and the chemical potentials of components follow from the form of the free energy function  $f$  (see Eq. 10) by definition:

$$S = - \left( \frac{\partial f}{\partial T} \right)_{N_k, V_p, \epsilon_{ij}} = - \left( \frac{\partial f^0}{\partial T} \right)_{\epsilon_{ij}=0} + \epsilon_{mm} \frac{\partial(Kw\rho^{-1})}{\partial T} - \epsilon_{ij}\epsilon_{ij} \frac{\partial(\mu\rho^{-1})}{\partial T} - \frac{\epsilon_{mm}}{2} \frac{\partial(\lambda\rho^{-1})}{\partial T}$$

$$g_k = \left( \frac{\partial f}{\partial N_k} \right)_{N_{j \neq k}, T, V_p, \epsilon_{ij}} = \left( \frac{\partial f^0}{\partial N_k} \right)_{\epsilon_{ij}=0} - \epsilon_{mm} \frac{\partial(Kw\rho^{-1})}{\partial N_k} + \epsilon_{ij}\epsilon_{ij} \frac{\partial(\mu\rho^{-1})}{\partial N_k} + \frac{\epsilon_{mm}^2}{2} \frac{\partial(\lambda\rho^{-1})}{\partial N_k}$$

In constructing and analyzing specific models, particular attention is paid to the coherent character of all processes and nonlinear correlations between variables as well as to the correct "substitution" of micro-mechanisms into macro-models (involving models of continuum medium mechanics).

Consider now an application of the approach described to the calculation of ignition characteristics of a deformable solid energetic material.

### INITIATION OF CHEMICAL REACTION IN A PREHEATED LAYER

Let us consider a chemical transformation which is described by the simplest reaction scheme:



We will assume that all information about the changes in properties of substance upon transformation is contained in the coefficients of the concentration expansion of both a reactant,  $\alpha_a$ , and a product,  $\alpha_b$ ; there is no pronounced destruction in the preheated layer; the strains are small and the reaction rate is temperature-dependent according to the Arrhenius law. Under these assumptions a one-dimensional model for initiation of reaction at the surface of solid material heated by external heat flux can be described by a system of equations:

$$\begin{aligned} c_\epsilon \rho_0 \left(1 + \omega \frac{T}{T^*}\right) \frac{\partial T}{\partial t} &= \lambda_T \frac{\partial^2 T}{\partial x^2} + Q_0 k_0 \varphi_1(y) \varphi_2(T) \left(1 - \omega g_{BA} \frac{T}{T^*}\right) \\ \frac{\partial y}{\partial t} &= k_0 \varphi_1(y) \varphi_2(T) \\ x=0, \quad -\lambda_T \frac{\partial T}{\partial x} &= q_c; \quad x \rightarrow \infty, \quad T = T_0; \\ t=0, \quad T - T_0, \quad y &= 0. \end{aligned} \quad (12)$$

Here  $y = N_B / (N_{B0} + N_{A0})$ ;  $\varphi_1(y)$  is the kinetic function;  $\varphi_2(T) = \exp(-E_0/RT)$ ;  $T^*$  is the reference temperature which is typical of the problem, e.g., the ignition temperature. Parameter  $\omega$  is the coherence coefficient for strain and temperature fields defined as:

$$\omega = \frac{(3K\alpha_T)^2 T^*}{(\lambda + 2\mu) c_\epsilon \rho_0} \quad (13)$$

Parameter  $g_{BA}$  is the dimensionless coefficient of concentration expansion defined as:

$$g_{BA} = \frac{(\alpha_B - \alpha_A) c_\epsilon \rho_0}{\alpha_T |Q_0|} \quad (14)$$

Unlike the classical theory of elasticity, in which the coefficient  $\omega$  is calculated at the initial temperature, and where typically  $\omega \ll 1$ , in the case under consideration the estimates of  $\omega$  for energetic materials at  $T=T^*$  give the value  $\omega \approx 1$ . Parameter  $g_{BA}$  reflects the system behavior in the course of chemical transformations: if reaction proceeds with volume expansion, i.e.  $\alpha_B > \alpha_A$ , then  $g_{BA} > 0$ , and vice versa,  $g_{BA} < 0$  if the reaction proceeds with a decrease of volume. The stresses and

deformations in the model described by the system of Eqs. (12) completely follow the change in the temperature and concentration fields and are explicitly expressed via the function  $w$ :

$$w = 3[\alpha_T(T - T_0) + (\alpha_B - \alpha_A)(N_{A0} + N_{B0})y]$$

A detailed analysis of the problem for various particular cases is given in Ref. 7. We discuss here only some specific findings of the study.

First, the "ignition" regime is realized in this model if the reaction is exothermic, with  $Q_0 > 0$  and  $\omega < 1/g_{BA}$ , or, in the case of endothermic reaction which runs with high increase of volume, i.e.  $Q_0 < 0$  but  $\omega > 1/g_{BA}$ . The approximate analytical solution of the problem with use of the adiabatic criterion gives the formulas to estimate the global kinetic parameters ( $E_0, Q_0, k_0$ ) of the global-reaction with allowance for thermal and concentration expansion using experimental data on ignition delay times.<sup>8</sup> The adiabatic criterion states that at the moment of ignition,  $t^*$ , the rate of surface temperature rise due to external heating becomes equal to that due to chemical-reactions heat release. The resulting approximate formulas may be written as:

$$\ln\left(\frac{t^*}{1 - T_0/T^*}\right) = \ln\left[\frac{(1 + \omega)}{2(1 - \omega g_{BA})} T^* \frac{c_\epsilon \rho_0}{Q_0 k_0}\right] + \frac{E_0}{R} \left(\frac{1}{T^*}\right) \quad (15)$$

$$T^* - T = \left[\frac{4}{\pi} q_c^2 t^* / c_\epsilon \rho_0 \lambda_T (1 + \omega)\right]^{1/2}$$

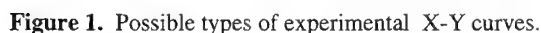
where  $t^* = t_a$  is the period of adiabatic induction;  $T^* = T_a$  is the adiabatic ignition temperature determined by taking the inflexion point on the temperature-time curve. As it is known, similar characteristics may be distinguished on an appropriate experimental curve. According to Eqs. (15), the experimental data on ignition can be described in coordinates  $X = \ln(t_a / (1 - T_0/T_a))$  and  $Y = 1/T_a$  by a straight line (Fig. 1, curve 1) whose slope gives the effective activation energy  $E_0$  for the global reaction (11). It has been shown that treatment of experimental data in such a way gives an estimate for  $E_0$  greater by 20-25% than that obtained using a purely thermal model.<sup>7</sup>

Second, there are cases when it is impossible to easily "fit" experimental data in the X-Y coordinates. Sometimes we have two straight lines with different slope whose possible mutual arrangement is illustrated in Fig. 1. Thus, treating experimental data in terms of purely thermal ignition theory, one finds two different sets of global kinetic parameters when  $\Delta E = E_2 - E_1 > 0$  and  $\Delta E' = E_2' - E_1' < 0$ . This can be attributed to a change of activation energy for global chemical reaction due to a change in the reaction mechanism, for example. However, the behavior of  $\Delta E$  can be explained in terms of a constant activation energy taking into account the effect of chemically induced mechanical deformations.

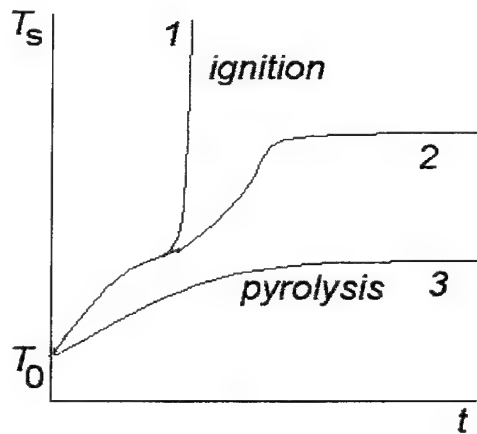
Consider for simplicity the case of zero-order reaction with  $(\omega g_{BA} T/T^*) \ll 1$ . The effective function of heat release can be represented in the particular case as:

$$\varphi_2' = \varphi_2(1 - \omega g_{BA} \frac{T}{T^*}) \equiv \exp\left(-\frac{E_0 + RT^2 \omega g_{BA}/T^*}{RT}\right) = \exp\left(-\frac{E_{eff}}{RT}\right) \quad (16)$$





769



**Figure 2.** Qualitative temporal behavior of surface temperature with different parameters of the model: 1.  $Q_0 > 0$ ,  $\omega < 1/g_{BA}$  or  $Q_0 < 0$ ,  $\omega > 1/g_{BA}$ ; 2. One of the conditions 1 does not hold at given  $T_S$ ; 3.  $Q_0 > 0$ ,  $\omega > 1/g_{BA}$  or  $Q_0 < 0$ ,  $\omega < 1/g_{BA}$ .

In Equation (17),  $\eta_0 = V_{p0}/V_0$  is the initial porosity of material;  $r = V_p/V_{p0}$  is the damage extent; and  $g_s = \alpha_s(c_s \rho_0 / |\chi_p| \alpha_r \eta_0) < 0$  is the dimensionless coefficient of structural expansion. To calculate damage growth, the fracture mechanics kinetic law can be used in the form:

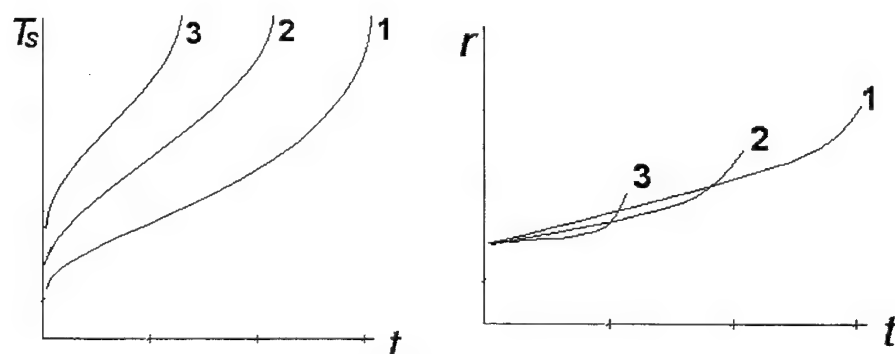
$$\dot{r} = -\frac{P}{\kappa} \left[ r + \exp\left(-\frac{P}{P_0}\right) \right], P < 0$$

Here  $P$  is the pressure,  $P = -\frac{1}{3} \sigma_{kk}$ ;  $P_0$  is an empirical constant which corresponds to a critical level of pressure causing crack formation. With allowance for the kinetic law for  $r$  and with the condition  $r(0, x) = 1$ , the model, complicated by destruction, has been analyzed for some particular cases.<sup>7,12</sup>

In particular, this model was used to account for certain experimental observations. It was shown in Ref. 12 that samples of pyroxilin powder did not exhibit significant surface damage before ignition, when gradually cooled to an initial temperature of about 170 K and exposed to pulses of irradiation. Conversely, in the case of nitroglycerin powder, the irradiated surface became covered with a network of cracks. Similar irradiated surface behavior was also observed at initial room temperature when using pulses of powerful radiant flux (more than 250 J/cm<sup>2</sup>s). Detailed experimental studies of dependence of ignition parameters upon initial temperature and radiant flux were not conducted. Since these data are not currently available in the literature, a comparison between theoretical and experimental results can be performed only qualitatively. Note that the suggested model describes the initial stage of the ignition process in a simplified manner. Possible effects of phase transitions during fast heating are also not taken into consideration by the model. Unfortunately, there is no reliable information in the available literature which shows how melting occurs at heating rates of 10<sup>3</sup> K/s and higher.

The calculation of ignition parameters was made using the following reference parameters:  $E_0 = 146.7 \text{ J/mole}$ ,  $\lambda_T = 2.35 \cdot 10^{-3} \text{ J/cm s K}$ ,  $k_0 = 8.6 \cdot 10^{-13} \text{ s}^{-1}$ ,  $\alpha_T = 10^{-4} \text{ K}^{-1}$ ,  $\lambda = 2 \cdot 10^4 \text{ J/cm}^3$ ,  $\mu = 4.15 \cdot 10^3 \text{ J/cm}^3$ ,  $P_0 = 5 \cdot 10^2 \text{ J/cm}^3$ ,  $\kappa = 2 \cdot 10^3 \text{ g/cm s}$ ,  $\rho_0 = 1.6 \text{ g/cm}^3$ ,  $Q_0 = 1200 \text{ cal/g}$ ,  $c_E = 1.46 \text{ J/g K}$ ,  $q_c = 15 \text{ J/cm}^2\text{s}$ ,  $(\alpha_b - \alpha_a) = 5 \cdot 10^{-2} \text{ cm}^3/\text{g}$ .

Calculated dependencies of surface temperature and damage extent typical for ignition are shown in Fig. 3. The calculations show that the rate of damage growth increases after the chemical reactions in the solid start to accelerate (before ignition event). In accordance with the experiment the ignition temperature ( $T_s$  at  $t = t^*$ ) rises with increase of initial temperature, while the magnitude of damage extent decreases. Note that the  $T_s(t)$  curves similar to that for ignition may be obtained in numerical tests when modeling heating of an inert material with destruction of a surface layer. The reason for this is a change of sign of the third term on the right hand side of Eq. 17. Indeed, at  $T > T^* / \omega |g_s|$  this term, which accounts for destruction of material, becomes a source of heat release instead of heat loss. On the other hand, the combined action of chemical heat release and relatively strong heat absorption due to fracture of solid material may lead to effective  $T_s(t)$  behavior corresponding to the behavior of a material with global endothermic reactions. The same material in heating conditions that prevent occurrence of deformations and destruction (e.g., uniform slow rate heating) can exhibit pronounced exothermic thermal decomposition behavior.



**Figure 3.** Temporal behavior of surface temperature and damage dependencies for different initial temperatures;  $T_0 = 170 \text{ K}$  (1);  $273 \text{ K}$  (2);  $350 \text{ K}$  (3).

Concerning application to real systems, the coherent ignition models that take into account any phase transition in the preheated layer are of interest. It should be mentioned that the problem of phase transition of the 1st type (melting, change of crystal structure) is relevant for numerous important components of solid rocket propellants, e.g. ammonium perchlorate, nitramines, ADN, HNF, etc. Analysis of phase equilibrium within the framework of this approach that takes into account coupling between the thermal and mechanical processes (Eqs. 1-10) leads to some interesting generalization of the equations of Clausius-Clapeyron and Poynting. In particular, it gives a dependence of the phase transition heat on conditions of mounting a specimen of solid material, leads to blurring of the region of phase transition, etc. The ignition model of solid energetic material with hexogen characteristics and the phase transition of the first type has been analyzed.<sup>10</sup> It was shown that in the coherent model

the influence of the phase transition on ignition characteristics cannot be reduced to either a change in heat capacity at the transition point or studying the Stefan problem with a distinct (sharp) interface. The appearance of a blurred region of phase transition is determined by the temperature dependence of the phase transition on stresses and deformations which are, in turn, affected by the temperature and concentration variations in the preheated and reaction zones.

### CONCLUDING REMARKS

The above considerations show that coupling between heat transfer in the condensed phase and chemically induced deformations may play an important role in the initiation of chemical transformations in energetic materials. Several conclusions were drawn on the basis of the results of this study.

Before determining the role of different stages in ignition, one could estimate the effect of intrinsic "mechanical" processes using this simple model. Small magnitude of the coherence coefficient or a relatively small value of strain cannot be the criterion for neglecting the coherence relationship between heat transfer and deformations in the description of transient combustion processes including ignition.

The global kinetic parameters determined using a purely thermal model may not correspond directly to chemical transformations; the energy of activation of the global reaction, because of the action of mechanical processes, could appear either higher or lower than the true value for unloaded material.

The temporal behavior of the surface temperature during heating of a solid material depends on contributions of chemical heat release and mechanical destruction heat loss. This behavior should not be considered as a unique source of information about exothermicity of the material thermal decomposition. In the case of pronounced heat loss due to mechanical destruction an apparent behavior may look similar to one for endothermic decomposition in spite of the existence of finite rate exothermic transformations in the condensed phase. On the other hand, the estimates show that even in the case of an endothermic reaction, a process similar to ignition (rapid rise of surface temperature) may occur in the solid energetic material if the reaction proceeds with a high increase of volume.

### REFERENCES

1. Gusachenko, L.K., Zarko, V.E., Zyryanov, V.Ya., and Bobryshev, V.P., Modeling of combustion of solid fuels, *Nauka*, Novosibirsk, 1985.
2. Knyazeva, A.G., Introduction to the local equilibrium thermodynamics of physicochemical transformations in deformable media, *Tomsk State University*, Tomsk, 1996.
3. Knyazeva, A.G., Coherent equations of heat and mass transfer in chemically reacting solid mixture with regard to deformation and destruction, *Journal of Applied Mathematics and Technical Physics* (Russian), 3, 1996, pp. 92-101.

4. D'yarmati, I., Non-Equilibrium Thermodynamics. Field theory and variational principles, *Springer Verlag*, Berlin, 1970.
5. De Groot, S. and Masur, P., Non-Equilibrium Thermodynamics, *North Holland Publ. Co.*, Amsterdam, 1964.
6. Petrov, N., and Brankov, I., Modern Problems of Thermodynamics, *Mir*, Moscow, 1986.
7. Knyazeva, A.G. and Zarko V.E., Modeling of combustion of energetic materials with chemically induced mechanical processes, *Journal of Propulsion and Power*, 4, 1995, 791-803.
8. Vilyunov, V.N., and Zarko, V.E., Ignition of Solids, *Elsevier*, Amsterdam, 1989.
9. Knyazeva, A.G., Ignition of the condensed substance by hot plate with regard to thermal stresses, *Combustion, Explosion, and Shock Waves*, 1, 1992, 13-18.
10. Knyazeva, A.G., Coherent models of physicochemical transformations in solids with regard to deformation and destruction, *Doct. Sci. Thesis, Tomsk State University*, Tomsk, 1996.
11. Knyazeva, A.G. and Zarko, V.E., Combustion of crystals with destruction in the reaction front, Theory and experiment, *Book of abstracts, Intern. Workshop on mathematical methods in physics, mechanics, and mesa mechanics of fracture*, Tomsk, 1996.
12. Knyazeva, A.G., and Kuznetsov, V.T., Destruction of the surface of nitroglycerin powder under ignition at different initial temperatures, *Combustion, Explosion, and Shock Waves*, 3, 1995, 27-36.

# MATHEMATICAL MODELING OF OPERATION OF AN ACOUSTIC DAMPER WITH GAS IN ITS INTERNAL CAVITY

N.G. Alkov

Keldysh Research Center, Moscow, Russia

**ABSTRACT:** A mathematical model has been developed of operation of an acoustic damper, based on Helmholtz's resonator principles, when a gas comes into its internal cavity and flows out through passages. Such an acoustic damper rather effectively suppresses oscillations in the chemical propulsion. The purposeful arrangement of a supply of gas with given properties into the internal cavity of the acoustic damper enables considerable decrease in the dimensions of the damper, thus providing its efficient use to suppress low - frequency oscillation. A solid propellant grain, placed in the cavity of the acoustic damper, can be used as the gas mass source.

The operation of the acoustic damper has been analysed based on the model proposed. The experimentally-observed effect of a significant increase in the efficiency of operation of the acoustic damper with increase in the velocity of the steady - state flow through the damper passages has been shown to be related to increase in friction in the passages, and the threshold velocity of the steady - state flow, at which this effect appears, has been shown to be determined by equality of the velocities of the pulsation and steady- state flows. The use of a solid propellant as a gas mass source in the damper cavity results in more efficient operation of the damper.

## Nomenclature

$P, T, \rho$  - gas pressure, temperature and density, respectively  
 $U, V$  - solid propellant burning rate and gas velocity in connecting channel (gas velocity is positive indirection of damper inner cavity)  
 $W, F$  - volume of cavity of acoustic damper and total area of its channels' cross section  
 $R, C, \gamma$  - gas constant, sonic velocity and adiabatic index in damper cavity  
 $l, d, \Pi$  - length, diameter and perimeter of connecting channels  
 $S, \rho_0$  - solid propellant burning area and density  
 $\tau_w, \xi$  - tangential stress on channel wall and channel friction resistance coefficient  
 $t, \omega$  - time and acting oscillation dimensionless frequency  
 $Z, Y$  - impedance and acoustic conductivity of conditional surface  
 $R, A$  - resistance and damping coefficient

## Subscripts and Superscripts

$0$  - stagnation  
 $'$  - pulsation  
 $\phi$  - effective  
 $m, k$  - solid propellant and combustion chamber  
 $r, i$  - real and imaginary

An acoustic damper, whose operation is based on the principles of the Helmholtz resonator, is an effective means for oscillation suppression in the combustion chambers of various chemical rocket engines. Experimental data of investigations of acoustic dampers, generalized, e. g., in [ 1 ], show that the efficiency of dampers substantially increases when the gas flows through connecting channels. Intentional arrangement of such a flow can also provide stability in damper parameters during operation.

This study is aimed to elaborate upon a mathematical model of an acoustic damper with the gas flowing through its channels and analyze its key parameters as a function of its steady-state velocity in the connecting channels. In particular, the gas flow through the channels is arranged by burning a solid grain in the damper cavity. This provides stable gas dynamic parameters in the damper cavity and allows one to intentionally establish damper parameters by choosing a propellant with required thermodynamic properties of its combustion products and to consider the effect of solid propellant combustion on damper characteristics. Generally, the efficiency of an acoustic damper operation with the gas flowing through its channels should be analyzed on the basis of comprehensive consideration of the processes occurring in its cavity and in the chambers where it is installed [ 2 ]. However, parameters (the resistance, impedance and damping coefficient ), giving a rather substantiated idea of the efficiency of such a damper and allowing one to compare results obtained with available experimental results.

A mathematical model of the acoustic damper is based on linearized gas mass balance equations for the acoustic damper cavity and gas flow equations for the connecting channels with the assumption that the process in the damper cavity is adiabatic and that the length of the connecting channels is negligible with comparison to the oscillation wave length. The work especially emphasizes the effect of the gas steady-state flow through the damper connecting channels on the damper efficiency. For this purpose, relationships are used for friction in a channel with a pulsation flow. The interaction between the gas, flowing from the channels, and the damper and combustion chamber cavities is not considered, but the conventional channel effective length is employed.

The equations are as follows:

$$W \frac{d\rho'}{dt} = S\rho_m U' + \frac{F}{RT} (V_0 \rho' + \rho_0 V') \quad (1)$$

$$\rho_0 l_{\text{eff}} \frac{dV'}{dt} = P'_k - P' - \frac{\Pi}{4F} l \tau'_w \quad (2)$$

Let us define the pulsation component of the tangential stress on the channel wall as it is done in [3] with the assumption that the hydraulic resistance coefficient in turbulent steady-state flow conditions is not affected by flow oscillation:

$$\tau'_w \equiv \pm \xi_* [(2(\rho V)_0 * (\rho V)') / (8 * \rho_0) + ((\rho V)')^2 / (8 * \rho_0)] \quad (3)$$

where the sign in the expression corresponds to that of  $(\rho * V)'$ .

The non-linear term in this expression significantly complicates further calculations, so let us follow the results [3] and perform harmonic linearization of this expression that consists in its approximation with a sinusoidal function under the condition of the equality of the channel wall friction force, determined by both relationship, in an oscillation half-period. The wall tangential stress pulsation value is then determined as follows:

$$\tau'_w = \xi \left( \frac{V_0}{d} + \frac{\pi}{8d} |V'| \right) \rho V' \quad (4)$$

where  $|V'|$  is the velocity pulsation amplitude in the channel.

Let us scale key parameters on the basis of the average pressure in the damper cavity, the sonic velocity in the gas filling the damper cavity and channels, and the steady-state solid propellant burning rate at a preset damper cavity pressure. Let us choose the chamber oscillation period as the time scale.

Then we have:  $u' = U' / U_o$ ,  $v' = V' / C$ ,  $\eta' = P' / P_o$ ,  $\tau = t / t_s$ .

Also, let us determine a characteristic time for emptying the damper cavity in the form:

$t_c = W / (F \cdot C)$ , a characteristic time for disturbance propagation in the channel in the form:

$t_p = l / c$ , and associated scaled parameters.

$$\chi = t_c / t_s, \quad \psi = t_p / t_s. \quad (5)$$

We shall consider propellant burning rate pulsations in the damper cavity to be related only to pressure pulsations. For the case of a harmonic oscillation, such a relationship between dimensionless parameters will be determined as:

$$u' = \eta' f(\omega) \quad (6)$$

where  $f(\omega)$  is generally a frequency complex function. Considering the above-mentioned and the designation  $\alpha = (\Pi l_{sp} \xi) / (4 F)$ , the system of equation relative to dimensionless variables is as follows.

$$\begin{aligned} \chi \frac{d\eta'}{d\tau} &= V_o \eta' (1 - f(\omega)) + v' \\ \Psi \frac{dv'}{d\tau} &= \eta'_k - \eta' - \alpha \left( V_o + \frac{\pi}{8} |v'| \right) v' \end{aligned} \quad (7)$$

The system of equations entirely describes operating conditions of an acoustic damper of the design under consideration in the framework of the assumption adopted under the action of constrained oscillation in the combustion chamber. For harmonic oscillation, when gas dynamic parameters can be presented in the form, e.g., of  $\eta^* = \eta \exp(i\omega \tau)$ , the associated equations describing relations between the amplitudes of the pressure and velocity, will be as follows:

$$\begin{aligned} v \left[ i\Psi\omega + \frac{1}{i\chi\omega - V_o(1 - f(\omega))} + \alpha V_o \right] + \alpha \frac{\pi}{8} |v| v &= \eta_i \\ \eta &= \frac{v}{i\chi\omega - V_o(1 - f(\omega))} \end{aligned} \quad (8)$$

To analyse these equations further, let us separate their real and imaginary parts, representing the associated complex numbers, e.g., in the form of  $\eta = \eta_r + i \eta_i$  and the following:

$$\begin{aligned} \Psi_0 &= (\chi \omega + V_o f_i)^2 + V_o^2 (f_r - 1)^2 \\ \Psi_1 &= \alpha V_o + V_o (f_r - 1) / \Psi_0 \\ \Psi_2 &= \psi \omega - (\chi \omega + V_o f_i) / \Psi_0 \end{aligned}$$

After transformation, we have two algebraic equations with respect to the real and imaginary parts of pulsations of the flow scaled velocity in the damper channel:



$$\begin{aligned} v_r \left( \frac{\alpha\pi}{8} \sqrt{v_r^2 + v_i^2} + \Psi_1 \right) - v_i \Psi_2 &= \eta_e \\ v_i \left( \frac{\alpha\pi}{8} \sqrt{v_r^2 + v_i^2} + \Psi_1 \right) + v_r \Psi_2 &= 0 \end{aligned} \quad (9)$$

The solution of this system results in a transcendental equation to be solved by the iteration method. As the zero approximation a relationship is used between the dimensionless flow velocity pulsation and pressure in conditions close to resonance without a steady-state flow in the connecting channels. This relationship is obtained from Eqs. (9) and is as follows at  $V_0 \approx 0$ :

$$v_r = \sqrt{\frac{8\eta_k}{\alpha\pi}} \quad \text{при } \omega_c \Rightarrow \omega_0 \quad (10)$$

where  $\omega_c$  and  $\omega_0$  are the natural frequency of the Helmholtz resonator. This relationship shows that there is no frequency shift between the combustion chamber and channels pressure oscillation in resonance. It is similar to the relationship between the acoustic conductivity of the conditional surface, separating the damper and the combustion chamber, and the amplitude of the combustion chamber pressure oscillation [1]; that relationship shows a inverse dependency between the acoustic conductivity and the square root of the dimensionless amplitude of the combustion chamber pressure oscillation.

The natural frequency of the damper under consideration can be presented as:

$$\omega_c = \sqrt{\left( \frac{V_0 f_i}{2\chi} \right)^2 + \frac{1}{\chi\Psi}} - \frac{V_0 f_i}{2\chi} \quad (11)$$

When there is neither combustion nor other processes determining mass oscillation of the gas coming into the damper cavity, the natural frequency of the damper under consideration is identically equal to the natural frequency of the Helmholtz resonator:

$$\omega_c \equiv \omega_0 = \sqrt{\frac{1}{\chi\Psi}} \quad (12)$$

The parameters, characterizing the efficiency of the damper operation, are defined as:

$$Z = v / \eta_k, \quad R = Z_r, \quad A = 4*Z_r / [(Z_r + 1)^2 + Z_r^2] \quad (13)$$

In the calculations, the following values of the damper parameters were adopted:  $w = 2.6 \times 10^{-3} \text{ m}^2$ ,  $F = 9.6 \times 10^{-5} \text{ m}^2$ ,  $l = 0.05 \text{ m}$ ,  $c = 600 \text{ m/s}$ ,  $P_k = 10 \text{ MPa}$ , the natural frequency of the damper being 500 Hz. The dimensionless velocity of the steady-state flow through the channels varied from 0 to 0.6. In the calculations, the influence was analyzed of the frequency of the acting oscillation (the frequency varied in a range of  $\pm 30\%$  of the resonant frequency of the damper) and of the amplitude of the combustion chamber pressure oscillation on damper parameters.

Most calculations were performed without consideration of propellant combustion in the damper cavity on its operation to find out basic features related to a steady-state flow through the connecting channels. Fig.1 shows curves  $A/A_0$  of the ratio of the damping coefficient with

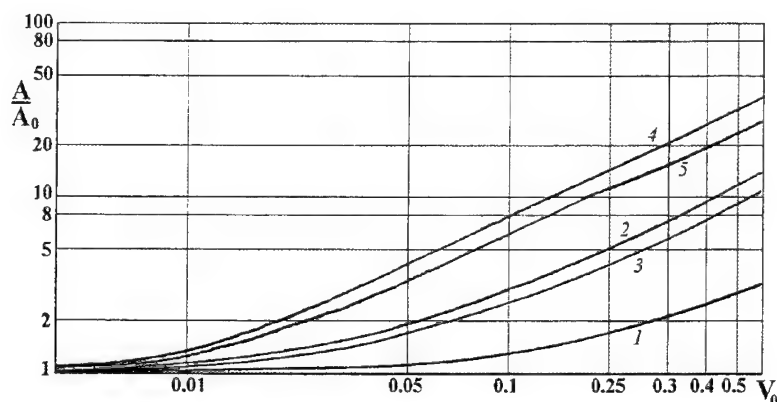


Figure 1. Variations of the damping coefficient as a function of the flow velocity for  $|P'_k| = 10^5$  (curve 1 -  $\omega_c \equiv \omega_0$ , curves 2, 3 -  $\omega_c = \omega_0 (1 \pm 0.1)$ , curves 4, 5 -  $\omega_c = \omega_0 (1 \pm 0.3)$ ).

a steady-state flow through the channels to its value without a steady-state flow through the channels for a number of frequency values of the acting pressure oscillation that characterize the accuracy of the adjustment of the damper for the frequency of the oscillation to be suppressed. The amplitude of the combustion chamber pressure oscillation is a set of a value of  $|P'_k| = 10^5$  Pa. A significant increase is observed in the damping coefficient rates as the flow velocity increases. The dependencies are non-linear and obviously have starting sections of a negligible effect of the steady-state flow velocity at its small values. When the frequency of the acting oscillation equals the natural frequency of the damper (curve 1), e.g., a 1.5 - time increase in the damping coefficient is achieved at a dimensionless flow velocity of 0.125, and is of 3.3 at the flow velocity equal to 0.6. When the frequency of the combustion chamber pressure oscillation does not coincide with the natural frequency of the damper, the damping coefficient ratio grows with the steady-state flow velocity more intensively, the negligible-effect starting section of being shorter. Thus, with the frequency of the combustion chamber oscillation differing from the natural frequency by  $\pm 10\%$  (curves 2 and 3), the damping coefficient increases by a factor of 11 to 15 at a flow velocity of 0.6, and it increases by a factor of 1.5 at a flow velocity of 0.04. When the frequencies differ from each other by  $\pm 30\%$  (curves 4 and 5), the damping coefficient increases by a factor of 30 to 40, and it increases by a factor of 1.5 at a flow velocity of 0.015. The curves of the resistance ratio ( $R/R_0$ ) varying with the flow velocity practically coincide with those of the damping coefficient ratio.

Fig. 2 shows a variation of the absolute damping coefficient and resistance with the flow velocity in a range of small dimensionless velocities (from 0 to 0.0125) for the cases when the damper is adjusted for the pressure oscillation frequency to be suppressed precisely and when these parameters are discrepant with each other by  $\pm 10\%$ . The results show that when there is no gas flow through the channels, the damping coefficient and resistance are 2.75 higher for the well-adjusted damper than for the  $\pm 10\%$  - discrepancy damper, which indicates the importance of precisely adjusting the damper for the oscillation frequency to be suppressed to provide its efficient operation. However, when there is a steady-state gas flow through the channels, the efficiency of the damper operation is less sensitive to the adjustment precision and it can remain to high in a wide range of its adjustment.

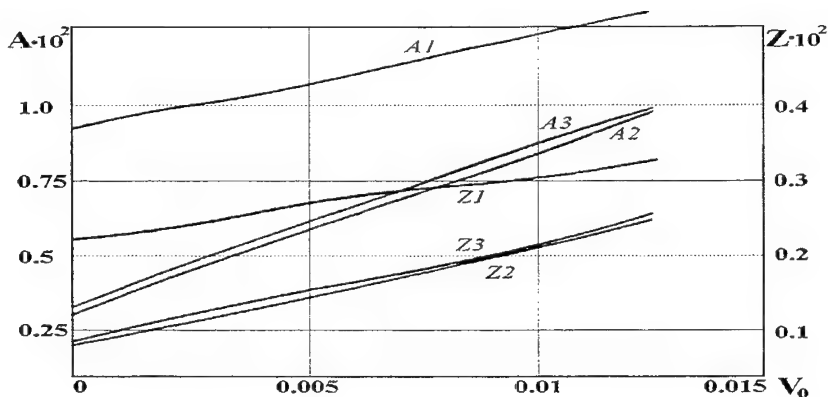


Figure 2. Variations of the damping coefficient and the resistance as a function of the flow velocity

This is of great importance, as it is rather hard to preliminarily choose design parameters of the damper because of the uncertainty in real parameters of the combustion pressure oscillation for suppression of which the damper is adjusted; and of the instability in gas parameters (mainly, temperature) in the damper cavity and channels.

Fig.3 shows variations of the damping coefficient as a function of the flow velocity for a oscillation amplitude of  $|P_k| = 10^{-4}$  Pa. The nature of the damping coefficient variations with the steady-state flow velocity in the channels is similar to the previous case, however, a significant increase is observed in the intensity growth of the damping coefficient ratio with the flow velocity for any damper adjustment levels for the acting oscillation frequency. As compared to the previous case, the damping coefficient ratio increases by a factor of 3 for the precisely-adjusted damper, to by a factor of 6 for the 30% - discrepancy damper. The absolute damping coefficient for this case is therewith 3.2 times lower than in the previous case as it follows from Eq.(10).

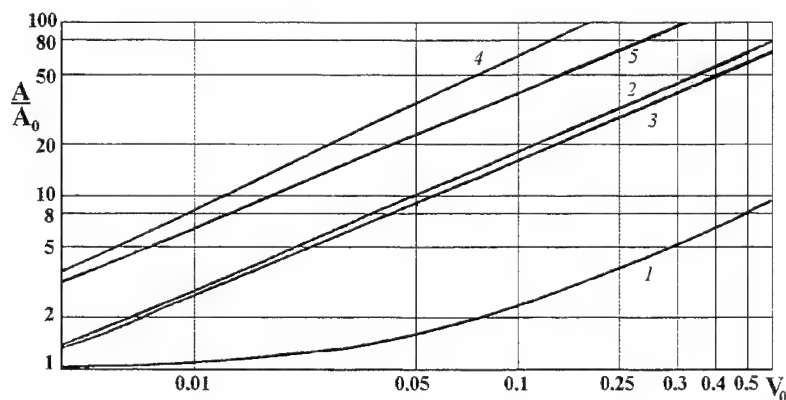


Figure 3. Variations of the damping coefficient as a function of the flow velocity for  $|P_k| = 10^{-4}$  (curve 1 -  $\omega_c = \omega_0$ , curves 2, 3 -  $\omega_c = \omega_0 (1 \pm 0.1)$ , curves 4, 5 -  $\omega_c = \omega_0 (1 \pm 0.3)$ ).

Analysis of the results presented enables making the following conclusions on the effect of the presence of a steady-state flow in the damper channels. An increase in the velocity of the gas flowing through the channels results in a considerable increase in the efficiency of the damper adjusted for the frequency to be suppressed. The presence of a gas flow and an increase in its velocity allows attaining a high efficiency of oscillation suppression even in the case of a substantial difference between the natural frequency of the damper and the frequency of the oscillation to be suppressed. The highest increase in the damper efficiency with the gas velocity in the channels occurs when the damper is adjusted for the frequency rather poorly, which allows efficient use of such a damper at widely-ranging parameters of the combustion chamber oscillation and parameters of the gas in the damper cavity. The suppression of the oscillation by the damper of the type under consideration is characterized by a high stability to the amplitude of the oscillation to be suppressed. At a preset flow velocity in the channels, its efficiency increases as the amplitude of the oscillation to be suppressed decreases. Thus, such a damper can entirely suppress the oscillation in the combustion chamber.

The peculiarities of the process established are qualitatively validated by known experimental data and allow accounting for a number of features of operation of an acoustic damper with a gas flowing through its channels, that are observed in experiments. Fig.4 shows experimental curves for a variation of the resistance ratio with the gas flow velocity, obtained under various conditions and generalized in [1]. In that work, mentioned are a considerable difference between the results presented and the existence of a flow velocity threshold ( $\geq 1\text{m/s}$ ), when the effect appears of an increase in the efficiency of oscillation suppression. As follows from an analysis of the model presented and calculation results, it is necessary to consider specific gas dynamic parameters in the damper cavity and combustion chamber to compare experimental data obtained in different conditions. Thus, it is advisable to use the flow velocity to gas sonic velocity ratio when reducing data of the channel resistance variation. Such a parameter is more universal than the absolute velocity. In addition, it is important to know a reliable value of the oscillation amplitude in the combustion chamber where a damper is installed. Correction of experimental data with these parameters results in the possibility to horizontally displace associated curves in the plane of the figure. As mentioned above, the level of damper adjustment for the frequency of the oscillation to be suppressed is of great importance, first of all, for determination of the conditional start of an essential increase in the resistance ratio with the steady-state flow velocity in the channels. It should be noted that the intensities of the growth (i.e., curve inclination angle) of the dimensionless resistance at high velocities obtained in this work and in [1] are in good agreement.

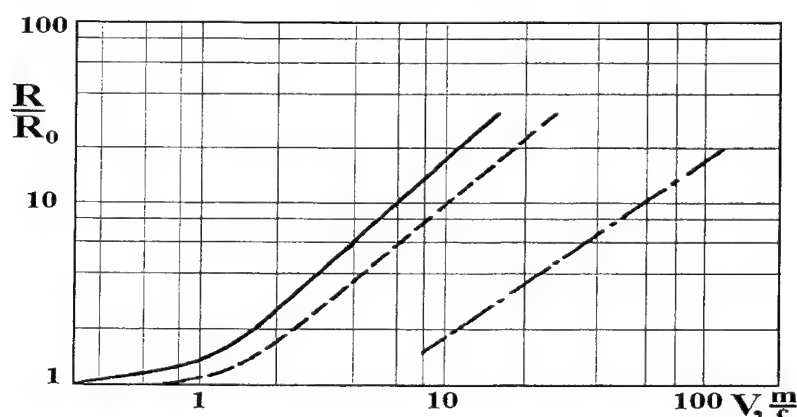


Figure 4. Variations of the damping coefficient as a function of the flow velocity ( experimental curves from [1] )

An important consequence of the model proposed is the possibility to physically substantiate and account for the behavior of the dimensionless resistance and damping coefficient as functions of the flow velocity at small values of the latter. Direct estimates of gas parameters in the channels yield no reason to consider the channel flow regime to be laminar near the zone of the sharp change of the resistance and damping coefficient, and the sharp change proper, to be caused by a laminar-to-turbulent transition. In this model, a resistance law, corresponding to developed turbulent flow [4], is adopted. As follows from it, the behavior of the tangential stress on the channel wall drastically changes when the steady-state flow velocity achieves a value exceeding the amplitude of the velocity oscillation in the channel. In this case, the term in the equation for the tangential stress, which contains the steady-state flow velocity, becomes more ponderable than the term, containing the velocity oscillation amplitude. The relation between a change in the damping coefficient and the steady-state flow velocity in the channels is determined by the law of variation in the tangential stress with the steady-state flow velocity, so the threshold steady-state velocity, at which exceeding a sharp growth in the damping coefficient is observed, can conditionally be considered to be the velocity from the condition:

$$V_0 \geq |V'| * \pi/8 \quad (14)$$

One way to intentionally arrange a steady-state gas flow through the damper channels is positioning the damper inside the solid propellant grain. Despite the fact that the damper natural frequency varies as the grain burns, the steady-state flow of the combustion products through the damper cavity and its channels will support a predicted stability in its parameters. The need in efficient operation of the damper is actually confined to some periods in combustion chamber operation, with consideration of which initial parameters of the damper and grain should be chosen. In this connection, an evaluation of the influence of solid propellant combustion inside the damper on its operation is of interest.

As follows from Eqs. (13), the efficiency of combustion chamber oscillation suppression is determined by the gas velocity oscillation in the connecting channels. Fig.5 shows versions of individual calculations of the velocity oscillation amplitude as a function of the steady-state flow velocity in the channels, determines the mass income into the gas damper cavity, for some numerical values of the real and imaginary parts of the influence function in Eq.(6). The velocity oscillation amplitude dependence of the steady-state flow velocity can be of various forms for various specific influence function parameters in Fig.5.

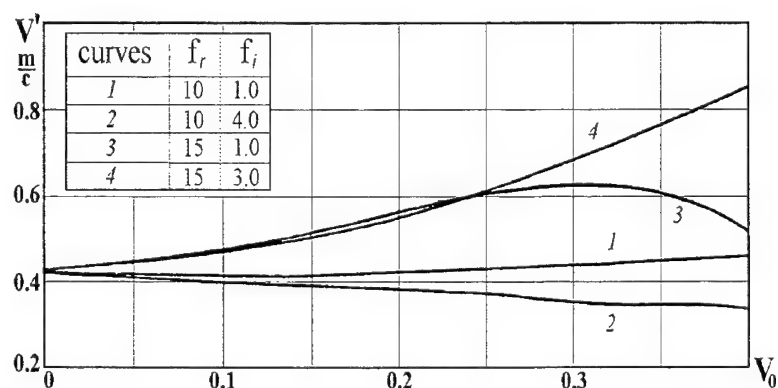


Figure 5. The velocity oscillation amplitude as a function of the steady-state flow velocity in the channels.

The velocity oscillation amplitude is observed to decrease (curve 2), to increase with various intensities (curves 1 and 4) , and to vary non-monotonously, having a maximum (curve 3) as the steady-state flow velocity increases . Taking into account the damper natural frequency dependence of the influence function parameters, such behavior of the curves is quite explicable and indicates the possibility to enhance the damper efficiency using this effect.

Intentional selection of the geometry of an acoustic damper and of thermodynamic parameters of the gaseous products filling its cavity and connecting channels in operation, as well as arrangement of a steady-state gas flow through the channel, enable widening the application area for acoustic dampers of the type under consideration. This allows using such a design to suppress the combustion chamber oscillation with comparatively low frequencies. An acoustic damper of the type under consideration was manufactured and tested to suppress the combustion chamber acoustic oscillation of about 100 Hz frequency and up 0.3 MPa amplitude. Such an acoustic damper of 0.012 m<sup>3</sup> cavity volume enabled reduction in the oscillation amplitude down to the noise level (less than 0.05 MPa). The above-described mathematical model for operation of an acoustic damper allowed rather accurate determination of its parameters and efficiency.

#### References

1. Harrie, D.T. and Reardon, F.H., Liquid propellant rocket combustion instability, *National Aeronautics and Space Administration*, 558, 1972.
2. Natanzon, M.S., Combustion Instability, *Mashinostroyenie*, Moscow, 122, 1986, (in Russian).
3. Galitseysky, B.M., Ryzhov, Y.A., and Yakush, E.V., Thermal and Hydrodynamic Processes in Oscillating Flows, *Mashinistroyenie*, Moscow, 17, 1977, (in Russian).

## IGNITION OF PROPELLANTS: SHAPING AND DEVELOPMENT OF BURNING WAVE AND ITS CHARACTERISTICS

**Victor S.Abrukov<sup>1</sup>, Stanislav V.Ilyin<sup>1</sup>, Vladimir M.Maltsev<sup>2</sup>**

<sup>1</sup>Chuvash State University, 15, Moskovsky ave, Cheboksary 428015, Russia;

<sup>2</sup>Institute of Structural Macrokinetics of the Russian Academy of Sciences, Chernogolovka 142432, Russia

**ABSTRACT:** The results of the experimental investigation of ignition processes for various propellant models are presented. The investigations have been made by interferometric techniques in terms of process visualization and qualitative analysis as well as in determining the various local and integral, time and space characteristics. The investigations have been made by new approaches. Their fundamentals are presented shortly with reference on the author's papers which have been published recently. These approaches have not been used earlier by other investigators in the ignition process research.

### 1. INTRODUCTION

In [1-5] new approaches to interferometric techniques (IT) in research of combustion processes, in particular in research of propellant ignition and burning in terms of process visualization as well as in determining the local and integral characteristics, have been presented.

In [1] possibilities of the visualization of the ignition process of transparent (glassy) propellant models both in the condensed phase (c-phase) and gaseous phase (g-phase) of a burning wave by means of the holographic IT are shown. The holographic IT permits to study the heat release and heat transfer in a transparent solid substance with surfaces which have not high optical quality.

In [2,3] a new approach to the solution of the problem of the flame temperature field determination based on the refractive index field is presented. This approach is as follows. As estimations, which have been done for various reacting systems, have shown, there is an a priori relationship between the temperature variation in the burning wave and the molar refraction variation. By examining this a priori relationship in conjunction with a reacting system state equation one can obtain a formula of the flame temperature field determination.

In [3-5] possibilities of determining the integral characteristics of a burning wave by IT are shown. They describe the g-phase of the burning wave (and the burning process) as a whole. They include: gas mass and heat quantity in the g-phase of the burning wave, mass burning rate and heat release power during the propellant ignition process and other characteristics. The eikonal of the g-phase of the burning wave (the integral of the function of the phase difference distribution in the interferogram recording plane) are used for the determination of the integral characteristics.

All approaches and experimental results are discussed in detail in [6,7]. The present paper generalizes only some experimental data obtained.

## 2. INVESTIGATION OF PROPELLANT TRANSPARENT MODELS. VIZUALIZATION OF ENTIRE STRUCTURE OF BURNING WAVE

IT is employed traditionally only in research of the part of the burning wave which is in the g-phase, except [8] and other papers by Ito and Kashiwagi [8], in which the holographic IT are used for the visualization and analysis of the process of the liquid burning flame spread both in the c- and the g-phases simultaneously.

The results demonstrating the potentialities of the holographic IT in the burning wave visualization in the c- and g-phases simultaneously during the laser radiation ignition (LRI) process of the solid propellant transparent (glassy) models are presented below. Under investigation was LRI of the polymethylmethacrylate (PM) and celluloid (weakly nitrated cellulose - NC) samples (laser radiation wavelength was 10.6 microns, laser spot size was 5 mm, radiation flow density is  $80 \text{ W/cm}^2$ ). The PM samples were parallelepiped ( $20 \times 30 \times 30 \text{ mm}$ ). The NC samples were 1 mm thick plates.

Figures 1 and 2 show the film frames representing typical features of the burning wave shaping and development during LRI process (numbers under frames show moments of the time  $t$  in seconds with the origin at the onset of the laser radiation). The time of laser radiation was 15 sec. (Figure 1) and 8 sec. (Figure 2). After the radiation was turned-off, the PM samples were extinguished, the NC samples were continued to burn.

The qualitative analysis of the holographic interferometric films has revealed the number of LRI stages taking place both sequentially and concurrently, among which the following stages may be pointed out:

- formation in the c-phase of the "cone" layer heated by the laser radiation, the simultaneous generation of stresses within the sample (the elastic strain of the sample as a whole) and gasification of the sample substance (see  $t=0.1 \dots 3 \text{ sec.}$  - Figure 1 and  $t=0.1 \dots 1 \text{ sec.}$  - Figure 2);
- inflammation of the gasification products, the expansion of the inflammation front to the sample and stabilization of the flame near the sample surface (see  $t=3 \dots 4.5 \text{ sec.}$  - Figure 1 and  $t=1 \dots 3 \text{ sec.}$  - Figure 2);
- formation of the "hemisphere" layer heated due to the heat transfer from the flame (see  $t=4.5 \text{ sec.}$  - Figure 1 and  $t=3 \text{ sec.}$  - Figure 2);
- restructuring of the heated layer (see  $t=4.5 \dots 6 \text{ sec.}$  - Figure 1 and  $t=3 \dots 5 \text{ sec.}$  - Figure 2);
- development of the stresses after the stabilization of the flame over the sample (see  $t=4.5 \dots 9 \text{ sec.}$  - Figure 1 and  $t=3 \dots 5 \text{ sec.}$  - Figure 2);
- burning-out of the sample substance, the development of a burnt-out "cone" (it appears as a result of self-focusing of the laser radiation) and restructuring of the general heated layer (see  $t=6 \dots 15 \text{ sec.}$  - Figure 1 and  $t=5 \dots 8 \text{ sec.}$  - Figure 2). The burnt-out "cone" can be definitely observed on the frame  $t=34 \text{ sec.}$  (Figure 1);



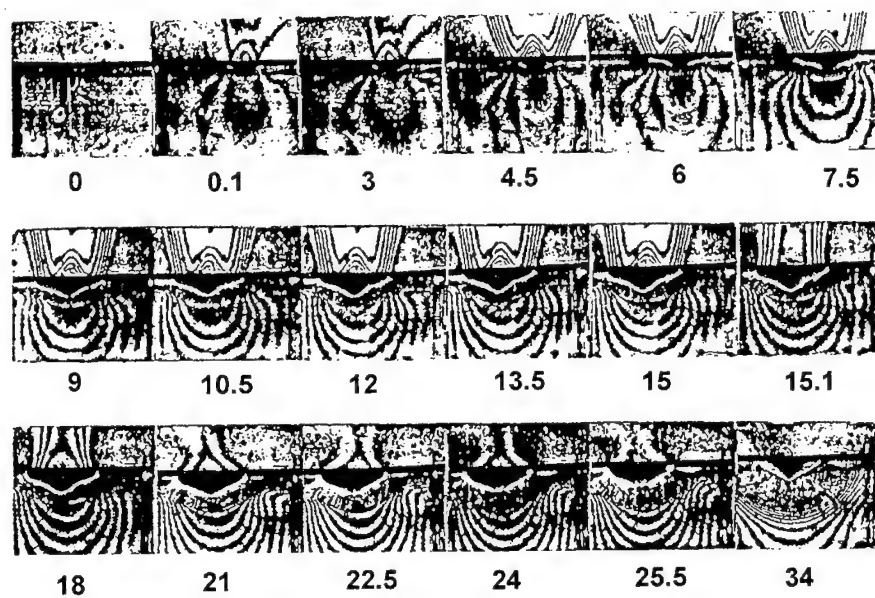


Figure 1. The film frames showing typical features of the PM sample burning wave shaping and development.

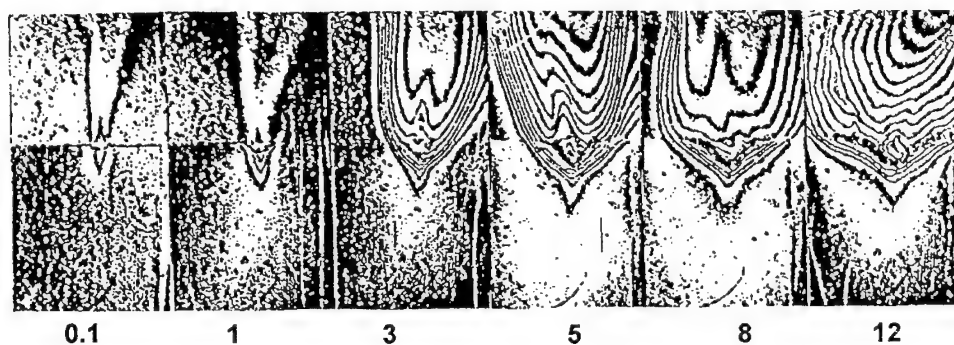


Figure 2. The film frames showing typical features of the NC sample burning wave shaping and development.

-formation and development of the phase transition zone (see the dark zone:  $t=0.1 \dots 15$  sec. - Figure 1);

-various transition processes in the g- and the c-phases after the interruption of the laser radiation followed by the flame extinction and dissipation of the heat accumulated in the sample (see  $t=15.1 \dots 34$  sec. - Figure 1).

As Figures 1 and 2 show, the burning wave structure formed during LRI, is not one-dimensional due to the laser radiation self-focusing in the sample substance.

The quantitative analysis of stages, observable in the c-phase calls for a further theoretical elaboration of the interferogram calculation techniques and the discussion of experimental problems and set up.

### 3. INVESTIGATION OF REAL PROPELLANT MODELS

#### 3.1 EXPERIMENTAL CONDITIONS

The LRI process of the following real propellant models was investigated: 1 - Cellulose Nitrate, 2 - AP+PS,  $a=1.0$ ; 3 - AP+PM,  $a=1.5$ ; 4 - AP+PM+2% $\text{Fe}_2\text{O}_3$ ,  $a=1.0$ ; 5 - AP+PM+10%Al,  $a=1.0$  (AP is ammonium perchlorate, PM is polymethylmetacrylate, PS is polystyrene, "a" is oxydizer-fuel equivalence ratio). The experiments were conducted in the air surroundings under the pressure 1 atm. The cylindric samples with diameter of 3.4 mm (sample 1), 5 mm (2, 3) and 7 mm (4, 5) were used. Two types of lasers with the two different radiation wavelengths were used. The surface of samples 1, 2, 3 was covered by the thin ( $\approx 0.01$  mm) graphite layer. The laser spot size at the sample surface was  $\approx 2$  mm (1, 2, 3),  $\approx 3$  mm (4) and  $\approx 4$  mm (5). Special means for the equation of the flux density distribution in the cross-section of the laser beam were not applied except the installation of the diaphragm at the beam exit from the laser. Different powers and flux densities of the laser radiation were applied in experiments (the data is in Tables 1, 2, 3). The polarization shift interferometer was applied for the production of the interference films (the speed was about 1000 frames per second).

Figure 3 shows the film frames representing the initial period of LRI process of samples 1-5 (numbers under frames show moments of the time  $t$  in seconds with the origin at the onset of the laser radiation).

#### 3.2. TEMPERATURE FIELDS

The g-phase temperature  $T$  fields were determined in the period from the emergence of the gasification products to the establishment of the quasi-stationary burning conditions.

The Figure 4 shows the temperature fields obtained for the LRI initial period of the sample 1. For this sample the temperature fields indicate that the gasification intensity from the sample surface is periodic in character. For other samples some temperature data are presented in Table 1.

#### 3.3 INTEGRAL THERMODYNAMIC AND DYNAMIC CHARACTERISTICS OF LRI PROCESS

The quantitative analysis of the LRI process as a whole was done for real propellant models by

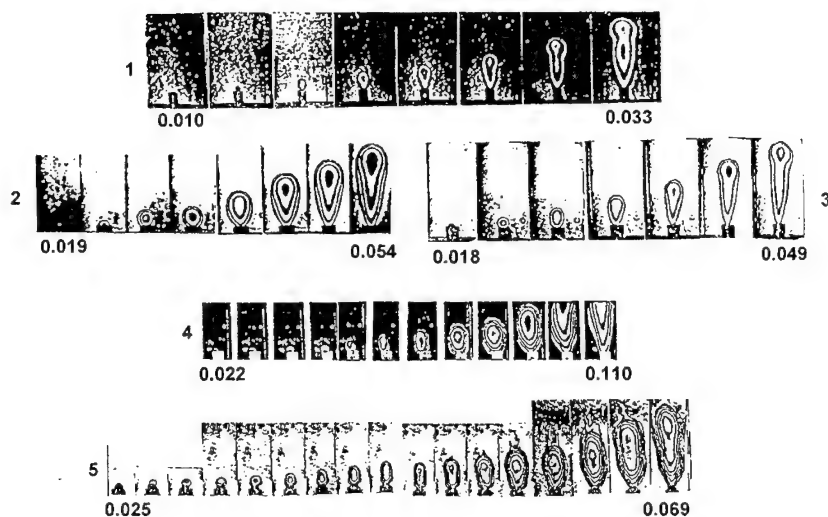


Figure 3. The film frames representing the initial period of LRI process of the samples 1-5.

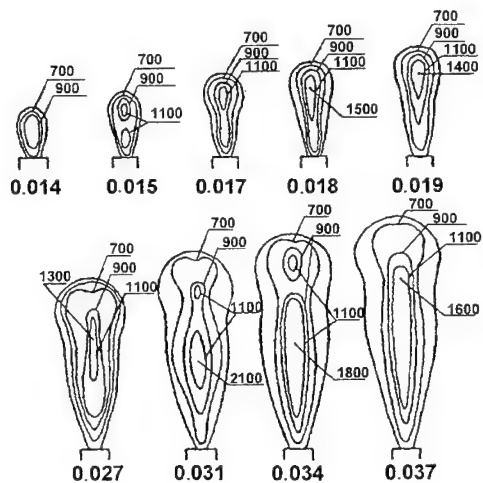


Figure 4. The temperature fields ( $T$  in K) in the gasification and burning products flow (g-phase of burning wave) during the initial period of LRI process of sample 1 ( $t=0.014 \dots 0.037$  sec.).

means of the measurement of parameters of the gaseous products flow emerging after the laser radiation onset.

The LRI initial period and the response period dealing with the laser radiation turn-off was studied. The period, while the emerging gasification and burning products "cap" was seen as a whole within the viewing area of the interferometer was taken as initial. The methodologies stated in Ref [3-5] and described in length in [6,7] were applied. The determination of the "cap" gas mass  $m$ , its "average" temperature, enthalpy  $H$ , the burnt-out sample mass burning rate  $m'$ , heat release power  $H'$  and other quantities by means of the "cap" eikonals lies in the base of these methodologies.

Some of the findings are given in Table 1. Figure 5 shows how  $m$ ,  $H$  and the average specific enthalpy  $H_m$  of the "cap" vary in time during the initial period of LRI process of sample 4 (see the curves for  $t=0 \dots 0.07$  sec.).

TABLE 1

	Cellulose Nitrate	AP+PM	AP+PM+ 2%Fe <sub>2</sub> O <sub>3</sub>	AP+PM+ 10% Al	AP+PS
$l$ , microns	1.06	1.06	10.6	10.6	1.06
$q_s$ , W/cm <sup>2</sup>	300	300	150	420	300
$dt_i$ , sec.	0.2	0.5	0.2	0.2	0.5
$dt$ , sec.	0.037	0.051	0.078	0.069	0.059
(the time being analysed: the period of the time during which the calculations were made. The results of measurements $m'(t)$ and $H'(t)$ showed that at the end of this period the quasi-stationary burning of samples 1-4 has formed)					
$h$ , mm	0.23	0.26	0.34	0.38	0.41
(the average thickness of the sample layer which burnt-out during $dt$ )					
max $m'$ , g/sec.	0.06	0.07	0.12	0.70	0.10
(at the end of the time being analysed)					
max $U$ , mm/sec.	10	10	15	29	14
(at the end of the time being analysed)					
max $H'$ , W	16	20	105	1050	35
(in the g-phase during the gasification products inflammation)					
max $T$ , K	1500	>2700	2600	-	>2700
	( $y=10$ mm)		( $y=19$ mm)		
(in the g-phase during the gasification products inflammation, $y$ is the distance from the the sample surface)					
$h$ , mm	0.024	0.010	0.040	0.070	0.010
(the average thickness of the sample layer which burnt-out to the max $H'$ moment)					
max $T$ , K	-	2700	1900	-	2700
		( $y=1$ mm)	( $y=8$ mm)		( $y=1$ mm)
(in the g-phase after the quasi-stationary burning under laser radiation sets in)					
$H'$ , W	16	20	49	200	32
(at the end of the time being analyzed)					
$q$ , W	4	$\approx 20$	42	150	$\approx 32$
(the resulting heat release power through chemical reactions in the system consisting of the sample and the g-phase, $q=H'-q_i$ ),					
$Q$ , J/g	70	280	350	214	330

(the resulting thermal effect of chemical reactions  $Q=q/m'$ )

$Q_l, \text{J/g}$	210	$\approx 0$	60	70	$\approx 0$
(the thermal effect of the laser radiation $Q_l = q_l/m'$ ; samples 2, 3, as experiments show, did not absorb the laser radiation with the wavelength 1.06 microns)					
$v, \text{m/sec.}$	6,2	4,8	5,8	-	3,5
$F, \text{J/kg}$	185000	215000	300000	475000	250000
$V, \text{m}^3/\text{kg}$	1.85	2.15	2.80	4.60	2.50
$E \cdot 10^{-9}, \text{J/m}^3$	0.6	1.0	1.4	4.2	1.4

Notes:  $l$  is the laser radiation wavelength,  $q_s$  is the laser radiation flux density ( $q_l$  is the power),  $dt_l$  is the whole laser radiation time, "max" is the maximum rate,  $v$  is the flow-section-average linear gas velocity near the sample surface,  $F$  and  $V$  are intraballistic characteristics of propellants (the force of powder  $F$ , the specific gas production  $V$ ),  $E$  is the quantity of the heat released when a unit volume of the sample substance is burned, the sign "-" indicates that the quantity is not measured.

### 3.4. CHARACTERISTIC TIMES OF SOME STAGES OF LRI INITIAL PERIOD

Based on the qualitative analysis of the interference films (Figure 3), the measurements of the characteristic times  $dt_i$  of the individual successive stages of the LRI initial period were made: the gasification delay (index  $i = 1$ ), the duration of the endothermic (2) and low-exothermic (3) gasification and the duration of the inflammation of the gaseous product (4). The results are given in Table 2 (the samples numbers are shown in the table top).

TABLE 2

	4	5	5	5
$q_s, \text{W/cm}^2$	150	420	350	200
$dt_1, \text{sec.}$	0.022	0.022	0.032	0.055
$dt_2, \text{sec.}$	0.029	0.018	0.018	0.022
$dt_3, \text{sec.}$	0.004	0.008	0.010	0.009
$dt_4, \text{sec.}$	0.007	0.009	0.012	0.008

### 3.5. CHARACTERISTIC TIMES OF SOME STAGES OF RESPONSE PROCESS ON LASER RADIATION TURN-OFF

Figure 5 shows the film frames representing sample 4 response process dealing with the laser radiation turn-off and the curve  $H_m(t)$  of the burning products flow (see  $t=0.20 \dots 0.30$  s). On Figure 6 the curves of  $m'(t)$  and  $H'(t)$  are shown. The methodologies of their determination have been discussed in [9].

The qualitative and quantitative (Figures 5 and 6) analysis of the interference films allowed the characteristic times  $dt_i$  and the burning-area-average thicknesses  $h_i$  of the burning-out layers of five individual stages to be revealed and evaluated: the response of the g-phase reaction zone (index  $i = 5$ ), the stage of the delay of the c-phase response (6), the response of the c-phase reaction zone (7), the response of the c-phase heat layer that developed upon exposure to the laser radiation

(8) and the stage of the establishment of the new level of the burning rate (9). These evaluations allow one to judge indirectly about the burning wave structure and its zones sizes.

The results are given in Table 3. Some  $dt_i$  are shown on Figures 5 and 6.

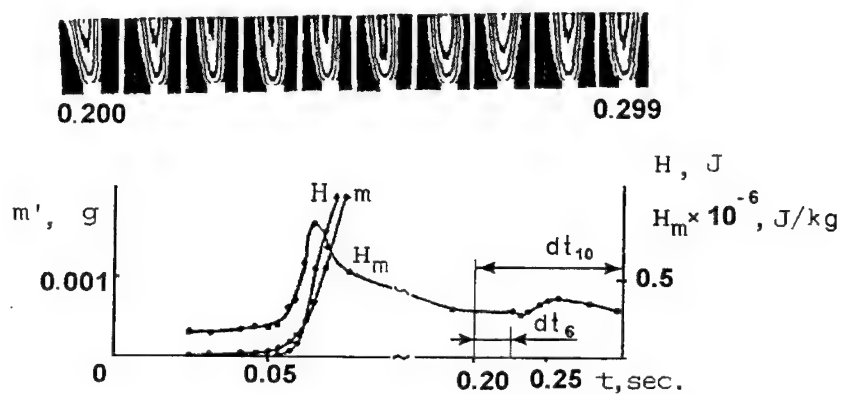


Figure 5. The film frames representing the response process of LRI of sample 4 after the laser radiation turned-off and the curves of the g-phase mass, enthalpy and specific enthalpy in the initial period of LRI ( $t=0 \dots 0.07$  sec.) and the curve of the specific enthalpy during the response process ( $t=0.020 \dots 0.030$  sec.).

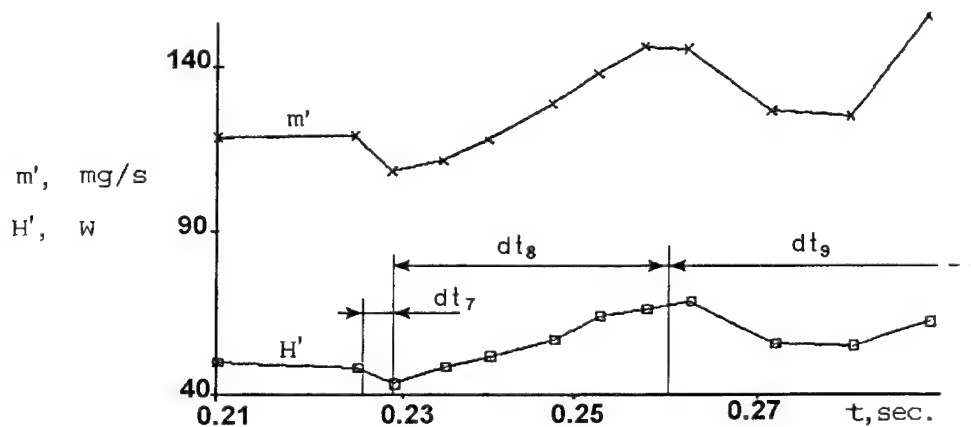


Figure 6. The curves of the mass burning rate and the heat release power during the response process of the LRI of sample 4.

The quantities  $h_i$  are evaluated by the following formula:

$$h_i = \langle m'_i \rangle dt_i / S d$$

where  $\langle m'_i \rangle$  is the average mass burning rate during  $dt_i$ ;  $S$  is the burning area of the sample surface,  $d$  is the sample substance density,  $i = 6, 7, 8, 9, 10$ . The quantity  $h_5 = v dt_5$ , where  $v$  is the average linear gas velocity near the sample surface.

TABLE 3

	4	5		4	5
$q_s, W/cm^2$	150	420		150	420
$dt_5, sec.$	0.001	-	$h_5, mm$	6	-
$dt_6, sec.$	0.026	0.009	$h_6, mm$	0.400	0.400
$dt_7, sec.$	0.003	0.025	$h_7, mm$	0.045	0.280
$dt_8, sec.$	0.030	0.095	$h_8, mm$	0.450	1.120
$dt_9, sec.$	0.040	0.080	$h_9, mm$	0.110	0.200
$dt_{10}, sec.$	0.099	0.209	$h_{10}, mm$	1.050	2.000

Notes:  $dt_{10}$  is the general time from the interruption of the laser radiation to the establishment of the new purely "independent" quasi-stationary burning conditions,  $h_{10}$  is the thickness of the layer which has burned-out during that period of time.

#### 4. CONCLUSION

The undeniable advantages of IT for the diagnostics of LRI are non-intrusiveness, fast response, and obviousness. However, in our opinion, the most fundamental advantage of IT is the determinability of the wide variety characteristics of LRI.

Unfortunately, in this paper, the authors can not provide examples of the realization of other potentials of IT (the evaluations of the resulting thermal effects of chemical reactions in the c- and g-phases, thermal effect of the convective heat loss from the burning sample surface, the conductive heat flux from the g-phase to the burning sample surface, the effective absorption index of the c-phase) due to the limited volume of the paper which may be presented to publication. Besides this, there are some problems associated with maintaining the conditions under which some particular procedure may be employed and problems dealing with the authors' limited capabilities for implementing the needed ignition process scenario. Authors hope that joint efforts of them and of other investigators who will take interest in the practical implementation of IT will permit to solve a number of problems of the IT ignition research. The authors would like to invite experts in the fields of the ignition research to participate in IT-related project frameworks.

#### References

1. Abrukov, V.S., Ilyin, S.V., Maltsev, V.M., Tarasov, N.A., "New ways in Combustion Interferometry: Quantitative Analysis of the Burning Wave Formation During Ignition of Condensed Systems", *Abstract of Symposium Papers and Abstract of Poster Session*

*Presentations/ Twenty-Fifth Int. Symp. on Combustion (July 31-August 5, 1994), The Combustion Inst., Pittsburgh, USA, 1994, p.419.*

2. **Abrukov, V.S., Maltsev, V.M.**, "Temperature Fields of Gas and Condensed System Flames", *Book of Proceedings of 15th Int. Colloquium on the Dynamics of Explosion and Reactive Systems/ University of Colorado, Boulder, USA, 1995, p.579.*

3. **Abrukov, V.S., Ilyin, S.V., Maltsev, V.M.**, "Interferometric Technique and Other Optical Methods in Combustion Research. New Approach", *Optical Techniques in Fluid, Thermal, and Combustion Flow, edited by Soyoung Stephen Cha and James D.Trolinger, Proceedings of SPIE Int. Symp., Vol. 2546, 1995, 420-426.*

4. **Abrukov, V.S., Ilyin, S.V., Maltsev, V.M.**, "Interferometric Techniques in Combustion Research", *Proceedings of the 3rd Int. Symp. "Non-Intrusive Combustion Diagnostics" (May 10-14, 1993, Scheveningen, The Netherlands), edited by Kenneth K.Kuo, The Pennsylv. State Univ., USA, 1993, 134-136.*

5. **Abrukov, V.S., Maltsev, V.M.**, "Determination of Intraballistic and Energy Characteristics of Condensed Systems Using Interferometry Techniques", *Int. Conference on Combustion (21-26 June, 1993, Moscow-St.Petersburg, Russia)/ Abstracts, The Semenov Institute of Chemical Physics, Moscow, Russia, 1993, p.83.*

6. **Abrukov, V.S.**, "Interferometric Techniques in Combustion Research", Thesis of Dr. Sci. dissertation, The Semenov Institute of Chemical Physics, Moscow, Russia, 1994, 48 pp. (in Russian)

7. **Abrukov, V.S.**, "Interferometry Techniques in Combustion Research", Dr. Sci. dissertation, The Semenov Institute of Chemical Physics, Moscow, Russia, 1994, 173 pp. (in Russian)

8. **Ito, A., Majidi, V., Saito, K.**, "Temperature Measurement by Holographic Interferometry in Liquids for Transient Flame Spread", *Laser Application in Combustion and Combustion Diagnostics, edited by Randy J. Locke, Proceedings of SPIE Int. Symp., Vol. 2122, 1994, 176-185.*

9. **Abrukov, V.S., Ilyin, S.V., Matveyev, V.V.**, "Determination of Laser Radiation Turn-off Response Characteristics During a Condensed System Ignition Process by Interferometry", *Proceedings of the Russian-Japanese Seminar on Combustion (Joint Meeting of the Russian and Japanese Sections, Chernogolovka, Moscow Region, 2-5 October, 1993), The Semenov Institute of Chemical Physics, Moscow, Russia, 1993, 34-36.*



## ON CHEMICAL KINETICS OF THE IGNITION OF AP / NSAN / INERT BINDER COMPOSITE PROPELLANTS

<sup>1</sup>Frota, Octávia and <sup>2</sup>Araújo, Luis

1 - Laboratory of Energetic and Detonic, 3150 Condeixa Portugal; 2 - National Institute of Engineering and Industrial Technology - Est. Paço do Lumiar - Ed. J1 - 1699 Lisboa, Codex - Portugal

**ABSTRACT.** This work concerns the ignition behaviour of ammonium perchlorate / non-stabilized ammonium nitrate / hydroxyl terminated polybutadiene and ammonium perchlorate / non-stabilized ammonium nitrate / polyurethane composite propellants. All the compositions were formulated with 80 % by weight of solid oxidant mass and 20 % by weight of bulk (pre-polymer, plasticizer and curing agent) binder system. In both type of compositions the cases 0 %, 20 %, 40 % and 60 % of non-stabilized ammonium nitrate weight content, of the total solid mass, were studied.

The experimental apparatus used in this work for the measurement of ignition delays of the propellants, in ambient air and at atmospheric pressure, was composed of an electrical furnace, a pneumatic system for rapid introduction of the propellant samples and peripheral devices allowing real time control of the process and data acquisition.

The results obtained showed that increasing non-stabilized ammonium nitrate content caused shorter values of the ignition delay. Further interpretation of the experimental data was made assuming a first order rate controlling reaction, with constant reactants' consumption during the pre-ignition period. As the calculated values of the activation energy in the lower temperature range were always lower than those obtained for the higher experimental temperature, this type of evolution indicated that the ignition mechanism of this type of composite propellants could be described in two independent phases, corresponding Phase I to the occurrence of heterogeneous ignition reactions while homogeneous gas phase ignition reactions were characteristic of Phase II. The transition temperatures between Phases I and II were calculated. The results obtained demonstrate clearly that partial substitution of ammonium perchlorate by non-stabilized ammonium nitrate in the propellants' formulation shifts the transition temperature to lower levels, increasing in this way the domain of occurrence of homogeneous ignition.

### 1 - INTRODUCTION

Significant efforts are been undertaken in the field of rocket propulsion aimed at the development of a new generation of less polluting propellants, with low signature and reduced sensitivity to shock and thermal stimuli. In fact, the exhaust gases resulting from the combustion of composite ammonium perchlorate-based propellants include a large amount of hydrogen chloride, as well as some other chlorine components, which are the main source of high levels of toxicity for most living forms, and of equipment corrosion damages [1]. Furthermore, the formation of hydrochloric acid, by

combination of hydrogen chloride with atmospheric water vapour, is the origin of visible and infrared optically dense secondary smoke, which is a major disadvantage for military applications [2]. Partial substitution of ammonium perchlorate (AP) by non-stabilized ammonium nitrate (NSAN) as oxidizer component in composite propellants is one of the possibilities which has been under study for some time at the Laboratory of Energetic and Detonic [3 - 4]. The use of non-stabilized ammonium nitrate is not free of problems, namely the contribution to the depletion of the ozone layer by the formation of  $\text{NO}_x$  compounds, its high hygroscopicity, the existence of crystalline phase transitions with important volume changes, and the low  $I_{sp}$  of NSAN/Inert Binder composite propellants. Nevertheless, one must consider that the absence of chlorine in NSAN composition and its low sensitivity to impact and friction make this component an attractive oxidizer candidate for those applications where increased insensitivity and a significant reduction of the emission of acid compounds, specially HCl, is of concern and high specific impulse is not a determinant parameter. This work concerns the ignition characteristics of AP/NSAN/Hydroxyl terminated polybutadiene (HTPB) and AP/NSAN/ Polyurethane (PU) composite propellants. Several compositions, with increasing NSAN content, were submitted to constant heating, in ambient air and at atmospheric pressure, until ignition occurred. The analysis of the ignition delays, as a function of temperature and NSAN content, provided additional evidence of the existence of two alternative, temperature-dependent, rate determining mechanisms, characterised by different activation energy and  $\beta$  factor, whose characteristic values were calculated, as well as the transition temperatures. The results also explained the fundamental role of the thermal degradation of NSAN in the ignition of this type of propellants.

## 2 - EXPERIMENTAL

### Propellants Test Samples - Composition and Preparation

All the compositions were formulated with 80 % by weight of solid oxidant charge and 20 % weight of bulk (pre-polymer, plasticizer and curing agent) binder system. In both AP/NSAN/HTPB and AP/NSAN/PU propellants, the cases 0 %, 20 %, 40 % and 60 % of non-stabilized ammonium nitrate by weight, of the solid oxidant mass total weight, were studied (Table 1).

**Table 1**  
Weight Composition of the Propellants

PROPELLANT	COMPOSITION (% wt)
<b>B1</b>	80 AP / 20 PU
<b>B2</b>	64 AP / 16 NSAN / 20 PU
<b>B3</b>	48 AP / 32 NSAN / 20 PU
<b>B4</b>	32 AP / 48 NSAN / 20 PU
<b>C1</b>	80 AP / 20 (HTPB + IPDI + DOA)
<b>C2</b>	64 AP / 16 AN / 20 (HTPB + IPDI + DOA)
<b>C3</b>	48 AP / 32 AN / 20 (HTPB + IPDI + DOA)
<b>C4</b>	32 AP / 48 AN / 20 (HTPB + IPDI + DOA)

Compositions containing only AP were bimodal with a 50 % fine/coarse weight proportion of the AP particles, but in the formulations including NSAN the compositions used were trimodal, with the same fine/coarse AP weight composition (Table 2).

**Table 2**  
Particle Sizes Used in the Formulations

<b>AP fine</b>	$45 < d_{AP} < 90 \mu\text{m}$
<b>AP coarse</b>	$106 < d_{AP} < 150 \mu\text{m}$
<b>NSAN</b>	$150 < d_{NSAN} < 180 \mu\text{m}$

The particle size distribution curves of both oxidizers were established by Laser Diffraction Spectrometry. The particle sizes presented in Table 2 were obtained by sieving and the material was kept at  $333 \pm 5 \text{ K}$  and  $11 \pm 2 \%$  relative humidity for the propellants formulations. Two different polymers, hydroxyl terminated polybutadiene (HTPB R45), from France Elf Atochem, and polyurethane (PU), from CPB Portugal, were used as binders. The propellants were obtained by mixing under vacuum at  $333 \text{ K}$  in an anchor blade type mixer, cast in small boxes ( $50 \text{ mm} \times 50 \text{ mm} \times 30 \text{ mm}$ ) and cured at  $333 \text{ K}$  for 5 days. Slice-like strands were cut from the cured propellant blocks and its uniformity was verified by optical microscopy and bulk density measurements of the various strands.

The test samples cut from the strands had the form of circular pellets  $10 \text{ mm}$  in diameter and  $0.8 \text{ mm}$  thick. In order to reduce possible ignition spots, which would increase data scatter, the surface of the samples was rubbed with fine emery paper and brushed in order to dust out any loose particles. The test samples were conditioned at  $298 \pm 2 \text{ K}$  and  $11 \pm 2 \%$  relative humidity before testing.

### Experimental Set-up

Strong differences of opinion exist about the ideal set-up for ignition delay studies of solid propellants [5, 6]. Nevertheless, the simplest and most reliable systems, like the hot plate and the electrical furnace, are still used in the majority of large scale applications, even if the results obtained are often believed to be limited to comparative purposes. In fact, due to the good reproducibility of testing conditions, a large amount of information can be inferred from the results obtained.

The experimental apparatus (Figure 1) used in this work for the measurement of ignition delays of the propellants, in ambient air and at atmospheric pressure, is essentially composed of an electrical furnace, a pneumatic system for rapid introduction of the propellant samples, and peripheral devices allowing real time control of the process and data acquisition. The furnace, composed of a ceramic cylindrical ignition chamber,  $115 \text{ mm}$  long and  $65 \text{ mm}$  in diameter, heated by a  $650 \text{ Watt}$  electrical element and externally isolated with ceramic fibre, has a maximum temperature of  $1573 \text{ K}$ . The temperature of the ignition chamber is controlled by a PID temperature controller associated with a Chromel-Alumel thermocouple.

The possibility of the non-uniformity of the superficial temperature of the test samples, due to natural convective flows and possible influence of the furnace end opening on radiation reaching the upper surface of the pellet, was considered.

In previous studies performed with similar equipment and similar test samples, it has been demonstrated that, with regard to natural convection, the heat transfer coefficient at a given pressure scarcely varies in approximately  $200 \text{ K}$  temperature intervals, and, therefore, the consideration of global heat transfer and mean surface temperature introduces very little error [7]. The fact that the solid angle defined by the furnace end opening and the test pellet was very small led to the assumption that the radiation losses could be assumed to be negligible in the total surface heating. Nevertheless, and in order to verify temperature uniformity, axial and radial measurements of the temperature inside the furnace were made using a K-type thermocouple that was displaced one millimeter between measurements.

The results of the calibration (Figure 2) allowed the determination of a cylindrical test zone ( $10 \text{ mm}$  high and  $20 \text{ mm}$  in diameter), where the maximum axial and radial temperature gradients proved to be always lower than  $0.05 \%$  of the lower test temperature ( $\Delta T_{\text{rad max}} = 3.5 \text{ K}$  and  $\Delta T_{\text{ax max}} = 2 \text{ K}$ ).

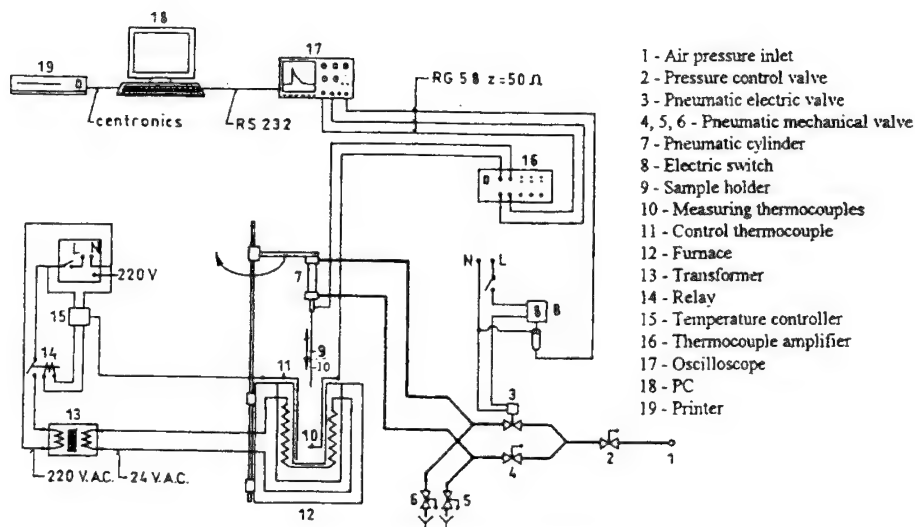


Figure 1. Experimental apparatus.

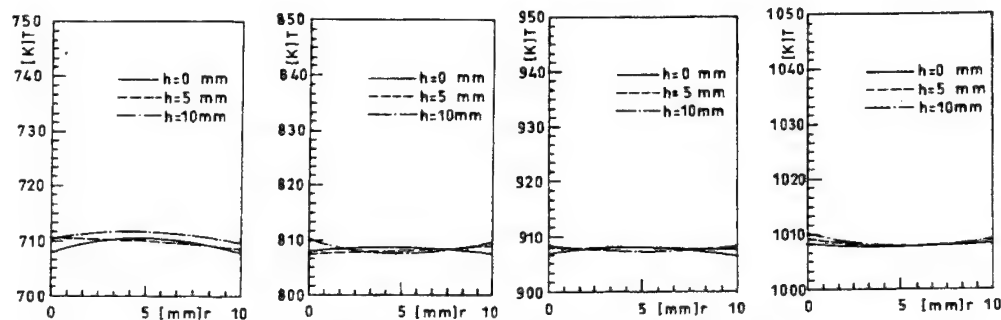
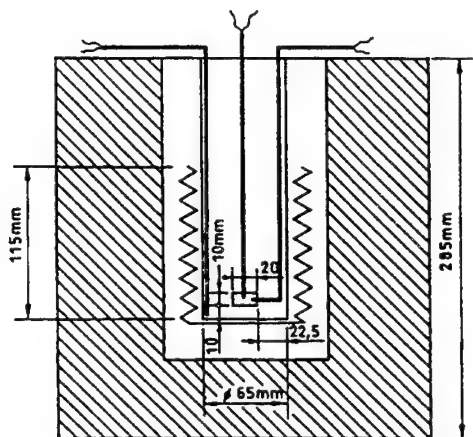


Figure 2. Examples of calibration results of the test zone.

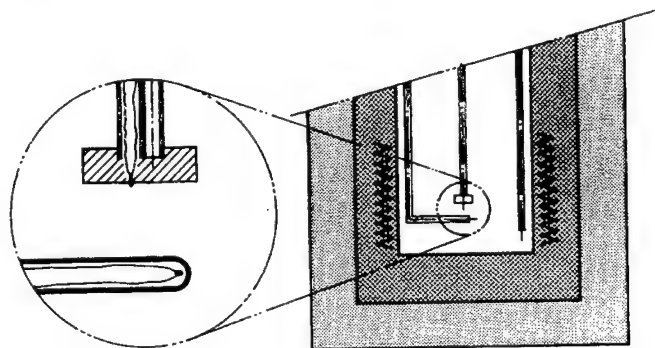
During the ignition tests, the temperature of the measuring zone was monitored by a shielded K-type thermocouple perpendicular to its axis (Figure 3). A pneumatic cylinder was used for the rapid introduction of the propellant samples in the test zone. The pneumatic system is attached to a support that allows its axial and radial displacement away from the furnace entrance in order to avoid heating by convection of the propellant samples during the installation period and to enable the coaxial alignment of the injecting piston with the furnace axis, before injection. The test samples were fixed to the extremity of a thin wire isolated with Teflon, which is axially connected with the piston of the pneumatic cylinder. The length of the wire is such that, at the piston maximum displacement, the sample is positioned at the center of the furnace measuring zone (Figure 3).

The time evolution of the surface temperature of the sample was measured with a 78  $\mu\text{m}$  K-type thermocouple. Due to the fact that ignition reactions of classic solid composite propellants always occur at a few microns distance from the surface of the propellants, and in order to optimize the accuracy of the measurements, the thermocouple was threaded up to the inferior side of the test pellet, in such a way that the sensitive junction, in close contact with the solid through the characteristic elasticity of the propellant, was positioned as close as possible to its surface. A detailed view of the sample and thermocouple installation can be seen in Figure 4.



**Figure 3.** Schematic representation of the furnace and location of the test zone.

The electrical output of the control and measuring thermocouples was amplified by an AD595AQ RS Data Control K-type thermocouple amplifier, with cold junction compensation, and registered by a Tektronix 320 TDS oscilloscope which allows a maximum sample-rate of 500 MSamples/s. Specific software is used to transfer all the data to a personal computer for further analysis.



**Figure 4.** Position of the thermocouple in the test sample.

### Time Response of the Equipment

Calibration tests were performed in order to measure the time response of the measuring equipment,  $\Delta t$ , which should be deducted from the experimental ignition delay measurements:

$$\Delta t = \delta t_1 + \delta t_2 \quad (2.1)$$

$\delta t_1$  and  $\delta t_2$  are, respectively, the mechanical time of injection of the test sample inside the furnace, and the time delay characteristic of the measuring chain.

As the operation of the pneumatic system was made by actuation on an electric valve and the same input voltage was used to trigger the oscilloscope (Figure 1), the calibration tests were executed injecting the thermocouple into several pure molten substances (paraffin, ammonium nitrate, and lead) and boiling bi-distilled water. The moment of contact of the thermocouple with the free surface of the standard substances was clearly defined by a very sharp rise of the temperature measured by the thermocouple (Figure 5). A series of five runs was executed for each standard substance. The results obtained, with an acquisition rate of 500 Samples/s, allowed the determination of the mechanical injection time  $\delta t_1 = 38 \pm 2$  ms.

The time delay of the measuring chain,  $\delta t_2$ , was identified as the time interval between the moment of contact of the thermocouple with the free surface of the standard substances ( $t_0$ ) and the moment when the temperature measured by the thermocouple was 95 % of the characteristic phase change temperature of the substance ( $t_f$ ), with the final value of  $\delta t_2$  the arithmetic mean of the results obtained in each case (Figure 6).

This procedure proved that the  $\delta t_2(T)$  evolution was linear and could be represented by the equation:

$$\delta t_2 = 53.189 - 0.049 T \quad (\text{ms}) \quad (2.2)$$

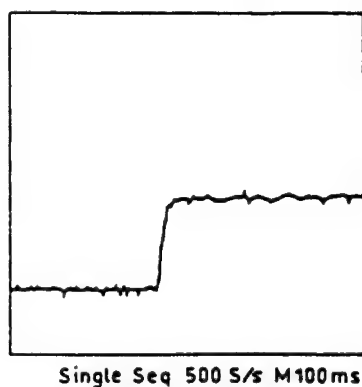


Figure 5. Thermocouple output of a calibration test.

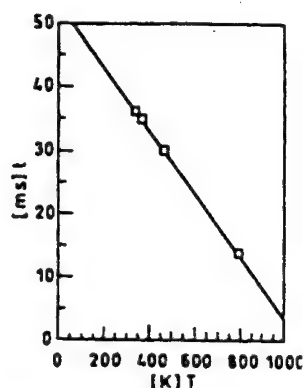


Figure 6. Evolution of  $\delta t_2$ , as a function of temperature.

### Ignition Tests

The measurement of the ignition delays of the formulations shown in Table 1 were made in the temperature range 600 K - 1100 K. The procedure to obtain ignition delay data started with the radial displacement of the injection system, followed by the heating period of the ignition chamber up to the desired temperature. The measuring thermocouple was threaded through the sample and the pellet was positioned on the support wire. Once thermal equilibrium inside the furnace was attained, the injection cylinder was displaced to the furnace axis and the propellant sample was injected into the measuring zone, until ignition occurred. The obtained data were transferred to a personal computer for further analysis.

### Definition of the Instant of Ignition

The occurrence of a very fast increase in the temperature of the propellant sample is a common criterion for the determination of the ignition delay when thermocouples are used as measuring devices. In this work, a supplementary condition has been introduced, in order to add to the

information concerning the influence of partial substitution of ammonium perchlorate by non-stabilized ammonium nitrate on the ignition delay of the composite propellants.

As the temperature of thermal degradation of NSAN (443 K) is significantly lower than the correspondent for AP (713 K), and in agreement with several authors who refer to be the ignition delay of composite propellants controlled by the thermal degradation of the oxidizer, the ignition instant of the sample was determined by the simultaneous obtainment of a sharp rise of the output of the measuring thermocouple and a minimum surface temperature,  $T_s \geq T_{mNSAN}$ , where  $T_{mNSAN}$  is the melting temperature of NSAN [8].

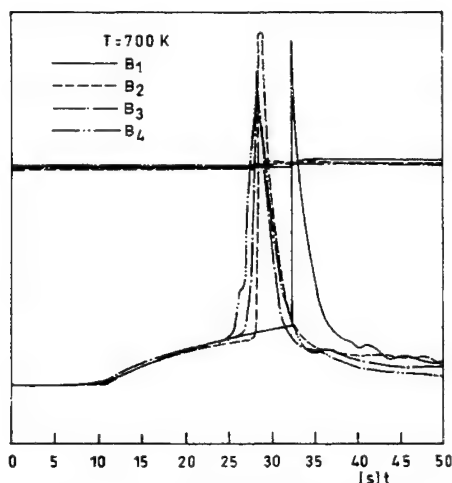


Figure 7. Output of the measuring and control thermocouples.

### 3 - RESULTS OBTAINED AND THEORETICAL ANALYSIS

The ignition delay data obtained for the propellants are plotted in Figure 8. The ignition delays, as a function of temperature, were calculated using the equation:

$$\tau_i(T) = \Delta t_{exp}(T) - \delta t_1 - \delta t_2(T) \quad (3.1)$$

where  $\Delta t_{exp}$  represents the time interval between the injection instant ( $t_0$ ) and the moment of ignition ( $t_{fi}$ ). The results presented are the arithmetic mean of the 10 closest values obtained for each formulation, within  $\pm 3\%$  reproducibility, at each temperature level.

In a first analysis it can be observed that, as expected, the ignition delay,  $\tau_i$ , of all the tested propellants increases with decreasing temperature levels. Furthermore, the results obtained show the dependence of the ignition delay on the type of binder used in the formulations. In fact, for the same experimental conditions, the  $\tau_i(T)$  values for any given AP/NSAN/PU propellant are always shorter than the corresponding AP/NSAN/HTPB formulation.

Considering the effect of the oxidizer composition alone, it is also apparent from Figure 8 that increasing non-stabilized ammonium nitrate content causes shorter values of  $\tau_i$ , for the same temperature levels.

Further interpretation of the experimental data was made considering a bulk analysis of the ignition phenomenon, that is, assuming a first order rate controlling reaction, with constant reactants' consumption during the pre-ignition period [9]. The reaction rate can thus be correlated by an Arrhenius law:

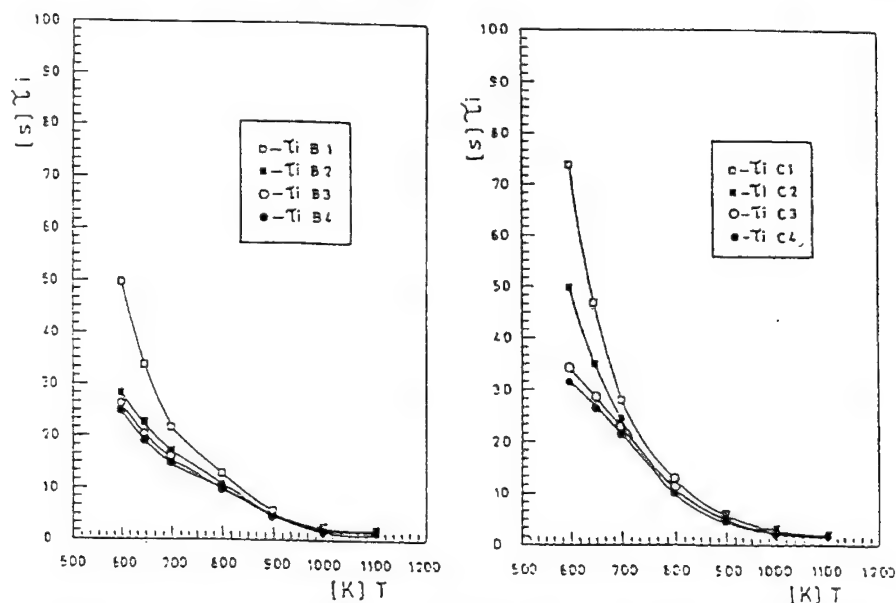
$$\frac{d[X]}{dt} = K[X] e^{-\frac{E}{RT}} \quad (3.2)$$

where  $[X]$  represent the reactants' concentration,  $K$  the Arrhenius pre-exponential factor,  $T$  the temperature of the measuring zone and  $E$  the activation energy of ignition. Based on the simple assumption that the ignition delay is, in a first analysis, inversely proportional to  $d[X]/dt$ ,  $\tau_i$  can be expressed by

$$\tau_i = \beta e^{\frac{E}{RT}} \quad (3.3)$$

where  $\beta$  is a constant related to the pre-exponential Arrhenius constant, for each formulation. A  $\ln \tau_i$  vs.  $1/T$  plot will thus originate a straight line expressed by the equation:

$$\ln \tau_i = \ln \beta + \frac{E}{RT} \quad (3.4)$$



**Figure 8.** Ignition delay of the propellants as a function of composition and temperature.

The application of this type of analysis to the experimental results showed that, in all formulations, the evolution of  $\ln \tau_i = \ln \tau_i (1/T)$  presented in fact a discontinuity and could be broken down into two linear Phases (Figure 9), with different values for the activation energy and  $\beta$  factor.

As the calculated values of the activation energy for Phase I of the evolution  $\ln \tau_i = \ln \tau_i (1/T)$  are always lower than those of Phase II (Table 3), and keeping in mind that homogeneous gas phase reactions generally occur at higher temperature, with high levels of activation energy, whereas heterogeneous reactions, with lower activation energy, predominate at lower temperature, this type of evolution seems to indicate that the ignition mechanism of AP/NSAN/HTPB and AP/NSAN/PU composite propellants is strongly dependent on the heating rate, representing Phase I the occurrence



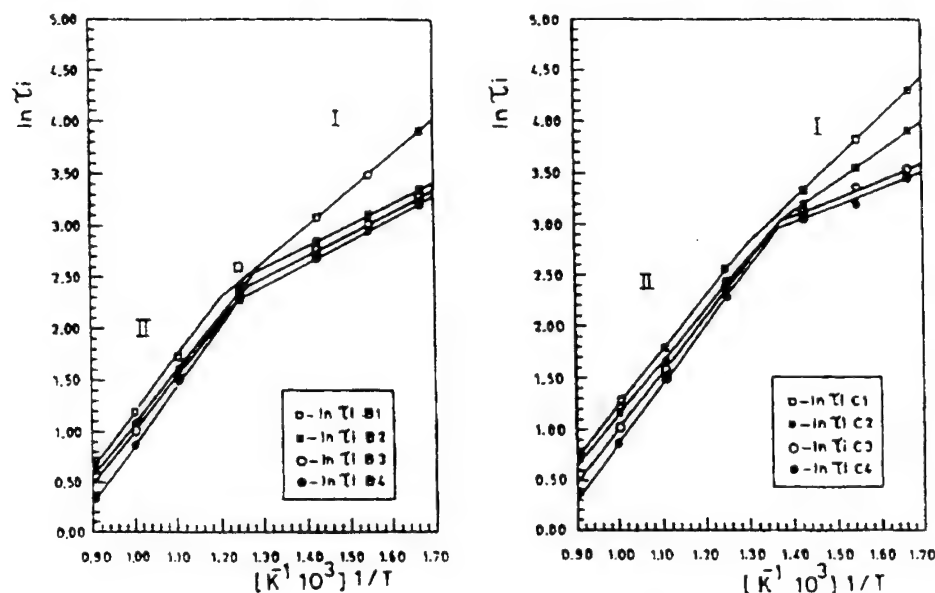


Figure 9. Evolution of  $\ln \tau_i$  ( $1/T$ ). Definition of Phases I and II.

of heterogeneous ignition reactions while homogeneous gas phase ignition reactions are characteristic of Phase II [9, 10].

The transition temperatures ( $T_{tr}$ ) between Phases I and II were calculated, solving the system of equations formed by the polynomial regression of the experimental results, identified as belonging to each phase. The results obtained (Table 3) clearly show that partial substitution of ammonium perchlorate with non-stabilized ammonium nitrate in the propellants' formulation shifts the transition temperature to lower levels, increasing in this way the domain of occurrence of homogeneous ignition.

**Table 3**  
Calculated Values of  $E$  and  $\beta$  for Phases I and II and Transition Temperatures Between Heterogeneous and Homogeneous Ignition Mechanisms.

PROPELLANT	$E_I$ (kJ mol <sup>-1</sup> )	$\beta_I$ (s)	$E_{II}$ (kJ mol <sup>-1</sup> )	$\beta_{II}$ (s)	$T_{tr}$ (K)
B1	28.6	$1.58 \cdot 10^{-1}$	44.8	$1.49 \cdot 10^{-2}$	825
B2	17.2	$8.98 \cdot 10^{-1}$	42.9	$1.66 \cdot 10^{-2}$	776
B3	17.8	$7.36 \cdot 10^{-1}$	43.1	$1.54 \cdot 10^{-2}$	786
B4	18.3	$6.29 \cdot 10^{-1}$	47.2	$0.81 \cdot 10^{-2}$	799
C1	33.6	$0.86 \cdot 10^{-1}$	43.3	$1.90 \cdot 10^{-2}$	767
C2	24.6	$3.59 \cdot 10^{-1}$	41.8	$2.07 \cdot 10^{-2}$	726
C3	14.2	1.96	44.4	$1.77 \cdot 10^{-2}$	727
C4	13.6	2.05	47.0	$0.85 \cdot 10^{-2}$	730

The values of the activation energy and of the experimental factor  $\beta$  are also affected by the presence of NSAN (Table 3). In fact, for both types of composite propellants, the calculated values present a significant decrease of  $E$  values of Phase I while  $\beta_I$  factors are increased. A similar analysis of the results obtained for Phase II shows that, after an initial slight reduction of  $E_{II}$  due to the presence of

NSAN, the values of this parameter increase, becoming superior to the correspondent of the formulation with AP only.

This same type of evolution can be observed for the  $\beta_{II}$  factor where values decrease, after a minimum value for formulations containing 20 % NSAN, becoming inferior to the  $\beta_{II}$  of the formulation with AP only.

#### 4 - SYNTHESIS AND CONCLUSIONS

AP/NSAN/HTPB and AP/NSAN/PU propellants containing 0 % to 60 % of non-stabilized ammonium nitrate by weight were submitted to radiative heating, in air and at atmospheric pressure, until ignition occurred and their ignition delays measured as a function of temperature. The results obtained in this work showed that non-stabilized ammonium nitrate plays an important role in the ignition of AP/NSAN/HTPB and AP/NSAN/PU composite propellants.

The experimental results, which confirmed, as expected, that the ignition delays of the formulations increase with decreasing temperature levels, have also shown that increasing non-stabilized ammonium nitrate content results in shorter values of  $\tau_i$ . Furthermore, the experimental results obtained also indicated that for the same experimental conditions, the  $\tau_i(T)$  values for any given AP/NSAN/PU propellant are always shorter than those of the corresponding AP/NSAN/HTPB formulation. A theoretical analysis of the experimental results, based in a first order Arrhenius reaction, showed that the evolution  $\ln \tau_i = \ln \tau_i (1/T)$  could be broken down into two linear phases with values of the activation energy in the lower temperature interval (Phase I) always lower than those obtained for the higher heating rates (Phase II). This behaviour indicates that the propellants can ignite heterogeneously or homogeneously, depending on the temperature level.

The calculated values of  $E$ ,  $T_{tr}$  and  $\beta$  present a similar evolution, with an inflection point.  $E$  and  $T_{tr}$  are minimum for formulations containing 20 % NSAN, while  $\beta$  attains its maximum value for these formulations.

The transition temperatures between heterogeneous (Phase I) and homogeneous (Phase II) ignition were calculated. The results obtained for both types of propellants,  $776 \text{ K} \leq T_{trB} \leq 825 \text{ K}$  and  $726 \text{ K} \leq T_{trC} \leq 767 \text{ K}$  showed that the partial substitution of AP with NSAN shifts the inferior limit of occurrence of homogeneous ignition to lower temperature levels.

#### REFERENCES

1. Manelis, G. B., Possible ways of development of ecologically safe solid rocket propellants, *Proceedings of the AGARD Conference on Environmental Aspects of Rocket and Gun Propulsion, Propulsion and Energetics Panel (PEP) 84th Symposium*, Aalesund, Norway, 1994, 13/1-13/6.
2. Lessard, P., Druet, L., Villeneuve, S., Thiboutot, S., Benchabane, M. and Alexander, D., Development of a minimum smoke propellant based on glycidyl azide polymer and ammonium nitrate, *NATO/AGARD - CP 511, 78th Spec. Meeting*, Bonn, 1991.
3. Araújo, L. and Frota, O., Thermochemical characteristics of AP/AN based composite propellants, *Proceedings of the 25th International Annual Conference of ICT (Energ. Mater. - Analysis, Characterisation and Test Techniques)*, Karlsruhe, Germany, 1994, 51/1-51/11.
4. Campos, J., Araújo, L., Góis, J. C., Pires, A., Mendes, R. and Nina, M., Gas pollutants from ammonium nitrate based propellants, *Proceedings of the AGARD Conference on Environmental Aspects of Rocket and Gun Propulsion, Propulsion and Energetics Panel (PEP) 84th Symposium*, Aalesund, Norway, 1994, 18/1-18/7.

5. Hasue, K., Tanabe, M., Watanabe, N., Nakahara, S., Okada, F. and Iwama, A., Initiation of some energetic materials by microwave heating, *Propellants, Explosives, Pyrotechnics*, 15, 181-186, 1990.
6. Saito, T., Shimoda, M., Yamaya, T. and Iwama, A., Ignition of AP based composite solid propellants containing nitramines exposed to CO<sub>2</sub> laser radiation at subatmospheric pressures, *Combustion and Flame*, 85, 68-76, 1991.
7. Roth, J. F. and Wachtell, G. P., Heat transfer and chemical kinetics in the ignition of solid propellants, *I & EC Fundamentals*, 1, 62-67, 1962.
8. Kishore, K. and Gayathri, V., Ignition and combustion of AP based propellants, *Progress in Astronautics and Aeronautics*, 90, 53-119, 1984.
9. Girdhar, H. L. and Arora, A. J., Ignition delay of composite solid propellants by the hot plate technique, *Combustion and Flame*, 31, 245-250, 1978.
10. Essenhigh, R. H., Fundamentals of coal combustion, *Chemistry of Coal Utilization, Second Supplementary Volume*, 1153-1312, 1981.

***Area 7:***

***Combustion Diagnostics***

## PROPELLANT COMBUSTION DIAGNOSTICS VIA MULTICHANNEL ABSORPTION SPECTROSCOPY

J. A. Vanderhoff<sup>1</sup>, A. J. Kotlar<sup>1</sup>, S. H. Modiano<sup>2</sup> and M. W. Teague<sup>3</sup>

1. US Army Research Laboratory, Aberdeen Proving Ground, MD 21005-5066; 2. SCEEE Postdoctoral Fellow; 3. IPA Faculty Fellow from Hendrix College, Conway, AR 72032

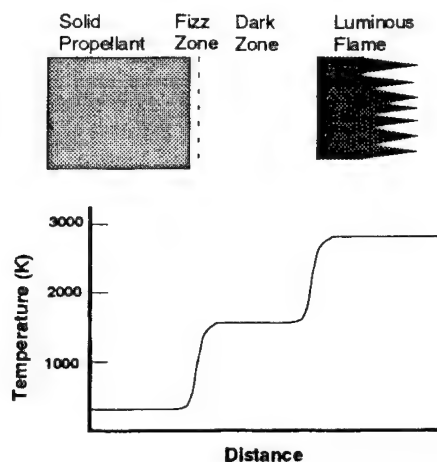
**ABSTRACT:** Multichannel absorption spectroscopy has been developed and used to non-intrusively probe the hostile environment of solid propellant combustion. A windowed pressure vessel, broadband light source, and a spectrometer-array detector system are the major components of the experiment. Gas phase absorption spectra obtained during the steady-state combustion of double-base and nitramine propellants can be analyzed to determine temperature and absolute concentration profiles. The analysis requires only fundamental spectroscopic data incorporated into the differential absorption law.

Ultraviolet-visible sensitive multichannel detectors have been used to obtain absorption spectra of NO, OH, NH, and CN during the combustion of solid propellants and their ingredients. Focus has been primarily on the propellant dark zone with simultaneous tracking capability for NO and OH. Vibrationally resolved transitions in the  $A^2\Sigma-X^2\Pi$  electronic system of NO allow determination of temperature and absolute NO concentration. Rotationally resolved transitions in the  $A^2\Sigma-X^2\Pi(0,0)$  vibrational band system of OH allow determination of OH concentration and luminous flame temperature. An infrared-sensitive multichannel detector has been used to obtain rotational-vibrational absorption spectra for CO, HCN, H<sub>2</sub>O, CO<sub>2</sub>, N<sub>2</sub>O, and CH<sub>4</sub> in the dark-zone region. Substantial HCN concentrations occur in the dark zone of nitramine propellants, but not in the dark zone of double base propellants. Dark-zone temperatures derived from fitting the infrared absorption spectra of HCN and H<sub>2</sub>O are in good agreement with those obtained from fitting NO in the ultraviolet region. Concentrations of these infrared active species have been determined.

Multichannel absorption spectroscopy, along with other experimental diagnostic techniques such as microprobe mass spectrometry, FT-IR spectroscopy and use of thermocouples, have greatly expanded the propellant database for quantitative gas-phase composition and temperature profiles. This information is presently being used to refine reduced reaction mechanisms for propellant dark-zone chemistry as well as to validate models of solid propellant combustion.

### INTRODUCTION

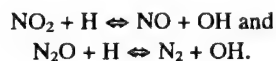
One of the oldest optical techniques is absorption spectroscopy, having its beginnings in the 18th century, where changes in light intensity with absorber thickness were being observed. However, the application of this technique for quantitative combustion diagnostic information requires a quantum mechanical formalism and molecule-specific information which has been mostly developed and accumulated in this century. On the experimental side, development of the multichannel array detectors over the last twenty years has made absorption spectroscopy useful for time-constrained experiments such as solid propellant



**Figure 1.** Sketch of the propellant flame structure showing the fizz zone, dark zone and a representative temperature profile. The sharp temperature breaks indicate the reaction stages.

flames. Photodiode arrays or charge coupled devices connected to spectrometers enable simultaneous sampling of preselected wavelength regions. Moreover, absorption changes within these regions can be recorded and updated on a millisecond time scale. Different multichannel detectors are available which cover the wavelength range from the ultraviolet (uv) to the infrared (ir) and thus can be used to monitor gas phase molecules by their electronic or vibrational transitions.

Before going further, a brief description of the gas phase structure of double-base and nitramine solid propellant flames is in order. Many of these propellants (M9, JA2, DB1, DB2 and XM39, see Table A for composition) exhibit two flame stages in the gas phase which are separated at low pressure by a visually distinct "dark zone". A simple sketch of this structure and associated temperature profile is shown in Fig. 1. The length of this zone increases with decreasing pressure and for sufficiently low pressure ( $\leq 1$  MPa) the second stage luminous flame may not appear. At atmospheric pressure these propellants do not burn in an inert environment. At high pressure, the two stages merge into one. Typical surface temperatures range from about 500 to 700 K depending upon propellant. There is an abrupt rise in temperature in the first combustion stage (fizz zone or primary reaction zone). Although this region is of small spatial extent (less than 1 mm at 1 MPa) much of the chemistry occurs here. The condensed phase evaporates and/or decomposes to produce fuels and oxidizers where  $\text{NO}_2$  is the primary oxidizer for double-base propellants. For nitramines, the primary oxidizers are  $\text{NO}_2$  and  $\text{N}_2\text{O}$ . Reactions of these oxidizers with fuels elevate the temperatures to the 1150 to 1600 K range in the dark zone. These values are dependent on propellant composition and pressure. These propellants burn fuel rich and under such conditions important early reactions<sup>1</sup> in the conversion of  $\text{NO}_2$  and  $\text{N}_2\text{O}$  are



Substantial concentrations of the intermediate species NO and, in the case of nitramine propellants, HCN fuel are present in the dark zone region suggesting that their low reactivity is responsible for its formation. In this region, temperature and species concentration gradients are much smaller than in either the first or second stage of reaction. In other words, experimental spatial resolution requirements are relaxed. After a certain distance (induction time), the temperature and dark-zone species again change rapidly in what is called the second stage of reaction. Here, NO and HCN are converted to final products and the temperature increases to the adiabatic flame temperature. A

luminous region is formed. Species concentrations in this region should agree with those predicted from adiabatic thermochemical equilibrium calculations. In contrast, some nitramine propellants burn without a dark zone and a common triple-base propellant M30 also burns with no dark zone. It is not known with certainty the mechanisms which cause the elimination of the dark zone. For propellants with  $\text{NO}_2/\text{N}_2\text{O}$  as the primary oxidizers, increased formation of the  $\text{N}_2\text{O}$  oxidizer could reduce the extent of the zone. Production of species which are highly reactive with NO may also remove this zone. For M30, the nitroguanidine ingredient may produce sufficient  $\text{NH}_x$  species<sup>1</sup> to accelerate the conversion of NO to  $\text{N}_2$ . Some of our early studies involved attempts to measure NH profiles in M30. Later studies concentrated on the dark zone where the spatial gradients are much smaller.

A paper by Lempert<sup>2</sup> stimulated our development of multichannel absorption spectroscopy for the purpose of studying the flame structure of solid propellants. These investigations have been ongoing for the last eight years. Advantages of the technique are that it can be applied *in-situ* and is non-intrusive. Moreover, the technique is applicable within the time frames of interest for these steady-state-combustion experiments and quantitative information can be derived from the resultant spectra. A disadvantage of the absorption technique is that it is useful only where line-of-sight measurements are meaningful. Additionally, absorption cannot detect  $\text{H}_2$  and  $\text{N}_2$ .

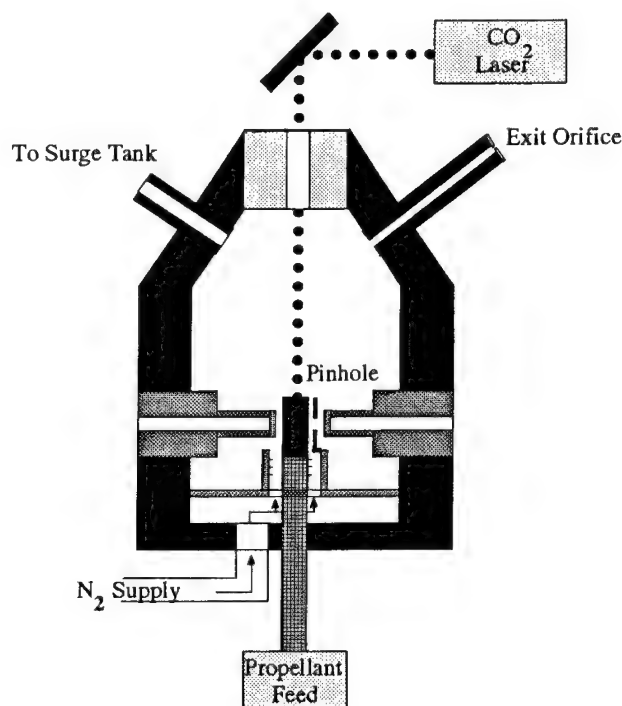
Initial, self-sustained, steady-state propellant combustion studies were aimed at determining the temperature and absolute concentration profiles of the diatomic species OH, NH and  $\text{CN}^{3-5}$  in propellants without a dark zone (M30 and HMX1). Here, the entire NH and CN intermediate species profiles peak and decay over a distance of about 1 mm or less and while the OH species peaks within this small distance, easily measurable equilibrium concentrations are continued where the propellant flame temperature is above about 2300 K. Further studies on NH and CN were not pursued due to perceived difficulties with maintaining one-dimensional flame structure to a precision necessary for probing the fizz zone. On the other hand, Parr and Hanson-Parr<sup>6-12</sup> at China Lake have profiled NH, CN, OH, NO,  $\text{NO}_2$ , HONO and  $\text{H}_2\text{CO}$  while performing extensive propellant ingredient flame structure investigations using multichannel absorption spectroscopy to quantify their planar laser induced fluorescence (PLIF) work. A majority of these studies on propellant or propellant ingredient combustion involved laser assistance where a  $\text{CO}_2$  laser is kept on for the duration of the experiment. Thus, in addition to providing the ignition stimulus, an energy flux maintains combustion. In this fashion, combustion of propellants can be made to occur at lower pressures. These laser supported studies have the benefits of an expanded first stage combustion region, improved combustion stability and improved one-dimensionality for uniform energy flux on the combusting surface. An important aspect of laser-assisted combustion is that the flame structure is different than self-sustained combustion and these differences may be difficult to model.

Subsequent propellant absorption work centered on the dark zone where spatial resolution requirements are relaxed. Temperature and NO and OH concentration profiles were obtained from least-squares fitting uv absorption spectra of NO and OH<sup>13-16</sup>. The Penn State group also applied multichannel absorption spectroscopy and least-squares fitting to OH and NO<sup>17-19</sup> to further probe flame zone structures of solid propellants. Some important dark-zone combustion species do not have absorptions easily accessible in the uv-visible region. Therefore an infrared sensitive multichannel detector has been incorporated. With this detector, infrared absorption spectra have been experimentally measured and then simulated to estimate dark-zone temperatures and concentrations for HCN,  $\text{H}_2\text{O}$ ,  $\text{CH}_4$ , CO and  $\text{N}_2\text{O}^{20,21}$ . More recently, least squares fitting<sup>22</sup> has been used to obtain dark zone temperature and concentrations for HCN,  $\text{H}_2\text{O}$ ,  $\text{CH}_4$ , CO,  $\text{CO}_2$  and  $\text{N}_2\text{O}$ . Details are given later. Related work in this spectral regime involves the use of an FTIR technique to measure absorption spectra during self deflagration of nitramine propellants.<sup>23,24</sup> These absorption spectra are least-squares analyzed to determine quantitative dark zone temperature and species profiles.

An application of these experimental measurements has been to advance the understanding of detailed chemical processes occurring in gun propellant combustion. Current gun ballistic codes contain no finite rate chemistry for combustion. In these codes, once the propellant reaches a certain surface temperature there is instant gasification to final products and the propellant starts burning according to  $r \propto p^n$  ( $r$  is the burn rate,  $p$  the pressure and  $n$  an experimentally determined exponent). While this approximation works well over most of the pressure range of the ballistic cycle, it is a poor approximation in the low-pressure region ( $\sim 2$  MPa) where the transition from ignition to full combustion occurs. In this pressure region, anomalies such as ignition time delays arise for  $\text{NO}_2$  oxidized propellants burning as a two-stage flame. Quantitative combustion diagnostic information (i.e., temperature and species profiles, burning rates and dark-zone lengths) are valuable for developing and testing chemical mechanisms that adequately describe the conversion of the dark zone mixture to final products. Reduced chemical mechanisms that describe this process have been recently developed for double base and nitramine propellants.<sup>25</sup>

### EXPERIMENTAL

A windowed combustion vessel has been developed to provide the elevated-pressure inert environment for conducting self-deflagrating propellant flame studies. A sketch of this stainless steel vessel is shown in cross-section on Fig. 2. This vessel allows for a constant pressure nitrogen flow to



**Figure 2.** Details of combustion vessel used to burn solid propellant samples in an inert (nitrogen) environment at elevated pressure.



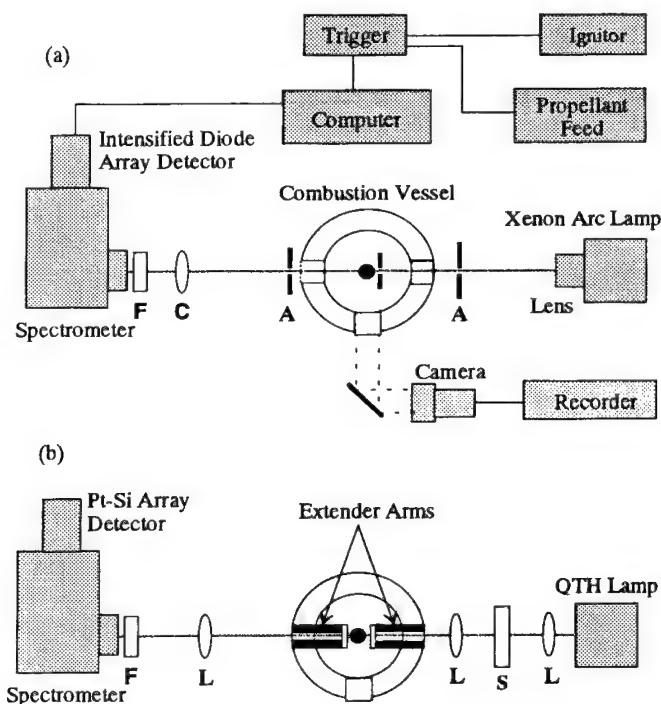
act as a shroud around the cylindrical propellant sample. This flow rate has been set with an exit orifice to be  $\leq 4$  times the propellant gasification rate. In the current configuration, the vessel has been operated over a pressure range from 0.1 to 2.0 MPa. A surge tank is used to minimize pressure fluctuations of ignition and combustion transients and the total pressure has been monitored to be constant to within 5%. In early work, a hot wire was used to point ignite the top end of the propellant sample at the centerline. Unsatisfactory aspects of this technique were that the ignition wire pulled out on occasion during positioning, the remnant wire could act as a flame holder and the burning surface of the propellant retained a slightly concave hemispherical shape. A zinc selenide window was later added to provide optical access for a 25-Watt CO<sub>2</sub> laser ignition source. This added feature increased the success rate for experiments and allowed initial ignition to occur on about a 0.3 cm diameter circle on the propellant surface. While improving the flatness of the burn some concavity still occurred due to nonuniformity of the ignition source over the complete top surface as well as edge cooling from the flowing shroud gas. A bi-directional propellant feed mechanism has been incorporated into the experiment to perform several functions. The main purpose is to extend the data acquisition time by advancing the propellant sample at a rate close to the propellant burn rate. Also, this mechanism is used to move the propellant sample below the light beam for reference light intensity measurements under pressure. Extender arms, made to position the optical access windows close to the sample and pinhole, minimize the pathlength in the combustion vessel. For the uv-visible work the total pathlength in the combustion vessel is about twice the propellant diameter. For the ir work the pinhole was eliminated and the pathlength reduced to about 1.5 times the propellant diameter. Some of the recent ir work reported here on CO and N<sub>2</sub>O overtones describes a technique to extend the pathlength in the combustion vessel by partially gold coating the sapphire optical access windows<sup>26</sup>.

There is a more acute concern about possible pathlength effects for the ir studies than the uv-visible studies for the following reasons. The radical species NH, CN and OH will only exist in high temperature combustion regions and thus are limited to reside above the combusting surface of the sample propellant. There also exists sufficiently large NO concentrations in the dark zone to cause 100 percent absorption of light from ground state NO molecules and thus absorption spectra are obtained for two vibrationally excited states. These excited state NO molecules are only expected to occur in regions of elevated temperature (above the propellant combusting surface). The ir absorption spectra, on the other hand, are obtained from ground state transitions of molecules which can be present at room temperature. Hence, it is important to minimize the population of these molecules in the combustion vessel pathlength outside the combustion region.

Top views of the optical paths for absorption and video are shown in Fig. 3. A video record is taken for each propellant burn experiment where burn rates, dark-zone lengths and estimates of the one-dimensionality of the burn can be determined. The uv-visible experiment is shown in part a where all the optics for absorption are quartz. A 500-Watt cw xenon arc lamp with close electrode spacing is the light source. Light from this source is focussed and apertured with the spatial resolution being set by either a 0.1 or 0.2 mm pinhole in close proximity to the propellant sample. Emission interference signals are made negligible by a small aperture (A) between the propellant flame and the detector. A cylindrical lens focusses the apertured light to a line on the entrance slit of a 0.32-m spectrometer (ISA Model HR-320). The wavelength dispersed light is detected with an intensified photodiode array (IPDA) consisting of 1024 elements in a line (EG&G PAR Model 1420). This detector is sensitive over a wavelength range from about 200 to 800 nm and can capture a wavelength range of about 6 or 12 nm depending on whether the spectrometer with a 2400 grooves/mm grating is operated in first or second order. Actually, only about 800 of the photodiodes are intensified and the wavelength range is dispersed among these photodiodes with an element to element spacing of 0.025 nm. Second order operation, with a spectral resolution of 0.03 nm, requires a glass filter (F) to eliminate first order light. Repetitive spectra were obtained at rates  $\leq 62$  Hz for a 14-bit dynamic

range. After acquisition, the absorption data are digitized and stored for further analysis. When it is advantageous to monitor two or more significantly different spectral regions simultaneously, the transmitted beam is split and additional spectrometer-IPDA systems added. This variation has been used successfully for simultaneous measurements of OH and NO<sup>14,15</sup>.

Modifications for obtaining absorption data in the infrared region of the spectrum are shown in Fig. 3b and discussed in more detail elsewhere<sup>21</sup>. A 250-Watt quartz-tungsten-halogen (QTH) lamp (Osram HLX 64655) was used as the light source and chosen for its stability as well as for its small filament size (7.0 x 3.5 mm). Although the quartz lamp envelope cuts off direct radiation from the filament at wavelengths longer than about 3500 nm, the hot envelope acts as a broad band emitter with output further into the ir. Very recently<sup>26</sup>, a silicon carbide Globar inserted into a flashlight reflector has been used for improved source intensity at wavelengths longer than 3000 nm. CaF<sub>2</sub>



**Figure 3.** Light paths for the multichannel optical absorption experiments; (a) uv-visible and video and (b) ir.

lenses were used to direct the light into the combustion vessel, and then collect and focus the transmitted light onto the entrance slit of the 0.32-m spectrometer. Sapphire windows terminated the extender arms and provided optical access into the combustion vessel. Spatial resolution is controlled by the 2.5-mm inside diameter of the extender arm on the spectrometer side of the experiment. Again, a long wavelength pass filter (F) was used to remove any higher-order light as well as any visible emission emanating from the burning propellant. The 75 groove/mm spectrometer grating blazed at 4000 nm dispersed about a 1000-nm wavelength region onto 1024 linear elements of liquid nitrogen-cooled, infrared-sensitive platinum silicide detector (Princeton instruments Model PtSi - 1024). These detector elements have a 0.025 mm spacing and are sensitive over a wavelength

region from about 900 to 4500 nm. When operated in first order with a 0.125-mm entrance slit the system has a spectral resolution of about 7 nm. Emission from the propellant flame turned out to be more of a problem in the ir region and its removal was necessary for obtaining quantitative transmission data. A fast shutter (S), with a minimum opening time of 1.8 ms (Vincent Associates Model LS6), was placed between the light source and vessel so a background spectrum, consisting of the background, the dark charge, and any emission from the sample, could be subtracted from the spectrum of transmitted light. With this arrangement a pair of spectra (14-bit dynamic range) consisting of the transmitted light spectrum and the background emission spectrum could be obtained in 31.5 ms. When possible, propellant samples with a larger diameter (1.08 versus 0.65 cm) were used to increase the ratio of the sample length to the total combustion vessel pathlength.

A typical experimental run involves the following sequence of events. A propellant sample (cylindrical with diameters of 0.65 or 1.08 cm and total lengths from 2 to 4 cm) is glued to the pushrod of the propellant feed mechanism. After the combustion vessel is sealed and pressurized, a reference spectrum ( $I_0$ ) is taken. The propellant is then advanced until it completely blocks the light beam. The video recording system is turned on and a 0.1-s pulse from the CO<sub>2</sub> laser ignites the propellant sample. After a predetermined time the propellant feed mechanism, absorption detector and shutter are triggered on. As the propellant burns downward in a cigarette fashion, the light beam becomes unblocked. This first appearance of light in the data acquisition cycle marks the propellant surface position.

## DATA ANALYSIS

A nonlinear least-squares fitting procedure has been developed to extract quantitative species concentration and temperature information from absorption spectra by including a complete segment of data in the fit. Many single detector techniques extract diagnostic information from one or a few isolated absorption lines. Spectral data obtained with an array detector can include many lines and consequently a full spectrum data analysis has been developed.

Based on the differential absorption law for parallel light of frequency  $\nu$  traveling in the +x direction through a homogeneous medium with absorption coefficient ( $k_\nu + b_\nu$ ), the intensity of the incident beam  $I_0$ , is attenuated along a path of length  $l$  according to

$$I(\nu) = I_0 \exp[-k_\nu l - b_\nu l] \approx I_0 B(\nu) \exp[-k_\nu l] \quad (1)$$

where  $k_\nu$  refers to the absorption coefficient of the molecule of interest and  $b_\nu$  refers to all the other light attenuating processes which are pathlength dependent. Sources for  $b_\nu$  are broadband absorption of light from other molecules and scattering from particulates. It is assumed that  $b_\nu$  is a weak function of frequency and thus is approximated by a multiplicative factor,  $B(\nu)$ . The observed shape of the experimental baseline is used to determine the appropriate form of  $B(\nu)$ .

Assuming a Boltzmann distribution of states, the transmitted intensity of a group of lines can be written as

$$I(\nu) = I_0 B(\nu) \exp\{-(h\nu/c)[N_i/Q(T)][\sum_j B_j g_j \exp(-E_j/kT) P_j(\nu)]\}, \quad (2)$$

where  $h$  is Planck's constant,  $k$  is the Boltzmann constant,  $T$  is the temperature,  $B_j$  is the absolute Einstein coefficient for absorption for the  $j$ th transition in energy density units,  $g_j$  is the degeneracy of the  $j$ th sublevel and  $E_j$  its energy.  $N_i$  is the total number density,  $Q(T)$  is the partition function and  $P_j$  is the transition lineshape. For conditions where the light source and spectrometer bandwidth are

much larger than the width of a typical absorption transition  $P_j$  is approximated with a delta function<sup>27</sup> and an instrument function  $S(\nu, \nu_0)$ , centered at  $\nu_0$  and normalized to unit area is introduced to give

$$\tau(\nu_0) = I/I_0(\nu_0) = \int S(\nu, \nu_0) I(\nu) d\nu, \quad (3)$$

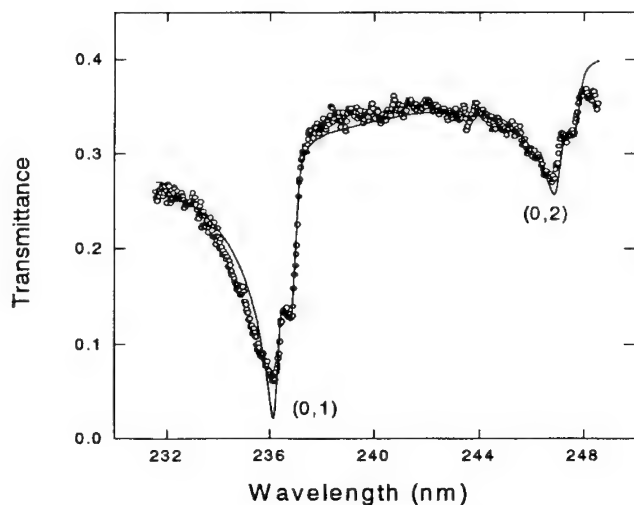
where  $\tau$ , the integrated light transmitted or the transmittance, is a function of  $\nu_0$ , the index frequency of the diode array detector. A Lorentzian lineshape has been found to be a good representation of the instrument function for the uv-visible detector and a Gaussian lineshape is the better representation for the ir detector. When applying the delta function approximation for the transition lineshape, the above integral reduces to a sum. Equation (3) is fitted with a nonlinear, multivariate, least-squares-fitting program to determine optimum values of temperature and species concentration for given absorption spectra. This program was written in Fortran and made use of a Levenberg-Marquardt algorithm.<sup>28,29</sup> The time to fit a typical spectrum was  $\leq 5$  minutes on a 486/33 PC.

Many of the molecule specific parameters, in particular the partition function, for the species studied come from Huber and Herzberg<sup>30</sup>. For OH, the molecular constants come from fitting the data of Diecke and Crosswhite<sup>31</sup> and the Einstein coefficients are from Dimpfl and Kinsey<sup>32</sup>. Ground state constants for NO are from Henry et al.<sup>33</sup> and the upper state constants are from Engleman and Rouse<sup>34</sup>. The radiative lifetime is taken from McDermid et al.<sup>35</sup>

The HITRAN database<sup>36</sup> with associated PC programs has been used to synthetically simulate experimentally obtained ir absorption spectra<sup>20,21</sup>. Recently<sup>22</sup>, a nonlinear, multivariate, least-squares-fitting program using a Simplex algorithm<sup>37</sup> has been written for use within the Galactic Industries' GRAMS/386 environment. This program uses transition line strengths and molecular parameters within the HITRAN database. In general, best values are obtained for species concentration and temperature. Some ir spectra did not have sufficient fidelity to fit for both temperature and concentration. In these cases only the species concentration was fitted, with the temperature being preset to a value determined from prior fits to other molecules having more spectral detail with better signal-to-noise characteristics.

## RESULTS

The purpose for development of this absorption technique was to obtain quantitative species and temperature information in the the gas phase of propellants self-deflagrating in an inert environment. Examples of NO and OH absorption data, taken above the surface of a double-base propellant (M9) burning in 1.7 MPa nitrogen are shown on Figs. 4 and 5, respectively. The NO spectrum, taken in the dark zone, covers a wavelength range where absorptions from the (0,1) and (0,2) vibrational hot bands are observed. A least-squares fit to this spectrum involved 2079 possible transitions and resulted in a dark zone temperature of 1550 K and a NO mole fraction of 0.30. These values are consistent with other measurements<sup>38,39</sup>. Sufficient OH density for reasonable absorption spectra is only found in the luminous flame region and Fig. 5 represents one luminous flame spectrum. A least-squares fit of this rotationally resolved spectrum includes 128 transitions and best values for temperature and concentration are 3100 K and an OH mole fraction of 0.01. This temperature is in good agreement with the adiabatic flame temperature and the OH concentration is about a factor of two lower than the equilibrium value. During a single experiment many absorption spectra, such as shown on Figs. 4 and 5, are recorded as a function of time. A concurrent burn rate measurement obtained from the video recording allows conversion of time to a distance scale and a temperature profile as a function of distance from the M9 propellant surface is shown on Fig. 6. It can be seen that the temperature is relatively constant out to about 0.4 cm (the dark zone length) and abruptly rises to the adiabatic temperature in the luminous flame. The dashed line indicating the 3028 K adiabatic flame temperature. Regions of double values for the temperature result from movement of the luminous flame. From these type of experiments, burn rates, dark zone lengths, temperature and species concentration are measured. The data of Fig. 6 indicate that only about half of the propellant thermal energy is released in the formation of the dark zone. Measurements of high oxidizer

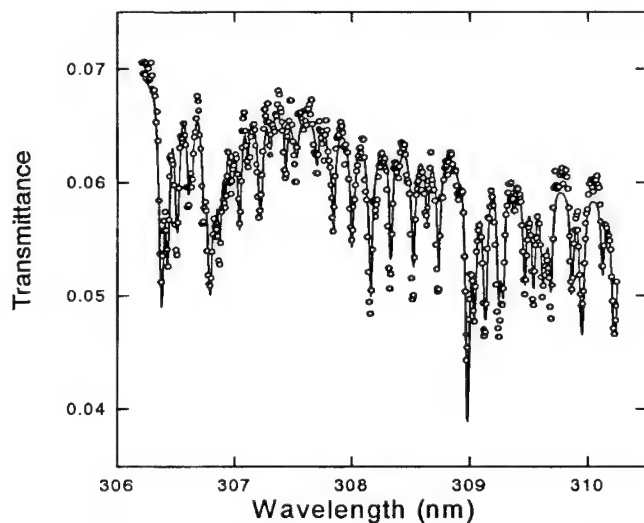


**Figure 4.** NO absorption spectrum from the dark-zone region of M9 burning in 1.7 MPa nitrogen

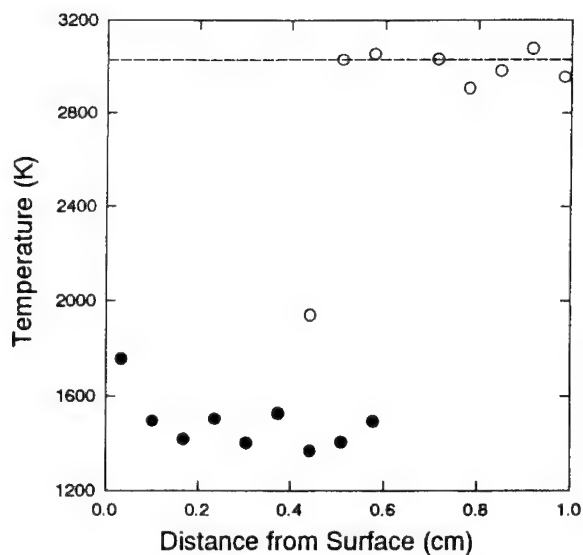
(NO) concentrations in this zone provide evidence that this zone is formed from the slow conversion of NO to  $N_2$ . Other Army gun propellants have been studied in analogous fashion<sup>14-16</sup>.

The propellant flame structure data base has recently been expanded and now three different investigators<sup>11,16,18</sup> have made use of multichannel absorption to obtain dark-zone temperature and NO concentration profiles for the self-deflagration of XM39. Mole fractions of NO range from 0.075 to 0.15 and temperatures from 1100 to 1400 K depending on pressure and surrounding environment.

Most of the major dark-zone species do not have easily accessible uv-visible spectra. One species of concern with respect to nitramine propellant combustion was HCN. Reports by Kubota<sup>40</sup> did not indicate

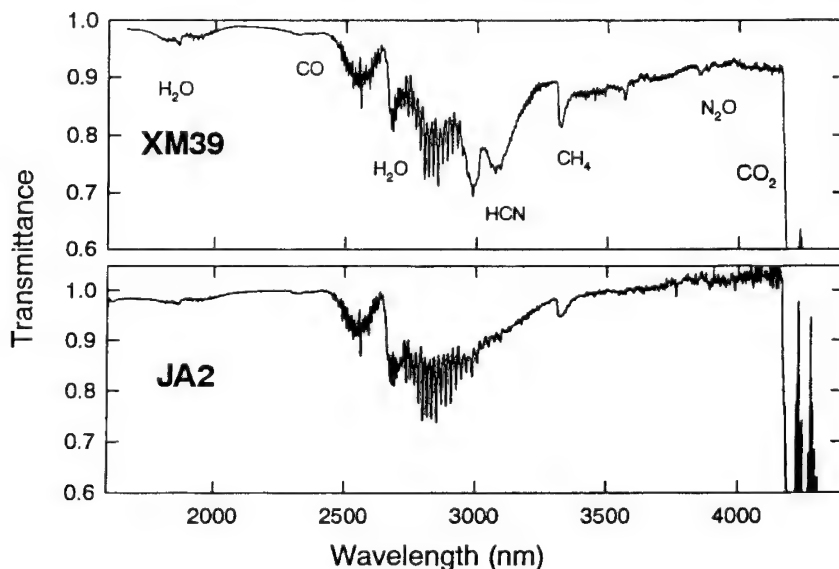


**Figure 5.** OH absorption from the luminous flame region of M9 burning in 1.7 MPa nitrogen

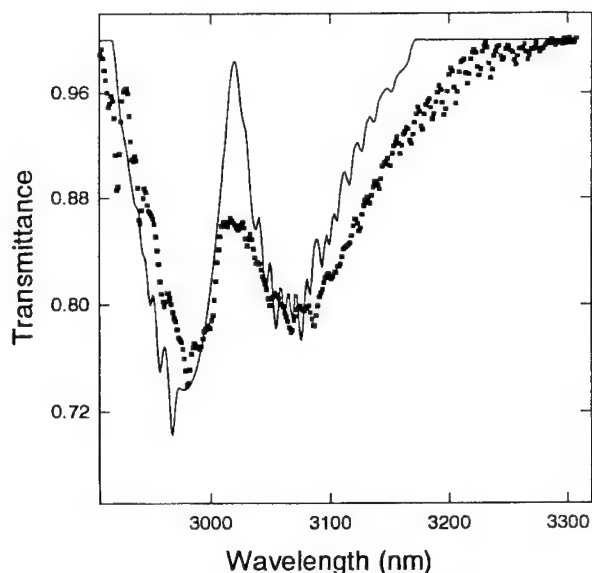


**Figure 6.** Temperature vs distance for M9 burning in 1.7 MPa nitrogen. NO absorption(●) and OH absorption (○) spectra obtained from the dark zone and luminous flame, respectively. The dashed line is the adiabatic flame temperature

the presence of HCN in an HMX propellant where results of Korobeinechev<sup>41</sup> and later others<sup>24,42</sup> showed substantial HCN concentrations in the dark zone of neat RDX and RDX composite propellants. An ir sensitive diode array was used to obtain absorption spectra in the dark zones of XM39 and JA2 propellants and representative spectra are shown on Fig. 7. A range of approximately 1000 nm could be obtained using

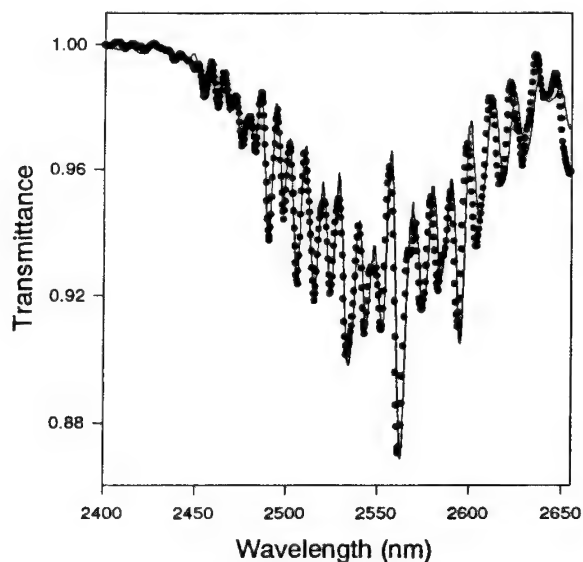


**Figure 7.** Dark zone absorption spectra for XM39 and JA2 propellants under self-sustained combustion conditions in 1.0 MPa nitrogen. These infrared absorption spectra were taken at an average distance of 0.25 cm from the propellant surface.

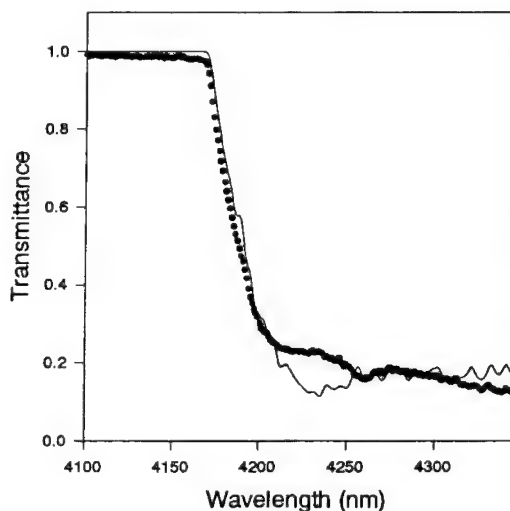


**Figure 8.** Absorption spectrum of HCN taken in the dark zone of XM39 burning in 1.0 MPa nitrogen. A best fit for temperature and concentration are 1173 K and 0.14 mole fraction, respectively.

the ir multichannel array with 7 nm spectral resolution, consequently four spectra were pieced together to form the wavelength coverage depicted in Fig. 7. Six species, HCN, H<sub>2</sub>O, N<sub>2</sub>O, CO, CO<sub>2</sub> and CH<sub>4</sub>, have been identified as having absorptions over the wavelength range from 1600 to 4400 nm. CO and N<sub>2</sub>O are discussed elsewhere<sup>25</sup> in this text. Fundamental CH stretch wavelengths at 3020 and 3311 are for HCN and CH<sub>4</sub>, respectively. Prominent absorptions for H<sub>2</sub>O occur in the 2400 to 3100 nm and the 1700 to 2000 nm regions and are fundamental and combination bands, respectively. The largest absorption observed starts around 4250 nm and is a fundamental CO<sub>2</sub> stretch. As can be seen from Fig. 7, the spectrum for XM39 exhibits a prominent absorption in the region appropriate for HCN while JA2 does not. A more detailed HCN spectrum obtained in the dark-zone region of XM39 burning in 1.0 MPa nitrogen is shown on Fig. 8 together with a least squares fit to the data. Solid points represent the data and a line indicates the fit. The best fit to these data results in a temperature of 1173 K and an HCN mole fraction of 0.14. The largest deviation between the data and the fit occurs around 3020 nm where the fit indicates a much more pronounced separation of the P and R branches. A possible cause for the difference is that the HITRAN database does not contain all the spectral line data at high temperature. Supportive evidence comes from HCN spectra obtained just after the completion of the propellant burn. Sufficient HCN still resides in the combustion vessel for absorption measurements, but at a substantially lower temperature. Least squares fitting of these spectra result in a much improved data match with a fitted temperature of 314 K. Prominent absorption features for H<sub>2</sub>O and CO<sub>2</sub> are found in both the XM39 and JA2 spectra. Fitted results for JA2 burning in 1.0 MPa nitrogen are shown on Figs. 9 and 10. *In-situ* optical measurements of H<sub>2</sub>O in the combustion region eliminate the condensation problems that must be addressed in experiments where the measurements are performed on extracted gas samples. A good fit is obtained for the rotational structure and a fitted temperature of 1402 K is close to the average results of other absorption measurements on NO<sup>15</sup> for an equivalent pressure. Absorption spectra for CO<sub>2</sub> do not include sufficient structure to confidently extract both temperature and concentration from fitting. Thus the temperature was set to 1400 K (results here and previous work 14) and a best fit for concentration was determined to be 0.10 mole fraction. These results as well as others not shown are tabulated in Table 1 and compared with other work in the next section.



**Figure 9.** Absorption spectrum of  $\text{H}_2\text{O}$  taken in the dark zone of JA2 burning in 1.0 MPa nitrogen. A best fit for temperature and concentration are 1402 K and 0.22 mole fraction, respectively.



**Figure 10.** Absorption spectrum of  $\text{CO}_2$  taken in the dark zone of JA2 burning in 1.0 MPa nitrogen. The temperature is fixed at 1400 K and a best fit for  $\text{CO}_2$  concentration is 0.10 mole fraction.

Uncertainties in the obtained data are estimated in the following fashion. It is assumed that no large systematic error is present in either the determination of pathlength or in the molecular database used to least-squares-fit the experimental absorption spectra. The largest variations come from the run-to-run repeatability of the experiment and include changes in the flatness of the burning surface and the combustion intensity. Run-to-run variations in the concentration are about  $\pm 20\%$ , except for  $\text{CH}_4$  and about  $\pm 5\%$  for temperature. The HITRAN database did not provide a good Q-branch representation for



the experimental spectra at high temperatures. Thus the CH<sub>4</sub> concentrations contain larger uncertainty, estimated as a factor of two.

## DISCUSSION

Table 1 contains dark-zone temperature and concentration data for a nitramine composite propellant (XM39). The experimental data come from both uv-visible and ir absorption. The temperature and NO concentrations for all three data columns come from uv-visible absorption data and the other species are obtained by ir absorption. FTIR absorption<sup>24</sup> is used for the results of the middle column and multichannel absorption for the first and third columns. It should be noted that not all of the possible major species are listed in this Table. Two major species molecules, H<sub>2</sub> and N<sub>2</sub>, are not measurable with an ir technique and hence are not listed. The data of Parr and Hanson-Parr<sup>11</sup> were taken in room air, whereas the other data were obtained in a pressurized nitrogen environment. In addition each of the three columns represent data taken at a different pressure. With these differences, a general agreement in dark-zone temperature is observed and good agreement is shown for NO, CO, CO<sub>2</sub>, N<sub>2</sub>O and CH<sub>4</sub>. with respect to the first two columns. Differences occur for HCN and H<sub>2</sub>O. Evidence in support of larger values comes from mass-spectrometric-sampling, laser-assisted-combustion data of Tang, et. al.<sup>42</sup> who report HCN and H<sub>2</sub>O mole fractions of about 0.2 for XM39 at 0.1 MPa argon pressure. A small concentration of N<sub>2</sub>O is reported with one value being an upper limit. This upper limit is a result of an unknown absorber<sup>26</sup>. In addition, N<sub>2</sub>O is known to exist in the primary reaction zone and any perturbations of flat geometry could give rise to an appearance of a small amount of N<sub>2</sub>O in the dark zone. Further work is needed on N<sub>2</sub>O since the dark zone is fuel rich and any reactive oxidizers will have a magnified effect on dark-zone chemistry. Nonetheless, as experimental data are being obtained for nitramine-based propellants for a variety of conditions, an improved picture of the flame structure is emerging.

**Table 1.**

Comparison of XM39 dark zone major species and temperatures with published results for self-sustained combustion conditions. Concentrations in mole fraction.

Parameter	XM39 <sup>a</sup>	XM39 <sup>b</sup>	XM39 <sup>c</sup>
P (MPa)	1.0 - 1.2	2.2	0.1
Height (cm)	0.15	0.1	0.15
T (K)	1150	1090	1250
NO	0.15	0.15	0.08
CO	0.12	0.10	
H <sub>2</sub> O	0.15	0.09	
CO <sub>2</sub>	0.04	0.04	
HCN	0.14	0.04	
N <sub>2</sub> O	≤ 0.02	0.03	
CH <sub>4</sub>	~ 0.005	~0.004	

a. present results and Refs. 16 and 26.

b. Refs. 18, 23 and 24

c. Ref. 11.

Double-base propellant dark zones have been previously investigated with sampling probes. The results of Heller & Gordon<sup>38</sup> are a landmark study and have often been used to test and develop combustion models. Lengelle et al.<sup>39</sup> have also investigated double-base propellants with sampling probes. In these studies, all of the major species with the exception of H<sub>2</sub>O were measured. The results normalized for an assumed 0.2 mole fraction H<sub>2</sub>O are shown in Table 2. Non-intrusive optical absorption results for JA2 are shown for comparison purposes. Both measurements of species concentration and temperature are in good agreement for these three investigations. It can be said that the double-base propellant dark zone database is in better

shape than the nitramine composite propellant's database. Some of the reasons are: the double-base

**Table 2.**

Comparison of double-base dark-zone species and temperatures with published results for self-sustained combustion conditions. Concentrations in mole fraction

Parameters	DB1 <sup>d</sup>	DB2 <sup>e</sup>	JA2 <sup>f</sup>
P (MPa)	1.6	0.9	1.0
T (K)	1600	1500	1400
NO	0.24	0.21	0.22
CO	0.33	0.38	0.38
CO <sub>2</sub>	0.10	0.09	0.11
H <sub>2</sub> O	0.20	0.20	0.23
CH <sub>4</sub>	0.008	0.026	~ 0.005
N <sub>2</sub>	0.04	0.02	--
H <sub>2</sub>	0.08	0.08	--
HCN	0.004	--	0
C <sub>2</sub> H <sub>4</sub>	0.008	0.008	0

d. Ref. 38

e. Ref. 39

f. present results and Ref. 14.

propellants have been studied over a longer period of time, nitramine-composite propellants (XM39) were developed for low vulnerability applications and thus exhibit poorer burning characteristics than double-base propellants at the low pressures required for diagnostic experiments with spatial meaning, and another major non-equilibrium species (HCN) is participating in the dark zone chemistry of nitramine propellants.

## SUMMARY AND FUTURE CONSIDERATIONS

A non-intrusive optical absorption technique has been developed to perform combustion diagnostics on a time scale relevant to self-sustained solid propellant combustion. Multi-featured absorption spectra have been least-squares-fitted to obtain quantitative species concentrations and temperatures through exclusive use of basic spectroscopic molecular information. No calibration factors are required.

This technique has been applied to the dark zone of nitramine and double-base propellants. These results with other published work are resulting in a chemically specific database of sufficient size to provide direct benefit to ongoing modelling efforts of the detailed chemistry occurring in solid propellant combustion.

Array detector technology is constantly being improved both in obtaining better signal-to-noise characteristics and a better spatial resolution capability. Digital readout circuitry is becoming faster so measurements can be performed on shorter time scales. These improvements will allow absorption experiments to address an increasing variety of problems. With respect to solid propellant combustion, an enhanced spatial resolution may allow probing the thin primary reaction zone. On the other hand, efforts to improve spatial resolution by clever techniques to expand the reaction zone have been ongoing. Preheating the propellant will allow self-sustained combustion at lower pressures and thus larger reaction zones. This technique is preferred since it should be easy to model. However, sufficient reaction zone expansion may not be attainable. Another method used to expand the reaction zone is through laser-assisted combustion. Larger expansion has been demonstrated with this technique<sup>6-12</sup>. If laser-assisted combustion can be modelled and related to self-sustained combustion it could be the technique of choice for spatial detail.

Efforts have begun on incorporating the capabilities of a 2-D array for absorption work. A pulsed arc lamp is used to provide a more intense light source for a rectangular sheet of light. This sheet of light passes vertically through the combustion region and is imaged onto multiple strips of the array detector. In this way a snapshot of absorption at various heights above the propellant surface can be obtained. If the sheet of light is made to pass horizontally through the combustion region a tomographic analysis might be applied to realize added spatial information.

With the speed of the present day computer, it is possible to incorporate detailed kinetics to model solid propellant flames. Hence, in the future, models may be predicting kinetically controlled parameters such as burn rate and temperature sensitivity. These models must be carefully tested and validated during the developmental period and thus experiments which produce quantitative results are essential for this validation process. Multichannel absorption spectroscopy is one technique which fulfills this need.

## APPENDIX

**Table A.**

Major ingredients for the propellants discussed in the text. The values are given in weight percent and the numbers in parentheses give the percent nitration level of the nitrocellulose.

Ingredient	M9	JA2	DB1	DB2	XM39	HMX1	M30
Nitrocellulose	57.6	58.2	55	52	4.0		28.0
nitration level	(13.3)	(13.0)	(12.6)	(11.6)	(12.6)		(12.7)
Nitroglycerin	40.0	15.8	45	43			22.5
Nitroguanidine							47.7
Potassium Nitrate	1.63						
Ethyl Centralite	0.73			3	0.4		
RDX*					76		
Cellulose Acetate Butyrate					12		
Acetyl Triethyl Citrate					7.6		
DEGDN*		25.2					
HMX*						73	
TMETN*						17	
Polyester Binder						10	

\* These abbreviations are RDX, cyclotrimethylene-trinitramine, DEGDN, diethyleneglycoldinitrate, HMX, cyclotetramethylene-tetranitramine and TMETN, trimethylethanedinitrate.

## REFERENCES

1. Anderson, W. R., 1996. Chemistry discussions.
2. Lempert, W. R., 1988. "Microwave Resonance Lamp Absorption Technique for Measuring Temperature and OH Number Density in Combustion Environments," *Combustion & Flame*, Vol. 73, pp. 89-98.
3. Vanderhoff, J. A., 1988. "Spectral Emission and Absorption Studies of Solid Propellant Combustion," *25th JANNAF Combustion Meeting*, CPIA Publ. 498, vol. IV, p. 537.
4. Vanderhoff, J. A., 1989. "Spectral Studies of Solid Propellant Combustion II. Emission and Absorption Results for M30 and HMX1 Propellants," BRL-TR-3055.
5. Vanderhoff, J. A., 1991. "Species Profiles in Solid Propellant Flames Using Absorption and Emission Spectroscopy," *Combustion & Flame*, Vol. 84, pp. 73-92.

6. Parr, T. P. and Hanson-Parr, D.M., 1989. "Nitramine Flame Structure as a Function of Pressure," *26th JANNAF Combustion Meeting*, CPIA Publ. 529, Vol. I, p. 27.
7. Parr, T. P. and Hanson-Parr, D.M., 1991. "Absorption Measurements in Propellant Flames," *28th JANNAF Combustion Meeting*, CPIA Publ. 573, Vol. II, p. 369.
8. Parr, T. P. and Hanson-Parr, D.M., 1993. "Solid Propellant Flame Chemistry and Structure," *Non-Intrusive Combustion Diagnostics*, Begell House Publishing Co.
9. Parr, T. P. and Hanson-Parr, D.M., 1993. "RDX Flame Structure and Chemistry," *30th JANNAF Combustion Meeting*, CPIA Publ. 606, Vol. I, p. 31.
10. Parr, T. P. and Hanson-Parr, D.M., 1994. "RDX Laser Assisted Flame Structure," *31st JANNAF Combustion Meeting*, CPIA Publ. 620, Vol. II p. 407.
11. Parr, T. P. and Hanson-Parr, D.M., 1995. "RDX, HMX, and XM39 Self-Deflagration Flame Structure," *32nd JANNAF Combustion Meeting*, CPIA Publ. No. 631, Vol. I, pp. 429-438
12. Parr, T. P. and Hanson-Parr, D.M., 1995, "Solid Propellant Flame Structure," Materials Research Society Meeting, Paper No. 663.9, Boston, MA
13. Vanderhoff, J. A. and Kotlar, A. J., 1990. "Simultaneous Determination of Temperature and OH Concentrations in a Solid Propellant Flame," *23rd Symposium (Int) on Combustion*, The Combustion Institute, pp. 1339-1344.
14. Vanderhoff, J. A., Teague, M.W., and Kotlar, A. J., 1992. "Determination of Temperature and NO Concentrations through the Dark Zone of Solid Propellant Flames," *24th Symposium (Int) on Combustion*, The Combustion Institute, pp. 1915-1922.
15. Vanderhoff, J. A., Teague, M. W., and Kotlar, A. J., 1992. "Absorption Spectroscopy through the Dark Zone of Solid Propellant Flames, BRL-TR-3334.
16. Teague, M. W., Singh, G. and Vanderhoff, J. A., 1993. "Spectral Studies of Solid Propellant Combustion IV: Absorption and Burn Rate Results for M43, XM39 and M10 Propellants," ARL-TR-180.
17. Lu, Y. C., Freyman, T. M. and Kuo, K. K., 1995. "Measurement of Temperatures and OH Concentrations of Solid Propellant Flames Using Absorption Spectroscopy," *Combustion Science and Technology*, Vol. 104, No. 1-3, pp. 193-205.
18. Y. C. Lu, Ulas, A., Kuo, K. K. and Freyman, T. M., 1995. "Absorption Spectroscopy of Solid Propellant Flames," AIAA Paper 95-2713, 31st AIAA/ASME/SAE/ASEE Joint Propulsion Conference, San Diego, CA.
19. Ulas, A., Lu, Y. C., Kuo, K. K. and Freyman, T. M., 1995. "Measurement of Temperatures and NO and OH Concentrations of Solid Propellant Flames Using Absorption Spectroscopy," *32nd JANNAF Combustion Meeting*, CPIA Publ. No. 631, Vol. I, pp. 461-470.
20. Modiano, S. H. and Vanderhoff, J. A., 1994. "Multichannel Infrared Absorption Spectroscopy of Solid Propellant Flames," *Combustion & Flame*, Vol. 99, pp. 187-189.
21. Modiano, S. H. and Vanderhoff, J. A., 1995. "Multichannel Infrared (IR) Absorption Spectroscopy Applied to Solid Propellant Flames," ARL-TR-900.
22. Modiano, S. H. and Vanderhoff, J. A., 1995. "Multichannel IR Spectroscopy of Solid Propellant Flames: CO and N<sub>2</sub>O Concentration Measurements," *32nd JANNAF Combustion Meeting*, CPIA Publ. No. 631, Vol. I, pp. 439-447.
23. Mallery, C. and Thynell, S. T., 1994. "Species and Temperature Profiles of Propellant Flames Obtained from FTIR Absorption Spectrometry," *31st JANNAF Combustion Meeting*, CPIA Publ. 620, Vol. II, pp. 291-305.
24. Mallery, C. and Thynell, S. T., 1995. "Further Improvements to FTIR Absorption Spectroscopy of Propellant Flames for Profiling of Species and Temperature," *32nd JANNAF Combustion Meeting*, CPIA Publ. No. 631, Vol. I, pp. 449-460.
25. Anderson, W. R., Ilincic, N., Meagher, N. E., Seshadri, K. and Vanderhoff, J. A., 1995. "Detailed and Reduced Chemical Mechanisms for the Dark Zones of Double Base and Nitramine Propellants in the Intermediate Temperature Regime," *32nd JANNAF Combustion Meeting*, CPIA Publ. No. 638, Vol. I, pp. 197-214.

26. Vanderhoff, J. A., Modiano, S. H., Homan, B. E. and Teague, M. W., 1996. "Overtone Absorption Spectroscopy of Solid Propellant Flames: CO and N<sub>2</sub>O Concentrations," *Fourth International Symposium on Special Topics in Chemical Propulsion*, Stockholm, Sweden.
27. Vanderhoff, J. A. and Kotlar, A. J., 1990. "Temperature and OH Concentrations in a Solid Propellant Flame Using Absorption Techniques," BRL-TR-3098.
28. Levenberg, K., 1944. "A Method for the Solution of Certain Problems in Least Squares," *Quarterly of Applied Mathematics*, Vol. 2, pp164-168.
29. Marquardt, D. 1963. "An Algorithm for Least-Squares Estimation of Nonlinear Parameters," *SIAM Journal on Applied Mathematics*, Vol. 11, pp 431-441.
30. Huber, K. P. and Herzberg, G., 1979. *Molecular Spectra and Molecular Structure. IV. Constants of Diatomic Molecules*, Van Nostrand Reinhold Company.
31. Dieke, G. and Crosswhite, H., 1963. "The Ultraviolet Bands of OH: Fundamental Data," *J. Quant. Spec. Radiat. Transfer*, Vol. 2, p. 97.
32. Dimpfl, W. L. and Kinsey, J., 1979. "Radiative Lifetimes of OH ( $A^2\Sigma$ ) and Einstein Coefficients for the A - X system of OH and OD," *J. Quant. Spec. Radiat. Transfer*, Vol. 21, p. 233.
33. Henry, A., LeMoal, M. F., Cardinet, Ph. and Valentin, A. 1978. "Overtone Bands of 14N16O and Determination of Molecular Constants," *J. Mol. Spectrosc.*, Vol. 70, p. 18.
34. Engleman, R. and Rouse, P. E., 1971. "The  $\beta$  and  $\gamma$  Bands of Nitric Oxide Observed During the Flash Photolysis of Nitrosyl Chloride," *J. Mol. Spectrosc.*, Vol. 37, p. 240.
35. McDermid, S. and Laudenslager, J. B., 1982. "Radiative Lifetimes and Electronic Quenching Rate Constants for Single-Photon-Excited Rotational Levels of NO ( $A^2\Sigma^+$ ,  $v'=0$ )," *J. Quant. Spec. Radiat. Transfer*, Vol. 27, p. 483.
36. Rothman, L. S., Gamache, R. R., Tipping, R. H., Rinsland, C. P., Smith, M. A., Benner, D. C., Malathy Devi, V., Flaud, J. M., Brown, L. R. and Toth, R. A., 1992. "The HITRAN Molecular Database: Editions of 1991 and 1992," *J. Quant. Spec. Radiat. Transfer*, Vol. 48, p. 469.
37. Daniels, R. W., 1978. *An Introduction to Numerical Methods and Optimization Techniques*, North Holland Publ. Amsterdam.
38. Heller, C. A. and Gordon, A. S. 1955. "Structure of the Gas Phase Combustion Region of a Solid Double Base Propellant," *J. Phys. Chem.*, Vol. 59, p. 773.
39. Lengelle, G., Bizot, A., Duterque, J. and Trubert, J. F., 1984. "Steady-State Burning of Homogeneous Propellants," in *Fundamentals of Solid-Propellant Combustion*, edited by Kuo, K. K. and Summerfield, M. AIAA Progress in Astronautics and Aeronautics Series, Vol. 90, pp. 361-407.
40. Kubota, N. 1982. "Physicochemical Processes of HMX Propellant Flame Structure," *Nineteenth Symposium (Int) on Combustion*, The Combustion Institute, pp. 777-785.
41. Korobeinichev, O. P., Kuibida, L. V., Orlov, V. N., Tereshchenko, A. G., Kutsenogii, K. P., Mavliev, R. A., Ermolin, N. E., Fomin, V. M. and Emel'yanov, 1985. "Mass Spectrometric Probe Study of the Flame Structure and Kinetics of Chemical Reactions in Flames," *Mass-Spektrom. Khim. Kinet.* pp. 73-93.
42. Tang, C. J, Lee, Y. J. and Litzinger, T. A., 1994. "A Study of Gas-Phase Processes During the Deflagration of RDX Composite Propellants," *31st JANNAF Combustion Meeting*, CPIA Publ. No. 620, Vol. II, pp. 307-316.

## COMMENTS

Q. Brewster, Univ. of Illinois, Urbana, IL, USA: Could you comment on the degree of accuracy expected for the IR bands with the HITRAN database for these conditions given that the HITRAN data is based on atmospheric conditions, may be missing hot bands, and includes only nitrogen and self-broadening?

Author's Reply: This is an interesting and complex question. We have indeed applied the HITRAN database to a regime of elevated temperature and pressure. A main reason for application of this database is that (to our knowledge) it is the most complete database available. Testing of the database at these conditions has not been done, thus a definitive uncertainty cannot be assigned. There are reasons to believe that the database can perform reasonably well under these experimental conditions. For the HITRAN database, a temperature dependence has been incorporated into the line intensities as well as the internal partition sums and extends to 3000 K. Use of an array detector allows simultaneous sampling of large chunks of spectra. In other words, there are many transitions that contribute to the observed spectra. For HCN, H<sub>2</sub>O and CO<sub>2</sub> there are 90, 1375 and 350 transitions considered, respectively. Missing bands of non-negligible strength would readily appear in a comparison of experimental and fitted spectra. The resolution of the experiment is much less than that of an isolated line thus the experimental spectra are usually contours which consist of sums of individual transitions. These contours are well represented by the experimentally determined linewidth of an Ar lamp. Fitted values for temperature have less uncertainty than concentration since they depend on ratios, not absolute values.

V. Abrukov, Chuvash State Univ., Cheboksazy, Russia: Recently a new integral approach to various optical techniques has been developed (interferometry, spectroscopy, Mie scattering, etc.). For example, a total number of molecules (radicals, etc.) M absorbing a particular light wavelength can be determined by the following formula:

$$M = (1/B_\lambda) \iint \ln[\Gamma_{0,\lambda} / \Gamma_\lambda(x,y)] dx dy,$$

where B is the average absorption cross section of the molecule,  $\Gamma_{0,\lambda}$  is the initial illumination, and  $\Gamma_\lambda(x,y)$  is the illumination distribution in the recording plane (with coordinates x,y). I think this approach will be able to solve some of the practical problems in propellant combustion research.

Reference: Abrukov, V. S. et al., 1995. "Interferometric techniques and other optical methods in combustion research. New approach", in *Optical Techniques in Fluid, Thermal, and Combustion Flow*, edited by S. S. Cha and J. D. Trolinger, Proc. SPIE, Vol. 2546, pp. 420-426.

Author's Reply: This approach involves measurements in two spatial dimensions. Our technique involves only one spatial dimension, but with wavelength resolution via a spectrometer. We thus rely on wavelength specific information for the calculation of the molecule absorption coefficient.

# OPTICAL DIAGNOSTICS OF ATOMIZATION AND COMBUSTION FOR CRYOGENIC LIQUID ROCKET PROPULSION

M. Oschwald R. Lecourt<sup>1</sup>, U. Brummund, A. Cessou<sup>2</sup>, O. Haidn

DLR Forschungszentrum Lampoldshausen, Space Propulsion Division

## Abstract

The M3 micro-combustor is a test facility for basic investigations of cryogenic oxygen/hydrogen rocket propulsion. The model combustor is operated at pressures up to 2MPa and has full optical access to study in detail the LOX-spray combustion phenomena with nonintrusive optical diagnostic techniques. Oxygen and hydrogen are injected at 77 K through a single coaxial injection element. The phenomenology of LOX-jet break up and the topology of the flowfield has been investigated by flashlamp and laser light-sheet photography to determine the distribution of the liquid phase and by droplet tracking to measure the droplets velocities. Location and structure of the flamefront has been investigated by laser-induced fluorescence and the detection of the spontaneous emission of the OH radical.

## 1 INTRODUCTION

At DLR research center Lampoldshausen the M3 micro-combustor test facility is operated for basic investigations on liquid oxygen/gaseous hydrogen combustion. The combustor is designed for pressures up to 2MPa. The work up to now has largely been focused on using a single coaxial injection element, whereas a three-injector element has been investigated in preliminary work.

The aims of the experiments presented here are twofold. First, they are dedicated to develop and test the performance of optical diagnostic techniques for the application in reactive two-phase flows at high pressures. Second, the investigations are part of a series of experiments to characterize the phenomenology of jet atomization, vaporization, mixing, combustion, and also combustion instabilities and the interaction between these processes. Detailed information is needed to identify the dominating physical and chemical processes and to contribute to a data base for CFD-code validation.

In this paper, we focus primarily on the performance of the optical diagnostic techniques. The implications of the results of the applied diagnostics for the understanding of the flow and combustion processes are briefly discussed at the end of the paper.

<sup>1</sup>ONERA ,Centre du Fauga-Mauzac, 31410 Noe, France

<sup>2</sup>Université de Rouen / CORIA, 76821 Mont-Saint-Aignan, France

## 2 THE M3 MICRO-COMBUSTOR

A detailed description of the micro-combustor can be found in [1] and [2]. A sketch of the combustor cross section is shown in figure 1. The model combustor has full optical access to permit diagnostics by non-intrusive optical methods. For laser light-sheet applications, the flow can be illuminated through slit windows in the upper and lower walls. Fluid supply lines, flow meters, and valves are placed in a bath of  $\text{LN}_2$  to reach propellant temperatures similar to real rocket engine conditions. Additionally, the propellant injection system is in thermal contact with the  $\text{LN}_2$  to prevent long-lasting transients caused by heating of  $\text{LO}_2$  during the startup of an experiment. Together with specially designed fast opening valves steady state operation is guaranteed after about 50ms.

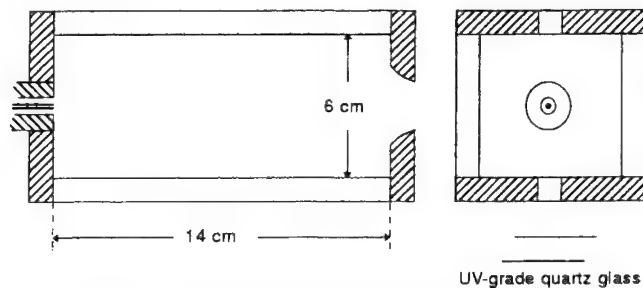


Figure 1: Cross sectional view of the model combustor.

The dimensions of the injector are chosen to be similar to the HM7B type (see figure 2) leading to rather small momentum flux ratios at low combustion chamber pressures. Several injection elements are used with the same dimensions of the  $\text{LOX}$ -post but different outer diameters of the annular hydrogen slit to achieve different  $\text{H}_2$ -mass flows necessary for the different combustion chamber pressures. In any case, the length to diameter ratio of the  $\text{LOX}$ -post and of the annular hydrogen gap is kept above 20 to ensure a fully developed turbulent flow profile.

The experiments discussed in this paper were done at four test cases: cases A and A' at 150 kPa, case B at 500 kPa and case C at 1.2 MPa. Weber numbers  $We = \rho(v_{H_2} - v_{LOX})^2 d_{LOX} / \sigma_{LOX}$  and the momentum flux ratios  $J = (\rho v^2)_{H_2} / (\rho v^2)_{LOX}$  as calculated for injector exit conditions for these test cases are shown in figure 3.

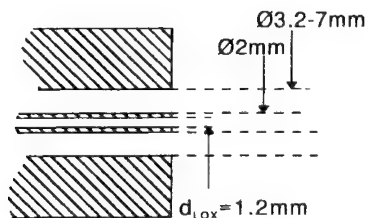


Figure 2: Sketch of the single coaxial injection element.

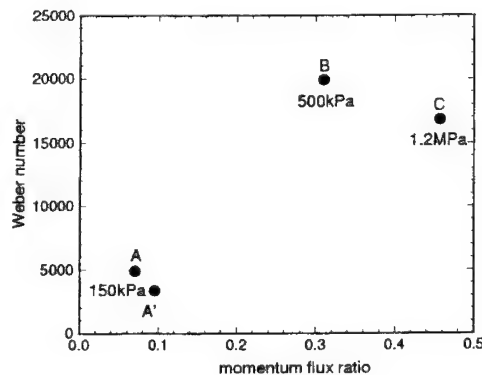


Figure 3: Pressures, Weber numbers and momentum flux ratios for the test cases A, A', B, and C.



### 3 PHENOMENOLOGY OF LOX-JET BREAKUP

Several optical methods were used to investigate the phenomenology of jet breakup and to visualize the gas flow in the combustor.

Shadow- und Schlieren photography were applied to map the topology of the gas flow. Although the LOX-distribution could be obtained with these line-of-sight methods, turbulence and strong gradients in the cryogenic two-phase flow result in images with strong gray value variations. Flow structures, for example the shear layer between hydrogen and oxygen, could not be resolved with satisfying quality in the outer gas flow region.

The distribution of the LOX-phase was recorded with a 300ns flash lamp in a line-of-sight configuration [1] and by laser light-sheet photography (see figure 4). Both methods yield reasonable information about the distribution of the liquid phase. The quality of the laser light-sheet measurements is superior to flash-lamp photography in terms of contrast and spatial resolution.

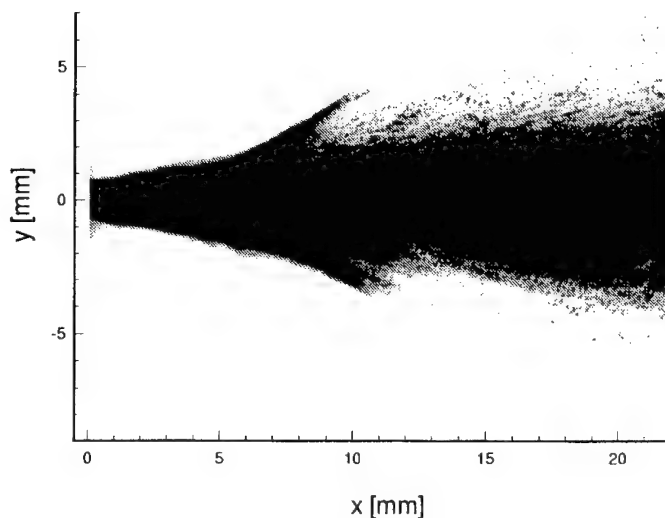


Figure 4: LOX-phase distribution for test case A as obtained with laser light-sheet photography.

### 4 2D-LOX-DROPLET VELOCIMETRY

Injection velocities for hydrogen (300-500 m/s) are always high compared to the velocities of liquid oxygen at the injector exit (15-35 m/s). The shear layer between these two flows is essential for the phenomenology of the LOX-jet break up, evaporation of the liquid phase and the mixing of hydrogen and oxygen. We use the LOX-droplets as tracers to get information about this region. Due to the droplets inertia the droplet velocity is not identical with the gas velocity. But droplets penetrating into the hydrogen flow will be accelerated and therefore the droplet velocity will be influenced by the gas velocity. An estimation of the relaxation time  $\tau = \rho D^2 / 18\eta$  of a  $10 \mu\text{m}$  droplet gives an order of 1 ms, clearly longer than the shortest turbulent time scales expected. The droplet velocity therefore depends on the droplets mass and on its history in the flow field, no unique flowfield for all the droplet can be expected. An evaluation of the velocity of individual droplets is done in this work instead of taking ensemble averages. Velocity measurements of

LOX-droplets with phase-Doppler anemometry (PDA) in LOX/GH<sub>2</sub>-combustion chambers were carried out at ONERA Palaiseau [3] and Pennsylvania State University [4]. In our experiment, droplet tracking velocimetry (DTV) is used to determine instantaneous droplet velocities in a 2D-field. The method is similar to particle tracking velocimetry that has been widely used in PIV applications with low image densities [5]. DTV uses the LOX-droplets in the flow as tracers. The velocity is determined by recording their position at two times on a single frame. The flow is therefore illuminated with a pulsed light-sheet. From the displacement of the droplet images and the known time interval between the exposure times the velocity can be determined. Preliminary experiments demonstrated the feasibility of droplet velocimetry by droplet tracking in this cryogenic two phase flow with combustion [6]. The results presented were obtained with optimized parameters for the photographic recording of the droplet images and with an automated data reduction scheme.

#### 4.1 Experimental Setup

Two pulsed frequency doubled Nd:YAG-lasers were used as light sources. Each laser is triggered by the same clock, the trigger for the second laser is delayed by an adjustable time which was chosen to be 7  $\mu$ s in this application. The laser light was formed into a light-sheet of a width of 4 cm and a thickness of 500  $\mu$ m in the measurement plane. Since no recirculation zone was present in regions where the measurements were done it was not necessary to resolve the directional ambiguity. The images were recorded on a 24mm x 36mm photographic film (Kodak Technical Pan). The magnification was 1, so that the size of the area in the flow recorded and the size of the photographic film matched. Four images were necessary to map the total length of the combustion chamber. The camera shutter was opened for 1/125 s, during this time interval the two lasers were triggered. An interference filter was mounted in front of the camera lens system to avoid light from the H<sub>2</sub>/O<sub>2</sub>-flame exposing the film. The camera was able to record 2.5 frames/second.

#### 4.2 Data Reduction

The frames were digitized to 3072 x 2320 pixels with a dynamic range of 8 bit for the grey values, hence each pixel corresponds to 11.5 x 11.5  $\mu$ m<sup>2</sup> in laboratory coordinates. For data reduction, these images were divided in 512 x 512 pixel subimages. Several sources contributed to the exposure of the film: light scattered from the liquid jet, from ligaments and droplets, but also stray light from water and ice condensating on the windows of the combustion chamber. After contrast enhancement and binarization of these subimages, connected pixels were identified as individual objects. The positions of the objects were determined by calculating the center of gravity of their binarized images. Also the area  $A$  and the perimeter  $P$  of the objects were evaluated. To discriminate droplets from the liquid core, ligaments and stray light, objects with a size  $A$  above a threshold size were deleted. In a second step, objects with a  $P/\sqrt{A}$ -ratio differing from the ratio for spheres for more than 40% were deleted too. The mean displacement of the droplet images was now determined by calculating the autocorrelation function by performing two subsequent 2D-FFT on the 512 x 512 pixel subimage. This mean displacement was used as an initial starting value in the search algorithm for identifying pairs of droplet images.

For each identified droplet pair, the position and the area of the two images were stored. It is not expected that from the image area a droplet size can be deduced; for example, due to non-linear image filtering for contrast enhancement, the size of a binarized image is not proportional to the droplet size. Nevertheless, we think that at least trends of size-dependent effects may be found by looking at the image areas.

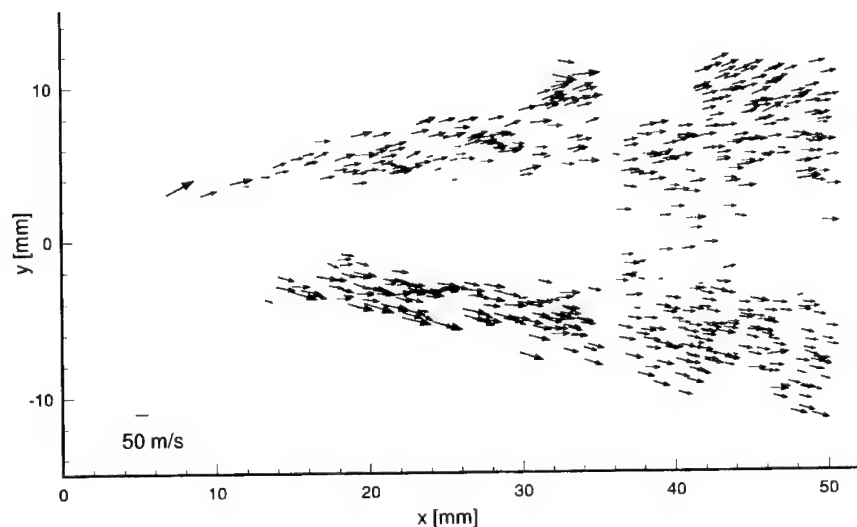


Figure 5: Vector plot of droplet velocities in the range  $0\text{mm} < x < 50\text{mm}$ . The injector is at position  $x = 0\text{mm}$ ,  $y = 0\text{mm}$ .

### 4.3 Velocity Fields

Due to the improved optical set up and the increased droplet density at test case A compared to the previous measurements at test case A' [6], a much higher number of droplet images could be analysed on the recorded photographs in this work. A total of 2700 droplet image pairs were identified by the automated analysis software in nine images mapping the total combustor length. Two to three images were obtained at the same location in the combustion chamber. The large number of droplets permits to calculate significant mean values and variances.

Figure 5 shows the flowfield for test case A for the first 5 cm downstream the injector. Each vector represents the velocity of an individual droplet. An analysis of the velocities shows that in a small area the velocities of the droplets may be very different. This confirms that no flowfield can be attributed to the droplets, each droplet has its individual velocity corresponding to its mass and history in the gas flowfield.

To see how the flowfield develops downstream the injector, the velocities were analyzed for the two droplet groups with  $y > 0$  and  $y < 0$ , i.e. droplets above and below the central flow axis. Figure 6a-f shows the probability density function of the  $v_y$ -component, i.e. the radial velocity component for droplets of these two subgroups for different  $x$ -intervals downstream the injector. Near the injector, the velocity distribution for each subgroup is rather broad and asymmetric to  $v_y = 0$ , indicating that the majority of the droplets is moving away from the central LOX-core (figure 6a,b). The mean value  $\bar{v}_y$  and the width of the distribution are decreasing further downstream (figure 6c,d). For  $x > 8\text{cm}$  the distributions are almost symmetric to  $v_y = 0$  (see figure 6e,f). All droplets are now moving mainly parallel to the central axis.

The probability density function for the  $v_x$ -components were analysed for droplets having  $x$ -components in an interval  $[x, x + 5\text{mm}]$  at several  $x$  positions downstream the injector. The mean value and the width of the distribution were determined by fitting a Gaussian distribution to the probability density function. As can be seen in figure 7, the mean value of  $v_x$  is increasing over the first few centimeters downstream of the injector and is decreasing for  $x > 4\text{cm}$ . The vertical bars show the width of the  $v_x$ -distribution. Data corresponding to different experiments are marked with different symbols. The ratio of the standard deviation  $\sigma$  of the distribution to

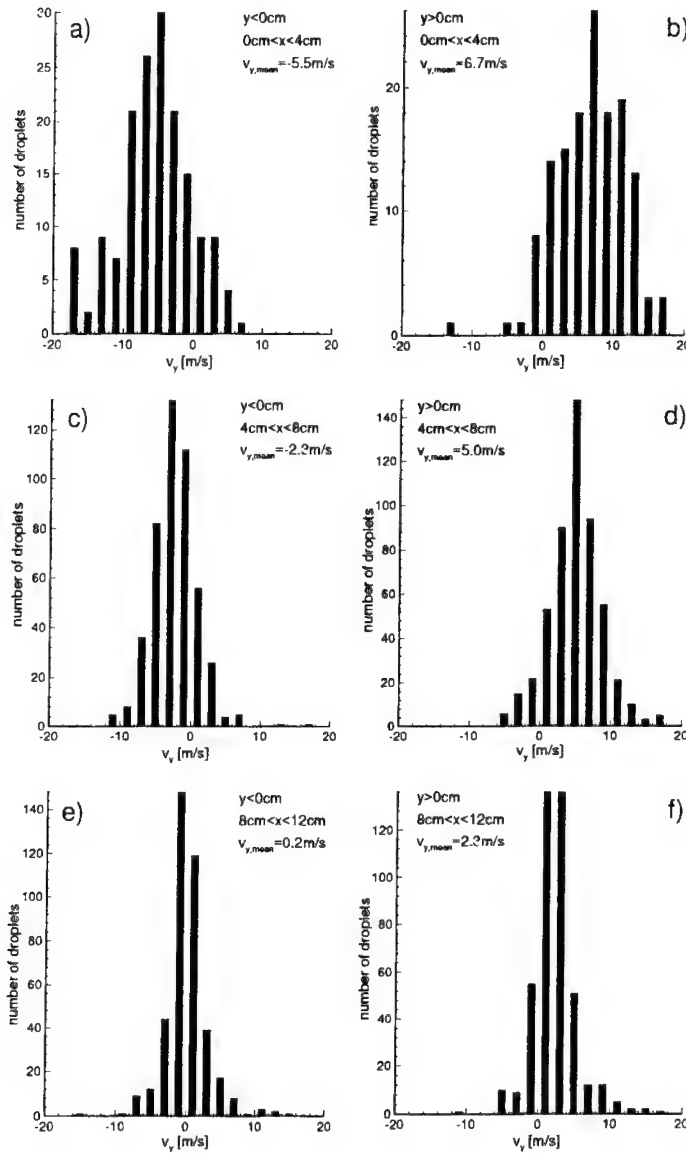


Figure 6: Probability density function of the  $v_y$ -component for droplets below and above the liquid core.

the mean  $\bar{v}_x$  may be as high as 0.6 near the injector. At the end of the combustion chamber  $\sigma/\bar{v}_x$  decreases to typical values of  $\sigma/\bar{v}_x \approx 0.1$ , the flowfield in the center becomes uniform.

No significant correlation of image size and position of droplets could be found. In figure 8, the droplet velocity is plotted as a function of its area for all the 2700 evaluated droplets. It can be seen that for small droplets the velocity distribution is broader than for large ones, indicating that small droplets may be more strongly influenced turbulent structures within the gas flow than large ones.

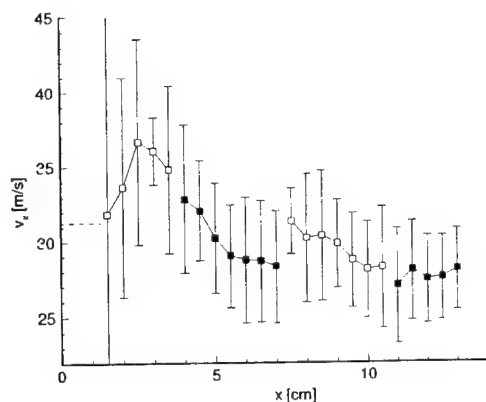


Figure 7: Mean value of the  $v_x$ -velocity component of droplet ensembles in an interval of  $[x, x + 5\text{mm}]$ . The vertical bars correspond to the standard deviation of the  $v_x$ -distribution. The injection velocity of LOX was 30.3 m/s.

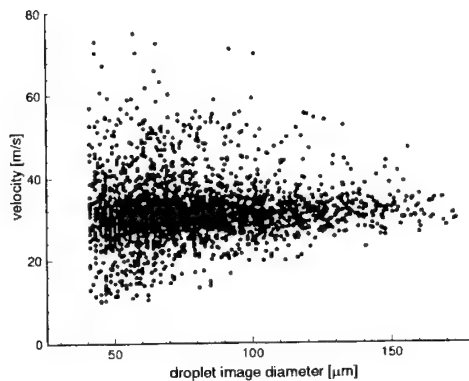


Figure 8: Correlation of droplet image size and velocity.

## 5 Location and Structure of Flamefront

There are several questions that can be addressed by the determination of the location of the flame front. Are the LOX-core, the droplets and ligaments and the evaporated oxygen contained in a well defined volume in the central region of the combustion chamber and surrounded by a conical flame front? Or do individual droplets or groups of droplets penetrate in the hydrogen flow leading to a complex flame structure and interaction of jet-break up and combustion? The determination of the position of the flame near the injector exit should help to answer the question of the process responsible for the flame anchoring. We applied planar laser induced fluorescence (PLIF) to measure the OH-radical distribution. OH is produced in the reaction zone and therefore is a marker for the flame front. Downstream the flame front OH may be present in relevant equilibrium concentrations due to the high temperatures reached in stoichiometric  $\text{H}_2/\text{O}_2$  combustion.

### 5.1 The UV-Laser Diagnostic System

The PLIF experiments were carried out with an injection-locked narrowband, tunable excimer laser (Lambda-Physik LEX 150T), operating at the KrF wavelength of 248 nm. It yields tunable radiation between 248 nm and 249 nm with an energy of 250 mJ/pulse and a bandwidth of  $0.4\text{ cm}^{-1}$ . The pulse duration is 20 ns which is essentially instantaneous in comparison to the combustion and turbulence time scales. To image a large part of the flame the rectangular laser output beam is transformed into a laser sheet of approximately 40 mm width and 0.3 mm thickness using a combination of a spherical and a cylindrical lens. The laser beam is focused by this lens combination, so that the beam waist is located in the center line of the combustion chamber axis. This sheet traverses the combustion chamber from the top to the bottom and is limited on the left side by the injector. The power density necessary for single shot measurements sometimes led to damaged windows when water vapour is condensed on the inner window surfaces. An intensified CCD camera placed at right angle to the laser sheet detected the induced fluorescence. Different filter combinations were chosen for the measurements. For the induced fluorescence images a combination of a 20 mm high-pass liquid butyl acetat filter and four dielectrical bandpass filters centered at 297 nm are put in front of the CCD camera. The gate time of the intensifier is always set to 100 ns. To obtain dispersed fluorescence spectra,

a high pass Schott WG 280 filter or the liquid butyl acetat filter is put in front of the entrance slit of the spectrometer. A pair of quartz lenses focusses the imaged part of the spray flame onto the entrance slit of a  $f/\# = 4$  spectrometer. The spectrometer is mounted so that the entrance slit is parallel to the laser beam axis. After dispersion of the entrance slit image by a grating with 1200 lines/mm the resulting fluorescence spectrum is projected by the refocussing mirror of the spectrometer onto the exit plane where it is detected by an ICCD camera. The spectrometer grating is adjusted to display a wavelength range of approximately 35 nm from 270 - 305 nm, calibrated with a Hg pen lamp. The slit width is set to 100  $\mu\text{m}$ , and the gate time of the intensifier is 10  $\mu\text{s}$ .

## 5.2 Excitation Wavelengths and Interferences

A lot of problems may arise in applying the laser induced fluorescence technique in high pressure, two-phase combustion systems, i.e. fluorescence interferences of the OH signal with  $\text{O}_2$  transitions, beam attenuation due to high OH number density and strong Mie scattering and stray light problems from the liquid oxygen core. The beam attenuation problem is significantly reduced when using the excitation of the OH  $\text{A}^2\Sigma (v'=3) \leftarrow \text{X}^2\Pi (v''=0)$  transition because no self-absorbing states are excited [7]. The KrF excimer laser is ideally suited for this OH transition leading to negligible attenuation. The Mie scattering can be strongly reduced by effective filtering with the butyl acetat filter having a steep cut-off at 248 nm and small bandwidth detection of the OH fluorescence with the dielectrical filters. In this way effective stray light suppression (rejection ratio better than  $10^{-10}$ ) is achieved. To reduce interferential effects arising from  $\text{O}_2$  fluorescence with increasing chamber pressures we calculated the OH and  $\text{O}_2$  absorption spectra to locate wavelength ranges of interferential free regions. From these synthetic spectra, we decided to choose the  $\text{P}_1(9)$  and  $\text{Q}_2(10)$  absorption lines to excite the OH radical in order to experimentally investigate the interferential effects with increasing chamber pressure. This investigation was done in the LOX/ $\text{GH}_2$  flame by acquiring dispersion spectra. The same laser-sheet illumination geometry as for the PLIF imaging has been used. OH fluorescence spectra, integrated on chip for typically fifty laser shots, have been obtained for the  $\text{P}_1(9)$  line at the test cases A, B, and C for the  $\text{Q}_2(10)$  line at test cases A and B and at a pressure of 0.8 MPa. The P-, Q-, and R-lines within the  $3 \leftarrow 2$  band of OH in the wavelength range of 300 nm are clearly resolved and can be identified on the basis of the known spectral behaviour of the OH-radical.

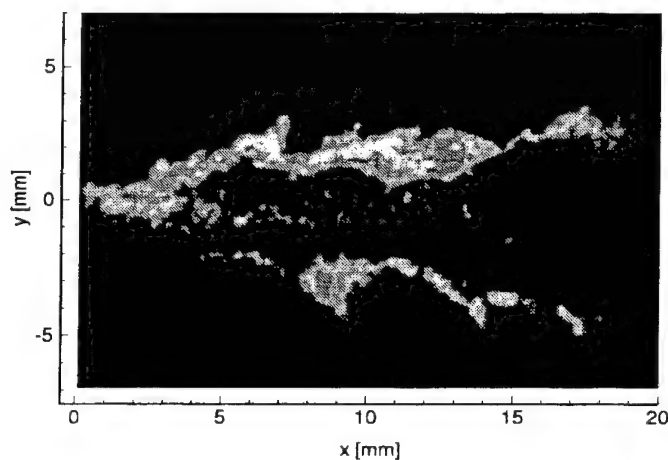


Figure 9: OH distribution as measured with PLIF at 150kPa (test case A').

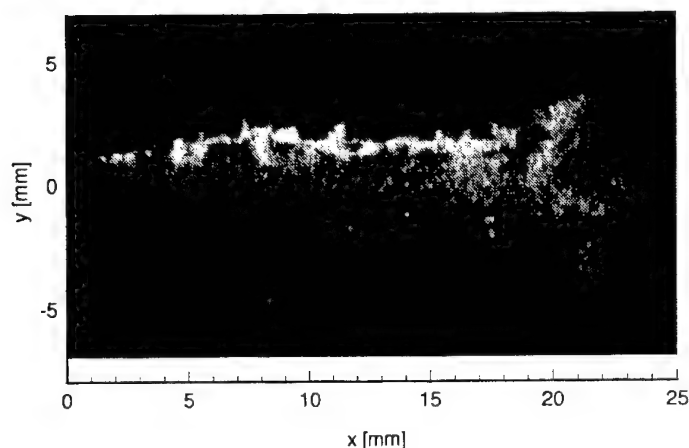


Figure 10: OH distribution as measured with PLIF at 500kPa (test case B).

Between these single strong lines some weaker and considerably broader emission appears in the range of 285 nm to 295 nm. This weaker emission originates from fluorescence of lower vibrational states ( $v'=0, 1, 2$ ). As pressure increases, the fluorescence intensity emitted by these states increases due to vibrational energy transfer. The background level is much higher and enhances with increasing chamber pressure when using the  $P_1(9)$  excitation line. At 1.2 MPa the  $3 \leftarrow 2$  band begins to diminish for the  $P_1(9)$  excitation line, whereas for the  $Q_2(10)$  line at 0.8 MPa the spectral structure and the relative emission intensities of P, Q, and R lines are still pronounced and well separated. Spectral lines originating from  $O_2$  appearing with increasing pressure can definitely not be observed in the spectral range of 295–305 nm. From these experimental and synthetic spectra we conclude that with the  $Q_2(10)$  excitation line it is possible to perform OH-PLIF measurements in a LOX/GH<sub>2</sub> combustion chamber at least at pressures up to 1.2 MPa.

### 5.3 OH-PLIF Images

Single-pulse OH PLIF images have been acquired with the KrF excimer laser tuned to the  $Q_2(10)$  absorption line, allowing interference free visualization of the laser-induced OH fluorescence. All PLIF images have been obtained with a fixed field of view of 25mm x 16mm. The main aim of this part of the work was to identify the location of the flame front and the spatial structures in dependence of the chamber pressure.

Figure 9 and figure 10 show typical PLIF images of the OH radical at a combustion chamber pressure of 150kPa (test case A') and 500kPa (test case B), respectively. A thin conical flame expands downstream the injector and gets thicker and wrinkled. The high turbulence associated with the flowfield is reflected by the convoluted flame zone. The thickness of the flame varies strongly, in some images at test conditions B and C the flame contour is even interrupted whereas at other locations there are zones of very high OH signal. Due to high stretch forces the flame may extinguish locally. The PLIF signal intensity is generally higher in the upper half of the combustion chamber because of strong attenuation of the laser sheet scattered by the dense liquid oxygen core in all directions. Travelling a long way through the dense spray, this effect will be much enhanced.

By signal averaging 50 laser shots the averaged intensity distributions were obtained. In these images turbulent structure is smoothed out due to the temporal integration process.

A surprising feature of the PLIF images is that on the centerline in the region of the LOX-core the signal is not zero. In the middle of the liquid oxygen jet there cannot be any OH fluorescence, and elastic scattering has been suppressed. The signal may be a shifted emission from the liquid oxygen, either stimulated Raman scattering and only partially blocked by the interference filter, or fluorescence from impurities in the liquid oxygen. In any case it indicates the presence of the dense liquid.

## 6 Results and Discussion

For all injection conditions with combustion we observed a liquid LOX-core extending several centimeters downstream the injector. These observations are consistent with results for small momentum flux ratios in reference [9]. The liquid core has been observed to be completely disintegrated downstream  $x > 8$  cm but there is still liquid oxygen at the exit of the combustor, i.e. 14 cm downstream the injector. A comparison of the LOX-spray without and with combustion exhibits the disappearance of the smallest droplets due to the heat release in the burning spray. With increasing chamber pressure, aerodynamic forces raise making the liquid jet look more compact along its movement downstream with a decreasing size of ligaments and droplets.

DTV has been shown to be a promising tool for velocimetry in the central region of the LOX/GH<sub>2</sub> combustor where the relevant processes of jet-breakup, evaporation, and mixing occur. The analysis of individual droplet velocities show that the mean value  $\bar{v}$  is a continuous function of the spatial coordinates but even in small areas in the flow the droplet velocities show a distribution around the mean reflecting the individual droplet's history due to the dynamics of jet disintegration and the interaction of the gasflow with the droplets.

Both velocity components show a decreasing width of their probability distribution function downstream the injector. For  $x > 8$  cm in the region mapped by the double exposures, i.e. from 12 mm below to 12 mm above the central axis the flow becomes rather uniform and parallel to the combustor axis and exhibits no velocity gradients. The LOX-jet is already disintegrated in this region, the LOX-phase is present in the form of droplets and ligaments. Evaporation and potential secondary droplet break-up will not be influenced by a shear layer in the surrounding gas flow. The observed decrease in the mean  $v_x$ -velocity of the droplets indicates that the cross section of the oxygen flow confined by the flow of reaction products and hydrogen is increasing. Assuming complete combustion and calculating the mean velocity of the reaction products for test case A yields 144 m/s. The presence of droplets at the injector exit and the measured velocity of about 28 m/s near the chamber exit clearly shows that combustion is incomplete.

It has been shown that with an appropriate choice of an excitation line, OH-LIF is possible with the KrF-laser without interferences with O<sub>2</sub>-LIF for pressures up to 1.2 MPa. The flame, as detected with PLIF, exhibits a conical shape. At 150 kPa conditions, the flame zone does not lie directly on the liquid oxygen core, but is well separated from it. For higher pressure conditions, the expansion angle of the flame cone decreases, and the flame is much more confined to the center line and continues to burn near the surface of the liquid oxygen core. For both high pressure cases, the flame burns more effectively further downstream leading to high OH fluorescence spreading over expanded regions which come in close connection to the liquid oxygen. For these conditions, the averaged images show a confined flame zone lying close to the liquid core. This is in accordance with results from flame visualization experiments in a 10 MPa LOX/GH<sub>2</sub> model combustor [8].

LIF-images as well as DTV results indicate that large-scale fluctuations are present in the flow. The step in the mean value of  $v_x$  at  $x = 7$  cm in figure 7 shows that the mean values of the velocity at a given position may fluctuate from run to run although the injection conditions were rather reproducible and stable from one experiment to another. This is in agreement with the observed spatial structure of the OH-distribution in the wrinkled flame front which varies in intensity and width.



Neither from instantaneous nor from the averaged images is it unambiguously clear that the flame is anchored directly at the outlet of the LOX injector due to the very small OH signal at that location. Spontaneous OH emission, which we ambiguously detected at a combustion pressure of 500 kPa, indicates that the flame begins at the lip of the injector, as has been observed in the LOX/GH<sub>2</sub>-spray at ONERA, Palaiseau [6]. It is therefore assumed that the flame is anchored at the injector, probably due to a recirculation zone between the LOX-post and the H<sub>2</sub>-annular slit.

A comparison of the LIF-images and the light-sheet images showing the distribution of the liquid phase for test case A shows that no or only a small number of droplets are outside the flame cone. Droplets leaving the central LOX-core have not enough momentum to cross the flame front and penetrate into the hydrogen flow.

## 7 Future Work

In further experiments, the DTV measurements will be continued at test cases B and C to complete the data set for comparison with the PLIF data. In the present experiments the LOX- and hydrogen mass flows are injected in a model combustor of a 6cm x 6cm cross section, by far larger than that available for the reactants in a real rocket combustor where they are injected through a matrix of injectors. In further experiments this situation will be approximated by two approaches. First, the micro-combustor will be modified to reduce the cross section by 60%. Second, a triple injector element will be investigated. The cross section available for each injection element will be reduced and the investigation of injector/injector interaction will be possible.

## Acknowledgement

The contribution of A. Cessou is part of the outcome of a one year stay in Lampoldshausen founded by Centre National d'Etudes Spatiales (CNES, France). The work of R. Lecourt is supported by Office National d'Etudes et de Recherches Aerospatiales (ONERA, France).

## References

- [1] Vogel A., 1994. "Investigations on Atomization of a Coaxial Injected H<sub>2</sub>/LOX Jet under Hot Fire Conditions", *Proceedings of ICLASS-94*, Rouen, France, paper VII-8, pp. 742-749.
- [2] Haidn O., Vogel A., Mayer W., Pal S., Gökalp I., Chauveau C., 1995. "Experimental Investigation of Liquid Propellant Spray Combustion", *2nd International Symposium on Liquid Rocket Propulsion*, ONERA-Chatillon, France, June 19-21, 1995.
- [3] Ledoux M., Care I., Micci M., Glogowski M., Vingert L., Gicquel P., 1995. "Atomization of Coaxial-Jet Injectors", *2nd International Symposium on Liquid Rocket Propulsion*, ONERA-Chatillon, France, June 19-21, 1995.
- [4] Pal S., Moser M. D., Ryan H. M., Foust M. J., Santoro R. J., 1993. "Flowfield Characteristics in a Liquid Propellant Rocket", *AIAA 93-1882*, 29th Joint Propulsion Conference and Exhibit, June 28-30, 1993, Monterey, CA.
- [5] Adrian R. J., 1991. "Particle-Imaging Techniques for Experimental Fluid Mechanics", *Annual Review of Fluid Mechanics*, 23, pp. 261-304.
- [6] Brummund U., Vogel A., Oschwald M., Grisch F., Bouchardy P., Pealat M., Vingert L., Candel S., Herding G., Scoufflaire P., Snyder R., Rolon C., 1995. "Laser Diagnostics for Cryogenic Propellant Combustion Studies", *2nd International Symposium on Liquid Rocket Propulsion*, ONERA-Chatillon, France, June 19-21, 1995.

- 
- [7] Quagliaroli T. M., Laufer G., Krauss R. H., McDaniel J. C., 1993. "Laser Selection Criteria for OH Fluorescence Measurements in Supersonic Combustion Test Facilities", *AIAA Journal*, 31, pp. 520-527.
- [8] Mayer W., Tamura H., 1995. "Flow Visualization of Supercritical Propellant Injection in a Firing LOX/GH<sub>2</sub> Rocket Engine", *AIAA 95-2433*, 31st Joint Propulsion Conference and Exhibit, July 10-12, 1995 / San Diego, CA.
- [9] Hopfinger E. J., Lasheras J. C., 1994. "Breakup of a Water Jet in High Velocity Co-Flowing Air", *Proceedings of ICLASS-94*, Rouen, France, paper I-15, pp. 110-117.

## COMMENTS

G. Smeets, ISL, France: Which was the temperature of the injected hydrogen?

Author's Reply: The temperature of the injected hydrogen is similar to the liquid oxygen and is about 100K at the injector exit.

G. Smeets, ISL, France: How was the combustion initiated?

Author's Reply: The combustion was initiated by a pilot flame which was switched off after ignition.

# DIAGNOSTICS OF NON-REACTING AND REACTING SUPERSONIC FLOWS IN A SCRAMJET MODEL COMBUSTOR USING NON-INTRUSIVE SPECTROSCOPIC METHODS

R. Hönig<sup>1</sup>, D. Theisen<sup>2</sup>, R. Fink<sup>2</sup>, G. Kappler<sup>1</sup>, D. Rist<sup>2</sup>, P. Andresen<sup>3</sup>

<sup>1</sup>BMW Rolls-Royce, Eschenweg 11, 15827 Dahlewitz, Germany

<sup>2</sup>Lehrstuhl für Flugantriebe, Technische Universität München, Arcisstr. 21,  
80333 München, Germany

<sup>3</sup>Lehrstuhl für angewandte Laserphysik, Universität Bielefeld, Universitätsstr. 25,  
33615 Bielefeld, Germany

## ABSTRACT

The research on SCRAMJET combustors motivated the work on new non-intrusive measurement approaches to study the flowfield inside a combustor during operation. This was made possible by the development of new powerful laser systems and cameras with high spatial and time resolution. In this paper, we report an investigation of the swept ramp injector concept in a nonreacting as well as a reacting flowfield of a hydrogen-fueled supersonic model combustion chamber. To visualize the structure of the flame and the distribution of  $OH$  and  $O_2$  as well as to determine the averaged temperature and pressure field within the combustor, we used natural fluorescence (without laser excitation) and different laser-induced predissociative fluorescence (LIPF) excitation/detection schemes.

## INTRODUCTION

Research has been conducted for a number of years in several laboratories all over the world, to develop a hydrogen fuelled supersonic combustion ramjet (scramjet) for propelling an aerospace transport system at hypersonic speed [1]. To gain maximum thrust, the most complete fuel-air mixing and fuel chemical energy release must be achieved during the very short residence time within the combustor and, at the same time, losses due to injection, mixing and combustion of the fuel must be kept to a minimum. Therefore a considerable number of advanced injection and mixing techniques [2] have been proposed and investigated in experimental and theoretical studies. Vortex enhanced mixing involves the use of streamwise vortices generated by free stream spilling around an unswept or swept ramp. The technique has been studied in several works [3,4] and significant mixing enhancement was found with greater streamwise vorticity and better mixing for the swept ramp injectors. However, large momentum losses occur with swept ramps.

To overcome the problem of point measurements in turbulent flames and to avoid low Raman signal levels and the very intensive computation for CARS data reduction, two dimensional imaging techniques based on laser-induced fluorescence excitation have been extensively studied during the last years (see e.g. [6]). Although quantification of LIF results is difficult because of quenching problems, the proposed LIF approaches have been applied successfully to a wide range of combustion systems. LIF measurements for scramjet combustor development have mainly been performed in cold flow studies, especially using iodine tracer molecules (LIIF-technique) [6,7], and in the reacting flow of shock tubes [8,9]. The swept ramp injector was studied by Hartfield et al. [7] in a  $Ma = 2.0$  and a  $Ma = 2.9$  nonreacting flow. Injection concentration measurements, conducted in cross flow planes with the LIIF-method, clearly illustrated the domination of the mixing process by streamwise vorticity generated by the swept ramp.

### DETECTION SCHEMES

To perform these measurements with only one experimental setup we used the UV-LFP (UV laser flash photography) approach based on tunable excimer lasers and intensified, gated cameras as discussed by Koch et al. [10]. In general (except for the natural fluorescence) the laser beam is expanded by cylindrical lenses to a lightsheet which crosses the flowfield in the plane of interest. The various subsequent emissions from this area are imaged on a highly sensitive fast gated camera system. Spectral filtering of the emissions and state selective excitation in the case of LIF allows us to determine the structure of the flame and the spatial distributions of  $OH$  and  $O_2$ . Details of the different detection schemes are discussed elsewhere (e.g. [10,11]). In the following section we briefly summarize these approaches.

Spontaneous emission of  $OH$  molecules  $A^2\Sigma^+(v' = 0,1) \rightarrow X^2\Pi(v'' = 1,0)$ , excited by previous collisions or chemical reactions (natural fluorescence), was used to obtain the instantaneous flame structure (reaction zone and post combustion zone) within the combustion chamber. To suppress unwanted emissions from other sources, a Schott UG-11 filter with maximum transmission wave lengths around  $325\text{ nm}$  and a bandwidth of  $100\text{ nm}$  was mounted in front of the camera. The imaging time was  $0.1\text{ ms}$ .

For species and quantum state selective detection with the laser-induced fluorescence approach the pulsed excimer laser has to be tuned in order to resonantly excite a particular electronic transition of a molecular species present in the flow. The excited molecules may undergo subsequent processes like stimulated emission, rotational, vibrational and electronic energy transfer, predissociation and a fraction of the laser-populated upper state decays by spontaneous emission of a photon from the upper to a lower energy level. Assuming weak excitation of an isolated transition and fluorescence emission into  $4\pi$  steradians, the resulting temporally integrated signal on the CCD array is given by

$$N_p = q_{DET} \frac{\Omega}{4\pi} n x_i f_{osc}(T) V_c g B_{12} E_v \left( \frac{A_{21}}{A_{21} + Q_2 + P_2} \right) \quad (1)$$

where  $N_p$  is the number of photoelectrons of the detector,  $q_{DET}$  the overall efficiency of the detector (e.g. transmission efficiency of the collecting optics and quantum efficiency of the photocathode),  $\Omega$  is the collection solid angle and  $n$  is the total gas number density.  $f_{v',j'}(T)$  is the Boltzmann population fraction of the absorbing state and  $x_i$  is the mole fraction of the absorbing species  $i$ .  $V_c$  is the collection volume. The overlap between laser and absorbing transition is described by the overlap integral  $g$ , while  $A_{21}$ ,  $B_{12}$  are the Einstein rate coefficients.  $E_v$  is the spectral laser pulse energy,  $Q_2$  is the total quenching rate and  $P_2$  is the rate of predissociation which has to be taken into account if repulsive upper states cause dissociation of the excited molecules. If the predissociation rate dominates the fluorescence yield  $\Phi = (A_{21} / (A_{21} + Q_2 + P_2))$ , the fluorescence signal can be assumed to be unaffected by collisions within a certain pressure range [11]. Therefore, the signal  $N_p$  is proportional to the quantum state specific number density  $n_i$  of the excited molecules.

The temperature can be determined from the relative Boltzmann fractions in the ground electronic state by exciting two transitions from different ro-vibrational states within the same electronic system and calculating the fluorescence ratio  $R_{12} = N_{p,1} / N_{p,2}$  and the temperature on a pixel by pixel basis.

$$T = - \frac{E_1(v'', J'') - E_2(v'', J'')}{k \ln(R_{12} / C)} \quad (2)$$

Implicit is the assumption that the primary temperature dependence results from the Boltzmann fractions and that the various spectroscopic terms are independent from  $T$  and can be summarized with other optical parameters by a constant  $C$ .

In case of a spatial and temporal constant oxygen mole fraction (as given for the nonreacting flow without hydrogen injection), the pressure can be calculated on a pixel by pixel basis by rearranging equation (1) and using the equation of state for perfect gases to express the total number density  $n$ .

$$p = C' \frac{S_{LIPF} \cdot T}{f(T)} \quad (3)$$

$S_{LIPF}$  is the measured fluorescence signal in [counts] when exciting a singular oxygen quantum state,  $T$  is the temperature calculated from equation (2) and  $C'$  is a calibration constant which summarizes all constant optical, spectroscopic and setup parameters. The Boltzmann population fraction  $f(T)$  of the absorbing state can be calculated from known spectroscopic parameters and the previously calculated temperature.

### Hydroxyl Radical

Laser-induced fluorescence of OH is performed using 248 nm KrF-excimer-laser light to excite the strongest line within the tuning range,  $A^2\Sigma^+(v'=3) \leftarrow X^2\Pi(v''=0)$ ,  $P_1(8)$ . The excited molecules predissociate with the rate  $P \approx 10^{10} s^{-1}$  [12] whereas the quenchrate at atmospheric

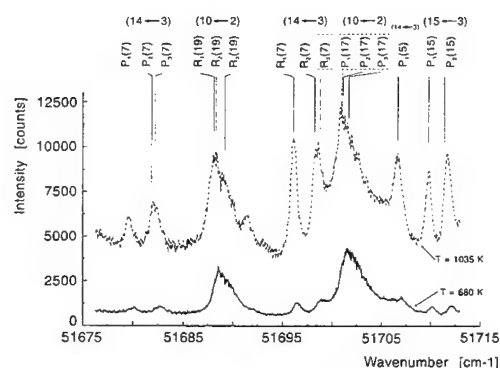
pressure is about  $Q \approx 0.5 \cdot 10^9 \text{ s}^{-1}$  [13-14]. Therefore only 5% of the excited molecules are influenced by quenching and the OH-LIPF signal can be considered "quench-free" at atmospheric pressure. An additional advantage of the probed  $v'' = 0, J'' = 8$  state is that its population fraction shows only a small temperature dependance within typical flame conditions. The upper state fluorescence was detected via a broadband Schott UG-11 transmission filter. Subsequent studies showed that it is better to detect only the fluorescence via the (3-2) band to keep the systematic error low which is caused by vibrational energy transfer in the excited state to non-predissociative levels ( $v' = 2, 1$ ).

## Oxygen

Laser-induced fluorescence of  $O_2$  is performed using the 193 nm ArF-excimer-laser light to excite several transitions within the Schumann-Runge band system  $B^3\Sigma_u^- - X^3\Sigma_g^-$ . The B-state of  $O_2$  is subject to significant predissociation with lifetimes for  $v' = 0-19$  and  $J' = 0-20$  varying from 1.4 - 48 ps [15] so that again quenching effects can be neglected in these measurements. To obtain the averaged temperature due to the described two-line approach, we excited successively the transitions  $v' = 10 \leftarrow v'' = 2, P_2(17)$  and  $v' = 14 \leftarrow v'' = 3, R_3(7)$ . Of course, implicit in the described approach is the limitation that excitation from  $v'' = 2$  and  $v'' = 3$  detects only "hot" oxygen molecules; but as Koch [10] pointed out, this is still possible at temperatures as low as 600 K and pressures of 200 mbar. The imaging of the  $O_2$  emissions, which are strongest around 200 to 250 nm, was done via two 45° dielectrically coated mirrors with high reflectivity (> 90%) at 210 nm and a bandwidth of about 20 nm. Another 0° mirror with high reflectivity at 193 nm was mounted in front of the UV lens to block diffusely scattered light and Rayleigh scattering originating from the flame.

## Calibration

As previously outlined, the two-line approach follows the idea to compare the population density of two singular quantum states and to calculate the temperature from the density ratio via the Boltzmann equation. Consequently, line ratios at known temperatures have to be measured in a reference object which simulates the expected temperature range of the object under investigation, to calibrate the measurement and to determine the constant  $C$  from equation (2). For the nonreacting flow studies, a hot fan and a heated cell ( $600 \text{ K} \leq T \leq 1100 \text{ K}$ ) were used as calibration objects. To get the line ratios, numerous oxygen excitation spectra like those shown in Fig. 1 were recorded. In Fig. 1, it can clearly be seen that the line ratio of the transitions  $v'' = 2, P(17)$  and  $v'' = 3, R(7)$  varies by 400 to 500% with increasing temperature from 680 K to 1035 K. Consequently, the temperature sensitivity of this line pair is quite high. The obtained accuracy of the calibration measurement was 3.5% when averaged over 5 lasershots.



**Figure 1.** Oxygen excitation spectrum within the Schumann-Runge band system  $B^3\Sigma_u^- - X^3\Sigma_g^-$  by LIPF at 193 nm (ArF-laser) at a pressure of 1 bar and a temperature of 680 K and 1035 K.

To set the pressure measurement on an absolute scale the calibration constant  $C'$  in equation (3) has to be determined. Therefore, the pressure has to be known at a certain point within the measurement field, e.g., by a measurement with an independent technique. Otherwise, equation (3) has to be normalized to give the relative pressure distribution. To perform the described *in situ* calibration in the nonreacting flow studies we used the inactive hydrogen injection nozzle to determine the static pressure behind the ramp.

## EXPERIMENTAL APPARATUS

### Model Combustion Chamber

A complete schematic of the scramjet model combustor is given in Fig. 2. Flow is from left to right. Vitiated air ( $T_i = 1375$  K,  $p_i = 6.7$  bar) expands in a two dimensional Laval-nozzle and enters the combustor at a Mach number of  $Ma = 1.9$ , a static temperature of  $T = 850$  K and a static pressure of 0.96 bar. The rectangular combustor consists of an exchangeable injection module and a  $3^\circ$  divergent expansion duct, both with optical access from all sides at different axial locations. The complete structure is uncooled, which limited the burning time of the combustor to about 15 seconds. Details of the injection module and the swept ramp are shown in Fig. 3. The geometry of the ramp is similar to that described in reference [3] (ramp angle:  $\varphi = 11^\circ$ , ramp width at the end of the injector block:  $b = 10$  mm), but the injector nozzle, which is integrated in the ramp, can be replaced to investigate different injection Mach numbers. In all experiments reported in this paper hydrogen was injected at a Mach number of  $Ma_{H_2} = 1.6$ , but the total hydrogen pressure  $p_{t,H_2}$  has been varied from  $4.5 \leq p_{t,H_2} \leq 35$  bar to vary the expansion ratio as well as the equivalence ratio.

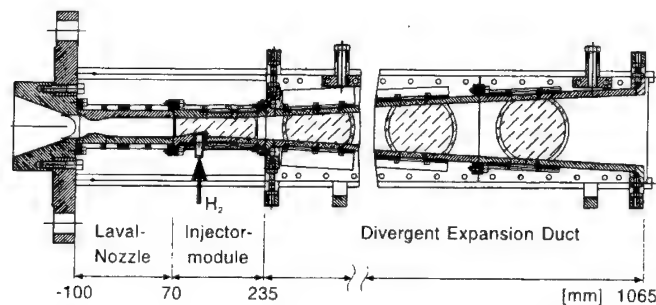


Figure 2. Schematic of the scramjet model combustion chamber.

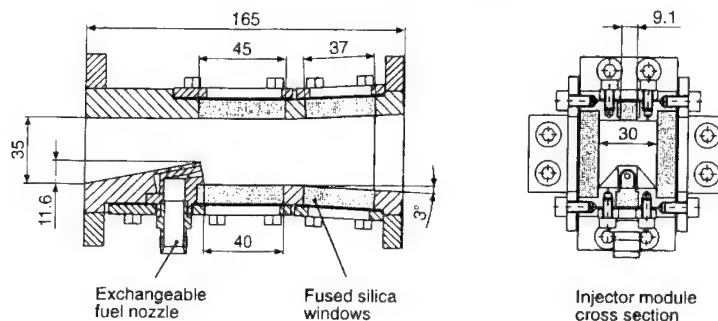


Figure 3. Schematic of the injector module with the swept ramp and the exchangeable fuel injector nozzle.

### LIF / LIPF Setup

Figure 4 shows a schematic of the LIF/LIPF arrangement used for two dimensional concentration and temperature measurements. A tunable excimer laser (1), (Lambda Physik EMG 150 T-MS-C) is used to produce a  $25 \times 5 \text{ mm}$  laser beam (2) at the ArF-transitions ( $\sim 193 \text{ nm}$ ) or the KrF-transitions ( $\sim 248 \text{ nm}$ ). The pulse duration is  $20 \text{ ns}$  and its energy is about  $110 \text{ mJ}$  in the ArF mode and  $250 \text{ mJ}$  in the KrF mode. The beam passes a calibration section (3-4), some plane mirrors (5), cylindrical lenses to form the laser sheet (6), an adjustable slit (7)  $0.5$  to  $2 \text{ mm}$  wide and  $25 \text{ mm}$  in length and finally enters the test section as a sheet with the slit dimensions. The laser sheet passes through the combustion chamber (8) from bottom to top or vice versa, to get additional information of laser beam absorption. The induced light emissions from the area of interest (see shaded area in Fig. 4) leave the test section through the side windows. The light emissions to be imaged are, if necessary, filtered with a combination of dielectrically coated mirrors (9), (see chapter "detection schemes") and additional transmission filters (9), to reduce scattered light at the laser wavelength. The two-dimensional fluorescence distributions are imaged onto a photometric digital camera (11) (LaVision Flamestar II), via a  $105 \text{ mm f}/\#4.5$  Nikkor UV lens (10). The Flamestar camera system consists of an UV sensitive high gain image intensifier (S20 photocathode,



P20 phosphor) fibroptically coupled with the CCD-chip (Thomson TH7863). The intensifier is gated for 50 to 500 ns after each laser pulse to suppress unwanted natural fluorescence. The resulting grayscale pictures are digitized, stored in a computer (12) and presented in false colors on an online monitor. Triggering of the laser and the photometric cameras as well as controlling the stepmotor to tune the laser frequency is done by a programmable input/output card of the system computer and an external camera multiplexer (13).

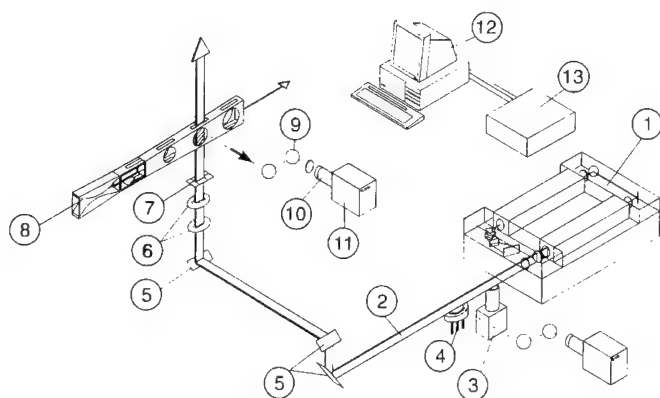


Figure 4. Overall schematic of the LIF setup for two dimensional imaging.

For measurement of spatial, state-selective density distributions of  $O_2$  and  $OH$  in the reacting flowfield of the combustion chamber fluorescence images at three different locations along the central plane and in selected cross sections of the chamber were recorded. "Cross-sectional" images were obtained by orienting the laser sheet perpendicular to the flow direction. The image was viewed through the same side window through which the light sheet passed. The viewing angle of the camera was set to  $35^\circ$  relative to the plane of the laser sheet. Distortion of the aspect ratio of the images was corrected by a horizontal spreading of the digitized images. To realize a short overall measurement time, the laser beam forming optics together with the complete detection system are mounted on a movable device, driven by a computer controlled stepmotor. One set of pictures was recorded with the laser on-resonance, the other at off-resonance condition. The off-resonance pictures were subtracted from the on-resonance ones. Laser beam profile correction was done for all images. Typical on/off-resonance ratios are in the order of 2.5 to 4.5 depending on the flame zone and the species under investigation. No attempt was done to correct the images for the Beer's law absorption of the laser beam within the combustion chamber.

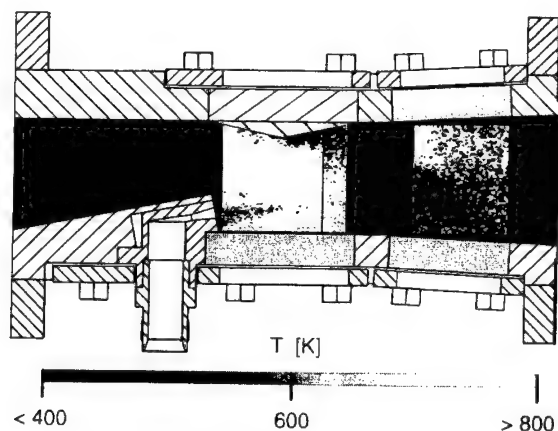
## RESULTS AND DISCUSSION

All images printed in this paper are presented in gray scale pictures with intensity levels according to the scale given beneath the image. The pictures are recorded with 12-bit accuracy (0 - 4095

counts) and a chosen intensity range is displayed in 64 gray levels. Lower and higher intensities are grouped together to one color (black or white).

### Nonreacting flow studies

To provide data for comparison and validation of CFD-calculations, non-intrusive quantitative temperature and pressure measurements in the nonreacting flowfield were performed with the approaches described in the previous sections of this paper. The obtained averaged temperature distribution for the flowfield with hydrogen injection, but without combustion, is given in Fig. 5.



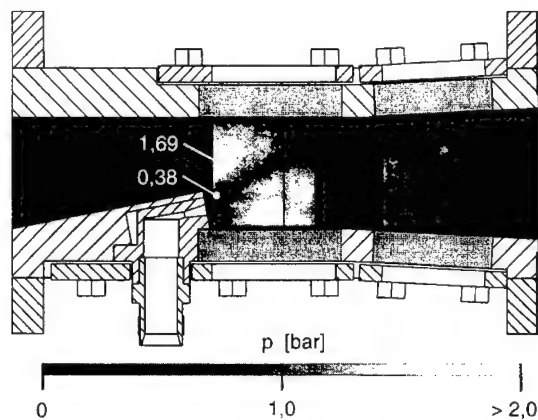
**Figure 5.** Temperature distribution in the central vertical plane of the flow with hydrogen injection ( $p_{0, H_2} = 30 \text{ bar}$ ,  $\phi = 0.5$ ) but without combustion. The temperature is calculated from the relative Boltzmann fractions in the ground electronic state of oxygen by exciting successively the transitions  $v' = 10 \leftarrow v'' = 2$ ,  $P_2(17)$  and  $v' = 14 \leftarrow v'' = 3$ ,  $R_3(7)$  within the Schumann-Runge band system  $B^3\Sigma_u^- - X^3\Sigma_g^-$  by LIPF at  $193 \text{ nm}$ . The temperature is encoded according to the gray scale given beneath the image.

Maximum static temperatures are found close to the wedge, where the boundary layer is thick or has separated from the upper wall. The temperature of the air flow decreases from top to bottom by about  $200 \text{ K}$  because of the expansion behind the ramp. Close to the injector the black region marks the pure hydrogen jet or mixing regions with very little oxygen concentrations where no temperature could be measured. The temperature decrease behind the wedge, caused by the flow expansion, is clearly visible in Fig. 5, but can not be quantified with this approach, because the population density of the used  $v'' = 3$  vibrational state is too low at temperatures below  $600 \text{ K}$  to give sufficient signal to noise ratios. Consequently, at points within the measurement field with S/R-

ratios below 1.5, no temperature calculation has been performed and the value of these pixels was set to zero. A temperature measurement is possible again further downstream, where the temperature increase caused by the oblique compression shock becomes visible in the right portion of the measurement area.

To demonstrate the feasibility of nonintrusive, two dimensional pressure measurements in the nonreacting supersonic flow without hydrogen injection and wedge, the temperature field was determined (different from that in Fig. 5) with the two-line approach. Then this temperature information was used to calculate the two-dimensional distribution of the Boltzmann population fraction for one of the two excited oxygen quantum states on a pixel by pixel basis. Finally the Boltzmann population fraction distribution, the corresponding measured oxygen number density image and the temperature field were used to calculate the pressure distribution from equation (3). The result of this evaluation process for the combustor configuration without wedge is given in Fig. 6.

An analysis of Fig. 6 shows that several essential gasdynamical features of the supersonic flowfield can be found in the pressure distribution. First, flow expansion behind the ramp is accompanied by a decrease of the static pressure from about 1.69 bar to about 0.38 bar. Geometry of the Prandtl-Meyer-expansion (angle of the first and the end-characteristic) can be estimated from the image. Second, maximum pressure is found in an area 15 mm downstream of the ramp, where the supersonic flow due to the converging duct is getting slower accompanied by a static pressure rise. Finally as the flow slightly expands in the 3° divergent section of the injector module, an additional small pressure decrease can be found in the streamwise flow direction.



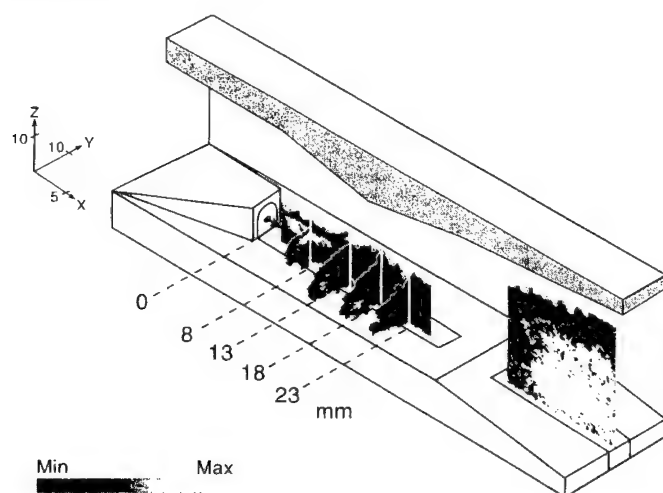
**Figure 6.** Static pressure distribution in the central vertical plane of the flow within the model combustor without wedge and without hydrogen injection. The pressure is encoded according to the gray scale given beneath the image.

## Reacting flow studies

To improve the ignition process, a small wedge was mounted at the top of the injection module to realize a "shock induced ignition". Due to the static temperature rise across the shock induced at the end of the wedge, the flame could be ignited and stabilized over a wide range of equivalence ratios ( $0.07 \leq \Phi \leq 0.6$ ).

The model combustor was equipped with an exchangeable injection module with a swept ramp as described earlier. This ramp induces a pair of counterrotating swirls which transport the injected hydrogen from the center-axis plane towards the side walls of the combustion chamber. To study this three-dimensional hydrogen-air mixing process, fuel concentration profiles had to be determined in axial as well as in cross-sectional planes. As one of the most important reaction intermediates,  $OH$  was chosen to indicate the combustion zone due to the fact that the imaging of hydrogen with this setup was not possible. The  $OH$  distribution in the central-axis plane of the flow as well as in four cross-sectional planes was recorded with LIPF and combined to a three-dimensional map of the flame, shown in Fig. 7.

By looking at the distribution of the  $OH$  radicals in the measuring planes 8, 13, 18 and 23 mm downstream of the injection point, the dominant influence of the induced swirls on the flame can be seen. After  $x=13$  mm, the flame fills the width of the injection module and is extinguished by the expansion behind the wedge at about  $x=23$  mm. Downstream, the flame is relighted by the recompression shock structure from the wedge. In this part of the model combustor, the flame nearly fills the total height. This sudden expansion of the flame after a shock/shear-layer interaction is also found in the work of Menon [16] and shows that the oblique shock impinges on the mixing boundary layer and enhances its spreading.



**Figure 7.** Spatial flame structure within the model combustor indicated by the distribution of the  $OH$  molecules ( $p_{O_2/H_2} = 29.5$  bar,  $\phi = 0.48$ ). The images are averaged over 50 lasershots. The emission intensities are encoded according to the gray scale given beneath the image.

## CONCLUSIONS

The investigation of the nonreacting and reacting flowfield of a scramjet model combustor with swept ramp injector by nonintrusive two-dimensional fluorescence measurements can be summarized as follows:

1. Quantitative, two-dimensional, averaged temperature and pressure distributions achieved by sequential excitation of two ro-vibronic states of  $O_2$  allow a detailed study of the gasdynamical features of the nonreacting flowfield within the model combustor.
2. The structure of the supersonic hydrogen-air diffusion flame, characterized by the spatial hydroxyl radical distribution, is dominated by the vortical induced mixing process, generated by the three-dimensional flow around the swept ramp.
3. Mixing can be further improved by a shock/shear-layer interaction.

## ACKNOWLEDGMENT

This research was supported by the Deutsche Forschungsgemeinschaft under responsibility of the Sonderforschungsbereich 255. The authors wish to thank Dr.-Ing. M. Valk now at ABB Baden / Switzerland, for his assistance in preparing and performing these experiments.

## REFERENCES

1. Billig, F.S., 1993. "Research on Supersonic Combustion," *Journal of Propulsion and Power*, Vol. 9:4, pp.499-514.
2. Bogdanoff, D.W., 1994. "Advanced Injection and Mixing Techniques for Scramjet Combustors," *Journal of Propulsion and Power*, Vol. 10:2, pp.183-190.
3. Northam, G.B., Greenberg, J., Byington, C.S., 1989. "Evaluation of Parallel Injector Configurations for Supersonic Combustion," *AIAA/ASME/SAE/ASEE 25th Joint Propulsion Conference*, Monterey, CA, AIAA-89-2525.
4. Drummond, J.P., Carpenter, M.H., Riggins, D.W., Adams, M.S., 1989. "Mixing Enhancement in a Supersonic Combustor," *AIAA/ASME/SAE/ASEE 25th Joint Propulsion Conference*, Monterey, CA, AIAA-89-2794.
5. Hanson, R.K., 1986. "Planar Imaging Techniques," *Twenty-first Symposium (International) on Combustion*, The Combustion Institute, Pittsburgh, PA, pp.1677-1691.
6. Hartfield Jr., R.J., Hollo S.D., McDaniel J.C., 1990. "Planar Measurement of Flow Field Parameters in a Nonreacting Supersonic Combustor using Laser-Induced Iodine Fluorescence," *28th Aerospace Science Meeting*, Reno, NV, AIAA 90-0162.

7. Hartfield Jr., R.J., Hollo S.D., McDaniel J.C., 1990. "Experimental Investigation of a Supersonic Swept Ramp Injector using Laser-Induced Iodine Fluorescence," *AIAA 21st Fluid Dynamics, Plasma Dynamics and Laser Conference*, Seattle, WA, AIAA 90-1518.
8. Allen, M.G., Parker, T.E., Reinecke, W.G., Legner, H.H., Foutter, R.R., Rawlings, W.T., Davis, S.J., 1992. "Instantaneous Temperature and Concentration Imaging in Supersonic Air Flow Behind a Rear-Facing Step with Hydrogen Injection," *30th Aerospace Sciences Meeting*, Reno, NV, AIAA 92-0137.
9. McMillin, B.K., Palmer, J.L., Seitzman J.M., Hanson, R.K., 1993. "Two-line Instantaneous Temperature Imaging of NO in a SCRAMJET Model Flowfield," *AIAA 31st Aerospace Sciences Meeting*, Reno, NV, AIAA-93-0044.
10. Koch, A., Chrysosostomou, A., Andresen, P., Bornscheuer, W., 1993. "Multi Species Detection in Spray Flames with Tunable Excimer Lasers," *Applied Physics B* 56, pp.165-176.
11. Andresen, P., Meijer, G., Schlüter, H., Voges, H., Koch, A., Hentschel, W., Oppermann, W., Rothe, E., 1990. "Fluorescence imaging inside an internal combustion engine using tunable excimer lasers," *Applied Optics*, Vol. 27:2, pp. 2392-2404.
12. Gray, J.A., Farrow, R.L, 1991. "Predissociation Lifetime of OH  $A^2\Sigma^+(v'=3)$  Obtained from Optical-Optical Double-Resonance Linewidth Measurements," *Journal of Chemical Physics* 5:10, pp. 7054-7060.
13. Schwarzwald, R., Monkhouse, P., Wolfrum, J., 1987. "Picosecond Fluorescence Lifetime Measurement of the OH Radical in an Atmospheric Pressure Flame," *Chemical Physics Letters*, Vol. 142:1/2, pp. 15-18.
14. Köller, M., Monkhouse, P., Wolfrum, J., 1990. "Time Resolved LIF of OH ( $A^2\Sigma^+, v'=1$  and  $v'=0$ ) in Atmospheric-Pressure Flames using Picosecond Excitation," *Chemical Physics Letters*, Vol.168:3/4, pp. 355-360.
15. Kim, G.S., Hitchcock, L.M., Rothe, E.W., Reck, G.P., 1991. "Identification and Imaging of Hot  $O_2(v''=2,3$  or  $4$ ) in Hydrogen Flames using 193 nm - and 210 nm Range Light," *Applied Physics B* 53, pp. 180-186.
16. Menon, S., 1989. "Shock-Wave-Induced Mixing Enhancement in Scramjet Combustors," *AIAA 27th Aerospace Sciences Meeting*, Reno, NV, AIAA-89-0104.

#### COMMENTS

G. Smeets, French-German Research Institute of Saint-Louis, France: Which was the static temperature of the air at the entrance of the combustor?

Author's reply: The air enters the combustor at a static temperature of  $T=900K$ .

## GAS TEMPERATURE MEASUREMENTS IN A FLAT FLAME

### BY TUNABLE DIODE LASER SPECTROSCOPY

by M. Charpenel, C. Brossard

ONERA, Energetics Department, Fort de Palaiseau, 91120 Palaiseau, France

**ABSTRACT** Due to their very fine spectral linewidth, lower than  $10^{-3} \text{ cm}^{-1}$ , tunable infrared diode lasers offer the opportunity to explore the whole absorption line profile of a chemical species, even for very narrow lines existing in low-pressure environments. Therefore, its temperature and absolute density, averaged along the laser beam path, can be calculated, if the molecular properties are known, by using the Beer-Lambert law of radiation absorption. In this investigation, the Tunable Diode Laser Spectroscopy (TDLS) technique was applied to measure the temperature profile in a one-dimensional, low-pressure (5700 Pa), premixed  $\text{H}_2/\text{CO}/\text{O}_2/\text{Ar}$  flat flame. For this purpose, a pair of two spectrally adjacent absorption lines of carbon monoxide was used. The concentration profile of this species could then also be deduced from the measurements.

To achieve high accuracy in the temperature measurement, the difference between the values of the lower energy level for the two selected rovibrational transitions should be as high as possible. In order to satisfy this condition, as well as to provide a sufficient absorption in the broad range of temperature investigated (400 - 1400 K), the pair of two adjacent lines 1-2 P(35) and 0-1 P(40) of carbon monoxide, respectively located at 1963.6607 and 1963.7290  $\text{cm}^{-1}$ , was chosen. One of the major TDLS problems, the Fabry-Pérot effects due to lens reflection, was avoided by using an optical setup based on metallic mirrors instead of lenses. This optical arrangement allowed a 2 mm measurement spatial resolution along the burner axis. This value was shown to cause a temperature overestimation by only 5 % in the lower and also steeper part of the profile.

The highest measured temperature was 1420 K, at a location of about 2.5 cm above the burner surface. The level of temperature in the experimental profile was lower than in the theoretical profile. This was attributed to the cooling effect caused by both two-dimensional heat transfer and radiation heat losses from the flame. These effects were not accounted for in the theoretical model. The analyzed pair of absorption lines provided accurate temperature measurements ( $\pm 3.7 \%$ ) in the whole axial flame profile, but the absorption level was insufficient to allow the measurement of the CO concentration in the lower part of the profile.

### 1. INTRODUCTION

Tunable infrared Diode Lasers provide the means to perform extremely high resolution absorption Spectroscopy (TDLS) on a wide variety of molecules, and to measure their absolute density averaged along the laser beam pathlength. Because it is quite simple to use, this technique is attractive in

many remote sensing applications, especially in combustion environments, and has been used for several years [1-4].

A diode laser is a semi-conductor element based on a lead salt, such as  $\text{Pb Sn}(x) \text{Te}(1-x)$ , whose nature and composition ( $x$ ) both determine the working spectral range of the diode. The emission wavelength for the currently available infrared diode lasers ranges from 3 to 30  $\mu\text{m}$  (or 300 to 3000  $\text{cm}^{-1}$  in terms of the wavenumber range). For a given diode laser, the tuning interval of the emission wavenumber is about 40  $\text{cm}^{-1}$ . This tuning is obtained via the polarization current strength variation, which produces a responding variation of the diode temperature. The laser emission composes of several modes, separated by 1 to 2  $\text{cm}^{-1}$ , whose power output varies between 100 and 500 microwatts. The most important feature of these modes is a very fine spectral linewidth, lower than  $10^{-3} \text{ cm}^{-1}$ . For comparison, the spectral resolution of a classical spectrometer is about  $10^{-1} \text{ cm}^{-1}$ . This feature offers the opportunity to explore the whole absorption line profile, even for very narrow ones existing in low-pressure environments. Therefore, by using the Beer-Lambert law of radiation absorption, the density of the absorbing species can be calculated if the following parameters are known: 1. the line strength at a reference temperature, 2. the laser beam pathlength across the flame, and 3. the gas temperature.

In this paper, the experimental setup and the data reduction and analysis are described, and some of the results obtained by Brossard are reported [3]. The TDLS technique was applied to measure the temperature profile in a one-dimensional, low-pressure (5700 Pa), premixed  $\text{H}_2/\text{CO}/\text{O}_2/\text{Ar}$  flat flame. For this purpose, a pair of two spectrally adjacent absorption lines of carbon monoxide was used. The concentration profile of this species could then also be deduced from the measurements.

The burner setup, briefly described below, provided a stable and reproducible experimental configuration. It was also equipped with a probe sampling mass spectrometer, in order to measure the different stable species concentration profiles. Some of the results obtained by this technique for carbon monoxide concentration are included in this paper for comparison with the TDLS results. The complete results for all species are reported in [3].

## 2. FLAT-FLAME BURNER SETUP AND FLAME FEATURES

The flat-flame burner consists of a cylindric 35 mm in diameter bundle of 90 mm long stainless steel tubes (1 mm internal diameter). The bundle is surrounded by a sintered porous bronze shroud ring of 10 mm width. This ring was used to provide a surrounding argon flow, in order to isolate the flame from the burnt gases flow inside the burner chamber and to limit the edge effects on the flame. The value of the argon flow velocity was chosen at the value of the flame cold unburnt gases velocity at the burner surface. The burner was enclosed in a low-pressure cylindrical chamber made of "Altuglas" material (475 mm height, 18.4 mm thickness and 396 mm internal diameter). The burner could be translated vertically along its axis on a 100 mm distance, thus avoiding any displacement of the optical setup when a flame profile was being investigated. The passage of the infrared diode laser beam was obtained by two opposite fluorspar windows. These windows were located very close to the burner (80 mm distance between the two windows), in order to avoid any undesirable absorption along the laser beam optical pathlength across the burnt gases flow inside the chamber.

The value of the cold unburnt gases mixture mass flowrate was  $7.7 \times 10^{-2} \text{ g.s}^{-1}$  at a chamber pressure of 5700 Pa. The following composition (in mole fraction) of this mixture was chosen to simulate the composition of the combustion products of a homogeneous propellant:



H <sub>2</sub>	CO	O <sub>2</sub>	Ar
0.1143	0.1820	0.1400	0.5637

Argon was chosen for the diluent species instead of nitrogen, in order to increase the flame temperature, and to simplify the reaction mechanism involved in the investigated flame by avoiding the production of nitrogen oxides.

### 3. CO ABSORPTION SPECTROSCOPY

In this investigation, the diode laser was used as an energy source, whose absorption by gaseous carbon monoxide was analyzed. The spectral resolution of the laser emission allowed an accurate record of the whole absorption line spectral profile. In the infrared spectrum, the absorption lines correspond to rovibrational energy transitions. Information on the temperature is mainly contained in the strength of the absorption line. Assuming a Maxwell-Boltzmann distribution, i.e the molecules are in thermal equilibrium at the temperature T, the ratio of the areas A1 and A2 respectively of two absorption lines 1 and 2 observed simultaneously, and centered in spectral positions very close to one another, is given by:

$$\frac{A_1}{A_2} (T) = \frac{S_1}{S_2} (T) = \frac{S_1}{S_2} (T_s) [ \alpha (T_s) - \alpha (T) ] \quad (1)$$

where S is the line strength, and T<sub>s</sub> is a reference temperature.

$\alpha (T)$  is the temperature sensitivity factor defined by:

$$\alpha (T) = \exp \left( - \frac{E''_1 - E''_2}{kT} \right) \quad (2)$$

where E'' is the lower energy level of the transition, and k is the Boltzmann constant.

Equation (1) can be used to deduce the temperature T from the experimental record of the spectral profiles of the two transmission lines, the values of the line strengths at the reference temperature S<sub>1</sub>(T<sub>s</sub>) and S<sub>2</sub>(T<sub>s</sub>) being known. This method is named the "two lines method" [1-5].

Once the temperature T is determined by this method, the strength of one of these lines for this temperature can be calculated, by using the Maxwell-Boltzmann distribution law. The value of the mole fraction X of the absorbing species (carbon monoxide in this investigation) can then be deduced from the relation:

$$A (T) = X P S (T) \quad (3)$$

Relation (3) expresses the proportionality of the absorption line area with the line strength, the mole fraction X and the pressure P.

In practice, it is more accurate to calculate, thanks to a least-squares method, the theoretical

spectrum of the two absorption lines corresponding to the experimental spectrum, by adjusting the temperature and concentration to be identified. The application of this method requires the knowledge of input data for the Lorentz collisional broadening coefficients, in order to calculate the value of  $\alpha_L$ , the Lorentz Half-Width at Half-Maximum (HWHM) broadening. This broadening is given by:

$$\alpha_L(T) = \sum_k \alpha_{L,k}^R X_k P (T_r / T)^{\gamma_k} \quad (4)$$

where:  $\alpha_{L,k}^R$  is the Lorentz HWHM per pressure unit, at the reference temperature  $T_r$ , due to the broadening by the species  $k$ ;  $X_k$  is the mole fraction of the species  $k$ ;  $\gamma_k$  is the temperature dependence factor.

However, the exact values corresponding to the broadening by the stable species existing in the flame gases ( $H_2$ ,  $O_2$ ,  $H_2O$ ,  $CO_2$  and Ar) are still uncertain. The values available in the literature reveal a significant scatter, especially for the temperature dependence factor, for which only a few references were found. The values used in this investigation are given in table 1 [3, 6-14]. For each measurement height location above the burner surface, the values of the species mole fractions in the relation (4) were set to the values calculated by an aerothermochemical code [15].

**Table 1**  
Values of Lorentz broadening coefficients used ( $T_r = 300$  K) [3].  
 $J$  is the lower rotational level in the transition

	$O_2$	$H_2O$	$CO_2$	$H_2$	Ar	CO
$\alpha_{L,k}^R$ ( $10^{-3} \text{ cm}^{-1} \cdot \text{atm}^{-1}$ ) $J = 35$	41.8	36.9	37.4	63.14	29.87	40.32
$\gamma_k$ $J = 35$	0.545	0.580	0.5	0.5	0.6	0.6
$\alpha_{L,k}^R$ ( $10^{-3} \text{ cm}^{-1} \cdot \text{atm}^{-1}$ ) $J = 40$	39.7	82.1	35.0	61.66	26.66	36.10
$\gamma_k$ $J = 40$	0.515	0.577	0.440	0.5	0.6	0.6

#### 4. CHOICE OF THE PAIR OF CO ABSORPTION LINES

To achieve high accuracy in the temperature measurement, the most appropriate pair of absorption lines has to be determined. The following selection criteria were applied [4-5]:

- \* The value of the spectral interval separating the two line central positions should be optimized. On the one hand, it should be lower than  $1 \text{ cm}^{-1}$ , so that the two lines could be recorded on the same diode emission mode. On the other hand, it should exceed the linewidth in order to avoid lines overlapping.

- \* The absorption line strength should be sufficient for each of the two lines in the temperature range investigated.
- \* The spectrum should not include any atmospheric water absorption line in the vicinity. Such lines are very wide and could overlap the analyzed lines.
- \* The difference between the values of the lower energy level for the two selected rovibrational transitions should be as high as possible, in order to increase the temperature measurement accuracy. A criterion suggested by Ouyang and Varghese is that the temperature sensitivity factor  $\chi(T)$  should be greater than 1 [5].

The proper choice is difficult, since it depends on the measured values, which are initially unknown. The characteristics of six pairs of lines fitting the selection criteria are given in table 2. The percentage of absorption in CO/air mixtures at  $P = 5000$  Pa was calculated at the line center wavenumber  $\sigma_0$  for three different temperature levels: 500 K, 1000 K and 2000 K. A lower value of the CO mole fraction was used for 2000 K, in order to simulate the combustion of CO in the flame. The spectroscopic data for CO were obtained from the data bases available at the Physics Department of ONERA [2]. The absorption line strengths are known with an accuracy of about  $\pm 3\%$  [16]. The three pairs of lines centered at a wavenumber greater than  $2000\text{ cm}^{-1}$  exhibit a better measurement sensitivity at high temperatures (higher values of  $\chi(T)$ ). However, these absorption lines are based on the vibration level 2; therefore, their absorption level becomes very weak at low

**Table 2**

Comparison of six pairs of CO lines characteristics. Absorption level calculated in CO/air mixtures at  $P = 5000$  Pa [3]

Pair Number	Lower Vibrational Level	Line center Wavenumber $\sigma_0$ ( $\text{cm}^{-1}$ )	Lower Energy Level of Transition $E^*$ ( $\text{cm}^{-1}$ )	Temperature Sensitivity Factor $\chi(1500\text{ K})$	Temperature Sensitivity Factor $\chi(2000\text{ K})$	Absorption Level at $\sigma_0$ (%)		
						$X_{\text{CO}} = 0.14$ $T = 500\text{ K}$	$X_{\text{CO}} = 0.14$ $T = 1000\text{ K}$	$X_{\text{CO}} = 0.01$ $T = 2000\text{ K}$
1	0	1953.4496	3452.1573	1.302	0.977	0.761	22.7	2.78
	1	1953.7452	4809.6553			0.251	5.66	1.84
2	0	1958.6038	3292.4744	1.321	0.991	1.18	27.9	3.05
	1	1958.7178	4669.9210			0.0885	6.76	1.99
3	0	1963.7290	3136.5105	1.340	1.005	1.80	34.2	3.34
	1	1963.6607	4533.8993			0.479	7.98	2.13
4	1	2034.1355	2942.3033	1.644	1.233	3.18	45.5	3.88
	2	2034.4086	4656.1731			0.0240	4.05	1.18
5	1	2038.5827	2866.2980	1.666	1.250	3.76	48.3	3.90
	2	2038.6253	4603.3896			0.0260	4.06	1.15
6	1	2042.9977	2794.0748	1.688	1.266	4.39	50.9	3.90
	2	2042.8089	4554.3678			0.0276	4.03	1.10

temperatures. This property could exclude the opportunity to measure the complete temperature profile. Consequently, the pair of lines number 3 of table 2, whose spectroscopic denominations are 1-2 P(35) and 0-1 P(40) for the lower vibrational levels 1 and 0 respectively, were selected.

Their respective strengths at 296 K are  $8.498 \times 10^{-25}$  and  $1.661 \times 10^{-27}$  cm.molecule<sup>-1</sup>. The variation with temperature of the strengths ratio S1/S2 for these two lines exhibits an inflexion point at  $T^* = 1005$  K, corresponding to a temperature sensitivity factor  $\chi(T^*)$  equal to 2.  $T^*$  is the temperature level at which the two-lines method is the most accurate [3].

## 5. DESCRIPTION OF THE OPTICAL SETUP

A schematic top view of the optical arrangement is shown in Fig. 1. This arrangement included only metallic mirrors. Indeed, lens reflection could generate feedback (energy return to the diode) or Fabry-Pérot effects, which could affect the quality of the signals.

The diode laser was placed at the focal point of an off-axis parabolic mirror with a focal length of  $f' = 200$  mm and a reception diameter of 55 mm. The use of a long focal length was related to the small emission solid angle observed for some diodes in a previous study [2]: it allowed a sufficient coverage of the 52 mm side grooved surface of the monochromator grating. The blaze wavelength of the 150 lines/mm grating is  $10 \mu\text{m}$  in the first order (blaze angle =  $48.6^\circ$ ). The image of the interference figure was formed in the plane of a slit by a 40 mm diameter spherical mirror with a focal length of 490 mm. The slit was used to spectrally isolate an emission mode.

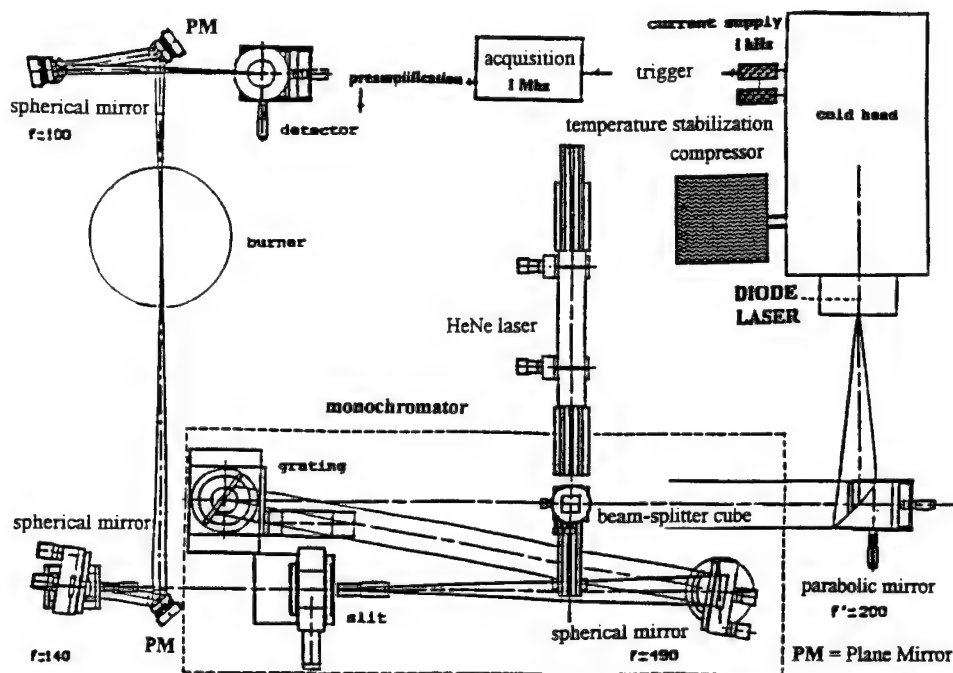


Figure 1 Schematic top view of the optical arrangement (focal length values are indicated in mm)[3].

The spectral resolution was determined by its aperture, which was set according to the spectral interval separating two adjacent modes of the diode laser. The resolution could be increased to 0.5

$\text{cm}^{-1}$  while preserving an acceptable signal-to-noise ratio. The image of the slit was formed in the flame axis by a spherical mirror with a 140 mm focal length. The image of the pupil, materialized by this mirror, was formed on the active surface of an HgCdTe infrared detector by a spherical mirror with a 100 mm focal length. This active surface is a 2 mm diameter disk, whose detectivity is uniform in a frequency band ranging from  $10^2$  to  $10^5$  Hz. The detector was associated with a preamplifier equipped with analog high-pass and low-pass filters with cutoff frequencies of 72 Hz and 400 kHz, respectively. This latter value was sufficiently high to prevent any signal distortion [3].

After preamplification and filtering, the signals delivered by the infrared detector were amplified in a 0-2 V range; they were then acquired and 12-bit digitized at a sampling rate of 1 MHz by a Metrabyte DAS 50 card. The acquisition bursts were triggered by each rising edge of a reference signal synchronized with the diode laser polarization current signal. Any desired number of bursts could be recorded. The acquisition time per burst could be chosen at any value less than or equal to the polarization current modulation period.

The parabolic mirror, the two spherical mirrors located on either side of the slit and the detector were mounted on precision 3-D positioners in order to ensure the reproducibility of the adjustments. The grating was mounted on a DC motor driven precision rotator (resolution of  $0.001^\circ$ ).

Prior to the optical alignment for the diode laser infrared beam, a first alignment was carried out by using a visible helium neon laser beam oriented by a beam-splitter cube. This laser was also used to precalibrate the monochromator by an original method developed at ONERA [3]. The adjustments were then refined for the infrared diode laser beam by using the precision positioners.

The time variation of the recorded transmission signal was converted into a wavenumber variation by using a Fabry-Pérot interferometer. This interferometer was placed into the optical arrangement when the burner was not active. It consists of a 2.5012 cm thick cylindrical germanium bar with parallel surfaces. The interfringe is equal to approximately  $0.05 \text{ cm}^{-1}$ , but its exact value depends on the wavelength and the germanium refractive index variation with temperature. Based on the monochromator calibration curve, the identification of the pair of CO lines was verified by measuring the spectral interval between the two line centers, deduced from the Fabry-Pérot signal.

In order to estimate the measurement spatial resolution along the burner axis, the height of the optical beam passing across the flame was measured by moving the burner surface at several locations, in order to create different beam cutting conditions. A 3 mm total height was estimated; however, about 90 % of the beam radiation intensity was concentrated within 2 mm.

## 6. LASER EMISSION FEATURES

Temperatures in the cryogenic range (typically lower than 50 K) are required to operate the infrared diode lasers, in order to sufficiently reduce the radiation losses by absorption inside the crystal. The diode laser was placed inside the cold head, cooled by an helium gas compression / expansion cycle at a 3 Hz frequency. Due to the low thermal conductivity of the diode, the wavenumbers of the emitted modes are very sensitive to the temperature ( $\sim 1$  to  $4 \text{ cm}^{-1} \cdot \text{K}^{-1}$ ). Therefore, a very accurate stabilization of the diode temperature was achieved ( $\pm 3 \times 10^{-4}$  K for a temperature level lower than 25 K).

An infrared diode laser (Muetek MDS 2020) was selected among four ones, in order to record the two investigated absorption lines over a high-quality emission mode. The value of the diode laser central emission wavenumber was  $1939 \text{ cm}^{-1}$ . Its tuning interval was large ( $1888 - 1991 \text{ cm}^{-1}$ ) and corresponded to a diode temperature level ranging from 25 K to 50 K. The tuning interval of the

selected mode was  $2.7 \text{ cm}^{-1}$ . It was separated from the two adjacent modes by wavenumber intervals of  $2.6$  and  $2.9 \text{ cm}^{-1}$ . These values were higher than the typical values specified by the manufacturer. This was an advantage, because the spectral resolution of the monochromator could be decreased without affecting the isolation of the selected mode. Therefore, the transmitted diode laser radiation intensity was increased by using a higher value of the slit aperture. This value corresponded to a spectral resolution of  $1 \text{ cm}^{-1}$ , which was only  $0.4$  time the distance to the closest adjacent mode.

A wavenumber modulation was obtained by creating a temperature modulation of the diode laser associated with a polarization current strength modulation. Indeed, the diode laser temperature level is dictated by the thermal equilibrium between the cooling provided by the cold head and the heating by Joule effect due to the polarization current. The shape of the polarization current was "chopped": its strength was constant over the first half-period, and zero over the second one. The trend of the wavenumber time response to that kind of polarization signal is illustrated in Fig. 2. The modulation frequency was set to  $400 \text{ Hz}$ . For each acquisition burst, the diode laser radiation intensity signals were recorded from the beginning of the modulation period within a time interval  $\Delta t$  equal to  $1300 \mu\text{s}$ . The additional  $50 \mu\text{s}$  interval from the beginning of the second half-period was used to check the zero level of the recorded signals.

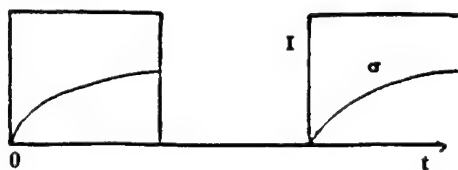


Figure 2. "Chopped" polarization current and trend of the wavenumber time response.

In spite of a high  $1 \text{ MHz}$  sampling rate, it was still desirable to have more data points in each absorption line profile. This was achieved by tuning the selected emission mode near the end of the periodic intensity-time traces, where the emission wavelength versus time variation associated with the diode temperature was the slowest (about  $2.5 \times 10^{-3} \text{ cm}^{-1} \cdot \mu\text{s}^{-1}$ ). Under this arrangement,  $10$  data points could be obtained for each absorption line. The time interval necessary to record the two absorption line profiles was about  $40 \mu\text{s}$ . Therefore, the validity of the recorded profiles required the assumption that during these  $40 \mu\text{s}$ , no disturbance occurred in the emission wavenumber versus time variation, i.e., the noise spectrum included no significant contribution of frequencies higher than  $25 \text{ kHz}$ .

## 7. TEST AND DATA REDUCTION PROCEDURES

The data reduction procedure detailed in this section was applied to three kinds of signals:

- \* the Fabry-Pérot interference signal, recorded at the beginning of the test;
- \* the radiation intensity signal transmitted after passage of the diode laser beam across the flame. These signals were recorded at different height locations in the flame, in order to obtain a detailed flame profile; and,
- \* the incident radiation intensity signal emitted by the diode laser, recorded at the end of the test.

The data reduction procedure included four steps:

1- The time-variable filtered detector output signal  $x(t)$  is a derived signal due to the low-pass filter, whose cutoff frequency is 72 Hz. It was rectified numerically by applying the relation:

$$X_r(t) = X(t) + \int_0^t [X(t) - X_t] / \tau_r \quad (5)$$

where  $X_r$  is the rectified signal;  $\tau_r$  is the rectification time constant (equal to 2220  $\mu$ s in this investigation). The value of  $X_t$  was calculated from the acquisition time per burst  $\Delta t$  (equal to 1300  $\mu$ s in this investigation):

$$X_t = [X(\Delta t) - X(0)] \cdot \tau_r / \Delta t + \int_0^{\Delta t} X dt / \Delta t \quad (6)$$

Relation (6) requires both that the acquisition time per burst is shorter than the signal modulation period, and that the rectified signal level is zero between the end of the burst and the end of the modulation period.

2- The transmitted radiation intensity signal was divided by the incident radiation intensity signal, averaged over several acquisition bursts, in order to obtain a dimensionless transmission signal. This step was not absolutely necessary to the data analysis procedure, since the least-squares fit of the experimentally measured transmission spectrum did not require a dimensionless signal; therefore, the transmitted radiation intensity signal could be directly fitted. However, this step was especially useful at lower temperatures, in order to detect in the measured spectrum the location of the two low-strength absorption lines.

3- For each burst, was identified the acquisition point for which the center of the 0-1P(40) absorption line was recorded. The 0-1P(40) absorption line was used because its strength is higher than the 1-2 P(35) absorption line. This procedure was used to discard any burst for which the identified acquisition point differed from the points identified in the other bursts. Indeed, such a difference revealed a wavenumber shift with respect to the other bursts; therefore, the burst should not be included in the averaging step. In general, the fluctuation was found to be  $\pm 1$  acquisition point, corresponding to a wavenumber fluctuation of about  $\pm 3 \times 10^{-3} \text{ cm}^{-1}$ , with a slightly higher value for only a few bursts. However, in order to achieve a higher accuracy, any burst revealing any fluctuation of the identified acquisition point with respect to the most frequently recorded position in the bursts was systematically discarded. This step was essential in this investigation, since the absorption lines were narrow. However, it could be applied only to spectra with an absorption line strength high enough for the absorption line central position to emerge from the signal noise. In practice, such spectra were obtained at beam height locations in the flame greater than or equal to 0.5 cm above the burner surface.

4- The signals selected after the third data reduction procedure step were averaged to increase their signal-to-noise ratio. This averaging step was allowed in this investigation, since the analyzed flame was very stable. The value of the residual noise was measured for different numbers of averaged bursts. For a single burst, the ratio of the peak-to-peak noise to the signal was about  $\pm 1$  to 2 %. It fell to  $\pm 0.02$  % and  $\pm 0.01$  % after averaging 100 and 300 bursts respectively. The value of the ratio remained constant when the number of averaged bursts was increased from 300 to 500 bursts. Therefore, the number of acquired bursts was chosen to be limited to 300. This resulted in a number of averaged bursts greater than 90 for each measurement.

## 8. RESULTS AND DISCUSSION

The measured CO temperature and concentration were deduced from a least-squares fit of the averaged spectrum by a theoretical spectrum based on a Voigt profile. Figure 3 reveals the typical quality of a fit.

Figure 4 presents the comparison between the experimental and theoretical profiles along the burner axis. The experimental profile was obtained with two TDLS tests carried out under the same conditions. The highest measured temperature was 1420 K, at a location of about 2.5 cm above the burner surface. The slopes of the experimental and theoretical profiles between 0 and 10 mm are similar. However, the level of experimental temperatures is lower; the value of the temperature difference is about 130 K at 20 mm above the burner surface, and becomes larger for higher height locations. This result was attributed to two main factors:

\* The cooling effect in the experimental flame, caused by both radiation heat losses from the flame and a two-dimensional heat transfer associated with species dilution in the surrounding cold argon flow, was not accounted for in the theoretical flame aerothermochemical model. The larger temperature difference between the two profiles at higher height locations in the flame was attributed to a stronger cooling by two-dimensional effects. Indeed, the occurrence of species dilution at higher height locations in the flame ( $> 2$  cm above the burner surface) was confirmed by the stable species concentration profiles results obtained by probe sampling mass spectrometry [3].

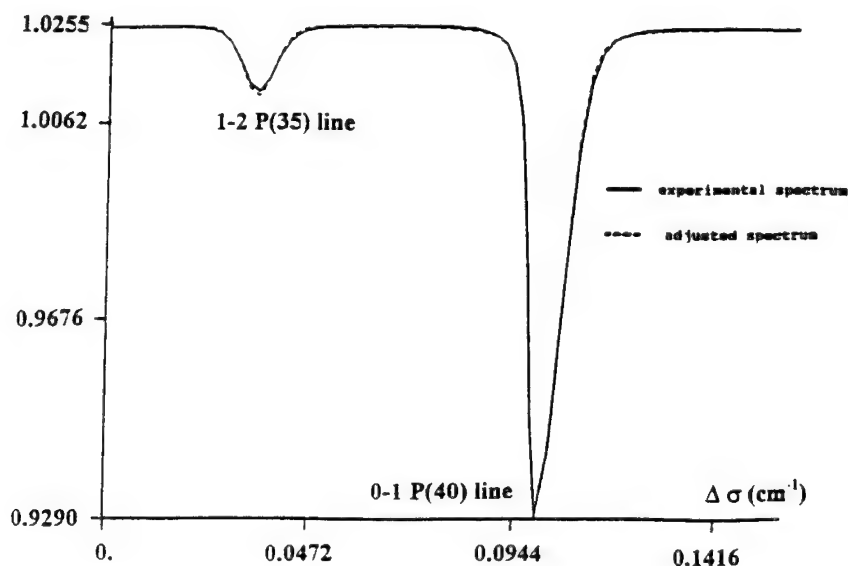


Figure 3. Comparison of TDLS experimental and adjusted spectra at a location of 0.5 cm above the burner surface. Deduced quantities:  $T = 809$  K,  $X_{CO} = 0.1122$  [3].

\* The temperature level measured by the TDLS technique is lower than the temperature level existing in the flame axis, due to integration along the optical pathlength across the flame. This effect is more pronounced at higher height locations in the flame, due to the two-dimensional heat



transfer mentioned above. However, it is unlikely that the significant temperature difference level of 200 K between the experimental and theoretical profiles near the burner surface should be attributed only to the experimental underestimation resulting from this effect. Indeed, very high radial gradients, leading to non-flat temperature and concentration profiles, would then exist; however, the flame appears to be very flat visually in this region.

Figure 5 shows the comparison between experimental and theoretical CO concentration profiles. Two experimental profiles were obtained, by TDLS and probe sampling mass spectrometry. The error bars indicate the accuracy limits estimated for each mass spectrometry measurement result. Within these limits, the agreement between these two profiles is good. Two theoretical profiles are also presented. They were calculated by an aerothermochemical code [3, 15]. One profile was calculated based upon the theoretical temperature profile; the other was based upon the experimentally measured temperature profile. In order to be compared with the concentration values relative to argon concentration measured by mass spectrometry, the absolute CO concentration values obtained by TDLS were divided by the argon concentration values calculated based upon the theoretical temperature profiles [3]. Below a location of 0.5 cm above the burner surface, the CO concentration could not be measured by TDLS (see section 9); the value obtained at 0.5 cm is shown in Fig. 5, but is clearly unreliable.

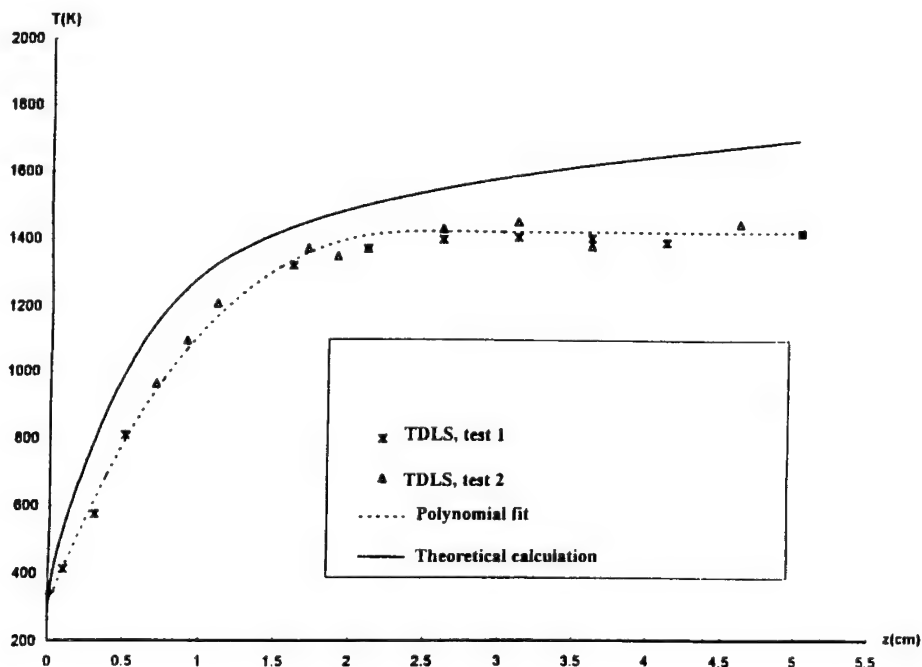


Figure 4. Comparison of theoretical and TDLS experimental temperature profiles [3].

The scattering of the mass spectrometry measurements results was quite large. Therefore, it could not be concluded whether the measured stable species concentration profiles were more similar to the calculated profiles based upon the experimentally measured temperature profile than those based upon the theoretical temperature profile, or not.

## 9. DISCUSSION OF THE MEASUREMENT ACCURACY

The measurement accuracy is intrinsically dictated by both the choice of the pair of CO absorption lines, and the accuracy with which the Lorentz collisional broadening and absorption line strengths are known.

As mentioned in section 4, the intrinsic accuracy of the temperature measurement for the selected pair of absorption lines is optimal when  $T = T^* = 1005$  K. In the least-squares fit procedure of one of the absorption spectra measured at a higher temperature level ( $\sim 1350$  K), the value of CO concentration was imposed and varied within a range of  $\pm 3\%$  around the value obtained when both the temperature and concentration are adjusted. The deduced temperature varied within a range of  $\pm 3.7\%$ , i.e. approximately  $\pm 50$  K. Within this range, the graphic agreement between the measured and deduced theoretical spectra remained good. Out of this range, although the least-squares fit algorithm continued to converge, the rms difference between the spectra increased and the quality of the graphic agreement decreased.

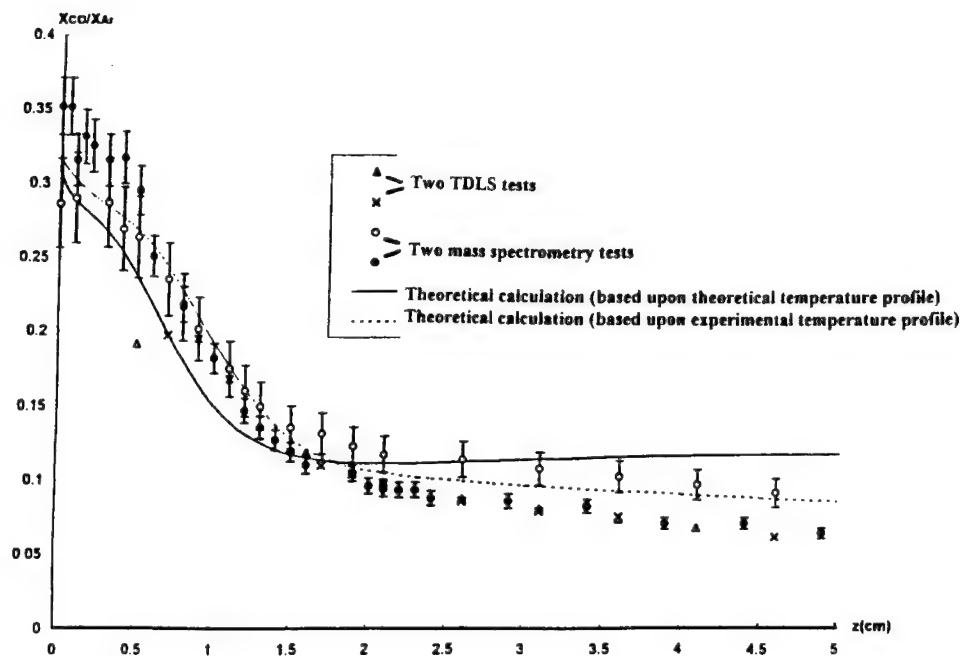


Figure 5. Comparison of theoretical and experimental CO concentration profiles [3].

A comprehensive review of the possible sources of experimental errors was established, and their effects were analyzed [3]. These sources are:

- \* The effects of integration along the optical pathlength and along the height of the optical beam, in a spatially non-uniform medium. These effects can introduce both a bias of the temperature measurement results, and an uncertainty on the actual pathlength to be considered for the concentration measurement;
- \* The wavenumber fluctuations of the diode laser emission mentioned in section 7, whose control depends on the signal sampling rate;

\* The signal-to-noise ratio.

In the lower part of the profile, where the axial gradients are higher, integration along the height of the optical beam led to a temperature overestimation by only about 5 %. In the upper part of the profile, the measured temperature tended to be underestimated due to the radial gradients (edge cooling effects); however, the value of this underestimation is difficult to estimate. In this region, the quantifiable errors due to the other experimental sources (wavenumber fluctuations, signal-to-noise ratio) on the temperature were estimated at about  $\pm 3$  %.

In the lower part of the profile ( $z < 0.5$  cm), the CO concentration could not be measured, due to an insufficient strength of the two absorption lines at low temperatures, and an uncertain knowledge of the Lorentz collisional broadening value. In the upper part of the profile, the uncertainty on the concentration measurement results was estimated at about  $\pm 15$  %.

To confirm the measurement results, another pair of absorption lines, centered at  $1958.66\text{ cm}^{-1}$  (see Table 2), and whose spectroscopic denominations are 0-1 P(41) and 1-2 P(36), was used. Two consecutive tests involving the two pairs of lines were carried out at the same location in the flame (for which  $T \approx 1300\text{K}$ ). Similar results were found, with differences of only  $\pm 1.4$  % for the temperature and  $\pm 2.8$  % for the CO concentration.

## 10. CONCLUSION

A quite accurate temperature profile in a one-dimensional, low-pressure (5700 Pa) premixed  $\text{H}_2/\text{CO}/\text{O}_2/\text{Ar}$  flat flame was measured by tunable diode laser infrared absorption spectroscopy. The measurement spatial resolution of 2 mm caused a temperature overestimation by only 5 % in the lower and also steeper part of the profile.

The highest measured temperature was 1420 K, at a location of about 2.5 cm above the burner surface. However, this value was probably underestimated. Indeed, the flatness of the upper part of the flame is doubtful, due to stronger edge cooling effects by a two-dimensional heat transfer, associated with the dilution of the flame species in the cold argon flow surrounding the flame. Therefore, the measured apparent temperature was lower than the temperature in the flame axis, due to integration of the absorption along the optical pathlength across the flame.

The analyzed absorption lines allowed an accurate temperature measurement in the broad range of temperature investigated (400 - 1400 K). However, their strengths were too weak at the low temperatures existing in the lower part of the profile (below 0.5 cm above the burner surface) to allow an accurate measurement of the CO concentration. In order to achieve a higher accuracy in this region, a better knowledge of the value of the Lorentz collisional broadening involved is required. In the upper part of the flame, involving higher temperatures, the CO concentration measurement became reliable; its accuracy was estimated at about  $\pm 15$  %.

**Acknowledgements:** the authors would like to thank J. F. Trubert, P. Comas and P. Roux from ONERA for the technical help they provided during the burner tests.

## REFERENCES

- [1] Schoenung, S.M. and Hanson, R.K., 1981. "CO and Temperature Measurements in a Flat Flame by Laser Absorption Spectroscopy and Probe Techniques", *Combustion Science And technology*, Vol. 24, pp. 227-237.

- [2] Rosier, B. et al., 1988. "Carbon Monoxide Concentration and Temperature Measurements in a Low-pressure  $\text{CH}_4$  -  $\text{O}_2$  -  $\text{NH}_3$  Flame", *Applied Optics*, Vol. 27, N° 2, pp. 360-364.
- [3] Brossard, C., 1995. "Contribution à l'étude de l'inhibition de la post-combustion: caractérisation aérothermochimique d'une flamme plane basse pression enssemencée en potassium", Doctoral Thesis, Rouen University, France.
- [4] Ouyang, X. and Varghese, P.L., 1989. "Line-of-sight Absorption Measurements of High Temperature Gases with Thermal and Concentration Boundary Layers", *Applied Optics*, Vol. 28, N° 18, pp. 3979-3984.
- [5] Ouyang, X. and Varghese, P.L., 1990. "Selection of Spectral Lines for Combustion Diagnostics", *Applied Optics*, Vol. 29, N° 33, pp. 4884-4890.
- [6] Hartmann, J.M. et al., 1988. "Accurate Calculated Tabulations of CO Line Broadening by  $\text{H}_2\text{O}$ ,  $\text{N}_2$ ,  $\text{O}_2$ , and  $\text{CO}_2$  in the 200 - 3000 K Temperature Range", *Applied Optics*, Vol. 27, N° 15, pp. 3063-3065.
- [7] Hunt, R.H. et al., 1968. "High resolution Determination of the Widths of Self-broadened Lines of Carbon Monoxide", *Journal of Chemical Physics*, Vol. 49, N° 9, pp. 3909-3912.
- [8] Bouanich, J.P. and Hauesler, C., 1972. "Linewidths of Carbon Monoxide Self-broadening and Broadened by Argon and Nitrogen", *Journal of Quantitative Spectroscopy and Radiative Transfer*, Vol. 12, pp. 695-702.
- [9] Bouanich, J.P. and Broadbeck, C., 1973. "Mesure des largeurs et des déplacements des raies de la bande 0-2 de CO autoperurbé et perturbé par  $\text{N}_2$ ,  $\text{O}_2$ ,  $\text{H}_2$ ,  $\text{HCl}$ ,  $\text{NO}$ , et  $\text{CO}_2$ ", *Journal of Quantitative Spectroscopy and Radiative Transfer*, Vol. 13, pp. 1-7.
- [10] Bouanich, J.P., 1984. "On the Temperature Dependence of Self-broadening in the First Overtone Band of CO", *Journal of Quantitative Spectroscopy and Radiative Transfer*, Vol. 31, pp. 561-567.
- [11] Sun, J.N-P. and Griffiths, P.R., 1981. "Temperature Dependence of the Self-broadening Coefficients for the Fundamental Band of Carbon Monoxide", *Applied Optics*, Vol. 20, N° 9, pp. 1691-1695.
- [12] Nakazawa, T. and Tanaka, M., 1982. "Intensities, Half-widths and Shapes of Spectral Lines in the Fundamental Band of CO at Low Temperatures", *Journal of Quantitative Spectroscopy and Radiative Transfer*, Vol. 28, pp. 471-480.
- [13] Bonamy, J. et al., 1984. "Simplified Models for the Temperature Dependence of Linewidths at Elevated Temperatures and Applications to CO Broadened by Ar and  $\text{N}_2$ ", *Journal of Quantitative Spectroscopy and Radiative Transfer*, Vol. 31, pp. 23-34.
- [14] Lowry III, H.S. and Fisher, C.J., 1984. "Line Parameter Measurements and Calculations of CO Broadened by  $\text{H}_2\text{O}$  and  $\text{CO}_2$  at Elevated Temperatures", *Journal of Quantitative Spectroscopy and Radiative Transfer*, Vol. 31, pp. 575-581.
- [15] Giovangigli, V. and Smooke, M.D., 1992. "Application of Continuation Techniques to Plane Premixed Laminar Flames", *Combustion Science and Technology*, Vol. 87, pp. 241-256.
- [16] Chackerian, C., Jr. et al., 1983. "CO 1-0 Band Isotopic Lines as Intensity Standards", *Journal of Quantitative Spectroscopy and Radiative Transfer*, Vol. 30, pp. 107-112.

## THE RESPONSE OF A PYROTECHNIC POWDER UNDER DYNAMIC LOADING CONDITIONS

A. I. Atwood,<sup>1</sup> C. F. Price,<sup>2</sup> S. A. Finnegan,<sup>1</sup> P. O. Curran,<sup>1</sup> J. Wiknich<sup>2</sup>

<sup>1</sup>Naval Air Warfare Center Weapons Division, China Lake, CA 93555-6001;

<sup>2</sup>Sverdrup INS Aegir, Ridgecrest, CA 93555

**ABSTRACT:** Experimental and analytical results describing the combustion response of a porous pyrotechnic powder under dynamic loading conditions are described. Pyrotechnic powder samples were subjected to dynamic loading using a piston driven porous bed configuration. Piston impact velocities ranged from about 80 to 300 m/sec. The initial loading density of the porous bed ranged from 54 to 56 percent of theoretical maximum density (TMD). The porous bed of pyrotechnic material ignited and burned at all but the lowest impact velocity tested (81 m/sec) where no reaction was observed. Two impact velocity dependent combustion modes were observed in the high speed motion pictures. No accelerating reactions were observed in either the motion pictures or the pressure gage data for the conditions tested. Traditional analytical porous bed combustion techniques were used in the evaluation of the pyrotechnic response under dynamic loading conditions. The NWCCDT porous bed code was used to model the response of the pyrotechnic powder to mechanical stimulus. Calculations of the pyrotechnic powder were complicated by the rebounding of the initial compaction wave off of the end of the confining tube.

### INTRODUCTION

Pyrotechnic materials are commonly used in military applications as igniters and incendiary devices. Pyrotechnic powder in an igniter configuration often serves two functions: as part of an ignition train (e.g. as a primary ignition source or delay composition) and as a fire-setting (incendiary) material.

Pyrotechnic materials are composed of a mixture of ingredients including an oxidizer, a fuel and a binder, not unlike the basic components of a solid rocket propellant. They differ from the rocket propellant in the relative amounts of these basic components, usually containing high levels of a metallic fuel. The high level of condensed phase products resulting from the combustion of these materials presents a challenging contrast to the traditional energetic solids being studied. Most blends are formulated to burn rather than explode or detonate, as is the case of the pyrotechnic powder used in this study.<sup>1-3</sup> Due to the heterogeneity of the mixture, reaction rates depend on migration or diffusion distances, hence on the powder characteristics.

Impact initiation is the principal mode of ignition for the pyrotechnic used in this study. Under high-rate loading conditions, reactivity may be enhanced as a result of both micro- and macro-scale changes within the powder. Reactivity is also altered on a microscopic level by crystallographic defects and phase transformations and on a macroscopic level, by deformation, fracturing, comminution, mixing processes and compaction effects.<sup>4,5</sup>

The processes associated with impact induced initiation of a pyrotechnic powder are not unlike the response encountered in a deflagration to detonation transition of traditional porous high energy

Approved for public release; distribution is unlimited.

materials. In both cases, the event begins with the development of convective burning within the material. In order to achieve this effect, there must be an adequate amount of surface area available accompanied by the development of combustion upon these surfaces. The critical stages of the convective combustion/DDT process have been identified as a result of these studies: (1) ignition with pre-ignition products traveling through the bed, (2) the formation of a weak compaction wave which travels into the unreacted porous material, (3) the reaction of the pre-ignition products to final products forming a strong compaction wave, shutting off the bed to the combustion gases, accelerating the reaction, and (4) the coalescence of the waves to build a shock leading to detonation.<sup>6,7</sup>

In order to model the pyrotechnic porous bed response, a basic material characterization was required to provide a number of the input parameters to the code. The thermochemistry, thermal conductivity, ignition and combustion properties, and compaction behavior under quasi-static loading conditions are a few of the basic characteristics that were generated for this analysis.<sup>8</sup> A detailed description of the material characteristics of the pyrotechnic material is beyond the scope of this paper.

### SAMPLE

The pyrotechnic powder examined in this study consisted of a 50/50 mixture of potassium perchlorate, magnesium-aluminum alloy with calcium resinate as binder. The formulation is given in Table 1. Particle sizes of the oxidizer and alloy were similar, ranging between approximately 70-150  $\mu\text{m}$  for the perchlorate and 60-125  $\mu\text{m}$  for the metal.

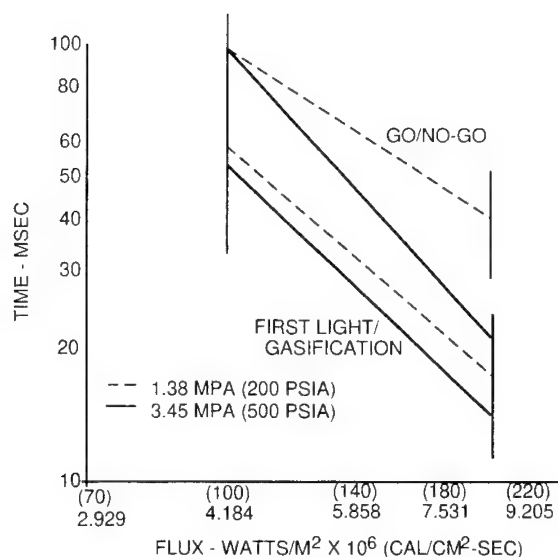
TABLE I  
Pyrotechnic Powder Mixture Specifications.

Ingredient	Wt %
Magnesium/aluminum alloy powder <sup>a</sup>	49.0
Potassium perchlorate	49.0
Calcium resinate	2.0

<sup>a</sup>50/50 composition by weight

Characterization studies of the pyrotechnic powder revealed that it is thermally stable, with exothermic decomposition beginning at about 530°C. The powder was also difficult to ignite by radiant means. Log-time versus log flux data at two pressures are plotted in Figure 1. It is interesting to note that the material demonstrates a pre-ignition region (time between first gasification and go/no-go) at 1.38 MPa. The presence of a pre-ignition zone is important in the porous bed convective combustion process, in that a source of reactive gasses are being generated which can then penetrate into the bed enhancing the combustion process. Pressed pellets of the pyrotechnic material would not reliably ignite by hot wire initiation at pressures below 3.45 MPa, again demonstrating the high thermal stability of this material. Due to the thermal stability of the pyrotechnic powder being examined, some doubts were raised as to whether the standard piston driven compaction arrangement would be capable of delivering a piston at high enough velocity to initiate the bed.

A second interesting physical property of this material was observed during the quasi-static loading experiments. The pyrotechnic powder was considerably more difficult to compact under the standard quasi-static conditions.<sup>9</sup> Compressive loading forces which compact the pyrotechnic material to 77% TMD, result in an equivalent AP powder compaction of over 90% TMD. At these low levels of TMD, a large elastic component was observed in the pyrotechnic powder.



**Figure 1.** Log-Time Versus Log-Flux Ignition Data of Porous Pyrotechnic Material.

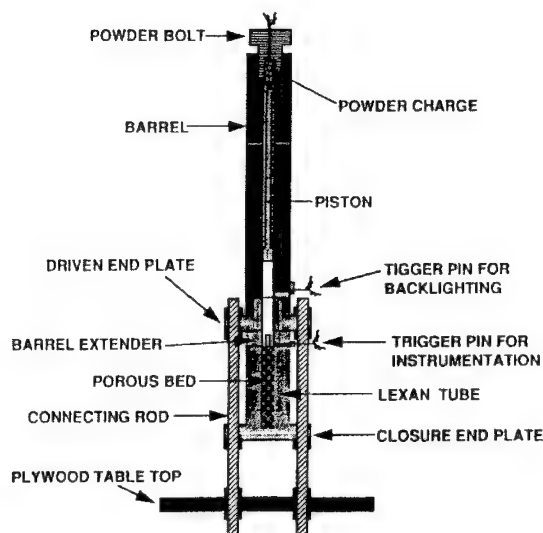
### EXPERIMENT

A piston driven compaction experiment was selected in order to examine the response of the pyrotechnic powder under high strain rate conditions approximating those encountered upon projectile impact. The dynamic compaction design of Sandusky<sup>10</sup> was used for this study. A schematic of the test apparatus is shown in Figure 2. A smooth bore gun barrel was used to propel a polycarbonate piston approximately 305 mm in length into a 25.4 mm diameter bed of pyrotechnic, incendiary powder 165 mm in length. Polycarbonate tubes were also used as the confining medium for these experiments to allow for photographic observation of the events occurring down the length of the bed upon piston impact.

A barrel extender was screwed into the barrel and clamped onto the top of the porous bed tube. The barrel extender protected the end of the barrel from damage and was instrumented with Dynasen model 26CA-1059-C self-shorting pins which were used to estimate the piston velocity and to trigger an Imacon image converter camera operating in the streak mode. Slots in the barrel extender provided venting of the air from the barrel. The top of the porous bed was protected by a 0.25 mm thick plastic disk. The slots in the barrel extender were also used to photographically measure the piston velocity as it entered the porous bed.

The pyrotechnic material was loaded into a polycarbonate tube (Lexan) of 76.2 mm outer diameter and with a 25.4 mm inner diameter in 13 mm increments. Porous beds of the pyrotechnic were tested at pour density (55-57% TMD). A polished polycarbonate tube was used for its transparency allowing for viewing of the porous bed experiment.

Red Dot smokeless powder, shift 2, lot 733-12/94, ignited with an SQ-80 igniter was used to propel the piston down the barrel into the porous bed. Piston velocity was varied by adjusting the amount of Red Dot propelling charge. Propellant powder charges were varied from 0.5 gram to a maximum of 4.2 grams.



**Figure 2.** Schematic of Dynamic Compaction Test Apparatus.

High speed motion picture photography was used to evaluate entry of the piston into the pyrotechnic powder bed and to track any subsequent combustion response down the length of the tube. A Photec IV high speed motion picture framing camera operating at approximately 8000 pps in the quarter framing mode produced a framing rate range between 31,000 and 36,000 pictures per second. This framing rate resulting in an interframe picture time of 28 to 32  $\mu$ sec for these experiments. Initial piston velocity, luminous gasification front and sustained combustion rate data were determined from the high speed motion picture film with the aid of a Vanguard Motion Analysis System. The initial piston velocity was calculated by tracking the piston movement prior to contact with the porous bed. The luminous and sustained combustion fronts were calculated by tracking the flame fronts after the piston impacted and ignited the porous bed. A Reynolds header mounted at the base of the porous bed arrangement was fired with closure of the firing circuit and provided a temporal fiducial for data collection.

Streak records of the piston as it passed through the barrel extender were made using an Imacon Model 792 camera system operating at 990 nsec/mm. The streak records were reduced using a Micro-Vu Metrology Computer by calculating the velocity of the piston as it passed through a known distance in the barrel extender.

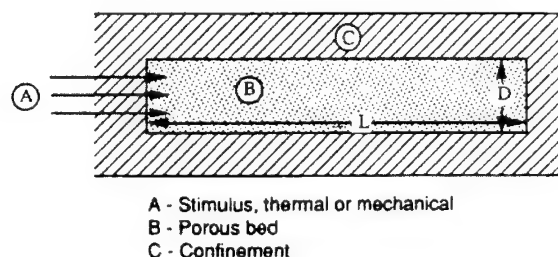
Kistler piezo electric transducers were used to record the pressure response of the combustion reaction as it proceeded down the bed in two of the experiments. The transducers were located at positions 25.4 mm and 76.2 mm from the top of the porous pyrotechnic bed. The electronic pressure signal was amplified through a Kistler 504E amplifier and simultaneously recorded on a Nicolet 4094 and Multipro system. Self-shorting pin data were also recorded on the digital oscilloscope systems.

### MODEL

The NAWC DDT porous bed code was used in the design and interpretation of the pyrotechnic powder response under dynamic loading.<sup>11,12</sup> This model is a major modification of that used by Pilcher et al.,<sup>13</sup> based partially on the earlier work of Krier.<sup>14</sup> The code includes the effects of confinement as well as gas flow, ignition, flame spread, and pressure build up due to burning within the porous



material. It incorporates a transient analysis, solving the conservation equations of mass, momentum, and energy in both the solid and gas phases.<sup>15</sup>



**Figure 3.** Situation Being Modeled: (a) stimulus, thermal or mechanical; (b) porous bed; and (c) confinement.

The test case being modeled is shown in Figure 3. The igniter (A), in this study, a moving piston, provides the stimulus to the sample (B) and the tube (C) the confinement. The igniter is described as a mass and energy input to the tube. The sample is described in terms of initial loading density, compaction properties (intragranular stress relationship), material decomposition/pyrolysis kinetics and energetics, thermal properties of the solid, particle diameter and nonsphericity, and any void, or ullage condition. The geometric and material description of the tube must be included to describe the wall dilation.<sup>16</sup>

## RESULTS

### Experiment

Six dynamic compaction firings were made using the pyrotechnic powder. The initial firing conditions for the six firings are given in Table 2. The bed of pyrotechnic powder were not preloaded for these firings. Piston data for each experiment are given in Table 3. Piston velocity was varied by adjustment of the amount of Red Dot loaded into the powder bolt.

TABLE 2  
PDC Sample - Filled In  $\approx 12.7$  mm Increments.

Experiment	Weight, grams	Initial % TMD
PDC3	105.18	55.8
PDC4	106.85	56.8
PDC5	106.46	56.5
PDC6	107.48	57.1
PDC7	105.34	56.0
PDC8	105.72	56.2
PDC9 (Inert)	95.23	54.5

TABLE 3  
Lexan Piston Data.

Test #	Weight, grams	Length, cm
PDC3	174.1744	30.554
PDC4	174.3689	30.526
PDC5	174.1322	30.523
PDC6	167.4497	30.505
PDC7	174.8503	30.528
PDC8	175.9555	30.582
PDC9	174.6049	30.493

Piston velocity as it passed through the barrel extender was measured using three different techniques: self-shortening pins, Imacon streak records, and high speed motion pictures. Velocity data from each of these techniques can be compared in the plot of powder loading versus piston velocity in Figure 4.

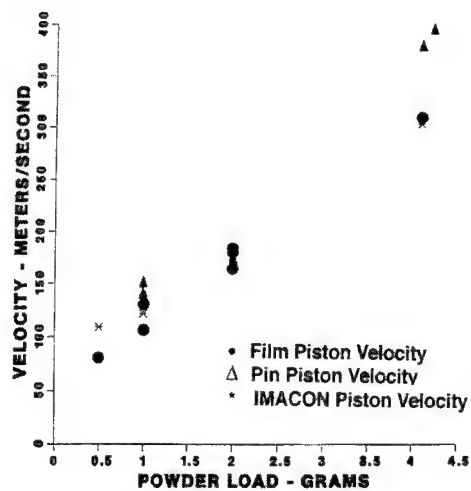


Figure 4. Impact Piston Velocity Data as a Function of Propellant Powder Load.

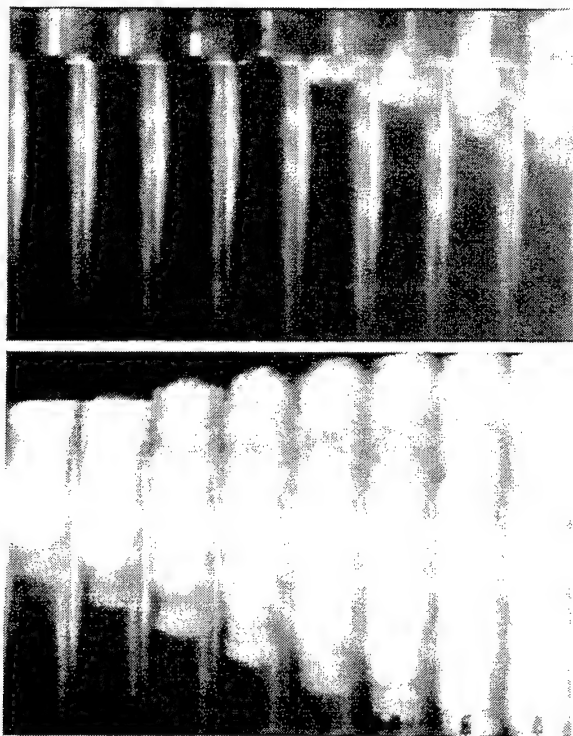


Figure 5. A Series of Photos Showing Piston Impacting Bed (Frame 8) with Ignition of the Porous Pyrotechnic Bed.

Figure 5 shows a series of photos for a typical piston compaction experiment. The photos show the impact piston travel through the barrel extender and entering the bed of pyrotechnic material. A luminous reaction front is immediately visible upon piston impact. The piston velocity taken from film data for this test was 307 m/sec. The time between individual pictures was 32  $\mu$ sec. Two distinct combustion phenomena can be seen. A luminous gasification front precedes a dense sustained combustion front. The entire tube is engulfed in flame by picture 16. Figure 6 illustrates the flame location relative to the point of impact down the length of the porous bed for the 307m/sec firing (PDC3). The flame propagation down the length of the porous bed was linear in all but the lowest velocity firing (107m/sec, PDC5) which is shown in Figure 7. This firing shows an ignition delay between the luminous gasification and the appearance of a sustained reaction of over 100  $\mu$ sec. The relationship between flame propagation rates and piston velocity is shown in Figure 8. No acceleration of the combustion front was observed in any of the experiments.

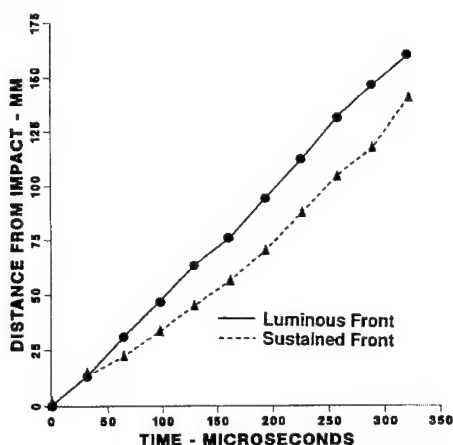


Figure 6. Flame Location Relative to Piston Impact for 307 m/sec Firing.

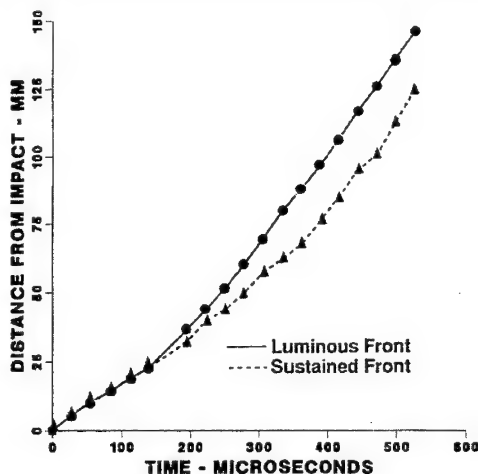


Figure 7. Flame Location Relative to Piston Impact for 107 m/sec Firing.

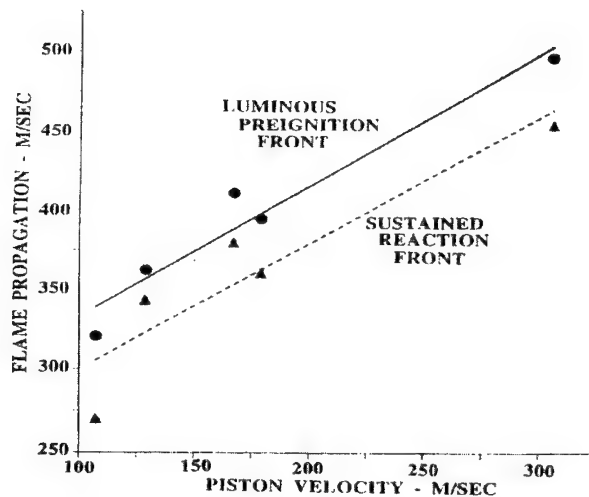


Figure 8. Relationship Between Flame Propagation Rates and Piston Velocity.

The pressure-time histories for gages one and two of the firing with an impact velocity of 179 m/sec (film), PDC8, is plotted in Figure 9. A Piston to bed impact time of 6.99 msec from the test initiation signal was measured from the film record.

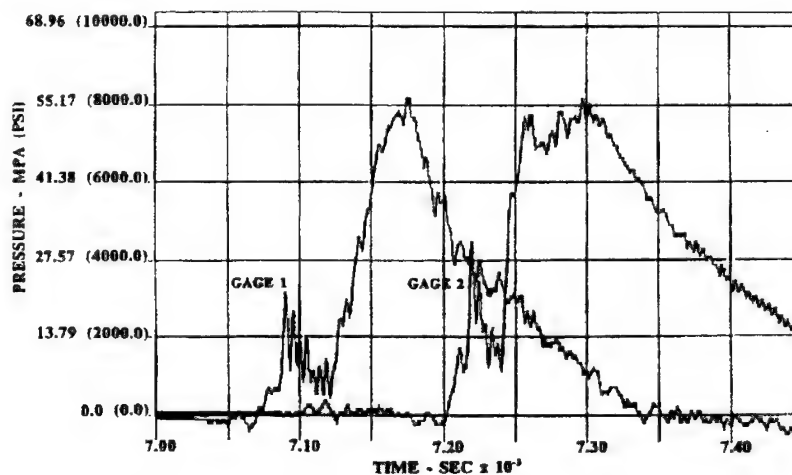


Figure 9. Pressure-Time Histories for Gages 1 (25.4 mm) and 2 (76.2 mm) of PDC8, Impacted at 179 m/sec (Film).

In evaluating the pressure gage data it is assumed that the pressure changes result from chemical reaction and not from mechanical effects (i.e., compaction wave processes). Whether that assumption is correct is not known as we have no pressure data at the present time for inert systems under comparable loading conditions.

The evaluation consisted largely of a simple comparison between data derived from pressure histories and photographic records. It was assumed that the first two pressure pulses represent the effects of the luminous precursor and sustained reaction region, respectively. Assuming the piston impact time of 6.99 ms is correct, the luminous front arrived at gage 1 approximately 74  $\mu$ s after piston impact while the main reaction front arrived about 57  $\mu$ s later. These times agree fairly closely with those based on photographic evidence (60  $\mu$ s and 60  $\mu$ s, respectively). A comparison of luminous front and main reaction front velocities (374 m/s and 416 m/s, respectively) between gages 1 and 2, with average values from photographic measurements (395 m/s and 360 m/s) also shows reasonable agreement (A comparison of velocity values for the two fronts, from photographic data, shows both to be approximately the same, 402 m/s, between gages 1 and 2.) Additionally, a comparison of peak pressure levels for the two pulses at gages 1 and 2 (22.06 MPa and 56.54 MPa, respectively at gage 1 versus 31.03 MPa and 56.54 MPa at gage 2) also shows no significant change over that distance. The pressure data again verify the observed steady state combustion of the pyrotechnic material with no accelerating phenomena.

At a piston velocity of 81 m/sec (film) the pyrotechnic did not ignite. No luminous gasification was observed in the high speed motion pictures but the rebound of the piston off of the bed was observed. A post-test bed height of 130 mm was measured for the pyrotechnic material (165.4 mm initial bed height). An average TMD of 72.58 percent was calculated assuming a uniformly compacted bed; however, upon dissection of the impacted pyrotechnic filled tube, a highly nonuniform bed was discovered. About 13 mm of material at the top of the bed was very loose, showing no visible compaction. The second 13 mm of material was lightly compacted in the center, with increased compaction on the walls. This would indicate a wall friction effect on the porous bed compaction behavior. A solid uniform plug of pyrotechnic material was encountered at about the 26 mm level. The solid plug was about 66 mm thick followed by about 25 mm of material which was compacted tighter on the walls than in the center of the sample. The final 13 mm of material was lightly compacted and easily removed from the confining tube. The lack of compaction on the top of the bed may be the result of a deconsolidation as a result of the compaction wave rebounding off of the end of the tube.

### **Model**

The best available kinetic and compaction data for the pyrotechnic powder were input into the NWCCDDT code and a series of piston-driven compaction experiments, at initial piston velocities of 84, 151, 240 and 303 m/sec were modeled. Both a standard (165 mm) length and a long (330 mm) bed length were run at each piston velocity. The piston velocity was allowed to decrease in accordance with the momentum-force balance, except for a single comparison case in which it was held constant. The peak compaction loci for the standard length piston cases at the four piston velocities is shown in Figure 10. The "wave" velocities resulting from the compaction are plotted as a function of piston velocity in Figure 11. The calculated wave velocities are comparable to the combustion front velocities observed experimentally.

Previous calculations showed that the compaction wave reached the end of the standard length tube and reflected, causing the piston to compact more highly compressed material. Piston rebound was observed at the lowest velocity (81m/sec) firing. These observations provided the motive for some porous bed calculations at double the original bed length. The calculations made at a piston impact velocity of 84m/sec with the standard resulted in a compaction wave reflecting at about 500  $\mu$ sec after piston impact, while no reflection occurred in the longer bed at 1200  $\mu$ sec. Compaction profiles are shown in Figure 12 at times of 400, 800, 1200 and 1600  $\mu$ sec for both porous bed lengths. The standard bed length data (solid lines) clearly show the reflection, while the longer bed (dashed lines) shows reflection only after more than 1200  $\mu$ sec.

Comparative calculations were made for the experimental porosity (56%) and for lower porosities of 63.5% and 73% of TMD for a piston impact velocity of 303m/sec. The calculated peak compaction loci for the three porosity levels are shown in Figure 13. The wave velocity was increased somewhat

by increasing the density to 63.5% TMD, but the further increase to 73% causes much more particle heating, leading to a higher velocity reaction than was calculated at the lower porosity levels.

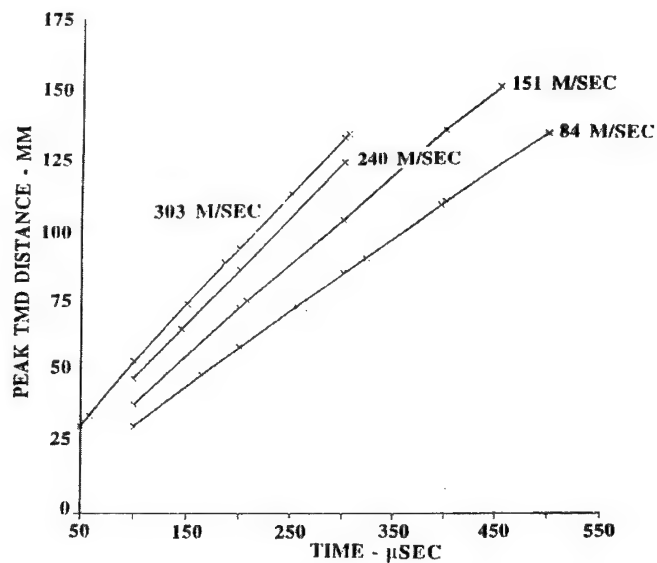


Figure 10. Peak Compaction Loci for Standard Length Piston Impacting the Porous Pyrotechnic Bed at Four Impact Velocities.

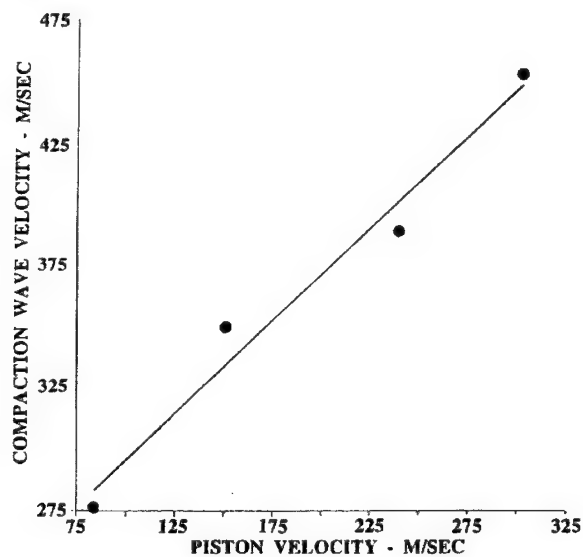


Figure 11. Calculated Compaction Wave Velocities as a Function of Piston Velocity.

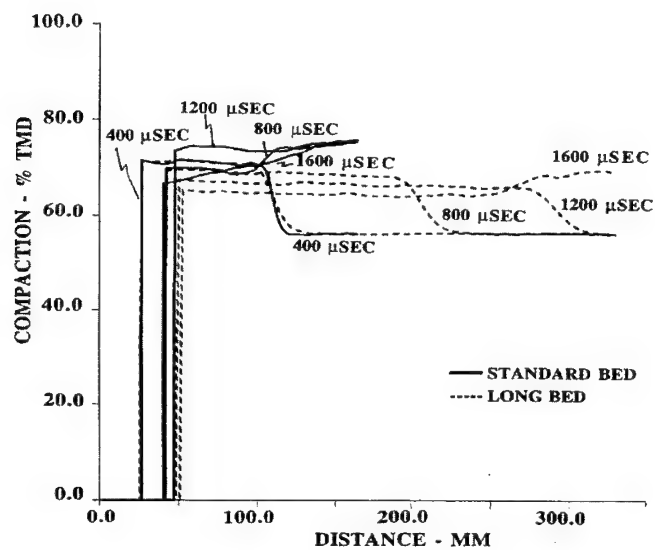


Figure 12. Calculated Compaction Profiles for Two Porous Bed Lengths.

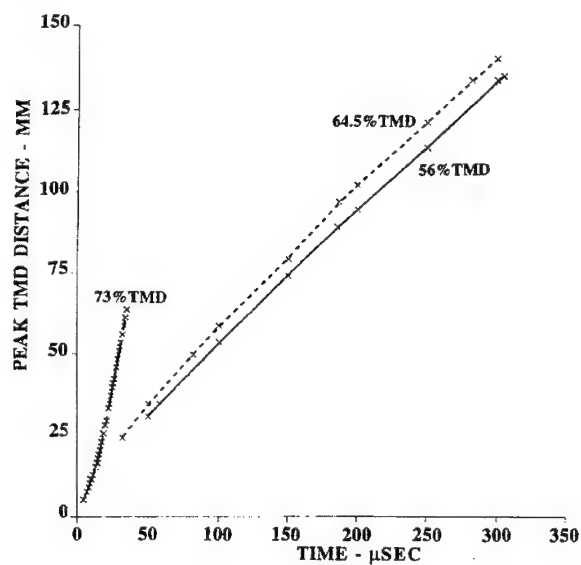


Figure 13. Calculated Peak Compaction Loci for the Pyrotechnic Powder at Three Porosity Levels. (Piston impact velocity = 303 m/sec.)

## SUMMARY

Ignition and combustion mechanisms of a porous pyrotechnic powder due to dynamic loading have been examined at piston impact velocities up to 307 m/sec. The analysis of the material using standard convective combustion/DDT techniques provides a tool in guiding and interpreting the experimental data.

Six dynamic compaction experiments were performed on a pyrotechnic powder. The porous pyrotechnic was ignited under dynamic conditions at piston velocities as low as 107 m/sec. Two distinct combustion phenomena were observed in the impacted pyrotechnic beds. A luminous gasification front preceded a dense sustained combustion region. This type of luminosity has been observed in porous beds of potassium perchlorate and aluminum.<sup>17</sup> In that study, the luminosity in the preignition region was attributed to local chemical reaction heating of the porous medium.

Assuming the pressure changes observed in the 179 m/sec (PDC8) impact experiment resulted from chemical reaction, reasonable agreement between photographic and pressure data was found. The luminous preignition front arrival time corresponds to the initial rise of the pressure gage with the sustained reaction zone arriving about 50  $\mu$ sec later.

Model calculations have proven to be a valuable tool in the design of the experimental test conditions. Luminous preignition front velocities were comparable to the compaction wave velocities calculated in the model. Calculated compaction wave reflections add a complexity to the calculations that require verification by experiment. The calculations indicate that at low piston impact velocities the reflected wave may have a considerable influence on the combustion response of the pyrotechnic powder.

## FUTURE PLANS

Future plans call for the modification of the experiment in accordance with the analysis. The length of the porous bed will be doubled in an effort to reduce the effect of a retro-wave on the low velocity results. A series of short piston impact experiments are planned to increase the momentum of the piston in order to make future experiments more like a typical porous bed experiment.

The current pyrotechnic powder studies were performed at pour density. Future studies will examine dynamic properties of porous beds of pyrotechnic material at lower porosity levels in order to improve and verify the model calculations.

## REFERENCES

1. Conkling, J.A., *Chemistry of Pyrotechnics*, Marcel Dekker, New York, New York, 1985.
2. McLain, J.H., *Pyrotechnics*, The Franklin Institute Press, Philadelphia, Pennsylvania, 1980.
3. Barnes, P., de Yong, L.V., Queay, J., and Valenta, F.J., Pyrotechnic ignition transfer problems encountered in ordnance related applications, *Proceedings of the 15th International Pyrotechnics Seminar*, IIT Research Institute, Chicago, Illinois, 1989, pp. 61-78.
4. Thadhani, N.N., Shock-induced chemical reaction and synthesis of materials, *Progress in Materials Science*, Vol. 37, No. 4, 1972, pp. 595-597.
5. Kiselev, A.N., Plyusnin, V.I., Boldyreva, A.V., Deribas, A.A., and Boldrev, V.V., Effect of preliminary treatment of ammonium perchlorate by a shock wave on its rate of thermal decomposition and burning of mixtures on its base, Translated from *Fizika Goreniya I Vzryva*, Vol. 8, No. 4, 1972, pp. 595-597.
6. Bernecker, R.R., The deflagration-to-detonation transition process for high-energy propellants-a review, *AIAA Journal*, Vol. 24, No. 1, 1986, pp. 82-91.
7. Bradley, H.H. and Boggs, T.L., Convective burning in propellant defects: a literature review, Naval Weapons Center, NWC TP 6007, 1978.



8. Atwood, A.I., Lindfors, A.J., Finnegan, S.A., Lee, I., Boteler, J.M., and Covino, J., Overview of the static and dynamic properties of a pyrotechnic powder mixture, *Proceedings of the 32nd JANNAF Combustion Subcommittee Meeting*, NASA Marshall Space Flight Center, Huntsville, Alabama, 1995.
9. Atwood, A.I., Curran, P.O., Price, C.F., and Wiknich, J., Quasi-static compaction studies of a porous pyrotechnic powder, *Proceedings of the 1995 APS Topical Conference on Shock Compression of Condensed Matter*, Seattle, Washington, 1995.
10. Sandusky, H.W., Elban, W. L., Coyne, P. J., Jr., and Clairmont, A. R., Jr., Compaction Studies on Cross-Linked Double-Base, High-Energy Propellant Shreds, Naval Surface Warfare Center, TR 88-124, Silver Spring, MD, 1988.
11. Boggs, T.L., Price, C.F., Atwood, A.I., Zurn, D.E., and Derr, R.L., Role of Gas Phase Reactions in Deflagration to Detonation Transition, *Proceedings of the Seventh Symposium (International) on Detonation*, Naval Surface Weapons Center, White Oak, Maryland, MP82-334, 1981, pp. 216-224.
12. Beckstead, M.W., *A computer user's manual for NWCCDDT-2*, Brigham Young University, 1995.
13. Pilcher, D.T., Beckstead, M.W., Christensen L.W., and King, A.J., A comparison of model predictions and experimental results of DDT tests, *Sixth Symposium (International) on Detonation*, Naval Surface Weapons Center, White Oak, Maryland, 1976, pp. 258-266.
14. Krier, H., and Gokhale, S.S., "Modeling of convective mode combustion through granulated propellant to predict detonation transition, *AIAA Journal*, Vol. 16, No. 2, 1978, pp. 177-183.
15. Price, C.F., and Boggs, T.L., Transient combustion: An important aspect of deflagration-to-detonation transition, *Progress in Astronautic and Aeronautics*, AIAA, Washington, DC, ISBN 1-56347-014-4, 1991.
16. Price, C.F., Atwood, A.I., and Boggs, T.L., An improved model of the deflagration-to-detonation transition in porous beds, *Proceedings of the 9th Symposium (International) on Detonation*, Vol. I, 1989, pp. 363-376.
17. Hershkowitz, J., Schwartz, F., and Kaufman, J.V.R., Combustion in loose granular mixtures of potassium perchlorate and aluminum, *Proceedings of the 8th Symposium (International) on Combustion*, California Institute of Technology, Pasadena, California, 1960, pp. 720-727.

## OVERTONE ABSORPTION SPECTROSCOPY OF SOLID PROPELLANT FLAMES: CO AND N<sub>2</sub>O CONCENTRATIONS

J. A. Vanderhoff<sup>1</sup>, S.H. Modiano<sup>2</sup>, B.E. Homan<sup>2</sup>, and M.W. Teague<sup>3</sup>

<sup>1</sup>US Army Research Laboratory, Attn: AMSRL-WT-PC, Aberdeen Proving Ground, MD 21005;

<sup>2</sup>SCEEE Postdoctoral Fellow; <sup>3</sup>IPA Faculty Fellow from Hendrix College

**ABSTRACT:** In a continuing investigation of the chemical composition of the dark zones of double-base and nitramine solid propellants, additional multichannel infrared absorption experiments have been performed. The experiment has been improved by the addition of mirrors on a portion of the chamber windows effecting a "triple-pass" of the beam through the sample region. Overtone absorptions for CO at 2.3  $\mu\text{m}$  and N<sub>2</sub>O at 3.9  $\mu\text{m}$  were measured and analyzed to determine absolute concentration and temperature. Least-squares fitting routines using the HITRAN database were developed and used for this analysis. The solid propellants, JA2 and XM39, were probed under steady-state combustion conditions in a nitrogen environment of 1.0-1.3 MPa pressure. CO is a major gas species in these propellant flames and concentrations of about 0.35 and 0.12 mole fraction were obtained in the dark zones of JA2 and XM39, respectively. Small absorption signals were found in the spectral region appropriate for N<sub>2</sub>O and an upper limit of 0.02 mole fraction was determined for XM39. No absorption in this region was observed for JA2. These results are in qualitative agreement with published values.

### INTRODUCTION

The combustion of solid propellants has been under investigation for many years; however, the detailed chemical and physical processes are still not completely understood. Many solid propellants burn as a two-stage flame with a luminous portion and a non-luminous "dark zone".<sup>1</sup> The length of this dark zone increases with decreasing pressure and for sufficiently low pressures the luminous flame is not formed. Common gun propellants, i.e., single-base (nitrocellulose), double-base (nitrocellulose-nitroglycerin), and low-vulnerability nitramine propellants exhibit dark zones which arise from the slow conversion of NO to N<sub>2</sub>. The delayed ignitions which are found to take place in some gun firings are thought to be related to the chemistry occurring in the dark zone.

Over the last eight years, this laboratory has developed a multichannel optical absorption technique and applied it to the study of gas-phase, steady-state propellant combustion processes. Results for NO and OH have been obtained for double-base and nitramine propellants using a multichannel array detector sensitive in the ultraviolet-visible spectral region.<sup>2,3</sup> More recently, an infrared sensitive photodiode array detector has been used to obtain absorption spectra from which concentration estimates were obtained for HCN, CH<sub>4</sub>, H<sub>2</sub>O, CO, and N<sub>2</sub>O.<sup>4-7</sup> We report here updated results for CO and N<sub>2</sub>O using symmetric stretch overtone absorptions and a least-squares fitting technique.

## EXPERIMENTAL

The absorption experiment as well as the windowed pressure vessel used in this study have been described in detail previously,<sup>2,7</sup> so only pertinent features or changes to the experiment will be described here. One aspect that is very useful is the rapid rate of data collection. Typically, runs were made at a repetition rate of approximately 25 Hz. During this period, a spectrum was taken with the light passing through the sample region and one taken with the beam blocked. This means that a background corrected spectrum was obtained every 40 ms. Although most of the least-squares fitting results were obtained from averages of a few seconds of data, an example of a "single-shot" spectrum will be presented. At wavelengths beyond about 3  $\mu\text{m}$ , the quartz envelope of the quartz tungsten halogen lamp used previously limits the exiting radiation. This lamp was replaced by a silicon carbide Globar, commonly used as a light source in commercial FTIR instruments, fitted with an ordinary flashlight reflector. About a factor of two increase in intensity was realized at the  $\text{N}_2\text{O}$  wavelength of interest, 3.9  $\mu\text{m}$ .

Another modification involved mounting the entrance and exit chamber windows at a slight angle to the beam normal and mirroring a portion of them to produce multiple passes through the sample area, effectively increasing absorption pathlength.

The "triple-pass" experimental setup is shown in Figure 1. This setup consists of extenders into the chamber with rectangular apertures and partially gold-coated sapphire windows set at an angle to the centerline. The effective path length,  $l$ , can be calculated:

$$l = D + (4 \times X) = D + (4 \times \sqrt{(D/2)^2 - h^2}) \quad (1)$$

$$l = 10.8 \text{ mm} + (4 \times \sqrt{5.4^2 - 2.7^2}) \text{ mm} = 29.31 \text{ mm}$$

The expected path length for triple pass is  $\sim 2.6$  times single pass experiments. Figure 2 shows spectra with the triple-pass absorption data, which is linear with path length,  $\sim 2.7$  times the single pass.

In order to test the data analysis procedure of least-squares fitting absorption spectra using the HITRAN<sup>8</sup> database, a temperature-controlled, windowed, stainless-steel sample cell was incorporated into the experiment. Pure gases of  $\text{N}_2\text{O}$  and  $\text{CO}$  were introduced into the 1-cm pathlength cell and the gas pressure and temperature set to desired values. The absorption spectra obtained were then least-squares fitted and the results compared to the known values. These comparisons are discussed in the data analysis section.

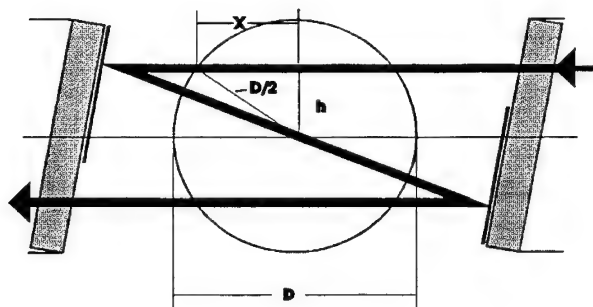
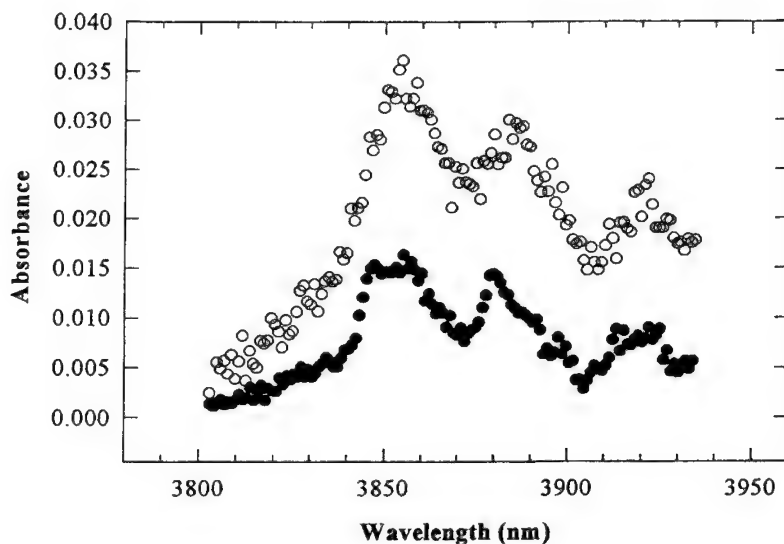


Figure 1. Diagram of triple-pass beam



**Figure 2.** Absorption spectra of  $N_2O$  in XM39 dark zone at 1.25 MPa with single- and triple-pass beams. Open circles are for the triple pass; solid circles, single pass.

#### DATA ANALYSIS

The change in intensity of a parallel beam of light with frequency  $\nu$  traveling through a medium in the  $+x$  direction with an absorptivity  $k(\nu)$ , is given by the differential absorption law,

$$-\frac{dI}{I} = k(\nu)dx \quad (2)$$

By integrating along the path length  $l$ , the intensity, after having transversed the region of interest, is given by

$$I = I_0 \exp[-k(\nu)l] \quad (3)$$

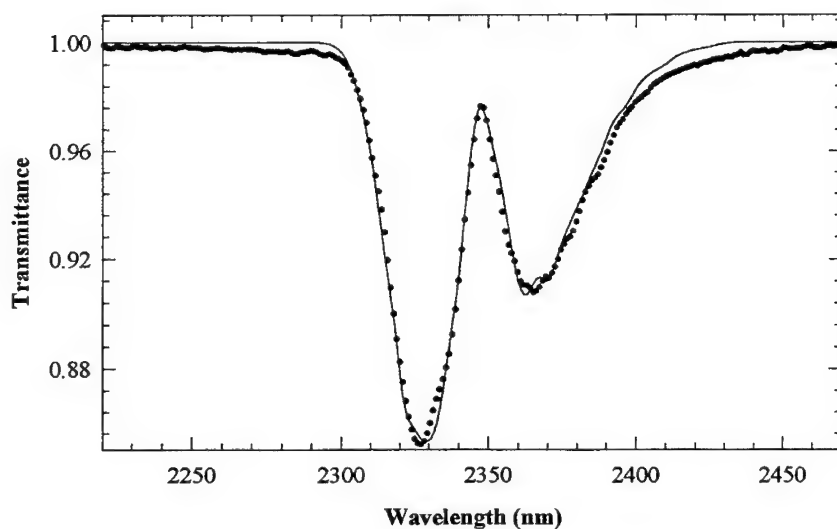
If a background absorption occurs over the pathlength and is only weakly dependent on  $\nu$ , the transmitted intensity  $I(\nu)$ , can be written as

$$I(\nu) = I_0 B(\nu) \exp[-k_w l] \quad (4)$$

where  $k_w$  is the absorption coefficient of the molecule of interest and  $B(\nu)$  represents a multiplicative background correction for a broadband attenuation along the path length. For conditions where the light source and spectrograph bandwidths are much larger than the width of a typical absorption line an instrument function,  $S(\nu, \nu_0)$ , centered at  $\nu_0$  is introduced to give

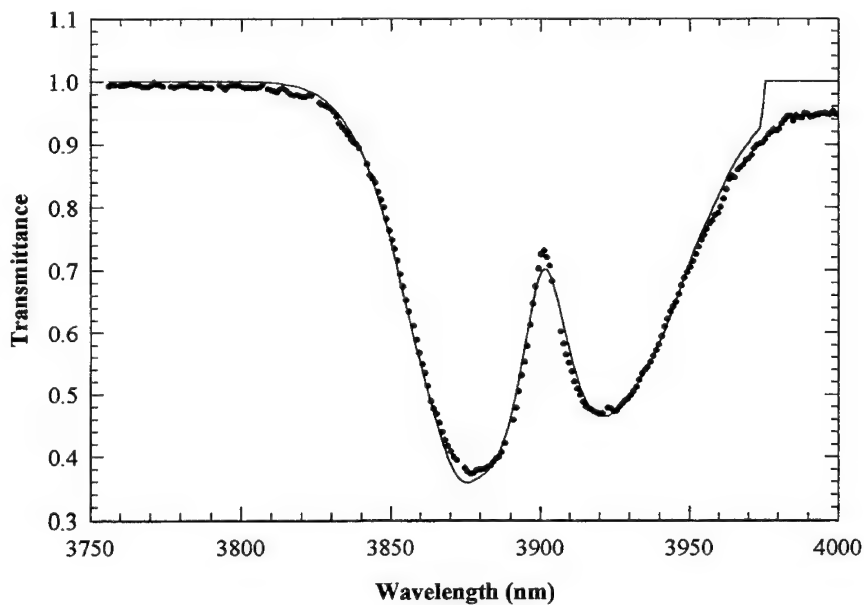
$$I_i = \int S(\nu, \nu_0) I(\nu) d\nu \quad (5)$$

where  $I_i$  is the integrated light transmitted.



**Figure 3.** Transmittance spectrum for the  $2\nu_1$  overtone of CO in a static cell at 423 K and 1.033 MPa. The points are the data and the solid line is the least-squares fit.

A nonlinear, multivariate, least-squares-fitting program using a Simplex algorithm<sup>9</sup> has been written for use within the Galactic Industries' GRAMS/386 environment. Molecular parameters and transition line strengths needed for the calculation of  $k_w$  are obtained from the HITRAN<sup>8,10</sup> database.



**Figure 4.** Transmittance spectrum for the  $2\nu_1$  overtone of N<sub>2</sub>O in a static cell at 370 K and 0.174 MPa. The points are the data and the solid line is the least-squares fit

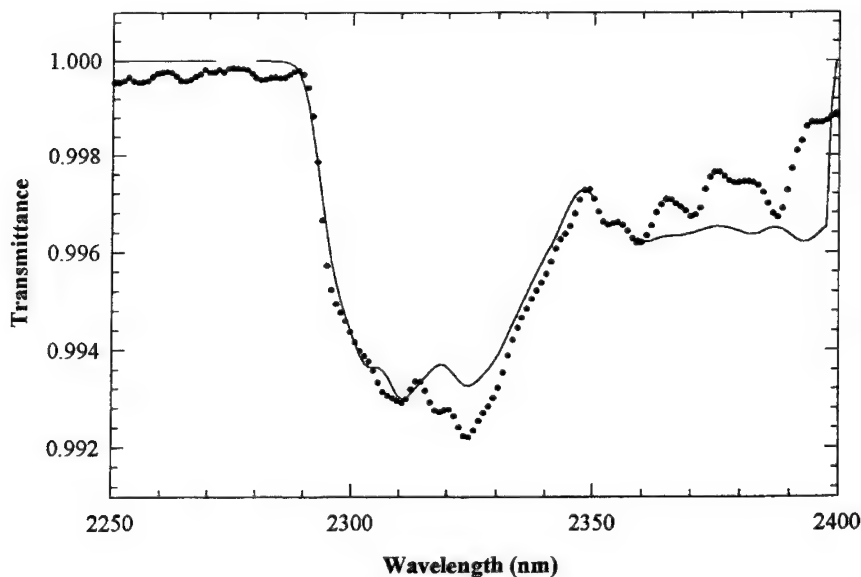
To test the fitting program, the static test was employed. A typical test-cell transmittance spectrum and fit for CO is shown in Figure 3. For this experiment the temperature and pressure conditions were set to 423 K and 1.033 MPa, respectively. A least-squares fit to these data gives a temperature of 419 K and pressure of 1.018 MPa. If it is assumed there is no error in the thermocouple and pressure gauge measurements, then the least-squares fit for temperature and pressure agrees to within 2%.

Likewise, Figure 4 illustrates a transmittance spectrum and fit for N<sub>2</sub>O where the test cell conditions are  $T = 370$  K and  $P = 0.174$  MPa. Least-squares fitting results in a temperature of 375 K and a pressure of 0.194 MPa. Here the agreement in temperature is within 2% and the pressure 6%.

The spectral resolution (2.3 nm) required as an input for fitting was obtained by measuring the width of a helium or argon emission line in the appropriate wavelength region. The shape of the emission lines were well represented by a Gaussian. Hence a Gaussian lineshape function was used to convolute the calculated spectrum to best approximate the effects of the instrument response. Additionally, the individual molecular transitions were approximated by a delta function shape since the light source is broad band and the resolution of the spectrometer is much broader than that of the molecular-rotational-transitions. These simplifications allowed for fitting on a personal computer486 processor, personal computer with common fitting times of a few minutes.

## RESULTS

A transmittance spectrum for the  $2\nu_1$  overtone of CO taken during steady-state combustion conditions of JA2<sup>11</sup> is shown in Figure 5. This spectrum was taken in the center section of the dark zone during combustion at 1.03 MPa nitrogen pressure. The JA2 propellant sample was a 0.64-cm diameter solid cylinder which was burned in a cigarette fashion, and the absorption pathlength was



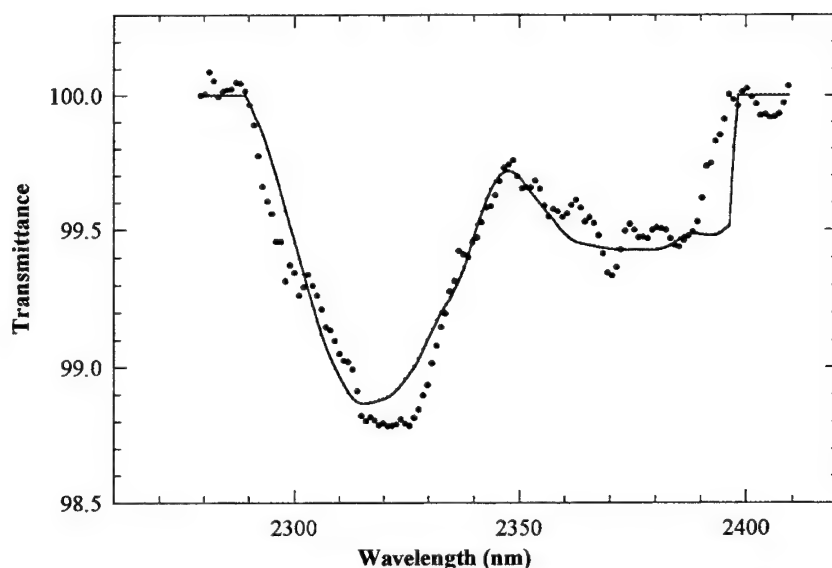
**Figure 5.** Transmittance spectrum for the  $2\nu_1$  overtone of CO taken in the dark zone of JA2 propellant burning in a 1.03 MPa nitrogen environment. The points are the data and the solid line is the least-squares fit.

assumed to be the propellant diameter. Maximum spatial resolution for these experiments was 0.25 cm, which is the diameter of the light beam. For these small absorptions, less than 1%, averaging of spectra was required. Typically 100 emission corrected spectra were obtained which takes about 4 seconds. While spectra gathering occurs, the propellant feed mechanism is feeding the propellant at about the same rate it is being consumed. This process lowers the spatial resolution somewhat and a conservative estimate for the overall resolution is 0.5 cm. Least-squares fitting of the data results in a temperature of 1476 K and 0.36 mole fraction of CO. Several other experimental runs were made for these conditions and the averages are reported in Table 1 along with other published results. No signals attributable to  $N_2O$  absorption could be identified in the dark zone of JA2 burning at 1.03 MPa pressure.

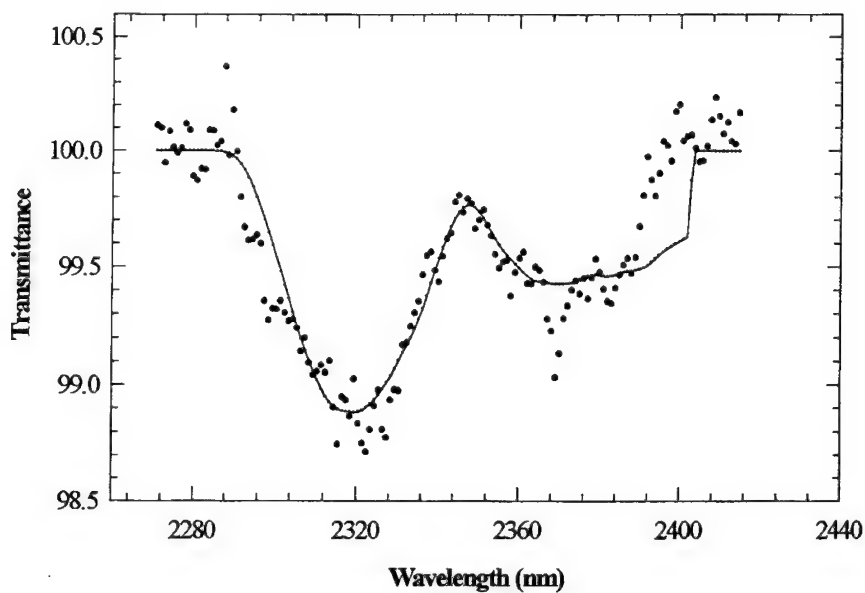
A nitramine propellant, XM39<sup>12</sup>, was also investigated. This propellant gave larger variations in combustion intensity behavior during the course of an experimental run as well as producing more smoke, often obscuring the beam. Lower CO concentration in the dark zone make measurement even more problematic. It was found that somewhat higher pressure (1.25 MPa) produced cleaner burns. A larger propellant diameter (1.08 cm) was used to increase the absorption zone; this also decreased the cold zone traversed by the beam in the chamber, reducing possible interference from cold gases. Use of the triple-pass optics was also beneficial in increasing the absorption signal. The transmittance spectrum for CO is shown in Figure 6. The least-squares fit for the data in Figure 6 gave values of 1040 K and 0.10 mole fraction CO. However, the experimental uncertainty was rather high, so the data were also fitted at a fixed temperature of 1150 K, an average value obtained previously from both IR<sup>5</sup> and uv-visible<sup>13</sup> absorption studies. This produced a CO mole fraction of 0.12.

Figure 7 shows a "single shot," a spectrum obtained over one cycle of the data collection. This spectrum is corrected for background within 20 ms of data collection, eliminating interference from all but very short term flame events. The fit produced values of about 1000K and 0.09 mole fraction CO.

Using similar techniques, absorption at 3900 nm, due at least in part to  $N_2O$ , produced the spectrum

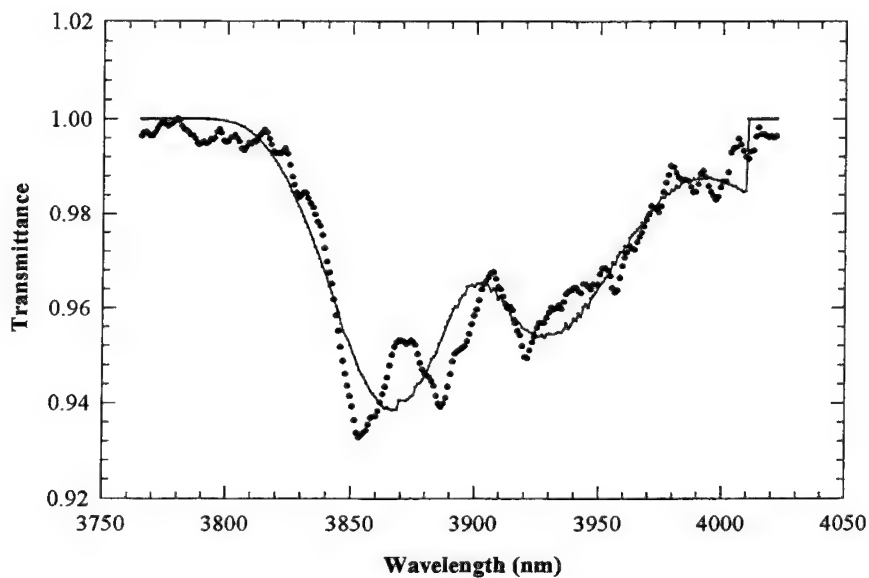


**Figure 6.** Transmittance spectrum for the  $2v_1$  overtone of CO taken in the dark zone of XM39 propellant burning in a 1.25 MPa nitrogen environment using the triple-pass optics. The points are



**Figure 7.** A "single shot" transmittance spectrum for the  $2v_1$  overtone of CO taken in the dark zone of XM39 propellant burning in a 1.25 MPa nitrogen environment using the triple-pass optics. The points are the data and the solid line is the least-squares fit.

shown in Figure 8. For the same reasons as above, these data were fitted at a fixed temperature of 1150 K, producing an upper limit of 0.018 for the mole fraction of  $N_2O$ .



**Figure 8.** Transmittance spectrum for the  $2v_1$  overtone of  $N_2O$  taken in the dark zone of XM39 propellant burning in 1.25 MPa nitrogen using the triple-pass optics. The points are the data and the



**Table 1**

Comparison of CO and N<sub>2</sub>O mole fractions measured in XM39 and JA2. A. Mallery and Thynell<sup>14</sup>, B,C. Present work, D. Lengelle et. al.<sup>15</sup>. d is the distance above the surface of the solid propellant.

Molecule	A - XM39 P = 21 atm d = 1.25 mm	B - XM39 P = 12.1 atm (1.25 MPa) d = 1.25-2.75 mm	C - JA2 P = 10 atm (1.03 MPa) d = 1.25 mm	D - DB2 <sup>16</sup> P = 9 atm d = 2 mm
CO	0.10	0.12	0.38	0.38
N <sub>2</sub> O	0.03	≤ 0.018	0	0
T	1200 K	1150 K (fixed)	1448 K	1500 K

### COMPARISON OF RESULTS

Several factors were considered for inclusion of published results. All the data in Table 1 are for steady-state unassisted combustion conditions. A direct comparison is available for XM39; in the case of JA2, a similar type propellant, DB2, was chosen. Both propellants are homogeneous and the experimental pressures used are almost identical, and the agreement for CO concentration is good for both comparisons. The dark zone temperature for JA2 was fitted in the present study and the comparison with DB2 is quite good. Our previously determined temperature<sup>5,13</sup> for the XM39 dark zone is similar to that of Mallery and Thynell<sup>14</sup>. While detectible quantities of N<sub>2</sub>O were found in XM39, the signal was noisy due to combustion intensity changes and a low detector quantum efficiency. Moreover it appears that another species is causing some absorptions. The comparisons indicate about a 40 per cent difference and this variation is probably within the experimental error considering the noisy nature of the data in both experiments. With the other species interference that we observe, the N<sub>2</sub>O concentration value given in Table 1 should more appropriately be considered an upper limit.

### SUMMARY

Improvements in the near-infrared overtone absorption spectroscopy experiment at Army Research Laboratory have permitted better measurement of two minor species, CO and N<sub>2</sub>O, concentrations in the dark zone of burning representative nitramine propellants (XM39) and homogeneous propellants (JA2). When compared with published work excellent agreement is found for CO concentrations but less satisfactory agreement for N<sub>2</sub>O. From a detailed chemical kinetic modeling standpoint, establishing an accurate value for this latter species is quite important. The gas composition of the propellant dark zone is fuel rich and thus an oxidizer such as N<sub>2</sub>O can play a pivotal role in major chemical steps. Infrared detection with InSb elements would give higher efficiency in this wavelength region and provide a more accurate determination of N<sub>2</sub>O concentration.

## REFERENCES

1. Kubota, N., Combustion Mechanisms of Nitramine Composite Propellants, in *Eighteenth Symposium (International) on Combustion*, The Combustion Institute, pp. 187-194, 1980
2. Vanderhoff, J.A., Species Profiles in Solid Propellant Flames Using Absorption and Emission Spectroscopy, *Combustion & Flame*, Vol. 84, pp. 73-92, 1991.
3. Vanderhoff, J.A., Teague, M.W. and Kotlar, A.J., Determination of Temperature and NO Concentrations through the Dark Zone of Solid-Propellant Flames, in *Twenty-Fourth Symposium (International) on Combustion*, The Combustion Institute, p. 1915-1922, 1992.
4. Modiano, S. H. and Vanderhoff, J. A., Multichannel Infrared Absorption Spectroscopy of Solid Propellant Flames, *Combustion & Flame*, Vol. 99, p. 187-189, 1994.
5. Modiano, S. H. and Vanderhoff, J. A., Multichannel Infrared Absorption Spectroscopy Applied to Solid Propellant Flames, *30th JANNAF Combustion Meeting*, CPIA Publ. No. 606, Vol. II, pp. 227-234, 1993.
6. Modiano, S. H. and Vanderhoff, J. A., Improvements in Infrared Absorption of Solid Propellant Flames, *31st JANNAF Combustion Meeting*, CPIA Publ. No. 620, Vol. II, p. 325-332, 1994.
7. Modiano, S. H. and Vanderhoff, J. A., Multichannel Infrared Absorption Spectroscopy Applied to Solid Propellant Flames, ARL Technical Report, Army Research Laboratory, in press.
8. Rothman, L. S., Gamache, R. R., Tipping, R. H., *et al.*, The HITRAN Molecular Database: Editions of 1991 and 1992, *J. Quant. Spectrosc. Radiat. Transfer*, Vol. 48, No. 5/6, p. 469-507, 1992.
9. Daniels, R. W., *An Introduction to Numerical Methods and Optimization Techniques*, North Holland Publ., Amsterdam, 1978.
10. We used an updated HITRAN database for the CO molecule. This database was developed to be able to better represent higher temperature conditions. HITRAN 1992 was used for the N<sub>2</sub>O molecule.
11. The major ingredients for JA2 propellant are (by weight per cent): nitrocellulose, 58.2%, nitroglycerin, 15.8%, and diethyleneglycoldinitrate, 25.2%. The nitration level of the nitrocellulose is 13.04%.
12. The major ingredients for XM39 propellant are (by weight per cent): cyclotrimethylene-trinitramine, 76%, cellulose acetate butyrate, 12%, acetyl-triethyl- citrate, 7.6%, and nitrocellulose, 4%. The nitration level of the nitrocellulose is 12.6%.
13. Teague, M. W., Singh, G. and Vanderhoff, J. A., Spectral Studies of Solid Propellant Combustion IV: Absorption and Burn Rate Results for M43, XM39, and M10 Propellants, ARL-TR-180, pg 8, 1993.
14. Mallory, C. F. and Thynell, S. T., Solid Propellant Flame Diagnostics Using Fourier Transform Infrared (FT-IR) Spectrometry, ARO/URI Program Review, Sandia National Laboratory, 1995.
15. Lengelle, G., Bizot, A., Duterque, J., and Trubert, J. F., Steady State Burning of Homogeneous Propellants, in *Fundamentals of Solid Propellant Combustion*, edited by K. Kuo and M. Sommerfield, AIAA Progress in Astronautics and Aeronautics Series, Vol. 90, 1984.
16. The major ingredients for DB2 propellant are (by weight per cent): nitrocellulose, 52%, and nitroglycerin, 43%. The nitration level of the nitrocellulose is 11.6%. The reported gas composition was renormalized to include 0.2 mole fraction H<sub>2</sub>O.

# DETERMINATION OF TEMPERATURE AND OH CONCENTRATION PROFILES OF RDX/CAB PSEUDO PROPELLANTS USING UV/VISIBLE ABSORPTION SPECTROSCOPY

Abdullah Ulas, Yeu-Cherng Lu, and Kenneth K. Kuo  
Mechanical Engineering Department  
The Pennsylvania State University  
University Park, PA 16802, USA

**ABSTRACT:** In this paper, burning rates, temperature and OH concentration profiles of pure RDX and pseudo propellants containing RDX with CAB binder having 8, 11, and 14 percent by weight were determined. UV/Visible absorption spectroscopy was used as the diagnostic technique to determine the gas-phase temperature and OH species concentration profiles. The deduced final flame temperatures from absorption measurements are 3062 K for pure RDX, 2990 K for RDX/CAB (92/8%), 2806 K for RDX/CAB (89/11%), and 2742 K for RDX/CAB (86/14%) at 0.45 MPa. In order to examine the pressure dependency of final flame temperatures and OH mole fractions, absorption measurements were also conducted at 0.17 and 0.79 MPa for pure RDX. The results showed that pure RDX has a final flame temperature of around 2950 K at 0.17 MPa and 3220 K at 0.79 MPa. The deduced final flame temperatures are in good agreement with equilibrium calculations. The deduced OH concentrations from absorption measurements are lower than equilibrium calculations due to the non-one-dimensionality of the flame causing uncertainties in the effective pathlength of the light beam. During the tests, it was observed that there was no multi-stage flame structure for both pure RDX and pseudo propellants with RDX/CAB mixtures. Thermocouple measurements for pure RDX indicated that the surface temperature is about 600 K at 0.17 MPa and 675 K at 0.79 MPa.

## INTRODUCTION

Understanding the physics and chemistry of solid propellant combustion process is challenging, since solid propellant combustion involves complex heat and mass transfer processes with chemical kinetics. Nonetheless, the formulation of new highly energetic propellants requires a complete understanding of the chemical and physical mechanisms controlling their ignition and combustion processes. Determination of temperature and species concentration profiles of solid-propellant flames under various operating conditions is the first step in understanding the combustion of solid propellants. These data are used to build up detailed chemical kinetic mechanisms of solid propellant combustion. Theoretical models are also necessary in the prediction of combustion

behavior of energetic propellants since testing and optimization are expensive and sometimes difficult to achieve.

Solid propellants are designed by combining energetic materials [e.g., RDX (cyclotrimethylene trinitramine) and HMX (cyclotetramethylene tetranitramine)] with polymeric binders that provide the necessary mechanical properties to form certain grain shapes with acceptable densities. These binder materials and other additives, such as stabilizers and plasticizers, generally have a major effect on propellant ignition and combustion processes. The model simulation of solid propellants with all ingredients is very difficult for several reasons. The major limitation is that thermal decomposition processes and associated chemical kinetic rates are not known for many propellant ingredients. The decomposition processes of only a few propellant ingredients have been studied.[1] Furthermore, complex physico-chemical interactions between propellant ingredients could occur when they are mixed. One of the possible processes is the formation of solid solution (e.g., between RDX and CAB) which changes the purity and properties of propellant ingredients.[2]

Recently, many research programs have focused on modeling and testing of pure RDX ( $C_3H_6N_6O_6$ ), since RDX has been widely adopted in low vulnerability ammunition (LOVA) propellants due mainly to its low vulnerability to thermal initiation of ignition, and partly to its low cost.[1-8,15,16] During the combustion of RDX, a large amount of thermal energy is released and a high percentage of low molecular weight product gases is generated. These characteristics make RDX very attractive in the formulation of new gun and rocket propellants. In a companion study, a 1-D computational model developed by Liao and Yang successfully simulated the steady-state combustion processes of pure RDX.[3] A logical way of advancing combustion models for composite propellants is to study a pseudo propellant which contains only a few ingredients. In this experimental work and a companion theoretical modeling effort, pseudo propellants containing RDX and CAB (cellulose acetate butyrate,  $C_{15}H_{22}O_8$ ) were selected since these two ingredients have been widely used in LOVA propellants.

The objectives of this research are: (1) to provide experimental data on burning rate, temperature and OH concentration profiles of pure RDX and pseudo propellants containing different amount of RDX and CAB binder for guiding model development and validation, (2) to observe the ignition and combustion behavior of these pseudo propellants, and (3) to examine the pressure dependency of final flame temperatures and OH mole fractions. In order to determine the effect of percentage of CAB on the ignition and combustion processes, four different formulations were studied: pure RDX, RDX/CAB (92/8%), RDX/CAB (89/11%), and RDX/CAB (86/14%).

Absorption spectroscopy was used as the diagnostic technique to measure the gas-phase temperature and OH concentration profiles of pure RDX and three RDX/CAB pseudo propellants. Absorption spectroscopy is a non-intrusive optical diagnostic technique for simultaneous determination of temperature and absolute concentration of chemical species from one measured spectrum. Although it is a simple and relatively inexpensive technique, it has sufficient sensitivity even for the detection of the transient species with low concentrations in the flame zone. Spatial resolutions as low as 50  $\mu m$  can be achieved to probe species which are found in a very thin propellant flame zone.[5] Absorption spectroscopy does not suffer from the collisional quenching effect, which is a major limitation for other linear optical techniques such as laser induced fluorescence (LIF), especially at higher pressures. This technique has been successfully applied for the measurements of diatomic molecules, such as OH, NH, CN, and NO.[5,8-10,15,16] The basic limitation of the absorption spectroscopy is that it is a line-of-sight measurement method which requires the flame-zone structure to be one-dimensional. When the flame structure is not one-dimensional, determination of the effective pathlength of the light beam becomes very difficult, which in turn causes discrepancies in the deduced species concentration since assumed pathlength and species concentration are almost inversely proportional.

## EXPERIMENTAL SETUP

The experimental setup used for this work is very similar to that reported in Lu et al.[9] Therefore, only a brief description of the test facility is given below.

Absorption transitions of OH molecules in solid propellant flames were achieved by passing a 450-Watt Xenon arc-lamp light beam across the flame zone. A portion of the light energy is absorbed by OH molecules in the propellant flame. The transmitted component of the light is focused onto a 100  $\mu\text{m}$  pinhole and then onto the entrance slit of the spectrometer through fused-silica lenses. The pinhole reduces the emission signals from the propellant flame which reach the entrance of the spectrometer and its diameter governs the spatial resolution of the measurements (around 150  $\mu\text{m}$ ).

The focal length of the fused-silica lenses is a function of the wavelength of the light beam. At 589.3 nm, the focal length is 25.4 cm and it varies significantly when the wavelength decreases to the UV range. The focal length at any other wavelength  $\lambda$  can be computed by using the thin lens formula:

$$f_{\lambda} = f_{589.3} (n_{589.3} - 1) / (n_{\lambda} - 1) \quad (1)$$

where  $n_{\lambda}$  is the index of refraction at wavelength  $\lambda$ . For OH measurements, the focal length was taken as 23.9 cm at 306 nm. Then, the distances between the lens and the focal point on each focusing side were adjusted accordingly.

The spectrometer has a focal length of 75 cm and a grating with 1200 grooves/mm. The grating is blazed at 250 nm on the first order with about 65% efficiency at 230 nm and about 73% at 250 nm. The spectral resolution was around 0.36 Angstroms at full width half maximum (FWHM) when the slit opening was set at 38  $\mu\text{m}$  for OH measurements. The dispersed light was detected by a thermoelectrically cooled CCD camera and stored in a microcomputer for data processing. The CCD camera covered a 28 nm band of light when the grating was operated in the first order.

Pseudo propellants were prepared by pressing shock precipitated mixtures of recrystallized RDX and CAB powders in a cylindrical presser system. The recrystallized RDX powder was extracted from military grade RDX which also contains 5 to 10% of HMX.[7] A recrystallization process was applied to remove the HMX. After this process, the amount of HMX was reduced to a range below 0.3%.[7] The procedure for recrystallization of RDX is explained in detail in Ref. 8. After obtaining pure RDX powder, a shock precipitation procedure used by Boyer et al. was followed to prepare RDX/CAB mixtures.[2] In this process, the desired amount of pure RDX and pure CAB powders were mixed in acetone until they dissolved completely. The amount of acetone was determined from the solubility of RDX and CAB in acetone. To achieve shock precipitation of the RDX/CAB mixture, the solution was then dumped into distilled water which was about ten times larger in volume than the acetone. Immediately after dumping, it was observed that the white colored RDX/CAB powder started to precipitate to the bottom of the container. After 10 to 20 minutes, the solution was filtered to remove RDX/CAB powder. The wet RDX/CAB powder was dried at 55°C for at least 4 hours to remove moisture. The RDX/CAB mixtures were then pressed at 274.8 MPa into cylindrical pellets of 0.64 cm in diameter and 0.8 to 1.5 cm in length in a specially designed computer-controlled presser system.[7]

Propellant samples were ignited by a CO<sub>2</sub> laser and burned inside a windowed-high-pressure strand-burner under well-controlled operating conditions. A linear actuator system was employed to feed the propellant sample at a pre-specified speed so that the propellant surface could be either kept at a fixed position or controlled to regress downward at a slow speed relative to the light beam location during burning. Thus, either multiple sampling at a fixed position or scanning through the flame

zone could be conducted in a single test. Nitrogen purge gas flow was supplied during tests to carry combustion product gases out of the test chamber. Sampling time was 0.04 seconds with 28-34 samplings of spectra per test.

## DATA ANALYSIS

The data-reduction program was exactly the same as that presented in Ref. 9. This program was based on Beer's law to extract temperature and concentration from the measured absorption spectrum. Since the spectrometer's bandwidth was larger than the linewidth of a typical transition line, convolution between molecular absorption and instrument function was required and considered. Due to scattering and absorption by soot particulates and large molecules, strong attenuation of the transmitted light was observed; the attenuation effect was displaced by shifting the baseline away from unity in either linear or non-linear fashion. By assuming Boltzmann distribution, the observed transmittance  $\tau$  at any wavenumber  $\nu_0$   $\text{cm}^{-1}$  can be described by the following equation.[10]

$$\tau(\nu_0) = (A_0 + A_1\nu_0 + A_2\nu_0^2) \times \int_{-\infty}^{\infty} S(\nu, \nu_0) \exp\left[-\frac{h\nu b}{c} \frac{N_T}{q(T)} \sum_j B_j g_j e^{-E_j/kT} P_j(\nu)\right] d\nu \quad (2)$$

where  $h$  is the Planck constant,  $b$  the path length,  $c$  the speed of light,  $k$  the Boltzmann constant,  $T$  the absolute temperature,  $B_j$  the Einstein coefficient for the  $j$ th transition in energy density units,  $g_j$  the degeneracy of the  $j$ th energy level,  $E_j$  the energy of the  $j$ th level,  $P_j(\nu)$  the transition line shape,  $N_T$  the total number density,  $q(T)$  the partition function, and  $S$  the normalized instrument function. The summation  $j$  was performed over all of the energy transitions which contribute to the light absorption at wavenumber  $\nu_0$ . The second-order polynomial  $A_0 + A_1\nu_0 + A_2\nu_0^2$  was used to account for the baseline shift.

Each transitional line was treated as a Dirac-Delta function to improve the efficiency of data analysis. As demonstrated in Ref. 9, line broadening at elevated pressures as high as 6.99 MPa does not change the characteristics of absorption signals nor deteriorate the quality of the curve fit; thus, the Delta-function treatment for transitional lineshape is acceptable for 0.17-0.79 MPa range considered in this paper. Since the calibration between wavelengths and CCD pixels using the Hg lamp was only an approximation, adjustment of wavelengths in measured spectra was considered in data analysis.[9] To further simplify the data reduction, an average instrument bandwidth was used for the wavelength range of interest. The final equation for curve-fitting the observed transmittance at any wavenumber  $\nu_0$  is given below.[9]

$$\tau(\nu_0) = (A_0 + A_1\nu_0 + A_2\nu_0^2) \times \left\{ 1 - \sum_j S(\nu_j, \nu_0) \times \left[ 1 - \exp\left(-\frac{h\nu_j b}{c} \frac{N_T}{q(T)} B_j g_j e^{-E_j/kT}\right) \right] \right\} \quad (3)$$

The measured absorption spectra were used as the input files for the data analysis program. The program analyzed the measured spectrum and adjusted a set of parameters including temperature, number density, etc. to best fit the data by the least-squares method. The Einstein coefficients, degeneracies, and energy levels for OH were obtained from Kotlar.[11] One hundred fifty three transitions in the  $A^2\Sigma - X^2\Pi$  (0,0) vibrational band system were considered in the data analysis. Other molecule-specific parameters were obtained from Huber and Herzberg.[12] Levenberg-Marquardt's algorithm was used to perform the least-squares analysis for the measured absorption spectra.[13] Absolute number density was converted to mole fraction and molar concentration using the perfect gas law.

## RESULTS AND DISCUSSION

### 1. In-Situ Observations of Pure RDX and RDX/CAB Pseudo Propellants

OH absorption measurements for pure RDX and the three pseudo propellants were conducted at 0.45 MPa. At a higher pressure of 0.79 MPa, the flame spread down the lateral side surfaces of RDX/CAB (92/8%) pellets even under high purge flow rates. For pure RDX, tests were also conducted at 0.17 and 0.79 MPa to examine the effect of pressure on temperature and OH concentration. An attempt was made to study the RDX/CAB (84/16%) pseudo propellant; however, no adequate OH absorption was detected.

At 0.17 MPa, there was a very thick, bubbling foam layer on the burning surface region of pure RDX with a maximum thickness of about 0.4 to 1 mm (which is inherently unsteady). The foam layer exhibited a dome shape due to the effects of surface tension and cooling of the nitrogen purge gas. At 0.17 MPa, a dark zone with a thickness of about 0.1 to 0.2 mm was present between the luminous flame and the burning surface. The flame structure of pure RDX at 0.17 MPa was not uniform, i.e. there were few (one or two) bright columns of flame (flamelets) surrounded by a less luminous zone. At higher pressures (i.e., 0.45 and 0.79 MPa), the size of the foam layer was reduced and there was no visible dark zone. Figure 1 shows a typical flame structure of pure RDX at 0.45 MPa. As can be seen, bright flamelets still existed at this high pressure and became much elongated and isolated. The luminosity of the flame was greater than those at 0.17 MPa. The number of bright flamelets increased with an increase of pressure.

The flame structure of RDX/CAB (92/8%) pseudo propellant at 0.45 MPa was quite different than that of pure RDX. Again, there was no visible dark zone and foam layer at 0.45 MPa. However, the flame structure of RDX/CAB (92/8%) pseudo propellant was more uniform than that of pure RDX. There were one or two flamelets having nearly uniform luminosity as shown in Fig. 2. The flame width was smaller than the pellet diameter of 0.64 cm. As the percentage of CAB was increased to 11%, there was intermittent appearance of flamelets in the gas-phase region. These flamelets were much narrower, less bright and shorter in length than those of RDX/CAB (92/8%). At other times, there was no visible flame in the gas-phase region as can be seen in Fig. 3. In some tests, flame spreading down the lateral side surface of the pellet was observed. The increase of the CAB percentage to 14% further reduced the occurrence of the visible flame. During each test (about 15 seconds), the visible flame was seen for only two or three times and the flame was almost invisible during the rest of the test. These visible flames were short-lived and less bright than those of RDX/CAB (89/11%) pseudo propellant.

### 2. Burning Rates

Burning rates of pure RDX and three pseudo propellants were determined from video records. At 0.45 MPa, the burning rates were found to be  $0.95 \pm 0.05$  mm/s for pure RDX,  $0.71 \pm 0.05$  mm/s for RDX/CAB (92/8%),  $0.68 \pm 0.07$  mm/s for RDX/CAB (89/11%), and  $0.52 \pm 0.02$  mm/s for RDX/CAB (86/14%). These burning rates can be fitted into the following equation as shown in Fig. 4:

$$r_b = 0.9543 - 0.029 \times [\% \text{ CAB}] \quad (4)$$

At 0.17 and 0.79 MPa, burning rates of RDX are  $0.42 \pm 0.05$  mm/s and  $1.52 \pm 0.06$  mm/s, respectively. Burning rates of pure RDX can be fitted to the equation  $r_b = a P^n$  with  $n = 0.836 \pm 0.002$  and  $a = 1.850 \pm 0.002$ .

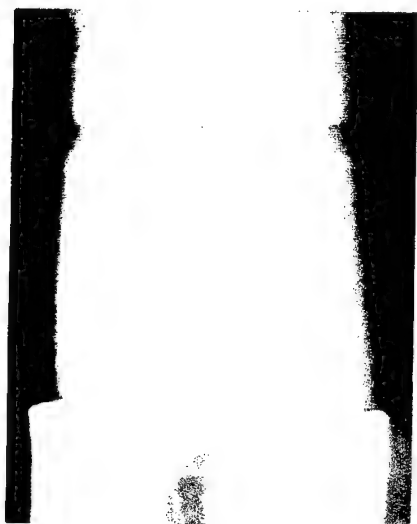


Figure 1. RDX flame at 0.45 MPa

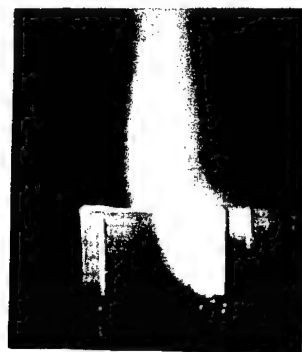


Figure 2. RDX/CAB (92/8%) flame at 0.45 MPa

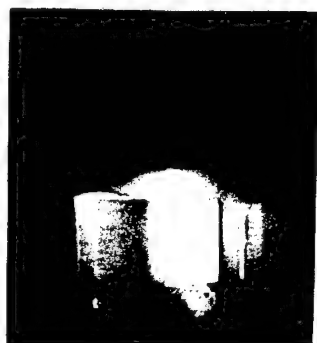


Figure 3. RDX/CAB (89/11%) flame at 0.45 MPa

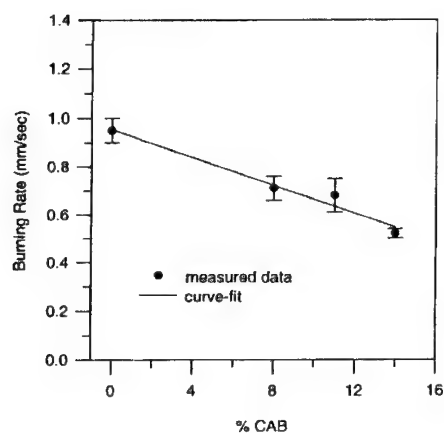


Figure 4. Burning rates of RDX/CAB pseudo propellants as a function of percentage of CAB at 0.45 MPa



### 3. Absorption and Thermocouple Measurements

Figures 5 and 6 show typical absorption spectra for OH molecule in RDX/CAB (92/8%) and RDX/CAB (86/14%) pseudo propellants taken at 0.45 MPa, respectively. The circles represent the measured transmittance which were used as input data for the data reduction program. The solid line represents the curve fit by the data reduction program. The deduced temperature and OH concentration are 2970 K and  $4.44 \times 10^{16}$  molecules/cm<sup>3</sup> for Fig. 5 and 2477 K and  $1.70 \times 10^{16}$  molecules/cm<sup>3</sup> for Fig. 6. Figures 5 and 6 also show the baseline shift and the quality of the resolved rotational transition lines. From these two figures, it is clear that as the percentage of CAB increases, the absorption by OH molecules decreases since the absolute concentrations of OH decrease with an increase in CAB percentage. Many similar tests were conducted to obtain the OH concentration and temperature profiles for the pure RDX and three pseudo propellant flames.

Figures 7 through 12 show the temperature and OH concentration profiles of pure RDX flames at 0.17, 0.45, and 0.79 MPa and the three pseudo propellant flames at 0.45 MPa. In Fig. 7, the temperatures and OH concentrations of pure RDX flame at 0.17 MPa increase from the surface and reach their maximum values at about 1.38 mm above from the surface. The decreasing trend of the temperature and OH concentration in the luminous region (beyond 2 mm) is due mainly to the heat and mass transfer processes between the flame and the purge gas. Figures 8 and 9 show the temperature and OH concentration profiles of pure RDX flame at 0.45 and 0.79 MPa, respectively. The profiles are similar to that at 0.17 MPa, except the plateau regions are reached at locations closer to the burning surface (i.e., 0.42 mm at 0.45 MPa and 0.29 mm at 0.79 MPa). Figures 10 through 12 show the temperature and OH concentration profiles of RDX/CAB (92/8%), RDX/CAB (89/11%), and RDX/CAB (86/14%) pseudo propellant flames at 0.45 MPa. The plateau temperature and OH concentration zones occur at locations about 0.76 mm for RDX/CAB (92/8%), 1.15 mm for RDX/CAB (89/11%), and 0.8 mm for RDX/CAB (86/14%) above from the surface. The pronounced cooling effect on the flame starts beyond 2.7 mm for RDX/CAB (92/8%), 1.9 mm for RDX/CAB (89/11%), and 1.6 mm for RDX/CAB (86/14%).

According to these profiles, the final flame temperatures of pure RDX are 2950 K at 0.17 MPa, 3062 K at 0.45 MPa, and 3220 K at 0.79 MPa and for the three pseudo propellants the final flame temperatures at 0.45 MPa are 2990 K for RDX/CAB (92/8%), 2806 K for RDX/CAB (89/11%), and 2742 K for RDX/CAB (86/14%). The equilibrium flame temperatures and OH mole fractions for these pseudo propellants and pure RDX were calculated using the CEC76 code and are indicated in Figs. 7 through 12.[14] The heat of formation of RDX and CAB were taken as +14,690 and -117,950 cal/mole in these calculations. It is evident that there are good agreements between the deduced final flame temperatures and the calculated equilibrium temperatures. The deduced OH mole fractions are lower than the equilibrium values by a factor of 2 to 3 for pure RDX and 28 - 48% for the three pseudo propellant. The difference is mainly caused by the highly non-one-dimensional nature of the pure RDX flame and uncertainties in the pathlength of the light beam. From the video records, it was observed that the flame structures of pure RDX were highly non one dimensional and the flame widths of pure RDX and the three pseudo propellants were smaller than the pellet diameter. In the data analysis, the pellet diameter of 0.64 cm was used as the pathlength. The propellant diameter is greater than the effective pathlength due to the above mentioned effects. Therefore, the deduced OH concentrations are lower than the equilibrium calculations since concentration and pathlength are nearly inversely proportional to each other for a given transmittance. The determination of the effective pathlength of the light beam is not easy, especially in non-one-dimensional flames. To achieve consistency in data reduction, a constant pathlength of pellet diameter was thus used for all tests. It is noted that pathlength has a greater effect on deduced species concentration than on temperature; therefore, the actual flame temperatures can still be determined without appreciable error.

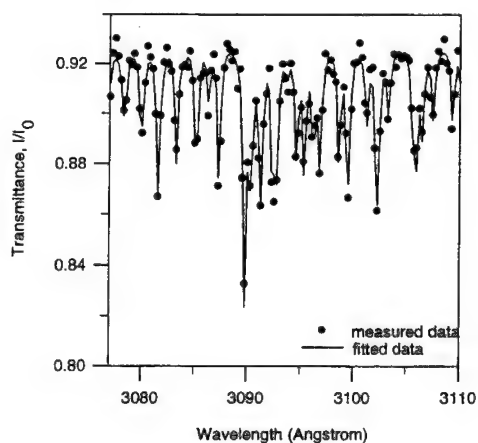


Figure 5. A typical absorption spectrum of RDX/CAB (92/8%) pseudo propellant at 0.45 MPa for deducing one pair of temperature and number density (dots: measured data, line: fitted result)

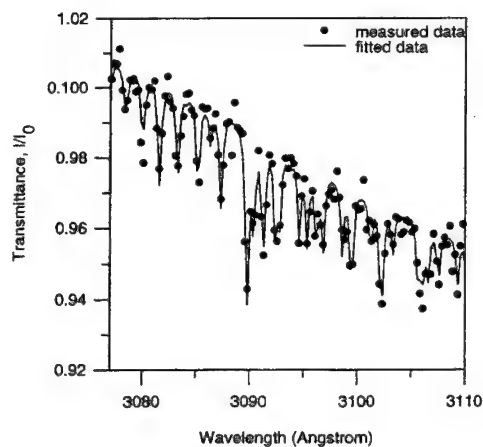


Figure 6. A typical absorption spectrum of RDX/CAB (86/14%) pseudo propellant at 0.45 MPa for deducing one pair of temperature and number density (dots: measured data, line: fitted result)

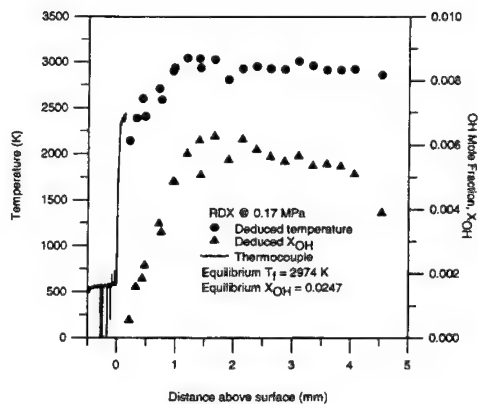


Figure 7. Deduced gas-phase temperature and OH mole fraction profiles of RDX flame at 0.17 MPa

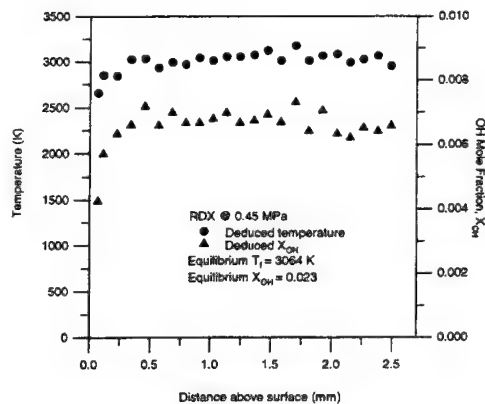


Figure 8. Deduced gas-phase temperature and OH mole fraction profiles of RDX flame at 0.45 MPa

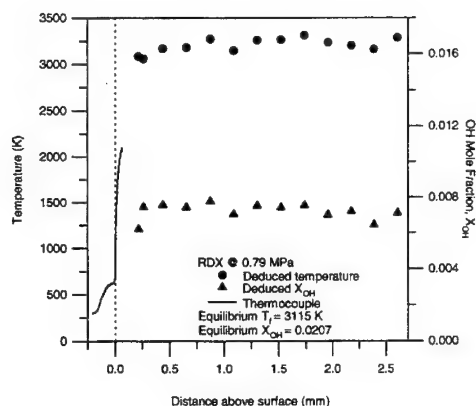


Figure 9. Deduced gas-phase temperature and OH mole fraction profiles of RDX flame at 0.79 MPa

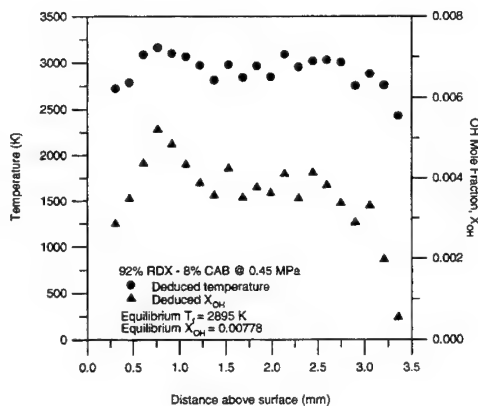


Figure 10. Deduced gas-phase temperature and OH mole fraction profiles of RDX/CAB (92/8%) pseudo propellant flame at 0.45 MPa

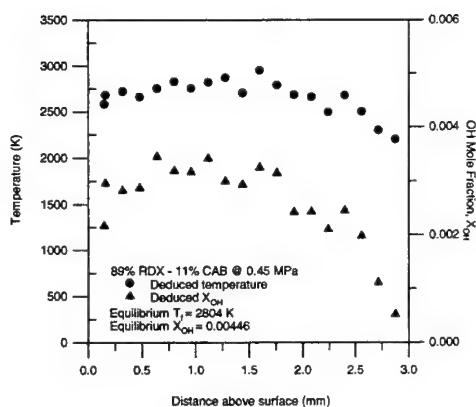


Figure 11. Deduced gas-phase temperature and OH mole fraction profiles of RDX/CAB (89/11%) pseudo propellant flame at 0.45 MPa

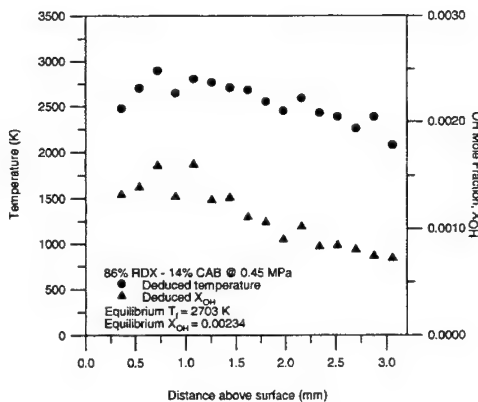


Figure 12. Deduced gas-phase temperature and OH mole fraction profiles of RDX/CAB (86/14%) pseudo propellant flame at 0.45 MPa

Fine wire tungsten/rhenium thermocouples (25  $\mu\text{m}$  in diameter) were used to measure temperature profiles of pure RDX at 0.17 and 0.79 MPa. These profiles are also shown in Figs. 7 and 9. Tests indicated that the surface temperature of RDX is about 600 K at 0.17 MPa and about 675 K at 0.79 MPa. The final flame temperatures could not be measured due to the burn out of thermocouples.

## CONCLUSIONS

UV/Visible absorption spectroscopy was applied to simultaneously determine temperature and OH concentration profiles of the flames of pure RDX at 0.17, 0.45, and 0.79 MPa and three RDX pseudo propellants containing CAB (8%, 11%, and 14% by weight) at 0.45 MPa. The deduced final flame temperatures of pure RDX are about 2950 K at 0.17 MPa, 3062 K at 0.45 MPa, and 3220 K at 0.79 MPa and the deduced final flame temperatures of three pseudo propellants are about 2990 K for RDX/CAB (92/8%), 2806 K for RDX/CAB (89/11%), and 2742 K for RDX/CAB (86/14%). These values are in good agreement with the results of equilibrium calculations. The line-of-sight averaged OH concentrations are lower than those predicted by equilibrium calculations due to the non-one-dimensionality of the flames causing an uncertainty in the effective pathlength of the flame. From the recorded video images, it was observed that only pure RDX flame at 0.17 MPa exhibited a thin dark zone region (0.1 to 0.2 mm in thickness); none of the pseudo propellants containing RDX/CAB mixtures exhibited a dark-zone region at 0.45 MPa. Thermocouple tests for pure RDX indicated that the surface temperature is about 600 K at 0.17 MPa and 675 K at 0.79 MPa. In addition, the final flame temperatures and OH mole fractions of RDX/CAB pseudo propellant flames decrease with an increase in CAB content.

## ACKNOWLEDGMENTS

This work was performed under the sponsorship of the Army Research Office, Contract No. DAAL03-92-G-0118. The support and encouragement of Dr. Robert W. Shaw of ARO are highly appreciated.

## REFERENCES

1. Oyumi, Y. and Brill, T. B., Thermal Decomposition of Energetic Materials 3. A High-Rate, In-Situ, FTIR Study of the Thermolysis of RDX and HMX with Pressure and Heating Rates as Variables, *Combustion and Flame*, 62, pp. 213-224, 1985.
2. Boyer, E., Brown, P. W., and Kuo, K. K., Phase Relationships Involving RDX and Common Solid Propellant Binders, 4-060-PP-R, Fourth International Symposium on Special Topics in Chemical Propulsion: Challenges in Propellants and Combustion 100 Years After Nobel, Stockholm, Sweden, 1996.
3. Liao, Y. C. and Yang, V., Analysis of Nitramine Propellant Combustion with Two-Phase Subsurface Reactions, *Proceedings of the 31<sup>st</sup> JANNAF Combustion Meeting*, 1994.
4. Melius, C. F., The Gas Phase Chemistry of Nitramine Combustion, *Proceedings of the 25<sup>th</sup> JANNAF Combustion Meeting*, 1988.
5. Donna Hanson-Parr and Tim Parr, RDX Flame Structure, *Proceedings of the 25<sup>th</sup> International Symposium on Combustion (The Combustion Institute)*, Paper 25-329, 1994.
6. Litzinger, T. A., Lee, Y. J., and Tang, C. J., A Study of the Gas-Phase of RDX Combustion Using a Triple Quadrupole Mass Spectrometer, *Proceedings of the 31<sup>st</sup> JANNAF Combustion Meeting*, 1994.

7. Boyer, E., Lu, Y. C., Desmarais, K., and Kuo, K. K., Observation and Characterization of Burning Surface Reaction Zones of Solid Propellants, *Proceedings of the 31<sup>st</sup> JANNAF Combustion Meeting*, 1994.
8. Ulas, A., Master Thesis, Mechanical Engineering Department, The Pennsylvania State University, 1996.
9. Lu, Y. C., Freyman, T., and Kuo, K. K., Measurement of Temperatures and OH Concentrations of Solid Propellant Flames Using Absorption Spectroscopy, *Combustion Science and Technology*, 104, pp. 193-205, 1995.
10. Vanderhoff, J. A. and Kotlar, A. J., Simultaneous Determination of Temperature and OH Concentrations in a Solid Propellant Flame, *Proceedings of the 23<sup>rd</sup> Symposium (International) on Combustion*, pp. 1339-1344, 1990.
11. Kotlar, A. J., Private communication, U.S. Army Research Laboratory, 1994.
12. Huber, K. P. and Herzberg, G., *Molecular Spectra and Molecular Structure IV. Constants of Diatomic Molecules*, Van Nostrand Reinhold., 1979.
13. Press, W.P., Flannery, B. P., Teukolsky, S. A. and Vetterling, W. T., *Numerical Recipes*, Cambridge University Press, Chap. 14, 1986.
14. Gordon, S. and McBride, B. J., Computer Program for Calculation of Complex Chemical Equilibrium Compositions, Rocket Performance, Incident and Reflected Shocks, and Chapman-Jouguet Detonations, NASA SP-273, Interim Revision, 1976.
15. Lu, Y. C., Ulas, A., Kuo, K. K., and Freyman, T. M., Absorption Spectroscopy of Solid Propellant Flames, AIAA 95-2713, 31<sup>st</sup> AIAA/ASME/SAE/ASEE Joint Propulsion Conference and Exhibit, July 10-12, 1995, San Diego, CA.
16. Ulas, A., Lu, Y. C., Kuo, K. K., and Freyman, T. M., Measurement of Temperatures and NO and OH Concentrations of Solid Propellant Flames Using Absorption Spectroscopy, *Proceedings of the 32<sup>nd</sup> JANNAF Combustion Meeting*, 1995.

## COMMENTS

**Viktor S. Abrukov, Cheboksary, Russia:** Recently a new integral approach to various optical techniques have been developed (interferometry, spectroscopy, Mie scattering, etc.). For example, a total number of molecules (radicals, etc.)  $M$ , absorbing a particular light wavelength can be determined by the following formula:

$$M = (1/b_\lambda) \iint \ln[I_{0,\lambda}/I_\lambda(x,y)] dx dy$$

where  $b$  is the average absorption cross-section of the molecules,  $I_{0,\lambda}$  is the initial illumination,  $I_\lambda(x,y)$  is the illumination distribution in the recording plane (with coordinates  $x$  and  $y$ ). I think this approach will be able to solve some practical problems in propellant combustion research.

**Author's Reply:** The measurement of intensity distribution in the recording plane as a function of both  $x$  and  $y$  is practically impossible. In the line-of-sight spectroscopic techniques, intensity is assumed to be constant along the pathlength. However, one can still measure intensity at different radial positions and then have an average number of molecules. But, when you conduct measurements away from the centerline, the cooling effect along the outer rim of the flame would increase and the average number of molecules would still be far from the actual one. Therefore, it would be much preferable to measure intensity along the centerline of the propellant where the pathlength is maximum and effect of cooling is relatively minimum.

## COMBUSTION PHENOMENA OF BORON CONTAINING PROPELLANTS

W. Eckl, N. Eisenreich, W. Liehmann, K. Menke, Th. Rohe, V. Weiser

Fraunhofer-Institut für Chemische Technologie  
Joseph-von-Fraunhofer-Str. 7  
76327 Pfinztal 1(Berghausen), F.R.G.

### ABSTRACT:

The combustion of boron containing propellants, based on AP/GAP and AP/HMX/GAP formulations, have been investigated by applying fast spectroscopic, pyrometric and photographic techniques. The propellants burn at a rate of 17mm/s at 5 MPa. Addition of an iron oxide catalyst increased the rate to 20 mm/s at the same pressure. The determined average pressure exponents are 0.66 without and 0.57 with iron oxide as catalyst. At pressures higher than 5 MPa, a strong decrease in the exponent is observed. The reaction zones show high particle concentrations with temperatures from 1500 to 2000 K, varying with the nitrogen pressure. Reacting with air, the particle temperatures increase close to the evaporation temperature (2200 K) of boron oxide. The reaction of boron with oxygen is proved by the results of spectroscopic data. Considering an application in a ducted rocket, the boron is heated to the desired reaction temperature.

### INTRODUCTION

The range of missiles is mainly limited by the weight of transported propellant. Therefore, air-breathing concepts for rocket propellants aim to develop low-weight formulations only carrying the fuel. The oxidiser being supplied from the ambient air. One approach for realising such a technique is the ducted rocket concept, a propulsion system based on two separate combustion chambers

- the first for producing preheated fuel,
- the second where the fuel is oxidised by air.

Boron is a favourite fuel with low molar weight and high reaction enthalpy [1-3]. An overview on boron ignition and burning behaviour is published in [1].

In the present work, the combustion behaviour of boron and high boron containing propellants (FS 280, FS 314, FS 315), developed at ICT, was investigated in a so-called optical bomb using two different atmospheres:

- Nitrogen, to simulate the first chamber
- Air, to simulate the first reactions in the secondary chamber.

Results comprise burning rates, flame geometry, temperatures and emitted radiation to allow interpretations with reference to applications in rocket propulsion.

### EXPERIMENTAL

The experiments were carried out in an optical bomb equipped with two opposing windows, allowing simultaneous observation of propellant combustion up to 10 MPa by different methods (Figure 1) [4]. The propellant formulations were pressed to strands of 4 x 4 x 40 mm and electrically ig-

nited. Visualisation of the combustion was obtained, using an automatically exposing camera (4 frames per second). The emitted radiation was detected with a Tracor Northern TN 6500 optical multichannel spectrometer (time resolution: 10 ms). Simultaneously, the combustion was observed applying a fast two colour pyrometer developed at ICT (time resolution < 0.1 ms) [5]. The high time resolution allows the detection of single boron particles. For determining the combustion rate under nitrogen atmosphere, the strand's image was focused onto a diode array, detecting the progressing flame front [6].

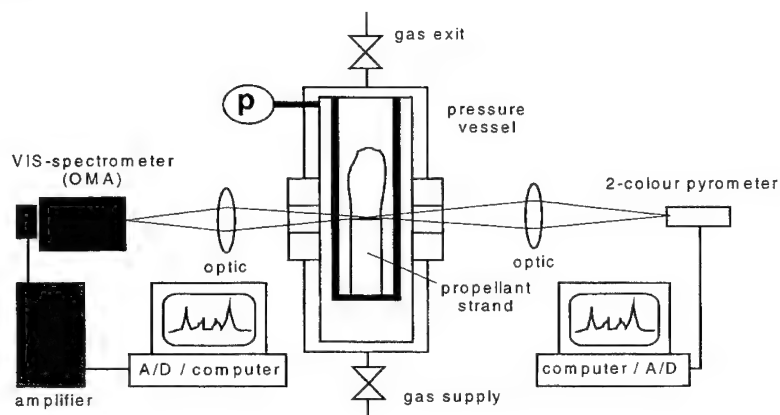


Figure 1. Experimental set-up for simultaneous spectroscopic and pyrometric investigation of propellant combustion

The investigated propellants FS 280, FS 314 and FS 315 are based on boron containing AP/GAP formulations. FS 314 and FS 315 are additionally blended with HMX (Table 1). The propellants were burned in the optical bomb both in nitrogen and air atmospheres at pressures of 0.5, 2, 4 and 7 MPa. Thermodynamic calculations based on the ICT code [7], showed the results for adiabatic flame temperatures listed in table 3 (in K).

Additional amounts of oxygen increases the flame temperature about 500 K, proving a gain of power in the second combustion chamber without oxidiser in the propellant (reduction of weight).

The calculated reaction products of FS 280 in the first and after the second reaction chamber are shown in Table 3. The calculation assumes a pressure of 7 MPa in first reaction chamber, and an adiabatic relaxation to standard conditions at frozen equilibrium for the combustion with air.

TABLE 1  
Composition of the investigated propellants (in Ma%)

Sample	AP	HMX	GAP	BDNPA-F	Boron	N100	Fe <sub>2</sub> O <sub>3</sub>
FS 280	20	--	25.6	12	40	2.4	--
FS 314	20	5	25.2	12	35	2.8	--
FS 315	20	5	24.5	11.7	35	2.8	1

The results show, that boron is not expected reacting in nitrogen atmosphere and, therefore, preserved for oxidation in air (second reaction chamber). Only partially oxidised components in the gas

phase, like CO or H<sub>2</sub> are additional reactants supplied to the second burning chamber. It is expected that the boron is even less oxidised before entering the second chamber.

TABLE 2  
Adiabatic flame temperatures in K (combustion with air: stoichiometric conditions)

Sample	2 MPa, N <sub>2</sub>	7 MPa, N <sub>2</sub>	2 MPa, Air	7 MPa, Air
FS 280	2340	2350	2840	2890
FS 314	2350	2350	2830	2880
FS 315	2350	2350	2830	2880

TABLE 3  
Equilibrium composition of important reaction products of FS 280 after the first and second combustion chamber (in mol%) assuming complete combustion of boron

	comb. chamber, 7 MPa	nozzle exit, 0.1 MPa
Temperature in K	2350	1610
reaction products in mol%:		
CO <sub>2</sub>	0	5.7
H <sub>2</sub> O	0	2.3
N <sub>2</sub>	0	77.2
CO	15.9	0.2
H <sub>2</sub>	18.7	0
BOH	2.9	0
HBO <sub>2</sub>	0.2	8.1
BO <sub>2</sub>	0	0.1
B <sub>2</sub> O <sub>2</sub>	0.8	0
B <sub>2</sub> O <sub>3</sub>	0.3	5.3
HCl	2.5	0.8
C	3.2	0
B	36.6	0
BN	18.4	0



## RESULTS AND DISCUSSION

The investigations aimed at:

- characterising the process for determining combustion rate and temperature,
- verifying that boron is not burned in air free conditions but produced with a temperature high enough to react in the second one
- investigating the reaction zone (geometry, emitted radiation, intermediate products) to clear up reaction mechanisms.

### Combustion Rate

Figure 2 shows the experimental combustion rates vs. pressure (nitrogen atmosphere). As a consequence of iron oxide catalysis, FS 315 shows maximum rates and minimum mean pressure exponents (FS 315: 0.57, FS 280 and FS 314: 0.65 at 0.5 to 10 MPa). At relevant higher pressures (> 2 MPa), an even stronger effect is observable (pressure exponent: 0.4 for FS 315). Therefore, the FS 315 formulation is advantageous, both in pressure exponent and performance.

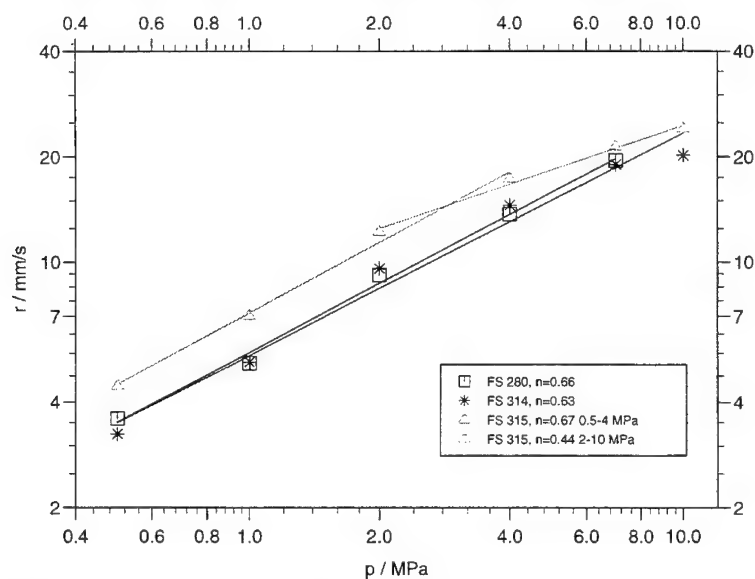


Figure 2. Combustion rate vs. chamber pressure of investigated propellants

### Flame Geometry

The shape of the reaction zone of the three investigated propellants are not significantly different as shown in Figure 3. Originated from hot particles, a lot of luminescent traces are observable (probably glowing boron particles). No melting layer was observed on the propellant surface. It emits with low intensity. The dark spots above the FS 315 surface point to ejected small propellant fractions. No dark zone (fizz zone) is observable.

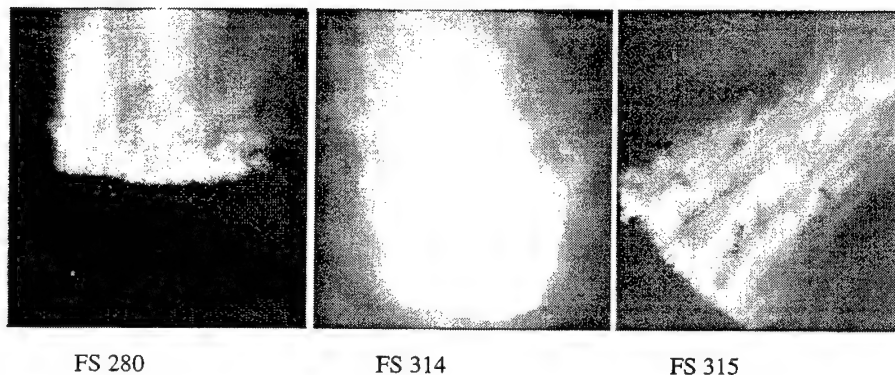


Figure 3. Combustion zones of FS 280, FS 314 and FS 315 propellants in 0.5 MPa nitrogen atmosphere

The photographic investigations in an air atmosphere were disturbed by strong fogging caused from water condensation at HCl molecules. Additionally, the air induces a strong non homogeneous combustion front. Single fractions are ejected. The observed luminescent traces are generated by hot boron particles reacting with air.

### Spectroscopy

The spectroscopic investigations aimed at the question, whether the boron from the propellants is hot enough to react in air or not. Therefore, the combustion was investigated employing air and nitrogen.

Figure 4 shows spectra of FS 280 with nitrogen supplied at pressures of 0.5, 2, 4 and 7 MPa. Corresponding spectra of FS 315 burned in air are shown in Figure 5.

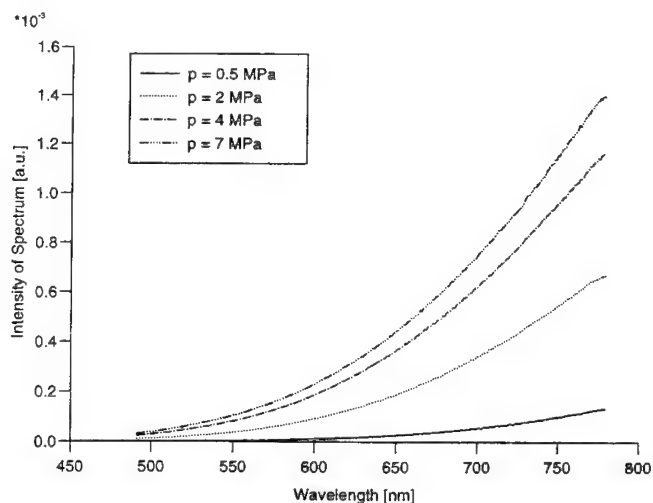


Figure 4. Spectra obtained from the gaseous phase above FS 280 propellant at different nitrogen pressures

Pure continuous radiation spectra are observable in nitrogen atmosphere, comparable to that obtained from hot condensed matter or gas phases with high particle concentrations. Above the propellant's

surface the intensity is increasing with pressure caused from a higher particle temperature or particle density along the line-of-sight.

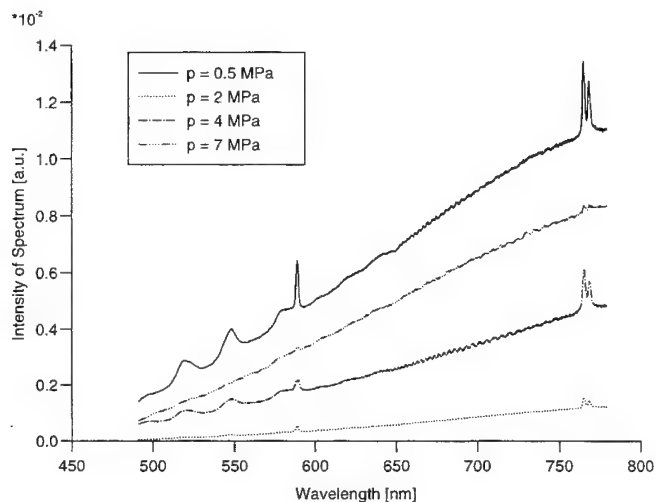


Figure 5. Spectra obtained from the reaction area above FS 315 propellant at different air pressures

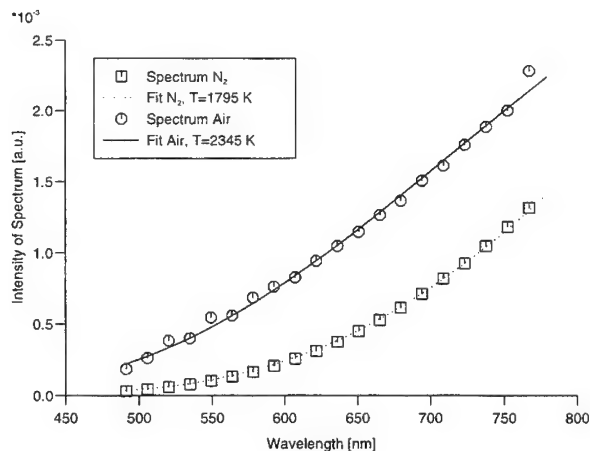


Figure 6. Least-Squares-Fit of grey radiation (Planck's radiation law) to FS 280 spectra (air and nitrogen atmosphere)

In an air atmosphere (Figure 6), the spectra show strong atomic lines (sodium 589 nm, potassium 766.5 and 769.9 nm) and band profiles caused by the  $\text{BO}_2$  molecule (between 400 and 600 nm). The boron particles are reacting with air. The heating of boron by the propellant reaction in the first chamber is sufficient.

The temperatures can be determined by fitting Planck's radiation law with constant emission coefficient to the experimental data (Figure 7). The temperatures obtained at various pressures are summa-

rised in Figure 8. Compared with nitrogen atmosphere, the temperatures of all propellants are 700 to 1200 K higher supplying air. This proves the additional amount of energy by boron oxidation.

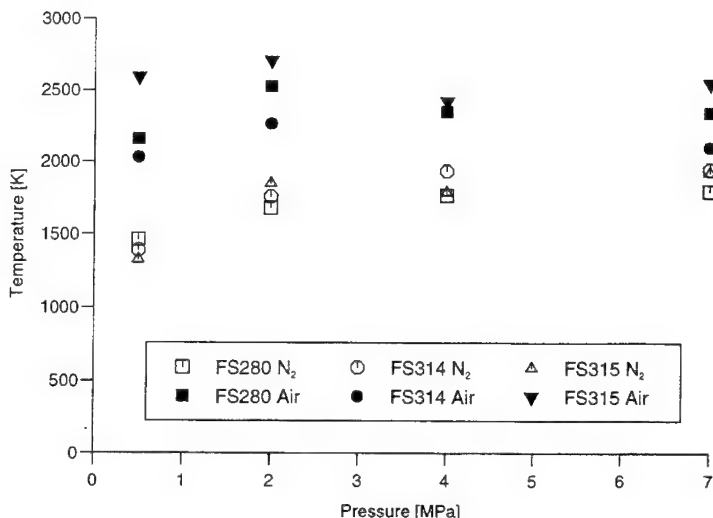


Figure 7. Temperatures at FS-propellants combustion at different pressures of air and nitrogen obtained from a grey radiation fit

### Pyrometry

The applied two colour pyrometer allows measuring temperature and integrated radiation of the reaction front with a time resolution  $\Delta t < 0.1$  ms [4]. Single particles are detectable. Figures 9 shows examples of temperature profiles under nitrogen (left) and air (right) atmosphere at 0.5 MPa.

At 0.5 MPa nitrogen pressure, the intensity strongly increases in the first zone, where the hot reaction zone (burning surface) is located. Strong peaks are observable in all experiments, caused by the small micron-sized boron particles. The peak frequency is constant. During the first 5 to 10 seconds, temperatures of 1400 to 1600 K were measured moderately decreasing up-stream. The spectroscopic investigations showed no boron oxidation in nitrogen atmosphere, indicating that the boron can be considered as nearly inert under these conditions. 10 mm above the surface the particles are slowly cooling down.

At 7 MPa nitrogen atmosphere, the complete reaction zone and the area of constant temperature are extremely shortened. Higher particle temperatures of 1800 to 2000 K are obtained. Temperature conditions are reached that enable a stable combustion of boron particles.

The combustion in air atmosphere shows a symmetrical reaction zone. The obtained temperatures are 1900 to 2000 K and are distinctively higher than in nitrogen atmosphere combustion. The temperatures increase 2000 to 2100 K at 7 MPa pressure.

Temperatures measured in the optical bomb experiments are considerably lower than calculated by the thermodynamic code. The optical bomb can not be compared with a ducted rocket, so the results are limited to the ignition phase and to partial combustion as the burning products are too early diluted up-stream. A temperature close to adiabatic conditions can only be obtained in a burning chamber designed for complete combustion.

Figure 8 shows in detail temperature and intensity measurements in the upper and lower reaction zone. The upper is determined by the area of constant temperature. In the lower zone of reaction, particle peaks and temperature maxima of 1500 K coincide. In the upper zone, the minima of temperature (about 1450 K) coincide with the intensity maxima of emitting particles. This is attributed to a cooling of the larger boron particles.

## CONCLUSIONS

The following conclusions can be drawn:

- The propellants show a burning behaviour and burning rate which makes them applicable for ducted rockets.
- The propellants feed heated boron to the secondary burning chamber in a way that boron can be ignited.
- The boron particles do not agglomerate and form a hot particle stream.
- The experiments in the optical bomb enable investigations simulating the conditions of the primary combustion chamber in a ducted rocket.
- The spectroscopic and pyrometric equipment allows the measurement of temperatures of the gas phase and single particles in a hot particle stream.

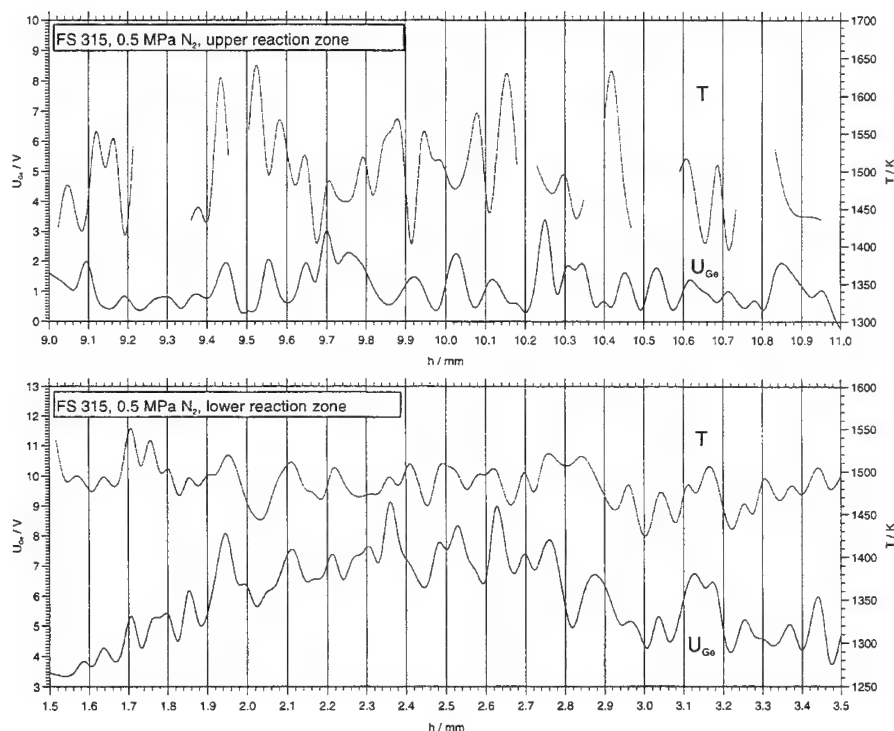


Figure 8. Intensity and temperature progress (FS 315 propellant, 0.5 MPa nitrogen) in the reaction zone 2.5 mm and 10 mm above propellant strand surface.

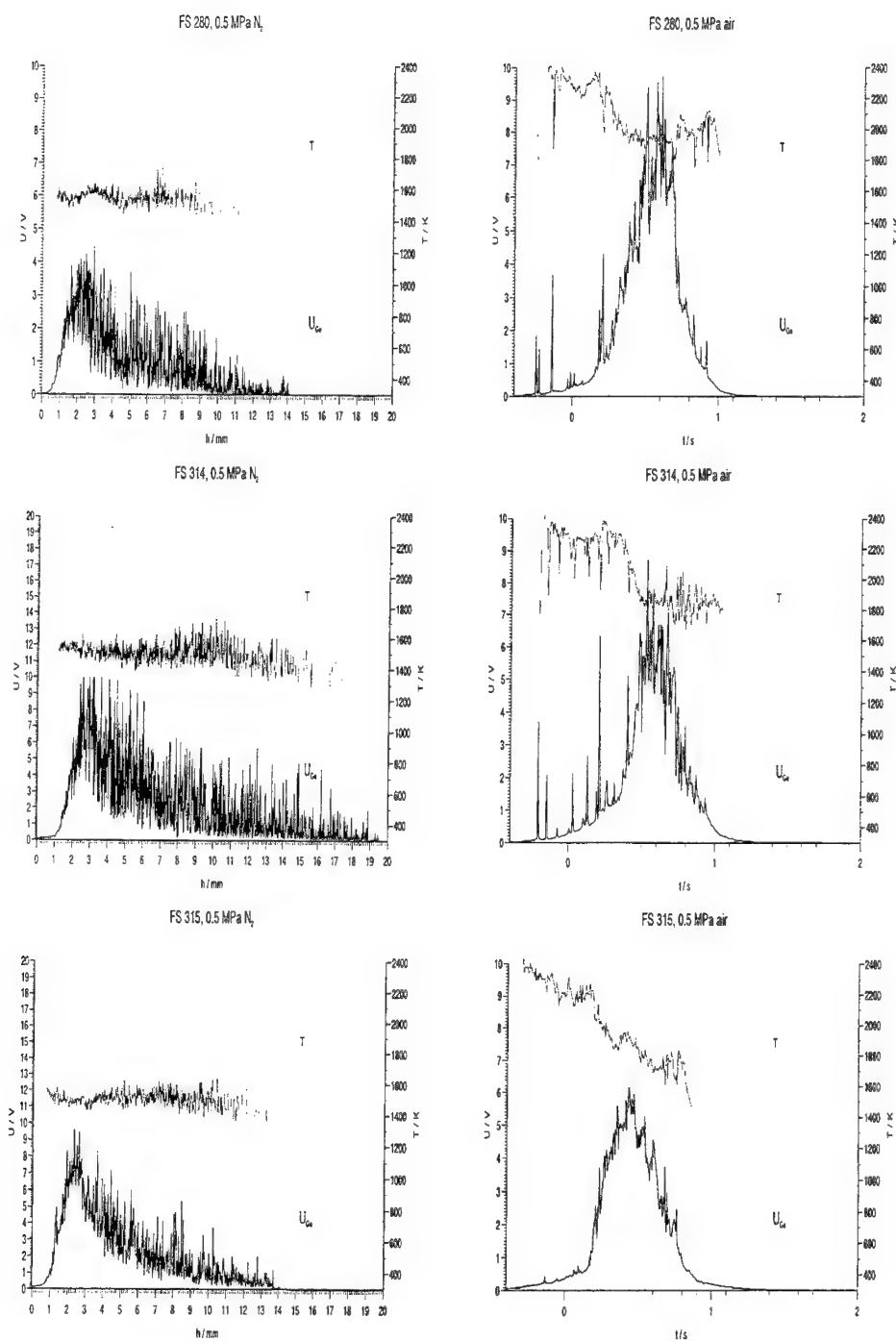


Figure 9. Progression of temperature and intensity at 0.5 MPa in nitrogen (left) and air (right)

## REFERENCES

1. **Kuo, K. K.; Pein, R. (Ed.);** Boron-based solid propellants and solid fuels; CRC Press, 1993
2. **Liehmann, W.;** Combustion of Boron-Based Slurries in a Ramburner; Propellants, Explosives, Pyrotechnics 17, 14-16 (1992)
3. **King, M. K.;** A review of studies of boron ignition and combustion phenomena at Atlantic Research Corporation over the past decade; Boron-based solid propellants and solid fuels; K. K. Kuo; R. Pein (Ed.); CRC Press, 1993
4. **Weiser, V.; Eckl, W.; Eisenreich, N.; Pfeil, A.;** Untersuchungen zum Abbrandverhalten von PSAN/GAP-Mischungen mit verschiedenen Phasenstabilisatoren; 25th International Annual Conference of ICT, 1994, pp. 25-(1-15)
5. **Eckl, W.; Eisenreich, N.; Liehmann, W.; Schneider, H.; Weiser, V.;** Emission Spectroscopy and Pyrometry of Propellant Flames and Rocket Plumes; Non-Intrusive Combustion Diagnostics; (Kuo K. K., Parr T. P. ed.), Begell House, Inc. New York
6. **Eckl, W.; Rohe, Th.; Weiser, V.;** Characterizing the combustion process of new gasgenerator propellant; 2. International Symposium on Sophisticated Car Occupant Safety Systems (AIRBAG 2000); 1994, November 29/30, Karlsruhe, Germany; pp. 35-(1-9)
7. **Volk, F.; Bathelt, H.;** Rechenprogramm zur Ermittlung thermochemischer und innenballistischer Größen, sowie von Gasdetonationsparametern, ICT-Report 3/82, 1982
8. CRC-Handbook of Chemistry and Physics (72nd edition), Lide, D.R. (ed.); CRC Press, 1991

## CHARACTERIZATION OF CONDENSED-PHASE CHEMICAL REACTIONS OF RDX AND NITRAMINE-BASED PROPELLANTS

E. Boyer, Y. C. Lu, and K. K. Kuo

Department of Mechanical Engineering, The Pennsylvania State University  
University Park, PA 16802

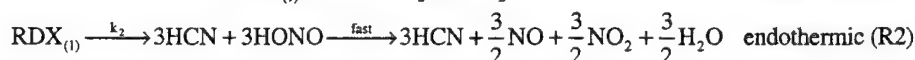
**ABSTRACT:** A microprobe mass spectrometer was used to measure decomposition products from the subsurface region of two RDX-based propellants: XM39 and one (MZ) containing an energetic plasticizer. The microprobe was inserted into a hole drilled axially in the centerline of each propellant sample. Gaseous species released in the subsurface region were collected in the cavity and sucked into the probe and analyzed. Tests were conducted in Ar at 1 and 3 atm, with a CO<sub>2</sub> laser external heat flux of 100, 200, and 275 W/cm<sup>2</sup>. An insignificant amount of solid-phase decomposition products was detected for MZ, and only a very minute amount of OST was detected from XM39 at very low heat flux conditions. At the time of burn through, the major species detected had masses of 30, 28, 44, and 27 amu, believed to be CH<sub>2</sub>O, CO, N<sub>2</sub>O, and HCN. These products suggest that the RDX decomposition pathway to form CH<sub>2</sub>O and N<sub>2</sub>O is more dominant for the condensed-phase reactions at the operating conditions studied. The binders of these two propellants showed relatively inactive behavior under the conditions tested.

### INTRODUCTION

Because of its many favorable characteristics, cyclotrimethylene trinitramine (RDX) has been utilized as an important ingredient in both gun and solid rocket propellants. RDX is used in low vulnerability ammunition (LOVA) propellant formulations due to its relative insensitivity to accidental energy stimuli. The large amount of gas generated and high energy released during combustion make it very attractive for both rocket and gun applications. The absence of HCl in the combustion products makes RDX desirable on an environmental basis as well. It is useful to characterize the condensed-phase pyrolysis behavior and achieve better understanding of the combustion processes of RDX and RDX-based propellants so that detailed simulation of the burning phenomena of RDX-based propellants can be achieved.

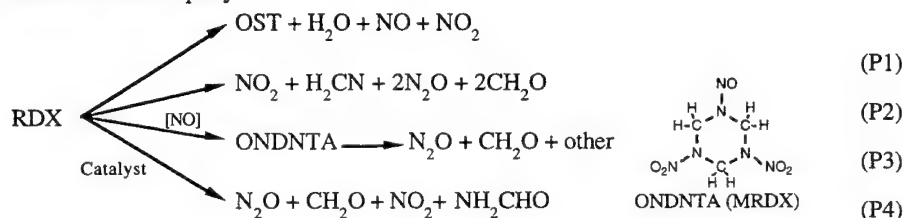
Since the regression rate of solid propellants can be greatly influenced by surface and subsurface reactions, better knowledge of condensed phase reactions is vital to gain a more in-depth understanding of the combustion of nitramine solid propellants. Surface and near-surface phenomena of RDX-based propellants have not been fully studied, mainly due to the difficulties in probing the thin surface reaction zone. Any intrusive probing of the reaction zone having a relatively small characteristic length on the order of 100  $\mu$ m could significantly disturb the localized combustion phenomena.

Many previous studies have focused on experiments at non-combustion conditions to investigate thermal decomposition rates and mechanisms of solid propellants and their ingredients.<sup>1-5</sup> Melius<sup>1</sup> suggested a pair of competing reactions, shown below, for the liquid-phase decomposition of RDX.

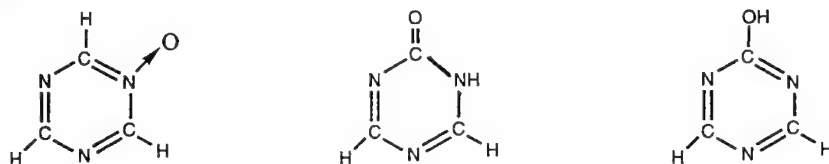




These two competing reactions were also supported by T-jump/FTIR studies of Brill et al.<sup>2,3</sup> By comparison of the  $\text{N}_2\text{O}/\text{NO}_2$  ratio at different temperatures, the reaction R1 was found to be favored at lower temperatures. Behrens and Bulusu<sup>5</sup> studied RDX condensed-phase decomposition under low heating rates ( $< 0.6^\circ\text{C}/\text{min}$ ), with detailed mechanisms developed for both liquid and solid phases. It was found that the rate of solid-phase decomposition was very much slower than that of liquid phase. Solid-phase decomposition produced only 1-nitroso-3,5-dinitrohexahydro-*s*-triazine (ONDNTA), also known as MRDX, in the initial decomposition stage, and  $\text{N}_2\text{O}$  and a lesser amount of  $\text{CH}_2\text{O}$  in later stages. Production rates of these species increase slowly until the temperature reaches a level that the following four liquid-phase decomposition pathways become active; thereafter, formation rates of all gaseous products increase rapidly.



In reaction pathway P1, the product species OST represents oxy-*s*-triazine; the exact structure of this compound is not presently known and can be represented by any one of the following three molecular structures:<sup>5</sup>



**Table 1**  
Ingredients in XM39 Propellant

Propellant	Material	%
XM39	RDX	76.0
	Cellulose Acetate Butyrate (CAB)	12.0
	Acetyl Triethyl Citrate (ATEC)	7.6
	Nitrocellulose (NC) (12.6% N)	4.0
	Ethyl Centralite (EC)	0.4

Some other studies have focused on nitramine composite propellants such as XM39 and another LOVA propellant containing an energetic plasticizer, identified here as MZ. The ingredients of XM39 propellant is given in Table 1. Schroeder, et al.<sup>6</sup> detected significant amounts of RDX-derived nitrosamines (ONDNTA and DRDX--hexahydro-1,3-dinitroso-5-nitro-triazine) near the burned surface of recovered XM39 samples. Wormhoudt, et al.<sup>7</sup> used infrared absorption spectroscopy coupled with embedded thin fiber optics (nominal diameter 200  $\mu\text{m}$ ) to detect NO and  $\text{NO}_2$  in the condensed phase. They concluded that the detected NO and  $\text{NO}_2$  were formed by the decomposition of RDX trapped in the propellant binder matrix that melts at a higher temperature than RDX. Using a method similar to the current study, Fetherolf et al.<sup>8</sup> found a sudden appearance of several gas species at 100–400  $\mu\text{m}$  below the burning surface of XM39 at 1 atm argon gas environment under 100  $\text{W}/\text{cm}^2$   $\text{CO}_2$  laser heating. NO was found in the greatest quantity, with  $\text{N}_2\text{O}$  having the second highest mole fraction, then followed by species at 28 amu, HCN,  $\text{NO}_2$ , and  $\text{CH}_2\text{O}$  with lowest concentrations. It was hypothesized that these species were released by a bubble bursting in the foam layer. However, comparison of these results with the current study could suggest that the probe probably became blocked part way through the test, thus possibly skewing the species profiles.

The major objectives of this study were to use a microprobe mass spectrometer system to detect gaseous species evolved in the subsurface region of nitramine composite propellants and to use this information to identify any condensed phase decomposition and its reaction mechanisms.

### METHOD OF APPROACH

A schematic diagram of the experimental setup is shown in Fig. 1. The propellant sample was mounted directly onto a quartz microprobe inside a sealed test chamber filled with argon gas. A CO<sub>2</sub> laser provided a uniform heat flux normal to the sample surface to initiate and support laser-assisted combustion. Subsurface gas species were sucked into the microprobe and flowed into the mass spectrometer for analysis. A high resolution Pulnix video camera coupled with a 60 mm micro lens and a Super-VHS VCR were used to record the test event.

### Mass Spectrometer

An Extrel C50 triple quadrupole mass spectrometer was used to analyze gases sampled through the microprobe. However, the mass spectrometer was only run in the single quadrupole mode. This instrument can measure gaseous species ranging from 1 to 500 amu at a variable scan speed of 0.2 to 1,000 amu/sec. The available sampling rates allow fast and localized diagnostic capability. Since the largest species expected to be present was RDX, the highest amu scanned was 222. An ionization energy of 22 eV was used because it produced enough ions to generate strong signals but yet limited the extent of molecular fragmentation. A 486-66 MHz PC-compatible computer equipped with a high-speed I/O board was used for real-time data acquisition, analysis, and control of the system.<sup>9,10</sup> The microprobe was fabricated from 0.32 cm (1/8 inch) diameter quartz tubing and tapered to an orifice of approximately 25  $\mu$ m diameter at the tip. This small orifice controlled the amount of mass flow into the instrument. In addition, the expansion downstream of the orifice cooled the sampled gases, quenching reactions within the system and freezing the composition of the sample gases.

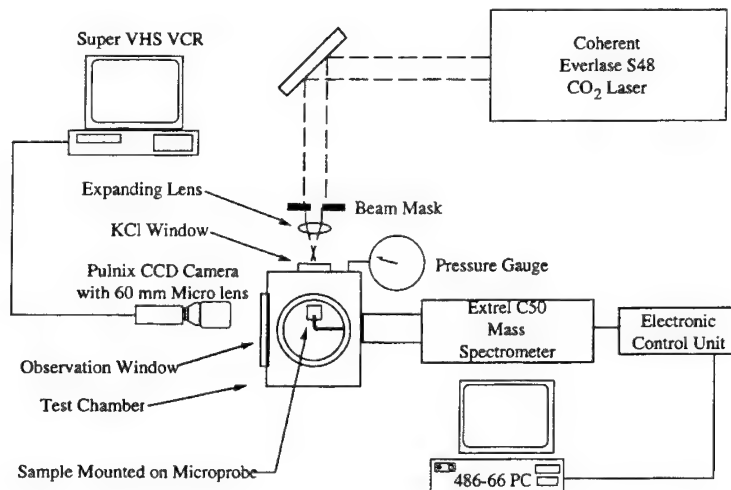


Figure 1. Schematic diagram of Microprobe Mass Spectrometer

### Sample Configuration

Both XM39 and MZ propellants were supplied as extruded sticks with a diameter of 0.64 cm (0.25 inch). Cylindrical samples approximately 0.71 cm (0.28 inch) long were cut from the supplied propellant sticks with a sharp blade, and the ends were carefully sanded to a flat and uniform surface. A 0.208 cm (0.082 inch) diameter hole was drilled axially along the centerline of the sample, leaving a

thickness of 0.23 cm (0.09 inch) of material underneath the initial burning surface. A quartz microprobe was inserted into the drilled hole until stopped by the tapered surface; a fast-drying thick cement was then applied around the junction section to provide a gas-tight seal. The cement prevented combustion product gases from leaking into the cavity around the tip of the microprobe in the subsurface region. The embedded probe inside the sealed cavity allowed immediate drawing of any gases produced in the subsurface region into mass spectrometer. A vacuum pump was used to provide a sufficient suction effect. The vacuum reading (averaging  $6 \times 10^{-3}$  torr) from the microprobe prior to tests indicated the effectiveness of the seal provided by the mounting method, thus ensuring that the analyzed subsurface gases were not contaminated by gaseous species formed in the gas-phase region. A cross-sectional diagram of a mounted pellet is shown in Fig. 2.

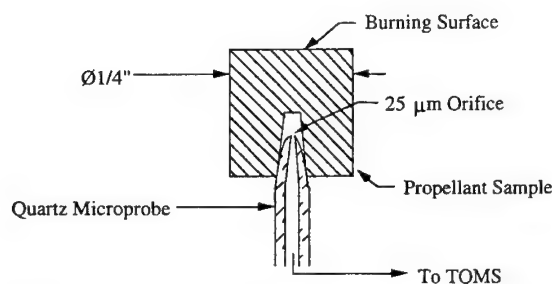


Figure 2. Cross-sectional detail of sample pellet mounted on microprobe

### CO<sub>2</sub> Laser Heating

A CO<sub>2</sub> laser heat flux was projected onto the surface of the sample to provide a steady, uniform regression of the solid propellant after the attainment of ignition. A Coherent Everlase S48 CO<sub>2</sub> laser in continuous wave mode was used, with the beam masked and focused to about twice the diameter of the sample. It was confirmed that the laser beam had a uniform intensity at the cross-section where the sample surface was located. Computer control ensured synchronization of the laser with mass spectrometer sampling.

### Test Conditions

Tests were conducted on both XM39 and MZ propellants at several heat fluxes and pressures to examine the effect of different operating conditions on condensed phase decomposition and subsurface gas generation. Heat fluxes of 100, 200, and 275 W/cm<sup>2</sup> were applied at chamber pressures of 1 and 3 atm. Analysis of the video records provided time correlated information at the instant of propellant surface burn through. For the purpose of comparison, pressed RDX pellets with subsurface cavities in the form of a truncated cone were tested. In some tests, "U"-shaped 25 μm diameter fine-wire thermocouples were embedded in the sample with the bead on the centerline for thermal wave profile measurements.

## RESULTS AND DISCUSSION

Most of the results obtained in this study are presented in terms of intensity of chemical species of interest versus time measured from time of burn through. Although not converted to mole fractions due to some calibration uncertainty, previous calibration coefficients allowed a rough comparison of the intensity levels to be made. The time of burn through was defined when the burning surface reached the top portion of sample cavity containing the microprobe (see Fig. 2). Thereafter, gases from the surface reaction zone were able to flow into the probe. In fact, the experimental setup is capable of detecting gaseous chemical species produced by thermal decomposition even before the sample burns through. It was experimentally verified that at the time of burn through there was a sudden jump in the measured species intensities. The time scale used in the figures presented was referenced to the time of burn through. By doing so, these figures can clearly show any decomposition activities near the time of burn through.

### MZ Propellant

The major species observed were at masses of 18, 27, 28, 30, 44, and 46 amu under all conditions. As shown in Fig. 3a, masses of 18, 27, and 46 could be assigned to a definite species,  $\text{H}_2\text{O}$ ,  $\text{HCN}$ , and  $\text{NO}_2$ , respectively. However, it was not possible to separate the signals of the multiple molecules at the same mass for other species due to the mode the mass spectrometer was operated. For mass 28, possible species are  $\text{CO}$  and  $\text{N}_2$ , with  $\text{CO}$  as the most probable decomposition product.  $\text{H}_2\text{CN}$ , another expected decomposition product, also has mass 28 but cannot be reliably detected by the mass spectrometer because of its unstable nature. For mass 30, the possible decomposition species are  $\text{CH}_2\text{O}$  and  $\text{NO}$ , but a greater amount of  $\text{CH}_2\text{O}$  was expected due to the decomposition pathways reported in the literature.<sup>1</sup> For mass 44, there are several possible product species including  $\text{N}_2\text{O}$ ,  $\text{H}_2\text{CNO}$ , and  $\text{CO}_2$ , with  $\text{N}_2\text{O}$  being the most likely decomposition product. Minor species of interest in decomposition reactions, as shown in Fig. 3b were  $\text{HNO}$  at mass 31,  $\text{HONO}$  at 47,  $\text{H}_2\text{CNNO}_2$  at 74, and oxy-s-triazine (OST) at 97. Masses up to that of RDX (222 amu) were scanned in some cases to detect decomposition products such as ONDNTA (206 amu), DRDX (190 amu) and RDXR (176 amu). Nevertheless, no species above 97 were detected. In fact, no  $\text{H}_2\text{CNNO}_2$  or OST was found in any of the MZ tests, as shown in Figs. 3-6. This represents a significantly different result from that of Behrens and Bulusu,<sup>5</sup> although they noted that their results pertained to lower reaction temperature conditions in their experiments. The lack of ONDNTA seems to preclude any significant solid-phase decomposition, since it is the primary product. However, ONDNTA may become trapped in the solid phase and continue decomposition into  $\text{N}_2\text{O}$  and  $\text{CH}_2\text{O}$ .<sup>5</sup> These results may also be due to the tendency of larger molecules to fragment during the mass spectrometer ionization process, even at low energies. It is known that RDX is not stable after losing an electron,<sup>12</sup> and this may be true for the other large species of interest as well. In fact, masses 75 and 81, believed to be possible products of RDX fragmentation within the mass spectrometer,<sup>12,13</sup> were observed when scanned for at the 275  $\text{W}/\text{cm}^2$  and 3 atm condition (Fig. 6b), suggesting the presence of RDX vapor in the subsurface region.

At all conditions, the levels of mass 30 (mostly  $\text{CH}_2\text{O}$ ) were higher than those of  $\text{HCN}$  and  $\text{NO}_2$ . Since the cooler subsurface region was the area under study, this observation tends to agree with Brill et al.<sup>2,3</sup> in that the R1 pathway is more preferred than the R2 pathway at lower temperatures. The relative concentration of  $\text{NO}_2$  was very low in comparison with other decomposition product species. This finding also indicated that the R1 pathway was the more active one, since  $\text{NO}_2$  was a product of the R2 competitive reaction.

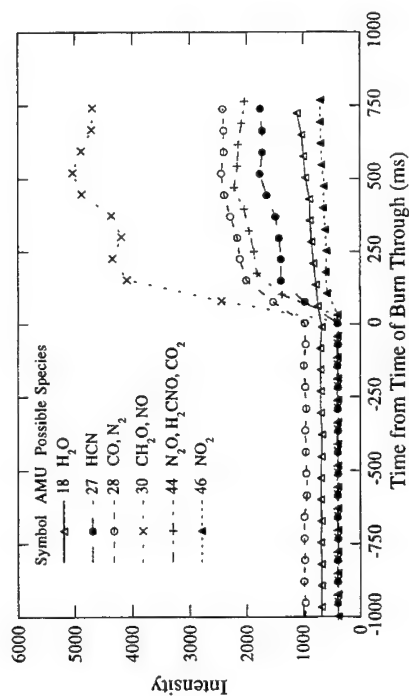
The ratio of mass 28 to 30, assumed to be  $\text{CO}$  to  $\text{CH}_2\text{O}$ , was found to decrease with increasing heat flux. There are two possible, but not exclusive explanations. The increase in the binder product of mass 30 ( $\text{CH}_2\text{O}$ ) at higher heat fluxes could be one possible reason. The second possible reason could be the increased production rate of  $\text{CH}_2\text{O}$  and  $\text{N}_2\text{O}$  at higher heat fluxes, since the R1 pathway has a lower activation energy than that of the R2 pathway. The relative concentrations of both  $\text{H}_2\text{O}$  and  $\text{HONO}$  seem to decrease at higher heat fluxes; this observation further supports the conclusion that R1 is preferred in the near surface region.

In view of the above-mentioned observations, it is believed that the solid-phase decomposition of MZ propellant is negligible and the most important decomposition reaction of the condensed phase is the R1 pathway for RDX. The binder decomposition could occur to generate similar decomposition products as those of RDX. However, due to extremely low amount of  $\text{NO}_2$  observed, decomposition of the energetic binder must not be significant.

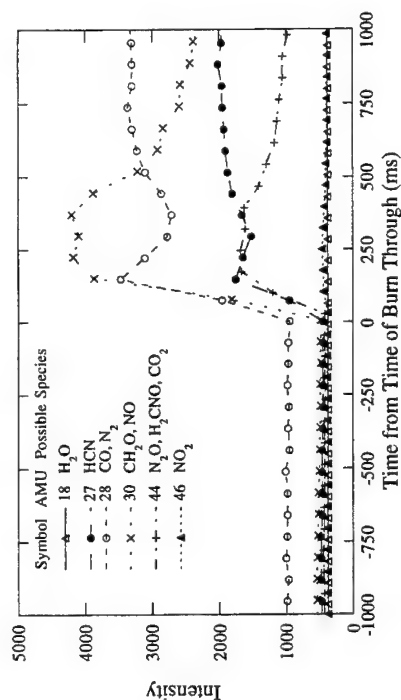
### XM39 Propellant

Decomposition product species generated from XM39 propellant tested under different operating condition are shown in Figs. 7-10. In general, these traces were somewhat similar to those of MZ. However, in 2 of the 3 cases at 3 atm (Figs. 8a and 9a), a small amount of species at 44 amu was detected under the surface, before burn through. This is believed to be  $\text{N}_2\text{O}$  generated from the condensed phase decomposition of RDX. Also, in Fig. 7b, a very small amount of OST was detected when the sample was under low heat flux of 100  $\text{W}/\text{cm}^2$  at 1 atm.

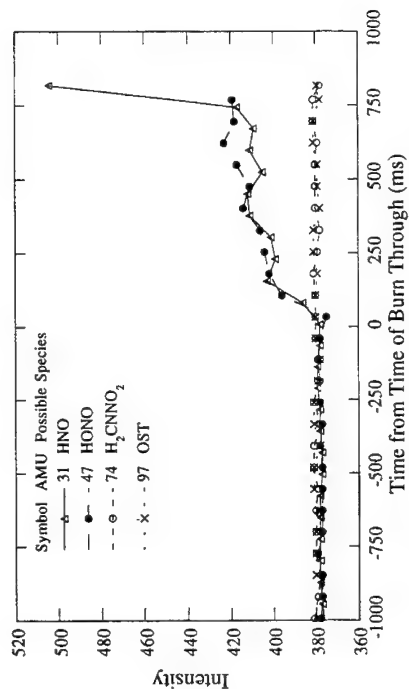
The discovery of OST seems to agree with the findings of Behrens and Bulusu<sup>5</sup> that it may appear under low heating rates by P1 liquid-phase decomposition. For XM39, mass 75, believed to be an ionization-induced fragmentation product of RDX vapor, was only observed at the low heating rate test in which OST was also observed (Fig. 7b). Overall, these results indicate that the replacement of the



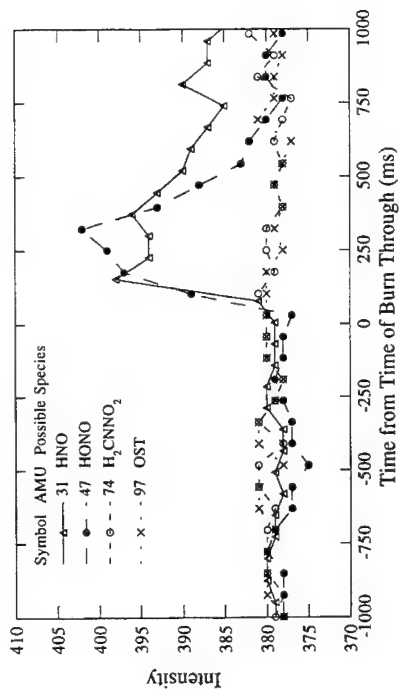
**Figure 3a.** Major decomposition species of MZ at 100 W/cm<sup>2</sup> heat flux and 1 atm pressure



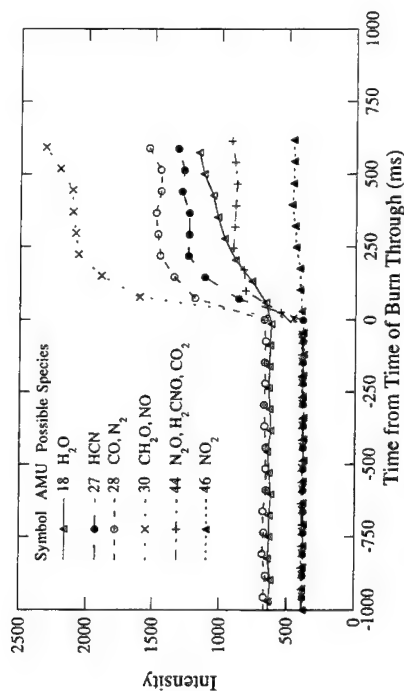
**Figure 4a.** Major decomposition species of MZ at 100 W/cm<sup>2</sup> heat flux and 3 atm pressure



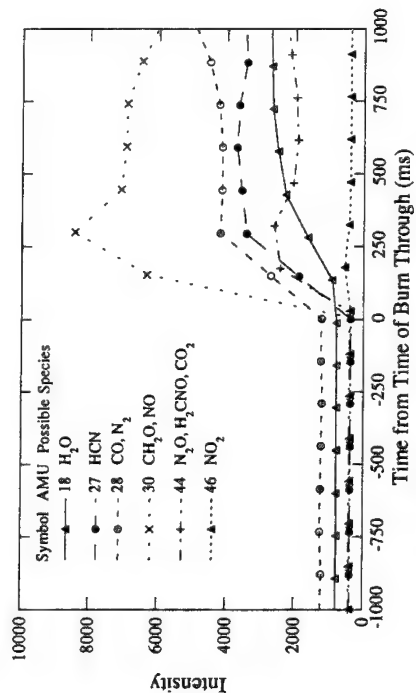
**Figure 3b.** Minor decomposition species of MZ at 100 W/cm<sup>2</sup> heat flux and 1 atm pressure



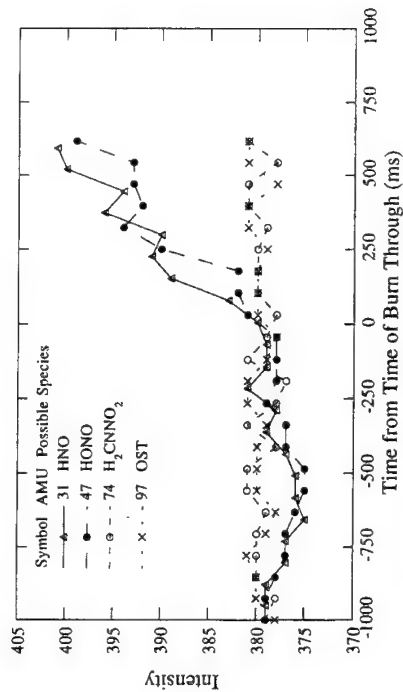
**Figure 4b.** Minor decomposition species of MZ at 100 W/cm<sup>2</sup> heat flux and 3 atm pressure



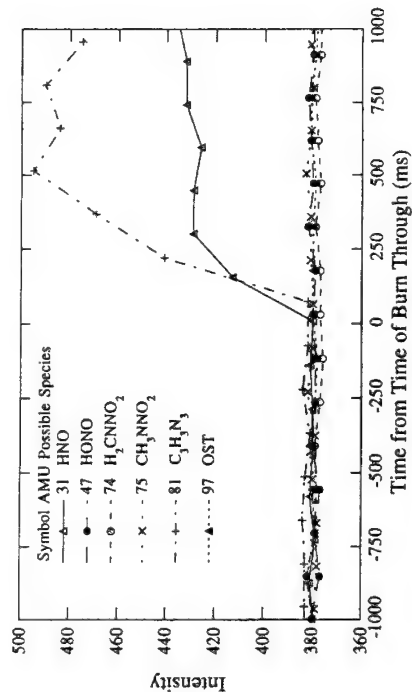
**Figure 5a.** Major decomposition species of MZ at 200 W/cm<sup>2</sup> heat flux and 3 atm pressure



**Figure 6a.** Major decomposition species of MZ at 275 W/cm<sup>2</sup> heat flux and 3 atm pressure



**Figure 5b.** Minor decomposition species of MZ at 200 W/cm<sup>2</sup> heat flux and 3 atm pressure



**Figure 6b.** Minor decomposition species of MZ at 275 W/cm<sup>2</sup> heat flux and 3 atm pressure

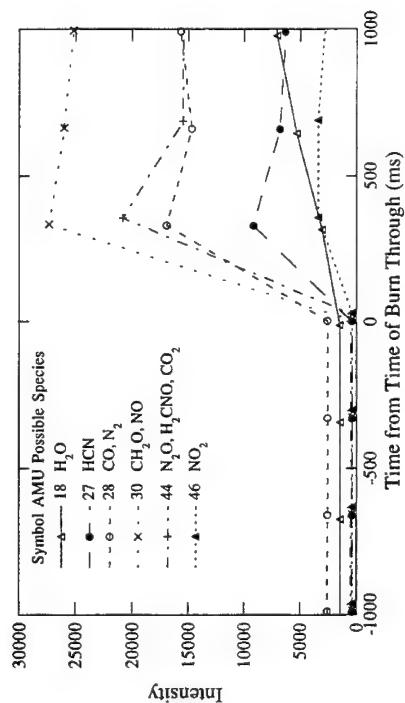


Figure 7a. Major decomposition species of XM39 at 100 W/cm<sup>2</sup> heat flux and 1 atm pressure

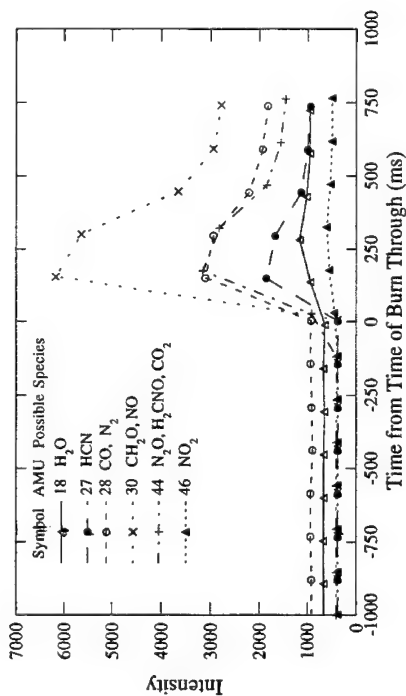


Figure 8a. Major decomposition species of XM39 at 100 W/cm<sup>2</sup> heat flux and 3 atm pressure

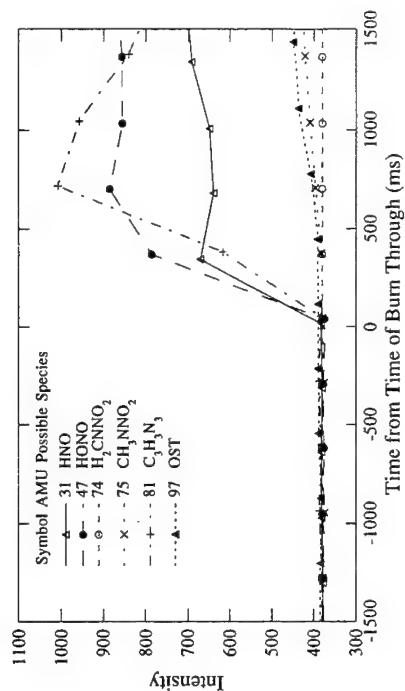


Figure 7b. Minor decomposition species of XM39 at 100 W/cm<sup>2</sup> heat flux and 1 atm pressure

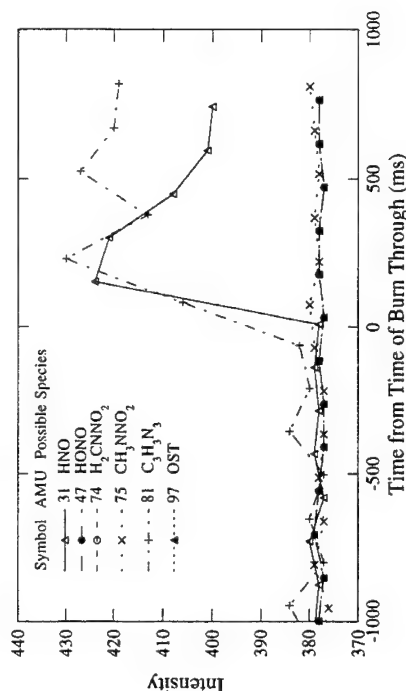
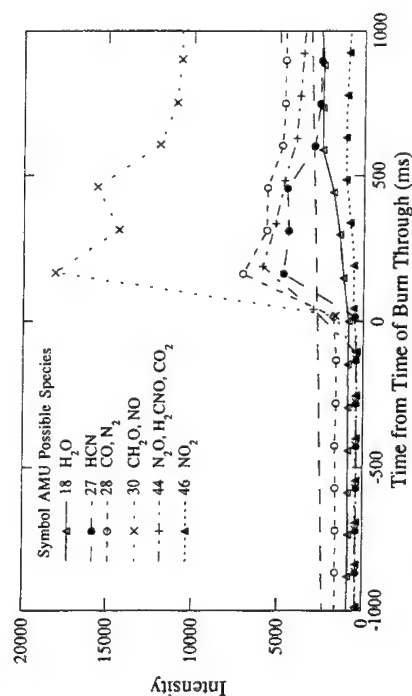
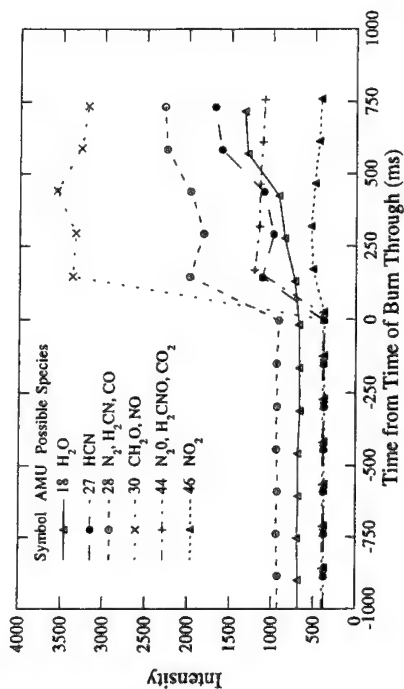


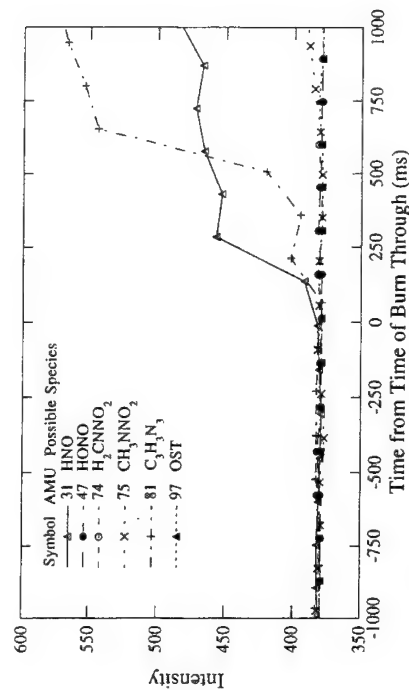
Figure 8b. Minor decomposition species of XM39 at 100 W/cm<sup>2</sup> heat flux and 3 atm pressure



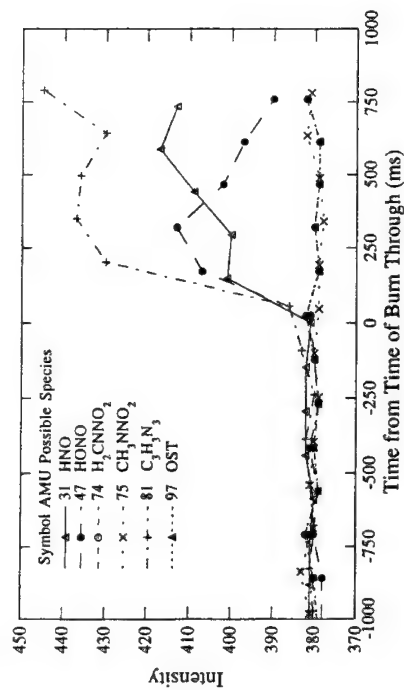
**Figure 9a.** Major decomposition species of XM39 at 200 W/cm<sup>2</sup> heat flux and 3 atm pressure



**Figure 10a.** Major decomposition species of XM39 at 275 W/cm<sup>2</sup> heat flux and 3 atm pressure



**Figure 9b.** Minor decomposition species of XM39 at 200 W/cm<sup>2</sup> heat flux and 3 atm pressure



**Figure 10b.** Minor decomposition species of XM39 at 275 W/cm<sup>2</sup> heat flux and 3 atm pressure



binder ATEC in XM39 with an energetic plasticizer in MZ does not cause a significant difference in the subsurface reaction mechanisms.

## RDX

To compare results obtained from RDX-based propellants, a few limited test runs of pressed RDX pellets were conducted. Fig. 11 shows the time traces of the major decomposition species detected from a self-deflagrating RDX sample at 2 atm. In this particular run, minor species were not scanned. The relative magnitudes of the major species in Fig. 11 show the same trends as those of RDX-based propellants. Because of this observation, either the binder of the propellant does not have significant decomposition products in the subsurface region, or the binder products are similar to those of RDX. Several recorded temperature-time traces from fine-wire thermocouples embedded in RDX samples are shown in Fig. 12. These profiles indicate a burning RDX surface temperature around 620 K, which is very close to the value reported by Zenin.<sup>11</sup> The long flat region is caused by the thick foam layer that forms on the surface of burning RDX at low pressures. The difference in residence times in this region is believed to have two possible causes. First, surface tension may have flexed the 2.9 mm thermocouple span down, retaining the temperature-sensitive bead at the middle of the span in the foam zone for a longer time. Second, a small amount of liquid might have remained as a coating on the bead after the foam zone regressed below it. The coating could have depressed the temperature below the gas-phase value until it burnt off, followed by a rapid rise to the actual temperature. Further tests correlated with high-magnification video are underway to resolve the cause.

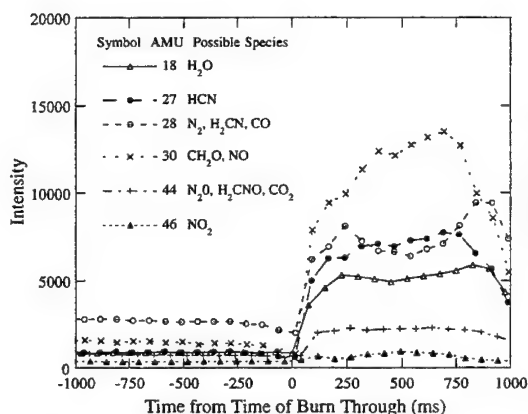


Figure 11. Major decomposition species of RDX at steady-state burn in 2 atm pressure

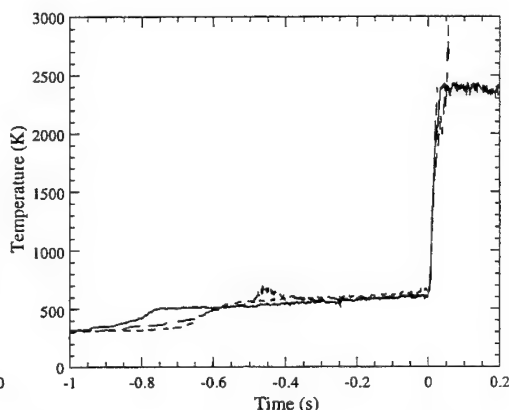


Figure 12. RDX W/Re fine-wire thermocouple temperature traces at 10 psig  $N_2$

## CONCLUSIONS

1. Based upon microprobe mass spectrometer measurements in the subsurface region of MZ, an insignificant amount of subsurface reactions was detected. Only minute amounts of the condensed-phase decomposition product OST were detected from XM39 under very low heat fluxes.
2. Major species observed during burn through of the RDX-based propellants are species with amu of 30, 28, 44, and 27. These species are believed to be predominantly  $CH_2O$ ,  $H_2CN$ ,  $N_2O$ , and  $HCN$ , respectively. Between the two competitive decomposition pathways proposed by Melius and Brill, these observations tend to suggest that the R1 pathway is more dominant in the condensed-phase reaction region where the temperature is relatively low.
3. Different binders used in these two RDX-based propellants (XM39 and MZ) did not yield any major difference in the measured evolution of decomposed species concentrations. The relative concentration of  $NO_2$  detected was extremely low under the operating conditions considered.

4. Based upon the results of this study, it is reasonable to consider the subsurface energy release term in the solid-phase heat equation to be negligible for these RDX-based propellants.

### FUTURE WORK

Based on the results of this study, further examination of large RDX decomposition intermediate products such as ONDNTA, DRDX, OST, etc. is warranted to achieve a better understanding of the thermal decomposition mechanisms. Use of the triple quadrupole mode of the mass spectrometer will resolve the identities of species at masses 28, 30, and 44. More precise calibration can allow mole fractions to be calculated more accurately. Finally, broadening the range of conditions examined will allow the effects of changing heat flux and pressure to be better quantified.

### ACKNOWLEDGMENTS

This work has been sponsored by the Army Research Office under Contract Nos. DAAH04-93-G-0364 and DAAL03-92-G-0118. The program manager is Dr. Robert W. Shaw. His interest and support are gratefully acknowledged.

### REFERENCES

1. Melius, C.F., Thermochemical Modeling: II. Applications to Ignition and Combustion of Energetic Materials, in *Chemistry and Physics of Energetic Materials*, edited by Bulusu, S. N., Kluwer Academic Publishers, Dordrecht, The Netherlands, 1990, 51-78.
2. Brill, T. B., Brush, P. J., Patil, D. G., et al., Chemical Pathways at a Burning Surface, *Twenty-Fourth Symposium (International) on Combustion*, The Combustion Institute, Pittsburgh, PA, 1992, 1907-1914.
3. Brill, T. B. and Brush, P. J., Condensed Phase Chemistry of Explosives and Propellants at High Temperature: HMX, RDX, and BAMO," *Phil. Trans. R. Soc. London*, 339, 377-385, 1992.
4. Oyumi, Y., Melt Phase Decomposition of RDX and Two Nitrosamine Derivatives, *Propellants, Explosives, and Pyrotechnics*, 13, 42-47, 1988.
5. Behrens, Jr., R. and Bulusu, S., Thermal Decomposition of Energetic Materials. 3. Temporal Behaviors of the Rates of Formation of the Gaseous Pyrolysis Products from Condensed-Phase Decomposition of 1,3,5-trinitrohexahydro-s-triazine, *Journal of Physical Chemistry*, 96, 8877-8891, 1992.
6. Schroeder, M. A., Fifer, R. A., Miller, M. S., et al., Condensed-Phase Processes During Solid Propellant Combustion. Part II: Chemical and Microscopic Examination of Conductively Quenched Samples of RDX, XM39, JA2, M30, and HMX-Binder Compositions, Technical Report BRL-TR-3337, Ballistic Research Laboratory, Aberdeen Proving Ground, Maryland, May 1992.
7. Wormhoudt, J., Kebabian, P. L., and Kolb, C. E., Embedded Infrared Fiber Optic Absorption Studies of Nitramine Propellant Strand Burning, ARI-RR-1099, Aerodyne Research, Inc., Billerica, Massachusetts, October 1994.
8. Fetherolf, B. L., Litzinger, T. A., Lu, Y. C., et al., A Comparison of the Physical and Chemical Processes Governing the CO<sub>2</sub> Laser-Induced Pyrolysis and Deflagration of XM39 and M43, *Proceedings of 30th JANNAF Combustion Subcommittee Meeting*, CPIA Publication 606, Vol. 2, November 1993, 183-193.
9. Lee, Y. J., Tang, C. J., and Litzinger, T. A., A Study of the Gas-Phase Processes of RDX Combustion Using a Triple Quadrupole Mass-Spectrometer, *Proceedings of 31st JANNAF Combustion Subcommittee Meeting*, October 1994.

10. **Tang, C. J., Lee, Y. J., and Litzinger, T. A.,** A Study of the Gas-Phase Processes During the Deflagration of RDX Composite Propellants Using a Triple Quadrupole Mass Spectrometer, *Proceedings of 31st JANNAF Combustion Subcommittee Meeting*, October 1994.
11. **Zenin, A. A.,** Personal communication, 1995.
12. **Behrens, Jr., R.,** Personal communication, 1995.
13. **Lee, Y. J.,** The Pennsylvania State University, Personal communication, 1995.

## **X-RAY DIAGNOSTICS FOR LOCAL BURNING RATE MEASUREMENT OF SOLID PROPELLANTS**

**Masahiro Kohno,<sup>1</sup> Angelo Volpi,<sup>2</sup> Shin-Ichiro Tokudome<sup>1</sup>**

<sup>1</sup>ISAS-Institute of Space and Astronautical Science, Sagami-hara, Kanagawa 229, Japan;

<sup>2</sup>ISAS, Visiting Associate Professor from CNPM-C.N.R., Peschiera Borromeo, Milano, Italy

**ABSTRACT:** Combustion products flowing in the free port of a solid-rocket motor are responsible for the erosive burning effect. To improve the knowledge of the mechanism governing erosive burning, a nonintrusive X-ray diagnostic system is utilized with the objective of acquiring burning rate data with high temporal and spatial resolutions. The motor has a rectangular cross section, and it is loaded with two solid-propellant slabs parallel to each other. The X-ray source is placed above the motor. The X-ray beam passes through the aluminum windows, which are inserted in the top side of the motor case, and the component transmitted through the slabs is collected by three sensors inserted in the case on the opposite side of the windows. By means of an experimentally determined calibration curve of the attenuation of the X-ray beam through various thicknesses of an unburned propellant, the local time history of the propellant thickness can be deduced and the erosive burning can be evaluated. Results demonstrate a diagnostic reliability and provide data for improving model development and validation of the erosive burning characteristics of the tested solid propellant.

### **INTRODUCTION**

When a rocket motor is operating under nonstationary conditions, the simple knowledge of its pressure history is of limited use for predicting the local burning rate of the solid propellant. Furthermore, erosive burning can significantly affect the propellant combustion, and an accurate evaluation of the local burning rate can not easily be obtained through numerical simulations.<sup>1</sup> Despite the causes for erosive burning are quite well known, their effects on the overall solid propellant pyrolysis are still very difficult to predict. In addition, the erosive effect in the motor needs to be predicted locally rather than globally, and a precise map of its influence on the combustion of the propellant grain must be known.

A direct measurement at different positions of the local burning rate is therefore indispensable and X-ray diagnostics is a suitable tool for burning rate measurement,<sup>2</sup> nonsteady combustion study<sup>3</sup> and in-motor propellant combustion investigation. The experimental set-up described here is based on X-ray absorption by the solid propellant loaded in a laboratory scale slab motor, and it allows a simultaneous measurement at different positions along the motor axis. Furthermore, some parameters of the motor configuration can be changed to allow local pressure and burning rate measurements over a wide range of operating conditions.

## EXPERIMENTAL SET-UP

After a preliminary assessment of various system configurations designed to carry out erosive combustion tests, the following one has been adopted. It mainly consists of a slab rocket motor, X-ray source and data acquisition system. As shown in Fig. 1, the first two components are placed on a test stand located inside a lead cage with a port only for the exhaust of combustion gases, whereas the third component is placed in an adjacent control room. Figure 2 represents the main concept on which this measurement system is based.

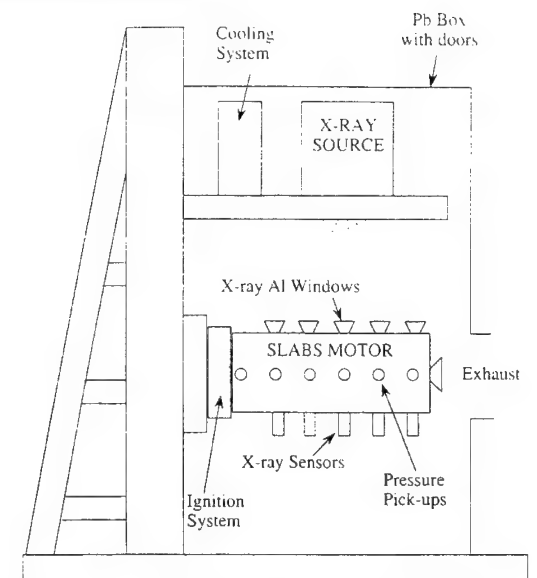


Fig. 1 Layout of Test Stand

## X-RAY SOURCE AND SENSORS

The X-ray source shown in Fig. 2 has a square emission area of  $0.6 \times 0.6 \text{ mm}^2$  and  $40^\circ$  emission angle. The tube voltage can be varied over the range from 20 to 100 kV, while the tube current can be set from 1 to 4 mA. The position of the source, placed on a support mounted 50 cm above the motor, can be moved depending on the position of the selected test section. The source is equipped with a closed-circuit cooling system. Due to the source emission angle, the propellant thickness and measurement point location, this source allows the simultaneous use of three adjacently placed X-ray sensors. They are placed in housings that are inserted in the removable bottom side of the motor.

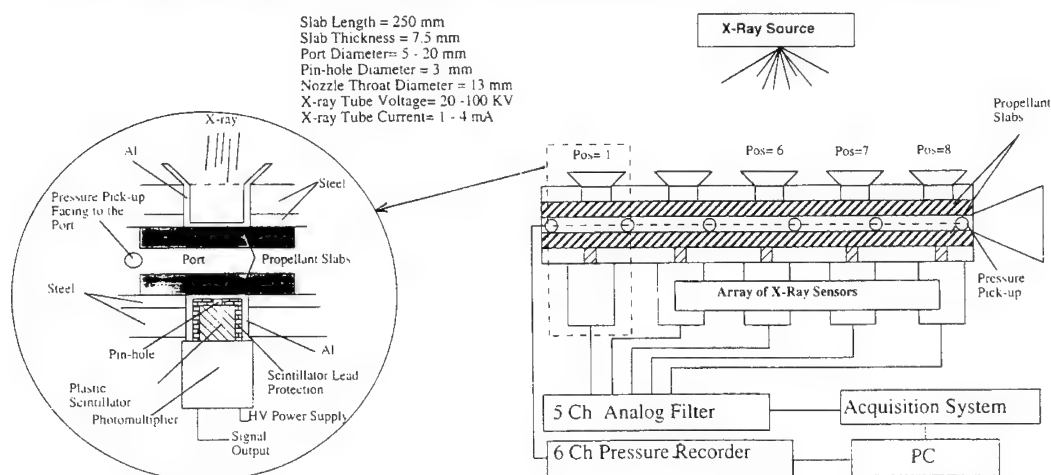


Fig. 2 Sketch of Motor with Sensors

The sensor consists of a plastic scintillator which is connected to phototube located inside an aluminum housing. The sensitive surface area is reduced by using a lead diaphragm having a circular aperture with a diameter of 3 mm, and the applied tube voltage is 1100 V.

### SLAB MOTOR

The slab motor is a modular steel structure that allows a modification of its configuration by changing the distance between the two parallel solid-propellant slabs, the nozzle throat area, and the X-ray sensors and pressure pick-up positions along the longitudinal axis of the motor case (see Fig. 3). The main body of the motor is properly mounted to the test stand in order to leave access for the igniter plug, and a disposable nozzle is inserted on the opposite side. The nozzle itself is made of graphite and is attached to a flange that can be easily mounted and removed from the main body. Also the top and bottom sides of the rocket motor are removable and each of them houses one of the propellant slabs and eight access areas. The top side (Fig. 4) is equipped with five screw taps and three aluminum windows, whose positions can be selected depending on the longitudinal positions under investigation. These aluminum windows do not significantly attenuate the power of the X-ray beam. The bottom side (Fig. 5) shows the same feature as the top one, except that three X-ray sensors are positioned just below the three aluminum windows of the top side. On one side of the main body, six pressure measurement points have been obtained allowing six pressure transducers to monitor the static pressure inside the free port at different pre-selected positions. The motor case is constructed of stainless steel and has been pressure tested up to 14 MPa.

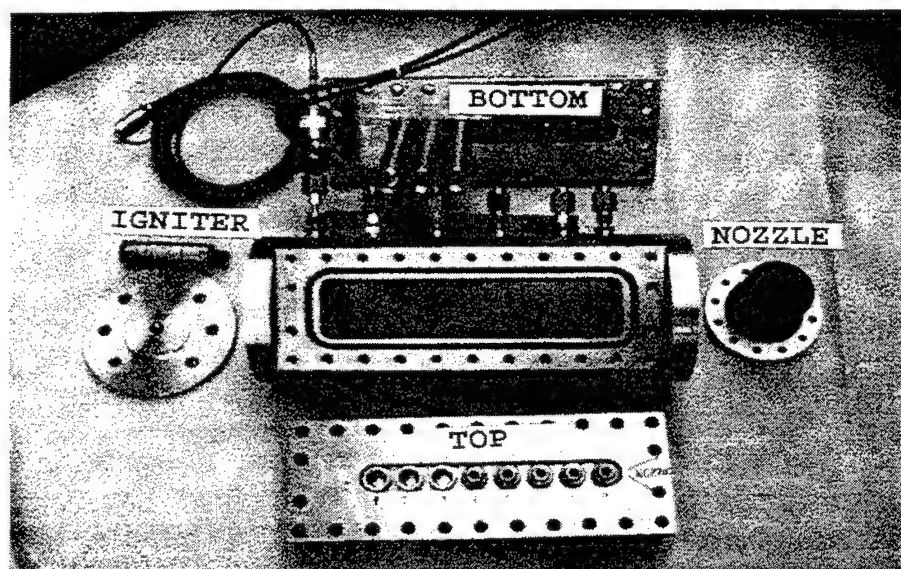


Fig. 3 Components of Motor

### DATA ACQUISITION SYSTEM

The actually employed version of the data acquisition system shown in Fig. 6 consists of a controller interfaced with a personal computer, where standard data acquisition and presentation packages are

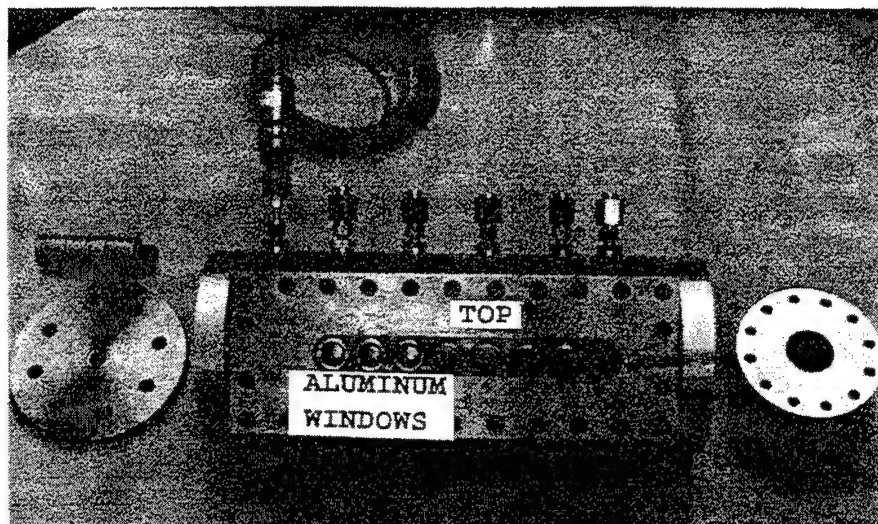


Fig. 4 Top Side of Motor

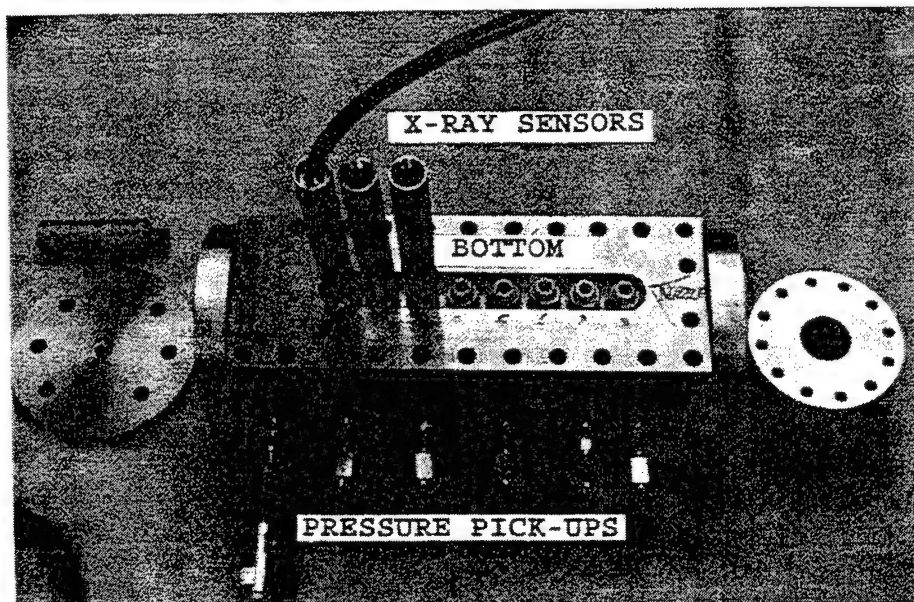


Fig. 5 Bottom Side of Motor

installed. The controller is equipped with a 12-bit AD converter (12.5kHz - 8 channels), a hard disk (1 GB), power relays and a sequencer. Signals from three X-ray sensors and those coming from the strain-gage pressure pick-ups are, respectively, 2 and 10 kHz low-pass filtered before reaching the controller. All the procedures starting from the ignition of the motor until data storage are PC controlled, and a digital tape recorder (DAT) serves as the back up to the acquisition system.

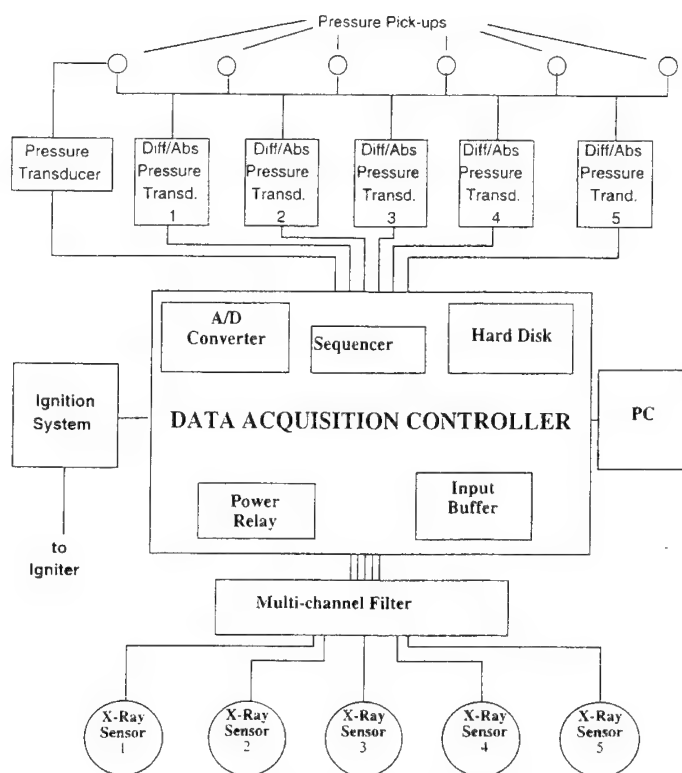


Fig. 6 Data Acquisition System

### SOLID PROPELLANT SLABS

The reported experiments were conducted by using only one propellant formulation whose composition and characteristics are specified in Table 1. The propellant is currently in practical use, and it is highly aluminized which produces a high burning rate. The slabs with a length  $L = 250$  mm, width  $W = 50$  mm, thickness  $t = 7.5$  mm are fitted into their supports after being cured and attached by using proper adhesive.

### IGNITER

Motor ignition is achieved by using a pyrogen igniter loaded with a polyester-based composite propellant whose amount is measured to be less than that required for usual negligible ignition delay. The ignition system is rather sophisticated, and the simultaneous ignition over the complete propellant surface is obtained after the pressure in the motor, raised by the firing of the igniter, has dropped again to the ambient pressure level.



TABLE 1  
Propellant Properties

<b>Composition (mass%)</b>		
Oxidizer	AP.....	68
Fuel Binder	HTPB.....	12
Fuel	Al.....	20
Additive	Fe <sub>2</sub> O <sub>3</sub> .....	0.3 - 0.5
by parts		
<b>Density</b> (@20°C/50°C), g/cm <sup>3</sup> .....		1.82
<b>Linear Burning Rate</b>		
(@50Kg/cm <sup>2</sup> , 20°C), mm/s.....		9.2
Pressure Exponent.....		0.4
Temperature Sensitivity, %/°C.....		0.076
<b>Combustion Gas Properties</b>		
(@5MPa, Frozen equilibrium)		
Adiabatic Flame Temperature, T <sub>f</sub> , K.		3529
Mean Molecular Weight, W <sub>p</sub> , g/mol..		29.66

## EXPERIMENTAL PROCEDURES

The formulation of a detailed experimental procedure is critical to the success of the motor firing and data collection. First, the propellant slabs must be properly mounted on their support. The adhesive also serves to minimize flame propagation along the side and in between the slab and its support. Once the adhesive has cured, the calibration procedure is carried out. Pressure transducers are always calibrated before every test firing, and the same is done for the X-ray sensors. For this purpose, immediately before the test firing, the X-ray apparatus is *in situ* calibrated by using slabs of known thicknesses; then the aluminum windows and sensors are removed from the supports used for the calibrations and placed in their respective housings on the top and the bottom side of the motor. This operation should be performed within a time period as short as possible in order to reduce the effects of power fluctuations of the X-ray source.

Assembling and fixing of all the motor components must be carefully conducted, and fiber reinforced polymer (FRP) spacers must be inserted between the edges of the slab supports to avoid heat losses to the side walls of the free port. As one of the spacers is properly perforated, its position must be carefully fixed in order to allow the pressure transducers to face into the port.

Special attention has been paid to the reductions of the electric noise on the sensors due to the presence of the X-ray source with its high-voltage power supply and its cooling system inside the lead box; therefore the pressure pick-ups are insulated from the motor body by means of a short plastic tube and the X-ray sensors are properly shielded.

All the components and cables inside the lead box are protected from the combustion gases (often coming back into the box after the burn-out), and the camera for monitoring the firing test is placed close to the test stand. At last, the igniter is inserted and, after the final check, the motor is fired under the control of the PC interfaced with the data acquisition system. The data collected are real time presented, but further processing is needed to store the data in the back-up system (DAT).

## RESULTS

A typical calibration plot is shown in Fig. 7, and the three curves can be fitted by the following exponential functions:

$$\text{Pos. 6: } V = 8.9 \exp(-0.0535 w),$$

$$\text{Pos. 7: } V = 7.5 \exp(-0.0487 w),$$

$$\text{Pos. 8: } V = 8.9 \exp(-0.0545 w).$$

Here, the maximum value assumed by the variable  $w$  is  $W$ . Some nonlinearities are shown and are due to small fluctuations over time of the X-ray power. The raw data collected in one test firing are illustrated in Fig. 8. By means of the related calibration curve and a proper filtering procedure, the collected data can be reduced to such shown in Fig. 9 and are used for further analysis. Filtering procedures can be as sophisticated as needed, but in this work only a standard low-pass filter has been applied.

Depending on the data acquisition rate, the details of the combustion of the slabs can be investigated and the local burning rate can be measured and averaged on the needed scale even if the limited number of tests carried out so far can not precisely evaluate data reproducibility. The result presented in Fig. 9 shows that the average burning rate (at Pos. 6 and Pos. 7,  $r_b = 9.7 \pm 0.2$  mm/s; at Pos. 8,  $r_b = 9.8 \pm 0.2$  mm/s at 4 MPa) is higher than the burning rate measured at a steady-state condition,  $r_b = 8.4 \pm 0.1$  mm/s, and therefore the effect of the erosive burning can be evaluated. Moreover, the three curves linearly fitted in the first 0.2 s of the combustion event give a burning rate which at Pos. 6 and 8 is  $r_b = 9.8 \pm 0.2$  mm/s and at Pos. 7,  $r_b = 9.9 \pm 0.1$  mm/s. Close to the burn-out (averaging time = 0.2 s), they show a burning rate  $r_b = 9.7 \pm 0.1$  mm/s at Pos. 6 and 7 and  $r_b = 9.8 \pm 0.1$  mm/s at Pos. 8.

The results also suggest that the erosive burning effect has, in this type of motor, a scale larger than the distance between the three sensors. Information on the ignition process can also be obtained by evaluating the ignition time. In the present case, the curves suggest a spontaneous ignition driven by hot spots or areas.

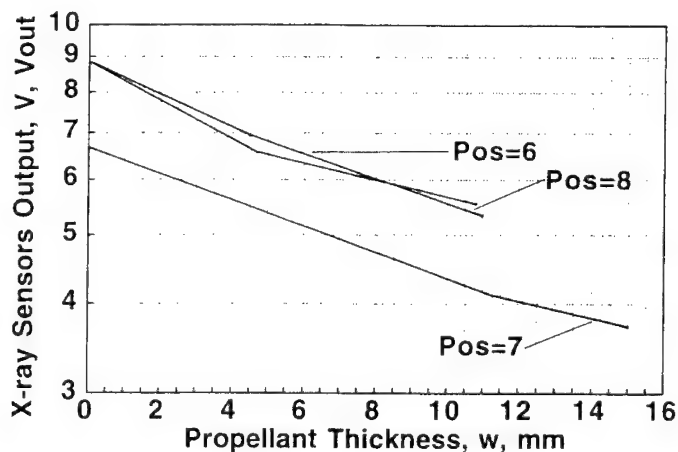


Fig. 7 Example of Results from Calibration

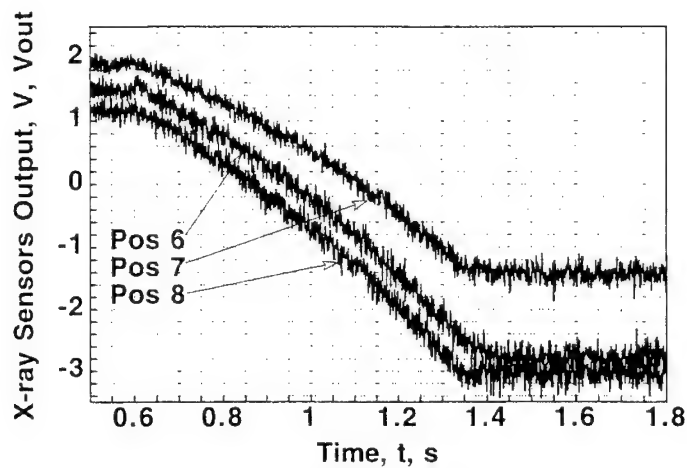


Fig. 8 Raw Data for a Gap Distance of 4 mm

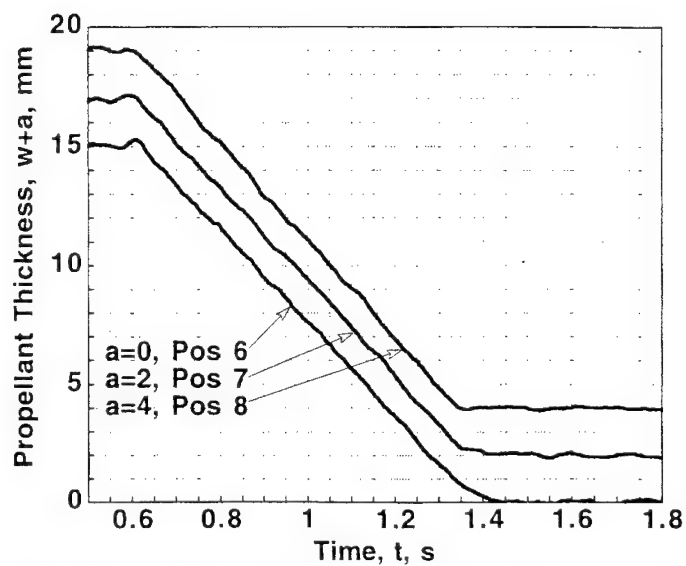


Fig. 9 Propellant Thickness versus Time for a Gap Distance of 4 mm

### CONCLUSIONS

The collected results have demonstrated the reliability of the diagnostic system and its suitability for investigation of situations where accurate knowledge of the local nonsteady burning rate is required. This implies that the present diagnostic system is quite promising as a methodology for investigating the erosive burning characteristics of aluminized composite propellants due to its high spatial and temporal resolutions. The reliability of the diagnostic system is mainly dependent on the determination of the calibration curve and the stability of the X-ray source. High accuracy of the calibration curve is required in regions where the regression of the slab is of strong interest for an

examination of the physical phenomena involved. Digital filtering techniques can also be helpful for improving the overall performance of the diagnostic system, even when the combustion process is highly transient. Future work will include a numerical simulation of the flowfield near the nozzle and the development of a method to scale the results. This X-ray diagnostic technique can also be useful for providing information about other related phenomena, such as ignition, burn-out and aluminum particle combustion.

### ACKNOWLEDGMENTS

The authors wish to thank Dr. Takei (A.D. Consulting Co.), Mr. Kayuta together with Mr. Murata (Toreck Co. Ltd.) for the preliminary work, Mr. Kobayashi for his assistance during the firing tests, Mr. Kitazaka (Tokai Giken Co.) for the preparation of the motor with related hardware and Mr. Hasegawa for his active help in data acquisition and processing. Special thanks are due to Nissan Motor Co. and NOF Co. for having supplied the solid propellant.

### REFERENCES

1. **Razdan, M.K. and Kuo, K.K.**, "Erosive Burning of Solid Propellant," *Fundamentals of Solid-Propellant Combustion*, edited by Kuo, K.K. and Summerfield, M., Progress in Astronautics and Aeronautics, AIAA, New York, 90, 515-598, 1984.
2. **Hsieh, W.H, Char, J.M., Zanoliti, C. and Kuo, K.K.**, "Erosive Burning of Stick Propellants, Part I: Measurement of Burning Rate and Thermal Wave Structure," *Journal of Propulsion and Power*, 6, 4, 400-406, 1990.
3. **Kuo, K.K., Lu, Y.C., Yim, Y.J. and Schwam, F.R.**, "Transient Burning Behavior of Solid Propellants," *Non-Intrusive Combustion Diagnostics*, edited Kuo, K.K. and Parr, T.P., Begell House Publishing Co., 389-402, 1994.

### COMMENTS

B. Stokes, NATO Hq., Brussels, Belgium. What was the Mach number and area ratio at the downstream end of your propellant sample? Could you do a CFD calculation of the test apparatus to evaluate the effect of a 2-D (rectangular) port changing to a circular nozzle? Perhaps the flow is disturbed at P3, P4 and P5 locations.

Author's reply. Sorry, but I could not evaluate it. I think it is a good question because I found in the nozzle some deposit of  $\text{Al}_2\text{O}_3$  suggesting distortion of the flow. My colleagues will be utilizing a CFD code to investigate the flowfield in close vicinity to the nozzle.

## SPECTROSCOPIC INVESTIGATION OF SOLID ROCKET SIGNATURES

L. Deimling, W. Eckl, N. Eisenreich, W. Liehmann, M. Weindel

Fraunhofer-Institut für Chemische Technologie

Joseph-von-Fraunhofer-Str. 7

76327 Pfinztal 1(Berghausen), F.R.G.

### ABSTRACT

The objective was to investigate the signature of various types of solid rocket propellants. The emission and transmission characteristics of the plumes were studied experimentally, the results were analysed based on molecular bands and continuum radiation. The model formulations include a nitramine propellant, a double-base propellant and a composite propellant. Applied were rapid-scanning filter wheel spectrometers for the wavelength region from 1.2 to 14  $\mu\text{m}$  with a time resolution of 50 spectra/s and a wavelengths resolution of 1% of actual wavelength. The UV/VIS wavelengths region was recorded by an OMA system with wavelength resolution of 0.1 and 1 nm and time resolution of 10 spectra / s. Molecular bands of water and carbon dioxide dominate in the near infrared and infrared. Depending on composition, continuous radiation indicates particles in the rocket exhaust. A code was developed to calculate molecular bands and continuous radiation using temperature and species distributions found by thermodynamic estimation to obtain the radiance of the plume. Comparison with experimental data delivered plume temperatures.

### INTRODUCTION

The signature of rocket plumes contains information about hot gases and particles present in the exhaust of rockets. The plumes strongly scatter, emit and transmit light. The effects can be used for detection, identification and guidance of missiles. In addition, the analysis of the signature evidently delivers information about the exhaust of air pollutants which are for example important at high altitudes.

In principle, it would be possible to obtain all data needed from theoretical calculations. The chemical in a rocket plume can be estimated from thermodynamic codes and the interaction with light obtained from models describing the radiative properties of the species and the temperatures in the plume. However, the conditions of the plumes seem to be more complicated to be described by models based on equilibrium with sufficient accuracy.

- The final products of the combustion in the chamber expand at the nozzle by a factor of 100 or more. So non-equilibrium distribution of temperatures have to be taken into account which reduces the applicability of codes for species and radiance.
- The particle density which is responsible for the strong continuous radiation cannot exactly be predicted.

- The after burning of the plume leads to further conversion of species not completely oxidized. It increases temperature depending on air entrainment.
- The chemical analysis is limited due to condensation and reactions when sampling at transient conditions if experiments are performed in vacuum vessels.

As a consequence, experimental data have to be acquired and compared to theoretical calculations. For measurement of radiative properties of plumes and propellant flames, spectroscopic equipment is available to cover the wavelength regions of interest from the UV to the mid-infrared with sufficient sensitivity and time resolution. The codes could be improved by comparison with experimental data. It is the objective of the reported work to describe an experimental set up for spectroscopic measurements, theoretical models to predict the radiance of hot gases including particles, two and three atomic molecules and to present first results. The most important types of propellants are taken into account by using simplified compositions with the main components.

## EXPERIMENTAL

Emission spectra in the UV and VIS have been detected using a Tracor Northern rapid-scan spectrometer TN 6500 with a Jarrel Ash monochromator (focal length 275 mm, entrance slit 50 microns). To get rotationally resolved spectra, a grating with 2400 lines/mm has been chosen (wavelength resolution  $20 \text{ cm}^{-1}$ ). The detector is equipped with an intensified 1024 element diode array. Minimum time resolution of the system is 10 ms. Assumed stationary conditions, experimental spectra were recorded with 100 ms per scan. If no rotational resolution was needed, a grating with 300 lines/mm has been used which gives spectra with a wavelength resolution of ca 1 nm. Spectra in the NIR (1000 to 2500 nm) have been recorded applying a rotating filter wheel spectrometer developed at ICT [1] (wavelength regions from 1.2 to 14  $\mu\text{m}$  with a time resolution of 50 spectra / s and a wavelength resolution of 1% of actual wavelength. A bomb equipped with windows (quartz or  $\text{CaF}_2$ ) was utilized to acquire spectra of propellant flames and a small standardized rocket motor was utilized to obtain spectra of plumes.

## DATA ANALYSIS

Determination of rotational and vibrational temperatures of various diatomic is based on the calculation of line intensities and profiles. The intensity of a spectral line is given by [2]:

$$I_{em} = N_n h c \nu_{nm} A_{nm} \quad (1)$$

where  $N_n$  are the atoms in the initial state,  $h c \nu_{nm}$  is the energy of each emitted photon of the transition and  $A_{nm}$  is the Einstein transition probability of spontaneous emission. Taking into account thermal equilibrium, Born-Oppenheimer approximation and the explicit expression for Einstein coefficients, equation (1) can be written as:

$$I_{em} = C \cdot q_{j,j'} \cdot S_{j,j'} \cdot \nu^4 \cdot \exp(-E_{vib} / kT_{vib} - E_{rot} / kT_{rot}) \quad (2)$$

where  $q_{j,j'}$  and  $S_{j,j'}$  are, respectively, the vibrational and rotational line strength,  $E_{vib}$  and  $E_{rot}$  are, respectively, the vibrational and rotational energy of the upper level,  $k$  is the Boltzmann constant and  $T_{vib}$  and  $T_{rot}$  are, respectively, the vibrational and rotational temperatures. The constants and parameters for the different molecules and transitions are taken from literature [3-5].

**Table 1.**

Temperatures and main reaction products calculated from ICT thermodynamic code for different propellant formulations at 10 and 0.1 MPa simulating a rocket exhaust plume including secondary combustion with air

Propellant	Nitramine		Double base		Composite	
composition	85% HMX 15% binder		50% NC (13.3% N) 35% NG 11% Triacetine 2% Centralite 2% CuO		80% AP 10% Al 10% binder	
atmosphere	inert	air	inert	air	inert	air
pressure	10	0.1 MPa	10	0.1 MPa	10	0.1 MPa
temperature	2293 K	1227 K	2508 K	1317 K	3470 K	1909 K
main reaction products in wgt. %	CO <sub>2</sub>	5.931 27.700	CO <sub>2</sub>	21.790 37.832	Cl	2.332 0.261
	H <sub>2</sub> O	9.132 10.111	H <sub>2</sub> O	17.215 10.746	CO <sub>2</sub>	8.362 19.647
	N <sub>2</sub>	32.551 62.168	N <sub>2</sub>	13.332 50.743	H <sub>2</sub> O	20.720 18.089
	CO	49.946 0.001	CO	45.021 0.013	N <sub>2</sub>	9.509 34.100
	H <sub>2</sub>	2.421 0.000	H <sub>2</sub>	1.008 0.000	CO	14.724 0.228
					OH	1.487 0.034
					HCl	22.166 15.492

Temperatures have been determined by comparing calculated line profiles to experimental data [6]. Therefore, a line profile must be taken into account. In case of our spectral resolution (about 20 cm<sup>-1</sup>), the line profile is dominated by the slit function of the spectrometer and can be approximated by a single Lorentzian. The broadened lines are overlapped by adding the contribution of each line at a given wavenumber.

A quantitative data analysis of infrared spectra has been applied by band modelling. The used computer program BAM can calculate NIR/IR-spectra (1 - 10 µm) of inhomogeneous gas mixtures of H<sub>2</sub>O (with bands around 1.3, 1.8, 2.7 and 6.2 µm), CO<sub>2</sub> (with bands around 2.7 and 4.3 µm), CO, NO and HCl and can take into account emission of soot particles. It is based on the single line group model and tabulated data of H<sub>2</sub>O and CO<sub>2</sub> (see [7]). Because there are many unknown parameters influencing the emission spectrum of an inhomogeneous gas mixture, only a simplified model can be applied. Therefore we have assumed that there is just one emitting layer of undefined thickness, constant temperature, constant concentration of the various gases and soot particles which are in thermal equilibrium.

## RESULTS AND DISCUSSION

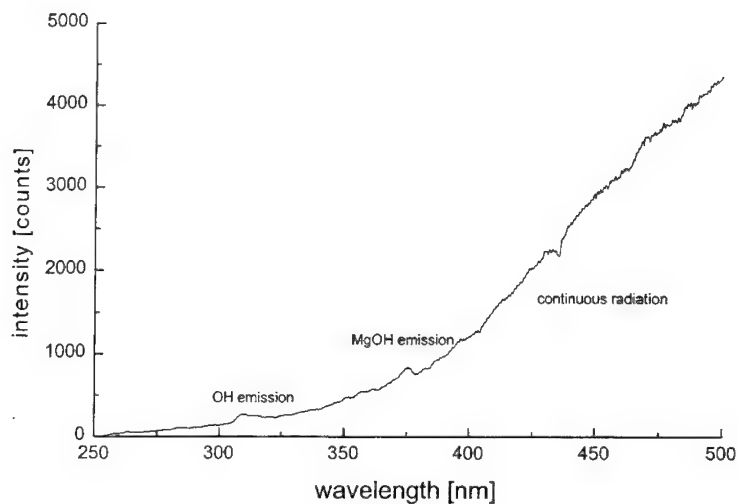
The adiabatic flame temperature and equilibrium compositions of model propellant formulations has been calculated using a thermodynamical code developed at ICT [8]. Results and description of the basic formulations are shown in table 1. Reaction products and temperatures were obtained assuming

- an inert atmosphere at 10 MPa
- a combustion in air (stoichiometric) after expanding to 0.1 MPa.

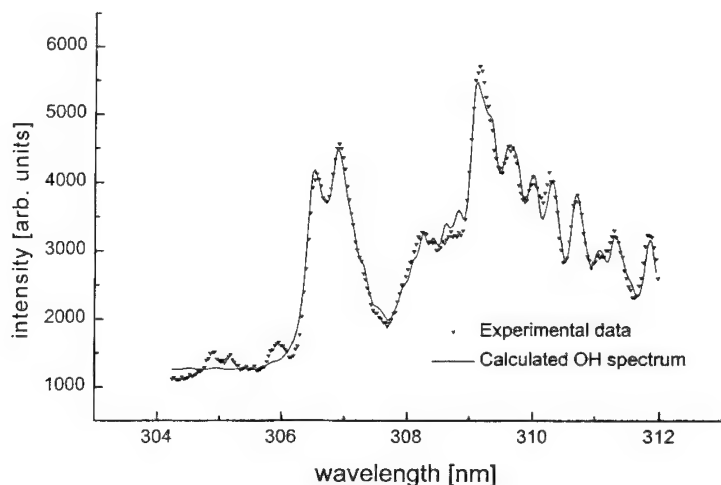
The latter data should account for after burning of the species in the rocket plume.

A medium resolved UV/VIS spectrum recorded from a rocket exhaust plumes of a composite propellant is shown in fig. 1. The spectrum is dominated by continuous radiation emitted from particles. Observable radiation of hot gases are band profiles of the OH radical and MgOH (present

because of impurities). The continuous spectrum can be approximated by a gray body radiation of particles and the temperature estimated to 2600 K.



**Figure 1.** UV/VIS spectrum of a composite propellant exhaust plume acquired at a spectral resolution of 1 nm.



**Figure 2.** Rotationally resolved OH 0-0 band for temperature determination in a composite propellant exhaust plume

The band profile of OH has been rotationally resolved by using a 2400 g/mm grating. The 0-0 band of OH has been compared to calculated intensity distribution for temperature determination (see fig. 2). Average rotational temperatures 15 cm behind the nozzle were about 2500 to 3000 K. The



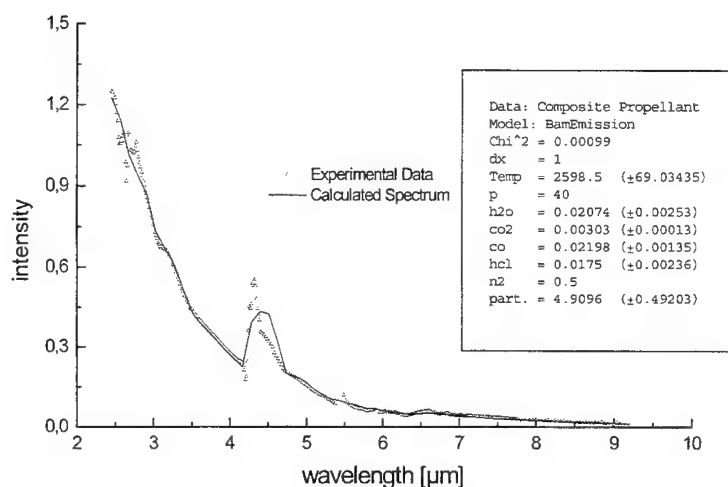
calculated adiabatic temperature at a pressure of 10 MPa (pressure in the burning chamber) is 3500 K. Taking into account expansion to 0.1 MPa, temperatures of 2000 K are expected (see table 1).

Nitramine and double-base propellants show no radical emission in the plumes. Experimental investigation of nitramine and double base propellants in an optical bomb allowed temperature determination from UV/VIS band profiles of various molecules. The results can be found in [9, 10]. The thermodynamical data of the ICT code [8] were used for modelling of infrared spectra and compared to experimental data. Fig. 3 shows a spectrum of a composite propellant flame. The calculated spectrum has been obtained assuming a single-emitting-layer-model:

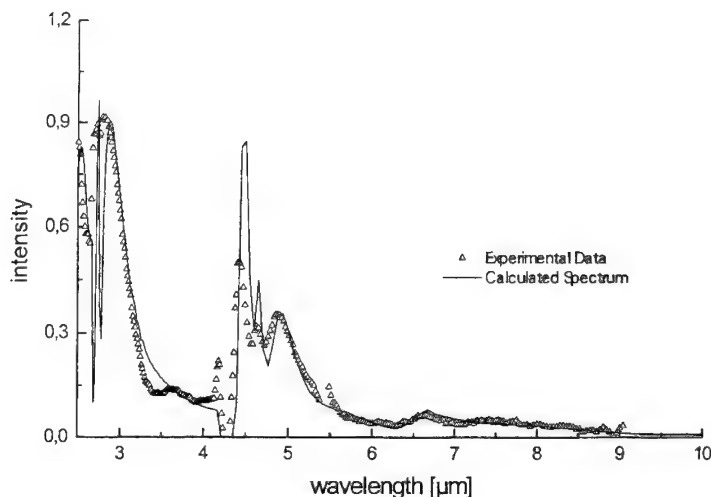
$$T_{\text{detected}} = CI_{b,\lambda} [1 - \exp(-k_{\lambda} L)] \quad (3)$$

$L$ =path lengths,  $k_{\lambda}$ =absorption coefficient;

Comparing calculated intensity distributions to the emitted radiation of a double base propellant, a multi-layer-model has to be applied taking into account a temperature and concentration gradient in the flame and exhaust (see Fig. 4). Fig. 5 shows a comparison of a measured and a calculated spectrum of a nitramine propellant flame.



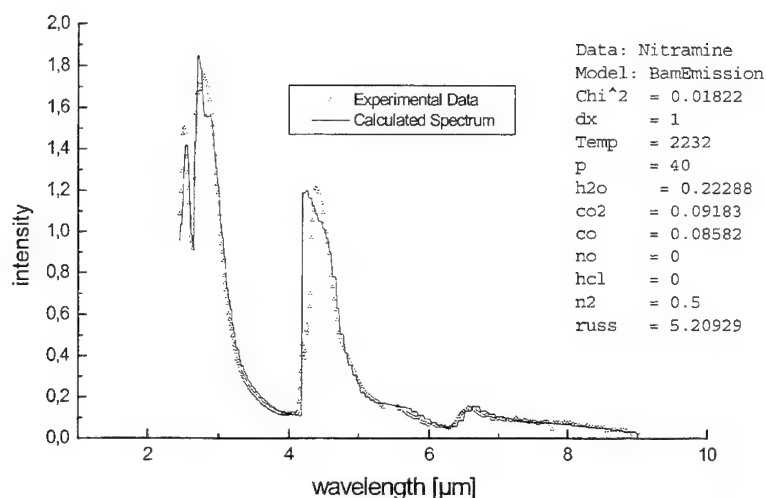
**Figure 3.** Comparison of a calculated and experimental spectrum of a composite propellant flame, (the peak at 5.5  $\mu\text{m}$  is caused by the change of the detector InSb to HgCdTe)



**Figure 4.** Comparison of a calculated and experimental spectrum of a double base propellant flame ( $T = 2200\text{ K}$ )

As expected, the infrared region of spectra from propellant flames is dominated by the emission of  $\text{H}_2\text{O}$  and  $\text{CO}_2$ . The spectra of the nitramine and the double-base show a weak continuum with respect to the bands of the combustion products. The spectra confirm that these propellant types produce very low signatures. A strong CO emission is found in the spectra of the double-base caused by the low oxygen balance of the composition. It agrees qualitatively with the result of the calculation. Spectra of double base rocket plumes indicate the strong after burning of especially CO by the increase of the observed temperature at some distance after the nozzle and an additional weak broad band in the blue wavelengths region. The agreement of experimental and calculated spectra is low in the region of the  $\text{CO}_2$  band, because of self absorption and atmospheric absorption, which have not been accounted for. The bands of the nitramine are better approximated by the model. The temperature is found to be close to the calculated one. The temperatures obtained for the flames of double-base propellants are 200 to 300 K below the adiabatic value obtained from the thermodynamic code. The difference can be assigned to the heat loss of the flame by radiation cooling, but the error of the measurement is estimated to be about 5 %.

The emission of the composite propellant is governed by continuous radiation. The molecular bands are small including the  $\text{CO}_2$  band. The temperature derived mainly from the continuous emission deviated strongly from the data calculated by the thermodynamic code. The cooling of the flame by radiation could be high but cannot explain the difference. The molecular bands are too small and too affected by noise to give reliable data.



**Figure 5.** Comparison of a calculated and experimental spectrum of a nitramine propellant flame ( $T = 2200\text{ K}$ )

## REFERENCES

- [1] **Blanc, A. et al.**, "Charakterisierung von Verbrennungsprozessen mittels zeitaufgelöster IR-Spektroskopie im Bereich 1 - 14  $\mu\text{m}$ ", 19th Int. Annual Conf. of ICT, 1988.
- [2] **Herzberg, G.**, "Molecular Spectra and Molecular Structure I. Spectra of Diatomic Molecules", D. van Nostrand Company Inc., Princeton, New Jersey, 1950.
- [3] **Dieke, G.H., Crosswhite, H.M.**, "The Ultraviolet Bands of OH", J. Quant. Spectrosc. Radiat. Transfer, Vol. 2, 97 - 199, 1961.
- [4] **Coxon, J. A.**, "Optimum Molecular Constants and Term Values for the  $X^2\Pi$  and  $A^2\Sigma$  States of OH", Canadian Journal of Physics, Vol. 25 pp. 676, 1980.
- [5] **Chidsey, I. L., Crosley D.R.**, "Calculated Rotational Transition Probabilities for the A-X System of OH", Journal of Quant. Spec. and Rad. Transfer, Vol. 23, pp 187, 1980.
- [6] **Eckl, W., Eisenreich, N.**, "Temperature of Flames Obtained from Band Profiles of Diatomic Molecules," Bull. Soc. Chim. Belg. Vol. 101, n° 10, pp 851., 1992.
- [7] **Ludwig, C.B. et al.**, "Handbook of Infrared Radiation from Combustion Gases," NASA SP-30980, 1973
- [8] **Volk, F.; Bathelt, H.**, "Rechenprogramm zur Ermittlung thermochemischer und innenballistischer Größen, sowie von Gasdetonationsparametern," ICT-Report 3/82, 1982.
- [9] **Eckl, W., Eisenreich, N.**, "Determination of the Temperature in a Solid Propellant Flame by Analysis of Emission Spectra," Propellants, Expl., Pyrotech., 17, 202 - 206, 1992.
- [10] **Eckl, W., Eisenreich, N., Liehmann, W.**, "Non-Intrusive Temperature Measurement of Propellant Flames and Rocket Exhausts Analysing Band Profiles of Diatomic Molecules", Non-Intrusive Combustion Diagnostics; (Kuo K. K., Parr T. P. ed.), Begell House, Inc. New York, pp. 673, 1994.
- [11] **Vanderhoff, J.A., Kotlar, A.J., Beyer, R.A.**, "Temperature and Concentration Measurements in Hostile Combusting Flows Using Multichannel Absorption Spectroscopy", Non-Intrusive Combustion Diagnostics; (Kuo K. K., Parr T. P. ed.), Begell House, Inc. New York, pp. 227, 1994.

## CARS MEASUREMENTS OF TEMPERATURE FLUCTUATIONS IN A HIGH PRESSURE GAS TURBINE COMBUSTOR

B. Hemmerling, R. Bombach, and W. Kreutner  
Paul Scherrer Institut, CH-5232 Villigen PSI, Switzerland

**ABSTRACT:** A mobile CARS system has been used to determine temperatures and their fluctuations in a high-pressure combustion test rig with a maximum thermal power of 8 MW. Probability density functions of the temperature, each based on 1000 single-shot measurements, have been determined at different radial and axial locations within the combustion chamber in turbulent natural gas and oil flames up to a pressure of 14 bar. Analysis of the frequency spectrum of the temperature probability density functions reveals periodic fluctuations of the flame.

A high degree of turbulence, an increased pressure together with an extended size of the combustion chamber caused beam propagation effects to become a serious problem for this measuring technique. Temperature determinations in sooty oil flames became even more difficult due to the strong absorption of a part of the fundamental band of the  $N_2$  CARS spectrum by  $C_2$  radicals.

### Introduction

The constraints on pollutant production by fossil combustion processes have increased during the last years enforcing the development of sophisticated combustion technologies. Proven to successfully reduce the emission of nitrous oxides, the lean premixed technique has emerged as a concept for gas turbine combustors. A high degree of turbulence is employed to mix fuel and oxidizer. High pressure and a macro scale of the turbulence of some centimeters lead to very high turbulent Reynolds numbers ( $>10^6$ ). Such conditions are not easily achieved in laboratory-based combustors. To validate numerical models for gas turbine combustors working under realistic conditions, optical diagnostic methods have to be applied. Such measurements at industrial sites and large-scale test rigs became feasible by the development of mobile systems which remain operational even under harsh conditions.<sup>1-3</sup>

Coherent Anti-Stokes Raman Scattering (CARS) is a well-established and accepted tool for non-intrusive determination of gas temperature in combustion processes.<sup>4,5</sup> Because of its natural abundance in air fed flames,  $N_2$  is widely used as temperature probe molecule. With multiplex CARS, the complete Q-branch spectrum of nitrogen and therefore the temperature can be measured with a single laser shot. Hence, the temporal resolution of this technique exceeds the needs dictated by the fluid dynamic time scales in a flame. The obtainable spatial resolution typically ranges from parts of a millimeter to some ten millimeters, depending on the optical accessibility of the process under investigation and the signal level required to deduce a reasonable accurate temperature from the recorded spectra. Commercial combustors are often limited in their optical accessibility in order to avoid a change in the operating behaviour by too extensive modifications of the construction. This may result in a spatial resolution which is too poor for measurements in media exhibiting high

temperature gradients. However, the spatial resolution commonly realized for measurements within large-scale combustors at realistic conditions ends up with several millimeters rendering CARS, in most of the cases, unable to resolve the flame front. Different approaches have been studied to cope with such situations.<sup>6-8</sup> However, in turbulent environments single shot CARS data are recorded to establish temperature histograms which deliver reliable temperature information as long as the size of the turbulence exceeds the spatial resolution.

The applicability of the CARS technique for temperature measurements in high-pressure environments has already been shown for a number of technically relevant systems, such as internal combustion engines, jet engines, and solid propellant flames.<sup>9-11</sup> Nevertheless, some difficulties in the evaluation of high-pressure CARS spectra are still under investigation. These concern the proper description of the collision dynamics for a number of collision partners over a wide range of temperature and pressure and the contribution of the nonresonant background to the CARS signal.<sup>12</sup>

In this report preliminary results of measurements carried out at a high pressure test rig on turbulent natural gas/air, and sooty oil/air flames are presented. Caused by the size of the combustion chamber the most serious limitations for optical diagnostics stem from beam-propagation effects. Ray-bending effects, increase of beam divergence, and appearance of speckles are obstacles in the conversion process of the incident light waves into the CARS signal.

### Experimental

The mobile CARS system used for the measurements outlined in this contribution has been built at the Paul Scherrer Institute. It has already been described elsewhere.<sup>3</sup> Therefore, only the most salient features will be repeated here. The apparatus consists of a laser unit, a beam handling and delivery section, and a detection unit. The laser unit includes the laser sources necessary for nitrogen CARS thermometry, their power supplies and the beam alignment optics in a stable frame, 2 m long, 0.8 m wide, and 1.35 m high. Temperature stabilization and insulation against mechanical vibrations allow its employment even under harsh conditions. The system is built around a frequency-doubled Nd:YAG laser running at a repetition rate of 20 Hz. A two-stage broadband dye laser using Rhodamine 101 dye dissolved in methanol provides the Stokes beam. Different phase matching configurations can be employed for signal generation. To allow measurements of temperature profiles, the lens that focuses the laser beams into the burner can be translated on a motorized table by 200 mm. A second, identical device is used to move the recollimating lens. The resonant signal is focused into a glass fiber bundle and guided to the monochromator. A part of the laser light is used to generate a nonresonant reference signal in a gas cell filled with butane at a pressure of 2 bar. This signal is used to reference the resonant signal to the spectral profile of the broadband dye laser, the individual sensitivity of the camera diodes and the transmission characteristics of the optical components of the detection unit. The reference signal is focused into a second fiber bundle. The two bundles are merged in a "Y" junction and formed into a rectangular array about 2 mm high and 50 mm wide. The exit face of the combined fiber bundle is imaged onto the entrance slit of the monochromator (1 m focal length, 2400 grooves/mm grating). Resonant and nonresonant CARS signals are alternatively detected with a gated, intensified diode array camera. The translation of the measurement volume and the acquisition of reference and single-pulse resonant spectra are automated and run under control of a PC program.

With each shot of the laser system a spectrum can be recorded and stored, resulting in a maximum data acquisition rate of 20 Hz. The temporal resolution, given by the duration of the laser pulse (approx. 10 ns), comfortably exceeds the demands encountered in the investigation of turbulent flames. The obtainable spatial resolution depends on the angle at which the laser beams are focused into the measurement volume, and also on the phase matching geometry employed. Beam steering effects originating from changes in the refractive index in the medium under investigation may lead to an imperfect overlap of the beams at the focus and therefore to a reduced CARS signal intensity.

The USED CARS beam geometry<sup>4</sup> is somewhat less affected by beam steering effects than the folded BOXCARS<sup>4</sup> configuration at the expense of a reduced spatial resolution. The USED CARS geometry is realized by a doughnut shaped pump beam accommodating the Stokes beam. Focused by a lens the beams overlap each other and create the sampling volume. With a focal length of 400 mm, 90% of the CARS signal is generated within a volume extending 11 mm in direction of the laser beams. To some extent, the spatial resolution determined under laboratory conditions has to be relaxed for measurements in processes subjected to strong turbulence.

The precision of the single-pulse measurements has been validated in a stable, laminar laboratory flame. For an isothermal medium the repeated determination of the temperature results in a Gaussian shaped distribution of the temperatures around the true value. At 2000 K, a standard deviation of the temperature measurement of 70 K has been determined. The width of the distribution is mainly caused by mode fluctuations of the broadband Stokes laser. Furthermore, the accuracy of the CARS temperature measurement has been cross-checked in a graphite tube furnace against pyrometric temperature determinations. The discrepancy was smaller than 70 K at 2000 K.

### Measurements

CARS measurements of temperature fluctuations were carried out in a test rig which was built as a joint test facility for high-pressure combustion by Asea Brown Boveri (ABB), Switzerland, the Federal Institute of Technology, Zurich, and the Paul Scherrer Institute. The test rig was equipped with a double cone burner developed by ABB.<sup>13</sup> A double-cone burner comprises two halves of a cone that are shifted with respect to each other in radial direction such that two inlet slits of constant width are formed. Preheated air enters the burner via these slits producing a strong swirl. The swirl mixes the fuel, which is injected in axial direction, with the burner air. The degree of swirl is chosen such that near the burner outlet the flow undergoes a sudden vortex breakdown, resulting in a zone of recirculation, which acts as an hydrodynamic flame holder.

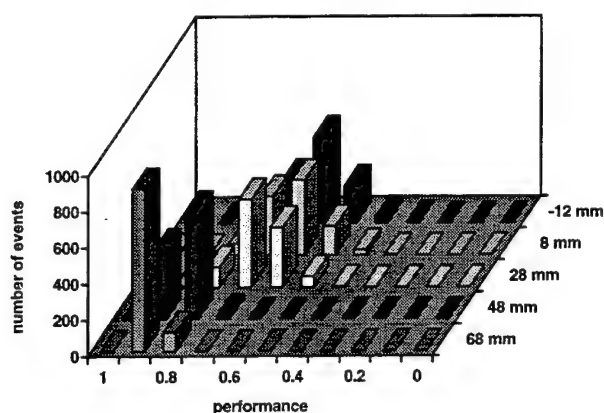
The double-cone burner had an outlet diameter of 100 mm. It was mounted in a liner with a diameter of 155 mm. Holes in the wall of the liner allowed for the optical access. Within the liner, the burner could be translated in the axial direction with respect to the axis of optical access.

At 18 bar, the maximum operating pressure of the test rig, a thermal power of 8 MW is achieved with a fuel throughput of 200 g per second, and an air mass flow of 4.5 kg per second. The burner air can be preheated up to 500 °C. Typically, an air/fuel ratio around  $\lambda=2$  has been used. The turbulent Reynolds number exceeds  $10^6$ , and the Karlovitz and Damköhler numbers are larger than one. Little is known about flames under this condition. However, thick turbulent flames are expected.

In turbulent flames, there are strong fluctuations of the CARS signal amplitude which are caused both by the intrinsic temperature dependence of the CARS signal and by beam propagation effects. The decay time of the phosphor used in the camera intensifier sets a limit on the rate at which individual spectra can be read out sequentially, because a low-intensity spectrum may be obscured by the residual lag from a preceding high-intensity spectrum. However, in this burner the expected temperatures lie within the relatively narrow range of 650 K and 2000 K, corresponding to an intensity change at the signal maximum of only about a factor of 130. Therefore, the maximum data acquisition rate of 20 Hz could be used for the single-shot spectra. A standard temperature measurement of one point within the radial profile consists of 1000 single-pulse spectra. The temperature information is extracted from the flame spectra by comparison with a library of theoretical CARS spectra, pre-calculated for 25 K increments. The resulting temperatures are compiled in normalized histograms with 10 K bin width as so called probability density functions (pdf's) of the temperature. Measurements have been carried out for different pressures in gas-and oil-fed flames.

## Results and Discussion

Even employing a USED CARS phase matching geometry which minimizes the influence of ray-bending on the CARS signal intensity, the signal-to-noise ratio was worse than could be expected. There have been two obvious reasons for that. First, we found that the divergence of a laser beam passing the combustion chamber is proportional to the gas pressure. Going from atmospheric pressure up to 14 bar, the divergence has tripled. Furthermore, at high pressure, the transmitted laser beams show a well-developed granular pattern of the intensity, so called speckles. They arise when the beam of a coherent light source passes areas of strong turbulence. Increasing divergence and appearance of speckles are obstacles in the conversion process of the incident light waves to the Anti-Stokes beam, thus contributing to the low signal level.

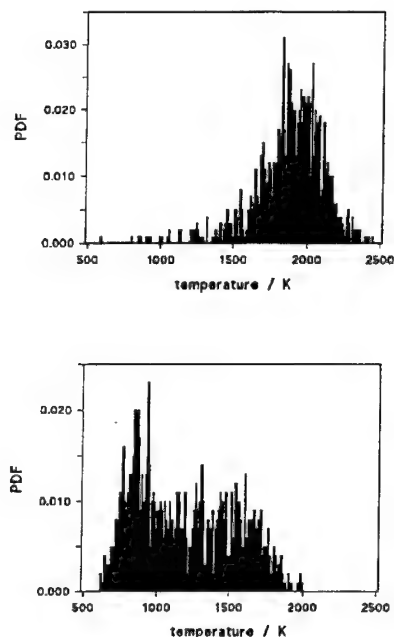


**Figure 1.** 3D-histogram of the performance index of the temperature determination for a series of radial measurements at the axial position  $x=216$  mm.

To characterize the quality of the temperature measurement, we introduced a performance index  $p$  defined by  $p = 1 - \text{sq}(\chi^2)/I_{\text{tot}}$ , where  $\chi^2$  is the sum of squared differences of measured and calculated CARS spectrum, and  $I_{\text{tot}}$  is the total intensity of measured spectrum. A performance index of zero is attached to spectra which did not match a theoretical spectrum. For a series of radial measurements at the position of two burner diameters downstream of the burner outlet, the performance indices of temperature measurements carried out in a natural gas flame at 9 bar are compiled in a 3D-histogram (see Fig. 1). The bin width is 0.1. High-quality temperature measurements are possible near the wall of the combustion chamber, at the entrance side of the laser beams. Closer to the center of the combustion chamber, the quality of the temperature measurements deteriorates more and more. The crossing of the flame front by the measurement volume is indicated by the drastic change of the performance index between the radial positions 48 mm and 28 mm. For an oil-fed flame, the performance index of the temperature measurement behaves similarly.

Radial profiles of CARS temperatures were measured at various axial positions in the burner chamber. To illustrate the results, Fig. 2 shows temperature pdf's obtained at two locations along the burner axis for a natural gas/air flame ( $p=9$  bar,  $\lambda=1.95$ , air preheat temperature 420 °C). Near the burner outlet ( $x=16$  mm, the  $x$ -axis starts at the burner outlet and points along the gas flow), the pdf is rather broad and strongly skewed, with a maximum slightly above the reactant temperature. Only a fraction of the fuel has reacted yet. The mean temperature is  $T_{\text{av}} = 1197$  K with a standard deviation of  $\sigma = 338$  K. Further downstream ( $x=116$  mm), the average temperature has increased

substantially. A mean temperature of  $T_{av} = 1884$  K and a standard deviation of  $\sigma = 245$  K are established. The high mean temperature indicates almost complete conversion of the fuel.



**Figure 2.** Single Pulse CARS temperature pdf's obtained in the middle of the combustion chamber. The upper pdf was recorded at  $x=116$  mm, the lower at  $x=16$  mm, see text.

Periodic, temporal oscillations of the temperature can be recognized by analyzing the frequency spectrum. Figure 3 shows the power spectral densities (psd's) of the temperature determinations which have been used to construct the pdf's displayed in Fig. 2. We removed the DC part of the spectrum to obtain a better representation of the other frequency components. While there is no evidence for a periodic fluctuation of the temperature for the measurement carried out at  $x=116$  mm,  $r=8$  mm ( $r$  is measured from the axis of the combustion chamber), the psd of the temperature determination at the burner outlet ( $x=16$  mm,  $r=8$  mm) exhibits a strong and sharp peak at 2.3 Hz. At this point, the temperature oscillates periodically between 800 K and 1600 K. The flame moves across the measurement point. If the flame front lies within the measurement volume an intermediate temperature is indicated. Figure 4 shows an overview of the locations in the combustion chamber where pronounced peaks in the psd of the temperature measurement were found. The height of the bar is proportional to the intensity of the assigned frequency in the psd. Open bars, hatched bars, and solid bars correspond to a pressure of 3 bar, 9 bar, and 14 bar in the combustion chamber.

At constant pressure and for one axial position, temperature measurements at different radial positions exhibit a pronounced peak in the psd at the same position. For the oil fed flame the behaviour is similar. However, the peaks in the psd of the temperature measurement appear not so pronounced as in the case of the gas-fed flame.

At each measurement location the temperature is sampled, according to the repetition rate of the laser system, with a time interval  $\Delta t = 50$  ms. The bandwidth of the measurement is limited to frequencies smaller or equal to the Nyquist frequency, given by  $f_N = 1/2\Delta t$ . No obvious reasons limit the frequencies of temperature fluctuations occurring in the flame to frequencies below the Nyquist frequency.<sup>14</sup> Therefore, it is very likely that frequencies outside of the frequency range  $(-f_N, f_N)$  are mirrored into that range by the process of discrete sampling. This phenomenon is called aliasing. Two frequencies differing by a multiple of the sampling frequency lead to a peak at the same position in the psd.

The sharpness of the peak in the psd indicates that the oscillation period is very stable. Especially, if the measured oscillation is due to aliasing of a much higher frequency. There are several reasons which can cause a periodic fluctuation of the flame. The most trivial one might be an oscillating flow controller. On the other hand, from pulsation measurements at the same burner under similar conditions, it is known that there are flame oscillations of some 100 Hz corresponding to the



resonance frequencies of the liner. Unfortunately, no pulsation measurements, which could resolve this ambiguity, have been carried out synchronously with the temperature determinations.

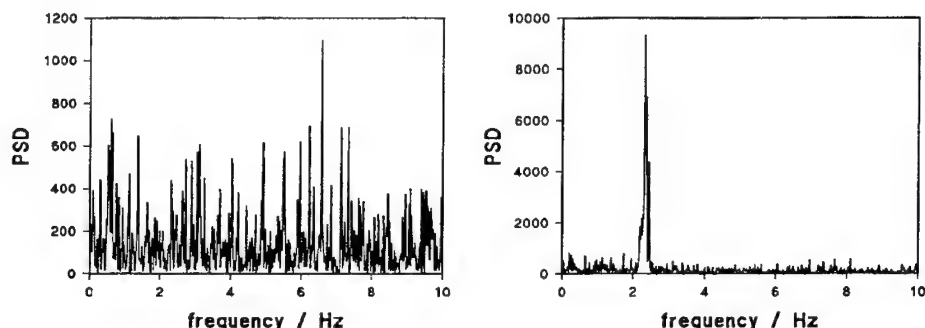


Figure 3. Frequency spectra of the temperature measurements displayed in Fig. 2.

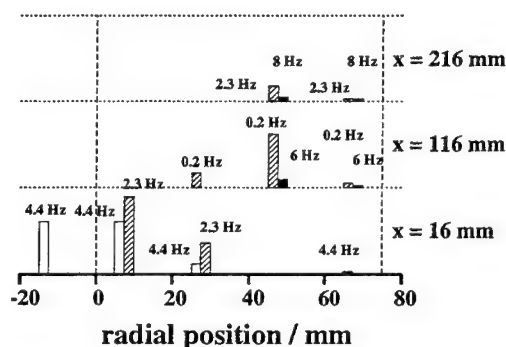


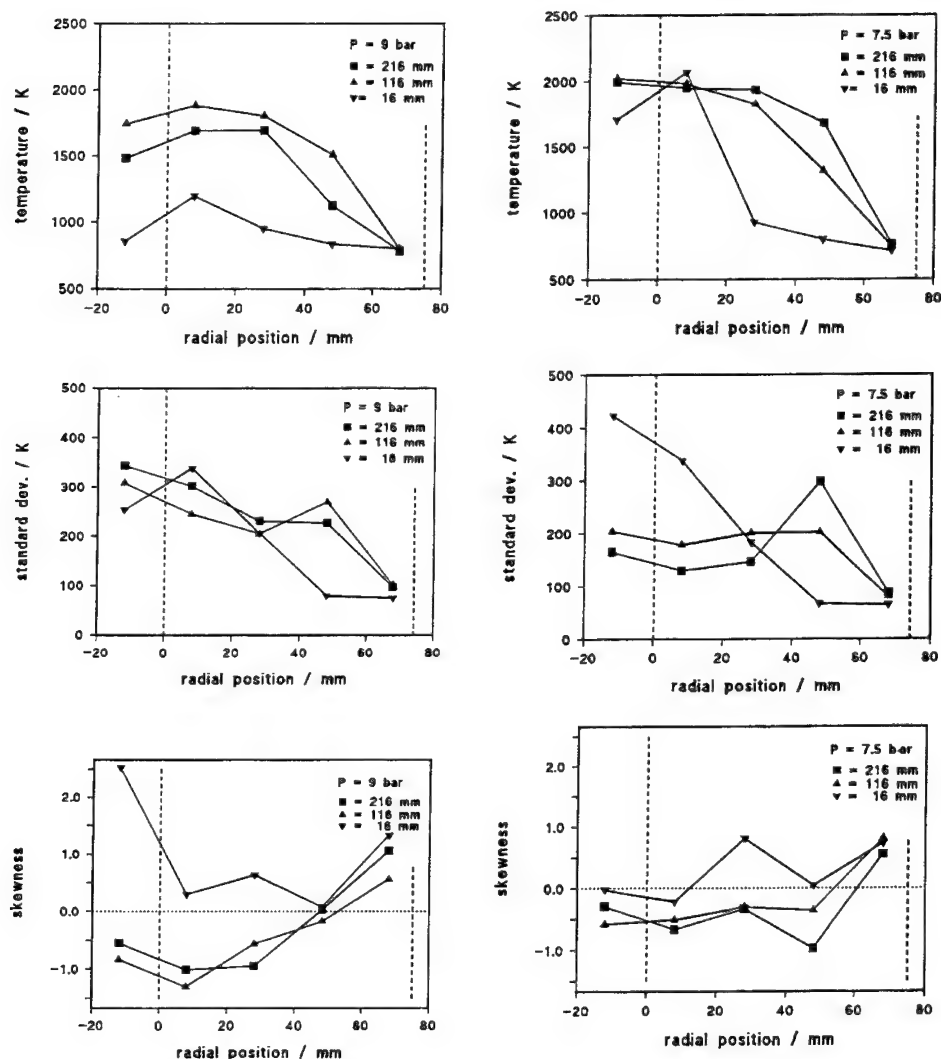
Figure 4. Overview of the fluctuation frequencies of the flame observed at different axial and radial positions. Open, hatched, and solid bars correspond to pressures of 3 bar, 9 bar, and 14 bar, respectively.

Probability density functions are used as input for probabilistic combustion models. However, for illustrative purposes it is necessary to reduce the data material. This is accomplished by characterizing the temperature pdf's by the first three moments of the distribution, the mean, the standard deviation, and the skewness. In Fig. 5 the resulting mean temperatures, standard deviations, and skewness of three radial profile measurements (at  $x = 16$  mm, 116 mm, and 216 mm) are summarized for a gas flame at 9 bar and an oil flame at 7.5 bar. The broken lines indicate the center axis and the wall position of the combustion chamber, respectively. For all three axial locations the temperature is highest a small distance away from the center, and drops towards the wall to a value corresponding to the preheat temperature. There is no great

difference in the temperature profile of the two axial positions farthest away from the burner outlet, indicating that the combustion process has already finished. The same conclusion can be drawn from the behaviour of the standard deviation and the skewness. Clearly, the measurements suggest that there is no recirculation of hot product gases along the wall of the combustion chamber in contrast to this burner under atmospheric pressure.<sup>3</sup>

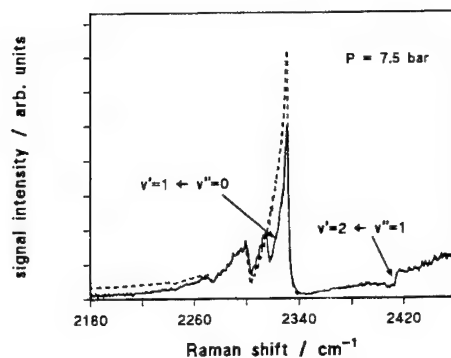
There are no significant problems for temperature measurements by CARS up to a pressure of 9 bar. Broad temperature pdf's ranging from the temperature of preheated air to adiabatic flame temperature indicate that there are hot and cold zones larger than the temperature sampling volume.

At 14 bars there are only small changes of mean temperature and standard deviation with respect to the measurement position within the combustion chamber. The homogeneity of the measured temperature, which lies clearly below the adiabatic flame temperature, allows the conclusion that there are cold and hot regions in the flame which are smaller than the temperature sampling volume.



**Figure 5.** Radial profiles of the mean temperature, standard deviation, and skewness obtained for a natural gas/air flame at 9 bar (left side) and for an oil flame at 7.5 bar (right side).

Another difficulty was encountered during CARS measurements in sooty oil flames. Figure 6 shows a time averaged nitrogen Q-branch CARS spectrum which has been recorded in the middle of the combustion chamber close to the burner exit at a pressure of 7.5 bar. Comparison with a calculated spectrum shows that the fundamental band is strongly distorted. It is well known<sup>15</sup> that for a



**Figure 6.** Nitrogen Q-branch CARS spectrum (theoretical spectrum - dashed line; measured spectrum - solid line).

Nd:YAG based CARS system the nitrogen Q-branch coincides with the  $v'=1 \leftarrow v''=0$  transitions of the  $A^3\Pi_g-X^3\Pi_g$  system of the  $C_2$  radical at about  $2320\text{ cm}^{-1}$ . The  $v'=2 \leftarrow v''=1$  transitions of the same system can also be seen at about  $2420\text{ cm}^{-1}$ . Serious errors in temperature determination may result from fitting such spectra, unless that part of the spectrum, which is influenced by the  $C_2$  absorption, is excluded from the fit. The best fit to the whole spectrum shown in Fig. 6 results in a temperature of about 2130 K. A temperature of 1480 K is obtained by a fit to the unaffected part of the spectrum. In this way, unfortunately, the strongest part of the signal has to be rejected from the evaluation process leading to a deterioration in accuracy and precision of the measured temperatures. However,  $C_2$  absorption was only a problem for measurements in the middle of the combustion chamber in close proximity to the burner exit.

### Summary

CARS measurements of temperatures and their fluctuations have been carried out in large-scale, turbulent, high-pressure flames fueled by natural gas and oil. Especially for the natural gas/air flame, we found periodic fluctuations of the flame. A high degree of turbulence, an increased pressure together with an extended size of the combustion chamber caused beam propagation effects to become a serious problem for this measurement technique. At the center of oil flames,  $C_2$  absorption has to be taken into account.

### Acknowledgements

Financial support by the Swiss Federal Office of Energy (BEW) is gratefully acknowledged.

### References

1. Goss L.P., Trump D.D., MacDonald B.G., Switzer G.L., 1983. "10-Hz Coherent Anti-Stokes Raman Spectroscopy Apparatus for Turbulent Combustion Studies," *Rev. Sci. Instrum.* Vol. 54(5), pp. 563-571.
2. Lueckerath R., Kreutner W., Meier W., Stricker W., 1993. "CARS  $N_2$  Thermometry in Industrial Flames up to 350 kW Thermal Load," in: *Coherent Raman Spectroscopy - Applications and New Developments*, edited by Castellucci, E.M., Righini, R. and Foggi, P., World Scientific Publishing Co., Singapore, pp. 159-164.

3. **Bombach R., Hemmerling B., Kreutner W.,** 1994. "CARS Temperature Measurements in a Lean, Turbulent, 120 kW Natural Gas Flame," in: *Non-Intrusive Combustion Diagnostics*, edited by Kuo K.K. and Parr T.P., Begell House, Inc., pp. 145-151.
4. **Eckbreth, A.C.,** 1988. *Laser Diagnostics for Combustion Temperature and Species*, Abacus Press, Cambridge, Mass..
5. **Greenhalgh, D.A.,** 1988. "Quantitative CARS Spectroscopy," in: *Advances in Non-Linear Spectroscopy*, edited by Clark R.J.H. and Hester R.E., Wiley, New York pp. 193-251.
6. **Bradley D., Lawes M., Scott M.J., Sheppard C.G.W., Greenhalgh D.A., Porter F.M.,** 1992. "Measurement of Temperature PDFs in Turbulent Flames by the CARS Technique," "Twenty-fourth Symposium (International) on Combustion, The Combustion Institute, pp. 527-535.
7. **Singh J.P., Yueh F.Y.,** 1992. "Comparative Study of Temperature Measurement with Folded BOXCARS and Collinear CARS," *Combust. Flame* Vol. 89, pp. 77-94.
8. **Zhu J.Y., Dunn-Rankin D.,** 1993. "CARS Thermometry in High Temperature Gradients," *Appl. Phys.*, Vol. B56, pp. 47-55.
9. **Eckbreth A.C., Dobbs G.M., Stufflebeam J.H., Tellex P.A.,** 1985. "CARS Temperature and Species Measurements in Augmented Jet Engine Exhausts," *Appl. Optics*, Vol. 23, pp. 1328-1338.
10. **Lucht R.P., Teets R.E., Green R.M., Palmer R.E., Ferguson C.R.,** 1987. "Unburned Gas Temperatures in an Internal Combustion Engine I: CARS Measurements," *Combust. Sci. Technol.*, Vol. 55, pp. 41-61.
11. **Fleming J.W., Barber W.H., Wilmont G.B.,** 1984. "Applications of Laser Chemistry and Diagnostics," *SPIE* Vol. 482, p. 74.
12. **M. Woyde** 1992. "Temperaturbestimmung hoher Genauigkeit mit CARS in Hochdruckverbrennungssystemen Untersuchungen an einer vorgemischten CH<sub>4</sub>/Luft-Hochdruckflamme," PhD Thesis, University of Stuttgart, Germany.
13. **Sattelmayer Th., Felchlin M.P., Haumann J., Hellat J., Styner D.,** 1990. "Second Generation Low-Emission Combustors for ABB Gas Turbines: Burner Development and Tests at Atmospheric Pressure," Paper 90-GT-162 presented at the ASME Gas Turbine and Aeroengine Congress and Exposition, June 11-14, 1990, Brussels, Belgium.
14. **Press W.H., Flannery B.P., Teukolsky S.A., Vetterling W.T.** 1990. *Numerical Recipes*, Cambridge University Press, New York, p. 386.
15. **Bengtsson P.E., Aldén M.,** 1991. "C<sub>2</sub> Production and Excitation in Sooting Flames Using Visible Laser Radiation: Implications for Diagnostics in Sooting Flames," *Combust. Sci. Technol.* Vol. 77, pp. 307-318.

## DIAGNOSTICS AND ACTIVE CONTROL OF ACOUSTIC INSTABILITIES IN COMBUSTORS BY ELECTRICAL DISCHARGES AND PLASMA JETS

V.V. Afanasiev, V.A. Frost,\* N.I. Kidin,\* A.K. Kuzmin, and A.A. Terentiyev

Chuvash State University, 15, Moskovsky ave, 428015, Cheboksary, Russia;

\*Institute for Problems in Mechanics of Russian Academy of Sciences

101, Vernadsky ave, 117526, Moscow, Russia

**ABSTRACT:** Electro-acoustic characteristics of various acoustic oscillators operating on the basis of modulated electrical discharges are studied. The results of experimental studies of acoustic instability in model and real ram-jet and liquid-rocket combustors are presented in the form of the spectrum of the pressure-oscillation response to a harmonic perturbation generated by modulated discharges. A new promising method for active control of unstable combustion modes is developed based on the use of electrical discharges using a current- or voltage-stabilized power source. A selective sensitivity of the combustion zone to external perturbation is discovered in experiments with premixed hydrocarbon flames exposed to modulated discharges. Experiments performed in model combustors revealed that combustion instability arises when the fuel resonance coincides with the acoustic combustor resonance. The developed method and results are also applicable to propellant combustors and hybrid solid propellant chambers.

### INTRODUCTION

During the burning of gaseous, liquid or solid fuels in the combustion chambers of various power units, unstable regimes of combustion can appear spontaneously [1, 2]. Such regimes are undesirable in rocket and air-jet engines as they can lead to a disturbance of the normal combustion process and in extreme cases to the actual destruction of the combustor. The level of understanding of this problem is, at present, not yet sufficiently advanced to be able to predict the possible occurrence of such instabilities, as for example, the buildup of a self-oscillating regime.

It is common knowledge that a system is considered to be dynamically stable if it returns to its initial state after a disturbance is introduced by some internal or external perturbing mechanism. This gives an approach to the study of normal process stability in combustors, supported by a large number of laboratory and on-site tests, which can predict the probability for onset of instability in many cases.

It is noted [1] that for the best estimation of stability, it is necessary that all modes of unstable combustion are excited artificially to obtain oscillations of the required amplitude. However, it is also noted that the realization of this approach is extremely difficult for several reasons. First, there exists only an approximate theoretical model of the exciting oscillation mechanism. Second, there

are so far no reliable methods for initiating disturbances in a combustion chamber which give known and controllable characteristics. For this aspect, the development of new devices which would excite an operating combustion system with disturbances of the required frequency and amplitude, but without destroying the working process in the chamber, is very important and desirable. To reduce unsteady combustion modes, it is also essential to develop entirely new predictive methods which could in turn lead to active control of such combustion instabilities in the chamber.

This paper presents results of an analysis of the characteristics of various electro-acoustic oscillation generators, used at normal and higher pressures, for the diagnosis and active control of acoustic instabilities in combustion systems. The generators were all based on a modulated electrical discharge with amplitude and frequency modulation of the current in the acoustic range. The theoretical and experimental results of a continuing joint research program into new and sophisticated methods for the control of unsteady combustion are presented. The paper also considers results of combustion zone sensitivity for premixed hydrocarbon fuels of different reagents to harmonic disturbances created by the modulated electric discharge. It considers the consequences of changing the modulation frequency and compares the results obtained with experimental data on excitation by sound in a model combustion chamber burning air-propane and air-petrol mixtures.

### THE ARC DISCHARGE AS AN ACOUSTIC GENERATOR

Figure 1 shows the experimental arrangement used to determine the electro-acoustic characteristics of a modulated high frequency arc discharge localized in the combustion zone. It consisted of three main parts: the acoustic emitter or generator which was a modulated gas-discharge plasma, an electric power supply, and a recording and measuring device. The modulated electric discharge was created between carbon electrodes placed in the ionized combustion products of an oxygen-propane mixture (see also [3, 6]). The conductivity of the combustion products was increased by seeding it with COH additives. The modulated discharge was powered by a high-frequency amplifier with a carrier frequency of 440 kHz and an output power of 25 kW. The generator 3 was used as a source of voltage with the signal modulated by the acoustic generator 2.

Preliminary experiments showed that the modulated high-frequency arc discharge would not operate readily in boosted high-intensity combustors as the arc tended to become detached from the electrodes in the high-flow velocity of the combustion products. To prevent this the modulated arc discharge was maintained in the electro-discharge channel of a plasmatron (see Fig. 2).

Oscillations were brought about by three methods: 1) by amplitude modulation of the output high voltage of a high-frequency generator (Fig. 1); 2) by current modulation of a continuous arc by a variable magnetic field at acoustic frequencies (Fig. 3); and 3) by inputting a voltage from a powerful high-frequency amplifier into a continuous duty arc (Fig. 4).

Figure 5 presents a typical frequency response for an acoustic emitter consisting of a modulated high-frequency arc (HFA) discharge between carbon electrodes operating in the free field and for various values of electric power dissipated in the discharge. For frequencies up to 4 kHz (Fig. 5), the dependence is linear, then up to 10 kHz it is practically constant although the modulating frequency is varied. Such behavior of the frequency response could be explained by the size of generator.

When the acoustic wave length exceeds the dimensions of the acoustic generator the reactive component of the acoustic impedance becomes dominant and the acoustic energy does not propagate into the surrounding space but remains close to the radiator. The reason for the diminishing acoustic

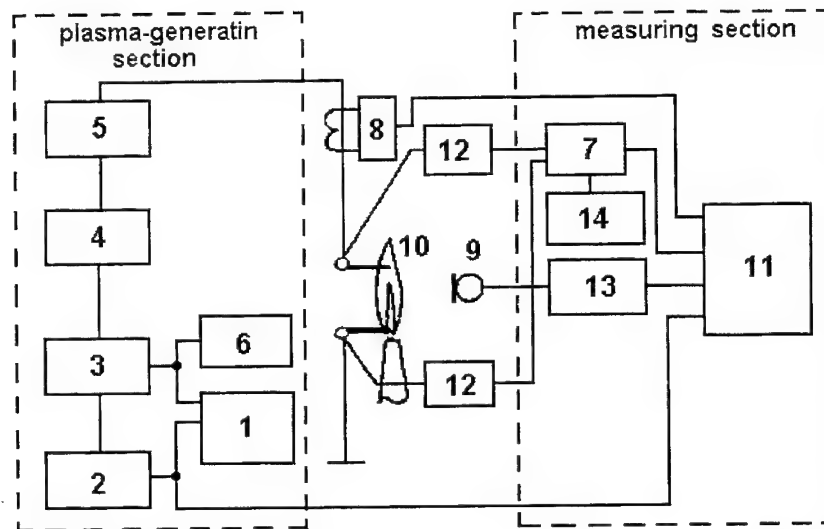


Figure 1. Diagram of electro-acoustic high-frequency arc-discharge radiator; 1 - oscillograph; 2 - audio-frequency oscillator; 3 - high-frequency oscillator; 4 - pre-amplifier; 5 - high-frequency amplifier, up to 25 kW; 6 - frequency meter; 7 - voltage detector; 8 - current detector; 9 - microphone; 10 - acoustic radiator as a modulated gas-discharge plasma; 11 - magnetograph; 12 - low-frequency filter; 13 - noise-level meter; 14 - vacuum-tube voltmeter.

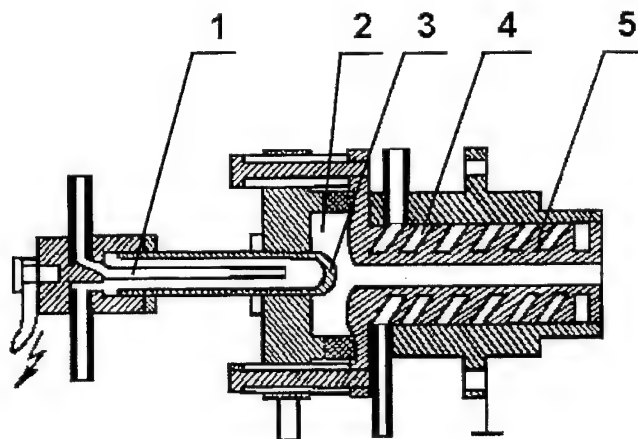


Figure 2. Diagram of the vortex-stabilized arc plasmatron with a smooth output electrode; 1 - water supply tube; 2 - vortex chamber; 3 - end-face electrode; 4 - water supply and discharge groove; 5 - output electrode.

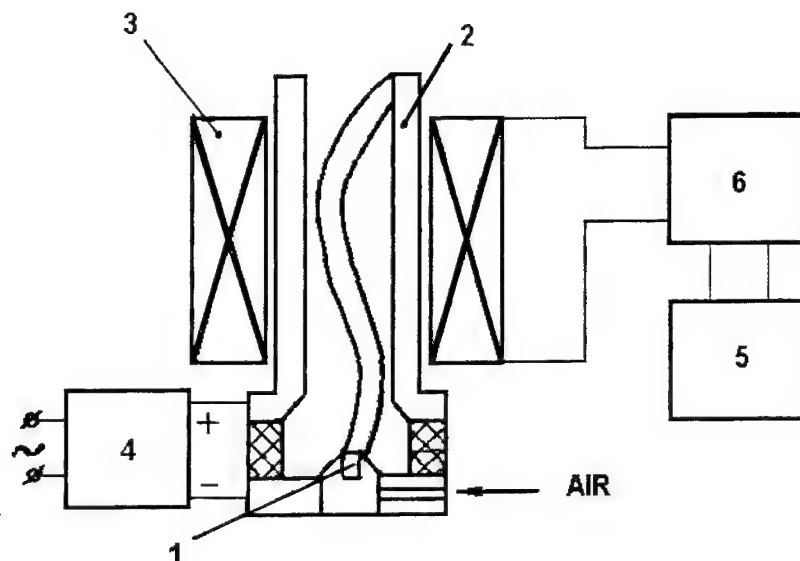


Figure 3. Diagram of an acoustic oscillator based on the magnetic modulation of the discharge current; 1 - end-face electrode; 2 - output electrode; 3 - solenoid; 4 - plasmatron power supply; 5 - acoustic modulation-frequency oscillator; 6 - low-frequency amplifier, 5 kW.

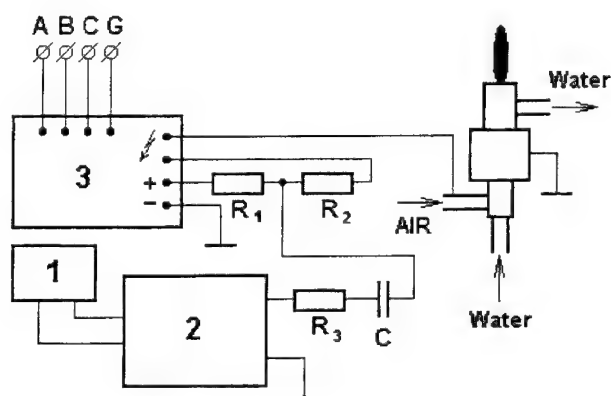


Figure 4. Diagram of an acoustic amplitude voltage-modulation oscillator with a continuous-duty arc; 1 - acoustic oscillator; 2 - low-frequency amplifier, 5 kW; 3 - plasmatron power supply;  $R_1$ ,  $R_2$ ,  $R_3$  - ballast resistances.

pressure level at low frequencies could be in the non-fulfillment of the adiabatic expansion condition for the pulsating plasma (Fig. 6).



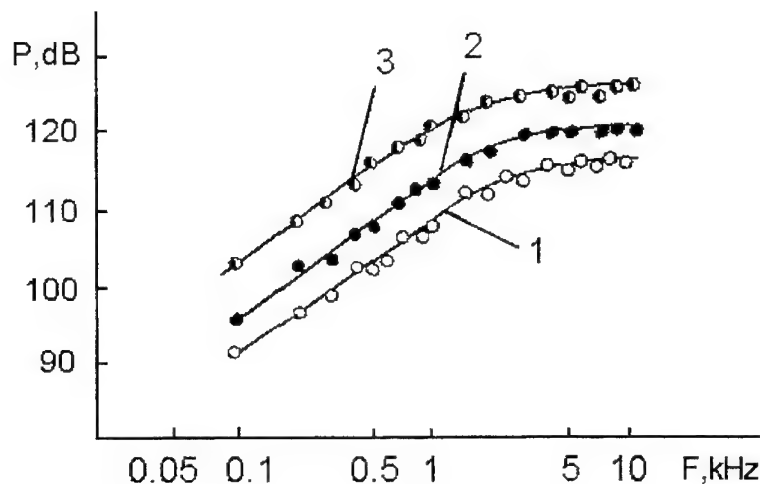


Figure 5. The acoustic amplitude-frequency response for different high-frequency arc discharges; 1 - 0.5 kW; 2 - 1.5 kW; 3 - 5.0 kW.

Figure 7 shows the directivity characteristics of the acoustic radiation for various frequencies. The radiation directivity is shown over  $180^\circ$  only as the acoustic generator has a cylindrical symmetry. It should be noted that the directivity characteristics at low frequencies have a spherical shape which is deformed when the frequency increases. The spherical character at low frequencies is explained simply by the fact that the characteristic dimension of the acoustic oscillation source is much smaller than the wave length, and thus it behaves as a point source.

Figure 8 presents the frequency response of the modulated HFA-discharge plasma jet device which shows the same general shape as that for the magnetic modulation arc and the modulated continuous duty arc. The frequency response in this case remains practically constant over the whole range of frequencies and is independent of the electric power dissipated in the space between the electrodes.

### DIAGNOSTIC TESTS

Diagnostic tests for instability on a model liquid jet engine combustion chamber were carried out using the modulated plasma jet and the arc. The model combustion chamber consisted of an injection head, a cylindrical part 270mm in length and a nozzle with a critical diameter of 30mm. The cylindrical part of the combustor was equipped with transducers to record internal pressure oscillations. The plasma jet generator was fixed at the center of the combustion chamber, and the pressure transducer signals were recorded graphically.

A kerosene-oxygen mixture was used with a flow rate of 1.5 kg/sec and the pressure inside the combustor was about 10 atm. The maximum operating time for the combustion chamber for each experiment was 3 sec, in order to study the combustion response to harmonic disturbances over the frequency range from 200 Hz to 10 kHz. The duration of the frequency modulation to the plasma jet generator in the above range was 1 sec.

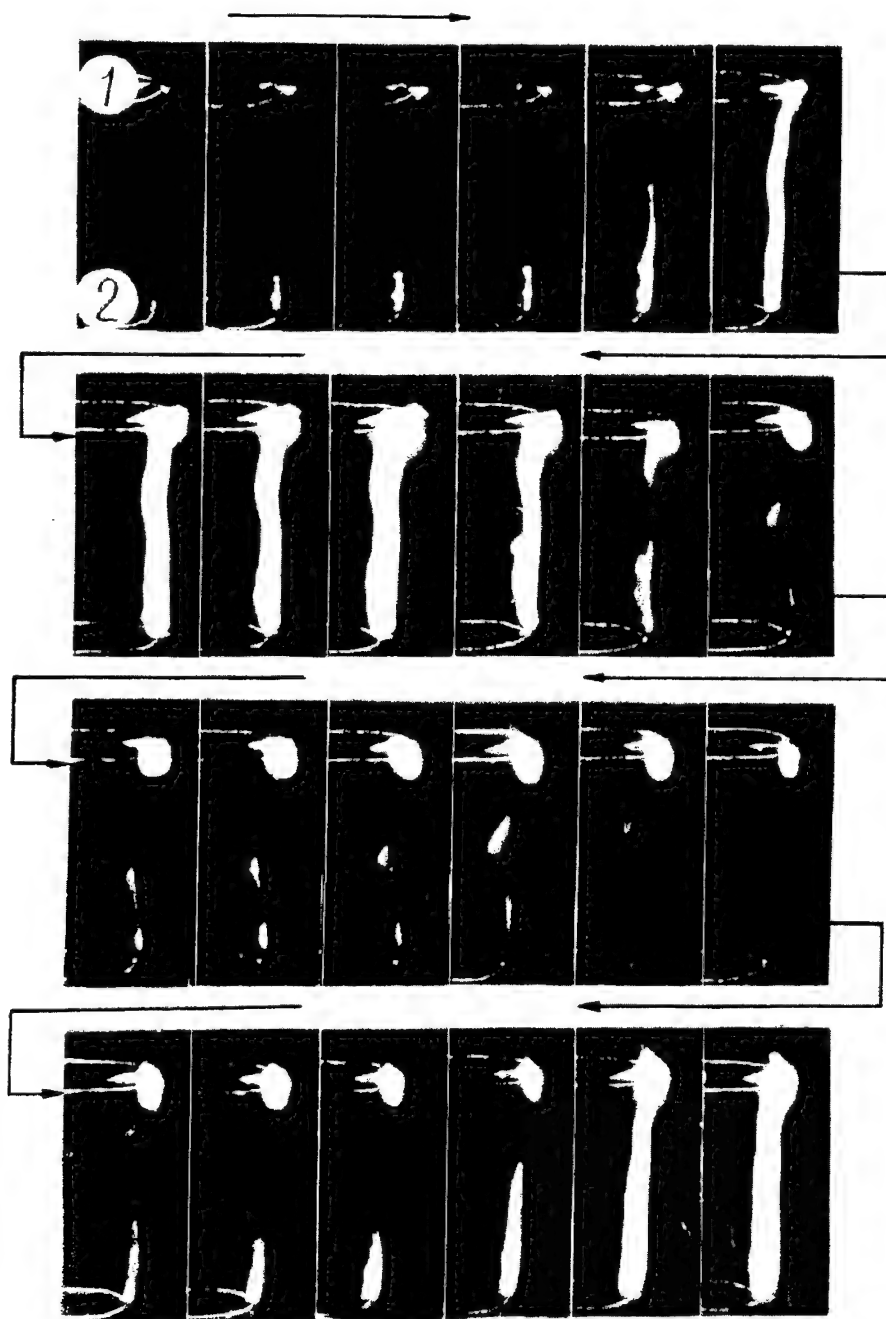


Figure 6. A motion picture fragment illustrating a high-frequency arc discharge of 1.5 kW; 1, 2 - carbon electrodes.

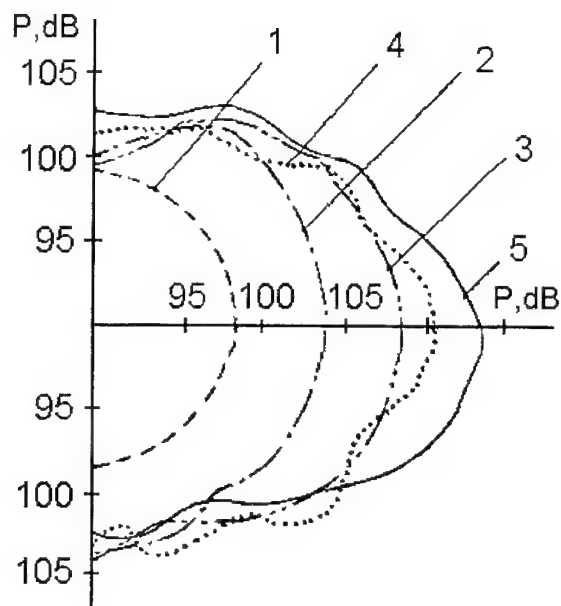


Figure 7. The directional characteristic of the audio-frequency radiator for different modulation frequencies.  
1 - 200 Hz; 2 - 600 Hz; 3 - 1 kHz; 4 - 3 kHz; 5 - 7 kHz.

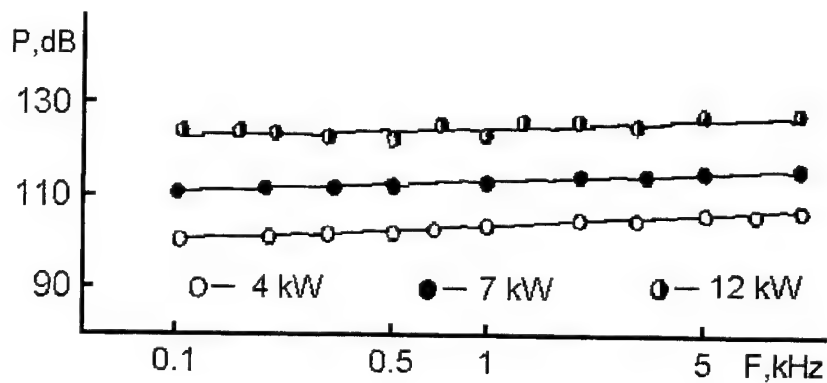


Figure 8. The amplitude-frequency response of the modulated HF arc-discharge plasmatron.

Figure 9 presents a typical three-dimensional spectrum of the amplitude of pressure oscillations at the injector head versus time, without the plasma jet generator operating. The process time (sec) from start-up is drawn as the  $Y$  coordinate. It is clear that combustion in the chamber is characterized by a developing pressure oscillations at a frequency of 2.55 kHz. At this frequency, there exists a so-called resonance combustion corresponding to the first longitudinal mode of the combustion chamber. The same results are presented for a pressure transducer located near the nozzle (Fig. 10). A comparison of the two spectra (Figs. 9 and 10) shows a marked increase in the resonance frequency from 500 to 600 Hz at the nozzle. This shift of frequency is fully explained by the Doppler effect.

The results of an experiment to determine the influence of plasma flow upon the operating processes in the combustion chamber shows that the maximum resonant frequency of the pressure oscillations near the injector is slightly displaced to the higher frequency of 2.7 kHz with plasma flow as compared to 2.55 kHz without. Such a shift of frequency is connected to the fact that the plasma flow is displaced by the high-velocity combustion products towards the nozzle. As a result, in this part of the combustion chamber there might be considerable acceleration of the combustion process. The pressure transducer at the nozzle does indicate a displacement of the resonance frequency by 1.2 kHz in comparison with the first case. The mechanisms of influence of a modulated discharge on the chemical reaction rates were described in [6], and a theoretical analysis of the problem is given in [3,5,7 - 9]. However, according to the results of recent investigations the arrangement of the discharge and the condition of the voltage source has a strong influence on the combustion zone and plays a definite role in the operating conditions (see also [10]).

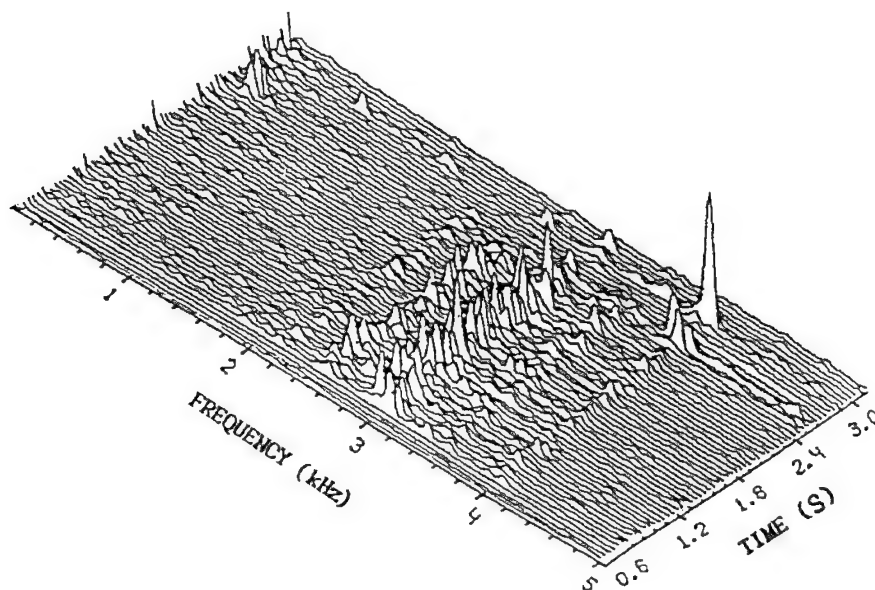


Figure 9. The spectrum of pressure oscillations at the injector for the case of a kerosene-oxygen mixture burning in a liquid-propellant engine combustor.

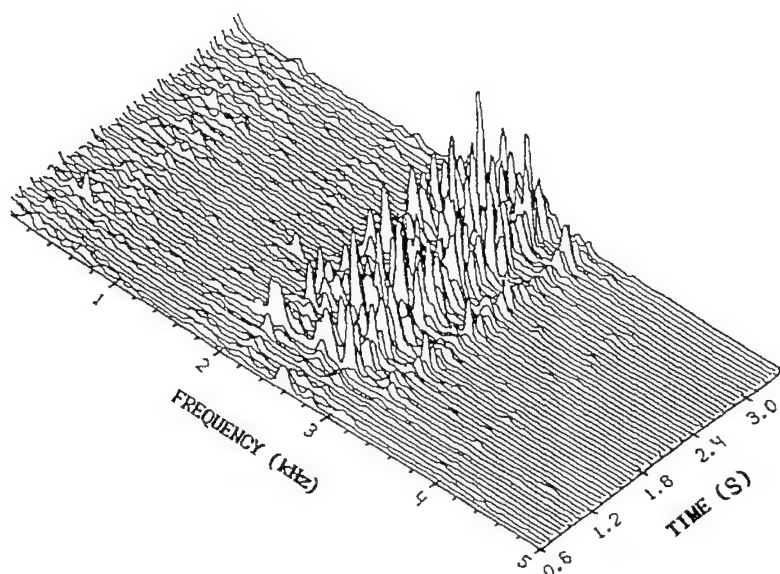


Figure 10. The spectrum of pressure oscillations at the nozzle for the case of a kerosene-oxygen mixture burning in a liquid-propellant engine combustor.

### THEORETICAL ASPECTS

Consider the system of gas dynamic equations of continuity, momentum and energy with various heat release sources included (see also [3, 5, 7 - 9]).

$$\frac{\partial \rho}{\partial t} + \nabla \cdot (\rho \mathbf{V}) = 0$$

$$\rho \frac{\partial \mathbf{V}}{\partial t} + \rho (\mathbf{V} \cdot \nabla) \mathbf{V} = -\nabla p$$

$$\frac{\partial}{\partial t} \left( \rho V^2 / 2 + \rho c_v T \right) = -\nabla \cdot \left[ \rho \mathbf{V} (V^2 / 2 + p / \rho + c_v T) \right] + \Psi + W_{ch}$$

$$p = \rho R T, \text{ and } W_{ch} = Q k T^n \exp(-E / RT)$$

Here,  $\Psi$  is a term to describe the influence of the electric discharge and is a function of temperature  $T$  and electron concentration;  $W_{ch}$  is the macroscopic heat release rate due to the chemical reactions of combustion (Arrhenius Law) with a heat effect  $Q$ ;  $k$  is the effective macroscopic constant of chemical reaction;  $E$  is the activation energy,  $R$  is the gas constant, and  $c_v$  is the heat capacity at constant volume.

For simplicity, the resistance dependence of the electrically augmented flame on temperature,  $R_e(T)$ , could be presented as an empirical dependence  $R_e = R_o \exp(-\beta T)$ , where  $R_o$  is the resistance at steady conditions without any electric voltage, and  $\beta$  is a coefficient determined experimentally, which takes into account the dependence of resistance on electron and "active center" concentrations in the combustion zone. In fact this is the modified Saha equation for low-temperature plasmas and the finding of  $\beta$  is reduced to simple current and voltage measurements and the recording of the temperature. Using Ohm's Law and substituting the values obtained into the initial equation one

could derive the value of  $\beta$ . This relationship lets us simplify the calculations as this resistance dependence which is a function of only one parameter (the temperature) can approximately take into account many aspects at the ionization processes.

The set of equations may be linearized and a solution obtained in the form of plane waves for any of the variables  $P$ ,  $T$ ,  $V$ , for example

$$T = T_0 + T' \exp(i\omega t - iky)$$

where  $y$  is in a direction perpendicular to the direction of the gas-discharge current. As a result of appropriate transformations, an algebraic equation of third order was obtained and solved to give the known Cordano solution. Three modes or roots to the equation were determined, two of them being acoustic and the third one corresponding to the development or attenuation of an "overheat-ionization" instability.

Solutions were obtained for the two extreme cases of the discharge supply source having an infinite output impedance and with the impedance tending to zero. An analysis of the solutions obtained showed that for the supply source with an infinite output impedance the diffusion electric discharge, at supply currents above a certain value, became unsteady relatively to the overheat-ionization factor and any local temperature or density fluctuations in the discharge lead to the "cording" of the discharge and to an abrupt decrease of its effectiveness in the combustion zone, (the flame in this case streamlines the discharge like an absolutely solid body). However, at the same time, the two acoustic modes tended to fade and consequently at this moment any pressure oscillations of acoustic waves would be damped. On the other hand, for the power source with zero impedance the increment of over-heat ionization instability is negative and this provides a stable operating mode for the diffusion discharge, but in this case the amplitude of the acoustic modes tend to increase.

### STABILITY CONTROL

Figure 11 presents curves of the electric discharge instability increment of the applied power for the two operating conditions of the power source: 1) with an infinite output impedance, and 2) with the impedance tending to zero. Similar features appear in the curves for the acoustic modes but differing only in the fact that the two curves are interchanged.

Combining in practice the two supply modes for the electric discharge, one can obtain effective control of combustion instabilities for flames in combustors. The implementation of this concept has made it possible (compared with a previously known system) to organize a short inner feedback loop in the control system of discharge and flame and to let it amplify or suppress acoustic oscillations in model combustion chambers according to the control problems in hand.

The results of the experiments as typical records of time dependencies of acoustic oscillations, current and voltage, are shown in Fig. 12a. The control element in this experiment was a multi-nozzle propane-oxygen star-type burner with a carbon electrode fixed coaxially above it. The carbon electrode was at a positive potential with respect to the burner with the latter acting as the second electrode. As is evident from the records, the acoustic intensity decreases by 20 dB from instant  $t_1$ , at which the process of the discharge-combustion zone interaction starts, until instant  $t_2$  and remains essentially unchanged until instant  $t_3$ , at which the discharge is quenched. After the discharge quenching, the acoustic oscillations are observed to further decrease by 6 dB until instant  $t_4$ , whereupon the pressure oscillations are self-excited until the original level is restored. Certain decrease in the acoustic intensity after the discharge quenching until instant  $t_4$  was observed to occur

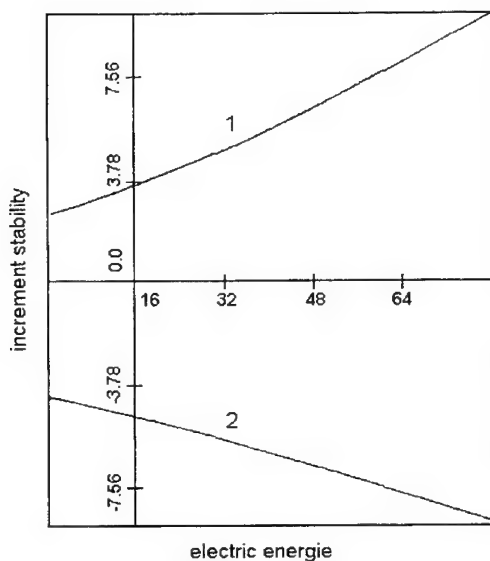


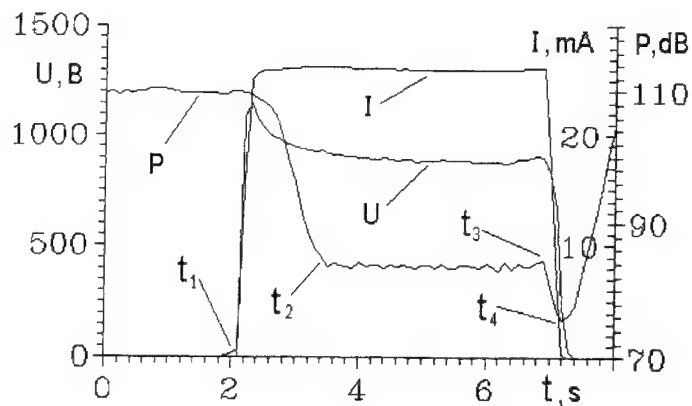
Figure 11. Calculated electric discharge instability increment as a function of applied electric power; 1, 2 - operation with an infinite and zero impedance power-supply, respectively.

in all the experiments. As the experimental evidence suggests, suppression of combustion instabilities will occur at any combustor resonant frequency thanks to the internal negative feedback loop. This is clearly shown by the amplitudes of the spectral harmonics as a function of the discharge-combustion zone interaction time (Fig. 12b).

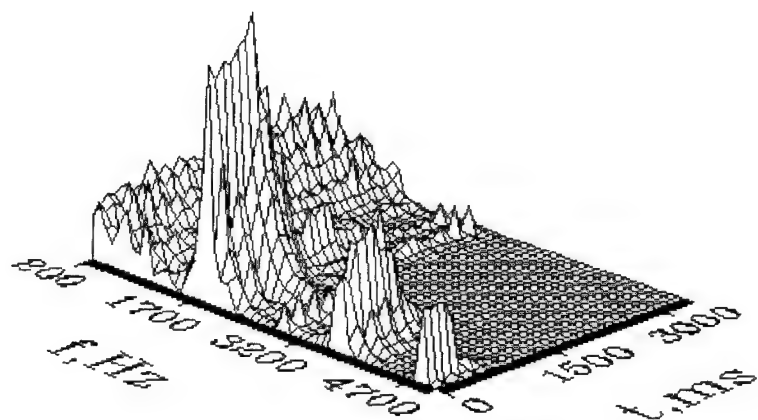
To set combustion into an unstable regime, the burner unit was located inside a resonance tube. The resonance system was of high quality and produced an intense resonant mode with combustion with sound pressure levels in excess of 100 dB. After the appearance of this resonant condition, the discharge was established in the space between the two electrodes causing the operating condition to change with the complete suppression of the oscillation (Fig. 12). Up to the present time, there is no unified model to describe mechanisms of unsteady combustion and its appearance and development in combustors and, as it was noted above, there is no reliable methodology for diagnosing instability in general nor to predict the unstable operation of a particular combustor with certainty.

### SENSITIVITY OF THE COMBUSTION ZONE TO OSCILLATION

The authors have analyzed the sensitivity of the combustion zone to the input of external harmonic disturbances aimed at developing a new method for diagnosing and predicting unsteady combustion. A flame's sensitivity to acoustic oscillations was studied by Rayleigh [10, 11]. Later this problem was considered in a number of theoretical and experimental investigations which essentially searched for the influence of external periodic disturbances on laminar and diffusion flames. For instance, in [11] it is noted that one of the mechanisms of vibrational combustion of homogenous mixtures in laminar and turbulent flows is the so called kinetic one, connecting the gas pressure oscillations in the acoustic waves with the heat release rate in the laminar front of the flame. The results of theoretical and experimental researches for homogenous mixtures showed that the laminar flame front represented a wide-band sound amplifier with the amplification coefficient changing slowly as the frequency increases.



a



B

Figure 12. **a** - Dependence of the level of sound oscillations  $P$ , current  $I$  and voltage  $U$  on time.  
**b** - Dependence of the amplitude of spectral harmonics on the time of combustion zone exposure to discharge.

It is known that the primary cause for developing and maintaining acoustic instability in combustors is a variation in the chemical reaction rate, producing a variable heat release in phase with the associated pressure oscillations in the combustion zone. It is therefore essential to study the kinetic interaction mechanisms of acoustic oscillations upon the combustion process in order to reveal the mechanisms and provide a better understanding of the processes involved.



To simplify the calculations, the combustion of premixed fuels in combustion chambers can be modeled on the basis of a homogeneous chemical reactor [3, 5-8], and proceeding from the Arrhenius Law it turns out that it is possible to affect chemical reaction rates most easily through the temperature. It is estimated that to do the same through pressure would need such an intense acoustic fields that it would disturb the hydrodynamic balance of the flames being analyzed and mask the kinetic combustion interaction response being sought.

Here the most appropriate method for affecting combustion seems to be in the use of the diffused electric discharge modulated at acoustic frequencies and superimposed on the combustion zone. Here the Joulian dissipation of energy in the combustion zone is said to be the main affecting mechanism [3-8]. The estimations given in [12] shows that in this case comparatively small amounts of energy (of the order 100 to 300 W) are sufficient for the discharge to influence combustion. The estimated results and the experiments prove that the chemical reaction rate variation due to the temperature oscillations provides a far greater change than the pressure oscillations  $p$ , developed by the discharge in the ratio given by the equation:

$$\frac{\partial k(\bar{T})}{\partial k(\bar{P})} = \left( \frac{E}{R\bar{T}} - 1 \right) \frac{\partial T}{\partial P}, \quad \left( \frac{n\bar{P}}{\bar{T}} > 1 \right)$$

where  $\bar{T}$  and  $\bar{P}$  are, respectively, the average values of temperature and pressure in the combustion zone, and  $n$  is the order of reaction.

To conduct experiments to study the influence of the diffused modulated electric discharge on the combustion zone, an experimental stand was constructed equipped with automatic control and a microcomputer-based data processing system. A modulated discharge, which would be applied to the gap between the burner and the electrode above it, was generated by an amplifier with the following output characteristics: voltage  $U=300$  V, current  $I=0.5$  to  $1.0$  A. The experiments were conducted in a sound-absorbing chamber. The experimental technique involved a systematic variation of the modulation frequency and detection of the respective response as pressure oscillations by a *Robotron* noise-level meter, with a consequent computer aided processing of the data. During the progress of the experiments, the fuel concentration was varied and, for each concentration, the amplitude-frequency response (AFR) was identified by spectral processing using fast Fourier transformation algorithms. With this done, the AFRs for different fuel concentrations were combined to form a single three-dimensional plot, with one axis being the discharge modulation frequency, another the fuel concentration and a third the pressure oscillation amplitude.

Figure 13 presents an AFC plot for a propane-air mixture. Proceeding from the present conception of the combustion zone as a wide-band amplifier one would expect a gradual increase in the amplitude of the combustion zone response with frequency over the range 300-500 Hz. However, according to Fig.13, the combustion response to the disturbances introduced has quite a different character. One can clearly see a selective sensitivity of combustion towards disturbances both on frequency dependency and mixture composition. For a better illustration, Fig.14 presents a topogram of the observed experimental dependence. One can see that the response amplitude depends strongly on the concentration of the propane, and there are clearly defined concentric areas where the probing signal is amplified in the combustion zone. Moreover, these areas are situated approximately at an equal distance (by the mixture composition) from each other and the arrangement of areas resembles very much a periodic process with an increasing amplitude achieving a maximum in the region of the stoichiometric ratio (4.1%).

Intensive amplification of the disturbances takes place only in the concentration regions drawn in the topogram. It is worth noting that propane-air mixtures have quite a few frequency intervals where

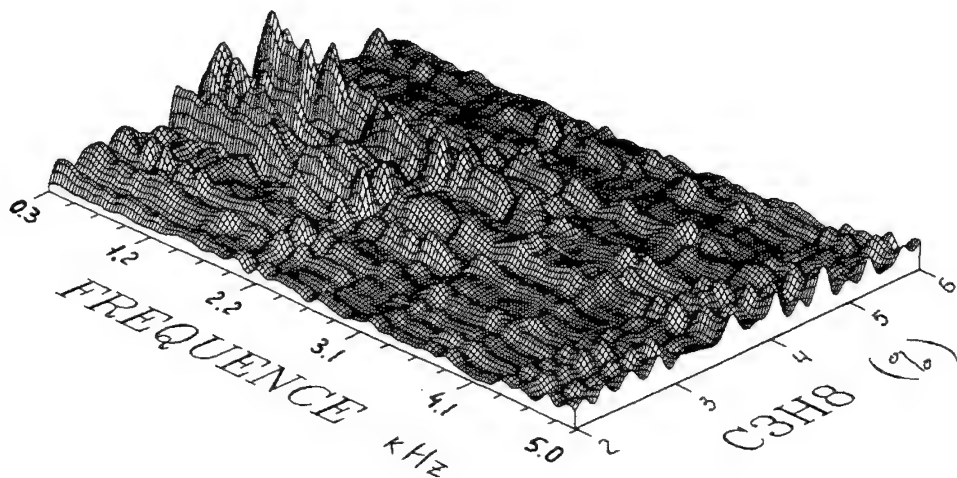


Figure 13. The amplitude-frequency response of the propane-air combustion zone to modulated-discharge perturbations as a function of the fuel concentration.

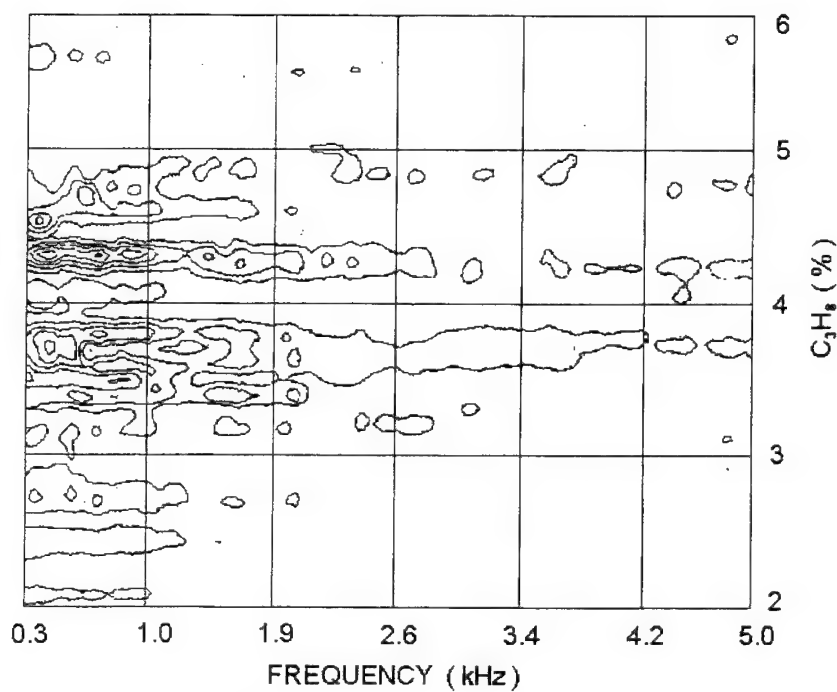


Figure 14. Topogram of Figure 13.

one could observe disturbance amplification. These intervals are called sensitive zones of the flame AFC. Figures 15 and 16 present the AFC and topogram for petrol-air flames. In these figures one can see five sensitive zones where there is amplification of the probing signal. The most active

reaction of the flame to the imposed disturbance is observed at a frequency of 1550 Hz. The other zones give more uniform amplification. The experiments lead to the conclusion that the combustion zone in its relation to external disturbances is not a wide-band amplifier but has a selective sensitivity both by frequency and by mixture composition. Hence, the possibility exists of predicting combustion instability by studying the AFR of fuels used with laboratory burners, the ambient pressure being equal to that associated with the combustor operating conditions.

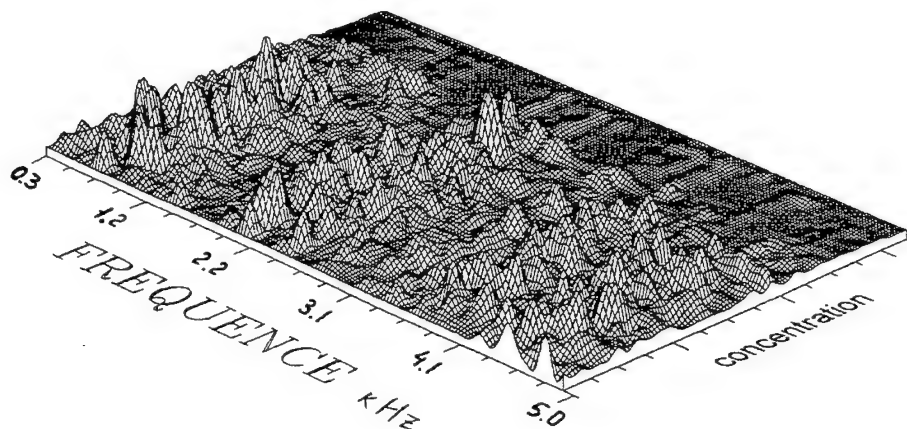


Figure 15. The amplitude-frequency response of the gasoline-air combustion zone.

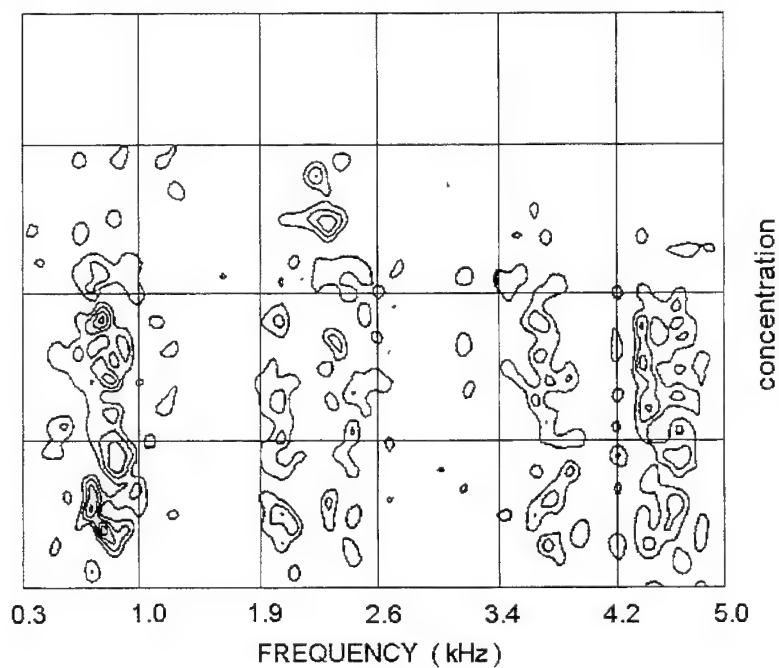


Figure 16. Topogram of figure 15.

## THE PREDICTION OF CHAMBER RESONANCE

Experimental study of the predictability of combustion instability was performed using a model variable-length combustor, whose length can be smoothly varied from 10 to 60 cm. To this end, the cylindrical part of the combustor was displaced relative to the fixed injector. Acoustic measurements were made basically in the injector plane at about 2 m. Again, the experimental results were processed by the computer and presented as three-dimensional plots.

Figures 17 and 18 present typical results of the combustion chamber runs for propane-air and petrol-air mixtures, respectively. Figure 17 shows intense acoustic radiation at low frequencies in the range from 200 to 300 Hz. Along with the low frequency spectrum components, one can observe their gradual increase towards higher frequencies as the combustor length is decreased. However, the amplitudes of these harmonics do not change continuously with frequency but have clearly defined maxima for certain chamber lengths. That is, there exist determined zones at given chamber lengths (and, consequently, at definite frequencies) where there takes place amplification at the natural resonant frequency of the chamber. Moreover, the frequencies at which this amplification occurs are well coordinated with the frequency zones discovered in the experiments for determining the AFC of the propane-air flames (Fig. 13, 14).

Table 1 presents a statistical analysis of all the chamber results for each mixture and their comparison with AFC. On the left hand side are the results of the combustor measurements, and on the right side are the experimental results for the determination of the AFC (Fig. 15, 16). The columns headed " $F$  (Hz)" and " $L$  (cm)" are the frequencies at which resonant pressure amplification occurs by the combustion zone and the corresponding combustor length (4), respectively. The columns "frequency interval" and "zone" correspond to the flame AFC and are intervals of the maximum amplification of external disturbances by the combustion ZONES and their index number. One can see good correspondence between the combustor excitation frequency of various lengths with the sensitivity zones of the flame AFC, i.e., resonance amplification of a pressure oscillation in the combustor takes place only within strictly determined frequency intervals falling into one of the 12 AFC zones characterizing the given type of fuel. These sensitivity zones could be predicted in advance from the flame AFC for the type of fuel used following the methodology described above.

Figure 18 presents one of the combustor runs with petrol-air fuel and one can single out the peculiarity of this plot; that is, a visible absence of the gradual variation of the spectrum harmonic frequencies, characteristic of the experiments with propane-air mixtures. This is apparently connected to the fact that the combustion of sprayed or dispersed liquids mixed with air is characterized by more intensive combustion rates and more intensive acoustic radiation, thus the gradual change of the chamber resonance frequency resulting from the flow gas dynamics is of smaller amplitude and is hidden by larger signals. Here, one can note the frequency intervals at which amplification occurs, as with the propane-air mixtures. Moreover, due to the reasons given above these areas are much more clearly defined. Also, one can observe the determined frequencies at which amplification takes place. Having classified these frequencies for all the runs, one can see that they correspond only to the sensitive areas identified in the AFC of the petrol-air flame.

Following this study, one could draw the important conclusions, resulting from the confirmation of the experimentally discovered zones in the flame AFC measurements: the development of instability is first and foremost connected with the type of fuel, and that the flame is sensitive only to oscillations at a certain set of frequencies. Consequently, the appearance and development of a combustion-chamber instability is possible only when there is coincidence between one of the chamber resonant frequencies and the frequency of a sensitive flame zone for that type of fuel. This

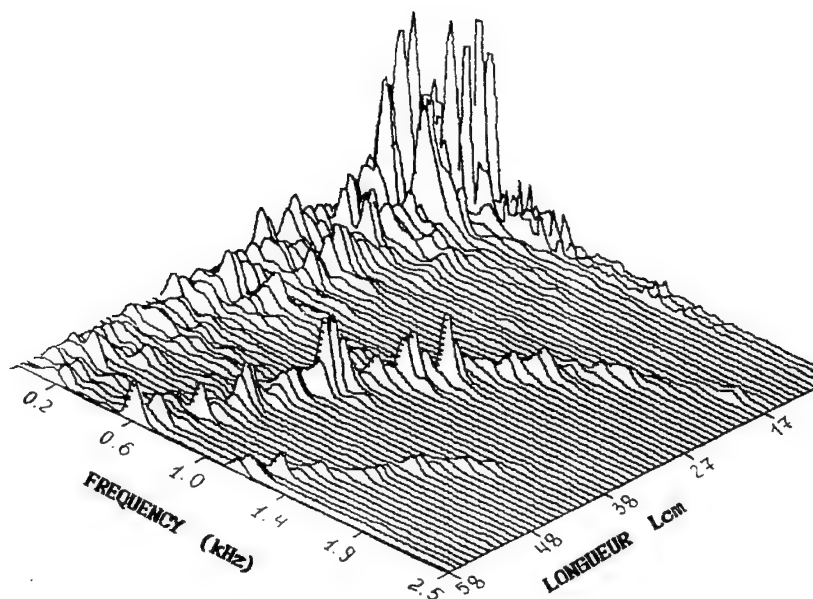


Figure 17. The spectrum of the pressure oscillations in the combustor cavity as a function of its length for a propane-air mixture.

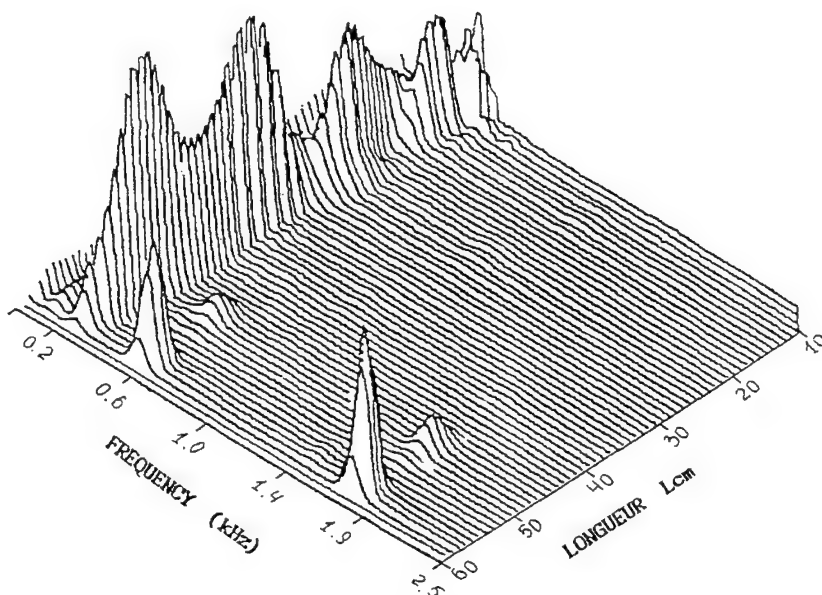


Figure 18. The spectrum of the pressure oscillations in the combustor cavity as a function of its length for a gasoline-air mixture.

the mechanism of unsteady combustion, leading to an increase in system reliability from the design stage and thus remove the need for expensive remedial measures to be carried out on newly constructed combustors which suffer from this particular defect.

TABLE 1  
Analysis of Chamber Results

COMBUSTION CHAMBER						AFC	
START	<i>L</i> (cm)	<i>F</i> (Hz)	C <sub>3</sub> H <sub>8</sub> (cm <sup>3</sup> /s)	AIR (cm <sup>3</sup> /s)	C <sub>3</sub> H <sub>8</sub> (%)	Frequency Interval	Zone
1.	39.2	200	520	5420	7.0	200 - 330	1
	32.2	310				200 - 330	1
	24.1	400				390 - 470	2
	15.6	600				530 - 630	3
2.	38.6	200	260	3330	5.6	200 - 330	1
	14.6	400				390 - 470	2
	55.7	590				530 - 630	3
	46.6	720				710 - 800	4
	24.5	1340				1300 - 1380	6
	45.9	1460				1400 - 1480	7
3.	13.2	319	430	4580	6.7	200 - 330	1
	58.3	620				530 - 630	3
	42.7	970				930 - 1030	5
	32.3	1330				1300 - 1380	6
	25.9	1460				1400 - 1480	7
	47.4	1550				1540 - 1680	8
4.	41.0	330	490	4440	7.8	200 - 330	1
	15.3	470				390 - 630	2
	41.3	620				530 - 630	3
	40.3	800				710 - 800	4
	41.8	1600				1400 - 1480	7
	19.8	1470				1540 - 1680	8

### CONCLUSIONS

1. The investigation showed that acoustic radiation can take place from the discharge due to Joulian heat release and the subsequent adiabatic expansion of the pulsating plasma at a frequency equal to the modulation frequency.
2. A new theoretical foundation for an earlier original method of active control for unsteady combustion is offered using electrical discharge and plasma jets under various operating conditions of the supply source.
3. The experiments on control have shown that it is to reduce or completely suppress the resonance pressure oscillations of all modes. Also if amplification is required, one can observe oscillation being increased by 30 to 40 dB.
4. The experiments investigating the influence on the combustion of premixed hydrocarbon fuels of a diffused modulated discharge with modulation frequency variation, revealed a selective sensitivity of the combustion zones to this external disturbance. This showed that the flame cannot be a linear wide-band amplifier of external disturbances (pressure, velocity, temperature etc.), but is sensitive at certain frequencies depending on the fuel mixture reactants, the pressure and the temperature.

### ACKNOWLEDGMENT

The investigation is supported by the U.S. Office of Naval Research, under Contract No. N68171-96-C-9024.

### REFERENCES

1. *Unsteady Combustion in Liquid Rocket Engines*. Edited by D.T. Harriew and P.G. Rirdon, Moscow, Mir, 1975 (in Russian).
2. Natanson, M.S., *Unstable combustion*. Moscow, Mashinostroenie, 1986 (in Russian).
3. Abrukov, S.A., Librovich, V., Medvedev, N., Roberts, J., and Vuillermoz, M., On the use of a sound probe technique for investigating the acoustic characteristics of model combustion chambers. *Archivum Combustionis*, 3, 47-64, 1983.
4. Nedvedev, N., Vuillermoz, M., and Roberts, J., An experimental study of sound generation by modulated electrical discharge within a flame. *Combustion and Flame*, 44, 337-346, 1982.
5. Kidin, N., Librovich, V., Roberts, J., and M. Vuillermoz, M., A theoretical model for sound output from a pulsating arc discharge, Progress in Astronautics and Aeronautics, AIAA, New York, 88, 305-313, 1988.
6. Afanasiev, V.V., A study of resonance combustion excitation mechanisms in a combustion zone being influenced by harmonic disturbances of various physical natures in a model combustion chamber. *Low Temperature Plasma and Combustion*, Cheboksary, 84-86, 1989 (in Russian).
7. Kidin, N., Medvedev, N., Vuillermoz, M., and Roberts, J., A spherically symmetrical model for sound emission from an oscillating arc in combustion flow. *Acoustic Letters*, 3, 12, 212-214, 1989.
8. Kidin, N., On acoustic waves emission by electric discharges in the combustion zone. In book investigations of unsteady combustion processes, Cheboksary, 70-82, 1987 (in Russian).
9. Kidin, N., Generation of sound by modulated electric discharge localized in the combustion zone. *Physics of Combustion and Explosions*, 3, 26-30, 1985 (in Russian).
10. Lord Rayleigh. *Phil. Mag*, 13, 340 and Scientific papers, 11, 101, 1882.
11. Lord Rayleigh. *Theory of Sound*, Macmillan, London, 1894.
12. Afanasiev, V.V., Kidin, N., and Frost, V.A., The effects of electric discharge on the combustion zone of hydrocarbon fuels, All-Union Conference on Electric Machining of Materials. Kishinev, 300-301, 1990 (in Russian).

## COMPOSITE PROPELLANT EXTINCTION BY LASER ENERGY PULSE

C. Zanotti and P. Giuliani

TEMPE - National Research Council  
Via Cozzi 53, 20125 Milano, Italy

**ABSTRACT:** Knowledge of the dynamic response characteristics of burning propellants to the variation of external parameters permits an evaluation of their capability to reach, through a combustion transient, the steady-state burning regime. In this experimental study, a transient combustion event is induced by employing externally incident laser radiation. The objective is to determine propellant extinction characteristics and its dependency on the working pressure. Fast deradiation of the burning propellant surface is utilized to achieve propellant extinction, because only the combustion process itself is perturbed; the flow field in the combustion chamber is unaffected. Tests were carried out using an AP/HTPB (86/14) propellant and a CO<sub>2</sub> laser system, whereas laser Doppler velocimetry was used to measure the velocity of product gases from the burning propellant. Further qualitative information was obtained by a photodiode which collected light emitted by the burning surface and flame. Results of tests performed over pressures ranging from 12 to 50 kPa indicate that the transient propellant behavior upon deradiation depends on the laser pulse duration and that burning propellant extinction was achieved only if the form of the laser pulse was properly chosen. Two final solutions were found after laser cut off: continuous burning or extinction defining, for any working pressure, the curves separating the distinct burning propellant response. These boundary limits were drawn for different pressure values: 12, 15, 20 and 30 kPa.

### INTRODUCTION

Rapid excursion of different external parameters may cause a transient combustion event that modifies the thermal wave structure within the solid propellant;<sup>1</sup> under this condition, unsteady burning may occur. The finite time required for temperature profile adjustment in the condensed phase to the final operating condition depends largely on the thermophysical propellant properties, whereas the final solution of the transient (extinction or continuous burning) is largely associated with propellant dynamic stability.<sup>2</sup>

Dynamic extinction of solid rocket propellants can be achieved by removing the burning propellant from its steady-state burning condition either by depressurizing the combustion chamber or decreasing the radiant energy incident on the burning propellant surface. Fast depressurization of the combustion chamber is a popular approach,<sup>2</sup> because it allows an exploration of a wide range of pressures and to study the effect of different final conditions. Unfortunately, the interpretation of the results is complicated by the effects of fluid dynamic phenomena that occur inside the combustion chamber which are controlled by its volume and geometry.



The ability to extinguish a burning propellant by deradiation, even if it steadily burns at the prescribed operating condition, offers an opportunity for research; however, deradiation of the burning propellant surface is not a common technique. This method has the advantage that it perturbs only the combustion process itself, without directly modifying the fluid dynamic field around the burning propellant sample. Hence, results can be obtained that are easier to analyze. A variety of theoretical studies, addressed to understand and predict the unsteady burning propellant behavior, are available and different numerical codes are able to simulate the combustion transient.<sup>2,3</sup> Experimental investigations on the dynamic extinction by laser energy pulse of double-base propellants burning in a steady-state regime are reported.<sup>4,5</sup> To the best of the authors' knowledge, no experimental results are available in the literature for composite propellants.

In this paper, combustion transients of an AP/HTPB (86/14) composite propellant caused by a laser energy pulse are investigated to determine the operating conditions which yield extinction. Of particular interest is to examine the effects of temporal shape of laser pulse and operating pressure on the propellant behavior.

There are many different approaches for transferring radiant energy to the surface of the propellant, but the use of lasers is generally preferred.<sup>6</sup> It is a nonintrusive technique that renders laser systems very flexible and convenient. In particular, the CO<sub>2</sub> laser guarantees a good beam intensity distribution and power stability. Hence, it is an indispensable tool in the study of inert heating, ignition and combustion of solid propellants.<sup>7</sup> To determine the velocity of product gases departing from the burning surface, it is required to use nonintrusive diagnostic techniques that operate at a high frequency (at least larger than 10 kHz). Laser Doppler velocimetry (LDV) is capable of such operation and is utilized in this work. Details are available about the application of this method in steady-state propellant combustion.<sup>8</sup>

## EXPERIMENTAL APPARATUS AND PROCEDURE

Tests were performed by using a CO<sub>2</sub> laser as the external power source (TEM00, 70 W, 10.6  $\mu$ m). The employed apparatus is depicted in Fig. 1. Here, the vertical axis of the combustion chamber is parallel to the CO<sub>2</sub> laser beam. Along the optical line is an electro-mechanical shutter, a laser-beam analyzer and a power meter to control the laser power intensity and distribution. The laser beam enters the combustion chamber through a ZnSe window. The propellant sample can be moved horizontally to provide the best alignment with the CO<sub>2</sub> laser beam.

The laser is operated in its continuous wave mode to guarantee power stability and to obtain a Gaussian intensity distribution of the laser beam power. In order to achieve fast deradiation, it is necessary to utilize a fast shutter to turn on and off the power of the beam. In our case, a home made electro-mechanical shutter, controlled by a personal computer, is used. The working principle is based on a movable knife, which travels forward and backward through the focused CO<sub>2</sub> laser beam; it takes less than 20  $\mu$ s for turning on and about 40  $\mu$ s for turning off the power. The exposure time can be selected by the computer and sequences of pulses with different duration and interval can be designed in order to conduct different radiation-driven transient events during the same test.

The velocity of the gases coming out from the burning surface was measured by the LDV technique, and very fast changes of the velocity are detectable because of the high frequency of system (625 kHz). The main part of the LDV system is shown in Fig. 1, where the split beams of a He-Ne laser are focused by a lens on the propellant sample axis to obtain the probe volume at a distance of about 20 mm from the propellant sample holder. The light scattered by the particles crossing the probe volume is transmitted through a narrowband filter centered at 632.8 nm and collected by a photomultiplier. The signal is recorded by a burst spectrum analyzer (BSA). The transient

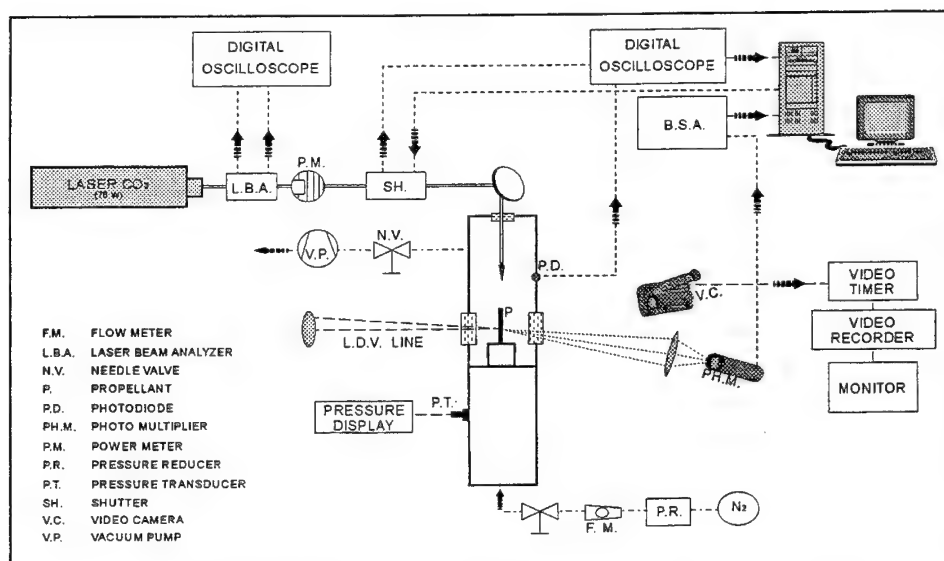


Figure 1. Experimental apparatus

combustion event can also be analyzed by observing the intensity variation of the light emitted by the flame and burning propellant surface by using a photodiode. Qualitative results are usually obtained and provide useful information for describing the propellant burning behavior.

To run tests at subatmospheric pressures, a special combustion chamber with a total internal volume of 30 dm<sup>3</sup> was designed. The subatmospheric pressure inside the burner was measured by a piezoresistive transducer facing the propellant sample. Propellant ignition was obtained by an electrically heated nichrome wire. The unsteady combustion process was recorded by a TV system, which permitted observation of the event by slow motion playback. Tests were carried out according to the following procedure.

First, the laser power and its intensity distribution were controlled and adjusted to get the best power stability and a Gaussian distribution in order to be able to estimate the value of the radiant flux intensity incident on the burning propellant sample. Second, the combustion chamber was evacuated by a vacuum pump to a minimum pressure of about 2 kPa. Third, nitrogen gas was used to purge and fill the burner up to the prescribed test pressure. Fourth, ignition was obtained by increasing the current through the nichrome wire. Fifth, once steady burning was achieved, the burning surface was moved to permit spatial measurements of the gas velocity by the LDV system. Finally, the data acquisition systems and laser-shutter motion were triggered to achieve a sequence of shots having different lengths and intervals. At the end of the test, the data acquired were transferred to the computer for processing.

## RESULTS

The cylindrically shaped propellant sample has diameter of 6 mm and length of 40 mm. In order to simplify the presentation of results, the data reported are referenced to the value of the incident flux ( $I_0$ ), which corresponds to the maximum value of the power distribution. No corrections were introduced for gas-phase radiation absorption or reflection or by the propellant's surface.

Experiments were performed at pressures equal to or lower than 30 kPa. At higher pressures and using the maximum power output from the CO<sub>2</sub> laser, propellant extinction could not be achieved. At first, tests were carried out by using the photodiode and shutter in a sequence of ten shots to find out whether the CO<sub>2</sub> laser pulse was able to extinguish the burning propellant. Once the burning propellant behavior was determined, data were collected by the LDV system using sequences of no more than five shots in order to store the data in the BSA memory. In the following, results of gas velocity versus time are presented, because they contain more quantitative information.

Figure 2 depicts the propellant burning behavior when a laser pulse of 0.11 s was used at a pressure of 50 kPa. The results show that the heat addition caused a 50-70% increase in gas velocity, but extinction was not achieved. This implies that the external energy input was not large enough to change the energy coupling between the condensed phase and the gas phase at the burning surface to produce a significant modification of the thermal wave structure. Figure 3 shows the result of a test carried out at a lower pressure, and it indicates that deradiation induces a small gas velocity undershoot, demonstrating that the burning propellant is less able to withstand the effect of the external stimulus at this operating condition.

By reducing the pressure by an additional 5 kPa, the trend is more evident as shown in Fig. 4. In this case, the minimum gas velocity, after the laser cut off, is about half of the one measured under steady-state condition. By maintaining the same laser power and pulse duration, Fig. 5 shows that the further decrease in the working pressure yields extinction. In this case, the heat-feedback from the flame to the surface decreases and is comparable to that of the externally incident laser flux. Thus, the operating condition which can induce the different propellant responses to the laser pulse was deduced. In fact, if the pulse duration is increased, burning propellant extinction also occurs as shown in Fig. 6. On the other hand, if the pulse length is reduced (0.09 s) as depicted in Fig. 7, extinction does not occur. It is important to note that propellant combustion after laser cut off is characterized by an oscillatory burning regime which is damped in time. The frequencies of these oscillations are similar to those obtained in the study of the oscillatory behavior of burning propellant under steady-state condition.<sup>9</sup>

Reduction of the pulse duration yields, at the same operating condition, a decrease in the dynamic effect following the laser cut off. Such a burning propellant behavior can be explained by saying that the pulse duration is not long enough to allow the deflagration wave to reach the new steady state. Results obtained at a fixed pressure with a different laser power indicate that it is possible to achieve extinction if the pulse form (duration and intensity) is properly chosen. Comparison between Figs. 8 and 9 points out that if the laser pulse intensity is diminished, the laser pulse duration must be augmented to reach extinction. These pictures indicate that the sequential laser pulsing has no effect on extinction if the time elapsed between two shots is long enough to allow the burning propellant to recover the steady-state regime (in this case, 2 s are adequate).

Dependency of the laser pulse duration ( $t_p$ ) on the intensity of the incident flux ( $I_o$ ) at a pressure of 15 kPa is illustrated in Fig. 10. A curve separating the two different final solutions (extinction, no extinction) can be drawn. This boundary is characterized by a vertically asymptotic trend when the laser flux intensity approaches  $\sim 3.5 \text{ cal/cm}^2 \text{ s}$ , meaning that no extinction can be achieved regardless of the pulse length. For increasing laser flux, there is a flat region that can be caused by a change in the propellant burning features. This peculiar aspect has already been observed in studies of propellant extinction by rapid depressurization.<sup>11</sup>

The observed trend is also common for other operating pressures as shown in Fig. 11, which depicts the boundary at 12, 15, 20, and 30 kPa. Comparisons of these results with data obtained in the study of propellant extinction associated with go/no-go boundary limits after the ignition transient<sup>7</sup> indicate that, in the tested pressure range, this propellant presents opposite dependencies on the

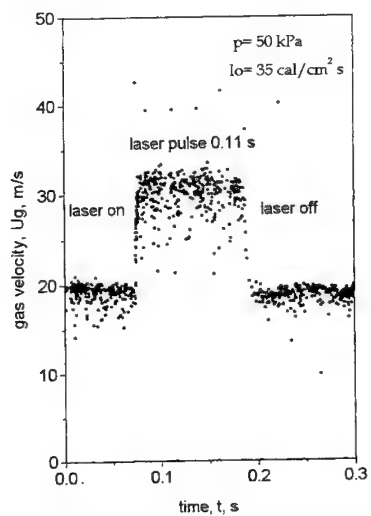


Figure 2. Combustion transient driven by radiant pulse (no extinction).

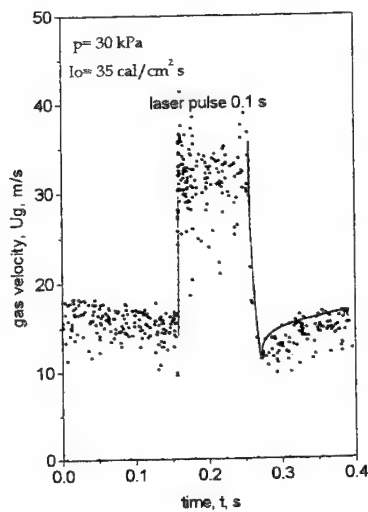


Figure 3. Combustion transient driven by radiant pulse (no extinction).

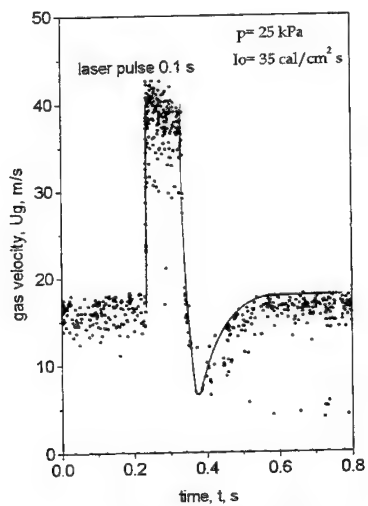


Figure 4. Combustion transient driven by radiant pulse (no extinction).

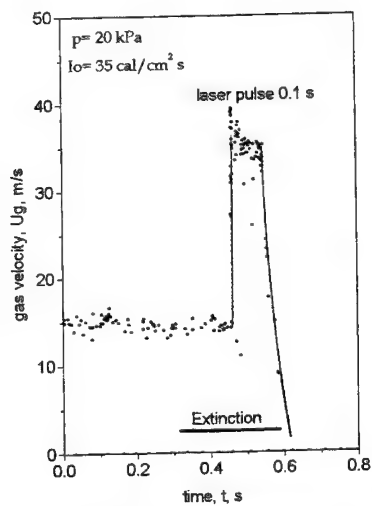


Figure 5. Combustion transient driven by radiant pulse (extinction).

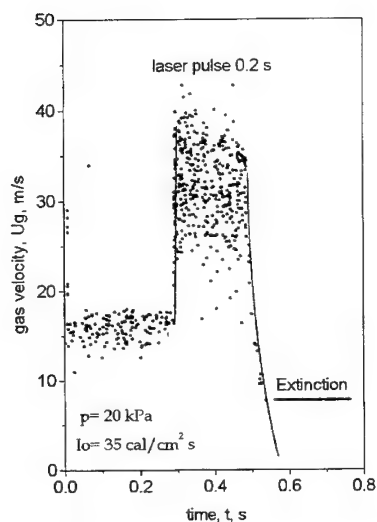


Figure 6. Combustion transient driven by radiant pulse (extinction).

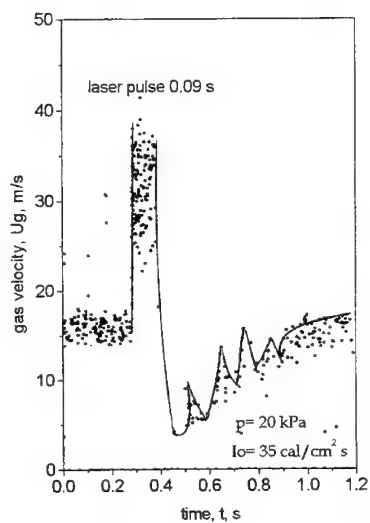


Figure 7. Combustion transient driven by radiant pulse (no extinction).

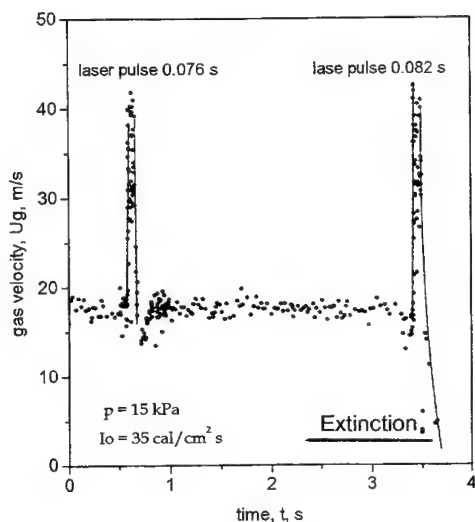


Figure 8. Combustion transients by radiation pulse (no extinction and extinction solutions).

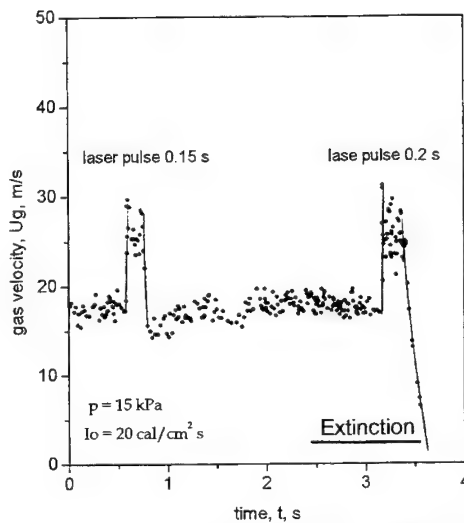


Figure 9. Combustion transients by radiation pulse (no extinction and extinction solutions).

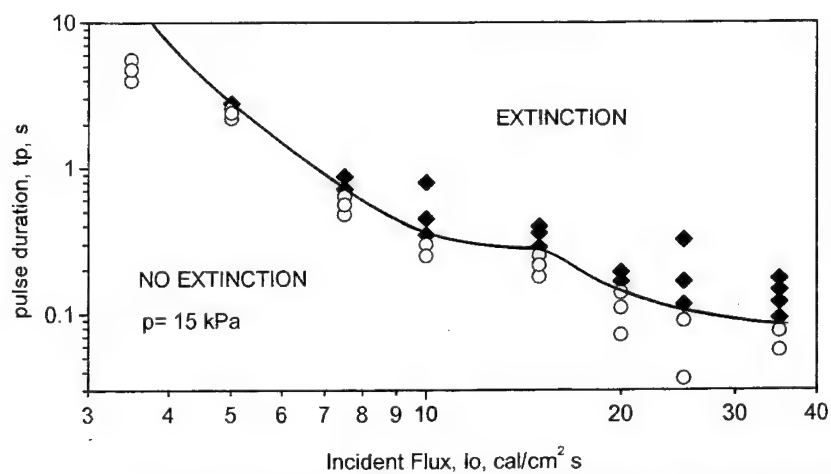


Figure 10. Extinction boundary for burning propellant subject to laser radiation pulses

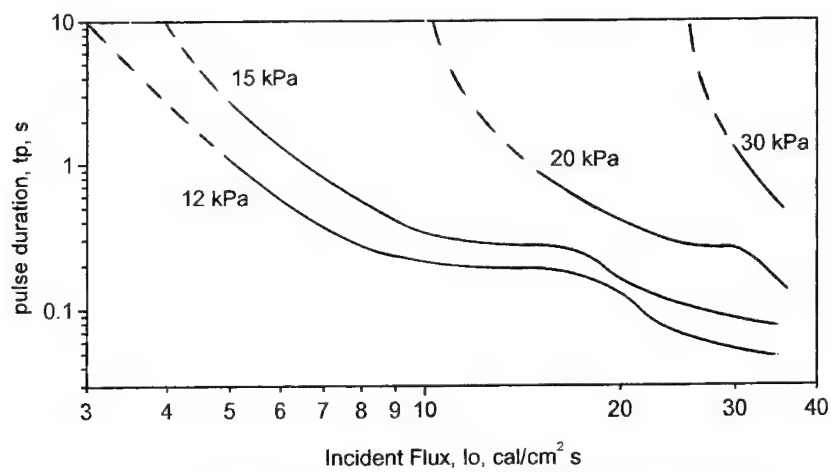


Figure 11. Extinction boundaries for different working pressures.

pressure. Differences are also present in the general trend of these curves. However, all the results indicate that burning propellant extinction by a laser energy pulse does not only depend on the deradiation transient but also on the integrated effect in time of the laser incident flux.

As previously mentioned, it is possible to determine the minimum incident flux value below which the extinction is not achieved. The curve separating the region where extinction does not occur from the one where extinction is possible is plotted in Fig. 12. The trend of this curve shows that when the operating pressure approaches the pressure deflagration limit,<sup>10</sup> the intensity of the laser pulse necessary for extinction decreases. It is evident that even a small disturbance, having a heat flux of approximately  $1 \text{ cal/cm}^2 \text{ s}$  or less, has the ability to extinguish the combustion process. In other words, the combustion occurs in an unstable regime, and it is strongly affected by the deradiation transient.

Finally, results obtained using a photodiode, at a working pressure where the oscillatory combustion behavior is pronounced, permit the observation that this phenomenon can influence extinction as illustrated in Fig. 13. In fact, from these results, it is possible to notice that if deradiation occurs when the oscillation is growing, the deradiation transient is almost canceled while for the opposite case it is enhanced. This peculiarity has been previously described in numerical simulations.<sup>2</sup>

Records made by the video system of the burning propellant sample have allowed a definition of two final configurations: continuous burning and extinction. A frame by frame analysis of the recorded combustion transient permits an examination of the effect of the radiation pulse on the flame structure. In fact, when the laser flux impinges on the burning surface, the flame length and luminosity reaches their maximum (highest gas velocity) while after the deradiation the lowest luminosity and flame length were observed (lowest gas velocity). No quantitative data can be obtained from these observations at this time.

## CONCLUSIONS AND FUTURE WORK

Experiments were performed using a pulsed  $\text{CO}_2$  laser as a forcing function for the purpose of studying extinction of an AP/HTPB (86/14) propellant burning in its steady-state regime. Laser Doppler velocimetry was utilized to measure the velocity of the gas departing from the burning surface, and the obtained results provided information about the phenomena occurring during the combustion transient.

Experimental evidence shows that extinction can be achieved if the duration and power of the laser pulse are properly chosen, and that two different final conditions are established after laser cut off; continuous burning in a steady-state regime or propellant extinction because reignition phenomena were not observed testing this propellant.

Curves separating the different propellant response to the external radiant stimulus were constructed for different operating pressures and laser pulse intensities below which extinction did not occur. Dependence of the propellant response on the laser intensity indicates that the pulse duration, required for the propellant extinction, generally must decrease as the  $\text{CO}_2$  laser intensity increases. Future work will involve the use of a more powerful  $\text{CO}_2$  laser (150 W) which will allow an investigation of a wider pressure range and different final conditions. Aluminized composite propellants will be tested and reignition phenomena, often observed in some of our preliminary tests, will be studied.

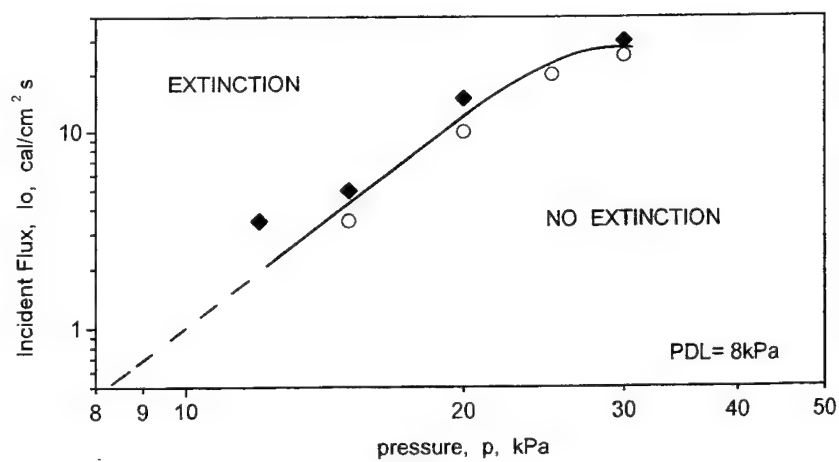


Figure 12. Extinction limit curve.

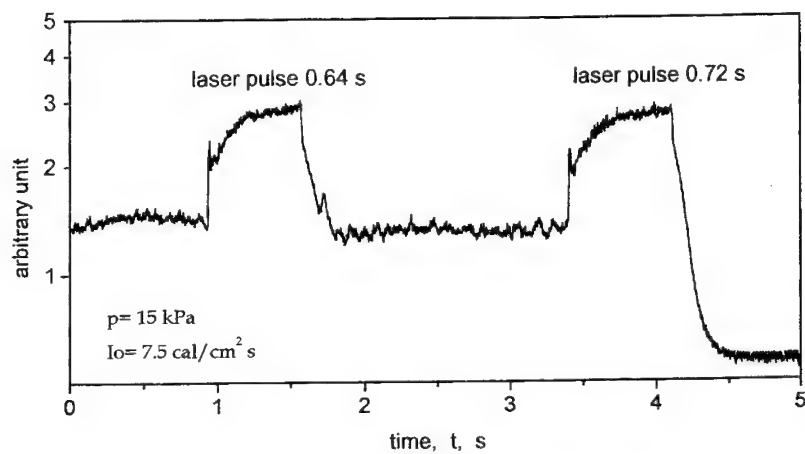


Figure 13. Light intensity collected by photo diode.



## REFERENCES

1. **Kuo, K.K. and Summerfield, M.**, *Fundamentals of Solid-Propellant Combustion*, AIAA Progress in Astronautics and Aeronautics, Vol. 90, New York, 1984.
2. **De Luca, L., Riva, G. and Zanotti, C.**, "Nonlinear Burning Stability of Solid Propellants," dipartimento di Energetica, Politecnico di Milano, Final Technical Report to European Research Office, 2nd Reprint, April 1984.
3. **De Luca, L., Price, E. W. and Summerfield, M.**, *Nonsteady Burning and Stability of Solid Propellants*, AIAA Progress in Astronautics and Aeronautics, 143, 1992.
4. **Mikheev, V. F. and Levashov, Yu. V.**, "Experimental Study of Critical Conditions during the Ignition and Combustion of Powders," *Combustion, Explosion and Shock Waves*, 9, 438-441, 1973.
5. **Ohlemiller, T. J., Caveny, L. H., De Luca, L. and Summerfield, M.**, "Dynamic Effects of Ignitability Limits of Solid Propellants Subjected to Radiative Heating," *Fourteenth Symposium (International) on Combustion*, 1297-1307, 1972.
6. **Vilyunov, V. N. and Zarko, V. E.**, *Ignition of Solid*, Elsevier Ed., 1989.
7. **Zanotti, C. and Giuliani, P.**, "Driven Ignition and Combustion of Solid Propellants by CO<sub>2</sub> Laser," *Proceedings of the XX International Pyrotechnics Symposium*, Colorado, 1994.
8. **Zanotti, C., Volpi, A., Bianchessi, M. and De Luca, L.**, "Measuring Thermodynamic Properties of Burning Propellants," *Nonsteady Burning and Combustion Stability of Solid Propellants*, AIAA Progress in Astronautics and Aeronautics, 143, 145-196, 1992.
9. **Zanotti, C., Carretta, U., Grimaldi, C. and Colombo, G.**, "Self-Sustained Oscillatory Burning of Solid Propellants: Experimental Results," *Nonsteady Burning and Combustion Stability of Solid Propellants*, AIAA Progress in Astronautics and Aeronautics, 143, 399-439, 1992.
10. **Zanotti, C. and Giuliani, P.**, "Pressure Deflagration Limit of Solid Rocket Propellants: Experimental Results," *Combustion and Flame*, 98, 35-45, 1994.
11. **De Luca, L., Zanotti, C., Grimaldi, C., Caslini, M. and Dondš, R.**, "Studio Sperimentale e Numerico dei Transitori d' Ignizione ed Estinzione di Propellenti Solidi," Final Technical Report prepared for the PSN/CNR 13, October 1988.

# **IN-CYLINDER MEASUREMENTS OF NO IN A RUNNING DIESEL ENGINE BY MEANS OF LIF DIAGNOSTICS**

**G.G.M. Stoffels, Th.M. Brugman, C.M.I. Spaanjaars, N. Dam, W.L. Meerts and  
J.J. ter Meulen**

Department of Molecular and Laser Physics, University of Nijmegen  
Toernooiveld, NL-6525 ED Nijmegen, The Netherlands

**ABSTRACT:** Two-dimensional NO distributions in a steadily running optically accessible diesel engine are observed by laser-induced-fluorescence using a tunable ArF excimer laser at 193 nm. Simultaneous excitation at 226 nm revealed that no sizeable photo-chemical effects influencing the NO distribution are induced by the excimer laser. The measurements are performed in both a directly injected two-stroke engine and an indirectly injected four-stroke engine. The in-cylinder attenuation of the laser beam due to absorption and scattering by particles as well as the reduced transparency of the quartz windows due to soot deposits are taken into account in the evaluation of the NO distributions. Hereto correction procedures are applied involving the measurement of Mie scattered laser light distributions in the motored and the running engine. Results for the corrected NO-LIF distributions are presented as a function of crank angle and load. The consistency of the obtained results is verified by performing measurements with reversed laser beam direction. The NO-LIF distributions show a reproducible evolution as a function of crank angle. The averaged LIF intensity decreases strongly with increasing crank angle, as expected for an early NO formation followed by an expansion.

## **INTRODUCTION**

In the study of combustion processes, laser induced fluorescence (LIF) has proven to be a powerful technique to extract information about molecular density and temperature distributions. The development of high power tunable excimer lasers in combination with sensitive intensified CCD cameras has enabled the application of LIF in even the most hostile environments such as the combustion chamber of an engine. Whereas the applicability of LIF detection to the study of the combustion process in Otto engines has been widely recognized, there are only few studies involving LIF in diesel engines. To a great deal this is due to the reduction of window transmission by sticky soot deposits and extinction of the laser beam in the cylinder, which reduce the signal strength and complicate the interpretation of the obtained data. In most experiments, therefore, mostly low-sooting

fuels or (mixtures of) single component fuels such as n-heptane are used. Moreover, the test engines are usually operated in skip-fired mode (i.e., the combustion in the motored engine only takes place every selectable number of cycles) in order to prolong the optical transparency of the windows of the combustion chamber.

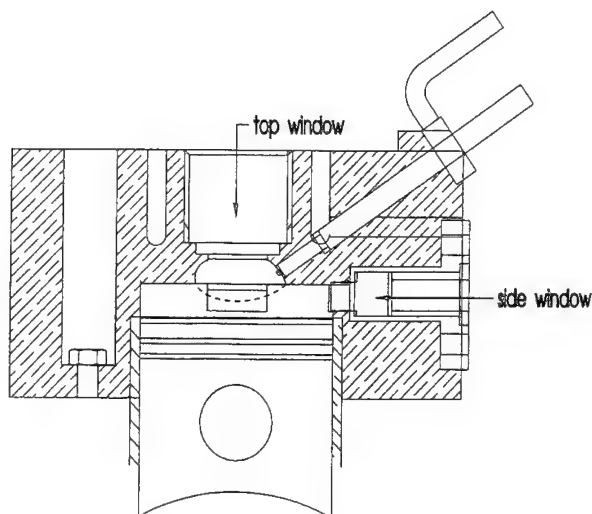
In-cylinder NO distributions have been visualized by means of 2D-LIF as described by Arnold et al. [1], Alataş et al. [2] and Brugman et al. [3]. Alataş et al. [2] using a 50/50 mixture of iso-octane and tetradecane in a square combustion chamber, found evidence that the NO formation ceased at 30 to 40 degrees after top dead center (ATDC). In a previous paper, LIF spectra of NO at 193 nm were reported for a 4-stroke engine operated on both n-heptane and standard diesel fuel [3]. These measurements were performed at low pressures around bottom dead center (BDC). Subsequently, experiments were extended to higher pressures with the objective of exploring 2D-LIF for its capability to obtain relative 2D distributions of NO during the complete combustion cycle.

In this paper, 2D-LIF measurements of NO in a directly injected 2-stroke and an indirectly injected 4-stroke engine are presented. Attention is paid to the effects of attenuation by the soot contaminated windows and the in-cylinder extinction of the laser beam. In order to verify the non-intrusive character of the LIF measurements a two-colour experiment was performed to check the possible occurrence of excimer laser induced photo-chemical processes by which NO is produced or destroyed, which would result in erroneous NO distributions.

## EXPERIMENTAL

Measurements are performed on two different single cylinder diesel engines: a directly injected 2-stroke engine (Sachs, swept volume of 412 cc, bore of 81 mm diameter, stroke of 80 mm) and an indirectly injected 4-stroke engine (Hatz-Samofa, swept volume 580 cc, bore 86 mm, stroke 100 mm). Details of the experimental setup including the 4-stroke engine are available in [3]. The NO molecules are excited at 193 nm using a tunable ArF excimer laser (Lambda Physik EMG 150). The laser beam is shaped into a 3 mm x 25 mm sheet and traverses the combustion chamber through an entrance and an exit window. The 4-stroke engine was made optically accessible by mounting three quartz windows in the cylinder wall. In this case, the laser sheet is oriented in a vertical plane (i.e., parallel to the piston axis) and the fluorescence is coupled out in a direction perpendicular to this plane. In the 2-stroke engine, the outcoupling window is mounted in the cylinder head, as shown in Fig. 1, and the laser sheet is in a horizontal plane (i.e. perpendicular to the piston axis). Whereas in the 4-stroke engine the optical access is strongly limited due to the blocking of the windows by the moving piston, this is no longer the case in the 2-stroke engine. Full access is obtained by using a piston with a shallow slot to allow the laser sheet traversing. The experiments described in this paper, however, have been performed by using a flat piston allowing measurements at crank angles larger than 25° ATDC.

Within the 300 cm<sup>-1</sup> wide tuning range of the laser, NO produced in the cylinder of the running engine can effectively be excited through a series of rotational channels of the  $D^2\Sigma^+(v'=0) \leftarrow X^2\Pi(v''=1)$  transition. The 2D-LIF measurements are performed at a fixed laser wavelength (193.588 nm) corresponding to the coinciding  $R_1(23.5)/Q_1(29.5)$  transitions of NO. At this wavelength, no disturbance by oxygen absorption is expected [4]. During the measurements, the laser is kept on resonance by monitoring the simultaneously induced fluorescence from NO in an oxy-acetylene flame, produced by a small fraction of the pulse energy. The remaining pulse energy ( $\approx 60$  mJ/pulse) is directed to the entrance window of the engine. In one experiment on the 4-stroke engine the propagation direction of the laser beam was reversed in order to check the consistency of the obtained NO distribution.



**Figure 1.** Schematic view of the optically accessible cylinder head of the 2-stroke engine. The entrance and exit windows are out of the plane of the drawing. The laser sheet is oriented perpendicular to the piston axis. The fluorescence radiation is coupled out via the top window. The side window, shown in the figure, is not used in the present measurements.

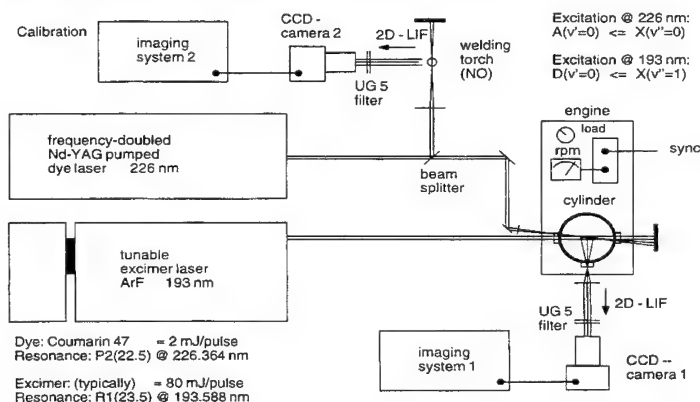
The imaged in-cylinder area has a diameter of 2.5 cm and 4.0 cm for the 2- and the 4-stroke engine, respectively. The 2D-LIF signal is separated from the resonantly scattered laser radiation by means of a 10 nm bandwidth interference filter (Laser Optik) adjusted to maximum transmission ( $\approx 80\%$ ) at 208 nm. The 2D-LIF signal is then fed into the 50 ns gated image intensifier of a CCD-camera. The images from the 4-stroke engine are recorded by a video CCD camera (Theta) and digitized by an 8 bit frame grabber (Matrox). In the experiments with the 2-stroke engine, a more sensitive 12-bit slow-scan camera (LaVision) is used. The background of the recorded 2D-LIF signal (if the laser beam is blocked or the laser is tuned off-resonant) is observed to be sufficiently low [3] to make background subtraction procedures redundant. An opto-electronic device continuously measures the crank position of the engine and triggers a delay generator, which in turn synchronizes the laser pulses, the LIF calibration section and the 2D-LIF imaging system. An electric brake mounted on the flywheel of the engine provides adjustable load conditions. Most of the imaging of NO presented in this work is performed while the engine is running steadily ( $\approx 1000$  rpm for the 4-stroke engine and  $\approx 2000$  rpm for the 2-stroke engine) on standard diesel fuel. In the 4-stroke engine, a fixed amount of oxygen (circa 12%) is added to the air-inlet of the running engine in order to raise the combustion temperature, resulting in an increased population of the probed  $v''=1$  state of NO. The increased combustion temperature also leads to decreased soot formation and as a consequence a sufficiently high optical transparency of the quartz windows can be maintained over almost unlimited periods of time. The 2-stroke engine is operated without extra oxygen. Nevertheless there are no soot deposits formed on the windows during operation. Probably this is caused by a higher temperature of these windows due to the neighbouring diesel sprays. The pressure in the cylinder of the running engine is monitored by a water-cooled pressure transducer (AVL QC 32) connected to a charge amplifier.

## VALIDATION OF THE DETECTION METHOD

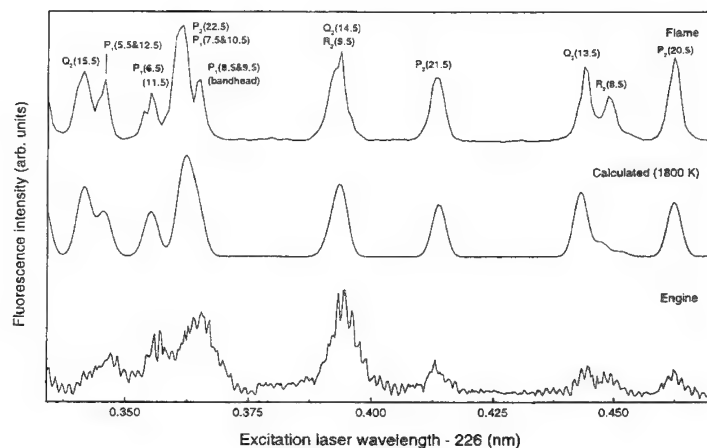
### Laser induced photochemistry

In the two-colour excitation experiment, a setup is used as schematically depicted in Fig. 2. In addition to the ArF excimer laser a frequency doubled Nd:YAG pumped dye laser (Quantel) is applied to excite the NO molecules via the transition  $A^2\Sigma^+(v'=0) \leftarrow X^2\Pi(v''=0)$  at 226 nm. A spherical lens ( $f=30$  cm) focuses the dye laser beam at the axis of the cylinder in such a way that both laser pulses have maximum spatial overlap. The dye laser induced fluorescence from the  $A^2\Sigma^+(v'=0) \rightarrow X^2\Pi(v''\geq 3)$  bands, observed above 250 nm through a UG 5 filter, is measured both in the presence and in the absence of the excimer laser beam. This way the possible occurrence of photochemical effects on the NO distribution induced by the excimer laser is checked.

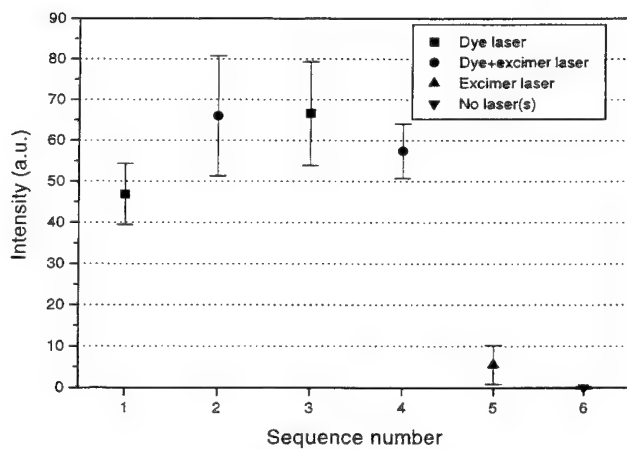
In Fig. 3, two NO excitation scans of the 226 nm region measured with the frequency-doubled dye laser in the running engine and in the welding torch are presented. A simulated spectrum, calculated for  $T=1800$  K using data from Reisel et al. [5], is given in the middle row. The three spectra show very good agreement. Evidently, the spectrum obtained from the engine is much weaker than the flame spectrum. The strongest transition ( $P_2(22.5)$  at 226.364 nm [5]) was selected to detect any photochemical effects of the excimer laser radiation. The effect of the presence of the excimer laser radiation on the dye laser induced LIF signal strength from the running engine (1000 rpm, no load) is depicted in Fig. 4. As can be clearly deduced from this figure, the influence of the excimer laser radiation on the dye laser induced LIF signal strength is negligible, which leads to the conclusion that excimer laser induced photo-chemical processes, if they occur at all, have no observable influence on the population of the  $X^2\Pi(v''=0)$  state under the present experimental circumstances. In view of the fast vibrational relaxation of NO [6] this most probably holds for the  $X^2\Pi(v''=1)$  state (probed by the excitation at 193 nm) as well. A three-level double resonance experiment is in preparation to directly monitor the depletion of the lower level of the excimer laser transition.



**Figure 2.** The experimental setup for the two-colour experiment. The NO molecules are probed via the  $A-X(0, 0)$  band by a frequency doubled dye laser, operated at Coumarin 47, delivering 2 mJ/pulse at 226 nm. The subsequent fluorescence in the  $A-X(0, 3)$  band at 270 nm is measured in the absence and in the presence of the ArF excimer laser beam (80 mJ/pulse), exciting the  $D-X(0, 1)$  band of NO.



**Figure 3.** Two excitation scans of NO around 226 nm in the welding torch (top scan) and in the running 4-stroke engine (bottom scan), respectively. In the middle a simulated spectrum is shown, calculated with the data of Reisel et al. [5]. The  $P_2(22.5)$  transition is used for the two-colour measurements.



**Figure 4.** A typical result of the two-colour measurements. Within the experimental accuracy no change in the A-X fluorescence intensity is observed when the excimer laser is switched on or off. It makes no difference whether the excimer laser is set on or off the D-X,  $R_1(23.5)/Q_1(29.5)$  transition of NO.

## Linearity

In the processing of the NO-LIF signals linearity of the signal strength with the laser pulse energy is a prerequisite. Measurements as a function of the laser intensity showed that within the spread of the experimental results this condition is fulfilled up to the highest energy used in the experiments.

## Saturation

The observed linearity of the NO signal strength on the pulse energy does not imply that there are no saturation effects present. An estimate of the degree to which saturation plays a role can be obtained by comparing the actual laser intensity with the calculated saturation intensity,  $I_s$  [7]. Since the Einstein coefficient for absorption,  $B_{12}$  is not known for the D - X transition only a lower limit can be calculated for  $I_s$  by using the known radiative lifetime of the D state. This results in  $I_s > 9 \cdot 10^8 \text{ W/m}^2$  at the present laser bandwidth of  $0.5 \text{ cm}^{-1}$ . This is about equal to the estimated laser intensity in the imaged area in the combustion chamber. Therefore saturation effects are expected to be of minor importance in the present experiments. It should be noted that even in case of (not too strong) saturation, the LIF signal strength is still linearly proportional to the local NO density.

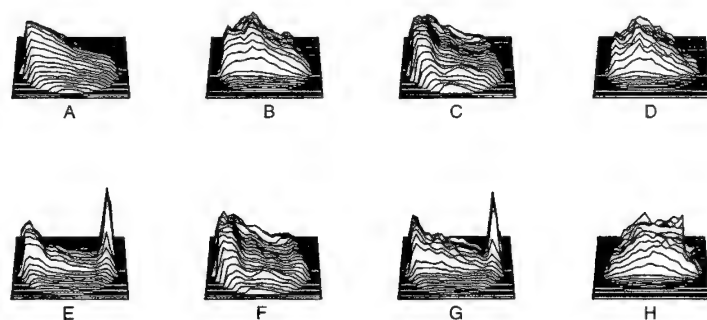
## MEASUREMENT PROCEDURE

A complete measurement, at given crank angle and engine conditions, comprises one NO fluorescence distribution and four Mie scattering images, recorded in a specific order which facilitates post-processing of the NO-LIF distributions [8]. First, with all windows thoroughly clean, a Mie scattering distribution is measured in the motored engine (A in Figs. 5 and 6 below). Then the NO-LIF image is recorded in the running engine (B), immediately followed by a second Mie scattering distribution from the motored engine (C). Finally, a Mie scattering image is recorded in the running engine (E), once again followed by a (third) Mie scattering distribution from the motored engine (F). All individual images are averages over about 300 (4-stroke) or 25 (2-stroke) laser pulses. The Mie scattering images are recorded by bypassing the interference filter in front of the CCD camera. A complete series takes about 15 minutes. The Mie scattering images from the motored engine are used to derive correction factors for locally decreasing window transmission due to soot deposits building up while the engine is running. Local window transmission changes during, for instance, the NO fluorescence measurement, can be detected by a comparison of the two Mie scattering images before and after the 2D-LIF measurement. Since the locations of the soot deposits are observed not to change during the runs, this allows for a correction of the NO-LIF distributions for the attenuation of both the laser beam and the fluorescence radiation due to window fouling.

In addition to the correction for the reduced window transmissions, the measured NO LIF distributions have to be corrected for in-cylinder attenuation of the laser beam. At the pressures considered ( $< 10$  bar) the attenuation is mainly due to Mie scattering and absorption by particles. The scattered signal is linearly proportional to both the laser intensity and the local particle density. If it is assumed that the particles are more or less uniformly distributed in the imaged area, the Mie scattering image reflects the laser intensity distribution, which then can be used to obtain more realistic NO-LIF distributions[8].

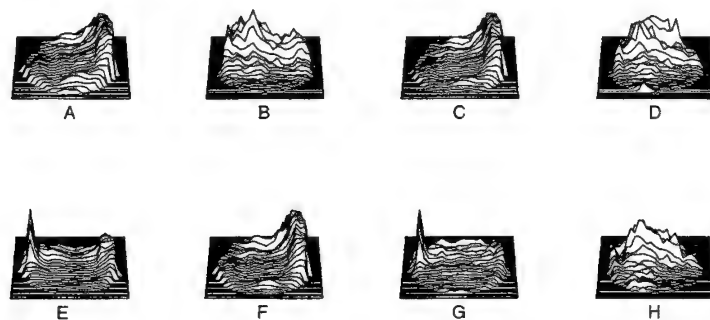
Presently, it is not yet possible to correct for the effects of collisional quenching on the measured NO fluorescence distributions. Inelastic collisions induce a considerable decrease of the number of excited NO molecules and as a consequence the intensity of the induced fluorescence is reduced (quenched). This will affect the total signal strength of the observed NO-LIF distributions, thus making the determination of absolute NO densities difficult. Therefore the present experiments are aimed at the study of relative NO density distributions as a function of crank angle and load.

Laser propagation direction: >>> Engine running @ 1000 rpm / no load



**Figure 5.** Measured 2D images of Mie scattered laser light and of NO fluorescence in the 4-stroke engine at 135° ATDC. The laser sheet enters the imaged area from the left hand side. In picture A, a Mie scattering image is shown, measured in the motored engine with clean windows; picture B shows a NO-LIF image, recorded in the running engine; pictures C and F show images of Mie scattered distributions in the motored engine after running, i.e. with dirty windows; in picture E, a Mie scattering image is shown, measured in the running engine. Pictures D and G represent images of NO-LIF and Mie scattering distributions after correction for the soot deposits on the windows. The final result for the NO-LIF distribution corrected for both window fouling and in-cylinder laser extinction is given in picture H. All individual images are averages over about 300 laser pulses.

Laser propagation direction: <<< Engine running @ 1000 rpm / no load



**Figure 6.** The same as in Fig. 5, but with the opposite laser sheet direction. The laser beam enters the imaged area from the right hand side.

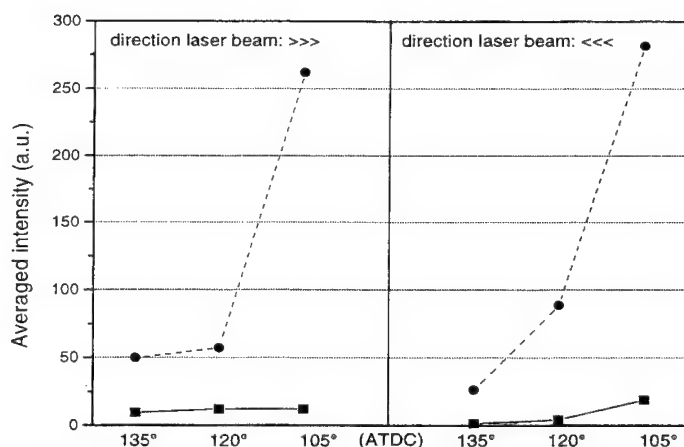


The correction procedures are described in detail in [8]. Their application is based on the assumption that the sampled 2D-LIF signal strength depends linearly on both the laser pulse energy as well as on the NO population density in the imaged area. As discussed above, the in-cylinder laser intensity is low enough to preclude any observable photochemical processes. Within the experimental accuracy, the NO-LIF signal is linearly dependent on the laser intensity at the considered engine operating conditions and saturation is not expected to play an important role.

## RESULTS AND DISCUSSION

Demonstrations of the measurement procedure applied to two NO fluorescence distributions recorded in the running 4-stroke engine (no load, 135° ATDC) are given in Fig. 5 and Fig. 6 for the two directions in which the laser beam can traverse the combustion chamber. Both figures consist of 8 three-dimensional representations of the measured and corrected images. The plots labelled A were measured first, and they display the laser intensity distributions in the motored engine with previously cleaned windows as imaged by Mie scattering. The plots labelled B are depictions of the (unprocessed) measured NO fluorescence distributions. The plots labelled C show the in-cylinder laser intensity distributions measured immediately after the NO fluorescence measurement in the running engine. Plots 5D and 6D display the results of applying the correction procedure for window fouling to the measured NO fluorescence distribution. Comparing Fig. 6B with Fig. 6D, one observes a shift of the corrected NO distribution towards the centre of the imaged area, whereas in this particular case (with apparently little window fouling) this first correction hardly affects the initially imaged NO fluorescence distribution for the other direction (Fig. 5B). The plots labelled E are the (uncorrected) results of the Mie scattering measurements of the laser intensity distribution in the cylinder of the running engine. The high intensities at the laser exit sides are most probably artefacts caused by reflections of the laser sheet at the laser exit window. The plots labelled F are Mie scattered images from the motored engine measured immediately after the measurements which produced the plots E. The plots A and F are used to apply the same correction procedure for window fouling, mentioned above, to the plots E and the results are shown in Fig. 5G and Fig. 6G. The latter, in combination with the corrected NO fluorescence distributions (plots D), form the ingredients of the second correction procedure, which accounts for the decreasing laser intensity [8]. Finally, the plots labelled H are depictions of the fully corrected NO fluorescence distributions. It should be noted here that the NO distributions of Fig. 5H and Fig. 6H are very similar in contrast to the original, uncorrected, NO fluorescence distributions Fig. 5A and Fig. 6A. Thus, after two corrections, an in-cylinder NO fluorescence distribution is found which, at least qualitatively, is independent of the propagation direction of the laser sheet. This is a strong indication for the reliability of the correction procedures and the resulting in-cylinder NO distributions.

Comparing Fig. 5E with Fig. 5A and Fig. 6E with Fig. 6A, one might conclude that the decay of the laser intensity in the motored engine is much larger than the decay observed in the running engine. In order to verify this, the overall transmission of the laser through both windows and the cylinder was measured. It turned out that the transmission of the laser is about two times better if the engine is running ( $\approx 20\%$ ) instead of being motored ( $\approx 10\%$ ). An explanation is most likely to be found in the higher in-cylinder temperature of the running engine, causing vaporization of the lubricant and other scattering particles. This will reduce the scattering losses in the cylinder of the running engine. At high pressures, absorption by oxygen is expected [9], due to broadening of the individual lines in the Schumann-Runge band. For the pressure range in the present experiments ( $< 10$  bar) no line broadening larger than the  $0.5\text{ cm}^{-1}$  bandwidth of the laser is expected and no indication of absorption by oxygen is found.



**Figure 7.** The averaged NO LIF densities for the two opposite laser sheet directions as a function of crank angle in the 4-stroke engine, before (●) and after (■) correction for window fouling and laser beam extinction.

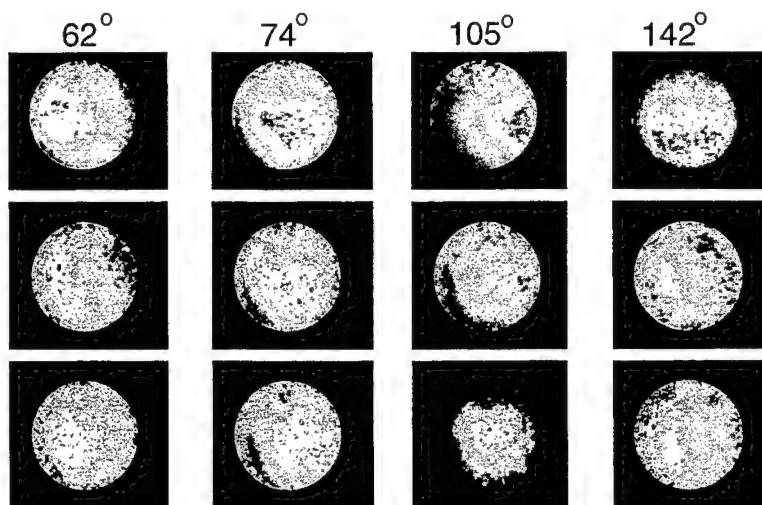
The effect of the correction procedures is shown in Fig. 7, where the averaged NO-LIF densities are plotted as a function of the crank angle before and after the signal processing. The two parts of the figure correspond to the two opposite directions of the laser beam through the combustion chamber. The largest effect is seen at 80° ATDC (not shown in the figure), the smallest angle where measurements are possible in the 4-stroke engine. The corrected signal is here more than 20 times stronger as compared to the unprocessed signal. The increase of the NO density towards higher pressures (i.e. earlier in the expansion stroke) is in agreement with the expectation that the NO is formed early in the combustion and expands with the volume during the stroke. The results for both laser beam directions are in qualitative agreement to each other. The quantitative differences might be due partly to the spread of the experimental data and partly to a larger concentration of scattering particles at the exhaust valve, which is situated close to one of the windows, as explained in more detail in [8].

In Fig. 8, three series of two-dimensional NO-LIF distributions are shown in false colours, measured in the 2-stroke engine as a function of the crank angle. The series were measured at the same engine conditions, a few minutes after each other. All images are averaged distributions measured during 1.25 seconds (25 strokes). In all these images, the laser beam travelled from top to bottom; the position of the fuel injector is at the right hand side of each image. Because the scaling factors are different for each image, only the distributions and not the absolute values of these pictures should be compared among themselves. Although the series differ from each other, due to the highly turbulent character of the combustion process, some reproducible pattern is observed: the NO seems to move from the top (at 62° ATDC) to the bottom in the image (at 105° ATDC). Possibly this effect is caused by a specific gas flow circulation in the cylinder during the stroke. If the different scaling factors are taken into account the average NO LIF densities are obtained as given in Fig. 9. In this figure, the results are also shown for another diesel fuel with a different cetane number. A behaviour similar to the result obtained for the 4-stroke engine is obtained: the amount of NO is almost zero at the point where the exhaust and inlet port are both open and increases strongly at higher pressures, corresponding to an expanding amount of NO at increasing crank angle.

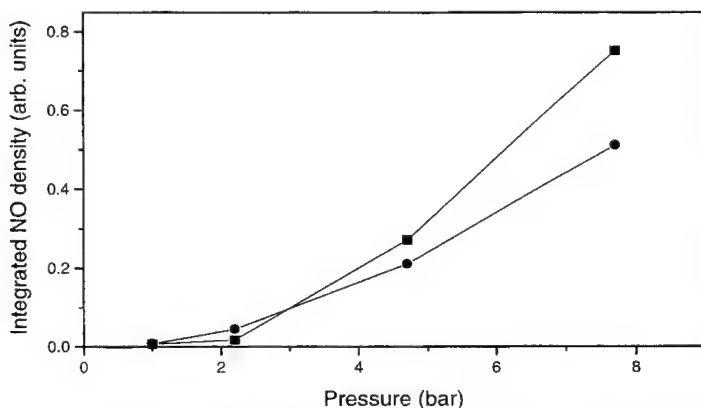
The averaged NO LIF densities in Figs. 7 and 9 are not corrected for the change in fluorescence quenching and temperature during the stroke. The effect of the temperature is expected to be small

as explained above. The fluorescence quenching will be stronger at higher pressure, which would result in steeper curves in Figs. 7 and 9 after correction.

In the 4-stroke engine, measurements were also performed at different loads, yielding an increase of the in-cylinder NO amount with load, as expected. Measurements are in progress to follow the NO-LIF distribution towards higher pressures.



**Figure 8.** Three series of corrected NO-LIF density distributions in the 2-stroke engine at four crank angles. The series were measured immediately after each other at the same fuel and engine conditions. The laser beam traverses the imaged area from top to bottom. The fuel injector is at the right hand side of each image.



**Figure 9.** Averaged NO-LIF densities as a function of pressure in the 2-stroke engine for two fuels with different cetane number.

## CONCLUSIONS

Nitric oxide distributions inside the cylinder of a running diesel engine operated on standard diesel fuel can be visualized by 2D-LIF detection at 193 nm. This is demonstrated for both a directly injected and an indirectly injected engine. Despite the high energy of the excimer laser pulse, the measured NO LIF distribution is not influenced by possible photochemical effects. After correction for window fouling and in-cylinder laser beam extinction, relative NO distributions are obtained, showing the expected behaviour of an expanding gas in the expansion stroke. Qualitatively, the results are independent of the direction of the laser beam. Future experiments will, amongst others, address the dependence of the NO distribution on engine load and fuel composition during as large a part of the combustion cycle as possible.

## ACKNOWLEDGEMENTS

This research is supported by the Technology Foundation (STW). We would like to thank Ch. Spaanjaars, E. van Leeuwen, L. Gerritsen, R. and E. Merkus and the workshop of the Faculty of Science for their expert technical assistance. The financial support of TNO, NOVEM and Esso is gratefully acknowledged.

## REFERENCES

1. Arnold, A., Dinkelacker, F., Heitzmann, T., Monkhouse, P., Schäfer, M., Sick, V., Wolfrum, J., Hentschell, W., and Schindler, K.P., DI Diesel engine combustion visualized by combined laser techniques, *Twentyfourth Symposium (International) on Combustion*, The Combustion Institute, 1605-1612, 1992.
2. Alataş, B., Pinson, J.A., Litzinger, T.A., and Santavicca, D.A., A study of NO and soot evolution in a DI Diesel engine via planar imaging, SAE Paper 930973, 1993.
3. Brugman, Th.M., Klein-Douwel, R., Huigen, G., van Walwijk, E., and ter Meulen, J.J., Laser-induced-fluorescence imaging of NO in an n-heptane and diesel-fuel-driven Diesel engine, *Appl. Phys. B57*, 405-410, 1993.
4. Lee, M.P., and Hanson, R.K., Calculation of O<sub>2</sub> absorption and fluorescence at elevated temperatures for a broad band argon-fluoride laser source, *J. Quant. Spectrosc. Radiat. Transfer* 36, 425, 1986.
5. Reisel, J.R., Carter, C.D., and Laurendeau, N.M., Einstein coefficients for rotational lines of the (0,0) band of the NO A<sup>2</sup>Σ<sup>+</sup> - X<sup>2</sup>Π system, *J. Quant. Spectrosc. Radiat. Transfer* 47, 43-54, 1992.
6. Frost, M.J., Islam, M., Smith, I.W.M., Infrared-ultraviolet double resonance measurements on the temperature dependence of rotational and vibrational self-relaxation of NO(X<sup>2</sup>Π, v=2, j), *Can. J. Chem.* 72, 606-611, 1994.
7. Demtröder, W., *Laser Spectroscopy*, Springer, Berlin, 104, 1981.
8. Brugman, Th.M., Stoffels, G.G.M., Dam, N., Meerts, W.L., and ter Meulen, J.J., to be published in *Appl. Phys.*
9. Schulz, C., Yip, B., Sick, V., and Wolfrum, J., A laser-induced fluorescence scheme for imaging nitric oxide in engines, *Chem. Phys. Letters*, 242, 259-264, 1995.

---

***Area 8:***

***Theoretical Modeling and  
Numerical Simulation of  
Combustion Processes of  
Energetic Materials***

## NUMERICAL SIMULATION OF DETONATIONS: FUNDAMENTALS AND APPLICATION

Elaine S. Oran

Laboratory for Computational Physics and Fluid Dynamics  
U.S. Naval Research Laboratory, Washington, DC

**ABSTRACT:** This paper presents results from a series of numerical simulations of detonations for a range of energetic materials and applications. A brief discussion is given of the computers and computational capabilities that allow such simulations. Then results are presented for simulations of cellular structure in gas-phase detonations, detonations in supernovae, and the effects of lattice structure on initiation and propagation of detonations in solid explosives. The paper concludes with a description of a new project whose objective is to develop environmentally sound ways of detonating the hundreds of megatons of surplus energetic materials.

### INTRODUCTION

A detonation is the fastest, most intense form of energy release that occurs in an energetic material. Detonations occur in confined natural gases in caves or mines, in the use of condensed-phase explosives and propellants. Astrophysical detonations are supernovae, which have created most of the heavy elements in the universe. After many years of concentrated efforts, fundamental questions about the properties of the initiation, propagation, and extinction of detonations in many materials remain. Ignition from a shock wave is perhaps the best understood process. But the transition from laminar burning to deflagration (turbulent flames) to detonation poses many fundamental unanswered questions. In the simplest theories, a propagating detonation front can be considered as a discontinuity moving through the material at a speed characteristic of the energetic and background materials. Closer examination reveals the importance of the much more complex and dynamic structure of interacting and intersecting shock waves, contact surfaces, and continuously changing reaction zones. On the microscopic scales of condensed phase explosions, there are fundamental questions about the mechanisms of heat transfer in the crystals, the effects and importance of inhomogeneities, and how these affect ignition and propagation.

The basic physics of an idealized detonation on a macroscopic scale can be described by the set of continuum conservation equations of mass, momentum, and energy, coupled to an expression for energy release as the material is heated and compressed by a leading shock wave. At one extreme, the simplest solution of these equations, for a planar geometry and in free space, gives the steady-state jump conditions across the detonation front. This type of analysis provides information; for example, an estimate of the detonation velocity based on the energy content of the material. At the other extreme, the more complex solutions of multidimensional, time-dependent, compressible flows with various rates of chemical transformations and forms of energy release in and different types of materials must be solved numerically. The reliability of these simulations is severely limited by the quality of the chemical reaction rates and equations of state. For some condensed-phase systems, these continuum equations cannot properly describe the system and when used, much of the input is ad hoc and phenomenological. Recently there have been attempts to simulate condensed-phase detonations at the microscopic

level using molecular dynamics, to obtain qualitative information about microscopic manybody effects.

Performing such computations requires a confluence of tools and information from a number of disciplines, including fluid dynamics, chemical kinetics, computer science, and numerical analysis. The field of computational fluid dynamics (CFD) brings together those aspects that involve all but the chemical and some physical inputs. We have been calling the science and engineering that includes the details of the multispecies interactions computational reacting fluid dynamics. Detonation simulations are computationally intensive, and often their extent and validity are a function of the available computer resources.

### HIGH-SPEED, LARGE-SCALE COMPUTING

The detail and, for some properties, the accuracy we can expect from a numerical simulation of a chemically reacting flow depends on the interplay of a number of factors. These include the availability of high-speed computers, specialized numerical algorithms, and methods of visualizing or analyzing the output.

For example, the major advances in CFD have come from using the more accurate monotone methods on massively parallel computers that allow high-resolution simulations. Fifteen years ago, a two-dimensional computation with  $10^6$  computational cells was considered large. Today, computations have been done with  $10^9$  cells. This not only reflects an advance in computer memory, but also reflects greatly increased computational speeds. Problems that previously could only be attempted on large supercomputers at very few institutions can now be done on readily obtainable workstations. Similarly, there have been changes in our expectations of computing for chemically reacting flows. Fifteen years ago we could regularly do a one-dimensional calculation with a full chemical reaction model for hydrogen combustion. Today, we can almost regularly do the same computation in two dimensions.

A graph of the advances in computer speed and memory as a function of year [1] appears as a straight line on a semi-log scale, indicating that the computer power and memory available seems to be going up exponentially. This is due to a series of innovations, not one new development. The straight line is the result of the superposition of a series of curves, each reaching a peak and then leveling off. Each partial curve represents the introduction of a new technology. For example, early breakthroughs have included going from vacuum tubes to transistors and from magnetic cores to semiconductor memory. More recently, we have gone from scalar to vector architectures, and now from serial to parallel computing. Such a curve is typical of the growth of an enabling technology, which here is the high-performance computer. The time-dependent change is necessarily short term, and slows down at some point. The leveling occurs because the particular technology that allowed the growth becomes too expensive and time-consuming to improve. The result is the series of piecewise logistic curves. One rather frightening feature of this type of analysis is that in order to continue to grow, and not stagnate, we constantly need new technologies.

There has been much said and written on the characteristics of currently available large-scale computers, and, in particular, on vector and parallel supercomputers. Their availability and capabilities, and their manufacturers, are in constant flux. The most powerful computers generally use the same types of computer chips that are in the most powerful workstations. Issues in parallel computing are whether the computer memory is global or distributed, whether codes are portable from one type of machine to another, whether computations scale well from a few processors to many processors, and how data is communicated among processors. Figure 1 gives the information on current computers, and also shows some of the limits on computing. Computer speeds are given in units of Mflops (megaflop, or millions of floating point operations per second), and the computers are shown in terms of their maximum number of processors. The current goal is a teraflop or larger computer, which, as shown with the proposed T3E, could be achieved if enough fast processors are combined.

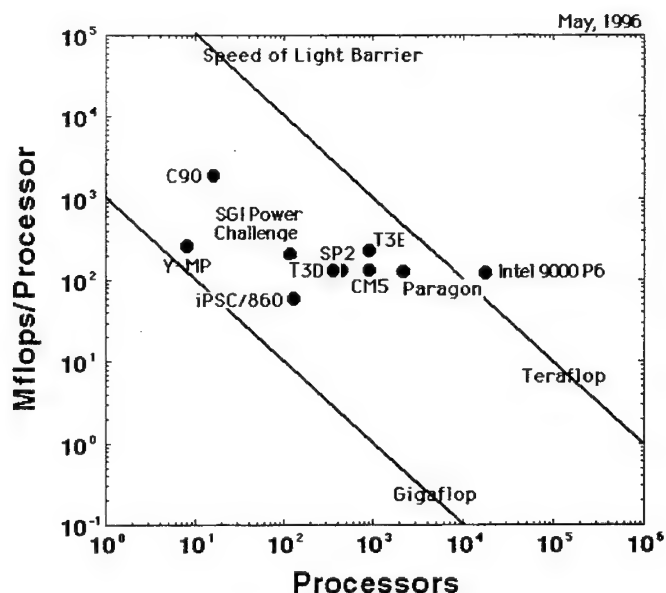


Figure 1. Speed of a component processor (Mflops), as a function of the maximum number of processors available in the largest configuration of currently available or projected massively parallel supercomputers.

New advances in computers, and particularly in computer architectures, have made a significant contribution to computation of chemically reacting flows. The improvements are impressive, as we show later. Part of this development has come through the straightforward application of various existing algorithms, and some has come from new procedures that combine the standard algorithms with specific features of the new architectures. Future advances could also come from simultaneously combining different kinds of computers, each of which is best suited for a different kind of operation, an approach called heterogeneous computing.

### CELLULAR STRUCTURE OF GAS-PHASE DETONATIONS

It has become well known in the last twenty years that the front of a self-sustained gas-phase detonation propagating in an energetic gas is not uniform and planar. Its structure is complex and multidimensional, involving interactions between incident shocks, Mach stems, transverse waves, and boundaries of the regions through which the detonation is moving. The triple points, formed at the intersection of the transverse wave with the Mach stem and the incident shock, trace out patterns called detonation cells. These structures may be obscured for certain material conditions or if the detonation is heavily overdriven, but they seem to occur consistently in self-sustained gas-phase detonations. Extensive experimental data show that the size and regularity of this cellular structure is characteristic of the particular combination of initial material conditions, such as composition, density and pressure.

There are two major contributing physical processes in gas-phase detonations – chemical reactions with local energy release and compressible fluid dynamics – that need to be coupled to represent a detonation. To first approximation, the various physical diffusion processes may be neglected in regions of the detonation far from bounding walls. However, the apparent simplicity disappears and the subject becomes infinitely more complex and dramatic when multi-dimensional fluid interactions, multispecies, multistep chemical kinetics, or nonideal equations of state must be considered. Because of the apparent simplicity of the contributing physical processes, there have been extensive efforts in recent years to simulate detonation structure.



Detonation simulations have advanced in complexity as computer resources have become available and as our understanding of the phenomena expanded. Ten years ago, we could, with great effort, perform a computation of a two-dimensional detonation with a rather simplified parametric chemistry model. Now, with relatively less effort, we can perform this computation with a full, detailed, multispecies chemical model, with orders of magnitude better resolution on a much larger computational domain. Figures 2 and 3 are part of a simulation describing the development and propagation of a detonation in a low-pressure, mixture of hydrogen and oxygen heavily diluted with argon. [2,3]. This type of mixture has become fairly standard for studies of detonations because it displays a regular, repeating structure and the chemical model is fairly well known. The computation was initiated by computing the properties of a highly resolved, detailed one-dimensional detonation, using a detailed hydrogen-oxygen chemical reaction scheme, placing it onto a two-dimensional grid, and perturbing the solution in the transverse direction. The solution evolves into a propagating multidimensional detonation.

Figure 2 shows contours of pressure, streamwise velocity, and specific energy release for the entire computational grid after 24000 timesteps. The notable features of these figures are the propagation of the rarefaction wave from the left endwall into the wake of the detonation, the downstream propagation of the weak transverse waves, the presence of embedded jets that result from the re-ignition of the detonation at the collision of two triple points, and the formation of large eddies due to slip-line interactions. The location of the detonation front as a function of time was used to give the average computed velocity of the detonation wave. The average computed detonation velocity is 1625 m/s, which agrees well with the Chapman-Jouguet velocity ( $D_{CJ}$ ) of 1618 m/s predicted by a standard equilibrium model. The instantaneous velocity ranged from 1.38  $D_{CJ}$  to 0.85  $D_{CJ}$ , showing the effects of the time-varying detonation rate due to changes in the local structure of the detonation front.

The energy release is due to chemical reactions behind the shock front. Figure 3 shows the time history of the triple points, which gives a regular, cellular pattern similar to those observed in previous simulations and experiments. In addition to the primary energy release behind the Mach stem, near the trip point, the figure shows a secondary energy release inside the detonation cell. The secondary energy release is due to transverse wave detonations, as observed in the experiments of marginal detonations.

One innovative feature of these computations is the approach to implementing the chemical reaction algorithm on the massively parallel computer. In the paradigm used here, each processor can be thought of as a computational cell, or divided into  $2^n$  "virtual" computational cells, when  $n > 1$ . If chemical reactions occur in the material in a computational cell, the integration naturally occurs within the processor associated with that computational cell. There is no problem when there are chemical reactions occurring in all computational cells: then all of the cells are simultaneously working and the procedure is very efficient. When little or no chemical reactions occurs in many cells, processors are idle and the computation is extremely inefficient. In the case of the propagating detonation, most of the reaction occur in relatively few computational cells, near the propagating front in the reaction zone. In front of the detonation, there are no reactions; far enough behind the detonation, the reactions are complete. For this kind of calculation, straightforward application of the algorithms leads to very inefficient calculations.

The solution to this problem is to find ways of improving the processor load balancing. In the detonation problem, the approach has been to develop a way to scatter the work of the integration onto all of the processors, then gather it back to its appropriate place. This minimizes the time when any are idle and less work is done in each processor. Figure 4 shows that, using this approach, the ratio of computer time required for integration of the chemical reactions to the time required to compute the convective transport,  $\tau_{chem}/\tau_{conv}$ , has been reduced to less than one [4]. this opens up tremendous possibilities for detailed reactive-flow computations.

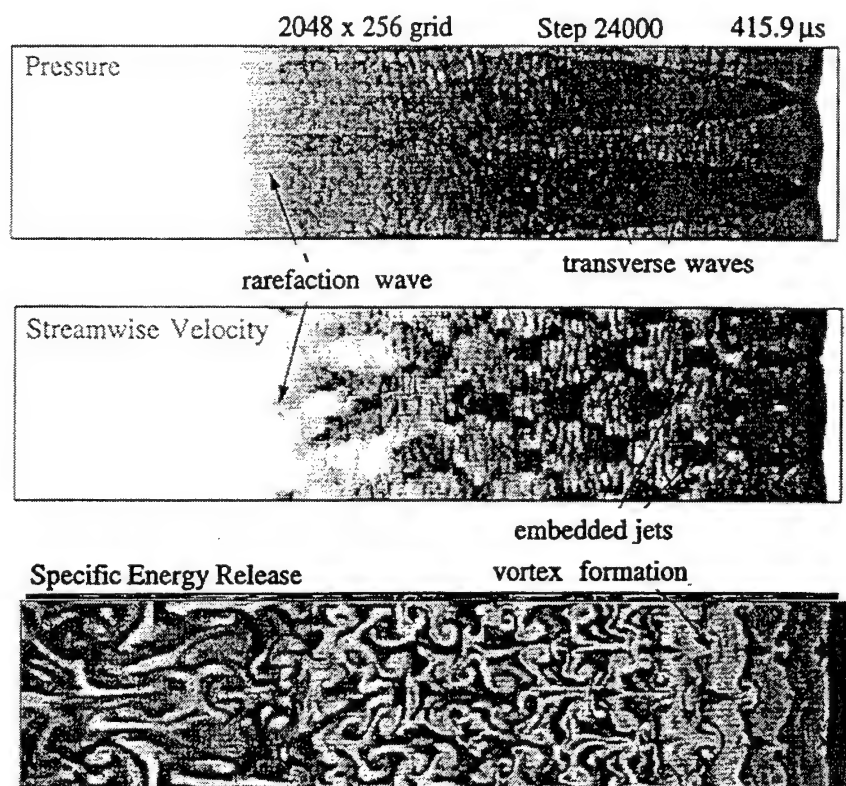


Figure 2. Instantaneous flow field of a detonation propagating (from left to right) in a mixture of  $\text{H}_2:\text{O}_2:\text{Ar}/2:1:7$ , 298 K and 6.67 kPam in a channel 6 cm in height. Computations performed with a fully parallelized code on a the CM-5 [2,3].

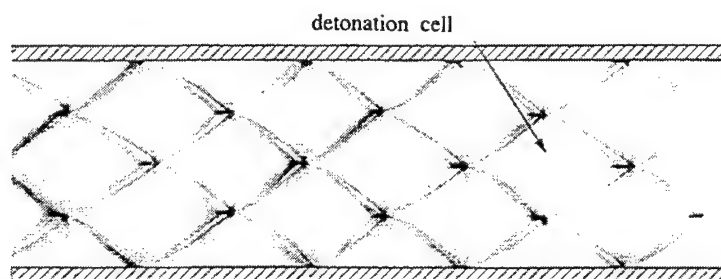


Figure 3. Energy release contours showing cellular pattern [2,3], taken from the evolution of the detonation shown in Figure 2.

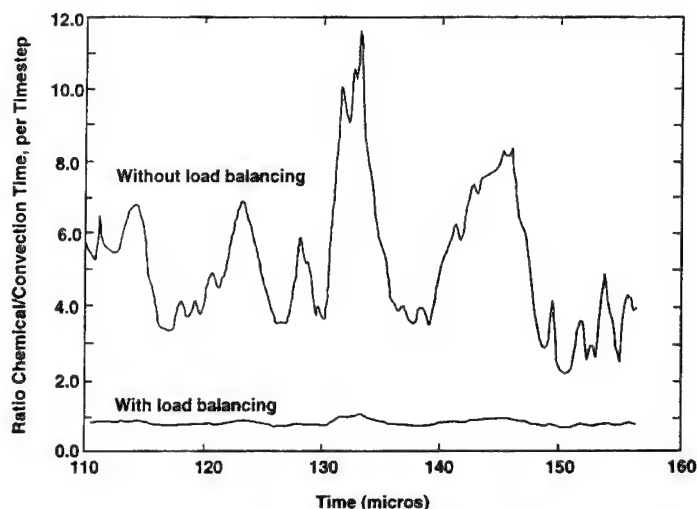


Figure 4. The importance of load balancing the chemical integration is shown by the reduction of the successful ratio of the chemical to convection times required in the course of the detonation calculation shown in Figures 2 and 3 [4].

## NUCLEAR DETONATIONS IN SUPERNOVAE

Type Ia supernovae, believed to be explosions of white dwarf stars, are the brightest and most frequent type of supernovae observed. A single explosion releases approximately  $10^{51}$  ergs of energy into the interstellar medium, and these explosions are the major source of all iron-group elements formed in the universe. Since they are the brightest known stellar objects, they are used to estimate the age, size, and curvature of the universe by comparing their intrinsic luminosity to their apparent brightness.

Typical densities and temperatures in a supernova are  $\rho \simeq 10^5 - 10^{10}$  g/cc and  $T \simeq 10^9 - 10^{10}$  K, respectively. Under these conditions, matter is fully ionized and composed of ideal Fermi-Dirac gases of electrons and positrons, equilibrium Planck radiation, and practically ideal Boltzmann gases of ions. Thermonuclear burning in supernovae involves many reactions of nuclei from hydrogen to zinc. The main reaction in the explosion is  $^{12}\text{C} + ^{12}\text{C}$ , which produces oxygen and releases  $\simeq 50\%$  of the available nuclear energy. The remaining energy is released by a subsequent complicated reaction chain that produces nuclei from carbon to nickel with protons, neutrons and  $\alpha$ -particles.

Even though the absolute values of physical quantities and the nature of the reactions are so different between explosions in terrestrial gases and supernovae, many common or analogous physical mechanisms control the processes. Burning starts near the dense center of the star at zero gravity. As the flame burns and the star expands, it is distorted by hydrodynamic instabilities, and then propagates outward into a regime with higher gravity and lower densities and temperatures. At the radius where the Rayleigh-Taylor instability begins to dominate, the flame becomes a turbulent deflagration [Khokhlov, 1995].

The subsequent behavior is the subject of active study because there are several possibilities after the deflagration forms. First, the turbulent deflagration could be strong enough to burn through and release enough energy to unbind the star. Another possibility is the transition of the deflagration to a detonation, which continues the energy release process in the mate-

rial. However, it now appears most likely that the deflagration is quenched as it moves into less reactive, expanding outer material. In this case, the star will eventually implode in a recompression phase. During this phase, the unreacted material will detonate [6].

In some ways, numerically simulating a supernova blast is less difficult than any but the most idealized terrestrial combustion systems. At the energies of supernovae, many of the nuclear reactions have been directly measured in accelerator experiments, and reasonably good theories calibrated by experiments exist for those reactions that have not been measured directly. It is safe to say that all key reactions determining the energy release and production of major nuclear species during the explosion are known to within a factor of two or better. The typical dependence of nuclear reaction rates on temperature is  $\simeq \exp(-Q/T)$  or  $\simeq \exp(-Q/T^{1/3})$ . This exponential temperature dependence of nuclear reactions makes them qualitatively similar to terrestrial chemical reactions, though the typical nuclear burning time scales,  $\simeq 10^{-5} - 10^{-11}$  s, are much shorter. The equation of state has a simple form,  $P = (\gamma - 1)E$  with  $\gamma \simeq 1.3 - 1.6$ , and is known with accuracy better than 1%. There is thermal conduction which is well known, but there are no molecular diffusion effects ( $Le = \infty$ ).

The difficulty is that the disparities in scales are even larger than in terrestrial problems. The radius of an unexploded white dwarf, is  $\simeq 2 \times 10^8$  cm, which is much larger than any terrestrial combustion apparatus. (This expands during the burning phase to  $\simeq 10^9$  cm.) Depending on the density, the thickness of a laminar nuclear flame in a carbon-oxygen white dwarf is  $\simeq 10^{-3} - 10$  cm, and the thickness of the carbon detonation front is about one hundred times larger,  $\simeq 10^{-1} - 10^3$  cm. These are comparable with the thickness of gas-phase terrestrial combustion processes. Ratios of temperature, density, and pressure across these fronts are comparable to those in terrestrial combustion systems. Any theory of supernovae explosions must be consistent with the observed spectra and their variations with time.

Recent numerical simulations have examined some of the fundamental properties of the propagation of flames and detonations in Type Ia supernovae, and other simulations have attempted to model the complete explosion process. Figure 5 is taken from a series of computations that investigate the manner in which multidimensional detonations propagate through supernovae material at various densities. As the reaction proceeds through the material, the original carbon material burns out [7]. The irregularity of the structure at the front shows that a somewhat regular cellular structures forms, and that the transverse waves cut off large pockets of unburned material that appear to persist for some time in the flows. This work is the first demonstration that thermonuclear material supports detonation cells.

## DETONATIONS IN CONDENSED PHASE EXPLOSIVES

Detonations in gases, liquids, and solids are usually modeled by fluid models with appropriate modification for differences such as the equations of state and elastic-plastic effects. There are, however, important differences between the fluid and solid states which indicate that the mechanisms of heat transfer and shock-wave propagation may be very different. In a fluid, heat transfer occurs by collisions between the molecules, while in a nonconducting solid, heat propagates as vibrational motions of the crystal lattice. In a solid, the intermolecular interactions that play a large role in shock-wave propagation are more coherent. The importance of these differences between fluids and solids is suggested by crystallographic studies which indicate that specific structural characteristics, perhaps structural inhomogeneities, may be required for a detonation to propagate in a solid.

There is a major difference in the spatial scales of detonations in the condensed and gas phases. The width of a shock front in a condensed phase is of the order of a few atomic distances. The important scales of a condensed-phase detonation are on scales from a few crystallographic unit cells to microns. Such microscopic phenomena might be represented in a molecular dynamics calculation, in which atoms, molecules, or molecular clusters are treated as particles which interact according to specified potentials. Then given the interaction potential, the particles

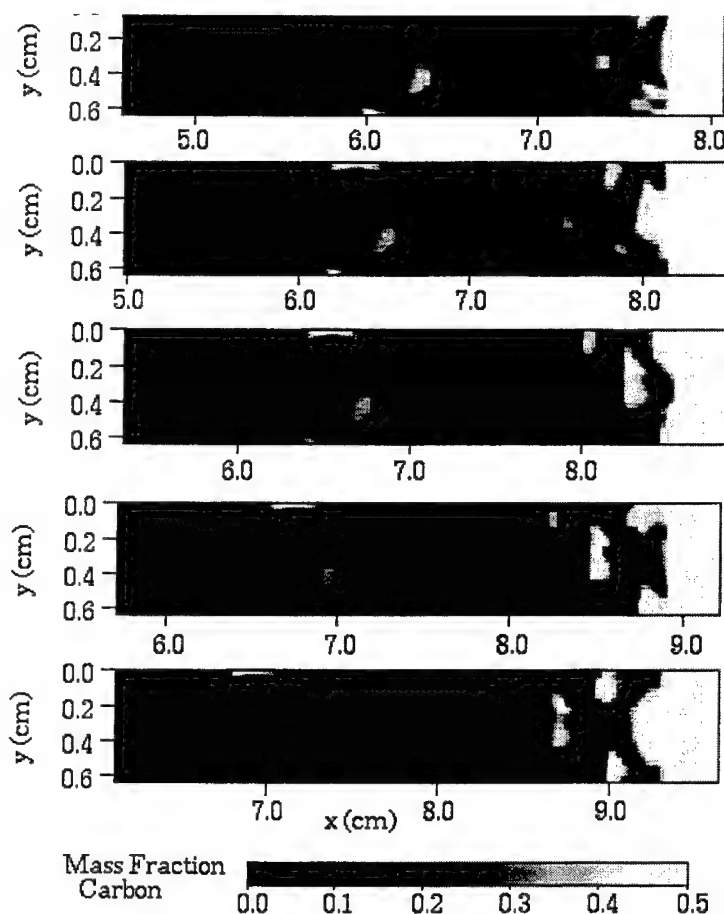


Figure 5. Computation of the instantaneous contours of carbon mass fraction destroyed by a thermonuclear detonation in supernova material at  $3 \times 10^7$  g/cc [7].

are allowed to interact according to Newtonian dynamics, constrained by initial and boundary conditions. If many particles are included or the interaction is complex, the problem becomes extremely computer-intensive. It has generally been found that this approach provides insight into the manybody dynamics of very different types of systems, ranging from condensation phenomena in cryogenic materials to the behavior of proteins in solution.

The application of molecular dynamics to solid-phase detonations is extremely computer intensive. A microscopic study of detonation structure has to consider: the effects of the lattice geometry, including the unit cell structure and interparticle bond strength; the multidimensionality of the system; the interaction between the different regions that make up a detonation wave; the characteristic response time of potentially dissociative molecules subjected to stress fields in a lattice; and the chemistry of the reaction path from reactants to products. To produce really quantitative results from molecular dynamics would thus require input information that is not likely to be available for complex explosive molecules, and computer resources which at best may be available in the middle of the next century.

As a consequence, this field has proceeded more along the lines of physics than engineering: simplified models have been proposed for molecular structures and interactions, based on real

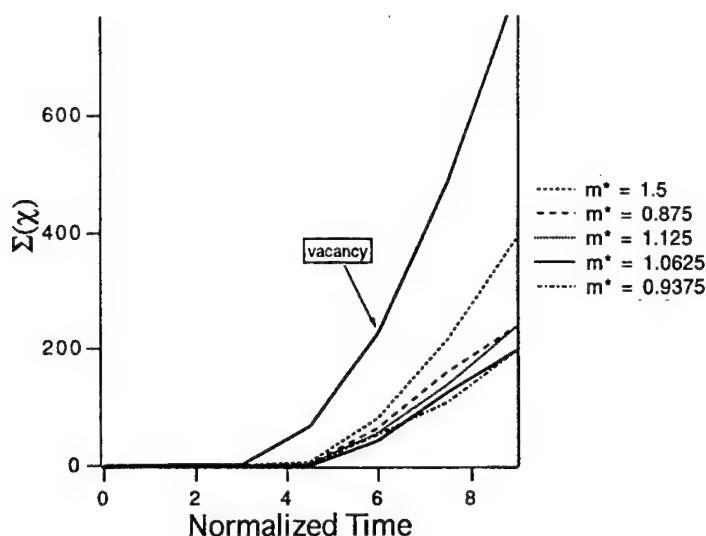


Figure 6. Results of two-dimensional Molecular dynamics computations of the effects of impurities compared to a vacancy in a stable hexagonal lattice [11,12]. The quantity  $\Sigma$  is a disruption factor. The masses of the impurities tested are normalized to one.

and proposed concepts for the input data, and small systems have been examined, often with shortened length and time scales. These unphysical modifications are done in the belief that useful information comes from studying the dynamics of a very small sample of the material. This is all done with the knowledge that we would expect quite different quantitative results from those of real macroscopic explosive samples.

For example, the first computations that used molecular dynamics to study detonation in solids, investigated a two-dimensional monatomic crystal consisting of atoms bound to each other by a predissociative exothermic potential [8]. They found that the widths of the induction zone and of the shock front may be of the order of a few unit cells. Subsequent studies, for example, investigated the coherence of a multidimensional lattice consisting of essentially diatomic molecules [9,10]. Their idea was to represent crystalline nitromethane as a  $\text{CH}_3$  group and an  $\text{NO}_2$  group, and bond-breaking would involve splitting the C-N bond under the right circumstances. This model, which attempted to use physically correct parameters for crystal nitromethane, produced interesting information about detonation propagation and crystal motions.

One important experimental observation is that there may be a significant variation in the response of a series of explosive samples to what appears to be the same macroscopic impulse. For example, in an experiment in which crystals are detonated by mechanical impact, a wide range of impact energies might be necessary to detonate what seem to be identical samples of material. A possible explanation for this might be some uncontrolled variation in the experimental conditions, presenting different samples with an unknown variation in initial conditions. Another explanation might lie in the material itself. A solid is characterized not only by its chemical composition and its thermodynamic state, but also by its particular crystal structure.

More recent studies have examined the effects of inhomogeneities on the multidimensional structure of model crystal lattices. Two-dimensional simulations have shown the strong effects of inhomogeneities on initiating and strengthening a detonation. One interesting result, summarized in Figure 6, shows that in a stable, shocked, two-dimensional lattice, a void has a

much stronger effect than any impurity of finite mass. [11,12]. Subsequent computations of the effects of a void in a three-dimensional nitromethane lattice showed how a void might enhance the shock sensitivity of a single crystal of energetic material [13]. As the shock passes, the bonds between molecules on the void boundary interact with the shock and to form a dense, hot, liquid phase. The presence of the defect then increases the reaction rate, which in turn leads to the temperature increase that form this hot spot. Such hot spots might reenforce the strength of shocks whose strength is on the borderline of being able to initiate a detonation.

A fundamental inconsistency in simulation and experiments of solid-phase detonations is the experimental evidence that a detonation cannot propagate in a single crystal without inhomogeneities. Furthermore, the required inhomogeneities might have to be on a mesoscale of crystalline grains, and not on the microscale generally modeled by molecular dynamics. However, most molecular dynamics simulations have been able to initiate and propagate detonations in lattices with no inhomogeneities. There are several reasons for this apparent disagreement. First, the molecular dynamics models are simplistic in the way they model the lattice and molecular interactions. It is possible the more complex molecules and a better representation of energy-transfer in the lattice is required. Another problem may be of size. Possibly if the full size of the sample could be modeled, other hydrodynamic effects would appear that would affect the system.

## **A PRACTICAL APPLICATION OF SHOCK AND DETONATION PHYSICS**

During the Cold War, over nine million tons of conventional propellants, explosives and munitions, and pyrotechnic materials accumulated in the United States and Europe, including the Former Soviet Union. Now we are faced with eliminating large inventories of unneeded or unserviceable energetic materials in an environmentally sound manner. For example, the United States alone has over 450,000 tons in its "demil inventory" which is increasing at the rate of 40,000 to 50,000 tons per year. The three methods of disposing of the surplus energetic materials are: incineration; disassembly, recovery and recycling (DRC); and open-air burning or detonation (OB,OD). Although incineration and DRC are the environmentally preferred methods of disposal, they cannot presently be used on all of the items in the inventory, and for this reason, OB and OD remain an integral part of all energetic materials disposal programs.

However, in the United States, the disposal of energetic materials by OB and OD is very restricted. In some states, it is prohibited because of concerns about: (1) the degree to which they convert the materials into innocuous chemicals; (2) the toxicities and dispersion in the environment of the ash, soil, and chemical pollutants released; and (3) the impact of the blast waves and sound waves released. These restrictions and prohibitions have contributed to the increase in the demil inventory.

To address the above concerns, the United States Army, Navy and Environmental Protection Agency are cooperating in an effort to use computational and experimental methods to identify and quantify the emission products released by OB and OD activities [14,15]. These products must be evaluated as a function of such variables as: type and quantity of energetic material, stacking configuration, site geology and meteorology, and pollutant and noise reduction procedures. The objectives are to: (1) obtain a quantitative understanding of the chemical and physical processes which occur when energetic materials are destroyed by OB and OD; (2) combine this information with that from previous studies to develop methods that minimize and control the noise, heat, shrapnel, blast wave and toxic inorganic and organic compounds released by OB and OD activities; and (3) improve the environmental safety of OB and OD activities.

To this end we have been developing a large-scale OB/OD facility that would take advantage of carefully designed partial confinement of the blast, and would flash incinerate large quantities of explosive. Several designs have been evaluated by a series of simulations using the FAST3D



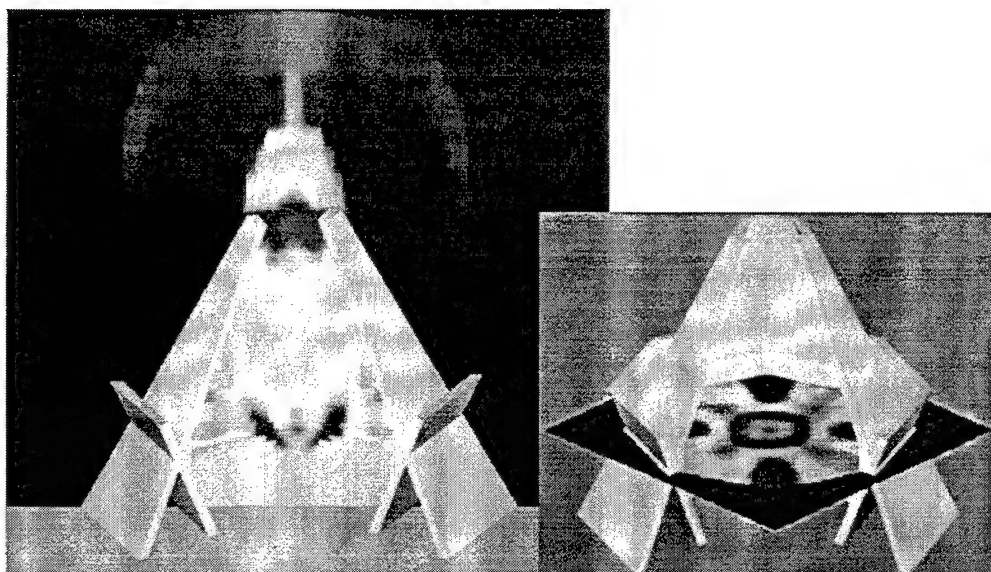


Figure 7. Planes showing computations of instantaneous contours of pressure for a proposed open-air detonation facility. Left figure: vertical plane through the center. Right figure: horizontal slice through a center plane.

reactive flow code. This is a time-dependent, multiphase reactive-flow code based on the flux-corrected transport (FCT) algorithm for convective transport and a generalized, calibrated induction parameter model (GIPM) to represent chemical energy release, species conversion, and post explosion afterburn of potential pollutants. To date, the geometries considered have been either octagonal or circular configurations, with variable-sized openings to the outside.

Figure 7 shows a preliminary design of an octagonal explosion facility that would take a series of shots of from 50 to 300 lbs of explosive. The computation is initialized with a 300 lb spherical charge centered 3 m above the ground. The simulation uses an  $80 \times 80 \times 80$  grid to simulate one quarter of the facility, so that the uniform grid consists of cubes 15 cm on a side. Pressure contours are shown at 10 ms for one vertical and one horizontal plane. At this time, the initial blast has reflected from the sidewalls and refocused, as shown in the horizontal contour map. The vertical contour map shows that the blast has left the facility and is in the outside atmosphere. At 10 ms, the maximum pressure in the chamber is just over 13 atm, having decayed from an initial high of thousands of atm.

The computations have been used to determine the optimal sizes and placements of the explosive charge and to evaluate the loading on the walls of the structure. This loading is being evaluated to determine the types and the strengths of the materials necessary to build this reusable facility. The use of partial confinement by water cover placed on the outside vent (a water bag) is being investigated as a way to absorb pollutants and particles and to mitigate some of the problems of noise propagation.

Of particular interest are the time-histories of the temperature and flow fields in the facility. The facility must be designed so that the temperatures can be kept high enough for a long period of time to decompose the resulting harmful materials. The flow fields must ensure rapid mixing of explosion byproducts with the ambient (possibly enriched) air in the facility to ensure efficient afterburn. Such partial confinement is expected to produce sufficiently high internal temperature profiles, so that the facility could, in principle, be used to eliminate other types of harmful materials such as chemical weapons.



The current work involves combining the results of the FAST3D computations and a structural analysis to design a prototype, scaled facility than will be tested at Dugway Proving Ground during the summer of 1996.

#### ACKNOWLEDGMENTS

This material in this paper is based on the efforts of many scientists with whom I have worked on the various projects over many years. In particular, the work presented here is based on collaborations with Drs. Jay P. Boris, K. Kailasanath, Michel Lefebvre, James W. Weber, Jr., J.R. (Jay) Boisseau, Alexei Khokhlov, J. Craig Wheeler, Robert Sinkovits, Lee Phillips, Charles Lind, William Mitchell, J.L. (Casey) Wilcox, and Christopher Biltoft. Various portions of this work were supported by the Office of Naval Research, the Defense Advanced Research Projects Agency, the National Aeronautics and Space Agency, the U.S. Army, and the Environmental Protection Agency.

#### REFERENCES

1. Worlton, J., Some Patterns of Technological Change in High-Performance Computing. This material is based on the work of Worlton, as presented at the Symposium *Advances and Trends in Computational Structural Mechanics and Fluid Dynamics*, Washington, DC, organized by A.K. Noor, 1988.
2. Weber, J.W. (Jr.), *Physical and Numerical Aspects of Two-Dimensional Detonation Simulations including Detailed Chemical Kinetics on a Massively Parallel Connection Machine*, Ph.D. dissertation, Department of Aerospace Engineering, University of Maryland, 1994.
3. Weber, J.W. (Jr.), Oran, E.S., Lefebvre, M., and Anderson, J.D. (Jr.), Numerical Study of a Two-Dimensional  $H_2/O_2/Ar$  Detonation Wave with a Detailed Chemical Model, submitted to *Combust. Flame*, 1996.
4. Weber, J.W. (Jr.), Anderson, J.D. (Jr.), Oran, E.S., Patnaik, G., and Whaley, R., Load Balancing and Performance Issues for the Data Parallel Simulation of Stiff Chemical Nonequilibrium Flows, AIAA Paper No. 95-0570, American Institute of Aeronautics and Astronautics, Washington, DC; to appear in *AIAA Journal*, 1997.
5. Khokhlov, A.M., Propagation of Turbulent Flames in Supernovae, *Astrophys. J.* Vol. 449, pp. 695-713, 1995.
6. Khokhlov, A.M., Oran, E.S., and Wheeler, J.C., Deflagration to Detonation Transition in Thermonuclear Supernovae, to appear in *Astrophysical J.*, 1996.
7. Boisseau, J.R., Khokhlov, A.M., Oran, E.S., and Wheeler, J.C., The Multidimensional Structure of Detonations in Type Ia Supernovae, *Astrophysical J.*, Vol. 471, pp. L99-L102, 1996.
8. Karo A.M., Walker F.E., DeBoni T.M., and Hardy J.R., The Simulation of Shock-Induced Energy Flux in Molecular Solids, *Prog. Aero. Astro.*, Vol. 94, pp. 405-415, 1983.
9. Peyrard, M., Odier, S., Oran, E., Schnur, J., and Boris, J., Microscopic Model for Propagation of Shock-Induced Detonations in Energetic Solids, *Phys. Rev. B.*, Vol. 33, pp. 2350-2362, 1986.
10. Lambrakos, S.G., Peyrard, M., Oran, E.S., and Boris J.P., Molecular-Dynamics Simulations of Shock-Induced Detonations in Solids, *Phys. Rev. B*, Vol. 39, pp. 993-1005, 1989.
11. Sinkovits, R.S., L. Phillips, L., Oran, E.S., and Boris J.P., Molecular Dynamics Simulations of Shock-Defect Interactions in Two-Dimensional Nonreactive Crystals, *Structure and Properties of Energetic Materials*, edited by Armstrong, R.W., and Gilman, J.J., Materials Research Society, Pittsburgh, Vol. 296, pp. 161-166, 1993.

12. Phillips, L., Sinkovits, R.S., Oran, E.S., and Boris J.P., The Interaction of Shocks and Defects in Lennard-Jones Crystals, *Journal of Physics - Condensed Matter*, Vol. 5, pp. 6357-6376, 1993.
13. Phillips, L., Molecular Dynamics Simulations of Shocks and Detonations in a Model 3D energetic Crystal with Defects, *Structure and Properties of Energetic Materials*, edited by Armstrong, R.W., and Gilman, J.J., Materials Research Society, Pittsburgh, Vol. 296, pp. 155-160, 1993.
14. Biltoft, C.A., Oran, E.S., Boris, J.P., Lind, C.A., Mitchell, W.J., Source Characterization Modeling for Demil Operations, to appear in *Proceedings of the 20th Army Science Conference*, 1996.
15. Mitchell, W.J., Wilcox, J.L., Biltoft, C., Oran, E.S., Boris, J.P., Techniques to Improve the Environmental Safety of OB and OD Operations, to appear in *Proceedings of the 89th Annual Meeting and Exhibition*, Air and Waste Management Association, 1996.

## SOME DYNAMICS OF ACOUSTIC OSCILLATIONS WITH NONLINEAR COMBUSTION AND NOISE

V. S. Burnley<sup>1</sup>, F. E. C. Culick<sup>2</sup>

<sup>1</sup>U. S. Air Force Phillips Laboratory; <sup>2</sup>California Institute of Technology

**ABSTRACT:** The results given in this paper constitute a continuation of progress with nonlinear analysis of coherent oscillations in combustion chambers. We are currently focusing attention on two general problems of nonlinear behavior important to practical applications: the conditions under which a linearly unstable system will execute stable periodic limit cycles; and the conditions under which a linearly stable system is unstable to a sufficiently large disturbance. The first of these is often called 'soft' excitation, or supercritical bifurcation; the second is called 'hard' excitation, 'triggering,' or subcritical bifurcation and is the focus of this paper. Previous works extending over more than a decade have established beyond serious doubt (although no formal proof exists) that nonlinear gasdynamics alone does not contain subcritical bifurcations. The present work has shown that nonlinear combustion alone also does not contain subcritical bifurcations, but the combination of nonlinear gasdynamics and combustion does. Some examples are given for simple models of nonlinear combustion of a solid propellant but the broad conclusion just mentioned is valid for any combustion system.

Although flows in combustors contain considerable noise, arising from several kinds of sources, there is sound basis for treating organized oscillations as distinct motions. That has been an essential assumption incorporated in virtually all treatments of combustion instabilities. However, certain characteristics of the organized or deterministic motions seem to have the nature of stochastic processes. For example, the amplitudes in limit cycles always exhibit a random character and even the occurrence of instabilities seems occasionally to possess some statistical features. Analysis of nonlinear coherent motions in the presence of stochastic sources is therefore an important part of the theory. We report here a few results of power spectral densities of acoustic amplitudes in the presence of a subcritical bifurcation associated with nonlinear combustion and gasdynamics.

### NOMENCLATURE

Symbol	Description
$\bar{a}$	speed of sound
$f$	function defined with Eq. (1.2)
$F_n$	forcing function defined in Eqs. (1.5) and (1.6)
$\mathcal{F}'$	defined in Eq. (2.1)
$F(u)$	defined in Eq. (2.3)
$h$	function defined with Eq. (1.1)

$k_n$	wavenumber of $n^{\text{th}}$ mode
$\dot{m}_{\text{pc}}$	pressure-dependent mass flux, Eq. (2.3)
$\hat{n}$	unit outward normal vector
$p'$	pressure fluctuation
$\mathcal{P}'$	defined in Eq. (2.1)
$r_n(t)$	magnitude of the time-dependent amplitude $\eta_n(t)$
$R_{\text{vc}}$	constant defined in Eq. (2.3)
$s'$	entropy fluctuation
$\mathbf{u}'$	velocity fluctuation
$u_t$	threshold velocity (Figures 2 and 3)
<i>Greek Symbols</i>	
$\alpha_n$	linear growth rate of $n^{\text{th}}$ mode
$\eta_n(t)$	time-dependent amplitude of $n^{\text{th}}$ mode
$\rho'$	density fluctuation
$\theta_n$	linear frequency shift of $n^{\text{th}}$ mode
$\phi_n$	phase of the time-dependent amplitude $\eta_n(t)$
$\psi_n(\mathbf{r})$	mode-shape of $n^{\text{th}}$ mode
$\omega_n$	frequency of $n^{\text{th}}$ mode
$\Omega'$	vorticity fluctuation
<i>Subscripts</i>	
( ) <sub>a</sub>	acoustic waves
( ) <sub>s</sub>	entropy waves
( ) <sub><math>\Omega</math></sub>	vorticity waves

## 1 INTRODUCTION

Coherent oscillations have been a constant problem in the design of combustion systems. There are two general types of oscillations which are commonly found in combustion chambers: spontaneous oscillations and pulsed oscillations. A spontaneous oscillation occurs when the system is linearly unstable. As a result, any perturbation of the system grows exponentially in time. Under the influence of nonlinear effects, the pressure field may reach a periodic motion, or limit cycle. This type of instability is also known as an intrinsic instability or a soft excitation. In the field of dynamical systems, the change of behavior from linearly stable to linearly unstable is called a supercritical bifurcation. The problem of linear instability has been widely treated and will not be covered in this paper.

A pulsed oscillation, on the other hand, is a true nonlinear instability of a linearly stable system. Small perturbations in the pressure field decay exponentially to zero, while larger perturbations may lead to stable or unstable periodic motions. Common terminology used to describe this type of oscillation includes triggered instability, hard excitation, and subcritical bifurcation. In the field of combustion instabilities, Sirignano and Crocco<sup>1,2</sup> were the first to examine pulsed oscillations using the method of characteristics and the  $n - \tau$  model for the combustion dynamics. However, the calculations were quite complex and restrictive approximations were required in order to obtain results. No assessment was made as to the consequences of using these approximations. For several reasons, then, it is impossible to determine the general applicability of these results. Moreover, it is not possible to determine whether or not the pulsed oscillations were stable or unstable. Zinn and his students<sup>3-7</sup> also studied pulsed oscillations in liquid propellant rocket motors using many of the same approximations used by Sirignano and Crocco (notably

the combustion model). As a result, those investigations suffer from the same shortcomings as the earlier works.

In the current study, we are primarily interested in the conditions under which stable pulsed oscillations can occur. We base the analysis on an approximate formulation which was developed over two decades ago by Culick.<sup>8</sup> The formulation has been covered in many other works, so only a brief overview of the method is presented here; for more details, see, e.g., the review by Culick.<sup>9</sup> The numerical calculations consist in applying a continuative method such that the results are guaranteed to represent stable limit cycles.

In order to keep the analysis as general as possible, the formulation begins with the conservation equations for two-phase flow. These equations are then rewritten into an equivalent form for a single medium having the mass-averaged properties of the two phases. Subsequently, a wave equation for the pressure is developed, along with the corresponding boundary condition.

$$\nabla^2 p' - \frac{1}{\bar{a}^2} \frac{\partial^2 p'}{\partial t^2} = h \quad (1.1)$$

$$\hat{n} \cdot \nabla p' = -f \quad (1.2)$$

The functions  $h$  and  $f$  are linear and nonlinear functions of the pressure and velocity perturbations. As an approximation, these perturbations are expanded as a synthesis of classical acoustic modes with time-varying amplitudes,

$$p'(\mathbf{r}, t) = \bar{p} \sum_{n=1}^{\infty} \eta_n(t) \psi_n(\mathbf{r}) \quad (1.3)$$

$$\mathbf{u}'(\mathbf{r}, t) = \sum_{n=1}^{\infty} \frac{\dot{\eta}_n(t)}{\bar{\gamma} k_n^2} \nabla \psi_n(\mathbf{r}) \quad (1.4)$$

where  $\psi_n$  is the mode shape and  $\eta_n(t)$  is the time-dependent amplitude of the  $n^{\text{th}}$  classical acoustic mode. After substituting Eq. (1.3) in Eq. (1.1), the equations are spatially averaged, resulting in a system of ordinary differential equations describing the amplitudes of the acoustic modes.

$$\frac{d^2 \eta_n}{dt^2} + \omega_n^2 \eta_n = F_n \quad (1.5)$$

where  $\omega_n = \bar{a} k_n$  and

$$F_n = -\frac{\bar{a}^2}{\bar{p} E_n^2} \left\{ \int \psi_n h dV + \oint \psi_n f dS \right\} \quad (1.6)$$

Thus, the problem is reduced to solving for the amplitudes,  $\eta_n(t)$ . This approach is very general and can accommodate all damping and amplification mechanisms. The most difficult part of the problem is in the identification and modeling of the important physical processes.

Much of the earlier work using this analysis has concentrated on the effects of nonlinear contributions from gasdynamics only. Some of these include Yang et al.,<sup>10</sup> Paparizos and Culick,<sup>11</sup> and Jahnke and Culick.<sup>12</sup> These works have convincingly shown that nonlinear gasdynamics alone does not contain the possibility of pulsed oscillations. It has also been shown that results for nonlinear gasdynamics to second-order is qualitatively similar to results obtained using gasdynamics to third-order; we will therefore include nonlinear gasdynamics to second-order only. In this work, we will present results for systems with additional contributions from nonlinear combustion response and noise.

## 2 NONLINEAR COMBUSTION RESPONSE OF SOLID PROPELLANTS

Combustion of a solid propellant is nonlinear chiefly for two reasons: chemical processes depend nonlinearly on both temperature and pressure; and the conversion of condensed material to gaseous products is a nonlinear function of the properties of the local flow field. In the past, analysis of unsteady burning has been directed largely to investigating the response of burning to small fluctuations of the flow field in order to satisfy the need to predict linear stability. In particular, the response of burning to fluctuations in pressure has received the most attention; see Culick<sup>13</sup> for a review of calculations of the linear response function. In this section, we will show results for models of the nonlinear response of solid propellants.

In order to be used in the present analysis, any model of unsteady combustion must be put in such a form as to fit into the appropriate terms in the forcing function given by Eq. (1.6). For gasdynamics up to second-order, the right-hand side of Eq. (1.5) can be written:

$$-\frac{\bar{p}E_n^2}{a^2}F_n = \bar{\rho} \int (\bar{\mathbf{u}} \cdot \nabla \mathbf{u}' + \mathbf{u}' \cdot \nabla \bar{\mathbf{u}}) \cdot \nabla \psi_n dV + \frac{1}{a^2} \frac{\partial}{\partial t} \int (\bar{\gamma} p' \nabla \cdot \bar{\mathbf{u}} + \bar{\mathbf{u}} \cdot \nabla p') \psi_n dV$$

linear gasdynamics

$$+ \bar{\rho} \int \left[ \mathbf{u}' \cdot \nabla \mathbf{u}' + \frac{\rho'}{\bar{\rho}} \frac{\partial \mathbf{u}'}{\partial t} \right] \cdot \nabla \psi_n dV + \frac{1}{a^2} \frac{\partial}{\partial t} \int (\bar{\gamma} p' \nabla \cdot \mathbf{u}' + \mathbf{u}' \cdot \nabla p') \psi_n dV \quad (2.1)$$

nonlinear gasdynamics

$$+ \oint \bar{\rho} \frac{\partial \mathbf{u}'}{\partial t} \cdot \hat{\mathbf{n}} \psi_n dS - \int \left[ \frac{1}{a^2} \frac{\partial \mathcal{P}'}{\partial t} \psi_n + \mathcal{F}' \cdot \nabla \psi_n \right] dV$$

linear and nonlinear      other contributions  
surface processes

As a means of accommodating nonlinear combustion of solid propellants, we are concerned with the term labeled "linear and nonlinear surface processes." Because this term is nearly equal to the time derivative of the second-order fluctuation of mass flux inward, it provides a means through which contributions from nonlinear combustion may be included. The mass flux at the surface is defined as  $\dot{m} = \rho \mathbf{u}$  so that the fluctuating part becomes

$$\begin{aligned} \dot{m}' &= \dot{m} - \bar{\dot{m}} \\ &= (\bar{\rho} + \rho')(\bar{\mathbf{u}} + \mathbf{u}') - \bar{\rho}\bar{\mathbf{u}} \\ &= \bar{\rho}\mathbf{u}' + \rho'(\bar{\mathbf{u}} + \mathbf{u}') \end{aligned}$$

Assuming  $\bar{\mathbf{u}}$  is independent of time, a form which can be directly substituted in Eq. (2.1) is obtained by taking the time derivative of the above equation and rearranging terms.

$$\bar{\rho} \frac{\partial \mathbf{u}'}{\partial t} \cdot \hat{\mathbf{n}} = \frac{\partial \dot{m}'}{\partial t} \cdot \hat{\mathbf{n}} - \rho' \frac{\partial \mathbf{u}'}{\partial t} \cdot \hat{\mathbf{n}} - \frac{\partial \rho'}{\partial t} (\bar{\mathbf{u}} + \mathbf{u}') \cdot \hat{\mathbf{n}} \quad (2.2)$$

It happens that analysis and modeling of unsteady combustion leads to results for mass fluctuation, but as shown by Eq. (2.1), the gasdynamics problem within the chamber requires the

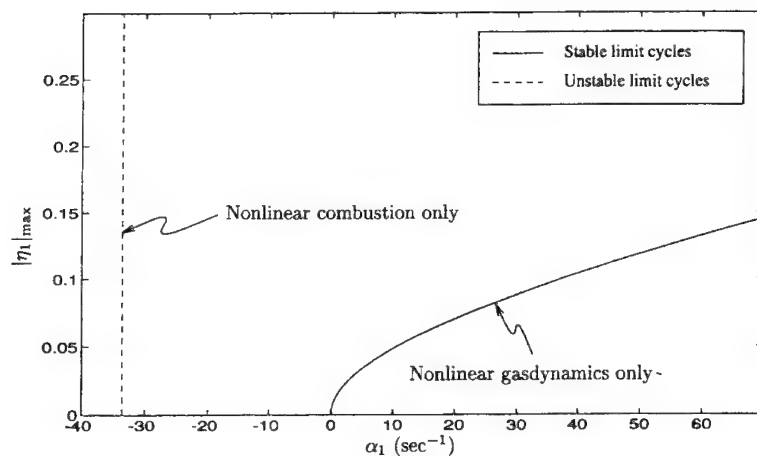


Figure 1. Maximum amplitude in limit cycle of first acoustic mode showing contributions of nonlinear gasdynamics and combustion

unsteady velocity as the boundary condition. Thus, we can include contributions from nonlinear combustion by use of Eq. (2.2).

For the results here, we assume that all linear processes are accounted for and that nonlinear contributions arise only from gasdynamics and/or combustion. When only nonlinear gasdynamics is included in the analysis, a supercritical bifurcation, characteristic of spontaneous oscillations, is produced; see Fig. 1. The basic input data for Figs. 1, 3 and 4 are those used by Culick and Yang<sup>14</sup> except for the special values needed in the representation of the nonlinear combustion response.

When combustion provides the only nonlinear contributions, the possibility of pulsed oscillations has also not been found. For the nonlinear combustion model used in Fig. 1, described in the following section, a shifted stability boundary was produced. No stable limit cycles are found on either side of this boundary. Other models of nonlinear combustion have produced similar results. Therefore, we have subsequently investigated the combination of nonlinear gasdynamics and combustion, and some of those results will be reproduced here.

Most of the work concerning combustion instabilities has dealt with linear stability of pressure oscillations. As a result, many models of the linear response of combustion to pressure oscillations have been developed.<sup>15</sup> In order to study the possible influences of nonlinear pressure coupling, one of these linear response functions was extended by retaining terms to second-order.<sup>16</sup> For reasonable values of parameters, this model did not produce triggering to stable limit cycles and will not be covered here; see Burnley<sup>17</sup> for details. Instead, we will concentrate on the response of combustion to velocity oscillations parallel to the burning surface, i.e., velocity coupling.

## 2.1 Velocity Coupling

In the experimental and theoretical investigation of pulsed instabilities by the Air Force Propulsion Laboratory, Baum and Levine<sup>18</sup> introduced a model of nonlinear combustion response based on the idea of velocity coupling. To obtain agreement between predicted behavior and observations, one parameter representing the response of combustion to the velocity parallel to the

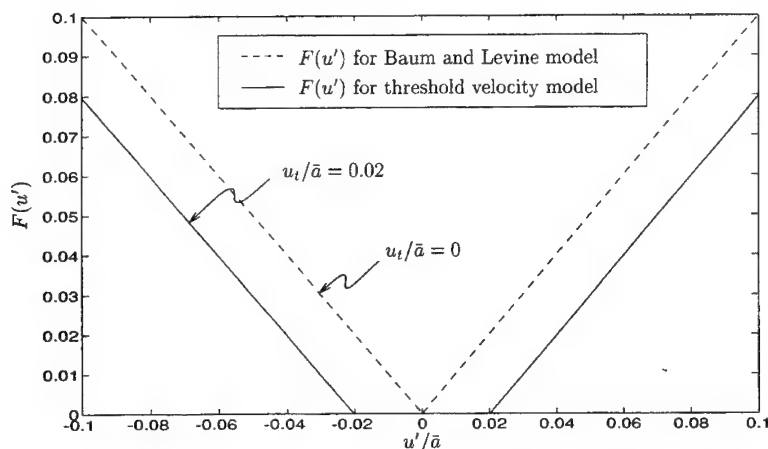


Figure 2. Function of velocity to be used in the threshold velocity model;  $u_t/\bar{a} = 0.02$

burning surface was changed. By changing only this parameter, they were able to match the growth rates, the limit cycle amplitudes, the mean pressure shift, and the waveform quite accurately. This suggests that the chosen nonlinearity must be fairly close to the important physical processes present in the experiments.

The Baum and Levine model is an ad hoc model in which the mass burning rate is directly modified by some function of the velocity.<sup>18</sup> For that reason it was originally called the 'burn rate augmentation model.' The total mass burning rate is written as a combination of linear pressure coupling and nonlinear velocity coupling.

$$\dot{m} = \dot{m}_{pc}[1 + R_{vc}F(u)] \quad (2.3)$$

where  $\dot{m}_{pc}$  is the mass flux due to pressure only and  $R_{vc}$  is a constant related to the sensitivity of burning to velocity parallel to the surface. As the evolution rate of solid to gas should depend on the magnitude but not the direction of the scouring flow, and the simplest assumption is linear dependence,  $F(u)$  is taken equal to  $|u'|/\bar{a}$ . We will restrict  $R_{vc}$  to positive values, i.e., cases in which the mass flux decreases due to velocity fluctuations will not be considered.

A second model which will be discussed in this section is based on the idea of a threshold velocity. Threshold effects have been observed in experimental investigations of velocity coupling. Ma et al.<sup>19</sup> used subliming dry ice to simulate the flow in a solid propellant rocket motor. A piston was used to generate acoustic waves in the chamber. The investigation found a threshold acoustic velocity above which the mean mass flux increased linearly with the Reynolds number of the acoustic fluctuations. Below the threshold value, the mean mass flow was approximately constant. The increased mass flux was determined to be a result of increased heat transfer to the surface after transition to turbulent flow had occurred.

The function of velocity shown in Figure 2 will be used in the Baum and Levine model (2.3) to construct the threshold velocity model. This function introduces a dead zone in which the nonlinear contributions from combustion do not affect the system. When the amplitudes of oscillations become larger than the chosen threshold value  $u_t$ , the nonlinear effects are then felt.



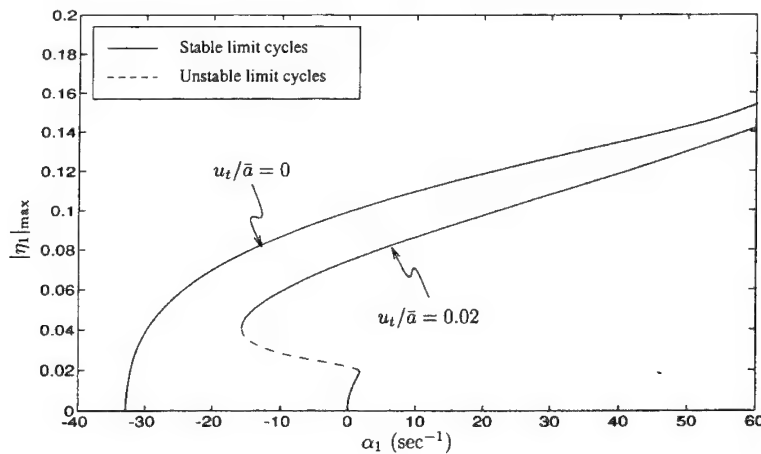


Figure 3. Maximum amplitude in limit cycle of first acoustic mode with and without a normalized threshold velocity of 0.02; four modes;  $R_{vc} = 5.32$

### 2.1.1 Results for velocity coupling

The Baum and Levine model as originally formulated did not satisfactorily explain pulsed oscillations. Although regions of possible triggering were found when the system was truncated to two modes, this region is greatly reduced or is no longer present when more modes are included. The threshold velocity model, on the other hand, produces sizeable regions of possible triggering. In Fig. 3, results for the Baum and Levine model is compared with results for a normalized threshold velocity ( $u_t/\bar{a}$ ) of 0.02.

For velocity oscillations with amplitudes less than the chosen threshold velocity, the effect of nonlinear combustion is nonexistent. Therefore, the path of periodic solutions should be identical to the case of linear pressure coupling, i.e., a supercritical bifurcation occurring at the origin. This is precisely the behavior shown in Fig. 3 for the threshold velocity model. Once the magnitude of the velocity oscillations reaches the threshold value, nonlinear combustion quickly

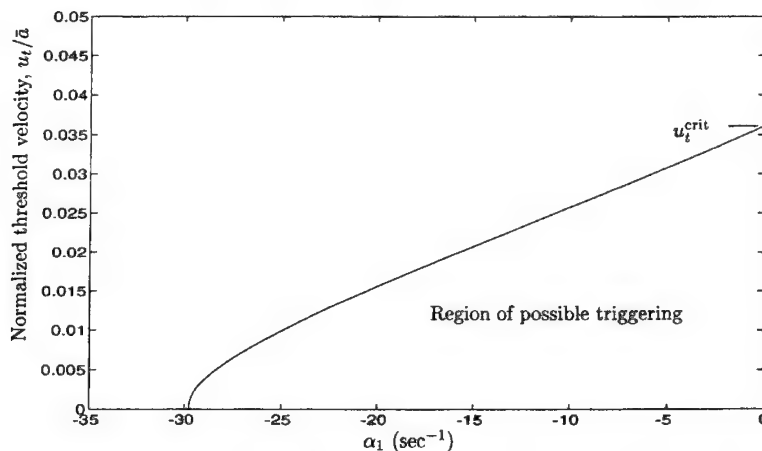


Figure 4. Influence of the threshold velocity  $u_t$  on the region of possible triggering;  $R_{vc} = 5.32$

becomes important, and a fold in the path is produced. The unstable path remains nearly horizontal until other nonlinear contributions become strong enough to produce a second fold, thereby producing a path of stable periodic solutions. Another observation from Fig. 3 is that the amplitudes of oscillations are lower than the amplitudes for a zero threshold velocity. The total energy provided by nonlinear combustion during one cycle is less when a threshold velocity is present. Thus, lower amplitudes are required in order to dissipate the energy and maintain a stable limit cycle.

Using the methods of dynamical systems theory, the location of the upper turning point was determined as a function of the threshold velocity. For a value of  $R_{vc} = 5.32$ , a plot of this dependence is provided in Fig. 4. (Note that there is a discrepancy between Figs. 3 and 4 for  $u_t/\bar{a} = 0$ . This is due to the quantitative inaccuracy of the original oscillator equations when using the threshold velocity model in the methods of dynamical systems theory; see Burnley<sup>17</sup> for details. The plot of  $u_t/\bar{a} = 0$  in Fig. 3 was generated using time-averaged equations, while Fig. 4 was produced using the original oscillator equations. For  $u_t/\bar{a} \approx 0$ , the time-averaged equations are slightly more accurate than the original oscillator equations.) There is actually no triggering for  $u_t/\bar{a} = 0$ , although a large region of possible triggering exists for  $u_t/\bar{a}$  infinitesimally greater than zero. As  $u_t$  is increased, the region becomes increasingly smaller until finally, a critical value is reached above which triggering is no longer possible. This phenomenon was noted by Levine and Baum,<sup>18</sup> but no possible explanations were given.

If the threshold velocity is greater than  $u_t^{\text{crit}}$ , the rate of energy production by nonlinear combustion cannot equal the rate at which energy is transferred to higher modes by nonlinear gasdynamics. Therefore, for a stable limit cycle to exist, additional energy must be provided by linear processes, i.e.,  $\alpha_1 > 0$ . For this reason, a propellant with a very high threshold velocity will be impossible to trigger. It was also determined that the critical value of  $u_t$  depends directly on the value of the velocity coupled response function, as one would expect. The rate of energy production is proportional to  $R_{vc}$ . As the coupling to velocity oscillations becomes stronger, i.e.,  $R_{vc}$  increases,  $u_t^{\text{crit}}$  increases accordingly.

### 3 THE INFLUENCE OF COMBUSTION NOISE

Combustion chambers are inherently noisy environments. This is apparent from inspection of the power spectra of pressure records from test firings, as well as from simply listening to the test. When a combustion instability is present, the power spectrum exhibits well-defined peaks in addition to background noise over the entire range of frequencies. Substantial noise sources in rocket motors include flow separation, turbulence, and combustion processes. It is expected that the presence of noise will affect in some way the amplitudes and possibly the qualitative behavior of coherent oscillations. That is precisely the purpose of this section: to determine the influence of noise on combustion instabilities.

Only a small amount of work has been done on the interactions between noise and acoustic instabilities. Culick et al.<sup>20</sup> studied the influence of noise on combustion instabilities, but only for a very simple case: two acoustic modes with noise present only in the first mode. In addition, the formulation was flawed, and the form of the resulting noise terms is not quite correct. Clavin et al.<sup>21</sup> studied the influence of turbulence on instabilities in liquid rocket motors. Using only one mode in the analysis and third-order nonlinearities, it was reported that the inclusion of noise can lead to the possibility of triggering. It is a well-known result that a single third-order equation may produce a subcritical bifurcation. When more acoustic modes are considered, this may not be the case, as demonstrated by Yang et al.<sup>10</sup> for third-order gasdynamics. Therefore, the results of Clavin et al. may not be applicable in general.

The present analysis is an extension of the previous work by Culick et al.<sup>20</sup> We will first decompose the flow field into acoustic and non-acoustic parts using a method developed by Chu and Kovásznay.<sup>22</sup> This will allow the general form of the noise terms to be determined. Finally, we will simplify the equations in order to study the possible influences of noise on combustion instabilities.

### 3.1 Splitting the Unsteady Flow Field Into Acoustic, Vortical, and Entropic Modes of Propagation

Fluctuations in a compressible fluid can be decomposed into three types of waves: acoustic waves, vorticity waves, and entropy waves. A thorough discussion of this idea is presented by Chu and Kovásznay.<sup>22</sup> The three waves propagate independently in linearized theory of a uniform mean flow, but are coupled when the mean flow is non-uniform.<sup>23</sup> For example, the pressure in an acoustic wave is changed slightly by the presence of a vorticity or entropy wave if the mean flow is not uniform. Coupling between modes may also occur at the boundaries of the chamber.

Although noise is detected as pressure waves, the *sources* of noise are associated with the presence of vorticity fluctuations (e.g., turbulence, flow separation, etc.) and entropy or non-isentropic temperature fluctuations. Therefore, decomposing the unsteady flow field into the three types of waves allows both noise and acoustic instabilities to be handled in the same analytical framework discussed in Sec. 1. The contributions from vorticity and entropy waves will appear as additional force terms on the right-hand side of the acoustic equation.

Following the analysis of Chu and Kovásznay,<sup>22</sup> the thermodynamic and kinematic variables can be written as a sum of fluctuations in the three waves as follows.

$$p' = p'_a + p'_\Omega + p'_s \quad (3.1)$$

$$\Omega' = \Omega'_a + \Omega'_\Omega + \Omega'_s \quad (3.2)$$

$$s' = s'_a + s'_\Omega + s'_s \quad (3.3)$$

$$\mathbf{u}' = \mathbf{u}'_a + \mathbf{u}'_\Omega + \mathbf{u}'_s \quad (3.4)$$

In general, all of the fluctuations will be nonzero, but not all terms are the same order. If we restrict the analysis to small amplitude motions, the three waves have the following characteristics:<sup>22</sup>

- ( )<sub>a</sub> acoustic waves: pressure and velocity fluctuations, no entropy change
- ( )<sub>Ω</sub> vorticity waves: velocity fluctuations, no pressure or entropy changes
- ( )<sub>s</sub> entropy waves: entropy and velocity fluctuations, no pressure change

Thus, to zeroth-order, the fluctuations in the three waves are given by

$$p' = p'_a \quad (3.5)$$

$$\Omega' = \Omega'_\Omega \quad (3.6)$$

$$s' = s'_s \quad (3.7)$$

$$\mathbf{u}' = \mathbf{u}'_a + \mathbf{u}'_\Omega + \mathbf{u}'_s \quad (3.8)$$

An equation for the density fluctuation is obtained by expanding the formula for the entropy of a perfect gas.

$$\frac{\rho'}{\bar{\rho}} = \frac{1}{\bar{\gamma}} \frac{p'_a}{\bar{p}} - \frac{1}{\bar{c}_p} s' \quad (3.9)$$

As an approximation to the acoustic pressure and velocity perturbations, we will once again use a superposition of the classical acoustic modes so that

$$p'_a = \bar{p} \sum_{n=1}^{\infty} \eta_n(t) \psi_n(\mathbf{r}) \quad \mathbf{u}'_a = \sum_{n=1}^{\infty} \frac{\dot{\eta}_n(t)}{\bar{\gamma} k_n^2} \nabla \psi_n(\mathbf{r})$$

Substitution of Eq. (3.5) in the left-hand side of the nonlinear wave equation (1.1), followed by application of Galerkin's method, leads to a set of coupled nonlinear oscillator equations.

$$\ddot{\eta}_n + \omega_n^2 \eta_n = F_n \quad (3.10)$$

The right-hand side will be slightly different from the previous derivation with  $F_n$  given by:<sup>23</sup>

$$-\frac{\bar{p} E_n^2}{\bar{a}^2} F_n = \bar{p} I_1 + \frac{1}{\bar{a}^2} I_2 + \bar{p} I_3 + \frac{1}{\bar{a}^2} I_4 + \int \bar{p} \frac{\partial \mathbf{u}'}{\partial t} \cdot \hat{\mathbf{n}} dS - \int \left[ \frac{1}{\bar{a}^2} \frac{\partial \mathcal{P}'}{\partial t} \psi_n + \mathcal{F}' \cdot \nabla \psi_n \right] dV \quad (3.11)$$

where

$$\begin{aligned} I_1 &= \int (\bar{\mathbf{u}} \cdot \nabla \mathbf{u}' + \mathbf{u}' \cdot \nabla \bar{\mathbf{u}}) \cdot \nabla \psi_n dV & I_2 &= \frac{\partial}{\partial t} \int (\bar{\gamma} p' \nabla \cdot \bar{\mathbf{u}} + \bar{\mathbf{u}} \nabla \cdot p') \psi_n dV \\ I_3 &= \int \left( \mathbf{u}' \cdot \nabla \mathbf{u}' + \frac{\rho'}{\bar{\rho}} \frac{\partial \mathbf{u}'}{\partial t} \right) \cdot \nabla \psi_n dV & I_4 &= \frac{\partial}{\partial t} \int (\bar{\gamma} p' \nabla \cdot \mathbf{u}' + \mathbf{u}' \cdot \nabla p') \psi_n dV \end{aligned}$$

In the original development of the approximate analysis, the zeroth-order approximations for the pressure and velocity were used to evaluate  $F_n$ . The same idea will be applied here, although additional contributions to the velocity fluctuation from coupling to vorticity and entropy waves will be included. Once these quantities are substituted in the right-hand side, the set of forced oscillator equations eventually takes the general form

$$\begin{aligned} \ddot{\eta}_n + \omega_n^2 \eta_n &= 2\alpha_n \dot{\eta}_n + 2\omega_n \theta_n \eta_n - \sum_{i=1}^{\infty} \sum_{j=1}^{\infty} [A_{nij} \dot{\eta}_i \dot{\eta}_j + B_{nij} \eta_i \eta_j] \\ &+ (F_n)_{\text{other}}^{\text{NL}} + \sum_{i=1}^{\infty} [\xi_{ni}^v \dot{\eta}_i + \xi_{ni} \eta_i] + \Xi_n \quad (3.12) \end{aligned}$$

This system of equations is very complex, and there are many free parameters. For instance, if we truncate the system to  $N$  modes, there are  $2N$  linear parameters and an additional  $2N^2 + N$  unknown functions. In order to simplify the equations somewhat, we will therefore neglect cross-coupling terms in  $\xi_{ni}^v$  and  $\xi_{ni}$ , i.e., terms with  $n \neq i$ . These terms may turn out to be important, but neglecting them will allow for easier initial computation of results and will suffice for the purposes here. The simplified set of equations is

$$\begin{aligned} \ddot{\eta}_n + \omega_n^2 \eta_n &= 2\alpha_n \dot{\eta}_n + 2\omega_n \theta_n \eta_n - \sum_{i=1}^{\infty} \sum_{j=1}^{\infty} [A_{nij} \dot{\eta}_i \dot{\eta}_j + B_{nij} \eta_i \eta_j] \\ &+ (F_n)_{\text{other}}^{\text{NL}} + \xi_n^v(t) \dot{\eta}_n + \xi_n(t) \eta_n + \Xi_n(t) \quad (3.13) \end{aligned}$$

### 3.2 Modeling of the Stochastic Sources

The problem has now been reduced to solving Eq. (3.13) for the time-dependent amplitudes  $\eta_n(t)$  which are subjected to additive and multiplicative white noise. The source terms  $\xi_n^v(t)$ ,  $\xi_n(t)$ , and  $\Xi_n(t)$  represent stochastic processes of some sort and are responsible, in this formulation,

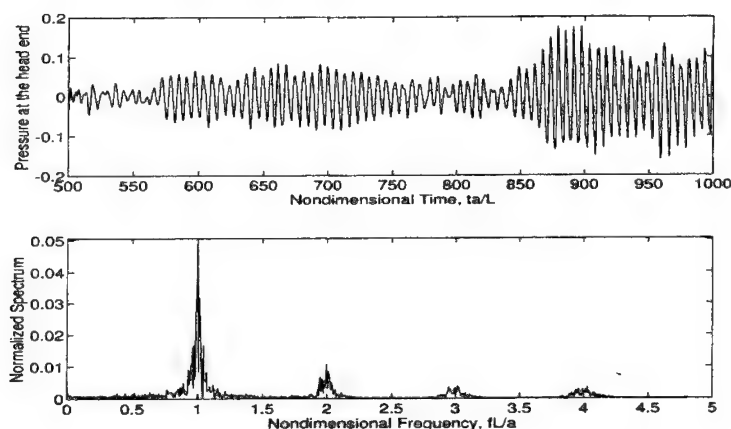


Figure 5. Sample pressure trace and spectrum for a simulation

for the background noise found in the power spectra of test firings. The problem of modeling these processes, however, remains. This requires specification of both the spatial and temporal distribution of the velocity and the entropy. At the present time, no models exist for these fluctuations.

There are several other paths that can be followed at this point which include obtaining approximate representations for the velocity and entropy fluctuations based on experimental data or numerical simulations. The approach that will be taken here is to assume forms for the source terms which are based on observations of experiments. By inspection of the pressure traces of test firings, it is apparent that the stochastic processes in real systems are broadband with very small correlation times,  $\tau_c$ . (The correlation time is the time above which the autocorrelation function is zero. This is a measure of the dependence of the process on its past.) The limit  $\tau_c \rightarrow 0$  represents a delta correlated process, i.e., a process which is totally uncorrelated with itself. It is thus interesting to study this limiting case and assume that the stochastic terms are represented by *white noise*.

The definition of a white noise process is a process whose spectral density is flat, i.e., all frequencies are present at the same amplitude. Although such a process cannot occur in a real system, white noise can be a very useful tool for studying real processes which have very small correlation times compared to the macroscopic times of the system. This is true of the random processes and systems of interest.<sup>20</sup> Therefore, we will approximate  $\xi_n^v$ ,  $\xi_n$ , and  $\Xi_n$  by mutually independent white noise processes with zero mean values and intensities  $\sigma_n^{\xi^v}$ ,  $\sigma_n^{\xi}$ , and  $\sigma_n^{\Xi}$ .

An example of a simulation with white noise excitations is presented in Fig. 5. A sample pressure trace is shown along with the corresponding normalized spectrum. Inspection of the spectrum shows the distinct frequencies which are associated with an acoustic instability, along with broadband background noise. This is characteristic of actual test data of a case when an instability is present.

### 3.3 The Effects of Noise and Nonlinear Combustion

In Section 2, we were interested only in deterministic systems. Since we are now studying nondeterministic systems, it is natural to use the probability density functions of the amplitudes

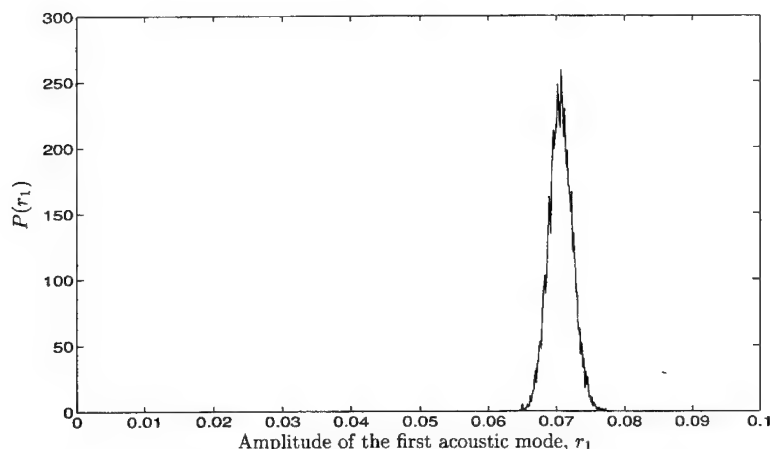


Figure 6. Probability density function for a system with a noisy linear growth rate in the fundamental mode only; 2 modes,  $\sigma_1^v = 0.005 \text{ sec}^{-3/2}$ ,  $\alpha_1 = 25 \text{ sec}^{-1}$

of acoustic modes to investigate the dynamics of the system. In addition, we will use the amplitude  $r_n$  which is defined in the following equation.

$$\eta_n(t) = r_n(t) \cos(\omega_n t + \phi_n(t)) \quad (3.14)$$

This amplitude will have a nonzero mean value so that quantitative changes will be more evident.

A Monte-Carlo method will be used to obtain an approximation to the probability density functions of the acoustic amplitudes. In this method, a series of numerical "experiments" is conducted, usually in the same manner that one would conduct actual experiments. After the flow field has become well-developed (say 1000 periods of the fundamental mode or so), the amplitudes of the acoustic modes are sampled. The results are then used to construct histograms which, after normalization, approximate the instantaneous probability density functions of the modal amplitudes. The approximation becomes better as the number of experiments is increased.

In the current study, each Monte-Carlo simulation will consist of 10000 numerical experiments. The linear parameters will be fixed throughout a series of experiments, while the initial conditions for the simulations will be varied systematically. In particular, a square initial pulse which is nonzero from  $0 \leq x/L \leq .25$  will be used. The size of the pressure pulse  $p'/\bar{p}$  will be varied from 0 to .2 linearly so as to include all likely values.

It is to be expected that the inclusion of combustion noise may well change the quantitative and perhaps even the qualitative behavior of solution. A previous investigation<sup>17</sup> was unable to find cases consistent with subcritical bifurcations when only nonlinear gasdynamics were included. All cases had only one apparent attractive state; see Fig. 6 for an example of a case with a noisy linear growth rate of the fundamental mode. As no examples of triggering were found for the case of noise and nonlinear gasdynamics, nonlinear combustion in the form of the threshold velocity model was also included in the analysis. The results are reproduced here.

When nonlinear combustion is added to the stochastic system (3.13), the resulting probability density functions can be quite different, as one might expect. We have previously shown in Section 2 that this model can produce regions of possible triggering in which two stable solutions exist simultaneously. In a stochastic system, this corresponds to a bimodal probability density

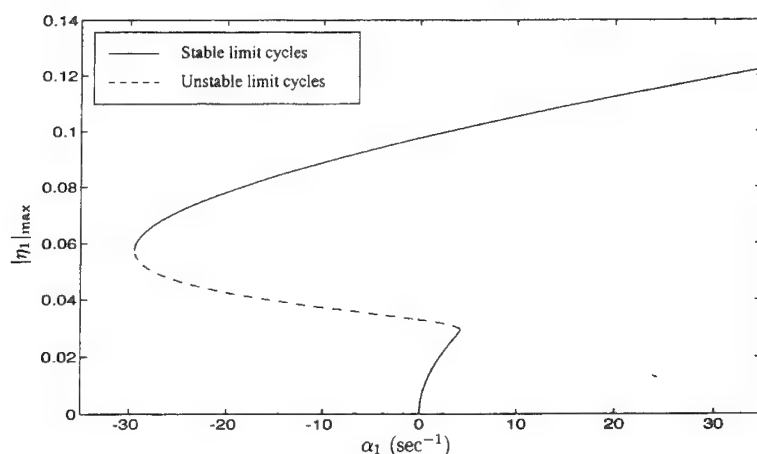


Figure 7. Bifurcation diagram for the deterministic system; threshold velocity model,  $u_t/\bar{a} = 0.03$ ,  $R_{vc} = 7.8$ , 4 modes

function such that there is a high probability of low and high amplitudes and a low probability of intermediate values.

For the parametric values in the threshold velocity model, we will use  $u_t/\bar{a} = 0.03$  and  $\bar{R}_{vc} = 7.8$  for the parameters in the threshold velocity model. Using these values, the bifurcation diagram for the deterministic system is shown in Fig. 7. This diagram will be useful in the discussion of results. In addition, the following values were chosen for the intensities of the stochastic sources:  $\sigma_n^{\xi_v} = 0.005 \text{ sec}^{-3/2}$ ,  $\sigma_n^{\xi} = 0.025 \text{ sec}^{-1/2}$ , and  $\sigma_n^{\Xi} = 0.0005 \text{ sec}^{-3/2}$ , for  $n = 1, 2$ . The parameter  $\alpha_1$  will be varied while all other parametric values remain fixed. By changing this parameter, we will demonstrate a variety of the possible forms of the probability density functions.

From inspection of Fig. 7, we see that the region of possible triggering begins at approximately  $\alpha_1 = -30 \text{ sec}^{-1}$  for the deterministic system. Below this value, the deterministic system is stable to any size perturbation. To illustrate the effect of noise on such a system, a linear growth rate of  $-35 \text{ sec}^{-1}$  was chosen. Figure 8a shows the resulting probability density function for the first acoustic mode. For this case, the attractor of the deterministic system, i.e., the trivial steady state, is so strong that the amplitudes never reach large values. Therefore, the parametric excitations, i.e.,  $\xi_n^v$  and  $\xi_n$ , have a very small effect on the system. Most of the noise contribution is a result of the external excitations,  $\Xi_n$ .

As the linear growth rate is increased to a value above  $-30 \text{ sec}^{-1}$ , we enter the region of possible triggering where an additional attractive state is present. Three values of  $\alpha_1$  were chosen in order to show how the probability density of the fundamental mode changes throughout this region. As the value of  $\alpha_1$  is varied, the regions of attraction of the stationary states will change. This will have a noticeable effect on the probability density functions.

The first value of  $\alpha_1$  was chosen very close to the lower boundary of the region of possible triggering. For a value of  $\alpha_1 = -25 \text{ sec}^{-1}$ , Figure 8b shows the probability density function of the fundamental mode. The low amplitude attractive state is dominant because the region of attraction for this state is larger. However, the effect of the high amplitude attractive state is still present, resulting in a long tail in the probability density function.

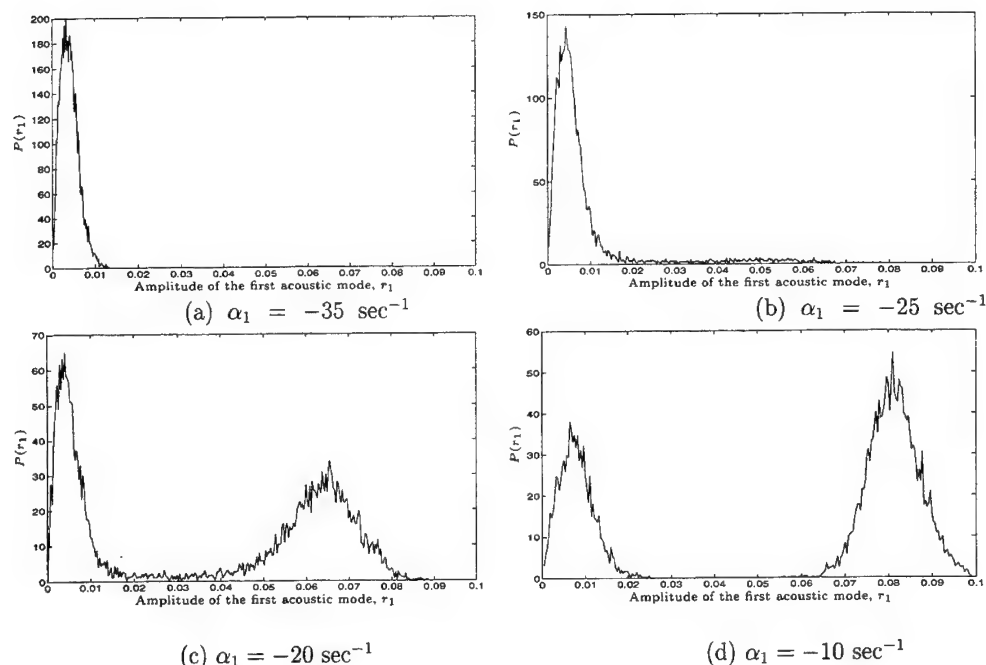


Figure 8. Probability density function of the first acoustic mode for various values of  $\alpha_1$ ; threshold velocity model,  $u_t/\bar{a} = 0.03$ ,  $R_{vc} = 7.8$ , 4 modes

As we increase  $\alpha_1$  further to a value of  $-20 \text{ sec}^{-1}$ , the effect of the high amplitude state becomes more noticeable, as shown in Figure 8c. The regions of attraction of the two states are becoming more equal so that amplitudes surrounding both states have high probabilities. Note that the probability density function is continuous, and the intermediate values are nonzero. This means that the background noise can lead to a qualitative change in the behavior of the system. This is not consistent with the usual definition of triggering in which a larger amplitude perturbation is necessary.

Figure 8d corresponds to  $\alpha_1 = -10 \text{ sec}^{-1}$ . This figure is a good example of triggering in the presence of noise. The background noise is generally insufficient to cause transition from the low amplitude state to the high amplitude state. However, since we are assuming Gaussian distributed noise, even large amplitude perturbations are possible, and the stationary probability density function will in fact be continuous. The probability of intermediate amplitudes will, nonetheless, be very small.

#### 4 CONCLUDING REMARKS

In this paper, we have presented some recent results of a continuing investigation on coherent oscillations in combustion chambers. Past studies have established that nonlinear gasdynamics alone does not explain pulsed oscillations. Using several models of nonlinear combustion, we have shown that nonlinear combustion alone does not apparently contain subcritical bifurcations either. The combination of the two, however, can produce the type of coupling between combustion processes and acoustic oscillations necessary for this type of behavior to occur. We



have reproduced some results obtained using a model of velocity coupling with a threshold. This model, which is based on a physically observed phenomenon, is sufficient to explain pulsed oscillations.

Most past studies of acoustic oscillations have neglected vortical and entropic waves. (For important recent exceptions, see Flandro<sup>24</sup> and Roh et al.<sup>25</sup>) We have relaxed that assumption and developed the general form for the noise terms which arise from vorticity, etc. In order to determine if the combination of combustion noise and nonlinear gasdynamics is sufficient to produce pulsed oscillations, a systematic study was performed. No cases of bimodal probability density functions were located, and it appears that combustion noise alone cannot produce that type of behavior. When the threshold velocity model is also included in the analysis, bimodal probability density functions are possible, as demonstrated here.

### REFERENCES

- [1] Sirignano, W. A., *A Theoretical Study of Nonlinear Combustion Instability: Longitudinal Mode*, Ph.D. thesis, Princeton Univ., Princeton, NJ, 1964.
- [2] Sirignano, W. A. and Crocco, L., "A Shock Wave Model of Unstable Rocket Combustors," *AIAA Journal*, Vol. 2, No. 7, pp. 1285-1296, 1964.
- [3] Zinn, B. T. and Powell, E. A., "Application of the Galerkin Method in the Solution of Combustion Instability Problems," *Proceedings of the 19th International Astronautical Congress*, Vol. 3, pp. 59-73, 1970.
- [4] Powell, E. A. and Zinn, B. T., "A Single Mode Approximation in the Solution of Nonlinear Combustion Instability Problems," *Combustion Science and Technology*, Vol. 3, pp. 121-132, 1971.
- [5] Powell, E. A., Padmanabhan, M. S., and Zinn, B. T., "Approximate Nonlinear Analysis of Solid Rocket Motors and T-Burners: Volume 1," Air Force Rocket Propulsion Laboratory, Technical Report AFRPL-TR-77-48, Edwards AFB, CA 93523, 1977.
- [6] Zinn, B. T. and Lores, E. M., "Application of the Galerkin Method in the Solution of Nonlinear Axial Combustion Instability Problems in Liquid Rockets," *Combustion Science and Technology*, Vol. 4, No. 6, pp. 269-278, 1972.
- [7] Lores, E. M. and Zinn, B. T., "Nonlinear Longitudinal Instability in Rocket Motors," *Combustion Science and Technology*, Vol. 7, No. 6, pp. 245-256, 1973.
- [8] Culick, F. E. C., "Nonlinear Growth and Limiting Amplitude of Acoustic Oscillations in Combustion Chambers," *Combustion Science and Technology*, Vol. 3, No. 1, pp. 1-16, 1971.
- [9] Culick, F. E. C., "Some Recent Results for Nonlinear Acoustics in Combustion Chambers," *AIAA Journal*, Vol. 32, No. 1, pp. 146-169, 1994.
- [10] Yang, V., Kim, S. I., and Culick, F. E. C., "Third-Order Nonlinear Acoustic Waves and Triggering of Pressure Oscillations in Combustion Chambers, Part I: Longitudinal Modes," in *AIAA 25th Aerospace Sciences Meeting*, AIAA Paper 87-1873, 1987.
- [11] Pappas, L. and Culick, F. E. C., "The Two-Mode Approximation to Nonlinear Acoustics in Combustion Chambers. I. Exact Solutions for Second Order Acoustics," *Combustion Science and Technology*, Vol. 65, No. 5, pp. 39-65, 1989.

- [12] **Jahnke, C. C. and Culick, F. E. C.**, "An Application of Dynamical Systems Theory to Nonlinear Combustion Instabilities," *Journal of Propulsion and Power*, Vol. 10, No. 4, pp. 508-517, 1994.
- [13] **Culick, F. E. C.**, "A Review of Calculations of Unsteady Burning of a Solid Propellant," *AIAA Journal*, Vol. 6, No. 12, pp. 2241-2255, 1968.
- [14] **Culick, F. E. C. and Yang, V.**, "Prediction of the Stability of Unsteady Motions in Solid Propellant Rocket Motors," Chapter 18 in *Nonsteady Burning and Combustion Stability of Solid Propellants*, Progress in Astronautics and Aeronautics, Vol. 143, p. 719, 1992.
- [15] **Culick, F. E. C.**, "Some Problems in the Unsteady Burning of Solid Propellants," Naval Weapons Center, Research Report NWC TP 4668, China Lake, CA, 1969.
- [16] **Burnley, V. S., Swenson, G., and Culick, F. E. C.**, "Pulsed Instabilities in Combustion Chambers," in *31st AIAA/ASME/SAE/ASEE Joint Propulsion Conference*, AIAA Paper 95-2430, 1995.
- [17] **Burnley, V. S.**, *Nonlinear Combustion Instabilities and Stochastic Sources*, Ph.D. thesis, California Institute of Technology, Pasadena, CA, 1996.
- [18] **Levine, J. N. and Baum, J. D.**, "A Numerical Study of Nonlinear Instability Phenomena in Solid Rocket Motors," *AIAA Journal*, Vol. 21, No. 4, pp. 557-564, 1983.
- [19] **Ma, Y., Moorhem, W. K. Van, and Shorthill, R. W.**, "Experimental Investigation of Velocity Coupling in Combustion Instability," *Journal of Propulsion and Power*, Vol. 7, No. 5, pp. 692-699, 1991.
- [20] **Culick, F. E. C., Paparizos, L., Sterling, J., and Burnley, V.**, "Combustion Noise and Combustion Instabilities in Propulsion Systems," in *Proceedings of the AGARD Conference on Combat Aircraft Noise*, AGARD CP 512, 1992.
- [21] **Clavin, P., Kim, J. S., and Williams, F. A.**, "Turbulence-Induced Noise Effects on High-Frequency Combustion Instabilities," *CST*, Vol. 96, pp. 61-84, 1994.
- [22] **Chu, B.-T. and Kovásznyai, L. S. G.**, "Nonlinear Interactions in a Viscous Heat-conducting Compressible Gas," *Journal of Fluid Mechanics*, Vol. 3, No. 5, pp. 494-514, 1958.
- [23] **Culick, F. E. C.**, "Nonlinear Acoustics in Combustion Chambers With Stochastic Sources," Guggenheim Jet Propulsion Center, California Institute of Technology, Documents on Active Control of Combustion Instabilities CI95-6, 1995.
- [24] **Flandro, G. A.**, "Effects of Vorticity on Rocket Combustion Stability," *Journal of Propulsion and Power*, Vol. 11, No. 4, pp. 607-625, 1995.
- [25] **Roh, T.-S., Tseng, I.-S., and Yang, V.**, "Effects of Acoustic Oscillations in Flame Dynamics of Homogeneous Propellants in Rocket Motors," *Journal of Propulsion and Power*, Vol. 11, No. 4, pp. 640-650, 1995.

## MODELING OF TRANSIENT COMBUSTION REGIMES OF ENERGETIC MATERIALS WITH SURFACE EVAPORATION

V.E. Zarko<sup>1</sup>, L.K. Gusachenko<sup>1</sup>, A.D. Rychkov<sup>2</sup>

<sup>1</sup>Institute of Chemical Kinetics and Combustion, Russian Academy of Sciences, Novosibirsk 630090, Russia; <sup>2</sup>Institute of Computational Technologies, Russian Academy of Sciences, Novosibirsk 630090, Russia

**ABSTRACT:** A one-dimensional transient model of the combustion of energetic material (EM) with surface evaporation is formulated. The model considers heat propagation and EM condensed phase decomposition via a 1st order reaction. In the gas phase, it considers heat propagation, species diffusion, exothermic decomposition of vapor via a 1st order reaction and exothermic conversion of gas components via a 2nd order reaction. The matching condition at the surface corresponds to equilibrium evaporation in the form of the Clausius-Clapeyron equation. An external radiant flux is assumed to be absorbed in the bulk of EM and not to be absorbed in the gas phase. When simulating radiative ignition, it has been revealed that it can occur in one-, two- or three-stages. First, under irradiation, the evaporation and exothermic reaction in the condensed phase is initiated with a gas flame being formed far from the burning surface. The conductive heat flux from the gas to the EM surface is vanishingly small and the low rate gasification regime is realized. If the radiant flux gradually decreases up to zero, the flame approaches the EM surface and the heat feedback from the gas phase increases several times. A sustaining combustion is governed by heat feedback from the gas flame with burning rate several times higher than the gasification rate. Numerical experiments performed with the combustion model under study have revealed the intrinsic instability of steady-state combustion in case of EM with the rate controlling zone in the condensed phase.

### INTRODUCTION

To create a combustion model of energetic materials (EM) for predicting the dynamic behavior of a concrete EM, one should describe the processes occurring in combustion zones. Although this was recognized many decades ago, it is still impossible to elucidate a detailed combustion mechanism by direct experimental methods for a considerable number of EM. The reason is that the processes under study occur in narrow zones (hundreds, and at high pressures tens of micron) at the width of which the temperature is varied by 2000 – 3000 K. The high gradients of temperature and component concentration make difficult the correct measurements in combustion zones. As a rule, for EM available with a good precision are only stationary burning rate  $r_b$  and its dependencies on pressure  $p$ , initial temperature  $T_0$  and external radiant heat flux  $q_r$ . The temperature profile and  $r_b$  response to time-dependent radiant flux may be measured to less accuracy (by microthermocouple technique, usually in steady-state regime, and by the measurements of the reactive force of issued gases). There is a great need in the techniques

for getting reliable information at least on global kinetics of combustion processes. The natural way to do this is to develop the comprehensive combustion models and the optimal means to compare them with experimental observations.

A steady-state combustion model of evaporating EM is likely to be first proposed by A.F. Belyaev for secondary explosives for which the reactions occurring in the condensed phase may be neglected.<sup>1,2</sup> For ammonium perchlorate a stationary combustion model has been developed with taking consideration of a partial depletion and evaporation of condensed phase and assuming a negligibly small role of the gas phase reactions.<sup>3</sup> The method of small perturbations has been employed to study the stability of steady-state combustion regimes of EM with evaporation on the surface without reactions in the condensed phase and assuming the infinitely thin reaction zone in the gas phase.<sup>4,5</sup> The up-to-date models take into account the global reactions in the liquid phase, the detailed reaction kinetics in gas, and non-equilibrium evaporation at the surface.<sup>6-9</sup>

We consider that the refusal of phase equilibrium at the surface causes unjustified complications of the model (see discussion below). Besides, taking consideration of a detailed kinetics of reactions in the gas phase as one of the current problems of combustion theory we think that today it cannot substantially improve the consumers' characteristics of an "engineering" variant of the model because of the lack of knowledge about processes in the condensed phase. These remarks are especially important for nonsteady combustion models. Below we discuss a relatively simple transient model in which we have tried to allow for the basic phenomena observed in combustion of melting and evaporating EM. A detailed comparison with experimental data for particular EM is beyond the scope of the present paper.

## PROBLEM FORMULATION

In the condensed phase a physical model includes heat propagation in solid and liquid states (heat capacity and density are taken equal for both of the states while thermal conductivity coefficients for solid  $\lambda_s$  and for liquid  $\lambda_l$  are assumed to be different); melting at temperature  $T_m$  with endothermic effect  $Q_m$ ; global exothermic reaction of decomposition in the liquid phase of a 1st order with thermal effect  $Q_c$ ; thermal sources spatially distributed in the bulk of condensed phase according to the Beer law  $q_r \alpha e^{-\alpha x}$ .

The model neglects the change in the liquid layer density due to reactions. This assumption is of minor importance in case of liquid decomposition products. However, in the presence of gaseous products it implies an effective removal of gas from the liquid layer. For example, this removal may occur via molecular diffusion of dissolved gas from a very thin subsurface layer.

On the surface the phase equilibrium is assumed according to the Clausius-Clapeyron condition. Actually, there is no exact equality between the mass flow rates of evaporation  $M_+^*$  and condensation  $M_-^*$

$$M_+^* - M_-^* = y_{cs} m \quad (1)$$

where  $m$  is the mass burning rate;  $y_{cs}$  is the mass fraction of vapor in total mass flow rate generated by the condensed phase. Equation (1) is known to be used for calculating  $m$ .<sup>6-9</sup> However, we consider the arguments given by Ben-Reuven and Caveny in favour of equilibrium evaporation sufficiently convincing.<sup>10</sup> They analyze the relationship obtained for the rates by division of Eq.(1) by gas density near the surface

$$y_{1s}(V_+^* - V_-^*) = V y_{cs} \quad (2)$$

Here  $V$ ,  $V_+^*$ ,  $V_-^*$  are the gas velocity (the arithmetical mean velocity of all molecules both approaching and receding from the surface) and the mean velocities of molecules moving from

the surface and falling on it, correspondingly;  $y_{1s}$  is the mass fraction of vapor above the surface. The estimate is given<sup>10</sup>

$$V/V_-^* \ll 1 \quad (3)$$

Indeed,  $V_-^*$  is of the order of sound velocity. At surface temperature it amounts to hundreds of  $m/s$ . Velocity of gas in EM combustion at atmospheric pressure is usually of the order of  $m/s$  which gives inequality (3). As the pressure increases, it strengthens. Equations (1) and (2) yield

$$M_+^*/M_-^* - 1 = V_+^*/V_-^* - 1 = (V/V_-^*)(y_{cs}/y_{1s}) \quad (4)$$

In EM combustion the condition  $y_{1s} < y_{cs}$  holds due to the dilution of vapor near the surface by the combustion products from gas flame. However, for typical set of input parameters the values  $y_{1s}$ ,  $y_{cs}$  are always of the same order of magnitude (the difference in case of the pronounced rate controlling role of the gas phase amounts 20-40%). Thus, from Equations (3) and (4) it follows that

$$M_+^*/M_-^* - 1 \ll 1 \quad (5)$$

Using advanced approach one should take into account that a certain portion of falling molecules does not stick to the surface but is elastically reflected. This portion, however, is assumed to be small and taking it into account will not change a given qualitative estimate. Note that a sticking coefficient is usually taken to be equal to unity.<sup>7</sup>

Expression (5) confirms the validity of the Clausius-Clapeyron relationship for EM combustion and shows inconvenience of using Eq.(1) as a key expression for computing burning rate because it represents the difference of large numbers.

Thus, we assume that on the surface the following condition holds

$$(M/M_1)y_{1s}p \approx Ae^{-L/RT_s} \quad (6)$$

Here  $(M/M_1)y_{1s}$  is the mole fraction of vapor above the surface;  $M_1$  and  $M$  are the molecular masses of vapor and gaseous mixture, respectively;  $A = const$ ;  $L$  is the evaporation latent heat.

In the gas phase the model takes into account heat propagation, diffusion and two successive global reactions with thermal effects  $Q_i$ ,  $i = 1, 2$ . The products of the first reaction (vapor decomposition via a 1st order kinetics) are assumed to coincide in their composition with the products of decomposition of the liquid phase. The second reaction generates final combustion products via a 2nd order kinetics.

A mathematical model represents a system of differential equations in partial derivatives describing the above physical processes within the framework of a one-dimensional nonsteady approximation, and closing initial and boundary conditions, see Appendix.

The model takes into account the dependence of the coefficients of thermal conductivity and diffusion in the gas phase on temperature and component composition. The EM burning rate is determined from the condition of heat balance at the interface between the gas and condensed phases. In numerical solution this causes certain difficulties which may be overcome by the new special iteration process.

To solve the energy equation with a convective term a quasi monotonous difference scheme of second-order accuracy has been developed that effectively operates on rough (real) difference grids. Its essence may be explained taking the model equation as an example

$$\frac{\partial T}{\partial t} + u \frac{\partial T}{\partial x} = \kappa \frac{\partial^2 T}{\partial x^2} + \beta T \quad (7)$$

where  $T$  is the temperature;  $u$  is the medium velocity;  $\kappa$  is the thermal diffusivity coefficient,  $\beta$  is the heat exchange coefficient. The presence of a convective term leads to the fact that the application of "standard" difference schemes with central differences of the Crank-Nicolson scheme type in case of fairly rough grids causes nonphysical oscillations in the numerical solution in the vicinity of its sharp change (for a given class of problems this is usually the combustion front in which the temperature gradients are large enough). To avoid these oscillations one may apply a difference scheme based on "hyperbolic" approximation. To this end we write the left-hand side of Eq. (7) along line  $dx/dt = u$  that is conventionally called the characteristic line and construct the following difference scheme

$$\frac{T_i^{n+1} - T_i^n}{\tau} = \delta \kappa_i^{n+1} \left( \frac{\partial^2 T}{\partial x^2} \right)_i^{n+1} + (1 - \delta) \kappa_*^n \left( \frac{\partial^2 T}{\partial x^2} \right)_*^n + \delta \beta_i^{n+1} T_i^{n+1} + (1 - \delta) \beta_*^n T_*^n \quad (8)$$

where  $\tau$ ,  $h$  are the grid steps over spatial and time variables so that  $t = n\tau$ ;  $x = ih$ ;  $n = 0, \dots, M$ ;  $i = 0, \dots, N$ . The values with subscript  $*$  are calculated at the cross-points of the characteristic lines coming from the point  $(n+1, i)$  with the straight lines forming the difference grid (with the horizontal ones at  $h/\tau > u$  and with the vertical ones at  $h/\tau < u$ ) using the appropriate interpolations. When  $\delta = 1/2$  the second-order accuracy is attained. For either the variable coefficients of equation or nonlinear source term, one should take advantage of the "predictor-corrector" method.

A combination of computer codes developed for numerical modeling of nonsteady-state processes allows one to realize the permanent output of temperature and concentration profiles to the display as well as the time-dependence of several (up to five) combustion parameters, e.g., the linear velocities of motion of liquid-gas and solid-liquid interfaces, heat flux from gas to the burning surface, the thickness of melted layer, and reactive force produced by issued gases. Besides, the required numerical and graphical information may be recorded on a hard disc. This model was used in a series of numerical experiments during which some new effects specific of the given model have been revealed.

## RESULTS OF CALCULATIONS

In numerical experiments the reference data were chosen based on information reported on combustion of nitramines under atmospheric pressure. These data were changed (see Figures 1-3) in certain range in order to study the effect of kinetic coefficients on transient combustion behavior.

### Ignition peculiarities.

The ignition of EM by thermal radiation was modeled as follows. For semi-transparent EM ( $\alpha = 1000 \text{ cm}^{-1}$  in terms of the Beer law) we assumed time-dependent heat absorption  $q_r(t)$  which is constant  $q_r = q_0$  within the time interval  $0 < t < t_1$ , linearly decreases to zero with  $t_1 < t < t_2$  and at last vanishes. It appears that depending on the relation of parameters  $q_0$ ,  $t_1$ ,  $t_2$  and kinetic parameters (the gas phase, first of all) possible are one-, two- or even three-stage ignition regimes. All regimes have the same beginning phase, i.e. "inert" heating when all reactions may be neglected. This phase continues until the surface temperature reaches the EM boiling (a bit lower) temperature  $T_b$ . When  $T_s$  approaches  $T_b$ , noticeable are the rates of evaporation from surface and reacting in liquid and gas.

To demonstrate the effects of multi-stage ignition the calculations were conducted with following reference parameters:  $n_c = 18.3$ ,  $E_c = 198000 \text{ J/mol}^{17}$ ,  $Q_c = 420 \text{ J/g}$ ,  $E_{g1} = E_{g2} =$

$147420 \text{ J/mol}^{19}$ ,  $Q_{g1} = 1050 \text{ J/g}$ ,  $Q_{g2} = 2982 \text{ J/g}$ ,  $D = 0.15 \text{ cm}^2/\text{s}$ ,  $\lambda = 8.4 \cdot 10^{-4} \text{ W/cmK}^{16}$ ,  $\lambda_c = 2.31 \cdot 10^{-3} \text{ W/cmK}$ ,  $c_p = c_c = 1.26 \text{ J/gK}$ ;  $n_{g1} = 14$ ,  $n_{g2} = 13.5$  for Figure 1;  $n_{g1} = n_{g2} = 13.5$  for Figure 2;  $n_{g1} = 13.5$ ,  $n_{g2} = 12.3$  for Figure 3.

One-stage ignition is realized with sufficiently strong heat release of reactions in the gas phase, in the time interval  $0 < t \sim t_1$  (Figure 1). The gas flame is stabilized in close vicinity of surface and provides heating and evaporation of the condensed phase. When the  $q_r$  gradually vanishes, the steady-state regime of self-sustaining combustion can be established if the deradiation time ( $t_2 - t_1$ ) is not much shorter than the characteristic relaxation time of preheat layer in this regime (in opposite case the flame quenches).

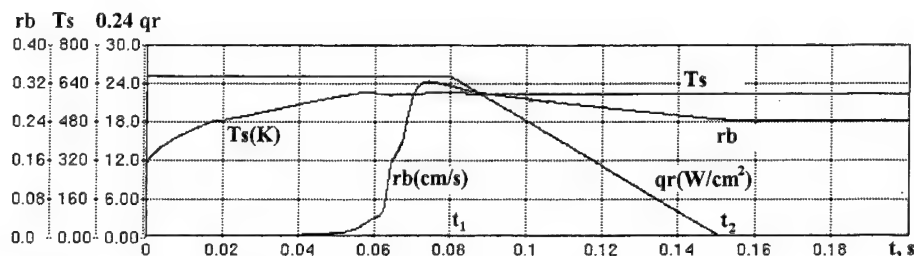


Figure 1. One-stage ignition ( $q_0 = 105 \text{ W/cm}^2$ ,  $t_1 = 0.08 \text{ s}$ ,  $t_2 = 0.15 \text{ s}$ ).

In self-sustaining regime a regression rate is relatively high, conversion degree in liquid is small.

Two-stage regime is possible (Figure 2) with relatively slow kinetics of the first gas phase reaction. The gas flame arises when the  $T_s \approx T_b$  and evaporation starts. However, the flame is realized in the "zone separation regime", i.e. far from the surface at a distance  $h \approx V_g t_{ign}$ . In this case  $V_g \sim q_r$  is the velocity of gas flowing from the surface;  $t_{ign}$  is the time of thermal explosion in gas at characteristic temperature  $T_s$ . When  $h > \lambda/(c\rho V_g)$ , the heat from gas flame does not effectively feed to the surface. In these conditions the gasification regime is observed presumably under the action of the external heat flux  $q_r$ . When  $q_r$  decreases the degree of conversion in condensed phase increases (for used reference parameters it reaches  $\sim 0.2$ ),  $r_b$  decreases too.

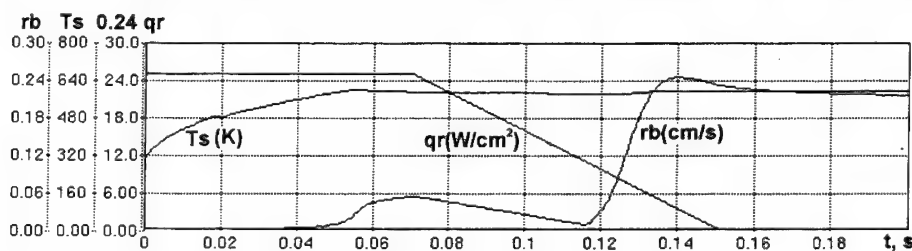


Fig.2. Two-stage ignition ( $q_0 = 105 \text{ W/cm}^2$ ,  $t_1 = 0.07 \text{ s}$ ,  $t_2 = 0.15 \text{ s}$ ).

With  $q_r(t)$  decreasing, the gas velocity and distance  $h$  also decrease and the flame approaches the surface. When  $q_r$  vanishes, the flame provides the heat flux to the surface that is necessary for the steady-state self-sustaining regime (if deradiation was not too fast). In this case, the mass fraction of vapor above the surface  $y_{1s}$ , which in the zone separation regime of combustion or in gasification regime coincides with  $y_{cs}$ , becomes smaller due to the diffusion dilution of vapor by combustion products that according to expression (6) leads to a small drop in  $T_s$ . As a result, the value  $(1 - y_{cs})$  decreases compared to gasification regime.

Three-stage regime is possible (Figure 3) with fairly "slow" kinetics of the second reaction in the gas phase (burning in a far zone). In this case, at the first stage in the gasification regime the gas flame of the first reaction is separated from the surface and from the flame of the second

reaction in a far zone. As  $q_r$  decreases, the flame in a far zone approaches the first flame and merges with it. Finally, the merged flame approaches the surface.

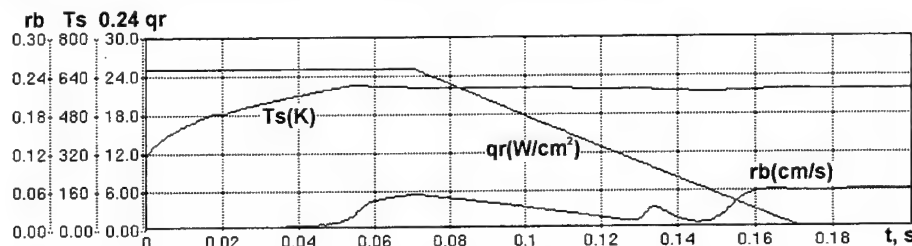


Figure 3. Three-stage ignition ( $q_0 = 105 \text{ W/cm}^2$ ,  $t_1 = 0.07 \text{ s}$ ,  $t_2 = 0.17 \text{ s}$ ).

It should be noted that the regime of flameless gasification under irradiation by Nd-YAG laser was experimentally observed in our laboratory with pressed samples of RDX burning at atmospheric pressure.

### Reactive force response to sinusoidal oscillations of radiant flux

Several research groups from different countries study the response of the reactive force (recoil)  $F(t)$  to oscillations of radiant flux  $q_r(t)$  supplied to the sample surface.<sup>12-14</sup> This approach was developed more than 20 years ago in the hope that the method will be found to obtain the pressure driven burning rate response by a simple recalculation from measured radiation driven response.<sup>15</sup> At present, these researches are not finalized. However, experimental data can be used for comparison with the results of calculation by a model in order to validate the model parameters. Obviously, it is profitable to examine the variants with the minimum number of matched parameters. One of the variants is determination of combustion response in gasification regime. In this case, it may be neglected heat feedback from the gas phase. Below the calculated results are presented for the modulus and the phase shift of recoil response function versus frequency in gasification regime for evaporated EM.

It is noteworthy that similar calculations have been performed for the model with a detailed description of gas-phase kinetics.<sup>8</sup> Rather good qualitative agreement was obtained with experimental results on oscillating combustion of RDX under  $CO_2$ -laser irradiation. However, principled feature of the approach with use of  $CO_2$ -laser is the absence of low rate gasification regime.

The most of the reference parameters for calculations were chosen on the basis of literature data for nitramines:  $\lambda_c = 2.31 \cdot 10^{-3} \text{ W/cmK}$ <sup>16</sup>,  $c_p = c_c = 1.26 \text{ J/gK}$ <sup>16</sup>;  $A_c = 10^{18.3}$ ,  $E_c = 198000 \text{ J/mol}$ <sup>17</sup>;  $Q_c = 2520 \text{ J/g}$ ,  $Q_m = 160 \text{ J/g}$ <sup>11</sup>,  $T_m = 477 \text{ K}$ <sup>11</sup>;  $L = 470 \text{ J/g}$ <sup>18</sup>,  $T_b = 613 \text{ K}$ <sup>18</sup>;  $A_1 = 10^{13.5}$ ,  $E_1 = 147400 \text{ J/mol}$ <sup>19</sup>;  $\lambda_g = 8.4 \cdot 10^{-4} \text{ W/cmK}$ <sup>16</sup>.

Several parameters were chosen from a condition of best correspondence to experimental data on burning rate for RDX under pressure lower than 0.5 MPa<sup>16</sup>:  $Q_1 = 420 \text{ J/g}$ ,  $A_2 = 10^{13.1}$ ,  $E_2 = 99750 \text{ J/mol}$ ,  $Q_2 = 2980 \text{ J/g}$ ,  $D = 0.15 \text{ cm}^2/\text{s}$ . Initial calculations were conducted for opaque material.

When ignited with relatively high constant radiant flux ( $q_r = 83.3 \text{ W/cm}^2$ ), the reference propellant reacts in gasification regime with weak heat feedback from the gas phase. Being subjected to oscillating irradiation with  $\Delta q_r/q_0 = 0.15$  and  $q_0 = 83.3 \text{ W/cm}^2$  the propellant exhibits unusual response from the point of view of typical transient combustion behavior for non-evaporated energetic materials with non-constant surface temperature (see Table 1).



**Table 1**  
Characteristics of Recoil Response Function in Gasification Regime ( $\alpha = \infty$ )

$f, \text{ Hz}$	2	5	12	50
$(\Delta F/F)(q_0/\Delta q_r)$	0.959	1.239	1.413	1.450
Phase shift	+18°	+14.4°	+7.2°	+3.6°

More correctly, the results of calculations correspond qualitatively to expected ones in case of forced pyrolysis of inert evaporated material. It follows from the analysis of solution of the linearized problem:

$$\begin{aligned}
 c\rho \frac{\partial T}{\partial t} &= cm(t) \frac{\partial T}{\partial z} + \lambda \frac{\partial^2 T}{\partial z^2} \\
 m(t) &= [q_r(t) + \lambda \frac{\partial T}{\partial z}(0, t)]/L \\
 T(0, t) &= T_s = \text{const}, \quad T(\infty, t) = T_0, \quad q_r(t) = q_0 + \Delta q \exp(i\omega t) \\
 R_q &\equiv \frac{\Delta m}{m} / \frac{\Delta q_r}{q_r} = \frac{(l+1)2\Omega}{2\Omega l - i(1 + \sqrt{1 + 4i\Omega})} \\
 \Omega &= \omega(\lambda/c\rho)/r_b^2, \quad l = \frac{L}{c(T_s - T_0)} \\
 R_{q(\omega \rightarrow 0)} &\approx i\Omega(l+1), \quad R_{q(\omega \rightarrow \infty)} \rightarrow 1 + 1/l
 \end{aligned}$$

It is seen from the expression for  $R_q$  that in the limit of zero frequency the modulus of  $R_q$  equals zero and phase shift equals  $\pi/2$ . With increasing frequency of oscillations the  $R_q$  modulus approaches monotonously  $(1 + 1/l)$  but phase shift diminishes up to zero.

Thus, the evaporated opaque propellant with relatively slow kinetics in gas phase and weak heat release in condensed phase exhibits trivial combustion response to oscillating irradiation. It was of interest to study the effect of transparency of the material on its combustion behavior.

The calculations revealed drastic change in qualitative behavior of combustion response to oscillating irradiation. In addition, it was revealed strong dependence of transient combustion behavior on transparency of the condensed phase. The reason for this is high sensitivity of combustion stability of evaporated EM on transparency of the material. Special estimates have shown that with given extinction coefficient there are lowest and upper limiting values of radiant flux allowing stable combustion.<sup>20</sup> Therefore, if oscillating combustion response is tested near the boundary of stable combustion it may lead to unsteady combustion of propellant under study. The numerical tests made with different extinction coefficients keeping the same parameters of oscillating radiant flux ( $q_0 = 83.3 \text{ W/cm}^2$  and  $\Delta q_r/q_0 = 0.15$ ) demonstrated this effect. Table 2 presents data on combustion response for propellant with  $\alpha = 2000 \text{ cm}^{-1}$ .

**Table 2**  
Characteristics of Recoil Response Function in Gasification Regime ( $\alpha = 2000 \text{ cm}^{-1}$ )

$f, \text{ Hz}$	2	5	12	20	50	200
$(\Delta F/F)(q_0/\Delta q_r)$	0.961	1.213	1.476	1.586	1.404	1.261
Phase shift, $r_{b, \max}$	+14.4°	+21.6°	+14.4°	$\sim 0^\circ$	-7.2°	-14.4°
Phase shift, $r_{b, \min}$	+14.4°	+10.8°	+7.7°	$\sim 0^\circ$	-7.2°	-10.8°

It is seen that in contrast to data for  $\alpha = \infty$  the recoil response function exhibits resonance-type behavior with maximum of response at frequency 20 Hz and with changing the sign of phase shift lag at the same frequency. Another important feature of transient recoil behavior for transparent propellant is that the phase shift is different for maximum and minimum of burning rate. This is

a consequence of nonlinear response of combustion to finite amplitude perturbations of external heat flux.

The value of the lowest radiant flux for stable combustion of propellant with  $\alpha = 2000 \text{ cm}^{-1}$  equals  $32 \text{ W/cm}^2$ . With  $\alpha = 1000 \text{ cm}^{-1}$  the lowest radiant flux equals  $70 \text{ W/cm}^2$  that is more close to the boundary of stable combustion if using the same  $q_0 = 83.3 \text{ W/cm}^2$ . The data on combustion response for propellant with  $\alpha = 1000 \text{ cm}^{-1}$  are presented in Table 3.

**Table 3**  
Characteristics of Recoil Response Function in Gasification Regime ( $\alpha = 1000 \text{ cm}^{-1}$ )

$f, \text{ Hz}$	2	5	10	12	30	50
$(\Delta F/F)(q_0/\Delta q_r)$	1.008	1.382	2.347	$\infty$	2.34	1.472
Phase shift, $r_{b, \max}$	+21.6°	+28.8°	+39.6°		-34°	-43.2°
Phase shift, $r_{b, \min}$	+21.6°	+18°	+10.8°		-18°	-32.4°

A distinctive feature of radiation driven oscillating combustion of propellant with  $\alpha = 1000 \text{ cm}^{-1}$  is pronounced unstable behavior at resonance frequency. In the vicinity of this frequency the oscillations of burning rate, started with relatively small amplitude, increase their amplitude with time that finally leads to failure of computations. Diminishing spatial and time steps does not improve situation because this behavior is caused by the loss of combustion stability at high amplitude of oscillations.

To obtain more detailed information about oscillating combustion behavior in the vicinity of resonance frequency one may decrease the magnitude of perturbations of radiant flux. Calculations made with  $\Delta q_r/q_0 = 0.05$  (instead of 0.15) gave at  $f = 12 \text{ Hz}$  finite value of recoil response,  $(\Delta F/F)(q_0/\Delta q_r) = 2.18$  and appropriate values of phase shift: Phase shift,  $r_{b, \max} = +25^\circ$ ; Phase shift,  $r_{b, \min} = +14.4^\circ$ .

### The limitations of the model.

Describing the model we have underlined its weak point. The assumption on effective gas removal from reaction zone in the liquid phase can be fulfilled in a very restricted number of cases. The particular mechanisms of gas removal and its possible influence on heat-and-mass transfer in the reaction zone should be discussed and elaborated.

Several mechanisms of gas removal may be considered: 1) by bubbles motion due to the Marangoni effect or due to their diffusion to the surface; 2) by convective diffusion of dissolved gas caused by the motion of bubbles; 3) by gas jets. Obviously, when the formation of bubbles or gas jets is considered it becomes necessary to analyze the subsurface layer structure and to derive the dependence of subsurface layer density on problem parameters.

It was experimentally established that for several EM there is a range of parameters where the rate controlling zone is in the liquid surface layer (e.g., this holds for hexogen and octogen at  $p > 5 \text{ MPa}$ ).<sup>16</sup> In this case, the discrepancy between the model and a physical pattern described by this model arises.

The heat balance is fulfilled on the liquid-gas interface

$$q_g = Lmy_{cs} + q_c \quad (9)$$

Here  $q_g$ ,  $q_c$  are the heat fluxes from gas to surface and from surface into the bulk of liquid, respectively;  $Lmy_{cs}$  is the heat loss due to evaporation. It is reported that with  $P = 9 \text{ MPa}$  for RDX heat feedback from gas  $q_g/m \approx 113 \text{ J/g}$ , while evaporation heat  $L \approx 470 \text{ J/g}$ .<sup>16</sup> As follows

from Eq.(9), even at  $y_{cs} = 0.3$  (liquid phase depletion by 70%) the  $q_c$  value must be negative, i.e. the heat should be supplied to the surface from the bulk of liquid. According to the Fourier law this means that the temperature maximum must occur beneath the burning surface.

The attempts to numerically simulate the combustion regimes with evaporation on the surface and with the rate controlling zone in liquid layer have confirmed the existence of temperature maximum in the bulk of material but only in nonsteady-state regime which quenched after series of flashes. The analytical study of the model by the method of small perturbations has verified the instability of these combustion regimes.<sup>21</sup>

### Concluding remarks

As it was stated in Introduction the goal of this study was to create rather simple but informative model for transient combustion of evaporated energetic materials. At present the model has been formulated and some numerical tests have been fulfilled. Validation and step-by-step improvement of the model can be achieved by comparison with experimental data.

However, such comparison should be accompanied with thorough analysis of the experimental data. In fact, the available experimental data are obtained with EM of different sources having different purity and density that leads to significant scatter in experimental results. When changing floating parameters in the model (first of all, global kinetics parameters), it is relatively easy to fit published in the literature data on burning rate dependencies on pressure and initial temperature. However, it does not guarantee the ability of model to predict adequately transient combustion behavior and adequacy of predictions for substances with the same title.

Unfortunately, there is a lack of detailed and reliable experimental data on transient radiation driven combustion of evaporated EM that prevents direct comparison between theoretical and experimental results. Therefore the main attention in this study was paid to understanding the effects of kinetic parameters and external factors on qualitative combustion behavior of evaporated EM.

It has been shown that depending on kinetic parameters and temporal behavior of a radiant flux an ignition of evaporated EM with two global exothermic gas phase reactions may occur in one-, two-, and three-stages. Obviously, the number of stages depends on the number of global reactions under consideration. It means that the experimental data, if available, may give reliable background for choosing the global kinetic mechanism for particular EM in specified conditions of combustion.

Another finding of this study is that the radiation driven combustion of evaporated EM may occur in gasification regime, i.e. with negligible heat feedback from the gas phase. The reason for such behavior is rather simple: with sufficiently high velocity of gases issued from the surface characteristic reaction time in gas products becomes larger hydrodynamic time that prevents development of exothermic reactions in close vicinity of the regressing surface. When realized in experiments, the steady-state radiation driven gasification regime may serve a source of important information on global kinetics of reaction in the condensed phase.

Valuable information can be obtained in experiments with measurement of combustion response to time-dependent external radiant flux. Theoretical study of such response should be extended to the case of step-wise time history of radiant flux and be accompanied with analytical investigations in order to generalize theoretical predictions. At the same time, there is an urgent task of developing comprehensive experimental approaches and techniques to obtain reliable quantitative data on transient combustion response of EM under study.

**Acknowledgement.** The authors thank the European Research Office of the US Army for partial support of this study.

## REFERENCES

1. Belyaev, A.F., On combustion of explosives, *J. Phys. Chem.* (in Russian), 12, 93-96, 1938.
2. Belyaev, A.F., On combustion of nitroglycol, *J. Phys. Chem.* (in Russian), 14, 1009-1014, 1940.
3. Manelis G.B., Strunin V.A., The mechanism of ammonium perchlorate burning, *Combustion and Flame*, 17, 69-77, 1971.
4. Novozhilov, B.V., The effect of gas phase thermal inertia on combustion stability of evaporated condensed systems, *Chemical Physics* (in Russian), 7, No.3, 388-396, 1988.
5. Novozhilov, B.V., Combustion of evaporating condensed systems at harmonically varied pressure, *Chemical Physics* (in Russian), 8, No.1, 102-111, 1989.
6. Melius, C.F., Thermochemical modeling: I & II, *Chemistry and Physics of Energetic Materials*, Ed. by S.N. Bulusu, Kluwer Academic Publishers, Netherland, 21-78, 1990.
7. Liau, Y.-C., Yang, V., Analysis of RDX monopropellant combustion with two-phase subsurface reactions, *JPP*, 11, No.4, 729-739, 1995.
8. Erikson, B., Beckstead, M.W., A numerical model of monopropellant deflagration under unsteady conditions, *AIAA paper*, 96-0652, 1996.
9. Davidson, J., Beckstead, M.W., Improvements to RDX combustion modeling, *AIAA paper* 96-0885, 1996.
10. Ben-Reuven, M., Caveny, L.H., Nitramine flame chemistry and deflagration interpreted in terms of a flame model, *AIAA Journal*, 19, 1276-1285, 1981.
11. Hall, P.G., Thermal decomposition and phase transitions in solid nitramines, *Trans. Farad. Soc.*, 67, No.578, Part 2, 556-562, 1978.
12. Mikheev, V.F., Zarko V.E. et al., Measurement of burning rates in transient combustion processes under the influence of external radiation, *Experimental Diagnostics in Combustion of Solids*, edited by Thomas L. Boggs and Ben T. Zinn, V.63, Progress in Astronautics and Aeronautics, AIAA, New York, 173-187, 1978.
13. Finlinson, J.C., Parr, T. and Hanson-Parr, D., Laser recoil, plume emission, and flame height combustion response of HMX and RDX at atmospheric pressure, *Twenty-Fifth Symposium (International) on Combustion*, Irvine, CA, 1994.
14. Son, S.F. and Brewster, M.Q., Unsteady combustion of homogeneous energetic solids using the laser-recoil method, *Twenty-Fifth Symposium (International) on Combustion*, Irvine, CA, 1994.
15. Muhlfeith, C.M., Baer, A.D. and Ryan, N.W., Propellant combustion instability as measured by combustion recoil, *AIAA Journal*, 10, No.10, 1280-1285, 1972.
16. Zenin, A.A., HMX and RDX: combustion mechanism and influence on modern double-base propellant combustion, *JPP*, 11, No.4, 752-758, 1995.
17. Rogers, R.N. and Daub, G.W., Scanning calorimetric determination of vaporphase kinetic data, *Anal. Chem.*, 45, 596-600, 1973.
18. Scheludjak, Yu.E., Kaschporov L.Ya, et al., *Thermophysical Properties of Combustible System Components*, NPO "InformTEI", (in Russian), 1992.
19. Burov, Yu.M., and Nazin, G.M., Effect of structure on decay rate of secondary nitroamines in gas phase, *Kinetics and Catalysis*, (in Russian), 23, No.1, 12-17, 1982.
20. Gusachenko, L.K., Zarko, V.E. and Rychkov, A.D., Modeling of gasification under irradiation, *INTAS Workshop*, Milan, July, 1996.
21. Gusachenko, L.K., Zarko, V.E. and Rychkov, A.D., Instability on combustion model with vaporization on surface and overheat in condensed phase, *Combustion, Explosion, and Shock Waves*, 33, No.1, 1997.

## APPENDIX

Let choose movable coordinate system  $(x, t)$  attached to the burning surface to derive the system of equations describing heat propagation in the condensed phase:

a) solid state  $(x_m(t) \leq x \leq x_R)$

$$C_c \rho_c \left( \frac{\partial T_c}{\partial t} - r_b \frac{\partial T_c}{\partial x} \right) = \lambda_c \frac{\partial^2 T_c}{\partial x^2} + q_r(t) \alpha \exp(-\alpha x) \quad \text{I}$$

$$T_c(x, 0) = T_0, \quad T_c(x_m, t) = T_m, \quad \text{at } x = x_R \quad \partial T_c / \partial x = 0$$

b) liquid state  $(0 \leq x \leq x_m)$

$$C_c \rho_c \left( \frac{\partial T_c}{\partial t} - r_b \frac{\partial T_c}{\partial x} \right) = \lambda_c \frac{\partial^2 T_c}{\partial x^2} + \Phi_c + q_r(t) \alpha \exp(-\alpha x) \quad \text{II}$$

$$\rho_c \left( \frac{\partial y_c}{\partial t} - r_b \frac{\partial y_c}{\partial x} \right) = -\omega_c \quad \text{III}$$

$$\Phi_c = Q_c \omega_c, \quad \omega_c = A_c \rho_c y_c \exp(-E_c / RT_c) \quad \text{IV}$$

$$y_c(x_m, t) = 1, \quad T_c(x, 0) = T_0$$

$$T_c(x_m, t) = T_m, \quad -\lambda_c \frac{\partial T_c}{\partial x} \Big|_{x=x_m-0} = -\lambda_c \frac{\partial T_c}{\partial x} \Big|_{x=x_m+0} + Q_m V_m \rho_c$$

Assume that the condensed phase reaction produces combustible gas and there are 3 components in the gas phase: vapor, combustible gas, and final combustion product. The vapor decomposes in the reaction of a 1st order and generates combustible gas the chemical transformation of which follows the reaction of a 2nd order yielding final combustion product. The temperature of the components is uniform at the given point of space.

The system of equations for gas phase is as follows  $(x_L \leq x \leq 0)$ :

$$C_p \rho \left[ \frac{\partial T}{\partial t} + (V - r_b - \sum_{i=1}^3 \frac{C_{pi}}{C_p} D_i \frac{\partial y_i}{\partial x}) \frac{\partial T}{\partial x} \right] = \frac{\partial}{\partial x} \left( \lambda \frac{\partial T}{\partial x} \right) + \Phi_1 + \Phi_2 \quad \text{V}$$

$$\rho \left( \frac{\partial y_1}{\partial t} + (V - r_b) \frac{\partial y_1}{\partial x} \right) = \frac{\partial}{\partial x} \left( \rho D_1 \frac{\partial y_1}{\partial x} \right) - \omega_1 \quad \text{VI}$$

$$\rho \left( \frac{\partial y_2}{\partial t} + (V - r_b) \frac{\partial y_2}{\partial x} \right) = \frac{\partial}{\partial x} \left( \rho D_2 \frac{\partial y_2}{\partial x} \right) - \omega_2 + \omega_1 \quad \text{VII}$$

$$\frac{\partial \rho}{\partial t} - r_b \frac{\partial \rho}{\partial x} + \frac{\partial (\rho V)}{\partial x} = 0 \quad \text{VIII}$$

$$p = R \rho T / M \quad \text{IX}$$

$$\frac{1}{M} = \frac{y_1}{M_1} + \frac{y_2}{M_2} + \frac{y_3}{M_3}$$

$$\Phi_1 = Q_1 \omega_1, \quad \Phi_2 = Q_2 \omega_2$$

$$\omega_1 = A_1 \rho y_1 \exp(-E_1 / RT), \quad \omega_2 = \frac{A_2}{M_2} (\rho y_2)^2 \exp(-E_2 / RT)$$

$$T(x, 0) = T_0, \quad y_1(x, 0) = y_2(x, 0) = 0$$

$$\text{at } x = x_L \quad \partial T / \partial x = \partial y_1 / \partial x = \partial y_2 / \partial x = 0$$

Boundary conditions at  $x = 0$  are as follows:

$$\begin{aligned}\lambda \frac{\partial T}{\partial x} \Big|_{x=-0} &= \lambda_c \frac{\partial T_c}{\partial x} \Big|_{x=+0} + q_r - y_{cs} \rho_c r_b L \\ -\rho(V - r_b)y_{1s} + D_1 \rho \frac{\partial y_1}{\partial x} &= \rho_c r_b y_{cs} \\ -\rho(V - r_b)y_{2s} + D_2 \rho \frac{\partial y_2}{\partial x} &= \rho_c r_b (1 - y_{cs}) \\ \rho(V - r_b) &= -\rho_c r_b, \quad y_{1s} = \frac{M_1}{M} \exp \left[ -\frac{LM_1}{R} \left( \frac{1}{T_s} - \frac{1}{T_b} \right) \right]\end{aligned}$$

Mass fraction of the combustion product and its effective diffusion coefficient are determined on the basis of mass conservation equation and condition of zero sum of individual diffusion fluxes:

$$y_1 + y_2 + y_3 = 1, \quad D_1 \frac{\partial y_1}{\partial x} + D_2 \frac{\partial y_2}{\partial x} + D_3 \frac{\partial y_3}{\partial x} = 0$$

In order to solve numerically the problem I-IX with closing initial and boundary conditions a spatial domain  $x_L < x < x_R$  should be chosen on the basis of physical considerations or numerical experiment.

### Nomenclature

$t$  – time [s]  
 $x$  – spatial coordinate [cm]  
 $r_b$  – burning rate [cm/s],  
 $V$  – gas velocity [cm/s],  
 $T$  – temperature [K],  
 $\rho$  – density [g/cm<sup>3</sup>],  
 $p$  – pressure [MPa],  
 $y_i$  – mass fraction of species  $i$ ,  
 $C_c$  – specific heat of condensed phase [J/(g·K)],  
 $C_{pi}$  – constant-pressure heat capacity of species  $i$  [J/(g·K)],  
 $\lambda$  – thermal conductivity [W/(cm·K)],  
 $Q$  – heat release per unit mass [J/g],  
 $M_i$  – molecular weight of species  $i$  [g/mol],  
 $R$  – universal gas constant [J/(mol·K)],  
 $L$  – latent heat of evaporation [J/g],  
 $A$  – pre-exponential factor of rate constant ( $A_1 \sim [1/s]$ ,  $A_2 \sim [cm^3/(mol \cdot s)]$ ),  
 $E$  – energy of activation [J/mol],  
 $D$  – diffusion coefficient [cm<sup>2</sup>/s],  
 $q$  – external heat flux [W/cm<sup>2</sup>],  
 $f$  – frequency of oscillations [1/s],  
 $\alpha$  – extinction coefficient in the Beer law [1/cm].

### Subscripts

$c$  – parameters of the condensed phase, 1, 2, 3 – species in a gas phase,  $s$  – propellant surface,  $m$  – the melting point. 0 corresponds to the initial condition. Variables without index correspond to the bulk of gas.

## ANOMALOUS GROUP COMBUSTION THEORY - TRANSIENT DUALITY IN GROUP COMBUSTION -

H. H. Chiu, C. L. Lin and T. S. Li

Aerospace Science and Technology Research Center; Institute of Aeronautics and Astronautics  
National Cheng Kung University  
Tainan, Taiwan

**ABSTRACT:** Polydisperse octane fuel droplet clusters preheating, igniting, and combusting in a hot environment are simulated to the probability of anomalous group combustion in premixed clusters in the broad ranges of initial group combustion number and cluster stoichiometry. Numerical analysis employs updated droplet laws accounting for the effects of relative motion and drop-drop interaction. The results reveal that the establishment of a single flame generally suffers flame bifurcation by which the inner flame propagates into the cluster interior and the other branch propagates into the exterior of the cluster. The appearance of external flame in low- $G$  clusters and the inward propagation of the premixed flame into the cluster for intermediate to high- $G$  clusters are perceived to be a possible mechanism of the anomaly observed in the recent experimental observation. Numerical analysis reveals pronounced anomalous group combustion occurring in a broad range of initial group combustion numbers when the cluster initial equivalence ratio is 0.5 to 50 for a cluster with a 1cm radius.

### 1. INTRODUCTION

Utilization of liquid fuel in broad areas of human activities has brought world wide attention to questions about the future energy reserve, environmental pollution, and global economic issues related to petroleum resources. These concerns have promoted extensive research and development programs devoted to an efficient and clean utilization of liquid fuel through better understanding of the nature of combustion which would then facilitate the design and development of improved spray combustion systems.

One basic development in liquid fuel combustion is the concept of group combustion, which classifies the burning of practical sprays into sheath combustion, external, and internal group modes, and dropwise combustion, according to the extent of collective interaction among the droplets and their environment (Chiu et al. [1-3], and Kuo [4]). Each combustion mode exhibits different burning characteristics and performance. Many aspects of the group combustion of fuel sprays and fuel droplet clouds have been reported over the past decades, see for example [5-9].

In a series of experimental investigations on turbulent premixed sprays, Mizutani and coworkers compared the spectra of  $OH$  and  $CH$  light emissions with those of Mie scatterings of droplets from clusters in a premixed turbulent spray [10,11]. Their experimental results, which provided evidence of excitation and transition of the group combustion modes, along with correlations relating the excited group combustion modes to the corresponding group combustion numbers, are found to be in good qualitative agreement with the theoretical predictions of Chiu et al. [1-3]. However, Chiu and Lin observed that there are distinct discrepancies between the results of the experimental measurement and the analytical model [12]. For example, the experimental

data [11], reveals that although 90% of the clusters with high group combustion numbers burn as external group flames, as predicted by theoretical analysis, yet nearly 10% of these high clusters burn as an internal group flames. Likewise, the experimental results also reveal that the majority of low-group combustion number clusters burn as internal group flames, as analytically predicted, but a small fraction of clusters combust as external group flames. Chiu and Lin demonstrated that there is anomalous behavior in the transient combustion of a premixed cluster [12], in which captured air in the cluster and a gasified vapor initiate in the interior and exterior of the cluster simultaneously upon the splitting of an initial flame. These dual bifurcated flames in the exterior and interior of the cluster are termed "anomalous group combustion," which is predicted to occur in practical premixed sprays [12]. Anomalous group combustion is perceived to be a basic process preceding quasi-steady state group combustion of droplet clusters. However, this study does not examine the probability of the appearance of anomalous group combustion.

The objectives of this paper are (1) to examine the probability of the occurrence of anomalous combustion behavior of premixed clusters in broad ranges of initial group combustion numbers and cluster mixture ratios and (2) to examine the transition from anomalous group combustion to normal group combustion. Our numerical simulation of the transient processes involves ignition, flame spreading, splitting of a combustion zone into a dual flame configuration, and the ultimate transition to quasi-steady group combustion. This is followed by an extensive numerical simulation to facilitate the identification of various anomalous group combustion modes and the probability of the excitation of anomalous modes in a broad range of group combustion numbers and initial fuel/air ratios of clusters.

This paper concludes with a comment on the need for future experimental and analytical research on the validation of the anomalous behavior in many cluster systems in practical turbulent sprays.

## 2. THEORETICAL DESCRIPTIONS

The present analysis adopts a two-phase flow model for the description of the transient combustion processes of a spherical droplet cluster, thus preserving point symmetry exposed in a hot, stationary environment. The governing equations for the gas and liquid phase consist of time-dependent conservation laws supplemented by major physico-chemical processes describing interphase exchange behavior between gas and dispersed phases. In particular, major criteria required for the identification of droplet states, and updated laws of droplets accounting for the effects of drop-drop interaction and convective motion are adopted. For details of the mathematical description, one presented in [12] and will not be reproduced here.

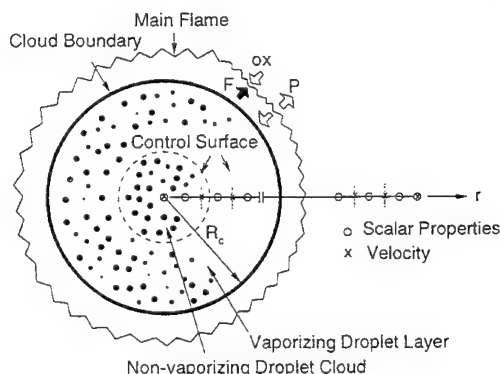


Figure 1. Schematic diagram and grid system for both gas and liquid phase of a droplet cloud in a hot environment



### 3. NUMERICAL METHOD

A numerical method based on control volume formalism is used in this work. The first step is the formulation of the discretized algebraic equations. Then the power-law scheme in conjunction with a staggered grid system is employed to avoid zigzag pressure field and gas velocity distributions. Subsequently, the SIMPLER algorithm [13], incorporated with the TDMA (TriDiagonal-Matrix Algorithm) method, is used to solve the algebraic equations. The grid system inside and outside the droplet cluster is shown in Fig.1. Time-step size of  $10^{-3} \text{ sec}$ , which is smaller than the smallest characteristic time involved, is used. The grid size is  $\frac{R_c}{100}$  inside the initial droplet cluster, and the grid size outside the initial droplet cluster is calculated according to  $r(i) = r(i-1) + \frac{R_c}{100} \times (i-1)$ . All the numerical results obtained in the analysis are checked for their dependence on grid size, time-step, and convergence criteria. Furthermore, the temperature dependence of the heat conductivity, the viscosity, and the diffusion coefficient used by Reid [14], are adopted in this analysis to treat the effects of variable properties.

Droplets in a cluster which is initially at room temperature,  $T_{\ell 0}$ , are suddenly exposed to an elevated temperature,  $T_{\infty}$ , at  $t = 0^+$ . The temperature and oxidizer concentration at  $r \rightarrow \infty$  are  $T_{\infty}$  and  $Y_{ox, \infty}$ , respectively. Since the flow structure preserves spherical symmetry, all the derivatives of flow variables vanish at  $r = 0$ .

### 4. EVOLUTIONARY ANOMALOUS GROUP COMBUSTION IN PREMIXED CLUSTERS

Numerical analysis is conducted to examine the transient dual combustion characteristics of three selected clusters with the same initial group combustion number but different cluster equivalence ratios. These cluster equivalence ratios consist of polydisperse octane droplets with a 2 cm diameter, Table 1 shows the operating conditions for three clusters.

TABLE 1  
Summary of Premixed Clusters Selected for Parametric Study

Case	$D_{30,0}(\mu m)$	$n_{k,0}(cm^{-3})$	$T_{\infty}(K)$	$G_0$	$\phi_{cl,0}$	$m_f \times 10^4(g)$
A	60	476	1200	50	1.8	1.5
B	100	286	1200	50	5.2	4.3
C	200	143	1200	50	10.5	8.6

Group combustion number  $G(t)$  is defined by

$$G(t) = \frac{\int_{V_c} \dot{m}_{\ell} dV}{\int_{\Sigma_c} \rho_g D_{ox} \nabla Y_{ox} d\Sigma} \quad (4.1)$$

and the cluster equivalence ratio is given by

$$\phi_{cl,0} = \frac{m_f}{m_a Y_{ox,\infty}} \left( \frac{M_{ox} \nu_{ox}}{M_f \nu_f} \right) \quad (4.2)$$

in which  $m_a$  is the mass of captured air, and  $m_f$  is the total mass of liquid fuel inside the cluster at the initial state.

The detailed evolutionary behavior of clusters with different cluster equivalence ratios is presented in the following subsections.

#### Cluster Gasification, Consumption, and Ignition

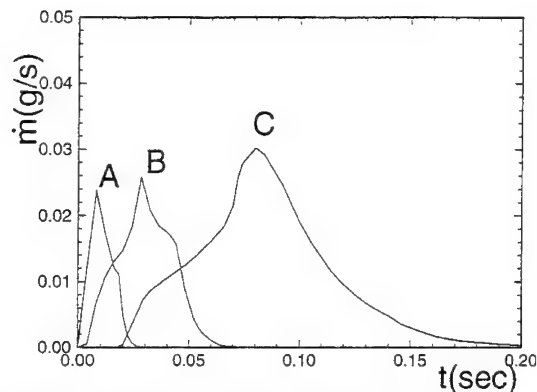


Figure 2 Total evaporation rate ( $\dot{m}$ ) vs. time ( $t$ ) for cases A, B, C.

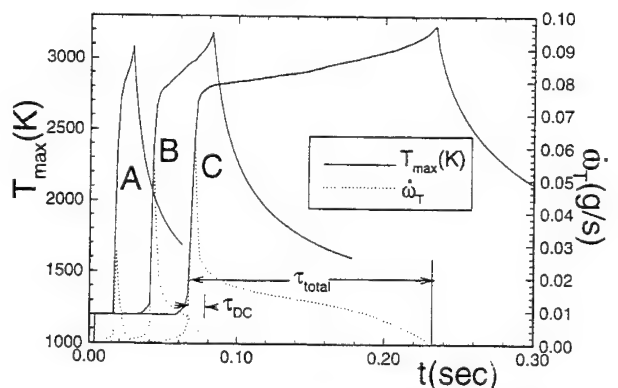


Figure 3. Maximum gas temperature ( $T_{\max}$ ) and fuel consumption rate ( $\dot{\omega}_T$ ) vs. time ( $t$ ) for cases A, B, C.

The time history of the gasification rates of three clusters, and the variations in the maximum temperature achieved in the field, and the fuel consumption rate are presented in Fig.2 and 3, respectively. Gasification starts earlier for the low- $\phi_{cl,0}$  cluster than it does in the fuel-rich clusters because of the smaller droplet size and a shorter preheating time in the former. The ignition of a cluster is marked by sharp rises in both fuel consumption rate and maximum gas temperature, as shown in Fig.3. One finds that the ignition delay and fuel consumption increase with the increase of  $\phi_{cl,0}$ , which is due to large droplets and a long preheating time. This makes the gasification slower in the initial state, but also make it increase after ignition. Figure 3 shows the time periods of dual and quasi-steady combustion in cluster C according to the variation of the fuel consumption rate. Dual combustion is marked by a brief period of a distinctly high fuel consumption rate immediately after ignition. The ratio of the time period in dual and total combustion is defined as  $P_{DC}$ , i.e.  $P_{DC} = \tau_{DC}/\tau_{total}$ , which has an important effect on the probability of anomalous group combustion, as is discussed later.

#### Low- $\phi_{cl,0}$ Cluster

The transient behavior of low- $\phi_{cl,0}$  cluster A is summarized below.

**Preheating and vaporization** Figure 4(a) shows that at  $t = 0.016\text{sec}$ , the zone of preheating and vaporization spreads over the cluster, and the  $\dot{\omega}_T$  distribution suggests that a weak reaction occurs at this time.

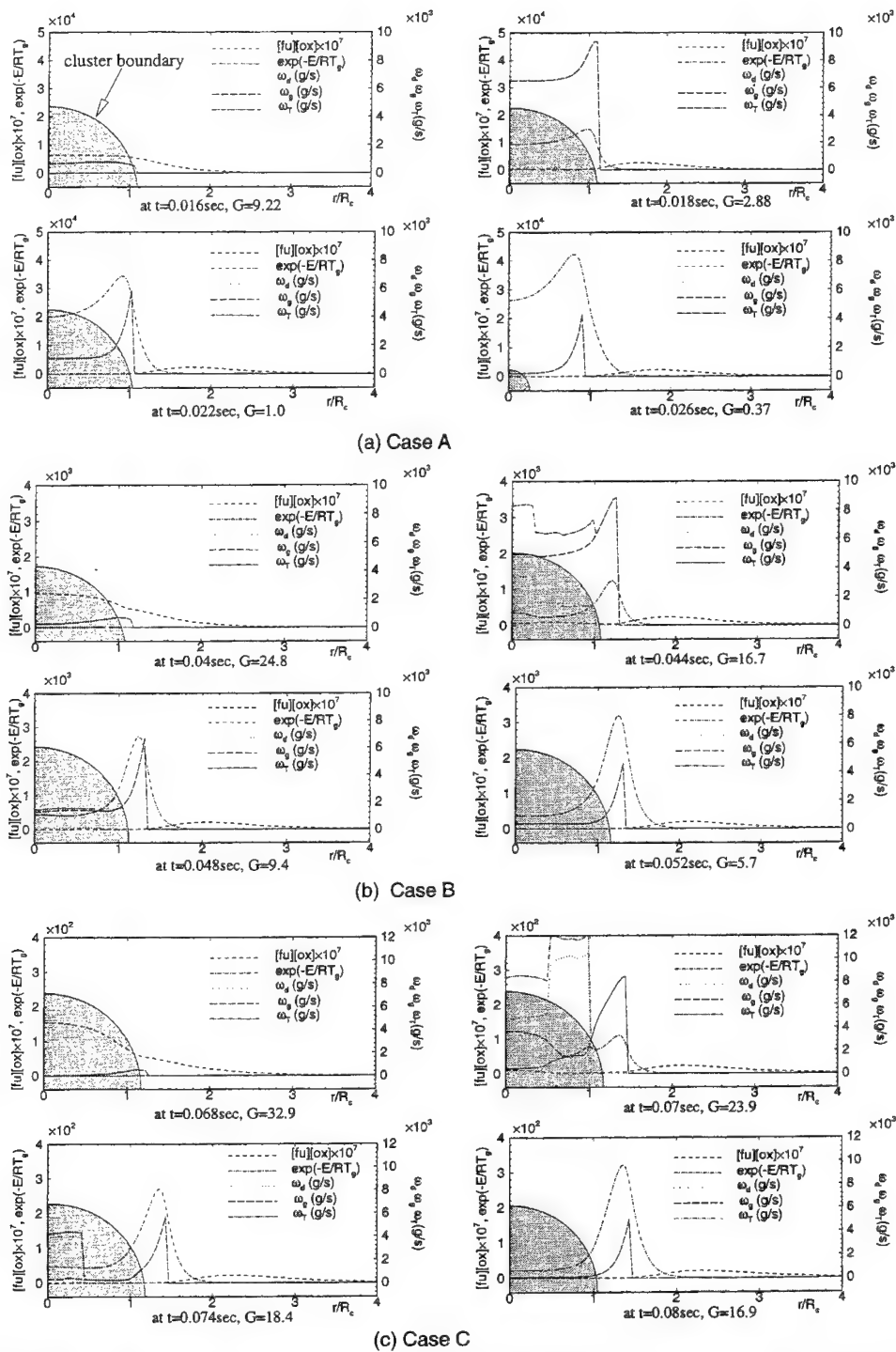


Fig.4 Fuel consumption rate( $\omega_d, \omega_g, \omega_t = \omega_d + \omega_g$ ) distributions and the contribution of concentration( $[fu][ox]$ ), gas temperature( $\exp(-E/RT_p)$ ) on  $\omega_g$  during the evolution processes of a droplet cluster in a hot environment. Cluster boundary indicated.

Ignition and flame spreading Figure 4(a) reveals that at  $t = 0.016\text{sec}$ , the flame is initiated inside the cluster. Subsequently, the flame front also propagates outwardly to burn as a diffusion flame, which also burns inside the cluster.

Normal external group combustion The concentration of captured air decreases to a low level at  $t = 0.022\text{sec}$ , result in the reduction in the internal combustion intensity whereas an external group combustion becomes the primary mechanism. Note that the average droplet number density at this time is about 15 *drop/cc*.

External group combustion At  $t = 0.026\text{sec}$ , the internal group flame extinguishes, whereas the external group flame continues to burn until all the droplets are consumed.

### High- $\phi_{cl,0}$ Clusters

The transient behavior and the combustion structure of moderately high- $\phi_{cl,0}$  cluster *B* and high- $\phi_{cl,0}$  cluster *C* are both affected by droplet state modulation due to collective interaction. Their combustion behaviors and structures are compared below.

Preheating and vaporization Time histories of the evaporation rates of clusters *B* and *C* show that the peak gasification of cluster *B* is  $0.028\text{g/s}$ , whereas the corresponding values of cluster *C* are  $0.032\text{g/s}$ , as shown in Fig.2. Note that cluster *C* is the last to begin gasification among these selected clusters, because larger droplets in cluster *C* have a longer preheating time.

Ignition and flame spreading Non-dilute clusters *B* and *C* are ignited in the exterior space of the cluster. The ignition delay for cluster *B* and *C* are  $0.044\text{sec}$  and  $0.068\text{sec}$ , respectively, see Figs.2, 3. Figure 4(b) for cluster *B* shows that at  $t = 0.04\text{sec}$  the reaction zone spreads outwardly to  $r/R_c = 1.2$  and inwardly to the cluster core. The reaction zone does not penetrate into cluster *C*, Fig.4(c)( $t=0.066\text{sec}$ ), because the fuel rich cluster acts as a strong heat sink and a source of the formation of fuel rich mixture.

Flame splitting and dual combustion Observation of cluster *B*, Fig.4(b), at  $t = 0.044\text{sec}$ , reveals that the outwardly propagating flame front and the inwardly propagating flame zone are sufficiently separated so that the original thick flame progressively splits into two flames from the distribution of  $\exp(-E/RT_g)$  and  $\dot{\omega}_T$ . The outer flame is a group flame primarily supported by the air transported from the environment, as is shown by the oxidizer concentration gradient present near the flame front. In contrast, the inner flame is a premixed type combustion involving both gas and droplet phase combustion. Although  $G = 16.7$  at this moment, it is clear that combustion still takes place inside the cluster. The dual combustion, i.e. interior and exterior combustion in this cluster, is also a prospective source of anomalous group combustion for the moderately dense clusters observed in experimental measurements.

Cluster *C*, Fig.4(c), at  $t = 0.068\text{sec}$  has an outer diffusion controlled flame and an inner premixed flame. Note that the drop-phase reaction rate for cluster *C* is larger than that of cluster *B*, because of its larger droplets.

Depletion of captured air and normal external group combustion For cluster *B*, Fig.4(b), the depletion of captured air which occurs slightly after  $t = 0.048\text{sec}$  marks the termination of the premixed interior flame. The outer flame, however, continues to burn as a normal external group flame. The above phenomena happens in cluster *C* at  $t = 0.08\text{sec}$ . The flame outside the cluster, nevertheless, continues to burn as a normal external group flame at  $r/R_c \sim 1.4$  for cluster *B* and at  $r/R_c \sim 1.5$  for cluster *C*.

### Probability of Anomalous Group Combustion ( $P_{AG}$ )

According to the previous study, the probability of exhibiting anomalous group combustion during cluster combustion [12],  $P_{AG}$ , is defined in terms of the ratio of the characteristic time of exterior and interior combustion to that of total combustion time. Figure 5 shows the inner and outer flame location and cluster boundary vs. time for a special case. The result reveals that the outer flame is always outside the cluster.  $\tau_{io}$  is defined as the time interval when  $R_{fo} > R_c$  and  $R_{fi} < R_c$ , i.e. the time where anomalous group combustion may occur;  $\tau_{DC}$

is defined as the time interval when both outer and inner flames exist; and  $\tau_{total}$  is the total combustion time. By the above definitions,

$$P_{AG} = \epsilon P_{DC}, \quad \text{where} \quad \epsilon = \tau_{io}/\tau_{DC} \quad (4.3)$$

The definition of  $P_{DC}$  is shown in Fig.3. Further calculation of  $P_{AG}$  vs.  $\phi_{cl,0}$  for different group combustion numbers according to Eq.(4.3) is shown in Fig.6, which reveals that  $P_{AG}$  is relatively low in the low- $\phi_{cl,0}$  and high- $\phi_{cl,0}$  regions, due to the short  $\tau_{DC}$  and long  $\tau_{total}$ , respectively. It is of particular interest to note that rich clusters,  $\phi_{cl,0} > 10$ , with higher group combustion numbers appear to have a higher probability of anomalous group combustion. However,  $1.2 < \phi_{cl,0} < 2.0$  clusters with initial group combustion numbers lower than 50 appear to have a higher probability of anomalous group combustion than clusters with high group combustion numbers. This latter trend is attributed to the increase of total combustion time for high- $G$  clusters.

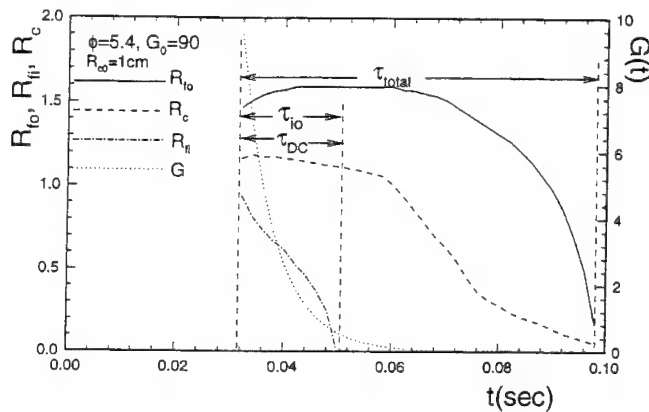


Figure 5. Outer flame location( $R_{oi}$ ) and inner flame location( $R_{ii}$ ) vs. time  $\tau_{io}$  is the time interval when  $R_{oi} > R_c$  and  $R_{ii} < R_c$ ,  $\tau_{DC}$  is the time interval when outer and inner flame both exists,  $\tau_{total}$  is the total combustion time for the cluster

$$\text{Define } \epsilon = \tau_{io}/\tau_{DC} \quad P_{AG} = \frac{\tau_{io}}{\tau_{DC}} \frac{\tau_{DC}}{\tau_{total}} = \epsilon P_{DC}$$

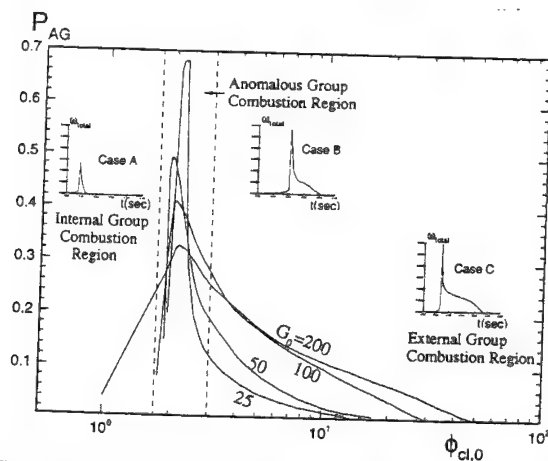


Figure 6. Probability of anomalous group combustion ( $P_{AG}$ ) vs.  $\phi_{cl,0}$  for different initial group combustion numbers( $G_0$ ), and the fuel consumption rate( $\omega_{Total}$ ) vs. time for different range of  $\phi_{cl,0}$  indicated.

## 5. CONCLUSIONS

This study indicates that the transient dual combustion process involving simultaneous excitation of dual combustion modes in the exterior and interior of clusters is a principal source of anomalous group combustion in the clusters formed in a premixed spray, as is experimentally observed. The study also identifies two types of combustion which occur in dual combustion: (1) a premix dominated combustion initiated by the combustion of air captured with the fuel vapor produced during the pre-ignition period; and (2) a primarily diffusion-controlled flame that consumes the air transported by diffusion, and the fuel vapor produced by sustained gasification.

It is further established that anomalous group combustion occurs in clusters whose initial group combustion numbers are within a range of critical values determined by the cluster configuration, stoichiometry, and temperature, and the probability of anomalous group combustion is defined in consistence with the physical phenomena, i.e. very dense clusters with a cluster equivalence ratio  $\gg 1$  do not exhibit anomalous combustion, because the sheath phenomenon which limits vaporization to droplets near the edge of the cluster precludes cluster interior combustion. On the other hand, very dilute clusters burn out without external group combustion because the outer flame does not exist in the lifetime of cluster combustion. Additionally, one finds that the characteristic time for quasi-steady (Q.S.) group combustion in moderately dilute clusters is relatively short, because the transition period occupies a large fraction of the total combustion time. The transition period of a dense cluster has a relatively short transition period, compared with the life-time of the cluster, hence it has a longer period of Q.S. group combustion to dilute clusters.

Research on the transitional evolution of convecting clusters promises to be complicated by many factors, such as the appearance of envelope flame, wake flame, side flame, and multiple state phenomena. Understanding and predicting transient phenomena remains to be a challenging area for further research on the group combustion of many-droplet systems.

## NOMENCLATURE

$D$	diffusivity
$E$	activation energy
$G$	group combustion number
$i$	the grid number extended from the initial cluster surface
$M$	molecular weight
$\dot{m}_l$	evaporation rate of a droplet
$n$	droplet number density
$P_{AG}$	probability of anomalous group combustion
$R$	ideal gas constant
$R_c$	radius of droplet cluster
$R_{fo}$	flame initiated outside the cluster
$R_{fi}$	flame initiated inside the cluster
$r$	radial coordinate
$T$	temperature
$t$	time
$Y$	mass fraction
$\rho$	density
$\phi_{cl}$	equivalence ratio
$\nu$	stoichiometric reactant coefficient
$\tau_{DC}$	dual combustion time
$\tau_{total}$	total combustion time
$\dot{\omega}_d$	reaction rate of droplet phase
$\dot{\omega}_g$	reaction rate of gas phase
$\dot{\omega}_T$	total reaction rate

## Subscripts

0	initial state
$\infty$	far-field state
$f$	fuel
$g$	gas phase
$k$	$k$ th size group of droplets
$l$	liquid phase
$ox$	oxidizer

## REFERENCES

1. Suzuki, T. and Chiu, H.H., Multi-Droplet Combustion of Liquid Propellants, *Proc. of the Ninth Symposium on Space Tech. and Sci.*, 145-153, 1971.
2. Chiu, H.H. and Liu, T.M., Group Combustion of Liquid Droplets, *Combustion Science Technology*, 17, 127-142, 1977.
3. Chiu, H.H., Kim, H.Y. and Croke, E. J., Internal Group Combustion of Liquid Droplets, *19th Symposium on Combustion*, The Combustion Institute, Pittsburg, 971-980, 1982.
4. Kuo, K.K., Principles of Combustion, A. Wiley-Zulerscience publication, John Wiley & Sons, 1986.
5. Chigier, N.A. and McCreath, C.G., Combustion of Droplets in Spray, *ACTA Astronautica*, 687-710, 1974.
6. Chigier, N., Group Combustion Models and Laser Diagnostic Methods in Sprays: A Review, *Combustion and Flame*, 51, 127-139, 1983.
7. Sirignano, W.A., Fuel Droplet Vaporization and Spray Combustion Theory, *Prog. Energy Combust. Sci.*, 9, 291-322, 1983.
8. Bellan, J. and Harstad, K., Evaporation, Ignition, and Combustion of Nondilute Clusters of Drops, *Combustion and Flame*, 79, 272-286, 1990.
9. Chigier, N.A., Future Research in Atomization and Spray, in *Atomization and Spray 2000 NSF Workshop*, 1991.
10. Mizutani, Y., Akamatsu, F., Katsuki, M., and Tabata, T., Optical Observation of Group Combustion Behaviors of Premixed Sprays with and without a Circular Rod, in *Mechanism and Combustion of Droplets and Sprays*, edited by H.H. Chiu and N.A. Chigier, Begell house Inc. NY, 1996.
11. Akamatsu, F., Mizutani, Y., Katsuki, M., Tsushima, S., Chao, Y.T., *Proceedings of the Thirty-Third Japanese Symposium on Combustion*, The Japanese Combustion Society, Tokyo, 37-39, 1995.
12. Chiu, H.H. and Lin, C.L., Anomalous Group Combustion of Premixed Clusters, Accepted for publication in *26th Symposium on Combustion*, The Combustion Institute, Pittsburgh, 1996.
13. Patankar, S.V., Numerical Heat Transfer and Fluid Flow, *Series in Computational Methods in Mechanics and Thermal Science*, McGraw-Hill, New York, 1982.
14. Reid, R.C., Prausnitz, J.M., and Poling, B.E., *The Properties of Gases and Liquids*, 4ed. McGraw-Hill International Editions, 1988.

# A PHENOMENOLOGICAL THEORY OF PROPELLANTS' IGNITION AND SUBSEQUENT UNSTEADY COMBUSTION IN HIGH PRESSURE CHAMBERS

I.G. Assovskii

Semenov Institute of Chemical Physics RAS,  
Kosygin St. 4, Moscow 117977 Russia;  
e-mail: iga@icp.msk.ru

**ABSTRACT:** The goal of this paper is to show significant influence of ignition conditions on subsequent combustion of a condensed propellant and on the pressure diagram of combustion chamber. Emphasis is placed on the effect of accelerated combustion (AC-effect) after ignition in a high pressure closed bomb and in a chamber with moving piston. An analysis of such typical problems is carried out using an original phenomenological theory. Intermediate asymptotic solutions for the temperature and composition of combustion products as well as for the transitional combustion rate are presented. These asymptotic solutions show how the ignition conditions influence the subsequent unsteady combustion and pressure diagram in a high pressure chamber. The AC-effect of propellant surface layers and its dependence on ignition characteristics is demonstrated. A modification of Drozdov's solution of the basic problem of gun interior ballistics has been obtained taking into account the AC-effect. It is shown that AC-effect can be responsible for the anomalous increasing of pressure-peak with decreasing of initial temperature of propellant charge in a gun-chamber.

## INTRODUCTION

Sufficiently fast pressurization of combustion chamber causes the instant combustion rate  $R(t)$  of a gasifiable propellant to deviate from its quasi-steady state (QS) dependence on gas pressure  $P$  and on initial temperature  $T_0$  of propellant:

$$R^{\circ} = R^{\circ}(P, T_0) \quad (1)$$

This phenomenon, first predicted by Zel'dovich [1], is related to the thermal relaxation of condensed phase (c-phase) of propellant. Zel'dovich's theory (Z-theory) was based on the negligibly small thermal inertia of the gas-phase of propellant (QS-approximation of the gas-phase) and used the phenomenological approach: the non-steady state rate was calculated by substituting into the known dependence (1) the instantaneous pressure value and some effective initial temperature  $T_e$ :



$$R(t) = R^{\circ}(P(t), T_e(t)). \quad (2)$$

This Z-theory and its extensions: to propellants with variable surface temperature (Novozhilov [2]), to non-adiabatic combustion (Gostintsev et al. [3]), and to combustion under irradiation (Assovskii and Istratov [4]) are widely used to calculate the effects of unsteady combustion under pressures up to hundreds atmospheres [5-8]. The Z-theory and its modifications based on the QS-approximation of the gas-phase, are not applicable to combustion under pressure of order of thousand atmospheres and higher. In such a case the density and thermal inertia of the gas-phase are comparable with the density and thermal inertia of the c-phase, and the main assumption of those theories is broken.

However the phenomenological approach is fruitful to construct more advanced theory applicable to the unsteady combustion under the pressure increasing up to thousands of atmospheres and higher, as it was shown by author in [9]. This theory is also applicable to all transitional combustion processes, where the temperature distribution in c-phase changes from the initial one  $T_i(x/L)$ , with a large spatial scale  $L$ , to the final distribution  $T_f(x/l)$  with small spatial scale  $l$  ( $l \ll L$ ), see Fig.1. In such cases it is possible to construct intermediate asymptotics for the combustion rate and other time-variants of combustion process. These asymptotics are hold during times of order  $t_m$  satisfying to conditions:

$$L^2/k \gg t_m \gg l^2/k, \quad (3)$$

where  $k$  is the thermal diffusivity of c-phase,  $\text{cm}^2/\text{s}$ .

In the present paper this advanced phenomenological theory has further development for application to some typical problems of the solid propellant unsteady combustion in high pressure chambers, for example in constant volume bombs and in chambers with moving piston.

#### THE TIME-SCALES OF TRANSITIONAL COMBUSTION

Let a transitional combustion process be accompanied by a rearrangement of the temperature distribution in the c-phase  $T(x, t)$  from the initial  $T(x, 0) = T_i(x/L)$  to the final  $T_f(x/l)$ . For example, the initial and final states can correspond to QS-combustion at pressures  $P_i$  and  $P_f$ . In such a case  $L = k / R^{\circ}(P_i, T_0)$  and  $l = k / R^{\circ}(P_f, T_0)$ .

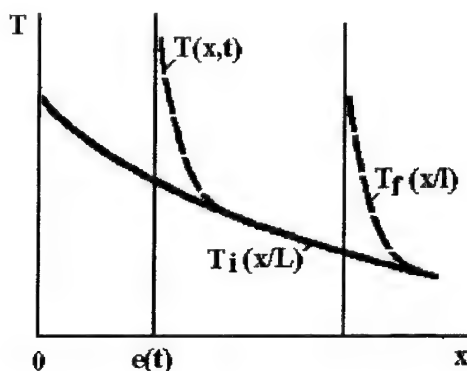


Figure.1. Transformation of the propellant temperature distribution during transitional combustion.

If the final pressure is much greater than initial one then the scales  $L$  and  $l$  are significantly different. The presence of two spatial scales for the temperature distribution leads to existence of three time scales of the c-phase thermal relaxation:

$$t_i = L^2/k, \quad t_m = L/R_m, \quad t_f = l/R_m = l^2/k, \quad (4)$$

where  $R_m$  is a characteristic combustion rate, e.g.,  $R_m = R^0(P_f, T_0)$ . At a sufficiently high pressure  $P_f$  (and consequently at a high rate  $R_m$ ) the values of time-scales  $t_i$ ,  $t_m$ , and  $t_f$  are significantly different from one to another:

$$t_i \gg t_m \gg t_f. \quad (5)$$

Thus, the scales for the transitional combustion of nitrocellulose propellant, starting from  $P_i \sim 10$  atm and ending at  $P_f \sim 1000$  atm, are characterized by following values (data from [5,10,11]):  $L \sim 100 \mu\text{m}$ ,  $l \sim 1 \mu\text{m}$ ,  $t_i \sim 100$  ms,  $t_m \sim 1$  ms,  $t_f \sim 10^{-2}$  ms that satisfy conditions (4).

The thermal relaxation times for the propellant gasification zone and for the gas-phase are comparable to  $t_f$  as it was shown by author in [9]. That is why we can not neglect the thermal inertia of these processes on times of order of  $t_f$ . However, we can consider the thermal relaxation of these zones as QS-process on times that are much bigger than the relaxation time-scale  $t_f$  of the final temperature distribution.

In high pressure chambers, as a rule, the characteristic time of transitional combustion  $t_m$  (4) is comparable to the time-scale of pressure diagram  $t_p = 1/(d(\ln P)/dt)$ . Moreover, both of them are much bigger than  $t_f$  and satisfy the conditions (3) and (5). Such ratio of the time-scales is responsible for existence of an intermediate asymptotic solution for problems of transitional combustion.

### INTERMEDIATE ASYMPTOTIC SOLUTION

According to the phenomenological approach, the effective initial temperature  $T_e$  has to be found to calculate the unsteady combustion rate. In the Z-theory and in its mentioned above modifications the effective temperature  $T_e$  (2) is defined as:

$$T_e = T_s - k F / R, \quad (6)$$

where  $T_s$  and  $F$  are the temperature and the derivative of temperature at the c-phase surface, determined by solution of the heat transfer equation:

$$\partial T / \partial t + R \partial T / \partial x = k \partial^2 T / \partial x^2 \quad (7)$$

having the boundary and initial conditions:

$$x \rightarrow -\infty : T \rightarrow T_0; \quad x \rightarrow 0 : T \rightarrow T_s; \quad t \rightarrow 0 : T \rightarrow T_i(x/L). \quad (8)$$

In the present theory for the transitional combustion, the temperature  $T_e$  is defined as a temperature in the bulk of c-phase on long distance from the surface (much more than the smallest spatial scale  $l$ ). The mathematical analysis of the problem (7), (8) under conditions (5) shows the existence of an intermediate asymptotic solution on time of order of  $t_m$  (4). The initial heated layer of c-phase (its depth  $\sim L$ ) burns out during this period (Assovskii [9, 12]). The thermal inertia of the gas-phase, the gasification zone, and inertia of a surface layer having a depth  $\sim l$  is negligible on this period of transitional combustion. At the same time the initial temperature distribution  $T_i(x/L)$  can not change significantly, and the combustion wave propagates over the propellant having a "quasi-frozen" distribution of initial temperature, Fig. 1.

Thereat, the effective temperature  $Te(t)$  is connected with the initial temperature distribution and with a thickness  $e(t)$  of burnt layer by asymptotic ( $z \rightarrow 1$ ) relationship [9,12]:

$$Te = Ti(e/L) - (Ts - Ti(e/L)) \cdot (1 - z) / 2z, \quad (9)$$

$$e = \int_0^t R(t') dt', \quad z = \text{erf}(e/(2\sqrt{kt})).$$

If the steady-state dependencies for the surface temperature  $Ts^\circ(P, To)$ , the flame temperature  $Tf^\circ(P, To)$ , and for the combustion products composition  $Aj^\circ(P, To)$  are known as the combustion law (1), then the appropriate equations for unsteady characteristics can be written similarly to the form (2):

$$Ts(t) = Ts^\circ(P(t), Te(t)), \quad Tf = Tf^\circ(P, Te), \quad (10)$$

$$Aj = Aj^\circ(P, Te).$$

Since the main reason for existence of the asymptotic solutions (2), (9), and (10) is the great difference between the initial and final thickness of heated layer in c-phase, these solutions are applicable not only to unsteady combustion under the high pressurization. For example, this intermediate asymptotic solution can describe the stabilization of the steady-state combustion after ignition at moderate pressures. For this, the extent of warm-up upon ignition  $Li$  should be much greater than the final steady-state layer  $l=k/Rf^\circ$ .

Thus, if warm-up takes place by conductive or convective heat exchange over a time interval  $ti$ , then  $Li \sim \sqrt{ti}k$ , and conditions (5) of application of (9) are equivalent to :

$$R^\circ(P, To) \sqrt{(ti/k)} \gg 1. \quad (11)$$

Especially deep heating of the surface layer takes place during a thermal irradiation of semi-transparent propellant. In such a case the condition (5) can be presented in a form:  $RfL/k \gg 1$ , where  $L$  is the depth of radiation absorption. The numerical calculations show, that  $R(t)$ -curves of transitional combustion, determined by expressions (2), (9) and by (2), (6), (7), differ only slightly already when  $L/l = 10$  (see, for example, further consideration of combustion under a pressure-step, Figs. 2 and 3). This is true both for the constant  $Ts$  (Zel'dovich [1]) and for the variable  $Ts$  (Novozhilov [2]) models. Thereto, even the first term of the intermediate asymptotic expression (9) represents itself a good approximation for the effective initial temperature  $Te(t)$ .

#### APPLICATION TO SOME TYPICAL PROBLEMS

Let us consider application of the presented theory to some typical problems of unsteady combustion in high pressure chambers. In a number of such cases Eq. (9) gives a possibility to find the changes of combustion parameters in a clear analytical form and to determine the influence of unsteady combustion on the pressure-time curve of combustion chamber.

##### The Basic Relationship Between Pressure and Combustion Rate Curves.

The combustion law (1) can usually be presented in a form of product:

$$R^\circ(P, To) = Rp(P) \cdot RT(To). \quad (12)$$

Using the first approximation for  $Te(e)$  (9), we can derive from Eqs. (2), (12), and (9) the basic integral relationship between curves  $P(t)$  and  $e(t)$  :

$$\int_0^e \frac{de}{R_T(T_i(e/L))} = \int_0^t R_P(P(t))dt \quad (13)$$

The left and right parts of Eq. (13) contain separately the pressure-time function and the combustion rate. Such a form of the basic relationship is very convenient especially to solve so called the forward and inverse problems of unsteady combustion.

*The forward problem of unsteady combustion.* If the pressure curve is known from experiment then it needs find how the combustion rate and other combustion characteristics change with time (the forward problem). For definiteness, let the combustion law (1) have the form:

$$R^\circ(P, T_0) = R_0 P (1 + b T_0), \quad (14)$$

and the curves  $T_i(e/L)$  and  $P(t)$  be approximated by exponential functions:

$$T_i = T_0 + (T_{si} - T_0) \exp(-x/L), \quad (15)$$

$$P = P_f - (P_f - P_i) \exp(-t/t_p). \quad (16)$$

After substitution of Eqs. (14) and (15) into Eq. (13) and its integration we find an expression for the burnt layer:

$$e(t) = L \ln[ (1+g) \exp(t/t_m - (R_f - R_i)t_p(1 - \exp(-t/t_p))/L) - g ], \quad t_m = L/R_f, \quad (17)$$

$$g = b(T_{si} - T_0)/(1 + bT_0), \quad R_i = R^\circ(P_i, T_0), \quad R_f = R^\circ(P_f, T_0).$$

Substituting Eq. (17) into Eqs. (9), (2) and (10) we obtain the rate and other characteristics of combustion as clear time-functions. Thus for the temperature of the combustion products  $T_f$ , that is additively related to the initial temperature:

$$T_f^\circ(P, T_0) = T_f^\circ(P, T_0') + (T_0 - T_0'),$$

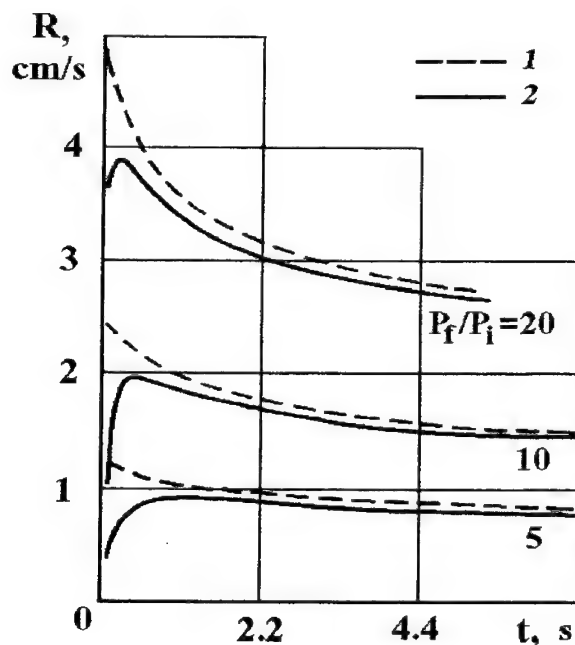
we obtain a divergence between  $T_f(t)$  and the QS-value  $T_f^\circ$ :

$$T_f - T_f^\circ = (T_{si} - T_0) / [(1+g)\exp(t/t_m - t_p(R_f - R_i)(1 - \exp(-t/t_p))/L) - g].$$

In a limit case, when pressure changes like step-function ( $t_p \rightarrow 0$ ,  $L = k/R_i$ ,  $t_m = L/R_f \gg t_p$ ), we have rather simple expressions for the combustion characteristics:

$$\begin{aligned} e &= L \ln[ (1+g) \exp(t/t_m) - g ], \\ R(t) &= R_f / (1 - g(1+g)^{-1} \exp(-t/t_m)), \\ T_f - T_f^\circ &= (T_{si} - T_0) / [(1+g)\exp(t/t_m) - g]. \end{aligned} \quad (18)$$

The solution (18) demonstrates the effect of accelerated combustion under fast pressurization. Some curves  $R(t)$  taken from (18) are presented at Figs. 2 and 3 as dotted lines. On the plane  $(R/R_f, t/t_m)$  the  $R(t)$ -curves (18) look like one-parameter family. The combustion rate reaches its maximum value  $R_M$  just after the pressure-jump and then decreases to the final QS-value  $R_f$ . The characteristic time of combustion transition  $t_m$  is equal to the burning out time of initially heated layer (having a depth  $L$ ), if combustion



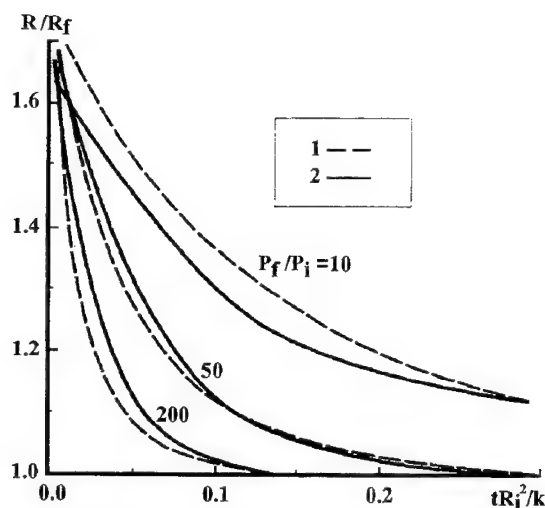
**Figure 2.** The accelerated combustion effect under step-pressurization.  
1-analytical asymptotic solution (18), 2- numerical solution.

wave would propagate with the final rate  $R_f$ . The maximum rate is equal to a QS-rate at  $T_o = T_{si}$  (as the first approximation):

$$R_M = R^o(P, T_{si}) = (1+g)R_f.$$

The higher is an initial surface temperature  $T_{si}$  and the temperature sensitivity of combustion rate  $b$  the higher is the relative maximum of combustion rate  $R_M/R_f$ . That is why it is important to know the initial temperature distribution and also the combustion law (1) at the high initial temperatures  $T_o$  (up to the surface temperature in ignition or even combustion).

Meanwhile, it must be noticed as an interesting fact, that AC-effect (18) does not depend on the surface temperature during the transitional combustion. To check this result the asymptotic solution (18) has been compared with numerical solutions based on different models of unsteady combustion. These numerical solutions are presented on Figs. 2 and 3 as solid lines. The curves on Fig. 2 are obtained using the Novozhilov model [2] (variable temperature  $T_s$ ) and correspond to combustion of double-base propellant N [5, 6] under step-pressurization starting from a steady state at  $P_i=10$  atm,  $T_o=293$  K. The computational method has been described in [6]. The numerical solutions on Fig.3 are taken from [13] and correspond to the Zel'dovich model [1] (constant  $T_s$ ). A comparison of presented solutions testifies that there is not any significant difference between the appropriate solutions, except at the very beginning of transitional combustion, if the pressure increase is high enough.



**Figure 3.** Combustion rate variation under step-pressurization.

1-asymptotic solution (18), 2-numerical solution [13] based on Zel'dovich model [1].

*The inverse problem.* In the control of combustion process the reverse problem arises (see, for example, Zel'dovich et. al [6]), to determine the pressure change  $P(t)$  ensuring the given curve  $R(t)$ . Using Eqs. (9) and (12) we obtain a solution of such a problem in a general form:

$$R_p(P(t)) = R(t) / R_T \left( T_i \left( \int_0^t R(t) dt' / L \right) \right).$$

For example, in a case of an exponential distribution of the initial temperature, Eq. (15), and for QS-combustion law:

$$R_T = R_0 \exp(b T_0), \quad n = d(\ln R^0)/dP = \text{const}, \quad (19)$$

the rule for the pressure change is:

$$P(t) / P^0(t) = \exp(-b(T_{si}-T_0) / n \exp(e(t)/L)),$$

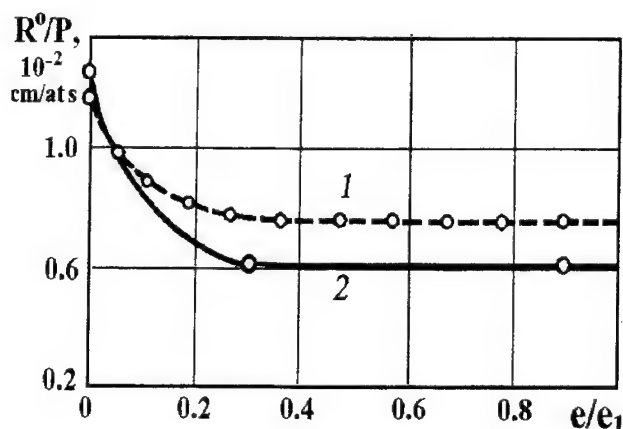
where  $P^0(t)$  is the condition of pressure change that corresponds to the QS-correlation between pressure and combustion rate:

$$n \ln P^0 = \ln(R(t)/R_0) - b T_0.$$

In a common case the pressure or combustion rate curve is not preliminarily known, but there is an additional relationship between the pressure, combustion rate and other parameters of intrachamber combustion.

#### Accelerated Combustion after Ignition in a Closed Chamber.

Combustion in a constant volume chamber (the closed-bomb test) is frequently used to determine the combustion law (1) in high pressure conditions [10,11,14-16]. Here we consider the problem of ignition influence on the combustion rate and the pressure diagram in a closed bomb.



**Figure 4.** The accelerated combustion of surface layer of single-base gun propellant.  
Data derived from the closed bomb test by Serebryakov [13].  
 $2e_1 = 1.0$  (1),  $6.0$  (2) mm

The pressure of combustion products in a chamber is determined by the gas-state equation. The Noble-Abel equation is usually used for pressures of order of thousand atmospheres [14-16]. It is useful for further purposes to present this state-equation in the form:

$$Y = (P - P_i)(1 - \Delta/\rho) / (R_g T_g / M - (1/\rho - \alpha)(P - P_i)). \quad (20)$$

Here  $P_i$  is an ignition pressure;  $\alpha$  is the powder gas covolume;  $T_g$  and  $M$  are the temperature and average molecular weight of the gas;  $R_g$  is the universal gas constant;  $\Delta$  is the loading density (the ratio of the charge weight to the chamber volume);  $\rho$  is the propellant density; and  $Y = Y(e)$  is the fraction of burnt out part of the propellant charge.

At the initial stage of combustion ( $Y \ll 1$ ) we can assume in Eq. (20) that  $Y(e) = e(dY(0)/de)$ . Using Eq. (20) we find the function  $e(P)$ . Substituting  $e(P)$  together with Eq. (15) into Eqs. (9) (first approximation) and (10) we find the dependence of unsteady combustion characteristics on current pressure and ignition conditions (initial temperature distribution). Thus, for the combustion law (19) the final equation for the rate of subsequent combustion after ignition is:

$$R(t) = R^0(P(t), T_0) \exp(b(T_{si} - T_0) \exp(-Y(P)/Y_i)), \quad (21)$$

where  $Y_i = Y(L_i)$  is the fraction of charge part corresponding  $e = L_i$ .

The equation (21) specifies the relationship between the effect of accelerated combustion of propellant surface layer and the conditions of propellant ignition. Such an AC-effect has been first observed by Serebryakov [14] in tests of single base gun-powders in a closed bomb. He found that external layers of powder grains had the burning rate  $R_t$  that was much higher than combustion rate of internal layers (see Fig. 4). Also, it has been found that more intensive combustion of external layers depends on nature of powder as well as on ignition conditions. Using the formula (21) with an appropriate value of pre-heated layer depth  $L_i$  one can describe Serebryakov's experimental data with good agreement.

## Combustion in Chamber with Moving Piston

The effect of accelerated combustion after the propellant ignition (21) can significantly influence the pressure maximum,  $P_M$ , in a semi-closed bomb and in a chamber with moving piston. This problem is very interested for interior ballistics of such systems, especially for systems safety [18,19]. Here we consider how the AC-effect influence the pressure peak in a large caliber artillery system, and its dependence on initial temperature of propellant.

For a large-caliber gun typical values of ignition time delay  $t_i$  are much more than characteristic times of the ballistic cycle (see, for example, Fisher [18]). That is why the condition (11) for application of the asymptotic solution (9) is satisfied. Therefore, the way to determine the rate of unsteady combustion in gun-chamber is similar to that one for constant volume systems. In this case, in addition to the gas state equation (20), there is the system of equations of interior ballistics [14,15]. Putting off the details of solution for this system, we present here some final results.

At first, the well known Drozdov's solutions for basic problem of interior ballistics of guns and for the pressure peak in gun-chamber [14] can be extended taking into account the unsteady combustion law. For this purpose, we have to substitute in Drozdov's formula (derived assuming the QS-combustion law) instead of QS-rate  $R^\circ$  the average rate  $R^\wedge$ :

$$R^\wedge = e / \int_0^e \frac{de}{R^\circ(P, T_e(e))}. \quad (22)$$

Further, this result gives possibility to determine influence of the initial temperature  $T_0$  and ignition characteristics on the pressure peak  $P_M$ . Following equation can be derived to describe this influence:

$$d(\ln P_M)/dT_0 = 2Cr(1 - 2Bi + Bt) + 2C_f, \quad (23)$$

where  $Bi$  and  $Bt$  are non-dimensional criterions:

$$Bi = Cr(T_{si} - T_0)L_i / e^*, Bt = Ct(T_{si} - T_0)L_i / e^*,$$

$Cr$ ,  $Ct$ , and  $C_f$  are coefficients characterizing the temperature sensitivity of QS-combustion rate, the ignition time-delay  $t_i$  and the QS-temperature of combustion products:

$$Cr = d(\ln R^\circ)/dT_0, Ct = d(\ln t_i)/dT_0, C_f = d(\ln T_f^\circ)/dT_0;$$

$e^*$  is the thickness of burnt layer at pressure peak under QS-combustion of propellant.

As it follows from Eq. (22), the value of the pressure peak can increase with decreasing of initial temperature, if time-delay  $t_i$  increases too fast with decreasing  $T_0$ .

## CONCLUSION

It needs to underline in conclusion three distinguishing features of performed analysis.

In combustion theory and in interior ballistics the ignition process is usually involved into consideration only to estimate the time-delay and critical conditions of ignition. Influence of ignition conditions on combustion rate is ordinary neglected. In contrast to such a viewpoint, the presented analysis shows that ignition conditions can significantly influence as the subsequent combustion rate as the pressure peak that is so far from the combustion beginning. It is a reason to pay more attention to ignition process in high-pressure combustion chambers. It is important



to know the initial temperature distribution and the combustion law at high initial temperatures  $T_0$  up to the surface temperature in ignition.

The traditional methods to analyze such a nonlinear and multiscale problem as the unsteady combustion is a linearization of equations, assuming relatively small amplitudes of deviation of combustion characteristics. The smaller is deviation of pressure and other characteristics of combustion, the more exact is such a solution. In contrast to the linearization-method, the presented theory and asymptotic solutions are applicable to problems dealing with great amplitudes of the pressure or combustion rate increasing. The greater is amplitude of increase the more exact are these asymptotic solutions.

It needs also to underline a methodological sense of the performed analysis. The results show that transitional combustion process has own measure as for time and spatial scales as for pressure and combustion rate deviation. The performed analysis assists to understand the dynamics of transition from ignition to steady-state combustion as well as the asymptotic sense of such a basic idea as the quasi-steady state combustion.

In practice, the obtained relationships between ignition conditions and subsequent accelerated combustion of propellant allow one to understand more deeply the origination and amplification of pressure waves in combustion chamber [18,19] during the charge ignition. It will be useful for the charge design to avoid anomalous pressure peak in combustion chamber.

#### NOMENCLATURE

$\alpha$	gas covolume, $\text{m}^3/\text{kg}$
$A_j$	substance $j$ content in combustion products, $\text{mol/kg}$
$B_i$	non-dim. criterion of ignition
$B_t$	non-dim. criterion of temperature sensitivity of ignition time delay
$b, C_r$	temperature sensitivity of the steady-state combustion rate, $1/\text{K}$
$C_t, C_f$	temperature sensitivity characteristics for the ignition time-delay, and combustion products temperature respectively, $1/\text{K}$
$\Delta$	ratio of charge mass to chamber volume, $\text{kg/m}^3$
$e$	thickness of burnt layer of propellant, $\text{m}$
$2e_1$	initial thickness of propellant grain, $\text{m}$
$F$	temperature derivative at the C-phase surface, $\text{K/m}$
$g$	non-dim. criterion of initial temperature influence on combustion rate
$\rho$	propellant density, $\text{kg/m}^3$
$k$	thermal diffusivity of propellant, $\text{m}^2/\text{s}$
$l, L$	spatial scales for temperature distribution in propellant, $\text{m}$
$M$	average molecular weight of combustion products, $\text{AMU/mol}$
$n$	exponent in combustion rate dependence on pressure
$P_M$	pressure maximum in combustion chamber, $\text{N/m}^2$
$P_i, P_f$	initial and final values of pressure, $\text{N/m}^2$
$R_g$	$8.31 \text{ J/mol}\cdot\text{K}$ , universal gas constant
$R$	combustion rate, $\text{m/s}$
$R_p$	multiplier-function in combustion law; depends on pressure, $\text{m/s}$
$R_t$	non-dim. factor in combustion law; depends on initial temperature
$T$	temperature, $\text{K}$
$t$	time, $\text{s}$
$t_p$	characteristic time-scale for pressure diagram, $\text{s}$

x	space variable, m
Y	fraction of burnt part of charge
z	non-dim. function, depending on time and burnt out layer e

#### Subscripts.

o	initial state
i	ignition or initial state
f	final state or flame
M	maximum value
m	characteristic value
s	surface
p	pressure
t	temperature
g	gas

#### Superscripts.

'	steady state
*	pressure peak
^	average value

#### REFERENCES

1. Zel'dovich, Ya. B., Zh. Eksp. Teor. Fiz., 12, 11-12, 498-512, 1942.
2. Novozhilov, B. V., Journal of Applied Mechanics and Technical Physics (ZPMTF), 1, 54-59, 1967.
3. Gostintsev, Yu. A., Sukhanov, L. A. and Pokhil, P. F., Dokl. Akad. Nauk SSSR, (Proc. Acad. Scien. USSR), 195, 137-141, 1970.
4. Assovskii, I. G. and Istratov, A. G., ZPMTF, 12(5), 692-698, 1971.
5. Zel'dovich, Ya. B., Leypunskii, O. I., and Librovich, V. B., The Theory of Unsteady Combustion of Powder, Nauka, Moscow, Russia, 1975.
6. Assovskii, I.G., Zakirov Z.G. and Leypunskii, O.I., Sov. J. Chem. Phys., 4(10), 2342-2353, 1989.
7. DeLuca, L., Price E.W. and Summerfield, M., (Co-Editors), Nonsteady Burning and Combustion Stability of Solid Propellants, Progress in Astronautics and Aeronautics, vol. 143, AIAA, Washington, DC, USA, 1992.
8. Son S.F. and Brewster M.Q., Combustion Explosion and Shock Waves (FGV), 29(3), 31-36, 1993.
9. Assovskii, I. G., Dokl. Phys. Chem., Proc. Acad. Scien. USSR, 294 (1-3), 421-424, 1987.
10. Glazkova A.P., Catalysis in Combustion of Explosives, Nauka, ICP, Moscow, USSR, 1976, 14-15.
11. Aksenov, V. S., Leonov G. N., Lyubimov A. V., et al., FGV, 15(2), 103-106, 1979.
12. Assovskii, I. G., 24th Int. Symp. on Combustion, Abstracts, The Comb. Inst., Pittsburgh, USA, 366, 1992.
13. Novozhilov, B. V., ZPMTF, 5, 83-86, 1962.
14. Serebryakov, M. E., Interior Ballistics, Oborongiz, Moscow, USSR, 1949, 43-140.
15. Corner, J., Theory of The Interior Ballistics of Guns, Wiley, New York, 1950.
16. Stiefel, L., in Interior Ballistics of Guns, Vol. 66 of Progress in Astronautics and Aeronautics, AIAA, Washington, DC, USA, 1979, 307-324.
17. Powell, E.G., Wilmot, D., Haar, L., and Klein, M., ibid., 325-346.
18. Fisher, E. B., ibid., 281-306.
19. Wildegger-Gaissmaier, A.E., and Johns', I.R., Combustion and Flame, 106, 219-230, 1996.

## **Ignition and Unsteady Combustion of AP-based Composite Propellants in Subscale Solid Rocket Motors**

**A. Bizot**

Office National d'Etudes et de Recherches Aéronautiques  
Chatillon, France

**ABSTRACT :** The description of the unsteady combustion mechanisms of solid propellants and the numerical solution of the solid rocket internal flow are the two key factors in determining the unsteady behavior during the ignition transient inside a solid rocket motor. The objective of this study is to develop a numerical tool able to predict the flow-solid propellant interaction responsible for the ignition process. The numerical package developed for the simulations comprises a multi-dimensional CFD code using a  $k-\epsilon$  turbulence model which is associated with two main components: a one-dimensional unsteady heat conduction analytical solution for the propellant surface temperature or burning rate and a one-dimensional Couette flow solution for the wall boundary layer. In addition, one considers that an ignition propagation occurs by conduction at the gas side propellant surface when the critical inflammation conditions to sustain such a propagation are satisfied.

This paper presents the details of the modules created to simulate the ignition transient period and the applications conducted to predict the ignition delay and the flow field in selected subscale solid rocket motor configurations.

### **INTRODUCTION**

The ignition mechanisms controlled by the internal flow of solid rocket motors have long been studied in depth and the basic information derived from these studies have produced a very good understanding of ignition phenomena. However, only recently, both the development of multi-dimensional CFD codes with robust flow solvers and the widespread use of fast computers allow one to accurately predict the internal flow field during the ignition process inside a solid rocket motor.

The numerical approach consists mainly of three modules: the main module is the CFD code (flow solver), the second module describes the boundary layer near the propellant wall (Couette flow model) and the third solves the heat transfer inside the propellant (an integral equation is used for the surface temperature or the burning rate).

In the present work, emphasis is placed upon the ignition transient phenomena related to the unsteady combustion which lasts less than 100 ms. Consequently, the propellant is assumed to be undeformable as the pressure increases and the grid mesh boundaries used in the computations are assumed not to move. The grain deformation could easily be taken into account since the CFD module, which solves the Navier-Stokes equations, has already been developed for an arbitrary grid mesh with moving boundary surfaces. However, the addition of a grid generation module was not part of the present study.

## DESCRIPTION OF THE IGNITION TRANSIENT SIMULATIONS

The two geometric configurations of the subscale rocket motor studied in this work are shown in Fig. 1. The igniter at the head-end of the rocket generates a supersonic mass flow at a very high temperature depending on the propellant used in the rocket motors ( $T_{f \text{ igniter } 1} = 2350 \text{ K}$ ,  $T_{f \text{ igniter } 2} = 3770 \text{ K}$ ). This flow produces a very strong convective heat transfer ( $\Phi_{w1} = 2.0 \text{ MW/m}^2$ ,  $\Phi_{w2} = 6 \text{ MW/m}^2$ ) which initiates the propellant ignition. Although alumina particles are present in the igniter propellant combustion products, the radiative heat transfer is nevertheless moderate and assumed to be a constant which is computed separately. The internal flow structure of the motor shows regions of flow separation upon which the heat transfer at the propellant surface is strongly dependent. Since the wall heat flux is a dominant parameter in determining the ignition delay, the interaction between the flow field and the propellant is of great importance.

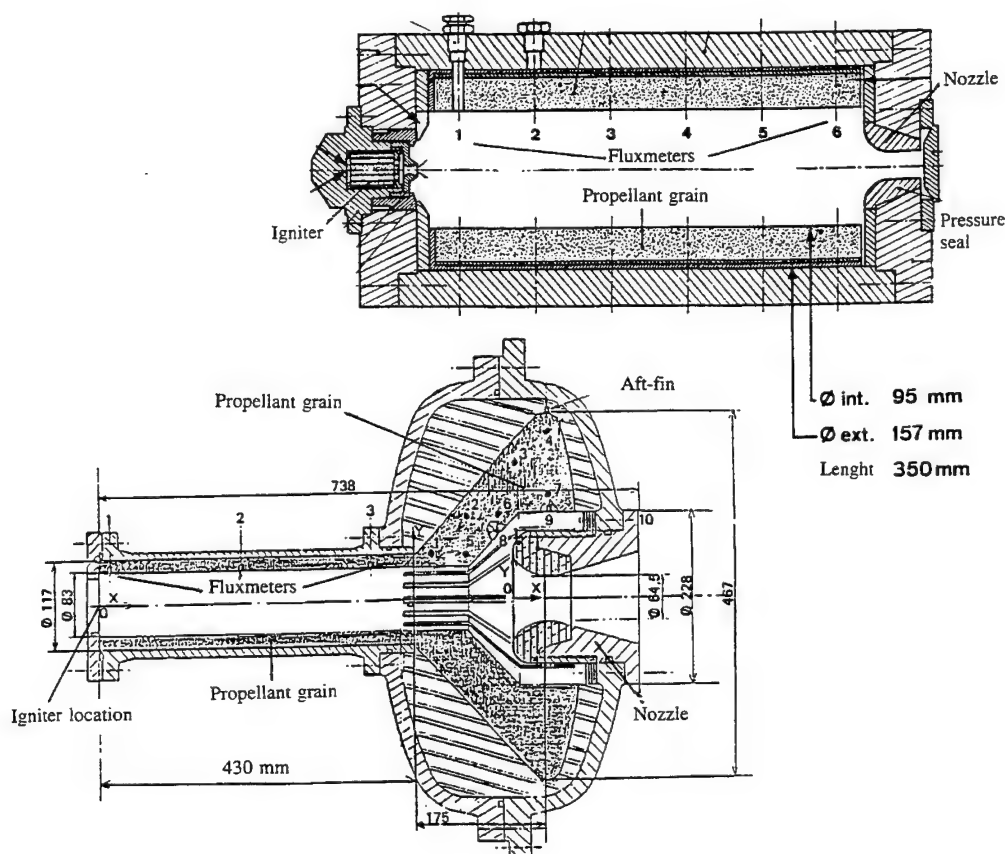


Figure 1. Schematic Diagrams of the Subscale Solid Rocket Motors

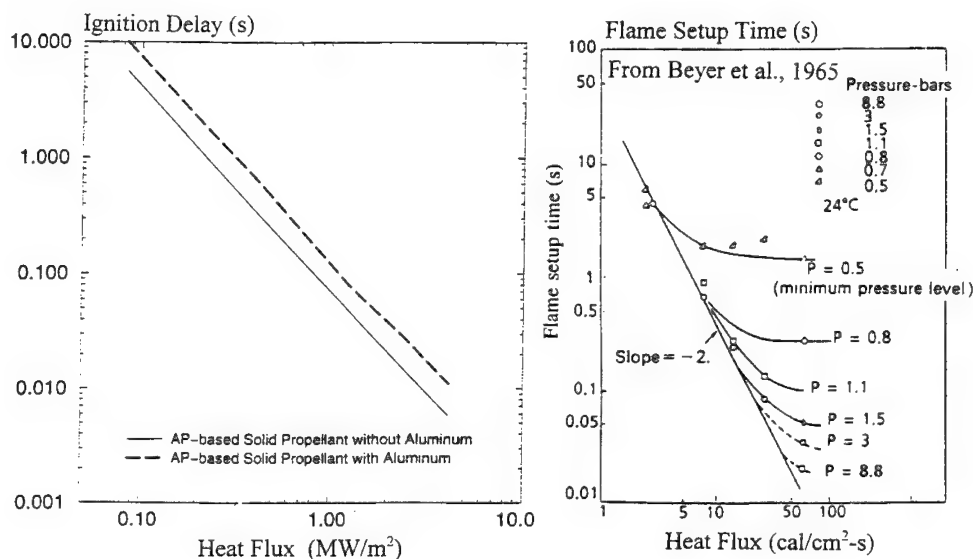
The igniter is responsible for the slow pressure increase (a few bars) inside the motor until the ignition is effective. Then the propellant burning rate rises slowly (in comparison to the ignition delay). The gas flow produced by the propellant combustion progressively provides an additional mass flow which becomes stronger as the burning surface spreads longitudinally inside the motor.

The ignition propagation is due to the convection of the hot gases in the boundary layer. For most applications, the heat transfer by convection is the dominant ignition propagation mechanism. However, when the convection in the boundary layer is not strong enough, a secondary propagation mechanism at the propellant surface bypasses the main propagation mechanism. This could happen in low velocity flow regions inside solid rocket motors or in operculated motors.

The unsteady combustion disappears when the pressure evolution reaches a steady regime. The regression of the propellant surface tends to increase the volume of the combustion chamber. Since the propellant grain is assumed to be undeformable, the boundaries of the grid mesh are not redefined. This restriction can be eliminated for industrial applications.

### THEORY

The description of the ignition process is based on an ignition delay which is mainly influenced by the temperature level needed to initiate the chemical reactions [1]. This critical temperature is dependent of the heat flux supplied to the propellant and corresponds to the observation of exothermal reactions at the propellant surface. Such evolution of the ignition delay with respect to the heat flux allows one to describe the initiation of the propellant degradation. The experimental results obtained by ONERA are given in Fig.2 which shows the ignition delay of two types of AP composite propellants (an AP-CTPB propellant and an aluminized AP-CTPB composite propellant) and the pressure influence on flame setup time [2].



**Figure 2.** Ignition Delay and Flame Setup time vs. Heat flux for AP-based Composite Propellants

The main conclusion that can be deduced from this results (taking into account also some results published in the literature which are not presented in this paper - see [1] for details) is that the AP degradation is the limiting process of the ignition. Hence, the chemical mechanism responsible for the ignition can be described by a single reaction. The kinetic characteristics of this reaction deduced from the plot in Fig.2, are given according to the following equations :

$$T_{s_{ign}} = \frac{E_p}{R \ln \left( \frac{Q_s B_{ign}}{\alpha \Phi_{ign}} \right)} \quad (1)$$

$$t_{ign}^{1/2} = \frac{\pi^{1/2}}{2} \frac{\sqrt{\lambda_p \rho_p C_p}}{\Phi_{ign}} (T_{s_{ign}} - T_0)$$

with  $E_p = 125.4$  KJ/mole and  $B_{ign} Q_s = 3.05 \cdot 10^{15}$  W/m<sup>2</sup>,  $\alpha = 0.15$ .

From this simplified analysis, it can be seen that the ignition temperature is influenced by the heat flux received by the propellant. The higher the heat flux, the higher the ignition temperature. That means that, as the heat flux increases, the conduction time required to ignite the propellant in the degradation zone, is not sufficient enough to allow the chemical reaction to occur. Consequently, the ignition temperature has to rise enough in order to increase the residence time of the degradation products.

Another conclusion deduced from the experimental results is that the type of binders does not affect the ignition delay, except if the change of the propellant composition modifies the propellant thermal diffusivity, which is not usually the case for propellants with practical polymer binders. However, a typical example of such an influence is encountered with aluminized composite propellants. Due to the aluminum mass fraction, the propellant diffusivity is increased by a factor of 3, compared to the equivalent non-aluminized propellant. In this case, it was found that the experimental results shown in Fig. 2 could be correlated with the same kinetic parameters previously obtained. The increase of the ignition delay is caused by the increased of the propellant diffusivity (or, more precisely, by the propellant effusivity as seen in Eq. 1). The conduction time necessary to reach the ignition temperature is increased because the heated propellant thickness is greater.

The integration of this data in the description of the ignition is a key factor in the elaboration of the numerical code developed for the simulations in subscale solid rocket motors.

### Computation Fluid Dynamics Module

The flow solver developed at ONERA is an approximate Riemann solver based on a 3D finite volume technique using structured meshes. The numerical conservative upwind implicit scheme features the shock-capturing Roe's method. The fluxes decomposition is based on the flux difference splitting method. This approach is not the most efficient numerical scheme but is sufficiently robust to compute compressible flows over a wide range of Mach numbers. It can capture discontinuities such as pressure waves which move forward and backward in a rocket motor during ignition or strong shock waves at the head end of the motor due to the supersonic igniter flow.

### Couette Flow Module

The turbulent boundary layer near the solid propellant is of great importance in the heat flux evaluation. Because of the very high temperature gradient at the propellant surface, a one-dimensional numerical model, based on Couette flow assumptions, is used for computing the boundary layer. The energy and momentum equations are integrated with a one-dimensional finite volume technique from the wall to the nearest cell center of the mesh. The turbulence model consists of an extension of Van Driest's mixing length damping function and an extension of Cebecchi's correction factor. Integration of the Couette flow model is performed with a grid mesh of about 150 cells in the direction normal to the wall. In order to maintain computational efficiency, a process which puts the numerical integration into algebraic form has been developed. The resulting formulae obtained (wall-functions) allow for the computation of the

heat flux. The results are very close to those obtained with the Couette flow model.

This analytical and numerical work leads to the development of a wall-function relationship which takes into account the very high temperature gradient encountered in the boundary layer inside solid rocket motors. The turbulent viscosity, which is based on Boussinesq and Prandtl mixing length hypothesis, and the shear stress are written as follows :

$$\begin{aligned}\mu_t &= \rho l^2 \left| \frac{\partial u}{\partial y} \right| \\ \tau_t &= \rho (\chi y f_\mu)^2 \left( \frac{\partial u}{\partial y} \right)^2\end{aligned}\quad (2)$$

As can be seen from the above equations, the evolution of the density in the boundary layer modifies the shear stress at the wall and, consequently, according to the Reynolds analogy, the heat flux.

The wall-function used for propellant ignition applications is an extension of a wall-function established to describe the behavior of a quasi-adiabatic boundary layer [3] :

$$\alpha_{ad} = 1 + c_0 \left( \frac{Re_c}{403} \right)^{0.825} = \tau_w \frac{y_c}{\mu_{t,c}}, \quad Re_c = 2 \frac{\rho_c u_c y_c}{\mu_{t,c}} \quad (3)$$

where  $c_0$  is a correction function which allows the use of the wall-function even in the laminar boundary layer ( $\alpha_{ad} = 1$  corresponds rigorously to the laminar regime).

$$c_0 = \frac{\frac{Re_c}{400}}{1 + \frac{Re_c}{400}} \quad (4)$$

The wall heat flux is defined with the non-dimensional parameter  $\beta_{ad}$  :

$$\begin{aligned}\beta_{ad} &= 1 + g_{ad} (\alpha_{ad} - 1) = \Phi_w \frac{y_c}{\lambda_{t,c} (T_c - T_w)} \\ g_{ad} &= \frac{Pr_{t,c}}{Pr_t} \frac{1}{1 + p_{ad} \sqrt{\frac{2(\alpha_{ad} - 1)}{0.75 Re_c}}} \\ p_{ad} &= 9.24 \left[ \left( \frac{Pr_{t,c}}{Pr_t} \right)^{0.75} - 1 \right] \left[ 1 + 0.28 \exp \left( -0.7 \frac{Pr_{t,c}}{Pr_t} \right) \right]\end{aligned}\quad (5)$$

In the particular case where  $Pr_{t,c} = Pr_t$  ( $p_{ad} = 0$  and  $g_{ad} = 1$ ), one obtains :

$$\beta_{ad} = \alpha_{ad},$$

which corresponds strictly to the Reynolds analogy.

The extension adopted for strongly non-adiabatic flows has the following form :

$$\begin{aligned}
\alpha &= 1 + c_0 \left( \frac{Re_c}{403} \right)^{0.825} \left( \frac{T_c}{T_w} \right)^{0.3} \\
\beta &= 1 + g (\alpha - 1) \\
g &= \frac{Pr_{l_c}}{Pr_t} \frac{1}{1 + p \sqrt{\frac{2(\alpha - 1)}{0.75 Re_c}}} \\
p &= p_{ad} \left( \frac{T_w}{T_c} \right)^{0.3}
\end{aligned} \tag{6}$$

This relation shows clearly that the influence of the temperature profile in the boundary layer could be of great importance. For a wall temperature of 500 K and a near wall cell temperature of 3000 K, which is commonly encountered in the numerical simulations of flows in rocket motors, the correction factor  $(T_c/T_w)^{0.3}$  is equal to 1.7. Consequently, the heat flux at the wall is approximatively increased by the same factor.

### Heat Transfer and Unsteady Combustion Module

This module provides the time-dependent propellant surface temperature or burning rate. Integration of the energy equation in the solid phase is conducted using an analytical method, assuming a superficial degradation reaction in the solid phase. The unsteady combustion model which includes a detailed explicit description of the gas phase determines the change of the flame temperature due to the unsteady behavior of the solid phase.

The complete modeling of the propellant degradation comprises the description of the solid phase which is considered as an unsteady semi-infinite medium, and, the gas phase which is assumed to react instantaneously to the sollicitations of the solid phase ( $\rho_g C_g \partial T / \partial t|_{\text{gas}} \ll \rho_p C_p \partial T / \partial t|_{\text{solid}}$ ).

The description of the heat transfer inside the solid propellant correspond to the heat equation to which is added a term related to the coordinate system that moves with the regressing surface :

$$\frac{\partial^2 T}{\partial x^2} + \frac{R_b}{a_p} \frac{\partial T}{\partial x} = \frac{1}{a_p} \frac{\partial T}{\partial t} \tag{7}$$

where  $R_b$  is the burn rate and  $a_p$  the propellant diffusivity.

This implies that the reactive zone is very small compared to the heated propellant thickness. The high value of the activation energy justifies this assumption.

The energy balance at the propellant surface reads as :

$$-\lambda_p \frac{\partial T}{\partial x}|_s = \dot{m}_p Q_s + q_f + \Phi_{ign} \tag{8}$$

where  $Q_s$  is the heat released by the superficial degradation reaction,  $q_f$ , the heat flux issuing from the flame and  $\Phi_{ign}$  the ignition flux.



This set of equations can be reduced to an integral equation for the surface temperature (or the burn rate) [4]. The solution is :

$$\theta_s = \frac{1}{\sqrt{\pi}} \int_0^{\tau} \left[ \frac{I(\tau, \tau')}{2(\tau - \tau')} \theta_s(\tau') - \xi(\tau') C(\tau') \right] \exp \left[ -\frac{I^2(\tau, \tau')}{4(\tau - \tau')} \right] \frac{d\tau'}{\sqrt{\tau - \tau'}}$$

$$\theta_s = \frac{T_s - T_0}{\bar{T}_s - T_0}, \quad \xi = \frac{R_b}{R_b}, \quad \tau = \frac{\bar{R}_b^2 t}{\alpha_p}$$

$$I(\tau, \tau') = \int_{\tau'}^{\tau} R_b(\tau'') d\tau''$$

$$C = \frac{\left[ T_s - \frac{Q_s}{C_p} - \frac{q_f}{\dot{m}_p C_p} - \frac{\Phi_{ign}}{\dot{m}_p C_p} \right] - T_0}{\bar{T}_s - T_0}$$
(9)

The mass balance equation integrated in the superficial degradation zone leads to the following burn rate relationship :

$$R_b = A_p \exp \left( -\frac{E_p}{RT_s} \right)$$
(10)

where  $A_p$  and  $E_p$  are the kinetic characteristics of the steady state degradation reactions.

The simplified modeling of the gas phase which is assumed to be a premixed flame (diffusion phenomena are ignored) and governed by a single reaction is given by the following mass flow rate relationship :

$$\dot{m}_p = A_g P^n \exp \left( -\frac{E_g}{2RT_f} \right) \left( \frac{\lambda_g}{C_g} \frac{(T_f - T_s)}{\frac{Q_g}{C_g(T_f - T_s)} - 1} \right)^{\frac{1}{2}}$$
(11)

The physical and chemical processes involved in the gas phase are very complex. However, the controlled ignition phenomena are the exothermic chemical reactions which can be modeled using a single flame mechanism. Further studies, which will be presented in a future paper, show very clearly that the flame structure (single flame sheet, single distributed flame, single diffusion flame, multiple flames of various types similar to BDP-type model [5]) does not significantly affect the ignition process. The previous equation can be expressed in terms of the unsteady flame temperature which is determined using an iterative procedure. Therefore, one obtains from Eq. (11) :

$$T_f - T_s = \frac{(-\delta + \sqrt{\delta^2 + 4\delta a_1})}{2}$$

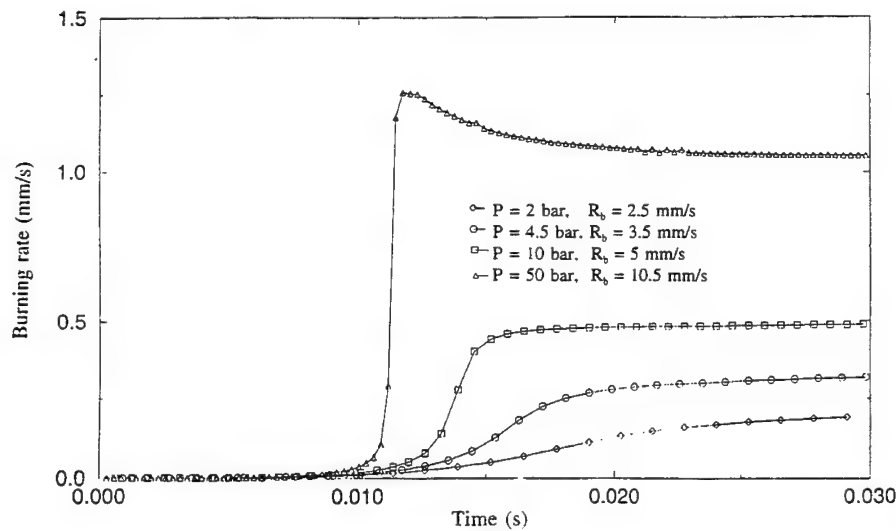
$$\delta = \left( \frac{\dot{m}_p}{A_g p^n \exp(-\frac{E_g}{2RT_f}) \sqrt{\frac{\lambda_g}{C_g}}} \right)^2 \quad (12)$$

$$a_1 = \frac{Q_g}{C_g}$$

The proposed form of Eq. (12) is less likely to cause numerical instabilities, especially in the early phase of ignition when the unsteady flame temperature,  $T_f$ , is close to the surface temperature,  $T_s$ .

Finally, the heat flux issuing from the flame is deduced from the energy balance between the propellant surface and the the end of the flame :

$$q_f = \dot{m}_p [Q_g - C_g (T_f - T_s)] \quad (13)$$

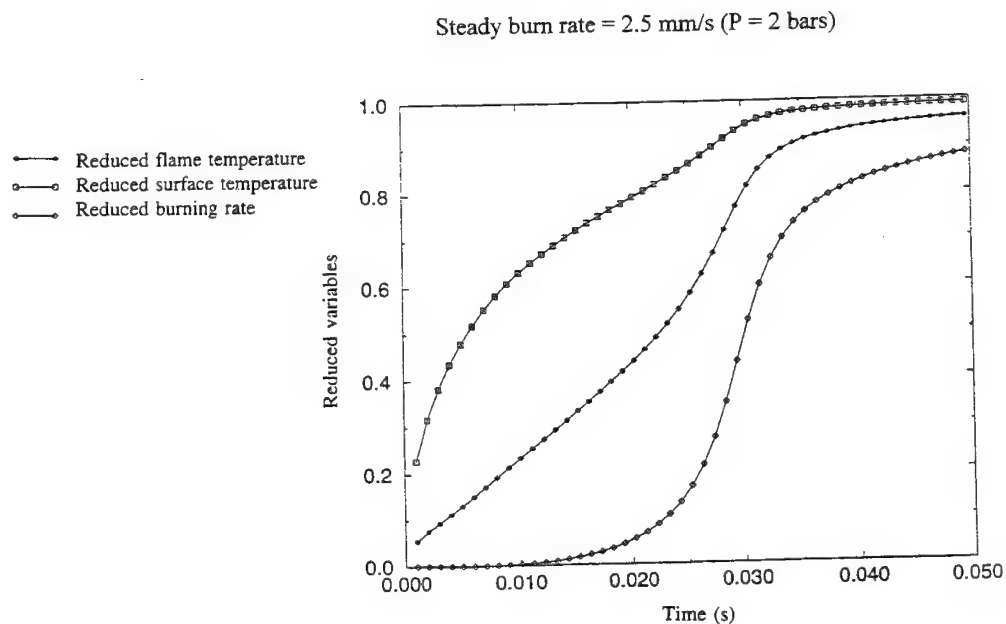


**Figure 3.** Unsteady Burn Rate of an Aluminized AP-based Composite Solid Propellant during Ignition

An important factor that affects significantly the ignition transient is the interaction between the flame and the neighboring fluid. Eq. (8) indicates that the heat flux at the propellant surface is divided into three terms: the heat flux due to the superficial degradation reactions, the flame heat flux,  $q_{f1}$ , and the the ignition heat flux,  $\Phi_{ign}$ , which represents the influence of the neighboring fluid. The flame model is

implemented through the wall boundary conditions of the flow governing equations (assuming that  $T_f = T_{wall}$ ). The ignition flux is modeled using a wall-function (Eq.(6)), which is based on  $T_{wall}$  and  $T$  (near wall cell temperature). The wall temperature,  $T_w$ , rises from  $T_0$ , the propellant initial temperature, to  $T_{ign}$ , the ignition temperature, and to  $T_f$ , the flame temperature. In the model, one implicitly assumes that the wall-function is not modified by the flame, which is clearly not true in solid rocket motor applications. This weakness of the model will be eliminated in future studies.

The complete description of the combustion avoids taking an ignition temperature criterion into account to evaluate the ignition delay and, in addition, allows one to predict the delay necessary to sustain a steady combustion burning rate. However, for the sake of simplicity and to avoid time-consuming computations (as described in [6-7]), an algebraic relationship giving the unsteady propellant burning rate and, consequently, the surface temperature, has been established and used for most industrial applications. From the previous set of equations, a series of parametric numerical computations were conducted to describe the unsteady behavior of AP-based composite propellants with and without aluminum, from ignition to the steady regime. An example of such a calculation is reported in Figs.3 and 4.



**Figure 4.** Unsteady Behavior of an Aluminized AP-based Composite Solid Propellant During Ignition

The plots show the three different regimes : the heating of an inert material (ignition regime), the progressive apparition of the flame and the burn rate (transition regime) and the steady state. The final relationship deduced from this study can be written as :

if  $t \leq t_{ign}$

$$R_{burn} = 0$$

if  $t_{\text{ign}} < t < t_{\text{ign}} + dt^*$

$$R_{b_{\text{unst}}} = a p^n \left( \frac{t - t_{\text{ign}}}{dt^*} \right)$$

$$dt^*(s) = \frac{(10^3 dt_{\text{unst}}(s))^{c_2}}{10^3} \quad (15)$$

$$c_2 = \left( \frac{50 - p(\text{bar})}{48} \right)^3$$

if  $t \geq t_{\text{ign}} + dt^*$

$$R_{b_{\text{unst}}} = a p^n$$

where the term  $a p^n$  is the standard steady burn rate and  $dt^*$  is at a given pressure the necessary delay to reach the steady state from ignition.

That means that the steady state burn rate relationship can be used only after this delay which corresponds to the establishment of the propellant flame. Eq. (15) shows that the parameter  $dt^*$  is independent of the ignition heat flux (contrary to the ignition delay  $t_{\text{ign}}$ ) and decreases as the pressure increases inside the rocket motor.  $dt^*$  also depends on the parameter  $dt_{\text{unst}}$  which is by definition the delay of the flame establishment at low pressure ( $P = 2$  bar) and can be obtained by computation or experimental results for a given propellant. By way of example, for AP-CTBP composite propellants with aluminum,  $dt_{\text{unst}} = 21$  ms ( $dt^* = 1$  ms at  $P \sim 50$  b). For AP-CTBP composite propellants without aluminum,  $dt_{\text{unst}} = 7$  ms.

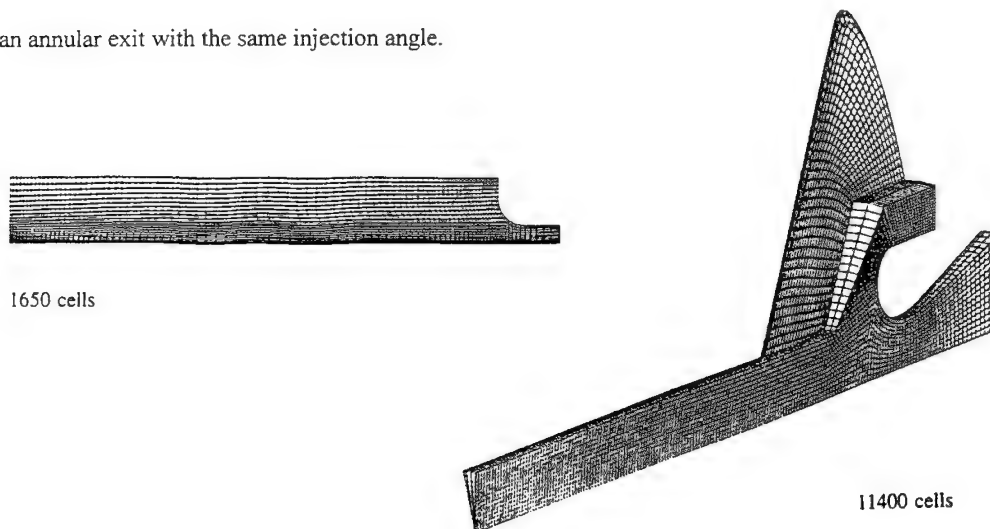
Included in this modelization is a two-dimensional ignition propagation at the surface propellant. This propagation corresponds to the spread of the ignition along the gas-side propellant surface, by gas conduction from cell to cell, due to the apparition of reactive gases at the propellant surface. The chemical reactions which occurs in this thin zone very close to the propellant surface are related to the propellant degradation. The propellant-side ignition propagation is assumed to be negligible because the solid propellant density is very large compared to the gas phase density. The details of the model are given in annex 1.

## NUMERICAL CALCULATIONS AND EXPERIMENTAL RESULTS

Two types of AP-based composite propellants were used for the comparison of theory and experiment: one propellant with aluminum (AP weight fraction  $\sim 68\%$ , Al  $\sim 18\%$ ) and one without aluminum (AP  $\sim 73\%$ ). Because of the cost of the experiments, these two propellants were tested in different configurations of rocket motors: the first was tested in a solid rocket motor with 12 aft-fins and the second one in a more simple rocket (see Fig. 1) with an operculated nozzle (the rupture pressure is  $\sim 40$  bars). In both cases, igniter and motor grains were made with the same propellant.

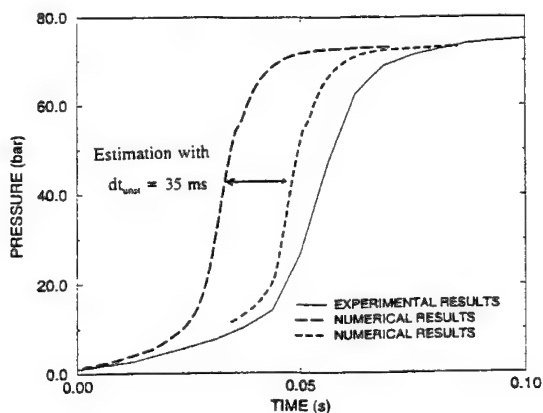
Fig. 5 shows the two computational grids used for the internal flow numerical simulations. The three-dimensional grid consists of three domains which represent the axisymmetrical longitudinal chamber, the exhaust nozzle and the aft-fins. The igniter geometry is limited to the nozzle exit of which the injection angle is  $13^\circ$ . Because of the geometrical symmetry, only  $1/24$  of the motor is computed. The 2D axisymmetrical grid represents the geometric configuration of the second motor. The igniter system produces hot gases which flow through a multiperforated nozzle with 6 ports at a  $35^\circ$  angle with respect to the motor axis. To keep the axisymmetrical configuration, it was decided to represent the nozzle by

an annular exit with the same injection angle.



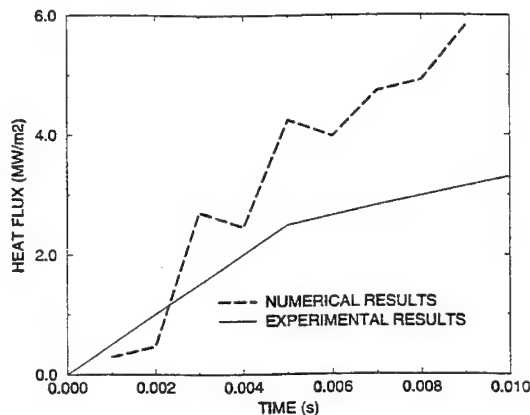
**Figure 5.** Computational Grids of the two Solid Rocket Motors

The comparison between experimental and numerical chamber pressure evolutions of the firing test corresponding to the motor with aft-fins is shown in Fig.6. The pressure measurement indicates three different regimes which are quite different from those previously mentioned. The first regime is the preheating of the inert propellant which lasts about 10 ms. This delay corresponds to the first ignited point which is located in the second half of the longitudinal chamber. The experimental ignition, which is not measured but estimated from the surface temperature measurement of a inertial fluxmeter, is  $\sim 10$  ms. The propagation of the ignition and the flame inside the chamber occurs almost instantaneously ( $\sim 3$  ms) with a quasi-linear pressure increase. The unsteady behavior of the propellant combustion adds  $\sim 20$  ms to the delay before reaching a pseudo-stationary combustion regime ( $dt_{unst} = 21$  ms for the aluminized AP-based composite propellant used). The following regime is the sharp pressurization rise of the motor which corresponds to the ignition propagation in the aft-fins. The pressure stabilizes at  $\sim 80$  bars which is the motor operating condition.



**Figure 6.** Experimental and Numerical Pressure Evolutions of the Afts-fins Rocket Motor

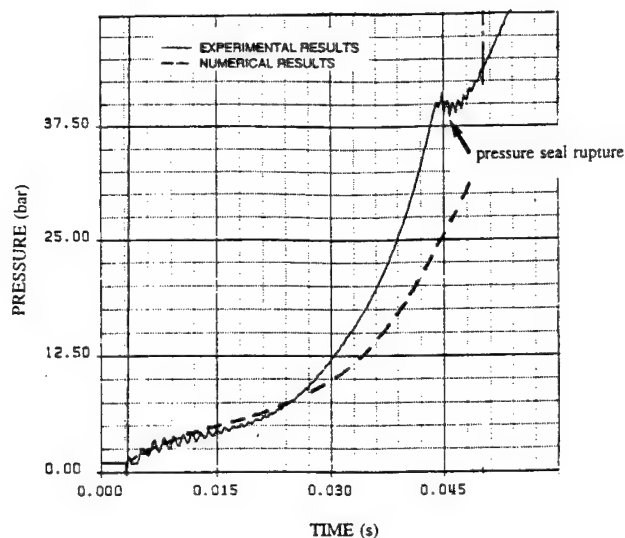
The numerical results and the data show that the calculated pressure rise occurs too early. In fact, the calculated unsteady combustion delay ( $dt_{unst}$ ) has been probably underestimated. This assertion is deduced from the experimental results obtained by [8]. It has been observed by means of laser propellant ignition studies that  $dt_{unst} = 35$  ms for the operating conditions of the rocket motor studied (same mean heating flux and same pressure). However, this ignition delay is the so-called go/no-go ignition delay which does not correspond exactly to the ignition delay defined in the present work. If one takes into account the experimental unsteady combustion delay in the unsteady burn rate relationship, the calculated pressure evolution is in good agreement with the measurement. This curve is presented in dashed-line in Fig. 6. However, the calculated pressure rise can also be attributed to the neglect of the interaction between the flame and the neighboring fluid. The wall mass transfer due the propellant degradation tends to decrease the heat flux received by the propellant. The investigations of the calculated and experimental wall heat fluxes show that the prediction is accurate (see Fig. 7). This observation is confirmed by the fact that the first ignition point is very well predicted.



**Figure 7.** Wall Heat Flux of the Afts-fins Rocket Motor during Ignition Transient

The comparison between experimental and numerical chamber pressure evolutions of the firing test corresponding to the simplified motor is shown in Fig.8. The calculations have been made from ignition until the rupture of the pressure seal (the rupture is progressive and it is difficult to predict the evolution of the crack except by matching the calculated pressure with the measurements). The first ignition delay observed is  $\sim 28$  ms. Taking discrepancies into account, the experimental delay can be estimated between 12 and 27 ms. The mean value of 20 ms is probably a good estimation.

The comparison between data and calculated wall heat flux indicates an underprediction of the wall heat flux which corresponds in fact to the underestimation of the ignition delay (see Fig. 9). This deficiency is caused by the wall-function relationship of the numerical code which is well adapted for flows parallel to the wall. Due to the  $35^\circ$  angle of the igniter ports, the injection flow probably creates, at the impact with the wall, a heat flux stronger than the predicted one. The unsteady behavior of the propellant combustion has been taken into account in the unsteady burn rate relationship with an unsteady combustion delay ( $dt_{unst}$ ) of  $\sim 7$  ms (corresponding to AP-based composite propellants without aluminum). Although the calculated ignition delay is not very well estimated, the shape of the pressure evolution with respect to time is well predicted. The axial flame propagation in the motor chamber is much slower than the flame propagation in the first motor and is not complete when the pressure seal is ejected at 40 bars.



**Figure 8.** Experimental and Numerical Pressure Evolutions of the Simplified Rocket Motor

Finally, in both cases, the surface propagation of the ignition appears to be of secondary importance compared to the propagation of the flame by convection in the main flow and can be neglected.

### CONCLUSIONS

A study of the ignition propagation inside subscale solid rocket motors was conducted by developing a multi-dimensional numerical tool suited to the simulation of internal flows induced by propellant combustion and igniter supersonic flows. The solution procedure treats the igniter supersonic flow, the boundary layer at the propellant surface and the unsteady behavior of the propellant combustion during ignition transient period.

The results of the calculations indicate that the code is able to accurately describe the main features of the phenomena involved during ignition transient. The evolution of the pressure and the propagation of the ignition inside the motor are fairly well predicted. Some discrepancies have been mentioned and suggest room for improvements in the future. The wall-function relationship should be adapted to wall boundary layers with mass transfer (due the propellant degradation) and regions of non-boundary layer type flows. Another improvement would be to incorporate the complete numerical resolution of the unsteady combustion model in the CFD code. The influence of the pressure seal rupture is a study in itself and can not be modeled successfully.

### REFERENCES

- [1] **Lengellé, G., Bizot, A., Duterque, J., Amiot, C.,** "Ignition of Solid Propellants." La Recherche Aéronautique, N°2, 1991.
- [2] **Price, E.W., Bradley, H. H., Dehotity, G. L., and Ibricu, M. M.,** "Theory of Ignition of Solid Propellants," AIAA Journal, Vol.4, N°7, pp.1153-1181, 1966..
- [3] **Bizot, A.,** "Turbulent Boundary layer with Mass Transfer and Pressure Gradient in Solid

- Propellant Rocket Motors," AIAA Paper 95-2707, 1995.
- [4] **Bizot, A., Gobbo-Ferreira, J., Lengellé, G.,** "Modelisation of the Ignition Process of Homogeneous Propellants," AIAA/ASME/SAE 21<sup>st</sup> Joint Propulsion Conference, 1985.
- [5] **Beckstead, M. W., Derr, R. L., and Price, C. F.,** "A Model of Composite Solid Propellant Combustion Based on Multiple Flames," Vol. 8, pp. 2200-2207, 1970.
- [6] **Johnston, W.A.,** "A Numerical Procedure for the Analysis of Internal Flow in a Solid Rocket Motor During Ignition," AIAA Paper 91-1655, 1965.
- [7] **Lu, Y., Kuo, K. K.,** "Modeling and Numerical Simulation of Combustion Process Inside a Solid-Propellant Crack," Propellants, Explosives, Pyrotechnics, 19, pp. 217-226, 1994.
- [8] **Shannon, L. J.,** "Composite Solid Propellants Ignition by Radiation," AIAA Journal, Vol. 8, N° 2, 1970.

### NOMENCLATURE

$a_p$	propellant thermal diffusivity [ $m^2/s$ ]
$A_g$	pre-exponential factor of the gas phase reaction
$A_p$	pre-exponential factor of the steady state degradation reaction
$B_{ign}$	pre-exponential factor of the ignition reaction
$C$	specific heat [ $J/kg.K$ ]
$E_p$	activation energy of the ignition and steady state degradation reactions [ $J/mole$ ]
$E_g$	gas phase reaction activation energy [ $J/mole$ ]
$f_\mu$	damping function
$\dot{m}_p$	propellant mass flow rate [ $Kg/m^2.s$ ]
$p$	pressure (Pa)
$Pr$	Prandtl Number
$Q_s$	heat released by the ignition and steady state degradation reactions [ $J/kg$ ]
$Q_g$	heat released by the gas phase reaction [ $J/kg$ ]
$q_f$	heat flux issuing from the flame [ $W/m^2$ ]
$Re$	Reynolds Number
$R$	universal gas constant
$R_b$	burning rate [ $m/s$ ]
$t$	time [ $s$ ]
$T$	temperature [ $K$ ]
$T_0$	solid propellant initial temperature
$T_c$	temperature at the near wall cell center [ $K$ ]
$u$	longitudinal velocity [ $m/s$ ]
$u_c$	longitudinal velocity at the near wall cell center [ $m/s$ ]
$x$	distance [ $m$ ]
$y$	distance to the wall [ $m$ ]
$y_c$	distance from the cell center to the wall [ $m$ ]
$\lambda$	conductivity [ $W/m.K$ ]
$\rho$	density [ $Kg/m^3$ ]
$\mu$	viscosity [ $Kg/m.s$ ]
$\tau$	shear stress [Pa]
$\Phi$	heat flux [ $W/m^2$ ]
$\chi = 0,41$	

### Subscripts

ad	adiabatic
b	burning rate
c	cell center adjacent to the wall
f	flame



g	gas phase
ign	ignition
l	laminar
p	solid propellant
s	propellant surface
t	turbulent
unst	unsteady
w	related to the wall boundary of the computational grid

Superscript

- steady values

## ANNEX 1

### Ignition propagation at the propellant surface

The ignition propagation velocity is the result of the heat transfer by conduction in the gases issuing from the propellant surface. The simplified unsteady model used to evaluate the velocity concerns the heat transferred by conduction which causes the inflammation of the gases produced by the propellant degradation. The energy balance of the gases at the propellant surface can be written as :

$$\begin{aligned} \rho_g C_g \frac{\partial T}{\partial t} &= \lambda_g \frac{\partial^2 T}{\partial x^2} + B_{ign} \exp\left(-\frac{E_p}{RT}\right) \\ t = 0, \quad T &= T_i \\ x = 0, \quad T &= T_{ign} \\ x \rightarrow \infty, \quad \frac{\partial T}{\partial x} &\rightarrow 0 \end{aligned} \quad (17)$$

where x is the direction parallel to the propellant surface.

The propagation occurs close to the propellant surface in a thin zone that is assumed to be at a temperature  $T_i$  close to the ignition temperature. This is a condition necessary for the ignition propagation. Therefore, one can linearize the chemical term which can be expressed as :

$$\begin{aligned} B_{ign} \exp\left(-\frac{E_p}{RT}\right) &= B_{ign} \exp(-E^*) \left(1 - E^* \frac{T_{ign} - T}{T_{ign}}\right) \\ E^* &= \frac{E_p}{R T_{ign}} \end{aligned} \quad (18)$$

One obtains the following solution :

$$T - T_i = \frac{1}{2} \left[ \exp\left(-x \sqrt{\frac{v}{a_p}}\right) \operatorname{erfc}\left(\frac{x}{2\sqrt{a_p t}} - \sqrt{vt}\right) + \exp\left(+x \sqrt{\frac{v}{a_p}}\right) \operatorname{erfc}\left(\frac{x}{2\sqrt{a_p t}} + \sqrt{vt}\right) \right] \quad (19)$$

$$v = -B_{ign} \exp(-E^*) \frac{E^*}{\rho_g C_g T_{ign}}$$

This reduces to the approximated relation which gives the delay  $t_i$  necessary for the ignition to propagate on a distance  $\Delta L$  and, consequently, the propagation velocity :

$$\begin{aligned} \frac{\Delta L}{2\sqrt{a_p t_f}} &= \alpha \sqrt{B_{ign}^* t_f} \\ V_{prop} &= \frac{\Delta L}{t_f} = 2 \alpha \sqrt{a_p B_{ign}^*} \\ B_{ign}^* &= \frac{B_{ign} \exp(-E^*) E^*}{\rho_g C_g T_{ign}} \end{aligned} \quad (20)$$

where  $\alpha$  is a constant adjusted from the exact calculation of the solution ( $\alpha = 0.65$ ).

The difficulty in determining the propagation velocity is the estimation of the low temperature reaction mechanism at the propellant surface. The assumption made is that the reaction mechanism is the ignition mechanism previously established (the values used are in-depth reaction kinetic parameters instead of superficial reaction kinetic parameters). The temperature in the propagation zone is chosen as the ignition temperature ( $T_{ign} = 690$  K). The propellant gas characteristics estimated at low pressure are:

$$\lambda_p = 0.05 \text{ W/m.K}, \rho_p = 5 \text{ Kg/m}^3, C_p = 1250 \text{ J/Kg.K},$$

which gives  $V_{prop} = 15$  m/s. This combustion propagation velocity is the value used in the numerical calculations

# EVALUATION OF THERMOCHEMICAL EROSION OF THE SOLID PROPELLANT ROCKET GRAPHITE NOZZLE THROATS BY INTEGRAL BOUNDARY LAYER TECHNIQUE

Hüseyin Vural<sup>1</sup> and M. Ali Ak<sup>2</sup>

<sup>1</sup>Middle East Technical University Mechanical Engineering

Fax: (90) - 312- 210 1266 e-mail: hvural@rorqual.cc.metu.edu.tr

<sup>2</sup>TÜBİTAK Defence Industries Research and Development Institute  
ANKARA-TÜRKİYE

**ABSTRACT-** An aerothermochemical model for the graphite nozzle erosion of the rocket motors was developed. The theoretical modeling of the problem is similar to the approach of Kuo and Keswani and the solution technique differs in modeling of the boundary layer over the nozzle. In this study, the integral formulation and solution of the boundary layer equations for highly accelerating flow in rocket nozzles derived by D.R. Bartz was used in the throat erosion calculations. The integral energy equation was modified by including heterogeneous wall reactions. It was assumed that the mass transfer Stanton number is equal to heat transfer Stanton number and diffusion controlled erosion was calculated accordingly. Predicted results showed good agreement with Geisler's experimental data and the theoretical predictions made by Kuo and Keswani. The integral method used in this study is found to be yielding the results faster than the differential method.

## INTRODUCTION

Carbon-carbon composites and graphitic materials (pyrolytic and crystalline) have found increasing use in the manufacture of nozzles and nozzle throats for the solid propellant rocket motors due to their high resistance and strength to high temperatures and high pressures. It was observed that these materials were subjected to erosion during the operation of the solid propellant rocket motors. The erosion of the material in the throat region results with the increase in the throat area, and hence, decrease in the motor performance. The decrease in the performance due to throat erosion must be determined and the result must be used in the development of the solid propellant rocket motor. One way to determine the throat erosion is to perform full scale test firing. This method requires considerable time and expense. The other method is numerical simulation that is cheap and fast compared to the first method.

The identification and description of the major significant mechanisms taking place in the nozzle regression constitute a relatively recent field of study in solid rocket technology. There are several experimental and theoretical works reported in the literature. Geisler [2] used an experimental motor to measure the recession rate of carbon-carbon composites and bulk graphites as a function of aluminum content of the propellant. Geisler found out that the recession rate was proportional to the concentration of H<sub>2</sub>O, OH and CO<sub>2</sub> and inversely proportional to H<sub>2</sub> concentration. Geisler also concluded that chemical attack was the only significant mechanism for the throat erosion. Klager [3] had conducted experimental firings and found the similar results.

Recently, Kuo and Keswani [4] developed a comprehensive model for the carbon-carbon erosion. Keswani solved the problem with boundary layer solution method developed by Spalding and Patankar [5]. In this model, gas phase conservation equations were Favre averaged to account for variable density effects. Two equations (k-ε) turbulence closure model was used for the final averaged gas-phase conservation equations. Keswani showed that recession was strongly influenced

by propellant composition, chamber pressure and motor geometry and the recession was due to the oxidation of carbon to carbon monoxide by water vapor and carbon dioxide. The analysis also showed that the influence of chemical kinetics was predominant only when surface temperature was low. The recession rate was largely determined by the diffusion rate of oxidizing species when the nozzle surface temperature has reached about 2500 K.

Borie, Brulard and Lengelle [6] investigated the same problem but they assumed that only  $H_2O$  reacts with the carbon-carbon surface,  $CO_2$  being in very small amount. Because of the complexity of the problem, they solved the boundary layer equations by a two step process:

1. Reference (k- $\epsilon$ ) boundary layer calculations on a smooth wall.
2. Practical integral boundary layer calculations with coefficients adjusted on the results of the (k- $\epsilon$ ) solutions.

They compared the theoretical model with the experiments and found out that the surface roughness induced by the erosion has significant effect on the heat and mass transfer. They showed that the controlling mechanism of the erosion was intermediate; 30% chemical and 70% diffusion controlled.

The objective of this study is to establish a physical and mathematical model for the carbon-carbon erosion. The model includes the effect of the propellant composition, chamber pressure, kinetically and diffusion controlled regimes, as well as transient effects are considered in the model.

## THEORETICAL FORMULATION

### A. Physical Model for Carbon-Carbon Erosion

As the solid propellant motor operates, carbon-carbon nozzle is exposed to the hot combustion gases that form a turbulent boundary layer over the nozzle surface. Species like  $CO_2$  and  $H_2O$  diffuse all along the boundary layer and reach to the surface. These species react with the surface and heterogeneous surface reactions take place. They are assumed to react with carbon as follows:



The erosion of the graphite is forced with kinetically and diffusionally controlled reactions. In order to account both diffusion and chemical kinetics the following conventional formula is employed in the analysis:

$$\dot{r}_c = \left[ \frac{1}{\dot{r}_{c,d}} + \frac{1}{\dot{r}_{c,ch}} \right]^{-1} \quad (3)$$

The kinetic recession rate  $\dot{r}_{c,ch}$  depends on the kinetics of the heterogeneous reactions, the concentrations of the various reactants and the surface temperature of the nozzle. The surface temperature is determined by the transient heat-conduction response of the graphite nozzle and the heat transfer from the combustion gases.

### B. Modelling of the Heterogeneous Chemical Reactions

#### B.1 Kinetically Controlled Erosion

For kinetically controlled erosion regime the burning of the graphite with each species can be expressed as a function of surface temperature through the use of the Arrhenius law of surface pyrolysis:

$$\dot{r}_{c,chl} = \frac{A_s p_i}{\rho_c} \exp\left(-\frac{E_{a,s}}{R_u T_s}\right) \quad (4)$$

where  $p_i$ ,  $\rho_c$ ,  $R_u$  and  $T_s$  represent partial pressure of steam or carbon dioxide, nozzle material density, universal gas constant and surface temperature, respectively. The activation energy  $E_{a,s}$  and the pre-exponential factor  $A_s$  are taken to be 41.9 kcal/mole and 2470 kg/(m<sup>2</sup>·s·atm), [4]. Using this equation, the recession rate of graphite in the limit of chemical kinetics control can be expressed as

$$\dot{r}_{c,chl} = \sum_i \dot{r}_{c,chl,i} \quad (5)$$

As it can be seen from the equation (4) kinetically controlled erosion regime is strongly dependent on the surface temperature and reactants partial pressure. As time proceeds, the surface temperature increases due to the convective heat transfer from the hot combustion gases to the solid wall and infinitely fast kinetic rates are obtained at the nozzle surface, thus, the recession is controlled by diffusion only. The surface temperature  $T_s$ , can be found from the transient heat transfer analysis in a semi-infinite solid:

$$\frac{T_s - T_i}{T_\infty - T_i} = 1 - \left[ \exp\left\{\frac{h^2 \alpha t}{k^2}\right\} * \left(1 - \operatorname{erf}\left\{\frac{h\sqrt{\alpha t}}{k}\right\}\right) \right] \quad (6)$$

where  $T_i$ ,  $T_\infty$ ,  $h$ ,  $\alpha$ ,  $k$  and  $t$  are initial graphite surface temperature, free stream gas temperature, convective heat transfer coefficient, thermal diffusivity and thermal conductivity and time, respectively.

## B.2 Diffusionally Controlled Erosion

In the diffusionally controlled erosion regime the rate of the surface recession is obtained by assuming the analogy between heat and mass transfer. It is assumed that both temperature and the concentration profiles develop together in the same manner, hence, the driving potential for both heat and mass transfer is the same. So the formulation that was used in order to find the heat transfer is also valid for the diffusion. The empirical Stanton number was utilized for both heat and mass transfer. The following equations were employed in order to find the diffusion controlled erosion as follows:

$$h_m \cong U_\infty St_m \quad (7)$$

where  $h_m$ ,  $U_\infty$  and  $St_m$  are convective mass transfer coefficient, free stream gas velocity and the mass transfer Stanton number, respectively. Thus, the reactants consumption rate  $\dot{m}$ , at the surface are found by the following formula.

$$\dot{m} = \sum_i h_m (\rho_i - \rho_s) \quad (8)$$

where  $\rho_i$  and  $\rho_s$  are free stream and surface densities of  $i^{\text{th}}$  species, respectively. Since infinite reaction rates are obtained at the nozzle surface, the concentration at the nozzle surface is very small compared to free stream concentration values, and it is neglected. Finally, the recession of the graphite surface is obtained by the following formula :

$$\dot{r}_{c,d} = \frac{1}{\rho_c} \sum_i \dot{m}_i \frac{W_c}{W_i} \quad (9)$$

where  $W_c$  and  $W_i$  represent molecular weights of carbon and species  $i$ . For the kinetically controlled and diffusional controlled erosion for the graphite surface, convective heat transfer and mass transfer coefficients must be known. In order to find these transfer coefficients, boundary layer flow in the nozzle must be solved. The following part describes the method that was used in this analysis.

### C. Governing Equations for the Boundary Layer Region

The simplest and the fastest method for the solution of the turbulent boundary layer development is the simultaneous solution of the integral forms of the boundary layer momentum and energy equations. The weakness of the solution technique is that it needs experimental or empirical relations for the coefficients within the differential equations. The formulation can be simplified by reasonable assumptions. The integral formulation and solution of the boundary layer equations for highly accelerating flow (for rocket nozzles) had been used by numerous researchers successfully and among them the method derived by D.R. Bartz [1] was used in the boundary layer calculations in this analysis.

The following assumptions were made in the derivation of the equations:

1. The flow is axisymmetric and steady and there is no swirl in the flow.
2. The boundary layer is confined to a distance from the wall which is small compared with the distance from the symmetry axis.
3. The axial momentum was balanced with the pressure and the wall friction.
4. The flow outside the boundary layer is isentropic and parallel to wall.
5. The pressure does not change in the radial direction.
6. The laminar viscosity depends exponentially upon temperature (Sutherland's Law).
7. The flow is turbulent all along the nozzle.

#### C.1 The Integral Momentum Equation

The basic form of the integral momentum equation is given by:

$$\frac{d}{dx}(\rho U_\infty^2 \theta) = r \rho \tau_s - r \rho U_\infty \delta^* \frac{dU_\infty}{dx} \quad (10)$$

where  $r$ ,  $x$ ,  $\tau_s$ ,  $\theta$  and  $\delta^*$  are coordinate in radial direction, distance along the nozzle wall in the flow direction, retarding wall shear stress, momentum and the displacement thicknesses respectively. It can be expressed in a more convenient form by differentiating and introducing the skin-friction coefficient  $C_f$ . Under assumptions (4) and (5), the expressions involving  $\rho$  and  $U_\infty$  can be written in terms of Mach number  $M$ , as follows:

$$\frac{1}{\rho U_\infty} \frac{d(\rho U_\infty)}{dx} = \frac{1 - M^2}{M \left[ 1 + \frac{\gamma - 1}{2} M^2 \right]} \frac{dM}{dx} \quad (11)$$

Transforming the independent variable to  $z$ , the distance along the nozzle axis the following can be derived:

$$\frac{dx}{dz} = \left[ 1 + \left( \frac{dr}{dz} \right)^2 \right]^{1/2} \quad (12)$$

The final form of the momentum equation will be as shown below:

$$\frac{d\theta}{dz} = \frac{C_f}{2} \left[ 1 + \left( \frac{dr}{dz} \right)^2 \right]^{1/2} - \theta \left[ \frac{2 - M^2 + \frac{\delta^*}{\theta}}{M \left( 1 + \frac{\gamma - 1}{2} M^2 \right)} \frac{dM}{dz} + \frac{1}{r} \frac{dr}{dz} \right] \quad (13)$$

## C.2 Integral Energy Equation

The basic form of the boundary layer integral energy equation is given by:

$$\frac{d}{dx} \left[ (r \rho U_\infty C_p (T_\infty - T_s) \phi) \right] = r q + r q_c \quad (14)$$

where  $C_p$ ,  $\phi$ , represent specific heat of free stream gas and boundary layer energy thickness respectively. The term  $q$  is used for the surface heat transfer rate that occurs due to the temperature gradient between the wall and the free stream. The term  $q_c$  is calculated by finding the net change of enthalpy due to erosion of the graphite surface with hot reactive gases. Equation (14) is the integral energy equation for thin axi-symmetric boundary layers in terms of energy thickness  $\phi$ . It can be put in a more convenient form by differentiating by parts, introducing the definition of the Stanton number,  $St_h$ , substituting Eq.(11) and transforming the independent variable to  $z$  and rearranging to give

$$\begin{aligned} \frac{d\phi}{dz} = & \left\{ St_h \left( \frac{T_{as} - T_s}{T_\infty - T_s} \right) + \frac{q_c}{\rho U_\infty C_p (T_\infty - T_s)} \right\} \left[ 1 + \left( \frac{dr}{dz} \right)^2 \right]^{1/2} \\ & - \phi \left[ \frac{1}{\rho U_\infty} \frac{d(\rho U_\infty)}{dz} + \frac{1}{r} \frac{dr}{dz} - \frac{1}{T_\infty - T_s} \frac{dT_s}{dz} \right] \end{aligned} \quad (15)$$

In order to solve these two differential equations (13) and (15) simultaneously, it is necessary to specify the expressions for  $C_f$  and  $St_h$  in terms of the variables  $\theta$  and  $\phi$ . The evaluation of these parameters was described by Bartz et al [1]. With the specification of  $C_f$  and  $St_h$  only the local Mach number at the edge of the boundary layer and the boundary layer shape parameter  $\delta^*/\theta$  need to be determined in order to proceed with the solution of the integral momentum and integral energy equations for  $\theta$  and  $\phi$ , respectively. In (15) the adiabatic wall temperature was calculated by using the recovery factor of 0.9.

## RESULTS

The coupled differential equations were solved simultaneously to predict the erosion rate of the carbon-carbon nozzles and the results were compared with the differential model used by Kuo and Keswani. In the differential formulation the turbulent boundary layer over the nozzle was solved by Patankar Spalding technique and the methodology suggested by Kuo and Keswani was used to run the program. In the program standart (k-ε) turbulence model was used. It was detected that the modification of von-Driest according to the surface roughness did not affect the results and because of this fact the law of the wall was used for evaluation of the surface boundary conditions of (k-ε). Laminar to turbulent flow transition was not considered and the computations were started for the turbulent flow at the inlet. Turbulent Prandtl and Lewis numbers of 0.9 were used.

The nozzle configuration for which the results of the computations were obtained is given below. The nozzle has an elliptic entrance region and a conic exit cone.

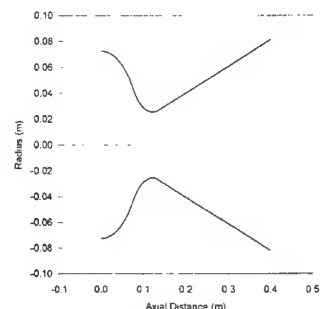


Figure 1. Nozzle Geometry

The results of the integral technique is compared to that of Patankar Spalding technique in the following figures.

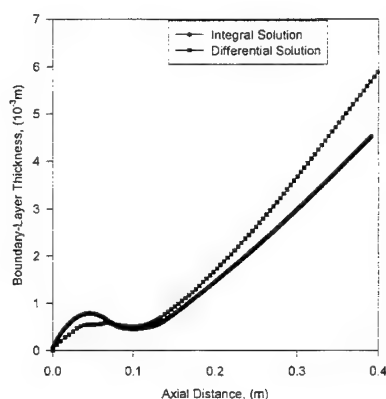


Figure 2. Variation of Boundary Layer Thickness in Nozzle

Figure 2 shows the variation of the boundary layer thickness along the nozzle. The boundary layer thickness, that begins to increase at the entrance of the nozzle, has been affected by the variation of mass flux. It reaches a maximum in the entrance region and thereafter is forced to decrease before approaching to the throat. As mass flux decreases in the exit cone, the boundary layer thickness increases again. Differential and integral solutions deviate from each other in the exit cone region. It was assumed that the integral formulation fails to predict mass entrainment rates through the boundary layer. This problem, however, does not influence erosion at the throat, since both methods predicts the same thickness at the throat.

Figure 3 and 4 represents the variation of the velocity, turbulent kinetic energy and eddy viscosity at the throat location. As it can be seen from Figure 3, the assumed power law velocity profile for the integral solution is consistent with the velocity profile obtained from the exact formulation.



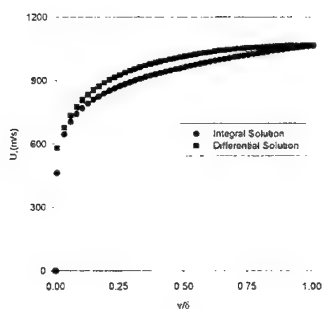


Figure 3. Velocity Profiles at Throat

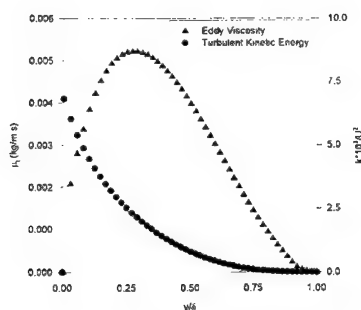


Figure 4. Turbulent Kinetic Energy and Eddy Viscosity at Throat

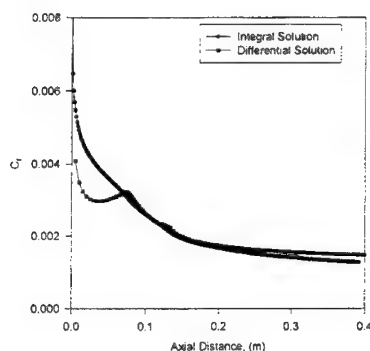


Figure 5. Variation of Skin Friction Coefficient in Nozzle

Figure 5 shows the variation of the skin friction coefficient along nozzle axis. The skin friction coefficient obtained from the differential solution deviate from that of the integral solution at the nozzle entrance. Both methods predict the same skin friction coefficient at the throat. It was assumed that the difference between the solutions at the entrance region is due to the skin friction data used in integral formulation. The skin friction coefficient data of Coles [1] is not adequate for the entrance region because it is applicable for flat wall flow at constant pressure. In the entrance region, the local flat wall assumption can not represent the correct picture since in this region the flow accelerates very fast in a short distance which is due to the elliptic geometry. In the differential formulation, however, the axial pressure drop term was taken into account in the calculation of wall shear as proposed by Spalding [5]. The secondary peak in the differential formulation is due to the increase of wall shear and momentum flux in the entrance region.

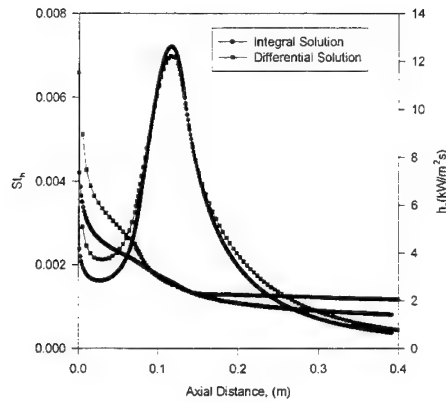


Figure 6. Variation of Convective Heat Transfer Coefficient and Stanton Number in Nozzle

The variation of convective heat transfer coefficient and erosion rate of graphite along nozzle axis are shown in Figures 6 and 7. The convective heat transfer coefficient in the nozzle reaches its maximum value at the throat due to higher mass flux, as shown in Figure 6. A similar argument is valid for the graphite erosion rate at the throat. The convective heat transfer Stanton numbers monotonically decreases along the nozzle, and the values at the throat location are the same for integral and differential solutions. Both integral and differential solutions have predicted the same heat transfer and erosion rates at the throat, and also results obtained for exit cone and entrance regions are very close to each other.

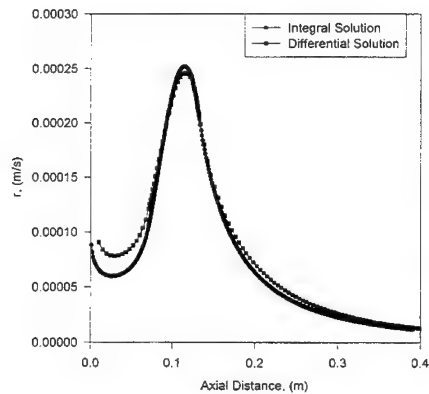


Figure 7. Variation of Graphite Erosion Rate in Nozzle

Finally, Figure 8 compares the results of the integral solution with the Geisler's experimental data. As it can be seen the experimental findings are in good agreement with the integral formulation solutions.

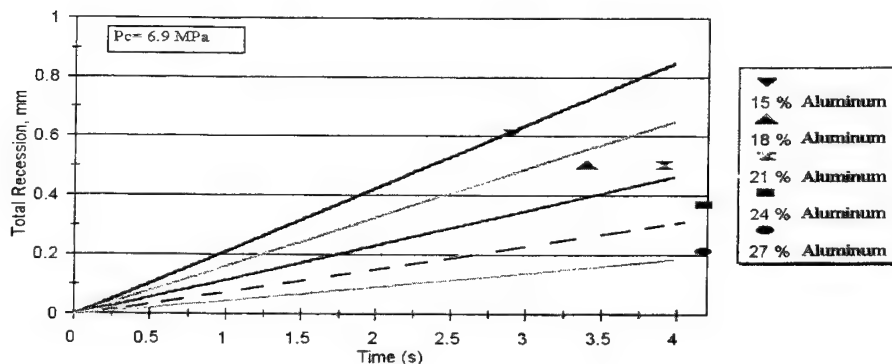


Figure 8. The Effect of Aluminum Content in Total Erosion

### DISCUSSION AND CONCLUSION

In the present study, aerothermochemical erosion of graphite nozzle throats were investigated. The diffusion controlled erosion regime was solved by using integral boundary layer approach. This modeling resulted with two ordinary differential equations for the momentum and energy. The parameters appear in both equations were obtained by experimentally and these are skin friction coefficient and the heat transfer Stanton number found from the von-Karman type of analogy. Diffusional fluxes of oxidizing species through the boundary layer was evaluated by using the heat transfer Stanton number for mass transfer process.

The solution of the new technique compared well with the differential solution technique proposed by Kuo and Keswani. It was found out that both models predicted the same behavior for the boundary layer thickness variation up to throat location and the solutions were found to be different in the exit cone region. The reason for this discrepancy was regarded to be that the integral formulation failed to predict the entrainment rate in to the boundary layer. From the differential solution technique, it was detected that the temperature profile in the entrance region and near the throat region resembles to that of turbulent pipe flow profile and in the exit cone region. This similarity vanishes and temperature changes almost linearly from the nozzle wall to the edge of boundary layer. In the integral boundary layer solution technique, however, the temperature profile does not change. This means that mass flow rate calculated with in the boundary layer was confined to a narrower thickness compared to the thickness calculated in differential solution. This explains the difference between the two models in the exit cone region.

The calculated skin friction coefficient and the heat transfer Stanton number variation in the entrance region were found to be relatively different in the integral and differential solution technique. In the integral formulation the correlation used for the skin friction coefficient and the Stanton number hold for the gradual nozzle contours. In the experimental nozzle for which the computations were performed, the entrance region geometry has not a gradual contour and this explains the reason of this discrepancy.

Although there are some differences between the two models in the entrance region and exit cone, both models converge to the same solution near the throat location. This means that the integral

formulation is satisfactory for graphite erosion simulations and can be used in nozzle design. The integral method is preferred, since it calculates the results faster than the differential method.

## REFERENCES

1. **Bartz, D.R.**, Survey of the Relationship Between Theory and Experiment for Convective Heat Transfer from Rocket Combustion Gases, *Advances in Tactical Rocket Propulsion, AGARD CP-1*, pp. 293-381, 1968.
2. **Geisler, R.L.**, The Relationship Between Solid Propellant Formulation Variables and Nozzle Recession Rates, presented at the JANAF Rocket Nozzle Technology Subcommittee Workshops, 1978, Lancaster, CA.
3. **Klager, K.**, The Interaction of Efflux of Solid Propellants with Nozzle Materials, *Propellants and Explosives*, Vol. 2, pp. 55-63, 1977.
4. **Kuo, K.K., and Keswani, S.T.**, A Comprehensive Theoretical Model for Carbon Carbon Composite Nozzle Recession, *Combustion Science and Technology*, Vol. 42, pp. 145-164, 1985.
5. **Patankar, S.V. and Spalding, D.B.**, Heat and Mass Transfer in Boundary Layers, Intertext Books, London, 1970.
6. **Borie, V., Brulard, J., and Lengelle, G.**, Aerothermochemical Analysis of Carbon-Carbon Nozzle Regression in Solid-Propellant Rocket Motors, *Journal of Propulsion and Power*, Vol. 5, pp. 665-673, 1989.

## COMMENTS

Prof. H. H. Chiu, Institute of Aeronautics and Astronautics, National Cheng Kung University, Tainan, Taiwan, R.O.C.:

The heat transfer and skin friction depend on the drag law used. In the presence of erosive gasification, drag law must be corrected for the wall gasification because of the increased effective boundary layer thickness. Does the drag law used in your calculation account for the effect of gasification at the wall?

Authors' Reply:

The erosion rate of graphite is not very fast, and thus the effect of gasification and mass addition to the boundary layer is not significant. Because of this, the drag law used in the model is quite adequate. If the material used in the nozzle insert had been thermoset, we would have included the mass addition effect, since the ablation rate would have been very large compared to graphite.

Dr. Elaine Oran, Naval Research Lab, Washington, DC, USA:

(1) Why do you think the boundary integral method is giving as good a result as it is? (2) What are the weak points of the input in the differential model? (3) Can you quantify how valid it is to use a  $k-\epsilon$  model?

Authors' Reply:

The boundary layer integral method uses appropriate turbulent velocity and temperature profiles with acceptable experimental skin-friction data. These parameters allow us to solve the turbulent boundary layer quite precisely. Although the differential method is more reliable than that of integral method, it is very slow (regarding computational speed), and hence it cannot be used in the preliminary design stage of solid rocket motors. The  $k-\epsilon$  turbulence model is one of the most widely used models, especially in accelerating nozzle flows. We believe that it is a valid model.

## A NUMERICAL STUDY ON UNSTEADY PRESSURE FLUCTUATIONS OF DAVIS GUN

Han-Chang CHO<sup>1</sup>, Jae-Kun YOON<sup>2</sup>, and Hyun Dong SHIN<sup>1</sup>

<sup>1</sup> : Department of Mechanical Engineering, Korea Advanced Institute of Science and Technology,  
371-1, Kusong-dong, Yuseong-gu, Taejeon, 305-701, KOREA

<sup>2</sup> : School of Industrial and System Engineering, Hansung University, 389, 2-ga, Samsun-dong,  
Sungbuk-gu, Seoul, 136-792, KOREA

**ABSTRACT :** Interior ballistics code for unsteady pressure fluctuations in a Davis gun with two moving boundaries was developed using two-phase fluid dynamic model. Numerical simulation results were compared with experimental values to evaluate the feasibility of the interior ballistic code. By comparing numerical analysis with the experimental data, the numerical pressure-time history and muzzle velocities of the projectile and the counter mass closely agreed with the experimental data. The strong pressure waves were not observed unlike other works. It was considered that this was owing to the high initial porosity and charge ignition near the center of the gun. The pressure wave amplitude was increased exponentially by the lower initial porosity.

### INTRODUCTION

At the gun interior ballistics, interest in the longitudinal structure of the pressure field has been intensified for the generation of strong pressure waves in the gun. The strong pressure waves have been associated with charges in which malfunctions, catastrophic overpressure, have occurred. Also, the presence of large-amplitude pressure waves is associated with increased muzzle velocity variability. The previous works on the unsteady pressure fluctuation generally carried out in a conventional gun with a moving boundary. However, the numerical analysis in this study are conducted in a Davis gun with two moving boundaries.

Davis gun<sup>1</sup> is a special type of recoilless gun. In a Davis gun, a counter mass made of some particulate material, e.g. metal powder, plastic, liquid and solid moving masses, etc., is ejected to the rear, in addition to, or instead of, the combustion gases. The projectile and the counter mass are subjected to approximately equal but opposite direction forces, and this gun has little or no recoil force.

The main objective of this study is to develop the interior ballistic code of Davis gun for the analysis of the unsteady pressure fluctuations. The predictive code, using the one-dimensional two-phase model, has been developed. By comparing the numerical analysis results with the experimental data, we would like to evaluate the validation and usefulness of the interior ballistics code. Also, the combustion behavior in the gun are numerically examined.

## ANALYSIS

Figure 1 illustrates the schematic calculation domain of test gun. The size of the gun is 6.0 cm i.d. and 100 cm long. The longitudinal coordinate is imposed on the distance from the center of the granular bed. The left boundary ( $x = x_c$ ) and the right boundary ( $x_p$ ) of the bed are called the counter-mass base and the projectile base, respectively. The primer which has 10 g BKNO<sub>3</sub> is used to ignite 45 g of disk plate shaped M9 propellant. The propellant is initially charged up with 7.5 cm length, from  $x_c = -3.75$  cm to  $x_p = 3.75$  cm. Both the counter-mass and the projectile, which are made of the same rigid metal, have similar masses. (3848 g, 3841 g)

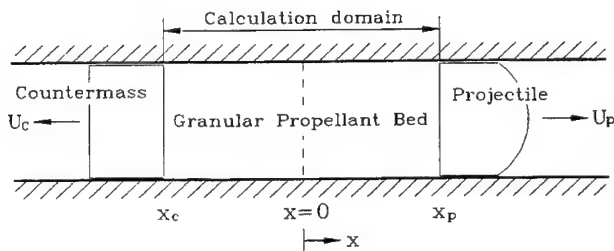


Figure 1. Schematic calculation domain

### Basic Assumptions and Governing Equations

Kuo's two-phase fluid dynamic model<sup>2</sup> is selected among the one-dimensional two-phase models.<sup>2-4</sup> This model was developed by formulating the governing equations on the basis that the fluxes were balanced over the control volumes occupied separately by gas and particle phases.

The assumptions for this model are as follows: a) penetrating hot primer gas do not make energy gradient in the radial direction by well-distributed penetration, b) the propellant gas mixture is described by the Noble-Abel equation of state, c) after the ignition, the propellant grain has uniform burning velocity and the steady-state burning rate law can be used to describe the recession rate of the propellant grains, and d) propellant grains are incompressible, and all of them have the same size and configuration.

Under the above assumptions, the governing equations are formulated as follows. The mass equations are

$$\frac{\partial(\phi\rho_g)}{\partial t} + \frac{\partial(\phi\rho_g U_g)}{\partial x} = A_s \rho_s r_b + m_{ign} \quad (1)$$

$$\frac{\partial[(1-\phi)\rho_s]}{\partial t} + \frac{\partial[(1-\phi)\rho_s U_s]}{\partial x} = -A_s \rho_s r_b \quad (2)$$

where the subscripts  $g$  and  $s$  denote gas phase and particle phase, respectively,  $r_b$  is the rate of propellant burning and  $m_{ign}$  is the mass flow rate of the penetrated hot primer gas. The bed porosity  $\phi$  is the ratio of void gas volume to total control volume. And the specific surface area  $A_s$  represents the effective propellant's surface area exposed to the fluid per unit volume. That is,

$$A_s = (1-\phi) \cdot \frac{S_s}{V_s} \quad (3)$$

where  $S_s$  and  $V_s$  represent the propellant surface area and the volume, respectively.

The momentum equations are

$$\frac{\partial(\phi \rho_g U_g)}{\partial t} + \frac{\partial(\phi \rho_g U_g^2)}{\partial x} + \frac{\partial(P\phi)}{\partial x} = A_s \rho_s r_b U_s - A_s D_v + m_{ign} U_{ign} - \frac{\tau_{wg} P_{wg}}{A} \quad (4)$$

$$\frac{\partial[(1-\phi)\rho_s U_s]}{\partial t} + \frac{\partial[(1-\phi)\rho_s U_s^2]}{\partial x} - \frac{\partial[(1-\phi)\tau_p]}{\partial x} = -A_s \rho_s r_b U_s + A_s D_v - \frac{\tau_{wp} P_{wp}}{A} \quad (5)$$

where  $\tau_p$  is intergranular normal stress to account for the particle-particle interaction,  $D_v$  is the interphase drag force,  $\tau_{wg}$  and  $\tau_{wp}$  are the shear stress between the gas and the wall of the gun and that between the particle and the wall, respectively.  $P_{wg}$  and  $P_{wp}$  are the perimeter between the wall and the gas phase and that between the wall and the particle phase, respectively.

The gas-phase energy equation is

$$\begin{aligned} \frac{\partial(\phi \rho_g E)}{\partial t} + \frac{\partial(\phi \rho_g U_g E)}{\partial x} + P \frac{\partial \phi}{\partial t} + \frac{\partial(q\phi)}{\partial x} \\ = A_s \rho_s r_b (h_f + 0.5 U_s^2) - A_s D_v U_s - A_s h_t (T - T_{ss}) - Q_w + m_{ign} E_{ign} \end{aligned} \quad (6)$$

where  $E$  is the sum of internal energy and kinetic energy,  $q$  is gas phase heat transfer by conduction,  $h_f$  is heat of combustion,  $T_{ss}$  is the particle surface temperature, and  $Q_w$  is heat loss through the chamber wall.

Propellant temperature should be obtained to determine the ignition condition and the rate of heat transfer from the gas to the particle phase. For low heat conductivity coefficient and short transient process, the temperature profile in a grain has a steep gradient as shown in Figure 2. Therefore, in order to decide more precise ignition time and the heat transfer rate, the propellant surface temperature instead of propellant's bulk temperature should be required. Using the disc plate type grain in the present study, an equation similar to Kuo's one<sup>5</sup> for ball type propellant was derived. The disc plate type grain can be represented by the cylindrical coordinate, as shown in Figure 2. Since heat transfer depends on the interphase area, the heat transfer along the longitudinal direction is much greater than that along the radial direction. The heat equation in the longitudinal direction written in the Lagrangian time derivative is

$$\left. \frac{DT_s}{Dt} \right|_s = \alpha_s \frac{\partial^2 T_s}{\partial z^2} \quad (7)$$

The initial condition and the boundary conditions are

$$\begin{aligned} T_s(0, z) &= T_o \\ T_s(t, z_o - \delta) &= T_o \\ \frac{\partial T_s}{\partial z}(t, z_o - \delta) &= 0 \\ \frac{\partial T_s}{\partial z}(t, z_o) &= \frac{h_t(t)}{k_s} [T(t) - T_{ss}(t)] \end{aligned} \quad (8)$$

where  $\delta$  is the theoretical thermal penetration depth in a disc type propellant. The temperature distribution inside a propellant is assumed to be a second-order polynomial profile, as follows

$$T_s(t, z) - T_o = C_0(t) + C_1(t)z + C_2(t)z^2 \quad (9)$$

The coefficients  $C_0$ ,  $C_1$ , and  $C_2$  are determined by the previous three boundary conditions in equation(8), and the temperature profile is obtained, i.e.,

$$T_s - T_o = \frac{h_t}{k_s} \frac{(z - z_o + \delta)^2}{2\delta} \cdot (T - T_{ss}) \quad (10)$$

After the procedure of the integral method is taken, a final form is obtained,

$$\left. \frac{DT_{ss}}{Dt} \right|_s = \frac{6 \frac{\alpha_s}{\delta} \frac{h_t}{k_s} (T - T_{ss}) + \frac{h_t}{k_s} \left( \frac{DT}{Dt} \right)}{4 + h_t \delta / k_s} \quad (11)$$

where  $\delta$  as a function of time is given by:

$$\delta = 2 \frac{k_s (T_{ss} - T_o)}{h_t (T - T_{ss})}$$

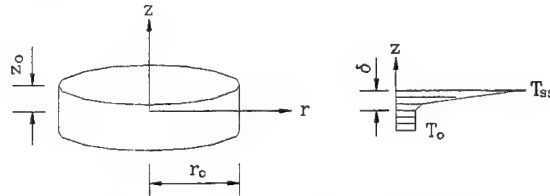


Figure 2. Propellant surface temperature

The governing equations for the each phase can be simplified further through an order of magnitude analysis. The neglected higher-order terms are: a) the gas phase heat conduction term  $q$ , b) the heat loss  $Q_w$  to the chamber wall in the extremely short transient combustion, and c) the shear stress term in momentum equations. And the source term by the igniter at the gas-phase momentum equation is assumed as zero because both the values of this term are not measured exactly from the experimental works and from the sensitivity analysis, the effects of this term is very small.

### Closure and the Constitutive Laws

The six balance equations involve the eleven unknown quantities. Thus, one must specify a) the equation of state; b) the rate of propellant burning  $r_b$ ; c) intergranular normal stress  $\tau_p$ ; d) interphase heat transfer coefficient  $h_t$ ; and e) the interphase drag force  $D_v$ .

At first, the Noble-Abel dense gas law<sup>1</sup> is used as gas-phase state equation. That is,

$$P(1/\rho_g - b) = RT \quad (12)$$

where  $R$  is gas constant and  $b$  is covolume.

For burning rate correlations, the steady-state burning rate<sup>6</sup> is used a simple pressure-dependent law:

$$r_b = aP^n \quad (13)$$

The intergranular normal stress  $\tau_p$  is based on Koo's correlation.<sup>5</sup> Thus,

$$\tau_p = \begin{cases} -\frac{\rho_s C^2 \phi}{(1-\phi)\phi_c} (\phi_c - \phi) - P \frac{(1-\phi_c)}{1-\phi}, & \text{if } \phi \leq \phi_c \\ -P, & \text{if } \phi > \phi_c \end{cases} \quad (14)$$



where  $C$  is the speed of sound transmitted in the granular material and  $\phi_c$  is the critical porosity, which means that there is no direct contact between particles.

To compute interphase heat transfer, only convective and radiative heat transfers are considered because conduction heat transfer is negligible compared to the others. The convective heat transfer coefficient is defined as follows. For the packed bed, we used the correlation of Denton<sup>3</sup>

$$h_c = 0.58(k_g / d) \cdot \text{Re}^{0.7} \text{Pr}^{0.3} \quad (15)$$

and for the fluidized bed, we used the correlation of Gelperin and Einstein<sup>6</sup>

$$h_c = (k_g / d)[2 + (\text{Re}/d)^{2/3} \text{Pr}^{1/3}] \quad (16)$$

where  $\text{Re}$  is Reynolds number ( $\text{Re} = \rho_g \phi d |U_g - U_s| / \mu$ ) and  $d$  is the radius of propellant that is assumed to be a sphere. The total heat transfer coefficient,  $h_t$  is the sum of convective and radiative heat transfer coefficients, i.e.,

$$h_t = h_c + h_r = h_c + \varepsilon_s \sigma [T(t) - T_{ss}(t)] \cdot [T(t)^2 + T_{ss}(t)^2] \quad (17)$$

Viscous drag force  $D_v$  is induced by velocity difference between solid phase and gas phase. Applicable  $D_v$ 's correlations are divided by packed bed and fluidized bed. The viscous drag force for the packed bed is generally larger than that for the fluidized bed. But the difference is too small,<sup>4</sup> hence we use Ergun's equation in all cases as

$$D_v = \frac{\rho_g (U_g - U_s) \cdot |U_g - U_s|}{6} \cdot \left[ 1.75 + \frac{150(1 - \phi)}{\phi \text{Re}} \right] \quad (18)$$

We can neglect the second term in the brackets for very large Reynolds number and take a simplified Ergun's equation.

$$D_v = 1.75 \rho_g (U_g - U_s) \cdot |U_g - U_s| / 6 \quad (19)$$

## Numerical Procedure

The system of governing equations becomes a set of six first order, coupled, nonlinear equations. As the balance equations are hyperbolic type, two-step MacCormack explicit scheme, incorporated with predictor-corrector calculations, is used to solve the governing equations. MacCormack scheme is satisfactory with the Courant condition as follows;

$$\beta = |\max(U_g) + c| (\Delta t / \Delta x) \leq 1 \quad (20)$$

where  $\max(U_g)$  is the maximum velocity of gas phase and  $c$  is the speed of sound. The mesh size  $\Delta x$  is uniform as 0.05 cm throughout the interior region and  $\Delta t$  is determined by  $\beta \Delta x / |\max(U_g) + c|$  where  $\beta$  is 0.8.

The boundary conditions for solving the set of governing equations are assumed that the gas and particle velocities at the both ends of the chamber are, at all times, equal to those of moving boundary and the symmetric conditions are applied to the other variables.

The velocity of moving boundary can be determined from the cross section area of the gun and the local pressure at the moving boundary. At that time, the friction force between the wall of the gun and moving mass exists but can not be measured accurately from the experimental tests. However, as the wall of the gun and moving masses are made with precision, the friction force between them may be

small as applied by Chen.<sup>4</sup> So, at the numerical analysis, the friction force is assumed to be a shear disc which is fractured at 50 atm. Once the local pressure at the moving boundary reaches the 50 atm, the friction force disappears and this boundary begins to move out.

Initially, the both bases of the chamber are closed and the gas and particle velocities are zero. The problem is specified after a time, chosen as  $t = 0$ , in which the hot primer gas  $m_{ign}$  for propellant's ignition penetrates from  $x = -1.25$  cm to 1.25 cm, by a step distribution. The igniter mass flow rate begins with a value of 100 g/s and increases linearly to a constant value of 11,000 g/s in 0.04 ms. It begins to decrease linearly at 0.90 ms and it is completely cutoff at 0.95 ms.

Other input data used in the computations are summarized Table 1. The initial porosity of the granular bed is so high as 0.8674.

**Table 1**  
Input Data for the Numerical Code

$m_p = 3841$ (g)	$m_c = 3848$ (g)
$\phi_c = 0.6500$	$k_s = 5.30 \times 10^4$ (cal/cm s K)
$a = 0.005240$ (in/s) (psi) <sup>n</sup>	$n = 0.72044$
$\alpha_s = 0.945 \times 10^3$ (cm <sup>2</sup> /s)	$\rho_s = 1.5999$ (g/cm <sup>3</sup> )
$r_o = 0.075$ (cm)	$z_o = 0.0275$ (cm)
$T_{ign} = 620$ (K)	$h_f = 5.42 \times 10^9$ (J/g)
$Pr = 0.7$	$\epsilon_s = 1.0$
$\mu = 0.44615 \times 10^3$ (g/cm s)	$b = 0.89566$ (cm <sup>3</sup> /g)
$k_g = 0.265 \times 10^3$ (cal/cm s K)	$E_{ign} = 4.3 \times 10^9$ (J/g)
$P_o = 1013250$ (g/cm s <sup>2</sup> )	$T_o = 277.91$ (K)
$\phi_o = 0.8674$	

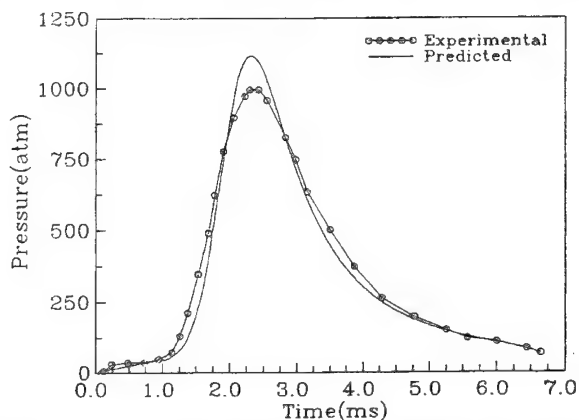
## RESULTS AND DISCUSSION

To clarify the details of the unsteady behavior in the one-dimensional gun, the pressure trace with time is investigated. Figure 3 shows the pressure-time curves by the experiment<sup>7</sup> and computations at the center of the bed. The pressure increases slowly by the penetrated hot primer gas until the propellant is ignited. From near  $t = 1.2$  ms, the pressure begins to increase steeply by propellant burning. The peak pressure occurs at  $t \approx 2.3$  ms, and then the pressure decreases slowly due to both propellant regression by the combustion and the elongation of the bed by boundary's movement.

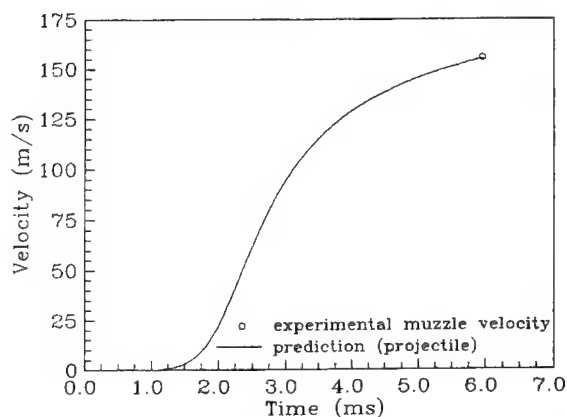
The numerical pressure-time curve agrees closely with the experimental data, but the largest difference between two curves occurs at the region of peak pressure. Measured and predicted peak pressures are 994.7 atm and 1116.8 atm, respectively. Also, it can be noted that the pressure gradient of the numerical result is steeper than that of the experiment. This slope of pressure-time curve is directly influenced by the burning rate of the propellant. Hence the burning rate coefficients used in the computations seem to be overestimated compared to the real condition.

Figure 4 represents the muzzle velocity by experiment and the projectile velocity trace with times by numerical analysis. From the numerical results, the projectile begins to move out at  $t \approx 1.1$  ms and it is quickly accelerated by the steeply increasing pressure, as shown in Figure 3. Around  $t = 5.95$  ms, moving masses get out of the bed. The experimental and numerical muzzle velocities of the projectile are 155.5 m/s and 155.1 m/s, respectively and those of the counter mass are 155.4 m/s and 154.8 m/s,

respectively. From Figure 3-4, it can be concluded that the predictions are closely consistent with the experimental results.



**Figure 3.** Pressure-time curves of the experimental results and the predictions at  $x=0$

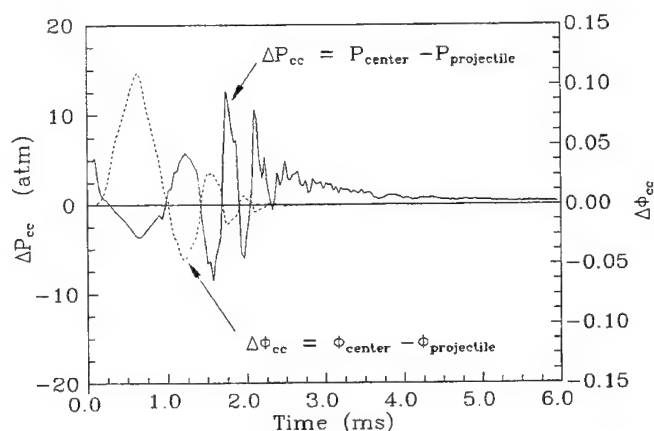


**Figure 4.** The predicted projectile velocity profile with experimental muzzle velocity

Figure 5 displays the history of the differences in pressure  $\Delta P_{cc}$  and porosity  $\Delta \phi_{cc}$  between the center ( $x=0$ ) of the bed and the projectile base ( $x=x_p$ ). The pressure and porosity differences between the center of the bed and the counter mass base ( $x=x_c$ ) are the same magnitude as  $\Delta P_{cc}$  and  $\Delta \phi_{cc}$ , respectively. In Figure 5, the maximum value of the  $\Delta P_{cc}$  is about 13 atm and after several oscillations, the  $\Delta P_{cc}$  disappears. Also, owing to the granular bed's movement resulting from the pressure gradient, it can be seen that the porosity difference  $\Delta \phi_{cc}$  has inverse trend to the pressure difference  $\Delta P_{cc}$ .

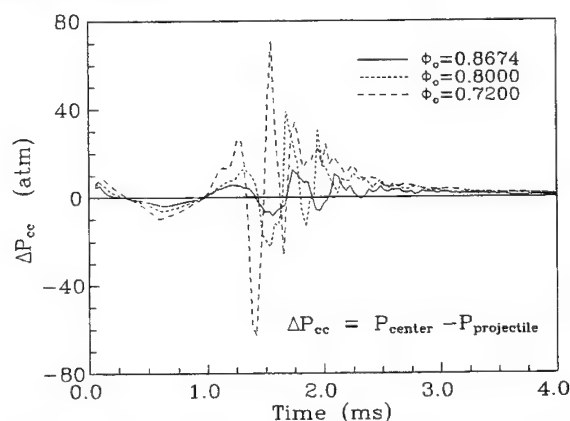
The essential qualitative description of the generation and growth of pressure waves may be represented in the following manner. At first, the pressure gradient is driven by flame spreading of the granular bed. This pressure gradient and drag force move the granular bed to the moving boundary, compacting in against moving boundary. The pressure waves driven by the propellant combustion reach the moving boundary, stagnate, and are reflected toward the center point. The pressure waves continue to reflect between the center of the bed and the moving boundaries until dissipated. The

pressure and porosity differences of the present study have the similar characteristics with upper description, but the strong pressure wave which is observed by other previous researchers<sup>8-10</sup> does not appear as shown in Figure 5. The previous work<sup>11</sup> explained that distributing the free space at both ends of the charge and igniting the charge in the center gave small pressure wave amplitude. In this study, as the charge is ignited near the center of the bed and the granular bed may be regarded as the free space by high initial porosity ( $\phi_0 = 0.8674$ ), it is considered that the large pressure waves would not be appeared.



**Figure 5.** The history of the differences in pressure and porosity between the center of the bed and the projectile base

To know the relation between the  $\Delta P_{cc}$  and propellant charge weight, the pressure differences  $\Delta P_{cc}$  with the various initial porosity are plotted in Figure 6. As shown in Figure 6, the maximums of  $\Delta P_{cc}$  at  $\phi_0 = 0.8000$  and  $0.7200$  are  $41 \text{ atm}$  and  $72 \text{ atm}$ , respectively. Thus the maximum of  $\Delta P_{cc}$  decays exponentially as the initial porosity. Also, it is shown that the period of the pressure wave in low initial porosity is faster than that in high one.



**Figure 6.** Pressure difference between the center of the bed and the projectile base with various initial porosities

The last predictions are the corresponding porosity distribution histories, which are shown in Figure 7. The initial porosity is presented in a dashed line. It is noted that the porosity have different behavior depending on time. At  $t = 0.6 \text{ ms}$ , the porosity is the lowest at the moving boundaries, according to

forward motion of particles by pressure waves. Later, the porosity is the lowest at the center of the bed by backward flow. From this results, it can be suggested that the oscillation of the porosity profiles is affected by the pressure waves. After  $t = 1.8 \text{ ms}$ , the porosity shows almost flat distributions by fast burning propellants and elongation of the granular bed.

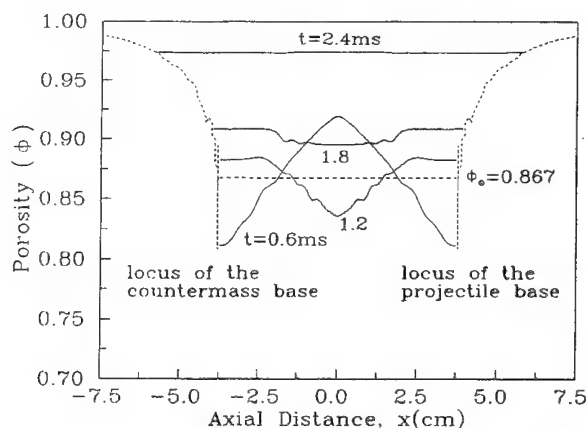


Figure 7. Predicted porosity distributions at various times

## CONCLUSIONS

The development of the interior ballistics code for Davis gun is carried out using two-phase fluid dynamic model. By comparing numerical analysis with the experimental data, the numerical pressure-time trace and muzzle velocities of the projectile and the counter mass closely agree with the experimental data. The pressure in the gun are predicted to be very uniform distributions unlike other works. It is supposed that this is owing to the high initial porosity and charge ignition near the center of the gun. The maximum pressure difference between the center of the bed and the projectile base decays exponentially according to the initial porosity and the period of the pressure wave in low initial porosity is faster than that in high one. The porosity distributions move to the inverse direction with the pressure distributions.

## REFERENCES

1. A. K. Celmins, Mathematical modeling of recoilless rifle interior ballistics, in *Interior ballistics of guns*, edited by H. Krier and M. Summerfield, Progress in Aeronautics and Astronautics, 66, AIAA, 113-134, 1979
2. K. K. Kuo, eds., *Principles of combustion*, John Wiley & Sons, Inc., 1986
3. H. Krier and S. S. Gokhale, Modeling convective mode combustion through granulated propellant to predict detonation transition, *AIAA Journal*, 16, 177-183, 1978
4. P. S. Gough and F. J. Zwartz, Modeling heterogeneous two-phase reacting flow, *AIAA Journal*, 17, 17-25, 1979
5. K. K. Kuo, J. H. Koo, T. R. Davis, and G. R. Coates, Transition combustion in mobile gas-permeable propellants, *Acta Astronautica*, 3, 573-591, 1976
6. H. Krier and M. J. Adams, An introduction to gun interior ballistics and a simplified ballistics code, in *Interior ballistics of guns*, edited by H. Krier and M. Summerfield, Progress in Aeronautics and Astronautics, 66, AIAA, 1-36, 1979

7. **J. C. Kim and M. K. Yi**, *Study on the launching techniques by Davis gun principle*, ADD Report No. GWSD-519-93218, 1993
8. **D. Y. Chen, V. Yang, and K. K. Kuo**, Boundary condition specification for mobile granular propellant bed combustion processes, *AIAA Journal*, 19, 1429-1437, 1981
9. **W. F. V. Tassell and H. Krier**, Combustion and flame spreading phenomena in gas-permeable explosives materials, *Int. J. Heat Mass Transfer*, 18, 1377-1386, 1975
10. **P. S. Gough**, Modeling of two-phase flow in guns, in *Interior ballistics of guns*, edited by H. Krier and M. Summerfield, Progress in Aeronautics and Astronautics, 66, AIAA, 176-196, 1979
11. **I. W. May and A. W. Horst**, Charge design considerations and their effect on pressure waves in guns, in *Interior ballistics of guns*, edited by H. Krier and M. Summerfield, Progress in Aeronautics and Astronautics, 66, AIAA, 197-227, 1979

### Comments and Answers

1. In Eq. 4, the momentum associated with the igniter gas is not included. However, the mass and energy provided by the igniter are included in the equation for conservation of mass and energy. If this momentum term can be neglected, the reasons should be presented by the authors.

*Answer.* The source term by the igniter at the gas-phase momentum equation is generally included as  $+m_{ign}U_{ign}$ . But in the experimental works, values of the momentum source term by the igniter gas are not measured accurately. Also, although the gas velocity of the penetrated hot igniter gas have been used as  $U_{ign}=0.0m/s$  and  $U_{ign}=100.0m/s$ , the results of both cases are almost the same. For example, the maximum pressures at these conditions are 1116 atm and 1118 atm, respectively. So, in this study, it is assumed that this term is zero.

2. The way in which the frictional force between the projectile and the barrel is handled seems to be quite arbitrary. A better explanation of why 50 atm was chosen as the fracture point would be helpful. In addition, the kinetic frictional force was ignored altogether, without proper justification.

*Answer.* The friction force between the wall and moving mass can not be obtained accurately from the experimental works. However, the wall of the gun and the moving mass are made with precision, the friction force between them may be very small as applied by Chen\*. Also, according to the numerical analysis using the present code, the results with respect to friction force, have a similar trend and only slight increase of the maximum pressure and muzzle velocity. For example, in case of the friction pressure at 50 atm and 100 atm, the maximum pressures are 1116 atm and 1152 atm. And the kinetic friction force are neglected by order of magnitude analysis like Kuo\*\*.

\* : **D. Y. Chen, V. Yang, and K. K. Kuo**, "Boundary condition specification for mobile granular propellant bed combustion processes", *AIAA Journal*, 19, 1429-1437, 1981

\*\* : **K. K. Kuo**, eds., *Principles of combustion*, John Wiley & Sons, Inc., 1986

3. Equation 6 may be incorrect and should be checked.

*Answer.*  $A_s \rho_s r_b (h_f - 0.5U_s^2) \rightarrow A_s \rho_s r_b (h_f + 0.5U_s^2)$

## UNSTEADY COMBUSTION OF HOMOGENEOUS ENERGETIC SOLIDS

M. Q. Brewster and T. B. Schroeder  
University of Illinois at Urbana-Champaign  
Urbana, Illinois

**ABSTRACT:** The classical, linearized quasi-steady (QS) theory of unsteady combustion of homogeneous energetic solids is examined for three materials: nitrate ester (NC/NG) double base propellants, ammonium perchlorate (AP) and cyclo-trimethylene-trinitramine (RDX). Single step, zero order, high activation energy decomposition is shown to be a superior condensed phase model compared with the usual *ad hoc* Arrhenius surface pyrolysis model. Favorable comparison with T-burner and laser-recoil response function data provides evidence of compatibility of the zero order QS decomposition model for NC/NG and AP at 1 atm and higher pressures and for frequencies approaching the characteristic frequency of the condensed phase reaction layer. RDX appears not to satisfy the QS assumptions at 1 atm but may at higher pressures.

### INTRODUCTION

The premise of this paper and our recent research is that in trying to understand combustion of energetic materials, unsteady combustion represents a significant opportunity that is not being sufficiently exploited. Unsteady combustion is not important simply because important unsteady phenomena (such as instability) occur in real systems but also because transient burning offers the more difficult challenge for modeling. Any combustion model should be compared with the full range of observable data. The fact that the full range of even steady observations cannot yet be predicted for any material by any model should not be considered a valid reason for postponing unsteady comparisons but should be taken as an indication of insufficient understanding of the processes and/or flaws in the present models. Unsteady combustion offers a significant opportunity for making more rapid progress in understanding the necessary fundamental processes and achieving a predictive modeling capability.

### Classical Theory of Unsteady Combustion

The classical linearized theory of oscillatory combustion of homogeneous propellants and energetic materials is based on the assumption of quasi-steady (QS) reaction zones in *both* the gas and condensed phases. In the U.S. and Europe this theory (also called QSHOD for quasi-steady, homogeneous, one-dimensional) was developed in the context of the flame modeling (FM) approach whereas in the former Soviet Union the phenomenological Zeldovich-Novozhilov (ZN) approach was used. The two approaches are essentially equivalent. In both cases the tacit assumption is that condensed phase reaction is a quasi-steady surface phenomenon. Interpreted in the framework of the FM approach, this assumption implies that the effective non-dimensional activation energy of initial decomposition is large (which is generally true for real energetic materials). This suggests that the results of activation energy asymptotics (AEA) theory should hold for the decomposition process, at least over an appropriate (low) frequency range. While rigorous results for AEA-decomposition have been available for many years [1-3] they apparently have not been applied to unsteady combustion of solids until recently [4]. Instead, an *ad hoc* Arrhenius surface pyrolysis relation,  $\dot{r}_p = A_s p^{n_s} \exp(-E_s/RT_s)$ , has been almost universally assumed in FM studies, usually with  $n_s=0$ . However, recent results for nitrate ester (double base) propellants [4, 5] have shown that a simple but

formally derived AEA formula based on single-step, zero order decomposition is clearly superior to the Arrhenius surface pyrolysis formula for describing oscillatory burning.

In this paper a summary of results is given for several energetic materials which have been investigated for compatibility with the QS zero order decomposition AEA description. These materials include uncatalyzed and catalyzed double base propellant, ammonium perchlorate (AP), and cyclo-trimethylene-trinitramine (RDX).

## EQUATIONS

The classical QS model is based on the phenomenological approach developed by Soviet researchers, especially Novozhilov [6], and originated by Zeldovich in 1942. It assumes quasi-steady gas and condensed phase reaction zones, homogeneous solid, and a one-dimensional flame (*i.e.*, one-dimensional heat feedback). Thermal relaxation in the inert condensed phase, with time scale  $t_c$ , is the only non-quasi-steady process. The condensed phase reaction layer and the gas phase region (if included) are considered to respond instantly to changing external conditions. This formulation implicitly assumes that condensed phase reactions are confined to the interface between the unreacted condensed phase and the gas phase (*i.e.*, surface reaction). This assumption is justified only if two important conditions are met. First, the effective activation energy of the condensed phase decomposition must be large enough that a relatively thick inert convective-diffusive zone develops, followed by a thin reactive-diffusive zone ( $E_c/RT \gg 1$ ;  $x_c = \alpha_c/\bar{v}_b \gg x_R = x_c/(E_c/2RT_s)$ ). Typical values of  $E_c/2RT_s$  for energetic materials are 5 to 15. For steady burning, even the smallest realistic values ( $\sim 5$ ) are large enough that AEA formulas (leading term only) are accurate to within a few percent. This does not guarantee similar accuracy for oscillatory burning, however, which depends on the frequency of the imposed perturbation. Therefore, the second necessary condition is that the frequency of the perturbation be less than the characteristic frequency of the reaction layer ( $f \ll f_R$ )—how much less depends on the magnitude of  $E_c/2RT_s$  and is something which has been only recently addressed [7]. Nevertheless it is to be expected that at some sufficiently large frequency the QS model will fail by virtue of non-QS (*i.e.*, distributed) reaction effects in the condensed phase, if not by some other mechanism.

Under these assumptions the unsteady energy equation in the condensed phase is

$$\rho_c C \frac{\partial T}{\partial t} + \rho_c C v_b \frac{\partial T}{\partial x} = \lambda_c \frac{\partial^2 T}{\partial x^2} + f_r q K_a \exp(K_a x) \quad (1)$$

The initial temperature condition is

$$T(-\infty, t) = T_o \quad (2)$$

The energy equation includes Fourier conduction and Beer's law for radiative transport of a collimated incident radiative flux. The incident radiative flux can represent either "artificial" radiation (*e.g.*, laser radiation in a laboratory test) or natural thermal radiation from combustion products. The absorption coefficient in the condensed phase,  $K_a$ , is assumed to be spatially constant. No description of spectral variation of  $K_a$  is made; therefore in the case of broadband thermal radiation  $K_a$  must be viewed as some appropriate effective value. Thermal emission by the condensed phase and scattering are neglected. It is assumed that a fraction of the radiant flux  $f_r$  is transmitted through the reactive-diffusive zone (*i.e.*, absorbed below the reactive-diffusive zone) while the remainder  $1-f_r$  is absorbed in the reactive-diffusive zone (this assumption has been justified in [8]). (It is not inconsistent to allow for radiation absorption in a vanishingly thin surface region just like it is not inconsistent to allow for chemical heat release in such a region. It follows from the asymptotic approximation.) The reaction layer transmissivity  $f_r$  is given by Beer's law based on an average path length equal to the approximate reaction layer thickness.

$$f_r = \exp(-K_a x_R) \quad (3)$$

Using the steady state integral energy equation

$$\bar{f}_s = \frac{\bar{\Gamma}_b}{\alpha_c} (\bar{T}_s - T_o) - \frac{f_r q}{\lambda_c} \quad (4)$$



and linearizing Eq. 1 ( $\Delta r_b \ll \bar{r}_b$ ), the linear frequency response functions for pressure-perturbed burning (constant radiant flux) and radiation-perturbed burning (constant pressure) can be obtained [9] as

$$R_p = \frac{v + \delta(\lambda - 1)}{\lambda r + k / \lambda - (r + k) + 1 - \frac{k\bar{Q}_r(\lambda - 1)}{\lambda(\beta + \lambda - 1)}} = \frac{nAB + n_s(\lambda - 1)}{\lambda + A / \lambda - (1 + A) + AB - \frac{A\bar{Q}_r(\lambda - 1)}{\lambda(\beta + \lambda - 1)}} \quad (5)$$

$$R_q = \frac{v_q + \delta_q(\lambda - 1) - \frac{k\bar{Q}_r(\lambda - 1)}{\beta + \lambda - 1}}{\lambda r + k / \lambda - (r + k) + 1 - \frac{k\bar{Q}_r(\lambda - 1)}{\lambda(\beta + \lambda - 1)}} = \frac{v_q AB + n_q(\lambda - 1) - \frac{A\bar{Q}_r(\lambda - 1)}{\beta + \lambda - 1}}{\lambda + A / \lambda - (1 + A) + AB - \frac{A\bar{Q}_r(\lambda - 1)}{\lambda(\beta + \lambda - 1)}} \quad (6)$$

Equations 5 and 6 assume  $f_r$  (the surface reaction layer transmissivity) is a constant parameter. The steady state sensitivity parameters,  $k$ ,  $r$ ,  $v$ ,  $\delta$ ,  $v_q$ , and  $\delta_q$  ( $A=k/r$ ,  $B=1/k$ ,  $n=v$ ,  $n_s=\delta/r$ ,  $n_q=\delta_q/r$ ) are obtained from steady state burning information. While in principle all the sensitivity parameters could be obtained from measurements, in practice this has proven to be unfeasible. The parameters which require highly precise surface temperature measurement ( $r$ ,  $\delta$ , and  $\delta_q$ ) are better represented by a reasonably accurate condensed phase decomposition model. Single-step, zero order decomposition appears to be adequate for this purpose.

### Zero Order Condensed Phase Decomposition

Activation energy asymptotic analysis of the condensed phase reactive-diffusive zone, assuming single-step, zero order decomposition, gives the following steady state result [2].

$$\bar{r}_b^2 = \frac{A_c \alpha_c \exp\left(\frac{-E_c}{RT_s}\right)}{\frac{E_c}{RT_s} \left[ 1 - \frac{T_o}{T_s} - \frac{Q_c}{2CT_s} - \frac{f_r \bar{q}}{\rho_c \bar{r}_b C T_s} \right]} = \frac{A_c \alpha_c \exp(-2\bar{E}_c)}{2\bar{E}_c (1 - T_o / T_s) (1 - \bar{Q}_c / 2 - \bar{Q}_r)} \quad (7)$$

The accuracy of this result has been verified elsewhere [7] by numerical analysis to be within a few percent when  $E_c/2RT_s > 5$ . Assuming  $f_r$  is a constant parameter, Eq. 7 can be differentiated to give the following sensitivity parameter relations.

$$r = \frac{k[2 - \bar{Q}_c - \bar{Q}_r] - 1}{\left(1 - \frac{T_o}{T_s}\right)(1 + \bar{E}_c)(2 - \bar{Q}_c - 2\bar{Q}_r) - 1} \quad (8)$$

$$\delta = \frac{-v}{\left(1 - \frac{T_o}{T_s}\right)(1 + \bar{E}_c)(2 - \bar{Q}_c - 2\bar{Q}_r) - 1} ; \delta_q = \frac{-v_q + k\bar{Q}_r}{\left(1 - \frac{T_o}{T_s}\right)(1 + \bar{E}_c)(2 - \bar{Q}_c - 2\bar{Q}_r) - 1} \quad (9,10)$$

In these equations  $k$ ,  $v$ , and  $v_q$  need to be specified in order to determine  $r$ ,  $\delta$ , and  $\delta_q$ . This requires either measured steady state burning rate data or a gas phase model. An accurate model for the gas phase, one which matches all available experimental observations and is therefore comparable to the zero order model for the condensed phase, has not been demonstrated for any energetic material yet. Therefore, until a reliable gas phase model is demonstrated it seems more productive to rely on measured or assumed values for  $k$ ,  $v$ , and  $v_q$ . In the results presented below measured values for  $v$  and  $v_q$  and reasonable assumed values for  $k$  are used.

## RESULTS

### Double Base Propellant

For double base propellant, measurements of both  $R_p$  and  $R_q$  are available. T-burner measurements of  $\text{Re}\{R_p\}$  for uncatalyzed propellant N4 [10] and model comparisons are shown in Fig. 1. Measured steady state burning rate data were used for  $k$ ,  $v$ , and  $v_q$  where such data were available; otherwise values were assumed. Most of the model parameters were taken from [10] (see Table 1). The steady state surface temperature was estimated from Eq. 7 using reported burning rates with constant  $A_c$ . The heat of reaction  $Q_c$  was assumed based on the values given by Zenin [11] for similar propellant. The  $\sigma_p$  value for N4 ( $2.8\text{e-}3 \text{ K}^{-1}$ ) was obtained by correcting the value given by Ibricic and Williams [2] ( $3.5\text{e-}3 \text{ K}^{-1}$ ) to account for combustion gas thermal radiation in the T-burner. It can be seen in Fig. 1 that over the frequency range plotted for each pressure the zero order

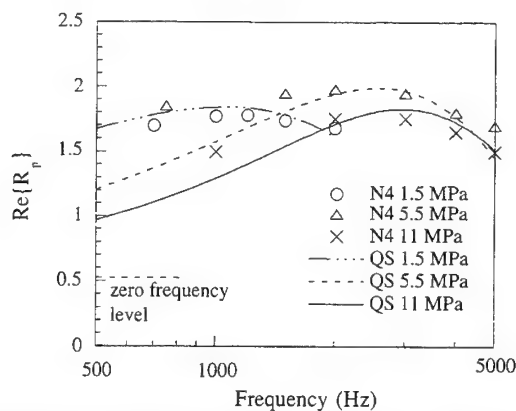


Figure 1. In-phase (real) part of linear frequency response (pressure-driven) for N4 double base propellant; data points are T-burner results [10]; quasi-steady (QS) predictions based on parameters in Table 1 [4].

TABLE 1  
Propellant Properties ( $T_0=300 \text{ K}$ )

	N4			N5	AP
	15 atm	55 atm	110 atm	1 atm	1 atm
$\rho_c, \text{g/cm}^3$	1.55	1.55	1.55	1.55	1.95
$C, \text{cal/g-K}$	0.35	0.35	0.35	0.35	0.40
$\alpha_c, \text{cm}^2/\text{s}$	$1.2\text{e-}3$	$1.2\text{e-}3$	$1.2\text{e-}3$	$1.2\text{e-}3$	$5.7\text{e-}4$
$E_c, \text{kcal/mole}$	40	40	40	40	29.1
$A_c, \text{s}^{-1}$	$1\text{e}17$	$1\text{e}17$	$1\text{e}17$	$1\text{e}17$	$3\text{e}9$
$K_a, \text{cm}^{-1}$	50	50	50	500	370
$Q_c, \text{cal/g}$	95	100	75	40	-39
$\bar{q}, \text{cal/cm}^2\text{-s}$	6.5	12	13	10	37
$\bar{T}_s, \text{K}$	630	659	676	609	800
$\bar{r}_b, \text{cm/s}$	0.43	0.86	1.21	0.23	0.084
$\sigma_p, \text{K}^{-1}$	$2.8\text{e-}3$	$2.8\text{e-}3$	$2.8\text{e-}3$	$3.6\text{e-}3$	$1.8\text{e-}3$
$\bar{q}_c / \bar{m}, \text{cal/g}$	11	17	50	41	12
$v$ or $v_q$	0.51	0.51	0.51	0.43	0.71
$k$	0.93	1.00	1.05	1.1	0.90
$r$	0.0021	0.016	0.042	0.057	0.10
$\delta$ or $\delta_q$	-0.064	-0.061	-0.048	-0.020	0.030
$A$	440	62	25	19	9.0
$B$	1.1	1.0	0.95	0.91	1.1
$n_s$ or $n_q$	-30	-3.8	-1.1	-0.35	0.30

QS model gives a close match to the experimental data except at the lowest non-zero frequency data points. As discussed in [10], at low frequencies heat losses and other effects result in erroneously high experimental values. The experimental data reported were not corrected for these effects. Therefore this disagreement is not unexpected. If the comparisons were carried to higher frequencies than those shown in Fig. 1 it would be seen that agreement would become steadily worse with increasing frequency. This also is not unexpected, since the quasi-steady assumptions (both gas and condensed phase) will begin to fail with increasing frequency. The characteristic frequency of the condensed phase reaction layer, as estimated from the scaling  $\tau_R = x_R / \bar{r}_b$ , is 2460, 9430, and 18,180 Hz for 1.5, 5.5, and 11 MPa, respectively. Significant deviation from the QS theory would not be expected until the frequency reached some fraction, say 1/4, of these values, 600, 2500, and 4500 Hz for 1.5, 5.5, and 11 MPa. Figure 1 shows that this is indeed the case, at least with regard to the in-phase component of the response (subsequent results show that the response phase may give a clearer indication of the onset of non-QS effects).

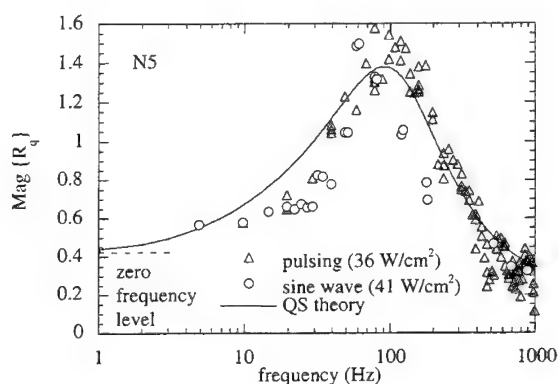


Figure 2. Magnitude of linear frequency response (radiation-driven) for N5 double base propellant at 1 atm; data points are laser-recoil results [12]; quasi-steady (QS) prediction based on parameters in Table 1 [5].

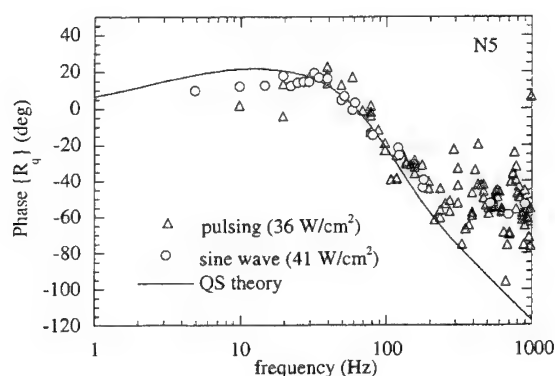


Figure 3. Phase of linear frequency response (radiation-driven) for N5 double base propellant at 1 atm; data points are laser-recoil results [12]; quasi-steady (QS) prediction based on parameters in Table 1 [5].

CO<sub>2</sub> laser-recoil measurements of  $R_q$  for catalyzed N5 propellant [12] are compared with model predictions in Figs. 2 (magnitude) and 3 (phase). Most of the model parameters were taken from [10-12]; see Table 1. The temperature sensitivity was assumed to be  $\sigma_p = 3.6e-3 \text{ K}^{-1}$ . The absorption coefficient ( $500 \text{ cm}^{-1}$ ) was obtained from FTIR absorption spectroscopy measurements at  $10.6 \text{ } \mu\text{m}$  (CO<sub>2</sub> laser). Other condensed phase thermophysical and kinetic parameters are the same as for N4

since, except for the catalyst, both propellants are the same. (The catalyst is presumed to affect the primary ("fizz zone") gas flame.) One source of discrepancy is the uncertainty of a few key steady state parameters which need to be better characterized, such as  $Q_c$  and  $\sigma_p$ . In this regard it is important for  $\sigma_p$  to be measured at the same radiant flux condition since it decreases with increasing radiant flux (particularly at low fluxes) for many energetic materials. Nevertheless, even for these approximate (yet realistic) parameters the agreement in Figs. 2 and 3 is good. For frequencies approaching the characteristic condensed phase reaction layer frequency ( $f_R \approx 730$  Hz), the deviation in the QS predictions, particularly phase, increases due to non-QS effects, as expected. To improve the model agreement in the higher frequency range the QS assumption could be relaxed in the condensed phase (this has been demonstrated in [7]). It should be noted that the measured thrust response magnitude data were scaled by a constant to give the best fit in Fig. 2. This scaling is made necessary by uncertainty in the momentum balance which relates burning rate to recoil force (thrust). We have found that by assuming one-dimensional flow and reasonable estimates for gas temperature and molecular weight (i.e., density) it is possible to convert oscillatory thrust magnitude to burning rate magnitude to within a factor of two (this is verified by independent measurement of  $v_q$ ). Because of this uncertainty, thrust response magnitude data are scaled. No correction is necessary for the phase data; it is assumed in Fig. 3 that the thrust is in phase with the burning rate.

Aside from frequency regions of expected disagreement, the QS zero order decomposition model gives good agreement with the measured double base response data--much better than can be obtained from the Arrhenius surface reaction model. It should be emphasized that all parameters used here are reasonable measured or assumed values. It should also be noted that the Jacobian parameters ( $n_s$  or  $n_q$ ) are both negative for N4 and N5, respectively. The goodness of the fit and the realistic values of all the parameters present a favorable argument for the validity of the zero order model and the QS assumptions (both gas and condensed phases) for double base propellants in the frequency range from dc through  $f_R/4$  (or some fraction of the characteristic gas phase frequency if it is smaller than  $f_R$ ).

### Ammonium Perchlorate

CO<sub>2</sub> laser-recoil data for  $R_q$  [13] and model comparisons are shown in Figs. 4 (magnitude) and 5 (phase) for AP. Model parameters are listed in Table 1. Surface temperature was measured by microthermocouples embedded in pressed pellets [13]. Specific heat and thermal diffusivity were extrapolated from data [14] for the cubic phase. The absorption coefficient ( $370 \text{ cm}^{-1}$ ) is estimated from a room temperature measurement ( $240 \text{ cm}^{-1}$ ) using KBr-FTIR spectroscopy [15]. The CO<sub>2</sub> laser lines ( $10.6 \mu\text{m}$ ) fall near the perchlorate ion "breathing" frequency, where the absorption coefficient varies rapidly with wavelength. This absorption structure probably shifts with temperature. Therefore the uncertainty in  $K_a$  for a hot, burning AP surface is probably rather large (at least 50%).

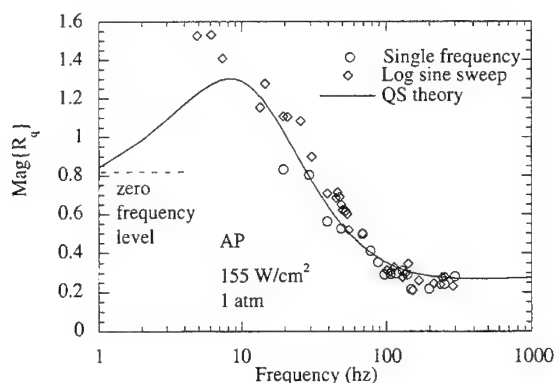


Figure 4. Magnitude of linear response function for AP with mean radiant flux of  $155 \text{ W/cm}^2$ , 1 atm; data points are laser-recoil measurements [13]; quasi-steady (QS) prediction based on parameters in Table 1.

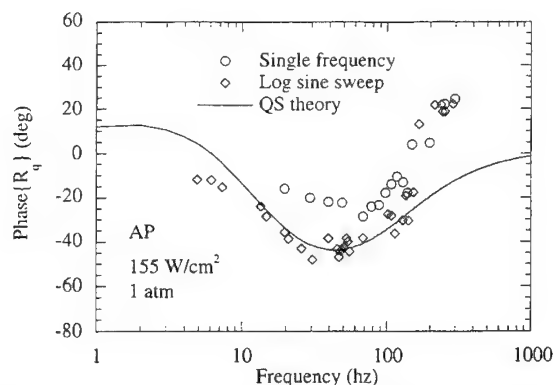


Figure 5. Phase of linear response function for AP with mean radiant flux of  $155 \text{ W/cm}^2$ , 1 atm; data points are laser-recoil measurements [13]; quasi-steady (QS) prediction based on parameters in Table 1.

Figure 4 shows that the scaled magnitude data match well except at the 5-6 Hz frequency points. (Again the measured thrust magnitude data were scaled for best fit in Fig. 4; this required a factor of two multiplier in addition to the one-dimensional momentum conversion.) Figure 5 shows that the phase matches well up to 100 Hz. (The value of  $E_c=29 \text{ kcal/mole}$  gives  $f_R=110 \text{ Hz}$ .) Above 100 Hz, the deviation in phase is presumably due to non-QS effects. At low frequencies (a few Hz), laser-recoil measurements are subject to systematic error for two reasons. First, there is a transducer time constant limitation at low frequencies due to charge loss on the piezo-electric crystal. Second, there is an unsteady mass loss effect in the momentum balance that introduces a frequency-dependent term (including phase lag) between the momentum flux and recoil force [16]. This effect has not been well characterized yet, but it appears to be more important with low mean mass flux and is thus probably more evident in the low frequency AP data than in the low frequency N5 data.

Therefore the low frequency AP data (except, of course, the dc sensitivity measurement  $v_q$ ) are discounted somewhat relative to the higher frequency data. The zero order QS model fit results in global parameters that seem realistic, an activation energy of  $E_c=29 \text{ kcal/mole}$  and overall endothermic condensed phase chemistry ( $Q_c=-39 \text{ cal/g}$ ). The detailed chemical steps which these global parameters represent are at present unknown; however, the  $E_c=29$  value seems compatible with both a proton transfer initiation process from  $\text{NH}_4^+$  to  $\text{ClO}_4^-$  giving  $\text{NH}_3$  and  $\text{HClO}_4$  [18] and the subsequent homolytic bond scission of  $\text{HClO}_4$  to give  $\text{ClO}_3$  and  $\text{OH}$  [19]. Further investigation is needed to determine the decomposition process of AP, particularly the condensed phase chemistry. Nevertheless, it appears that the zero order QS model is a reasonable representation of AP decomposition, at least at 1 atm (and probably at higher pressures).

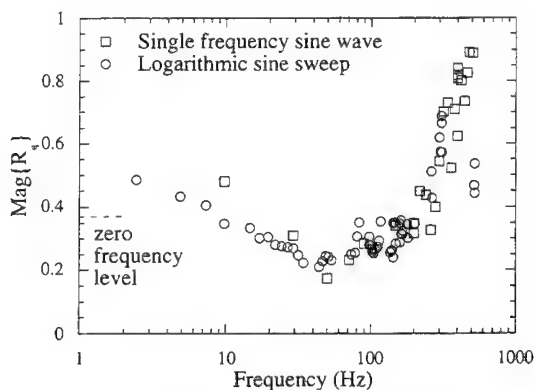


Figure 6. Magnitude of linear response function (laser-recoil [13, 17]) for RDX with mean absorbed  $\text{CO}_2$  laser flux of  $48 \text{ W/cm}^2$ , 1 atm.

## RDX

Laser-recoil measurements for RDX at 1 atm [13, 17] are shown in Figs. 6 and 7. These data do not fit the zero order QS model as do double base propellants and AP. This is probably due to the violation of one or more of the QS model assumptions. Temperature measurements from microthermocouples embedded in RDX pellets indicated a region near the sample surface in which there were significant temporal temperature fluctuations but which was spatially isothermal on a time-averaged basis. This region corresponded to a relatively thick (100's of  $\mu\text{m}$ ) liquid layer that was observed on the burning surface. (In the laser-recoil and other tests this liquid layer was confined to maintain one-dimensionality.) The temporal temperature fluctuations were probably due to bubbling action and the time-averaged, spatially isothermal condition was probably due to two-phase, bubble-induced convective recirculation. These conditions violate the simple QS model assumption of a single phase, convective-diffusive energy balance in the condensed phase, suggesting that any fit by the QS model might be of questionable meaning, at least at 1 atm. At higher pressures, the liquid layer thickness decreases and it may be that the QS model becomes applicable.

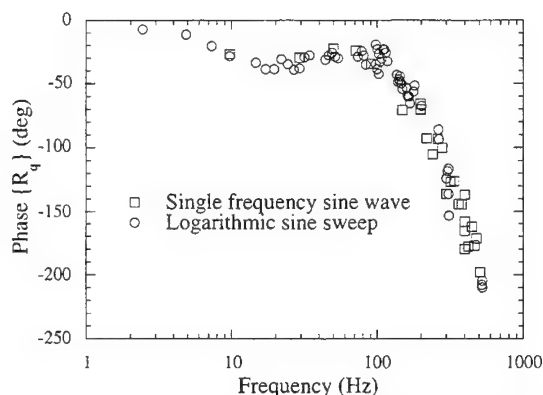


Figure 7. Phase of linear response function (laser-recoil [13, 17]) for RDX with mean laser flux of  $48 \text{ W/cm}^2$ , 1 atm.

In spite of the lack of applicability of the QS model to RDX combustion at 1 atm, the response data of Figs. 6 and 7 represent additional unsteady combustion data which should prove useful for model validation. The increase in magnitude of  $R_q$  beyond 100 Hz (Fig. 6) has been verified to be a real effect (i.e., it is not transducer resonance). It was also observed that without confinement the RDX liquid layer would run off the sample surface. To model such a process would presumably require a multi-dimensional advective transport mechanism. The data of Figs. 6 and 7 were obtained with the liquid layer confined, such that, although the quasi-one-dimensional bubbling, recirculative mechanism may not be a trivial modeling exercise, at least the multi-dimensional, advective mass and energy loss mechanism would not be a factor.

## CONCLUSIONS

The classical, linearized quasi-steady (QS) theory of unsteady combustion of homogeneous energetic solids has been examined for three energetic materials, NC/NG, AP, and RDX. The important conclusions are as follows.

1. The use of rigorous AEA decomposition formulas (such as zero order decomposition) in classical QS theory appears to be not only justified for many energetic materials but the key to achieving a useful predictive capability. It is hard to defend continued use of the old, *ad hoc* Arrhenius surface pyrolysis relation except for steady state curve-fitting (i.e., Arrhenius plots) only.
2. At 1 atm and higher pressures double base propellant and AP appear to be compatible with the usual QS assumptions and single-step, zero order decomposition.

3. At 1 atm RDX has a bubbly, recirculative liquid layer which, unless confined, flows off the surface. These effects probably render the QS model invalid for RDX at 1 atm. At higher pressures it is likely that these effects become less important.
4. The frequency domain of applicability of the QS model is limited by the characteristic frequency of the surface reaction layer,  $f_R$  (or that of the gas phase, whichever is smaller). Scaling estimates indicate that for NC/NG and AP the QS theory is valid up to  $f_R/4$  with non-QS effects becoming clearly noticeable at  $f_R$ .
5. Even within the frequency domain of applicability of QS theory ( $f < f_R/4$ ), the accuracy of the theory depends on the magnitude of the non-dimensional activation energy of decomposition. Furthermore, the activation energy criterion (or alternatively the need to include higher order terms) for a given level of accuracy appears to be more stringent for oscillatory than for steady burning.
6. Preliminary computational studies indicate that the initial deviation (error) in response phase for QS theory, which becomes noticeable as frequency approaches  $f_R$ , can be accounted for by resolving the distributed reaction zone in the condensed phase. Gas phase unsteadiness (at least for homogeneous materials) is possibly a secondary consideration.

#### ACKNOWLEDGMENTS

The support of ONR (N00014-91-J-1977), Dr. R. S. Miller, and BMDO (N00014-95-I-1339), Dr. L. Caveny, is gratefully acknowledged along with J. Finlinson and D. Hanson-Parr of NAWC for assistance with RDX samples.

#### NOMENCLATURE

$A_c$	=	pre-exponential factor of single-step, zero order decomposition reaction
$A$	=	$(\bar{T}_s - T_o)(\partial \ln \bar{r}_b / \partial \bar{T}_s)_{p,q} (=k/r)$
$B$	=	$1/[(\bar{T}_s - T_o)(\partial \ln \bar{r}_b / \partial T_o)_{p,q}] (=1/k)$
$C$	=	specific heat of condensed phase
$E_c$	=	effective activation energy of condensed phase decomposition
$E_s$	=	$E_c/2$
$\bar{E}_c$	=	$E_c / 2R\bar{T}_s$
$f$	=	frequency (Hz)
$f_{c,R}$	=	$1/t_{c,R}$
$f_r$	=	fraction of $\bar{q}$ absorbed below surface reaction zone, Eq. 3
$f_s$	=	surface temperature gradient on condensed phase side, $(\partial T / \partial x)_s$ .
$J$	=	dimensionless mean radiant heat flux, $\bar{q} / [\bar{m} C (\bar{T}_s - T_o)]$
$K_a$	=	absorption coefficient of condensed phase
$k$	=	$(\bar{T}_s - T_o)(\partial \ln \bar{r}_b / \partial T_o)_{p,q}$
$m$	=	mass burning rate, $\rho_c \bar{r}_b$
$m'$	=	$\Delta m e^{i(\omega t + \phi)}$
$n_q$	=	$(\partial \ln \bar{r}_b / \partial \ln \bar{q})_{T_s,p} (= \delta_q / r)$
$n_s$	=	$(\partial \ln \bar{r}_b / \partial \ln \bar{p})_{T_s,q} (= \delta / r)$
$n$	=	$(\partial \ln \bar{r}_b / \partial \ln \bar{p})_{T_o,q} (=v)$
$p$	=	pressure
$q$	=	absorbed radiant heat flux in condensed phase
$q_c$	=	conductive heat flux to surface from gas phase
$q'$	=	$\Delta q e^{i\omega t}$
$Q_c$	=	condensed phase heat release (positive exothermic)
$\bar{Q}_c$	=	$Q_c / C(\bar{T}_s - T_o)$
$\bar{Q}_r$	=	$f_r J$
QS	=	quasi-steady gas and condensed phase reaction zone assumption
$R$	=	universal gas constant, 1.987 cal/mole-K
$R_p$	=	pressure-driven frequency response function = $(m'/\bar{m})/(p'/\bar{p})$ at constant $q$

$R_q$	=	radiation-driven linear frequency response function = $(m'/\bar{m})/(q'/\bar{q})$ at constant $p$
$r$	=	$(\partial \bar{T}_s / \partial T_o)_{p,q}$
$r_b$	=	burning rate
$t_{c,R}$	=	characteristic times, $x_{c,R}/\bar{r}_b$
$T_{o,s}$	=	initial or surface temperature
$x$	=	coordinate normal to surface, positive into gas phase
$x_c$	=	conduction zone length scale, $\alpha_c/\bar{r}_b$
$x_R$	=	reaction zone length scale, $x_c/\bar{E}_c$
$\alpha_c$	=	condensed phase thermal diffusivity
$\beta$	=	optical thickness (absorption only) of conduction zone ( $K_a x_c$ )
$\delta, \delta_q$	=	Jacobian parameters, $v_r - \mu k, v_{qr} - \mu_q k$
$\Delta$	=	amplitude of fluctuating quantity
$\lambda$	=	$1/2 + (1/2)(1 + 4i\Omega)^{1/2}$
$\lambda_c$	=	thermal conductivity
$\mu$	=	$[1/(\bar{T}_s - T_o)](\partial \bar{T}_s / \partial \ln \bar{p})_{T_o,q}$
$\mu_q$	=	$[1/(\bar{T}_s - T_o)](\partial \bar{T}_s / \partial \ln \bar{q})_{T_o,p}$
$v$	=	$(\partial \ln \bar{r}_b / \partial \ln \bar{p})_{T_o,q}$ (same as $\bar{n}$ )
$v_q$	=	$(\partial \ln \bar{r}_b / \partial \ln \bar{q})_{T_o,p}$
$\rho_c$	=	condensed phase density
$\sigma_p$	=	$(\partial \ln \bar{r}_b / \partial T_o)_{p,q} (= k / (\bar{T}_s - T_o))$
$\Omega$	=	dimensionless frequency: $2\pi f \alpha_c / \bar{r}_b^2$

#### SUBSCRIPTS AND SUPERSSCRIPTS

$c$	=	condensed phase, convective-diffusive, or conduction
$r$	=	radiation
$R$	=	reaction zone in condensed phase
$s$	=	surface
$-$	=	overbar denotes the steady condition or mean value
$\sim$	=	nondimensional quantity
$'$	=	complex fluctuating quantity

#### REFERENCES

1. **Lengelle, G.**, "Thermal Degradation Kinetics and Surface Pyrolysis of Vinyl Polymers," *AIAA J.*, 8, 1989-98, 1970.
2. **Ibircu, M. W. and F. A. Williams**, "Influence of Externally Applied Thermal Radiation on the Burning Rates of Homogeneous Solid Propellants," *Combustion and Flame*, 24, 185-198, 1975.
3. **Williams, F. A.**, *Combustion Theory*, 2<sup>nd</sup> Edition, Addison-Wesley Publishing Company, 1985.
4. **Brewster, M. Q. and S. F. Son**, "Quasi-Steady Combustion Modeling of Homogeneous Solid Propellants," *Combustion and Flame*, 103, 11-26, 1995.
5. **Brewster, M. Q., M. A. Zebrowski, T. B. Schroeder, and S. F. Son**, "Unsteady Combustion Modeling of Energetic Solids," AIAA 95-2859, AIAA/ASME/SAE/ASEE Joint Propulsion Conference, San Diego, CA, 1995.
6. **Novozhilov, B. V.**, *Nonstationary Combustion of Solid Propellants*, Nauka, Moscow, (English translation available from NTIS, AD-767 945), 1973.
7. **Zebrowski, M. A. and M. Q. Brewster**, "Theory of Unsteady Combustion of Solids: Investigation of Quasi-Steady Assumption," *J. Prop. Power*, 12, 564-573, 1996.
8. **Son, S. F. and M. Q. Brewster**, "Radiation-Augmented Combustion of Homogeneous Solids," *Comb. Sci. Tech.*, 107, 127-154, 1995.
9. **Son, S. F. and M. Q. Brewster**, "Linear Burning Rate Dynamics of Solids Subjected to Pressure or External Radiant Heat Flux Oscillations," *J. Propulsion and Power*, 9 (2), 222-232, 1993.
10. **NWC TP 4393**, *Experimental Studies on the Oscillatory Combustion of Solid Propellants*, Naval Weapons Center, China Lake, CA, 1969.



11. **Zenin, A. A.**, In *Prog. in Astro. and Aero.*, (L. DeLuca, E. W. Price, and M. Summerfield, Eds.), AIAA, Vol. 143, Chap. 6, 1992.
12. **Son, S. F. and M. Q. Brewster**, "Unsteady Combustion of Homogeneous Energetic Solids Using the Laser-Recoil Method," *Combustion and Flame.*, 100, 283-291, 1995.
13. **Schroeder, T. B.**, "Laser Augmented Combustion of AP and RDX Using the Laser Recoil Technique," M. S. Thesis, University of Illinois at Urbana-Champaign, 1995.
14. **Zanotti, C., A. Volpi, M. Bianchessi, and L. De Luca**, In *Prog. in Astro. and Aero.*, (L. DeLuca, E. W. Price, and M. Summerfield, Eds.), AIAA, 143, Chap. 5, 1992.
15. **Isbell, R. A.**, "Optical Properties of Energetic Materials: AP, RDX, HMX, HTPB Binder and N5," M. S. Thesis, University of Illinois at Urbana-Champaign, 1995.
16. **Schroeder, T. B. and M. Q. Brewster**, "Steady and Unsteady Laser Augmented Combustion of AP at Atmospheric Conditions," 30th JANNAF Combustion Meeting, CPIA Publ. 606, I, 327-336, 1993.
17. **Schroeder, T. B. and M. Q. Brewster**, "Experimental Study of Steady and Unsteady Combustion of RDX," 32nd JANNAF Combustion Meeting, CPIA Publ. 638, I, 85-94, 1995.
18. **Jacobs, P. W. M. and H. M. Whitehead**, "Decomposition and Combustion of Ammonium Perchlorate," *Chem. Rev.*, 69, 551-590, 1969.
19. **Politzer, P.**, private communication, 1996.

## IMPROVEMENTS TO MODELING OF HOT FRAGMENT CONDUCTIVE IGNITION OF NITRAMINE-BASED PROPELLANTS\*

E. S. Kim, S. T. Thynell, and K. K. Kuo

Department of Mechanical Engineering  
The Pennsylvania State University  
University Park, PA 16802

**ABSTRACT:** Hot fragments generated during the impact of shaped charge jets may penetrate the cartridge casing and induce propellant ignition. To simulate hot fragment conductive ignition, a comprehensive model has been formulated and validated by conducting detailed experiments. The model has been based on an assumed decomposition behavior of the various binder ingredients contained in the nitramine-composite propellant. The objective of this work is to describe the effects of incorporating an improved knowledge about the thermal decomposition behavior of these binder ingredients into the existing model. Rapid thermolysis experiments have revealed that essentially no decomposition occurs of the major ingredients CAB and ATEC over the range of temperatures from 450 to 600 K. The use of these findings has enabled an improved predictive capability of the propellant's rate of gasification, as well as the location of the Go/No-Go ignition boundary for both partially and fully confined enclosures. It should also be noted that the use of different reactions among  $\text{CH}_2\text{O}$  and  $\text{NO}_2$  for describing the ignition event has shown only a limited impact on the location of Go/No-Go ignition boundary.

### INTRODUCTION

Accidental ignition of solid-propellant charges in confined environments is of great concern for reducing thermal sensitivity of certain weapon systems. Such an ignition may be caused by either electrostatic discharges, or heat generation due to friction. In combat situations, hot spall fragments from a shape charge jet impact may induce ignition of the propellant bed. In these situations, confinement has a strong effect on the ignition susceptibility. Effects initiated by an internal electrostatic discharge have been attributed to the cause of fires within solid rocket motors, although the energy available in the electrostatic discharge is small. Owing to the relatively short event and difficulty in establishing a sufficient volume for study, it has been quite challenging to study electrostatic discharge phenomena. On the other hand, ignition due to hot fragments has been much easier to analyze.

In a recent series of works,<sup>1-5</sup> a detailed model of partially confined hot fragment conductive ignition (PCHFCl) process has been formulated and solved numerically. Validation of results with carefully conducted experiments has been performed, and, in general, agreement appears to be quite

---

\* This work was performed under Grants No. DAAL-03-92-G-0020 and No. DAAH04-94-G-0202 with the Army Research Office, Research Triangle Park, NC, with Dr. David M. Mann serving as the contract monitor. It should be noted that the content of the information contained in this work does not necessarily reflect the position or the policy of the government, and no official endorsement should be inferred.

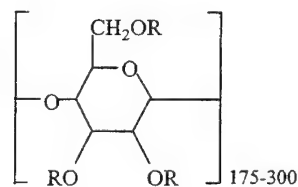
reasonable. This model has been used to demonstrate that the Go/No-Go ignition boundary can be strongly dependent on the type of confinement of the evolved decomposition gases for the XM39 nitramine-composite propellant.

Although the model considers a detailed treatment of physical and chemical phenomena in a foam layer, including a separate analysis of the gas bubbles and liquid, the short residence time of the energetic material in this layer precludes ignition within the gas bubbles. Instead, the thermal decomposition product gases accumulate in the free volume above propellant's surface, and the pressure rises until spontaneous ignition occurs due to reaction among the decomposition products  $\text{CH}_2\text{O}$  and  $\text{NO}_2$ . Regarding the ignition susceptibility of the XM39 propellant, assumptions were required to describe its thermal decomposition behavior. Unfortunately, only a limited amount of data was available to describe the decomposition behavior of the binder ingredients. Hence, data from differential scanning calorimetry were incorporated.<sup>6</sup>

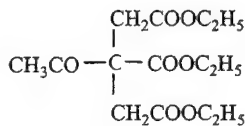
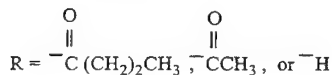
To more fully understand the role of the binder ingredients during the hot fragment conductive ignition, isothermal decomposition experiments have been performed at both the Pennsylvania State University and at the University of Delaware.<sup>7</sup> These studies have been focused on examining the binder ingredients contained in the XM39 propellant. The objectives of this work are: (1) to describe and adopt the results obtained from rapid thermolysis experiments on binder ingredients in the model simulation, (2) to outline the relevant improvements to the existing model of PCHFCI, and (3) to summarize changes in the predicted Go/No-Go ignition boundary for the XM39 propellant.

#### DECOMPOSITION BEHAVIOR OF XM39 BINDER INGREDIENTS

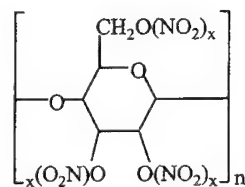
The XM39 propellant contains five different ingredients: 76% of cyclotrimethylenetrinitramine (RDX) whose average crystal size is  $5\mu\text{m}$ , 12% of cellulose-acetate-butyrate (CAB), 7.6% of acetyltriethylcitrate (ATEC), 4% of nitrocellulose (NC), and 0.4% of ethylcentralite (EC), which is a stabilizer for the NC. A reasonable amount of data has emerged on the decomposition<sup>8</sup> and combustion behavior of RDX<sup>9,10</sup>, and a comprehensible model of its flame structure has been established<sup>11</sup>. Virtually no data are available on the thermal decomposition behavior of ATEC relevant to either steady-state propellant burning conditions or the slow cook-off situations of PCHFCI. Recently, Gongwer et al.<sup>12</sup> have conducted T-jump/FTIR experiments using CAB. The results from their comprehensive study suggest that the major species formed include methyl acetate, methyl butyrate, butyric acid,  $\text{CO}_2$ , and  $\text{CO}$ . The minor species formed are acetic acid, formaldehyde, acetaldehyde, ketene, ethyl ketene, and CAB oligomers. A dark residue also remained on the heated filament. In order to observe the thermal decomposition, the filament temperatures ranged from 738 to 873 K. The molecular structures of CAB, ATEC, and NC are shown below.



CAB



ATEC



NITROCELLULOSE

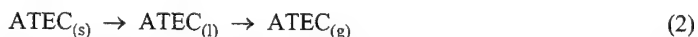
$$x = 2.5$$

In view of the complex molecular structure of these compounds, it is evident that elucidating the thermal decomposition behavior becomes very difficult. In CAB, the molecular weight and decomposition behavior depend on the extent of acetyl and butyryl substitutions. An approach for measuring the extent of butyryl substitution is available.<sup>13</sup> To study the thermal decomposition behavior of these binder ingredients, the test rig used previously for conducting the PCHFCI experiments<sup>5</sup> has also been utilized for conducting studies of the pyrolysis behavior of the binder ingredients. The temperature of the heated surfaces was varied over the range from 450 to 600 K, which is typical to the temperatures measured within the foam layer during the PCHFCI experiments. However, the evolved gases from these thermal decomposition experiments revealed that neither CAB nor ATEC decomposed to any significant extent over this range of temperatures, which is more than 200 K below those utilized by Gongwer et al.<sup>12</sup> In the case of ATEC, the required temperatures for achieving rapid thermal decomposition appears to be higher than those required to thermally decompose CAB, but the experiments are difficult to perform due to ATEC's propensity to rapidly vaporize.

It is now evident that thermal decomposition of CAB and ATEC can be neglected in the PCHFCI model, because the temperatures are low and the residence time are short of the liquid/gas within the foam layer. Hence, it is reasonable to assume that CAB and ATEC undergo a melting process that is followed by an evaporation process. This assumption should be valid for ATEC, but it is more questionable for CAB which is a very long polymer. Furthermore, studies are underway to assess the decomposition behavior of known mixtures of RDX/CAB as well as mixtures of RDX/ATEC, in order to assess the extent of catalytic effects.<sup>7</sup> Hence, it is useful to consider the following phase changes for both CAB and ATEC

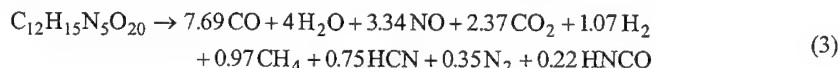


and



At standard pressure and temperature, CAB appears as a solid, whereas ATEC is a liquid. In the model, latent heats associated with the polymerization process during propellant manufacturing are assumed to be small and are neglected. Thus, the enthalpy of formation of liquid ATEC is equal to that of the solid; in other words, in the solid we treat ATEC as a dissolved liquid.

NC is a much more reactive compound than either CAB or ATEC. As discussed by Brill and Gongwer,<sup>14</sup> the decomposition rate and controlling processes are highly dependent upon the temperature. For temperatures above 523 K, the decomposition rate is very high, and the results are considerably scattered. At temperatures below 523 K, the results indicate the importance of first-order decomposition kinetics and autocatalysis. However, for autocatalysis to be important, long residence times are required to allow an accumulation of species. Hence, it is reasonable to assume first-order decomposition kinetics of NC. Preliminary results from Gongwer and Brill<sup>7</sup> indicate that the following decomposition mechanism of NC (12.43% N) is a reasonable approximation:



### MODEL MODIFICATION

A detailed description of the model of PCHFCI is available;<sup>4,5</sup> therefore, only the major features are briefly mentioned here. Figure 1 shows the five regions considered in the model. In region 1, a transient one-dimensional heat conduction process was considered inside the solid propellant. Region 2 involved a lumped parameter analysis of the liquid, and it also accounted for thermal decomposition of RDX. Region 3 treated physical and chemical effects within the bubbles,

including thermal decomposition of RDX and subsequent reactions among its highly reactive products ( $\text{NO}_2 + \text{CH}_2\text{O}$ ), by using a lumped parameter analysis. In region 4, a two-dimensional heat conduction model accounted for transient temperature distributions in the axial and radial directions within the spall fragment. Finally, gas accumulation occurred in region 5, which was simulated by a lumped parameter model including a consideration of the conservation equations for mass, species, and energy. Since convective heat losses to the surrounding chamber walls are considered to be relatively small and continuous heating occurred from the spall fragment, the ignition occurred in this region rather than inside the bubbles. Ignition did not occur inside the gas bubbles within the foam layer due to large heat transfer rates to the surrounding liquid layer; small bubble sizes established large convective heat-transfer coefficients. Modifications to this model were performed both in regards to heat transfer and chemical kinetics. Modifications in the chemical kinetic mechanism were made to incorporate the new information about the thermal decomposition behavior of the binder ingredients, as well as to consider the effect of different reactions and rates between  $\text{CH}_2\text{O}$  and  $\text{NO}_2$ .<sup>15,16</sup> Since the ignition delay times on the order of 60 s were recorded in our experiments, thermal decomposition of  $\text{NO}_2$  was also considered according to the reaction



However, the consideration of this reaction has produced very limited impact on the predicted results.

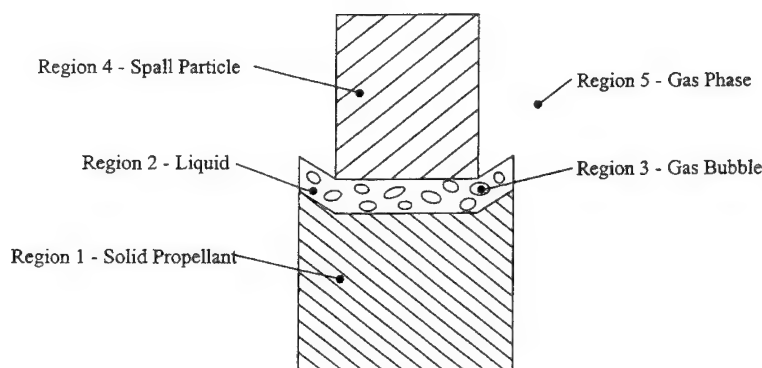


Figure 1. Schematic diagram of the five different regions considered in the model of PCHFCL.

The flow field established between the chamber walls and propellant sample inside the test rig was very complex. The velocities of the gas evolving from the foam layer decayed rapidly, and combined natural and forced convection cooling occurred along the chamber walls. It was assumed that these walls were isothermal. In order to account for the effects of pressure on the convective heat transfer, it was shown that the pressure dependency on the heat-transfer coefficient could be approximately accounted for according to

$$h_c = h_{c,\text{ref}} (p / p_{\text{ref}})^{1/2} \quad (5)$$

This expression was readily developed by using the equation of state for an ideal gas and also accounting for the effect of temperature on viscosity in convective heat transfer correlations. Here,  $p_{\text{ref}} = 0.1$  MPa. Since the gas was largely in contact with plexiglass, which served as a poor heat conductor, a relatively low value of the reference heat transfer coefficient  $h_{c,\text{ref}} = 2$  W/m<sup>2</sup>K was utilized. The resulting model involved a total of 45 dependent variables coupled in a highly

nonlinear manner. This model was readily solved numerically using an adaptive 4-th order Runge-Kutta method adopted from Press et al.<sup>17</sup>

## DISCUSSION OF RESULTS

In this section, an assessment is presented on the effects of the changes made on the predicted results. These major changes include the vaporization of CAB and ATEC, decomposition of NC, and the use of a different global reaction as well as rate among  $\text{CH}_2\text{O}$  and  $\text{NO}_2$  species. A detailed summary of the chemical kinetic model incorporated in the existing PCHFCI model is shown in Table 1, and the associated kinetic data are given in Table 2.

Figure 2 shows a comparison of the sinking distance of the spall fragment obtained both from experiments and modeling. In the experiments, the sinking distance was obtained by measuring the time it took for the spall fragment to traverse through the propellant sample. This time was indicated by a thermocouple placed at the bottom of the sample, and samples of different heights were used. The results shown in Fig. 2 apply to a spall fragment having an initial temperature  $T_{si} = 1203 \text{ K}$ , and height  $L_s = 1.27 \text{ cm}$ , whereas the large exit area of the chamber for the gaseous pyrolysis products ( $A_{\text{exit}} = 3.17 \times 10^{-5} \text{ m}^2$ ) prevented chamber pressurization. Examination of this figure reveals that results from both the previous and modified models underpredict the results obtained from experiments by about 30%. Much of that discrepancy is due to uncertainties associated with the inert heating period, which typically lasts for about 1 to 2 s. More importantly, however, the sinking velocity was somewhat more accurately predicted with the use of the modified model. The sinking velocity was obtained by evaluating the slope of these lines. In general, the sinking velocity could be closely related to the pressurization rate of decomposition product gases within the chamber, but in this case, the pressure remained steady at 0.1 MPa.

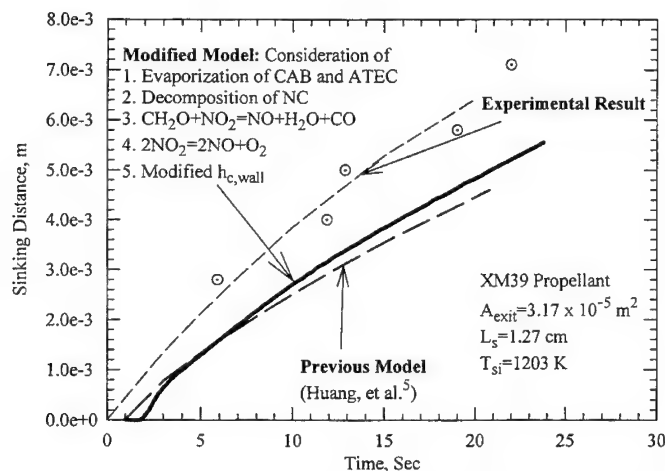
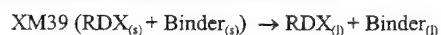


Figure 2. Comparisons of modified and previous calculated time variations of sinking distance with experimental data.

Figure 3 shows the evolution of the temperature within the gas-phase region of the totally confined chamber ( $A_{\text{exit}} = 0$ ), as well as within the bubbles and liquid of the foam layer. Examination of this figure reveals that the gas temperatures inside the bubbles were higher than those of the liquid

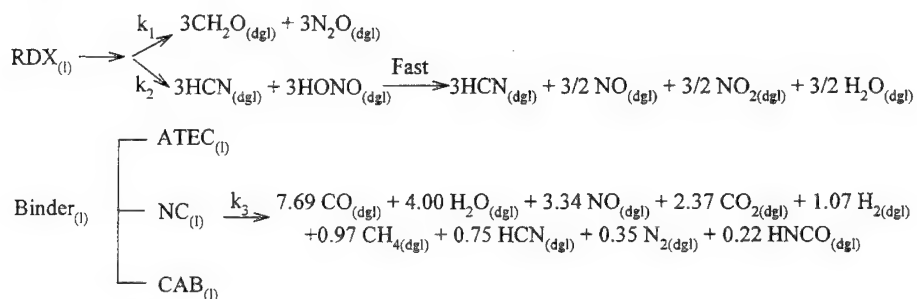
TABLE 1  
Modified Chemical Kinetic Scheme for Ignition Study of XM39 Propellant

### 1. XM39 Solid Propellant / Foam Layer Interface:

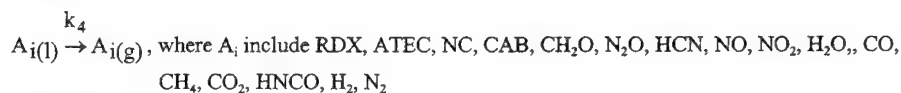


## 2. Foam Layer:

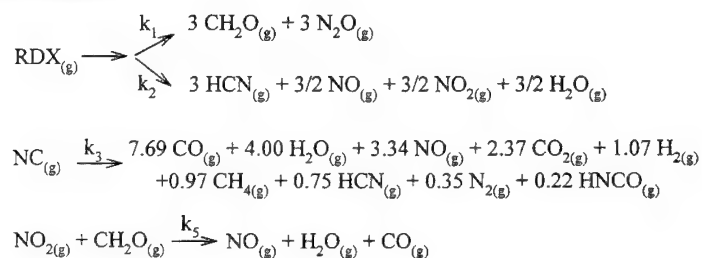
Liquid:



**Liquid/Gas Bubble Interface:**



**Gas Bubbles:**



### 3. Gas-Phase Region:

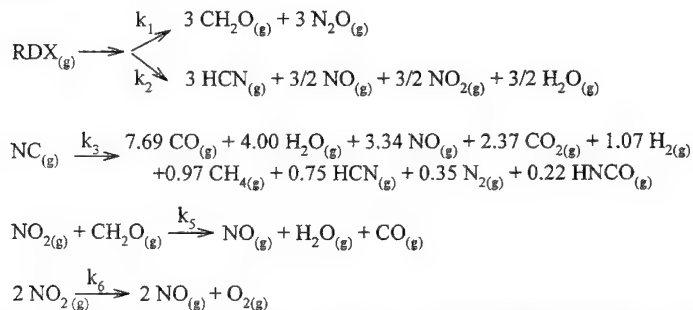


TABLE 2  
Specification of Preexponential Factors and Activation Energies

$k_i = A \exp(-E/R_u T)$	A	E (kcal/g-mole)	Ref.
$k_1$	$1 \times 10^{13}$ , (1/s)	36	9, 10
$k_2$	$2 \times 10^{16}$ , (1/s)	45	9, 10
$k_3$	$1 \times 10^{13.3}$ , (1/s)	37.1	7
$k_4$	$1.98 \times 10^{14}$ , (1/s)	38.2	8
$k_5$	$802 \times T^{2.77}$ , (cm <sup>3</sup> /g mole-s)	13.7	16
$k_6$	$2 \times 10^{12}$ , (cm <sup>3</sup> /g mole-s)	26.8	10

in the foam layer due to their immediate contact with the high-temperature spall fragment and exothermic decomposition of RDX. The low-temperature decomposition pathway, associated with the formation of CH<sub>2</sub>O and N<sub>2</sub>O, contributed to these high temperatures due to its exothermicity. The relatively low temperature of the liquid was caused by its high thermal conductivity, which provided a high heat-transfer rate to the solid propellant. As the decomposition products accumulated within the gas-phase region of the test chamber, the temperature increased and a more rapid decomposition of gas-phase RDX occurred. Since convective heat transfer to the surrounding chamber walls was much smaller than the rate of heat release from chemical reactions, ignition occurred within the gas-phase region (Region 5, Fig. 1). The gas-phase temperature approached 850 K but dropped rapidly due to the endothermicity of the high-temperature decomposition pathway, represented by the formation of HCN and other species, the increased convective heat-transfer to the chamber walls, and depletion of reactants. At these high temperatures, decomposition of binder ingredients could occur relatively rapidly and extensively in view of the findings from the

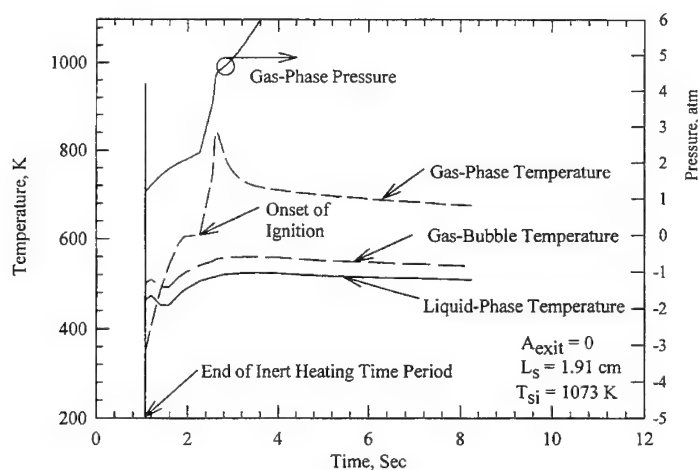


Figure 3. Calculated time variations of temperatures and pressure when ignition of XM39 propellant occurs.



thermolysis work conducted by Gongwer et al.<sup>12</sup> Hence, the accuracies of the calculated temperatures within the gas-phase region beyond the time of ignition could have some degree of uncertainty.

Figure 4 shows the evolution of species within the gas-phase region also for the case of a totally confined chamber. Since prior to ignition, the temperatures within the bubbles were higher than those within the gas-phase region over a portion of the time, the thermal decomposition products were primarily formed within the bubbles of the foam layer. To keep this figure in a relatively readable format, only the most relevant species are included. It is observed from this figure that RDX became essentially depleted upon ignition, and its replenishment was due to evaporation of the foam layer. At these temperatures, NC underwent extensive decomposition. The relative roles of the low- and high-temperature decomposition pathways are also evident: in this case, it can be seen that  $\text{CH}_2\text{O}$  and  $\text{NO}_2$  evolved at about the same rate prior to ignition. After ignition, the high-temperature decomposition pathway became dominant and  $\text{NO}_2$  appeared in quantities several orders-of-magnitude larger than those of  $\text{CH}_2\text{O}$ .

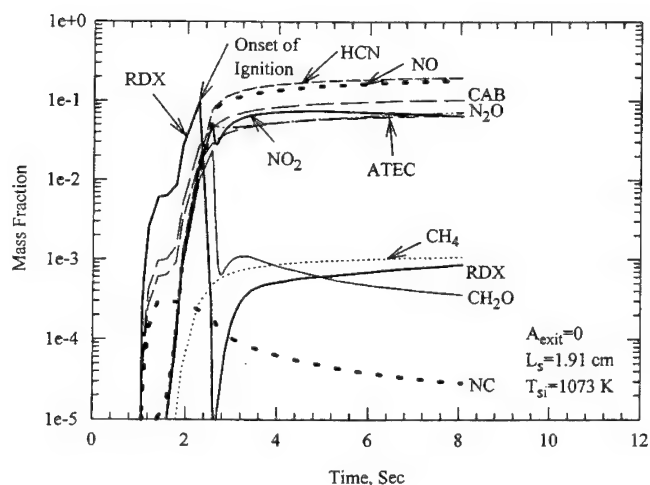


Figure 4. Calculated time variations of species concentration in the gas-phase region in the simulation of conductive ignition of XM39 propellant.

The remaining discussion of results is focused on the prediction of the Go/No-Go ignition boundary. In Fig. 5, the Go/No-Go ignition boundaries for the totally confined enclosure are presented. Above an individual curve in this figure, ignition is either observed or predicted. Examination of Fig. 5 reveals that an improved agreement with the experimental data was obtained with the modification of the model described previously. This improved agreement is attributed to better knowledge both of decomposition species and of convective heat transfer to the chamber walls. In particular, knowledge about heats of formation and a smaller species conversion rate have caused the upward shift in the calculated ignition boundary. In addition, in the previous model,<sup>5</sup> the convective heat-transfer coefficient was assumed to be independent of pressure, which also affected the location of the modelled ignition boundary.

An accurate prediction of the Go/No-Go ignition boundary for the partially confined enclosure, as shown in Fig. 6, was much more difficult to obtain. The difference in the predicted ability between fully and partially confined enclosures was noted for both the modified and previous models. An

improved agreement was obtained in regards to the overall dependency of the mass of spall fragment on the location of the ignition boundary. For an increased spall mass, a decrease in initial spall temperature was required for ignition. In the case of a partially confined enclosure, the ignition delays were significantly longer compared to the fully confined enclosure; therefore, accurate prediction of Go/No-Go ignition boundary requires more detailed knowledge of the rate of heat losses to the surrounding walls. Further improvements to such modeling of heat transfer will most likely come from a more accurate modeling of the flow field within the enclosure, which is beyond the scope of this report.

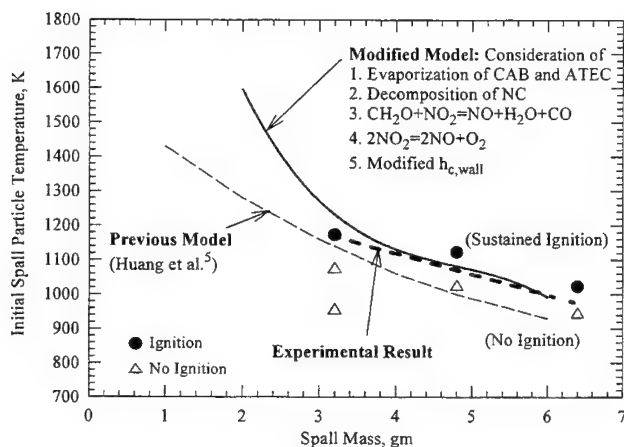


Figure 5. Comparisons of experimental result with modified and previous calculated GO/NO-GO ignition boundaries for XM39 propellant in a totally confined enclosure.

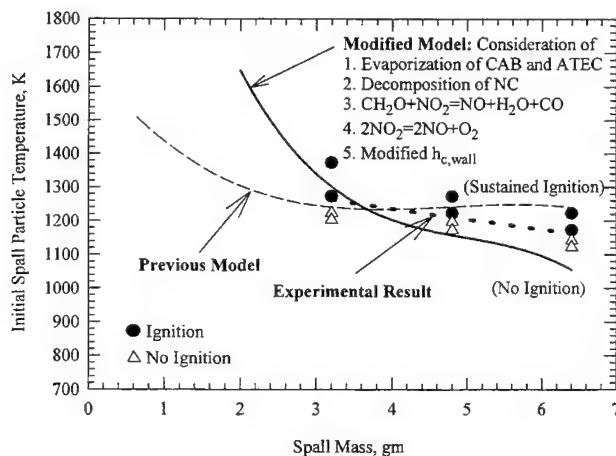


Figure 6. Comparisons of experimental result with modified and previous calculated GO/NO-GO ignition boundaries for XM39 propellant in a partially confined enclosure.

The final set of results shown in Fig. 7 describes uncertainties associated with the use of a global reaction among  $\text{CH}_2\text{O}$  and  $\text{NO}_2$  species. The reaction between these species was attributed to cause ignition within the gas-phase region. It should be emphasized that all the calculations shown in Fig. 7 were determined using the previous model.<sup>5</sup> Inspection of Fig. 7 shows that over the range of experimental data there is essentially very little difference in the predicted ignition boundaries. This observation implies that the reaction among  $\text{CH}_2\text{O}$  and  $\text{NO}_2$  may not be the limiting step in the ignition sequence. Instead, the decomposition of RDX and thus the formation of  $\text{CH}_2\text{O}$  and  $\text{NO}_2$  could be the limiting step to the ignition. However, in cases of a small mass of the spall fragment, a noted difference is predicted. Hence, it is believed that in the range of small spall masses, where reactions among  $\text{CH}_2\text{O}$  and  $\text{NO}_2$  species control the location of the ignition boundary, the differences in the rates of these reactions become important.

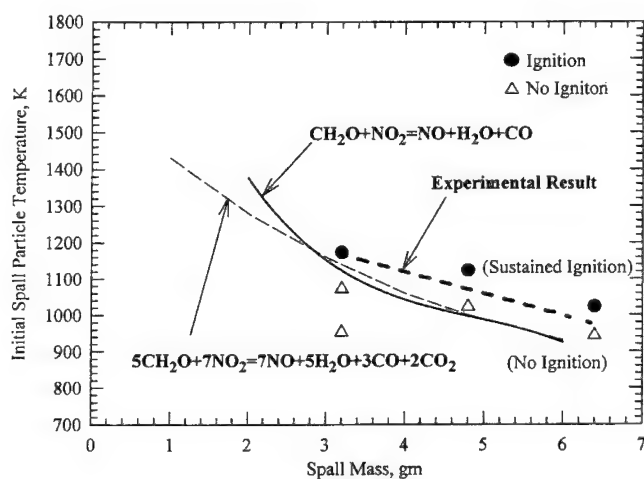


Figure 7. Comparisons of experimental result with calculated Go/No-Go ignition boundaries using different reactions between  $\text{CH}_2\text{O}$  and  $\text{NO}_2$  for XM39 propellant in a totally confined enclosure.

## SUMMARY AND CONCLUSIONS

An existing model of hot fragment conductive ignition was modified to more accurately reflect heat transfer and binder decomposition product evolution of the XM39 propellant. For the binder ingredients of the XM39 propellant, thermal decomposition experiments revealed that the extent of decomposition of these binders was very limited due to the low temperature experienced prior to ignition and short residence times of bubbles within the foam layer. The effects of initial temperature of spall particle, size of spall particle, and size of chamber exhaust port (governing the degree of confinement) were examined for comparison with experimental results. The Go/No-Go ignition boundaries were predicted under various degrees of confinement. An improved agreement was obtained between the calculated and experimentally determined Go/No-Go ignition boundary in both the fully and partially confined enclosure in which the pressure was maintained at one atmosphere prior to ignition. Both calculated results and experimental data showed the shift of the Go/No-Go ignition boundary from the highly confined case to that of a partially (weakly) confined condition. In addition, the use of either a reaction among  $\text{CH}_2\text{O}$  and  $\text{NO}_2$  species attributed to BenReuven et al.,<sup>15</sup> or a more recently established one by Lin et al.<sup>16</sup> from shock-tube experiments showed no appreciable differences.

## REFERENCES

1. Kuo, K. K., Hsieh, W. H., Hsieh, K. C., and Miller, M. S., Modeling of Hot Fragment Conductive Ignition of Solid Propellants with Applications to Melting and Evaporation of Solid, *ASME Journal of Heat Transfer*, 110, 670-679, 1988.
2. Hsieh, K. C., Hsieh, W. H., Kuo, K. K., and Miller, M. S., Modeling of Hot Fragment Conductive Ignition Processes of LOVA Propellants, *Proceedings of the 24th JANNAF Combustion Meeting*, Naval Postgraduate School, Monterey, CA, October 5-9, 1987.
3. Hsieh, K. C., Hsieh, W. H., Kuo, K. K., and Miller, M. S., Validation of a Theoretical Model for Hot Fragment Conductive Ignition Processes of LOVA Propellants, *Proceedings of the 10th International Symposium on Ballistics*, San Diego, CA, October 27-29, Vol. 1, Section 2, 1987.
4. Huang, T. H., Thynell, S. T., and Kuo, K. K., Modeling of Partially Confined Hot Fragment Conductive Ignition, *25th Symposium (International) on Combustion*, The Combustion Institute, 1595-1601, 1994.
5. Huang, T. H., Thynell, S. T., and Kuo, K. K., Hot Fragment Conductive Ignition of Nitramine-Based Propellants, *Journal of Propulsion and Power*, 11, 4, 781-790, 1995.
6. Miller, M. S., Effective Ignition Kinetics for LOVA Propellant, *Proceedings of the 23rd JANNAF Combustion Meeting*, CPIA Publ. 457, Vol. II, 55-62, 1986.
7. Gongwer, P., and Brill, T. B., Personal Communication, 1995.
8. Brill, T. B., and Brush, P. J., Condensed Phase Chemistry of Explosives and Propellants at High Temperature: HMX, RDX, and BAMO, *Philosophical Transactions of the Royal Society*, London, A, 339, 377-385, 1992.
9. Melius, C. F., Theoretical Studies of the Chemical Reactions Involved in the Ignition of Nitramines, *Proceedings of the 24th JANNAF Combustion Meeting*, CPIA Publ. 476, Vol. 1, 359-366, 1987.
10. Melius, C. F., Thermochemical Modeling: I & II, in *Chemistry and Physics of Energetic Materials*, Bulusu, S. N., ed., Kluwer Academic, Norwell, MA, 21-78, 1990.
11. Liao, Y.-C., and Yang, V., Analysis of RDX Monopropellant Combustion with Two-Phase Subsurface Reactions, *Journal of Propulsion and Power*, 11, 4, 729-739, 1995.
12. Gongwer, P. E., Arisawa, H., and Brill, T. B., Kinetics and Species of Flash Pyrolysis of Cellulose Acetate Butyrate: The Binder of LOVA, in *Decomposition, Combustion and Detonation Chemistry of Energetic Materials*, Brill, T. B., Russell, T. P., Tao, W. C., and Wardle, W. C., eds., Materials Research Society, Vol. 418, Pittsburgh, PA, 233-238, 1996.
13. Saunders, C. W., and Taylor, L. T., Solution Infrared Spectra of Cellulose Acetate Butyrate, *Applied Spectroscopy*, 44, 6, 967-969, 1990.
14. Brill, T. B., and Gongwer, P. E., Thermal Decomposition of Energetic Materials 69. Analysis of the Kinetics of Nitrocellulose at 50 - 500°C, *Propellants, Explosives and Pyrotechnics*, in press, 1997.
15. BenReuven, M., Caveny, L. H., Vichnevetsky, R. J., and Summerfield, M., Flame Zone and Sub-Surface Reaction Model for Deflagrating RDX, *Sixteenth Symposium (International) on Combustion*, The Combustion Institute, 1223-1233, 1976.
16. Lin, C.-Y., Wang, H.-T., Lin, M. C., and Melius, C.F., A Shock Tube Study of the  $\text{CH}_2\text{O} + \text{NO}_2$  Reaction at High Temperatures, *International Journal of Chemical Kinetics*, 22, 455-482, 1990.
17. Press, W. H., Teukolsky, S. A., Vetterling, W. T., and Flannery, B. P., *Numerical Recipes*, Cambridge University Press, Cambridge, MA., Chap. 15, 1992.

## AN EIGENVALUE METHOD FOR COMPUTING THE BURNING RATES OF RDX AND HMX MONOPROPELLANTS

Kuldeep Prasad<sup>1</sup>, Richard A. Yetter<sup>2</sup> and Mitchell D. Smooke<sup>3</sup>

<sup>1</sup>Naval Research Laboratory, Washington DC 20375, <sup>2</sup>Princeton University, Princeton, NJ 08544, <sup>3</sup>Yale University, New Haven, CT 06520

**ABSTRACT:** A mathematical model for a three-tiered system consisting of solid, liquid and gas is derived for studying the combustion of RDX and HMX monopropellants. The resulting nonlinear two-point boundary value problem is solved by Newton's method with adaptive gridding techniques. In this study the burning rate is computed as an eigenvalue, which removes the uncertainty associated with employing evaporation and condensation rate laws in its evaluation. Results are presented for laser-assisted and self-deflagration of HMX monopropellants and are compared with experimental results. The burning rates are computed over a wide range of ambient pressures and compare well with experimental results from one to ninety atmospheres. The burning rate is found to be proportional to the pressure raised to the 0.82 power. Sensitivity of the burning rate to initial propellant temperature is calculated and found to be extremely low, in agreement with past theoretical predictions and experimental data. Results for laser-assisted combustion show a distinct primary and secondary flame separated by a dark zone, the length of which is dependent upon the incident laser flux intensity.

### 1. INTRODUCTION

Numerous chemicals have been used in making solid propellants with the goal of optimizing combustion characteristics for different purposes. The cyclic nitramines cyclotrimethylenetrinitramine ( $C_3H_6N_6O_6$ ), commonly called RDX, and cyclotetramethylenetetranitramine ( $C_4H_8N_8O_8$ ), commonly called HMX are important ingredients in solid propellants. The addition of nitramine particles such as RDX and HMX to double-base homogeneous propellants increases the flame temperature and energy release. It is widely known that the use of these ingredients offers many advantages. Due to the high energy release of these compounds and the large amount of low molecular weight gaseous combustion products, high values of specific impulse for rocket propellants and impetus for gun propellants can be achieved.

Due to the lack of understanding of the various elementary chemical and physical processes involved during the combustion of HMX monopropellants, little work has been done in the area of detailed numerical modeling. Microscopic observations, mostly by Boggs and Hanson-Parr and Parr, of quenched samples using a scanning electron microscope and of burning samples

using high speed motion-picture photography have revealed many aspects of the deflagration process that can aid in the development of theories [1-2]. Ben-Reuven et al. have incorporated basic nitramine flame chemistry into theoretical models for studying the self-deflagration of HMX [3]. A simplified theoretical model was also developed by Mitani and Williams for describing the flame structure and deflagration of nitramines, which included exothermic decomposition in a liquid layer, equilibrium vaporization, and exothermic combustion in the gas [4].

The problem of modeling the deflagration of a homogeneous solid propellant becomes especially difficult if it is necessary to account for two-phase flow that occurs in liquid melt layers as well as the gas-phase region above the liquid melt layer. The combustion of double-base propellants usually involves reactions occurring in the condensed-phase, in the dispersed-phase and in the gas-phase. Li, Williams and Margolis used asymptotic analysis to extend the Mitani-Williams model to account for the presence of bubbles and droplets in a two-phase layer at the propellant surface [5]. They again report good agreement with measured burning rates and pressure and temperature sensitivities using an overall chemical-kinetic parameter for describing gas-phase reactions. These models do not predict a dark zone as observed in experimental results. Additional work considering RDX combustion with two-phase subsurface reactions is included in [6].

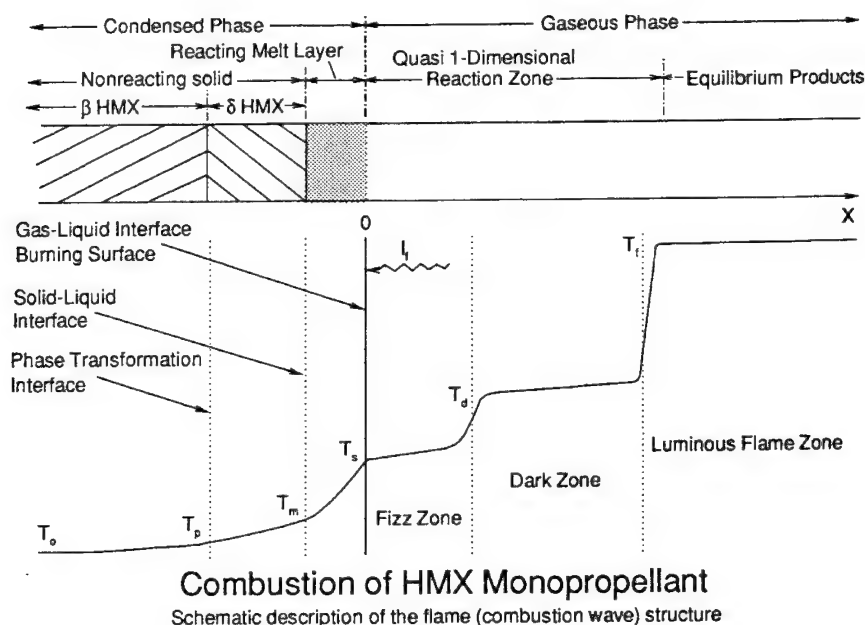
Melius developed a two-layer solid-gas model for studying the ignition and self-deflagration of RDX [7-8]. He constructed a gas-phase model with an evaporation-condensation rate law that was used to model the regressing planar interface separating the solid and the gas-phase. In the solid-phase there was a single irreversible reaction whose rate was pertinent to liquid phase RDX. Fetherolf and Litzinger have studied the  $CO_2$  laser-induced pyrolysis of HMX using both experimental studies and kinetic modelling of the gas-phase processes [9]. Hatch has developed a steady-state one-dimensional combustion model to study the gas-phase chemistry of a nitrate-ester flame and has recently applied this approach for studying the deflagration of HMX [10]. The effects on combustion of different mechanisms of decomposition were determined and some of the more important gas-phase reactions were identified.

More recently, Prasad, Yetter and Smooke have developed a detailed three-layered model for studying RDX self- and laser-assisted deflagrations using detailed finite rate chemistry in the gas-phase and a three-step liquid-phase decomposition mechanism [11]. This model accurately predicts the burn rates over a wide range of ambient pressures and initial propellant temperatures under self-deflagration conditions. In the present study, we apply the approach used in [11] to develop a detailed model for studying the combustion of HMX homogeneous monopropellants.

## 2. PROBLEM FORMULATION

Figure 1 shows a schematic diagram of the physical model we will employ for describing the steady-state burning of a homogeneous solid propellant. It consists of a three-layered (solid, liquid and gas) model with sharp planar boundaries, with the liquid layer sandwiched between the other two phases. HMX monopropellant combustion is modeled with a solid region followed by a liquid reaction zone followed by a fizz zone and then, after a dark zone, by a luminous gas-phase flame. Unlike RDX, there are four polymorphic forms of HMX [1]. The  $\beta$ HMX is the commonly encountered stable form at room temperature, whereas  $\delta$ HMX is most relevant to the thermal decomposition of HMX.

The  $\beta \rightarrow \delta$  phase transformation is again modeled as a sharp planar interface within the solid-phase to account for the different enthalpies and specific heats associated with the two polymorphs. Under certain conditions the gas-phase shows a clearly separated primary flame (fizz zone) and a secondary flame (luminous zone) separated by a dark zone which exhibits essentially isothermal chemical reactions.



**Figure 1.** Schematic diagram of a three-tiered (solid, liquid and gas) combustion model for HMX monopropellant. Also shown is the structure of the combustion wave obtained under laser-assisted conditions.

We consider the steady-state deflagration of a semi-infinite piece of pure HMX monopropellant. It is assumed that the propellant is mounted on a platform moving at a velocity equal but opposite to the regression velocity of the propellant. As a result, during steady-state HMX deflagration, the locations of the gas-liquid interface, the solid-liquid interface, and the primary and secondary flames are all fixed in the laboratory frame of reference. We further choose that the gas-liquid interface is located at the origin of the coordinate frame of reference. Thus in Figure 1,  $x$  is the coordinate normal to the surface; the interface is located at  $x = 0$ ; the solid extends to  $x = -\infty$ , and the gas extends to  $x = +\infty$ . We are interested in computing the burning rate (determined from the mass flux  $\dot{m}$  ( $gm/cm^2/sec$ ) and the local value of the density) with which the solid must move in the  $+x$  direction so that the interface will remain at  $x = 0$ .

The burning rate or the rate of decomposition of liquid HMX can be obtained as a difference between the rate of evaporation for liquid HMX and the rate of condensation for the gaseous products. The evaporation and condensation rates are generally complicated empirically derived expressions that involve the temperature and the various species concentrations at the interface. The evaporation and condensation rates are large numbers  $O(10^2)$  with a very small difference  $O(10^{-2})$ . The result of employing this approach in a computational model is that numerical instability/convergence difficulties can occur. In the approach taken in this paper, the mass flux (and hence the burning rate) is obtained as an eigenvalue of the problem [11].

Our goal is to predict theoretically the mass fractions of the species and the temperature as functions of the independent coordinate,  $x$ , together with the mass flux. If in the gas-phase we neglect viscous effects, body forces, radiative heat transfer and the diffusion of heat due to concentration gradients, the equations governing the structure of a steady, one-dimensional,

gas-phase, isobaric flame [12] are

$$\dot{m} = \rho v A = K1 = \text{constant} \quad (2.1)$$

$$\dot{m} \frac{dY_k}{dx} = -\frac{d}{dx}(\rho A Y_k V_k) + A \dot{\omega}_k W_k, \quad k = 1, 2, \dots, K \quad (2.2)$$

$$\dot{m} c_p \frac{dT}{dx} = \frac{d}{dx} \left( \lambda A \frac{dT}{dx} \right) - A \sum_{k=1}^K \rho Y_k V_k c_{pk} \frac{dT}{dx} - A \sum_{k=1}^K \dot{\omega}_k h_k W_k \quad (2.3)$$

where

$$\rho = \frac{p \bar{W}}{RT} \quad (2.4)$$

In these equations,  $x$  denotes the independent spatial coordinate;  $\dot{m}$ , the mass flux;  $T$ , the temperature;  $Y_k$ , the mass fraction of the  $k^{\text{th}}$  species;  $p$ , the pressure;  $v$ , the velocity of the fluid mixture;  $\rho$ , the mass density;  $W_k$ , the molecular weight of the  $k^{\text{th}}$  species;  $\bar{W}$ , the mean molecular weight of the mixture;  $R$ , the universal gas constant;  $\lambda$ , the thermal conductivity of the mixture;  $c_p$ , the constant pressure heat capacity of the mixture;  $c_{pk}$ , the constant pressure heat capacity of the  $k^{\text{th}}$  species;  $h_k$ , the enthalpy of the  $k^{\text{th}}$  species;  $\dot{\omega}_k$ , the molar rate of production of the  $k^{\text{th}}$  species; and  $V_k$ , the diffusion velocity of the  $k^{\text{th}}$  species.  $A$  represents the local cross-sectional area of the stream tube encompassing the flame.

In the liquid layer, sometimes referred to as the foam zone, temperatures are high enough for molecular degradation to take place. Simultaneous secondary reactions occur so that a mixture of soluble and liquid-phase species emerge from the surface and the net energy balance of the degradation is exothermic. For the liquid-phase, it is assumed that the diffusion velocities are negligible. The equations of motion therefore simplify into the form

$$\dot{m} = \rho v A = K1 = \text{constant}, \quad \rho = \text{constant} = K2 \quad (2.5)$$

$$\dot{m} \frac{dY_k}{dx} = A \dot{\omega}_k W_k, \quad k = 1, 2, \dots, K \quad (2.6)$$

$$\dot{m} c_p \frac{dT}{dx} = \frac{d}{dx} \left( \lambda A \frac{dT}{dx} \right) - A \sum_{k=1}^K \dot{\omega}_k h_k W_k + \dot{Q} A \quad (2.7)$$

The term  $\dot{Q} A$  represents the energy input due to laser flux heating.

The solid-phase (both  $\beta$  and  $\delta$  HMX) consists of a homogeneous propellant with no chemical reactions. The diffusion velocities in the condensed phase are again zero. The equations further simplify to

$$\dot{m} = \rho v A = K1 = \text{constant}, \quad \rho = \text{constant} = K2 \quad (2.8)$$

$$Y_{\text{HMX}} = 1.0, \quad Y_k = 0, \quad k \neq \text{HMX} \quad (2.9)$$

$$\dot{m} c_p \frac{dT}{dx} = \frac{d}{dx} \left( \lambda A \frac{dT}{dx} \right) + \dot{Q} A \quad (2.10)$$

To complete the specification of the problem, boundary conditions must be imposed on each end of the computational domain ( $-L_1, L_2$ ) and at the interfaces. The temperature and the species mass flux fractions are prescribed at the unreacted solid boundary. In the hot stream outflow boundary the gradient of temperature and species mass fractions are assumed to be negligibly small.

Calculation of the mass flux proceeds by introducing the trivial differential equation

$$\frac{d\dot{m}}{dx} = 0 \quad (2.11)$$



and an additional boundary condition. We have considered several possibilities all of which close the problem mathematically. One possibility is to use experimental information regarding the "boiling point" or the "evaporation" temperature at the gas - liquid interface, the location of which is fixed at the origin in the chosen coordinate system. Another choice is to impose the fact that the monopropellant concentration is negligibly small at the far stream boundary. Other possibilities exist but these are the two we most often use. In addition, one needs to specify specialized interface conditions that account for the transition from the liquid to the gas-phase as well as any laser flux heating that might occur at the interface. Energy balance at this interface is maintained by solving the difference form of the energy equation

$$\dot{m} \frac{d}{dx} \left( \sum_{k=1}^K Y_k h_k \right) = \frac{d}{dx} \left( \lambda A \frac{dT}{dx} \right) - A \sum_{k=1}^K \rho Y_k V_k c_{pk} \frac{dT}{dx} + \dot{Q} A \quad (2.12)$$

The term  $\dot{Q}A$  represents the heat input due to laser flux heating, whereas the difference form of the convective term  $\dot{m} \frac{d}{dx} \left( \sum_{k=1}^K Y_k h_k \right)$  takes account of the heat of vaporization associated with the phase transition from the liquid to the gas-phase.

Unlike the gas-liquid interface, whose location remains fixed at a specified grid point, the locations of the  $\delta$ HMX-liquid (melt point) and the  $\beta$ HMX- $\delta$ HMX (phase transformation point) interfaces are not known a-priori. The temperature decides the location of these interfaces and the algorithm uses thermodynamic properties relevant to that phase for evaluating the interface conditions. Energy balance is maintained across the  $\delta$ HMX-liquid and the  $\beta$ HMX- $\delta$ HMX interfaces by solving equation (2.12) without the diffusion velocity term.

The governing equations (2.1-2.12) are solved by Newton's method with adaptive gridding techniques [12]. The various diffusion coefficients in the gas-phase are evaluated using vectorized and highly optimized transport and chemistry libraries. The specific heats and thermal diffusivities for  $\beta$ HMX,  $\delta$ HMX and liquid HMX were obtained from the work of Shoemaker [13]. The liquid-phase reaction mechanism is based on the work of Brill and Thynell et al. [14-15]. The mechanism consists of three steps in which HMX thermally decomposes through two global channels to form either  $CH_2O$  and  $N_2O$  or  $H_2CN$  and  $NO_2$ . The third global step describes low temperature secondary chemistry of  $CH_2O$  and  $NO_2$  and is derived from the gas-phase studies of Lin et al. [16].

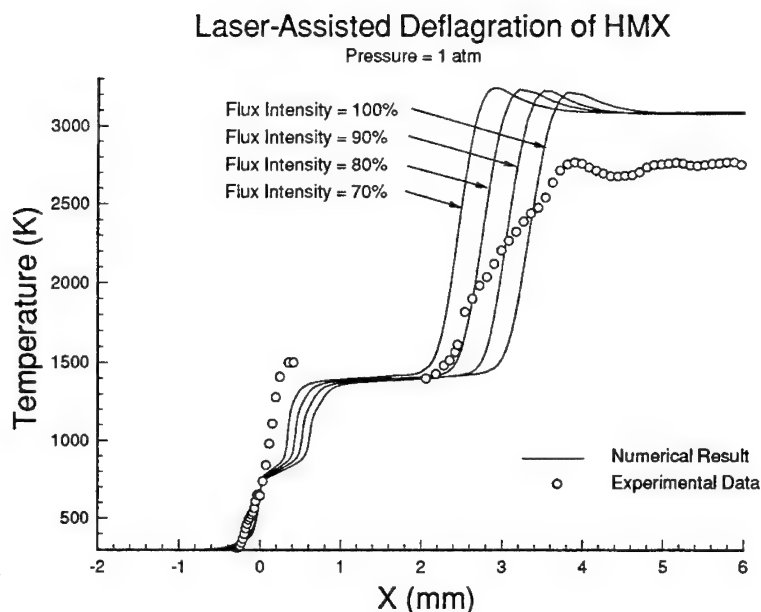
The gas-phase reaction mechanism consists of 48 chemical species and 228 reactions and was formulated from the original RDX mechanism of Melius [7-8] and the RDX mechanism in [11]. The gas-phase kinetic parameters for thermal decomposition of HMX were obtained from Shaw and Walker [17]. Rate parameters for reactions of the species HMXR, the radical formed by removing a nitro group from HMX, and the species HMXRO, the ring open-structure of HMXR, were estimated to be the values used in the RDX mechanism. We realize that with further study, these rates could be subject to change.

### 3. RESULTS AND DISCUSSION

In this section we present results for the case of self-deflagration and laser-assisted combustion of HMX monopropellants.

#### 3.1 Laser-assisted combustion

Experimental studies often employ laser heating for ignition purposes and for obtaining higher burning rates [2]. In particular, the added laser flux energy significantly affects the energy balance at the gas-liquid interface, which results in larger mass flux values (burning velocities) and also higher final flame temperatures. It is assumed that gas-phase species do not absorb at a laser wavelength of 10.6 microns and that the laser flux energy is completely absorbed in the condensed-phase [2]. Furthermore, the absorptivity of solid HMX at 10.6



**Figure 2.** Comparison of numerical and experimental results for laser-assisted combustion of HMX monopropellant at 1 atm. Temperature profiles in the gas, liquid and solid phase. Numerical results are illustrated for 70%, 80%, 90% and 100% of the peak laser flux intensity. Results show a distinct fizz zone followed by a dark zone and a flame zone.

microns is such that the  $\frac{1}{e}$  depth is only  $1\mu m$ . Employing Beer's law, the reduction in beam irradiance brought about by absorption in the condensed-phase can be described as

$$I(x) = I(0)e^{-\alpha x} \quad (3.1)$$

where  $I(0)$  is the irradiance of the beam at the input to the gas-liquid interface,  $\alpha = 1/(1\mu m)$  is the absorption coefficient, and  $x$  is the absolute distance measured from the gas-liquid interface. The energy input ( $\dot{Q}$ ) at any node point in the condensed-phase is obtained by subtracting the beam irradiance leaving the cell from that at the input to the cell.

The laser-assisted experiments show that the HMX flame is not a truly one-dimensional flame but a quasi-one-dimensional system. Measurements of the variation in cross sectional area were obtained experimentally by generating streamlines from particle image velocimetry (PIV) data and measuring the relative change in area of these streamlines. It was shown that the area increases by a factor of about five between the surface and the region in the burnt gas where the flame stops expanding radially. A curve fit was developed for this area variation normalized to the region of the burnt gases very far from the gas-liquid interface.

Numerical simulations for laser-assisted combustion have been performed at 1 atm with 70%, 80%, 90% and 100% of the peak value ( $337 \text{ cal/cm}^2/\text{sec}$ ), and have been compared with experimental results. The lower values used in the numerical simulations implicitly account for losses in the experiments such as reflection at the surface as well as the Gaussian distribution of the laser flux profile. The reactant stream temperature was  $T_u = 298K$  and the computational length was given by  $L = 8mm$ .

Figure 2 shows the temperature profile in the solid, liquid and gas-phases. The experimental temperature at which evaporation occurs is  $T_{evap} = 660K$ . Based on the structure of the thermal wave propagating into the condensed-phase, we find that the temperature rises

monotonically from the initial propellant temperature ( $T_u = 298K$ ) to the melting point temperature ( $T_{melt} = 555K$ ). During this portion HMX exists in solid forms ( $\beta$  or  $\delta$  crystals), and it is assumed that there are no chemical reactions taking place in this regime. This region is followed by the melt layer in which the temperature further increases from 555K to the surface temperature. The thickness of the melt layer based on these calculations is approximately 40  $\mu m$ . This compares reasonably well with results published in the literature. We also find approximately 53% decomposition of liquid HMX in the melt layer. This is in contrast to 43% found for laser-assisted RDX deflagration.

The liquid melt layer is followed by gas-phase combustion of gases evaporating from the melt layer. The temperature profile in the gas-phase shows three distinct regions termed in the literature as fizz, dark and flame zones. The fizz zone temperature steadily rises from the surface temperature to 1500K. The temperature of the dark zone which follows the fizz zone remains almost constant throughout its width (2 mm), while that of the flame zone rises from the end of the dark zone to nearly the adiabatic flame temperature.

The symbols in Figure 2 represent temperature measurements from the experiments of Hanson-Parr and Parr [2]. Temperature profiles were obtained by piecing together *OH* and *NO* rotational temperature data in the gas phase and thermocouple measurements in the condensed phase. In general, there is good agreement between experimental and numerically computed temperatures in the gas, liquid and solid-phases.

As the laser flux intensity is increased, the calculations suggest that the burning rate increases correspondingly, with small changes in the final flame temperatures. The burning rates corresponding to 70%, 80%, 90% and 100% were 0.135, 0.152, 0.165 and 0.182 cm/sec, respectively. Hanson-Parr and Parr have reported a burning rate value of 0.18 cm/sec for the laser-assisted combustion experimentally studied [2]. This increase in the mass flux (as compared with those for self-deflagration) is responsible for increasing the length of the dark zone as shown in Figure 2. Experimental results also indicate that the length of the dark zone varies as a function of the laser flux intensity.

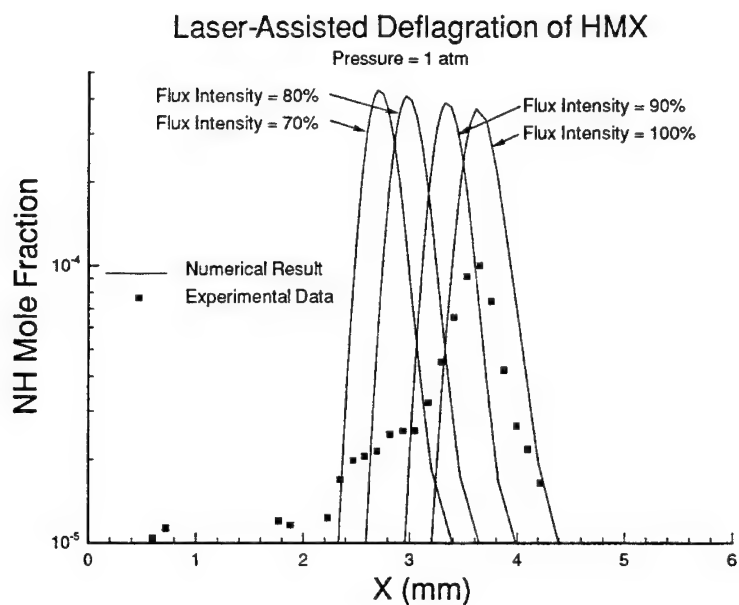
The profiles for the *NH*, *OH* and *CN* mole fraction are shown in Figures 3, 4 and 5, respectively, and show good agreement between the numerical and the experimental results. The *CN* profile is indicative of the location of the flame zone. Although the experimental measurements are slightly lower than the numerical values, the location of peak concentrations as well as the width of the *CN* profile again compare well with the experimental results. The *OH* profile peaks outside the *CN/NH* flame sheet. For  $CO_2$  laser-assisted deflagration, experiments indicate that the narrow *NH* profile peaks at 3.6 mm above the surface at a value of 100 ppm.

### 3.2 Self-Deflagration

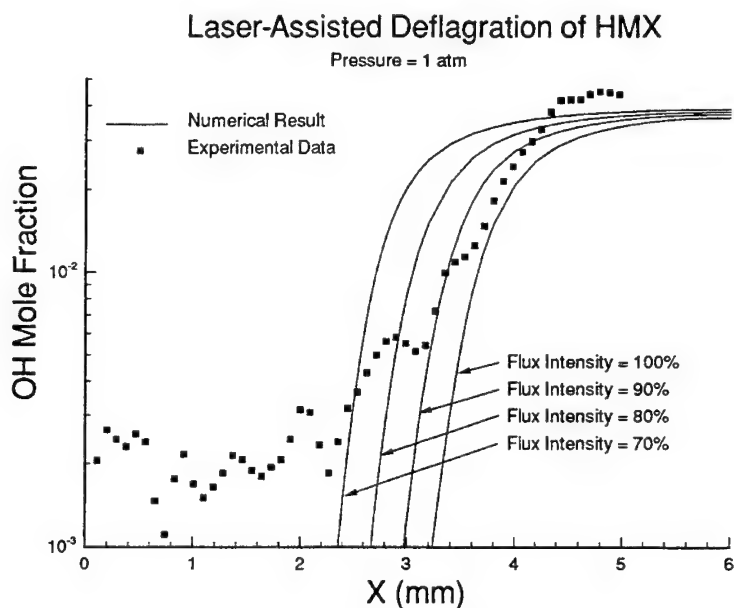
Numerical calculations have also been performed for self-deflagrating HMX monopropellants. When the laser flux heating is removed, the mass burning rate is reduced and, as a result, the primary and the secondary flames superimpose on each other producing a single flame. The temperature profile for self-deflagration at 1 atm illustrated in Figure 6 shows that the two-zone flame structure is no longer present. This finding is in accordance with experimental results [2].

Calculations have also been performed for self-deflagration of HMX monopropellants over a wide range of ambient pressures ranging from one to ninety atmospheres. The dependence of the burning rate on ambient pressure is shown in Figure 7 for both model and experiment [1], [18-19]. The pressure sensitivity  $n$  was found to be approximately 0.82, and matches very well with experimental results and theoretical work [3-5], [20].

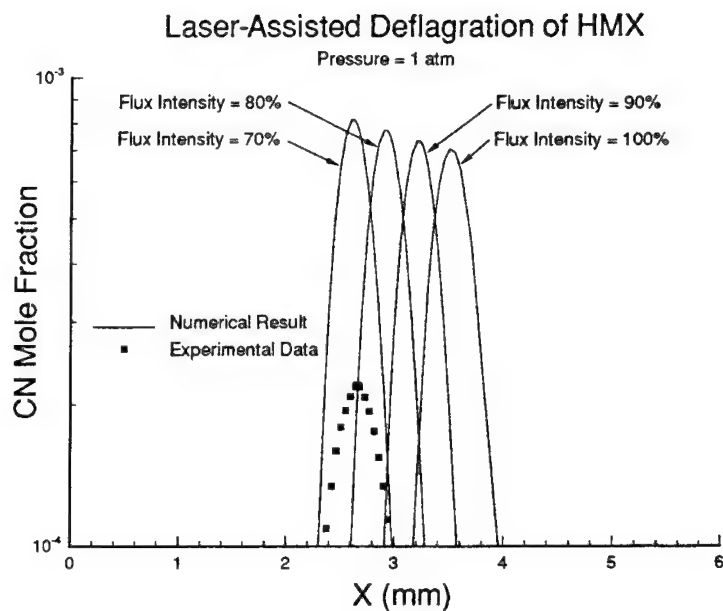
As the ambient pressure increases, the flame comes closer to the gas-liquid interface result-



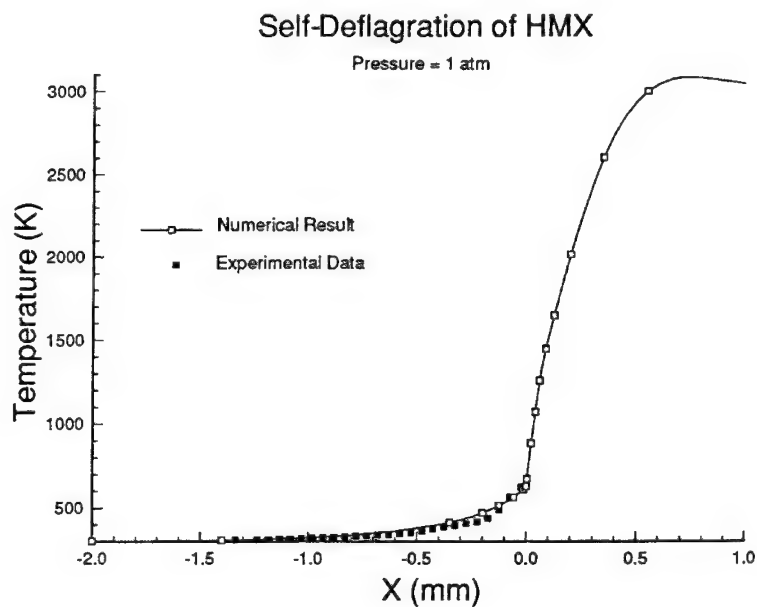
**Figure 3.** Comparison of numerical and experimental results for laser-assisted combustion of HMX monopropellant at 1 atm. Numerically computed  $NH$  mole fraction profile is for 70%, 80%, 90% and 100% of the peak laser flux intensity.



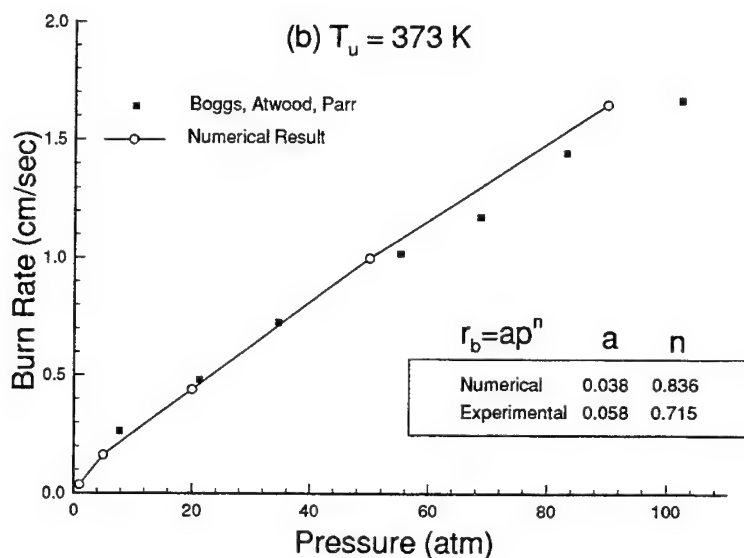
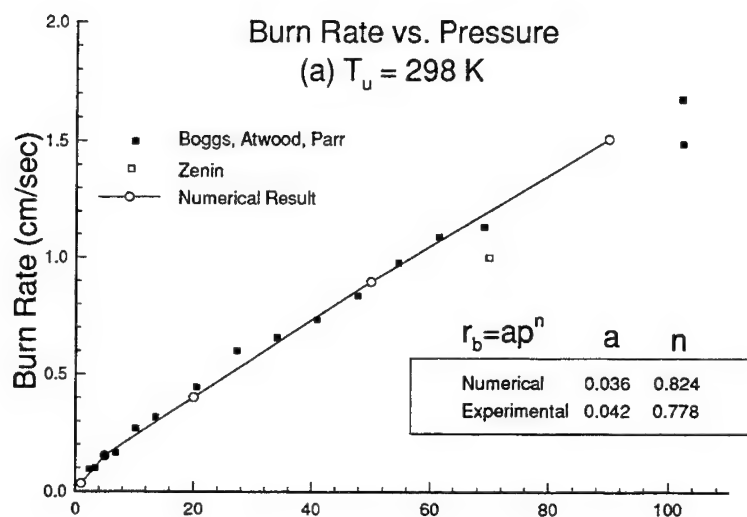
**Figure 4.** Comparison of numerical and experimental results for laser-assisted combustion of HMX monopropellant at 1 atm. Numerically computed  $OH$  mole fraction profile is for 70%, 80%, 90% and 100% of the peak laser flux intensity.



**Figure 5.** Comparison of numerical and experimental results for laser-assisted combustion of HMX monopropellant at 1 atm. Numerically computed  $CN$  mole fraction profile is for 70%, 80%, 90% and 100% of the peak laser flux intensity.



**Figure 6.** Self deflagration of HMX monopropellant at 1 atm. Temperature profiles in the gas, liquid and solid phase. Also shown is the experimentally measured temperature profile in the condensed phase. The gas phase profile does not show the presence of a dark zone.



**Figure 7.** Variation of burn rate as a function of ambient pressure for self-delfagration conditions of HMX monopropellant. The numerical results have been compared with experimental results obtained from Atwood, Boggs, Parr and Zenin. The surface temperatures used in the numerical calculations were obtained from the experimental data of Zenin. (a) Initial propellant temperature = 298 K, (b) Initial propellant temperature = 373 K.

ing in higher temperature gradients in the gas and the condensed-phases. Due to the higher burning rates associated with higher ambient pressures, we find that the thickness of the melt layer and the  $\delta$ HMX layer decreases as the ambient pressure increases. Although the surface temperature increases as the ambient pressure increases, the amount of decomposition in the liquid-phase decreases from about 59% at one atmosphere to almost 0% at 90 atmospheres. This is due to a combination of smaller melt layer thickness and higher burning rates at higher ambient pressures.

The burning rate has been computed at initial propellant temperatures ( $T_u$ ) ranging from 173 K to 423 K over a wide range of ambient pressure. These results compare favourably with experimental results from Atwood et al. [18]. (Burning rate comparisons for  $T_u = 373\text{K}$  are also shown in Figure 7.) When the initial propellant temperature is increased from 298 K to 373 K, the temperature gradient in the gas and liquid-phase reduces, but the thickness of the melt layer, the amount of liquid-phase decomposition and the burn rate increase slightly. The average value of temperature sensitivity ( $\sigma_p$ ) obtained for HMX monopropellant is approximately 0.0008/K, and compares favourably with experimental results. The value for  $\sigma_p$  predicted in [3-5] and [20] was significantly higher.

#### 4. CONCLUSIONS

Research in the field of solid rocket propellants over the past few decades has focused on obtaining a detailed understanding of the various physical and chemical processes involved during the burning of homogeneous and heterogeneous propellants. In this paper, a mathematical model for a three-tiered system consisting of solid, liquid and gas was derived for studying the combustion of HMX monopropellant. The resulting non-linear two-point boundary value problem was solved by Newton's method and adaptive gridding techniques. In this study, the burning rate was computed as an eigenvalue, which removes the uncertainty associated with employing evaporation and condensation rate laws in its evaluation. Self-deflagration burning rates were computed over a wide range of ambient pressures and were shown to compare favourably with experimental results. Results for laser-assisted combustion showed a distinct primary and secondary flame separated by a dark zone.

#### Acknowledgement

This work was supported by the Office of Naval Research.

#### REFERENCES

- [1] BOGGS, T.L., in *Fundamentals of Solid-Propellant Combustion*, Progress in Astronautics and Aeronautics (K.K. Kuo, and M. Summerfield, Eds.), New York, 1984, Vol. 90, p. 121.
- [2] PARR, D.H., and PARR, T., in *Twenty-Fifth Symposium (International) on Combustion*, The Combustion Institute, 1994, p. 1281.
- [3] BEN-REUVEN, M., and CAVENY, L.H., *AIAA J.*, Vol. 19, No. 10 (1981), p. 1276.
- [4] MITANI, T., and WILLIAMS, F.A., in *Twenty-First Symposium (International) on Combustion*, The Combustion Institute, 1988, p. 1965.
- [5] LI, S.C., WILLIAMS, F.A., and MARGOLIS, S.B., *Comb. Flame*, Vol. 80 (1990), p. 329.
- [6] LIAU, Y.-C., and YANG, V., *Journal of Propulsion and Power*, Vol. 11, No. 4 (1995), p. 729.
- [7] MELIUS, C.F., in *Chemistry and Physics of Energetic Materials*, (S.N. Bulusu, Ed.), The Netherlands, 1990, p. 51.

- [8] MELIUS, C.F., *Proceedings of the Twenty-Fifth JANNAF Combustion Meeting*, 1988.
- [9] FETHEROLF, B.L., and LITZINGER, T.A., *Proceedings of the Thirtieth JANNAF Combustion Meeting*, 1993.
- [10] HATCH, R. L., *Proceedings of the Twenty-Fourth JANNAF Combustion Meeting*, 1987.
- [11] PRASAD, K., YETTER, R.A., and SMOOKE, M.D., to be published in, *Comb. Sci. & Tech.*, 1997.
- [12] SMOOKE, M.D., *J. Comp. Phy.*, Vol. 48 (1982), p. 72.
- [13] SHOEMAKER, R.L., STARK, J.A., and TAYLOR, R.E., *High Temperature-High Pressures*, Vol. 17 (1985), p. 129.
- [14] BRILL, T.B., *Journal of Propulsion and Power*, Vol. 11 (1995), p. 740.
- [15] THYNELL, S.T., GONGWER, P.E., and BRILL, T.B., submitted, *Comb. Flame*, 1995.
- [16] LIN, C.Y., WANG, H.T., LIN, M.C., and MELIUS, C.F., *Int. J. Chem. Kin.*, Vol. 22 (1990), p. 455.
- [17] SHAW, R., and WALKER, F.E., *J. Phys. Chem.*, Vol. 81 (1977), p. 2572.
- [18] ATWOOD, A., PRICE, C., CURRAN, P., and WIKNICH, J., *Proceedings of the Thirty-Second JANNAF Combustion Meeting*, 1995.
- [19] ZENIN, A.A., *Combustion Explosion and Shock Waves*, Vol. 2 (1966), p. 67.
- [20] PRICE, C.F., BOGGS, T.L., and DERR, R.L., *AIAA Paper 79-0164*, 1979.

#### COMMENTS

Mr. Thomas L. Boggs, Naval Air Warfare Center Weapons Division, China Lake, CA, USA:  
 You showed results for your predictions of  $r=r(p)$  to 100 atm for RDX and HMX. Have you made predictions to higher pressures? If not, it would be interesting for you to do so for two reasons: (1) experimental data exist, e.g.  $r=r(p)$  for HMX from 1 atm to 50,000 psi, and (2) your predictions seem to start to deviate from experimental data at approximately 80-100 atm.

#### Authors' Reply:

We have carried out a series of calculations for HMX burn rates at pressures up to 3,500 atm (Prasad, Tanoff, Smooke and Yetter, "Modeling the Deflagration of HMX at High Pressures," 33rd JANNAF Meeting, Monterey, CA, 1996). Specifically, by replacing the ideal gas law with a Becker-Kistiakowski-Wilson equation of state, we have been able to incorporate real gas effects into our burn rate model. For pressures in the 500-1000 atm range, we predict differences up to 20% in the burn rate over the ideal gas model. Agreement with the experimental data of Atwood and Boggs is excellent over the pressure range 100-3500 atm.



## A COMPARISON OF SOLID MONOPROPELLANT COMBUSTION AND MODELING

M. W. Beckstead, J. E. Davidson and Q. Jing

Brigham Young University

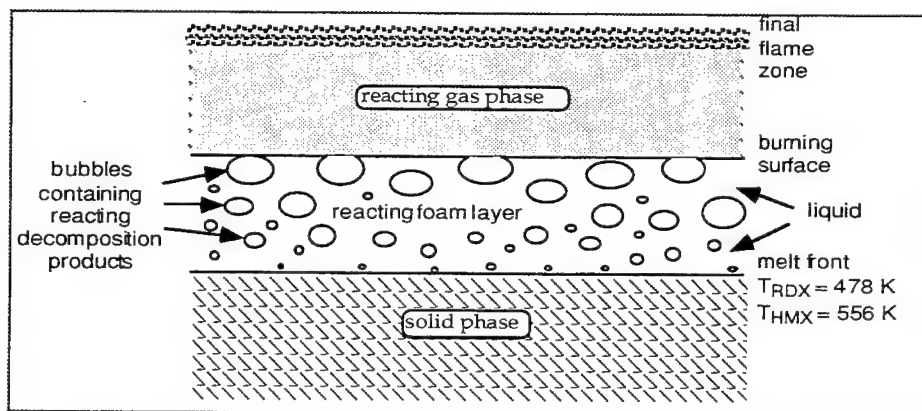
Provo, Utah USA

**ABSTRACT:** Many of the ingredients in solid propellants burn as monopropellants. This paper focuses on the combustion characteristics of two nitramine monopropellants, RDX and HMX. Monopropellant modeling efforts are reviewed. Early models describing monopropellants were primarily based on global kinetics. Although different physical pictures were assumed, the calculated burning rates of most of the models were very reasonable, compared to experimental data. Because of the agreement many authors have claimed their models to be correct. Other investigators have been more objective, and have used their models to evaluate more detailed combustion characteristics, such as  $\sigma_p$ , flame stand-off distances, etc. More recent models have been based on much more detailed kinetic mechanisms, and more detailed modeling of the condensed phase. One such model has recently been developed at BYU, building on the pioneering work of Melius, Yetter, and others. The model has been applied to RDX and HMX, comparing the modeling calculations with available experimental data. The agreement is very reasonable for burning rate, surface temperature, temperature sensitivity, temperature profile, major species profiles and many minor species profiles. Both experimental data and modeling calculations show a two stage flame when the combustion is augmented by an external heat flux. A single stage flame with no evidence of a dark zone is observed, and calculated, for normal combustion.

### INTRODUCTION

To understand the mechanisms of solid propellant combustion, it is important to understand the fundamental mechanisms involved in the combustion of monopropellants. This paper will focus on the combustion characteristics of RDX and HMX as typical solid monopropellants (some examples will also refer to AP and nitroglycerin or double base binders). As a monopropellant burns there are complex interactions between the gas-phase flame, the liquid layer on the surface and the unreacted solid. The heat released in the flame provides a heat flux to the surface. This energy causes the propellant to melt, evaporate and/or decompose, providing a flow of reacting species to the gas flame. This fuel reacts, providing an energy flux back to the surface. The increase in heat flux to the condensed propellant causes an increased mass flux away from the surface. The increased mass flux has the effect of "blowing" the gas-phase reactions away from the surface which reduces the heat flux to the surface. Steady-state deflagration occurs when the heat flux from the gas flame is in balance with the mass flux away from the surface.

Combustion of a monopropellant can be broken into three regions (solid, liquid-gas two-phase region and the gas region) as illustrated in Figure 1. Monopropellants can sublime and/or decompose while in their solid form, but the rates associated with these processes are small compared to the decomposition and evaporation rates after the propellant has melted. For other propellants, it is disputed whether there is an actual phase change from solid to liquid but rather rapid solid decomposition to liquid and gas-phase species.<sup>1</sup> Because of the temperatures and rate involved, it is difficult to find experimental values for  $\Delta H_{\text{melt}}$  in the literature. The two-phase (molten) region consists of liquid and gaseous species resulting from the melting and/or decomposition of the solid phase. Apparently there can be several parallel steps occurring in the molten region, some exothermic and others endothermic. The molten phase has been difficult to understand because of the many processes occurring and the gas phase molecules generated. At high pressures and high heat fluxes, the burn rate is sufficiently fast that bubble formation appears to be less important.<sup>2</sup>



**Figure 1.** Schematic illustration of the burning zones of a solid monopropellant (not to scale).

The division between the two-phase and gas-phase region is also not well defined due to chemical reactions, bubbles, and condensed material being convected away from the surface. In the gas phase region of a monopropellant, the flame is essentially premixed. The species coming from the surface react with each other and/or decompose to form other species. Thousands of reactions involving hundreds of species can be occurring in the gas flame.<sup>3</sup> The reactions continue until equilibrium is reached at the final flame zone.

## MODELING REVIEW

The evolution of steady-state propellant combustion modeling can be divided into three general categories: 1) models based on global kinetics; 2) semi-global models based on some finite kinetic mechanism in either, or in both gas and condensed phase; and finally 3) multi-phase models with detailed kinetic mechanisms. Naturally some models will overlap two of the categories. The global kinetics-type models typically only solve an energy equation using a flame sheet or flame stand-off distance approach. Semi-global models using some kind of finite kinetic mechanisms have usually (but not always) relaxed the flame sheet assumption replacing it with a distributed energy release

associated with solving both the energy and species equations. The most recent models include detailed reaction mechanisms in the gas phase coupled with a detailed reaction mechanism describing the condensed phase.

### Global Kinetics-Type Models

For the global kinetics-type of models, the combustion processes is usually described by a one-dimensional energy equation spanning a condensed (generally assumed to be solid) and gas region. The species equations are neglected and the reactions are represented by heat releases at both the surface and at a flame, approximated at some flame stand-off distance from the surface. Beckstead and McCarty summarized many of the global monopropellant models published prior to 1975<sup>4</sup>. Eleven of those models were applied to AP and one was applied to both AP and HMX. All of the models were able to match the experimental burning rate data with reasonable accuracy in spite of the diverse assumptions relative to the physical picture being modeled. As a result most researchers then claimed that their physical model was 'correct' based on the agreement. In all of the models there are parameters that have not been quantified experimentally, and thus these parameters must be estimated. These parameters thus become optimization parameters, ensuring a reasonable fit of the data.

In 1982 Miller<sup>5</sup> reviewed monopropellant modeling approaches comparing various models to a generalized approach. He observed that most models give the correct burning rate and pressure dependence, but not necessarily the correct temperature sensitivity. Again, within the format of using some form of an energy equation there is enough flexibility, especially with unknown kinetics constants, that the burning rate characteristics can be correctly reproduced using a variety of different physical models. In 1985 Gusachenko and Zarko<sup>6</sup> published a book reviewing solid propellant modeling. Approximately one third of the book (117 references) is dedicated to reviewing homogeneous materials (monopropellants for the context of this paper), with specific applications to the Russian powder N, AP and nitramines (RDX and HMX). These authors also recognize that most models are able to achieve a reasonable fit with the experimental burning rate data, and that it is not justifiable to claim that a model is 'physically correct' based on a comparison with burning rate data.

Some typical global kinetics-type models and their general characteristics are summarized in Table 1 (the list is not comprehensive, but is representative). Most models listed in Table 1 were based on a form of the energy equation, but neglected the species equation. Most also modeled the complexity of the gas phase chemistry with a simple flame sheet, although a few integrated the gas phase equations. The Manelis/Strunin model assumed that the condensed phase reactions control the burning rate rather than the gas phase. Most of the models assumed that significant reaction and heat release occurs in both the gas and condensed phase. In the recent work of Li and Williams, they assume that evaporation dominates the surface process and that there is an inner flame at ~1300 K followed by a dark zone (similar to the BenRueven model discussed in the following section). The dark zone and inner flame are not observed experimentally.

Again, there is enough flexibility within the models summarized in Table 1, that the burning rate characteristics are correctly reproduced using a variety of different physical models.

## Semi-Global Models

As computer capabilities have increased, models have abandoned the surface reaction and flame sheet assumptions of the global-type models, and kinetic mechanisms of a few steps began to be developed.

**Table 1**  
Typical Global-Kinetics Models

Year	Researchers	Ingredient	General Assumptions and/or Results
1971	Manelis & Strunin <sup>7</sup>	AP	1. Assume that condensed phase is 'the' controlling step. 2. Develop an equation for $\sigma_p$ but no results are presented.
1971	Beckstead, Derr & Price <sup>8</sup>	AP, HMX	1. For AP, 75% of energy release occurs in surface reaction. 2. $\sigma_p$ is calculated and compared to existing data. 3. Apparently first monopropellant model for HMX.
1971	Guirao & William <sup>9</sup>	AP	1. A 14 step mechanism which is reduced to a one-step gas reaction. 2. 70% of surface reaction forms final products. 30% forms $\text{NH}_3$ and $\text{HClO}_4$ .
1975	Sohn <sup>10</sup>	AP	1. Develops model to predict pressure deflagration limit. 2. Claims success.
1976	Beckstead & McCarty <sup>4</sup>	HMX	1. Determined parameters via optimization to experimental data. 2. Calculate HMX $\sigma_p$ .
1977	Price, Boggs & Bradley <sup>11</sup>	AP	1. Integrate gas phase for 2 parallel reactions (global kinetics) 2. Include the species equations for the global species.
1977	Strunin & Manelis <sup>12</sup>	AP	1. Extend their previous model assuming condensed phase control.
1979	Price, Boggs & Derr <sup>13</sup>	AP, HMX	1. Compare their model to others' results. 2. Compare their calculations to an extended set of data.
1980	Beckstead <sup>14</sup>	DB	1. Studies the effect of propellant energy on model predictions.
1981	Miller and Coffee <sup>15</sup>	general	1. They conclude that most 1-D models cannot correctly predict all combustion characteristics
1983	Miller and Coffee <sup>16</sup>	general	1. They compare several modeling approaches to data for 5 propellants, concluding that one must compare to more than just the burning rate.
1986	Mitani and Williams <sup>17</sup>	HMX	1. HMX model similar to Guirao/Williams AP model, but with inner flame (dark zone). 2. 20 to 40 % of HMX decomposed in the condensed phase. 3. They get reasonable results for rate, $\sigma_p$ , etc.
1989	Beckstead <sup>18</sup>	AN, AP, HMX, DB	1. Same assumptions as Beckstead 1971 except for DB. The dark zone temperature was chosen as the flame temperature.
1990	Li, Williams and Margolis <sup>19</sup>	RDX and HMX	1. Based on 1986 Mitani and Williams model but using AEA. 2. Assume an inner flame and dark zone. 3. Evaporation in RDX is 99.9% of surface process (less for HMX) 4. Predict reasonable values of rate, $\sigma_p$ , $T_s$ , flame standoffs, etc.

BenReuven, et al.<sup>20</sup> included an in-depth condensed reaction zone in their modeling of RDX and HMX. They assumed that decomposition began after melting, describing it by a single first-order reaction. The gaseous species formed by this reaction were assumed dissolved in the liquid, thus bubble formation was neglected. Evaporation was calculated using a Clausius-Clapeyron expression assuming vapor-liquid equilibrium. In addition, one reaction between the decomposition products was considered in the gas phase. The gas phase was described essentially by the basic conservation equations with the Lewis number for the individual species and the mixture assumed to be unity. The gas-phase calculations proceed from the surface until all the RDX vapor decomposes, at which point the authors assume that the remaining portion of the flame has a negligible effect on the surface. This results in a low temperature (~1000K) inner flame that controls the burning rate. The surface temperature and burn rate are determined by matching the energy gradient and evaporation mass flux at the surface. The model also predicts the melt layer thickness, temperature profile and the species profiles. For RDX, the model accurately predicted the burn rate over the pressure range of 10-40 atm, but for HMX<sup>21</sup> the authors had to specify the burn rate. Based on the HMX model results, the authors speculate that bubble formation is an important factor that should be considered. Major contributions of BenReuven, *et al.* are the inclusion of the in-depth liquid reaction and solving the gas phase species equation, for their semi-global mechanism. Cohen, et al.<sup>22</sup> updated the chemistry of BenReuven's HMX model (but it was still global) and the model was able to match experimental burn rates.

Bizot and Beckstead modeled double base<sup>23</sup> and HMX<sup>24</sup> propellants by dividing the combustion process into two regions (condensed and gas). In both regions, their reactions were semi-global and the products were not specified. They neglected mass diffusion, phase changes, and assumed constant properties. But even with such a simple model, the calculations agreed fairly well with experimental data for burn rate, surface temperature, and dark zone length. The authors conclude that the only way to match experimental data is to adjust kinetic parameters and/or use a more complex mechanism. While more correlative than predictive, this model gives sufficiently realistic characteristics that it has been incorporated in models of multidimensional, unsteady combustion in rocket motors.<sup>25</sup>

Li and Williams<sup>26</sup> have recently extended their previous model to include a 15 step near surface, kinetic mechanism. They then reduce the mechanism to a single global step as in their previous models, but no results are presented.

#### Development of Multi-Phase Models with Detailed Kinetic Mechanisms

Models utilizing elementary step mechanisms are summarized in Table 2. Again the list is representative, but not completely comprehensive. In 1982, Korobeinichev, et al.<sup>27</sup> measured concentration profiles in perchloric acid/methane flames. They proposed an 18-step mechanism for this system. In subsequent work, Ermolin, Korobeinichev, et al.,<sup>3</sup> measured concentration profiles for AP and proposed an elementary mechanism composed of 80 steps and 24 species. They modeled the gaseous flame conservation equations, but, neglected heat and mass diffusion. The agreement between the model and their experimental data was fair, and their model indicated which reactions needed further review. In 1984<sup>28</sup>, they included thermal and mass diffusion in their equations and concluded that thermal and mass diffusion play an important role in the overall flame structure. They then developed a 90 step mechanism for RDX combustion and were able to match their experimental species profiles to within 10% at 0.5 atm.<sup>29</sup> They have neglected any condensed-

phase interaction other than assuming the feed concentrations going into their gas-phase model came from the decomposition of the monopropellant, either AP or RDX.

**Table 2**  
Elementary Step Mechanisms for Monopropellant Combustion.

Year	Researchers	Ingredient	# of Species	# of rxns	Comments
1969	Jacobs & Pearson <sup>30</sup>	AP	19	17	Only gave a possible kinetic path but no kinetic constants nor actual calculations.
1971	Guirao & Williams <sup>9</sup>	AP	19	14	Developed a global one-step expression from calculations made with a 14-step mechanism under iso-thermal conditions.
1972	Korobienichev, et al. <sup>31</sup>	AP			Assume $\text{NH}_3 + \text{HClO}_4$ at the surface and a 2 step gas phase mechanism
1984	Ermolin et al. <sup>28</sup>	AP	24	80	Qualitative agreement with mass spec. data at 0.58 atm
1984	Narahari et al. <sup>32</sup>	AP	14	17	Linked condensed phase to 14 step mechanism
1990	Sahu et al. <sup>33</sup>	AP	18	22	$\text{ClO}$ , a species considered by many to be important is not included. Some rate constants are not reasonable.
1992	Cohen <sup>34</sup>	AP	35	136	Reviewed several AP mechanisms and proposes his own, but does not provide rate constants for several important reactions.
1986	Hatch <sup>35</sup>	NG	21	60	Predicts dark zone for double base application
1995	Anderson et al. <sup>36</sup>	Double Base	41	189	Mechanism for predicting the chemistry of the dark zone (1-30 atm)
1986	Ermolin et al. <sup>29</sup>	RDX	23	90	Mechanism produced reasonable agreement with experiment at 0.5 atm.
1987	Hatch <sup>37</sup>	HMX	25	77	Assumed HMX decomposed to $\text{CH}_2\text{O}$ , $\text{NO}_2$ , $\text{N}_2\text{O}$ and HCN in condensed phase.
1990	Melius <sup>38,39</sup>	RDX	38	158	Calculated properties and kinetics from BAC-MP4
1994	Li & Williams <sup>26</sup>	RDX		15	Describe a primary flame mechanism but do not provide any rate constants.
1995	Yetter et al. <sup>40</sup>	RDX	45	232	Improvements on Melius Mechanism

In 1986, Hatch<sup>35</sup> developed a model for NG/binder combustion similar to the BenReuven model for RDX. Three major differences between the models were: 1) the gas was assumed to form voids in the liquid, thus, allowing it to react; 2) a 60 step gas phase mechanism was developed; and 3) the gas-phase calculations proceed to the final flame products. Although the model failed to accurately predict experimentally determined burn rates, sensitivity analysis indicated which parameters were affecting the burn rate significantly. His model did predict a dark zone, characteristic of NG (and double base propellant) combustion.

Hatch also applied his model to HMX<sup>37</sup>, but again failed to match burn rate measurements quantitatively. Hatch's major contribution to the modeling effort was allowing for the formation of voids (or bubbles) in an inviscid liquid/two-phase region. With this assumption the liquid and gas velocities can then be calculated by dividing the mass burning rate by the individual densities. This leads to void velocities a couple orders of magnitude higher than the liquid velocity. The other extreme is to assume that the gas and liquid have equal velocities.

Margolis and Williams<sup>41</sup> studied the two-phase flow in burning solids, focusing their attention on the reacting melt layer. Their model considered two species, a liquid reactant and a gaseous product, taking into account the momentum equation with viscous terms, surface tension and pressure gradient effects. They concluded that the void velocity will be in excess of the liquid velocity though it is unclear as to what extent.

Melius, et al.<sup>38,39</sup> developed an approach to calculate thermodynamic properties and reaction rate constants for the decomposition of RDX vapor and for other intermediate decomposition products. Based on this work, he proposed a 158 step mechanism involving 38 species to describe the ignition of RDX<sup>42</sup>. The model consisted of a simple condensed model supplying the cold boundary conditions to the PREMIX code. He allowed for one decomposition reaction and an evaporation/condensation relation at the surface. The model under predicted the burn rate and surface temperature at 1 and 20 atmospheres. The burning rate was largely controlled by the net flux between the evaporation and condensation which becomes the difference between two very large numbers, neither of which is known very accurately. Many improvements have been made to the original Melius RDX mechanism, primarily by Yetter, Dryer, et al.<sup>40</sup>. Their changes to the RDX mechanism have greatly improved its predictive power. The mechanism is still being improved and currently has approximately 230 reactions and 45 species.<sup>43</sup>

### MOST RECENT PROPELLANT COMBUSTION MODELS

Recently, three models (Liau and Yang<sup>44</sup>, Prasad, Smooke and Yetter<sup>45</sup>, and Davidson and Beckstead<sup>46,47</sup>) have been developed for the one-dimensional steady-state combustion of RDX. These models solve the basic conservation equations in the three regions, neglecting mass diffusion in the condensed regions and the radiation term in the energy equation. There has been a lot of communication and sharing of ideas between the three modeling groups and between modelers and those doing experiments. This has resulted in unprecedented agreement between experiment and model predictions for a wide variety of conditions. These models use an improved Melius/Yetter RDX mechanism<sup>39</sup> in the gas region and a global mechanism proposed by Brill<sup>48</sup> for the liquid region. The method of numerical convergence differs between the three models but these differences will not be discussed.

The models divide the combustion process into three regions: solid, melt layer (liquid and gas) and gas. In the solid region, it is assumed that the propellant does not decompose, and only the energy equation is solved for this region with boundary conditions of a known initial temperature and a known melt temperature at the solid/liquid interface.

As in most models<sup>20,44,45</sup> mass diffusion is neglected in the two-phase region. Both the Davidson-Beckstead and the Liau-Yang models include the gas phase in the two-phase region as a void fraction following the approach of Hatch<sup>35</sup>. Yang and Liau developed an expression based on the

kinetic theory of gases at low pressure to describe the evaporation-condensation of RDX inside the bubbles and at the burning surface, which has also been incorporated into the Davidson-Beckstead model. The Prasad-Smooke model assumes that all the decomposition products produced in the liquid remain dissolved in the liquid, thus neglecting sub-surface evaporation. This greatly simplifies the equations describing the two-phase region, allowing them to solve the liquid region simultaneously with the gas region. One additional constraint is required to close the system of equations. The Davidson-Beckstead and the Liao-Yang models use a vapor pressure relationship which allows the surface temperature and surface void fraction to be predicted. In the Prasad-Smooke model, the surface temperature is specified. When this temperature is reached, any remaining liquid is mathematically vaporized. Thus their model does not predict a surface temperature *a priori*. The surface temperature and mass flux fractions serve as boundary conditions for the gas region.

The gas region equations are solved using a modified version of PREMIX. The correct burning rate will satisfy the energy balance at the two-phase/gas interface including the heat flux from the gas phase flame plus any additional energy from a laser.

#### COMPARISON OF RECENT MODELS WITH TYPICAL COMBUSTION DATA

The three models have been applied to RDX and show reasonable agreement with much of the experimental data available. The Davidson-Beckstead model has also been applied to HMX<sup>49</sup> by converting the stoichiometric coefficients and thermophysical properties used for RDX to the appropriate HMX values. Only a few figures comparing experimental results with predictions for RDX and HMX from the Davidson-Beckstead model are included here. Figure 2 shows burn rate as a function of pressure, comparing several sources of experimental data<sup>50,51,52,53</sup> to the model. The difference in burning rate between RDX and HMX (both experimental and theoretical) is essentially within the data scatter.

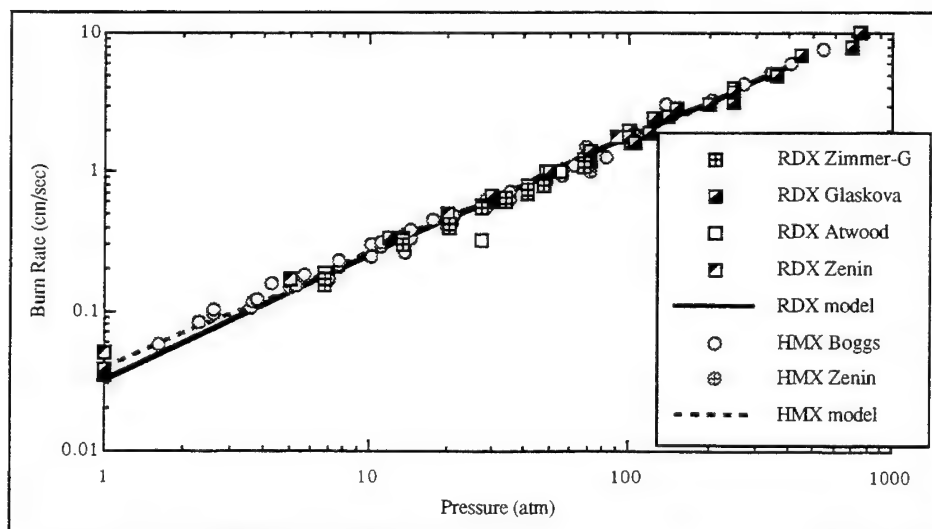
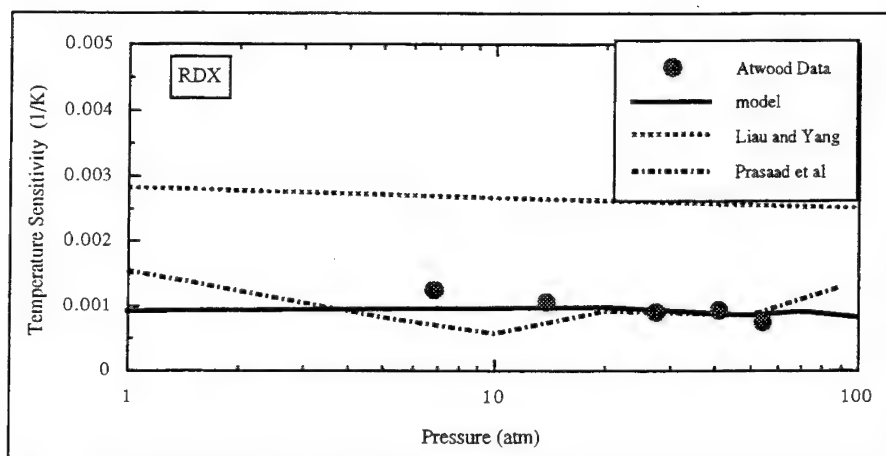


Figure 2. Comparison of experimental and theoretical RDX and HMX burning rate versus pressure.



Figure 3 contains the RDX temperature sensitivity data by Atwood<sup>52</sup> compared to calculated values by the three models. It is significant to note that even though all three models use the same gas phase mechanism, their predicted temperature sensitivity is somewhat different. The Davidson-Beckstead and Prasad-Smooke models are the correct magnitude, but the Liao-Yang model over predicts the  $\sigma_p$  value by a factor of  $\sim 2$ . It appears that the sensitivity of the burn rate to initial temperature is quite dependent on the condensed phase reaction. The differences in the calculated  $\sigma_p$  values would then be attributed to the differences in the modeling of the condensed phase between the three models.



**Figure 3.** A Comparison of Experimental and Theoretical RDX Temperature Sensitivity

Five experimental studies measuring the surface temperature of HMX<sup>53,54,55,56,57</sup> were found in the literature, but only one comprehensive study of RDX<sup>53</sup>. The scatter of the data, especially between investigators is discouraging. Normalizing the data (the different investigators used different techniques) gives values of  $\pm 100$ - $150^\circ$ . Most of the measurements were made at relatively low pressures due to the difficulty in obtaining data at pressures above  $\sim 10$ - $20$  atm. The lower temperature data appear to be more consistent, and most of the higher temperatures were reported by Mitani. Extrapolating his data to pressures of interest ( $\sim 60$  atm) results in temperatures well over  $1000^\circ\text{K}$ , which is considered to be unrealistic. Neglecting his data the remainder still show scatter of  $\pm 70$ - $90^\circ$ . Thus, comparing modeling results with surface temperature data is somewhat less than satisfactory, due to the uncertainty of the data.

Zenin measured both RDX and HMX surface temperatures, and his data appeared to be consistent. Also, he made measurements up to very high pressures. Thus, the model has been compared with Zenin's data in Figure 4. Within the scatter of the data, the agreement is very reasonable. If the other data were included in the plot, it becomes very confusing due to the excessive scatter, so they have been excluded.

At one atm the calculated HMX surface temperature of  $634^\circ\text{K}$  is  $40^\circ$  greater than that of RDX, and at 100 atm it is  $27^\circ$  greater, in spite of the fact that the burning rates are essentially the same. The

increased surface temperature of HMX is due to a combination of increased melting temperature and reduced vapor pressure of the HMX. The melting temperatures of the two compounds are indicated in the figure. At one atm the surface temperatures are 116° and 78° higher than the melting temperatures of RDX and HMX, respectively.

RDX melt layer thickness were calculated to be ~170  $\mu\text{m}$  at 1 atm and ~5 $\mu\text{m}$  at 100 atm. For HMX the values were 70 and 5 for the same pressures. These values are within reason compared to values measured by Zenin. These predictions for surface temperature and melt layer thickness showed better agreement with Zenin's data than those values predicted by the Liao-Yang model. The authors attribute the better agreement to their choice of RDX liquid physical properties which dominate these two combustion characteristics.

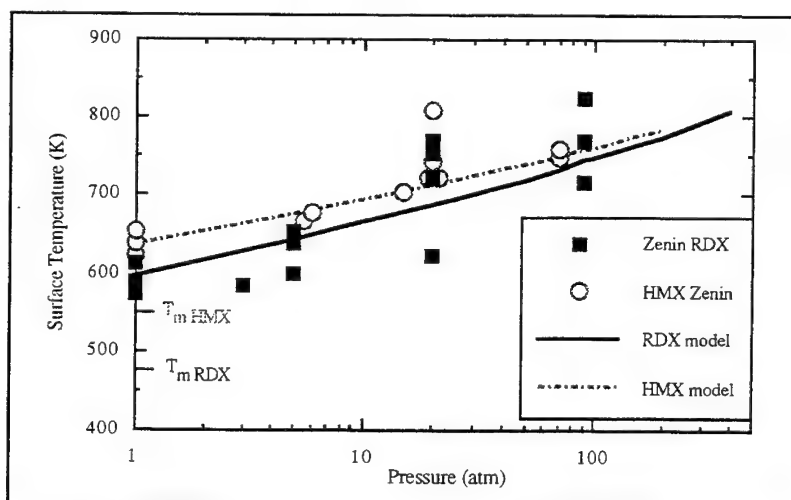


Figure 4. Experimental and Calculated Surface Temperatures for HMX and RDX.

#### COMPARISONS WITH SPECIES AND TEMPERATURE PROFILES DATA

To quantitatively verify a model, the flame structure (species and temperature profiles) needs to be known. Litzinger, et al.<sup>58,59,60</sup>, Brewster, et al.<sup>61</sup> and Parr and Hanson-Parr<sup>62,63,64</sup> have used mass spectrometers and UV-Visible absorption measurements to quantify the gas phase flame structure of RDX. Kuo, et al.<sup>65,66</sup> and Brill<sup>48</sup> have focused on the initial decomposition mechanism and melt region of RDX using mass spectrometry and T-Jump experiments. Using thermocouples Zenin<sup>53</sup> measured temperature profiles, surface temperature, and melt layer thicknesses of both RDX and HMX. Examples of experimental data available for monopropellant model validation for several energetic materials is summarized in Table 3.

Parr has shown that the RDX flame extends only about 1 mm from the burning surface (at 1 atm), whereas the HMX flame extends between 2 to 3 mm, and neither show a dark zone nor a plateau of any kind in the temperature profile. This is significant as it invalidates assumptions made by BenReuven et al. and by Li, et al., that there should be an inner flame which controls the burning rate. This observation also indicates that experimental measurements at one atm will be very

difficult due to the very small diagnostic space available. Therefore, Litzinger, et al. and Parr, et. al imposed a laser heat flux on the burning propellant surface to spread out the reaction zone. With the added heat flux a two-stage flame developed similar to that seen in double base combustion. At that time none of the models were modeling a laser flux or seeing a dark zone. To validate the models with experimental data, the effect of the laser flux on the burn rate had to be included within the models. As shown in Figure 5, the models are now able to predict the two-stage flame structure observed experimentally for the laser assisted conditions.

**Table 3**

Examples of experimental data available for model validation. (X(species) are concentrations)

Researchers	Propellant	Type of Data	Comments
Ermolin et al. <sup>3</sup>	AP	X(H <sub>2</sub> O, HCl, O <sub>2</sub> , HClO <sub>4</sub> , Cl <sub>2</sub> , ClOH, NO, NO <sub>2</sub> , N <sub>2</sub> O, ClO <sub>2</sub> )	0.5 atm
Brewster & Schroeder <sup>61</sup>	RDX	T <sub>s</sub> , r <sub>b</sub> (laser)	
Ermolin, et al. <sup>29</sup>	RDX	X(CO, H <sub>2</sub> CO, NO <sub>2</sub> , HCN, CO <sub>2</sub> , N <sub>2</sub> O, H <sub>2</sub> O, NO, N <sub>2</sub> , H <sub>2</sub> )	0.5 atm. Species concentrations do not approach equilibrium values.
Zenin <sup>53</sup>	HMX, RDX	T(x), r <sub>b</sub> , T <sub>s</sub> , I <sub>melt</sub>	1-90 atm
Parr & Hanson-Parr <sup>60,61,62</sup>	RDX, HMX, XM39, HNF	T(x), X(NO, CN, OH, NH, NO <sub>2</sub> , H <sub>2</sub> CO), r <sub>b</sub> (laser)	With and without laser augmentation at 1 atm.
Litzinger et al. <sup>58,59,60</sup>	RDX, HMX, XM39, M43	T(x), X(H <sub>2</sub> O, HCN, CO, N <sub>2</sub> , NO <sub>2</sub> , CO <sub>2</sub> , H <sub>2</sub> , N <sub>2</sub> O, CH <sub>2</sub> O, NO) r <sub>b</sub> (laser)	With high laser flux, atomic balance not closed.
Boggs <sup>1,13</sup>	HMX, AP	r <sub>b</sub> (P, T <sub>init</sub> )	
Atwood <sup>51</sup>	RDX	r <sub>b</sub> (P, T <sub>init</sub> )	
Brill <sup>48</sup>	RDX, HMX	Relative initial decomposition specie concentrations.	Limited number of species. 1 atm.

It is significant to note that a dark zone is not observed experimentally unless there is additional heat flux. The models are in agreement, in that they only calculate the two stage flame for conditions with laser augmentation. With no additional heat flux, the calculated and observed temperature profiles do not show a dark zone. Those results have been presented previously.<sup>44,45,47</sup> For both RDX and HMX the final flame temperature and specie concentrations (of N<sub>2</sub>, CO<sub>2</sub>, H<sub>2</sub>O, etc.) agree with those calculated by thermochemical equilibrium codes (NASA-Lewis, Edwards) over the range of pressures to within a percent.

Figure 6 shows the calculated species concentration profiles corresponding to the laser assisted tests, demonstrating the relationship between the formation and destruction of NO and the dark zone. Experimentally determined species concentration profiles at low pressures as a function of distance from the burning surface are also available for comparison (See Table 3). Most of this data was taken under laser-assisted combustion conditions. Some of the experimental species data do not approach equilibrium flame values (i.e. Ermolin, et al.); some of the data fail to close elemental balances (Litzinger, et al. ); and some of the data differ from one experiment to another, but all can be used to indicate the strengths and weaknesses in the model. For the species CN, HCN, OH, N<sub>2</sub>O, CO, CO<sub>2</sub>, H<sub>2</sub> and NH, there is very reasonable agreement between experiment and model. The

agreement is poor for some of the key intermediate species. The model over predicts the experimental NO concentration by approximately 40% and under predicts the NO<sub>2</sub> by over 80% for both RDX and for HMX. There are many steps within the kinetic mechanism that involve NO and NO<sub>2</sub>. It is apparent that the kinetic parameters affecting these two species need review.

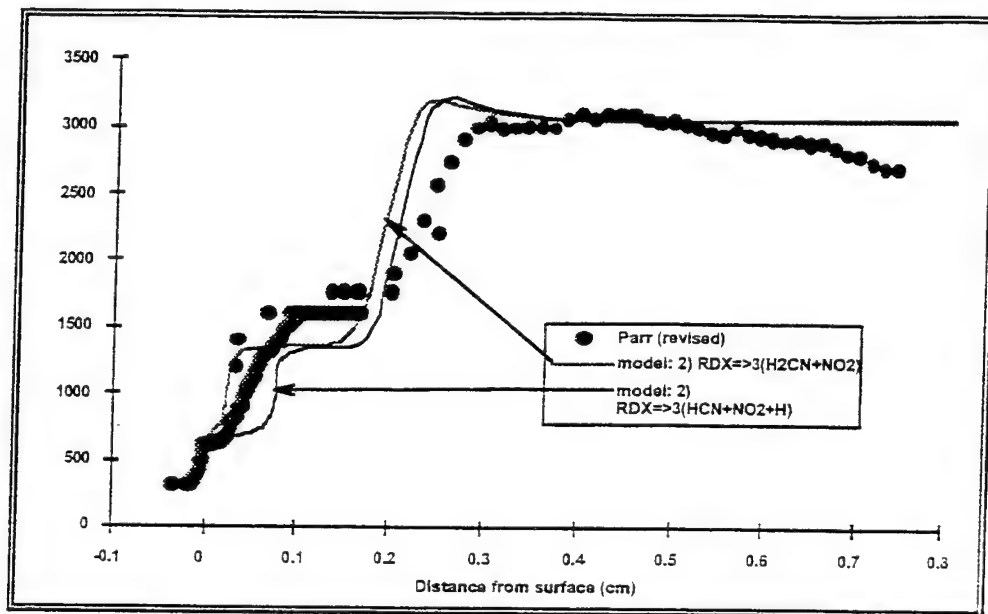


Figure 5. RDX at 1 atm under laser assisted combustion conditions.

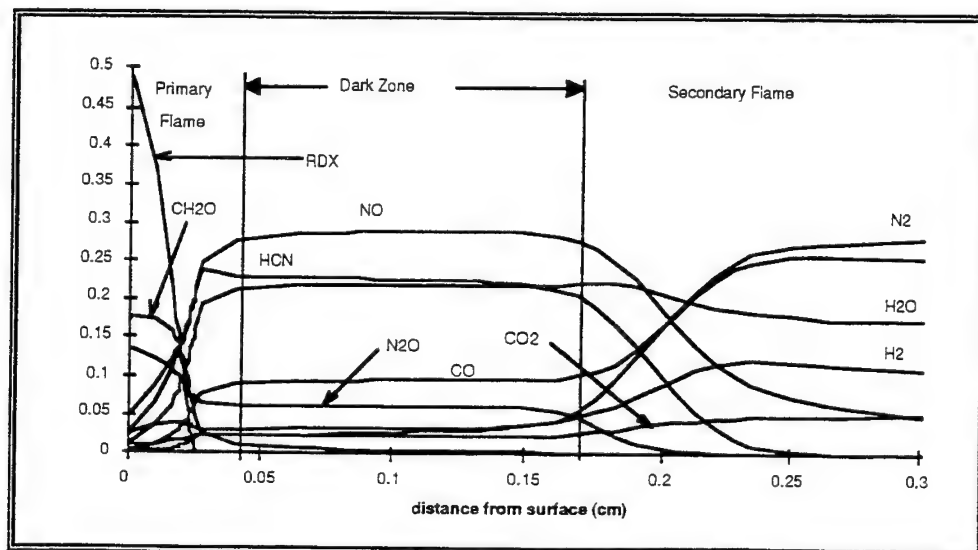


Figure 6. RDX dark zone under laser assisted conditions (1 atm)

## SUMMARY AND CONCLUSIONS

Modeling solid monopropellants has been divided into three categories; global models, semi-global models and models based on detailed kinetics. Global kinetics-type of models are able to match the experimental burning rate data with reasonable accuracy in spite of the diverse assumptions relative to the physical picture being modeled. This is due to the fact that the models are usually based on some form of the energy equation which gives the model a reasonable functional form. Also, all of the models contain uncertain parameters that are estimated from known data, thus becoming optimization parameters. Some researchers have naively claimed that their physical model was 'correct' based on their agreement with burning rate data. Other investigators have been more objective, and have used their models to evaluate more detailed combustion characteristics, such as  $\sigma_p$ , flame stand-off distances, etc.

Semi-global models evolved, based on simplified kinetic schemes involving more than one step global models, presumably including the most important steps or species. These models have been compared to more detailed combustion data contributing to the overall understanding. However, they have also been very dependent on having prior knowledge of the results.

The most recent models include detailed reaction mechanisms in the gas phase coupled with a detailed reaction mechanism describing the condensed phase. These models are not only able to predict burning rate,  $\sigma_p$ , surface temperature, and melt thickness, but they also can calculate temperature and species profiles through the reaction zone, identifying dominant steps in the mechanism and important species. These models will be very valuable in interacting with researchers doing experimental work to aid in interpreting the more advanced experimental measurements.

The current model has been used to describe the combustion of RDX and HMX showing the excellent agreement with experimental burning rate data,  $\sigma_p$  data, measured temperature profiles and species profiles for data taken with and without laser augmentation. However, there are still some discrepancies in temperature sensitivity and certain species concentration profiles, specifically with  $\text{NO}_2$  and  $\text{NO}$ . Some of these discrepancies might be attributed to experimental error but others are apparently the result of erroneous model inputs.

## REFERENCES

1. Boggs, T. L. "Thermal Behavior of RDX and HMX," *Progress in Astronautics and Aeronautics*, (eds: Kuo, K. and Summerfield, M.) Vol 90. (1984), pp. 121-176.
2. Wilson, S. J., Fetherolf, B. L., Brown, P. W. and Kuo, K. K., "Surface Microstructure Resulting from Laser-induced Pyrolysis and Combustion of M43 and XM39," *30th JANNAF Comb Mtg.* (1993).
3. Ermolin, N. E., Korobeinichev, O. P., Tereshchenko, A. G. and Fomin, V. M., "Kinetic Calculations and Mechanism Definition for Reactions in an Ammonium Perchlorate Flame," *Combustion, Explosion & Shock Waves*, Vol 18. No. 2. pp. 61-70, Mar-Apr, 1982.

4. Beckstead, M. W. and McCarty, K. P., "Calculated Combustion Characteristics of Nitramine Monopropellants", *13th JANNAF Combustion Meeting*, (1976), Vol. I, pp.57-68.
5. Miller, M. S., "In Search of an Idealized Model of Homogeneous Solid Propellant Combustion", *Combustion and Flame*, (1982), 46, pp.51-73.
6. Gusachenko, L. K. , and Zarko, V.E., "Modeling the Combustion Processes Solid Fuels", Nauka, Novosibirsk, 1985 (in Russian); see also, Gusachenko, L. K. , and Zarko, V.E., "Analysis of Contemporary Models of Steady State Combustion of Composite Solid Fuels", *Combustion, Explosion & Shock Waves*, (1986), Vol. 22, No. 6, pp.643-653.
7. Manelis, G. B. and Strunin, V.A., "The Mechanism of Ammonium Perchlorate Burning", *Combustion and Flame*, (1971), 17, pp.69-77.
6. Beckstead, M. W. , Derr, R. L. and Price, C. F., "The Combustion of Solid Monopropellants and Composite Propellants", *13th Symposium (Int'l) on Combustion*, (1971), The Combustion Institute, Pittsburgh, PA, pp.1047-1056.
9. Guirao, C. and Williams, F. A., "A Model for Ammonium Perchlorate Deflagration between 20 and 100 atm," *AIAA Journal*, Vol 9, No. 7, (1971), pp. 1345-1356.
10. Sohn, H. Y., "A Unified Theory of Ammonium Perchlorate Deflagration and the Low Pressure Deflagration Limit", *Comb. Sci. and Tech.*, (1975), 10, pp.137-154.
11. Price, C. F. , Boggs, T.I. and Bradley, H.H., Jr., "Modeling the Combustion of Monopropellants", *14th JANNAF Combustion Meeting* , (1977), Vol. I, CPIA No. 292, pp.307-324.
12. Strunin, V. A. , Firsov, A.N., Shkadinskii, K.G. and Manelis, G.B., "Stationary Combustion of Decomposing and Evaporating Condensed Substances", *Combustion, Explosion & Shock Waves*, (1977), Vol. 13, No. 1, pp.3-9.
13. Price, C. F. , Boggs, T.L. and Derr, R.L., "The Steady-State Combustion Behavior of Ammonium Perchlorate and HMX", AIAA-79-0164, (1979),.
14. Beckstead, M. W., "Model for Double-Base Propellant Combustion", *AIAA Journal*, (Aug. 1980), Vol. 18, No. 8, pp.980-985.
15. Miller, M. S. and Coffee, T.P., "Numerical Reliability of Solid Monopropellant Combustion Models", *18th JANNAF Combustion Meeting*, (1981), CPIA #347, pp.373-382.
16. Miller, M. S. and Coffee, T.P., "A Fresh Look at the Classical Approach to Homogeneous Solid Propellant Combustion Modeling", *Combustion and Flame*, (1983), 50, pp.65-74.
17. Mitani, T. and Williams, F. A., "A Model for the Deflagration of Nitramines," *21st Symposium (Int'l) on Combustion*, The Combustion Institute, (1986), pp. 1965-1974.
18. Beckstead, M. W., "Modeling AN, AP, HMX, and Double Base Monopropellants," *26th JANNAF Combustion Mtg.* CPIA No 529, Vol 4, (1989), pp 255-268.
19. Li, S. C. , Williams, F.A. and Margolis, S.B., "Effects of Two-Phase Flow in a Model for Nitramine Deflagration", *Combustion and Flame*, (1990), 80, pp. 329-349.
20. BenReuven, M., Caveny, L., Vichnevetsky, R., and Summerfield, M., "Flame Zone and Sub-surface Reaction Model for Deflagrating RDX," *16th Symposium (Int'l) on Combustion*, The Combustion Institute, pp. 1223-1233, 1976.
21. BenReuven, M. and Caveny, L., "HMX Deflagration and Flame Characterization," Report AFRPL-TR-79-94, Vol II, Oct. 1980.
22. Cohen, N., Lo, G. and Crowley, J., "Model and Chemistry of HMX Combustion," *AIAA Journal*, Vol 23, No. 2 pp. 276-282, Feb 1985.
23. Bizot, A. and Beckstead, M., "A Model for Double Base Propellant Combustion," *22nd Symposium (Int'l) on Combustion*, The Combustion Insititute, pp. 1827-1834, 1988.

24. Bizot, A. and Beckstead, M., "A Model for HMX Propellant Combustion," *Flame Structure*, (ed. Korobeinichev, O. P.) Vol 1, pp. 230-235, 1991.
25. Roh, T., Tseng, I., and Yang, V., "Effects of Acoustic Oscillations on Flame Dynamics of Homogeneous Propellants in Rocket Motors," *J. Propulsion and Power*, Vol 11. No. 4, pp. 640-650, Jul-Aug. 1995.
26. Li, S. C., and Williams, F. A., "Nitramine Deflagration: A Reduced Chemical Mechanism for the Primary Flame," AIAA Report 94-3031, 30th AIAA Joint Propulsion Conference, June 1994.
27. Korobeinichev, O. P., Orlov, V. N., and Shifon, N. Ya., "Mass-Spectrometric Study of the Chemical Structures of Flames of Perchloric Acid in Lean and Rich Mixtures with Methane," *Combustion, Explosion & Shock Waves*, Vol 18, No 5, pp 77-83, 1982.
28. Ermolin, N. E., Korobeinichev, O. P., Tereshchenko, A. G. and Fomin, V. M., "Simulation of Kinetics and Chemical Reaction Mechanism of Ammonium Perchlorate Burning," *Sov. J. Chem. Phys.*, Vol 1(12), pp 2872-2883, 1984.
29. Ermolin, N. E., Korobeinichev, O. P., Kuibida, L. V. and Fomin, V. M., "Study of the Kinetics and Mechanism of Chemical Reactions in Hexogen Flames," *Combustion, Explosion & Shock Waves*, Vol. 22, No. 5, pp. 54-64, 1986.
30. Jacobs, P. W. M. and Pearson, G.S., "Mechanism of the Decomposition of Ammonium Perchlorate", *Combustion and Flame*, (1969), 13, 4, pp.419-430.
31. Korobeinichev, O. P. , Shmelev, A.S., and Tatevosyan, A.V., "Model of the Catalysis of Burning of a Monopropellant (With Reference to Ammonium Perchlorate)", *Combustion, Explosion & Shock Waves*, (1972), Vol. 8, No. 3, pp.378-388.
33. Narahari, H. K, Mukunda, H. S. and Jain, V. K, "A Model for Combustion Monopropellants (AP) with Complex Gas Kinetics," *20th Symposium (Int'l) on Combustion*, The Combustion Institute, pp. 2073-2082, 1984.
33. Sahu, H., Sheshadri, T. and Jain, V., "Novel Kinetic Scheme for Ammonium Perchlorate Gas Phase," *J. Phys. Chem.* Vol. 94, pp. 294-295, 1990.
34. Cohen, N. "A Review of Kinetic Models for High Temperature Gas Phase Decomposition of Ammonium Perchlorate," *Aerospace Report* No. ATR-92(9558)-3, The Aerospace Corporation. Sep. 1992
35. Hatch, R. L., "Chemical Kinetics Combustion Model of the NG/Binder System," *23rd JANNAF Combustion Mtg.*, Vol 1, CPIA 457, Oct. 1986, pp. 157-165.
36. Anderson, W. R., Ilincic, N. and Meagher, N. E., "Detailed and Reduced Chemical Mechanisms for the Dark Zones of Double Base and Nitramine Propellants in the Intermediate Temperature Regime," *32nd JANNAF Combustion Mtg.* 1995, Vol. I, CPIA No. 638.
37. Hatch, R. L., "Chemical Kinetics Modeling of HMX Combustion," *24th JANNAF Combustion Mtg.*, Vol 1, CPIA# 476, 1987, pp. 383-391
38. Melius, C. F. and Binkley J. S., "Thermochemistry of the Decomposition of Nitramines in the Gas Phase," *21st Symposium (Int'l) on Combustion*, The Combustion Institute, 1986, pp. 1953-1963,
39. Melius, C. F., "Thermochemical Modeling: I. Application to Decomposition of Energetic Materials," *Chemistry and Physics of Energetic Materials*, (ed. S. N. Bulusu) pp, 21-49, 1990.
40. Yetter, R. A., Dryer, F. L., Allen, M. T., Gatto, J. L., "Development of Gas-Phase Reaction Mechanism for Nitramine Combustion," *J. Propulsion and Power*, Vol. 11, No. 4, pp.683-697, 1995.
41. Margolis, S., Williams, F., and Armstrong, R., "Influences of Two-Phase Flow in the Deflagration of Homogeneous Solids," *Combustion and Flame*, Vol 67, pp. 249-258, 1987.

42. Melius, C. F., "Thermochemical Modeling: II. Application to Ignition and Combustion of Energetic Materials," *Chemistry and Physics of Energetic Materials*, (ed. S. N. Bulusu) pp, 51-78, 1990.
43. Yetter, Personal Communication. Aug 1995.
44. Liao, Y. and Yang, V., "Analysis of RDX Monopropellant Combustion with Two-Phase Subsurface Reactions," *J. Propulsion and Power*, Vol 11, No. 4, pp. 729-739, 1995.
45. Prasad, K., Yetter, R., and Smooke, M., "An Eigenvalue Method for Computing the Burning Rates of RDX Propellants," Submitted for publication, *Combustion Science and Technology*, 1996.
46. Davidson, J. E. and Beckstead, M.W., "Improvements in RDX Combustion Modeling," *32nd JANNAF Combustion Mtg.*, 1995, Vol. I, CPIA No. 638, pp. 41-53.
47. Davidson, J. E. and Beckstead, M.W., "Improvements in RDX Combustion Modeling," AIAA No. 96-0885, 34th Aerospace Sciences Meeting, 1996.
48. Brill, T. B., "Multiphase Chemistry Considerations at the Surface of Burning Nitramine Monopropellants," *J. Propulsion and Power*, Vol 11:4, pp 740-751, 1995.
49. Davidson, J. E. and Beckstead, M.W., "A Three-Phase Model of HMX Combustion," *26th Symposium (Int'l) on Combustion*, 1996 (in publication).
50. Glaskova, A. P., Rozantsev, E.G., Bobolev, V.K., and Skripko, L.A., "Effect of the Chemical Structure of the Inhibitor on the Combustion of RDX", *Combustion, Explosion & Shock Waves*, (1970), No. 4, pp.584-585.
51. Zimmer-Galler, R. "Correlations between Deflagration Characteristics and Surface Properties of Nitramine-Based Propellants", AIAA J., Vol. 6, No. 11 (1968), pp. 2107-2110.
52. Personal Communication from A. Atwood Aug. 1995.
53. Zenin, A., "HMX and RDX: Combustion Mechanism and Influence on Modern Double Base Propellant Combustion," *J. Propulsion and Power*, Vol 11. No. 4, pp. 752-758, 1995
54. Parr, D. M. and Parr, T.P., "Condensed Phase Temperature Profiles in Deflagrating HMX", *20th JANNAF Combustion Meeting*, (1983), Vol. I, CPIA No 383, pp.281-291.
55. Mitani, T. and Takahashi, M., "Temperature Measurements of Monopropellants Using a Counterflow Burner Method", WSS/CI Spring Mtg. Hawaii, (1988), 3C-050, pp.161-163.
56. Lengelle, G. and Duterque, J., "Combustion des Propergols a Base D'Octogene", (1986), AGARD-CP-391, Smokeless Propellants, pp.8-1 to 8-17.
57. Kubota, N. and Sakamoto, S., "Combustion Mechanism of HMX", *Combustion and Detonation Phenomena*, 19th Int'l Conference of ICT, (1988), Germany, pp.65-1 to 65-12; see also, Kubota, N., "Nonsteady Burning and Combustion Stability of Solid Propellants, *Progress in Astronautics and Aeronautics*, Vol 143, pp. 233-259.
58. Fetherolf, B. L., and Litzinger, T. A., "Chemical Structure of the Gas Phase Above Deflagrating RDX: Comparison of Experimental Measurements and Model Predictions," *30th JANNAF Combustion Mtg*, Vol II. CPIA No. 606, 1993.
59. Tang, C., Lee, Y. and Litzinger, T., "A Study of Gas-Phase Processes During the Deflagration of RDX Composite Propellants Using Triple Quadrupole Mass Spectrometer," *31st JANNAF Combustion Mtg.*, Vol II, CPIA No. 620, 1994.
60. Lee, Y., Tang, C., Kudva, G., Litzinger, T., "The Near-Surface Gas-Phase Structure of RDX During CO<sub>2</sub> Laser-Assisted Combustion," *32nd JANNAF Combustion Meeting*, 1995, Vol. I, CPIA No. 638.
61. Brewster, M., and Schroeder, T., "Experimental Study of Steady and Unsteady Combustion of RDX," *32nd JANNAF Combustion Mtg.* 1995, Vol. I, CPIA No. 638.



62. Hanson-Parr, D., and Parr, T., "RDX Laser-Assisted Flame Structure," *31st JANNAF Combustion Mtg.*, Vol II, CPIA No. 620, 1994.
63. Hanson-Parr, D., and Parr, T., "RDX Flame Structure," *25th Symposium (Int'l) on Combustion*, The Combustion Institute, pp. 1635-1643, 1994.
64. Parr, T., and Hanson-Parr, D., "RDX, HMX, and XM39 Self-Deflagration Flame Structure," *32nd JANNAF Combustion Mtg.*, 1995, Vol. I, CPIA No. 638.
65. Boyer, E., Lu, Y., and Kuo, K., "Characterization of Condensed-Phase Chemical Reactions of RDX and Nitramine-Based Propellants," *32nd JANNAF Combustion Mtg.*, 1995, Vol. I, CPIA No. 638.
66. Ritchie, S. J., Thynell, S. T., and Kuo, K., "Modeling and Experiments of Laser-Induced Ignition of Nitramine Propellants," *32nd JANNAF Combustion Mtg.*, 1995, Vol. I, CPIA No. 638.

## MODELING AND NUMERICAL SIMULATION OF PHYSICOCHEMICAL PROCESSES OCCURRING IN THE TWO-PHASE FOAM LAYER OF BURNING RDX

Kenneth K. Kuo, Yeu-Cherng Lu, and Yang-Sheng Tseng

Department of Mechanical Engineering  
The Pennsylvania State University  
University Park, PA 16802, USA

**ABSTRACT:** The two-phase phenomena in the surface region of RDX could have significant effects on low-pressure burning rate and ignition behavior of RDX-based propellants. A model describing the physicochemical processes occurring in the two-phase foam layer of burning RDX was developed. An analysis based upon Lagrangian formulation, incorporating vaporization, heat transfer, and gas-phase chemical reactions was applied to a single bubble in the two-phase region. A multi-bubble analysis was also developed using a statistical treatment of families of single bubbles. The results of the single bubble simulation indicate pronounced vaporization of RDX in the foam layer; however, very little decomposition of RDX occurs in the gas bubbles even though the growth of the bubbles is significant, and the gas bubble temperature is largely governed by the surrounding liquid temperature.

### INTRODUCTION

During combustion, RDX develops a complex flame structure, involving a gas-phase flame zone and a two-phase foam layer which is formed on the surface of the solid RDX. An overall depiction of the structure of a burning RDX monopropellant, from Kuo et al. [1], is provided in Fig. 1. The solid RDX first liquefies and then bubbles begin to nucleate in the liquid layer. The existence of a molten foam zone on the surface of burning RDX has been observed in several research studies. A micrograph, from Wilson et al. [2] is provided in Fig. 2. This micrograph of a recovered XM39 composite propellant containing 76% RDX clearly shows bubbles have nucleated in the liquid.

Most of the earlier models of RDX combustion did not incorporate any detailed two-phase analysis of the foam zone, except the model of Li et al. [3], which offered a simplified treatment of this layer. The physicochemical processes occurring in the foam layer are of interest because heat release in the foam layer could play an important role in the ignition and combustion behavior of RDX. The recent model developed by Kuo and Lu [4] provided very detailed analysis of the surface foam layer. In a parallel work, team members Liao and Yang [5] solved a simplified version of this model, with the consideration of void fractions in the surface reaction zone and bypassed detailed treatment of bubble dynamics. The major objectives of this work are (1) to solve a portion of the comprehensive model developed by Kuo and Lu for simulating the physicochemical processes associated with a single bubble in the foam layer, and (2) to extend the single bubble analysis to a statistical description of multi-bubble phenomena in the two-phase foam layer. This model can be further incorporated into a comprehensive model of propellant combustion in the near future. Figure 3 shows the model development process for prediction of flame structure and ignition behavior of energetic materials.

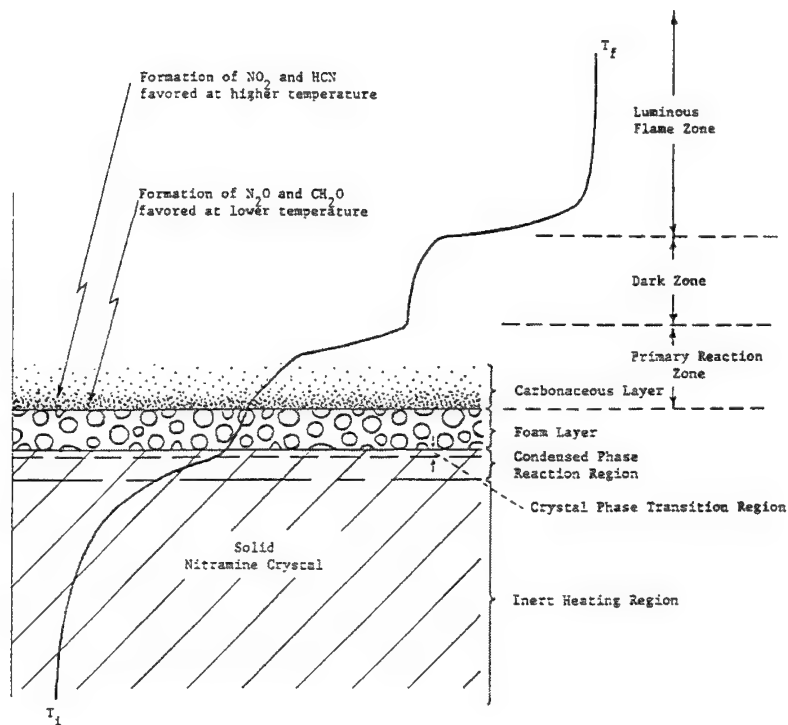


Figure 1. A schematic diagram showing various flame zones and condensed phase reaction regions as well as a typical temperature profile.

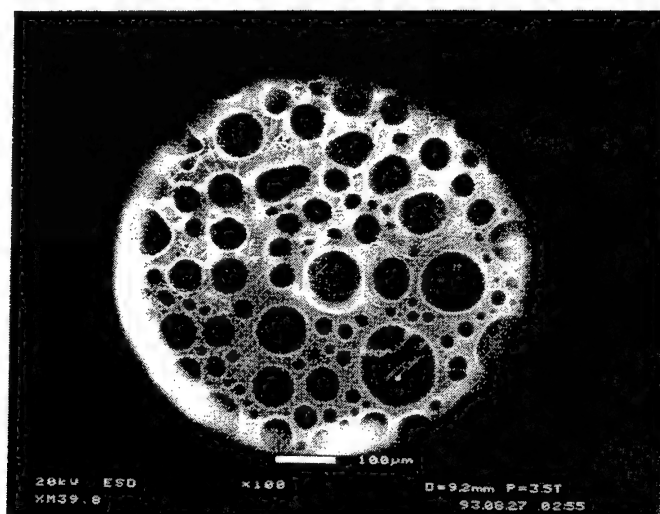


Figure 2. A typical micrograph showing bubble formation on the surface of XM39 propellant

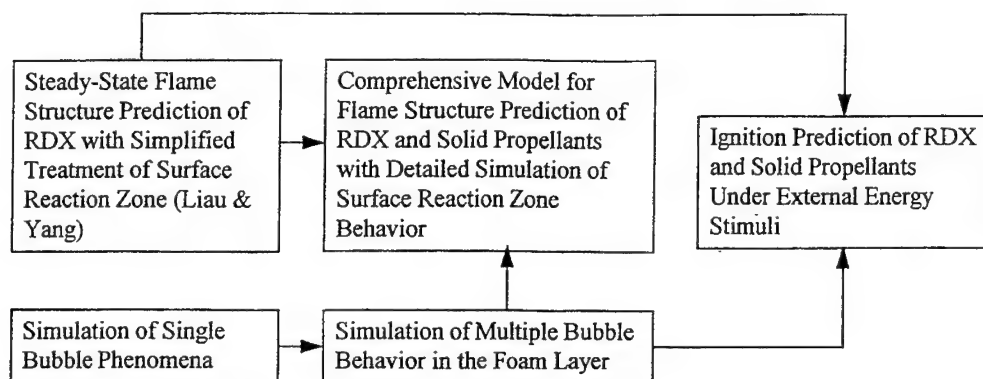


Figure 3. Model development process for prediction of flame structure and ignition behavior of energetic materials

In this work, the single bubble analysis considered the time history of a gas bubble from its formation to the instant prior to its bursting at the top of the foam layer based on the Lagrangian formulation. A simplified chemical reaction scheme was adopted to describe the reactions occurring inside the gas bubble. The extension of the single bubble analysis to a multiple bubble description of the two phase foam layer was accomplished using statistical methods. The mathematical expressions for area-averaged properties at any specified distance from the burning surface were derived for the purpose of coupling with solutions from comprehensive flame structure models. [5]

### SINGLE BUBBLE ANALYSIS

The model used in this study is a simplification of Kuo and Lu's model. From an order-of-magnitude analysis, the buoyancy force was found to be much smaller than the drag force acting on the bubble. Thus, the bubble can be considered stationary and free to grow while the burning surface is regressing downward. Under this assumption, the formulation simplifies to a set of ordinary differential equations, greatly reducing the amount of computational time required.

The characteristics of a single gas bubble are modeled from its nucleation until the top surface of the foam layer is reached. Nucleation of the gas bubble is assumed to occur at the instant the vapor pressure of RDX is equal to the ambient pressure. The characteristics of the gas bubble that are determined by this model include the time variations of the gas temperature, bubble diameter, gas density, species concentrations inside the bubble, and heat released by chemical reactions in the gas bubble.

The governing equations are derived from the first principles of mass, energy, and species conservation using control volume analysis. The basic assumptions of this model are:

1. Due to the relatively low temperature of the liquid in the foam layer, the liquid consists of pure RDX with no chemical reactions.
2. For the same reason, no heterogeneous chemical reactions occur on the liquid-bubble boundaries.
3. No dissolved chemical species exist in the liquid phase, since the foam layer behavior is associated only with ignition or low-pressure combustion processes.

4. The shape of the bubble is considered to be spherical.
5. Dufour and Soret effects are negligibly small.

As mentioned above, the bubble is stationary inside the foam zone and the surface regression is considered to be the only cause of the relative motion of the bubble with respect to the melt front and burning surface. Figure 4 summarizes all the physicochemical processes considered for the bubble.

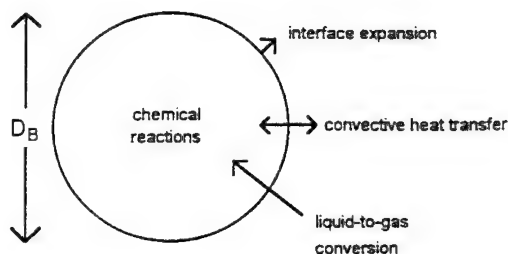


Figure 4. Physicochemical processes considered in single bubble analysis

The rate of mass production of the  $i$ th species due to gas-phase chemical reactions is equal to  $(\pi/6)D_B^3 \dot{\omega}_{g,i}$ , where  $\dot{\omega}_{g,i}$  is the mass production of the  $i$ th species per unit volume. The rate of liquid-to-gas conversion can be written as  $D_B^2 \rho_l (r_{l-g})_B$ , where  $(r_{l-g})_B$  is the rate of advancement of the liquid-gas interface. The heat transfer between the liquid and bubble is written as  $D_B^2 \bar{h}_c (T_l - T_g)$ .

The rate of energy accumulation inside the gas bubble is then equal to the sum of rate of enthalpy increase due to vaporization of liquid RDX at the interface and the rate of heat transfer from liquid to gas by convection. Therefore, the energy equation can be written in the following form

$$\left(\frac{D}{Dt}\right)_B \left[ \frac{\pi}{6} D_B^3 \rho_g h_g \right] = \pi \rho_l D_B^2 (r_{l-g})_B h_{g,RDX} + \pi D_B^2 \bar{h}_c (T_l - T_g) \quad (1)$$

In the above equation, the specific enthalpy of the gaseous mixture inside the gas bubble,  $h_g$ , is defined as

$$h_g = \sum_{i=1}^N Y_i h_i = \sum_{i=1}^N Y_i \left( \int_{T_{ref}}^{T_g} c_{p,i} dT + \Delta h_{f,i}^0 \right) \quad (2)$$

Under the assumption of no dissolved gas species in the liquid, the continuity equation can be written as:

$$\left(\frac{D}{Dt}\right)_B \left[ \frac{\pi}{6} D_B^3 \rho_g \right] = \pi D_B^2 \rho_l (r_{l-g})_B \quad (3)$$

The species conservation equation for the  $i$ th species in the bubble is

$$\left(\frac{D}{Dt}\right)_B \left[ \frac{\pi}{6} D_B^3 \rho_g Y_{g,i} \right] = \pi D_B^2 \rho_l (r_{l-g})_B \epsilon_{g,i} + \frac{\pi}{6} D_B^3 (\dot{\omega}_{g,i})_B \quad (4)$$

where  $\epsilon_{g,i}$  is equal to one for RDX and zero for all other species, since 100% of the gaseous species generated from the liquid-bubble interface is RDX vapor. The summation of mass fractions of all gaseous species in the bubble is unity, i.e.,

$$\sum_{i=1}^N Y_{g,i} = 1 \quad (5)$$

The equation of state is

$$P = \rho_g R_u T_g \sum_{i=1}^N \frac{Y_i}{W_i} \quad (6)$$

The liquid-to-gas conversion rate in Eqs. (1), (3) and (4) is given by

$$r_{l-g} = \sqrt{\frac{W_{RDX}}{2\pi RT_i}} \gamma (p_v - X_{RDX} p_\infty) \quad (7)$$

where  $W_{RDX}$  is the molecular weight of RDX,  $T_i$  the interface temperature,  $p_v$  the vapor pressure of RDX,  $p_\infty$  the ambient pressure, and  $X_{RDX}$  the mole fraction of RDX inside the bubble.

The convective heat transfer coefficient can be determined using the Nusselt number definition

$$\overline{Nu} \equiv \frac{\overline{h_c} D_B}{k} \quad (8)$$

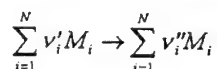
The Nusselt number used in this model is that of a sphere in a quiescent condition, which gives

$$\overline{Nu} = 2 \quad (9)$$

therefore,

$$\overline{h_c} = \frac{2k}{D_B} \quad (10)$$

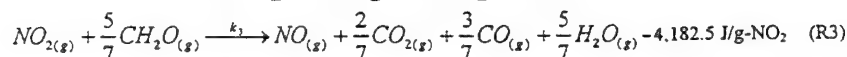
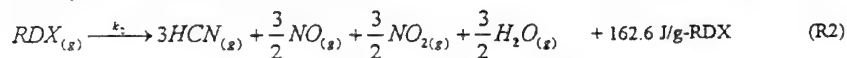
The mass production rate of the  $i$ th species due to chemical reactions,  $\dot{\omega}_{g,i}'''$ , is determined by the molar concentrations of the gas species,  $C_i$ , and the rate constants of the chemical reactions,  $k_i$ . Each of the chemical reactions can be represented by the following symbolic form,



where  $\nu_i'$  and  $\nu_i''$  represent the stoichiometric coefficients of the reactants and products, respectively, and  $M_i$  represents the  $i$ th species. The mass production rate of the  $i$ th species can now be written as

$$\dot{\omega}_i''' = W_i \sum_{l=1}^M [(\nu_{i,l}'' - \nu_{i,l}') k_l \prod_{j=1}^N C_{M_j}^{\nu_{j,l}'}] \quad (11)$$

where  $M$  is the total number of chemical reactions. In this model, there are three reactions considered: two RDX decomposition reactions and one gas-phase reaction. The reaction mechanism suggested by Brill and Brush [6] and kinetic data from Melius [7] were adopted to describe RDX decomposition. The global kinetic rates from BenReuven et al. [8] were adopted to describe reactions between  $\text{NO}_2$  and  $\text{CH}_2\text{O}$ . These reactions were utilized successfully in a nitramine propellant ignition study conducted by Huang et al. [9] The chemical reactions are as follows:



The general form of the reaction rate constants  $k$  follows the Arrhenius form

$$k = A \exp\left(-\frac{E_a}{R_u T}\right) \quad (12)$$

where  $E_a$  is the activation energy of chemical reactions and  $A$  is the frequency factor. The values of  $E_a$  and  $A$  for the three reactions considered in this model are given in Table 1.

TABLE 1  
Chemical Reaction Rate Constants

$k_i = A \exp\left(-\frac{E_a}{R_u T}\right)$	A	$E_a$	Ref.
R1	$1 \times 10^{13} \text{ sec}^{-1}$	36.0 Kcal/gmole	7
R2	$2 \times 10^{16} \text{ sec}^{-1}$	45.0 Kcal/gmole	7
R3	$1 \times 10^{12} \text{ cm}^3 \text{ gmole}^{-1} \text{ sec}^{-1}$	19.0 Kcal/gmole	8

Based upon the above reactions, nine chemical species were considered in the gas bubble. These species are: RDX,  $CH_2O$ ,  $N_2O$ , HCN, NO,  $NO_2$ ,  $H_2O$ ,  $CO_2$ , and CO.

The single bubble model was solved using a fourth-order Runge-Kutta method. Combustion pressure was specified as an input to the program. Other parameters that are input include the initial diameter of a nucleated bubble, the melting temperature of RDX, and a realistic temperature profile of the liquid in the foam layer. The time variations of key parameters (including bubble diameter, bubble temperature, gas density, and mass fractions of various chemical species) were solved on computer by numerical integration of the differential equations. A set of sample input data and results is included in the Results and Discussion section.

### MULTI-BUBBLE ANALYSIS

The single bubble analysis was extended using statistical method for describing multiple-bubble phenomena. In the multi-bubble analysis, the number of nucleation sites at the nucleation plane can be determined experimentally or obtained from literature. An example for the number of nucleation sites per unit volume per unit time (defined as  $J$ ) is given by the following expression [10].

$$J = N \left( \frac{\sigma}{\pi m B} \right)^{1/2} \exp \left[ -\frac{16\pi\sigma^3}{3kT(p_v - p_\infty)^2} \right] \quad (13)$$

where  $N$  is the number density of the liquid molecules,  $\sigma$  the surface tension,  $k$  the Boltzmann constant,  $m$  the mass of one liquid molecule,  $p_v$  the vapor pressure of RDX at temperature  $T$ ,  $p_\infty$  the pressure in the liquid at the nucleation plane, and  $B$  an empirical constant. The radius of the nucleated bubble is given by

$$r = \frac{2\sigma}{p_v - p_\infty} \quad (14)$$

If the sizes of nucleated bubbles are assumed to follow a normal distribution function (e.g. Gaussian or Upper Limit), the number of bubbles of each distinct size family that nucleate per unit time,  $J_k$ , can be calculated. The sum of all  $J_k$  for the total number of size families ( $K$ ) should be equal to  $J$ , determined from Eq. (13).

Consider a given bubble as it travels through the  $x = X$  plane. In order for this bubble to be intersected by the  $X$ -plane, it must be located between the two extreme cases denoted in Fig. 5. When the center of the bubble reaches  $x_{b,min}$ , the top edge of the bubble just intersects the horizontal plane. When the center of the bubble reaches  $x_{b,max}$ , the bottom edge of the bubble just about to depart the horizontal plane. For any bubble located between these two extreme cases, the bubble is intersected by the  $x = X$  plane.

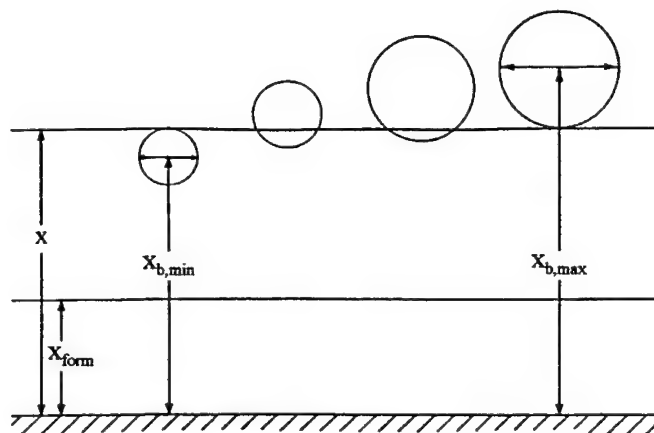


Figure 5. Illustration of plane intersection of a bubble as it travels between two extreme locations

From the single bubble analysis, the time history of the bubble  $[D_b(t), x(t)]$  is known. Therefore, the amount of time ( $t_1$ ) required for the bubble to travel from its nucleation station to  $x_{b,min}$  location and the time ( $t_2$ ) required to travel from its nucleation station to  $x_{b,max}$  are known. If these two time periods are subtracted, a time period  $\Delta t$  is obtained.

$$\Delta t_{21} = t_2 - t_1 \quad (15)$$

This time period represents the time interval during which the bubble will be intersected by the  $x = X$  plane. Additionally, this time period also represents the time period during which all bubbles of the same family formed will be intersected by the same plane. Knowing the bubble travel time ( $t_1$ ) and the interaction time interval ( $\Delta t_{21}$ ), it is possible to relate any bubble in the foam layer to its nucleation time. The probability of bubble formation at a given axial location normal to the foam layer can then be described by a counting process.

Let us consider the nucleation of one bubble. This process can be modeled statistically as a counting



process, where  $M(t)$  represents the total number of events that have occurred up to time  $t$ . A counting process must satisfy the following conditions:

1.  $M(t) \geq 0$ ;
2.  $M(t)$  is an integer;
3. If  $s < t$ , then  $M(t) \geq M(s)$ ; and
4. For  $s < t$ ,  $M(t) - M(s)$  is the number of events that have occurred in the interval  $(s, t]$  up to and including time  $t$ .

Condition (1) means that the process can never have a negative number of events at any time  $t$ . Condition (2) means that the process occurs in discrete steps, not continuously. In other words, a bubble forms instantly, so that there will never be a fraction of a bubble at any time  $t$ . Condition (3) means that the number of events that have occurred never decreases with increasing time. Condition (4) implies that if the number of events that have occurred is known at two times, the number of events that have occurred between these two times is simply the difference between the two values. In the following derivation, the bubble nucleation process is assumed to satisfy all of these conditions. Therefore, bubble nucleation can be modeled as a counting process.

The nucleation of bubbles can be modeled statistically as a Poisson process, a common type of counting process [11]. A Poisson process must satisfy the following conditions:

1.  $M(0) = 0$
2. The process has independent time increments
3. The number of events in any interval of length  $t$  is Poisson distributed with the expected value equal to  $\lambda t$ , where  $\lambda$  is defined as the rate of the process

These conditions imply that (1) the process begins at time zero with no events having occurred, (2) events that occur in one time interval do not influence the events that occur in a different time period, and (3) the expected value of the process is equal to the rate multiplied by the time period. Once again, the bubble nucleation process is assumed to satisfy these conditions.

According to the Poisson process, the probability of an event occurring in a time interval between  $(t+s)$  and  $(s)$  is

$$P\{M(t+s) - M(s) = m\} = \exp(-\lambda t) \frac{(\lambda t)^m}{m!} \quad (16)$$

where  $m = 0, 1, 2, \dots$ . Therefore, the probability that one bubble of the  $k$ th family forms over the time interval  $\Delta t$  is

$$P\{M(\Delta t) = 1\} = \lambda_k \Delta t \exp(-\lambda_k \Delta t) \quad (17)$$

If one is interested in the number of bubbles which interact with  $x = X$  plane, it is useful to consider the number of bubbles formed during the time interval of  $\Delta t_{21}$ , regardless of the absolute ages of this group of bubbles. The total number of bubbles ( $N_k$ ) of the  $k$ th family formed during the time interval of  $\Delta t_{21}$ , which will intersect the  $x = X$  plane with an area of  $A$ , can be calculated as

$$N_k = AS \lambda_k \Delta t_{21,k} \exp(-\lambda_k \Delta t_{21,k}) \quad (18)$$

where  $S$  is the number of nucleation sites at the nucleation plane per unit area. Since there are different initial bubble sizes, each with different interaction times,  $\Delta t_{21}$  will be different for each bubble family.

To determine the area averaged diameter of the intersected bubbles, the average cross-sectional area of each bubble family at the  $x = X$  plane must be calculated. Assuming that the bubbles of each family are

randomly distributed across the  $x = X$  plane, an average diameter can then be calculated from a geometric relationship based upon the Pythagorean theorem:

$$\overline{D}_k^2(X) = \frac{\int_{x_{B\min}}^{x_{B\max}} \left\{ D_k^2(x_B) - 4[X^2 - 2Xx_B + x_B^2] \right\} dx_B}{x_{B\max} - x_{B\min}} \quad (19)$$

The average cross-sectional area for the  $k$ th bubble at the  $x = X$  plane can then be calculated as

$$\overline{A}_k(X) = \frac{\pi}{4} \overline{D}_k^2(X) \quad (20)$$

and the total cross-sectional area intercepted by the  $x = X$  plane due to bubble family  $k$  is

$$\overline{A}_{t_k} = N_k \overline{A}_k(X) \quad (21)$$

The void fraction  $\phi$  at the chosen  $X$ -plane can then be determined from

$$\phi = \frac{\text{total area occupied by gas phase materials}}{\text{cross sectional area of the foam layer}} = \frac{\sum_{k=1}^K \overline{A}_{t_k}}{A} \quad (22)$$

where  $\overline{A}_{t_k}$  is total cross sectional area of the bubble family  $k$ , and  $K$  is total number of bubble families. The area averaged gas density ( $\overline{\rho}_g$ ) can then be calculated from

$$\overline{\rho}_g = \frac{\text{mass of gas phase material}}{\text{volume occupied by gas phase material}} = \frac{\int_x^{x+\Delta x} \overline{A}_{t_1} \rho_1 dx + \int_x^{x+\Delta x} \overline{A}_{t_2} \rho_2 dx + \dots + \int_x^{x+\Delta x} \overline{A}_{t_K} \rho_K dx}{\int_x^{x+\Delta x} \overline{A}_{t_1} dx + \int_x^{x+\Delta x} \overline{A}_{t_2} dx + \dots + \int_x^{x+\Delta x} \overline{A}_{t_K} dx}$$

$$\overline{\rho}_g = \frac{\sum_{k=1}^K \int_x^{x+\Delta x} \overline{A}_{t_k} \rho_k dx}{\sum_{k=1}^K \int_x^{x+\Delta x} \overline{A}_{t_k} dx} \quad (23)$$

where  $\rho_k$  is the calculated gas density of the  $k$ th family bubble from single bubble analysis, and  $\Delta x$  is the thickness of the  $x$ -level. Similar expressions to Eq. (23) can be obtained for area-averaged mass fraction and area-averaged gas-phase temperature. The average temperature in the foam layer can be given by

$$\overline{T} = \frac{\phi c_{p_g} \overline{T}_g \overline{\rho}_g + (1-\phi) \overline{c}_l \overline{T}_l \overline{\rho}_l}{\phi c_{p_g} \overline{\rho}_g + (1-\phi) \overline{c}_l \overline{\rho}_l} \quad (24)$$

These area-averaged quantities can be utilized to interface the multi-bubble analysis with comprehensive numerical solution of the companion study of Liao and Yang [5].

## RESULTS AND DISCUSSION

A set of sample results from the single-bubble analysis is provided in Figs. 6-11. These plots show the time variation of several important parameters including: bubble diameter, bubble temperature, gas density, and mass fractions of various chemical species. The input parameters used to generate these results are summarized in Table 2.

TABLE 2  
Input Parameters

Parameter	Value
Pressure	5 ATM
Liquid Temperature Profile	632.84 K
Initial Bubble Diameter	2 microns
RDX melting temperature	477 K

From the single bubble results, several major observations are summarized below:

1. Similar to the physical situation observed by Wilson et al. [2], the model predicts a large amount of bubble growth at low pressures.
2. The amount of decomposition of RDX is quite small due to the relatively low temperature of the gaseous mixture inside the bubble.
3. The gas-phase reaction (R3) between  $\text{CH}_2\text{O}$  and  $\text{NO}_2$  is negligible inside the bubble for the conditions considered, as evidenced by the low mass fractions of CO and  $\text{CO}_2$  inside the bubble. This is due to the relatively low temperature of the gaseous mixture inside the bubble and the low concentrations of decomposition products  $\text{CH}_2\text{O}$  and  $\text{NO}_2$  inside the bubble.
4. Due to effective heat transfer between the liquid and gas bubble, the gas bubble temperature is largely governed by the liquid temperature. This implies that for RDX-based composite propellants, if the RDX liquid can react exothermically with the binder melt in the foam layer of a burning propellant, the gas-phase reactions inside the bubble can easily be triggered by these exothermic reactions. Conversely, if the RDX liquid and binder melt react endothermically, the gas-phase reaction in the bubbles can be suppressed.

### SUMMARY

A detailed model of the physicochemical processes occurring in the two-phase foam layer of burning RDX monopropellant has been developed. This model considers the time history of one bubble from its nucleation to the instant prior to its bursting at the top surface of the foam layer. The single bubble model has been solved numerically and extended to describe multi-bubble phenomena using a statistical treatment of families of single bubbles. The multiple-bubble model is being solved numerically and will be incorporated into a comprehensive model of RDX combustion in the near future.

The modeling approach developed in this work could also be applied to other energetic materials, besides RDX. With limited modification, this detailed foam layer analysis can be extended for prediction of nitramine based composite propellants. Additionally, the complicated surface burning phenomena of liquid propellants (e.g. XM46) could be treated with this approach.

### ACKNOWLEDGMENT

This work has been sponsored by the Army Research Office under Contract Nos. DAAH04-93-G-0364 and DAAL03-92-G-0118. The program manager is Dr. Robert W. Shaw. His interest and support are gratefully acknowledged. The participation of J. A. Laxton is also appreciated.

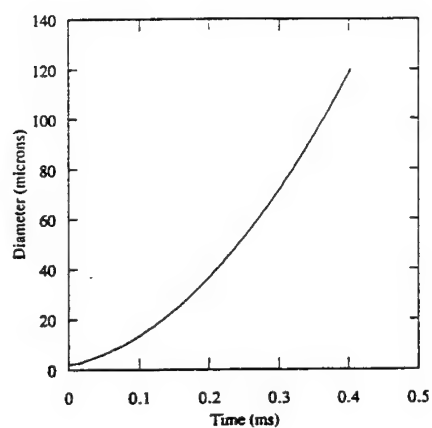


Figure 6. Gas bubble diameter

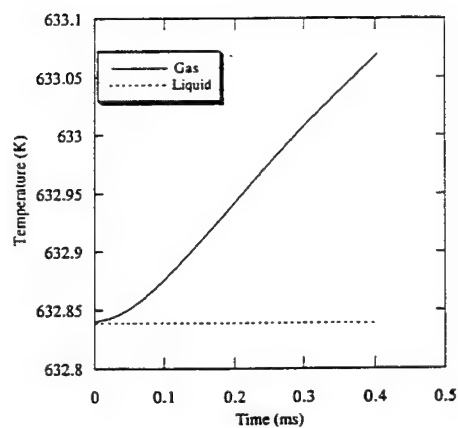


Figure 7. Bubble temperature

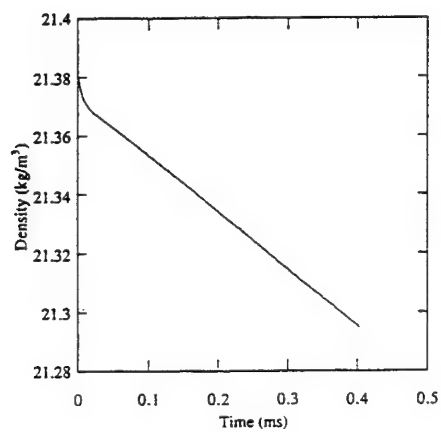


Figure 8. Gas density inside bubble

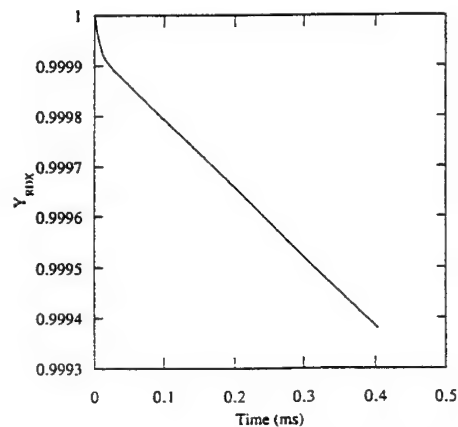


Figure 9. RDX mass fraction inside bubble

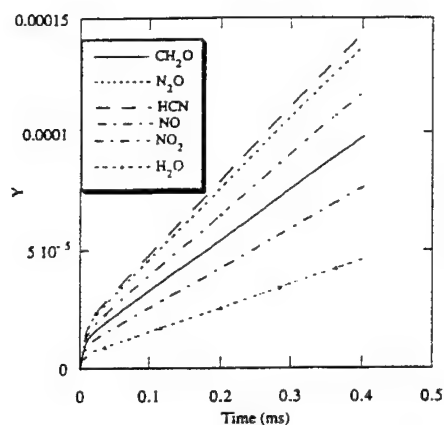


Figure 10. Mass fractions of various species

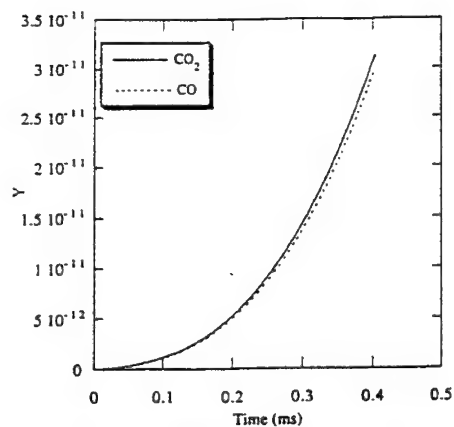


Figure 11. Mass fractions of CO and CO<sub>2</sub>

#### NOMENCLATURE

$A$	Arrhenius factor $[(N/L^3)^{1-m}/t]$
$B$	Empirical constant
$c_l$	Specific heat of liquid $[Q/(MT)]$
$c_{p,i}$	Specific heat of $i$ th species $[Q/(MT)]$
$C_i$	Molar concentration $[N/L^3]$
$D_B$	Diameter of gas bubble $[L]$
$E_a$	Activation energy $[Q/N]$
$\bar{h}_c$	Average convection heat transfer coefficient $[Q/L^2T]$
$h_g$	Enthalpy of gas mixture inside bubble $[Q/M]$
$J$	Total bubble nucleation rate $[1/L^3]$
$J_k$	Nucleation rate of $k$ th bubble family $[1/L^3]$
$k$	Thermal conductivity of gas mixture $[Q/LT]$
$k_i$	Chemical reaction rate constant $[(N/L^3)^{1-m}/t]$
$K$	Number of bubble families
$M$	Number of chemical reactions
$N$	Number of chemical species
$N_k$	Number of bubbles in the $k$ th family
$p_v$	Vapor pressure $[F/L^2]$
$p_\infty$	Ambient pressure $[F/L^2]$
$(r_{l-g})_B$	Liquid-to-gas regression rate $[L/t]$
$T_g$	Gas temperature $[T]$
$T_l$	Liquid temperature $[T]$
$r$	Bubble radius $[L]$
$R_u$	Universal gas constant $[Q/NT]$
$t$	Time $[t]$
$W_i$	Molecular weight of $i$ th species $[M/N]$
$Y_i$	Mass fraction of the $i$ th species

#### Greek Symbols

$\varepsilon_{z,i}$	Fraction of $i$ th species vaporizing at interface
$\Delta h_{f,i}$	Heat of formation, species $i$ $[Q/M]$
$\Delta t$	Time interval $[t]$
$\phi$	Void fraction
$\gamma$	Sticking coefficient
$\lambda$	Rate of Poisson process $[1/t]$
$\rho_g$	Gas density inside bubble $[M/L^3]$
$\rho_l$	Liquid density $[M/L^3]$
$\sigma$	Surface tension $[F/L]$
$\nu_i$	Stoichiometric coefficient $[N]$
$\dot{\omega}_{a,i}$	Rate of gas-phase chemical reactions $[M/L^3]$

#### Dimension Symbols

$F$	Force
$L$	Length
$M$	Mass
$N$	Mole
$Q$	Heat
$t$	Time
$T$	Temperature

Overbars represent averaged properties

## REFERENCES

1. **Kuo, K. K., Litzinger, T. A., and Hsieh, W. H.**, Interrelationship Between Solid-Propellant Combustion and Material's Behavior, *Proceedings of Materials Research Society Symposium*, Vol. 296, pp. 331-348, 1993.
2. **Wilson, S. J., Fetherolf, B. L., Brown, P. W., and Kuo, K. K.**, Surface Microstructure from Laser-induced Pyrolysis of M43 and XM39, *Proceedings of 30th JANNAF Combustion Subcommittee Meeting*, CPIA Publication, Vol. 11, pp. 269-281, November 1992.
3. **Li, S. C., Williams, F. A., and Margolis, S. B.**, Effects of Two-Phase Flow in a Model for Nitramine Deflagration, *Combustion and Flame*, Vol. 80, pp. 329-349, 1990.
4. **Kuo, K. K. and Lu, Y. C.**, Modeling of Physicochemical Processes of Burning RDX Monopropellant with Detailed Treatments for Surface Reaction Zone, *Proceedings of the Twentieth International Pyrotechnics Seminar*, Colorado Springs, Colorado, pp. 583-600, July 25-29, 1994.
5. **Liau, Y. C. and Yang, V.**, Analysis of RDX Monopropellant Combustion with Two-Phase Subsurface Reactions, *Journal of Propulsion and Power*, Vol. 11 No. 4, pp. 729-739, Jul-Aug 1995.
6. **Brill, T. B. and Brush, P. J.**, Condensed Phase Chemistry of Explosives and Propellants at High Temperature: HMX, RDX, and BAMO, *Philosophical Transactions of the Royal Society of London, A*, Vol. 339, pp. 377-385, 1992.
7. **Melius, C. F.**, Theoretical Studies of the Chemical Reactions Involved in the Ignition of Nitramines, *Proceedings of the 24th JANNAF Combustion Meeting*, Vol. 1, CPIA Publ. 476, pp. 359-366, 1987.
8. **BenReuven, M., Caveny, L. H., Vichnevetsky, R. J., and Summerfield, M.**, Flame Zone and Sub-Surface Reaction Model for Deflagrating RDX, *Proceedings of the 16th Symposium (International) on Combustion*, The Combustion Institute, Pittsburgh, PA, pp. 1223-1233, 1976.
9. **Huang, T. H., Thynell S. T., and Kuo, K. K.**, Hot Fragment Conductive Ignition of Nitramine Based Propellants, *Journal of Propulsion and Power*, Vol. 11, No. 4, pp. 781-790, Jul-Aug 1995.
10. **Blander, M. and Katz, J. L.**, Bubble Nucleation in Liquids, *AIChE Journal*, Vol. 21, pp. 833-848, 1975.
11. **Spiegel, M. R.**, *Schaum's Outline of Theory and Problems of Probability and Statistics*, McGraw-Hill, Inc., Chapter 4, 1975.

## NONLINEAR TRANSIENT BURNING OF COMPOSITE PROPELLANTS: THE EFFECT OF SOLID PHASE REACTIONS

Jeroen Louwers and Guy M.H.J.L. Gadiot

TNO Prins Maurits Laboratory, P.O. Box 45, 2280 AA Rijswijk, The Netherlands

**ABSTRACT:** The phenomenon of transient burning of solid propellants is a topic which still contains a large number of questions. In this paper the transient burning of AP composite propellants is calculated within the QSHOD approach (Quasi Steady gas phase, Homogeneous One-Dimensional condensed phase). This paper focuses on the effect of the condensed phase on the transient burning of solid propellants by showing the effect of temperature dependent thermal properties, phase transitions and chemical reactions in the solid phase. Nonlinear effects are conserved, as governing equations are solved numerically.

### NOMENCLATURE

$A$	frequency factor [1/s]	$\epsilon$	heat release rate [W/m <sup>3</sup> ]
$c$	specific heat [J/kgK]	$\rho$	density [kg/m <sup>3</sup> ]
$E$	activation energy [J/mole]	$\tau$	nondimensional time
$k$	thermal conductivity [W/mK]		
$n$	integer 0, 1, 2, ...	<i>Subscripts and superscripts:</i>	
$p$	pressure [Pa]	$c$	condensed phase
$Q$	heat release [J/kg]	$g$	gas phase
$R$	universal gas constant [J/molK]	$m$	melting of AP
$R_p$	pressure driven response function	$s$	surface
$r_b$	propellant regression rate [m/s]	$tra$	crystallographic transition of AP
$T$	temperature [K]	0	initial
$t$	time [s]	+	on the positive side of
$x$	space coordinate [m]	-	on the negative side of
$\alpha$	thermal diffusivity [m <sup>2</sup> /s]		

### INTRODUCTION

In the past a lot of effort has been put into the development of models for transient burning of solid propellants. With the exception of a few models, most models share the same basic assumptions, of which the most important are: homogeneous propellant, quasi-steady gas phase and neglect of solid phase reactions. Several researchers suggested that the existing models could be improved by accounting for the chemical reactions in the solid phase [1] [2]. For this reason, an extended model for the solid phase of ammonium perchlorate (AP) composites was

developed within the flame description approach, similar to the transient burning models developed by DeLuca and coworkers [3]. The model presented here, accounts for the solid phase reactions, the melting of AP and the crystalline transformation of an orthorhombic to a cubic state of AP. The latter causes an abrupt change of thermal properties at the transitions.

### THE MODEL

Fig. 1 shows the model considered. Deep in the propellant solid phase, the propellant has its initial temperature  $T_0$ . Due to the conductive heating by the gas phase, and chemical reactions in the solid, the temperature in the solid increases up to the surface temperature  $T_s$ . At the surface gasification of the solid takes place. Above the surface, the decomposition products of oxidizer and fuel react, until the gases reach the flame temperature  $T_f$ .

When the condensed phase is assumed to move with the burning rate  $r_b$  to the right, the surface will remain at a fixed position ( $x = 0$ ). For this situation the energy equation of the condensed phase is given by the following parabolic partial differential equation [3]:

$$c_c \rho_c \left[ \frac{\partial T}{\partial t} + r_b \frac{\partial T}{\partial x} \right] = \frac{\partial}{\partial x} \left[ k_c \frac{\partial T}{\partial x} \right] + Q_c \epsilon_c(T), \quad \text{for } -\infty < x < 0 \quad (1)$$

where  $c_c$  is the heat capacity of the condensed phase,  $\rho_c$  is the density of the condensed phase,  $k_c$  is the thermal conductivity of the propellant,  $T$  is the temperature,  $t$  and  $x$  are the time and space coordinate respectively, and  $Q_c \epsilon_c$  is the heat release distribution due to chemical reactions in the solid phase. The regression rate is calculated from a zero-th order Arrhenius law. This equation is nonlinear because of the terms  $r_b \partial T / \partial x$ , and  $Q_c \epsilon_c(T)$ .

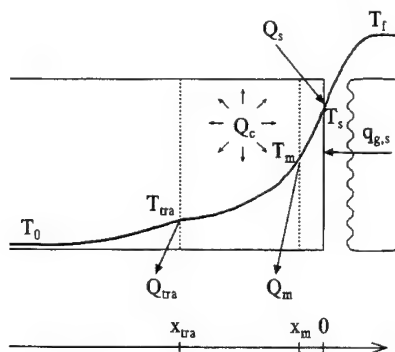


Figure 1. Schematic of the temperature distribution in an AP-propellant.

On the cold boundary side,  $x \rightarrow -\infty$ , the boundary condition is given by

$$T(x \rightarrow -\infty, t) = T_0 \quad (2)$$

From an energy balance at the burning surface, the boundary condition at  $x = 0$  is found

$$\left[ k_c \frac{\partial T}{\partial x} \right]_{0-} = q_{g,s} + r_b Q_s \quad (3)$$

where  $q_{g,s}$  is the heat flux from the gaseous phase to the surface of the propellant. At the surface, heat is released which is described by the term  $Q_s$ . In most models the surface heat release accounts for the total heat released in the condensed phase which is then assumed to be



collapsed at the surface. This allows for simple calculations, because this term does not appear in the energy equation but in its boundary conditions. In the model presented here, the surface heat release  $Q_s$ , and the condensed phase heat release  $Q_c$  are considered both.

Because of the presence of AP in the solid, two phase transitions take place. The first one is a crystallographic transition (at  $x = x_{tra}$ ) and the second one is the melting of AP (at  $x = x_m$ ). These transitions require energy, and act as heat sinks in the solid phase ( $Q_{tra}$  and  $Q_m$  respectively).

Apart from the phase transitions, the temperature dependence of the thermal conductivity and heat capacity is also accounted for. The thermal conductivity of AP, e.g., is reduced by a factor of three during the transition from orthorhombic to cubic AP as is illustrated by Fig. 2. The temperature dependent thermal properties used for the calculations were obtained from Ref.[4]. The gas phase is considered to be quasi-steady, which holds for low frequencies and low pressure. The heat feedback from the gaseous phase to the condensed phase ( $q_{g,s}$ ) is calculated using the  $\alpha\beta\gamma$ -model with  $\alpha = 0$ ,  $\beta = 1$ , and  $\gamma = 0, 1, 2, \dots$  [3]. It is assumed further that this conductive heat transport is only pressure dependent. From these assumptions it becomes clear that the gas phase is modelled very crude, however, it is the objective of this study to analyze the effects of the processes in the condensed phase on the transient burning.

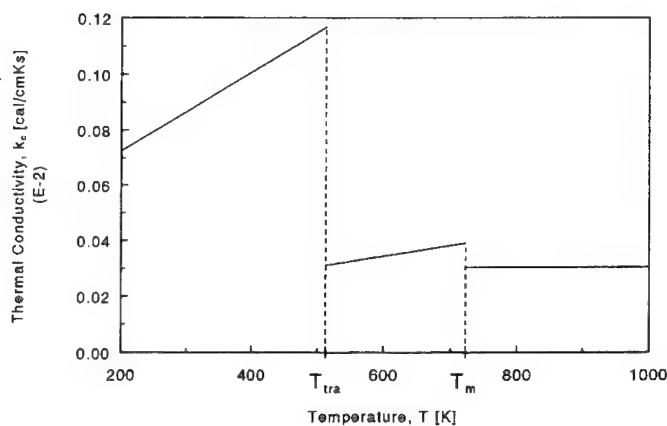


Figure 2. Thermal conductivity of a typical nonaluminized AP-propellant.

The heat release distribution function  $\epsilon_c$  may be assumed to be exponentially dependent on the temperature in the condensed phase

$$Q_c \epsilon_c(T) = A_c Q_c e^{-E_c/RT} \quad (4)$$

where  $E_c$  is the activation energy of the condensed phase reactions,  $R$  is the universal gas constant, and the pre-exponential factor  $A_c$  can be deduced from the normalization condition [3]

$$\int_{-\infty}^0 \epsilon_c(T(x)) dx = 1 \quad (5)$$

The thermophysical properties of the propellant considered are given in Table 1.

## NUMERICAL SOLUTION

The equations are solved numerically by the use of an implicit finite difference method similar to that as described in Ref.[5]. In essence this is a modified Crank-Nicholson method, with an

TABLE 1  
Properties of the AP:HTPB 86:14 propellant used as reference propellant.  
All heat releases positive if exothermic.

	Symbol	Value	Unit
AP weight fraction		86	%
AP crystalline transition temperature	$T_{tra}$	513	K
AP melting temperature	$T_m$	723	K
Condensed phase density	$\rho_c$	1.630	g/cm <sup>3</sup>
Gas specific heat	$c_g$	0.33	cal/g K
Gas thermal conductivity	$k_g$	$2.0 \cdot 10^{-4}$	cal/cm s K
$\alpha\beta\gamma$ -flame model parameters	$\alpha$	0	-
	$\beta$	0	-
	$\gamma$	0, 1, 2, 3, ...	-
Surface pyrolysis pressure exponent	$n_s$	0	-
Surface pyrolysis activation energy	$\bar{E}_s$	21000	cal/mole
Initial sample temperature	$T_a$	300	K
Reference pressure	$p_{ref}$	0.1013	MPa
Steady-state burning rate	$\bar{r}_b$	$1.074 \cdot (p/p_{ref})^{0.53}$	cm/s
Steady-state surface temperature	$\bar{T}_s$	$945.2 \cdot (p/p_{ref})^{0.045}$	K
Adiabatic flame temperature	$\bar{T}_f$	$2763 \cdot (p/p_{ref})^{0.019}$	K

improved stability of the time derivative by a weighted average of the points next to the point to be solved. Because of the steep gradients near the burning surface, and the very slowly varying temperature near the cold end, a scale transformation was applied. This transformation enlarges intervals near the surface, and intervals far away from the surface are reduced.

The finite difference equations were implemented in a FORTRAN-77 computer program. This program first calculates the steady-state solution, which serves as a starting point for the transient calculations. This steady solution is then perturbed by a prescribed time dependent (e.g. sinusoidal) pressure disturbance.

Unless noted otherwise, all calculations are performed at a pressure of 1.0 MPa.

## RESULTS

### Steady State Burning

Because of the dependence of the thermophysical properties on the temperature, the steady-state temperature distribution in the condensed phase is different from the analytical solution of Eq.(1) which holds for constant thermal properties, see Fig.3. Because of the lower thermal conductivity of the propellant at higher temperatures, less energy is conducted away from the surface, resulting in a steeper temperature profile in the condensed phase. When the latent heats of the phase transitions are introduced the profile becomes steeper, because of the condition

$$\left[ k_c \frac{\partial T}{\partial x} \right]_{x=x_{tra}^-} = \left[ k_c \frac{\partial T}{\partial x} \right]_{x=x_{tra}^+} + r_b Q_{tra} \quad (6)$$

at the crystallographic transition point, and analogous at the melting point. The melting heat of AP was not found in the open literature, and is approximated by that of potassium perchlorate [6]. The location of the crystallographic transition is found to be 13  $\mu\text{m}$  below the

surface, which agrees well with experiments of AP composite propellants, which yielded a value of  $18 \mu\text{m}$  [4].

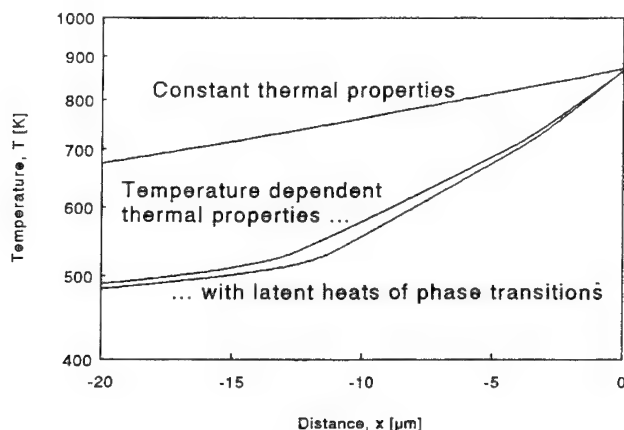


Figure 3. Steady-state temperature profile in the condensed phase for several situations.

### Transient Burning

In order to be able to calculate the transient burning of a solid rocket propellant, it is necessary that the propellant parameters are known accurately. The value of the total subsurface heat release by chemical reactions ( $Q_s + Q_c$ ) is a quantity which is difficult to measure. It was shown that the surface heat release  $Q_s$  is a very sensitive parameter for steady state burning [7], as well as for transient burning for which this sensitivity can be shown easily by linearized calculations. For these linearized calculations the maximum of the pressure driven response function is increased by a factor 2.5, when the surface heat release is increased from 100 to 125 cal/g [3]. It will be shown here that apart from the value of the total heat release in the condensed phase, the *distribution* of this heat release is also an important aspect.

To verify the effect of the distribution of condensed phase reactions on the transient burning of solid propellants, the response of the propellant on a pressurization was calculated. The calculations started from a steady state at  $t = 0$ , followed by an increase in pressure according to

$$p(\tau) = \bar{p} + \Delta p (1 - e^{-\tau}) \quad (7)$$

where  $\tau$  is the nondimensional time, defined as  $\tau = t/t_{ref} = t/(\alpha_c/r_{b,ref}^2)$ . For these calculations  $\bar{p} = \Delta p = 1 \text{ MPa}$ . The total heat released by chemical reactions is assumed to be 150 cal/g. This value is somewhat larger than the realistic values (100...125 cal/g), but was chosen because it clearly demonstrates the effect of the different distributions.

Fig.4 contains several typical results. Curve 1 shows the fluctuating surface temperature for a propellant with all the chemical reactions collapsed to the surface ( $Q_s \neq 0, Q_c = 0$ ). Curve 2 is obtained from calculations with all chemical reactivity in the condensed phase ( $Q_s = 0, Q_c \neq 0$ ). For these calculations a high activation energy has been used (28.9 kcal/mole, according to Ref.[8]), i.e. the heat is released in a thin layer close to the surface, and falls to exponentially small values, even at short distances from the surface. As expected for this high value of the activation energy the response is similar, showing a damped response. This shape can be attributed to the increase in burning rate during the increase in pressure. At higher burning rates the thermal zone in the condensed phase is smaller. Because the temperature distribution is in its steady state at  $t = 0$ , the layer is too thick during the transition. Thus a preheated zone exists, which burns away fast (the maximum in the response). After this period almost no thermal layer exists, and it takes time to build a new thermal layer by heat conduction from the gaseous

phase (minimum in the response). Note that the response of the propellant resembles a typical response of an underdamped second order mass-spring-dashpot system on a step response. This analogy can be shown by approximation of the partial differential equation (1) by an ordinary differential equation [3]. Finally, curve 3 shows the results of calculations with a much lower activation energy of 10 kcal/mole. Because the reaction rate is less temperature sensitive for the low activation energy situation, the heat is released more gradually in the subsurface zone, this results in a broader thermal zone.

The three responses show that even for a narrow chemical zone, the approximation of this zone by a heat release at the surface is not correct (difference between curves 1 and 2). For real propellants the reaction zone is spatially distributed over a wider thermal layer, which exhibits a different response. These calculations illustrate that the transient burning of solid rocket propellants is largely affected by a spatial distribution of the heat release due to chemical reactions.

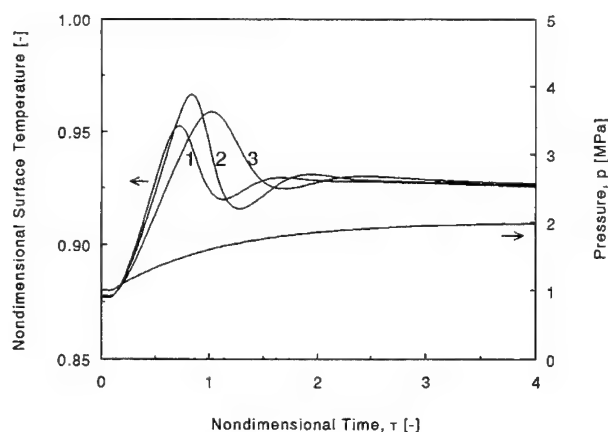


Figure 4. Surface temperature transient during an exponential increase of pressure for several different condensed phase heat release distributions; 1. surface reactions, 2. condensed phase reactions, high activation energy, 3. condensed phase reactions, low activation energy.

For different perturbing signals the response of the three situations mentioned above might be reversed. This is because the response of the system is a function of the spectrum of the applied signal. The effect of the frequency on the response of the propellant is expressed by the response function. In the next section these response functions will be discussed. From these results it will become clear that the response of the propellant to an external disturbance is frequency dependent, and that the response is therefore dependent on the perturbing signal.

### Response Functions

From the transient calculations the response function of the propellant can be calculated. The pressure driven response function is computed by perturbing the steady state with a sinusoidal fluctuating pressure, with an amplitude of 10% of its mean value. After a few cycles a situation of dynamic equilibrium develops. Fig. 5 is an example of such a calculation. The relative change in burning rate,  $\bar{r}_b$ , during this equilibrium divided by the relative change in pressure defines the pressure coupled response function, according to:

$$R_p = \frac{\bar{r}_b' / \bar{r}_b}{p' / \bar{p}} \quad (8)$$

To verify the numerical calculations under limit conditions, a comparison has been made with the familiar linearized analysis [1]. Fig. 6 is an example of such a calculation. For these calculations

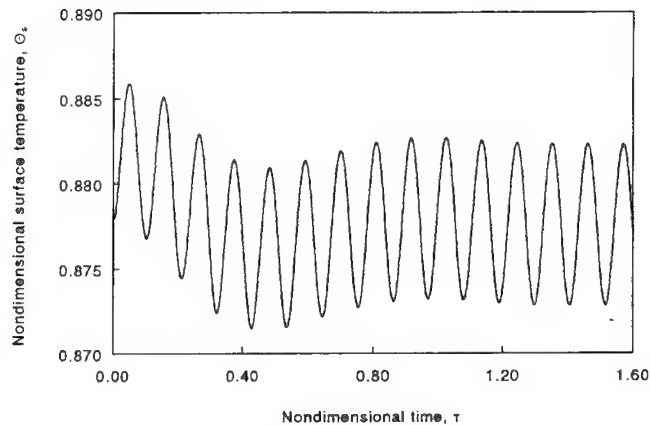


Figure 5. Surface temperature during a sinusoidal pressure transient. After a few initial cycles a situation of dynamic equilibrium develops.

the condensed phase is assumed to be inert, with no phase transitions, and constant thermal properties. It is seen that the response function for a disturbance amplitude of 10% predicts a larger response than that for an amplitude of 1%. So even for the usual  $\Delta p/\bar{p} = 0.1$ , nonlinearity plays an important role. This is an important restriction when pressure coupled experiments are compared with linearized analysis. From an experimental point of view, large disturbance amplitudes are desirable for acceptable signal to noise ratios.

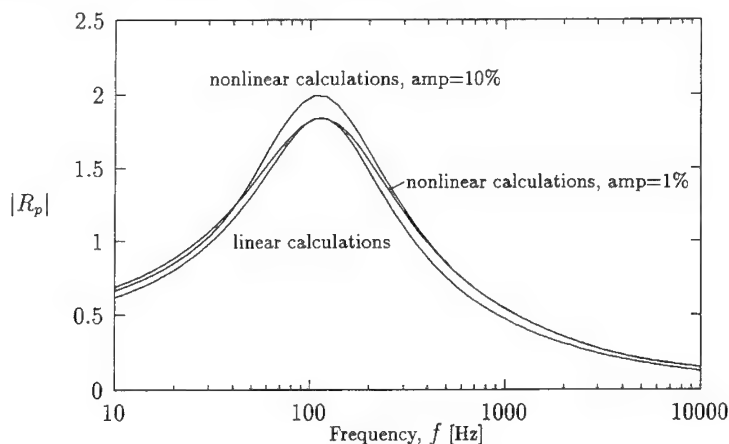


Figure 6. Nonlinear pressure driven response function versus linear calculated response function (constant thermal properties).

The nonlinearity from Fig. 6 is confirmed by the Fast Fourier Transform (FFT) calculations of the propellant response on a sinusoidal pressure disturbance with a frequency of 500 Hz, see Fig. 7. This figure demonstrates that a second harmonic is introduced for an amplitude of 10% of the mean signal. For a larger amplitude even more harmonics appear.

The effect of the temperature dependent properties on the pressure driven response functions is shown in Fig. 8. As seen from Fig. 3, the thermal layer thickness of the analytical temper-

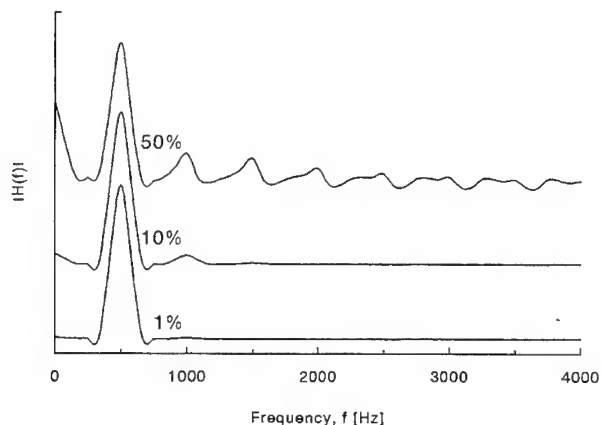


Figure 7. Effect of the amplitude of a 500 Hz sinusoidal disturbance on the FFT-spectrum. For perturbing amplitudes larger than 10% harmonics appear.

ature profile is much larger than that of the other two profiles because of the reduced thermal conductivity of AP. This thermal layer stores information of foregoing disturbances. Because of the smaller affected zone of the condensed phase for a propellant with temperature dependent thermal properties, the response is smaller. This smaller zone has a higher resonance frequency, expressed by the shifting of the maximum of the response function to higher frequencies.

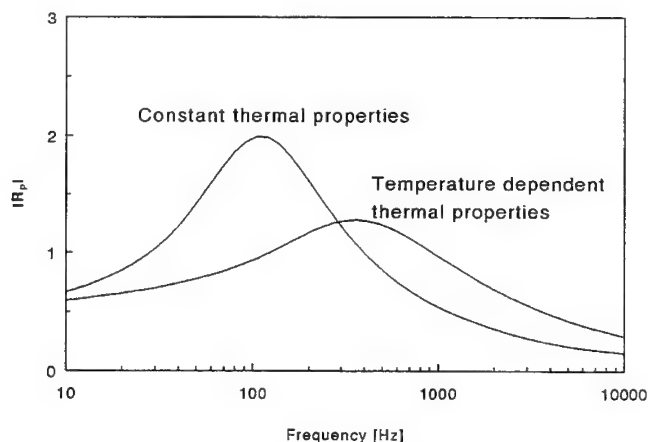


Figure 8. Effect of temperature dependent properties on the pressure response function.

The effect of phase changes of AP are not only found in the thermal properties, but coupled with it are the latent heats of transition,  $Q_{tra}$  and  $Q_m$ . As seen from Fig. 3, this leads to a smaller thermal layer, with an accompanying higher resonance frequency. This is confirmed by the calculations of Fig. 9. The propellant for which phase transitions are accounted for has a smaller maximum of the response function, indicating that this propellant is more stable, as compared to the propellant for which the latent heats are assumed to be zero.

Fig. 10 shows the effect of the heat release distribution on the response function, for the same cases of Fig. 4, however, now the more realistic heat release of 125 cal/g has been used. It is seen

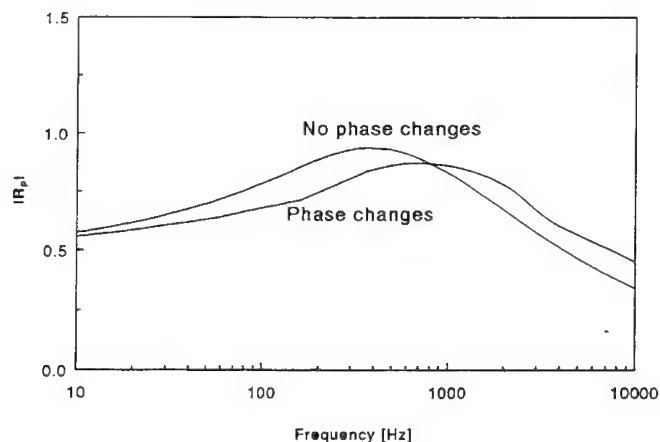


Figure 9. Effect of phase changes on the pressure response function.

that the condensed phase reactions lower the maximum response. So, when subsurface reactions are approximated by surface reactions, the propellants appears to be less stable. The maxima of the response function decrease and shift to lower frequencies, because the thermal layer is larger for subsurface reactions.

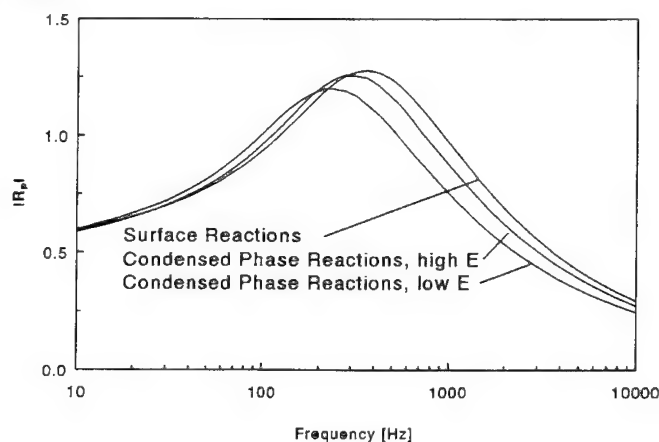


Figure 10. Effect of the heat release distribution on the pressure response function.

Similar effects were found when the condensed phase heat release was distributed as

$$Q_c \epsilon_c(X) = \begin{cases} 0 & \text{if } x < x_{tra} \\ A_c Q_c (x - x_{tra})^n & \text{if } x_{tra} < x < 0 \end{cases} \quad (9)$$

where  $n$  an integer,  $n = 0, 1, 2, \dots$ . For  $n = 0$  a constant heat release is found. For  $n > 0$  a heat release which increases towards the burning surface is found. In this definition an implicit temperature dependence is present because  $x_{tra}$  is defined as  $T(x_{tra}) = T_{tra}$ . Fig. 11 shows calculations for situations where all heat is released in the condensed phase. For  $n \rightarrow \infty$  the surface heat release situation is recovered. As in the previous calculations, situations with the energy release close the the surface have the highest response, occurring at the highest resonance frequency. So a large heat release close to the surface results in less intrinsic stability. Based

on linearized calculations, DeLuca et al. derived the same conclusions for an exothermic and endothermic heat release of 20 cal/g [9].

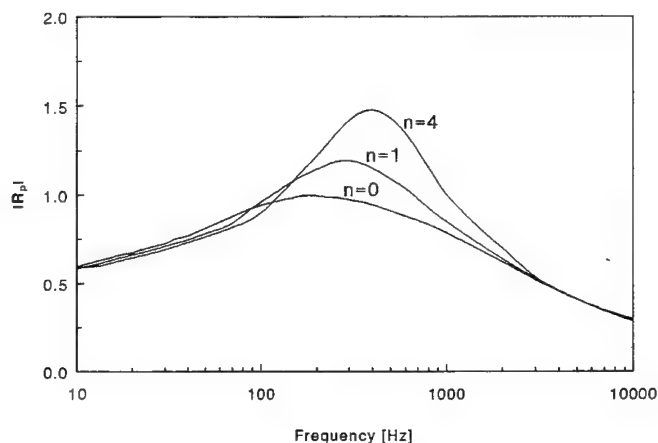


Figure 11. Effect of heat release distribution on the pressure coupled response function. By collapsing the condensed phase reactions to the surface (increase of parameter  $n$ ) the intrinsic stability decreases, and the resonance peak shifts towards higher frequencies.

## CONCLUSIONS

- The approximation of constant thermal properties is too crude to predict the response of a propellant accurately.
- Phase changes in the condensed phase yields a more stable propellant, lowering the maximum of the response function and shifting it to higher frequencies.
- Solid phase reactions have a similar effect on the transient burning as the surface heat release. Subsurface reactions demonstrate an decrease in maximum and resonance frequency for an increase in chemical reaction zone width.
- For small disturbance amplitudes of 1%, the response of the propellant is linear, for 10% disturbances the nonlinearity cannot be neglected anymore, and differences can be found from small amplitude calculations.

## REFERENCES

- [1] Zarko, V.E., Simonenko, V.N. and Kiskin, A.B., Radiation-Driven Transient Burning: Experimental Results, in *Nonsteady Burning and Combustion Stability of Solid Propellants*, edited by DeLuca, L., Price E.W. and Summerfield, M., AIAA Progress in Astronautics and Aeronautics Vol. 143, Chapter 10, 1992



- [2] **Son, S.F. and Brewster M.Q.**, Unsteady Combustion of Homogeneous Energetic Solids Using the Laser-Recoil Method, *Combustion and Flame*, 100, 283-291, 1995
- [3] **DeLuca, L.**, Theory of Nonsteady Burning and Combustion Stability by Flame Models, in *Nonsteady Burning and Combustion Stability of Solid Propellants*, edited by Deluca, L., Price E.W. and Summerfield, M., AIAA Progress in Astronautics and Aeronautics Vol. 143, Chapter 14, 1992.
- [4] **Zanotti, C. and Volpi A.**, Measuring Thermodynamic Properties of Burning Propellants, in *Nonsteady Burning and Combustion Stability of Solid Propellants*, edited by Deluca, L., Price, E.W. and Summerfield, M., AIAA Progress in Astronautics and Aeronautics Vol. 143, Chapter 5, 1992.
- [5] **Galfetti, L., Riva, G. and Bruno, C.**, Numerical Computations of Solid-Propellant Nonsteady Burning in Open or Confined Volumes, in *Nonsteady Burning and Combustion Stability of Solid Propellants*, edited by Deluca, L., Price E.W. and Summerfield, M., AIAA Progress in Astronautics and Aeronautics Vol. 143, Chapter 16, 1992.
- [6] **Guirao C. and Williams F.A.**, A Model for Ammonium Perchlorate Deflagration between 20 and 100 atm, *AIAA Journal*, 9, 1345-1356, 1971.
- [7] **Hermance, C.E.**, A Model of Composite Propellant Combustion Including Surface Heterogeneity and Heat Generation, *AIAA Journal*, 4, 1629-1637, 1966.
- [8] **Kumar, R.N. and Culick, F.E.C.**, Role of Condensed Phase Details in the Oscillatory Combustion of Composite Propellants, *AIAA Paper*, 73-218, 1973.
- [9] **DeLuca, L., Di Silvestro, R. and Cozzi, F.**, Intrinsic Combustion Instability of Solid Energetic Materials, *J. Propulsion and Power*, 11, 804-815, 1995.

## THE MODEL OF POROUS CARBONIZED PARTICLE COMBUSTION

V.M.Gremyachkin

Head of the laboratory of the Institute for Problems in Mechanics,  
Russian Academy of Sciences  
(101, ave. Vernadskii, Moscow 117526, Russia)

### Abstract

The theoretical model of porous carbonized particle combustion in air is discussed. The model considers equations of heat and mass transfer in the gas phase and inside porous particles. The heat flux from the particles surface to the wall of the furnace is taken into account. The different regimes of particle combustion are investigated. It is shown that the gas-phase regime of particles combustion, in which the heterogeneous chemical reaction of carbon interaction with oxygen is absent and the homogeneous chemical reaction occurs above particle surface, is realized when the furnace walls temperature is rather high. In this regime of the particle combustion the heterogeneous chemical reaction of carbon interaction with carbon dioxide takes place inside particle, because the oxygen is almost totally supplied in homogeneous chemical reaction above the particle surface. For lower furnace wall temperature the kinetic regime of particle combustion, in which the heterogeneous chemical reaction of carbon interaction with oxygen as well as with carbon dioxide takes place inside porous particle, is observed. In the kinetic regime of the particle combustion the rate of the particle burning out is increased with furnace wall temperature increasing and that practically achieves the maximum particle burning out rate in the diffusing regime of particle combustion. In the gas-phase regime of the particle combustion the rate of the particle burning out is smoothly increased achieving the maximum rate of the particle combustion at the very high furnace wall temperature. Thus, there is some crisis of the particle burning out rate, when the rate of the particle burning out is very sharply fallen down in the narrow range of the furnace wall temperature (from 1300 K to 1400 K for particle having size about  $100\text{ }\mu\text{m}$  and burning out in air).

### Main Equations and Solutions

The process of the carbon particle interaction with oxygen is kinetic process up to rather high temperature.<sup>1-3</sup> Thus, the determination of chemical reaction kinetics taking place in process of carbon particle interaction with oxygen is the basis for the development of the theory of carbon particle combustion.

Four chemical reactions can take place in process of carbon combustion:



The kinetics of gas-phase chemical reaction have been determined:<sup>4</sup>

$$\Phi_g = 1.05710^{-5} \exp(-27544/T) [\text{CO}] [\text{O}_2]^{0.5} [\text{H}_2\text{O}]^{0.25} \quad (1)$$

where concentrations are determined in [moll/liter].

It may be considered that the kinetics of the heterogeneous chemical reaction of carbon interaction with carbon dioxide have been rather well determined too.<sup>5</sup>

$$\Phi_c = 740 \exp(-16748/T)[\text{CO}_2] \quad (2)$$

As regards, the kinetics of the heterogeneous chemical reactions of carbon interaction with oxygen that the results receiving in the different experiments are very contradictory. Besides, it is necessary to determine the correlation of the rate of the carbon oxide and the carbon dioxide formation in the products of the chemical reaction of carbon with oxygen. The absence of the kinetics of the heterogeneous chemical reaction of carbon interaction with oxygen is the main hindrance for development of the theory of the porous carbonized particle combustion and gasification.

Let us consider the equations which determine the process of porous carbon particle interaction with air in a furnace with wall heated. These conditions are the condition in what the experiments are as a rule realized. Such equations are first of all the equations of carbon atoms and oxygen atoms and heat conservation:

$$\text{div} \sum \frac{m_j I_j}{\mu_j} = \frac{\Phi S}{\mu_c} \quad (3)$$

$$\text{div} \sum \frac{n_j I_j}{\mu_j} = 0 \quad (4)$$

$$\text{div}(\sum I_j h_j + I_h) = \Phi S h_c - I_R \delta(r - R) \quad (5)$$

Here  $I_j$ —are the flows of gaseous substances with molecular mass  $\mu_j$ , ( $j = 1$  corresponds to  $\text{CO}_2$ , 2— $\text{CO}$ , 3— $\text{O}_2$ ) and  $I_h$  is the heat flux;  $\Phi S$  is the summary rate of carbon consumption in the heterogeneous chemical reaction per unit of the volume inside particle;  $I_R = \sigma(T_s^4 - T_w^4)$  is the heat flux by radiation from the particle surface to furnace wall;  $h_j$  и  $h_c$  are the enthalpy of the of gaseous substances formation and solid carbon,  $m_j$  и  $n_j$  are the numbers of the carbon atoms and oxygen atoms in the molecular of the substance  $\text{C}_{m_j}\text{O}_{n_j}$ .

The next equations may be also considered:

the equation for the velocity alteration of the mass gas

$$\text{div}(\varepsilon \rho u) = \Phi S \quad (6)$$

the condition of sum of the relative concentration, including the inert gas, equality to unit

$$z_i + \sum z_j = 1 \quad (7)$$

and the equation for pressure alteration inside particle, as the flux of the products of the heterogeneous chemical reaction inside porous medium is connected with gradient pressure by Dapcy's law

$$\varepsilon u = -\frac{k}{\mu} \text{grad} P \quad (8)$$

For solution of the task it is necessary to consider the additional equation which includes the kinetics of the homogeneous and heterogeneous chemical reactions. Such equation may be the equation of oxygen diffusion

$$\text{div} I_3 = -\left(\frac{\mu_3}{\mu_c} \Phi_{o1} S + \frac{\mu_3}{2\mu_c} \Phi_{o2} S + \frac{\mu_3}{2\mu_1} \Phi_g\right) \quad (9)$$

where  $\Phi_{o1}$  is the rate of carbon consumption in reaction with oxygen when the carbon dioxide is formed, and  $\Phi_{o2}$ —when the carbon oxide is formed

The system of the equations (3)–(9) may be solved with boundary conditions:

$$\begin{aligned} r = 0, \quad u = 0, \quad I_j = 0, \quad I_h = 0; \\ r = \infty, \quad z_j = z_j^0, \quad T = T_0 \end{aligned} \quad (10)$$

if the kinetics of the all heterogeneous and homogeneous chemical reactions are determined.

Excluding the rate of carbon consumption  $\Phi$  from the equations (3) и (6) and integrating the equations (3)–(5) on coordinate with boundary conditions in the particle center, we receive the correlation between fluxes of the gaseous substances taking into account that the enthalpy of the solid carbon is zero

$$\sum \frac{m_j I_j}{\mu_j} = \frac{m}{\mu_c} \quad (11)$$

$$\sum \frac{n_j I_j}{\mu_j} = 0 \quad (12)$$

$$\sum I_j h_j + I_h = -I_R R^2 \theta(r - R) \quad (13)$$

where  $m = \varepsilon \rho u$ ,  $\theta(r - R)$  is the function which is equaled to zero at  $r < R$  and unit at  $r \geq R$ .

The expressions for fluxes of gaseous substances may be written in form

$$I_j = m z_j - \varepsilon \rho D \text{grad} z_j, \quad I_h = m c T - [\lambda_g \varepsilon + \lambda_c (1 - \varepsilon)] \text{grad} T$$

where  $\lambda_g$  и  $\lambda_c$  are coefficients of heat conduction in the gas and in the solid substances of the particle, correspondingly.

### The kinetic regime of the particle combustion.

Let us consider the solution of the equation in the gas phase where the heterogeneous chemical reaction is absent. Substituting the expressions for substances fluxes in the equations (11)–(13), and assuming that the criteria Lewis  $Le = \lambda / \rho c D = 1$  in the gas, after integrating the equations (11)–(13) with boundary conditions in the ambient gas, we receive the next expressions:

$$\sum \frac{m_j z_j}{\mu_j} = e^{-\eta} \left( \sum \frac{m_j z_j^0}{\mu_j} + \frac{1}{\mu_c} \right) - \frac{1}{\mu_c} \quad (14)$$

$$\sum \frac{n_j z_j}{\mu_j} = e^{-\eta} \sum \frac{n_j z_j^0}{\mu_j} \quad (15)$$

$$\begin{aligned} \sum \left( \frac{z_j}{\mu_j} [H_j + (C_j - C_i \frac{\mu_j}{\mu_i}) T] + C_i T \right) = \\ = e^{-\eta} \left\{ \sum \frac{z_j^0}{\mu_j} [H_j + (C_j - C_i \frac{\mu_j}{\mu_i}) T_0] + C_i T_0 + \frac{I_R}{m_g} \right\} - \frac{I_R}{m_g} \end{aligned} \quad (16)$$

where  $H_j$  и  $C_j$  are the enthalpies and the heat capacities on the molar of a substances and  $m_g$  is the mass flux of the gas at the particle surface and

$$\eta = \int_r^\infty \frac{m}{\varepsilon \rho D} dr = \frac{m_g R}{\varepsilon \rho D} \frac{R}{r} = \eta_0 \frac{R}{r}$$

in gas phase above particle surface.

The system of the equations (14)–(16), (9) determines the distributions of the temperature and the concentrations on the coordinate in gas phase above particle surface if the temperature and gas composition at the particle surface are known. If  $r = R$ ,  $T = T_s$  and  $\eta = \eta_0$  in the equations (14)–(16) that the system equations receiving determines the dependence the composition of

gas phase at the particle surface on the particle temperature and on the parameter  $\eta_0$ , what determines the particle burning out rate.

The results of the experimental investigations of carbonized particle combustion are as a rule expressed in form of the particle burning out rate dependence on the particle surface temperature and on the ambient oxygen concentration. The dependence most known and utilized in the last years is the dependence <sup>6</sup>

$$m_g = 7.0 \exp(-9908/T_s)(z_3^0)^{1/2} \quad (17)$$

If such dependence of the particle burning out rate on the particle temperature is taken into account that the dependence of the gas phase composition at the particle surface may be determined on the particle surface temperature only. It is necessary to mark that the particle surface temperature must be simply determined if the ambient temperature and gas composition and furnace wall temperature are fixed. In the experiments the alteration of the particle temperature was connected with alteration of the ambient particle temperature and the furnace wall temperature. For determination of the correlation between particle surface temperature and furnace wall temperature it is necessary to consider the processes inside porous particle. Such consideration is impossible if the kinetics of heterogeneous chemical reaction of carbon with oxygen is unknown. Nevertheless, the solution of the equations (14)–(17) for ambient gas composition (air) and for particle diameter about  $100 \mu\text{m}$  may be only found for furnace wall temperature  $T_w$  and ambient gas temperature  $T_\infty = T_w$  below 1300 K. It is first of all connected with equality of the oxygen concentration to zero at the particle surface and with the achievement of maximum rate of particle combustion near the rate of particle combustion in the diffusing regime ( $\eta_0 = 0.1599$ ) where the rates of all chemical reactions are infinite.<sup>7</sup>

The concentration of the oxygen is near the ambient concentration at the low furnace wall temperature and that is decreasing with the furnace wall temperature increasing and that equals to zero at the limit of the solution existence. It is connected with more extensive consumption of oxygen in the gas phase chemical reaction above particle surface. The temperature of the particle surface achieves the value a little more than 1800 K at the limit of the solution existence.

### The gas-phase regime of the particle combustion

On the further increasing of the furnace wall temperature the oxygen does not achieve the particle surface and the heterogeneous chemical reactions of carbon with oxygen do not take place inside porous particle. In this case the heterogeneous chemical reaction of carbon interaction with carbon dioxide takes only place inside porous particle. This regime of particle combustion may be considered in the theory as the kinetics of the reaction of carbon with carbon dioxide is known.

The equation describing the process of heterogeneous interaction of carbon with carbon dioxide may be received from equations (6) и (9) and may be written in form

$$\frac{1}{\xi^2} \frac{d}{d\xi} \xi^2 \frac{d\eta}{d\xi} = -W_c \quad (18)$$

where  $W_c = \Phi_c S R^2 / \varepsilon \rho D$  and  $\xi = r/R$ .

The boundary conditions for this equation are:

$$\xi = 0, \quad \frac{d\eta}{d\xi} = 0; \quad \xi = 1, \quad \eta = \eta_0, \quad \frac{d\eta}{d\xi} = \eta_0 \quad (19)$$

Besides the equations (14)–(15) the additional equation

$$= e^{-\eta} \left\{ \sum_j \frac{z_j^0}{\mu_j} [H_j + (C_j - C_i \frac{\mu_j}{\mu_i}) T_0] + C_i T_0 + \frac{I_R}{m_g} (1 - e^{\eta_0}) \right\}, \quad (20)$$

which is received in the assumption that the heat flux in the solid porous media is negligible in comparison with flux of the full enthalpy in gas, must be considered. In these equations the oxygen concentration is zero. Thus the equations (14)–(15), (20) determine the gas composition and the gas temperature in dependence on function  $\eta$ , and the dependence of the function  $\eta$  on coordinate  $\xi$  is determined from the solution of the equation (18) with boundary conditions (19). Besides the value of parameter  $\eta_0$  may be determined from the solution of the equation (18) also as the number of the boundary conditions (19) are more than two.

In case of molecular regime of flow in the particle porous media the function  $\eta$  does not depend on the media porosity while in the regime of the Knudsen's flow, when  $D \sim \varepsilon^2$ , the dependence of this function on porosity is necessary to take into account. Besides, the dependence of the porosity on coordinate inside particle is necessary to consider in common case as the carbon inside particle is consumed nonuniformly [6]. Nevertheless, here we shall assume that the molecular regime of flow inside particle takes place and the porosity  $\varepsilon = 0.55$  does not depend on coordinate.

The dependence of function  $\eta$  on coordinate  $\xi$  is determined from the task (19)–(21). This task determines the value  $\eta_0$  what is the rate of particle combustion. The dependence of the rate of the chemical reaction of carbon interaction with carbon dioxide (1) is utilized and the dependence of the temperature, pressure and gas composition on function  $\eta$  is determined from the solution of the system equations (14)–(17), where the oxygen concentration is zero, what is valid for combustion regime considering. The solution of this task may be only received for the furnace wall temperature higher 1400 K.

## Results and Discussions

The dependence of the particle combustion rate on the particle temperature for particle diameter near to  $100 \mu\text{m}$  and burning out in air is shown in the Figure. 1. The curve 1 corresponds to kinetic regime of the particle combustion what is described by equation (17), but the curve 2 corresponds to gas-phase regime what is described by equations (14)–(15), (18)–(20). It may be seen that the rate of the particle combustion is sharply increased in the kinetic regime of the combustion attaching the maximum possible rate of the particle combustion in the diffusing regime ( $\eta_0 = 0.1599$ ). In the gas-phase regime the rate of the particle burning out is smoothly increased achieving the maximum rate of the particle combustion at the very high temperature. The minimum rate of the particle combustion in this regime is about half of the maximum particle combustion rate. Thus the very sharply decreasing of the particle combustion rate must be taken place in the very narrow range of the particle temperature. Such sharp decreasing of the particle combustion rate is connected with carbon consumption rate decreasing. In the kinetic regime the carbon is consumed as in the reaction of carbon with oxygen so in the reaction of carbon with carbon dioxide, but in the gas-phase regime the carbon is consumed in the chemical reaction of carbon with carbon dioxide only. It is necessary to mark that such sharp decreasing of the particle burning out rate was observed in the experiments where the dependence of time of the particle burning out on the particle size was investigated in the furnace with high temperature.<sup>8</sup>

For determination of the correlation between particle temperature and the furnace wall temperature it is necessary to consider the heterogeneous chemical reaction proceeding inside porous particle. It is hard to make in the kinetic regime as the kinetics of the heterogeneous chemical reaction of carbon interaction with oxygen is unknown. However, in the gas-phase regime it may be done as the heterogeneous reaction of carbon with oxygen is absent in this case and the kinetics of the heterogeneous reaction of carbon with carbon dioxide is known (1).

The dependence of the gas composition at the particle surface (curve 1 is the relived mass concentration of  $\text{CO}_2$ ; 2,  $\text{CO}$ ; 3,  $\text{O}_2$ ) and the particle surface temperature  $T_s$  (curve 4) and the rate of the particle combustion  $\eta_0$  (curve 5) on the furnace wall temperature  $T_w$  are received from the solution of the task (14)–(15), (18)–(20) and that is shown in the Figure 2 for particle having diameter about  $100 \mu\text{m}$  and burning out in air. Thus, the concentration of the oxygen at the particle surface is negligible when the furnace wall temperature is rather high but that is increased and the concentration of the carbon oxide is decreased achieving zero when the furnace wall temperature is decreased. It is the main reason why the solution of the task does

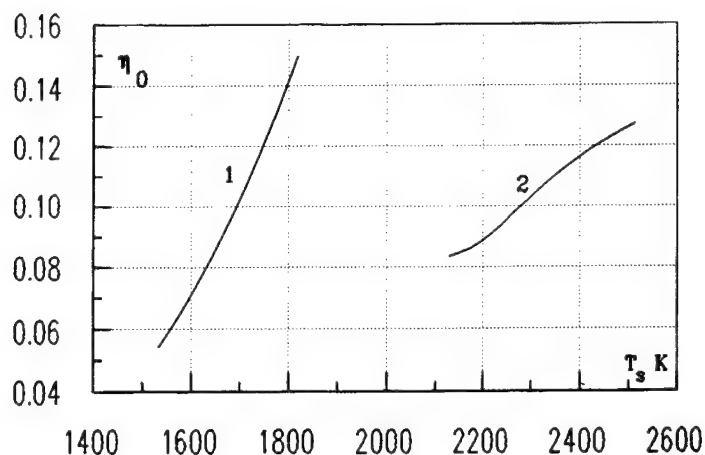


Figure 1. The dependence of the rate of the particle having size about  $100\mu\text{m}$  and burning out in air on particle surface temperature for kinetic regime of combustion (1) and for gas-phase regime (2).

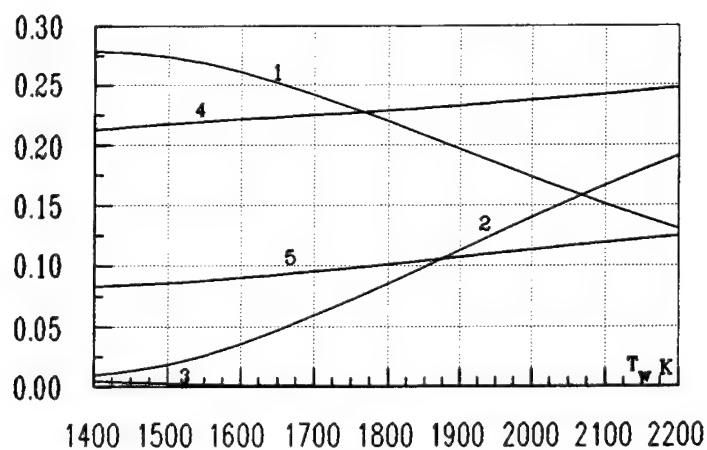


Figure 2. The dependence of the concentrations  $CO_2$  (curve 1),  $CO$  (2),  $O_2$  (3) at the particle surface and the particle surface temperature  $T_s$  (4) and the rate of the particle burning out  $\eta_0$  (5) on the furnace wall temperature  $T_w$  for particle having size  $100\mu\text{m}$  and burning out in air in the gas-phase regime.

not exist.

## Conclusion

The model of porous carbonized particle combustion is considered. The model is based on the consideration of heat and mass transfer equations in the gas phase above the particle surface and inside the porous particle.

Two regime of the particle combustion are considered: (1) the kinetic regime in what the

heterogeneous chemical reactions of carbon interaction with oxygen and with carbon dioxide take place inside porous particle and (2) the gas-phase regime in what the heterogeneous chemical reaction of carbon with carbon dioxide takes place inside porous particle only and the oxygen is practically totally consumed in the homogeneous chemical reaction over the particle surface.

The rate of the particle burning out is sharply increased in the kinetic regime and that achieves the value near the maximum possible rate of the particle combustion in diffusing regime where all rates of the chemical reactions are infinite. In the gas-phase regime of the particle combustion the rate of the particle burning out is smoothly increased from the minimum rate of the particle burning out what is approximately half of the maximum possible rate of the particle combustion to the maximum possible rate of the particle burning out. The transition from the kinetic regime to gas-phase regime of the particle combustion occurs at the furnace wall temperature from 1300 K to 1400 K for carbonized particle having size about 100  $\mu\text{m}$  and burning out in air.

Thus the crisis of the rate of the particle combustion when the rate of the particle burning out is sharply fallen down, must be observed. The reason of the such phenomenon is the decreasing of rate of the carbon consumption inside porous particle as in the kinetic regime the carbon consumes as in heterogeneous reaction of carbon with oxygen so with carbon dioxide but in the gas-phase regime the carbon consumes in the heterogeneous chemical reaction of carbon with carbon dioxide only.

## References

1. Predvoditelev A.S., Khitrin L.N., Tsukhanova O.A., et al. The carbon combustion, Moscow, AS USSR Press, 1949 (in Russian).
2. Golovina E.S., High-temperature combustion and gasification of carbon, Moscow, Energoatomisdat Press, 1984 (in Russian)
3. Laurendau N.M., Heterogeneous Kinetics of coal Gasification and Combustion, *Progress in Energy and Combustion Sciences*, 4, 221-270, 1978.
4. Lavrov N.V., Rosenfeld E.I., Khaustovich G.N., The processes of the fuel combustion and the defence of the ambient media, Moscow, Metallurgia Press, 1981 (in Russian).
5. Lee S., Angus J.C., Edwards R.V., Gardner N.C., Noncatalytic Coal Char Gasification, *AIChE Journal*, 30, 583-593, 1984.
6. Young B.C., Smith I.W., The Kinetics of Combustion of Petroleum Coke Particles at 1000 to 1800 K: the Reaction Order." *Eighteenth Symposium (International) on Combustion. The Combustion Institute, Pittsburgh*, 1249-1255, 1981.
7. Gremyachkin V.M., The Model of Coke Combustion and Gasification in a Mixture of Gaseous Reactances, *Combustion, Explosion and Shock Waves*, 30, 2-9, 1995.
8. Babiy V.I., Kuvaev U.F., The coal dust combustion and the calculation of the coal-dust torch, Moscow, Energoatomisdat Press, 1986 (in Russian).



# **NUMERICAL SIMULATION OF THE NONSTATIONARY SPATIAL GASDYNAMICS PROCESSES ACCOMPANYING THE PELLETIZED SOLID PROPELLANT COMBUSTION IN A GAS GENERATOR**

**Alexey M. Lipanov, Alexander N. Lukin, Ali V. Aliyev**

Institute of Applied Mechanics, Ural Branch of the Russian Academy of Sciences

222, Gorky Str., Izhevsk, Udmurt Republic, 426001, Russia

Tele.: +7-(3412)-752731; Fax: +7-(3412)-231713; E-Mail: lam@lam.ipm.udm.ru

**ABSTRACT:** In the present paper, the laws of sequential distribution of the parameters of nonstationary two-dimensional flows of the mixture of pelletized solid propellant (PSP) combustion products (CP) along the gas generator (GG) cavity is investigated numerically. For imitation of the exploitation conditions the GG is placed in an cylindrical imitation chamber. Two-dimensional gas-dynamic equations of motion of the CP mixture between the granulated elements (GE), are written in the axisymmetrical statement for the multicomponents biphasic mixture of ideal gases. A peculiarity of the model is that the physical processes accompanying the CP filtration through granular propellant are taken into account. Calculation of the solid phase temperature state and its non-stationary burning-out is carried out on the method, made up in accordance with the model of Prof. R.Ye.Sorkin of Russia. The heat problem is solved in each of gas-dynamics knots for a separately taken propellant pellet. The equations, describing the gas-dynamic processes, are solved numerically by the Large Particles Method, developed by Prof. Yu.M.Davydov of Russia, with using of a number of modifications. For the complex check-up of the developed mathematical model of physico-chemical processes, the numerical calculation results have been compared with the fire stand tests. The analysis of results of numerical investigations of laws of the physico-chemical processes evolution in the GG reveals that the flows patterns in the GG cavities are characterized by substantial inhomogeneity, increasing as the process develops and expressed temperature sensitivity. After the pelletized propellant complete ignition, the flow non-one-dimensionality degenerates gradually and parameters in the GG volume can be averaged. Using of two-dimensional gas-dynamic model opens a possibility for obtaining the information on processes proceeding in the GG at a new qualitative level, gives a more comprehensive idea about the physico-chemical processes essence and permits to abandon the use of a number of empirical relations.

## **INTRODUCTION**

Numerical investigation of the non-stationary spatial gasdynamics processes, accompanying the PSP combustion in the GG presents considerable interest for the wide class of technical devices.

As an examples of such GG it is possible to name the solid propellant gas generator, which is used for airbag, belt restraint systems or other means for safety ensuring in case of any transport crash or airbag dispersion system, which is used in new techniques for dispersing the submunition from the carrier vehicle (warhead).<sup>1,2</sup> For such GG a considerable dependence of technical characteristics and respectively the operational safety from passing quality of aggregate of physico-chemical processes is characteristic: the PSP heating-up and combustion, distribution of the gaseous reaction products along the GG volume, passing of aggregate of heterogeneous reactions with emission or absorption of energy, heat-mass exchange processes. There are a few theoretical models reported in the literature.<sup>3-8</sup> In comparison with works<sup>3,8</sup>, the more detailed investigation of spatial gasdynamics processes development laws in GG is presented below. The GG body is made from composite nonmetallic materials and is filled in by the PSP. The paper takes care with two-dimensional statement of intraballistic problems in the GG volume on the basis of Euler's equations.

### PROBLEM STATEMENT

Solution of the problem is carried out for one of the most widespread schemes of the GG.<sup>3</sup> A schematic drawing of a typical pyrotechnic GG, which having a parallel scheme shown in Figure 1.<sup>3</sup>

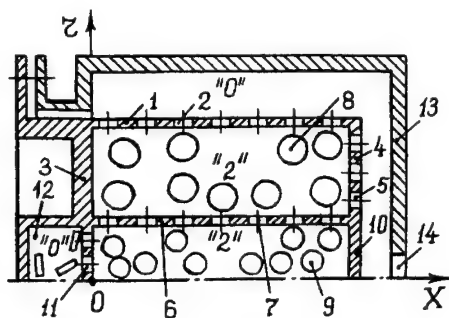


Figure 1. A schematic drawing of a typical pyrotechnic GG

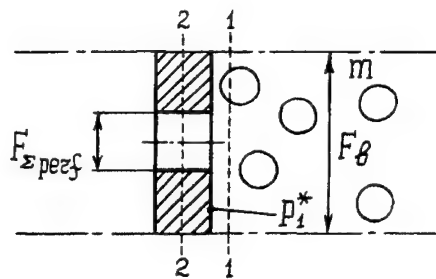


Figure 2. A schematic drawing of the GG perforated boundary

The GG consists of the main cylindrical channel (MC) 1 having uniform perforation 2 over the lateral surface. The left MC boundary 3 is deaf and in the right boundary 4 there is a uniform perforation 5. Whole perforation is hermetically sealed outside. The additional cylindrical channel (AC) 6 (an initial impulse amplifier) with uniform perforation 7 over the lateral surface is installed into the MC cavity 1, coaxially to MC. The GE 8,9 having the spherical form and pressed from the pyrotechnic mixture (PTM) are placed with the bulk density in the cavities of the channels 1, 6. The right AC boundary 10 is deaf, and the time-varying high-temperature gas flow, containing incandescent particles is supplied from initiator 12 equipped with a fast burning compound through left perforated boundary 11. Ratios of channels length to their diameters are more than one and preset to be equal to 1.2 - for MC, and 10 - for AC. The GG is installed in the imitation chamber (IC) 13, which intended for imitating service conditions, for example, of a free volume and geometrical sizes of any device. At the right end of the IC 13 there is hole 14

intended for exhausting the differential pressure up to the normal level. The process in the GG, and then in the IC is developed by the following way. From the initiator 12 CP arrive at AC 6, where they heating-up and ignite the PSP 9. From the AC 6 the CP arrive in the MC 1, where they heating-up and ignite the PSP 8. When the pressure in the MC 1 achieves the level, exceeds the destruction pressure of the hermetic sealing, occurs destruction of the hermetic sealing and the CP begin to arrive in the front volume of the IC (Figure 1).

### MATHEMATICAL MODEL

When constructing the mathematical model of physico-chemical processes proceeding in the GG and IC, the following assumptions system was accepted:

- cold gas originally occupied the pore space of the ducts, hot combustion products coming through the AC left boundary, into the estimated ranges, and CP of the PSP, all form the chemically non-reacting mixture the flow of which is nonstationary and follows the laws of flow of ideal gas;
- in CP mixture the condensed (c) particles can be present, the rate and the temperature of which coincide with the corresponding parameters of the gas;
- losses by friction and heat transmission from the CP mixture into PSP and ducts walls are taken into account by introducing into the equations right parts the amount of motion and energy of the source-type members;
- all of the c-particles generated by PSP combustion deposit right away on the GE surface, for that reason a convective term in the continuity equation for the c-phase is dropped;
- GE are fixed in space, and only their geometrical sizes change gradually in burning. No particular flow over each GE is considered;
- initial porosity of the PSP is considered to be prescribed.

With allowance of these assumptions, two-dimensional differential equations of the CP mixture non-stationary motion between the GE, along the AC and MC are written in the following form (in axisymmetrical statement for the multicomponents biphasic mixture of the ideal gases):

$$\frac{\partial}{\partial t}(F_p \cdot \rho_{mix} \cdot j \cdot r) + \frac{\partial}{\partial x}(F_p \cdot \rho_{mix} \cdot U \cdot r) + \frac{\partial}{\partial r}(F_p \cdot \rho_{mix} \cdot V \cdot r) = M_j, \quad t > 0, \quad (1)$$

$$0 \leq x \leq L, \quad 0 \leq r \leq D_{MC} / 2, \quad j = 1 \div 3$$

$$\frac{\partial}{\partial t}(F_p \cdot \rho_{mix} \cdot U \cdot r) + \frac{\partial}{\partial x}(F_p \cdot \rho_{mix} \cdot U^2 \cdot r) + \frac{\partial}{\partial r}(F_p \cdot \rho_{mix} \cdot U \cdot V \cdot r) + F_p \cdot r \cdot \frac{\partial P_{mix}}{\partial x} =$$

$$= G_U^i - p_U \cdot \tau_U^U \cdot \bar{S}_U \quad (2)$$

$$\frac{\partial}{\partial t}(F_p \cdot \rho_{mix} \cdot V \cdot r) + \frac{\partial}{\partial x}(F_p \cdot \rho_{mix} \cdot V \cdot U \cdot r) + \frac{\partial}{\partial r}(F_p \cdot \rho_{mix} \cdot V^2 \cdot r) + F_p \cdot r \cdot \frac{\partial P_{mix}}{\partial r} =$$

$$= G_V^i - p_V \cdot \tau_V^V \cdot \bar{S}_V \quad (3)$$

$$\frac{\partial}{\partial t}(F_p \cdot \rho_{mix} \cdot E_{sp} \cdot r) + \frac{\partial}{\partial x}(F_p \cdot \rho_{mix} \cdot U \cdot E_{sp} \cdot r) + \frac{\partial}{\partial r}(F_p \cdot \rho_{mix} \cdot V \cdot E_{sp} \cdot r) +$$

$$+ \frac{\partial}{\partial x}(F_p \cdot P_{mix} \cdot U \cdot r) + \frac{\partial}{\partial r}(F_p \cdot P_{mix} \cdot V \cdot r) = Q_E + G^E \quad (4)$$

$$\frac{\partial}{\partial t}(F_p \cdot \rho_{mix} \cdot r \cdot \gamma_c) = [(p_U + p_V) \cdot r] \cdot \rho_c \cdot u_c \cdot \gamma_c - \dot{G}_c \cdot \gamma_c \quad (5)$$

$$E_{sp} = C_{ef} \cdot T_{mix} + 0.5 \cdot (U^2 + V^2) \quad (6)$$

$$C_p = C_{p0} \cdot (1 - a - b) + C_{p2} \cdot a + C_{p3} \cdot b \quad (7)$$

$$a = \rho_{mix2} / \rho_{mix} \quad (8)$$

$$b = \rho_{mix3} / \rho_{mix} \quad (9)$$

$$C_V = C_{V0} \cdot (1 - a - b) + C_{V2} \cdot a + C_{V3} \cdot b \quad (10)$$

$$C_{ef} = C_V \cdot (1 - \gamma_c) + C_c \cdot \gamma_c \quad (11)$$

$$R = C_p - C_V \quad (12)$$

$$k = C_p - C_V \quad (13)$$

$$\rho_g = \rho_{mix} \cdot (1 - \gamma_c) \quad (14)$$

$$F_p = \begin{cases} F_x \cdot m_x, & \text{axial direction,} \\ F_r \cdot m_r, & \text{radial direction} \end{cases} \quad (15)$$

$$P_{mix} = \rho_{mix} \cdot (1 - \gamma_c) \cdot (k - 1) \cdot (E_{sp} - 0.5 \cdot (U^2 + V^2)) \quad (16)$$

$$\bar{S}_U = (1 - \bar{S}_c^U) + \bar{S}_c^U \cdot \psi(\delta_U) \quad (17)$$

$$\bar{S}_V = (1 - \bar{S}_c^V) + \bar{S}_c^V \cdot \psi(\delta_V) \quad (18)$$

$$\bar{S}_c^U = 0 \quad \text{and} \quad \bar{S}_c^V = 0, \quad \text{when} \quad u_c = 0 \quad (19)$$

$$0 < \bar{S}_c^U \leq 1 \quad \text{and} \quad 0 < \bar{S}_c^V \leq 1, \quad \text{when} \quad u_c > 0 \quad (20)$$

$$\psi(\delta_U) = \left[ 1 - \frac{\delta_U}{\delta_{cr}} \right]^2 \quad (21)$$

$$\delta_U = \frac{2}{C_{fo}^U} \cdot \frac{\rho_c \cdot u_c}{\rho_{mix} \cdot |U|} \quad (22)$$

$$\psi(\delta_V) = \left[ 1 - \frac{\delta_V}{\delta_{cr}} \right]^2 \quad (23)$$

$$\delta_V = \frac{2}{C_{fo}^V} \cdot \frac{\rho_c \cdot u_c}{\rho_{mix} \cdot |V|} \quad (24)$$

$$\delta_{cr} = 4.0 \quad (25)$$

$$\text{If } \delta_{(U,V)} / \delta_{cr} > 1, \quad \text{assumed that } \delta_{(U,V)} / \delta_{cr} = 1 \quad (26)$$

$$\tau_t^U = \eta_{IU} \cdot \rho_{mix} \cdot U^2 / 8 \quad (27)$$

$$\tau_t^V = \eta_{IV} \cdot \rho_{mix} \cdot V^2 / 8 \quad (28)$$

A peculiarity of the written model is that the physical processes accompanying the CP filtration through the GE are taken into account. For description of the temperature distribution inside and on the surface of the GE separately taken in each of gas-dynamics knots, as well as to find the moment of the GE inflammation, the one-dimensional heat conduction equation written in terms of the spherical coordinate system is used. In this case supposed, that the heterogeneous exothermic chemical zero-order reactions, localized in the GE thin surface layer, are leading in the ignition process.<sup>9,10</sup> Therefore, the thermal effect from the chemical reactions in the warmed up layer can be attributed to the GE surface and taken into account in boundary conditions, and in the right part of the heat conduction equation not to take into account:

$$\frac{\partial T_c}{\partial t} = \frac{\lambda_c}{C_c \cdot \rho_c} \cdot \frac{1}{z^2} \cdot \frac{\partial}{\partial z} \left( z^2 \cdot \frac{\partial T_c}{\partial z} \right), \quad 0 \leq z \leq (d_{AC}, d_{MC}) / 2, \quad t > 0 \quad (29)$$

The equation (29) is utilized up to the moment, when on the GE surface there will be conditions, which providing intensive gasification. For the ignition criterion, a condition of achievement on the GE surface of some critical temperature  $T_{ig}$  is accepted:

$$T_s \geq T_{ig} \quad (30)$$

In the conditions of the GE non-stationary combustion with the linear rate  $u_c$ , the heat conduction equation in the solid phase is recorded in the movable coordinates system, connected with the GE combustion surface and moving to the GE centre, on normal to its surface with the rate  $u_c$ :

$$\frac{\partial T_c}{\partial t} = u_c \cdot \frac{\partial T_c}{\partial z} + \frac{\lambda_c}{C_c \cdot \rho_c} \cdot \frac{1}{z^2} \cdot \frac{\partial}{\partial z} \left( z^2 \cdot \frac{\partial T_c}{\partial z} \right), \quad 0 \leq z \leq (d_{AC}, d_{MC}) / 2, \quad t > 0 \quad (31)$$

Boundary conditions:

$$\text{On } z = (d_{AC}, d_{MC}) / 2, \quad \partial T_c / \partial z = 0 \quad (32)$$

$$\text{On } z = 0 \quad \text{and } t > 0$$

$$\partial T_s / \partial z = q_{cp} + q_h = \alpha_{cp} \cdot (T_{mix} - T_s) / \lambda_c + Q_h \cdot K_h(T_c) / \lambda_c \quad (33)$$

$$K_h(T_c) = \begin{cases} K_{0h} \cdot \exp \left\{ -\frac{E_h}{R_0 \cdot T_c} \right\}, & \text{on } T_c > T_h \\ 0, & \text{on } T_c \leq T_h \end{cases} \quad (34)$$

For the GE burning surface ( $u_c > 0$ ), as additional boundary condition, the equation for temperature on the surface (burning condition) is accepted:

$$T_s = \theta(P_{mix}, T_0) \quad (35)$$

Integral dependences suggested by Prof. V.P. Bobrishev of Russia (1973) are used to account for the possible erosive effect in GE burning. In the basis of this procedure is the solution of the asymptotic equations of heat conduction and diffusion in the gas phase of the burning propellant. The distinctive feature of Bobrishev's model consists in the fact, that for every particular solid propellant there is no need to know a threshold (critical) value of the velocity of the flowing-over gas flux, below which there is no erosive burning. According to this procedure, the erosive coefficient  $\varepsilon$ , is determined on the basis of the following relationships:

$$\varepsilon = \sqrt{0.5 + \sqrt{0.25 + [\kappa_o \cdot \eta_T \cdot th(-\eta_T / 30)]^2}} \quad (36)$$

$$\eta_T = (0.675 \cdot \eta_s + 2.1) \cdot th(\eta_s / 3.25) \quad (37)$$

$$\eta_s = 2.2 \cdot \rho_{mix} \cdot |W| \cdot \sqrt{C_{fo} / 2} \cdot \frac{1}{\rho_c \cdot u_c^{st}} \quad (38)$$

$$\kappa_o = 0.39 \quad (39)$$

$$\sqrt{C_{fo} / 2} = \left[ 5.5 + 2.5 \cdot \ln \left( Re \cdot \sqrt{C_{fo} / 2} \right) \right]^{-1} \quad (40)$$

The last equation is solved by the iterations method. For the first approximation it is believed that  $C_{fo} = 0.04$ .

For determination of  $Re$  value, the next dependence was used:

$$Re(U, V) = l(U, V) / \sqrt{K_p(U, V) \cdot \rho_{mix}} / \mu \quad (41)$$

For description of the hydrodynamics processes and the heat exchange processes in the porous medium the authors use the procedure, which based on the model of the integral characteristics of the systems.<sup>11,12</sup> For determination of the  $\eta_1$  value, the next criterion dependence was used:

$$\eta_1(U, V) = \left( \frac{3 \cdot \pi}{m_{(x,r)}} \right) \cdot \frac{Nu_T^3}{(Pr \cdot Re_{(U,V)}^2)} \quad (42)$$

In accordance with Ergun's and Vitkov's works, the  $K_p$  value is determined on the following dependence:<sup>11,13</sup>

$$K_{p(x,r)} = \frac{(d_{ef} \cdot m_{(x,r)}^3)}{\beta \cdot (1 - m_{(x,r)})^2} \quad (43)$$

where  $\beta$  - is the constant,  $\beta = 215$ .

The heat exchange coefficient  $\alpha_{cp}$  consists of three components: they are convective  $\alpha_f$  realized in the CP filtering through the PSP pores; owing to CP radiation,  $\alpha_{rad}$ ; owing to the deposition of incandescent particles on the PSP surface,  $\alpha_{cont}$ .<sup>3</sup> To find the value  $\alpha_f$  the following correlation is used:<sup>11</sup>

$$\alpha_f = Nu_T \cdot \lambda_{mix} \cdot \bar{S}_c / \sqrt{K_p} \quad (44)$$

As far as the intensity of the gasdynamics parameters changes on AC and MC volumes considerably greater than velocity of thermal parameters variation, at determination of the last (including and a heat exchange coefficient) utilization of the criteria relations, obtained in stationary conditions is allowable. This statement is coordinated with data, obtained by B.P.Zhukov, V.V.Vengerskiy, Yu.N.Kovalyov and A.M.Lipanov of Russia.<sup>12</sup> According to these data, application of the stationary criteria relations for calculation of the processes on the initial stage of solid propellant gas generation system operation is correctly in case, if:

$$\lambda_{mix} \cdot P_{mix} \cdot C_p \cdot \frac{1}{6 \cdot \alpha_f^2} \cdot \left( \frac{\partial}{\partial t} (\ln T_{mix}) + r_f \cdot \frac{\partial}{\partial t} (\ln / W /) \right) \leq 0.03 \quad (45)$$

In case of laminar mode of the CP mixture flow, a coefficient  $r_f = 0.2$ , and at turbulent mode  $r_f = 0.5$ .

The physico-chemical processes proceeding in the initiator 12 and IC 13 (Figure 1) are simulated in the thermodynamic statement.<sup>3,12</sup> All the mass flow rate through the nozzles characteristics are determined in accordance with the dependencies given in Shapiro's and Sorkin's works.<sup>14,15</sup>

### BOUNDARY CONDITIONS

"Joint" of gas-dynamic parameters in boundaries of adjacent ranges with different dimensions (Figure 1, "0" - "2" - "2" - "0") is carried out by the means of the algorithm of "decay of a random breakage".<sup>12,16</sup> In the same way the boundary conditions are formulated on the other AC and MC boundaries. For determination of the flow parameters on internal surfaces of the calculated ranges boundaries "2" (Figure 1, AC, MC), the conditions of dynamic compatibility are used.<sup>3</sup> We shall consider the singularity of application of these conditions for perforated boundary, which is partially covered by the GE. The influence of the separation phenomenon, which is observed at the CP flowing through the GG perforation, do not take into account, as far as the GG has small walls thickness. The conditions of dynamic compatibility, which express the laws of conservation of mass, impulse and energy at reduction of the section area by "jump", connect CP parameters on a surface of perforated boundary (Figure 2, "1") and in openings of perforated boundary ("2").

$$F_b \cdot m \cdot [\rho_{mix} \cdot U]_1 = F_{\Sigma perf} \cdot \theta_o \cdot [\rho_{mix1} \cdot U]_2 \quad (46)$$

$$F_b \cdot m \cdot [\rho_{mix} \cdot U^2]_1 + F_b \cdot m \cdot P_{mix1} = F_{\Sigma perf} \cdot \theta_o \cdot [\rho_{mix} \cdot U^2]_2 + F_{\Sigma perf} \cdot \theta_o \cdot P_{mix2} + (F_b - F_{\Sigma perf} \cdot \theta_o) \cdot P_{mix1}^* - (1 - m) \cdot F_b \cdot P_{mix1} \quad (47)$$

$$\frac{U_2^2}{2} + \left( \frac{k_b}{k_b - 1} \right) \cdot \frac{P_{mix2}}{\rho_{mix2}} = \frac{U_1^2}{2} + \left( \frac{k_b}{k_b - 1} \right) \cdot \frac{P_{mix1}}{\rho_{mix1}} \quad (48)$$

In the equation of impulses we shall assume that  $P_{mix}^* \approx P_{mix1}$ . The recorded system of equations (46 - 48) has two decisions. And, only one of these decisions, which corresponds to the supersonic mode of the CP flowing ( $U_1 > C_1$ , where  $C$  - is a sound velocity), will satisfy to a condition of entropy  $\Delta S$  increase:

$$\begin{cases} \Delta S = \frac{R_b}{k_b - 1} \cdot \ln \left[ \frac{P_{mix1}}{P_{mix2}} \cdot \left( \frac{\rho_{mix2}}{\rho_{mix1}} \right)^{k_b} \right] \\ \Delta S > 0 \end{cases} \quad (49)$$

Starting from it, at  $t = 0$ , from system (46 - 48) it is possible to receive:

$$U_1 = \frac{U_2}{\left( 2 \cdot \left( 1 - \psi \cdot \frac{k_b - 1}{2 \cdot k_b} \right) \right) \cdot \left[ \frac{k_b + 1}{k_b} + \sqrt{\left( \frac{k_b + 1}{k_b} \right)^2 - 2 \cdot \left( 1 - \psi \cdot \frac{k_b - 1}{2 \cdot k_b} \right) \cdot \psi \cdot \frac{k_b + 1}{k_b}} \right]} \quad (50)$$

$$\rho_{mix1} = \psi \cdot \frac{\rho_{mix2} \cdot U_2}{U_1} \quad (51)$$

$$P_{mix1} = P_{mix2} + \rho_{mix2} \cdot U_2 \cdot (U_2 - U_1)$$

$$\text{where } \psi = \frac{\theta_o \cdot F_{\Sigma \text{ perf}}}{m \cdot F_b} \quad (52)$$

The process of the CP flow through flowing boundaries of regions in a greater part of a period of PSP ignition is critical. In case, when the critical conditions of the outflow will be broken, the perturbations introduced by the CP, which flowing through the boundary, will not already render the essential influence on the character of the process. Therefore, later, on flowing boundaries nonflowing conditions can be given.

## NUMERICAL METHOD

The stated mathematical model is substantially non-linear, that is why it will be solved by numerical methods. The equations, describing the gas-dynamic processes, represent the system of differential equations with partial derivatives of a hyperbolic type. These equations are solved numerically by the Large Particle Method, developed by Prof. Yu.M.Davydov of Russia, with using of a number of modifications.<sup>12,17,18</sup> These modifications in particular, allow to increase the stability and the accuracy of solution of problems for the CP filtered with a small rates.<sup>18</sup> The thermal problem is solved by means of the finite difference method by the conservative nonexplicit scheme using the scalar fit method.<sup>19</sup> The approximation of difference equations is carried out on the non-uniform grid. The less step of the GE surface is chosen, and then it is increased according to the geometric progression law. All the rest equations of the system in the initiator and in the imitation chamber are not complex to solve. The results of the model are presented later in the paper.



### COMPARISON WITH TEST DATA

For the complex check-up of the developed mathematical model of physicochemical processes, the numerical calculation results have been compared with the fire stand tests. The tests have been executed for the special pyrotechnical GG (Figure 1), mounted in the largesized imitation chamber (Figure 1). Figure 3 shows dependences of pressures on time (continuous lines) - in the GG body  $P_{GG}^{test}$  (a pressure gauge was installed in the GG flange plug), and in the front volume of the IC -  $P_{IC}^{test}$  (two pressure gauges were installed in the IC front volume. Each of average curves represents the mathematical expectation, found by 5 tests.

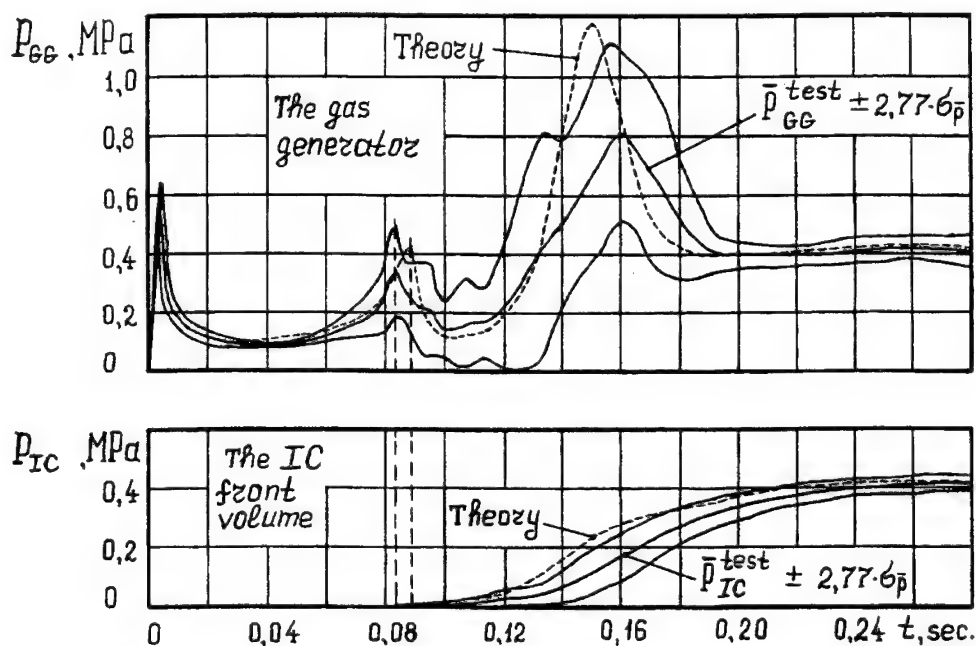


Figure 3. Comparison of the numerical calculation results with the fire stand tests

Lowermost and uppermost curves characterize the bilateral symmetrical confidence interval of the pressure spread  $\bar{P}_{GG}^{test}$  and  $\bar{P}_{IC}^{test}$ , and with confidence probability of 0.95. Curves, corresponding to the calculated pressures are shown by dashed lines. It is directly clear, that calculated and experimental curves (Figure 3) are in good agreement both in on the amplitude, and on the frequency.

### SIMULATION RESULTS AND DISCUSSIONS

Numerical investigations was carried out for PTM with the following chemical compositions: technical barium nitrate - 60 %, titanium powder - 35 %, binding solution containing Mg compounds and graphite - 5 %. The basic initial data used in the computer model are as follows:

$\rho_c = 2900 \text{ kg/m}^3$ ;  $T_{ig} = 1090 \text{ K}$ ;  $T_{mix} = 3500 \text{ K}$ ;  $k = 1,276$ ;  $\gamma_c = 0,62$ ;  $L = 0,24 \text{ m}$ ;  $d_{AC} = 0.0095 \text{ m}$ ;  $d_{MC} = 0.0120 \text{ m}$ ;  $F_{AC} = 0.5 \cdot 10^{-3} \text{ m}^2$ ;  $F_{MC} = 28.5 \cdot 10^{-3} \text{ m}^2$ ;  $F_{AC}^p = 0.0065 \text{ m}^2$ ;  $F_{MC}^p = 0.040 \text{ m}^2$ ;  $\omega_{AC} = 0.09 \text{ kg}$ ;  $\omega_{MC} = 5.0 \text{ kg}$ ;  $\omega_{AC1} = 0.0010 \text{ kg}$ ;  $\omega_{MC1} = 0.0017 \text{ kg}$ ;  $u_c^{st} = 0,02 \text{ m/s}$  at  $P_{mix} = 1 \text{ mPa}$ ;  $\Delta H_{298} = -2414 \text{ kJ/kg}$ ;  $\lambda_{mix} = 8.494 \cdot 10^{-5} \text{ kJ/(m} \cdot \text{sec} \cdot \text{K)}$ ;  $C_{ef} = 1387 \text{ J/(kg} \cdot \text{K)}$ . The analysis of the results of numerical investigations of laws of the physico-chemical processes evolution in the GG reveals following. The PSP inflammation in the ducts occurs under substantially nonstationary conditions and the flows patterns in the GG AC and MC are characterized by substantial inhomogeneity, increasing as the process develops and expressed temperature sensitivity. After the PSP complete inflammation a gradual degeneration of combustion nonstationarity is observed. A patterns of the GG charges gradual ignition are shown in Figure 4 ( for the GG AC ) and in Figure 5 ( for the GG MC ).

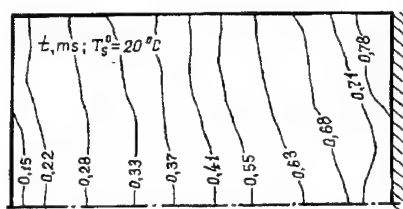


Figure 4. The pattern of the GG AC charge gradual ignition

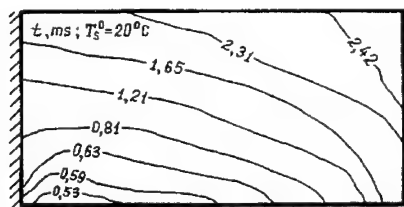


Figure 5. The pattern of the GG MC charge gradual ignition

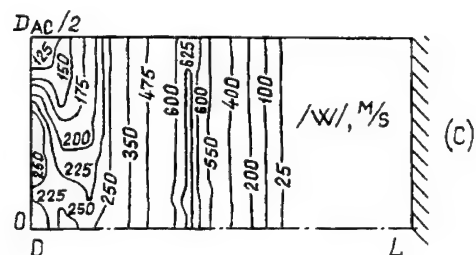
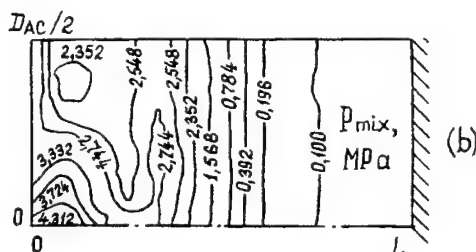
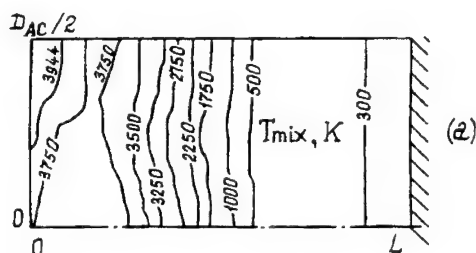
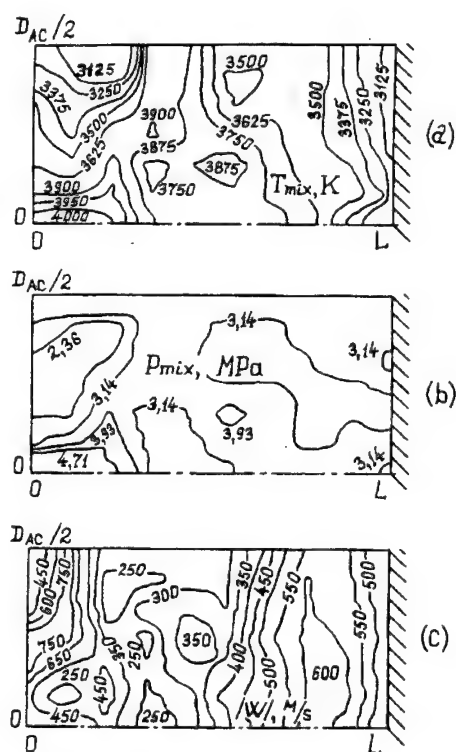


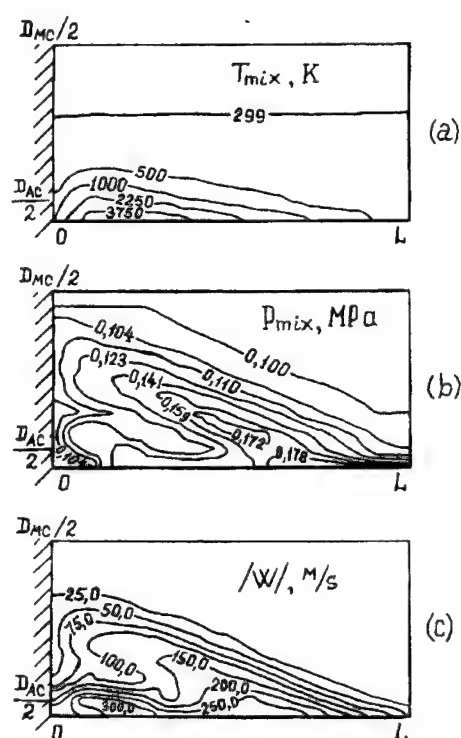
Figure 6. The lines of identical values of the CP mixture flow parameters in the GG AC

On initial stage of the process (  $t = 0.1 \text{ ms}$  ), the main influence are render the CP, which arriving from the initiator. By means of flow into of these CP with the sound velocity at the left-hand AC boundary, a compression wave is formed. On Figure 6 are submitted an example of the

development of the two-dimensional wave processes in GG AC - the lines of identical values of the temperature (a), the pressure (b) and the modulus of the velocity vector (c) of the CP mixture flow, at  $T_s^0 = 20^\circ \text{C}$ , formed to the time moment  $t = 0.3 \text{ ms}$ . From figures it is clear, that as the process develops the flow gradually acquires two-dimensional character. As well as in the one-dimensional flow, ahead of the top of a compression wave (Figure 6, (b),  $P_{\text{mix}} = 2,744 \text{ MPa}$ ) there is the top of the flow velocity module (Figure 6, (c),  $|W| = 625 \text{ m/sec.}$ ). Figure 7 shows the lines of identical values of the temperature (a), pressure (b) and modulus of the vector of the flow velocity (c) of the CP mixture, at  $T_s^0 = 20^\circ \text{C}$ , formed to a time moment  $t = 0.8 \text{ ms}$ .



**Figure 7.** The lines of identical values of the CP mixture flow parameters in the GG AC



**Figure 8.** The lines of identical values of the CP mixture flow parameters in the GG MC

From the Figure 7 (a) and (b) it is visible, that practically all the PSP in the AC was connected to combustion, and the pressure distribution on the AC volume has become more uniform. A similar results referred to the GG MC, is presented on Figure 8 - Figure 10. On Figure 8 are submitted the lines of identical values of the temperature (a), pressure (b) and the modulus of the velocity vector (c) of the CP mixture flow, at  $T_s^0 = 20^\circ \text{C}$ , which formed in the MC to the time moment  $t = 0.6 \text{ ms}$ . Here, from the very beginning of the process the flow patterns has a non-one-dimensional character, due to irregularity of the development of the process of the CP flow from AC to the MC.

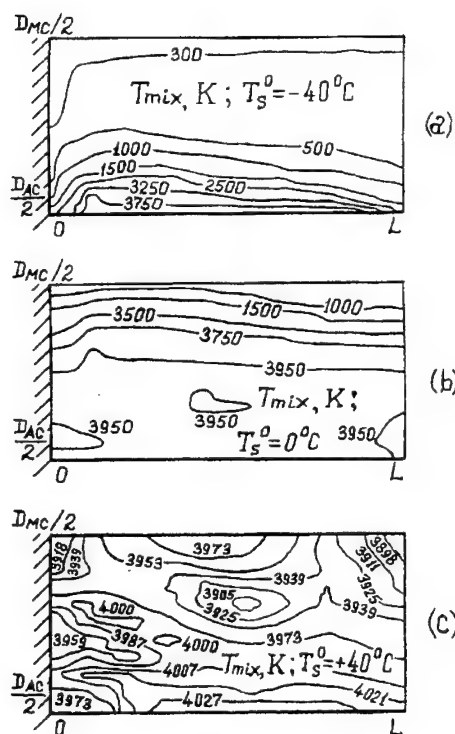


Figure 9. The lines of identical values of the CP mixture flow temperatures in the GG MC

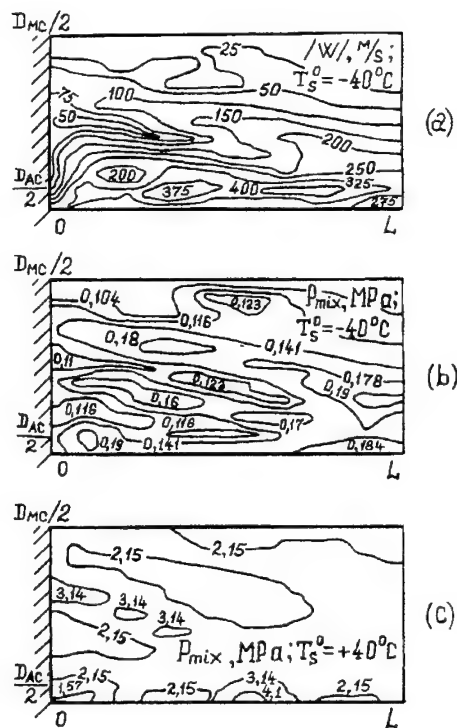


Figure 10. The lines of identical values of the modules of vector of the CP mixture flow velocity in the GG MC

Also, the influence of the PSP initial temperature on the flow picture in the MC was investigated. The investigations were executed for a temperatures interval from  $-40^{\circ}\text{C}$  up to  $+40^{\circ}\text{C}$ . On the Figure 9 are submitted the lines of identical values of the temperatures of the CP mixture flow, which formed to a time moment  $t = 1\text{ ms}$ . (a) -  $T_s^0 = -40^{\circ}\text{C}$ ; (b) -  $0^{\circ}\text{C}$ ; (c) -  $+40^{\circ}\text{C}$ ). On Figure 10 are submitted the lines of identical values of the modules of vector of the CP mixture flow velocity, at  $T_s^0 = -40^{\circ}\text{C}$  (a) and the pressure of the CP mixture at  $T_s^0 = -40^{\circ}\text{C}$  (b) and  $T_s^0 = +40^{\circ}\text{C}$  (c). From Figure 9 and Figure 10 it is obviously, that the consecutive increase of the PSP initial temperature are results in considerable modification of the flow picture and acceleration of the process development. After the PSP complete ignition, the flow non-one-dimensionality are degenerates gradually and the parameters in the GG volume can be averaged.

## CONCLUSION

The flows patterns in the GG AC and MC are characterized by substantial inhomogeneity, increasing as the process develops and expressed temperature sensitivity. After the PSP complete ignition, the flow non-one-dimensionality is degenerated gradually. The using of two-dimensional gas-dynamic models opens the possibility for obtaining the information about processes proceeding in the GG and IC at a new qualitative level, and gives a more comprehensive idea about the

physico-chemical processes essence and permits to abandon the use of a number of empirical relations.

## NOMENCLATURE

$a, b$  - are the mass concentrations of the CP, coming into the AC through its left boundary and formed in GP burning;  $C_p, C_V, C_C$  - are the specific heat capacities of the CP mixture gas phase and the condensed phase;  $C_{f0}$  - is the friction resistance coefficient;  $d_{AC}$  and  $d_{MC}$  - are the initial diameters of the pelletized elements, placed in AC and MC cavities;  $d_{ef}$  - is the effective (current) GE diameter;  $D_{MC}$  - is the diameter of MC;  $E$  - is the total energy;  $E_{sp}$  - is the specific energy of the CP mixture;  $E_h$  - is the activation energy of the "heterogeneous" reaction;  $F$  - is the area;  $F_{AC}$  and  $F_{MC}$  - are the cross-section areas of the GG AC and MC;  $F_{AC}^p$  and  $F_{MC}^p$  - are the total perforation areas in the AC and MC;  $F_p$  - is the pores area;  $F_b$  - is the external surface of the identify length boundary;  $F_{\Sigma perf}$  - is the total perforation openings area per unit boundary length;  $F_x, F_r$  - are the areas on the boundaries between knots in the calculated region, in the longitudinal and lateral directions;  $G_U^i, G_V^i, G^E$  - are the losses and income of the amounts of motion and energy owing to the CP flow between spaces,  $G^E$  also takes into account the work, done when CP flow-out through the perforation;  $\dot{G}_c$  - is the CP mass flow rate through the MC nozzles into the IC combustion chamber;  $\Delta H_{298}$  - is the specific enthalpy of 1 kg. of the PSP;  $k$  - is adiabatic exponent;  $K_p$  - is the PSP penetration factor;  $\sqrt{K_p}$  - is the characteristic size;  $K_h(T_c), K_{0h}$  - are the rate coefficient and pre-exponent of the "heterogeneous" reaction;  $L$  - is the length of the GG (AC and MC);  $m$  - is the PSP porosity;  $M_j$  - is the rate of the mass interphase exchange (the sum of the CP entering and the CP flow rates);  $Nu_T$  - is the Nusselt thermal criterion;  $P$  - is the pressure;  $P_0$  - is the environmental pressure;  $P_1^*$  - is the damping pressure on the surface with area ( $F_b - F_{\Sigma perf}$ );  $Pr$  - is the Prandtl thermal criterion;  $p_U, p_V$  - are the total perimeters of the PSP pores in the directions of the CP motion velocity components  $U$  and  $V$ ;  $Q_E$  - is the rate of the interphase energy exchange;  $Q_h$  - is the thermal effect of the "heterogeneous" reaction;  $q_{cp}, q_h$  - are the thermal flows from the CP and from "heterogeneous" chemical reaction;  $r$  - is the lateral coordinate;  $R$  - is the gas constant;  $R_0$  - is the universal gas constant;  $Re$  - is the Reynolds criterion;  $S$  - is the entropy;  $\bar{S}_c$  - is the PSP surface relative area joined up to combustion;  $t$  - is the time of the process;  $T$  - is a temperature;  $T_h$  - is the temperature of the beginning of the "heterogeneous" exothermic reaction;  $T_{ig}$  - the critical temperature;  $u_c$  - is the linear rate of the GE combustion;  $U, V$  - are the longitudinal and lateral components of the flow velocity;  $W = \sqrt{U^2 + V^2}$  - is the modules of the CP mixture flow velocity vector;  $x$  - is the longitudinal coordinate;  $z$  - is the radial distance, which reading from the GE surface, to its center.

## Greek Symbols

$\alpha$  - is the heat exchange coefficient;  $\beta$  - is the constant;  $\gamma_c$  - is the relative mass concentration of the c-phase in the CP mixture;  $\eta_1$  - is a dimensionless coefficient of the hydrodynamic resistance;  $\pi$  - is the constant ( $\pi = 3.1415$ );  $\theta_0$  - is the coefficient of the perforation openings contraction;  $\lambda$  - is the thermal conductivity coefficient;  $\mu$  - is the dynamic viscosity coefficient;  $\rho$  - is the density;  $\tau_t^U, \tau_t^V$  - are the tangential stresses of the CP friction in filtering through the PSP pores in the directions of the CP motion velocity components U and V;  $\omega_{AC1}, \omega_{MC1}$  - is the masses of the one pelletized element of the PSP, placed in the GG AC and MC;  $\omega_{AC}, \omega_{MC}$  - is the masses of PSP, which placed in the AC and MC cavities.

## Subscripts & Superscripts

b - corresponds to the parameters on the boundary; c - corresponds to the parameters of the condensed (solid) phase; ef - corresponds to effective value of the parameter; g - corresponds to the parameters of the gas phase; h - corresponds to the parameters of the "heterogeneous" chemical reaction; j = 1 - corresponds to the CP mixture; j = 2 - corresponds to the CP coming from the initiator, through the AC left boundary; j = 3 - corresponds to the PSP CP; mix - corresponds to the parameters of the gas phase and the c - phase mixture; o - corresponds to initial conditions, the parameters of the gas, originally filling PSP pores; perf - corresponds to the parameters of the openings; r - corresponds to the parameters in the direction of lateral coordinate; s - corresponds to the parameters at the GE surface; st - corresponds to the stationary values of parameters; u, v - corresponds to the parameters in the directions of the CP motion velocity components U and V; x - corresponds to the parameters in the direction of longitudinal coordinate.

## REFERENCES

1. **Katoh, M., Ishii, T. and Nagaoka, T.**, Combusting device for generation of a combustion gas, *Pat 4249673 USA, B01J 7/00, F42B 3/04, Offic. Gaz*, 1003, N 3, 1981.
2. **Hwang, J.S. and Kim J.S.**, Application of air bag technology for submunition dispersion, *Proceedings of 20th International Pyrotechnics Seminar*, Chicago, Illinois, USA, July 25-29, 1994, 471-482.
3. **Kalinin, V.V., Kovaliyov, Yu.N. and Lipanov, A.M.**, Non-stationary processes and methods of designing of the SPRM units, *Mashinostroyeniye*, Moscow, 216, 1986, (in Russian).
4. **Wang, J.T. and Nefske, J.**, A new CAL3D airbag inflation model, *SAE Paper No. 880654, SAE International Congress*, February, 1988, 267-282.
5. **Wang, J.T.**, Recent advances in modeling of pyrotechnic inflators for inflatable restraint systems, *ASME Publication AMD-Vol. 106 and BED-Vol. 13*, December, 1989, 89-93.
6. **Materna, P.**, Advances in analytical modeling of airbag inflators, *SAE Paper No. 920120, SAE International Congress*, February, 1992, 382-403.

7. **Butler, P.B. and Krier, H.**, Numerical simulation of passenger-side automotive airbag inflators, *SAE Paper No. 920848, SAE International Congress*, February, 1992, 507-531.
8. **Chan, S.K.**, A lumped-parameter airbag gas generator model, *Proceedings of 20th International Pyrotechnics Seminar*, Chicago, Illinois, USA, July 25-29, 1994, 153-166.
9. **Viliyunov, V.N.**, The theory of the condensed materials ignition, *Nauka*, Novosibirsk, 189, 1984, (in Russian).
10. **Matveiyev, V.V., Grechanyi, A.N.**, About heterogeneous ignition of the solid propellant particle by the hot gas, *J. Physics of Combustion and Explosion*, Vol. 20, N 5, 61-64, 1984, (in Russian).
11. **Vitkov, G.A., Sherstnev, S.N.**, On calculation of the filtration and convective heat and mass-exchange in the porous medias, *VNIGIK, Deposited in the VINITI 31.01.84*, N 602, 51, 1984, (in Russian).
12. **Lipanov, A.M., Bobryshev, V.P., Aliyev, A.V., et al.**, Numerical experiment in the theory of the SPRM, *Ural publishing firm "Nauka"*, Ekatherinburg, 303, 1994, (in Russian).
13. **Ergun, S.**, Fluid flow through packed columns, *Chem. Engr. Progress*, Vol. 48, N 2, 89, 1952.
14. **Shapiro, A.H.**, The dynamics and thermodynamics of compressible fluid flow, Vol. 1, *The Ronald Press Co.*, New York, 82, 1953.
15. **Sorkin, R.Ye.**, The theory of the intrachamber processes in the solid propellant rocket systems: internal ballistics, *Nauka*, Moscow, 288, 1983, (in Russian).
16. **Grin, V.T., Kraiyko, A.N., Miller, L.G.**, On disintegration of the arbitrary rupture on the perforated partition, *J. Applied Mechanics and Technical Physics*, N 3, 1981, 95-103, (in Russian).
17. **Davydov, Yu.M.**, Large particles method, *Encyclopaedia of Mathematics*, Vol. 5, *Kluwer Academic Publishers*, Dordrecht / Boston / London, 350-360, 1990.
18. **Lipanov, A.M., Lukin, A.N. and Aliyev A.V.**, Non-stationary burning of granulated propellant in a cylindrical channel, *J. Physics of Combustion and Explosion*, Vol.30, N 6, 43-51, 1994, (in Russian).
19. **Samarskii, A.A., Gulin, A.V.**, Numerical methods, *Nauka*, Moscow, 432, 1989, (in Russian).

# AUTHORS INDEX

Abrukov, V.S.	783	Chizhevskii, O.T.	587
Afanasiev, V.V.	943	Cho, H.-C.	1072
Ageev, N.	486	Coffey, C.S.	268
Aguesse, T.	106	Cohen, D.	368
Ak, M.A.	1062	Colombo, G.	493
Alimi, R.	668	Cor, J.J.	70
Aliyev, A.V.	1164	Covino, J.	302
Alkov, N.G.	774	Cozzi, F.	493
Allen, M.T.	58	Culick, F.E.C.	998
Ampleman, G.	135	Cunliffe, A.V.	706
Ananiev, A.V.	145	Curran, P.O.	863
Anderson, D.W.	706	Dam, N.	972
Andresen, P.	837	Davidson, J.E.	1116
Araújo, L.	118, 793	Deimling, L.	927
Arisawa, H.	3	Dell'Orco, P.C.	213
Armstrong, R.W.	313	De Luca, L.	493
Assovskii, I.G.	587, 1035	DeMay, S.C.	337
Asthana, S.N.	594	Doriath, G.	646
Atwood, A.I.	863	Dorofeev, E.I.	290
Baxter, L.	167	Dreyer, C.B.	70
Beckstead, M.W.	1116	Dryer, F.L.	58
Behrens, R.	278	Du, L.	661
Bennett, R.R.	92	Duterque, J.	693
Bishop, R.L.	213	Eck, G.	177
Bizot, A.	1046	Eckl, W.	896, 927
Boggs, T.L.	233	Eisenreich, N.	896, 927
Bombach, R.	934	Elban, W.L.	313
Boteler, J.M.	302	Elliott, J.P.	221
Boughton, J.W.	48	Fifer, R.A.	83
Boyer, E.	387, 906	Fink, R.	837
Branch, M.C.	70	Finnegan, S.A.	863
Brewster, M.Q.	1082	Flesner, R.L.	213
Brill, T.B.	3	Fortov, V.E.	476
Brossard, C.	849	Frost, V.A.	943
Brown, P.W.	387	Frota, O.	118, 793
Brugman, Th.M.	972	Fujita, M.	753
Brummund, U.	825	Gadiot, G.M.H.J.L.	430, 1146
Bulusu, S.	278	Gilion, J.B.	177
Burnley, V.S.	998	Giuliani, P.	962
Campbell, C.	395	Goldenberg, C.	668
Caulder, S.M.	574	Golovitchev, V.I.	734
Cessou, A.	825	Gongwer, P.E.	3
Chan, M.L.	627	Greer, C.W.	135
Chan, S.K.	413, 465	Gremyachkin, V.M.	1157
Charpenel, M.	849	Guiot, S.R.	135
Chen, T.	395	Gusachenko, L.K.	1014
Chiaverini, M.J.	719	Haidn, O.	825
Chiu, H.H.	1026	Hawari, J.	135



Heimerl, J.M.	83	Li, T.S.	1026
Hemmerling, B.	934	Liang, Y.	395
Hoffmans, D.W.	430	Liehmman, W.	896, 927
Homan, B.E.	876	Lin, C.L.	1026
Honey, P.J.	706	Lin, M.C.	48
Hönig, R.	837	Lindfors, A.J.	302
Hsu, C.-C.	48	Liparov, A.M.	1164
Huey, S.	167	Lipkin, J.	167, 177
Hurley, J.A.	221	Louwers, J.	1146
Ikezaki, T.	743	Lu, Y.C.	356, 368, 719, 885, 906, 1133
Ilyin, S.V.	783	Lukin, A.N.	1164
Istratov, A.G.	145	Machacek, O.	177
Ivanov, G.V.	636	Maltsev, V.M.	783
Iwama, A.	442	Marshakov, V.N.	145
Jalongo, A.	493	McDonald, A.J.	92
Jing, Q.	1116	McKenzie, A.	177
Johnson, D.K.	719	McNair, J.M.	221
Jones, A.M.	135	Mead, C.	627
Kappler, G.	837	Mebel, A.M.	48
Kato, H.	743	Meerts, W.L.	972
Kidin, N.I.	943	Melik-Gaikazov, G.V.	145
Kim, E.S.	1093	Melnik, D.	668
Kim, F.S.	574	Mench, M.M.	465
Kishimoto, J.	442	Menke, K.	896
Knyazeva, A.G.	762	Merrill, C.	345
Kohno, M.	918	Merwin, L.	627
Kolesnikov, V.I.	145	Michalak, R.	177
Kondrikov, B.N.	290	Miller, P.L.	199
Kopicz, C.	559	Mintsev, V.B.	476
Korobeinichev, O.P.	38	Mitchell, A.R.	189
Korting, P.A.O.G.	430	Modiano, S.H.	807, 876
Kostishin, Yu.	486	Morgan, M.E.	199
Kotlar, A.J.	807	Morgan, L.	177
Kramer, J.F.	213	Moy, B.K.	574
Krause, H.	205	Muthiah, Rm.	129
Kreutner, W.	934	Nazare, A.N.	594
Krishnamurthy, V.N.	129	Nguyen, T.T.	679
Krülle, G.	734	Ninan, K.N.	129
Kubota, S.	753	Olive, R.	413
Kuibida, L.V.	38	Oran, E.S.	985
Kuo, K.K.	356, 368, 387, 465, 559, 719, 885, 906, 1093, 1133	Oschwald, M.	825
Kurochkin, A.I.	145	Östmark, H.	616
Kuzmin, A.K.	943	Ostrom, G.	627
Kyro, S.	486	Pagoria, P.F.	189
Langlet, A.	616	Paletsky, A.A.	38
Lecourt, R.	825	Perelmutter, L.	668
Leenders, A.P.M.	430	Perry, R.	177
Leiper, G.A.	413	Pesce-Rodriguez, R.A.	83
Lengellé, G.	515	Polikarpov, Yu.N.	290

Prasad, K.	1104	Tepper, F.	636
Price, C.F.	863	ter Meulen, J.J.	972
Ramaswamy, A.L.	313	Terentiyev, A.A.	943
Rao, S.S.	129	Teselkin, V.A.	145
Reynaud, J.	549	Theisen, D.	837
Rising, S.A.	221	Thelen, C.J.	337
Rist, D.	837	Thiboutot, S.	135
Ritchie, S.J.	356, 368	Thynell, S.T.	559, 1093
Rohe, Th.,	896	Tod, D.A.	706
Ross, J.	167	Tokudome, S.-I.	918
Rotshin, A.V.	145	Tseng, Y.S.	1133
Rychkov, A.D.	1014	Turner, A.	627
Saitoh, T.	442	Uher, K.	213
Schmid, H.	453	Ulas, A.	885
Schmidt, R.D.	189	Vanderhoff, J.A.	807, 876
Schroeder, T.B.	1082	Varghese, T.L.	129
Schubert, H.	453	Verri, M.	493
Sclippa, G.	167	Volk, F.	457
Serin, N.	719	Volpi, A.	918
Sergeev, V.V.	587	Vural, H.	1062
Shah, D.	167	Wang, H.	661
Sharma, J.	268	Wanninger, P.	155
Shen, C.F.	135	Watson, T.J.	559
Shin, H.D.	1072	Weindel, M.	927
Shmakov, A.G.	38	Weiser, V.	896
Shrotri, P.G.	594	Whimpey, J.R.	92
Simmons, R.L.	24	Wiknich, J.	863
Singh, H.	594	Wingborg, N.	616
Skidmore, C.B.	213	Wood, S.	627
Smith-Kent, R.	92	Wu, C.Cm.	313
Smooke, M.D.	1104	Yang, W.	661
Song, M.	661	Yeh, C.L.	465
Spaanjaars, C.M.I.	972	Yetter, R.A.	58, 1104
Spinks, G.A.	706	Yoon, J.-K.	1072
Spontarelli, R.L.	213	Yuasa, S.	743, 753
Spritzer, M.H.	221	Zanotti, C.	962
Stesik, L.N.	145	Zarko, V.E.	762, 1014
Stoffels, G.G.M.	972	Zeigarnik, V.A.	476
Sunahara, G.I.	135	Zigmund, J.	607
Teague, M.W.	807, 876	Zoler, D.	668
Teipel, U.	205		